Valery V. Tuchin

Editor

VOLUME 1

Handbook of Coherent-Domain Optical Methods

Second Edition

Biomedical Diagnostics,
Environmental Monitoring,
and Materials Science

Springer Reference

Handbook of Coherent-Domain
Optical Methods

Valery V. Tuchin

Editor

Handbook of Coherent-Domain Optical Methods

Biomedical Diagnostics, Environmental Monitoring, and Materials Science

Second Edition

With 714 Figures and 27 Tables

Springer

Editor
Valery V. Tuchin
Department of Optics and Biophotonics
Saratov State University, and
Precision Mechanics and Control
Institute of the Russian Academy of Sciences
Saratov, Russian Federation
Optoelectronics and Measurement Techniques Laboratory
University of Oulu
Oulu, Finland

Preface

This handbook deals with laser and coherent-domain methods as applied to biomedical diagnostics, environmental monitoring, and materials inspection. It is a second edition of the two-volume *Handbook of Coherent-Domain Optical Methods for Biomedical Diagnostics*, *Environmental and Material Science* published by Kluwer Academic Publishers in 2004.

The appearance of this book was stimulated by the recent rapid progress in novel photonics technologies on the basis of diode lasers, broadband femtosecond lasers (Ti: Sapphire or Cr: Försterite), light-emitting diodes (LEDs), and superluminescence diodes (SLDs). Such technologies are applicable in many fields, namely, biomedical, environmental, and material diagnostics and monitoring. The main reason that prompted me to edit this book is my many years co-chairing of the Conference on *Optical Coherence Tomography and Coherence Domain Optical Methods in Biomedicine* (SPIE Photonics West Symposia, San Jose/San Francisco, USA) together with Joseph Izatt and James Fujimoto, and the intensive work of my research group in collaboration with many leading groups throughout the world. These activities provided the possibility of inviting world-renowned experts to write the book chapters.

The problem of light interaction with scattering media, including biological tissues, is of great interest in medicine, environmental studies, and industry, and therefore it is often discussed in the monographic literature [1–15]. Since the publication of the first edition of the handbook, a number of new books, handbooks, and tutorials were published (see [16–57]). This expanded edition is genetically linked with the mentioned literature. However, this handbook has some important specific features making it different from these other books. In particular, for the first time in one book a variety of coherent-domain optical methods are discussed in the framework of various applications, which are characterized by a strong light scattering. Readers are provided with the opportunity to learn the fundamentals of light interaction with random media and to obtain an overview on basic research containing the latest results on coherent and polarization properties of light scattered by random media, including tissues and blood, on speckle formation in multiple scattering media, and on other nondestructive interactions of coherent light with rough surfaces and tissues. Readers can then understand the principles of coherent diagnostics techniques as presented in many other chapters of this book.

This handbook is divided into six parts – Part 1: *Speckle and Polarization Technologies* (▶ Chaps. 1–5); Part 2: *Holography, Interferometry, Diffractive Imaging, and Wavefront Measurements* (▶ Chaps. 6–11); Part 3: *Light Scattering Methods* (▶ Chaps. 12–15); Part 4: *Optical Coherence Tomography* (▶ Chaps. 16–26); Part 5: *Microscopy* (▶ Chaps. 27 and ▶ 28); and Part 6: *Applications* (▶ Chaps. 29–31).

The recent and prospective methods of coherent and polarization optical imaging, tomography, and spectroscopy, including polarization-sensitive optical coherent tomography, polarization diffusion wave spectroscopy, and elastic and quasi-elastic light scattering spectroscopy and imaging, are presented. The holographic, interferential, coherent light scattering, and diffractive techniques in application to diagnostics of tissues and turbid materials are also discussed. The basics of wavefront measurements, aberration and adaptive optics in application to ophthalmology, are given in two chapters. Eleven chapters describe various aspects of optical coherence tomography (OCT) – a very new and growing field of coherent optics. Therefore, these chapters serve as a good addition and update to *Handbook of Optical Coherence Tomography* [13] and the recent Springer book *Optical Coherence Tomography: Technology and Applications* [30]. Readers will find the chapter on laser scanning confocal microscopy, which is characterized by recent extraordinary results of in vivo imaging, useful. Raman and OCT microscopies as tools for tissues and various materials inspection are also analyzed in this book.

In comparison with the first edition, this edition is significantly updated with a few new chapters that more or less replace former chapters of authors who no longer work in the field, as well as a few chapters that cover new research fields such as digital holographic microscopy, Fourier transform light scattering method, coherent diffractive imaging, wavefront sensing, aberration measurement and adaptive optics in ophthalmology, and laser remote sensing in medicine and environmental monitoring.

This book represents a valuable contribution by well-known experts in the field of coherent-domain light scattering technologies for diagnostics of random media and biological tissues. The contributors of this volume are drawn across the globe from countries such as Australia, Austria, Bulgaria, Canada, China, Denmark, Finland, Germany, Italy, the Netherlands, New Zealand, Russia, Sweden, the UK, Ukraine, and the USA.

Volume 1 consists of 15 chapters. ▶ Chapter 1 describes the approaches to multiple scattering media characterization on the basis of correlation and polarization analysis of scattered radiation, including fundamentals of diffusing-wave and polarization spectroscopies. Results of basic research on speckle and polarization phenomena, industrial and biomedical applications of the speckle correlation, and polarization diagnostic techniques in the framework of their universality are also presented.

New feasibilities for metrology of coherence and polarization of light fields with consideration of novel approaches to singular optics are dealt in ▶ Chap. 2. The authors discuss new techniques based on the studies of completely or partially coherent/polarized complex fields that can be of use in optical correlation diagnostics.

In ▶ Chap. 3, optical techniques for the study of tissue structures are classified on the basis of polarization and correlation characteristics for real object fields of tissue samples and their images. The authors discuss novel approaches to the analysis of tissue optical images based on polarization, interference, and correlation characterization of structures associated with the tissue physiological state.

▶ Chapter 4 describes the diffusing wave spectroscopy (DWS) methodology and its application to noninvasive quantitative monitoring of blood microcirculation important for diabetes studies, pharmacological intervention for failing surgical skin flaps or replants, assessing burn depth, diagnosing atherosclerotic disease, and investigation of mechanisms of photodynamic therapy in cancer treatment.

In ▶ Chap. 5, the authors introduce a laser speckle imaging (LSI) method for dynamic, high-resolution monitoring of cerebral blood flow (CBF) which is crucial for studying the normal and pathophysiologic conditions of brain metabolism. Three LSI data processing frameworks based on graphic processing unit (GPU), digital signal processor (DSP), and filed programmable array (FPGA) are discussed. By illuminating the cortex with laser light and imaging the resulting speckle pattern, relative CBF images with tens of microns spatial and millisecond temporal resolution were obtained.

▶ Chapter 6 presents methods for digital holographic microscopy (DHM) which provide label-free, multi-focus quantitative phase imaging of living cells. The DHM instrumentation and numerical processing of digitally captured holograms are explained in this chapter. The use of partial coherent light and multi-wavelength approaches are also discussed. This chapter demonstrates that DHM can be used for automated tracking of migrating cells and cell thickness/refractive index monitoring and determination, as well as for label-free analysis in fluidics.

The authors of ▶ Chap. 7 discuss the concept that diagnosis of a certain disease (e.g., cancer) is based on modification of one of the light (scattering) properties and translation of that optical information into data of clinical relevance. The basics of tissue scattering and analysis of existing scattering methods, as well as Fourier transform light scattering, a method recently developed by the authors, are presented in this chapter.

▶ Chapter 8 is an overview of the principles and basic concepts of coherent diffractive imaging (CDI), a novel technique for inspecting matter from nanometric down to picometric resolution. The plane wave CDI, focused beam Fresnel CDI, Bragg CDI, keyhole CDI, and TEM CDI experiments are discussed.

In ▶ Chap. 9, it is shown that wavefront sensing or aberration measurement in the eye is a key problem in refractive surgery and vision correction with laser; the origins of laser-based wavefront sensing technologies and new opportunities for their wider implementation in optometry and vision correction with customized contact and intraocular lenses are analyzed and discussed.

▶ Chapter 10 describes current trends in laser remote sensing and laser Doppler velocimetry, including principles and optical systems of wind sensing, flow and vibration measurement and mapping. Coherent Doppler and direct detection lidars with applications for environmental monitoring and flow velocity and vibration measurements in biomedicine are presented.

The impact of several important factors, such as speckle modulation, temporal aberrations, and anisoplanatic effects, on the performance of ophthalmic diagnostic systems with adaptive optics compensation of human eye aberration is investigated in ▶ Chap. 11. The authors also consider the implementation of a fundus camera with adaptive optics.

▶ Chapter 12 reviews light scattering spectroscopic techniques in which coherent effects are critical because they define the structure of the spectrum. Particularly in the case of elastic light scattering, the targets themselves, such as aerosol particles in environmental science or cells and subcellular organelles in biomedical applications, play the role of microscopic optical resonators. In the case of Raman spectroscopy, the spectrum is created due to light scattering from vibrations in molecules or optical phonons in solids.

The principles of speckle and Doppler measurements, as well as particle image velocimetry are considered in ▶ Chap. 13. The authors discuss the basic physics of speckle microscopy, analyze the output characteristics of dynamic speckle microscope for measurements of parameters of biological flows, provide in vivo measurements of velocity of blood and lymph flows in microvessels using speckle-microscopic and cross-correlation techniques, and show the difficulties of the absolute velocity measurements.

In ▶ Chap. 14, the possibility to diagnose ocular and systemic diseases through the eye is demonstrated. Recent progress in quasi-elastic light scattering (QELS) is described from a laboratory technique routinely used in the characterization of macromolecular dispersions to novel QELS instrumentation which has become compact, more sensitive, flexible, and easy to use. These developments have made QELS an important tool in ophthalmic research where diseases can be detected early and noninvasively before the clinical symptoms appear.

The Monte Carlo simulation program developed for modeling of light scattering in turbid media is described in ▶ Chap. 15. Various options for light transport and scattering, reflection and refraction at boundaries, light sources and detection, and some special features, like laser Doppler velocimetry, photoacoustics, and frequency-modulation scattering, are described.

Volume 2 presents a very new and growing field of coherent optics: optical coherence tomography (OCT). Various aspects of OCT techniques and applications, particularly those used in biomedicine, are discussed. Readers also will find the description of laser scanning confocal microscopy, which is characterized by recent extraordinary results on in vivo imaging, to be informative. OCT endoscopy and microscopy as tools for tissues and materials inspection are also analyzed in this volume.

In comparison with the first edition, significant updates will be found together with a few new chapters on basic research and applications of OCT, and a new section on applications with three chapters on Mueller matrix polarimetry applications to material science, medicine, and environmental monitoring, nonlinear laser fluorescence spectroscopy of natural organic compounds, and triplet-triplet annihilation-assisted upconversion as an optical tool for probing physical parameter of materials.

The fundamentals of OCT, methods providing enhanced probing depth and higher contrast, as well as brief descriptions of applications in medicine, biology, and material science, are presented in ▶ Chap. 16. The impact of multiple scattering in tissues on the OCT imaging performance is analyzed. The developments and mechanisms for reducing the overwhelming multiple scattering effects and improving imaging capabilities by the use of optical immersion technique are discussed. A novel technique based on the use of biocompatible and hyperosmotic chemical agents to impregnate the tissue and to enhance the OCT images is described.

Analytical and numerical models for describing the light propagation in scattering samples imaged by OCT systems are given in ▶ Chap. 17. Analytical and numerical models based on the extended Huygens-Fresnel principle and advanced Monte Carlo technique are derived and used for calculating the OCT signal. For improvement of OCT images, the so-called true-reflection algorithm in which the OCT signal may be corrected for the attenuation caused by scattering is developed and verified experimentally and by Monte Carlo modeling. A novel method of OCT imaging is proposed on the basis of derived Wigner phase-space distribution function.

The so-called en face OCT, which delivers slices in the tissue of coherence length thickness with an orientation similar to that of confocal microscopy is presented in ▶ Chap. 18. The versatile operation in A, B, C scanning regimes; simultaneous OCT and confocal imaging; and simultaneous OCT imaging at different depths are considered. B-scan and C-scan images from different types of tissues are presented. A number of OCT innovations, such as adaptive optics-assisted en face OCT/CM(SLO), coherence-gated wavefront sensors, en face OCT imaging with adjustable depth resolution, and 3D imaging of tissue and en face non-scanning systems, can be found in this chapter.

The implementation of a real-time fiber-based polarization-sensitive OCT (PS-OCT) system, the associated behavior of polarization states in single-mode fibers, and optimal polarization modulation schemes are described in ▶ Chap. 19. The principle of Stokes parameters determination in OCT, processing of PS-OCT signals to extract polarization properties of tissue, such as birefringence, optical axis orientation, and diattenuation, and results of in vivo determination of skin birefringence and birefringence of the retinal nerve fiber layer for glaucoma detection are discussed.

▶ Chapter 20 describes a noninvasive optical method for tomographic imaging of in vivo tissue structure and hemodynamics with high spatial resolution. The principles of D-OCT, system design and implementation, and clinical application are described. The recent advances in imaging speed, spatial resolution, and velocity sensitivity as well as potential applications of D-OCT for mapping of 3-D microvasculature for tumor diagnosis and angiogenesis studies are discussed.

Doppler OCT signals for low and high scattering regimes are analyzed in ▶ Chap. 21. A Monte Carlo simulation is proposed for description of the Doppler OCT signal which allows the readers to analyze the distortions in the measured Doppler OCT flow profile connected with the multiplicity of light scattering. Simulations are compared with phantom and blood measurements.

OCT microvascular imaging and quantification is the topic of ► Chap. 22 with discussion of fundamentals of phase-resolved and power-based methods, and exogenous contrast agents. Examples of microvascular OCT imaging, with emphasis on treatment monitoring and tissue response assessment, are discussed.

The ultrahigh resolution, ultrahigh speed, and wide-field OCT system for corneal and retinal imaging is described in ► Chap. 23. The authors demonstrate unique capabilities of the system that include the thickness determination of the tear film, corneal epithelium, and Bowman's layer over a wide field of view, as well as high-resolution retinal microscopy.

► Chapter 24 discusses the theoretical issues of OCT imaging on the basis of the wave and energy approaches, and presents the development of polarization maintaining fiber optical elements for the OCT Michelson interferometer and various modifications of OCT such as "two-color," 3D, cross-polarized, and endoscopic OCT modalities. It also summarizes clinical applications of OCT, discusses criteria of norm and pathology, diagnostic value, and clinical indications in OCT. Compression of tissues and their impregnation by chemical agents are used for improvement of OCT images. An effective mathematical algorithm for postprocessing of OCT images accounting for tissue scattering is demonstrated.

The development and innovations of OCT needle-probe technologies are reviewed in ► Chap. 25. Several different clinical applications, including demarcation of margins of breast cancer tumor and lung imaging, demonstrate OCT needle-probe capabilities for optical biopsy.

The authors of ► Chap. 26 discovered that OCT is a well-suited imaging modality for conducting permeation trials to quantify diffusivity of molecules and particles through human and animal vascular tissue. It was demonstrated that such studies could improve the understanding of the penetration and accumulation of lipoproteins in arterial wall and thus could help in the prevention and treatment of atherosclerosis.

► Chapter 27 discusses the development of a compact optical coherence microscope (OCM) with ultrahigh axial (3.4 μm) and lateral (3.9 μm) resolution for imaging internal structures of biological tissues at the cellular level. Such resolution is achieved due to combined broadband radiation of two spectrally shifted SLDs and implementation the dynamic focus concept which allows for in-depth scanning of a coherence gate and beam waist synchronously. Results of a theoretical investigation of OCM axial and lateral resolution degradation caused by light scattering in tissues are also presented.

The principles and instrumentation of confocal scanning laser microscopy (CSLM) are described in ► Chap. 28. It discusses reflectance-mode CSLM (rCSLM), where the images are based on the scattering properties of the cell or tissue. The mechanisms of image contrast and rCSLM application to study tissue properties are considered.

► Chapter 29 describes the fundamentals of polarized beam interaction with natural scenes and informative polarimetric identifiers of objects of various natures. It presents the Mueller matrix ideology. The multiplicative and additive matrix models of deterministic and depolarizing objects are discussed. Several

applications of optical and radar polarimetry for the investigation of biological tissues, vegetation, soil, atmosphere, and oil and chemical contaminations are considered.

The principles of nonlinear laser fluorescence spectroscopy of organic compounds are reviewed in ▶ Chap. 30. The roles of intramolecular energy transfer and localized donor-acceptor pairs (LDAPs) within a single fluorophore in fluorescent response to pulsed laser excitation are discussed.

A description of the energetically conjoined triplet-triplet annihilation upconversion (TTA-UC) process in a soft matter environment is presented in ▶ Chap. 31. Material parameters of the organic system assuring efficient TTA-UC and TTA-UC-based sensing of local temperature in thin polymer films and the water environment are discussed.

This handbook is aimed at researchers, postgraduate and undergraduate students, laser engineers, biomedical engineers, and physicians who are interested in designing and applying laser and coherent optical methods and instruments in medicine and the medical device industry, in materials characterization, and in environmental monitoring. Because of the large amount of fundamental and basic research on coherent light interactions with inhomogeneous media presented in this book, it should be useful for a broad audience including students and physicians. Investigators in the field will find new or updated information and results throughout the second edition. Physicians and biomedical engineers will be particularly interested in the chapters covering clinical applications and instrumentation. Laser engineers will also find many critical applications to stimulate novel ideas of laser design.

I greatly appreciate the cooperation and contribution of all the authors of this book, who have done great work on the preparation of their chapters.

I would like to thank all those authors and publishers who freely granted permissions to reproduce their copyrighted material.

I am grateful to David Packer for his suggestion to prepare the second edition of this handbook and Sara Kate Heukerott for her assistance.

It should be mentioned that these two volumes also present the results of the international collaboration and exchange of ideas between all participating research groups. In particular, the collaboration of the authors of ▶ Chap. 16 was supported by grant REC-006 of CRDF (U.S. Civilian Research and Development Foundation for the Independent States of the Former Soviet Union) and the Russian Ministry of Education and Science and a few Royal Society grants (UK). Chapters 16 and 17 also represent work done in the past 4 years through funding from PHOTONICS4LIFE of FP7-ICT-2007-2 (grant № 224014). ▶ Chapter 21 is related to FiDiPro TEKES Program (40111/11, Finland). The ideas in ▶ Chap. 25 are an outgrowth of RF Governmental contract 11.519.11.2035 supporting collaboration with Australia. The technology presented in ▶ Chap. 26 partly originated under the collaborative CRDF grant RUB1-2932-SR-08.

Support from FiDiPro TEKES Program (40111/11, Finland) allowed the editor the time to complete this handbook. The editor believes that this handbook will be very helpful in creating an institutional partnership between Switzerland, Russia, and Uzbekistan (SCOPES, IZ74ZO_137423/1, Swiss NSF), with regard to grants

1177.2012.2 "Support for the Leading Scientific Schools" from the President of the RF, RFBR-11-02-00560-a, and RF Governmental contracts 02.740.11.0770, 02.740.11.0879, 11.519.11.2035, 14.B37.21.0728, and 14.B37.21.0563.

I greatly appreciate the cooperation, contribution, and support of all my colleagues from Department of Optics and Biophotonics of Saratov State University, Precision Mechanics and Control, Institute of the Russian Academy of Sciences, and Optoelectronics and Measurement Techniques Laboratory of University of Oulu.

Last, but not least, I express my gratitude to my wife, Natalia, and all my family, especially to grandkids Dasha, Zhenya, Stepa, and Serafim for their indispensable support, understanding, and patience during my writing and editing the book.

June 2012   Valery V. Tuchin
Saratov, Russia

References

1. A.P. Ivanov, E.P. Zege, I.L. Katsev, *Image Transfer Through a Scattering Medium* (Springer, Heidelberg, 1991)
2. G. Müller, B. Chance, R. Alfano et al. (eds.), *Medical Optical Tomography: Functional Imaging and Monitoring*, vol. IS11 (SPIE Press, Bellingham, 1993)
3. A. Katzir, *Lasers and Optical Fibers in Medicine* (Academic Press, San Diego, 1993)
4. D.H. Sliney, S.L. Trokel, *Medical Lasers and their Safe Use* (Academic Press, New York, 1993)
5. G. Müller, A. Roggan (eds.), *Laser–Induced Interstitial Thermotherapy* (SPIE Press, Bellingham, 1995)
6. A.J. Welch, M.J.C. van Gemert (eds.), *Optical–Thermal Response of Laser–Irradiated Tissue* (Plenum Press, New York, 1995)
7. M.H. Niemz, *Laser-Tissue Interactions. Fundamentals and Applications*, 3rd edn. (Springer, Berlin, 2007).
8. O.V. Angelsky, S.G. Hanson, P.P. Maksimyak, *Use of Optical Correlation Techniques for Characterizing Scattering Objects and Media* (SPIE Press, Bellingham, 1999)
9. V.V. Tuchin, *Tissue Optics: Light Scattering Methods and Instruments for Medical Diagnosis*, vol. PM 166, 2nd edn. (SPIE Press, Bellingham, 2007)
10. M.I. Mishchenko, J.W. Hovenier, L.D. Travis (eds.), *Light Scattering by Nonspherical Particles* (Academic, San Diego, 2000)
11. M.I. Mishchenko, L.D. Travis, A.A. Lacis, *Scattering, Absorption, and Emission of Light by Small Particles* (Cambridge University Press, Cambridge, 2002)
12. V.V. Tuchin (ed.), *Handbook of Optical Biomedical Diagnostics*, vol. PM107 (SPIE Press, Bellingham, 2002)
13. B.E. Bouma, G.J. Tearney (eds.), *Handbook of Optical Coherence Tomography* (Marcel Dekker, New York, 2002)
14. D.R. Vij, K. Mahesh (eds.), *Lasers in Medicine* (Kluwer Academic, Boston/Dordrecht/London, 2002)
15. T. Vo-Dinh (ed.), *Biomedical Photonics Handbook* (CRC Press, Boca Raton, 2003)

16. J.S. Schuman, C.A. Puliafito, J.G. Fujimoto, *Optical Coherence Tomography of Ocular Diseases*, 2nd edn. (Slack, Thorofare, 2004)

17. M.I. Mishchenko, L.D. Travis, A.A. Lacis, *Multiple Scattering of Light by Particles: Radiative Transfer and Coherent Backscattering* (Cambridge University Press, New York, 2006)

18. A.A. Kokhanovsky, *Polarization Optics of Random Media* (Springer, Berlin/Heidelberg/New York, 2003)

19. A.A. Kokhanovsky, *Light Scattering Media Optics. Problems and Solutions*, 3rd edn. (Springer, Berlin/Heidelberg/New York, 2004)

20. B. Wilson, V. Tuchin, S. Tanev (eds.), *Advances in Biophotonics*, NATO Science Series I. Life and Behavioural Sciences, vol. 369 (IOS Press, Amsterdam, 2005)

21. A.A. Kokhanovsky (ed.), *Light Scattering Reviews* (Springer, Berlin/Heidelberg/New York, 2006)

22. V.V. Tuchin, L.V. Wang, D.A. Zimnyakov, *Optical Polarization in Biomedical Applications* (Springer, Berlin/Heidelberg/New York, 2006)

23. V.V. Tuchin, *Optical Clearing of Tissues and Blood*, vol. PM 154 (SPIE Press, Bellingham, 2006)

24. A. Kishen, A. Asundi (eds.), *Photonics in Dentistry. Series of Biomaterials and Bioengineering* (Imperial College Press, London, 2006)

25. J. Popp, M. Strehle (eds.), *Biophotonics: Visions for Better Health Care* (Wiley-VCH Verlag GmbH & Co. KGaA, 2006)

26. L.V. Wang, H.-I Wu, *Biomedical Optics: Principles and Imaging* (Wiley-Intersience, Hoboken, 2007)

27. R. Splinter, B.A. Hooper, *An Introduction to Biomedical Optics* (Taylor and Francis, New York/London, 2007)

28. J.W. Goodman, *Speckle Phenomena in Optics: Theory and Applications* (Roberts & Co., Englewood, 2007)

29. L. Pavesi, Ph.M. Fauchet (eds.), *Biophotonics* (*Biological and Medical Physics*, *Biomedical Engineering*) (Springer, Berlin/Heidelberg, 2008)

30. W. Drexler, J.G. Fujimoto (eds.), *Optical Coherence Tomography: Technology and Applications* (Springer, Berlin, 2008)

31. B.R. Masters, P.T.C. So (eds.), *Handbook of Biomedical Nonlinear Optical Microscopy*, (Oxford University Press, New York, 2008)

32. S. Tanev, B.C. Wilson, V.V. Tuchin, D. Matthews (guest eds.),Special issue on biophotonics. Adv. Opt. Technol. (2008). doi: 10.1155/2008/134215

33. V.V. Tuchin (ed.) *Handbook of Optical Sensing of Glucose in Biological Fluids and Tissues* (CRC Press/Taylor & Francis Group, London, 2009)

34. K.-E. Peiponen, R. Myllylä, A.V. Priezzhev, *Optical Measurement Techniques, Innovations for Industry and the Life Science* (Springer, Berlin/Heidelberg, 2009)

35. V.V. Tuchin, A. Tarnok, V.P. Zharov (guest eds.), Special issue on towards *in vivo* flow cytometry. J. Biophoton. **2** (8–9), 457–458 (2009)

36. J.W. Shim, *Measurement of Cell/Tissue-Biomaterial Interface Strength: The Laser Spallation Technique for Measurement of Tensile Strength of Cell/Tissue-Biomaterial Interface and its Applications* (VDM Verlag Dr. Müller, 2009)

37. F. Martelli, S. Del Bianco, A. Ismaelli, G. Zaccanti, *Light Propagation through Biological Tissue and Other Diffusive Media: Theory, Solutions, and Software*, vol. PM193 (SPIE Press, Bellingham, 2009)

38. F. Lin, M. Olivo, S.-Y. Kung (eds.), *Biomedical Imaging* (Springer, New York, 2009)

39. A.A. Kokhanovsky (ed.) *Light Scattering Reviews* 4: *Single Light Scattering and Radiative Transfer* (Springer, Heidelberg, 2009)

40. A.A. Kokhanovsky (ed.), *Light Scattering Reviews* 5: *Single Light Scattering and Radiative Transfer* (Springer, Heidelberg, 2010)

41. A. Wax, V. Backman (eds.), *Biomedical Applications of Light Scattering* (McGraw-Hill, New York, 2010)

42. V.V. Tuchin (ed.), *Handbook of Photonics for Biomedical Science* (CRC Press/Taylor & Francis Group, London, 2010)

43. V.V. Tuchin, A.N. Yaroslavsky, S.L. Jacques, R. Anderson (eds.), Biophotonics for dermatology: science and applications. J. Biophoton. **3** (1–2), 9–88 (2010)

44. F.S. Pavone (ed.), *Laser Imaging and Manipulation in Cell Biology* (Wiley-VCH Verlag GmbH & Co. KGaA, Weinheim, 2010)

45. V.V. Tuchin, M. Leahy, D. Zhu (eds.), Optical clearing for biomedical imaging in the study of tissues and biological fluids. J. Innov. Opt. Health Sci. **3**(3) (2010)

46. V.V. Tuchin, *Lasers and Fibre Optics in Biomedical Science*, 2nd edn. (Fizmatlit, Moscow, 2010)

47. V.V. Tuchin (ed.), *Advanced Optical Cytometry: Methods and Disease Diagnoses* (Wiley-VCH Verlag GmbH & Co. KGaA, Weinheim, 2011)

48. V.V. Tuchin, A. Tárnok, V.P. Zharov (eds.), In vivo flow cytometry. Cytometry A **79A**(10), 737–883 (2011)

49. D.A. Boas, C. Pitris, N. Ramanujam (eds.), *Handbook of Biomedical Optics* (CRC Press/Taylor & Francis Group, London, 2011)

50. J. Popp, V.V. Tuchin, A. Chiou, S.H. Heinemann, (eds.) *Handbook of Biophotonics. Vol.1*: *Basics and Techniques* (Wiley-VCH Verlag GmbH & Co. KGaA, Weinheim, 2011)

51. J. Popp, V.V. Tuchin, A. Chiou, S.H. Heinemann (eds.) *Handbook of Biophotonics. Vol. 2*: *Photonics for Health Care* (Wiley-VCH Verlag GmbH & Co. KGaA, Weinheim, 2011)

52. J. Popp, V.V. Tuchin, A. Chiou, S.H. Heinemann (eds.), *Handbook of Biophotonics*, *Vol. 3*: *Photonics in Pharmaceutics, Bioanalysis and Environmental Research* (Wiley-VCH Verlag GmbH & Co. KGaA, Weinheim, 2012)

53. V.V. Tuchin, *Dictionary of Biomedical Optics and Biophotonics* (SPIE Press, Bellingham, 2012)

54. J.S. Suri, S.V. Sree, K.-H. Ng, R.M. Rangayyan (eds.), *Diagnostic and Therapeutic Applications of Breast Imaging*, vol. PM211 (SPIE Press, Bellingham, 2012)

55. M.T. Eismann, *Hyperspectral Remote Sensing*, vol. PM210 (SPIE Press, Bellingham, 2012)

56. R.K. Tyson, B.W. Frazier, *Field Guide to Adaptive Optics*, vol. FG24 (SPIE Press, Bellingham, 2012)

57. G. Popescu, *Quantitative Phase Imaging of Cells and Tissues* (McGraw-Hill, New York, 2011)

Contents

Volume 2

List of Contributors

Peter E. Andersen Department of Photonics Engineering, Technical University of Denmark, Kongens Lyngby, Denmark

Oleg V. Angelsky Department of Correlation Optics, Chernivtsi National University, Chernivtsi, Ukraine

Rafat R. Ansari NASA John H. Glenn Research Center at Lewis Field, Cleveland, OH, USA

V. T. Bachynsky Department of Pathomorphology and Forensic Medicine, Bukovinian State Medical University, Chernivtsi, Ukraine

Gert von Bally Center for Biomedical Optics and Photonics Muenster, University of Münster, Münster, Germany

Stanislav B. Baluschev Max–Planck–Institute for Polymer Research, Mainz, Germany

Organic Optoelectronics Laboratory, Optics and Spectroscopy Department, Sofia University, "St. Kliment Ochridski", Sofia, Bulgaria

Johannes F. de Boer Institute for Lasers, Life and Biophotinics (LaserLaB) Amsterdam, Department of Physics, VU University, Amsterdam, The Netherlands

T. M. Boychuk Department of Cytology and Embryology, Bukovinian State Medical University, Histology, Chernivtsi, Ukraine

Alexander V. Bykov Optoelectronics and Measurement Techniques Laboratory, University of Oulu, Oulu, Finland

Elvio Carlino IOM CNR Laboratorio TASC, Trieste, Italy

Liberato De Caro Istituto di Cristallografia (IC-CNR), Bari, Italy

Zhongping Chen Department of Biomedical Engineering, Beckman Laser Institute, University of California, Irvine, Irvine, CA, USA

Haiying Cheng Huazhong University of Science and Technology, Wuhan, People's Republic of China

Christian Dierker Biomedical Technology Center, University of Münster, Münster, Germany

Lev S. Dolin Institute of Applied Physics of the Russian Academy of Sciences, Nizhny Novgorod, Russian Federation

Victor V. Fadeev Moscow State University, Moscow, Russian Federation

Ivan V. Fedosov Department of Optics and Biophotonics, Saratov State University, Saratov, Russian Federation

Grigory V. Gelikonov Institute of Applied Physics of the Russian Academy of Sciences, Nizhny Novgorod, Russian Federation

Valentin M. Gelikonov Institute of Applied Physics of the Russian Academy of Sciences, Nizhny Novgorod, Russian Federation

Mohamad G. Ghosn Department of Medicine, Baylor College of Medicine, Houston, TX, USA

Department of Biomedical Engineering, University of Houston, Houston, TX, USA

Cinzia Giannini Istituto di Cristallografia (IC-CNR), Bari, Italy

Natalia D. Gladkova Medical Academy, Nizhny Novgorod, Russian Federation

A. S. Goncharov M.V. Lomonosov Moscow State University, Moscow, Russian Federation

Eugene B. Hanlon Department of Veterans Affairs, Medical Research Service, Bedford, MA, USA

Rashid R. Iksanov Institute of Applied Physics of the Russian Academy of Sciences, Nizhny Novgorod, Russian Federation

N. G. Iroshnikov M.V. Lomonosov Moscow State University, Moscow, Russian Federation

Steven L. Jacques Oregon Health & Science University, Portland, OR, USA

Chao Jiang Huazhong University of Science and Technology, Wuhan, People's Republic of China

Thomas M. Jørgensen Department of Photonics Engineering, Technical University of Denmark, Kongens Lyngby, Denmark

Jeroen Kalkman Biomedical Engineering & Physics, Academic Medical Center, University of Amsterdam, Amsterdam, The Netherlands

Vladislav A. Kamensky Institute of Applied Physics of the Russian Academy of Sciences, Nizhny Novgorod, Russian Federation

Björn Kemper Center for Biomedical Optics and Photonics Muenster, University of Münster, Münster, Germany

Taewoo Kim Quantitative Light Imaging Laboratory, Department of Electrical and Computer Engineering, Beckman Institute for Advanced Science & Technology, University of Illinois at Urbana-Champaign, Urbana, IL, USA

Sebastian Kosmeier Center for Biomedical Optics and Photonics Muenster, University of Münster, Münster, Germany

Sergey U. Ksenofontov Institute of Applied Physics of the Russian Academy of Sciences, Nizhny Novgorod, Russian Federation

Roman V. Kuranov Institute of Applied Physics of the Russian Academy of Sciences, Nizhny Novgorod, Russian Federation

Patrik Langehanenberg Center for Biomedical Optics and Photonics Muenster, University of Münster, Münster, Germany

Andrey V. Larichev M.V. Lomonosov Moscow State University, Moscow, Russian Federation

Kirill V. Larin Department of Biomedical Engineering, University of Houston, Houston, TX, USA

Department of Optics and Biophotonics, Saratov State University, Saratov, Russian Federation

Rainer A. Leitgeb Center for Medical Physics and Biomedical Engineering, Medical University Vienna, Vienna, Austria

Michael K. K. Leung Departments of Medical Biophysics and Radiation Oncology, University of Toronto, Toronto, Canada

Pengcheng Li Huazhong University of Science and Technology, Wuhan, People's Republic of China

Gangjun Liu Department of Biomedical Engineering, Beckman Laser Institute, University of California, Irvine, Irvine, CA, USA

Dirk Lorenser Optical + Biomedical Engineering Laboratory, School of Electrical, Electronic, and Computer Engineering, University of Western Australia, Perth, WA, Australia

Qingming Luo Huazhong University of Science and Technology, Wuhan, People's Republic of China

Peter P. Maksimyak Department of Correlation Optics, Chernivtsi National University, Chernivtsi, Ukraine

Adrian Mariampillai Department of Electrical and Computer Engineering, Ryerson University, Toronto, Canada

Maleeha Mashiatulla Department of Biomedical Engineering, University of Houston, Houston, TX, USA

Robert A. McLaughlin Optical + Biomedical Engineering Laboratory, School of Electrical, Electronic, and Computer Engineering, University of Western Australia, Perth, WA, Australia

Igor Meglinski Department of Physics, University of Otago, Dunedin, New Zealand

O. P. Mincer Department of Medical Informatics, National Medical Academy named after P.L. Shupyka, Kiev, Ukraine

Mark D. Modell Beth Israel Deaconess Medical Center, Harvard University, Boston, MA, USA

Igor I. Mokhun Department of Correlation Optics, Chernivtsi National University, Chernivtsi, Ukraine

Vasyl Molebny Academy of Technological Sciences of Ukraine, Kiev, Ukraine

Andrey N. Morosov Institute of Applied Physics of the Russian Academy of Sciences, Nizhny Novgorod, Russian Federation

Joel D. Morrisett Department of Medicine, Baylor College of Medicine, Houston, TX, USA

Frits F. M. de Mul Department of Applied Physics, University of Twente, AE Enschede, The Netherlands

Alexey V. Myakov Institute of Applied Physics of the Russian Academy of Sciences, Nizhny Novgorod, Russian Federation

Lev T. Perelman Beth Israel Deaconess Medical Center, Harvard University, Boston, MA, USA

Adrian Podoleanu School of Physical Sciences, University of Kent at Canterbury, Canterbury, UK

Peter V. Polyanskii Department of Correlation Optics, Chernivtsi National University, Chernivtsi, Ukraine

Gabriel Popescu Quantitative Light Imaging Laboratory, Department of Electrical and Computer Engineering, Beckman Institute for Advanced Science & Technology, University of Illinois at Urbana-Champaign, Urbana, IL, USA

Yury P. Potapov Institute of Applied Physics of the Russian Academy of Sciences, Nizhny Novgorod, Russian Federation

Christian Remmersmann Center for Biomedical Optics and Photonics Muenster, University of Münster, Münster, Germany

Christina Rommel Biomedical Technology Center, University of Münster, Münster, Germany

David D. Sampson Optical + Biomedical Engineering Laboratory, School of Electrical, Electronic, and Computer Engineering, University of Western Australia, Perth, WA, Australia

Centre for Microscopy, Characterisation and Analysis, University of Western Australia, Perth, WA, Australia

Veronika V. Saposhnikova Institute of Applied Physics of the Russian Academy of Sciences, Nizhny Novgorod, Russian Federation

Sergey N. Savenkov Department of Radiophysics, Kyiv Taras Shevchenko University, Kyiv, Ukraine

Frank Schlichthaber Center for Biomedical Optics and Photonics Muenster, University of Münster, Münster, Germany

Tilman Schmoll Center for Medical Physics and Biomedical Engineering, Medical University Vienna, Vienna, Austria

Jürgen Schnekenburger Biomedical Technology Center, University of Münster, Münster, Germany

Alexander M. Sergeev Institute of Applied Physics of the Russian Academy of Sciences, Nizhny Novgorod, Russian Federation

Ekaterina A. Sergeeva Institute of Applied Physics of the Russian Academy of Sciences, Nizhny Novgorod, Russian Federation

Dmitry V. Shabanov Institute of Applied Physics of the Russian Academy of Sciences, Nizhny Novgorod, Russian Federation

Natalia M. Shakhova Institute of Applied Physics of the Russian Academy of Sciences, Nizhny Novgorod, Russian Federation

Evgeny A. Shirshin Moscow State University, Moscow, Russian Federation

Dritan Siliqi Istituto di Cristallografia (IC-CNR), Bari, Italy

Shamira Sridharan Quantitative Light Imaging Laboratory, Department of Electrical and Computer Engineering, Beckman Institute for Advanced Science & Technology, University of Illinois at Urbana-Champaign, Urbana, IL, USA

Beau A. Standish Department of Electrical and Computer Engineering, Ryerson University, Toronto, Canada

Ove Steinvall Swedish Defence Research Agency, Stockholm, Sweden

Lars Thrane Department of Photonics Engineering, Technical University of Denmark, Kongens Lyngby, Denmark

Valery V. Tuchin Department of Optics and Biophotonics, Saratov State University, Saratov, Russian Federation

Precision Mechanics and Control, Institute of the Russian Academy of Sciences, Saratov, Russian Federation

Optoelectronics and Measurement Techniques Laboratory, University of Oulu, Oulu, Finland

Ilya V. Turchin Institute of Applied Physics of the Russian Academy of Sciences, Nizhny Novgorod, Russian Federation

Andrey A. Turshatov Max-Planck-Institute for Polymer Research, Mainz, Germany

Andreas Tycho Department of Photonics Engineering, Technical University of Denmark, Kongens Lyngby, Denmark

Yurii A. Ushenko Department of Correlation Optics, Chernivtsi National University, Chernivtsi, Ukraine

I. Alex Vitkin Departments of Medical Biophysics and Radiation Oncology, University of Toronto, Toronto, Canada

Division of Biophysics and Bioimaging, Ontario Cancer Institute/University Health Network, Toronto, Canada

Edward Vitkin Beth Israel Deaconess Medical Center, Harvard University, Boston, MA, USA

Ruikang K. Wang University of Washington, Seattle, WA, USA

Zhen Wang Huazhong University of Science and Technology, Wuhan, People's Republic of China

Zheng Wang Huazhong University of Science and Technology, Wuhan, People's Republic of China

Harold T. Yura Electronics and Photonics Laboratory, The Aerospace Corporation, Los Angeles, CA, USA

Elena V. Zagainova Medical Academy, Nizhny Novgorod, Russian Federation

Dmitry A. Zimnyakov Saratov State Technical University, Saratov, Russian Federation

Precision Mechanics and Control, Institute of the Russian Academy of Sciences, Saratov, Russian Federation

Part 1

Speckle and Polarization Technologies

Light Correlation and Polarization in Multiply Scattering Media: Industrial and Biomedical Applications

1

Dmitry A. Zimnyakov

Contents

Abstract

This chapter describes approaches to multiply scattering media characterization on the basis of correlation and polarization analysis of scattered probe radiation.

1.1 Introduction: Interference and Polarization Phenomena at Multiple Scattering

This chapter considers of some the important phenomena that appear as a result of the interaction of coherent light with optically dense disordered media. When a coherent light propagating significant distances in a random medium scatters numerous times

D.A. Zimnyakov
Saratov State Technical University, Saratov, Russian Federation

Precision Mechanics and Control, Institute of the Russian Academy of Sciences, Saratov, Russian Federation
e-mail: zimnyakov@mail.ru

and finally loses information about its initial propagating direction but nevertheless preserves its coherence in certain conditions, the situation is not obvious. However, there are a number of classical examples of coherence persisting despite multiple scattering by the random media. These examples are the existence of temporal, spatial, and angular correlations of the multiply scattered light revealing the information on the microscopic dynamic and structure properties of the scattering system. It should be noted that an abundance of theoretical and experimental papers related to different manifestations of coherence in multiple scattering have been published in the last two decades, beginning with the classical works of Golubentsev [1], Stephen [2], and John [3]. It is impossible to cite all of these works here, and only the common aspects of coherence of light in multiple scattering that are important from the viewpoint of gaining a better understanding of the optics of condensed media and of practical applications in industrial and medical diagnostics will be briefly reviewed. Statistical (correlation) properties of the multiply scattered light and methods of studying the optically dense disordered and weakly ordered systems by means of correlation spectroscopy are considered in this chapter. Some fundamental relations between correlation and polarization characteristics of the multiply scattered coherent light that can be interpreted as the existence of self-similarity in multiple scattering are also analyzed.

Among these phenomena, the decay of polarization of multiply scattered light is one of the most important features of the radiative transfer in random media related to the vector nature of electromagnetic waves running through a scattering system. From the physical picture, it can be expected that the specific relaxation scale characterizing the rate of suppression of initial polarization of light propagating in a multiply scattering medium will be closely related to other relaxation scales that characterize an increase of uncertainty of other fundamental parameters of electromagnetic radiation. The obvious way is to establish the relations between the polarization relaxation parameters, which can be introduced as the characteristic spatial scales of decay of the polarization characteristics chosen to describe the scattered field [4–6], and the relaxation parameter that characterizes the spatial scale in which the almost total loss of information about the initial direction of light propagation occurs. In terms of the radiative transfer theory, the latter parameter is defined as the mean transport free path (MTFP, [7]). The relations between the MTFP and the polarization decay parameters are controlled by the individual properties of each scattering medium and, consequently, the given scattering system can be specified with adequate reliability by measurements of the polarization decay rate for given scattering and detection conditions. Thus, the introduction of the additional polarization measurement channels in the systems traditionally used for optical diagnostics and visualization of optically dense scattering media provides a novel quality and spreads the functional ability of these systems.

The object of particular interest is the appearance of polarization effects in the case of stochastic interference of electromagnetic waves traversing random media. One of the most familiar examples of such appearance is the polarization dependence of temporal correlations of the electric field fluctuations induced by multiple scattering of coherent light by non-stationary media. These phenomena indicate the vector character of electromagnetic radiation propagating in random media.

In this chapter, the correlation and polarization properties of multiply scattered light are considered from the viewpoint of their application for optical diagnostics of scattering systems with complex structures such as the biological tissue.

1.1.1 Temporal and Angular Correlations of Light Scattered by Disordered Media

The existence of finite spatial and temporal correlation scales for amplitude and intensity fluctuations of coherent light propagating in optically dense random media is the direct manifestation of the coherence property of light multiply scattered by disordered and weakly ordered media. If coherent light is scattered by a non-stationary disordered medium, then the statistical properties of a scattered field can be characterized by simultaneous analysis of the correlation of the complex amplitude values for two spatially separated observation points and for different moments of time. In this way, the spatial-temporal correlation function of scattered-field fluctuations is introduced as follows [8, 9]:

$$G_1(\bar{r}_1, t_1, \bar{r}_2, t_2) = \langle E_1 E_2^* \rangle = \langle E(\bar{r}_1, t_1) E^*(\bar{r}_2, t_2) \rangle, \qquad (1.1)$$

where the symbol * denotes complex conjugation. For many cases, the spatial-temporal fluctuations of scattered-field amplitude can be considered as the stationary random fields; this leads to the following form of the field correlation function:

$$G_1(\bar{r}_1, t_1, \bar{r}_2, t_2) = G_1(\bar{r}_1, \bar{r}_2, t_1 - t_2) = G_1(\bar{r}_1, \bar{r}_2, \tau). \qquad (1.2)$$

In the similar manner, the spatial-temporal correlation function of scattered light intensity fluctuations can be introduced:

$$G_2(\bar{r}_1, \bar{r}_2, \tau) = \langle I_1 I_2 \rangle = \langle I(\bar{r}_1, t) I(\bar{r}_2, t + \Delta\tau) \rangle. \qquad (1.3)$$

Moreover, for statistically homogeneous speckle patterns, the field and intensity correlation functions depend only on $\Delta\bar{r} = \bar{r}_2 - \bar{r}_1$:

$$G_1(\bar{r}_1, \bar{r}_2, \tau) = G_1(\Delta\bar{r}, \tau); \ G_2(\bar{r}_1, \bar{r}_2, \tau) = G_2(\Delta\bar{r}, \tau). \qquad (1.4)$$

If a scattered optical field is characterized by the Gaussian statistics of complex amplitude that has zero mean value, then the normalized correlation functions of amplitude and intensity fluctuations,

$$g_1(\Delta\bar{r}, \tau) = \langle E_1 E_2^* \rangle \Big/ \left(\left(|E_1|^2 \right) \left(|E_2|^2 \right) \right)^{1/2},$$

$$g_2(\Delta\bar{r}, \tau) = \langle I_1 I_2 \rangle / \langle I_1 \rangle \langle I_2 \rangle$$

are related to each other as follows (the well-known Siegert relation) [8, 9]:

$$g_2(\Delta\bar{r}, \tau) = 1 + \beta|g_2(\Delta\bar{r}, \tau)|^2, \tag{1.5}$$

where the factor β depends on the detection conditions and is equal to 1 under ideal circumstances.

Let us analyze only the temporal fluctuations of a multiple scattered coherent light in a fixed detection point. For simplicity, the scalar wave approach is frequently used to describe the statistics of a multiple scattered coherent light. It should be noted that, despite the obvious physical restrictions of this approach, it provides adequately valid results for the vast majority of scattering systems, provided appropriate scattering and detection conditions are chosen. Moreover, the scalar wave formalism can be appropriately modified to describe the propagation of polarized light in disordered media.

Propagation of a coherent electromagnetic wave in random media can be considered as a sequence of statistically independent scattering events, taking place in the moment t at positions $\bar{r}_1(t), \bar{r}_2(t), \ldots$. Each scattering event is characterized by the wavevector $\bar{k}_i$. This discussion will follow the physical picture first outlined by G. Maret and P. Wolf [10]. The scattered field interferes with itself but at time $t + \tau$. In this analysis, the time delay of light propagation is neglected; correspondingly, displacements of scatterers during this propagation time are also neglected.

In this case, each partial contribution to the scattered field is considered as the result of sequence of n scattering events:

$$E_k(t) = \exp(j\omega t) \prod_{i=1}^{N_k} E_i \exp(-j\bar{q}_i \bar{r}_i(t)), \tag{1.6}$$

and the total scattered field in the detection point is expressed as follows:

$$E(t) = \sum_k E_k(t).$$

In further analysis, the *single-path* correlation function of field fluctuations is introduced as

$$G_2^k(\tau) = \langle E_k(t) E_k^*(t + \tau) \rangle \approx \exp(-j\omega\tau) \left\langle \prod_{i=1}^{N_k} |a_i|^2 \exp\{j\bar{q}_i \Delta\bar{r}_i(\tau)\} \right\rangle$$

$$\approx \exp(-j\omega\tau) \left\langle |a_i|^2 \right\rangle \exp\{-\langle\bar{q}^2\rangle \langle\Delta\bar{r}^2(\tau)\rangle N_k/6\}.$$

For the discussed case, the mean value of $\bar{q}^2$ estimated for a sequence of scattering events can be expressed as

$$\langle\bar{q}^2\rangle = 2k^2 l/l^*,$$

where l is the scattering mean free path and l^* is the mean transport free path for the scattering medium [7]. The number of scattering events for each partial contribution can be expressed as $N_k \approx s_k/l$, where s_k is the corresponding propagation path for k-th partial component inside a scattering medium. Thus, the single-path correlation function has the following form:

$$G_1^k(\tau) \approx \exp(-j\omega\tau)\left\langle |a|^2 \right\rangle \exp\left\{-k^2\left\langle \Delta\bar{r}^2(\tau)\right\rangle s_k/3l^*\right\}. \qquad (1.7)$$

The total temporal correlation function of field fluctuations in the detection point can be obtained by the statistical summation of the single-path correlation functions over the ensemble of partial contributions:

$$G_1(\tau) \approx \sum_k P(k)G_1^k(\tau),$$

where $P(k)$ are the statistical weights characterizing contributions of partial components to formation of a scattered field in a detection point. This expression may be modified for multiple scattering systems characterized by the continuous distribution of optical paths s by integration over the range of all possible values of s:

$$G_1(\tau) \approx \int_0^\infty \exp\left(-\frac{k^2\left\langle \Delta\bar{r}^2(\tau)\right\rangle s}{3l^*}\right)\tilde{\rho}(s)ds, \qquad (1.8)$$

where $\tilde{\rho}(s)$ is the probability density of optical paths of scattered partial waves and the following normalization condition takes place:

$$\int_0^\infty \tilde{\rho}(s)ds = \langle I \rangle.$$

The normalized temporal correlation function can be introduced as

$$g_1(\tau) = \int_0^\infty \exp\left(-k^2\left\langle \Delta\bar{r}^2(\tau)\right\rangle s/3l^*\right)\rho(s)ds \qquad (1.9)$$

by using the following normalization condition:

$$\rho(s) = \tilde{\rho}(s)\bigg/\int_0^\infty \tilde{\rho}(s)ds.$$

In particular, for Brownian scattering systems the argument of the exponential kernel in the right-hand side of (1.9) has the well-known form:

$$2\tau s/\tau_0 l^*,$$

where τ_0 is the so-called single-scattering correlation time defined as

$$\tau_0 = \left(4\pi^2 D/\lambda^2\right)^{-1} = \left(k^2 D\right)^{-1},$$

where D is the diffusion coefficient of scattering sites and λ is the wavelength of the probe light.

Thus, analysis of the time-dependent correlation decay of the scattered light fluctuations allows us the characterization of non-stationary multiple scattering media through the reconstruction of the path length distribution function dependent on optical properties and geometry of the probed medium or through the reconstruction of the time-dependent variance of scattering sites' displacements. The diagnostic approaches based on this principle will be discussed in Sect. 1.1.4.

The existence of long-range spatial or angular correlations, a fundamental property of optical fields multiply scattered by random media, can be considered in terms of "angular memory" effect (Feng et al., Ref. [11]). The possibility to use this effect as the physical basis for tomographic imaging of optically dense disordered media is discussed in Ref. [12]. The relations between angular correlations of multiply scattered coherent light and optical properties of scattering media for the transmittance mode of light propagation were studied theoretically and experimentally by Hoover with co-workers [13]. In this study, the potentiality to use the angular correlation analysis for disordered scattering media characterization was investigated. Also, an original approach to this problem, considered in Ref. [14] (see ▶ Chap. 7), is based on the influence of angular correlation decay on an interference of optical fields induced by two illuminating coherent beams incoming in the scattering medium at different angles of incidence. In this case, the probed medium is illuminated by a spatially modulated laser beam formed by overlapping the two collimated beams. The spatial modulation of the resulting illuminating beam has the form of a regular interference pattern with the fringe spacing determined by the angle between the overlapping beams. In the absence of scattering, the angular spectra of incident beams have the δ-like forms; the appearance of scattering causes the broadening of these angular spectra and decay in the interference pattern contrast of the outgoing spatially modulated beam. Analysis of the interference pattern contrast for the outgoing beam and its dependence on the distance between the scatter and the observation plane and interference fringe period allows one to characterize the scattering properties of the probed medium.

1.1.2 Damping of Polarization of Light Propagating Through the Disordered Media

The relations between statistical properties of the path length distributions for partial waves propagating in random media, and statistical properties of multiply scattered vector optical fields manifest themselves in a number of theoretically predicted and experimentally observed effects [1–3, 15–20]; one is the appearance of the similarity in multiple scattering. A group of relaxation phenomena, in the case of coherent light propagation in the disordered systems, can be considered as manifestations of the similarity in multiple scattering. This similarity is related to the same forms of dependences of certain statistical moments of scattered optical fields on the specific spatial scales that characterize the decay of the corresponding moments in the course of the coherent light propagation in the disordered media. The following relaxation effects can be considered [21–23]:

– The existence of temporal correlations of amplitude and intensity fluctuations of scattered optical fields in the fixed detection point for non-stationary systems of scattering particles;
– The decay of polarization of light propagating in the disordered systems;
– The manifestation of Bougier's law in the case of multiple scattering with noticeable absorption.

The relaxation of the statistical moments of the scattered optical fields can be considered in terms of the path length distributions, i.e., by statistical analysis of ensembles of optical paths for partial waves, which propagate in the scattering medium and from which the observed scattered field can be constructed. For the diffusion scattering mode, each partial component of the multiply scattered optical field is associated with a sequence of a great number N of statistically independent scattering events and is characterized by the path s. The statistical moments of scattered field can be considered as the integral transforms of the probability density function $\rho(s)$. In the weak scattering limit, when $l, l^* \gg \lambda$, such second-order statistical moments as the average intensity of scattered light, the temporal correlation function of the field fluctuations, and the degree of polarization of multiply scattered light in the arbitrarily chosen detection point can be expressed in the case of $N = s/l \gg 1$ as the Laplace transforms of $\rho(s)$. In particular, the average intensity of the scattered light for multiply scattering medium with non-zero absorption can be written using the modified Bougier's law:

$$\langle I \rangle \cong \int\limits_0^\infty \exp(-\mu_a s)\rho(s)ds = \int\limits_0^\infty \exp(-s/l_a)\rho(s)ds, \qquad (1.10)$$

where the averaging is carried out over all possible configurations of the scattering sites. The normalization condition can be written in the following form:

$$\int\limits_0^\infty \rho(s)ds = \langle I \rangle_0,$$

where $\langle I \rangle_0$ is the average intensity in the absence of absorption.

For non-stationary disordered media consisting of moving scattering particles, the normalized temporal autocorrelation function of the scattered field fluctuations is expressed as [10, 24, 25]

$$g_1(\tau) \approx \frac{\int_0^\infty \exp[-B(\tau)s/l]\rho(s)ds}{\int_0^\infty \rho(s)ds}, \tag{1.11}$$

where $B(\tau)$ is determined by the variance of the displacements of the scattering sites for the time delay τ. As considered above, in the particular case of Brownian systems the exponential kernel of the integral transform (1.11) is equal to $\exp(-2\tau\, s/\tau_0\, l^*)$.

The relaxation of the initial polarization state of the coherent light propagating in the disordered multiply scattering medium is caused by the energy flux interchange between partial waves with different polarization states. In particular, for initial linear polarization of the propagating light linearly "co-polarized" and "cross-polarized" partial components of the scattered field can be considered; the former is characterized by the same direction of polarization azimuth as the incident illuminating beam and the latter by the orthogonal direction. In a similar way, the interrelation between the left circularly polarized component and right circularly polarized component can be analyzed if the illuminating light with the initial circular polarization is used. Propagation of linearly polarized light in a strongly scattering disordered medium can be considered with the use of a solution of the Bethe-Salpeter equation for the case of transfer of a linearly polarized partial, "single-path" contribution, which undergoes n scattering events in a disordered medium with isotropic scattering [17]. This consideration leads to the following expressions for intensities of the "single-path" cross-polarized and co-polarized components [5]:

$$\begin{aligned} I_{II}^s &= f_{II}^s(n)I^s(n), \\ I_\perp^s &= f_\perp^s(n)I^s(n), \end{aligned} \tag{1.12}$$

where the single-path "scalar" intensity $I^s(n)$ can be obtained by evaluating the photon density for a scalar wave propagating at the distance corresponding to n scattering events and the weighting functions $f_{II}^s(n)$, $f_\perp^s(n)$ can be determined in the dependence on the number of scattering events as [5, 17]

$$f_{II}^s(n) = \left[\left(\frac{10}{15}\right)^{n-1} + 2\left(\frac{7}{15}\right)^{n-1}\right]\Big/3,$$

$$f_{II}^s(n) = \left[\left(\frac{10}{15}\right)^{n-1} - \left(\frac{7}{15}\right)^{n-1}\right]\Big/3.$$

Thus, introducing a value of the polarization degree for the arbitrary single-path contribution of a scattered optical field with a propagation path equal to $s \approx nl$ as $P^s(n) = \left[I_{II}^s(n) - I_\perp^s(n)\right] / \left[I_{II}^s(n) + I_\perp^s(n)\right]$, one obtains the following:

$$P^s(n) = \frac{f_{II}(n) - f_\perp(n)}{f_{II}(n) + f_\perp(n)} = \frac{3\left(\frac{7}{15}\right)^{n-1}}{2\left(\frac{10}{15}\right)^{n-1} + \left(\frac{7}{15}\right)^{n-1}}$$

$$= 3\left[2\exp\left\{(n-1)\ln\frac{10}{7}\right\} + 1\right]^{-1}.$$

Correspondingly, the single-path polarization degree $P^s(n)$ for linearly polarized light obeys the exponential decay $P^s(n) \cong 1.5\exp\{(n-1)/n'\}$ with the decay parameter equal to $n'_L \approx 2.804$ for long propagation distances with a great number of scattering events $n \gg 1$.

If a multiple scattering disordered medium is illuminated by circularly polarized light, then the single-path degree of circular polarization of multiple scattered light can be introduced as the ratio $P_C^s(n) = [I_+(n) - I_-(n)]/[I_+(n) + I_-(n)]$, where $I_+(n), I_-(n)$ are the intensities of circularly polarized partial contributions that undergo n scattering events and have the same helicity as an incident circularly polarized light (+) and the opposite helicity (−). Similar considerations for the case of multiple scattering of circularly polarized light also lead to the exponential decay of the single-path degree of circular polarization with the value of the decay parameter equal to $n'_C \approx \ln 2 \approx n'_L/2$ [5].

If polarized light propagates in the disordered medium characterized by the sufficiently non-zero value of the anisotropy parameter g (the case of anisotropic scattering), then the decay parameter $n'_{L,C}$ should be replaced by the effective value $\tilde{n}'_{L,C}$ determined by optical properties of scattering particles, which form a scattering system. Introducing the depolarization length $\xi_{L,C} = \tilde{n}'_{L,C}l$ as one of the dimension scales that characterize the scattering system, one can find the relation between $\xi_{L,C}$ and another important scale – the mean transport free path l^*. This relation is strongly influenced by the optical properties of the scattering medium as well as by the illumination and detection conditions.

The degree of residual polarization of a scattered optical field in the arbitrarily chosen detection point can be determined by averaging the single-path polarization degree over the ensemble of partial components of a scattered optical field characterized by the path length density distribution $\rho(s)$:

$$P_{L,C} = \int\limits_0^\infty P_{L,C}^s(s)\rho(s)ds \approx \frac{3}{2}\int\limits_0^\infty \exp\left(-\frac{s}{\xi_{L,C}}\right)\rho(s)ds, \qquad (1.13)$$

where the probability density function $\rho(s)$ is determined by the conditions of light propagation in a scattering medium between a source of polarized light and a detection system which allows the polarization discrimination of scattered light.

Theoretically predicted exponential decay of the single-path polarization degree with the increasing path length s was directly observed in the experiments with time-resolved intensity measurements for co-polarized and cross-polarized components of a backscattered light in the case of optically dense media illumination by a short pulse of linearly polarized laser light [26]. In these experiments, the colloidal systems with volume fractions ranging from 5 % to 54 % and consisting of aqueous suspensions of 1-μm-diameter silica spheres with an ionic strength of 0.03 m/L $NaNO_3$ and pH = 9.5. Scattering samples were probed by laser pulses with a duration of 150 fs emitted by a dispersion-compensated, self-mode-locked Ti:sapphire laser pumped by a frequency-doubled Nd:YAG laser. The backscattered light pulses were analyzed with the use of a background-free cross-correlation technique. The Ti:sapphire laser, which had a repetition frequency of 76 MHz, was tuned to a wavelength of 800 nm, and its output was split into two beams by a 50:50 beam splitter. One beam passed through a delay stage and served as the gating pulse in the cross correlator. Data runs were typically recorded with a 3-mm (20-fs) step size. The other beam passed through a mechanical chopper, a second beam splitter, and a 15-cm-focal-length converging lens to a sample placed at the focus of the beam. The estimated value of the photon density corresponding to a single pulse of probe light was found equal to 5.3×10^{13} cm^{-2}/pulse.

The degree of polarization of the backscattered light was determined by use of a half-wave plate and a Glan-Thompson polarizer. Typical shapes of the detected pulses for co-polarized and cross-polarized components of the backscattered light from two scattering samples with strongly differing values of the scattering coefficient are illustrated by Fig. 1.1. The inset illustrates the tendencies in decay of the time-dependent degree of linear polarization of the backscattered light.

The analysis of the obtained experimental results allows for the single-path degree of linear polarization to be expressed in the simple exponential form $P_L^s(n) \approx \exp(-n/n'_L)$, where n'_L is regarded as the average number of scattering events needed to depolarize the optical wave. For an effective speed of light, v_{eff}, and the mean elastic scattering free path l, the time scale of the depolarization process can be estimated to be of the order of $\tau = n'_L l / v_{eff}$.

Also, the validity of the exponential decay model for the description of dissipation of the initial polarization state of light propagating in multiple scattering random media was confirmed by experimental studies of the depolarizing properties of optically thick random media with the slab geometry, which were probed in the transmittance mode [5, 21, 22]. Being calculated with the use of the diffusion approximation, the path length density distributions $\rho(s)$ for optically thick slabs in the transmittance mode are characterized by the single-sided Laplace transformation:

$$L_\rho(m) = \int\limits_0^\infty \exp(-s/ml^*)\rho(s)ds,$$

which, analyzed for the fixed value of m, exponentially decays with the increasing dimensionless slab thickness L/l^*. This tendency is illustrated by Fig. 1.2.
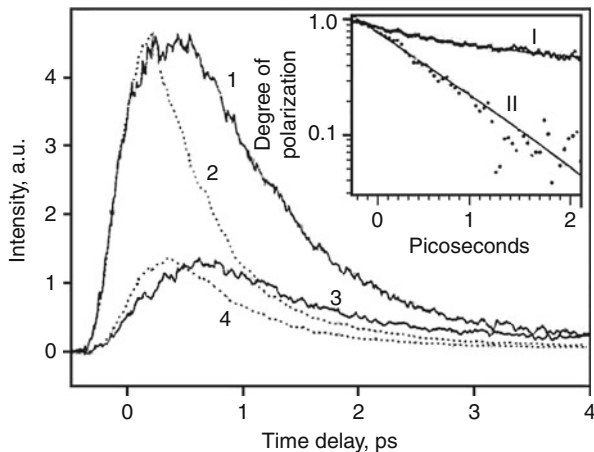
Fig. 1.1 The pulse shapes for co-polarized and cross-polarized components of backscattered light. *Solid lines* – the scattering sample with 5 % volume concentration of silica spheres; *dotted line* – the scattering sample with 25 % volume concentration of silica spheres. *1*, *2* – intensity of the co-polarized component; *3*, *4* – intensity of the cross-polarized component. *Inset* shows the evolution of the time-dependent degree of linear polarization of backscattered light for both samples (*I* – 5 % volume concentration of the scattering sites; *II* – 25 % concentration of the scattering sites) [26]

Fig. 1.2 The Laplace transformations of the path length density distributions for probe light, which is transmitted through a scattering slab as depending on the normalized slab thickness [21, 22]. The probability density functions $\rho(s)$ were calculated with the use of the diffusion approximation
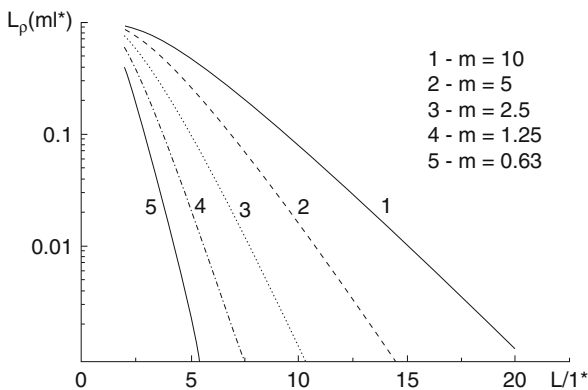
The above-discussed exponential decay of the "single-path" degree of polarization should lead to the approximately exponential decay of the degree of polarization of light transmitted through an optically thick slab ($L/l^* \geq 5$) with the increasing ratio L/l^*. Indeed, the dependences of the degree of polarization for linearly or circularly polarized light transmitted through the optically dense scattering slabs on the dimensionless slab thickness, which were obtained in the experiments with mono-disperse aqueous suspensions of polystyrene beads of various sizes, evidently show that $P_{L,C}$ falls as

$$P_{L,C} \sim \exp(-KL/l^*)$$

with K depending on the size of scattering particles and the type of polarization of the incident light (Fig. 1.3).

The principle of similarity in multiple scattering following from the exponential form of the "single-path" parameters of multiply scattered optical fields such as the "single-path" degree of polarization and the "single-path" temporal correlation function of scattered field fluctuations in the case of non-stationary scattering media is manifested as the equality of spatial scales that characterize the decay rate for corresponding parameter.

In particular, such equality allows the specific parameter for non-stationary scattering media such as the characteristic correlation time [27, 28] to be introduced. This parameter establishes the relation between the characteristic spatial scale of dissipation of optical field correlation due to multiple scattering in fluctuating random medium, the depolarization length, and the dynamic properties of Brownian scattering medium and can be written as follows:

$$\tau_{cd} \approx \frac{l^*}{2\xi_L D k_0^2},$$

where ξ_L is the depolarization length for linearly polarized radiation in scattering medium, D is the translation diffusion coefficient of scattering particles, and k_0 is the wave-number of probe light.

It is easy to conclude that the characteristic correlation time is independent on the concentration of scattering sites but is determined only by their optical and dynamic properties and thus can be considered as the universal parameter of multiple scattering dynamic media. Figure 1.4 illustrates the principle of evaluation of τ_{cd} with the use of results of simultaneous measurements of the temporal correlation function and the degree of polarization of multiply scattered light.

The experiments with the aqueous suspensions of polystyrene spheres irradiated by linearly polarized light from an Ar-ion laser evidently demonstrate the independence of the characteristic correlation time on the volume fraction of scattering particles (Fig. 1.5). The values of τ_{cd} were determined by the method illustrated in Fig. 1.4. Normalized values of module of the field correlation functions were obtained from experimentally measured intensity correlation functions by using the Siegert relation. Moreover, measurements of the "conventional" correlation time as the half-width of the normalized field correlation functions were performed. Figure 1.5 shows a logarithmic plot of the experimentally measured concentration dependences of τ_{cd} and $\Delta\tau_{0.5}$ ("conventional" correlation time estimated as the halfwidth of the correlation peak).

Analysis of the experimental data shows that, in the experimental range of concentrations of the aqueous suspensions of polystyrene beads, the concentration dependences $\Delta\tau_{0.5} = \varphi(c)$ are close to power-law functions $\Delta\tau_{0.5} \sim c^{-\alpha}$. The exponents α in the power-law functions approximating the experimental values of $\Delta\tau_{0.5}$ in Fig. 1.5 are ≈ 2.21 and ≈ 1.96 for polystyrene beads of diameters 0.46 and
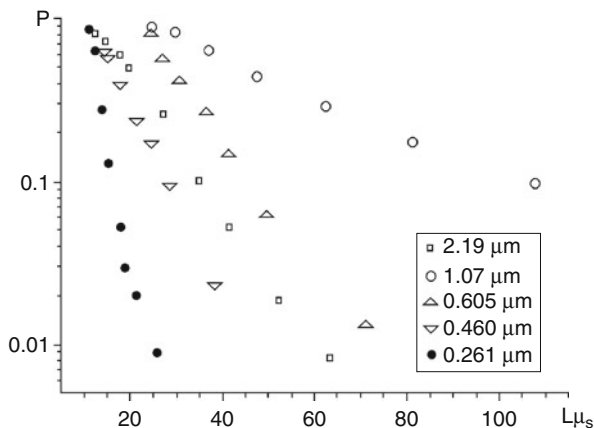
Fig. 1.3 The measured values of the degree of linear polarization of light transmitted through the scattering slabs [21]. Scattering systems are the aqueous suspensions of polystyrene beads of various sizes. The values of the degree of polarization are plotted against the dimensionless scattering coefficient of corresponding scattering system. The used wavelength and cuvette thickness: 514 nm (Ar-ion laser) and 10 mm – for 0.460 and 1.07 μm particles; 532 nm (diode-pumped Nd-laser) and 20 mm – for 0.261, 0.605, and 2.19 μm particles
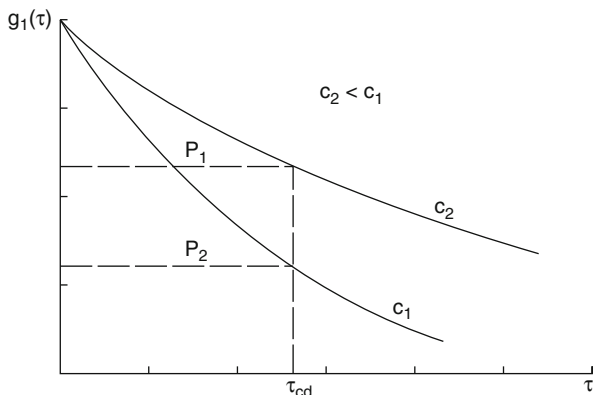
Fig. 1.4 The method for determining the characteristic correlation time for multiply scattering Brownian medium

1.07 μm, respectively. These values are in satisfactory agreement with the value $\alpha = 2$ given by the diffusion approach. Specifically, as was mentioned in Ref. [3], for an optically thick layer of thickness L consisting of Brownian scattering particles the normalized autocorrelation function of the amplitude fluctuations of the scattered coherent radiation allows the following approximation:

$$g_1(\tau) \approx \exp\left(-\sqrt{6\tau/\tau_0}\frac{L}{l^*}\right).$$
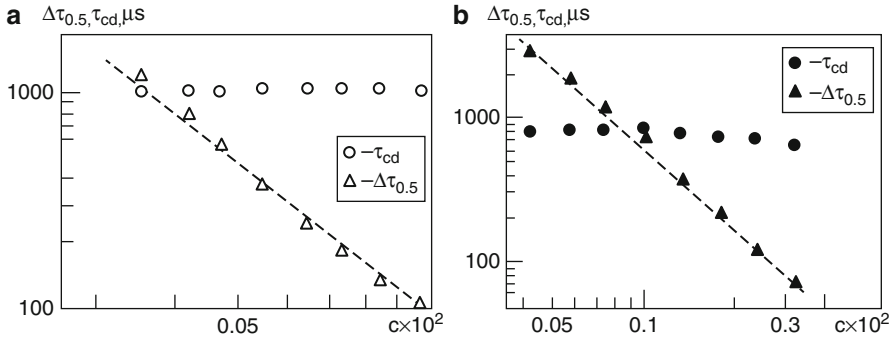
Fig. 1.5 Concentration dependences of the characteristic correlation time and the half-width of the autocorrelation function of intensity fluctuations for aqueous suspensions of polystyrene beads (*left* – bead diameter 0.46 μm; *right* – bead diameter 1.07 μm) [27].

Thus, analysis of polarized light transfer on the basis of principle of similarity gives the additional possibilities for the description of scattering properties of probed media. In particular, the influence of the size parameter of scattering sites on the decay of polarization of propagated light can be studied with this approach, as it was shown in Ref. [27].

The consideration of influence of the size parameter of scattering centers on decay of the initial polarization state of coherent light backscattered by random media was pioneered by MacKintosh et al. [19]. On the basis of measurements of the intensity of backscattered light corresponding to opposite polarization channels (co-polarized and cross-polarized light in the case of linearly polarized probe light and components of scattered light with the opposite helicity in the case of circularly polarized light), they concluded that backscattering of the linearly polarized light from random medium consisting of the large-sized dielectric particles (Mie scattering regime) is accompanied by the significant suppression of polarization of outgoing multiple scattered light (i.e., the backscattered light is almost totally depolarized). On the contrary, backscattering by random media consisting of the small-sized dielectric particles (Rayleigh scattering regime) is characterized by the significant degree of polarization of backscattered light. If the circularly polarized light is used to probe the scattering media in the backscattering mode, then scattering ensembles consisting of the small-sized particles are characterized by close values of the intensity of backscattered light in polarization channels with the opposite helicity. In contrast, the backscattering of circularly polarized light by media with the expressed scattering anisotropy exhibits a high degree of polarization memory, which is manifested as the noticeable difference between the values of intensity for helicity-preserving polarization channel and polarization channel with the opposite helicity: $\langle I_+ \rangle / \langle I_- \rangle = 1.40$ for scattering system with $l^* = 10l$ [19].

The Monte Carlo simulation was used to analyze the influence of the size parameter of scattering dielectric spheres on the decay of linear polarization in the backscattering mode [29]. In the procedure followed, a transformation of the
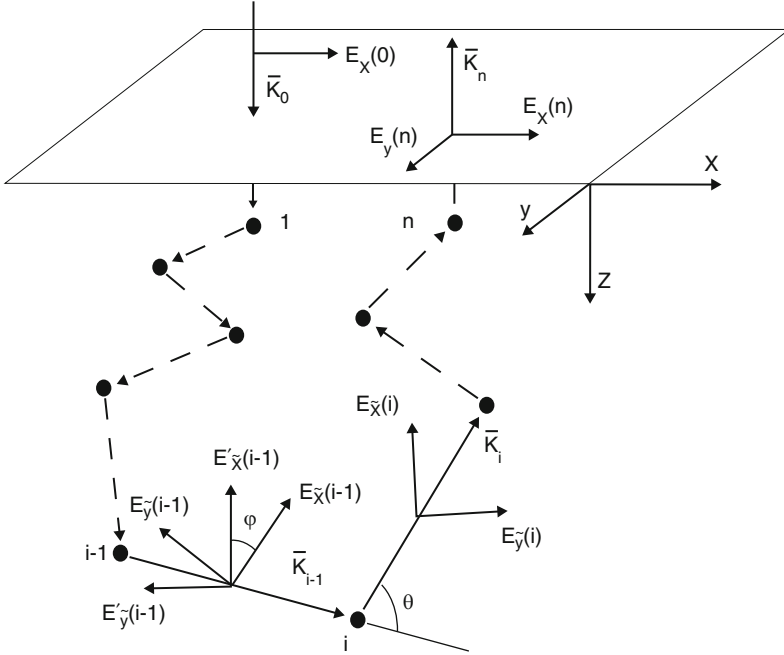
Fig. 1.6 The scheme of transformation of polarization state of partial wave due to the random sequence of scattering events (Monte-Carlo simulation) [29]

complex amplitude of partial waves, which form a backscattered optical field due to random sequences of scattering events, was simulated (Fig. 1.6). Each partial wave was induced by an incident linearly polarized monochromatic plane wave propagating along the z-axis of the "fundamental" coordinate system (x, y, z). The electric field of an incident wave was directed along the x-axis. A scattering medium was considered as the disordered ensemble of non-absorbing dielectric particles with a given value of the size parameter. The relative refractive index of spheres was taken to be 1.2; this value is approximately equal to the refractive index for polystyrene beads in water. The direction of propagation of the incident linearly polarized plane monochromatic wave relative to the "fundamental" coordinate system was characterized by the normalized wave-vector:

$$\bar{k}_0 / |\bar{k}_0| = (0, 0, 1),$$

where the z-axis was oriented normal to the scattering medium surface.

Transformation of the electric field of the propagating partial wave was analyzed for a sequence of n scattering events. For each i-th step, transformation of the complex amplitude for both orthogonally polarized components of the propagating wave was described by a (2×2) scattering matrix:

$$(S_{km}(\theta, \phi, i)) = (S''_{km}(\theta, i)) \times (S'_{km}(\phi, i)).$$

The complex elements of the scattering matrix were calculated for simulated random values of the scattering angle θ and azimuth angle ϕ by use of the current coordinates $(\tilde{x}_i, \tilde{y}_i, \tilde{z}_i)$ related to the i-th scattering event.

The $\tilde{z}_i$-axis is directed along the wavevector of the partial wave propagating after the i-th scattering event and the $\tilde{x}_i$-axis is directed normal to the scattering plane. The scattering angle distribution that corresponds to the Mie phase function for single scatter with a given value of the size parameter was used for simulation of the random value of θ for each scattering event. Random values of the azimuth angle ϕ were considered to be uniformly distributed within the range $(0, 2\pi)$. The $\left(S'_{km}(\phi, i)\right)$ matrix characterizes transformation of the $\tilde{x}$ and $\tilde{y}$ components of the electric field of the partial wave, which propagates after the $(i-1)$ th scattering event, due to rotation by the angle ϕ during conversion of the $(\tilde{x}_{i-1}, \tilde{y}_{i-1}, \tilde{z}_{i-1})$ current coordinates to the $(\tilde{x}_i, \tilde{y}_i, \tilde{z}_i)$ ones (see Fig. 1.6):

$$\left(E_{\tilde{x}}(i-1), E_{\tilde{y}}(i-1) \Rightarrow E'_{\tilde{x}}(i-1), E'_{\tilde{y}}(i-1)\right).$$

During the simulation only the n-times scattered partial waves, which were characterized by a z component of the normalized wavevector with values between -0.985 and -1 (relative to the "fundamental" coordinates), were selected for further analysis. The magnitudes $I_x = |E_x|^2$ and $I_y = |E_y|^2$ were evaluated by calculating the x and y components of the electric field in the "fundamental" coordinates for each selected n-times scattered outgoing partial wave. After this, values $\langle I_{II} \rangle = \langle I_x \rangle$ and $\langle I_\perp \rangle = \langle I_y \rangle$ were calculated by averaging over the whole ensemble of the selected partial waves with

$$-1 \leq k_{zn} / |\hat{k}_n| \leq -0.985$$

and a single-path value of P_L^s for a given number of scattering events was obtained as

$$P_L^s = (\langle I_{II} \rangle - \langle I_\perp \rangle) / (\langle I_{II} \rangle + \langle I_\perp \rangle).$$

Figure 1.7 illustrates the typical dependences of the degree of single-path linear polarization on the number of scattering events as a result of the simulation procedure described above for two different scattering regimes [the Rayleigh scattering regime for small values of the anisotropy parameter, Fig. 1.7a, and the Mie scattering regime for large values of g, Fig. 1.7b].

For a given number of scattering events, values of $\langle I_{II} \rangle$, $\langle I_\perp \rangle$ and $P_L^s(n)$ were calculated for a simulated scattering system, which was characterized by a given value of the size parameter, by averaging over the ensemble of 10,000 outgoing partial waves; after this, the obtained values of the single-path residual polarization were plotted in semi-logarithmic coordinates against the number of scattering events n. Bars show an increase in the deviation of the obtained $P_L^s(n)$ values with respect to the mean value of the single-path residual polarization with an
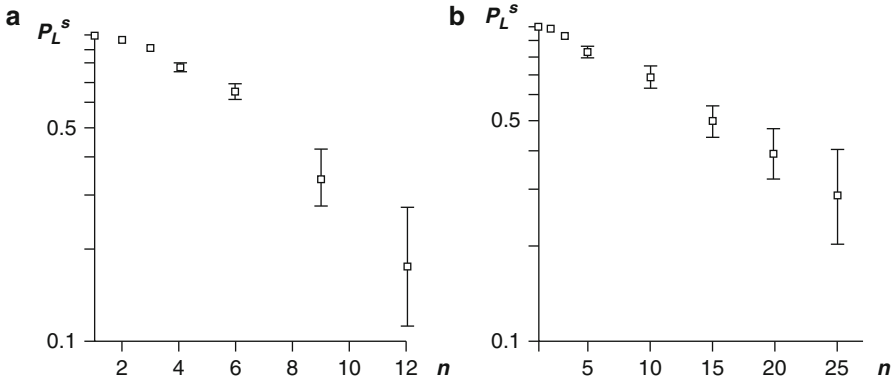
Fig. 1.7 The dependences of the "single-path" degree of residual linear polarization in the backscattering mode on the number of scattering events (results of Monte-Carlo simulation). (**a**) isotropic scattering ($ka = 1$, $g \approx 0.178$); (**b**) anisotropic scattering ($ka = 6.5$, $g \approx 0.915$) scheme of transformation of polarization state of partial wave due to the random sequence of scattering events (Monte-Carlo simulation) [29]

increase in the number of scattering events. The value of the anisotropy parameter for each simulated scattering system was calculated as the mean cosine of the scattering angle by using Mie theory.

Typically, all curves obtained by the simulation procedure are characterized by the presence of two specific regions: a relatively small "low-step scattering" region with values of the single-path polarization degree that are close to 1, and a "diffusion scattering" region characterized by an approximately exponential decay of the single-path polarization degree $P_L^s(n)$. The location of the overlap between these regions, as well as the polarization decay rate for the diffusion scattering region, strongly depends on the anisotropy parameter of the scattering particles.

Values of the normalized depolarization length m_L, which were estimated as $m_L = (1 - g)\bar{n}'_L$ using the exponential approximation $P_L^s \propto \exp(-n/\bar{n}'_L)$, are presented in Fig. 1.8 by full circles depending on the anisotropy parameter.

In order to obtain the dependence of the normalized depolarization length on g, the dependences of the single-path residual polarization on n, which are similar to those presented in Fig. 1.8, were obtained by use of the above-described Monte Carlo procedure for scattering systems characterized by given values of the size parameter and, correspondingly, the anisotropy parameter. After this, values of $\bar{n}'_L$ were determined versus g by evaluation of the slope of the corresponding dependences $\ln P_L^s = f(n)$ for the "diffusion scattering" region.

For small scatterers (the Rayleigh scattering regime), the value of m_L was obtained approximately equal to 4.2. This magnitude diverges from the above-presented theoretical value $m_L \approx \bar{n}'_L \approx 2.8$ [5] by approximately 35 %. With an increase in the anisotropy parameter up to values of the order of 0.6–0.8, m_L decreases insignificantly; for larger values of g the decay rate becomes large and
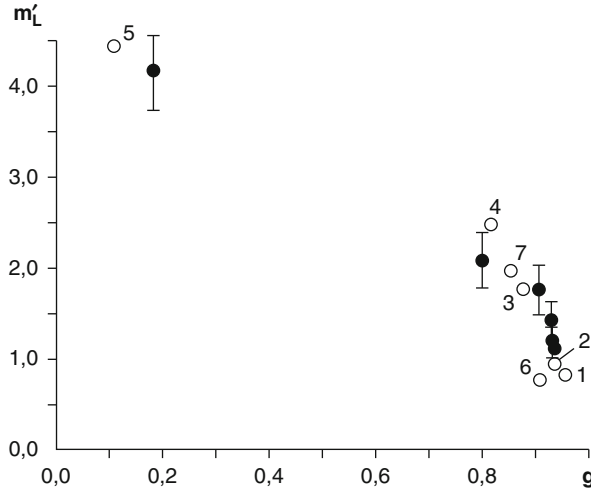
Fig. 1.8 The normalized depolarization length for linearly polarized light in the backscattering mode versus the parameter of scattering anisotropy: full circles – results of Monte Carlo simulation; *open circles* – experimental data; 1 – 1.07 μm polystyrene beads in water, volume fraction is 10 %, $\lambda = 3$ mm, $\lambda = 488$ nm; 2 – the same as 1, but $\lambda = 633$ nm; 3 – Teflon, $L = 30$ mm, $\lambda = 488$ nm; 4 – the same as 3, but $\lambda = 633$ nm; 5 – 0.091 μm polystyrene beads in water, volume fraction is 5 %, $\lambda = 488$ nm [19]; 6 – 0.605 μm polystyrene beads in water, volume fraction is 2 %, $\lambda = 488$ nm [19]; 7 – 0.46 μm polystyrene beads in water, volume fraction is 10 %, $L = 3$ mm, $\lambda = 515$ nm [30]

m_L falls to values of the order of 1.0–1.2 in the vicinity of the first Mie resonance ($ka \approx 8, g \approx 0.93$).

In the case of "forward-scattering" mode (i.e., when the simulated partial waves are selected using the condition:

$$0.985 \leq k_{zn} / |\hat{k}_n| \leq 1)$$

the dependences of the single-path polarization degree on the number of scattering events obtained by Monte-Carlo simulation for the Rayleigh scattering system are similar to those obtained for the backscattering mode (Fig. 1.9).

Thus, it can be concluded that the estimates of the depolarization length for linearly polarized light in the case of scattering systems characterized by $ka << 1$ are insensitive to the regime of scattered light collection. On the contrary, the depolarization length for linearly polarized light estimated under similar conditions for the forward scattering system consisting of large-sized particles significantly exceeds the value of the mean transport free path (Fig. 1.9). The results of experimental studies of the polarization decay in the case of forward scattering of linearly polarized light by optically thick disordered layers of dielectric spheres [5, 21] give the depolarization length ξ_L, increasing with an increase in the size parameter ka of scattering sites.
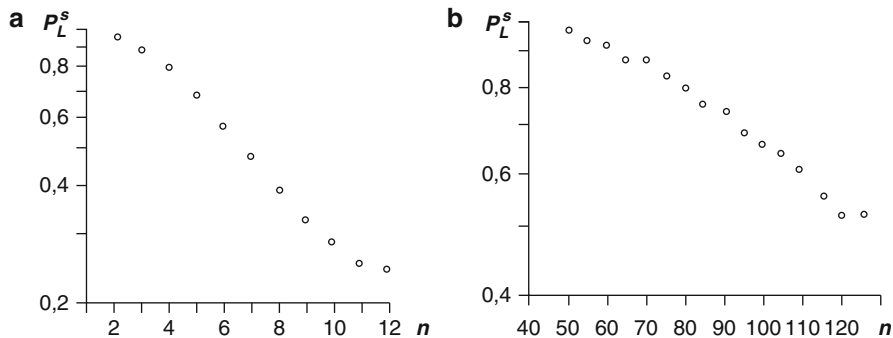
Fig. 1.9 The dependences of the "single-path" degree of residual linear polarization in the forward scattering mode on the number of scattering events (results of Monte Carlo simulation). (**a**) isotropic scattering ($ka = 1$, $g \approx 0.178$); (**b**) anisotropic scattering ($ka = 6.5$, $g \approx 0.915$) [29]

For multiple scattering systems consisting of the optically soft dielectric spheres (e.g., aqueous suspensions of polystyrene spheres), the maximal value of ξ_L in the forward scattering mode was found in the vicinity of the first Mie resonance [5]. Theoretical analysis of the polarization decay for linearly polarized light multiply scattered in the forward direction by disordered media [31, 32] also shows the better preservation of linear polarization of the forward scattered light in the case of random media with the expressed scattering anisotropy.

Compared with the phantom scattering media, the propagation of polarized light in tissue is characterized by some features related to the rate of polarization dissipation. These features were studied by Jacques et al. [33–36], Sankaran et al. [37–39], L. Wang, J. Schmitt, and many other researchers (see, e.g., Refs. [40–42]) in experiments with various in vivo and in vitro tissues such as the human skin, porcine adipose tissue, and whole blood.

The difference between the values of the depolarization length for linearly or circularly polarized light estimated in the experiments with tissue layers and corresponding parameters of phantom scattering media (for instance, the aqueous suspensions of polystyrene beads) with the same optical properties (the mean transport free path and the parameter of scattering anisotropy) as the examined tissue samples can be considered as the main peculiarity of polarization decay in biological tissues. Figure 1.10 shows the values of the degree of linear and circular polarization for light transmitted through the porcine adipose layer in the dependence of the layer thickness.

As in the case of the phantom monodisperse scattering systems consisting of dielectric spheres of equal size, the dependencies of P_L and P_C (the degree of circular polarization) on the thickness of tissue layer demonstrates the presence of two characteristic regions: the region of non-diffuse scattering in the case of optically thin ($L \leq l^*$) tissue samples, which is characterized by slow decay of the initial polarization, and the region in which the abrupt decrease of the degree of polarization takes place with the increasing thickness of tissue layer. It is necessary

Fig. 1.10 The degree of linear and circular polarization in sections of porcine adipose tissue as a function of tissue thickness [39]
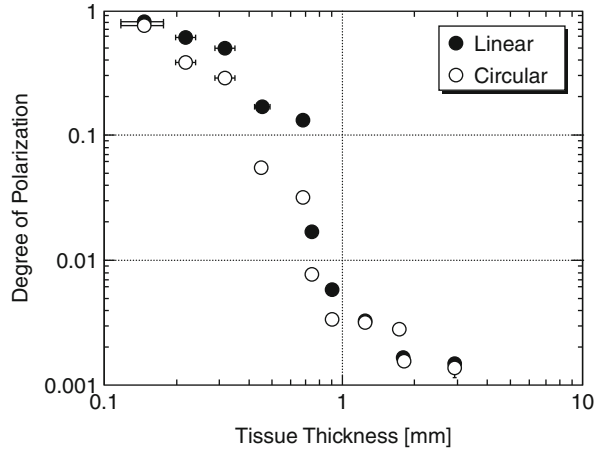
to note that the decay rates for linear and circular polarization in the latter case are characterized by the close values and appear significantly smaller in comparison with scattering phantoms with similar optical properties. In any case, at present the peculiarities of polarized light transfer in real tissues at the cellular and subcellular levels of spatial scales are still far from complete understanding and thus require further theoretical and experimental investigations.

1.1.3 Industrial and Biomedical Applications

Correlation analysis of temporal fluctuations of light propagated in optically dense, weakly absorbing, non-stationary media carried out in order to study the dynamic properties of the scattering system is the basis for a set of applied methods usually termed *correlation spectroscopy*, or *diffusing-wave spectroscopy* (DWS). Similar information about scattering media can be obtained using spectral analysis of the intensity fluctuations of multiply scattered dynamic speckles, but in the case of optically dense media characterized by a strong extinction of the probe light and very broad spectra of the speckle intensity fluctuations, the DWS methods are preferable because of the more developed instrumentation for the analysis of the detected intensity fluctuations (photon-counting, digital correlators, etc.).

A typical scheme for a DWS experiment is illustrated by Fig. 1.11. Light emitted by a single-mode laser propagates through a multiply scattering dynamic medium (sample). As a result of superposition of the partial components of the scattered light, a random non-stationary interference pattern appears, which is associated with the spatial-temporal fluctuations of the scattered optical field. This interference pattern, or *dynamic speckle pattern*, contains information about the dynamic properties of the scattering system. Part of the scattered light is selected by the collimator (a collimating system can consist of two pinhole diaphragms, as in Fig. 1.11) and falls onto the photosensitive area of photodetector.

Fig. 1.11 Typical scheme of DWS experiment with use of the transmitted light detection


A photomultiplier tube (PMT) operating in photon counting mode is usually necessary to obtain sufficient sensitivity to optically dense media. In this case, the output PMT signal is a random sequence of amplified electron pulses that is then processed by a digital correlator. Commercially available digital correlators allow for analysis of temporal fluctuations of the scattered light with a bandwidth on the order of 100 MHz, or, correspondingly, with a temporal resolution of 10 ns.

In order to perform analysis at shorter time scales, different approaches are necessary. A good example of such an approach is the application of interferometers in order to induce the light beatings by mixing of the two identical optical signals with a controlled phase delay in one of channels of the interferometer (see, e.g., Ref. [43]). The principles of such *diffusing wave interferometry* are illustrated in Fig. 1.12. This scheme, as applied to the analysis of the dynamics of multiply scattering media such as aqueous suspensions of polystyrene beads, enables a temporal resolution on the order of 1 ns, which is comparable with the time scale of hydrodynamic interactions for the scattering particles [44]. In this case, the time lag τ is determined by the optical path difference between two arms of the optical interferometer. The sample is illuminated by the single-mode laser beam, just as in the case of conventional DWS experiments. The major difference is that the output dynamic speckle field, $E(t)$, is collected, collimated, and directed into a Michelson interferometer. If the lengths of arms are equal, respectively, to L_1 and L_2, then, after recombination, the beams will be delayed by $\tau = 2(L_1 - L_2)/c$. If the intensities of both beams are equal to each other, then the intensity of light detected by PMT can be written as

$$I(\tau) = \frac{1}{4} \left\langle |E(t)|^2 \right\rangle \left\{ 1 + \left[\langle E^*(t+\tau)E(t) \rangle \Big/ \left\langle |E(t)|^2 \right\rangle \right] \cos \omega\tau \right\}, \qquad (1.14)$$

where ω is the angular frequency of the probe light. The envelope multiplying the oscillating term is usually considered the visibility of the observed interference pattern. At the same time, this is the temporal correlation function of the scattered light evaluated for the given value of τ. Thus, analyzing the decay of the envelope with an increase of τ due to changing the position of mirror M_2, one can reconstruct the form of the normalized field correlation function for the required range of time scales.

Modification of the original DWS technique with a selection of partial contributions of the scattered optical field, characterized by the given value of the path length s, has been developed by D. Boas et al. [45]. This method is based on the usage of a low-coherence interferometer in order to discriminate the short-path and long-path components of the scattered field. The corresponding instrumentation is shown in Fig. 1.13. In this case, the cut-on and cut-off values of the effective optical
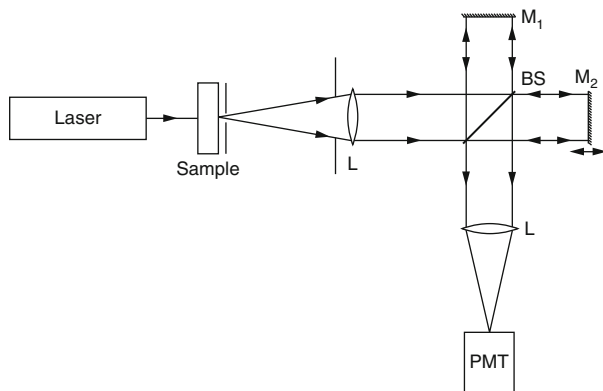
Fig. 1.12 Optical scheme of the diffusing-wave interferometer for correlation analysis of scattered light with small time scales (Ref. [43])
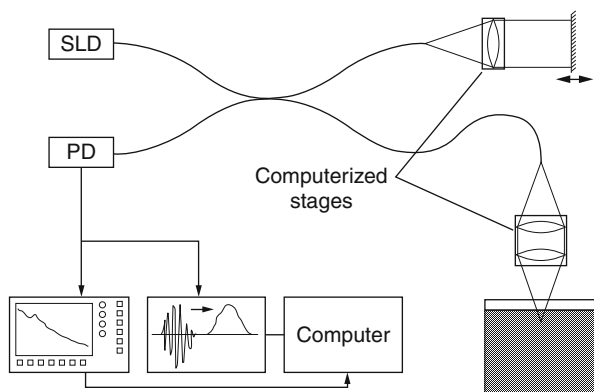
Fig. 1.13 Schematic of the dynamic low-coherence interferometer system (Ref. [45])

paths are determined by the optical path difference between two arms of the low-coherence interferometer as well as by the spectral bandwidth and the central wavelength of the light source. In this system, the single-mode fiber-optic interferometer is illuminated with an 850-nm superluminescent diode (SLD). Interferometer adjustment is provided by changing the position of the retroreflector in the reference arm. Focusing lenses in the sample and reference arms of the interferometer are mounted on computer-controlled stages in order to provide the possibility of exact matching of the optical paths in both arms. It can be concluded that, in the case of probing Brownian multiply scattering media, the detected ac signal is characterized by the single-path temporal correlation function, which has the typical exponential form:

$$G_1^s(\tau) \sim \exp(-K\tau), \tag{1.15}$$

and the corresponding spectral density is the Lorentzian one.

The value of K in the discussed case should strongly depend on scattering conditions: in the case of small sample depths (i.e., small path lengths), which are of the order of the transport mean free path for scattering medium, only single- and low-order-scattered components of the diffuse retroreflected light will be selected by the low-coherence interferometer. In this case, the single-path temporal correlation function has the typical "single-scattering" form and the parameter K, which is related to the Lorentzian linewidth of the detected light beatings, does not depend on the sample depth. But with increasing path length, when it becomes significantly larger than l^*, light beatings will be induced by contributions that are scattered many times. In this case, the single-path temporal correlation function has the typical "multiple-scattering" form:

$$G_1^s(\tau) \sim \exp\left[-\frac{2\tau s_{sel}(\Delta z)}{\tau_0 l^*}\right]. \tag{1.16}$$

Thus, dependence of the selected value s_{sel} of the path length of partial components, which induce the light beatings, on the sample depth Δz leads to the increase of the spectral width of the detected signal, when Δz increases. Such a physical picture is in qualitative agreement with experimental results obtained with a two-layer scattering system [45]. The first 580-μm-thick layer consists of 1.20 μm polystyrene (PS) beads (0.5 % volume fraction) separated from the second layer (4 % suspension of 0.22 μm PS beads) by a 150-μm-thick glass cover. Volume fractions for both layers were chosen to provide a mean scattering length equal to $\approx$100 μm. Due to anisotropic scattering in the first layer (mean cosine of the scattering angle is approximately equal to 0.89 at 830 nm), its thickness is less than the transport mean free path ($\approx$1,000 μm) and, consequently, single-scattered contributions strongly dominate in the formation of the detected light beating signal. On the contrary, the second layer, consisting of smaller particles, is characterized by a significantly smaller value of the anisotropy parameter ($g \approx 0.267$) and $l^* \approx 140$ μm for this scattering medium. Thus, if the sample depth exceeds this value, transition from the single- to the multiple-scattering mode of the formation for the detected optical signal takes place and the spectral width of the observed light beatings becomes dependent on the sample depth. In this experiment, such a transition was observed when the beam waist in the sample was embedded into the second layer at depths larger than 300 μm.

An effective approach in diffusing-wave spectroscopy of non-stationary turbid media is analysis of correlation transport viewed as a propagation of a correlation "wave" outwards from sources and its scattering by macroscopic inhomogeneities associated with spatial variations of dynamical or optical properties. It should be noted that evolution of the spatial-temporal correlation function of the optical field fluctuations due to the light propagation in free space was analyzed in early works of E. Wolf. Later, it was shown by Ackerson et al. [46] that certain analogies exist between the transport of correlation in disordered scattering media and transport of photons, which can be described by the well-known radiative transport equation.

The main feature of correlation transport relates to the accumulation of the decay of correlation function caused by each scattering event during the propagation of the correlation wave in the scattering system. In this case, considering the "stationary correlation transport" through the scattering medium (steady state) probed by continuous-wave source, one can modify the radiative transfer equation in its usual form in order to obtain the corresponding correlation transport equation:

$$\nabla G_1(\bar{r}, \tilde{\Omega}, \tau) + \mu_t G_1(\bar{r}, \tilde{\Omega}, \tau) =$$
$$\mu_s \int G_1(\bar{r}, \tilde{\Omega}', \tau) g_1{}^s f(\tilde{\Omega}, \tilde{\Omega}') d\tilde{\Omega}' + S(\bar{r}, \tilde{\Omega}). \tag{1.17}$$

The temporal correlation function of the scattered field fluctuations $G_1(\bar{r}, \tilde{\Omega}, \tau)$ depends on the detection point position ($\bar{r}$) and direction in turbid medium ($\tilde{\Omega}$) chosen for correlation analysis: $\mu_t = \mu_s + \mu_a$. The term

$$g_1'(\tau) = \exp\left(-\frac{1}{6}q^2\langle\Delta\bar{r}^2(\tau)\rangle\right),$$

which corresponds to single scattering, describes the accumulation of correlation decay due to sequences of scattering events; $f(\tilde{\Omega}, \tilde{\Omega}')$ is the phase function of the scattering medium and $S(\bar{r}, \tilde{\Omega})$ is the light source distribution.

In the case of validity of the standard diffusion approximation, the stationary correlation transport (1.17) can be rewritten in the following form [47]:

$$\left(D_\gamma \nabla^2 - c\mu_a - \frac{1}{3}c\mu_s' k_0{}^2\langle\Delta\bar{r}^2(\tau)\rangle\right)G_1(\bar{r}, \tau) = -cS(\bar{r}), \tag{1.18}$$

where $D_\gamma = cl^*/3$ is the photon diffusion coefficient, c is the light speed in the scattering medium, and μ_s' is the reduced scattering coefficient. It should be noted that the term

$$\frac{1}{3}v\mu_s' k_o{}^2\langle\Delta\bar{r}^2(\tau)\rangle$$

describes additional losses of correlation due to dynamic scattering in disordered media and can be interpreted as "correlation absorption" caused by the dynamic processes.

The presence of any kind of scattering medium dynamics is manifested as the appearance of the additional "absorbance" term in the correlation diffusion equation. Thus, numerical solution of this equation for given source and detector positions with respect to embedded dynamic inhomogeneities can be used as the basis for an inverse problem solution (reconstruction of the inhomogeneity "image"). This technique was applied by D. Boas et al. [48] and was verified in experiments with a multiply scattering "static" object (titanium dioxide–resin cylinder)

containing a "dynamic" inhomogeneity (spherical space filled by a water solution of Intralipid). The sample was illuminated by an Ar-ion laser through a fiber-optic light-guiding system; scattered light was collected by a single-mode fiber-optic light collector and detected by a photon-counting system. The scattered light intensity fluctuations as random sequences of photo-count pulses were processed by a digital autocorrelator to obtain $G_2(\tau)$ for given illumination and detection conditions. Apart from the geometry of the scattering system, angular scanning of the object was carried out; measurements were made every 30° at the surface of the cylinder with source-detector angular separations of 30° and 170°. Results of the inhomogeneity image reconstruction are shown in Fig. 1.14.

A typical example of the potential applications of the DWS technique in medicine is burn depth diagnostics. The main idea of this approach is based on the well-known dependence of the penetration of the light propagation paths on the source-detector separation in the case of backscattering (Fig. 1.15).

For such a configuration, the regions of maximum density of light paths have a typical "banana-like" shape and the penetration depth for each "banana" can be expressed as [49]:

$$z \approx d/2\sqrt{2}, \tag{1.19}$$

where d is the source-detector separation.

When the probe light propagates through the burnt layer, the lack of blood microcirculation means that the scattering is predominantly from stationary scatterers. As a result, there is only a slow decay of the correlation function of scattered light with increasing τ. Thus, in the case of surface burn diagnostics by a pair of closely adjacent light-emitting and light-collecting fibers (as shown in Fig. 1.15), only the upper, necrotic layer of the burnt tissue will be probed and the DWS technique will show a slowly decaying $g_1(\tau)$. But with an increase in the distance between source and detector, the "banana-shaped" region of the maximum concentration of the photon paths will reach the underlying layers of tissue where there is blood flow. This will be manifested as an increase in the slope of the intensity correlation function and, correspondingly, $g_1(\tau)$. This promising possibility of DWS burn depth diagnostics was demonstrated by D. Boas and A. Yodh [50] using the pig burn model suggested by N. Nishioka and K. Schomacker at the Wellman Institute in Boston (Fig. 1.16).

A He-Ne laser with an output power of 8 mW was used as the light source in their experiments. The laser light was coupled into a multi-mode optical fiber with a core diameter of 200 μm. This fiber delivered the probe light to the burn surface being diagnosed; after passing through the layer of burnt tissue, the backscattered laser light was collected by the light-collecting system consisting of a single mode fiber assembly: several single mode fibers were positioned at different distances varying from 0.2 to 2.4 mm with respect to the source fiber. The light-collecting fibers were connected to a photodetector (photon-counting photo-multiplier tube (PMT)) via an electronically controlled fiber-optical switch. The PMT output signal
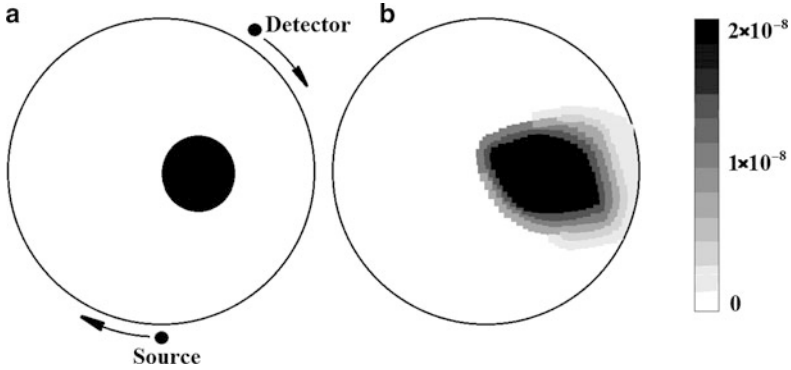
Fig. 1.14 Imaging of the dynamic multiply scattering inhomogeneity embedded in the static scatterer by means of correlation diffusion analysis (Ref. [48]). (**a**) Static scatterer is a 4.6 cm diameter cylinder with $l^* = 0.25$ cm and $\mu_a = 0.002$ cm^{-1}. Dynamic scatterer is a 1.3 cm diameter spherical cavity filled with a colloid with $l^* = 0.25$ cm, $\mu_a = 0.002$ cm^{-1} and $D_B = 1.5 \times 10^{-8}$ cm^{2}s^{-1}. A slice of the image is presented in (**b**). The values of the reconstructed particle diffusion coefficient are imaged using the presented gray-level scale
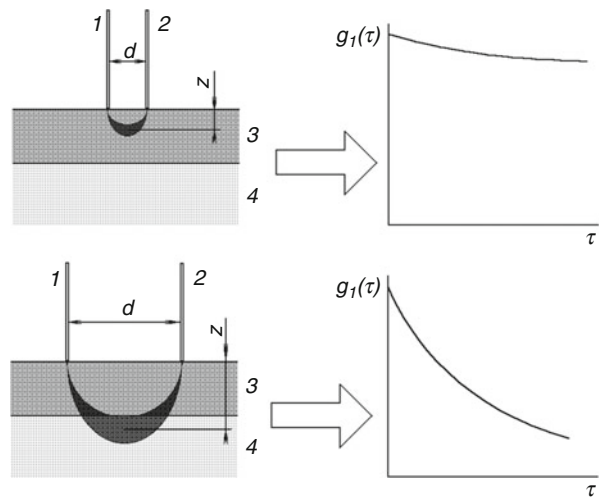
Fig. 1.15 Burn depth diagnostics by means of speckle correlation measurements; *1* – source fiber; *2* – detector fiber; *3* – burned tissue; *4* – normal tissue

was processed by a digital autocorrelator to obtain the temporal correlation function for a given burn depth and source-detector separation. The burn depth was controlled by applying a hot metal block (100°C) to the surface of a pig skin for a given duration. In this experiment, five different durations of burn with consequently increasing depth (60–100 μm; 400–500 μm; 500–600 μm; 1,500–2,000 μm, and 2,100–2,200 μm) were used. The strong dependence of the decay rate of the correlation function on the burn depth for a given source-detector separation allows the different grades of tissue burn to be distinguished (Fig. 1.17).

Fig. 1.16 Schematic of the burn depth diagnostics (By Boas et al. [50])
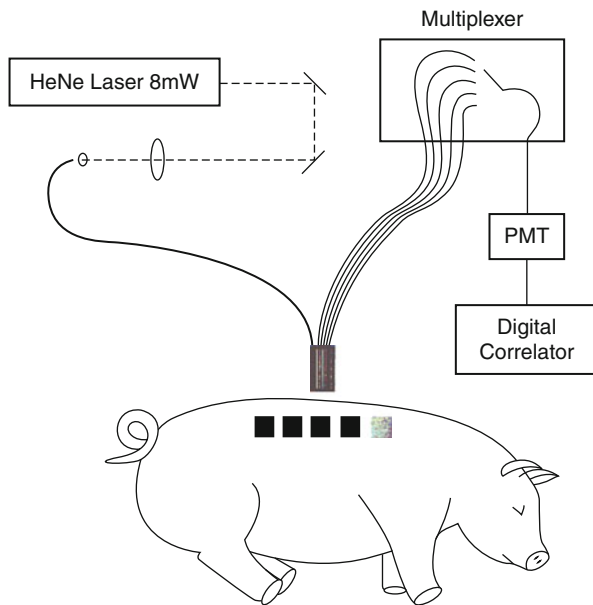
Fig. 1.17 Temporal field correlation functions obtained from 48-h-old burns for a source-detector separation of 800 μm (By Boas et al. taken from Ref. [50]); the correlation functions for burn duration times of 3 s (*solid line*), 5 s (*dotted line*), 7 s (*dashed line*), 12 s (*dot–dash line*), and 20 s (*dot-dot-dot–dash line*) are presented
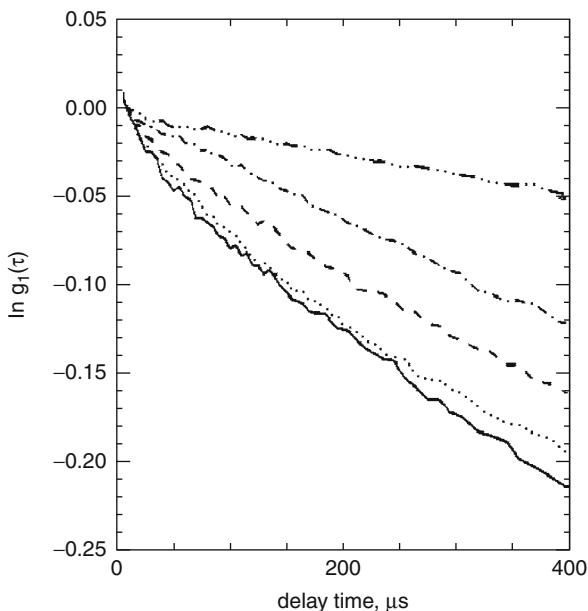
To summarize the data for all source-detector separations and to produce the criteria for burn depth estimations, the following technique was suggested: decay rates of the field correlation functions were determined for $0 < \tau < 100$ μs by fitting a line to the data, and these values of decay rate were plotted against the

source-detector separation. The tendencies of the decay rate behavior can be summarized as follows (Fig. 1.18): for shallow burns, the decay rate increases linearly with the source-detector separation as observed for healthy tissue and as would be expected for a homogeneous system, i.e., the shallow burn does not perturb the correlation function.

On the contrary, for deeper burns, the decay rate is smaller and no longer increases linearly with the source-detector separation. In recent years, the principle of polarization discrimination of multiply scattered light was fruitfully applied by many research groups for morphological analysis and visualization of the subsurface layers in strongly scattering tissues [35, 51–57]. One of the most popular approaches to polarization imaging of heterogeneous tissues is based on use of linearly polarized light to irradiate an object (the chosen area of the tissue surface) and rejection of scattered light with the same polarization state (co-polarized radiation) by an imaging system. Typically, such polarization discrimination is simply achieved by use of a polarizer between an imaging lens and the object. The optical axis of the polarizer is oriented perpendicular to the polarization plane of incident light. Thus, only a cross-polarized component of scattered light contributes to formation of the object image. Despite its simplicity, this technique was demonstrated to be an adequately effective tool for functional diagnostics and imaging of the subcutaneous tissue layers.

Moreover, the separate imaging of the object with co-polarized and cross-polarized light allows the separation of structural features of the shallow tissue layers (such as, e.g., skin wrinkles, papillary net, etc.) and the deep layers (such as the capillaries in derma). The elegant simplicity of this approach has led to its widespread application in laboratory and clinical medical diagnostics.

In the imaging system developed by Demos et al. [55], a dye laser with Nd:YAG laser pumping was used as an illumination source. The probe beam diameter is 10 cm and the average intensity was approximately equal to 5 mW/cm^2. A cooled CCD camera with a 50-mm focal length lens is used to detect retroreflected light and to capture the image. A first polarizer placed after the beam expander is used to ensure illumination with linearly polarized light. A second polarizer is positioned in front of the CCD camera with its polarization orientation perpendicular or parallel to that of the illumination.

The similar camera system, but with an incoherent white light source such as xenon lamp, is described in Ref. [36], where the results of a pilot clinical study of various skin pathologies with use of polarized light are presented. The image processing algorithm used is based on evaluation of the degree of polarization $\left(I_{par} - I_{per}\right)\big/\left(I_{par} + I_{per}\right)$, which is then used as the imaging parameter. The polarization images of pigmented skin sites (freckle, tattoo, pigmented nevi) and unpigmented skin sites (nonpigmented intradermal nevus, neurofibroma, actinic keratosis, malignant basal cell carcinoma, squamous cell carcinoma, vascular abnormality (venous lake), burn scar) were analyzed to find differences caused by various skin pathologies. Also, the point-spread function of backscattered polarized light was analyzed for images of a shadow cast from a razor blade onto a forearm

Fig. 1.18 Dependence of the
decay rates of the field
correlation functions on the
source-detector separations
for different burn depths
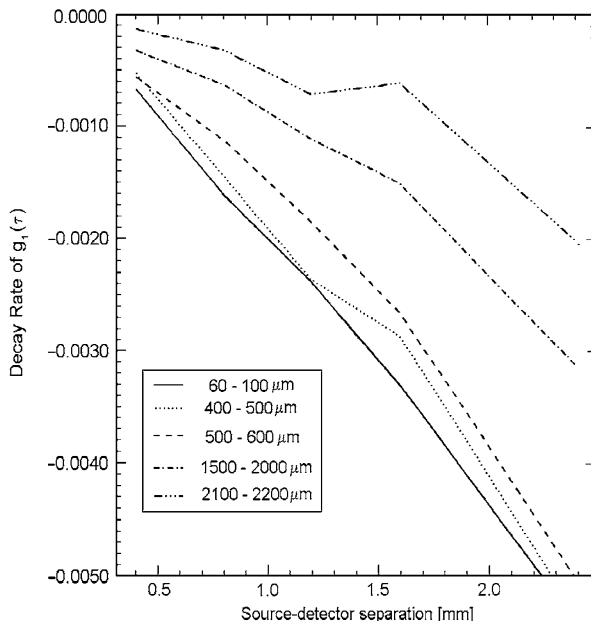
skin site. This function describes the behavior of the degree of polarization as an
imaging parameter near the shadow edge. It was found that near the shadow edge,
the degree of polarization approximately doubles in value because no I_{per} photons
are superficially scattered into the shadow-edge pixels by the shadow region, while
I_{par} photons are directly backscattered from the superficial layer of these pixels.
This result suggests that the point-spread function in skin for cross-talk between
pixels of the polarization image has a half-width-half-max of about 390 μm.

The comparative analysis of the polarization images of normal and diseased
human skin has shown the ability of the discussed approach to emphasize image
contrast on the basis of light scattering in the superficial layers of the skin. The
polarization images can visualize the disruption of the normal texture of the
papillary and upper reticular layers by skin pathology. The polarization imaging
has demonstrated itself as an adequately effective tool for identification of skin
cancer margins and guidance of surgical excision of skin cancer.

Various modalities of the polarization imaging were also considered in Ref. [58].
In particular, the polarization-difference imaging technique was demonstrated to
improve the detectability of target features that are embedded in scattering media.
The improved detectability occurred for both passive imaging in moderately scat-
tering media (<5 optical depths) and active imaging in more highly scattering
media. These improvements are relative to what is possible with equivalent
polarization-blind, polarization-sum imaging under the same conditions. In this
study, the point-spread functions for passive polarization-sum and polarization
imaging in single-scattering media were studied analytically, and Monte

Carlo simulations were used to study the point-spread functions in single- and moderately multiple-scattering media. The obtained results indicated that the polarization-difference point-spread function can be significantly narrower than the corresponding polarization-sum point-spread function, implying that better images of target features with high-spatial-frequency information can be obtained using differential polarimetry in scattering media. Although the analysis was performed for passive imaging at moderate optical depths, the results lend insight into experiments that have been performed in more highly scattering media with active imaging methods to help mitigate the effects of multiple scattering.

One of the promising approaches to early cancer diagnostics can be based on analysis of a single scattered component of light perturbed by tissue structure. Wavelength dependence of the intensity of radiation elastically scattered by tissue structure appears sensitive to changes in tissue morphology typical for pre-cancerous lesions. In particular, it was established that specific features of malignant cells such as the increased nuclear size, increased nuclear/cytoplasmic ratio, pleomorphism, etc. [59] are markedly manifested in the elastic light scattering spectra of the probed tissue [60]. A specific fine periodic structure in the wavelength of backscattered light was observed for mucosal tissue [61]. This oscillatory component of light scattering spectra are attributed to single scattering from surface epithelial cell nuclei and can be interpreted within the framework of Mie theory. Analysis of the amplitude and frequency of the fine structure allows one to estimate the density and size distributions of these nuclei. It should be noted, however, that the major problem is related to extraction of the single scattered component from the masking multiple scattering background. Also, absorption of the stroma caused by hemoglobin distorts the single scattering spectrum of the epithelial cells. Both these factors should be carefully taken into account in order to provide an adequate interpretation of the measured spectral dependencies of backscattered light.

The negative effect of the diffuse background and hemoglobin absorption can be significantly reduced by application of the polarization discrimination technique in the form of illumination of the probed tissue with linearly polarized light and separate detection of the elastic scattered light at parallel and perpendicular polarization (i.e., the co-polarized and cross-polarized components of backscattered light) [62, 63]. This approach, called polarized elastic light scattering spectroscopy or polarized reflectance spectroscopy (PRS), can potentially provide a quantitative estimate not only of the size distributions of cell nuclei but also the relative refractive index of the nucleus. These potentialities demonstrated in a series of experimental works with tissue phantoms and in vivo epithelial tissues allow one to classify the PRS technique as a new step in the development of noninvasive optical devices for real-time diagnostics of tissue morphology and, consequently, for improved early detection of pre-cancers in vivo. An important point in further development of the PRS method is the design of portable and flexible instrumentation applicable for in situ tissue diagnostics. In particular, use of fiber optic probes can "bridge the gap between benchtop studies and clinical applications of polarized reflectance spectroscopy" [64].

Over a past decade, a new level of quality has been achieved in the area of speckle correlation probes of multiple scattering media with complex scatter dynamics. Substantial progress in this field primarily relates to the adoption of novel robust analytical and imaging techniques. In particular, the sounding contribution is associated with work by V. Viasnoff, F. Lequeux, and D. Pine [65], in which the principle of diffusing wave spectroscopy was combined with the principle of parallel processing using a multi-pixel detector of multiply scattered speckle-modulated light with real-time calculation of the great number of intensity correlation functions. Each correlation function is referenced to its own reference time; in combination with ensemble averaging over the set of pixels, this approach provides the unique possibility for the analysis of slow and time-dependent processes in dynamic scattering media. The multi-speckle diffusing-wave spectrometer (MS-DWS) can readily span the range of correlation times from 1 ms up to 1,000 s; combination of the MS-DWS technique with a two-cell technique allows one to shift the lower limit of the measuring range down to 10 ns.

Further development of the MS-DWS technique took place by way of the modification of the scheme design and supporting algorithms of data processing; for instance, one of modifications is related to application of a fast rotating diffuser in the optical path between laser and sample [66]. In this case, the recorded multi-speckle correlation echoes provide an ensemble-averaged signal that does not require additional time averaging. Also, novel parameters for quantification of the evolution of dynamic speckle patterns were introduced in addition to the traditional correlation parameters, such as, e.g., an "inter-mage distance" and a "speckle rate" [67]. The real-time estimates of these parameters together with an adaptive algorithm, which continuously adjusts the camera acquisition rate to trace in real time the speckle dynamics with high reactivity, dynamic range, and accuracy, are key principles of an extension of MS-DWS technique defined as "Adaptive Speckle Imaging Interferometry" (ASII) [67].

Simultaneous correlation analysis of multi-speckle data in time and space domains provides an opportunity to study the slow spatial-temporal dynamics of soft matter (in particular, the slow dynamics of a quasi-two-dimensional coarsening foam made of highly packed, deformable bubbles and a rigid gel network formed by dilute, attractive colloidal particles [68]). Generated sequences of "Dynamic Activity Maps" reflect slow changes in the morphology and dynamics of examined dispersive systems; the authors defined this approach as "photon correlation imaging" (PCI) and stressed that PCI could also be extended to different kinds of radiation, to probe, for instance, molecular glass formers. For example, the optical layout used is similar to the one used in fluctuation electron microscopy, and the PCI method could be adopted to analyze the FEM speckle images to monitor the dynamics with spatial resolution.

Recent advances in the multi-speckle light-correlation technologies have resulted in their widespread use for various applications in material science and biomedical optics (see, e.g., Refs. [69–74]).

1.1.4 Correlation Spectroscopy of Scattering Systems with Specific Scatter Dynamics

A vast majority of the above-considered cases are characterized by translational dynamics of scattering sites in random media probed with various modifications of the correlation spectroscopy method. In addition, the examined ensembles of scattering particles, despite the randomness of spatial-temporal distributions of their mobility and directions of movement, are characterized by stationary or quasi-stationary scatter dynamics, which is continuous in time. On the contrary, quite different, "discrete" scatter dynamics can occur in certain cases, when a scattering ensemble remains for a significant period of time in a metastable state, but small groups of scatters undergo the abrupt short-time transitions to new configurations. Such spike-like scatter dynamics in local zones of the scattering ensemble, which appears against the background of a stable state of the ensemble as a whole, should manifest itself in specific behavior of the correlation properties of fluctuations of multiply scattered coherent light depending on the state of the scattering system. Another type of the "exotic" behavior may be related to the case of dynamic scattering systems with suppressed translational motion of scatters (e.g., due to high viscosity of a host medium), in which the light beating is induced by continuing changes in the optical properties and/or the sizes of scatters.

This section will consider the possibilities of correlation spectroscopy analysis for characterization of the microscopic dynamics of scatters in the scattering systems with "exotic" behavior such as:

1. The porous media at the late stages of the imbibition process, when a liquid–gas interface in the porous layer is close to the *pinned state*, and the interphase motions in single pores or in small groups of pores have a spike-like, or avalanche-like character;
2. Two-component systems in which heterogenization occurs due to a phase separation process such as, e.g., the "dispersing polymer–liquid crystal" (DPLC) composites obtained by UV irradiation of a LC–prepolymer mixture (see, e.g., Refs. [75–77]).

In both cases, the developing interphase boundaries (the liquid–gas boundaries in pores or the boundaries of LC droplets in polymer as a host medium) play the role of dynamic scatters, which cause the phase or amplitude-phase modulation of propagating light.

1.1.4.1 Non-coherent Light Probing and Correlation Spectroscopy of the Critical Behavior of Liquid–Gas Interfaces in Porous Media

The critical behavior of various non-ideal systems with weak structural order is one of the fundamental phenomena in the physics of condensed state and statistical physics, which have been intensively studied for several decades. For example, this behavior is typical of charge-density waves [78], domain walls in ferromagnetic materials [79], and contact lines at the interface between liquid and solid phases [80]. A typical manifestation of critical behavior is the growth of an interface between liquid and gaseous phases in disordered porous media under

non-stationary mass transfer with small values of the average velocity on a macroscopic level (on a spatial scale on the order of the characteristic size of the medium in a direction perpendicular to the velocity of the interface) [81–83]. When the resulting force F_Σ that controls the motion of a phase interface in a porous medium is close to a certain threshold value F_c, which depends on the structural characteristics of the medium and the parameters of interaction between the liquid phase and the medium, the function $\bar{v}(F_\Sigma)$ exhibits scaling behavior:

$$\bar{v} \propto (F_\Sigma/F_c - 1)^\theta, \qquad (1.20)$$

which is indicative of the critical behavior of the system [84]. When the critical parameter tends to zero, the phase interface is pinned. At the pinning stage, the evolution of the interface represents a series of acts of appearance, growth, and decay of local instabilities (avalanches) whose characteristic size and rate of appearance are also described by power law functions of the critical parameter. Note that the studies of interface dynamics in porous media are of interest not only for further developing the physics of the critical state, but also for solving a number of practical problems related to non-stationary mass transfer in disordered media (e.g., monitoring the transport of biologically active substances in biological tissues).

The critical behavior of the interface between liquid and gaseous phases in disordered porous media can be studied, for example, with the use of non-coherent and coherent radiation incident on the interface. In the latter case, the scattering of laser radiation by dynamic irregularities (local phase interfaces in pores in unstable regions of the global interface) is responsible for the dynamic speckle-modulation of images of an object. A correlation analysis of the intensity fluctuations of the speckles that modulate the images makes it possible to describe the evolution of an ensemble of local instabilities of the interface as $f \to 0$. A similar approach was applied to analyzing the dynamics of local phase interfaces in pores during evaporation of a liquid from porous layers [85].

The growth dynamics of an interface between liquid and gaseous phases in porous layers during capillary rise of a liquid was examined by a projection method under non-coherent illumination of samples and speckle-correlation analysis of the total field [86]. In the first case, sequences of images of the surface of a porous layer were detected under diffuse illumination by broadband light sources (luminescent lamps). For the speckle-correlation analysis, speckle-modulated images of the surface of a layer were formed by laser radiation scattered forward at small angles when a collimated laser beam with a uniform intensity distribution was incident on the layer. Figure 1.19 shows the experimental setup, which implements both methods. Sequences of images of the layer surface near the phase interface were detected by a VS-CTT-075-2000 monochrome CCD camera (the number of pixels in the CCD sensor is 782×582, eight bits per pixel, and the linear size of a pixel is 8.3×8.3 μm). The optical system (National CC TV objective lens) formed a reduced image of the sample surface on the CCD sensor. When studying the growth of local instabilities of the phase interface under non-coherent illumination,
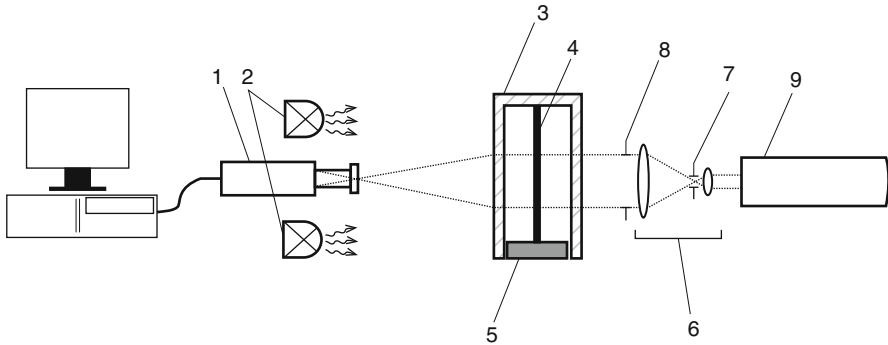
Fig. 1.19 Scheme of the experimental setup for analysis of the critical behavior of phase interfaces in porous layers with the use of the projection method under noncoherent illumination and the speckle correlation analysis; (*1*) CCD camera, (*2*) luminescent lamps for non-coherent illumination, (*3*) container with plane-parallel glass walls, (*4*) sample under examination, (*5*) vessel with a liquid, (*6*) telescopic system (collimator and expander for a laser beam), (*7*) pinhole aperture (spatial filter), (*8*) aperture, confining the cross-section of the incident beam, and (*9*) He–Ne laser (5-mW output, linear polarization)

a linear magnification of $0.2^{\times}$ was used. When studying the dynamics of the global phase interface under non-coherent illumination and in the case of speckle-correlation measurements under coherent illumination, a magnification of $0.048^{\times}$ was used. The larger magnification in the first case was chosen because the characteristic size of instabilities at the initial stage of growth was no greater than 0.10–0.15 mm in all samples. The diameter of the lens aperture for recording speckle-modulated images was chosen so that the average size of the speckles approximately corresponded to the pixel size of the CCD camera.

In diffuse, reflected non-coherent and transmitted coherent light, the image sequences of the sample surfaces were recorded in the course of interface growth in various porous layers. Because the maximal height of a liquid in a layer in the experiments was much greater than the size of the field of view of the objective lens–CCD camera system in the vertical direction, the rise of the interface was recorded fragmentarily, by timing each sequence of images to the starting point of the process and referring the position of the system to the vertical direction. To choose the number of fragments (video clips), their duration, and the approximate starting time of recording for each fragment at the stage of planning an experiment, the results of a preliminary analysis of the interface dynamics were used. Preliminary analysis of the experimental data showed that the Lucas–Washburn model [87] is an approximation with acceptable accuracy (see below) at the stage preceding the interface pinning. This allowed the recording of the fragments at this stage without partial overlapping of the record regions for successive fragments, followed by interpolation of the average velocity of the interface for time intervals between the end and beginning of fragments.

When processing image sequences under non-coherent illumination, the sequences of frames obtained were smoothed with the use of a median filter and

then converted to a binary form. The cutoff level was chosen as $\left(\langle I_{dry}\rangle + \langle I_{wet}\rangle\right)/2$, where $\langle I_{dry}\rangle$ and $\langle I_{wet}\rangle$ are the mean values of the brightness of image fragments in dry and wet regions of the porous layer near the phase interface. Then, the binarized images $\delta^k(i,j)$($\delta^k(i,j) = 1$ in a wet region of the layer and $\delta^k(i,j) = 0$ in a dry region, where k is the frame number in a sequence and i and j are the numbers of columns and rows in the frame) of the layer surface, were used (a) for analysis of the data obtained during preliminary experiments with the test samples to determine the number and the length of the image sequences necessary for analyzing the behavior of the phase interface at different growth stages; and (b) for analysis of the average velocity of the phase interface as a function of the critical parameter by means of the experimental data obtained from results of preliminary experiments.

Note that, in the general case of growth of an interface between liquid and gaseous phases in thick porous layers, the distribution of the liquid near the interface is three-dimensional; however, for thin paper samples used in the experiment, the characteristic dimensions of irregularities of the interface in a direction perpendicular to its propagation are, as a rule, greater than the layer thickness. The comparison of the shape of the interface at the stage of pinning for binarized images of two surfaces of different samples, made during preliminary experiments by rotating container with samples (see Fig. 1.19) through 180°, showed that these images are nearly identical. The difference in the vertical positions of the interface for the same value of the longitudinal coordinate (perpendicular to the preferred direction of growth of the interface) measured from the boundary of a layer was no greater than 1–3 pixels, which can be attributed to small defocusing of the recorded image due to rotation, to the difference in the sensitivity of the pixels of the CCD camera, and to other factors. Thus, in further analysis the distribution of the liquid phase in the domain of growth of the interface was assumed as quasi-two-dimensional.

For the sequences of binarized images obtained in the preliminary experiments, the average height of the upper boundary of the interface, $\bar{h}_{max} \approx K \sum_i j_{max}(i)_{\delta=1}/\hat{L}$, was determined as a function of time $t = t_{st} + k\Delta T$. Here, $j_{max}(i)_{\delta=1}$ is the maximal row number for the ith column in the binarized image with $\delta^k(i,j) = 1$, $\hat{L}$ is the number of columns in the image, K is the scaling factor depending on the magnification of the optical system and on the pixel size of the CCD sensor (in our case, $K = 173$ µm), t_{st} is the time interval between the start of capillary rise of a liquid and the start of recording a video clip, and ΔT is the recording frame-to-frame interval, 83 ms. For two binarized images of the interface that correspond to time instants $t_{st} + k_2\Delta T$ and $t_{st} + k_1\Delta T$, the average velocity of interface as a function of time $t = t_{st} + (k_1 + k_2)\Delta T/2$ was determined as

$$\bar{v} \approx K \frac{\sum_{i,j} \delta^{k_2}(i,j) - \sum_{i,j} \delta^{k_1}(i,j)}{\hat{L}(k_2 - k_1)\Delta T}. \tag{1.21}$$

One can easily verify that, in the case of a quasi-two-dimensional distribution of a liquid in a layer, the calculation of the increment of the area of a liquid-saturated

region of the layer makes it possible to adequately estimate the increase in the liquid volume in the interface growth region within time $(k_2 - k_1)\Delta T$, even when the binarized image contains non-convex regions. Using the values obtained in the experiment and determined by the interpolation of time intervals between image sequences, the average interface height $\bar{h}(t)$ was reconstructed by numerically integrating the expression

$$\bar{h}(t) \approx \int_0^t \bar{v}(t')dt'.$$

When analyzing binarized images under non-coherent illumination, the average number of local instabilities of the front (avalanches) was also considered as the number of nonoverlapping domains in the difference image $\delta^{k_2}(i,j) - \delta^{k_1}(i,j)$ as a function of $t = t_{st} + (k_1 + k_2)\Delta T/2$, $\Delta t = (k_2 - k_1)\Delta T$, and $\bar{h}$.

The sequences of speckle-modulated images of the surface of a porous layer obtained under coherent illumination were processed by calculating the local values of the normalized autocorrelation function of intensity fluctuations, $g_2(i,j,t,\Delta k) = G_2(i,j,t,\Delta k)/G_2(i,j,t,0)$, where

$$
\begin{aligned}
G_2(i,j,t,\Delta k) &= \sum_{k=k_1}^{k_2} \left[I^{k+\Delta k}(i,j) - \bar{I}(i,j) \right] \\
&\quad \times \left[I^k(i,j) - \bar{I}(i,j) \right], \\
\bar{I}(i,j) &= \sum_{k=k_1}^{k_2} \frac{I^k(i,j)}{k_2 - k_1}, \\
t &= t_{st} + \frac{\Delta T}{2}(k_1 = k_2).
\end{aligned}
\tag{1.22}
$$

Using these values of $g_2(i,j,t,\Delta k)$, the local values of the first cumulant of the correlation function of intensity fluctuations were calculated:

$$\Gamma_1(i,j,t) = \ln\{g_2(i,j,t,\Delta k = 1)\}/T. \tag{1.23}$$

Samples of filter paper labeled as FM (moderate filtering, "white band"), FS (slow filtering, "blue band"), and FF (fast filtering, "red band") according to GOST 12026–76 were used as porous layers with disordered fibrillar structure; distilled water was used as a saturating liquid. Paper strips 150 mm long with a width ranging from 35 to 60 mm were placed vertically in a fixing frame so that the lower margin of a sample was in contact with the saturating liquid, whose level in vessel 5 (see Fig. 1.19) was kept constant. To reduce the effect of evaporation of the liquid from the surface of a porous layer on the growth of phase interface, the fixing frame and the vessel were placed in a closed glass container with plane-parallel

glass walls. Ten series of measurements both under non-coherent and coherent illumination were carried out for each type of filter paper.

Figure 1.20 represents the time dependence of the experimental average velocity of the boundary of a liquid-saturated layer for one of the test samples (filter paper FM).

This dependence shows that there exist two characteristic modes of stationary flow of a liquid in a porous layer under capillary forces. When $t < t_{cr}$, the data obtained admit a high-accuracy exponential approximation $\bar{v}(t) \propto \exp(-t/t_{rel})$, where t_{rel} is a characteristic time determined by the structural characteristics of the porous layer. Many authors (see, for example, [88]) pointed out that, at its early stage, the capillary rise of a liquid phase in a porous layer can be adequately described by the Lucas–Washburn model [87] with appropriately chosen parameters. The Lucas–Washburn equation, which describes the dynamics of rise of a liquid in an isolated capillary, is expressed as

$$A(t) = -Bh(t) - \ln[1 - Bh(t)], \tag{1.24}$$

where $h(t)$ is the current height of the liquid in a capillary; $A = \rho^2 g^2 r^3 / 16\sigma\eta \cos\vartheta$; $B = \rho g r / 2\sigma \cos\vartheta$; and ρ, η, and σ are, respectively, the density, viscosity, and surface tension of the liquid; r is the capillary radius; and ϑ is the contact angle determined by the interaction between the liquid and the capillary walls. For a capillary rise of a liquid with known ρ, η, and σ in a porous layer, the approximation of the experimental dependence $\bar{h}(t) = \int_0^t \bar{v}(\tau)d\tau$ with the use of (1.24) allows one to determine the effective value of the capillary radius r_{eff}, which is determined by the characteristic size of pores in the layer and the porosity of the layer, and the value of $\cos\vartheta$.

As $t \to \infty$, the Lucas–Washburn equation describes the asymptotic behavior of the interface, which tends to an equilibrium state, $\bar{h}(t)_{t\to\infty} \to \bar{h}_{eq} = 1/B$, which is independent of the viscosity of the liquid. It can be shown that, within the Lucas–Washburn model, the time dependence of the absolute value of the average velocity $|\bar{v}|$ on the saturation time of a layer at large time scales is described by the expression $|\bar{v}(t)| \approx (A/B)\exp(-At)$, which corresponds to the experimentally observed behavior of the phase interface in all test samples for $t < t_{cr}$ (see Fig. 1.20). A sharp decrease in $|\bar{v}|$ for $t > t_{cr}$ corresponds to the critical interface pinning mode as $f \to 0$, which is characterized by a power law dependence of the average velocity of interface growth on the critical parameter: $\bar{v} \propto f^\theta$. Note that the values of $\bar{h}_{pin}$ determined in the experiment for the pinned interface in porous layers are substantially less than the equilibrium values of the rise height of the liquid, which are determined by the Lucas–Washburn model for $t \to \infty$: $\bar{h}_{pin} << \bar{h}_{eq}$ [89].

Figure 1.21 shows the values of $\bar{v}$, measured with the use of a projection method under non-coherent illumination, as a function of the critical parameter at the stage of interface pinning in the samples; the values of f were determined from the current value of $\bar{h}(t)$ and the value of $\bar{h}_{pin}$ measured as $t \to \infty$ for the pinned interface: $f = \bar{h}_{pin}/\bar{h}(t) - 1$ [89]. All the experimental functions $\bar{v}(f)$ admit

Fig. 1.20 Average velocity
of interface $\bar{v}$ as a function of
time for an FM sample
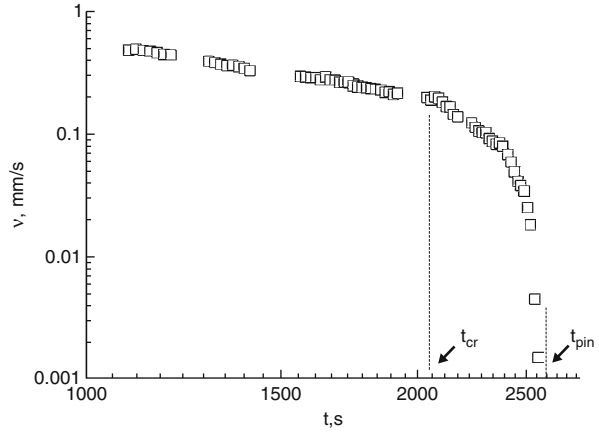
Fig. 1.21 The average
velocity of interface $\bar{v}$ as
a function of the critical
parameter f at the stage of
interface pinning for different
samples; (*1*) FS, (*2*) FF, and
(*3*) FM
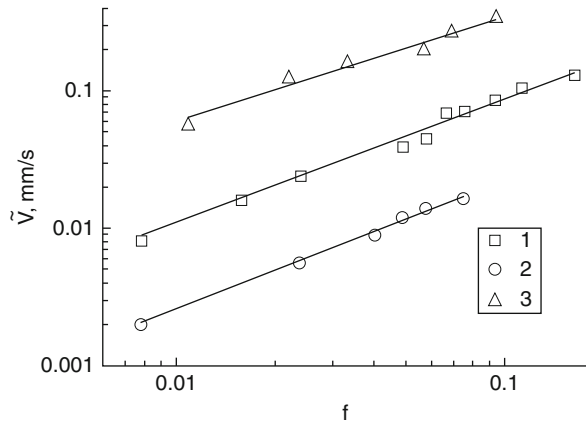
a power law approximation of reasonable accuracy as $f \rightarrow 0$, which is indicative of
the critical behavior of the phase interface. Table 1.1 presents the values of θ, t_{cr},
t_{pin}, and $\bar{h}_{pin}$ for the test samples.

The values of $\theta < 1$ correspond to a finite duration of the interface pinning
process under capillary rise of a liquid in thin, disordered porous layers. Note that
the experimental data presented in [89] on the growth of the interface under
capillary rise of a liquid in a cylindrical porous column of diameter 8 mm consisting
of densely packed glass spheres with diameters of 180, 253, 359, and 510 μm are
evidence for a different scenario of the critical behavior of the phase interface. In
particular, the value of θ for a porous medium, evaluated according to the exper-
imental data, is substantially greater than unity, which corresponds to an infinitely
large pinning time of the phase interface. At larger time scales, one can observe
a power law decay of $\bar{v}$ as a function of t with an index of about 0.75 (according to
the experimental data, the average velocity of the interface exhibits power law
time dependence in a time interval of more than three orders of magnitude).

Table 1.1 Critical indices, transition times to the critical mode, and to the interface pinning mode; and the height of a pinned interface for test samples (results of statistical processing over ten series of experimental data for each type of paper; the significance level is 0.9)

Sample	θ	t_{cr}, s	t_{pin}, s	$\bar{h}_{pin}$, mm
FF	0.89 ± 0.06	$2{,}150 \pm 110$	$3{,}300 \pm 170$	127.4 ± 3.6
FM	0.76 ± 0.07	$2{,}050 \pm 106$	$2{,}600 \pm 135$	93.0 ± 2.9
FS	0.93 ± 0.07	$1{,}800 \pm 98$	$2{,}900 \pm 150$	64.5 ± 1.7

It is noteworthy that the porous system studied in [89] is characterized by a higher degree of structural ordering and greater dimension compared with our samples: the phase interface cannot be represented by a fractal line like in the case of quasi-two-dimensional flow of a liquid in a thin porous layer; it is, rather, a surface (three-dimensional flow of a liquid).

The transfer of the liquid phase in paper layers strongly depends on the interaction between the saturating liquid and cellulose fibers (e.g., swelling due to saturation of a paper layer with water). Therefore, the effect of interaction between the saturating liquid and the hydrophilic fibers that form the porous layer on the growth of the phase interface in the layer requires a more comprehensive analysis. The authors of [21] point to two basic factors that determine the process of saturation of paper layers with water: the absorption of water by the fiber surface and the swelling of fibers. Due to the formation of an additional channel for mass transfer in a porous medium and due to a change in the dimensional characteristics of the system of pores in time and over the bulk of the medium, these factors may affect the growth of the global phase interface in a porous layer. During the initial stage of rise of the liquid in the layer, which is described by the Lucas–Washburn equation, these factors should lead to a nontrivial time dependence of the model parameters A and B (expression (1.24)) and, consequently, to a slightly different form of the function $\bar{h}(t)$ compared with the classical Lucas–Washburn equation with $A(t) = const$ and $B(t) = const$. In [90], the authors present experimental data on the swelling kinetics of cellulose fibers during hydration, which make it possible to evaluate the characteristic time of this process as 40–50 s; the maximal increase in the fiber diameter is no greater than 15 %. Assuming that the average size of pores during the hydration of cellulose fibers changes by a value on the same order of magnitude and taking into account that the effective capillary radius in the Lucas–Washburn model depends on the average size of pores and the porosity of a layer, a slight variation (by about 10–20 %) in the equilibrium height $\bar{h}_{eq}$ of the liquid compared with the stationary Lucas–Washburn model with $A(t) = const$ and $B(t) = const$ can be predicted.

In Refs. [91–93], using computer simulation methods, the authors investigated the formation of a phase interface in disordered porous media by two- and three-dimensional stochastic grid models that do not take into account how filling of the grid cells affect their parameters. Nevertheless, similar model systems exhibit critical behavior of their characteristics (including the behavior of the average velocity of propagation of the global interface) as the control parameter tends to zero. Investigations of the propagation of the interface between liquid and gaseous

phases in three-dimensional media formed by hydrophilic ceramic materials (see, for example, Ref. [92]), in which phenomena like the swelling of cellulose fibers in paper are completely excluded, are also evidence for the critical behavior and fractal properties of the developing interface at small propagation velocities. These phenomena cannot be described within continual concepts about fluid transfer in porous media (see, for example, Ref. [94]).

Thus, the critical behavior of interfaces and the pinning effect as $f \rightarrow 0$ in disordered porous systems are a fundamental property of these systems, which is associated precisely with the structural disorder of a system rather than with the variations in the structure and the properties of the system due to interaction with the liquid phase. Note also that, in paper layers at the stage of interface pinning, rather slow processes of hydration and swelling of fibers immediately below the interface may substantially affect the kinetics of the appearance of local instabilities (avalanches), thus affecting the value of the critical index θ. However, the saturation of these regions with a liquid phase up to the maximal concentration occurs in a finite time [90]; for paper layers, this rules out the possibility that a phase interface will exhibit behavior similar to that described in [89].

The following qualitative interpretation can be proposed for the significant difference in the critical behavior of two types of porous systems: in the case of disordered systems considered in the present section, when the velocity of the phase interface reaches a certain value $\bar{v}_{ch}$ characteristic of the medium, continuous motion of the phase interface described by the Lucas-Washburn model is suppressed and it changes to discrete decaying motion controlled by the appearance, growth, and decay of local instabilities (avalanches). In the case of a porous system with a higher degree of structural ordering [89], the continuous motion of the phase interface presumably is not completely suppressed; however, for average velocities of the interface lower than $\bar{v}_{ch} \approx 100 \, \mu m/s$, an increase in the spatial-temporal fluctuations of a local velocity $v(x, t)$ leads to a power law time dependence at large time scales (which was obtained in [89]), rather than to the critical behavior.

As $f \rightarrow 0$ and, accordingly, $\bar{h}(t) \rightarrow \bar{h}_{pin}$, the motion of the interface represents the sequence of appearance, growth, and decay of local instabilities of the interface. Figure 1.22, which presents a sequence of binarized difference images of the surface of a sample in the localization region of the interface, illustrates the evolution of an ensemble of localized instabilities for small values of the critical parameter. Each of the 19 fragments of this image, separated by lines, represents a region of a difference image of a localization domain of the interface obtained for different values of $k_2 - k_1$ (an increment of $k_2 - k_1$ during the image synthesis is 20). From considerations of compact representation of a set of difference images, the vertical coordinate L' perpendicular to the propagation direction of the phase interface (to a horizontal direction in the recorded images) was chosen. The size of a region in the direction of L' corresponds to the width of the field of view (300 pixels, or 12.45 mm for a linear magnification of the system of $0.2^{\times}$); in the direction in which the interface propagates (the vertical direction in the images of surface of
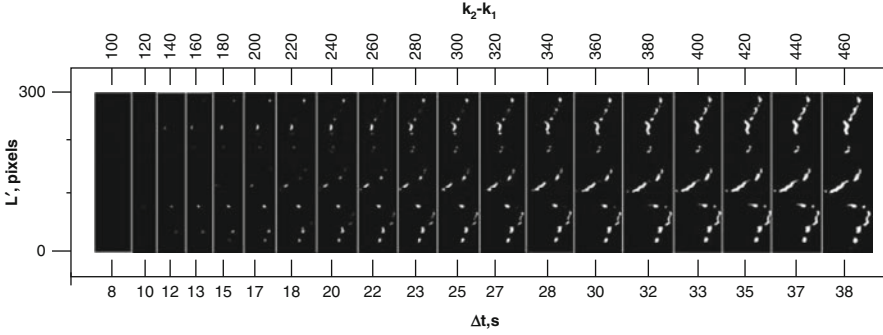
Fig. 1.22 Growth of local instabilities at the stage of interface pinning. FM sample, $f \approx 0.1$. Linear magnification of the optical system is $0.2\times$. L' and L'' are measured in the number of pixels

a paper layer), the size of the regions was chosen according to the criterion $L''_{max} \approx 1.1(h_{max} - h_{min})$, where h_{max} and h_{min} are the maximal and minimal values of the height of the interface within the analyzed region at the starting point at which the sequence of images was recorded. For the example shown in Fig. 1.22, the value of L''_{max} is 90 pixels, or ≈ 3.74 mm.

The analysis of difference images in Fig. 1.22 shows that the interface remains stable during the first 9 s after the start of recording of a sequence of raw images; at the tenth second, a local instability with coordinates $L' \approx 86$ pixels and $L'' \approx 63$ pixels arises; at the 12th second, one can observe three growing irregularities, and, at the 15th second, seven irregularities. Further, the existing irregularities grow and merge together, and new irregularities arise in different regions of the interface; as a result, for large values of $k_2 - k_1$, a considerable part of the entire interface is covered by zones of active growth. For example, at $k_2 - k_1 = 480$ (for a time interval of 38.18 s between the images used to construct the last fragment in Fig. 1.22), the total area of active growth zones amounts to 55 % of the interface within the region considered. Other regions of the interface remain stable for a given time interval.

In the case shown in Fig. 1.22, the time t_{st} is 2,120 s and the critical parameter is $f \approx 0.1$. This corresponds to the transition region (see Fig. 1.20) from the Lucas–Washburn mode of flow of a liquid to the growth of an interface via the appearance and growth of local instabilities, which is illustrated in Fig. 1.22. A further decrease in the critical parameter leads to a sharp decrease in the probability that local instabilities will appear in a finite observation time, which ultimately leads to pinning of the interface. The average velocity of the interface for small values of the critical parameter can be represented as

$$\bar{v}(t) \approx \frac{\bar{N}_{aval}(t)}{L} \overline{\left\langle \frac{\partial S_{i,aval}(t)}{\partial t} \right\rangle}, \tag{1.25}$$

Fig. 1.23 $\bar{N}_{aval}$ and $\bar{v}$ as the functions of the critical parameter f at the stage of interface pinning for the FM sample
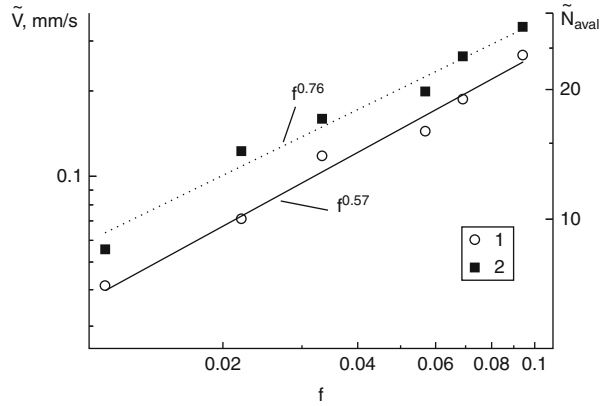
where $\bar{N}_{aval}(t)$ is the average number of intensely growing local instabilities in a region of interface having a length of L; $S_{i,aval}(t)$ is the area covered by the i th local instability at moment t; and the averaging $\langle \partial S_{i,aval}(t)/\partial t \rangle$ is performed both over the ensemble of instabilities and over the time interval used to determine $\bar{v}(t)$. According to the general principles of the behavior of critical systems as $f \rightarrow 0$ [84], one can naturally assume that, at the pinning stage, $\bar{N}_{aval}(t)$ and $\overline{\langle \partial S_{i,aval}(t)/\partial t \rangle}$, as functions of the critical parameter, exhibit scaling behavior:

$$\bar{N}_{aval} \propto f^{\gamma}, \overline{\langle \partial S_{i,aval}/\partial t \rangle} \propto f^{\delta},$$

and that the following relation holds between the critical indices θ, γ, and δ, which characterize the behavior of the interface: $\theta = \gamma + \delta$. Figure 1.23 shows the functions $\bar{v}(f)$ and $\bar{N}_{aval}(f)$ for an FM sample obtained by analyzing binarized difference images of the surface in the localization region of the interface. For the critical index γ, the function $\bar{N}_{aval}(f)$ gives an estimate of 0.57 ± 0.05, which is comparable with the critical index θ of the average velocity of the interface; this suggests that the critical index δ is much smaller than γ and, hence, the effect of the critical parameter on $\langle \partial S_{i,aval}/\partial t \rangle$ is insignificant.

The relatively small effect of f on $\overline{\langle \partial S_{i,aval}/\partial t \rangle}$ is also confirmed by analysis of the growth of individual local instabilities of the interface. Figure 1.24 shows the initial regions of the functions $S_{i,aval}(t)$ for arising and growing local instabilities at various values of the critical parameter; these functions are obtained by processing sequences of binarized difference images of the surface of samples in the localization region of the interface. These functions characterize the growth of a single local instability within a considered region and admit a piecewise linear approximation of the form:

$$S_{i,aval}(t') = \begin{cases} 0, & t' \leq t'_{0i} \\ \alpha_i(t' - t'_{0i}), & t' > t'_{0i}, \end{cases}$$

Fig. 1.24 Functions $S_{i,aval}(\Delta t)$ for small values of the critical parameter f for the FM sample; (1) $f \approx 0.07$, (2) $f \approx 0.03$, and (3) $f \approx 0.01$. The area is measured in the number of pixels in a region of local instability. The linear magnification of the optical system is $0.2^{\times}$
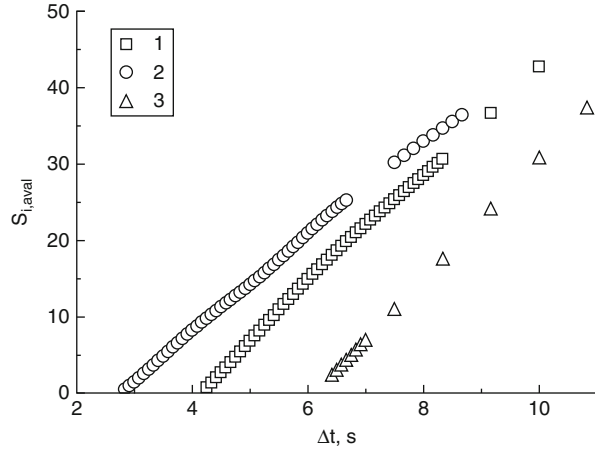
where the time t' is measured from the start of recording of a sequence of images, t'_{0i} is the time interval determined by a random delay of the moment at which instability appears (a value of $\langle t'_{0i} \rangle$, averaged over an ensemble of local instabilities, monotonically increases as f decreases), and α_i is the rate of growth of the area of the layer surface covered by a local instability during the growth of this instability (at the initial stage, $\alpha_i = \partial S_{i,aval}/\partial t \approx const$; that large time scales, $\partial S_{i,aval}/\partial t$ slowly decreases, thus leading to decay of the instability). For the functions shown in Fig. 1.24, the velocities α_i have close values; that is, a significant decrease in the critical parameter does not lead to significant variations in the growth dynamics of the instabilities, which were chosen randomly for the analysis (at least at the initial stage of their growth). This result agrees with the conclusion, made by comparing the experimental values of the critical indices θ and γ, that $\overline{\langle \partial S_{i,aval}/\partial t \rangle}$ weakly depends on f.

The dynamic speckle modulation of images of the surface of a porous layer under coherent illumination is associated with quasi-elastic scattering of light by moving local phase boundaries in the pores in the region of active growth of the global boundary of the liquid-saturated bulk of the layer. The first cumulant $\Gamma_1(t)$ (see formula (1.23)) of the correlation function of intensity fluctuations of scattered radiation is related to the halfwidth of the spectrum $S(\omega)$ of intensity fluctuations, which, in turn, is determined by the mobility of the dynamic scattering centers in the medium. In the multiple scattering regime, the multiplicity of scattering in the expression for the first cumulant as a function of the mobility of scatterers should be taken into account. For approximate estimates one may assume that $\Gamma_1(t) \propto \langle n \rangle/\tau_\lambda$, where $\langle n \rangle$ is the average number of scattering events for propagating light under fixed detection conditions and τ_λ is the characteristic time of displacement of scattering centers to a distance on the order of the wavelength. Note that, in the case of diffuse propagation of radiation, when the characteristic dimensions of the scattering medium are much greater than the transport mean free path l^* for the medium, the parameter $\Gamma_1(t)$ does not depend on the angle between the incident and

detected beams; this is attributed to the nearly isotropic character of propagation of light in the medium.

Under the experimental conditions (detection of light scattered forward at small angles), the correlation time of intensity fluctuations for different regions of an image is determined by the mobility of the scattering centers (moving phase boundaries in the pores [85]) in a local volume of the porous layer under this region. The correlation time is substantially different in different regions and attains its maximum in the zones of active growth of the global interface in the layer. Local estimates of the correlation time (or another parameter that determines the decay rate of the correlation function of intensity fluctuations) calculated at different time instants over image regions with a size on the order of an average speckle size can be used for visualizing the mobility of the liquid on a microscopic level in different active growth zones of the interface. The cumulant analysis of speckle-modulated images used to study the interface growth was based on the local estimates of the first cumulant $\Gamma_1(x, y, t)$ with the use of a moving window in the time domain over short (on the order of 40–50 frames) fragments of image sequences. The choice of the method was determined by its efficiency as applied to analysis of non-stationary dynamic speckles (especially at the stage of interface pinning, when its average velocity changes by a factor of 30–100 within times of 200–400 s; see Fig. 1.20).

Figure 1.25a illustrates substantial differences in the dynamics of speckles recorded in the growth region of the interface in a porous layer (*1, 2*) and outside this region (*3, 4*). Normalized correlation functions of intensity fluctuations were calculated over a time interval of 4 s (over 50 frames). The correlation time of intensity fluctuations estimated by the decay of normalized correlation function $g_2(\tau)$ down to a level of $1/e$ (Fig. 1.7b) for an active growth region ranges from 0.2 to 0.4 s, whereas for the regions *3* and *4* this time is about 1.3 s. The decorrelation of speckles outside the active growth zone is mainly associated with the noise in the measurement system (fluctuations of the laser radiation frequency, noise of the CCD camera, and vibrations). When laser radiation is scattered in a liquid-saturated volume of a layer, processes in the layer with large characteristic times (variation in the cellulose fiber volume due to hydration) also lead to a slow decorrelation of detected speckles. The negative values of $g_2(\tau)$ (Fig. 1.25b; functions *1* and *2* for $\tau > 0.8\,s$) are due to the relatively small sample size of the raw data.

Local estimates for $\Gamma_1(x, y, t)$ obtained by the analysis of sequences of speckle-modulated images were used for the visualization of the region of active growth. Figure 1.26 represents the images corresponding to the initial stage of growth, that is, to the Lucas–Washburn mode with the viscosity of the liquid significantly affecting the rise of the liquid in the layer (Fig. 1.26a), and to the stage of exponential decay of the interface velocity $\bar{v}$, which precedes its pinning (Fig. 1.26b). The coordinate y is the direction of propagation of the phase interface in the layer. Four brightness grades (the appropriate scales are shown in Fig. 1.26) are used to give a clear representation of the active growth region of an interface and eliminate redundant details. Figure 1.26a is characterized by considerable values of the first cumulant in the zone of active growth of the interface. In Fig. 1.26b, the
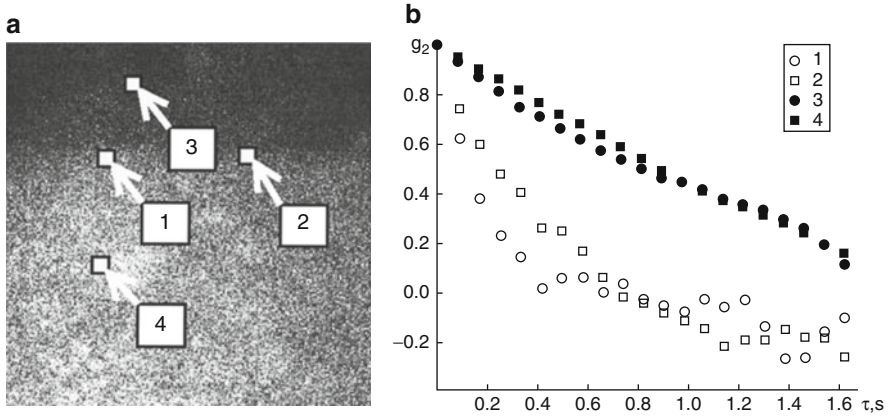
Fig. 1.25 (**a**) Speckle-modulated image of the surface of a porous layer in the growth region of the interface between the liquid and gaseous phases (linear magnification of the optical system is $0.048^\times$); (**b**) normalized time correlation functions of intensity fluctuations of speckles in different regions of the image of Fig. 1.7a

growth zone is characterized by much smaller values of Γ_1. Individual domains in the images outside the active growth zone are due to the noise in the measurement system, which leads to a slow decorrelation of speckles and determines the sensitivity threshold of the system with respect to the values of Γ_1.

Since the value of $\Gamma_1(i,j,t = const)$ is determined by the characteristic time of displacement of dynamic scattering centers in a local volume of a porous layer over a distance of λ:

$$\Gamma_1(i,j,t = const) = C_C/\tau_\lambda(i,j,t = const),$$

where C_C is a dimensionless normalization factor for the scheme used, the averaging of $\Gamma_1(i,j,t = const)$ over the active growth zone of the interface in the layer makes it possible to characterize the mean mobility of the dynamic scatterers (phase boundaries in individual pores) for a given growth stage of the interface. When calculating the mean values $\langle \Gamma_1(t) \rangle$, summation was performed only over those elements of the matrix $\Gamma_1(i,j,t)$ whose values were greater than the preliminary established threshold value:

$$\langle \Gamma_1(t) \rangle = \frac{1}{N_{th}(t)} \sum_{i=1}^{N_{th}(t)} \Gamma_1(i,j,t).$$

The analysis of $\langle \Gamma_1(t) \rangle$ as a function of $\bar{h}(t)$ makes it possible to consider variations in the microscopic mobility of local instabilities of the interface at different stages. Figure 1.27 presents this function for one of the samples (filter paper FM). Note that, at the initial stage of growth, when the average velocity of the interface is rather high and the growth of the interface significantly depends on the
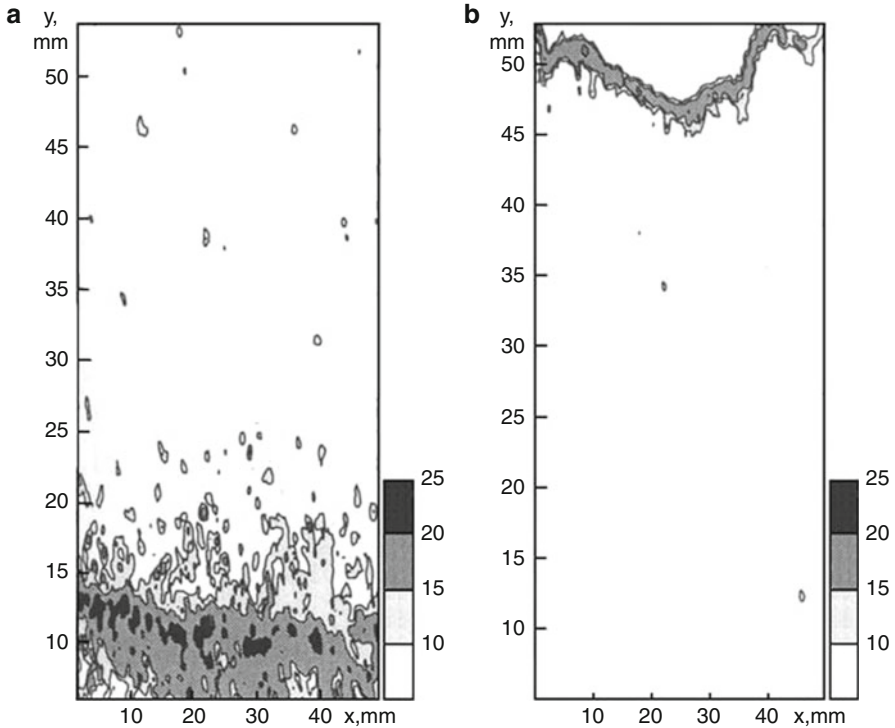
Fig. 1.26 Visualization of a growing interface between liquid and gaseous phases with the use of local estimates for the first cumulant Γ_1 as a visualization parameter; (**a**) the initial stage of capillary rise of a liquid; (**b**) a stage corresponding to exponential decay of the interface velocity as a function of time. FM sample. Linear magnification of the optical system is $0.048^\times$

viscosity ($0 < \bar{h} < 30\,\text{mm}$), the mean value of the first cumulant decays relatively rapidly; the values of $\langle \Gamma_1(t) \rangle$ are stabilized during transition to the exponential decay mode of $\bar{v}$ and decay during transition to the critical mode of interface pinning ($\bar{h} > 50\,\text{mm}$).

The dependence of τ_λ on the parameter that determines the mobility of the scattering centers is determined by the character of their motion at a microscopic level. Analysis of the growth dynamics of local instabilities of the interface under non-coherent illumination (see Figs. 1.22 and 1.24) points to a predominantly diffusive character of microscopic motion of the liquid phase in the growing local instabilities of the interface in the critical mode (as $f \to 0$). The parameter $S_{i,aval} \propto \xi_{i,aval}^2$ ($\xi_{i,aval}$ is the characteristic size of the ith instability) is a linear function of time, at least at the initial stage of the growth of instabilities (see Fig. 1.24), which is typical of diffusive growth processes $\xi_{i,aval}^2 \propto Dt$, where D in this case is the effective diffusion coefficient of the liquid phase in a porous layer.

The decay of autocorrelation functions of the intensity fluctuations of speckles in the region of active growth of the interface (Fig. 1.25b), which admits an

Fig. 1.27 $\langle \Gamma_1 \rangle$ as a function of the average height of the interface and the critical parameter f for the FM sample. The *dashed line* shows the limit value $\langle \Gamma_1 \rangle^{noise}$ determined by the noise of the measurement system. The *arrow* shows the limit state corresponding to the pinned state
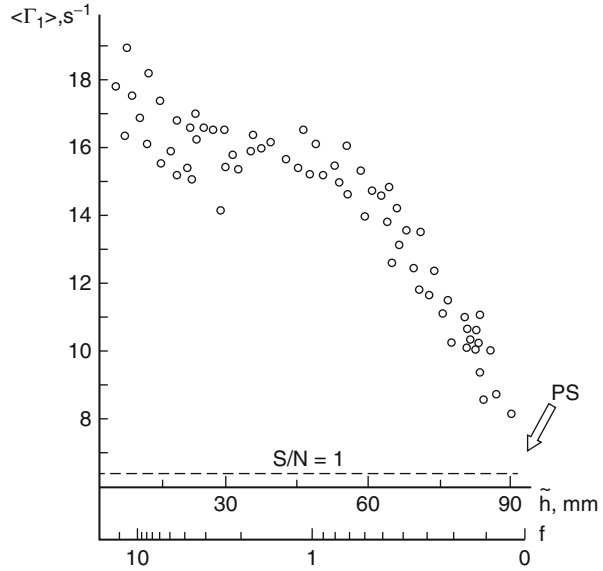
exponential approximation of the form $g_2(\tau) \approx \exp(-\Gamma|\tau|)$ with satisfactory accuracy, is also evidence in favor of the diffusive type of motion of the scattering centers as $f \to 0$. Note that a nearly exponential decay of $g_2(\tau)$ with the increase in τ is indeed typical of single and small-angle multiple scattering of laser radiation in systems with diffusive motion of scattering centers. However, a substantial difference in the diffusion coefficients for different scattering centers should lead to a deviation in $g_2(\tau)$ from the canonical exponential form [95]. Therefore, the experimental behavior of $g_2(\tau)$ serves only as indirect evidence of the diffusive character of motion of the liquid phase. At the same time, the results of analysis of images of local inhomogeneities under non-coherent illumination are indisputable evidence for the above conclusion.

Under the assumption of the scaling behavior of $\langle \Gamma_1 \rangle \propto f^{\delta'}$, analysis of the data shown in Fig. 1.27 for $f \to 0$ allows the evaluation of the corresponding critical index as $\delta' \approx 0.242 \pm 0.080$, which agrees satisfactorily with the value of the critical index $\delta \approx 0.19$ obtained from the analysis of the functions $\bar{N}_{aval}(f)$ and $\bar{v}(f)$ (see Fig. 1.23).

According to an approach considered by many authors (see, for example, [92, 93]), the scaling properties of the interface between liquid and gaseous phases in a disordered porous medium with $f \to 0$ can be described by a set of critical indices z, v, and α. The dynamic critical index z determines the relation between the characteristic size L of a porous system and the characteristic time t_x of interface growth: $t_x \propto L^z$. At the stage of interface pinning, for a growth time of the interface much greater than t_x, the interface width, defined as $W(L, t) = \left\langle \sqrt{\overline{(h^2(x,t))} - \left(\overline{h(x,t)} \right)^2} \right\rangle$, depends on the characteristic size of the system as

$W_{sat} \propto L^{\alpha}$, where the critical index α describes the fractal properties of the developing interface. When determining the interface width, the following notation is used: $h(x, t)$ is a random height of the phase interface at point x at instant t, the x axis is perpendicular to the direction of motion of the interface, and the averaging is performed both over coordinate x and over an ensemble of configurations of the interface that are randomly implemented at instant t. The critical index v determines the scaling of the characteristic size ξ of pinned regions of the interface (and, hence, the local instabilities of the interface) as $f \to 0$: $\xi \propto f^{-v}$. The relation between ξ and the characteristic time of the appearance and growth of a local instability of the interface is also determined by the dynamic critical index: $\tau_{aval} \propto \xi^{z}$ (see, for example, [89]). It should be noted [92, 93] that the characteristic longitudinal $\xi_{II} = \xi$ (in the direction x) and transverse $\xi_{\perp}$ dimensions of local instabilities of the interface exhibit different scaling behavior: $\xi_{\perp}/\xi_{II} = f^{v(1-\alpha)}$. Many authors (see, for example [92]) give a fundamental relation between the critical indices z, v, and α and the critical index of the average velocity of the interface at the stage of pinning: $\theta = v(z - \alpha)$. The above-presented considerations allow one to obtain the following relationships between two sets of indices (γ, δ and z, v, α): $\delta = v(z - 1 - \alpha)$ and $\gamma = v$.

In Refs. [92, 93], the authors discuss the critical exponents obtained from numerical simulation of the motion of phase interfaces in disordered media with the different models (in particular, models of directed percolation corresponding to the Kardar–Parisi–Zhang equation [96] and quenched Edwards–Wilkinson models corresponding to the Edwards–Wilkinson equation [97]). Note that the critical index θ for two-dimensional directed percolation depinning (DPD) models, which ranges from 0.47 to 0.82 (depending on the simulation error), agrees much better with the discussed results than the appropriate values for quenched Edwards–Wilkinson models, which range from 0.21 to 0.33. The weak dependence of $\overline{\langle \partial S_{i,aval}/\partial t \rangle}$ on the critical parameter, which was established by interpreting experimental data, is attributed to the factor $z - 1 - \alpha$ in the expression given above, which establishes the relation between the critical indices δ and z, α. Note that, in [92], which was devoted to analysis of the scaling properties of the interface between liquid and gaseous phases by numerical simulation on the basis of DPD models and full-scale experiments (capillary rise of a liquid in paper sheets), the authors obtained the following value of the critical index: $\alpha \approx 0.63$. The dynamic critical index z for critical systems similar to the considered systems is usually assumed to be about 14/9 [89, 93]. For this value of the dynamic critical index, the value of $z - 1 - \alpha$ is close to zero, although the authors of [92] give smaller values of z (in particular, for two-dimensional systems, simulation yields a value of 1.01). On the other hand, the authors of [89], using an experimental value of $\theta > 1$, suggest that the values of the dynamic critical index are greater than 14/9.

The value of $\gamma \approx 0.57$, which was obtained for an FM sample, is much smaller than the critical index $v = v_{II}$ determined by numerical simulation on the basis of the two-dimensional DPD model [92, 93] ($v_{II} \approx 1.73$). On the other hand, analysis of the Kardar–Parisi–Zhang equation by the renorm group method [98] yields the

following relation between v and α: $v = 1/(2 - \alpha)$. Thus, for $\alpha \approx 0.63$ the value of v is equal to ≈ 0.73, which agrees satisfactorily with the above-presented value of γ. Note also that v strongly depends on the dimension of the system: when $\xi_{II}, \xi_{\perp} \leq H$, where H is the layer thickness, the three-dimensional character of the interface motion in a layer should be taken into account. According to the results of simulation in [92], this should lead to a decrease in v_{II} and $v_{\perp}$ and to an increase in z. Nevertheless, the problem of the relationship between γ and v, as well as the problem of scaling the average growth rate of local instabilities of the interface as $f \rightarrow 0$, requires further experimental and theoretical investigation.

The discussed results are of interest for describing the transport properties of porous systems of different natures in the case of the critical mode of liquid transfer in such objects.

1.1.4.2 Correlation Spectroscopy of Dispersive Media in the Course of Phase Separation

This section presents the results of correlation analysis of multiply scattered laser light for characterization of the microscopic dynamics of scattering sites in random media such as two-component systems in which heterogenization occurs due to phase separation process (e.g., the "dispersing polymer–liquid crystal" (DPLC) composites obtained by photo-polymerization of a LC–prepolymer mixture). In this case, the developing interphase boundaries between the liquid-crystalline phase and the polymer phase cause the amplitude-phase modulation of propagating light. Formation of such dispersive substances as DPLC composites in the course of the polymerization-induced phase separation in mixtures of prepolymer and liquid crystal has been the subject of numerous theoretical and experimental studies in the last decade [75–77, 99–101]. One of the reasons for such research activity is that these substances can be considered as the basis for new types of electrically and thermally controlled optical materials. The typical structure of DPLC composite is an ensemble of randomly distributed LC droplets in a host polymer medium. The kinetics of formation, as well as the size distribution and concentration of the droplets, depends on the volume fractions of components in the mixture and their physicochemical properties. During the formation, three characteristic stages of the process can be marked: the relatively long "latent" stage with the absence of any observable changes in optical properties of the mixture, the short-term stage of structure formation, and the prolonged stage of structure stabilization. In the course of irradiation of the formed DPLC composite by laser light, the expressed dynamic modulation of scattered light occurs at the last two stages of formation; the correlation properties of fluctuating light should be related to the kinetic properties of the droplet ensemble formation (in particular, the rate of increase in the average size of droplets, their concentration, etc.).

Light beating induced by dynamic scattering of laser radiation (single-mode He-Ne laser emitting at the wavelength of 633 nm, linear polarization, 5 mW output) in 40-μm layers of photo-polymerized mixtures of nematic liquid crystal (LC-807, a product of NIOPIK, Russia, which is a quinary mixture of R-oxycianobiphenyls, where R is methyl, or amyl, or propyl, or hexyl, or heptyl; the

Fig. 1.28 Schematic of the experimental setup. *1* – the He–Ne laser; *2* – the beam expander with the pinhole diaphragm; *3* – the sample under study between two quartz substrates; *4* – the CMOS camera with the lens; wavy arrows indicate irradiation of the sample for activation of photo-polymerization
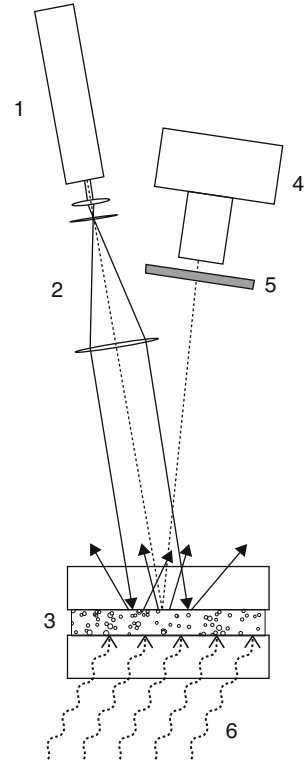
melting point is $-5°C$, the bulk viscosity is ≈ 35 mm^2/s, the refractive indices are $n_o \approx 1.52$ and $n_e \approx 1.72$, and the optical anisotropy is ≈ 0.22) and prepolymer (NOA65, the product of Norland Products Inc., USA, the refractive index in visible region at $25°C$ is ≈ 1.52, the viscosity is 1,200 mPa/s) was studied in the experiment. The weight fraction of the LC component in mixtures varied from 0.35 to 0.65. The scheme of experimental setup is presented in Fig. 1.28. The collimated laser beam (8 mm in diameter) was formed by the beam expander 2 (the telescopic system with 10 μm pinhole diaphragm as the beam cleaner) and fell on the upper surface of the layer placed between the quartz substrates (1.5 mm in thickness). Photo-polymerization was provided by irradiation of a layer through the lower substrate by light with the power density ≈ 700 mW/cm^2 at the wavelengths in the range from 400 to 500 nm. Speckle-modulated backscattered light was detected by CMOS camera (Basler 602f) in the subframe mode (50 pixels $\times$ 50 pixels) with the frame rate of 50 fps. The camera lens was focused onto the upper surface of the probed layer. The captured frame sequences were processed for retrieval of the dependencies of fluctuating intensity of backscattered light in an arbitrarily chosen small area of the detection zone on the time lapse after beginning UV irradiation.

Figure 1.29 displays these dependencies obtained for the various weight fractions of the LC component in the mixture. The above-mentioned three stages of the DPLC formation, the latent stage, the formation stage, and the stabilization stage,

Fig. 1.29 The values of intensity of detected signal (in arbitrary units) versus the time interval after the beginning of photo-polymerization; *1* – (40 % of LC807)/(60 % of NOA65); *2* – (50 % of LC807)/(50 % of NOA65); *3* – (60 % of LC807)/(40 % of NOA65)
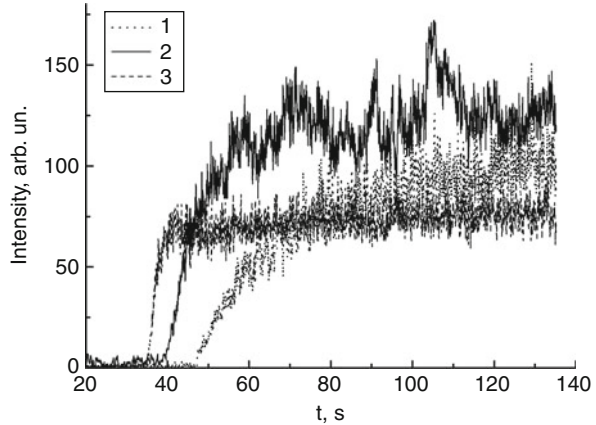

are clearly identified on these graphs. In order to analyze the correlation properties of speckle intensity fluctuations, or equivalently, light beating, the dependencies $I(t)$ were detrended using the Savitsky-Golay procedure with further subtraction of the smoothed data from the raw data. The window width for smoothing was chosen equal to 4 s, which is considerably greater than the characteristic time of intensity fluctuations in our experiments. The fluctuating components $\tilde{I}(t)$ of detected signals were analyzed using the formalism of Kolmogorov structure functions. The second-order structure function can be defined as $D_{\tilde{I}}(t, \tau) = \left\langle \{\tilde{I}(t + \tau) - \tilde{I}(t)\}^2 \right\rangle$; if the statistical characteristics of the fluctuating signal insignificantly change during the time of analysis (quasi-stationary behavior of the signal, $\left\langle \tilde{I}^2(t) \right\rangle \cong \left\langle \tilde{I}^2(t + \tau) \right\rangle$), then $D_{\tilde{I}}(t, \tau) \cong D_{\tilde{I}}(\tau)$. The structure function is closely related to the correlation function $G_{\tilde{I}}(\tau) = \left\langle \tilde{I}(t + \tau)\tilde{I}(t) \right\rangle$ as

$$D_{\tilde{I}}(\tau) = 2\left\{ \left\langle \tilde{I}^2 \right\rangle - G_{\tilde{I}}(\tau) \right\}. \tag{1.26}$$

The reason for choosing the structure function $D_{\tilde{I}}(t, \tau)$ for fluctuating signal analysis instead of the correlation function $G_{\tilde{I}}(\tau)$ is that the structure function is more appropriate for the analysis of signals at small time scales, especially for the study of scaling properties of fluctuations (see, e.g., Ref. [102]).

Figure 1.30 displays the experimentally obtained normalized structure functions $D_{\tilde{I}}(\tau) \big/ 2\left\langle \tilde{I}^2 \right\rangle$ for the examined DPLC samples at the stabilization stage, when the average intensity of detected signals varies insignificantly. Note that the behavior of $D_{\tilde{I}}(\tau) \big/ 2\left\langle \tilde{I}^2 \right\rangle$ in the region $0.1 \div 0.3 < D_{\tilde{I}}(\tau) \big/ 2\left\langle \tilde{I}^2 \right\rangle < 0.8 \div 0.9$ allows the power-law approximation $D_{\tilde{I}}(\tau) \big/ 2\left\langle \tilde{I}^2 \right\rangle \sim \tau^{\alpha_I}$ with the adequate accuracy; the values of the index of structure function are approximately equal to 0.49 and 0.48 for the samples with the weight fractions of the LC component equal to 0.4 and 0.5, respectively. In contrast, this value is equal to ≈ 0.88 for the sample with a larger

Fig. 1.30 Empirical normalized structure functions $D_{\bar{I}}(\tau)\big/2\langle\tilde{I}^2\rangle$. The notations of curves are the same as in Fig. 1.29
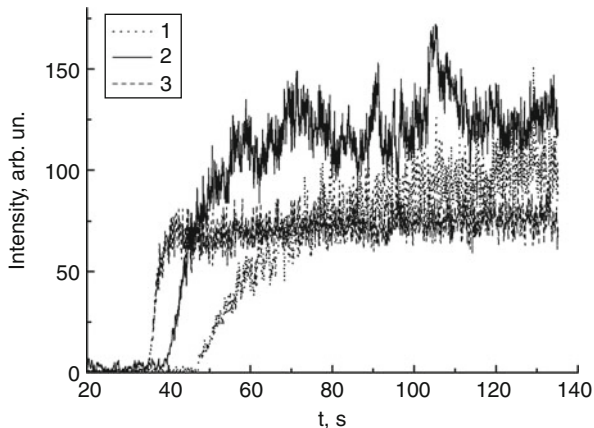
amount of LC component (0.6). For two samples with the weight fractions of LC component equal to 0.4 and 0.6, respectively, the values of $D_{\bar{I}}(\tau)\big/2\langle\tilde{I}^2\rangle$ smaller than 0.2 have not been obtained because of the limited frame rate of the used CMOS camera. Despite this limitation, the values of α_I for these samples can also be estimated with acceptable accuracy.

Compared with many other dynamic scattering systems, the DPLC composites are characterized by a specific type of modulation of propagating laser light during the structure formation. The modulation is not due to the changes in the scatter positions, as in the case of systems with translational dynamics of scattering particles, but due to the non-correlated variations of the S-matrix elements [103] of scattering sites (LC droplets in a prepolymer matrix) in the course of their formation and growth. In this case, the time-varying parameter of propagating partial contributions to the scattered optical field in the medium is not only the phase (as, for example, in the case of Brownian scattering systems) but also the amplitude. Joint amplitude-phase variations of interfering partial contributions cause the light beating in an any arbitrarily chosen detection point with the correlation parameters depending on the scattering geometry, the average number of scattering events $\langle N \rangle$, and the kinetic parameters of LC droplets formation (in particular, the average rate of droplet growth $d\langle r \rangle/dt$, where $\langle r \rangle$ is the average droplet radius). Decorrelation of intensity fluctuations in the detection point, which can be considered in terms of the increased rate of structure function $D_{\bar{I}}(\tau) \cong K_{\bar{I}}\tau^{\alpha_{\bar{I}}}$ with the increasing τ, may be related to the current state and the kinetics of formation of the examined scattering system in the framework of the random walk model.

Numerical simulation of the random walk process was carried out, including the propagation of partial contributions to a multiply scattered optical field in a random ensemble of spherical scattering particles characterized by the lognormal distribution of the radius (as follows from Ref. [75], these statistics can be used for approximation of the empirical size distributions for LC droplets in DPLC composites). The input parameters for the considered model were the number of

scattering events N, the mean value $\langle r \rangle$ and the standard deviation σ_r of the scatter radius at the origin, the wavelength of probe light λ_0, the refractive indices of scatters n_p and host medium n_h, and the average rate of scatter growth $d\langle r \rangle/dt$ (we assumed for simplicity that the ratio $\sigma_r/\langle r \rangle$ does not vary in the course of scatter growth). At the beginning of each cycle of simulation process a linearly polarized plane wave of unit amplitude entering into the scattering system was considered. For the partial component characterized by the given number of scattering events N, the random value of scatter radius r_i was generated for each scattering event and, after this, the random value of scattering angle θ_i was obtained using the Mie phase function. On the base of the set of r_i and θ_i values, the array of elements of amplitude scattering matrix $\{S_{1i}, S_{2i}\}$ (see, e.g., Ref. [103]) was calculated. Accordingly, the transformation of the complex amplitude of propagating wave in the sequence of N scattering events was considered under the assumption of the uniform distribution of the azimuthal angle φ_i in the range from 0 to 2π for each scattering event. Finally, the intensity of the linearly polarized component of N-times scattered wave, which leaves the scattering system in the backward direction with the same polarization direction as the incoming wave, was calculated. After this, the array of scatter radii was modified by incrementation of each value with a small additive Δr_i, which was calculated from the given value of $d\langle r \rangle/dt$ under the assumption of $\sigma_r/\langle r \rangle = const$. The arrays of θ_i and φ_i values were unchanged, which corresponded to the stability of scatter positions in time. The described procedure was repeated K times and the intensity values $I_m(0), I_m(1), ..., I_m(K)$, which correspond to times $t, t + \Delta t, ..., t + K\Delta t$, were obtained for m-th partial contribution.

This simulation procedure was repeated M times for various partial contributions with the same values of N but with the different sets r_i, θ_i, and φ_i, and the obtained ensemble of intensity values was used to calculate the normalized *single-path* structure function of intensity fluctuations $D_{\tilde{I}}(\tau, N) = \left\langle \left\{ \tilde{I}(t + \tau, N) - \tilde{I}(t, N) \right\}^2 \right\rangle / 2 \left\langle \left\{ \tilde{I}(t, N) \right\}^2 \right\rangle$ for the given initial value of scatter radius $\langle r \rangle$ and the average rate of scatter growth $d\langle r \rangle/dt$.

Before discussing the simulation results in comparison with the obtained experimental data, it is necessary to give some comments on the considered model. First, it does not include the effect of optical anisotropy of the scattering sites (LC droplets) on the formation of multiply scattered optical field in the examined system. The reason for such an assumption is that the droplets, which are randomly distributed in the host medium, will be presumably characterized by randomness in orientations of the symmetry axes for molecular configurations into the droplet volume from one droplet to another in the absence of macroscopic orienting factor. Optical anisotropy of the scattering site should affect the phase function and scattering cross section depending on the state of polarization of the scattered wave. Consequently, the transport parameters of a multiple scattering random medium consisting of anisotropic scatters with orientational disorder can differ from those of a medium with the same structural characteristics and consisting of isotropic scatters. In this way, the results of light transfer analysis, which were

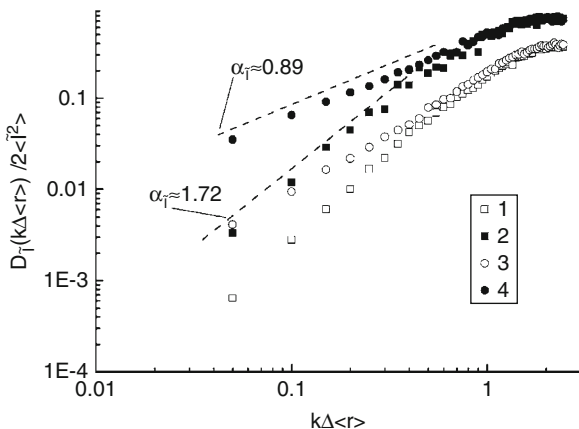**Fig. 1.31** The calculated normalized structure functions $D_{\bar{I}}(k\Delta\langle r\rangle, N)\big/2\langle\tilde{I}^2\rangle$;

$1 - N = 5, k\langle r\rangle = 25$;
$2 - N = 30, k\langle r\rangle = 25$;
$3 - N = 5, k\langle r\rangle = 250$;
$4 - N = 30, k\langle r\rangle = 250$

obtained for the multiple scattering ensemble of isotropic scattering sites, can be transferred to the case of anisotropic scattering sites. Thus, only the effect of structural changes (the average radius $\langle r\rangle$ and the volume fraction of LC droplets in the scattering system) on the light-beating-induced decorrelation of the detected intensity was considered.

Figure 1.31 displays the calculated values of the normalized single-path structure function of intensity fluctuations $D_{\bar{I}}(\Delta\langle q\rangle, N)\big/2\langle\tilde{I}^2\rangle$ depending on the increment of average wave parameter of scattering sites $\Delta\langle q\rangle = k\Delta\langle r\rangle = (2\pi/\lambda)\Delta\langle r\rangle$ for the scattering systems consisting of "small" $((2\pi/\lambda)\langle r\rangle = 5)$ and "large" $((2\pi/\lambda)\langle r\rangle = 50)$ scattering sites and for the values of N equal to 5 and 30. The relative refractive index of scatterers was assumed equal to 1.15 that is close to the ratio n_e/n_h, where n_e is the extraordinary index of LC component, and n_h is the refractive index of the host medium (polymer). Note that the characteristic value of the relative index of LC droplets in the host medium is rather less than the used value, but our estimates showed a less significant effect of this parameter on $D_{\bar{I}}(\Delta\langle q\rangle, N)\big/2\langle\tilde{I}^2\rangle$ in comparison with other model parameters (especially $\langle r\rangle$ and N).

Renormalization of the structure function argument of the wave parameter domain to the time domain (i.e., the replacement of $\Delta\langle q\rangle$ by the time lapse τ) can be performed on the basis of experimental data on the kinetics of LC droplet growth in DPLC composites (the results of optical microscopy, see Ref. [75]) and the results of molecular modeling of the phase separation [101]. In both cases, the dependence $\langle r\rangle = f(t)$ (t is the time interval from the beginning of phase separation process) at the stage of structure stabilization allows with the appropriate accuracy the power-law approximation $\langle r\rangle \approx Kt^\alpha$ with K and $\alpha < 1$ depending on the physical-chemical properties of components of a phase-separating system. Hence, $\Delta\langle r\rangle \approx K\{(t+\tau)^\alpha - t^\alpha\}_{\tau \ll t} \approx K\alpha t^{\alpha-1}\tau = K^{2-\frac{1}{\alpha}}\langle r\rangle^{\frac{1-\alpha}{\alpha}}\tau$ and the linear dependence of the wave parameter decrement $\Delta\langle q\rangle$ and the time lapse τ can be established for $\Delta\langle r\rangle \ll \langle r\rangle$. In particular, theoretical predictions on the basis of the

Ostvald coarsening model give $\alpha = 1/3$ [75]; molecular modeling of phase separation in two-component systems predicts the lesser values of α at the structure stabilization stage.

Comparison of the experimental structure functions of intensity fluctuations (see Fig. 1.30) with the model structure functions (Fig. 1.31) allowed us to point to the following key features and differences in the behavior of empirical and theoretical dependencies:

1. Typically, the indices α for the calculated single-path structure functions (Fig. 1.31) are comparable with 1 and vary from ≈ 0.89 ($k\langle r \rangle = 50$) to ≈ 1.72 ($k\langle r \rangle = 5$), while the experimental curves are characterized by approximately two times lower values of the index ($\alpha \approx 0.88$ for sample 1, ≈ 0.48 for sample 2, and ≈ 0.49 for sample 3);
2. Among the examined samples, the sample with the equal volume fractions of LC and prepolymer (#2) is characterized by the expressed low-frequency and high-amplitude light beating at the stage of structure stabilization (see Fig. 1.29).

Approximately two-fold difference between the simulation and experimental data on the structure function indices is presumably caused by peculiarities of the pathlength statistics for detected probe light in the backscattering mode; a similar behavior was observed in the case of diffusing wave spectroscopy of multiply scattering Brownian media with the detection of backscattered light [3]. It was found that the field correlation function of detected light has the stretched exponential form $g_1(\tau) \sim \exp(-C'\sqrt{\tau})$ (this corresponds to the normalized structure function of intensity fluctuations varying as $D_I(\tau) \sim \tau^{0.5}$ at small time scales), while the single-path field correlation function for Brownian multiply scattering media is defined as $g_1(\tau, s) \sim \exp(-C''\tau s)$ (this corresponds to $D_I(\tau) \sim \tau$). Here C' and C'' are the coefficients depending on the dynamical and optical properties of the scattering medium. Thus, the transformation of the single-path correlation function $g_1(\tau, s)$ to the correlation function of detected light with the pathlength probability density $\rho(s)$ for the backscattering geometry is accompanied by the decrease in the structure function index α: $1 \rightarrow 1/2$. The same trend occurs in our case (compare Figs. 1.30 and 1.31).

The observed difference between the parameters of light beating for sample 2 and samples 1, 3 can be interpreted on the basis of available data (see, e.g., Refs. [75, 100]) on the effect of the LC volume fraction f_{LC} on the structure of UV-cured DPLC composites (namely, the average radius $\langle r \rangle$ and the concentration c of the droplets). The droplet formation in polymerizing host medium can occur when the LC volume fraction exceeds a certain threshold value related to the LC solubility limit in a prepolymer for given conditions: $f_{LC} > \chi$ [100]. In our experiments, we found the value of χ slightly larger than 0.3. Following Ref. [100], the relative amount of LC component, which is released in the form of droplets during the polymerization, can be approximated by the following expression:

$$f'_{LC} = \frac{1}{f_{LC}} \frac{f_{LC} - \chi}{1 - \chi}. \tag{1.27}$$

The average droplet radius $\langle r \rangle$ in DPLC composites depends significantly on f_{LC} increasing by several times when the value of f_{LC} rises up from χ to $0.65 \div 0.70$. At larger volume fractions, a coalescence of droplets takes place and the formation of large-sized LC domains in the host medium occurs. Note the expressed non-linear or even non-monotonic behavior of $\langle r \rangle$ with the increase of f_{LC}. The average droplet radius rapidly increases at the intermediate values $\chi < f_{LC} \leq 0.50 \div 0.55$; in particular, the E7 droplets in NOA65 as the host medium are characterized by $\langle r \rangle \approx 0.39\,\mu m$ at the weight concentration of E7 equal to 40 % and $\langle r \rangle \approx 1.18\,\mu m$ at the weight concentration equal to 50 % (these estimates were obtained using experimental data presented in Ref. [75]). A further increase in the concentration of the LC component leads to significant changes in the structure of DPLC composites; in particular, optical polarization micrographs of PEHA/E7 structures [100] (PEHA is the polymerized 2-ethyl hexyl acrylate) obtained with 50 % and 65 % weight concentration of E7 show the dramatic changes in the droplet size distribution for the PEHA/E7 (35:65) structure in comparison with the (50:50) structure. These changes are associated with the increase in the variance and the skewness of droplet size distribution because of the large number of small-sized droplets and the appearance of a small amount of very large LC drops ("pre-domains"). Statistical analysis of polarization images presented in Ref. [100] has shown that $\langle r \rangle_{50:50} \approx 4.74\,\mu m$, $\langle r \rangle_{35:65} \approx 4.33\,\mu m$, and $(\delta_r / \langle r \rangle)_{50:50} \approx 0.33$, $(\delta_r / \langle r \rangle)_{35:65} \approx 0.47$. Note that the molecular modeling of phase separation in two-component systems [101] also predicts the decrease in $\langle r \rangle$ under the change of the concentration ratio towards the predominance of released component.

Considering the light transport parameters of the examined systems, one can evaluate the mean scattering free path as

$$
\begin{aligned}
l = \frac{1}{\sigma_s n} &= \frac{1}{\left(Q_{sca} \pi \langle r \rangle^2 \right) \left\{ f'_{LC} \Big/ \rho_{LC} \left(\frac{4}{3} \pi \langle r \rangle^3 \right) \right\}} \\
&\approx \frac{2 \rho_{LC} \langle r \rangle f_{LC} (1 - \chi)}{3 (f_{LC} - \chi)}.
\end{aligned}
\tag{1.28}
$$

Here, σ_s and Q_{sca} are the scattering cross-section and the scattering efficiency of LC droplets and n is their volume concentration. The approximation $Q_{sca} \approx 2$ is used for the large-sized spherical scattering particles and (1.27) for the fraction of LC component released in the form of droplets. Rough estimates show that the following relationship is typical for the examined scattering systems due to the high scattering anisotropy: $l^* >> L$, where l^* is the mean transport free path for propagating light in the medium, and L is the thickness of the medium. In this case, the "snake-like" contributions propagating with small angular deviations with respect to the probe beam axis will be a significant part of the detected signal due to Fresnel reflections from the lower substrate. Consequently, one can roughly estimate the average number of scattering events for the "snake-like" contributions as $\langle N \rangle_{snake} \approx 2L/l \approx 3(f_{LC} - \chi)/\rho_{LC} \langle r \rangle f_{LC} (1 - \chi)$. It should also be noted that

diffusing components of multiply scattered light propagate in a scattering system at a distance of the order of Λ^2/l, where Λ is the characteristic size of the scattering system, $\Lambda \sim L$. Thus, the average number of scattering events for the diffusing components $\langle N \rangle_{dif} \sim (L/l)^2 \approx [3(f_{LC} - \chi)/2\rho_{LC}\langle r \rangle f_{LC}(1 - \chi)]^2$ is more strongly influenced by variations in l in comparison with $\langle N \rangle_{snake}$. Finally, the average number of scattering events for detected light can be considered as

$$
\begin{aligned}
\langle N \rangle \approx\ & p_{snake}[3(f_{LC} - \chi)/\rho_{LC}\langle r \rangle f_{LC}(1 - \chi)] \\
& + p_{dif}[3(f_{LC} - \chi)/2\rho_{LC}\langle r \rangle f_{LC}(1 - \chi)]^2,
\end{aligned}
\tag{1.29}
$$

where p_{snake} and p_{dif} are the weighting coefficients that characterize contributions of the snake-like and the diffusing components. Thus, taking into account the above-mentioned changes in DPLC morphology with increasing f_{LC} in the range $\chi < f_{LC} < f_{LC}^{coal}$ (the weight fraction f_{LC}^{coal} corresponds to the expressed coalescence of droplets), one can assume the appearance of a pronounced minimum of $\langle N \rangle$ for a certain weight fraction of LC component and, consequently, a narrowing of the spectrum of detected signal. An indirect confirmation of this hypothesis is related to the appearance of pronounced, large-scale fluctuations of detected signal (see curve 2 in Fig. 1.29), which are expected with the decrease in the number of scattering sites in the scattering system.

The question arises about the role of phase shifts, which are accumulated by propagating partial contributions in random sequences of scattering events, in the formation of scintillating detected signal. In a "classic" case of dynamic random media with the translational movement of the scattering sites, the single-path correlation function is expressed as

$$
\begin{aligned}
g_1(\tau, s) &= \exp(-j\omega\tau)\exp\left(-\langle \bar{q}^2 \rangle \langle \Delta \bar{r}^2(\tau) \rangle s/6l\right) \\
&= \exp(-j\omega\tau)\exp\left(-\langle \Delta\varphi^2(\tau) \rangle s/6l\right),
\end{aligned}
$$

where $\langle \Delta\varphi^2(\tau) \rangle$ is the variance of the phase shift of propagating partial contribution per one scattering event. For Brownian scattering systems $\langle \Delta\varphi^2(\tau) \rangle \sim \tau$, the single-path correlation function decays exponentially, and the corresponding structure function of intensity fluctuations $D_I(\tau, N) = D_I(\tau, s = lN) \sim \tau^{\alpha_I}$ is characterized by the index $\alpha_I = 1$. Analysis of the scaling behavior of the phase shift variance $\langle \Delta\varphi^2(\tau) \rangle$ for the examined DPLC scattering system, which was carried out using the considered simulation model, has shown the quadratic dependence of $\langle \Delta\varphi^2(\tau) \rangle$ on $\Delta\langle q \rangle = (2\pi/\lambda)\Delta\langle r \rangle$ and, correspondingly, on the time lapse τ. Thus, it can be concluded that the stochasticity of the detected signal fluctuations, which is characterized for large-sized scattering particles by the value of $\alpha_I \leq 1$ (see Fig. 1.31), is mainly due to the random amplitude modulation of partial contributions in the sequences of scattering events. The dominant role of random amplitude modulation in the formation of fluctuating detected signal is also presumably manifested in relatively small values of the oscillation index of the detected speckle

modulated signals (Fig. 1.29) at the stage of DPLC structure formation. Note also that a much larger value of $\alpha_{\bar{l}}$ for sample 1 as compared with samples 2 and 3 satisfactorily agrees with the simulation results, which predict a significant increase in $\alpha_{\bar{l}}$ with decreasing $\langle r \rangle$ (Fig. 1.31).

Thus, the structure functions of intensity fluctuations of scattered light, which are caused by interphase dynamics in two-component systems with phase separation such as the photo-polymerized mixtures of liquid crystal and pre-polymer, demonstrate a fairly high sensitivity to changes in the morphology of synthesized DPLC composites (in particular, to variations in the average size and the concentration of LC droplets). It was found that the stochastic modulation of laser light in such scattering systems is mainly caused by the random changes in the amplitude of propagating partial contributions to the multiply scattered optical field in the sequences of scattering events. Note that only the effect of structural changes in the probed system was considered, neglecting the influence of the optical anisotropy of the scattering centers. Such an assumption is justified because of the high degree of randomness in the positions of scattering centers, as well as in the orientations of the symmetry directions of the LC molecular structures in these centers in the absence of macroscopic orienting factors. Nevertheless, the optical anisotropy of scattering sites can manifest itself in the polarization structure of scattered speckle-modulated optical field, especially in the case of optically thin probed samples with the weight fractions of LC components, which are close to f_{LC}^{coal} (i.e., in the region of crossover between the regime of formation of separate LC droplets and the regime of their expressed coalescence).

1.1.5 Summary

The approaches presented in this chapter to characterization of strongly scattering media with complicated structure and dynamics exhibit high sensitivity to the correlation and polarization characteristics of multiply scattered light to structural and dynamical features of probed objects. The relatively simple instrumentation and data processing algorithms necessary to provide the correlation or polarization diagnostics and visualization provide the opportunity for successful implementation of these techniques in industrial and clinical practice.

References

1. A.A. Golubentsev, On the suppression of the interference effects under multiple scattering of light. Pis'ma Zh. Eksp. Teor. Fiz. **86**, 47–59 (1984)
2. M.J. Stephen, Temporal fluctuations in wave propagation in random media. Phys. Rev. B. **37**, 1–5 (1988)

3. F.C. MacKintosh, S. John, Diffusing-wave spectroscopy and multiple scattering of light in correlated random media. Phys. Rev. B. **40**, 2382–2406 (1989)

4. D. Bicout, C. Brosseau, Multiply scattered waves through a spatially random medium: entropy production and depolarization. J. Phys. I **2**, 2047–2063 (1992)

5. D. Bicout, C. Brosseau, A.S. Martinez, J.M. Schmitt, Depolarization of multiply scattering waves by spherical diffusers: influence of size parameter. Phys. Rev. E **49**, 1767–1770 (1994)

6. W.C. Brosseau, *Fundamentals of Polarized Light: a Statistical Optics Approach* (Wiley, New York, 1998)

7. A. Ishimaru, *Wave Propagation and Scattering in Random Media* (Academic, New York, 1978)

8. H.Z. Cummins, E.R. Pike (eds.), *Photon Correlation and Light-Beating Spectroscopy*. NATO Advanced Study Institute Series B: Physics, vol. 3 (Plenum, New York, 1974)

9. S.M. Rhytov, U.A. Kravtsov, V.I. Tatarsky, *Introduction to Statistical Radiophysics, Part 2. Random Fields* (Nauka, Moscow, 1978)

10. G. Maret, P.E. Wolf, Multiple light scattering from disordered media. The effect of Brownian motions of scatterers. Z. Phys. B **65**, 409–413 (1987)

11. S. Feng, C. Kane, P.A. Lee, A.D. Stone, Correlations and fluctuations of coherent wave transmission through disordered media. Phys. Rev. Lett. **61**, 834 (1988)

12. R. Berkovits, S. Feng, Theory of speckle-pattern tomography in multiple-scattering media. Phys. Rev. Lett. **65**, 3120 (1990)

13. B.G. Hoover, L. Deslauriers, S.M. Grannell et al., Correlations among angular wave component amplitudes in elastic multiple-scattering random media. Phys. Rev. E **65**, 026614–1 (2002)

14. V.V. Tuchin, V.P. Ryabukho, D.A. Zimnyakov et al., Tissue structure and blood microcirculation monitoring by speckle interferometry and full-field correlometry. Proc. SPIE **4251**, 148–155 (2001)

15. S. John, M. Stephen, Wave propagation and localization in a long-range correlated random potential. Phys. Rev. B. **28**, 6358–6380 (1983)

16. S. John, Electromagnetic absorption in a disordered medium near a photon mobility edge. Phys. Rev. Lett. **53**, 2169–2172 (1984)

17. E. Akkermans, P.E. Wolf, R. Maynard, G. Maret, Theoretical study of the coherent backscattering of light by disordered media. J. Phys. **49**, 77–98 (1988)

18. M.J. Stephen, G. Cwillich, Rayleigh scattering and weak localization: effects of polarization. Phys. Rev. B **34**, 7564–7572 (1986)

19. F.C. MacKintosh, J.X. Zhu, D.J. Pine, D.A. Weitz, Polarization memory of multiply scattered light. Phys. Rev. B **40**, 9342–9345 (1989)

20. V.L. Kuz'min, V.P. Romanov, Coherent phenomena in light scattering from disordered systems. Sov. Phys. Usp. **166**, 247–277 (1996)

21. D.A. Zimnyakov, On some manifestations of similarity in multiple scattering of coherent light. Waves Random Media **10**, 417–434 (2000)

22. D.A. Zimnyakov, Effects of similarity in the case of multiple scattering of coherent light: phenomenology and experiments. Opt. Spectrosc. **89**, 494–504 (2000)

23. D.A. Zimnyakov, Coherence phenomena and statistical properties of multiply scattered light, in *Handbook of Optical Biomedical Diagnostics*, ed. by V.V. Tuchin (SPIE Press, Belligham, 2002), pp. 265–310

24. D.J. Pine, D.A. Weitz, P.M. Chaikin, E. Herbolzheimer, Diffusing wave spectroscopy. Phys. Rev. Lett. **60**, 1134–1137 (1988)

25. I. Freund, M. Kaveh, M. Rosenbluh, Dynamic light scattering: ballistic photons and the breakdown of the photon-diffusion approximation. Phys. Rev. Lett. **60**, 1130–1133 (1988)

26. A. Dogariu, C. Kutsche, P. Likamwa, G. Boreman, B. Moudgil, Time-domain depolarization of waves retroreflected from dense colloidal media. Opt. Lett. **22**, 585–587 (1997)

27. D.A. Zimnyakov, V.V. Tuchin, About interrelations of distinctive scales of depolarization and decorrelation of optical fields in multiple scattering. JETP Lett. **67**, 455–460 (1998)
28. D.A. Zimnyakov, V.V. Tuchin, A.G. Yodh, Characteristic scales of optical field depolarization and decorrelation for multiple scattering media and tissues. J. Biomed. Opt. **4**, 157–163 (1999)
29. D.A. Zimnyakov, Y.P. Sinichkin, P.V. Zakharov, D.N. Agafonov, Residual polarization of non-coherently backscattered linearly polarized light: the influence of the anisotropy parameter of the scattering medium. Waves Random Media **11**, 395–412 (2001)
30. P. Wolf, G. Maret, Weak localization and coherent backscattering of photons in disordered media. Phys. Rev. Lett. **55**, 2696–2699 (1985)
31. E.E. Gorodnichev, D.B. Rogozkin, Small-angle multiple scattering of light in a random medium. JETP Lett. **80**, 112–126 (1995)
32. E.E. Gorodnichev, A.I. Kuzovlev, D.B. Rogozkin, Depolarization of light in small-angle multiple scattering in random media. Laser Phys. **9**, 1210–1227 (1999)
33. S.L. Jacques, M.R. Ostermeyer, L. Wang, D. Stephens, Polarized light transmission through skin using videoreflectometry: toward optical tomography of superficial tissue layers. Proc. SPIE **2671**, 199–210 (1996)
34. S.L. Jacques, K. Lee, Polarized video imaging of skin. Proc. SPIE **3245**, 356–362 (1998)
35. S.L. Jacques, R.J. Roman, K. Lee, Imaging superficial tissues with polarized light. Lasers Surg. Med. **26**, 119–129 (2000)
36. S.L. Jacques, J.C. Ramella-Roman, K. Lee, Imaging skin pathology with polarized light. J. Biomed. Opt. **7**, 329–340 (2002)
37. V. Sankaran, M.J. Everett, D.J. Maitland, J.T. Walsh, Comparison of polarized light propagation in biologic tissue and phantoms. Opt. Lett. **24**, 1044–1046 (1999)
38. V. Sankaran, J.T. Walsh, D.J. Maitland, Polarized light propagation through tissue phantoms containing densely packed scatterers. Opt. Lett. **25**, 239–241 (2000)
39. V. Sankaran, J.T. Walsh, D.J. Maitland, Comparative study of polarized light propagation in biologic tissues. J. Biomed. Opt. **7**, 300–306 (2002)
40. A.H. Hielscher, J.R. Mourant, I.J. Bigio, Influence of particle size and concentration on the diffuse backscattering of polarized light from tissue phantoms and biological cell suspensions. Appl. Opt. **36**, 125–135 (1997)
41. R.C. Studinski, I.A. Vitkin, Methodology for examining polarized light interaction with tissues and tissue-like media in the exact backscattering direction. J. Biomed. Opt. **5**, 330–337 (2000)
42. G. Jarry, E. Steiner, V. Damaschini, M. Epifanie, M. Jurczak, R. Kaizer, Coherence and polarization of light propagating through scattering media and biological tissues. Appl. Opt. **37**, 7357–7367 (1998)
43. A.G. Yodh, N. Georgiades, D.J. Pine, Diffusing-wave interferometry. Opt. Commun. **83**, 56–59 (1991)
44. M.H. Kao, A.G. Yodh, D.J. Pine, Observation of Brownian motion on the time scale of hydrodynamic interactions. Phys. Rev. Lett. **70**, 242–245 (1993)
45. D.A. Boas, K.K. Bizheva, A.M. Siegel, Using dynamic low-coherence interferometry to image Brownian motion within highly scattering media. Opt. Lett. **23**, 319–321 (1998)
46. B.J. Ackerson, R.L. Dougherty, N.M. Reguigui, U. Nobbman, Correlation transfer: application of radiative transfer solution methods to photon correlation problems. J. Thermophys. Heat Trans. **6**, 577–588 (1992)
47. D.A. Boas, A.G. Yodh, Spatially varying dynamical properties of turbid media probed with diffusing temporal light correlation. J. Opt. Soc. Am. A **14**, 192–215 (1997)
48. D.A. Boas, L.E. Campbell, A.G. Yodh, Scattering and imaging with diffusing temporal field correlations. Phys. Rev. Lett. **75**, 1855–1858 (1995)
49. S. Feng, F. Zeng, B. Chance, Monte Carlo simulations of photon migration path distributions in multiple scattering media. Proc. SPIE **1888**, 78–89 (1993)

50. D.A. Boas, A.G. Yodh, Spatially varying dynamical properties of turbid media probed with diffusing temporal light correlation. J. Opt. Soc. Am. A **14**, 192–215 (1997)
51. R.R. Anderson, Polarized light examination and photography of the skin. Arch. Dermatol. **127**, 1000–1005 (1991)
52. P.F. Bilden, S.B. Phillips, N. Kollias, J.A. Muccini, L.A. Drake, Polarized light photography of acne vulgaris. J. Invest. Dermatol. **98**, 606 (1992)
53. S.G. Demos, W.B. Wang, R.R. Alfano, Imaging objects hidden in scattering media with fluorescence polarization preservation of contrast agents. Appl. Opt. **37**, 792–797 (1998)
54. N. Kollias, Polarized light photography of human skin, in *Bioengineering of the Skin: Skin Surface Imaging and Analysis*, ed. by K.-P. Wilhelm, P. Elsner, E. Berardesca, H.I. Maibach (CRC Press, New York, 1997), pp. 95–106
55. S.G. Demos, W.B. Wang, J. Ali, R.R. Alfano, New optical difference approaches for subsurface imaging of tissues, in *Advances in Optical Imaging and Photon Migration*, ed. by J.G. Fujimoto, M.S. Patterson. OSA TOPS, vol. 21 (OSA, Washington, DC, 1998), pp. 405–410
56. A. Muccini, N. Kollias, S.B. Phillips, R.R. Anderson, A.J. Sober, M.J. Stiller, L.A. Drake, Polarized light photography in the evaluation of photoaging. J. Am. Acad. Dermatol. **33**, 765–769 (1995)
57. O. Emile, F. Bretenaker, A. LeFloch, Rotating polarization imaging in turbid media. Opt. Lett. **21**, 1706–1709 (1996)
58. J.S. Tyo, Enhancement of the point-spread function for imaging in scattering media by use of polarization-difference imaging. J. Opt. Soc. Am. A **17**, 1–10 (2000)
59. G.A. Wagnieres, W.M. Star, B.C. Wilson, *In vivo* fluorescence spectroscopy and imaging for oncological applications. Photochem. Photobiol. **68**(5), 603–632 (1998)
60. J.R. Mourant, T. Fuselier, J. Boyer, T.M. Johnson, I.J. Bigio, Predictions and measurements of scattering and absorption over broad wavelength ranges in tissue phantoms. Appl. Opt. **36**, 949–957 (1997)
61. L.T. Perelman, V. Backman, M. Wallace, G. Zonios, R. Manoharan, A. Nustar, S. Shields, M. Seiler, C. Lima, T. Hamano, I. Itzkan, J. Van Dam, J.M. Crawford, M.S. Feld, Observation of periodic fine structure in reflectance from biological tissue: a new technique for measuring nuclear size distribution. Phys. Rev. Lett. **80**, 627–630 (1998)
62. K. Sokolov, R. Drezek, K. Gossage, R. Richards-Kortum, Reflectance spectroscopy with polarized light: is it sensitive to cellular and nuclear morphology. Opt. Express **5**, 302–317 (1999)
63. V. Backman, R. Gurjar, K. Badizadegan, I. Itzkan, R. Dasari, L.T. Perelman, M.S. Feld, Polarized light scattering spectroscopy for quantitative measurements of epithelial cellular structures *in situ*. IEEE J. Sel. Top. Quantum Electron. **5**, 1019–1026 (1999)
64. A. Myakov, L. Nieman, L. Wicky, U. Utzinger, R. Richards-Kortum, K. Sokolov, Fiber optic probe for polarized reflectance spectroscopy *in vivo*: design and performance. J. Biomed. Opt. **7**(3), 388–397 (2002)
65. V. Viasnoff, F. Lequeux, D.J. Pine, Multispeckle diffusing-wave spectroscopy: a tool to study slow relaxation and time-dependent dynamics. Rev. Sci. Instrum. **73**(6), 2336–2344 (2002)
66. P. Zakharov, F. Cardinaux, F. Scheffold, Multispeckle diffusing-wave spectroscopy with a single-mode detection scheme. Phys. Rev. E **73**(1), 011413 (2006)
67. L. Brunel, A. Brun, P. Snabre, L. Cipelletti, Adaptive speckle imaging interferometry: a new technique for the analysis of microstructure dynamics, drying processes and coating formation. Opt. Express **15**(23), 15250–15259 (2007)
68. A. Duri, D.A. Sessoms, V. Trappe, L. Cipelletti, Resolving long-range spatial correlations in jammed colloidal systems using photon correlation imaging. Phys. Rev. Lett. **102**, 085702 (2009)
69. P. Zakharov, A.C. Völker, M.T. Wyss, F. Haiss, N. Calcinaghi, C. Zunzunegui, A. Buck, F. Scheffold, B. Weber, Dynamic laser speckle imaging of cerebral blood flow. Opt. Express **17**(6), 13904–13917 (2009)

70. J.S. Paul, H. Al Nashash, A.R. Luft, T.M. Le, Statistical mapping of speckle autocorrelation for visualization of hyperaemic responses to cortical stimulation. Ann. Biomed. Eng. **34**(7), 1107–1118 (2006)

71. G. Dietsche, M. Ninck, C. Ortolf, J. Li, F. Jaillon, T. Gisler, Fiber-based multispeckle detection for time-resolved diffusing-wave spectroscopy: characterization and application to blood flow detection in deep tissue. Appl. Opt. **46**(35), 8506–8514 (2007)

72. P. Ballesta, C. Ligoure, L. Cipelletti, Temporal heterogeneity of the slow dynamics of a colloidal paste, in *Slow Dynamics in Complex Systems: Third International Symposium on Slow Dynamics in Complex Systems*, vol. 708 (AIP, Melville, 2004), pp. 68–71

73. A. Duri, H. Bissig, V. Trappe, L. Cipelletti, Time-resolved-correlation measurements of temporally heterogeneous dynamics. Phys. Rev. E **72**(5), 051401 (2005)

74. L. Cipelletti, L. Ramos, Slow dynamics in glassy soft matter. J. Phys. Condens. Matter **17**, R253–R285 (2005)

75. L. Lucchetti, F. Simoni, Coarsening and phase separation in ultraviolet curing polymer dispersed liquid crystals. J. Appl. Phys. **88**, 3934–3940 (2000)

76. T. Bouchaour, M. Benmouna, X. Coqueret, U. Maschke, V. Rachet, P. Le Barny, P. Feneyrou, UV-cured polymer dispersed liquid crystals with nanosized droplets. Mol. Cryst. Liq. Cryst. **413**, 2165–2170 (2004)

77. F. Roussel, C. Canlet, B.M. Fung, Morphology and electro-optic properties of polymer-dispersed liquid-crystal films. Phys. Rev. E **65**, 021701 (2002)

78. S. Bhattacharya, M.J. Higgins, J.P. Stokes, Harmonic generation and scaling behavior in sliding-charge-density-wave conductors. Phys. Rev. Lett. **63**(14), 1503–1506 (1989)

79. P.-Z. Wong, J.W. Cable, Hysteretic behavior of the diluted random-field Ising system $Fe_{0.70}$ $Mg_{0.30}Cl_2$. Phys. Rev. B **28**(9), 5361–5364 (1983)

80. J.P. Stokes, M.J. Higgins, A.P. Kushnick, S. Bhattacharya, M.O. Robbins, Harmonic generation as a probe of dissipation at a moving contact line. Phys. Rev. Lett. **65**(15), 1885–1888 (1990)

81. J. Koplik, H. Levine, Interface moving through a random background. Phys. Rev. B **32**(1), 280–292 (1985)

82. T. Natterman, S. Stepanow, L.-H. Tang, H. Leschhorn, Dynamics of interface depinning in a disordered medium. J. Phys. II **2**(8), 1483–1488 (1992)

83. O. Narayan, D.S. Fisher, Threshold critical dynamics of driven interfaces in random media. Phys. Rev. B **48**(10), 7030–7042 (1993)

84. D.Y. Ivanov, *Critical Behavior of Non-ideal Systems* (Wiley, Weinheim, 2008), section 1.2

85. D.A. Zimnyakov, P.V. Zakharov, V.A. Trifonov, O.I. Chanilov, Dynamic light scattering study of the interface evolution in porous media. JETP Lett. **74**(4), 216–221 (2001)

86. D.A. Zimnyakov, A.V. Sadovoy, M.A. Vilenskii, P.V. Zakharov, R. Myllylä, Critical behavior of phase interfaces in porous media: analysis of scaling properties with the use of noncoherent and coherent light. J. Exp. Theor. Phys. **108**(2), 311–325 (2009)

87. E.W. Washburn, The dynamics of capillary flow. Phys. Rev. **17**(3), 273–283 (1921)

88. A. Marmur, R.D. Cohen, Characterization of porous media by the kinetics of liquid penetration: the vertical capillaries model. J. Colloid Interface Sci. **189**, 299–304 (1997)

89. T. Delker, D.B. Pengra, P.Z. Wong, Interface pinning and the dynamic of capillary rise in porous media. Phys. Rev. Lett. **76**(16), 2902–2905 (1996)

90. M. Alava, K. Niskanen, The physics of paper. Rep. Prog. Phys. **69**, 669–723 (2006)

91. S.V. Buldyrev, A.-L. Barabási, F. Caserta, S. Havlin, H.E. Stanley, T. Vicsek, Anomalous interface roughening in porous media: experiment and model. Phys. Rev. A **45**(12), R8313–R8316 (1992)

92. L.A.N. Amaral, A.-L. Barabási, S.V. Buldyrev, S.T. Harrington, S. Havlin, R. Sadr-Lahijany, H.E. Stanley, Avalanches and the directed percolation depinning model: experiments, simulations, and theory. Phys. Rev. E **51**(5), 4655–4673 (1995)

93. L.A.N. Amaral, A.-L. Barabási, H.A. Makse, H.E. Stanley, Scaling properties of driven interfaces in disordered media. Phys. Rev. E **52**(4), 4087–4104 (1995)

94. O. Zic, T. Kustanovich, E. Moses, Z. Olami, Defects in wetting fronts: experimental and theoretical results. Phys. Rev. E **58**(1), 689–699 (1998)
95. H. Cummins, E. Pike (eds.), *Photon Correlation and Light Beating Spectroscopy* (Plenum, New York, 1974)
96. Z. Csahók, K. Honda, T. Vicsek, Dynamics of surface roughening in disordered media. J. Phys. A: Math. Gen. **26**(5), L171–L178 (1993)
97. R. Bruinsma, G. Aeppli, Interface motion and nonequilibrium properties of the random-field Ising model. Phys. Rev. Lett. **52**(17), 1547–1550 (1984)
98. G. Grinstein, S.K. Ma, Surface tension, roughening, and lower critical dimension in the random-field Ising model. Phys. Rev. B **28**(5), 2588–2601 (1983)
99. K. Amundson, A. van Blaaderen, P. Wiltzius, Morphology and electro-optic properties of polymer-dispersed liquid-crystal films. Phys. Rev. E **55**, 1646–1654 (1997)
100. F. Roussel, J.-M. Boussine, U. Maschke, X. Coqueret, F. Benmouna, Phase diagrams and morphology of polymer dispersed liquid crystals based on nematic-liquid-crystal-monofunctional-acrylate mixtures. Phys. Rev. E **62**, 2310–2316 (2000)
101. K. Luo, The morphology and dynamics of polymerization-induced phase separation. Eur. Polym. J. **42**, 1499–1505 (2006)
102. D.A. Zimnyakov, V.V. Tuchin, Fractality of speckle intensity fluctuations. Appl. Opt. **35**, 4325–4333 (1996)
103. C.F. Bohren, D. Huffman, *Absorption and Scattering of Light by Small Particles* (Wiley, New York, 1998)

Metrology of Coherence and Polarization in Sight of Singular Optics

2

Oleg V. Angelsky, Peter V. Polyanskii, Peter P. Maksimyak, and Igor I. Mokhun

Contents

Abstract

This chapter considers new feasibilities for metrology of coherence and polarization of light fields and reviews novel approaches to singular optics from the point of view of researchers. New possible techniques are discussed that can be involved in the study and implementation of completely and partially coherent/ polarized complex fields and that can be of use in optical correlation diagnostics.

O.V. Angelsky (✉) • P.V. Polyanskii • P.P. Maksimyak •
I.I. Mokhun
Department of Correlation Optics, Chernivtsi National University, Chernivtsi, Ukraine
e-mail: angelsky@itf.cv.ua, polyanskii@itf.cv.ua, maksimyak@itf.cv.ukrtel.net, mokhun@itf.cv.ua

These considerations were inspired by revived attempts to develop generalized classical theory of partial coherence and partial polarization (Emil Wolf), as well as by achievements in quantum theory of optical coherence (for which Roy Jay Glauber was awarded the Nobel Prize in 2005).

2.1   Introduction

The notion of coherence is the most fundamental concept of modern optics. As has been shown by E. Wolf [1], this notion is intrinsically connected with other characteristics of light, such as intensity and polarization. One can distinguish between these characteristics mainly for didactic purposes. But in every practically important case, we meet the problem of their tight, inseparable interconnection. So, one cannot define coherence, aspiring in part to associate it with visibility of interference pattern, while ignoring the states of polarization of superposed beams. Note that attempts to explain Young's interference experiment for "completely unpolarized" light lead sometimes to questionable conclusions [2]. At the same time, the most fundamental definition of polarized light is given through the measure of mutual coherence of the orthogonally polarized components of a beam. Finally, all three mentioned characteristics of a light beam are comprehensively expressed through known combinations of the Wolf's coherency matrix elements [3].

Incidentally, the impulse to associate coherence only with obvious interference (intensity modulation) effect does not always lead to true understanding of the coherence phenomena. It is not enough that interference fringes are absent in superposition of completely mutually coherent but orthogonally polarized beams (it is well-known from the Fresnel-Arago laws and experiments). There are quite new concepts showing the absence of interference effect for superposing two waves of equal frequencies with strictly (*deterministically*) connected complex disturbances, even with the same state of polarization. A refined example of this kind was given by L. Mandel in his concept of "anticoherence" [4]. In very simplified form, Mandel's concept can be formulated in terms of conventional (static) holography.

As is well known, a simple thin hologram reconstructs in plus-minus first diffraction orders two conjugate fields producing so-called main and conjugate images [5]. Having reliable techniques for optical phase conjugation, one can try to add two complex conjugated copies of the signal at one plane to a plane of a hologram. What is the result? Intensity of superposition of two such waves is determined as

$$I = < |a \exp[i(\omega t - \mathbf{k r} + \varphi_1)] + b \exp[-i(\omega t - \mathbf{k r} + \varphi_2)]|^2 >, \qquad (2.1)$$

where a and b are amplitudes of two conjugated waves that are believed constants (stationary optical fields [6]), $\omega = 2\pi/T$ is angular frequency of oscillations (T being a time period) that is the same for both superposed counterparts, $\mathbf{k}$ is the

Fig. 2.1 Superposition of two complex conjugated replicas of a signal results in a real signal of constant amplitude along the Arrow of time, without interference effect
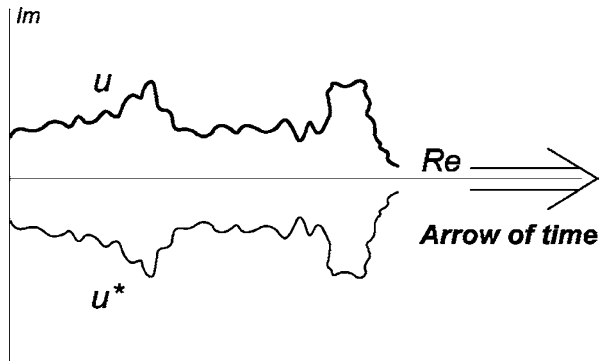
wave vector, **r** is the position vector of the observation point, $\phi_{1,2}$ are the initial phases of two waves, and $< \ldots >$ denotes time averaging. It is easy to see that, in contrast with common interference, the temporal multiplier does not vanish in this expression:

$$I = a^2 + b^2 + 2ab < \cos[2(\omega t - \mathbf{kr}) + (\varphi_1 - \varphi_2)] > \equiv a^2 + b^2, \qquad (2.2)$$

so that the averaging results in vanishing the "interference" term. This conclusion is illustrated in Fig. 2.1, from which one can see that summation of two complex conjugated beams, u and u^*, everywhere along the arrow of time gives rise to the real value of constant magnitude. Thus, interference between deterministically, unambiguously connected two waves of equal frequency and identical state of polarization is absent. Of course, if one implements phase conjugation of one of two waves figuring in (2.1), the interference effect will be provided due to compensation of the temporal multiplier and, as a consequence, inefficiency of time averaging.

Less discussed within the framework of classical (wave) theory of partial coherence is the influence of an "observer" on coherent properties of studied beams. This problem is typical for quantum optics [7–9] (as well as for quantum physics in general [10]). But the results obtained in the last quarter of a century compel one to take into account the influence of the conditions of observation and detector characteristics on evaluation of the coherence of light in the classical approach also. Some arguments for this point follow.

When we consider interference of two waves with close but non-equal frequencies ($\omega_1 \neq \omega_2, \Delta\omega << \bar{\omega}$), we observe moving intensity fringes. This effect is widely used in the optical heterodyning (optical nonlinear mixing) technique. If the "register" is stationary and possesses low temporal resolution, averaging over a large enough temporal interval results in smoothing of interference fringes, so that visibility $V \to 0$; we conclude that two waves are mutually incoherent. On the other hand, using a "register" with higher temporal resolution, which moves in the direction and with speed of propagation of moving intensity waves, one recognizes

the same two waves as mutually coherent that *form* observable interference fringes in moving coordinates! Therefore, one can register a hologram forms such waves at the properly moving "register" (though this task is not simple in practice).

Another example related to the problem of interest is the influence of *spectral* resolution (or, more strictly, inhomogeneous spectral sensitivity) of the detector on our conclusions concerning *spatial* coherence of the elaborated optical field. If one uses a source with uniform spectral density in the classical Young's two-pinhole interference arrangement, then a detector with uniform spectral sensitivity "evaluates" the field as completely spatially incoherent for arbitrary sampling points at the beam cross-section due to superposing numerous scaled in wavelength spectral interference patterns, so that minima of intensity (of the field of homogeneous spectral distribution!) are absent in the resulting pattern. *Such a detector is "blind" to spatial coherence of such an optical field*. Nevertheless, the human eye detects spatial coherence of a field due to non-uniform spectral sensitivity of visual receptors and inhomogeneous spatial distribution of *colors* over the analyzed field. Of course, the same is true for evaluation of *temporal* coherence, for example, in the arrangement of the Newton's rings in white light.

A less trivial case has been considered by Wolf ([11,12], see also numerous useful references therein) in the context of induced spectral changes resulting in remarkable transformations of temporal coherence of polychromatic optical fields due to the presence of a material *intermediary* as diffraction or a scattering object.

The next example, which is closer to our circumstances, is *pseudo-depolarization* [13] (in modern terminology, "global" depolarization [2]) resulting from stationary scattering of laser radiation in multiply scattering media, such as turbid media, multi-mode waveguides, and most natural objects, including biological ones. Here, the role of the detector is fundamental. The universal approach to determining all polarization characteristics of a field (both the state of polarization and the degree of polarization [14]) consists of Stokes polarimetry of the analyzed field. Stokes polarimetric analysis provides different results for local and "global" (space-averaged) measurements. Thus, the point-wise measuring Stokes parameters show a complete (unity) degree of polarization, but the state of polarization changes from point to point. Space averaging over ten or more speckles seemingly shows depolarization. This is the central subject of study of vector singular optics [15].

These examples illustrate, in part, the importance of taking into account the temporal and spatial resolution of the detector used, as well as a choice of the coordinates (stationary or moving) for metrological estimation of coherence and polarization of light, and even understanding (*definition*) of these phenomena.

Two other positions require consideration. First, as has been pointed out by Isaak Freund [16], tone cannot investigate experimentally the problem of coherence and polarization of optical light in the general, 3D case when paraxial approximation is violated nor can one neglect any of three Cartesian coordinates in describing the behavior of the electric vector. As an example, Freund references the study of polarization of relict–cosmic microwave radiation (CMR) [17] that is believed to be almost *isotropic* (nondirectional) [18]. Measuring the Stokes parameters for such radiation is, to all appearances, not well grounded. It is the same as measuring

the Stokes parameters in various directions from the interior of a cloud of light-scattering small particles, an approach that is not generally accepted [19, 20]. Nevertheless, it is the only one that we have!

The second example relates directly to one of the problems that will be discussed below, the so-called *optical currents* [21]. Though it is premature to solve this problem comprehensively, especially the experimental aspect, it is clear that micro- or nanoparticles serving for diagnostics of an inhomogeneously polarized and partially coherent optical field [22–27] affect this field as absorbing and retransmitting particles with their own characteristics, so that the state of a field, in general, changes under the influence of such secondary radiators.

Pronouncing call of the times in the topic under consideration consists in involving the ideas, approaches and techniques of singularoptics [28]. This is seen in an important review [29] devoted to the structure of partially coherent optical fields. Investigations in this scientific domain have been stimulated, in part, by the literature [30–33]. For that, many usual and new results of the theory of partial coherence and partial polarization become essentially urgent just in the singular optics concept. On the other hand, there are good reasons to expect that applying the fundamentals of the theory of partial coherence will eventually lead to development of new practical applications of singular optics.

Moreover, as it has been argued in papers [34–36], "Usual beam parameters either characterize a beam 'in a whole' (power, momentum, beam size and divergence angle) or describe its 'shape' via certain spatial distributions (amplitude, phase, polarization state, etc.)... Usual beam parameters provide only rough and, sometimes, distorted picture of internal processes that constitute a real 'inner life' of a light beam. These processes are related to the fundamental dynamical and geometrical aspects of light fields, and are associated with the permanent energy redistribution inside the beam 'body', which underlies the beam evolution and transformations. The internal energy flows provide a natural and efficient way for 'peering' into the light fields and studying their most intimate and deep features." It is of interest, in the context of this chapter, to correlate this statement with Wolf's methodology of *observable quantities* that is the most influential concept of physical optics since 1954: "optics of observable quantities, such as correlation functions and averaged in time intensities" [14]. Paradoxical contradiction between two undoubtedly true statements is apparent. In fact, this contradiction is eliminated when one takes into account that internal energy flows ("optical currents" [21]) may be revealed only by carrying out the experiments with observable quantities. Similarly, the vibration phase [15] of an optical wave is unobservable, whereas its difference with a phase of coherent reference phase is liable to register simply as the phase of the mutual coherence function of two waves. More globally, two mentioned approaches are complementary, being *intimately* interconnected, similarly to approaches of statistical physics and thermodynamics.

Organization of the review is not typical. Most review papers written to date on this topic are of a theoretical nature, sometimes with a valued simulation background. Relatively less attention is paid to experimental aspects of

the problem. This gap is filled, in part, by recent books and book chapters written by the authors of this chapter [37, 38]. But the scope of experimental results rapidly grows, and this outlook does not repeat our previous papers. So, we represent here several independent experimental current views on the problem of metrology of coherent and polarization properties of optical fields, with especial emphasis on singular optical prerequisites and consequences of our experimental approaches. In spite of the unavoidable incompleteness of this consideration, the authors hope that it stimulates further experimental investigations in this field and leads to a broadening of practically significant applications of *singular optics of partially coherent and inhomogeneously polarized optical fields*.

2.2   Investigation of Optical Currents in Completely Coherent and Partially Coherent Vector Fields

In this section, the computer simulation results on the spatial distribution of the Poynting vector are presented and the motion of micro- and nanoparticles in spatially inhomogeneously polarized fields is illustrated. The use of small particles for diagnostics of the microstructure of light is a widely used approach [22–27], but mainly in approximation of complete coherence of an optical field. Here, the influence of phase relations and the degree of mutual coherence of superposing waves in two-wave and four-wave configurations on the characteristics of the microparticle's motion are analyzed. The possibility of diagnostics of optical currents in liquids caused by polarization characteristics of an optical field alone is demonstrated using nanoscale metallic particles. The prospects of studying temporal coherence using the proposed approach are also discussed.

The motivation for this study is that experimental investigation and computer simulation of the behavior of small spherical particles embedded in optical fields provide a deeper understanding of the role of the Poynting vector for description of optical currents in various media [21, 36]. Interference between waves polarized in the plane of incidence has been shown to be effective in creation of polarization micro-manipulators and optical tweezers. On the other hand, this is a vital step in optimal metrological investigation of optical currents in vector fields [39–42]. In addition, the study of spatial and temporal peculiarities of the motion of particles embedded in optical fields with various spatial configurations and with various scale distributions of the Poynting vector leads to new techniques for estimating the temporal coherence of optical fields [43].

Computation of the spatial distribution of the time-averaged Poynting vector determining the forces affecting microparticles and their movement is performed following the algorithm proposed by M. Berry [21], who has shown that the vector force affecting a small particle in an optical field is proportional to the time-averaged Poynting vector. It will be shown that the study of the motion of microparticles in inhomogeneously polarized fields provides reconstruction of the spatial distribution of the time-averaged Poynting vectors, viz. the optical currents.

Fig. 2.2 Superposition of plane waves of equal amplitudes linearly polarized in the plane of incidence having an interference angle of 90°. Periodical spatial polarization modulation takes place in the plane of incidence
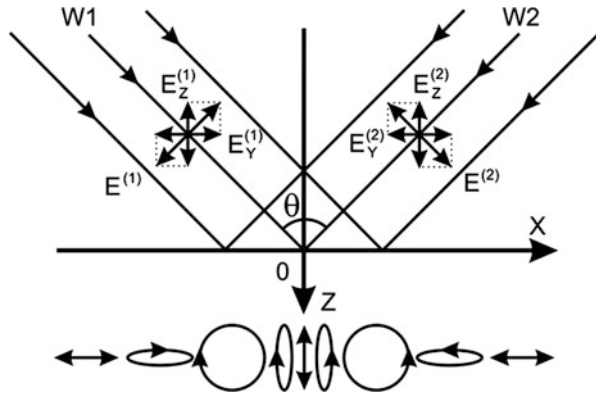
Fig. 2.3 Spatial distribution of the time-averaged Poynting vectors resulting from superposition of two orthogonally linearly polarized waves with an interference angle of 90°
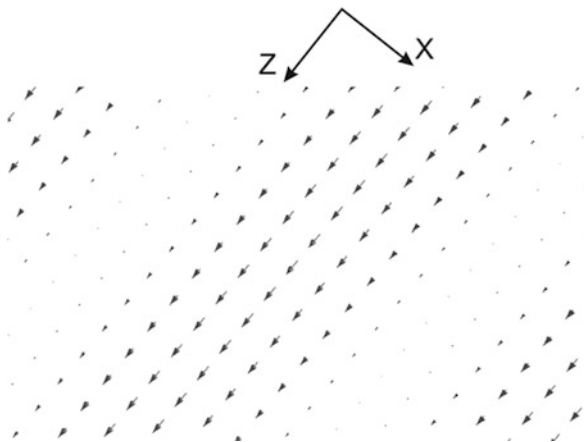
2.2.1 Two-Wave Superposition for Changeable Degree of Mutual Coherence of the Components

Superposition of two plane waves of equal amplitudes polarized in the plane of incidence (Fig. 2.2) results in the distribution of the Poynting vector shown in Fig. 2.3. Such distribution arises when the interference angle is equal to 90°, and the only periodical polarization modulation of the field (in the absence of intensity modulation) takes place in the plane of observation [44].

The coherency matrix $W(\mathbf{r_1}, \mathbf{r_2}, t)$ describes the coherence properties of vector optical fields, characterizing the correlation of two fields at two different spatial points $\mathbf{r_1}$ and $\mathbf{r_2}$ [45, 46], and is determined as

$$W(\mathbf{r_1}, \mathbf{r_2}, t) = < E^{(1)}{}_i(\mathbf{r_1}, t) E_j^{(2)^*}(\mathbf{r_2}, t) >$$

where $i, j = x, z$. Within the framework of such an approach, the degree of mutual coherence of the field is defined as [12]

$$\eta_{ij}(\mathbf{r_1}, \mathbf{r_2}, t) = \frac{W_{ij}(\mathbf{r_1}, \mathbf{r_2}, t)}{\sqrt{\text{tr}[W(\mathbf{r_1}, \mathbf{r_1}, 0)]} \cdot \sqrt{\text{tr}[W(\mathbf{r_2}, \mathbf{r_2}, 0)]}} = \frac{W_{ij}(\mathbf{r_1}, \mathbf{r_2}, t)}{\sqrt{\sum_{ij} W_{ii}(\mathbf{r_1}, \mathbf{r_1}, 0) W_{jj}(\mathbf{r_2}, \mathbf{r_2}, 0)}}.$$

$$(2.3)$$

The distribution of the time-averaged density of the energy current in space determines the current magnitude at different points of the plane of observation, being unambiguously determined by the degree of coherence of the superposing waves.

The direction of the resulting current is set by the directions of the Poynting vectors of these waves.

An analysis of the spatial distribution of the time-averaged Poynting vectors shown in Fig. 2.3 reveals the periodicity of this distribution, where the lengths of lines shown in the figure are proportional to the absolute magnitudes of the vectors. The lines corresponding to the singularities of the Poynting vector are shown by the indicated set of points [47–49].

Spatial distribution of the time-averaged Poynting vectors, cf. Fig. 2.3, shows the trajectories of energy transfer. The points on the map of the time-averaged Poynting vectors (Fig. 2.3) correspond to the areas through which energy transfer is absent, showing (1) the loci of singularities of the Poynting vector; (2) the points (with constant intensity) forming the directions along which light energy is non-vanishing, but is conserved; and (3) the points where the vector $\mathbf{H}$ vanishes due to interference, while in this arrangement (90°-superposition of plane waves) superposition of strictly coaxial vectors $\mathbf{H}$ of equal amplitudes associated with two superimposed plane waves takes place.

On the other hand, the instantaneous magnitude of the electric (magnetic) field strength's vector of the resulting distribution, which is formed in the plane of observation, is written as

$$\mathbf{E} = \left| \mathbf{E}^{(1)} + \mathbf{E}^{(2)} \right| \cos(\omega t + \delta_e) \mathbf{a_e}$$

$$(\text{or } \mathbf{H} = \left| \mathbf{H}^{(1)} + \mathbf{H}^{(2)} \right| \cos(\omega t + \delta_h) \mathbf{a_h}),$$
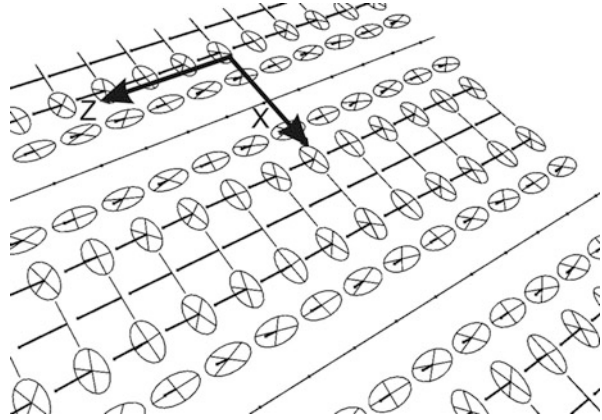
where, $\mathbf{a_e}$, $\mathbf{a_h}$ are the unit vectors in the direction of propagation of the electric (magnetic) components for the resulting field in the plane of observation; $\delta_e(\delta_h)$ is the phase difference of the electric (magnetic) field components of superposed waves. In this case, the instantaneous magnitude of the Poynting vector is

$$\mathbf{S}_{inst} = \mathbf{E} \times \mathbf{H} = |\mathbf{E}| \cdot |\mathbf{H}| \cos(\omega t + \delta_e) \cos(\omega t + \delta_h)(\mathbf{a_e} \times \mathbf{a_h}),$$

and the time-averaged magnitude of the Poynting vector is

Fig. 2.4 The polarization distribution in the registration plane is marked by thin lines. The direction and magnitude of the Poynting vector are marked by bold lines. The point at the end of the vector determines the energy transfer direction. The modulation of the Poynting vector takes place according to the polarization modulation at the plane of observation

$$\mathbf{S}_{ave} = \frac{|\mathbf{E}| \cdot |\mathbf{H}|}{2} (\mathbf{a_e} \times \mathbf{a_h}) \cos(\delta_e - \delta_h) = \frac{1}{2} (\mathbf{E} \times \mathbf{H}) \cdot \cos(\delta_e - \delta_h). \quad (2.4)$$

Because the phase difference of the electric field changes from point to point (polarization modulation), the time-averaged magnitude of the Poynting vector is modulated in space, taking the maximum (minimum) at different points of the plane of observation, as is seen from (2.4).

Homogeneous intensity distribution and periodical spatial modulation of the Poynting vector simultaneously realized in the observation region have previously been discussed within the framework of Refs. [50, 51]. Spatial polarization modulation at the plane of observation is caused by superposition of the E_x and E_z field components by changing the phase difference from point to point, cf. Fig. 2.2. A photodetector registers only intensity, $I = E_x^2 + E_z^2$. The sum of the squared amplitudes of the electrical field components is constant at the plane of observation, though the state of polarization changes. The Poynting vector is defined, as mentioned above, by the vector product, $\mathbf{S} = \mathbf{E} \times \mathbf{H}$. One observes the dependence of the result on the phase relation between vectors $\mathbf{E}$ and $\mathbf{H}$ through the vector magnitude and its direction. This relation changes from point to point in the plane of observation and manifests itself in polarization modulation. An obvious explanation for this follows from consideration of the vector product of the components of vector $\mathbf{E}$ (E_x and E_z components) with vector $\mathbf{H}$. Both the magnitudes of projections E_x and E_z and their phases change from point to point in the observation plane. As a consequence, the vector product as well as the Poynting vector change. The result of modulation is shown in Fig. 2.4.

The results of simulating the motion of particles embedded in the field of the considered distribution of the Poynting vector are shown in Fig. 2.5. We have here tacitly assumed the particles to be absorbing and of size 0.1 μm. One observes that, in the case of the distribution resulting from superposition of completely mutually coherent waves, the velocities of particle motion along the lines of the maxima and zeroes of the Poynting vector are considerably different from one another.

Fig. 2.5 The change of the particle motion velocity with time obtained for different magnitudes of the degree of coherence of superposing waves in the case of particles moving along the peak (**a**) and the minimum (**b**) of the field of time-averaged Poynting vector magnitude: curves 1, 2, and 3 correspond to the degree of coherence, which equals 1, 0.5, and 0.25, respectively
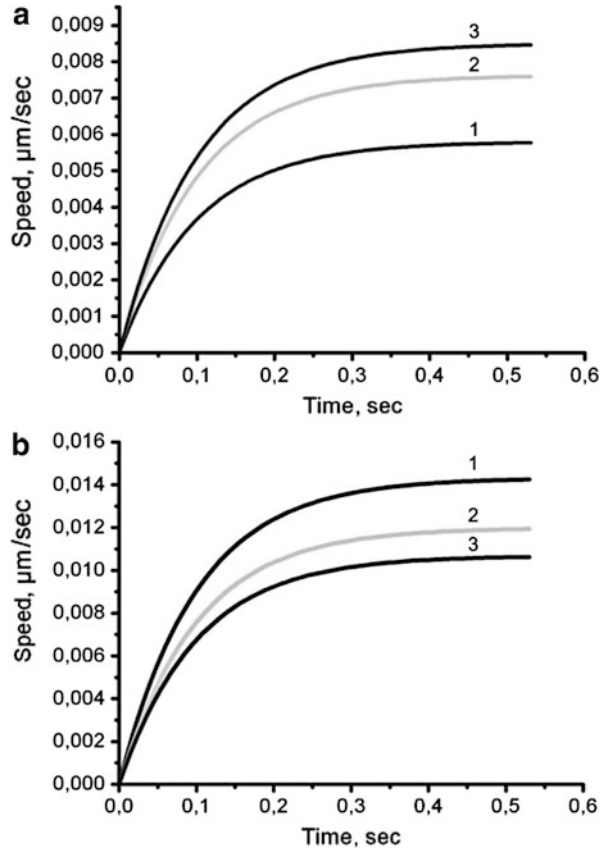

The particle size is here comparable with a half-period of the corresponding distribution; however, the resultant force giving rise to the particle motion along the lines close to the Poynting vector maxima exceeds the resultant force for lines close to the zeroes of the Poynting vector. The results of modulation of particle movement velocity along the peaks and zeroes of the averaged field of the Poynting vector are shown in Fig. 2.5a, b, respectively.

If the degree of mutual coherence of the superposed waves equals 0.2, the spatial distribution of the averaged Poynting vectors becomes more homogeneous, the modulation depth decreases considerably, and the velocities of microparticles become almost identical.

When the degree of mutual coherence equals 0.5, the relative velocities of the microparticles along the same trajectories are lower in comparison with velocities in the case of complete mutual coherence of the superposed waves and lie in the vicinity of the average magnitudes for coherent and incoherent cases [52]. One observes the dependence on the coherent properties of the superimposed waves for the motion velocities of microparticles with constant size and form in

Fig. 2.6 The diagram of
particles velocity distribution
with time
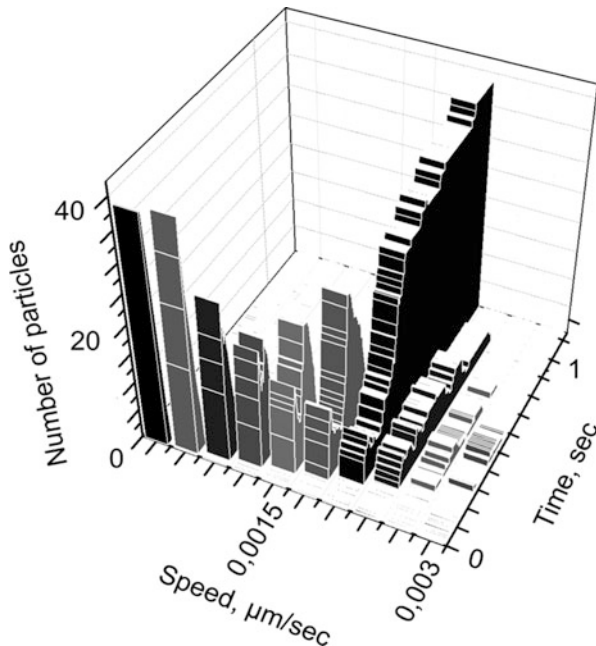
media with constant viscosity [52]. When analyzing the motion of test particles in
the region of distributed magnitude of the Poynting vector, the influence of the
parameters of superposing fields on the character of particle motion can be deter-
mined, cf. Fig. 2.5a, b.

As shown in the literature [44, 51, 52], the degree of coherence of superposing
waves determines not only the visibility of an interference distribution but also the
structure of the polarization field, viz. it determines the distribution of the Poynting
vector. Under the same other conditions of the wave superposition, changing the
degree of coherence results in changing motion velocity of the test particles, which
can serve as an estimating parameter for determining the coherence properties of
superposing waves. These differences in velocities of motion of microparticles are
explained physically in the following manner: Increasing the share of incoherent
radiation in the resulting field distribution causes a decrease of the modulation
depth of the Poynting vector's spatial distribution, as well as a decrease of
the resultant force magnitude along the lines of energy transfer, which induces
the motion of the microparticles. The increase of the degree of coherence brings
about an accelerated particle motion in the field of averaged energy magnitudes.

Figure 2.6 shows the particle velocity distribution (in this case, 39 particles),
embedded into the field formed by the averaged magnitudes of the Poynting vector
in the case of superposition of completely mutually coherent waves. With time
($\sim$1.2 s), practically all particles gain equal velocity magnitudes (see column 7);
redistribution of particles in the direction of the resultant force and uniform motion
along the zero value of the Poynting vector take place.

Fig. 2.7 Arrangement of superposition of four plane waves
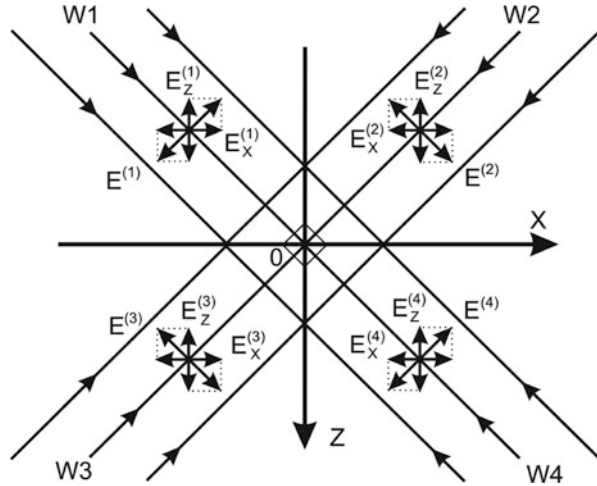
Fig. 2.8 2D distribution of the averaged Poynting vectors resulting from the superposition of four waves shown in Fig. 2.7
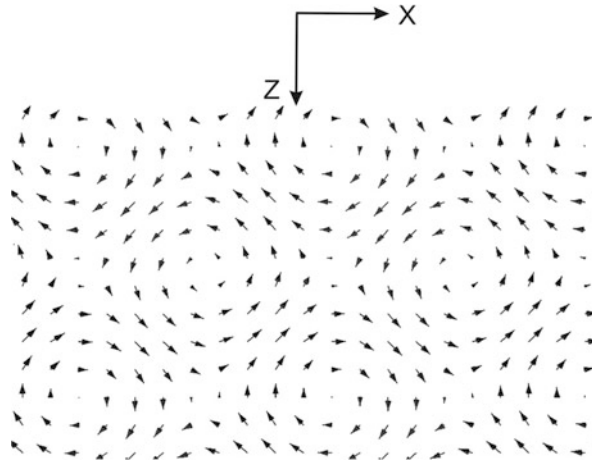

2.2.2 Superposition of Four Waves for a Changeable Degree of Mutual Coherence of the Components

In the case of superposition of four waves, see Fig. 2.7, involving two sets of counter-propagating plane waves of equal intensities, linearly polarized in the plane of incidence and oriented at an angle of 90° with respect to each other, the spatial distribution of the time-averaged Poynting vectors is formed as shown in Fig. 2.8.

The 2D periodicity of the Poynting vector's distribution is evident. As in the previous case, the lengths of the time-averaged Poynting vectors are proportional to their magnitudes. The nodal points in this distribution correspond to zero magnitudes of the Poynting vector, i.e., singularities of the Poynting vector.

Fig. 2.9 The variation of motion velocity of a test particles in an averaged field of distributed Poynting vectors with the change of the degree of mutual coherence of the waves (four superposing waves are in phase): curve 1 – one of the waves is incoherent; curves 2, 3, 4 correspond to the degree of coherence 0.25, 0.5, and 0.75, respectively
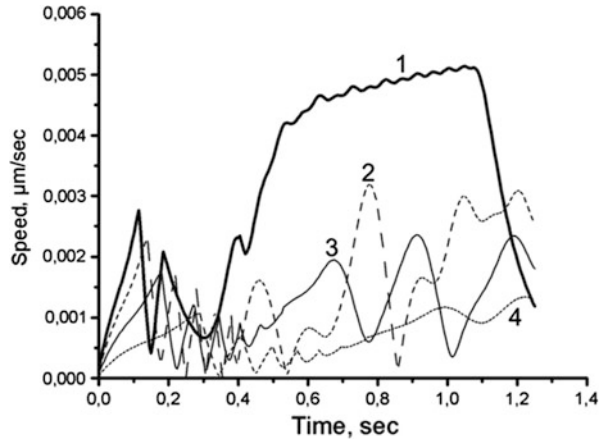
In the following simulation, the diameters of the particles are changed to be comparable with a half-period of the corresponding spatial distribution of the Poynting vector.

In order to compare the influence of the temporal and spatial parameters of coherence on the motion of the microparticles, we have analyzed the maps of the time-averaged Poynting vector with a superposition of four plane waves over a large area. Meanwhile, we have tracked the microparticles' motion. The dependence of microparticles' velocities on the phase difference of the superposing beams has thus been revealed. So, in the case of pair-by-pair four opposite-in-phase superposed beams, particles become motionless. For that, the "opposite-in-phase" configuration covers the situation where two sets of mutually orthogonal standing waves are characterized by the fact that their nodes strictly coincide.

This follows from the presence of the minimum of the modulation depth at the spatial distribution of the Poynting vector. If the phase relations between four superposed beams are such that the modulation depth of the spatial distribution of the Poynting vector is maximal, the particle velocities will depend on the degree of mutual coherence between the interfering beams, see Fig. 2.9.

Increasing the degree of mutual coherence of the waves sets a more uniform velocity magnitude of moving particles. The magnitude of the resultant force causing this motion under an increasing degree of coherence does not change with time, see Fig. 2.10. The maximum depth of modulation for coherent equiphase waves determines the stable position of particles. *The chaotic state and the average particle velocity value can be taken as a possible guideline in estimating the degree of coherence of superposing waves.*

It is worth emphasizing two issues for the case of superposition of four plane waves. The first is the dependence of the depth of modulation for the distribution of the time-averaged Poynting vectors on the phase relation of superposing waves. It is assumed here that changing the phase relation between the superposed waves causes a transition (in the observed pattern) from the situation when the maxima

Fig. 2.10 The change of the resultant force of the test particle motion in the time-averaged field of distributed Poynting vectors with the change of the degree of mutual coherence of the waves (four superposing waves are in phase): curve 1 – one of the waves is incoherent with all other waves; curves 2, 3 and 4 correspond to the degree of coherence of the waves 0.25, 0.5, and 0.75, respectively
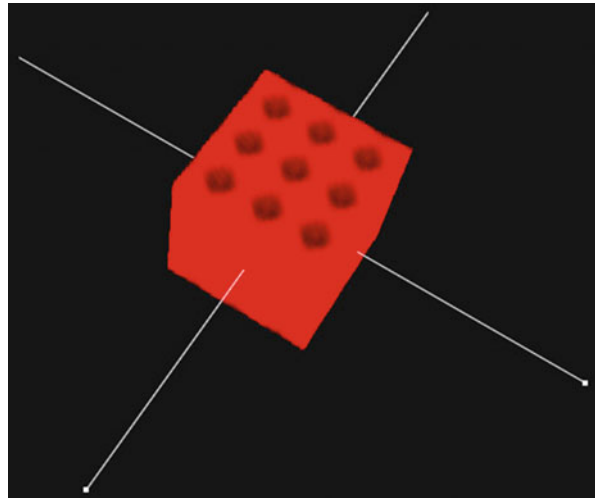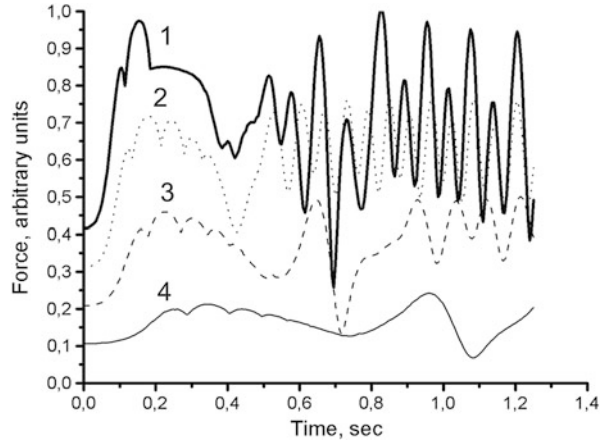
Fig. 2.11 "Cellular" distribution of the potential traps for microparticles in the case of superposition of four waves

of two systems of mutually orthogonal standing waves coincide with the case when the nodes of two such systems coincide. Thus, the velocities of particles in such fields depend on the depth of modulation of the distribution of the time-averaged Poynting vector, as seen in Fig. 2.10. The second is that the superposition of four waves linearly polarized in the plane of incidence results in the formation of a so-called "cellular" structure in the resulting field distribution, see Fig. 2.11, which can be used for transfer (transporting) of the set of periodically positioned microparticles *as an entity* to a desired zone.

One considers a future deeper investigation of the peculiarities of motion of microparticles to reveal the coherent characteristics of the waves constituting certain spatial polarization distributions.
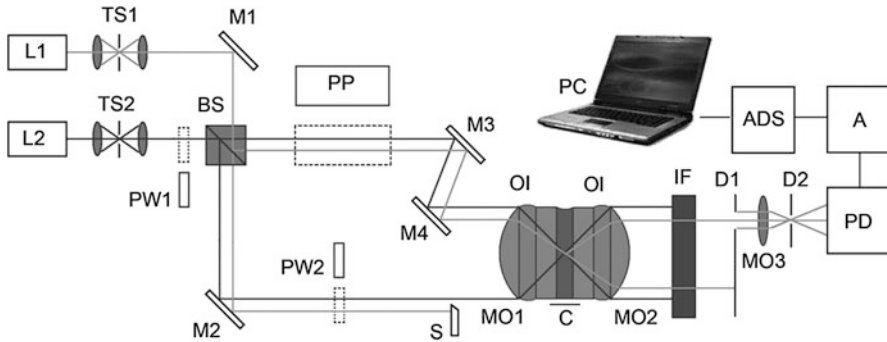
Fig. 2.12 Experimental setup: L1, L2 – lasers; TS1, TS2 – telescopic systems; M1, M2, M3, M4 – mirrors; PW1, PW2 – half-wave plates for $\lambda = 635$ nm; PP – plane-parallel plate; BS – beam-splitter; MO1, MO2, MO3 – microobjectives; C – cuvette with gold hydrosol; IF – interference filter at $\lambda = 532$ nm; D1(0.7-diam), D2 – diaphragms; S – opaque screen; PD – photodetector; A – amplifier; ADC – analog-to-digit converter; PC – computer

The use of strongly reflected test spherical particles provides a more realistic notion of movement of particles in the field modulated in polarization in the incidence plane. So, the test particles are concentrated in zones (planes) of minima of the time-averaged Poynting vector and move along these planes. This situation reflects in the most adequate manner the processes of a particle moving in the fields spatially modulated in polarization.

2.2.3 Experimental Technique and Results

Direct experimental verification of the results of computer simulation is rather difficult. The spatial period of the polarization distribution resulting from superposition of plane waves meeting at a right angle is less than a wavelength of the laser radiation of the visible range. In this case, diagnostics of optical currents presumes the use of test particles (preferably spherical) of a size much less than the period of polarization distribution. For this reason, direct visualization and diagnostics of such particle currents is hampered.

To verifying these results and the computer simulation, we have studied experimentally the influence of the field resulting from superposition of two plane waves meeting at a right angle with various combinations of their states of polarization on the test particles. Experimental arrangement is shown in Fig. 2.12. To provide a right angle between the beam axes, we use an immerse oil microobjective 90^x with NA 1.25. Two parallel linearly polarized beams converge at the focus of microobjective 1. If the electrical vectors of two beams are parallel, the intensity distribution as a set of interference maxima and minima is formed at the area of superposition of such beams. We used radiation from a semiconductor laser RLTMRL-III-635 ($\lambda = 635$ nm). For that, the period of an interference pattern is 449 nm. For investigation of the influence of the field distribution with such a period on the particles, the particle's size must be much less than the mentioned period.

We have used spherical particles of hydrosol of gold with approximate diameter 40 nm. Hydrosol has been obtained following the standard technique [53], by mixing of chlorauric acid (H[AuCl$_4$]) and sodium citrate (Na$_3$Cyt).

Periodical intensity distribution causes movement of the particles and formation of the periodical distribution of concentration of particles as the planes coinciding with interference minima of the intensity distribution at the area of superposition of two beams. These planes can be regarded as the analog of crystallographic planes in crystals. Direct visualization of particles and their currents is hampered due to small particle size. However, at planes of dense packing of particles, self-diffraction takes place. We have observed this phenomenon for angles of meeting of two beams less than 40°. For a right angle of meeting of the beams, each self-diffracted beam propagates *along* and *contrary to* the propagation direction of other of two superposing beams. Thus, it is impossible to discriminate the initial and self-diffracted beams. That is why, taking into account Bragg's law, we use, for diagnostics of periodical distributions of particles, the test laser beam with another wavelength, $\lambda = 532$ nm. To form the same interference distribution (with the period 449 nm) with such wavelength the angle of meeting of two beams could be 72.6°. So, the angle of incidence of the probing beam must be 36.3° in respect to the bisector of the writing beams. In this case, Bragg's law is fulfilled strictly for the probing beam. The mentioned angles are the angles of propagation in light-scattering media, in our case in water.

Two shifted beams from a green laser (marked by the thin line in Fig. 2.12) propagate in parallel to the beams of red laser (marked by the thick line). The external green beam is stopped by the screen S, while the inner probing beam passes the microobjective MO1 and falls at the angle 36.3° into the area of interference extrema. Diameters of the focused beams of red and green lasers are approximately 12 and 10 μm, respectively. Glass cuvette C with gold hydrosol is placed at the area of interference pattern. Thickness of the cuvette walls is 0.15 mm, and thickness of the swept volume is 18 μm. Oil immersion with refraction index 1.515 is placed between microobjectives MO1 and MO2. Microobjective MO2 is used to adjust the optical arrangement and output of the radiation diffracted on periodical distribution of gold particles.

Optical lengths of two legs of an interferometer BS-M2-M3-M4-MO2 are strictly identical. So, two beams from the red laser are mutually coherent and interfere at the focus of the microobjective MO2. Placing a perfect plane-parallel plate PP of thickness 19 mm into one interferometer leg leads to disappearance of interference, while the corresponding optical path difference exceeds the coherence length of red laser. It is important that introducing the plate PP must not be accompanied by shifting beams into the interferometer. In such a manner, one can control appearance and disappearance of interference extrema at the focus of MO1.

The change of the position of the plate leads to the change of the photodetector signal. Thus, under superposition of radiation from lasers L1 and L2, which are linearly polarized at the plane perpendicular to the figure plane, removal the plate PP results in increasing signal from a photodetector. It shows forming periodical spatial distribution of gold particles and appearance of the diffracted probing beam. The diffracted signal appears for radiation power of a red laser more than 2 mW.

However, it has been observed that for radiation power exceeding 50 mW, non-linear effects occur in light-scattering medium. So, gold particles absorb radiation and heat environment, acting as a thermal lens. That is why we have carried out our experiment for radiation power of red laser 5 mW. Radiation power of the probing beam was 0.5 mW, so that it can not affect gold particles.

If two beams of a red laser are polarized in the figure plane (half-wavelength plate PW1 for $\lambda = 635$ nm is inserted) and their convergence angle is equal to $90°$, only polarization modulation takes place in the incidence plane. In this case, the diffracted probing beam is present as well. The signal at the photodetector output with and without a plane-parallel plate is shown in Fig. 2.13b. The diffracted probing beam is present but is approximately of half the intensity in comparison with the case illustrated in Fig. 2.13a. This experimental result is also in accordance with the result of computer simulation. The field modulated in polarization (in the plane of incidence) is correlated with the concentration of the test particles at the planes of minima of the time-averaged magnitude of the Poynting vector, and particles move along these planes.

If two beams from a red laser are linearly polarized, but one is in the figure plane while the other is perpendicular to this plane (a half-wave plate PW2 for $\lambda = 635$ nm is inserted), the diffracted probing beam is absent, cf. Fig. 2.13c. This shows that at the focal plane where the beams from the red laser superpose, the periodical distributions of gold particles are absent. This experimental result is also in agreement with an earlier computer simulation [42]. In other words, there are no ordered optical currents liable to optical diagnostics, as has been made in the previous case.

Thus, temporal and space peculiarities of a particle's motion in optical fields without intensity modulation, but only due to polarization modulation causing the spatial modulation of the time-averaged Poynting vector (depending on the degree of mutual coherence of superpose waves), opens up new possibilities for the use of such field characteristics and the parameters of microparticles' motion for estimating the temporal coherence of the tested field. Here, we have demonstrated of the potential influence of only the polarization factor on formation of optical currents in liquids by the use of the principles of spatial polarization modulation in the observation plane. In addition, we have shown the possibility of diagnostics of optical currents using nanoscale test particles.

The explained metrology of microstructure of optical fields may be extended on polychromatic waves. The initial steps in this direction have been recently made in other studies [52, 54–60].

2.3 Polarization Singularities in Partially Coherent Light Beams

In this section we describe specific polarization singularities arising in incoherent superposition of coaxial orthogonally polarized laser beams. It is shown that in a transversal cross-section of paraxial combined optical beams of this class, instead

Fig. 2.13 Relative signal of a photodetector (a plate PP is inserted on 2 s and then removed) in the case when radiation of red laser is linearly polarized: (**a**) both beams are polarized in the plane perpendicular to the figure plane; (**b**) both beams are polarized in the figure plane; (**c**) one beam is polarized at the figure plane, while another one is polarized perpendicularly to this plane
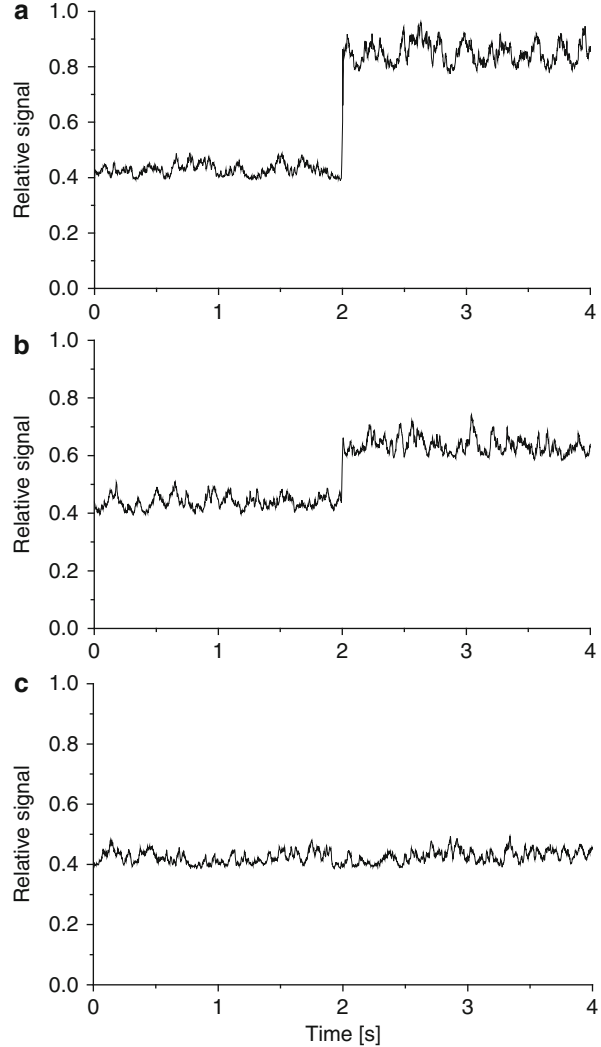
of common singularities, such as amplitude zeroes (optical vortices) inherent in scalar fields [28], and polarization singularities such as C points and L lines inherent in completely coherent vector fields [15], *phase singularities of the complex degree of polarization* (CDP) arise, whose description and investigation have been initiated by papers [61–65] basing on earlier studies [66–68] concerned with Young's concept of the edge diffraction wave in connection with diagnostics of phase singularities of spatial correlation functions of optical fields. There are U contours along which the degree of polarization equals zero and the state of polarization is undetermined (singular), and isolated P points where the degree of polarization equals unity and the state of polarization is determined

by the non-vanishing component of the combined beam. (Note, the notion of CDP discussed here differs from the definition of the complex degree of mutual polarization, CDMP [2] that is two-point function of an optical beam).

Let us briefly argue the relevance of the introduced approach.

It is known [69] that each level of description of optical phenomena possesses its own set of singularities, i.e., the set of elements of a field (points, lines, surfaces, depending on considered dimension) where some parameter of a field is undetermined. The importance of detecting such elements of a field is due to the fact that such elements form the peculiar skeleton of a field, so that if one knows behavior of a field at such singular elements (and at the their nearest vicinities), one can predict, at least in a qualitative manner, but with a high level of validity, the behavior of a field at all other areas.

Conditionally, one can classify singularities of optical fields in the following manner [69]:

– Singularities of geometrical optics,
– Singularities of completely coherent scalar (homogeneously polarized) wave fields – optical vortices,
– Singularities of completely coherent vector (inhomogeneously polarized) wave fields – optical vortices,
– Singularities of partially coherent wave fields,
– Singularities of quantum optics – "quantum cores."

Singularities of geometrical optics are caustics where the field amplitude reaches infinity. Singularities of completely coherent wave fields are divided into two sub-classes: (1) for scalar (homogeneously polarized) fields and (2) for vector (inhomogeneously polarized) fields. In scalar fields, when polarization can be neglected, so-called wave front dislocations take place (which are also referred to as amplitude zeroes or optical vortices). Phase of the complex amplitude is undetermined at such elements and is step-like changed at the crossing of them. In vector fields optical vortices are absent, though they remain in any polarization ("scalar") component. Instead of vortices, polarization singularities arise at the cross-section of a field, viz. field elements where azimuth of polarization (C points), or handedness (L lines), are undetermined [15]. Vector skeletons of coherent inhomogeneously polarized fields are elaborated in detail in Refs. [70–72]. By crossing L lines, handedness is step-like changed into the opposite one; by crossing C point, the azimuth of polarization is changed into the orthogonal one. These types of singularities are blurred in the quantum-mechanical description being "camouflaged" by the so-called quantum vacuum [69], though the distance of influence of such a quantum core is rather small. Its linear size is of order of magnitude λ^{-3} (about 6 Å for a He–Ne laser).

All mentioned singularities disappear in the case of partially coherent wave fields (though they remain in each completely coherent component), the mode in a set of which partially coherent radiation is decomposed. Instead, in addition, new singularities appear inherent only in partially coherent fields. Let us emphasize that singularities of partially coherent fields created a new topic in the field of singular optics just at the beginning of the twenty-first century [29].

Fig. 2.14 Mixing of vortex-supporting LG01 mode and plane wave with intensity less than peak intensity of a mode
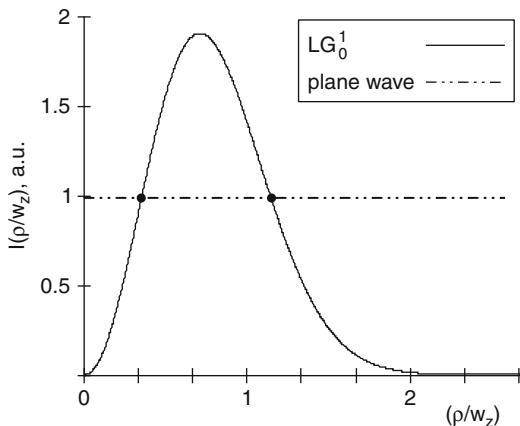

Thus, two situations arise again: (1) the scalar case when polarization can be ignored while the state of polarization is the same at all points of a field, and (2) the vector case when the state of polarization of a *partially coherent* field changes from point to point, which requires explicitly taking into account the vector nature of light. The first (scalar) case has been the subject of intense investigations [67, 73–76]. As a result of these investigations, a new phase of singularities of spatial and temporal correlation functions of quasi-monochromatic light fields has been revealed, as well as singularities of spectral components of polychromatic ("white-light") radiation [68, 77–82]. Vector singularities of partially coherent light fields have been revealed [61–65]. Such singularities are elaborated in this section.

2.3.1 U and P Singularities in Partially Spatially Coherent Combined Beams

Let us consider vector singularities in partially coherent optical beams by giving the following simple instructive example. Mutually incoherent and orthogonally polarized Laguerre-Gaussian mode LG01 and a plane wave are coaxially mixed. Such components can be obtained from one laser (using a computer-generated hologram for forming LG01 mode) in interferometric arrangement with optical delay, Δl, considerably exceeding a coherence length of the used laser, l, or using two different lasers. Intensity of a plane wave is set deliberately to be less than the peak intensity of the mode, see Fig. 2.14.

Thus, we consider two component mixture co-directional orthogonally polarized beams, one of which contains a common phase singularity, viz. optical vortex. Interference between such beams forming common interference fringes is excluded for two reasons: (1) specified mutual incoherence of the components and (2) their polarization orthogonality. Note, only the second condition *per se* determines that, independent of the degree of mutual coherence of two beams over the whole interval from zero (for optical path difference exceeding the coherence length)
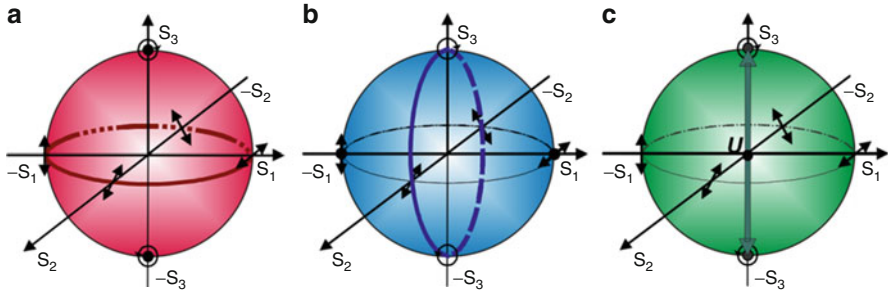
Fig. 2.15 The lines of equal intensities of orthogonally polarized beams at Stokes space: equator of the Poincare sphere for circular polarization basis, coherent mixing (**a**); 45°-meridian including the poles for linear polarization basis, coherent mixing (**b**); diameter of the Poincare sphere connecting the poles for circular polarization basis, incoherent mixing (**c**)

to unity (for zero optical path difference), the *visually* observed and *photometrically* measured pattern remains unchangeable. However, more delicate polarization analysis of the combined beam enables differentiation of two limiting cases, viz. completely coherent and completely incoherent mixing of orthogonally polarized components.

Let us firstly consider the limiting case, when two components are completely mutually coherent. For the sake of distinctness (and for substantiveness of further consideration), we consider coherent mixing of orthogonally *circularly* polarized LG01 mode and a plane wave. In addition, choice of circular polarization basis has the advantage that it is invariant in respect to rotation of the coordinates, in contrast to the linear or elliptical basis, which are relative [83].

In general, the combined beam, everywhere with the unit polarization degree ($\sqrt{s_1^2 + s_2^2 + s_3^2} = 1$, where s_1, s_2, s_3 are the normalized second, third, and fourth Stokes parameters, respectively [14, 83, 84]), is elliptically polarized. But at the center of the vortex of LG01 mode the field is circularly polarized with the state of polarization of a plane wave. A common phase singularity (vortex) of the orthogonally polarized component of the combined beam lies at the bottom of this circular polarization. At the same time, the resulting field is polarized linearly at two contours where amplitudes of two components become equal to each other, see Fig. 2.15a. For that, owing to the helicoidal structure of a wave front of the LG01 mode, the azimuth of linear polarization changes with changing phase difference of a mode and a plane wave. Such a topological structure can be considered as an elementary experimental model of the assemblage of C point and, surrounding it, the L contour of conventional singular optics of vector fields. Similar to the case of random vector fields, the crossing L line where handedness is undetermined is accompanied by step-like changing handedness into the opposite one, corresponding to the predominant intensity component with unchangeable azimuth of polarization. For comparison, Fig. 2.15b illustrates the line of equal intensities of coherently mixed components in the linear polarization basis.

Fig. 2.16 The complex
circular polarization plane.
The center of coordinates
corresponds to left-circular
polarization (C point); the
circle of unite radius
separating *red* and *blue* areas
corresponds to linear
polarizations with changeable
azimuth of polarization
(L contours), its contours
separate the area of the beam
with left handedness (*red*) and
right handedness (*blue*); right-
circular polarization point lies
at infinity
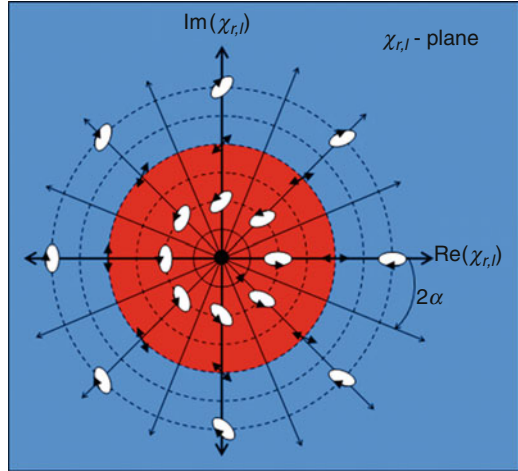
It is of interest that the elementary structure shown in Fig. 2.15a is directly
related to the description of polarized light at the circular complex polarization
plane that is a stereographic projection of the Poincare sphere [84]. So, the C point
and L contours correspond to the pole of the Poincare sphere and its equator,
see Fig. 2.16.

Let us support this intuitive consideration by formal description. Proceed from
the Jones vectors of two components, the right-circularly polarized LG01 mode and
left-circularly polarized plane wave,

$$\mathbf{E}_{LG} = c(w/\rho)e^{i\Delta}\begin{bmatrix} e^{i\phi} \\ e^{i(\phi+\pi/2)} \end{bmatrix}, \mathbf{E}_P = \begin{bmatrix} e^{i\phi} \\ e^{i(\phi-\pi/2)} \end{bmatrix}, \tag{2.5}$$

where c is the amplitude factor corresponding to inhomogeneous amplitude
distribution of a mode as a function of dimensionless radial coordinate, and $e^{i\Delta}$
is associated with the helicoidal change of a phase of a mode under circumference
of the central vortex (its explicit form for the Laguerre-Gaussian mode is
well known but is not relevant here). There is the Jones vector of the combined
beam:

$$\mathbf{E}_{Total} = \mathbf{E}_{LG} + \mathbf{E}_P = \begin{bmatrix} E_x \\ E_y \end{bmatrix} = \begin{bmatrix} ce^{i\Delta} + 1 \\ ce^{i\Delta}e^{i\frac{\pi}{2}} + e^{-i\frac{\pi}{2}} \end{bmatrix} e^{i\phi}. \tag{2.6}$$

General coherency matrix of the beam is found as

$$\{\mathbf{J}\} = \mathbf{E}_{Total} \cdot \mathbf{E}_{Total}^* = \begin{bmatrix} E_x \\ E_y \end{bmatrix} \begin{bmatrix} E_x^* & E_y^* \end{bmatrix} = \begin{Vmatrix} J_{xx} & J_{xy} \\ J_{yx} & J_{yy} \end{Vmatrix}, \tag{2.7}$$

or in explicit form:

$$\{\mathbf{J}\} = \left\| \begin{matrix} c^2 + 2c\cos\Delta + 1 & c^2 e^{-i\frac{\pi}{2}} + 2c\sin\Delta + e^{i\frac{\pi}{2}} \\ c^2 e^{i\frac{\pi}{2}} + 2\sin\Delta + e^{-i\frac{\pi}{2}} & c^2 - 2c\cos\Delta + 1 \end{matrix} \right\|. \tag{2.8}$$

Combining the elements of coherency matrix, one can find the *full* Stokes parameters:

$$S_0 = J_{xx} + J_{yy} = 2(c^2 + 1); \quad S_1 = J_{xx} - J_{yy} = 4c\cos\Delta;$$
$$S_2 = J_{xy} + J_{yx} = 4c\sin\Delta; \quad S_3 = i(J_{xy} - J_{yx}) = 2(c^2 - 1). \tag{2.9}$$

Here we are especially interested in the case $c = 1$. One only obtains for this case the *normalized* Stokes parameters:

$$s_0 = 1; \ s_1 = \cos\varDelta; \ s_2 = \sin\varDelta; \ s_3 = 0. \tag{2.10}$$

Vanishing of the fourth Stokes parameter means that the polarization at all points of the contour where intensities of the mixed components are equal to each other is equally distanced from the states of polarization of the components, i.e., neither right-circular nor left-circular predominate in intensity. This is in direct correspondence with 2.15a. At all points of such an L contour, polarization is linear with the polarization azimuth $\alpha = 0.5\tan^{-1}(s_2/s_1) = \Delta/2$, while the angle of ellipticity $\beta = 0.5 \ \arcsin s_3 = 0$. In addition, the degree of polarization $P = \sqrt{s_1^2 + s_2^2} \equiv 1$. In correspondence with the helicoidal structure of a wave front of LG01 mode, a phase difference of the components changes along the contour of equal intensities that results in changing azimuth of polarization. Thus, we obtain the direct analog of the L contour. Further, at the center of vortex of LG01 mode we have $c = 0$. Again, proceeding from (2.9) we find the normalized Stokes parameters $1, 0, 0, -1$, i.e., left-circular polarization of a plane wave. In the vicinity of such C point, polarization is elliptical, with the azimuth of polarization changing with azimuthal coordinate and ellipticity decreasing from the vortex to L contour, (2.10), where handedness is undetermined in a step-like changing by crossing this contour. This corresponds with Fig. 2.16.

Thus, for the circular polarization basis, moving along the contour of the combined beam "LG01 mode + plane wave" where intensities of the components become equal corresponds to moving along the equator of the Poincare sphere that is determined only by the ratio of the second and third Stokes parameters. (For comparison, using the linear polarization basis, to say $0°$ and $90°$, one obtains by the same way the normalized Stokes parameters for the combined beam $1, 0, \cos[\Delta + (\varphi_0 \ \varphi_{90})], \ \sin[\Delta + (\varphi_0 \ \varphi_{90})]$ that corresponds to points of $45°$-merdian of the Poincare sphere, see Fig. 2.15b.)

Before consideration of the most general case of partial mutual coherence of the mixed orthogonally polarized components in the following section, let us consider another limiting case, viz. completely incoherent mixing of such components.

There is no necessity to proceed now from Jones vectors and to form a coherency matrix of the combined beam. One can at once determine the Stokes parameters of mutually incoherent components and sum them directly, without accounting phase relations that are irrelevant for incoherent summation. The normalized Stokes parameters of orthogonally polarized beams differ only in the sign of the second, third and fourth parameters: $\{1, s_1, s_2, s_3\}$ and $\{1, -s_1, -s_2, -s_3\}$. It is clear that when two components become equal in intensities, the normalized Stokes parameters of the combined beam becomes $\{1, 0, 0, 0\}$. The field at such elements of a field is completely unpolarized. There are only U singularities [61, 63]. This is shown in Fig. 2.15c for the case of incoherent mixing of orthogonally circularly polarizer components. The trajectory of the imaging point for the combined beam in this case is the diameter of the Poincare sphere connecting two poles. U singularity is imaged by the center of this sphere, and all other points (beside the center and poles) image partially circularly polarized fields. Here, the length of a vector drawn from the center of the Poincare sphere to the imaging point inside it equals the degree of polarization. The point where the degree of polarization equals unity is referred to as the P (completely polarized) point [61, 63]. Its location is determined by the vortex of the orthogonally polarized (scalar singular) component. The set of P points and U contours corresponding to extrema of the degree of polarization of a field are *the singularities of the degree of polarization* forming the vector skeleton of the two-component mixture of orthogonally polarized beams. Note, in Refs. [61–64] consideration is carried out using the notion of the complex degree of polarization – CDP, associated with orientation of the vector of polarization in the Stokes space and undergoing the phase singularity at the center of this space. So, U singularities can be considered only as vector singularities, viz. singularities of the vector of polarization, when its magnitude equals zero and a phase (orientation of the vector) is undetermined.

Let us emphasize that the condition of occurring U singularity is equal to the condition of the occurring L contour in completely coherent limit. This means that loci of C and L singularities in completely coherent fields and P and U singularities in partially coherent fields arising from completely incoherent orthogonally polarized components, correspondingly, coincide.

Displacement from U singularity results in predomination of one of two orthogonal components in intensity. The state of (partial) polarization is only determined by the predominant component. For this reason, the degree of polarization can be determined in similar form as visibility:

$$P = \left| \frac{I_1 - I_2}{I_1 + I_2} \right|. \tag{2.11}$$

In other words, at each point of the combined beam equal in intensities, parts of orthogonal components form unpolarized background at which a completely polarized part manifests itself corresponding to the component that is predominant in

intensity. This is in complete agreement with classical decomposition of a partially polarized beam into completely coherent and completely incoherent parts, which are added on intensities, without accounting for phase relations [14, 84]. Note, there are no devices providing such decomposition in practice. However, the share of the completely polarized part can be determined experimentally through the Stokes polarimetric experiment, $P = \sqrt{s_1^2 + s_2^2 + s_3^2}$, or, equivalently, following (2.11). In theory, one puts in correspondence to such beams the set of two coherency matrices – for completely polarized and completely unpolarized parts of a beam [3, 14].

Thus, only two orthogonal states of polarization take place in combined beams of the kind considered, which are separated by U singularities where the state of polarization is undetermined.

So, the considered limiting cases show the same location of C and P singularities and L and U singularities for the same set of components. However, vicinities of such singularities are essentially different. Only two orthogonal states of polarization are present in spatially partially coherent combined beams, and only the degree of polarization changes from point to point within the areas separated by U singularities.

2.3.2 Vector Singularities for Partially Mutually Coherent Mixed Components

Let us consider now the most general case, when two mixed components shown in Fig. 2.14 are orthogonally (circularly) polarized and are partially mutually coherent, so that the degree of mutual coherence of the components can be gradually changed from unity to zero. It can be implemented in the arrangement of the Mach-Zehnder interferometer with controllable optical pass difference between the legs of an interferometer, as shown in Fig. 2.17.

A half-wave plate at the interferometer input serves for fine balancing of the intensity ratio between the legs of an interferometer without changing total intensity at its output. Two polarizers inside an interferometer are controllers setting the orthogonal linear polarizations. The LG01 mode is generated by a computer-synthesized hologram. A quarter-wave plate at the output of an interferometer transforms an orthogonal linear polarization into an orthogonal circular one. A quarter-wave plate and linear analyzer at the receiving end, together with a CCD-camera matched with personal computer serve for Stokes-polarimetric analysis of combined beams. Two prisms at one of legs of an interferometer enable control of optical path difference and mutual coherence of the mixed components. Namely, one can control path delay Δl from zero to magnitude exceeding a coherence length (length of wave train) l of the used laser. Change of the ratio $\Delta l / l$ corresponds to change degree of mutual coherence of orthogonally polarized components. Thus, for $0 < \Delta l / l < 1$, the combined beam is *simultaneously* partially spatially coherent (due to changing intensity ratio at the cross-section of the resulting field) and partially temporally coherent (due to the non-zero optical
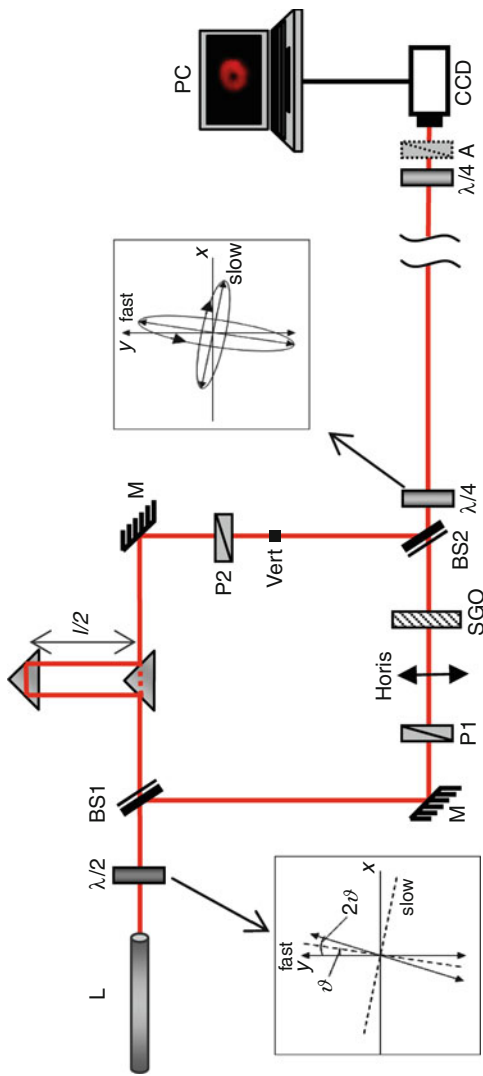
Fig. 2.17 General arrangement for generation and detection of vector singularities in partially coherent beams: L – He–Ne laser; and – half-wave and quarter-wave plates, respectively; P – polarizers; A – linear analyzer; SGO – singularity generating object (computer synthesized hologram); BS – beam splitters; M – mirrors; CCD – CCD-camera; PC – personal computer. *Insets* show action and plates at the input and at the output of an interferometer; two prisms form optical path delay loop

path difference between the components), one expects for increasing optical path difference the following.

As already mentioned, the condition of the arising of L contours and U contours in the limiting cases of mixing of orthogonally circularly polarized beams is the same: intensities of the components must be equal to each other. If the optical path difference increases from zero, the field at the L contour remains linearly polarized, but the degree of polarization decreases. It follows from that the degree of polarization of a beam is determined by the degree of mutual coherence of its arbitrary orthogonal components [3,14], here right-hand and left-hand circular components. This means that *the U contour nucleates just at the bottom of the L contour*.

The degree of polarization can be represented equivalently in terms of the *measured* Stokes parameters (which will be used in the next section) or *theoretically*, viz. through the invariants of the coherency matrix, which at the same time determine coherence properties of a field [14]:

$$P = \sqrt{1 - \frac{4 \det\{\mathbf{J}\}}{Sp^2\{\mathbf{J}\}}}. \tag{2.12}$$

In general, the degree of polarization is always not less than the modulo of the degree of mutual coherence of the components, for circularly polarized components

$$|\mu_{rl}| = \left| \frac{J_{rl}}{\sqrt{J_{rr}J_{ll}}} \right|. \tag{2.13}$$

In the general case, $P \neq |\mu_{rl}|$, as the degree of coherence depends on the decomposition basis while the degree of polarization is invariant [1]. However, it has been shown [3, 14] that the degree of polarization is equal to the *maximal* degree of coherence, $P \equiv |\mu_{rl}|_{\max}$, in the case when the components are of equal intensities. This is only the case for L singularities and U singularities. It is important that a change of the optical path difference changes weights $|\mu_{rl}|$ of the completely coherent (and completely polarized) part of the combined beam and $1 - |\mu_{rl}|$ of its completely incoherent part. Increasing $\Delta l/l$ difference corresponds to an increase of weight of U singularity against L singularity, so that one can follow gradual transformation of the L contour into the U contour.

2.3.3 Experimental Reconstruction of "Pure" and "Mixed" Polarization Singularities

Mixing of the LG01 mode and the plane wave was performed in the arrangement seen in Fig. 2.17 [66]. Intensity of a plane wave was considerably (approximately by the order of magnitude) less than the peak intensity of a mode, both circularly (orthogonally) polarized. The following results have been obtained under such conditions.

Fig. 2.18 The partially
coherent combined beam
(*left*) and its vector skeleton
formed by P and
U singularities (*right*) for
completely incoherent mixing
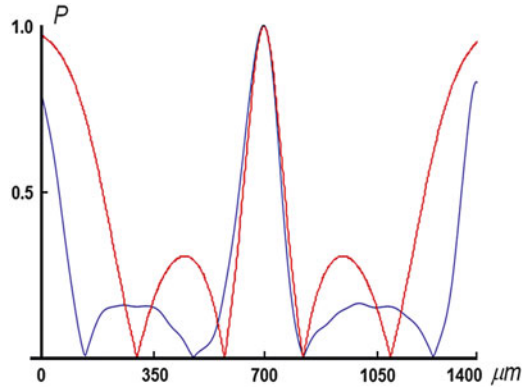of circularly polarized
components
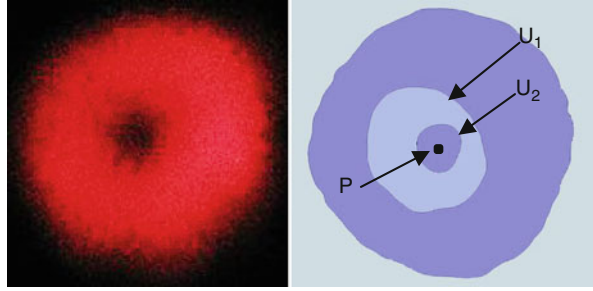
Figure 2.18 shows the combined beam whose view, as mentioned above, within experimental accuracy remains the same at the arbitrary optical path delay set in the interferometer. This photo has been obtained for incoherent mixing of two components for $\Delta l/l \approx 3$ (under the condition realized in Ref. [68]). We measured spatial distribution of the Stokes parameters and looked for the elements where $s_1 = s_2 = s_3 = 0$ ($P = 0$, U contours), and $s_3 = 1$ (P point), see the discussion after (2.10). In such a manner, we were in a position to reconstruct a vector skeleton of a partially spatially coherent combined beam formed by completely mutually incoherent components, as in Refs. [61–64]. Experimental error in determining the normalized Stokes parameters was at the level 7 %; this determines reliability with which we reconstructed the P point and U contours. P and U singularities for this case are shown in the right fragment of Fig. 2.18. Two U contours separate the areas, with right-circular and left-circular polarization shown by different colors. Within these areas, $\sqrt{s_1^2 + s_2^2} = 0$, while $s_3 < 1$. The full Stokes-polarimetric experiment over combined beam cross-section is necessary in this case, as operating only with a rotating linear analyzer does not provide differentiation of partial circular polarization from complete elliptical polarization.

Separate maps of the Stokes parameters are less representative, being only row material for finding out the degree of polarization, ellipsometric parameters of a field, and vector singularities. For this reason, we demonstrate separately from the 2D pattern shown in the right fragment of Fig. 2.18 1D cross-section of the degree of polarization of this combined beam, see Fig. 2.19. The red curve shows two-lateral radial dependence of P computed following (2.11). The blue curve shows experimentally obtained distribution found as the combination of measured Stokes parameters, here $P = |s_3|$. Quantitative discrepancy of two curves (both in positions of zeroes and in heights of side-lobes) is obvious and is explained by anisotropy of the vortex. Nevertheless, behavior of the experimental dependence is in quite satisfactory qualitative agreement with the simulation results. Namely, one observes two zeroes of the degree of polarization at the each side of the central optical vortex that are the signs of the two U contours. Moreover, the experiment has proved typical conical vicinity of the U contours predicted and observed in Ref. [61], which are a reliable sign of true singularity of any kind, in contrast to the local minimum.

Fig. 2.19 1D distribution of the degree of polarization of the combined beam formed by two mutually incoherent orthogonally polarized components defined in Fig. 2.14 and shown in Fig. 2.18

Fig. 2.20 C and L singularities in combined beam assembled from completely mutual coherent orthogonally (circularly) polarized LG01 mode and plane wave. At L lines, where intensities of two mixed component are equal, the azimuth of polarization changes in agreement of prediction illustrated in Fig. 2.16 Areas of different colors correspond to opposite handedness
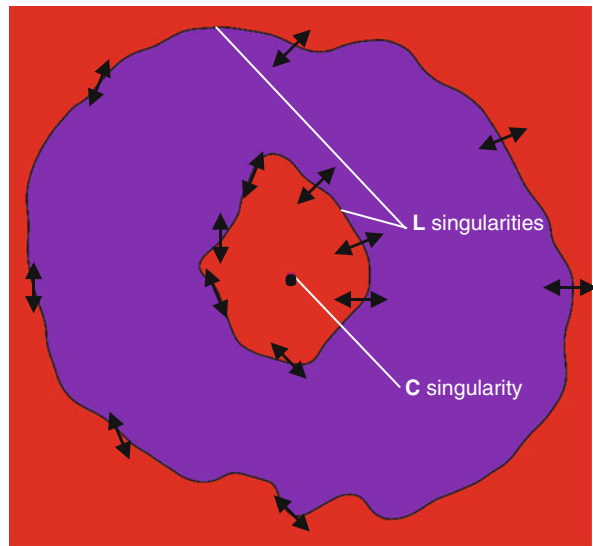
Another limiting case (completely mutually coherent components) for $\Delta l/l < 1$ (approximately 0.05) is illustrated in Fig. 2.20. Again, spatial maps of the Stokes parameters were obtained and the elements $s_3 = 0$ and $\sqrt{s_1^2 + s_2^2} = 1$ were selected. There are lines of linear polarization. In several selected points of such L lines, we determined the azimuth of polarization in two ways: first as $\tan^{-1}(s_2/s_1)$, and, second as direct measurement of the azimuth of polarization by rotating a linear analyzer up to complete extinction of a field at the specified point that corresponds to the crossed azimuth of polarization of the combined beam and the axis of maximal transmittance of the analyzer. Description between two results for determining of the azimuth of polarization do not exceeded 0.1 rad.
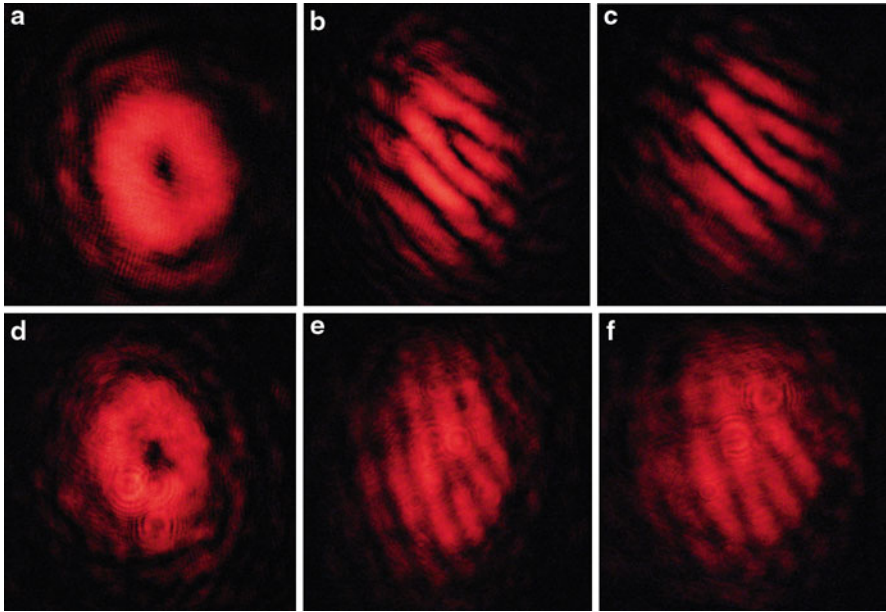
Fig. 2.21 The combined beams "LG01 mode + plane wave" with relative optical path differences $\Delta l/l \approx 0.05$ (**a**) and $\Delta l/l \approx 0.56$ (**d**); the corresponding intensity distributions behind a linear analyzer for determining the third Stokes parameters: $+45°$ (**b** and **e**) and $-45°$ (**c** and **f**). Decreasing visibility of interference fringes in fragments e and f corresponds to decreasing in parallel the degree of mutual coherence of the mixed components and the degree of polarization of the combined beam

Perfect extinction of a beam at the specified points shows that the degree of polarization $P = 1$ (in contrast to the previous case of completely mutually incoherent components, where intensity at the analyzer output is independent on its orientation). Also, for certain orientations of a quarter-wave plate and analyzer, the field at every other point can be extinguished that shows that everywhere the degree of (elliptical) polarization equals unity. Comparing Fig. 2.20 with a view of the circular complex polarization plane (Fig. 2.16) shows such polarization distribution over of a combined beam is a close experimental analogue of the circular polarization plane.

We have elaborated experimentally the intermediate case, when $0 < \Delta l/l < 1$, lying between the ones considered above. For step-by-step increasing optical path difference between the same orthogonally (circularly) polarized components, we obtained spatial distributions for the Stokes components $I_0, I_{90}, I_{+45}, I_{-45}, I_r, I_l$ and found from them the Stokes parameters. Further, the degree of polarization and ellipsometric parameters of the combined beam were determined as the combinations of these parameters.

Before formulating the conclusions from our observations, let us represent one of the row (intermediate) results undergoing the following processing. Figure 2.21 illustrates combined beams "LG01 mode + plane wave" (with large intensity ratio,

so that one does not visualize a plane wave) for relative optical path differences close to unity (coherent limit illustrated in Fig. 2.20) and slightly exceeding a half of the coherence length of the utilized laser, left fragments of Fig. 2.21. Other fragments of this figure are the intensity distributions I_{+45} (central column) and I_{-45} (right column) used for forming the third Stokes parameters. (Other pairs of intensity distributions show the same tendency). Though two orthogonally polarized components do not interfere, their equal polarization projections selected by the properly oriented polarizer *can* interfere, depending on their mutual coherence. If the degree of mutual coherence of the components is not zero, their equally polarized projections interfere with forming typical patterns, indicating phase singularity. To have enough spatial resolution for determining the place of the vortex, we set a non-zero interference angle between the components (which is small enough to not influence the accuracy of the polarization measurements). Here, instead of the snail-like pattern typical of coaxial mixing of the LG01 mode and a plane wave, we obtained interference forklets. Comparison of the central and left columns of Fig. 2.21 shows that spatial intensity distributions for orthogonal polarization projection of the combined beam are complementary in the sense that a dark forklet is replaced by a bright one.

The main conclusion follows from comparison of fragments b and e (c and f). A decrease in the mutual coherence of the mixed components and a decrease in the degree of polarization of the combined beam are accompanied by a decrease in the ability of equal polarization projections of the mixed components to interfere that manifests itself in a decrease in visibility of interference pattern. So, in fragments b and c of Fig. 2.21 ($\Delta l/l \approx 0.05$) the measured visibility is 0.97, while in the fragments Fig. 2.21e and f ($\Delta l/l \approx 0.56$) visibility is 0.24 (with experimental error non exceeding 5 %). It shows the feasibility allows one to determine *the degree of mutual coherence* of two orthogonally polarized beams by measuring *the degree of polarization* of the combined beam formed by such components found from Stokes parameters. Namely, in our experiment, $|\mu_{rl}|$ for $\Delta l/l \approx 0.56$ also equals 0.24. For the reasons discussed in Sect. 2.3, such measurements are preferably performed at the elements of the combined beam where intensities of two beams are equal to each other (where L and U singularities co-exist in the case of partial mutual coherence of the components), while at such singular elements of the combined beam $P \equiv |\mu_{rl}|$.

Thus, vector singularities occurring in light fields, which are simultaneously partially spatially and partially temporally coherent, have been considered. It has been shown that in the case of partially coherent mixing of two orthogonally *circularly* polarized components, conventional vector singularities, viz. C points and L lines submerged in a field of elliptical polarizations, coexist with singularities arising only in partially coherent fields, such as U and P singularities as the extrema of the degree of polarization. Gradual transformation of C and L singularities into P and U singularities, respectively, accompanying a decreasing degree of mutual coherence of the components has been experimentally shown. So, conventional polarization singularities of completely coherent fields (C points and L lines) vanish in the incoherent part of the combined beam, so that the only polarization of the component predominant in intensity remains in the vicinities of P points and U lines.

2.4 Feasibilities for Experimental Analysis of Characteristics of the Poynting Vector Components

In this section, potentiality of experimental analysis for the time-averaged Poynting vector is considered. In part, we will show that combined application of conventional interferometry and Stokes polarimetry should allow for unambiguous determination of the characteristics of the time-averaged Poynting vector components at each point of electromagnetic field.

One of theoretical aspects in a rapidly developing area of the modern optical technology, elaboration of new kinds of optical tweezers [22–27, 85] is connected with the fact that the vortex beams and polarized waves (both homogeneous and inhomogeneous) possess an angular momentum [85–87]. Existence of controlled angular momentum provides a possibility for controlled rotation of micro-objects locked by corresponding optical traps. Angular momentum of a field can be specified at each spatial point. One may also consider angular momentum averaged over some spatial area. As is known [86, 88], angular momentum may be divided into a spin momentum associated with elliptical polarization and an orbital one produced by specific beam structure. However, density of the angular momentum, j_z (at least of its orbital part), depends upon the location of the axis $\mathbf{r} = 0$ (i.e., "purchase") with regard to which the parameter j_z is calculated. As a result, some ambiguity appears. At the same time, another physical value closely associated with the angular momentum, viz. the space distribution of characteristics of the time-averaged Poynting vector (more accurately, its transverse component), represents a univocal function of coordinates of each field point.

Distribution of parameters of the time-averaged Poynting vector for Laguerre-Gaussian beams is considered in Refs. [89, 90]. However, the behavior of the time-averaged Poynting vector was analyzed only for homogeneously polarized fields and "symmetrical" beams [86, 89].

At the same time, analyzed fields may be more complicated, in part, when their polarization is inhomogeneous. Distribution of the transverse component of the Poynting vector for such fields may be characterized by a set of certain points, i.e., by the net of Poynting singularities [7]. The importance of these points comes from the fact that the characteristics of this singular net, such as the Poynting field skeleton, determine qualitative behavior of the Poynting vector at each of the field points [37]. For instance, vortex Poynting singularities [91] are the points around which circulation of the transverse component of the Poynting vector takes place. In other words, one deals here with the points that are the intersections of the observation plane and the axis of the angular momentum. Thus, spatial distributions of characteristics of the time-averaged Poynting vector components would contain important information on the field, which is concerned with the energy flows [21, 34–36].

Nevertheless, one can state that the technique for experimental analysis of the time-averaged Poynting vector components and their singularities has been developed up to now. Here we demonstrate that the components of the time-averaged Poynting vector can be experimentally analyzed by using conventional optical methods.

It has been shown [37, 87] that the instantaneous components of the Poynting vector may be written as

$$
\begin{cases}
P_x \approx \frac{c}{4\pi k}\{E_x T_2\ E_y T_1\}; \\
P_y \approx \frac{c}{4\pi k}\{E_y T_2 + E_x T_1\}; \\
P_z \approx \frac{c}{4\pi}\{E_x^2 + E_y^2\},
\end{cases}
\tag{2.14}
$$

where

$$
\begin{cases}
T_1 = E_x \Phi_x^y\ E_y \Phi_y^x + \frac{A_x^y}{A_x} E_{x,\frac{\pi}{2}}\ \frac{A_y^x}{A_y} E_{y,\frac{\pi}{2}}; \\
T_2 = E_x \Phi_x^x + E_y \Phi_y^y + \frac{A_x^x}{A_x} E_{x,\frac{\pi}{2}} + \frac{A_y^y}{A_y} E_{y,\frac{\pi}{2}},
\end{cases}
\tag{2.15}
$$

$$
\begin{cases}
E_i = A_i \cos(\omega t + \Phi_i\ kz); \\
E_{i,\frac{\pi}{2}} = A_i \sin(\omega t + \Phi_i\ kz),
\end{cases}
\tag{2.16}
$$

$i = x, y$, A_i, Φ_i denote, respectively, amplitudes and phases of the corresponding field components, and A_i^l, Φ_i^l are their partial derivatives, and $k = \omega/c$ represents the wave number. Here, the axis z coincides with the preferential direction of the wave propagation.

One can show after some algebraic transformations that the averaged components of the Poynting vector are as follows:

$$
\begin{cases}
\bar{P}_x \approx \frac{c}{8\pi k}\{[A_x^2 \Phi_x^x + A_y^2 \Phi_y^x]\ A_x A_y(\Phi_x^y\ \Phi_y^y)\cos\Delta\ (A_x A_y^y + A_y A_x^y)\sin\Delta]\}; \\
\bar{P}_y \approx \frac{c}{8\pi k}\{[A_x^2 \Phi_x^y + A_y^2 \Phi_y^y] + A_x A_y(\Phi_x^x\ \Phi_y^x)\cos\Delta + (A_x A_y^x + A_y A_x^x)\sin\Delta]\}; \\
\bar{P}_z \approx \frac{c}{8\pi}\{A_x^2 + A_y^2\}.
\end{cases}
\tag{2.17}
$$

The second and the third terms in the brackets appearing in the first two rows of (2.17) may be rewritten as follows:

$$
A_x A_y(\Phi_x^i\ \Phi_y^i)\cos\Delta + (A_x A_y^i + A_y A_x^i)\sin\Delta == \frac{\partial}{\partial i}(A_x A_y \sin\Delta),
\tag{2.18}
$$

where $i = x, y$. Then, the system of (2.17) is transformed to the form

$$
\begin{cases}
\bar{P}_x \approx \frac{c}{8\pi k}\{[A_x^2 \Phi_x^x + A_y^2 \Phi_y^x]\ \frac{\partial}{\partial y}(A_x A_y \sin\Delta)\}; \\
\bar{P}_y \approx \frac{c}{8\pi k}\{[A_x^2 \Phi_x^y + A_y^2 \Phi_y^y] + \frac{\partial}{\partial x}(A_x A_y \sin\Delta)\}; \\
\bar{P}_z \approx \frac{c}{8\pi}\{A_x^2 + A_y^2\}.
\end{cases}
\tag{2.19}
$$

It follows from (2.19) that one of the possible methods of vector Poynting component measurement is complete analysis of orthogonal components:

- Measurement of the components' intensities (for defining the components' amplitudes and their corresponding derivatives).
- Phasometry (interferometry) of the components (for the defining components' phases and their corresponding derivatives).

However, the phase difference between orthogonal components Δ is included in relations (2.19). Note that:

1. As is known [14], measurement of the "absolute" phase in optics is problematic. Only the phase difference between object wave and reference one is fixed. In other words, the phase is measured within the constant component.
2. The experimental arrangement for simultaneous measuring of component phase with the same constant components is practically impossible.

Consequently, the phase difference Δ cannot be measured with enough accuracy by the components' analysis. Such value may be easily measured by the Stokes polarimetry [83]. Stokes parameters for the monochromatic wave have the form [14]:

$$
\begin{aligned}
s_0 &= A_x^2 + A_y^2; \\
s_1 &= A_x^2\, A_y^2; \\
s_2 &= 2A_x A_y \cos \Delta; \\
s_3 &= 2A_x A_y \sin \Delta.
\end{aligned}
\tag{2.20}
$$

Value Δ may be determined as:

$$
\Delta = \tan^{-1} \frac{s_3}{s_2},
\tag{2.21}
$$

and the (2.19) may be used for the analysis of Poynting vector components. If one takes into account (2.20), the relations (2.19) are transformed to the form:

$$
\begin{cases}
\bar{P}_x \approx \frac{c}{16\pi k} \left\{ \left[(s_0 + s_1)\Phi_x^x + (s_0\, s_1)\Phi_y^x \right] \frac{\partial s_3}{\partial y} \right\}; \\
\bar{P}_y \approx \frac{c}{16\pi k} \left\{ \left[(s_0 + s_1)\Phi_x^y + (s_0\, s_1)\Phi_y^y \right] + \frac{\partial s_3}{\partial x} \right\}; \\
\bar{P}_z \approx \frac{c}{8\pi} s_0.
\end{cases}
\tag{2.22}
$$

Thus, the Poynting vector's components can be defined by the Stokes parameters and derivatives of the components phases. Note that phasometry of only one component (let us use the y-component for certainty) is necessary, because a phase of the orthogonal component is determined as $\Phi_x = \Delta + \Phi_y$. Obviously, in the practical sense, the phasometry of the smooth component (without any singularity in the analyzed area) is preferable.

As is known (see, for example, Ref. [92], which is the closest to the topic of our study), three kinds of measurement are necessary for defining of phase of scalar field at each field point:

1. Intensity of component field $I_i = A_i^2$.
2. Intensity of referent wave $I_r = A_r^2$.
3. Intensity of total field I_s.

The component phase (within the constant component) may be derived from the relation:

$$\Phi_i = \arccos \frac{I_s - (I_i + I_r)}{2\sqrt{I_i I_s}}. \tag{2.23}$$

Naturally, the phase derivatives Φ_i^k, included in (2.19) and (2.22), are independent of the constant component.

Thus, jointly applying the conventional interferometry and Stokes-polarimetry allow us to unambiguously determine the characteristics of the Poynting vector components at each point of an optical field.

Let us now represent the results of measuring the Poynting vector's components of the homogeneously polarized Gaussian beam. As is known [86], such a beam possesses the spin impulse momentum that reaches its maximal magnitude in the case of circular polarization of a beam. It is natural to expect that the vortex-like Poynting vector's singularity might be observed at the center of a beam, while at some distance from the center the transverse component possesses the corresponding circulation.

What is of special interest, the problem of measuring the Poynting vector's components of a Gaussian beam, is considerably simplified owing to constant phases of the orthogonal components. For that, the phase derivatives of the Poynting vector of the orthogonal components vanish and one obtains:

$$\begin{cases} \bar{P}_x \approx \frac{c}{16\pi k} \frac{\partial s_3}{\partial y}\}; \\ \bar{P}_y \approx \frac{c}{16\pi k} \frac{\partial s_3}{\partial x}\}; \\ \bar{P}_z \approx \frac{c}{8\pi} s_0. \end{cases} \tag{2.24}$$

Thus, measuring magnitudes of the Poynting vector components is reduced to determining *two* Stokes parameters, viz. s_0 and $I_r = A_r^2$. Moreover, to analyze the transverse component, one must determine the third Stokes parameter alone. Proper measurements can be carried out in the arrangement shown in Fig. 2.22.

A beam from a He–Ne laser *1* is transformed to a circular state (polarization pair *2* to *3*) and is expanded by the collimator *4* to *6*. Then, a circularly polarized Gaussian beam enters the Stokes polarimeter (elements *7* and *8*). Relevant intensity distributions needed for determining the Stokes parameters are registered by a CCD-camera.

The beam intensity distribution at the output of a collimator is shown in Fig. 2.23a. Figure 2.23b illustrates distribution of the transverse component of the Poynting vector. Altering modulus is shown by levels of gray and length of arrows. Azimuths of the component correspond to arrow orientations.

One can see from Fig. 2.23b that, really, the transverse component of the Poynting vector circulates around the beam center, where its magnitude vanishes while its azimuth is undetermined.

Fig. 2.22 *1* – He–Ne laser,
2 – polarizer, *3* $-\lambda/4$-plate,
4 and *6* – beam expander with
a pinhole 5, 7, and 8 – Stokes
polarimeter, 9 – CCD-camera
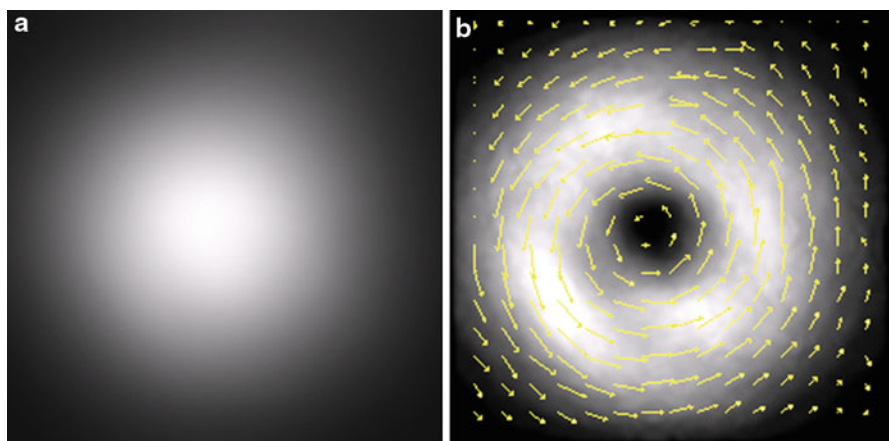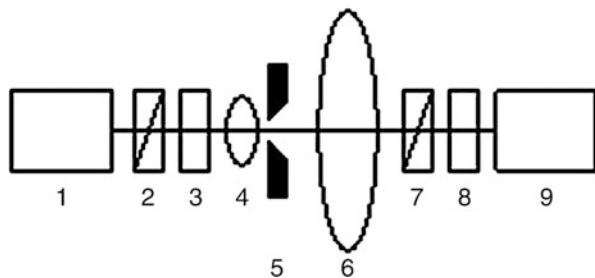
Fig. 2.23 (**a**) intensity distribution of a beam behind of collimator, (**b**) distribution of the transverse component of the Poynting vector

2.5   Conclusions

Two new approaches to metrology of partially coherent and partially polarized light fields are derived from a singular optics concept. The first approach, discussed in Sect. 2.2, concerns exploring the spatial modulated time-averaged Poynting vector in completely and partially coherent non-paraxial light fields for control the motion of nano- and microparticles in optical currents. The second approach, detailed in Sect. 2.3, reveals the interconnection between polarization singularities inherent in completely polarized and partially polarized optical beams for the general case of partial mutual coherence of orthogonally polarized components. Section 2.4 explains the feasibility of experimental analysis of the Poynting vector components by combining interferometric and polarimetric techniques. The represented approaches show the fruitfulness of employing the concepts of singular optics in formation and investigation of unconventional polarization distributions that can be used in problems of optical correlation diagnostics and optical telecommunications.

References

1. E. Wolf, Unified theory of coherence and polarization of random electromagnetic beams. Phys. Lett. A**312**, 263–267 (2003)
2. J. Ellis, A. Dogariu, Complex degree of mutual polarization. Opt. Lett. **29**, 536–538 (2004)
3. E. Wolf, L. Mandel, Coherence properties of optical fields. Rev. Mod. Phys. **37**, 231–287 (1965)
4. L. Mandel, Anticoherence. Pure Appl. Opt. **7**, 927–932 (1998)
5. R. Collier, L. Burckhardt, L. Lin, *Optical Holography* (Academic, New York, 1971)
6. J.W. Goodman, *Statistical Optics* (Wiley-Interscience, New York, 1985)
7. R.J. Glauber, in *Lectures in Theoretical Physics*, ed. by W.E. Brittin, J. Downs, vol. 4 (Interscience, New York, 1962)
8. R.J. Glauber, The quantum theory of optical coherence. Phys. Rev. **6**, 2529–2539 (1963)
9. R.J. Glauber, Optical coherence and photon statistics, in *Quantum Optics and Electronics*, ed. by C. deWitt, A. Blandin, C. Cohen-Tannoudji (Gordon & Breach, New York, 1965), pp. 65–185
10. P.A.M. Dirac, *Principles of Quantum Mechanics*, 4th edn. (Oxford University Press, Oxford, 1958)
11. E. Wolf, Non-cosmological redshifts of spectral lines. Nature **326**, 363–365 (1987)
12. E. Wolf, D.F.V. James, Correlation-induces spectral changes. Rep. Progr. Phys. **59**, 771–818 (1996)
13. V.K. Polyanskii, L.V. Kovalskii, On fine structure of the scattered radiation field. Opt. Spectrosc. **35**, 345–350 (1973)
14. M. Born, E. Wolf, *Principles of Optics*, 7th edn. (Cambridge University Press, Cambridge, 1999) (expanded)
15. J.F. Nye, *Natural Focusing and Fine Structure of Light: Caustics and Wave Dislocations* (Institute of Physics Publishing, Bristol/Philadelphia, 1999)
16. I. Freund, Coherency matrix description of optical polarization singularities. J. Opt. A: Pure Appl. Opt. **6**, 229–234 (2004)
17. A.D. Dolgov, A.G. Doroshkevich, D.I. Novikov, I.D. Novikov, Classification of singular points in the polarization of the cosmic microwave background and eigenvectors of the Stokes matrix. J. Exp. Theor. Phys. Lett. **69**, 427–433 (1999)
18. S. Hawking, *A Brief History of Time* (Bantam Press, London, 1988). ISBN 055305340X
19. H.C. van de Hulst, *Light Scattering by Small Particles* (Wiley, New York, 1957)
20. C.F. Bohren, D.R. Huffman, *Absorbing and Scattering of Light by Small Particles* (Wiley, New York, 1983)
21. M.V. Berry, Optical currents. J. Opt. A: Pure Appl. Opt. **11**, 094001 (2009)
22. H. He, M.E.J. Friese, N.R. Heckenberg, H. Rubinsztein-Dunlop, Direct observation of transfer of angular momentum to absorbtive particles from a laser beam with a phase singularity. Phys. Rev. Lett. **75**, 826–829 (1995)
23. N.B. Simpson, K. Dholakia, L. Allen, M.J. Padgett, Mechanical equivalence of spin and orbital angular momentum of light: an optical spanner. Opt. Lett. **22**, 52–54 (1997)
24. A.T. O'Neil, I. MacVicar, L. Allen, M.J. Padgett, Intrinsic and extrinsic nature of the orbital angular momentum of a light beam. Phys. Rev. Lett. **88**, 053601 (2002)
25. V. Garces-Chavez, D. McGloin, M.D. Summers, A. Fernandez-Nieves, G.C. Spalding, G. Cristobal, K. Dholakia, The reconstruction of optical angular momentum after distortion in amplitude, phase and polarization. J. Opt. A: Pure Appl. Opt. **6**, S235–238 (2004)
26. S.N. Khonina, V.V. Kotlyar, R.V. Skidanov, V.A. Soifer, K. Jefimovs, J. Simonen, J. Turunen, Rotation of microparticles with Bessel beams generated by diffractive elements. J. Mod. Opt. **51**, 2167–2184 (2004)

27. A. Bekshaev, M. Soskin, M. Vasnetsov, *Paraxial Light Beams with Angular Momentum* (Nova, New York, 2008)
28. M.S. Soskin, M.V. Vasnetsov, Singular optics, in *Progress in Optics*, ed. by E. Wolf, vol. 42 (Elsevier, Amsterdam, 2001), pp. 219–276
29. G. Gbur, T.D. Visser, The Structure of partially coherent fields, in *Progress in Optics*, ed. by E. Wolf, vol. 55 (Elsevier, Amsterdam, 2010), pp. 285–341
30. A. Friberg, C. Gao, B. Eppich, H. Weber, Generation of partially coherent fields with twist. Proc. SPIE **3110**, 317–328 (1997)
31. J. Tervo, T. Setala, A.T. Friberg, Degree of coherence of electromagnetic fields. Opt. Express **11**, 1137–1142 (2003)
32. T. Setala, J. Tervo, A.T. Friberg, Complete electromagnetic coherence in the space-frequency domain. Opt. Lett. **29**, 328330 (2004)
33. J. Tervo, T. Setala, A.T. Friberg, Theory of partially coherent electromagnetic fields in the space-frequency domain. J. Opt. Soc. Am. A**21**, 2205–2215 (2004)
34. A.Ya. Bekshaev, "Spin" and "orbital" flows in a circularly polarized paraxial beam: orbital rotation without orbital angular momentum. ArXiv: 0908.252v1 [physics.optics]
35. A.Y. Bekshaev, Oblique section of a paraxial light beam: criteria for azimuthal energy flow and orbital angular momentum. J. Opt. A.: Pure Appl. Opt. **11**, 094003 (2009)
36. A.Y. Bekshaev, K.Y. Bliokh, M.S. Soskin, Internal flows and energy circulation in light beams. J. Opt. **13**, 053001 (2011). doi:10.1088/2040-8978/13/5/053001 (32pp)
37. O.V. Angelsky (ed.), *Optical Correlation Techniques and Applications – TA 1630, A6* (SPIE Press, Bellingham, 2007)
38. O.V. Angelsky, P.V. Polyanskii, P.P. Maksimyak, Speckles and phase singularities in polychromatic fields (chapter 3), in *New Directions in Holography and Speckle*, ed. by H.J. Caulfield, C.S. Vikram (Kluwer Academic Publishers, Boston, 2008), pp. 37–53
39. O.V. Angelsky, N.N. Dominikov, P.P. Maksimyak, T. Tudor, Experimental revealing of polarization waves. Appl. Opt. **38**, 3112–3117 (1999)
40. T. Tudor, Polarization waves as observable phenomena. J. Opt. Soc. Am. A**14**, 2013–2020 (1997)
41. M.V. Berry, K.T. Donald, Exact and geometrical optics energy trajectories in twisted beams. J. Opt. A: Pure Appl. Opt. **10**, 035005 (2008)
42. M.V. Berry, M.R. Dennis, Polarization singularities in isotropic random vector waves. Proc. R. Soc. Lond. **A456**, 2059–2079 (2001)
43. O.V. Angelsky, S.G. Hanson, C.Y. Zenkova, M.P. Gorsky, N.V. Gorodyns'ka, On polarization metrology (estimation) of the degree of coherence of optical waves. Opt. Express **17**, 15623–15634 (2009)
44. C.Y. Zenkova, M.P. Gorsky, P.P. Maksimyak, A.P. Maksimyak, Optical currents in vector fields. Appl. Opt. **50**, 1105–1112 (2010)
45. M. Mujait, A. Dogariu, E. Wolf, A law of interference of electromagnetic beams of any state of coherence and polarization and the Fresnel-Arago interference laws. J. Opt. Soc. Am. A**21**, 2414–2417 (2004)
46. J. Ellis, A. Dogariu, S. Ponomarenko, E. Wolf, Degree of polarization of statistically stationary electromagnetic fields. Opt. Commun. **248**, 333–337 (2005)
47. R. Khrobatin, I. Mokhun, Shift application point of angular momentum in the area of elementary polarization singularity. J. Opt. A: Pure Appl. Opt. **10**, 064015 (2008)
48. R. Khrobatin, I. Mokhun, J. Victorovskaya, Potentiality of experimental analysis for characteristics of the Poynting vector components. Ukr. J. Phys. Opt. **9**, 182–186 (2008)
49. A.Y. Bekshaev, M.S. Soskin, Transverse energy flows in vectorial fields of paraxial light beams. Proc. SPIE **6729**, 67290G (2007)
50. O.V. Angelsky, S.B. Yermolenko, C.Y. Zenkova, A.O. Agelskaya, Polarization manifestations of correlation (intrinsic coherence) of optical fields. Appl. Opt. **47**, 5492–5499 (2008)
51. O.V. Angelsky, C.Y. Zenkova, M.P. Gorsky, N.V. Gorodyns'ka, On the feasibility for estimating the degree of coherence of waves at near field. Appl. Opt. **48**, 2784–2788 (2009)

52. O.V. Angelsky, M.P. Gorsky, P.P. Maksimyak, A.P. Maksimyak, S.G. Hanson, C.Y. Zenkova, Investigation of optical currents in coherent and partially coherent vector fields. Opt. Express **19**, 660–672 (2011)
53. J. Turkevich, P.C. Stevenson, J. Hiller, A study of the nucleation and growth processes in the synthesis of colloidal gold. J. Discuss. Faraday Soc. **11**, 55–75 (1951)
54. O.V. Angelsky, S.G. Hanson, P.P. Maksimyak, A.P. Maksimyak, A.L. Negrych, Experimental demonstration of singular-optical colouring of regularly scattered white light. J. Eur. Opt. Soc. Rap. Public. **3**, 08029 (2008)
55. O.V. Angelsky, S.G. Hanson, A.P. Maksimyak, P.P. Maksimyak, Feasibilities of interferometric and chromascopic techniques in study of phase singularities. Appl. Opt. **44**, 5091–5100 (2005)
56. O.V. Angelsky, A.P. Maksimyak, P.P. Maksimyak, S.G. Hanson, Interference diagnostics of white-light vortices. Opt. Express **13**, 8179–8183 (2005)
57. O.V. Angelsky, S.G. Hanson, A.P. Maksimyak, P.P. Maksimyak, On the feasibility for determining the amplitude zeroes in polychromatic fields. Opt. Express **13**, 4396–4405 (2005)
58. O.V. Angelsky, S.G. Hanson, A.P. Maksimyak, P.P. Maksimyak, Optical correlation diagnostics of rough surfaces with large surface inhomogeneities. Opt. Express **14**, 7299–7311 (2006)
59. O.V. Angelsky, P.V. Polyanskii, S.G. Hanson, Singular-optical coloring of regularly scattered white light. Opt. Express **14**, 7579–7586 (2006)
60. O.V. Angelsky, H.V. Bogatyryova, P.V. Polyanskii, Interference coloring of regularly scattered white light. Opt. Appl. **38**, 431–444 (2008)
61. C.V. Felde, A.A. Chernyshov, H.V. Bogatyryova, P.V. Polyanskii, M.S. Soskin, Polarization singularities in partially coherent combined beams. J. Exp. Theor. Phys. Lett. **88**, 418–422 (2008)
62. A.A. Chernyshov, K.V. Felde, G.V. Bogatyreva, P.V. Polyanskii, M.S. Soskin, Vector singularities of superposition of mutually incoherent orthogonaly polarized beams. Opt. Spectrosc. **107**, 645–650 (2009)
63. A.A. Chernyshov, C.V. Felde, H.V. Bogatyryova, P.V. Polyanskii, M.S. Soskin, Vector singularities of the combined beams assembled from mutually incoherent orthogonally polarized components. J. Opt. A: Pure Appl. Opt. **11**, 094010 (2009)
64. P.V. Polyanskii, C.V. Felde, A.A. Chernyshov, Polarization degree singularities. Proc. SPIE **7388**, 7388OA (2010)
65. M.S. Soskin, P.V. Polyanskii, New polarization singularities of partially coherent light beams. Proc. SPIE **7613**, 7613OG (2010)
66. P.V. Polyanskii, G.V. Bogatiryova, EDW: edge diffraction wave, edge dislocation wave, or whether tertio est datur? Proc. SPIE **4607**, 109–124 (2001)
67. G.V. Bogatyryova, C.V. Felde, P.V. Polyanskii, S.A. Ponomarenko, M.S. Soskin, E. Wolf, Partially coherent vortex beams with a separable phase. Opt. Lett. **28**, 878–880 (2003)
68. M.S. Soskin, P.V. Polyanskii, O.O. Arkhelyuk, Computer-synthesized hologram-based rainbow optical vortices. New J. Phys. **6**, 196 (2004)
69. M.V. Berry, M.R. Dennis, Quantum cores of optical phase singularities. J. Opt. A.: Pure Appl. Opt. **6**, S178 (2004)
70. I. Freund, A.I. Mokhun, M.S. Soskin, O.V. Angelsky, I.I. Mokhun, Stokes singularity relations. Opt. Lett. **27**, 545–547 (2002)
71. O.V. Angelsky, I.I. Mokhun, A.I. Mokhun, M.S. Soskin, Interferometric methods in diagnostics of polarization singularities. Phys. Rev. E **65**, 036602(5) (2002)
72. O.V. Angelsky, A.I. Mokhun, I.I. Mokhun, M.S. Soskin, The relationship between topological characteristics of component vortices and polarization singularities. Opt. Commun. **207**, 57–65 (2002)
73. S.A. Ponomarenko, A class of partially coherent vortex beams carrying optical vortices. J. Opt. Soc. Am. A **18**, 150–156 (2001)

74. G. Gbur, T.D. Visser, Coherence vortices in partially coherent beams. Opt. Commun. **222**, 117–125 (2003)
75. H.F. Schouten, G. Gbur, T.D. Visser, E. Wolf, Phase singularities of the coherence functions in Young's interference pattern. Opt. Lett. **28**, 968–970 (2003)
76. G.A. Swartzlander Jr., J. Schmit, Temporal correlation vortices and topological dispersion. Phys. Rev. Lett. **93**, 093901 (2004)
77. G. Gbur, T.D. Visser, E. Wolf, Anomalous behavior of spectra near phase singularities of focused waves. Phys. Rev. Lett. **88**, 013901 (2002)
78. G. Popescu, A. Dogariu, Spectral anomalies at wave-front dislocations. Phys. Rev. Lett. **88**, 183902 (2002)
79. M.V. Berry, Colored phase singularities. New J. Phys. **4**, 66 (2002)
80. M.V. Berry, Exploring the colors of dark light. New J. Phys. **4**, 74 (2002)
81. A.V. Volyar, T.A. Fadeyeva, Generation of singular beams in uniaxial crystals. Opt. Spectrosc. **94**, 260–270 (2003)
82. Y.A. Egorov, T.A. Fadeyeva, A.V. Volyar, The fine structure of singular beams in crystals: colors and polarization. J. Opt. A.: Pure Appl. Opt. **6**, 217 (2004)
83. R.M.A. Azzam, N.M. Bashara, *Ellipsometry and Polarized Light* (North-Holland, Amsterdam, 1977)
84. W.A. Shurcliff, *Polarized Light: Production and Use* (Harvard University Press, Cambridge, Massachusetts, 1962)
85. M.J. Lang, S.M. Block, Resource letter: LBOT-1: laser-based optical tweezers. Am. J. Phys. **71**, 201–205 (2003)
86. L. Allen, M.J. Padgett, M. Babiker, The orbital angular momentum of light, in *Progress in Optics*, ed. by E. Wolf, vol. 39 (Elsevier, Amsterdam, 1999), pp. 219–236
87. I. Mokhun, R. Brandel, J. Viktorovskaya, Angular momentum of electromagnetic field in areas of polarization singularities. Ukr. J. Phys. Opt. **7**, 63–73 (2006)
88. M.V. Berry, Paraxial beams of spinning light. Proc. SPIE **3487**, 6–11 (1998)
89. L. Allen, M.J. Padgett, The Poynting vector in Laguerre-Gaussian beams and the interpretation of their angular momentum density. Opt. Commun. **18**, 67–71 (2000)
90. M.V. Berry, Phase vortex spirals. J. Phys. A**38**, 745–751 (2005)
91. I. Mokhun, R. Khrobatin, A. Mokhun, J. Viktorovskaya, The behavior of the Poynting vector in the area of elementary polarization singularities. Opt. Appl. **37**, 261–277 (2007)
92. N. Shvartsman, I. Freund, Speckle spots ride phase saddles side saddle. Opt. Commun. **117**, 228–234 (1995)

Diagnostics of Structure and Physiological State of Birefringent Biological Tissues: Statistical, Correlation and Topological Approaches

3

Yurii A. Ushenko, T. M. Boychuk, V. T. Bachynsky, and O. P. Mincer

Contents

Abstract

Optical techniques for investigation of the structure of biological tissues are classified. Both polarization and correlation characteristics for real object fields

Y.A. Ushenko (✉)
Department of Correlation Optics, Chernivtsi National University, Chernivtsi, Ukraine
e-mail: ushenko@itf.cv.ukrtel.net, yuriyu@gmail.com

T.M. Boychuk
Department of Cytology and Embryology, Bukovinian State Medical University, Histology, Chernivtsi, Ukraine
e-mail: rector@bsmu.edu.ua

V.T. Bachynsky
Department of Pathomorphology and Forensic Medicine, Bukovinian State Medical University, Chernivtsi, Ukraine
e-mail: mf3@bsmu.edu.ua

O.P. Mincer
Department of Medical Informatics, National Medical Academy named after P.L. Shupyka, Kiev, Ukraine
e-mail: spie@ukr.net

of tissues, including their images, are analyzed. The development of novel approaches to the analysis of tissue optical images and the search for the novel polarization, interference, and correlation diagnostics of BT structure associated with the tissue physiological state is the main goal of this chapter.

3.1   Introduction

3.1.1   Polarimetric Approach

Optical techniques for investigation of the structure of biological tissues (BTs) can be classified into three groups: (1) spectrophotometric techniques [1] based on the analysis of spatial or temporal changes of intensity of a field scattered by BTs; (2) polarization techniques based on the use of the coherency matrix for a complex amplitude [2, 3] and the analysis of the degree of polarization as the factor of correlation of the orthogonal complex components of electromagnetic oscillations at the specified point of scattered field; and (3) correlation techniques based on the analysis of correlations of the parallel polarization components at different points of the object field [4–6].

Both polarization and correlation characteristics are typically changed for real object fields of BTs, including their images [5]. One of the most promising techniques for obtaining such images is the optical coherence tomography and its new branch – polarization-sensitive optical coherence tomography [7]. This diagnostic approach is based on measuring of the coordinate distributions of the Stokes parameters at the BT's images providing important data both on the BT microstructure and on magnitude and coordinate distributions of the parameters of optical anisotropy of the architectonic nets formed by birefringent protein fibrils.

Further progress of the polarization-sensitive optical coherence tomography is connected with the development of new techniques for analysis and processing of inhomogeneously polarized BT images. For this reason, the development of novel approaches to the analysis of laser images of BTs and the search for new techniques for polarization, interference, and correlation diagnostics of BT's structure for determining the efficient criteria of estimation of birefringence associated with the BT's physiological state is the topic of this discussion.

Laser radiation, similarly to natural light, can be absorbed and scattered by a BT, and the each of these processes results in filling of the field with information on micro- and macrostructure of the studied medium and its components [8]. The spectrophotometric techniques for BT diagnostics based on the analysis of the spatial and temporal changes of intensity of the field scattered by such optically inhomogeneous objects are the most widespread and approbated nowadays. At the same time, other diagnostic techniques based on the fundamental concepts, such as "polarization" and "coherence," are also intensively developed.

Historically, the spatial changes of optical fields have been characterized in terms determining the coherent properties of fields. The concept of "measure of

coherence" between two light oscillations is defined as their ability to form an interference pattern and is associated with the visibility of interference fringes [9]. This value is the measure of the sum of correlations between parallel components of electrical fields at two points of space. Another type of correlation characteristics of scattered laser fields is the degree of polarization defined as the magnitude of the maximal correlation between the orthogonally polarized components of the electrical field at one point [10]. Polarization properties of light are studied experimentally by measuring the intensity of radiation passing various optically active elements.

Techniques based on the use of the coherency matrix and the degree of polarization are referred to as polarization techniques; let us consider them in more detail. Much development of the vector approach to investigations of the morphological structure and physiological state of various BTs [11, 12] calls for the development of model notions of optically anisotropic and self-similar structure of BTs.

Thus, the hierarchical self-similar (tropocollagen, microfibril, subfibril, fibril, fascia, etc.) structure of typical connective tissue, tendons, has been analyzed in [13]. The filiform structural elements are discrete, being of the scale repeated within the large interval of "optical sizes," from 1 to 10^3 μm. For that, the optical characteristics of such a structure of various BTs correspond to "frozen" optically uniaxial liquid crystals [13].

A similar approach to the description of the BT's morphological structure has been used in Ref. [14], where a BT is considered at the two-component amorphous-crystalline structure. The amorphous component of a BT (fat, lipids, non-structured proteins) is isotropic in polarization (optically non-active). The crystalline component of a BT is formed by oriented birefringent protein fibrils (collagen proteins, myosin, elastin, etc.). The properties of an isolated fibril are modeled by an optically uniaxial crystal whose axis is oriented along the direction of packing at the BT plane, and the birefringence index depends on the fibril matter. The architectonic net formed by differently oriented birefringent bundles is the higher level of the BT organization.

Within the framework of this model one can explain the mechanisms causing polarization inhomogeneity of the fields of various BTs, such as osseous and muscular tissue and tissues of the female reproductive system [14, 15]. The interconnections between the magnitudes of the azimuth of polarization and ellipticity of light oscillations, on the one hand, and the direction (angle) of packing of fibrils and the parameters characterizing birefringence of the corresponding matter, on the other hand, have been also found [16]. This enables improvement of the technique of polarization visualization of the architectonic net of BTs of various morphological types and the use of statistical analysis of the coordinate distributions of the polarization parameters of the scattered fields [17].

The results of the investigation of interconnections between the set of the statistical moments of the first to the fourth orders characterizing microgeometry of a surface and orientational and phase structure of birefringent architectonics of human BT, on the one hand, and the set of the corresponding statistical moments of

the coordinate distributions of the magnitudes of the azimuth of polarization and ellipticity (polarization maps) of the images of such objects, on the other hand, have been represented in Refs. [18–20]. It has been found that growing magnitudes of kurtosis and skewness of the azimuth of polarization and ellipticity result from growing dispersion of orientation of the optical axes of birefringent fibrils of BTs. Decreasing magnitudes of kurtosis and skewness correspond to increasing dispersion of phase shifts caused by biological crystals of the architectonic nets [20].

Further development of laser polarimetry includes the development of new techniques for processing of two-dimensional tensors of polarization parameters characterizing the nets of various biological crystals of human tissues [17–22].

So, in part, statistical analysis of the coordinate distributions of the Stokes parameters provides new information on microstructure (magnitudes and coordinate distributions of the parameters of optical anisotropy of architectonic nets formed by collagen and myosin) of physiologically normal and pathologically changed BTs [18–22].

As a whole, rapid development of techniques for diagnostic use of coherent laser radiation is reflected in optical coherent tomography as the most convenient and elaborated instrument for noninvasive study of BT structure [23]. The use of a new informative parameter, viz. the polarization of laser beam carrying out contrasting of the BT images, opens up new directions in optical coherent tomography, often referred to as the polarization-sensitive coherence tomography [21–23].

Note, the peculiarity of "laser polarimetry of distributions of azimuth and ellipticity" consists, in point-by-point analysis, of the polarization parameters of the object field and searching for their interconnection with the orientation and anisotropic parameters of the BT architectonics. In this situation, information on the peculiarities (statistical and fractal) of two-dimensional distributions of the polarization parameters of the field, on the one hand, and the orientation and phase characteristics of the object, on the other hand, remains undetermined.

In this connection, development of laser polarimetry requires further elaboration of the techniques for non-destructive macrodiagnostics of the BT geometrical-optical structure through improving modern techniques of BT polarization-interference mapping and development of new techniques for reconstruction of BT architectonics. In addition, the development of new approaches for both statistical and local topological (singular) analysis of two-dimensional polarization images of BTs is urgently needed.

3.1.2 Correlation Approach

It is known [24, 25] that polarization properties of light at some spatial point are comprehensively described by the coherency matrix. This formalism is also adequate for characterization of a beam as a whole, if the characteristics of scattered radiation are unchanged in space, i.e., if the beam is homogeneous. However, it is not sufficient for the description of spatially inhomogeneous polarization scattered

optical fields. Consideration of not only coordinate distributions of the polarization parameters of a field but also the search for interconnections between the state of polarization and the degree of coherence at different points of a field must be carried out in this case.

The initial attempt to describe spatially inhomogeneous polarization object fields as the direct generalization of the two-point coherency matrix was performed by Gori [26]. The author shows that some visibility of interference fringes results from superposition of radiation from two point sources whose polarization characteristics are formed by the set of polarizers and phase plates corresponding to each matrix element.

The unified theory of coherence and polarization provides a description of changes of the state of polarization of freely propagating light and was developed by Wolf in 2003 [27].

Within the framework of the approach based on the generalized coherency matrix, a new parameter has been proposed [28, 29], namely, the degree of mutual coherence characterizing the correlation similarity of the electric vector at two points and experimentally determined by measuring the visibility of the corresponding interference distributions.

This approach has been further developed by Ellis and Dogariu [30]. They introduced the complex degree of mutual polarization (CDMP), determining the correlation between the points of a field with different states of polarization and different intensities. Statistics of intensity fluctuations at the field resulting from scattering of partially coherent beams are analyzed in Ref. [31]. The matrix technique proposed by Gori [32] generalizes the description of inhomogeneously polarized coherent fields on the basis of the CDMP. It extends the description of light-scattering phenomena to more general cases, when partially polarized light is not obviously completely spatially coherent.

Proceeding from the unified theory of coherence and polarization of random electromagnetic waves, it has been proved theoretically and experimentally that partially polarized light can be described using the correlation of unpolarized components [33]. The technique for determination of the polarization parameters of light from measured intensity fluctuation contrast has been proposed in [34]. This technique presumes parallel measurements of the degree of polarization and the second Stokes parameter directly connected with the azimuth of polarization and ellipticity. Matrix analysis of correlation properties of scattered coherent radiation has been extended on the vector (inhomogeneously polarized) fields. The notion of a 3×3 correlation matrix has been introduced [35, 36] for a completely polarized electromagnetic field that is stationary in the statistical sense.

Another prospective direction is connected to solving the problem of direct measurement of the CDMP for problems of biomedical optics, namely, processing of coherent inhomogeneously polarized images of BTs obtained by the optical coherence tomography technique. It has been shown [37] that the CDMP of a coherent image of a BT is the parameter sensitive to orientation and phase changes of the BT's architectonics. Experimental studies of 2D distributions of the degree of mutual polarization of the BT's laser images for examples of muscular

tissue, skin tissue, and osseous shin have proved the interconnection between coordinate distribution of the CDMP of laser images and the geometrical-optical structure of birefringent architectonic nets of physiologically normal and dystrophically changed BTs.

Accounting for the potential diagnostic importance and steadiness of the CDMP, it is necessary to continue searching for the peculiarities of correlation structure of the coordinate distributions of this parameter for various types of BTs. Special attention must be paid to the development of unified criteria for differentiation of morphological and physiological structure of BTs based on the CDMP. In addition, the combination of the formalism of coordinate distributions of the Mueller matrix elements and the CDMP is also a prospective direction that may reveal the new diagnostic criteria of physiological state of BTs.

3.1.3 Topological or Singular Optical Approach

At inhomogeneous vector electromagnetic fields, lines or surfaces exist at which one of the parameters characterizing the state of polarization is undetermined [38, 39]. Crossing by the observation plane perpendicular to the propagation direction, these singular lines (surfaces) go over to points (lines), respectively. Generally, the object field resulting from scattering of laser radiation in phase-inhomogeneous media is elliptically polarized. At the transversal cross-section of a beam, however, other (limiting) states of polarization are also taking place [40], viz. (1) at points where the polarization ellipse degenerates into circle and polarization is circular (C points), the azimuth of polarization (orientation of the major axis) is undetermined; (2) lines with linear polarization (S lines) where the direction of rotation of the electric vector is undetermined.

General principles of the singular analysis of vector fields have been initially formulated by Nye and Hajnal [39, 41–45]. Further consideration of polarization singularities at optical fields has been carried out by Mokhun and Angelsky [46–48]. A detailed theoretical investigation of an optical field with the set of C points has been performed by Freund, Soskin, and Mokhun [49], whose results have been confirmed experimentally [50]. Three morphological forms of distribution of polarization ellipses are possible at speckle fields [51–53], which determine the field behavior in the vicinity of the C point: "star" (S), "lemon" (L), and "monostar" (M). These forms differ in the number and positions of lines, at the each point of which major and minor axes of the surrounding ellipses are oriented to C point.

Experimental study of the influence of C points on the polarization structure of a field in their closest vicinity has been carried out in [54–56], where all three mentioned morphologically allowed forms of the polarization ellipse distributions in the vicinity of isotropic points with circular polarization have been revealed, and their statistical weights have been estimated, for example, for a random vector field resulting from light scattering at inhomogeneous media. The obtained results show skewness and considerable angular dispersion of "forming" straight lines

for S and M structures in comparison with their canonical forms. The experimental data directly prove universality of the laws of topology and morphology.

It has been shown within the framework of the topological approach [39, 42] that analysis of the polarization structure of object fields presumes that the areas with right-hand circular and elliptic polarizations are separated from the areas with left-hand circular and elliptical polarizations by the contours (at the observation plane) where polarization is linear; S surfaces correspond to such S lines at 3D space.

The system of singular points of the vector object field determines its structure as a skeleton and reflects in such a manner polarization properties of a media. It shows importance for a biomedical optics searching for the conditions for forming polarization singularities by biological objects. In addition, the experimental study of the coordinate distribution of singularities at polarization images of BTs provides diagnostic data on polarization properties of media. It also shows the importance of new singular optical criteria for differentiating the physiological state of histological slices of BTs.

The considered approaches [41–43, 54–56] have been taken into account in Ref. [49] for analytical determination of the conditions for forming singly (linear) and doubly (circular) degenerated polarization singularities and experimental investigation of the coordinate distributions of singularities at images of BTs of various morphological structures and states. It has been demonstrated that the third and fourth statistical moments of the distributions of the number of singular points are the most sensitive to changes of the geometrical-optical structure of BTs [57]. It has been also established that the coordinate structure of polarization singularities at images of physiologically normal BT is self-similar (fractal), while for pathologically changed it is random [49].

Thus, the topicality of the materials represented here is the result of the necessity for more general polarization diagnostics of changes of coordinate and local structure (including distributions of optical axes orientations of and magnitude of birefringence) of the nets of organic crystals of BTs with various morphological structures and physiological states.

3.2 Biological Tissue as the Converter of Parameters of Laser Radiation

3.2.1 Crystal Optical Model of the Anisotropic Component of the Main Types of Biological Tissues

It is assumed within the framework of notions of the geometrical-optical structure of BT that it consists from two components, viz. optically isotropic (amorphous) and anisotropic (architectonic), that are formed by birefringent, optically uniaxial fibrils, see Fig. 3.1.

Let us characterize interaction of coherent radiation with the amorphous $\{A\}$ and architectonic $\{C\}$ components of a BT by the following Jones operators:

Fig. 3.1 Birefringent (Δn) fibril with cross-section diameter d; ρ_i – directions of packing of fibrils at the plane of a BT sample
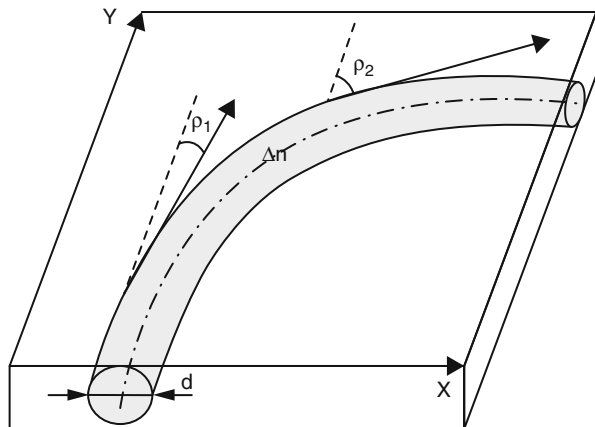
$$\{A\} = \left\| \begin{matrix} a_{11} & a_{12} \\ a_{21} & a_{22} \end{matrix} \right\| = \left\| \begin{matrix} \exp(-\tau l) & 0 \\ 0 & \exp(-\tau l) \end{matrix} \right\|; \tag{3.1}$$

$$\{C\} = \left\| \begin{matrix} c_{11} & c_{12} \\ c_{21} & c_{22} \end{matrix} \right\| = \left\| \begin{matrix} \cos^2\rho + \sin^2\rho \exp(-i\delta); & \cos\rho\sin\rho[1 - \exp(-i\delta)]; \\ \cos\rho\sin\rho[1 - \exp(-i\delta)]; & \sin^2\rho + \cos^2\rho \exp(-i\delta); \end{matrix} \right\|. \tag{3.2}$$

Here τ – absorption coefficient for laser radiation and amorphous layer of a BT with geometrical thickness l; ρ – direction of packing of anisotropic (birefringent index Δn) fibrils at the BT plane, introducing a phase shift Δn between the orthogonal components (E_x and E_y) of the electrical vector of the probing laser beam with wavelength λ. It is shown in [1, 17] that the Jones matrix of a geometrically thin layer of a BT where isotropic and anisotropic formations lie at the same plane is represented as the superposition of the operators $\{A\}$ and $\{C\}$:

$$\{M\} = \left\| \begin{matrix} a_{11} + c_{11}; & a_{12} + c_{12}; \\ a_{21} + c_{21}; & a_{22} + c_{22}. \end{matrix} \right\|. \tag{3.3}$$

Within the model formalized by (3.1–3.3) one can find complex amplitude U of a laser beam transformed by a BT. At the output of the BT layer the magnitudes of the orthogonal components of an amplitude of a laser beam, U_x and U_y, are determined from the following matrix equation:

$$\begin{aligned} \begin{pmatrix} U_x \\ U_y \end{pmatrix} &= \left\| \begin{matrix} a_{11} + c_{11}; & a_{12} + c_{12}; \\ a_{21} + c_{21}; & a_{22} + c_{22}. \end{matrix} \right\| \begin{pmatrix} E_x \\ E_y \end{pmatrix} \\ &= \begin{pmatrix} c_{11}E_x + c_{12}E_y \exp(i\delta) \\ c_{21}E_x + c_{22}E_y \exp(i\delta) \end{pmatrix} + \exp(-\tau l) \begin{pmatrix} E_x \\ E_y \end{pmatrix}, \end{aligned} \tag{3.4}$$

Solution of (3.4) with account of (3.2) and (3.3) gives the following dependences for the each, with coordinate r at the boundary field:

$$U_x(r) = \left(\cos^2\rho + \sin^2\rho \exp(-i\delta)\right)E_x + \cos\rho\sin\rho(1 - \exp(-i\delta))\exp(i\varphi))E_y;$$
$$U_y(r) = \cos\rho\sin\rho(1 - \exp(-i\delta))E_x + \left(\sin^2\rho + \cos^2\rho \exp(-i\delta)\right)\exp(i\varphi))E_y.$$
$$(3.5)$$

Let us, for simplicity (but without loss of generality of the analysis), consider the mechanisms of formation of the polarization structure of the BT's speckle image when a BT is illuminated by a linearly polarized laser beam with the azimuth of polarization $\alpha = 0^0$,

$$\begin{pmatrix} E_x \\ E_y \end{pmatrix} \Rightarrow \begin{pmatrix} 1 \\ 0 \end{pmatrix}. \qquad (3.6)$$

In this case, (3.5) are rewritten in the form:

$$U_x^A = \exp(-\tau l);$$
$$U_y^A = 0. \qquad (3.7)$$

$$U_x^C = \left[\cos^2\rho + \sin^2\rho \exp(-i\delta)\right];$$
$$U_y^C = \left[\cos\rho\sin\rho(1 - \exp(-i\delta))\right]. \qquad (3.8)$$

Here, $U^A{}_x, U^A{}_y$ and $U^C{}_x, U^C{}_y$ – the orthogonal components of amplitude of the object field formed by amorphous (A) and anisotropic (C) components of a BT. To determine the magnitudes of the azimuth of polarization and ellipticity at the points of the boundary field $r(X, Y)$, we write the coherency matrices for the BT's amorphous $\{K^A\}$ and crystalline $\{K^C\}$ components:

$$\{K^A\} = \left\| \begin{matrix} \exp(-\tau l) & 0 \\ 0 & 0 \end{matrix} \right\|; \qquad (3.9)$$

$$\{K^C\} = \left\| \begin{matrix} U_x^C U_x^{*C}; & U_x^C U_y^{*C}; \\ U_x^{*C} U_x^C; & U_y^C U_y^{*C}. \end{matrix} \right\|. \qquad (3.10)$$

It follows from (3.9) and (3.10) that the coordinate distributions of the azimuth of polarization α and ellipticity β at the BT speckle image consist of two parts, viz. homogeneously polarized

$$\begin{cases} \alpha^A = 0^0; \\ \beta^A = 0^0 \end{cases} \qquad (3.11)$$

and inhomogeneously polarized

$$
\begin{cases}
\alpha^C = 0.5 arctg \left[\dfrac{U_x^C U_y^{*C} - U_x^{*C} U_y^C}{U_y^C U_x^{*C} - U_y^C U_y^{*C}} \right]; \\[4mm]
\beta^C = 0.5 \arcsin \left[\dfrac{i \left(U_x^C U_y^{*C} - U_x^{*C} U_y^C \right)}{(q_1 + q_2 + q_3)^{\frac{1}{2}}} \right],
\end{cases}
\tag{3.12}
$$

where

$$
\begin{aligned}
q_1 &= \left[U_x^C U_x^{*C} - U_y^C U_y^{*C} \right]^2; \\
q_2 &= \left[U_x^C U_y^{*C} - U_x^{*C} U_y^C \right]^2; \\
q_3 &= i \left[U_x^C U_y^{*C} - U_x^{*C} U_y^C \right]^2.
\end{aligned}
\tag{3.13}
$$

Thus, the performed analysis provides the notions on the mechanisms of formation of the inhomogeneous polarization structure of the boundary object field of a BT at the each point by (1) decomposition of amplitude of laser wave U into orthogonal linearly polarized coherent components $\begin{pmatrix} U_x(r) \\ U_y(r) \end{pmatrix}$; (2) formation of a phase shift $\delta(r)$ between these components due to birefringence; (3) superposition of these components, resulting, generally, in an elliptically polarized field with the polarization ellipse described as

$$
\frac{X^2}{U_x^2(r)} + \frac{Y^2}{U_y^2(r)} - \frac{2XY}{U_x(r)U_y(r)} \cos \delta(r) = \sin^2 \delta(r).
\tag{3.14}
$$

3.2.2　Techniques for Analysis of the Structure of Inhomogeneous Polarized Object Fields

Distributions $N(x, y)$ of parameters of interest in laser images of phase inhomogeneous layers (PhIL) are characterized with the set of statistic moments of the first to the fourth orders $Z_{j=1,2,3,4}$ calculated using the following relations [2]:

$$
\begin{aligned}
Z_1 &= \tfrac{1}{M} \sum_{i=1}^{M} |N(x, y)|, & Z_2 &= \sqrt{\tfrac{1}{M} \sum_{i=1}^{M} [N(x, y) - Z_1]^2}, \\
Z_1 &= \tfrac{1}{Z_2^3} \tfrac{1}{M} \sum_{i=1}^{M} [N(x, y)]^2, & Z_4 &= \tfrac{1}{Z_2^4} \tfrac{1}{M} \sum_{i=1}^{M} [N(x, y)]^4.
\end{aligned}
\tag{3.15}
$$

where $N = 800 \times 600$ is the amount of pixels in the CCD camera 10 (Fig. 3.2).
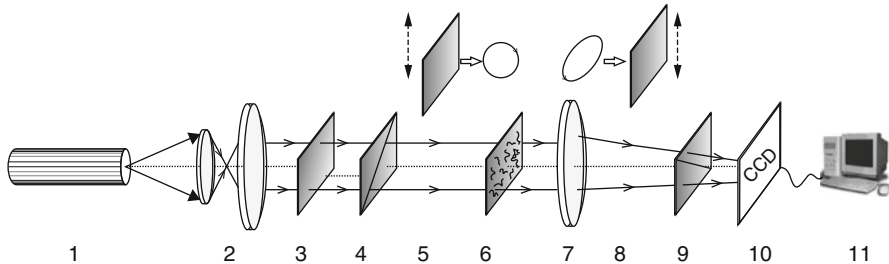
Fig. 3.2 Optical arrangement of a polarimeter: *1* – He–Ne laser; *2* – collimator; *3* – stationary quarter-wave plate; *5* and *8* – mechanically moving quarter-wave plates; *4* and *9* – polarizer and analyzer, respectively; *6* – studied object; *7* – microobjective; *10* – CCD-camera; *11* – personal computer

Our analysis of the coordinate structure for $N(x, y)$ distributions was based on the autocorrelation method by using the function [20, 21]

$$K_{N(x,y)}(m) = \frac{1}{(n-m)\sigma^2} \sum_{t=1}^{n-m} [X_t - \mu][X_{t+m} - \mu]. \qquad (3.16)$$

Here, n is the length of discrete sampling $N(x, y) = X_1, X_2, \ldots, X_n$; μ – average value, σ^2 – the dispersion; m, n – positive integers; $(m = 1\ pix)$ is the step for changing the coordinate $x = 1 \div m$.

As correlation parameters that characterize the dependences $K_{N(x,y)}(\Delta x)$, we chose:

• Correlation area $S_{N(x,y)}$

$$S_{N(x,y)} = \int_{1}^{m} K_{N(x,y)}(m)\,dm, \qquad (3.17)$$

• Normalized fourth statistic moment $Q_{N(x,y)}$ that determines the kurtosis of the autocorrelation function $K_{N(x,y)}(m)$

$$Q_{N(x,y)} = \frac{N}{\left(\sum_{i=1}^{N} \left(K_{N(x,y)}(m)\right)_i^2\right)^2} \sum_{i=1}^{N} \left(K_{N(x,y)}(m)\right)_i^4; \qquad (3.18)$$

The fractal analysis of the distributions $N(x, y)$ was performed using the calculation of logarithmic dependences $\log J[N(x, y)] - \log d^{-1}$ for the power

spectra $J[N(x, y)]$, which was calculated as a discrete Fourier transform of the corresponding autocorrelation function $K_{N(x,y)}(m)$ using MATLAB software

$$J[N(x, y)] = S_{xx}(w) = \sum_{m=1}^{n} K_{N(x,y)}(m) e^{-j\omega m}, \qquad (3.19)$$

where ω are the normalized frequencies, which correspond to a spatial frequencies ($\omega = d^{-1}$) that are determined by geometrical sizes (d) of PhIL structural elements.

The dependences $\log J[N(x, y)] - \log d^{-1}$ are approximated using the least-squares method into the curves $\Phi(\eta)$, straight parts of which serve to determine the slope angles η and calculate fractal F dimensions by using the relations [21, 53]

$$F_{N(x,y)} = 3 - tg\eta. \qquad (3.20)$$

Classification of coordinate distributions $N_{L,\pm C}(x)$ should be performed using the following criteria [49, 58]:

- They are fractal on the condition of a constant slope angle value $\eta = const$ for 2–3 decades of changing sizes d;
- They are multi-fractal, if several slope angles $\Phi(\eta)$ are available;
- They are random when any stable slope angles are absent within the whole range of changing sizes d.

In the latter case, the distributions $\log J[N(x, y)] - \log d^{-1}$ are characterized with the dispersion

$$D_z = \sqrt{\frac{1}{m} \sum_{i=1}^{m} \left[\log J(N(x, y)) - \log d^{-1}\right]^2}. \qquad (3.21)$$

3.3   Polarization 2D Tomography of Biological Tissues

This section is devoted to the analysis of the feasibilities for solving the inverse problem of laser polarimetry, viz. separate determination of the coordinate distributions of the orientational, $\rho(r)$, and phase, $\delta(r)$, parameters of the BT's architectonics.

Optical arrangement for measuring the coordinate distributions of the azimuth of polarization and ellipticity at the images of histological slices of BTs is shown in Fig. 3.2. Illumination is performed by collimated beam ($\otimes = 10^4 \, \mu m$, $\lambda = 0.6328 \, \mu m$, $W = 5.0 \, mW$). The polarization illuminator consists of quarter-wave plates 3 and 5 and polarizer 4 providing the forming of the laser beam with arbitrary azimuth of polarization $0^0 \leq \alpha_0 \leq 180^0$ and ellipticity $0^0 \leq \beta_0 \leq 90^0$. Polarization images of BTs are projected using the microobjective 7 to the plane

of light-sensitive area of the CCD-camera 10 ($m \times n = 800 \times 600$ pixels with coordinates $\begin{pmatrix} r_{11}, \ldots, r_{1m} \\ \ldots\ldots\ldots \\ r_{n1}, \ldots, r_{nm} \end{pmatrix} \equiv r_{m,n}$) providing the interval of the measured structural image elements from 2 to 2,000 μm.

The experimental conditions are chosen to provide minimization of the spatial-angular aperture filtration under BT imaging. It is ensured by matching of the angular characteristics of the scattering indicatrices of a BT and the angular aperture of a microobjective.

3.3.1 Orientation Tomography of Architectonics Nets

Basing on the proposed model notions on the mechanisms of interaction of laser radiation with the nets of biological crystals (3.1–3.12), one can see that for the crossed polarizer 4 and analyzer 9 (see Fig. 3.2) and probing with a linearly polarized laser beam with the azimuth of polarization $\alpha_0 = 0^0$, intensity at the each point of the image of BT's histological tome r can be found by solving the following matrix equation:

$$
U(r) = 0.25\{A\}\{M\}\{P\}D_0 = 0.25 \left\| \begin{matrix} 1 & -1 \\ -1 & 1 \end{matrix} \right\|
$$
$$
\times \left\| \begin{matrix} \cos^2\rho(r) + \sin^2\rho(r)\exp[-i\delta(r)] & \cos\rho(r)\sin\rho(r)\{1 - \exp[-i\delta(r)]\} \\ \cos\rho(r)\sin\rho(r)\{1 - \exp[-i\delta(r)]\} & \sin^2\rho(r) + \cos^2\rho(r)\exp[-i\delta(r)] \end{matrix} \right\|
$$
$$
\times \left\| \begin{matrix} 1 & 1 \\ 1 & 1 \end{matrix} \right\| \begin{pmatrix} 1 \\ 0 \end{pmatrix},
$$

$$(3.22)$$

where D_0, $U(X, Y)$ are the Jones vectors of the probing and object beams, and $\{A\}$, $\{M\}$, and $\{P\}$ are the Jones matrices of the analyzer, BT, and polarizer, respectively. Intensity of the object field is determined from (3.22) as

$$
I(r) = U(r)U^\otimes(r) = I_0 \sin^2 2\rho(r)\sin^2[\delta(r)/2], \qquad (3.23)
$$

where I_0 is intensity of the probing beam.

Analysis of (3.23) shows that, for the rotating azimuth of polarization of the probing beam (ω is the rotation angle of the axes of crossed polarizer and analyzer), the azimuth of polarization may coincide with the optical axis of a biological crystal, $\alpha_0(\omega) = \rho(r)$. In this case, lines of zero intensity, $I_\rho^*(r, \omega) = 0 \big|_{\alpha_0(\omega)=\rho(r)}$, or "polarizophotes" occur at the corresponding image of

a BT. Thus, for matched rotation of the transmission axes of the crossed polarizer and analyzer one can obtain the set of the distributions of polarizophotes, which we call the orientation tomograms of the BT's architectonics. Such a set of the orientation tomograms of the BT's architectonics contains the data on the coordinate distribution of optical axes of protein fibrils. Such information is important for early (preclinical) diagnostics of degenerative-dystrophic (disordering structure) and pathologic (forming the directions of growth) changes of the BT's architectonics [59].

Additional information on the properties of birefringent nets of biological crystals is given by the coordinate distribution of phase shifts introduced by their matter between the orthogonal components of amplitude of laser radiation. Hereinafter, such distributions $\delta(r)$ are referred to as the phase tomograms.

3.3.2 Phase Tomography of Biological Tissues

For selecting of the phase component (phase tomogram) at the polarization image of a BT, one must place the BT sample into a polarization system consisting of two crossed filters, viz. quarter-wave plates 5, 8 and polarizers 4, 9, the angles of transmission axes of which with the axes of the maximal velocity of the plates are $+45°$ and $-45°$, respectively (see Fig. 3.2). In this case, the coordinate intensity distribution at the BT image, $I_\delta(r)$, is determined from the Jones vector of the object field, $E(r)$, through solving the following equations:

$$
\begin{aligned}
E(r) = 0.25\{A\}\{\Phi_2\}\{M\}\{\Phi_1\}\{P\}D_0 = 0.25 \left\|\begin{matrix} 1 & -1 \\ -1 & 1 \end{matrix}\right\| \left\|\begin{matrix} i & 0 \\ 0 & 1 \end{matrix}\right\| \\
\times \left\|\begin{matrix} \cos^2\rho(r) + \sin^2\rho(r)\exp[-i\delta(r)] & \cos\rho(r)\sin\rho(r)\{1 - \exp[-i\delta(r)]\} \\ \cos\rho(r)\sin\rho(r)\{1 - \exp[-i\delta(r)]\} & \sin^2\rho(r) + \cos^2\rho(r)\exp[-i\delta(r)] \end{matrix}\right\| \\
\times \left\|\begin{matrix} 1 & 0 \\ 0 & i \end{matrix}\right\| \left\|\begin{matrix} 1 & 1 \\ 1 & 1 \end{matrix}\right\| \begin{pmatrix} 1 \\ 0 \end{pmatrix},
\end{aligned}
$$

$$(3.24)$$

where $\{\Phi_1\}$ and $\{\Phi_2\}$ are the Jones matrices of quarter-wave plates; $\{A\}$ and $\{P\}$ are the Jones matrices of the analyzer and polarizer, respectively. It follows from (3.24) that the coordinate intensity distribution as filtered in the polarization image of a BT is unambiguously connected with the phase shifts as

$$I_\delta(r) = E(r)E^\otimes(r) = I_0 \sin^2\left[\frac{\delta(r)}{2}\right]. \qquad (3.25)$$

Thus, this approach provides the information on the phase-shifting ability of birefringent matter of a BT irrespective from the direction of packing of its anisotropic fibrils.
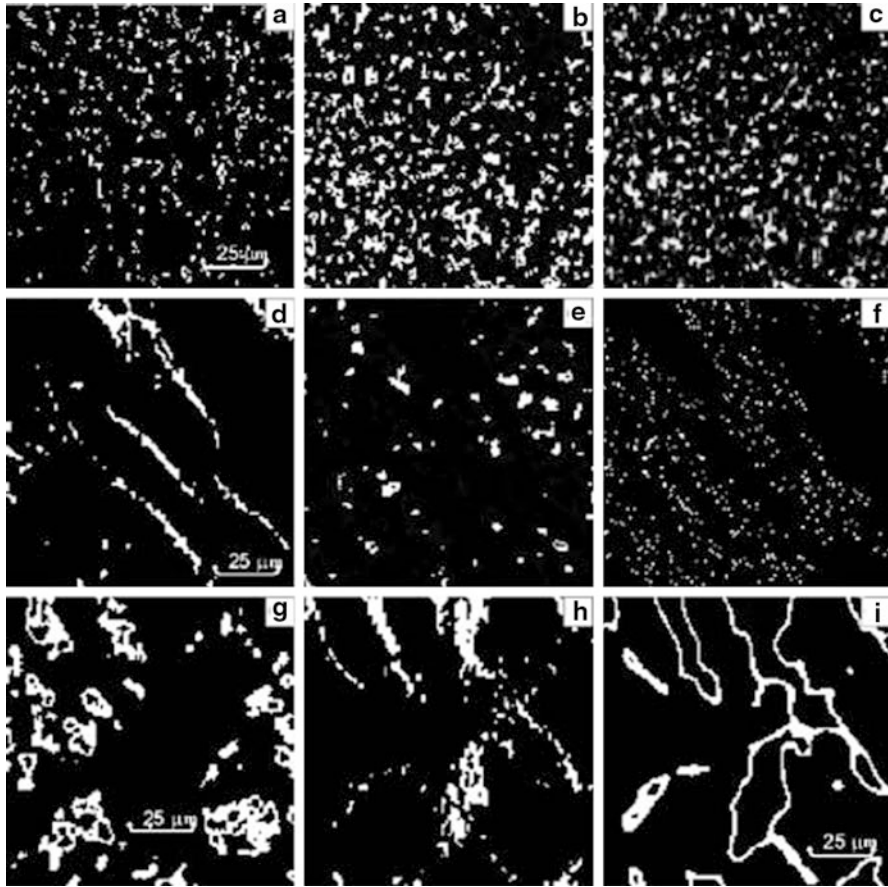
Fig. 3.3 Orientation tomograms of physiologically normal (**a–c**) and pathologically changed (**d–i**) myometrium

3.3.3 Experimental Implementation of Orientation Tomography

Efficiency of the orientation tomography for diagnostics of pathological structures of BTs, for example, of the architectonics of myometrium (a BT of the female reproductive system) is illustrated by the tomograms shown in Fig. 3.3.

This figure shows the orientation tomograms of a collagen net of physiologically normal (fragments a to c) and pathologically changed (fragments d to i) samples of myometrium, namely, with directed (fragments d, e, f) and diffuse (fragments g, h, i) growth of pathologically changed protein fibrils. The left column of the orientation tomograms corresponds to the angle $\omega = 45^0$, middle column – $\omega = 25^0$, and right column – $\omega = 0^0$.

The obtained polarizophotes illustrate in qualitatively efficient manner the polarization technique for orientation selection of the directions of optical nets of birefringent biological crystals for BTs with various physiological states. These data lead to the following conclusions.

- All orientation tomograms for a polarization image of the architectonics of a physiologically normal sample of myometrium are the ensembles of small-scale (5–10 μm) areas of polarizophotes uniformly distributed over a sample area (Fig. 3.3a–c). Such a structure shows statistical, with practically uniform distribution, orientation structure of collagen net.
- Areas with large-scale (20–200 μm), optically anisotropic structures, such as the ensembles of similarly oriented collagen fibers, correspond to pathological processes of diffuse forming fibromyoma. Similar birefringent domains are optically visualized as the corresponding polarizophotes whose set is shown in Fig. 3.3g–i.
- Comparison of the set of orientation tomograms shows their topological skewness. It is seen that for large interval of changes of the angle ω, the ensembles of polarizophotes have individual structure connected with both localization of pathologically changed self-similar (fractal) domains of the architectonics of myometrium and with the directions of their growth.
- Asymmetry of polarizophotes is pronounced, illustrated by the comparison of the orientation tomograms for the sample of myometrium with the directed growing fibromyoma (Fig. 3.3d–f). It is seen from Fig. 3.3d that, the angle of rotation of the crossed polarized and analyzer ω equals 45°, coinciding with the main direction of growth of collagen fibers, as the corresponding orientation tomogram consists from larger polarizophotes.

The feasibilities of correlation analysis of the orientation structure of the BT's architectonics are illustrated by 2D autocorrelation functions in Fig. 3.4 obtained for the orientation tomograms of physiologically normal (Fig. 3.3a–c) and pathologically changed (sprouts of fibromyoma, Fig. 3.3d–f) myometrium.

The azimuthal structure of 2D autocorrelation functions $\left\{\hat{G}_{xxyy}(\Delta x, \Delta y)\right\}$ (Fig. 3.4b, d) is characterized by the asymmetry coefficient $\zeta(\varphi)$ of the following form:

$$\zeta(\varphi) = \frac{\Re\left\{\hat{G}_{xxyy}(\varphi)\right\}}{\Re\left\{\hat{G}_{xxyy}(\varphi + 0.5\pi)\right\}}, \qquad (3.26)$$

where $\Re\left\{\hat{G}_{xxyy}(\varphi)\right\}$ and $\Re\left\{\hat{G}_{xxyy}(\varphi + 0.5\pi)\right\}$ are half-widths of the function $\left\{\hat{G}_{xxyy}(\Delta x, \Delta y)\right\}$ determined for the orthogonal azimuthal directions of polar angle φ at level $0.5\left[\max\left\{\hat{G}_{xxyy}(\Delta x, \Delta y)\right\}\right]$.

Architectonics of physiologically normal myometrium is almost uniform on the directions of packing of collagen fibers construction. Thus, the function $\left\{\hat{G}_{xxyy}(\Delta x, \Delta y)\right\}$ is close to the azimuthally symmetric one (Fig. 3.4a), and the coefficient $\zeta(\varphi) \cong 1$ over all the angular range (Fig. 3.4b). Tomograms of pathologically changed myometrium are characterized by the azimuthally asymmetrical 2D correlation function (Fig. 3.4c) with the corresponding azimuthal coefficient
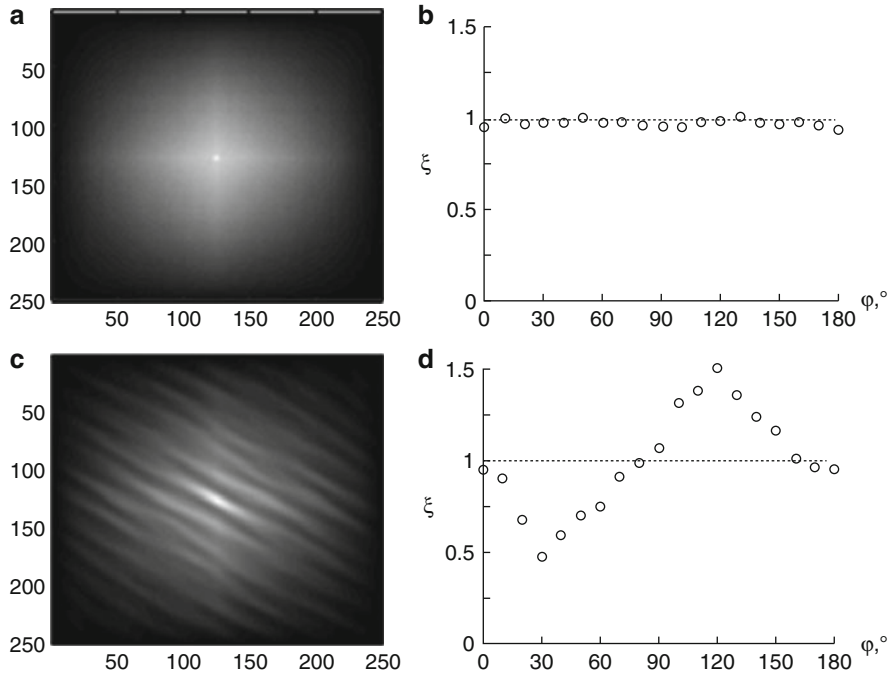
Fig. 3.4 Autocorrelation functions (**a**, **c**) and corresponding asymmetry coefficients (**b**, **d**) of the orientation tomograms for samples of myometrium of normal (**a**) and pathologically changed (sprouts of fibromyoma) (**c**) tissue

$\zeta(\varphi)$, see (3.26) (Fig. 3.4d). It can be seen that its extremal magnitudes correspond to the angles of the directions of growth of pathologically changed areas of a collagen net of myometrium (Fig. 3.3d, h correspondingly).

Thus, orientation tomography of the BT's architectonics enables effective detection of the processes of transformation of its orientation-phase structure, which is promising in the development of medical techniques for preclinical diagnostics of the physiological state of a BT.

3.3.4 Experimental Implementation of the Phase Tomography of the Architectonics Nets of Biological Tissues

The development of pathological and degenerative-dystrophic processes in BTs at preclinical stages is accompanied by the following morphological changes of their architectonics [59]: (1) decreasing concentration of mineral matter and disorientation of an architectonic net (rachitis, osteoporosis etc.); (2) growing collagen structures and calcinosis of soft tissues (psoriasis, collagenoses, myomes, fibromyomes). The tendency of such changes in the first case can be determined
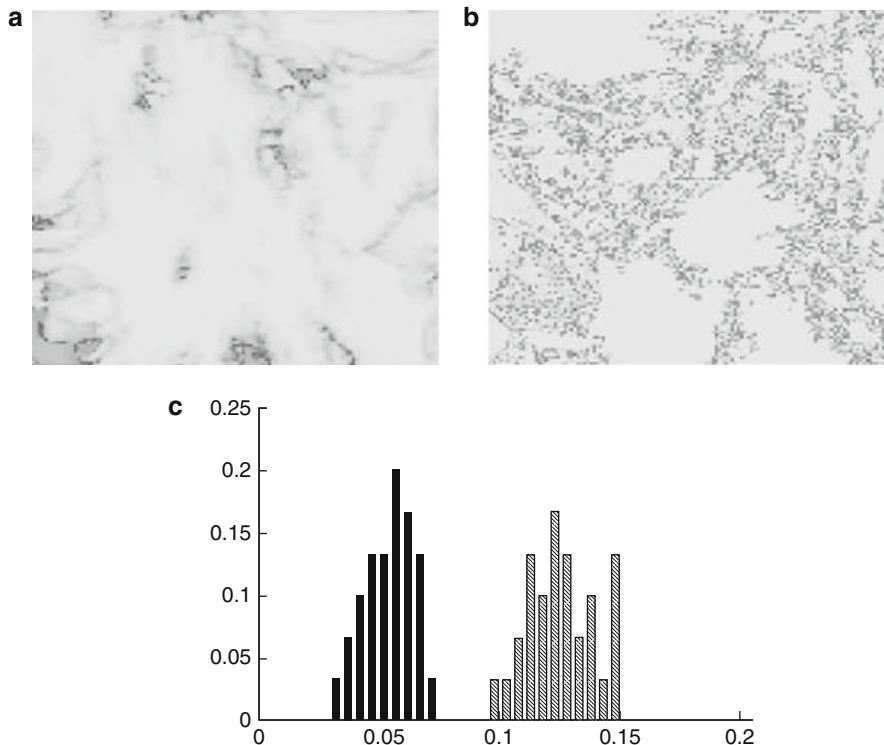
Fig. 3.5 Diagnostic feasibilities of phase tomography in determination of degenerative-dystrophic changes (osteoporosis) of the structure of osseous tissue

as decreasing of the birefringence index $\Delta n \rightarrow \Delta n_{\min}$, while in the second case as increasing of its value, as $\Delta n \rightarrow \Delta n_{\max}$. The results, illustrating the feasibilities for selection of the phase component at the images of BTs for preclinical diagnostics of degenerative-dystrophic changes of osseous tissue, are represented in Fig. 3.5.

The obtained data on the coordinate distributions of the magnitudes of the birefringence coefficients leads to the following conclusions. For the sample of physiologically normal osseous slice (Fig. 3.5a), the magnitude of the birefringence index, $\Delta n(r)$, of the architectonics matter within the areas of its crystalline domains (40–200 μm) is almost uniform. A different structure is seen for the phase tomogram for a sample of osseous tissue with forming osteoporosis (decalcinating architectonics). The coordinate distribution $\Delta n(r)$ is transformed into the set of small-scaled (5–30 μm) areas (Fig. 3.5b). The birefringence index of the architectonics of an osseous tissue decreases by one order of magnitude, $\Delta n(r) \approx 0.2 \times 10^{-2} - 1.2 \times 10^{-2}$.

The statistics of such changes are illustrated by the set of diagrams of change of dispersion of fluctuations, $\Delta n(r)$, obtained from the phase tomograms of an osseous tissue (Fig. 3.5c).

Experimental data are presented for physiologically normal osseous tissue (solid columns, 30 samples) and degeneratively changed this (dashed columns, 28 samples). Comparison of these diagrams shows that, within the statistically trustworthy groups of the studied samples, they do not overlap. Thus, this statistical parameter of the phase tomograms of the BT architectonics can be used for preclinical diagnostics of degenerative-dystrophic changes of BTs.

3.4 Structure of Polarized Fields of Biological Tissues

3.4.1 Main Mechanisms and Scenarios of Forming Singular Nets at Laser Fields of Birefringent Structures of Biological Tissues

Interaction of laser radiation with the set of optically uniaxial anisotropic fibrils (see Fig. 3.1) may be considered as the process of generation of polarization singularities (linear and circular states) by a birefringent biological object. In the general case of an elliptically polarized probing beam $E_{0x} + E_{0y} \exp(-i\delta_0)$ (3.1–3.13), the orthogonal amplitudes U_x and U_y of light oscillations at points (r) of an image of the anisotropic components of BT are of the form

$$
\begin{aligned}
U_x(r) &= \cos\rho\left(E_{0x}\cos\rho + E_{0y}\sin\rho\exp(-i\delta_0)\right) \\
&+ \sin\rho\left(E_{0x}\sin\rho - E_{0y}\cos\rho\exp(-i\delta_0)\right)\exp(-i\delta); \\
U_y(r) &= \sin\rho\left(E_{0x}\sin\rho + E_{0y}\cos\rho\exp(-i\delta_0)\right) \\
&+ \cos\rho\left(E_{0x}\cos\rho - E_{0y}\sin\rho\exp(-i\delta_0)\right)\exp(-i\delta).
\end{aligned}
\tag{3.27}
$$

It follows from (3.27) that elliptical polarization is most probable at the image of a BT. Classification of singular states of polarization has been performed in Ref. [43–51]. One distinguishes the singly degenerated trajectory when $\beta(r) = 0; \delta(r) = 0$, polarization is linear with undetermined direction of turning of the electrical vector, and the doubly degenerated trajectory when $\beta(r) = 0.25\pi; \delta(r) = 0.5\pi$, polarization is circular with undetermined azimuth of polarization. Let us determine the conditions of formation of the singly degenerated polarization singularities:

$$
\sin^2\rho\cos^2\rho\left(E_{0x}^2\cos^2\rho - E_{0y}^2\sin^2\rho\exp(-2i\delta_0)\right)\sin^2\delta = 0;
\tag{3.28}
$$

$$
\begin{aligned}
\rho &= arctg\left[\exp(-2i\delta_0)\frac{E_{0y}}{E_{0x}}\right]; \\
\delta &= 2q\pi, \quad q = 0, 1, 2\ldots
\end{aligned}
\tag{3.29}
$$

The following relation is justified for the doubly degenerated polarization singularities:

$$\sin^2\rho\ \cos^2\rho\left(E_{0x}^2\cos^2\rho - E_{0y}^2\sin^2\rho\ \exp(-2i\delta_0)\right)\sin^2\ \delta = 1, \qquad (3.30)$$

from which one determines the conditions of formation of circularly polarized points at BT images:

$$\rho = \pi/4 + arctg\left[\exp(-2i\delta_0)\frac{E_{0y}}{E_{0x}}\right];$$
$$\delta = \pi/2 + 2q\pi, q = 0, 1, 2, 3, \dots. \qquad (3.31)$$

Experimentally, the coordinate distributions of such points can be found by selection of linear and circular states of polarization at various points of the BT images from all possible states of the polarization distributions. The map of the singly degenerated singular points is determined as

$$\delta(r) = arctg\left[\frac{tg2\beta(r)}{tg\alpha(r)}\right] = 2q\pi;$$
$$\beta(r) = 0. \qquad (3.32)$$

and the map of the doubly degenerated singular points is determined as

$$\delta(r) = arctg\left[\frac{tg2\beta(r)}{tg\alpha(r)}\right] = 0.5\pi + 2q\pi;$$
$$\beta(r) = 0.25\pi. \qquad (3.33)$$

3.4.2 Statistical and Fractal Approaches to Analysis of Singular Nets at Laser Fields of Birefringent Structures of Biological Tissues

We illustrate in this section the feasibilities for polarization singularometry at BT images for preclinical diagnostics of inflammatory processes whose detection by the above-considered techniques of laser polarimetry is difficult. We use as the samples for this study optically thin (extinction coefficient $\tau \leq 0.1$) histological slices of normal (Fig. 3.6a, b) and pathologically changed (early stage of sepsis, Fig. 3.6c, d) dog kidney. The samples of the selected tissues of dog kidney are almost identical from a medical point of view, namely, conventional histochemical techniques do not distinguish them one from another. Pathological changes of kidney were formed experimentally, by inserting special chemical preparations causing septic inflammation. Similarity of the morphological structure of such tissues is proved by the comparative analysis of images (Fig. 3.6) obtained with matched and crossed polarizer and analyzer.

Fig. 3.6 Polarization images of histological slices of physiologically normal (**a**, **b**) and pathologically changed (**c**, **d**) kidney tissue. Fragments (**a**, **c**) correspond to the situation with matched polarizer and analyzer; fragments (**b**, **d**) – crossed polarizer and analyzer
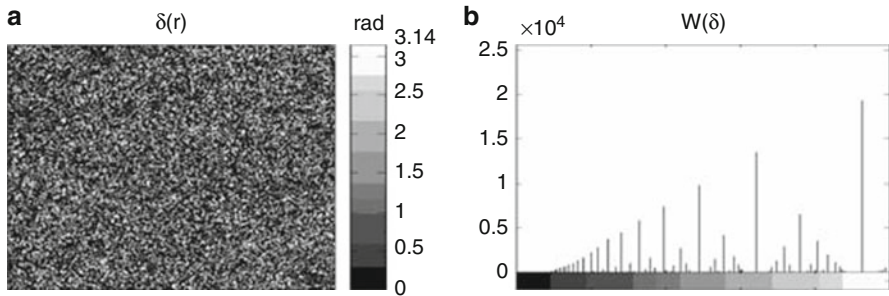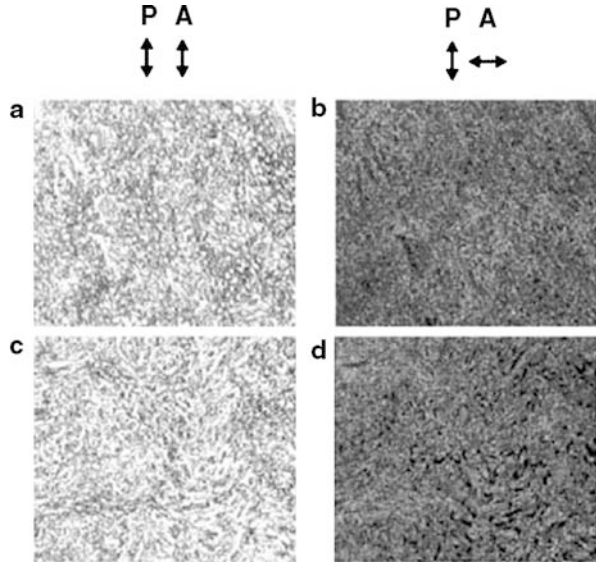
Fig. 3.7 Coordinate distributions (**a**) of phase shifts δ and histograms of their magnitudes (**b**) for polarization image of physiologically normal tissue of dog kidney

To obtain new and more detailed information on optical anisotropic properties of such objects, one determines the nets of polarization singularities (3.32, 3.33) of their laser images based on measurements of the coordinate distributions of the azimuth of polarization, $\alpha(r)$, and ellipticity, $\beta(r)$, see Sect. 3.3.3, and following computing (3.25) of the 2D tensor of magnitudes of phase shifts $\delta(r)$.

The coordinate distributions (fragments a) and histograms of the distributions of phase shift magnitudes $\delta(r)$ between the orthogonal components of laser radiation transformed by layers of histological slices (fragments b) are shown in Figs. 3.7 and 3.8, respectively, for normal and septically inflamed dog kidney.
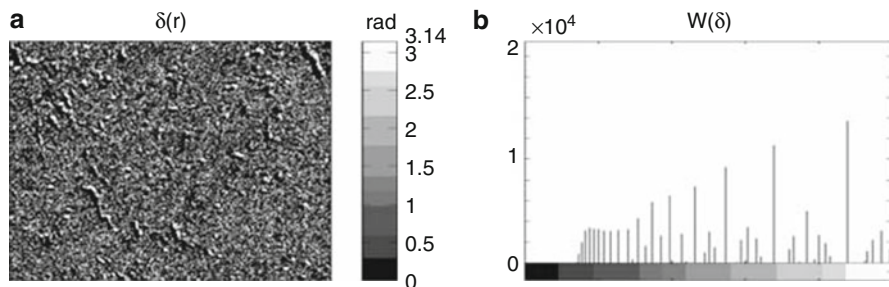
Fig. 3.8 Coordinate distributions (**a**) of phase shifts δ and histograms of their magnitudes (**b**) for a polarization image of tissue of dog kidney with early septic symptoms
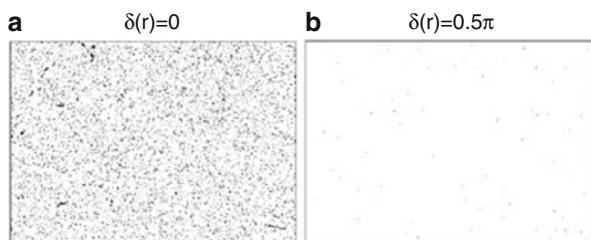
Fig. 3.9 Coordinate distributions of the singly (**a**) and doubly (**b**) degenerated polarization singularities at image of physiologically normal kidney tissue
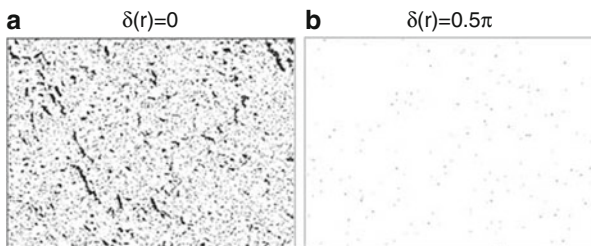
Fig. 3.10 Coordinate distributions of the singly (**a**) and doubly (**b**) degenerated polarization singularities at image of pathologically changed kidney tissue

Comparison of the PMs (Figs. 3.7 and 3.8) shows that the intervals of change of phase shifts $\delta(r)$ are almost the same for images of the samples of kidney tissue of both types. Histograms for $W(\delta)$ of the distribution of magnitudes $\delta(r)$ also have similar structure.

Much larger differences are observed for the polarization-phase properties of kidney tissues of two types, as is seen from comparison of the coordinate distributions of singular points at their images, see Figs. 3.9 and 3.10.

There is the algorithm for statistical analysis of the nets of singularly polarized points at the images of kidney tissue:
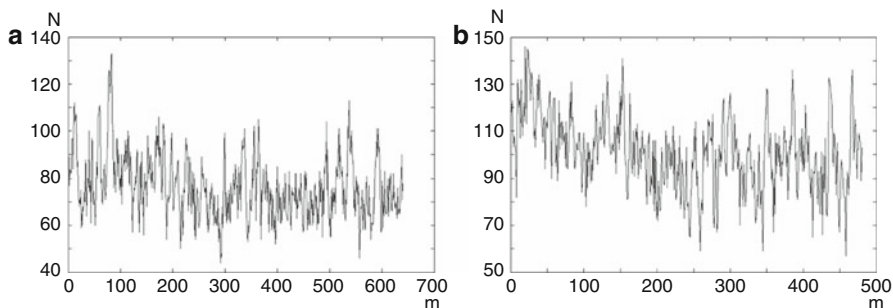
Fig. 3.11 Distributions on number N of singularly polarized points ($\delta(r) = 0$; $\delta(r) = 0.5\pi$) at image of physiologically normal (**a**) and pathologically changed (**b**) kidney tissue

Table 3.1 Statistical moments of the first to the fourth orders for distribution of the number of polarization singularities at image of kidney tissue

S_i	Norm (37 samples)	Pathology (36 samples)
S_1	0.634 ± 0.032	0.706 ± 0.065
S_2	0.198 ± 0.0045	0.149 ± 0.053
S_3	2.689 ± 0.21	21.75 ± 3.11
S_4	3.8 ± 0.34	46.8 ± 5.47

- Determination of the distribution $N(m)$ of the number of singularly polarized points at the BT image, that corresponds to the each column $m_{i=1,2,\dots800}$ of pixels of the sensitive area of CCD-camera (Fig. 3.11);
- Computation of the statistical moments of the first to the fourth orders for $N(m)$ (Table 3.1);
- Determination of the log-log dependences ($\log J - \log(1/r)$) of power spectra of J of $N(m)$ of singularly polarized points (Fig. 3.12).

The distributions of the number of singularly polarized points $N(m)$ at images of physiologically normal and pathologically changed samples of kidney tissue are shown in Fig. 3.11, fragments a and b, respectively.

One can see that the dependences $N(m)$ determined for images of the samples of kidney tissue of both types have a complex statistical structure. Comparison of the distributions of the number of points with singularly polarized states shows that the number of such points at the image of kidney tissue with early collagenosis exceeds their number at the physiologically normal tissue by 10–15%.

More detailed quantitative information on the distribution of polarization singularities $N(m)$ at images of kidney tissue with various physiological states is contained in the statistical moments of the first to the fourth orders shown in Table 3.1.

One can see from these data that the statistical distribution of the number of singularly polarized points at the image of normal kidney tissue is close to the normal one, viz. the magnitudes of skewness, S_3, and kurtosis, S_4, of the distributions $N(m)$ are rather small.
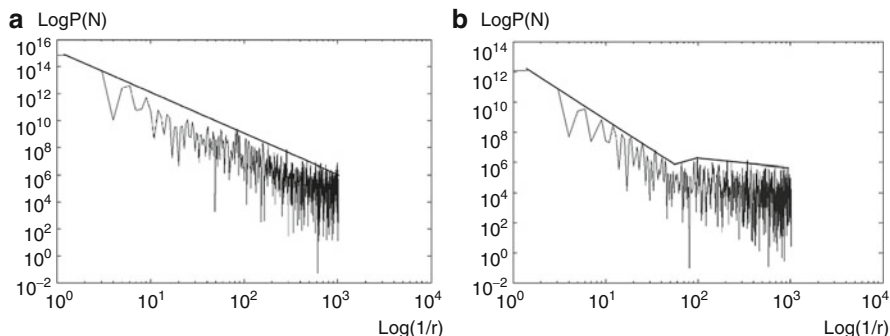
Fig. 3.12 Log–log dependences of power spectrum J for the distribution of the number $N(m)$ of polarization singularities at image of physiologically normal (**a**) and pathologically changed (**b**) kidney tissues

Another is observed for the set of the statistical moments characterizing the distribution $N(m)$ of the points with singular states of polarization at the image of pathologically changed kidney tissue.

The statistical moments S_3 and S_4 increase by approximately one order of magnitude in comparison with such parameters for the polarization image of normal kidney tissue. Such change of the higher-order statistical moments for the distribution of density of singularly polarized points at the image of physiologically changed kidney tissue can be caused by transformation of its optically anisotropic component.

Septic changes of kidney tissue manifest themselves morphologically by growing birefringence due to forming swells, microhematomas, etc. Optically, such processes are accompanied by increasing phase shifts $\delta(r)$ between the orthogonal components of amplitude of a laser beam passing through such pathologically changed structures of kidney tissue.

The same phase modulation manifests itself in formation of an additional number of singularly polarized points (3.27–3.33) at image of pathologically changes kidney tissue. As a consequence, skewness S_3 and kurtosis S_4 of the distributions grow considerably.

Additional information on differences in the coordinate distributions of the singularly polarized ($\delta(r) = 0; \delta(r) = 0.5\pi$) points at images of kidney tissue of both types is contained in power spectra of such distributions. The $\log(J) - \log(1/r)$ dependences illustrated in Fig. 3.12 were obtained for the coordinate distributions of the number $N(m)$ of polarization singularities at images of physiologically normal (a) and pathologically changed (b) kidney tissue.

Analysis of the obtained data shows that interpolation of the $\log(J) - \log(1/r)$ dependences by the least-square technique for polarization singularities of images of physiologically normal kidney tissue gives one straight line with a constant slope (Fig. 3.12a).

With regard to polarization, the image structure of pathologically changed tissue gives a set of broken lines with several magnitudes of local slopes, viz. statistical processing of the $\log(J) - \log(1/r)$ dependences (Fig. 3.12b).

Thus, it has been shown that the coordinate structure of polarization singularities at the image of physiologically normal BT is self-similar (fractal), while for pathologically changed one it is random (stochastic).

3.5 Polarization-Singular Processing of Laser Images of Biological Layers in Order to Diagnose and Classify Their Optical Properties

3.5.1 Model Conceptions and Analytical Relations

As a basis for analytical description of processes providing formation of polarization-inhomogeneous images for various types of PhIL, we have used the model conceptions developed in Refs. [2, 3, 8]:

- Surface-scattering PhIL is a rough surface (superficial layer of the skin epithelium) consisting of an ensemble of quasi-plane, chaotically oriented micro-areas with optical dimensions $l > \lambda$ – *group 1*;
- PhIL with surface and subsurface scattering – ground glass with rough external and subsurface (the layer of collagen fibrils of the skin derma) components – *group 2*;
- PhIL with bulk scattering – optically thick layer of the skin derma of a various optical thickness – *group 3*.

3.5.1.1 Mechanisms Providing Formation of Polarization-Inhomogeneous Images for Rough Surface

Optical properties of each micro-area of rough layer of the epithelium are exhaustively characterized with the Jones operator of the following look:

$$\{R\} = \left\| \begin{array}{cc} 1 & 0 \\ 0 & \frac{p_y}{p_x} \end{array} \right\|. \tag{3.34}$$

It is possible to show that within the sizes $(\Delta x, \Delta y)$ of one micro-area there takes place the change of polarization azimuth α inherent to the refracted plane-polarized laser wave with the initial azimuth α_0

$$\alpha(\Delta x, \Delta y) = arctg\left(\frac{p_y U_{0y}}{p_x U_{0x}}\right) = arctg\left[(\Delta p_{xy})tg\alpha_0\right], \tag{3.35}$$

where U_{0x}, U_{0y} are orthogonal components of the amplitude U_0, p_x, p_y – Fresnel amplitude coefficients for transmission [3].

Thus, in the approach of single scattering the polarization image of rough surface may be considered as coordinate-distributed parts of L-polarized states [16, 35].

3.5.1.2 Model Structure of PhIL with Surface and Subsurface Components – Ground Surfaces

The process providing formation of a local polarization state can be considered as superposition of "influences" of an optically strained subsurface of an optically anisotropic layer of collagen fibrils as well as the surface rough micro-relief one disposed in sequence. From the analytical viewpoint, this scenario can be described by superposition $\{F\}$ of the Jones matrix operators for these partial layers (subsurface $\{T\}$ and surface $\{R\}$)

$$\{F\} = \{R\}\{T\} = \left\| \begin{matrix} f_{11} & f_{12} \\ f_{21} & f_{22} \end{matrix} \right\| = \left\| \begin{matrix} (r_{11}t_{11} + r_{12}t_{21}); & (r_{11}t_{12} + r_{12}t_{22}); \\ (r_{21}t_{11} + r_{22}t_{21}); & (r_{21}t_{12} + r_{22}t_{22}) \end{matrix} \right\|, \quad (3.36)$$

$$\{T\} = \left\| \begin{matrix} t_{11} & t_{12} \\ t_{21} & t_{22} \end{matrix} \right\| = \left\| \begin{matrix} [\cos^2\gamma + \sin^2\gamma \exp(i\delta)]; & [\cos\gamma \sin\gamma \exp(i\delta)]; \\ [\cos\gamma \sin\gamma \exp(i\delta)]; & [\sin^2\gamma + \cos^2\gamma \exp(i\delta)] \end{matrix} \right\|. \quad (3.37)$$

Here, γ is the direction of the optical axis of fibril; δ – phase shift between orthogonal components (U_x, U_y) of the amplitude (U) of laser wave with the wavelength λ that arises as a consequence of birefringence in the matter Δn.

If taking into account (3.34), (3.36) and (3.37), it follows that within the limits $(\Delta x, \Delta y)$ of a local bulk formed is an elliptically polarized part of the object field with the following parameters:

$$\tilde{\alpha}(\Delta x, \Delta y) = \arccos \left(\frac{\sin\delta}{\cos 2\left(arctg\left\{ \left[\frac{(f_{21} + f_{22})^2}{(f_{11} + f_{12})^2} \right] tg\alpha_0 \right\} \right)} \right); \quad (3.38)$$

$$\tilde{\beta}(\Delta x, \Delta y) = \arcsin \left(\frac{tg\delta}{\sin 2\left(arctg\left\{ \left[\frac{(f_{21} + f_{22})^2}{(f_{11} + f_{12})^2} \right] tg\alpha_0 \right\} \right)} \right). \quad (3.39)$$

As it follows from the analytical relations (3.38) and (3.39), interaction of the plane-polarized (α_0) wave with the PhIL of this type provides formation of a polarization-inhomogeneous laser image. Among the whole set of values $\left(\tilde{\alpha}, \tilde{\beta} \right)$, formation of L and $\pm C$ polarization states seems to be probable [47, 49]

$$L- \Leftrightarrow \delta(\Delta x, \Delta y) = q\pi, \quad q = 1, 2, \ldots; \quad (3.40)$$

$$\pm C- \Leftrightarrow tg\delta(\Delta x, \Delta y) = \sin 2 \left(arctg \left\{ \left[\frac{(f_{21}(\Delta x, \Delta y) + f_{22}(\Delta x, \Delta y))^2}{(f_{11}(\Delta x, \Delta y) + f_{12}(\Delta x, \Delta y))^2} \right] tg\alpha_0 \right\} \right). \quad (3.41)$$

3.5.1.3 Polarization Structure of Laser Fields Inherent to PhIL with Bulk Scattering

When analyzing the processes of interaction of laser radiation with these PhIL, we have used the method of superposition of the Jones matrix operators (3.36) for the set of sequentially disposed optically thin layers

$$\{\Phi\} = \left\{ \Phi^{(p)} \right\} \left\{ \Phi^{(p-1)} \right\} \times \ldots \times \left\{ \Phi^{(1)} \right\}. \quad (3.42)$$

Having calculated the set of Jones matrix elements for an optically thick PhIL, one can define analytical expressions (like to (3.40)–(3.41)) to find L and $\pm C$ polarization states in the laser image

$$L- \Leftrightarrow \delta^*(\Delta x, \Delta y) = q\pi, \quad q = 1, 2, \ldots; \quad (3.43)$$

$$\pm C- \Leftrightarrow tg\delta^*(\Delta x, \Delta y)$$
$$= \sin 2 \left(arctg \left\{ \left[\frac{(\phi_{21}(\Delta x, \Delta y) + \phi_{22}(\Delta x, \Delta y))^2}{(\phi_{11}(\Delta x, \Delta y) + \phi_{12}(\Delta x, \Delta y))^2} \right] tg\alpha_0 \right\} \right). \quad (3.44)$$

Thus, the above analytical consideration (3.34–3.44) for various scenarios of transformation of laser radiation by PhIL in all the cases enabled to reveal the principled possibility of formation of polarization-singular states ($\beta = 0$, $\beta = \pm\frac{\pi}{4}$) in respective laser images.

In Sect. 3.4, to describe coordinate (x, y) distributions for polarization-singular $(L, \pm C)$ states in laser images for all the types of PhIL [47, 49]

$$\begin{cases} V_4(x, y) = 0 \leftrightarrow L(\beta = 0); \\ V_4(x, y) = \pm 1 \leftrightarrow \pm C \left(\beta = \pm \frac{\pi}{4} \right). \end{cases} \quad (3.45)$$

It served as a basis to calculate coordinate distributions of the fourth parameter in the Stokes vector $V_4(m \times n)$ describing the laser image of PhIL, if using the relation

$$V_4 = \frac{I_\otimes - I_\oplus}{I_\otimes + I_\oplus}. \quad (3.46)$$
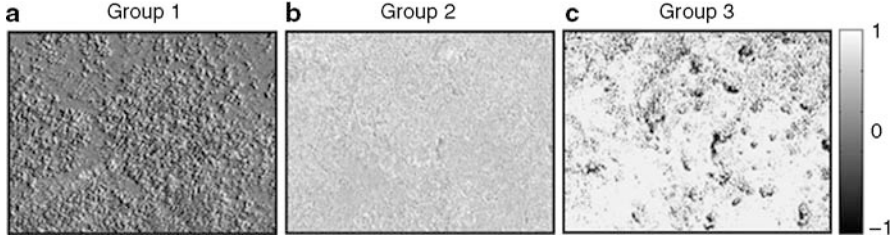
Fig. 3.13 Coordinate distributions of $V_4(m \times n)$ of laser images inherent to PhIL

Here, $I_\otimes, I_\oplus$ – intensities of right- and left-circulated polarization components of laser beam in pixel with coordinate r_{ik}.

The two-dimensional array (3.46) was scanned along the horizontal direction $x \equiv 1, \ldots, m$ with the step $\Delta x = 1pix$ (see Sect. 3.3.3, Fig. 3.2). Within the limits of each local sample $\left(1_{pix} \times n_{pix}\right)^{(k=1,2,\ldots,m)}$, we calculated the amount (N) of characteristic values $V_4(k) = 0, - (N_L^{(k)})$ and $V_4(k) = \pm 1, - (N_{\pm C}^{(k)})$.

Thus, we determined the dependences $N_L(x) \equiv \left(N_L^{(1)}, \quad N_L^{(2)}, \quad \ldots, \quad N_L^{(m)} \right)$ and $N_{\pm C}(x) \equiv \left(N_{\pm C}^{(1)}, \quad N_{\pm C}^{(2)}, \quad \ldots, \quad N_{\pm C}^{(m)} \right)$ for amounts of polarization-singular $L -$ and $\pm C -$ points within the limits of a laser image for PhIL.

3.5.2 Investigation Objects Characteristics

Figure 3.13 illustrates coordinate $(100 \times 50\,pix)$ distributions of the fourth parameter for the Stokes vector $V_4(m \times n)$ inherent to laser images of PhIL in all the groups.

Our qualitative analysis of coordinate distributions $V_4(m \times n)$ for laser images of PhIL (Fig. 3.13) revealed the following:

- Practically all the images of the rough surface of skin (Fig. 3.13a) are linearly polarized field $V_4(m \times n) = 0$ (3.34, 3.35). Availability of a small amount of the parts $V_4(m \times n) \neq 0$ polarized otherwise can be related to interferential effects of multiple interaction of coherent waves with adjacent micro-roughnesses.
- The image of the rough skin surface with a subsurface layer of the derma (Fig. 3.13b) is characterized with a developed polarization-inhomogeneous structure formed both by linearly $(V_4(m \times n) = 0)$ and elliptically $(V_4(m \times n) \neq 0)$ polarized states, including the circularly $(V_4(m \times n) = 1)$ polarized ones (3.36–3.39).
- The images of the optically thick layer of skin are characterized with the widest range of changing the azimuth and polarization due to multiple bulk scattering (3.43–3.45), $-1 \leq V_4(m \times n) \leq 1$.
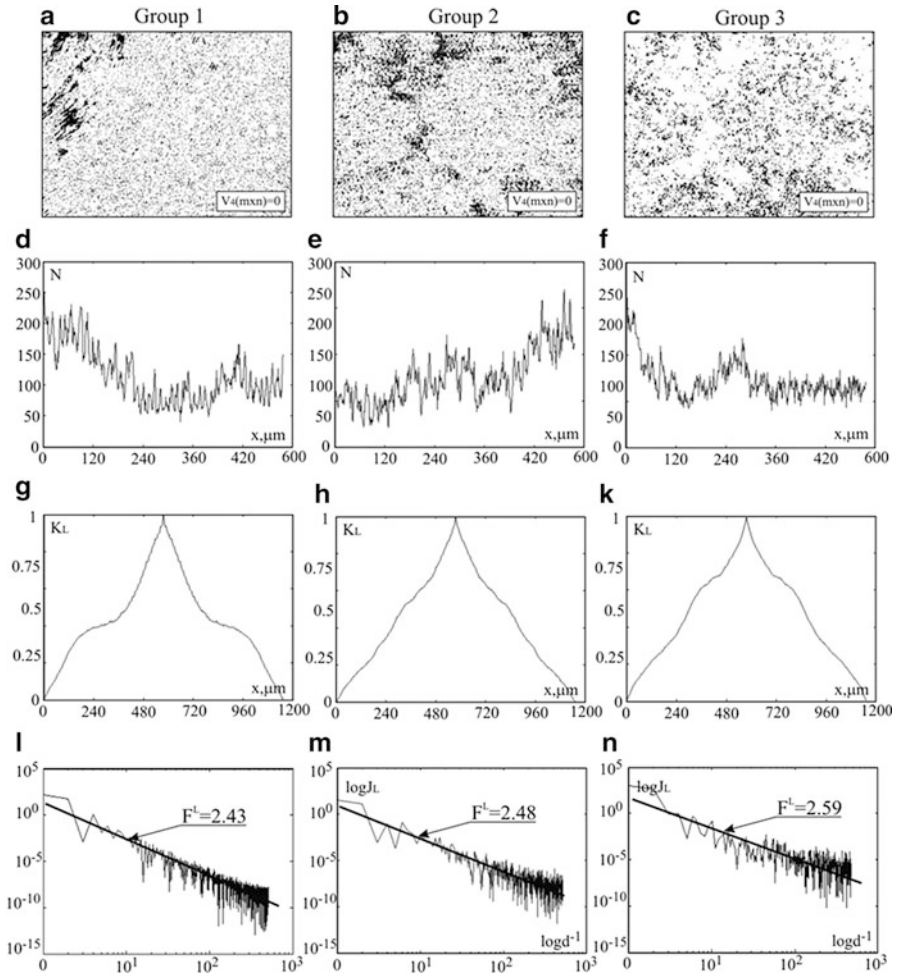
Fig. 3.14 Coordinate $V_4(m \times n) = 0$ (fragments **a–c**) and quantitative $N_L(x)$ distributions (fragments **d–f**) of L states in polarization; autocorrelation functions $K_L(\Delta x)$ (fragments **g, h, k**) and $\log J_L - \log d^{-1}$ dependencies (fragments **l, m, n**) for power spectra $J(N_L)$ of the distribution $N_L(x)$ for laser images of the PhIL

3.5.3 Statistic, Correlation, and Fractal Analysis for Distributions of Polarization-Singular States in Laser Images of PhIL

3.5.3.1 L States of Laser Images

Summarized in Fig. 3.14 is a series of coordinate ($V_4(m \times n) = 0$), quantitative ($N_L(x)$), autocorrelation ($K_L(\Delta m)$), and logarithmic ($\log J_L - \log d^{-1}$) distributions for polarization-singular L states in laser images of PhIL.

Our comparative analysis of the obtained dependences $N_L(x)$ for the amount of polarization-singular L states in laser images of PhIL in all the groups (Fig. 3.14d–f) revealed similarity of their statistic, correlation, and fractal structures.

For instance, all the $N_L(x)$ distributions are close to the equiprobable ones – the condition $Z_{j=3,4}^L << Z_{j=1,2}^L$ is valid for the values of statistic moments (3.15). Distinctions between the distributions of L states in laser images of various PhIL are observed as variations of the first and second statistic moments – $Z_1^L = 0.62$, $Z_2^L = 0.13$, $Z_3^L = 0.07$, $Z_4^L = 0.09$ (group 1); $Z_1^L = 0.39$, $Z_2^L = 0.19$, $Z_3^L = 0.06$, $Z_4^L = 0.085$ (group 2) and $Z_1^L = 0.19$, $Z_2^L = 0.28$, $Z_3^L = 0.04$, $Z_4^L = 0.07$ (group 3).

As seen, for PhIL of the first, second and third groups, the mean value Z_1^L is 1.5 and 3.3 times decreased. And vice versa, the dispersion Z_2^L is 1.5 and 2.5 times increased. These changes in $N_L(x)$ distributions are related to the mechanisms of optically anisotropic (group 2) and interferential phase modulation (group 3) as well as formation (3.39, 3.43) of elliptically polarized states in laser images of PhIL. Due to these processes, the total amount of polarization L states is decreased with simultaneous conservation of their equiprobable disposition in the image plane of various PhIL.

The investigated statistic structure of L states for polarization of PhIL laser images is confirmed by a monotonous drop of dependences for autocorrelation functions $K_L(\Delta m)$ (3.16) of all the distributions $N_L(x)$ (Fig. 3.14g, h, k). In this case, values of the correlation area S and correlation moment Q trend to their boundary values ($S^L \to 0.33$, $Q^L \to 0$, (3.17) and (3.18)) that are characteristic just to equiprobable distributions: $S^L = 0.26$, $Q^L = 0.11$ (group 1); $S^L = 0.22$, $Q^L = 0,14$ (group 2) i $S^L = 0.19$, $Q^L = 0,18$ (group 3).

The performed analysis of logarithmic dependences $\log J_L - \log d^{-1}$ (Fig. 3.14I, m, n) for the power spectra $J(N_{\pm C})$ (3.19) of the distribution $N_{\pm C}(x)$ inherent to laser images of the group 1, group 2, and group 3 revealed a common regularity – the approximating curves are characterized with stable slope angles that corresponded with fractal dimensions increasing in value (3.20): $F^L = 2.43$ (group 1); $F^L = 2.48$ (group 2) and $F^L = 2.59$ (group 3).

3.5.3.2 $\pm$C States of Laser Images

Summarized in Fig. 3.15 is the series of coordinate ($V_4(m \times n) = 1$), quantitative ($N_{\pm C}(x)$), autocorrelation ($K_{\pm C}(\Delta m)$), and logarithmic ($\log J_L - \log d^{-1}$) distributions for polarization-singular $\pm C -$ states in laser images of PhIL.

In the laser image of the group 1 $\pm C -$ states of polarization are absent (Fig. 3.15, left column – fragments a, b, d, l), which corresponds to model conceptions of mechanisms providing transformation of laser radiation by the set of chaotically oriented micro-areas of the rough surface (3.34, 3.35).

Optical manifestations of the anisotropic layer of collagen fibrils are illustrated with the network of $\pm C -$ points in the laser image (Fig. 3.15b). It is seen that the total amount of circularly polarized points (Fig. 3.15c) is practically one order less than the amount of linearly polarized states (Fig. 3.14b, c). All the static moments $Z_{j=1,2,3,4}^{\pm C} = 0.48$ that characterize the distribution $N_{\pm C}(x)$ of the amount of
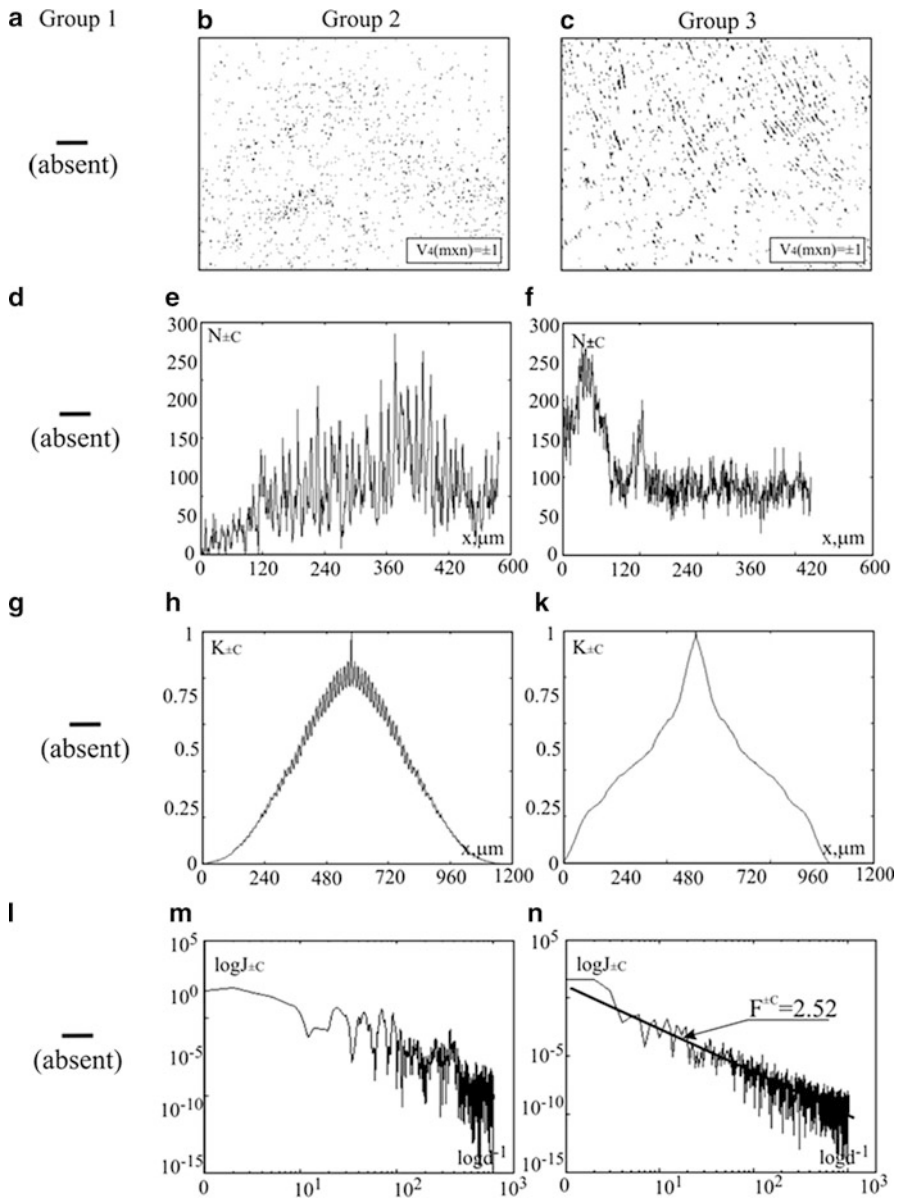
Fig. 3.15 Coordinate $V_4(m \times n) = 1$ (fragments **b**, **c**), and quantitative $N_L(x)$ distributions (fragments **e**, **f**) of $\pm C$ − states in polarization; autocorrelation functions $K_{\pm C}(\Delta x)$ (fragments **h**, **k**), and $\log J_L - \log d^{-1}$ dependencies for power spectra $J(N_{\pm C}(x))$ (fragments **m**, **n**) of the distribution $N_{\pm C}(x)$ for laser images of PhIL

circularly polarized singular states differ from zero: $Z_1^{\pm C} = 0.09$, $Z_2^{\pm C} = 0.33$, $Z_3^{\pm C} = 0.48$, $Z_4^{\pm C} = 0.52$. In this case, the values of statistic moments of higher orders $Z_{j=2,3,4}^{\pm C}$ are commensurable: $Z_2^{\pm C} \approx Z_3^{\pm C} \approx Z_4^{\pm C}$.

This fact is indicative of another, more complex, statistic distribution for the amount of $\pm C$ polarization states as compared with the equiprobable distribution of L polarization states in laser images of the PhIL (group 2).

The autocorrelation function $K^{\pm C}(\Delta m)$ of the dependence $N_{\pm C}(x)$ (Fig. 3.15h) rapidly drops with increasing the scanning step Δx, which shows the random distribution of states with circular polarization in laser images of the ground PhIL. The correlation area $S^{\pm C}$ and correlation moment $Q^{\pm C}$ of the distribution $N_{\pm C}(x)$ as compared with similar correlation parameters of $N_L(x)$ distributions (Fig. 3.14h) experience changes in inverse proportion: $S^{\pm C}(\downarrow) = 0.16$ and $Q^{\pm C}(\uparrow) = 0.96$.

The random character of the $N_{\pm C}(x)$ distribution is also confirmed by the absence of a stable value for the slope angle of the approximating curve to the logarithmic dependence $\log J_{\pm C} - \log d^{-1}$ (Fig. 3.15m, n). In this case, the dispersion value $D^{\pm C}$ grows up to 2.1 times as compared with the data obtained for logarithmic dependences of power spectra for distributions of the amount of linearly polarized states: $D^{\pm C} = 0.49$.

The phase modulation of multiply scattered laser radiation by the optically thick layer of the skin derma is characterized by the network of $\pm C -$ states (Fig. 3.15c). The total amount of L- and $\pm C -$ states of polarization for the respective laser image is approximately the same (Figs. 3.14f, 3.15f). As with the case of $N_L(x)$ distribution for the amount of linearly polarized states, the $N_{\pm C}(x)$ distribution is close to the equiprobable one: $Z_{j=3;4}^{\pm C} << Z_{j=1;2}^{\pm C}$. Differences between statistic moments $Z_{j=1,2,3,4}^{L}$ and $Z_{j=1,2,3,4}^{\pm C}$ are insignificant and lie within 25–35%: $Z_1^{\pm C} = 0.14$, $Z_2^{\pm C} = 0.31$, $Z_3^{\pm C} = 0.08$, $Z_4^{\pm C} = 0.14$.

Our analysis of the logarithmic dependences (Fig. 3.15n) for the power spectra $J(N_{\pm C})$ of the $N_{\pm C}(x)$ distribution in laser images of the PhILs of group 3 found a stable slope of the approximating curve: $F^{\pm C} = 2.52$. The dispersion value of the distribution $\log J_{\pm C} - \log d^{-1}$ is 1.7 times larger as compared with the analogous statistic moment that characterizes the dependence $\log J_L - \log d^{-1}$ ($D^{\pm C} = 0.285$).

3.5.4 Polarization-Singular Classification and Differentiation of Optical Properties Inherent to PhIL

In order to define the possibilities of polarization-singular classification and differentiation of optical properties of all types biological layers, the comparative investigation of laser images within the reliable amount of histological sections samples (confidence interval for each group $p \leq 0.01$) was performed.

The statistically averaged (within the limits of groups 1–3) values and ranges of changing statistic moments $Z_{j=1;2;3;4}^{L;\pm C}$, correlation $Q^{L;\pm C}$, $S^{L;\pm C}$ and fractal $F^{L;\pm C}$, $D^{L;\pm C}$ parameters that characterize the $N_{\pm C}(x)$ dependences for the amount of singular states in laser images of PhIL are illustrated in Table 3.2.

Table 3.2 Statistic, correlation, and fractal parameters for the distribution of the amount of polarization-singular states in laser images of PhIL

Parameters	Group 1		Group 2		Group 3	
$(L-; \pm C-)$	$L-$	$\pm C-$	$L-$	$\pm C-$	$L-$	$\pm C-$
Z_1	0.71 ± 0.079	–	0.43 ± 0.045	0.14 ± 0.032	0.25 ± 0.035	0.21 ± 0.041
Z_2	0.12 ± 0.034	–	0.23 ± 0.042	0.39 ± 0.091	0.32 ± 0.045	0.26 ± 0.034
Z_3	0.05 ± 0.008	–	0.07 ± 0.009	0.41 ± 0.12	0.05 ± 0.007	0.08 ± 0.01
Z_4	0.17 ± 0.044	–	0.08 ± 0.009	0.49 ± 0.23	0.08 ± 0.03	0.07 ± 0.05
S	0.27 ± 0.012	–	0.24 ± 0.02	0.18 ± 0.045	0.21 ± 0.032	0.26 ± 0.028
Q	0.08 ± 0.01	–	0.01 ± 0.0149	1.01 ± 0.35	0.18 ± 0.034	0.14 ± 0.019
F	2.43 ± 0.11	–	2.48 ± 0.012	Statistic	2.59 ± 0.08	2.52 ± 0.11
D	0.25 ± 0.073	–	0.27 ± 0.012	0.49 ± 0.021	0.22 ± 0.019	0.25 ± 0.021

Table 3.3 The differentiation possibilities

PhIL	Groups 1–3	
Parameters	N_L	$N_{\pm C}$
Z_1	$\oplus$	$\oplus$
Z_2	$\oplus$	$\oplus$
Z_3	$\otimes$	$\oplus$
Z_4	$\otimes$	$\oplus$
S	$\otimes$	$\oplus$
Q	$\otimes$	$\oplus$
F	$\otimes$	$\oplus$
D	$\otimes$	$\oplus$

Note: $\otimes$, here differentiation is impossible; $\oplus$, possible

The performed analysis of results presented in Table 3.2 for statistic ($Z_{j=1,2,3,4}^{L,\pm C}$), correlation ($S^{L,\pm C}$, $Q^{L,\pm C}$), and fractal ($F^{L,\pm C}$, $D^{L,\pm C}$) parameters has shown:

- *Statistic parameters.* The most sensitive appears to be both the first and the second statistic moments, which characterize the distributions of $L-$ polarization states, and the third and the fourth statistic moments, which characterize the distributions of $\pm C-$ polarization states. The difference between them reaches 2–3 times for $L-$ states and 5–7 times for $\pm C-$ states;
- *Correlation parameters.* The most sensitive appears to be the normalized fourth statistic moment $Q_{L,\pm C}$ that determine the kurtosis of the autocorrelation function $K_{L,\pm C}(m)$. The intergroup difference reaches one order of magnitude as for $L-$ states as for $\pm C-$ states;
- *Fractal parameters.* The fractal analysis appears to be effective in differentiation of optical properties of different PhIL too. The difference between the dispersion $D^{\pm C}$ values reaches two times.

The possibility to differentiate "group" optical properties of PhIL with surface, subsurface, and bulk light scattering is illustrated in Table 3.3.

3.5.5 Wavelet Approach to the Analysis of Distributions for a Fourth Stokes Vector Parameter of Laser Images Inherent to Blood Plasma

It is noteworthy that there exists a widespread group of optically anisotropic biological objects for which the methods of laser polarimetric diagnostics are not so efficient. Optically thin (coefficient of extinction $\tau \leq 0.1$) layers of various biological fluids (bile, urine, liquor, synovial fluid, blood plasma, etc.) can be related to these objects. All these layers possess considerably less optical anisotropy (the possibility of C-points forming is sufficiently small) of the biological component matter as compared with birefringent biological tissue structures [47]. On the other hand, biological fluids are more available for a direct laboratory analysis as compared with traumatic methods of biological tissues biopsy. Thus, searching for new, additional parameters for laser diagnostics of optically anisotropic structures in biological fluids makes sense.

Additional possibilities have been considered of wavelet diagnostics of polycrystalline networks structure with weak phase fluctuations in samples of blood plasma in order to differentiate a human's physiological state.

If a prototype function is taken as a specific wavelet function possessing a finite base both in coordinate and frequency spaces, then one can expand into series the one-dimensional distribution of the fourth Stokes vector parameter V_4

$$V_4(x) = \sum_{a,b=-\infty}^{\infty} C_{ab} \Psi_{ab}(x), \qquad (3.47)$$

where $\Psi_{ab}(x) = \Psi(ax - b)$ is a base function formed from the function-prototype by shifting b and scaling a, while the coefficients of this expansion are determined as follows:

$$C_{ab} = \int V_4(x) \Psi_{ab}(x) dx. \qquad (3.48)$$

The result of this wavelet transformation for the one-dimensional distribution of polarization parameters is a two-dimensional array of the coefficients $W_{V_4}(a, b)$ that are defined by the following relation:

$$W(a,b) = \frac{1}{|a|^{1/2}} \int\limits_{-\infty}^{+\infty} f(V_4)(\frac{x - b}{a}) dx. \qquad (3.49)$$

In our work, we have used as a wavelet function the so-called MHAT function, i.e., the second derivative of the Gaussian function. It has been shown that the MHAT wavelet possesses a narrow energy spectrum and two moments (zero and first) that are equal to zero. It satisfies the analysis of complex

Fig. 3.16 Polarization images of liquid-crystalline optically anisotropic network inside blood plasma of healthy (**a, b**) and oncologic (**c, d**) patients. The images were obtained for co- (**a, c**) and cross-oriented (**b, d**) polarizer and analyzer
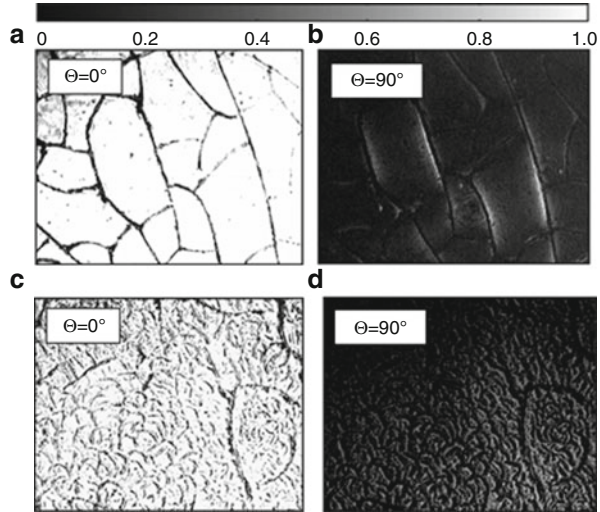
signals rather well. The mathematical expression for the MHAT wavelet is of the following form:

$$\Psi(x) = \frac{d^2}{dx^2} e^{-x^2/2} = (1 - x^2)e^{-x^2/2}. \tag{3.50}$$

3.5.6 Brief Characteristic of the Investigation Objects

The main optically anisotropic elements of blood plasma are albumin and globulin that form networks of liquid crystals in the process of crystallization. The structure of these networks is superposition of albumin crystals with spatially ordered directions of optical axes and spatially disordered globulin crystals.

The above model assumptions can be qualitatively illustrated by the results of comparative investigation of structures in laser images of blood plasma taken from healthy and sick patients (Fig. 3.16).

As seen from these images, the blood plasma of a healthy patient is characterized by the domination of a large-scale network consisting of albumin crystals with ordered directions of their optical axes. In the laser images of the blood plasma taken from a patient with cervical carcinoma, one can observe domination of small-scale disordered networks consisting of albumin crystals.

3.5.7 Wavelet Analysis of Polarization Distributions of Laser Images for Polycrystalline Networks in Blood Plasma

The locally scaled analysis of coordinate distributions $V_4(m \times n)$ (Fig. 3.17) for laser images of blood plasma is provided using linear $k_1, \ldots, k_m, k = 1 \div n$
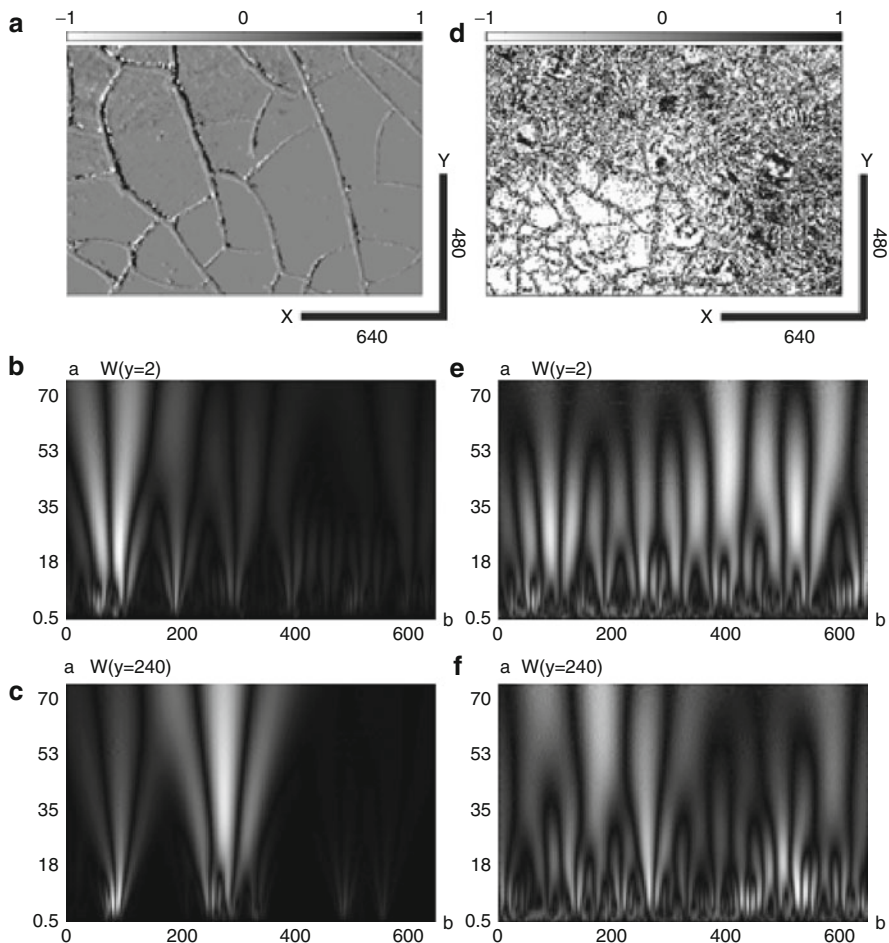
Fig. 3.17 Distributions of wavelet coefficients $W(a_{\min}; b = k_1 \div k_m)$ of the $V_4(m \times n)$ parameter observed in blood plasma of a healthy (*left* column) and sick (*right* column) patient's blood plasma for various lines $k = 2, 240$ of CCD-camera

scanning by the MHAT wavelet with the step $b = 1pix$ and window width $1~\mu m \leq a_{\min} \leq 70~\mu m$. The result of this scanning can be represented (see Eq. (3.49)) as a two-dimensional set of wavelet coefficients

$$W_{a,b} = \begin{pmatrix} W(a_{\min}, b_1) & \dots & W(a_{\min}, b = m) \\ \dots & \dots & \dots \\ W(a_{\max}, b_1) & \dots & W(a_{\max}, b = m) \end{pmatrix} \text{ for each } k\text{-th line of pixels}$$

(Fig. 3.17a,d) in the light-sensitive area of CCD camera.

Thus, the obtained set of wavelet coefficients $W(a_{\min}; b = k_1 \div k_m)$ should be averaged using the following algorithm:

$$
\overline{W}_{a,b} = \begin{pmatrix} \overline{W}(a_{\min}, b_1) = \dfrac{\sum\limits_{j=1}^{m} W_j(a_{\min}, b_1)}{m} & \ldots & \overline{W}(a_{\min}, b = m) = \dfrac{\sum\limits_{j=1}^{m} W_j(a_{\min}, b=m)}{m} \\ \ldots & \ldots & \ldots \\ \overline{W}(a_{\max}, b_1) = \dfrac{\sum\limits_{j=1}^{m} W_j(a_{\max}, b_1)}{m} & \ldots & \overline{W}(a_{\max}, b = m) = \dfrac{\sum\limits_{j=1}^{m} W_j(a_{\max}, b=m)}{m} \end{pmatrix}.
$$

(3.51)

The algorithm (3.51) is an analog of two-dimensional wavelet transformation that characterizes coordinate distributions for $V_4(m \times n)$ (Fig. 3.17a,d) observed in laser images within the range of small scales 1 μm $\leq a_{\min} \leq$ 70 μm in polycrystalline structures of blood plasma.

Shown in Fig. 3.18 are the results of experimental investigations of statistical (statistical moments of the first to fourth orders $M_{j=1,2,3,4}(W_{a,b})$, correlation (autocorrelation functions $K(W_{a,b})$) and fractal (logarithmic dependences of the power spectra $\log J(W_{a,b}) - \log d^{-1}$) parameters that characterize the distributions $W(a_{\min}; b = k1 \div km)$ for a scale $a_{\min} = 30 \mu m$ of the MHAT wavelet for $V_4(m \times n)$ parameter describing blood plasma of a healthy (left column) and sick (right column) patients. As seen from the data obtained, the distributions for wavelet coefficients $\overline{W}[(a_{\min}); (b = k1 \div km)]$ of $V_4(m \times n)$ for the polycrystalline network of amino acids from healthy patient's blood plasma, which is ordered along the directions of optical axis, are individual.

Our analysis of the data obtained for statistical, correlation, and fractal parameters that characterize sets of wavelet coefficients for various scales of MHAT functions for distributions of $V_4(m \times n)$ parameter of laser images of the albumin-globulin polycrystalline network in blood plasma of a patient with cervical carcinoma enabled us to find:

1. An essential decrease of statistical moments of the third (2.7–3.5 times) and fourth (3.4–5.7 times) orders for the distributions $\overline{W}_{[(a_{\min});(b=k1 \div km)]}(V_4)$ determined on larger scales ($a_{\min} = 2\mu m - 70\mu m$) of the MHAT wavelet.
2. A faster drop in the autocorrelation dependences $K\{\overline{W}(V_4)\}$ as well as a decrease in their fluctuation amplitudes.
3. The absence of any stable slope of the approximating curves $\Phi(\eta)$ for the logarithmic dependences $\log J(W_{a,b}(V_4)) - \log d^{-1}$ determined on all the scales of the MHAT wavelet.

The above-mentioned differences between statistical moments, autocorrelation functions, and logarithmic dependences that characterize the distributions $\overline{W}_{[(a_{\min});(b=k1 \div km)]}(V_4)$ can be related with growth of the albumin concentration in blood plasma of a patient with the oncological process. This biochemical process results in growth of the birefringence coefficient for partial albumin crystals disordered as to directions of their optical axes. This transformation of the polycrystalline structure begins from small sizes ($d = 1\,\mu m \div 50\,\mu m$) of structural elements in the polycrystalline network.

From the viewpoint of polarization, these processes become apparent via formation of random distributions for $V_4(m \times n)$ in respective blood plasma laser
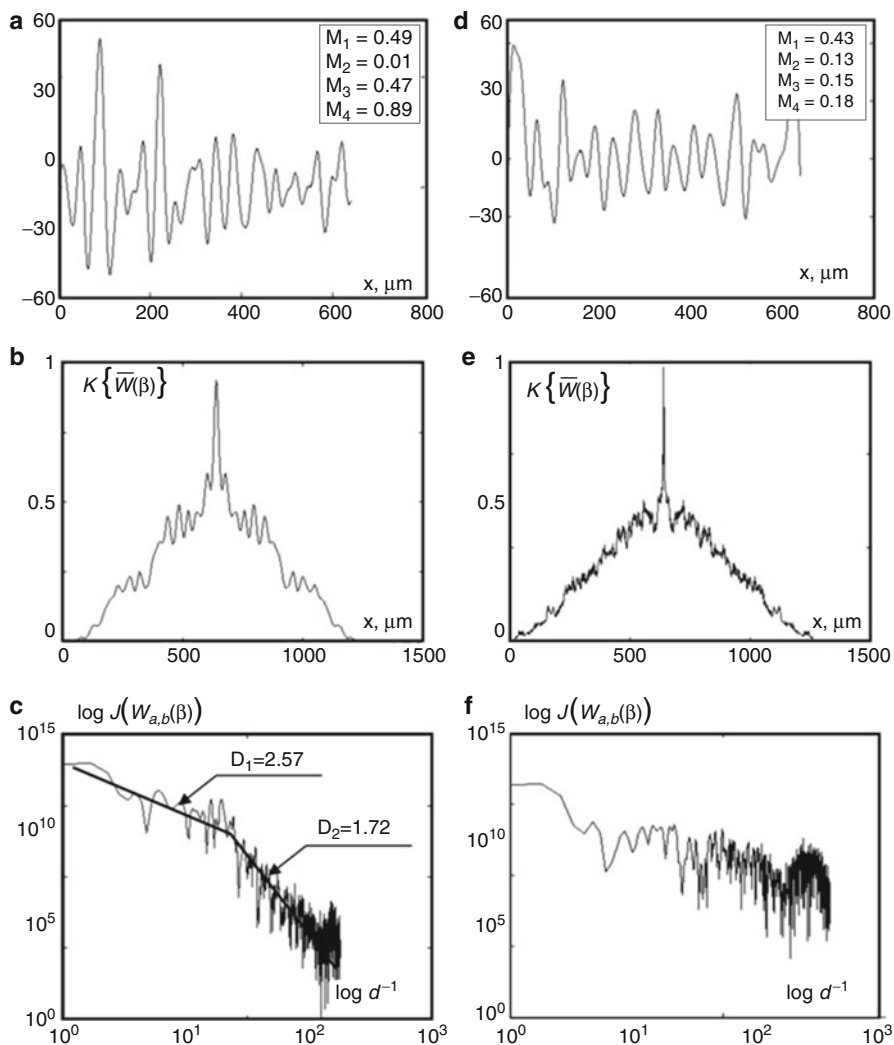
Fig. 3.18 Statistical (*left* column), correlation (*central* column), and fractal (*right* column) parameters of distributions inherent to wavelet coefficients $\overline{W}[(a_{min} = 30\mu m); (b = k1 \div km)]$ describing the $V_4(m \times n)$ parameter of a healthy (*left* column) and sick (*right* column) patient's blood plasma

images obtained in the case of an oncologically sick patient. It results in a decrease of the values inherent to statistical moments of the third and fourth orders that characterize the distributions $\overline{W}_{[(a_{min});(b=k1 \div km)]}(V_4)$. For the same reason, autocorrelation functions experience a faster drop of their intrinsic values, while the approximating curves $\Phi(\eta)$ for the logarithmic dependences $\log J\left(W_{a,b}(V_4)\right) - \log d^{-1}$ are characterized with the absence of a stable slope angle.

Table 3.4 Statistic moments of the first to the fourth orders for distributions of wavelet coefficients related to $V_4(m \times n)$ parameter of laser images describing blood plasma of healthy and oncologically sick patients

	Statistic moments	Norm	Oncology
$a_{\min} = 2$	M_1	0.24 ± 0.028	0.27 ± 0.032
	M_2	0.09 ± 0.01	0.08 ± 0.009
	M_3	0.16 ± 0.024	0.14 ± 0.018
	M_4	0.09 ± 0.009	0.07 ± 0.0085
$a_{\min} = 30$	M_1	0.49 ± 0.053	0.43 ± 0.051
	M_2	0.1 ± 0.017	0.13 ± 0.017
	M_3	0.47 ± 0.058	0.15 ± 0.019
	M_4	0.89 ± 0.092	0.16 ± 0.018

Possibilities to diagnose pathological processes in a human organism by using the wavelet analysis of $V_4(m \times n)$ parameter of laser images describing blood plasma have been illustrated in Table 3.4, where the values of statistical moments that characterize distributions on two scales $a_{\min}$ of the MHAT wavelet for two groups of healthy (21 samples) and sick (22 samples) patients are summarized.

From the analysis of obtained data one can conclude that:

1. Analyzed in this section are the main physical mechanisms providing formation of polarization singularities in laser images of PhIL with surface, subsurface, and bulk light scattering.
2. Offered are statistical, correlation, and fractal parameters for polarization-singular estimating the optical properties inherent to PhIL of all types.
3. Determined are the ranges for changing the set of criteria that characterize distributions of the amount of polarization-singular states in laser images, which enabled us to realize both "intergroup" classification and differentiation of optical properties related to PhIL of various types.

3.6   Conclusion

The interconnection has been established between the set of the statistical moments of the first to the fourth orders and fractal parameters (log–log dependences of power spectra) characterizing geometrical-optical structure of the architectonic component of a BT, on the one hand, and the set of statistical and fractal characteristics of its polarization map, i.e., 2D distribution of the azimuth of polarization and ellipticity, on the other hand.

Physical mechanisms and conditions of formation of polarization singularities, such as linearly and circularly polarized states, at BT images have been established, and the technique for polarimetry of singularities at such images has been developed.

The coordinate distributions of the number of singularly polarized points at images of normal BTs have statistical (stochastic) structure. Changing the

parameters of optical anisotropy accompanying the formation of pathological states manifests itself in transformation of the log-log dependences of power spectra of the number of singularly polarized points into self-similar (fractal) dependences.

Scenarios of formation of topological structure of inhomogeneously polarized images of the nets of biological crystals at human tissues have been analytically substantiated and experimentally investigated. The connection between the peculiarities of orientational and phase structure of the net of biological crystals and polarization singularities of the Stokes parameters of their images has been revealed.

For the case of weak phase fluctuations, diagnostic efficiency has been demonstrated of wavelet analysis applied to coordinate distributions for $V_4(m \times n)$ parameter in laser images inherent to amino acid polycrystalline networks in blood plasma of patients with oncological changes (cervical carcinoma) in the female reproductive system.

References

1. V.V. Tuchin, *Tissue Optics: Light Scattering Methods and Instruments for Medical Diagnosis*, vol. PM 166 (SPIE Press, Bellingham, 2007)
2. O.V. Angelsky, A.G. Ushenko, Y.A. Ushenko, V.P. Pishak, Statistical and fractal structure of biological tissue Mueller matrix images, in *Optical Correlation Techniques and Applications*, ed. by O.V. Angelsky (Society of Photo-Optical Instrumentation Engineers, Washington, 2007), pp. 213–266
3. A.G. Ushenko, V.P. Pishak, Laser polarimetry of biological tissue: principles and applications, in *Handbook of Coherent-Domain Optical Methods: Biomedical Diagnostics, Environmental and Material Science*, ed. by V.V. Tuchin (Kluwer, Boston, 2004), pp. 93–138
4. E. Wolf, Unified theory of coherence and polarization of random electromagnetic beams. Phys. Lett. A **312**, 263–267 (2003)
5. O.V. Angelsky, A.G. Ushenko, G.Y. Ushenko, Investigation of the correlation structure of biological tissue polarization images during the diagnostics of their oncological changes. Phys. Med. Biol. **50**, 4811–4822 (2005)
6. J. Ellis, A. Dogariu, S. Ponomarenko, E. Wolf, Interferometric measurement of the degree of polarization and control of the contrast of intensity fluctuations. Opt. Lett. **29**, 1536–1538 (2004)
7. J.F. de Boer, T.E. Milner, M.G. Ducros, S.M. Srinivas, J.S. Nelson, Polarization-sensitive optical coherence tomography, in *Handbook of Optical Coherence Tomography*, ed. by B.E. Bouma, G.J. Tearney (Marcel Dekker, New York, 2002), pp. 237–274
8. O.V. Angel'skii, A.G. Ushenko, A.D. Arkhelyuk, S.B. Ermolenko, D.N. Burkovets, Structure of matrices for the transformation of laser radiation by biofractals. Quantum Electron. **29**, 1074–1077 (1999)
9. F. Zernike, The concept of degree of coherence and its applications to optical problems. Physica **5**, 785–795 (1938)
10. G. Parrent, P. Roman, On the matrix formulation of the theory of partial polarization in terms of observables. Nuovo Cimento **15**, 370–388 (1960)
11. A.G. Ushenko, Polarization structure of laser scattering fields. Opt. Eng. **34**, 1088–1093 (1995)
12. A.G. Ushenko, Laser polarimetry of polarization-phase statistical moments of the object field of optically anisotropic scattering layers. Opt. Spectrosc. **91**, 313–316 (2001)
13. S.C. Cowin, How is a tissue built? J. Biomed. Eng. **122**, 553–568 (2000)
14. A.G. Ushenko, Correlation processing and wavelet analysis of polarization images of biological tissues. Opt. Spectrosc. **91**, 773–778 (2002)

15. A.G. Ushenko, Laser probing of biological tissues and the polarization selection of their images. Opt. Spectrosc. **91**, 932–936 (2001)
16. A.G. Ushenko, The vector structure of laser biospeckle fields and polarization diagnostics of collagen skin structures. Laser Phys. **10**, 1143–1149 (2000)
17. A.G. Ushenko, Polarization contrast enhancement of images of biological tissues under the conditions of multiple scattering. Opt. Spectrosc. **91**, 937–940 (2001)
18. A.G. Ushenko, Polarization correlometry of angular structure in the microrelief pattern or rough surfaces. Opt. Spectrosc. **92**, 227–229 (2002)
19. O.V. Angelsky, P.P. Maksimyak, S. Hanson, *The Use of Optical – Correlation Techniques for Characterizing Scattering Object and Media*, vol. PM71 (SPIE Press, Bellingham, 1999)
20. A.G. Ushenko, I.Z. Misevich, V. Istratiy, I. Bachyns'ka, A.P. Peresunko, O.K. Numan, T.G. Moiysuk, Evolution of statistic moments of 2D-distributions of biological liquid crystal net Mueller matrix elements in the process of their birefringent structure changes. Adv. Opt. Technol. **2010**, 423145 (2010)
21. O.V. Dubolazov, A.G. Ushenko, V.T. Bachynsky, A.P. Peresunko, O.Y. Vanchulyak, On the feasibilities of using the wavelet analysis of Mueller matrix images of biological crystals. Adv. Opt. Technol. **2010**, 162832 (2010)
22. J.F. de Boer, T.E. Milner, Review of polarization sensitive optical coherence tomography and Stokes vector determination. J. Biomed. Opt. **7**, 359–371 (2002)
23. A.F. Fercher, Optical coherence tomography – principles and applications. Rep. Prog. Phys. **66**, 239–303 (2003)
24. N. Wiener, Generalized harmonic analysis. Acta Math. **55**, 117–258 (1930)
25. E. Wolf, Coherence properties of partially polarized electromagnetic radiation. Nuovo Cimento **13**, 1165–1181 (1959)
26. F. Gori, M. Santarsiero, S. Vicalvi, R. Borghi, G. Guattari, Beam coherence-polarization matrix. Pure Appl. Opt. **7**, 941–951 (1998)
27. E. Wolf, Unified theory of coherence and polarization of random electromagnetic beams. Phys. Lett. A **312**, 263–267 (2003)
28. J. Tervo, T. Setala, A. Friberg, Degree of coherence for electromagnetic fields. Opt. Express **11**, 1137–1143 (2003)
29. J.M. Movilla, G. Piquero, R. Martínez-Herrero, P.M. Mejías, Parametric characterization of non-uniformly polarized beams. Opt. Commun. **149**, 230–234 (1998)
30. J. Ellis, A. Dogariu, Complex degree of mutual polarization. Opt. Lett. **29**, 536–538 (2004)
31. C. Mujat, A. Dogariu, Statistics of partially coherent beams: a numerical analysis. J. Opt. Soc. Am. A **21**, 1000–1003 (2004)
32. F. Gori, Matrix treatment for partially polarized, partially coherent beams. Opt. Lett. **23**, 241–243 (1998)
33. M. Mujat, A. Dogariu, Polarimetric and spectral changes in random electromagnetic fields. Opt. Lett. **28**, 2153–2155 (2003)
34. J. Ellis, A. Dogariu, S. Ponomarenko, E. Wolf, Interferometric measurement of the degree of polarization and control of the contrast of intensity fluctuations. Opt. Lett. **29**, 1536–1538 (2004)
35. A.G. Ushenko, Stokes-correlometry of biotissues. Laser Phys. **10**, 1286–1292 (2000)
36. O. Korotkova, E. Wolf, Spectral degree of coherence of a random three-dimensional electro-magnetic field. J. Opt. Soc. Am. A **21**, 2382–2385 (2004)
37. O.V. Angelsky, A.G. Ushenko, Y.G. Ushenko, Complex degree of mutual polarization of biological tissue coherent images for the diagnostics of their physiological state. J. Biomed. Opt. **10**, 060502 (2005)
38. J.F. Nye, M. Berry, Dislocations in wave trains. Proc. R. Soc. Lond. A **336**, 165–190 (1974)
39. J.F. Nye, *Natural Focusing and Fine Structure of Light: Caustics and Wave Dislocations* (Institute of Physics, Bristol, 1999)
40. M. Soskin, V. Denisenko, R. Egorov, Topological networks of paraxial ellipse speckle-fields. J. Opt. A: Pure Appl. Opt. **6**, S281–S287 (2004)

41. J.F. Nye, Polarization effects in the diffraction of electromagnetic waves: the role of disclinations. Proc. R. Soc. Lond. A **387**, 105–132 (1983)
42. J.F. Nye, The motion and structure of dislocations in wave fronts. Proc. R. Soc. Lond. A **378**, 219–239 (1981)
43. J.F. Nye, Lines of circular polarization in electromagnetic wave fields. Proc. R. Soc. Lond. A **389**, 279–290 (1983)
44. J.V. Hajnal, Singularities in the transverse fields of electromagnetic waves. I. Theory. Proc. R. Soc. Lond. A **414**, 433–446 (1987)
45. J.V. Hajnal, Singularities in the transverse fields of electromagnetic waves II. Observations on the electric field. Proc. R. Soc. Lond. A **414**, 447–468 (1987)
46. O.V. Angelsky, I.I. Mokhun, A.I. Mokhun, M.S. Soskin, Interferometric methods in diagnostics of polarization singularities. Phys. Rev. E **65**, 036602 (2002)
47. O.V. Angelsky, A.G. Ushenko, Y.G. Ushenko, Y.Y. Tomka, Polarization singularities of biological tissues images. J. Biomed. Opt. **11**, 054030 (2006)
48. O. Angelsky, A. Mokhun, I. Mokhun, M. Soskin, The relationship between topological characteristics of component vortices and polarization singularities. Opt. Commun. **207**, 57–65 (2002)
49. O.V. Angelsky, A.G. Ushenko, Y.A. Ushenko, Y.G. Ushenko, Polarization singularities of the object field of skin surface. J. Phys. D: Appl. Phys. **39**, 3547–3558 (2006)
50. M.S. Soskin, V. Denisenko, I. Freund, Optical polarization singularities and elliptic stationary points. Opt. Lett. **28**, 1475–1477 (2003)
51. M.R. Dennis, Polarization singularities in paraxial vector fields: morphology and statistics. Opt. Commun. **213**, 201–221 (2002)
52. M.V. Berry, J.H. Hannay, Umbilic points on Gaussian random surfaces. J. Phys. A: Math. Gen. **10**, 1809–1821 (1977)
53. Y.O. Ushenko, Y.Y. Tomka, I.Z. Misevich, A.-P. Angelsky, V.T. Bachinsky, Polarization-singular processing of phase-inhomogeneous layers laser images to diagnose and classify their optical properties. Adv. Electr. Comp. Eng. **11**, 3–10 (2011)
54. M.S. Soskin, V.G. Denisenko, R.I. Egorov, Singular elliptic light fields: genesis of topology and morphology. Proc. SPIE **6254**, 625404 (2006)
55. R.W. Schoonover, T.D. Visser, Polarization singularities of focused, radially polarized fields. Opt. Express **14**, 5733–5745 (2006)
56. M.V. Berry, M.R. Dennis, Polarization singularities in isotropic random vector waves. Proc. R. Soc. Lond. A **457**, 141–155 (2001)
57. O.V. Angelsky, A.G. Ushenko, Y.G. Ushenko, 2-D Stokes polarimetry of biospeckle tissues images in pre-clinic diagnostics of their pre-cancer states. J. Hologr. Speckle **2**, 26–33 (2005)
58. D.J. Whitehouse, Fractal or fiction? Wear **249**, 345–353 (2001)
59. A.G. Ushenko, Laser diagnostics of biofractals. Quantum Electron. **29**, 1–7 (1999)

Diffusing Wave Spectroscopy: Application for Blood Diagnostics

4

Igor Meglinski and Valery V. Tuchin

Contents

Abstract

This chapter describes the application of diffusing wave spectroscopy (DWS) for noninvasive characterization of skin blood flow and skin blood microcirculation in vivo. The DWS is a simple but ingenious approach, utilizing the loss of correlation of scattered laser light to observe the structural changes and displacement of scattering particles, such as red blood cells (RBC) within the biological tissues. This approach has the potential to be so specific that it can revolutionize the currently developed techniques for blood flow monitoring. Developments in DWS are likely to lead it to be used for characterization of skin blood microcirculation, to assess burn depth, to diagnose atherosclerotic

I. Meglinski (✉)
Department of Physics, University of Otago, Dunedin, New Zealand
e-mail: igor@physics.otago.ac.nz

V.V. Tuchin
Department of Optics and Biophotonics, Saratov State University, Saratov, Russian Federation

Precision Mechanics and Control, Institute of the Russian Academy of Sciences, Saratov, Russian Federation

Optoelectronics and Measurement Techniques Laboratory, University of Oulu, Oulu, Finland
e-mail: tuchinvv@mail.ru

disease, and investigate mechanisms of photodynamic therapy for cancer treatment, as well as to monitor pharmacological intervention for failing surgical skin flaps or replants.

4.1   Introduction

Noninvasive probing of skin tissues at the cells scale and mapping of blood flow in the microvascular network in vivo are common objectives for physicians, biologists, physiologists, and pharmacists. The disturbances of vascular circulation, typically, are due to malformations of the structure of the capillary loops and aggregation of red blood cells (RBC). Such disturbances are a frequent complication of various common diseases, including diabetes [1], arteriosclerosis [2], venous leg ulceration [3], anemia [4], ischemia [5], etc. The World Health Organization has reported that these diseases are more prevalent than cancer [6]. Thus, new clinical methods are urgently required for their diagnosis and effective treatment.

Due to the recent advancements in technology and miniaturization of solid-state optical and laser devices, a number of new revolutionary diagnostic techniques have become available for noninvasive screening and 2/3D imaging of biological tissues, e.g., optical coherence tomography (OCT) [7], confocal microscopy [8], optical spectroscopy [9], and others [10]. However, when applied to the skin, which strongly scatters light, these techniques fail to provide high-quality information on the skin's structural and/or physiological changes associated with blood flow and blood microcirculation changes.

In the last decades, a number of emerging technologies have been suggested and applied for noninvasive studies of skin blood flow and blood microcirculation; these include Doppler ultrasound [11], conventional and magnetic resonance angiography [12], laser Doppler flowmetry (LDF) [13], laser speckle contrast analysis (LASCA) [14], capillaroscopy [15], laser-scanning confocal imaging [16], optical Doppler tomography (ODT) [17], color Doppler optical coherence tomography (CDOCT) [18], and a combination of few or more imaging modalities, so-called multimodal imaging [19, 20]. These diagnostic techniques offer a unique opportunity for researchers working in various branches of biology, medicine, cosmetics, and the health-care industry. Nevertheless, the problem of implementing these techniques in day-to-day clinical practice in order to solve a wide range of actual diagnostic tasks remains unresolved.

Doppler ultrasound provides a means to resolve flow velocities at different locations in a tissue, but a long acoustic wavelength required for deep tissue penetration limits spatial resolution to 200 μm. Conventional and magneto resonance angiography provides information mainly about large blood vessels, such as coronary artery.

Application of capillaroscopy and laser-scanning confocal microscopy requires tissues to be thin enough (less than 400 μm) and transilluminated. Images obtained using laser-scanning confocal microscopy can only be collected at a fraction of the
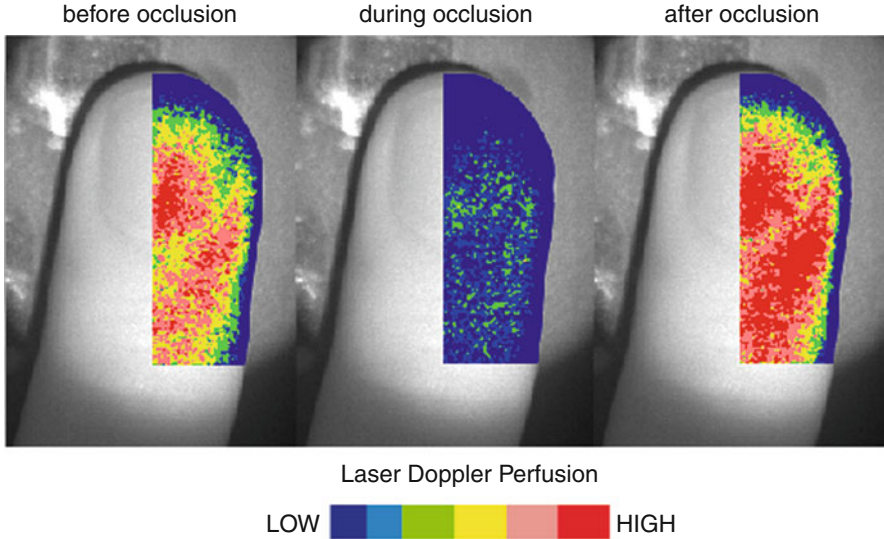
Fig. 4.1 128×256 pixels CMOS-LDF perfusion images of human finger before, during, and after occlusion of the blood at the forearm. Six-level color scale representing low-to-high tissue perfusion is displayed below (The figure is adapted from [21])

normal video rate. Strong scattering in skin tissue limits spatially resolved flow measurements by LDF and LASCA. As a result, these techniques can provide only an average characteristic of blood flow in a unit of tissue per unit of time, so-called perfusion (Fig. 4.1).

The disadvantages of ODT and CDOCT are high sensitivity to patient movements and an inability to quantify flow value in small vessels with a diameter of ∼50 μm or less, where blood flows with velocities less than ∼100 μm/s.

In contrast, diffusing wave spectroscopy (DWS) – a modern laser-based diagnostic technique – is uniquely suited for measurement of the average size of particles and their motion within the turbid highly scattering media, such as colloidal suspensions, particle gels, aerosols, foams, emulsions, and biological media [22, 23]. DWS is sensitive to fluctuations of the media on length-scales much smaller than the wavelength of sounding laser radiation (often as small as several Angstroms, Å) [23]. Potentially, this allows providing information on the scattering particle motion within highly scattering tissue-like medium avoiding the above-mentioned limitations.

This chapter describes the DWS technique and its application for noninvasive characterization of skin blood flow and skin blood microcirculation in vivo. We emphasize that we have not tried to include references for all significant and interesting research papers and monographs in the area of noninvasive screening of blood flow and blood microcirculation. We have provided references to the basic monographs and reviews that offer the most systematic and fundamental consideration of various aspects of DWS and/or blood microcirculation, both at highly qualified and

comprehensive levels. As most monographs do not cover these issues, we refer to the original papers to gain an insight into the operation principles of the experimental setup and some practical aspects.

4.2   Principles of the Diffusing Wave Spectroscopy

Introduced in 1987 [24], DWS has rapidly evolved in recent years and is currently applied to study various types of turbid media [22, 23, 25]. It is an extension of the conventional photon correlation spectroscopy [26], also known as dynamic light scattering (DLS) [27, 28].

The development of DLS with respect to the diagnostics of optically inhomogeneous dynamic scattering media originates at the end of the 1960s [27]. The technique is based on the statistical analysis of the intensity of laser radiation scattered by moving particles [29], when the Doppler shift is sufficiently small in comparison with the own frequency of incident light. The DLS approach is also known as the method of quasi-elastic light scattering [30], optical mixing spectroscopy and photon correlation [31], light beating spectroscopy [27], and laser correlation spectroscopy [32]. All of the above reflect some methodological and technical details, but in fact correspond to the same type of experiment when the fluctuations of intensity of light scattered by moving particles within a medium are analyzed.

Despite the definite similarity between the experiments on DWS and conventional experimental schemes of photon correlation spectroscopy [27, 28], the DWS theory is based on a qualitatively different concept. In DWS, the propagation of coherent laser light through a highly scattering medium is described in terms of diffusion approximation [33] and coherent scattering channels theory [34]. It is assumed that each photon experiences a great number of scattering events, N, within the medium before reaching the observation point at the detector (Fig. 4.2). The multiple scattered photons accumulate the phase shift:

$$\Delta\phi(t) = \sum_{i=0}^{N} k_i(t)[r_{i+1}(t) - r_i(t)], \qquad (4.1)$$

which is dependent on the total photons path length in the medium:

$$s = \sum_{i=0}^{N} |r_{i+1}(t) - r_i(t)| = \sum_{i=0}^{N} \left(\frac{k_i}{|k_i|}\right)(r_{i+1}(t) - r_i(t)). \qquad (4.2)$$

Here, $r_i(t)$ is the coordinate of scattering events (particles) at the instant of time t, k_i is the wave vector, and s is related to the number of scattering events N by the obvious relation $s = Nl^*$, where l^* is the mean free path of a photon (the reciprocal of the medium scattering coefficient μ_s, i.e., $l^* = (\mu_s)^{-1}$).

In a highly scattering medium, such as the human skin, where μ_s in visible/near-infrared region of spectra varies in the range of 50–100 mm^{-1} [35], s can be

Fig. 4.2 Schematic diagram representing a trajectory of light propagated from the source area (S) toward the detector (D) within a semi-infinite scattering medium: (●) indicates the location of scattering particles at the instant of time $(t + \tau)$ and (○) indicates the location of the same scattering particles at the instant of time t, $(t \gg \tau)$
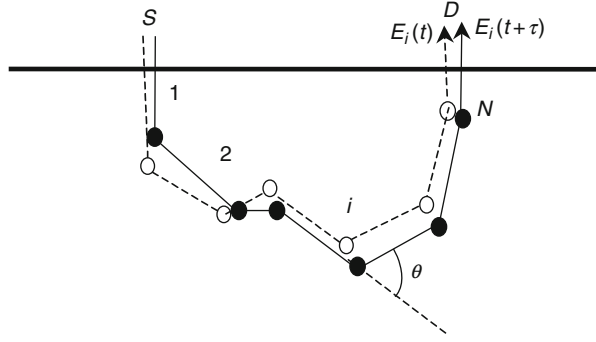
considered as a statistically independent random walk of photon. The distribution function of the photon migration paths $P(s)$ is determined as the probability that light covers the optical paths s, moving from point r_0 to point r_{N+1} [33] (see Fig. 4.2):

$$P(s) = \left(\frac{\upsilon}{4\pi s D}\right)^{3/2} \exp\left(\frac{\upsilon|r_0 - r_{N+1}|^2}{4sD}\right). \tag{4.3}$$

Here, $D = \frac{\upsilon l}{3}$ is the photon diffusion coefficient, υ is the speed of light in the medium, and l is the transport length of free path $l = (\mu'_s)^{-1}$, where μ'_s is the reduced scattering coefficient determined as follows: $\mu'_s = \mu_s(1 - <\cos\theta>)$, where $<\cos\theta>$ is the mean cosine of scattering angle.

The electromagnetic field $E(t)$ results from the sequential scattering events in the points $r_1(t), r_2(t), \ldots r_i(t), \ldots r_N(t)$ interferes with the field $E^*(t + \tau)$ scattered slightly later at the same series of the scattering events but at the instant of time $t + \tau$ (see Fig. 4.2). The time it takes the photons to travel the entire optical path in the medium is much shorter than the time of displacement of scattering particles in the medium. Since scattering particles move, i.e., the scattering events are displaced to the points $r_1(t + \tau), r_2(t + \tau), \ldots r_i(t + \tau), \ldots r_N(t + \tau)$, when compared to $s(t)$, the optical path $s(t + \tau)$ is changed. As a result, the phase shift between fields $E(t)$ and $E^*(t + \tau)$ will be different at different instants of time. This predetermines temporal fluctuations of the intensity of scattered light recorded at the detector in the far zone.

Quantitatively, these fluctuations are analyzed by the temporal field correlation function

$$G_1(\tau) = <E(\tau)E^*(t + \tau)>, \tag{4.4}$$

defined as

$$G_1(\tau) = I_0 \sum_{j=0,\infty} P(s_j) \exp\left(-\frac{N}{6}\langle q^2\rangle\langle\Delta r^2(\tau)\rangle\right), \tag{4.5}$$

where $I_0 = <|E(t)|^2>$, $P(s)$ is the probability density function of the photon migration paths defined by (4.3), $<\ldots>$ denotes an ensemble average, and q is the change in the wave vectors k_i and k_{i+1} as follows:

$$q = |k_i - k_{i+1}| = 2k_0 \sin\frac{\theta}{2}. \tag{4.6}$$

Respectively,

$$\left\langle q^2 \right\rangle = \left\langle 4k_0^2(1 - \cos\theta) \right\rangle = 2k_0(1 - \langle\cos\theta\rangle) = 2k_0\frac{l^*}{l}, \tag{4.7}$$

where $k_0 = |k_i| = |k_{i+1}|$, and θ is the angle between the directions $k_i = k_{i+1}$ (i.e., angle of the ith scattering event).

Substituting (4.7) in (4.5), we obtain that the normalized temporal field autocorrelation function, $g_1(\tau) = G_1(\tau)/<|E(t)|^2>$, which has the form

$$g_1(\tau) = \int_0^\infty P(s)\exp\left(-\frac{1}{3}k_0^2 < \Delta r^2(\tau) > \frac{s}{l}\right)ds. \tag{4.8}$$

Thus, similar to the conventional DLS [27, 28], in DWS $g_1(\tau)$ is determined in terms of the mean-square displacement of scattering particles $<\Delta r^2(\tau)>$, and proportioned to the average number of scattering events N that results in a significant increase in the slope of $g_1(\tau)$. This has been verified directly by using pulsed laser and by gating the broadened response to select specific photon path lengths [36]. For the continuous wave illumination, (4.8) is valid given the assumption that the coherence length of probing laser light, propagated through the medium, is much longer than the width of the photon path length distribution [37].

For a medium that multiply scatters laser light, the transport of temporal field correlation function is well defined by the correlation diffusion equation [38]

$$\left(D\nabla^2 - \upsilon\mu_a - 2\upsilon\mu'_s D_B k_0^2 \tau\right) \cdot G_1(\mathbf{r}, \tau) = -\upsilon S(\mathbf{r}). \tag{4.9}$$

Here, $G_1(\mathbf{r}, \tau)$ is determined by (4.4), is a function of position $\mathbf{r}$ and correlation time τ; and it has units of intensity and energy per area per second. D is the photon diffusion coefficient, υ is the speed of light in the medium, and $S(\mathbf{r})$ is the light source intensity distribution in the units of photons per volume per second. Similar to μ_a, describing losses of intensity of probing light due to photon absorption, $\left(2\mu'_s D_B k_0^2 \tau\right)$ defines loss of correlation due to particle motion and can be interpreted as a "dynamical absorption."

The correlation diffusion equation (4.9) is valid for turbid samples with the dynamics of scattering particles governed by the Brownian motion. When $\tau = 0$, there is no "dynamical absorption" and (4.9) reduces to the steady-state photon diffusion equation [39].

The correlation diffusion equation can be generalized to account other dynamic processes, including random flow and shear flow [40]:

$$\left(D\nabla^2 - \upsilon\mu_a - \frac{1}{3}\upsilon\mu'_s k_0^2 <\Delta r^2(\tau)> - \frac{1}{3}\upsilon\mu'_s <\Delta V^2> k_0^2\tau \right.$$

$$\left. - \frac{1}{15}\upsilon\mu'^{-1}_s \Gamma^2_{eff} k_0^2\tau^2 \right) G_1(\mathbf{r}, \tau) = -\upsilon S(\mathbf{r}). \tag{4.10}$$

Here, the fourth and fifth terms on the left-hand side arise from random and shear flows, respectively. $<V^2>$ is the second moment of the particle velocity distribution (assuming the velocity distribution is isotropic and Gaussian) and Γ_{eff} is the effective shear rate. D_B, $<V^2>$, and Γ_{eff} appear separately because the different dynamical processes are uncorrelated.

As one can see, in (4.10) the "dynamic absorption" for the flow increases as τ^2 compared to the τ increase for the Brownian motion. The "dynamic absorption" terms for random flow and Brownian motion are both defined by $\frac{1}{3}\upsilon\mu'_s k_0^2<\Delta r^2(\tau)>$, where $<\Delta r^2(\tau)>$ is the mean square displacement of a scattering particle. For the Brownian motion $<\Delta r^2(\tau)> = D_B$ and for random flow $<\Delta r^2(\tau)> = <V^2>\tau^2$.

Thus, for the different dynamics of scattering, particle motion within the turbid medium $G_1(\tau)$ consists of different independent time scales, representing a weighted average of dynamics of particles within the sample. When the flow significantly dominates under the Brownian motion, the logarithmic plot of $g_1(\tau)$ versus $\tau^{1/2}$ gives a straight line with a slope proportional to the velocity of particle flow. This approach is well known and has been widely applied to probe the flow localized within the colloidal suspension [41] and to measure and visualize Poiseuille, random, and turbulent flows and Brownian motion within a stationary environment [42–44].

4.3 DWS Experimental Approach and Data Analysis

An example of DWS experimental setup used in the studies of dynamic media [42, 44–46] is schematically presented in Fig. 4.3. A coherent laser light generated by Argon ion laser in the TEM$_{00}$ mode (wavelength $\lambda = 514$ nm, coherence length over 3 m) has been used as the laser light source. Multimode optical fiber (with numerical aperture 0.16 and 100 μm core diameter) has been used to deliver laser light to the surface of the sample. Diffusely scattered within the sample, laser light is collected at the "detector" – a single-mode optical fiber (3 μm in diameter and narrow numerical aperture 0.13) separated from the source area. Passing along the single-mode fiber, scattered light is detected in the single photon counting regime by a photomultiplier tube (PMT) or by avalanche photodiode (APD) connected to a digital multichannel autocorrelator.

Fig. 4.3 Schematic diagram of the DWS experimental setup: *1* – source of laser radiation, *2* – fiber-optic probe, *3* – detecting system and computer, *4* – sample of investigation
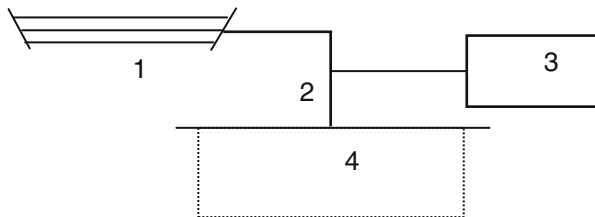
The use of optical fibers with narrow numerical aperture to deliver the laser radiation to/from the sample makes it possible to obtain a high signal-to-noise ratio in the measurement process. The spatial separation of source and detector fibers on the surface of the sample (in a range of distances from micrometers to centimeters) allows shallow or deep detection of the medium, like human skin [47, 48].

The output signal is then processed with an autocorrelator to the temporal intensity correlation function $g_2(\tau) = <I(\tau)I(t+\tau)>/<I>^2$, which is related to the normalized temporal field autocorrelation function $g_1(\tau)$ by the Siegert relation [26]:

$$g_2(\tau) = 1 - \beta|g_1(\tau)|^2. \tag{4.11}$$

Here, $<I>$ is the ensemble-averaged intensity and β is the aperture function, a dimensionless parameter ($0 \leq \beta \leq 1$), which depends on the number of speckles detected and the coherence length of incident laser light, also known as correlation function "interception" [49]. In an ideal DLS/DWS experimental setup, $\beta = 1$. The Siegert relation is valid for the Gaussian random optical fields only, when the scattering field's phase and amplitude variations are statistically independent of each other.

Further subsequent analysis of measured temporal field autocorrelation functions can be performed as a semilogarithmic plot, as mentioned above:

$$Y(\tau) = -\frac{1}{\tau} \ln(g_2(\tau) - 1) = D_B q^2 + v^2/2\omega^2. \tag{4.12}$$

Similar to the conventional DLS approach, the plot of $Y(\tau)$ versus τ gives a straight line with the slope equal to the inverse beam transit time squared and intercept equal to the inverse correlation time. The data analysis for the Brownian motion with the conventional DLS approach [50] becomes relatively easy because the intersection with the ordinate, by the Stokes-Einstein relation $D_B = \frac{k_B T}{6\pi\eta r}$, is a measure of the particle size, whereas for the flow, the slope is proportional to the convection velocity of scattering particles $\frac{v^2}{2\omega^2}$ [50]. Here, k_B denotes the Boltzmann constant, T the absolute temperature, η the shear velocity, and r the radius of the particles. A similar approach can be applied in the case of multiple scattering.

This opens up the possibility of imaging an object consisting of scattering particles undergoing a motion which differs from the particle's motion outside the object even if there is no static scattering contrast between the object and its environment.

4.4 Results and Discussion

The approach described above has been systematically applied for measurements of velocity gradients of laminar shear flow [40], Poiseuille flow, and Brownian motion of particles inside the particles in Brownian motion with different sizes [41, 43], and to Brownian motion and Poiseuille, random, and turbulent flows inside a stationary scattering environment [42, 44]. The results of these studies agree well with the results of correlation diffusion equation for systems with Brownian motion, Poiseuille, and shear flows.

Figure 4.4 presents an example of typical temporal field autocorrelation functions, measured for a Poiseuille flow ($\Gamma_{eff} = 0$) localized inside a solid slab of TiO_2 suspended in resin [42, 44]. The slab contains a single cylindrical vein containing 0.5 % water solution of Intralipid. (Intralipid is a polydisperse suspension of fat particles ranging in diameter from 0.1 to 1.1 μm [51] typically used to simulate highly scattering biological media/flows.). The Intralipid is pumped through the cylindrical vein in the slab with pump speeds of 0.08, 0.62, and 3.22 cm s^{-1}.

The decay at short correlation time ($\tau \sim 1-300$ μs) corresponds to the flow dynamics while the decay for long correlation time ($\tau \sim 1,000-10,000$ μs) results from the ensemble averaging [42]. The three plots come from three different flow speeds, 0.08, 0.62, and 3.22 cm s^{-1}. As one can see, the short τ decay rate increases with the flow speed. The longer τ decay depends only on the rate of ensemble averaging and is constant.

Figure 4.5 presents a comparison of the experimental results and the results of Monte Carlo simulation for the same experimental geometry, parameters of source-detector, and properties of the medium and flow [44].

The results presented in Fig. 4.5 demonstrate a good agreement. A priori knowledge of flow parameters is used in the simulation. The best fit to the experimental data indicates that shear rate Γ_{eff} is approximately 6.8 cm^{-1} times the flow speed. Since the shear rate is given by the change in speed per unit length in the direction perpendicular to the flow, one might expect that the effective shear rate would be the flow speed divided by the radius of the vein. This simple calculation gives an effective shear rate that is a factor of 2 smaller than the measured Γ_{eff}. This difference results from the mismatches in optical indices of refraction and sensitivity to the semi-infinite boundary condition.

Thus, as one can see from Fig. 4.5, the part of the correlation function in the bounded range of time delay ($1 < \tau < 400$ μs) is most sensitive to a change in velocity of scattering particles in the dynamic region. This agrees well with the results obtained in [41].

Fig. 4.4 An example of
measured temporal field
autocorrelation functions for
three different values of flow
hidden within a highly
scattering medium: $1 - 0.08$,
$2 - 0.62$, and $3 - 3.22$ cm s^{-1}
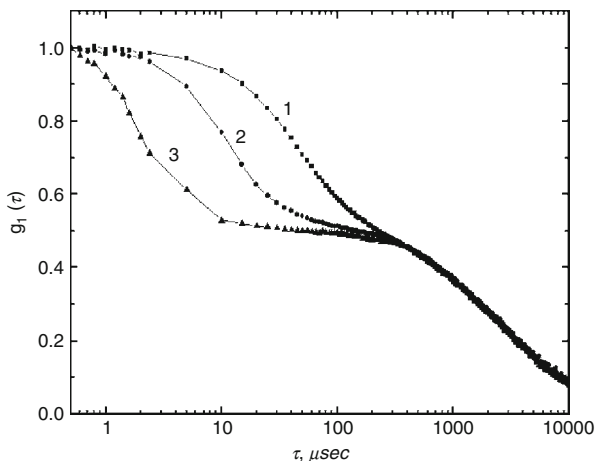
Fig. 4.5 Comparison of the
experimental results
(*symbols*) with the results of
Monte Carlo simulation
(*lines*) of the normalized
temporal field autocorrelation
functions for the same values
of flow as presented in
Fig. 4.4
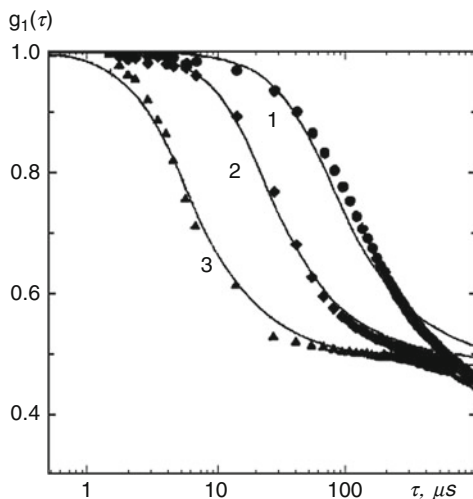
For $\tau < 1$ μs, the slope of the correlation function is determined mainly by nonzero absorption of light in the medium. In the experiment and Monte Carlo modeling, the absorption both inside and outside the vein is the same.

For the longer time delay, $\tau < 50-300$ μs, the change of slope of $g_1(\tau)$ tends to "saturate" at a constant level ("plateau") that is independent of the flow velocity (see Figs. 4.4 and 4.5). This was predicted theoretically [52] and can be easily explained qualitatively on the basis of the correspondence between the short trajectories of photons in the medium and the long delay times τ [24]. For larger τ, the rate of slope decrease of $g_1(\tau)$ is determined mainly by photons with relatively short trajectories, since photons with long trajectories are now completely de-correlated. Photons with short trajectories are mainly those that do not reach the capillary, and since the particles in the medium surrounding the capillary are

Fig. 4.6 Temporal field autocorrelation functions $g_1(\tau)$ measured for different suppressions of the human arm in vivo [45, 55]
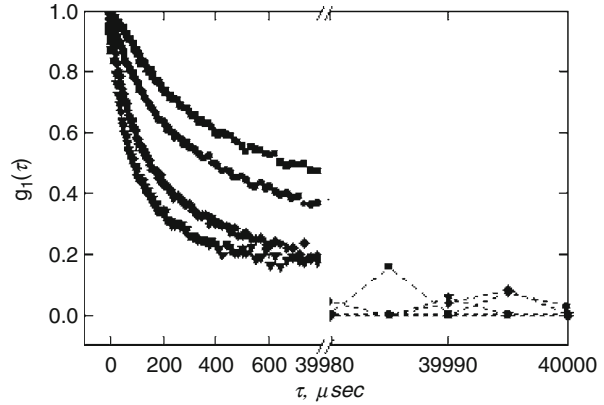
immobile, the theoretically computed function $g_1(\tau)$ approaches a constant different from zero as $\tau \rightarrow \infty$. The value of this constant is determined solely by the depth at which the capillary is located. In other words, the intermediate "plateau" (see Figs. 4.4 and 4.5) shows fraction of the detected photons sampled in the dynamic region.

A number of phantom studies and development of the theoretical model carried out in terms of temporal field correlation functions based on the DWS approach show good agreement between the experimental and theoretical results. Thus, the generalized diffusion correlation approach is expected to be used more actively to monitor the flows in complex turbid media. Currently, there are a number of experimental systems where DWS micro-rheology measurements agree well quantitatively with the traditional macroscopic mechanical rheometry over the time scales at which these techniques are overlapped [53, 54].

Having carried out the evaluation of the technique via the theoretical and phantom studies, an attempt to monitor the dynamics of time variations in the skin blood flow and skin blood microcirculation has been made [45, 55, 56]. These studies were made on the human skin with the same experimental system as described above (see Fig. 4.3), but using the laser light at a near-infrared range of wavelength 632.8 and 805 nm with a coherence length 4 cm and incident intensity of laser radiation 10 μW. The measurements of skin blood flow clearly demonstrate a reproducible drop of $g_1(\tau)$ in blood perfusion changes with the cuff pressure (Fig. 4.6).

For the different dynamics of scattering, particles within the multiple scattering medium $g_1(\tau)$ consist of different independent time scales (Fig. 4.4), e.g., τ_B and τ_S for the Brownian motion and convective shear flow [40]:

$$g_1(\tau) = \int\limits_0^\infty P(s) \exp\left(-2\left[\frac{\tau}{\tau_B} + \left(\frac{\tau}{\tau_S}\right)^2\right]\frac{s}{l^*}\right)ds. \qquad (4.13)$$

Fig. 4.7 Semilogarithmic
plot of temporal field
autocorrelation functions,
presented in Fig. 4.6, versus
$\tau^{1/2}$ [45, 55]
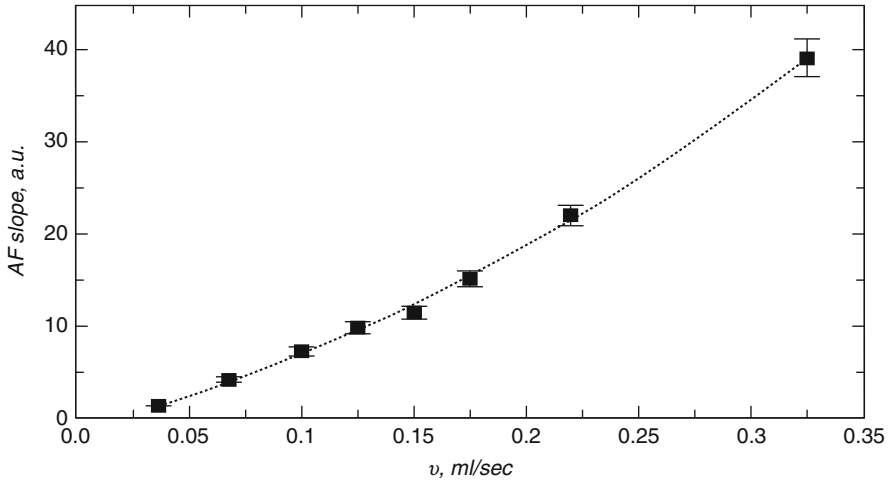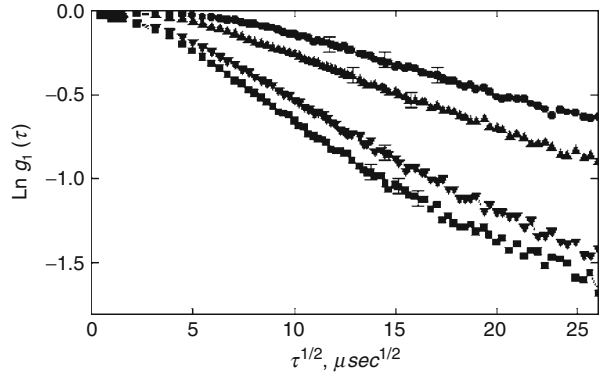
Fig. 4.8 The measured slopes of the temporal field autocorrelation functions versus average
velocity of flows (phantom measurements)

When shear flow significantly dominates under the Brownian motion, taking into
account (4.10), a semilogarithmic plot of $g_1(\tau)$ versus $\tau^{1/2}$ is considered, which
gives a straight line slope (Fig. 4.7) proportional to the velocity of flow of scattering
particles confirmed experimentally (Fig. 4.8).

The changes in the relative slope of temporal field autocorrelation function
(see Fig. 4.7) measured in vivo during the human arm suppression [45, 55].
The decay rate of the correlation function decreases as the cuff pressure is increased.
There is a small decrease when the cuff pressure is increased to 50 mmHg, a larger
decrease when the arm suppression is increased to 100 mmHg, and a small decrease
again when the cuff pressure is increased to 150 mmHg. The change in the slope
results from venous occlusion.

Fig. 4.9 The relative slope of temporal field autocorrelation functions measured for arm suppression changes in real time
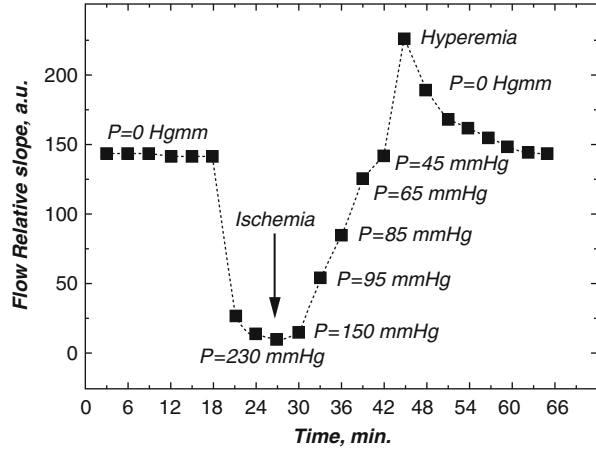
Fig. 4.10 Blood volume and deoxygenation measured simultaneously with the measurements of slope of temporal field autocorrelation function changes (see Fig. 4.9)
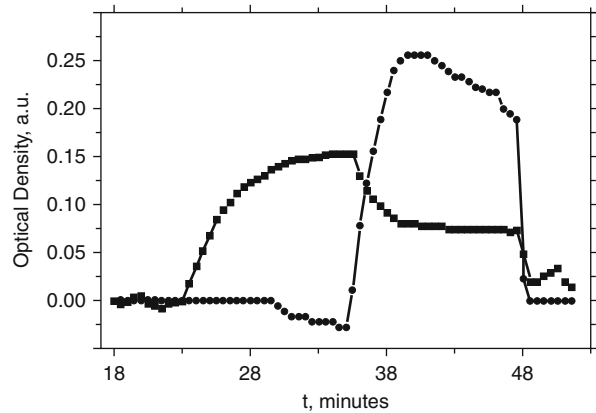
Figure 4.9 represents the changes in relative slope of temporal field autocorrelation functions in time. The ischemia refers to the use of a pressure cuff to occlude blood flow in a limb, preventing the delivery of oxygen. The initial baseline refers to un-cuffed measurements for the first 20 min, when the arm, blood flow, blood volume, and deoxygenation are at normal conditions.

The arm suppression is quickly raised to 230 mmHg that simultaneously occludes veins and arteries. The changes in average blood volume and oxygenation simultaneously monitored by the "Runman" device (NIM Inc. Philadelphia, PA) are presented in Fig. 4.10. Each DWS measurement was performed in 2 min, while blood volume and oxygenation measurements were gathered continuously. In 12 min time, the cuff pressure was slightly released and the measurements continued until the blood flow, volume, and oxygenation returned to normal.

The results presented in Fig. 4.9 clearly show the post-occlusive reactive hyperemic overshoot after the cuff pressure was released. Comparing these results to the

results of blood volume and oxygenation measurements, presented in Fig. 4.10, it is easy to see that during venous and arterial occlusion, the volume did not change, but blood deoxygenation increased, while blood flow decreased rapidly. No change in blood volume occurs because blood flow has been abruptly halted (see Fig. 4.10).

The deoxygenation of blood increases, corresponding to a decrease in oxygenation. When the arteries are opened by dropping the pressure below 150 mmHg, a significant increase in blood volume is observed, as well as drop in blood deoxygenation. This is due to arteries' ability to deliver more blood to the tissues when the venous pathways are still occluded. As the pressure drops further, the blood volume drops a little because of incomplete venous occlusion, allowing blood to leak back to the body's vascular system. This notion of leakage is supported by an increase in measured flow as the pressure decreases. Under normal circumstances, the veins remain occluded and the blood volume and flow rate remain fixed until the pressure drops below 80 mmHg. When the pressure drops to zero, the blood volume and oxygenation are seen to return to normal but the blood flow first increases above the baseline because of a hyperemic response.

Thus, the DWS can be used to determine the blood flow rate of various human tissues in vivo. Alternatively, so-called *diffuse laser Doppler velocimetry* (DLDV) [57] can be applied for a similar purpose. DWS and DLDV are related to each other according to the Wiener-Khintchine theorem [58]:

$$S(\omega) = \frac{\langle I \rangle^2}{2\pi} \int_{-\infty}^{+\infty} [g_1(\tau)]^2 \cos(i\omega_0 \tau) d\tau. \tag{4.14}$$

The DWS and DLDV may seem identical, but the main distinctions between them are technical requirements and convenience rather than fundamental differences. However, for the weak optical signals (at the single photon counting rate), photon correlation approach is preferable. Recent technology breakthroughs and development of digital multichannel autocorrelators based on high-speed processors lifted many technical restrictions from the correlation method, and now medium fluctuations may be probed over an extraordinarily wide range of time scales, from 10^{-8} to 10^5.

In addition, to convert DWS and DLDV measured signals to the actual blood flow parameters, analysis of the path length distribution within the skin tissues and skin vascular bed is required. The uncertainty of the sampling depth leads to ambiguities in the interpretation of what fraction of the recorded signal is generated by capillary blood flow and by flow through arterioles, venules, arteriovenous anastomosis, etc.

Based on the results of computer modeling [47, 48], it can be assumed that for the small distance between source and detector fibers (~ 0.3–0.5 mm), the detected photons are predominantly scattered in the topical vascularized skin layers, such as *papillary dermis*, *upper blood net dermis*, and the upper part of the *reticular dermis*. Similar to the results of phantom studies (see Fig. 4.8), computer modeling allows finding out the observed changes of the correlation function slope in comparison to blood flow in various groups of vessels. This allows to reliably decompose

measured correlation function into the components corresponding to the contribution of different compartments of the blood vascular net.

Instead of the fiber-optic-based DWS system presented above, which analyzed the intensity fluctuations at a single point (one-speckle spot), a large area of the intensity pattern (hence multispeckle) of scattered light can be analyzed using a CCD camera [59, 60].

The main advantage of this setup is the significant reduction in the data acquisition time, since a large number of one-speckle spot DWS experiments are performed simultaneously. This instrument should be capable of measuring the values of flow parameters in the medium with high precision and accuracy. However, this approach requires spatially resolved analysis and developing an algorithm to convert accurately the measured autocorrelation function to blood flow values.

4.5 Summary

DWS is a modern technique uniquely suited for the measurement of the average size of particles and their spatial displacement within a randomly inhomogeneous highly scattering and absorbing medium, including bio-tissues. The technique is based on illuminating of the medium with a coherent laser light and analyzing the loss of coherence of the scattered field arising from motion of the scattering particles with respect to each other.

This chapter reviews the experimental fiber-optic-based DWS approach developed for noninvasive quantitative monitoring and functional diagnostics of skin blood flow and skin blood microcirculation in vivo. The presented technique encourages developing and validation of the methodology further to the point that skin blood microcirculation measurements can be routinely and accurately obtained in normal skin, and to estimate its changes before, during, and after medical procedures. This is likely to lead to noninvasive quantitative monitoring of the effectiveness of general diagnostics [61], diabetes studies [62], pharmacological intervention for failing surgical skin flaps or replants [63], blood microcirculation monitoring during sepsis, burn depth assessment [64], and diagnosis of atherosclerotic disease as well as to investigate mechanisms of photodynamic therapy for cancer treatment [65]. Apart from this, this method can be effectively applied in preclinical studies of blood samples in vitro [66] and in colloid chemistry and material science [53, 54].

References

1. A.A. Rossini, W.L. Chick, Microvascular pathology diabetes mellitus, in *Microcirculation*, ed. by G. Kaley, B.M. Altura, vol. III (University Park Press, Baltimore, 1980), pp. 245–271
2. E. Davis, Hypertension and peripheral vascular diseases, in *Microcirculation*, ed. by G. Kaley, B.M. Altura, vol. III (University Park Press, Baltimore, 1980), pp. 223–234
3. P.D. Coleridge-Smith, P.R.S. Thomas, J.D. Scurr, J.A. Dormandy, The etiology of venous ulceration – a new hypothesis. Br. Med. J. **296**, 1726–1727 (1988)
4. P.C. Hübert, L. Qun Hu, G.P. Biro, Review of physiologic mechanisms in response to anemia. CMAJ **156**, S27–S40 (1997)
5. B. Fagrell, Microcirculatory methods for the clinical assessment of hypertension, hypotension, and ischemia. Ann. Biomed. Eng. **14**(2), 163–173 (1986)
6. 2001 Heart and Stroke Statistical Update (American Heart Association, Dallas, 2000), www.americanheart.org/statistics/index.html
7. B.E. Bouma, G.J. Tearney, *Handbook of Optical Coherence Tomography* (Marcel Dekker, New York, 2002)
8. J.B. Pawley, *Handbook of Biological Confocal Microscopy* (Springer, New York, 2006)
9. N.V. Tkachenko, *Optical Spectroscopy: Methods and Instrumentations* (Elsevier Science, Amsterdam, 2006)
10. V.V. Tuchin (ed.), *Handbook on Optical Biomedical Diagnostics*, vol. PM107 (SPIE Press, Bellingham, 2002)
11. J.V. Chapman, G.R. Sutherland, The noninvasive evaluation of hemodynamics, in *Congenital Heart Disease. Doppler Ultrasound Applications in the Adult and Pediatric Patient with Congenital Heart Disease*. Developments in Cardiovascular Medicine Series, vol. 114 (Kluwer, Dordrecht, 1990)
12. W.J. Manning, W. Li, R.R. Edelman, A preliminary-report comparing magnetic-resonance coronary angiography with conventional angiography. New Eng. J. Med. **328**, 828–832 (1993)
13. R.F. Bonner, R. Nossal, Principles of laser-Doppler flowmetry, in *Laser-Doppler Blood Flowmetry*, ed. by A.P. Shepherd, P.A. Oberg (Kluwer, Dordrecht, 1990), pp. 17–45
14. J.D. Briers, Laser Doppler, speckle and related techniques for blood perfusion mapping and imaging. Physiol. Meas. **22**, R35–R66 (2001)
15. B. Fagrell, A. Bollinger, Application of microcirculation research to clinical disease (Chapter 11), in *Clinically Applied Microcirculation Research*, ed. by J.H. Barker, G.L. Anderson, M.D. Menger (CRC Press, Boca Raton, 1995), pp. 149–160
16. M. Rajadhyaksha, M. Grossman, D. Esterowitz, R.H. Webb, R.R. Anderson, In vivo confocal scanning laser microscopy of human skin: Melanin provides strong contrast. J. Invest. Dermatol. **104**, 946–952 (1995)
17. Z. Chen, Y. Zhao, S.M. Srinivas, J.S. Nelson, N. Prakash, R.D. Frostig, Optical Doppler tomography. IEEE J. Sel. Top. Quant. Elect. **5**, 1134–1142 (1999)
18. J.A. Izatt, M.D. Kulkarni, S. Yazdanfar, J.K. Barton, A.J. Welch, In vivo bidirectional color Doppler flow imaging of picoliter blood volumes using optical coherence tomography. Opt. Lett. **22**(18), 1439–1441 (1997)
19. V. Kalchenko, N. Madar, I. Meglinski, A. Harmelin, In vivo characterization of tumor and tumor vascular network using a multi-mode imaging approach. J. Biophotonics **4**(9), 645–649 (2011)
20. Y.L. Kuznetsov, V.V. Kalchenko, I.V. Meglinski, Multi-modal imaging of vascular network and blood microcirculation by optical diagnostic techniques. Quantum Elect. **41**(4), 308–313 (2011)
21. A. Serov, B. Steinacher, T. Lasser, Full-field laser Doppler perfusion imaging and monitoring with an intelligent CMOS camera. Opt. Express **13**, 3681–3689 (2005)

22. W. Brown (ed.), *Dynamic Light Scattering. The Method and Some Applications* (Oxford University Press, New York, 1993)
23. J.L. Harden, V. Viasnoff, Recent advances in DWS-based micro-rheology. Curr. Opin. Colloid In. **6**(5–6), 438–445 (2001)
24. G. Maret, E. Wolf, Multiple light scattering from disordered media. The effect of Brownian motion of scatterers. Z. Physik B – Condens. Matter **65**, 409–413 (1987)
25. W.V. Meyer, A.E. Smart, R.G.W. Brown, Special issue on photon correlation and scattering. Appl. Opt. **40**(24), 3965–4242 (2001)
26. H.Z. Cummins, E.R. Pike, *Photon Correlation and Light Beating Spectroscopy* (Plenum Press, New York, 1973)
27. R. Pecora, *Dynamic Light Scattering: Applications of Photon Correlation Spectroscopy* (Plenum Press, New York, 1985)
28. B. Crosignani, P.D. Porto, M. Bertolotti, *Statistical Properties of Scattered Light* (Academic, New York, 1975)
29. M. Giglio, in *Laser in Biology and Medicine*, ed. by F. Hillenkamp, R. Pratesi, C.A. Sacchi. Series A: Life Sciences, vol. 34 (Plenum Press, New York, 1980), p. 111
30. H.Z. Cummins, H.L. Swinney, in *Progress in Optics*, ed. by E. Wolf, vol. VIII (American Elsevier, North Holland, 1970), p. 135
31. A.D. Lebedev, Y.N. Levchuk, A.V. Lomakin, V.A. Noskin, *Laser Correlation Spectroscopy in Biology* (Naukova Dumka, Kiev, 1987)
32. D.J. Pine, D.A. Weitz, G. Maret, P.E. Wolf, E. Herbolzheimer, P.M. Chaikin, Dynamical correlations of multiply scattered light, in *Scattering and Localization of Classical Waves in Random Media*, ed. by P. Sheng. World Scientific Series on Direction in Condensed Matter physics, vol. 8 (World Scientific Publishing, Singapore, 1990), pp. 312–372
33. K.M. Watson, Multiple scattering of electromagnetic waves in an underdense plasma. J. Math. Phys. **10**, 688–702 (1969)
34. D.A. Weitz, D.J. Pine, Diffusing-wave spectroscopy (Chapter 16), in *Dynamic Light Scattering The Method and Some Applications*, ed. by W. Brown (Oxford University Press, New York, 1993), pp. 652–720
35. V.V. Tuchin, *Tissue Optics: Light Scattering Methods and Instruments for Medical Diagnosis*, vol. PM 166, 2nd edn. (SPIE Press, Bellingham, 2007)
36. A.G. Yodh, P.D. Kaplan, D.J. Pine, Pulsed diffusing-wave spectroscopy: High resolution through nonlinear optical gaiting. Phys. Rev. B **42**, 4744–4747 (1990)
37. T. Bellini, M.A. Glaser, N.A. Clark, V. Degiorgio, Effects of finite laser coherence in quasi-elastic multiple-scattering. Phys. Rev. A **44**(8), 5215–5223 (1991)
38. D.A. Boas, L.E. Campbell, A.G. Yodh, Scattering and imaging with diffusing temporal field correlations. Phys. Rev. Lett. **75**(9), 1855–1858 (1995)
39. A. Isimaru, *Wave Propagation and Scattering in Random Media* (Wiley, New York, 1999)
40. X.-L. Wu, D.J. Pine, P.M. Chaikin, J.S. Huang, D.A. Weitz, Diffusing-wave spectroscopy in shear flow. J. Opt. Soc. Am. B **7**(1), 15–20 (1990)
41. M. Heckmeier, S.E. Skipetrov, G. Maret, R. Maynard, Imaging of dynamic heterogeneities in multiple-scattering media. J. Opt. Soc. Am. A **14**(1), 185–191 (1997)
42. D.A. Boas, I.V. Meglinski, L. Zemany, L.E. Campbell, B. Chance, A.G. Yodh, Diffusion of temporal field correlation with selected applications. Proc. SPIE **2732**, 34–46 (1996)
43. M. Heckmeier, G. Maret, Visualization of flow in multiple-scattering liquids. Europhys. Lett. **34**(4), 257–262 (1996)
44. S.E. Skipetrov, I.V. Meglinski, Diffusing-wave spectroscopy in random inhomogeneous media with spatially localized scatterer flow. J. Exp. Theor. Phys. **86**(4), 661–665 (1998)
45. I.V. Meglinski, D.A. Boas, A.G. Yodh, B. Chance, In vivo measuring of blood flow changes using diffusing wave correlation techniques, in *Advances in Optical Imaging and Photon Migration*, ed. by R.R. Alfano, J.G. Fujimoto, vol. 2 (Optical Society of America, Washington, DC, 1996), pp. 195–197

46. D.A. Boas, I.V. Meglinski, L. Zemany, L.E. Campbell, B. Chance, A.G. Yodh, Flow properties of heterogeneous turbid media probed by diffusing temporal correlation, in *Advances in Optics Imaging and Photon Migration*, ed. by R.R. Alfano, J.G. Fujimoto, vol. 2 (Optical Society of America, Washington, DC, 1996), pp. 175–178

47. I.V. Meglinski, S.J. Matcher, Modelling the sampling volume for skin blood oxygenation measurements. Med. Biol. Eng. Comp. **39**(1), 44–50 (2001)

48. I.V. Meglinski, S.J. Matcher, The analysis of spatial distribution of the detector depth sensitivity in multi-layered inhomogeneous highly scattering and absorbing medium by the Monte Carlo technique. Opt. Spectrosc. **91**(4), 654–659 (2001)

49. E. Overbeck, C. Sinn, Three-dimensional dynamic light scattering. J. Mod. Opt. **46**(2), 303–326 (1999)

50. D.P. Chowdhury, C.M. Sorensen, T.W. Taylor, J.F. Merklin, T.W. Lester, Application of photon-correlation spectroscopy to flowing Brownian-motion systems. Appl. Opt. **23**(22), 4149–4154 (1984)

51. H.J. van Staveren, C.J.M. Moes, J. van Marle, S.A. Prahll, M.J.C. van Gemert, Light scattering in intralipid – 10 % in the wavelength range of 400-1100 nm. Appl. Opt. **30**(31), 4507–4514 (1991)

52. S.E. Skipetrov, R. Maynard, Dynamic multiple scattering of light in multilayer turbid media. Phys. Lett. A **217**(2–3), 181–185 (1996)

53. M.J. Solomon, Q. Lu, Rheology and dynamics of particles in viscoelastic media. Curr. Opin. Colloid In. **6**(5–6), 430–437 (2001)

54. F.C. MacKintosh, C.F. Schmidt, Microrheology. Curr. Opin. Colloid In. **4**, 300–307 (1999)

55. I.V. Meglinski, D.A. Boas, A.G. Yodh, B. Chance, V.V. Tuchin, The development of correlation of intensity fluctuations technique for the non-invasive monitoring and measurements of the blood flow parameters. Izv. VUZ. Appl. Nonlinear Dynam. **4**(6), 72–81 (1996)

56. D.A. Boas, A.G. Yodh, Spatially varying dynamical properties of turbid media probed with diffusing temporal light correlation. J. Opt. Soc. Am. A **14**, 192–215 (1997)

57. P. Snabre, J. Dufaux, L. Brunel, Diffuse laser Doppler velocimetry from multiple scattering media and flowing suspensions, in *Waves and Imaging through Complex Media*, ed. by P. Sebbah (Kluwer, New York, 2001), pp. 369–382

58. S.M. Rytov, Y.A. Kravtzov, V.I. Tatarskii, *Introduction to Statistical Radiophysics. I. Random Processes* (Nauka, Moscow, 1978)

59. L. Cipelletti, D.A. Weitz, Ultralow-angle dynamic light scattering with a charge coupled device camera based multispeckle, multitau correlator. Rev. Sci. Instrum. **70**, 3214–3221 (1999)

60. V. Viasnoff, F. Lequeux, D.J. Pine, Multi-speckle diffusing-wave spectroscopy: A tool to study slow relaxation and time-dependent dynamics. Rev. Sci. Instrum. **73**(6), 2336–2344 (2002)

61. J.E. Tooke, L.H. Smaje, The microcirculation and clinical disease, in *Clinically Applied Microcirculation Research*, ed. by J.H. Barker, G.L. Anderson, M.D. Menger (CRC Press, Boca Raton, 1995), pp. 3–15

62. A.J. Jaap, J.E. Tooke, Diabetes and the microcirculation, in *Clinically Applied Microcirculation Research*, ed. by J.H. Barker, G.L. Anderson, M.D. Menger (CRC Press, Boca Raton, 1995), pp. 31–44

63. P.C. Neligan, Monitoring techniques for the detection of flow failure in the postoperative period. Microsurgery **14**, 162–164 (1993)

64. Z.B.M. Niazi, T.J.H. Essex, R. Papini, D. Scott, N.R. Mclean, M.J.M. Black, New laser-Doppler scanner, a valuable adjunct in burn depth assessment. Burns **19**, 485–489 (1993)

65. M. Korbelik, G. Krosl, Cellular-levels of photosensitizers in tumors – the role of proximity to the blood-supply. Brit. J. Cancer **70**, 604–610 (1994)

66. A.N. Korolevich, I.V. Meglinski, The experimental study of the potentialities of diffusing wave spectroscopy for the investigating of the structural characteristics of blood under multiple scattering. Bioelectrochemistry **52**, 223–227 (2000)

Laser Speckle Imaging of Cerebral Blood Flow

5

Qingming Luo, Chao Jiang, Pengcheng Li, Haiying Cheng, Zhen Wang, Zheng Wang, and Valery V. Tuchin

Contents

Abstract

Monitoring the spatio-temporal characteristics of cerebral blood flow (CBF) is crucial for studying the normal and pathophysiologic conditions of brain metabolism. By illuminating the cortex with laser light and imaging the resulting speckle pattern, relative CBF images with tens of microns spatial and millisecond temporal resolution can be obtained. In this chapter, a laser speckle imaging (LSI) method for monitoring dynamic, high-resolution CBF is introduced. To improve the spatial resolution of current LSI, a modified LSI method is proposed. To accelerate the speed of data processing, three LSI data processing

Q. Luo (✉) • C. Jiang • P. Li • H. Cheng • Z. Wang • Z. Wang
Huazhong University of Science and Technology, Wuhan, People's Republic of China
e-mail: qluo@mail.hust.edu.cn, jchaoer@gmail.com, pengchengli@mail.hust.edu.cn, chhyibp@sina.com, zhenwang@mail.hust.edu.cn, nirvana_wz@sina.com

V.V. Tuchin
Department of Optics and Biophotonics, Saratov State University, Saratov, Russian Federation

Precision Mechanics and Control, Institute of the Russian Academy of Sciences, Saratov, Russian Federation

Optoelectronics and Measurement Techniques Laboratory, University of Oulu, Oulu, Finland
e-mail: tuchinvv@mail.ru

frameworks based on graphics processing unit (GPU), digital signal processor (DSP), and field-programmable gate array (FPGA) are also presented. Applications for detecting the changes in local CBF induced by sensory stimulation and thermal stimulation, the influence of a chemical agent on CBF, and the influence of acute hyperglycemia following cortical spreading depression on CBF are given.

5.1   Introduction

Monitoring the spatio-temporal characteristics of cerebral blood flow (CBF) is crucial for studying the normal and pathophysiologic conditions of brain metabolism. At present there are several techniques for velocity measurement. One of these is laser-Doppler flowmetry (LDF), which provides information about CBF from a limited number of isolated points in the brain (approximately 1 mm^3) [1, 2]. Scanning laser-Doppler can be used to obtain spatially resolved relative CBF images by moving a beam across the field of interest, but the temporal and spatial resolution of this technique is limited by the need to mechanically scan the probe or the beam [3, 4], such as with laser Doppler perfusion imaging (LDPI). Another method is time-varying laser speckle [5–7], which suffers from the same problems as LDF. Single photon emission computed tomography (SPECT) uses the tracer 99mTC-HMPAO to obtain quantitative CBF values (mL/100 g/min). However, its disadvantage is the injection of exogenous substances [8, 9]. Positron emission tomography (PET) scanning is currently the most versatile and widely used functional imaging modality both in health and disease. The spatial resolution is quite limited, being about 0.5 cm^3 [10, 11]. The recently developed thermal diffusion technique is based on the thermal conductivity of cortical tissue, allowing continuous recordings of CBF in a small region of the cortex. The spatial resolution is determined by the placement of the sensor [12, 13]. Although autoradiographic methods provide three-dimensional spatial information, they contain no information about the temporal evolution of CBF changes [14]. Methods based on magnetic resonance imaging, such as functional magnetic resonance imaging (fMRI), provide spatial maps of CBF but are limited in their temporal and spatial resolution [15, 16]. Therefore, a noninvasive, simple method without the need for scanning and providing full-field dynamic CBF images would be helpful in experimental investigations of functional cerebral activation and cerebral pathophysiology.

One such technique is the laser speckle imaging technique (LSI) using the first-order spatial statistics of time-integrated speckle, which was first proposed by the group of A.F. Fercher and J.D. Briers [17, 18]. The speckle method has been used to image blood flow in the retina [19] and skin [20]. Later, a group at Harvard medical school applied this method to image blood flows during focal ischemia and cortical spreading depression (CSD) [21, 22]. In this chapter, we will introduce the principles of laser speckle imaging method and provide some experimental results on various animal models for dynamic, high-resolution CBF monitoring.

5.2   Principles of Laser Speckle Imaging

Laser speckle is an interference pattern produced by the light reflected or scattered from different parts of the illuminated rough (i.e., nonspecular) surface. When the area illuminated by laser light is imaged onto a camera, a granular or speckle pattern is produced. If the scattered particles are moving, a time-varying speckle pattern is generated at each pixel in the image. The faster the blood flow velocity changes, the faster the speckle pattern fluctuates and a more blurred speckle pattern is recorded by a CCD camera during the exposure time.

We can use the electric field autocorrelation function $g_1(\tau)$ to quantify the temporal fluctuation of speckle. The absolute normalized temporal electric field autocorrelation is denoted as

$$g_1(\tau) = |\langle E(t)E^*(t+\tau)\rangle|/\langle E(t)E^*(t)\rangle, \tag{5.1}$$

where τ is the delay time and $E(t)$ is electric field. In fact, the temporal fluctuation of the electric field is difficult to measure directly. However, the electric field autocorrelation function can be deduced from the light intensity autocorrelation function, which is easily obtained by recording the light intensity $I(t)$. The light intensity autocorrelation function $g_2(\tau)$ is defined as

$$g_2(\tau) = \langle I(t)I(t+\tau)\rangle/\langle I\rangle^2. \tag{5.2}$$

There is a Siegert relation for relating the light intensity autocorrelation function to the electric field autocorrelation function:

$$g_2(\tau) = 1 + \beta[g_1(\tau)]^2, \tag{5.3}$$

where β is a constant that is determined by the ratio of detector size to speckle spot size.

For each exposure, the CCD camera returns a frame of raw speckle image. The intensity for the ith pixel in a small region of image (usually 5×5, 7×7 pixels square) consisting of total N pixels with the index i can be quantified as follows:

$$I_{i,T} = \frac{1}{T}\left\{ \int_0^T \int_0^T I_i(t')I_i(t'')dt'dt'' \right\}^{\frac{1}{2}}, \tag{5.4}$$

where T is duration of the exposure time.

During the exposure, the nth moment of the intensity of the pixels in the small region is defined as $\langle I^n\rangle_T = \frac{1}{N}\sum_{i=1}^{N}(I_{i,T})^n$. With the assumption of ergodicity, we can

replace the temporal estimation by the spatial estimation. Therefore, combining (5.2), (5.3), and (5.4), the second moment can be deduced as follows:

$$\langle I^2 \rangle_T = \frac{\langle I \rangle^2}{T^2} \int_0^T \int_0^T \left\{ 1 + \beta[g_1(t' - t'')]^2 \right\} dt' dt'' \tag{5.5}$$

We can further deduce the relationship between the local speckle contrast C in a small region and the electric field autocorrelation function as follows [23]:

$$C = \sqrt{\langle I^2 \rangle - \langle I \rangle^2} / \langle I \rangle = \left\{ \frac{\beta}{T} \int_0^T 2(1 - t/T)[g_1(t)]^2 dt \right\}^{\frac{1}{2}} \tag{5.6}$$

Note that (5.6) is a correction to the primal definition of Fercher and Briers [17], in which the β was defined as 1. Under this condition, without considering the finite size of detector, they give a relation as $C = \left\{ \frac{1}{T} \int_0^T [g_1(t)]^2 dt \right\}^{\frac{1}{2}}$ without the term $2(1 - t/T)$ [17].

The normalized autocorrelation function of a electric field can often be approximated by a negative exponential function (for the case of a Lorentzian spectrum, for example, it is an exactly negative exponential) as

$$g_1(t) = \exp(-t/\tau_c) \tag{5.7}$$

where τ_c is the autocorrelation time of light fluctuation. The less the τ_c is, the faster the scattering granule moves.

Substituting expression (5.7) in (5.6), we can obtain the relation of the spatial local contrast and τ_c as follows:

$$C = \sqrt{(\exp(-2x) - 1 + 2x)/2x^2} \tag{5.8}$$

where x is the ratio of T to τ_c ($x = T/\tau_c$).

Equation (5.8) gives us an expression for the speckle contrast in a time-integrated speckle pattern as a function of the exposure time T and the correlation time $\tau_c = 1/(ak_0v)$, where v is the mean velocity of scatterers, k_0 is the light wavenumber, and a is a factor that depends on the Lorentzian width and scattering properties of the tissue [24]. As in laser-Doppler measurements, it is theoretically possible to relate the correlation time values τ_c, to the absolute velocities of the red blood cells, but this is difficult to do in practice, inasmuch as the number of moving particles that light interacted

Fig. 5.1 Schematic of system for laser speckle imaging. A He:Ne laser ($\lambda = 632.8$ nm, 3 mW) beam is expanded to illuminate the area of interest in the brain, which is then imaged onto a CCD camera. The computer acquires raw speckle images and computes relative blood flow maps [27]
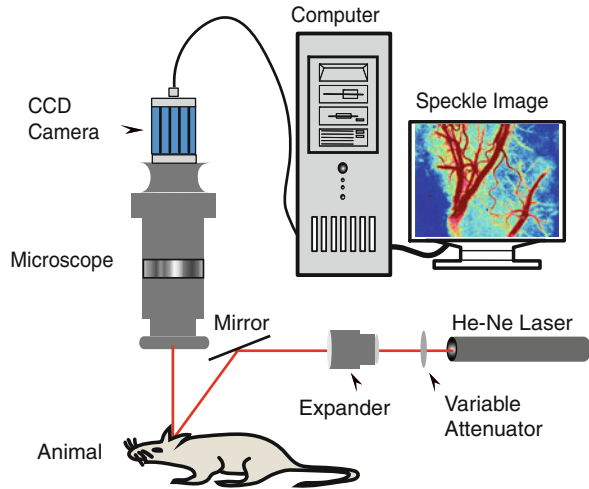
with and their orientations are unknown [24]. However, relative spatial and temporal measurements of velocity can be obtained from the ratios of $2T/\tau_c$ that is proportional to the velocity and defined as measured velocity in present chapter.

5.3 Instrumentation and Performances

5.3.1 LSI System

The schematic diagram of the experimental set-up is shown in Fig. 5.1. A He:Ne laser beam ($\lambda = 632.8$ nm, 3 mW) was coupled into an 8-mm-diameter fiber bundle, which was adjusted to illuminate the area of interest evenly. The illuminated area was imaged through a zoom stereo microscope (SZ6045TR, Olympus, Japan) onto a CCD camera (PIXELFLY, PCO Computer Optics, Germany) with 480×640 pixels, yielding an image of 0.8–7 mm depending on the magnification. The exposure time T of the CCD was 20 ms. Images were acquired through the easy-control software (PCO Computer Optics, Germany) at 40 Hz.

5.3.2 Data Analysis

The raw speckle images were acquired to compute the speckle contrast images. The number of pixels used to compute the local speckle contrast can be selected by the user: lower numbers reduce the validity of the statistics, whereas higher numbers limit the spatial resolution of the technique. To ensure proper sampling of the speckle pattern, the minimum size of a single speckle should be double the size

Table 5.1 Time consumptions comparison between GPU and CPU for processing each frame [26]

Image resolution	Window size: 5×5 pixels, $1/C^2$			Window size: 7×7 pixels, $1/C^2$			Window size: 5×5 pixels, T/τ_c		
	CPU (ms)	GPU (ms)	Speed-up	CPU (ms)	GPU (ms)	Speed-up	CPU (ms)	GPU (ms)	Speed-up
320×240	11.0	0.09	12.2×	16.5	1.30	12.7×	110	2.10	52.4×
480×320	22.3	1.52	14.7×	33.5	2.31	14.5×	290	3.80	76.3×
640×480	45.2	2.88	15.7×	67.9	4.43	15.3×	480	8.31	57.8×
800×600	70.6	4.25	16.6×	106	6.59	16.1×	927	11.3	82.0×
$1,024 \times 768$	123	6.86	17.9×	173	10.7	16.2×	1,162	18.1	64.2×
$1,280 \times 1,024$	209	11.5	18.2×	306	18.4	16.6×	1,938	34.2	56.7×
$1,600 \times 1,200$	283	16.6	17.0×	431	26.0	16.6×	3,073	44.8	68.6×
$1,920 \times 1,440$	409	24.0	17.0×	621	37.9	16.4×	4,347	72.3	60.1×

Note: The results are from three different kernels, and the operations each kernel performed are shown in the first row. $1/C^2$ denotes the approximation method and T/τ_c denotes the Newton iteration method using (5.8).

of a single pixel in the image, according to the Nyquist criterion [25], which is the width of the diffraction-limited spot size and is given by 2.44 $\lambda f/D$, where λ is the wavelength and f/D is the f number of the system. In our system, the pixel size was 9.9 μm. With a magnification of unity, the required f/D is 12.8 at a wavelength of 632.8 nm. Squares of 5×5 pixels were used according the theoretical studies [17, 18]. The software calculated the speckle contrast (k) for any given square of 5×5 pixels and assigned this value to the central pixel of the square. This process was then repeated to obtain a speckle contrast map. For each pixel in the speckle contrast map, the measured velocity ($2T/\tau_c$) was obtained through (5.8), which describes the relationship between the correlation time and velocity, and therefore measures velocity map.

To compute the relative blood flows in vessels of interest, first a threshold was set in a region of interest from the measured velocity image and then the vessels of interest were identified by the pixels with values above this threshold. The mean values of the measured velocity in those pixels were computed at each time-point. The relative velocity in the vessel of interest was expressed as the ratio of the measured velocity in the condition of stimuli to that of control condition.

In order to accelerate the speed of data processing and achieve a fast blood flow visualization of high-resolution laser speckle imaging, we introduced a graphics processing unit (GPU)-equipped personal computer into the data processing framework of laser speckle imaging [26]. In recent years, the rapid increase in the performance of graphics hardware, coupled with recent improvements in programmability, has made graphics hardware a compelling platform for computationally demanding tasks in a wide variety of application domains [27]. By using a GPU, a 12–60 fold performance enhancement is obtained in comparison to the optimized CPU implementations. Table 5.1 provides a detailed performance comparison between GPU and CPU for LSI.

Fig. 5.2 Schematic illustration of the portable laser speckle perfusion imaging system [28]
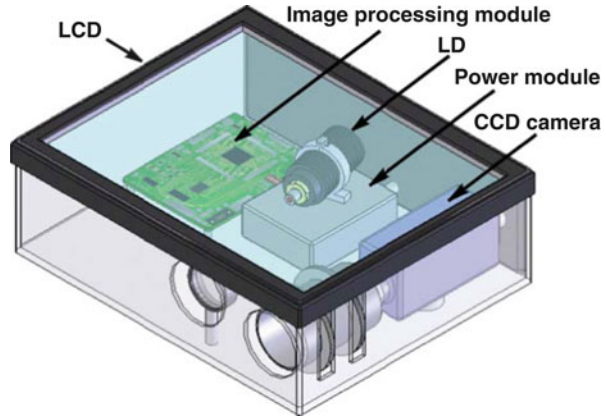
5.3.3   Portable LSI System

The LSI system illustrated above is based on a personal computer for image processing with large size, which potentially limits the widespread clinical utility. The need for a portable laser speckle imaging system that does not compromise processing efficiency is crucial in clinical diagnosis. However, the processing of laser speckle images is time consuming because of the heavy calculation required for enormous high-resolution image data. To address this problem, two methods using a DSP (digital signal processor) and FPGA (field-programmable gate array) have been introduced to accomplish portable real-time LSI systems [28, 29].

5.3.3.1 DSP-Based LSI System

A portable laser speckle imaging system based on a digital signal processor (DSP) is described in this section, including the corresponding hardware and software [28].

As shown in Fig. 5.2, the portable laser speckle perfusion imaging system is composed of a laser diode (LD), charge-coupled device (CCD) camera, image processing module, and liquid crystal display (LCD). A laser diode (660 nm, 30 mW) illuminates the surface of the tissue and the speckle pattern is captured by a monochrome CCD camera (OB-1280, Oved, China; pixel size $= 6.5 \times 6.25\,\mu m$) with 8-bit resolution. The output format of CCD camera is phase alternating line (PAL) video standard at 25 frames per second. The image processing module provides high-speed calculation with a laser speckle spatial contrast analysis algorithm and a laser speckle temporal contrast analysis algorithm. It has flexibility to modify the parameters or analysis algorithms of a system through the graphical user interface on the on-screen display (OSD) and to display blood flow images on LCD in real time.

The block diagram of the image processing module is depicted in Fig. 5.3. It includes TVP5150, TMS320DM6446, and the peripherals. The TVP5150, an ultralow power video decoder, converts baseband analog PAL video signal from a CCD camera into a digital YUV 4:2:2 component video signal. As a highly
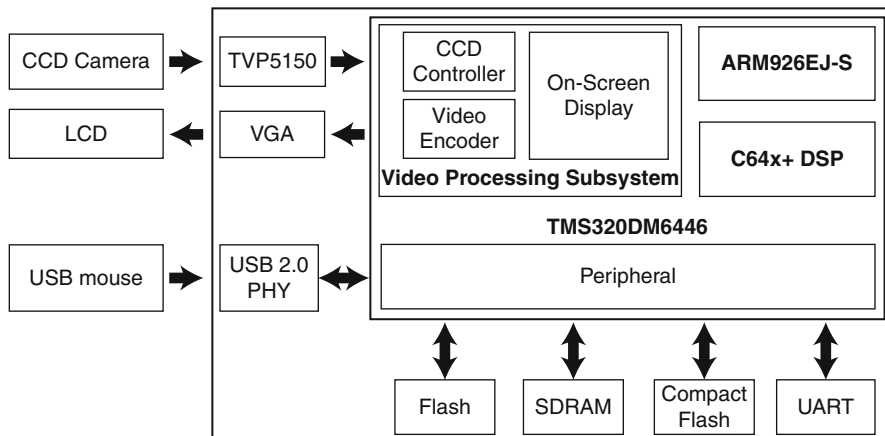
Fig. 5.3 Block diagram of image processing module [28]

integrated digital media system-on-chip, TMS320DM6446 (Texas Instruments Inc.) consists of an ARM926 core, a C64x+ DSP core, a video processing subsystem, and some other peripherals. The ARM926EJ-S, a 32-bit RISC processor capable of supporting a full operating system such as LINUX, features flexible size instruction and data caches, tightly coupled memory interfaces, and a memory management unit. The C64x+ DSP core, which is based on advanced very-long-instruction-word (VLIW) architecture developed by Texas Instruments (TI), is the highest-performance fixed-point DSP generation in the TMS320C6000 DSP platform. The internal memory of C64x+ consists of a two-level cache based memory architecture and external memory. The cache size of Level 1 data memory (L1D) and Level 2 data memory (L2D) can be configured up to 32 and 64 K, respectively. The video processing subsystem provides an input interface for a video decoder and an output interface for a display device. The CCD controller is responsible for accepting digital data from the video decoder TVP5150. The function of the OSD module is to blend video data and bitmap data into a single display frame. The video encoder module provides four analog DACs that run at 54 MHz, providing a PAL video output. A 64 M-byte NAND flash memory is used to store a bootloader, operating system, and application program. A 256 M-byte synchronous dynamic random access memory (SDRAM) is designed to store the original digital image data before processing and run program code with high speed of reading and writing. The image processing module makes full use of the advantages of dual-core architecture of the TMS320DM6446. The application program runs on the ARM core, which also controls all peripherals through LINUX device drivers, while real-time tasks such as the laser speckle contrast analysis algorithm is assigned to the DSP core.

Figure 5.4 illustrates the software architecture of a portable laser speckle imaging system. The eXpressDSP Digital Media compliant LSCI algorithms are packaged in a codec server and executed on the DSP core. The application program calls the Video, Image, Speech, and Audio application programming interfaces (VISA APIs),

Fig. 5.4 Software architecture of portable laser speckle perfusion imaging system [28]
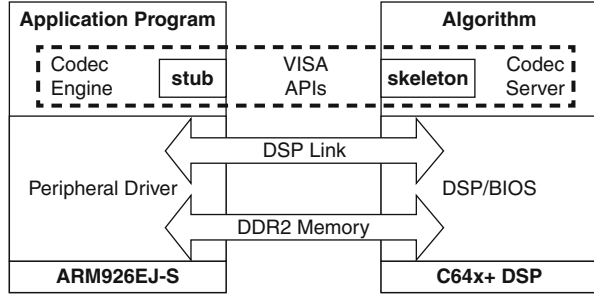
which use stubs and skeleton to access the algorithms. Communication between the ARM and DSP is managed by DSP/BIOS Link. All of the DDR2 memory is shared between the ARM and the DSP. The application program consists of four separate threads: the main thread, the capture thread, the video thread, and the display thread. In order to have a user-friendly interface, the main thread adopts MiniGUI, a cross-operating-system graphical user interface (GUI) under the GNU General Public License, to draw buttons and texts on the OSD and take input from USB mouse to send commands. The capture thread reads image data from TVP5150, which decodes the raw data of the CCD camera through the Video 4 LINUX 2 (V4L2) device driver; the video thread receives frame buffers from the capture thread and controls the DSP core to perform a laser speckle spatial contrast analysis algorithm or laser speckle temporal contrast analysis algorithm under the DSP/BIOS real-time operating system, and the display thread is responsible for copying the video buffer into the frame buffer of the display device driver.

With this highly integrated DSP method, we have markedly reduced the size and weight of the system, as well as its energy consumption, while preserving the high processing speed. In vivo experiments demonstrate that our portable laser speckle imaging system can obtain blood flow images at 25 frames per second with the resolution of 640×480 pixels. The portable and lightweight features make it capable of being adapted to a wide variety of application areas, such as the research laboratory, operating room, ambulance, and even disaster sites.

5.3.3.2 FPGA-Based LSI System

To further improve the processing capability of this kind of portable LSI system, we developed a novel hardware-friendly algorithm for the real-time processing of laser speckle imaging. Based on this algorithm, a dedicated hardware processor for real-time processing of laser speckle imaging data in the FPGA is designed. The pipeline processing scheme and parallel hardware architecture are introduced into the design of this type of LSI hardware processor in order to further improve the processing performance. When the LSI hardware processor is implemented in a low-cost FPGA running at the maximum frequency of 130 MHz, up to 85 raw images with the resolution of 640×480 pixels can be processed per second. Compared with the DSP solution, this hardware-based LSI processor can achieve real-time processing at very low clock frequency and power dissipation but with high performance.

In addition, we also present a system-on-chip (SOC) solution for LSI processing by integrating the CCD controller, memory controller, LSI hardware processor, and LCD display controller into a single FPGA chip [29].

As illustrated in Fig. 5.5, the circuit of the LSI processor mainly consists of a three-stage pipeline and one divider array. The modules of stage 1 to stage 3 in the pipeline correspond to calculate the simplified LSI estimation equation's [29] numerator and denominator that are output by the module of stage 3 in a pipeline before the divider array. All the modules in the pipeline run separately at the same time. For example, when module (c) of stage 2 is calculating the square value of the raw data accumulation out from module (a) of stage 1, module (a) is calculating the new accumulation of pixels in the next adjacent sliding window. When the size of the sliding window is 5×5, each module in the pipeline performs a part task of a sliding window in five clock cycles. This means that for every five cycles, a pair of numerator and denominator of a sliding window will be output from the module of stage 3 in the pipeline waiting for a dividing operation. The divider unit of this LSI hardware processor is designed using the scheme of the shift-and-subtraction method. So completing a dividing operation costs more than five clock cycles. For instance, when the raw data width is 12 bits in binary and the relative velocity value is at the precision of 0.01 in decimal, one dividing operation costs 45 clock cycles. Therefore, in order to keep pace with the output speed for the numerator and denominator from the module of stage 3 in the pipeline, a divider array containing nine hardware dividers is integrated into the LSI processor circuit. This parallel architecture consisting of multiple hardware dividers ensures that each pair of numerator and denominator can be processed in time. For every five clock cycles, a relative velocity value will be output from one divider of the divider array. In addition, a gatherer module follows the divider array that gathers the relative velocity values from the dividers and outputs these values in chronological order.

The method of reading the pixels of a raw image into the pipeline is illustrated in Fig. 5.6. At the rising edge of each clock cycle, a pixel value of a sliding window is read into the pipeline from the raw image memory. The reading order is one pixel after one pixel in the vertical direction in a sliding window. We define that the sliding window's five pixels in the vertical direction make up a vertical strip. The two adjacent sliding windows have the same four vertical strips, so that only a new vertical strip needs to be read into the pipeline when computing the new adjacent is possible. Because module (a) and module (d) of the LSI hardware processor's circuit can cache the temporary results of the strips from 2 to 5 of the last sliding window, these strips are the first, the second, the third, and the fourth strip of the new adjacent sliding window at the same time. This scheme allows that computing one sliding window only needs to read the fifth vertical strip of the current sliding window into the pipeline, as the former four vertical strips are cached in the circuit when computing the last sliding window. Of course, there is no adjacent sliding window for the first sliding window in each line of the raw image, so the first one must read all five vertical strips while the following ones only need to read one vertical strip. With this method, computing a raw image with the
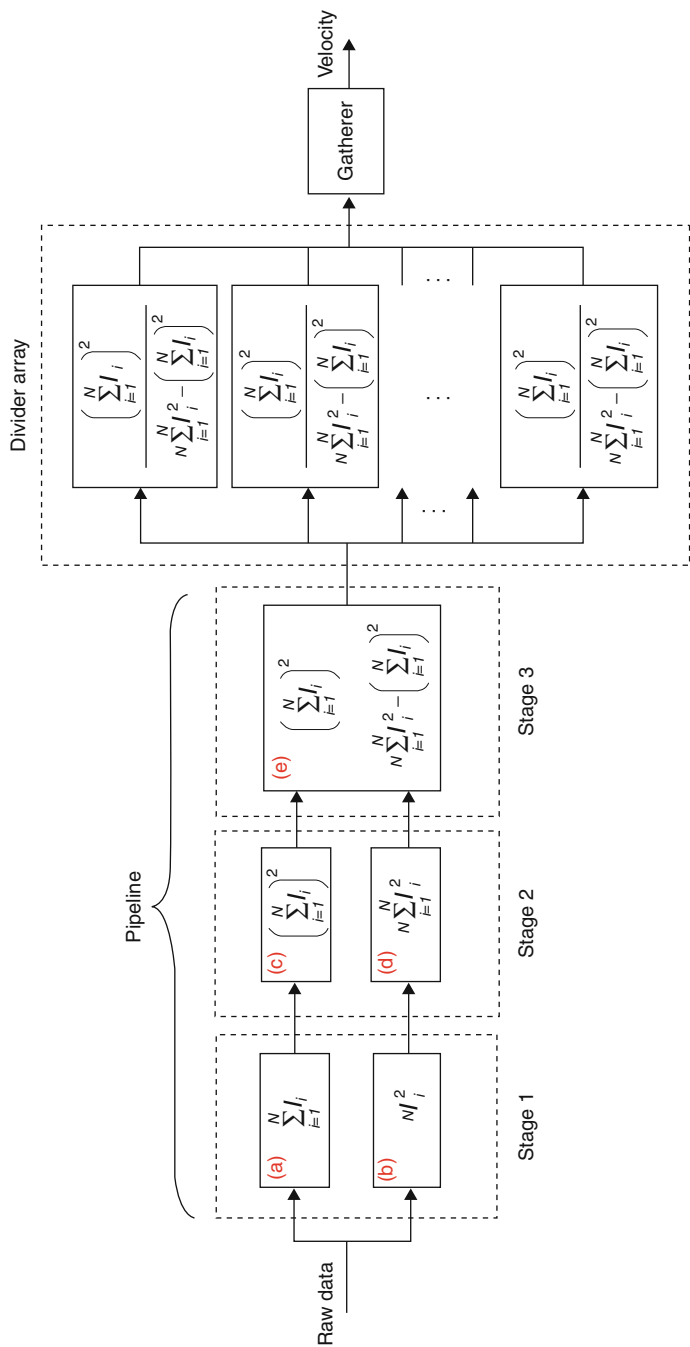
Fig. 5.5 The circuit architecture of an LSI hardware processor mainly consists of a three-stage pipeline and a divider array. Module (*a*) and module (*b*) of stage 1 in the pipeline calculate the accumulation and the square multiplied with constant N of raw data within a sliding window separately. Module(*c*) and module (*d*) of stage 2 in the pipeline calculate the square of the data out from module (*a*) and the accumulation of the data out from module (*b*) separately. Module (*e*) calculates the subtraction of the data out from module (*c*) and module (*d*). In addition, module (*e*) caches the accumulation of module (*c*) waiting for outputting with the subtraction value at the same time as numerator and denominator. The divider array contains multiple divides to keep pace with the output speed of module (*e*) in the pipeline. The gatherer module gathers the relative velocity value out from dividers in the divider array and outputs these values in chronological order [29]
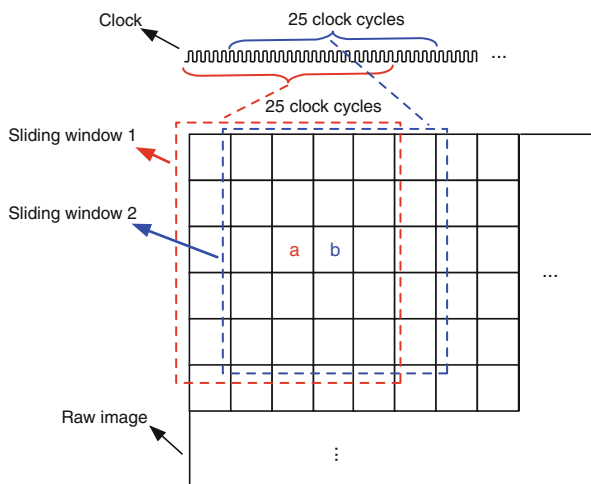
Fig. 5.6 The illustration describes the method of reading the raw data into the pipeline of the LSI hardware processor. The size of sliding window is 5×5. The small black rectangles stand for pixels of raw image. The *colored rectangles* with a *dashed line* stand for two adjacent sliding windows. Symbols *a* and *b* mark the center positions of sliding window 1 and sliding window 2. Clock sequence diagrams are also presented to tell how many cycles for reading each sliding widows' pixels into the pipeline [29]

resolution of $M \times N$ pixels needs $5 \times (M - 4) \times N + 55$ clock cycles when the size of the sliding window is 5×5, where M is the number of rows of the raw image and N is the number of columns of the raw image. The number 55 is the latency for the last sliding window from having been read into the pipeline to outputting the relative velocity value in the hardware divider of the divider array.

Based on the LSI hardware processor above, we further designed a SOC for LSI system by integrating the CCD camera controller, memory controller, LSI hardware processor, and LCD display controller in a single FPGA chip. The CCD camera controller controls the work mode of the CCD camera and receives the image data captured by CCD camera. The memory controller consisting of a saver module and a reader module caches the raw image data out from CCD controller module into the image memory and reads the raw image data to the LSI processor. The LSI processing unit containing a LSI hardware processor converts the raw data into the relative velocity value based on the algorithm described above. The relative velocity values out from the LSI processor are normalized into color index values and the color index values are stored in the video memory to make up a blood flow map image. The LCD controller reads the blood flow image in the video memory and displays it in a LCD. This SOC-based LSI system can achieve the real-time data acquisition, processing, and display. The main architecture of this SOC design is illustrated in Fig. 5.7.
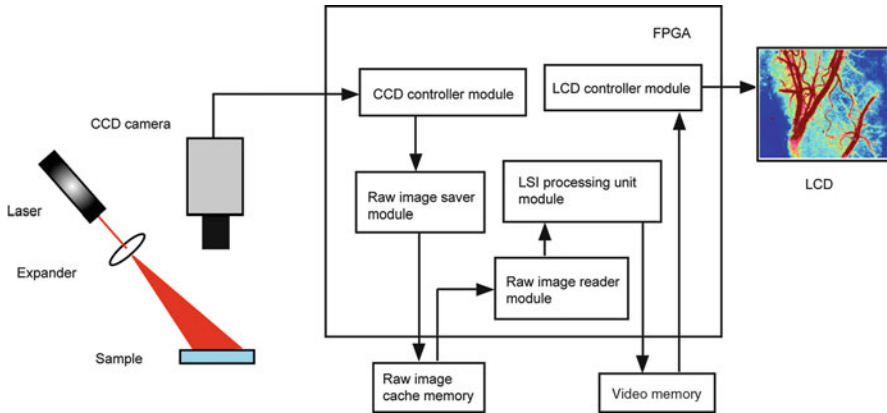
Fig. 5.7 The main architecture of the SOC solution for the LSI system. The direction of the arrow stands for the direction of the data that flows in the main modules [29]

5.4   Applications

LSI is a noninvasive full-field optical imaging method with high spatial and temporal resolution, which is a convenient technique in measuring the dynamic of CBF [21, 22]. In this chapter, we present the application of the LSI method to monitor the dynamics of CBF in several animal models.

5.4.1   Speckle Imaging of CBF Dynamics During Sciatic Nerve Stimulation

The postulation by Roy and Sherrington in 1890 that the brain possesses an intrinsic mechanism by which its vascular supply can be varied locally in correspondence with locally variation of functional activity provided a principal basis of neurophysiology and neuroenergetics for modern functional neuroimaging techniques [30, 31]. The change in local cerebral blood flow (CBF) induced by sensory stimulation is considered as an index to investigate the effects of activated neural activity based on the above hypothesis. The response of evoked regional CBF to somatosensory stimulation in rats has been studied using some techniques such as laser-Doppler flowmetry (LDF) and functional MRI (fMRI) [32, 33]. In addition, quantitative and temporal relationship between regional CBF and neuronal activation has also been reported, which combined electrophysiological and LDF techniques [34]. It is well documented that CBF at the level of individual capillaries and the coupling of neuronal activity to flow in capillaries are fundamental aspects of homeostasis in the normal and the diseased brain [35]. However, it is hard for most present techniques to probe the dynamics of blood flow at this level due to their limitations of temporal or spatial resolution. Therefore, a new alternative

approach is needed to assess the intrinsic hemodynamic response in the corresponding cortical areas and elucidate the role of CBF in circulatory and metabolic correlates of functional activation in the brain [36]. Here we apply the laser speckle imaging method to image CBF dynamics during sciatic stimulation.

5.4.1.1 Animal Preparation

Male adult Sprague–Dawley rats weighing from 350 to 400 g ($n = 16$) were anesthetized with an intraperitoneal injection of 2 % α-chloralose and 10 % urethane (50 and 600 mg/kg, respectively) to execute craniotomy. Atropine (0.4 mL/kg per hour) was administered to reduce mucous secretion during surgery. A closed cranial window (4 × 6 mm) over the parietal cortex was created as follows: a midline incision was made to expose the surface of the skull, then the skull overlying the hindlimb sensory cortex was bored to translucency with a dental drill under constant cooling with saline. The thinned skull preparation has the advantage over a full craniotomy since it keeps the dura mater intact and allows a long-term investigation into the changes in a somatosensory cortex within a single animal while preserving the integrity of the brain surface environment. The cranial window fully exposed the hindlimb sensory cortex in an area of 2.46 × 3.28 mm^2, centered at 2 mm caudal and 1.5 mm lateral to the bregma.

The animals were mounted in a stereotaxic frame, and body temperature was maintained at 37.0 ± 0.5 °C with a thermostatic heating blanket. A tracheotomy was performed to enable mechanical ventilation using a ventilator (TKR-200C, Animal Mechanical Respirator, China) with a mixture of air and oxygen (20 % O_2, 80 % N_2) to achieve physiological arterial blood levels of O_2 and CO_2 tension. The right femoral artery and vein were cannulated for measurement of blood pressure (PcLab Instruments, China) and intravenous administration of drugs. Periodically, a small volume of blood was drawn from the femoral artery, and the blood gas pressure (pO_2, pCO_2) and pH value were analyzed (JBP-607, Dissolved Oxygen Analyzer, China). After surgery, the animals were left for at least half an hour before the experiment began and supplemental doses of anesthetic (one-fifth initial dose/h) were also needed.

Stimulation of the sciatic nerve was similar to that used in conventional physiological studies. The contralateral sciatic nerve was dissected free and cut proximal to the bifurcation into the tibial and peroneal nerves. Then the proximal end was placed on a pair of silver electrodes and bathed in a pool of warm mineral oil. We stimulated the single sciatic nerve on the left with a rectangular pulse of 350 mV intensity, 0.5 ms duration, and at a rate of 5 Hz frequency for a continuous duration of 2 s (Multi Channel Systems, Germany). These parameters were chosen to optimize vessel response without affecting systemic blood pressure and were kept constant during each experiment. The single sciatic nerve on the left was stimulated for 2 s with rectangular pulses of 0.5 ms duration, 350 mV amplitude, and 5 Hz frequency (Multi Channel Systems, Germany). In all animals, a single-trial procedure was repeated 15–20 times and separated by an interval of at least 4 min. Four hundred frames of raw images were obtained in one 10-s single-trial; the electrical stimuli started at 2 s and the images in the first 2 s were recorded as
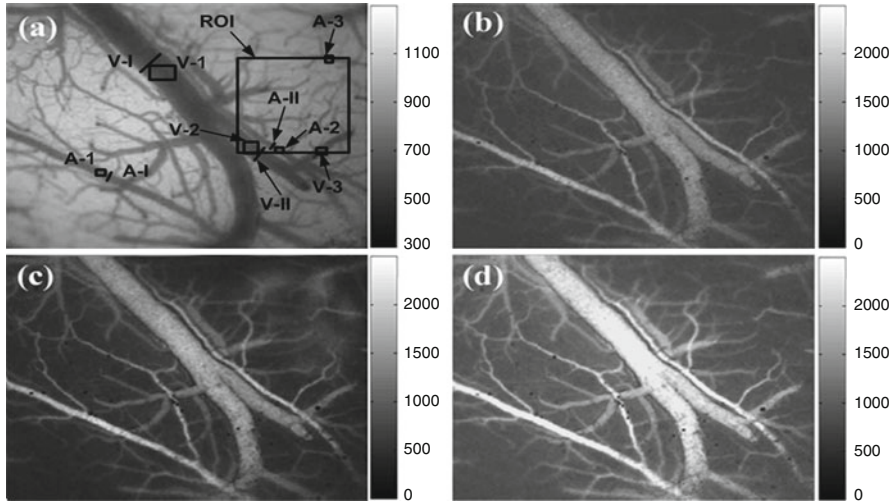
Fig. 5.8 Blood flow change in contralateral somatosensory cortex of rats under unilateral sciatic nerve stimulation. (**a**) A vascular topography illuminated with green light (540 ± 20 nm); (**b–d**) blood activation map at prestimulus, 1 and 3 s after the onset of stimulation (the relative blood-flow images are shown and converted from the speckle-contrast images, in which the brighter areas correspond to the area of increased blood flow.), respectively. A-1, 2, 3 and V-1, 2, 3 represent the arbitrarily selected regions-of-interest for monitoring changes in blood flow. A-I,II and V-I,II represent the selected loci on the vessel whose diameters are measured in the experiment [30]

baseline. Images were acquired through the Easy-control software (PCO Computer Optics, Germany) at 40 Hz and synchronized with Multi Channel Systems. Notably, here data acquisition was synchronized with the electrical signal via an appropriate trigger circuit, and therefore the procedures of data analysis described below could improve the reproducibility of our results and enhance the signal-to-noise ratio. All recorded data were finished within 3–4 h after the beginning of chloralose-urethane anesthesia.

5.4.1.2 Results

With the LSI technique we monitored blood flow in somatosensory cortex in a total of 16 rats under electrical stimulation of the sciatic nerve, and obtained the activated blood flow distribution at different levels of arteries/veins and the change of activated areas. Although slight differences existed in individual anatomic features in the rat cortex, we could eliminate this influence because the imaged area was much bigger than the scope demarcated by Hall et al. [37]. One example of our results is shown in Fig. 5.8, in which the brighter areas correspond to the area of increased blood flow. In comparison with LDF, an area of 1 mm^2 ROI in Fig. 5.8a was chosen to evaluate its mean velocity (Fig. 5.9): the evoked CBF started to increase at 0.7 ± 0.1 s, peaked at 3.1 ± 0.2 s, and then returned to the baseline level. This is consistent with the conclusions obtained from the LDF technique [32, 34].
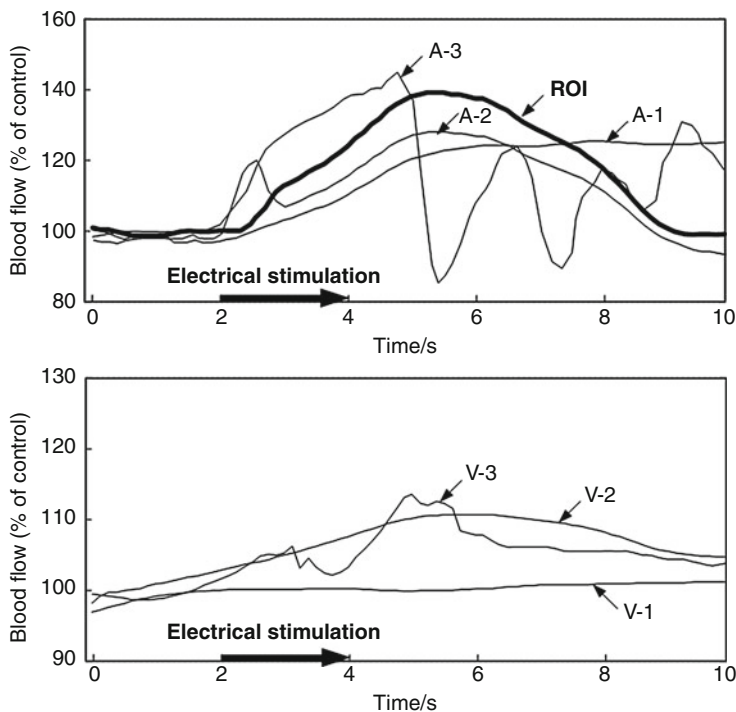
Fig. 5.9 The relative change of blood flow in 6 areas indicated in Fig. 5.8a (divided by the values of prestimulus) [30]

In order to differentiate the response patterns of artery/vein under the same stimulus, we labeled six distinct levels of vessels in Fig. 5.8a and displayed their changes of blood flow. The results clearly showed that the response patterns of arteries and veins in the somatosensory cortex were totally different: vein 1 (V-1, $\sim$140 μm in diameter) almost remained unaffected, and arteriole 1 (A-1, $\sim$35 μm in diameter) responded slowly; arteriole 2 (A-2, $\sim$35 μm in diameter) peaked at 3.5 ± 0.5 s after the onset of stimulation and then reached the steady-state plateau, and vein 2 (V-2, $\sim$70 μm in diameter) presented a delay and mild response; blood flow in the capillaries (A-3 and V-3, $\sim$10 μm in diameter) surged readily and increased significantly. We also measured the changes in arteries and veins with different diameters, and the results are shown in Fig. 5.10. The statistical results exhibited that arterioles (A-II, $\sim$35 μm in diameter) dilated abruptly ($p < 0.05$) but arteriole 1 (A-I) did not change and dilated slightly at 5–6 s after the end of stimulation ($p < 0.05$). No alterations in vein with diameter of >70 μm were observed during sciatic nerve stimulation ($p > 0.05$). We found that the blood flow in capillaries in hindlimb sensory cortex was firstly activated to increase at (0.5 ± 0.2) s; then arterioles with diameter of >70 μm began to respond at
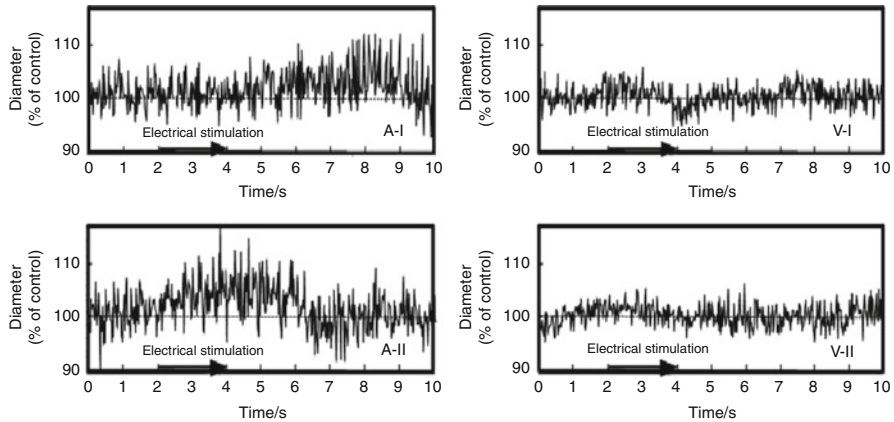
Fig. 5.10 Relative alterations in vessel diameter during sciatic nerve stimulation (divided by the values of prestimulus) [30]

(2.5 ± 0.5) s, dilated up to maximum at (3.5 ± 0.5) s and came back to the prestimulus level; and finally the activation propagated to the entire scope of somatosensory cortex. Blood flow in arteriole 1 did not increase until after 5–6 s end of stimulation since it was situated farther from the hindlimb cortex. The activation pattern of cerebral blood flow is discrete in spatial distribution and highly localized in the evoked cortex with the temporal evolution. This is consistent with the hypothesis of Roy and Sherrington and the conclusions drawn by other research groups [32–34, 38].

5.4.1.3 Discussion

The present study is influenced by various kinds of experimental conditions due to the complicacy of biological experiments. The first factor is stimulation parameters that should reach the threshold of response, and not affect systemic blood pressure and evoke the maximal magnitude of vascular response. The optimal parameters (350 mV, 0.5 ms, and 5 Hz) were adopted in our experiments. The second is anesthesia condition of animals. It was proved by the former investigations that chloralose-urethane is most suitable for the study on neurovascular coupling since it induces minimal cardiovascular effects [34, 38]. In order to minimize spontaneous oscillations (also known as "vasomotion"), it is important to maintain an adequate anesthesia and keep blood pressure above 80 mmHg. Anesthesia would exert direct influence on the animals' respiration and probably cause CBF fluctuating in nearly synchrony with the respiratory cycle. Third, tissue pH and blood composition also influence regional CBF. Acids and bases cause cerebral vasodilation and vasoconstriction, respectively. When functional activity in blood-perfused tissue is activated, the rate of energy metabolism is increased and the gas tension of CO_2 is elevated to cause cerebral vasodilation and increase local CBF. Electrical stimulation of unilateral sciatic nerve is a classical biological model that was used to probe effects of increased functional activity in somatosensory cortex [32, 38, 39].

In our experiments, several physiological parameters (including body temperature, femoral blood pressure, pO_2, pCO_2, and pH) were monitored for keeping a normal physiological status during the experiment. This improved the reliability and reproducibility of our results.

Until now, the response of evoked CBF to somatosensory stimulation in rats has been studied using some techniques such as laser-Doppler flowmetry (LDF) [32] and functional magnetic resonance imaging (fMRI) [33] under laboratory or clinical conditions. However, these conventional methods have their own limitations, like lower temporal/spatial resolutions in fMRI, or radioactive effects in positron emission tomography (PET), or limited information from isolated points in LDF. It is difficult to understand comprehensively behaviors of CBF during brain functional activity. It is almost certain that the dynamic regulation of the cerebral circulation is not mediated by a single exclusive mechanism but is achieved by numerous factors acting in concert. Most of the effects of these neural vasomotor pathways were observed in pial arteries and might not apply to the small parenchymal resistance vessels that regulate the blood flow, which is also known as the "spatial heterogeneity of microcirculation" [31]. The sample tissue volume of conventional LDF technique is approximately 1 mm^3 [32, 34, 40], which exerted great limitations on its application [41].

5.4.2 Speckle Imaging of CBF Dynamics under the Effect of a Hyper-Osmotic Chemical Agent

Optical clearing of tissue technique alters the optical properties of normally turbid tissues, offering many potential advantages in laser surgery and phototherapy [42–44]. The idea is that by reducing the scattering effect of the tissue by means of physical or chemical manipulation, among which are compression, coagulation, dehydration, and immersion into osmotically active chemical agents [45–47], imaging and surgical techniques can probe deeper into the tissue than is normally possible. This effectively opens a window into the tissue for more effective treatment, aiding diagnosis of deeper-lying tumors, for example.

In the application of light-based cerebral surgery and diagnostics, one of the problems deals with transport of the laser beam through the dura mater tissue. As dura mater, a typical fibrous tissue, is turbid due to the random scattering within tissue caused by variations in refractive index, depth penetration of optical methods is limited [43, 44]. Through application of hyper-osmotic chemical agents, the scattering effect of tissue can be temporarily modified, which is demonstrated in many studies [48, 49], and imaging modalities would benefit from an increased penetration depth [50, 51]. As tissue clearing is a reversible process, usually after a short time, interstitial liquid is reabsorbed into the tissue and the scattering returns to normal, the clearing effects and period of time of the chemical agents action are the focuses in these studies. The influence of chemical agents on tissue normal physiological function is investigated rarely. In the present chapter, optical

properties of in vitro and in vivo rabbit dura mater with the application of a hyper-osmotic chemical agent, glycerol, were measured, and the influence of epidurally applied hyper-osmotic glycerol on in vivo resting cerebral blood flow (CBF) was investigated by laser speckle imaging method based on our previous studies [30, 52–54].

5.4.2.1 Materials and Methods: Animal Preparation

Healthy rabbits, weighting 4–5 kg, were used for the experiments. Before the experiments, the animals were housed in individual cages in a specialized animal department where they were allowed free access to food and water. The experimental design has been approved by the local ethics committee. Rabbits were narcotized by 20 % urethane (0.5 mL/kg). Animals were divided into three groups for in vitro transmittance spectra, in vivo reflectance spectra and in vivo CBF measurement separately. In in vitro experiments, dura mater was removed from anesthetic rabbits. In in vivo experiments, rabbits were fixed on a stereotaxic apparatus. Body temperature was kept constant at 37 °C with a thermostablizing stage during experiments. The left femoral artery was cannulated for continuous blood pressure monitoring. Animals were ventilated and breathed room air supplemented with oxygen. The skull was removed and intact dura mater was exposed. The reflectance spectra were measured to investigate the optical clearing effect of glycerol on in vivo rabbit dura mater. The photographs were taken by digital video camera (Panasonic, Japan) in above two cases. To study the influence of glycerol to in vivo CBF, a small area of dura mater was removed. Warm dehydration glycerol was administrated near the exposed area. CBF in the exposed area was monitoring by laser speckle imaging method.

Transmission and Diffuse Reflectance Measurements

Optical property measurements were performed on in vitro and in vivo samples of rabbit dura mater with a computer-controlled PC1000 spectrometer (Fiber Optic Spectrometer, Ocean Optics Inc., U.S.A.) of scanning wavelengths of 370–2,000 nm. Native dura mater, which had not been treated with any chemical agents, and samples immersed in dehydration glycerol placed between two glass-slides were measured separately. Transmission spectra were obtained. To assess the optical property change of in vivo dura mater under the action of glycerol, glycerol was directly applied on the intact dura mater of the rabbits and reflectance spectra were measured.

Speckle Imaging Measurement

The instrument for speckle imaging measurement is shown in Fig. 5.1. As described above, images were acquired through the easy-control software (PCO Computer Optics, Germany) at 40 Hz. Conversion of the raw speckle image to blood flow maps was controlled by our written software that computed the speckle contrast and correlation time values at each pixel according to the principle of LSI [18].
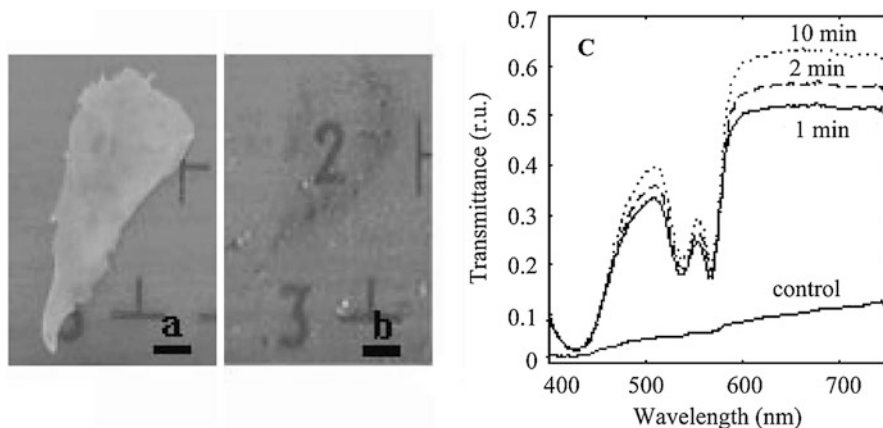
Fig. 5.11 Visual changes in the in vitro turbid rabbit dura mater and the measured optical changes before and after application of glycerol. (**a**) Native dura mater placed over the resolution target, bar = 1 mm. (**b**) 1-min application of glycerol, bar = 1 mm. (**c**) Transmittance spectra for native dura mater measured at application of glycerol for 1, 2, and 10 min

5.4.2.2 Results

Figure 5.11 illustrates the dynamic changes in in vitro dura mater turbidity after application of glycerol. A resolution target was placed under a dura mater sample. After the treatment of glycerol for 1 min, the target, which was not visible under the native dura mater (Fig. 5.11a), was seen through the dura mater specimen (Fig. 5.11b). Optical property measurement results (Fig. 5.11c) confirmed the visually observed reduction in scattering. Fig. 5.11c shows the increase in transmittance within the wavelength range of 400–750 nm as a function of time the dura mater was soaked in glycerol. The hemoglobin absorption became much more prominent after application of glycerol due to the blood on the dura mater (Fig. 5.11b).

In vivo experiment results are demonstrated in Fig. 5.12. Epidurally applying glycerol changed the turbidity of dura mater. The vasculature under the dura mater became visible after the treatment of glycerol (Fig. 5.12a, b). The reflectance decreased as a function of time glycerol action, which proved the visually observation. In Fig. 5.12c, it was seen that, the dura mater nearly recovered to native condition after 1 min.

Velocity images of in vivo CBF under the effect of glycerol are shown in Fig. 5.13. Glycerol was applied around the exposed area. When glycerol diffused in brain tissue and influenced CBF under the dura mater, CBF in the exposed area would also change. Figure 5.13 illustrates the spatio-temporal characteristics of CBF changes under the treatment of glycerol. Under the action of glycerol, blood flow first decreased while the blood vessels underneath the dura mater became increasingly visible. Then blood flow increased to near baseline, at the same time the turbidity of the dura mater returned.
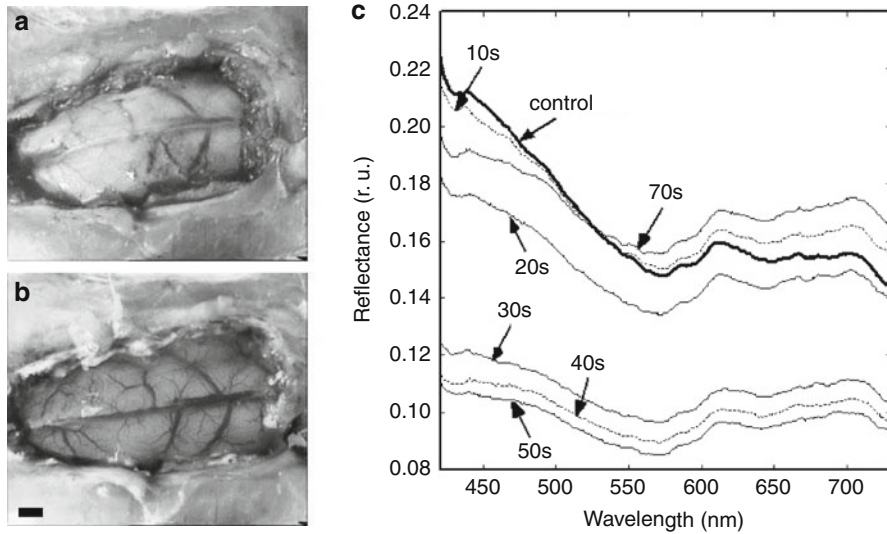
Fig. 5.12 Visual changes and the measured optical changes for in vivo rabbit dura mater before and after treatment with glycerol epidurally. (**a**) Native in vivo turbid dura mater, bar = 1 mm. (**b**) Fifty-second application of glycerol, bar = 1 mm. (**c**) Reflectance spectra for native dura mater, application of glycerol epidurally for 10, 20, 30, 40, 50, and 70 s

Figure 5.14 gave the time course of changes in four different vessels, which was expressed as the ratio of the measured velocity in the conditions of treatment with glycerol to that of control condition. Vessel 2 was an arteriole. Vessels 1, 3, and 4 were venules. Blood flow in vessel 2 (arteriole) began to decrease after 20-s application of glycerol, whereas in other vessels (venules) it decreased immediately after application with glycerol. The blood flow in vessel 1 decreased slower than that in other vessels, which suggested that blood flow in the arteriole had different response from that in the venules. Blood flow in all vessels decreased to 70–80 % of baseline after treatment with glycerol.

5.4.2.3 Discussion
Optical Clearing Effects on In Vitro and In Vivo Dura Mater
After treatment with glycerol, the in vitro dura mater specimen became increasingly transparent, which lasted for a long period of time. However, in vivo dura mater became transparent and then recovered to be turbidity within short period of time. This may be due to different interactions between tissue and the agent under in vitro and in vivo conditions.

The optical effect caused by glycerol is a time-dependent process in that it occurs as a consequence of the transport of chemical agent and water in and out of the tissue, respectively. The mass transport occurs when experiencing an osmotic stress. Interstitial water travels from areas of high water potential and a lower osmotic potential to a lower water potential and higher osmotic potential.
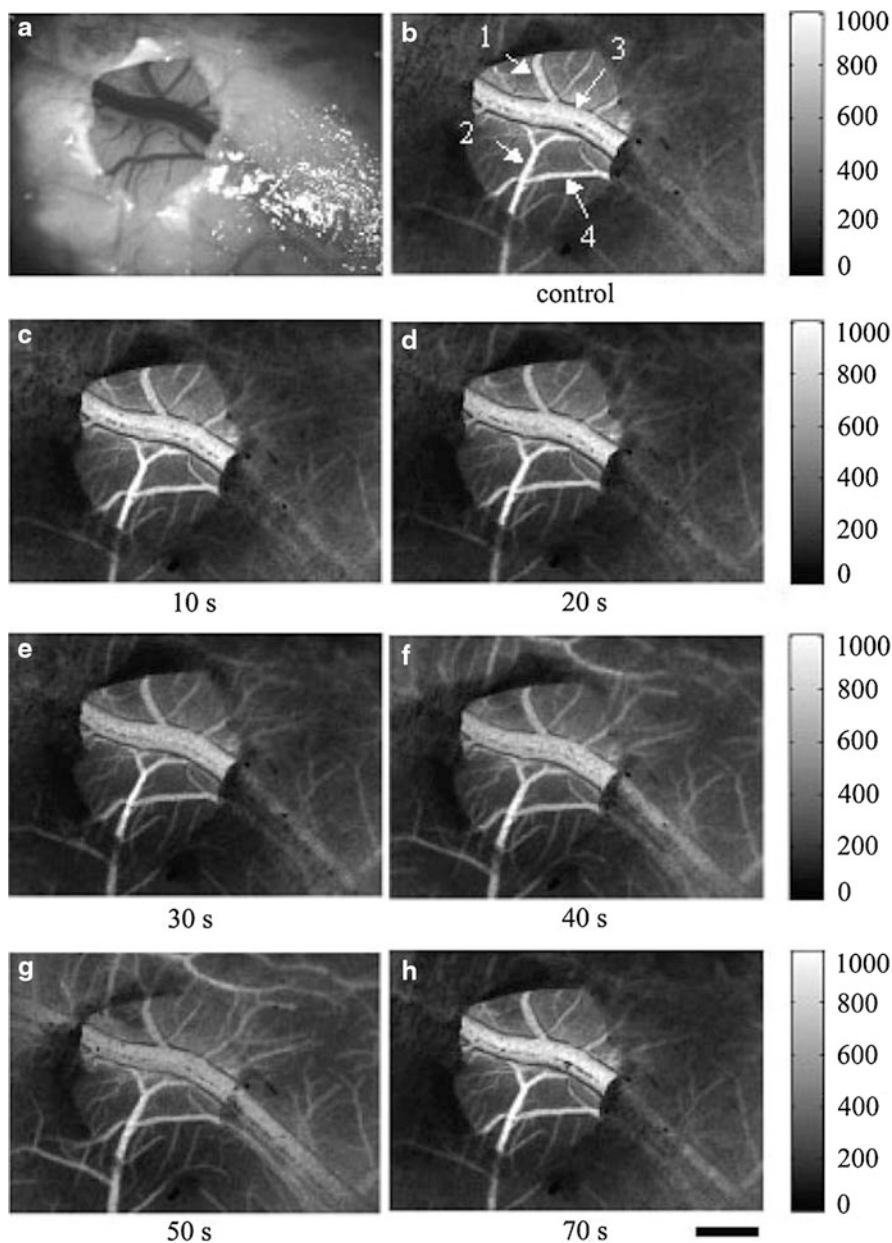
Fig. 5.13 Blood–flow images following the epidurally applied glycerol around the exposed area of in vivo dura mater. (**a**) White light picture of the interest area. Four vessels are indicated in (**b**). (**b–h**) Blood flow maps expressed as measured velocity, which is proportional to the blood flow velocity, during the treatment with glycerol and represented by images at the time-points shown in Fig. 5.14. (**b**) Imaged blood flow before the application with glycerol (control). (**c**) Ten-second application of glycerol. No obvious change in blood flow was observed. (**d**) Twenty-second
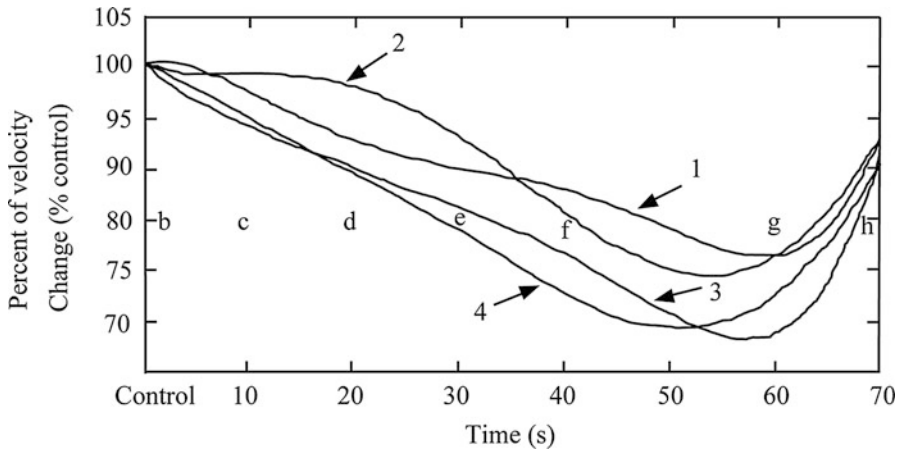
Fig. 5.14 Time course of change in relative blood flow in vessel 1, 2, 3, and 4, which are indicated in Fig. 5.13b, before and after the application of glycerol epidurally. After 20 s, the blood flow in vessel 2 (arteriole) began to decrease, while blood flow in other vessels (venules) decreased immediately after application with glycerol. Decreases of blood flow in these vessels were 20–30 % of baseline. (**b–h**) denote the time points of corresponding images in Fig. 5.13b–h

This indicates water leaves interstitial (extrafibrillar) spaces in the case of topical application of a hyper-osmotic agent and leaves the bulk tissue when the agent surrounds it. Due to the high affinity of glycerol to water and its much higher viscosity in comparison with water, local tissue dehydration takes place, and collagen fibrils may become more closely packed. This will reduce multiple scattering if the packed fibers act as a single scatterer. In in vivo studies at the point when equilibrium is reached, water will begin reentering the extrafibrillar space over the treated area, while glycerol is washed out. The change in optical properties of tissue with variations in fiber and/or cell size, refractive index mismatch between the extrafibrillar or extracellular and intrafibrillar or intracellular spaces, and fibrillar and/or cellular volume fraction are still under investigation [45–48, 55]. In spite of the high viscosity of glycerol, it cannot be assumed that in the in vivo setup it only acts on dura mater tissue as a dehydration agent. Diffusion into brain tissue has to be considered. In addition, glycerol was applied epidurally at high concentrations due to no protection in its surface and a high tension in the present study, not like studies [50] using glycerol to reduce scattering in skin, in which glycerol

Fig. 5.13 (continued) application of glycerol. Blood flow began to decrease. (**e**) Thirty-second application of glycerol. The blood vessels underneath dura mater began to be clear. (**f**) Forty-second application of glycerol. Blood flow decreased and the transparency of surrounding dura mater increased. (**g**) Fifty-second application of glycerol. More blood vessels could be seen through dura mater and the blood flow decreased significantly. (**h**) Seventy-second application of glycerol. Blood flow increased and dura mater became turbid again. Bar = 1 mm

required subdermal injection because the penetration of glycerol through the epidermis was quite limited due to the protective (cellular) nature of the stratum corneum.

Influence of Glycerol to Resting CBF

In our study, glycerol was applied on the dura mater surface around the exposed area. When it diffused into brain tissue and influenced the CBF, the blood flow of exposed area also changed. LSI was a noninvasive full-field optical imaging method for the measurement of blood flow, which provided high-resolution maps of spatial and temporal evolution of CBF changes. The dynamic change of CBF in the exposed area monitored by LSI reflected the effect of glycerol. From our results (Fig. 5.13), the CBF perfusion decreased as the transparency of dura mater increased, which was also proved by the in vivo optical measurement (Fig. 5.12). The increase of tissue transmittance may be due to the index matching between the ground substance and the collagen fibrils, caused mostly by tissue dehydration induced by glycerol [50]. The release of neurotransmitters or vasoactive substances during glycerol application [56], although glycerol is biologically inert and is widely used in cosmetics and medicine [57, 58], may affect CBF. The mechanism of glycerol's influence on in vivo CBF requires further research.

LSI

LSI is a noninvasive full-field optical imaging method with high spatial and temporal resolution, which was found to be a convenient technique in measuring the dynamic of CBF [23, 24]. As with other optical imaging methods, LSI can only provide the velocity information on the surface of the turbid tissues due to the high scattering properties of the light in the biological tissue. In brain studies, as dura mater on the surface of the brain cortex is a typical fibrous tissue and turbid for the light between visible and NIR spectra range, which limits the depth penetration of optical methods, it is usually removed [59, 60]. This destroys the normal physiological condition of CBF and creates the need for a complex method to maintain normal encephalic pressure. Our study can be viewed as an attempt to find a suitable agent to improve optical properties while measuring cerebral blood flow in vivo.

Existing studies showed that the technique of reduced tissue scattering by optical clearing agents can be of benefit to a number of optical diagnostic or therapeutic applications. For example, the potential of the method to enhance penetration depth in imaging had been shown for the specific case of OCT, which demonstrated that the glycerol reduced excessive scattering in the tissue enough to image an underlying area that was previously not visible [50]. This method was also used to study the effects of transient tissue scattering on the remitted fluorescence emission intensity from a target placed under a tissue sample. The detected fluorescent signal was found to increase as the scattering in tissue samples was substantially reduced. Although the increase was different between different chemical agents, it was not statistically different between in vivo skin and in vitro skin [51]. In our study, the LSI method was used to image the regional blood flow. After application with glycerol, the blood flow in blood vessels

underneath in vivo dura mater became clearly visible, which suggested that the light penetration increased. The optical immersion technique could increase the light penetration of LSI. However, administration with glycerol decreased 20–30 % of control cerebral blood flow at the same time. This indicated that glycerol was not suitable for our purposes. In our experiment, as glucose (40 %) and mannitol (156 mg/mL) solutions have no significant clearing effect by epidural application on in vivo dura mater (data not shown), only glycerol's effect was studied in the present chapter.

5.4.3 Acute Hyperglycemia Compromises Cerebral Blood Flow Following Cortical Spreading Depression in Rats Monitored by Laser Speckle Imaging

Hyperglycemia and cortical spreading depression (CSD) can worsen the outcome of ischemic stroke and also influence cerebral blood flow (CBF) [61–63]. It is demonstrated that acute or chronic hyperglycemia can lead to the decrease in CBF in animals in the previous studies [62]. Hyperglycemia might have a long-term effect on CBF, especially under the condition of cerebral ischemia. There is also evidence that CSD plays an important role in ischemic stroke, and it has been commonly believed that CSD increases the ischemic volume and aggravates ischemic injury [63]. Therefore, perhaps both hyperglycemia and CSD have a prolonged cooperative effect on CBF in ischemic stroke. In this application, laser speckle imaging is used to investigate the long-term effect of acute hyperglycemia and the additional effect of CSD during acute hyperglycemia on CBF for different vascular compartments in an acute rat hyperglycemic model.

5.4.3.1 Materials and Methods

Intraperitoneal anesthesia was implemented with a mixture of α-chloralose (50 mg/kg) with urethane (600 mg/kg) in adult male Sprague–Dawley rats (200–300 g). The body temperature of the rats was kept constant at $37.0 \pm 0.5\ ^{\circ}$C. A 6.0×8.0 mm cranial window with intact dura was produced by removing the skull bone overlying the parietal cortex. In order to induce CSD by electrical stimulation, a burr hole (2 mm diameter) was drilled in the ipsilateral frontal bone. Acute hyperglycemia in rats ($n = 10$, n is the number of the rats) was produced by giving a 50 % solution of D-glucose in water at 15 mL/kg intraperitoneally. The same volume of normal saline was given by intraperitoneal injection to the control rats ($n = 10$).

The administration of agents (50 % D-glucose or saline) was performed immediately after the acquisition of baseline imaging of laser speckle. Laser speckle imaging was repeated at 30-min intervals after the administration of agents. Ninety consecutive raw speckle images were acquired for each measurement (20 ms exposure time). The whole observation period was 180 min. Speckle contrast images were acquired by analyzing the raw speckle images using the method of laser speckle temporal contrast analysis that will be described later in this chapter. Relative changes in CBF at each time in a region were calculated as a percentage of the baseline.

In five rats of each group, CSD was initiated by intracortical electrical stimulation (5 mA, 1-s duration, 1 pulse). Optical reflectance and direct current potential were simultaneously recorded to characterize CSD waves, as mentioned in Ref. [41]. At the start, just before the injection of glucose or saline (0 min), a laser speckle image was obtained and then the first CSD was immediately induced. CSD waves were again induced immediately after laser speckle imaging at 30, 60, 90, 120, and 150 min after experimental intervention.

For data analysis, different vascular compartments were manually chosen by selecting subregions of the blood velocity image. These vascular compartments are arterioles, capillaries, and venules, respectively. Three subregions of the image were selected for each of the three vascular compartments. Relative change in CBF at each time in a subregion was expressed as percent change from its baseline. The same process as that reported here was done in each experiment (including five rats). Statistical analysis was then performed on this dataset, consisting of 15 samples for each vascular compartment at each time point. The relative changes in CBF at each of the three vascular compartments were obtained by averaging over 15 samples, yielding three curves for the time courses of relative changes in CBF for the three vascular compartments.

5.4.3.2 Results

Effect of Acute Hyperglycemia on CBF in Normal Rat Cortex

Figure 5.15a, b illustrate the status of CBF before and after the administration of agents (saline or D-glucose) in a representative subject. The redder the region in the pseudo color image, the higher the blood flow is in this region. This shows that the CBF in the rat with acute hyperglycemia exhibited a distinct increase, peaking about 90–120 min after glucose injection, and finally recovered toward the baseline level (Fig. 5.15b).

The time courses of the relative changes in CBF for three vascular compartments (as drawn in Fig. 5.15a – 0 min or Fig. 5.15b – 0 min] are shown in Fig. 5.15c and Fig. 5.15d, correspondingly. These curves in Fig. 5.15c show that the relative changes in CBF after saline administration at different vascular compartments had slight fluctuation over 180-min periods, ranging from 88 % to 108 % baseline value. Generally, it is believed that normal CBF levels always vary from 80 % to 120 % baseline. However, the relative changes of CBF during acute hyperglycemia had a significant difference among the various vascular compartments as shown by Fig. 5.15d. First, the relative changes of CBF at the arteriole and parenchyma showed significant increase, but the amplitudes of the arterial response were larger than that of parenchyma. Second, the relative changes of CBF in the arteriole rose from 30 min (111 % baseline), peaking at 150 min (183 % baseline value). Increases in CBF at the parenchyma began at 60 min (108 % baseline value), peaking at 120 min (162 % baseline value) after the glucose injection. Whereas there is no significant changes in CBF at the venule, the relative changes of CBF varied from 89 % to 108 % baseline value (Fig. 5.15d).
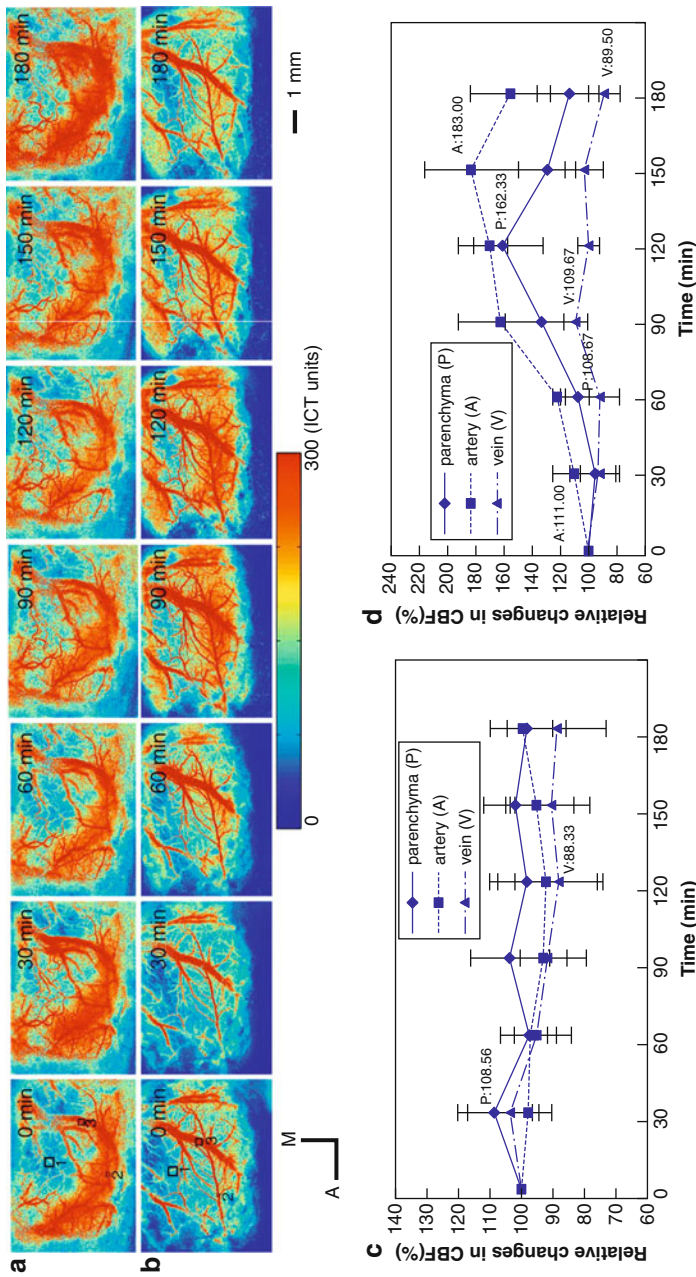
Fig. 5.15 The effect of acute hyperglycemia on CBF in a normal rat cortex. (**a**) The distribution of CBF perfusion was measured by laser speckle imaging before and after saline administration in a representative subject. (**b**) The distribution of CBF perfusion was measured by laser speckle imaging before and after glucose administration in a representative subject. Three vascular compartments (parenchyma, arteriole, and venule) (**a**) – 0 min or (**b**) – 0 min are indicated as three solid squares numbered 1, 2, and 3. (**c**) The time courses of saline-induced relative changes in CBF at the three vascular compartments are shown. (**d**) The time courses of glucose-induced changes in CBF at the three vascular compartments are denoted. Direction: A, anterior; M, median. Scale bar, 1 mm. All of the images share the same direction and color bar [61]

Effect of Acute Hyperglycemia on CBF Following CSD in Rat Cortex

The length of time for a wave to first appear in the imaged cortex was usually ~2 min after delivering electrical stimulation into the frontal cortex. CBF 30 min after each CSD wave was also monitored using laser speckle imaging. Figure 5.16a, b illustrate spatial and temporal changes in CBF following each CSD in the rats of the control group and the hyperglycemia group, respectively. Two series of blood flow images in Fig. 5.16a, b were acquired at a 30-min interval. In the control group, CBF following each CSD was usually close to the baseline level during the experiment, as shown in Fig. 5.16a; however, CBF following each CSD in the hyperglycemia rats had a stepwise reduction within 180 min after glucose injection (Fig. 5.16b).

Figure 5.16c, d show the time courses of the saline (glucose) induced changes in CBF following CSD for all vascular components, as the same as that illustrated in Fig. 5.15c, d. From Fig. 5.16c, we obtained that the relative changes of CBF in the three vascular compartments (parenchyma, arteriole, and venule), respectively, were 100–124 %, 96–124 %, and 95–108 % of the baseline value, which were all close to the baseline level. There were no significant differences between them.

The relative changes of CBF following each CSD gradually fell off in the vascular compartments during acute hyperglycemia. These decreases in CBF for all compartments first appeared at 30 min after glucose administration and reached their minimums at 150 min. The minimums of relative changes were, respectively, 49 %, 56 %, and 60 % of the baseline value (Fig. 5.16d). There were not significant differences in relative changes of CBF among the various vascular compartments.

5.4.3.3 Conclusion

In this application, laser speckle imaging is utilized to study influences of acute hyperglycemia on CBF at the level of individual vascular compartments for 3 h in normal rats and those with CSD. It is shown that there are extensive increases of CBF at the arteriole and parenchyma over the normal rat cortex during acute hyperglycemia, whereas there is no significant change in CBF at the venule. Moreover, at all vascular compartments, after the glucose administration there is a stepwise reduction of CBF following CSD, but after saline injection CBF following CSD is close to the baseline. These results indicate that acute hyperglycemia could aggravate the severity of decrease in CBF following CSD, suggesting possible mechanisms by which hyperglycemia exacerbates cerebral damage after ischemic stroke.

5.4.4 Speckle-Correlation Analysis of the Microcapillary Blood Circulation in Nail Bed

Many diseases are accompanied by functional and morphological changes in the microcirculation, such as cardiovascular complications, atherosclerosis, and diabetes mellitus [64]. Therefore, it is of great significance to investigate the mechanisms of the microcirculation for clinical diagnosis. The study of the microcirculation
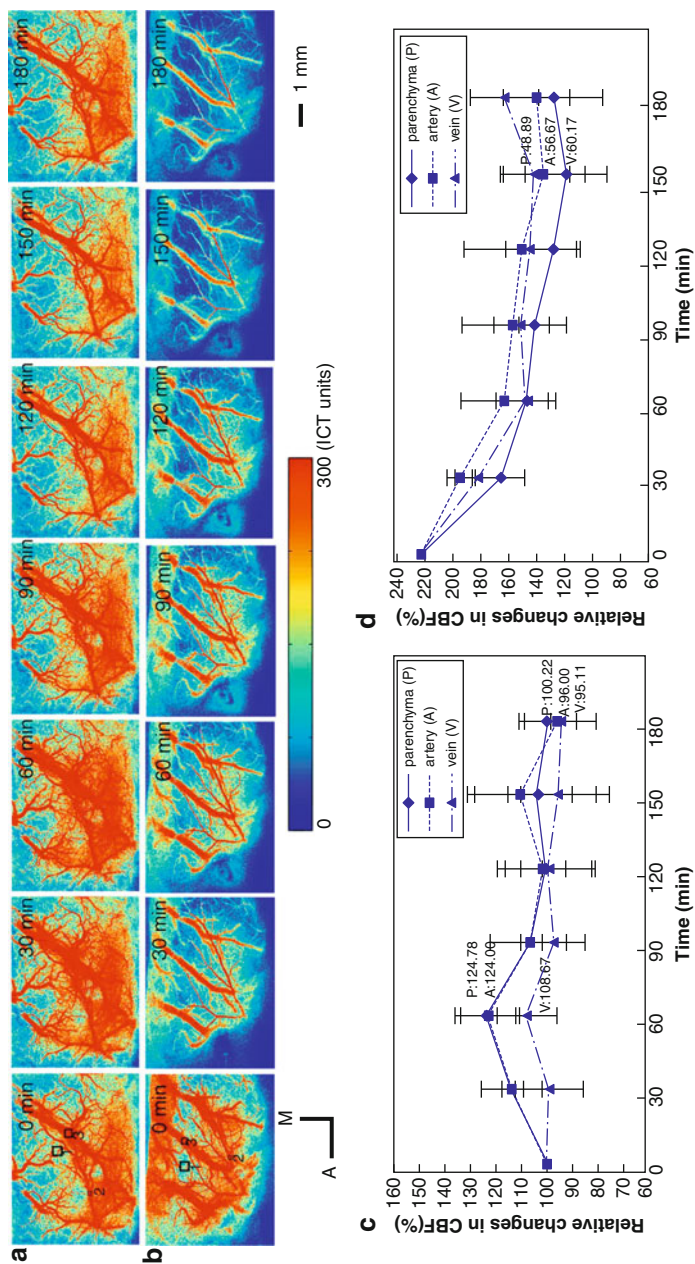
Fig. 5.16 The effect of acute hyperglycemia on CBF after CSD in rats. (**a**) The distribution of CBF perfusion was measured by laser speckle imaging before or after saline administration in a representative subject. (**b**) The distribution of CBF perfusion was measured by laser speckle imaging before or after glucose administration in a representative subject. Three vascular compartments (parenchyma, arteriole, and venule) in (**a**) – 0 min or (**b**) – 0 min are indicated as three solid squares, numbered 1, 2, and 3. (**c**) The time courses of saline-induced relative changes in CBF after CSD monitored at the selected region are shown. (**d**) The time courses of glucose-induced changes in CBF after CSD monitored at the region [(**b**) – 0 min] are denoted. Direction: A, anterior; M, median. Scale bar, 1 mm. All of the ICT images share the same direction and color bar [61]

Fig. 5.17 Experimental setup: (*1*) helium–neon GN-5P laser, (*2*) beam expander, (*3*) camera objective, (*4*) Basler A602f CMOS camera, (*5*) computer, and (*6*) object [64]
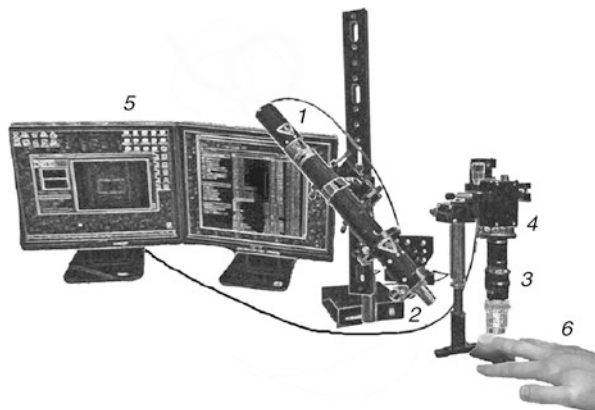
system can be performed using morphological and functional analytical methods. The morphological microcirculation studies, which were performed in most cases by the biopsy method, reflect the microcirculation state only at some specific point and cannot reflect dynamic processes. Some methods have made it possible to study the dynamic processes of microcirculation, such as laser Doppler flowmetry [65, 66], capillaroscopy [67, 68], intravital microscopy [69], optical coherent tomography [70], magneto-resonance tomography [71], radioisotope arteriography, and so on. However, there are more or less limitations when using these methods to study microcirculation. Here, an application of laser speckle imaging is presented using the speckle-contrast method to monitor the hemodynamics of blood in nail bed capillaries. This application may possibly be used to reveal irregularities of the pathological process caused by diabetes and to control treatment.

5.4.4.1 Method

The architecture of a full-field speckle-correlation capillaroscope for monitoring of microhemodynamic variations in nail bed is illustrated in Fig. 5.17. The coherent light source was a single-mode helium-neon GN-5P laser. An LOMO microlens ($20^{\times}$, NA $= 0.40$) was used to expand the laser beam. Speckle-modulated images of the area analyzed were recorded by a Basler A602f monochromatic CMOS camera (656×491 pixels in the matrix, pixel size 9.9×9.9 mm, 8 bit pixel^{-1}), equipped with an LOMO objective with a focal distance $f = 30$ mm. A Labview program is specially written for collecting the raw image data captured by the camera. Data was detected with a frame frequency of 40 Hz in the subframe regime with a window size of 1×5 pixels and frame exposure time of 20 ms. Fig. 5.18 shows as an example the full-frame images of recorded speckle structures for a human nail bed under the conditions of short-term hemodynamics suppression and at normal blood circulation.

When processing the speckle-modulated images of an area of internal-organ surface the contrast $V_k = \sigma_{Ik}/\overline{I}_k$ is calculated, where k is the frame number in the
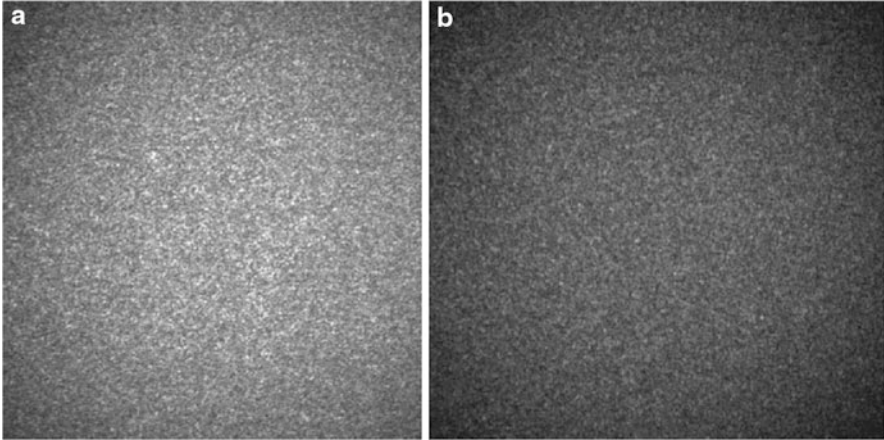
Fig. 5.18 Full-frame images of recorded speckle-structures (**a**) under the conditions of short-term suppression of hemodynamics and (**b**) at normal blood circulation [64]

sequence of speckle-modulated images, $\bar{I}_k$ is the frame-averaged intensity, and σ_{Ik} is the rms value of the fluctuation component of pixel intensity. Furthermore, the average velocity can be deduced by the relation of the contrast and the normalized time correlation function of intensity fluctuation, which is explained in the principal section above in detail.

The experiment was carried out in the fourth finger of the left hand of five volunteers without diseases of the cardiovascular system at normal blood circulation and under partial blockage. Blood circulation was blocked by crossclamping the main arteries with an elastic cuff of a Medica CS-105 tonometer. The microcirculation was decreased by the blood circulation blockade. After the blockade, reactive postocclusive hyperemia appears at once; under normal conditions it shows an increase in blood circulation to a level exceeding the initial one.

The morphological changes in capillaries under partial blockage were also monitored using a computer capillaroscope that is equipped with a Basler A602f monochromatic CMOS camera and a LOMO microlens ($8\times$ NA $= 0.20$). To reduce the effect of light scattering in cellular structures and biological tissues, an antireflection agent was used to create optical blooming. Figure 5.19 shows images of a nail bed area with capillaries before and after depositing an antireflection agent.

5.4.4.2 Speckle-Correlation Analysis of the Capillary Blood Circulation in Nail Bed

According to the microscopy data, the diameter of visible capillary before and after the blood circulation blockade was, respectively, 7.5 and 11 mm, which indicated a partial decrease in the microcirculation level in the tissue. As shown in Fig. 5.20, there are three steady-state hysiological regimes. During the first 10 s of the blood circulation blockade (the first physiological regime), the contrast corresponded to a level of 0.6; then postocclusive hyperemia develops during the next 10 s
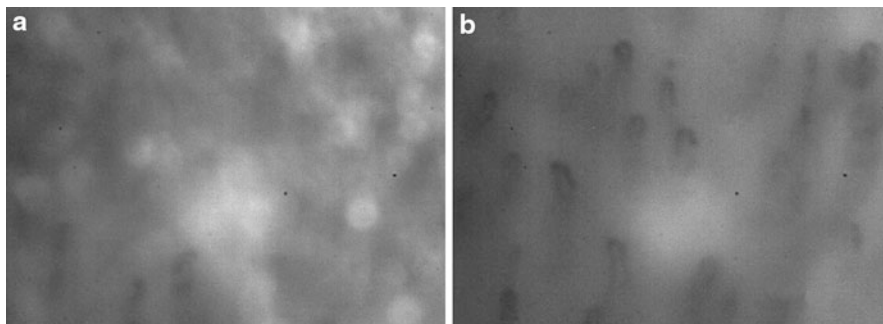
Fig. 5.19 Images of a nail bed area with capillaries (**a**) before and (**b**) after depositing an antireflection agent [64]
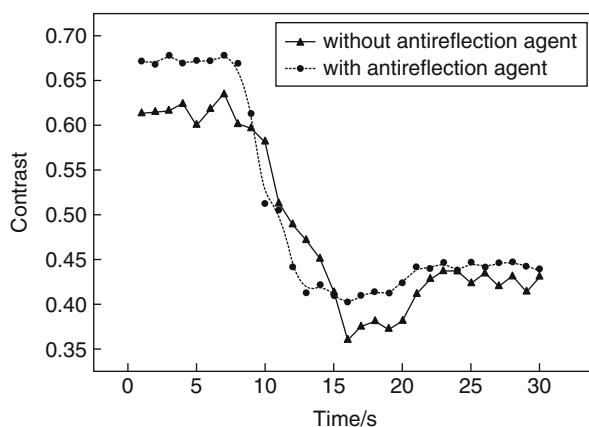
Fig. 5.20 Time dependence of the contrast of averaged dynamic speckle fields [64]

(the second physiological regime), with a decrease in contrast to 0.38; and, finally, the microcirculation restored to the initial level with a slight increase in contrast to 0.42. In addition, using an antireflection agent could bring a higher accuracy and sensitivity for the microscopic measurements without affecting the ratio of the obtained values of the speckle-image contrast before and after the blood circulation blockade.

5.4.4.3 Conclusion

In this application, the efficiency is demonstrated of monitoring the microhemo-dynamics of nail bed capillaries using full-field speckle correlometry. This method is likely to be used in clinical practice for monitoring of microhemodynamics in diabetes and other diseases that affect microcirculation for diagnostics and monitoring therapy performed.

5.5 Modified Laser Speckle Imaging Method with Improved Spatial Resolution

As described above, laser speckle imaging (LSI) was based on the first-order spatial statistics of time-integrated speckle [72]. The main disadvantage of LASCA is the loss of resolution caused by the need to average over a block of pixels to produce the spatial statistics used in the analysis, although it actually has higher resolution than other techniques such as scanning laser Doppler. In this chapter, we presented a modified laser speckle imaging (LSI) method utilizing the temporal statistics of the time-integrated speckle based on our previous studies [52, 53, 73]. First a model experiment was designed to validate this method, and then imaging of the rat cerebral blood flow distribution was performed. Also, the influences of temperature to the rat cerebral blood flow (CBF) were investigated by this method compared with LSI.

5.5.1 Materials and Methods

5.5.1.1 Model Experiment

A porcelain plane, which was pushed by a stepping motor (SC3, Sinoptek, China), moved with velocity that ranged from 0.018 to 2.3 mm/s. The laser beam illuminated evenly on the surface of the plane and the imaged area was about 2.46×3.28 mm^2. Three measurements were performed under each velocity condition.

5.5.1.2 In Vivo CBF Measurement

The experiment was performed on Sprague–Dawley rats (350–450 g), which were anesthetized with α-chloralose and urethane (50 and 600 mg/kg, respectively). The right femoral artery was cannulated for measurement of mean arterial blood pressure (Pclab Instruments, China) and blood sampling. A tracheotomy was executed to enable mechanical ventilation with a mixture of air and oxygen (20 % O_2, 80 % N_2, TKR-200C, China). Periodically, blood gases analysis was performed to ensure that normoxia was maintained at normal physiological levels (pO_2, pCO_2 and pH) (JBP-607, Dissolved Oxygen Analyzer, China). The animals were mounted in a stereotaxic frame, and rectal temperature was maintained at 37.0 ± 0.5 °C with a thermostatic heating blanket. The skull was thinned to translucency using a dental drill under constant cooling with saline. Following surgical preparation, the animals were left for at least 30 min before the experiment began. In all animals, the physiologic parameters were kept within normal range throughout the experiments. The temperature of the rat cortex was changed locally by constant application of warm saline solution to the cortex for 10 min under each temperature condition: 35 °C, 45 °C, and 50 °C. The raw speckle images were acquired first under control condition (38 °C) and then under other temperatures to obtain the CBF map.

5.5.1.3 Speckle Imaging Processing

Laser speckle is an interference pattern produced by the light reflected or scattered from different parts of the illuminated rough (i.e., nonspecular) surface. When the area illuminated by laser light is imaged onto a camera, a granular or speckle pattern is produced. If the scattered particles are moving, a time-varying speckle pattern is generated at each pixel in the image. The intensity variations of this pattern contains information of the scattered particles.

Analysis of LASCA (Laser Speckle Contrast Analysis)

In the current version of LSI [18], to quantify the blurring of the speckles, the local speckle contrast was defined as the ratio of the standard deviation to the mean intensity in a small region of the image:

$$k = \frac{\sigma_s}{<I>}. \tag{5.9}$$

Here, k, σ_s, and $<I>$ represent speckle contrast, the standard deviation, and the mean value of light intensity, respectively. This method uses the spatial intensity variations in the speckle pattern to obtain the relative blood flow map. In practice, a 5×5 or 7×7 region of pixels is used: lower numbers reduce the validity of the statistics, whereas higher numbers limit the spatial resolution of the technique. In this section, squares of 5×5 pixels were used. The software computes the speckle contrast k for any given square and assigns this value to the central pixel of the square. The process is then repeated for 5×5 squares centered on each pixel in turn. This results in a smoothing of the contrast map, but the spatial resolution is lost for the averaging over a block of pixels.

Theory and Analysis of Modified LSI

The first-order temporal statistics of time-integrated speckle patterns can be used to provide velocity information, and are described in detail in Ref. [74]. In the previous research woks, only the velocity of a single point area (a single speckle size in the detected plane) is measured by this method.

$$N_t = \frac{<I^2> - <I>^2}{<I>^2}, \tag{5.10}$$

where $<I>$ and $<I^2>$ are the mean and square-mean values of time-integrated speckle intensity variations during the time interval t, N_t is inversely proportional to the velocity of scattering particles [74].

Here we utilized the first-order temporal statistics of time-integrated speckle to obtain the 2-D blood flow distribution. Each pixel in the speckle image can be viewed as the single point area in the previous study. Then the signal processing consists of calculation of the temporal statistics of the intensity of each pixel in the image:

Fig. 5.21 The value of $1/N$ under different velocity (V) conditions calculated through different frames. The solid line was a least squares fit between $1/N$ and V when m equaled 25 [72]
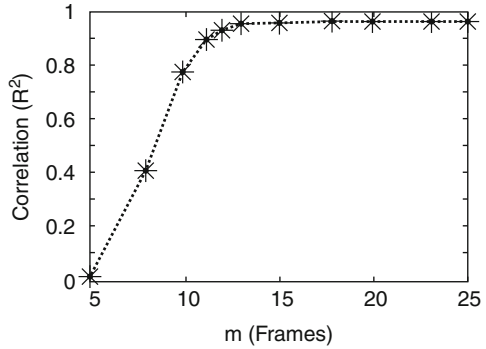
$$N_{i,j} = [<I_{i,j,t}^2>_t - <I_{i,j,t}>_t^2]/<I_{i,j,t}>_t^2$$

$$i = 1 \div 480, j = 1 \div 640, t = 1 \div m, \qquad (5.11)$$

where $I_{i,j,t}$ is the instantaneous intensity of the i- and j-th pixels at the t-th frame of raw speckle images, and $<I_{i,j,t}>_t$ is the average intensity of the i- and j-th pixels over the consecutive m frames. $N_{i,j}$ is inversely proportional to the velocity of scattering particles. The value $N_{i,j}$ of each pixel in the consecutive m frames ($I_{i,j,t}$) of raw speckle pattern is computed according to (5.11). The process is then repeated for the next group of m frames. The results are given as 2-D grayscale (65,536 shades) or false-color (65,536 colors) coded maps that describe the spatial variation of the velocity distribution in the area examined.

5.5.2 Results and Discussion

5.5.2.1 Validation of the Modified LSI Method
In the model experiment, the N values of the center pixel of the interest area under the conditions of different velocities were computed according to (5.11). Figure 5.21 shows the value of the reciprocal of $N(1/N)$ computed from different number of frames (m) of consecutive images under different velocity conditions (V).

The correlation value (R^2) between V and $1/N$ are given in Fig. 5.22. It is obvious to see that the correlation value (R^2) increased with m. When m is larger than 15, the high correlation ($R^2 = 0.96$) is obtained. This can be explained because, for small number of integrated speckles, the experimental results of the probability density function are slightly different from the theoretical ones (gamma distribution), which may be due to the statistical uncertainty associated with the experiments [74], and therefore the linearity is only for high m. The linearity is not as good as that of LDPI, for (5.11) is obtained under an ideal condition of fully developed speckle pattern [17, 74], and actual experiment conditions are usually contiguous to the ideal one, which does not influence much in measuring the relative velocity change.

Fig. 5.22 The correlations (R^2) between the actual velocity and the $1/N$. R^2 increases with m [72]
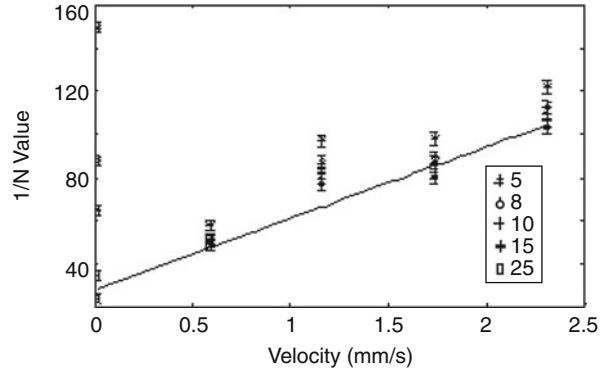
In Fig. 5.22, the high $1/N$ values obtained for the lower m may be due to that for small number of integrated speckles, the fluctuation of the moving porcelain plane becomes significant and its effect cannot be neglected [74], i.e., for lower m, the value of $[<I^2> - <I>^2]^{1/2}/<I>$ (between 0 and 1, reflecting the fluctuation) would be larger and N would be smaller, and thus the corresponding $1/N$ value became larger. To insure the temporal resolution, we could choose m larger than 15. Assuming ergodicity, the principle of modified LSI method was similar to that of LASCA. In theory, to obtain the same the signal-to-noise ratio (SNR) as LASCA, 25 temporal samplings used, i.e., m equaled 25. In the present section, we would compare the blood flow map obtained when m equaled 25 with that obtained by LASCA. The least squares fit between V and $1/N$ is displayed when m equaled 25 (Fig. 5.22), which suggests that the change of $1/N$ value could be used to reflect the velocity change of scatterers effectively in the illuminated area. The same problem of it being difficult to measure the absolute velocity of scatterers from the time-integrated speckle pattern was met, which was the problem shared with all time-varying speckle techniques, as well as with laser Doppler [18, 24, 75].

As stated in previous studies of image speckle [75, 76], each point in image plane is the superposed result of the points near the corresponding point in object plane, i.e., the size of single speckle is approximately equal to the size of a single pixel in the image acquired by CCD and the captured images from different speckles do not interact with others, which was different from that in case of laser Doppler. Each $1/N_{i,j}$ value reflected the velocity change of one pixel (i, j) in imaged area. If velocities of the imaged plane were diversiform, just like the inhomogeneities in CBF model, the N value of each pixel would be different, forming the velocity map of CBF. We chose a moving porcelain plane as the model for the convenience of controlling the speed by computer. Of course, a tube model using a layer of static scatter above with different velocities and concentrations of Intralipid (or blood) would be better than this model for its similarity to a real CBF model.

Further research is needed to clarify the relationship between the signal and the velocity and concentration by a tube model.
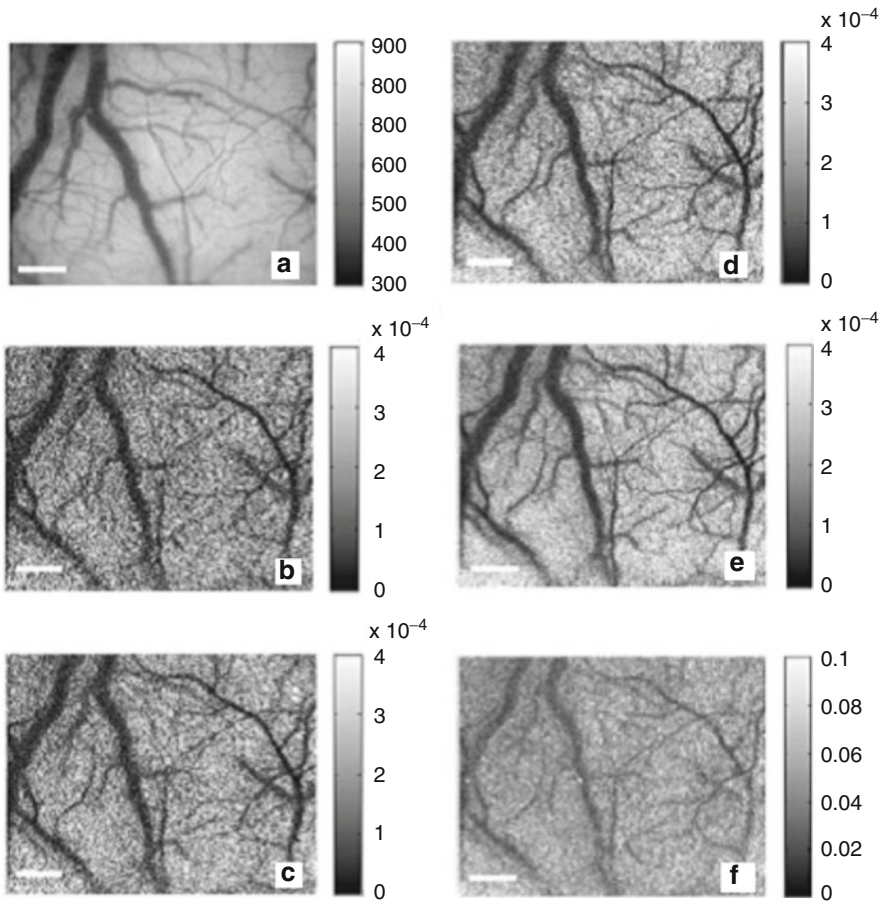
Fig. 5.23 The blood flow maps obtained by the methods of modified LSI and LASCA under control condition. (**a**) Vascular image of the interest area of rat brain under control condition. (**b–e**) – The blood flow maps obtained by the modified method when *m* chosen as 5, 8, 15, and 25, respectively (*gray* bar indicated as *N* value on the *right* side of the picture). (**f**) The blood flow map obtained by LASCA (*gray* bar indicated as *k* value on the *right* side of the picture). Bar = 500 μm. Figure (**a**) is a white light picture, and (**b–e**) the scale is 0–4 × 10^{-4}, which is the value of *N*. Figure (**f**) is indicated by value of *k*, the scale is 0–0.1 [72]

5.5.2.2 CBF Maps Obtained by Modified LSI

The white light image of the vasculature is shown in Fig. 5.23a. By illuminating the expanded laser beam on the interest areas (2.46 × 3.28 mm^2), the raw speckle images were captured. The CBF maps obtained by the modified LSI method are represented in Fig. 5.23b–e, which are the blood flow maps obtained by 5, 8, 15, and 25 frames (*m*), respectively. It is easy to see that as *m* increases, the signal-to-noise ratio (SNR) of blood flow map increases.

5.5.2.3 Spatial Resolution of Modified LSI

In the in vivo CBF experiment, the field of view was approximately 2.46×3.28 mm^2. The size of each raw speckle image was 480×640 pixels. According to the principle of modified LSI, the resolution of the map was 5 μm (246/480). The resolution of the map obtained by LASCA was effectively reduced by the use of 5×5 squares of pixels from 480×640 (pixels) to approximately 96×128 (pixel blocks). Hence, the spatial resolution was approximately 25 μm, which was as low as one-fifth that of the modified LSI in theory. Compared with the work by Linden et al. [77], in which an enhanced high-resolution laser Doppler imaging (EHR-LDI) technique intended for visualization of separate microvessels was evaluated by use of in vitro flow models, the resolution of the modified LSI is much higher than that of EHR-LDI (about 40 μm). The modified LSI and LASCA were utilized respectively to measure the CBF under the same conditions. According to (5.11), the maps of flows represented by N values under control condition (38 °C) were achieved (Fig. 5.23e, $m = 25$). Compared with the map obtained by LSI (Fig. 5.23f), we could see that the spatial resolution of the modified method was much higher, and more small blood vessels appeared clearly in the case of modified LSI, although both methods could well resolve the statically and dynamically scattering regions in the map of flow.

5.5.2.4 Influence of Temperature on CBF

The CBF distributions of the rats under different temperatures (35 °C, 45 °C, 50 °C) were examined in this study. The results are illustrated in Fig. 5.24. When the temperature increased from 35 °C to 50 °C, the map of flow gained by the modified LSI became darker (Fig. 5.24a–c), indicating N value became smaller, therefore the blood perfusion increased. In some small blood vessels, indicated by panes in Fig. 5.24a, the blood perfusion increased obviously. However, these vessels could not be clearly seen in the map obtained by LSI (Fig. 5.24d–f) due to the lower spatial resolution, although these two methods showed the same tendency of the thermal influence to CBF. Hence, in the physiological studies, the modified LSI could provide more information about small blood vessels. As in brain studies, brain homeostasis depended on adequate levels of blood flow to ensure the delivery of nutrients and to facilitate the removal of metabolites and excess heat, the exchange of material between constituents in the blood and neurons and glia occurred at the level of individual capillaries [78]. Our modified LSI with improved spatial resolution would be helpful for this brain research.

5.5.2.5 Temporal Resolution of Modified LSI

The sampling frame of our CCD was 40 Hz. From the principle of modified LSI method, the temporal resolution was about 0.4–0.6 s (15/40, 25/40), which was determined by the sampling frequency of CCD camera and the value of m.
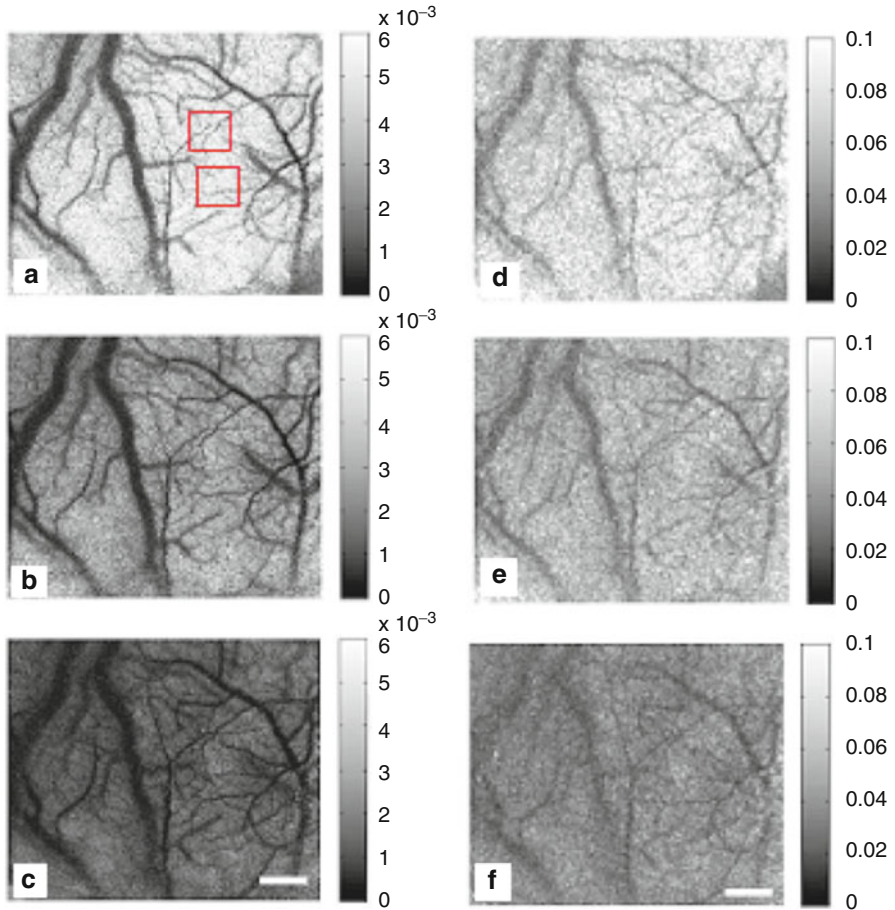
Fig. 5.24 The blood flow maps obtained by two methods. (**a–c**) – The blood flow distributions obtained by the modified LSI when *m* equaled 25 under the temperatures of 35 °C, 45 °C and 50 °C, respectively (the indicated as *N* values). (**d–f**) – The blood flow distributions obtained by LASCA under the temperatures of 35 °C, 45 °C 50 °C, respectively (the indicated as *k* values). The pane areas in (**a**) were used to notice the blood perfusion change of small blood vessels under the thermal influence. *Darker* areas in the maps obtained by two methods both represented increased cerebral blood flow. Bar = 500 μm [72]

As described in above, the temporal resolution of LSI was only determined by the sampling frequency (1/40 s), which was higher than that of modified LSI. In many cases of physiological studies, the CBF response was a slow change [21, 78], and the temporal resolution of second was enough for the measurement. The data processing time with this method was reduced significantly, which was advantageous to real-time operation.

5.6   Conclusion

In this chapter, we present a LSI technique, which is a new alternative approach in measurement of blood flow. Three LSI systems are introduced which are built by personal computer, DSP, and FPGA respectively. The latter two portable laser speckle imaging systems that do not compromise processing efficiency are crucial in clinical diagnosis. This LSI technique develops the spatial statistical characteristics of time-varying image speckle, extracts the velocity information from speckle signals within an area of 5×5 pixels and obtains the velocity distribution in the whole region. Its spatial resolution is equal to the area in the image plane corresponding to 5×5 pixels, far better than LDF. LSI is capable of accurately imaging the cortical blood flow response over an area ranging from a few millimeters to a centimeter over time scales of milliseconds to hours. For its higher temporal and spatial resolution (here 25 ms and 27 μm, respectively), we can choose small regions-of-interest in two-dimensional maps of blood vessels so as to analyze the spatial patterns of different vessels response to sciatic nerve stimulation and also show their evolution along the time axis, as can furnish more information to characterize the regulation mechanism of microcirculation associated with cerebral functional events. The finding of this study is that spatial response of CBF is highly localized in cortical anatomic distribution and discretely coupled to the microvasculature in the targeted cortex. Different levels of arteries, veins, and capillaries are activated successively with the time varying. Compared with the former conclusions, we found more elaborated details besides those accordant results and offered a new proof to the hypothesis proposed by Roy and Sherrington more than 100 years ago.

As with other optical imaging methods, LSI can only provide the velocity information on the surface of the turbid tissues due to the high scattering properties of the light in the biological tissue. The optical immersion method is a technique using chemical agents to alter the optical properties, established as immersion into index-matching fluids greatly reduced the amount of specular scattering of a dispersive system. Our present study tried to combine the optical immersion and LSI method to obtain deeper CBF information through intake dura mater. Before this we investigated the chemical agents' influence on CBF. Here we demonstrated a hyperosmotic agent of glycerol causing a reduction in scattering in the dura mater and its influence on in vivo CBF revealed by LSI. Optical property changes are given for in vitro and in vivo clearing of dura mater. The differences between the in vivo and in vitro cases indicate that the processes of reduction in scattering might be different for the two conditions. Clearly, the agent drastically increased the optical depth of the tissue in the case of LSI. At the same time, it decreased 20–30 % blood flow of baseline. These suggest that although glycerol is biocompatible, it does irritate tissue and is not the agent of choice for in vivo procedures. It is not a suitable agent for in vivo CBF imaging. Further experiments of the mechanism of the chemical agent's influence on CBF are required; not only the optical clearing effects and period of time of the chemical agents action but also

the influence to tissue normal physiological function are challenges in the optical clearing technique.

We also utilized laser speckle imaging to study influences of acute hyperglycemia on CBF at the level of individual vascular compartments for 3 h in normal rats and those with CSD. It was shown that there are extensive increases of CBF at the arteriole and parenchyma over the normal rat cortex during acute hyperglycemia, whereas there were no significant change in CBF at the venule. We also found that, at all vascular compartments, after the glucose administration there was a stepwise reduction of CBF following CSD, but after saline injection CBF following CSD is close to the baseline. Our results indicate that acute hyperglycemia could aggravate the severity of decrease in CBF following CSD, suggesting possible mechanisms by which hyperglycemia exacerbates cerebral damage after ischemic stroke. In addition, an application is presented for monitoring the blood microcirculation in human finger nail bed with an LSI technique. The problems and prospects of this application under laboratory and clinical conditions are discussed [64].

To improve the spatial resolution of the current LSI, we proposed a modified LSI based on the temporal resolution of time-integrated speckle. Compared with other laser Doppler perfusion imaging (LDPI), this modified LSI method did not require the moving scanning components, and the spatial resolution was highly improved to five times of that of LSI thus being able to discriminate the small blood vessels and providing more spatial information under the same condition. The temporal resolution of this method was much lower than that of LSI and the laser Doppler perfusion imaging with a complimentary metal oxide semiconductor sensor proposed by Serov et al. [79] for the limitation of the frame rate of a CCD camera. However, this method could be used to measure the relative slow change of blood flow. By use of a CCD camera with high sampling frame rate, the temporal resolution would increase. In addition, our system was an easy-to-use instrument for whole-field blood flow imaging.

References

1. K.U. Frerichs, G.Z. Feuerstein, Laser Doppler flowmetry: a review of its application for measuring cerebral and spinal cord blood flow. Mol. Chem. Neuropathol. **12**, 55–61 (1990)

2. U. Dirnagl, B. Kaplan, M. Jacewicz, W. Pulsinelli, Continuous measurement of cerebral cortical blood flow by laser-Doppler flowmetry in a rat stroke model. J. Cereb. Blood Flow Metab. **9**, 589–596 (1989)

3. B.M. Ances, J.H. Greenberg, J.A. Detre, Laser Doppler imaging of activation-flow coupling in the rat somatosensory cortex. Neuroimage **10**, 716–723 (1999)

4. M. Lauritzen, M. Fabricius, Real time laser-Doppler perfusion imaging of cortical spreading depression in rat neocortex. Neuroreport **6**, 1271–1273 (1995)

5. D.A. Zimnyakov, J.D. Briers, V.V. Tuchin, Speckle technologies for monitoring and imaging of tissues and tissuelike phantoms, in *Handbook of Optical Biomedical Diagnostics*, ed. by V. V. Tuchin, vol. PM107 (SPIE Press, Bellingham, 2002), pp. 987–1036

6. D.A. Zimnyakov, V.V. Tuchin, Laser tomography, in *Medical Applications of Lasers*, ed. by D.R. Vij, K. Mahesh (Kluwer, Boston, 2002), pp. 147–194

7. E.I. Galanzha, G.E. Brill, Y. Aizu, S.S. Ulyanov, V.V. Tuchin, Speckle and Doppler methods of blood and lymph flow monitoring, in *Handbook of Optical Biomedical Diagnostics*, ed. by V.V. Tuchin, vol. PM107 (SPIE Press, Bellingham, 2002), pp. 881–937

8. R. Bullock, P. Statham, J. Patterson, D. Wyper, D. Hadley, E. Teasdale, The time course of vasogenic oedema after focal human head injury-evidence from SPECT mapping of blood brain barrier defects. Acta Neurochir. Suppl. **51**, 286–288 (1990)

9. M. Schröder, J.P. Muizelaar, R. Bullock, J.B. Salvant, J.T. Povlishock, Focal ischemia due to traumatic contusions, documented by SPECT, stable Xenon CT, and ultrastructural studies. J. Neurosurg. **82**, 966–971 (1995)

10. A. Alavi, R. Dann, J. Chawluk et al., Positron emission tomography imaging of regional cerebral glucose metabolism. Semin. Nucl. Med. **16**, 2–34 (1996)

11. W.D. Heiss, O. Pawlik, K. Herholz et al., Regional kinetic constants and cerebral metabolic rate for glucose in normal human volunteers determined by dynamic positron emission tomography of [18 F]-2-fluoro-2-deoxy-D-glucose. J. Cereb. Blood Flow Metab. **3**, 250–253 (1984)

12. L.P. Carter, Surface monitoring of cerebral cortical blood flow. Cerebrovasc. Brain Metab. Rev. **3**, 246–261 (1991)

13. C.A. Dickman, L.P. Carter, H.Z. Baldwin et al., Technical report. Continuous regional cerebral blood flow monitoring in acute craniocerebral trauma. Neurosurgery **28**(467–472) (1991)

14. O. Sakurada, C. Kennedy, J. Jehle, J.D. Brown, G.L. Carbin, Sokoloff measurement of local cerebral blood flow with iodo [14C] antipyrine. Am. J. Physiol. **234**, H59–H66 (1978)

15. D.S. Williams, J.A. Detre, J.S. Leigh et al., Magnetic resonance imaging of perfusion using spin inversion of arterial water. Proc. Natl. Acad. Sci. U.S.A. **89**, 212–216 (1992)

16. F. Calamante, D.L. Thomas, G.S. Pell, J. Wiersma, R. Turner, Measuring cerebral blood flow using magnetic resonance imaging techniques. J. Cereb. Blood Flow Metab. **19**, 701–735 (1999)

17. A.F. Fercher, J.D. Briers, Flow visualization by means of single-exposure speckle photography. Opt. Commun. **37**, 326–329 (1981)

18. J.D. Briers, S. Webster, Laser speckle contrast analysis (LASCA): a nonscanning, full-field technique for monitoring capillary blood flow. J. Biomed. Opt. **1**, 174–179 (1996)

19. K. Yaoeda, M. Shirakashi, S. Funaki, H. Funaki, T. Nakatsue, H. Abe, Measurement of microcirculation in the optic nerve head by laser speckle flowgraphy and scanning laser Doppler flowmetry. Am. J. Ophthalmol. **129**, 734–739 (2000)

20. B. Ruth, Measuring the steady-state value and the dynamics of the skin blood flow using the non-contact laser speckle method. Med. Eng. Phys. **16**, 105–111 (1994)

21. A.K. Dunn, H. Bolay, M.A. Moskowitz, D.A. Boas, Dynamic imaging of cerebral blood flow using laser speckle. J. Cereb. Blood Flow Metab. **21**, 195–201 (2001)

22. H. Bolay, U. Reuter, A.K. Dunn, Z. Huang, D.A. Boas, A.M. Moskowitz, Intrinsic brain activity triggers trigeminal meningeal afferernts in a migraine model. Nat. Med. **8**, 136–142 (2002)

23. R. Bandyopadhyay, A.S. Gittings, S.S. Suh, P.K. Dixon, D.J. Durian, Speckle-visibility spectroscopy: a tool to study time-varying dynamics. Rev. Sci. Instrum. **76**, 093110 (2005)
24. R. Bonner, R. Nossal, Model for laser Doppler measurements of blood flow in tissue. Appl. Opt. **20**, 2097–2107 (1981)
25. J.K. Sean, D.D. Donald, M.W. Elaine, Detrimental effects of speckle-pixel size matching in laser speckle contrast imaging. Opt. Lett. **33**, 2886–2888 (2008)
26. S. Liu, P. Li, Q. Luo, Fast blood flow visualization of highresolution laser speckle imaging data using graphics processing unit. Opt. Express **16**, 14321–14329 (2008)
27. J. Owens, A survey of general-purpose computation on graphics hardware. Comput. Graph. Forum **26**, 80–113 (2007)
28. X. Tang, N. Feng, X. Sun, P. Li, Q. Luo, Portable laser speckle perfusion imaging system based on digital signal processor. Rev. Sci. Instrum. **81**, 125110 (2010)
29. C. Jiang, H.Y. Zhang, J. Wang, Y.R. Wang, H. He, R. Liu, F.Y. Zhou, J.L. Deng, P.C. Li, Q.M. Luo, Dedicated hardware processor and corresponding system-on-chip design for real-time laser speckle imaging. J. Biomed. Opt. **16**(116008) (2011)
30. Z. Wang, Q.M. Luo, H.Y. Cheng, W.H. Luo, H. Gong, Q. Lu, Blood flow activation in rat somatosensory cortex under sciatic nerve stimulation revealed by laser speckle imaging. Prog. Nat. Sci. U.S.A. **13**(7), 522–527 (2006)
31. R. Greger, U. Windhorst, *Comprehensive Human Physiology* (Springer, Berlin, 1996), pp. 561–578
32. A.C. Ngai, J.R. Meno, H.R. Winn, Simultaneous measurements of pial arteriolar diameter and Laser-Doppler Flow during somatosensory stimulation. J. Cereb. Blood Flow Metab. **15**, 124–127 (1995)
33. A.C. Silva, S. Lee, G. Yang, C. Iadecola, S. Kim, Simultaneous blood oxygenation level-dependent and cerebral blood flow function magnetic resonance imaging during forepaw stimulation in the rat. J. Cereb. Blood Flow Metab. **19**, 871–879 (1999)
34. T. Matsuura, I. Kanno, Quantitative and temporal relationship between local cerebral blood flow and neuronal activation induced by somatosensory stimulation in rats. Neurosci. Res. **40**, 281–290 (2001)
35. D. Kleinfeld, P.P. Mitra, F. Helmchen, W. Denk, Fluctuations and stimulus-induced changes in blood flow observed in individual capillaries in layers 2 through 4 of rat neocortex. Proc. Natl. Acad. Sci. U.S.A. **95**, 15741–15746 (1998)
36. M.E. Raichle, Neuroenergetics: relevance for functional brain imaging, in *Human Frontier Science Program* (Bureaux Europe, Strasbourg, 2001), pp. 65–68
37. R.D. Hall, E.P. Lindholm, Organization of motor and somatosensory neocortex in the albino rat. Brain Res. **66**, 23–28 (1974)
38. A.C. Ngai, K.R. Ko, S. Morii, H.R. Winn, Effects of sciatic nerve stimulation on pial arterioles in rats. Am. J. Physiol. **269**, H133–H139 (1988)
39. A.C. Ngai, M.A. Jolley, R. D'Ambrosio, J.R. Meno, H.R. Winn, Frequency-dependent changes in cerebral blood flow and evoked by potentials during somatosensory stimulation in the rat. Brain Res. **837**, 221–228 (1999)
40. J.A. Detre, B.M. Ances, K. Takahashi, J.H. Greenberg, Signal averaged Laser Doppler measurements of activation-flow coupling in the rat forepaw somatosensory cortex. Brain Res. **796**, 91–98 (1998)
41. R. Steinmeier, I. Bondar, C. Bauhuf, R. Fahlbusch, Laser Doppler flowmetry mapping of cerebrocortical microflow characteristics and limitations. Neuroimage **15**, 107–119 (2002)
42. G. Taubes, Play of light opens a new window into the body. Science **27**, 1991–1993 (1997)
43. A.N. Bashkatov, E.A. Genina, V.I. Kochubey, Y.P. Sinichkin, A.A. Korobov, N.A. Lakodina, V.V. Tuchin, *In vitro* study of control of human *dura mater* optical properties by acting of osmotical liquids. Proc. SPIE **4162**, 182–188 (2000)
44. A.N. Bashkatov, E.A. Genina, Y.P. Sinichkin, V.I. Kochubey, N.A. Lakodina, V.V. Tuchin, Glucose and mannitol diffusion in human *dura mater*. Biophys. J. **85**, 3310–3318 (2003)

45. E. Chan, B. Sorg, D. Protsenko, M. O'Neil, M. Motamedi, A.J. Welch, Effects of compression on soft tissue optical properties. IEEE J. Select. Topics Quantum. Electron. **2**, 943–950 (1997)
46. I.F. Cilesiz, A.J. Welch, Light dosimetry: effects of dehydration and thermal damage on the optical properties of the human aorta. Appl. Opt. **32**, 477–487 (1993)
47. V.V. Tuchin, I.L. Maksimova, D.A. Zimnyakov, I.L. Kon, A.K. Mavlutov, A.A. Mishin, Light propagation in tissues with controlled optical properties. J. Biomed. Opt. **2**, 401–417 (1997)
48. V.V. Bakutkin, I.L. Maksimova, T.N. Semyonova, V.V. Tuchin, I.L. Kon, Controlling of optical properties of sclera. Proc. SPIE **2393**, 137–141 (1995)
49. B. Nemati, A. Dunn, A.J. Welch, H.G. Rylander, Optical model for light distribution during transscleral cyclophotocoagulation. App. Opt. **37**, 764–771 (1998)
50. G. Vargas, E.K. Chan, J.K. Barton, H.G. Rylander, A.J. Welch, Use of an agent to reduce scattering in skin. Lasers Surg. Med. **24**, 133–141 (1999)
51. G. Vargas, K.F. Chan, S.L. Thomsen, A.J. Welch, Use of osmotically active agents to alter optical properties of tissue: effects on the detected fluorescence signal measured through skin. Lasers Surg. Med. **29**, 213–220 (2001)
52. H.Y. Cheng, Q.M. Luo, S.Q. Zeng, J. Cen, W.X. Liang, Optical dynamic imaging of the regional blood flow in the rat mesentery under the effect of noradrenalin. Prog. Nat. Sci. **13**, 198–201 (2003)
53. H.Y. Cheng, Q.M. Luo, Z. Wang, S.Q. Zeng, Laser speckle imaging system of monitoring the regional velocity distribution. Chinese J. Sci. Instrum. **25**(3), 409–412 (2004)
54. E.I. Galanzha, V.V. Tuchin, A.V. Solovieva, T.V. Stepanova, Q.M. Luo, H.Y. Cheng, Skin backreflectance and microvascular system functioning at the action of osmotic agents. J. Phys. D: Appl. Phys. **36**, 1739–1746 (2003)
55. H. Liu, B. Beauvoit, M. Kimura, B. Chance, Dependence of tissue optical properties on solute-induced changes in refractive index and osmolarity. J. Biomed. Opt. **1**, 200–211 (1996)
56. Y.R. Tran Dinh, C. Thurel, A. Serrie, G. Cunin, J. Seylaz, Glycerol injection into the trigeminal ganglion provokes a selective increase in human cerebral blood flow. Pain **46**, 13–16 (1991)
57. E. Jungermann, N.O.V. Sonntag, *Glycerine: A Key Cosmetic Ingredient* (Marcel Dekker, New York, 1991)
58. J.B. Segur, Uses of glycerine, in *Glycerol*, ed. by C.S. Miner, N.N. Dalton (Reinhold, New York, 1953), pp. 238–330
59. A. Grinvald, R.D. Frostig, R.M. Siegel, E. Bartfeld, High-resolution optical imaging of functional brain architecture in the awake monkey. Proc. Natl. Acad. Sci. U.S.A. **88**, 11559–11563 (1991)
60. L.M. Chen, B. Heider, G.V. Williams, F.L. Healy, B.M. Ramsden, A.W. Roe, A chamber and artificial dura method for long-term optical imaging in the monkey. J. Neurosci. Methods **113**, 41–49 (2002)
61. Z. Wang, W.H. Luo, P.C. Li, J.J. Qiu, Q.M. Luo, Acute hyperglycemia compromises cerebral blood flow following cortical spreading depression in rats monitored by laser speckle imaging. J. Biomed. Opt. **13**, 064023 (2008)
62. A.L. McCall, Cerebral glucose metabolism in diabetes mellitus. Eur. J. Pharmacol. **490**(1–3), 147–158 (2004)
63. A. Gorji, Spreading depression: a review of the clinical relevance. Brain Res. Rev. **38**(1–2), 33–60 (2001)
64. M.A. Vilensky, D.N. Agafonov, D.A. Zimnyakov, V.V. Tuchin, R.A. Zdrazhevskii, Speckle-correlation analysis of the microcapillary blood circulation in nail bed. Quantum Electron. **41**(4), 324–328 (2011)
65. M.J. Leahy, F.F.M. de Mul, G.E. Nilsson, R. Maniewski, Principles and practice of the laser-Doppler perfusion technique. Technol. Health Care **7**, 143–162 (1999)
66. K. Yaoeda, M. Shirakashi, S. Funaki, T. Nakatsue, H. Abe, Measurement of microcirculation in the optic nerve head by laser speckle flowgraphy and scanning laser Doppler flowmetry. Am. J. Ophthalmol. **129**, 734–739 (2000)

67. S. Hanazawa, R.L. Prewitt, J.K. Terzis, The effect of pentoxifylline on ischemia and reperfusion injury in the rat cremaster muscle. J. Reconstr. Microsurg. **10**, 21–26 (1994)
68. J.B. Dixon, D.C. Zawieja, A.A. Gashev, G.L. Coté, Measuring microlymphatic flow using fast video microscopy. J. Biomed. Opt. **10**, 064016 (2005)
69. H.H. Lipowsky, N.U. Sheikh, D.M. Katz, Intravital microscopy of capillary hemodynamics in sickle cell disease. J. Clin. Invest. **80**, 117–127 (1987)
70. Z.P. Chen, T.E. Milner, D. Dave, J.S. Nelson, Optical Doppler tomographic imaging of fluid flow velocity in highly scattering media. Opt. Lett. **22**, 64–66 (1997)
71. P.R. Schvartzman, R.D. White, Magnetic resonance imaging, in *Textbook of Cardiovascular Medicine*, ed. by E.J. Topol (Lippincott Williams & Wilkins, Philadelphia, 2002)
72. H.Y. Cheng, Q.M. Luo, S.Q. Zeng, S.B. Chen, J. Cen, H. Gong, A modified laser speckle imaging method with improved spatial resolution. J. Biomed. Opt. **8**, 559–564 (2003)
73. H.Y. Cheng, D. Zhu, Q.M. Luo, S.Q. Zeng, Z. Wang, S.S. Ul'yanov, Optical monitoring of the dynamic change of blood perfusion. Chin. J. Lasers **30**, 668–672 (2003) (in Chinese)
74. J. Ohtsubo, T. Asakura, Velocity measurement of a diffuse object by using time-varying speckles. Opt. Quantum Electron. **8**, 523–529 (1976)
75. J.D. Briers, Laser Doppler and time-varying speckle: reconciliation. J. Opt. Soc. Am. A **13**, 345–350 (1996)
76. P.S. Liu, *The optical bases of speckle statistic* (Science Press, Beijing, 1987) (in Chinese)
77. M. Linden, H. Golster, S. Bertuglia, A. Colantuoni, F. Sjoberg, G. Nilsson, Evaluation of enhanced high-resolution laser Doppler imaging in an *in vitro* tube model with the aim of assessing blood flow in separate microvessel. Microvasc. Res. **56**, 261–270 (1998)
78. D. Kleinfeld, P.P. Mitra, F. Helmchen, W. Denk, Fluctuations and stimulus-induced changes in blood flow observed in individual capillaries in layers 2 through 4 of rat neocortex. Proc. Natl. Acad. Sci. U.S.A. **95**, 15741–15746 (1998)
79. A. Serov, W. Steenbergen, F.F.M. de Mul, Laser Doppler perfusion with a complimentary metal oxide semiconductor image sensor. Opt. Lett. **27**, 300–302 (2002)

Part 2

Holography, Interferometry, Diffractive Imaging, and Wavefront Measurements

Digital Holographic Microscopy: Quantitative Phase Imaging and Applications in Live Cell Analysis

6

Björn Kemper, Patrik Langehanenberg, Sebastian Kosmeier, Frank Schlichthaber, Christian Remmersmann, Gert von Bally, Christina Rommel, Christian Dierker, and Jürgen Schnekenburger

Contents

Abstract

The analysis of complex processes in living cells creates a high demand for fast and label-free methods for online monitoring. Widely used fluorescence methods require specific labeling and are often restricted to chemically fixated samples. Thus, methods that offer label-free and minimally invasive detection of live cell processes and cell state alterations are of particular interest. In combination with light microscopy, digital holography provides label-free, multi-focus quantitative phase imaging of living cells. In overview, several methods for digital holographic microscopy (DHM) are presented. First, different experimental setups for the recording of digital holograms and the modular integration of DHM into common microscopes are described. Then the numerical processing of digitally captured holograms is explained. This includes the description of spatial and temporal phase shifting techniques, spatial filtering

B. Kemper (✉) • P. Langehanenberg • S. Kosmeier • F. Schlichthaber • C. Remmersmann • G. von Bally
Center for Biomedical Optics and Photonics Muenster, University of Münster, Münster, Germany
e-mail: bkemper@uni-muenster.de, patrik@uni-muenster.de, sebastian.kosmeier@uni-muenster.de, f.schlichthaber@uni-muenster.de, remmersmann@googlemail.com, bally@uni-muenster.de

C. Rommel • C. Dierker • J. Schnekenburger
Biomedical Technology Center, University of Münster, Münster, Germany
e-mail: rommelc@uni-muenster.de, cdierker@uni-muenster.de, schnekenburger@uni-muenster.de

based reconstruction, holographic autofocusing, and the evaluation of self-interference holograms. Furthermore, the usage of partial coherent light and multi-wavelength approaches is discussed. Finally, potentials of digital holographic microscopy for quantitative cell imaging are illustrated by results from selected applications. It is shown that DHM can be used for automated tracking of migrating cells and cell thickness monitoring as well as for refractive index determination of cells and particles. Moreover, the use of DHM for label-free analysis in fluidics and micro-injection monitoring is demonstrated. The results show that DHM is a highly relevant method that allows novel insights in dynamic cell biology, with applications in cancer research and for drugs and toxicity testing.

6.1   Introduction

The imaging of living single cells with light microscopy is important for many research areas in biology and medicine. This includes in particular the ranges of stem cell, development, and cancer sciences as well as the analysis of infection and inflammation processes. Here, capabilities for dynamic analysis, for example, to study the temporal dependency of morphology changes, and the intracellular solute concentrations, are of particular interest. Microscopic life cell imaging can give new insights into cell motility, biomechanical properties on the cellular or subcellular level, and the response of cells to drugs and toxins. In order to affect the living specimen under investigation as little as possible, ideal imaging methods for the investigation of life cell processes should be minimally invasive. Moreover, quantitative measurement data should be provided. On a molecular level, live cell imaging aspects have been widely addressed by using a variety of fluorescence microscopy techniques [1, 2]. These methods have been found highly suitable for 3D imaging of subcellular structures like, for example, the cell membrane, proteins of the cytoskeleton, mitochondria, or vesicles, with a resolution down to several nanometers (see [3, 4] and references therein). However, although the specificity of fluorescence signals is high due to a large number of available dyes [5], specific auto fluorescence mechanisms [6], fluorescence life time imaging (FLIM) [7], and a wide experience with the techniques, there still remain challenges in the application of these methods for live cell imaging. For example, long-term in vitro investigations and in vivo applications are restricted as many fluorescence dyes are toxic. The engineering of fluorescent proteins like the green fluorescent protein (GFP) [8] allow extended investigations of living cells. However, for this purpose cells have to be (genetically) modified, e.g., by chemical [9] or optical [10] transfection. Furthermore, in several cases, a low quantum efficiency of, for instance, the available dyes or the relevant auto fluorescence mechanisms results in the need for long exposure times or a high light intensity. This limits the temporal resolution and the application on living specimens. Thus, in the past years other label-free methods like Optical Coherence Tomography (OCT) [11, 12] and

Coherent Amplified Raman Spectroscopy (CARS) [13] have been transferred to life sciences. In addition, to make use of the high accuracy of diffraction and interferometry-based metrology, the activities of a growing number of research groups focus on techniques for quantitative phase imaging (QPI). QPI provides label-free data with low demands on light exposure and high data acquisition rates. As opposed to the above-mentioned fluorescence techniques, such methods detect changes of the optical path length (OPL) that are caused by the specimen under investigation.

This chapter focuses on quantitative phase imaging with digital holographic microscopy (DHM). Holographic interferometric metrology is well established in industrial nondestructive testing and quality control [14–16]. In combination with microscopy, digital holography provides label-free, quantitative phase imaging [17–22] that is also suitable for modular integration into common research microscopes [23]. In this way, DHM facilitates a combination with other microscopy techniques like laser scanning microscopy, fluorescence imaging, and optical laser micromanipulation [24–26]. The reconstruction of digitally captured holograms is performed numerically. Thus, in comparison with other phase contrast methods [27, 28], related interferometry-based techniques [29–32], and optical coherence tomography (OCT) or microscopy (OCM) [33–38], DHM provides quantitative phase contrast with subsequent numerical focus correction (multi-focus imaging) from a single recorded hologram.

In an overview, several methods for digital holographic microscopy are presented. First, different experimental setups for the recording of digital holograms and the modular integration of DHM into common microscopes are described. Then, the numerical processing of digitally captured holograms is explained. This includes the description of spatial and temporal phase shifting techniques, spatial filtering based reconstruction of the object wave, the evaluation of self-interference holograms, and holographic autofocusing. Furthermore, the use of partial coherent light and multi-wavelength approaches in DHM are discussed. Finally, potentials of DHM for quantitative cell imaging are illustrated by results from selected applications. It is shown that DHM can be used for automated tracking of migrating cells and cell thickness monitoring as well as for refractive index determination of cells and particles. Moreover, the use of the quantitative holographic phase contrast for label-free flow analysis in fluidics and for micro-injection monitoring is demonstrated. The results show that DHM represents a QPI method that is highly relevant to achieve novel insights in dynamic cell biology, with applications in cancer research and for drugs and toxicity testing.

6.2   Principles of Digital Holographic Microscopy

In this section, the principle of DHM and the evaluation of digital holograms are illustrated with focus on the investigation of transparent microscopic specimens like living cells in transmission mode.
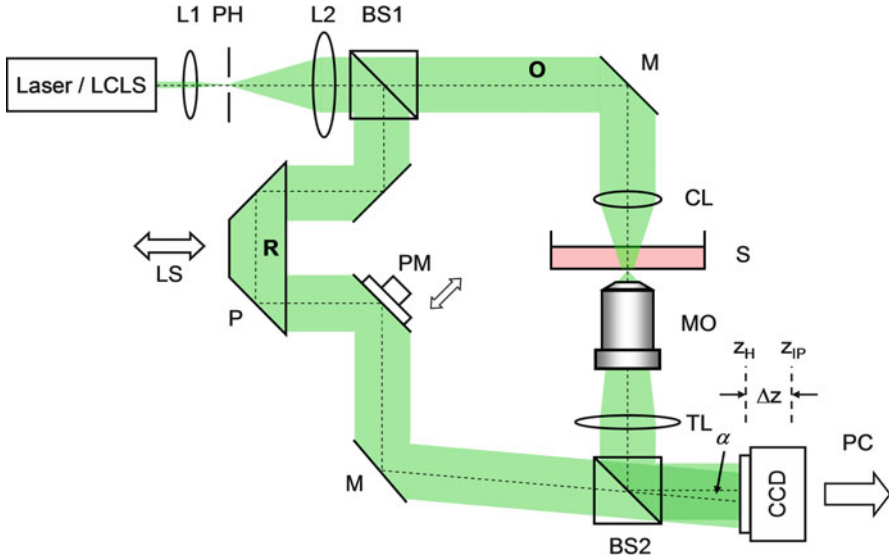
Fig. 6.1 Mach-Zehnder setup for digital holographic microscopy in transmission mode. *LCLS*: low coherence light source; *O*: object wave; *R*: reference wave; α: phase gradient between *O* and *R*; *M*: mirror; *BS1*, *BS2*: non-polarizing beam splitter cubes; *CL*: condenser lens; *MO*: microscope lens; *CCD*: hologram recording device (CCD image sensor); *L1*, *L2*: lenses; *PM*: piezo actuated mirror; *P*: Porro prism; *LS*: motorized linear translation stage; *PH*: pin-hole aperture (spatial filter); *TL*: tube lens; Δ*z*: distance between the hologram plane at $z = z_H$ and the image plane at $z = z_{IP}$; *S*: sample; *PC*: computer [40]

6.2.1   Experimental Implementation

Digital holographic microscopy is based on the classic holographic principle, the difference being that the hologram recording is performed with a digital sensor, e.g., a charge coupled device (CCD) or a complementary metal oxide semiconductor (CMOS) [39]. First, the design of a free-space Mach-Zehnder measurement setup for temporal phase shifting and off-axis digital holography is explained. Then, the fiber optical integration of Mach-Zehnder-based DHM into common research microscopes is described. Finally, a Michelson interferometer approach for simplified implementation of DHM by self-interference is presented.

6.2.1.1 Mach-Zehnder Setup for Imaging of Transparent Samples with Coherent and Partially Coherent Light

Figure 6.1 depicts the principle of a Mach-Zehnder-based digital holographic microscopy setup [40]. The shown transmission mode setup enables investigations on transparent samples such as living cell cultures.

The emitted light of a laser (e.g., a frequency doubled Nd:YAG, $\lambda = 532$ nm) or a low-coherence light source *LCLS* (e.g., a light emitting diode (LED) or a superluminescence diode (SLD)) is spatially filtered (*L1*, *PH*), collimated (*L*),

and divided into an object illumination wave (O) and a reference wave (R). The intensity ratio between O and R is adjusted by adequately chosen optical density filters (not shown) or, alternatively, by substituting *BS1* by a polarizing beam splitter cube in combination with two $\lambda/2$-wave plates. A condenser lens (*CL*) provides an optimized illumination of the sample. The reference wave is guided directly by a beam splitter to the image recording device (typically a charge-coupled device sensor, CCD), which is applied for the digitization of the holograms in the hologram plane located at $z = z_H$. Holographic off-axis geometry (see also Sects. 6.2.2.4–6.2.2.6) is achieved by a phase gradient of the reference wave front relative to the object wave front, which can be performed by a slight tilt of a mirror (see angle α in Fig. 6.1) or by the beam splitter *BS2*. The adjustment of the optical path length difference for the *LCLS* can be performed by a Porro prism that is mounted onto a translation stage. For temporal phase shifting-based digital holographic reconstruction (see Sect. 6.2.2.3), a calibrated piezo-actuated mirror (*PM*) is applied. To enhance the lateral resolution, the object wave is magnified by a microscope lens (*MO*). The magnification is chosen in such a way that the recorded image of the specimen is oversampled by the image recording device [41]. In this way, the maximum (diffraction-limited) resolution of the optical imaging system is not decreased by spatial phase shifting-based reconstruction as described in Sect. 6.2.2.4. The digital holograms are recorded with a digital image recording device and transferred to a computer (*PC*). The piezo-actuated mirror *PM* and the translation stage are synchronized with the hologram acquisition by a digital interface.

6.2.1.2 Modular Digital Holographic Microscopy for Live Cell Imaging

In this section, the principle of DHM is illustrated by a modular setup to be used in combination with commercial research microscopes [23].

The upper panel of Fig. 6.2 depicts the concept of an inverse digital holographic microscopy system, designed for the integration into common commercial research microscopes and investigations on transparent specimens such as living cells [23]. In analogy to the schematic depicted in Fig. 6.1, the light of a laser (e.g., a frequency-doubled Nd:YAG laser, $\lambda = 532$ nm with a large coherence length > 1 m) is divided into object illumination wave (object wave) and reference wave. For variable light guidance, polarization-maintaining single-mode optical fibers are applied. The illumination of the sample with coherent laser light is performed in transmission by coupling the object wave into the microscope's condenser. Thus, an optimized (Koehler-like) illumination is achieved. For imaging, common microscope objectives are utilized. The reference wave is guided directly to an interferometric unit that is adapted to one of the microscope's camera ports. Off-axis holography is achieved by a beam splitter that tilts the reference wave front against the wave front of the object wave. The interferogram that is formed by the superposition of object wave and reference wave is recorded by a CCD camera and transferred to an image processing system for the reconstruction and the evaluation of the digitized holograms. The lower panel of Fig. 6.2 illustrates modular DHM by an experimental
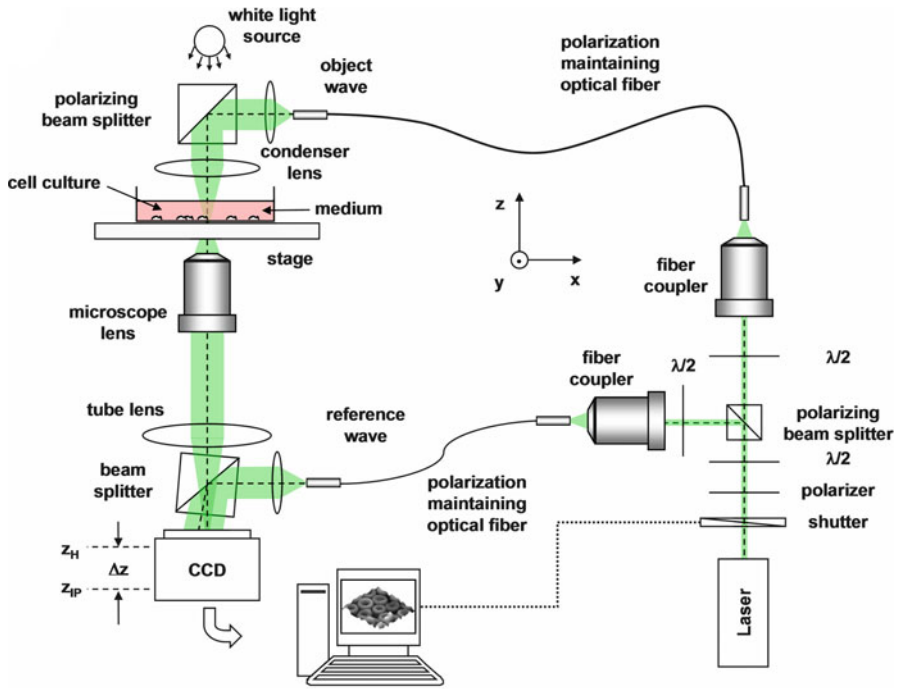
Fig. 6.2 *Upper panel*: schematic of the modular integration of digital holography into an inverted microscope (Modified from [23]), *lower panel*: photo of an experimental setup (iMIC, TiLL Photonics GmbH, Munich, Germany, modified for DHM) with included heating chamber (Solent Scientific Ltd., Segensworth, United Kingdom) for live cell imaging

setup consisting of an inverted microscope (iMIC, TiLL Photonics GmbH, Munich, Germany) with an included heating chamber (Solent Scientific Ltd., Segensworth, United Kingdom) for live cell imaging that has been modified for DHM.
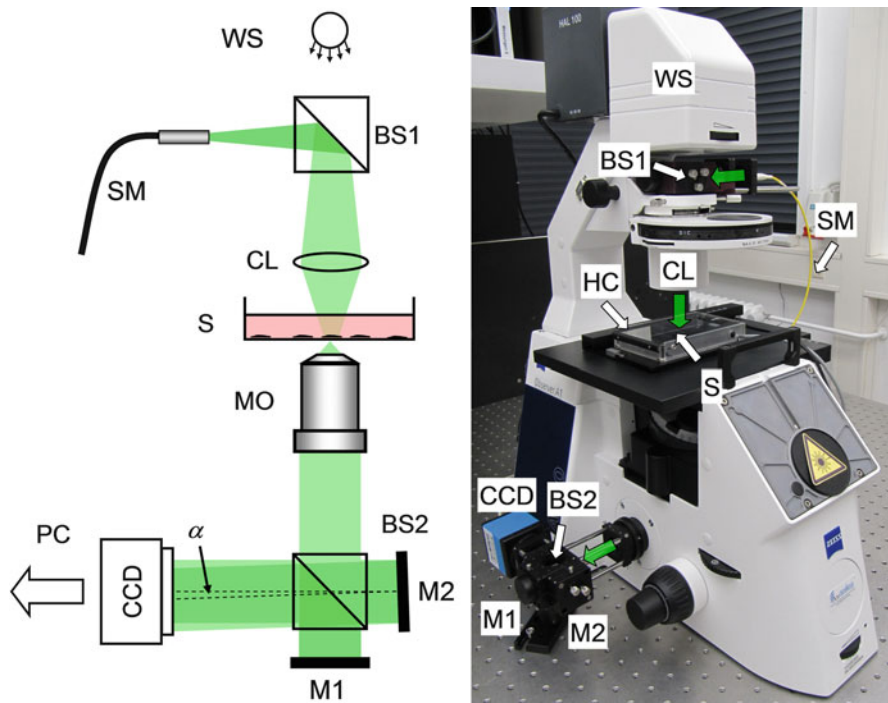
Fig. 6.3 Schematic (*left*) and photo (*right*) of an experimental setup for Michelson-interferometer-based self-interference DHM. *WS*: white light source; *BS1*, *BS2*: beam splitter cubes; *CL*: condenser lens; *SM*: single mode fiber; *S*: sample (here: Petri dish with adherent cells); *MO*: microscope lens; *M1*, *M2*: mirrors; *CCD*: charge-coupled device sensor; α: tilt angle; *PC*: computer; *HC*: heating chamber for live cell imaging [46]

6.2.1.3 Michelson-Interferometer-Based Self-Interference DHM

A drawback of many Mach-Zehnder-interferometer-based quantitative phase imaging arrangements [17, 19–21, 31, 41] is the requirement for a separate reference wave, which results in a phase stability decrease and the demand for a precise adjustment of the intensity ratio between object and reference wave. To overcome these problems several approaches were reported [31, 42–45]. Here, in order to avoid a separately generated reference wave, a Michelson interferometer approach for DHM is presented [46]. The advantage of the this setup is that, opposed to other self-interference or common path-based approaches, no additional components like temporal phase shifting devices [31], lenses [43], or customized reflective surfaces [44] are required. Furthermore, no diffractive optical elements (DOEs) [47] or spatial light modulators (SLMs) [31, 42] are needed, which may be expensive or possibly affect the object wave by spatial filtering and thus may influence the lateral resolution.

Figure 6.3 shows a sketch and a photo of a Michelson interferometer-based DHM arrangement setup that was attached to an inverted research microscope

(Zeiss Axio Observer A1, Carl Zeiss Micro Imaging GmbH, Göttingen, Germany) [46]. The sample is illuminated by a frequency-doubled Nd:YAG laser via a single-mode optical fiber (*SM*) by inserting a non-polarizing beam splitter cube (*BS1*) into the illumination path of the microscope's white light source (*WS*). Behind the microscope lens (*MO*) the light is coupled into a Michelson interferometer that has been attached to the camera side port of the microscope. Mirror *M2* was tilted by an angle α in such a way that an area of the sample that contained no object was superposed with the image of the specimen to create a suitable spatial carrier fringe pattern (for illustration see Figs. 6.6 and 6.7 in Sects. 6.2.2.4 and 6.2.2.5) for off-axis holography. Note that, due to the Michelson interferometer design in areas without specimen, two wave fronts with nearly identical curvatures are superimposed. This is even fulfilled for an imaging geometry with two slightly divergent waves that differs from the collimated arrangement, which is sketched on the left panel of Fig. 6.3 to simplify the illustration of the measurement principle. The digital holograms are recorded by a CCD sensor. The numerical calculation of the quantitative DHM phase contrast images from the resulting self-interference digital holograms can be performed as described in Sects. 6.2.2.4–6.2.2.6.

6.2.2 Recording and Reconstruction of Digital Holograms

6.2.2.1 Description of the Intensity Distribution in the Hologram Plane

The intensity distribution I_H of the interferogram in the hologram plane that is created with the experimental setups in Figs. 6.1–6.3 by the interference of the object wave and the reference wave is:

$$
\begin{aligned}
I_H(x,y,z_0) &= O(x,y,z_H)O^*(x,y,z_H) + R(x,y,z_H)R^*(x,y,z_H) \\
&\quad + O(x,y,z_H)R^*(x,y,z_H) + R(x,y,z_H)O^*(x,y,z_H) \\
&= I_O(x,y,z_H) + I_R(x,y,z_H) \\
&\quad + 2\sqrt{I_O(x,y,z_H)I_R(x,y,z_H)}\cos\Delta\phi_{HP}(x,y,z_H)
\end{aligned}
\tag{6.1}
$$

with $I_O = OO^* = |O|^2$ and $I_O = RR^* = |R|^2$ (* represents the conjugate complex terms). The parameter $\Delta\phi_H(x,y,z_H) = \phi_R(x,y,z_H) - \phi_O(x,y,z_H)$ is the phase difference between O and R at $z = z_H$. In the presence of a sample in the optical path of O, the phase distribution represents the sum $\phi_O(x,y,z_H) = \phi_{O_H}(x,y,z_H) + \Delta\varphi_S(x,y,z_H)$ with the pure object wave phase $\phi_{O_H}(x,y,z_H)$ and the phase change $\Delta\varphi_s(x,y,z_H)$ that is effected by the sample. In the following section it is explained how the sample-induced phase change $\Delta\varphi_s(x,y,z_{IP})$ in the image plane $z = z_{IP}$ is retrieved from the intensity distribution in (6.1).

6.2.2.2 Principles of Object Wave Retrieval and Numerical Propagation

Various methods for the numerical reconstruction of temporal phase shifted and digital off-axis holograms have been developed (for an overview see, e.g., [22, 39, 48–51]). Here, the numerical reconstruction is performed in two steps. First, the

complex object wave O is reconstructed in the hologram plane. This can be performed by temporal or spatial phase shifting methods as well as in the spatial frequency domain by Fourier transformation-based spatial filtering (see Sects. 6.2.2.3–6.2.2.6). These three methods provide the retrieval of the object wave without the disturbing terms "twin image" and "zero order intensity" and were found highly applicable for quantitative phase imaging in live cell analysis. In case of the imaging of objects that have been recorded out-of-focus, numerical refocusing is required. Thus, in an optional subsequent step, O is numerically propagated to the image plane. This typically is performed by the numerical implementation of the Fresnel-Huygens principle [39, 52]. Here, the numerical wave propagation is illustrated by an approach of the convolution method in which the convolution theorem is applied after the Fresnel approximation [41, 53]. The propagation of $O(x, y, z_H)$ to the image plane z_{IP} that is located at $z_{IP} = z_H + \Delta z$ in the distance Δz to the hologram plane (see Fig. 6.1) is performed by using the equation:

$$O(x, y, z_{IP} = z_H + \Delta z) = \mathrm{F}^{-1}\left\{\mathrm{F}\{O(x, y, z_H)\}\exp\left(i\pi\lambda\Delta z\left(v^2 + \mu^2\right)\right)\right\}. \quad (6.2)$$

In (6.2), λ is the applied laser light wavelength, v, μ are the coordinates in frequency domain, and F denotes a Fourier transformation. The advantage of this approach is that the size of the propagated wave field is preserved during the refocusing process. This is a particular advantage for numerical autofocusing as described in Sect. 6.2.2.7 because it simplifies the comparison of the image definition in different focal planes. Furthermore, in contrast to propagation by digital Fresnel transformation [17, 19], (6.2) allows the refocusing of only slightly defocused images of the sample near the hologram plane [54]. However, numerical refocusing also may be performed with other common numerical propagation methods, including in particular more general approaches of the convolution method [39] and the angular spectrum method [51, 55]. During the propagation process the parameter Δz in (6.2) is chosen so that the holographic amplitude image $|O|$ appears sharply, like a microscopic image under white light illumination. In the special case that the image of the sample is sharply focused in the hologram plane with $\Delta z = 0$ and thus $z_{IP} = z_H$ the reconstruction process can be accelerated because no propagation of O by (6.2) is required.

From the numerically reconstructed and optionally propagated complex object wave $O(x, y, z_{IP})$, in addition to the absolute amplitude $|O(x, y, z_{IP})|$ that represents the image of the sample, the phase information $\Delta\varphi_S(x, y, z_{IP})$ of the sample is retrieved:

$$\Delta\varphi_S(x, y, z_{IP}) = \arctan\frac{\mathrm{Im}\{O(x, y, z_{IP})\}}{\mathrm{Re}\{O(x, y, z_{IP})\}}(\mathrm{mod}\ 2\pi). \quad (6.3)$$

After removal of the 2π ambiguity by phase unwrapping [14], the data obtained by (6.3) can be used for QPI.
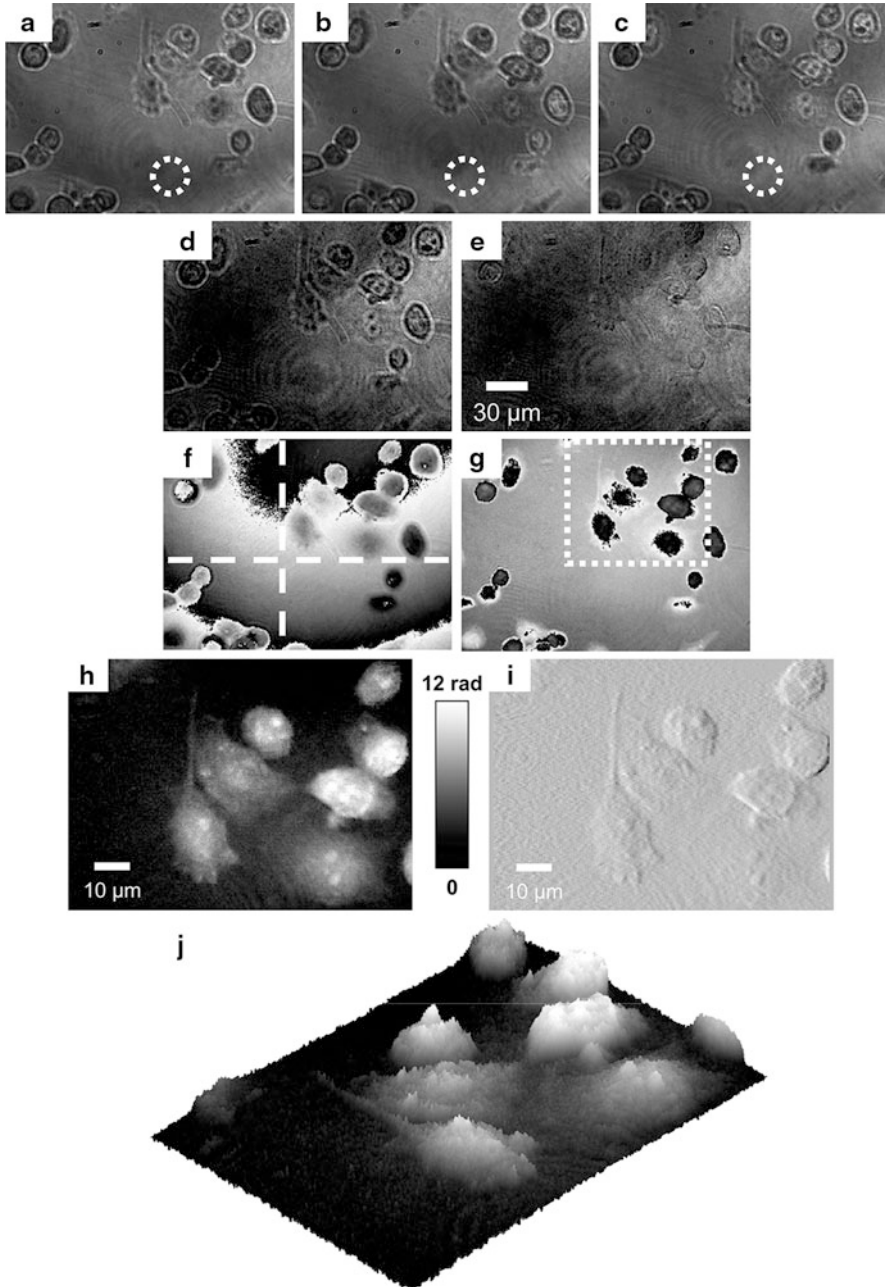
Fig. 6.4 Temporal phase shifting holography-based multi-focus quantitative phase imaging. (**a–c**): Temporal phase shifted digital holograms of fixed human pancreatic adenocarcinoma cells (PaTu 8988T); (**d**): reconstructed unfocused holographic amplitude distribution; (**e**): numerically refocused holographic amplitude distribution; (**f**): reconstructed phase distribution modulo

In *transmission mode* as depicted in Figs. 6.1–6.3, induced phase change $\Delta\varphi_S(x, y, z_{IP})$ of a semi-transparent sample is influenced by the sample thickness, by the refractive index of the sample, and the refractive index of the medium surround the investigated specimen. Thus, for quantitative cell imaging, information about the cellular refractive index is required. Several interferometric and holographic methods for the determination of the refractive index have been developed (see, for example, Refs. in [22, 56, 57] and Sect. 6.3.2). However, it is not possible to perform a decoupling of the parameters' thickness and refractive index in every measurement case. For cells in cell culture medium with the refractive index n_{medium}, and the assumption of a known homogeneously distributed integral cellular refractive index n_{cell}, the cell thickness $d_{\mathrm{cell}}(x, y, z_{IP})$ can be determined by measuring the optical path length change $\Delta\varphi_{\mathrm{cell}}$ of the cells to the surrounding medium [20, 41]:

$$d_{\mathrm{cell}}(x, y, z_{IP}) = \frac{\lambda\Delta\varphi_{\mathrm{cell}}(x, y, z_{IP})}{2\pi} \cdot \frac{1}{n_{\mathrm{cell}} - n_{\mathrm{medium}}}. \tag{6.4}$$

The parameter λ in (6.4) represents the wavelength of the applied laser light. For fully adherently grown cells, the parameter d_{cell} can be interpreted as the cell shape. Nevertheless, the results from (6.4) have to be handled critically, e.g., if toxically and osmotically induced reactions of cells [41, 58] are analyzed that may affect dynamic changes of the cellular refractive index.

6.2.2.3 Temporal Phase Shifting Holography

In temporal phase shifting digital holography (TPS DH), the intensity distribution in the hologram plane that is described by (6.1) typically is evaluated for several known (or unknown but equidistant) phase shifts of the reference wave (or alternatively of the object wave) [59, 60]. Thus, a system of linear equations is formed that can be solved for the required parameters' intensity, modulation, and phase, from which the complex object wave is obtained. Therefore, common interferometric phase-shifting algorithms can be used (for an overview see, e.g., [14] and [61]). For a given field of view, with TPS DH, a higher lateral resolution than with off-axis-based holographic methods as described in Sects. 6.2.2.4–6.2.2.6 can be achieved. Moreover, TPS DHM has been found suitable for use with low coherent light sources [62–64]. Figure 6.4 illustrates the numerical reconstruction by TPS DH for the example of fixed human pancreatic adenocarcinoma cells (PaTu 8988T) that have been recorded slightly out-of-focus with the setup in Fig. 6.1 by using a light-emitting diode (LED) as light source (central

Fig. 6.4 (continued) 2π corresponding to (**e**); (**g**): numerically refocused and background corrected phase distribution modulo 2π; (**h**): unwrapped phase distribution obtained from the area marked with a *dotted white box* in (**g**); (**i**): DHM DIC image obtained by calculation of the first derivative in *x*-direction of the data in (**h**); (**j**): gray level coded pseudo-3D representation of the phase distribution [65]

wavelength: $\lambda = 624$ nm, spectral width: $\Delta\lambda = 18$ nm, coherence length $l_c \approx$ 18 μm, [63]). Figures 6.4a–c show temporal phase-shifted holograms of the cells. The marked areas in Fig. 6.4a–c visualize the spatial intensity variations (see (6.1)) due to the temporal phase shifts $\phi_{R,1}(x, y) = -\Theta = -\pi/2$, $\phi_{R,2}(x, y) = 0$, $\phi_{R,3}(x, y) = +\Theta = +\pi/2$ of the reference wave between two subsequent recorded holograms that are generated by the piezo-actuated mirror PM in Fig. 6.1. Figure 6.4d shows the reconstructed (still unfocused) holographic amplitude $|O(x, y, z = z_H)|$ of the sample in the hologram plane that has been obtained by a variable three-step algorithm (see detailed description and references in [63, 64]. The complex object wave $O(x, y, z_H) = |O(x, y, z_H)| \times \exp(i\Delta\phi_O(x, y, z_H))$ in the hologram plane is calculated from $|O(x, y, z = z_H)|$ and the simultaneously retrieved phase $\Delta\phi_O(x, y, z_H)$. Then, the complex field $O(x, y, z_H)$ is propagated by (6.2) to the image plane that is located at $z = z_{IP}$. Figure. 6.4e depicts the sharply focused amplitude $|O(x, y, z = z_{IP})|$ in the image plane. As the investigated cells represent phase objects $|O(x, y, z = z_{IP})|$ appears with minimum contrast for the sharply focused image. Figure 6.4f shows the simultaneously reconstructed phase information $\phi_O(x, y, z_{IP})$ modulo 2π (coded to 256 gray levels) that was obtained as explained in Sect. 6.2.2.2.

After subtraction of the phase distribution of the pure object wave front $\Delta\phi_{O_H}(x, y, z_{IP})$ modulo 2π that is retrieved by fitting a polynomial model along the dotted white lines in Fig. 6.4f, the variation of the optical path length $\Delta\varphi_s(x, y, z = z_{IP})$ that is caused by the sample in comparison with the surrounding medium is obtained. Figures 6.4h, j show the unwrapped phase distribution in 256 gray levels, and a corresponding pseudo-three-dimensional representation that is obtained from the area marked with a dotted white box in Fig. 6.4g. Figure 6.4i represents a DHM differential phase contrast image (DHM DIC image) that has been obtained by calculation of the differential quotient in the x-direction of the data in Fig. 6.4h. DHM DIC is comparable to Nomarski differential interference phase contrast [66] with the advantage of an adaptable sensitivity due to a variable digital shear. Note that the cells and subcellular structures such as the nucleoli are clearly resolved in the DHM phase contrast images as well the DHM DIC image.

6.2.2.4 Spatial Phase Shifting Reconstruction of Off-Axis Holograms

In contrast to temporal phase shifting holography, where several holograms are recorded to retrieve the object wave (see Sect. 6.2.2.3), in spatial phase shifting holography neighboring pixels of single off-axis holograms are evaluated. Therefore, the same numerical algorithms as for temporal phase shifting can be used. The required spatial phase shift between object wave and reference wave is generated by an adequate off-axis tilt of one of the waves. For minimized phase noise, in analogy to TPS DHM [64], the optimum spatial phase shift should be chosen near 90° per pixel [67]. In addition to the variable three-step algorithm that has been used in Sect. 6.2.2.3 for the illustration of temporal phase shifting holography, the interferogram equation in (6.1) can also be solved pixel-wise within a squared area of

pixels (in practice usually 5×5 pixels) around a given hologram pixel using the least square principle. As described in detail in [68] and [19] by definition of appropriate substitutions the resulting nonlinear problem is transferred to a form that can be solved by linear algorithms. The resulting robust reconstruction method for O was found particularly suitable for the application in DHM and has been reported to be applied successfully for the analysis of living cells in [19, 41]. If the sample is not imaged sharply onto the hologram acquisition device during the hologram recording, in analogy to temporal phase shifting holography, a propagation of the object wave to the image plane can be performed as described in Sect. 6.2.2.2.

Figure 6.5 illustrates the reconstruction process of a digital off-axis hologram by spatial phase shifting-based reconstruction. Figure 6.5a shows a digital hologram of human red blood cells (RBCs) in phosphate-buffered saline (PBS). The cells were recorded slightly defocused with a $63\times$ microscope lens (NA = 0.75) with a setup as sketched in Fig. 6.1 using a frequency-doubled Nd:YAG laser ($\lambda = 532$ nm) as the light source. The enlarged area in Fig. 6.5a shows a part of the carrier fringe pattern of the digital off-axis hologram that was used for holographic coding of the object wave. Figure 6.5b depicts the unfocused reconstructed amplitude image of the RBCs in the CCD sensor plane. Figure 6.5c displays the sharply focused amplitude after numerical refocusing with (6.2). This image corresponds to a microscopic bright field image under coherent illumination. Figure 6.5d shows the phase distribution modulo 2π. The quantitative phase image after removal to the 2π ambiguity is displayed in Fig. 6.5e. Figure 6.5g illustrates the cell thickness measurement along a cross-section through the phase data. The thickness values d_{cell} of the RBC were calculated from the phase contrast $\Delta\varphi_{\text{cell}}$ with (6.4) as explained in Sect. 6.2.2.2 by estimating an integral cellular refractive index $n_{\text{RBC}} = 1.400$ [70] and a refractive index $n_{\text{medium}} = 1.337$ of the buffer solution that was obtained by an Abbe refractometer. Figure 6.5g also illustrates the cell thickness by a pseudo-3D representation of the data in Fig. 6.5e.

6.2.2.5 Hologram Evaluation by Spatial Filtering

In addition to phase-shifting techniques that are described in Sects. 6.2.2.3 and 6.2.2.4, spatial filtering based on Fourier transformation represents another efficient approach for the retrieval of the object wave in digital holography. Fourier transformation methods were first applied in optical holography for fringe pattern analysis and phase retrieval from double-exposure interferograms [71, 72]. In order to reconstruct the object wave in the hologram plane from digital off-axis holograms by spatial filtering, the intensity distribution $I_H(x, y, z_H)$ in (6.1) is evaluated by a two-dimensional Fourier transform following [21, 71]. Figure 6.6 illustrates the principle of digital off-axis holograms by spatial filtering for the example of suspended human fibrosarcoma cells (HT-1080, [73]) with internalized silica micro particles (diameter ≈ 3.44 µm). Figure 6.6a shows an off-axis hologram of the cells that was recorded with the experimental setup shown in Fig. 6.3 by using a frequency-doubled Nd:YAG laser ($\lambda = 532$ nm). Figure 6.6b shows an enlarged part of the carrier fringe pattern of the off-axis hologram (see box in Fig. 6.6a) that is utilized for holographic coding of the object wave.
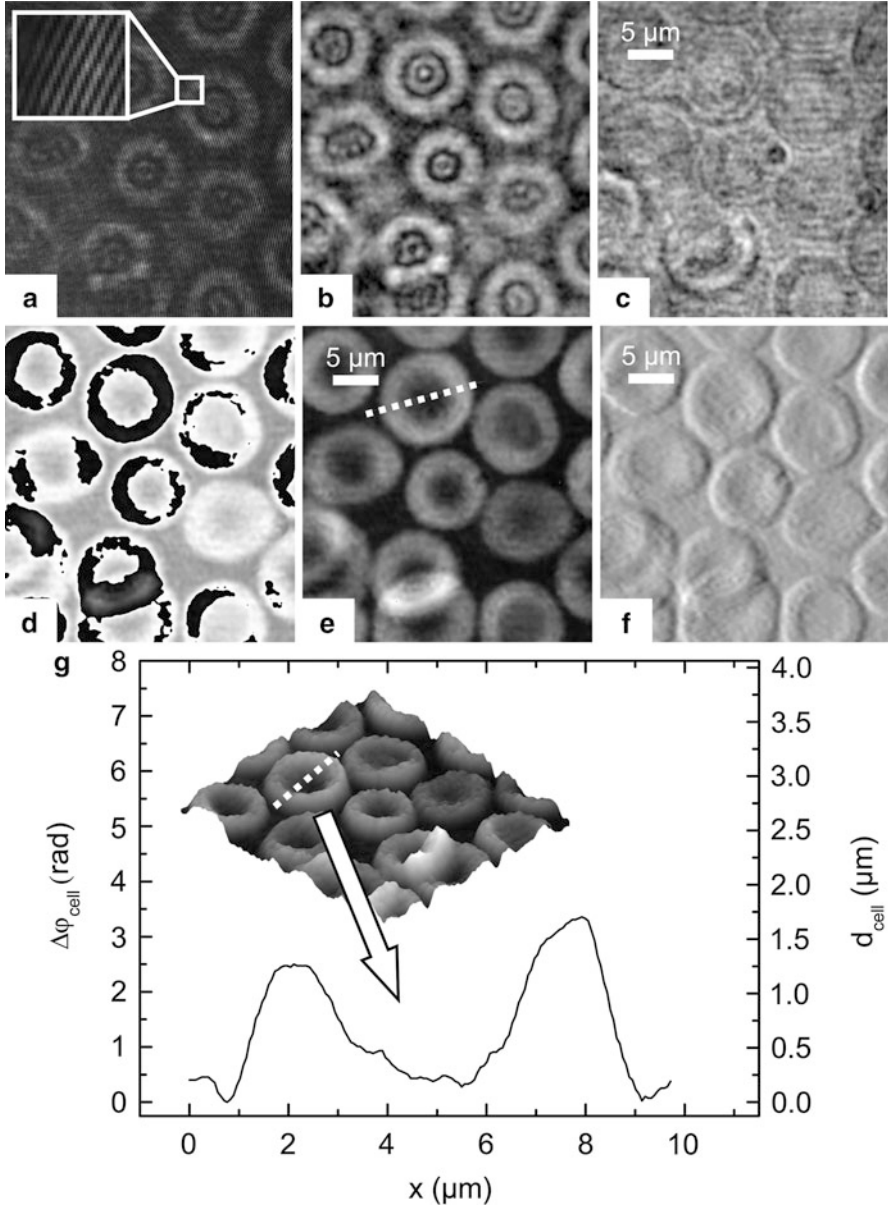
Fig. 6.5 Evaluation of digital holograms by spatial phase shifting: (**a**): slightly defocused recorded digital hologram of living human red blood cells, (**b**): reconstructed amplitude in the hologram plane (defocused), (**c**): numerically refocused amplitude distribution, (**d**): reconstructed phase distribution modulo 2π corresponding to (**c**) coded to 256 gray levels; (**e**) unwrapped phase distribution coded to 256 gray levels; (**f**): first derivative of (**e**) in x-direction, (**g**): pseudo-3D representation of the phase distribution in (**e**) with cross section through a cell [69]
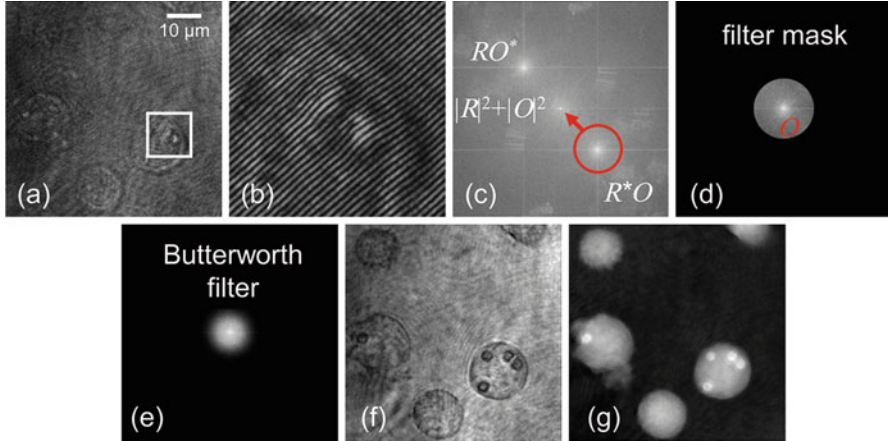
Fig. 6.6 Evaluation of off-axis holograms by spatial filtering. (**a**): digital off-axis hologram of suspended human fibrosarcoma cells (HT-1080) with internalized silica micro particles (diameter ≈ 3.44 μm), (**b**): enlarged part of the hologram (see *box* in (**a**)), (**c**): 2D frequency spectrum of (**a**) with the spatial separated "zero order intensity" ($|R|^2 + |O|^2$), image (R^*O) and twin image (RO^*), (**d**): spectrum of the object wave after application of a spatial filter and removal of the phase shift due to the carrier fringe pattern, (**e**): data in (**d**) after Butterworth filtering, (**f**): reconstructed amplitude $|O|$, (**g**): quantitative phase image

Figure 6.6c depicts the 2D frequency spectrum that is retrieved numerically by a fast Fourier transformation (FFT) from (a) for an adequately chosen off-axis angle between object wave for which the terms "zero order intensity" ($|R|^2 + |O|^2$), image (R^*O), and twin image (RO^*) appear spatially separated. In the next step of the evaluation, the terms $|R|^2 + |O|^2$ and RO^* are eliminated by application of a suitable spatial filter. Then, the contribution of the phase-conjugated reference wave is removed by a shift of the term R^*O to the center of the spectrum. The remaining spectrum parts (Fig. 6.6d) are filtered with a Butterworth filter to reduce disturbing spatial frequencies and numerical artifacts like the ringing effect (Fig. 6.6e). Afterwards, the object wave O in spatial domain is calculated by an inverse FFT. Figure 6.6f shows the resulting amplitude distribution $|O|$. In Fig. 6.6c the unwrapped phase contrast image is shown that was obtained as explained in Sect. 6.2.2.2 after background correction by a two-dimensional polynomial fit (for illustration, see Fig. 6.4f in Sect. 6.2.2.3). If the sample is not imaged sharply onto the image sensor during the hologram recording, as described in Sects. 6.2.2.3 and 6.2.2.4, a numerical propagation of O to the image plane can be performed.

6.2.2.6 Evaluation of Self-Interference Off-Axis Holograms

The evaluation of digital self-interference holograms that are generated by using the setup in Fig. 6.3 for the case that cells are imaged by different mirrors is illustrated by results from suspended pancreatic adenocarcinoma cells. The upper left panel of Fig. 6.7 shows a digital hologram of three PaTu 8988T cells in cell culture medium
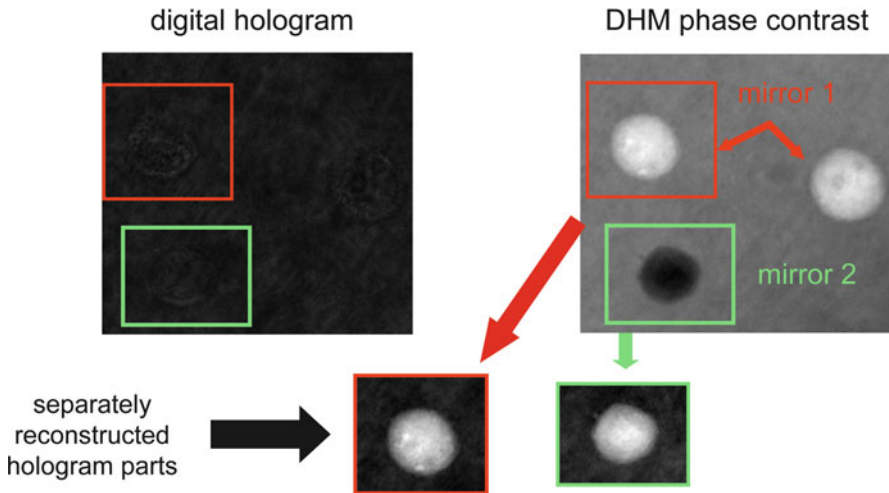
Fig. 6.7 Evaluation of digital self-interference holograms. *Upper left panel*: digital hologram of three suspended pancreatic adenocarcinoma cells (PaTu 8988T) that are imaged onto the image recording device by different mirrors; *upper right panel*: reconstructed DHM phase contrast image; *lower panel*: DHM phase contrast images from separately reconstructed hologram parts [74]

that are imaged onto the image recording device by different mirrors and thus appear in inverted phase contrast [74].

The upper right panel of Fig. 6.7 depicts a quantitative DHM phase image obtained by spatial phase shifting numerical reconstruction as explained in Sect. 6.2.2.4. Alternatively, the reconstruction also could be performed by spatial filtering (Sect. 6.2.2.5). The lower panel of Fig. 6.7 presents quantitative phase images of two cells that were obtained by the separate reconstruction of selected hologram parts (see red and green boxes in Fig. 6.7). The results in Fig. 6.7 illustrate that, in case of partial hologram reconstruction, the same gray-level range like for a Mach-Zehnder interferometer-based setup is achieved. However, the analysis of the spatial phase noise within the quantitative phase contrast images shows that the accuracy for the detection of optical path length changes for the Michelson interferometer-based DHM arrangement is lower than for a Mach-Zehnder setup [46]. This can be explained by the circumstance that in the Michelson interferometer setup both waves are affected by coherent disturbances due to scattering effects from the microscope imaging system and the medium in which the specimen is embedded. However, in [46] it is demonstrated that even subcellular structures like the nuclear envelope and the nucleoli are resolved. Furthermore, the setup is particular suitable for low-cost light sources with short coherence lengths $l_c < 1$ mm [74].

6.2.2.7 Holographic Autofocusing

In digital holography, refocusing can be performed numerically by variation of the propagation distance Δz (6.2). The combination of this feature with image

sharpness quantification algorithms yields subsequent autofocusing (for an over-view see, e.g., [69] and references therein). Pure phase objects with negligible absorption such as technical reflective specimens or biological cells are sharply focused at the setting with the least contours in the amplitude distributions [75, 76]. In contrast to the bright-field case, in digital holography this setting is of particular interest, as the amplitude and phase distributions are accessible simultaneously, and the focal setting with the least contrasted amplitude image corresponds to the best-resolved structures in the quantitative phase contrast distribution.

Different numerical methods that calculate a scalar focus value for the quanti-fication of the image sharpness were compared in [76]. Therefore, common criteria to evaluate the image sharpness in bright field microscopy [77, 78] were used. In agreement with previously reported results for microscopic imaging with white light illumination [79, 80], in [76, 81] the evaluation of the weighted and band-pass-filtered power spectra was identified to be most suitable for a robust determination of the image sharpness in digital holographic microscopy in combination with the convolution method described in Sect. 6.2. Thus, the principle of holographic autofocusing is illustrated by using the band-pass-filtered power spectra for image sharpness quantification. Figure 6.8 shows results from investigations on formalin-fixed pancreatic adenocarcinoma cells (PaTu 8988S) on a glass carrier with a setup as depicted in Fig. 6.2 (frequency-doubled Nd:YAG laser: $\lambda = 532$ nm, 63x microscope lens, NA = 0.75). An off-axis hologram of the slightly defocused cells was recorded and evaluated by spatial phase shifting as described in Sect. 6.2.2.4. Figures 6.8a–f show the impact of (de-)focusing on the reconstructed amplitudes (Fig. 6.8a–c) and the unwrapped phase distributions (Fig. 6.8d–f). In case of focused imaging, the phase specimens nearly disappear in the reconstructed amplitude distribution (Fig. 6.8b) while the reconstructed structures in the unwrapped phase distribution in Fig. 6.8e appear sharply with maximized contrast. In both defocused cases, the amplitude distributions show diffraction patterns and thus are visible with enhanced contrast (Fig. 6.8a, c) while the phase distributions appear blurred (Fig. 6.8d, f). In Fig. 6.8g the normalized focus value function obtained by spectral weighted analysis is plotted. A global minimum of the focus value is reached for a propagation distance $\Delta z = \Delta z_{AF} = 0.1$ cm that corresponds to the sharply focused amplitude and phase distributions of the sample.

The black vertical lines in the unwrapped phase distributions in Fig. 6.8f show further that defocusing-induced diffraction patterns can lead to phase singularities. These artifacts can induce phase-unwrapping errors that inhibit further data evaluation. This also illustrates the need of digital holographic autofocusing for optimized and automated data processing in DHM, which is required for the application of microscope lenses with a high numerical aperture and time-lapse live cell imaging as described in Sect. 6.3.1.

6.2.2.8 Multi-Focus Imaging

As already described in Sect. 6.2.2.7, digital holography enables the reconstruction of different focal planes from a single hologram. This multi-focus imaging feature is particularly suitable for investigations of particles and cells in suspension [57]

$\Delta z = (0.1 - 4.2)\,cm$ $\Delta z = \Delta z_{AF} = 0.1\,cm$ $\Delta z = (0.1 + 4.2)\,cm$
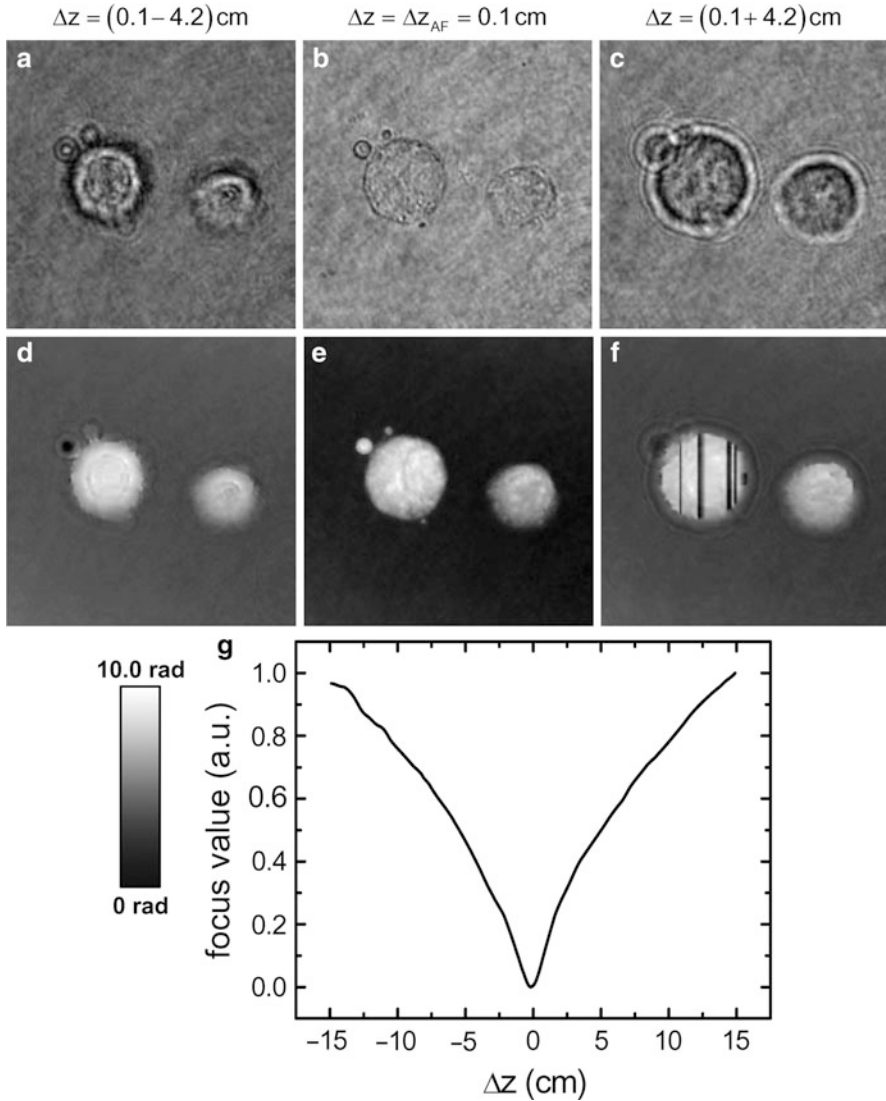
Fig. 6.8 Holographic autofocusing of a phase specimen (fixed PaTu 8988S cells). (**a**), (**c**): defocused amplitude distributions, (**d**), (**f**): defocused unwrapped phase distributions, (**b**) focused amplitude, (**e**): focused unwrapped phase distribution, (**g**): focus values calculated by spectral weighted analysis in dependence of the propagation distance Δz ([69])

or in a three-dimensional environment ([82] and Sect. 6.3.1) as several specimens in different planes can be recorded simultaneously. Furthermore, in combination with numerical autofocusing, the determination of relative object positions in the z-direction is provided. Figure 6.9 illustrates quantitative digital holographic
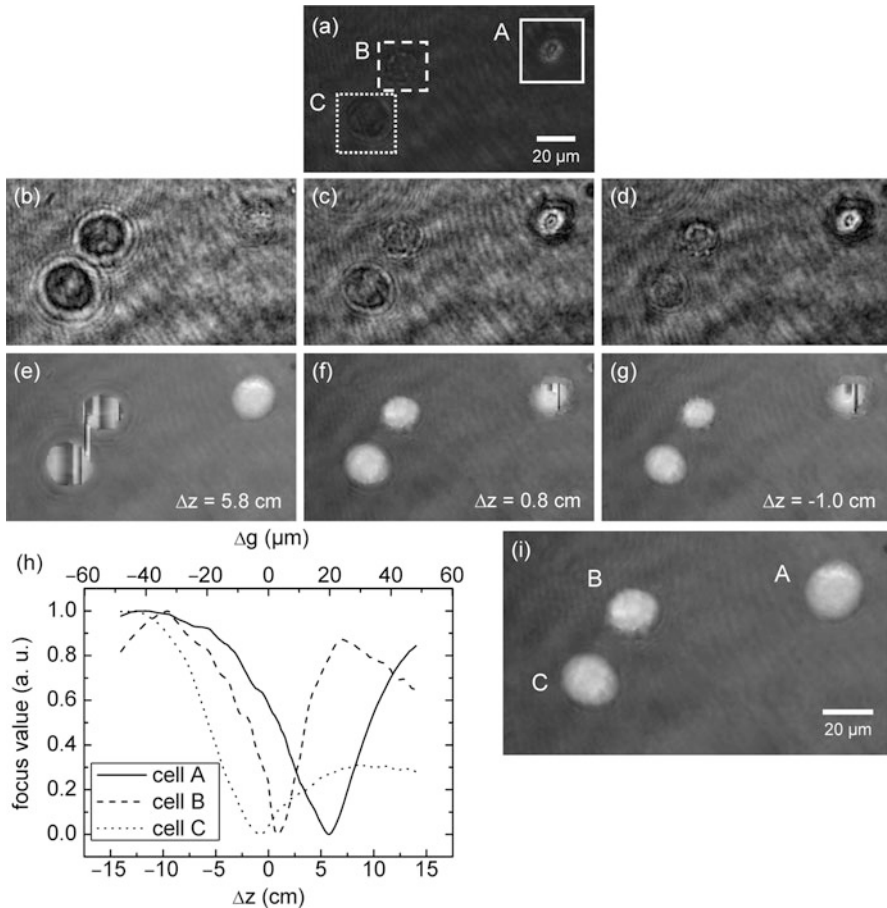
Fig. 6.9 Subsequent multi-focus imaging of suspended cells. (**a**): digital hologram of three pancreatic adenocarcinoma cells (PaTu 8988S) in different focal planes denoted as *A*, *B*, *C*; (**b–d**): amplitude distributions of the cells for different propagation distances obtained by numerical autofocusing in the regions of interest (ROIs) marked with *boxes*, (**e–g**): *gray* level coded unwrapped phase contrast images corresponding to (**b–d**). (**h**): focus values in dependence of the propagation distance Δz and the corresponding distance Δg in object space in the areas marked with *boxes*, (**i**): enlarged phase distribution merged from the sharply focused parts in (**e–g**). The minima of the curves in (**h**) indicate the propagation distances for the sharply focused imaging of the cells [69]

multi-focus imaging by results from pancreatic adenocarcinoma cells in suspension. Therefore, living trypsinized PaTu 8988S cells in cell culture medium were investigated using an inverted digital holographic microscopy setup as sketched in Fig. 6.2 ($\lambda = 532$ nm, 63x microscope lens, NA $= 0.75$). Figure 6.9a shows a digital off-axis hologram of three cells. The three diffraction patterns indicate that the cells denoted as A, B, and C were located in different planes. For the numerical

reconstruction in a region of interest (ROI) around each cell the maximum image definition was determined by calculation of a focus value in dependence of the propagation distance Δz.

Figure 6.9b–d show the amplitude distributions obtained by application of numerical autofocusing in the ROIs around each cell that are marked with boxes. In each ROI one of the cells appears sharply focused with minimum contrast (autofocus criterion). Figure 6.9e–g display the corresponding unwrapped quantitative phase contrast images of the cells and illustrate the requirement for precise subsequent numerical focus correction. The phase distributions caused by the unfocused imaged cells contain unwrapping artifacts that prevent a further data evaluation. In contrast, the sharply imaged samples appear clearly resolved and deliver qualitative data with minimized unwrapping errors. In Fig. 6.9h the focus values are plotted for each ROI in dependence of the propagation distance Δz. The corresponding distance Δg in object space is obtained as described in [82]. The minima of the curves (cell A: $\Delta z_{AF} = 5.8$ cm, cell B: $\Delta z_{AF} = 0.8$ cm, cell C: $\Delta z_{AF} = 1.0$ cm) indicate the propagation distances for the sharply focused imaging of each cells and are in agreement with the appearance to the amplitude and phase distributions in Fig. 6.9b–g. The relative axial distance of the cells in z-direction are: A:B $\approx$ 17 µm, A:C $\approx$ 23 µm, B:C $\approx$ 6 µm. Finally, Fig. 6.9i shows the phase distribution as results from merging the numerically refocused images of the cells in Fig. 6.9e–g in which all cells appear sharply focused. The results demonstrate that for an optimized imaging of cells in suspension, numerical multi-focus imaging is indispensable. The minimal error for the detection of the axial sample position is restricted by the depth of field of the applied microscope lens (here, approximately 0.4 µm). In practice, the precision is further decreased by the shape of the investigated specimen and the noise in the reconstructed amplitude distributions that depend on the individual measurement conditions. Thus, for the described experiment the error for the determination of relative axial positions can be estimated to be in the range of $\approx$2 µm.

6.2.3 DHM with Partial Coherent Light and Multi-Wavelength Techniques

The main drawbacks of the use of laser light in DHM are coherent noise and parasitic reflections in the experimental setup, as these disturbances affect the reconstructed images and restrict the measurement accuracy for the detection of optical path length changes. Partially coherent light sources [40, 62–64] and multi-wavelength techniques [83, 84] reduce such effects and prospect the selection of light from different sample layers [40, 85, 86]. Thus, in this section the benefit of partially coherent light and multi-wavelengths principles in DHM-based live cell imaging is illustrated.

6.2.3.1 Influence of the Coherence Length on Hologram Formation

The influence of the coherence properties of different light sources is illustrated for the example of spatial phase shifting digital holography (for a detailed description

see [40]). Therefore, the spatial distribution of the intensity modulation within the off-axis holograms and the lateral resolution in the corresponding reconstructed amplitude distributions was analyzed. The experiments were carried out with a transmission setup as depicted in Fig. 6.1 (microscope lens 20×, NA = 0.4) using a transparent USAF 1951 resolution chart with absorbing test structures. For illumination, four different light sources were used. Two fiber-coupled superluminescent diodes with different central wavelength λ, spectral width $\Delta\lambda$, and coherence lengths l_c emitting in the visible spectral range (SLD-VIS, $\lambda = 682.1 \pm 0.1$ nm, $\Delta\lambda = 4.8 \pm 0.2$ nm, $l_c = 68.2 \pm 0.2$ μm) and in the near infrared range (SLD-NIR, $\lambda = 835.5 \pm 0.1$ nm, $\Delta\lambda = 5.8 \pm 0.2$ nm, $l_c = 81.5 \pm 0.2$ μm) were used [40]. In addition, the SLD-NIR was spectrally band-pass filtered by a filter F (denoted as SLD-NIR-F in the further text). The band-pass filter limited the emission spectrum of SLD-NIR to a width of $\Delta\lambda = 1.2 \pm 0.2$ nm. This results in a coherence length of $l_c = 232.1 \pm 4.9$ μm that enables an increased spatial phase gradient over the whole field of view. The source for coherent light was a frequency-doubled Nd:YAG laser ($\lambda = 532$ nm, $\Delta\lambda < 1 \times 10^{-5}$ nm, $l_c > 25$ m).

After precise adjustment of the optical path length difference between object wave and reference wave for maximum hologram contrast by the movable Porro prism in the setup in Fig. 6.1, with all light sources digital off-axis holograms of the test chart were recorded. During the hologram recording the test chart was subjectively imaged sharply in the hologram plane. After hologram recording, the numerical reconstruction was carried out by spatial phase shifting as explained in Sect. 6.2.2.4. Figure 6.10 shows the experimental results. The first column of Fig. 6.10 presents the holograms that were obtained with the different light sources. In the middle column of Fig. 6.10 the normalized intensities along the cross-sections that are marked in the holograms by dashed lines are plotted. The right column of Fig. 6.10 presents the reconstructed amplitude images of the observed test chart structures.

The intensity plots in the middle column visualize the impact of the limited coherence lengths of SLD-VIS and SLD-NIR on the hologram formation: the modulation of the interference fringes is inhomogeneous and decreases to the hologram borders. Furthermore, for SLD-VIS and SLD-NIR in regions that correspond to a low spatial phase gradient (upper area) or a low hologram modulation (lower area) the reconstructed image parts appear with artifacts and slightly blurred. In contrast, for SLD-NIR+F, the decrease of the hologram modulation to the upper and lower border areas is only moderate while for the laser (Nd:YAG) no spatial dependency of the modulation is observed. For both light sources this results in sharply reconstructed test chart structures for the whole investigated area. In the amplitude distribution resulting from the Nd:YAG laser a fringe pattern due to multiple reflections in the experimental setup is visible that is not observed for the partially coherent light sources SLD-VIS, SLD-NIR, and SLD-NIR+F. For all light sources the smallest line width (group 7.6 of the USAF resolution test chart) amounts to 2.2 μm and is visible in all reconstructed amplitude distributions.
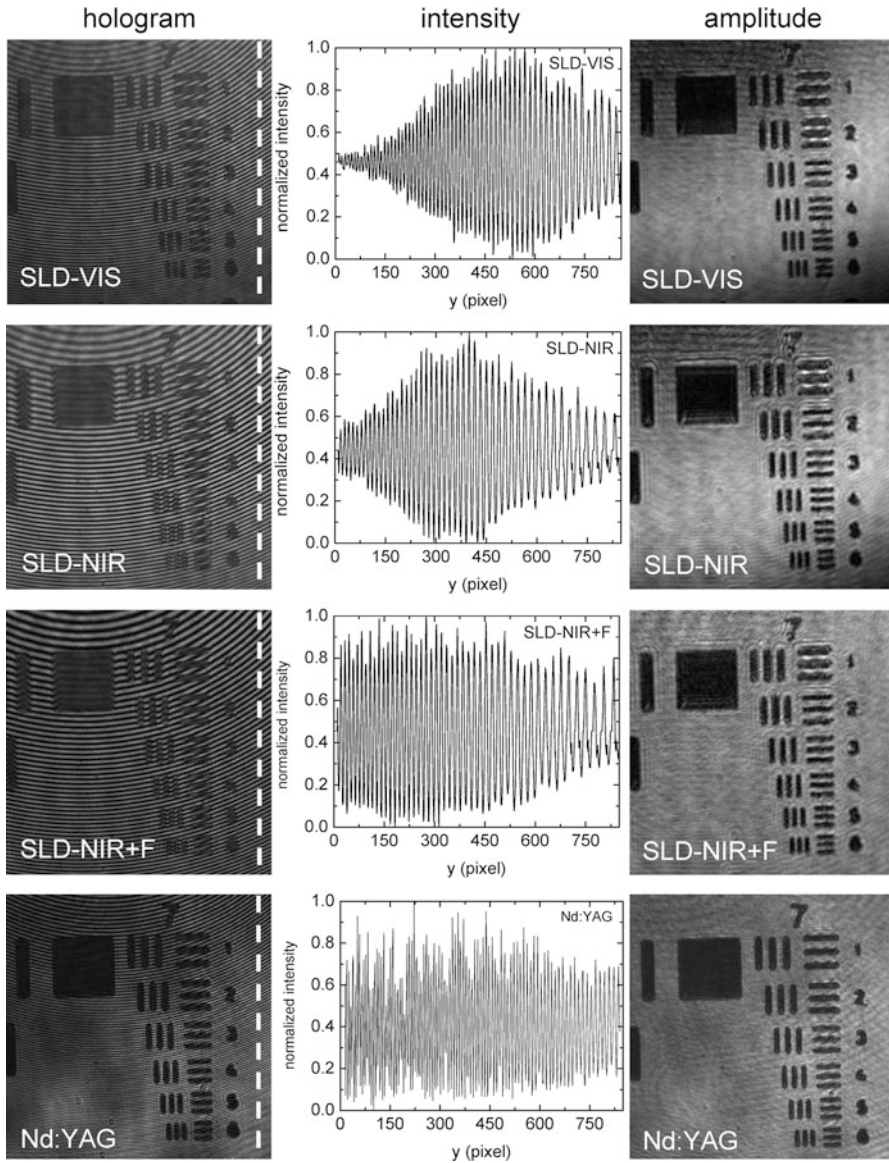
Fig. 6.10 Spatial dependency of the hologram modulation and lateral resolution of the reconstructed amplitude images for the light sources SLD-VIS, SLD-NIR, SLD-NIR+F, and Nd:YAG for the example of a transparent USAF 1951 test chart. *Left column*: digital off-axis holograms, *middle column*: cross-sections through the intensity distributions along the *vertical dashed lines* that are marked in the holograms, *right column*: corresponding amplitude images obtained by spatial phase shifting reconstruction [40]
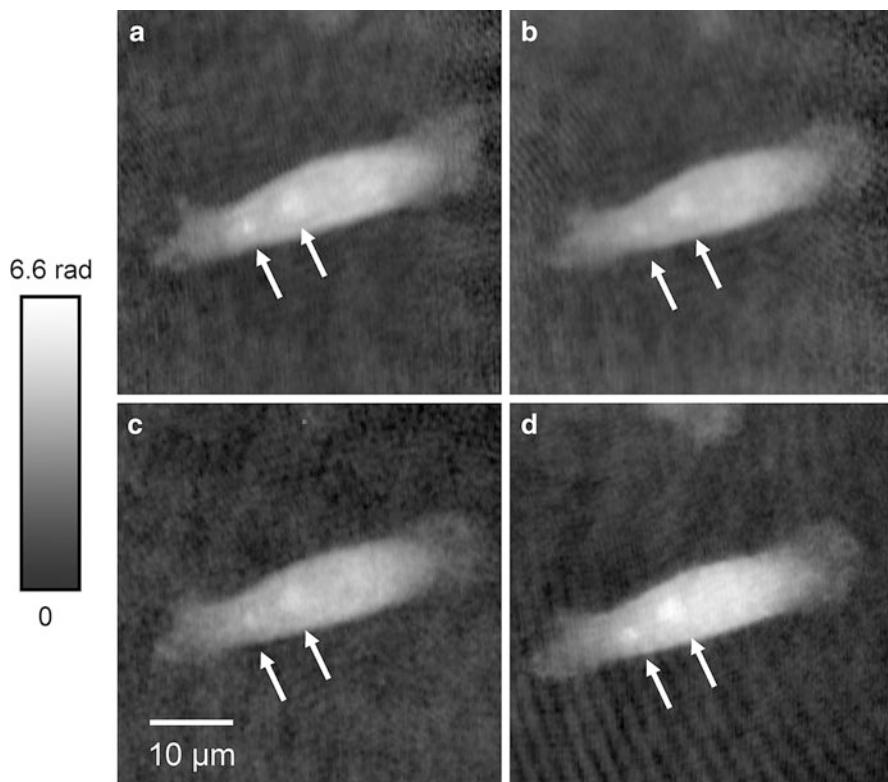
Fig. 6.11 Quantitative DHM phase contrast images of a living HT-1080 cell obtained from digital off-axis holograms recorded with different light sources. (**a**): SLD-VIS, (**b**): SLD-NIR, (**c**): SLD-NIR+F, (**d**): frequency-doubled Nd:YAG laser. The nucleoli are marked with *white arrows* [40]

6.2.3.2 Impact of the Coherence Length in Quantitative Phase Imaging

The influence of light sources with different coherence properties in live cell imaging with DHM is demonstrated by using the same transmission setup and light sources as described in Sect. 6.2.3.1. The USAF test chart was replaced by a Petri dish with adherent human fibrosarcoma cells (HT-1080) in cell culture medium. In analogy to the experiments with the USAF test chart with all light sources digital off-axis holograms were captured.

Figure 6.11 shows the obtained quantitative DHM phase contrast images of an investigated HT-1080 cell. Figure 6.11a, b depict phase data that result from SLD-VIS and SLD-NIR. Figure 6.11c, d show phase contrast images measured by SLD-NIR+F and Nd:YAG. In all four phase distributions the cells, subcellular compartments, and organelles like the nucleoli (see arrows) are visible. In Fig. 6.11d (frequency doubled Nd:YAG laser), as seen in Fig. 6.10, an additional interference pattern becomes visible that does not appear in Fig. 6.11a–c. In order to

quantify the quality of the DHM phase contrast images, the phase noise was determined in areas without the cellular specimen as described in [64]. The phase noise for the light sources with short coherence lengths (SLD-VIS, SLD-NIR) was found lower than for SLD-NIR+F and the frequency-doubled Nd:YAG laser. The comparison of the phase noise values $\sigma_{\Delta\varphi}$ with the error for the detection of optical path length changes $\sigma_{\Delta OPL}$ (for details, see [40]) shows that the absolute sensitivity of the DHM setup depends on both the phase noise $\sigma_{\Delta\varphi}$, which depends on the experimental setup, and the central wavelength of the light source. For SLD-VIS and SLD-NIR, the sensitivity for optical path length (OPL) changes is enhanced for 31 % and 26 % in comparison to Nd:YAG. In comparison to SLD-NIR+F, the sensitivity is increased by 82 % and 75 %. The lowest phase noise is achieved for the light sources SLD-VIS and SLD-NIR as the low coherence lengths prevent the formation of coherent noise and disturbing interference patterns due to multiple reflections. In contrast, for SLD-NIR+F a higher phase noise level than the Nd:YAG is determined, although the coherence length amounts only to $l_c = 232.1 \pm 5.9$ µm. However, the disturbing interference pattern that appears in the laser-generated phase contrast images is not visible. Furthermore, the enhanced coherence length of SLD-NIR+F resulted in a significantly simplified alignment of the experimental setup in comparison to SLD-VIS and SLD-NIR.

From the data in Figs. 6.10 and 6.11 it can be concluded that in off-axis DHM with partial coherent light sources a noise reduction in quantitative DHM phase contrast images can be achieved. Moreover, the results indicate that with a sufficient light intensity in the visible range around 532 nm and a coherence length in the range of $l_c \approx 250$ µm, a further resolution enhancement in quantitative DHM phase contrast imaging is prospected while, simultaneously, an adequate handling of the partially coherent DHM system is achieved.

6.2.3.3 Selection of Reflected Light from Different Sample Layers

The applicability of DHM for quantitative phase contrast imaging by selection of light from different sample layers was investigated by observation of living cells in a Petri dish filled with cell culture medium. The experiments were performed in incident light configuration with the inverse microscopy setup similar to the transmission setup in Fig. 6.1 (for details, see [40]).

The sample under investigation was a Petri dish with living human pancreatic adenocarcinoma cells (PaTu 8988T) in cell culture medium (DMEM). The cells were illuminated with partially coherent light through the bottom of the Petri dish by using a superluminescent diode with a coherence length of 68.2 ± 0.2 µm (see SLD VIS in Sects. 6.2.3.1 and 6.2.3.2). Figure 6.12a illustrates the illumination with incident partially coherent light and the reflective interfaces between the three different layers of the sample (1: air and Petri dish bottom, 2: Petri dish bottom and cell culture medium, 3: cell culture medium and air). Spatial-phase-shifted digital holograms of the cells were recorded with fixed mechanical focus while the optical path length difference between object wave and reference wave $\Delta\tilde{z}$ was changed in steps of 12.5 µm. Subsequently, the different interfaces were identified
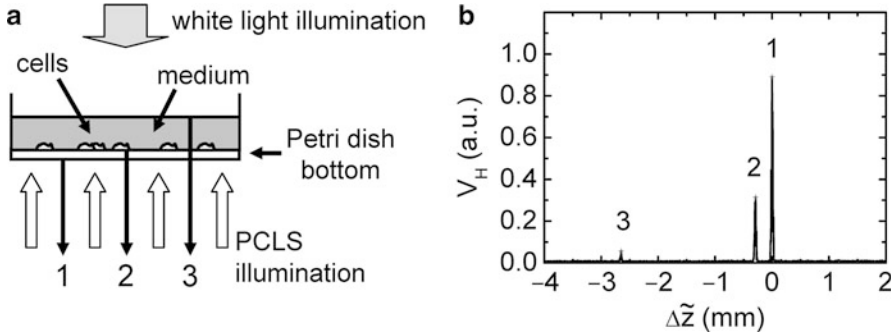
Fig. 6.12 Quantitative DHM phase contrast imaging of living PaTu 8988T cells in incident light configuration. (**a**) Sketch of the experimental setup, (**b**) hologram contrast V$_H$ versus the optical path length difference $\varDelta\tilde{z}$ between object wave and reference wave (the maxima of V$_H$ indicate the reflected light intensities at the different interfaces *1*: air and Petri dish bottom, *2*: Petri dish bottom and cell culture medium, *3*: cell culture medium and air) [40]

by analyzing the hologram contrast V_H in dependence of $\Delta\tilde{z}$. Figure 6.13b shows the resulting plot $V_H(\Delta\tilde{z})$. The origin of the abscissa ($\Delta\tilde{z} = 0$) was set to the coordinate of the global maximum of V_H. In the plot, three contrast maxima $V_{H,1}(\Delta\tilde{z}_1 = 0)$, $V_{H,2}(\Delta\tilde{z}_2 = 0.29$ mm), and $V_{H,3}(\Delta\tilde{z}_2 = 2.62$ mm) appear. The distances between the maxima correspond to the optical path length differences that are expected from the interfaces 1, 2, and 3. Thus, $\Delta\tilde{z}_1$ is identified as the interface air and Petri dish bottom. The values $\Delta\tilde{z}_2$ and $\Delta\tilde{z}_3$ correspond to the interfaces Petri dish bottom and cell culture medium and cell culture medium and air. For subsequent evaluation, the three holograms recorded at $\Delta\tilde{z}_1$, $\Delta\tilde{z}_2$, $\Delta\tilde{z}_3$ were reconstructed by spatial phase shifting as explained in Sect. 6.2.2.4.

Figure 6.13a depicts a white light image of the cells recorded by illumination in transmission, the obtained amplitude distributions (Fig. 6.13b–d) as well as the corresponding phase contrast images (Fig. 6.13e–g). In the amplitudes that are reconstructed from the holograms recorded at $\Delta\tilde{z}_1$ and $\Delta\tilde{z}_2$, no sample structures appear and the corresponding phase distributions are homogeneous. In contrast, for $\Delta\tilde{z}_3$ the cells are marginally visible in the amplitudes and appear clearly resolved the phase contrast images. Disturbances by diffraction patterns from the first pass of the light through the sample were not observed due to the limited depth of field of the applied microscope lens.

From the images in Fig. 6.13 it can be concluded that the use of partial coherent light enables the application of DHM in cases in which an illumination of semi-transparent samples in transmission is not possible. Furthermore, due to the DHM feature of subsequent numerical refocusing, the alignment for an optimized illumination with incident light and focusing of the sample can be performed independently. Thus, the handling of the experimental setup is significantly simplified in comparison with other interferometry based QPI techniques like for example presented in [85].
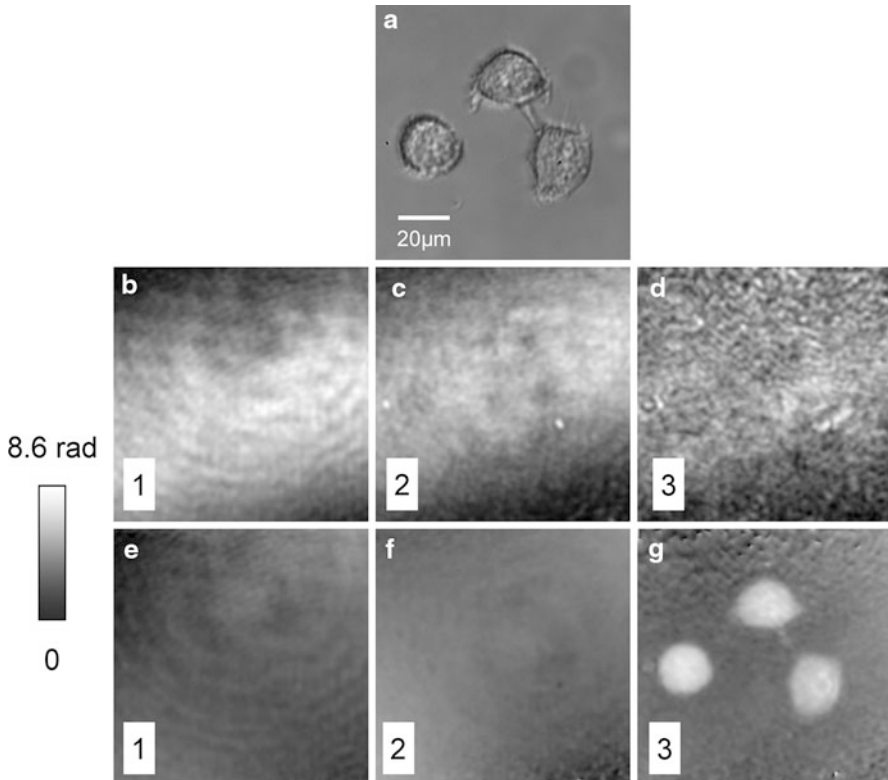
Fig. 6.13 Quantitative DHM phase contrast imaging of living PaTu 8988T cells in incident light configuration. (**a**): white light image of the sample (illumination in transmission), (**b–d**): amplitude distributions corresponding to the contrast maxima *1*, *2*, and *3* in Fig. 6.12, (**e–g**): corresponding reconstructed phase contrast images [40]

6.2.3.4 Reduction of Coherent Noise by Multi-Wavelength Techniques

In this section, the generation of short coherent properties by the superposition of amplitude and phase distributions that have been reconstructed separately from digital holograms recorded at different laser wavelengths are presented. In this way, the advantages of the robust alignment of a laser-based experimental setup due to long coherence lengths are combined with the noise reduction due to partial coherent light properties.

For the experiments, a fiber-coupled tunable diode laser ($\lambda \approx 780$ nm) is applied (for details see [84] and [87]) in a Mach-Zehnder-based DHM setup as shown in Fig. 6.1 ($63\times$ microscope lens, $NA = 0.75$). The evaluation of the acquired off-axis holograms was performed by spatial phase shifting-based reconstruction. Here, the variable three-step algorithm is used for spatial phase shifting DHM [87]. For a wavelength independent superposition, the digital holographically obtained phase distributions are converted to optical path length (OPL) distributions.
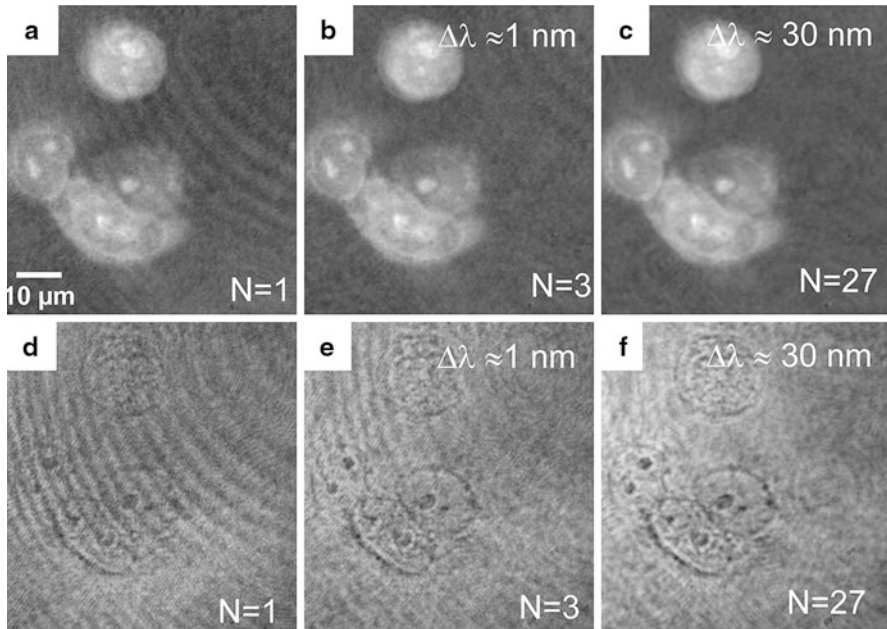
Fig. 6.14 Reconstructed and superposed OPL (*first row*) and amplitude (*second row*) distributions obtained from fixed pancreatic adenocarcinoma cells (PaTu 8988T). (**a**, **d**): from a single hologram ($N = 1$); (**b**, **e**): from $N = 3$ holograms; (**e**, **f**): from $N = 27$ holograms [84]

The corresponding averaged amplitude distributions are obtained from the hologram modulation. In the next step, the averaged images of N normalized OPL and amplitude distributions are calculated.

Figure 6.14 shows the OPL (a–c) and amplitude (d–f) distributions of fixed pancreatic adenocarcinoma cells (PaTu 8988T) for a single wavelength ($N = 1$, $\lambda_{i=1} = 780$ nm, Fig. 6.14a, d) for $N = 3$ wavelengths ($\lambda_{i=\{1,2,3\}} = \{779\,\text{nm}, 779.5\,\text{nm}, 780\,\text{nm}\}$, Fig. 6.14b, e) and $N = 27$ wavelengths ($\lambda_{i=\{1,2,\dots,27\}} = \{765\,\text{nm}, \dots, 791\,\text{nm}\}$, $\Delta\lambda_i = 1$ nm, Fig. 6.14c, f). For $N = 1$, the visibility of subcellular structures is decreased by parasitic interferences due to multiple reflections in the optical setup in both OPL and amplitude distributions. In comparison, for $N = 3$ and $N = 27$ the images appear with significant enhanced contrast. Furthermore, for $N = 3$ and $N = 27$ also, organelles like the nucleus and the nucleoli are clearly resolved. Compared with $N = 1$, the superposed OPL and amplitude distributions for $N = 3$ and $N = 27$ show a significant noise decrease up >63 percent [84].

In conclusion, the results in Fig. 6.14 demonstrate that, by superposition of amplitude, in OPL images that are retrieved from holograms that are recorded at different wavelengths an efficient reduction of disturbing coherence effects in DHM is achieved. In [87] it is shown that the principle can be applied also for the improvement of dynamic life cell imaging with DHM.

6.3   Selected Applications

In this section, the potentials of multi-focus DHM quantitative phase imaging are illustrated by selected applications. It is shown that DHM is suitable for automated tracking of migrating cells and cell thickness monitoring as well as for refractive index determination of cells and particles. Moreover, the use of DHM for label-free flow analysis in fluidics and for micro-injection monitoring is demonstrated. The results prove that DHM is highly relevant to achieve novel insights in dynamic cell biology, in cancer research, and in drugs and toxicity testing.

6.3.1   Cell Tracking and Thickness Monitoring

Results from experiments on living pancreatic adenocarcinoma cells (PaTu 8988T) demonstrate the applicability of digital holographic microscopy for the visualization and quantitative analysis of dynamic morphology changes and two-dimensional dynamic cell tracking. DHM was used in order to analyze cell morphology during drug-dependent cell death. Pancreatic adenocarcinoma cells grown in a Petri dish were exposed to the anti-cancer-drug taxol and monitored with a setup as depicted in Fig. 6.2 ($\lambda = 532$ nm, $40\times$ microscope lens, NA $= 0.65$). Digital holograms of selected cells were recorded in time-lapse series every 2 min for 14.2 h in a temperature-stabilized environment ($T = 37\,^\circ$C). The upper panel of Fig. 6.15 shows the results for the obtained unwrapped quantitative phase distributions $\Delta\varphi_{cell}(x, y, z_{IP})$ of a PaTu 8988T cell at $t = 0$, $t = 3.5$ h, $t = 5$ h, $t = 8.3$ h, and $t = 14.2$ h after taxol addition. The temporal dependence between application of taxol and the maximum phase contrast $\Delta\varphi_{cell,\,max}$ (black cross in quantitative phase contrast images in the upper panel of Fig. 6.15) as well as the corresponding cell thickness ($n_{medium} = 1.337$ and $n_{cell} = 1.38$, $\lambda = 532$ nm) are depicted in the lower left panel of Fig. 6.15. The lower right panel displays the two-dimensional cell migration trajectory that is determined from coordinates of the maximum phase contrast. From these results it is clearly visible that taxol induces morphological changes in pancreatic adenocarcinoma cells. As a first reaction, cell rounding is observed that causes an increase in cell thickness while, finally, cell collapse can be detected by a significant phase contrast decrease (see lower left panel of Fig. 6.15).

In further investigations on the applicability of DHM for 3D cell migration, monitoring was performed by observing the trajectory of two mouse fibroblasts (NIH 3T3) within a three-dimensional collagen matrix in a Petri dish by using the same experimental setup for 2D cell tracking and temperature stabilization at 37 °C. A series of holograms and white light images was recorded with fixed mechanical focus for a period of 100 min ($\Delta t = 2$ min). For both cells, digital holographic 3D tracking was performed as described [82]. Figure 6.16a depicts representative (image) results for $t = 0$, $t = 18$ min, $t = 36$ min, $t = 54$ min, and $t = 72$ min.

The first row of Fig. 6.16a shows bright-field images of two murine fibroblasts under white light illumination. The corresponding DHM phase contrast images are depicted in the second (cell A) and third (cell B) row of Fig. 6.16a. The dotted boxes
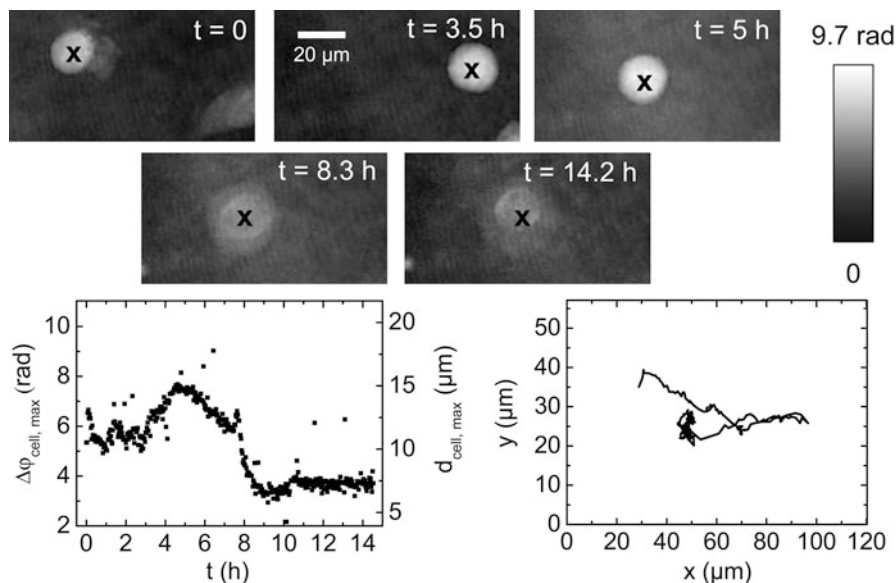
Fig. 6.15 Cell thickness monitoring and two-dimensional cell tracking illustrated by monitoring of a living pancreatic adenocarcinoma cells (PaTu 8988T) after addition of taxol to the cell culture medium (40× microscope lens, NA = 0.6). *Upper panel*: gray-level coded unwrapped phase distributions at $t = 0$, $t = 3.5$ h, $t = 8.3$ h, and $t = 14.2$ after toxin addition; *lower left panel*: temporal dependence between application of taxol and the maximum phase contrast (*black cross* in quantitative phase contrast images in the *upper panel*) and related cell thickness, *lower left panel*: cell migration trajectory obtained by the determination of the coordinates of the maximum phase contrast [88]

in the phase contrast images mark the ROIs that were evaluated for 3D tracking. As seen in the white light images, cell A only slightly moves out of focus whereas cell B descends to a different collagen layer, leaving the focus plane during the observation. In the second row of Fig. 6.16a, the ROI for digital holographic autofocusing was set to cell A, which appears sharply focused in the resulting quantitative phase contrast images. Likewise, in the third row the ROI was set to cell B. After digital holographic autofocusing, as explained in Sect. 6.2.2.7, cell B is sharply resolved in all phase distributions. Furthermore, morphological and cell thickness changes due to the migration process become visible. The x-y migration trajectories and the corresponding temporal dependency of the axial displacements of the cells are plotted in Fig. 6.16b, c, respectively. Figure 6.16d presents the 3D migration trajectories as results from the combination of the data in Fig. 6.16b, c. Cell A moves almost in parallel to the x-y-plane, but scarcely in the z-plane. In contrast, cell B migrates to a collagen layer approximately located 65 μm below its initial position.

In summary, the results in Fig. 6.16 show that DHM is appropriate to label-free 3D tracking of cells in a three-dimensional environment. In practice, the
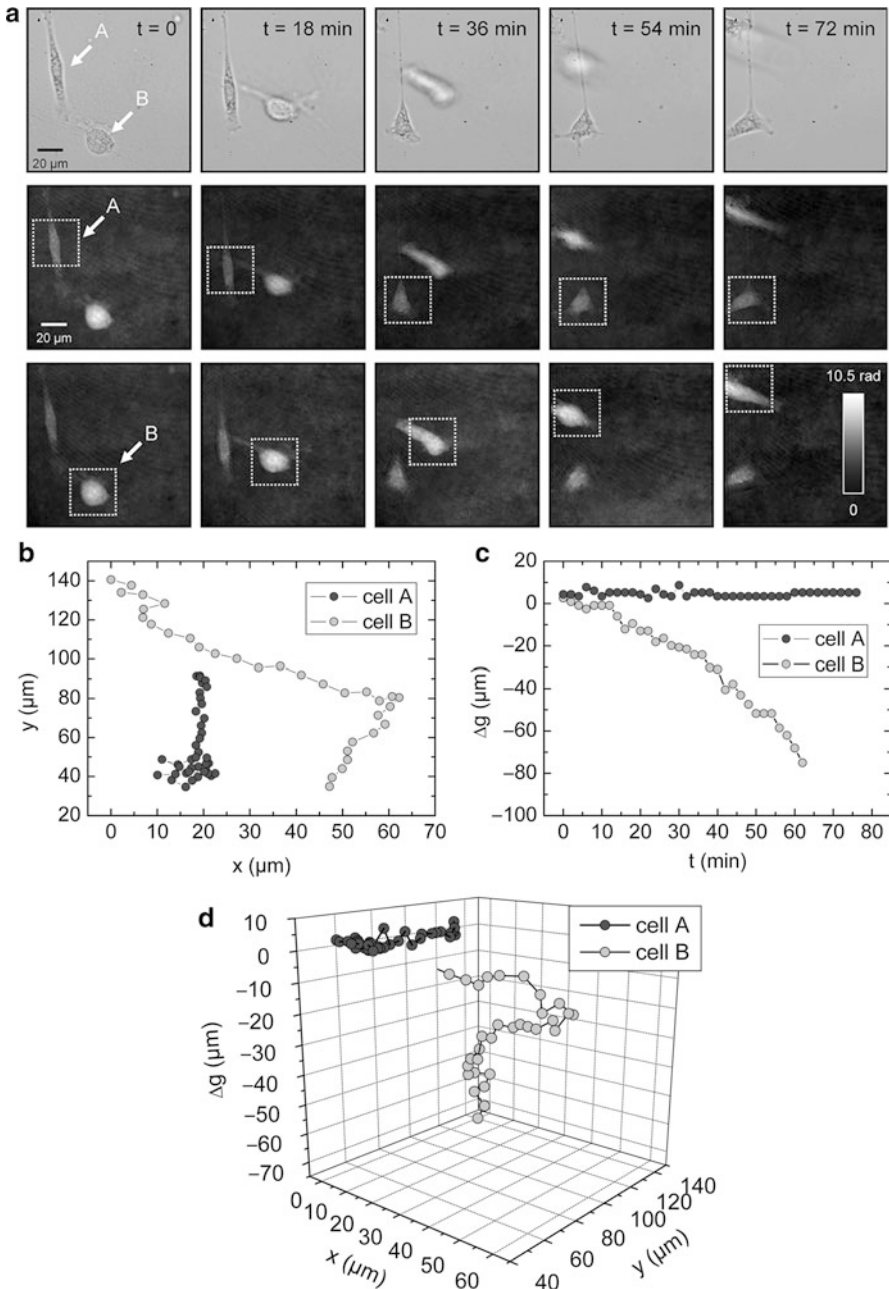
Fig. 6.16 3D migration monitoring of fibroblasts in a collagen matrix. (**a**) *first row*: bright-field images (white light illumination); (**a**) *second row*: DHM phase contrast images with 3D tracking ROI set to cell A; (**a**) *third row*: DHM phase contrast images with 3D tracking ROI set to cell B. (**b**): lateral displacement, (**c**): axial displacement, (**d**): 3D trajectories resulting from the data in (**c**) and (**d**) [69]

typical accuracy for the detection of 3D displacements can be estimated to be in the range of 1–2 µm. Furthermore, due to the underlying principles of the presented DHM configurations, integral information is obtained. Thus, specimens in different planes at the same lateral position with axial distances near the depth-of-field of the applied imaging system cause diffraction patterns. This can lead to misinterpretations in the image sharpness quantification process. Furthermore, these disturbances affect the correct determination of the lateral object position from the quantitative phase contrast images. This limits the density of objects under investigation to an amount in which the specimens are imaged laterally separated. However, the DHM 3D tracking feature suggests future applications in quantitative label-free cell migration and chemotaxis monitoring.

6.3.2 Refractive Index Determination of Cells and Particles

The cellular refractive index is an important parameter in DHM phase contrast imaging of living cells. The cellular refractive index influences the visibility of cells and subcellular structures in the quantitative phase images and represents the main limit of the accuracy for the determination of the thickness of transparent samples [41]. Furthermore, the determination of the cellular refractive indices are useful for the utilization with optical tweezers and related optical manipulation systems as the individual cellular refractive index values influence the resulting optical forces [89, 90]. Although, in many cases, a high measurement accuracy can be achieved, the refractive index determination of adherent cells with QPI methods, as described exemplarily in Refs. [41, 91–93], can be time consuming or requires special experimental equipment. Thus, DHM methods for the determination of the integral refractive index of suspended cells have been developed [57, 94, 95], which can be carried out without further sample preparation. Another advantage of DHM is that, due to the numerical multi-focus feature, increased data acquisition rates can be achieved by simultaneous recording of suspended cells that are located laterally separated in different focal planes (for illustration, see Fig. 6.9). Here, the determination of the integral refractive index of suspended cells is illustrated by a method in which a two-dimensional model is fitted to the DHM phase contrast data.

For sharply focused spherical cells in suspension, located at $x = x_0$, $y = y_0$, with radius R the cell thickness $d_{\text{cell}}(x, y)$ is

$$
d_{\text{cell}}(x, y) = \begin{cases} 2 \cdot \sqrt{R^2 - (x - x_0)^2 - (y - y_0)^2} & \text{for} \quad (x - x_0)^2 + (y - y_0)^2 \leq R^2 \\ 0 & \text{for} \quad (x - x_0)^2 + (y - y_0)^2 > R^2 \end{cases}.
$$

(6.5)

Insertion of (6.4) in (6.5) yields:

$$\Delta\varphi_{\text{cell}}(x,y)$$

$$= \begin{cases} \frac{4\pi}{\lambda} \cdot \sqrt{R^2 - (x-x_0)^2 - (y-y_0)^2} \cdot (n_{\text{cell}} - n_{\text{medium}}) & \text{for} \quad (x-x_0)^2 + (y-y_0)^2 \leq R^2 \\ 0 & \text{for} \quad (x-x_0)^2 + (y-y_0)^2 > R^2 \end{cases}.$$

$$(6.6)$$

with the unknown parameters n_{cell}, R, x_0, and y_0. In order to obtain the parameters n_{cell}, R, x_0, and y_0, Eq. 6.6 is fitted iteratively with the Gauss-Newton method [94, 96] to the measured phase data of spherical cells in suspension.

Figure 6.17 illustrates the evaluation process of the phase data by a representative result that has been obtained from a trypsinized cell in suspension with spherical shape. Figure 6.17a shows the phase contrast image of the cell, coded to 256 gray levels (8-bit). Figure 6.17b depicts a rendered pseudo-3D plot of the data in Fig. 6.17a. In a next step, a second-degree function is fitted to the data and subtracted from the phase distribution shown in Fig. 6.17b. Afterwards, the data of $\Delta\varphi_{\text{cell}}(x,y)$ for the fitting of Eq. 6.6 is selected from the background corrected data by application of a threshold value (Fig. 6.17c) that considers the phase noise in the area around the cell. Figure 6.17d depicts the resulting fit. The absolute difference between the experimentally obtained data and fit is shown in Fig. 6.17e.

The refractive index determination is illustrated by results from simulated spheres, micro particles, and different types of pancreatic adenocarcinoma cells (for illustration of the simulated data and the investigated specimens, see Fig. 6.18). Therefore, simulated phase contrast images with radii similar to cells in the range from 0.5 to 10 μm, a constant refractive index of $n_{\text{sim}} = 1.38$ and $n_{\text{medium}} = n_{\text{water}} = 1.334$ were generated by application of (6.6). Figure 6.19a shows the plot of the refractive index n_{sim} versus the radius R_{sim} of the simulated holographic phase contrast data that have been obtained by the fitting algorithm. A constant average refractive index $\bar{n}_{\text{sim}} = 1.38006 \pm 0.00002$ ($N_{\text{sim}} = 64$) is obtained. Then, experiments with beads (Cytodex 1 Microcarrier, GE Healthcare, Uppsala, Sweden) of different size in water ($n_{\text{water}} = 1.334 \pm 0.001$) were carried out (20× microscope lens, NA = 0.4). The obtained plot of n_{bead} versus R_{bead} is depicted in Fig. 6.19b. The refractive index of the micro carriers is found to be independent from the radius with an average refractive index $\bar{n}_{\text{bead}} = 1.3383 \pm 0.0003$ ($N_{\text{bead}} = 27$). In a third experiment, three different types of living pancreatic adenocarcinoma cells (PaTu 8988T, PaTu 8988S, and PaTu 8988T pLXIN E-Cadherin [41]) in suspension were investigated. For the experiments, cells were trypsinized and holograms of the cells in culture medium (DMEM containing 5 % FCS and 5 % horse serum, $n_{\text{medium}} = 1.337 \pm 0.001$) were recorded by application of a 40× microscope lens (NA = 0.6). For data evaluation, only cells with spherical shape have been selected, which were mainly observed in the recorded holographic phase contrast images for all investigated cell lines. Figure 6.19c depicts the integral cellular refractive index n_{cell} in dependence of the cell radius R_{cell}. The plot in Fig. 6.19c shows that n_{cell} decreases
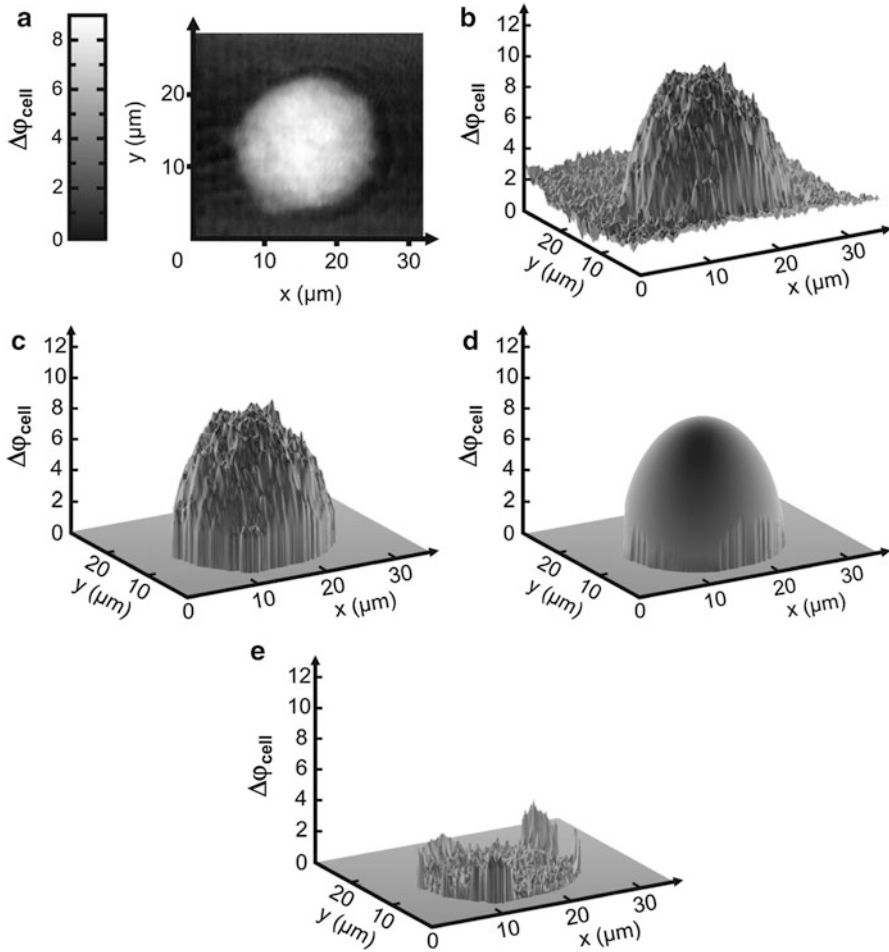
Fig. 6.17 Refractive index determination of a spherical cell in suspension: (**a**) reconstructed quantitative digital holographic phase contrast image ($\Delta\varphi$) of a trypsinized cell, (**b**) rendered pseudo-3D plot of (**a**, **c**) data for the fitting of (6.3) that is selected from (**b**) after background subtraction and application of a threshold value, (**d**) fit of (6.3) to the data in (**c**, **e**) absolute difference between (**c**) and (**d**) (Modified from [94])

with increasing R_{cell}. The decrease of the refractive index with increasing cell radius, and thus the cell volume, may be explained by cellular water content [29].

6.3.3   Label-Free Flow Analysis in Fluidics

Quantitative digital holographic phase contrast can be used for label-free imaging in fluidics. This is demonstrated by results from an experiment in which glycerol
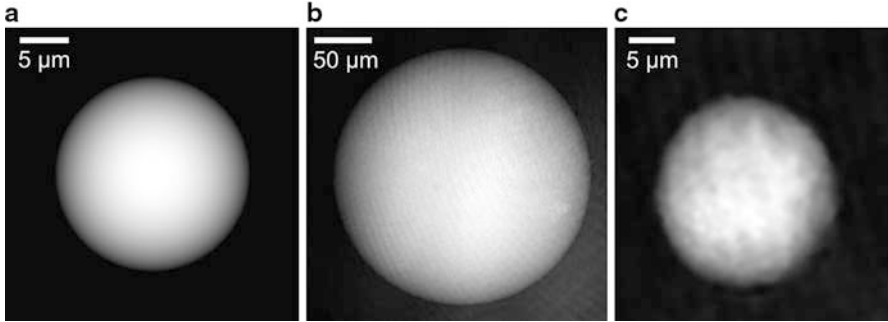
Fig. 6.18 Phase contrast images of (**a**) a simulated sphere, (**b**) a bead (Cytodex 1 Microcarrier, GE Healthcare, Uppsala, Sweden), and (**c**) a trypsinized PaTu 8988T pLXIN E-cadherin cell [94]
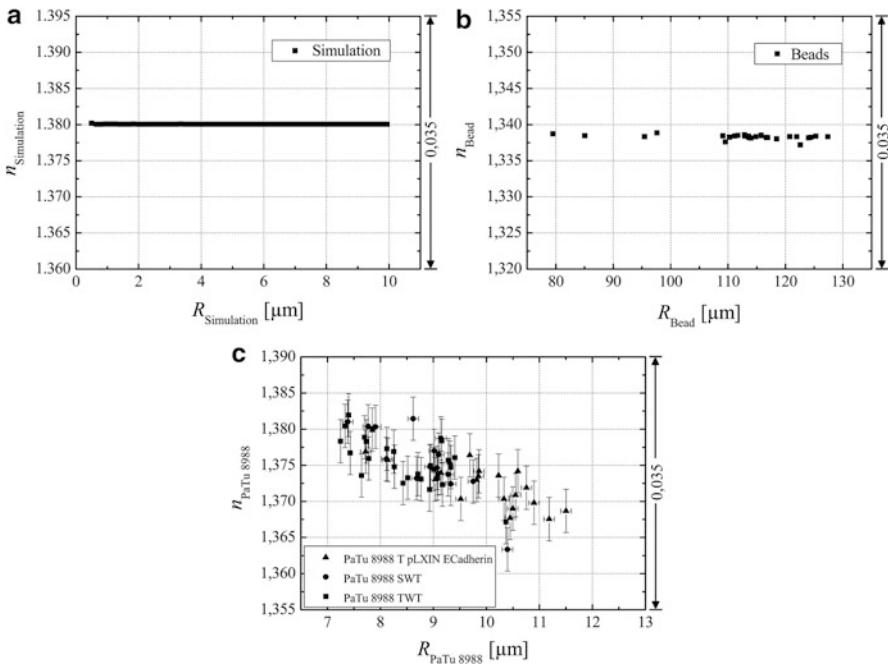
Fig. 6.19 Refractive index n in dependence of radius R for (**a**) simulated data, (**b**) beads, and (**c**) suspended PaTu 8988 cells [94]

was injected into phosphate-buffered saline (PBS). The observation of the fluidic process was performed with a setup as shown in Fig. 6.2 ($\lambda = 532$ nm), which is described in detail in [97]. Due to high viscosity and refractive index of the pure substance, glycerol has been diluted with PBS (50 %, v/v), leading to a refractive
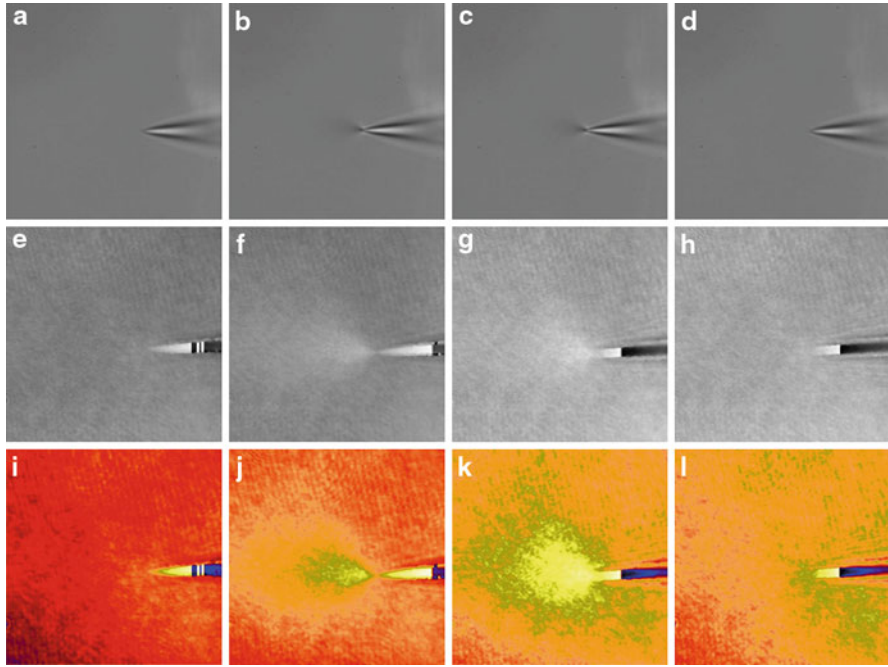
Fig. 6.20 DHM monitoring of the injection of a glycerol/PBS mixture (50 %, v/v) into pure phosphate-buffered saline (PBS). The injection pressure was set to 500 Pa with an injection time of 1 s. (**a–d**) Bright field images under white light illumination, (**e–h**) DHM phase contrast images, and (**i–l**) corresponding false color plots [97]

index of 1.408. For imaging, a $60\times/1.35$ oil immersion microscope objective was used. In a time-lapse series, bright field images under white light illumination and digital off-axis holograms were captured throughout the injection process with a micro pipette (injection pressure: 20 hPa, injection time: 1 s, compensation pressure: 15 hPa). The numerical evaluation of the resulting digital holograms was performed by spatial phase shifting reconstruction as described in Sect. 6.2.2.4. Figure 6.20 shows bright field images (first row), the quantitative DHM phase images (second row), as well as corresponding false color plots of the DHM phase contrast (third row) that result from the injection process. The first column in Fig. 6.20 depicts the micrographs immediately before injection. The next two columns show the images obtained during micro-injection, and, finally, the last column shows the area around the micropipette 3 s after this process. While in the white light images the injection process only becomes visible near the tip of the micropipette (see Fig. 6.20b–c), in the quantitative DHM phase images the distribution of the glycerol mixture appears with increased contrast.

The different gray levels in the DHM phase contrast images (Fig. 6.20e–h) represent the local changes in the refractive index distribution. High gray values correlate with a high refractive index, while the lowest values display a refractive

index of the pure PBS ($n_{PBS} \approx 1.337$). Obviously, the injection of the glycerol/PBS dilution leads to a maximum concentration of the mixture at the tip of the needle, which is indicated by the brightest gray levels and highest refractive index, respectively (Fig. 6.20f, g). The false color-coded representation of the phase images in Fig. 6.20j, k illustrate these findings with increased contrast. The gentle transition from the tip to distant areas demonstrates the fast mixing process of both liquids to a finally homogeneous mixture (Fig. 6.20h, l) within three seconds. In conclusion, the results in Fig. 6.20 demonstrate the capability of DHM to detect fast mixing processes of liquids with different refractive indices in fluidics.

6.3.4 Micro-Injection Monitoring

The feasibility of DHM phase contrast for the live cell monitoring of micro-injection is illustrated by an experiment in which a glycerol mixture was injected into living pancreatic adenocarcinoma cells (PaTu 8988T). The experimental investigations were carried out with a DHM setup as depicted in Fig. 6.2. For details on the micro-injection unit used, see Ref. [97].

The micro-injection of the glycerol solution (Glycerol/PBS: 50 %, v/v) was performed with a glass micropipette at an injection pressure of 20 hPa for 1 s. Bright field images and digital off-axis holograms were recorded before, during, and after the micro-injection process. Quantitative phase images were calculated by spatial phase shifting reconstruction as described in Sect. 6.2.2.4. Figure 6.21 shows a typical result of a PaTu 8988T cell before (a and e), directly after (b and f), 1 min after (c and g), and 8 min after (d and h) injection. The first row (Fig. 6.21a–d) represents bright field images of the cell with corresponding DHM phase images in the second row.

Figure 6.21a shows a typical healthy PaTu 8988T cell after 24 h cultivation on a Petri dish under cell culture conditions with flat membrane extension and lamellipodia. These cell features and the cell border can also be resolved in the corresponding DHM phase contrast image (21e), where the gray-level map (8-bit) represents the optical path length changes that are affected by the cell in comparison to the surrounding medium due to its thickness and inner refractive index distribution. Nevertheless, only few intracellular structures are visible, and a correlation to specific intracellular compartments is not possible. In order to enhance the intracellular refractive index, a mixture of glycerol/PBS is injected into the perinuclear region of the cell. Thereafter, the resolution of the lamellipodia at the cell border only slightly changes, whereas the central part of the cell around the nucleus appears with enhanced phase contrast, and structures of brighter gray levels become visible. These are surrounded by an area with only smooth gray value changes and with a partly visible border to the ambient cell body (arrow in Fig. 6.3f). Comparisons with the bright field image (captured 1 s after the hologram, Fig. 6.3b) allow their identification as the nucleus with nucleoli. Moreover, this image verifies the successful injection of the glycerol/PBS mixture, as a fluid-filled membrane bleb occurs in the right part of the cell. Additionally, small blebs at the distal parts of the
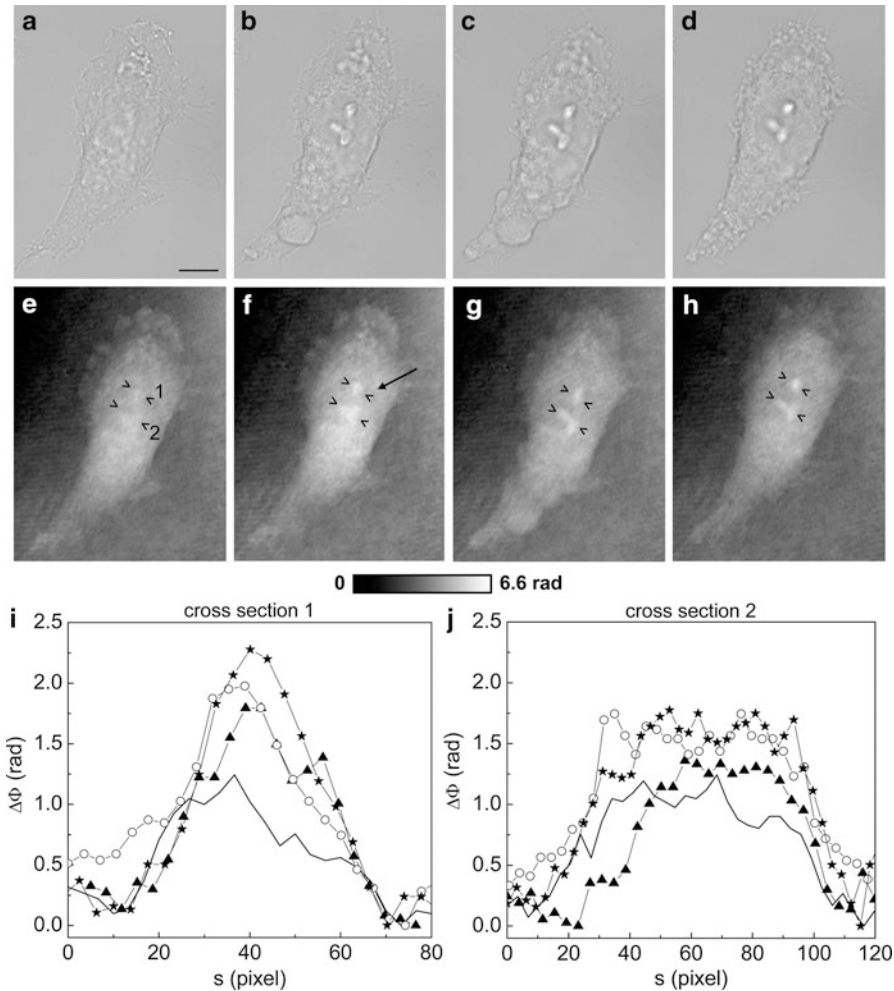
Fig. 6.21 Injection of a glycerol/PBS mixture (50 %, v/v) into a PaTu 8988T cell. (**a–d**) Bright field images and (**e–h**) corresponding DHM phase contrast images showing a PaTu 8988T cell (**a**) and (**e**) before, (**b**) and (**f**) directly after, (**c**) and (**g**) 1 min after, and (**d**) and (**h**) 8 min after injection (20 hPa, $t_i = 1$ s). In (**e–h**), *black arrowheads* indicate the positions of two cross sections to quantify the relative phase contrast of two different nucleoli 1 and 2 at each time step. The *black arrow* in (**f**) marks the nuclear envelope. (**i**) The plots for cross section 1 and (**j**) cross section 2 illustrate the alteration of the relative phase contrast in rad, with the *solid line* representing the nucleolus prior to injection, the *triangle line* representing the nucleolus directly after injection, the *circle line* representing the nucleolus 1 min after injection, and the *asterisk line* representing the nucleolus 8 min after injection. The phase range of 6.6 rad is coded to 256 gray levels. Scale bar: 10 μm [97]

membrane extensions are visible, revealing a continuous connection to the cytosol. One minute after injection (Fig. 6.3c, g), the cellular reaction appears increased and the membrane curled and rather low local differences of the refractive index in the blebs and the cytosol indicate a fast mixing (see Sect. 6.3.3) of the injected glycerol/PBS.

Eight minutes after the micro-injection, blebs have regressed and the cell surface appears somewhat rougher (Fig. 6.3d). Moreover, fine, long membrane extensions are still visible and indicate a living cell. To quantify the enhanced intracellular contrast, the DHM phase contrast images were analyzed by cross sections through the two nucleoli and surrounding parts of the nucleus (cross sections between the arrowheads in Fig. 6.3e–h). The results in Fig. 6.3i, j depict the relative phase contrast differences ($\Delta\Phi$ in rad) for the cross sections at all four moments. The solid line in Fig. 6.3i represents the situation before the injection, and the relative phase contrast of nucleolus 1 is about 1.2 rad higher than the surrounding area. Directly after the injection of the glycerol/PBS mixture, $\Delta\Phi$ rises to 1.8 rad in maximum, 1 min later to 2.0 rad, and 8 min after the injection process to 2.3 rad. The results for the second analyzed nucleolus confirm this measurement. Here, before the injection, the relative phase contrast amounts to 1.2 rad in maximum, and 8 min after the injection it shows an increase to 1.7 rad. These results of quantitative phase contrast analysis support the effect of contrast enhancement for the nucleoli inside the living cell after injection of a glycerol/PBS mixture.

In summary, the micro-injection of small amounts of glycerol leads to significant enhancement of the intracellular phase contrast of living cells in DHM. This can be explained by an underlying process of gentle cell swelling due to a glycerol-induced osmotic disequilibrium, resulting in a decrease of the refractive index of the cytosol. These changes of the refractive index are reproducible and controllable [97]. Furthermore, we conclude the possibility to induce cellular contrast enhancement by osmotic swelling of the cells in hypotonic buffer, but this has to be proved in further experiments. However, the injection of a glycerol mixture directly into the cell might be preferred because of the advantage to work with established cell culture conditions in the extracellular medium. Moreover, the swelling is a transient and reversible process, as glycerol can diffuse slowly out of the cell and intracellular pathways can be used to metabolize remaining material. Finally, due to the principles of the contrast enhancement approach, the method can be applied with other quantitative phase contrast methods and interferometry-based techniques, and thus prospects enhanced application fields in label-free live cell imaging.

6.4   Conclusion

The presented results show that DHM allows high-resolution, multi-focus quantitative phase contrast imaging of adherent and suspended cells. Although the presented DHM methods do not achieve the resolution as obtained from atomic force microscopy (AFM), scanning optical near field microscopy (SNOM), scanning electron microscopy (SEM), or super resolution fluorescence imaging (STED, PALM, STORM), they overcome some particular limitations of these techniques, for example, the scanning process, the requirement of fixed cells, or investigations in a vacuum. DHM in off-axis configuration enables a vibration insensitive (hologram capture time in or below the ms range) and non-contact full-field measurement of living cells. The results further demonstrate that the presented DHM

concepts can be utilized for investigations of dynamic cell morphology changes and for the quantitative analysis of cellular reactions on drug treatment. The obtained information opens up new quantitative ways for label-free dynamic cell monitoring, and may help access new parameters, for example, for apoptosis recognition or for control in micro-injection. Future prospects include the use of DHM for multimodal imaging, in fluidics, and for 3D cell tracking in a three-dimensional environment. In combination with fluorescence microscopy techniques, new possibilities for multifunctional microscopy systems for imaging and analysis of fixed and living cells are opened up. A higher specificity of the technology and improvement the lateral and axial resolution can be expected by the integration of nonlinear effects like second harmonic generation [98, 99] and by recently developed novel algorithms for the deconvolution of the holographically retrieved wave fields [100, 101] and the corresponding quantitative phase images [102]. In conclusion, the presented methods have the potential to form versatile microscopy tools for life sciences and biophotonics, and are highly relevant to achieve novel insights in dynamic cell biology and cancer research as well as in drugs and toxicity testing.

References

1. E.M. Goldys (ed.), *Fluorescence Applications in Biotechnology and the Life Sciences* (Wiley-Blackwell, New-Jersey, 2009)
2. V. Ntziachristos, Fluorescence molecular imaging. Annu. Rev. Biomed. Eng. **8**, 1–33 (2006)
3. L. Schermelleh, R. Heintzmann, H. Leonhardt, A guide to super-resolution fluorescence microscopy. J. Cell Biol. **190**, 165–175 (2010)
4. B. Huang, M. Bates, X. Zhuang, Super-resolution fluorescence microscopy. Annu. Rev. Biochem. **78**, 993–1016 (2009)
5. *The Molecular Probes*® *Handbook*, 11th edn. (2011). www.invitrogen.com
6. M. Monici, Cell and tissue autofluorescence research and diagnostic applications, in *Biotechnology Annual Review*, ed. by M.R. El-Gewely (Elsevier, Amsterdam, 2005), pp. 227–256
7. C.W. Chang, D. Sud, M.A. Mycek, Fluorescence lifetime imaging microscopy. Methods Cell Biol. **81**, 495–524 (2007)
8. O. Shimomura, The discovery of aequorin and green fluorescent protein. J. Microsc. **217**, 3–15 (2005)
9. P.L. Felgner et al., Lipofection: a highly efficient, lipid-mediated DNA-transfection procedure. Proc. Natl. Acad. Sci. U.S.A. **84**, 7413–7417 (1987)
10. X. Tsampoula et al., Fibre based cellular transfection. Opt. Express **16**, 17007–17013 (2008)
11. A.F. Fercher, Optical coherence tomography. J. Biomed. Opt. **1**, 157–173 (1996)
12. W. Drexler, Ultrahigh-resolution optical coherence tomography. J. Biomed. Opt. **9**, 47–74 (2004)
13. L.G. Rodriguez, S.J. Lockett, G.R. Holtom, Coherent anti-stokes raman scattering microscopy: a biological review. Cytometry A **69**, 779–791 (2006)
14. T. Kreis, in *Holographic Interferometry: Principles and Methods*, ed. by W. Osten, vol. 1 (Akademie-Verlag, Berlin, 1996)
15. V.P. Shchepinov, V.S. Pisarev, *Strain and Stress Analysis by Holographic and Speckle Interferometry* (Wiley, New York, 1996)

16. M.-A. Beeck, W. Hentschel, Laser metrology – a diagnostic tool in automotive development processes. Opt. Lasers Eng. **34**, 101–120 (2000)
17. E. Cuche, P. Marquet, C. Depeursinge, Simultaneous amplitude-contrast and quantitative phase-contrast microscopy by numerical reconstruction of Fresnel off-axis holograms. Appl. Opt. **38**(24), 6694–7001 (1999)
18. F. Charrière et al., Characterization of microlenses by digital holographic microscopy. Appl. Opt. **45**, 829–835 (2006)
19. D. Carl et al., Parameter-optimized digital holographic microscope for high-resolution living-cell analysis. Appl. Opt. **43**, 6536–6544 (2004)
20. P. Marquet et al., Digital holographic microscopy: a noninvasive contrast imaging technique allowing quantitative visualization of living cells with subwavelength axial accuracy. Opt. Lett. **30**, 468–470 (2005)
21. C.J. Mann et al., High-resolution quantitative phase-contrast microscopy by digital holography. Opt. Express **13**, 8693–8698 (2005)
22. B. Kemper, G. von Bally, Digital holographic microscopy for live cell applications and technical inspection. Appl. Opt. **47**, A52–A61 (2008)
23. B. Kemper et al., Modular digital holographic microscopy system for marker free quantitative phase contrast imaging of living cells. Proc. SPIE **6191**, 61910T (2006)
24. G. von Bally et al., New methods for marker-free live cell and tumor analyis, in *Biophotonics: Vision for Better Healthcare*, ed. by J. Popp, M. Strehle (Wiley, Berlin, 2006), pp. 301–360
25. B. Kemper et al., Monitoring of laser micromanipulated optically trapped cells by digital holographic microscopy. J. Biophoton. **3**, 425–431 (2010)
26. M. Esseling et al., Multimodal biophotonic workstation for live cell analysis. J. Biophoton. **5**, 9–13 (2012)
27. L.G. Alexopoulos, G.R. Erickson, F. Guilak, A method for quantifying cell size from differential interference contrast images: validation and application to osmotically stressed chondrocytes. J. Microsc. **205**, 125–135 (2001)
28. A. Barty et al., Quantitative optical phase microscopy. Opt. Lett. **23**(11), 817–819 (1998)
29. J. Farinas, A.S. Verkman, Cell volume and plasma membrane osmotic water permeability in epithelial cell layers measured by interferometry. Biophys. J. **71**, 3511–3522 (1996)
30. T. Ikeda et al., Hilbert phase microscopy for investigating fast dynamics in transparent systems. Opt. Lett. **30**(10), 1165–1167 (2005)
31. G. Popescu et al., Fourier phase microscopy for investigation of biological structures and dynamics. Opt. Lett. **29**, 2503–2505 (2004)
32. V.P. Tychinskii, Coherent phase microscopy of intracellular processes. Phys. Usp. **44**, 617–629 (2001)
33. A.D. Aguirre et al., High-resolution optical coherence microscopy for high-speed, in vivo cellular imaging. Opt. Lett. **28**, 2064–2066 (2003)
34. E.A. Swanson et al., In vivo retinal imaging by optical coherence tomography. Opt. Lett. **18**, 1864–1866 (1993)
35. Y. Zhao et al., Real-time phase-resolved functional optical coherence tomography by use of optical Hilbert transformation. Opt. Lett. **27**, 98–100 (2002)
36. C.G. Rylander et al., Quantitative phase-contrast imaging of cells with phase-sensitive optical coherence microscopy. Opt. Lett. **29**(13), 1509–1511 (2004)
37. A.K. Ellerbee, T.L. Reazzo, J.A. Izatt, Investigating nanoscale cellular dynamics with cross-sectional spectral domain phase microscopy. Opt. Express **15**, 8115–8124 (2007)
38. C. Joo, K.H. Kim, J.F. de Boer, Spectral-domain optical coherence phase and multiphoton microscopy. Opt. Lett. **32**, 623–625 (2007)
39. U. Schnars, W.P.O. Jüptner, Digital recording and numerical reconstruction of holograms. Meas. Sci. Technol. **13**, 85–101 (2002)
40. P. Langehanenberg, G. von Bally, B. Kemper, Application of partial coherent light in live cell imaging with digital holographic microscopy. J. Mod. Opt. **57**, 709–717 (2010)

41. B. Kemper et al., Investigation of living pancreas tumor cells by digital holographic microscopy. J. Biomed. Opt. **11**(3), 034005–034008 (2006)
42. H. Ding, G. Popescu, Instantaneous spatial light interference microscopy. Opt. Express **18**, 1569–1575 (2010)
43. J. Jang et al., Self-reference quantitative phase microscopy for microfluidic devices. Opt. Lett. **35**, 514–516 (2010)
44. N.T. Shaked et al., Reflective interferometric chamber for quantitative phase imaging of biological sample dynamics. J. Biomed. Opt. **15**, 030503 (2010)
45. G. Popescu et al., Diffraction phase microscopy for quantifying cell structure and dynamics. Opt. Lett. **31**, 775–778 (2006)
46. B. Kemper et al., Simplified approach for quantitative digital holographic quantitative phase contrast imaging of living cells. J. Biomed. Opt. **16**, 026014 (2011)
47. P. Bon et al., Quadriwave lateral shearing interferometry for quantitative phase microscopy of living cells. Opt. Express **17**, 13080–13094 (2009)
48. T.-C. Poon (ed.), *Digital Holography and Three-Dimensional Display* (Springer, New York, 2006)
49. L. Yaroslavsky, *Digital Holography and Digital Image Processing: Principles, Methods, Algorithms* (Kluwer, Boston, 2004)
50. T. Kreis, *Handbook of Holographic Interferometry: Optical and Digital Methods* (Wiley, Weinheim, 2005)
51. M.K. Kim, L. Yu, C.J. Mann, Interference techniques in digital holography. J. Opt. A **8**, 518–523 (2006)
52. J.W. Goodman, *Introduction to Fourier Optics* (McGraw-Hill, San Francisco, 1996)
53. T. Colomb, F. Montfort, C. Depeursinge, Small reconstruction distance in convolution formalism, paper DMA4, in *Digital Holography and Three-Dimensional Imaging, OSA Technical Digest*, ed. by C. Depeursinge (Optical Society of America, Washington, DC, 2008)
54. M.K. Kim, Principles and techniques of digital holographic microscopy. SPIE Rev. **1**, 018005 (2010)
55. S. De Nicola et al., Angular spectrum method with correction of anamorphism for numerical reconstruction of digital holograms on tilted planes. Opt. Express **13**, 9935–9940 (2005)
56. N.T. Shaked et al., Whole-cell-analysis of live cardiomyocytes using wide-field interferometric phase microscopy. Biomed. Opt. Express **1**, 706–719 (2010)
57. B. Kemper et al., Integral refractive index determination of living suspension cells by multifocus digital holographic phase contrast microscopy. J. Bio. Med. Opt. **12**, 054009 (2007)
58. J. Klokkers et al., Atrial natriuretic peptide and nitric oxide signaling antagonizes 2 vasopressin-mediated water permeability in inner medullary 3 collecting duct cells. Am. J. Physiol. Renal Physiol. **297**(3), F693–703 (2009)
59. T. Zhang, I. Yamaguchi, Three-dimensional microscopy with phase-shifting digital holography. Opt. Lett. **23**, 1221–1223 (1998)
60. I. Yamaguchi et al., Image formation in phase-shifting digital holography and applications to microscopy. Appl. Opt. **40**, 6177–6186 (2001)
61. K. Creath, Temporal phase measurement methods, in *Interferogram Analysis*, ed. by D. Robinson, S. Reid (Institute of Physics Publishing, Bristol, 1993), pp. 94–140
62. F. Dubois, L. Joannes, J.-C. Legros, Improved three-dimensional imaging with a digital holography microscope with a source of partial spatial coherence. Appl. Opt. **38**(34), 7085–7094 (1999)
63. B. Kemper et al., Characterisation of light emitting diodes (LEDs) for application in digital holographic microscopy for inspection of micro and nanostructured surfaces. Opt. Lasers Eng. **46**, 499–507 (2008)
64. C. Remmersmann et al., Phase noise optimization in temporal phase-shifting digital holography with partial coherence light sources and its application in quantitative cell imaging. Appl. Opt. **48**, 1463–1472 (2009)

65. B. Kemper et al., Application of 3D tracking. LED illumination and multi-wavelength techniques for quantitative cell analysis in digital holographic microscopy. Proc. SPIE **7184**, 71840R (2009)
66. G. Nomarski, Differential microinterferometer with polarized waves. J. Phys. Radium. **16**, 9–13 (1955)
67. B. Kemper et al., Optimization of spatial phase shifting in endoscopic electronic-speckle-pattern-interferometry. Opt. Commun. **217**, 151–160 (2003)
68. M. Liebling, T. Blu, M. Unser, Complex-wave retrieval from a single off-axis hologram. J. Opt. Soc. Am. A **21**(3), 367–377 (2004)
69. P. Langehanenberg, G. von Bally, B. Kemper, Autofocussing in digital holographic microscopy. 3D Res. **2**, 01004 (2011)
70. P. Marquet et al., Analysis of cellular structure and dynamics with digital holographic microscopy. Proc. SPIE **6633**, 66330F (2007)
71. M. Takeda, H. Ina, S. Kobayashi, Fourier-transform method of fringe-pattern analysis for computer-based topography and interferometry. J. Opt. Soc. Am. **72**, 156–160 (1982)
72. T. Kreis, Digital holographic interference-phase measurement using the Fourier-transform method. J. Opt. Soc. Am. A **3**, 847–855 (1986)
73. S. Rasheed et al., Characterization of a newly derived human sarcoma cell line (HT-1080). Cancer **33**, 1027–1033 (1974)
74. B. Kemper et al., Self interference digital holographic microscopy approach for inspection of technical and biological phase specimens. Proc. SPIE **8082**, 808207 (2011)
75. F. Dubois et al., Focus plane detection criteria in digital holography microscopy by amplitude analysis. Opt. Express **14**, 5895–5908 (2006)
76. P. Langehanenberg et al., Autofocusing in digital holographic phase contrast microscopy on pure phase objects for live cell imaging. Appl. Opt. **47**, D176–D182 (2008)
77. Y. Sun, S. Duthaler, B.J. Nelson, Autofocusing in computer microscopy: selecting the optimal focus algorithm. Microsc. Res. Tech. **65**, 139–149 (2004)
78. F.C. Groen, I.T. Young, G. Ligthart, A comparison of different focus functions for use in autofocus algorithms. Cytometry A **6**, 81–91 (1985)
79. L. Firestone et al., Comparison of autofocus methods for automated microscopy. Cytometry **12**, 195–206 (1991)
80. M. Bravo-Zanoguera et al., High-performance autofocus circuit for biological microscopy. Rev. Sci. Instrum. **69**, 3966–3977 (1998)
81. P. Langehanenberg, B. Kemper, G. von Bally, Autofocus algorithms for digital-holographic microscopy. Proc. SPIE **6633**, 66330E (2007)
82. P. Langehanenberg et al., Automated 3D-tracking of living cells by digital holographic microscopy. J. Biomed. Opt. **14**, 014018 (2009)
83. J. Kühn et al., Axial sub-nanometer accuracy in digital holographic microscopy. Meas. Sci. Technol. **19**, 074007 (2008)
84. S. Kosmeier et al., Multi-wavelength digital holographic microscopy for high resolution inspection of surfaces and imaging of phase specimen. Proc. SPIE **7718**, 77180T (2010)
85. H. Iwai et al., Quantitative phase imaging using actively stabilized phase-shifting low-coherence interferometry. Opt. Lett. **29**, 2399–2401 (2004)
86. J. Kühn et al., Sub-micrometer tomography of cells by multiple-wavelength digital holographic microscopy in reflection. Opt. Lett. **34**, 653–655 (2009)
87. S. Kosmeier et al., Reduction of parasitic interferences in digital holographic microscopy by numerically decreased coherence length. Appl. Phys. B **106**(1), 107–115 (2012)
88. B. Kemper, P. Langehanenberg, G. von Bally, Methods and applications for marker-free quantitative digital holographic phase contrast imaging in life cell analysis. Proc. SPIE **6796**, 6796E (2007)
89. A. Ashkin, Optical trapping and manipulation of neutral particles using lasers. Proc. Natl. Acad. Sci. U.S.A. **94**, 4853–4860 (1997)

90. J. Guck et al., Optical deformability of soft biological dielectrics. Phys. Rev. Lett. **84**(23), 5451 (2000)
91. B. Rappaz et al., Measurement of the integral refractive index and dynamic cell morphotometry of living cells with digital holographic microscopy. Opt. Express **13**, 9361–9373 (2005)
92. W. Choi et al., Tomographic phase microscopy. Nat. Methods **4**, 717–719 (2007)
93. M. Debailleul et al., High-resolution three-dimensional tomographic diractive microscopy of transparent inorganic and biological samples. Opt. Lett. **34**, 79–81 (2009)
94. S. Kosmeier et al., Determination of the integral refractive index of cells in suspension by digital holographic phase contrast microscopy. Proc. SPIE **6991**, 699110 (2008)
95. M. Kemmler et al., Noninvasive timedependent cytometry monitoring by digital holography. J. Biomed. Opt. **12**, 064002 (2007)
96. Å. Björk, *Numerical Methods for Least Squares Problems* (SIAM, Philadelphia, 1996)
97. C.E. Rommel et al., Contrast enhanced digital holographic imaging of cellular structures by manipulating intracellular refractive index. J. Biomed. Opt. **15**, 041509 (2010)
98. E. Shaffer et al., Label-free second-harmonic phase imaging of biological specimen by digital holographic microscopy. Opt. Lett. **35**, 4102–4104 (2010)
99. E. Shaffer, P. Marquet, C. Depeursinge, Real time, nanometric 3D-tracking of nanoparticles made possible by second harmonic generation digital holographic microscopy. Opt. Express **18**, 17392–17403 (2010)
100. Y. Cotte et al., Realistic 3D coherent transfer function inverse filtering of complex fields. Biomed. Opt. Express **2**, 2216–2230 (2011)
101. Y. Cotte et al., Microscopy image resolution improvement by deconvolution of complex fields. Opt. Express **18**, 19462–19478 (2010)
102. S.D. Babacan et al., Cell imaging beyond the diffraction limit using sparse deconvolution spatial light interference microscopy. Biomed. Opt. Express **2**, 1815–1827 (2011)

Fourier Transform Light Scattering of Tissues

7

Taewoo Kim, Shamira Sridharan, and Gabriel Popescu

Contents

Abstract

We review the basic principles of light-tissue interaction and common methods of investigation. The mathematical framework for describing weakly scattering regime (the Born approximation) as well as the strong scattering regime (the diffusion equation) are described. Traditional techniques based on polarization, time-resolved, single and multiple scattering are reviewed. We then introduce

T. Kim • S. Sridharan • G. Popescu (✉)
Quantitative Light Imaging Laboratory, Department of Electrical and Computer Engineering, Beckman Institute for Advanced Science & Technology, University of Illinois at Urbana-Champaign, Urbana, IL, USA
e-mail: gpopescu@illinois.edu

Fourier transform light scattering (FTLS), which is a recent development from our own laboratory. FTLS is the spatial analogue of Fourier transform spectroscopy, in the sense that it provides angular scattering (spatial frequency) data from phase and amplitude measurements in the spatial (image) domain. We show that FTLS can be used as a diagnostic tool by translating the quantitative phase information into data of clinical relevance. Further, FTLS allows us to extract scattering parameters of the tissue from imaging unlabeled, thin tissue slices, using a relationship which we call the scattering-phase theorem. Using these measurements, FTLS can predict the outcome of many other experiments, including time resolved and enhanced backscattering experiments.

7.1 Introduction to Tissue Scattering

Biological tissues are optically inhomogeneous, which makes the understanding of light-tissue interaction challenging and, for the same reason, interesting [1, 2]. Upon propagation through tissues, optical fields suffer modifications in terms of irradiance, phase, spectrum, direction, polarization, and coherence, which can reveal information about the sample of interest [3–5]. The *elastic* interaction, in which the frequency (or wavelength) of light is conserved, is generally called *scattering*. Sometimes *elastic light scattering* (ELS) is used to specifically distinguish this type of scattering from *dynamic* (or *quasi-elastic*) light scattering [6], in which the light frequency changes slightly due to Doppler shifts induced by the dynamic specimen. This type of interaction, together with other inelastic processes, such as absorption and emission, is outside the scope of this entry and will not be discussed in detail.

For diagnosis applications, the starting assumption is that a certain disease (e.g., cancer) modifies one of these light properties, such that optical information can be translated into data of clinical relevance. Thus, developing methods for accessing tissue scattering parameters has been an area of great interest and active research. In this chapter, we first review the basics of tissue scattering (Sect. 7.1), followed by a review of existing scattering methods (Sect. 7.2) and a review of the recent Fourier transform light scattering method developed in our laboratory (Sect. 7.3). We will summarize and conclude in Sect. 7.4.

7.1.1 Optical Window of Tissues

Biological cells abound in structures of different refractive indices, which makes it possible to study the cell using light scattering. Essentially, the optical microscope, which is the most common method of investigation in biomedicine [7], can be regarded as a powerful scattering instrument. The only difference between an imaging system, e.g., microscopes, and a common angular scattering instrument, e.g., goniometer, is that, in the first case, the measurement is performed in the real space (x, y, z) while, in the second, the measurement is in the spatial frequency domain (k_x, k_y, k_z).
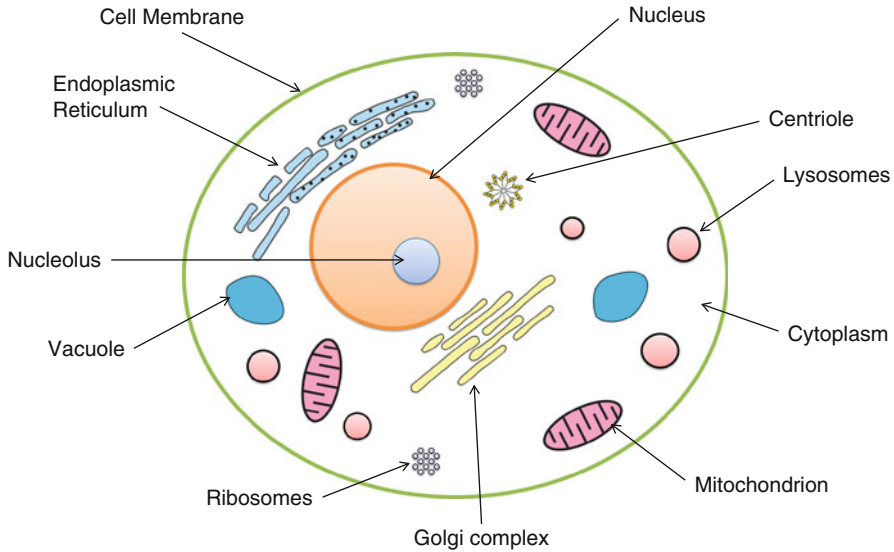
Fig. 7.1 Illustration of cellular substructures that can potentially contribute to light scattering signals

There are three major structures in a cell: *cell membrane*, *cytoplasm*, and *nucleus* (see Fig. 7.1) [8]. Cell membrane is the structure that serves as a "wall" for the entire cell structure to separate it from the surroundings. The structure of cell membrane is described with the fluid mosaic model introduced by Singer and Nicolson [9]. According to this model, cell membrane consists of protein molecules "floating" on lipid bilayer structure such that the hydrophobic tails of lipid molecules are sandwiched by the hydrophilic heads. Cytoplasm includes three major elements: cytosol, organelles, and cytoplasmic inclusions. Cytosol refers to the inter-structure fluid that the subcellular structures such as mitochondria, endoplasmic reticulum, and Golgi apparatus are suspended in. Organelles are the subcellular "organs" that are suspended in cytosol and cytoplasmic inclusions are small insoluble particles suspended in cytosol. Lastly, the cell nucleus is a spherical organelle separated from the cytoplasm by a layer called the nuclear envelope. The nucleus includes the chromosomes and also is the place where DNA replication happens.

All these different structures in a cell provide refractive index differences inside the cell and make it a scattering medium [10, 11]. Thus, large cellular structures, e.g., nucleus, generally scatter light at small angles, while large angle scattering is due to contributions from small organelles such as mitochondria.

Light can also be absorbed by cells. Beer–Lambert law states the intensity change as the light travels along a distance L through a material characterized by the extinction coefficient, ε, and the concentration of the absorbing material, ρ,

$$
\begin{aligned}
I &= I_0 e^{-\varepsilon \rho L} \\
&= I_0 e^{-\alpha L},
\end{aligned}
\tag{7.1}
$$

Fig. 7.2 Optical window in biological tissues
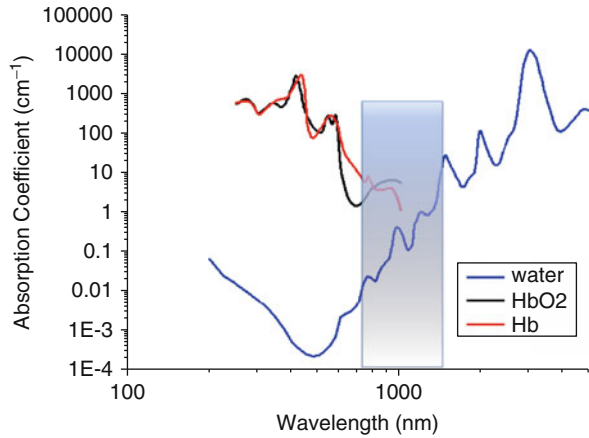
where α is the absorption coefficient, which gives the decrease rate of the intensity as light travels further into the material. Since human body is mostly composed of water, it is important to understand how water absorbs light over various spectral regions (see Fig. 7.2). From the studies of extinction constants of water done by Hale and Querry [12], we can see that within the spectral region 200–1,300 nm, water does not absorb light significantly.

Besides water, *hemoglobin* is another major contributor to light absorption in human tissue. This protein contained in red blood cells delivers oxygen by binding the oxygen molecules to its iron atoms. As red blood cells travel through the lung and make hemoglobin molecules oxygenated (*oxyhemoglobin*), the absorption spectrum of hemoglobin changes from its deoxygenated state (*deoxyhemoglobin*). In Fig. 7.2, we show the absorption spectrum of oxygenated and deoxygenated hemoglobin from 250 to 1,000 nm wavelength region [13] together with the water absorption spectrum. Hemoglobin absorbs the most in blue and green and this absorption drops significantly at longer wavelength, where water's contribution becomes important. Therefore, there is a window of opportunity, around 800–1,300 nm, sometimes referred to as the *tissue optical window*, where overall the tissue exhibits low absorption. In this window, the contribution of light absorption becomes insignificant compared to light scattering. Not surprisingly, this is the spectral region where most tissue scattering experiments are performed. In the following sections, we discuss the main concepts in light scattering theory, as it applies to tissue scattering experiments.

7.1.2 Light Scattering Basics

Light scattering refers to the interaction between the electromagnetic wave and inhomogeneous media. When studying light scattering in cells and tissues, our general goal is to solve the *inverse scattering problem*, i.e., from the experimental data, i.e., to obtain information about the refractive index distribution, $n(\mathbf{r})$, of the structure.

Here, we restrict the discussion to scalar fields, which is the relevant situation whenever the tissue scatters light isotropically. The wave propagation in a medium can be represented by the (inhomogeneous) Helmholtz equation, (7.2).

$$\nabla^2 U(\mathbf{r}, \omega) + \beta^2(\mathbf{r}, \omega) U(\mathbf{r}, \omega) = 0, \tag{7.2}$$

where

$$\begin{aligned} \beta(\mathbf{r}, \omega) &= n(\mathbf{r}, \omega)\beta_0 \\ &= n(\mathbf{r}, \omega)\frac{\omega}{c}. \end{aligned} \tag{7.3}$$

In (7.2)–(7.3), U is the complex field, β is the inhomogeneous *wave number* (a material property), β_0 the wave number of vacuum, $\mathbf{r}$ the spatial coordinate, ω the angular frequency, and n the refractive index (generally a function of both $\mathbf{r}$ and ω).

We can rearrange (7.2) to isolate a new term describing the inhomogeneous medium, $F(\mathbf{r},\omega)$, referred to as *scattering potential* [14],

$$\nabla^2 U(\mathbf{r}, \omega) + \beta_0^2 U(\mathbf{r}, \omega) = -4\pi F(\mathbf{r}, \omega) U(\mathbf{r}, \omega) \tag{7.4}$$

$$F(\mathbf{r}, \omega) = \frac{1}{4\pi} \beta_0^2 \left[n^2(\mathbf{r}, \omega) - 1 \right] \tag{7.5}$$

Solving the Helmholtz equation for a point source, i.e., inserting a 3D delta function, $\delta^{(3)}(\mathbf{r})$, on the right hand side of (7.4), provides the well-known *spherical wave* as the Green's function,

$$g(\mathbf{r}, \omega) = \frac{e^{i\beta_0 r}}{r} \tag{7.6}$$

Furthermore, using the superposition (or the Huygens-Fresnel) principle, the convolution of the spherical wave and the source term in (7.4) gives the *scattered field* solution,

$$U(\mathbf{r}, \omega) = \int \int \int_V F(\mathbf{r}', \omega) U(\mathbf{r}', \omega) \frac{e^{i\beta_0 |\mathbf{r} - \mathbf{r}'|}}{|\mathbf{r} - \mathbf{r}'|} d^3\mathbf{r}' \tag{7.7}$$

By applying the *Fraunhofer approximation*, the *far-field* approximation of the scattered field is obtained as:

$$U(\mathbf{r}, \omega) = \frac{e^{i\beta_0 r}}{r} \int \int \int_V F(\mathbf{r}', \omega) U(\mathbf{r}', \omega) e^{-i\mathbf{k}_s \cdot \mathbf{r}'} d^3\mathbf{r}' \tag{7.8}$$

This equation indicates that the far field behaves as a spherical wave perturbed by the *scattering amplitude*, $f(\mathbf{k}_s, \omega)$, defined as (7.9).

$$f(\mathbf{k}_s, \omega) = \int \int \int_V F(\mathbf{r}', \omega) U(\mathbf{r}', \omega) e^{-i\mathbf{k}_s \cdot \mathbf{r}'} d^3 \mathbf{r}'. \tag{7.9}$$

Without further approximation, this integral remains difficult to evaluate. However, in the case of single layers of cells and thin tissue slices, it is reasonable to assume that the light scatters weakly. Below we show that under these circumstances, (7.8) can be inverted, i.e., an expression for F can be obtained in terms of the measured scattered field U.

7.1.3 The Born Approximation

7.1.3.1 Diffraction Tomography

Following our assumption that the scattering is weak, the (first) *Born approximation* states that the field inside the inhomogeneous medium remains approximately equal to the incident plane wave,

$$U_i(\mathbf{r}', \omega) = e^{i\mathbf{k}_i \mathbf{r}'} \tag{7.10}$$

Therefore, inserting this plane wave under the integral of (7.9), the scattering amplitude can be simplified to:

$$f(\mathbf{q}, \omega) = \int_v F(\mathbf{r}', \omega) e^{-i\mathbf{q} \cdot \mathbf{r}'} d^3 \mathbf{r}', \tag{7.11}$$

Equation (7.11) now is a 3D Fourier transform, where $\mathbf{q} = \mathbf{k}_s - \mathbf{k}_i$ is the Fourier variable. The quantity $\mathbf{q}$ represents the difference between the scattered wave vector, $\mathbf{k}_s$, and the incident wave vector, $\mathbf{k}_i$, and is geometrically illustrated in Fig. 7.3a. Note that the modulus of the scattering wave vector depends on both the wavelength and scattering angle, $q = 2\beta_0 \sin(\theta/2)$.

Equation (7.11) ultimately provides the solution to the inverse scattering problem because of the reversibility of the Fourier integral,

$$F(\mathbf{r}', \omega) = \int_{-\infty}^{\infty} U(\mathbf{q}, \omega) e^{i\mathbf{q} \cdot \mathbf{r}'} d^3 \mathbf{q} \tag{7.12}$$

This equation implies that the structure of the inhomogeneous medium can be completely retrieved by taking the Fourier transform of the measured *complex scattered field* over an *infinite range* of spatial frequencies. Equation (7.12) is the main result of *diffraction tomography*, in which a 3D object is reconstructed via measurements of angular scattering.
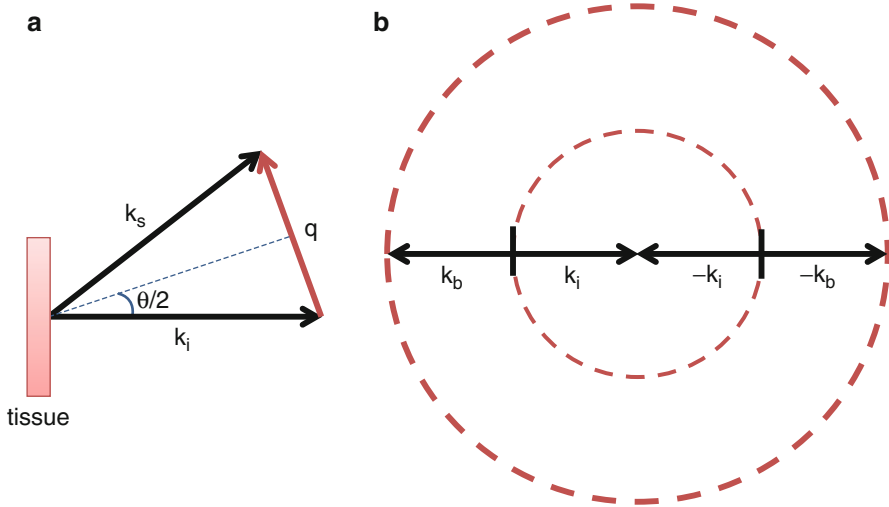
Fig. 7.3   Momentum transfer of (**a**) scattering event. (**b**) The Ewald sphere

However, in practice, these conditions are not satisfied and the reconstruction of the structure of the sample is always limited. Currently, most measurements are made by observing the intensity of the scattered field, not the complex scattered field itself. Taking the Fourier transform of the intensity of the scattered field and using the correlation theorem [15], we obtain autocorrelation of the scattering potential rather than the potential itself,

$$\int_{-\infty}^{\infty} \left| U(\mathbf{q}, \omega) \right|^2 e^{i\mathbf{q} \cdot \mathbf{r}'} d^3\mathbf{q} = F(\mathbf{r}', \omega) \otimes F(\mathbf{r}', \omega) \tag{7.13}$$

Thus, (7.13) states that intensity measurements, without phase information, are insufficient for retrieving the structure of scattering objects. Note that this problem has been known in X-ray diffraction for many decades, it is called the "phase problem" (for review, see the recent account by Wolf [16]).

Furthermore, we only have access to a limited spatial frequency range. For an incident wave vector $\mathbf{k}_i$, the highest magnitude of the momentum transfer vector (Fig. 7.3a) we can obtain experimentally is $2k_i$ which is the case of backscattering. For arbitrary incident wave vectors, the largest possible $\mathbf{q}$ appears in backscattering with magnitude $2\beta_0$, and direction opposite to the incident vector. Thus, the largest possible $\mathbf{q}$ covers a sphere of radius $2\beta_0$, which is known as the *Ewald sphere* (Fig. 7.3b). The meaning of this coverage is that we can only measure the frequency components within this sphere, and the accessible *propagating* field is truncated in frequency. Note that frequencies above $2\beta_0$ are evanescent and can only be accessed in *near field*.

This truncated field can be written as the multiplication of the scattered field and a *ball function*, which describes the Ewald sphere and is mathematically defined as:

$$\Pi\left(\frac{q}{4\beta_0}\right) = \begin{cases} 1, \text{when } |\mathbf{q}| \leq 2\beta_0 \\ 0, \text{elsewhere} \end{cases} \tag{7.14}$$

Thus, we can write the measured, truncated field, $\underline{U}$, as:

$$\underline{U}(\mathbf{q}, \omega) = U(\mathbf{q}, \omega) \cdot \Pi\left(\frac{q}{4\beta_0}\right) \tag{7.15}$$

Now the scattering potential can be obtained by taking the Fourier transform of the truncated field,

$$\begin{aligned} \underline{F}(\mathbf{r}', \omega) &= F(\mathbf{r}', \omega) \oslash \widetilde{\Pi}(r') \\ &= F(\mathbf{r}', \omega) \oslash \frac{\sin(2\beta_0 r') - 2\beta_0 r' \cos(2\beta_0 r')}{r'^3} \end{aligned} \tag{7.16}$$

In the equation above, $\oslash$ indicates the 3D convolution. From the 3D Fourier transform of a ball function, $\widetilde{\Pi}(r')$, we notice that the new scattering potential after frequency truncation is a smoothed-out version of the object. We can conclude that diffraction tomography requires the measurement of both the phase and amplitude of the scattered field and the reconstruction is, at best, band-limited to a sphere of radius $2\beta_0$.

7.1.3.2 Single Particle Under the Born Approximation

Now, we define some parameters that characterize single particle scattering. The generalized form of scattered field in the *far zone* (Fraunhofer approximation of (7.8)) can be written as:

$$\mathbf{U}_s(\mathbf{r}) = \mathbf{U}_i(\mathbf{r}) \frac{e^{ikr}}{r} f(\mathbf{k}_s, \mathbf{k}_i). \tag{7.17}$$

Incident field, scattered field, and the position in the space are now in vector forms. Also, the scattering amplitude, $f(\mathbf{k}_s, \mathbf{k}_i)$, now includes polarization information as well. The scattering by single particles is efficiently described by *cross sections*. First, the *differential cross section* is defined as follows:

$$\sigma_d(\mathbf{k}_s, \mathbf{k}_i) = \lim_{r \to \infty} r^2 \left|\frac{\mathbf{S}_s}{\mathbf{S}_i}\right|, \tag{7.18}$$

where $\mathbf{S}_{s,i}$ are the Poynting vectors for the scattered and incident field. Since the moduli of the Poynting vectors are $(1/2\eta)|U_{s,i}|^2$, the differential cross section can be written as a function of the scattering amplitude, (7.19).

$$\sigma_d(\mathbf{k}_s, \mathbf{k}_i) = |f(\mathbf{k}_s, \mathbf{k}_i)|^2. \tag{7.19}$$

By normalizing the differential cross section, we can obtain the *phase function*, $p(\mathbf{k}_s, \mathbf{k}_i)$, which provides the angular probability density function of the scattered light.

$$p(\mathbf{k}_s, \mathbf{k}_i) = 4\pi \frac{\sigma_d(\mathbf{k}_s, \mathbf{k}_i)}{\int\limits_{4\pi} \sigma_d(\mathbf{k}_s, \mathbf{k}_i) d\Omega}. \tag{7.20}$$

Furthermore, the *scattering cross section* is defined by integrating the differential cross section over the solid angle (the denominator of the phase function in (7.20)),

$$\sigma_s = \int\limits_{4\pi} \sigma_d(\mathbf{k}_s, \mathbf{k}_i) d\Omega. \tag{7.21}$$

In general, absorption through the scattering particle also gives rise to an *absorption cross section*, σ_a, which also contributes to the *total cross section*, σ,

$$\sigma = \sigma_s + \sigma_a. \tag{7.22}$$

Next, we will discuss some specific cases where the Born approximation is applied to single spherical particles. These are known as Rayleigh-Gans particles and are characterized by a small phase shift, i.e., $k_0(n-1)2r << 1$, where r is the radius of the particle.

When a scattering particle has a well-defined shape such as sphere, cylinder, or cube, the Born approximation discussed in the previous section allows analytic solutions. In case of a spherical particle with radius r, the scattering potential can be written as a ball function and the scattering amplitude is simply the 3D Fourier transform of the scattering potential with $\mathbf{q} = \mathbf{k}_s - \mathbf{k}_i$.

$$\begin{aligned} F_p(\mathbf{r}') &= \Pi\left(\frac{r'}{2r}\right) F_0 \\ &= \frac{1}{4\pi}\beta_0^2(n^2 - 1)\Pi\left(\frac{r'}{2r}\right). \end{aligned} \tag{7.23}$$

Thus, we obtain the scattering amplitude by simply taking the 3D Fourier transform of the particle scattering potential, F_p. The Fourier transform of the "ball" function is well known, such that the scattering amplitude is:

$$f(\mathbf{q}, \omega) \propto (n^2 - 1)\beta_0^2 r^3 \frac{\sin(qr) - qr\cos(qr)}{(qr)^3}. \tag{7.24}$$

Note that the differential cross section depends on the size of the particle and also on the modulus of the scattering wave vector, $q = 2\beta_0 \sin(\theta/2)$,

$$\sigma_d(\mathbf{k}_s, \mathbf{k}_i) = |f(\mathbf{k}_s, \mathbf{k}_i)|^2$$
$$\propto (n^2 - 1)V^2\beta_0^4 \left[\frac{\sin(qr) - qr\cos(qr)}{(qr)^3}\right]^2. \tag{7.25}$$

This formula establishes the angular scattering generated by a weakly scattering spherical particle. When $qr \to 0$, i.e., either the particle is very small ($r \to 0$) or the measurement is made at very small angles $[q = 2\beta_0 \sin(\theta/2) \to 0]$, (7.25) can be further simplified to:

$$\sigma_d(\mathbf{k}_s, \mathbf{k}_i)\big|_{qr \to 0} \propto (n^2 - 1)V^2\beta_0^4 \left[\frac{\sin(qr) - qr\cos(qr)}{(qr)^3}\right]^2 \simeq \frac{1}{9}(n^2 - 1)V^2 k_0^4. \tag{7.26}$$

Therefore, by measuring the scattering at small angles, i.e., *forward scattering*, we can determine the volume of the scattering particle. Also, for very small particles, or *Rayleigh particles*, the differential cross section is independent of the angle of measurement, which defines *isotropic scattering*. The result also states that the Rayleigh scattering is isotropic and strongly depends on the size of the particle and the wavelength,

$$\sigma_s(\omega) \propto (n^2 - 1)^2 \beta_0^4 V^2$$
$$\propto \frac{r^6}{\lambda^4}. \tag{7.27}$$

For other particle shapes, such as a cube, a cylinder, etc., we can follow the same procedure of determining the scattering potential to analyze the scattering properties.

7.1.3.3 Ensemble of Particles Under the Born Approximation

When a measurement on a biological object is made, there are many "particles" that contribute to the light scattering. Therefore, studying light scattering from ensembles of particles is relevant to biomedical measurements. In this section, we look at the cases where identical particles are randomly distributed in space.

With the assumption that all the particles are identical and the distribution of these particles in space is expressed as a sum of delta functions, the scattering potential of the ensemble can be written as a convolution between the sum of delta functions and the scattering potential of a particle, $F_0(\mathbf{r})$,

$$F(\mathbf{r}) = F_0(\mathbf{r}) \otimes \sum_i \delta(\mathbf{r} - \mathbf{r}_i). \tag{7.28}$$

Consequently, the scattering amplitude can be obtained by taking a 3D Fourier transform of the scattering potential

$$f(\mathbf{q}) = f_0(\mathbf{q})S(\mathbf{q}), \tag{7.29}$$

where S is the so-called *structure function*, defined as,

$$S(\mathbf{q}) = \sum_i e^{i\mathbf{q}\cdot\mathbf{r}_i}. \tag{7.30}$$

We can immediately see that the scattering amplitude of an ensemble is just the scattering amplitude of a single particle multiplied by the *structure function*, $S(\mathbf{q})$, which contains the information about the particle distribution in space. As expected, since the particles are separated by distances larger than their diameter, S contributes at high spatial frequencies, or q-values, hence the term "structure." The single scattering feature, described by f_0, is called *form factor (function)* and acts as the envelope of the angular scattering signal. If the particles are separated by large distances, the structure contribution can be neglected at appropriately low angles. However in cells and tissues, this is hardly the case.

7.1.4 Multiple Scattering

So far, we discussed the case of *single scattering* where the average dimension of the scattering medium is smaller than the characteristic mean free path, l_s. For a distribution of particles, l_s is defined by the density of the scattering particles and the scattering cross section of each particle,

$$l_s = \frac{1}{N\sigma_s}. \tag{7.31}$$

For small particles under Rayleigh scattering regime, the scattering event happens in an isotropic manner and the average step between two scattering events is defined by l_s. The scattering mean free path allows us to define the intensity decay of a plane wave propagating through a medium of thickness L via Lambert-Beer equation similar to the one used for absorption (see (7.1)),

$$\begin{aligned} I &= I_0 e^{-\frac{l_s}{L}} \\ &= I_0 e^{-\mu_s L}, \end{aligned} \tag{7.32}$$

where μ_s is called scattering coefficient.

However, when the single scattering event is *anisotropic*, we have to take the average direction of a scattering wave vector into account, which gives a new average characteristic distance. This new average distance, l_t, the *transport mean free path*, includes not only the scattering cross section and the density of the particles, but also the anisotropy factor, g, which is defined as the average cosine of a single scattering event,

$$l_t = \frac{l_s}{(1-g)} = \frac{1}{N\sigma_s(1-g)} \tag{7.33a}$$

$$\begin{aligned} g &= \langle \Omega \cdot \Omega' \rangle \\ &= \langle \cos\theta \rangle_\theta. \end{aligned} \tag{7.33b}$$

For highly scattering media, when the dimensions of the medium are much larger than l_t, the light propagation resembles a *random walk*, or diffusion process, which can be described by a diffusion equation:

$$\frac{\partial\Phi}{\partial t} - \nabla[D(r)\nabla\Phi(\mathbf{r},t)] + \mu_a\Phi(\mathbf{r},t) = S(\mathbf{r},t). \tag{7.34a}$$

Here, $\Phi(\mathbf{r},t)$, $D(r)$, μ_a, and $S(\mathbf{r},t)$ are, respectively, the energy flux, diffusion constant, absorption coefficient, and the light source. For a statistically homogeneous medium, i.e., $D = const.$, and in the absence of absorption and sources, the diffusion equation simplifies to:

$$\nabla^2\Phi(\mathbf{r},t) - \frac{1}{D}\frac{\partial\Phi(\mathbf{r},t)}{\partial t} = 0. \tag{7.34b}$$

In (7.34b), the diffusion equation is directly related to the transport mean free path, $D = cl_t/3$. This equation is heavily used in bulk tissue scattering experiments, e.g., in vivo, because through measurements of Φ, either in space- or time-resolved manner, D becomes a measurable quantity of potential clinical relevance.

Below, we review some of the common light scattering methods, operating both in single scattering and diffusion regimes.

7.2 Traditional Scattering Methods

Here we discuss some traditional scattering methods used to solve inverse problems and study tissues.

7.2.1 Polarized Light Scattering

Polarization of the light scattered from an inhomogeneous scattering medium depends on many different factors: wavelength of the light, type of the scattering

medium, time of travel, and traveling distance [17, 18]. Especially, the traveling distance, which tells us if the light scattering is in the single scattering regime or in the multiple scattering regime, plays an important role in the polarization state of the scattered light. The polarization state is preserved in the backscattered field if it originates from a thin region in the tissue, i.e., within an l_s – thick slice from the surface. However, multiply scattered backscattered light, which underwent at least two scattering events before exiting the tissue, loses its polarization [19, 20]. Thus, for linearly polarized incident light, the backscattered light from the near-surface region is still linearly polarized in the same direction as the incident light while the backscattered light from deeper region is unpolarized. This means that if we use an analyzer that is parallel to the incident polarization, we will obtain the field scattered from the near-surface region plus half of the field multiply scattered from the deeper region. Furthermore, using an analyzer that is perpendicular to the incident polarization, we will only get the multiply scattered field, which is identical to the multiply scattered field from the parallel polarization except for the cross-polarization direction. Therefore, by subtracting the perpendicular polarized field from the parallel polarized field, we can retrieve only the backscattering from the near-surface region [21, 22],

$$I_{\parallel} - I_{\perp} \simeq \frac{I_0}{k^2 r^2} \int_{\pi}^{\pi - \theta_0} \mathrm{Re}\left[S_{\perp}^*(\theta)S_{\parallel}(\theta)\right] \sin\theta d\theta. \tag{7.35}$$

In this equation, $S_{\perp,\parallel}$, θ_0, θ, r, and k are the scattering amplitudes, linearly polarized incident angle, scattering angle, the distance from the scatterer to the detector, and the wave number, respectively. Thus, polarization properties of light can be used to filter out the diffusive background and analyze only the single scattering regime, for which the Born approximation may be applicable [22–25]. Other differential methods for selectively removing the diffusive background have been developed [26, 27].

7.2.2 Single Scattering

7.2.2.1 Angular Scattering

Unlike Rayleigh scattering regime discussed earlier (Sect. 7.1.3.2.), the scattering is anisotropic when the particle size is sufficiently large compared to the wavelength of the incident light. In this case, we need the complete angular distribution of the scattered field from the biological tissue. Measurements on the angular dependence of scattering, $P(\theta, \lambda)$, can be directly used to calculate the anisotropy factor, which in turn gives the transport mean free path of the scattering medium,

$$g(\lambda) = \int P(\theta, \lambda) \cos\theta d\Omega \tag{7.36}$$

Fig. 7.4 Goniometer-based angle-resolved light scattering setup
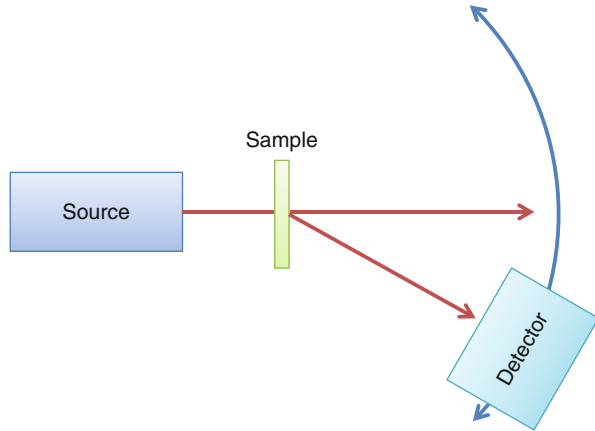
Figure 7.4 shows a traditional, goniometer-based measurement of angular scattering. As already mentioned in Sect. 7.1.3, studying the angular distribution of light scattered from weakly scattering specimens, such as monolayers of cells and thin tissue sections, can provide us with valuable morphological information. This information can then be used to diagnose abnormalities in biological tissues, including various types of cancer [25, 28–30].

7.2.2.2 Light Scattering Spectroscopy

As shown above, light scattering depends on not only the scattering sample, but also the wavelength of the incident light. Therefore, by taking the spectral density of the scattered light using a spectrometer, the characteristics of the scatterer can be determined. Perelman et al. [31] proposed a technique to take the wavelength dependence into account in studying the light backscattered from biological tissue. In this paper, the normalized reflectance of the field is measured in terms of the incident intensity and the backscattered diffused intensity of the field from deeper part of the field. This reflectance is ultimately used to calculate the size distribution of the cell nuclei. Clearly, angular and spectroscopic scattering measurements are equivalent, because the scattering wave number, $q = 4\pi \sin(\theta/2)/\lambda$, is a function of both angle and wavelength. However, recently, it has been emphasized that interpretation of the single scattering signal has to be done carefully [32].

7.2.3   Diffusive Scattering

7.2.3.1 Enhanced Backscattering

When a plane wave illuminates a semi-infinite scattering medium, every backscattered wave has its time-reversed pair which takes the same optical path but in opposite direction (see Fig. 7.5). For this class of backscattered field, the phase difference between the pair of waves approaches zero as the angle approaches 180° (backscattering) [33–35]. Due to constructive interference, the angular

Fig. 7.5 Time-reversed photon pairs in enhanced back scattering
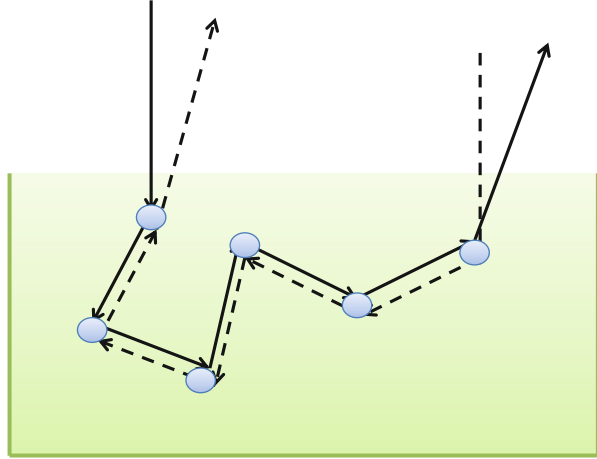
distribution of the backscattered field will exhibit a bright spot, or *enhancement*, in the backscattering direction, which seats on a diffusive background. Since all the different possible pathlengths within the medium are governed by the diffusion equation, the enhanced backscattering peak width depends on the transport mean free path l_t as [34]:

$$\alpha(\theta) = \frac{3}{8\pi} \left[1 + \frac{2z_0}{l_t} + \frac{1}{(1 + q_\perp l_t)^2} \left(1 + \frac{1 - e^{-2q_\perp z_0}}{q_\perp l_t} \right) \right], \qquad (7.37)$$

where l_t transport mean free path, z_0 trapping plane location, $q_\perp = 2\pi\theta/\lambda$ is the component of q normal to the z-axis. Thus the information about l_t is carried by the angular width, $\delta\theta$, of the enhancement cone, $\delta\theta \propto \lambda/3\pi l_t$, which is obtained by expanding (7.37) around $q_\perp z_0 = 0$ [36]. Because of this, enhanced backscattering can be used to characterize tissue properties [36]. Note that typical experimental values are $l_t \simeq 1\,\text{mm}$ and $\lambda \simeq 1\,\mu\text{m}$, which indicates that the angular spread of the enhancement cone is extremely small, of the order of 0.1 mrad. This fact adds tremendous constraints on the experimental execution of these measurements. Due to the uncertainty principle, resolving such a small angle requires a correspondingly large beam, of the order of $N\lambda/\delta\theta \simeq N10l_t$, i.e., the illumination beam waist must be larger than N centimeters (!), where N is the number of points sampling the enhancement cone.

Due to the interference law, the enhancement is a factor of 2 higher than the diffussive, incoherent background [33–35]. However, if the illumination field has a coherence area that is smaller than the illumination beam, the incoherent background raises, roughly by a factor equal to the ratio between the beam area and coherence area. The net effect of this incoherent illumination effect is to effectively diminish the enhancement factor and broaden the cone. In essence, a partially coherent field is characterized by a certain distribution of **k**-vectors (or angles), each generating an enhancement distribution. Thus, the resulting enhancement is

Fig. 7.6 OCT setup
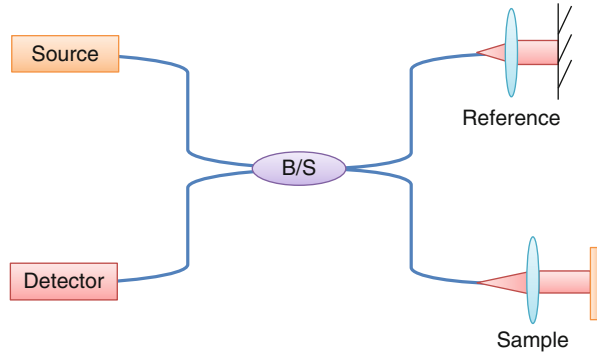
the angular convolution between the coherent enhancement profile and the angular distribution of illumination. Note that this angular distribution of illumination acts as the Green's function (or impulse response) of the instrument, limiting the angular resolution of the measurement in the same way the point spread function limits the spatial resolution in a microscope. The spatial coherence length has to be at least l_t; otherwise, the coherent effect is lost. Recently, Kim et al. investigated this incoherent illumination in the extreme case of very low spatial coherence [36].

7.2.3.2 Diffuse Reflectance

A diffusive model can be used to study the diffuse reflectance versus point-detector separation or wavelength and extract scattering parameters of bulk tissues. This steady-state measurement has been used extensively due to its simplicity (see, e.g., [37–41]). A more detailed description of the diffusion phenomenon in semi-infinite media, including the full, time-resolved solution, is presented below, in Sect. 7.2.4.2. Averaging the time-resolved solution over time gives the steady-state, *diffuse reflection* solution.

7.2.4   Time-Resolved Scattering

7.2.4.1 Optical Coherence Tomography

Optical coherence tomography (OCT) uses low-coherence light to interferometrically retrieve echo-type measurements from deep tissues [42]. Typical setup for OCT is based on the Michelson interferometer which consists of a broadband source, beam splitter, reference arm, sample arm, and a detector (Fig. 7.6). Light scattered from the sample arm is analyzed with the light from reference arm to give the object information. Because of its low-coherence from the broadband source, OCT obtains the depth sectioning comparable to the coherence length of the light source. In other words, only the part of the sample that produces the same pathlength as the reference field, within the coherence length, is studied at any one time. Therefore, OCT usually measures one small region defined by the fiber optic and the depth section per measurement. In order to reconstruct an entire 3D volume, raster scanning is necessary.

OCT measures the cross-correlation of the field from the reference arm and the field from the sample arm,

$$\Gamma_{12}(\tau) = \int\limits_{-\infty}^{\infty} U_{sample}(t)U_{ref}(t+\tau)dt \tag{7.40}$$

$$= U_{sample}(t) \otimes U_{ref}(t).$$

In the frequency domain, the Fourier transform of the cross-correlation, i.e., the *cross spectral density*, can be expressed as a product of source spectrum, $S(\omega)$, and the spectral modifier, $h(\omega)$, due to the sample.

$$W_{12}(\omega) = U_{sample}(\omega)U_{ref}^*(\omega)$$
$$= U_{ref}(\omega)U_{ref}(\omega)h(\omega) \tag{7.41}$$
$$= S(\omega)h(\omega).$$

Back in the time domain, now the cross-correlation function can be written as a convolution of the autocorrelation of the source, $\Gamma(\omega)$, and the time response function, $h(\tau)$.

$$\Gamma_{12}(\tau) = \Gamma(\tau) \otimes h(\tau) \tag{7.42}$$

Assuming that the sample is just a single reflective flat surface, the time response function can be expressed as a single delta function. In this case, the cross-correlation function becomes:

$$\Gamma_{12}(\tau) = \Gamma(\tau) \otimes \delta(\tau - \tau_0)$$
$$= \Gamma(\tau - \tau_0) \tag{7.43}$$

where $\tau_0 = z/2c$ is the time delay from the location of the reflector, z, with respect to the reference mirror. Finally, the OCT time-profile is obtained by taking the modulus of the cross-correlation function, $|\Gamma_{12}(\tau)|$, defined by:

$$\Gamma_{12}(\tau) = |\Gamma_{12}(\tau)|e^{i[\omega_0\tau + \phi(\tau)]} \tag{7.44}$$

Thus, the envelope of the correlation function, $|\Gamma_{12}(\tau)|$, acts as the Green's function of the measurement, i.e., the time response of the tissue is "smoothed" by this function that is narrower for broader spectra.

OCT has been used primarily as an imaging tool, with ophthalmology being the main field of applications. This is so because the eye is transparent and contains many surfaces producing specular reflections, which can be resolved unequivocally, according to (7.43). However, OCT can be used as an effective scattering method. It has been recognized 12 years ago that the OCT signal from a diffusive

medium can be very well characterized by the time-resolved diffusion equation as reported in Ref. [43]. In essence, OCT can provide the pathlength distribution of light scattered by a diffusive tissue, with a time resolution given by the coherence length divided by the speed of light, which can easily reach in tens of femtoseconds. Using OCT for time-resolved diffusion measurements is superior to using mode-locked Ti:Saph lasers in the point of view of not only time resolution, but also sensitivity and dynamic range (due to the interferometric, heterodyne detection). The solution to the time-resolved diffusion equation is discussed below.

7.2.4.2 Time-Resolved Reflectance

The reflectance at any point in the tissue as a function of time can be calculated from the scattering coefficients by using a diffusive light transport model in reference [44]. The diffuse energy flux rate is assumed to satisfy the diffusion equation (with negligible absorption for now):

$$\frac{\partial}{\partial t}\phi(r,t) - D\nabla^2\phi(r,t) = S(r,t), \tag{7.45}$$

where D is the diffusion coefficient. We assume that the absorption coefficient of tissue is zero, such that D is given by (see also Sect. 7.1.4):

$$D = \frac{cl_s}{3(1-g)} \tag{7.46}$$
$$= cl_t/3.$$

If we assume that all incident light is scattered at depth z_0, where $z_0 = l_t$, the source term becomes a delta function $S(r,t) = \delta(0,0)$, which allows us to find the Green's function of the system. We also assume that at the boundary of the tissue, $\phi = 0$. The Green's function of (7.45) can be used to obtain the 3D solution in spherical coordinates:

$$\phi(r,t) = (4\pi Dt)^{-\frac{3}{2}}e^{\frac{-r^2}{4Dt}}. \tag{7.47}$$

This solution can be converted to cylindrical coordinates:

$$\phi(\rho,z,t) = (4\pi Dt)^{-\frac{3}{2}}\left[e^{-\frac{(z-z_0)^2+\rho^2}{4Dt}} - e^{-\frac{(z+z_0)^2+\rho^2}{4Dt}}\right]. \tag{7.48}$$

Using Fick's law, $J(\rho,0,t) = -D\nabla\phi(\rho,z,t)|_{z=0}$, we can obtain the final expression for the time-resolved reflectance:

$$R(\rho,t) = |J(\rho,0,t)| = (4\pi D)^{-\frac{3}{2}}z_0 t^{-\frac{5}{2}}e^{-\frac{\rho^2+z_0^2}{4Dt}}. \tag{7.49}$$

Fig. 7.7 Geometry consideration for time-resolved reflectance calculation
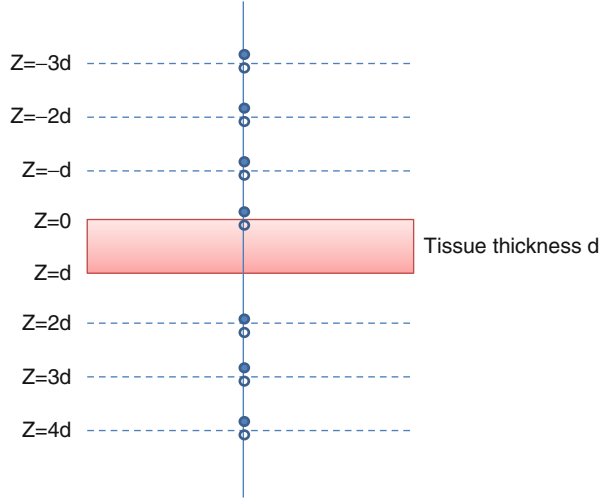
Tissue thickness d

By integrating over the entire surface, the final expression for the time-resolved reflectance can be obtained as:

$$R(t) = \int_0^\infty R(\rho, t)2\pi\rho d\rho = (4\pi D)^{-\frac{1}{2}}z_0 t^{-\frac{3}{2}}e^{-\frac{z_0^2}{4Dt}}. \quad (7.50)$$

In finite tissue of thickness d, boundary conditions can be met by addition of dipoles as shown in Fig. 7.7 [44]:

$$R(d, t) = (4\pi D)^{-\frac{1}{2}}t^{-\frac{3}{2}}\left\{ z_0 e^{-\frac{z_0^2}{4Dt}} - (2d - z_0)e^{-\frac{(2d-z_0)^2}{4Dt}} + (2d + z_0)e^{-\frac{(2d+z_0)^2}{4Dt}} \right\}. \quad (7.51)$$

Clearly, performing time-resolved measurements, via OCT, pulsed lasers, or otherwise, offers yet another path toward retrieving the scattering mean free path, l_t, which in this case is contained in the diffusion equation, D.

7.3 Fourier Transform Light Scattering

As described in the previous sections, light scattering techniques provide information that is intrinsically averaged over the measurement volume. Thus, the spatial resolution is compromised and the scattering contributions from individual components are averaged. However, recently, *phase-sensitive* methods have

been employed to directly extract the refractive index of cells and tissues [45–49]. From this *quantitative phase imaging* information, the angular scattering can be obtained via the Born approximation (see Sect. 7.1.3.), as described in Ref. [50].

Based on quantitative phase imaging (QPI) [51], we developed Fourier transform light scattering (FTLS) as an approach to study static and dynamic light scattering. FTLS combines the high spatial resolution associated with optical microscopy and intrinsic averaging of light scattering techniques. FTLS is not particular to a single method of QPI, i.e., it is not important how the phase and amplitude information was obtained from the imaging field. Below, we review FTLS briefly.

7.3.1 Quantitative Phase Imaging Methods

Recently, new QPI techniques have been developed for spatially resolved investigation of biological structures [52]. Combining phase-shifting interferometry with Horn microscopy, DRIMAPS (digitally recorded interference microscopy with automatic phase-shifting) has been proposed as a new technique for quantitative biology [53, 54]. This *quantitative phase imaging* technique has been successfully used for measuring cell spreading [55], cell motility [56], cell growth, and dry mass [57]. A full-field quantitative phase microscopy method was developed also by using the transport-of-irradiance equation [58, 59]. The technique is inherently stable against phase noise because it does not require using two separate beams as in typical interferometry experiments. This approach requires however recording images of the sample displaced through the focus and subsequently solving numerically partial differential equations.

Digital holography has been developed a few decades ago [60] as a technique that combines digital recording with traditional holography [61]. Typically, the phase and amplitude of the imaging field are measured at an out-of-focus plane. By solving numerically the Fresnel propagation equation, one can determine the field distribution at various planes. For optically thin objects, this method allows for reconstructing the in-focus field and, thus, retrieving the phase map characterizing the sample under investigation. This method has been implemented in combination with phase-shifting interferometry [62]. More recently, digital holography has been adapted for quantitative phase imaging of cells [63–65].

In recent years, new full-field quantitative phase imaging techniques have been developed for studying live cells. The advance of Fourier phase microscopy (FPM) [66, 67], Hilbert phase microscopy (HPM) [68, 69], and diffraction phase microscopy (DPM) [70, 71] came in response to the need for high phase stability over broad temporal scales. Spatial light interference microscopy (SLIM) has been developed in our laboratory to enhance the phase sensitivity to unprecedented levels by eliminating the speckles due to the laser illumination [72–75]. The principles of operation of DPM and SLIM are described below.
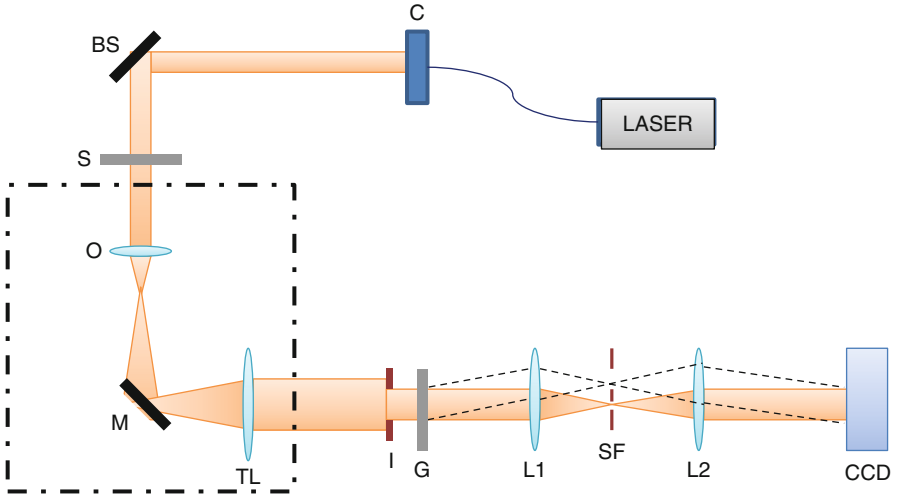
Fig. 7.8 DPM, FTLS setup: C: Collimator, BS: Beam splitter, S: Sample plane, O: Objective, M: Mirror, TL: Tube Lens, I: Iris, G: Phase grating, L1-L2: Lenses, DF: Spatial filter

7.3.1.1 Diffraction Phase Microscopy

Diffraction phase microscopy (DPM) [76] combines the single shot feature of Hilbert phase microscopy (HPM) [68, 69] with the common path interferometry of Fourier phase microscopy (FPM) [67, 77, 78], making it stable to sub-nanometer scale while reducing longitudinal noise. The experimental setup (Fig. 7.8) consists of illumination from the second harmonic of Nd:YAG laser ($\lambda = 532$ nm) which is the source for an inverted microscope. The image is formed at the output port. The image appears to be illuminated by a virtual point source. The field for this point source is further collimated by a relay lens and replicated at the image plane. The phase grating at the image plane generates multiple diffraction orders containing full spatial field information. The Mach-Zehnder spatial filtering setup with two lenses L1-L2 is used to filter the 0th order beam which acts as the reference and the 1st order diffraction beam which acts as sample field. The 0th order beam is low pass filtered, so the field is uniform at the CCD plane. The entire frequency content of the 1st diffraction order is allowed to pass to the CCD by the spatial filter in the Fourier plane of L1 forming an interferogram at the CCD plane. The common path geometry reduces longitudinal phase noise. If the spatial modulation is at 45° with respect to both X and Y axes, the field is of the form [76]:

$$E(x, y) = \left|E_0\right| e^{i[\phi_0 + \beta(x+y)]} + \left|E_1(x, y)\right| e^{i\phi(x,y)}. \tag{7.52}$$

where $\left|E_{0,1}\right|$ and $\phi_{0,1}$ are the amplitudes and the phase of the 0th and 1st diffraction orders while β is the spatial frequency shift induced by the grating to the 0th order.

Fig. 7.9 SLIM setup
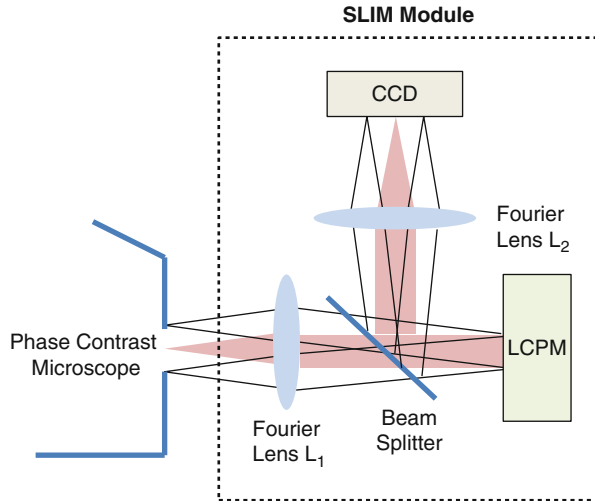
The reference field is proportional to the spatial average of the microscope image field (central ordinate theorem):

$$\left|E_0\right|e^{i\phi_0} \propto \frac{1}{A} \int \left|E_1(x,y)\right|e^{i\phi(x,y)}dxdy, \tag{7.53}$$

where A is the total image area.

By performing a spatial high pass filter, the cross-term can be isolated as $\left|E_0\right|\left|E_1(x,y)\right|\cos[\phi(x,y) - \beta(x+y) - \phi_0]$. For transparent objects, $E_1(x,y)$ does not vary significantly. Using a Hilbert transform, the quantitative phase map, $\phi(x,y)$, can be obtained from a single recording [79].

7.3.1.2 Spatial Light Interference Microscopy (SLIM)

Zernike's phase contrast microscopy is a *qualitative* method of imaging transparent objects, also termed as phase objects [80–82]. Gabor's holography enables recoding of phase and amplitude information of such objects [61]. By combining the two principles, we developed SLIM, spatial light interference microscopy, which is a quantitative phase imaging method that uses the white light, spatially coherent field from a phase contrast microscope [72–75].

A schematic of the SLIM instrument is depicted in Fig. 7.9. SLIM functions by adding spatial modulation to the image field of a commercial phase contrast microscope. Besides the conventional $\pi/2$ shift introduced in phase contrast between the scattered and unscattered light from the sample [82], we generated further phase shifts by increments of $\pi/2$. The objective exit pupil, containing the phase-shifting ring, is imaged via lens L1 onto the surface of a reflective liquid crystal phase modulator (LCPM, Boulder Nonlinear). The active pattern on the LCPM is calculated to precisely match the size and position of the phase ring

Fig. 7.10 Scattering-phase theorem: (a) Light passes through tissue of thickness L; l_s is the scattering mean free path length. (b) $\mathbf{k_i}$, $\mathbf{k_s}$ are the scattered and incident wave vectors, $\mathbf{q}$ is the momentum transfer
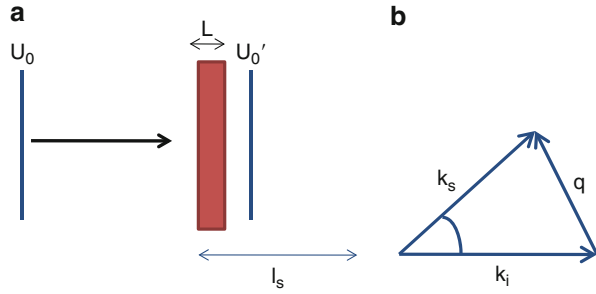
image, such that additional phase delay can be controlled between the scattered and unscattered components of the image field. In this setup, four images corresponding to each phase shift are recorded (Fig. 7.1b), to produce a quantitative phase image that is uniquely determined [75].

7.3.2 Scattering-Phase Theorem

The *scattering-phase theorem* relates the phase distribution of a tissue slice of thickness $L \ll l_s$, and scattering parameters l_s and g. l_s, the scattering mean free path length when averaged over a certain area, is inversely proportional to the variance of the phase in that area. The anisotropy factor g is related to the phase gradient distribution [83]. The derivations are as follows.

7.3.2.1 Proof of the l_s-ϕ Relationship

l_s is defined as the length over which the irradiance of unscattered light drops to $1/e$ of its original value, which is the Beer–Lambert's law [83]

$$I_0' = I_0 e^{-L/l_s}, \tag{7.62}$$

where I_0' is the intensity of unscattered light passed through the sample and I_0 is the intensity of incident light. In (7.62), $I_0 = |U_0|^2$ and $I_0' = |U_0'|^2$, where U_0 and U_0' represent the corresponding amplitudes shown in Fig. 7.10. The measured field U' is a combination of the scattered and unscattered light that passes through the sample. This contains the phase information measured in quantitative phase measurement techniques:

$$U'(\mathbf{r}) = U_0' + U_1'(\mathbf{r}). \tag{7.63}$$

The unscattered component is the zero frequency or DC component of the field which is U_0, and U_1 represents the scattered high-frequency component of light. This implies that U_0' is the spatial average,

$$U_0' = \left\langle U_0 \cdot e^{i\phi(\mathbf{r})} \right\rangle_{\mathbf{r}}. \tag{7.64}$$

If the phase shifts are normally distributed and the Gaussian function takes the form $\exp\left[-\phi^2/2\langle\Delta\phi^2\rangle_{\mathbf{r}}\right]/\sqrt{2\pi\langle\Delta\phi^2\rangle_{\mathbf{r}}}$, the average field in (7.64) is expressed as:

$$
\begin{aligned}
U_0' &= \frac{U_0}{\sqrt{2\pi\langle\Delta\phi^2\rangle_{\mathbf{r}}}} \int_{-\infty}^{\infty} e^{i\phi}e^{-\frac{\phi^2}{2\langle\Delta\phi^2\rangle_{\mathbf{r}}}}d\phi \\
&= U_0 e^{-\frac{\langle\Delta\phi^2\rangle_{\mathbf{r}}}{2}}.
\end{aligned}
\tag{7.65}
$$

In (7.65), $\langle\Delta\phi^2\rangle_{\mathbf{r}}$ is the *variance* in the phase shift distribution. We also know that:

$$
U_0'/U_0 = \sqrt{I_0'/I_0}.
\tag{7.66}
$$

By combining (7.63), (7.65), (7.66) we get the final expression for scattering mean free path:

$$
l_s = \frac{L}{<\Delta\phi^2(\mathbf{r})>_{\mathbf{r}}} \quad (q.e.d.).
\tag{7.67}
$$

While the assumption of Gaussian distribution of phase shifts is made for the purpose of this derivation, l_s can also be calculated in samples with non-Gaussian phase distribution if the quantitative phase is known.

7.3.2.2 Proof of the g-ϕ Relationship

g is defined as the average cosine of the scattering angle for *a single scattering event*. Since l_s is the distance over which light scatters once, g is the average cosine of the field transmitted through l_s [83].

$$
g = <\cos\theta>_\theta.
\tag{7.68}
$$

The scattering angle θ connects the incident and scattered wave vector with $\mathbf{q} = \mathbf{k_s} - \mathbf{k_i}$, where q is the momentum transfer (Fig. 7.10b), as:

$$
\begin{aligned}
\cos\theta &= 1 - \frac{q^2}{2\beta_0{}^2} \\
q &= 2\beta_0 \sin\frac{\theta}{2}
\end{aligned}
\tag{7.69}
$$

The average cosine from (7.68) and (7.69) is:

$$
g = 1 - \frac{1}{2\beta_0{}^2} \int\int q^2 P(q) q\, dq,
\tag{7.70}
$$

where $P(q)$ is the normalized angular scattering probability distribution of the field exiting the sample slice with a thickness of l_s. $P(q)$ is represented as:

$$P(q) = \frac{\left|\tilde{U}'(q)\right|^2}{\int\int\left|\tilde{U}'(q)\right|^2 qdq},$$
(7.71)

where $\tilde{U}'$ is the spatial Fourier transform of U'. From (7.70) and (7.71), we get:

$$g = 1 - \frac{1}{2\beta_0^2}\int\int\left|q\tilde{U}'(q)\right|^2 qdq \Big/ \int\int\left|\tilde{U}'(q)\right|^2 qdq.$$
(7.72)

By differentiating the numerator and using Parseval's theorem on the entire term, we can express g via spatial-domain integrals [84],

$$g = 1 - \frac{1}{2\beta_0^2}\int\int\left|\nabla U'(r)\right|^2 rdr \Big/ \int\int\left|\tilde{U}'(r)\right|^2 rdr.$$
(7.73)

U' is spatially dependent on phase, $U'(\mathbf{r}) = U_0 \cdot e^{i\phi_{ls}(\mathbf{r})}$, the gradient can be expressed as:

$$\nabla U'(\mathbf{r}) = U'(\mathbf{r})\nabla\phi_{ls}(\mathbf{r}).$$
(7.74)

From (7.73) and (7.74), the expression for g can be simplified to:

$$g = 1 - \frac{\left\langle\left|\nabla[\phi_{ls}(r)]\right|^2\right\rangle_{\mathbf{r}}}{2\beta_0^2}.$$
(7.75)

Equation (7.75) applies to a slice of thickness l_s. For a phase image $\phi(\mathbf{r})$ obtained over a thickness L, with $L \ll l_s$, $\phi_{ls} = \phi\, l_s/L$. The anisotropy factor depends on the measurable phase image as:

$$g = 1 - \left(\frac{l_s}{L}\right)^2 \frac{\left\langle\left|\nabla[\phi(r)]\right|^2\right\rangle_{\mathbf{r}}}{2\beta_0^2}\,(q.e.d.).$$
(7.76)

In summary, the scattering-phase theorem relates the phase map of a tissue slice with the scattering parameters. These quantitative phase imaging maps can be obtained by any QPI method, e.g., DPM and SLIM described in Sects. 7.3.1.1–7.3.1.2. The scattering mean free path and phase relation states that the attenuation caused by scattering is stronger when the tissue roughness increases, i.e., greater inhomogeneity leads to stronger scattering. The phase gradient g is the tilt in the light propagation direction. The relation states that as the square averaged gradient increases, the probability of higher scattering angles and smaller g increases [83].

Below, we illustrate the capability of QPI and scattering-phase theorem to provide new insights into scattering properties of tissues.
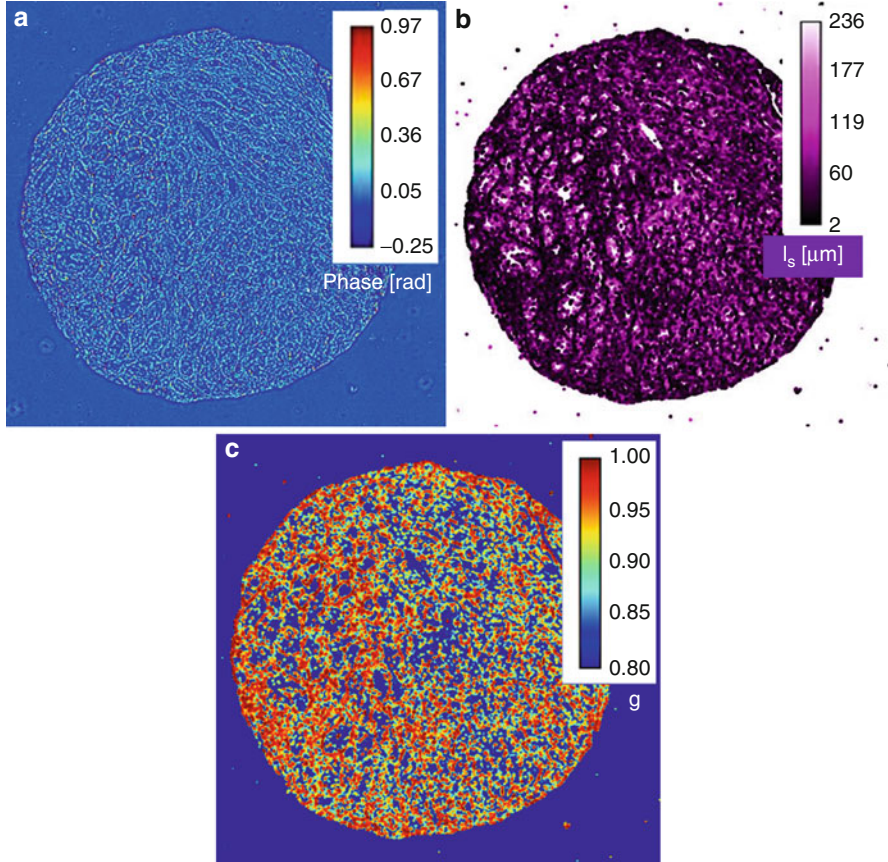
Fig. 7.11 Prostate tissue microarray core with cancer. (**a**) SLIM montage; (**b**) l_s map; (**c**) g map

7.3.3 Scattering Parameters of Prostate Tissue

We imaged a tissue microarray slide obtained from University of Illinois at Chicago using SLIM. Using SLIM equipped with a 10X (0.3NA) objective, we imaged 30 cores in a final mosaic of 1,025 images, that were stitched together, each containing $1,388 \times 1,040$ pixels. In Fig. 7.11a, we show a core with cancer of Gleason score 7 (3 + 4). The grade 3 region is concentrated on the left side of the image and grade 4 (higher grade) is concentrated on the right side. Using the phase information of the core, we were able to employ the scattering-phase theorem and calculate the scattering mean free path (l_s) and the anisotropy factor (g) as shown in Fig. 7.11b and c, respectively. From the maps, it is visible that *stroma* has a higher scattering mean free path than epithelial tissue and the degree of anisotropy is higher in the region with a higher grade of cancer.

Finally, we show next that using the l_s and g information from quantitative phase imaging, we can now simulate the results of a number of other methods, including time-resolved reflectance, diffuse reflectance, and enhanced backscattering.
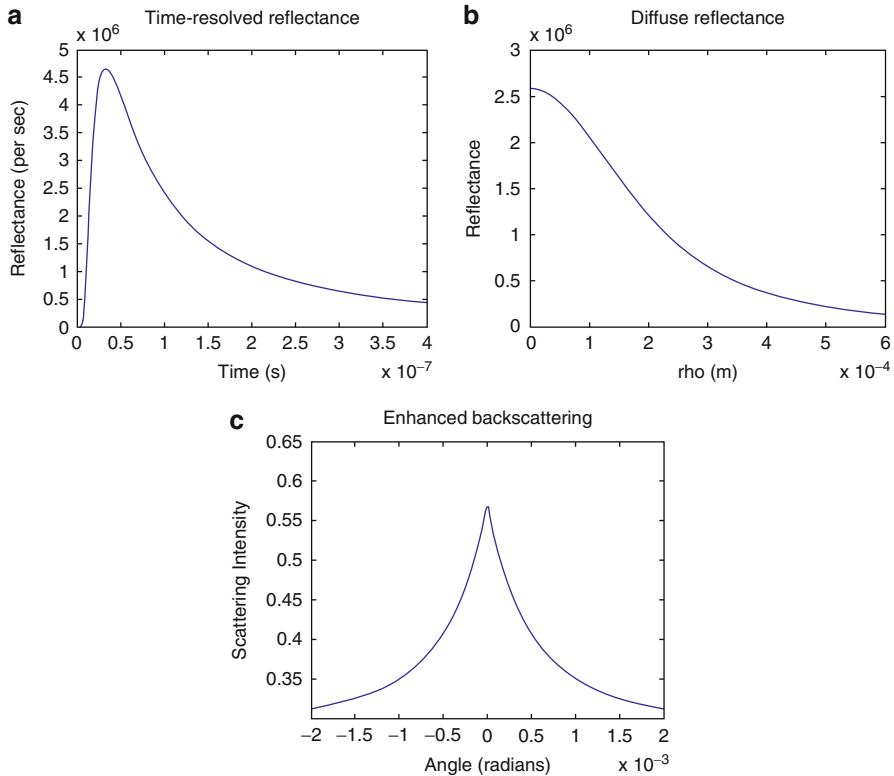
Fig. 7.12 Simulations of traditional methods using l_s, g values measured via SLIM and the scattering-phase theorem: (**a**) Time-resolved reflectance versus time; (**b**) Reflectance versus source-detector separation; (**c**) Enhanced backscattering versus angle

7.3.4   Simulation of Traditional Methods

The ability to calculate scattering parameters of tissue is significant as it enables us to calculate, for example, the time-resolved reflectance and angular backscattering data for various tissue, regions of interests, and disease states, with great flexibility provided by our imaging geometry. For these simulations, shown in Fig. 7.11, we calculated the mean value of l_s and g distributions shown in Fig. 7.11, which were 63.89 μm and 0.742, respectively. We plotted the reflectance of tissue versus time (7.49), reflectance versus ρ (7.49), as well as the angular enhanced backscattering (7.37), as shown in Fig. 7.12a–c, respectively.

7.4   Summary

Here we reviewed the main concepts in tissue light scattering and some of the main experimental methods used in the field. Then, we focused on a new approach to

measuring tissue scattering properties, which is Fourier transform light scattering (FTLS). The principle in FTLS can be regarded as the spatial equivalent of Fourier transform infrared (FTIR) spectroscopy, in the sense that it provides angular scattering information from measurements in the conjugate space (image space) [48, 50, 85–87]. The most recent advancement in FTLS is the ability to *map* a tissue slice in terms of its scattering properties, which is a result established by the *scattering-phase theorem* [88, 89]. We believe that this capability of retrieving scattering parameters from particular regions of interest in a biopsy will be key to overcoming current challenges in optical diagnosis, which are mainly due to insufficient knowledge and agreement over baseline parameters in healthy and diseased tissues. We anticipate that our FTLS approach will make a positive impact into areas of research that employ a variety of other techniques (see Fig. 7.12), by predicting outcomes of these measurements.

References

1. V.V. Tuchin, *Tissue Optics: Light Scattering Methods and Instruments for Medical Diagnosis* (SPIE Press, Bellingham, 2007)
2. A. Wax, V. Backman (eds.), *Biomedical Applications of Light Scattering* (McGraw-Hill, New York, 2010)
3. C.F. Bohren, D.R. Huffman, *Absorption and Scattering of Light by Small Particles* (Wiley, New York, 1983)
4. H.C. van de Hulst, *Light Scattering by Small Particles* (Dover Publications, New York, 1981)
5. A. Ishimaru, *Electromagnetic Wave Propagation, Radiation, and Scattering* (Prentice Hall, Englewood Cliffs, 1991)
6. B.J. Berne, R. Pecora, *Dynamic Light Scattering with Applications to Chemistry, Biology and Physics* (Wiley, New York, 1976)
7. Milestones in light microscopy. Nat. Cell Biol. **11**, 1165 (2009)
8. B. Alberts, *Essential Cell Biology: An Introduction to the Molecular Biology of the Cell* (Garland, New York, 2004)
9. S.J. Singer, G.L. Nicolson, Fluid mosaic model of structure of cell-membranes. Science **175**, 720 (1972)
10. A. Dunn, R. Richards-Kortum, Three-dimensional computation of light scattering from cells. IEEE J. Sel. Topics Quant. Electron. **2**, 898–905 (1996)
11. J.R. Mourant, J.P. Freyer, A.H. Hielscher, A.A. Eick, D. Shen, T.M. Johnson, Mechanisms of light scattering from biological cells relevant to noninvasive optical-tissue diagnostics. Appl. Opt. **37**, 3586–3593 (1998)
12. G.M. Hale, M.R. Querry, Optical-constants of water in 200-nm to 200-μm wavelength region. Appl. Opt. **12**, 555–563 (1973)
13. S. Takatani, M.D. Graham, Theoretical-analysis of diffuse reflectance from a 2-layer tissue model. IEEE Trans. Biomed. Eng. **26**, 656–664 (1979)
14. M. Born, E. Wolf, *Principles of Optics: Electromagnetic Theory of Propagation, Interference and Diffraction of Light* (Cambridge University Press, Cambridge/New York, 1999)
15. R.N. Bracewell, *The Fourier Transform and Its Applications* (McGraw Hill, Boston, 2000)
16. E. Wolf, in *Advances in Imaging and Electron Physics*, ed. by P.W.E. Hawkes (Academic, San Diego, 2011)
17. S.G. Demos, R.R. Alfano, Temporal gating in highly scattering media by the degree of optical polarization. Opt. Lett. **21**, 161–163 (1996)

18. S.G. Demos, H. Savage, A.S. Heerdt, S. Schantz, R.R. Alfano, Time resolved degree of polarization for human breast tissue. Opt. Commun. **124**, 439–442 (1996)
19. K.M. Yoo, R.R. Alfano, Time resolved depolarization of multiple backscattered light from random-media. Phys. Lett. A **142**, 531–536 (1989)
20. R.R. Anderson, Polarized-light examination and photography of the skin. Arch. Dermatol. **127**, 1000–1005 (1991)
21. S.G. Demos, R.R. Alfano, Optical polarization imaging. Appl. Opt. **36**, 150–155 (1997)
22. V. Backman, R. Gurjar, K. Badizadegan, L. Itzkan, R.R. Dasari, L.T. Perelman, M.S. Feld, Polarized light scattering spectroscopy for quantitative measurement of epithelial cellular structures in situ. IEEE J. Sel. Topics Quant. Electron. **5**, 1019–1026 (1999)
23. I. Georgakoudi, B.C. Jacobson, J. Van Dam, V. Backman, M.B. Wallace, M.G. Muller, Q. Zhang, K. Badizadegan, D. Sun, G.A. Thomas, L.T. Perelman, M.S. Feld, Fluorescence, reflectance, and light-scattering spectroscopy for evaluating dysplasia in patients with Barrett's esophagus. Gastroenterology **120**, 1620–1629 (2001)
24. R.S. Gurjar, V. Backman, L.T. Perelman, I. Georgakoudi, K. Badizadegan, I. Itzkan, R.R. Dasari, M.S. Feld, Imaging human epithelial properties with polarized light-scattering spectroscopy. Nat. Med. **7**, 1245–1248 (2001)
25. M. Hunter, V. Backman, G. Popescu, M. Kalashnikov, C.W. Boone, A. Wax, G. Venkatesh, K. Badizadegan, G.D. Stoner, M.S. Feld, Tissue self-affinity and light scattering in the born approximation: a new model for precancer diagnosis. Phys. Rev. Lett. **97**, 138102 (2006)
26. A. Amelink, M.P.L. Bard, S.A. Burgers, H.J.C.M. Sterenborg, Single-scattering spectroscopy for the endoscopic analysis of particle size in superficial layers of turbid media. Appl. Opt. **42**, 4095–4101 (2003)
27. A. Wax, C.H. Yang, J.A. Izatt, Fourier-domain low-coherence interferometry for light-scattering spectroscopy. Opt. Lett. **28**, 1230–1232 (2003)
28. T.H. Foster, J.D. Wilson, Characterization of lysosomal contribution to whole-cell light scattering by organelle ablation. J. Biomed. Opt. **12**, 030503 (2007)
29. J.R. Mourant, J.P. Freyer, A.H. Hielscher, A.A. Eick, D. Shen, T.M. Johnson, Mechanisms of light scattering from biological cells relevant to noninvasive optical-tissue diagnostics. Appl. Opt. **37**, 3586–3593 (1998)
30. V. Backman, M.B. Wallace, L.T. Perelman, J.T. Arendt, R. Gurjar, M.G. Muller, Q. Zhang, G. Zonios, E. Kline, J.A. McGilligan, S. Shapshay, T. Valdez, K. Badizadegan, J.M. Crawford, M. Fitzmaurice, S. Kabani, H.S. Levin, M. Seiler, R.R. Dasari, I. Itzkan, J. Van Dam, M.S. Feld, Detection of preinvasive cancer cells. Nature **406**, 35–36 (2000)
31. L.T. Perelman, V. Backman, M. Wallace, G. Zonios, R. Manoharan, A. Nusrat, S. Shields, M. Seiler, C. Lima, T. Hamano, I. Itzkan, J. Van Dam, J.M. Crawford, M.S. Feld, Observation of periodic fine structure in reflectance from biological tissue: a new technique for measuring nuclear size distribution. Phys. Rev. Lett. **80**, 627–630 (1998)
32. C. Lau, O. Scepanovic, J. Mirkovic, S. McGee, C.-C. Yu, J. Stephen Fulghum, M. Wallace, J. Tunnell, K. Bechtel, M. Feld, Re-evaluation of model-based light-scattering spectroscopy for tissue spectroscopy. J. Biomed. Opt. **14**, 024031 (2009)
33. P.-E. Wolf, G. Maret, Weak localization and coherent backscattering of photons in disordered media. Phys. Rev. Lett. **55**, 2696 (1985)
34. E. Akkermans, P.E. Wolf, R. Maynard, Coherent backscattering of light by disordered media – analysis of the peak line-shape. Phys. Rev. Lett. **56**, 1471–1474 (1986)
35. F.C. Mackintosh, S. John, Coherent backscattering of light in the presence of time-reversal-noninvariant and parity-nonconserving media. Phys. Rev. B **37**, 1884–1897 (1988)
36. Y.L. Kim, Y. Liu, R.K. Wali, H.K. Roy, V. Backman, Low-coherent backscattering spectroscopy for tissue characterization. Appl. Opt. **44**, 366–377 (2005)
37. F. Bevilacqua, C. Depeursinge, Monte Carlo study of diffuse reflectance at source-detector separations close to one transport mean free path. J. Opt. Soc. Am. **16**, 2935–2945 (1999)

38. G. Zonios, L.T. Perelman, V. Backman, R. Manoharan, M. Fitzmaurice, J. Van Dam, M.S. Feld, Diffuse reflectance spectroscopy of human adenomatous colon polyps in vivo. Appl. Opt. **38**, 6628–6637 (1999)

39. N. Subhash, J.R. Mallia, S.S. Thomas, A. Mathews, P. Sebastian, Oral cancer detection using diffuse reflectance spectral ratio R540/R575 of oxygenated hemoglobin bands. J. Biomed. Opt. **11**, 014018 (2006)

40. C.F. Zhu, G.M. Palmer, T.M. Breslin, J. Harter, N. Ramanujam, Diagnosis of breast cancer using diffuse reflectance spectroscopy: comparison of a Monte Carlo versus partial least squares analysis based feature extraction technique. Lasers Surg. Med. **38**, 714–724 (2006)

41. Z. Volynskaya, A.S. Haka, K.L. Bechtel, M. Fitzmaurice, R. Shenk, N. Wang, J. Nazemi, R.R. Dasari, M.S. Feld, Diagnosing breast cancer using diffuse reflectance spectroscopy and intrinsic fluorescence spectroscopy. J. Biomed. Opt. **13**, 024012 (2008)

42. D. Huang, E.A. Swanson, C.P. Lin, J.S. Schuman, W.G. Stinson, W. Chang, M.R. Hee, T. Flotte, K. Gregory, C.A. Puliafito, J.G. Fujimoto, Optical coherence tomography. Science **254**, 1178–1181 (1991)

43. G. Popescu, A. Dogariu, Optical path-length spectroscopy of wave propagation in random media. Opt. Lett. **24**, 442–444 (1999)

44. M.S. Patterson, B. Chance, B.C. Wilson, Time resolved reflectance and transmittance for the noninvasive measurement of tissue optical-properties. Appl. Opt. **28**, 2331–2336 (1989)

45. N. Lue, J. Bewersdorf, M.D. Lessard, K. Badizadegan, K. Dasari, M.S. Feld, G. Popescu, Tissue refractometry using Hilbert phase microscopy. Opt. Lett. **32**, 3522 (2007)

46. B. Rappaz, P. Marquet, E. Cuche, Y. Emery, C. Depeursinge, P.J. Magistretti, Measurement of the integral refractive index and dynamic cell morphometry of living cells with digital holographic microscopy. Opt. Express **13**, 9361–9373 (2005)

47. Y.K. Park, M. Diez-Silva, G. Popescu, G. Lykotrafitis, W. Choi, M.S. Feld, S. Suresh, Refractive index maps and membrane dynamics of human red blood cells parasitized by *Plasmodium falciparum*. Proc. Natl. Acad. Sci. U.S.A. **105**, 13730 (2008)

48. H. Ding, F. Nguyen, S.A. Boppart, G. Popescu, Optical properties of tissues quantified by Fourier transform light scattering. Opt. Lett. **34**, 1372 (2009)

49. N. Lue, W. Choi, G. Popescu, Z. Yaqoob, K. Badizadegan, R.R. Dasari, M.S. Feld, Live cell refractometry using Hilbert phase microscopy and confocal reflectance microscopy. J. Phys. Chem. A **113**, 13327–13330 (2009)

50. H.F. Ding, Z. Wang, F. Nguyen, S.A. Boppart, G. Popescu, Fourier transform light scattering of inhomogeneous and dynamic structures. Phys. Rev. Lett. **101**, 238102 (2008)

51. G. Popescu, in *Methods in Cell Biology*, ed. by B.P. Jena (Academic, San Diego, 2008), pp. 87–115

52. G. Popescu, *Quantitative phase imaging of cells and tissues* (McGraw-Hill, New York, 2011)

53. D. Zicha, G.A. Dunn, An image-processing system for cell behavior studies in subconfluent cultures. J. Microsc. **179**, 11–21 (1995)

54. G.A. Dunn, D. Zicha, in *Cell Biology: A Laboratory Handbook*, ed. by J.E. Celis (Academic, San Diego, 1998)

55. G.A. Dunn, D. Zicha, P.E. Fraylich, Rapid, microtubule-dependent fluctuations of the cell margin. J. Cell Sci. **110**, 3091–3098 (1997)

56. D. Zicha, E. Genot, G.A. Dunn, I.M. Kramer, TGF beta 1 induces a cell-cycle-dependent increase in motility of epithelial cells. J. Cell Sci. **112**, 447–454 (1999)

57. G.A. Dunn, D. Zicha, Dynamics of fibroblast spreading. J. Cell Sci. **108**, 1239–1249 (1995)

58. T.E. Gureyev, A. Roberts, K.A. Nugent, Phase retrieval with the transport-of-intensity equation – matrix solution with use of Zernike polynomials. J. Opt. Soc. Am. A Opt. Image Sci. Vis. **12**, 1932–1941 (1995)

59. T.E. Gureyev, A. Roberts, K.A. Nugent, Partially coherent fields, the transport-of-intensity equation, and phase uniqueness. J. Opt. Soc. Am. A Opt. Image Sci. Vis. **12**, 1942–1946 (1995)

60. J.W. Goodman, R.W. Lawrence, Digital image formation from electronically detected holograms. Appl. Phys. Lett. **11**, 77 (1967)

61. D. Gabor, A new microscopic principle. Nature **161**, 777 (1948)
62. I. Yamaguchi, T. Zhang, Phase-shifting digital holography. Opt. Lett. **22**, 1268–1270 (1997)
63. C.J. Mann, L.F. Yu, C.M. Lo, M.K. Kim, High-resolution quantitative phase-contrast microscopy by digital holography. Opt. Express **13**, 8693–8698 (2005)
64. D. Carl, B. Kemper, G. Wernicke, G. von Bally, Parameter-optimized digital holographic microscope for high-resolution living-cell analysis. Appl. Opt. **43**, 6536–6544 (2004)
65. P. Marquet, B. Rappaz, P.J. Magistretti, E. Cuche, Y. Emery, T. Colomb, C. Depeursinge, Digital holographic microscopy: a noninvasive contrast imaging technique allowing quantitative visualization of living cells with subwavelength axial accuracy. Opt. Lett. **30**, 468–470 (2005)
66. N. Lue, W. Choi, G. Popescu, R.R. Dasari, K. Badizadegan, M.S. Feld, Quantitative phase imaging of live cells using fast Fourier phase microscopy. Appl. Opt. **46**, 1836 (2007)
67. G. Popescu, L.P. Deflores, J.C. Vaughan, K. Badizadegan, H. Iwai, R.R. Dasari, M.S. Feld, Fourier phase microscopy for investigation of biological structures and dynamics. Opt. Lett. **29**, 2503–2505 (2004)
68. G. Popescu, T. Ikeda, C.A. Best, K. Badizadegan, R.R. Dasari, M.S. Feld, Erythrocyte structure and dynamics quantified by Hilbert phase microscopy. J. Biomed. Opt. Lett. **10**, 060503 (2005)
69. T. Ikeda, G. Popescu, R.R. Dasari, M.S. Feld, Hilbert phase microscopy for investigating fast dynamics in transparent systems. Opt. Lett. **30**, 1165–1168 (2005)
70. Y.K. Park, G. Popescu, K. Badizadegan, R.R. Dasari, M.S. Feld, Diffraction phase and fluorescence microscopy. Opt. Express **14**, 8263 (2006)
71. G. Popescu, T. Ikeda, R.R. Dasari, M.S. Feld, Diffraction phase microscopy for quantifying cell structure and dynamics. Opt. Lett. **31**, 775–777 (2006)
72. M. Mir, Z. Wang, Z. Shen, M. Bednarz, R. Bashir, I. Golding, S.G. Prasanth, G. Popescu, Measuring cell cycle-dependent mass growth. Proc. Natl. Acad. Sci. U.S.A. **108**, 13124 (2011)
73. R. Wang, Z. Wang, J. Leigh, N. Sobh, L. Millet, M.U. Gillette, A.J. Levine, G. Popescu, One-dimensional deterministic transport in neurons measured by dispersion-relation phase spectroscopy. J. Phys.: Cond. Matter **23**, 374107 (2011)
74. Z. Wang, L. Millet, V. Chan, H. Ding, M.U. Gillette, R. Bashir, G. Popescu, Label-free intracellular transport measured by spatial light interference microscopy. J. Biomed. Opt. **16**, 026019 (2011)
75. Z. Wang, L.J. Millet, M. Mir, H. Ding, S. Unarunotai, J.A. Rogers, M.U. Gillette, G. Popescu, Spatial light interference microscopy (SLIM). Opt. Express **19**, 1016 (2011)
76. G. Popescu, T. Ikeda, R.R. Dasari, M.S. Feld, Diffraction phase microscopy for quantifying cell structure and dynamics. Opt. Lett. **31**, 775–777 (2006)
77. G. Popescu, K. Badizadegan, R.R. Dasari, M.S. Feld, Observation of dynamic subdomains in red blood cells. J. Biomed. Opt. Lett. **11**, 040503 (2006)
78. G. Popescu, Y. Park, N. Lue, C. Best-Popescu, L. Deflores, R.R. Dasari, M.S. Feld, K. Badizadegan, Optical imaging of cell mass and growth dynamics. Am. J. Physiol. Cell Physiol. **295**, C538–C544 (2008)
79. T. Ikeda, G. Popescu, R.R. Dasari, M.S. Feld, Hilbert phase microscopy for investigating fast dynamics in transparent systems. Opt. Lett. **30**, 1165–1167 (2005)
80. F. Zernike, Phase contrast, a new method for the microscopic observation of transparent objects, Part 1. Physica **9**, 686–698 (1942)
81. F. Zernike, Phase contrast, a new method for the microscopic observation of transparent objects, Part 2. Physica **9**, 974–986 (1942)
82. F. Zernike, How I discovered phase contrast. Science **121**, 345 (1955)
83. G. Popescu, Z. Wang, H.F. Ding, Scattering-phase theorem. Opt. Lett. **36**, 1215–1217 (2011)
84. R.N. Bracewell, *The Fourier Transform and its Applications* (McGraw Hill, Boston, 2000)

85. H.F. Ding, Z. Wang, F.T. Nguyen, S.A. Boppart, L.J. Millet, M.U. Gillette, J.M. Liu, M.D. Boppart, G. Popescu, Fourier transform light scattering (FTLS) of cells and tissues. J. Comput. Theor. Nanosci. **7**, 2501–2511 (2010)
86. H.F. Ding, E. Berl, Z. Wang, L.J. Millet, M.U. Gillette, J.M. Liu, M. Boppart, G. Popescu, Fourier transform light scattering of biological structure and dynamics. IEEE J. Sel. Topics Quant. Electron. **16**, 909–918 (2010)
87. H. Ding, L.J. Millet, M.U. Gillette, G. Popescu, Actin-driven cell dynamics probed by Fourier transform light scattering. Biomed. Opt. Express **1**, 260 (2010)
88. Z. Wang, H. Ding, G. Popescu, Scattering-phase theorem. Opt. Lett. **36**, 1215 (2011)
89. H. Ding, Z. Wang, X. Liang, S.A. Boppart, G. Popescu, Measuring the scattering parameters of tissues from quantitative phase imaging of thin slices. Opt. Lett. **36**, 2281 (2011)

Coherent Diffractive Imaging: From Nanometric Down to Picometric Resolution

8

Liberato De Caro, Elvio Carlino, Dritan Siliqi, and Cinzia Giannini

Contents

Abstract

Coherent diffractive imaging (CDI) is a novel technique for inspecting (crystal-line and non-crystalline) matter from nanometric down to picometric resolution. It was used originally with X-rays and, more recently, with electrons (so-called electron diffractive imaging, or EDI). This chapter introduces basic concepts concerning CDI and addresses the different types of X-ray CDI experiments that have been conducted, namely plane wave CDI from isolated objects in forward scattering, focused-beam Fresnel CDI from isolated objects in forward

L. De Caro • D. Siliqi • C. Giannini (✉)
Istituto di Cristallografia (IC-CNR), Bari, Italy
e-mail: liberato.decaro@ic.cnr.it, dritan.siliqi@ic.cnr.it, cinzia.giannini@ic.cnr.it

E. Carlino
IOM CNR Laboratorio TASC, Trieste, Italy
e-mail: carlino@iom.cnr.it

scattering, Bragg CDI from nanocrystals, and keyhole CDI and ptychography from extended objects. A CDI experiment with a transmission electron microscope, alternatively named an EDI experiment, is also introduced.

8.1 Coherent Diffractive Imaging: CDI

8.1.1 Introduction

According to the Huygens-Fresnel principle, the propagation of a wave can be described by considering that every point on a wavefront becomes a point source of secondary spherical waves. The subsequent propagation and addition of all these spherical waves form the new wavefront. When waves are added together, their coherent sum (interference) is determined by the relative phases as well as the amplitudes of the individual waves. If an object is placed along the wave propagation, every point on a wavefront impinging on it generates secondary waves, with moduli and phased related to the object size, shape, and composition. The interference of these secondary waves generated by the object forms the diffraction pattern that can be described mathematically by means of the Fourier transform (FT) formalism, if planar waves are used.

However, planar waves do not constitute a prerequisite to perform diffraction experiments. In fact, to probe matter, CDI experiments can be realized both using planar and curved wave fields. The former is obtained when the wave source is very far from the sample, the latter for source-sample distances smaller than the Fresnel distance, which is defined as a^2/λ, where a is the lateral size of the object and λ is the wavelength. When the detector is placed far from the sample ($\gg a^2/\lambda$), the diffraction experiment is realized in the far-field Fraunhofer regime; conversely, for sample-detector distances less than the Fresnel distance ($\leq a^2/\lambda$), the diffraction intensity is collected in the near-field Fresnel regime.

In both cases, only the intensity of the complex diffracted wave field is experimentally measurable, with a loss of the phase component. This loss of phase information prevents the use of the inverse FT to retrieve the unknown scattering function directly from the diffraction pattern. This experimental situation of loss of phase information is known as the *phase problem*. Nevertheless, phase retrieval techniques can be developed to reconstruct the object scattering function from the diffraction pattern.

For example, the diffraction pattern in a far-field configuration of an infinite crystal, here exemplified by a unidimensional periodic lattice [1], is concentrated into discrete Bragg spots (Fig. 8.1a). The localization of the intensity in a discrete number of reflections is due to the constructive interference among waves – scattered by the atoms in the periodically repeated unit cells – only for determined scattering wave-vectors satisfying Bragg's law. The intensity and width of the diffraction peaks depends on how many waves, diffracted by different unit cells, are actually interfering to form the diffraction pattern. The higher the number of unit cells – coherently illuminated by the incident waves – the sharper the

a

b
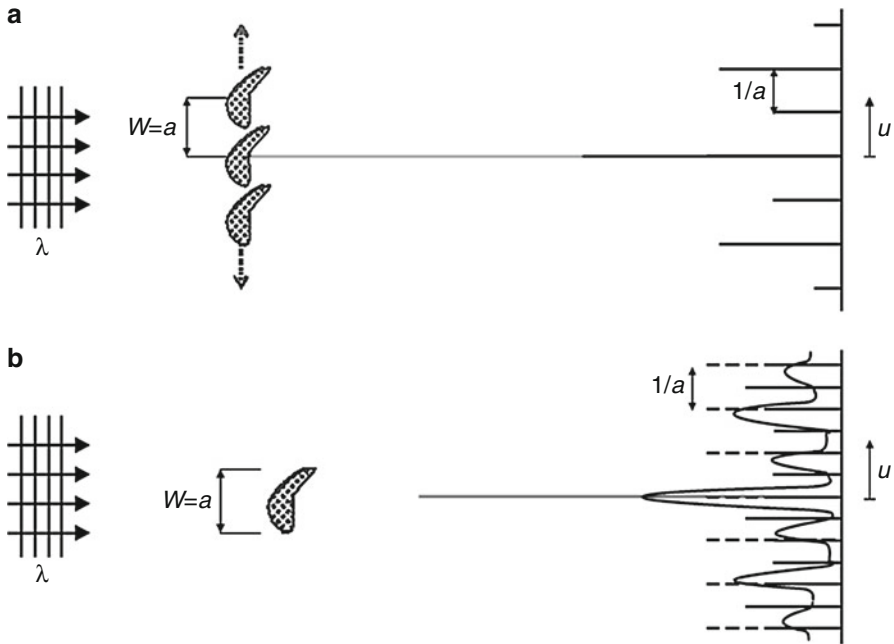
Fig. 8.1 Diffraction pattern of an infinite unidimensional periodic lattice crystal (**a**) and of a single-unit cell crystal (**b**) (Reprinted from [1])

interference peaks. In the case of a crystal, the object to be spatially reconstructed – by inverting the diffraction pattern – is the unit cell content, which means the atomic positions and atomic species with their proper symmetry (crystal structure). This job has been effectively realized by X-ray crystallographers for decades, achieving atomic-scale resolutions (Ångström scale), despite the mathematically ill-posed problem to retrieve the lost phase information [2].

In fact, diffraction effects are generally most pronounced for waves where λ is on the order of the size of the diffracting objects. This is the reason why hard X-rays must be used to study atomic crystal structure, being their wavelength on the Ångström scale. Moreover, the diffraction pattern contains only a part of the information needed to solve the crystal structure, as detectors can only register intensities, whereas the phases of the propagated complex-valued wavefronts are lost in the measurement process. However, crystallographers succeeded greatly in finding a way out, through phase retrieval [2].

To perform this mathematical reconstruction of the unknown phase, the spatial coherence of the scattering structure is a fundamental requirement for measuring the diffraction pattern with enough details up to the atomic resolution scale. The requirement is certainly satisfied in a crystal, but for ideal experiments without noise limitations the crystal is not needed. In principle, even the structure of a single molecule alone, i.e., a non-periodic object, could be reconstructed by its diffraction

pattern. The only requirement is the spatial coherence of the incident waves on an extension at least twice the object size.

The diffraction obtained by a non-periodic object is called coherent diffractive imaging (CDI) and can be realized by using either photons, mainly X-rays, or electrons. X-ray (CDI) was theoretically conceived by Sayre [3], who in 1952 first introduced the possibility of "crystallography without the need for a crystal." A reduction in the crystal lattice extension down to the extreme case of a single-unit cell, which means no periodic lattice and therefore no crystal, transforms the diffraction pattern into a continuous distribution of, unfortunately, extremely weak intensity (Fig. 8.1b). In order to register such a feeble signal, either very long acquisition times or extremely high-brilliance X-ray sources are needed. This explains why such a revolutionary idea waited until 1999, when J. Miao and coworkers [4] proved it experimentally. Over such a long period, X-ray sources improved their characteristics in terms of brilliance and coherence, a process that recently speeded up even more rapidly with the advent of free electron lasers, several orders of magnitude more intense sources than third-generation synchrotron radiation ones.

The possibility to record a continuous diffraction pattern, without losing the information *between* the Bragg spots, counterbalances the missing phases, thus allowing them to be determined. A single-unit cell crystal is not just an abstraction or a purely speculative example. On the contrary, it perfectly matches with the case of most of the biological specimens (virus, membrane proteins, etc.), where a crystal can hardly be obtained from these large molecules. This panorama of fundamentally and technologically interesting applications drove the acceleration in a number of experiments realized, since 1999, on both inorganic and biological samples [5–14].

8.1.2 Basic Principles

In the first X-ray CDI experiment [4], a sample, made of a nanometric non-periodic object assembly, was illuminated with a coherent high-flux beam, transferred through a pinhole. A typical *lens-less* imaging setup was used, as the scattered wave field freely propagated up to the detector, placed in a Fraunhofer diffraction regime. The absence of any lens between the sample and the detector was motivated by the intent to avoid typical lens aberrations and reach spatial resolutions ideally only wavelength limited. Thus, for a *lens-less* setup, the resolution was limited by the wavelength, by the numerical aperture and photon noise of the detector, by mechanical precision and stability of the entire setup, and by the sample radiation damage. In the image reconstruction, the role of the lens was indeed replaced by powerful phase retrieval algorithms: some call them, "virtual mathematical lenses."

Basic conditions of any CDI experiment are: (1) coherence of the beam, (2) high flux, and (3) thermal and mechanical stability of the setup.

Coherence and flux are related properties. The longitudinal/temporal coherence of an X-ray beam (along the propagation direction) is guaranteed by a bandpass

a

b
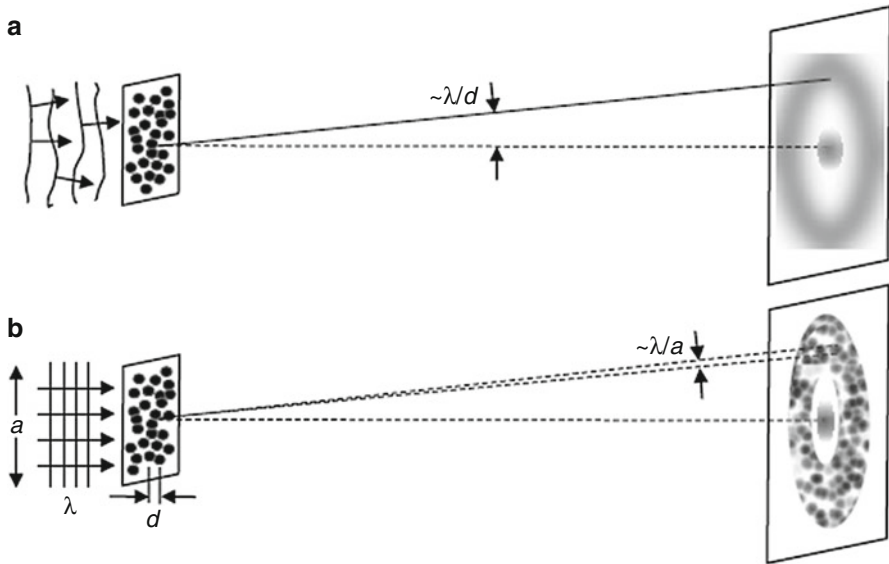
Fig. 8.2 Diffraction pattern of incoherently (**a**) and coherently (**b**) illuminated assemblies of non-periodic objects (Reprinted from [1])

frequency filter, typically a monochromator, while the transverse/spatial coherence of the beam is imparted by any spatial filter, such as a pinhole, and developed through wave propagation along large distances. As a consequence, the monochromator, the pinhole, and the large distances require a very intense X-ray source. The coherently illuminated lengths, along the longitudinal (ξ_λ) and transverse (ξ) directions, are simply estimated as:

$$\xi_\lambda \sim \frac{\lambda^2}{2\Delta\lambda}, \text{ with } \Delta\lambda \text{ spectral band width of the frequency filter;} \qquad (8.1)$$

$$\xi \sim \frac{\lambda}{w}R, \text{ with R the distance from the source and } w \text{ the source dimension.} \qquad (8.2)$$

Typical values of ξ_λ and ξ are in the range of 0.5–2 and 10–100 μm, respectively [15]. The very small longitudinal coherence length usually is not a problem in performing CDI experiments inasmuch as longitudinal optical wave-path differences are very small for hard X-rays.

The scattered 2D pattern of an incoherently illuminated assembly of non-periodic objects (here simply depicted as spheres) of size a is a set of few rings, as shown in Fig. 8.2a. Conversely, if the same sample is coherently illuminated, its diffraction patterns will contain typical speckles, each having an angular width λ/a, whose relative positions encode the original objects positions,

as shown in Fig. 8.2b. The speckles arise from the interferences between the wavefronts scattered from the different particles. If the position of a single particle is changed, all interferences are affected, and the complete speckle pattern changes. In principle, the inversion of the pattern – possible if the correct phase information is retrieved – could allow one to obtain these positions.

8.1.3 Oversampling

To simplify the mathematic formalism, let us consider a unidimensional lattice made by an infinite number of units cells of size a. The crystal and unit-cell electron density functions, $\rho(r)_{\text{cryst}}$ and $\rho(r)$, are related as:

$$\rho(r)_{\text{cryst}} = \rho(r) \otimes \sum_m \delta(r - ma), \tag{8.3}$$

where the symbol " $\otimes$ " denotes the convolution product and the sum of Dirac-delta functions $\sum_m \delta(r - ma)$ runs over all the unit cells.

If $F(u)_{\text{cryst}}^m = \text{FT}[\rho(r)_{\text{cryst}}]$ and $F(u) = \text{FT}[\rho(r)]$ are, respectively, the FT of the crystal and single unit-cell electron density function, then:

$$F(u)_{\text{cryst}} = F(u) \sum_h \delta\left(u - h\frac{1}{a}\right), \tag{8.4}$$

meaning that the diffraction pattern of an infinite unidimensional lattice, proportional to the structure factor modulus $\left|F(u)_{\text{cryst}}\right|^2$, is given by an array of delta function with a period $1/a$ modulated in intensity by $F(u)$. According to the Shannon sampling theorem [15], any function $\rho(r)$, non-zero within an interval a, can be fully reconstructed by sampling its Fourier transform $\text{FT}[\rho(r)]$ at a frequency $1/a$, called the Nyquist frequency and equal to the inverse of the size a. Unfortunately, in typical Bragg diffraction experiments, we do not sample $\text{FT}[\rho(r)] = F(u)$ every h/a but we do sample the square modulus $\left|F(u)_{\text{cryst}}\right|^2$ at the $1/a$ (phase information is lost). The inverse FT of $\left|F(u)_{\text{cryst}}\right|^2$ is the Patterson function $P(r) = \rho(r)_{\text{cryst}} \otimes \rho(-r)_{\text{cryst}}$ whose spatial extension is $2a$. Thus, to satisfy the Shannon sampling theorem [16–18] requirements, one should measure the modulus of FT of the scattering function $\rho(r)$ not only in correspondence of Bragg peaks (equispaced $1/a$) but also in between them (with a $1/2a$ sampling step). Bragg peaks are generated by the constructive interference of scattered waves whose transferred scattering wave vectors q_h – i.e., the difference between the scattered and incident wave vectors – satisfy Bragg's law: $q_h = 2 \sin \theta_h / \lambda = h/a$, with θ_h the Bragg angles. The $1/2a$ finer sampling is prevented by full destructive interference in-between Bragg peaks since the index h can assume only integral values (± 1, ± 2, ...) and not half-integral ones such as $\pm 1/2$, $\pm 3/2$, ... [17].
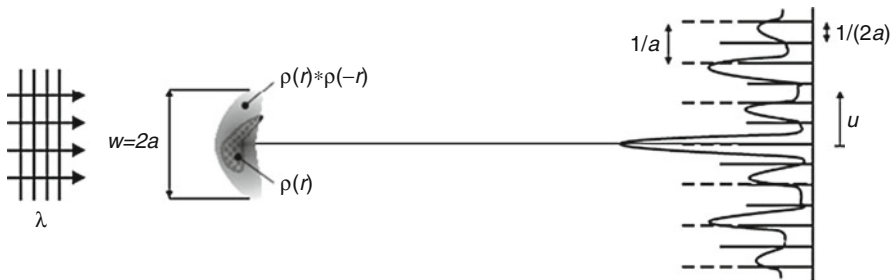
Fig. 8.3 Oversampling of the continuous diffraction pattern of a single object of electron density $\rho(r)$ and extension a. The autocorrelation function $\rho(r) \otimes \rho(-r)$ is also shown (Reprinted from [1])

This lack of information is compensated in crystallography by using other a priori knowledge of the scattering function, e.g., positivity and atomicity of the atomic electron density $\rho(r)$, which is just the scattering function probed by using X-rays.

Let us consider now a specimen made by a single unit cell of size a. As already stated, the diffraction pattern is continuously distributed between the diffraction peaks and can be measured at a frequency twice finer than the Nyquist one, i.e., every $1/2a$, or better. In this simpler case, $\left|F(u)_{\mathrm{cryst}}\right|^2 = |F(u)|^2$ and the Patterson function $P(r) = \rho(r)_{\mathrm{cryst}} \otimes \rho(-r)_{\mathrm{cryst}} = \rho(r) \otimes \rho(-r) = A(r)$ coincides with the autocorrelation function $A(r)$ of the unit cell electron density. If $\rho(r)$ is non-zero in an interval a, the autocorrelation function $A(r)$ is automatically confined in $2a$ (see Fig. 8.3) and it is a continuous function. Thus, the FT of this continuous function has to be known with a $1/2a$ sampling step to satisfy the Shannon sampling theorem. To perform this task, the scattering object $\rho(r)$ of size a has to be surrounded by a zero-scattering region of spatial extension a, at least as wide as the object size. If the impinging radiation has a spatial coherence length of at least of $2a$, the diffraction pattern will be proportional to the square modulus of FT$[\rho(r)]$ sampled just at the Nyquist frequency corresponding to the autocorrelation function $A(r)$ of the unit cell electron density (see Fig. 8.3), i.e., sampled every $H/2a$ with H integer. For even $H = 2h$ values, we obtain Bragg peaks that would correspond to the periodic repetition of $\rho(r)$, as in (8.3): $q_H = H/2a = h/a = q_h$. For odd $H = (2h + 1)$ values, we obtain the so-called half-integral reflections [17, 18], in between Bragg peaks. If the above conditions are satisfied, the $\rho(r)$ non-periodic scattering function can be computed by phase retrieval of its oversampled diffraction pattern.

8.1.4 Phase Retrieval

The virtual lens of every CDI experiment consists of a smart and effective combination of phase retrieval algorithms [19–21]. Several algorithms are available; the hybrid input–output (HIO) and the error reduction (ER) are among the first
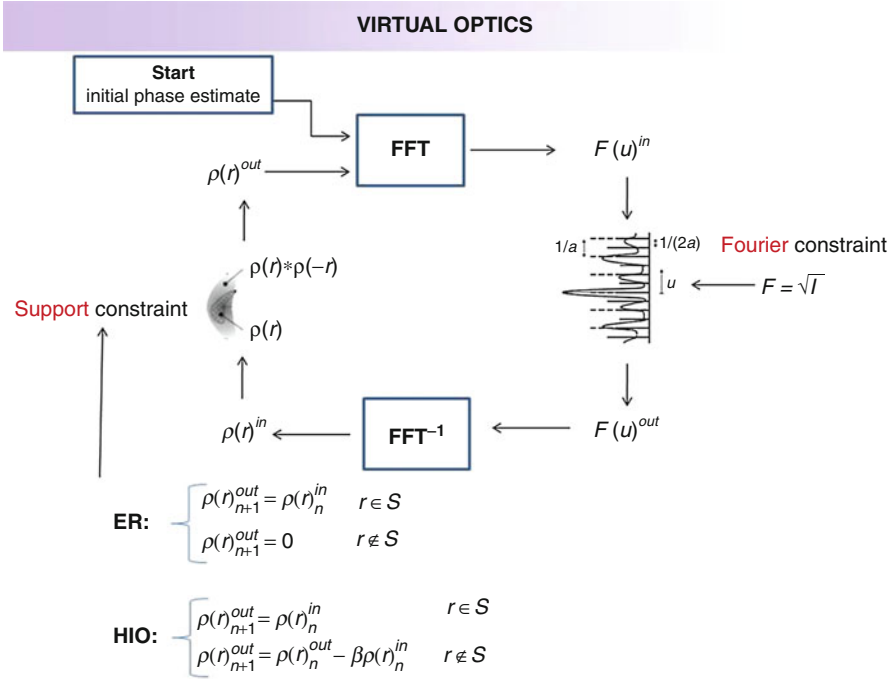
Fig. 8.4 Here, $\rho(r)$ is the real space image, $F(u)$ is the reciprocal space pattern, S is the support, and β is the feedback parameter

developed algorithms. Any algorithm makes use of two or more different constraints in two different spaces, the real and its dual space, conjugated by the fast Fourier transform (FFT). For example, for the error reduction algorithm one has

- A *support* constraint in the object space, which automatically means fixing within a *defined* support space region S the overall object position and physical extent, thus defining also the complementary no-scattering region, i.e., $\rho(r) \rightarrow P_s[\rho(r)]$, with $P_s(r) = 1$ for $r \in S$, $P_s(r) = 0$ otherwise.
- A modulus projection in its dual space (Fourier space), which means placing $|F(u)|^2$ *equal* to the measured intensity pattern (Fourier constraint), keeping unchanged the phases obtained by means of the fast FT (FFT) of $P_s[\rho(r)]$.

Thus, for the ER algorithm, the object scattering function $\rho(r)_{(n+1)}$ at the $(n + 1)$ iteration is obtained by that of the previous iteration, except for all points of the object scattering function out of the support region S, which are replaced by zeros: $\rho(r)_{n+1}^{out} = \rho(r)_n^{in}$ for $r \in S$ and $\rho(r)_{n+1}^{out} = 0$ for $r \notin S$ [20]. For the HIO [4, 20], the algorithm takes into account the errors in the estimates of the previous iteration, through a feedback parameter β ranging from 0.5 to 0.9: $\rho(r)_{n+1}^{out} = \rho(r)_n^{in}$ for $r \in S$ and $\rho(r)_{n+1}^{out} = \rho(r)_n^{out} - \beta\rho(r)_n^{in}$ for $r \notin S$. The feedback parameter will be close to 1 if the support region is correctly known (strong feedback), otherwise, it will take smaller values (weaker feedback). A schematic figure of the ER/HIO algorithms is depicted in

Fig. 8.4. As the phase errors lead to non-zero values for the $\rho(r)$ estimated out of the support region, the feedback correction $-\beta\rho(r)_n$ for $r\notin S$ in the HIO algorithm speeds up the convergence with respect to the ER algorithm and it is helpful to avoid phase stagnation around local minima [19, 20]. The reconstruction errors in both spaces, i.e., the object support error $\sum|\rho(r)_n|^2_{r\notin S}/\sum|\rho(r)_n|^2_{r\in S}$ in the real space and the normalized mean square error $\varepsilon_n = \sum||F(q)_n| - I(q)^{1/2}|^2/\sum I(q)$ in its dual space or, equivalently, the R-factor $R = \sum||F(q)_n|- I(q)^{1/2}|/\sum I(q)^{1/2}$, where q is the transferred scattering vector, can be used as reliable figures of merit (FOMs) to monitor the phasing process. In fact these two FOMs become smaller and smaller as phase improves. HIO is useful to overcome local minima and avoid phase stagnation, but it strongly perturbs phased maps and – for this reason – could not converge to the solution, leading to wrong estimates of the modulus $|F(q)|$ by FFT. ER is useful to evaluate correctly FOM values and unknown $|F(q)|$ by FFT, but when used alone it becomes trapped in local minima. Conversely, the ER used in synergy with the HIO is useful to avoid phase stagnation and to read only the FFT modulus of the phased maps obtained by the HIO algorithm. Thus, the alternation of different algorithms – e.g., N cycles of HIO (usually few tens) and few cycles of ER (also just one ER cycle every N cycles of HIO) – leads to more efficient phase-retrieval procedures.

8.2   X-Ray CDI

Different types of X-ray CDI experiments have been conducted [22]:
1. Plane wave CDI from isolated objects in forward scattering;
2. Focused-beam Fresnel CDI from isolated objects in forward scattering;
3. Bragg CDI from nanocrystals;
4. Keyhole CDI and ptychography from extended objects.

Isolated objects were first studied with planar incident beams. As previously described, a region equal to or larger than the object size was left empty around it to ensure the beam exiting the object to be of finite extent, a mandatory condition for a phase retrieval solution [22]. These kinds of experiments were performed in forward scattering geometry, either with plane waves using pinholes (Fig. 8.5a) or with X-ray optics and curved waves (Fig. 8.5b), or in Bragg geometry (Fig. 8.5c). The limitation to study isolated objects was definitively overcome with the implementation of keyhole CDI (KCDI) and ptychography CDI (PCDI), the latter shown in Fig. 8.5d.

The presence of a beam stopper is required to avoid detector saturation/damage caused by the incident unscattered beam when using planar incident waves (*a* and *d* configuration of Fig. 8.5). Two striking benefits have emerged by using nonplanar wavefronts (*b* configuration of Fig. 8.5): a faster convergence of the iterative phase-retrieval algorithms and the possibility to measure easily the diffracted intensity at low scattering vectors, which is lost in plane-wave configurations [23]. Another extremely important aspect to consider in CDI experiments is the degree of coherence of the incident wave. In practice, in most of the experiments, the beam that arrives onto the sample has encountered several optical elements on its path
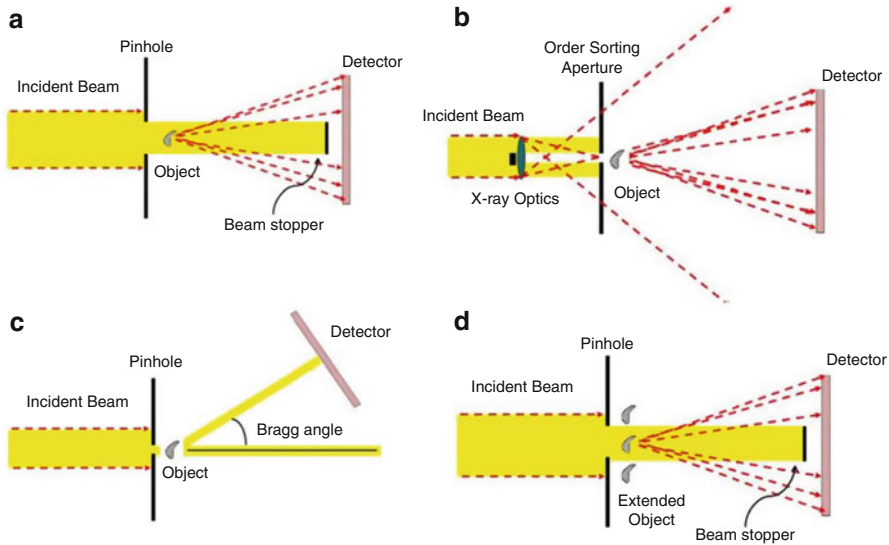
Fig. 8.5 Schematic representation of the different CDI experimental setups: (**a**) forward CDI on isolated objects with pinhole, (**b**) forward CDI on isolated objects with X-ray optics, (**c**) Bragg CDI on nanocrystals, (**d**) ptychography CDI (PCDI) on extended objects with pinhole [22]

from the source, e.g., monochromators, mirrors, slits, etc., that lead to coherence degradation at the sample position. This lack of coherence can severely disturb the convergence of the phasing process, as previously discussed [23], in plane wave configurations. Conversely the use of curved incident wave fields – to perform Fresnel X-ray CDI experiments – allows one to tolerate also a partial coherence of the incident wave field, instead of a full coherence, which is mandatory in the case of plane-wave configurations.

8.2.1 Forward Coherent Diffractive Imaging

Miao and coworkers did the first two-dimensional [4] and three-dimensional [5] reconstruction of a non-periodic assembly of objects, achieving ∼75 and ∼50 nm resolution, respectively. In both cases, plane waves were used to illuminate the sample and a forward-scattering geometry was adopted. The same group, a few years later, first applied the forward-scattering CDI with plane waves to imaging biological samples [9]. Another relevant experiment was the first CDI on "on-the-fly" nanometric particles, using single femtosecond soft-X-ray free electron laser pulses [7, 8].

Parallel to plane-waves CDI in forward geometry, as a very promising alternative, experiments were realized using X-ray optics to deliver a coherent but curved beam onto the samples. Fresnel zone plates [24], two crossed waveguides [25], refractive lenses [26], and mirrors [27] were used to have a nanofocused beam close
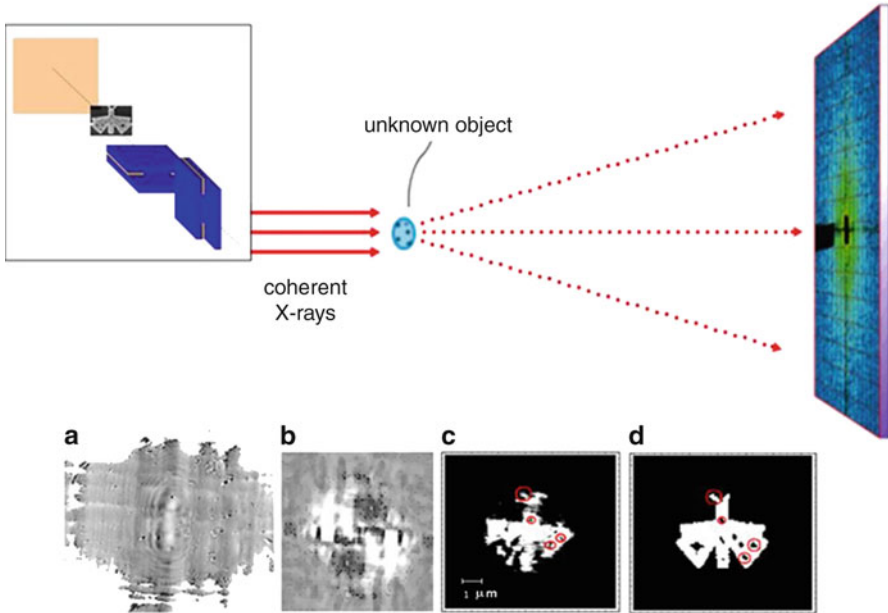
Fig. 8.6 The *inset* shows the experimental setup with two planar waveguides, crossed to have a limited beam of 200 × 200 nm^2 dimension. At about 1 cm from the waveguides, a lithographically printed butterfly was coherently illuminated and the diffraction pattern was recorded at about 4 m distance from the sample, with a Princeton CCD detector. The low scattering vectors data are shown in *a*, which gives, via a single FFT, a holographic reconstruction at a spatial resolution of about 200 nm, shown in *b* The phase-retrieved image, obtained from the entire CDI dataset, is showed in *c* to be compared with the digitalized SEM image in *d*

to the sample. In these peculiar setups, the wave field illuminating the sample is measured and phased separately. As already stated, the curvature of the wavefronts facilitates iterative phase-retrieval algorithms convergence. Furthermore, in most cases, the diffracted intensity at low-q is not obscured by the beam stopper, as for plane-waves CDI experiments with pinholes, and can be measured.

In the experiment of De Caro et al. [25], a 4.5-µm-wide and 600-nm-thick gold butterfly, lithographically printed onto a SiN membrane, was imaged with a 200 × 200 nm^2 focused beam, obtained by two crossed planar waveguides (see inset in Fig. 8.6). Figure 8.6a shows the experimental data acquired at low scattering vectors. Figure 8.6b shows a holographic reconstruction at a source limited spatial resolution via just one FFT. This holographic reconstruction is possible as the virtual source – formed by the crossing of the wave fields exiting the two waveguides – is point-like and slightly off-axis with respect to the object position [25]. The image obtained by phase retrieval is shown in Fig. 8.6c with a resolution of about 50 nm, fourfold improved with respect to Fig. 8.6b. For comparison, the digitalized scanning electron microscopy (SEM) image of the butterfly is shown in Fig. 8.6d.

Fig. 8.7 KCDI experiment: a finite-sized beam was used to image an extended object (Reprinted from [28])
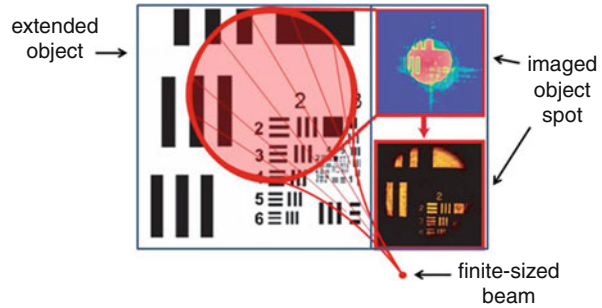
The main difference between CDI with nanofocused beams and plane wave experiments is that it offers the possibility to work without beam stopper and to record the precious low-resolution image (Fig. 8.6a). Actually, in these cases, it is more accurate to speak of extending phase information from the low-resolution phase-contrast image, recovered in the low scattering-vectors region, to a higher-resolution image (Fig. 8.6c) that is retrieved by phasing the entire CDI pattern. The final resolution of Fig. 8.6c depends on the data measured in the diffraction pattern image at the highest scattering vectors. The possibility to record the low-resolution data allows phase retrieval algorithms to easily converge towards a unique solution.

8.2.2 Ptychography and Keyhole CDI

A new form of imaging, called keyhole CDI (KCDI), was introduced by Abbey et al. [28]. They performed the same kind of experiment both with visible light (Fig. 8.7) and with a nanofocused X-ray beam, produced with Fresnel zone plates, to have a constrained nanometric illumination function. The experimental setups for the optical and X-ray experiments are conceptually identical. The experimental geometry is similar; however, the requirements for the source and detector are substantially different. The finite extension of the illuminating beam allowed study of extended samples instead of isolated objects.

A fundamental condition of KCDI is that the illumination function must rapidly fall off to an experimentally negligible value at its edges. This requires a high-quality focusing optics. Furthermore, the quality of the reconstruction depends critically on the knowledge of the illuminating beam, the latter being phased together with the unknown object. Actually, in KCDI the *zero-scattering* region around the area to be reconstructed by means of the phase retrieval – i.e., the scattering object – is replaced by a *zero-illumination* region around the scattering region we want to visualize, as schematically depicted in Fig. 8.7 by the red region superimposed on the extended object.

Ptychography is valid alternative to KCDI. This imaging mode was originally proposed by Hoppe in the field of electron microscopy [29]. With ptychographic CDI (PCDI) the sample is imaged by translating it at several positions with respect to the beam, to ensure specific overlapping conditions [30]. This allows redundant

information to be registered from the overlapping illumination areas on the sample. In this way, a ptychographical iterative engine (PIE) can be used [31, 32], combining data redundancy and iterative phase retrieval algorithms to phase simultaneously the illumination function and the object's complex transmission function. Relevant PCDI results include the tomographic reconstruction of a bone sample at 65×65 nm^2 resolution [33] and the imaging of a weak scattering biological specimen, *Magnetospirillum gryphiswaldense*, which was reconstructed at a 43.5×43.5 nm^2 resolution [34].

This idea to illuminate a sample with a finite-sized beam, guaranteed both by KCDI and by PCDI, enhanced the use of applications to any kind of extended specimen.

8.2.3 The Bragg Case: Imaging of Atomic Displacement Fields

Coherent diffractive imaging was used also in Bragg mode (Fig. 8.5c), not registering the forward-scattered intensity, as in the previously cited cases, but the intensity around precise reciprocal lattice points. A useful overview has been published by Robinson and Harder [35]. The main difference in recording data at Bragg angles, rather than in forward-scattering geometry – also called SAXS geometry – is that Bragg data include atomic information, whereas SAXS data only morphological (shape and size) ones. Therefore, Bragg-CDI is typically used to study strain fields inside nanocrystals as well as atomic displacement field due to defects. Some relevant experiments are shown in Fig. 8.8, on GaAs [36], InAs [37], and Si [38] nanostructures. The nanobeam size adopted in the experiments was reduced from 600, 150 down to 95 nm. A topological map of the elastic crystal strain or of defect-related atomic displacements can be derived with a spatial resolution basically limited by the smallest nanobeam that can be produced. This poses severe stability conditions on the entire experimental setup, which must be guaranteed in order to properly use such a small beam. The elastic or plastic strain crystal deformation is encoded in the Bragg diffracted amplitude, as a phase contribution, which must be extracted by the mapped intensity, using proper phase retrieval methods. This Bragg CDI application is strategically needed for many areas of nanotechnology and semiconductor device industry. Along with development of tools enabling programmable material fabrication with nanometer-level compositional and geometric precision, the unfolding of the local structure of nanomaterials with atomic resolution is increasingly emerging as a fundamental transition pathway towards control of their unique size-dependent properties and realization of their technological potential.

8.3 Electron Diffractive Imaging: EDI

In the case of electrons, the equipment suitable for electron diffractive imaging (EDI) experiments is the transmission electron microscope (TEM). Indeed the TEM is a powerful tool to investigate the structural, chemical, and electronic properties

J. Synchrotron Rad. (2009). 16
Biermanns et al
GaAs ∅ ~ 600 nm

phys. Rev. B 79, 125324 (2009)
Diaz et al
InAs ∅ ~ 150 nm

phys. Rev. B 79, 195401 (2009)
Favre-Nicolin et al
Si ∅ ~ 95 nm
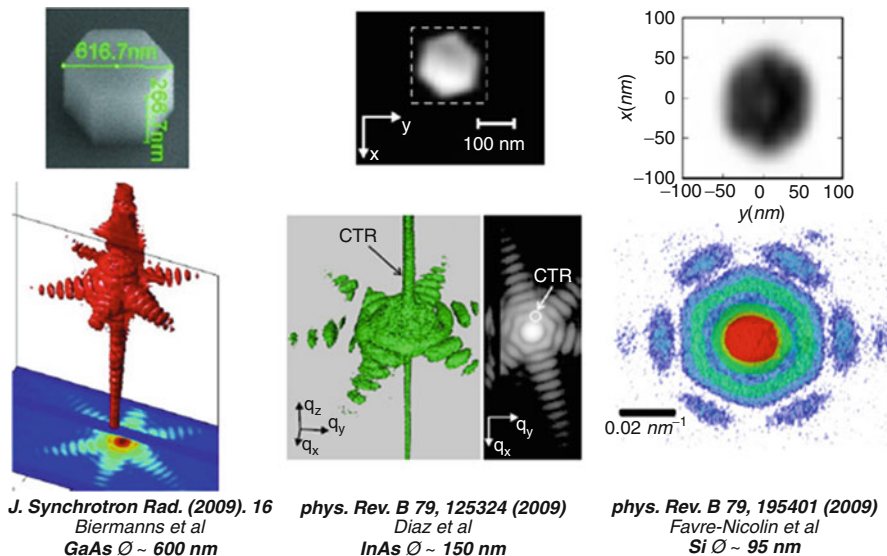
Fig. 8.8 Bragg CDI of GaAs (http://dx.doi.org/10.1107/S0909049509032889 IUCr's copyright permission), InAs and Si nanostructures imaged with nanobeam sizes of 600, 150 down to 95 nm, respectively (Figure assembled from the original papers cited in [36–38])

of the matter at the highest spatial resolution and it is an extremely flexible optical bench that can be tuned, as in the present case, to satisfy the requirement of the EDI experiments. The first example of atomic-resolution EDI was obtained on a carbon nanotube [39], as shown in Fig. 8.9a. More recently, individual single-domain Au [40], CdS [41], and TiO_2 [42] nanocrystals were imaged with EDI at resolutions of 100, 80, and 70 pm, respectively (see Fig. 8.9b–d). The introduction of EDI in the TEM allows detection of subtle properties of the matter not reachable by standard high-resolution TEM (HRTEM) experiments, overcoming the limits of resolution related to the aberrations of the electron lenses [43]. In fact, Zuo and co-workers imaged a double-wall carbon nanotube at 100 pm resolution, revealing the structure of two tubes of different helicities. Figure 8.9a summarizes the EDI experiments of Huang and co-worker, where contraction of surface atoms in an Au cluster was measured. The contraction was found to be coordination dependent and dominated by edge atoms and atoms on {100} facets. For the CdS quantum dot (Fig. 8.9b) and TiO_2 nanorod cases (Fig. 8.9c), the improved EDI image resolution enabled determination of the actual atomic structures, which were found to differ at the nanoscale from the bulk counterpart.

8.3.1   CDI in a TEM

The de Broglie wavelength of electrons in a standard TEM is of the order of picometers: for example, for a 200 keV microscope the electron wavelength is
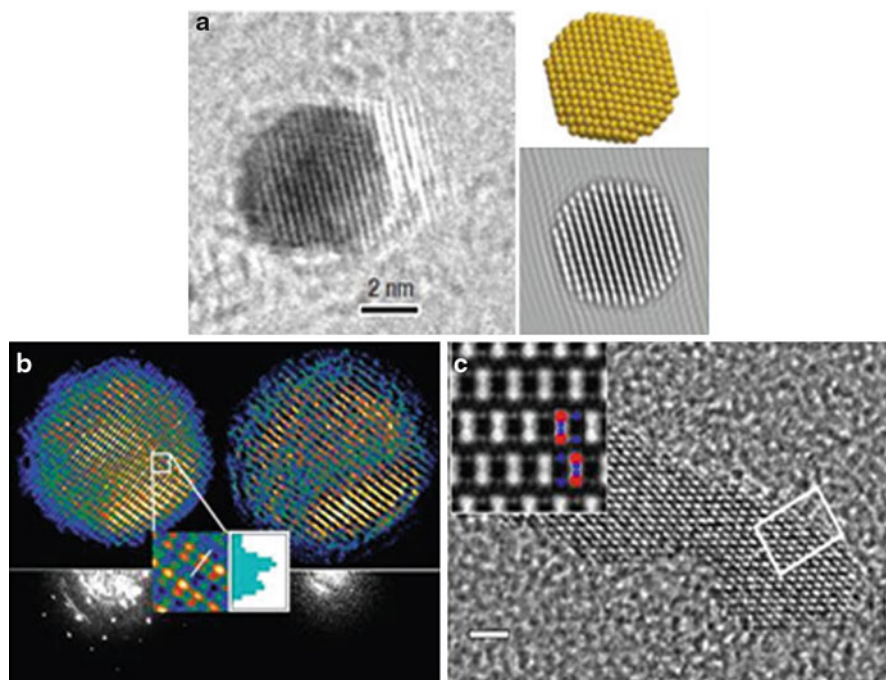
Fig. 8.9 EDI experiments of Au crystals of 3–5 nm in diameter (panel **a**), CdS quantum dot of 7 nm size (panel **b**), and TiO_2 nanorods of 20 nm length and 5 nm diameter (panel **c**) (Figure assembled from the original papers cited in [40–42])

$\lambda = 2.5$ pm. Hence, the resolution of a diffractive limited imaging experiment is well below the distance of atoms in a crystal lattice (≈ 100 pm). Unfortunately, the electron lenses are affected by severe third- and fifth-orders aberrations [44] and the resolution achievable in a standard HRTEM experiment is about two orders of magnitude worse than the diffraction limit. For example, for a high-quality microscope of acceleration voltage E = 200 keV, with low spherical aberration coefficient (Cs) objective lens (Cs = 0.47 ± 0.01 mm), the resolution at optimum defocus is 190 pm = 1.9 Å [42]. It may appear strange to perform a method such as CDI, developed for lens-less experiments, in a TEM where there are plenty of electro-magnetic lenses. However, as we will see, the approach allows one to overcome the limitation due to the lens aberration while allowing to one obtain all the information necessary for a reliable and efficient phase retrieval [39–42].

The EDI experiment in the TEM is a two-stage process based on recording the HRTEM image and the nano-electron diffraction (n-ED) from the same specimen area (see Fig. 8.10) [45]. The former represents the specimen in real space, allowing an excellent estimation of the support, while the diffraction pattern is a depiction in reciprocal space, both characterizing the crystal structure. The HRTEM is one of

Fig. 8.10 HRTEM and n-ED
images as recorded in
a transmission electron
microscope (Reprinted
from [45])

(a)

several ways in which an image of a specimen can be obtained in a TEM and allows
imaging of the structure of that sample at high spatial resolution but limited by the
aberrations of the lenses. The HRTEM image is obtained by the interaction between
the high-energy electron wave field with the electrostatic potential $\varphi(x,y)$ in the
specimens and the magnetic field of the objective lens in the microscope [46].
The phase of the wave field carries detailed information on the specimen structure.
The remarkable feature of a HRTEM image is that, if the specimen is thin enough to
satisfy the so-called weak phase object approximation (WPOA) [46], the contrast
carries information directly related to the phase of the electron wave field after the
interaction with the specimen and hence on the electrostatic crystal potential.

In fact, as a result of the interaction with the sample, the electron exit wave
directly below the sample is the superposition of the incident plane wave and
a multitude of diffracted waves characterized by different scattered wave vectors
with different in-plane spatial frequencies (u,v) where high spatial frequencies
correspond to large lateral distances from the optical axis. These waves, passing
through the imaging system of the microscope, undergo further phase changes and
interfere, before reaching the detector (image wave). Due to the objective lens
spherical aberration, the phase changes in these waves depend on the lateral
distance from the optical axis. Thus, the total exit wave – the coherent sum of the
incident and diffracted waves with their respective phases – will be strongly

dependent on the electro-optical parameters characterizing the image formation process. Also, the distance (defocus distance) along the propagation direction between the image plane and the lens focal plane plays an important role in the determination of the phase-contrast of the HRTEM image. For these reasons, the relationship between the exit wave and the image wave is, in general, highly nonlinear and it is described in the Fourier space by the *contrast transfer function* $T(u,v)$ [46]. In fact, HRTEM does not use amplitudes, i.e., absorption by the sample, for image formation. Instead, contrast arises only from the interference in the image plane of the incident and diffracted waves. Due to our inability to record the phase of these waves, we generally measure the amplitude resulting from this interference (phase contrast imaging). In particular, at the so-called Scherzer defocus, by choosing the right defocus value, one flattens the $T(u,v)$ to create a wide band where low spatial frequencies u,v are transferred into image intensity with a similar phase, to preserve as much as possible a direct proportionality between image contrast and projected atomic potential.

This, however, is true only if the sample is well-oriented in a zone-axis (high-symmetry crystallographic direction) and it is thin enough so that amplitude variations only slightly affect the image and the phase term can be well approximated by the first order of its Maclaurin expansion (the so-called *weak phase object approximation*, WPOA) [46]. In fact, if the specimen is thin enough to satisfy the WPOA, the HRTEM image intensity $I(x,y)$ is linear to the convolution of the projected potential $\varphi(x,y)$ and the inverse Fourier transform of the contrast transfer function (CTF) $T(u,v)$ of the electron microscope:

$$I(x, y) = 1 + 2\pi/\lambda E\varphi \ (x, y) \otimes \mathrm{FT}^{-1}[T(u, v) \times A(u, v)].$$

Here E is the energy of the electrons. $T(u,v)xA(u,v)$ is a function of limiting apertures, defocus distance, and aberrations of the microscope objective lens. The *aperture function*, $A(u,v) = 1$ for $|u| < u_{\max}$ and $|v| < v_{\max}$, and zero elsewhere, cuts off beams scattered above a certain critical angle (for which $|u| > u_{\max}$ and/or $|v| > v_{\max}$), thus effectively limiting the attainable resolution. However, it is the *envelope function* related to the spatial and temporal coherence of the electron waves that dampens the signal of beams scattered at high angles and imposes a maximum to the transmitted spatial frequency. Therefore, $T(u,v)$ acts as a low-frequency filter and HRTEM provides "low-resolution" information about the investigated sample ("low" if compared with the ultimate resolution related to the wavelength diffraction limit). Hence, in an EDI experiment, the HRTEM image information is combined with the relevant nano-electron diffraction (n-ED) pattern collected on the sample following proper sampling conditions [47]. The n-ED pattern is proportional to the FT of the projected potential $\varphi(x,y)$ if the thickness of the scattering object satisfies the so-called kinematical conditions [46], requiring that the diffracted wave amplitude is much smaller than the one of the incident wave. The reflections registered in the n-ED pattern correspond to significantly smaller lattice spacing than HRTEM, meaning a potential enhanced spatial resolution.

Sophisticated iterative phase retrieval algorithms, which are basically very similar to those used for X-ray CDI, use synergistically the HRTEM and n-ED data to retrieve the electron atomic potential of the imaged sample. EDI aims to extend the relatively low-resolution crystal potential information of the HRTEM image up to the best spatial resolution corresponding to the diffracted intensities at the highest scattering angles, accurately measured in the electron diffraction n-ED pattern above the noise level.

There are a series of advantages in performing an EDI experiment in a TEM, as we can apply all the potentiality of electron microscopy to gain the extra information necessary to retrieve the phase from the electron diffraction data. Moreover, a specimen area of few tens of nanometers or less can be illuminated with plane electron waves at very low dose. The support of the object can be determined very precisely from the HRTEM image of the object of interest and also the starting phases at low resolution can be calculated from the FFT of the relevant HRTEM image. All these benefits highly enhance the phase algorithm convergence.

The experimental setup of a TEM microscope and the collected data have to satisfy the oversampling condition – needed for phase retrieval methods – and to maximize the signal-to-noise ratio in collecting the n-ED pattern. Thus, for isolated objects, the particle to be imaged must be illuminated with a coherent electron wave with lateral coherence at least twice as large as the object, a condition already encountered with X-ray CDI. The coherence of the field emission guns, equipping standard TEM, leads to electron waves with a lateral coherence of some tenths of nanometers [48] and hence enough to illuminate coherently an isolated nanoparticle. Thus, the n-ED pattern and the relevant HRTEM image have to be acquired using the same illumination conditions producing a parallel electron beam with a size at least double that of the object in order to satisfy the oversampling conditions.

An experimental example of EDI is reported in Fig. 8.11. Figure 8.11a shows the HRTEM image of a TiO_2 anatase nanoparticle. Figure 8.11b shows a magnification of the region of the HRTEM image inside the black rectangle of Fig. 8.11a. Figure 8.11e is obtained by combining the experimental n-ED pattern (Fig. 8.11d) with the low-frequency information obtained by the FFT of the nanoparticle (Fig. 8.11c). The loss of low-frequency information in the n-ED in Fig. 8.11d is due to the presence of the beam stopper, used during this data acquisition to avoid the damage of the CCD detector. This information, lost in the diffraction pattern, is replaced by the relevant one derived from the FFT of the HRTEM image. To perform this task the projected object potential calculated from the HRTEM image in Fig. 8.11a was rotated and scaled in size in order to match its FFT (Fig. 8.11c) with the recorded n-ED pattern (Fig. 8.11d). The modulus of the so-obtained FFT was limited to half of the standard deviation value, rescaled in intensity, and finally merged with the n-ED pattern to complement it with the missing data cut by the beam stopper.

The highest frequency spacing in the n-ED in Fig. 8.11d are the {055} reflections corresponding to a distance of 70 pm in the anatase crystal lattice. Hence, if an appropriate phasing algorithm is now applied to the data in Fig. 8.11 the maximum
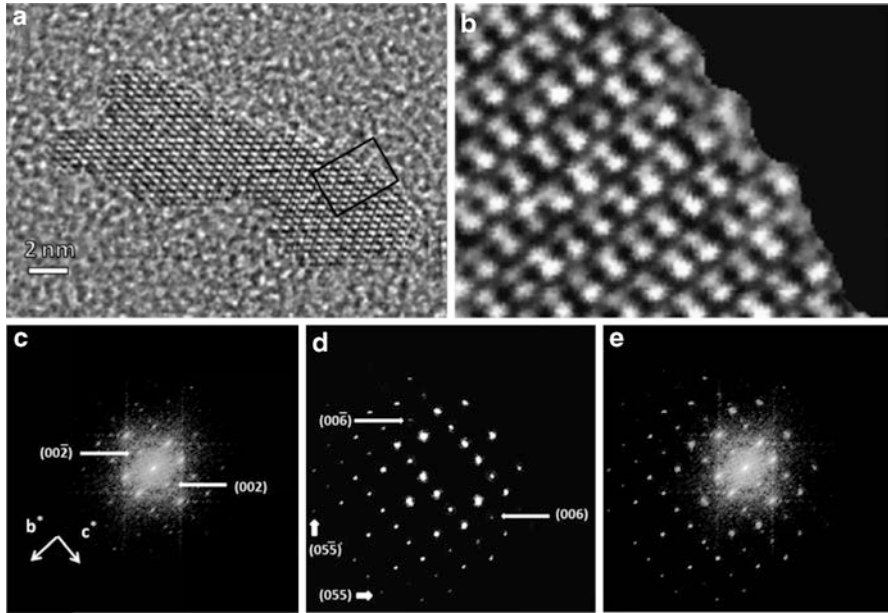
Fig. 8.11 TEM analysis of an anatase TiO$_2$ nanocrystal along its <1,0,0> zone axis. (**a**) "Low-resolution" phase-contrast HRTEM image taken at an objective lens defocus of −79 nm. (**b**) Enlarged view of the area marked in (**a**) without background contribution. (**c**) FFT of the HRTEM image shown in (**a**); the reciprocal lattice directions and some reflections forbidden for the anatase structure are marked; (**d**) n-ED pattern of the nanocrystal; *arrows* indicate the highest-frequency diffraction spots, namely the (0, 5, ±5). The *other arrows* indicate some weak diffraction spots, e.g., the (0, 0, ±6), which are kinematically forbidden for the tetragonal anatase structure. (**e**) Combination of (**c**) and (**d**) after scaling and rotating to achieve the best matching of the positions of the strongest diffraction spots (Reprinted from [42])

expected resolution is 70 pm, about three times better than the resolution 190 pm of the HRTEM image and able to distinguish the oxygen and titanium atomic column in the experimental crystal projection.

The object support (S) was derived as binary mask from the HRTEM image. Then, constrains for the phasing were as follows: a support projection in the object space (direct space) and a modulus projection in its dual space (reciprocal space). The oversampling condition was satisfied for the HRTEM and n-ED pattern in Fig. 8.11 as a region of about 40 nm was centered on the object whose maximum size is less than 20 nm. Usually, the modulus and support projections can both be suitably tuned to handle phase-retrieval processes involving complex objects and/or noisy and/or missing data.

The phasing process was monitored by root-mean-squared errors in the Fourier domain ε_R and in the object domain ε, which gave a measure of the object-reconstruction error out of the support, where the object function was known to be zero. At convergence of the phase-retrieval process, ε_R reached down to 8×10^{-4}, and the object-reconstruction error ε became of a few percent.
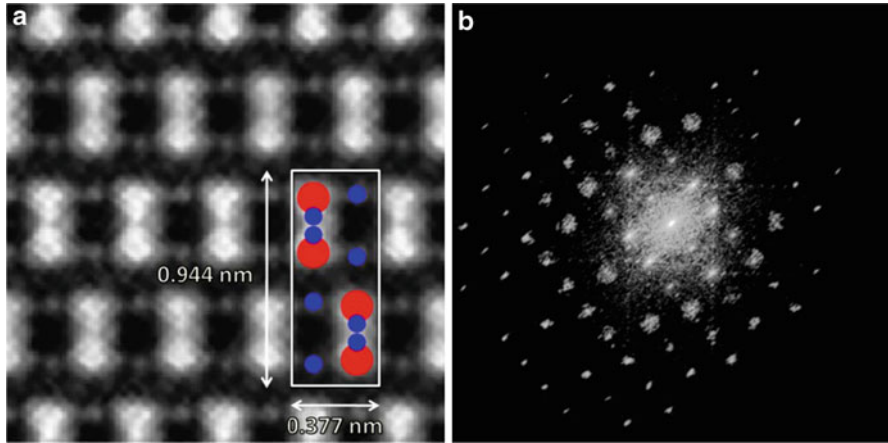
Fig. 8.12 Phase-retrieved diffractive image of a distorted anatase TiO_2 nanocrystal lattice along the <1,0,0> direction. (**a**) Phase-retrieved diffractive image of a portion of the TiO_2 nanocrystal shown in Fig. 8.11a, which has been rotated so as to allow the c-axis to be vertically oriented. A *rectangular box* has been superimposed, which depicts the tetragonal structure of bulk anatase (unit space group I4$_1$/amd, cell parameters: $a = b = 0.377$ nm, $c = 0.944$ nm), with the Ti and O atomic columns in *red* and *blue*, respectively. (**b**) Phase-retrieved diffraction pattern of the TiO_2 nanorod in Fig. 8.11a (Reprinted from [42])

The phase retrieved image is shown in Fig. 8.12 along with the retrieved diffraction pattern.

The phase-retrieved image in Fig. 8.12 was reconstructed at 70 pm resolution, in agreement with the highest resolution in the relevant experimental n-ED allowing one to detect the light atomic columns of oxygen separated from the titanium atomic column and to measure a small distortion in the crystal cell of TiO_2 very likely related to the oxygen vacancies in the anatase structure of nano clusters [42].

Also for EDI, as for the previous cited CDI with nanofocused beam, phase retrieval allows extension of the phase information of the HRTEM image, skipping the lenses' aberration problems affecting any microscope. EDI is an alternative to aberration-corrected microscopy [49], but the approach can be also applied to aberration-corrected experiments to rectify residual distortions, paving the way for the ultimate resolution by TEM and improving considerably the signal-to-noise ratio of the experimental image. The method so far has been applied to inorganic material, but it could be envisioned in the imaging of proteins and bio-particles, providing an opportunity to image radiation-sensitive materials with, possibly, reduced damage with respect to imaging by photons [50].

8.4   Conclusions and Outlook

Coherent diffraction imaging, either with X-rays or electrons, offers great promise for structural studies of biological or material science samples. The use of

a coherent beam to illuminate matter finally removes any constraint due to the crystalline nature of the specimens, opening the door to the always-difficult field of solving the atomic structure of protein molecules. However, this is not the only hot topic that could benefit from such a promising technique. In fact, there are several different types of meta materials [51], macroscopic composites of periodic and non-periodic structures, which could be imaged by CDI at atomic resolution. While sub-Ångström resolutions can be presently achieved only with electrons, femtosecond free-electron lasers spots have already been used to increase the best resolution achievable with X-rays. However, the most urgent unresolved issue for CDI both with X-ray and electrons, concerns the radiation dose limits matter can hold, especially soft matter. The ultimate spatial resolution will be definitively limited by the dose and, as proved for X-rays by Quiney and Nugent [52], the conditions under which biomolecular structures may be solved by X-ray CDI are unduly restrictive. The capability to generate new approaches for imaging matter at increasing higher resolutions and accuracy induces a kind of optimistic expectation in the comprehension of subtle and important open questions in materials science and biology. The future looks bright!

References

1. J.F. van der Veen, F. Pfeiffer, Coherent x-ray scattering. J. Phys.: Condens. Mat. **16**, 5003–5030 (2004)
2. D. Sayre, X-ray crystallography: the past and present of the phase problem. Struct. Chem. **13**, 81–96 (2002) (and reference therein)
3. D. Sayre, Some implications of a theorem due to Shannon. Acta Crystallogr. **5**, 843 (1952)
4. J. Miao, C. Charalambous, J. Kirz, D. Sayre, Extending the methodology of X-ray crystallography to allow imaging of micrometre-sized non-crystalline specimens. Nature **400**, 342–344 (1999)
5. J. Miao, T. Ishikawa, B. Johnson, E.H. Anderson, B. Lai, K.O. Hodgson, High resolution 3D X-ray diffraction microscopy. Phys. Rev. Lett. **89**, 088303 (2002)
6. A. Barty, S. Marchesini, H.N. Chapman, C. Cui, M.R. Howells, D.A. Shapiro, A.M. Minor, J.C.H. Spence, U. Weierstall, J. Ilavsky, A. Noy, S.P. Hau-Riege, A.B. Artyukhin, T. Baumann, T. Willey, J. Stolken, T. van Buuren, J.H. Kinney, Three-dimensional coherent X-ray diffraction imaging of a ceramic nanofoam: determination of structural deformation mechanisms. Phys. Rev. Lett. **101**, 055501 (2008)
7. H.N. Chapman, A. Barty, M.J. Bogan, S. Boutet, M. Frank, S.P. Hau-Riege, S. Marchesini, B.W. Woods, S. Bajt, W.H. Benner et al., Femtosecond diffractive imaging with a soft-X-ray free-electron laser. Nat. Phys. **2**, 839–843 (2006)
8. M.J. Bogan, W.H. Benner, S. Boutet, U. Rohner, M. Frank, A. Barty, M.M. Seibert, F. Maia, S. Marchesini, S. Bajt, B. Woods, V. Riot, S.P. Hau-Riege, M. Svenda, E. Marklund, E. Spiller, J. Hajdu, H.N. Chapman, Single particle X-ray diffractive imaging. Nano Lett. **8**(1), 310–316 (2008)
9. J. Miao, K.O. Hodgson, T. Ishikawa, C.A. Larabell, M.A. LeGros, Y. Nishino, Imaging whole *Escherichia coli* bacteria by using single-particle x-ray diffraction. Proc. Natl. Acad. Sci. U.S.A. **100**, 110–112 (2003)
10. D. Shapiro, P. Thibault, T. Beetz, V. Elser, M. Howells, C. Jacobsen, J. Kirz, E. Lima, H. Miao, A.M. Neiman, D. Sayre, Biological imaging by soft x-ray diffraction microscopy. Proc. Natl. Acad. Sci. U.S.A. **102**, 15343–15346 (2005)

11. C. Song, H. Jiang, A. Mancuso, B. Amirbekian, L. Peng, R. Sun, S.S. Shah, Z.H. Zhou, T. Ishikawa, J. Miao, Quantitative imaging of single, unstained viruses with coherent X rays. Phys. Rev. Lett. **101**, 158101 (2008)
12. Y. Nishino, Y. Takahashi, N. Imamoto, T. Ishikawa, K. Maeshima, Three-dimensional visualization of a human chromosome using coherent X-ray diffraction. Phys. Rev. Lett. **102**, 018101 (2009)
13. M.M. Seibert, T. Ekeberg, F.R.N.C. Maia, M. Svenda, J. Andreasson, O. Jönsson, D. Odić, B. Iwan, A. Rocker, D. Westphal, M. Hantke, D.P. DePonte, A. Barty, J. Schulz, C.L.N. Gumprecht, A. Aquila, M. Liang, T.A. White, A. Martin, C. Caleman, S. Stern, C. Abergel, V. Seltzer, J.-M. Claverie, C. Bostedt, J.D. Bozek, S. Boutet, A.A. Miahnahri, M. Messerschmidt, J. Krzywinski, G. Williams, K.O. Hodgson, M.J. Bogan, C.Y. Hampton, R.G. Sierra, D. Starodub, I. Andersson, S. Bajt, M. Barthelmess, J.C.H. Spence, P. Fromme, U. Weierstall, R. Kirian, M. Hunter, R.B. Doak, S. Marchesini, S.P. Hau-Riege, M. Frank, R.L. Shoeman, L. Lomb, S.W. Epp, R. Hartmann, D. Rolles, A. Rudenko, C. Schmidt, L. Foucar, N. Kimmel, P. Holl, B. Rudek, B. Erk, A. Hömke, C. Reich, D. Pietschner, G. Weidenspointner, L. Strüder, G. Hauser, H. Gorke, J. Ullrich, I. Schlichting, S. Herrmann, G. Schaller, F. Schopper, H. Soltau, K.-U. Kühnel, R. Andritschke, C.-D. Schröter, F. Krasniqi, M. Bott, S. Schorb, D. Rupp, M. Adolph, T. Gorkhover, H. Hirsemann, G. Potdevin, H. Graafsma, B. Nilsson, H.N. Chapman, J. Hajdu, Single mimivirus particles intercepted and imaged with an X-ray laser. Nature **470**, 78–82 (2011)
14. H.N. Chapman, P. Fromme, A. Barty, T.A. White, R.A. Kirian, A. Aquila, M.S. Hunter, J. Schulz, D.P. DePonte, U. Weierstall, R.B. Doak, F.R.N.C. Maia, A.V. Martin, I. Schlichting, L. Lomb, N. Coppola, R.L. Shoeman, S.W. Epp, R. Hartmann, D. Rolles, A. Rudenko, L. Foucar, N. Kimmel, G. Weidenspointner, P. Holl, M. Liang, M. Barthelmess, C. Caleman, S. Boutet, M.J. Bogan, J. Krzywinski, C. Bostedt, S. Bajt, L. Gumprecht, B. Rudek, B. Erk, C. Schmidt, A. Hömke, C. Reich, D. Pietschner, L. Strüder, G. Hauser, H. Gorke, J. Ullrich, S. Herrmann, G. Schaller, F. Schopper, H. Soltau, K.-U. Kühnel, M. Messerschmidt, J.D. Bozek, S.P. Hau-Riege, M. Frank, C.Y. Hampton, R.G. Sierra, D. Starodub, G.J. Williams, J. Hajdu, N. Timneanu, M.M. Seibert, J. Andreasson, A. Rocker, O. Jönsson, M. Svenda, S. Stern, K. Nass, R. Andritschke, C.-D. Schröter, F. Krasniqi, M. Bott, K.E. Schmidt, X. Wang, I. Grotjohann, J.M. Holton, T.R.M. Barends, R. Neutze, S. Marchesini, R. Fromme, S. Schorb, D. Rupp, M. Adolph, T. Gorkhover, I. Andersson, H. Hirsemann, G. Potdevin, H. Graafsma, B. Nilsson, J.C.H. Spence, Femtosecond X-ray protein nanocrystallography. Nature **470**, 73–78 (2011)
15. F. Mastropietro, D. Carbone, A. Diaz, J. Eymery, A. Sentenac, T.H. Metzger, V. Chamard, V. Favre-Nicolin, Coherent x-ray wavefront reconstruction of a partially illuminated Fresnel zone plate. Opt. Express **19**(20), 19223–19232 (2011)
16. C.E. Shannon, Communication in the presence of noise. Proc. Inst. Radio Eng. **37**(1), 10–21 (1949)
17. L. De Caro, C. Giacovazzo, D. Siliqi, Confined structures: basic crystallographic aspects. Acta Cryst A **58**, 415–423 (2002)
18. J. Miao, D. Sayre, H.N. Chapman, Phase retrieval from the magnitude of the Fourier transforms of nonperiodic objects. J. Opt. Soc. Am. A **15**, 1662–1669 (1998)
19. R.W. Gerchberg, W.O. Saxton, A practical algorithm for the determination of phase from image and diffraction plane pictures. Optik **35**, 237–246 (1972)
20. J.R. Fienup, Phase retrieval algorithms: a comparison. Appl. Opt. **21**, 2758–2769 (1982)
21. S. Marchesini, A unified evaluation of iterative projection algorithms for phase retrieval. Rev. Sci. Instrum. **78**, 011301 (2007)
22. H.N. Chapman, K.A. Nugent, Coherent lensless X-ray imaging. Nat. Photonics. **4**, 833 (2010)
23. K.A. Nugent, Coherent methods in the X-ray sciences. Adv. Phys. **59**, 1–99 (2009)
24. H.M. Quiney, A.G. Peele, Z. Cai, D. Paterson, K.A. Nugent, Diffractive imaging of highly focused X-ray fields. Nat. Phys. **2**, 101–104 (2006)

25. L. De Caro, C. Giannini, D. Pelliccia, C. Mocuta, T.H. Metzger, A. Guagliardi, A. Cedola, I. Burkeeva, S. Lagomarsino, In-line holography and coherent diffractive imaging with x-ray waveguides. Phys. Rev. B **77-R**, 081408 (2008)
26. C.G. Schroer, P. Boye, J.M. Feldkamp, J. Patommel, A. Schropp, A. Schwab, S. Stephan, M. Burghammer, S. Schöder, C. Riekel, Coherent X-ray diffraction imaging with nanofocused illumination. Phys. Rev. Lett. **101**, 090801 (2008)
27. Y. Takahashi, Y. Nishino, R. Tsutsumi, H. Kubo, H. Furukawa, H. Mimura, S. Matsuyama, N. Zettsu, E. Matsubara, T. Ishikawa, K. Yamauchi, High-resolution diffraction microscopy using the plane-wave field of a nearly diffraction limited focused x-ray beam. Phys. Rev. B **80**, 054103 (2009)
28. B. Abbey, K.A. Nugent, G.J. Williams, J.N. Clark, A.G. Peele, M.A. Pfeifer, M. De Jonge, I. Mcnulty, Keyhole coherent diffractive imaging. Nat. Phys. **4**, 394–398 (2008)
29. W. Hoppe, Diffraction in inhomogeneous primary wave fields: principle of phase determination from electron diffraction interference. Acta Crystallogr. A **25**, 495–501 (1969)
30. P. Thibault, M. Dierolf, A. Menzel, O. Bunk, C. David, F. Pfeiffer, High-resolution scanning X-ray diffraction microscopy. Science **321**, 379–382 (2008)
31. H.M.L. Faulkner, J.M. Rodenburg, Movable aperture lensless transmission microscopy: a novel phase retrieval algorithm. Phys. Rev. Lett. **93**, 023903 (2004)
32. J.M. Rodenburg, H.M.L. Faulkner, A phase retrieval algorithm for shifting illumination. Appl. Phys. Lett. **85**, 4795 (2004)
33. M. Dierolf, A. Menzel, P. Thibault, P. Schneider, C.M. Kewish, R. Wepf, O. Bunk, F. Pfeiffer, Ptychographic X-ray computed tomography at the nanoscale. Nature **467**, 436–439 (2010)
34. M. Dierolf, P. Thibault, A. Menzel, C.M. Kewish, K. Jefimovs, I. Schlichting, K. von König, O. Bunk, F. Pfeiffer, Ptychographic coherent diffractive imaging of weakly scattering specimens. New J. Phys. **12**, 035017 (2010)
35. I. Robinson, R. Harder, Coherent X-ray diffraction imaging of strain at the nanoscale. Nat. Mater. **8**, 291–298 (2009)
36. A. Biermanns, A. Davydok, H. Paetzelt, A. Diaz, V. Gottschalch, T.H. Metzger, U. Pietsch, Individual GaAs nanorods imaged by coherent X-ray diffraction. J. Synchrotron Rad. **16**, 796–802 (2009)
37. A. Diaz, C. Mocuta, J. Stangl, B. Mandl, C. David, J. Vila-Comamala, V. Chamard, T.H. Metzger, G. Bauer, Coherent diffraction imaging of a single epitaxial InAs nanowire using a focused x-ray beam. Phys. Rev. B **79**, 125324 (2009)
38. V. Favre-Nicolin, J. Eymery, R. Koester, P. Gentile, Coherent-diffraction imaging of single nanowires of diameter 95 nanometers. Phys. Rev. B **79**, 195401 (2009)
39. J.M. Zuo, I. Vartanyants, M. Gao, R. Zhang, L.A. Nagahara, Atomic resolution imaging of a carbon nanotube from diffraction intensities. Science **300**, 1419–1421 (2003)
40. W.J. Huang, R. Sun, J. Tao, L.D. Menard, R.G. Nuzzo, J.M. Zuo, Coordination-dependent surface atomic contraction in nanocrystals revealed by coherent diffraction. Nat. Mater. **7**, 308–313 (2008)
41. W.J. Huang, J.M. Zuo, B. Jiang, K.W. Kwon, M. Shim, Sub-ångström-resolution diffractive imaging of single nanocrystals. Nat. Phys. **5**, 129–133 (2009)
42. L. De Caro, E. Carlino, G. Caputo, D.P. Cozzoli, C. Giannini, Electron diffractive imaging of oxygen atoms in nanocrystals at sub-ängström resolution. Nat. Nanotechnol. **5**, 360–365 (2010)
43. P.W. Hawkes, Aberration correction past and present. Philos. Trans. R. Soc. A **367**, 3637–3664 (2009)
44. H.H. Rose, Optics of high-performance electron microscopes. Sci. Technol. Adv. Mater. **9**, 014107 (2008) (30pp)
45. N.D. Browning, S.J. Pennycook, *Characterization of High Tc Materials and Devices by Electron Microscopy* (Cambridge University Press, Cambridge, 2006). ISBN 052155490X
46. J.M. Cowley, *Diffraction Physics*, 2nd edn. (North-Holland, Amsterdam/Oxford/New York/Tokyo, 1990)

47. D. Sayre, H.N. Chapman, J. Miao, On the extendibility of X-ray crystallography to noncrystals. Acta Crystallogr. **A54**, 232–239 (1998)
48. J.M. Zuo, J. Zhang, W. Huang, K. Ran, B. Jiang, Combining real and reciprocal space information for aberration free coherent electron diffractive imaging. Ultramicroscopy (2010). doi:10.1016/j.ultramic.2010.10.013
49. K.W. Urban, Studying atomic structures by aberration-corrected transmission electron microscopy. Science **321**, 506–510 (2008)
50. L. Jiang, D. Georgieva, H.W. Zandbergen, J.P. Abrahams, Unit-cell determination from randomly oriented electron-diffraction patterns. Acta Crystallogr. D **65**(7), 625–632 (2009)
51. T.J. Cui, D.R. Smith, R. Liu (eds.), *Metamaterials: Theory, Design, and Applications* (Springer, New York, 2010)
52. H.M. Quiney, K.A. Nugent, Biomolecular imaging and electronic damage using X-ray free-electron lasers. Nat. Phys. **7**, 142–146 (2011)

Wavefront Measurement in Ophthalmology

Aberrometry Through the Eyes of an Engineer

9

Vasyl Molebny

Contents

Abstract

Wavefront sensing or aberration measurement in the eye is a key problem in refractive surgery and vision correction with laser. The accuracy of these measurements is critical for the outcome of the surgery. Practically all clinical methods use laser as a source of light. To better understand the background, we analyze the pre-laser techniques developed over centuries. They allowed new discoveries of the nature of the optical system of the eye, and many served as prototypes for laser-based wavefront sensing technologies. Hartmann's test was strengthened by Platt's lenslet matrix and the CCD two-dimensional

V. Molebny
Academy of Technological Sciences of Ukraine, Kiev, Ukraine
e-mail: molebny@gmail.com

315

photodetector acquired a new life as a Hartmann-Shack sensor in Heidelberg. Tscherning's aberroscope, invented in France, was transformed into a laser device known as a Dresden aberrometer, having seen its reincarnation in Germany with Seiler's help. The clinical ray tracing technique was brought to life by Molebny in Ukraine, and skiascopy was created by Fujieda in Japan. With the maturation of these technologies, new demands now arise for their wider implementation in optometry and vision correction with customized contact and intraocular lenses.

9.1 Introduction

It is difficult to determine a starting point in the history of wave front and geometrical aberration measurement, but the familiar names can be mentioned of the scientists who were involved in these studies. From the pre-laser era, the most significant findings were made by Scheiner, Young, Helmholtz, Hartmann, Gulstrand, Zernike, Le Grand, Smirnov, and other physicists and physiologists.

With the advent of laser, intensive development of instrumentation for ocular wavefront sensing began. The experience of several centuries was concentrated in the last decades, bringing to the clinics new instruments using the ideas of Donders and Tscherning, Hartmann, and Smirnov. All market-available instruments exploit the techniques of data processing and wave front reconstruction based on Zernike expansion, and eye models, so thoroughly studied by Donders, Helmholtz, Gullstrand, Le Grand, and others. The development of this kind of instrumentation would not be so extensive without the progress in the techniques of vision correction, be it by laser, or by contact lenses, inlays, or intraocular lenses.

The first results of the laser era were summarized in Ref. [1], with the description of general ideas of aberrometry and its clinical applications. Its second edition [2] paid more attention to the commercialized aberrometers and their comparison. Other books [3, 4] summarized clinical applications of the wavefront sensing. Complemented by earlier-introduced corneal topography, it became a topic of wider clinical studies [5]. A series of dissertations followed on instrumentation development [6, 7] and clinical studies [8]. The new techniques were reviewed for the audience of optometrists [9] and medical doctors [10].

9.2 Initial Steps of Understanding the Aberrations

The first explanation for why the eye can distort the outer image was by Scheiner [11], who proposed an experiment with a shield with two small holes through which an observer can look at a far object – a point source of light (Fig. 9.1). The idea of investigating the eye through small openings was widely used in many later studies.

In 1801, Thomas Young demonstrated the existence of aberrations by means of a simple experiment [12]. He extended a thread from a point close to the eye, nearly along its visual axis, to a considerable distance away. Then, he closed the eye with

OCVLVS

HOC EST:

FVNDAMENTVM OPTICVM,

IN QVO

EX ACCVRATA OCVLI

ANATOME, ABSTRVSARVM EX-
PERIENTIARVM SEDVLA PERVE-
ftigatione, ex inuifis fpecierum vifibilium tam
euerfo quam erecto fitu fpectaculis, nec-
non folidis rationum mo-
mentis

RADIVS VISVALIS ERVITVR,

SVA VISIONI IN OCVLO SEDES
DECERNITVR;

ANGVLI VISORII INGENIVM
APERITVR;

DIFFICVLTATES VETERES, NOVÆ, INNVMERÆ EXPE-
diuntur, abftrufa, obfcura, curiofa plurima in medium proferuntur; plura
depromendi eccafio harum rerum ftudiofis datur: Opus multorum votis diu ex-
petitum; Philofophis omnibus, præfertim qui naturæ vim in Medicina,
Phyfica aut Mathefi addifcendarim antur, neque inutile neque
ingratum, imò neceffarium futurum.

AVCTORE

CHRISTOPHORO SCHEINER,

SOC. IESV. &c.

OENIPONTI,

Apud Danielem Agricolam.

M. DC. XIX.
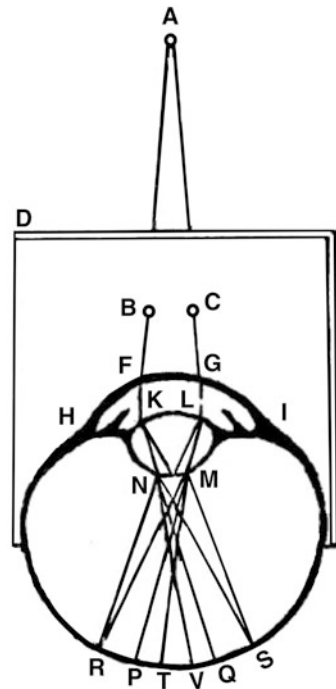
Fig. 9.1 Scheiner's book and the schematic of the experiment with an eye looking at for object through two openings in a non-transparent shield

a screen with four slits and observed four separate images of the thread with accommodated and relaxed eye, and saw the threads intersecting differently depending on the accommodation state.

In 1846, Volkmann [13], looked through four small openings placed across the eye pupil at a pin, which he moved to different distances. As a measure of the spherical aberration, he determined the distance at which the pin was in sharp focus, using first the two more centrally located openings, and then the two located more laterally. He tested several observers and found some of them having a positive spherical aberration and some having a negative aberration.

In his comments on the experiments of Young and Volkmann in a chapter on the history of monochromatic aberration, Helmholtz, recognizing their significance, noticed that Volkmann's results are opposite to the data received by other observers [14], and "in most meridians of most eyes the points of intersection of the rays refracted with the central ray do not form a continuous series at all, as if the conception of spherical aberration does not apply here."

Helmholtz commented also [14] on the results of investigations by Donders, who moved a small perforated screen in front of the eye so as to let light pass
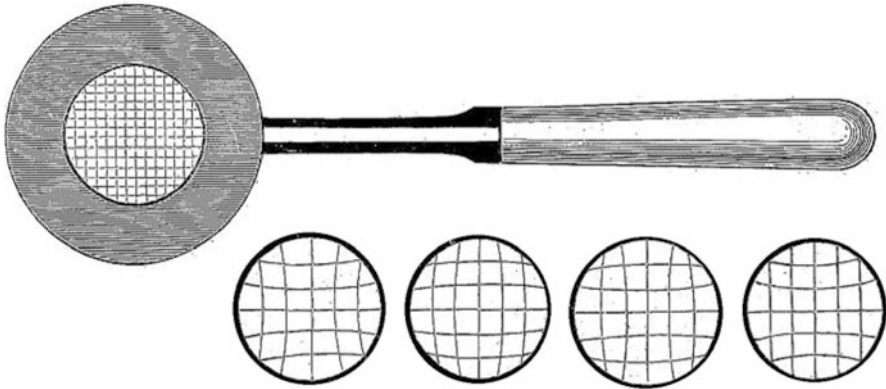
Fig. 9.2 Tscherning's aberroscope and examples of grid deformations resulting from several typical aberrations

through one sector of the lens or another, each sector of the lens converging the rays approximately to a focus, but the focus was not the same for different sectors. The accuracy of determination of the focus was unfortunately not good enough in his experiments.

Skiascopy was an approach used by Jackson, who described symmetrical positive and negative aberrations in 1885 [15]. Later [16], having measured skiascopically the aberration in 100 eyes, he published the accumulated statistics. According to him, 75 % of patients had positive aberration, and only 9 % had negative aberration, which was largely associated with conical corneas or with lens conditions leading to nuclear cataract.

In 1894, Tscherning devised his "aberroscope" as a rectangular grid of thin wires combined with a plano-convex lens [17]. With the lens in front of his eye, he observed a distant luminous point. The opaque lines cast shadows in the blur circle produced on the retina by the "artificial myopia." From the direction of the curvature of the shadows Tscherning concluded that the aberration was positive when his eye was relaxed, tending toward the negative as his eye accommodated. Its general view and several examples of distorted projections are shown in Fig. 9.2.

In 1910, Ames and his sister, who were both painters, began studies of scene reproduction in the eye; the war interrupted these studies, but after the service Ames returned to his work and, together with Proctor, published an article in 1921 [18]. The authors measured spherical aberrations along two meridians in the relaxed eye. They directed at the eye two beams of light of small cross section. The beams were cut of the wide parallel bundle from the exit of a concave mirror using two non-transparent sheets with slits, the sheets being made movable along orthogonal directions and installed in the path of the bundle (Fig. 9.3). One beam passed through the center of the pupil while the second was made to pass consecutively through a series of points along a given meridian due to sliding the sheets in X and/or Y directions. In this way, the observers could change the distance between
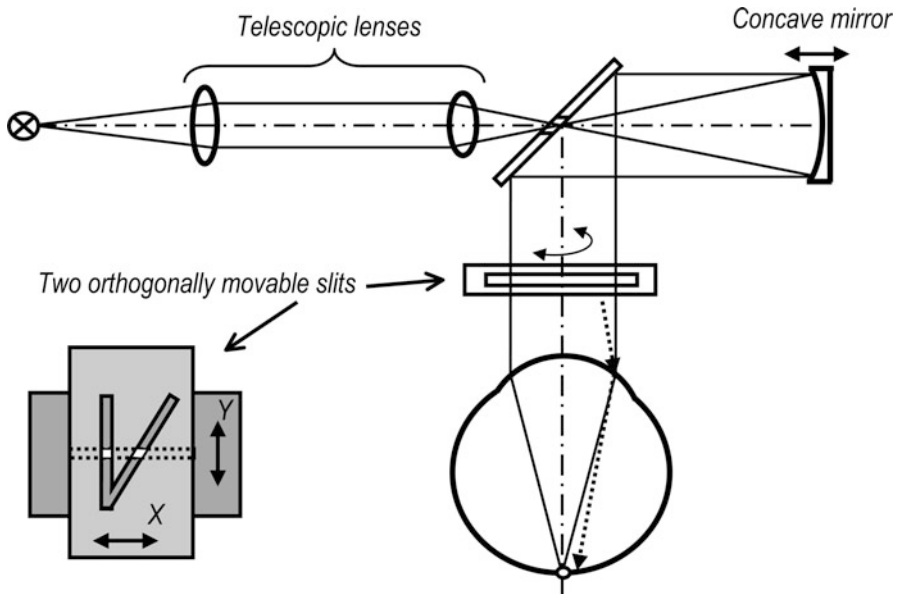
Fig. 9.3 Ames and Proctor's layout. Beam positioning is provided by orthogonally movable slits, the tilt adjustment is made by shifting the concave mirror

the beams. The configuration of the slits can be changed as well, giving the option of changing the traces of the beams if the observer decides to make another comparison. Rotation of the sheets resulted in changing the investigated meridian of the eye. The two beams were made to intersect on the retina by an adjustment of the inclination of one of them (or both). This adjustment was implemented by moving the concave mirror along the optical axis. The spherical aberration was calculated from the angle between the axial and the tilted beams.

In three eyes measured, Ames and Proctor found that, from the center of the pupil to a radius of about 1.5 mm, the eye became increasingly myopic; that is, it showed positive spherical aberration. From 1.5 mm to the pupil margin the aberration decreased, tending to become zero again at the very edge. The maximum observed values of the aberration were between 0.4 and 0.8 diopter.

In the period that followed, modifications of the earlier published approaches were made and tested. In 1925, Pi, using skiascopy, divided the pupil area of the eye into a central zone and four peripheral quadrants and measured the difference in refraction between the central zone and each quadrant in turn [19]. In 1930, Stine made a similar investigation of the refraction by quadrants in non-pathological eyes [20]. He found that differences between quadrants can be as high as eight diopters. Some degree of aberration was found in every eye, both positive and negative.

In 1944, Byram measured spherical aberration of his eye as a part of the study of the light distribution in the image on the retina [21]. He used a slightly different method than that of Ames, and each measurement includes the aberrations of both

the temporal and nasal zones (horizontal meridian). He reported that his eye became increasingly myopic from the center to the margin of the pupil, being more consistent with the model of the eye he described in his article.

In 1945, Bahr measured the aberration along the horizontal and vertical meridians of the pupil, using pairs of small pinholes to sample various zones along a meridian [22]. He found that most of the eyes exhibited positive spherical aberration, the zones of the pupil becoming gradually more myopic from the center of the pupil outward. Negative aberration was present in a few eyes. Some eyes exhibited negative aberration in one-half of a meridian only. Of all the eyes measured, there were none in which the aberration was completely symmetrical.

Otero and Duran [23] investigated the aberrations of the eye looking through each of a series of circular artificial pupils of different diameters. However, since the optical power was determined not zone by zone but for circular areas of progressively increasing size, the results do not give directly the spherical aberration of the eye.

Koomen et al. [24] modified these measurements, subdividing the eye pupil into a central circular area of 2 mm diameter and five to seven distinct annular areas of increasing mean diameter extending to the limit imposed by the fully dilated pupil. Measurements consisted of determining the spectacle lens power, which produced most acute vision while the observer was using, in turn, each of the chosen pupil areas. The spectacle corrections for the annular zones, considered relative to the correction required for the small central area, gave the magnitude and the sign of the aberration. The measurements were made under conditions of controlled accommodation.

A simplified setup is shown in (Fig. 9.4). Annular apertures used for dividing the eye pupil into selected zones are placed in turn in front of the eye-aperture. The annular apertures consist of transparent rings in an opaque background. The target observed through the annular aperture consists of a distant pair of point sources whose separation is held just above the resolution threshold for each annular zone. To fix the state of accommodation of the eye, there is a second target introduced by means of a small beam-splitter.

9.3 The Mid-Twentieth Century: Aberration Distribution in the Eye

In 1946–1953, Ivanoff published [25, 26] some parts of his doctoral work made under Le Grand's supervision (later, Le Grand used these results in his monographs). He modified the Ames and Proctor technique using two thin vertical wires (upper and lower ones) in front of the objective illuminated from two different sources of light. If the crystalline lens were ideal (without aberrations), a change in the place of entry into the pupil of the two light-beams would not cause a misalignment of the wire images. However, if the lens had aberrations, the wires had to be adjusted so that they were perceived to seem a continuation of each other. This adjustment is a measure of the aberration. Ivanoff's measurements
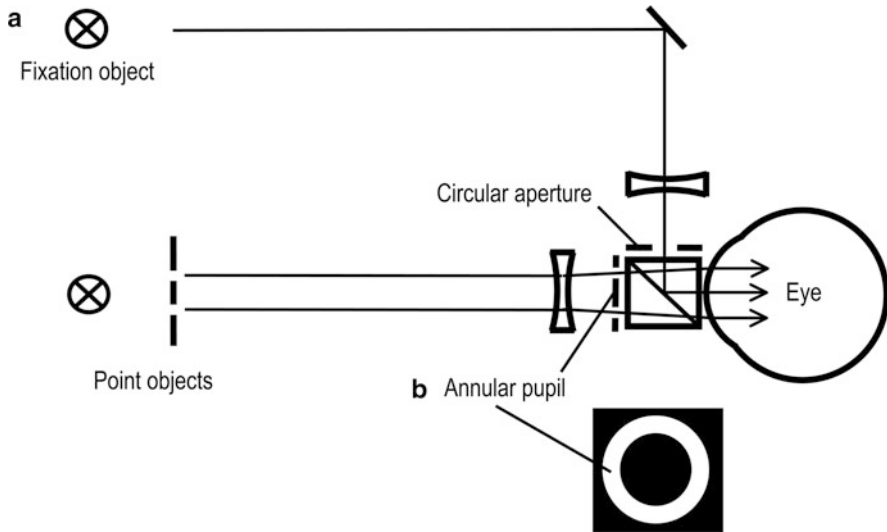
Fig. 9.4 Apparatus for measurement of spherical aberrations (**a**) with a set of annular pupils (**b**) of different sizes [24]

produced a number of smooth curves for several subjects and several states of accommodation (see example in Fig. 9.5). They showed the major change in refractive power occurring within 0.5 mm of the center of the pupil, with little additional change beyond this zone.

Along a single meridian, the outer zones of the average eye exhibited approximately 0.9 diopter of positive spherical aberration when in the relaxed state, and 1.25 diopters of negative spherical aberration when accommodated at 3.0 diopters. When accommodated at 1.5 diopters, there was practically no aberration present. While the magnitude of the aberration varied from individual to individual, the amount of the accommodation necessary to eliminate the aberration was about the same for all individuals.

The results published by Ivanoff evoked criticism on too large aberration close to the axis. No other observers were able to find such an effect within the central zone of 0.5 mm radius, using a method similar to his. This caused him to correct the data reconstruction [27], making the results compatible with other spherical aberration measurements (dotted regions in Fig. 9.5). Criticizing Ivanoff's data processing, Koomen et al. [28] paid attention to the fact that the choice of the reference axis, upon which the points of intersection of the various rays are determined in the process of measurement of the spherical aberration, has a strong effect on the shape of the curve of spherical aberration. An improper choice may lead to a highly non-symmetrical curve. Since spherical aberration is always referred to the axis of symmetry and since there is no axis of perfect symmetry in the real eye, even for a single meridian, Koomen et al. recommended referring to an axis relative to which the eye exhibits the greatest degree of

Fig. 9.5 Profiles of aberration along the eye meridian for different states of accommodation. *Dotted lines* – after correction (after the critics, Ivanoff abandoned the idea to suggest a zero error on the visual axis)
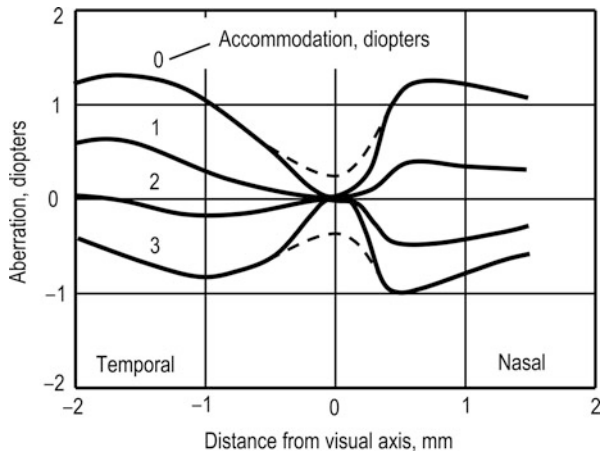
symmetry. It became clear from Ivanoff's results that dealing only with spherical aberration is not enough.

As a response to this conclusion, Smirnov in 1961 [29] and Van den Brink in 1962 [30] made pioneering works having not only measured the distribution of the optical power across certain meridians of the eye pupil but having reconstructed the maps of refraction non-homogeneity of the human eye. Their predecessors did it with similar data but they only made the conclusion on asymmetry of spherical aberrations and did not attempt to map the irregularity they were observing.

Van den Brink's experimental setup consisted of four channels, their optical axes being combined by means of half-mirrors and a mixing cube and brought together into the same ocular. The four light-paths provide (a) the test object, (b) an annular comparison field around the test object, (c) the fixation point for direction, which also provides a control of accommodation, and (d) an optical system to indicate the correct eye position. For the sake of simplification, only the test channel is shown in Fig. 9.6.

The test object consisted of a number of opaque stripes. The width and the separation of the stripes increased from the center towards the edge. The object was transilluminated and subtended an angle of 3″; the orientation of its stripes could be changed. The objective could be moved back and forth to adjust the focus. The position of the objective was recorded photographically via a mirror, which was rotated by the movement of the objective. A point of light was focused via this mirror on a recording drum, provided a shutter did not intercept the light beam. Following focusing, the shutter was opened for a short time to project the beam on the photo recorder. Just behind the movable objective, a frame for diaphragms was fixed. The plane of this frame was focused 10 mm behind the ocular, at the position of the eye. Focus settings were made for each position of the diaphragm. After each focus setting, a shutter was opened and the dioptric value was registered with the photo recorder.
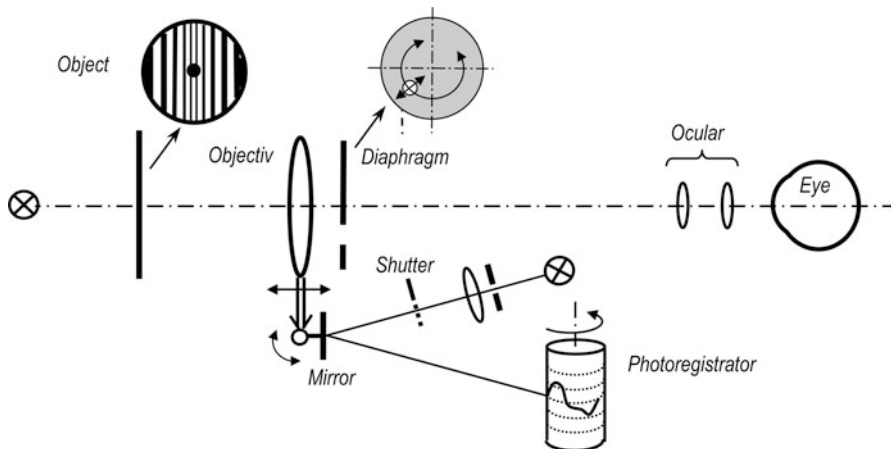
Fig. 9.6 A simplified arrangement of the van den Brink's apparatus (accommodation, fixation, and positioning channels are not shown)

An example of measured optical power of the eye as a function of the eccentricity for three different observers is given in Fig. 9.7 (we rotated the original author's axes to more logic orientation: Y direction being the function of X). Another example of the dioptric power as a function of the diaphragm position is shown in Fig. 9.8 (points of the same power are connected by iso-diopter lines).

Van den Brink paid attention to the changes of the distribution of the optical power with variation in the state of accommodation. With each state of accommodation, the standard deviation and the visual acuity were registered (Fig. 9.9). It is apparent from the graph that the visual acuity is maximal at that state of accommodation at which the distribution of the dioptric power over the eye aperture is most homogeneous, and that the visual acuity changes in the other direction when the standard deviation changes. From this it is clear that the course of the dioptric homogeneity of the focusing system of the eye, as a function of accommodation, is an important factor in the dependence of the visual acuity upon accommodation. Previously, this phenomenon had not been unambiguously explained.

With Smirnov's instrument (Fig. 9.10), the observer looks at the light-scattering shield (Sh) through a consecutively installed polarizer (P_2) with a small central opening, through an opening in the test object (an opaque white screen, Scr), crossed wires (CW), and a polarizer (P_1) (Fig. 9.10). A rectangular grid is drawn on the test object, which is illuminated with the lamp (L_1). Polarizers (P_1 and P_2) are installed with orthogonal orientation of their axes. The shield (Sh) is back illuminated with the lamp (L_2). With this layout, the observer can see the screen (Scr) through the polarizer (P_2) in a wide field of view and the crossed wires (CW) only through the opening in the polarizer (P_1) and through the opening in the test object (Scr). The dimensions in this layout are as follows: distance from the eye to the polarizer (L_2) is 15 cm, distance to the test object (Scr) is 1 m, the opening in the polarizer (L_2) is 0.4 mm in diameter, the diameter of the opening in the test object is 1 cm.
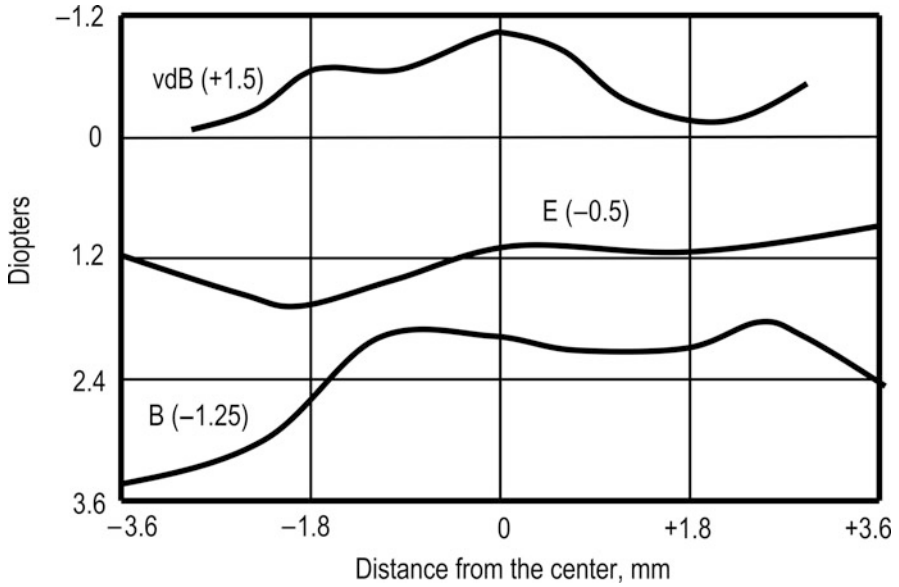
Fig. 9.7 Distribution of a local optical power of the eye as a function of the distance from the center for different accommodation states (compare with Fig. 9.5)
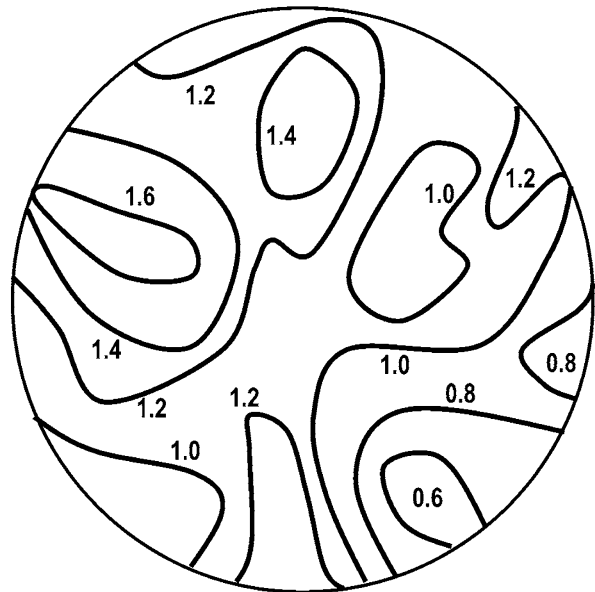
Fig. 9.8 Refraction map ("dioptric power as a function of place") reconstructed from the data acquired with the apparatus of Fig. 9.6
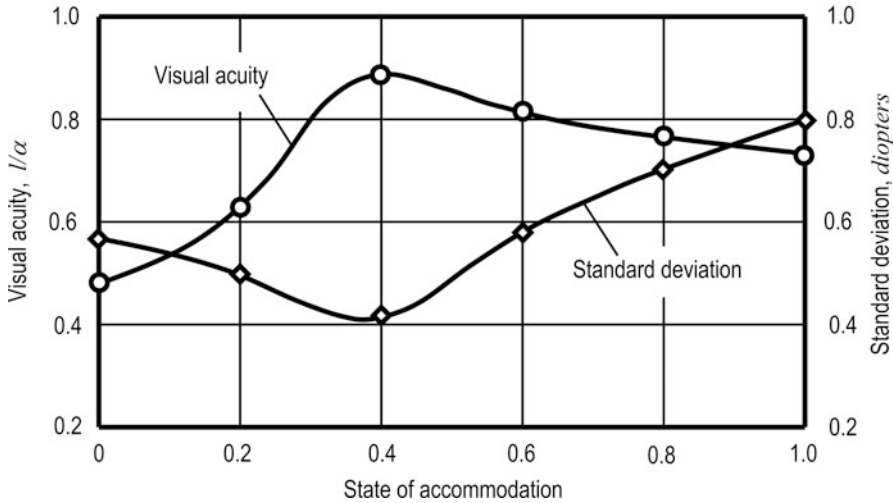
Fig. 9.9 Visual acuity as compared with the level of aberrations
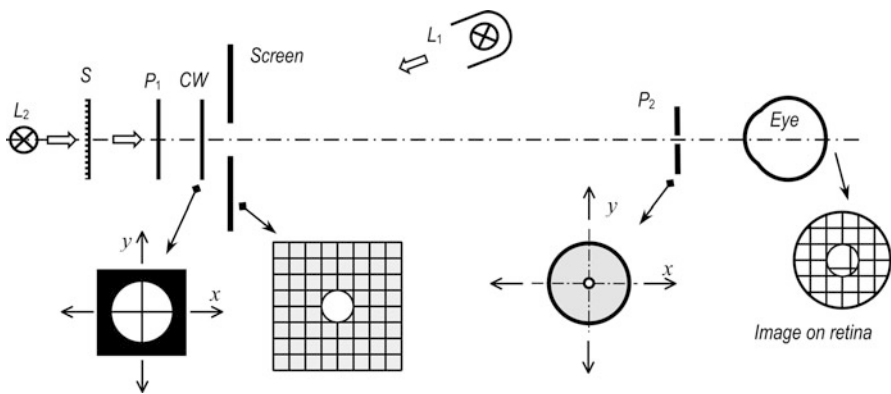
Fig. 9.10 A simplified set-up for aberration measurement made by Smirnov (auxiliary channels are not shown). The test object (screen) is seen through the polarizer P_2. Crossed wires CW can be seen only through a small (0.4 mm) aperture in the polarizer

Smirnov reconstructed the wavefront maps, calling them "plates of errors" (see an example in Fig. 9.11), analyzed and recalculated the results of Ivanoff, explained the causes of the discrepancies in Ivanoff's conclusions, compared his own results with the results of other authors, and came to the conclusion that, generally speaking, the wavefront errors of the eye cannot be described only in terms of defocusing or simple astigmatism. They, as a rule, are essentially non-symmetrical. He noted that the high level of aberrations correlates with the drop of visual acuity.

Fig. 9.11 An example of a wave front map ("plate of errors") reconstructed from the data acquired with the setup of Fig. 9.10
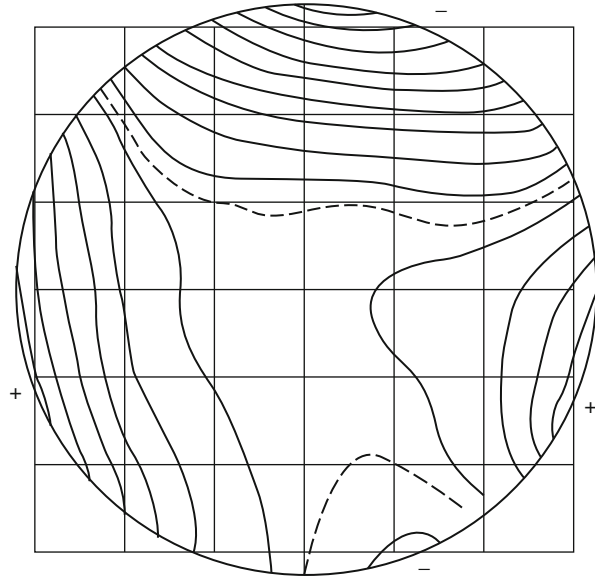
But for "not very high level of aberrations there does not seem to be a robust and direct relationship between the level of the aberrations and the visual acuity."

Based on his findings, Smirnov expressed a far-reaching idea: "In principle, it is possible to manufacture a lens compensating the wave aberration of the eye in the complex form of the plates of errors. The lenses must obviously be contact ones. Otherwise, even small turns of the eye will produce sharp increase in aberrations of the system." The time to implement this idea came about 40 years later [31].

As with the other above-described techniques, Smirnov's was quite laborious: the measurement took 1–2 h, and calculations in those days took 10–12 h. For these reasons, Smirnov suggested that it is unlikely that "such detailed measurements will ever be adopted by practicing ophthalmologists." He believed that principal value of his study was the understanding of the restrictions of the visual channel of information acquisition, and for these reasons, he abandoned further development of his technique (M.S. Smirnov, 2005, private communication to V. Molebny).

In 1968, an article appeared [32] on the technique of photographic lens evaluation. It was a modification of Tscherning's grid projection method, in which, instead of a pair of a grid and a spherical lens, a triplet was used consisting of a combination of plus and minus plano cylinder lenses, with the grid sandwiched between their plano surfaces (Fig. 9.12). The triplet was called an "aberroscope." Later, the technique was applied for eye investigation [33, 34]. A point source of light was generated by placing a fiber optic at the front focal plane of a microscope objective (Fig. 9.13). The lenses taken were +5D and −5D. The combination forms a single test lens element that fits into the front of a trial lens frame. The grid spacing is 1.25 mm. The diagonals of the grid coincide with the axes of the crossed cylinder lens combination.

Fig. 9.12 Crossed cylinder orientation with the grid sandwiched between their plano surfaces (diagonals of the grid are parallel to the axes of cylinders)
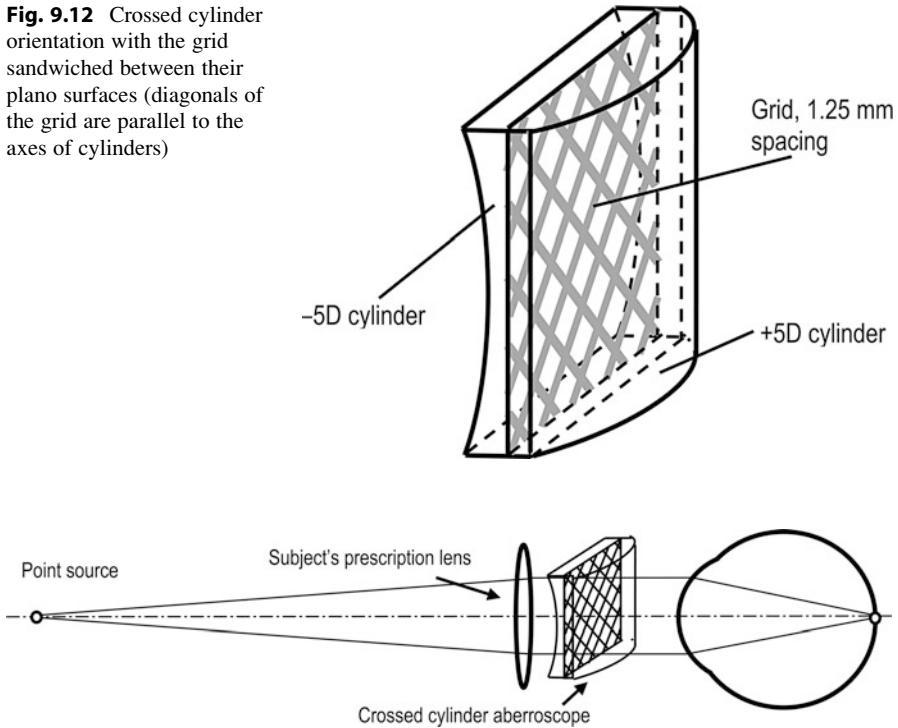
Fig. 9.13 Schematic of the subjective tests with the crossed cylinder aberroscope

The subject looks at a point source of light about 1 m distant in a darkened room. The subject's near prescription is placed in the trial frame. The lines in the central squares of the grid are seen as horizontal and vertical. Any change in spherical or cylindrical power causes a tilting of the grid lines. The subject is asked to memorize the grid's pertinent features so that he or she can later sketch the grid with these features. The sketch is then analyzed quantitatively to estimate the wave aberration.

This technique was modified by Walsh et al. [35] due to introduction of the optics necessary for photographing the grid on the subject's retina (Fig. 9.14), thus obviating the uncertainty of subjective sketches. Rather than asking the subject to reproduce the distortions that he or she perceives. In this modification, the grid samples the pupil on a 0.9 × 0.9 mm square mesh. Computer reconstruction of an aberroscope grid on retina and topographic representation of wave aberrations are illustrated by Fig. 9.15. The contours in the topographic maps are at 0.33-μm intervals.

Simulations of the optics of the Howland crossed-cylinder aberroscope technique show [36] that errors in alignment, data collection, and analysis can lead to unexpected asymmetries of the determined aberrations in a rotationally symmetric system. Large errors in measured aberrations occur from the incorrect choice of grid center and from errors in setting up the aberroscope. As an example, a 1-mm
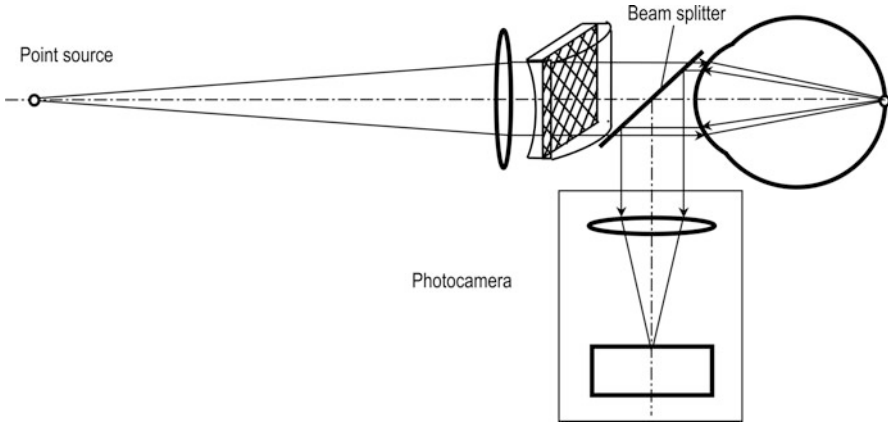
Fig. 9.14 Schematic of the objective tests with the crossed cylinder aberroscope

Fig. 9.15 Computer reconstruction of an aberroscope grid on retina and topographic representation of wave aberrations [35]
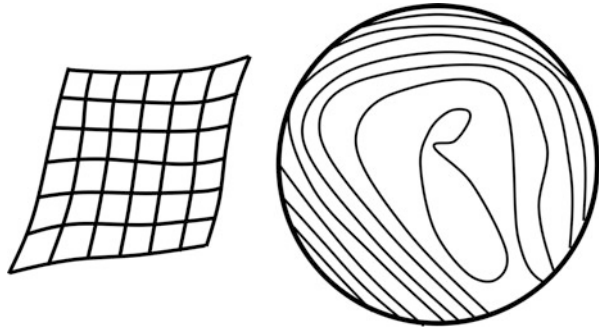
error in choice of grid center produces a coma error with a larger coefficient than that of the existing spherical aberration. Alignment errors and data collection–analysis errors tend to increase the measured aberrations and to affect the asymmetrical aberrations more than the symmetrical aberrations. It is not possible to predict the expected errors a priori. It is recommended therefore to make calibration, using schematic eyes with known aberrations.

9.4 Spatially Resolved Refractometry

The instrument described in Ref. [37] incorporates two independently adjustable apertures. One is imaged at a region near the corneal apex, and the other's corneal position is varied. The subject sees a reference image through the first aperture and a test image through the second. The subject's task is to align the test image (a bright dot) with the reference (a target pattern) by means of a joystick.
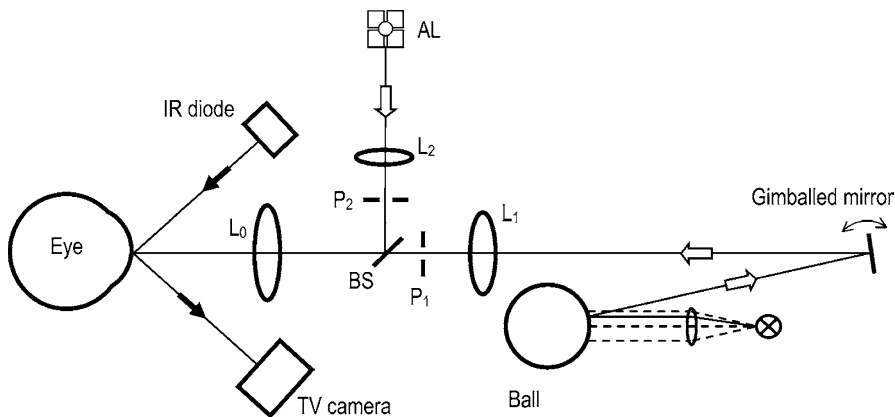
Fig. 9.16 Layout of the spatially resolved aberrometer [37]

The joystick changes the angle at which the incident light falls without changing its position at the cornea – as shown in Fig. 9.16. The orientation and magnitude of the angular change are recorded; then the test aperture is moved to a new position for another measurement. The authors took measurements at 30 separate positions on the cornea (having a dilated pupil 6–7 mm in diameter, and a probe beam being 1 mm in diameter).

Figure 9.16 shows the layout of the instrument. P_1 and P_2 are the pinholes, which are *XYZ* movable. Lens L_0 images the pinholes at the plane of the cornea, with the beam splitter (BS) transmitting light for P_1 and reflecting light for P_2. Light from a lamp shines on a steel bearing ball and is reflected in all directions so that there is a virtual point source inside the ball. Some of this light falls on the gimballed mirror and is reflected to lens L_1 and P_1. Lens L_1 forms an image of the virtual point source in the plane Q, which is at the focal length of L_0. Thus, this light, when it reaches the cornea, is collimated. It is stopped down by the pinhole P_1, and directed by the gimballed mirror. The gimballed mirror changes the beam's direction without changing its position at the cornea.

The instrument's program works as follows: after the initial alignment, the program selects randomly the locations (x, y) for P_1 and drives the position of P_1 to a reference position of beam projection established at alignment. The patient, who is looking at a retinal plane, sees the bright spot of reflected light from the bearing ball superposed on the cross of the alignment target. The patient's task is to use the joystick to bring the bright test spot into coincidence with the center of the cross. The procedure is repeated for all 30 points.

In Sergienko's astigmometer [38], bringing two images together was implemented by along-axis shifting of the target. Sixteen points were chosen in the eye aperture of 3 and 5 mm in diameter.

In one modification [39], a laser is used as a source of light followed by a rotating diffuser to model a point source, and a chopper is inserted on the beam path to
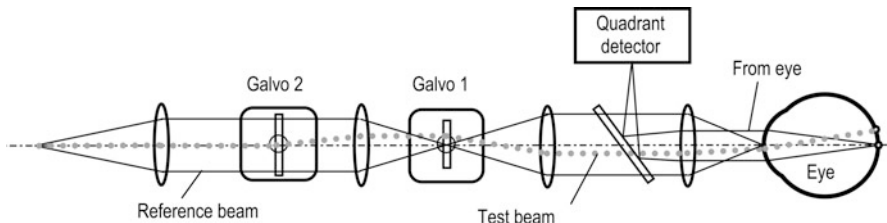
Fig. 9.17 Schematic of the automatic variant of a spatially resolved refractometer. One of the galvanometers, Galvo 1, is imaged at the cornea, the other at the retina. The quadrant detector is also imaged at the retina, its signal drives the retinal position of the laser spot to the null. The beam expander can adjust retinal focus to compensate for ametropia [41]

arrange a pulse mode of operation. A focusing block was also introduced to compensate for defocus. Separate channels are used for providing the test stimulus, a reference stimulus with adjustable pupil size, and a real-time view of the subject's pupil.

In another modification [40], an oscilloscope display is used as a source of light with a pupil sampling aperture randomly selecting the positions within the aperture (37 positions in the aperture sized about 6 mm, beam diameter being about 1 mm).

In a later work [41], the feasibility was tested of making the procedure of target alignment automatic. For this purpose, two beams are projected into the eye alternately, the first one as a reference and another one as a test beam (Fig. 9.17). A quadrant detector installed to look into the eye measures relative positions of the test beam and controls its positioning and tilt until the coordinates of its projection on the retina coincide with the coordinates of the reference beam. The authors analyzed several techniques, including bright cathode ray tubes and light-emitting diodes combined with spatial light modulators. They came to the conclusion that it is impractical to use liquid crystal modulators, since they have a relaxation time of 50 ms at room temperature. If using the galvanometer controlled mirrors having a resonance frequency above 1 kHz, an average time for large repositioning could be about 30 ms, resulting in 2 s for 65 corneal positions. To make the technique attractive for clinical use, the authors propose pupil tracking. This would scarcely be the solution since it would lead to further complications of the instrument.

9.5 Hartmann's Test of the Outgoing Light

A short summary on a lenticular Hartmann screen [42] was published in the program of the 1971 OSA Spring Meeting. It was a less-than-common 10-min presentation, and was marked with a note that the paper could be presented "only if the chairman of the session rules that time permits." The whole idea was formulated in two sentences: "The conventional perforated screen is replaced by an array of contiguous lenticular elements, each approximately 1 mm square and
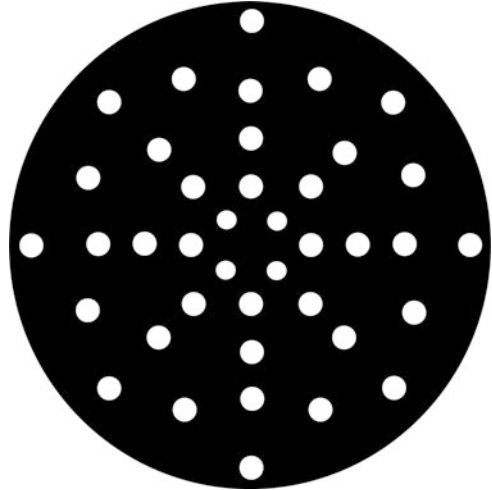
approximately 125 mm in focal length. The recording is made in the common focal plane of the lenticular elements." At that time, nobody could predict that the name of the first author would be fated to become a part of a widely used term, "Hartmann-Shack sensor" (some authors continue to use the term "Hartmann sensor" or "Shack-Hartmann sensor").

The Hartmann-Shack technique had nothing in common with ophthalmology until the late 1980s. The initial idea was proposed by J. Hartmann [43] at the beginning of the twentieth century to check the quality of large-size optics, mainly for astronomy. On the path of a bundle of light propagating through an optical component (lens), he installed an obscure screen with a series of small apertures (Fig. 9.18).

In the late 1960s, the US Air Force wanted to improve the images of satellites taken from earth [44]. The earth's atmosphere limits the image quality and exposure time of stars and satellites taken with telescopes. R. Shack soon came to the conclusion that the only workable solution was to replace the holes in the plate with lenses. After many trials, B. Platt manufactured crossed cylinder based lens arrays in his "wife's kitchen" (Fig. 9.19). The Air Force project was simulated in the laboratory using the satellites photographs. Modeling using a pinhole as a test target is demonstrated in Fig. 9.20 [44]. The left image shows a spot pattern (a) in the focal plane of the lenslets. The next image (b) is a vector representation of the wavefront tilts where the length of the arrow illustrates the magnitude of the tilt and the direction of the arrow illustrates the angle of the tilt. The wavefront (c) was recovered using Zernike polynomial fit. An attempt was made to file for a patent but the application was never filed. A complete system was designed, fabricated, and delivered to the Air Force in the early 1970s to be used on the satellite-tracking telescope at Cloudcroft, NM. The system was never installed and the facility was later decommissioned.

Fig. 9.19 Platt's construction of the wavefront sensor
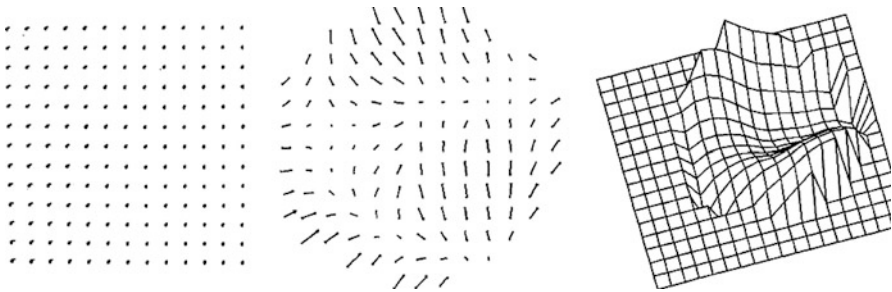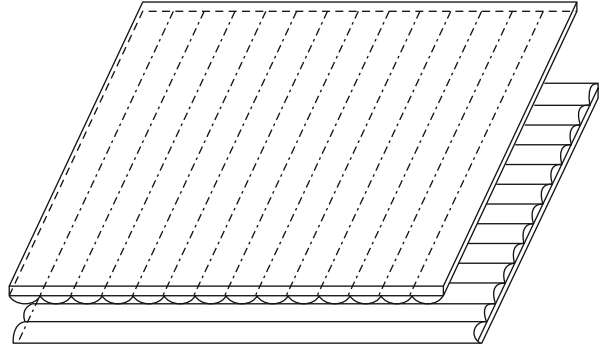
Fig. 9.20 Array of images formed by the Hartmann-Shack lens array from a single pinhole (**a**); graphical representation of the wavefront tilt vectors (**b**); 3-D plot of the measured wavefront (**c**) [44]

Shack also worked with astronomers in Europe. He gave lens arrays to R. Wilson, who having tested large telescopes published a paper on this work and sent a copy of the paper to Shack, thanking him for introducing this new tester to him and coining the name "Shack-Hartmann sensor."

In the mid-1980s, J. Bille, in Germany, started working with Shack to use the lens array for measuring the profile of the cornea. Later, he projected a laser beam onto the retina and analyzed the backscattered light with the Hartmann-Shack sensor [45]. In this classic layout, the laser beam projection plays the role of the secondary point source of light (Fig. 9.21). The more it is deformed (defocused or otherwise distorted), the less accurate is the initial sphere-shaped wavefront of this point source, whose distortions should be fixed by the lenslet array.

Simultaneously, several other groups were working on military applications of wavefront sensing. One of these applications was adaptive correction of the aberrations of the optical systems [46]. This experience was successfully transformed into ophthalmic wavefront sensing that used holograms instead of micro-lens arrays [47]. To exclude the manufacturing errors, an additional reference channel was incorporated into the layout (Fig. 9.22). As a result, each holographic microlens
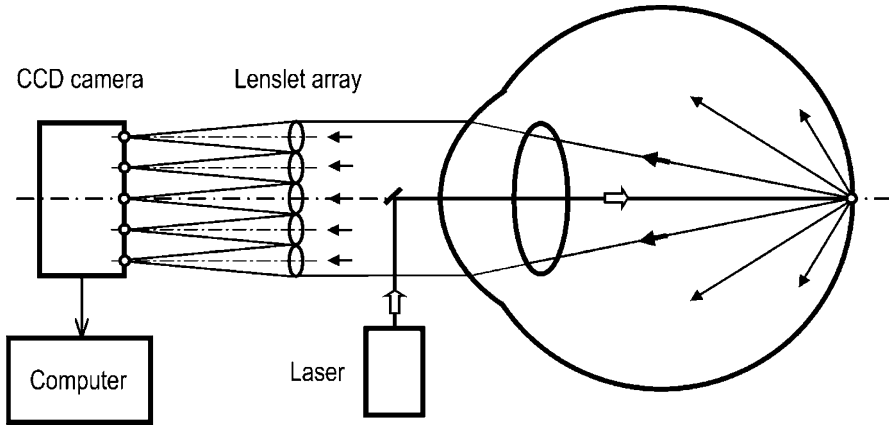
Fig. 9.21 Simplified schematic of the aberrometer using the Hartmann-Shack sensor
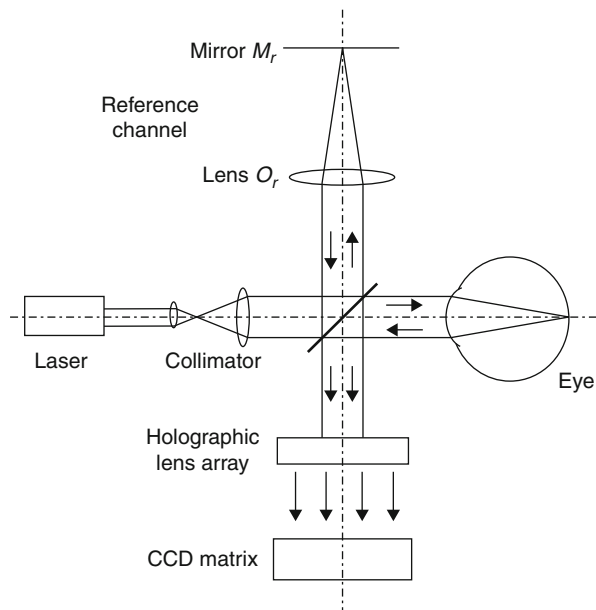
Fig. 9.22 Schematic of a wavefront sensor with a holographic lens array and a reference channel

produced two images: of the reference spot and of the test spot (Fig. 9.23). Distance between these spots is the measure of the transverse aberration.

The idea of analyzing the distortions of ray paths not of the light entering the eye but of the light coming back from the eye was the analog to that from the military systems acquiring the information about the wavefront from the light reflected by the target and propagating to the wavefront sensor along the same trace but in the

Fig. 9.23 Images of focal
spots of the reference and test
channels (only last rows and
columns are shown)
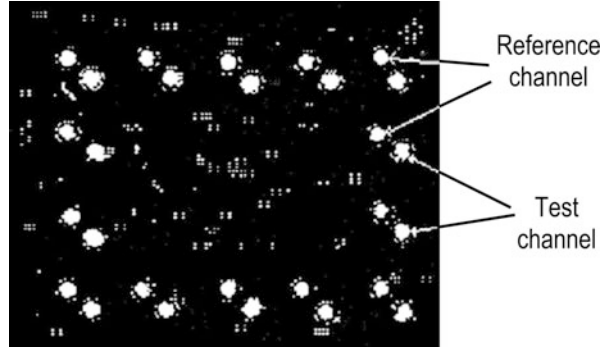
reverse direction. The atmosphere should be unchanged during the time of propagation there and back. This time of being "frozen" for the atmosphere is about 1 ms, restricting the range to 150 km. Fortunately, the eye does not change its characteristics so fast, but there is another problem: should the non-homogeneity of refraction be not identical along the paths inward and outward, the principle would not be applicable.

If we analyze the trajectories of the beams for the methods extracting aberration information acquired along the inward paths in the eye (spatially resolved refractometry and some other methods, to be discussed later) and the methods extracting the information acquired along the outward paths (based on Hartmann-Shack approach), we shall note that these paths are different (Fig. 9.24). Let us suggest, we want to have the information on the refractive power in point A. In inward methods, the beam is directed in the eye in point A hitting the retina in point R_1, comes back through the nodal point N and exits from the eye through point B. In outward methods, the radiation is caught in the point A coming from the retinal point R on the visual axis of the eye that is hit by the probing beam. It is evident that the paths AR_1B and ORA, both in myopic and hyperopic eyes, are different. There is the only situation when these paths coincide (this means that aberrations are measured correctly) – in an emmetropic eye when there are no aberrations. Still, commercial aberrometers using Hartmann-Shack sensors do not pay much attention to this non-correspondence.

A fundamental limitation of a Hartmann Shack wavefront sensor is created by a condition that each spot generated by a lenslet array must be within the virtual subaperture on a detector for spot centroiding. This limitation creates a trade-off between accuracy and dynamic range. The larger the focal length of the microlenses, the higher is the accuracy. But, when highly aberrated wavefronts are measured with a long-focal-length lenslet array, multiple spots or crossed-over spots could appear within the same virtual centroiding area due to a larger spot displacement. The simplest way to avoid this problem is to reduce the amount of spot displacement by using a significantly shorter focal length. However, this solution also decreases measurement sensitivity due to the inability to detect small spot displacements when relatively small amounts of aberration are
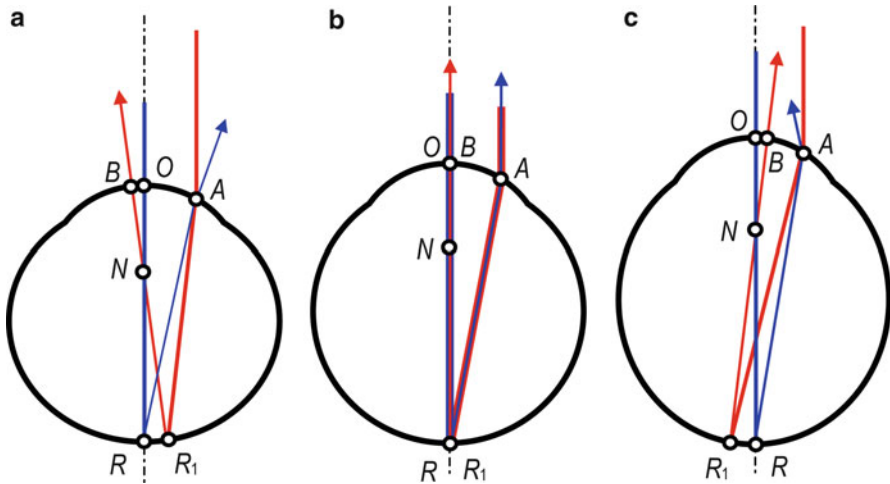
Fig. 9.24 Inward and outward beam trajectories in hyperopic (**a**), emmetropic (**b**), and miopic (**c**) eyes

measured. Therefore, an increase in the dynamic range results in a decrease in measurement sensitivity. A solution must include an increase in dynamic range without loss of measurement sensitivity. Several methods have been proposed that enable the detection of the subaperture violation. They can be divided into software-based methods and hardware-based methods. The advantage of the software-based methods is that no change of the hardware is necessary. The disadvantage is that they require more a priori knowledge about the smoothness of the wavefront than the hardware-based methods and that they are time consuming.

One of the hardware-based ways is to switch the subapertures on and off, so that a definite assignment of the spots to their subapertures is possible. Yoon et al. [48] proposed the blocking of adjacent lenslets using translatable plates. In the configuration shown in Fig. 9.25, every other lenslet is blocked by the translatable plate. In this prototype, the virtual centroiding area is increased by a factor of 2. After the first spot array pattern is captured, the translatable plate is translated by one lenslet spacing to capture the second spot array pattern that includes spots blocked by the plate previously. In the 2-D space, each complete measurement consists of four spot-array images after each of three translations of the plate in horizontal and vertical directions. The total acquisition time, including the time required to translate the plate, was approximately five times longer (470 ms) than with the conventional wavefront sensor.

Instead of mechanical switching, Lindlein et al. [49] proposed using spatial light modulators in front of the microlenses of the sensor to switch on and off the subapertures. It is done with a coding algorithm that also allows a definite assignment of the spots to their subapertures. Each subaperture of the Hartmann-Shack
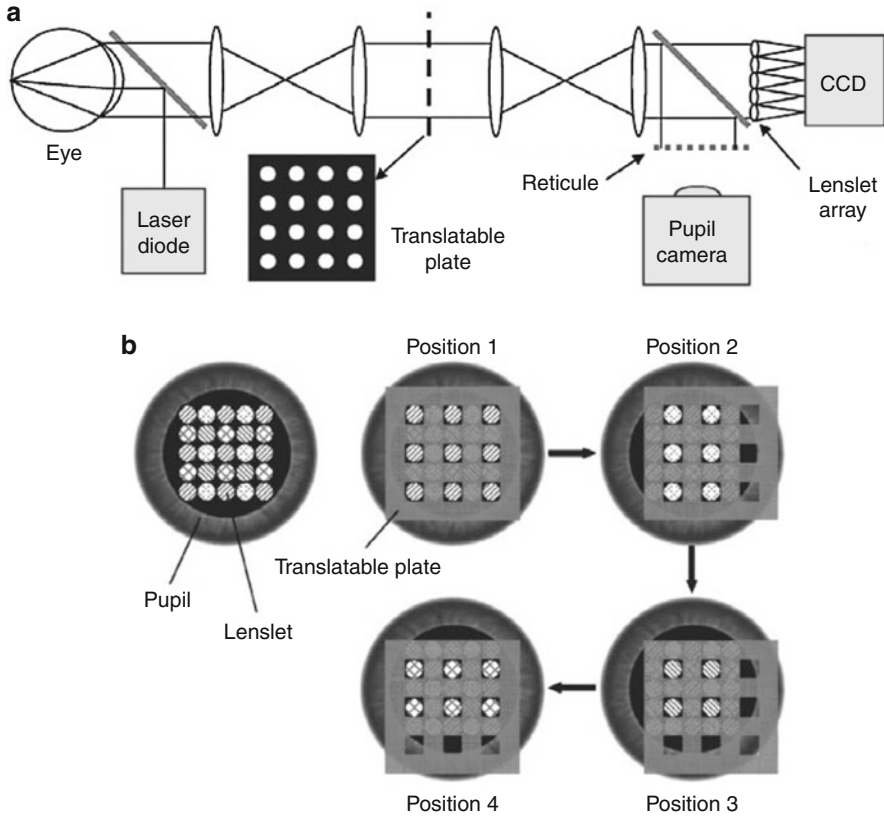
Fig. 9.25 Optical layout of the Shack-Hartmann sensor with a translatable plate blocking every other lenslet (**a**) and a schematic diagram of capturing spot pattern at each position of the plate after translations (**b**) [48]

sensor can be switched on or off with the help of an array of spatial light modulators, so two different states are possible for each subaperture. The state "subaperture switched off" is marked by a binary 0, and the state "subaperture switched on" by a binary 1. Examples of off-on subapertures are given in Fig. 9.26. With relaxation time 50 ms for liquid crystal modulators and 50 ms read-out time for CCD device, five-time switching and reading will result in at least 500 ms for measurement.

The time of switching can be reduced with faster devices. Molebny [50] described the solution with fast acousto-optic switching of the tilt of the probing beam (Fig. 9.27). With subaperture grouping like that with a translatable plate, each probing provides one fourth of the information. Switching four times with different tilts of the probing beam will complete the cycle. The tilt of the beam should correspond to the pitch of the lenslet array.

Not to spend time on switching, a parallel layout was proposed with astigmatic lenslets having different orientations of axes in such a way that no one neighbor of
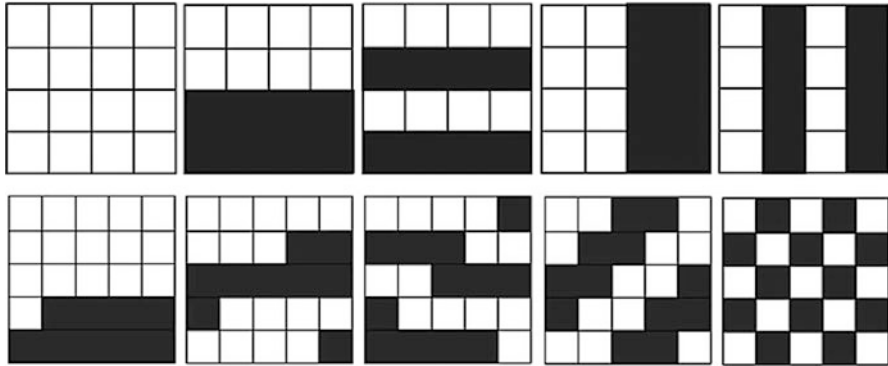
Fig. 9.26 Switching patterns for 4×4 and 5×5 arrays of subapertures. Five different switching patterns are necessary for a definite assignment of the spots to their subapertures in both patterns
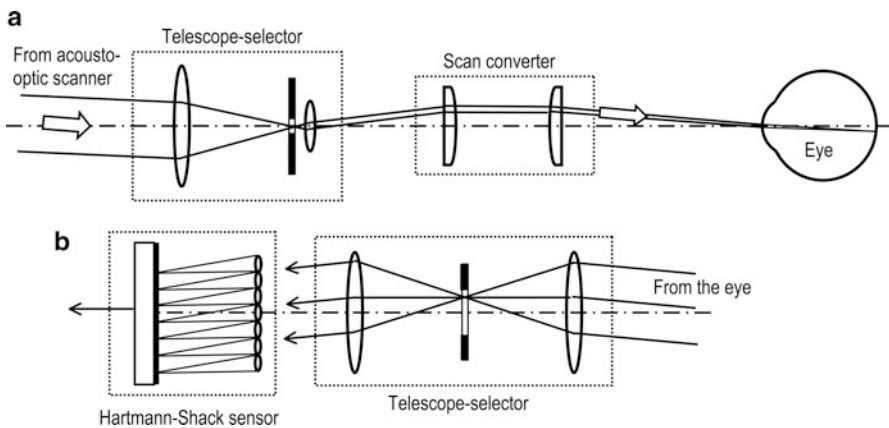
Fig. 9.27 Optical layout of the Hartmann-Shack sensor with a fast switching of the tilt of the probing beam [50]

any lenslet has the same orientation [51]. The orientations change in 10-degree steps (Fig. 9.28). Their identification should be made after detection during the processing of the spots and calculating their centroids.

Increasing the dynamic range, software-based approaches do not require any modification to existing systems and thus minimize the cost of system reconstruction.

Groening et al. [52] described an algorithm that assigns the spots to their reference points unequivocally even if they are situated far outside their subaperture. For this assignment a spline function is extrapolated in successive steps of the iterative algorithm. Starting with a number of spots that can be assigned to their reference points unequivocally (it is a central 3×3 matrix in the example presented in Fig. 9.29), the algorithm estimates the positions of the spots of neighboring microlenses by extrapolating a two-dimensional spline function that

Fig. 9.28 Schematic view of a 9×9 subarray where each lens has orientation of the principal axis $10°$ different of the neighbor
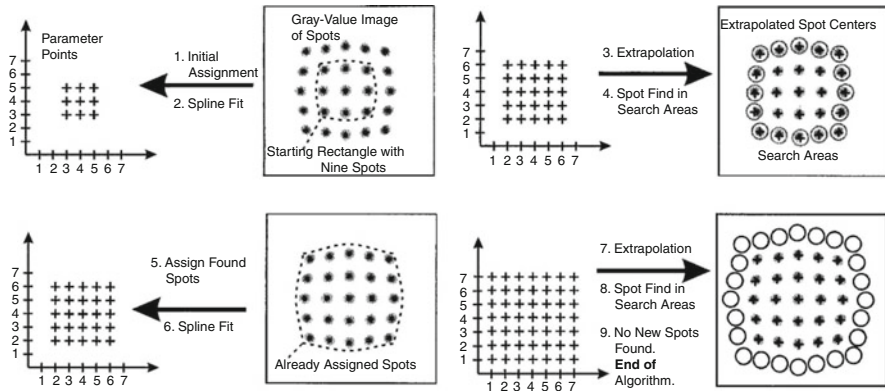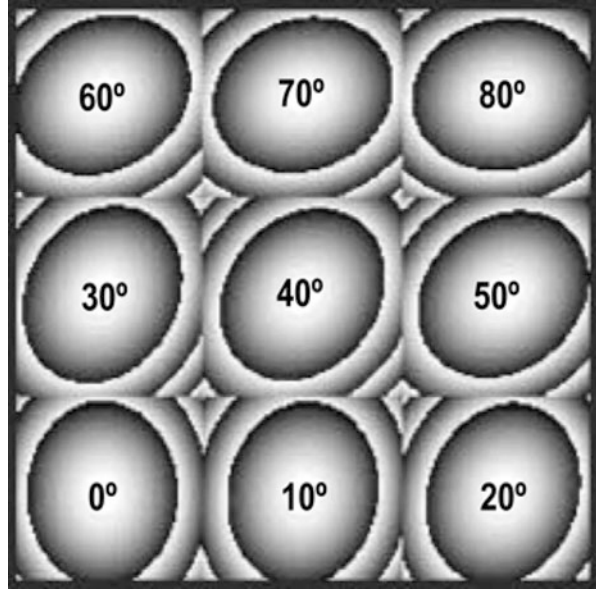
Fig. 9.29 Principle of the iterative spline-fitting algorithm

assigns the spots to their respective reference points. If spots are found in a small area around the extrapolated spot positions, they are used to recalculate the spline function. This procedure is carried on iteratively until no spots are found at the extrapolated spot positions.

Lundström and Unsbo [53] modified this "unwrapping algorithm." They made it to start by connecting the central Hartmann-Shack sensor (HS) spots to the central lenslets (Fig. 9.30). It then fits a B-spline function through a least squares estimate

Fig. 9.30 The structure of the unwrapping algorithm [53]
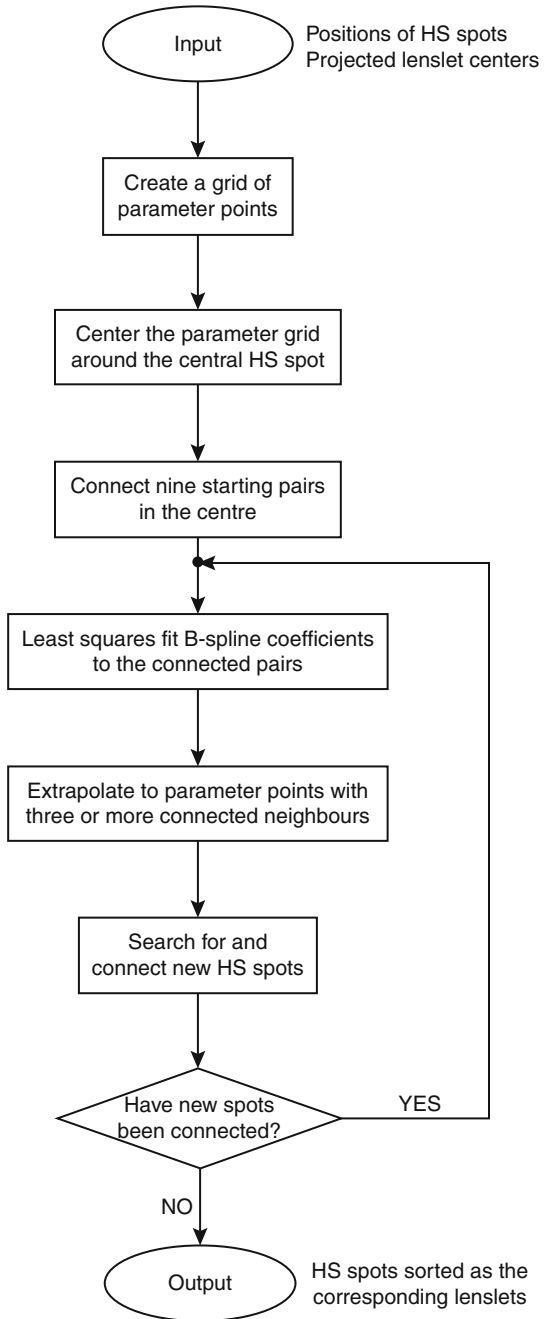
Fig. 9.31 Example
wavefront from the set of
1,000 randomly generated
wavefronts. *Large circles*
indicate spots that were
correctly located according to
the internal error checking of
each algorithm [57]
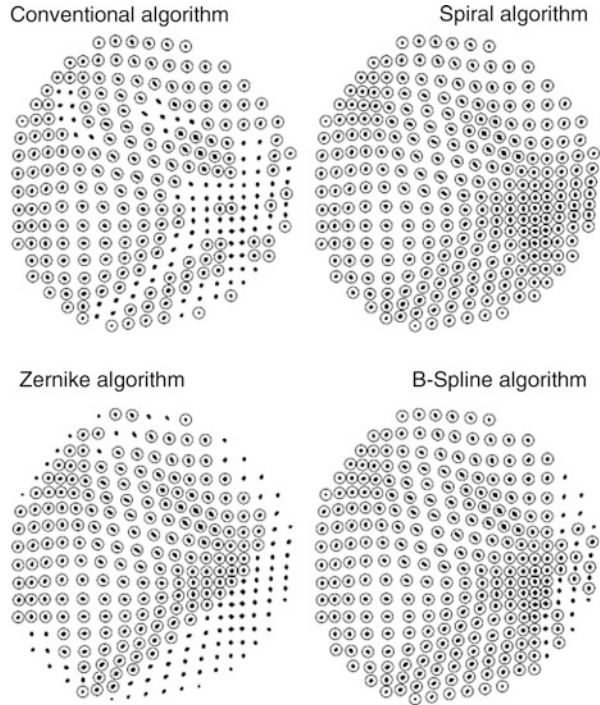
to the deviations of the central HS spots. This function is then extrapolated to find
the expected locations of HS spots for the unconnected lenslets. The extrapolation
is performed gradually in an iterative manner; the closest unconnected lenslets are
extrapolated and connected, and then the B-spline function is least squares fitted to
all connected HS spots and extrapolated again.

Leroux and Dainty [54] used a similar approach but fit Zernike polynomials to
the spot displacement data instead of a spline, producing a smoothing effect that
suppresses noise. Lee et al. [55] and Smith and Greivenkamp [56] described
algorithms in which spots are located in a predetermined order in such a way as
to reduce ambiguity as to lenslet-spot correspondence.

Bedggood and Metha [57] compared these software methods for different kinds
of errors and found that Leroux and Dainty ("Zernike") and Lundström and Unsbo
("B-spline") algorithms are more accurate in describing the aberrations they
modeled. Modeling the ability to avoid errors, they found that the most "correct"
is the "Spiral" algorithm (Lee at al., Smith and Greivenkamp). The results of this
last test are presented in Fig. 9.31. with an example wavefront from the set of 1000
randomly generated wavefronts. Large circles indicate spots that were correctly
located according to the internal error checking of each algorithm. One can see that,
in this specific example, the "Spiral" algorithm was able to correctly sort all the
spots; the other algorithms show varying amounts of error.

9.6 Clinical Ray Tracing

9.6.1 Acquiring the Hartmanngram with Ray Tracing

Lasers opened many of new opportunities for building precise instruments in optics and, specifically, in ophthalmology. In 1988, Häusler and Schneider [58] applied the principle of ray tracing known in theoretical optics to experimentally acquire the Hartmanngram. Fig. 9.32 demonstrates how the classic setup for acquiring the Hartmanngram can be transformed using a laser: instead of pinhole stops a laser beam is directed into the tested optics with the scanning (translatable) mirror (Fig. 9.32a). With this configuration, point-by-point probing of the test optics is implemented sequentially in time, not simultaneously like in a classic scheme. Measurement of the position of the beam projections is made with the position sensing detector (PSD) in two planes: in front of the focal point and behind it.

A further simplification of the layout consists of the use of the translation of the tested optics itself instead of the beam. In this case, the PSD is positioned in the focal plane of the tested optics (to be correct, it is a focal one only for a certain beam position, for example, on the optical axis). The tested optics is repositioned in a point-by-point manner. In each position, the coordinates of the beam projection on PSD are measured (Fig. 9.32b). The authors called this approach an experimental ray tracing. The procedure yields directly the local refracting power of spherical and even strong aspheric optics. As samples, aspheric spectacle lenses were used with a continuously varying refracting power from -0.5 to 2.0 diopters. An example of the reconstruction of the distribution of the local refractive power along a meridian in the pupil plane is given in Fig. 9.33.

It was demonstrated also that the experimental ray tracing can successfully be applied for reconstruction of a 3-D shape of the optical objects. The profile of a car windshield was reconstructed from the data of the beam displacement along the glass plate.

9.6.2 Ray Tracing the Retina

The ray tracing technique came to clinical ophthalmology from another field – laser radar – and was reported at the Conference on Laser Radar Technology and Applications [59] as a medical application of optical radars. It was the micro-scaling of a laser radar for the centimeter distances instead of kilometers. The solution was initially formulated by Molebny in his discussion with Pallikaris in 1995, and was implemented in 1996–1998 in the project supported by the governments of Sweden and Canada. The first ophthalmology-related publication was made in 1997 [60], and the technique was baptized as a retina ray tracing. The instrument went through the first clinical tests in 1998–1999. The results of these tests were made public in 2000 [61, 62].

Ray tracing technique uses measurement of the position of a thin laser beam onto the retina. A beam of light is directed into the eye parallel to the visual axis having
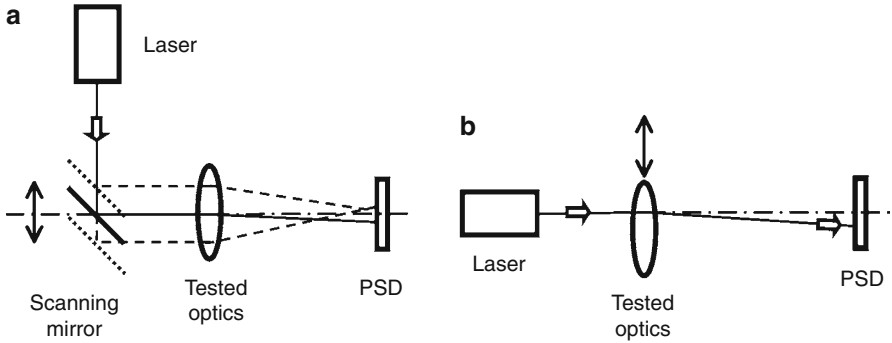
Fig. 9.32 Transformation of the setup using the basic principle of the Hartmann test into an experimental setup (**a**) for a modified Hartmann test using a PSD and into an experimental ray tracing setup (**b**) for measuring the local refraction of aspheric optics

Fig. 9.33 Local refractive power versus position x of the probing beam in the pupil plane of an aspheric spectacle lens
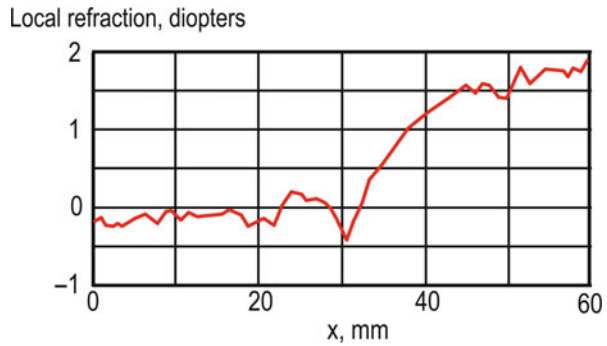
passed a two-directional (x,y) acousto-optic deflector and a collimating lens (Fig. 9.34). The front focal point of the collimating lens is positioned in the center of scanning of the acousto-optic deflector. Each entrance point, one at a time, provides its own projection on the retina. A set of entrance points overlaid on the image of the eye is shown in Fig. 9.35a. A green outer contour corresponds to the shape of the pupil, reconstructed from the eye image. The position sensing detector measures the transverse displacement δ_x, δ_y of the laser spot on retina. An objective lens is used to optically conjugate the retina and the detector plane. In the process of beam displacement over the eye aperture, data on the transverse aberration for each point of the beam entrance into the eye are collected. They are reconstructed into a two-dimensional distribution known as a retinal spot diagram (9.35b).

The iTrace visual function analyzer (Tracey Technologies, USA) is the instrument based on the ray tracing principle. It uses a narrow (0.30 mm) diode laser beam with the wavelength 785 nm being displaced over the entrance pupil of an eye
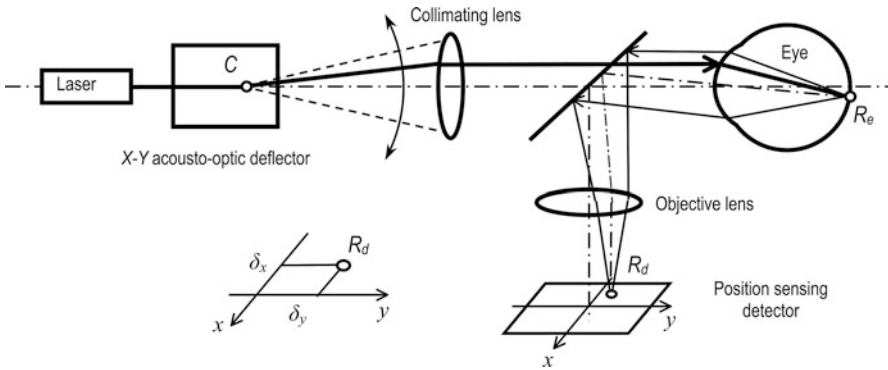
Fig. 9.34 Simplified schematic of the ray tracing aberrometer
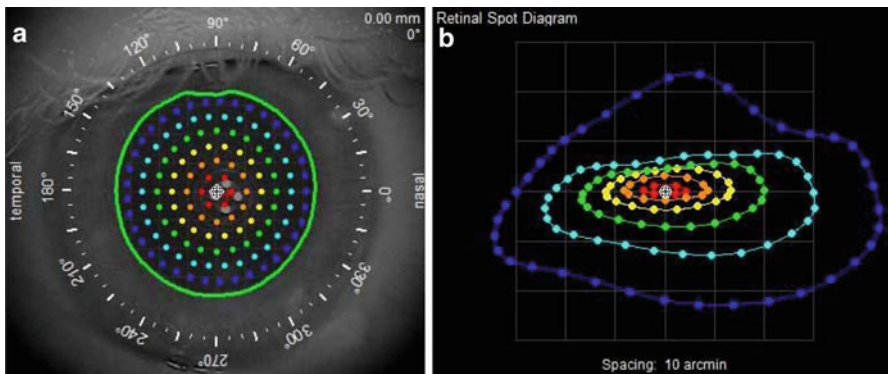
Fig. 9.35 Positions of the beam projected into the eye (**a**) and its positions on the retina (**b**) as measured by the position sensing detector (retina spot diagram)

while kept parallel to the visual axis (Fig. 9.36). To measure the positions of the laser spots on retina, two linear arrays of photodetectors are used, each with its cylinder optics. The signals from these photodetectors are processed to determine the centroids of the spots (Fig. 9.37).

In the process of measurement, an image of the pupil is captured, its size and position are automatically measured in each TV frame. From the size of the pupil, the software calculates optimal locations of all the probing points. The permission on firing the probing radiation is given by the software only when the positions of the pupil and visual axis are within a predetermined correspondence, as well as the data, captured with a position-sensing detector, are processed and transferred to the computer. The total time of scanning for the entire aperture of the eye is within 100 ms. The duration depends on the number of test points at the eye entrance pupil (64–256). Acousto-optic deflectors are very fast devices: transition time for switching a position is about 10 μs, i.e., for 256 points, less than 3 ms is necessary.

Fig. 9.36 Ray tracing
aberrometer developed at the
Institute of Biomedical
Engineering (Kiev, Ukraine)
combined with the placido-
based topographer
manufactured by Tracey
Technologies, USA

This is a great advantage of acousto-optics as compared to the much slower
scanners (no more than 20 rays/s), used in the laboratory studies of Navarro et al.
[63, 64]. For 256 points, this would take more than 10 s for one measurement, which
is unacceptable for clinical use.

9.6.3   Wavefront Reconstruction

Wavefront aberration $W(x, y)$ of the optical system of the eye is related to the
geometric transverse aberrations $\delta x'$, $\delta y'$ as follows:

$$\delta x' = \frac{R}{n'} \cdot \frac{\partial W(x,y)}{\partial x}, \tag{9.1}$$

$$\delta y' = \frac{R}{n'} \cdot \frac{\partial W(x,y)}{\partial y}, \tag{9.2}$$

where R is the radius of a reference sphere; n' is the refraction index of the eye
medium (suggesting the simple eye model).

In polar system of coordinates, the wavefront can be written in terms of Zernike
polynomials:

$$W(\rho, \varphi) = \sum_{n} \sum_{m} R_n^m(\rho) \left[C_n^m \cdot \cos m\varphi + S_n^m \cdot \sin m\varphi \right], \tag{9.3}$$

Fig. 9.37 Signals from horizontal and vertical linear-array photodetectors

Horizonatal Point Profile

11594

Vertical Point Profile

11894
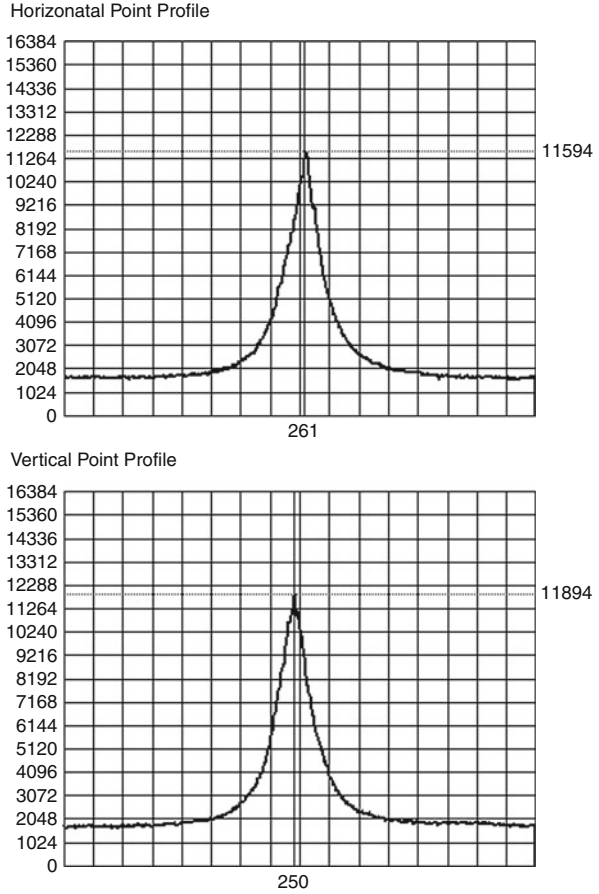
where ρ, φ are the polar coordinates of the beam in the pupil; $n \geq m$, $n + m -$ are even digits,

$$R_n^m(\rho) = \sum_{k=0}^{0.5(n-m)} (-1)^k \frac{(n-k)! \cdot \rho^{n-2k}}{k![0.5(n+m)-k]! \cdot [0.5(n-m)-k]!}, \quad (9.4)$$

C_n^m and S_n^m being the Zernike coefficients. With this in mind, the transverse aberrations can be presented as follows:

$$\delta x'(\rho, \varphi) = R' \cdot \sum_n \sum_m \left[a_{xc} \cdot C_n^m + a_{xs} \cdot S_n^m \right] \quad (9.5)$$

$$\delta y'(\rho, \varphi) = R' \cdot \sum_n \sum_m \left[a_{yc} \cdot C_n^m + a_{ys} \cdot S_n^m \right] \quad (9.6)$$

where

$$R' = \frac{R}{n'}, \tag{9.7}$$

$$a_{xc} = \frac{\partial R_n^m(\rho)}{\partial \rho} \cdot \cos\varphi \cdot \cos m\varphi + m\frac{R_n^m(\rho)}{\rho} \cdot \sin\varphi \cdot \sin m\varphi, \tag{9.8}$$

$$a_{xs} = \frac{\partial R_n^m(\rho)}{\partial \rho} \cdot \cos\varphi \cdot \sin m\varphi - m\frac{R_n^m(\rho)}{\rho} \cdot \sin\varphi \cdot \cos m\varphi, \tag{9.9}$$

$$a_{yc} = \frac{\partial R_n^m(\rho)}{\partial \rho} \cdot \sin\varphi \cdot \cos m\varphi - m\frac{R_n^m(\rho)}{\rho} \cdot \cos\varphi \cdot \sin m\varphi, \tag{9.10}$$

$$a_{ys} = \frac{\partial R_n^m(\rho)}{\partial \rho} \cdot \sin\varphi \cdot \sin m\varphi + m\frac{R_n^m(\rho)}{\rho} \cdot \cos\varphi \cdot \cos m\varphi. \tag{9.11}$$

In each node ρ_k, φ_k ($k = 1\ldots q$, where q is the number of nodes) of the scanning grid, $\delta x'$ and $\delta y'$ are measured representing the left side of the (9.5) and (9.6).

The total number N_e of equations is the doubled number of nodes, the number N_c of sought (unknown) coefficients of the Zernike polynomials can be derived from the formula:

$$N_c = \frac{2nm - m^2 + 2n + 2m + z}{4} - z_o, \tag{9.12}$$

where z_0 is the number of coefficients that do not influence the value of the wavefront deformation function.

In general, $N_e \neq N_c$; that is why the function of the wavefront deformation should be approximated. The most correct way is to use the least squares method. In the matrix form, the unknown coefficients are sought using the multiplication of the corresponding matrices:

$$\mathbf{C} = \left(\mathbf{A}^{\mathbf{T}}\mathbf{E}\mathbf{A}\right)^{-1}\mathbf{A}^{\mathbf{T}}\mathbf{E}\,\mathbf{X}, \tag{9.13}$$

where $\mathbf{C}$ is the vector of the sought coefficients C_{nm}, S_{nm}, $\mathbf{A}$ is the matrix of digital values at the sought coefficients C_{nm}, S_{nm}, $\mathbf{A}^{\mathbf{T}}$ is the transposed matrix $\mathbf{A}$, $\mathbf{E}$ is the unit matrix, $\mathbf{X}$ is the resulting vector of measured transverse aberrations $\delta x'$ and $\delta y'$, consisting of N_e elements. The wavefront tilt is represented by the coefficients C_{11} and S_{11}, the defocus is described by C_{20}.

The above-described method is called modal (or, sometimes, global, i.e., each component of the polynomial is relevant to the entire aperture) in contrast to zonal (sometimes called local), where the describing functions correspond only to a part

of the aperture (zone). It is typical to use polynomials for modal description. A typical zonal description is implemented with splines, but it does not mean that polynomials cannot be used for zonal description. Besides Zernike polynomials, among other option there are Seidel, Taylor, and Bhatia-Wolf polynomials, as well as Fourier decomposition. Zernike polynomials are recommended as the standard method for specifying wavefront error in the eye [65, 66].

Many aspects of eye structure and its functions were studied and described with Zernike polynomials including contributions of the cornea and the lens to the aberrations of the human eye [67], compensation of corneal aberrations by the internal optics in the human eye [68], correlation between dynamic processes in the eye and higher-order members of Zernike series [69], and so on.

It was demonstrated using different quality metrics [70] that Zernike decomposition is still not the best approach. Modeling of the corneal surfaces with radial polynomials [71] showed that Bhatia-Wolf polynomials [72] being orthogonal also in a radial direction fit the corneal surfaces better in comparison to Zernike polynomials. Fourier analysis was also applied to the description of refractive error [73, 74].

Several publications demonstrated effectiveness of the combination of modal and zonal approaches [75–77] in which the modal description embraces high-level aberration non-homogeneities (usually, those affected by lower-order aberrations), and zonal descriptors (polynomial or spline) are responsible for lower scale details (splines give better description of higher-order aberrations, but suffer more from noise).

The refraction aberration can be considered to consist of radial and tangential (rotational) components. The radial direction is attributed to the forces performed by ciliary muscles. The orthogonal direction is attributed to the orthogonal forces, appearing from the properties of the lens, or from the non-homogeneity of the forces delivered by the ciliary muscles.

As to details the mentioned above, the radial component can be produced by the spherical or aspheric surface (surface of rotation around the optical axis). If originated from the crystalline lens, this kind of aberration can be explained by non-ideal shape or non-homogeneous rigidity/refraction of the lens in radial direction or/and by the under- or over-drive of the ciliary muscles. The rotational component can originate from the non-ideal shape or non-homogeneous rigidity/refraction of the lens in tangent direction or/and from the non-homogeneous distribution of the forces applied by the ciliary muscles to the crystalline lens.

It was proposed earlier [78] to supplement the reconstructed refraction error map (derived from the wavefront map) with an additional map of the focal offset, that is the distribution of minimal distances at which the ray passes by the optical axis (minimal separation of the ray and the optical axis), the focal length being defined as a distance from the pupil to the point of minimal separation of the ray and the optical axis.

In the development of this approach, for each point (ρ, θ), the values of $\frac{\partial W(\rho,\theta)}{\partial \rho}$ and $\frac{\partial W(\rho,\theta)}{\partial \theta}$ are calculated [79]. Figure 9.38 illustrates the procedure. Radial

Fig. 9.38 A fragment of the wavefront map with decomposition in radial and tangential components
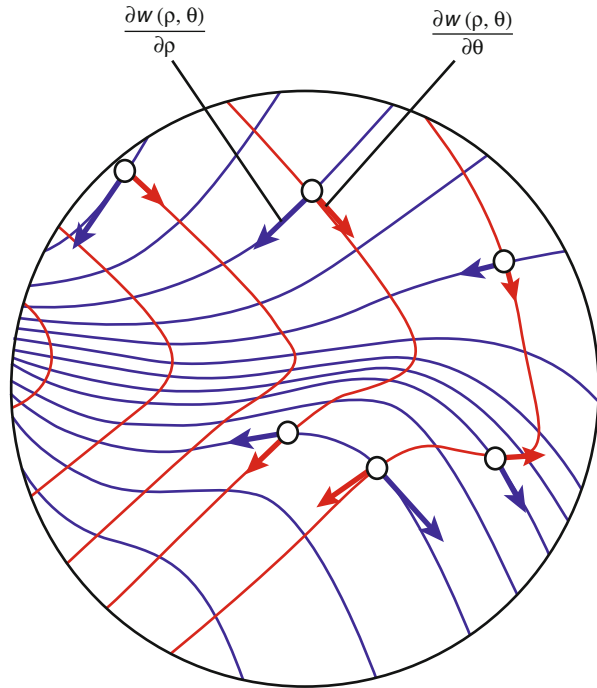
sectioning is in blue, circular (tangential) is in red. Correspondent colors illustrate the orthogonal values of both derivatives.

Examples of orthogonal decompositions for spherical aberrations and coma are presented in Fig. 9.39. The values of each component are taken from a real eye. Spherical aberrations being axially symmetric are constant over the whole map of the tangent component. A notice can be taken from the map for coma that the tangent component has higher values where the wavefront map has steeper variations in the tangent direction.

It was noticed that mean value of the tangent component is always zero. Standard deviation is the same with defocus and without it. This last fact originated the idea to use the standard deviation of the tangent component as a normalization value. The ratio of the standard deviation S_r of the radial component to the standard deviation S_t of the tangent component was proposed as "the eye shape quality factor Q" or "ocular Q-factor."

It was found that the Q-factor is significantly higher in the man-made model eye than in the natural eye. It becomes lower after surgeries of vision correction. Q-factor is higher in the dominating eye than in the lagging eye. It varies with changing the accommodation state, each eye having its own characteristics even for the same patient. Preliminary studies with different groups of patients showed practically unchanged value of the Q-factor within the age of 20–60 years, still, it becomes lower at the age after 80.

	Total	Radial	Tangential
Spherical aberrations 0.147μm			
Coma 0.143μm×232°			
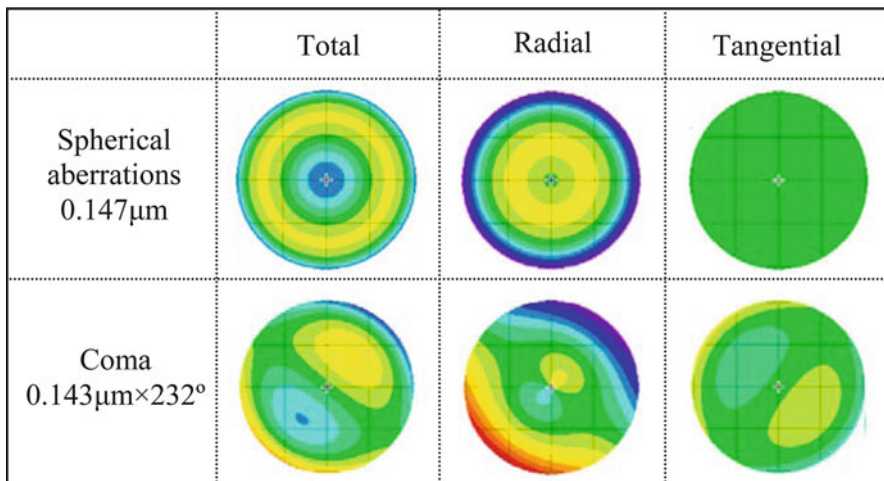
Fig. 9.39 Examples of wavefront maps with orthogonal decompositions for spherical aberrations and coma. The values of each component are taken from a real eye

An example of the wavefront aberration reconstruction from the retinal spot diagram ($\delta x'$ and δy) made by the iTrace aberrometer is represented in Fig. 9.40. The instrument calculates and displays also the modulation transfer function and the point spread function. For the convenience of the user, all these data can be displayed in 2D or 3D versions as a summary (four diagrams at once) or separately. The data can be compared with each other and the difference can be displayed. The aberrometer is combined with the topographer, thus bringing an opportunity to study the wavefront errors not only of the total eye, but also of the cornea separately and, when the cornea wavefront is subtracted, an error component due to crystalline lens.

The iTrace aberrometer also features a video camera and a special target (fixation point) to align the instrument with the eye and achieve a required accommodation state.

9.6.4 Compensation of Back-Path Distortions

Objective methods of measurement of aberrations suffer from the twofold role of the optical system of the eye as an object of study and as a part of the aberrometer. In the ray tracing technique, coordinates of the laser beam projection on the retina are the source of information for subsequent calculations, but they are distorted by the optical system of the eye itself when the coordinates are evaluated through the eye media, being the part of the optical system imaging the projection spot on the retina into its image on the position-sensitive detector.

The term "double-pass" was introduced [80] for treating the situation. It was shown that odd components of the Zernike decomposition compensate themselves on their path back [81]. These considerations are true only if the inward and
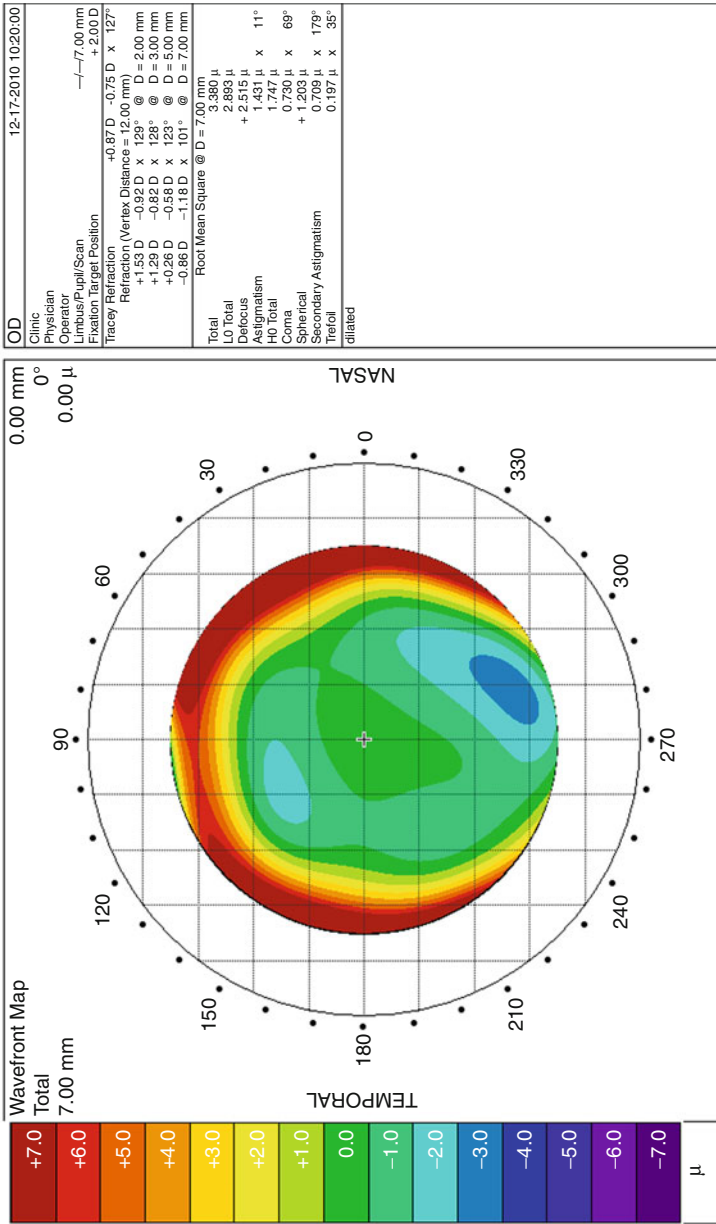
Fig. 9.40 Map of wavefront errors reconstructed from ray tracing measurements
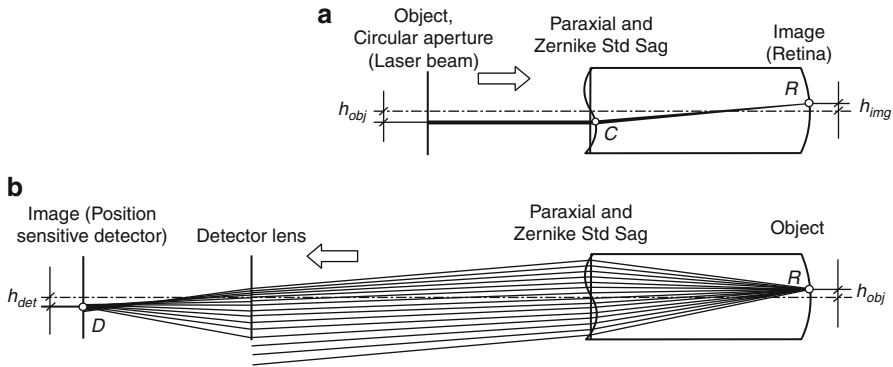
Fig. 9.41 The model of the ray tracing aberrometer

outward paths are the same. To resolve the "double-pass" problem, many efforts were made to modify the inward or outward paths in a way to decrease the influence of the pass, which distorts the information [82]. The term "one and a half pass" was even used to describe the layouts where the influence of the distorting pass was lessened. This term is hardly correct because there is no half passage in either forward or backward direction. In addition, the double pass in its strict definition practically never occurs. An interesting approach was tested [83] in which autofluorescence of retinal lipofuscin was used excited by the laser irradiation at shorter wavelength and detection of light signals with the longer wavelengths. This technique causes the same uncertainty of the beam propagation path to the retina with the only exception of different wavelengths in inward and outward directions.

Modeling the ray tracing aberrometer is interpreted in Fig. 9.41, with the ingoing (*a*) outgoing (*b*) ray course. The eye is modeled by the paraxial approximation to which polynomials are added describing the wavefront distortion. In the inward direction, the beam can change its position, corresponding to the coordinate of eye probing. In the outward direction, the front focus of the detector lens is set to coincide with the back focus of the paraxial eye.

The relative root mean square values related to the value of the corresponding Zernike coefficient for some Zernike coefficients containing sine and cosine members are given in Fig. 9.42. It is obvious that the optical system of the eye, when incorporated in the optical system of the aberrometer, can dramatically change the whole picture of measured aberrations. This distortion of the results needs to be compensated.

Figure 9.43 demonstrates solutions for two cases: *a*, a hyperopic type of non-homogeneity, and *b*, a myopic case. In the standard ray tracing mode, the beam exits the deflector center of deflection in the point O_1 and enters the eye in parallel to the optical axis of the instrument at the height h_1 crossing the anterior surface of the cornea in point C. The beam hits the retina in the point R_h at the height d_h from the central point R for the hyperopic type of non-homogeneity. For the myopic type, the retina is hit in the point R_m at the height d_m.

Fig. 9.42 Error of measurement of the aberrations with the ray tracing aberrometer versus the pupil coordinate in the eye having a single aberration of a Zernike standard sag
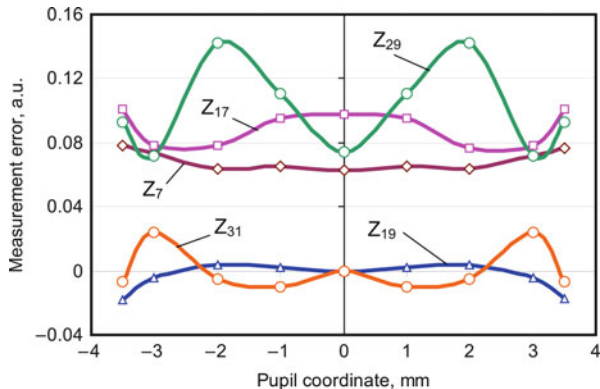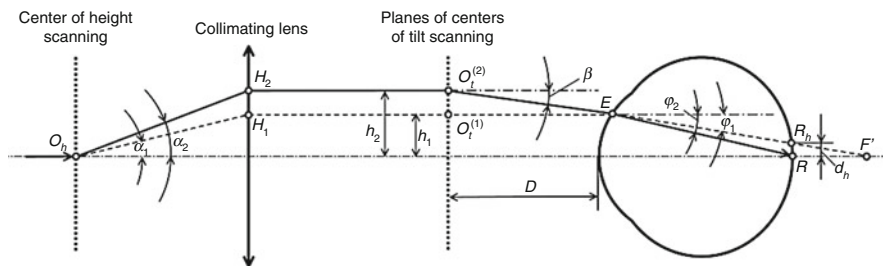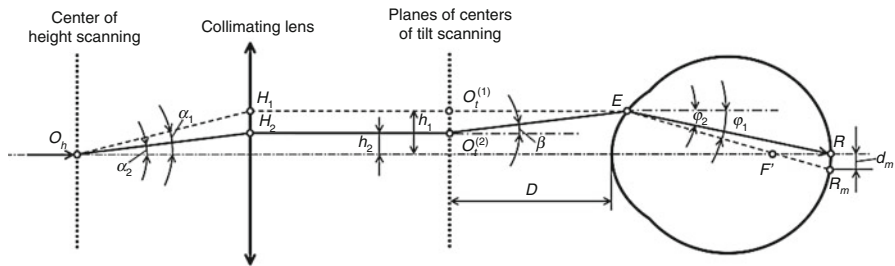
Fig. 9.43 Principle of the local wave front conjugation: hyperopic (**a**) and myopic (**b**) types of errors

To solve the problem of wave front conjugation in the point C of the entrance into the eye, the tilt of the beam inside the eye is to be changed from φ_1 to φ_2. This can be done by changing the height of the beam at the deflector center of deflection from h_1 to h_2 and inclining the beam by the angle β_h for the case of hyperopia or by β_m for myopia. This means that the height of the beam in the center of deflection must be shifted from point O_1 to point O_2. This can be done with an additional deflector and a collimating lens. Since the information on tilts β_h or β_m is obtained
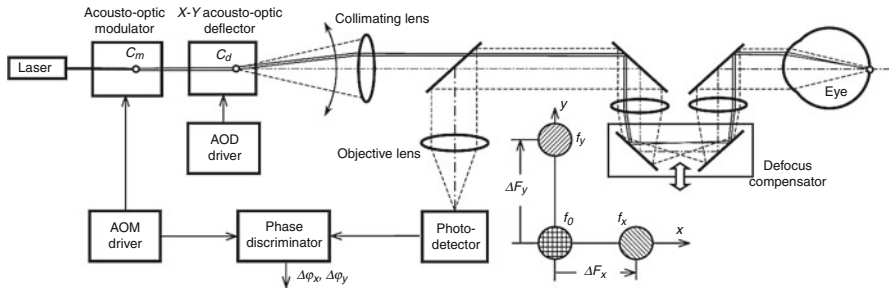
Fig. 9.44 Layout of the frequency-shifted ray tracing aberrometer

with errors, the correction of the position of R_h or R_m will not result in achieving zero values of d_h or d_m, in the very first correction, and another iteration may be necessary, similarly to the systems with the simultaneous total wave front conjugation. It is concluded that, depending on the type of aberration, the error can be reduced from 20 % to 2 % after the first iteration, and to 0.2 % after the second iteration. In most cases, a single iteration can be enough.

9.6.5 Interferometric Ray Tracing

Interferometric, or frequency-shifted ray tracing technique has its roots in phase microscopy and its further development for profile measurement based on phase difference measurement between two beams that passed different optical paths [84, 85]. In applications for ophthalmology, this technique was initially studied with frequency shifting along one of the two orthogonal axes, along which the scanning is provided [86, 87]. Later, a three-beam system was proposed for microprofilometry [88].

The layout of the frequency-shifted ray tracing aberrometer is explained in Fig. 9.44. Its principal difference from the simple ray tracing aberrometer consists of additional splitting of the beam into three components having the frequencies f_0, f_x, and f_y, and using the phase discriminator instead of a position-sensing detector to calculate the wavefront tilt. The splitting is provided by the acousto-optic modulator driven by the AOM driver. The configuration of the beams (shown in Fig. 9.44) contains the central beam having the frequency f_0 and two diffracted beams having the frequencies f_x and f_y, which originate from the central frequency being shifted by ΔF_x and ΔF_y. These two beams are scanned in X and Y directions by the acousto-optic deflector (the term "scan" means here repositioning from one point to another within a certain aperture, being unmoved in each position for a prescribed time interval). The beams interfere on the retina, whose plane is conjugated with the photosensitive plane of the photodetector. Two signals of the frequencies ΔF_x and ΔF_y are filtered at the output of the photodetector. Reference signals of the same frequencies ΔF_x and ΔF_y that are used for controlling the acousto-optic modulators are the reference inputs for the phase discriminator measuring the phase difference $\Delta\varphi_x$ and $\Delta\varphi_y$ at each of these two frequencies ΔF_x and ΔF_y.

The measured phase differences correspond to the optical path differences in X and Y directions, i.e., to the X and Y components of the wavefront tilt in the given point of the eye aperture where the beam is positioned in the moment of measurement. Due to the specificity of the data processing with this technique, a defocus compensator is introduced on the beam paths into and out of the eye. This is necessary to make plane the wavefronts of the beams on the retina. Defocus compensator can be recommended in any other aberrometer, but in intereferometric methods it is very important from the signal-to-noise considerations. The sensitivity of this technique is of the order of nanometers.

9.7 Skiascopic Aberrometer

The principle of skiascopy was used by Fujieda [89] to design the aberrometer that was combined with the corneal topographer [90]. Narrow strips of light are directed into the eye. These strips are the projections of the light propagating from inside the rotating cylinder-shaped drum (chopper wheel) with narrow slits in the generatrix (Fig. 9.45). Like in the ray tracing technique, the center of scanning (center of the drum cylinder) coincides with the front focus of the collimating lens. An objective lens conjugates the retina and a set of photodetectors. The strips running in the retina plane are imaged in the plane of this set of photodetectors. The set consists of two groups: (1) the delay measuring detector array and (2) the centering detectors. The first group is used to measure the sign and value of ametropia, the second to center the images of the strips.

As it is known from the principle of skiascopy that the direction of strip's run depends on whether the eye is myopic or hyperopic. For the direction of drum rotation shown in the Fig. 9.45, the directions of strip movement in the myopic and hyperopic eyes are indicated by arrows for the retina plane and for the plane of photodetectors. The time interval between the moments of light strip passing over individual detectors of the detector array depends on the distance between the detectors and the degree of ametropy for this given meridian of the eye. The measurements are taken between the pairs of detectors symmetrically positioned relative to the center (in Fig. 9.45, the detectors of the same pair are filled with the same texture). This ranging from the center corresponds to certain diameters in the corneal plane. In one of the versions of the instrument there are four pairs of detectors ranged as far as 2.0, 3.2, 4.4, and 5.5 mm in the plane of the cornea. The time difference in each pair of photodetectors is converted into the refractive power. In this way, four-ring data are accumulated for reconstruction of the refraction map. After having measured the time intervals, the meridian is changed by the rotation in the direction of arrows A and B, the rotation of both axes being matched. More detector pairs would result in more dense spatial data in the radial direction.

An infrared LED is used as a source of light. The projecting system of the chopper wheel rotates $180°$ in 0.4 s across both semi-meridians, so that 360
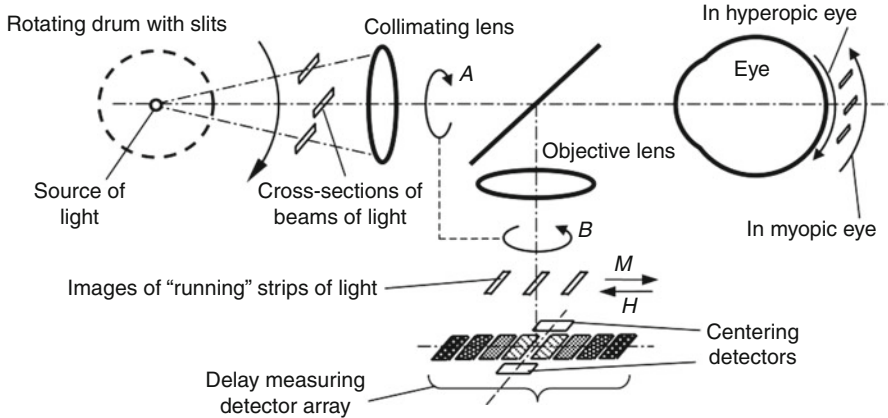
Fig. 9.45 Optical layout of the aberrometer based on the skiascopy principle

meridians are covered. The LED and photodetectors are conjugated with the cornea. The aperture stop (not shown in Fig. 9.45) is conjugated with the retina when the eye is emmetropic. In myopia, the aperture stop is in front of the retina; in hyperopia, the aperture stop is behind the retina.

9.8 Laser-Based Tscherning Approach

Seiler et al. modified the Tscherning idea of grid projection on the retina in such a way that the grid was substituted by a set of thin laser beams [91, 92]. They formed this set of a parallel bundle of light having split into a group of single thin parallel rays by means of a mask with a regular matrix of fine holes (Fig. 9.46). These rays are focused by a low-power lens in front of the eye so that the intraocular focus point is located about 2.5 mm in front of the retina. The purpose of the aberroscope lens is only to sufficiently enlarge the retinal spot pattern to separate and to identify the single light spots. Its optical power depends on the mean ocular spherical refraction. For example, an emmetropic eye needs this lens to be in the range from 14 to 15 D.

The light source for the measuring rays was a green 532 nm diode-pumped solid state laser with a beam diameter of about 2 mm and an output power of 10 mW. The measuring light is controlled by an electromechanical shutter with an opening time of about 60 ms. The laser beam is enlarged to a diameter of about 25 mm by means of a beam expander (a Keplerian telescope). Figure 9.47 (left) shows the configuration of the dot pattern mask that produces the system of test rays. The diameter of a single ray is about 0.3 mm. These rays are focused by a changeable aberroscope lens. The dot pattern masks are also changeable. They differ only in the dot spacing. Figure 9.47 (right) shows an example of a retinal light spot pattern.
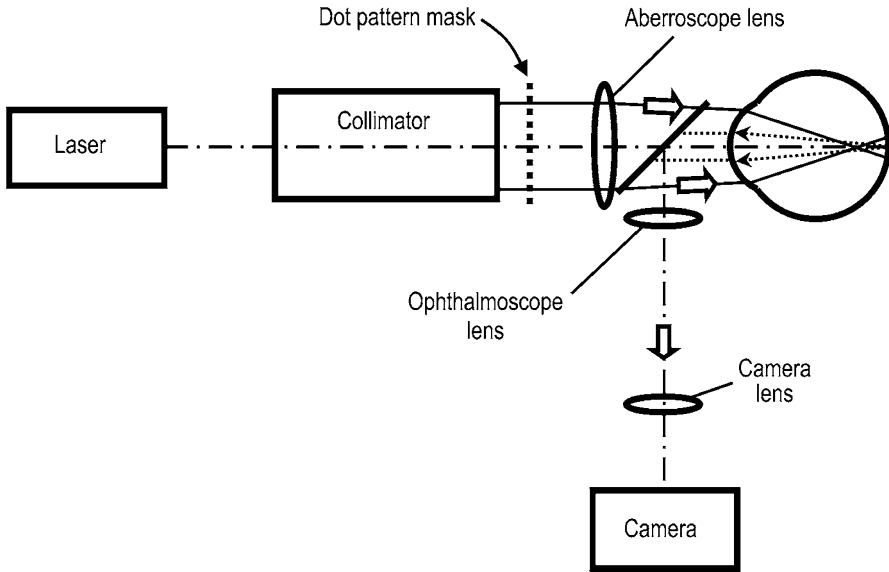
Fig. 9.46 Optical layout of the aberrometer using the Tscherning principle

Fig. 9.47 Dot pattern mask (hole diameters 0.33 mm, aberroscope lens +4 D, hole spacing 0.805 mm) and an example of images of retinal spots [92]
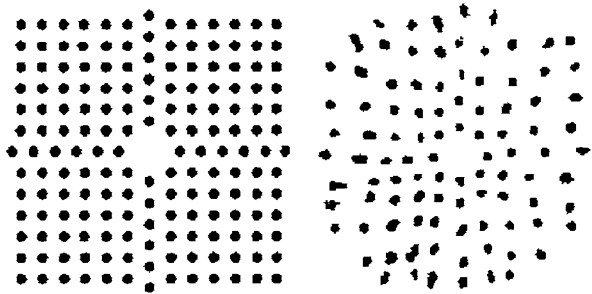
In an aberration-free eye, a projected spot configuration will have the same regularity as at its origin. With real eyes, the spot positions are measured. For this purpose, the retinal light pattern is imaged onto the sensor of a low-light CCD camera using the ophthalmoscopic approach with a central near paraxial channel about 1 mm in diameter within the eye. This optical channel is assumed to be approximately free of higher-order aberrations.

According to the opinion of the authors, the described aberrometer does not provide exact measurements because of some specific reasons. The assumption of

an approximately aberration-free paraxial ocular channel with a diameter of about 1 mm is not given in every individual case. Furthermore, some opacities of the ocular lens or the vitreous body can considerably diminish the intensity of the rays, and some spots cannot be detected by the image processing program.

The technique allows only the measurement of eyes with astigmatism of less than 3–4 D. In eyes with greater astigmatic differences, the retinal light spot separations in one of the main axes is so reduced that clear identification of the spots is not possible. Nevertheless, practical experience shows that this aberrometer is applicable under clinical conditions.

9.9 Discussion and Conclusions

Development of vision correction techniques based on the phenomenon of eye tissue ablation, evoked intensive engineering efforts to create the instruments providing high quality of vision correction from wavefront measurements. The majority of solutions used the earlier developed fundamentals. Hartmann test reincarnated into an instrument using a matrix of lenslets with a CCD camera which by inertia is called the Hartmann-Shack wavefront sensor, although the first who designed and tested it for ophthalmology purposes was the team of Bille, being advised and provided with the sensors designed and manufactured by Platt. Tscherning's idea of grid projection into the eye through an additional lens to disperse the projected grid on some area on the retina was successfully implemented by the team of Seiler. Smirnov's alignment of two projections found its new design in Webb's spatially resolved refractometer. Molebny concentrated his experience in optical radar to build the fast ray tracing instrument for clinical use. Fujieda as a professional working in the field of refractometry used the skiascopy principle to design an aberrometer without the laser, using only the light-emitting diode.

Leaving behind some problems and post-op complications, new revolutionizing technological solutions started in designing and manufacturing customized contact lenses and customized intraocular lenses (IOL), opening a whole new field of competition for the wavefront sensing techniques. To meet the requirements for customized IOL design, a series of additional data are necessary, like anterior chamber depth, axial eye length, and so on. The simplest way is to combine several instruments to make all these measurements, for example, making a combination of an aberrometer, a corneal topographer, and an optical coherence tomograph. But such a combination produces another problem (leaving behind the cost and time), which is the difference in alignment of these instruments with the patient's eye.

The best approach would be the incorporation of several solutions with the same technique in a single device. To our opinion, the ray tracing technique has a good chance to be advantageous due to its flexibility, having the potential to be easily combined with topography [93, 94] and to use the triangulation potential [95] for measurement of the geometrical parameters of the eye.

References

1. S.M. MacRae, R.R. Kruger, R.A. Applegate (eds.), *Customized Corneal Ablation. The Quest for SuperVision* (SLACK, Thorofare, 2001)
2. S.M. MacRae, R.R. Kruger, R.A. Applegate (eds.), *Wavefront Customized Visual Correction. The Quest for SuperVision II* (SLACK, Thorofare, 2004)
3. B.F. Boyd (ed.), *Wavefront Analysis. Aberrometers and Corneal Topography* (Highlights of Ophthalmology, Panama, 2003)
4. F. Caimi, R. Brancato, *The Aberrometers Theory. Clinical and Surgical Applications* (Fabiano Editore, Canelli, Italy, 2003)
5. M. Wang (ed.), *Corneal Topography in the Wavefront Era* (SLACK, Thorofare, 2006)
6. V.M. Sokurenko, Objective single-beam spatially resolved refractometry of the eye, PhD Dissertation, National Technical University of Ukraine, Kiev, 2000 (in Ukrainian)
7. I.H. Chyzh, Aberrometry of the optical system of the eye with ray tracing, DSc Dissertation, National Technical University of Ukraine, Kiev, 2006 (in Ukrainian)
8. J. Rosema, On the wavefront aberrations of the human eye and the search for their origins, PhD Dissertation, University of Antwerp, 2004
9. D. Atchison, Recent advances in measurement of monochromatic aberrations of human eyes. Clin. Exp. Optom. **88**, 5–27 (2005)
10. M. Lombardo, G. Lombardo, Wave aberration of human eyes and new descriptors of image optical quality and visual performance. J. Cataract Refract. Surg. **36**, 313–331 (2010)
11. C. Scheiner, *Oculus hoc est: fundamentum opticum in quo ex accurata oculi* (Oeniponti, Innsbruck, 1619)
12. T. Young, The Bakerian lecture. On the mechanism of the eye. Philos. Trans. R. Soc. Lond. **91**, 23–88 (1801)
13. A.W. Volkmann, *Wagner's Handwörterbuch der Physiologie* (Vieweg und Sohn, Brunswick, 1846)
14. H. von Helmholtz, *Optique Physiologique. 1. Dioptrique de l'oeil* (Edition Jacques Gabay, Paris, 1867). reimpression Jacques Gabay, Sceaux, 1989
15. E. Jackson, The measurement of refraction by the shadow-test, or retinoscopy. Am. J. Med. Sci. **89**, 404–412 (1885)
16. E. Jackson, Symmetrical aberration of the eye. Trans. Am. Ophthalmol. Soc. **5**, 141–150 (1888)
17. M. Tscherning, Die monochromatischen Aberrationen des menschlichen Auges. Z. Psychol. Physiol. Sinnesorg. **6**, 456–471 (1894)
18. A. Ames, C.A. Proctor, Dioptrics of the eye. J. Opt. Soc. Am. **5**, 22–84 (1921)
19. H.T. Pi, Trans. Ophthalmol. Soc. U K **45**, 393 (1925)
20. G.H. Stine, Am. J. Ophthalmol. **13**(Ser. 3), 101 (1930)
21. G.M. Byram, The physical and photochemical basis of visual resolving power. Part I. The distribution of illumination in retinal images. J. Opt. Soc. Am. **34**, 571–591 (1944)
22. G. von Bahr, Investigations into the spherical and chromatic aberrations of the eye, and their influence on its refraction. Acta Ophthalmol. **23**, 1–47 (1945)
23. J.M. Otero, A. Duran, Continuación del estudio de la miopia nocturna. An. Fis Quim **38**, 236 (1942)
24. M. Koomen, R. Tousey, R. Scolnik, The spherical aberration of the eye. J. Opt. Soc. Am. **39**, 370–376 (1949)
25. A. Ivanoff, Sur une méthode de mesure des aberrations chromatiques et sphériques de l'oeil en lumière dirigée. C. R. Acad. Sci. **323**, 170–172 (1946)
26. A. Ivanoff, *Les aberrations de l'oeil* (Editions de la Revue de l'Optique Theorique et Instrumentale, Paris, 1953)
27. A. Ivanoff, About the spherical aberration of the eye. J. Opt. Soc. Am. **46**, 901–903 (1956)
28. M.J. Koomen, R. Scolnik, R. Tousey, Spherical aberration of the eye and the choice of axis. J. Opt. Soc. Am. **46**, 903–904 (1956)

29. M.S. Smirnov, Measurement of the wave aberration of the human eye. Biophysics **6**, 687–703 (1961). Russian original: Biofizika **6**, 776–795 (1961)
30. G. van den Brink, Measurements of the geometrical aberrations of the eye. Vision Res. **2**, 233–244 (1962)
31. M. Dick, E. Schroeder, J. Fiedler, H. Maeusezahl, V. Molebny, Method and device for completely correcting visual defects of the human eye. US Patent 6,616,275, 9 Sept 2003
32. B. Howland, Use of crossed cylinder lens in photographic lens evaluation. Appl. Opt. **7**, 1587–1600 (1968)
33. B. Howland, H.C. Howland, Subjective measurement of high order aberrations of the eye. Science **193**, 580–582 (1976)
34. H.C. Howland, B. Howland, A subjective method for the measurement of monochromatic aberrations of the eye. J. Opt. Soc. Am. **67**, 1508–1518 (1977)
35. G. Walsh, W.N. Charman, H.C. Howland, Objective technique for the determination of monochromatic aberrations of the human eye. J. Opt. Soc. Am. A **1**, 987–992 (1984)
36. G. Smith, R.A. Applegate, D.A. Atchison, Assessment of the accuracy of the crossed-cylinder aberroscope technique. J. Opt. Soc. Am. A **15**, 2477–2487 (1998)
37. R.H. Webb, C.M. Penney, K.P. Thompson, Measurement of ocular local wavefront distortion with a spatially resolved refractometer. Appl. Opt. **31**, 3678–3686 (1992)
38. N.M. Sergienko, *Ophthalmologic Optics* (Meditsina, Moscow, 1991) (in Russian)
39. J.C. He, S. Marcos, R.H. Webb, S.A. Burns, Measurement of the wave-front aberration of the eye by a fast psychophysical procedure. J. Opt. Soc. Am. A **15**, 2449–2456 (1998)
40. S. Marcos, S.A. Burns, E. Moreno-Barriuso, R. Navarro, A new approach to the study of ocular chromatic aberrations. Vision Res. **39**, 4309–4323 (1999)
41. R.H. Webb, C.M. Penney, J. Sobiech, P.R. Staver, S.A. Burns, SRR (spatially resolved refractometer): a null-seeking aberrometer. Appl. Opt. **42**, 736–744 (2003)
42. R.V. Shack, B.C. Platt, Production and use of a lenticular Hartmann screen. J. Opt. Soc. Am. **61**, 656 (1971)
43. J. Hartmann, Objektivuntersuchungen. Z. Instrum. **24**, 1–21 (1904)
44. B.C. Platt, R.S. Shack, History and principles of Shack-Hartmann wavefront sensing. J. Refract. Surg. **17**, S573–S577 (2001)
45. J. Liang, B. Grimm, S. Goelz, J.F. Bille, Objective measurement of wave aberrations of the human eye with the use of a Hartmann-Shack wave-front sensor. J. Opt. Soc. Am. A **11** (1949–1957) (1994)
46. A.P. Vinnichenko, V.V. Molebny, Y.N. Filippov, Adaptive aberration correction of a telescope system, in *Proceedings of 11 All-Union Conference Coherence Non-Linear Optics*, Erevan, 1982, pp. 789–790
47. V.V. Molebny, V.N. Kurashov, I.G. Pallikaris, L.P. Naoumidis, Adaptive optics technique for measuring eye refraction distribution. Proc. SPIE **2930**, 147–157 (1996)
48. G. Yoon, S. Pantanelli, L.J. Nagy, Large-dynamic-range Shack-Hartmann wavefront sensor for highly aberrated eyes. J. Biomed. Opt. **11**(1–3), 030502 (2006)
49. N. Lindlein, J. Pfund, J. Schwider, Algorithm for expanding the dynamic range of a Shack-Hartmann sensor by using a spatial light modulator array. Opt. Eng. **40**, 837–840 (2001)
50. V.V. Molebny, Method of measurement of wave aberrations of an eye and device for performing the same. US Patent 6,715,877, 2004
51. N. Lindlein, J. Pfund, Experimental results for expanding the dynamic range of a Shack-Hartmann sensor using astigmatic microlenses. Opt. Eng. **41**, 529–533 (2002)
52. S. Groening, B. Sick, K. Donner, J. Pfund, N. Lindlein, J. Schwider, Wave-front reconstruction with a Shack-Hartmann sensor with an iterative spline fitting method. Appl. Opt. **39**, 561–567 (2000)
53. L. Lundström, P. Unsbo, Unwrapping Hartmann-Shack images from highly aberrated eyes using an iterative B-spline based extrapolation method. Optom. Vis. Sci. **81**, 383–388 (2004)
54. C. Leroux, C. Dainty, A simple and robust method to extend the dynamic range of an aberrometer. Opt. Express **17**, 19055–19061 (2009)

55. J. Lee, R.V. Shack, M.R. Descour, Sorting method to extend the dynamic range of the Shack–Hartmann wave-front sensor. Appl. Opt. **44**, 4838–4845 (2005)
56. D.G. Smith, J.E. Greivenkamp, Generalized method for sorting Shack-Hartmann spot patterns using local similarity. Appl. Opt. **47**, 4548–4554 (2008)
57. P. Bedggood, A. Metha, Comparison of sorting algorithms to increase the range of Hartmann-Shack aberrometry. J. Biomed. Opt. **15**(1–7), 067004 (2010)
58. G. Häusler, G. Schneider, Testing optics by experimental ray tracing with a lateral effect photodiode. Appl. Opt. **27**, 5160–5164 (1988)
59. V.V. Molebny, I.G. Pallikaris, L.P. Naoumidis, V.N. Kurashov, I.H. Chyzh, Eye investigation with optical microradar techniques. Proc. SPIE **3065**, 191–199 (1997)
60. V.V. Molebny, I.G. Pallikaris, L.P. Naoumidis, I.H. Chyzh, S.V. Molebny, V.M. Sokurenko, Retina ray-tracing technique for eye-refraction mapping. Proc. SPIE **2971**, 175–183 (1997)
61. V.V. Molebny, S.I. Panagopoulou, S.V. Molebny, Y.S. Wakil, I.G. Pallikaris, Principles of ray tracing aberrometry. J. Refract. Surg. **16**, 572–575 (2000)
62. I.G. Pallikaris, S.I. Panagopoulou, V.V. Molebny, Clinical experience with the Tracey Technology wavefront device. J. Refract. Surg. **16**, 588–591 (2000)
63. R. Navarro, M.A. Losada, Aberrations and relative efficiency of light pencils in the living human eye. Optom. Vis. Sci. **74**, 540–547 (1997)
64. R. Navarro, E. Moreno-Barriuso, Laser ray-tracing method for optical testing. Opt. Lett. **24**, 951–953 (1999)
65. American National Standard for Ophthalmics, *Methods for Reporting Optical Aberrations of Eyes. American National Standard for Ophthalmics.* ANSI Z80.28–2004 (American National Standards Institute, Merrifield, 2004)
66. International Standard ISO/FDIS 24157:2008 (E), Ophthalmic optics and instruments – reporting aberrations of the human eye (2008)
67. P. Artal, A. Guirao, Contributions of the cornea and the lens to the aberrations of the human eye. Opt. Lett. **23**, 1713–1715 (1998)
68. P. Artal, A. Guirao, E. Berrio, D.R. Williams, Compensation of corneal aberrations by the internal optics in the human eye. J. Vis. **1**, 1–8 (2001)
69. H. Hofer, P. Artal, B. Singer, J.L. Aragon, Dynamics of the eye's wave aberration. J. Opt. Soc. Am. A **18**, 497–508 (2001)
70. J. Tarrant, A. Roorda, C.F. Wildsoet, Determining the accommodative response from wavefront aberrations. J. Vis. **10**(5), 4, 1–16 (2010)
71. D.R. Iskander, M.R. Morelande, M.J. Collins, B. Davis, Modeling of corneal surfaces with radial polynomials. IEEE Trans. Biomed. Eng. **49**, 320–328 (2002)
72. A.B. Bhatia, E. Wolf, On the circle polynomials of Zernike and related orthogonal sets. Proc. Camb. Philos. Soc. **50**, 40–53 (1954)
73. L.N. Thibos, W. Wheeler, D. Horner, Power vectors: an application of Fourier analysis to the description and statistical analysis of refractive error. Optom. Vis. Sci. **74**, 367–375 (1997)
74. G. Dai, Zernike aberration coefficients transformed to and from Fourier series coefficients for wavefront representation. Opt. Lett. **31**, 501–503 (2006)
75. S. Molebny, V. Molebny, L.F. Laster, Method for measuring the wave aberrations of the eye. US Patent 7,380,942, 2008
76. M. Ares, S. Royo, Comparison of cubic B-spline and Zernike-fitting techniques in complex wavefront reconstruction. Appl. Opt. **45**, 6954–6964 (2006)
77. J. Espinosa, D. Mas, J. Pérez, C. Illueca, Optical surface reconstruction technique through combination of zonal and modal fitting. J. Biomed. Opt. **15**, 026022 (2010)
78. V.V. Molebny, O.V. Lutsenko, Displaying aberration errors as vectors. Electron. Commun. **14**, 103–106 (2002)
79. V. Molebny, S. Molebny, Ocular Q-factor: an approach to eye aberrations analysis. J. Mod. Opt. **58** (2011). doi:10.1080/09500340.2011.564318
80. D.R. Williams, D.H. Brainard, M.J. McMahon, R. Navarro, Double-pass and interferometric measures of the optical quality of the eye. J. Opt. Soc. Am. A **11**(3123–3135) (1994)

81. P. Artal, S. Marcos, R. Navarro, D.R. Williams, Odd aberrations and double-pass measurements of retinal image quality. J. Opt. Soc. Am. A **12**, 195–201 (1995)
82. V.N. Kurashov, V.V. Molebny, A.V. Kovalenko, I.G. Pallikaris, L.P. Naoumidis, Double-pass wave model in eye aberrations study. Proc. SPIE **3192**, 243–248 (1997)
83. L. Diaz Santana, J.C. Dainty, Single-pass measurements of the wave-front aberrations of the human eye by use of retinal lipofuscin autofluorescence. Opt. Lett. **24**, 61–63 (1999)
84. G.E. Sommargren, Optical heterodyne profilometry. Appl. Opt. **20**, 610–618 (1981)
85. C.W. See, M.V. Iravani, H.K. Wickramasinghe, Scanning differential phase contrast optical microscope: application to surface studies. Appl. Opt. **24**, 2373–2379 (1985)
86. V.V. Molebny, I.G. Pallikaris, L.P. Naoumidis, G.W. Kamerman, E.M. Smirnov, L.M. Ilchenko, V.O. Goncharov, Dual-beam dual-frequency scanning laser radar for investigation of ablation profiles. Proc. SPIE **2748**, 68–75 (1996)
87. V.V. Molebny, I.G. Pallikaris, L.P. Naoumidis, E.M. Smirnov, L.M. Ilchenko, V.O. Goncharov, High precision double-frequency interferometric measurement of the cornea shape. Proc. SPIE **2965**, 121–126 (1996)
88. V.V. Molebny, G.W. Kamerman, E.M. Smirnov, L.M. Ilchenko, S.O. Kolenov, V.O. Goncharov, Three-beam scanning laser radar microprofilometer". Proc. SPIE **3380**, 280–284 (1998)
89. M. Fujieda, Ophthalmic measurement apparatus having plural pairs of photoreceiving elements. US Patent 5,907,388, 1999
90. S. MacRae, M. Fujieda, Slit skiascopic-guided ablation using the Nidek laser. J. Refract. Surg. **16**, 576–580 (2000)
91. M. Mrochen, M. Kaemmerer, P. Mierdel, H.E. Krinke, T. Seiler, Principles of Tscherning aberrometry. J. Refract. Surg. **16**, 570–571 (2000)
92. P. Mierdel, M. Kaemmerer, M. Mrochen, H.E. Krinke, T. Seiler, Ocular optical aberrometer for clinical use. J. Biomed. Opt. **6**, 200–204 (2001)
93. V. Molebny, I. Pallikaris, Y. Wakil, S. Molebny, Method and device for synchronous mapping of the total refraction non-homogeneity of the eye and its refractive components. US Patent 6,409,345, 2002
94. V. Sokurenko, V. Molebny, Damped least-squares approach for point-source corneal topography. Ophthalmol. Physiol. Opt. **29**, 330–337 (2009)
95. C.E. Stewart, EVA hazard due to TPS inspection and repair. http://ntrs.nasa.gov/archive/nasa/casi.ntrs.nasa.gov/20070020343_2007018370.pdf

Laser Remote Sensing: Velocimetry Based Techniques

<div style="text-align:right">

10

</div>

Vasyl Molebny and Ove Steinvall

Contents

Abstract

Laser-based velocity measurement is an area of the field of remote sensing where the coherent properties of laser radiation are the most exposed. Much of the published literature deals with the theory and techniques of remote sensing. We restrict our discussion to current trends in this area, gathered from recent conferences and professional journals. Remote wind sensing and vibrometry are promising in their new scientific, industrial, military, and biomedical applications, including improving flight safety, precise weapon correction, non-contact mine detection, optimization of wind farm operation, object identification based on its vibration signature, fluid flow studies, and vibrometry-associated diagnosis.

V. Molebny (✉)
Academy of Technological Sciences of Ukraine, Kiev, Ukraine
e-mail: molebny@gmail.com

O. Steinvall
Swedish Defence Research Agency, Stockholm, Sweden
e-mail: ove.steinvall@foi.se

10.1   Introduction

In remote sensing, information about objects or phenomena is acquired without physical contact with the objects of sensing. There are two main types of remote sensing: passive and active. Passive sensors detect radiation that is emitted or reflected by the object of sensing, usually the sunlight. In active remote sensing systems, energy is emitted by the system itself to scan objects or areas. Scattered or reflected radiation thereupon is detected and measured to obtain information about these objects of sensing.

Unmanned balloons and rockets following messenger pigeons and kites were the early passive remote explorers. An important step in the development of passive systems began with the use of aerial photography for military purposes. Recent developments include small sensor pods in both manned and unmanned platforms. Artificial satellites in the last half of the twentieth century allowed remote sensing to progress to a global scale. Space probes to other planets have provided the opportunity to conduct remote sensing studies in extraterrestrial environments.

Another modality is represented by active remote sensing. Radar is an example of active remote sensing where the time delay between emission and return is measured, establishing the location and some other parameters of an object. Lidar, with its optical specificity, is used to detect and measure the concentration of various chemicals in the atmosphere, while airborne lidar can be used to measure heights of objects and features on the ground more accurately than with microwave radar technology. Vegetation remote sensing is a principal application of lidar.

Simultaneous multi-spectral platforms such as Landsat take images in multiple wavelengths of electromagnetic radiation and are usually found on Earth observation satellites. Hyperspectral imaging produces an image where each pixel has full spectral information with imaging narrow spectral bands over a contiguous spectral range.

Remote sensing in all its combinations, active and passive, microwave radar and optical lidar, multi-spectral and hyperspectral, makes it possible to collect data on dangerous or inaccessible areas and monitor different natural or man-activated processes [1]. From land-based instrumentation, as well as from instrumentation installed on satellites, aircraft, spacecraft, buoys, ships, or helicopter carriers, data is stored, processed, and analyzed to be observed, mapped, imaged, and tracked. Maps of land cover can be used to prospect for minerals and to monitor land usage and deforestation. Hyperspectral imaging is used in various applications, including mineralogy, biology, medicine, defense, and environmental measurements.

Development of searchlights during World War II pushed forward the theory of propagation of narrow beams of light in scattering media [2]. With the advent of laser, laser radar became a principal instrument of laser remote sensing. In addition to the terms laser radar or optical radar, two more terms are in use: ladar (laser detection and ranging) and lidar (light detection and ranging). Practically, in all optical radars, it is the laser who does its job, making all these terms the synonyms. There is no strictly defined limits for usage of the terms, still laser radar is in more general use while lidar often deals with studies of the media of light propagation. During the late 1960s and

Fig. 10.1 Civilian, military, and scientific purpose lidars for atmosphere investigation (from *left to right*): Lidar automatic system for remote air pollution monitoring in large industrial areas (Institute of Precision Instrumentation, Moscow); Laser system for remote chemical agents detection (Astrofizika Corp., Moscow); Raman lidar at the Pennsylvania State University

early 1970s, military research laboratories and industry began developing laser systems for range finding, proximity fuzes, and weapon guidance. The early lasers used ruby as the lasing medium at the cost of poor efficiency, eye safety issues, and noncovertness. Publications included fundamental books on the theory of laser radar [3–5], as well as on the engineering problems [6, 7]. The technology level in the field of laser radar of those times is described in Ref. [8].

The initial laser-to-target-and-return time-of-flight experiments were made in the mid-1960s. The first long-distance laser ranging was implemented in 1969 using a retroreflector positioned on the moon by Apollo 11 astronauts. Additional retroreflector packages were landed on the lunar surface during the Apollo 14 and Apollo 15 missions. Two French-built retroreflector packages were soft-landed on the lunar surface by Soviet landers.

In parallel to the military laser sensing, the research community studied lidar for atmospheric and ocean sensing. For example, lidar observations of the mesosphere were made using a ruby laser as early as 1963 [9]. Vertical water vapor distribution was studied [10] using a temperature-tuned ruby laser; it was the first experiment on DIAL (differential absorption lidar). In the early stages, many new measurements were made with lidars: atmosphere temperature [11], humidity profile of the atmosphere [12], and ocean water parameters [13]. We refer to the textbooks and reviews for further reading [14, 15]. Examples of lidars are shown in Fig. 10.1 [16–18].

Development of Raman lidar [18] enabled measurements of the optical and meteorological properties of the atmosphere based upon vibrational and rotational energy states of molecular species: water vapor and ozone, temperature, optical extinction, optical backscatter, multi-wavelength extinction, extinction/backscatter ratio, aerosol layers, and cloud formation/dissipation (see examples in Fig. 10.2). The angular scattering technique replenishes the information due to measurement of the scattering phase function for aerosols, including the polarization ratio of the scattering phase function, density versus size, size distribution, identification of multi-component aerosols, index of refraction, and so on. Multistatic aerosol lidar and multi-wavelength multistatic lidars are under intensive study.
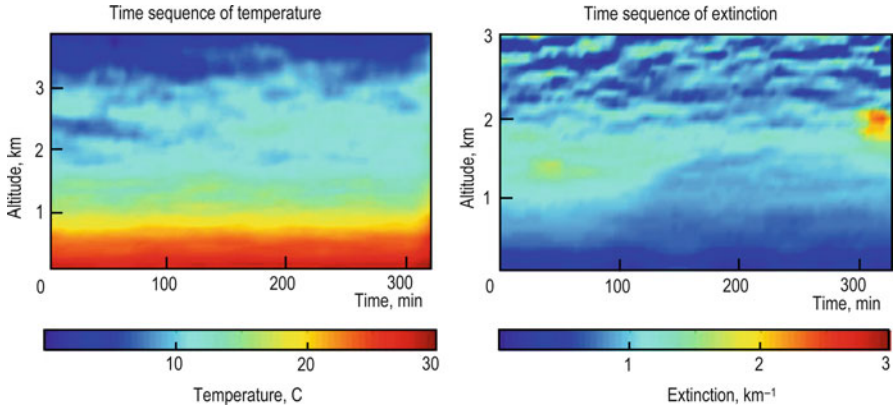
Fig. 10.2 Examples of data registration by the Pennsylvania State University lidar (dynamics of temperature and extinction)

Numerous books, periodicals, conference proceedings, and other types of publications are dedicated to the problems of remote sensing. It is not within the scope of this chapter to review all of this material. We shall restrict our interest to some current trends in laser remote sensing and note some innovative approaches in velocity and vibration measurement.

10.2 Laser Doppler Wind Sensing

Remote measurement of wind has a number of important applications, ranging from weather forecasting and air traffic safety to wind power utilization. Doppler laser radar has spatial and velocity resolution and accuracy higher then acoustic sodar and microwave radar. At short range, it can measure wind profiles, wind shear, clear air turbulence, and wake vortices generated by aircrafts. It is also considered for long-range profiling (at ranges 50 km or longer) from the ground and from space. It is believed that increased interest in wind power technologies will push the civilian development of Doppler wind lidar resulting in compact affordable systems. A Doppler lidar sends out a continuous wave (CW) or pulsed laser beam into the atmosphere and analyzes the backscatter radiation from aerosols and molecules to provide estimates of the wind velocity along the line of sight. By scanning the laser beam, the full wind vector may be retrieved.

The first remote wind measurements using the lidar technique were demonstrated in the last half of the 1960s [19, 20]. Since then, commercial Doppler lidar for wind sensing became a valuable tool for atmospheric research. We shall overview the principles of Doppler lidar with application examples and discuss its future prospects. A detailed review of Doppler lidar is given by Hendersson et al. [21] and Vaughan et al. [22].

10.2.1 Principles of Laser Doppler Velocity Measurements

10.2.1.1 Coherent Detection Methods

Doppler lidars can use coherent or non-coherent (direct) detection. Figure 10.3 illustrates the principle of coherent detection applicable for wind and fluid flow measurements, as well as for vibration sensing. A laser transmitter is focused at an appropriate range from which the wind velocity V is measured. The backscattered radiation interferes at the detector with the radiation from the master oscillator producing the signal containing a component of frequency difference v_D corresponding to the Doppler frequency shift. The laser frequency v_L is shifted by an amount given by the laser wavelength λ and the radial wind component V_r as:

$$v_D = \frac{2V_r}{\lambda}. \tag{10.1}$$

The sensitive region ΔL is defined [23] by:

$$\Delta L = \frac{8R^2\lambda}{\pi D^2}, \tag{10.2}$$

where R is the range to the focal region and D is the telescope diameter.

The laser radar equation for the received optical power P_{rec} can be represented by the following expression:

$$P_{rec} = \eta_{opt} \cdot P_L \cdot \Delta L \cdot \beta \cdot \frac{A_{rec}}{R^2} \cdot T^2_{atm}, \tag{10.3}$$

where η_{opt} is the optical system efficiency, P_L is the laser power, ΔL is the focal depth, $\beta(\mathrm{m}^{-1}\ \mathrm{sr}^{-1})$ is the atmospheric backscatter coefficient, $A_{rec} = \pi D^2$ is the receiver area, and T^2_{atm} is the transmission loss of the atmospheric double path.

As follows from (10.3), the strength of the backscattered signal is proportional to the backscatter coefficient β, which depends on the type of scattering involved. The Rayleigh scattering from molecules is rather weak and has a λ^{-4} dependence. Molecular scattering is a function of air density and temperature and has a predictable dependence on the altitude. For altitudes below 100 km, an approximate model for the molecular backscatter coefficient is [24]

$$\beta_M(\lambda) = (\lambda_0/\lambda)^{4.09} \exp(-z/z_0) \cdot 10^{-7}\,\mathrm{m}^{-1}\mathrm{sr}^{-1}, \tag{10.4}$$

where $\lambda_0 = 1.064\ \mu\mathrm{m}$ and $z_0 = 8$ km are the reference values. The wavelength dependence $\lambda^{4.09}$ differs from the pure molecular scattering λ^{-4} (considering the dispersion of the air index of refraction).

In general, aerosol scattering is much larger than molecular scattering, at least for low altitudes. The wavelength dependence falls between λ^{-1} and λ^{-2} in the optical region. A typical ground value for the aerosol backscatter is $10^{-6}\ \mathrm{m}^{-1}\ \mathrm{sr}^{-1}$
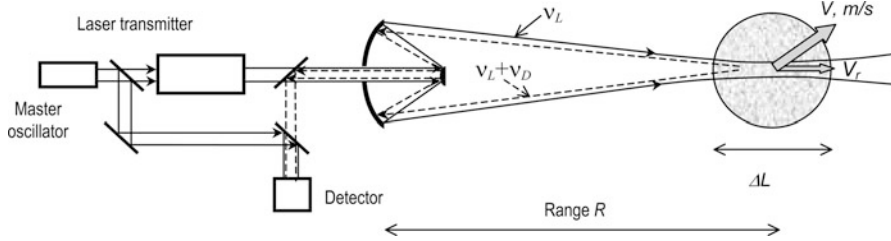
Fig. 10.3 Principle of Doppler laser wind sensing
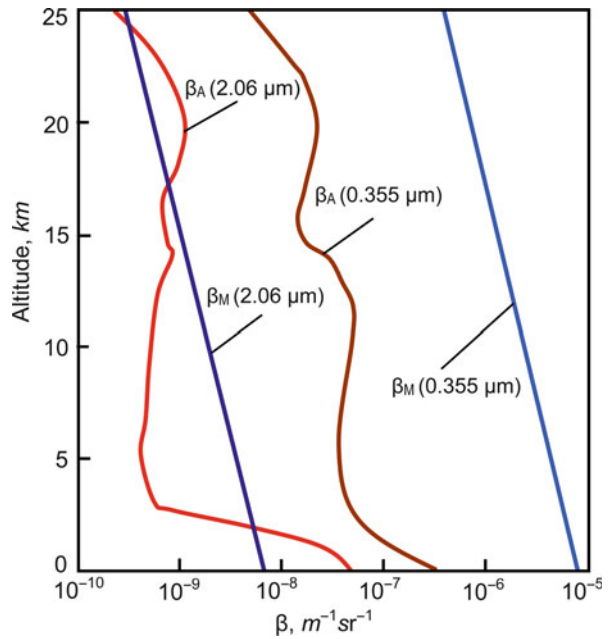
Fig. 10.4 Backscatter coefficients for molecular and aerosol scattering at 355 nm and 2.06 μm [21]

at 355 nm and 10^{-7} m^{-1} sr^{-1} at 2.06 μm. These values are 10–100 times higher than the corresponding molecular backscatter values.

Figure 10.4 shows model-based estimates of aerosol and molecular backscatter at the wavelengths 355 nm and 2.06 μm. The aerosol backscatter in this figure corresponds to the background model representing a geometric mean of a lognormal distribution of the "background" aerosol. In an enhanced model, the backscatter coefficient corresponds to the geometric mean of a lognormal distribution of the variable backscatter in excess of the "background" mode, sometimes referred to as the convective mode.

To get wind vector information, a so-called velocity-azimuth display (VAD) scan pattern can be used. In the VAD scan, three or more independent lines of sight have to be available due to beam scanning in azimuth at a fixed elevation angle.
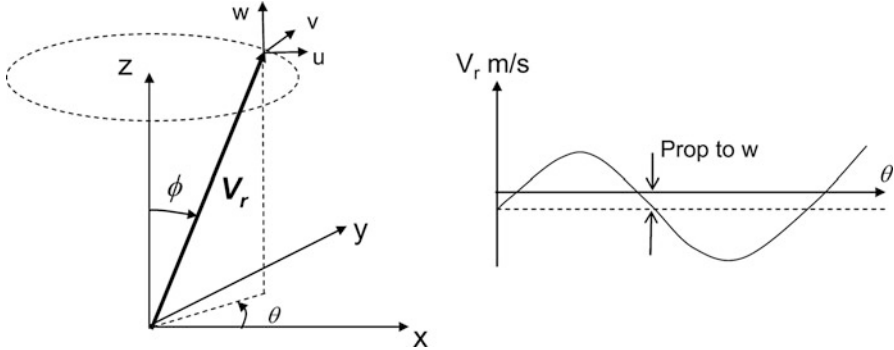
Fig. 10.5 *Left*: VAD scan geometry for a wind vector sensing Doppler lidar. *Right*: sinusoidal wind signal resulted from the VAD scan

Range-dependent radial velocity V_r is measured for each azimuth position and applied to a least-squares algorithm to estimate the wind vector:

$$V_r = |u\sin(\theta)\cos(\phi) + v\cos(\theta)\cos(\phi) + w\sin(\phi)| \qquad (10.5)$$

where u and v are horizontal components of the wind and w is its vertical component.

It is clear from (10.5) that at least two azimuth angles are needed for calculation of v. The vertical component w can be deduced from deviation of the velocity line from zero (Fig. 10.5, right). A least squares fit may be done on the whole or only on a part of the generated sinusoidal curve [25].

A typical CW system uses rather high Tm:LuAG laser power (10 W at 2.02 μm) being focused at 30 m and integrating 200 measurements. With the bandwidth 2 MHz, velocity uncertainty is ±1 m/s. There are numerous signal processing techniques for CW systems using spectrum analyzers, surface acoustic devices, filter banks, digital receivers, and so on. A comparison between these techniques for a CW Doppler lidar is given by Rothermel et al. [26]. The accuracy of measurement depends on measurement geometry, spatial and temporal wind variations, accuracy of frequency measurement, width of laser spectrum, signal-to-noise ratio, measurement time, and averaging, among others.

CW systems enable spectral averaging to a large extent. The laser frequency is also rather stable, supporting accurate wind measurements. However, they have shorter ranges and do not easily allow the range-resolved measurements.

In pulsed Doppler systems, a short pulse length is favored, keeping in mind the range resolution, whereas a longer pulse favors velocity resolution. For example, Frehlich [27] uses the following expression for the width of a Gaussian-type pulse:

$$\mathrm{FWHM} = 2\sqrt{\ln 2}\,\sigma_t, \qquad (10.6)$$

where $\sigma_t = \frac{1}{\sqrt{8\pi}w_f}$, and w_f is the spectral width. WFHM stands for full width half maximum time width.

Fig. 10.6 Range-height
dependence for a pulsed
Doppler lidar (with signal-to-
noise level 0 dB)
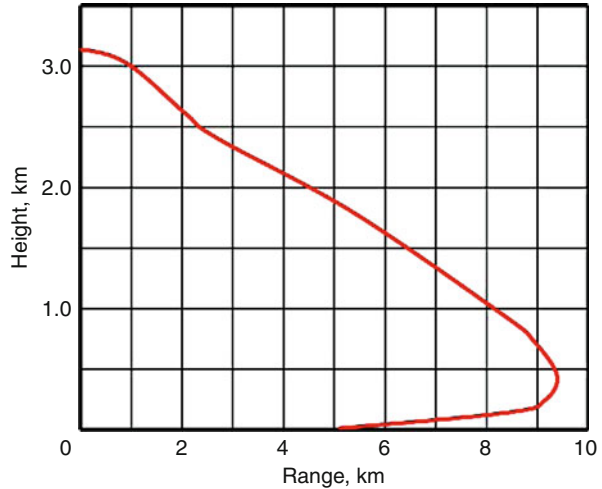
An example of data of a pulsed Doppler lidar is as follows: wavelength 2.02 μm of a Tm:LuAG laser, pulse energy 3.5 mJ, pulse duration 300 ns, 10 cm diameter of transmitter optics, receiver bandwidth 3 MHz, number of integrated pulses 5. A corresponding range diagram is shown in Fig. 10.6 (note the influence of the refractive turbulence close to ground on the range).

Pulsed systems are generally more complicated compared with their CW counterparts, but in general they offer better performance, especially concerning range resolution and long range. They can be successfully used for some short-range applications as well.

10.2.1.2 Direct Detection Methods

In direct detection Doppler lidars, the frequency of the Doppler-shifted lidars radiation is measured using a direct optical analyzer (like an optical interferometer, sharp edge molecular absorption filter, etc.) and the detected power or power spatial distribution transmitted through the analyzer gives a measure of the Doppler shift. There are several techniques using direct detection for wind sensing. Some examples include fringe imaging, spectral edge techniques, "sheet-pair" systems, and aerosol correlation techniques; some of them are described below.

The so-called edge technique [28–30] has recently been considered as an alterative for long-range wind sensing from satellite. According to this method, the received signal has to pass through a narrow-band optical filter designed in such a way that the laser line is centered on its slope (edge). Small changes of the laser frequency due to a Doppler shift result in a relatively large signal power change provided that the edge is sharp. The Doppler shift and thereby the wind is thus measured by the amplitude ratio between the outgoing and the received pulses. A modified layout can use a double-edge technique. With this modification, Flesia et al. [31] demonstrated around 2,000 wind measurements with 1–2 m/s accuracy at 10 km altitude (5 mJ laser energy, 25 cm telescope, integration over 750 pulses).

Gentry et al. [32] measured atmospheric wind profiles for 1.8–35 km with the vertical resolution 178 m. The range-dependent deviation of the horizontal wind speed was 0.4–6 m/s. Wang et al. [33] measured the along-line-of-sight wind velocity at ranges up to 8–10 km at night and 6–8 km during daytime with range resolution 10 m.

The ESA Aeolus mission will take an innovative wind lidar called ALADIN (Atmospheric LAser Doppler INstrument) [34] into space to measure wind profiles in the lowermost 30 km of the Earth's atmosphere. ALADIN is a direct detection wind lidar capable of using the backscatter signal from both molecular (Rayleigh) and aerosol (Mie) scattering to retrieve independent wind information. Reitebuch et al. report [35] on the first airborne demonstration of ALADIN.

Two intersecting laser beams create a fringe pattern in the zone of intersection, perpendicular to the flow direction where the passing particles will modulate the scattered laser light. The fringe spacing sets the velocity constant, and an object moving through the fringes creates a passing frequency proportional to the object velocity. A method of fringe generation was discussed [36] using printed optical masks, eliminating the need for interference techniques, and thereby making the velocity constant independent of laser beam parameters.

Wind velocity can be determined from the correlation between successive lidar returns. Pioneering work in this field was made by Eloranta [37] and Matvienko et al. [38]. By redirecting (scanning) the line of sight, two- and three-dimensional images of atmospheric structure including wind estimates can be reconstructed. Kunkel et al. [39] used aerosol lidar data to determine turbulence spectra and energy dissipation rates in the boundary layer. Ferrare et al. [40] used volumetric aerosol lidar data to monitor the evolution of convective structures in a convective boundary layer. Recently, Eloranta [41] reviewed Volume Imaging Lidar (VIL) to illustrate the potential of such measurements and described the necessary lidar performance requirements.

10.2.2 System Examples and Applications

10.2.2.1 Coherent Doppler Lidars

Wind sensing was realized to be a valuable application for coherent lidars. Measurements included various ground based programs, including local wind field measurement and wake vortex investigation at airfields. Airborne systems were used to investigate avionics problems of true airspeed, pressure error, wind shear warning, and collection of atmospheric backscattering over the North and South Atlantic.

One of the vitally important functions aboard a plane is warning about a windshear, especially during takeoff and landing. Entering a microburst and encountering a fast variation of the airspeed, the pilot's reaction can make the situation worse, leading to plane crash. An example of wind velocity distribution in the windshear cross-section measured with laser radar [42] and its effect is given in Fig. 10.7.

Spaceborne Doppler lidar provides accurate information on vertical and horizontal wind fields [43, 44], being unique especially over unpopulated areas like oceans, and
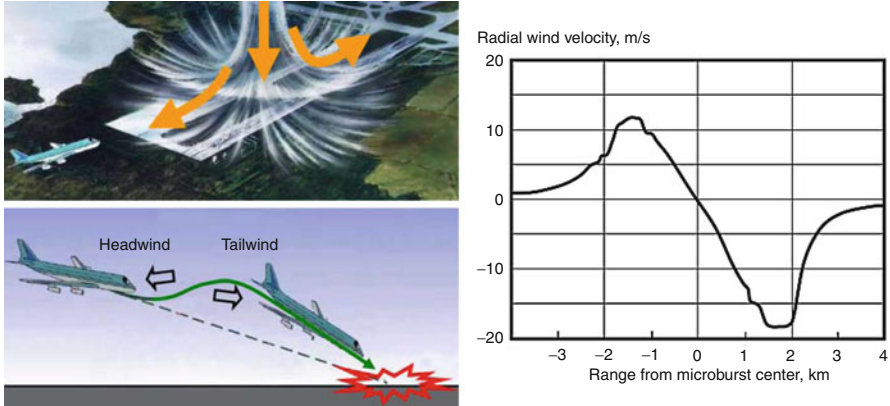
Fig. 10.7 Velocity distribution within the windshear and its effect [42]

a very valuable tool not only for direct use but also for long-term weather prediction. Direct use applications include improved track of hurricanes and severe storms, pollution motion, battlefield fog, and smoke and dust prediction. Long-term applications include improved understanding of climate and atmospheric processes, better weather prediction, and its hazards, which can provide loss mitigation.

The first airborne measurements of winds used a pulsed CO_2 laser [45, 46]. The lidar was oriented in the fore and aft directions in order to obtain the horizontal vector wind field. Another coherent lidar system CLASS (Coherent Lidar Airborne Shear Sensor) was developed in two versions: with a 10.6 μm CO_2 laser (CLASS-10) and with a solid state 2.02 μm Tm:YAG laser (CLASS-2). Both lidars showed a wind measurement accuracy better than 1 m/s [47]. Coherent airborne wind lidar system WIND (Wind INfrared Doppler lidar) was developed later in French-German cooperation [48, 49].

One of the early research activities in wind sensing was aimed at wake vortex detection and tracking for aircraft safety. An example from Vaughan et al. [22] is given in Fig. 10.8. At the left is a reconstruction from the lidar spectra of a vortex trajectory for a B747 aircraft arriving at Heathrow Airport. The lidar was scanned ±10° at a rate of nearly 3°/s. Note the initial descent of the near-wing vortex followed by ascent close to the glide slope about 70 s later. The right graph shows a sequence of Doppler spectra in which a transit is seen of a B757 vortex carried by the wind through a fixed lidar beam. The measurement rate was 2.5 spectra/s and the horizontal frequency scale is 0–6 MHz. Note the weak peak from the tangent region to the vortex rising close to the top of the scale near the core.

Lockheed Martin Coherent Technologies developed a system called WindTracer [50], whose specialty is remote sensing of winds in the critical 40–200 m height regime. With no sidelobes, WindTracer can scan the space near the ground, even adjacent to obstacles. It provides a 30–60 min warning of changes in the winds approaching a wind farm. This information is important for grid electric power operators and for turbine operators to optimize the operations. The wavelength is
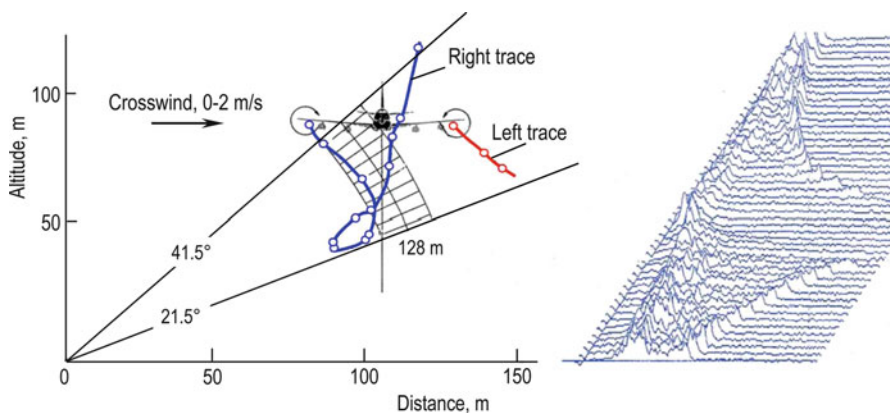
Fig. 10.8 Examples of data from coherent lidar [22]

the eye-safe 1.6 μm, the maximum operating range is up to 12 km, range resolution is about 50 m, the coverage area is 100–200 km^2, and a typical vector velocity accuracy is about 1 m/s. The combination of lidar and radar, called WTDS (WindTracer Terminal Doppler Solution) enables wind hazard detection under all weather conditions.

A general view of WindTracer is demonstrated in Fig. 10.9. The screenshot shows the radial velocity estimates over a 12-km-diameter circular area.

European companies Leosphere [51] and Halo Photonics [52] specialize in building compact Doppler lidars with emphasis on wind farming applications. A Windcube 200S model of the Doppler lidar from Leosphere and its radial speed display overlaid on the map are shown in Fig. 10.10. A streamline version of Halo Photonics Doppler velocimeter and an example of velocity-height dependency on time acquired with this instrument are demonstrated in Fig. 10.11. As the wind energy industry continues to grow, the need for more accurate and sophisticated wind data grows as well. Such lidars are used to explore the locations like ridgelines, oceans, lakes, and forested areas. Typically, the lidars provide 100–200 m vertical wind profiles with an accuracy down to 0.1 m/s. Maximum range of the Halo Photonics streamline instrument using 1500 nm laser wavelength is 9.0 km, range resolution 15 m, maximum measured velocity 19 m/s, velocity resolution 0.0384 m/s.

10.2.2.2 Direct Detection Lidars

An incoherent Doppler lidar capable of measuring winds and aerosols from the planetary boundary layer through the stratospheric aerosol layer during both day and night was built at the University of Michigan [53]. A schematic is shown in Fig. 10.12. The laser is a pulsed, frequency-doubled Nd:YAG with a 50 Hz repetition rate and 3.0 W average power. The beam is expanded to 1 cm diameter and the divergence angle is set to 0.2 mrad. Backscattered light is collected by a 44.5 cm in diameter, f/4.5 Newtonian astronomical telescope. The field of view of the

Fig. 10.9 WindTracer®
coherent Doppler lidar from
Lockheed Martin Coherent
Technologies and its display
with wind velocity map [50]
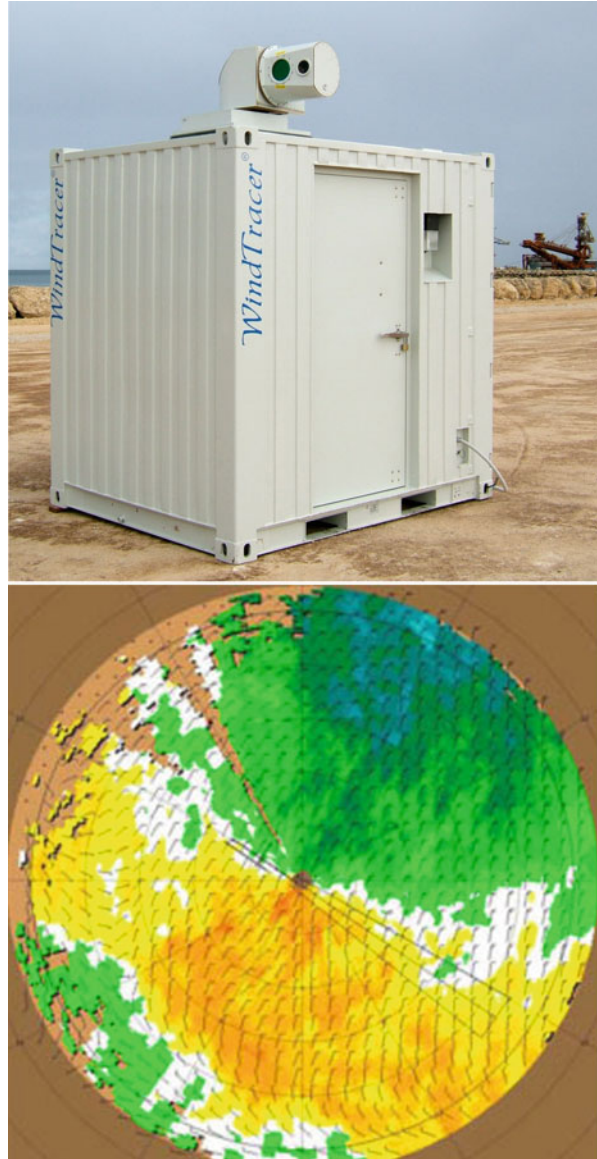
telescope is 0.5 mrad, which is somewhat larger than the laser divergence of
0.2 mrad to collect all of the laser light that may fall outside this angle because of
pointing jitter in the laser or slight instability in the mirror scanning system. The
collected light is focused by the telescope onto a 3.5 mm in diameter optical fiber
bundle.
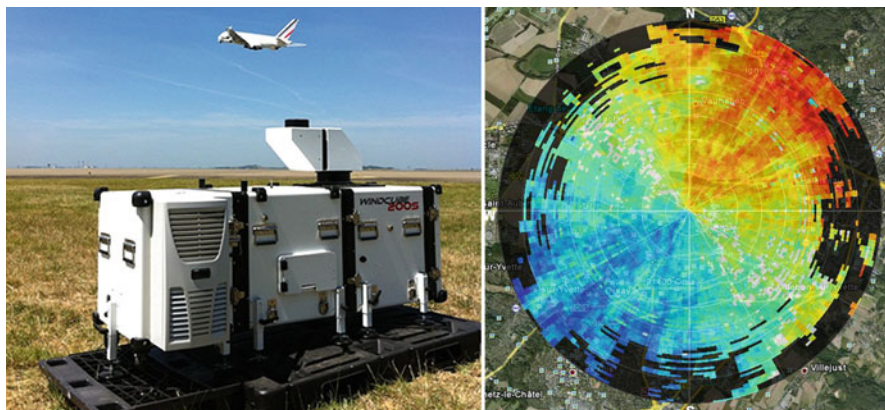
Fig. 10.10 A Windcube 200S model of the Doppler lidar from Leosphere (*left*) and its radial speed display overlaid on the map (*right*) [51]
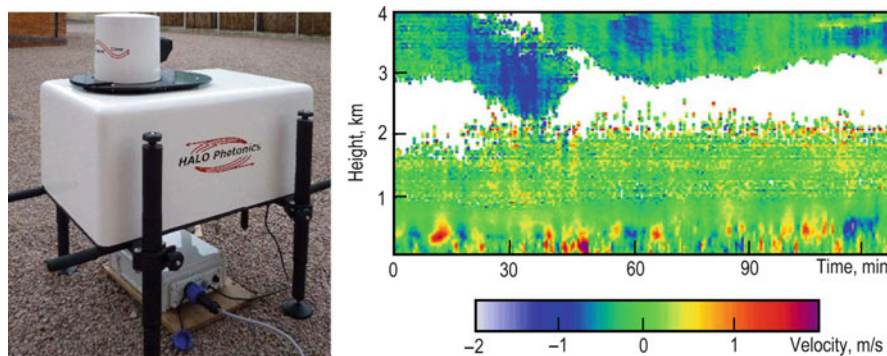
Fig. 10.11 Halo Photonics streamline V4 instrument (*left*) and an example of velocity-height dependency on time acquired with this instrument (*right*) [52]

The backscattered signal received by the lidar instrument is the superposition of aerosol and molecular components. The heavier aerosol particles broaden the laser line spectrally to only a small degree, whereas the faster-moving molecules broaden the laser line significantly. Fabry-Pérot étalons are used for filtration of the molecular and aerosol components. By varying the plate spacing of the highest resolution Fabry-Pérot étalon in the interferometer, it is possible to project either the narrow aerosol scattered spectrum or the broader molecular spectrum onto the detector. Both étalons are positioned in pressure-controlled canisters filled with dry nitrogen. The two étalons can be scanned in wavelength independently by controlling the pressure of each of them. The high-resolution étalon has a plate spacing of 10 cm, which allows the instrument to resolve the Doppler shift from aerosol backscattered light. The low-resolution étalon has a plate spacing of 0.49 cm, chosen to strongly attenuate the unwanted extra orders of the high-resolution étalon.
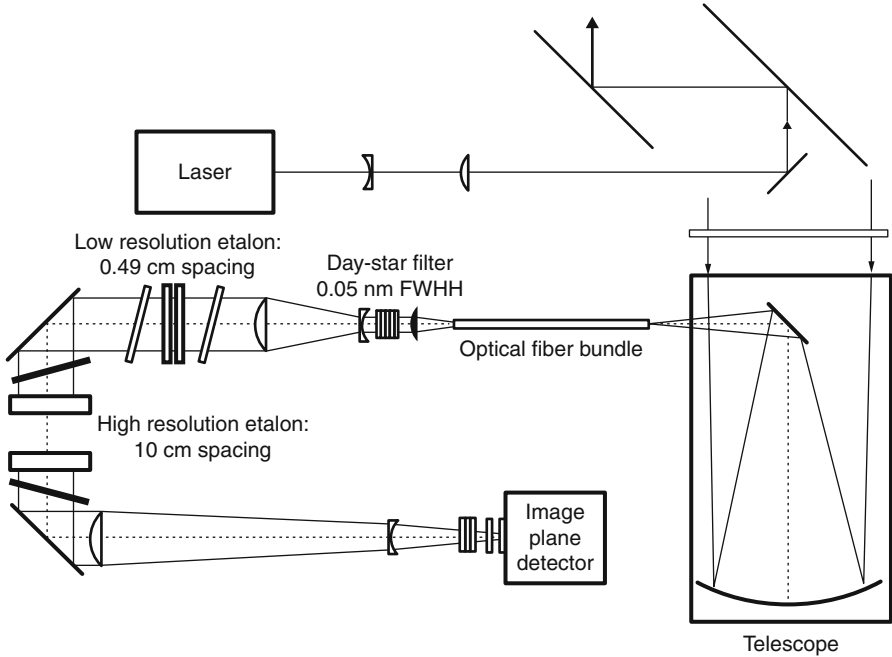
Fig. 10.12 Optical schematic of the transmitting and receiving parts of the incoherent (direct detection) Doppler lidar [53]
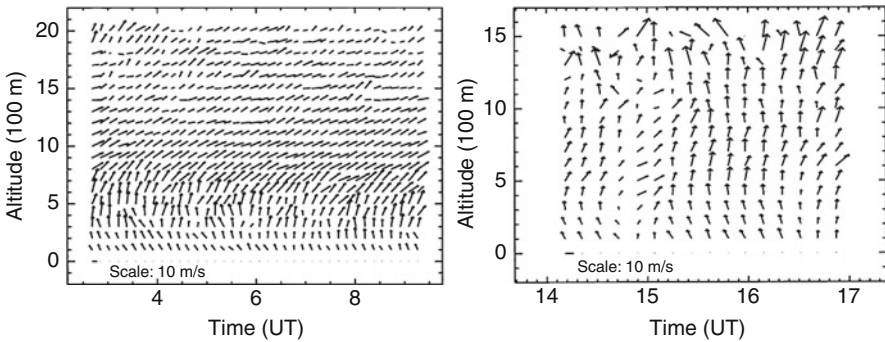
Fig. 10.13 Horizontal wind field map for night and daytime [53]

The detection system consists of a 32-channel image plane detector capable of single photon counting. The detector is a microchannel plate photomultiplier tube and provides a gain of 10^6.

Examples of horizontal wind field maps acquired with the described lidar are given in Fig. 10.13 for night and day. The length of each arrow is proportional to the horizontal wind speed and its direction indicates the compass direction in which the
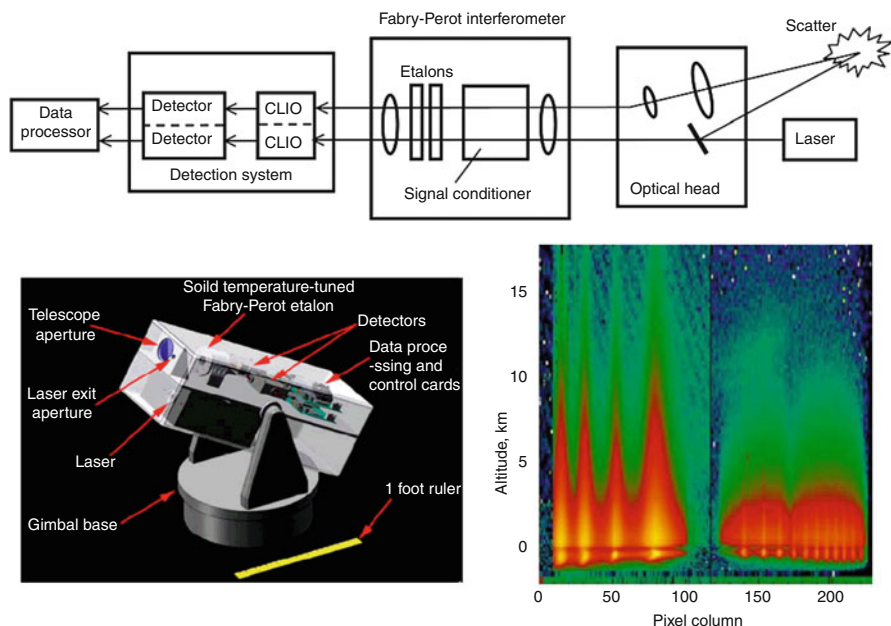
Fig. 10.14 Schematic, general view and a screenshot of a GroundWinds direct detection lidar [54]

wind is blowing. A classic Ekman spiral can be noted from the surface to 1,500 m in the night-time diagrams.

Another example of a wind measurement system based on direct detection with high spectral resolution is a GroundWinds lidar from Michigan Aerospace Corporation [54]. It uses a 355 nm or 255 nm laser source. The signal return of the GroundWinds lidar is injected into Fabry-Pérot étalons (one for Mie scattering, another for Rayleigh scattering). The étalons provide information about the spectral content of the light by generating an interference pattern that appears as a series of Haidinger fringes. The fringes correspond to a series of angles being a function of the wavelength of the light. For a given set of fringes illuminated with monochromatic light, the wavelength can be calculated by measuring the fringes. Another novelty is a so-called CLIO optics, transforming the circular Fabry-Pérot interferogram into a linear one, easily readable by a CCD detector. Still another solution, resulting in a higher signal-to-noise ratio, is light recycling due to use of monomode fibers enabling the off-axis light from the exit of the Fabry-Pérot resonator to recycle once more. Figure 10.14 shows a schematic, general view and a screenshot of the information from the described fringe-imaging Doppler lidar.

Unlike competing coherent detection systems, direct detection lidars utilize both molecular and aerosol scattering, allowing operation in clear air above the boundary layer and over oceans where there is a small amount or no aerosols. A Molecular Optical Air Data System (MOADS) collects the data from aircraft flying at high altitudes. MOADS operates in the ultraviolet at 266 nm, and can operate solely on
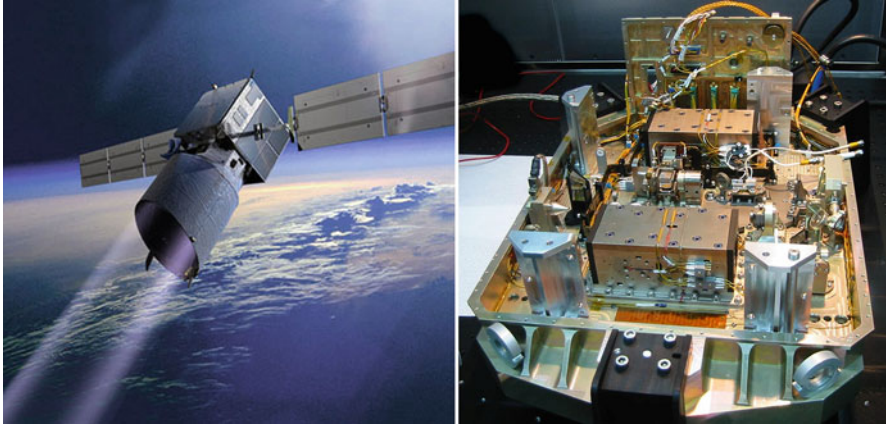
Fig. 10.15 Aeolus satellite and configuration of the power laser head of the ALADIN Doppler lidar [58]

molecular scattering of the atmosphere. A future modification of the MOADS will measure clear air turbulence ahead of an aircraft to give the pilot a one minute warning to avoid turbulent air regions [55–57].

Another direct detection lidar, the Aeolus-based spaceborne ALADIN lidar (Fig. 10.15), demonstrated high spectral resolution and accuracy of wind profile measurement in the troposphere and in the lower stratosphere (0–30 km). The lidar emits a laser pulse (wavelength 355 nm, pulse energy 150 mJ, pulse repetition frequency 100 Hz, optics diameter 1.5 m) towards the atmosphere, then collects, samples, and retrieves the frequency of the backscattered signal. The received signal frequency is Doppler-shifted from the emitted laser due to the spacecraft, Earth, and wind velocity. The lidar measures the wind projection along the laser line-of-sight, using a slant angle versus nadir [58]. The lidar has a potential to obtain about 3,000 globally distributed horizontal line-of-sight wind profiles daily. Additional geophysical products that will be retrieved from the satellite are cloud and aerosol optical properties.

10.3 Flow Measurement

Successful application of laser velocimetry for flow measurements was described with application to blood vessels. The feasibility of using laser Doppler velocimetry (LDV) to measure blood flow in individual retinal vessels was first demonstrated in 1972 by Riva et al. [59], who measured the Doppler-shift frequency spectrum of laser light scattered from red blood cells (RBCs) flowing in a retinal artery of an anesthetized rabbit. The maximum Doppler frequency shift arising from the light scattered by the RBCs flowing at the maximum speed was estimated from the spectrum and from the intraocular scattering geometry. Several years later, a new approach for determining blood velocity was proposed [60]. The procedure involves collecting the
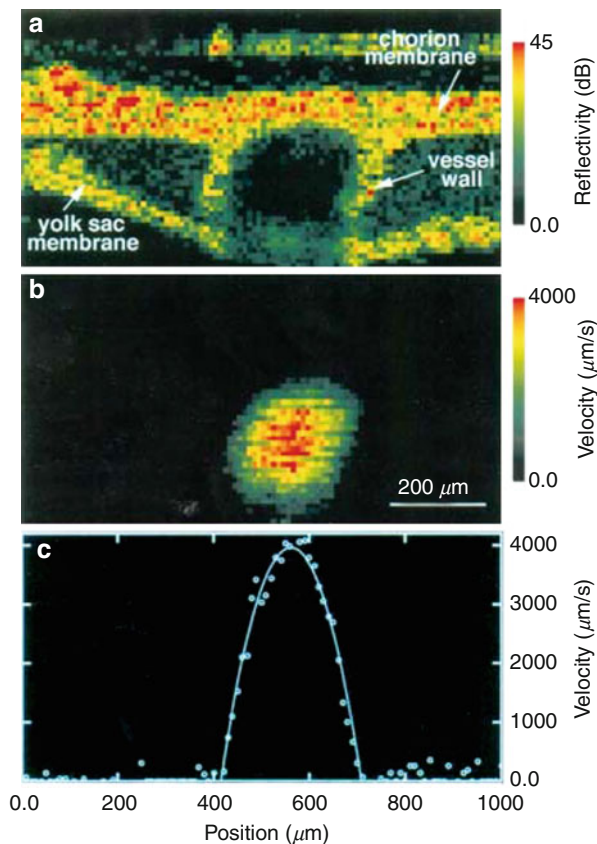
light scattered by the RBCs in two distinct directions separated by a known angle. Subsequent analysis yields an absolute measure of the velocity that is independent of the exact orientation of the vessel and of the relative angular orientation of the incident and scattered light beams with respect to the flow direction.

Conventional LDV found its application to measure mean blood perfusion in the peripheral microcirculation. However, strong optical scattering in biological tissue limits spatially resolved flow measurements by LDV. Further to that, coherence technique provided the instrument with simultaneous information regarding not only in vivo blood flow at discrete locations but also the tissue structure surrounding the vessel [61]. Fluid flow velocity at each pixel is determined by measurement of the Doppler frequency shift, which is defined as the difference between the carrier frequency established by the optical phase modulation and the centroid of the measured power spectrum at each pixel. Two-dimensional images are formed by sequential lateral scans at a constant horizontal velocity, followed by incremental probe movements in the axial direction.

Blood flow in a vein is imaged in Fig. 10.16, where A is a color-coded structural image, B is a color-coded velocity image, and C is a velocity profile along the vein cross
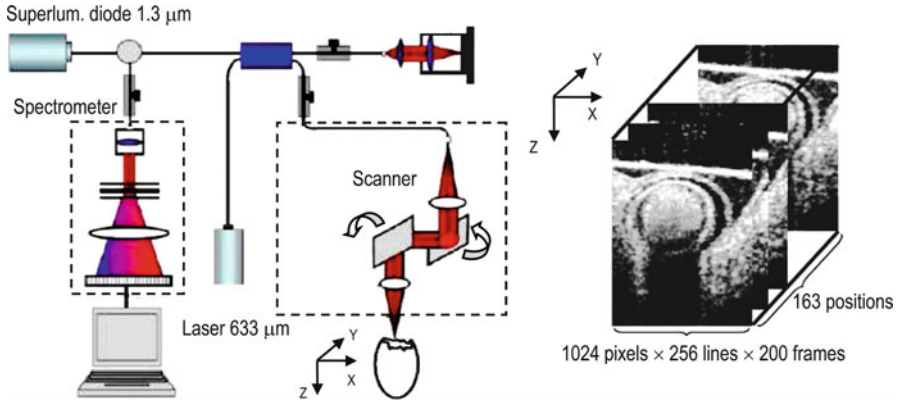
Fig. 10.17 *Left* – schematic of spectral-domain OCT. *Right* – strategy of 4D scan. Spatial volume: 4.6 (z) × 1.1(x) × 1.1(y) mm^3. Each position: 200 frames (~1.5 s) [62]

section. Structural and velocity images of blood flow are obtained simultaneously. In the velocity image, static regions (velocity is about zero) appear dark, and blood moving at different velocities is evident. The magnitude of blood flow velocity is maximal at the vessel center and decreases monotonically toward the peripheral wall. In a horizontal cross section of the velocity image near the vessel center, an excellent fit of the velocity profile to a parabolic function indicates that blood flow in the vein is laminar.

Ma et al. introduced [62] a novel method to measure absolute blood flow velocity in vivo. It is based on high-speed spectral domain optical coherence tomography, which measures the velocities of blood plasma across the heart outflow tract. In experiments involving a chicken, the authors acquired four-dimensional (4D) [(x, y, z) + t] images of absolute velocity distributions of the blood plasma with high spatial and temporal resolution in vivo. They reconstructed 4D microstructural images and obtained the orientation of the heart outflow tract at its maximum expansion, from which the centerline of the tract was calculated (Fig. 10.17). Assuming flow is parallel to the vessel orientation, the obtained centerline indicated the flow direction. The absolute flow velocity was evaluated based on the direction given by the centerline and the axial velocity obtained from Doppler OCT. Using this method, the flow velocity profiles were compared at various positions along the heart outflow tract of the chicken embryo.

10.4 Vibration Measurement and Mapping

Laser vibration sensing (LVS) has a number of civilian and military applications. It can be used for quality control in industrial applications in which vibration modes can help to identify machine malfunction, to detect excessive vibration, to identify harmful resonant frequencies, to monitor tool wear, and to predict impending tool failure. Laser-based optical measurement systems are used to measure civil

structures like bridges and houses. They opened many areas in medical applications, as well as in the security and military fields with the remote identification of targets like ground vehicles and ships. Laser vibrometry may be a candidate for detection of buried mines, hidden caves, and tunnels.

10.4.1 Basics of Laser Vibrometry

Laser vibrometry can be based on coherent or direct detection operating in CW or pulsed mode. A comparison of CW and pulsed lidars for vibration sensing is given by Hill et al. [63]. It has also been shown [64] that a pulse-doublet mode provides more accurate measurements. The processing techniques are of importance. Kachelmyer et al. [65] investigated a spectrogram-based frequency demodulation that outperformed the traditional FM discriminator in the presence of both target speckle and limited laser temporal coherence. Other spectral estimation methods are discussed by Rye and Hardesty [66, 67].

A compact solution is given by self-mixing laser diode velocimetry, a low-cost and compact technique for the measurement of the surface velocity of vibrating structures. Since the sensor is simply a photodiode, the whole system can be miniaturized. The principle is based on the interference produced when the light reflected or back-scattered by the target returns into the laser diode cavity and generates an amplitude modulated output from the diode itself. The first exploitation of the self-mixing effect for velocity measurements was described by Rudd [68]. Donati et al. [69] demonstrated a differential self-mixing vibrometer. Since there is no reference arm in the self-mixing configuration, the differential mode is obtained by electronic subtraction of signals from two (nominally equal) vibrometer channels, taking advantage that channels are servo stabilized and thus insensitive to speckle and other sources of amplitude fluctuation. The electronic subtraction is nearly as effective as field superposition. Common-mode suppression is 25–30 dB, the dynamic range is more than 100 μm, and a minimum measurable amplitude is 20 nm for 10 kHz bandwidth.

Instead of direct phase measurements, an incoherent system can measure the displacement of a beam or a speckle pattern caused by vibration. This can be done with a position-sensitive detector (PSD). The technique provides high-speed response, high dynamic range, very high resolution, and independence on spot size and shape [70].

Another option is to use the detector based on the photo-electromotive force (photo-emf) in the non-steady state [71]. It produces an output signal proportional to the transient lateral motion of an incident optical pattern on its surface. When the pattern is stationary, no output signal is produced, regardless of the location or amount of incident power. This principle can be used for a number of industrial, military, and security applications due to its high sensitivity. It allows the in-process ultrasonic inspection in industrial environment where background vibrations, high temperatures, and other hazards would foil both contact PZT transducers and traditional laser interferometers.

Fig. 10.18 Configuration of the system for vibration measurement using the photo-emf detector
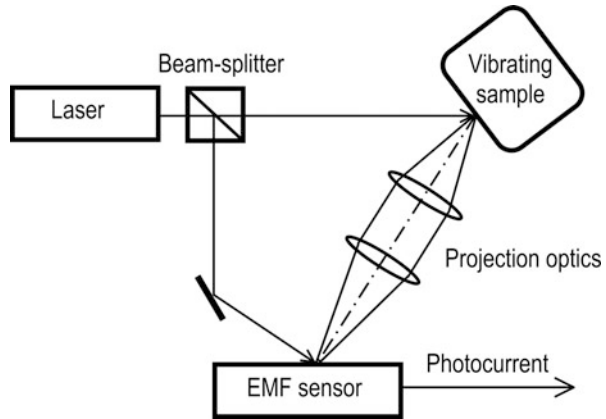
Figure 10.18 illustrates the principle of a photo-emf laser vibrometer [72]. Brimrose Technology Corporation demonstrates experimentally significant improvement in its sensitivity using pulsed-light sources. The vibrating surface is discretely sampled by individual laser pulses and recorded by the photo-emf sensor via the generation of photocurrent pulses whose magnitudes are proportional to the instantaneous surface displacements.

An important advantage of the pulse mode implies higher peak optical power levels of the probe laser pulses, leading to proportional enhancement in the photo-emf response and remarkable improvement in detection sensitivity, when the photodetection is noise current limited. At Brimrose, a 60 pm sensitivity was achieved with this approach.

Wang et al. [73] experimentally demonstrated a high-sensitivity pulsed laser vibrometer that was capable of detecting optically rough surfaces vibrating with the displacement value of 75 pm as well as its application as a laser microphone. By directing the probe light beam repeatedly onto the vibrating diaphragm and/or pressure sensing interface, the sensitivity of the pulsed laser vibrometer in detecting the displacement of the vibrating diaphragm is significantly improved down to an estimated value of less than 4 pm. By repeatedly bouncing the probe light beam N times onto the vibrating surface, the effective displacement of the vibrating diaphragm is amplified by a factor of N.

10.4.2 System Examples and Applications

Target classification and identification in the battlefield is an important issue, and large efforts have been put into development of methods based on target geometry and orientation. However, the performance of automatic target recognition methods can be sensitive to variability in target signature. Partly obscured targets, e.g., hidden by camouflage or foliage, can be difficult to recognize with imaging methods [74]. Also, target orientation may pose a problem to imaging methods, since target features may not be independent of target orientation. In such a case,
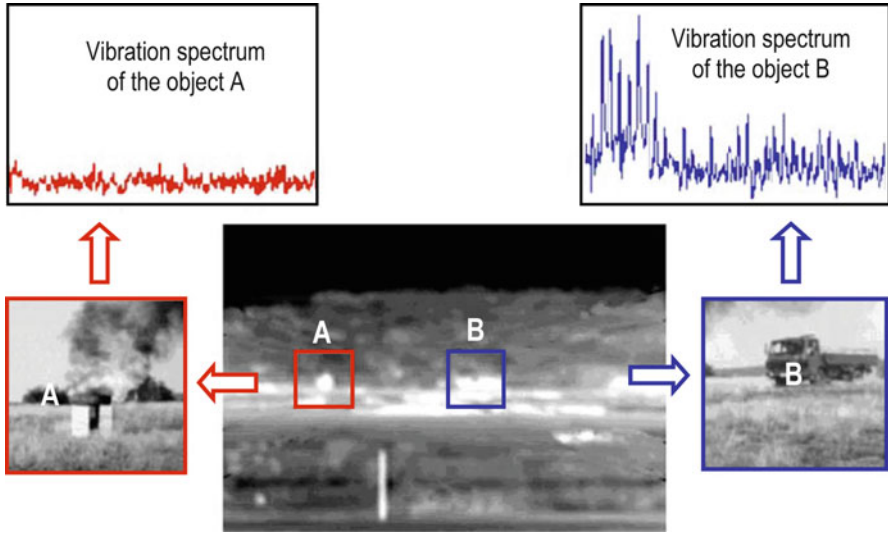
Fig. 10.19 Vibration spectra of a metal cube (object A) and of an idling truck (object B) measured by a laser vibrometer [75]

a point measurement to sense the target vibrations may be the solution. Vibration imaging offers a large potential for long-range target classification and identification. LDV, as a method for measuring the vibration signature of targets, offers the advantages of comparatively covert operation due to small beam divergence, of high geometrical resolution and high resolution of the vibration amplitude (due to the short wavelength). It is difficult to jam, and it is compatible with other electro-optical target-detection sensors.

Laser vibrometry can be used to discriminate between decoys and real targets (Fig. 10.19 [75]). A thermal image (a) shows a heated metal box (left white square) and an idling truck (right white square) at a distance of 3.2 km. Pictures (b) and (c) are the close-up images of these targets. The corresponding vibration spectra, measured with a CO_2 laser radar, are shown in (d) and (e), respectively. Another example is given in Fig. 10.20 [76], demonstrating a frequency spectrum from a command vehicle with an idling engine, taken with a laser vibrometer.

At long distances, the laser beam is spread across most, if not all, parts of the target. This results in spatially unresolved target vibration signatures. Lutzmann et al. [74] investigated a spatially resolved vibrometer to get the vibration signature of the investigated object. Resolution may be achieved by using a scan device or a multi-element receiver. With such a two-dimensional laser vibration sensing approach (2D-LVS), the target will be spatially resolved, giving a 2D map of vibration amplitudes across the target, one for each vibration frequency. An example of 2D-LVS signatures is given in Fig. 10.21. It should be noted that different frequencies give different signatures (Fig. 10.22).
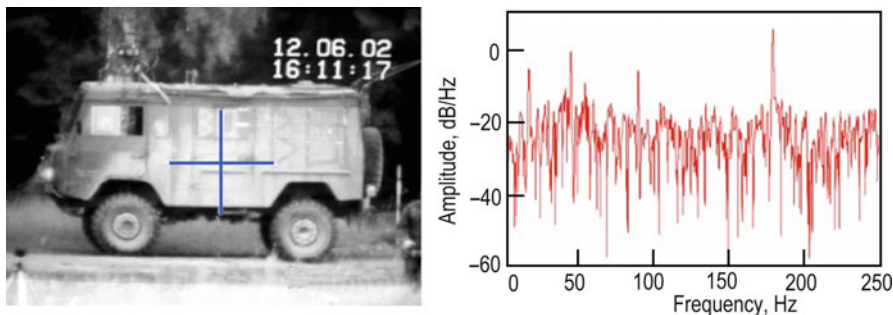
Fig. 10.20 A command vehicle with an idle engine and its vibration spectrum [76]
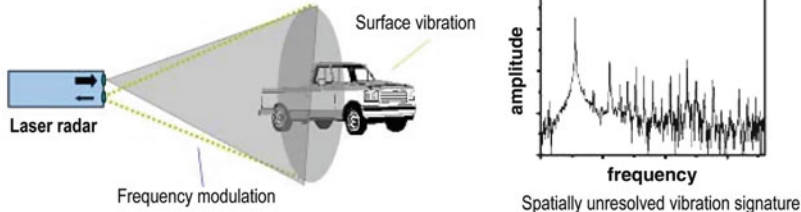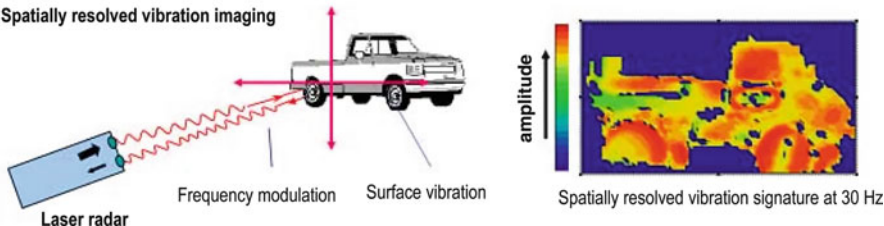
Fig. 10.21 Doppler velocity sensing and imaging. *Above*: the conventional broad illumination vibration sensing; *below*: spatially resolved vibration sensing using a scanning coherent lidar [74]

Investigating a spectrogram-based vibration data, Kachelmyer et al. [65] compared the spectrogram and FM-discriminator techniques and presented both theoretical and experimental results for a vibrating diffuse or glint target with simple or complex motion. Processed laser radar measurement data yielded vibration signatures of the Low-Power Atmospheric Compensation Experiment (LACE) satellite. Its simplified representation is given in Fig. 10.23. Three deployable/retractable booms each have a maximum extent of 50 m. A CO_2 laser vibrometer was used to measure the relative vibration between the germanium retroreflector located on the satellite body and the retroreflector located on the retroreflector boom tip. An example of the change in time vibration spectra, presented in the same Fig. 10.23, shows the dynamics of vibrations. The data have been aligned to the peak return. Vibration effects are clearly evident. The step in the oscillatory trajectory coincides with the termination of boom retraction.
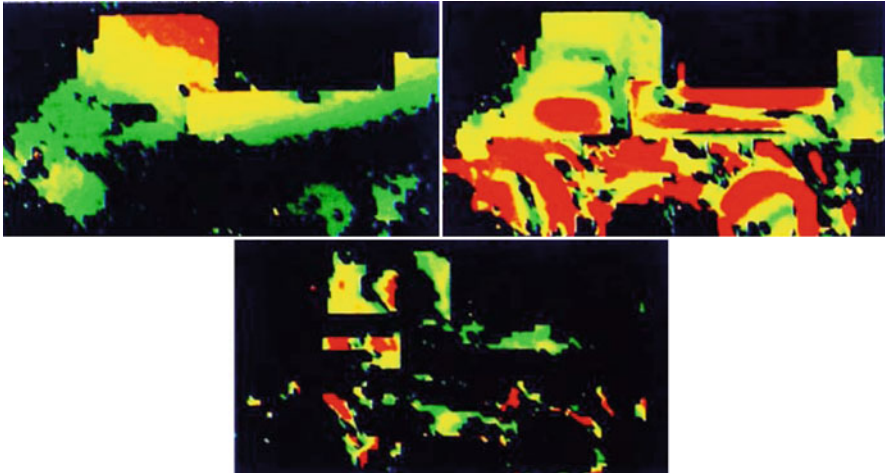
Fig. 10.22 Vibration maps of the same object at 8.5 Hz, 30 Hz, and 60.6 Hz [74]
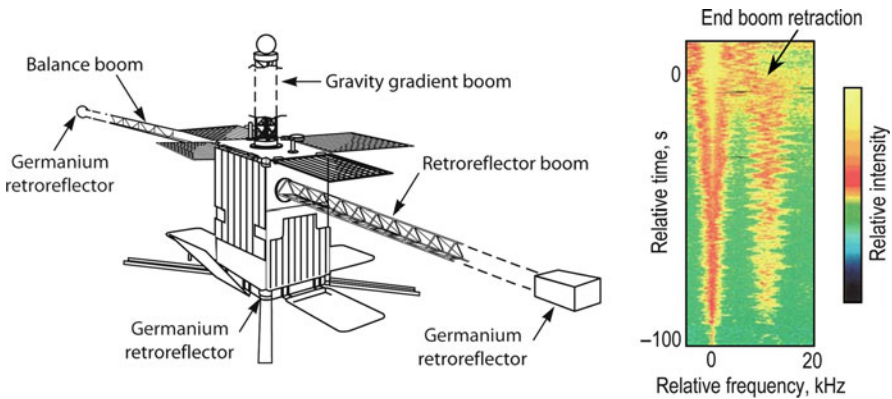
Fig. 10.23 Simplified representation of the LACE satellite and Doppler-time-intensity representation of the vibration spectra [65]

The laser Doppler velocimeter has attracted attention as a potential means for acoustic landmine detection [77–80]. The method consists of excitation of the ground with elastic waves in the frequency range from about 50–1,000 Hz and using a vibration sensor to obtain a vibrational velocity map of the ground surface. The interaction of a buried landmine with the elastic waves causes the landmine to vibrate. The mine has a compliance higher than the compliance of soil and natural objects like rocks and roots, because it is a complex mechanical structure. As a result, the vibration amplitude of the ground surface above the mine is higher than the vibration amplitude of the surrounding area. A vibrometer measures the vibration of the ground in many points to create a vibrational map of the ground

surface. Airborne sound created by loudspeakers, or seismic waves created by mechanical shakers, can be used to excite the ground vibration. The method does not depend on the metal content of landmines, hence, plastic mines (e.g., anti-personnel) can be also detected [79, 81].

The critical issue in landmine detection is the speed of measurements. If a single-beam scanning laser Doppler vibrometer is used, scanning a one-square-meter area with the required spatial resolution can take from 3 to 50 min. To reduce the measurement time, a multi-beam configuration was implemented. A schematic of such an instrument is shown in Fig. 10.24 [79, 81]. It uses a single-mode, solid-state, continuous-wave, frequency-doubled green Nd:YAG laser with a wavelength of 532 nm and an output power of 200 mW. The optical configuration is based on a Mach-Zehnder interferometer with polarization separation of the beams into reference beam and object beam.

The object beam is directed to a diffractive optical element, which divides it into 16 beams over an angle of 22°. The 16 beams illuminate a length of 1 m, with 63 mm separation between the beams. The scanning mirror allows the 16 beams to be scanned in the transverse direction. The light scattered from the target passes back through the optical system that collimates the light from each of the 16 object beams. The reference beam is frequency shifted by means of two acousto-optic modulators (AOMs) which operate at 80.1 and 80.0 MHz, respectively, to produce a net frequency shift of 100 kHz. Sixteen object beams and 16 reference beams are spatially overlapped and focused on 16 individual fiber-coupled pin photodiodes, producing 16 signals with a carrier frequency of 100 kHz.

Signal processing is illustrated in Fig. 10.25, where (a) shows the time domain vibration velocity signal for one of the channels, (b) its frequency spectrum, and (c, d) the velocity image of the buried landmine in the frequency band 140–145 Hz. Theoretical spatial profiles of the velocity image of an anti-tank mine buried 2.5 cm deep at different excitation levels are illustrated in Fig. 10.26 (top). Experimental profile for metal mine TM62M buried 10 cm deep is at the bottom.

Castellini et al. [82] reviewed industrial applications of the LDV that can be used in numerous application areas, including mechanical engineering, automotive, aeronautics, turbomachinery industries, biomedicine and clinical medicine, microsystems and MEMS, smart materials, artworks and archaeology, restoration, and civil engineering.

There are several commercial manufacturers of laser vibrometers, including Polytec [83], Ometron [84], and Metrovib [85]. The devices can either be single point, scanning, or multibeam for the creation of deflection shape of entire surfaces. The instruments can effectively detect vibration with a sensitivity of the order of 1 μm/s. These instruments are either designed for use in laboratories (0–5 m working distance) or field work (5–200 m).

An example of the Polytec 3D vibrometer is shown in Fig. 10.27, where the visualization of velocity and strain distributions are also illustrated (stress and strain are calculated from the measured velocities). Polytec developed the StrainProcessor as an extension of the PSV-400-3D Scanning Vibrometer to measure and analyze the dynamic strain and stress distribution on surfaces with high resolution and low
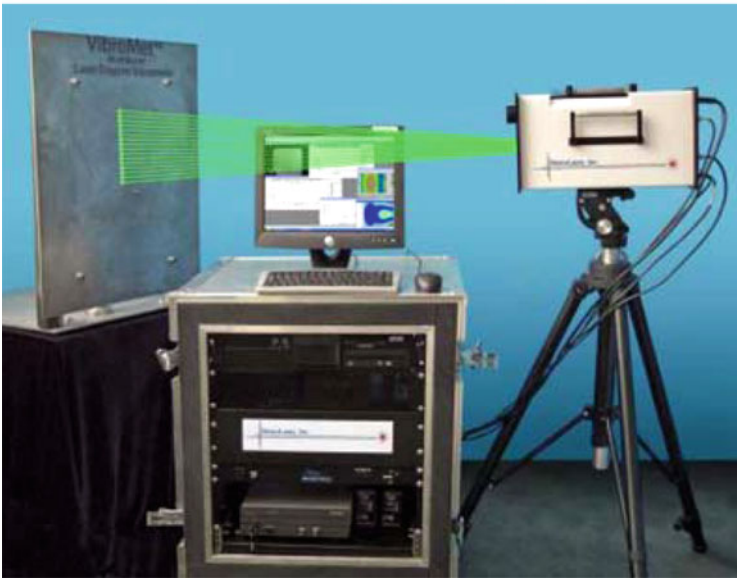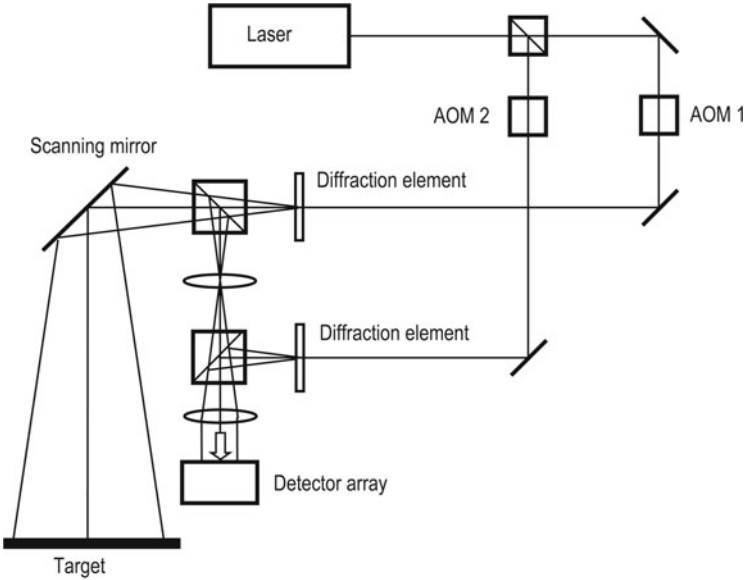
Fig. 10.24 Scanning multi-beam Laser Doppler vibrometer (MB-LDV) for buried mine detection [79, 81]

noise. The Scanning Vibrometer makes a series of non-contact deflection measurements on a predefined grid using the laser probe to characterize strain at each point instead of attaching individual strain gauges. The test setup is fast and repeatable, with no mass loading from an attached transducer.

Fig. 10.25 Processing of the vibration velocity signals: (**a**) time domain; (**b**) frequency spectrum; (**c**) segmented velocity image of the buried landmine; (**d**) smoothed velocity image [81]
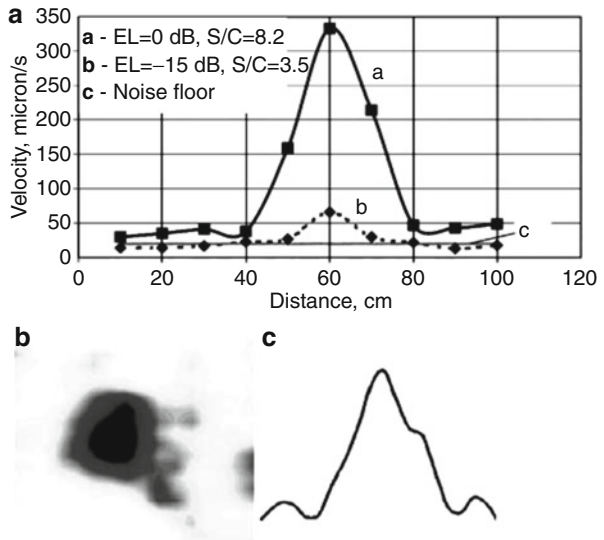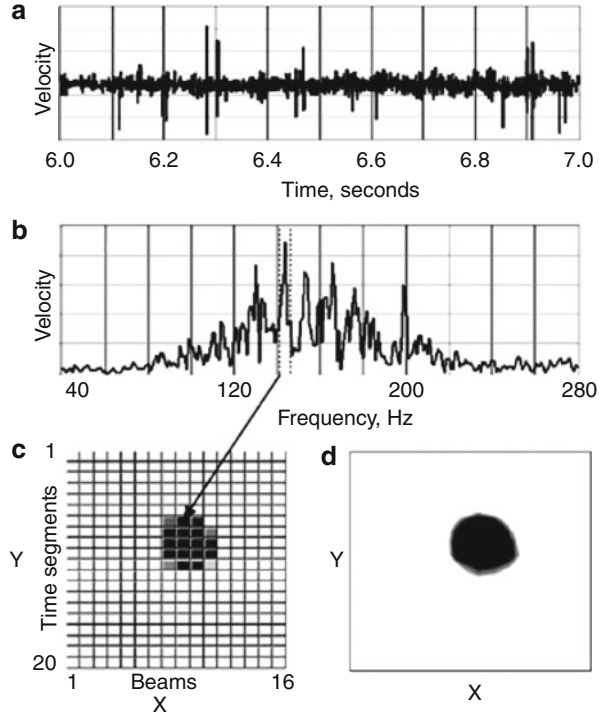
Fig. 10.26 Spatial profiles of the velocity image of a buried antitank mine: (**a**) theoretical and (**b**, **c**) experimental [81]

Fig. 10.27 3D scanning measurement of structural dynamics of a car body (**a**); vibration distribution over a car component (**b**); strain distribution in turbine blades (**c**)
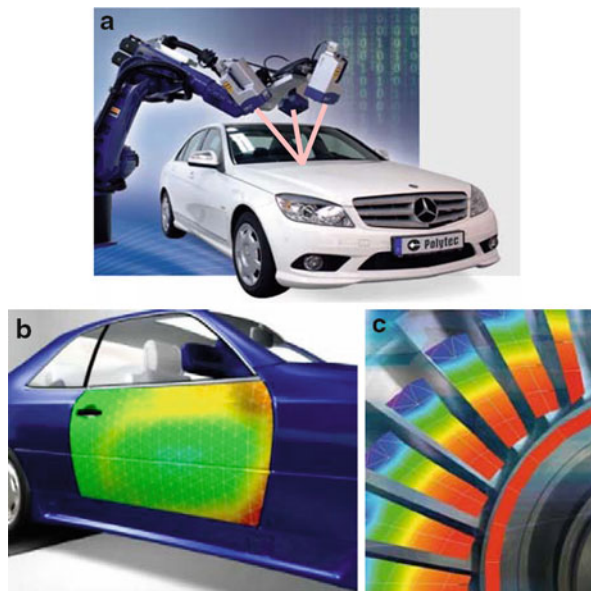
Diagnostics of building structures can be done according to the same principle as laser vibrometry for detection of buried objects. In particular, LDV has been used for the diagnostics of civil and historical buildings, with a special consideration for the so-called ventilated claddings [86]. This could also be applied to diagnostics of damaged buildings or other constructions, in order to determine the risk for a collapse or crash, before entering a structure.

Laser vibrometry for detection and classification of vehicles, both with clear line of sight and hidden behind vegetation and walls, has been demonstrated. The LDV technology can be used to detect voices from behind a window or inside a vehicle. The human voice causes the window or the body of a vehicle to vibrate, which could be readily detected by the LDV. Even if the engine is on and the volume of the speech is low (e.g., in cases of whispering), the human voice can still be extracted by signal decomposition, since the human voice and engine noise have different frequency-extracted ranges. Results with remote listening to conversation inside a car were reported by Zhu et al. [87].

Facilities like walls, pillars, lamp posts, large bulletin boards, and traffic signs vibrate very well with human voices. After enhancement by signal processing, involving Gaussian band pass filtering and adaptive volume scaling, the LDV voice signals can be picked up from targets without retro-reflective finishes at short or medium distances (<100 m).

Simple listening devices that are described in the literature have been used as far as 25 m away from a window and construction drawings are available on the Internet [88]. There is equipment on the commercial market today [89, 90], but the ability and quality of these systems is difficult to assess. However, due to limited
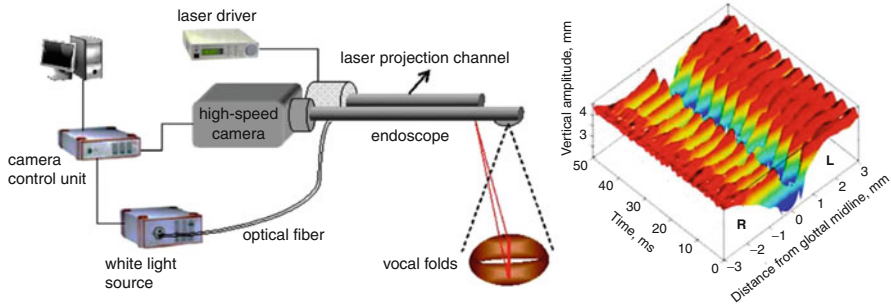
Fig. 10.28 Schematic view of the laser triangulation laryngoscope and color coded 3D vibration pattern of the vocal folds. The vertical amplitude is normalized with respect to the position of vocal folds surface at its lowest position. The closed phase of the glottis is visible as a continuous line between the left and right vocal folds [95]

SNR and/or limited ability to adopt the beam size and find the most vibrating parts of the target, non-cooperative vibration sensing is difficult, at least until coherent detector arrays have been fully developed. For some special applications, the Swedish Defense Research Agency (FOI) has developed a patented "laser microphone" [91] that allows speech and vibrations to be remotely transferred.

Laser Doppler vibrometry can provide advanced measurements in multiple physiological systems relevant to laboratory and field assessment of human stress and emotion [92, 93]. It can provide advanced recordings of myocardial and vascular performance, of respiratory efforts and sounds, and of tremor activity. It is responsive to laboratory stressors; muscle vibratory activity can be sensed from multiple muscles, including facial muscles, and the comparison is favorable with EMG. Laser velocimetry can reliably assess facial muscle activity, associated with emotion and stress at low levels – below the threshold for visible facial deformations.

Wang et al. [94] demonstrated the use of a high-sensitivity pulsed laser vibrometer based on photo-emf to remotely determine the detailed, time-phased mechanical workings of various parts of the human heart. Results reported were validated by electrocardiography and accelerometer readings.

An original technique was developed and used for clinical studies by George et al. [95]. To measure vibration dynamics of the vocal folds, they used a high-speed TV camera registration of a laser line projected onto the object in the triangulation mode and calculated the amplitude distribution for each frame (Fig. 10.28). The endoscopic laser projection system stretches a laser line beam in one direction and projects it as a thin laser sheet at an angle onto the vocal folds' surface. The laser projection channel consists of a semiconductor diode laser, a cylindrical optical system to focus the laser beam onto the vocal folds surface having stretched it in one direction.

The laser projection channel is firmly attached to a 90° rigid endoscope, which acts as the receiving channel. The optical axes of the two channels are separated by a distance of 9 mm at the tip of the system. Within a normal working distance of

60–70 mm from the tip of the endoscope, the laser line is 18–20 mm long and 0.4 mm wide. A semiconductor laser emits at 653 nm, delivering an effective laser power density of 1.8 mW/mm^2, keeping below the exposure limit of 2 mW/mm^2. The red laser is used because it gives minimum absorption and satisfactory reflectance by the tissue in the visible spectral region.

A compact high-speed digital color camera is used for recording the images. It can record images continuously for a maximum of 2 s at the rate of 4,000 fps with an image resolution of 256 × 256 pixels. Temporarily stored data in the camera memory is downloaded to the computer for further analysis. Vibration profiles in both horizontal and vertical directions were calibrated and measured with a resolution of ±50 μm.

10.5 Summary and Outlook

Laser remote sensing based on velocity measurements embodies the most of the coherent properties of laser light, both with coherent and direct detection techniques. Wind, flow, and vibration measurements were discussed in this chapter. Laser Doppler wind measurements have been developed from scientific instruments to unattended operational systems during the last decade. There are numerous applications in weather forecasting, including profiling and windshear and gust front detection. Aircraft wake vortex detection and tracking in the vicinity of airports is improving flight safety, as is clear air turbulence detection ahead of aircraft. Lidar-based optical air data systems for aircraft will replace Pitot tubes due to their better performance. Military applications include weapon corrections and precision cargo drop. The recent increase of wind farming has increased the operational small-scale wind measurement, and commercial systems are being deployed all over the globe.

Fluid flow velocimetry began with simple one-point sensing and has passed through several modifications to 4D measurements with time slicing, incorporating principles of the optical coherence tomography for in vivo biomedical studies in highly scattering media. It is vitally important for vessel blood flow measurements, hydrodynamic and aerodynamic studies, and modeling.

Laser vibration sensing has not yet become an established technique for industrial purposes, where it extends or even outperforms conventional methods like accelerometers and strain gauges and others. It allows non-contact rapid monitoring at substantial ranges. For defense and security the use of laser vibrometry is so far limited. The remote listening devices should be covert by using non-visible light. Sensor improvement is needed for long-range applications: increased laser power is needed to increase range performance. Classification of objects based on vibration signatures requires advances in signal processing and/or the development of focal plane arrays capable of simultaneous vibration sensing in several different pixels. LDV for remote measurement of pulse and muscle vibrations as indication of emotion requires further investigation but seems promising.

From a technology standpoint, both coherent Doppler lidars using homodyne or heterodyne schemes and direct detection Doppler lidars using high-resolution

spectral techniques will play a future role. Multifunctional lidars extending the wind measurement capability to aerosol and gas monitoring as well as temperature and humidity sensing have prospects for further development.

References

1. R.R. Navalgund, V. Jayaraman, P.S. Roy, Remote sensing applications: an overview. Curr. Sci. **93**, 1747–1766 (2007)
2. G.V. Rosenberg (ed.), *Searchlight Beam in the Atmosphere* (USSR Academic Science Publications, Moscow, 1960) (in Russian)
3. N.S. Shestov, *Signal Selection in Clutter* (Sovetskoe Radio, Moscow, 1967) (in Russian)
4. Y.G. Yakushenkov, *Basics of Theory and Design of Electro-Optical Devices* (Sovetskoe Radio, Moscow, 1971) (in Russian)
5. A.A. Kuriksha, *Quantum Optics and Optical Radar: Statistical Theory* (Sovetskoe Radio, Moscow, 1973) (in Russian)
6. I.N. Matveev, V.V. Protopopov, I.N. Troitsky, N.D. Ustinov, *Laser Radar Technology* (Mashinostroenie, Moscow, 1984) (in Russian)
7. V.V. Molebny, *Optical Radar Systems: Basics of Functional Layouts* (Mashinostroenie, Moscow, 1981) (in Russian)
8. V. Molebny, P. Zarubin, G. Kamerman, The dawn of optical radar: a story from another side of the globe. Proc. SPIE **7684** (2010)
9. G. Fiocco, L.O. Smullin, Detection of scattering layers in the upper atmosphere (60–140 km) by optical radar. Nature **199**, 1275–1276 (1963)
10. M. Schotland, The determination of the vertical profile of atmospheric gases by means of a ground based optical radar, in *Proceedings of Third Symposium on Remote Sensing of Environment, 1964*, U. Michigan, 1965
11. Y.F. Arshinov, S.M. Bobrovnikov, S.V. Sapozhnikov, On the method of lidar measurement of the atmosphere temperature from the signal ratio of the purely rotational specta of N_2 и O_2 (in Russian). Zh. Priklad. Spektrosk. (J. Appl. Spectrosc.) **32**, 725–731 (1980)
12. V.E. Zuev, Y.S. Makishkin, V.N. Matrichev, Laser sensing of the humidity profile of the atmosphere. Doklady Acad. Sci. USSR **257**, 1338–1342 (1981)
13. A.P. Ivanov, *Physical Fundamentals of Hydrooptics* (Nauka i Tekhnika, Minsk, 1975) (in Russian)
14. E.D. Hinkley (ed.), *Laser Monitoring of the Atmosphere* (Springer, Berlin, 1976)
15. T. Fujii, T. Fukuchi (eds.), *Laser Remote Sensing* (CRC Press Taylor & Francis Group, Boca Raton, 2005)
16. http://niipp-moskva.ru
17. http://www.popmech.ru/article/8352-vyizhigatel (Lazernyi nyukh)
18. C.R. Philbrick, H.D. Hallen, A.M. Wyant, T. Wright, M. Snyder, Optical remote sensing techniques to characterize the properties of atmospheric aerosols. Proc. SPIE **7684**, 76840J (2010)
19. J.A.L. Thomson, M.F. Dorian, Heterodyne detection of monochromatic light scattered from a cloud of moving particles. Tech Ret GDC-ERR-AN-1090, Convair Division of General Dynamics, San Diego (1967)
20. R.M. Huffaker, A.V. Jelalian, J.A. Thomson, Laser Doppler system for detection of aircraft trailing vortices. Proc. IEEE **58**, 322–326 (1970)
21. S.W. Hendersson, P. Gatt, D. Rees, R.M. Huffaker, Wind lidar, in *Laser Remote Sensing*, ed. by T. Fujii, T. Fukuchi (CRC Press Taylor & Francis Group, Boca Raton, 2005) (Chapter 7)
22. J.M. Vaughan, K.O. Steinvall, C. Werner, P.H. Flamant, Coherent laser radar in Europe. Proc. IEEE **84**, 205–226 (1996)
23. C.M. Sonneschein, F.A. Horrigan, Signal-to-noise relationships for coaxial systems that heterodyne backscatter from the atmosphere. Appl. Opt. **10**, 1600–1604 (1971)

24. J.M. Vaughan, Scattering in the atmosphere, in *Scattering and Inverse Scattering in Pure and Applied Wind Lidar*, ed. by E.R. Pike, P.C. Sabatier (Academic, San Diego, 2002) (Chapter 2.4.3)

25. R.L. Schwiesow, F. Köpp, C. Werner, Comparison of cw-lidar measured wind values obtained by full conical scan, conical sector scan and two-point technique. J. Atmos. Ocean. Technol. **2**, 3–14 (1985)

26. J. Rothermel, D.M. Chambers, M.A. Jarzembski, V. Srivastava, D.A. Bowdle, W.D. Jones, Signal processing and calibration of continuous-wave focused CO_2 Doppler lidars for atmospheric backscatter measurements. Appl. Opt. **35**, 2083–2095 (1996)

27. R.G. Frehlich, M.J. Yadlowsky, Performance of mean-frequency estimators for Doppler radar and lidar. J. Atmos. Ocean. Technol. **11**, 1217–1230 (1994)

28. C.L. Korb, B. Gentry, C. Weng, The edge technique – theory and applications to the lidar measurements of atmospheric winds. Appl. Opt. **31**, 4202–4213 (1992)

29. C.L. Korb, B. Gentry, S.X. Li, C. Flesia, Recent advances in Lidar wind measurements with the edge technique, in *Proceedings of 9th Conference on Coherent Laser Radar*, Linköping, 1997, pp. 32–35

30. M.J. McGill, J.D. Spinhirne, Comparison of two direct-detection Doppler lidar techniques. Opt. Eng. **37**, 2675–2686 (1998)

31. C. Flesia, C.L. Korb, C. Hirt, Double-edge molecular measurement of lidar wind profiles at 355 nm. Opt. Lett. **25**, 1466–1468 (2000)

32. B.M. Gentry, H. Chen, S.X. Li, Wind measurements with 355-nm molecular Doppler lidar. Opt. Lett. **25**, 1231–1233 (2000)

33. Z. Wang, Z. Liu, L. Liu, S. Wu, B. Liu, Z. Li, X. Chu, Iodine-filter-based mobile Doppler lidar to make continuous and full-azimuth-scanned wind measurements: data acquisition and analysis system, data retrieval methods, and error analysis. Appl. Opt. **49**, 6060–6078 (2010)

34. http://www.esa.int/esaLP/SEMM45ULWFE_index_0.html

35. O. Reitebuch, C. Lemmerz, E. Nagel, U. Paffrath, Y. Durand, M. Endemann, F. Fabre, M. Chaloupy, The airborne demonstrator for the direct-detection Doppler wind lidar ALADIN on ADM-Aeolus. J. Atmos. Ocean. Technol. **26**, 2501–2530 (2009)

36. C.I. Moir, Miniature laser Doppler velocimetry systems. Proc. SPIE **7356**, 73560I (2009)

37. E.W. Eloranta, J.M. King, J.A. Weinman, The determination of wind speeds in the boundary layer by monostatic lidar. J. Appl. Meteorol. **14**, 1485–1489 (1975)

38. G.G. Matvienko, I.V. Samokhvalov, Correlation method of wind velocity measurements with laser (in Russian), in *Remote Atmosphere Sensing*, ed. by V.E. Zuev (Nauka, Novosibirsk, 1978), pp. 113–124

39. K. Kunkel, E.W. Eloranta, J. Weinman, Remote determination of winds, turbulence spectra and energy dissipation rates in the boundary layer from lidar measurements. J. Atmos. Sci. **37**, 978–985 (1980)

40. R.A. Ferrare, E.W. Eloranta, R. Coulter, Lidar observations of banded convection during BLX83. J. Appl. Meteorol. **30**, 312–326 (1991)

41. E.W. Eloranta, Four dimensional lidar imaging of the atmosphere, in *American Geophysical Union, Fall Meeting 2010 Abstract #A12D-01* (2010). http://adsabs.harvard.edu/cgi-bin/author_form?author=Eloranta,+E&fullauthor=Eloranta,%20E.&charset=UTF-8&db_key=PHY

42. R. Targ, M.J. Kavaya, R.M. Huffaker, R.L. Bowles, Coherent lidar airborne windshear sensor: performance evaluation. Appl. Opt. **30**, 2013–2026 (1991)

43. W.E. Baker, G.D. Emmitt, F. Robertson, R.M. Atlas, J.E. Molinari, D.A. Bowdle, J. Paegle, R.M. Hardesty, M.J. Post, R.T. Menzies, T.N. Krishnamurti, R.A. Brown, J.R. Anderson, A.C. Lorenc, J. McElroy, Lidar-measured winds from space – a key component for weather and climate prediction. Bull. Am. Meteorol. Soc. **76**, 869–888 (1995)

44. U.N. Singh, S. Ismail, M.J. Kavaya, D.M. Winkler, F. Amzajerdian, Space-Based Lidar Chapter 9, in *Laser Remote Sensing*, ed. by T. Fujii, T. Fukuchi (CRC Press Taylor & Francis Group, Boca Raton, 2005)

45. J.W. Bilbro, W.W. Vaughan, Wind field measurement in the nonprecipitous regions surrounding severe storms by an airborne pulsed Doppler lidar system. Bull. Am. Meteorol. Soc. **59**, 1095–1100 (1978)
46. J. Bilbro, Airborne Doppler lidar wind field measurements. Bull. Am. Meteorol. Soc. **65**, 348–359 (1984)
47. R. Targ, B.C. Steakley, J.G. Hawley, L.L. Ames, P. Forney, D. Swanson, R. Stone, R.G. Otto, V. Zarifis, P. Brockman, R.S. Calloway, S.H. Klein, P.A. Robinson, Coherent lidar airborne wind sensor II: flight-test results at 2 and 10 μm. Appl. Opt. **35**, 7117–7127 (1996)
48. O. Reitebuch, C. Werner, I. Leike, P. Delville, P.H. Flamant, A. Cress, D. Engelbart, Experimental validation of wind profiling performed by the airborne 10-mu m heterodyne Doppler lidar WIND. J. Atmos. Ocean. Technol. **18**, 1331–1344 (2001)
49. C. Werner, O. Reitebuch, F. Köpp, J. Streicher, S. Rahm, E. Nagel, M. Klier, H. Herrmann, P.H. Flamant, C. Loth, P. Delville, P. Drobinski, B. Romand, C. Boitel, D. Oh, M. Lopez, M. Meissonnier, D. Bruneau, A. Dabas, Wind infrared Doppler lidar instrument. Opt. Eng. **40**, 115–125 (2001)
50. http://www.lockheedmartin.com/products/WindTracer/index.html
51. http://www.leosphere.com/8,wind-energy/
52. http://halo-photonics.com/index.htm
53. K.W. Fischer, V.J. Abreu, W.R. Skinner, J.E. Barnest, M.J. McGill, T.D. Irgang, Visible wavelength Doppler lidar for measurement of wind and aerosol profiles during day and night. Opt. Eng. **34**, 499–511 (1995)
54. http://www.michiganaero.com
55. P. Tchoryk, C. Watkins, S. Lindemann, P. Hays, C.A. Nardell, Molecular optical air data system (MOADS). Proc. SPIE **4377**, 194 (2001)
56. C.B. Watkins, C.J. Richey, P. Tchoryk, G.A. Ritter, P.B. Hays, C.A. Nardell, T.C. Willis, R. Urzi, Molecular optical air data system (MOADS) flight experiment. Proc. SPIE **5086**, 236–245 (2003)
57. C.B. Watkins, C.J. Richey, P. Tchoryk, G.A. Ritter, M. Dehring, P.B. Hays, C.A. Nardell, R. Urzi, Molecular optical air data system (MOADS) prototype II. Proc. SPIE **5412**, 10–20 (2004)
58. http://www.eumetsat.int/Home/Main/Publications/Conference_and_Workshop_Proceedings/groups/cps/documents/document/pdf_conf_p50_s1_12_straumel_p.pdf
59. C.E. Riva, B. Ross, G.B. Benedek, Laser Doppler measurements of blood flow in capillary tubes and retinal arteries. Invest. Ophthalmol. Vis. Sci. **11**, 936–944 (1972)
60. C.E. Riva, G.T. Feke, B. Eberli, V. Benary, Bidirectional LDV system for absolute measurement of blood speed in retinal vessels. Appl. Opt. **18**, 2301–2306 (1979)
61. Z. Chen, T.E. Milner, S. Srinivas, X. Wang, A. Malekafzali, M.J.C. van Gemert, J.S. Nelson, Noninvasive imaging of *in vivo* blood flow velocity using optical Doppler tomography. Opt. Lett. **22**, 1119–1121 (1997)
62. Z. Ma, A. Liu, X. Yin, A. Troyer, K. Thornburg, R.K. Wang, S. Rugonyi, Measurement of absolute blood flow velocity in outflow tract of HH18 chicken embryo based on 4D reconstruction using spectral domain optical coherence tomography. Biomed. Opt. Express **1**, 798–811 (2010)
63. C.A. Hill, M. Harris, K.D. Ridley, Fiber-based 1.5 μm lidar vibrometer in pulsed and continuous modes. Appl. Opt. **46**, 4376–4385 (2007)
64. S.M. Hannon, J.A.L. Thomson, S.W. Henderson, P. Gatt, R. Stoneman, D. Bruns, Agile multiple pulse coherent lidar for range and micro-Doppler measurement. Proc. SPIE **3380**, 259–269 (1998)
65. A.L. Kachelmyer, K.I. Schultz, Laser vibration sensing. Lincoln Lab. J. **8**(1), 3–28 (1995)
66. B.J. Rye, R.M. Hardesty, Discrete spectral peak estimation in incoherent backscatter heterodyne lidar, I: spectral accumulation and the Cramer-Rao lower bound. IEEE Trans. Geosci. Remote Sens. **31**, 16–27 (1993)
67. B.J. Rye, R.M. Hardesty, Discrete spectral peak estimation in incoherent backscatter heterodyne lidar, II: correlogram accumulation. IEEE Trans. Geosci. Remote Sens. **31**, 28–35 (1993)
68. M.J. Rudd, A laser Doppler velocimeter employing the laser as a mixer-oscillator. J. Phys. E **1**, 723–726 (1968)

69. S. Donati, M. Norgia, G. Giuliani, Self-mixing differential vibrometer based on electronic channel subtraction. Appl. Opt. **45**, 7264–7268 (2006)
70. D. Shetty, A. Ali, J. Hill, Optical instrumentation for vibration measurement and monitoring. Int. J. Preces. Eng. Manuf. **12**, 405–441 (2011)
71. M. Klein, B. Pouet, P. Mitchell, Photo-emf detector enables laser ultrasonic receiver, in *Optoelectronics World, A Supplement to Laser Focus World*, August 2000
72. http://www.brimrosetechnology.com/products/photo_emf_technology.html
73. C.-C. Wang, S. Trivedi, F. Jin, V. Swaminathan, P. Rodriguez, N.S. Prasad, High sensitivity pulsed laser vibrometer and its application as a laser microphone. Appl. Phys. Lett. **94**(051112) (2009)
74. P. Lutzmann, R. Frank, R. Ebert, Laser radar based vibration imaging of remote objects. Proc. SPIE **4035**, 436–443 (2000)
75. R.R. Ebert, P. Lutzmann, Vibration imagery of remote objects. Proc. SPIE **4821**, 1–10 (2002)
76. D. Letalick, T. Carlsson, H. Habberstad, M. Henriksson, Target recognition by vibration frequency analysis – a comparison of laser vibrometry and acoustic methods. Proc. SPIE **5086**, 246–252 (2003)
77. N. Xiang, J.M. Sabatier, An experimental study on antipersonnel landmine detection using acoustic-to-seismic coupling. J. Acoust. Soc. Am. **113**, 1333–1341 (2003)
78. J.C. van den Heuvel, V. Klein, P. Lutzmann, F.J.M. van Putten, M. Hebel, H.M.A. Schleijpen, Sound wave and laser excitation for acousto-optical landmine detection. Proc. SPIE **5089**, 569 (2003)
79. S. Lal, V. Aranchuk, A. Doushkina, C. Hurtado, J. Hess, D. Kilpatrick, N. L'Esperance, V. Luo, J. Markov, E.S. Sabatier, Advanced LDV instruments for buried landmine detection. Proc. SPIE **6217**, 621715 (2006)
80. D. Letalick, P. Jonsson, T. Carlsson, M. Henriksson, H. Habberstad, Detection of buried land mines with laser vibrometry. Scientific Report FOI-R-0909-SE (2003)
81. V. Aranchuk, A. Lal, C. Hess, J.M. Sabatier, Multi-beam laser Doppler vibrometer for landmine detection. Opt. Eng. **45**, 104302 (2006)
82. P. Castellini, M. Martarelli, E.P. Tomasini, Laser Doppler vibrometry: development of advanced solutions answering to technology's needs. Mech. Syst. Signal Process. **20**, 1265–1285 (2006)
83. http://www.polytec.com/
84. http://www.ometron.com/applications/index.html
85. http://www.metrolaserinc.com/vibrometer.htm
86. E. Esposito, S. Copparoni, B. Naticchia, Recent progress in diagnostics of civil structures by laser vibrometry, in *16th World Conference on NDT*, Montreal, 2004
87. Z. Zhu, W. Li, Integration of laser vibrometer and infrared video for multimedia surveillance display. TR-2005006, CUNY Graduate Center (2005)
88. J.M. Moses, K.P. Trout, A simple laser microphone for classroom demonstration. Phys. Teach. **44** (2006)
89. http://www.brickhousesecurity.com/lasermicrophonelisteningdevice-3000.html
90. http://www.global-security-solutions.com/index.htm
91. H. Habberstad, F. Kullander, O. Steinvall, Anordning för optisk fjärravlyssning samt system innefattande sådan anordning. Swedish Patent 0403074-8, 17 Dec 2004
92. J.W. Rohrbaugh, E.J. Sirevaag, J.A. Stern, A.H. Ryan, The physiology of threat: remote assessment using laser Doppler vibrometry. J. Credibil. Assess. Witn. Psychol. **7**(2), 135–145 (2006)
93. J.W. Rohrbaugh, E.J. Sirevaag, J.A. Stern, A.H. Ryan, The physiology of threat: remote assessment using laser Doppler vibrometry. Proc. SPIE **5778**, 567–573 (2005)
94. C.C. Wang, S. Trivedi, S. Kutcher, P. Rodriguez, F. Jin, V. Swaminathan, S. Nagaraj, S. Quoraishee, N.S. Prasad, Non-contact human cardiac activity monitoring using a high sensitivity pulsed laser vibrometer. OSA/CLEO paper CWB6 (2007)
95. N.A. George, F.F.M. de Mul, Q. Qiu, G. Rakhorst, H.K. Schutte, New laryngoscope for quantitative high-speed imaging of human vocal folds vibration in the horizontal and vertical direction. J. Biomed. Opt. **13**, 064024 (2008)

Retinal Imaging: Adaptive Optics

11

A. S. Goncharov, N. G. Iroshnikov, and Andrey V. Larichev

Contents

Abstract

This chapter describes several factors influencing the performance of ophthalmic diagnostic systems with adaptive optics compensation of human eye aberration. Particular attention is paid to speckle modulation, temporal behavior of aberrations, and anisoplanatic effects. The implementation of a fundus camera with adaptive optics is considered.

11.1 Introduction

Investigation of the features of the human eye optical system attracted researchers' attention for a long time [1]. The pioneering works of Smirnov [2] initiated studies of the aberrations arising due to imperfections of the optical structures of the eye. The relevance of such studies has grown recently with the development of various methods

A.S. Goncharov (✉) • N.G. Iroshnikov • A.V. Larichev
M.V. Lomonosov Moscow State University, Moscow, Russian Federation
e-mail: Goncharov@bk.ru, Nikita@optics.ru, larichev@optics.ru

for customized correction of refraction pathologies, such as intraocular lens implantation, laser refractive surgery, and so on. The efficiency of corrections of that kind is substantially determined by the reliability of the measurements of the optical parameters of the eye [3, 4].

Optical methods have also found widespread use in diagnosis of pathologies of the human retina. A human eye, which has no apparent pathology of refraction, can be considered as approximately diffraction-limited only for a small (2–3 mm) diameter of the pupil. In cases of a larger diameter, the spatial resolution is limited by random aberrations. Due to these aberrations, introduced by the cornea, crystalline lens, and vitreous body [5, 6], the diameter of the entrance pupil of devices for studying the eye fundus (fundus cameras) should be limited to 2 mm. Currently, the adaptive-optics-based techniques, which permit the compensation of random eye aberrations and, consequently, the extension of the entrance-pupil diameter of the device to 5–7 mm, are being intensely developed.

Several methods have been proposed for measuring the overall aberrations of the human eye, such as the double pass method [7], laser ray tracing [8], and the automated Tscherning technique [9]. Recently, aberrometers based on Shack-Hartmann wavefront sensors have gained popularity [10–13]. In such a device, a low-power laser produces a point reference light source on the eye retina. The optical radiation leaving the eye after being reflected off the retina is passed through a lenslet array in order to form a matrix of focal spots on the surface of a photodetector array. The lenslet array position is optically conjugated with the eye pupil plane. The shifts of the focal spots with respect to their reference positions are proportional to the local tilts of the measured wavefront within the corresponding subapertures of the sensor. The wavefront is reconstructed right from these tilts. It is assumed that the phase distribution thus retrieved represents the deviation of the optical system of the eye from the ideal one.

In 1994, Liang proposed for the first time the use of the Shack-Hartmann wavefront sensor for determining eye aberrations [10]. The first models of a Shack-Hartmann sensor did not allow eye aberrations to be measured at a high speed. This limitation arose from the fact that the speckle field, formed in the process of laser beam scattering by the retina, significantly lowered the quality of the detected signal [14]. The corresponding speckle field is both amplitude- and phase-modulated. Therefore, the wavefront profile measured by the sensor generally corresponds to the overall effect of the aberrations of the optical elements of the eye and the speckle field characteristics.

To suppress speckles in first models of a Shack-Hartmann sensor, the time integration over the range from 200 to 400 ms was applied. In 2001, the dynamic sensors, measuring phase distortions of the eye in real time, were fabricated. To suppress speckle structure in dynamic sensors, the authors of [12] scanned the position of the reference source on the retina, while the authors of [15] used a source with a low spatial coherence. Also in 2001, the possibility to compensate for the dynamic phase distortions by means of a membrane mirror [16] and a bimorph corrector [17] was demonstrated.

Hofer et al. [13] experimentally compared the quality of eye aberration correction in cases of static and dynamic control of a 37-electrode monolithic mirror.

The Shack-Hartmann wavefront sensor used in experiments measured aberrations with the 30-Hz rate. The analysis showed that the dynamic compensation increases the Strehl ratio by a factor of three and contrast of observable photoreceptors by 33% compared with the static compensation. The field of view of the system was 1° under these conditions. However, for clinical applications, devices with the field of view of 10°–30° are of the greatest interest. Therefore, the significant increase in the visual angle of adaptive systems is required for the retina imaging.

Generally, the field of view of the adaptive system, when examining the human eye, is limited by two factors: the imperfection of the image-forming optics and anisoplanar effects in the optical system of the eye. Analytical estimates, analogous to those in Ref. [18], showed that in most cases for the pupil diameter of 5 mm, sufficient to observe even the smallest eye-fundus details with respect to diffraction limitations, the isoplanar field of view reaches 7.5°–15° (depending on the amplitude of the eye aberrations and their distribution between the crystalline lens and the cornea). Thus, with an optical imaging system free of intrinsic aberrations in the angular field of about 15°, one can expect that the adaptive system will be able to compensate for distortions within the entire isoplanar area [19].

It is known that the amplitude of the eye aberrations decays sharply with the increase of their order number [20]. Low-order aberrations such as the defocus, astigmatism, coma, and spherical aberration have the maximum amplitude. Monolithic and membrane mirrors allow one to correct only for aberrations with relatively low amplitudes. In this connection, in experiments [16, 21, 22] the defocus and astigmatism were compensated before the feedback closure by means of the additional lens optics. In Ref. [23], the possibility to use a 69-segment liquid-crystal corrector for this purpose was examined. However, the authors failed to achieve a desirable effect and came to a conclusion that the dynamic range and the number of segments of a corrector should be significantly increased to compensate for real eye aberrations. Another type of wavefront correctors is a modal deformable mirror [24]. Using a small number of control channels, such correctors allow a high-precision modeling of low-order aberrations with relatively high amplitudes. This property of such correctors corresponds to the statistical properties of phase distortions of the eye.

11.2 Retina as a Scatterer

The human eye retina exhibits a complicated multilayer structure. In general, light is scattered by various layers of the retina, so that the penetration depth of the long-wavelength radiation (near-IR range) is significantly greater than the penetration depth of visible light. Normally, the radiation of the wavelength range 750–950 nm is used for the measurement of the eye aberrations. This is due to the relatively low sensitivity of photoreceptors in this spectral range, which provides low visual brightness of the source. In spite of the relatively deep penetration of IR radiation, the main contribution to the signal of the wavefront sensor is related to the scattering by the photoreceptor layer. In the case of laser scattering by the retina,
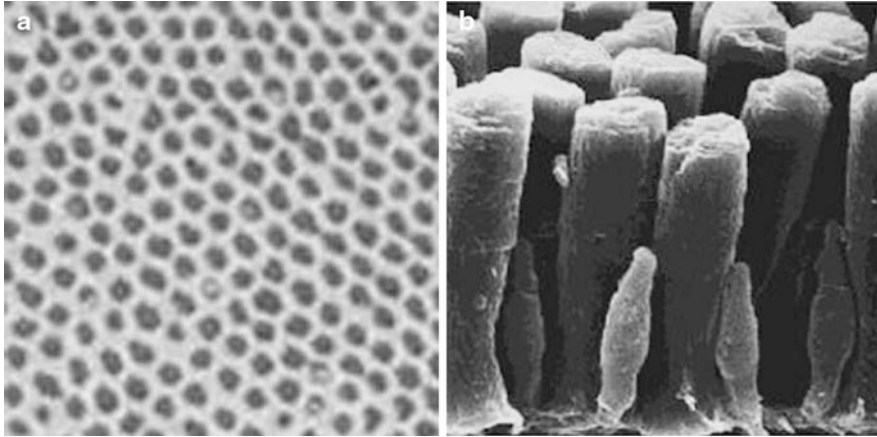
Fig. 11.1 (**a**) Front view of the photoreceptor mosaic; (**b**) electron microscope image of photoreceptors. The characteristic length and diameter of the cones are 40–60 μm and 1–5 μm, respectively [31]

its complicated microstructure [25, 26] (Fig. 11.1) resulted in a random phase shift of the scattered light waves. At the output of the ocular optical system, the interference of light waves gives rise to a spot structure known as the speckle field. Ocular photoreceptors work as waveguides and deliver incident light to the sensitive photopigments. Then, a part of the light is reflected back towards the pupil in the direction that is determined by the orientation of each photoreceptor [27]. The waveguide properties of the receptors and their location at the retina determine the light scattering pattern at the output of the ocular optical system [28, 29] as well as variations in the sensitivity of photoreceptors for the rays that pass through various zones of the pupil (Stiles–Crawford effect [30]).

To study the features of speckle modulation and to collect statistical data, many experiments are necessary. This work is not always expedient with a living human eye as the subject. Therefore, it is useful to develop simplified theoretical and nature models taking into account the specificity of laser radiation scattering by the human eye retina. For this purpose, the optical system shown in Fig. 11.2 was used as a basis for both implementing a nature model and building a numerical computation scheme [32].

Taking into account that the properties of photoreceptors are similar to those of waveguides [27, 28], a fiber-optic faceplate was used to experimentally model the scattering properties of the retina. The thickness of the faceplate was 8 mm, while the diameter of its fibers was 6 μm, which is close to the physical diameter of the human eye photoreceptors [31]. To investigate the speckle structure, the simplest reduced eye model [33] with a single refracting element (lens (2) in Fig. 11.2) was used. The input pupil of the eye model is formed by the lens aperture. The focal length f of the focusing lens (achromatic doublet) was 20 mm, being close to the
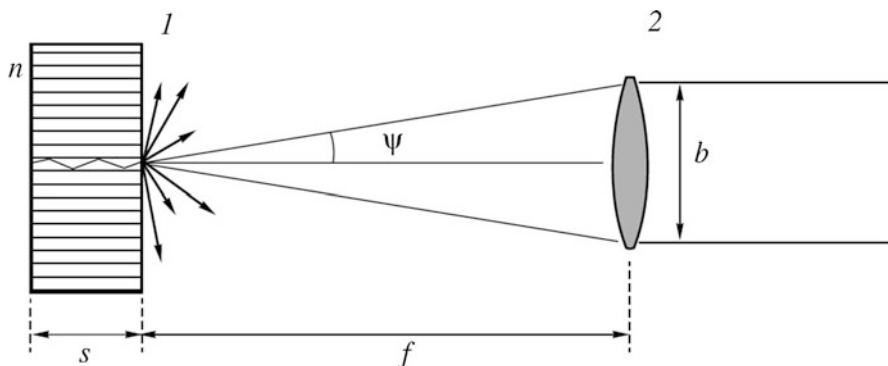
Fig. 11.2 Simplified equivalent scheme of the eye for the study of laser radiation scattering; (*1*) scatterer and (*2*) lens

average length of the human eye along its optical axis [34]. The light propagating through the fibers was reflected by the rear surface of the faceplate to propagate back and to form a reference source on the front surface of the faceplate. The phases of the sub-beams leaving different fibers of the faceplate differed from one another, making the scattered radiation have a speckle structure.

The numerical simulations were performed in the framework of the parabolic approximation for wave propagation [35], with the use of the fast Fourier transform. The input beam of probe radiation was considered as having a finite width. The input radiation was modeled by a super-Gaussian intensity distribution and a uniform phase. To get to the focal point formed on the eye retina, the Fourier transform of the initial beam was performed. The microstructure of the scatterer was defined by a hexagonal matrix that modeled the photoreceptor pattern (Fig. 11.3a). Each of these hexagonal elements introduced a random phase shift having a Gaussian distribution with a dispersion of 2π to the light wave it reflected. Thus, scattering of the light wave by the eye retina was modeled. The light field distribution at the plane of the model eye input pupil was obtained by the inverse Fourier transform. The intensity distribution contained a speckle structure (Fig. 11.3b) that was used to calculate the contrast and average size of the speckles.

It was possible to directly model the Hartmann pattern formed by the lenslet array within the parabolic approximation. For this purpose, the field distribution at the model eye pupil was split into the areas corresponding to the subapertures of the sensor. For each of these subapertures, the Fourier transform was performed with subsequent intensity calculation. Thus, the image at the focal plane of the lenslet array was generated (Fig. 11.3e). The modeling was performed with the following parameters: the photoreceptor diameter was set to 6 μm, being close to the physical diameter of human eye photoreceptors [31], the probe beam diameter was $b = 2$ mm, the focal distance was $f = 20$ mm, and the wavelength was $\lambda = 630$ nm.
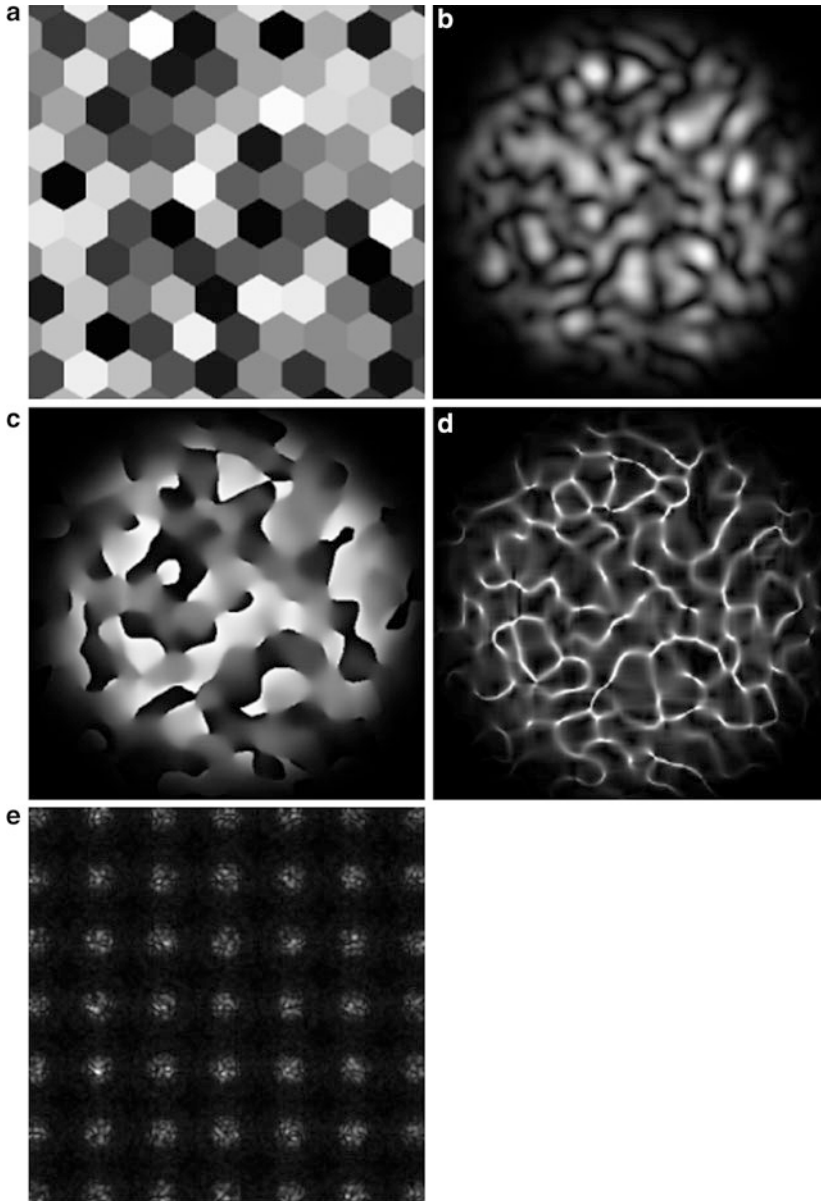
Fig. 11.3 Photoreceptor pattern model used in numerical simulations (**a**), numerically simulated speckle structure (**b**), phase speckle modulation (**c**), absolute value of the phase gradient (**d**) and fragment of Hartmannogram (**e**)

11.3   Influence of the Speckle Field on the Accuracy of Wavefront Reconstruction

In order to study the effect of speckles on the wavefront sensors, an experimental setup similar to one shown in Fig. 11.9 was constructed [12]. A diode laser beam ($\lambda = 0.67$ μm) passes through a diaphragm of diameter 0.8 mm. The diaphragm decreases the phase distortions acquired by the beam before its incidence on the retina, which makes it possible to satisfy the single-pass measurement conditions. After passing through the polarization beam splitter cube and spinning scanner, the beam falls on the eye model and is focused on the scatterer, forming a reference light source. Measurement of the eye aberrations consists of the measurement of large-scale phase distortions in the plane of the pupil of the eye model. The radiation emerging from the eye propagates in the reverse direction through the spinning scanner and is incident on the polarization cube. The cube is set in such a way that it eliminates polarized flare spots and directs only the depolarized part of the scattered radiation to the sensor. Then, the light passes through confocal lenses and falls on the lens array of the Shack-Hartmann wavefront sensor (placed instead of objective (8) and camera (10) in Fig. 11.9), which is placed in a plane optically conjugate to the plane of the pupil of the eye model.

Each lens of the array (subaperture) has a size $A_{sub} = 0.5$ mm and a focal length $F_{sub} = 25$ mm. For a pupil diameter equal to 6 mm, the radiation emerging from the eye illuminates about 80 subapertures of the array. The lenses of the sensor divide the wavefront being studied, forming an array of spots in the focal plane. Each spot of the Hartmannogram is an image of the reference source at the retina. The obtained Hartmannogram is recorded with a CCD camera located in the focal plane of the lens raster and is stored in the computer memory with a frequency of 30 fps and a resolution of 640×480 pixels. The processing time for a Hartmannogram is 8 ms. The wavefront is reconstructed by the method of least squares in the form of an expansion in 36 Zernike polynomials.

The beamsplitter was placed in front of the Shack-Hartmann wavefront sensor (not shown in the Fig. 11.9). The light deviated by the beamsplitter passes through the lens and is recorded by a second CCD camera located in a plane optically conjugate to the plane of the pupil of the eye. This camera is used for observing the speckle field.

The speckle structure of the field scattered by the retina lowers the accuracy of measurement of aberrations [37]. It was shown in Ref. [10] that owing to the eye movements, the speckles can be suppressed considerably due to time integration. However, such a regime of the system operation does not allow the measurement of aberrations of the eye at a high speed. In this system the scanning of the position of the reference source, is used. As the spinning scanner rotates, the laser beam describes a cone (0.5°), resulting in a displacement of the reference source on the retina and, consequently, in a change in the speckle structure.

In the general case, the wavefront tilt caused by the scanner may result in an undesirable displacement of the Hartmannogram spots. To eliminate this effect,

Fig. 11.4 Intensity distributions in the plane of the pupil of the eye model (**a**, **b**) and Hartmannograms (**c**, **d**) without (**a**, **c**) and with (**b**, **d**) scanner
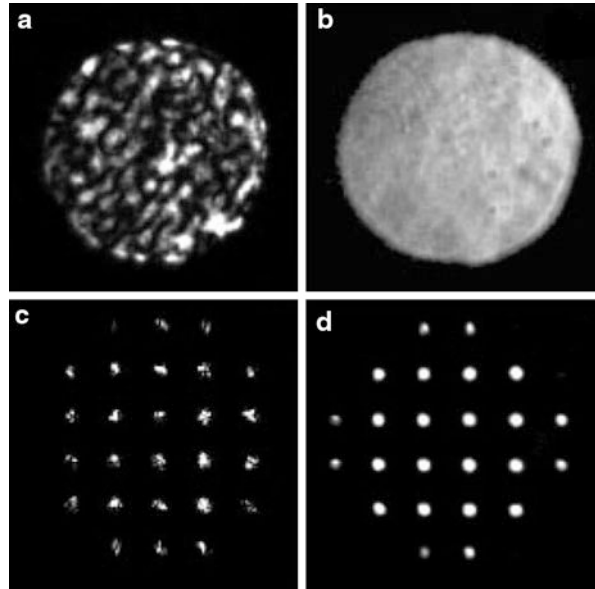
the optical diagram is organized in such a way that the beam leaving the eye is passed again through the scanner so that the tilts are compensated. In this case, the reference source describes on the retina a circle of diameter 150 mm, and the Hartmannogram spots remain stationary. For a rotation speed of 50 cycles/s of the electric motor, the characteristic time of speckle variation was much shorter than the integration time of the CCD camera (30 ms), and the speckles were effectively averaged. Figure 11.4 shows the intensity distributions in the plane of the pupil in the eye model, as well as the Hartmannogram obtained with and without the scanner. One can see that scanner allows an effective suppression of the speckle structure and improves the quality of the Hartmannogram.

The speckle field statistics depend on the diameter of the illuminated spot at the scatterer. For example, the speckle size is the largest when the front face of the fiber-optic faceplate coincides with the focal plane of the lens. A displacement of the lens along the optical axis leads to a change in the size of the illuminated spot and hence to a change in the speckle size.

The correlation radius r_{cor} of the speckle field is determined from the $1/e$ level of the structural intensity function: $G(\Delta r) = \left\langle [I(r + \Delta r) - I(r)]^2 \right\rangle$, where $I(r)$ is the intensity distribution in the speckle field, Δr is the transverse shift, and the angle brackets indicate space averaging. In the case of a statistically uniform field, the space averaging is equivalent to averaging over an ensemble of various realizations of speckles. This property was used for calculating the structure function and the error in the wavefront reconstruction.

The fiber-optic faceplate in the experiments was displaced in a plane perpendicular to the optical axis. The statistics of various realizations of the speckle field was

compiled in this manner. The characteristic scale of speckles, determined by the separation between the lens and the scatterer, remained unchanged in this case. Wavefront measurements for various realizations of the speckle field were carried out without the scanner. The set of Zernike coefficients determined in this way was used to determine their mean square deviation $\sigma_i = \left\langle (a_i - \langle a_i \rangle)^2 \right\rangle$ (a_i is the Zernike coefficient number i) characterizing the phase reconstruction error associated with the presence of speckles. After this, the fiber-optic faceplate was displaced longitudinally. The speckle size varied in this case, and the procedure for determining the error was repeated.

Figure 11.5 shows the intensity distributions in a speckle field and the Hartmannograms for two different ratios of the correlation radius to the size of the subaperture: $r_{cor}/A_{sub} = 0.3$ (large speckles, Fig. 11.5a and c) and $r_{cor}/A_{sub} = 0.07$ (fine speckles, Fig. 11.5b and d), as well as the structural intensity modulation functions (Fig. 11.5e). It should be noted that the visual size of the speckles is several times larger than the correlation radius r_{cor}.

One can see from Fig. 11.5d that the Hartmannogram spots are split when the characteristic size of the speckles becomes smaller than the subaperture size, and this leads to the emergence of additional extrema. In this case, the center-of-mass technique, which in the absence of noise gives a wavefront tilt averaged over the subaperture, irrespective of the size of phase inhomogeneity was used. If the characteristic size of the speckles exceeds the subaperture size, the intensity distribution inside each spot tends to the diffraction-limited distribution. However, one can see from Fig. 11.5c that some of the spots corresponding to the subapertures, on which dark speckles are incident, have a low intensity compared with the noise. The accuracy with which the centers of such spots are located is not high enough and, therefore, they should be discarded while processing the Hartmannogram. This leads to a decrease in the accuracy of phase evaluation.

Figure 11.6 shows the dependencies of the mean error σ in determining the Zernike coefficients of various orders (in the present case, the order of the polynomial is determined by the highest power of its radial argument r) (Fig. 11.6a) and the relative error $\sigma_{rel} = \sigma_3/a_3$ in determining the defocusing, on the ratio r_{cor}/A_{sub} of the correlation radius of the speckle field to the subaperture size of the Shack-Hartmann sensor (Fig. 11.6b). The experimental dependences were averaged over 20 different realizations of the speckle field. One can see from Fig. 11.6 that, as the speckle size decreases, the errors increase for polynomials of each order. This is due to a lower accuracy with which the positions of the spots are determined. For large speckles, the error in the wavefront reconstruction mainly comes from the random smooth phase distortions of the speckle field itself. In addition, the increased error is associated with a decrease in the number of spots whose intensity is sufficient to allow their processing. One can see from Fig. 11.6 that, in the range of variation of the ratio $r_{cor}/A_{sub} = 0.2$–0.7, the error in determining the Zernike coefficients varies insignificantly, and does not exceed 0.05 mm, while the relative error in determining the defocusing is no more than 10 %.
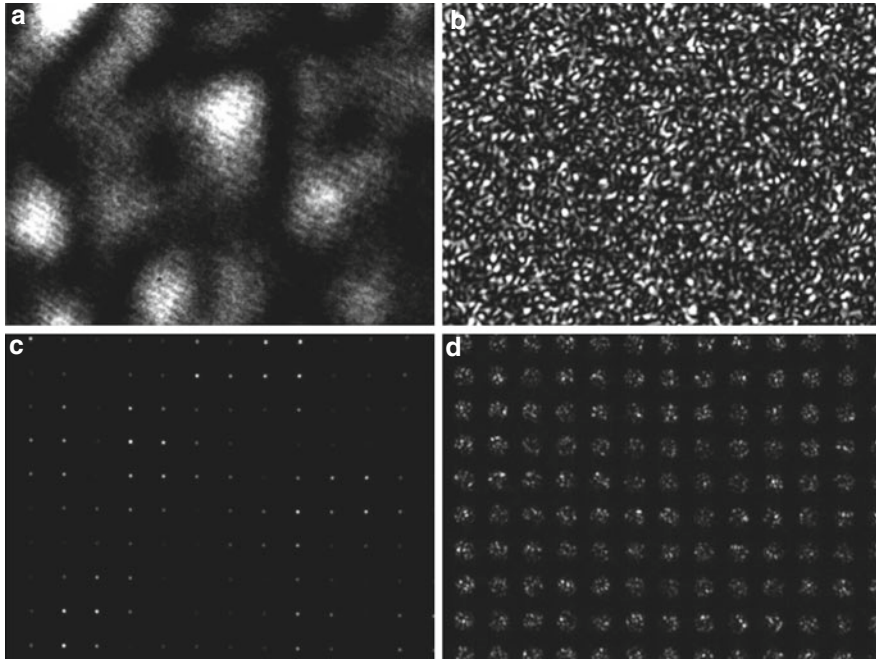
Fig. 11.5 Intensity distributions in the speckle field (**a**, **b**) and Hartmannograms (**c**, **d**) for large (**a**, **c**) and small (**b**, **d**) speckles, as well as the intensity modulation structural functions G corresponding to large (*solid line*) and small (*dashed line*) speckles

Fig. 11.6 (a) Dependences of the mean statistical deviation of the Zernike coefficient σ of the first ($\blacklozenge$), second ($\bullet$), third (Δ), fourth ($\square$), and fifth ($\bigcirc$) order and (b) the relative error in determining the defocusing σ_{rel} on the ratio r_{cor}/A_{sub} of the correlation radius of the speckle field to the size of the subaperture
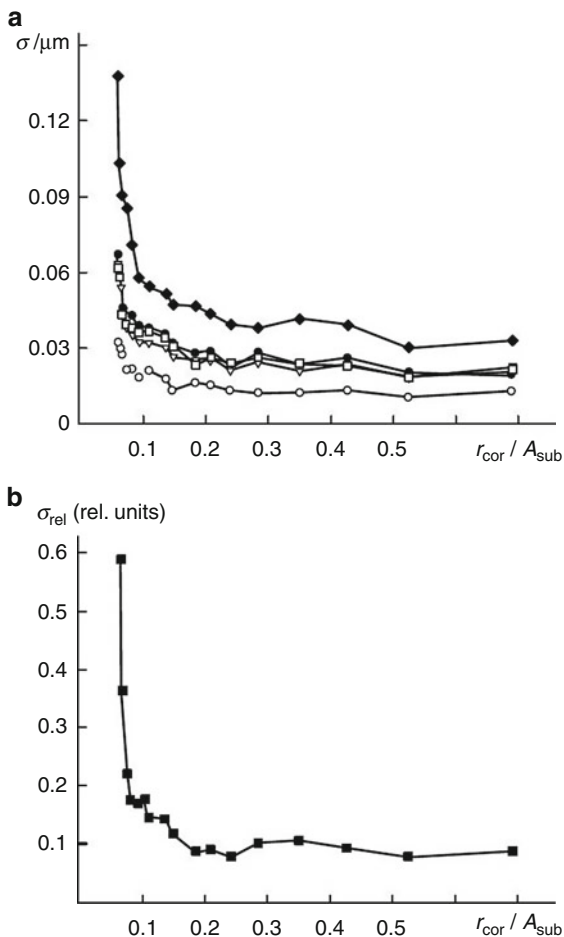
11.4 Characteristics of the Speckle Field

Consider the main characteristics of the speckle field that is generated in the optical systems under study. Normally, the contrast of the speckle pattern is represented as [36]

$$\gamma = \frac{\sigma_I}{\langle I \rangle},$$

where σ_I is the mean-square deviation of the intensity fluctuations in the beam cross section and $\langle I \rangle$ is the mean intensity.

A comprehensive theoretical analysis of the contrast of the speckle pattern and its dependence on the size of the irradiation region on the scatterer can be found in

Fig. 11.7 Plots of the mean speckle size ε versus defocusing D of the incident radiation
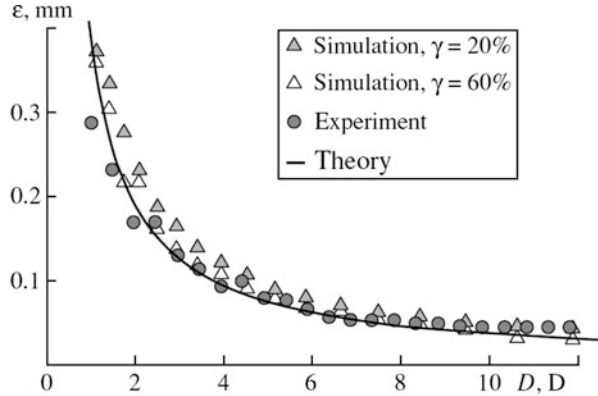
Ref. [36]. It is demonstrated that, at a relatively low phase modulation of the scattered radiation σ, the contrast decreases with an increasing size of the irradiated region: $\gamma \cong \sigma^2/\sqrt{M}$, where M is the number of uncorrelated fragments of the surface that contribute to the total intensity.

However, when the mean-square fluctuations of the phase are greater than π, this dependence reaches a saturation level of unity at virtually any size of the irradiated region.

The mean size of speckles depends on the diameter of the irradiated region on the scatterer (retina) and approximately equals the diameter of the diffraction pattern from the irradiated region [14]. The size of the irradiated region is determined by the divergence of the probe radiation and its defocusing. Figure 11.7 shows the dependence of the mean speckle size ε on defocusing D of the incident radiation. To simulate the defocusing, the phase modulation with a parabolic profile into the wavefront of the probe radiation was introduced. The results obtained for the speckle structures with the contrasts $\gamma = 20\%$ and $\gamma = 60\%$ (closed and open triangles, respectively) are compared with the theoretical curve (solid line) obtained with the formula

$$\begin{cases} \varepsilon \approx 2.44\lambda\dfrac{f}{a} = 2.44\lambda\dfrac{1}{Db}, \ D > \dfrac{2.44\lambda}{b^2} \\ \varepsilon \approx b, \ D \leq \dfrac{2.44\lambda}{b^2} \end{cases}, \tag{11.1}$$

where a is the diameter of the irradiated region on the retina, b is the probe beam diameter, and f is the focal length of the eye model lens. The mean speckle size is calculated based on the width of the light-field intensity autocorrelation function.

Figure 11.7 also demonstrates the experimental dependence (circles) obtained by means of setup shown in Fig. 11.9. The deviation of the theoretical curve plotted with formula (11.1) (solid line) from the experimental data (circles) at low defocusing is related to the inexact equality in the formula and the aberrations inherent in the optical system predominantly due to spherical lens ((6) in Fig. 11.9) with a relatively high power. Thus, the speckles do not reach the maximum size at zero defocusing, since the diameter of the irradiated region on the scatterer does not decrease to the diffraction-limited size.

Fig. 11.8 Plots of the cross correlation B of two speckle patterns versus shift s between two positions of the scatterer corresponding to these patterns
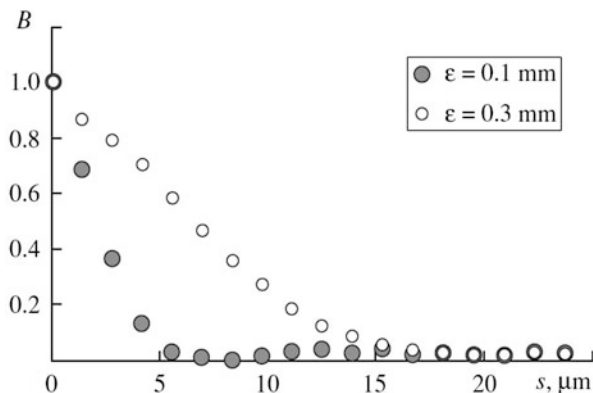
In the range of high defocusing, the difference between the curves is caused by the finite resolution of the photodetector array. The presence of small speckles leads to an increase in the error of their mean size. In particular, in the experiments, a defocusing of $10D$ corresponds to a mean speckle size of three pixels on the array.

Among the statistical properties of the speckle field, the cross correlation of speckle patterns obtained with a shift of the probe radiation spot on the scatterer surface is especially interesting. Statistically new realization of the speckle pattern is realized when its displacement equals one-half of the mean speckle size ε. Based on this assumption and using formula (11.1), an expression for the corresponding shift of the beam s_0 on the retina was derived:

$$s_0 \approx \frac{1.22\lambda f}{(1 - Df)b}.$$

This estimate is based on the following assumptions [32]. The shift s of the scatterer in the transverse direction with respect to the optical axis results in a shift of the speckle pattern by the distance sf/z [14], where $z = Df^2/(1-Df)$ is the distance between the scatterer and the focal plane at defocusing D. Note that the formulas are derived in the geometrical optics approximation and are valid at $D > 2.44\lambda/b^2$.

A similar estimate of the values of s_0 can be obtained based on the analysis of the data presented in Fig. 11.8, where we plot the cross correlation of two speckle patterns with the mean speckle sizes $\varepsilon = 0.1$ mm and $\varepsilon = 0.3$ mm (closed and open circles, respectively). On the abscissa axis, we plot the shift s between two positions of the scatterer corresponding to the data obtained. On the ordinate axis, we plot correlation B normalized to unity. The value of s_0 can be estimated using the value of s such that an increase in the scatterer shift relative to this value does not lead to a decrease in the cross correlation of two speckle patterns. For $\varepsilon = 0.1$ mm and $\varepsilon = 0.3$ mm ($b = 2.00$ mm and $b = 0.66$ mm, respectively) the estimated values of s_0 (6 and 16 μm, respectively) are close to the calculated values. The calculations are performed for the defocusing $D = 2$ dioptries.

Fig. 11.9 Scheme of the experimental setup. (*1*) Laser, (*2*) collimator, (*3*) diaphragm, (*4*) beamsplitter, (*5*) spinning scanner, (*6*) lens, (*7*) fiber-optic faceplate, (*8*) objective, (*9*) PC, (*10*) CCD camera
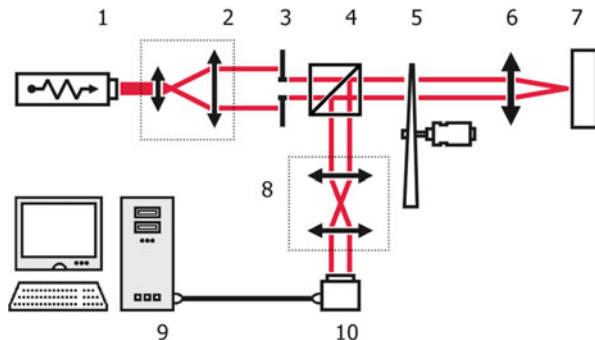
11.5 Efficiency of Methods for Suppressing Speckle Modulation

All methods of speckle modulation suppression are based on incoherent summation of a variety of speckle field realizations. One approach is the use of sources with short coherence length (such as superluminescent diodes) [15]. This approach will be further referred to as the spectral averaging. Another approach is based on averaging the speckle field realizations obtained when scanning the reference source over the retina surface [13] or when widening the beam slightly on the cornea and retina using acousto-optic cell [37]. This approach will be further referred to as the spatial averaging. Efficiency of these methods considerably depends on the parameters of the scatterer (human eye retina). For comparison efficiency of these methods, an experimental setup was constructed [32].

Figure 11.9 demonstrates the scheme of the experimental setup. A semiconductor laser (1) ($\lambda = 630$ nm) coupled with a single-mode fiber serves as the radiation source. The collimated (2) radiation passes through a pinhole (3) and beamsplitter (4) and is focused by a lens (6) on the front plane surface of the fiber-optic faceplate (7). The radiation backscattered by the faceplate is delivered with the beamsplitter (4) and objective (8) to CCD array (10) interfaced with a computer (9).

The size of the 720×576 pixel photodetector array is 6.4×4.8 mm. The focal length f of lens (6) is 20 mm, the diameter of diaphragm (3) is 4 mm, and the thickness of fiber-optic faceplate (7) is 8 mm. The faceplate is fixed in such a way that distance h between the faceplate and lens (6) can be varied and the defocusing of scattered radiation is given by

$$D = \frac{1}{f} \frac{h-f}{h}.$$

In the optical system, scanning is realized with the use of a scanner (5), which represents a transparent wedge plate. The light beam passing through this plate is deflected by the angle $\beta = 0.22°$ relative to the original direction. The plate is fixed at the axis of a DC motor. When the plate rotates, the transmitted beam moves along a cone so that the reference source on the scatterer is shifted and the speckle structure is varied.

Fig. 11.10 Examples of images measured (**a**) in the absence and (**b**) in the presence of scanning
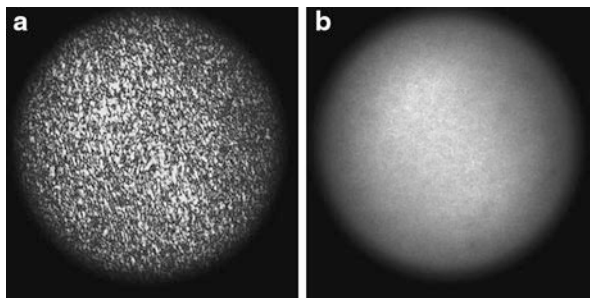
The tilts introduced by the scanner plate can give rise to undesired shifts of the image on the photodetector (10). To eliminate this effect, the optical system was constructed in such a way that the scattered radiation is refracted by the plate for the second time, which makes it possible to compensate for the tilts introduced by the scanner. In the proposed system, the reference source moves along a circle with diameter $d = 2\beta f = 0.15$ mm on the scatterer. At a motor rotation rate of 50 rps, the characteristic time of variations in speckles is significantly shorter than the photodetector integration time (30 ms). Hence, the variations are effectively averaged.

Figure 11.10 shows examples of images measured on the above setup. The images are obtained at a defocusing of $4D$ in the absence (Fig. 11.10a) and in the presence (Fig. 11.10b) of scanning.

Consider the scattering pattern of the fiber-optic faceplate. The angular width of the scattering pattern of the speckle field is determined by the diffraction divergence of radiation for a single fiber:

$$\Omega = 1.22 \frac{\lambda}{m} \approx 2.44 \frac{\lambda}{p},$$

where p is the fiber diameter, Ω is the angular width of the envelope at a level of $1/e$, and m is the diameter of the first mode of the fiber radiation, which approximately equals to $p/2$ [38].

Figure 11.11 demonstrates the transverse cross section of the speckle structure intensity for light scattered by the faceplate (circles) (the data presented are averaged over 10 realizations of the speckle field). The width of the envelope (solid line) is about 0.2 rad, which corresponds to a single fiber size of about 6 μm and, hence, agrees with the real size. The dashed line shows the curve that describes the Stiles–Crawford effect. This curve is calculated for a mean length of the eye axis of 24 mm [34] and the parameter $\rho = 0.05$ [30]. A minor peak at the center of the experimentally measured distribution is related to the incomplete suppression of the radiation that is mirror reflected by the front surface of the faceplate.

Fig. 11.11 Transverse cross
section and (*solid line*)
Gaussian approximation of
the speckle-structure intensity
for radiation scattered by the
fiber-optic faceplate with
averaging over 10 realizations
of the speckle field and
(*dashed line*) Stiles–Crawford
curve
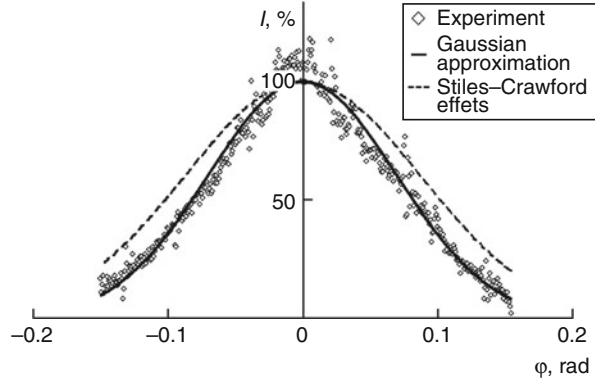
The efficiency of speckle suppressing with the circle scan method is illustrated in Fig. 11.12a. The dependence of the speckle pattern contrast γ upon the scan circle diameter d is compared for the probe beam diameter of $b = 2$ mm (●) and $b = 0.66$ mm (○) with the theoretical dependence (—) corresponding to the following formula:

$$\gamma \approx \frac{\gamma_0}{\sqrt{\frac{\pi d}{s_0} + 1}},$$

where γ_0 is the speckle pattern contrast without scanning. The denominator subduplicate is the number of statistically independent speckle pattern realizations averaged due to the incoherent summation on the photodetector [39]. Here, πd is the perimeter of the scan circle; s_0 is the spot shift on the retina surface, at which a statistically new speckle pattern realization is formed. The unity is added due to the fact that the zero scan diameter corresponds to measuring the only speckle field realization with the contrast γ_0. The theoretical curve is calculated for $s_0 = 6.5$ µm and $s_0 = 19.8$ µm. The simulation was performed for $D = 2$ dioptres.

The results of the experiment with the use of the reference spot scanning over the scatterer surface are shown in Fig. 11.13a. The contrast γ of the speckle pattern detected by the photodetector was measured for different values of the defocusing D with both enabled and disabled scanner ((5) in Fig. 11.9). The dependence of γ upon the probe beam defocusing (and, correspondingly, upon the mean speckle size) thus obtained was compared with the dependence numerically calculated for the same parameters of the optical system. The lower speckle pattern contrast experimentally obtained both with and without scanning is most likely due to individual characteristics of the photodetector.

Speckle suppression efficiency with the use of a broadband radiation source is illustrated by the plots presented in Fig. 11.12b. The dependence of the speckle pattern contrast γ upon the product of the scattered radiation spectral width $\Delta\lambda/\lambda$ by the factor Δ_G that characterizes the full OPD range for those rays forming the speckle pattern. The curves obtained for the cases $\Delta_G = 1.67\lambda$ (▲), 5λ (○), 15λ (♦),

Fig. 11.12 The dependences of the speckle pattern contrast γ on the scan circle diameter d (**a**) and on the product of the scattered radiation spectral width $\Delta\lambda/\lambda$ by the factor Δ_G (**b**), all compared with the corresponding theoretical curves
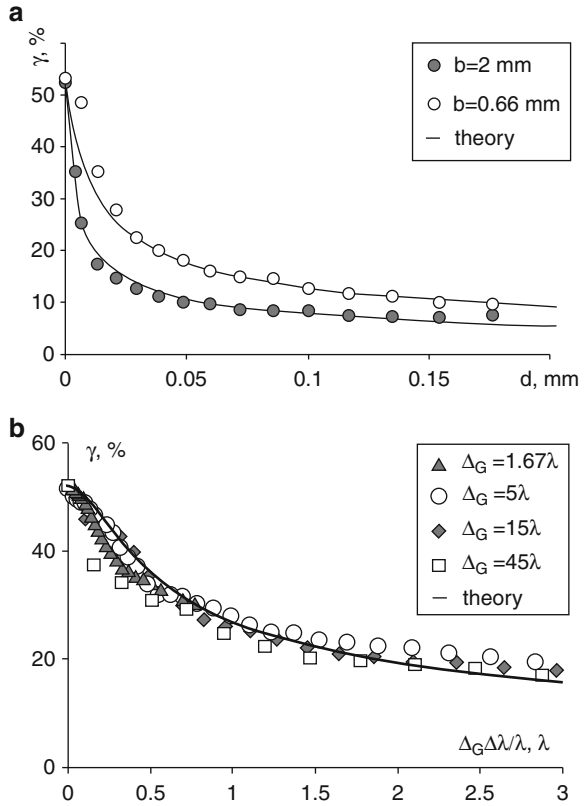
are 45λ ($\square$) are compared with the corresponding theoretical dependencies (—) [40]:

$$\gamma = \frac{\rho(k_0)}{\sqrt[4]{(2W\sigma)^2 + 1}} \approx \frac{\gamma_0}{\sqrt[4]{\left(\frac{4\pi\Delta\lambda\Delta_G}{\sqrt{3}\lambda^2}\right)^2 + 1}}.$$

Here, $\rho(k_0)$ is the contrast of the image obtained for $\Delta\lambda = 0$; W is the spectral width of the radiation recalculated to inverse nanometers (for a small $\Delta\lambda$, the recalculation yields $2\pi\,\Delta\lambda/\lambda^2$); σ is the standard deviation of the path difference of the rays forming the speckle pattern, the estimate of this deviation being $\Delta_G/\sqrt{3}$.

The results of the experiment with the use of a broadband light source are shown in Fig. 11.13b. As such a source, the superluminescent diode SLM-825-02M was employed. The diode emitted a light beam with the central wavelength $\lambda_0 = 825$ nm, and the spectral width $\Delta\lambda = 17$ nm. An aspheric lens with a focal distance of about 5 mm was used for collimating the diode beam. The diameter of the diaphragm ((3) in Fig. 11.9) was 1 mm. Other elements of the setup were not changed. The speckle pattern contrast γ was measured for different values of the

Fig. 11.13 Speckle pattern contrast γ versus the incident beam defocusing D with and without the use of the spatial (**a**) and spectral (**b**) averaging
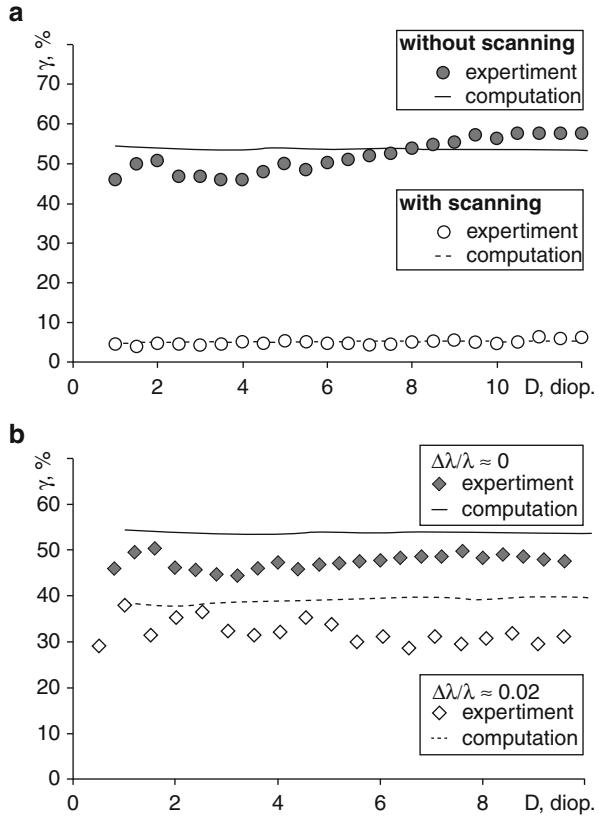
defocusing D and compared with the results of numerical simulations and the data obtained with the laser source.

The numerical simulations were performed for $\Delta_G = 16.7\lambda$, this estimate being based on the following considerations (Fig. 11.2). The light focused onto the front surface of fiber-optic faceplate is incident on it at different angles: from 0 (for the axial ray) to $\psi = \arctan b/2f$ (for the peripheral rays). Then, the light propagates through the faceplate fibers, is reflected by the rear surface of the faceplate, propagates back, and is finally scattered at the front surface. Therefore, the optical paths covered by different rays before the scattering range from $f + 2s$ to $(f + 2s)/\cos\psi$. The corresponding full range of the optical path differences is $\Delta_G = (f + 2sn)/\cos\psi - (f + 2sn)$, where n is the refractive index of the fiber core. Assuming $f \gg b$ and using the Taylor expansion of the cosine, we obtain:

$$\Delta_G \approx \frac{(f + 2sn)b^2}{8f^2}.$$

By substituting the parameters of the experimental setup into the above expression and choosing $n = 1.5$, one can obtain $\Delta_G = 13.7\ \mu m = 16.7\lambda$.

Fig. 11.14 RMS error of wavefront measurement by the Shack-Hartman sensor versus the speckle pattern contrast γ
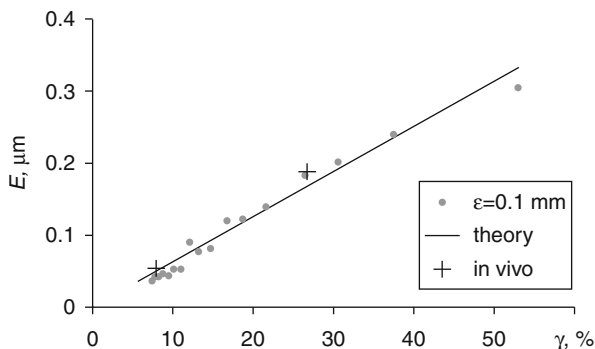
Fig. 11.15 In vivo experiment. The image of the radiation scattered by retina in the absence (**a**) and in the presence (**b**) of scanning
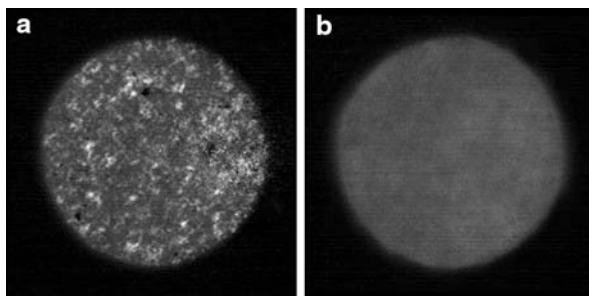
An important question is how the speckle modulation affects the accuracy of wavefront measurement by a Shack-Hartmann sensor. In order to clarify this point, numerical modeling with a light field containing a speckle modulation in the absence of regular phase distortions was performed. The corresponding Hartmannogram has been obtained by technique described above and the spot displacements were found by the conventional centroid technique, while the wavefront was restored in the form of Zernike polynomial decomposition (36 terms). The RMS deviation of the restored wavefront from the reference plane defines the error of measuring the eye aberrations with a Shack-Hartmann sensor in the presence of a speckle field. Figure 11.14 illustrates the dependence of the error E of wavefront measurement by the Shack-Hartmann sensor upon the speckle structure contrast. The calculations have been performed for the average speckle size $\varepsilon = 0.1$ mm, the diameter of the subaperture of the Shack-Hartmann sensor of 0.5 mm, and the pupil diameter of 6 mm. As one can see from the plot, the RMS measurement error is almost directly proportional to the speckle pattern contrast, reaching 0.3 μm ($\lambda/2$).

Figure 11.15 demonstrates result of the experiments with a human eye (in vivo). The image of the radiation scattered by the retina was obtained by means of aberrometer using laser of low power with beam diameter 1 mm and $\lambda = 785$ nm. The speckle pattern contrast without scanning is 26.6 % and root-mean-square error E of wavefront measurement is 0.18 μm. The same image with scanning is shown in

Fig. 11.15b. The scanning angle is 0.3°; hence diameter of circle of a focal spot scanning on a retina surface is about 0.2 mm. The speckle pattern contrast with scanning is 7.9 % and root-mean-square error E of wavefront measurement is 0.05 μm. Both values are put on the Fig. 11.14 (+) for comparison with results of numerical simulation.

It is noticeable that the speckle pattern contrast is almost independent on the defocusing and, therefore, on the size of the illuminated area of the scatterer. This fact argues that scattering at the model scatterer induces rather large phase fluctuations, implementing the regime for which the theory predicts the 100 % contrast of the speckle pattern. In reality, both in the experiments and numerical simulations, the 100 % contrast has never been detected. This is because, in the latter case, only a bounded region close to the scattering indicatrix was analyzed, while the theoretical results [36] were obtained for the scattering angles ranging from $-\pi$ to π.

11.6 Implementation of an Adaptive Optics Fundus Camera

The scheme of the multispectral fundus imager with adaptive compensation of human eye aberration [41] is shown in Fig. 11.16. The optical system is based on a KFG-2 fundus camera, series-produced by the Zagorsk Optics and Mechanics Plant joint-stock company (AO ZOMZ). Optical elements belonging to this device are circumscribed on the scheme by the dotted line. The standard fundus camera is supplemented with an adaptive unit, allowing the compensation of eye aberrations and retina imaging by means of a high-resolution digital camera. The adaptive unit has $23 \times 23 \times 30$cm dimensions.

The series model of KFG-2 underwent a number of modifications. To improve the diffraction-limited resolution of the system to 200 *lines per mm* (the resolution value is determined at the half-maximum of the modulation transfer function), the diameter of the entrance pupil of this device was extended from 2 to 4.8 mm. The illuminating halogen lamp and pulsed xenon lamp with the corresponding collecting optics, as well as power supplies of these lamps, were removed. The observation binocular, employed for pointing of the fundus camera at the human eye, was replaced by an IR guidance system including the lens (19) and the IR CCD camera (20).

To illuminate the fundus of the examined eye in both the guidance and the digital photo-registration regimes, the illuminator (26) was fabricated. A 300W CW xenon lamp with a small arc gap was used as a light source. Emission of the lamp was collimated by the built-in parabolic reflector and was incident on a movable mirror mounted on the axis of an electromagnetic drive (these elements are not shown in the scheme). In a stand-by mode, the mirror was removed from the light beam. When a control impulse was applied, the mirror turned, thus directing the beam to a focusing lens and further to the end of the fiberglass bundle (25), which coupled radiation into the optical unit of the fundus camera. Therefore, the duration of the light flash directed into the eye depended on the length of the control pulse applied to the mirror. Different narrowband filters could be mounted between the deflecting
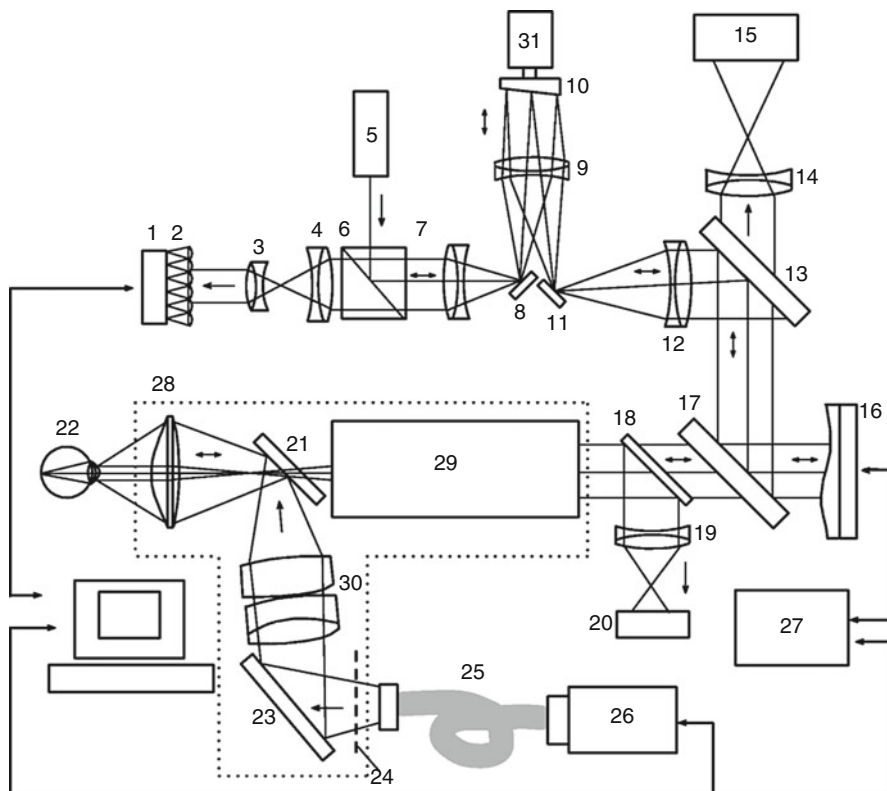
Fig. 11.16 Scheme of the multispectral fundus imager with adaptive compensation of human eye aberration: (*1*, *20*) CCD cameras; (*2*) lens raster; (*3*, *4*, *7*, *9*, *12*, *14*, *19*) lenses; (*5*) laser; (*6*) beamsplitter cube; (*13*, *17*, *18*) beamsplitters; (*8*, *10*, *11*, *21*, *23*) mirrors; (*15*) digital camera; (*16*) adaptive mirror; (*22*) eye; (*24*) annular diaphragm; (*25*) fiberglass bundle; (*26*) illuminator unit; (*27*) adaptive mirror control unit; (*28*, *30*) objectives; (*29*) fundus camera objectives; (*31*) electric motor

mirror and the focusing lens, thus making it possible to photograph the eye fundus in different spectral ranges. To filter the IR emission, a spectral beamsplitter transmitting only visible light and reflecting near infrared was mounted in the illuminator. This beamsplitter also directed the IR emission of the halogen lamp, used for the guidance of the fundus camera to the patient's eye, to the optical path.

The illuminating radiation, propagating in the fiberglass bundle, passed through the annular diaphragm (24). The objective (30) imaged this diaphragm on the deflecting annular mirror (21), which was used to separate the illuminating beams, propagating in forward and backward directions, from each other. The main objective (28) of the camera imaged the annular light source on the eye cornea (22), with the central part of the cornea remaining unlit. The entrance pupil of the device was located entirely inside the unlit area. This provided an additional selection of corneal flares. Thus, spurious reflections did not appear in

the area of the entrance pupil, and did not cause the artifacts in the retinal image. This illumination system also provided the uniform lighting of the eye fundus. A more detailed description of operation principles of such ophthalmologic devices can be found in Refs. [42, 43].

The radiation reflected by the retina emerges from the eye as a quasi-parallel beam. The eye-pupil image was constructed in the plane of the annular mirror (21) by the main objective (28) of the camera. The beam diameter corresponded to the central aperture of the annular mirror. Next, radiation propagated through the objective (29), fixed to the device, providing the transverse displacement and allowing the compensation of the eye ametropia within the range from $-20D$ to $+20D$.

After passing through the optical elements of the fundus camera, the light was incident on the spectral beamsplitter (18). A part of the emission, corresponding to the IR emission $(800 - 1,000$ nm) of the halogen lamp, was deflected by the beamsplitter to the guidance system. The lens (19) formed the retinal image in the plane of the IR video camera (20). The image registered by the video camera was displayed by the computer monitor and was used for the focusing of the fundus camera to the selected area of the retina.

Light, having passed through beamsplitters (18) and (17), was incident on the adaptive mirror (16). A modal bimorph corrector, which was similar to that described in Ref. [17] was used. Eighteen electrodes of the mirror made it possible to compensate for aberrations of up to the fifth order inclusive. The surface of the mirror was conjugate to the plane of the eye pupil and to the entrance pupil of the fundus camera.

The beam reflected by the deformable mirror was incident on the beamsplitter (13), transmitting the visible 440–670 nm light and reflecting the 680–800 nm radiation. The transmitted radiation passed through the lens (14), which formed the eye-fundus image on the matrix of the TsFK3020 digital video camera. One pixel of this camera corresponded to the retina region of size 2.7 μm. The photosensitive matrix had the resolution of $2,000 \times 3,000$ pixels. The signal of the matrix was digitized by means of the 14 bit ADC. For typical levels of the retina illumination, the camera provided the signal-to-noise ratio of 68 dB. The data transmission rate to the computer, provided by the digital interface, was one frame per second.

The configuration of the wavefront sensor is similar to the one described in first paragraph. The 780 nm radiation of the IR diode laser was used to form a reference light source on the retina. IR radiation of this range has the high coefficient of reflection from the eye fundus (10–12 %) [44], and is more comfort for a human eye than visible light. Moreover, having chosen such a wavelength of the reference source, we separated the channel of the forming of the visible-light image of the retina from the aberration-measuring channel using the coherent IR radiation, by selecting the spectral characteristics of optical elements of the system.

Preliminarily, the laser beam (5) passed through the diaphragm (not shown in Fig. 11.16) of diameter 0.8 mm. The reduction of the beam diameter provided the conditions of single-pass measurements [45]. The power of radiation incident on the eye was 50 μW, which was significantly lower than the maximum permissible

power [46, 47]. Then, the beam reflected from the inner face of the polarization cube (6), propagated through lenses (7, 9), and (12), reflected from the adaptive mirror (16), and was directed into the optical channel of the fundus camera. After passing through the objectives (29) and (28), the laser radiation was focused by the eye elements onto the retina, forming the reference source. The radiation scattered by the retina was brought back to the system, and was directed to the Shack-Hartmann wavefront sensor after the reflection from the adaptive mirror (16). The lens raster of the sensor (2) was placed in the plane, which was optically conjugated to the plane of the eye pupil. Each lens (subaperture) of the raster had a 0.25 mm diameter and a 7.8 mm focal length. For the pupil diameter equal to 4.8 mm, radiation emerging from the eye illuminated about 120 subapertures of the raster. The wavefront under study was divided by the lenses of the sensor, thus forming an array of spots (Hartmannogram) in the focal plane. Each spot of the Hartmannogram was an image of the reference source on the retina. The Hartmannogram was recorded by a CCD camera (1), located in the focal plane of the lens raster, and then was stored in the computer memory with the rate of 30 fps and the resolution of 640×480 pixels.

The wavefront was reconstructed from measured local wavefront slopes by the method of least squares [48] as an expansion in 36 Zernike polynomials [49] and in response functions of the adaptive mirror. The time of processing of a Hartmannogram was 8 ms. Thus, the maximum speed of aberration measurement was limited by the video camera parameters (30-Hz frame rate).

To suppress speckles in the system, the method of scanning of the reference-source position on the retina was used. For this purpose, the mirror (6) was attached to the electric-motor axis at a small angle equal to $0.5°$. The rotation of the mirror caused the displacement of the reference source on the retina, resulting in a change in the speckle structure. For the electric-motor rotation speed of 50 rps, the characteristic time of a change in the speckle structure (0.2 ms) was much shorter than the integration time of the CCD camera (1) (30 ms), and, therefore, speckles were efficiently suppressed.

Because the laser radiation was twice (in a forward and backward passage) reflected from the scanner mirror, the displacement of the reference source on the retina did not cause any displacement of the Hartmannogram spots. This is explained by the fact that the eye mainly works as a retro reflector, i.e., radiation scattered by the retina emerges from the eye at an angle equal to the angle of radiation incidence. Because the surface of the scanner mirror was optically conjugated to the entrance pupil of the system and the lens raster of the sensor, wavefront slopes caused by this mirror were compensated during the backward passage.

Note that the scanning technique, applied in phase distortion measurements, has an important feature, which does not concern speckle suppression. The human eye, as the most of optical systems, is not isoplanar [50]. This means that the measured phase distortions depend on the angular position of the reference source. In this case, it is impossible to determine aberrations in the entire field of view of the system by using a single reference source [51]. Therefore, the adaptive compensation improves the

Fig. 11.17 General view of the multispectral fundus imager with adaptive compensation of human eye aberration

image quality only within the isoplanatism region. In some cases, it is preferable to correct for average aberrations in a large field of view and to improve the image quality within the large area, than to achieve a high resolution within the small area.

The scanning technique, as distinct from other methods, gives an opportunity to determine average aberrations by using only one reference source. Thus, while a laser spot moves sufficiently fast, the phase distortions are being averaged over the scanning area. The size of this area can be varied by changing the mirror tilt angle. In this system, compensation of average aberrations is not required. The reference source described on the retina circle of 150 μm diameter is significantly smaller than the radius of isoplanatism [18].

The human-eye retina reflects a small part of the incident light [44]. In the experiment, the power of infrared radiation emerging from the eye did not exceed 5 μW. Although all lenses were covered with antireflection coatings, the intensity of light reflected from lenses was comparable with that of useful signal. To suppress spurious reflections, the polarization cube (6) was set in such a way as to transmit the depolarized radiation scattered by the retina and to reflect polarized radiation scattered from optical surfaces. A diaphragm (not shown in Fig. 11.16), which also partially suppressed defocused reflections, was placed in the focal plane between lenses (3) and (4).

A general view of the multispectral fundus imager with adaptive compensation of human eye aberration is shown in Fig. 11.17. In order to evaluate the quality of the adaptive system performance, the eye model similar to one shown in Fig. 11.2 was used. A standard USAF target, also known as a "3-barred mire," was fastened by optical adhesive to the flat rear facet of the fiber-optic faceplate. The laser beam passing through the objective was focused on the front face of the faceplate. Then, light propagated through the fibers, reflected from the mire, propagated in a backward direction and formed a reference source on the front facet of the faceplate. Phases of radiation emerging from different fibers were uncorrelated. The fiber-optic faceplate was fixed to a micrometer positioning stage, which provided the longitudinal displacement with the positioning accuracy of 10 μm.
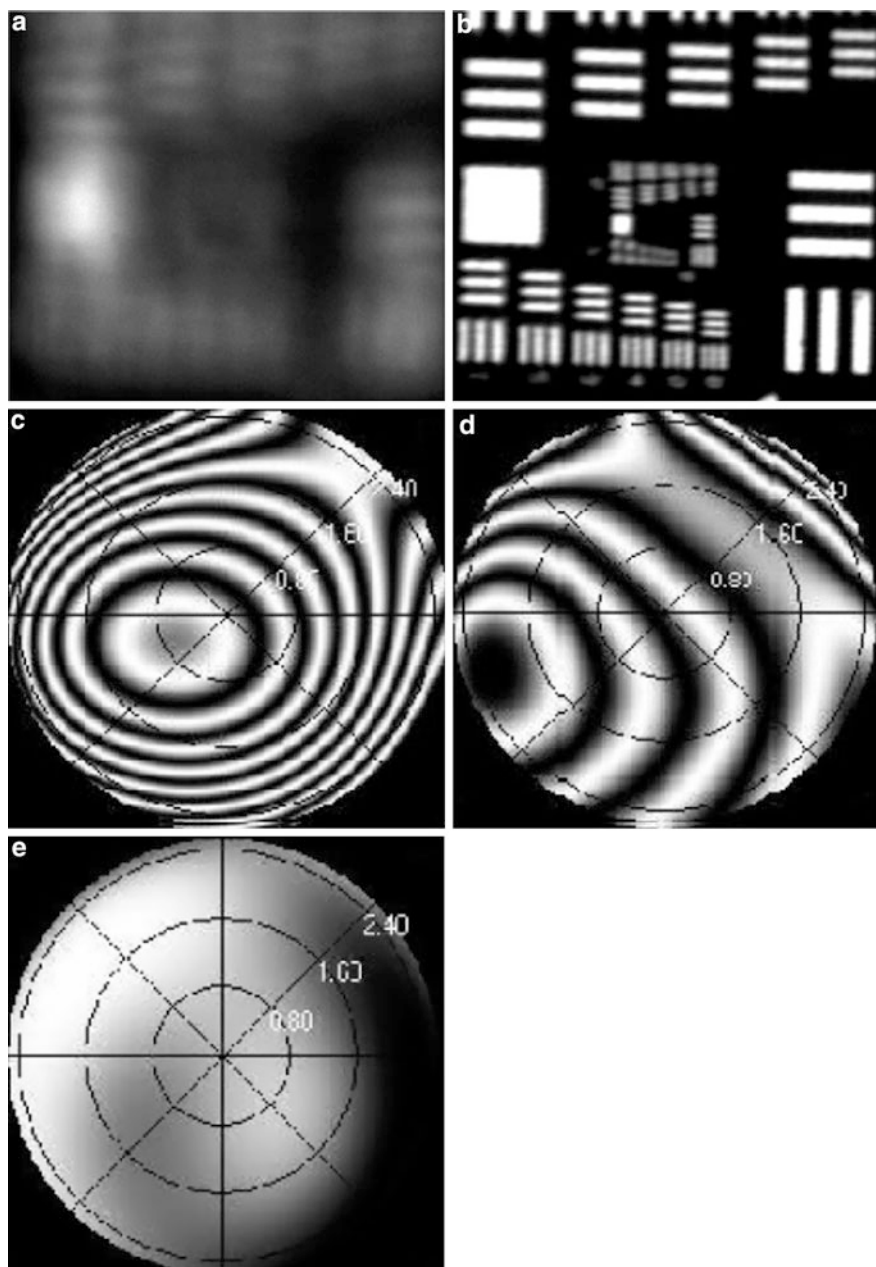
Fig. 11.18 Images of the central part of the standard USAF mire for opened (**a**), and closed (**b**) feedback loop, and wavefront interferograms before compensation (**c**), before compensation, with eliminated defocusing (**d**), and after compensation (**e**)

The performance of the adaptive system is demonstrated in Fig. 11.18. Here, the images of the central part of the mire are shown in cases of open and closed feedback loop. To introduce phase distortions, an eyeglass lens of poor quality was placed in the plane of the eye model pupil at an angle to optical axis of the system. No preliminary compensation of defocusing by means of an adjustable objective of the fundus camera was performed. The mire was illuminated in this experiment from the back (with respect to the pupil of the eye model) side. Despite strong initial aberrations (the wavefront root-mean-square deviation was 1.2 μm), the adaptive compensation made it possible to resolve the horizontal 6-6-group lines of the mire with the spatial frequency of 114 lines per millimeter.

Note that employing the fiber-optic faceplate in the eye model does not allow the resolution of seven-group elements, which have the spatial frequency greater than 128 lines per millimeter. We cannot discern the details of the mire with sizes less than the fiber diameter. Indeed, the direct observation of the faceplate surface under a microscope does not allow the resolution of seven-group elements as well. The interferograms of model eye-aberrations before the compensation, before the compensation with eliminated defocusing, and after the adaptive compensation, are also shown in Fig. 11.18. In the latter case, the wavefront root-mean-square deviation was reduced to 0.07 μm [41].

11.7 Compensation of Dynamic Aberrations

The eye pupil was preliminary dilated by mydriatic eye drops (phenylephrine hydrochloride, 2.5 %) that do not paralyze accommodation. The dilation of the pupil allowed the use of its external side for the eye-fundus illumination, and the internal side for the retina imaging. The patient's head was fixed by the face-holder of the fundus camera. All patients were instructed to look on a fixating needle (an infinitely far object) located inside the camera. The optical channel of the needle imaging and the channel of adaptive compensation were separated from each other; therefore, deformations of the adaptive mirror did not influence the eye accommodation.

The fundus camera was focused on the selected area of the retina by means of the CCD camera ((20) in Fig. 11.16). The eye aberrations were measured in real time, and the data were displayed on the monitor of the computer. As a preliminary to the feedback closure, the eye defocusing was compensated by means of the adjustable objective of the fundus camera. The Zernike coefficient corresponding to the defocusing was reduced to the minimum value under these conditions. This allows using the entire dynamic range of the adaptive mirror. After feedback closure, the compensation of eye aberrations was performed. The eye fundus was photographed when the residual root-mean-square error of the compensation σ was reduced below 0.15 μm. However, in some cases, when aberration amplitudes (usually the astigmatism amplitude) exceeded the dynamic range of adaptive mirror deformations, to achieve the satisfactory quality of suppression of phase distortions it was not possible. Another less common reason for poor-quality compensation was related

to the low-intensity level of the detected Hartmannogram, for example, due to the crystalline lens opacity.

During the xenon lamp flash, the laser and the illuminator lamp were switched off, and the control voltage applied to the mirror was "frozen." The light pulse duration was varied in the range from 30 to 100 ms. The eye fundus was photographed in different spectral ranges by filtering radiation of the xenon lamp emission at the output of the illuminator. The maximum intensity of the retinal illumination (in the absence of filters) was 0.08 J·cm^{-2}. According to the American standard (ANSI), the maximum admissible illumination for the white light is 0.924 J·cm^{-2} for the exposure time of 0.5 s [46].

Different spectral components of light are reflected from retinal layers lying at different depths. Because the laser wavelength was the same during the aberration measurement, the eye-fundus image was defocused when changing the spectral range of the light flash. To eliminate this effect (after the completion of the adaptive compensation), an additional voltage was applied to the main electrode of the deformable mirror just before photographing. In this way, the defocusing, compensating for the displacement of the reflecting retinal layer, was introduced into the image-forming channel. By using different spectral bands, images of the retina layers of different depths were obtained.

An illustration of the adaptive compensation of eye aberrations is given in Fig. 11.19 [41]. Aberrations were detected for 10 s. The feedback loop was closed at the third second. No preliminary compensation of the defocusing (by means of the tunable objective of the fundus camera) was performed; therefore, the defocusing (curve 7) was the predominant aberration (0.5 μm) before the feedback closure. The following-in-magnitude aberrations were the astigmatism (curve 2) and coma (curve 3). Aberrations of the order, higher than spherical, were low and are not shown in Fig. 11.19. One can see from the presented dependences that the process of the adaptive compensation lasted about 0.5 s. The root-mean-square phase deviation σ decreased under these conditions from 0.6 to 0.1 μm. The wavefront interferograms, written before and after the adaptive compensation, are shown in Fig. 11.19 as well. The interferogram of Fig. 11.19b corresponds to phase distortions before the feedback closure in the case of eliminated defocusing.

Figure 11.20 illustrates the improvement of the eye-fundus-image quality in the process of the adaptive compensation of eye aberrations. Here, two central parts of the retinal image, obtained in green light in cases of closed and opened feedback loop, are shown. For visual clarity, only a part of complete image of the eye fundus, involving the optical disk (6° visual angle) is shown.

The refraction of the patient's eye was 2*D* and the astigmatism was 1*D*. As a preliminary to the feedback closure, the eye defocusing was compensated by means of the adjustable objective of the fundus camera. Figure 11.20c and d also shows the interferograms of the wavefront before and after the correction of aberrations. After the feedback closure, the root-mean-square deviation of the wavefront decreased from 0.46 to 0.09 μm.

One can see from the given images that the compensation of eye aberrations substantially improved the image contrast and allowed the discerning of small details,
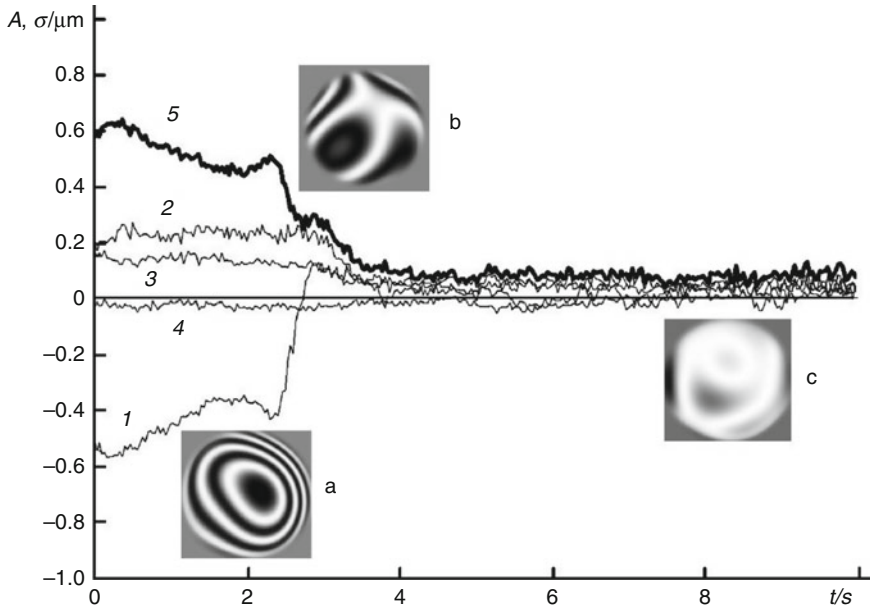
Fig. 11.19 Time dependences of aberration amplitudes A: defocusing (*1*), total astigmatism (*2*), total coma (*5*), spherical aberration (*4*), and root-mean-square phase deviation a (*5*). Aberration interferograms before compensation (*a*), before compensation, with eliminated defocusing (*b*), and after compensation (*c*)

being invisible on the first image with the compensation of eye defocusing. Thus, after the feedback closure, the nerve fibers lying on the retinal surface and directed to the centre of the optical disk can be discerned. Some separate nerve fibers, invisible in the blurred noncorrected image, are quite distinct against bright background of the optical disk. The characteristic width of these fibers is about 3 μm and is comparable with the size of the camera pixel (2.7 μm). Due to the spatial discretization of the image, the system cannot reliably resolve all nerve fibers (the details with the characteristic size of less than 6 μm suffer aliasing). Nevertheless, some fibers are distinctly visible, which seemingly corresponds to the case when a fiber falls exactly on camera pixels.

For comparison, Fig. 11.21 shows the intensity distributions in the digital-image cross sections, cut through white lines drawn in Fig. 11.20a and b. One can see that, after the adaptive compensation, a pair of strong local minima, corresponding to a pair vessels lying on the optical disk, appeared in the intensity distribution $I(x)$. The intensity distribution of the corrected image has more small (8 μm resolution) extrema as compared with the first image, which was obtained by compensating the eye defocusing only.

11.8 Anizoplanatic Effects in Wide-Field Retinal Imaging

One more limiting factor for the resolution is the anisoplanatism in the human eye, in which, according to the isoplanatic region [18] of the eye, an adaptive optical
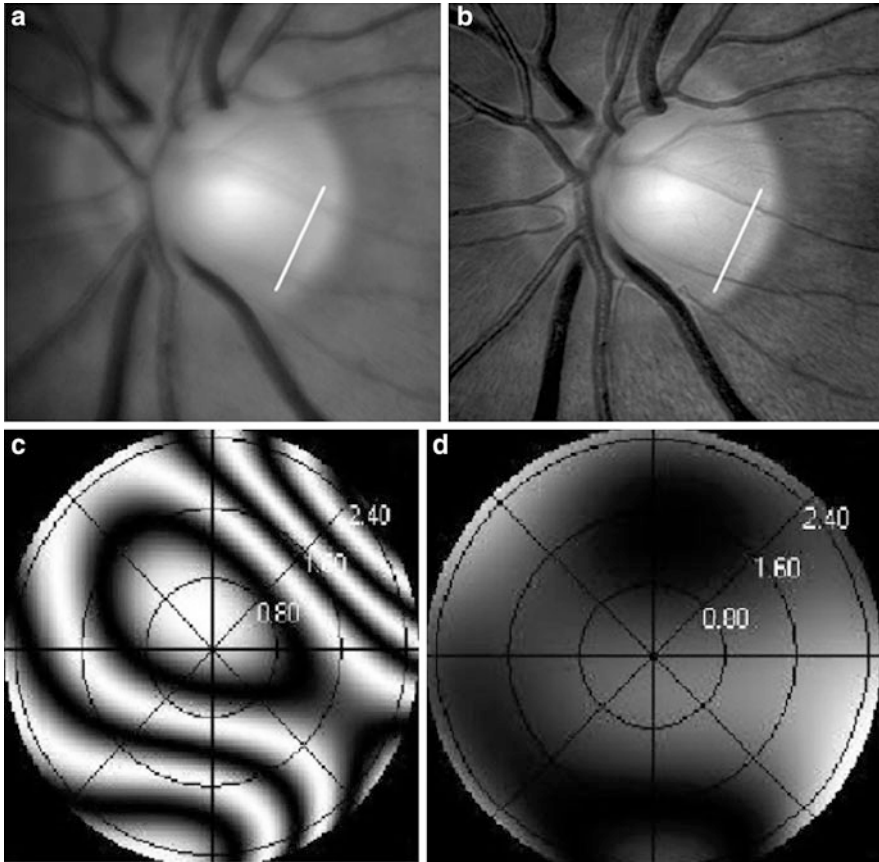
Fig. 11.20 Images of optical disk of the eye retina for opened (**a**), and closed (**b**) feedback loop, and wavefront interferograms (**c**, **d**). *White straight lines* (**a**, **b**) denote cross sections, whose intensity distributions are shown in Fig. 11.21

system is capable of measuring and compensating aberrations in a small angular region, determined by the system design and which is not larger than $1°$.

Instrumental limitation in astronomical adaptive optics due to its anisoplanatism is well studied [50, 52]. In most cases it restricts the angular size of the corrected zone up to a few arc seconds. The idea of enlarging the isoplanatic patch using a number of phase correctors [51] leads to complicated systems. If the distorting medium is stratified, the corrector location optimization and some modification of its control algorithm may give a good result [53]. These estimations are supposed to be useful, especially for non-astronomical applications, when phase distortions are usually concentrated in one or few layers. The main problem in such a case is that we usually have no reliable mathematical model of irregular aberrations, and the best thing one can do is to make up some heuristic model that does not contradict with experimental data.

Fig. 11.21 Intensity distributions $I(x)$ in the cross sections denoted in Fig. 11.20a and b by white straight lines for opened (*1*), and closed (*2*) feedback loop
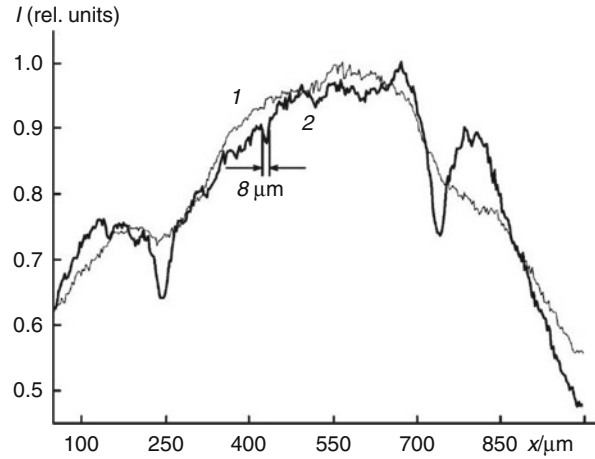
Fig. 11.22 The basic block diagram of a system. (*1*) adaptive optic unit, (*2*) phase corrector, (*3*) unhomogeneous layer
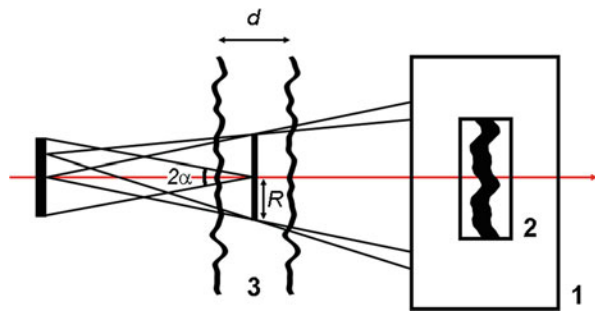
The basic diagram of a system under discussion is shown in Fig. 11.22. The optical unit (1) contains a phase corrector (2), the image of which is located within the unhomogeneous layer (3). It is supposed that the rays passing through that virtual corrector are not restricted by the other optical elements. Thus, the virtual corrector is the input pupil of the adaptive system. Phase distortions for all the rays outgoing from each object point are summarized along the ray and with the phase shift, introduced by corrector. Then the result is averaged over the pupil area. A similar approach can be used in the case of two or more layers. To perform those calculations the structure function of phase distortion should be known. For atmospheric turbulence it is taken in a conventional form: $D(r) = 6.88(r/r_0)$, where r_0 is the Fried's radius. For other applications we use "atmospheric-like" approximation $D(r) = (r/r_c)^\gamma$, where r_c is the correlation radius, and $l < \gamma < 2$.

The method of field-of-view widening discussed here is an alternative to another one where only a small number of lower aberrations are compensated by adaptive corrector and the rest are reduced by a deconvolution algorithm. The main difficulty is, in the absence of enough information to develop a reliable mathematical model for small-scale irregular aberrations, one can only speculate about it. Nevertheless,

Fig. 11.23 The basic block diagram of an eye inspection system. (*1*) adaptive optic unit, (*2*) phase corrector, (*3*) inhomogeneous layer
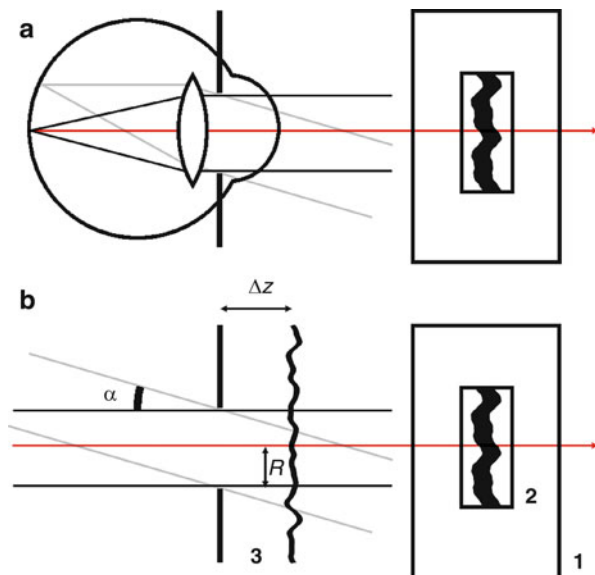
some plausible estimation can be done. Using available data [11] about the mean square aberration coefficients dependence on its number, we tried to approximate it by $\varepsilon^2 = N^{-b}$, where N is the aberration number and b is an empirical value. The authors of Ref. [18] have obtained $b = 1.4$–1.5, which is significantly less than for the atmospheric turbulence. It means that in case of the usage of an "atmospheric-like" structure function γ should be less than the common value of 5/3. The estimation gave $\gamma = 1.33$–1.56, but that result is not very reliable because of insufficient statistics. The basic block diagram of an eye inspection system and its equivalent scheme are presented in Fig. 11.23a and b. As the phase corrector and the distorting layer are placed now in parallel rays, the analysis of the isoplanatic angle leads to a universal dependence on a parameter η as it is shown in Fig. 11.24. Here, the mean square aberration suppression factor is depicted versus the normalized angle. Knowing the suppression factor required, one can estimate the size of the isoplanatic patch.

Let us try to apply the results above to estimate the size of field-of-view of an adaptive device for retinoscopy. According to [11, 21] mean square aberration caused by irregular distortions ($N > 4$) is about $\varepsilon^2 = 2.5$. The desired level of aberrations over the field-of-view for a diffraction limited image is $\varepsilon^2 = 0.15$. So the suppression factor should be $Q = 0.06$. This is an "optimistic" estimation. In the other case it may be supposed that a11 aberrations, including the large scale ones, are to be corrected. In that case we obtain a "pessimistic" estimation of the suppression factor of $Q = 0.005$. To make use of these estimations we approximated the upper curve in Fig. 11.24 by an empiric formula $Q = 0.78\eta^{1.2}$. That leads to an estimation of the isoplanatic patch angular size: $\alpha = (R/\Delta z)(Q/0.78)^{0.85}$, where R is the eye pupil radius (in our case it was $4.5/2 = 2.25$ mm) and Δz is the distance

Fig. 11.24 The mean square aberration suppression factor
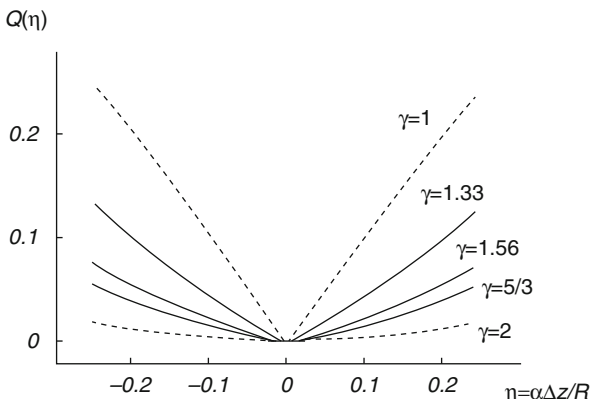
between the pupil and the distorting layer. Let us take here the worst possible situation when the most intensive distortions lay near the outer surface of the eye. In this case, Δz is also about 3.5 mm. These values lead to a field-of-view about of $4°$. These estimations are in a good accordance with experimental results [21].

Meanwhile, the typical fundus imager field of view is $15°$ and larger. Hence, it is necessary to get information on the aberrations outside the isoplanatic region in order to improve the resolution over the entire image.

For this purpose, first, it is necessary to make some theoretical estimations of aberration distribution of the human eye. Using the Gullstrand model of the eye, the dependence of the magnitudes of several aberrations on the angle was calculated (Fig. 11.25) [20].

To obtain experimental data on the aberrations, the following approach was used: first, the optical transfer function (OTF) according to the self-deconvolving data reconstruction algorithm (SeDDaRA), described in [54], was reconstructed. Then, Zernike polynomial amplitudes, which fit the OTF using a pyramidal recursive algorithm [55], were found. If the nondisturbed image is $f(x, y)$, OTF is $h(x, y)$, and the image taken by the system is $g(x,y)$, then in the Fourier space (u, v):

$$G(u, v) = F(u, v) \cdot H(u, v) + N(u, v),$$

where G, F, H are the Fourier spectra of g, f, and h, correspondingly, N is the noise spectrum. According to the original SeDDaRA algorithm, H can be estimated as:

$$H(u, v) = [K_G \cdot S\{|G(u, v) - N(u, v)|\}]^{\alpha(u,v)}, \tag{11.2}$$

where K_G is the real positive scalar chosen to ensure that $|H| \leq 1$, S is the smoothing operator and $\alpha(u,v)$ is a tuning parameter. In Ref. [54] it is shown that, although the best results require detailed knowledge of an averaged spectrum of undisturbed image, a rather good result can be achieved if α is chosen as a some function of angular coordinates. In our case, we used
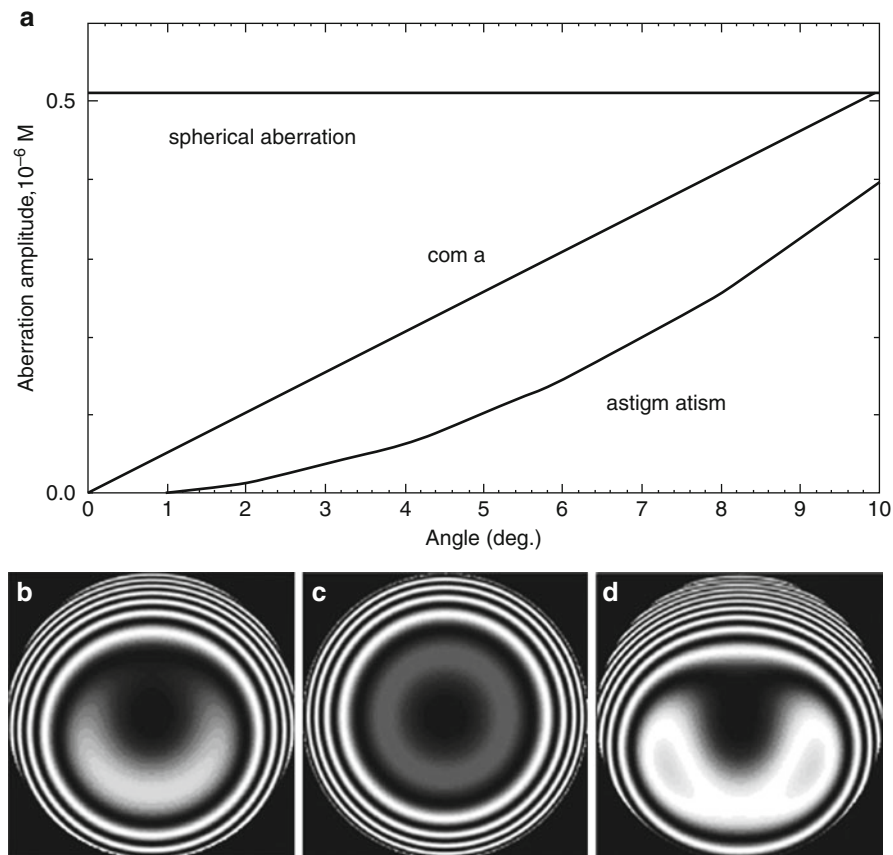
Fig. 11.25 Angular dependence of human eye aberrations, Gullstrand model (**a**), and simulated interferograms: $0°$ (**b**), $5°$ (**c**) and $10°$ (**d**)

$$\alpha(u, v) = \left(1 - e^{-\frac{u^2+v^2}{2 \cdot r_a^2}}\right) \cdot a_{\max},$$

where r_a and a_{max} can be found as an approximation of a spectrum of a rather good image. Such a function is chosen to leave low spatial frequency harmonics intact, and to augment the higher frequency harmonics, that must restore the initial image. Advantages of such an approach over iterative methods of blind deconvolution are the fastness of calculations and effectiveness of image restoration. Figure 11.26 shows an example of the use of SeDDaRA algorithm on the retina images.

The OTF, found from formula (11.2), was then approximated by an OTF calculated from the following equation:

$$\tilde{H}(u, v, \vec{a}) = \hat{F}\left\{m(x, y) \cdot e^{\frac{2\pi i \cdot \omega(x, y, \vec{a})}{\lambda}}\right\},$$
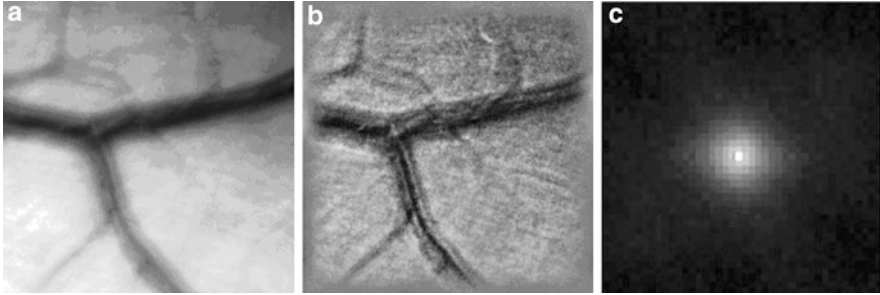
Fig. 11.26 Initial (**a**), deconvolved by the use of SeDDaRA algorithm (**b**) images and the PSF (**c**)
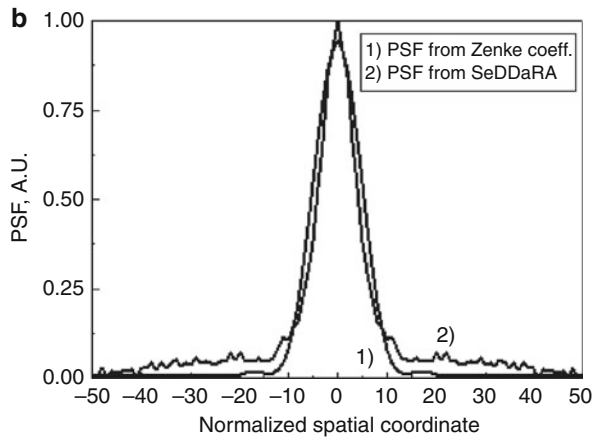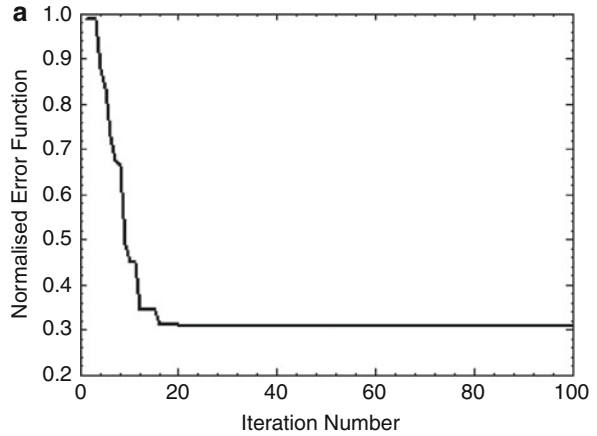
Fig. 11.27 Pyramidal
algorithm convergence (**a**),
PSFs found from SeDDaRA
deconvolution and pyramidal
approximation algorithms (**b**)

Fig. 11.28 Defocus (**a**) and astigmatism (**b**) magnitudes, found for different positions on the retina
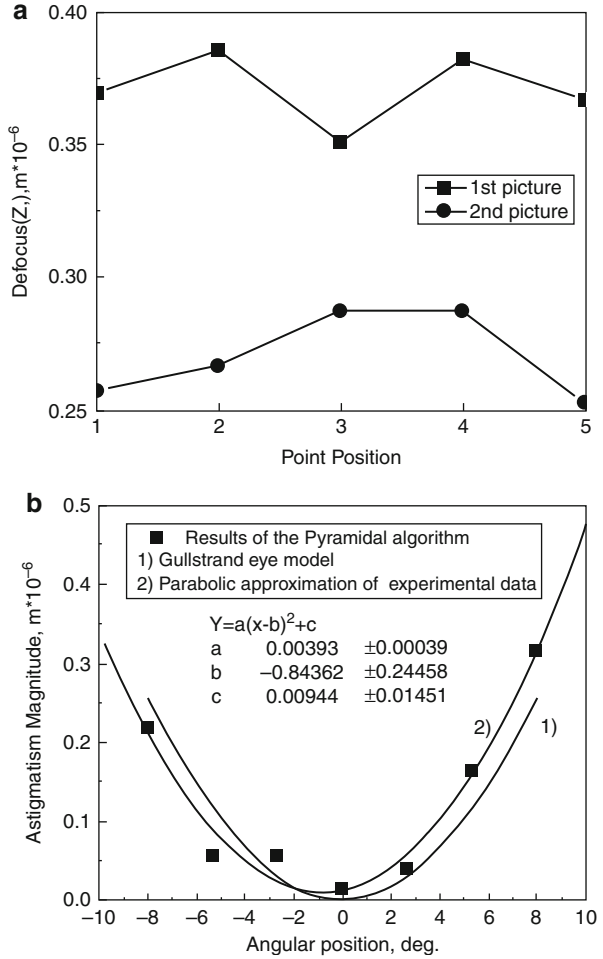
where $\vec{a} = \{a_0, a_1, a_2, \ldots, a_N\}$ is a set of Zernike coefficient amplitudes, $\hat{F}$ is a Fourier transformation, and

$$\omega(x, y, \vec{a}) = \sum_k a_k \cdot Z_k(x, y)$$

is the wavefront aberrations, expanded onto Zernike polynomials Z_k, $m(x,y)$ is the pupil function, and λ is the wavelength. We used a pyramidal approach [55] and the Nelder-Mead [56] algorithm for minimization of the error function

$$E(\vec{a}) = \sqrt{\sum_{u,v} \left(\tilde{H}(u, v, \vec{a}) - H(u, v) \right)^2}.$$

This algorithm showed good convergence in most cases (Fig. 11.27a).

Figure 11.28 shows dependencies of defocus and astigmatism magnitudes on the angular position over the central part of the eye. Up to nine regions on the retina were selected, each containing sharp details, like blood vessels seen in Fig. 11.26, in order to let the algorithm work convergently. Results for two images, taken with different focal adjustment, are shown. From Fig. 11.28b it is obvious that the dependence of astigmatism is in a good agreement with calculated theoretically from the Gullstrand model.

Thus, the angular behavior of aberrations is close to the model prediction. The matching of experimental results and model eye predictions suggests that the developed technique is suitable for investigations of spatially varied aberrations typical of the human eye. This, in turn, shows that non-iterative deconvolution can be a useful tool for increasing the field of view of the human eye AO systems, at least for moderate angles.

11.9 Summary

We have considered several factors that limit the performance of adaptive optics systems for ophthalmic diagnostics. While speckle effects can be successfully mitigated by the described approaches, the anisoplanatic effects are still the subject of investigations. The compensated field of view extension is crucial for successful implementation of these adaptive optics techniques in clinical ophthalmic diagnostics.

References

1. A. Gullstrand, Photographisch-ophthalmometrische und klinische Untersuchungen über die Hornhautrefraction Kongl Svenska vetenskapsakademiens handlingar. **28**(7), 64 (1896)
2. M.S. Smirnov, Izmerenie volnovoy aberracii chelovecheskogo glaza Biofisika. **6**, 687–703 (1961)
3. J.D. Marsack, L.N. Thibos, R.A. Applegate, Metrics of optical quality derived from wave aberrations predict visual performance. J. Vis. **4**, 322–328 (2004)
4. J.F. Bille, *Aberration-Free Refractive Surgery: New Frontiers in Vision* (Springer, Berlin, 2004)
5. P. Artal, A. Guirao, Contributions of the cornea and lens to the aberrations of the human eye. Opt. Lett. **23**, 1713 (1998)
6. P. Artal, E. Berrio, A. Guirao, P. Piers, Contribution of the cornea and internal surfaces to the change of ocular aberrations with age. J. Opt. Soc. Am. A **19**(1), 137–143 (2002)
7. P. Artal, S. Marcos, R. Navarro, D.R. Williams, Odd aberrations and double-pass measurements of retinal image quality. J. Opt. Soc. Am. A **12**, 195–201 (1995)
8. E. Moreno-Barriuso, S. Marcos, R. Navarro, S.A. Burns, Comparing laser ray tracing, spatially resolved refractometer and Hartmann-Shack sensor to measure the ocular wavefront aberration. Optom. Vis. Sci. **78**, 152–156 (2001)

9. M. Mrochen, M. Kaemmerer, P. Mierdel, H.-E. Krinke, T. Seiler, Principles of Tscherning aberrometry. J. Ref. Surg. **16**, S570–S571 (2000)

10. J. Liang, B. Grimm, S. Goelz, J.F. Bille, Objective measurement of wave aberrations of the human eye the use of a Hartmann-Shack wavefront sensor. J. Opt. Soc. Am. A. **11**, 1949–1957 (1994)

11. J. Liang, D.R. Williams, Aberrations and retinal image quality of the normal human eye. J. Opt. Soc. Am. A **14**, 2873–2883 (1997)

12. A.V. Larichev, P.V. Ivanov, N.G. Iroshnikov, V.I. Shmalgausen, Measurement of eye aberrations in a speckle field. Quantum Electron. **31**, 1108 (2001)

13. H. Hofer, P. Artal, B. Singer, J.L. Aragón, D.R. Williams, Dynamics of the eyes wave aberration. J. Opt. Soc. Am. A **18**, 497 (2001)

14. M. Françon, *La granularité laser (spekle) et ses applications en optique* (Masson, Paris, 1978)

15. D.R. Williams et al., Rapid automatic measurement of the eye's wave aberration, Patent Application Publication Pub. No.: US2003/0086063 A1, 2003

16. E.J. Fernandez, I. Iglesias, P. Artal, Closed-loop adaptive optics in the human eye. Opt. Lett. **26**, 746 (2001)

17. A. Larichev, N. Irochnikov, P. Ivanov, A. Kudryashov, Deconvolution of color retinal images with wavefront sensing. Proc. SPIE Int. Soc. Opt. Eng. **4251**, 102 (2001)

18. A.V. Larichev, N.A. Iaitskova, V.I. Shmalhausen, Field of view widening in non-astronomical adaptive systems, in *Adaptive Optics for Industry and Medicine*, ed. by G.D. Love. Proceedings of the 2nd International Workshop on Adaptive Optics for Industry and Medicine, Durham, Ingland. (World Scientific, Singapore, 1999), pp. 272–277

19. A.V. Larichev, J.J. Otten, N.G. Irochnikov, P. Soliz, G.R.G. Erry, V.Y. Panchenko, Anisoplanatic effects in human eye retinal imaging. Opt. Mem. Neural Networks **15**(N1), 35–44 (2006)

20. A. Guirao, J. Porter, D.R. Williams, I.G. Cox, Calculated impact of higher-order monochromatic aberrations on retinal image quality in a population of human eyes. J. Opt. Soc. Am. A **19**, 620–628 (2002)

21. J. Liang, D.R. Williams, D.T. Miller, Supernormal vision and high resolution retinal imaging through adaptive optics. J. Opt. Soc. Am. A **14**, 2884–2892 (1997)

22. H. Hofer, L. Chen, G.Y. Yoon, B. Singer, Y. Yamauchi, D.R. Williams, Improvement in retinal image quality with dynamic correction of the eye's aberrations. Opt. Express **8**, 631–643 (2001)

23. F. Vargas, P. Prieto, P. Artal, Correction of the aberrations in the human eye with a liquid crystal spatial light modulator: limits to the performance. J. Opt. Soc. Am. A **15**, 2552–2562 (1998)

24. J.C. Dainty, A.V. Koryabin, A.V. Kudryashov, Low order adaptive optical system with bimorph deformable mirror. Appl. Opt. LP **37**, 4663 (1998)

25. C.A. Curcio, K.R. Sloan, R.E. Kalina, A.E. Hendrickson, Human photoreceptor topography. J. Comp. Neurol. **292**, 497–523 (1992)

26. D.V. Norren, L.F. Tiemeijer, Spectral reflectance of the human eye. Vision Res. **26**, 313 (1986)

27. N.P.A. Zagers, T.T.J.M. Berendschot, D. van Norren, Wavelength dependence of reflectometric cone photoreceptor directionality. J. Opt. Soc. Am. A **20**, 18–23 (2003)

28. S. Marcos, S.A. Burns, He Ji Chang, Model for cone directionality reflectometric measurements based on scattering. J. Opt. Soc. Am. A **15**, 2012 (1998)

29. S. Marcos, S.A. Burns, Cone spacing and waveguide properties from cone directionality measurements. J. Opt. Soc. Am. A **16**, 995 (1999)

30. W.S. Stiles, B.H. Crawford, The luminous efficiency of rays entering the eye pupil at different points. Proc. R. Soc. London, Ser. B **112**, 428 (1933)

31. J. Porter, *Adaptive Optics for Vision Science: Principles, Practices, Design and Applications* (Wiley, Hoboken, NJ, 2006)

32. A.S. Goncharov, A.V. Larichev, Speckle Structure of a Light Field Scattered by Human Eye Retina. Laser Phys. **17**(N9), 1157–1165 (2007)

33. L.N. Thibos, A. Bradley, *Modeling the Refractive and Neuro-Sensor Systems of the Eye, in Visual Instrumentation: Optical Design and Engineering Principles* (McGraw-Hill, New York, 1999), pp. 101–159
34. H.-L. Liou, N.A. Brennan, Anatomically accurate, finite model eye for optical modeling. J. Opt. Soc. Am. A **14**, 1881–1891 (1997)
35. J.W. Strohbehn, *Laser beam propagation in the atmosphere* (Springer, Berlin/New York/ Heidelberg, 1978)
36. J.C. Dainty, *Laser speckle and related phenomena* (Springer, Berlin/New York/Heidelberg, 1975)
37. V. Albanis, E.N. Ribak, Y. Carmon, Reduction of speckles in retinal reflection. Appl. Phys. Lett. **91**, 054104 (2007)
38. M.A. Gladyshevskiy, O.E. Naniy, N.K. Sabinin et al. *Optical Fiber for Information Transmission System.* http://www.npi.msu.ru/structinc/lib/books/fiber01.pdf
39. J.W. Goodman, *Speckle Phenomena: Theory and Applications* (Roberts & Co, Englewood, 2006)
40. H.M. Pedersen, On the contrast of polychromatic speckle patterns and its dependence on surface roughness. Opt. Acta **22**, 15–24 (1975)
41. A. Larichev, P. Ivanov, I. Irochnikov, V. Shmalhauzen, L.J. Otten, Adaptive system for eye-fundus imaging. Quantum Electron. **32**, N10 (2002)
42. L.S. Urmakher, L.I. Aizenshtat, *Oftal'mologicheskie pribory (Ophthalmologic Instruments)* (Moscow, Meditsina, 1988)
43. R.M. Tamarova, *Opticheskie pribory dlya issledovaniya glaza (Optical Devices for Examination of Eye)* (Moscow, Meditsina, 1982)
44. F.C. Delori, K.P. Pflibsen, Spectral reflectance of the human ocular fundus. Appl. Opt. **28**, 1061 (1989)
45. L. Diaz Santana Haro, J.C. Dainty, Single-pass measurements of the wave-front aberrations of the human eye by use of retinal lipofuscin autofluorescence. Optics Lett. **24**, 61 (1999)
46. *American National Standard for the Safe Use of Lasers, ANSI Z136.1* (Laser Institute of America, Orlando, 1993)
47. Normy i pravila ustroistva i ekspluatatsii lazerov (Norms and Regulations for Laser Arrangement and Operation) No. 5804-91 (Moscow, 1991)
48. W.H. Southwell, Wave-front estimation from wave-front slope measurements. J. Opt. Soc. Am. A **70**, 998–1006 (1980)
49. M. Born, E. Wolf, *Principles of Optics* (Nauka, Moscow, 1973) (Pergamon Press, Oxford, 1969)
50. D. Fried, Anisoplanatism in adaptive optics. J. Opt. Soc. Am. A **72**(l), 52–61 (1982)
51. D. Johnston, B. Welsh, Analysis of multiconjugate adaptive optics. J. Opt. Soc. Am. A **11**, 394–408 (1994)
52. J. Hardy, Instrumentation limitation in adaptive optics for astronomy, in *Active Telescope System*. Proceedings of Photo-Optical Instrumentation, England, vol. 1114, pp. 2–13 (1989)
53. V.I. Shmalhausen, N.A. laitskova, Adaptive corection of the image in anisoplanatic condition for stratified atmosphere. Optika atmosferi i okeana **11**(4), 364–370 (1998)
54. J.N. Caron, N.M. Namazi, C.J. Rollins, Noniterative blind data restoration by use of an extracted filter function. Appl. Opt. **41**(32), 10 (2002)
55. I. Iglesias, Parametric wave-aberration retrieval from point-spread function data by use of a pyramidal recursive algorithm. Appl. Opt. **37**(23), 10 (1998)
56. J.A. Nelder, R. Mead, A Simplex method for function minimization. Computer J. **7**(4), 308–313 (1965)

Part 3

Light Scattering Methods

Light Scattering Spectroscopy: From Elastic to Inelastic

12

Lev T. Perelman, Mark D. Modell, Edward Vitkin, and
Eugene B. Hanlon

Contents

L.T. Perelman (✉) • M.D. Modell • E. Vitkin

Beth Israel Deaconess Medical Center, Harvard University, Boston, MA, USA
e-mail: ltperel@bidmc.harvard.edu, markmodell@erols.com, evitkin@bidmc.harvard.edu

E.B. Hanlon
Department of Veterans Affairs, Medical Research Service, Bedford, MA, USA
e-mail: Eugene.Hanlon@med.va.gov

Abstract

This chapter reviews light scattering spectroscopic techniques in which coherent effects are critical because they define the structure of the spectrum. In the case of elastic light scattering spectroscopy, the targets themselves, such as aerosol particles in environmental science or cells and subcellular organelles in biomedical applications, play the role of microscopic optical resonators. In the case of inelastic light scattering spectroscopy or Raman spectroscopy, the spectrum is created due to light scattering from vibrations in molecules or optical phonons in solids. We will show that light scattering spectroscopic techniques, both elastic and inelastic, are emerging as very useful tools in material and environmental science and in biomedicine.

12.1   Introduction

Optical spectroscopy is an important tool for understanding matter by means of its interaction with electromagnetic radiation. There are important spectroscopic methods where coherence of light does not play the essential role. At the same time, in light scattering spectroscopy (LSS), coherent effects are critical since they define the structure of the spectrum. In the case of elastic LSS, the targets themselves, such as aerosol particles in environmental science or cells and subcellular organelles in biomedical applications, play the role of microscopic optical resonators. Thus, the LSS spectrum depends on their size, shape, and optical properties, such as refractive indices and absorption coefficients. In case of inelastic light scattering spectroscopy or Raman spectroscopy, the spectrum is created due to light scattering from vibrations in molecules or optical phonons in solids. We will show that light scattering spectroscopic techniques, both elastic and inelastic, are emerging as very useful tools in material and environmental science and in biomedicine.

12.2   Principles of Light Scattering Spectroscopy

12.2.1 Light Scattering Spectroscopy

Not only does light scattered by cell nuclei have a characteristic angular distribution peaked in the near-backward directions, but it also exhibits spectral variations typical

for large particles. This information has been used to study the size and shape of small particles such as colloids, water droplets, and cells [1]. The technique which utilizes the fact that the scattering matrix, a fundamental property describing the scattering event, depends not only on the scatterer's size, shape, and relative refractive index but also on the wavelength of the incident light is called light scattering spectroscopy or LSS. LSS can be useful in biology and medicine as well.

Bigio et al. [2] and Mourant et al. [3] demonstrated that spectroscopic features of elastically scattered light could be used to detect the transitional carcinoma of the urinary bladder and adenoma and adenocarcinoma of the colon and rectum with good accuracy. In 1997, Perelman et al. observed characteristic LSS spectral behavior in the light backscattered from the nuclei of human intestinal cells [4]. The cells, approximately 15 μm long, affixed to glass slides in buffer solution, formed a monolayer of contiguous cells similar to the epithelial lining of the colon mucosa. In the experiments, an optical fiber probe (NA = 0.22) was used to deliver white light from a xenon arc lamp onto the sample and to collect the reflected signal. After the measurement was performed, the cells were fixed and stained with H&E, a dye that renders otherwise transparent cell nuclei visible under microscope examination and is widely used in biology and medicine to examine tissue morphology. Microphotographs of the monolayer were obtained, and the size distribution of the nuclei was measured. It centered at about 6 μm and had a standard deviation of approximately 0.5 μm. Comparison of the experimentally measured wavelength varying component of light backscattered by the cells with the values calculated using the Mie theory and the size distribution of the cell nuclei determined by microscopy demonstrated that both spectra exhibit similar oscillatory behavior. The fact that light scattered by a cell nucleus exhibits oscillatory behavior with frequency depending on its size was used to develop a method of obtaining the size distribution of the nuclei from the spectral variation of light backscattered by biological tissues. This method was then successfully applied to diagnose precancerous epithelia in several human organs in vivo [5, 6].

One very important aspect of LSS is its ability to detect and characterize particles, which are well beyond the diffraction limit. Detection and characterization of particles beyond the diffraction limit by LSS, specifically 260 nm particles, has been recently demonstrated experimentally by Fang et al. [7] and Backman et al. [8, 9]. As explained in Perelman and Backman [10], particles much larger than the wavelength of light give rise to a prominent backscattering peak, and the larger the particle, the sharper the peak. On the other hand, particles with sizes smaller than the wavelength give rise to very different scattering behavior. The small particle contribution dominates for large angles. It is important to note that this conclusion does not require an assumption that the particles are spherical or homogenous.

12.2.2   Interaction of Light with Cells

Studies of light scattering by cells have a long history. The first publications in this area investigated the angular dependence of the scattered light. Most of the

experiments were performed at a single wavelength, and the angular distribution of the scattered light was measured either with an array of photodetectors, fiber optics, or CCD. Brunsting et al. initiated a series of experiments aiming to relate the internal structure of living cells with the scattering pattern by measuring forward and near forward scattering by cell suspensions [11]. This turned out to be one of the first attempts to explain light scattering by cells using rigorous quantitative approaches.

The cell has complex structure with a very broad range of scatterer sizes: from a few nanometers, the size of a macromolecule, to 7–10 μm, the size of a nucleus, and to 20 μm, the size of the cell itself. Most cell organelles and inclusions are themselves complex objects with spatially varying refractive index. On the other hand, several studies have confirmed that many organelles such as mitochondria, lysosomes, and nuclei do posses an average refractive index substantially different from that of their surrounding and, therefore, viewing a cell as an object with continuously or randomly varying refractive index is not accurate either. A more accurate model acknowledges subcellular compartments of various sizes with refractive index, though not constant over the compartment's volume, but different from that of the surrounding.

Despite this diversity (more than 200 different cell types have been identified), cells have many common features [10]. A cell is bounded by a membrane, a phospholipid bilayer approximately 10 nm in thickness with integral and peripheral proteins embedded in it. Two major cell compartments are the nucleus and the surrounding cytoplasm. The cytoplasm contains organelles, which are metabolically active subcellular organs, and inclusions, which are metabolically inactive. Mitochondria typically have the shape of a prolate spheroid. Their size varies greatly even within a single cell. The large dimension of a mitochondrion may range from 1 to 5 μm. The larger diameter typically varies between 0.2 and 0.8 μm. The mitochondria are quite flexible and may easily change their shape. The numbers of mitochondria differ depending on the cell size and its energy needs.

Endoplasmic reticulum is composed of tubules and flat sheets of membranes distributed over the intracellular space. The outer diameter of these tubules ranges from 30 to 100 nm. Their wall thickness is about 10 nm. There are two types of endoplasmic reticulum: rough endoplasmic reticulum and smooth endoplasmic reticulum. The rough endoplasmic reticulum differs from the smooth endoplasmic reticulum in that it bears 20–25 nm spherical or sometimes spheroidal particles called ribosomes.

Golgi apparatus is composed of a group of 4–10 flattened parallel membrane-bounded cisternae and functions in the modification and packaging of the macromolecules. The overall thickness of this organelle can range from 100 to 400 nm.

Lysosomes are 250–800 nm organelles of various shapes. The numbers of lysosomes are highly variant for different cells as well: the cells of membranous epithelial lining of cervix, for example, contain just a few lysosomes, while hepatocytes may possess a few hundred ones.

Peroxisomes are 200 nm to 1.0 μm spheroidal bodies of lower densities than lysosomes that are more abandoned in the metabolically active cells such as hepatocytes where they are counted in hundreds.

Cytoskeleton is composed of filamentous arrays of proteins. Its three major components are microtubules, which are about 25 nm in diameter with a wall 9 nm thick and a 15 nm lumen, 10 nm in diameter intermediate filaments, and 7 nm in diameter microfilaments.

Various cytoplasmic inclusions, such as lipids, glycogen, secretory granules, and pigments, come in all different sizes ranging from 20 to 500 nm. They might be of various shapes but usually appear to be near spherical. The surface roughness of an inclusion can range from 2 to 40 nm.

Extensive studies of angular dependence of light scattering by cells using a goniometer were carried out by Mourant et al. [12]. Measurements of light scattering from cells and cell organelles were performed from 2° to 171° and from 9° to 168°, respectively. In both cases, the unpolarized light was delivered by a He-Ne laser at 632.8 nm. The angular resolution was about 0.5°, and most of the data was taken for every 2°. The concentration of the cells was 10^5 cells/ml. This concentration was chosen so that multiple scattering events would be rare. The researchers used two types of cells in their experiments: immortalized rat embryo fibroblast cells and a ras-transfected clone, which is highly tumorigenic. The cells were suspended in phosphate-buffered saline and kept on ice. Nuclei and mitochondria were isolated from MR1 cells by standard methods and resuspended mannitol sucrose buffer.

Not only organelles themselves but their components also can scatter light. Finite-difference time-domain (FDTD) simulations provide means to study spectral and angular features of light scattering by arbitrary particles of complex shape and density. Using FDTD and choosing proper models, one can learn a great deal about origins of light scattering.

Drezek et al. investigated the influence of cell morphology on the scattering pattern [13] and found that the internal structure of an organelle does affect the scattering at large angles but not in the forward or backward directions. In fact, this finding is not paradoxical and should be expected: light scattered in the forward or backward directions depends more on the larger structures within an organelle, for example, the organelle itself. It samples average properties of the organelle, which were kept constant in the simulations. On the other hand, smaller structures within the organelle scatter strongly in the intermediate angles. Thus, light scattering at these angles is influenced by its internal structure.

12.3   Applications of Light Scattering Spectroscopy

12.3.1 Measuring Size Distribution of Epithelial Cell Nuclei with Light Scattering Spectroscopy

Enlarged nuclei are primary indicators of cancer, dysplasia, and cell regeneration in most human tissues, and recent studies demonstrate that LSS can accurately detect dysplasia clinically in the esophagus, colon, and bladder [4–6, 9].

The hollow organs of the body are lined with a thin, highly cellular surface layer of epithelial tissue, which is supported by underlying, relatively acellular connective tissue. In healthy tissues, the epithelium often consists of a single, well-organized layer of cells with en face diameter of 10–20 μm and height of 25 μm. In dysplastic epithelium, cells proliferate and their nuclei enlarge and appear darker (hyperchromatic) when stained.

LSS can be used to measure these changes. Consider a beam of light incident on an epithelial layer of tissue. A portion of this light is backscattered from the epithelial nuclei, while the remainder is transmitted to deeper tissue layers, where it undergoes multiple scattering and becomes randomized before returning to the surface.

Epithelial nuclei can be treated as spheroidal Mie scatters with refractive index, n_n, which is higher than that of the surrounding cytoplasm, n_c. Normal nuclei have a characteristic diameter $l = 4$–7 μm. In contrast, dysplastic nuclei can be as large as 20 μm, occupying almost the entire cell volume. In the visible range, where the wavelength $\lambda \ll l$, the van de Hulst approximation can be used to describe the elastic scattering cross section of the nuclei:

$$\sigma_s(\lambda, l) = \frac{1}{2}\pi d^2 \left(1 - \frac{\sin(2\delta/\lambda)}{\delta/\lambda} + \left(\frac{\sin(\delta/\lambda)}{\delta/\lambda}\right)^2\right), \qquad (12.1)$$

with $\delta = \pi \cdot l \cdot (n_n - n_c)$. Equation (12.1) reveals a component of the scattering cross section, which varies periodically with inverse wavelength. This, in turn, gives rise to a periodic component in the tissue reflectance. Since the frequency of this variation (in inverse wavelength space) is proportional to particle size, the nuclear size distribution can be obtained from the Fourier transform of the periodic component.

To test this, Perelman et al. [4] studied elastic light scattering from densely packed layers of normal and T84 tumor human intestinal cells, affixed to glass slides in buffer solution (Fig. 12.1). The diameters of the normal cell nuclei ranged from 5 to 7 μm, and those of the tumor cells from 7 to 16 μm. The reflectance from the samples exhibits distinct spectral features. The predictions of the Mie theory were fit to the observed spectra. The fitting procedure used three parameters, average size of the nucleus, standard deviation in size (a Gaussian size distribution was assumed), and relative refractive index.

The solid line of Fig. 12.2 is the distribution extracted from the data, and the dashed line shows the corresponding size distributions measured morphometrically via light microscopy. The extracted and measured distributions for both normal and T84 cell samples were in good agreement, indicating the validity of the above physical picture and the accuracy of the method of extracting information.

Fig. 12.1 Microphotograph of the isolated normal intestinal epithelial cells (panel **a**) and intestinal malignant cell line T84 (panel **b**). Note the uniform nuclear size distribution of the normal epithelial cell (**a**) in contrast to the T84 malignant cell line, which at the same magnification shows larger nuclei and more variation in nuclear size (**b**). Solid bars equal 20 μm in each panel. The cells were stained after the LSS experiments were performed (From Ref. [14])
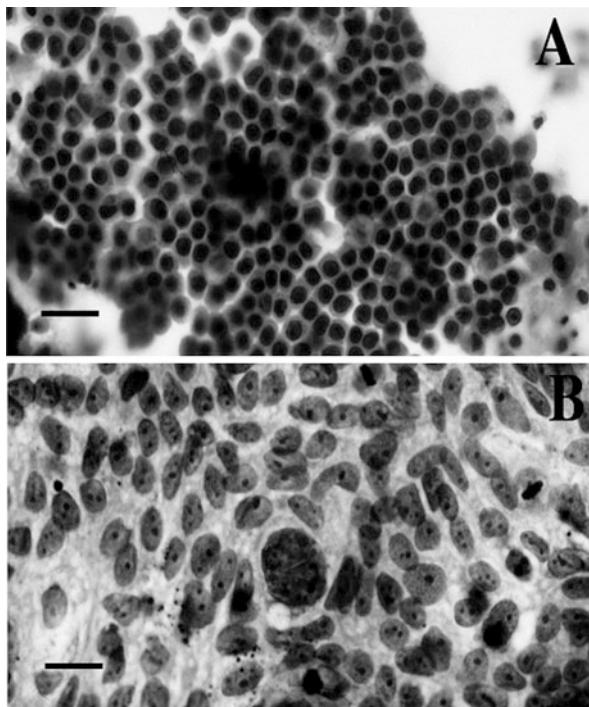
Fig. 12.2 Nuclear size distributions. (*a*) Normal intestinal cells; (*b*) T84 cells. In each case, the *solid line* is the distribution extracted from the data, and the *dashed line* is the distribution measured using light microscopy (From Ref. [4])
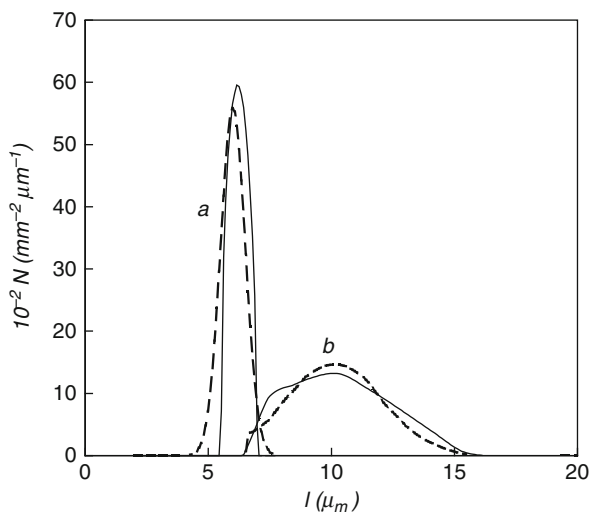
Fig. 12.3 Schematic diagram of the proof-of-principle LSS system (From Ref. [6])
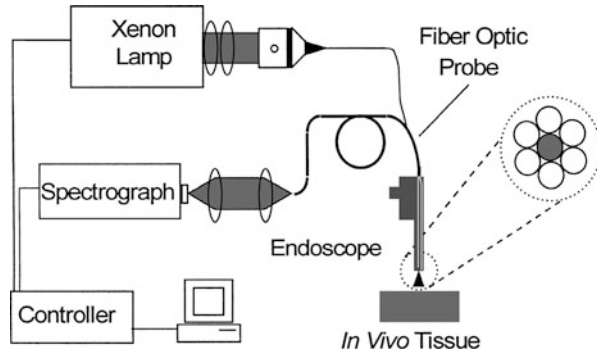
12.3.2 Noninvasive Diagnostic Technology for Early Cancer Detection

It is a well-known fact that often, when cancer is found, it is too late to treat it. Thus, the most effective method of fighting cancer might be its prevention at an early stage when precancerous changes are often confined to the superficial cellular layer called the epithelium. The question is what noninvasive diagnostic technology can be used to detect those early lesions, as they are microscopic, flat, and not readily observable. Over the last decades, substantial progress has been made in medical diagnostic technologies that target anatomic changes at the organ level. Such techniques as magnetic resonance imaging (MRI) and spectroscopy (MRS), X-ray computed tomography (X-ray CT), and ultrasound made it possible to "see through the human body." At the same time, there is clearly a need for the development of diagnostic techniques that use our current knowledge of the cellular and subcellular basis of disease. The diagnostic techniques applicable in situ (inside human body) that can provide structural and functional information about the tissue at the cellular and subcellular level – the kind of information that is currently obtainable only by using methods requiring tissue removal – will have great implications on the detection and prevention of disease as well as enabling targeted therapy.

12.3.3 Application of Light Scattering Spectroscopy to Barrett's Esophagus

Recently, Perelman et al. [6] observed periodic fine structure in diffuse reflectance from Barrett's esophagus (BE) of human subjects undergoing gastroenterological endoscopy procedures. A schematic diagram of the proof-of-principle system used to perform LSS is shown in Fig. 12.3. Immediately before biopsy, the reflectance spectrum from that site was collected using an optical fiber probe. The probe was inserted into the accessory channel of the endoscope and brought into gentle contact with the mucosal surface of the esophagus. It delivered a weak pulse of white light

to the tissue and collected the diffusely reflected light. The probe tip sampled tissue over a circular spot approximately 1 mm^2 in area. The pulse duration was 50 ms, and the wavelength range was 350–650 nm. The optical probe caused a slight indentation at the tissue surface that remained for 30–60 s. Using this indentation as a target, the site was then carefully biopsied, and the sample was submitted for histological examination. This insured that the site studied spectroscopically matched the site evaluated histologically.

The reflected light was spectrally analyzed, and the spectra were stored in a computer. The spectra consist of a large background from submucosal tissue, on which is superimposed a small (2–3 %) component that is oscillatory in wavelength because of scattering by cell nuclei in the mucosal layer. The amplitude of this component is related to the surface density of epithelial nuclei (number of nuclei per unit area). Because the area of tissue probed is fixed at 1 mm^2, this parameter is a measure of nuclear crowding. The shape of the spectrum over the wavelength range is related to nuclear size. The difference in nuclear size distributions extracted from the small oscillatory components for nondysplastic and dysplastic BE sites is pronounced. The distribution of nuclei from the dysplastic site is much broader than that from the nondysplastic site, and the peak diameter is shifted from $\sim$7 μm to about $\sim$10 μm. In addition, both the relative number of large cell nuclei ($>$10 μm) and the total number of nuclei are significantly increased.

However, single scattering events cannot be measured directly in biological tissue. Because of multiple scattering, information about tissue scatterers is randomized as light propagates into the tissue, typically over one effective scattering length (0.5–1 mm, depending on the wavelength). Nevertheless, the light in the thin layer at the tissue surface is not completely randomized. In this thin region, the details of the elastic scattering process can be preserved. Therefore, the total signal reflected from a tissue can be divided into two parts: single backscattering from the uppermost tissue structures such as cell nuclei, and the background of diffusely scattered light. To analyze the single scattering component of the reflected light, the diffusive background must be removed. This can be achieved either by modeling using diffuse reflectance spectroscopy [4, 15, 16] or by polarization background subtraction [14].

Polarization background subtraction has the advantage of being less sensitive to tissue variability. However, the diffuse reflectance spectroscopy has its own advantages since it can provide valuable information about biochemical and morphological organization of submucosa and degree of angiogenesis.

12.3.4 Diffuse Reflectance Spectroscopy of Colon Polyps and Barrett's Esophagus

A technique for modeling clinical tissue reflectance in terms of the underlying tissue scatterers and absorbers, which is called diffuse reflectance spectroscopy, was developed by Zonios et al. [15] in studies of colon polyps and applied by

Georgakoudi et al. [16] to Barrett's esophagus. This method provides both direct physical insight and quantitative information about the tissue constituents that give rise to the reflectance spectra.

The method described in Zonios et al. [15] is based on the diffusion approximation. It describes the tissue reflectance spectrum collected by a finite-sized probe with an effective probe radius r_c. Biological tissue is treated as a homogeneous medium with wavelength-dependent absorption coefficient μ_a and reduced scattering coefficient μ'_s. Incident photons are absorbed and scattered in the tissue, with the survivors eventually escaping from the tissue surface. A fraction of the escaping diffusely reflected light is collected by a probe of finite size.

Starting with an expression derived by Farrell, Patterson and Wilson [17], Zonios et al. [15] obtains analytical expression for the diffuse reflectance collected by the probe:

$$R_p(\lambda) = \frac{\mu'_s}{\mu'_s + \mu_a} \left\{ e^{-\mu z_0} + e^{-(1+\frac{4}{3}A)\mu z_0} - z_0 \frac{e^{-\mu r'_1}}{r'_1} - \left(1 + \frac{4}{3}A\right) z_0 \frac{e^{-\mu r'_2}}{r'_2} \right\}, \quad (12.2)$$

with $\quad \mu = (3\mu_a(\mu_a + \mu'_s))^{1/2}, \qquad z_0 = \frac{1}{\mu'_s + \mu_a}, \qquad r'_1 = \left(z_0^2 + r_c'^2\right)^{1/2}, \qquad$ and $r'_2 = \left(z_0^2(1 + \frac{4}{3}A)^2 + r_c'^2\right)^{1/2}$. The parameter A depends in the known way on the refractive index n of the medium. For a given probe geometry, there is an optimal value of the effective probe radius r_c, which can be determined by calibrating (12.2) using the reflectance measurement of a tissue phantom with known optical properties.

For the visible tissue reflectance spectra collected in colon [15] and BE [16], researchers found hemoglobin (Hb) to be the only significant light absorber. To account for both oxygenated and deoxygenated forms of Hb, the total absorption coefficient, $\mu_a(\lambda)$, is given by

$$\mu_a(\lambda) = \ln(c_{Hb} \left[\alpha \, \varepsilon_{HbO_2}(\lambda) + (1 - \alpha) \, \varepsilon_{Hb}(\lambda) \right]), \quad (12.3)$$

where α is the Hb oxygen saturation parameter and c_{Hb} the total hemoglobin concentration. The wavelength-dependent extinction coefficients (i.e., the ε's) of both forms of hemoglobin are well documented [18].

To test the model, Zonios et al. [15] measured the reflectance spectra of a series of tissue phantoms with known absorption and scattering properties. The phantom reflectance spectra were accurately modeled by (12.2), using the known absorption and scattering coefficients. By fitting (12.2) to the experimental phantom data obtained using various values of Hb concentration, oxygen saturation, scatterer size, and scatterer density, the authors found that the values of these parameters could be recovered with accuracy of better than 10 % over the full range of the four parameters. This established that the experimental spectra are adequately described by the diffusion model and that the model could be used in an inverse manner to extract the parameters from the spectra with reasonable accuracy.

Diffuse reflectance spectra were then collected from adenomatous polyps in 13 patients undergoing routine colonoscopy. The clinical data were analyzed using the model and the known spectra of oxy- and deoxyhemoglobin to extract values of Hb concentration and saturation and $\mu_s'(\lambda)$. For biological tissue, the reduced scattering coefficient is the sum of contributions from the various tissue scatterers. Detailed information about these individual scatterers is not presently known. Therefore, the reduced scattering coefficient can be presented in the form $\mu_s'(\lambda) = \rho_s \sigma_s'(\lambda)$, with the *effective* scattering density and $\sigma_s'(\lambda)$ the *effective* reduced scattering cross section. With this, tissue scattering properties were modeled in an average way, as if tissue contained a single, well-defined type of scatterer. In general, $\sigma_s'(\lambda)$ depends on the refractive index, shape, and size of the scatterer, as well as on the refractive index of the surrounding medium. Mie scattering theory was applied to evaluate $\sigma_s'(\lambda)$ [18], assuming the scatterers to be homogeneous spheres of diameter and relative refractive index n, $\sigma_s'(\lambda)$.

Figure 12.4a shows typical diffuse reflectance spectra from one adenomatous polyp site and one normal mucosa site. The model fits, also shown, are excellent. Both the absorption dips and scattering slopes are sensitive functions of the fit parameters, providing an inverse algorithm, which is sensitive to such features. The inverse algorithm was applied to the clinical spectra, and values of the four parameters for each site probed were obtained. These parameters provide valuable information about the tissue properties.

Figure 12.4b shows a binary plot of effective scatter size versus Hb concentration. Adenomatous colon polyps were characterized by increased Hb concentration, in agreement with the published results that precancerous tissues such as adenomatous polyps exhibit increased microvascular volume [19, 20]. The Hb oxygen saturation was found to be approximately 60 %, on average, for both normal mucosa and adenomatous polyps. This result is reasonable, inasmuch as the measurements were essentially performed in the capillary network of the mucosa, where oxygen is transferred from Hb to tissue. The authors also observed an intrinsic differentiation in the scattering properties between the two tissue types studied. For adenomatous polyps, the average effective scattering size was larger, and the average effective scatterer density was smaller, as compared to normal mucosa. The range of effective scattering sizes was in good agreement with that reported for average scatterer sizes of biological cell suspensions [12].

Figure 12.5 shows typical diffuse reflectance spectra from one nondysplastic BE site [16]. The analysis showed that the reduced scattering coefficient, μ_s', of Barrett's esophagus tissue changes gradually during the progression from nondysplastic, to low-grade, to high-grade dysplasia. Additionally, the wavelength dependence of μ_s' changes during the development of dysplasia. To describe these changes, the authors [16] fit a straight line to $\mu_s'(\lambda)$ and used the intercept at 0 nm and slope of this line as additional to LSS diagnostic parameters (Fig. 12.6b).

Georgakoudi et al. [16] found that the scattering coefficient of tissue decreases significantly during the development of dysplasia, suggesting that changes that are not observed histopathologically are taking place within the lamina propria and submucosa before the onset of invasion. The change in the slope of μ_s' as a function

Fig. 12.4 Diffuse reflectance analysis. (**a**). *Top*: reflectance spectra (*thick lines*), and modeled fits (*thin lines*). (**b**). *Bottom*: binary plot. *Open circle*: normal. *Filled circle*: polyp (From Ref. [15])
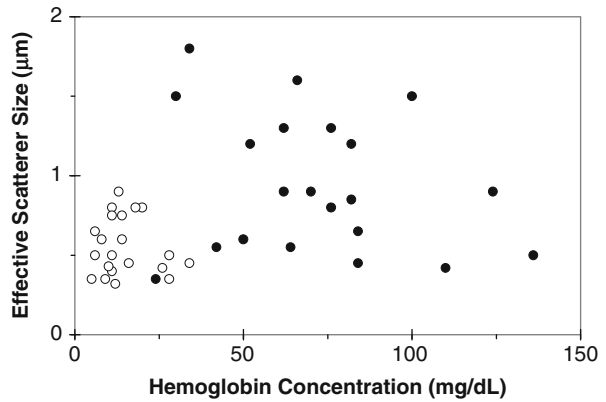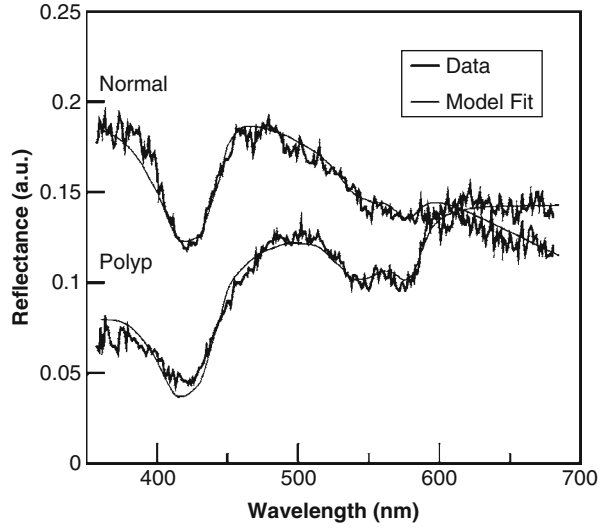
Fig. 12.5 Reflectance spectrum of a nondysplastic BE site. *Solid line*, experimental data; *dashed line*, model fit (From Ref. [16])
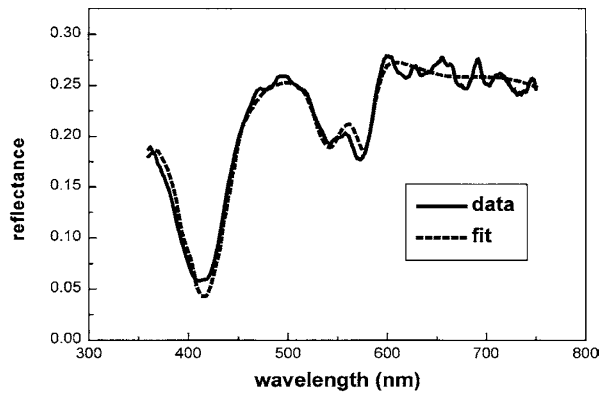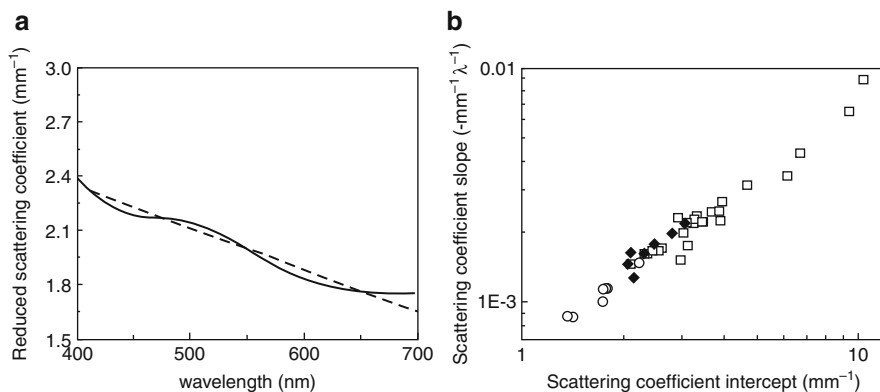
Fig. 12.6 (**a**) Reduced scattering coefficient as a function of wavelength for a representative nondysplastic BE site (*solid line*) and corresponding linear fit (*dashed line*). (**b**) Slopes and intercepts of linear fit to the wavelength-dependent tissue reduced scattering coefficient, μ_s', for nondysplastic ($\circ$), low-grade ($\blacklozenge$), and high-grade ($\square$) dysplastic BE sites. A log-log scale is used to facilitate visualization of all the data points (From Ref. [16])

of wavelength suggests that the mean size of the tissue scattering particles is changing. Crowding of the cells and nuclei of the epithelial layer may be responsible for this change.

12.3.5 Polarization Background Subtraction

To study the spectrum of polarized backscattered light, Backman et al. [14] employed an instrument that delivers collimated polarized light on tissue and separates two orthogonal polarizations of backscattered light. In the system described in [14] (Fig. 12.7), light from a broadband source (250 W CW tungsten lamp) is collimated and then refocused with a small solid angle onto the sample, using lenses and an aperture. A broadband polarizer linearly polarizes the incident beam. In order to avoid specular reflectance, the incident beam is oriented at an angle of $\sim$15° to the normal to the surface of the sample. The sample is illuminated by a circular spot of light of 2 mm in diameter. The reflected light is collected in a narrow cone ($\sim$0.015 rad), and two polarizations are separated by means of a broadband polarizing beam splitter cube, which also serves as the analyzer. The output from this analyzer is delivered through 200-μm-core-diameter optical fibers into two channels of a multichannel spectroscope. This enables the spectra of both components to be measured simultaneously in the range from 400 to 900 nm. The studies have shown that the unpolarized component of the reflected light can be canceled by subtracting $I_\perp$ from $I_\parallel$ allowing the single scattering signal to be extracted.

Backman et al. [14] performed experiments with cell monolayers. A thick layer of gel containing $BaSO_4$ and blood was placed underneath the cell monolayer to
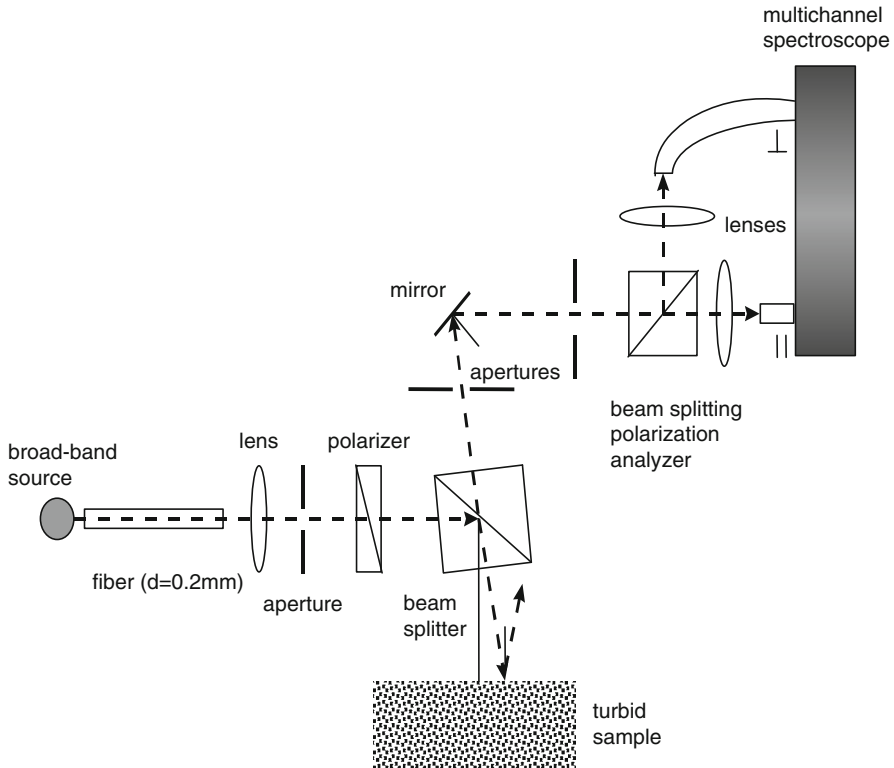
Fig. 12.7 Schematic diagram of the experiment with polarized light (From Ref. [14])

simulate underlying tissue. The predictions of Mie theory were fit to the observed residual spectra. The fitting procedure used three parameters, average size of the nucleus, standard deviation in size (a Gaussian size distribution was assumed), and relative refractive index. For normal intestinal epithelial cells, the best fit was obtained using $d = 5.0$ μm, $\Delta d = 0.5$ μm, and $n = 1.035$ (Fig. 12.8a).

For T84 intestinal malignant cells, the corresponding values were $d = 9.8$ μm, $\Delta d = 1.5$ μm, and $n = 1.04$ (Fig. 12.8b). In order to check these results, the distribution of the average size of the cell nuclei was measured by morphometry on identical cell preparations that were processed in parallel for light microscopy. The nuclear sizes and their standard deviations were found to be in very good agreement with the parameters extracted from Mie theory. A histogram showing the size distributions obtained for the normal intestinal epithelial cells and T84 cells is shown in Fig. 12.8c. The accuracy of the average size is estimated to be 0.1 μm, and the accuracy in n as 0.001. Note the larger value of n obtained for T84 intestinal malignant cells, which is in agreement with the hyperchromaticity of cancer cell nuclei observed in conventional histopathology of stained tissue sections.

The experiments [14] show that polarized light scattering spectroscopy is able to distinguish between single backscattering from uppermost cells and the diffusive
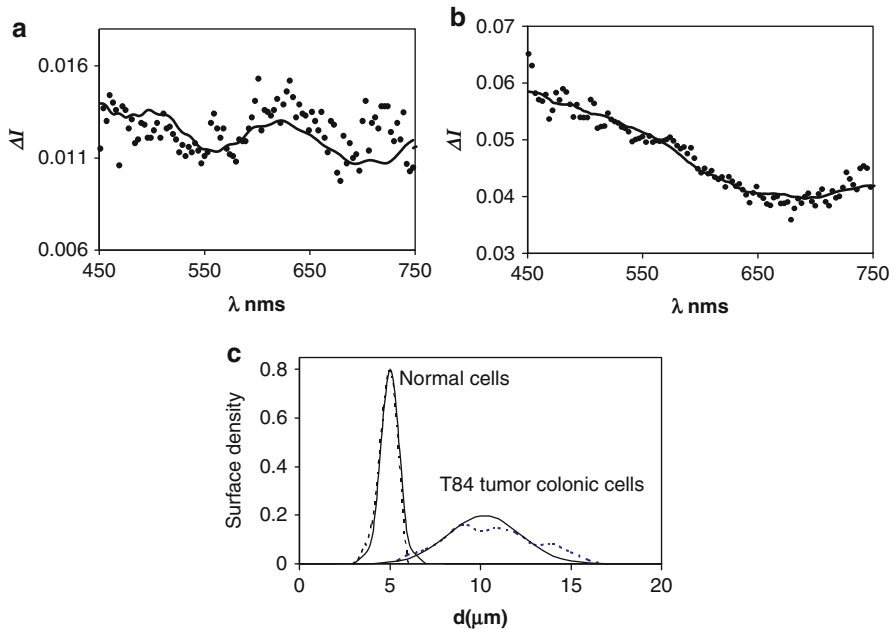
Fig. 12.8 Spectrum of polarized component of backscattered light from (**a**) normal intestinal cells, (**b**) T84 intestinal malignant cells, and (**c**) correspondent nuclear size distributions. In each case, the *solid line* is the distribution extracted from the data, and the *dashed line* is the distribution measured using light microscopy

background. It provides valuable information about the macroscopic properties of the tissue. On the other hand, the single scattering component provides morphological information about living cells, which potentially has valuable biomedical applications.

12.3.6 Clinical Detection of Dysplasia in Four Organs Using Light Scattering Spectroscopy

The ability of LSS to diagnose dysplasia and CIS was tested in in vivo human studies in four different organs and in three different types of epithelium: columnar epithelia of the colon and Barrett's esophagus, transitional epithelium of the urinary bladder, and stratified squamous epithelium of the oral cavity [5, 21]. All clinical studies were performed during routine endoscopic screening or surveillance procedures. In all of the studies, an optical fiber probe delivered white light from a xenon arc lamp to the tissue surface and collected the returned light. The probe tip was brought into gentle contact with the tissue to be studied. Immediately after the measurement, a biopsy was taken from the same tissue site. The biopsied tissue was prepared and examined histologically by an experienced pathologist in the
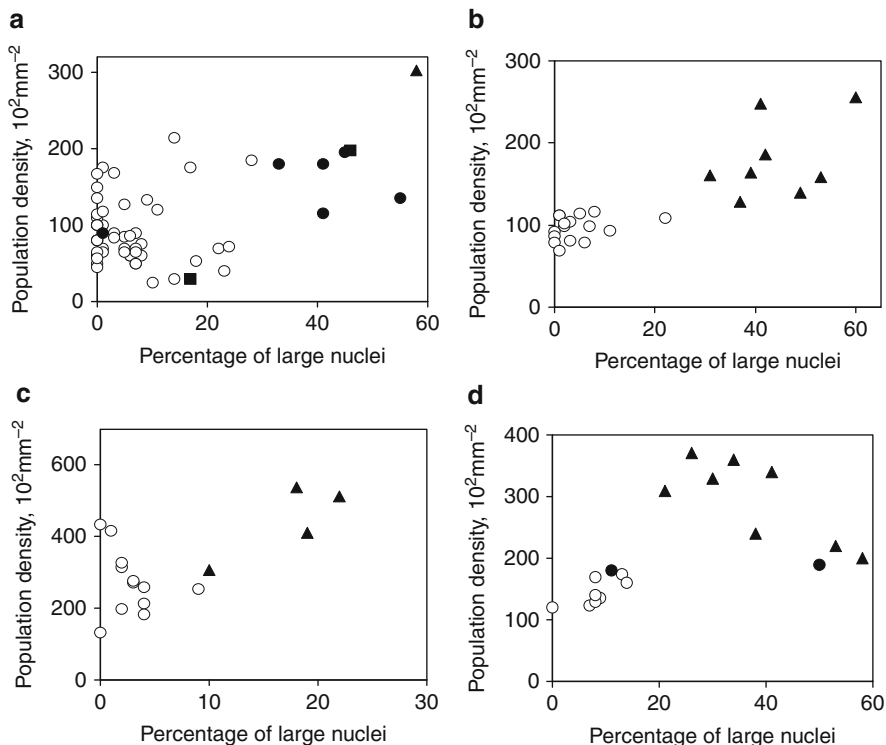
Fig. 12.9 Dysplasia/CIS classifications for four types of tissue obtained clinically with LSS, compared with histological diagnosis. In each case, the ordinate indicates the percentage of enlarged nuclei, and the abscissa indicates the population density of the nuclei, which parametrizes nuclear crowding. (**a**) Barrett's esophagus: nondysplastic Barrett's mucosa (○), indefinite for dysplasia (●), low-grade dysplasia (■), high-grade dysplasia (▲); (**b**) colon: normal colonic mucosa (○), adenomatous polyp (▲); (**c**) urinary bladder: benign bladder mucosa (○), transitional cell carcinoma in situ (▲); (**d**) oral cavity: normal (○), low-grade dysplasia (●), squamous cell carcinoma in situ (▲) (From Ref. [5])

conventional manner. The spectrum of the reflected light was analyzed, and the nuclear size distribution determined. The majority of distributions of dysplastic cell nuclei extended to larger size.

These size distributions were then used to obtain the percentage of nuclei larger than 10 μm, and the total number of nuclei per unit area (population density). As noted above, these parameters quantitatively characterize the degree of nuclear enlargement and crowding, respectively.

Figure 12.9 displays these LSS parameters in binary plots to show the degree of correlation with histological diagnoses. In all four organs, there is a clear distinction between dysplastic and nondysplastic epithelium. Both dysplasia and CIS have a higher percentage of enlarged nuclei and, on average, a higher population density, which can be used as the basis for spectroscopic tissue diagnosis.

These results show the promise of LSS as a real-time, minimally invasive clinical tool for accurately and reliably classifying invisible dysplasia. Although the presented data sets are limited in size, the effectiveness of LSS in diagnosing early cancerous lesions is again clearly demonstrated, and this suggests the general applicability of the technique.

12.3.7 Clinical Detection of Dysplasia in Barrett's Esophagus Using Light Scattering Spectroscopy

The studies in BE described in Perelman et al. [4], Backman et al. [5], and Wallace et al. [6] were conducted at the Brigham and Women's Hospital and the West Roxbury Veterans Administration Medical Center. Patients undergoing surveillance endoscopy for a diagnosis of Barrett's esophagus or suspected carcinoma of the esophagus were evaluated by systematic biopsy. In surveillance patients, biopsy specimens were taken in four quadrants, every 2 cm of endoscopically visible Barrett's mucosa. In patients with suspected adenocarcinoma, biopsy specimens for this study were taken from the Barrett's mucosa adjacent to the tumor.

Spectra were collected by means of an optical fiber probe, inserted in the biopsy channel of the gastroscope, and brought into gentle contact with the tissue. Each site was biopsied immediately after the spectrum was taken. Because of the known large interobserver variation [22], the histology slides were examined independently by four expert GI pathologists. Sites were classified as NDB, IND, LGD, or HGD. Based on the average diagnosis [23, 24] of the four pathologists, 4 sites were diagnosed as HGD, 8 as LGD, 12 as IND, and 52 as NDB.

To establish diagnostic criteria, eight samples were selected as a "modeling set," and the extracted nuclear size distributions were compared to the corresponding histology findings. From this, the authors decided to classify a site as dysplasia if more than 30 % of the nuclei were enlarged, with "enlarged" defined as exceeding a 10-μm threshold diameter, and classified as nondysplasia otherwise. The remaining 68 samples were analyzed using this criterion. Averaging the diagnoses of the four pathologists [22], the sensitivity and specificity of detecting dysplasia were both 90 %, with dysplasia defined as LGD or HGD, and nondysplasia defined as NDB or IND, an excellent result, given the limitations of interobserver agreement among pathologists.

To further study the diagnostic potential of LSS, the entire data set was then evaluated adding a second criterion, the population density of surface nuclei (number per unit area), as a measure of crowding. The resulting binary plot (Fig. 12.10) reveals a progressively increasing population of enlarged and crowded nuclei with increasing histological grade of dysplasia, with the NDB samples grouped near the lower left corner and the HGD samples at the upper right. Using logistic regression [25], the samples were then classified by histological grade as a function of the two diagnostic criteria. The percentage agreements between LSS and the average and consensus diagnoses (at least three pathologists in agreement) were 80 % and 90 %, respectively. This is much higher than that

Fig. 12.10 LSS diagnostic plots of Barrett's esophagus data. NDB (*circles*); IND (*squares*); LGD (*triangles*); HGD (*diamonds*). The decision threshold for dysplasia is indicated (From Ref. [6])
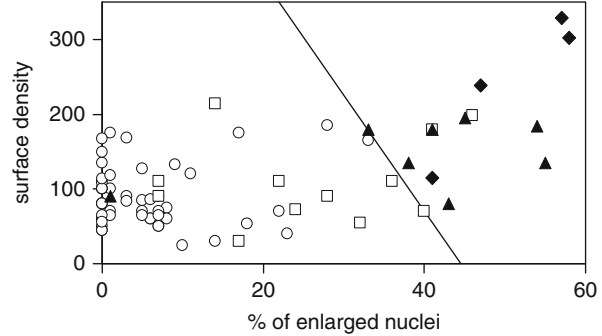
between the individual pathologists and the average diagnoses of their three colleagues, which ranged from 62 % to 66 %, and this was also reflected in the kappa statistic values [6].

12.3.8 Imaging Dysplasia in Barrett's Esophagus Using Endoscopic Polarized Scanning Spectroscopic Instrument

The instrument described in the above sections was capable of collecting data at randomly selected sites by manually positioning the probe. The sites were then biopsied, the data were processed off-line, and a comparison with biopsy results was made when the pathology information became available. The high correlation between spectroscopic results and pathology was sufficiently promising to justify the development of the clinical device, which is reviewed herein.

The clinical endoscopic polarized scanning spectroscopic (EPSS) instrument [26, 27] is compatible with existing endoscopes (Fig. 12.11). It scans large areas of the esophagus chosen by the physician and has the software and algorithms necessary to obtain quantitative, objective data about tissue structure and composition, which can be translated into diagnostic information in real time. This enables the physician to take confirming biopsies at suspicious sites and minimize the number of biopsies taken at nondysplastic sites.

The instrument detects polarized light coming primarily from the epithelial layer. Although principally using the polarization technique to extract diagnostic information about dysplasia, the EPSS instrument can also sum the two polarizations to permit the use of diffuse reflectance spectroscopy, which also can provide information about early stages of adenocarcinoma [16].

The EPSS instrument is a significant advance over the single-point fiber-optic instrument in that (1) it scans the esophagus and has the software and algorithms necessary to obtain quantitative, objective data about tissue structure and composition, which can be translated into diagnostic information and guide biopsy in real time; (2) it employs collimated illumination and collection optics, which enables the instrument to generate maps of epithelial tissue not affected by the distance
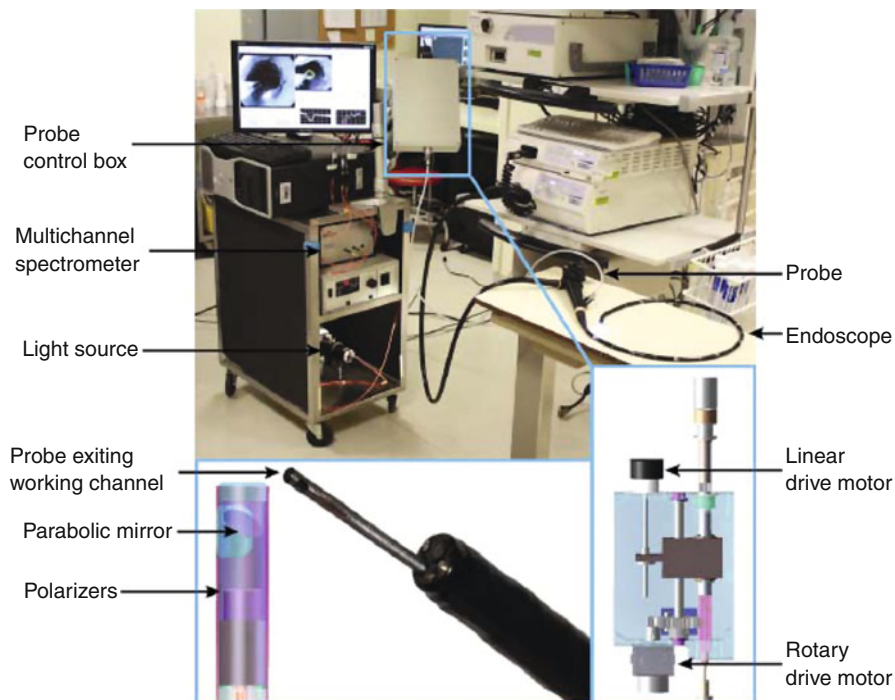
Fig. 12.11 Clinical EPSS instrument. The EPSS instrument is shown in the endoscopy suite before the clinical procedure, with the scanning probe inserted into the working channel of an endoscope. The *insets* show details of the scanning probe tip and the control box (From Ref. [26])

between the probe tip and the mucosal surface, making it dramatically less sensitive to peristaltic motion; (3) it incorporates both the polarization technique for removing the unwanted background in the LSS signal, and single backscattering in the diffuse reflectance spectroscopy signal; (4) it integrates the data analysis software with the instrument in order to provide the physician with real-time diagnostic information; and (5) it combines LSS information with diffuse reflectance spectroscopy information measured by the same instrument, thereby improving the diagnostic assessment capability.

The instrument makes use of commercially available gastroscopes and video processors. A standard PC is adapted to control the system. Commercially available spectrometers are also employed.

For use during endoscopy, the polarized scanning fiber-optic probe is inserted into the working channel of a standard gastroendoscope (e.g., Olympus GIF-H180 used in the procedures reported below) and the gastroenterologist introduces the endoscope through the mouth. Spectroscopy of the entire Barrett's segment is performed by scanning adjacent sections, 2 cm in length, with the polarized scanning probe as follows. The endoscope tip is positioned, and the probe is

extended 2 cm beyond the endoscope tip, placing it at the distal boundary of a BE region chosen for examination. One complete rotary scan of the esophageal wall is completed. The probe is withdrawn linearly 2 mm back into the endoscope tip, and another rotary scan is completed. This is repeated for 10 rotary scans so that an entire 2 cm length of BE is scanned; then, the endoscope tip is withdrawn 2 cm, and the next length of BE is examined. Currently, the instrument collects 30 data points for each rotary scan and performs ten steps during a linear scan (2 mm per step), collecting 300 data points in 2 min for each 2 cm segment of BE. We estimate that the scanning time can be reduced to as little as 20 s by utilizing a more efficient scanning mechanism.

We checked the performance of the EPSS instrument in experiments using freshly resected bovine esophagi. An intact bovine esophagus was mounted vertically, and an Olympus GIF-H180 clinical endoscope was inserted. The esophagus was scanned point-by-point, and the data were recorded. We then performed histological examination of the sites where the PLSS data were collected (see supplementary section of [26] for more detailed methods). Comparing nuclear sizes in the H&E image with the PLSS result, we observed reasonable agreement (Fig. 12.12).

We performed in vivo measurements using EPSS during ten routine clinical endoscopic procedures for patients with suspected dysplasia at the Interventional Endoscopy Center (IEC) at Beth Israel Deaconess Medical Center (BIDMC). Patients reporting to the IEC at BIDMC had undergone initial screening at other institutions and were referred with confirmed BE and suspicion of dysplasia. Our protocols were reviewed and approved by the BIDMC Institutional Review Board.

Patients reporting for routine screening of Barrett's esophagus who had consented to participate in our study were examined. The EPSS polarized fiber-optic probe was inserted into the working channel of the gastroendoscope, and the gastroenterologist introduced the endoscope through the mouth. The EPSS instrument performed optical scanning of each complete, continuous region of the luminal esophageal wall chosen for examination by the gastroenterologist. Data from the optical scans were recorded for each linear and angular position of the probe tip as parallel and perpendicular polarization reflectance spectra, corrected for light source intensity and lineshape. The backscattering spectrum at each individual spatial location was extracted by subtracting perpendicular from parallel polarized reflectance spectra. The backscattering spectra were then normalized to remove amplitude variations due to peristalsis. The mean of the normalized spectra was calculated. The difference from the mean for each site was calculated, squared, and summed over all spectral points. A site was considered likely to be dysplastic if this parameter was greater than 10 % of the summed mean squared. No data points are needed for calibration of this simple diagnostic rule. This analysis is straight-forward and can be done in real time. By extracting the nuclear size distributions from the backscattering spectra for each individual spatial location, we found that this simple rule is approximately equivalent to a contribution of greater than 25 % from enlarged nuclei over 10 µm in diameter (Fig. 12.13).

Fig. 12.12 Bovine lower-portion esophagus epithelium. (**a**) H&E staining. (**b**) Comparison of the nuclear size distributions extracted from the EPSS instrument measurements on intact epithelium (*solid curve*) and histological examination of the corresponding H&E stained sections (*dots*) (From Ref. [26])
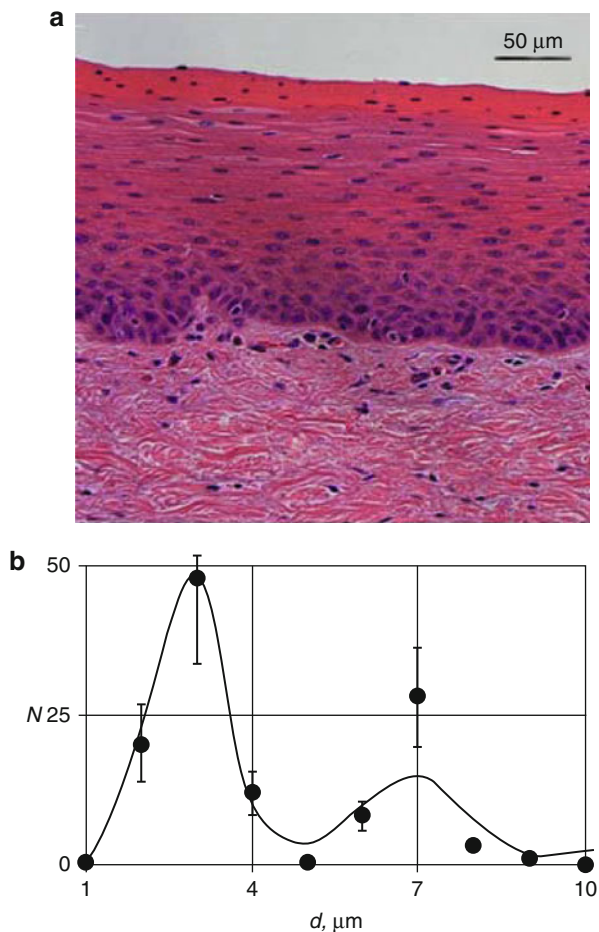
Two observations support the clinical feasibility of this method. First, spectroscopic data collected during clinical procedures confirm that the polarization technique is very effective in removing unwanted background signals. Second, the issue of peristaltic motion is addressed in the EPSS instrument. During a procedure, it is difficult to maintain a fixed distance between the optical probe head and the esophageal surface, due to peristaltic motion and other factors. Therefore, an important feature of the EPSS instrument is its ability to collect spectra of epithelial tissue that are not affected by the orientation or distance of the distal probe tip to the mucosal surface. This is achieved with collimated illumination and collection optics. Analysis of parallel polarization spectra collected at ten BE locations during a standard clinical procedure showed that although amplitudes of the spectra differ from point to point, the spectral shape is practically unchanged, and, more importantly, the oscillatory structure containing diagnostically significant information is intact.
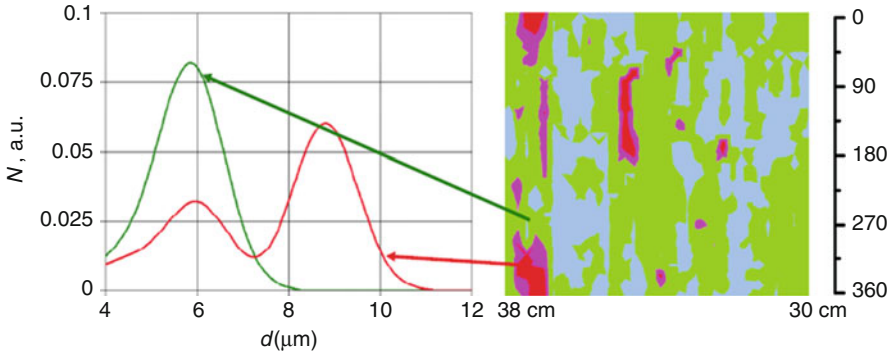
Fig. 12.13 Nuclear size distributions for one high-grade dysplasia site and one nondysplastic site in BE of one of the patients. Dark (*red* and *pink* online) regions of the map indicate areas suspicious for dysplasia based on nuclear size distributions extracted from the backscattering spectra for each individual spatial location. Nondysplastic BE sites had nuclear size distributions centered about 5–6 μm diameter, while sites marked as suspicious for dysplasia have nuclear size distributions with a main peak centered from 9 to 15 μm. The *arrows* indicate the specific locations on the esophageal surface from which the size distributions extracted from the polarized LSS data (From Ref. [26])

During the initial stage of the project, we collected a total of 22,800 EPSS spectra in ten clinical procedures, covering the entire scanned regions of the esophagus. We validated the capabilities of the clinical method by comparing EPSS data with subsequent pathology at each location where biopsies were taken. For the first two patients, pathology was reported per quadrant not per biopsy. For the other patients, 95 biopsies were collected at EPSS locations given by their distances from the mouthpiece of the endoscope and their angles relative to the start of the EPSS scan. Pathological examination revealed a total of 13 dysplastic sites out of which 9 were high-grade dysplasia (HGD). The rest of the sites were diagnosed as nondysplastic BE.

The diagnostic parameters for each EPSS location were extracted from the backscattering spectra, that is, the residuals of the parallel and perpendicular spectral components collected by the EPSS instrument. The results are presented in the form of pseudocolor maps. Double-blind comparison of the EPSS maps with the biopsy reports revealed 11 true positive (TP) sites, 3 false positive (FP) sites, 80 true negative (TN) sites, and 1 false negative (FN) site. Thus, EPSS measurements are characterized by sensitivity of 92 % and specificity of 96 %.

Several BE patients enrolled in our study who underwent routine endoscopy and biopsy with EPSS, pathology revealed no dysplasia, and the patients were dismissed. However, in some of these patients, the EPSS scan indicated probable sites of focal dysplasia, which were located in regions where biopsies had not been taken. One of the patients was recalled, and biopsies were taken at the three sites indicated by EPSS in addition to the standard-of-care protocol. Pathology confirmed HGD in all three EPSS-directed biopsies and one more HGD at a point located between two EPSS-indicated sites (Fig. 12.14). The latter site, considered to
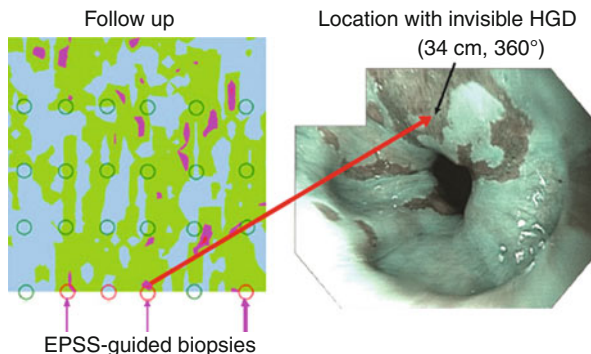
Fig. 12.14 Biopsies taken during the initial and follow-up endoscopy procedures for patient A, overlaid on the EPSS map acquired during the initial procedure (*left panel*). Three follow-up biopsies were guided by the EPSS map and pathology confirmed HGD for each (indicated at 360°). High-resolution endoscopic (HRE) image of a location with invisible HGD (*right panel*) with narrow band imaging (NBI) enabled. Video capture was acquired in subject A at one of the locations where invisible dysplasia was missed by visual examination by HRE with NBI, but located by EPSS, and later confirmed by pathology. The site is marked by an *arrow*. Note that the site is visually indistinguishable from the surrounding nondysplastic BE tissue (From Ref. [26])

be a false negative, is very close to the sites indicated by EPSS and may arise from imperfect correspondence of actual biopsy site with EPSS-mapped site (a problem which will be addressed in future instrument and algorithm development). The patient now has been given radio frequency ablation (RFA) treatment.

These focal dysplasias missed by standard-of-care procedures, which blindly biopsy a tiny fraction of esophageal tissue according to a prescribed protocol, but were caught and confirmed by the capability of EPSS to examine the entire esophageal epithelium millimeter-by-millimeter and detect dysplastic cells – enabling early treatment and in all likelihood saving patients' esophagi, and perhaps their lives.

The frequency of dysplasia in our patient sample is consistent with that of the prescreened patient population referred to the BIDMC IEC for confirmation and treatment but is higher than would be expected in the general BE patient population. In fact, the rarity of HGD detection in the general population of BE patients underscores the importance of having a more comprehensive and effective method for gastroesophageal cancer screening.

12.4 Confocal Light Absorption and Scattering Spectroscopic Microscopy

Recently, a new type of microscopy that employs intrinsic optical properties of tissue as a source of contrast has been developed [28]. This technique, called confocal light absorption and scattering spectroscopic (CLASS) microscopy, combines LSS with confocal microscopy. In CLASS microscopy, light scattering
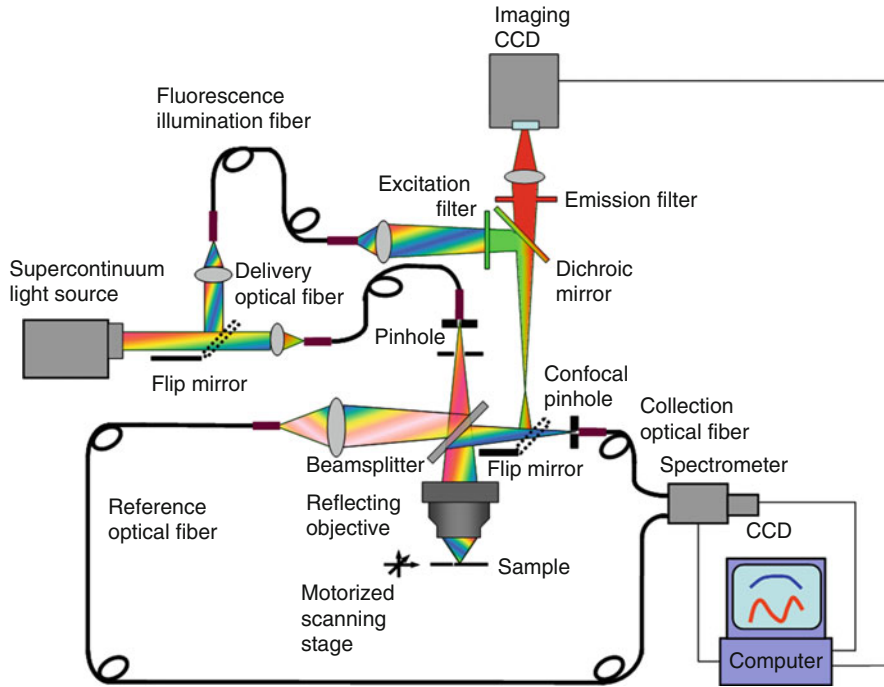
Fig. 12.15 Schematic of the prototype CLASS/fluorescence microscope (From Ref. [28])

spectra are the source of the contrast. Another important aspect of LSS is its ability to detect and characterize particles well beyond the diffraction limit.

A schematic of the CLASS microscope is shown in Fig. 12.15. System design of the CLASS microscope provided for broadband illumination with either a Xe arc lamp for the measurements performed on extracted organelles in suspension or a supercontinuum laser (Fianium SC-450-2) for the measurements performed on organelles in living cells. Both sources used an optical fiber to deliver light to the sample. To insure that CLASS microscopy detects organelles inside living cells and correctly identifies them, Itzkan et al. [28] complimented the CLASS instrument with a wide field fluorescence microscopy arm, which shares a major part of the CLASS optical train.

Depth-sectioning characteristics of a CLASS microscope can be determined by translating a mirror located near the focal point and aligned normal to the optical axis of the objective using five wavelengths spanning the principal spectral range of the instrument (Fig. 12.16). The half-width of the detected signal is approximately 2 μm, which is close to the theoretical value for the 30 μm pinhole and 36× objective used [29]. In addition, the shapes of all five spectra shown in Fig. 12.16 are almost identical (500, 550, 600, 650 and 700 nm), which demonstrates the excellent chromatic characteristics of the instrument. Small maxima and minima on

Fig. 12.16 Depth sectioning of CLASS microscope along vertical axis (From Ref. [28])
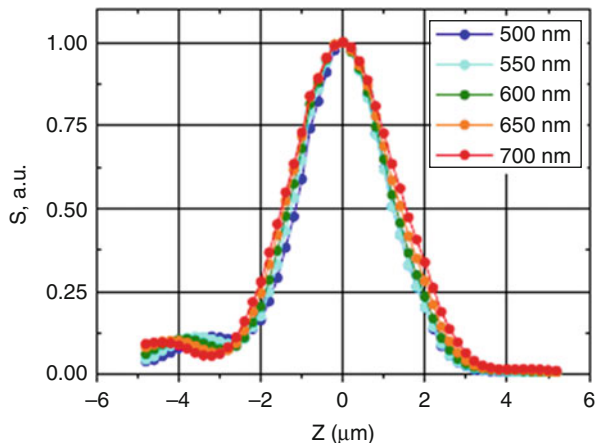
either side of the main peak are due to diffraction from the pinhole. The asymmetry is due to spherical aberration in the reflective objective [30].

Itzkan et al. [28] tested the combined CLASS/fluorescence instrument on suspensions of carboxylate-modified Invitrogen microspheres, which exhibit red fluorescence emission at a wavelength of 605 nm with excitation at 580 nm. The microspheres were effectively constrained to a single-layer geometry by two thin microscope slides coated with a refractive index matching optical gel. Figure 12.17a shows (from left to right) the fluorescence image of the layer of 1.9-μm-diameter microspheres, the image reconstructed from the CLASS data, and the overlay of the images. Figure 12.17b shows a mixture of three sizes of fluorescent beads with sizes 0.5, 1.1, and 1.9 μm mixed in a ratio of 4:2:1. Note the misleading size information evident in the conventional fluorescence images. A 0.5-μm microsphere which is either close to the focal plane of the fluorescence microscope or carries a high load of fluorescent label produces a spot which is significantly larger than the microsphere's actual size. The CLASS image (middle of Fig. 12.17b), on the other hand, does not make this error and correctly reconstructs the real size of the microsphere. One also can see that prior fluorescence labeling does not affect the determination of the objects with CLASS measurements.

To confirm the ability of CLASS to detect and identify specific organelles in a live cell, Itzkan et al. [28] performed simultaneous CLASS and fluorescence imaging of live 16HBE14o- human bronchial epithelial cells, with the lysosomes stained with a lysosome-specific fluorescent dye. The fluorescence image of the bronchial epithelial cell, the CLASS reconstructed image of the lysosomes, and the overlay of two images are provided in Fig. 12.17c. The overall agreement is very good; however, as expected, there is not always a precise, one-to-one correspondence between organelles appearing in the CLASS image and the fluorescence image. This is because the CLASS image comes from a single, well-defined confocal image plane within the cell, while the fluorescence image comes from several focal "planes" within the cell, throughout the thicker depth of field produced
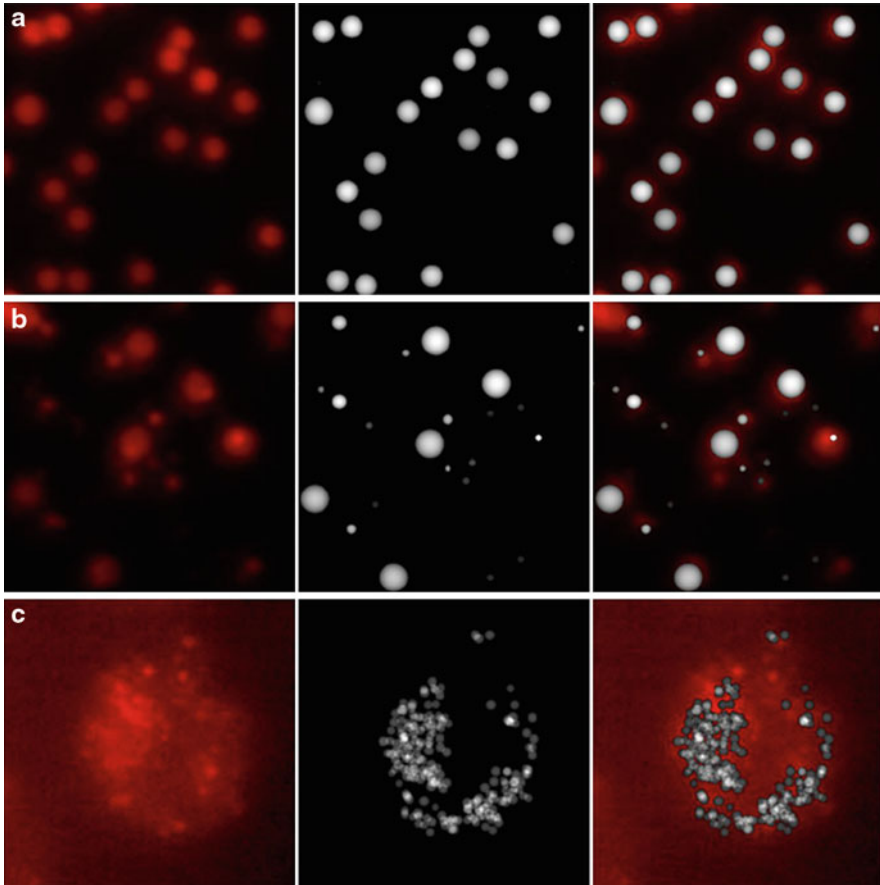
Fig. 12.17 Fluorescence image of the suspensions of carboxylate-modified 1.9-µm-diameter microspheres exhibiting red fluorescence (*left side*), the image reconstructed from the CLASS data (*middle*), and the overlay of the images (*right side*) (**a**). Image of the mixture of three sizes of fluorescent beads with sizes 0.5, 1.1, and 1.9 µm mixed in a ratio of 4:2:1 (*left side*), the image reconstructed from the CLASS data (*middle*), and the overlay of the images (*right side*) (**b**). Image of live 16HBE14o- human bronchial epithelial cells with lysosomes stained with lysosome-specific fluorescence dye (*left side*), the image reconstructed from the CLASS data (*middle*), and the overlay of the images (*right side*) (**c**) (From Ref. [28])

by the conventional fluorescence microscope. Thus, in the fluorescence image, Itzkan et al. [28] observe the superposition of several focal "planes" and therefore additional organelles above and below those in the single, well-defined confocal image plane of the CLASS microscope.

Figure 12.18 shows the ability of CLASS microscopy to do time sequencing on a single cell. The cell was incubated with DHA for 21 h. The time indicated in each image is the time elapsed after the cell was removed from the incubator. In this figure, the nucleus, which appears as the large blue organelle, has its actual shape
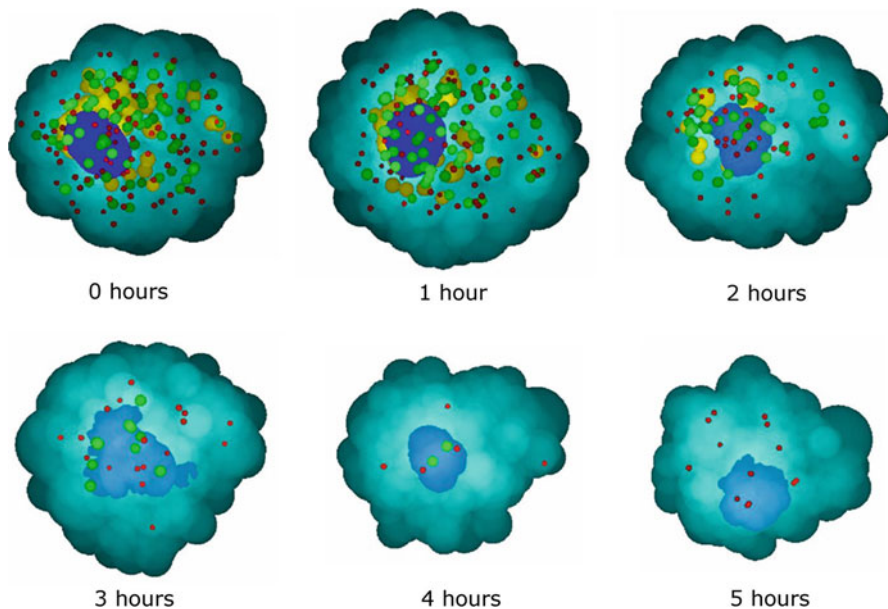
Fig. 12.18 The time sequence of CLASS microscope reconstructed images of a single cell. The cell was treated with DHA and incubated for 21 h. The time indicated in each image is the time elapsed after the cell was removed from the incubator (From Ref. [28])

and density reconstructed from the CLASS spectra. The remaining individual organelles reconstructed from the CLASS spectra are represented simply as spheroids whose size, elongation, and color indicate different organelles. The shape of the nucleus has changed dramatically by the third hour, and the nuclear density, indicated by color depth, has decreased with time. The organelles are almost completely vanished by 4 h.

Since CLASS microscopy requires no exogenous labels, thus avoiding their potential interference with cell processes, it is applicable to viable cell and tissue preparations, enabling the observation of cell and organelle functioning at scales on the order of 100 nm. Applications for CLASS microscopy in such diverse areas as prenatal diagnosis, in vitro fertilization (IVF), or drug discovery are all linked by the potential of this technique to observe functional intracellular processes nondestructively.

Human embryo development and quality, as well as response to environmental factors, might be monitored progressively at all critical stages, using CLASS. Since the CLASS measurement is nondestructive and requires no exogenous chemicals, a given embryo in vitro could be monitored over time before implantation. These kinds of progression studies are not possible with the techniques currently available.

An important part of the drug discovery process is to monitor changes in organelle morphology in cells treated with compounds being screened for

therapeutic or toxic effects. Currently, imaging using numerous fluorescence markers [31] and electron microscopy using nonviable cell preparations [32–34] are being used to detect these changes. However, CLASS could be used to monitor organelle responses in multiple cell lines in parallel, in real time, using viable cells with no exogenous markers. Not only would CLASS enable more rapid screening but also would provide results more likely to be predictive of animal and ultimately human outcomes.

12.5   Principles of Raman Scattering Spectroscopy

The Raman effect, known since the early 1920s, is an inelastic light scattering process. Energy is exchanged between the incident field and the scattering medium, leaving each in a different state as a result of the scattering event. Typically, the quanta exchanged are on the order of molecular vibrational energies. The frequency of the scattered light may be lower than (Stokes scattering) or higher than (anti-Stokes scattering) that of the incident light, and the scattering molecules will be left in higher or lower vibrational states, respectively.

The change in frequency in the scattered light corresponds to the energy difference between the initial and final vibrational states of the scattering molecule and is independent of the incident light wavelength. Hence, the typical Raman scattering spectrum represents the ground state vibrational spectrum of molecules in the scattering medium and is therefore unique to each molecular species. The Raman spectrum displays the intensity of scattered light as a function of the difference in frequency between the scattered and the incident light. Since each molecular species has its own unique set of molecular vibrations, the Raman spectrum of a particular species will consist of a series of peaks or bands of scattered light, each shifted from the incident light frequency by one of the characteristic vibrational frequencies of that molecule.

Though the effect has been known for almost a century, it is only within the last few decades that Raman spectroscopy has flourished as a powerful molecular spectroscopy technique. Widespread use had to await the advent of lasers and more recently high quantum efficiency detectors to compensate for the extremely low efficiency of Raman scattering. The intensity of Stokes Raman-scattered light is typically 10^{-7} to 10^{-15} the intensity of the excitation light, and for anti-Stokes Raman, it is even less. Thus, real-time monitoring or detection of Raman scattering spectra was not practical until the commercial development of lasers and subsequent advances in detector technology, which in turn facilitated an enormous number of applications and growth in the related Raman literature (see, e.g., Ref. [35] and its citations, Refs. [36, 37, 38]).

In this chapter, we will limit the discussion of Raman spectroscopy to two of the most exciting developments of the past decade: biomedical near-infrared Raman spectroscopy (NIRRS), for in vivo medical diagnosis, and surface-enhanced Raman spectroscopy (SERS) for biological, biomedical, and nanotechnology-related material science.

12.6 Applications of Raman Spectroscopy

12.6.1 Near-Infrared Raman Spectroscopy for In Vivo Biomedical Applications

Technological advances in excitation sources, spectrographs, detectors, and optical fibers, as well as realization that Raman spectroscopy can provide chemical composition, molecular structure, and molecular interactions in cells and tissues, brought substantial interest to the medical applications of near-infrared Raman spectroscopy. These applications and corresponding instrumentation have been most recently reviewed by several authors [38–43]. We will summarize major issues and successes of near-infrared Raman spectroscopy (NIRRS) using material from these reviews and adding results reported later.

Figure 12.19 is a depiction of a generic Raman system. The excitation source sends light to the sample. The collector directs the scattered light through the excitation rejection filter into the spectrograph. The excitation rejection filter blocks light at the excitation wavelength from reaching the spectrograph. The spectrograph disperses the scattered light so that light intensity at each wavelength can be measured. The detector transforms the light exiting the spectrograph into electrical signals so that the radiation at each wavelength is still distinguishable. The signals are then digitized and sent to a computer, where all signal processing and spectrum extraction is produced. Each component of the system has been dramatically improved in the last 5–10 years to enable successful in vivo biomedical applications. First, we will discuss the spectral range for the system.

12.6.2 Why Near-Infrared Excitation?

Most biological tissues fluoresce when excited by visible or near UV wavelengths (within 300–700 nm), and the fluorescence is usually a broadband signal within the same spectral range as the Stokes Raman spectrum. In most tissues, the fluorescence cross section is about 6 orders of magnitude stronger than the Stokes Raman cross section; thus, the fluorescence signal can overwhelm the tissue Raman spectrum. Two strategies for reducing fluorescence interference are to use near-infrared (NIR) excitation or UV resonance excitation (Fig. 12.20, modified from Ref. [40]).

As one can see from Fig. 12.20, Raman scattering at different excitation wavelengths, UV, visible, and NIR, produces the same change in vibrational energy; therefore, the excitation wavelength can be chosen to avoid spectral interference by fluorescence. For visible excitation, the fluorescence light frequency and Raman-scattered light frequency are similar. This leads to intense fluorescence background in visible excitation Raman spectra. NIR light has too low frequency to excite fluorescence, while for UV excitation, the fluorescence light frequency is much lower than the Raman-scattered light frequency. Hence, using UV or NIR excitation can reduce fluorescence background in the Raman spectrum.
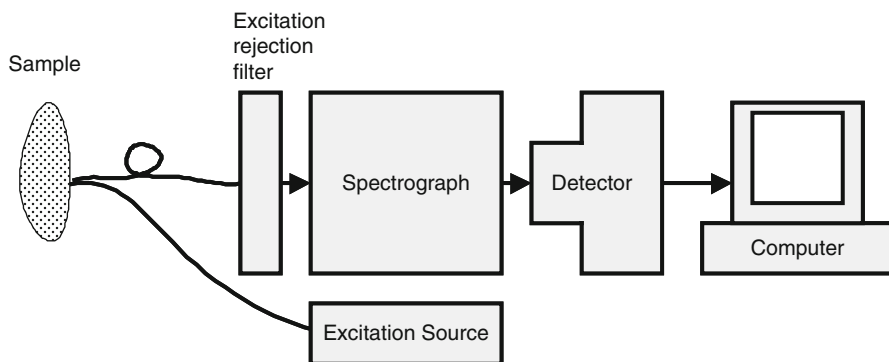
Fig. 12.19 Block diagram for generic Raman system
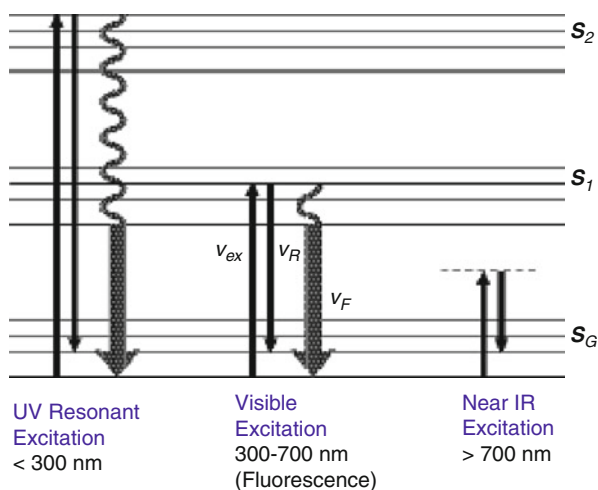
Fig. 12.20 Raman effect: UV, visible, and NIR excitation strategies. S_0, ground electronic state; S_1 and S_2, excited electronic states. The horizontal lines indicate vibrational energy levels. The diagram shows how a molecule in the ground state, S_0, can make a transition from the lowest vibrational level to the first excited vibrational level by means of Raman scattering. Thin *upper arrows* indicate the frequency of the laser excitation light; *thin down-arrows* indicate frequency of the Raman-scattered light. The difference in length between *thin up-* and *down-arrows* indicates molecular vibration frequency. *Thick arrows* indicate frequency of the fluorescence light

Most materials, including tissue, exhibit reduced fluorescence emission as the excitation wavelength increases into the NIR region. Thus, fluorescence interference in tissue Raman spectra can be greatly reduced by using NIR excitation. Another approach would be to use excitation wavelengths in the ultraviolet (UV) range. Background fluorescence is suppressed in tissue Raman spectra for

excitation wavelengths below about 270 nm. However, the tissue penetration of the UV excitation is limited (tens of microns), and, in addition, it has a risk of causing tissue damage through mutagenesis.

12.6.3 Near-Infrared Raman Spectroscopy System

Currently, the two most commonly used instrument design approaches for acquiring Raman spectra in the NIR spectral range are the Fourier transform (FT) spectrometer and the dispersive imaging spectrograph. The FT-Raman spectrometer was introduced earlier (in the 1980s). Usually a Nd:YAG laser (a flash lamp or diode-pumped solid-state laser emitting at 1,064 nm) is used to excite the sample, and the resulting Raman signal is detected using an interferometer with a single-element detector. Nd:YAG lasers have excellent beam quality and a range of available power. When diode lasers replace the lamp as a source of optical pumping for these lasers, it reduces thermal effects and improves pumping stability, thus increasing the overall S/N by reducing flicker noise.

High-throughput and averaging rate makes FT-Raman systems attractive for biomedical applications. In addition, the introduction of high-quality solid-state lasers and laser diodes at different wavelengths and detectors with high sensitivity, S/N, and broad dynamic range for these wavelengths provides the FT-based Raman spectrometer with flexibility unsurpassed by dispersive systems, especially, for in vitro applications. However, for in vivo applications, FT-based systems are much too bulky and vibration sensitive. There are some attempts to make the scanning interferometer for the Fourier transform without mechanically moving parts. So far, they have not reached an acceptable level of performance or cost-effectiveness.

The present state-of-the-art NIRRS instrument for in vivo applications capable of rapid collection of spectra in a mobile and physician-friendly setup is based on the dispersive system. This system consists of a NIR semiconductor laser, a suitable fiber-optic probe that illuminates the tissue with laser light and collects scattered light, and a high numerical aperture imaging spectrograph equipped with a cooled CCD camera that are both optimized for the NIR region. This system has a limitation of how far into the NIR spectral range the excitation can be moved to suppress fluorescence of tissue. Most CCD detectors in use today are silicon based. Their sensitivity rolls off sharply at 1,000 nm. There are specially developed silicon CCD arrays sensitive to 1,100 nm, with low quantum efficiency after 1,000 nm. Thus, excitation wavelengths longer than $\sim$800 nm would not be useful with this detector for observing vibrational transitions above about 2,500 cm^{-1}, although tissue fluorescence still can be substantial with this 800 nm excitation. Hanlon et al. [40] discussed several experimental and mathematical methods, which can be used for reducing the fluorescence component of biological Raman spectra. However, the fluorescence signal decreases the useful dynamic range of the CCD detector and that can be a critical issue for measurements of trace chemical species in the tissue or when high resolution of measurements is required.

Despite these limitations, cooled CCD-based systems with compact high-quality imaging spectrographs and semiconductor lasers are the preferred configuration for clinical NIRRS systems.

Recently, the advances in the integrated circuits development led to development of InGaAs photodiode array detectors hybridized with a CMOS readout multiplexer (e.g., Sensors Unlimited, Inc., Princeton, NJ) that should provide improved noise characteristics. The InGaAs photodiode has a spectral response from 900 to 1,700 nm with quantum efficiency greater than 70 % from 1,000 to 1,600 nm. Use of this type of detector should allow using semiconductor lasers with wavelengths well above 1,000 nm, further diminishing the tissue fluorescence background and broadening the range of biomedical applications for NIRRS.

In NIRRS, the two most widely used dispersive spectrograph configurations are the off-axis reflective and the axial transmissive [44, 45]. The off-axis reflective configuration is the Czerny-Turner design with off-axis mirrors as collimators and reflective gratings in the collimated space. The off-axis configuration suffers from strong astigmatism, which can be greatly reduced by using toroidal mirrors for collimation (see, e.g., SpectraPro series from Acton Research Corporation, Acton, MA). The spectrographs with this configuration are generally available with f-number not less than 4. As a result, the numerical aperture of the entering beam has to be limited to reduce the stray light in the spectrograph. This is especially important for fiber probe collection since the numerical aperture of the entering beam is limited by the probe fiber numerical aperture [46].

Relatively few design options are available on the market for the dispersive spectrograph with axial transmissive configuration (see, e.g., HoloSpec series from Kaiser Optical Systems, Inc., Ann Arbor, MI). This transmissive configuration uses lenses to collimate the beam and places them very close to a volume holographic transmissive diffraction grating. This permits f-numbers <4 without compromising on resolution and provides a very compact commercial package. As a result, this configuration allows for efficient coupling with fiber-optic probes. It was shown that this configuration has an advantage of about 2 or more over the off-axis reflective design [47]. Usually multielement lenses are required to provide adequate chromatic correction for Raman spectra and have good quality over the image plane [48].

The main disadvantage of the axial transmissive configuration is wavelength inflexibility. Fixed gratings may need to be changed for different excitation wavelengths or detection ranges. The low f-number lenses can be chromatically corrected only for a limited wavelength range, thus requiring refocusing or changing lenses for different excitation wavelengths as well.

12.6.4 Rejection Filter

Another critical component is the excitation rejection filter. The intensity of the Raman-scattered signal in NIR is about 10^{-10} times that of the excitation intensity; thus, the backscattered excitation light should be rejected from getting into the

spectrograph and, if possible, into the collection fiber. The current choice for achieving this rejection is a notch rejection filter. This filter usually transmits about 10^{-4} to 10^{-8} in a narrow band at the wavelength of the excitation laser and about 80 % for the wavelength regions of the Stokes and anti-Stokes Raman spectra. The most popular choice for excitation rejection filters in Raman spectroscopy is the holographic filters. Holographic notch filters are excellent filters for removing the laser line and are available in a variety of wavelengths (see, e.g., holographic notch filters from Kaiser Optical Systems, Inc., Ann Arbor, MI; www. kosi.com). They have practically replaced the second and third stages of traditional Raman spectrometers [49]. The holographic notch filters are widely used in a variety of NIRRS applications and provide excellent performance. It should be mentioned that another choice for the rejection notch filter could be a multiplayer dielectric interference filter (see, e.g., Omega Optical Inc., Brattleboro, VT; www. omegafilters.com). These filters can provide rejection on the laser wavelength greater than five orders with the Raman spectra ∼70 %. The advantage of these filters is that they are relatively inexpensive. The major drawback is that there is filter ringing at the Raman-scattered wavelengths caused by the multilayer structure of these filters. Also, the spectral width of the rejection notch is greater than that of the holographic notch filter. However, these filters offer reasonable alternatives that would be worth considering when the cost of the system is important.

12.6.5 Fiber Optics

The fiber probe can easily measure exposed areas of the body, such as skin, hair, nails, and areas of the mouth. Fiber probes can also be miniaturized and incorporated into endoscopic probes or biopsy needles or internal analysis. This is the most critical component of the NIRRS system. First of all, this component couples the system with the sample to be examined. Thus, it has to be implemented so as to maximize the system performance, requiring customization for the specifics of the measurement objective. Secondly, it is the component that brings the excitation light into the tissue and collects the emitted light from the tissue. Thus, this is the place in the system where both signals are present. The relative intensity of the Raman-scattered signal in NIR is about 10 orders of magnitude lower than the excitation intensity; thus, any interference of the excitation light with the optical and photoelectrical path of the Raman signal may create a background effectively completely obstructing the Raman signal. For example, the back reflection of the fiber end, even if antireflection coated, 1 % of the excitation light reflected through the fiber is still eight orders of magnitude greater than Raman signal. Though the reflected excitation light can be rejected with a notch filter, the fluorescence and Raman scattering induced by the excitation light traveling back through the fiber may be at about the same wavelength as the tissue Raman. There are processing methods to separate fast changing Raman spectra from slow changing fluorescence spectra, but these methods do not help against fiber Raman scattering. Again, these background signals due to the fiber itself use the available dynamic range of the

detector and induce shot noise which may decrease the signal-to-noise ratio for the tissue Raman signal to an unusable level. New fiber materials have reduced these effects, although very weak tissue Raman signals may still be obscured. Also, a beveled fiber exit surface has been explored and showed to decrease this reflection. The most common arrangement currently used in the NIRRS system is a probe using two separate paths for the excitation and scattered light. Also, some designs incorporate the rejection filter up front before the collection fiber to eliminate any backscattered excitation light from getting into the collection fiber. Utzinger et al. [46] presented a comprehensive analysis of fiber probe designs in the recent review.

NIRRS applications have been reported by a number of researchers for the in vivo cancer and precancerous conditions for various tissues (brain, breast, cervix, bladder), for other disease diagnosis (skin studies, Alzheimer's disease, atherosclerotic plagues), and blood analysis. We have cited earlier several recent reviews [38–43], where there are comprehensive discussions and citations of these reports. Here we will review the three latest reports of NIRRS applications for in vivo precancerous conditions of polyps [50], in vivo cervical precancers [51], and analysis of whole blood ex vivo [52].

12.7 Near-Infrared Raman Spectroscopy for In Vivo Disease Diagnosis

During the last decade, NIRRS has been applied for in vivo diagnosis of various diseases. To illustrate diagnostic potential of NIRRS, we will review three applications of this technique for detection of colon and cervical cancer and also blood analysis.

Recently, Molckovsky et al. [50] demonstrated that NIRSS can be used for in vivo classification of adenomatous and hyperplastic polyps in the GI tract. To achieve that, researchers used an in-house built NIRRS endoscopic system [53] comprised of a tunable laser diode emitting at 785 nm, a high-throughput holographic spectrograph, and a liquid nitrogen-cooled CCD detector. The schematic diagram of this system is presented in Fig. 12.21.

Researchers used custom-made fiber-optic Raman probes (Enviva Raman probes, Visionex, Inc., Atlanta, GA). The probes consisted of a central 400-μm-core-diameter excitation fiber surrounded by seven collection fibers 300 μm core diameter each. The probes employed internal filters, which significantly reduced interfering fluorescence and Raman background signals generated in the fiber optics.

An ex vivo study used for analysis a total of 33 polyps from 8 patients. When the large polyps were retrieved in multiple fragments, ex vivo Raman spectra were collected from individual polypectomy specimens. Thus, a total of 54 spectra were available for analysis (20 hyperplastic, 34 adenomatous). A preliminary in vivo study was carried out whereby a total of 19 spectra, each corresponding to a different measurement site, were collected from 9 polyps (5–30 mm in size) in 3 patients. The polyps were histologically classified as hyperplastic
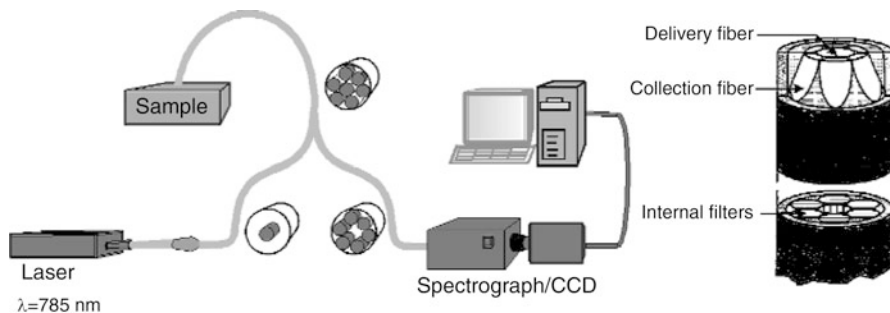
Fig. 12.21 Schematic diagram of Raman spectroscopic system and filtered fiber-optic probe (From Ref. [50])

(9 spectra/specimens, 5 polyps, 2 patients) or adenomatous (10 spectra/specimens, 4 polyps, 3 patients).

The average ex vivo Raman spectrum of adenomatous polyps versus that of hyperplastic polyps is shown in Fig. 12.22a (from Ref. [50]). Similarly, Fig. 12.22b contrasts the average in vivo Raman spectra of these 2 polyp types. In both ex vivo and in vivo settings, typical tissue Raman peaks were identified at 1,645–1,660, 1,450–1,453, 1,310, 1,260, and 1,003 cm^{-1}, which correspond, respectively, to the protein amide I band, CH_2 bending mode, CH_2 twisting mode, protein amide III band, and the phenyl ring breathing mode [53, 54].

The diagnostically important spectral differences found in the Molckovsky et al. [50] study were used to develop PCA/LDA-based diagnostic algorithm. With the limited number of samples, the predictive accuracy of the classification algorithm developed was estimated by using a leave-one-out cross-validation technique. Using this technique, the classification of colon polyps ex vivo identified adenomatous polyps with a sensitivity of 91 %, a specificity of 95 %, and an overall accuracy of 93 %. For the in vivo data set, the algorithm identified adenomas with a sensitivity of 100 %, a specificity of 89 %, and an accuracy of 95 %.

We believe the larger NIRRS studies in the GI tract should be very important. The reward of these studies (both in vivo and ex vivo) would be a step toward understanding what NIRRS is really measuring and how it relates to disease progression since it may establish the connection between the NIRRS extracted biochemical changes and the bimolecular chemistry and cell biology of the disease. Further development along these lines may advance our understanding of the connection between cancerous processes at the single cell level and various levels of neoplastic conditions and invasive tumors.

Detection of cervical precancer using NIRRS was recently reported by Utzinger et al. [51] in the in vivo pilot study where histopathologic biopsy was used as the gold standard. The block diagram of the system for collection of the spectra from the cervical epithelium in vivo is shown in Fig. 12.23 (from Ref. [51]).

It includes a diode laser at 789 nm coupled to a fiber-optic delivery and collection probe. The probe guides the illumination light onto the cervix and

Fig. 12.22 (a) Average Raman spectra of hyperplastic (n = 20; *solid line*) and adenomatous (n = 34; *broken line*) colon polyps collected ex vivo (power = 200 mW; 30-s collection time). (**b**) Average Raman spectra of hyperplastic (n = 9; *solid line*) and adenomatous (n = 10; *broken line*) colon polyps collected in vivo (power = 100 mW; 5-s collection time). The spectra have been intensity corrected, wavelength calibrated, and fluorescence background subtracted (From Ref. [50])
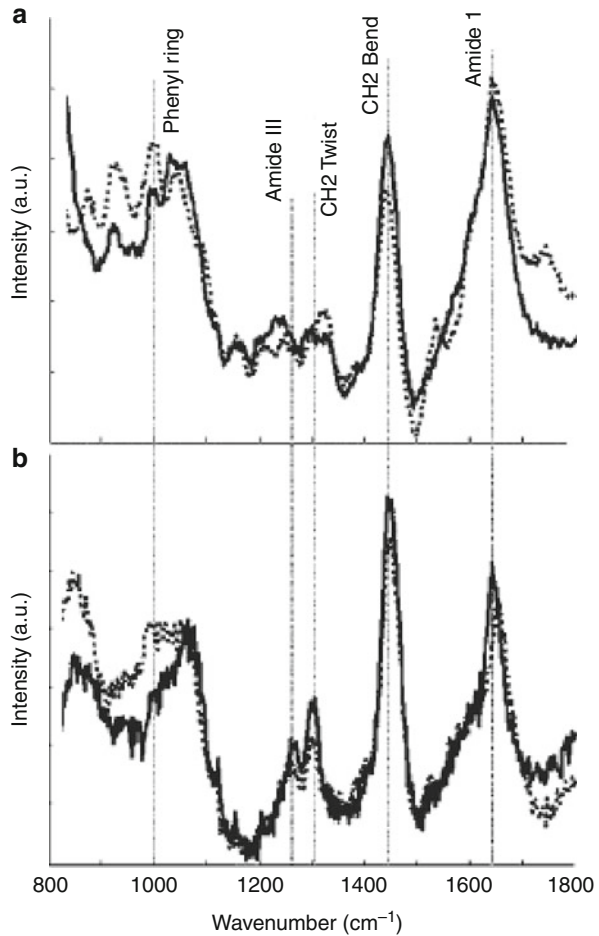
collects the resulting Raman-scattered light onto a holographic spectrograph coupled to a liquid nitrogen-cooled, back-illuminated, deep depletion, charge-coupled device (CCD) camera. The probe was optimized to measure epithelial tissue layers.

The probe was advanced through the speculum and placed in contact with a colposcopically normal and abnormal site on the cervix. Following the spectral measurement, each site was biopsied. During the cervical colposcopy, normal and abnormal areas were identified by the colposcopist, and Raman spectra were measured from one normal and one abnormal area of the cervix. Each of these sites was then colposcopically biopsied. Biopsies were submitted for routine histological analysis by a gynecologic pathologist. The pathological categories were normal cervix, inflammation, squamous metaplasia, low-grade squamous dysplasia (HPV and CIN 1), high-grade squamous dysplasia (CIN 2, CIN 3), and cancer. The pathologist was blinded to the Raman spectroscopic study.
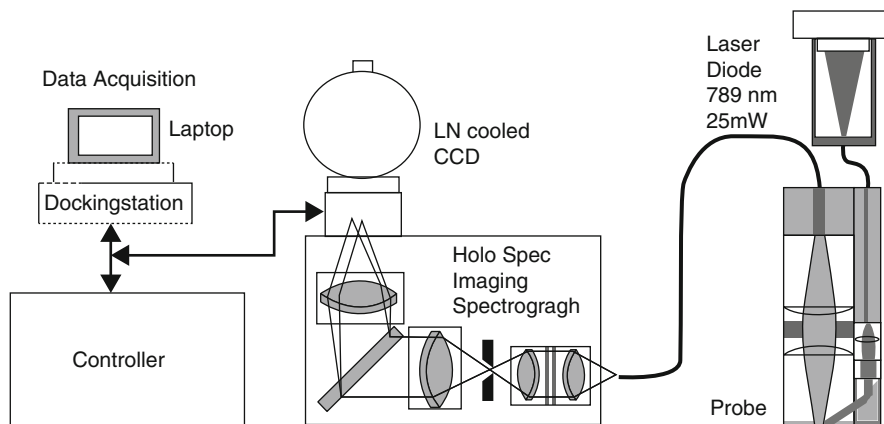
Fig. 12.23 Block diagram of system used to measure Raman spectra in vivo (From Ref. [51])

Raman spectra were grouped according to histopathologic findings, and average spectra were calculated. These average spectra were examined visually to identify a set of Raman peaks common to most spectra.

In the study, 24 measurements were made in 13 patients. Figure 12.24 (from Ref. [51]) shows average Raman spectra of each diagnostic category, normal, inflammation, metaplasia, and squamous dysplasia. The scatter plot presented in Fig. 12.25 (from Ref. [51]) shows performance of the diagnostic algorithms derived from the data.

The report [51] demonstrates the potential to measure near-infrared Raman spectra in vivo and extract potentially useful information. Spectra measured in vivo resemble those measured in vitro [55].

There are obvious visual differences in the spectra of normal cervix and high-grade squamous dysplasia in the same patient. Average spectra reveal a consistent increase in the Raman intensity at 1,330, 1,454, and 1,650 cm^{-1} as tissue progresses from normal to high-grade squamous dysplasia. These peaks are consistent with contributions from collagen, phospholipids, and DNA. However, because tissue is a complex, heterogeneous structure, definitive assignment is difficult.

The limitations of this study are that it is a pilot study with a small number of patients. The authors' experience shows that pilot studies are very useful in the development of emerging technologies; however, larger clinical trials are required to confirm these results. Improvements in hardware, measurement conditions, and training clinical staff to optimally participate in data collection are necessary and possible to allow these larger trials. Thus, NIRRS offers an attractive tool for surveying the biochemical changes that accompany the development of dysplasia.

We would add to the author's comments that perhaps a greater database of Raman spectra may allow to apply one of the statistical methods discussed in the previous report to identify differentiation criteria so that all six diagnostic categories (normal cervix, inflammation, squamous metaplasia, low-grade squamous
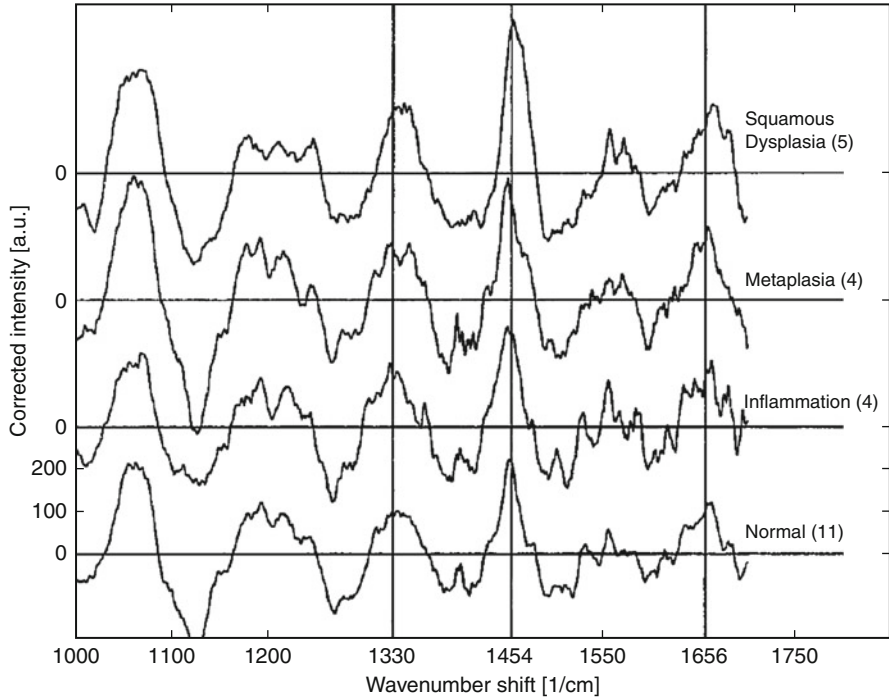
Fig. 12.24 Average Raman spectra of each diagnostic category: normal, inflammation, metaplasia, and squamous dysplasia (From Ref. [51])
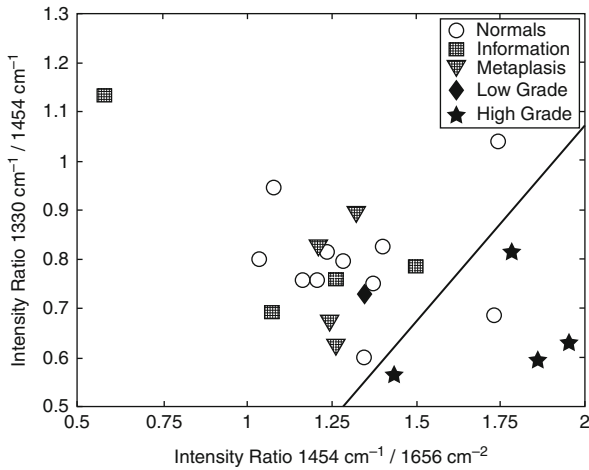
Fig. 12.25 This scatter plot indicates the intensity of each of the 24 sites measured by diagnostic category at three frequencies; the intensity ratio at 1,330/1,454 cm^{-1} is plotted against the ratio of intensities at 1,454/1,656 cm^{-1}. The straight-line algorithm separates high-grade squamous dysplasia from all others, misclassifying one normal sample (From Ref. [51])

Fig. 12.26 Schematic diagram of the Raman instrument (From Ref. [52])
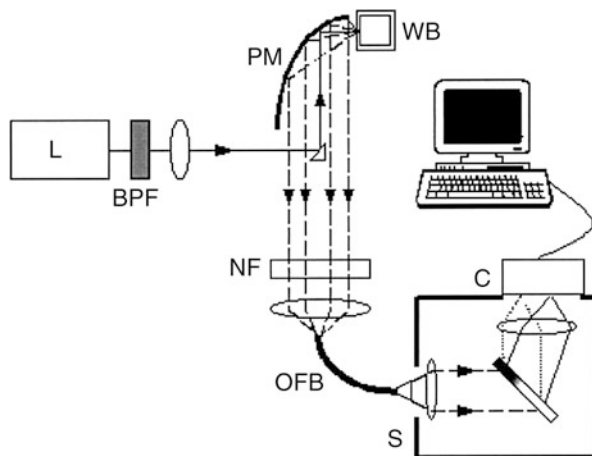
dysplasia (HPV and CIN 1), high-grade squamous dysplasia (CIN 2, CIN 3), and cancer) discussed in the report would be possible to differentiate. Also, it seems that even a simple model of the NIR Raman spectra including the Raman effective components in the tissue and the excitation and Raman radiation propagation in the tissue may provide useful improvement. Other comments made regarding the colon polyp differentiation apply here as well.

Near-infrared Raman spectroscopy has also been recently used for blood analysis. The major challenge in such analysis, even in a whole blood, lies in the presence of numerous low-concentration components, all with weak signals that are further distorted by the strong light absorption and scattering caused by the red blood cells. Enejder et al. [52] reported the application of NIRRS to analysis of whole blood with quantitative determination of multiple analytes in whole blood at clinically relevant precision. The analytes quantified are glucose, urea, cholesterol, albumin, total protein, triglycerides, hematocrit (hct), hemoglobin, and bilirubin, all of which are frequently ordered diagnostic tests used in connection with common medical conditions.

A block diagram of the NIRRS system for the whole blood measurements reported in [52] is shown in Fig. 12.26. A beam of 830-nm light from a diode laser is passed through a band-pass filter, directed toward a parabolic mirror by means of a small prism, and focused onto a quartz cuvette containing a whole blood sample. Raman-scattered light emitted from the whole blood surface (1-mm^2 area) is collected by the mirror, passed through a notch filter to reject backreflected 830-nm light, and coupled into an optical fiber bundle, which converts the circular shape of the collected light to rectangular to match the entrance slit of the spectrograph. The spectra were collected by a cooled CCD array detector.

The background subtracted Raman spectra from whole blood samples collected from 31 patients shown in Fig. 12.27 (from Ref. [52]). For each sample, 30 consecutive 10-s spectra were collected over a 5-min period. Conventional clinical laboratory methods, including absorbance spectrophotometry and automated cell counting, were used to assess the nine analytes concentration. These reference
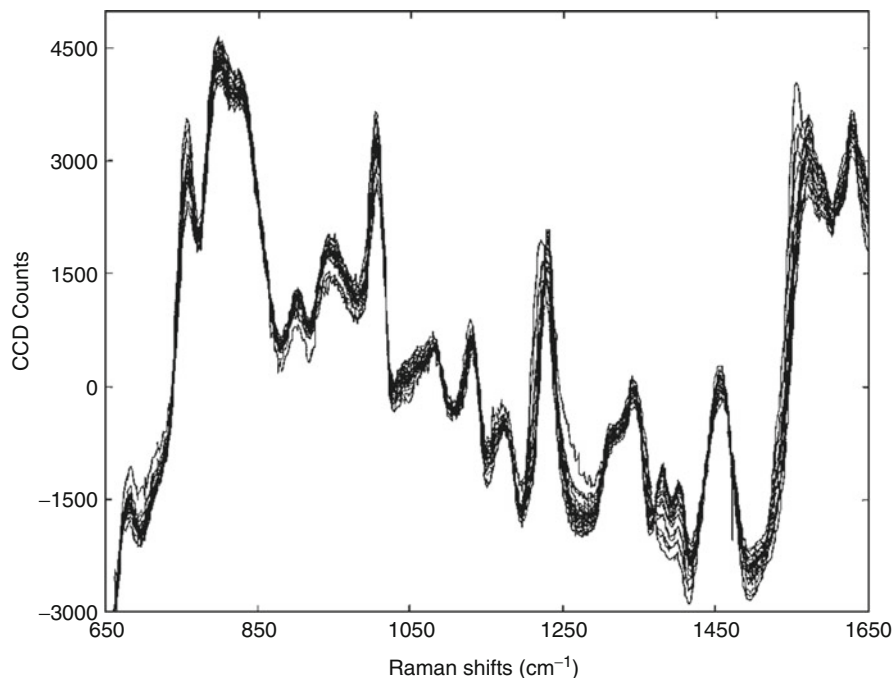
Fig. 12.27 Raman spectra of 31 whole blood samples after polynomial background subtraction (From Ref. [52])

concentrations were correlated with the recorded NIR Raman spectra and used for multivariate calibration and validation.

The accuracy of the technique was established using the cross-validation method. It was demonstrated that NIRRS could be used to extract quantitative information about bimolecular contents in whole blood at clinically relevant precision. The authors state that further improvement in prediction accuracy may be obtained by correction for variations in scattering and absorption. It is worth noting that for in vivo measurements, the tissue fluorescence may provide a very strong background. Although by subtracting the background fluorescence the effect of the background associated noise can be significantly reduced, the tissue fluorescence intensity may be high relative to the NIRRS signal from the blood. As a result, the dynamic range of the detector and the fluorescence-induced noise can complicate meaningful measurements. Further in vivo studies are required to demonstrate the applicability of the NIRRS for blood analyte measurements.

12.8 Surface-Enhanced Raman Spectroscopy

Surface-enhanced Raman scattering (SERS) is an intriguing technique based on a strong increase in Raman signals from molecules if those molecules are attached

to submicron metallic structures. Two effects are believed to contribute to the SERS enhancement mechanisms: electromagnetic effects and chemical effects [56].

When electromagnetic wave interacts with a smooth metal surface, there is a small enhancement of Raman intensities compared with that in the absence of the surface (on the order of 10 or less for metals like Ag) arising primarily from coherent superposition of the incident and reflected fields at the position of the molecule doing the scattering [57].

If the surface is rough, then enhanced local electromagnetic fields at the place of the molecule nearby the metal surface occur due to excitation of electromagnetic resonances by the incident radiation [58]. These resonances appear due to collective excitation of conduction electrons in the small metallic structures and also called surface plasmon resonances. Both the excitation and Raman-scattered fields contribute to this enhancement; thus, the SERS signal is proportional to the fourth power of the field enhancement factor [59].

The surface roughening effect can be achieved by isolated metal particle, by gratings, by assemblies of particles on surfaces, and randomly roughened surfaces. All these structures provide enhancement if the metal involved has narrow plasmon resonances at convenient frequencies for Raman measurements [57]. The chemical effects or "chemical mechanism" of enhancement is commonly defined to include any part of the surface enhancement that is not accounted for using the electromagnetic mechanism [57]. The "chemical mechanisms" include enhancements that arise from interactions between molecule and metal. The most commonly considered interaction that requires overlap between molecular and metal wavenumbers occurs when charge transfer between the surface and molecule leads to the formation of excited states that serve as resonant intermediates in Raman scattering [57]. Interactions that do not require overlap between molecular and metal wavenumbers arise from electromagnetic coupling between the vibrating molecule and the metal. These interactions can occur either at the vibrational frequency or at optical frequencies. The combined enhancement factors can be as high as 10^{14}, which is enough to observe SERS spectra from single molecules.

12.8.1   Single Molecule Detection Using Surface-Enhanced Raman Scattering

By exploiting this very high enhancement factor from surface-enhanced Raman scattering (SERS), Kneipp et al. [60] observed Raman scattering of a single crystal violet molecule in aqueous colloidal silver solution.

The excitation source was an argon-ion laser-pumped CW Ti:sapphire laser operating at 830 nm with a power of about 200 mW at the sample. Dispersion was achieved using a Chromex spectrograph with a deep depletion CCD detector. A water immersion microscope objective (363, NA 0.9) was brought into direct contact with a 30-ml droplet of the sample solution for both excitation and collection of the scattered light. Scattering volume was estimated to be approximately 30 pl.

Fig. 12.28 (**a**) Statistical analysis of 100 "normal" Raman measurements at 1,030 cm^{-1} of 1,014 methanol molecules. (**b**) Statistical analysis of 100 SERS measurements (1,174 cm^{-1} Raman line) of six crystal violet molecules in the probed volume. The *solid lines* are Gaussian fits to the data. (**c**) Statistical analysis of 100 SERS measurements (1,174 cm^{-1} Raman line) for an average of 0.6 crystal violet molecules in the probed volume. The peaks reflect the probability to find just 0, 1, 2, or 3 molecules in the scattering volume (From Ref. [60])
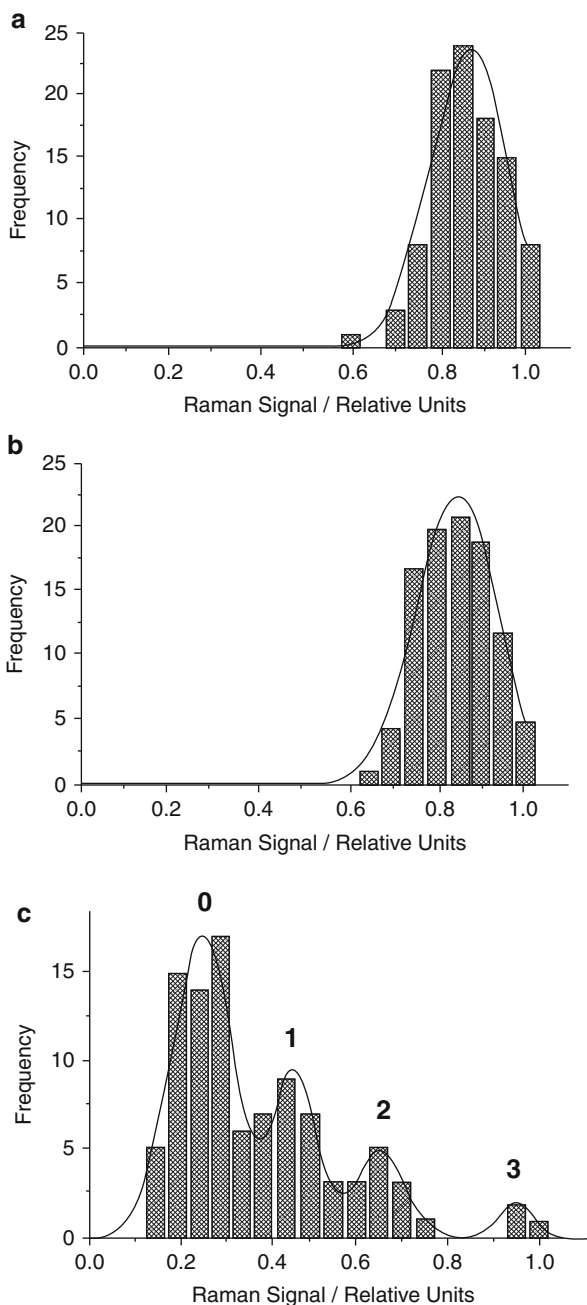
Fig. 12.29 Microscope view of (**a**) a section of a nanotube bundle touching a colloidal Ag cluster, and (**b**) SERS spectra collected along various points (1, 2, 3) on the bundle, using 830-nm CW Ti: sapphire laser excitation with a 1-mm spot size. The *black spots* in (**a**) are colloidal silver particles of different sizes that are aggregated by addition of NaCl (From Ref. [62])
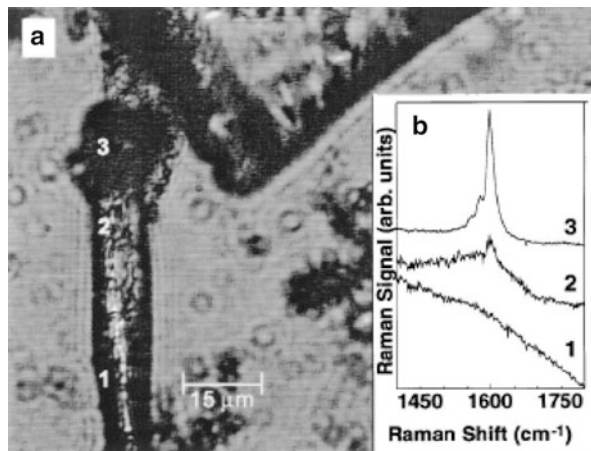
Using one second excitation time and 2×10^5 W/cm^2 nonresonant near-infrared excitation, researchers observed clear fingerprint of its Raman features between 700 and 1,700 cm^{-1}. Spectra observed in a time sequence for an average of 0.6 dye molecule in the probed volume exhibited the expected Poisson distribution for actually measuring 0, 1, 2, or 3 molecules (see Fig. 12.28).

The relatively well-"quantized" signals for 1, 2, or 3 molecules suggest relatively uniform enhancement mechanism(s) despite the nonuniform shape and size of the silver particles forming the clusters. The large SERS enhancement can be understood by favorable superposition of a very strong electromagnetic enhancement due to silver clusters, which is particularly effective at NIR excitation coupled with a strong chemical enhancement.

12.8.2 Surface-Enhanced Raman Spectroscopy of Carbon Nanotubes

Carbon nanotubes are macromolecules whose structure is honeycomb lattices rolled into the cylinders [61]. They also possess unique mechanical, electronic, and chemical properties. Raman scattering spectroscopy can be a very valuable tool in probing carbon nanotubes phonon spectra and also their electronic density of states. And since SERS is very sensitive and also it can provide information about high-energy anti-Stokes side of the excitation laser, it should be a perfect tool to study carbon nanotubes.

Recently, Kneipp et al. [62, 63] used SERS to measure narrow Raman bands corresponding to the homogeneous linewidth of the tangential C–C stretching mode in semiconducting nanotubes. Normal and surface-enhanced Stokes and anti-Stokes Raman spectra were discussed in the framework of selective resonant Raman contributions of semiconducting or metallic nanotubes to the Stokes or

anti-Stokes spectra, respectively, of the population of vibrational levels due to the extremely strong surface-enhanced Raman process and of phonon-phonon interactions.

Kneipp et al. [62] found that a very small number of tubes or perhaps even a single nanotube might be detected using SERS technique (Fig. 12.29). The strong enhancement and confinement of the electromagnetic field on a silver cluster, within domains that can be as small as 20 nm, may provide an additional high lateral resolution tool for selectively probing a small number of nanotubes that are adjacent to the interface just in such a domain. Kneipp et al. [63] expect that even stronger SERS enhancement could be observed at low Raman frequency shifts. Thus, it may be possible for SERS to reveal the radial breathing mode band for individual carbon nanotubes free from the inhomogeneous broadening effects observed for this mode in normal resonant Raman spectra.

12.8.3 Example of Biomedical Application of Surface-Enhanced Raman Spectroscopy: Glucose Biosensor

It was shown [52] (see Sect. 12.7) that NIR Raman spectroscopy could be used for whole blood analysis. In this section, we show that surface-enhanced Raman spectroscopy can potentially be utilized for measuring glucose in vivo. Shafer-Peltier et al. [64] reported detection of glucose using SERS.

The researchers prepared a novel SERS medium by using a self-assembled alkanethiol monolayer adsorbed on a silver film over nanosphere (AgFON) surface as a partition layer to concentrate glucose from solution within the $\sim$4-nm SERS activation distance of the silver. The SERS surface was fabricated by drop coating undiluted white carboxyl-substituted latex nanospheres (diameter 390 ± 19.5 nm) on glass substrates that had been cleaned and made hydrophilic. These were allowed to dry in ambient conditions then vapor deposited with Ag to a mass thickness of 200 nm. Since glucose SERS on this surface could not be observed, the authors used the alkanethiol monolayer assembled over the AgFON to concentrate glucose and increase its SERS interaction with AgFON. This is analogous to creating a stationary phase in high-performance liquid chromatography. The SERS substrate thus prepared should be stable electrochemically and thermally. A confocal microscope, a modified Nikon Optiphot (Frier Company, Huntley, IL) with a 20× objective in backscattering geometry, was used to measure spatially resolved SERS spectra. The laser light at 532 nm or 632.8 nm was coupled into a 200-µm-diameter fiber. The collected backscattered light was coupled by another fiber into a VM-505 monochromator (Acton Research Corporation, Acton, MA) with entrance slit set at 250 µm and Spec-10-400B liquid nitrogen-cooled CCD camera (Roper Scientific, Trenton, NJ).

Figure 12.30 (from Ref. [64]) shows example spectra from the different stages of glucose/1-decanethiol/AgFON surface. Figure 12.22a shows the SERS spectrum of 1-decanethiol on AgFON surface. In Fig. 12.22b, the SERS spectrum of the superposition of the SERS spectra of 1-decanethiol layer and glucose with features

Fig. 12.30 Spectra used in quantitative analysis. (**a**) 1-DT monolayer on AgFON substrate, $\lambda_{ex} = 532$ nm, $P = 1.25$ mW, acquisition time = 30 s. (**b**) Mixture of 1-DT monolayer and glucose partitioned from a 100 mM solution, $\lambda_{ex} = 532$ nm, $P = 1.25$ mW, acquisition time = 30 s. (**c**) Residual glucose spectrum produced by subtracting (**a**) from (**b**). (**d**) Normal Raman spectrum of crystalline glucose for comparison, $\lambda_{ex} = 632.8$ nm, $P = 5$ mW, acquisition time = 30 s (From Ref. [64])
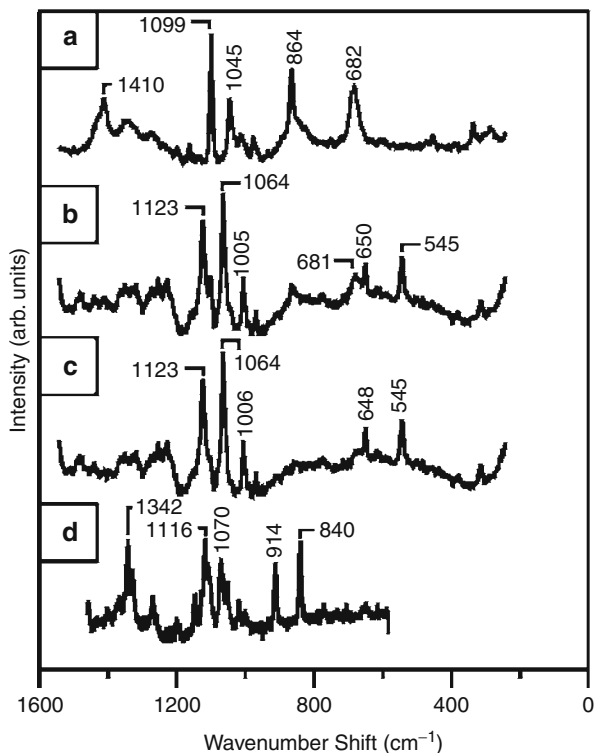
from glucose (1,123 and 1,064 cm^{-1}) and 1-decanethiol (1,099, 864, and 681 cm^{-1}) is shown.

The SERS spectra with the excitation laser at 632 nm were measured for 36 samples with glucose concentration from 0 to 250 mM. This data set was processed using partial-least squares analysis with leave-one-out cross validation. The resulting error of prediction was 3.3 mM. The results were repeated with multiple, similar data sets.

Similar measurements were carried out with the concentration within the clinically relevant range. Thirteen samples were measured. Performing partial-least squares analysis with leave-one-out cross validation rendered a corresponding prediction error of 1.8 mM (see Fig. 12.31, from Ref. [64]).

The authors concluded that the reported results demonstrate the feasibility of a SERS-based glucose sensor. They also observed that the expensive bulky equipment they used is already possible to down size to much smaller and less expansive instruments utilizing a linear array-based spectrometer. In the future, they suggest that micro- and nanophotonics approaches would produce a hand size apparatus for SERS measurement. They also projected that the SERS substrate can be miniaturized to become an implantable device not only for glucose but also for other analytes in the human body fluids. We would add to the author's comments that it is reasonable to assume that the nanophotonics will be
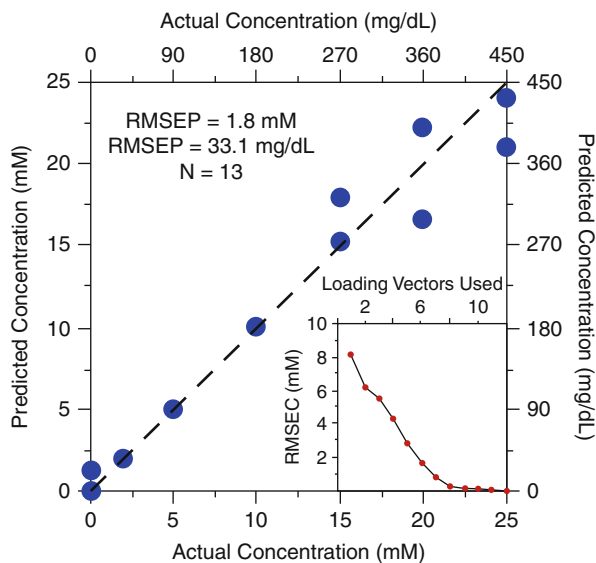
Fig. 12.31 Plot of PLS predicted physiologically relevant glucose concentrations versus actual glucose concentrations using leave-one-out cross validation (ten loading vectors). AgFON samples were made, incubated for 19 h in 1 mM 1-DT solution, and dosed in glucose solution (range: 0–25 mM) for 1 h. Each micro-SERS measurement was made, whereas samples were in an environmental control cell filled with glucose solution, using $\lambda_{ex} = 632.8$ nm (3.25 mW, 30 s). *Dashed line* is not a fit, but rather represents perfect prediction. *Inset* shows the root-mean-squared error of calibration as a function of number of loading vectors used in the PLS algorithm (From Ref. [64])

able to implement the entire device including a substrate as well as a SERS measurement apparatus in the scale amenable for implanting in the body. This could allow new levels for treating physiological conditions using implantable devices dispersing therapeutic agents with the real-time feedback and/or auto-adaptation, for example, an insulin-dispersing device, which could regulate the dose based on the glucose level continuously measured in the body by a nano-SERS device.

References

1. R.G. Newton, *Scattering Theory of Waves and Particles* (McGraw-Hill, New York, 1969)
2. I.J. Bigio, J.R. Mourant, Ultraviolet and visible spectroscopies for tissue diagnostics: fluorescence spectroscopy and elastic-scattering spectroscopy. Phys. Med. Biol. **42**, 803–814 (1997)
3. J.R. Mourant, J. Boyer, T. Johnson, J. Lacey, I.J. Bigio, Detection of gastrointestinal cancer by elastic scattering and absorption spectroscopies with the Los Alamos optical biopsy system. Proc. SPIE **2387**, 210–217 (1995)

4. L.T. Perelman, V. Backman, M. Wallace, G. Zonios, R. Manoharan, A. Nusrat, S. Shields, M. Seiler, C. Lima, T. Hamano, I. Itzkan, J. Van Dam, J.M. Crawford, M.S. Feld, Observation of periodic fine structure in reflectance from biological tissue: a new technique for measuring nuclear size distribution. Phys. Rev. Lett. **80**, 627–630 (1998)

5. V. Backman, M. Wallace, L.T. Perelman, R. Gurjar, G. Zonios, M.G. Müller, Q. Zhang, T. Valdez, J.T. Arendt, H.S. Levin, T. McGillican, K. Badizadegan, M. Seiler, S. Kabani, I. Itzkan, M. Fitzmaurice, R.R. Dasari, J.M. Crawford, J. Van Dam, M.S. Feld, Detection of preinvasive cancer cells. Early-warning changes in precancerous epithelial cells can be spotted in situ. Nature **406**(6791), 35–36 (2000)

6. M. Wallace, L.T. Perelman, V. Backman, J.M. Crawford, M. Fitzmaurice, M. Seiler, K. Badizadegan, S. Shields, I. Itzkan, R.R. Dasari, J. Van Dam, M.S. Feld, Endoscopic detection of dysplasia in patients with Barrett's esophagus using light scattering spectroscopy. Gastroenterology **119**, 677–682 (2000)

7. H. Fang, M. Ollero, E. Vitkin, L.M. Kimerer, P.B. Cipolloni, M.M. Zaman, S.D. Freedman, I.J. Bigio, I. Itzkan, E.B. Hanlon, L.T. Perelman, Noninvasive sizing of subcellular organelles with light scattering spectroscopy. IEEE J. Sel. Top. Quantum Electron. **9**, 267–276 (2003)

8. V. Backman, V. Gopal, M. Kalashnikov, K. Badizadegan, R. Gurjar, A. Wax, I. Georgakoudi, M. Mueller, C.W. Boone, R.R. Dasari, M.S. Feld, Measuring cellular structure at submicrometer scale with light scattering spectroscopy. IEEE J. Sel. Top. Quantum Electron. **7**, 887–893 (2001)

9. V. Backman, R. Gurjar, L.T. Perelman, V. Gopal, M. Kalashnikov, K. Badizadegan, A. Wax, I. Georgakoudi, M. Mueller, C.W. Boone, I. Itzkan, R.R. Dasari, M.S. Feld, Imaging and measurement of cell organization with submicron accuracy using light scattering spectroscopy, in *Optical Biopsy IV*, ed. by R.R. Alfano. Proceedings of SPIE, 4613 (SPIE Press, Bellingham, 2002), pp. 101–110

10. L.T. Perelman, V. Backman, Light scattering spectroscopy of epithelial tissues: principles and applications, in *Handbook on Optical Biomedical Diagnostics PM107*, ed. by V.V. Tuchin (SPIE Press, Bellingham, 2002), pp. 675–724

11. A. Brunsting, F. Mullaney, Differential light scattering from spherical mammalian cells. Biophys. J. **14**, 439–453 (1974)

12. J.R. Mourant, J.P. Freyer, A.H. Hielscher, A.A. Eick, D. Shen, T.M. Johnson, Mechanisms of light scattering from biological cells relevant to noninvasive optical-tissue diagnosis. Appl. Opt. **37**, 3586–3593 (1998)

13. R. Drezek, A. Dunn, R. Richards-Kortum, Light scattering from cells: finite-difference time-domain simulations and goniometric measurements. Appl. Opt. **38**, 3651–3661 (1999)

14. V. Backman, R. Gurjar, K. Badizadegan, R. Dasari, I. Itzkan, L.T. Perelman, M.S. Feld, Polarized light scattering spectroscopy for quantitative measurement of epithelial cellular structures in situ. IEEE J. Sel. Top. Quantum Electron. **5**, 1019–1027 (1999)

15. G. Zonios, L.T. Perelman, V. Backman, R. Manoharan, M. Fitzmaurice, M.S. Feld, Diffuse reflectance spectroscopy of human adenomatous colon polyps in vivo. Appl. Opt. **38**, 6628–6637 (1999)

16. I. Georgakoudi, B.C. Jacobson, J. Van Dam, V. Backman, M.B. Wallace, M.G. Muller, Q. Zhang, K. Badizadegan, D. Sun, G.A. Thomas, L.T. Perelman, M.S. Feld, Fluorescence, reflectance and light scattering spectroscopies for evaluating dysplasia in patients with Barrett's esophagus. Gastroenterology **120**, 1620–1629 (2001)

17. T.J. Farrell, M.S. Patterson, B.C. Wilson, A diffusion theory model of spatially resolved, steady-state diffuse reflectance for the non-invasive determination of tissue optical properties. Med. Phys. **19**, 879–888 (1992)

18. O.W. van Assendelft, *Spectrophotometry of Haemoglobin Derivatives* (C. C. Thomas, Springfield, 1970)

19. G.L. Tipoe, F.H. White, Blood vessel morphometry in human colorectal lesions. Histol. Histopathol. **10**, 589–596 (1995)

20. S.A. Skinner, G.M. Frydman, P.E. O'Brien, Microvascular structure of benign and malignant tumors of the colon in humans. Dig. Dis. Sci. **40**, 373–384 (1995)
21. V. Backman, L.T. Perelman, J.T. Arendt, R. Gurjar, M.G. Muller, Q. Zhang, G. Zonios, E. Kline, T. McGillican, T. Valdez, J. Van Dam, M. Wallace, K. Badizadegan, J.M. Crawford, M. Fitzmaurice, S. Kabani, H.S. Levin, M. Seiler, R.R. Dasari, I. Itzkan, M.S. Feld, Light scattering spectroscopy: a new technique for clinical diagnosis of precancerous and cancerous changes in human epithelia. Lasers Life Sci. **9**, 255–263 (2001)
22. B.J. Reid, R.C. Haggitt, C.E. Rubin, G. Roth, C.M. Surawicz, G. Vanbelle, K. Lewin, W.M. Weinstein, D.A. Antonioli, H. Goldman, W. Macdonald, D. Owen, Observer variation in the diagnosis of dysplasia in Barrett's esophagus. Hum. Pathol. **19**, 166–178 (1988)
23. R.H. Riddell, H. Goldman, D.F. Ransohoff, H.D. Appelman, C.M. Fenoglio, R.C. Haggitt, C. Ahren, P. Correa, S.R. Hamilton, B.C. Morson, S.C. Sommers, J.H. Yardley, Dysplasia in inflammatory bowel disease: standardized classification with provisional clinical applications. Hum. Pathol. **14**, 931–986 (1983)
24. R.C. Haggitt, Barrett's esophagus, dysplasia, and adenocarcinoma. Hum. Pathol. **25**, 982–993 (1994)
25. M. Pagano, K. Gauvreau, *Principles of Biostatistics* (Duxbury Press, Belmont, 1993)
26. L. Qiu, D. Pleskow, R. Chuttani, E. Vitkin, J. Leyden, N. Ozden, S. Itani, L. Guo, A. Sacks, J.D. Goldsmith, M.D. Modell, E.B. Hanlon, I. Itzkan, L.T. Perelman, Multispectral scanning during endoscopy guides biopsy of dysplasia in Barrett's esophagus. Nat. Med. **16**, 603–606 (2010)
27. L. Qiu, V. Turzhitsky, L. Guo, E. Vitkin, I. Itzkan, E.B. Hanlon, L.T. Perelman, Early cancer detection with scanning light scattering spectroscopy. IEEE J. Sel. Top. Quantum Electron. **99**, 1–11 (2011). doi:10.1109/JSTQE.2011.2161575
28. I. Itzkan, L. Qiu, H. Fang, M.M. Zaman, E. Vitkin, L.C. Ghiran, S. Salahuddin, M. Modell, C. Andersson, L.M. Kimerer, P.B. Cipolloni, K.-H. Lim, S.D. Freedman, I. Bigio, B.P. Sachs, E.B. Hanlon, L.T. Perelman, Confocal light absorption & scattering spectroscopic (CLASS) microscopy monitors organelles in live cells with no exogenous labels. Proc. Natl. Acad. Sci. U. S. A. **104**, 17255–17260 (2007)
29. T. Wilson, A.R. Carlini, Size of the detector in confocal imaging systems. Opt. Lett. **12**, 227–229 (1987)
30. B.A. Scalettar, J.R. Swedlow, J.W. Sedat, D.A. Agard, Dispersion, aberration and deconvolution in multi-wavelength fluorescence images. J. Microsc. **182**, 50–60 (1996)
31. J.C. Yarrow, Y. Feng, Z.E. Perlman, T. Kirchhausen, T.J. Mitchison, Phenotypic screening of small molecule libraries by high throughput cell imaging. Comb. Chem. High Throughput Screen. **6**, 279–286 (2003)
32. M. El Mouedden, G. Laurent, M.P. Mingeot-Leclercq, P.M. Tulkens, Gentamicin-induced apoptosis in renal cell lines and embryonic rat fibroblasts. Toxicol. Sci. **56**, 229–239 (2000)
33. F. Van Bambeke, C. Gerbaux, J.M. Michot, M.B. d'Yvoire, J.P. Montenez, P.M. Tulkens, Lysosomal alterations induced in cultured rat fibroblasts by long-term exposure to low concentrations of azithromycin. J. Antimicrob. Chemother. **42**, 761–767 (1998)
34. S. Carryn, H. Chanteux, C. Seral, M.-P. Mingeot-Leclercq, F. Van Bambeke, P.M. Tulkens, Intracellular pharmacodynamics of antibiotics. Infect. Dis. Clin. North Am. **17**, 615–634 (2003)
35. S.P. Mulvaney, C.D. Keating, Raman Spectroscopy. Anal. Chem. **72**, 145R–157R (2000)
36. J.M. Chalmers, P.R. Grifiths (eds.), *Handbook of Vibrational Spectroscopy* (Wiley, Chichester, 2002)
37. L.R. Lewis, H.G.M. Edwards (eds.), *Handbook of Raman Spectroscopy* (Marcel Dekker, New York, 2001)
38. D. Pappas, B.W. Smith, J.D. Winefordner, Raman spectroscopy in bioanalysis. Talanta **51**, 121–144 (2000)
39. L.P. Choo-Smith, H.G.M. Edwards, H.P. Endtz, J.M. Kroz, F. Heule, H. Barr, J.S. Robinson Jr., H.A. Bruining, G.J. Puppels, Medical applications of Raman spectroscopy: from proof of principle to clinical implementation. Biopolymers (Biospectroscopy) **67**, 1–9 (2002)

40. E.D. Hanlon, R. Manoharan, T.-W. Koo, K.E. Shafer, J.T. Motz, M. Fitzmaurice, J.R. Kramer, I. Itzkan, R.R. Dasari, M.S. Feld, Prospects for in vivo Raman spectroscopy. Phys. Med. Biol. **45**, R1–R59 (2000)
41. A. Mahavedan-Jensen, R. Richards-Kortum, Raman spectroscopy for the detection of cancers and precancers. J. Biomed. Opt. **1**, 31–70 (1996)
42. R. Petry, M. Schmitt, J. Popp, Raman spectroscopy – a prospective tool in the life sciences. Chemphyschem **4**, 14–30 (2003)
43. R.K. Dukor, Vibrational spectroscopy in the detection of cancer, in *Handbook of Vibrational Spectroscopy*, ed. by J.M. Chalmers, P.R. Grifiths (Wiley, Chichester, 2002)
44. M.J. Pelletier, Raman Instrumentation, in *Analytical Applications of Raman Spectroscopy*, ed. by M.J. Pelletier (Blackwell, Oxford, 1999), pp. 53–105
45. J.B. Slater, J.M. Tedesco, R.C. Fairchild, I.R. Lewis, Raman spectrometry and its adaptation to the industrial environment, in *Handbook of Raman Spectroscopy*, ed. by I.R. Lewis, H.G.M. Edwards (Marcel Dekker, New York, 2001), pp. 41–144
46. U. Utzinger, R. Richards-Kortum, Fiber-optic probes for biomedical optical spectroscopy. J. Biomed. Opt. **8**, 121–147 (2003)
47. J.B. Tedesco, K.L. Davis, Calibration of Raman process analyzers. Proc. SPIE **3537**, 200–212 (1998)
48. D.E. Bettey, J.B. Slater, R. Wludyka, H. Owen, D.M. Pallister, M.D. Morris, Axial transmissive f/1.8 imaging Raman spectrograph with volume-phase holographic filter and grating. Appl. Spectrosc. **47**, 1913–1919 (1993)
49. H. Owens, Holographic optical components for laser spectroscopy applications. Proc. SPIE **1732**, 324–332 (1993)
50. A. Molckovsky, L.-M. Wong Kee Song, M.G. Shim, N.E. Marcon, B.C. Wilson, Diagnostic potential of near-infrared Raman spectroscopy of colon: differentiating adenomatous from hyperplastic polyps. Gastrointest. Endosc. **57**, 396–402 (2003)
51. U. Utzinger, D.L. Heintselman, A. Mahadevan-Jansen, A. Malpica, M. Follen, R. Richards-Kortum, Near-infrared Raman spectroscopy for in vivo detection of cervical precancers. Appl. Spectrosc. **55**, 955–959 (2001)
52. A.K.M. Enejder, T.-W. Koo, J. Oh, M. Hunter, S. Sasic, M. Feld, Blood analysis by Raman spectroscopy. Opt. Lett. **27**, 2004–2006 (2002)
53. M.G. Shim, L.-M. WongKeeSong, N.N. Marcon, B.C. Wilson, In vivo near-infrared Raman spectroscopy: demonstration of feasibility during clinical gastrointestinal endoscopy. Photochem. Photobiol. **72**, 146–150 (2000)
54. Y. Guan, E.N. Lewis, I.W. Levin, Biomedical applications of Raman spectroscopy: tissue differentiation and potential clinical usage, in *Analytical Applications of Raman Spectroscopy*, ed. by M.J. Pelletier (Blackwell, Oxford, 1999), pp. 276–327
55. A. Mahadevan-Jansen, M. Follen Mitchell, N. Ramanujam, U. Utzinger, R. Richard Kortum, Development of a fiber optic probe to measure NIR Raman spectra of cervical tissue in vivo. Photochem. Photobiol. **68**, 427–431 (1998)
56. A. Otto, Surface-enhanced Raman scattering: 'classical' and 'chemical' origins, in *Light Scattering in Solids IV*, ed. by M. Cardona, G. Guntherodt (Springer, Berlin, 1984), p. 289
57. C.S. Schatz, R.P. Van Duyne, Electromagnetic mechanism of surface-enhanced spectroscopy, in *Handbook of Vibrational Spectroscopy*, ed. by J.M. Chalmers, P.R. Grifiths (Wiley, Chichester, 2002)
58. M. Moskovits, Surface-enhanced spectroscopy. Rev. Mod. Phys. **57**, 783–826 (1985)
59. K. Kneipp, H. Kneipp, I. Itzkan, R. Dasari, M.S. Feld, Ultrasensitive chemical analysis by Raman spectroscopy. Chem. Rev. **99**, 2957–2975 (1999)
60. K. Kneipp, Y. Wang, H. Kneipp, L.T. Perelman, I. Itzkan, R.R. Dasari, M.S. Feld, Single molecule detection using surface-enhanced Raman scattering (SERS). Phys. Rev. Lett. **78**, 1667–1670 (1997)

61. R. Saito, G. Dresselhaus, M.S. Dresselhaus, *Physical Properties of Carbon Nanotubes* (Imperial College Press, London, 1998)
62. K. Kneipp, H. Kneipp, P. Corio, D.M. Brown, K. Shafer, J. Motz, L.T. Perelman, E.B. Hanlon, A. Marucci, G. Dresselhaus, M.S. Dresselhaus, Surface-enhanced and normal stokes and anti-stokes Raman spectroscopy of single-walled carbon nanotubes. Phys. Rev. Lett. **84**, 3470–3473 (2000)
63. K. Kneipp, L.T. Perelman, H. Kneipp, V. Backman, A. Jorio, G. Dresselhaus, M.S. Dresselhaus, Coupling and intensity exchange between phonon modes observed in strongly enhanced Raman spectra of single-wall carbon nanotubes on silver colloidal clusters. Phys. Rev. B **63**, 6319 (2001)
64. K.E. Shafer-Peltier, C.L. Haynes, M.R. Glucksberg, R.P. Van Duyne, Toward a glucose biosensor based on surface-enhanced Raman scattering. J. Am. Chem. Soc. **125**, 588–593 (2003)
65. A. Ishimaru, *Wave Propagation and Scattering in Random media* (Academic, Orlando, 1978)
66. J. Landis, G. Koch, The measurement of observer agreement for categorical data. Biometrics **33**, 159–174 (1977)
67. N.B. Colthup, L.H. Daly, S.E. Wiberley, *Introduction to Infrared and Raman Spectroscopy*, 3rd edn. (Academic, Boston, 1990)
68. H. Martens, T. Naes, *Multivariate Calibration* (Wiley, New York, 1989)
69. M.J. Pelletier (ed.), *Analytical Applications of Raman Spectroscopy* (Blackwell, Oxford, 1999)

Bioflow Measuring: Laser Doppler and Speckle Techniques

13

Ivan V. Fedosov and Valery V. Tuchin

Contents

I.V. Fedosov (✉)

Department of Optics and Biophotonics, Saratov State University, Saratov, Russian Federation
e-mail: fedosov_optics@mail.ru

V.V. Tuchin
Department of Optics and Biophotonics, Saratov State University, Saratov, Russian Federation

Precision Mechanics and Control, Institute of the Russian Academy of Sciences, Saratov, Russian Federation

Optoelectronics and Measurement Techniques Laboratory, University of Oulu, Oulu, Finland
e-mail: tuchinvv@mail.ru

Abstract

This chapter describes optical imaging, particle image velocimetry, laser
Doppler anemometry, and the phenomenon of dynamic laser speckles within
the scope of the classical electromagnetic theory of light radiation. Several case-
specific practical solutions for optical bioflow diagnostics are overviewed and
discussed.

13.1   Introduction

Since the prehistoric human experience of observation of wooden chips that follow
the river stream, optical methods have played a central role in characterization of
gas and liquid flows. These methods are based on detection of a secondary light
field produced with a moving fluid due to light scattering or luminescence excited
with an incident light radiation. Normally, pure gases and fluids are transparent and
their motion does not result in any detectable variation of secondary light field.
Therefore, to measure the velocity of these fluids, they should be seeded with flow-
tracing particles that can be detected by means of optical methods.

An optical field produced with a flow-tracing particle at certain fixed observation
point depends on particle position and varies with time when a particle is in motion.
Displacement of a particle results in variation of light intensity and phase at the
observation point. Intensity of light means the energy that light transfers per unit of
time through a unit of area [1]. It determines all known actions of light and thus it is
the only physical quantity related to light that can be actually measured. Light
intensity decreases proportionally to the squared distance between particle and
observation point, thus small displacements of a particle result in no detectable
variations of light intensity at the observation point.

Phase is the intrinsic property of light that cannot be measured directly. However,
under certain conditions superposition of several light fields results in light intensity
that is strongly dependent on the difference in phases of superposed fields. The effect

of such phase-related light intensity redistribution is referred to as interference of light [1]. Phase of light is highly sensitive to particle displacement. And it covers its full range from 0 to 2π when distance between particle and observation point is changed to the wavelength of light, which is about half a micrometer.

Thus, position of a light source can be detected by means of an arrangement that employs interference to convert light field phase variations into that of light intensity, e.g., with a lens made of transparent material. The principle is implemented in the structure of human eye as well as in that of a great many living organisms, including vertebrates, mollusks, and insects. The natural eye is mimicked in lens-based imaging systems that have given rise to many optical imaging instrumentations developed extensively since the Renaissance. In all these devices, the effect of a transparent glass lens or a concave mirror on light field results in light intensity distribution over a flat surface that encodes angular data of light sources. The intensity distribution is referred to as an optical image. An optical image can be recorded as a distribution of lights and darks over a flat surface by means of a photographic process or electro-optical imaging arrangement.

Because lens-based imaging systems mimic human eye structure, the optical images they produce can be easily perceived with the human vision system. Over the centuries and today, despite current progress in natural sciences and digital computing, human vision is still a unique and unsurpassed instrument for image analysis and interpretation. But because of its subjective nature and relatively long response time, human vision is not well suited for quantitative measurements of moving object velocity.

Another way to encode light phase with light intensity was discovered at the beginning of nineteenth century, after the interpretation of light interference phenomenon as a wave process was proposed by Thomas Young. Young introduced the term *interference*, and he estimated for the first time the wavelength of light. After this seminal discovery, light interference was employed for light phase measurements by means of optical instruments referred to as *interferometers*, which have made possible measurements of linear distances to a fraction of light wavelength [1, 2].

In its early stages, light interferometry was used predominantly for precision measurements of static or slowly varying phase differences between light fields in various circumstances. The progress in optoelectronics and signal processing as well as the invention of highly coherent and intensive laser light sources in the 1960s gave raise to interferometric techniques for high-resolution spectroscopy. The so-called optical mixing spectroscopy technique made it possible to detect light field phase variation, which results from scattering of laser radiation by moving flow tracing particles [3]. It allows for measuring of both laser line broadening caused by random motion of light scattering particles and laser line shift as a result of ordered motion of scatterers. Soon after the invention of the technique, it was applied for experimental fluid mechanics and diagnostics of biological fluids. Because of its origin from spectroscopic techniques, the method is often referred to as laser Doppler anemometry due to its first interpretation in terms of light frequency shift [4].

The principle of operation of laser Doppler anemometers (LDAs) is based on interference or light beams propagating along different paths that include flow-tracing particles. Ordered movement of particles results in phase difference

between of these paths, which varies depending on time. Superposition of beams results in oscillation of light intensity due to interference. The oscillations are converted into an electrical signal with an optoelectronic detector and then processed by means of an analog or digital spectrum analyzer. Because of a limited number of detector channels, LDAs are typically used for point wise measurements of flow velocity averaged over a small measuring volume [4].

Flow velocity field measurements became possible after progress in digital imaging was made in the 1990s, with compact and powerful computers capable of processing large arrays of data, encoding two-dimensional light intensity distributions over optical images. The achievement was accompanied by the development of compact solid state digital image sensors, giving rise to the so-called particle image velocimetry (PIV) techniques for fluid flow diagnostics, which have replaced LDA instruments in the field of quantitative fluid flow velocity characterization. Typical PIV instruments employ software-based tracking of particle images through several consequently recorded pictures of a flow. As the single requirement to the pictures is the visibility of particles, the same PIV software can be used for evaluation of both a supersonic gas flow illuminated with short laser pulses and a microscopic water flow driven by a living cell filament [5].

As we mentioned earlier, the first application of laser-based Doppler anemometry was reported a few years after the invention of the method. But after decades of extensive studies in the field, these attempts have still not resulted in a clinically applicable diagnostic method. The main issue is related to high scattering of light from the biological tissues that living objects are made of and the biological fluids such as blood, the flow of which should be characterized. Although, practically, most living tissues do not absorb light energy and apparently transmit it into sufficient depth, they introduce huge variations of light field phase [6, 7]. The variations make impossible any reliable optical measurements of flow velocity through most significant biological tissues either by means of LDA or PIV. Therefore, applications of optical anemometry instrumentation for diagnostics of biological fluid flow are still challenging and case specific.

In recent decades, the method of optical coherence tomography (OCT) has been proposed to enhance imaging through biological tissues. It is based on selection of light that propagates along more or less straight paths from a certain depth of biological tissue and thus preserves its phase, critical for imaging. As OCT is based on the Michelson interferometer, it is potentially capable of detection of Doppler frequency shift caused by blood circulation through superficial blood vessels. But, as has been shown in multiple experiments, typical biological tissue attenuates such radiation for about 90 dB per millimeter of penetration depth. Therefore, the method could not provide image resolution better than 10 μm and thus it does not resolve superficial capillaries situated close to a tissue surface. However, larger vessels that potentially could be detected with the instrument normally lie deeper than 1 mm and thus are out of OCT penetration depth [6, 7].

Another approach in blood microcirculation assessment, referred to as laser Doppler flowmetry, is based on the measurements of laser light broadening, which results in multiple light scattering with a living tissue perfused with blood

[8–10]. The method is not capable of any quantitative characterization of blood microcirculation because multiple light scattering makes it impossible to define the differential wave vector that determines Doppler frequency shift. Thus, although some fluctuations of intensity of laser light scattered by a living tissue can be detected, they do not actually characterize blood flow dynamics only but also strongly depend on local tissue structure and optical properties. Because coherent light scattering with living tissue results in random phase variations and thus in formation of laser speckle field, nonquantitative laser-based methods for characterization of blood circulation are often referred to as laser speckle–based bioflow measurements [11–14].

The above led us to conclude that both coherent (laser Doppler and laser speckle) and non-coherent (imaging) optical velocimetry techniques should be used with care to obtain reliable results in bioflow characterization. These applications for study of clearly visible flows, and especially for flows carefully seeded with optimal tracers, which are discuss in this chapter, have been proved their high reliability and capability. But the application of these techniques for biological research and clinical diagnostics is still challenging and case specific. Therefore, the discussion here on the fundamental background of quantitative optical anemometry rather than providing a complete overview of the particular applications, as the former can give readers case-specific ideas related to their own particular tasks of bioflow characterization.

The first part of the chapter systematically discusses optical imaging, particle image velocimetry, laser Doppler anemometry, and the phenomenon of dynamic laser speckles within the scope of classical electromagnetic theory of light radiation. The second part illustrates considerations, with an overview of several case-specific practical solutions for optical bioflow diagnostics.

13.2 Fundamentals of Optical Techniques for Flow Velocity Measuring

13.2.1 Optical Measurements of Flow Velocity

Flow is a movement of a fluid-like gas or liquid from one point in space to another [15]. It can be characterized in terms of local velocity field, namely with three components of velocity determined at any point of a flow at each instant of time. As fluid flow is typically accompanied by variations of fluid temperature, density, and pressure, these parameters are also of interest in computational and experimental fluid mechanics. Among a number of approaches in experimental fluid mechanics, optical methods for flow characterization take an outstanding place because of their high reliability and non-contact nature. To date, optical methods have been employed for measurement of different flow parameters. For example, Schlieren imaging reveals gradients of fluid refractive index related to fluid density; and the laser-induced fluorescence (LIF) technique allows for measuring of liquid temperature. The main advantage of optical methods is their capability for non-contact measurements of flow

velocity field components, i.e., components of velocity vector that characterize displacement of element fluid volume at a fixed point of the flow.

Obviously, there are no practical ways to distinguish an individual volume of a homogenous fluid consisting of identical molecules and to track its motion. But one can modify some properties of a small fluid volume to make it traceable among the others, for example, by introducing into the fluid some particles with specific optical properties. These include smoke, consisting of small particles of soot in air, or plastic beads suspended in water, fluorescent nanoparticles, or even individual molecules diluted in a liquid. The particles can be expressly introduced in a flow for measurement purposes or they can be a natural part of multiphase fluid, like red blood cells (RBC) in a blood. In the former case, concentration, size, and optical properties of flow-tracing particles can be optimized in order to increase measurement performance. In the latter case, which is typical for experiments with biological fluids, properties of heterogeneous flow complicate and often makes impossible use of any optical instrumentation.

With respect to optical detection, a flow-tracing particle appears as a source of the light field. The particle either elastically scatters some incident radiation with the same wavelength or it emits light as a result of conversion of some other kind of energy, e.g., particle fluoresce being excited with a short-wave light radiation. The emitted light field reflects actual position of the particle and changes in space and time while the latter is in a motion. Thus, the detection of light originating from flow-tracing particles is the primary task of any optical technique for fluid flow velocity measurements. In practice, this can be performed through the use of the following optical phenomena: (1) the light source can be localized with an optical imaging system; (2) Doppler frequency shift of light emitted by moving particles can be detected; (3) spatial distribution and (or) dynamics of light field formed as a result of coherent light scattering by an ensemble of particles (so-called *speckle field*) can be analyzed. Below we will discuss the fundamental aspects of the methods for detection of light emitted by moving flow-tracing particles with respect to application of those for biological flow diagnostics.

13.2.2 Intensity of Light

Light radiation transfers energy between individual atoms or molecules. The latters should be considered as primary light sources which convert into light some other kinds of energy, like thermal, electrical of chamical one as well as they appears as unique primary light detectors which are capable for reverse conversion. Light energy is not converted continuously but in certain minimal portions, so-called quanta of light or photons [16]. There is no practical way to meddle with the interaction of light quantum with an atom and therefore only the energy flux associated with light radiation can be measured in an experiment [1]. Thus, the formal interpretation of optical phenomena is aimed at calculation of light energy flux in various circumstances.

A reliable method for interpretation of optical phenomena related to propagation of light can be provided within the scope of electromagnetic theory, which represents the light as a propagating in space and time disturbance of electric and

magnetic vector fields propagating in space and time. Electromagnetic theory expresses the energy flux of the electromagnetic field with Poynting vector [1]:

$$\mathbf{S} = \varepsilon_0 c^2 \mathbf{E} \times \mathbf{B}, \tag{13.1}$$

where ε_0 is the electric constant, c is the speed of light in vacuo, and $\mathbf{E}$ and $\mathbf{B}$ are the electric and magnetic fields, respectively. Both of these fields satisfy the general system of Maxwell's equations so they can be calculated in many circumstances. Neither an electric nor a magnetic field associated with light radiation can be measured directly, and thus they are used in optical theory as auxiliary variables introduced for mathematical interpretation only.

Classical electromagnetic theory fails in interpretation of light emission and absorption by individual atoms. Therefore, (1) is applicable to a propagating light only as light related energy flux through a certain closed surface of finite size that surrounds an elemental light source or receiver. In the particular case of an *electromagnetic wave propagating in free space*, $\mathbf{E}$ and $\mathbf{B}$ are at right angles to each other and to the direction of the wave propagation, and the magnitude of $\mathbf{B}$ is equal to $1/c$ times the magnitude of $\mathbf{E}$. The relation between fields gives unambiguous representation of a propagating light field at a certain point through three components of electric field $\mathbf{E}(\mathbf{r}, t)$ determined at any point of space given with position vector $\mathbf{r}$ at any instant of time t. In a mathematical sense, both $\mathbf{E}$ and $\mathbf{B}$ are equivalent but as it was shown in experiments with standing light waves that the maximal effect of light on atoms always coincides with maxima of $|\mathbf{E}|$.

Vector $\mathbf{E}$ is perpendicular to direction of light propagation and it represents the transverse nature of light waves that can be observed in experiments as *polarization of light*. Although polarization of light is critical for some applications, description of a light wave through vector $\mathbf{E}(\mathbf{r}, t)$ is still cumbersome and it makes us to look for further simplification.

Because any physical action of light requires finite quantity of energy, we should define light intensity as time averaged energy that passes per unit of time through area element perpendicular to light propagation direction. The averaging assumes here the fundamental quantum properties of light we mention above rather than response time of a particular detector. Taking into account that for a propagating light wave $|\mathbf{E} \times \mathbf{B}| = E^2/c$ and denoting the averaging over a time interval with $\langle \ldots \rangle$ we finally get the intensity of propagating light wave [1]:

$$I = \langle S \rangle = \varepsilon_0 c \langle E^2 \rangle. \tag{13.2}$$

As it follows from (13.2), light intensity is determined through modulus of electric field rather than through its components. Thus, if the effects of light polarization are not critical for a problem we can use scalar function of position vector and time $E(\mathbf{r}, t) = |\mathbf{E}(\mathbf{r}, t)|$ to find light intensity at $(\mathbf{r}, t)$.

Within the scope of electromagnetic theory, visible light is considered as oscillations of electromagnetic field with frequency ranging from 0.4×10^{15} to

0.8×10^{15} Hz. But for most practical applications like optical metrology, light with much narrower frequency interval is typically used to minimize possible uncertainties. Thus, as the first approximation we can represent electric field of light at any point with the cosine function:

$$E(\mathbf{r},t) = E_0(\mathbf{r})\cos(\omega t + \varphi(\mathbf{r})), \tag{13.3}$$

where $E_0(\mathbf{r})$ is the oscillation amplitude at the observation point, ω is the radian frequency of oscillations and $\varphi(\mathbf{r})$. Since cosine function (13.3) represents an infinite process, the field average can be calculated through limit:

$$\langle E^2(\mathbf{r})\rangle = \lim_{\tau\to\infty}\frac{1}{\tau}\int\limits_{-\tau/2}^{\tau/2} E^2(\mathbf{r},t)dt = \lim_{\tau\to\infty}\frac{1}{\tau}\int\limits_{-\tau/2}^{\tau/2} E_0^2(\mathbf{r})\cos^2(\omega t + \varphi(\mathbf{r}))dt = \frac{1}{2}E_0^2(\mathbf{r}),$$

$$\tag{13.4}$$

and finally assuming (13.2) the intensity is

$$I(\mathbf{r}) = \frac{\varepsilon_0 c}{2}E_0^2(\mathbf{r}). \tag{13.5}$$

The model that represents light field with infinite harmonic oscillations is referred to as *monochromatic light*. It corresponds to the situation when both amplitude and phase of oscillations remain constant during the entire time of observation and provides a simple way to find light intensity at any point as squared amplitude of oscillations there.

13.2.3 Interference of Monochromatic Light

According to electromagnetic theory, an electric field represents the sum of fields from all charges in the universe. Thus, to find the intensity of light at any point using (13.2), one should first summarize electric fields produced there with all light sources around. Let us consider the intensity resulting from the superposition of monochromatic light fields oscillating at the same frequency but each characterized with its specific amplitude and phase. To avoid summarization of trigonometric functions, it is useful to represent an electric field of light in terms of complex numbers. Actually, (13.3) is equal to the real part of a complex vector [1, 16]

$$V(\mathbf{r},t) = E_0(\mathbf{r})e^{i(\omega t + \varphi(\mathbf{r}))} = A(\mathbf{r})e^{i\omega t} \tag{13.6}$$

where $A(\mathbf{r}) = E_0(\mathbf{r})e^{i\varphi(\mathbf{r})}$ is referred to as complex amplitude of monochromatic light. $E_0(\mathbf{r})$ appears here as a magnitude of complex vector so its square can be

Fig. 13.1 The effect of two point sources
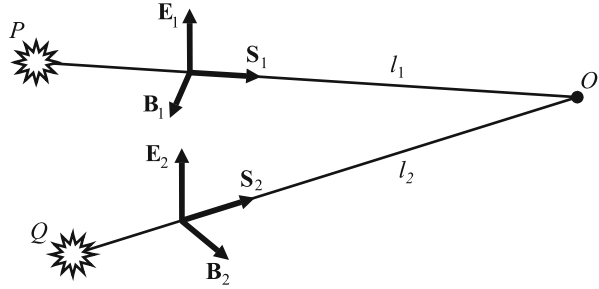
found as a product of $A(\mathbf{r})$ and its complex conjugate $A^*(\mathbf{r}) = E_0(\mathbf{r})e^{-i\varphi(\mathbf{r})}$, thus the intensity can be expressed through the complex amplitude of light as:

$$I(\mathbf{r}) = \frac{\varepsilon_0 c}{2} A(\mathbf{r})A^*(\mathbf{r}). \tag{13.7}$$

In complex representation, the field produced with n light sources can be found as

$$V_R(\mathbf{r}, t) = A_R(\mathbf{r})e^{i\omega t}, \tag{13.8}$$

where

$$A_R(\mathbf{r}) = \sum_n A_n(\mathbf{r}) \tag{13.9}$$

and $A_n(\mathbf{r})$ represents the complex amplitude produced at the observation point with nth source. Superposition of monochromatic light fields results in a monochromatic light field with the same frequency but characterized with some new amplitude and phase given with A_R. The intensity of resulting light can be expressed substituting (13.9) to (13.7).

Let us consider light intensity at the observation point O (Fig. 13.1), which results from the simultaneous effect of two point light sources P and Q. According to the principle of superposition, the electric field at an observation point is represented with the vector sum of those produced there by each light source, namely $\mathbf{E}_1$ and $\mathbf{E}_2$. In general, magnitude of the resulting vector is not equal to the sum of magnitudes of the components. However, for simplicity we suppose that $\mathbf{E}_1$ and $\mathbf{E}_2$ are always collinear at the observation point, so we can represent the electric field with scalar values of corresponding vector magnitudes E_1 and E_2. Let both fields oscillate with the same frequency ω, but each is characterized with its own amplitude and phase:

$$V_1(\mathbf{r}, t) = E_{01}(\mathbf{r})e^{i(\omega t + \varphi_1(\mathbf{r}))}, \quad V_2(\mathbf{r}, t) = E_{02}(\mathbf{r})e^{i(\omega t + \varphi_2(\mathbf{r}))}, \tag{13.10}$$

where $E_{01}(\mathbf{r})$, $E_{02}(\mathbf{r})$ are the oscillation amplitudes at the observation point; ω is the radian frequency of oscillations; and $\varphi_1(\mathbf{r})$, $\varphi_2(\mathbf{r})$ represent phases of oscillations at the observation point. Then, the summary complex amplitude of these fields is

$$A_R(\mathbf{r}) = \left(E_{01}(\mathbf{r})e^{i\varphi_1(\mathbf{r})} + E_{02}(\mathbf{r})e^{i\varphi_2(\mathbf{r})} \right). \tag{13.11}$$

Substituting it into (13.7) and opening brackets we get resulting intensity as

$$I(\mathbf{r}) = \frac{\varepsilon_0 c}{2} \left[E_{01}^2(\mathbf{r}) + E_{02}^2(\mathbf{r}) + E_{01}(\mathbf{r})E_{02}(\mathbf{r}) \left(e^{i(\varphi_1(\mathbf{r}) - \varphi_2(\mathbf{r}))} + e^{-i(\varphi_1(\mathbf{r}) - \varphi_2(\mathbf{r}))} \right) \right]. \tag{13.12}$$

Assuming $e^{i\theta} + e^{-i\theta} = 2\cos\theta$, we finally get the equation that represents the interference of the monochrome light at the point O [1]:

$$I_R(\mathbf{r}) = I_1(\mathbf{r}) + I_2(\mathbf{r}) + 2\sqrt{I_1(\mathbf{r})I_2(\mathbf{r})} \cos(\delta(\mathbf{r})), \tag{13.13}$$

where

$$I_1(\mathbf{r}) = \frac{\varepsilon_0 c}{2} \varepsilon_0 c E_{01}^2(\mathbf{r}), \quad I_2(\mathbf{r}) = \frac{\varepsilon_0 c}{2} E_{02}^2(\mathbf{r}), \tag{13.14}$$

are the intensities each source produces at the observation point separately and

$$\delta(\mathbf{r}) = \varphi_1(\mathbf{r}) - \varphi_2(\mathbf{r}) \tag{13.15}$$

is difference between field oscillation phases at observation point.

The result shows that the intensity of light resulting from the summary effect of two light sources is not equal to sum of the intensities each source produces there separately. The resulting intensity oscillates around its mean value of $I_1 + I_2$ depending on $\delta(\mathbf{r})$. It reaches its maxima $I_{max} = I_1 + I_2 + 2\sqrt{I_1 I_2}$ when $|\delta| = 0$, 2π, 4π, ...; and minima $I_{min} = I_1 + I_2 - 2\sqrt{I_1 I_2}$ when $|\delta| = \pi$, 3π, ... Maximal variation of the resulting intensity depending on phase difference can be observed when $I_1 = I_2$. In this case, $I_{min} = 0$ and $I_{max} = 4I_1 = 4I_2$.

To find the distribution of light intensity in space using (13.13), we must define functions $E_{01}(\mathbf{r})$, $E_{02}(\mathbf{r})$, $\varphi_1(\mathbf{r})$, and $\varphi_2(\mathbf{r})$ characterizing the light sources. A real light source consists of large number of light-emitting atoms. Therefore, the interference of light waves originating from diverse points of the source results in irregular distribution of phase and amplitude of the electric field over the so-called near-field region, which spreads from source to a radius of $R = D^2/\lambda$. D represents here characteristic size of a source and λ is light wavelength – namely a distance that light covers for a period of its oscillation. At distances $R > D^2/\lambda$, referred to as the far-field region, the electric field appears as a spherical wave. In particular,

the electric field produced in the far field region with an isotropic monochromatic light source can be expressed as

$$E(R,t) = \frac{E_0}{R} e^{i(\omega t - kR)},$$ (13.16)

where $R = |\mathbf{r} - \mathbf{r}_0|$ is the distance that separates the light source determined with its position vector $\mathbf{r}_0$ and an observation point given with $\mathbf{r}$; E_0 is an amplitude characterizing the electric field in far-field; and

$$k = \frac{\omega}{c} = \frac{2\pi}{\lambda}$$ (13.17)

is the wave number that describes phase variation with the distance separating light source and an observation point; λ is the light wavelength. As it follows from (13.16), the field phase at each instant of time is constant over any spherical surface corresponding to $R = $ const, which is referred to as the wave front. Depending on time, the wave front spreads along radii of the sphere; negative sign corresponds to wave expanding from the source towards infinity.

Particularly at large R, a light wave front can be considered as flat over a certain neighborhood of an observation point. In this case, a plane wave approximation can be used to describe the light field there:

$$E(\mathbf{r},t) = E_0 e^{i(\omega t - \mathbf{k}\mathbf{r})},$$ (13.18)

where $\mathbf{k} = k\mathbf{n}$ is referred to as the wave vector; and $\mathbf{n}$ denotes wave front normal.

Using (13.16), we can determine phases of electric field oscillation at point O (Fig. 13.1). Assuming for simplicity that oscillations at both sources are in phase and comparing (13.16) and (13.10)

$$\delta = \varphi_1 - \varphi_2 = k(l_2 - l_1).$$ (13.19)

Equation (13.19) defines the locus of the interference maxima as a family of parted rotation hyperboloids corresponding to $|\delta| = 0, 2\pi, 4\pi, \ldots$ with their foci collocated with light sources. Interference minima locus is defined with another family of hyperboloids $|\delta| = \pi, 3\pi, \ldots$. Thus, the interference of light results in complicated redistribution of light intensity in space, referred to as the interference pattern.

13.2.4 Coherence of Light

The model of monochromatic light represents the extreme case of infinitely long cosine oscillations of an electric field with stationary phase and amplitude. Intensity of such oscillation defined with a limit (13.4) is also stationary in time. Obviously,

such infinitely long and thus monochromatic oscillations could not be realized in any experiment, as the latter always takes a finite time. Moreover, in most cases, a light field results from the effect of a great many atoms emitting light independently of one another and therefore its amplitude and phase at any point randomly fluctuate depending on time. Because of its modulation, real light in any circumstances should not be considered as monochromatic and even as periodic in a fundamental sense [1, 16].

The spectral line of a modulated monochromatic signal is broadened with modulation bandwidth. Thus, a narrow spectral line corresponds to narrow-band modulation of amplitude and phase of light, depending on time which can be resolved with a particular detector. Light with narrow spectrum is referred to as quasi monochromatic as its intensity can be represented with the squared modulus of its complex amplitude, as for monochromatic light, to take into consideration fundamental averaging related to the quantum nature of light. In the case of stationary complex amplitude, (13.7) represents stationary intensity average over the infinite time interval. With respect to quasi monochromatic light characterized with fluctuating complex amplitude, the same equation gives an "instant intensity" [16], which is averaged only over time interval of $\tau_m \approx 4\pi/\Delta\omega$, where $\Delta\omega$ is width of the spectral line contour. We should note here that time interval τ_m corresponding to the period of highest modulation frequency is quite small. For example, the 0.1 nm wide contour of a spectral line peaked around the centerline wavelength of 500 nm corresponds to a modulation band about 60 GHz and τ_m is about 10^{-11}. Most real detectors are characterized by response time much longer than τ. Therefore, the observed intensity appears as squared modulus of complex amplitude averaged over detector response time $\tau_D >> \tau_m$:

$$I_D(\mathbf{r}, t) = \frac{\varepsilon_0 c}{2} \langle A(\mathbf{r}, t) A^*(\mathbf{r}, t) \rangle_D, \qquad (13.20)$$

where $A(\mathbf{r}, t) = E_0(\mathbf{r}, t) \exp(i\varphi(\mathbf{r}, t))$ is a complex amplitude of light at point $\mathbf{r}$; and $\langle \ldots \rangle_D$ denotes averaging over detector response time τ_D. By analogy with (13.12), we can express observed intensity resulting from superposition of two fields represented with complex amplitudes

$$A_1(\mathbf{r}, t) = E_{01}(\mathbf{r}, t) e^{i\varphi_1(\mathbf{r}, t)}, \quad A_2(\mathbf{r}, t) = E_{02}(\mathbf{r}, t) e^{i\varphi_2(\mathbf{r}, t)} \qquad (13.21)$$

as

$$I_D(\mathbf{r}, t) = \langle I_1(\mathbf{r}, t) \rangle_D + \langle I_2(\mathbf{r}, t) \rangle_D + \frac{\varepsilon_0 c}{2} \cdot 2\mathrm{Re}\langle A_1(\mathbf{r}, t) A_2^*(\mathbf{r}, t) \rangle_D, \qquad (13.22)$$

where

$$I_1(\mathbf{r}, t) = \frac{\varepsilon_0 c}{2} A_1(\mathbf{r}, t) A_1^*(\mathbf{r}, t), \quad I_2(\mathbf{r}, t) = \frac{\varepsilon_0 c}{2} A_2(\mathbf{r}, t) A_2^*(\mathbf{r}, t), \qquad (13.23)$$

are "instant intensities" of each field observed separately. As in (13.13), the first two terms of (13.22) represents a sum of intensities but the third term contains a correlation of field amplitudes $\langle A_1(\mathbf{r},t)A_2^*(\mathbf{r},t)\rangle_D$ that could not be reduced in the general case into a product of a part depending on amplitude of complex field and that depending on phase difference.

In most practical cases, light originates from light sources constituted of a great many elemental emitters independent one from another. The simultaneous effect of these emitters results in random fluctuations of field amplitude that are not correlated with fluctuations of field produced with any other light source. Thus, the third term of (13.22) is always equal to zero and superposition of light fields originating from distinct sources always results in the sum of intensities:

$$I_D(\mathbf{r},t) = \langle I_1(\mathbf{r},t)\rangle_D + \langle I_2(\mathbf{r},t)\rangle_D \tag{13.24}$$

Equation (13.24) is valid only while the detector response time is much less than the characteristic time of field fluctuations $\tau_D >> \tau_m$. Otherwise, the detector should resolve interference of light fields as random fluctuations of resulting intensity. It is possible to observe more or less regular interference of light fields emitted with distinct, highly stabilized single-frequency lasers. Construction of such lasers incorporates special measures to ensure extremely narrow emission bandwidth about 10^5 Hz or less.

The interference of light can be observed only when both superposed light fields originate from the same atom or molecule and thus their oscillations are completely correlated. It can be arranged by means of secondary light sources both excited by a single primary one. For example, one can replace light sources P and Q (Fig. 13.1) with a pair of particles illuminated with a primary light source. Such arrangements used to produce and superpose correlated light fields using the single primary source are referred to as interferometers.

Because an interferometer is potentially capable of arranging completely correlated secondary fields, we can discuss another extreme case of (13.22). If phase difference $\delta(\mathbf{r},t) = \varphi_1(\mathbf{r},t) - \varphi_2(\mathbf{r},t)$ varies depending on time, slow with respect to detector response time τ_D, cross correlation of fields can be factorized with regard to (13.21):

$$\langle A_1(\mathbf{r},t)A_2^*(\mathbf{r},t)\rangle_D = \langle E_{01}(\mathbf{r},t)E_{02}(\mathbf{r},t)\rangle_D e^{i\delta(\mathbf{r},t)}. \tag{13.25}$$

Then, if field amplitudes $E_{01}(\mathbf{r},t)$, $E_{02}(\mathbf{r},t)$ are completely correlated, we can use Cauchy–Bunyakovsky inequality $|\langle E_1(t)E_2(t)\rangle|^2 \leqslant \langle |E_1(t)|^2\rangle\langle |E_2(t)|^2\rangle$ to represent the cross correlation of field magnitudes with its maximal value:

$$\langle E_{01}(\mathbf{r},t)E_{02}(\mathbf{r},t)\rangle_D = \sqrt{\langle E_{01}{}^2(\mathbf{r},t)\rangle_D\langle E_{02}{}^2(\mathbf{r},t)\rangle_D}$$
$$= \frac{2}{\varepsilon_0 c}\sqrt{\langle I_1(\mathbf{r},t)\rangle_D\langle I_2(\mathbf{r},t)\rangle_D}. \tag{13.26}$$

Substituting (13.25) and (13.26) into (13.22), we finally get detected intensity of light:

$$I_D(\mathbf{r}, t) = \langle I_1(\mathbf{r}, t)\rangle_D + \langle I_2(\mathbf{r}, t)\rangle_D + 2\sqrt{\langle I_1(\mathbf{r}, t)\rangle_D \langle I_2(\mathbf{r}, t)\rangle_D} \cos(\delta(\mathbf{r}, t)). \quad (13.27)$$

Completely correlated optical fields are referred to as completely mutually *coherent* (from the Latin word *cohaerentia* – sticking together) [1, 16]. Otherwise, no correlated fields are referred to as mutually incoherent. Equation (13.27) has the same form as (13.13), which we obtained earlier for monochromatic light. Now we can state that monochromatic light corresponds to the trivial case of mutually coherent light as for any given point $\mathbf{r}$ field magnitudes $E_{01}(\mathbf{r})$, $E_{02}(\mathbf{r})$ and phases $\varphi_1(\mathbf{r})$, $\varphi_2(\mathbf{r})$ are constant.

Depending on mutual correlation of interference fields, the third (interference) term in (13.27) may vary continuously between zero for statistically independent light fields and $2\sqrt{\langle I_1(\mathbf{r}, t)\rangle_D \langle I_2(\mathbf{r}, t)\rangle_D} \cos(\delta(\mathbf{r}, t))$ for completely mutually coherent ones. Such light fields are referred to as partially coherent. Partially coherent light fields appear as a result of probing with an interferometer the radiation originating from an individual elemental light source. Thus, secondary light fields superposed at observation point $\mathbf{r}$ at time instant t can be expressed through primary field $A(\mathbf{r}, t)$ sampled at two points, $\mathbf{r}_1$ and $\mathbf{r}_2$, at time instants t_1 and t_2, respectively [1, 16]:

$$A_1(\mathbf{r}, t) = K_1 A(\mathbf{r}_1, t_1), \quad A_2(\mathbf{r}, t) = K_2 A(\mathbf{r}_2, t_2), \quad (13.28)$$

where K_1 and K_2 are some complex coefficients that represent the relation between complex amplitudes at sampling and observation points for a particular experimental arrangement. Strictly speaking, the field at an observation point is determined by the field at a certain neighborhood of these points, but the result obtained for a pair of points can then be extended for any set of points using, for example, the Kirchhoff method for light diffraction treatment. Equation (13.28) makes it possible to reduce cross correlation of light fields to autocorrelation of the primary light field complex amplitude [16]:

$$\Gamma(\mathbf{r}_1, \mathbf{r}_2, t_1, t_2) = \langle A(\mathbf{r}_1, t_1) A^*(\mathbf{r}_2, t_2)\rangle_D = \frac{\langle A_1(\mathbf{r}, t) A_2^*(\mathbf{r}, t)\rangle_D}{K_1 K_2^*}. \quad (13.29)$$

Autocorrelations of this kind represent the fundamental property of light fields, referred to as the coherence of light. Analysis of light field correlations is a subject of statistical theory of light coherence that is based on representation of light fields as complex random processes.

Within the scope of the electromagnetic model of light, the concept of partially coherent fields provides the best approximation for phenomena observed in optical experiments. But for a number of practically significant applications, extreme cases of light coherence, namely completely non-coherent and completely coherent light,

Fig. 13.2 Coherence length
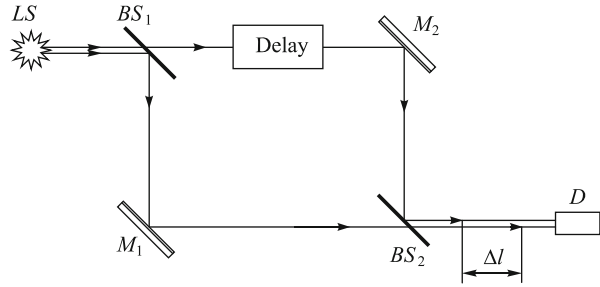
can be taken as a good approximation. Thus, we limit our further consideration to models concerning these two cases and simply supplement it with a phenomenological outline of conditions when each of them is applicable.

Evidently, autocorrelation (13.29) reaches its maximum value when $\mathbf{r}_1 = \mathbf{r}_2$ and $t_1 = t_2$ and gradually decreases to zero with the increase either of sampling point separation $\Delta \mathbf{r} = \mathbf{r}_1 - \mathbf{r}_2$ or delay between sampling time instants $\Delta t = t_1 - t_2$. The field of a propagating plane wave satisfies the wave equation when it is represented with a function of a single argument:

$$E(\mathbf{r}, t) = f\left(t - \frac{\mathbf{nr}}{c}\right), \tag{13.30}$$

where $\mathbf{n}$ is the unity vector indicating direction of wave propagation; c is the speed of light. Therefore, it is useful to represent both $\Delta \mathbf{r}$ and Δt as a combination of sampling point separation Δl along $\mathbf{n}$, which corresponds to $\Delta t = \Delta l / c$ and separation Δr perpendicular to $\mathbf{n}$. We assumed here that Δr is much less than the wave front curvature radius at sampling region.

Sampling of both secondary fields at the same point of the wave front at $\Delta r = 0$ can be performed with a semi-transparent mirror, for example, with a polished glass plate covered with a thin metal film. The metal film splits the energy flux of incident light between two secondary beams, one of which reflects from the mirror surface and another one passes through it. This method of light sampling is referred to as division of light field by its amplitude. Light sampled with a semi-transparent mirror can be then recombined with the second semi-transparent mirror (or with the same) to produce light interference. A typical arrangement used for such purposes is the so-called Mach-Zehnder interferometer [1] and is shown in Fig. 13.2. The light field produced with a source LS is sampled with semi-transparent mirror BS_1. Then, secondary beams are deflected with regular mirrors M_1 and M_2 towards a second semi-transparent mirror BS_2, which recombines both beams again and drops the resulting field towards light detector D.

When lengths of both paths are equal, $\Delta t = 0$, thus both light fields are mutually coherent and light intensity at the detector reaches its maximum given with (13.27)

Fig. 13.3 Spatial coherence
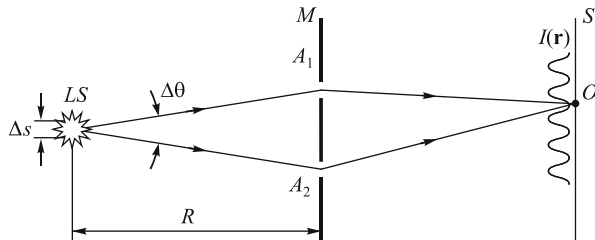
at $\delta(\mathbf{r}, t) = 0$. The delay of light propagating along one path with respect to another for interval Δt results in phase difference

$$\delta = \varphi_1 - \varphi_2 = \omega_0 \Delta t, \tag{13.31}$$

between light fields mixed on the detector. If the light is completely coherent, light intensity oscillates around its mean value with the increase of Δt. Thus, the Mach-Zehnder interferometer allows for detection of slight variations of optical paths caused by, for example, variation of gas refractive index along one of the paths. But the increase of Δt results in decrease of autocorrelation of light field [see (13.29)]. As has been well established with numerous experiments, interference could not observed if Δt exceeds the value referred to as coherence time:

$$\Delta t_c \approx \frac{1}{\Delta v}, \tag{13.32}$$

where $\Delta v = \Delta \omega / 2\pi$ is the width of the quasi monochrome light spectrum. Denoting speed of light propagation as c, we can find the distance light covers for the time interval of Δt_c

$$\Delta l_c = \Delta t_c c \approx \frac{c}{\Delta v}, \tag{13.33}$$

Referred to as coherence length, namely the maximal optical path difference that makes it possible to observe the interference. Coherence time has the physical interpretation as the time interval for which phase of light oscillations changes its value in a random way. Therefore, light field oscillations at two points within the light field are partially coherent while the distance separating them along the light propagation does not exceed Δl_c. Coherence length can be also expressed in terms of light wavelength $\lambda = c/v$; coherence length is expressed as [16]

$$\Delta l_c \approx \frac{\lambda^2}{\Delta \lambda}, \tag{13.34}$$

The second way to arrange interference is to divide the light wave front as is shown in Fig. 13.3. Light originated from light source *LS* passes through the small

apertures A_1 and A_2 in an opaque mask M. The apertures appear as secondary light sources like P and Q shown in Fig. 13.1. Because both apertures are exposed with a light field produced with the same light sources, the oscillations at each of them should be mutually coherent. Both apertures produce coherent oscillations at the surface of observation screen S, producing there an interference pattern $I(\mathbf{r})$ (Fig. 13.3). But, as was observed in experiments, the interference pattern is visible only until light source size Δs and the interference aperture $\Delta\theta$ – namely, the angle formed with rays emerging from light source toward center of each aperture satisfy the condition [16]

$$\Delta s\Delta\theta \leqslant \lambda, \tag{13.35}$$

where $\lambda = 2\pi c/\omega$ is light wavelength. The condition allows for calculating maximal possible distance Δr separating apertures A_1 and A_2; these can be considered as coherent light sources, namely the coherence radius [16]

$$\Delta r_c \approx \frac{R\lambda}{\Delta s}, \tag{13.36}$$

where R is the distance that separates the light source and opaque mask M (Fig. 13.3). The coherence between two points separated with a distance across light propagation is named transverse or spatial coherence by analogy with longitudinal or temporal coherence introduced above.

We can interpret the (13.36) in the following way [16]. Consider a pair of elementary light sources constituting an extensive light source and separated with certain distance. Both elementary sources produce at the aperture A_1 an effect that results from the superposition of the field each source produces there. It is clear that superposition depends on the difference of the paths connecting each source with A_1. However, with respect to aperture A_2, which is situated far enough from A_1, the path difference is not the same because there is some distance separating the sources. Therefore, the light disturbance that both atoms produce at A_2 is not correlated with those in A_1. Assuming that the maximal distance separating elementary light sources should not exceed a width of the macroscopic light source and supposing the superposition changes dramatically if the path difference is larger than the light wavelength, one can deduce the condition.

Coherence radius determines the size of a region one can draw around a certain point on a light wave front and within which light oscillations should be considered as coherent, the so-called coherence area. Then, we can lay the coherence length along the light propagation in order to define a cylindrical volume based on coherence area and called the volume of coherence. Light field oscillations within the volume should be considered as coherent (Fig. 13.4). Actually, coherence of light oscillations gradually degrades with the increase in the separation of observation points, so coherence volume has no uniquely defined surface and its actual shape strongly depends both on light source geometry and on the spectral distribution of light that it emits.

Fig. 13.4 Coherence volume
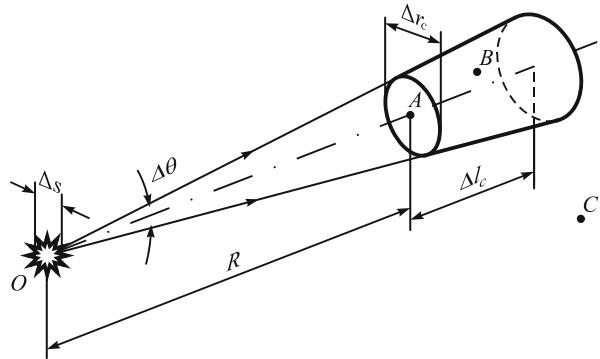
Coherence volume of natural light is typically small. For example, coherence radius of sunlight at the Earth's surface is about 60 μm, while coherence length of white visible light in the spectral range 400–700 nm is about 1 μm (in the case when a detector is not able to distinguish separate colors within the range). Coherence volume of laser light is quite large otherwise. As far as elementary light, sources within the laser active medium are synchronized by means of stimulated emission light oscillations across a single-mode laser beam and are quite coherent, i.e., radius of coherence is actually equal to that of the beam. Laser light is characterized by an extremely narrow spectrum of emission. Coherence length of laser radiation depends on the number of longitudinal modes excited within the laser cavity and may vary from several millimeters for solid-state lasers to several kilometers for stabilized single-mode ones.

13.2.5 Optical Image

An optical image is a representation of a light field originating from a scene with two-dimensional distribution of light intensity over a certain, typically flat, surface. Naturally, an optical image mediates visual perception of humans and higher animals as an optical system of eye forms it at the surface of the retina. Then, photosensitive cells of the retina detect light intensity distribution over its surface and transform it into perceptual neural activity. As follows from (13.20), the phase of the resulting light field does not affect the detected intensity and cannot be recognized with the eye. This means that artificial two-dimensional images projected with the optical system of the eye onto the retina can cause more or less a similar visual experience as direct observation of corresponding three-dimensional scenes. The effect makes it possible to use images to store, reproduce, and synthesize visual experience, as has been well known since the prehistoric era.

To ensure adequate perception, these images have to be performed on a flat surface in a manner that mimics the operation ofeye optics, namely through geometrical projection centered at the eye pupil. To acquire an image of an actual scene, certain optical arrangements should be used to convert light radiation into an
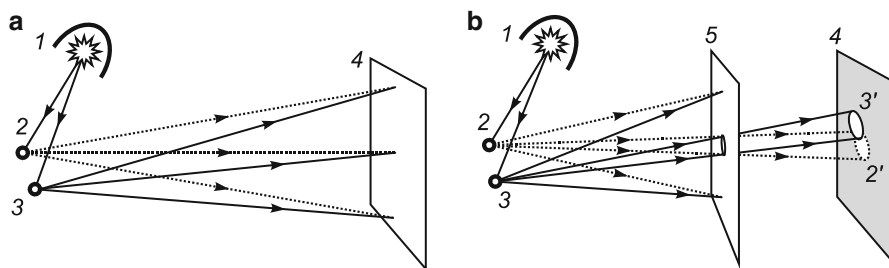
Fig. 13.5 Optical imaging. Light scattered by a particle produces a uniform illumination of a screen (**a**); image generation with a camera obscura (**b**); *1* – light source; *2, 3* – particle; *2′, 2″, 3′, 3″* – particle image; *4, 4′* – screen/image sensor; *5* – opaque screen with aperture

appropriate optical image that can be then recorded by means of a so-called image sensor or at least manually outlined with a pencil. The most common type of image sensor is an electro-optical device with its surface subdivided into identical elements referred to as pixels, i.e., picture elements. Electric circuitry of such a sensor encodes light energy captured with each pixel with a proportional digital electric signal. The totality of the signals that characterizes light intensity distribution over all pixels of a sensor is referred to as the digital image. As the digital image appears as common set of digital data, it can be processed with a digital computer, stored into its memory, and reproduced with an appropriate visualization device, e.g., a computer display or printer.

Independent of the actual manner of image sensor operation, it is the optical arrangement that is critical for adequately capturing the light field as an optical image. Consider a simple scene shown in Fig. 13.5a. Light source *1* illuminates a pair of small particles *2* and *3* that scatters light in particular towards an observation screen *4*. The scene represents the most common case of optical imaging of an object represented as a set of light-scattering particles that must be illuminated with a light source to become visible. We assume here that the light source is shaded in a proper way and this is only light scattered by the particles that falls on the screen.

Because light intensity at any point of the screen results from superposition of effects produced there with each particle, two extreme cases should be considered within the scope of our model of light fields: (1) particles act as mutually coherent light sources with respect to the observation screen, and superposition of light fields results in an interference pattern; (2) particles appear as independent light sources and superposition results in sum of intensities. The first case corresponds to illumination of particles with laser radiation characterized with a very large coherence volume. As will be discussed later, coherent superposition of secondary light fields scattered with real objects results in a complex interference pattern referred to as laser speckles.

We begin here with the second case as it represents the ordinary situation when an object is illuminated with natural light originating from an extended light source. Such radiation is characterized with a coherence volume size comparable with the

light wavelength and thus any macroscopic object can be considered as that built of a set independent elemental light sources. Assuming each particle is an isotropic point light source, we can find the intensity it produces at any given point by substituting (13.16) into (13.20):

$$I_D(R) \sim \frac{\langle E_0^2(t) \rangle_D}{R^2},\tag{13.37}$$

where $R = |\mathbf{r} - \mathbf{r}_0|$ is the distance that separates the light source determined with its position vector $\mathbf{r}_0$ and an observation point given with $\mathbf{r}$; E_0 is an amplitude that characterizes the electric field in far-field. Assuming the screen is tangent to wave front and its radius Δr is much smaller than R, we can find the relative variation or light intensity over its surface:

$$\frac{\Delta I}{I} \sim \frac{\Delta r^2}{R^2},\tag{13.38}$$

Thus, an isotropic light source produces uniform irradiation of an observation screen. As it follows from (13.38), intensity variation does not exceed 1 % over a screen with radius 1/10 of R. A second particle produces a similar smooth intensity distribution over the screen surface so the sum of the intensities also should be considered as uniform irradiation of the screen rather than an optical image that represents the positional relationship of the particles (Fig. 13.5a).

As is well known, light often appears as propagating along straight lines. Set an obstacle with an aperture 5 (Fig. 13.5b) between the particles and the observation screen. If aperture is much larger than light wavelength we can see that light originating from particle 2 passes straight through it and falls into a compact spot 2′ at the screen surface. By analogy, light scattered by particle 3 forms the other spot 3′. Each spot appears as a projection of the aperture onto the screen with straight rays emerging from the corresponding point light source. Spots corresponding to neighboring points of an object overlap one another, thus the optical image appears blurred. As it appears that light propagates along straight lines it might seem that the blur can be reduced with decrease of aperture diameter. But actually decrease of aperture size below certain value causes apparent deviation of light from straight-line propagation. This results in distortion of the light spot shape and in an increase of its size with further shrinking of the aperture in the obstacle.

The effect of obstacles on light propagation is referred to as diffraction of light [1]. Within the scope of electromagnetic theory, any material obstacle can be represented with a set of electric charges. The electric field of light incident upon the obstacle makes these charges produce some secondary field that superposes the incident one. Thus, the light field at any point of screen 4 (Fig. 13.5b) should be considered as a superposition of the electric field of light that can be observed there without obstacle 5 and the electric field produced with all charges constituting obstacle 5 that are excited with the incident field [1].

This model gives a qualitative interpretation for light matter interaction phenomena such as reflection, refraction, dispersion, and diffraction. But classical electromagnetic theory fails to describe interaction of light with atomic charges that constitutes material bodies because of the quantum nature of light and because none of theories can provide any method for calculating an exact electric field resulting from the effect of light radiation on the ensemble of a great many atoms interacting with each other. Therefore, electromagnetic theory uses a simplified phenomenological model of light diffraction based on the Huygens-Fresnel principle, with material bodies rather than an exact one [1].

The Huygens principle postulates that every point of a wave front may be considered as a center of a secondary disturbance that gives rise to spherical wavelets, and the wave front at any later instant may be regarded as the envelope of these wavelets. Fresnel improved the principle, stating that the intensity of light at any point can be found as a result of mutual interference that such wavelets produced, with virtual sources distributed over any arbitrary surface. This idea was put on a sounder mathematical basis by Kirchhoff within scalar representation of a light field. The Kirchhoff method was proved as quite adequate for the solution of the majority of the instrumental optics problems [1].

In order to assume the effect of obstacles on a light field, this theory of diffraction uses the following phenomenological interpretation of light-matter interaction. With respect to the light, any obstacle can be considered as opaque or transparent. An opaque obstacle shadows a certain spatial region behind it and no light can be detected there. Transparent objects let the light pass through but affect both amplitude and phase of the latter. Phase of the transmitted light appears to be delayed with respect to the incident one just as light propagates inside the body with speed n times less than that in vacuo. Index n is referred to as a refractive index of a transparent medium. Amplitude of transmitted radiation is attenuated because of partial light reflection on each surface of a transparent object it passes through and because of light energy absorption with transparent medium.

Within the scope of the theory, aperture *5* (Fig. 13.5b) in a flat opaque obstacle can be represented as a set of virtual sources distributed over the opening of the aperture. Light emitted with a point source of quasi monochromatic light *2* excites virtual light sources and makes them reradiate light energy towards the observation screen *4*. Virtual sources should be considered as mutually coherent because point light source *2* of infinitely small size ensures an infinitely large radius of coherence at the obstacle plane as it follows from (13.36). To find a light field at a certain observation point, we must summarize complex amplitudes of light fields produced there by each virtual source.

In general, the amplitude of each virtual source depends on the diffraction angle between the incident wave front normal at a virtual source location and the direction from that location towards the observation point. But, for the optical image produced with a small aperture shown in Fig. 13.5b, we can assume amplitudes of virtual source equal, as these are small diffraction angles that are of interest when examining the optical image. Denoting as a_n and b_n length of segments that connects the nth virtual source with the point light source *2* and the observation

point, respectively, we can denote the phase lag of oscillations at the observation point with that virtual source as $\varphi_n = k(a_n + b_n)$, where k is the wave number of light oscillations produced with point source. Namely, the phase is determined by length of optical path drawn through the nth virtual point source.

In general, all optical paths drawn through the aperture are not equal to one another. But we should expect that the interference of secondary light fields would result in local light intensity maximum at point that corresponds to minimal possible variation of path lengths. As can be shown, through appropriate integration, the intensity maximum is located at straight line connecting the point light source with the aperture centre. Thus, it corresponds to the apparent propagation of light along a straight line. The concept of virtual light sources also explains image blur resulting from shrinking of the aperture below a certain limit. Actually, if aperture size is comparable with light wavelength, it appears as a single point source that tends to emit light in all directions and thus produce uniform illumination of the observation screen, just like source 2 shown in Fig. 13.5a.

An optical system images a point light source with a spot of finite size. Overlapping of the spots corresponding to neighboring point light sources constituting a scene results in image blur and loss of small details. The minimal distance separating two equal point light sources that can be distinguished separately with a certain imaging system is referred to as resolution of the system. Obviously, the best resolution of an optical system can be achieved with most the compact image of a point light source. Because light enters into an optical system only through its aperture, the integral of light intensity over the image plane should be equal to that over the aperture. At a fixed aperture size, the most compact image of a point light source corresponds to the maximal possible peak of corresponding intensity distribution at the observation plane.

The peak of intensity distribution corresponds to maximum of interference of wavelets produced by virtual light sources. As it follows from (13.26) absolute interference maximum can be achieved when oscillations produced with all virtual light sources at observation point are in phase. In other words light should pass for the same time from light source S (Fig. 13.6a) to observation point S' along any path drawn through the aperture for example $SAA'S'$ or $SOO'S'$.

Although geometrical lengths of these paths are not equal, the difference can be compensated with a lens 3 made of transparent material and introduced into the aperture 2. As we mentioned above, transparent materials affect the phase of light, "slowing" the apparent propagation speed of light through them. Propagation of light through transparent material results in phase delay of $\varphi = \omega n d/c = k n d$, where d is geometrical path length, k is wave number, and n is refractive index of medium. Namely, the phase of light propagating through a transparent medium depends rather on the so-called optical path length nd than on its geometrical length d. Thus, the lens delays the phase of light propagating along shorter paths to ensure a interference maximum at point S'.

Equalizing the optical paths leading from S to S', the lens introduces a phase mismatch with respect to other points of the observation screen (e.g., Q' (Fig. 13.6a)). It results in certain distribution of light intensity over the surface of
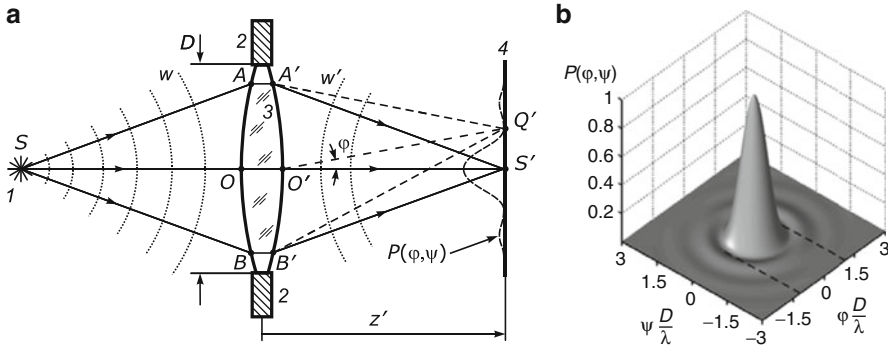
Fig. 13.6 Optical imaging with a lens (**a**) and normalized light flux distribution $P(\varphi, \psi)$ over the image plane (**b**). *1* – point light source; *2* – light stop with aperture; *3* – lens; *4* – image plane. D – is the aperture diameter

observation screen *4*, referred to as point spread function (PSF) of the optical system. The normalized theoretical PSF $P(\varphi, \psi)$, referred to as the Airy disk, which corresponds to the exact equalization of optical paths with the lens mounted into the circular aperture is shown in Fig. 13.6b. The angular radius of the central light spot of the distribution defines the minimal possible angular size of the point source image produced with the ideal optical system [1]:

$$\varphi_{\min} \approx \frac{\lambda}{D} \tag{13.39}$$

where D is the aperture diameter and λ is the light wavelength at the observation space. Angle $\varphi_{\min}$ determines the resolution of the optical system as the minimal angle separating the two point light sources that can be resolved as distinct light spots.

The diffraction of light on a lens results in an optical field that appears as a "cone of light" based on the lens aperture, like in the case of a camera obscura, which we discussed above. But vertex of the cone produced with the lens is located at point S', which is referred to as the optical conjugate of the point source S. When the cone vertex lies on the observation screen, it produces there the most compact spot with the radius of:

$$r_{\min} \approx \varphi_{\min} z' \approx \frac{\lambda}{D} z', \tag{13.40}$$

where z' is the separation between aperture *2* (Fig. 13.6a) and point S'. This light spot corresponds to the so-called "in-focus" image of the point light source. If point S' lays out of the observation screen light, the point light source is imaged with a broader light spot corresponding to the "out of focus" image. The center of the spot always represents the position of the point source as a projection with a straight
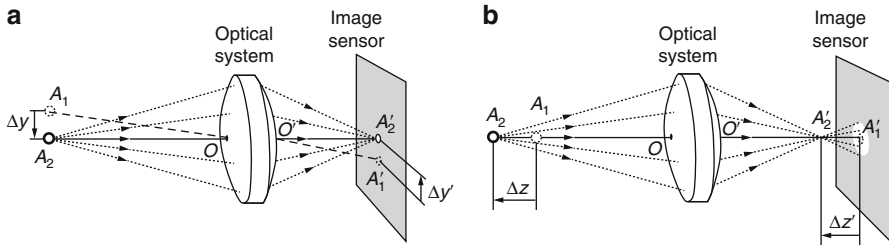
Fig. 13.7 Imaging of object that shifts perpendicular (**a**) and parallel (**b**) to principal ray

line referred to as the principal ray drawn from point S through the center of the aperture towards the observation screen.

Displacement of the light source immediately results in a corresponding movement of its image, therefore, optical imaging instruments can be used to determine the velocity of a flow-tracing particle. Displacement of an object perpendicular to the principal ray (Fig. 13.7a) results in an image shift within the image sensor plane as the light cone emitted with the source follows it. Image displacement is directly proportional to that of the light source, namely $\Delta y' = \beta \Delta y$, where β is the linear magnification of the imaging system. Thus, the lateral shift of the object can be easily detected by comparison of two consequently recorded images if the corresponding $\Delta y'$ exceeds the image sensor size. We should note here that β strongly depends on the distance between the light source and the entrance pupil of the system. In a real optical system, it also varies with the angle between the principal ray and the optical axis (axis of symmetry) of the optical system. It results in a distortion of the image shape.

Object shift along the principal ray is more difficult to detect as it results in changes of the diffraction pattern shape (Fig. 13.7b). In this case, the image (namely, the point corresponding to the local maximum of light intensity) moves along the principal ray in the image space and shifts out from the sensor plane. As far as the principal ray appears as the axis of symmetry of the light cone, it results in changes of diffraction pattern shape while its center remains at the same place. The expansion of diffraction pattern results in blurring of the image, which appears to be "out of focus." The axial displacement of image is directly proportional to that of object $\Delta z' = \gamma \Delta z$, where γ is referred to as longitudinal magnification. If the displacement is small and both object and image spaces are filled with the same medium, $\gamma \approx \beta^2$. In most cases, the actual position of an object along the principal ray could not be determined with reasonable precision from the optical image. One possible solution of the issue concerns the use of two imaging systems viewing an object from different points to obtain a so-called "stereo" image.

13.2.6 Particle Image Velocimetry

Over the millennia it was human vision that enabled detection and tracking of moving objects, which was critical to our survival. Thus, although it was

possible to acquire sequential images of flow-tracing particles by means of motion picture photography or videotape recording, there was only one way to evaluate flow velocity field through visual examination of the sequence. Progress in the field was achieved only in the early 1990s, with the development of powerful digital computers and reliable digital image sensors that gave rise to the computer-assisted particle image velocimetry (PIV) technique, which enables fast automated tracking of flow-tracing particles through sequential images of a flow. At present, PIV has became a versatile technique that is suitable for quantitative characterization of gas and fluid flows with velocities ranging from nanometers to kilometers per second and in different circumstances from airflow around an airplane to fluid circulation produced with a bacterial filament [5].

PIV is based on tracking of flow-tracing particles image through a series of consequently recorded pictures of a flow obtained with an appropriate imaging system. As an optical image represents a projection of an actual particle position onto the flat surface of an image sensor, the method is typically used for measurements of two-dimensional velocity fields within a plane that is optically conjugated with an image sensor surface. In order to simplify further analysis, we suppose here that the particle image is produced at the image sensor surface with an ideal optical system with unity magnification so we can assume that particle image coordinates x and y are equal to the actual particle coordinates within the conjugated flow cross section [5].

If two pictures were consequently recorded at instants separated with a certain time interval Δt, each particle image appears in the second picture displaced with respect to its position in the first one. Then, the first approximation velocity of a particle image can be calculated as

$$\mathbf{v}_i(\mathbf{r}_i) = \frac{(\mathbf{r}_i{}' - \mathbf{r}_i)}{\Delta t}, \tag{13.41}$$

where $\mathbf{r}_i = (x_i, y_i)$ and $\mathbf{r}_i' = (x_i', y_i')$ are position vectors of an individual particle i at the first and at the second image, respectively. If the picture contains N distinct images of the particle, the procedure results in an estimate $[\mathbf{v}_1(x_1, y_1) \ldots \mathbf{v}_N(x_N, y_N)]$ velocity vector field $\mathbf{V}(x, y)$. The main problem here is avoiding spurious displacement corresponding to the situation when $\mathbf{r}_i'$ and $\mathbf{r}_i$ points are images of distinct particles instead of the same one.

One way to ensure proper attribution of particles is to maintain particle seeding density low enough to ensure that the averaged distance separating particles sufficiently exceeds expected displacement of any flow tracing particle during the time interval of Δt (Fig. 13.7a). In this case, the particle position at the first picture is taken as a center of an interrogation region (IR) where only the same particle can be found at the next picture. Large particle separation guaranties proper attribution of the image because any unwanted particle could not enter into the interrogation region for Δt. The method referred to as particle tracking velocimetry (PTV) can be easily automated by means of computer-assisted digital image processing [5].
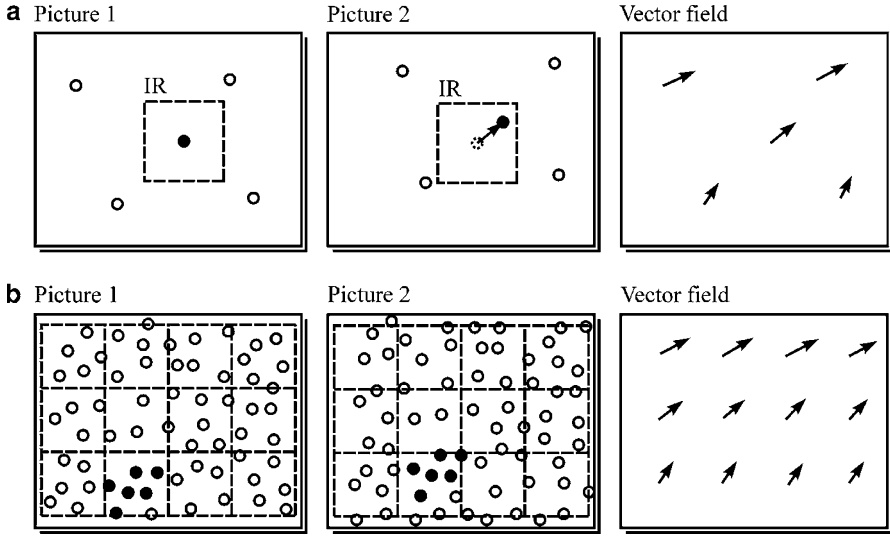
Fig. 13.8 Principle of particle tracking velocimetry (**a**) and particle image velocimetry (**b**); *IR* interrogation region

As is shown in Fig. 13.8a, the low seeding density required to avoid spurious displacements results in poor velocity field estimates.

On the other hand, if particle separation is less than length scale of any flow velocity gradient, neighboring particles retain their local positional relationship for a certain time. Thus, at high seeding density an image of particle group can be attributed properly through both images, so it should be considered as an elementary flow tracer rather than an image of a distinct particle (Fig. 13.8b). The principle gives a basis for the correlation-based technique referred to as particle image velocimetry (PIV).

PIV is based on subdividing of a picture with regular grid of identical interrogation areas that may partly overlap one another (Fig. 13.8b). Then, the mean displacement vector over each interrogation area is calculated with two-dimensional image correlations. The optical image recorded with a digital camera is represented with a two-dimensional array of numbers, each encoding mean light intensity over the corresponding image sensor element, referred to as pixel (namely *picture element*). Then, correlation of light intensity over the kth interrogation region is given with [5]

$$\Phi_k(m, n) = \sum_{j=1}^{q} \sum_{i=1}^{p} f_k(i,j) \cdot g_k(i+m, j+n), \qquad (13.42)$$

where $f_k(i, j)$ and $g_k(i, j)$ denote sub-arrays of $p \times q$ pixels, representing a light intensity distribution over the kth interrogation region at the first and the second pictures, respectively. The resulting estimate $\Phi_k(m, n)$ is represented with

a two-dimensional array with its maximal value position corresponding to the most likely displacement of a pattern representing a group of particles (e.g., one denoted with black circles in Fig. 13.8b). Thus, discrimination of the $\Phi_k(m, n)$ peak position gives the averaged fluid displacement over the IR for time interval of Δt, namely the mean displacement vector $\Delta \mathbf{r} = \mathbf{r}_i' - \mathbf{r}_i$. Repeating the procedure for each IR results in an estimate of velocity vector field as set of mean displacement vectors associated with the centers of corresponding IRs (Fig. 13.8b).

In order to optimize the image evaluation procedure, a fast Fourier transformation–based algorithm is used to get a cross correlation estimate $\Phi_k(m, n)$ rather than a sum calculation [see (13.42)], and more sophisticated methods of image evaluation may be implemented for specific applications like stereo PIV. Further details on PIV evaluation algorithms as well as comprehensive analysis of their performance can be found in Ref. [5].

PIV was initially developed for macroscopic fluid flow characterization with spatial resolution about 1 mm, but several years later it was extended to measure velocity fields of fluid motion within a length scale of 100 μm with a spatial resolution of 1–10 μm. The high-resolution technique, referred to as micro particle image velocimetry (μPIV), has found a number of applications in microfluidics, in particular related to chip development and life sciences [17, 18].

The extension of PIV to microscopic flows concerns not only the use of microscopic imaging systems for picture acquisition but also the fundamental difference between material particle motion in the macro and micro scale. It is well known that thermal fluctuations set small particles suspended in a fluid in endless stochastic motion, named Brownian motion after its discoverer. According to molecular-kinetic theory, Brownian motion results from collisions between fluid molecules and suspended particles. For time intervals Δt larger than particle inertial response time, the dynamics of Brownian motion is independent of inertial parameters such as particle and fluid density and should be considered as random walk of particles resulting in a great number statistically independent collisions. Thus, the random displacement of particles with respect to isotropic moving fluid can be considered as a Gaussian stochastic variable with the following probability distribution function [17]:

$$p(\Delta x, \Delta y, \Delta z) = \frac{1}{(2\pi)^{3/2}(2D\Delta t)^{3/2}} \exp\left[-\frac{(\Delta x^2 + \Delta y^2 + \Delta z^2)}{4D\Delta t}\right], \qquad (13.43)$$

where Δx, Δy, Δz are statistically independent displacement along corresponding Cartesian axes during the time interval of Δt; D is the particle diffusion coefficient. For a spherical particle subject to Stokes drag force, the particle diffusion coefficient was first given by Einstein as [19]

$$D = \frac{kT}{3\pi\mu d_p}, \qquad (13.44)$$

where d_p is the particle diameter; k is the Boltzmann constant; and μ and T represent dynamic viscosity and absolute temperature of a fluid.

Brownian motion of a particle with respect to moving fluid introduces an error in fluid velocity measurements. Assuming the above relative errors in measured x and y components of a fluid, velocity can be expressed as

$$\varepsilon_x = \frac{1}{u} \sqrt{\frac{2D}{\Delta t}}; \quad \varepsilon_y = \frac{1}{v} \sqrt{\frac{2D}{\Delta t}}. \tag{13.45}$$

While negligible in large length scales with respect to microscopic flows, the Brownian motion-related error establishes a lower limit on the measurement time interval Δt since, for shorter times, the measurements are dominated by uncorrelated Brownian motion. The uncertainty is more critical for PTV as the PIV approach means each displacement vector is an average over those of several particles within each IR. On the other hand, Brownian motion degrades positional relationship of particles within the IR, thus reducing cross correlation and even completely eliminating it for larger Δt. Thus, the "lifetime" of a particle positional relationship establishes a higher limit on the measurement time interval for PIV. In order to improve performance of PIV evaluation of microscopic flows, averaging of correlation estimates was proposed as the principal feature of the µPIV approach [17]. This means that the correlation estimate characterizing mean displacement over the kth is calculated as an average over the ensemble of picture pairs:

$$\bar{\Phi}_k(m, n) = \frac{1}{N} \sum_{l=1}^{N} \Phi_{k,l}(m, n), \tag{13.46}$$

where $\Phi_{k,l}(m, n)$ is the cross correlation of the kth IR through lth pair of pictures.

Although such correlation averaging improves the performance of the µPIV correlation-based particle, image velocimetry approaches (as with any of the other flow diagnostics technique we discuss later) fails when extended toward the sub-micrometer scale. This is because of the fundamental difference in the interpretation of term "motion" above and below the 1 µm length scale. In the macroscopic scale, we can assume the ordered motion of a particle from one point to another and consider Brownian motion as a source of errors. But at the sub-micrometer scale, the situation is reversed. Random motion of a particle should be considered as a principal while regular motion is just a drift of the probability distribution center. Therefore, the PIV approach originally suited to characterize ordered motion only no longer works at the length scale below 1 µm, while the PTV-like approach still can be used to track the random walk of single molecules with a spatial resolution of several nanometers [20].

13.2.7 Laser Doppler Anemometry

In 1842, Christian Doppler in his paper "On the Colored Light of Double Stars and Some Other Heavenly Bodies" formulated his principle, stating that the observed frequency of a radiation depends on the velocity of relative motion of the source

and detector. Thus, frequency of the observed radiation increases when the source moves towards the detector and decreases when it moves away from it. A fixed detector registers radiation with its original frequency. As Doppler's argument is applicable to wave process of any nature, he supposed that motion of the stars results in changes of their color. After the effect was confirmed in an experiment by W. Huggins in 1868, it was found that it could not affect the visible color of stars since it results only in a slight shift of spectral lines. In laboratory conditions, a similar shift of spectral lines was arranged for the first time in 1900 by A. Belopolsky, who utilized multiple light reflections from rotating mirrors to produce a virtual light source moving with respect to a spectroscope at a speed of 0.5 km/s. Since sufficient shift of spectral lines corresponds to very high velocities for a long time, the optical Doppler effect was only used in astronomy to measure the radial velocity of heavenly bodies [15, 21].

New applications of the Doppler effect became possible after the development of the laser-based technique of high-resolution optical mixing spectroscopy, enabling detection of very small, about a fraction of a cycle per second, variations of light oscillation frequency, which is about 10^{15} cycles per second. After the technique was used for the first time to detect the Doppler frequency shift resulting from light scattering from flow-tracing particles in 1964 [3], it gave rise to a variety of laser-based techniques for fluid diagnostics referred to as laser Doppler anemometry (LDA) [15]. For nearly four decades, LDA was the sole high-resolution non-intrusive method for localized fluid flow velocity measurements; the PIV technique replaced it for most of applications, as the latter is simpler to implement and allows for instant recording of the vector velocity field in contrast to point-wise measurements enabled by the former.

Although the Doppler effect manifests itself in wave processes of any nature, its interpretation within the scope of electromagnetic theory is different in a fundamental sense than that concerning, for example, acoustical waves. Mechanical waves are considered as propagating fluctuations of a property characterizing certain a material medium that transfers the wave from source to detector. In this case, Doppler frequency shift takes place two times: when the wave is excited in the medium with a source moving through it and when wave is registered with detector moving through the medium. Therefore, the same motion of a detector relative to a light source results in two different values of Doppler frequency shift: when medium is stationary relative to the source and when it is stationary relative to the detector. One value differs from another by the multiplier $(1 - (v/c)^2)$, where v is velocity of the detector motion relative to the source and c is the speed of wave propagation in the medium.

In acoustics, this difference can be easily observed in an experiment, because the speed of sound is relatively slow and even supersonic velocity of a source or a detector can be achieved. In optics, it is expected to be extremely small because of the extremely high speed of light. However, such small difference has not yet been detected in a reliable experiment concerning electromagnetic waves. Because no suitable interpretation of the phenomena was proposed, it was also postulated as a fundamental property of light and electromagnetic radiation in general.

Fig. 13.9 Laser light
scattering on a moving
particle: *1* – laser light source;
2 – moving particle, *3* –
detector, *4* – reference field
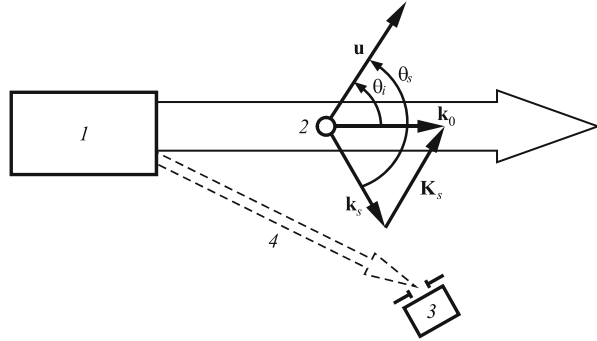
The postulation gives rise to the special theory of relativity, which states appropriate transformations of coordinates to avoid, with respect to electromagnetic waves, the difference in Doppler frequency shift mentioned above.

Thus, assuming the relativistic transformation of coordinates we obtain the same Doppler frequency shift for the observer either moving with the source or with the detector. In the one-dimensional case, the observer moves towards the light source and the observed radian frequency of light is expressed by any of the following equations [22]:

$$\omega = \omega_0 \frac{\sqrt{1 - v^2/c^2}}{(1 - v/c)} = \omega_0 \frac{1 + v/c}{\sqrt{1 - v^2/c^2}}, \qquad (13.47)$$

where ω_0 is the natural radian frequency of light source oscillations, v is the velocity of detector motion relative to the light source, and c is the speed of the light in vacuo. For most practically significant cases, one can take that $\sqrt{1 - v^2/c^2}$ is equal to unity. In this case, (13.47) are no longer identical but they are still equal to $(v/c)^2$, namely at the relative speed of about 1 m/s the error should not exceed 10^{-16}.

Now, using the (13.47), we can calculate the Doppler frequency shift of light radiation scattered by a moving flow-tracing particle. For simplicity, we consider a particle moving with a constant velocity **u** and illuminated with a beam of quasi monochromatic light with a central frequency of ω_0 emitted with light source *1* (Fig. 13.9). Light radiation scattered by a particle is collected with detector *3*. We suppose here that both the light source and detector are far enough from the particle, so we can assume that the wave vectors of incident and scattered light $\mathbf{k}_i$ and $\mathbf{k}_s$ produce constant angles θ_i and θ_s with velocity vector **u**. Due to the Doppler effect, the moving particle receives light radiation with shifted frequency that can be found from (13.47) assuming that the light source is moving relative to particle with velocity $\mathbf{u}' = -\mathbf{u}$ and u << c [21]:

$$\omega' = \omega_0[1 - (u/c)cos\Theta_i]. \qquad (13.48)$$

Now moving particle *2* appears as a moving secondary light source that emits light radiation with a central radian frequency of ω' towards stationary detector *3*. By using (13.47) once again, we express the frequency of light that reaches the detector as

$$\omega_s = \omega'[1 + (u/c)cos\Theta_s]. \tag{13.49}$$

Substituting (13.48) to (13.49) and leaving only terms linear in u/c we finally get

$$\omega_s = \omega_0\left[1 - \frac{u}{c}(\cos\Theta_i - \cos\Theta_s)\right] \tag{13.50}$$

or denoting Doppler frequency shift as $\Delta\omega = \omega_s - \omega_0$:

$$\Delta\omega = \frac{\omega_0}{c}u(cos\Theta_s - cos\Theta_i). \tag{13.51}$$

Taking for the non-relativistic case $\omega_0 \approx \omega_s$ and thus $|\mathbf{k}_0| = \frac{\omega_0}{c} \approx |\mathbf{k}_s|$, we can rewrite (13.51) as

$$\Delta\omega = (\mathbf{k}_s - \mathbf{k}_0)\mathbf{u} = \mathbf{K}_s\mathbf{u} \tag{13.52}$$

where $\mathbf{K}_s$ is vector difference between wave vectors of scattered and incident light radiation.

Maximal Doppler frequency shift corresponds to the case when wave vectors $\mathbf{k}_s$ and $\mathbf{k_0}$ are antiparallel and those both are collinear to the velocity vector $\mathbf{u}$. For particle velocity of 1 m/s and light wavelength of 500 nm, (13.45) gives the frequency shift $\Delta f = \Delta\omega/2\pi = 2u/\lambda = 4 \times 10^6$ Hz while the central frequency of light oscillations $f_0 = \omega_0/2\pi = c/\lambda= 6 \times 10^{14}$ Hz. Relative frequency shift about 10^{-8} could not be detected with conventional high-resolution spectroscopic techniques, but it can be detected through mixing of the scattered light field with a reference one oscillating at well-known frequency. If both fields are mutually coherent, their superposition results in light intensity oscillations with differential frequency, as follows from (13.20). The method referred to as heterodyning is widely used in radio electronics to detect differential frequency through mixing of electromagnetic fields originating from distinct oscillatory circuits [21].

In optics it is still very difficult to ensure mutual coherence of fields originating from different light sources, e.g., different lasers. Therefore, in the typical LDA arrangement, reference field *4* (Fig. 13.9) originates from the same source as the probing one. In this case, LDA arrangement should be considered as an interferometer that splits the light energy between two distinct optical paths connecting the light source and detector, namely *1-2-3* and *1-4-3* (Fig. 13.9). Interference of fields at the detector surface produces some light intensity distribution, the so-called interference pattern. Continuous motion of particle *2* changes the length of the first light path and thus it changes the phase difference $\Delta\varphi$ between optical fields

Fig. 13.10 Differential LDA
arrangement
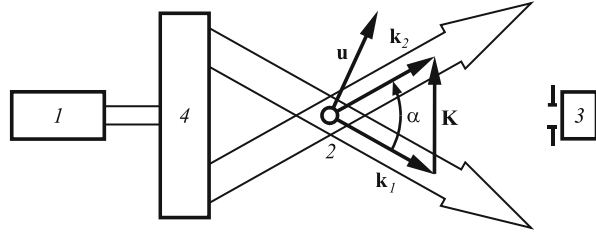
dropping at the detector surface. As can be shown, light intensity at each point of interference pattern in this case oscillates with frequency $\Delta\omega = \frac{\partial\Delta\varphi}{\partial t}$, which is equal to that given by (13.52).

The model of LDA as an interferometer is more useful than that based on the Doppler effect, because the former takes into consideration the full phase difference between optical fields mixed at the detector while the latter concerns only the time derivative of the phase difference, thus ignoring any phase relationships that do not depend on time. The full phase difference is critical for appropriate description of an LDA arrangement for at least of two reasons.

First of all, any arrangement must ensure mutual coherence of light fields mixing at the detector surface. For quasi monochromatic light (namely any light that can be observed in practice), this is possible only while the optical path difference introduced with arrangement does not exceed the coherence length of light radiation [see (13.34)].

Secondly, it is important to ensure that light intensity oscillations are in phase over the light detector surface. Output of any real light detector is proportional to light energy flux averaged over its sensitive surface of finite size. If light oscillations over a detector surface are not in phase, the overall modulation depth of the detected intensity decreases because a local intensity maximum at one part of detector could be balanced with a minimum at another one. Therefore, to provide an optimal signal-to-noise ratio of optical mixing, the detector size has to be much less than the period of phase variations over the observation plane.

The third factor affecting the modulation depth of the detector output is the ratio of reference and the scattered light field intensity. As follows from (13.13), the maximal difference between the intensity at the interference minimum and that at the corresponding minimum can be achieved if intensities of both fields are equal.

Evidently, the LDA arrangement shown in Fig. 13.9 is not ideal with respect to these issues inasmuch as special measures should be undertaken to ensure path equivalence; wave fronts of the reference wave are not parallel to that of light scattered with flow-tracing particles; and the reference field amplitude is constant while that of Doppler shifted light is determined only by optical properties of the particle and thus may vary from one particle to another.

To overcome the issues, differential LDA arrangement had been proposed (Fig. 13.10) [15]. Light radiation originating from laser *1* passes through an optical system *4*, which divides it between two mutually coherent beams and

then directs both of them onto a flow-tracing particle *2*. The moving particle scatters radiation of each beam subjected to Doppler frequency shift towards the light detector *3*. Superposition of the fields at the detector surface results in intensity oscillation with differential frequency $\Delta\omega_{12} = \Delta\omega_1 - \Delta\omega_2$, where $\Delta\omega_1$ and $\Delta\omega_2$ represent Doppler frequency shifts resulting from scattering of the first and the second beam by a moving particle towards the detector *3*. Using (13.52):

$$\Delta\omega_1 = (\mathbf{k}_{s1} - \mathbf{k}_1)\mathbf{u}; \quad \Delta\omega_2 = (\mathbf{k}_{s2} - \mathbf{k}_2)\mathbf{u}, \tag{13.53}$$

where $\mathbf{k}_1$ and $\mathbf{k}_2$ are wave vectors of incident beams; $\mathbf{k}_{s1}$ and $\mathbf{k}_{s2}$ denote wave vectors of scattered radiation corresponding to the first and the second beam, respectively; $\mathbf{u}$ is particle velocity. Because of Doppler frequency shift, frequencies of scattered waves are not equal, but because of very small shift magnitude we can assume that $\mathbf{k}_{s1} = \mathbf{k}_{s2}$ and then express differential frequency as

$$\Delta\omega_{21} = \Delta\omega_2 - \Delta\omega_1 = \mathbf{Ku}, \tag{13.54}$$

where $\mathbf{K} = \mathbf{k}_2 - \mathbf{k}_1$ is the differential wave vector of incident beams. Thus, the resulting light intensity at the detector surface oscillates with a frequency that is independent of the direction of light scattering by a particle. Light intensity frequency is determined here with a scalar product of the differential wave vector of incident beams and particle velocity. As follows from (Fig. 13.10), the differential wave vector magnitude can be expressed as

$$|\mathbf{K}| = \frac{4\pi n}{\lambda} \sin\left(\frac{\alpha}{2}\right), \tag{13.55}$$

where n is the refractive index of the surrounding medium; λ is the light wavelength in vacuo; and α is an angle between incident light beams.

The flow-tracing particle acts as a secondary source for both fields scattered towards the detector. Therefore, the differential LDA arrangement ensures matching of amplitudes and phases of mixed fields virtually at any observation point around the particle. It is obvious that modulation of light intensity at the detector surface takes place only when the particle is illuminated with both beams simultaneously. If the particle passes through only one beam, no intensity modulation is observed. Thus, differential LDA is suitable for local flow velocity characterization within a probe volume defined by the laser beams' intersection. Thus, narrower incident beams provide higher spatial resolution for local velocity measurements.

However, the Doppler-based model we used above does not assume any effect of finite beam size. Eventually it can be extended in the appropriate way to take into account the issues. But instead of following this elaborate method, we will examine the effect within the scope of the interference model of differential LDA.

Fig. 13.11 Interference
model of differential LDA
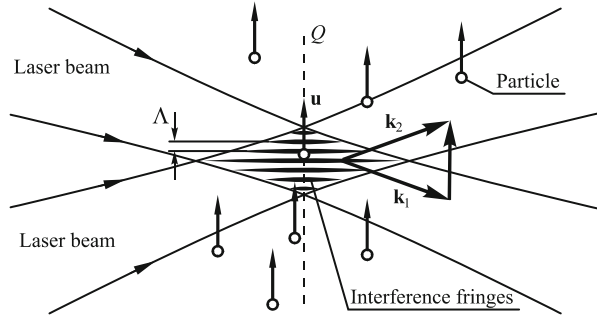
13.2.8 Interferential Model of Differential LDA

Say the probe volume of a differential LDA is formed by the intersection of two
mutually coherent Gaussian beams of laser radiation characterized by identical
amplitudes and frequencies. We also suppose that the intersection coincides with
the waist of each beam so the wave front of each beam is planar and wave vectors $\mathbf{k}_1$
and $\mathbf{k}_2$ are constant over the entire probe volume. As far as the beams are mutually
coherent, the interference should be observed over their intersection. According to
(13.27), the intensity at each point is determined by phase difference quasi mono-
chromatic light field oscillations

$$\delta(\mathbf{r}) = \varphi_1(\mathbf{r}, t) - \varphi_2(\mathbf{r}, t) = (-\mathbf{k}_2\mathbf{r}) - (-\mathbf{k}_1\mathbf{r}) = \mathbf{K}\mathbf{r}. \qquad (13.56)$$

The maxima of interference are expected at the point where $\delta(\mathbf{r}) = 2\pi m$, m is
integer. According to (13.56), their loci are represented with a set planes perpen-
dicular to $\mathbf{K}$ and spaced with period of $\Lambda = 2\pi/|\mathbf{K}|$. In (Fig. 13.11), the cross section
of the set of planes with the drawing plane is shown as a set of parallel horizontal
interference fringes.

As a result of interference, the light intensity over the probe volume appears to
be modulated in space. As follows from (13.27), the intensity at the maxima and
minima of the interference pattern depends on the ratio of intensities of superposed
light beams. Thus, because of nonuniform distribution of light intensity over the
beams, the modulation depth is nonuniform over the probe volume. It is close to
100 % at the points where the local intensities of both beams are equal. In the case
when a pair of identical Gaussian beams are used, the intensities should be equal at
the planes of symmetry of the probing volume, in particular in plane Q (Fig. 13.11)
where cross sections of the beams are matched.

When a particle moves across a probe volume it scatters light towards the
detector, which converts light energy flux through its sensitive surface into an
output voltage. Let us consider a detector output voltage corresponding to
a particle that crosses the probe volume with constant velocity of $\mathbf{u}$. Its position
varies depending on time as $\mathbf{r}(t) = \mathbf{r}_0 + \mathbf{u}t$ (Fig. 13.11), where $\mathbf{r}_0$ represents particle
position at $t = 0$. If particle size is much smaller than Λ and detector output is

Fig. 13.12 Simulated signal of differential LDA detector (**a**), low (**b**), and high (**c**) frequency components of the signal; and its power spectrum (**d**)
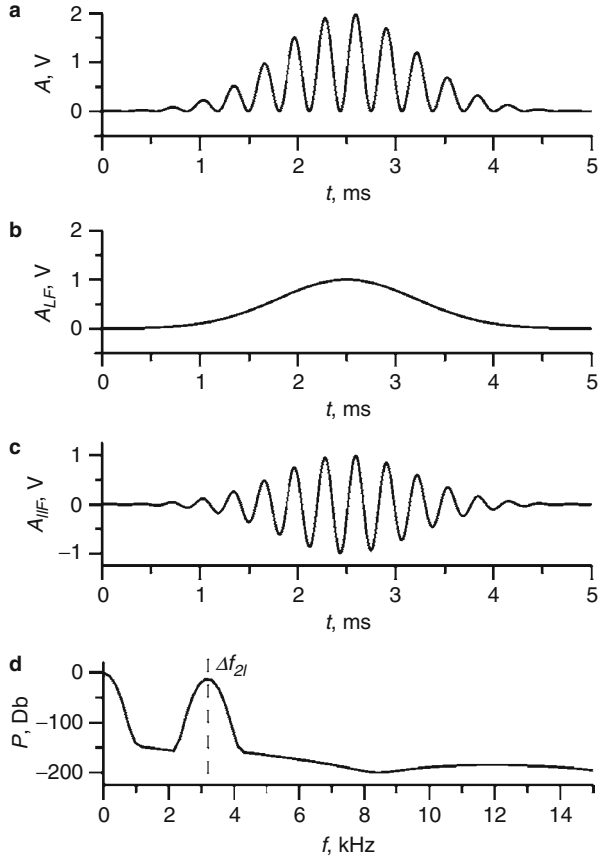
directly proportional to light energy flux through its surface, we can assume detector output at each instant of time is directly proportional to light intensity at the point corresponding to the current particle position. Then, if light intensity distribution over the first and the second laser beams is stationary and given with functions $I_1(\mathbf{r})$ and $I_2(\mathbf{r})$, we can express detector output using (13.39) and (13.56) as

$$A(t) \sim I_1(\mathbf{r}_0 + \mathbf{u}t) + I_2(\mathbf{r}_0 + \mathbf{u}t) + 2\sqrt{I_1(\mathbf{r}_0 + \mathbf{u}t)I_2(\mathbf{r}_0 + \mathbf{u}t)}\cos(\mathbf{K}\mathbf{u}t + \mathbf{K}\mathbf{r}_0).$$

$$(13.57)$$

A plot of $A(t)$ corresponding to particle movement parallel to $\mathbf{K}$ along the symmetry axis of probe volume formed with two identical Gaussian laser beams is shown in Fig. 13.12a. In that ideal case, the resulting signal modulation depth is 100 % because of $I_1(\mathbf{r}) = I_2(\mathbf{r})$ along whole particle trajectory.

The detector output appears as a sum of the low-frequency term $A_{LF}(t) \sim I_1(\mathbf{r}_0 + \mathbf{u}t) + I_2(\mathbf{r}_0 + \mathbf{u}t)$ corresponding to the averaged intensity

variation over cross sections of the superposed beam; and a high-frequency one
$A_{HF}(t) \sim 2\sqrt{I_1(\mathbf{r_0} + \mathbf{u}t)I_2(\mathbf{r_0} + \mathbf{u}t)}\cos(\mathbf{Ku}t + \mathbf{Kr_0})$ that represents intensity
oscillations with exactly the same frequency as (13.49) gives the Doppler fre-
quency shift: $\Delta\omega_{21} = \mathbf{Ku}$. The high-frequency component is also modulated with
an envelope that characterizes the light intensity distribution along the particle
trajectory. Plots of both low- and high-frequency components $A_{LF}(t)$ and $A_{HF}(t)$
are shown in Fig. 13.12b and c, respectively. The power spectrum of a signal
consists of a low-frequency component centered at zero frequency and a high-
frequency one peaking around $\Delta f_{21} = \Delta\omega_{21}/2\pi$. As follows from the fundamental
properties of Fourier transformation, the contours of both spectral components are
Gaussian because of the Gaussian shape of the intensity oscillation envelope.
Figure 13.12d represents an ideal case with 100 % intensity modulation.
However, in practice, for most of particles passing through the probe volume
the modulation rate is sufficiently less than 100%. Moreover, if a particle crosses
the light beams outside of the probe volume it produces light intensity variation
that consists of the low-frequency component only. Thus, the low-frequency
component of the LDA output spectrum is typically much higher than that at
high frequency. The superposition of spectral components introduces an error in
discrimination of a peak corresponding to Doppler frequency shift. As cos
$(-\mathbf{Ku}t) = \cos(\mathbf{Ku}t)$, the intensity variations do not reflect the actual direction of
particle velocity but only the modulus of its projection onto $\mathbf{K}$.

To overcome the issue, the frequency of one of the incident beams can be
shifted with respect to that of the other one in $\Omega = \omega_2 - \omega_1$ using, for example, an
acousto-optic modulator built in the optical setup of LDA. The constant prelim-
inary frequency shift results in translation of the interference maxima loci
into the probe volume along $\mathbf{K}$ with constant velocity. The translation does
not affect phase-independent low-frequency terms but shifts A_{HF} oscillation
frequency in Ω:

$$A_{HF}(t) \sim 2\sqrt{I_1(\mathbf{r_0} + \mathbf{u}t)I_2(\mathbf{r_0} + \mathbf{u}t)}\cos([\mathbf{Ku} + \Omega]t + \mathbf{Kr_0}). \qquad (13.58)$$

The shift of high-frequency spectral component ensures appropriate separation
between them and undesirable low-frequency pedestal centered on zero. It also
makes it possible to discriminate the sign of Doppler frequency shift $\Delta\omega_{21}$ because
the high-frequency component is centered now on $\Delta f'_{21} = (\Delta\omega_{21} + \Omega)/2\pi$.

After decades of intensive development of the LDA arrangement, many
improvements to the setup were proposed in order to enable simultaneous acquisi-
tion of three components of velocity vector: to reconstruct two- or even three-
dimensional velocity fields, to analyze particle size distribution in multi-phase
flows, and to provide velocimetry of microscopic flows, and so on. But, since
these improvements were achieved at the cost of complication of the optical
arrangements, each of them was application specific and thus reduced the versatility
of the approach [15, 21].
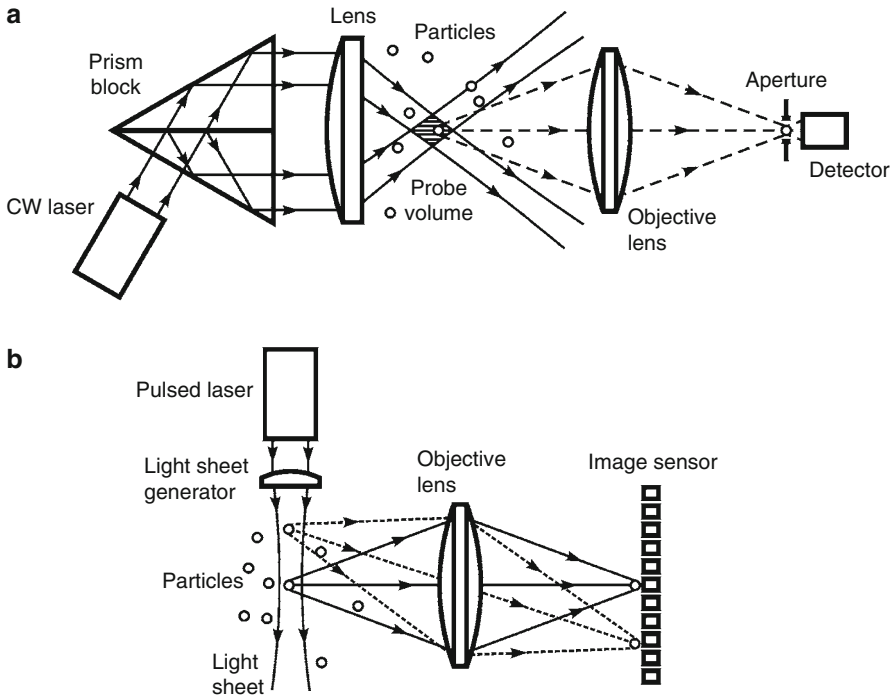
Fig. 13.13 Comparison of differential LDA (**a**) and light sheet based PIV (**b**)

13.2.9 Comparison of LDA and PIV Implementation

Originally, LDA and PIV techniques were developed for characterization of measurements of velocity of transparent media at low concentration of flow-tracing particles. Typical implementations of both techniques for such conditions are represented with structural diagrams shown in Fig. 13.13. As mentioned above, differential LDA (Fig. 13.13a) utilizes a cw laser light source to produce structured illumination of the probe volume with the interference pattern arranged with an interferometer constituted, e.g., of certain beam-splitting prism block and a lens that focuses laser beams and makes them intersect at their waist plane. To optimize collection of light scattered with the particle that crosses the probe volume, an objective lens is typically used to image the probe volume onto a plane of aperture that rejects unwanted radiation. A single light detector placed after the aperture converts light intensity into an electrical signal that is then analyzed with appropriate circuitry in order to discriminate its modulation frequency proportional to particle velocity. Actually, the differential LDA appears here just as a simple imaging system with specific structured illumination of the object space, which enables detection of particle displacement with a single detector.

By analogy with the above, PIV implementation can be considered as an imaging system that images particles onto an image sensor consisting of a two-dimensional array of light detectors (Fig. 13.13b). The replacement of a single detector with an image sensor PIV ensures measurement of the two-dimensional velocity field of flow-tracing particles in spite of point-wise measurements of the single-velocity component enabled with LDA shown in Fig. 13.13b. The PIV technique allows for tracking of any visible particles, so it is actually not critical to illumination setup. However, for large-scale flows, illumination with a laser "light sheet" is typically used to ensure exact localization of the velocity field along the imaging system axis. The "light sheet" produced with an optical system of a light sheet generator incorporating cylinder lenses is arranged to illuminate flow-tracing particles only within the plane optically conjugated with the image sensor. Because particles are in motion, it is necessary to ensure an exposure time that is as short as possible to avoid image smearing. Therefore, it is useful to illuminate flow-tracing particles with a pulsed laser, which "freezes" particle motion in a manner of a photographic flash lamp.

Actually, the use of a laser light source is not critical here as the only requirement for PIV processing concerns visibility of individual particles. For example, imaging of microscopic flows for PIV purposes does not require the use of light sheet illumination since the short depth of focus of high numerical aperture lenses efficiently suppresses images of out of plane particles. A laser light source ensures the best performance for LDA instrumentation because of the high intensity and monochromaticity of the radiation it emits. But the closer examination of the setup shown in Fig. 13.13a leads us to conclude that the replacement of the laser with any other light source of the equivalent intensity is not critical for proper operation of the Doppler anemometer. For example, the appropriate light intensity distribution over the probe volume can be obtained through projection with a lens of an appropriate pattern like diffraction grating. The use of an achromatic lens for projection makes it possible to use even white light for these purposes. Moreover, a reticle-shaped mask can be placed at the detector surface. Translation of the particle image across the mask will result in modulation of light reaching the detector surface.

Since both LDA and PIV can be considered as imaging-based techniques, we can state that they both enable quantitative measurements of flow-tracing particles' velocities under any conditions that make it possible to obtain optical images of these particles. Namely, they are suitable for characterizing flows in a transparent fluid seeded with flow-tracing particles of appropriate size and concentration to ensure visibility through the medium. Such criterion can be satisfied in most cases of experimental fluid dynamics studies as they leave the researcher a wide choice of working fluids and particles. However, the implementation of these techniques for characterization of biological fluids is not so easy because of the heterogeneous structure of both biological fluids and tissues introduces random phase modulation of the light propagating through. Since the phase of light is critical for localization of flow-tracing particles, the random modulation makes localization of flow tracing particles impossible and thus it cancels out any quantitative measurements of fluid

flow velocity. Thus, with respect to their applications for biomedical research, these techniques should be considered as task-specific methods for a limited number of applications like capillaroscopy or lab-on-a-chip testing, rather than as a versatile techniques for clinical diagnostics.

13.2.10 Scattering of Light

Interaction of light with material objects is the most complex problem of optics because it requires a model for interaction of light radiation with a huge ensemble of elemental light sources at atomic length scales. To date, quantum electrodynamics provides a formal interpretation of the interaction of an electromagnetic field with an individual atom or molecule, as well as with the set of limited number of such objects. But the direct extension of the microscopic approach for macroscopic objects is difficult because it is practically impossible to describe the exact positions of about 10^{23} atoms or molecules and to consider all interactions of each atom with the others. Therefore, some approximate models should be introduced to describe light propagation in the presence of macroscopic material bodies constituted with various media.

With respect to most practically significant problems, these media can be considered as deterministic or random. For deterministic media, distribution of elemental light sources can be described in terms of their macroscopic or microscopic structure. For example, gases and fluids can be considered as isotropic media with microscopically uniform spatial distribution of molecules; in a crystal, atoms and molecules or ions are arranged in an orderly and repeating pattern extended to all three spatial dimensions. Deterministic models are suitable for interpretation of the optical properties of homogeneous media such as refraction, dispersion, birefringence, and optical activity.

In contrast, a great deal of the media in nature could not be characterized in a deterministic manner as their local optical properties vary in a random way in space and time. These media introduce random variations of amplitude and phase in the field of light propagating through [23]. As a result, light energy is scattered in all directions. The models of random media are suitable for representation of optical properties of turbid objects with random or very complex internal structure like suspension of polydisperse particles or biological tissues. We consider here only some qualitative models of light propagation in random media in order to examine potential capabilities of imaging-based optical velocimetry with respect to optically heterogeneous media like these constituting biological objects.

Within the scope of electromagnetic theory, elemental light sources like atoms or molecules can be considered as certain oscillators that can be excited with incident light that makes them produce a secondary light field [23]. We suppose here that the intrinsic frequency of oscillators differs from that of incident light so they do not absorb light but scatter all incident energy due to forced oscillations. Let us consider a pair of such oscillators S_1 and S_2 illuminated with a point light source A (Fig. 13.14a). We suppose here that both oscillators fall into the same coherence
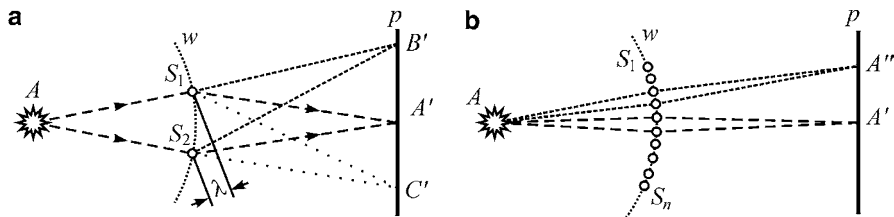
Fig. 13.14 Propagation of light through turbid (**a**) and transparent (**b**) medium

volume of incident light and thus they appear as mutually coherent secondary light sources. For example, we can suppose that both sources lie on the spherical wave front w. In this case, following the Huygens-Fresnel principle, we can represent the wave front as a set of virtual light sources as we did it for the empty space, except for points S_1 and S_2, where we should replace virtual light sources with real ones characterized by a different "oscillator force."

Superposition of coherent light fields produced with these real sources results in interference re-distribution of light energy over the screen surface, as discussed in Sect. 13.2.3. Following (13.19), we can expect interference maxima at points not only at A' for which optical lengths of paths AS_1A' and AS_2A' are equal, but also at points B', C', and so on, for which the optical path difference is equal to $m\lambda$, where m is an integer number and λ is light wavelength. Namely, diffraction of light on the elemental oscillators results in deflection of light from its initial direction, referred to as scattering of light.

The model also explains the propagation of light through homogeneous transparent media like air, water, glass, and clear plastics. Actually, as follows from geometry, the difference of optical paths leading from each oscillator to any given point in space could not exceed the length of segment $S_1 S_2$ separating these sources. Thus, if the separation between light sources is less than the light wavelength, the interference maximum is possible only when optical paths leading to the observation point are equal (Fig. 13.14b). In this case, densely packed oscillators act in the same manner as virtual light sources and they produce a light field that appears like a wave propagating along straight lines. As mentioned above, the secondary optical field produced with such densely packed oscillators superposes the incident one and the resulting field appears as propagating through the medium slower than through empty space.

This secondary field also appears as light reflected back from the transparent body surface, referred to as Fresnel reflection. We should note here that any variations of oscillator density result from light scattering. Such variations in length scale exceeding light wavelength makes a medium appear as turbid and non-transparent, while fluctuations of oscillator density at the molecular level, e.g., due to non-uniform distribution of molecules of gas as a result of thermal motion, produce weak scattering referred to as molecular scattering of light inside transparent media.
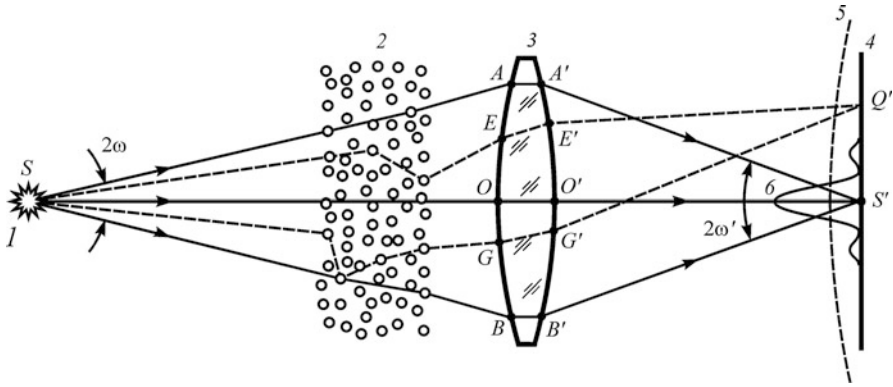
Fig. 13.15 Imaging trough turbid medium: *1* – light source; *2* – turbid medium; *3* – lens; *4* – observation screen; *5* – non-coherent light intensity distribution; *6* – coherent light intensity distribution (Airy disk)

Scattering of light inside turbid medium introduces random variation of the scattered light phase, which results in apparent deviation of light from its rectilinear propagation. Thus, in most cases it makes it impossible to obtain an optical image of an object with light propagating through a turbid medium. For example, an extreme case of light propagation through a strongly turbid medium results in diffusion, like transfer of light energy, because such a medium totally disorders any initial distribution of incident light field phase and amplitude. But, as discussed above, the opposite extreme case concerns the transparent medium that does not disturb rectilinear propagation of light, so a turbid medium in particular may allow for imaging through it even while it degrades image quality.

Consider the effect of a turbid medium on the optical image of a point light source of non-coherent light *1* (Fig. 13.15) covered with a turbid medium *2*. In order to obtain an optical image of the light source, a lens *3* is placed between the turbid medium and the observation screen *4*. Diffraction of light on heterogeneities causes it to deviate from its rectilinear propagation and pass along the curvilinear paths shown in Fig. 13.15 with dashed lines. But a certain fraction of light energy flow does not change its initial direction after it passes through the turbid medium, so it passes through the lens and reaches point *S'*. This light energy flow propagates along paths that are shown in Fig. 13.15 with solid lines.

As was shown in Fig. 13.6, the lens equalizes the optical length of these paths and produces an optical image of the light source as a result of constructive interference of the light oscillations passed along them. Thus, light oscillations passed through turbid medium along straight paths are mutually coherent and they result in interference pattern *6* (Fig. 13.15), which appears as an Airy disk, the same as that which represents the point light source image obtained without turbid medium introduced before the lens. Each oscillator constituting the turbid medium deflects a certain fraction of light energy away from the rectilinear trajectory

intensity of light, propagating along a straight path that exponentially degrades with the increase of turbid medium thickness following Beer's law:

$$I(l) = I_0 \exp(-\mu l), \tag{13.59}$$

where I_0 is the intensity of the parallel light beam incident to a slab of turbid medium; l is the slab thickness and I is the intensity of parallel light beam emerging from the slab at the same direction; μ is referred to as extinction coefficient, which represents the inverse optical path corresponding to the attenuation of incident light intensity by a factor of e.

Light passed through a turbid medium along curvilinear paths also reaches the observation screen. But since the optical length difference of these paths exceeds the coherence length of light emitted with the point source, these oscillations are incoherent at the screen surface. Thus, they produce a certain wide intensity distribution 5 (Fig. 13.15) over the screen surface. Because the incoherent distribution biases the coherent one, the latter remains visible despite the effect of the turbid medium [23].

The model shows us certain ways to enhance signal-to-noise ratio of the image obtained through a turbid medium. In particular, it can be increased with the increase of the imaging lens aperture ratio as it allows for collecting more coherent light that forms the image. Non-coherent light can be suppressed with an aperture placed at the image plane. But in this case, only one point of the object can be imaged at once and certain scanning is needed to resolve the whole object point-by-point. The effect of image quality enhancement with the increase of lens aperture and filtering of undesirable light with an aperture constitutes the fundamental background of laser scanning microscopy (LSM), which enables high-quality, three-dimensional imaging of living cellular structures through a 100-μm-thick layer of superposed tissue [6, 7].

The coherent component of scattered light can be also discriminated by means of certain interferometry techniques. This approach was implemented in so-called optical coherence tomography (OCT), which allows for imaging of supracellular structures through a 1-mm-thick layer of living tissue with resolution typically less than 10 μm limited with sufficient variations of optical paths inside living tissues. The penetration depth of both LSM and OCT is limited with exponential degradation of the coherent field rather than variation of optical paths. To date, LSM is used for optical tracking of polystyrene beads introduced into intracellular space and inside cells, while methods of LDA implemented in the OCT system allow for characterizing of blood circulation through individual arterioles and venula of superficial tissues [6, 7].

13.2.11 Laser Speckles

Light scattering results in deflection of light propagating through a turbid medium from its initial direction, namely in redistribution of light intensity in space.

The scattered field can be represented as the superposition of secondary fields produced with optical heterogeneities of the medium. Depending on the shape and size of the coherence volume characterizing the incident light field, the superposition can result in interference of secondary fields as well as in non-coherent addition of them. Thus, the most general case of light scattering should concern a certain combination of these two kinds of light field superposition, which can be treated using a model of so-called partially coherent light [1, 16].

Although the model of partially coherent light plays a central role in the theory of microscopic imaging, and thus can be useful for certain biomedical applications of optical techniques, we limit our consideration here to extreme cases of completely non-coherent and coherent light. The first case may correspond to diffuse non-filtered daylight originating from an extended diffuser. Using (13.34) and (13.36), we can find that coherence radius and coherence length of such radiation may be comparable with light wavelength, so optical heterogeneities constituting an object appear as mutually non-coherent secondary light sources (see Fig. 13.5a). Obviously, non-coherent superposition of light fields produced with a great many scattering centers results in so-called "diffuse" distribution of scattered light intensity, which smoothly varies from one point of space to another.

Another extreme case entails the complete coherence of the incident light field. It corresponds to irradiation of a turbid medium with laser light. As mentioned in Sect. 13.2.3, light oscillations produced with a laser are completely coherent over the whole wave front of the beam it emits and the coherence length of radiation is typically about several centimeters. Thus, one can treat the incident field as completely coherent when the object size is less than the coherence length of the laser radiation used.

In this case, scattered light intensity at any point results from interference of secondary waves produced with all scattered centers. Because light intensity that results from interference of light fields is sensitive to phase relationships between superposed oscillations, scattered light intensity varies quickly from one point to another and forms a random pattern of bright spots referred to as laser speckles [24], as is shown in Fig. 13.16. Figure 13.16a represents light scattering of a laser beam *1* with a set of randomly distributed scattering centers *2*. The scattered field appears as a speckled pattern on observation screen surface *3*.

Assuming both the incident and scattered light being linearly polarized, we can use scalar approximation of the light field to express the complex amplitude of light field $A(\mathbf{r})$ at observation screen *3* with (13.9) as a sum of complex phasors $a_1(\mathbf{r})$, $a_2(\mathbf{r})$, ..., $a_N(\mathbf{r})$ (as we assumed that all these phasors are completely mutually coherent), where $a_n(\mathbf{r})$ represents light field produced at observation point with scattering center S_n (Fig. 13.16a) and $\mathbf{r}$ denotes position vector of an observation point. Because scattering centers S_n are randomly distributed over space the sum can be found in a statistical sense rather than in deterministic one. The phasors can be considered as complex random variables characterized with its own specific probability distribution. Thus, a sum of them that represents the resulting field at the observation point should also be a random complex variable [24, 25].
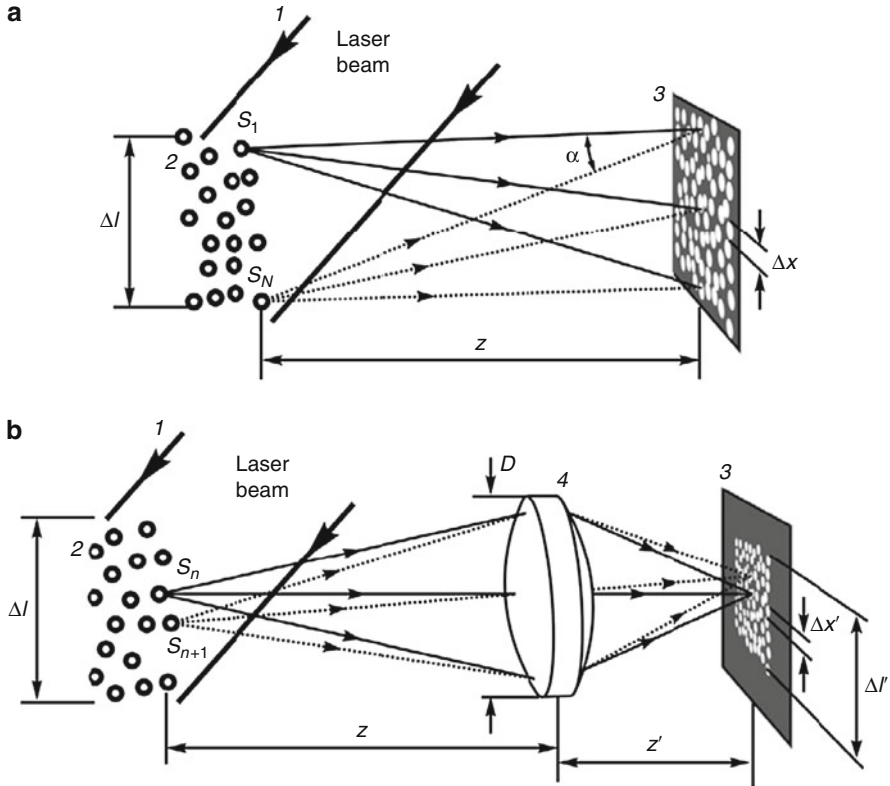
Fig. 13.16 Laser speckles in free space (**a**) and in imaging system (**b**). *1* – laser beam; *2* – turbid object; *3* – observation screen; *4* – optical system

Strictly speaking, the statistical properties of the resulting field depend on the specific structure of a scattering object as well as on the geometry of an experiment. But if the speckle field results in scattering of laser radiation by a great many scattering centers, the central limit theorem can be used to represent the resulting field with a Gaussian random variable that is independent of the actual structure of the object. The approximation postulates that that speckle pattern does not depend on the actual structure of the light scattering object. However, this asymptotical model is applicable to the vast majority of cases of practical interest with an extremely high degree of accuracy.

The model of laser speckles mentioned above is based on the following assumptions [24]: (1) the light field is completely mutually coherent and thus the light field at any point of the observation screen can be represented with the sum of complex amplitudes of phasors; (2) the light is linearly polarized and thus scalar approximation of the light field can be used; (3) the amplitude and the phase of each phasor are statistically independent of each other and of amplitudes and phases of all other elementary phasors; (4) the phases are uniformly distributed over the primary

interval of $(-\pi, +\pi)$; (5) the number of elementary phasor contributions is extremely large ($N \to \infty$). The assumptions make it possible to represent the complex amplitude of the resulting light field at an observation screen with a circular Gaussian random variable. The joint probability density function of real $A^{(r)}$ and imaginary $A^{(i)}$ is asymptotically approaching to [24]

$$p_{r,i}\left(A^{(r)}, A^{(i)}\right) = \frac{1}{2\pi\sigma^2} \exp\left[-\frac{\left(A^{(r)}\right)^2 + \left(A^{(i)}\right)^2}{2\pi\sigma^2}\right], \qquad (13.60)$$

where

$$\sigma^2 = \lim_{N \to \infty} \frac{1}{N} \sum_{k=1}^{N} \frac{\left\langle |a_k|^2 \right\rangle}{2} \qquad (13.61)$$

and $\left\langle |a_k|^2 \right\rangle$ modulus of the kth phasor amplitude averaged over macroscopically identical but microscopically different sets of scatterers. The probability density function, described by (13.60), plays a central role in the theory of so-called fully developed laser speckles. The intensity of light given with (13.7) as the squared modulus of complex amplitude and the probability density function of light intensity can be found from (13.60) as the negative exponential one. As can be shown, contrast of linearly polarized speckle field [24]

$$C = \frac{\sigma_I}{\langle I \rangle}, \qquad (13.62)$$

where σ_I is standard deviation and $\langle I \rangle$ is average value of light intensity over an observation screen, and is always unity.

Since intensity of the laser speckle pattern randomly varies along the observation screen, it can be characterized in terms of intensity autocorrelation:

$$R_I(\mathbf{r}_1, \mathbf{r}_2) = \langle I(\mathbf{r}_1)I(\mathbf{r}_2) \rangle, \qquad (13.63)$$

where $\langle \ldots \rangle$ denotes averaging performed over an ensemble of scattering objects [see (13.61)] and $\mathbf{r}_1 = (x_1, y_1)$ and $\mathbf{r}_2 = (x_2, y_2)$ represent coordinates of two distinct points on the observation screen plane (x, y). The "width" of this function, i.e., the minimal value of $\Delta\mathbf{r}$ corresponding to $R_I(\mathbf{r}_1, \mathbf{r}_1 + \Delta\mathbf{r}) = 0$, namely the intensity correlation distance characterizes the averaged size of a speckle at a point of screen given with $\mathbf{r}_1$. Although any measurements result in light intensity values, this is the amplitude of light field that can be calculated for each point of the observation screen. Thus, we should express intensity autocorrelation in terms of the corresponding field amplitude moments [24]:

$$R_I(\mathbf{r}_1, \mathbf{r}_2) = \langle A(\mathbf{r}_1)A^*(\mathbf{r}_1)A(\mathbf{r}_2)A^*(\mathbf{r}_2) \rangle, \qquad (13.64)$$

where $A_R(x, y)$ represents complex amplitude of the light field at a point of observation screen. Assuming $A_R(x, y)$ is a complex circular Gaussian random variable, we can simplify (13.64) utilizing the complex Gaussian moment theorem:

$$R_I(\mathbf{r}_1, \mathbf{r}_2) = \langle I(\mathbf{r}_1)\rangle\langle I(\mathbf{r}_2)\rangle + |J_A(\mathbf{r}_1, \mathbf{r}_2)|^2, \qquad (13.65)$$

where

$$J_A(\mathbf{r}_1, \mathbf{r}_2) = \langle A(\mathbf{r}_1)A^*(\mathbf{r}_2)\rangle \qquad (13.66)$$

is a so-called mutual intensity of light field and $I(\mathbf{r}) = A(\mathbf{r})A^*(\mathbf{r})$ is the intensity of light at a point of the observation screen (throughout this section we omit the constant term $\varepsilon_0 c/2$ because this is a relative intensity that is measured in the experiment rather than an absolute one). Thus, the Gaussian model of laser speckles allows for reducing the problem of the calculation of R_I to the calculation of J_A, which is much simpler. Because the complex amplitude of the light field at the observation screen can be expressed from that at the scattering object surface with appropriate diffraction integrals, the following important results can be obtained for the practically significant cases shown in Fig. 13.16.

In the particular case shown in Fig. 13.16a, the average size of laser speckle in free space light propagation can be estimated as [24]

$$\Delta x = \frac{\lambda z}{\Delta l}, \qquad (13.67)$$

where λ represents light wavelength; z is the distance between the light scattering object and the observation screen; and Δl is a separation of the outermost scattering centers denoted as A_1 and A_N. In other words, speckle size characterizes the distance corresponding to complete alteration of phase relationships between secondary fields originating from scattering centers.

When a scatterer is imaged with an optical system (Fig. 13.16b), the averaged speckle size is equal to the Airy disk diameter [24]

$$\Delta x' = \frac{\lambda z'}{D}, \qquad (13.68)$$

where D is the lens aperture diameter, z' is the distance between lens *4* (Fig. 13.16b) and the observation screen *3*, and λ is the light wavelength. Namely, each scattering center can be considered as a point light source imaged with a lens with aperture diameter D. Thus, the intensity distribution at the image plane results from interference of the Airy disks. If observation screen *3* is optically conjugated with an object *2*, a speckled image of the object can be observed there. Image size is $\Delta l' = \beta\Delta l$, where β is the linear magnification of the optical system.

Speckle size depends only on D and z'. It does not vary when the object moves along the optical axis. As mentioned in Sect. 13.2.4, the point spread function of the imaging system broadens when an object is displaced from the plane conjugated with the observation screen. But the speckles do not reflect this change because this is the aperture D that determines speckle size while it acts with respect to the observation screen as the illuminated object 2 shown in Fig. 13.16a.

Thus, scattering of coherent light with a large number of randomly distributed scattering centers always results in a random speckle pattern with averaged speckle size determined by scattering geometry rather than by a structure of the scatterer. In a free space geometry (Fig. 13.6a), speckle size is determined by the size of the object illuminated with laser light, and in imaging geometry (Fig. 13.6b) it is determined by the diameter of the imaging system aperture.

A high-contrast speckle pattern that superposes the optical image sufficiently degrades the images of objects illuminated with coherent light, and appears in this case as intensity noise. On the one hand, this noise makes it difficult to detect edges and other features of an object. But on the other, the speckles observed over the object image plane follow the object just as they would be drawn on its surface. This makes it possible to track displacements of surfaces which could not be tracked under non-coherent illumination as in the latter case they are looking smooth and featureless as far as one can see. The effect of "sticking" of speckle patterns to the optical image of an object underlies the versatile laser metrology technique referred to as speckle interferometry.

13.2.12 Dynamics of Laser Speckles

Because laser speckles represent positional relationships between scattering centers constituting an object, they vary depending on time as a result of any motion of the whole object or any part of it. The light field produced at the observation screen with an ensemble of moving scattering centers varies randomly depending on both time and observation point position. Throughout this section, we assume that movement of scattering centers result in slow fluctuations of resulting intensity at any point of the observation screen, which always can be resolved with a light detector. In the other words, the time constant of light intensity fluctuations $\tau_F = 1/\Delta\nu_F > \tau_D >> \tau_m = 1/\Delta\nu_m$, where $\Delta\nu_F$ is intensity fluctuation bandwidth; τ_D is detector bandwidth; τ_m and is time constant of random fluctuations of complex amplitude of the light field; and $\Delta\nu_m$ is laser spectral line bandwidth.

As above, we limit further consideration to completely coherent laser radiation and thus can ignore any fluctuations of the light complex amplitude with the exception of those resulting from the motion of scattering centers. Thus, we can modify the results of the previous section, assuming that the light field amplitude averaged over detector response time at the observation screen is represented with a random function

$$A(\mathbf{r}, t) = \langle A_m(\mathbf{r}, t) \rangle_D, \tag{13.69}$$

where $\mathbf{r}$ denotes position vector (x, y) of an observation point on the observation screen surface, and $A_m(\mathbf{r}, t)$ is the light field of quasi monochromatic light. Then, the light detector at any point registers instant intensity

$$I(\mathbf{r}, t) = A(\mathbf{r}, t)A^*(\mathbf{r}, t). \tag{13.70}$$

To shorten representation, we omit here the coefficient $\varepsilon_0 c/2$ because it is the relative intensity variations that are our primary interest. Because the detector can resolve all fluctuations of light intensity, we interpret $I(\mathbf{r}, t)$ as the time varying voltaic output of a point light detector placed at $\mathbf{r}$.

Random functions of time often represent fluctuations that do not change their character in time, even if any realization of the random process varies continuously depending on time. Such processes are referred to as statistically stationary. Strictly speaking, a random process is stationary if all probability density functions that describe fluctuations are independent of the choice of time origin. Using (13.65), we can express second-order statistics of light intensity with second order statistics of the field. For these purposes it is enough to assume the random process is stationary in a wide sense, namely that average $\langle A(\mathbf{r}, t) \rangle$ is independent of time and correlations like $\langle A(\mathbf{r}, t_1)A^*(\mathbf{r}, t_2) \rangle$ depend only on $\tau = t_1 - t_2$.

We also assume that the random process is ergodic, namely that time average of each realization is equal to the average across the ensemble of realization. Thus, we can interchange ensemble averages with these over time and express autocorrelation of the speckle pattern intensity as:

$$R_I(\mathbf{r}_1, \mathbf{r}_2, \tau) = \langle I(\mathbf{r}_1, t)I(\mathbf{r}_2, t + \tau) \rangle = \langle I(\mathbf{r}_1, t) \rangle \langle I(\mathbf{r}_2, t) \rangle + |J_A(\mathbf{r}_1, \mathbf{r}_2, \tau)|^2, \tag{13.71}$$

where angular brackets denote averaging over time and $\langle I(\mathbf{r}, t) \rangle$ is the time-averaged intensity (angular brackets denote average over recorded realization of $I(\mathbf{r}, t)$, which represents time-varying voltaic output of the light detector placed at $\mathbf{r}$). Because it does not depend on time, it is useful to normalize correlation, described by (13.71), dividing it by $\langle I(\mathbf{r}_1) \rangle \langle I(\mathbf{r}_2) \rangle$:

$$G_I(\mathbf{r}_1, \mathbf{r}_2, \tau) = \frac{\langle I(\mathbf{r}_1, t)I(\mathbf{r}_2, t + \tau) \rangle}{\langle I(\mathbf{r}_1, t) \rangle \langle I(\mathbf{r}_2, t) \rangle} = 1 + |g_A(\mathbf{r}_1, \mathbf{r}_2, \tau)|^2, \tag{13.72}$$

where

$$g_A(\mathbf{r}_1, \mathbf{r}_2, \tau) = \frac{\langle A(\mathbf{r}_1, t)A^*(\mathbf{r}_2, t + \tau) \rangle}{\sqrt{\langle A(\mathbf{r}_1, t)A^*(\mathbf{r}_1, t) \rangle}\sqrt{\langle A(\mathbf{r}_2, t)A^*(\mathbf{r}_2, t) \rangle}} \tag{13.73}$$

is the normalized autocorrelation of the light complex amplitude $A(\mathbf{r}, t)$ at the observation screen surface and angular brackets denote averaging over observation time. Thus, the particular case of the fully developed speckle pattern, described by (13.72), establishes a very simple relation between the normalized autocorrelation

of light intensity (detector output) $G_I(\mathbf{r}_1, \mathbf{r}_1, \tau)$ and the autocorrelation of complex amplitudes $g_A(\mathbf{r}_1, \mathbf{r}_1, \tau)$ resulting from scattering of coherent light on moving scatterers.

In most general cases, autocorrelations of the optical field in space and time should not be considered as independent of one another. This is true, for example, when the speckle pattern results from scattering of laser light by a moving rough surface. But for certain cases, like scattering of light with Brownian particles, g_A can be reduced to a product of a term depending only on the spatial coordinates and a term depending only on time delay [16, 26]:

$$g_A(\mathbf{r}_1, \mathbf{r}_2, \tau) = g_s(\mathbf{r}_1, \mathbf{r}_2)g_\tau(\mathbf{r}_1, \tau), \qquad (13.74)$$

where

$$g_s(\mathbf{r}_1, \mathbf{r}_2) = \frac{\langle A(\mathbf{r}_1, t)A^*(\mathbf{r}_2, t)\rangle}{\sqrt{\langle I(\mathbf{r}_1, t)\rangle\langle I(\mathbf{r}_2, t)\rangle}}, \qquad (13.75)$$

and

$$g_\tau(\mathbf{r}_1, \tau) = \frac{\langle A(\mathbf{r}_1, t)A^*(\mathbf{r}_1, t + \tau)\rangle}{\langle A(\mathbf{r}_1, t)A^*(\mathbf{r}_1, t)\rangle}. \qquad (13.76)$$

The factorization makes it possible to analyze each autocorrelation separately. As in the previous section, autocorrelation of the speckle field amplitude g_s sampled at points $\mathbf{r}_1$, $\mathbf{r}_2$ determines the autocorrelation of light intensity and thus averaged speckle size, which can be estimated using (13.67) or (13.68) for free space and imaging geometry, respectively. Temporal autocorrelation of light amplitude g_τ determines temporal autocorrelation of light intensity at single point of screen. And the product, described by (13.74), means that temporal fluctuations of intensity are correlated over the averaged speckle area. Thus, the best signal-to-noise ratio in intensity sampling can be achieved if detector size is equal to averaged size of speckle. A smaller detector is not efficient as it does not utilize all available light intensity. But a larger one would integrate statistically independent fluctuations of intensity over several speckles. Integration of speckles does not increase the magnitude of intensity fluctuations but biases it with a constant subset that rises with the broadening of the detector area.

As is well known from multiple experiments, the autocorrelations of light intensity produced with randomly moving particles show a nearly exponential decay with delay time τ. At very short time delays, particle positions are highly correlated and thus intensity autocorrelation $\langle I(t)I(t + \tau)\rangle$ is near to the mean square of intensity $\langle I^2(t)\rangle$. At long time delays, particle positions are no longer correlated and intensity correlation becomes the mean intensity squared $\langle I(t)\rangle^2$. As can be shown for coherent light scattering with an ensemble of spherical Brownian

particles of the same size, both the field and the amplitude autocorrelations have an exactly exponential decay delay time τ [27, 28]:

$$g_\tau(\mathbf{r}_1, \tau) = \exp(-\Gamma\tau), \tag{13.77}$$

and

$$G_I(\mathbf{r}_1, \tau) = 1 + 2\beta\exp(-\Gamma\tau), \tag{13.78}$$

where β is a parameter that characterizes the decrease of signal-to-noise ratio as a result of speckle field integration with the detector aperture. The decay constant Γ depends on the diffusion coefficient of particles D and the squared modulus of differential wave vector K:

$$\Gamma = DK^2. \tag{13.79}$$

The technique based on estimation of Γ is used for size characterization of small particles suspended in a fluid because the diffusion coefficient is directly proportional to hydrodynamic particle diameter. For monodisperse spherical non-interacting particles, the diffusion coefficient is given by the Stokes–Einstein equation.

$$D = \frac{kT}{3\pi\mu d_p}, \tag{13.80}$$

where k is the Boltzmann constant, T is the absolute temperature, μ is the fluid viscosity, and d_p is the apparent (hydrodynamic) diameter of a particle. A typical arrangement for particle size measurements is shown in Fig. 13.17. A collimated beam emitted with a laser light source 1 is passed through sample cell 2 filled with a suspension of small particles in a fluid. Scattered light is collected by means of an optical system that determines the angle of light scattering. In its simplest variant, the system consists of pair of apertures 3 that limit viewing angle of a detector 4. The detector converts light intensity into electric voltage transmitted to a stand-alone or PC-based autocorrelator 5. The differential wave vector in such an arrangement is determined by scattering angle θ:

$$K = \frac{4\pi n}{\lambda}\sin\frac{\theta}{2}, \tag{13.81}$$

where n is a refractive index of a fluid; λ is light wavelength in vacuo.

The laser-based method for particle size measurements, which is referred to as dynamic light scattering (DLS) or photon correlation spectroscopy, is typically used for characterization of monodisperse particles in a dilute suspension, which ensures detection of light scattered once with a particle [3, 27, 28]. Low concentrations of suspension result in fluctuations of particle number within the scattering volume, which distorts autocorrelation and affects quality of measurements. At high
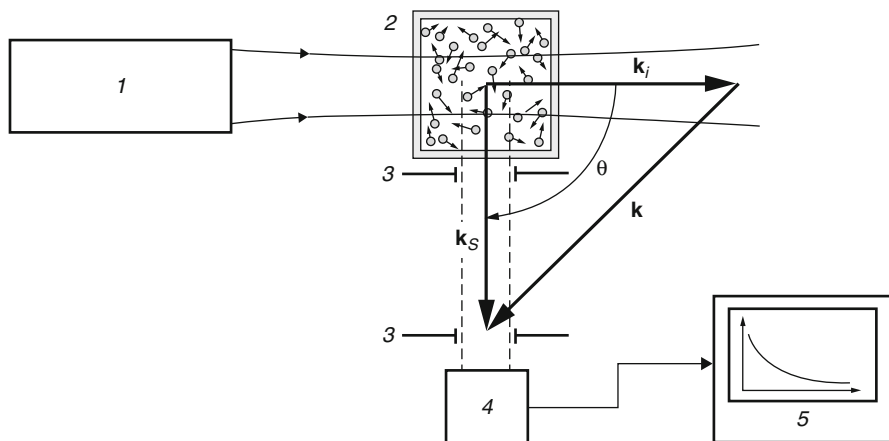
Fig. 13.17 Dynamic light scattering on Brownian particles. *1* – laser; *2* – sample chamber; *3* – aperture; *4* – light detector; *5* – autocorrelator

concentrations, measurements of particle size are impossible because of multiple scattering of light. This is because, when light is scattered two or more times with particles before it reaches the detector, the scattering angle each time depends on the instant positional relationship between particles, and thus it cannot be measured or determined with an optical arrangement. The only way to avoid the effect of multiple scattering is by filtering the single-scattered light by means of such techniques as cross correlation DLS or minimizing the probe volume through implementation of optical fiber-based miniature probes [27, 28].

DLS also fails at characterizing polydisperse suspensions. In this case, the autocorrelation function of scattered light is no longer exponentially decaying and only averaged particle size can be estimated with certain approximate methods. Although several methods were proposed for inversion of the autocorrelation function in order to obtain the size distribution of particles, all of them are highly sensitive to even a small amount of noise because of the ill-conditioned inversion of the sum of exponential functions with slightly different decay constants [27, 28].

Dynamic light scattering can also be used for blood perfusion assessment [8, 9]. The method is based on illumination of the surface layer of living tissue with laser radiation. The movement of red blood cells (RBCs) along small sub-surface blood vessels results in fluctuations of the scattered light intensity. As in the case of DLS, discussed above, the autocorrelation function of scattered light reflects the characteristic time of scatterer structure decorrelation related to blood microcirculation. The method referred to as laser Doppler flowmetry (LDF) is capable of detecting blood-related changes in microcirculation in response to occlusion of proximal blood vessels or application of vasoconstrictors [9, 11]. But, in contrast to DLS, laser Doppler blood flowmetry cannot provide any reproducible quantitative characteristic of blood circulation because of the strong multiple scattering on both moving tissue and moving red blood cells.

Fig. 13.18 Scattering of a Gaussian beam of laser radiation by a moving random phase screen
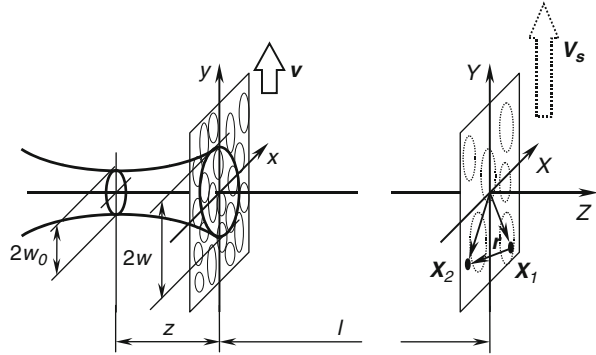
The multiple scattering makes it impossible to define the scattering angle for each scattering event. Since the LDF probe volume of tissue is typically as large as several cubic millimeters, it includes a number of blood vessels of different size from the smallest capillaries to relatively large arterioles and venules. Because RBC velocity depends on vessel size and type, each particular site of tissue is characterized by its own structure-specific distribution of RBC velocity. Thus, autocorrelation of scattered light fluctuations may vary sufficiently with probe volume displacement for a few millimeters along the tissue surface. Over the last decades, LDF has been applied in several instances of case-specific biomedical research, but the fundamental issues listed above still have not been overcome and all reported results concern only relative variations of blood microcirculation rate [9].

While uncorrelated movement of scattering centers results in non-correlated intensity fluctuations at the observation plane, movement of a turbid object as a single whole makes an effect of speckle field translation along an observation plane [26]. In the latter case, both intensity and amplitude correlation functions cannot be factorized to terms depending on spatial coordinates, which in turn depend on time delay. Thus, the intensity fluctuations of translating speckle field should be described in terms of space-time autocorrelation functions, described by (13.72) and (13.73), respectively.

Here we consider a particular case of a Gaussian beam of laser light scattering by a moving set of scatterers modeled with a deep random phase screen (RPS) (Fig. 13.18). The model of deep RPS includes an object constituting a large number of scattering centers, which does not affect the amplitude of incident light but introduces random phase fluctuations that obey the Gaussian statistics, with dispersion sufficiently exceeding 2π. As discussed in the previous section, speckle pattern structure depends on the size of the illuminated part of the random phase screen. For the particular case of illumination with a Gaussian beam of laser radiation, the light field at the RPS plane is given by (Fig. 13.18):

$$E_0(\mathbf{x}, t) = \frac{w_0}{w} \exp\left[-\frac{|\mathbf{x}|^2}{w^2} - i\left(\omega_0 t - k_{0z}z - \frac{\pi}{\lambda\rho}|\mathbf{x}|^2 - \varphi_0 \right) \right], \qquad (13.82)$$

where $\mathbf{x} = (x, y)$ is a position vector of a point at the RPS plane; w and ρ are, respectively, the radius of the beam spot and the wave front curvature radius in the RPS plane separated by a distance z from the position of the beam waist; and w_0 is the radius of the spot at the beam waist. Here, ω_0, k_{0z}, λ, and φ_0 are the angular frequency, the z component of wave vector, wavelength, and initial phase of the Gaussian beam, respectively. The beam spot radius w and radius of wavefront curvature ρ in object plane are determined by the following formulae:

$$w = w_0 \left[1 + \left(\frac{z}{a} \right)^2 \right]^{1/2}, \tag{13.83}$$

$$\rho = z \left[1 - \left(\frac{a}{z} \right)^2 \right], \tag{13.84}$$

where $a = \pi w_0^2 / \lambda$ represents the so-called beam waist length.

As can be shown, the normalized space-time correlation function of speckle field intensity at the observation plane (Fig. 13.18) is given by [26]:

$$G_I(\mathbf{r}, \tau) - 1 = \exp \left(-\frac{|\mathbf{v}|^2}{w^2} \tau^2 \right) \exp \left(-\frac{1}{r_s^2} \left| \mathbf{r} - \left(1 + \frac{l}{\rho} \right) \mathbf{v}\tau \right|^2 \right), \tag{13.85}$$

where $\mathbf{v}$ is velocity of RPS translation within its own plane; $\tau = t_1 - t_2$ is time delay; and $\mathbf{r} = \mathbf{X}_1 - \mathbf{X}_2$ is the distance separating two points at the observation plane. Here, $\mathbf{X} = (X, Y)$ represents a position vector of an observation point and l is the separation between RPS and the observation plane; $r_s = 2l/(k_0 w)$ represents averaged speckle size at the observation plane. Equation (13.85) was obtained with the assumption that speckle field fluctuations are stationary in both time and space. Although the latter statement should not be true for the whole observation plane, it provides a good approximation for a certain region around point $\mathbf{X} = 0$, namely the intersection of an observation plane and the incident beam axis (Fig. 13.18). As can be seen from the second multiplier of (13.85), speckles translate within the observation plane with velocity [26]:

$$\mathbf{V_s} = \frac{\mathbf{r}}{\tau} = \left(1 + \frac{l}{\rho} \right) \mathbf{v}. \tag{13.86}$$

The first multiplier of (13.85) represents decay of correlation related to the continuous replacement of one set of illuminated scatterers with another one as a result of RPS translation across the incident beam. Thus, translation of the speckle field along the observation plane is accompanied by gradual changing of its structure, so-called "speckle boiling." Obviously, displacement of RPS for a distance equal to

the light spot diameter w results in complete replacement of one set of scatterers with another one. Thus, (13.85) decays to zero for time interval of

$$\tau_T = \frac{w}{|\mathbf{v}|},$$

(13.87)

which corresponds to displacement of the speckle pattern within the observation plane for a distance of

$$r_T = \left(1 + \frac{l}{\rho}\right)w.$$

(13.88)

As follows from (13.85), no translation of speckle field is observed if $l = -\rho$. In this case, "pure boiling" of the speckle pattern takes place. The model discussed here allows for analysis of dynamic speckles under various conditions of illumination and observation.

The relation between the translational dynamics of the speckle field and the velocity of a light-scattering object is widely utilized in metrology. For example, it allows for visualization of flows of turbid fluids by means of PIV. In this case, the speckles that follow a fluid are tracked rather than images of individual flow-tracing particles. Tracking of speckles can be performed using imaging arrangement in free space geometry as well. In the latter case, it is enough to use a pair of detectors to measure fluid flow velocity.

In order to provide an overview of laser speckle properties, we have considered here a model of so-called fully developed speckles, which results from light scattering by a large number of independent scatterers, introducing large random variation of each phasor phase. We should note here, however, that some practically significant applications of laser speckles in biomedical diagnostics are beyond the scope of this useful model. For example, a model of single RPS represents light scattering of the light surface of a rough object rather than scattering of light by a three-dimensional set of scatterers constituting biological tissue. Thus, light scattering by blood flowing inside a blood vessel can be represented as a scattering with a set of RPSs. Regular translation of a speckle field can be observed only if detection of the single scattered light preserving its phase is still possible. Otherwise, no quantitative measurements of a flow velocity are attainable [12].

13.3 Particle Image Velocimetry for Capillary Blood Flow Assessment

13.3.1 Microscopic PIV Technique for Biofolow Velocity Measurements

The dynamic of blood microcirculation, namely blood flow through extremely narrow blood vessels, plays a key role in human metabolism and thus it is highly

sensitive to a number of pathological processes, including inflammation, intoxication, stress, shock, cancer, and edema. Being of great interest for both fundamental physiology and clinical diagnostics, the blood microcirculation rate is difficult to characterize quantitatively because of the lack of suitable methods for direct measurement of red blood cell velocity in individual vessels inside a living tissue. Since the smallest blood capillaries are less than 10 μm in diameter, quantitative measurements of microcirculation mean tracking of individual red blood cells that passes such a capillary one by one.

Optical imaging is the only method suitable for non-contact imaging of individual cells in vivo with resolution less than 10 μm. But, on the other hand, optical imaging performance is strongly affected by light scattering in tissues surrounding blood capillaries. Although optical imaging fails to detect individual capillaries deep inside tissue, it is useful for imaging of superficial blood capillaries of mucosa and even intact skin at certain sites. The human nailfold is one such site, typically used for microscopic visualization of blood capillaries, called capillaroscopy. The specific structure of the site includes capillary loops clearly visible with an optical microscope after application of glycerol or oil immersion at the skin surface in order to reduce light scattering.

Because of fluctuations of red blood cell concentration inside capillaries, microscopic imaging of the nailfold capillary loops reveals the motion of red blood cells along them, which can be recorded with a digital video camera. In this section, we report the pilot study based on application of PIV image processing instrumentation for quantitative assessment of capillary blood flow at the human nailfold.

The fundamental background of PIV was discussed in Sect. 13.2.4, while Sect. 13.2.5 provides an overview of the correlation-based image evaluation procedure. We implemented the procedure in our own custom-developed software suite for microanemetry developed with LabVIEW 8.5 Professional Development System (National Instruments Inc., USA), which includes image processing library NI Vision 8.5 (National Instruments Inc., USA).

Our software allows for processing of a series of flow-tracing particles' images captured at regular intervals of time. Figure 13.19 represents the typical results of PIV evaluation of a flow of water seeded with 1.5-μm polystyrene spheres through a micromixer prototype. Evaluation was performed over a series of 100 images obtained in transmitted light bright field with an upright Axio Imager A1 (Carl Zeiss, Germany) microscope using a $20\times$ long working distance lens with a numerical aperture of 0.4. Images were captured with an A602f (Basler, Germany) monochrome CMOS camera attached to microscope side video port. Image processing included preliminary subtraction of an averaged image from each image of the series and averaging of correlation estimates over all pairs of images, according with (13.46).

13.3.2 PIV Evaluation of Blood Circulation Through a Capillary Loop In Vivo

To evaluate the capability of the PIV technique for capillary blood circulation assessment, we used the same arrangement for imaging of the
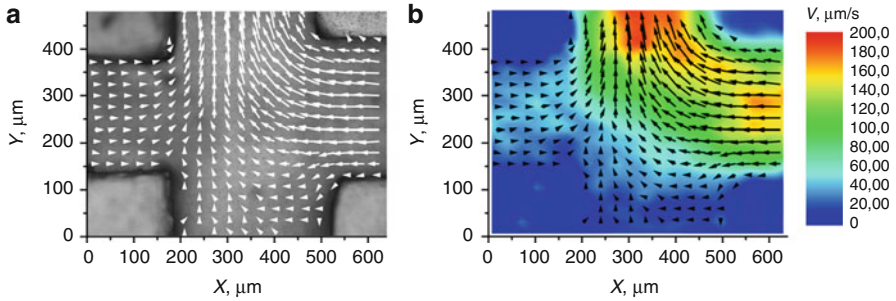
Fig. 13.19 PIV evaluation of fluid circulation inside a glass micromixer prototype. Original microscopic image superposed with velocity vectors (**a**) and false color velocity map (**b**)

left hand little finger nailfold of a healthy 33-year-old male volunteer. The little finger was gently fixed to a microscope stage with a rubber foam-coated clamp to prevent displacement. In order to reduce light scattering, the skin surface was covered with a drop of glycerol. Illumination of the object was performed in reflected light bright field mode with a green glass filter introduced into the illuminator optical path in order to enhance contrast of red blood cells.

The result obtained with the same PIV evaluation procedure as in previous example is shown in Fig. 13.20. The figure illustrates the effect of capillary thickness on PIV evaluation. The capillary loop is formed with connection of arterial and venous capillaries. As can be seen in Fig. 13.20a, the arterial capillary (right), which supplies blood into the loop, is thinner than the venous one (left). Normally, blood flow through the arterial branch is faster than that through the venous. But the arterial branch cross section is about 10 μm, which is comparable with the interrogation area's separation and thus current evaluation evidently underestimates flow velocity through it. In contrast, the venous branch is about two times thicker and thus the measured velocity of blood flow appears as more reliable. We also should note that insufficient density of PIV interrogation areas prevents blood flow evaluation at loop curve (Fig. 13.20b).

The presented results show the potential capability of PIV-based image evaluation for blood flow velocity characterization through optical capillaroscopy. However, because of light scattering by the superficial tissue layers, these are fluctuations of red blood cell density that can be tracked rather than individual cells. We also should note that spontaneous motion of a finger sufficiently affects PIV evaluation. For example, one can find in Fig. 13.20a several vectors located far outside of capillary loop that resulted from eventual displacements of the finger for several tens of micrometers during image sequence acquisition.
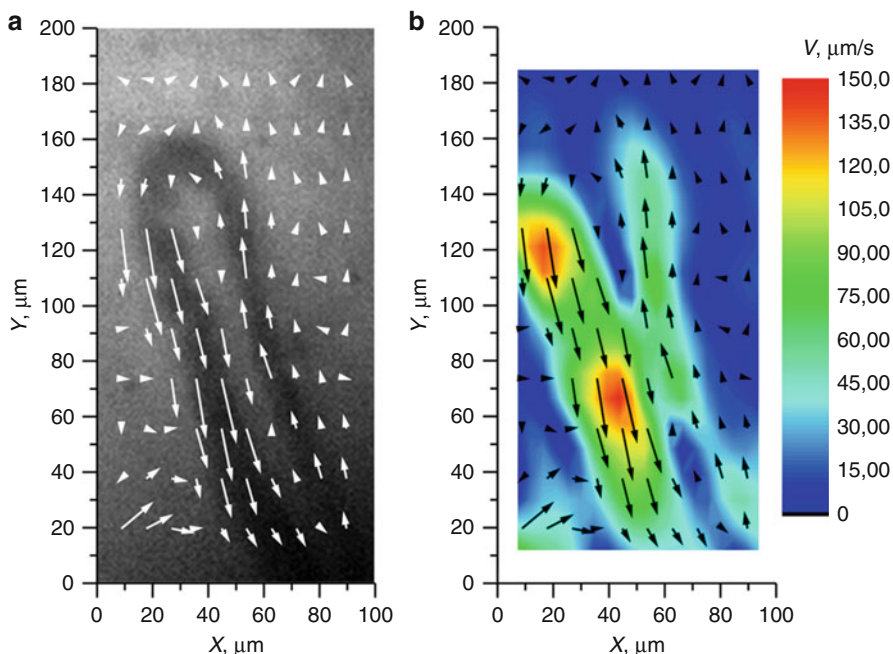
Fig. 13.20 PIV evaluation of blood microcirculation in human nailfold capillary loop. Original microscopic image superposed with velocity vectors (**a**) and false color velocity map (**b**)

13.4   Laser-Based Characterization of Blood Microcirculation

13.4.1 Blood Microcirculation Studies: Sites and Approaches

As already mentioned, two different approaches of blood microcirculation studies using optical methods have been developed. The first, laser Doppler flowmetry (LDF), is useful for assessment of blood microcirculation in a certain volume of tissue containing large number of blood capillaries. It was first developed by M.D. Stern in 1975 [8]. The LDF technique is based on the illumination of a tissue volume with coherent light. Since tissue contains blood cells moving in capillaries with different velocities and directions, the scattered light spectra becomes broader because of the Doppler effect. The width and shape of scattered light intensity fluctuation spectra are related to the blood perfusion in the sampling volume of tissue. Theoretical principles of LDF have been developed by Bonner and Nossal [9]. LDF allows extracting the information about the root mean square velocity of blood cells in the tissue volume. The LDF system could be used for in vivo microscopic, endoscopic, and intraoperational monitoring of local blood microcirculation.

The principal disadvantage of LDF technique is the strong dependence of the LDF output signal on the structure of the tissue site under investigation. It makes difficult any measurements of blood perfusion or absolute blood flow velocity [10, 29].

Another approach in blood microcirculation diagnostics is based on the investigation of blood flow in a single microvessel [7, 30–37]. Analysis of an isolated vessel provides detailed information about blood flow, but there are not many human organs where such measurements can be performed with the purposes of medical diagnostics. Only the nailbed, ocular fundus, and conjunctiva are available for noninvasive investigation of capillary blood flow. In this section, the application of the laser Doppler technique for examination of blood microcirculation in human eye conjunctiva is described.

13.4.2 Capillaries of Human Eye Conjunctiva

From the medical point of view, one of the most important sites for blood microcirculation assessment is the human eye.

Eye conjunctiva contains a single layer of blood vessels that are available for observation. Early diagnostics of disorders of retinal blood flow, caused by diseases such as diabetic retinopathy, hypertonic retinal angiopathy, or glaucoma, allows for blindness prevention. Blood vessels of different diameter are available for blood flow monitoring with LDF at two parts of the eye. The first is the retina, the light-sensitive inner side of the ocular fundus, and the second is the connective tissue layer covering the frontal surface of the eyeball (except thecornea) and the inner surface of the eyelids, called the eye conjunctiva. Blood vessels of the retina can be inspected through the optical system of the eye using the conventional technique of ophthalmoscopy. Vessels are situated directly on the surface of the light-sensitive layer of the retina. Diagnostics of blood flow in these vessels is important because they deliver blood directly to the retina. A number of commercial laser Doppler instruments are currently available for retinal blood flow assessment. However, laser Doppler diagnostics of retinal blood flow is still not simple procedure: the level of retinal irradiation is close to the maximal permissible limit [30], so measurements require a unique manipulation with the patient. It is convenient to investigate a single vessel on the part of conjunctiva that covers the frontal surface of the eyeball called the bulbar conjunctiva (Fig. 13.21) [38].

The bulbar conjunctiva has an attractive feature from the viewpoint of laser diagnostics: the single layer of blood vessels is situated on the surface of the homogeneous scattering sclera, which does not contain other blood vessels. This is a unique condition for investigation of blood vessels because blood vessels of the nailbed or retina are placed in tissues that contain other blood vessels. The presence of a large number of microvessels makes it difficult to separate a single vessel for microcirculation monitoring. Blood vessels of the conjunctiva are connected in general with the vasculatory of eyelid and a few vessels are related to that of inner structures of eye through the sclera [38]. Vascular pathology that can be observed in

Fig. 13.21 Bulbar conjunctiva of the human eye
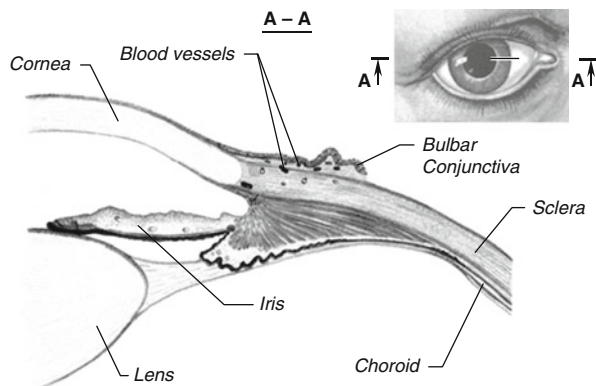
eye conjunctiva correspond to similar pathology in other parts of the eye (such as retinal and choroidal vessels) and other parts of the human organism as a whole. For example, it is important for diagnosis of cardiovascular diseases because the conjunctiva is the single site where vessels of different diameter can be investigated in detail. Moreover, in vivo measurements of blood flow in conjunctiva vessels are safer in comparison with the same measurements in retinal vessels.

13.4.3 Coherent Light Scattering by a Blood Vessel

Laser Doppler velocimetry was the first laser method applied for blood flow velocity measurement in retinal vessels. The use of the optical heterodyne technique for Doppler frequency shift of laser radiation scattering by particles moving in laminar flow was proposed in 1964, just several years later after the invention of lasers. Ten years later, in 1974, the first successful in vivo measurement of blood flow velocity in vessels of the human retina was described in Ref. [39].

There are some specific problems in laser Doppler measurements of blood flow in the human ocular fundus [30, 40]. The first is the strong limitation of the maximal permissible level of the retinal irradiation. This requires using low-power laser radiation for eye safety. On the other hand, the limitation of incident laser power makes it difficult to register the scattered light with sufficient signal-to-noise ratio. The second problem is the movement of the patient's head and eye. To eliminate blood vessel shifting during measurements, the sampling volume must be larger than the vessel cross-section. But this makes the investigation of the blood flow velocity profile impossible. If the vessel cross section is uniformly illuminated, the Doppler frequency shift power spectrum has a complicated structure due to the superposition of light fraction, scattered by blood cells moving with different velocities. The third problem concerns the influence of multiple light-scattering effects on the frequency bandwidth of Doppler spectra. Under some conditions, multiple scattering may cause failure of absolute flow velocity measurements [40].

Fig. 13.22 Arrangement for laser Doppler measurements of ocular blood flow
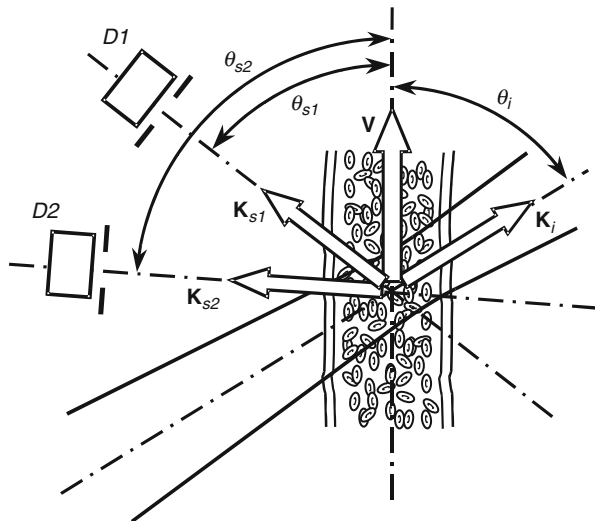
To solve these problems, a special kind of LDV arrangement was proposed by C.E. Riva that differs from the classical LDV schemes. It should be noted that classical schemes, overviewed in the first section of this chapter [33, 34], have been developed for technical applications.

The scheme for laser Doppler velocimetry of blood flow in the vessels of ocular fundus is shown in Fig. 13.22.

A blood vessel is illuminated by a laser beam. Laser light is scattered from the vessel wall and by moving blood cells. The scattered light is registered by two detectors: *D1* and *D2*. The resulting Doppler frequency shift can be calculated for each detector using (13.52), in the case of single scattering of light:

$$\omega_{D1} = (\mathbf{k}_{s1} - \mathbf{k}_i)\mathbf{v}, \quad \omega_{D2} = (\mathbf{k}_{s2} - \mathbf{k}_i)\mathbf{v}, \tag{13.89}$$

where, again, $\mathbf{k}_i$ is the wave vector of the incident laser radiation; $\mathbf{k}_{s1}$, $\mathbf{k}_{s2}$ are the wave vectors of light scattered toward the first and the second detectors, respectively; and $\mathbf{v}$ is the cell velocity vector. The magnitude of cell velocity vector in real flow changes with distance from the center of flow to the vessel's wall. In other words, the velocity profile of laminar flow of a Newtonian liquid in a cylindrical tube has a parabolic shape:

$$V(r) = V_{\max}\left[1 - \left(\frac{r_v}{r_0}\right)^2\right], \tag{13.90}$$

where r_v is the distance from the center of flow, r_0 is the vessel radius, and $V_{\max}$ is the maximal flow velocity at the center of the vessel. The maximal value of frequency shift corresponds to the centerline flow velocity $V_{\max}$

according to (13.90). Light, scattered by the vessel wall and the surrounding tissue, is used for heterodyning to measure Doppler frequency shift. Light, scattered by motionless structures, allows elimination of eye movements and the measurement of the velocity of blood cells relative to the vessel wall. As a result, the spectral density of scattered intensity fluctuations, which are caused by the interference of dynamic speckles scattered by moving cells and light fraction, scattered from vessel wall, has the constant value in the frequency range from zero to ω_{max} and then rapidly drops to the noise level for frequencies higher than ω_{max}. Such shape allows one to provide easy measurements of ω_{max}.

To calculate flow velocity, angles θ_i and θ_s have to be precisely measured. However, in real in vivo experiment this is not easy to do. To exclude these angles from formula for flow velocity, two detectors were separated by a constant angle $\alpha = \theta_{s1} - \theta_{s2}$. Maximal flow velocity may be calculated using the formula derived from (13.89):

$$V_{max} = \frac{\lambda[\omega_{max\,1} - \omega_{max\,2}]}{2\pi n \sin(\alpha)}, \qquad (13.91)$$

where ω_{max1}, ω_{max2} are the maximal Doppler frequency shifts evaluated from measured spectra of the first and the second detector signals, respectively; λ is the laser light wavelength in vacuum; and n is the refractive index of medium, which is surrounding the blood cells. The described principle serves as the basis of a special technique called bi-directional laser Doppler velocimetry.

Bi-directional LDV is a conventional technique for retinal blood flow monitoring, but it has some limitations. For one thing, blood is not a Newtonian liquid because it contains cells in high volume concentration (up to 45 %). It is not dramatic because, in practice, it simply causes some flattening of the velocity profile in vessel that does not sufficiently affect the spectrum of scattered light intensity fluctuations and ω_{max} is clearly measurable as a cutoff frequency. A much more serious limitation concerns the scattering properties of blood and the surrounding tissues. LDV works well only in the single scattering mode, when each photon reaches the detector after only one single scattering on a moving cell. But most biological tissues are high scattering structures and multiple light scattering is usually dominant. In the multiple scattering mode, light changes its direction in tissue two or more times, interacting with moving or motionless scattering centers. As a result, the angles of incidence and scattering of light by moving cell are defined by the random trajectory of light in tissue rather than the light source and detector position. In this case, absolute flow velocity measurement using bi-directional LDV is impossible because the scattered light intensity fluctuations spectra are distorted and cutoff frequencies are not clearly seen. As shown in the literature, bi-directional LDV allows for successful measurements of blood flow velocity only in vessels larger than 40 μm in diameter due to reasons described above [30, 41, 42].

In opposition to retinal vessels, multiple scattering is dominant when vessels of the conjunctiva are illuminated (Fig. 13.11). The sclera consists of thin collagen

Fig. 13.23 Scattering of
laser radiation by a blood
vessel of eye conjunctiva
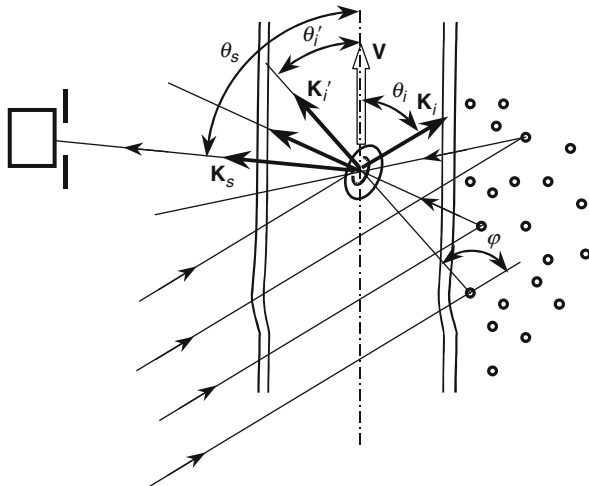
molecules that look like fibers with a refractive index $n_c = 1.47$, surrounded with
a base substance ($n_b = 1.345$). The sclera is a highly scattering medium with an
average thickness of about 1 mm [43].

Light scattering by a vessel of eye conjunctiva is schematically shown in
Fig. 13.23. There are several ways for light to be scattered. These are single back
scattering by moving cells, and multiple scattering by fixed scattering centers and
by moving cells. In Fig. 13.23, single scattering by a blood cell is depicted with
wave vectors $\mathbf{K}_i$ and $\mathbf{K}_s$. We can see that, in the case of double scattering,
wavevector $\mathbf{K}_i'$ is not determined by the direction of the incident laser radiation
but by the background scattering. Since the direction of incident light wave vector
θ_i' varies randomly in a wide range in cases of multiple scattering, the resulting
Doppler frequency shifts of light scattered by the cells are also random. So, the
shape of the Doppler spectrum is close to a negative exponent and the cutoff
frequency could not be measured.

It is not possible to carry out the measurement of absolute flow velocity in blood
vessels of eye conjunctiva using bi-directional LDV, in spite of the retinal vessels.
However, the width of the spectra depends on flow velocity. As was shown by
several authors, the zero- and first-order spectral moments can be used for charac-
terization of blood flow in the case of multiple light scattering in a tissue [9, 10, 32]:

$$M_0 = \int P(\omega)d\omega, \tag{13.92}$$

$$M_1 = \int \omega P(\omega)d\omega, \tag{13.93}$$

where ω is spectral frequency and $P(\omega)$ is the Doppler shift power spectrum. The
zero-order spectral moment is directly proportional to average number of blood

Fig. 13.24 Laser Doppler measuring system for blood flow measurements: *1* – computer and data acquisition board; *2* – photodetector module; *3* – objective; *4* – object plane; *5* – mirror of laser beam delivering module; *6* – microscope; *7* – photodiode detector; *8* – amplifier; *9* – field diaphragm [32]
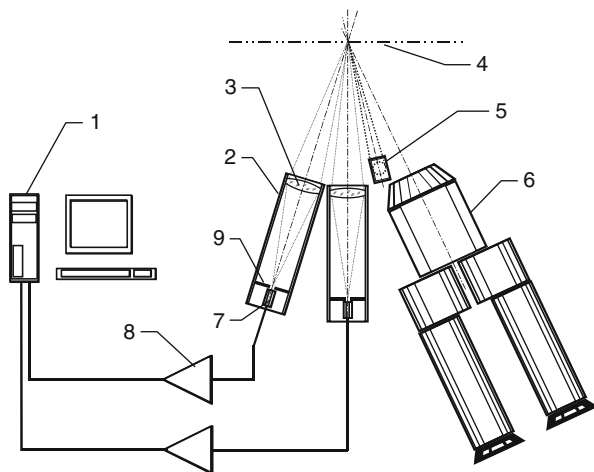
cells in the illuminated area, and the first moment is proportional to the product of the root mean square of blood cell velocity and the average number of cells. So, the first normalized spectral moment:

$$M_1' = \frac{M_1}{M_0} \tag{13.94}$$

is directly proportional to the root mean square of blood cell velocity. All coefficients of proportionality are usually unknown inasmuch as they are determined by a large number of different factors, including scattering geometry, structure and optical properties of tissue,and number and diameter of blood vessel in the illuminated area. But the human eye conjunctiva is a unique site for Doppler measurements because it has a very simple structure. This is an ideal situation for interpretation of LDF measurements: a single blood vessel located on the surface of a homogeneous scattering layer of sclera. Moreover, scattering properties of sclera are well known and vessel diameter can be precisely measured using a microscopic imaging technique [32].

13.4.4 Experimental Setup

The laser Doppler measuring system for investigation of blood flow in blood microvessels of the bulbar conjunctiva on the frontal surface of the human eye has been developed on the basis of a standard slit-lamp microscope (Fig. 13.14) [32].

A laser beam delivering module was mounted on the top of the microscope (not shown in Fig. 13.24). Two photodetectors of a bi-directional detecting system were placed at the left side of the microscope. The linearly polarized incident beam was provided by a red laser diode ($\lambda = 650$ nm). The incident laser power was

attenuated with a rotating polarizer to 30–50 μW to provide laser eye safety [44]. The incident beam was focused by laser beam delivering optics and directed to the object plane of the microscope with a mirror (5, Fig. 13.24). The laser spot size in the object plane was 30 μm in diameter.

Two similar photodiode modules were used to detect the light scattered in two different directions. The photodetector modules are separated by the angle of 17°. The scattered light passed through the aperture is collected by the FD256 photodiode detector. The linear field of each of photodetector module in the object plane was 100 μm. The output photocurrent signals from both photodiodes were amplified by the high-sensitivity current-to-voltage amplifiers ($5 \cdot 10^{10}$ V/A within the frequency range [0.5–20 kHz]). The resulting photocurrent signal was digitized by a Creative Labs Sound Blaster with 16-bit resolution at a sampling frequency of 44.1 kHz. Non-overlapping modified periodograms with a cosine time window were calculated using fast Fourier transform with a time period of 23 ms from 5 to 130 periodograms and were averaged to obtain a smooth power spectrum estimation. A microscope was used for visual guidance of the laser beam and measurement of the vessel diameter [32].

A series of experiments were performed with the model of the blood vessel to test the sensitivity of the instrument and to investigate the influence of multiple light scattering on the formation of Doppler frequency shift power spectra. A plastic tube with an internal diameter of 30 μm wasused as the model of a blood vessel. A 10 % suspension of erythrocytes in Ringer solution flowed through this capillary tube at a constant rate. In our experiments, the scattering geometry was close to that in real bulbar conjunctiva of the human eye. The plastic capillary tube was placed on the background of a 0.5-mm Teflon plate to reproduce the scattering from the sclera, and the space between the capillary tube and background was filled by an immersion oil ($n = 1.51$) to reduce the Fresnel reflection from the back side of the tube. These experiments, described in Ref. [32], showed that the multiple scattering by the background eliminates the angular dependence of scattered light fluctuations' spectra shape and makes impossible the use of the bi-directional laser Doppler technique for blood flow velocity in capillaries of the conjunctiva. It was also shown that the first normalized spectral moment of Doppler frequency shift power spectra is directly proportional to the flow velocity.

13.4.5 In Vivo Results

After testing of the measuring system using the models of blood vessels, in vivo measurements in human volunteer eye conjunctiva were performed. A spectrogram of Doppler frequency shift recorded when laser light is scattered by the human eye conjunctiva blood microvessels is shown in Fig. 13.25. The spectrogram was recorded during investigation of two vessels of 9 and 30 μm in diameter and part of conjunctiva containing no vessels.

Doppler spectra corresponding to light scattering by the vessel 30 μm diameter, by the vessel 9 μm diameter, and by the conjunctiva site containing no vessels are
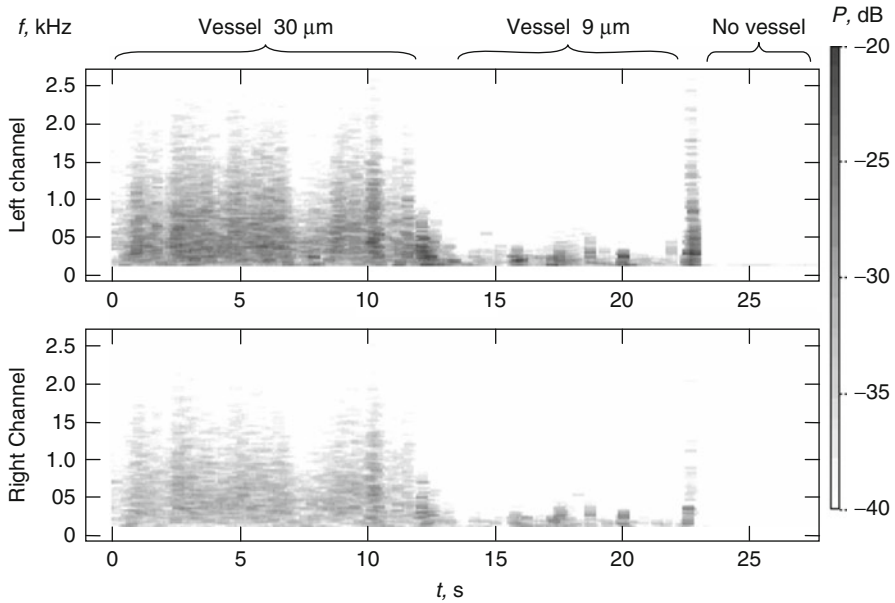
Fig. 13.25 Spectrogram of Doppler frequency shift

shown in Fig. 13.26 (curves 1, 2, and 3, respectively). Spectra have a negative exponential shape. They are not dependent on the angle of detection (left and right channels are separated by the angle of $17°$ as described in the previous section).

As already mentioned, the first normalized spectral moment is an informative parameter characterizing flow velocity in capillaries. The plot of dependence of the first normalized spectral moment on time is presented in Fig. 13.27. This plot corresponds to the spectrogram presented in Fig. 13.25. We can see that the first normalized spectral moment depends on the vessel diameter and flow velocity. Since vessel diameter can be easily measured, we can perform empirical calibration of dependence of spectral moment on vessel diameter in normal patients and for patients with different pathologies. This technique can be effectively used for cardiovascular diagnostics.

13.5 Speckle-Correlation Measurements of Lymph Microcirculation in Rat Mesentery Vessels

13.5.1 Peculiarities of Lymph Microcirculation

The microlymphatic system is a part of microcirculation. It constantly drains tissue and preserves the content and volume of the extracellular liquid, and it participates in the constant removal of proteins, cells, and fluid from tissue and their return to the bloodstream. Small lymphatics consist of segments (lymphangion), which are
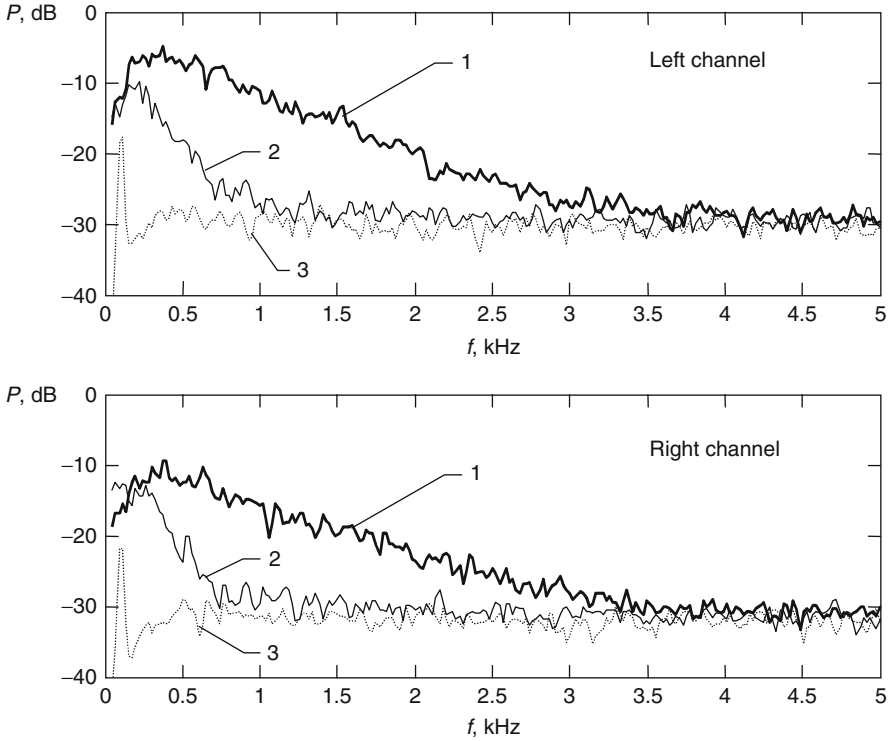
Fig. 13.26 Spectra of Doppler frequency shift of laser light scattered by blood vessels of human eye conjunctiva: *1* – vessel of 30 μm diameter; *2* – vessel of 9 μm diameter; *3* – site without vessels
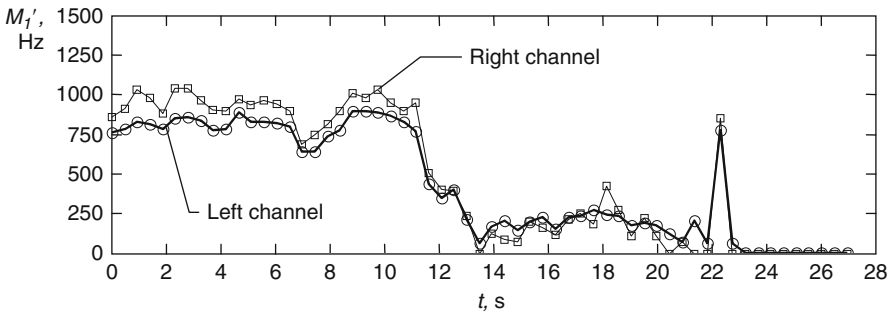
Fig. 13.27 First normalized spectral moment

isolated from each other by valves. As a result, lymphatics act as small pumps with alternating pressure and suction mechanisms [45]. Lymph flow and, correspondingly, effective lymph drainage are provided by a combination of passive (in response to muscle contractions, respiratory movements, intestinal peristalsis, etc.) and active driving forces (gradient of transmural pressure, phasic contractions, valve function)

[45–48]. The important role of the lymphatics in the pathogenesis of many diseases has been proved [49–52]. The importance of lymph drainage is increased significantly to compensate for different disturbances of blood microcirculation, including the increase in blood capillary pressure, the decrease of plasma colloid-osmotic pressure, and lesions of blood capillaries [53]. Some authors indicate that the efficacy of drug injection to the lymph versus the blood has been demonstrated [54–56].

The lymph flow in microvessels has some special features because of the specificity of the structure and function of the microlymphatics. The basic scattering element in a lymphatic vessel is a lymphocyte (white blood cell). Its size is about 3–5 µm [56]. As a rule, lymph flow differs from blood flow in its periodic oscillations, relatively lower velocity, markedly low cell concentration, and transparency of lymph [45, 57–59]. Thus, lymph flow dynamics essentially differs from the well-known blood flow dynamics [60–62].

13.5.2 Methods for Lymph Flow Monitoring

The structure and optical properties of the lymphatics of rat mesentery determine the choice of instrumentation for lymph flow monitoring. The most common technique for lymph microcirculation studies is light microscopy. Rat mesentery anatomy provides unique conditions for microscopic imaging in transillumination geometry. In this case, high-contrast microscopic images of mesentery allow not only for precise measurement of lymph vessel geometry but even tracking of single lymphocytes by means of videorecording. Dynamic parameters of lymphatics, such as valve activities, vessel diameter, cell velocity, concentration, and flow direction, can be determined from frame-by-frame analysis of video records [31, 36, 57, 59].

However, there are some limitations of this technique's application to microcirculation studies. The first is the possibility of cell velocity measurement only when a single cell can be tracked in several frames of a video record. This means that each cell has to cross over the eyesight of the microscope relatively slowly to be recorded at least two times. Since the frame rate and field of view are limited by both the video camera construction and the microscope magnification, some cells can be "lost" because they are moving too fast. Moreover, if cell concentration is high, the tracking of a single cell is impossible because the flow looks like smoothed moiré fringes. Another drawback of video microscopy is the amount of time and elaborate image processing required for flow dynamics monitoring [31].

Laser measuring techniques can be used in addition to light microscopy. The laser instrumentation must be able to: (1) measure flow velocity in a wide range in real time; (2) measure flow velocity in the vessels even in cases of high cell concentration; and (3) determine flow direction. Optical measurements of lymph flow velocity taking into account the direction of flow for a single scattering of light can currently be performed by the laser Doppler microscopy technique [10, 21, 35]. Laser Doppler microscopy is a well-developed way to obtain the flow parameters, including absolute flow velocity and flow direction. It is successfully applied to estimate lymph flow and sometimes to diagnose lymph node changes.

Specialized laser Doppler microscopes have been developed for research of biological flows in microvessels. But there are problems in the application of such techniques to monitoring bioflows in which velocity is low and the direction changes, as in lymphatic vessels. The use of comprehensive frequency shifting devices in laser Doppler microscopy is necessary to overcome this problem, but it requires quite complex and expensive equipment [21, 35].

Another approach in the laser measurement of lymph flow is the laser speckle technique. The speckle field of a laser beam scattered by a lymph vessel is the result of interference of light waves scattered by lymph cells moving at different velocities in the flow, as well as those scattered by immobile tissues surrounding a vessel [25, 26, 63, 64]. The fluctuations of the speckle field intensity have complicated form in this case. The properties of such a speckle field differ considerably from the properties of speckle fields that are formed, for example, upon a single scattering of laser radiation by a moving screen with a rough surface, and have been studied extensively. A special term, "biospeckles," was introduced to emphasize the peculiar nature of this speckle field. Because of the extreme complexity of biospeckles, a theoretical explanation of this effect has not been obtained so far [13, 14, 65, 66]. Even an exact relation between speckle field intensity fluctuations and the velocity of lymph flow has not been established. However, numerous experiments using microvessel models indicate that the width of the autocorrelation function or of the power spectrum of the speckle field intensity fluctuations is linearly connected with the mean velocity of flow of the cells [10, 30]. In blood and lymph flow studies, the speckle field intensity fluctuations are detected at one point, and the flow velocity is estimated from the width of the power spectrum of these fluctuations or from the width of their autocorrelation function. Measurements of this type, described in a previous section, cannot be used to determine the direction of flow in lymph vessels because the speckle field fluctuations recorded at one point do not depend on the direction of motion of the scattering object.

Another method of measurement of the velocity of motion of an object is based on the recording of intensity fluctuations of the speckle field at two points separated in space and on an analysis of their mutual correlation. The principle of this technique is overviewed in Sect. 13.3. This method makes it possible to determine the velocity as well as direction of motion of an object and is used in various technical applications. However, the possibility of using this method for measurement of lymph flow velocity has not been investigated so far. It has been experimentally shown that analysis of the spatial-temporal cross-correlation function of intensity fluctuations of single scattered dynamic speckles allows us to determine the velocity of the flow and its direction [31, 58, 67–69].

13.5.3 Experimental Setup for Lymph Flow Diagnostics

The optical scheme of the setup is shown in Fig. 13.28.

Radiation from a LG-207 633-nm He-Ne laser is delivered through the illuminator channel and focused by the objective of the microscope *2* onto a spot of

Fig. 13.28 Scheme of the experimental setup: *1* – digital video camera; *2* – micro-objective; *3* – He-Ne laser; *4* – beamsplitter; *5* – photodiodes; *6* – red light filter; *7* – photocurrent converters; *8* – PC; *9* – green light filters; *10* – mirror; *11* – illuminator; *12* – thermally stabilized table; *13* – lymph microvessel of mesentery. The *inset* shows illumination of a lymphatic vessel by a focused Gaussian laser beam (*a* is the length of the laser beam waist and *z* is the separation between the flow axis and the waist plane of the laser beam) [31]
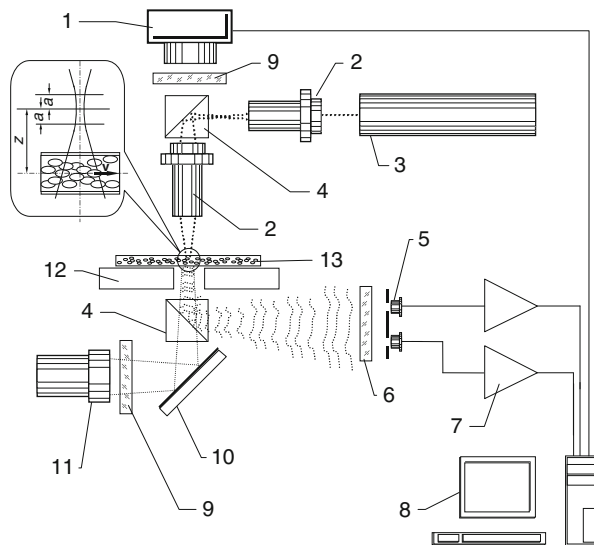
diameter about 2 μm in a plane situated at a distance $z = 100$ μm above the axis of the microvessel *13* [31]. The radius of curvature of the wavefront of the beam illuminating the microvessel is quite small to ensure the acceptable translation length of biospeckles *3*. The measuring volume is formed by the intersection of the diverging laser beam with the microvessel and has the shape of a truncated cone (whose elements have a slope $10°$ and a mean diameter of the order of 30 μm). The laser radiation scattered by the lymph flow is directed with the help of the beamsplitter *4* to the photodetector *5* placed at a distance of 300 mm from the objective plane of the microscope. The diameter of each photodetector is 3 mm, which corresponds to the mean speckle diameter in the observation plane. The distance between the centers of the photodetectors is about 7 mm. Signals from the photodetectors are amplified by the photocurrent transducers *7* and digitized with the help of a two-channel 16-bit analogue-to-digital converter with a sampling frequency 44.1 kHz. A PC is used to determine the cross-correlation function of the photodetector signals as well as the position of its peak.

Depending on the time resolution, the processing of realization of photodetector signals of duration 60 s takes between 90 and 300 s. The setup makes it possible to detect the changes of direction of the motion of cells and to measure the lymph flow velocity within the velocity range from 10 μm/s to 10 mm/s with a time resolution up to 50 ms. A digital video camera *1* combined with transmission microscope is used for analysis of lymph microvessel function in vivo in real time: estimating the mean flow velocity and its direction, measuring the diameter of microvessel, and registering the appearance of phasic contraction in the investigated lymphatic. Digital video images are processed with specially developed software. The cell velocity is determined as the ratio of the difference in cell coordinates in two consecutive frames to the time interval between two frames. The mean flow
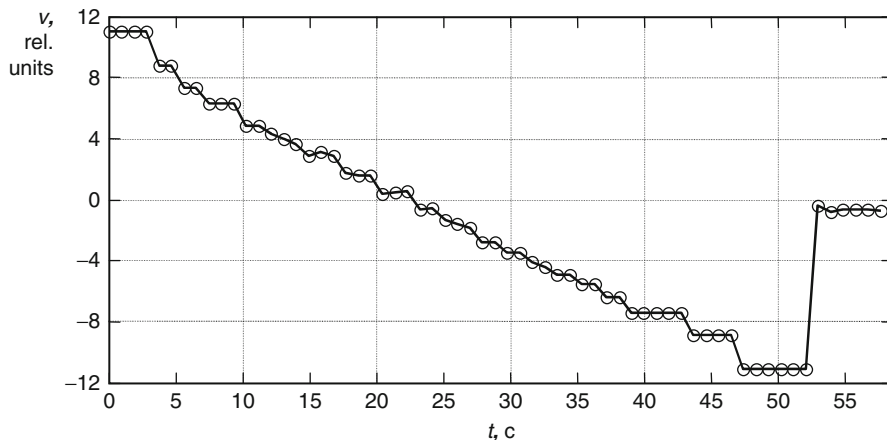
Fig. 13.29 Time dependence of the mean flow velocity in the lymph microvessel model [31]

velocity is calculated by averaging the velocities of four to six cells. This method allows us to record the lymph flow velocity in the range from 25 μm/s to 2–2.5 mm/s with a time resolution of 40 ms. The processing of a video recording of duration 15 s (375 frames) takes about 10 h and involves the tracking of the motion of about 2000 cells.

13.5.4 Experiments Based on the Lymph Vessel Model

The efficiency of the system was verified in a series of experiments using the lymph vessel model. A thin-walled plastic tube of diameter 200 μm serves as a model. Water, containing the suspension of particles of red pigment with an average diameter 3 μm, flows through the tube. The concentration of particles was about 1 %. Figure 13.29 shows the time dependence of the mean flow velocity (measured by a LDV) on the variation of the pressure difference at the ends of the capillary.

The sensitivity of the speckle-correlation method to the flow direction is illustrated because the mean flow velocity in the experiments is directly proportional to the difference in pressures at the ends of the capillary. The velocity measured by the velocimeter is expressed in relative units because the velocimeter described above does not allow measurement of velocity without a preliminary calibration. This is due to the fact that the radius of curvature r of the wave front of the laser beam in the plane of the microvessel, determined by the distance z between the axis of the vessel and the plane of the beam waist, cannot be determined accurately during in vivo measurements. In Fig. 13.30, a typical time series of speckle intensity fluctuations is shown.

Cross-correlation functions of scattered intensity fluctuations, corresponding to the 7th and 24th seconds of recording, are presented in Fig. 13.31. Test measurements confirmed the linear dependence between the measured flow velocity and the
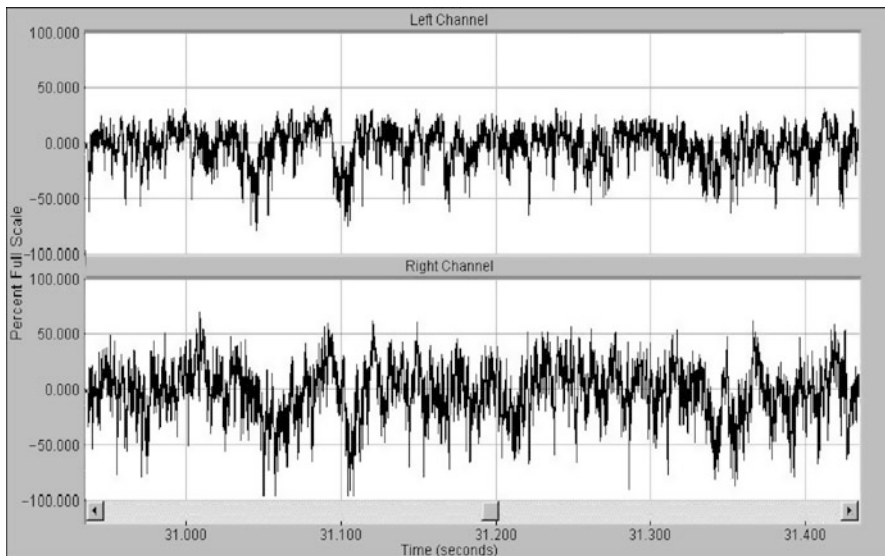
Fig. 13.30 Typical time series of speckle field intensity measured by left and right channel photodetectors are shown. Series are partially similar but one is delayed relative another due to speckle field translation
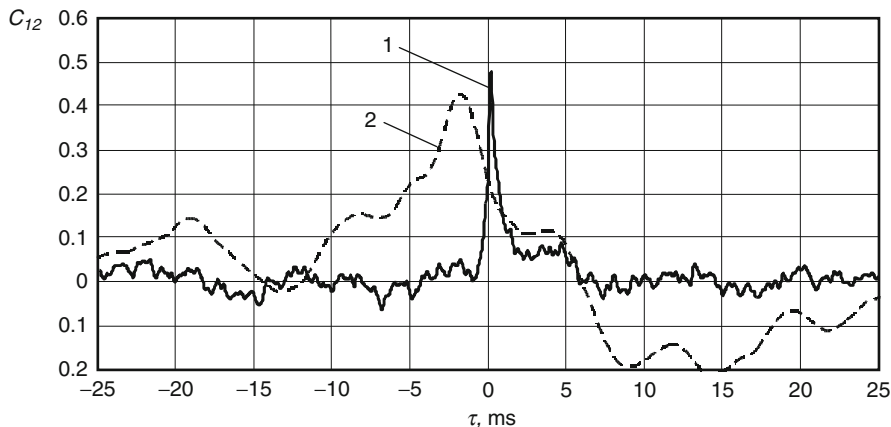
Fig. 13.31 Cross-correlation functions of signals corresponding to 7th (curve 1) and 24th (curve 2) seconds of the recording shown in Fig. 13.21, for delays 0.15 ms (curve 1) and −1.9 ms (curve 2) corresponding to the maxima of correlation functions [31]

difference in pressures at the ends of the capillary. The dependence (regression line) of the relative flow velocity on the difference in pressures at the ends of capillary is shown in Fig. 13.32a. The correlation coefficient equals 0.996, which confirms the validity of the model.
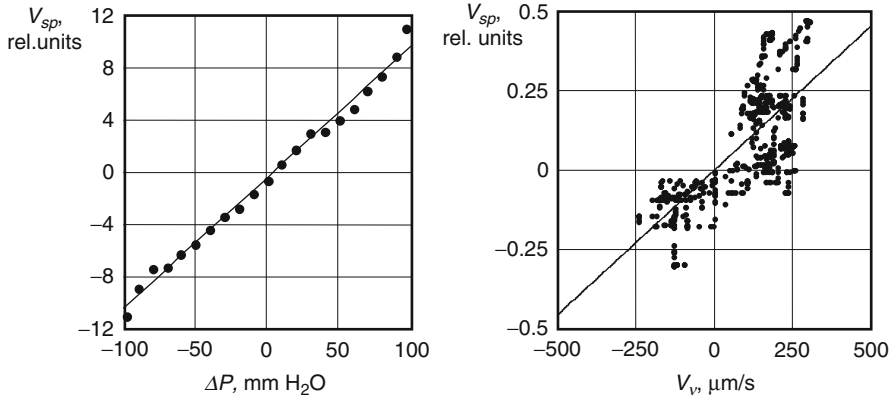
Fig. 13.32 Dependencies of the flow velocity determined by a laser velocimeter on the difference in pressures at the ends of a capillary (**a**), and on the lymph flow velocity in the lymphatic of rat mesentery, measured by the method of functional videomicroscopy (**b**). The solid line corresponds to linear regression, the correlation coefficient of linear regression being 0.996 (**a**) and 0.723 (**b**), respectively [31]

13.5.5 Measurement of the Lymph Flow Velocity in the Lymphatic of the Rat Mesentery

The described setup has also been tested for in vivo measurement of lymph flow velocity in the mesentery vessel of narcotized white rats. Animals were placed on a thermostabilized stage (37.7 °C) *12* of the microscope (see Fig. 13.28) and the mesentery and intestine were kept moist with Ringer's solution at 37 °C (pH ∼7.4). The images of microvessels were evaluated by transmission microscopy and laser velocimeter simultaneously.

Figure 13.33 shows the time dependence of the flow velocity in the investigated microlymphatic of mean diameter 170 ± 5 μm and mean lymph flow velocity 169 ± 4.6 μm/s [31]. This dependence was obtained by laser velocimeter and by processing of the video images as well. As mentioned, the laser velocimeter allows one to measure the lymphocyte velocity in relative units only. The proportionality coefficient between the data of laser velocimetry and the mean flow velocity, measured by the video microscope, was determined from the slope of the regression line (Fig. 13.32b). The correlation coefficient of linear regression between the velocities (measured by these two methods) is relatively high and equals 0.72.

13.5.6 Discussion of Advantages of Laser Diagnostics of Lymph Flow

Experiments on scattering of focused beams of coherent radiation from lymph microvessel models as well as native lymph microvessels in vivo revealed that
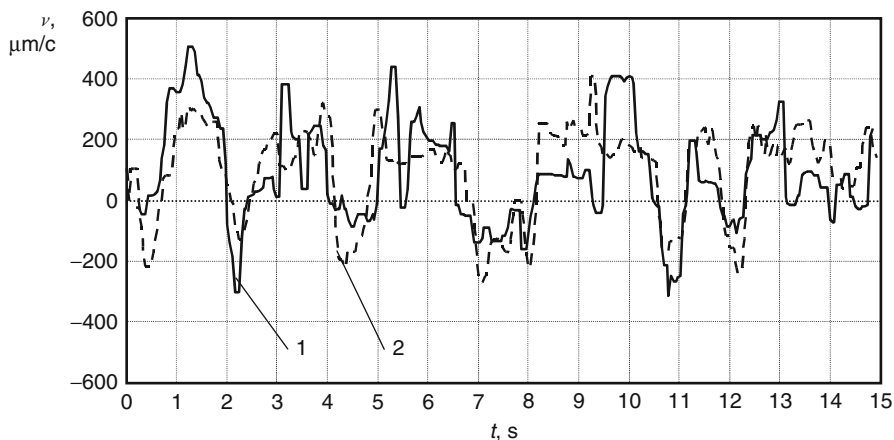
Fig. 13.33 Time dependence of the lymph flow velocity in the lymphatic vessel of mean diameter 170 ±5 μm of a white rat mesentery, recorded with a velocimeter (curve 1) and by processing of video recording (curve 2) [31]

a correlation exists between the speckle field intensity fluctuations recorded at two spatially separated points. This correlation indicates the manifestation of translation dynamics of the speckles. Moreover, a linear dependence is established between the flow velocity, radius of curvature of the laser beam wave front, and the speckle field translational velocity. The linear dependence between the mean flow velocity and the peak of the cross-correlation function of the intensities is confirmed, in particular, by the experimental results based on the lymphatic model presented in this work (see Fig. 13.23a). However, the cells in a lymphatic move with different velocities depending on their position relative to the flow axis. Therefore, further investigations must be carried out in order to find the relation between the flow velocity calculated in the moving random phase screen approximation and the mean flow velocity.

The velocity of the cell crossing the measuring volume may differ significantly from the mean velocity of the cells moving within a field of characteristic size of 150 μm. However, the results of measurements of velocities, made by two entirely independent methods, are quite convincing since the correlation coefficient between the results of velocity measurements is quit large.

The advantages of the proposed method are also supported by the fact that the time dependencies of the lymph flow velocity shown in Fig. 13.33 required an operator time of 10 h (videorecording of duration 15 s was processed), while the processing of the signals registered by photodetectors over the same period of time was completed in just 30 s.

Thus, we have studied experimentally the space-time correlation properties of the dynamic speckle fields formed upon a single scattering of a focused beam of coherent radiation by liquid flows containing scattering particles, and considered the possibility of their application for measurement of flow velocity. Optical measurements of the blood or lymph flow velocity taking into account the direction of flow for a single

scattering of light can be performed at present only by functional microscopy or the laser Doppler microscopy technique. It was mentioned above that functional microscopy requires a prolonged and cumbersome processing of images, while laser Doppler microscopy requires complex and expensive equipment. Of course, the method described here for measurement the lymph and blood flow velocities in biological and medical experiments requires a more detailed analysis of the properties of speckle fields formed as a result of scattering of coherent radiation beams from blood and lymph vessels of various diameters, and also a modification of the existing experimental equipment. However, even the experimental results presented in this work indicate that the changes in the velocity as well as the direction of lymph microflow can be recorded quite expediently by using relatively simple equipment.

13.6 Conclusion

In this chapter, principles of Doppler and speckle diagnostics of different types of microvessels have been presented. It has been demonstrated that measurement of absolute velocity of bioflow is a complicated problem. The measuring signal depends not only on the velocity of bioflow, but also on its scattering characteristics. It was demonstrated that it is possible to carry out the direct measurements of bioflow velocity in the case of single scattering.

Speckle or Doppler methods can be effectively applied for the relative measurement of bioflow velocity. But it also requires great caution because the bandwidth of the spectrum of scattered intensity fluctuations may vary not only as a result of relative changes of flow velocity. The same effect may be caused by the changes of scattering properties of the flow, which may be due to the influence of drugs and medical preparations.

Monitoring of relative spatio-temporal characteristics and images of cerebral blood flow (CBF) with tens of microns spatial and millisecond temporal resolution is possible using laser speckle imaging methods described in ▶ Chap. 5 of this book. In thick tissues with multiple scattering, another speckle-related technique, such as diffusing wave spectroscopy (DWS), is uniquely suited for the measurement of the average size of flowing cells and their spatial displacement (see ▶ Chap. 4). For skin, mucosa, and retinal blood flow, where depth of imaging does not exceed 1–3 mm, Doppler OCT techniques, described in ▶ Chaps. 22–24, are beneficial.

Comprehensive reviews and discussions of the advancements in blood flow imaging techniques and their capabilities for clinical applications, including in vivo cytometry, can be found in the literature (e.g., [70–75]).

References

1. M. Born, E. Wolf, *Principles of Optics*, 6th edn. (Pergamon, Oxford, 1980), 854 p
2. P. Hariharan, *Optical interferometry*. (Academic Press, San Diego, USA, 2003), 351 p
3. H.Z. Cummins, E.R. Pike (ed.), *Photon Correlation Spectroscopy and Velocimetry*. (Springer, New York, 1977), 590 p
4. Z. Zhang, *LDA Application Methods: Laser Doppler Anemometry for Fluid Dynamics*. (Springer, Berlin/Heidelberg, 2010), 272 p
5. M. Raffel, C.E. Willert, S.T. Wereley, J. Kompenhans, *Particle Image Velocimetry: A Practical Guide*, 2nd edn. (Springer, Berlin/Heidelberg, 2007), 445 p
6. V.V. Tuchin, *Tissue Optics: Light Scattering Methods and Instruments for Medical Diagnosis*, 2nd edn. (SPIE Press Book, Bellingham, WA, USA, 2007), 882 p
7. V.V. Tuchin (ed.), *Handbook of Optical Biomedical Diagnostics*, PM107. (SPIE Press, Bellingham, 2002)
8. M.D. Stern, In vivo evaluation of microcirculation by coherent light scattering. Nature **254**, 56–58 (1975)
9. R. Bonner, R. Nossal, Model for laser measurements of blood flow in tissue. Appl. Opt. **20**(12), 2097–2107 (1981)
10. A.P. Shepherd, P.A. Oberg (eds.), *Laser Doppler Blood Flowmetry*. (Kluwer, Boston/Dordrecht/London, 1989)
11. J.D. Briers, S. Webster, Laser speckle contrast analysis (LASCA): a nonscanning, full field technique for monitoring of capillary blood flow. J. Biomed. Opt. **1**(2), 174–179 (1996)
12. J.D. Briers, Laser Doppler and time-varying speckle: a reconciliation. J. Opt. Soc. Am. A **13**, 345–350 (1996)
13. Y. Aizu, H. Ambar, T. Yamamoto, T. Asakura, Measurements of flow velocity in microscopic region using dynamic laser speckles based on the photon correlation. Opt. Commun. **72**(5), 269–273 (1989)
14. Y. Aizu, T. Asakura, K. Ogino, T. Sugita, Y. Suzuki, K. Masuda, Measurements of retinal blood flow using biospeckles: experiments with glass capillary and in the normal human retina. Proc. SPIE **2678**, 360–371 (1996)
15. C. Tropea, A.L. Yarin, J.E. Foss (eds.), *Springer Handbook of Experimental Fluid Mechanics*. (Springer, Berlin/Heidelberg, 2007), 1557 p
16. L. Mandel, E. Wolf, *Optical Coherence and Quantum Optics*. (Cambridge University Press, Cambridge, 1995), 1166 p
17. S.T. Wereley, C.D. Meinhart, Micron-resolution particle image velocimetry, in *Microscale Diagnostic Techniques*, ed. by K.S. Breuer (Springer, Berlin/Heidelberg/New York, 2005), pp. 51–112
18. R. Lindken, M. Rossi, S. Große, J. Westerweel, Micro-Particle Image Velocimetry (mPIV): recent developments, applications, and guidelines. Lab Chip **9**, 2551–2567 (2009)
19. A. Einstein, *Theory of Brownian Movement* (Dover, New York, 1905)
20. P.E. Freudenthal, M. Pommer, C.D. Meinhart, B.D. Piorek, Quantum nanospheres for sub-micron particle image velocimetry. Exp. Fluids **43**, 525–531 (2007)
21. B.S. Rinkevichus, *Laser Techniques of Flow Diagnostics*. (MPEI, Moscow, 1990) (in Russian)
22. R.P. Feynman, R.B. Leighton; M.L. Sands, *Feynman Lectures on Physics*. (Addison-Wesley, Reading, c1963–1965)
23. A. Ishimaru, *Wave Propagation and Scattering in Random Media* (Wiley-IEEE Press, New York, 1999), 600 p
24. C. Dainty (ed.), *Laser Speckle and Related Phenomena*. (Springer, Berlin, Heidelberg, 1984)
25. J. Goodman, *Statistical Optics* (Wiley-Interscience, New York, 1985)
26. T. Yoshimura, Statistical properties of dynamic speckles. J. Opt. Soc. Am. A **3**(7), 1032–1054 (1986)
27. H.G. Merkus, *Particle Size Measurements: Fundamentals, Practice, Quality* (Springer Science+Business Media B.V., 2009)

28. R. Xu, *Particle Characterization: Light Scattering Methods* (Kluwer, New York/Boston/Dordrecht/London/Moscow, 2002)
29. A. Liebert, P. Lukasiewicz, D. Bogget, R. Maniewski, Optoelectronic standardization for laser Doppler perfusion monitors. Rev. Sci. Instrum. **70**, 1352–1354 (1999)
30. Y. Aizu, T. Asakura, Coherent optical techniques for diagnostics of retinal blood flow. J. Biomed. Opt. **4**(1), 61–75 (1999)
31. I.V. Fedosov, V.V. Tuchin, E.I. Galanzha, A.V. Solov'eva, T.V. Stepanova, Recording of lymph flow in microvessels using correlation properties of scattered coherent radiation. Quant. Electron. **32**(11), 970–974 (2002)
32. I.V. Fedosov, V.A. Galanzha, V.V. Tuchin, Blood flow assessment in capillaries of human eye conjunctiva using laser Doppler technique. Proc. SPIE **4427**, 104–108 (2001)
33. C.E. Riva, B.L. Petrig, G.E. Grunwald, Retinal blood flow, in *Laser Doppler Blood Flowmetry*, ed. by A.P. Shepherd, P.A. Oberg (Kluwer, Boston/Dordrecht/London, 1989), pp. 339–383
34. E. Logean, M.H. Geiser, B.L. Petrig, C.E. Riva, Portable ocular laser Doppler red blood cell velocimeter. Rev. Sci. Instrum. **68**(7), 2878–2882 (1997)
35. T. Eiju, M. Nagai, K. Matsuda, J. Ohtsubo, K. Homma, K. Shimizu, Microscopic laser Doppler velocimeter for blood velocity measurement. Opt. Eng. **32**(1), 15–20 (1993)
36. E.I. Galanzha, G.E. Brill, Y. Aizu, S.S. Ulyanov, V.V. Tuchin, Speckle and Doppler methods of blood and lymph flow monitoring, in *Handbook on Optical Biomedical Diagnostics*, **PM107**, ed. by V.V. Tuchin (SPIE Press, Bellingham, 2002), pp. 881–937
37. S.S. Ulyanov, Speckled speckle statistics with a small number of scatterers: implication for blood flow measurement. J. Biomed. Opt. **3**(3), 227–236 (1998)
38. R.D. Sinelnikov, Ya.R. Sinelnikov, *Atlas of Human Anatomy*, Issue 4 (Medicine Publishers, Moscow, 1994)
39. G.T. Feke, C.E. Riva, Laser Doppler measurement of blood velocity in human retinal vessels. J. Opt. Soc. Am. **68**(4), 526–531 (1978)
40. G.T. Feke, A. Yoshida, C.L. Schepens, Laser based instruments for ocular blood flow assessment. J. Biomed. Opt. **3**(4), 415–422 (1998)
41. C.E. Riva, J.E. Grunvald, B.L. Petrig, Laser Doppler measurements of retinal blood velocity: validity of the single scattering model. Appl. Opt. **24**, 605–607 (1985)
42. C.E. Riva, B.L. Petrig, R.D. Shonat, C.J. Pouranas, Scattering process in LDV from retinal vessels. Appl. Opt. **28**, 1078–1083 (1989)
43. A.J. Welch, M.C.J. van Gemert (eds.), *Tissue Optics* (Academic, New York, 1992)
44. D.H. Sliney, S.L. Torkel, *Medical Lasers and Their Safe Use* (Academic, New York, 1993)
45. K. Aukland, R.K. Reed, Interstitial-lymphatic mechanisms in the control of extracellular fluid volume. Physiol. Rev. **73**, 1–78 (1993)
46. W.L. Olszwski, Contractility patterns of normal and pathologically changed human lymphatics. Ann. N Y Acad. Sci. **979**, 52–63 (2002)
47. G.M. Johnston, The intrinsic lymph pump: progress and problems. Lymphology **22**, 116–122 (1989)
48. A.A. Gashev, Physiologic aspects of lymphatic contractile function: current perspectives. Ann N Y Acad Sci. **979**, 178–187 (2002)
49. L. Richard, M.D. McCann, Disorders of the lymphatic system. Chapter 47, in *Textbook of Surgery* (W.B. Saunders, London, 2000), pp. 1573–1577
50. D. Saito, M. Hasui, T. Shiraki, H. Kono, Effects of coronary blood flow, myocardial contractility, and heart rate on cardiac lymph circulation in open-chest dogs. Use of a direct cannulation method for subepicardial lymph vessel. Arzneimittelforschung **47**(2), 119–124 (1997)
51. J.B. Smith, N.C. Pederson, M. Dede, The role of the lymphatic system in inflammatory responses. Ser. Haematol. **3**, 2–7 (1970)
52. C.L. Witte, M.H. Witte, Disorders of lymph flow. Acad. Radiol. **2**, 324–334 (1995)
53. E. Foldi, M. Foldi, L. Clodius, The lymphedema chaos: a lancet. Ann. Plast. Surg. **22**, 505–515 (1989)

54. C.J.H. Porter, W.N. Charman, Uptake of drugs into the intestinal lymphatics after oral administration. Adv. Drug Deliv. Rev. **25**, 71–89 (1997)
55. A.A. Ramelet, Pharmacologic aspects of a phlebotropic drug in CVI-associated edema. Angiology **51**, 19–23 (2000)
56. R.F. Schmidt, G. Thews (eds.), *Human Physiology* (Springer, Berlin/Heidelberg, 1989)
57. E.I. Galanzha, V.V. Tuchin, A.V. Solov'eva, V.P. Zharov, Development of optical diagnostics of microlymphatics at the experimental lymphedema: comparative analysis. J. X-Ray Sci. Technol. **10**, 215–223 (2002)
58. I.V. Fedosov, E.I. Galanzha, A.V. Solov'eva, T.V. Stepanova, G.E. Brill, V.V. Tuchin, Laser speckle flow velocity sensor for functional biomicroscopy. Proc. SPIE **4707**, 206–209 (2002)
59. E.I. Galanzha, V.V. Tuchin, A.V. Solov'eva, T.V. Stepanova, G.E. Brill, V.P. Zharov, The diagnosis of lymph microcirculation on rat mesentery in vivo. Proc. SPIE **4965**, 325–333 (2003)
60. M.J. Lighthill, Pressure-forcing of tightly fitting pellets along fluid-filled elastic tubes. J. Fluid. Mech. **34**(1), 113–143 (1968)
61. J.M. Fitz-Gerald, Mechanics of red-cell motion through very narrow capillaries. Proc. Royal Soc. **B174**, 193–227 (1969)
62. A. Perlin, T.-K. Hung, Flow development of a train of particles in capillaries. J. Eng. Mech. Div. **EM1**, 49–66 (1978)
63. M. Francon, *Laser Speckle and Applications in Optics* (Academic, New York, 1979)
64. R. Jones, C. Wykes, *Holographic and Speckle Interferometry* (Cambridge University Press, Cambridge, 1983)
65. Y. Aizu, T. Asakura, Bio-speckle phenomena and their application to the evaluation of blood flow. Opt. Laser Technol. **23**(4), 205–219 (1991)
66. Y. Aizu, K. Ogino, T. Sugita, T. Yamamoto, N. Takai, T. Asakura, Evaluation of blood flow at ocular fundus by using laser speckle. Appl. Opt. **31**(16), 3020–3029 (1992)
67. I.V. Fedosov, V.V. Tuchin, The spatial-time correlation of the intensity of a speckle field formed as a result of scattering of focused coherent radiation by a capillary liquid flow containing scattering particles. Opt. Spectrosc. **93**(3), 473–477 (2002)
68. I.V. Fedosov, V.V. Tuchin, E.I. Galanzha, A.V. Solov'eva, Laser monitoring of the flow velocity in lymphatic microvessels based on a spatial-temporal correlation of the dynamic speckle fields. Tech. Phys. Lett. **28**(8), 690–692 (2002)
69. I.V. Fedosov, V.V. Tuchin, Use of dynamic speckle field space-time correlation function estimates for the direction and velocity determination of blood flow. Proc. SPIE **4434**, 192–196 (2001)
70. V.V. Tuchin, A. Tárnok, V.P. Zharov (eds.), Special issue: Towards in vivo flow cytometry. J. Biophoton. **2**(8–9), 457–547 (2009)
71. V.V. Tuchin (ed.), *Advanced Optical Cytometry: Methods and Disease Diagnoses* (WILEY-VCH Verlag GmbH & Co. KGaA, Weinheim, 2011)
72. V.V. Tuchin, A. Tárnok, V.P. Zharov (eds.), Special issue: In vivo flow cytometry. Cytometry A **79**(N10), 737–883 (2011)
73. V.V. Tuchin, A. Tárnok, V.P. Zharov, In vivo flow cytometry: a horizon of opportunities. Cytom. A **79**(N10), 737–745 (2011)
74. S.M. Daly, M.J. Leahy, Advances in blood flow imaging, in *Advanced Biophotonics: Tissue Optical Sectioning*, ed. by V.V. Tuchin, R.K. Wang (CRC Press/Taylor & Francis, London, 2012)
75. S.M. Daly, M.J. Leahy, 'Go with the flow': a review of methods and advancements in blood flow imaging. J. Biophotonics (2012). doi:10.1002/jbio.201200071

Quasi-Elastic Light Scattering in Ophthalmology

14

Rafat R. Ansari

Contents

Abstract

The eye is not just a "window to the soul"; it can also be a "window to the human body." The eye is built like a camera. Light which travels from the cornea to the retina traverses through tissues that are representative of nearly every tissue type and

R.R. Ansari
NASA John H. Glenn Research Center at Lewis Field, Cleveland, OH, USA
e-mail: rafat.r.ansari@nasa.gov

fluid type in the human body. Therefore, it is possible to diagnose ocular and systemic diseases through the eye. Quasi-elastic light scattering (QELS) also known as dynamic light scattering (DLS) is a laboratory technique routinely used in the characterization of macromolecular dispersions. QELS instrumentation has now become more compact, sensitive, flexible, and easy to use. These developments have made QELS/DLS an important tool in ophthalmic research where disease can be detected early and noninvasively before the clinical symptoms appear.

14.1 Introduction

The technique of quasi-elastic light scattering (QELS) was originally developed to study fluid dispersions of colloidal (size ≤ 1 μm) particles [1]. QELS is also known as dynamic light scattering (DLS), photon correlation spectroscopy (PCS), and/or homodyne/heterodyne light-beating spectroscopy. It was first used in the eye by Tanaka and Benedek to study cataract in the ocular lens over three decades ago [2, 3]. However, its use remained limited to a few research laboratories, and it did not find wide-scale commercial acceptance in ophthalmology. Thanks to the innovations in the fields of fiber optics and optoelectronics, QELS is now emerging as a potential ophthalmic tool, making the study of virtually every tissue type and fluid type comprising the eye possible thus pushing the envelope for broader applications in ophthalmology. The ability of QELS in the early detection of the changes in the molecular morphology of ocular tissues has the potential to help develop new drugs to combat not just the diseases of the eye such as cataract but to diagnose and study those of the body such as diabetes and the brain possibly Alzheimer's and Parkinson's disease [4].

14.1.1 Need for Noninvasive Diagnostics in Ophthalmology

Blindness is a global problem. According to the World Health Organization (WHO), 90 % of all blind people live in developing countries. In the United States alone, one person goes blind every 11 min. The current economic cost of blindness in India and the USA is estimated at 4.6 and 4.1 billion US dollars per year, respectively, and is rising. These are alarming figures since half of all blindness can be prevented if detected and treated early [5].

Ophthalmology is a specialized branch of medicine which deals with the study, detection, and treatment of eye diseases. Normal aging is the leading cause for ocular problems and refractive disorders such as cataract, age-related macular degeneration (AMD), vitreous liquefaction, glaucoma, and hyperopia. Certain systemic diseases can also lead to eye diseases early. For example, diabetes contributes to early formation of cataract and retinal disease (diabetic retinopathy), and hypertension (elevated blood pressure) can lead to glaucoma.

The visual function and ocular health is evaluated everyday by ophthalmologists with subjective (e.g., patient history) and objective methods that can include visual

acuity charts, direct and indirect ophthalmoscopy, retinoscopy, keratometry, and applanation tonometry. The classical principles of light scattering (Rayleigh, Mie, etc.) are employed virtually in every ophthalmic instrument in one form or another. The slit-lamp biomicroscope, based upon the optical principles of compound microscopy, is the most widely used ophthalmic instrument for examination from the cornea to the retina. This instrument, except for some mechanical designs and illumination techniques, has not changed in principle in the past 150 years [6]. The modern instruments employ direct illumination for the examination of lesions in conjunctiva, retro-illumination for corneal opacities, cataract, and iris atrophy in glaucoma, sclerotic scatter for corneal edema, and specular reflection for making the epithelium and endothelium cells in the cornea visible. A principle known as Scheimpflug is employed in slit-lamp biomicroscopes to generate stereoscopic images of the lens to study cataract. A recent review of the Scheimpflug imaging technique is given elsewhere [7]. Beyond these conventional methods, the modern techniques of optical coherence tomography (OCT), scanning laser ophthalmoscopy (SLO), confocal microscopy, and quasi-elastic light scattering (QELS) are some of the emerging tools that are showing potential in the early diagnosis of ocular disease.

14.1.2 Principles of QELS

In a QELS experiment, a constant fluctuating speckle pattern is seen in the far field when light passes through an ensemble of small particles suspended in a fluid [1]. This speckle pattern is a result of the interference in the light paths, and it fluctuates as the particles in the scattering medium perform random walks on a time scale of ≥ 1 μs due to the collisions between themselves and the fluid molecules (Brownian motion).

In the absence of particle-particle interactions (dilute dispersions), light scattered from small particles fluctuates rapidly while light scattered from large particles fluctuates more slowly. During a simple homodyne experiment, only scattered light is collected (absence of local oscillator) at a photodetector, assuming the particles are uniformly sized and spherically shaped, and an intensity-intensity temporal autocorrelation function (TCF) is measured.

$$g^2(\tau) = A[1 + \beta \exp(-2\Gamma\tau)], \tag{14.1}$$

where $A = <i>^2$ is the average DC photocurrent or the baseline of the autocorrelation function and β $(0 < \beta < 1)$ is an empirical experimental constant and is a measure of the spatial coherence of the scattering geometry of the collection optics which can be related to signal-to-noise (S/N). Γ is a decay constant due to diffusing motion of the particles in the scattering volume and τ is the delay time.

$$\Gamma = D_T \cdot q^2, \tag{14.2}$$

where D_T is the translational diffusion coefficient and q is the magnitude of the scattering wave vector

$$q = \frac{4\pi n}{\lambda} \sin\left(\frac{\theta}{2}\right),$$
(14.3)

where n is the refractive index of the solvent, λ is the wavelength of the incident light in vacuum, and θ is the scattering angle. Using the Stokes-Einstein relationship for spherical particles, D_T can be related to the hydrodynamic radius (R) of the particle

$$D_T = \frac{KT}{6\pi\eta R},$$
(14.4)

where K is Boltzmann's constant (1.38×10^{-23} J·K^{-1}), T is the absolute temperature of the scattering medium, and η is the solvent viscosity. In clinical ophthalmic applications, for n and η, value of water can be used at a body temperature of 37 °C. Equation 14.4 then can be used to extract average size of the particles in the transparent aqueous, lens, and vitreous. The lens and vitreous are polydisperse in nature and exhibit bimodal behavior. Today, commercial software packages are available to analyze eq. (14.1) in terms of bimodal and multimodal size distributions based upon the schemes reviewed by Stock and Ray [8].

Thus, a QELS or DLS experiment provides dynamic information such as diffusion, size, shape, and molecular interactions [1]. The most attractive features of this technique are that it is noninvasive and quantitative, works effectively for particle size ranging from few nanometers to few micrometers, requires small sample volume, and works reasonably well for polydisperse or multiple size (up to 2–3 component) dispersions. The new ocular QELS instrumentation is several orders of magnitude more sensitive than current ophthalmic instruments based on imaging and photographic techniques of slit-lamp biomicroscopy, retro-illumination, and Scheimpflug systems. These instruments are being used in clinical settings with better alignment and reproducibility to characterize the cornea, aqueous, lens, vitreous, and retina. Although still in experimental realm, many new applications have been realized to detect a diverse range of diseases early, noninvasively, and quantitatively. These include corneal evaluation of wound healing after refractive surgery, e.g., laser in situ keratomileusis (LASIK), pigmentary glaucoma, cataract, vitreopathy, diabetic retinopathy, and possibly Alzheimer's.

14.2 QELS and Disease Detection

Until recently, QELS or DLS instruments were physically bulky; required vibration isolation, index matching (for flare control), and tedious optical alignment; and were difficult to use. The new generation systems are compact and efficient due to new solid-state laser sources, sensitive photodetectors, and by using monomode optical fibers for launching and detecting low levels of laser light into the eye.
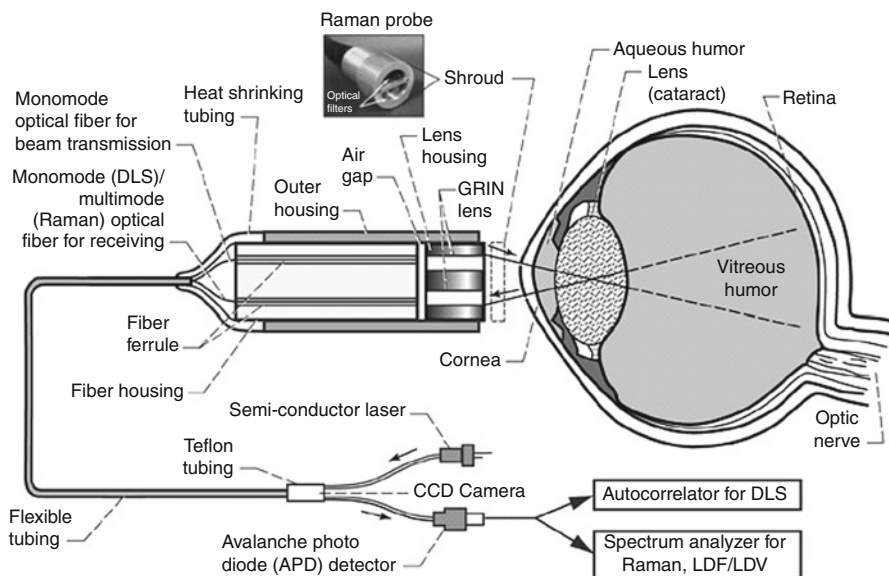
Fig. 14.1 QELS/DLS fiber-optic probe schematic diagram

The fiber-optic-based QELS design developments for studies of cataractogenesis are covered by Dhadwal et al. [9], Rovati et al. [10], Ansari et al. [11], and the references contained in their papers. The fiber-optic QELS probe, shown in Fig. 14.1, combines the unique attributes of small size, low laser power, and high sensitivity [β values in (14.1)]. The probe was originally developed to conduct fluid physics and biotechnology protein crystal growth experiments in the absence of gravity onboard a space shuttle or space station orbiter. The system is easy to use because it does not require sensitive optical alignment nor vibration isolation devices. The probe has been successfully employed in many ocular experiments to monitor the early symptoms of various eye diseases [4, 12–15].

A low-power (50–100 μW) light from a semiconductor laser, interfaced with a monomode optical fiber, is tightly focused in a 20-μm-diameter focal point in the tissue of interest via a GRIN (gradient index) lens. On the detection side, the scattered light is collected through another GRIN lens and guided onto an avalanche photodiode (APD) detector built into a photon-counting module. APD processed signals are then passed on to a digital correlator for analysis. The probe provides quantitative measurements of the pathologies of cornea, aqueous, lens, vitreous, and the retina. The device is modular in design. If needed, by suitable choice of optical filters, it can be converted into a device for spectral measurements (autofluorescence and Raman spectroscopy) and laser-Doppler flowmetry/velocimetry providing measurements of oxidative stress and blood flow in the ocular tissues. The device can easily be mounted onto many conventional ophthalmic instruments to significantly increase their diagnostic power. These instruments

Fig. 14.2 Modified slit-lamp
apparatus with QELS/DLS
probe mounted on a Hruby
lens holder (Courtesy of M.A.
DellaVecchia, MD)

QELS
Probe

Hruby
lens
holder
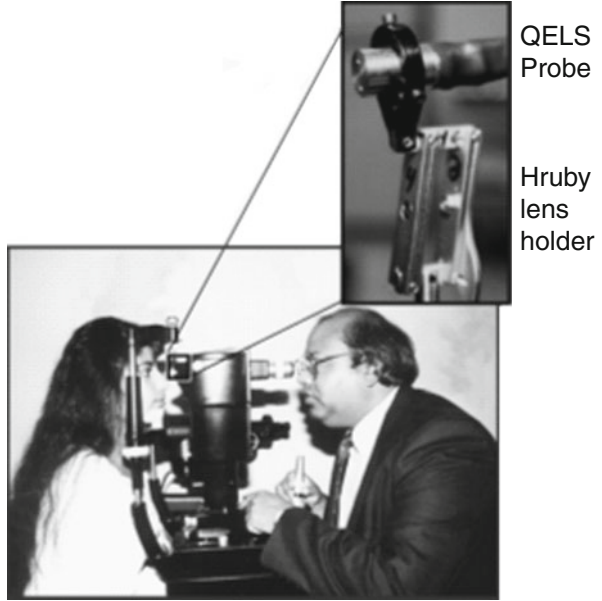
Fig. 14.3 Zeiss Scheimpflug
imaging set up with QELS at
NEI/NIH (Photo courtesy of
Manuel B. Datiles III, MD,
NEI/NIH)
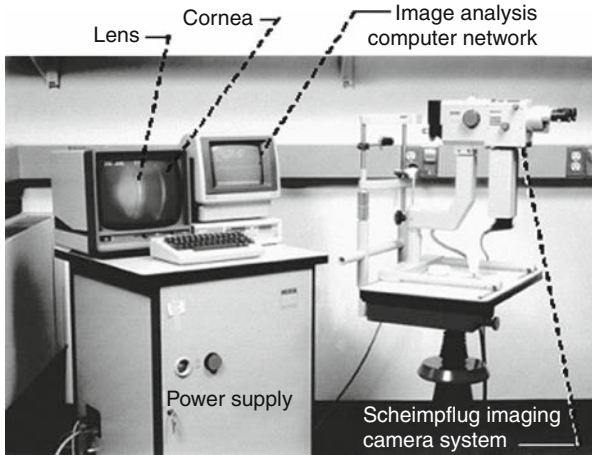
include slit lamps (Fig. 14.2), Scheimpflug cameras (Fig. 14.3), videokeratoscopy
(Figs. 14.4, 14.5), and a fluorometer (Fig. 14.6).

14.3   Early Detection of Ocular and Systemic Diseases

Table 14.1 represents various diseases and the respective ocular component of
interest in a QELS experiment.

Fig. 14.4 Modified corneal analyzer (Keratron videokeratoscope) with QELS probe (Photo courtesy of James S. Logan, MD, NASA Johnson Space Center, Houston)
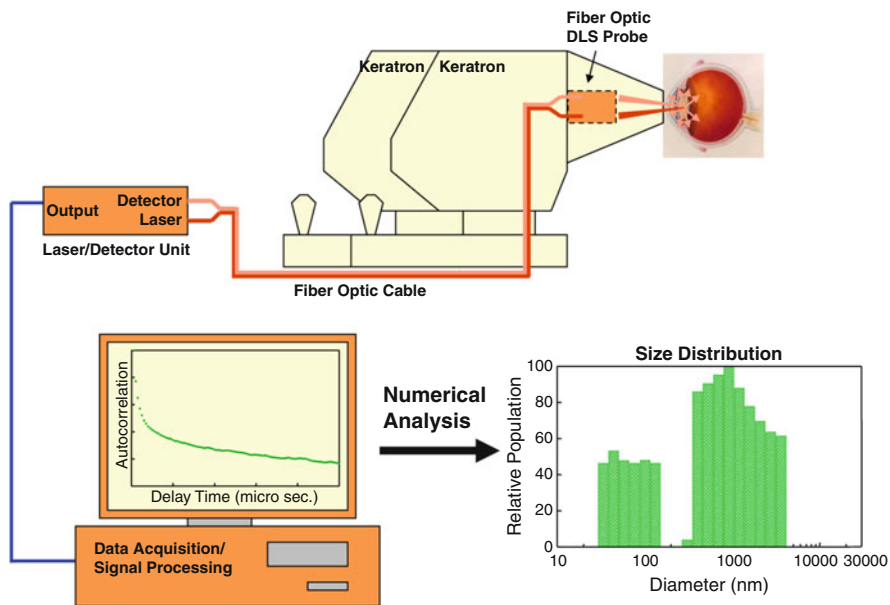
Fig. 14.5 Schematic diagram of the instrument shown in Fig. 14.4. The 100-μW solid state laser directs a beam of light to the lens in the patient's eye, and the light scattered by randomly moving protein crystallins in the lens is collected by an APD during a 5-s time interval. The time autocorrelation function of the measurement is then processed to estimate a distribution of particle sizes (Courtesy of M.B. Datiles III, MD)

Fig. 14.6 QELS probe integrated with fluorometry measurements in a fluorotron master (Photo courtesy of Luigi Rovati, Ph.D., University of Modena)

Table 14.1 Diseases and the ocular fluid/tissue components as measured by QELS

Disease	Cornea	Aqueous	Lens	Vitreous
Uveitis		Albumins		
Glaucoma		Pigments		
Cataract			Crystallins	
Diabetes			Crystallins	Hyaluronan and collagen
Diabetic retinopathy	Nucleotides pyridines			Hyaluronan and collagen
Wound healing (after refractive surgery)	Glycoproteins and collagen			
Oxidative stress (radiation, aging, etc.)	Nucleotides pyridines		Crystallins	
Alzheimer's		Amyloids	Amyloid-induced crystallin aggregation	Amyloids

14.3.1 Uveitis and Cholesterol Levels

The aqueous humor has a volume of about 250 μL and is located in a chamber between the cornea and the lens. It circulates at a rate of 2 μL/min and provides necessary metabolites to and transports the metabolic waste products from the lens, iris, and cornea. Therefore, aqueous can be considered an ultrafiltrate of blood since

it contains most of the molecules found in the serum at concentrations that are reflective of serum levels. For example, certain metabolites (glucose) and proteins (human serum albumin or HSA) are present in the aqueous. Since glucose molecules are much smaller ($\sim$0.6 nm in diameter) than the visible wavelength (λ) region, they do not contribute significantly to scattered light especially at the low laser power levels and at the normal physiological glucose concentration ($\sim$100 mg/dL). The HSA particles can scatter light appreciably since they are spherical in shape and their size ($\sim$7.0 nm in diameter) is comparable to λ frequently applied in QELS experiments.

Uveitis is an inflammatory disease of the anterior chamber. It can produce high numbers of protein particles in the aqueous humor. This increase in protein concentration gives rise to increased scattered light intensity or "flare." Clinically, flare and therefore the severity of uveitis can be easily detected and quantified by QELS.

Similarly, cholesterol levels in the body can also be evaluated through the aqueous as suggested by Bursell et al. [3]. But this important application has not been pursued thoroughly either in a laboratory or clinical setting. Cholesterol consists of two components: LDL (low density lipoprotein) and HDL (high density lipoprotein). Elevated level of LDL is a risk factor for coronary heart disease and stroke. In recent proof-of-concept experiments in the author's lab, both LDL and HDL levels were evaluated (unpublished data) in samples obtained post-cataract surgery. Recent research is now linking elevated cholesterol levels to increased risk of age-related macular degeneration (AMD).

14.3.2 Pigmentary Glaucoma

Glaucoma is a disease of the anterior chamber in which the intraocular pressure (IOP) increases. If IOP increase is not treated, it can lead to degeneration of the optic nerve and eventually loss of vision. Recently QELS was applied to study one specific type of glaucoma known as pigmentary dispersion glaucoma (PDG). The posterior layer of the iris epithelium contains high number of melanin granules. These granules are released into the aqueous as a consequence of natural epithelium cell death, infection, or trauma. The melanin granules can be trapped in the trabecular meshwork over time and block the aqueous outflow. This can cause an increase in IOP finally leading to PDG. Pollonini et al. [16] used QELS to detect and quantify melanin granules in a clinical pilot study of normal and PDG volunteer patients. The results showed in Fig. 14.7 indicated presence of small (1–10 nm) and large (up to 1 μm) particles in the aqueous of normal and the PDG patients, respectively, and therefore showed the potential of QELS in monitoring this type of glaucoma noninvasively.

14.3.3 Cataract

Cataract (lens opacification), its clinical evaluation, and classification are discussed in detail elsewhere by Datiles and Ansari [17].

Fig. 14.7 Detection of pigmentary glaucoma with QELS/DLS
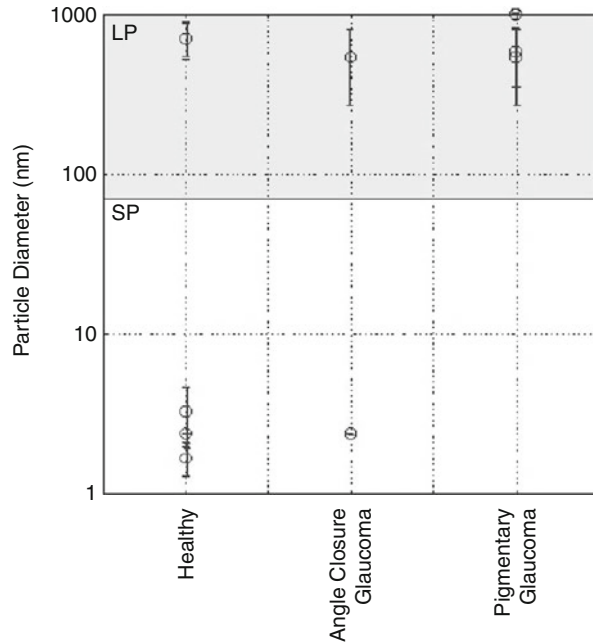
Cataract is the major cause of blindness worldwide. At the present time, clinical methods of classifying cataracts are based mainly upon visual acuity (Snellen charts) and photographic means (slit lamps). The inside of the eye is illuminated either directly or indirectly (retro-illumination) by a slit from an incandescent source of light. These approaches, however, are subjective because they cannot be accurately quantified. Furthermore, they do not have the ability to capture a growing cataract in its incipient stage. Therefore, by the time a cataract is diagnosed by these methodologies, it is too late to alter its course noninvasively or medically, e.g., using pharmaceuticals and/or nutraceuticals. QELS holds promise in "cracking the cataract code" by detecting it much earlier than the photographic techniques currently in use [18].

The normal lens in a human eye, situated behind the cornea, is a transparent tissue. It contains 35 % (by weight) protein and 65 % (by weight) water. Aging, disease (e.g., diabetes), smoking, dehydration, malnutrition, and exposure to UV and ionizing radiation can cause agglomeration of the lens proteins. Protein aggregation can take place anywhere in the lens causing lens opacity. The aggregation and opacification could produce nuclear (central portion of the lens) or cortical (peripheral) cataracts. Nuclear and posterior subcapsular (the membrane capsule surrounds the whole lens) cataracts, being on the visual optical axis of the eye, cause visual impairment, which can finally lead to blindness. The lens proteins, in their native state, are small in size. As cataract develops, this size grows from a few nm (transparent) to several microns (cloudy to opaque). Ansari and Datiles have

Fig. 14.8 QELS scanning
setup for laboratory animals
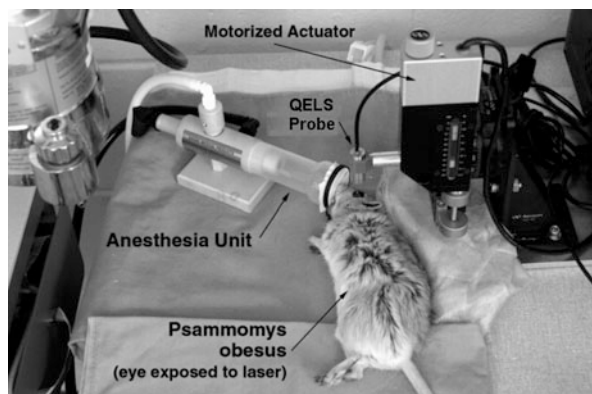
shown that QELS can detect cataracts at least two to three orders of magnitude earlier (noninvasively and quantitatively) than the best imaging (Scheimpflug) techniques in clinical use today [19].

Animal models are usually helpful in the validation of new instruments and testing of therapies prior to clinical use. Until recently, it was difficult to use QELS in small animal models due to instrument limitations, e.g., physical size, power requirements, and alignment problems. The compact probe described in Fig. 14.1 is proving to be very useful in this area of research. A generic experimental setup is shown in Fig. 14.8. Cataractogenesis is monitored in vivo by following TCF profiles (14.1) at different time lines. As an example, Philly mice were monitored. This animal develops cataract spontaneously between day 26 and 33 after birth.

The data includes a 45 days old normal mouse of the control FVB/N strain which does not develop a cataract and two Philly mice roughly 26–29 days old. The eye examinations of these mice with a slit-lamp biomicroscope concluded a normal (transparent) and two other eyes having trace to mild cataracts. Each measurement took 5 s at a laser power of 100 μW. The changing TCF slope is an indication of cataractogenesis as the lens crystallins aggregate to form high molecular weight clumps and complexes. The QELS autocorrelation data is converted into particle size distribution using an exponential sampling program and is shown in Fig. 14.9. Although, conversion of the QELS data into particle size distributions requires certain assumptions regarding the viscosity of the lens fluid, these size values do indicate a trend as the cataract progress. These measurements suggest that a developing cataract can be monitored quantitatively with reasonable reliability, reproducibility (5–10 %), and accuracy.

14.3.3.1 Drug Screening for Cataract

In the absence of a nonsurgical treatment, 50 % of all blindness is due to cataracts. At the present time, 34 million Americans over the age of 65 have cataracts. Foster predicts this figure to rise to 70 million by year 2030 [20]. According to Kupfer, "A delay in cataract formation of about 10 years would reduce the prevalence of
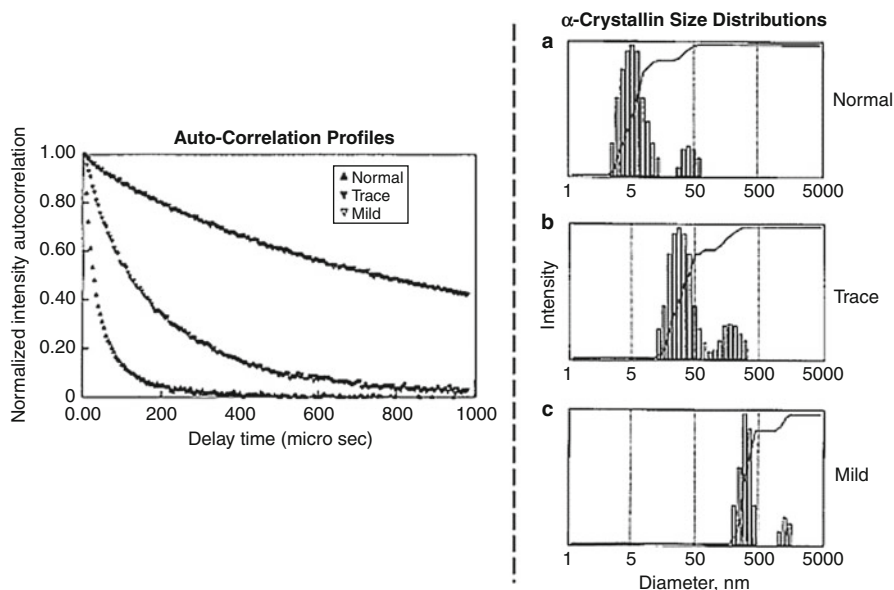
Fig. 14.9 In vivo cataract measurements in mice

visually disabling cataracts by about 45 %" [21]. QELS can help achieve this goal by detecting cataracts at very early stages and by screening potential anticataract drugs for their efficacy.

Pantethine is a metabolically active stable disulfide form of pantetheine and a derivative of pantothenic acid (vitamin B5). It can be used as an anticataract drug, but the clinical trial of pantethine was inconclusive with respect to effectiveness [22, 23]. The results of both preclinical and clinical tests of potential therapeutic agents indicate the need for more sensitive measures of protein aggregation and opacification in vivo. Studies in humans predicted that QELS will be useful in testing of anticataract drugs to inhibit or reverse the progression of cataract formation during longitudinal clinical trials [24, 25].

Ansari et al. [26], using QELS, demonstrated the efficacy of pantethine in very early stages (few hours to few days) of selenite-induced lens damage, well before formation of a mature cataract in the selenite model [27]. In this study, QELS measurements were made on 33 animals (rats) aged 12–14 days at the time of selenite or pantethine injection. Pantethine treatment resulted in a substantial decrease in dimensions of scattering centers in lens in vivo during the early stages of opacification prior to their detection with conventional ophthalmic instruments. An obvious opacity was not observed using a slit-lamp biomicroscope. Typical representative size distribution data is presented in Fig. 14.10 for control, Se-treated (12 and 60 h posttreatment) and Se-pantethine-treated animal (42 h posttreatment) at a distance of ∼2 mm from the lens anterior surface. The size distribution of scatterers in the control animal ranges from 60 to 80 nm in diameter. In the
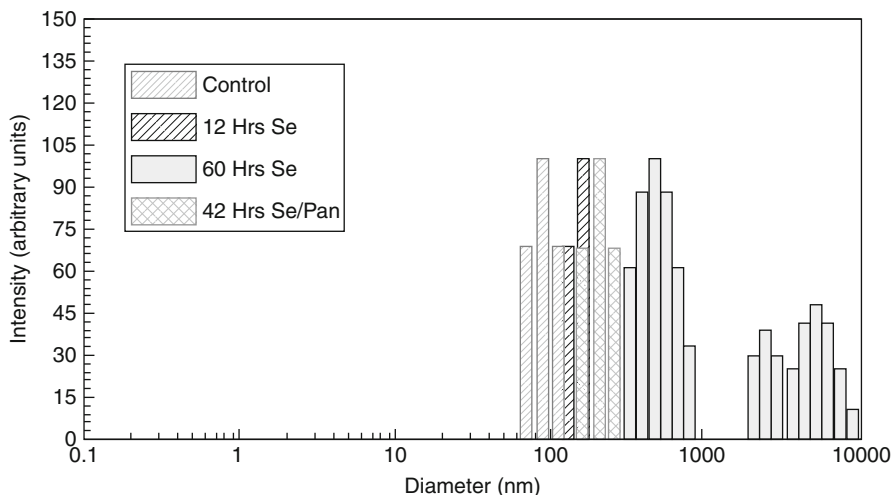
Fig. 14.10 Cataract treatment in rats. Exponential sampling particle size distribution analysis

Se-treated animals, the TCF shows bimodal behavior with aggregates ranging in size from 400 to 800 nm and 3,000 to 10,000 nm in diameter. The Se-pantethine-treated animal shows an aggregate size averaging around 200 nm. The experimental results indicated clearly that QELS was able to discern subtle molecular changes very early in cataract formation. The results suggested that pantethine may inhibit the initial aggregation process.

In conclusion, the results are encouraging. The future outlook for finding a medical cure for cataract seems optimistic when combined with advances in the detection technology, understanding of fundamental processes, and the efforts in designing new anticataract drug formulations [28–30].

14.3.4 Evaluation of Oxidative Stress in Humans

It would be most beneficial to have the ability to identify individuals at particular risk for developing cataracts and possibly other diseases by detecting early molecular (precataractous) changes in the lens. An early objective means of measuring early disease progression in vivo will give a good handle on controlling the oxidative stress. Oxidative stress is the main cause for aging and is involved in almost every disease (Fig. 14.11).

14.3.4.1 Human Study of Precataractous Lenses
In a recent clinical study [15] of 380 eyes at NEI/NIH, using the DLS/QELS device shown in Figs. 14.4, 14.5, Datiles et al. showed that significant loss of alpha crystallin proteins seen in clinically transparent lenses was associated with aging. The study further showed that a significant decrease in the alpha crystallin protein

Fig. 14.11 Oxidative stress leads to aging and disease because the whole-body cellular-level injuries occur with oxidative stress due to the formation of reactive oxygen species (ROS)

Oxidative Stress Sources:
Hyperoxia, Radiation, Noise, Exercise, Dust

Reactive Oxygen Species Formation (ROS)

Damage to Cells and Molecules
Lipids, Proteins, DNA

Anemia, Muscle Fatigue, Cancer, neurodegenarative Diseases, Cardiovascular & Respiratory Diseases, Diabetes, Cataract
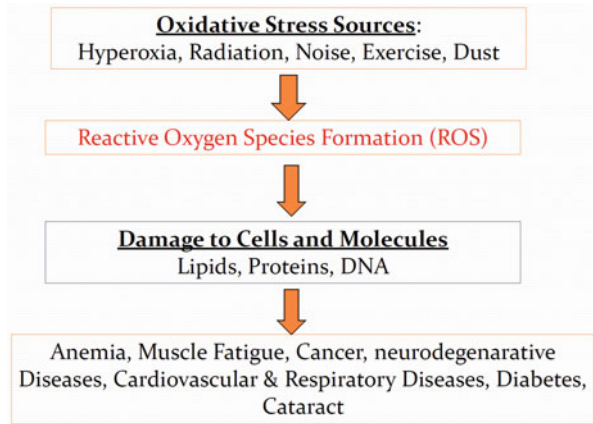
was associated with increasing nuclear lens opacity grades (Fig. 14.12). These findings confirm the potential of DLS/QELS as an early alarm system for oxidative damage.

14.3.5 Environmental Ocular Toxicity

It is a well-known fact that the cornea offers the first line of defense against external stresses. It can, however, be opacified and degenerated (like an onion peel) if exposed to toxic chemicals and biological agents (e.g., mustard gas). Exposure to X-ray and treatment under hyperbaric oxygen can lead to the formation of cataract in the lens. We will discuss these two examples and the ability of QELS to study the oxidative stresses early.

14.3.5.1 Exposure to X-ray

Figure 14.13 summarizes the effects of X-ray exposure in rabbit eyes as a function of time. Up until three weeks after the initial damage to the lens epithelium cells, few biochemical changes are expected to take place. However, these anticipated changes cannot be measured at the present time with conventional methods. From week 3 to 8, some biochemical changes can be measured postmortem by chemical assay. Matured nuclear cataract is visible at week 9 by photographing the lens. QELS is able to discern subtle differences very early.

The study animals were exposed to X-ray (one time only) at a radiation level of 2,000 rad for 15 min. The animals were anesthetized with an injection of xylazine (30 mg/kg) and ketamine (7 mg/kg). Their eyes were dilated using a 0.5 % solution of tropicamide. A laser power of 50 microwatts at a wavelength of 638 nm was used. Each TCF was collected for 5 s. The experiments were conducted at Oakland University under the NIH guidelines on handling and safety of animals.

The QELS experiments were concluded on day 54 after the irradiation. The relative change in the average protein crystallin size is plotted for one normal and

11 Month Follow up of Pre-Senile Nuclear Cataract

11 months earlier   AREDS Nucleus Grade = 1.5

11 months later   AREDS Nucleus Grade = 2.5
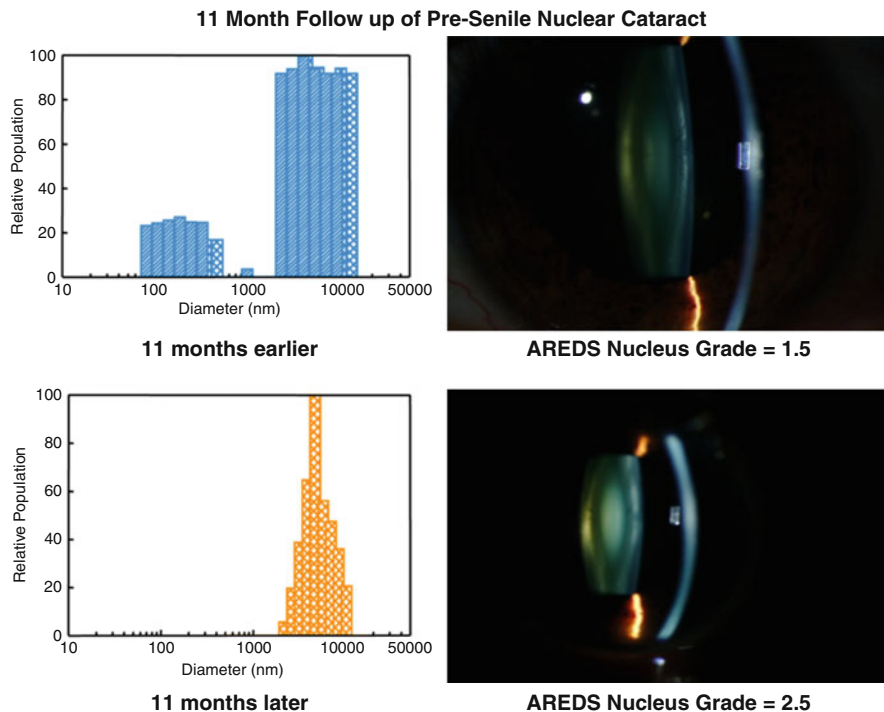
Fig. 14.12 Follow-up QELS/DLS data from a 42-year-old patient with early presenile nuclear cataract showing loss of the unbound alpha crystallin protein fraction (first peak) when a cataract developed 11 months later (see Ref. [15]). Alpha crystallin protein appears to prevent other damaged proteins from forming an opacity, but they are used up in the process. Once it drops below a critical level, a cataract can form (Images courtesy of M.B. Datiles III, MD)
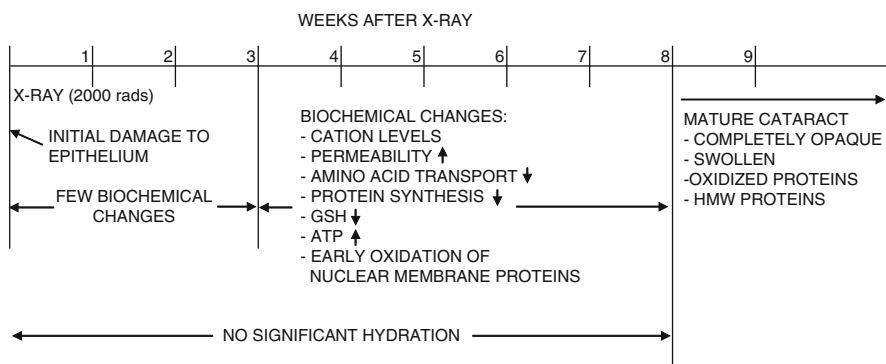
Fig. 14.13 Biochemical effects of X-ray in rabbit eyes (Courtesy of Frank Giblin, PhD, Oakland University)
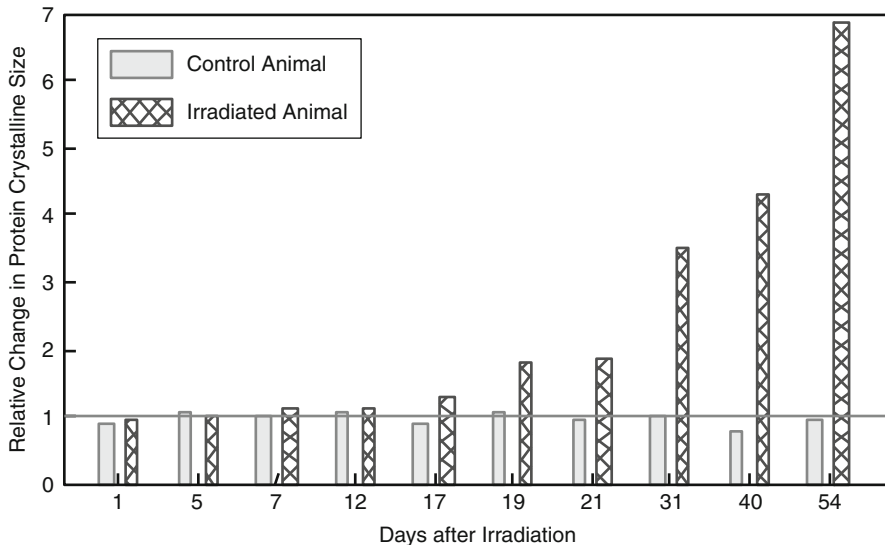
Fig. 14.14 Changes in rabbit lenses post-X-ray irradiation measured by QELS

one irradiated animal and is shown in Fig. 14.14. This was obtained by dividing each measured particle size, using the cumulant analysis method [8], by the mean value calculated from the average of all the values in the control or nonirradiated animal from day 1 to 54. The size remains constant (within 10–15 %) in the lens of the control animal (no radiation exposure). However, a significant increase in size can be noted in the experimental (irradiated) animal lens. Between day 1 and day 17, the protein aggregation seems to occur linearly. After a period of 2–2.5 weeks, the size increases almost exponentially. The average protein size in the lens of the animal exposed to ionizing X-ray radiation, compared with the control animal, increases by a factor of 2 by day 19, more than factor of 3 by day 31, more than factor of 4 on day 40, and almost by a factor of 7 by day 54. Slit-lamp imaging did not show any evidence of nuclear opacity until day 60.

14.3.5.2 Hyperbaric Oxygen (HBO)-Treated Animals

The role of oxygen in the formation of lens high molecular weight (HMW) protein aggregates during the development of human nuclear cataract was studied by Giblin et al. They measured lens crystallin aggregate formation in hyperbaric oxygen (HBO)–treated guinea pigs by using in vivo DLS/QELS (Fig. 14.15) and in vitro (HPLC) methods [12].

The results indicated average apparent diameter of proteins in the nucleus of lenses of HBO-treated animals was nearly twice that of the control animals. Size distribution analysis conducted at one selected point in the nucleus and cortex (the outer periphery of the lens) after dividing the proteins into small-diameter and large-diameter groups showed in the O_2-treated nucleus a threefold increase in
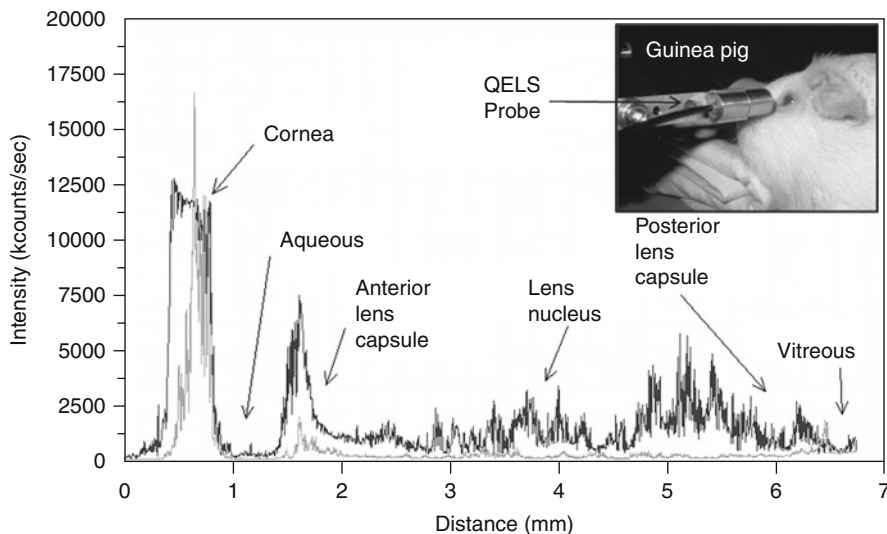
Fig. 14.15 QELS intensity scan showing enhanced light scattering in a guinea pig with HBO exposure (*dark line*: 67 treatments) compared with no HBO exposure (*light line*: no treatment) control animal

intensity and a doubling in apparent size of large-diameter aggregate proteins, compared with the same control group. These results were confirmed by well-established in vitro method of HPLC indicating that one half of the experimental nuclear WI protein fraction consisted of disulfide cross-linked aggregates, not present in control animals. Therefore, molecular oxygen in vivo can induce the cross-linking of guinea pig lens nuclear crystallins into large disulfide-bonded aggregates capable of scattering light. A similar process may be involved in the formation of human nuclear cataract [12].

14.3.5.3 Exposure to Ultraviolet Light

As described above, radiation (ionizing and nonionizing) is a source for oxidative stress. The DLS/QELS was used to investigate lens protein aggregation in vivo in the guinea pig post 5 months to a chronic low level of UVA light producing increased lens nuclear light scattering and elevated levels of protein disulfide. DLS size distribution analysis conducted at the same location in the lens nucleus of control and UVA-irradiated animals showed a 28 % reduction in intensity of small-diameter proteins in experimental lenses compared with controls. In addition, large-diameter proteins in UVA-exposed lens nuclei increased fivefold in intensity compared to controls. The UVA-induced increase in apparent size of lens nuclear small-diameter proteins was threefold, and the size of large-diameter aggregates was more than fourfold in experimental lenses compared with controls. It was presumed that the presence of a UVA chromophore in the guinea pig lens (NADPH bound to zeta crystallin), as well as traces of oxygen, contributed to UVA-induced crystallin aggregation. The results indicate a potentially harmful role
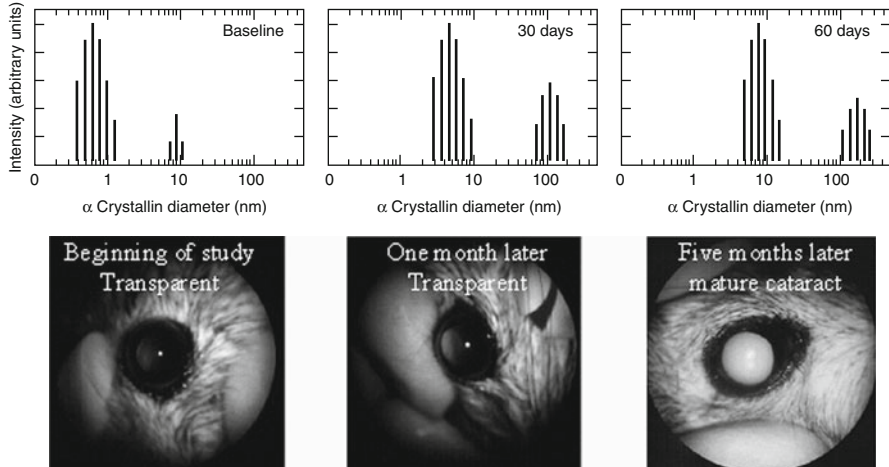
Fig. 14.16 Cataract formation due to diabetes in sand rats: (*top*) QELS particle size distribution; (*bottom*) slit lamp photographs (Photo courtesy of Michelle Chenault, PhD., FDA)

for UVA light in the lens nucleus. A similar process of UVA-irradiated protein aggregation may take place in the older human lens nucleus, accelerating the formation of human nuclear cataract [14].

14.3.6 Effects of Diabetes

QELS can be applied to detect effects of diabetes early through the transparent ocular lens. Chenault et al. have indicated that cataracts are 1.6 times more common in diabetic patients than nondiabetics [31]. The Food and Drug Administration (FDA) in the USA has a unique animal model to study type II diabetes. Psammomys obesus (sand rat) is a wild rodent found in the desert areas of the Middle East and Africa. It develops mild to moderate obesity, hyperglycemia, and the complications of diabetes such as cataracts and vision loss when it consumes a high caloric diet. In a recent study [31], blood glucose levels, insulin, and glycohemoglobin values in this animal were correlated with histopathology, traditional ophthalmology assessments, and QELS measurements toward developing a noninvasive means to detect early stages of eye damage due to diabetes mellitus. The control animal demonstrated no significant change in crystallin size distributions. Study animals exhibited significant increases in the sizes of crystallin-scattering centers and substantial shifts in the size distributions. No discernable difference was observed by ophthalmic examination or by histology between the control and study animals. The results demonstrated evidence of subtle changes in the lens of the diabetic sand rats after only two months on the diabetogenic diet using QELS (see Fig. 14.16 top graphs) Conventional ophthalmic instrumentation did not detect these changes
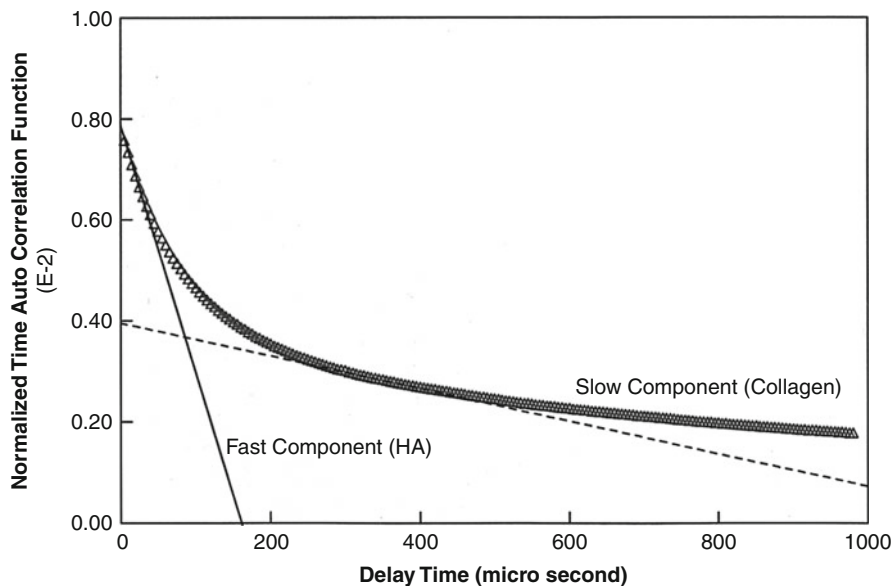
Fig. 14.17 Time relaxation of human vitreous gel

(see Fig. 14.16 bottom photographs). This animal model and QELS can be very helpful in screening of conventional and nonconventional drugs to control diabetes (hyperglycemia) for cataractogenic effect and its prevention.

14.3.6.1 Diabetic Vitreopathy

The vitreous body is the largest structure within the eye. Ansari et al. and Rovati et al. were the first to characterize vitreous structure with QELS and applied it to the study of diabetic vitreopathy [32, 33]. In a QELS measurement, the vitreous body truly exhibits a two exponential behavior consistent with its gel-like properties due to hyaluronan (HA) and collagen found, respectively, in the vitreous gel. A typical measurement is shown in Fig. 14.17. QELS can be a powerful tool to study the effects of diabetes on vitreous morphology due to the glycosylation of HA and collagen.

The effect of diabetes on the retina (diabetic retinopathy) is a leading cause of blindness in Americans between 20 and 74 years of age [34]. There has been little progress to diagnose this condition during early stages. Elevated levels of glucose affect tissues throughout the body by altering protein through the phenomenon of nonenzymatic glycation [35]. One of the most ubiquitous and important proteins altered by this process is collagen. Hyperglycemic effects on collagen underlie the basement membrane pathology in blood vessels throughout the body, including the retina. At present, there are no methods by which to evaluate glycation effects on collagen in the retinal vasculature. An alternative approach that could provide insight into this process would be to evaluate glycation effects upon collagen in ocular tissue, e.g., vitreous. In recent years, the vitreous has come to be recognized as an important
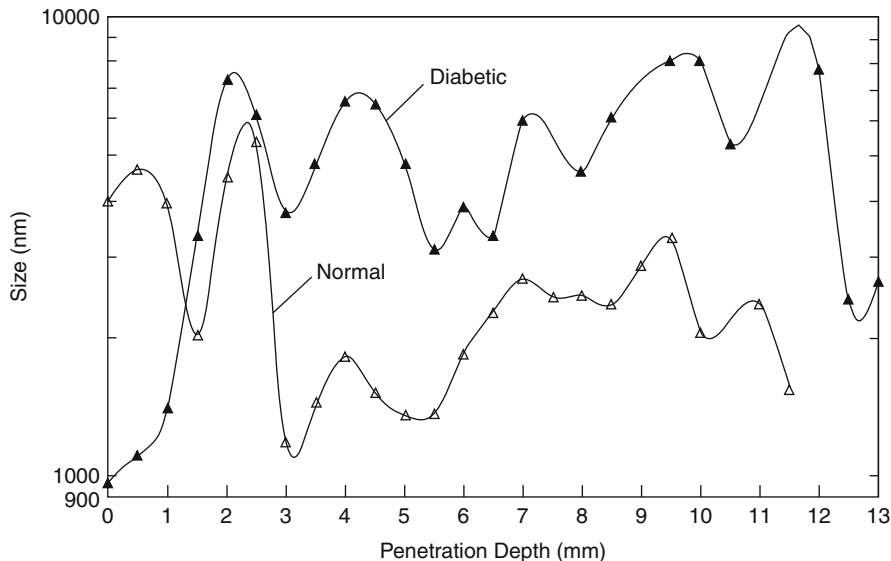
Fig. 14.18 Measurement of diabetic vitreopathy in normal and diabetic vitreous

contributor to advanced diabetic retinopathy. Studies have determined that there are elevated levels of glucose in the vitreous of diabetic patients. It is believed that these effects underlie the structural abnormalities in diabetic vitreopathy [36], similar to the effects of hyperglycemia on collagen elsewhere in the body [37]. Interestingly, these alterations appear to be quite similar to those observed in the vitreous during aging [38–41], consistent with the concept that diabetes induces accelerated aging in target tissues and organs [37]. Considering that the aforementioned effects of diabetes on vitreous collagen induce cross-linking and aggregation of fibrils into larger than normal fibers, it has been of interest to apply the methodology of QELS to assess the particle sizes found in diabetic vitreous and compare those to nondiabetic controls (see Fig. 14.18). Furthermore, QELS detected the structural changes [32] resulting from diabetic vitreopathy [40]. Interestingly, these QELS findings appear to corroborate the finding of dark-field slit microscopy where glycation of vitreous proteins resulted in cross-linking of collagen fibrils and aggregation into large bundles of fibrils. It is plausible that these are detected by QELS as particles of larger size with more variability than that seen in nondiabetic control in this preliminary study. Future studies in humans will determine if this phenomenon can be detected in a clinical setting, confirming these preliminary in vitro results.

14.3.6.2 Evaluation of Pharmacologic Vitreolysis

Pharmacologic vitreolysis is a new approach to improve vitreoretinal surgery and ultimately to liquefy and detach the vitreous from the retina to eliminate the contribution of the vitreous to retinopathy. The mechanism of action of the agents

being developed for pharmacologic vitreolysis remains unclear. The effect of microplasmin on vitreous diffusion coefficients was investigated using the noninvasive technique of QELS/DLS [13]. Pharmacologic vitreolysis with human recombinant microplasmin increases vitreous diffusion coefficients in vitro. The results of these studies have implications for the dosing, route of administration, duration of action, and methods of determining efficacy in future studies of pharmacologic vitreolysis to enhance vitreoretinal surgery, as well as the design of clinical trials to induce prophylactic posterior vitreous detachment [13]. This might be helpful in preventing the retinopathy of prematurity in neonates.

14.3.7 Evaluation of Corneal Surgery Outcomes

Corneal tissue is avascular composed primarily of collagen. The human cornea is about 500-μm thick at the apex and about 700 μm at the periphery or limbus [42]. Clearly, transparency is the most important corneal property to maintain good quality vision. Slight loss of transparency can cause problems such as haze and glare. A change in corneal shape can lead to myopic, astigmatic, and hyperopic vision.

Modern photorefractive surgeries, such as LASIK (laser-assisted in situ keratomileusis), have become popular to treat corneal refractive errors. The goal of refractive surgery is to sculpt the corneal surface, changing its physical shape. If successful, it will result in the elimination of refractive errors. In ~5 % post-LASIK cases, patients experience a variety of effects such as haze, glare, star bursts, dry-eye syndrome, and tissue healing issues. At present, no objective methods are available to evaluate quantitatively and noninvasively underlying molecular changes resulting in these corneal abnormalities after a LASIK procedure. McLeod [43], in his editorial, stressed the need for new diagnostic capabilities to better evaluate current refractive surgery outcomes.

QELS concepts discussed above were applied by Ansari et al. to the study of cornea as a molecular measure of clarity [44]. In a pilot study [45], excised but intact bovine eyes were treated with chemicals, cotton swabs, and radial and photorefractive surgeries. QELS measurements were performed as a function of the penetration depth into the corneal tissue. Topographical maps of corneal refractive power from untreated and treated corneas were also obtained using videokeratoscopy and the results compared.

The findings suggested the potential of QELS in measuring changes in the pre- and post-refractive surgeries. However, the ultimate aim for developing the technique using QELS for clinical applications in early evaluation of corneal complications after LASIK surgeries as well as other corneal abnormalities has yet to be proven. At the time of this writing, this validation work is being conducted at NEI/NIH.

14.3.8 Early Detection of Neurological Diseases

Ralf Dahm suggests "Studies of the eye not only could reveal ways to prevent cataracts but also might illuminate the biology of Alzheimer's, Parkinson's and

other diseases in which cells commit suicide (apoptosis)" [46]. Frederikse et al. [47] at NEI/NIH were the first to give a demonstration of Alzheimer's biology occurring in the lens. Alzheimer's disease (AD) sufferers loose cognitive abilities and thus serious deterioration in the quality of life. In simplistic terms, amyloid proteins forming plaques on the brain tissue lead to development of AD. Currently, these amyloid plaques or deposits can only be studied under a microscope by looking at the brain tissue at autopsy. Frederikse provided evidence of amyloid protein structure in the lens and its association with cataractogenesis [48]. A proof-of-concept experiment was conducted in vivo by measuring protein aggregation in the lenses of transgenic mice using NASA's QELS setup. The preliminary results indicated enhanced aggregation in study animals as opposed to controls [4]. This opens up an opportunity for QELS to be tried noninvasively in detailed studies of AD detection and treatments. Goldstein et al. [49] in a study of postmortem specimens of eyes linked amyloid proteins to the formation of supranuclear cataract in human lenses to AD. Recently, this group performed in vitro QELS measurements in protein suspensions and linked AD to lens and brain pathology in Down syndrome [50]. A recent article by Frost et al. presents a review of current literature on ocular morphology in AD and discusses the potential for an ocular-based screening test for AD [51].

14.4 QELS Limitations

Several things can go wrong in a QELS or DLS experiment. A few experimental tips are outlined below to avoid disappointments and artifacts.

14.4.1 Precise Control of Sample Volume

The lens and vitreous being transparent do not have any visible markers. Therefore, in longitudinal studies, reproducibility in repeat patient visits remains a big concern. QELS instrumentation must have the ability to precisely control and sample the same location inside the tissue of interest. The eye movements must be controlled, and the subject should remain well fixated during the QELS measurement cycle. In animal experiments, it is not much of a concern because animals can be sedated. However, they should be closely watched since some animals roll their eyes while sedated.

14.4.2 Laser Safety

In QELS ophthalmic applications, the major safety concern is the amount of light exposure to the retina. To minimize the risk of exposure, the power levels must be low and the exposure time must be short to satisfy the safety requirements set by ANSI (American National Safety Institute). Current ophthalmic QELS

instruments typically use a laser power of roughly 50–100 microwatts with exposure duration of 5 s. This makes it several orders of magnitude lower and therefore safer for use in animals and humans. However, every QELS instrument has its own unique optical arrangement for launching and receiving light signals, alignment procedures, and to maintain coherence conditions inside the scattering volume. Therefore, extra caution and care must be exercised in calculations for maximum possible exposure (MPE) limits set by ANSI and double checked by FDA to ensure patient safety.

14.4.3 Measurement of Visible Abnormalities

It is tempting to compare the QELS data, especially in clinical practice, with obvious ocular abnormalities. But one should bear in mind that QELS is only suitable for studies of very early ocular abnormalities in transparent tissues. It is not suitable to measure visible or mature lens or corneal opacities. Such measurements will introduce artifacts due to multiple scattering of light.

QELS can be used effectively in the determination of accurate particle size in water-based dispersions from transparent to extremely turbid ($\sim$7 orders of magnitude higher than the turbidity of water) samples ranging in size from few nanometers to almost a micron [11]. However, such analysis should be avoided in a cataractous eye because of unknown factors such as the changing viscosity. Therefore, it is acceptable to exploit the good dynamic range of QELS to follow a systematic trend as a marker for monitoring early ocular pathology, but due caution must be exercised in data interpretation when dealing with mild to mature pathologies. In clinical monitoring of a progressing disease, bimodal and multi-modal analyses are adequate to analyze autocorrelation data, and therefore, the calculation of a single parameter such as the alpha index [15] is very useful. However, there is room and need for improvement in software development. Recently, Nyeo and Ansari described a new method using the sparse Bayesian learning (SBL) algorithm to obtain an optimal and reliable solution to the Laplace transform inversion in dynamic light scattering (DLS) experiments [52, 53].

14.4.4 Eye Irrigation and Anesthesia in Animal Models

The drying of cornea and appearance of cold cataract, especially in animal measurements, produces artifacts. The corneas should be constantly irrigated (see Fig. 14.19) with saline solutions in between the QELS measurements to avoid corneal dehydration. In general, the body temperature drops in animals under anesthesia. This can cause cold-induced cataract especially in mice and rats. This can be avoided by using a heating pad and keeping the body temperature constant (37 °C) during the QELS experiments.
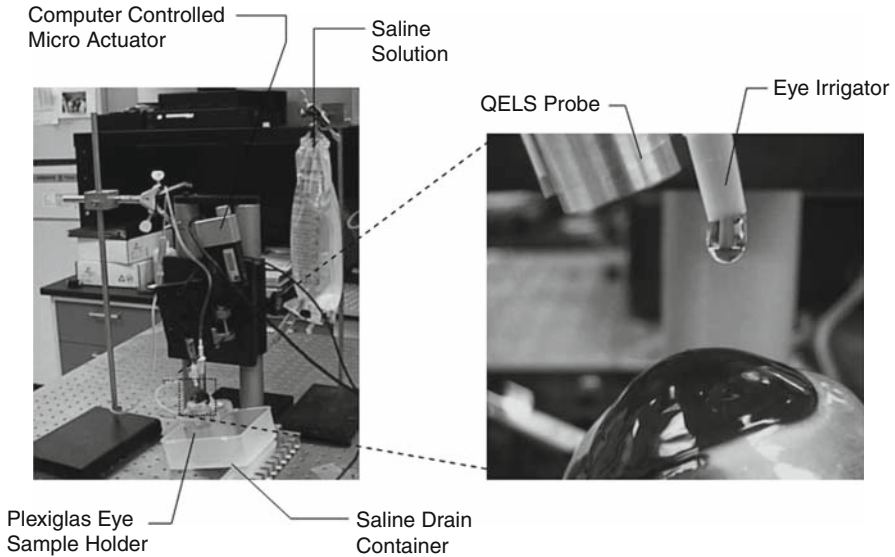
Fig. 14.19 Corneal irrigation system for QELS measurements

14.5   Conclusion and Future Outlook (Ophthalmic Tele-Health)

The effects of space travel on the human body are similar to those of aging here on earth, e.g., osteoporosis and cataract. The absence of gravity in space affects human physiology, and the development of cataract in astronauts is linked to the radiation exposure even in low earth orbit missions, e.g., on board the space shuttle and space station orbiters [54, 55]. This risk can be substantial if humans plan to travel to Mars or near-Earth Asteroid (NEA). A head-mounted goggles-like device with a suite of noninvasive optical technologies to ensure the mission safety and the health of astronauts can be developed. QELS is one technique among several others to be integrated in this device that may play an important role in monitoring ocular health remotely and noninvasively.

In the present economic climate, preventive medicine seems to be the direction of the future. Thus, the early detection of ocular diseases long before the appearance of clinical symptoms to help find medical cures is the most desired goal. The new developments in QELS ophthalmic research seem promising and indicate good potential to help achieve this goal. Hopefully, a system for both celestial and terrestrial applications, described earlier by Ansari and Sebag [56], will be available in not too distant future for use in astronauts and remote tele-health applications.

14.6 Disclaimer

The views and opinions expressed in this chapter are those of the author's and not those of the National Aeronautics and Space Administration (NASA) or the United States Government.

References

1. B. Chu, *Laser Light Scattering: Basic Principles and Practice* (Academic, New York, 1991)
2. T. Tanaka, G.B. Benedek, Observation of protein diffusivity in intact human and bovine lenses with application to cataract. Invest. Ophthalmol. Vis. Sci. **14**(6), 449–456 (1975)
3. S.E. Bursell, P.C. Magnante, L.T. Chylack, *In vivo* uses of quasi-elastic light scattering spectroscopy as a molecular probe in the anterior segment of the eye, in *Noninvasive Diagnostic Techniques in Ophthalmology*, ed. by B.R. Masters (Springer, New York, 1990), pp. 342–365
4. R.R. Ansari, Ocular static and dynamic light scattering: a non-invasive diagnostic tool for eye research and clinical practice. J. Biomed. Opt. **9**(1), 22–37 (2004)
5. D.S. Friedman et al., *Vision Problems in the US: Prevalence of Adult Vision and Age-Related Eye Disease in America* (National Eye Institute (National Institutes of Health)/Prevent Blindness America, Bethesda/Schaumburg, 2012). http://www.visionproblemsus.org
6. G.W. Tate, A. Safiz, The slit lamp, history, principle, and practice, in *Duane's Clinical Ophthalmology*, ed. by W. Tasman, E.A. Jaeger (J.B. Lippincott, Philadelphia, 1992)
7. A. Wegener, H. Laser-Junga, Photography of the anterior eye segment according to Scheimpflug's principle: options and limitations – a review. Clin. Experiment. Ophthalmol. **37**, 144–154 (2009)
8. R.H. Stock, W.H. Ray, Interpretation of photon correlation data: a comparison of analysis methods. J. Polym. Sci. A **23**, 1393–1447 (1985)
9. H.S. Dhadwal, R.R. Ansari, M.A. Dellavecchia, Coherent fiber optic sensor for early detection of cataractogenesis in a human eye lens. Opt. Eng. **32**(2), 233–238 (1993)
10. L. Rovati, F. Fankhauser II, J. Rick, Design and performance of a new ophthalmic instrument for dynamic light scattering in the human eye. Rev. Sci. Instrum. **67**(7), 2620 (1996)
11. R.R. Ansari, K.I. Suh, A. Arabshahi, W.W. Wilson, T.L. Bray, L.J. DeLucas, A fiber optic probe for monitoring protein aggregation, nucleation and crystallization. J. Cryst. Growth **168**, 216–226 (1996)

12. M.F. Simpanya, R.R. Ansari, K.I. Suh, V.R. Leverenz, F.J. Giblin, Aggregation of lens crystallins in an in vivo hyperbaric oxygen guinea pig model of nuclear cataract: dynamic light-scattering and HPLC analysis. Invest. Ophthalmol. Vis. Sci. **46**(12), 4641–4651 (2005)

13. J. Sebag, R.R. Ansari, K.I. Suh, Pharmacologic vitreolysis with microplasmin increases vitreous diffusion coefficients. Graefe's Arch. Clin. Exp. Ophthalmol. **245**, 576–580 (2007)

14. M.F. Simpanya, R.R. Ansari, V.R. Leverenz, F.J. Giblin, Measurement of lens protein aggregation in vivo using dynamic light scattering in a guinea pig/UVA model for nuclear cataract. Photochem. Photobiol. **84**, 1589–1595 (2008)

15. M.B. Datiles, R.R. Ansari, K.I. Suh, S. Vitale, G.F. Reed, J.S. Zigler, F.L. Ferris, Clinical detection of precataractous lens protein changes using dynamic light scattering. Arch. Ophthalmol. **126**(12), 1687–1693 (2008)

16. L. Pollonini, L. Rovati, R.R. Ansari, Dynamic light scattering and natural fluorescence measurements in healthy and pathological ocular tissues. Proc. SPIE **4611**, 213–219 (2002)

17. M.B. Datiles III, R.R. Ansari, Clinical evaluation of cataracts, in *Duane's Clinical Ophthalmology*, ed. by W. Tasman, E. Jaeger, vol. 73B (Lippincott, Philadelphia, 2003)

18. C. Kent, Cracking the cataract code, new technology, new hope. Rev. Ophthalmol. **XVI**(10), 80–87 (2009)

19. M.B. Datiles III, R.R. Ansari, G.F. Reed, A clinical study of the human lens with a dynamic light scattering device. Exp. Eye Res. **74**(1), 93–102 (2002)

20. A. Foster, Cataract – a global perspective: output, outcome and outlay. Eye **3**, 449–453 (1999)

21. C. Kupfer, Bowman lecture. The conquest of cataract: a global challenge. Trans. Ophthalmol. Soc. **104**(1), 1–10 (1984)

22. J.J. Harding, Drugs. Aging **18**(7), 473–486 (2001)

23. G.B. Benedek, J. Pande, G.M. Thurston, J.L. Clark, Theoretical and experimental basis for the inhibition of cataract. Prog. Retin. Eye Res. **18**, 391–402 (1999)

24. G.M. Thurston, D.L. Hayden, P. Burrows, J.I. Clark, V.G. Taret, J. Kandel, M. Courogen, J.A. Peetermans, M.S. Bowen, D. Miller, K.M. Sullivan, R. Storb, H. Stern, G.B. Benedek, Quasielastic light scattering study of the living human lens as a function of age. Curr. Eye Res. **16**(3), 197–207 (1997)

25. H. Dhadwal, J. Wittpen, *In vivo* dynamic light scattering characterization of the human lens: cataract index. Curr. Eye Res. **20**(6), 502–510 (2000)

26. R.R. Ansari, J.F. King, T. Seeberger, J.I. Clark, Early detection of cataract and response to pantethine therapy with non-invasive static and dynamic light scattering. Proc. SPIE **4951**, Ophthalmic Technologies XIII, 168 (2003)

27. J.I. Clark, J.C. Livesey, J.E. Steele, Delay or inhibition of rat lens opacification using pantethine and WR-77913. Exp. Eye Res. **62**, 75–85 (1996)

28. F.A. Bettelheim, R.R. Ansari, Q. Cheng, J.S. Zigler, The mode of chaperoning of dithiothreitol-denatured α lactalbumin by α crystallin. Biochem. Biophys. Res. Commun. **261**, 292–297 (1999)

29. J.S. Zigler, P. Russel, S. Tumminia, C. Qin, C.M. Krishna, Hydroxylamine compositions for the prevention or retardation of cataracts, U. S. Patent 6,001,853, 14 December 1999

30. J.S. Zigler, C. Qin, T. Kamiya, M.C. Krishna, Q. Cheng, S. Tumminia, P. Russell, Tempol-H inhibits opacification of lenses in organ culture. Free Radic. Biol. Med. **35**, 1194–1202 (2003)

31. V.M. Chenault, M.N. Ediger, R.R. Ansari, In vivo assessment of diabetic lenses using dynamic light scattering. Diabetes Technol. Ther. **4**(5), 651–659 (2002)

32. R.R. Ansari, K.I. Suh, S. Dunker, N. Kitaya, J. Sebag, Quantitative molecular characterization of bovine vitreous and lens with non-invasive dynamic light scattering. Exp. Eye Res. **73**, 859–866 (2001)

33. L. Rovati, F. Fankhauser II, F. Docchio, J. Van Best, Diabetic retinopathy assessed by dynamic light scattering and corneal autofluorescence. J. Biomed. Opt. **3**(3), 357–363 (1998)

34. R. Klein, B.E.K. Klein, S.E. Moss, Visual impairment in diabetes. Ophthalmology **91**, 1–9 (1984)

35. M. Brownlee, The role of nonenzymatic glycosylation in the pathogenesis of diabetic angiopathy, in *Complications of Diabetes Mellitus*, ed. by B. Drazin, S. Melmed, D. LeRioth (Alan R. Liss, New York, 1989), pp. 9–17

36. J. Sebag, Abnormalities of human vitreous structure in diabetes. Graefe's Arch. Clin. Exp. Ophthalmol. **231**, 257–260 (1993)

37. J. Sebag, Diabetic vitreopathy [guest editorial]. Ophthalmology **103**, 205–206 (1996)

38. J. Sebag, *The Vitreous – Structure, Function, and Pathobiology* (Springer, New York, 1989)

39. J. Sebag, Age-related changes in human vitreous structure. Graefe's Arch. Clin. Exp. Ophthalmol. **225**, 89–93 (1987)

40. J. Sebag, R.R. Ansari, S. Dunker, S.I. Suh, Dynamic light scattering of diabetic vitreopathy. Diabetes Technol. Ther. **1**, 169–176 (1999)

41. J. Aguayo, B. Glaser, A. Mildvan, H.M. Cheng, R.G. Gonzalez, T. Brady, Study of the vitreous liquefaction by NMR spectroscopy and imaging. Invest. Ophthalmol. Vis. Sci. **26**, 692–697 (1985)

42. C.W. Oyster, *The Human Eye Structure and Function* (Sinauer, Sunderland, 1999)

43. S.D. McLeod, Beyond Snellen acuity: the assessment of visual function after refractive surgery. Arch. Ophthalmol. **119**, 1371–1373 (2001)

44. L.B. Sabbagh, Dynamic light scattering focuses on the cornea. Rev. Ref. Surg. **5**, 28–31 (2002)

45. R.R. Ansari, A.K. Misra, A.B. Leung, J.F. King, M.B. Datiles III, Noninvasive evaluation of corneal abnormalities using static and dynamic light scattering. Proc. SPIE **4611**, 220–229 (2002)

46. R. Dahm, Dying to See. Sci. Am., 83–89 (October 2004)

47. P.H. Frederikse, D. Garland, J.S. Zigler, J. Piatigorsky, Oxidative stress increases production of beta-amyloid precursor protein and beta-amyloid (A beta) in mammalian lenses, and A beta has toxic effects on lens epithelial cells. J. Biol. Chem. **271**(17), 10169–10174 (1996)

48. P.H. Frederikse, Amyloid-like protein structure in mammalian ocular lenses. Curr. Eye Res. **20**(6), 462–468 (2000)

49. L.E. Goldstein, J.A. Muffat, R.A. Cherny, R.D. Moir, M.H. Ericsson, X. Huang, C. Mavros, J.A. Coccia, K.Y. Faget, K.A. Fitch, C.L. Masters, R.E. Tanzi, T. Chylack, A.I. Bush, Cytosolic β-amyloid deposition and supranuclear cataracts in lenses from people with Alzheimer's disease. Lancet **361**(9365), 1258–1265 (2003)

50. J.A. Moncaster, R. Pineda, R.D. Moir, S. Lu, M.A. Burton, J.G. Ghosh, M. Ericsson, S.J. Soscia, A. Mocofanescu, R.D. Folkerth, R.M. Robb, J.R. Kuszak, J.I. Clark, R.E. Tanzi, D.G. Hunter, L.E. Goldstein, Alzheimer's disease amyloid-b links lens and brain pathology in Down syndrome. PLoS ONE **5**(5), e10659 (2010). www.plosone.org

51. S. Frost, R.N. Martins, Y. Kanagasingam, Ocular biomarkers for early detection of Alzheimer's disease. J. Alzheimers Dis. **22**(1), 1–16 (2010)

52. S. Long, R.R. Ansari, Early cataract detection by dynamic light scattering with sparse Bayesian learning. J. Innov. Opt. Health Sci. **2**(3), 303–313 (2009)

53. S. Long, R.R. Ansari, Sparse Bayesian learning for the Laplace transform inversion in dynamic light scattering. J. Comput. Appl. Math. **235**, 2861–2872 (2011)

54. F.A. Cucinotta, F.K. Manuel, J. Jones, G. Izard, J. Murrey, B. Djojonegro, M. Wear, Space radiation and cataracts in astronauts. Radiat. Res. **156**(5), 460–466 (2001)

55. Z.N. Rastegar, P. Eckart, M. Mertz, Radiation-induced cataract in astronauts and cosmonauts. Graefe's Arch. Clin. Exp. Ophthalmol. **240**(7), 543–547 (2002)

56. R.R. Ansari, J. Sebag, Non-invasive monitoring of ocular health in space, in *Teleophthalmology*, ed. by K. Yogesan, S. Kumar, L. Goldschmidt, J. Cuadros (Springer, Berlin, 2006), pp. 267–273 (Chap. 32)

Monte-Carlo Simulations of Light Scattering in Turbid Media

15

Frits F. M. de Mul

Contents

The author Frits F. M. de Mul was previously at the Department of Applied Physics, University of Twente, AE Enschede, The Netherlands (now retired).

F.F.M. de Mul
Department of Applied Physics, University of Twente, AE Enschede, The Netherlands
e-mail: ffm@demul.net

Abstract

The physics behind the simulation program developed by our group are explained. The various options for light transport and scattering, reflection and refraction at boundaries, light sources and detection, and output are described. In addition, some special features, like laser Doppler velocimetry, photoacoustics, and frequency-modulation scattering, are described.

15.1 Introduction

In the past decade, much effort has been devoted to the elucidation of the optical properties of turbid media, especially tissue, of human and animal origin. This is worthwhile since these properties can reveal data and conclusions about the physiological condition of the tissue. These optical properties are the scattering and absorption characteristics, both as a function of position in the tissue and as a function of time, e.g., after administration of drugs, hydrogenation, or temperature treatment. In addition, the spectroscopic response of the tissue (e.g., Raman spectroscopy, induced or auto-fluorescence, absorption spectroscopy) can be used to obtain useful information.

Typical experiments to extract values for the optical properties of tissue include measuring the response of the tissue upon a stimulus from the outside. In the optical case, this mostly corresponds with measuring the properties of light (e.g., intensity) or of another suitable variable (e.g., sound, with photoacoustics) that will emerge from the tissue, as a function of the distance from the point of entrance of the light, or will pass through the tissue and eventually will appear at the backside of the sample.

In the case of "light in – light out," several interesting methods have been developed in addition to simple intensity measurements. Among these are frequency modulation of the light, enabling measurement of the phase delay upon passage through the sample, and optical coherence tomography, where single-scattered light is detected interferometrically.

In order to extract the optical properties from the measured data, it is necessary to have suitable analytical models relating those properties with general ideas about

the physics of the light transport in tissue. The best models for this purpose rely on the radiative transfer equation (RTE; also used in disciplines such as neutron physics) and the diffusion approximation (DA) derived from it [1–3]. The RTE describes the light transport in turbid media in the form of an integro-differential equation of the (place-time-dependent) radiance, arising from well-defined sources and subject to scattering and absorption. The DA takes into account that, in tissue, most scattering is predominantly in the forward direction. Then the light fluence is divided into two contributions: an isotropic term and a term describing the forward contribution. Several authors [4–10] have published sophisticated models for two- and even three-layered samples. For inhomogeneous samples, the models quickly become complex and difficult to apply, and the number of variables to be used in fitting to the experimental data will soon grow beyond manageability.

Therefore, it becomes difficult to produce tractable analytical models of the transport of light in these media, necessary to extract values for the optical properties from experimental data, especially when the media are more complex than homogeneous semi-infinite layers. This is the case with two- or three-layered samples, or when deviant structures, like vessels or plates, are present in those layers. Especially in those cases, Monte Carlo simulations of the light transport are helpful.

In Monte Carlo simulations, a completely different approach is followed. The light transport in tissue is described in the form of separate photons traveling through the sample. On its way, the photon might be scattered at (or in) particles, by which the direction of the photon is changed, or the photon is absorbed. The scattering phenomenon will be determined by suitable angle-dependent scattering functions. When a boundary between two layers, or between the sample and the surrounding medium, or between an internal structure and the surrounding layer, is encountered, the photon might be reflected or refracted. This is determined by the well-known Fresnel relations. In between these events, the photon will propagate, and the optical mean free path in that part of the sample will determine the length of the propagation path. The actual length of the contributions to the path, the angles of scattering, the choice between scattering and absorption, and between reflection and refraction, are determined by random number-based decisions.

Some extra features can be applied to the photons. For instance, photons can be thought of as scattering at particles at rest or at moving particles. This effect will cause a Doppler shift in the frequency of the photons, which can be registered. Afterwards, from the Doppler shift distribution of all suitably detected photons, the frequency power distribution can be derived. Several models are present for this velocity shift: unidirectional or random flow, various flow profiles, and so on. Another option is to use as the light source not a beam impinging from the outside world but a photon absorption distribution inside the sample. In this way, fluorescence or Raman scattering can be mimicked.

When recording the path of the photons through the sample, one might deduce the path length distribution, and from that the time-of-flight distribution. The latter can be used to predict the distributions of phase delays and modulation depths encountered when performing frequency-modulation experiments.

Further, the distribution of positions where photons were absorbed can be used as the distribution of sources for calculating the photoacoustic response, to be detected using suitable detector elements (or groups of elements, to take interference effects into account) at the surface of the sample.

With these applications in mind, we developed [11, 12] our Monte-Carlo light simulation package.

15.2 General Outline of the Program

We decided to build the package in a modular and self-explaining form, in the sense that all necessary input to run the simulations can be produced within the program itself. In addition, the output – in the form of parameter plots and other visualizations – can be obtained using the same program.

In overview, the program package consists of following parts:

- Calculation of angle-dependent scattering functions for all types of particles
- Definition of the light source, either a pencil beam, a broad divergent beam, or an internal source
- The sample system, consisting or one or more layers with different contents, with different optical characteristics and velocity profiles
- The contents may consist of (arrays of) cylinders, spheres, cones, rectangular blocks, and mirrors (see Fig. 15.1)
- Definition of the detection system, consisting of a poly-element detection window, and of its numerical aperture
- Definition of the calculation mode, e.g., reflection or transmission, absorption, or a combination of these
- Simulation, in which a preset amount of photons is injected in the sample and followed along their paths, until either detection or absorption
- Analysis, in which parameter plots can be produced and statistics can be calculated
- Extra features, like laser Doppler flowmetry, photoacoustics, and frequency modulation

These parts will be detailed in following sections.

15.3 Transport Algorithms

In order to describe the transport of photons through the sample, one needs algorithms for the various events that the photon may encounter. These are scattering or absorption, reflection or refraction at boundaries, and detection. In addition, a mechanism accounting for the destruction of irrelevant photons (e.g., photons that have traveled extremely far from the detection window) should be available.

We start with defining the basic optical properties relevant for this problem:

- σ_{sv}: scattering cross section [μm^2] of particle type v
- σ_{av}: absorption cross section [μm^2] of particle type v
- σ_{tv}: total cross section $= \sigma_{sv} + \sigma_{av}$ [μm^2] of particle type v
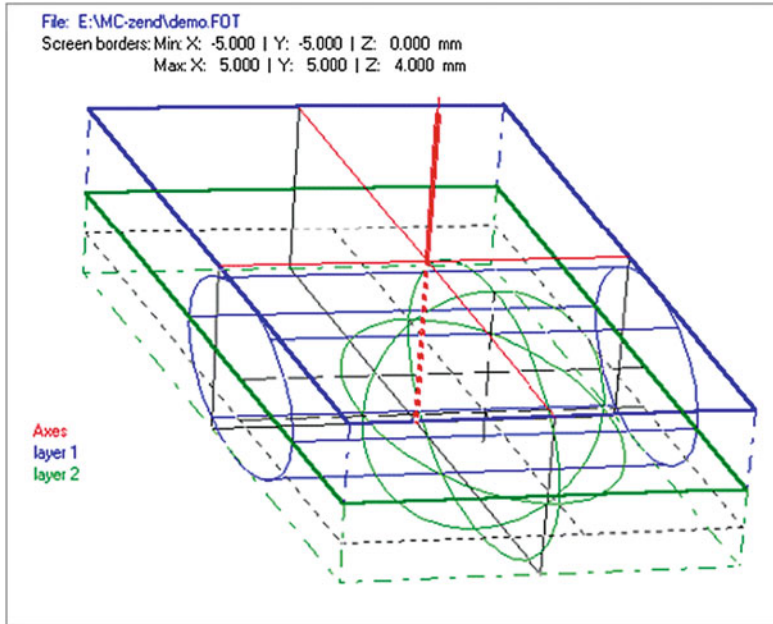
Fig. 15.1 Structure plot of a two-layer system with a horizontal cylindrical tube and a sphere (see Sect. 15.2), filled with various concentrations of scattering/absorbing particles. Laser light (here a diverging beam) injected around Z-axis

- a_v: albedo (= σ_{sv}/σ_{tv}) of particle type v
- c_{lv}: concentration [particles/mm^{-3}] of particle type v in layer l (or "block" l)
- μ_{sl}: scattering coefficient [mm^{-1}] of layer l (or "block" l)
- μ_{al}: absorption coefficient [mm^{-1}] of layer l (or "block" l)

All internal structures in a layer (vessels, tubes, blocks, mirrors, spheres, cones, etc.) will further be denoted as "blocks."

So, the probability f_{lv} to find a particle of type v in layer (or block) l is

$$f_{lv} = \frac{c_{lv}\sigma_{tv}}{\sum\limits_{v} c_{lv}\sigma_{tv}} \tag{15.1}$$

There are two basic algorithms for handling non-zero absorption in layers or particles. Frequently, the probability of absorption (given by $1 - a_v$) is taken into account as a "weight factor" for the photon. The cumulative effect of applying these subsequent factors at each scattering event will reduce its overall weight in calculating averages of relevant variables (such as intensity) over a set of emerged photons. An example is the work of Wang and Jacques [13]. An advantage is that no photons will be lost by absorption, which can be of importance when the absorption is relatively strong.

Fig. 15.2 The laboratory coordinate system. The +Z-axis is chosen as pointing inward. The *arrow* indicates the default direction of a pencil laser beam
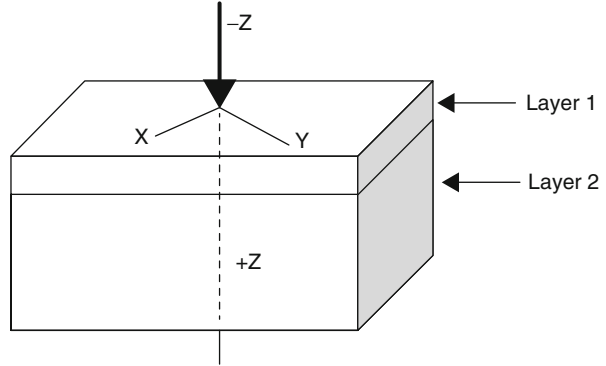
Another algorithm does not make use of weight factors but applies a "sudden death" method: the photon is considered to be completely absorbed at once and will thus be removed from the calculation process. This method might be a bit more time consuming, especially when absorption is not very low in a relative sense, but it offers the opportunity to study the positions where the photons actually are absorbed. In this way, extra features like photoacoustics or fluorescence response can be studied.

In view of this option, we have chosen the second method. The general laboratory coordinate system is chosen as shown in Fig. 15.2.

15.3.1 Propagation

Here we will describe the algorithm used for propagation. In addition, the correction to be made upon crossing an interface (between different layers, or between a layer and a block, or between a layer or block and the outside world) will be handled.

We may write down the average translation distance for a photon in a layer or block l with scattering particles of varying type, in the case of no absorption by that layer or block itself, as

$$L_l = \frac{1}{\sum\limits_{v} c_{lv} \sigma_{tv}}.$$ (15.2)

From this we deduce the expression for calculating the actual path length Δp:

$$\Delta p = -L_l . \ln(1 - R),$$ (15.3)

where R is a random number ($0 \leq R < 1$) and we have used for the probability f_{sl} to arrive at a path length Δp:

$$f_{sl} = 1 - \exp(-\Delta p / L_l).$$ (15.4)

The expression with $\ln(1 - R)$ is chosen to avoid the singularity in case R should equal 0. However, this path might end prematurely when a boundary at an interface is met. In this case, we can geometrically calculate a path fraction f_p using the distance between the previous event point and the intersection point of the path with the interface, and define the effective path Δp_{eff} by

$$\Delta p_{eff} = f_p . \Delta p. \tag{15.5}$$

In case $f_p < 1$, the path will partially stretch out into the medium at the other side of the interface. When dealing with this part of the path, it should be kept in mind that it has to be corrected in length according to the mean free path for the photons in the two media. See below for a full account.

Now we can define the probability f_{al} for absorption by the medium l (layer or block) before the photon has reached the end of path Δp_{eff}:

$$f_{al} = 1 - \exp(-\mu_{al} . \Delta p_{eff}). \tag{15.6}$$

This probability will lie between 0 and 1. Now we choose a fresh random number R. There are two possibilities:

- If this R is smaller than f_{al}, then absorption has occurred during path Δp_{eff}.
- It this is not the case, then absorption will occur within the particle at the end of path Δp_{eff} when

$$R < 1 - a_{vl}, \tag{15.7}$$

where R again is a fresh random number. If (15.7) is not fulfilled, then the photon will be scattered.

Since we handle the absorption by the particles in the medium as taking place within the particles themselves and the absorption by the medium itself separately, we can define the average translation length $L_{trans,l}$ for medium l:

$$L_{trans,l} = \left[\mu_{al} + \sum_v c_{lv} \sigma_{sv} \right]^{-1}, \tag{15.8}$$

and the average absorption length $L_{abs,l}$ caused by the medium and the scatterers in that medium:

$$L_{abs,l} = \left[\mu_{al} + \sum_v c_{lv} \sigma_{av} \right]^{-1}. \tag{15.9}$$
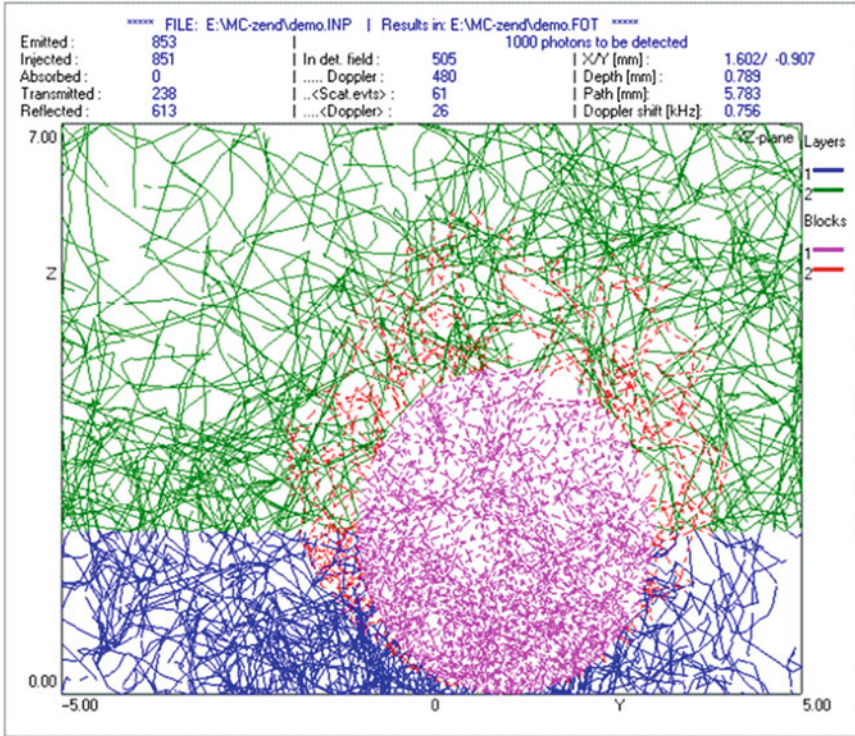
Fig. 15.3 Running graphics of the simulation process of the structure of Fig. 15.1. View in YZ-plane. Photons entering around pos (0,0,0). The tube (X-direction) and sphere can be seen

Now we can correct (15.3) and subsequent expressions for absorption, and find for the path with length Δp:

$$\Delta p = -L_{trans,l} . \ln(1 - R). \tag{15.10}$$

In a previous paper [14], we discussed two equivalent algorithms to determine the remaining path length after crossing an interface. In Fig. 15.3, we present a view of a running simulation in a sample with two layers and two blocks.

15.3.2 Scattering

In case the photon is not absorbed during or at the end of a translation step, the photon will be scattered. We define the angle θ as the polar angle of scattering, with the direction of the previous translation step as the Z-axis of the local coordinate system. For natural (unpolarized) light, the X-axis can be chosen at random in the
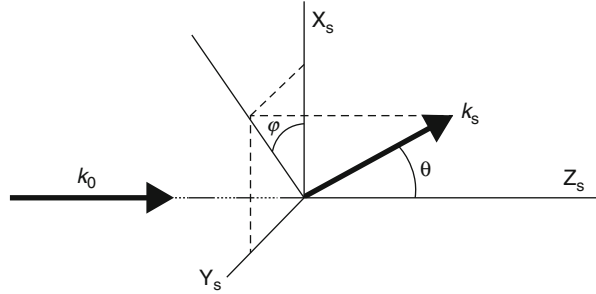
plane perpendicular to the Z-axis (see Fig. 15.4). For polarized light, the directions of the X- and Y-axes are determined by the polarization state of the incoming photon.

The probability of scattering to the direction given by the angles θ and φ is described by the *scattering function* $p(\theta, \varphi)$. This function is normalized in such a way that the total scattering over the whole 4π solid angle is unity:

$$\int\limits_0^{2\pi} d\varphi \int\limits_0^{\pi} d\theta . p(\theta, \varphi) \sin \theta = 1. \tag{15.11}$$

For the scattering function, several models are available: Dipole- or Rayleigh-scattering, Rayleigh-Gans scattering, Mie scattering, isotropic, or peaked-forward scattering. These scattering functions have been described in many textbooks. We refer here to the standard books of Van de Hulst [15]. They will be dealt with in detail in Sect. 15.4.

The standard method of determining the scattering angles θ and φ is as follows:

- The azimuthal angle φ is given by:

$$\varphi = R.2\pi \tag{15.12}$$

- For the polar angle θ, a normalized cumulative function $C(\theta, \varphi)$ is constructed:

$$C(\theta, \varphi) = \frac{C'(\theta, \varphi)}{C'(\pi, \varphi)} \text{ with } C'(\theta, \varphi) = \int\limits_0^{\theta} p(\theta', \varphi) . \sin \theta' . d\theta', \tag{15.13}$$

and the angle θ is obtained by taking a fresh random number R and determining the angle for which

$$C(\theta, \varphi) = R. \tag{15.14}$$

Fig. 15.5 Relation between the laboratory frame (subscript L) and the local scattering frame (subscript S). The circle indicates the set of possible vector directions for fixed θ and random φ
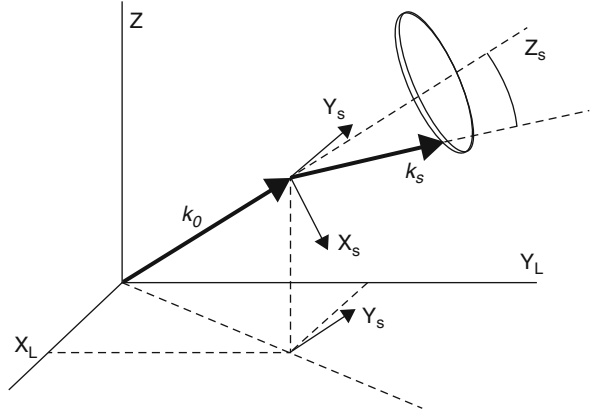
The determination of θ can be made by interpolation procedures or by constructing the inverse cumulative function, e.g., using a polynomial approximation. However, as we will see in Sect. 15.4, most relevant scattering functions decrease sharply for small angles, and then a simple polynomial approximation will not suffice. Since these small angles will occur frequently, an interpolation procedure will be more accurate (in the program, we have adopted this option).

In case polarization effects have to be taken into account, the choice of the angles θ and φ is coupled to the polarization state of the photon. We will deal with polarization in Sect. 15.3.5.

In order to connect the local scattering coordinate frame with the laboratory coordinate frame, we use Fig. 15.5.

The connection between the S-system and the L-system is constructed in three steps:

$$(1)\ \mathbf{z_S} = \frac{\mathbf{k_0}}{|\mathbf{k_0}|}; \quad (2)\ \mathbf{y_S} = \frac{\mathbf{z_L} \times \mathbf{z_S}}{|\mathbf{z_L} \times \mathbf{z_S}|}; \quad (3)\ \mathbf{x_S} = \frac{\mathbf{y_S} \times \mathbf{z_S}}{|\mathbf{y_S} \times \mathbf{z_S}|} \tag{15.15}$$

This means that

$$\mathbf{k_S} = |\mathbf{k_S}|\ [\mathbf{x_S} \cos \varphi \cdot \sin \theta + \mathbf{y_S} \sin \varphi \cdot \sin \theta + \mathbf{z_S} \cos \theta]. \tag{15.16}$$

The length of $\mathbf{k_s}$ is determined by the local wavelength, as $2\pi/\lambda_{local}$. With this, the scattered wave vector is fixed in the laboratory frame. In the program, the unit vector, along the scattered wave vector and expressed in the laboratory frame vectors, is updated at each event in which the photon direction is changed.

Fig. 15.6 Reflection or refraction at interfaces. Here the **k**-vectors denote unit vectors, and **n** is the unit vector perpendicular to the surface. $\theta_3 = \theta_1$
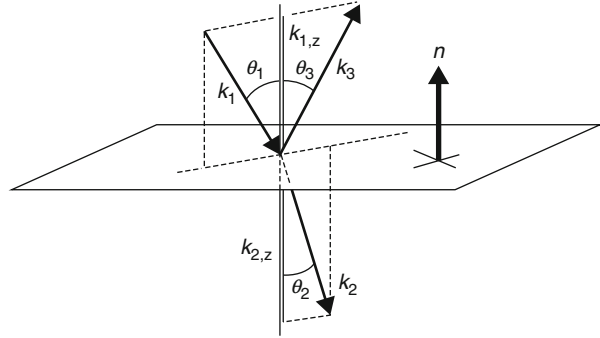
15.3.3 Boundaries

Because the program allows for insertion of special structures, like tubes, spheres, mirrors, and cones in the layer system, we have to deal with boundaries at flat surfaces (like those between layers) and at curved surfaces.

15.3.3.1 Flat Surfaces Perpendicular to the Z-axis

In this situation, the calculation of reflection or refraction angles is relatively simple: according to Snell's Law:

$$\frac{\sin\theta_2}{\sin\theta_1} = \frac{n_1}{n_2}, \tag{15.17}$$

where θ and n denote the angles with the surface normal and the refractive indices in the two media 1 and 2, respectively (see Fig. 15.6).

The fraction of reflected light is given by the Fresnel relations:

$$
\begin{aligned}
R_F(\theta_1) &= \left(\frac{n_1 - n_2}{n_1 + n_2}\right)^2 \quad \text{if} \quad \theta = 0 \\
&= \frac{1}{2}\left[\frac{\sin^2(\theta_1 - \theta_2)}{\sin^2(\theta_1 + \theta_2)} + \frac{\tan^2(\theta_1 - \theta_2)}{\tan^2(\theta_1 + \theta_2)}\right] \quad \text{if} \quad 0 < \theta_1 < \theta_c \\
&= 1 \quad \text{if} \quad \theta_1 > \theta_c; \quad \text{with} \quad \theta_c = \arcsin(n_2/n_1).
\end{aligned}
\tag{15.18}
$$

Reflection takes place if a fresh random number $R < R_F(\theta_1)$; otherwise, refraction occurs.

New unit vectors are calculated according to (see Fig. 15.4):

$$
\begin{aligned}
\boldsymbol{k}_{1,z} &= \cos\theta_1(\boldsymbol{n}); & \boldsymbol{k}_{1,\perp} &= \boldsymbol{k}_1 - \boldsymbol{k}_{1,z}; \\
\boldsymbol{k}_{2,z} &= \cos\theta_2(-\boldsymbol{n}); & \boldsymbol{k}_{2,\perp} &= (\boldsymbol{n}_1/\boldsymbol{n}_2)\boldsymbol{k}_{1,\perp}; \\
\boldsymbol{k}_{3,z} &= -\boldsymbol{k}_{1,z}; & \boldsymbol{k}_{3,\perp} &= \boldsymbol{k}_{1,\perp}.
\end{aligned}
\tag{15.19}
$$

where the symbol $\perp$ stands for the vector component parallel to the surface.

Fig. 15.7 Coordinate frame at curved surfaces. Vectors x' and y' are directed along the surface. M is the center point (or the point where the normal vector n intersects the symmetry axis) of the structure (tube, sphere, etc.)
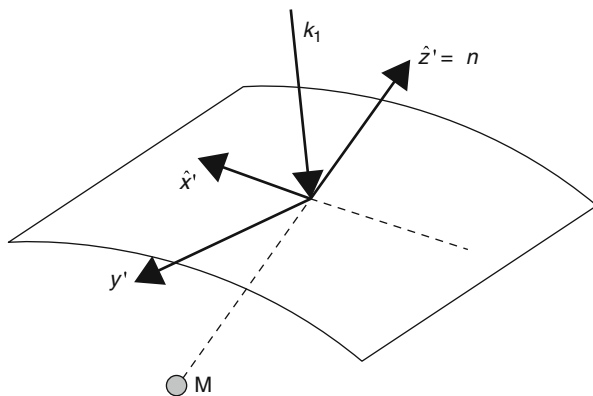
15.3.3.2 Curved Surfaces, or Flat Surfaces not Perpendicular to the Z-axis

For the general case of interfaces with a curved surface, at first a new coordinate frame is constructed as follows (see Figs. 15.6 and 15.7):

$$\hat{z}' = \boldsymbol{n}$$
$$\hat{\boldsymbol{y}}' = (\boldsymbol{k_1} \times \boldsymbol{n})/|\boldsymbol{k_1} \times \boldsymbol{n}| \tag{15.20}$$
$$\hat{\boldsymbol{x}}' = \hat{\boldsymbol{y}}' \times \hat{\boldsymbol{z}}'.$$

Then, the new vectors for refraction and reflection are found to be

$$\boldsymbol{k}_2 = k_{1,x}\hat{\boldsymbol{x}}' - k_{1,z}\hat{\boldsymbol{z}}'; \quad \boldsymbol{k}_3 = k_{2,x}\hat{\boldsymbol{x}}' + k_{2,z}\hat{\boldsymbol{z}}'$$
$$\text{with } k_{1,z} = -k_1.\sin\theta_1; \quad k_{1,z} = -k_1.\cos\theta_1; \tag{15.21}$$
$$k_{2,x} = -k_1\sin\theta_2; \quad k_{2,z} = \sqrt{k_1^2 - k_{2,x}};$$

and θ_1 and θ_2 are given by Snell's relation (15.17).

We will now deal with the geometry of how to determine the intersection points and normal vectors with special cases of curved surfaces.

15.3.3.3 An Oblique Cylinder

See Fig. 15.8. The point O' represents a point on the symmetry axis. Vector $\boldsymbol{b}$ is the direction vector (unit vector) and vector $\boldsymbol{r}$ points to the surface points.

The general equation for such a cylinder is

$$|\boldsymbol{r} - (\boldsymbol{r} \bullet \boldsymbol{b})\,\boldsymbol{b}| = R, \tag{15.22a}$$

which in fact is a quadratic equation in the coordinates of the cylinder wall points:

$$(x^2 + y^2 + z^2) - (xb_x + yb_y + zb_z)^2 = R^2. \tag{15.22b}$$

Fig. 15.8 Vectors for an oblique cylinder. R is the radius and $\boldsymbol{b}$ is the direction vector. $\boldsymbol{r}$ directs to a point at the surface
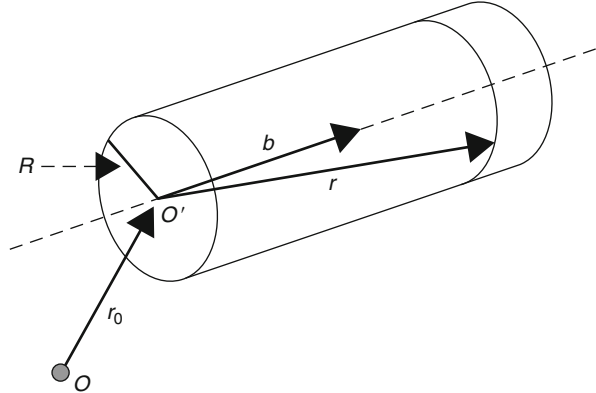
The vector expression between the absolute bars represents the direction of the normal vector on the surface at point $\boldsymbol{r}$.

Let vectors $\boldsymbol{p}_0$, $\boldsymbol{p}$, and $\boldsymbol{\Delta p}$ denote the "old new" position of the photon, $\boldsymbol{\Delta p} = \boldsymbol{p} - \boldsymbol{p}_0$ the path length vector, as determined in Sect. 15.3.2, respectively, and $\boldsymbol{p}_0{}'$ and $\boldsymbol{p}'$ the same vectors in the internal frame of the cylinder ($\boldsymbol{p}_0{}' = \boldsymbol{p}_0 - \boldsymbol{r}_0$ and $\boldsymbol{p}' = \boldsymbol{p} - \boldsymbol{r}_0$). Then, the crossing point $\boldsymbol{p}_S$ with the interface is given by insertion of

$$\boldsymbol{p}' = \boldsymbol{p}_0{}' + \lambda.\boldsymbol{\Delta p} \qquad (15.23)$$

as the vector $\boldsymbol{r}$ into (15.22b). Of the two resulting values of λ, only those between 0 and 1 are acceptable. The smallest of those λ-value(s) determines the intersection point $\boldsymbol{p}_S$.

In the following, we will use those primed vectors to indicate positions relative to the internal origin point of the block (tube, sphere, cone, etc.).

15.3.3.4 Cylinders Parallel to the Surface
As an example, we will discuss here the case of a straight cylinder parallel to the Y-axis. Insertion of (15.23) into (15.22) leads to

$$\left[(\Delta x)^2 + (\Delta z)^2\right]\lambda^2 + 2\left[p'_{0,x}.\Delta x + p'_{0,z}.\Delta z\right]\lambda + \left[(p'_{0,x})^2 + (p'_{0,z})^2\right] = R^2, \quad (15.24)$$

where Δx, Δy, and Δz are the components of $\boldsymbol{\Delta p}$.

In general, this equation will have two λ-roots; and, in order to be valid, intersection points should be real numbers between 0 and 1. Let us denote these with λ_m and λ_M, with $\lambda_m < \lambda_M$. The λ-value for the intersection point will be equal to λ_m if $0 < \lambda_m < 1$ and $\boldsymbol{p}_0$ is outside the cylinder, and to λ_M if $0 < \lambda_M < 1$ and $\boldsymbol{p}_0$ is inside the cylinder (in that case $\lambda_m < 0$), respectively. See Fig. 15.9 for clarification.
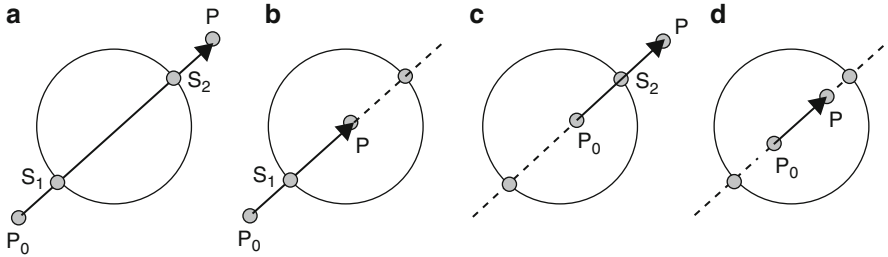
Fig. 15.9 Intersection points with a cylinder. P_0 and P are the begining and end of the path. In case (**a**), the intersection point is S_1 (at $\lambda = \lambda_m < \lambda_M$), (**b**) S_1 (at $\lambda = \lambda_m < \lambda_M$), (**c**) S_2 (at $\lambda = \lambda_M$; $\lambda_m < 0$), (**d**) no intersection ($\lambda_m < 0$ and $\lambda_M > 1$)

The direction of the normal vector $\boldsymbol{n_S}$ on the cylinder surface at the intersection point is given by

$$\boldsymbol{n_S} // \, (p_{S,x} - r_{0,x}, \; 0, p_{S,z} - r_{0,z}). \tag{15.25}$$

Similar expressions can be formulated for cylinders parallel to the X-axis. In the program, both X- and Y-cylinders have infinite length. For cylinders parallel to the Z-axis, one also has to take into account that those cylinders may have cover lids and bottom at an interface between layers or with the surface. We will deal with that shortly.

Now we will discuss the option of more than one cylinder, in the form of linear arrays of those cylinders. This means that the program can handle an infinite number of cylinders, arranged next to each other, with constant spacing distance, as shown in Fig. 15.10.

We denote the position vectors $\boldsymbol{p_0}'$ and $\boldsymbol{p}'$ with respect to the internal frame of the generating cylinder (located at the origin of the "rel" frame). The repetition distance is d and the radius is R. The generating cylinder has tube number $t_n = 0$; the adjacent tubes have numbers $t_n = +1, +2 \ldots$ and $-1, -2 \ldots$ for tubes at the right and left sides, respectively.

For the determination of intersections points, we take following reasoning:

- Does the path contain points with $-R < z_{rel} < +R$? In that case

$$\left(p_{0,z}' - R\right)\frac{dp_y}{dp_z} < 0 \quad or \quad \left(p_{0,z}' + R\right)\frac{dp_y}{dp_z} < 0, \tag{15.26}$$

and the path will cross one of the planes $z_{rel} = \pm R$, like path (1) or (2) in Fig. 15.8. If not, no intersection will take place (e.g., path (3) or (4) in Fig. 15.8).

- If (15.26) holds, does the path start inside the volume with boundaries $z_{rel} = \pm R$, or:

$$\left|p_{0,z}'\right| < R? \tag{15.27}$$
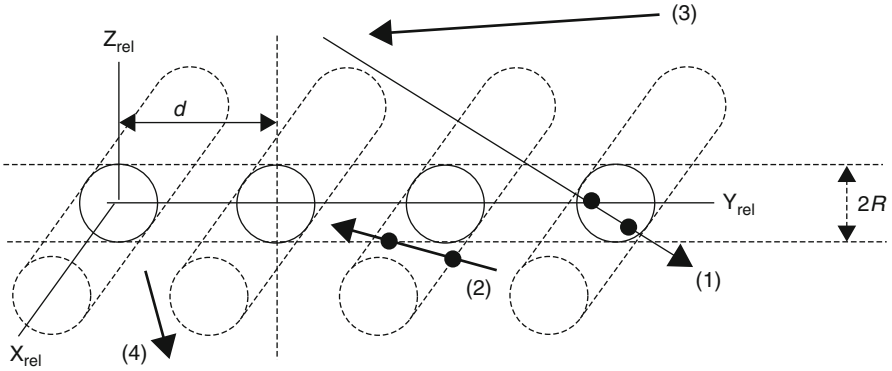
Fig. 15.10 An array of cylinders parallel to the X-axis. The dots indicate intersection points. With the subscript "rel" we denote relative coordinates with respect to the generating cylinder of the set. R = radius; d = repetition distance. For paths $1)\ldots4)$, see the text

- If (15.27) holds, does the path start inside one of the tubes? If so, the following expression must hold:

$$|\boldsymbol{p}_0' - t_n\, d\, \hat{\boldsymbol{y}}_{rel}| < R \qquad (15.28)$$

with

$$t_n = round\left(\frac{p_{0,y}'}{d}\right).$$

The operator "round" takes that integer value that is nearest to the argument between the brackets. Now we can solve the analogous (15.24) for cylinders parallel to the X-axis:

$$\left[(\Delta y)^2 + (\Delta z)^2\right]\lambda^2 + 2\left[p_{0,y}''.\Delta y + p_{0,z}''.\Delta z\right]\lambda + \left[(p_{0,y}'')^2 + (p_{0,z}'')^2\right] = R^2 \quad (15.29)$$

with $\boldsymbol{p}_0'' = \boldsymbol{p}_0' - t_n\, d\, \hat{\boldsymbol{y}}_{rel}$.

- If (15.28) does not hold, then the path starts outside all tubes. In that case, we solve (15.29) while taking for t_n the value

$$t_n = trunc\left(\frac{p_{0,y}'}{d}\right), \qquad (15.30)$$

where the operator "trunc" removes the fraction from its argument. However, because, according to (15.27), the starting point is inside the volume where $z_{rel} < \pm R$, the only tubes that can be intersected are those with tube numbers t_n and $t_n + 1$, we have to solve (15.29) for those two tubes only.

- However, in case (15.27) does not hold, the path will start outside the volume where $z_{rel} < \pm R$.
  Then, the intersection point with the nearest of the two planes $z_{rel} = \pm R$ is calculated first, and from there the procedure is followed as in the case of a valid (15.27).
- Finally, the intersection point is corrected for the coordinate shifts due to the tube number being $\neq 0$ and the relative position of the generating tube (at tube number $t_n = 0$).

15.3.3.5 Cylinders Parallel to the Z-axis

In the case of cylinders parallel to the Z-axis, the program offers the opportunity to insert two-dimensional arrays of cylinders, with equal repetition distance for the X- and Y-pitch. In addition, the cylinders do not have infinite length, as was the case for cylinders parallel to the surface, but will have a coverlid and a bottom lid. This will enlarge the intersection possibilities to be considered (see Fig. 15.11).

Now we must define two tube numbers, one for X-tubes and one for Y-tubes: t_{nx} and t_{ny}. In this cas e, the reasoning is as follows:

- Is the start position of the path in between the planes of the top and bottom lids of the tubes? If not, the nearest intersection, if any, will occur at the top or bottom lid of one of the tubes. See below.
- Is the start position of the path inside one of the tubes? This is equivalent to:

$$\left| \boldsymbol{p}_0' - t_{ny}\, d\, \hat{\boldsymbol{y}}_{\boldsymbol{rel}} \right| < R \text{ with } t_{ny} = round\left(\frac{p_{0,y}'}{d}\right), \qquad (15.31)$$

and simultaneously a similar question for the X-coordinate.

If so, we can calculate the intersection points with the curved wall and with the two lids of that tube and take the intersection point (if any) that is reached first. For the curved wall we use a similar expression as (15.29):

$$\left[(\varDelta x)^2 + (\varDelta y)^2 \right]\lambda^2 + 2\left[p_{0,x}''.\varDelta x + p_{0,y}''.\varDelta y \right]\lambda + \left[(p_{0,x}'')^2 + (p_{0,y}'')^2 \right] = R^2, \qquad (15.32a)$$

$$\boldsymbol{p}_0'' = \boldsymbol{p}_0' - t_{nx}d\, \hat{\boldsymbol{x}}_{\boldsymbol{rel}} - t_{ny}d\, \hat{\boldsymbol{y}}_{\boldsymbol{rel}}. \qquad (15.32b)$$

In case an intersection with curved wall exists, we check whether an intersection with one of the lids will occur earlier in the path. For the lids we first calculate the intersection points of the (relative) photon vector with the planes $z = z_{top}$ and $z = z_{bottom}$, given by

$$x_s = p_{0,x}'' + \frac{\varDelta x}{\varDelta z}.(z_{top} - p_{0,z}''); \quad y_s = p_{0,y}'' + \frac{\varDelta y}{\varDelta z}.(z_{top} - p_{0,z}'') \qquad (15.33)$$

(and similarly for the bottom lid) and check whether these points will lie on the lid of one of the tubes, i.e., have a distance to the axis of the nearest tube that is smaller
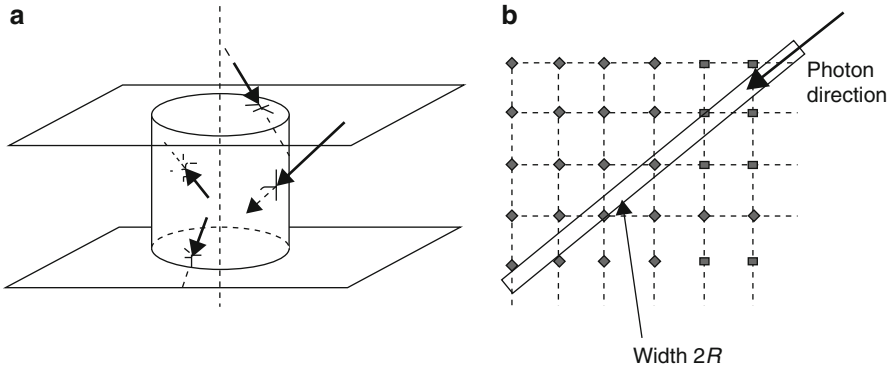
Fig. 15.11 Cylinders parallel to the Z-axis. (**a**) Several possibilities for intersections. (**b**) Two-dimensional array of cylinders; the dots indicate the symmetry axes, pointing into the plane of drawing. The photon will intersect with the nearest cylinder that is positioned within 2R distance of the photon propagation vector

than R. This procedure is also followed when a photon is approaching a layer with Z-tubes from another layer.

If (15.31) is not valid for one of the X or Y coordinates, the photon starts outside any tube. Now, the tube encountered first, with axis within $2R$ distance from the propagation vector of the photon, has to be determined. The tube number of the nearest tube will depend on the sign of $s_x = \Delta x/|\Delta x|$ and $s_y = \Delta y/|\Delta y|$, as is the number sequence of tubes to investigate for the existence of intersection points (going to higher or lower numbers). Following the photon path $\boldsymbol{\Delta p}$, the subsequent tubes most adjacent to the path are interrogated about intersection points by solving a similar equation as (15.32), until that equation has an acceptable solution (between 0 and 1) or the path has been completed (i.e., no intersection is found). This procedure is illustrated in Fig. 15.12.

15.3.3.6 Spheres

As with tubes parallel to the Z-axis, one might define sets of identical spheres arranged in a plane perpendicular to the Z-axis, with equidistant spacing. For these spheres, a similar procedure as for Z-tubes can be followed. Equation (15.32) is replaced by (see Fig. 15.13):

$$|\boldsymbol{p} - \boldsymbol{p}_0|^2 \lambda^2 + 2(\boldsymbol{p}_0 - \boldsymbol{m}) \bullet (\boldsymbol{p} - \boldsymbol{p}_0)\lambda + |\boldsymbol{p}_0 - \boldsymbol{m}|^2 = R^2, \tag{15.34}$$

which can be written as:

$$\left[(\Delta x)^2 + (\Delta y)^2 + (\Delta z)^2\right]\lambda^2 + 2\left[p_{0,x}''.\Delta x + p_{0,y}''.\Delta y + p_{0,z}''.\Delta z\right]\lambda + \\ \left[(p_{0,x}'')^2 + (p_{0,y}'')^2 + (p_{0,z}'')^2\right] = R^2 \tag{15.35}$$
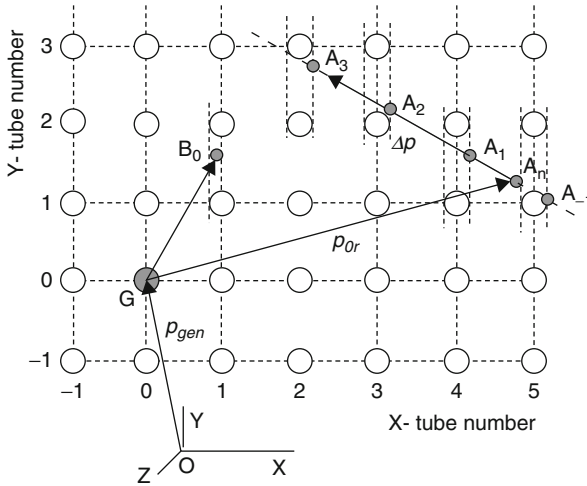
Fig. 15.12 The procedure for intersection points with Z-tubes. O is the origin of the layer system. G is the generating tube (position p_{gen}). A_0 is the starting point (at p_{0r}) of the actual photon path D_p. Subsequently, the existence of intersections is investigated with adjacent tubes. This is done by shifting point A_0 to A_{-1}, A_1, ..., A_3..., respectively, and solving a similar equation as (15.32) for both adjacent tubes along the Y-axis. In this case, points A_1 and A_2 will not lead to intersection points, and A_{-1} and A_3 would have led to intersection points, but outside vector D_p ($\lambda < 0$ and $\lambda > 1$, respectively). In case the starting point lies within a distance R from the axis (point B_0), that point is not shifted to B_{-1} (analogous to A_{-1})
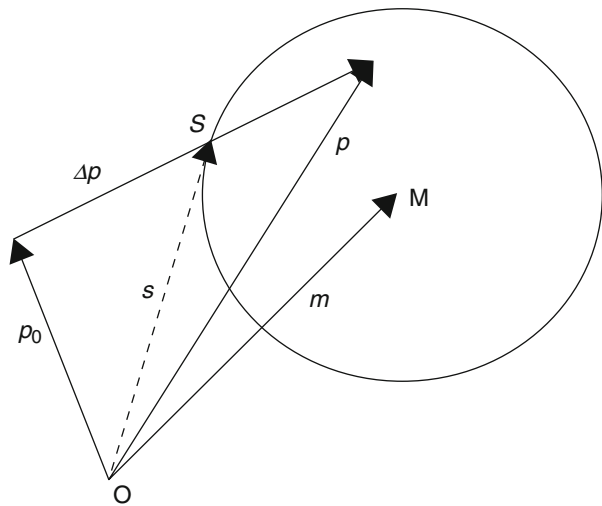
Fig. 15.13 Determination of the intersection point S with a sphere. p_0, p, and D_p are the photon vectors, m is the center point vector and s points at the (first encountered) intersection point

with p_0'' defined as above [see (15.32)]. With these equations the intersection point S can be calculated (if present). For calculating refraction and reflection, one needs the normal vector n_S and the angle of incidence θ_i of Δp with n_S at the sphere surface:

$$\cos\theta_i = \frac{\Delta p \bullet n_S}{|\Delta p \bullet n_S|}; \quad n_S // s - m. \tag{15.36}$$

The direction of the normal vector depends on the way the surface is crossed, with the photon arriving from the inside or outside. The other axes (l_S and m_S) of the coordinate system at point S can be found using

$$n_S \times \Delta p = m_S; \quad n_S \times m_S = l_S, \tag{15.37}$$

with m_S perpendicular to the plane of reflection or refraction and l_S lying in that plane, along the sphere surface.

15.3.3.7 Rectangular Blocks

Rectangular blocks, as used in the program, always have their side planes parallel to the laboratory coordinate axes. The position and dimensions are defined using maximum and minimum values for the coordinates of the side planes, e.g., x_{max} and x_{min}, and similarly for y and z. All six sides have to be interrogated for the presence of intersection points. For instance, for the block side at $z = z_{max}$, we calculate a ratio $f_{z,max}$ as

$$f_{z,\mathrm{max}} = \frac{z_{\mathrm{max}} - p_{0,z}}{\Delta z} \tag{15.38}$$

and similarly for all other sides. The smallest value of those six f-values, provided between 0 and 1, will determine the side where the first intersection will take place. If no such f-value can be found, no intersection point is present.

15.3.3.8 Cones

The equation for cones is:

$$(x - x_O)^2 + (y - y_O)^2 - \alpha(z - z_O)^2 = 0; \quad \alpha = (R/h)^2, \tag{15.39a}$$

for a cone directed along the Z-axis, as shown in Fig. 15.14. The relevant intersection points are given by

$$\left(p_{0,x}' + \lambda.\Delta x\right)^2 + \left(p_{0,y}' + \lambda.\Delta y\right)^2 - \alpha\left(p_{0,z}' + \lambda.\Delta z\right)^2 = 0. \tag{15.39b}$$

The smallest value of λ, if between 0 and 1, determines the valid intersection point S, provided the z-component of S is smaller than h. However, (15.38) also
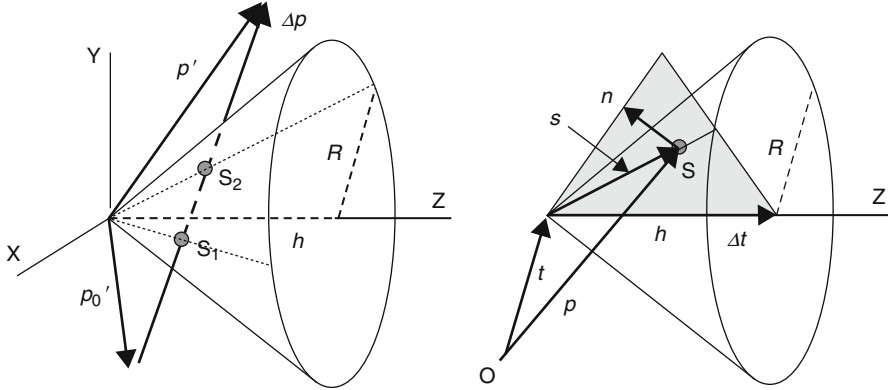
Fig. 15.14 Intersection with a cone (example: directed along the +Z-axis). The cone is characterized by its direction vector (along the axis) and its opening angle, or its radius R at height h. *Right*: construction of the normal vector

describes the other half of the cone, and therefore, for the intersection point to be accepted, this point should lie between top and bottom of the cone, which defines an additional condition for point S to exist.

For reflection and refraction, we have to construct the normal vector $\boldsymbol{n}$ on the surface in point S:

$$\boldsymbol{s} = \boldsymbol{p} - \boldsymbol{t}; \quad \boldsymbol{v} = (\Delta \boldsymbol{t} \times \boldsymbol{s}) \times \boldsymbol{s}; \quad \boldsymbol{n} = \boldsymbol{v}/|\boldsymbol{v}|, \tag{15.40}$$

with $\boldsymbol{t}$ and $\Delta \boldsymbol{t}$ as the position and direction vectors of the cone, and $\boldsymbol{v}$ as a vector in S parallel to the cone surface and perpendicular to the plane spanned by $\Delta \boldsymbol{t}$ and $\boldsymbol{s}$. The direction of $\boldsymbol{n}$ depends on the way the surface is crossed: arriving from the inside or outside. The determination of the angle of incidence is similar to the case of tubes and spheres.

With cones, an intersection with the bottom is also possible. In the coordinate frame of Fig. 15.12, we have two conditions to be fulfilled:

$$p'_{0,z} + \lambda.\Delta z = h \text{ with } 0 < \lambda < 1,$$
$$\left(p'_{0,x} + \lambda.\Delta x\right)^2 + \left(p'_{0,y} + \lambda.\Delta y\right)^2 \leq R^2 \tag{15.41}$$

In all cases the smallest of the λ-values of all possible intersections, if between 0 and 1, should be taken for the intersection point.

In the program, the available cones are those with the axis parallel to the $\pm X$, $\pm Y$, or $\pm Z$-axis.

15.3.3.9 Mirrors

The normal equation of a mirror plane is given, using the normal vector $\boldsymbol{a} = (a_1, a_2, a_3)$, by

$$a_1.x + a_2.y + a_3.z + d = 0, \tag{15.42}$$

where d is a constant. Vector $\boldsymbol{a}$ should point to the half plane where the starting point of the photon path is situated.

We can calculate the vector $\boldsymbol{p}_S$ to the intersection point S by insertion of the photon path $(\boldsymbol{p}_S = \boldsymbol{p}_0 + \lambda.\Delta\boldsymbol{p})$ into (15.42), which will render the λ-value corresponding to S. The direction vector $\boldsymbol{l}$ after reflection is given by

$$\boldsymbol{l}//\Delta\boldsymbol{p} - 2(\Delta\boldsymbol{p} \bullet \boldsymbol{a}).\boldsymbol{a}; \quad |\boldsymbol{l}| = (1 - \lambda).|\Delta\boldsymbol{p}|. \tag{15.43}$$

15.3.3.10 Entrance in a Block

When a photon enters a new layer, it is possible that it immediately will enter a block in that layer rather than first the material of the layer itself. An example is the entrance in a layer where a single Z-tube or a set of those tubes is present. This has to be checked separately. Therefore, the photon, after reaching that interface, is temporarily propagated further along its path over a very small distance, to ensure that it is placed inside. The next step is to check whether the following condition C is true (with $\boldsymbol{p}_c$ as the temporary position vector, $\boldsymbol{p}_c{}'$ as that vector relative to the block or to the generating block in case of an array, and d as the repetition distance):

- Rectangular block:

$$\begin{aligned}
C = (p_{cx} > x_{\min}) \wedge (p_{cx} < x_{\max}) \wedge (p_{cy} > y_{\min}) \wedge \\
(p_{cy} < y_{\max}) \wedge (p_{cz} > z_{\min}) \wedge (p_{cz} < z_{\max})
\end{aligned} \tag{15.44a}$$

- Cylindrical tube(s) parallel to the X-axis:

$$C = \left[(p'_{c,y} - q_y)^2 + (p'_{c,z})^2 < R^2 \right] \quad \text{with}$$
$$q_y = 0 \quad \text{if } d = 0; \text{ otherwise } q_y = round(p'_{c,y}/d).d \tag{15.44b}$$

- Cylindrical tube(s) parallel to the Y-axis:

$$C = \left[(p'_{c,x} - q_x)^2 + (p'_{c,z})^2 < R^2 \right] \quad \text{with}$$
$$q_x = 0 \quad \text{if } d = 0; \text{ otherwise } q_x = round(p'_{c,x}/d).d \tag{15.44c}$$

- Cylindrical tube(s) parallel to the Z-axis:

$$C = \left[(p'_{c,x} - q_x)^2 + (p'_{c,y} - q_y)^2 < R^2 \right] \wedge \left[p_{c,z} > z_{top} \right] \wedge \left[p_{c,z} < z_{bottom} \right], \tag{15.44d}$$

with z_{top} and z_{bottom} as the z-coordinates of the top and bottom lids of the tube(s),

- Spheres:

$$C = \left[(p'_{c,x} - q_x)^2 + (p'_{c,y} - q_y)^2 + (p'_{c,z})^2 < R^2 \right], \tag{15.45}$$

- Cones (e.g., with symmetry axis (bottom $\rightarrow$ top) pointing to +Z-axis):

$$C = \left(p'_{c,z} > 0 \right) \wedge (h > 0) \wedge (0 < p'_{c,z}/h < 1) \wedge$$
$$\left[(p'_{c,x})^2 + (p'_{c,y})^2 < (p'_{c,z} . R/h)^2 \right], \tag{15.46}$$

and analogously for the five other directions.
- Oblique cylinders (using $\boldsymbol{b}$ as the directional unit vector along the symmetry axis):

$$C = \left[(p'_{c,x})^2 + (p'_{c,y})^2 + (p'_{c,z})^2 - (\boldsymbol{p_c'} \bullet \boldsymbol{b})^2 < R^2 \right] \wedge$$
$$\left[p_{c,z} > z_{top} \right] \wedge \left[p_{c,z} < z_{bottom} \right]. \tag{15.47}$$

- Mirrors (with $\boldsymbol{b}$ as the normal vector on the mirror surface):

$$C = (\boldsymbol{p'} \bullet \boldsymbol{b} = 0). \tag{15.48}$$

15.3.4 Absorption

Normally, the position of the photon, together with its directional angles, is stored upon reflection or transmission. However, when in absorption mode, the position of absorption will be stored, together with the directional angles of the previous (last) photon path. These angles are stored using the normal convention for the polar angle θ and azimuthal angle φ:

$$\Delta\boldsymbol{p} = |\Delta\boldsymbol{p}|.(\sin\theta. \cos\varphi, \ \sin\theta.\sin\varphi, \ \cos\theta), \tag{15.49}$$

with $\theta = 0$, if the direction is pointing along the +Z-axis, inside the sample, and φ in the XY-plane, as the angle with the X-axis.

15.3.5 Polarization

15.3.5.1 Polarization in Scattering Events

To handle polarization effects in scattering events we use Van de Hulst's scattering matrix [15], with E_0 and E as the incoming and scattered electric field vectors:

$$\begin{pmatrix} E_l \\ E_r \end{pmatrix} = \frac{\exp(-ikr - i\omega t)}{i.4\pi\varepsilon_m kr} \begin{pmatrix} S_2 & S_3 \\ S_4 & S_1 \end{pmatrix} \begin{pmatrix} E_{l0} \\ E_{r0} \end{pmatrix}, \tag{15.50}$$

where the subscript l and r denote parallel and perpendicular polarization, respectively. In the following we will limit ourselves to spherical particles, where S_3 and S_4 are $= 0$. The other parameters S_1 and S_2 are functions of the polar scattering angle θ. The factor $(4\pi\varepsilon_m)$ can be inserted in the S-functions as well. Note that Van de Hulst uses Gaussian units instead of SI-units, which means that he does not take the factor $(4\pi\varepsilon_m)$ into account.

The Stokes vector $S^T = (I,Q,U,V)$ can be constructed from this matrix:

$$\begin{aligned}
I &= E_l E_l^* + E_r E_r^* \\
Q &= E_l E_l^* - E_r E_r^* \\
U &= E_l E_r^* + E_r E_l^* \\
V &= i(E_l E_r^* - E_r E_l^*).
\end{aligned} \tag{15.51}$$

With

$$\begin{aligned}
E_l &= a_l \exp(-ik_z - i\omega t - i\varepsilon_l) \\
E_r &= a_r \exp(-ik_z - i\omega t - i\varepsilon_r),
\end{aligned} \tag{15.52}$$

it follows:

$$\begin{array}{lll}
I = a_l^2 + a_r^2 & U = 2a_l a_r.\cos\delta & \delta = \varepsilon_l - \varepsilon_r \\
Q = a_l^2 - a_r^2 & V = 2a_l a_r.\sin\delta &
\end{array} \tag{15.53}$$

For normal (non-birefringent) materials $\varepsilon_l = \varepsilon_r$. The degree of polarization is defined as

$$\Phi_P = \frac{1}{I}\sqrt{Q^2 + U^2 + V^2}, \tag{15.54}$$

Transformation of the Stokes vector upon scattering (for spherical particles) is given by

$$S^T{}_n = \overline{\overline{F}}.S^T \tag{15.55}$$

with

$$\overline{\overline{F}} = \begin{pmatrix} \frac{1}{2}(M_2 + M_1) & \frac{1}{2}(M_2 - M_1) & 0 & 0 \\ \frac{1}{2}(M_2 - M_1) & \frac{1}{2}(M_2 + M_1) & 0 & 0 \\ 0 & 0 & S_{21} & -D_{21} \\ 0 & 0 & D_{21} & S_{21} \end{pmatrix} \qquad (15.56)$$

and

$$\begin{aligned} M_k &= S_k S_k^* = |S_k|^2; \; k = 1, 2 \\ S_{21} &= \tfrac{1}{2}(S_1 S_2^* + S_2 S_1^*) \\ D_{21} &= \tfrac{1}{2}i \, (S_1 S_2^* - S_2 S_1^*), \end{aligned} \qquad (15.57)$$

and so we arrive at the Mueller matrix $\overline{\overline{M}}$ replacing $\overline{\overline{F}}$:

$$\overline{\overline{M}} = \begin{pmatrix} m_{11} & m_{12} & 0 & 0 \\ m_{12} & m_{11} & 0 & 0 \\ 0 & 0 & m_{33} & m_{34} \\ 0 & 0 & -m_{34} & m_{44} \end{pmatrix}, \qquad (15.58)$$

where the parameters $m_{11} \ldots m_{44}$ depend on the particular scattering function and the scattering angles θ and φ. We will deal with those parameters in the next section.

Transformation of the Stokes vector upon scattering has to be preceded by a rotation from the actual coordinate system (given by the unit vectors e_l, e_r, e_p, with directions parallel and perpendicular to the actual polarization direction, and parallel to the direction of propagation, respectively) to that in the scattering plane (e_l', e_r', e_p', with $e_p' = e_p$). This rotation is determined by the rotation matrix $\overline{\overline{R}}$:

$$\overline{\overline{R}} = \begin{pmatrix} 1 & 0 & 0 & 0 \\ 0 & \cos 2\varphi & -\sin 2\varphi & 0 \\ 0 & \sin 2\varphi & \cos 2\varphi & 0 \\ 0 & 0 & 0 & 1 \end{pmatrix}, \qquad (15.59)$$

with φ as the azimuthal scattering angle (see Fig. 15.15).

Subsequent multiplication with the Mueller matrix produces the new Stokes vector in the coordinate frame (e_l'', e_r'', e_p'') connected to the new propagation direction e_p'' (with $e_p'' \bullet e_p' = \cos\theta$):

$$e_r'' = \begin{pmatrix} \cos \varphi \\ \sin \varphi \\ 0 \end{pmatrix}; \quad e_l'' = \begin{pmatrix} -\cos \theta . \sin \varphi \\ \cos \theta . \cos \varphi \\ \sin \theta . \end{pmatrix}; \quad e_p'' = \begin{pmatrix} \sin \theta . \sin \varphi \\ -\sin \theta . \cos \varphi \\ \cos \theta . \end{pmatrix}.$$

$$(15.60)$$

Fig. 15.15 Coordinate
frames of subsequent
scattering events. The
propagation vector e_p is first
transformed into $e_p{'}$ (by
rotation over φ) and then to
$e_p{''}$ (by rotation over θ). The
vectors e_l, e_r and $e_l{'}$, $e_r{'}$ are
frame vectors parallel and
perpendicular to the scattering
planes
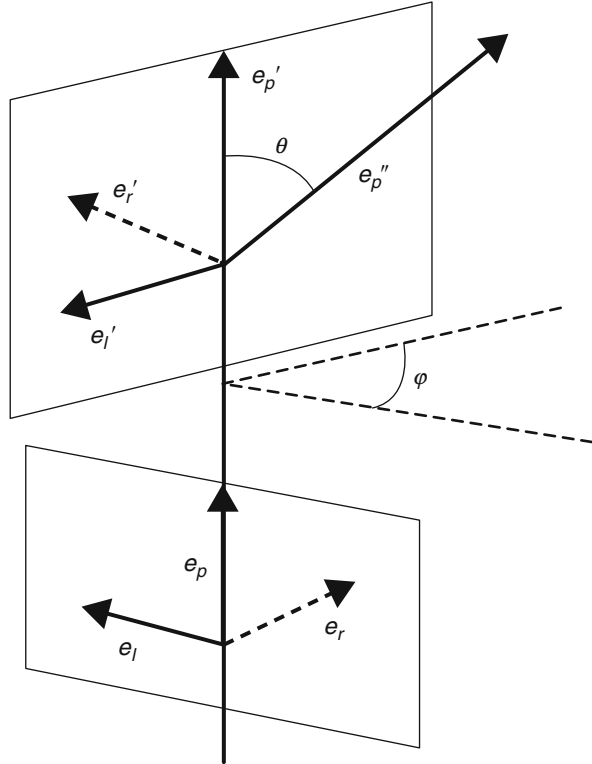
Subsequent scattering events (θ_i, φ_i, with $I = 1 \ldots n$) will result in

$$\boldsymbol{S}^T{}_{result} = \left[\prod_{i=1}^{n} \overline{\overline{\mathbf{M}}}(\theta_i) \overline{\overline{\mathbf{R}}}(\varphi_i) \right] . \boldsymbol{S}^T{}_0, \tag{15.61}$$

and this determines the polarization state of the emerging photon. Here, the vector $\boldsymbol{S}^T{}_0$ is the Stokes vector of the incoming photon, given by (15.47) after determination of the parallel and perpendicular directions corresponding to $E_{//}$ and $E_{\perp}$.

In the non-polarized case (natural light), the scattering angles can be determined using two subsequent random numbers. In the polarized state, that is no longer the case. When determining an angle φ using a random number, the angle θ is determined by the joint probability:

$$p(\theta, \varphi) = m_{11}(\theta) + m_{12}(\theta). \left(Q . \cos\ 2\varphi + U . \sin\ 2\varphi \right) / I. \tag{15.62}$$

Yao and Wang's approach [16] calculates θ with m_{11} (as, in fact, is done with natural light) and subsequently φ with (15.62). Several authors have dealt with polarization of light in turbid media [16–21].

15.3.5.2 Polarization at Interfaces

Changing of polarization direction may also occur at interfaces, where reflection or refraction takes place. With α_1, α_2, and α_3 as the angles of the electric vector $\boldsymbol{E}$ with the plane of incidence (formed by the incident propagation direction and the normal on the surface at the point of intersection) for the incident (1), refracted (2), and reflected (3) vector, respectively (see Fig. 15.4), and A as the field amplitude, it can be shown (see, e.g., Born and Wolf [22]) that

$$A_{1,l} = A_1 . \cos \alpha_1; \quad A_{1,r} = A_1 . \sin \alpha_1, \tag{15.63}$$

where α_1 can be derived from the components of the incident Stokes vector using

$$A_{1,l} = \tfrac{1}{2}(I + Q); \quad A_{1,r} = \tfrac{1}{2}(I - Q). \tag{15.64}$$

Now we calculate the amplitudes of the reflected and transmitted (refracted) wave

$$A_{3,l} = \frac{\tan(\theta_1 - \theta_2)}{\tan(\theta_1 + \theta_2)} A_{1,l}; \quad A_{3,r} = -\frac{\sin(\theta_1 - \theta_2)}{\sin(\theta_1 + \theta_2)} A_{1,r} \; \text{with} \; \frac{\sin \theta_1}{\sin \theta_2} = \frac{n_2}{n_1}$$

$$A_{2,l} = \frac{2 \sin \theta_2 . \cos \theta_1}{\sin(\theta_1 + \theta_2) . \cos(\theta_1 - \theta_2)} A_{1,l}; \quad A_{2,r} = \frac{2 \sin \theta_2 . \cos \theta_1}{\sin(\theta_1 + \theta_2)} A_{1,r} \tag{15.65}$$

$$\tan \alpha_3 = -\frac{\cos(\theta_1 - \theta_2)}{\cos(\theta_1 + \theta_2)} \tan \alpha_1; \quad \tan \alpha_2 = \cos(\theta_1 - \theta_2) . \tan \alpha_1.$$

From these we can derive the corresponding Stokes vector coefficients and Mueller matrices $\overline{\overline{M}}_R$ and $\overline{\overline{M}}_T$, where the subscripts R and T stand for reflection and transmission (refraction). However, to construct the new Stokes vector it is easier to use the amplitudes directly.

To find out whether reflection or refraction (transmission) will take place, we have to look at the reflectivity R and transmittivity T of the energy instead of those of the amplitude:

$$R = \frac{\left|A_{3,l}\right|^2}{\left|A_{1,l}\right|^2} \cos^2 \alpha_1 + \frac{\left|A_{3,r}\right|^2}{\left|A_{1,r}\right|^2} \sin^2 \alpha_1;$$

$$T = \frac{n_2 \cos \theta_2}{n_1 \cos \theta_1} \left[\frac{\left|A_{2,l}\right|^2}{\left|A_{1,l}\right|^2} \cos^2 \alpha_1 + \frac{\left|A_{2,r}\right|^2}{\left|A_{1,r}\right|^2} \sin^2 \alpha_1 \right], \tag{15.66}$$

where we can verify that

$$R + T = 1 \tag{15.67}$$

The procedure for handling reflection and refraction at interfaces is as follows:

- Rotate the coordinate frame of the incoming photon to the coordinates of the plane of reflection, using a rotation matrix as in (15.55).
- Determine whether reflection or refraction will take place, using (15.67) and a fresh random number R_N. Reflection will take place if $R_N \leq R$; otherwise, refractiontakes place.
- Construct the new coordinate frame for the photon and the new Stokes vector, using (15.65).

15.4   Scattering Functions

Now we introduce various scattering functions that are frequently used in light scattering simulations. In most cases, we will follow the treatment of Van de Hulst [15] and of Ishimaru [2, 3]. Further references can be found there.

In matters of light scattering by particles, two parameters are important: the aspect ratio x and the relative refractive index n_{rel}. The aspect ratio is given by

$$x = \frac{2\pi a}{\lambda_{med}} = ka; \quad \lambda_{med} = \frac{\lambda_{vac}}{n_{med}},$$ (15.68)

where a denotes the radius of the particle, λ the wavelength of the light, and k the modulus of the wave vector. The subscripts *med* and *vac* denote medium and vacuum, respectively. The relative index n_{rel} is the index of the particles with respect to the surrounding medium.

We start with very small particles (small compared to the wavelength: $x << 1$), giving rise to dipolar or Rayleigh scattering. When gradually increasing the radius, we encounter Rayleigh-Gans or Debije scattering, and, finally, scattering by large particles ($x >> 1$). Generally valid expressions were developed by Mie (Mie scattering). Finally, we have expressions of a more phenomenological nature, like Henyey-Greenstein scattering or peaked-forward scattering.

We will use the *geometrical* and *scattering cross sections* σ_g and σ_s [m^2], being the real and the apparent shadow of the particle, and the efficiency factor $Q_{sca} = \sigma_s/\sigma_g$, with $\sigma_g = \pi a^2$.

The ultimate way of treating scattering in numerical simulation is to use the *scattering coefficient* μ_s (in m^{-1}), defined as

$$\mu_s = n_s \sigma_s$$ (15.69)

with n_s as the particle concentration (in m^{-3}). The scattering coefficient is a measure for the average number of scattering events per unit of length. Normally in tissue the scattering is predominantly in the forward direction, which means that randomization of the photon direction only will occur after a relatively large
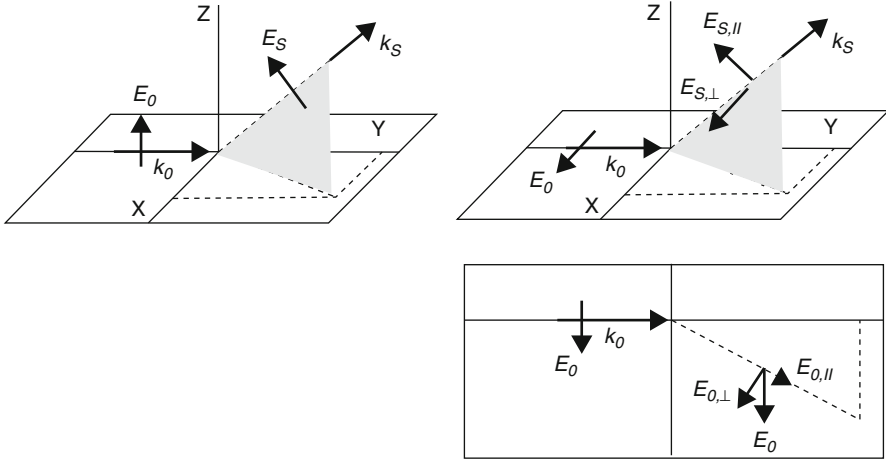
Fig. 15.16 The meaning of the double vector product in determining the direction of scattering and polarization, for two cases: polarization perpendicular to the XY-plane (*left*) and parallel to that plane (*right*). Here, ε is taken as a scalar

number of scattering events. Therefore, in those cases it is worthwhile to use the *reduced scattering coefficient* μ_s', defined as

$$\mu_s' = \mu_s(1 - g), \tag{15.70}$$

where g stands for the averaged cosine of the polar scattering angles during those events. This value will be 1 for perfectly forward scattering and 0 for isotropic scattering. For tissue $g \approx 0.8$–0.9 and for blood $g \approx 0.95$–0.99.

Standard electromagnetic theory for light scattered by dipoles leads to the expression:

$$\boldsymbol{E}_s(\boldsymbol{R}, t) = -\frac{1}{4\pi\varepsilon_0 R} \int \int \int_V d^3\boldsymbol{r} \quad \boldsymbol{k}_s \times \boldsymbol{k}_s \times \left[\overline{\overline{\boldsymbol{\varepsilon}}}(\boldsymbol{r}, t') \bullet \boldsymbol{E}_0(\boldsymbol{r}, t')\right] \tag{15.71}$$

with $\boldsymbol{E}_s$ and $\boldsymbol{E}_0$ as the scattered and the incoming electric field, respectively; $\boldsymbol{R}$ is the vector from the scattering volume V to the point of detection, $\boldsymbol{k}_s$ is the scattered wave vector in that direction, and $\overline{\overline{\varepsilon}}$ is the dielectric tensor (which frequently reduces to a scalar). The time t' is the reduced time, given by

$$t' = t - \frac{|\boldsymbol{R} - \boldsymbol{r}|}{c} \tag{15.72}$$

with c as the light velocity in the media. In (15.71), the dimensions of the scattering volume V are assumed to be small compared with R. The significance of the double vector product is illustrated in Fig. 15.16.
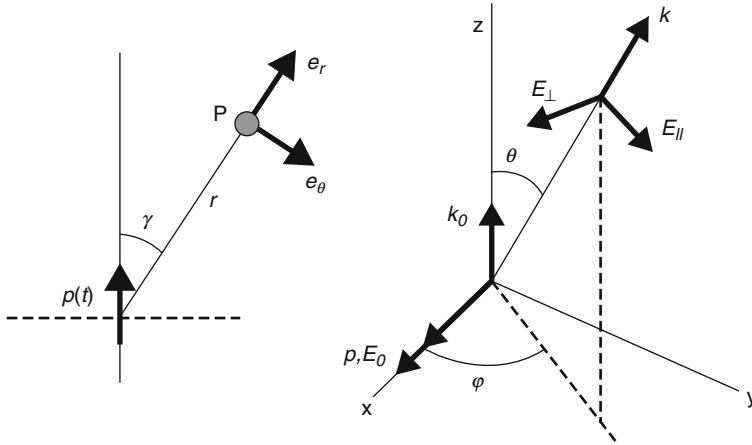
Fig. 15.17 (a) Electric dipole, radiating towards detection point P at distance r and with polar scattering angle γ. The vectors e_r and e_θ are unit vectors. Due to symmetry, the azimuthal angle does not play a role

15.4.1 Dipolar (Rayleigh)

With dipolar scattering, the particles are assumed to be so small that light scattered from different oscillating electrical dipoles in the particles will not lead to phase differences upon arrival at the point of detection. Using standard electromagnetic dipole radiation theory, or a standard Green's functions approach, we may derive for the radiative term E_{rad} of the scattered electric field strength (Fig. 15.17):

$$E_{rad} = -\frac{p_m k^2}{4\pi\varepsilon r} \sin\gamma \cdot \exp(i\omega t') \cdot e_\theta; \quad t' = t - \frac{r}{c}, \tag{15.73}$$

where p_m is the amplitude of the oscillating dipole $p(t) = p_m \exp(i\omega t)$, with ω as the frequency ($\omega = c/k$, with c the local light velocity). The parameter t' accounts for the time retardation upon arrival at detection, which generally could be the origin of phase differences. For clarity, Van de Hulst uses Gaussian rather than S.I.-units, which means that the factor $(4\pi\varepsilon_m)$ is set to unity.

Frequently, p_m can be considered as being related to the incoming electric field E_0, through the polarizability tensor α of the particle. In a number of cases this tensor reduces to a mere constant α, with

$$\alpha = 4\pi\varepsilon_m\alpha_H; \quad \alpha_H = a^3(\varepsilon_p - \varepsilon_m)f_p; \quad f_p = \frac{3\varepsilon_m}{\varepsilon_p + 2\varepsilon_m}, \tag{15.74}$$

where ε_p and ε_m are the dielectric constants of the particle and the medium, α_H is the polarizability as used by Van de Hulst (assuming $4\pi\varepsilon_m =$ unity) and f_p denotes the

correction for the internal enhancement of the incoming field (see standard EM textbooks). Note the dependence on the particle volume, through a^3.

We find for the two electric field components:

$$|E_{//}| = \frac{\alpha k^2}{4\pi\varepsilon_m r} \cos\theta.|E_{0,//}| = \frac{\alpha k^2}{4\pi\varepsilon_m r} \cos\theta.\cos\varphi.|E_0| = \frac{\alpha k^2}{4\pi\varepsilon_m r} \cos\theta.|E_{0,//}|$$

$$|E_\perp| = \frac{\alpha k^2}{4\pi\varepsilon_m r} |E_{0,\perp}| = \frac{\alpha k^2}{4\pi\varepsilon_m r} \sin\varphi.|E_0| = \frac{\alpha k^2}{4\pi\varepsilon_m r} .|E_{0,\perp}|$$

$$(15.75)$$

The intensities $I_{//}$ and $I_\perp$ are proportional to the squares of the field strengths $(I = \frac{1}{2}c\varepsilon_m E^2)$, thus,

$$I_{//} = \frac{\alpha^2 k^4}{(4\pi\varepsilon_m)^2 r^2} \cos^2\theta.\cos^2\varphi.\, I_0,$$

$$I_\perp = \frac{\alpha^2 k^4}{(4\pi\varepsilon_m)^2 r^2} \sin^2\varphi.\, I_0.$$

$$(15.76)$$

Due to the dependence on α^2 and k^4, the intensities are proportional to a^6 and $1/\lambda^4$.

The components of Van de Hulst's scattering matrix, (15.73), will read

$$S_2(\theta) = \alpha k^3 \cos\theta; \quad S_1(\theta) = \alpha k^3; \quad S_3 = S_4 = 0. \qquad (15.77)$$

This means that the component perpendicular to the scattering plane shows uniform scattering, but the parallel component has a cosine behavior: when viewing the scattering particle along a direction parallel to the polarization, no scattering will be observed.

For natural light the total intensity will be proportional to $\frac{1}{2}(S_1{}^2 + S_2{}^2)$, and thus

$$I_{nat}(\theta) = \frac{\alpha^2 k^4 I_0}{(4\pi\varepsilon_m)^2 r^2} \frac{1 + \cos^2\theta}{2}. \qquad (15.78)$$

Spatial integration of (15.74) over θ and φ leads to the total scattered intensity I_{tot} (now expressed in W/sr instead of W/m^2):

$$I_{tot} = \frac{8\pi}{3} \frac{\alpha^2 k^4 I_0}{(4\pi\varepsilon_m)^2}. \qquad (15.79)$$

The scattering cross section σ_s is defined (using Ω as the scattering solid angle and $F(\Omega)$ as the angle-dependent scattering function, but normalized to unity upon Ω-integration over 4π) with:

$$I(\Omega) = \sigma_s.F(\Omega).I_0, \qquad (15.80)$$

with $I(\Omega)$ expressed in W/sr and I_0 in W/m^2. This leads to

$$\sigma_s = \frac{8\pi}{3} \frac{\alpha^2 k^4}{(4\pi\varepsilon_m)^2} = \frac{8\pi}{3}\alpha_H{}^2 k^4. \tag{15.81}$$

The ratio Q_{sca} is given by

$$Q_{sca} = \frac{\sigma_s}{\sigma_g} = \frac{8}{3}a^4(\varepsilon_p - \varepsilon_m)^2\left(\frac{3\varepsilon_m}{\varepsilon_p + 2\varepsilon_m}\right)^2 k^4 \approx \frac{8}{3}x^4\left(\frac{m^2 - 1}{m^2 + 2}\right)^2, \tag{15.82}$$

where m^2 is the relative refractive index of the particles in the surrounding medium: $m^2 = \varepsilon_p/\varepsilon_m$.

15.4.2 Rayleigh-Gans

When particles grow larger, the phase differences of scattered waves arriving at the detection point from different source points in the scattering medium can no longer be neglected.

Here we will follow Van de Hulst, using the approximation $|\varepsilon_p - \varepsilon_m| \ll \varepsilon_m$. Also, the value of $x|\varepsilon_p - \varepsilon_m|/\varepsilon_m$ should be $\ll 1$. With these assumptions we may write for a volume element dV:

$$d\alpha_H = \frac{m^2 - 1}{4\pi}dV \approx \frac{m - 1}{2\pi}dV \tag{15.83}$$

where m is the relative refractive index of the particles in the medium: $m^2 = \varepsilon_p/\varepsilon_m$. The non-zero components of the scattering matrix will read:

$$S_2 = 4\pi\varepsilon_m\frac{m - 1}{2\pi}V.R(\theta, \varphi); \; S_1 = 4\pi\varepsilon_m\frac{m - 1}{2\pi}V.R(\theta, \varphi).\cos\theta \tag{15.84}$$

with $R(\theta.\varphi)$ obtained by integration over the volume V using a phase-dependent factor $i\delta$:

$$R(\theta, \varphi) = \frac{1}{V}\int\int\int \exp(i\delta).dV. \tag{15.85}$$

The phase-difference δ is given by $\mathbf{k}\cdot(\mathbf{r} - \mathbf{r}_O)$, where $\mathbf{r}$ and $\mathbf{r}_O$ are the position vectors from the scattering volume element under consideration and the origin in the sample. The scattering cross section will be (for natural incoming light):

$$\sigma_s = \frac{1 + \cos^2\theta}{2}k^4 V^2\frac{(m - 1)^2}{(2\pi)^2}|R(\theta, \varphi)|^2. \tag{15.86}$$

For special particles, the function $R(\theta, \varphi)$ can be expressed analytically:

$$R(\theta, \varphi) = \sqrt{\frac{9\pi}{2u^3}} J_{\frac{3}{2}}(u) = \frac{3}{u^2} (\sin u - u \cos u) \text{ with } u = 2x. \sin \tfrac{1}{2}\theta \qquad (15.87)$$

The factor Q_{sca} for spherical particles is given by:

$$Q_{sca} = \frac{32}{27}(m-1)^2 x^4 \quad (x<<1) \quad \text{and} \quad Q_{sca} = 2(m-1)^2 x^2 \quad (x>>1) \quad (15.88)$$

For other shapes, see Van de Hulst.

15.4.3 Mie

In principle, the rigorous scattering theory, as developed by Mie (see refs. in Ref. [15]), presents analytical expressions for all kind of particles. It departs from the Maxwell equations and solves the scalar part of the wave equation, taking boundary conditions into account. This leads to complicated expressions for the components of Van de Hulst's scattering matrix, which are only tractable when treated numerically.

In the Monte Carlo program we use a procedure developed by Zijp and Ten Bosch [23], which renders S_2 and S_1. Again, for natural light the total intensity will be proportional to $\tfrac{1}{2}(S_1{}^2 + S_2{}^2)$. See Fig. 15.18 for an example.

15.4.4 Henyey-Greenstein

The Henyey-Greenstein scattering function [24] originates from the astronomical field, to calculate the scattering by cosmic particle clouds. Since it can be written in a closed analytical form, it can be used as a fast replacement for the Mie functions. The function reads:

$$p_{HG}(\theta, \varphi) = \frac{1}{4\pi} \frac{1 - g^2}{(1 + g^2 - 2g.\cos\theta)^{3/2}}, \qquad (15.89)$$

where g is the averaged cosine of the polar angle θ of the scattering events. This function is normalized to unity upon integration over 4π solid angle.

A drawback of this expression is that the function only describes the angle-dependent behavior of the scattering. The calculation of the scattering cross section has to be done by other means. One option is to insert the total scattering cross section as obtained by Mie scattering (or another approach, if applicable) as a separate factor in the Henyey-Greenstein expression.

ME-File E:\MC\Mie\test1.MIE
Scattering function = f(theta) I (theta = polar scattering angle)
Nr.angles =   181 I Max. = 4.09657E+03 I 10-log. plot; blue: >0; green: <0
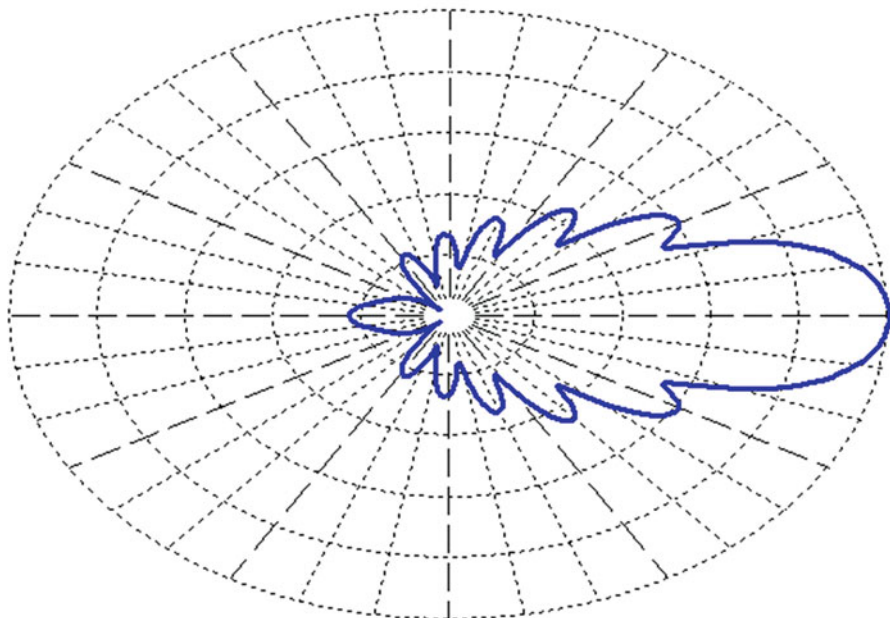
Fig. 15.18 Example of a MIE file. Scattering function according to the Mie formalism

15.4.5 Isotropic

Isotropic scattering can be described using the (normalized) function

$$p_{iso}(\theta, \varphi) = \frac{1}{4\pi}. \tag{15.90}$$

The normalized cumulative function $C(\theta)$ will read

$$C(\theta) = \frac{1}{2}(1 - \cos \theta). \tag{15.91}$$

and thus θ can be found from $\theta = \arccos(1 - 2R_N)$, with R_N as a fresh random number $(0 < R_N < 1)$. The value of g will be zero.

15.4.6 Peaked Forward

A peaked-forward scattering function is completely artificial. It can be useful for special applications. A possible functional form (not normalized) is

$$p_{PF} = \exp(-\theta^2/\theta_0^2). \tag{15.92}$$

15.5   Light Sources

For the injection of photons, one can imagine various mechanisms. Most general is
the pencil beam, entering from the top. However, other beam profiles can be used as
well. Here we offer a broad spectrum of those profiles.

15.5.1 Pencil Beams

Pencil beams are the simplest way to inject photons into the sample. The only
programmatic requisite is to define the point of injection at the sample surface. With
those beams, one still has to take care with proper handling of the transport through
the upper interface of the sample with the air, to take reflection losses into account.

Pencil beams can be tilted in two directions, which can be described using the
tilting polar and azimuthal angles θ and φ. See Sect. 15.5.2.

15.5.2 Broad Beams

Broad beams come in two forms: divergent beams and parallel beams. For diver-
gent beams, we have adopted the following procedure (see Fig. 15.19):

We define the divergence angles of the beam projection on the XZ- and YZ-
planes respectively, as α_x and α_y, and the tilting angles of the symmetry axis of the
beam with the Z-axis and the X-axis in the XY-plane, as θ and φ, respectively;

Then we may write (k is the length of $\boldsymbol{k}$):

$$k_x = k \sin \theta \cos \varphi; \; k_y = k \sin \theta \sin \varphi; \; k_z = k \cos \theta \qquad (15.93)$$

and for the tilting angles:

$$\tan \gamma_x = \frac{k_x}{k_z} = \tan \theta . \cos \varphi; \quad \tan \gamma_y = \frac{k_y}{k_z} = \tan \theta . \sin \varphi \qquad (15.94)$$

With adaptation for divergence:

$$\gamma_x{}' = \gamma_x + \alpha_x = \arctan(\tan \theta . \cos \varphi) + \alpha_x,$$

$$\gamma_y{}' = \gamma_y + \alpha_x = \arctan(\tan \theta . \sin \varphi) + \alpha_y. \qquad (15.95)$$

The new direction vector $\boldsymbol{k}'$ will be given by

$$k'_x = \tan \gamma_x{}' . k'_z; \; k'_y = \tan \gamma_y{}' . k'_z; \; |k'| = k. \qquad (15.96)$$

This approach offers the opportunity to define divergent beams with different
opening angles in X- and Y-directions, and with different profiles (Gaussian or uniform).

Fig. 15.19 Entrance of the beam. The surface of the sample is the XY-plane. F is the focus, and θ and φ are tilting angles of the symmetry axis of the beam
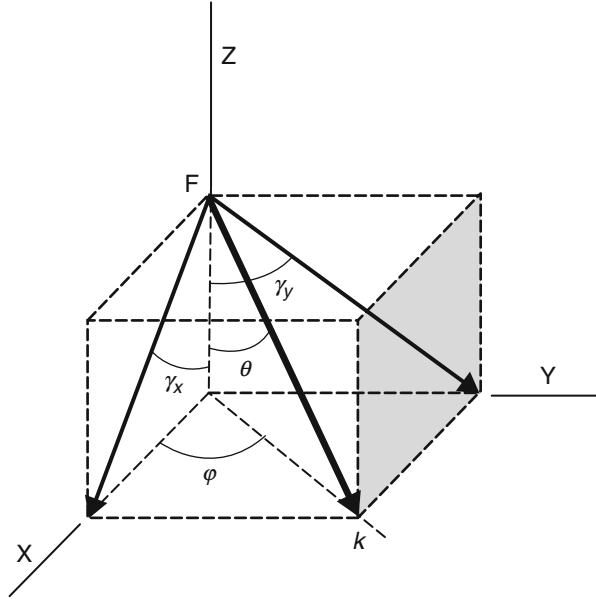
For parallel beams an ideal thin positive lens with focal point in F (see Fig. 15.19) is thought to be positioned horizontally on the surface.

15.5.3 Ring-Shaped Beams

Here we only apply ring-shaped beams with uniform filling, which means that the light intensity will be equal at all point in the ring. Then the amount of photons passing through a ring at distance r from the center and with width dr will be proportional to rdr. To define the actual distance of the photon we need to construct the cumulative function $C(r)$:

$$C(r) = \int_{R_1}^{r} c.r'.dr', \tag{15.97}$$

where c is a proportionality constant and $R_1 \leq r \leq R_2$ (R_1 and R_2 being the inner and outer ring radii), and normalize $C(R_2)$ to unity. This results in the cumulative function $C(r)$:

$$C(r) = \frac{r^2 - R_1{}^2}{R_2{}^2 - R_1{}^2}. \tag{15.98}$$

By equaling this function to a fresh random number between 0 and 1, the value of r is set. Subsequently, the φ-value is chosen randomly between 0 and 2π.

Fig. 15.20 Radiance and
power are supposed to be
emitted through area *dA* in
direction *p* in solid angle *dΩ*
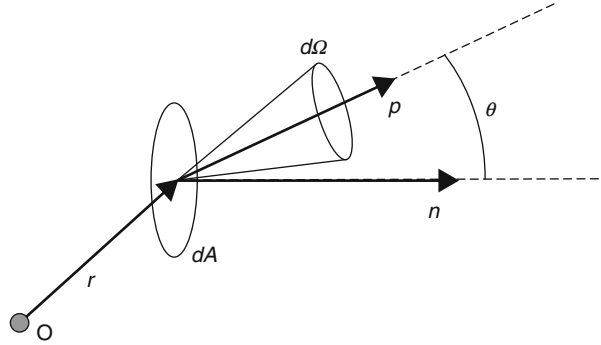
The ring-shaped beam can be combined with divergence and tilting as mentioned before.

15.5.4 Isotropic Injection

We can adopt several models for isotropic injection. The simplest model is:

$$I(\theta) = c; \quad c = \text{constant}. \tag{15.99}$$

Then we can construct the normalized cumulative function

$$C(\theta) = \frac{C'(\theta)}{C'(\pi)} = \tfrac{1}{2}(1 - \cos\theta) \quad \text{with} \quad C'(\theta) = \int\limits_{0}^{\theta} I(\theta').\sin\theta'.d\theta', \tag{15.100}$$

and by equaling this function to a fresh random number R_N, the value of θ can be derived, as $\theta = \arccos(1 - 2R_N)$. Again, the value of φ is obtained from a random number between 0 and 2π.

Another model uses isotropic radiances (see Fig. 15.20).

Using the radiance $L(p, r)$, expressed in $\text{W.m}^{-2}\ \text{sr}^{-1}$, we find for the emitted power contribution and the flux vector **F**:

$$dP = L(p, r).\cos\theta.dA.d\Omega$$

$$F(r) = \int_{\Omega} p.L(p, r).d\Omega \tag{15.101}$$

In the case of isotropic radiance, $L(p, r)$ will be a function of *r* only, and thus

$$F(r) = L(r).\int_{\Omega} p.d\Omega, \tag{15.102}$$

and for the component along the normal vector (Z-component):

$$F_z(\boldsymbol{r}) = L(\boldsymbol{r}) \int_\Omega \cos\theta.d\Omega = \pi.L(\boldsymbol{r}). \tag{15.103}$$

The other components will render zero, because of a zero result of the φ-integration of the function $\sin\varphi$ and $\cos\varphi$ over 2π. And so, using a constant value L_0 for $L(\boldsymbol{r})$, we find for the normalized cumulative function:

$$C(\theta) = \frac{C'(\theta)}{C'(\pi)} = \sin^2\theta \quad \text{with} \quad C'(\theta) = \int_0^\theta L_0.\cos\theta'.\sin\theta'.d\theta'.$$

By equaling a fresh random number (between 0 and 1) to $C(\theta)$, we find the corresponding value for θ (between 0 and π).

15.5.5 Internal Point Sources

For internal point sources, we may follow the same lines as with pencil beams or broad, divergent beams, if desired combined with a tilting angle. In this way, we are able to construct a layered sample with internal structures like spheres and cylinders, and to direct a beam either from the side or upwards, from the backside of the sample. It is also possible to combine this option with the option of internal detection, as will be described below.

15.5.6 Distributed Sources

Distributed sources will originate from points in a certain well-defined volume within the sample. These points will emit in random directions, and the light will not have a beam-like character. This type of photon source will be encountered, for instance, when calculating Raman or fluorescence scattering from within a scattering and absorbing volume. In those cases the calculations will consist of two steps:

- Absorption of light with wavelength λ_1 at relevant positions inside the medium.
- Scattering to the surface of the sample, using photons originating from the absorption positions of the previous step, but now with wavelength λ_2.

For fluorescence and Raman-Stokes emission λ_1 should be smaller than λ_2. This means that, in general, the optical characteristics of the sample and its internal structure will be different in the two steps.

Due to the absorption step that precedes the fluorescence or Raman emission, the direction of emission of the photon will be random. Then the procedure of isotropic scattering can be used, see Sect. 15.4.5. This means that the polar angle θ

can be found from $\cos\theta = 1 - 2R_N$, where R_N is a fresh random number. Now, $\cos\theta$ is identical to the Z-component of the direction unit vector, and from that the other components can be found, using a random number between 0 and 2π to find φ.

The polarization direction will be randomized as well, which will randomize the components of the Stokes vector. The Stokes vector $\boldsymbol{S}^T{}_0$, which starts the polarization procedure in (15.61), will now be defined on a local coordinate frame, with its Z-axis along the propagation vector of the photon and its X- and Y-axes perpendicular to that direction and to each other. Then the two components $E_{//}$ and $E_\perp$ might be chosen at random, as long as they satisfy $E_{//}{}^2\cos^2\theta + E_\perp{}^2\sin^2\theta = E_0{}^2$, where θ is the angle of the electric vector in the XY-plane with the X-axis.

15.6   Detection

Normally, the detection of emerging photons will take place at the surface, either at the top or at the bottom of the sample. We will denote these external detection options as reflection and transmission. Another method of detection is to make use of "internal" detectors. Here the photons are supposed to end their path at a certain position inside the sample.

A general property for both options is the presence of a limited numerical aperture (NA), with $NA = \sin\theta_D$, where θ_D is the (half) opening angle of the detection cone. NA ranges from 0 (pure pencil beam) to 1 (all incoming angles accepted). Its value can be set in the program.

The program stores the place of detection of the photon (x,y,z-coordinates) and the direction angles (θ and φ) with respect to the external laboratory coordinate frame. It also stores the number of scattering events and the percentage of Doppler scattering events, as well as the resulting Doppler frequency and the path length, either geometrical or optical. The latter is corrected for wavelength changes due to changes in the refractive index, by multiplication of the local contribution to the path with the refractive index of the local medium.

15.6.1 External Detection

In the case of external detection, either reflection or transmission, the photon is assumed to be detected if
- It passed the detection plane in the proper direction. This implies that the photon indeed has crossed the final interface between the sample and the medium where the detector is. This is to be decided using the proper Fresnel relations (see above).
- It passed that plane within the borders of the detection window. This window can be rectangular, circular, or ring-shaped.
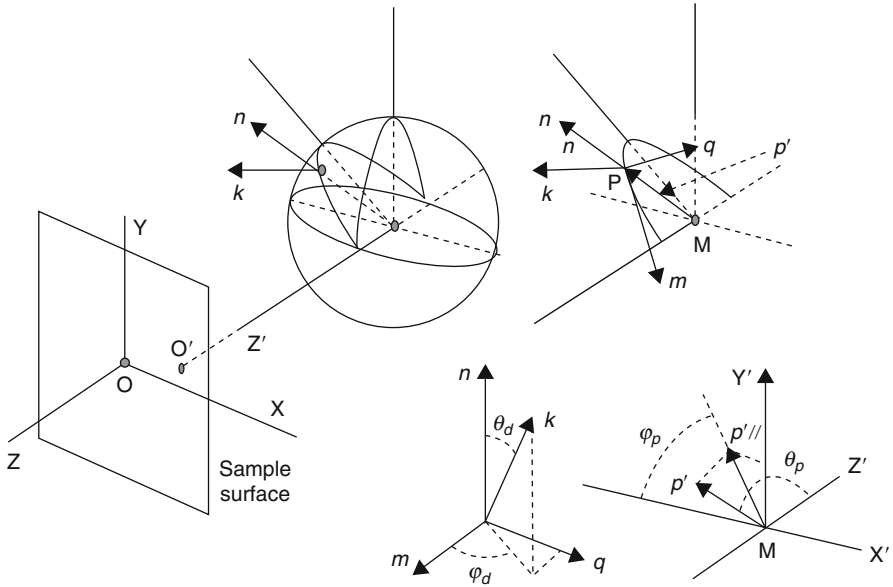
Fig. 15.21 Internal detection at the inside of a spherical surface. The vectors p', k, and n denote the position vector (relative to the origin of the sphere), the direction vector, and the normal on the surface, respectively. The vectors n, m, and q represent the local coordinate frame at the detection point P, with m in the plane spanned by n and the Z′-axis, and q // $n \times m$. All vectors except p' are here considered to be unit vectors. The subscripts p and d denote position and direction, respectively

Contrary to what is mentioned above with external detection, the program does not store the z-coordinate of detection, but the average depth of all scattering events along the path, or (as desired) the maximum depth along the path.

15.6.2 Internal Detection

With internal detection two options are present, one at the interface between two layers, and one at the internal interface of a structure (or block), like a sphere or cylinder.

- The first option is handled in the same way as with external detection, using reflection and transmission to denote the interface crossing direction necessary for detection.
- The second option is more complicated. This is elucidated in Fig. 15.21, where the situation is sketched for a sphere as an example. A cylinder can be described analogously.

With the definitions as in Fig. 15.21, the calculation of the position and direction angles proceeds as follows:

Fig. 15.22 Expressing k from the (X',Y',Z')-frame into the (X,Y,Z)-frame
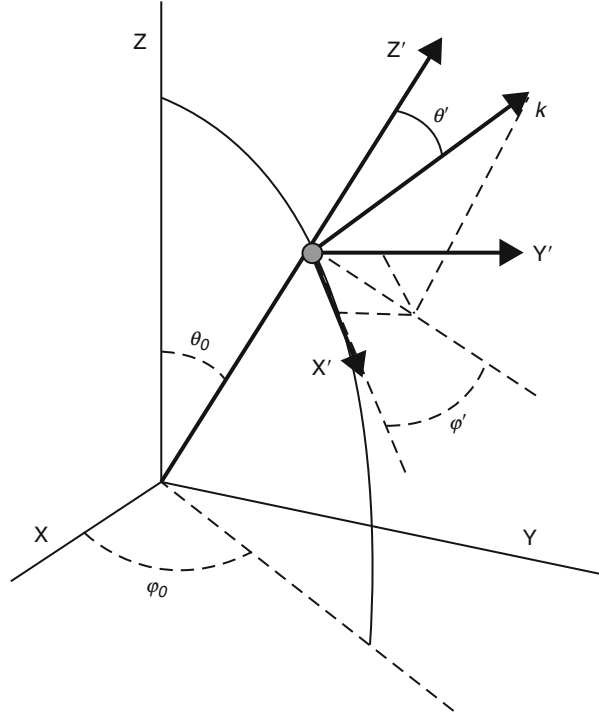
$$(1) \quad \boldsymbol{q} = \boldsymbol{n} \times \boldsymbol{e}_z,$$
$$(2) \quad \boldsymbol{m} = \boldsymbol{q} \times \boldsymbol{n},$$
$$(3) \quad \theta_d = \arccos\,(\boldsymbol{n} \bullet \boldsymbol{k}),$$
$$(4) \quad \boldsymbol{k}_{//} = \boldsymbol{k} - \boldsymbol{n}\,.\cos\theta_d = \boldsymbol{k} - \boldsymbol{n}\,.(\boldsymbol{n} \bullet \boldsymbol{k}),$$
$$(5) \quad \varphi_d = \left(1/\big|\boldsymbol{k}_{//}\big|\right).\arccos\,\left(\boldsymbol{m} \bullet \boldsymbol{k}_{//}\right), \qquad (15.104)$$
$$(6) \quad \boldsymbol{p}' = \boldsymbol{p} - \boldsymbol{r}_M = R.\boldsymbol{n},$$
$$(7) \quad \theta_p = \arccos\,(\boldsymbol{p}' \bullet \boldsymbol{e}_z),$$
$$(8) \quad \boldsymbol{p}'_{//} = \boldsymbol{p} - \boldsymbol{e}_z.\cos\theta_p,$$
$$(9) \quad \varphi_p = \left(1/\big|\boldsymbol{p}'_{//}\big|\right).\arccos\,\left(\boldsymbol{p}'_{//} \bullet \boldsymbol{e}_x\right).$$

Expressing $\boldsymbol{k}$ from the (X', Y', Z')-frame into the (X, Y, Z)-frame is as follows (Fig. 15.22):

$$
\begin{aligned}
\boldsymbol{k} &= \sin\theta'.\cos\varphi'.\boldsymbol{e}_x' + \sin\theta'.\sin\varphi'.\boldsymbol{e}_y' + \cos\theta'.\boldsymbol{e}_z', \\
\boldsymbol{e}_x' &= \cos\theta_0.\cos\varphi_0.\boldsymbol{e}_x + \cos\theta_0.\sin\varphi_0.\boldsymbol{e}_y - \sin\theta_0.\boldsymbol{e}_z \\
\boldsymbol{e}_y' &= -\sin\varphi_0.\boldsymbol{e}_x + \cos\varphi_0.\boldsymbol{e}_y \\
\boldsymbol{e}_z' &= \sin\theta_0.\cos\varphi_0.\boldsymbol{e}_x + \sin\theta_0.\sin\varphi_0.\boldsymbol{e}_y + \cos\theta_0.\boldsymbol{e}_z
\end{aligned}
\qquad (15.105)
$$

File: C:\MC\Eenbol2.FOT
Screen borders Min: X: -10.000 | Y: -10.000 | Z: 0.000 mm
                 Max: X: 10.000 | Y: 10.000 | Z: 6.000 mm
2000 of 2000 photons plotted

Axes
layer 1
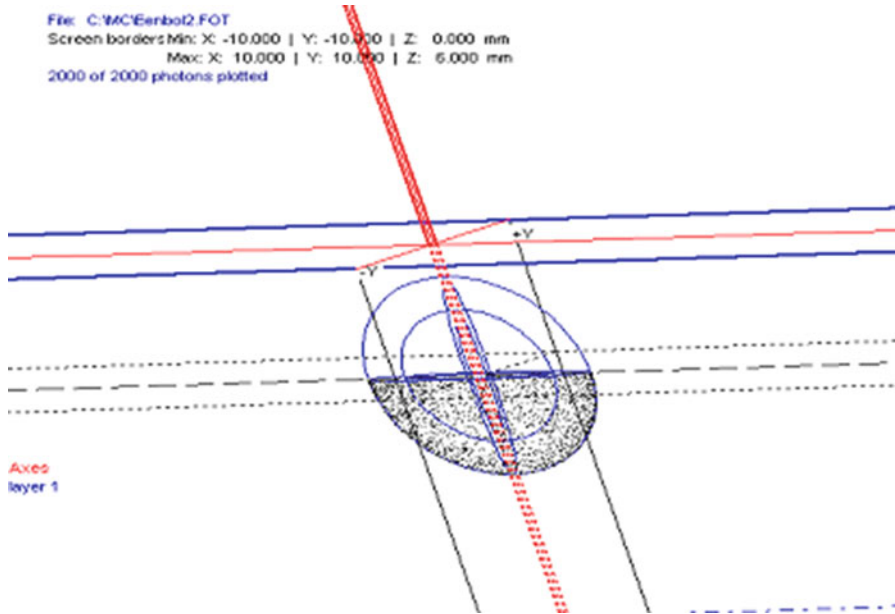
Fig. 15.23 Internal detection at the inside of a sphere. Settings: detection of photons arriving at the transmission side of the sphere only

The program offers the option to record internally detected photons in reflection mode (i.e., with direction angles $\theta > \pi/2$) or in transmission mode ($\theta < \pi/2$). It also allows calculation of the direction angles at the point of detection in both coordinate frames (laboratory frame and local frame). See Fig. 15.23.

15.6.3 Sampling of Photons

For the sampling of photons, some options for the maximum number of photons can be set:
- Emitted photons
- Injected photons
- Detected photons

In all cases we consider photons to be detected only when arriving at the plane of detection within the detection window (rectangular, circular, or ring-shaped). The difference between the options "emitted" and "injected" is due to the chance of reflection of the incoming beam at the surface of the sample and will be determined by the Fresnel relations.

Besides the recording of all properly detected photons, there also exists the option of recording the position of the photons during their paths, thus performing time-of-flight tracking. This can be done at a number of presettable time points, and the photons are stored in files similar to the files with detected photons.

15.6.4 Photon Path Tracking

The tracking of the path of the photon, i.e., recording the coordinates of the scattering events and of the intersections with interfaces, can easily result in enormous files. Consider a typical case of scattering in tissue, with a scattering coefficient μ_s of about 10–20 mm^{-1} and a g-factor (average of the cosines of the polar scattering angles) of about 0.80–0.90. Then in each millimeter of the path about $1/\mu_s \approx 10$ scattering events will take place. However, due to the large g-factor, the scattering will be predominantly in the forward direction and it will only be after about $1/\mu_s' \approx 1$ mm that the direction of the photon can be considered as randomized. When detecting reflected photons, the path length of the photons will depend on the distance d between the point of injection of the light in the sample and the point of detection. For homogeneous samples the average depth in the middle of that distance is about $\frac{1}{2}d$, and the average smoothed path length for perpendicular entrance and exit will be $\frac{1}{2}\pi d$. However, the actual paths are very irregular and the actual path lengths can range from about that value to tens or hundreds times as large. This means that, in most cases, the number of scattering events will be very large. As an example, for a thick homogeneous medium with $\mu_s' = 1$ mm^{-1} and without absorption, the average path length will be about $6d$, which for $d = 2$ mm means about 120 scattering events, thus per photon at least 120 × 3 × 4 bytes = 1,440 bytes. A typical simulation needs at least 10^4 photons, and thus in total 1,440 Mbytes. Therefore, in those cases it is better to register only part of the events, namely those at intervals of $1/\mu_s' = 1$ mm, which will decrease the storage space to 144 Mbytes per simulation.

The program therefore offers the options of recording the paths at intervals of $1/\mu_s$ or $1/\mu_s'$.

Photons originating from a pencil beam and emerging at equal distances d from the point of injection but at different positions on that ring are equivalent. However, visualization of those tracks will end up in a bunch that cannot be unraveled. Therefore, to clarify viewing we may rotate the whole paths around the axis of the pencil beam to such an orientation as if the photons all emerged at the same position on the ring, e.g., the crossing point with the X-axis. This particular rotation is given by

$$\begin{pmatrix} x' \\ y' \\ z' \end{pmatrix} = \begin{pmatrix} \cos\varphi & \sin\varphi & 0 \\ -\sin\varphi & \cos\varphi & 0 \\ 0 & 0 & 1 \end{pmatrix} \begin{pmatrix} x \\ y \\ z \end{pmatrix}. \tag{15.106}$$

See Fig. 15.24 for an example of the path tracking method.

15.7 Special Features

We now will describe some special features that are incorporated in the program. Laser Doppler flowmetry is the oldest feature, built in from the beginning of the development of the program, and meant to support measurements
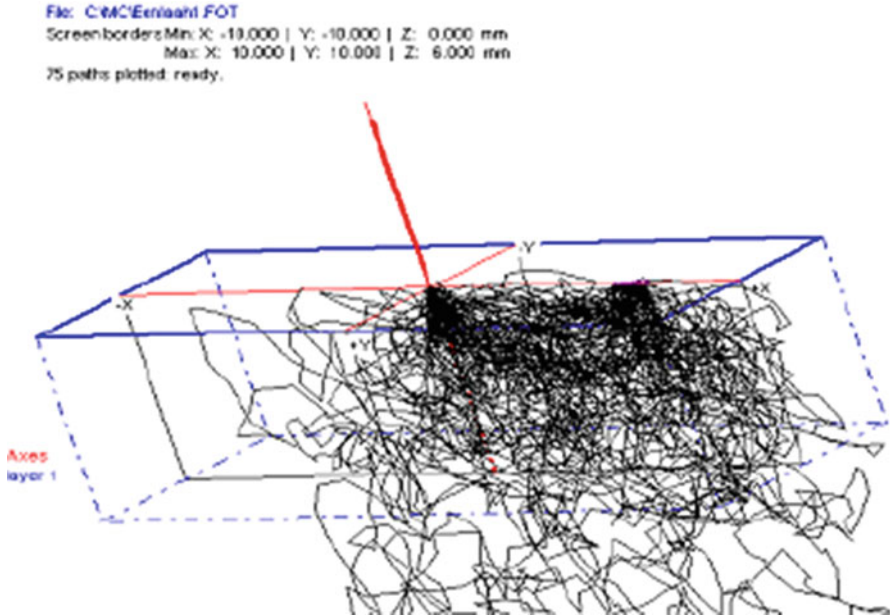
Fig. 15.24 Photon path tracking: Photon "bananas" arise by scattering from beam entrance point to exit area (between 5 and 6 mm). For clarity, all photon paths were rotated afterwards as if the photons had emerged on the +X-axis

of laser Doppler perfusion flowmetry in tissue. Photoacoustics has been added to simulate the acoustic response to pulsed light. Frequency modulation is a modality adding extra information using path length-dependent phase delay information.

15.7.1 Laser Doppler Velocimetry

15.7.1.1 Introduction

Laser Doppler flowmetry (LDF) makes use of the Doppler effect encountered with scattering of photons in particles when those particles are moving. The principles are shown in Fig. 15.25. Using the definitions of the variables given in that figure, the Doppler frequency is given by

$$\omega_D = (\boldsymbol{k}_s - \boldsymbol{k}_0) \bullet \boldsymbol{v} \qquad (15.107)$$

and with

$$|\delta \boldsymbol{k}| = 2k . \sin \tfrac{1}{2}\theta, \qquad (15.108)$$

Fig. 15.25 Principles of laser Doppler flowmetry. The particle has a velocity v. Vectors $\boldsymbol{k}_0$ and $\boldsymbol{k}_s$ denote the incoming and scattered light wave vectors, and $d\boldsymbol{k}$ is the difference vector
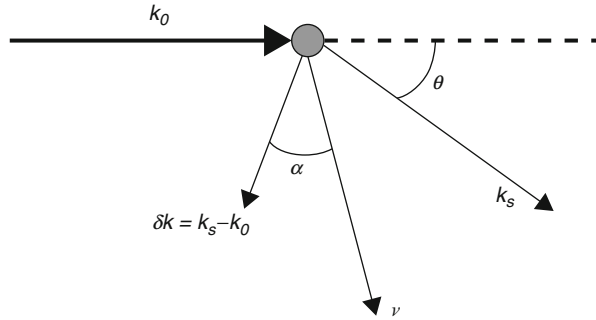
Fig. 15.26 A typical Doppler frequency spectrum as measured with LDF tissue perfusion (positive frequencies shown)
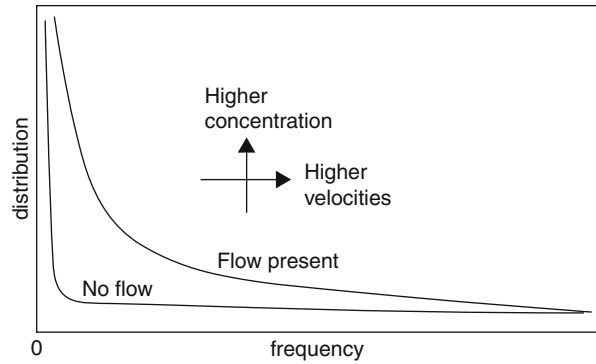
we find

$$f_D = \frac{kv}{\pi} \sin\tfrac{1}{2}\theta. \cos\alpha. \tag{15.109}$$

When applied to tissue, frequently the angles θ and α might be considered randomized. This is due to three reasons:

- Preceding scattering by non-moving particles might cause the direction of the photons to be randomized upon encountering moving particles.
- Most important moving particles are blood cells in capillaries. Due to the (more or less) random orientation of the capillaries, the velocities will have random directions.
- Traveling from injection point to detection point, in general the photons will encounter many Doppler scattering effects, with random velocities and orientations.

All three effects will broaden the Doppler frequency distribution, which ideally would consist of one single peak, to a smooth distribution, as in Fig. 15.26. This means that it is not possible to measure the local velocity, but we only may extract information about the averaged velocity over the measuring volume. The averaging concerns the three effects mentioned above.
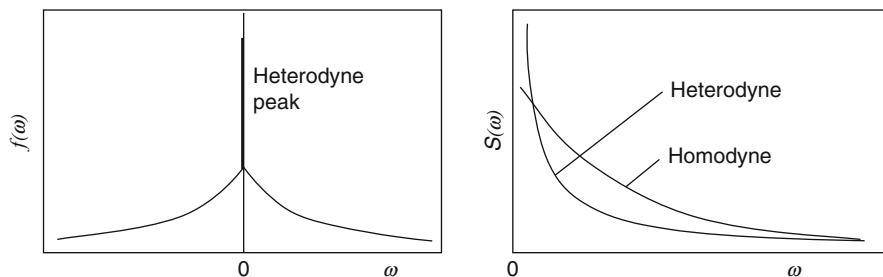
Fig. 15.27 Homodyne and heterodyne frequency spectra $f(\omega)$ and power spectra $S(\omega)$. Normally, the heterodyne peak is much higher than the signals at non-zero frequencies

There are two options to record these LDF-spectra: homodyne and heterodyne, depending on the relative amount of non-shifted light impinging on the detector. The first is the mutual electronic mixing of the Doppler-shifted signals, and the second is the mixing of those signals including mixing with non-shifted light, which can be overwhelmingly present. The resulting frequency and power spectra (which is the autocorrelation function of the frequency spectrum) will look as sketched in Fig. 15.27.

To characterize the frequency spectra use is made of moments of the power spectrum, defined as

$$M_n = \int\limits_0^\infty \omega^n . S(\omega) . d\omega, \tag{15.110a}$$

and the reduced moments

$$M_n{}' = \frac{M_n}{M_0}. \tag{15.110b}$$

The zeroth moment is the area under the power spectrum itself, and can be considered as proportional to the concentration of moving particles in the measuring volume. Bonner et al. [5] showed that the first moment M_1 is proportional to the averaged flow, while the ratio of the reduced moment $M_1{}' = M_1/M_0$ will be proportional to the averaged velocity. Analogously, the reduced moment $M_2{}' = M_2/M_0{}^2$ will be proportional to the average of the velocity-squared.

All three moments may be calculated within the package.

15.7.1.2 Construction of the Doppler Power Spectrum

For the construction [11] of the Doppler power spectrum from the frequency distribution, all photons detected within the detection window will be sorted into a discrete frequency distribution $N(\omega_i)$. Suppose we recorded a_i photons in the i-th spectral interval (width $\Delta\omega = 2\pi\Delta f$). This number is proportional to $I(f_i).\Delta f$, where I is the intensity, which is proportional to $|E^2|$, E being the electric field amplitude.

$$E(t) = \sum_{j=0}^{N} \sqrt{a_j} \exp\left[i(j\Delta\omega.t + \phi_j)\right], \tag{15.111}$$

where $N + 1$ is the number of intervals, and ϕ_j is the phase of the jth component. Since in the experiment we assume all photons to arrive at the same time, coherence between photons in the same frequency interval cannot be excluded. Therefore, ideally $\Delta\omega$ should be so small that the only values for a_j would be 0 and 1. However, to be able to work with tractable summations, a_j is to be read as the probability of the photon to arrive in that interval.

A square-law detector will at time $n\Delta t$ measure a current I proportional to E^*E:

$$i(n\Delta t) = c \sum_{v=0}^{N} \sum_{w=0}^{N} \beta_{vw} \sqrt{a_v a_w} \, \exp\{ i[(w-v)\Delta\omega.n\Delta t + \phi_w - \phi_v]\} + cc,$$

$$\tag{15.112}$$

where c is a proportionality constant, cc stands for complex conjugate (to ensure that i is real), and β is a constant related to the degree of coherence of the signals in the frequency intervals ($\beta = 1$ for perfect coherence, but $\beta < 1$ when the detector area is larger than a single coherence area). Assuming that β is not frequency dependent, one can write

$$I(n\Delta t) = c\beta \sum_{v=0}^{N} \sum_{w=0}^{N} \sqrt{a_v a_w} \, \exp\{ i[(w-v)\Delta\omega.n\Delta t + \phi_w - \phi_v]\} + cc. \tag{15.113}$$

Now we rename $v = p$, and define $k = w - v$ and the factor f_{pk} as

$$f_{pk} = c\beta \sqrt{a_p a_{p+k}} \, \exp\left[i\left(\phi_{p+k} - \phi_p\right)\right] \tag{15.114}$$

and find

$$I(n\Delta t) = \sum_{p=0}^{N} \sum_{k=0}^{N-p} f_{pk} \, \exp(i\Delta\omega.n\Delta t) + cc. \tag{15.115}$$

The Fourier transform $S(t)$ of the power spectrum $S(\omega)$, defined as

$$S(t) = <i^*(0).i(t)>, \tag{15.116}$$

can be written as

$$S(m\Delta t) = \frac{\Delta t}{N - m + 1} \sum_{n=0}^{N-m} I(n\Delta t) \, I((n+m)\Delta t), \tag{15.117}$$

with $\Delta\omega = 2\pi/[(N + 1).\Delta t]$. We construct the power spectrum $S(j\Delta\omega)$ using

$$S(j\Delta\omega) = \sum_{m=0}^{N} S(m\Delta t) \, \exp(-ij\Delta\omega.\Delta t), \tag{15.118}$$

and find

$$S(j\Delta\omega) = \sum_{m=0}^{N}\sum_{n=0}^{N-m}\sum_{p=0}^{N}\sum_{k=0}^{N-p}\sum_{p'=0}^{N}\sum_{k'=0}^{N-p}\frac{\Delta t}{N - m + 1}$$

$$\times \begin{bmatrix} f_{pk}.f_{p'k'}. \, \exp\{i\Delta\omega\Delta t[kn + k'(n + m) - mj]\}+ \\ f_{pk} * f_{p'k'} * . \, \exp\{-i\Delta\omega\Delta t[kn + k'(n + m) + mj]\}+ \\ f_{pk}.f_{p'k'} * . \, \exp\{i\Delta\omega\Delta t[kn - k'(n + m) - mj]\}+ \\ f_{pk} * f_{p'k'}. \, \exp\{-i\Delta\omega\Delta t[kn - k'(n + m) + mj]\} \end{bmatrix}. \tag{15.119}$$

Now, in the limit of $N \to \infty$, the phase factors will average out, except when their exponentials equal zero. Inasmuch as the sum $n + m$ appears in each exponential, in order to have the exponential equal zero for each combination of n and m, the variables n and m must not be present in the exponentials. This is possible only in the last term, under the condition that $k = k' = j$:

$$S(j\Delta\omega) = \sum_{m=0}^{N}\sum_{n=0}^{N-m}\sum_{p=0}^{N}\sum_{k=0}^{N-p}\sum_{p'=0}^{N}\sum_{k'=0}^{N-p'}\frac{\Delta t}{N - m + 1} \, f_{pk} * f_{p'k'} \, \delta(k - k') \, \delta(k - j). \tag{15.120}$$

Since $0 \leq k \leq N - p$, with $k = j$, it follows that $N - p \geq j$ or $p \leq N - j$. Then

$$S(j\Delta\omega) = \sum_{m=0}^{N}\sum_{n=0}^{N-m}\sum_{p=0}^{N-j}\sum_{p'=0}^{N-j}\frac{\Delta t}{N - m + 1} \, f_{pj} * f_{p'j} = \sum_{p=0}^{N-j}\sum_{p'=0}^{N-j} 2\pi \frac{f_{pj} * f_{p'j}}{\Delta\omega} \tag{15.121}$$

and

$$S(j\Delta\omega) = 2\pi \frac{c^2\beta^2}{\Delta\omega} \sum_{p=0}^{N-j}\sum_{p'=0}^{N-j} \sqrt{a_p a_{p'} a_{p+j} a_{p'+j}} \, \exp\left[i\left(\phi_p - \phi_{p'} + \phi_{p'+j} - \phi_{p+j}\right)\right]. \tag{15.122}$$

Now, suppose that all photons arrive at the detector with equal phases. Then the exponential in (15.122) becomes zero, and

$$S(j\Delta\omega) = 2\pi \frac{c^2\beta^2}{\Delta\omega} \left[\sum_{p=0}^{N-j} \sqrt{a_p a_{p'}} \right]^2. \tag{15.123}$$

However, in general, the photons will have different phases due to their different path lengths. The measured power will be the expectation value of (15.122) averaged over all phases. Thus, for the term in (15.122) with p and p', the expectation value will be zero unless $p = p'$. This leads to

$$S(j\Delta\omega) = 2\pi \frac{c^2\beta^2}{\Delta\omega} \sum_{p=0}^{N-j} \sqrt{a_p a_{p+j} a_p a_{p+j}} = 2\pi \frac{c^2\beta^2}{\Delta\omega} \sum_{p=0}^{N-j} a_p a_{p+j}. \tag{15.124}$$

This is the general expression for the calculation of the power spectrum from the simulated frequency distribution.

In the case of heterodyne detection, where one of the spectral components (normally that at zero frequency, set $p = 0$ for that frequency) is much more intense than all others, (15.123) and (15.124) will lead to the same result:

$$S(j\Delta\omega)_{het} = 2\pi \frac{c^2\beta^2}{\Delta\omega} a_0 a_j. \tag{15.125}$$

15.7.1.3 Implementation of Velocity Profiles

For the velocity profiles of the scattering particles, the following options are available:

- Velocity direction along X-, Y-, or Z-axis, or (in case of oblique blocks) along the block axis.
- Velocity direction randomized for each scattering event, with all particles equal velocities. The direction is determined with a similar procedure as with isotropic injection of light (see Sect. 15.5.4).
- Profiles can be uniform (equal velocity for all particles), or parabolic (in tubes and rectangular blocks only), or they can have a Gaussian distribution.
  With the parabolic distribution the actual velocity is calculated according to

$$v = 2v_0 \left(1 - \frac{r^2}{R^2} \right) \tag{15.126}$$

with v_0 as the average velocity value over the profile, r as the position of the particle with respect to the symmetry axis of the tube or block, or the mid-plane of the layer when relevant, and R as the radius of the tube, or the distance between the adjacent interfaces.

Fig. 15.28 Bipolar PA pulse response: function $P = x \cdot \exp(-x_2/x_0)$, with $-10 < x < 10$ and $x_0 = 5$
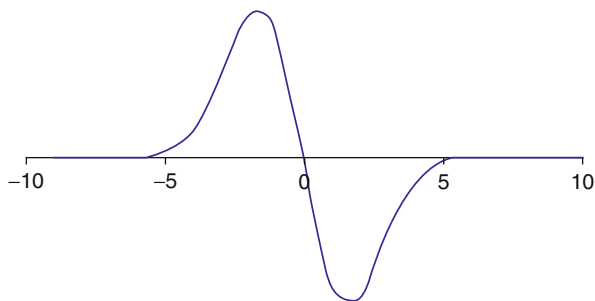
The Gaussian profile is handled using a cumulative function for the Gaussian profile. Here, the standard deviation is expressed as a percentage of v_0, being the maximum velocity in the profile. The actual value of the velocity is determined by equaling a fresh random number to that cumulative function.

15.7.2 Photoacoustics

With photoacoustics (PA) short light pulses are injected in the sample. At positions where absorbing particles are present, part of the light will be absorbed. Due to the short duration of the pulse, the particle will heat up adiabatically. Normally, this would result in volume dilatation, but since the surrounding medium is not heated, this dilatation will be prevented and a pressure shock wave will result. Some authors have investigated this mechanism. A review and some new theoretical aspects can be found in Hoelen's thesis and papers [25–28].

Typical values for the duration (FWHM) of the light pulses and the amount of energy to be injected are 15 ns and 1 mJ/cm^2. With these values, a safety factor of 20 from the European maxima for human tissue irradiation with this type of light pulses is maintained. Using a sound velocity of 1,500 m/s, this corresponds to a distance of 22.5 μm.

The PA response of a spherical source on a short laser pulse is given by:

$$P(r, t) = C \frac{v^2}{r} \left(t - \frac{r}{v} \right) \exp \left\{ - \left[\frac{v}{r_0} \left(t - \frac{r}{v} \right) \right]^2 \right\},$$ (15.127)

with r as the distance from PA source to the detector, r_0 as the source radius, t as the time after the pulse, and v as the acoustic velocity. Since for the calculations in this program we only have to deal with relative values, we have incorporated variables describing the dilatation, the heat capacity and the heat conduction of the source, and the laser pulse energy in the constant C.

This function is a bipolar function, as in Fig. 15.28.

We suppose that the sample can be subdivided into many 3D-voxels, which may serve as elementary PA sources, provided light absorbing material is present.

The voxels are supposed to be cubical, with sides da. It can be shown that the peak-peak time, i.e., the time τ_{pp} between the positive and negative peak of the bipolar pulse, is given by

$$\tau_{pp}{}^2 = (2\sigma)^2 = (2\sigma_l)^2 + (2\sigma_s)^2 = 2\tau_e{}^2, \qquad (15.128)$$

where σ_l is the standard deviation of the laser pulse, σ_s is that of the source voxel, σ is that of the bipolar pulse, and τ_e is the effective pulse length. The value of σ_l is given by FWHM/[2 $\sqrt{(2.\ln2)}$], with FWHM as the full width at half maximum of the (Gaussian) laser pulse. For a cubical voxel, σ_s is given by $\sigma_s = da/(2\sqrt{2}.v)$, with $da/\sqrt{2}$ as the effective diameter of the heat source element.

The expression for the pressure given by (15.127) has to be adapted for ultrasound attenuation during the time-of-flight to the detector. This will result in the corrected pressure pulse $P'(r, t)$:

$$P(r,t) = C \frac{v^2}{r}\left(t - \frac{r}{v}\right) \exp\left\{-\left(\frac{t - r/v}{\tau_e}\right)^2\right\} \cdot \exp(-\mu_{US}.r), \qquad (15.129)$$

where μ_{US} is the ultrasonic attenuation coefficient. This coefficient is slightly dependent on the ultrasound frequency. Here we take it as a constant, in view of the broad frequency bandwidth of the PA pulse.

This function has been implemented in the program, with $C = 1$. The pressure pulse is calculated as originating from the center of the source voxel and arriving at the centers of the elements of the detector array. Therefore, the resulting pressure signal has to be multiplied with the area of the detector element, and normalized to the volume of the voxel. However, in reality with elements that are not small, due to phase differences upon arrival of the pressure pulse at different positions on a detector element, some destructive interference might be present, which will decrease the multiplication factor. We may correct for this effect in two ways:

- The detector elements are first chosen very small (i.e., much smaller than the wavelength of the sound) and are afterwards grouped to larger detector elements, taking into account for each voxel the phase differences between the center points of the constituting elements in the group.
- The contribution from individual PA sources to individual detector elements is corrected using the Directivity, or the Numerical Aperture function, of the detector element. Normally, this is a Gaussian function, centered along the symmetry axis perpendicular to the element, with a certain opening angle given by the dimensions of the element and the characteristics of the laser pulse.

In the program both methods are implemented. For the Directivity, a Gaussian, uniform, or triangular function can be chosen. The groups are built from rectangles of single elements. See Fig. 15.29.

""" PHOTO-ACOUSTIC RESPONSE ; File: ABS19141 """
Plot normalized on absolute maximum: 1.403E-05
Signal Min: -1.161E-05 Max: 1.403E-05
Time window: -53.3 .. 3000.0 = 3053.3 ns ; start shift: 0.0 ns
Depth : -0.080 .. 4.500 = 4.580 mm .. 0.000 mm

Detectors : (X,Y)-groups: (1,1) ... (7,7)
... X-positions: -5.000 .. 5.000 mm ; 0.400 mm/det
... Y-positions: -5.000 .. 5.000 mm ; 0.400 mm/det
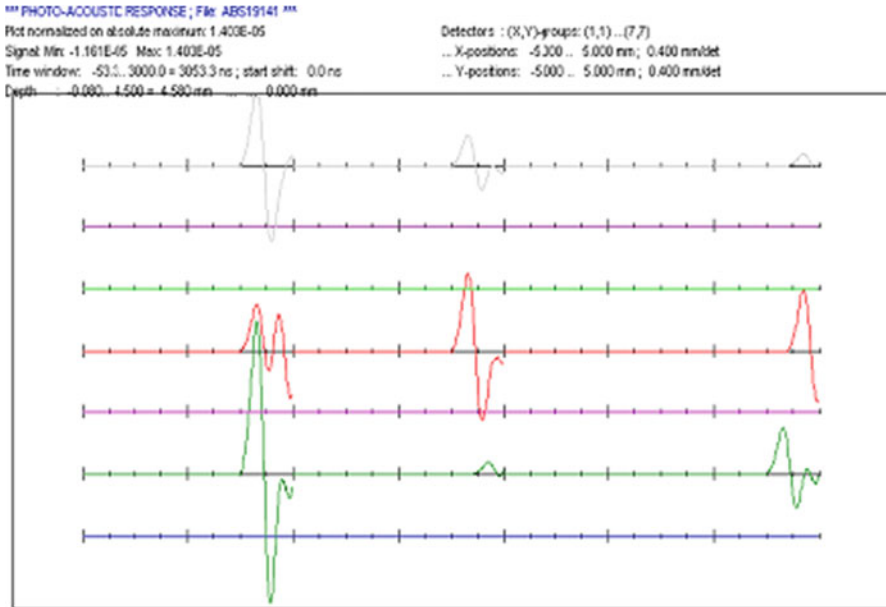
Fig. 15.29 Photoacoustic response at a 7×7 detector array of a sample consisting of several absorbing objects in a scattering (but not absorbing) medium

15.7.3 Time-of-Flight Spectroscopy and Frequency Modulation

A relatively new branch of the art of light scattering in tissue is time-of flight resolved scattering. The general idea is to distinguish between photons on the basis of their paths in tissue. This can be of help to elucidate the distribution of the optical properties, for instance, when dealing with samples consisting of various layers.

There are two main methods:

- Time-of-flight spectroscopy, in which the photon paths are registered using time-resolved detection, e.g., with ps- or fs-lasers and an ultrafast camera like a streak camera, or by using ultrafast time-windowing using Kerr's cells. A typical time is 3 ps for 1 mm resolution (light velocity $= 3 \times 10^8$ m/s).
- Frequency modulation spectroscopy, where the light source is modulated at very high frequencies, and the phase differences are recorded between photons arriving at the same detection point but after having traveling over different paths. The frequency range in use starts at 100 MHz and currently stops at about 1–2 GHz. For 100 MHz a path length difference of 1 mm will result in a phase difference of about 0.1°.

The first option of *time-of-flight spectroscopy* has been taken care of in two ways:

- By implementing the possibility to register the positions of the photons at certain presentable time points during the scattering process.

- Using the option of analyzing the registered time-of-flight distributions, which can be calculated from the simulated paths lengths (geometrical or optical) of the detected photons.

The second option of *frequency modulation spectroscopy* uses simple Fourier transformation of the path length distribution. For this purpose, the path length distribution is translated into a time-of-flight distribution, using the local light velocities. The Fourier transform of this distribution will result in the frequency response. When denoting that Fourier transform with $F_j(\omega)$, we can deduce for the phase delay $\varphi_j(\omega)$ and the AC/DC modulation depth $m_j(\omega)$:

$$\varphi_j(\omega) = \arctan\frac{\mathrm{Im}F_j(\omega)}{\mathrm{Re}F_j(\omega)} \quad \text{and} \quad m_j(\omega) = \sqrt{\frac{\mathrm{Im}^2F_j(\omega) + \mathrm{Re}^2F_j(\omega)}{\mathrm{Re}^2F_j(0)}}. \quad (15.130)$$

For the actual transform we may use the possibility of enlarging the number of points n in the time-of-flight distribution to an integer power of 2, named N, by filling the new points with zeros. Then fast Fourier transform algorithms will become possible. In doing this, the step size in the frequency spectrum will be smaller. When the time step in the time-of-flight distribution is given by Δt, then the maximum frequency is $f_{max} = 1/(2\Delta t)$ and the frequency step is $\Delta f = f_{max}/(\frac{1}{2}N) = 1/(N.\Delta t)$. This factor 2 is included due to the aliasing effect of this type of Fourier transform, by which the frequency spectrum ($f = 0\ldots f_{max}$) is folded out and copied to $f = f_{max}\ldots 2f_{max}$.

The program also offers facilities to calculate frequency modulation spectra using literature models, based on the diffusion approximation of the radiative transfer equation, from Haskell et al. [8] for one-layer samples and Kienle et al. [9, 10] for two-layer samples. Here we only list their results as far as implemented in the program.

We will use the notation (μ_a and μ_t are the absorption and total attenuation coefficients: $\mu_t = \mu_a + \mu_s'$, and ω is the frequency):

$$k_R = \mathrm{Re}(k) = K(1); \quad k_I = \mathrm{Im}(k) = K(-1),$$
$$K(p) = \sqrt{\frac{3}{2}\mu_a\mu_t}\sqrt{\sqrt{1 + \omega^2 t^2} + p}. \quad (15.131)$$

For small frequencies these functions can be approximated by

$$k_R = \sqrt{3\mu_a\mu_t}\left[1 + \tfrac{1}{8}\omega^2\tau^2\right]; \quad k_I = \tfrac{1}{2}\sqrt{3\mu_a\mu_t}\omega\tau; \quad \tau = \frac{1}{\mu_a c/n}.$$

Haskell et al. calculated five models, (a) through (e), for the one-layer case, and Kienle et al. added a general model (f) for the two-layer case. These models are implemented in the program.

(a) Infinite medium.

$$\Delta\varphi = k_I r; \quad m = \exp\left[-\left(k_R - \sqrt{2}q\right)r\right], \tag{15.132a}$$

where r is the source-detector distance and $q = \sqrt{(3\mu_a\,\mu_t/2)}$.

Using (15.131), we may see that for small frequencies $\Delta\varphi$ will start linear with ω and m will start as a (slowly decreasing) constant. When ω increases, the slope of $\Delta\varphi$ will decrease gradually and the value of m will decrease as well.

(b) Semi-infinite medium, taking refractive index differences at the interface into account:

$$\Delta\varphi = k_I r - \arctan(I/R); \quad m = (1/D).\sqrt{I^2 + R^2} \tag{15.132b}$$

with D, I and R complicated functions of r, μ_a, μ_t and of the refractive indices and the refraction angles.

(c) Semi-infinite medium, without interface correction.

$$\Delta\varphi = k_I r - \arctan\frac{k_I}{k_R + 1/r_0};$$
$$m = \frac{\sqrt{(k_R + 1/r_0)^2 + k_I^2}}{\sqrt{2}q + 1/r_0}\;\exp\left[-\left(k_R - \sqrt{2}q\right)r_0\right] \tag{15.132c}$$

with $r_0^2 = r^2 + (1/\mu_t)^2$.

(d) Extrapolated boundary condition, where the interface has been shifted over a distance dependent on the refractive indices at the interface (see Haskell et al. [8] for this and the following models).

(e) Partial current and extrapolated boundary unification.

(f) Two-layer model (Kienle et al. [9, 10]).

15.8 Output Options

The program offers several possibilities for output of the data. Apart from various ways to write photon data and corresponding statistics to file, we have several plot options. They will be described below. All plots can be exported in the form of *.BMP-files.

15.8.1 Parameter Plots

The fastest way of plotting data is to use parameter plots of photon distributions, in which the number of photons is plotted as a function of one out of a set of variables. These variables are:

(a) X-, Y-, or R-position at detection or at plane-crossings (see below; R is the radius of the circle around central Z-axis),
(b) (R-position)^2 (as above),
(c) Path length or time-of-flight distribution, followed by phase and modulation depth spectra using frequency modulation spectroscopy,
(d) Polar angle θ or azimuthal angle φ of the photon direction at the detection point,
(e) Z-position: several options (the averaging $<..>$ is performed over all detected photons):
   • Depth (in absorption mode or with photons-in-flight at plane-crossing points)
   • $<$Scattering depth$>$ (in reflection or transmission mode)
   • Maximum scatter depth
   • $<$Doppler scattering depth$>$ (Doppler-scattering events only)
(f) Number of scatter events (or number of plane crossings)
(g) Number of Doppler scatter events
(h) Doppler frequency
(i) With Internal detection: polar and azimuthal angles θ and φ
(j) Paths: crossings with X = c planes
(k) Paths: crossings with Y = c planes
(l) Paths: crossings with Z = c planes
(m) Paths: crossings with R = c (cylindrical) planes

15.8.1.1 Intensity Plots

Normally we may choose for plotting of photon distributions, as a function of one of the variables. However, in case the variable is R or R^2 we have the option for plotting the intensity instead, thus dividing distribution function by $2\pi R.dR$, with dR as the interval width of the horizontal variable.

We also have the option of comparing simulated intensity plots with theoretical ones. Several models are available for that purpose. See Sect. 15.8.4.1 and Fig. 15.30.

15.8.1.2 Parameters

In addition to their role as horizontal variables in the distribution plots, all variables may also be used as parameters in the plots. For instance, suppose we divide the value region of a parameter into n intervals. This will result in n lines in the plot.

There are two layers of parameters: the first offers the option of shifting the lines horizontally over a certain value, the second, vertically. We also may choose the option "Compare Files," by which different files (simulations) can be compared directly, as the second parameter.

15.8.1.3 Plane-Crossing Intersections

With the option "path tracking," the intersection points of the photon paths on their travel from source to detection point, with a set of planes perpendicular to the direction of the photons as seen at the surface, are recorded. The average coordinates of those intersections are calculated.
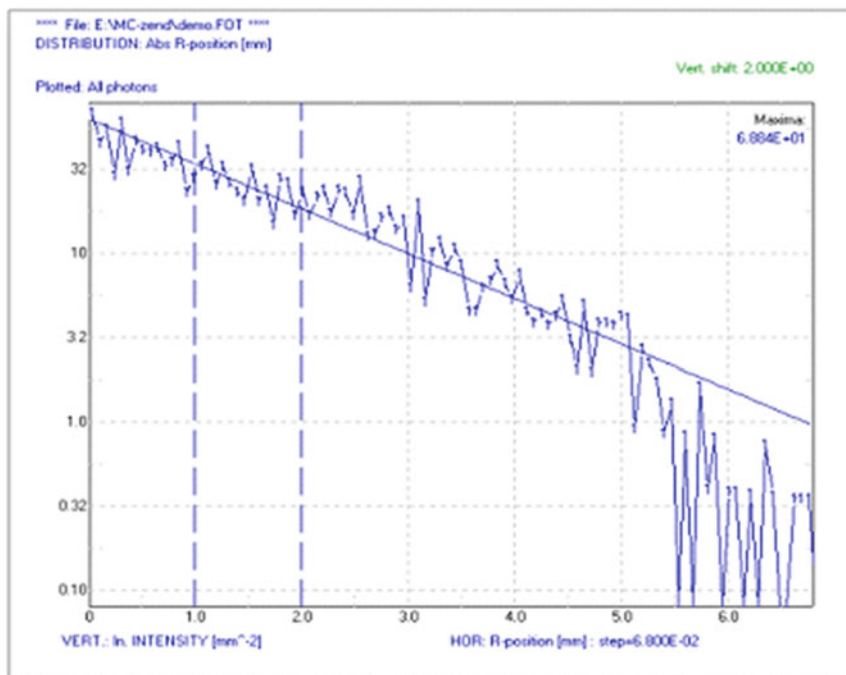
Fig. 15.30 Example of output plots. Here ln (Intensity) vs. R-position from the Z-axis. Also included: a model approximation (*solid line*)

For instance, when photons are tracked, for which the detection point lies at the surface on the X-axis, the crossing planes are defined parallel to the X-axis, ranging from the injection point to the detection point, and the Y- and Z-coordinates of those intersection points are recorded and (afterwards) averaged. This might be clarified with Fig. 15.31. Results are presented in Fig. 15.32.

In order to enhance the efficiency of the simulation process, photons emerging at positions with equal radii to the injection point might be taken together by rotating the whole path until an orientation as if the photon were emerging at that radius on the X-axis. See Sect. 15.6.4.

The options for crossing planes are flat planes perpendicular to the X- and Y-axis, and cylindrical planes around the central Z-axis at the injection point. All plots can be made on a linear or logarithmic scale, and in the form of lines or symbols or both. We may choose quadratic smoothing for the option of *n*-points.

15.8.1.4 Normalization

The plots may be normalized on their own maximum, or on the highest maximum of the set, or on the maximum of the first curve. We also may normalize on the number of detected, or injected or emitted, photons.
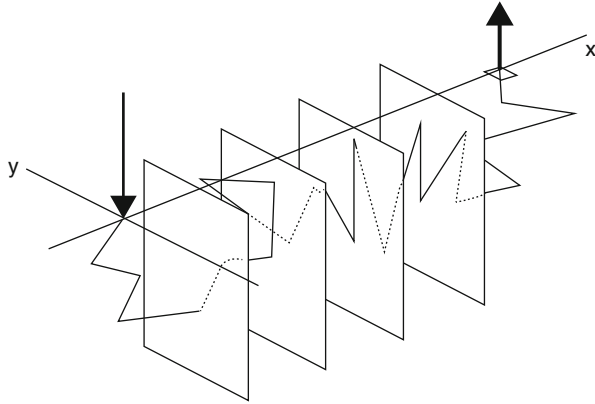
Fig. 15.31 Example of recording of path tracking of the photons, in which the photons are meant to emerge through a small window at the X-axis. The arrows indicate the injection and detection points. For analysis, we define a set of planes perpendicular to the X-axis and record the Y- and Z-coordinates of the intersections. Since photons can take steps in all directions, they might cross some planes more than once
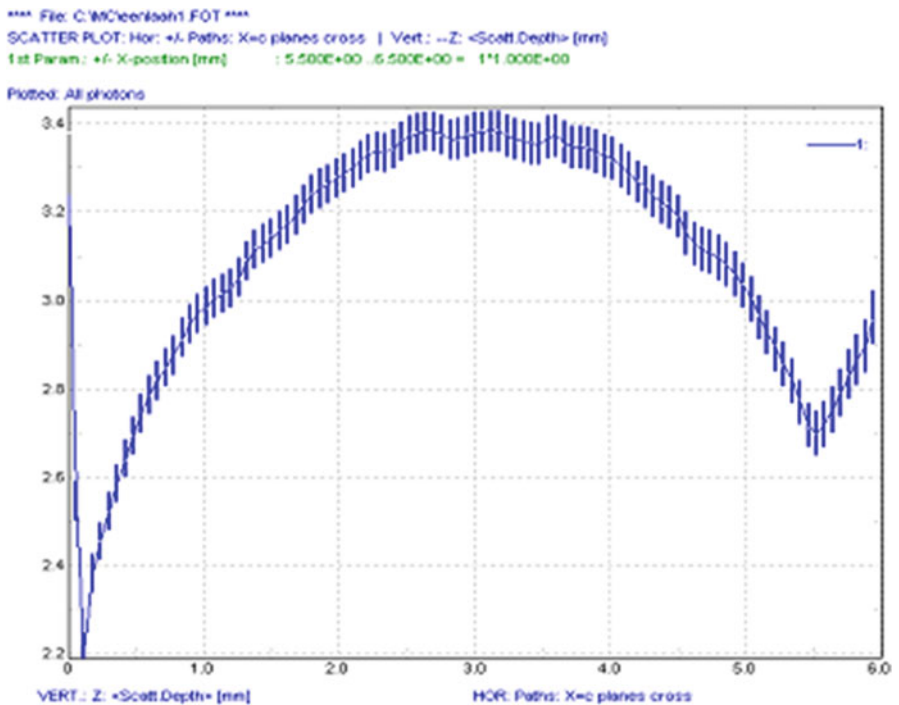
Fig. 15.32 Paths tracking: Averaged depths of photons, emerging between 5 and 6 mm from source origin, with standard deviation in the average. Settings: reduced scattering coefficient = 1/mm; absorption = 0. Plot for distance >5.5 mm is due to spurious photons
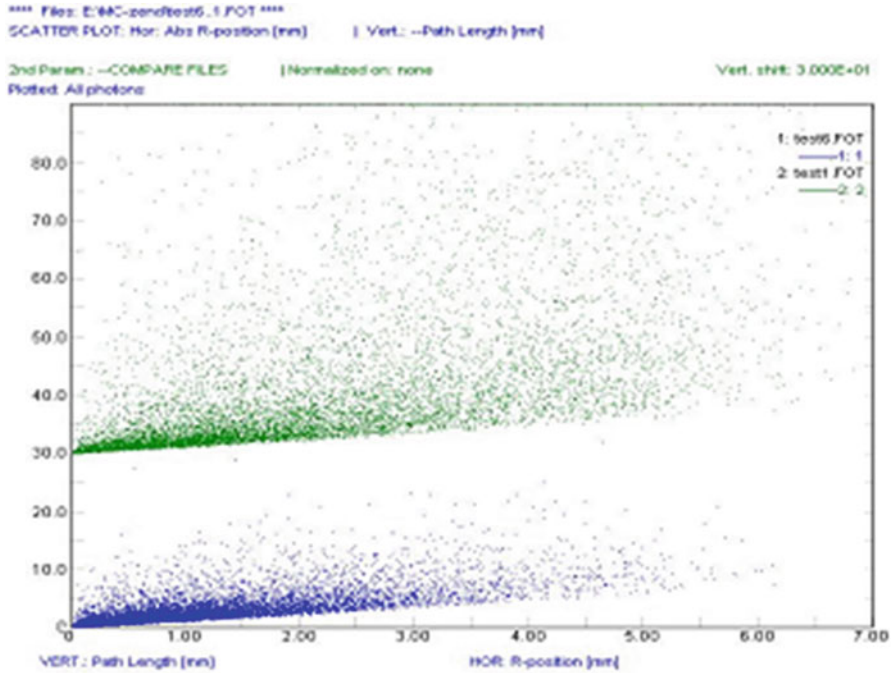
Fig. 15.33 Scatter plots of two samples, consisting of 1 layer with $\mu_s' = 1$ mm^{-1}; $\mu_a = 0$ (*upper*) and 0.1 (*lower*) mm^{-1}, respectively. Plotted: Path length vs. detection position. In both cases, 10,000 photons recorded. Higher absorption results in a broader path length distribution

15.8.1.5 Doppler Frequency Handling

The distributions as a function of the Doppler frequency, the frequency distribution, may be converted into "power spectra" using the formalism described in Sect. 15.7.1.2. From those spectra we may have the program calculate the moments of the power spectrum, as discussed in Sect. 15.7.1.1.

15.8.2 Scatter Plots

In addition to the distribution and intensity plots as described above, an option of producing scatter plots exists, in which the values of a second variable are on the vertical axis. The individual photons can be plotted as points, or their average values (per X-axis interval) as symbols or lines.

Again we have the opportunity to divide the set of points in subsets corresponding with different values of (two) parameters. The points belonging to different parameters are presented as two spatially separated clusters. We also may choose horizontal or vertical shifting per parameter value. See Fig. 15.33.
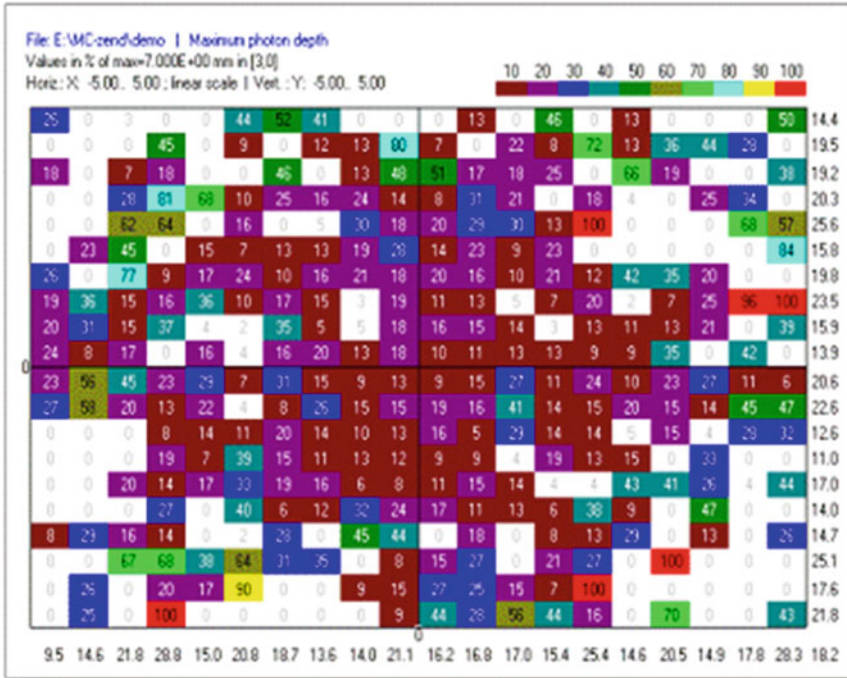
Fig. 15.34 Example of 2D-plot: Here the maximum photon depth plotted as function of (x, y)-position

15.8.3 2D/3D-plots

Another plot option is to produce 2D- or 3D-plots, based on the border values (see Figs. 15.34 and 15.35).

15.8.4 Approximations

As a final step in the simulations, one may want to compare the simulated results with theoretical curves. For this purpose we included several options in the program. The first option is to compare intensity data with published results of theoretical models based on the diffusion approximation. The second is to fit Doppler power spectra with exponential curves.

15.8.4.1 Intensity Approximations

In the literature, several approximate curves for the intensity as a function of the source-detector distance were investigated. Most important are those of Groenhuis and Ten Bosch [4], Bonner et al. [5], Patterson et al. [6], and Farrell et al. [7]. Here we will deal with those models and give their results.

PATH CROSSINGS [%] | −3.000<length < 3.000| 0.000<width/depth < 2.000| All photons
Values: 100 % = 2.340E+02 in plane: 5 ; this screen max = 5.600E+01

10 20 30 40 50 60 70 80 90 100

| Plane: | 0 | 1 | 2 | 3 | 4 | 5 |
| Coord.[mm]: | 0.500 | 1.000 | 1.500 | 2.000 | 2.500 | 3.000 |
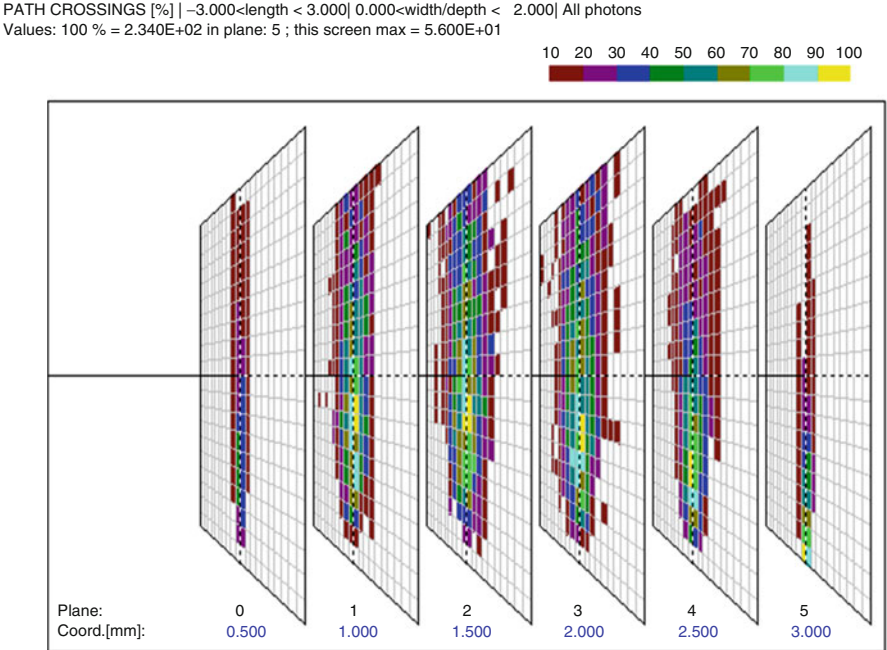
Fig. 15.35 3D-plot of path tracking: photon "bananas": average depths of photon paths. Entrance at position 0; photons emerging between positions 5 and 6 mm from entrance. Normalization per frame

Ishimaru [2, 3] notes for the light output as a function of the source-detector distance r:

$$I(r) = \frac{P\mu_{eff}^2}{4\pi\mu_a r^n}\,\exp(-\mu_{eff}.r), \qquad (15.133)$$

where $I(r)$ is the energy fluence rate (in W/m^2) or the photon fluence rate (in m^{-2} s^{-1}), depending on the definition of P, being the injected power (in W) or the number of injected photons (in s^{-1}), n is an exponential depending on the underlying physical model, and μ_{eff} is a characteristic effective attenuation coefficient, given by

$$\mu_{eff} = \sqrt{3\mu_a(\mu_a + \mu_s')}. \qquad (15.134)$$

There is some dispute about the value of the variable n. According to the diffusion approximation, n should be unity. However, Groenhuis et al. [4] arrive at $n = \frac{1}{2}$, on the basis of a simple scattering model consisting of a combination of an isotropic scattering term and a forward-scattering term. Bonner et al. [5]

use a probabilistic lattice model and derive an expression with $n = 2$. Using an expression for the time-of-flight intensity for homogeneous slab samples, Patterson et al. published a model containing effective light sources at depths $z_0 + k.d$ (d = sample thickness; $k = 1,2\ldots$) together with negative image sources at $-(z_0 + k.d)$ to ensure zero light flux at the surface:

$$I(r) = c\left[\sqrt{\frac{\pi}{a_+}}\exp\left(-2\sqrt{\mu_a a_+}\right) + \sqrt{\frac{\pi}{a_-}}\exp\left(-2\sqrt{\mu_a a_-}\right)\right], \qquad (15.135a)$$

where

$$a_\pm = \frac{(z \pm z_0)^2 + r^2}{4D}, \quad D = \frac{\mu_a}{\mu_{eff}^2}, \qquad (15.135b)$$

with D being a diffusion constant, and $z_0 = 1/\mu_s'$.

However, when integrating this function over volume, two singularities arise, at $z = \pm z_0$. This problem was tackled by Rinzema and Graaff [29], who included non-scattered photons. This leads to a change:

$$I(r) = \frac{P}{4\pi Dr}\exp(-\mu_{eff}.r) \quad \rightarrow$$
$$\frac{P}{4\pi}\left[\frac{a'}{D_a r}\exp(-\kappa_0 r) + \frac{1}{r^2}\exp(-\mu_t r)\right], \qquad (15.136a)$$

and it is seen that, as in Bonner's model, a term with $n = 2$ is present. In (15.136a) $\mu_t = \mu_s + \mu_a$, $a' = \mu_s/\mu_t$ (albedo) and $D_a = \mu_a/\kappa_0$, with κ_0 is the positive root of

$$a'.\arctan(\kappa_0/\mu_t) = \kappa_0/\mu_t. \qquad (15.136b)$$

The model of Patterson et al. was extended by Farrell et al. [7], who, starting byassuming an effective source at $z = z_0 = 1/(\mu_a + \mu_s')$ (with corresponding negative image source at $-z_0$), calculated the photon current leaving the tissue as the gradient of the fluence rate at the surface times D, and arrived at

$$I(r) = \frac{1}{4\pi}\sum_{k=1,2} z_{0k}\left(\mu_{eff} + \frac{1}{r_k}\right)\frac{\exp(-\mu_{eff}r_k)}{r_k^2} \qquad (15.137a)$$

with

$$r_1 = \left[(z - z_0)^2 + r^2\right]^{\frac{1}{2}}; \quad r_2 = \left[(z + z_0 + 2z_b)^2 + r^2\right]^{\frac{1}{2}} \qquad (15.137b)$$
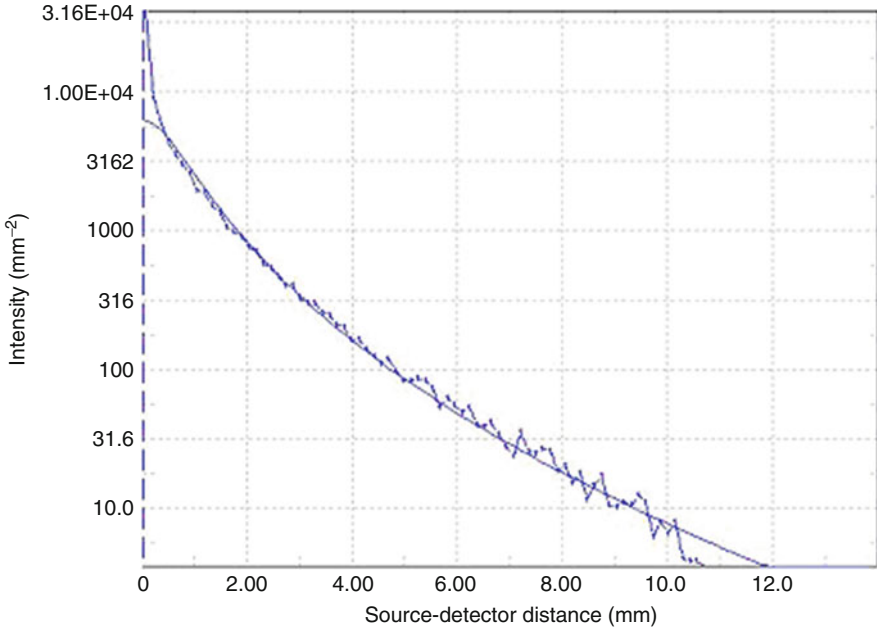
Fig. 15.36 Comparison of the Farrell model with simulations, for a one-layer semi-infinite sample with $\mu_s' = 1$ mm^{-1} and $\mu_a = 0.01$ mm^{-1}. In simulations: Henyey-Greenstein phase scattering function, $g = 0.90$. Detected photons: 50,000. Detection window radius: 0–12 mm. Ratio of reflected vs. injected photons: in the simulation: 0.748, in the model: 0.749. At small r-values deviations occur due to the limited applicability of the diffusion approximation in that region

The depth correction z_b arises from taking refractive index mismatch at the surface interface into account [4, 30]

$$z_b = 2AD; \quad A = \frac{1 + r_d}{1 - r_d} \tag{15.137c}$$

and

$$r_d = -1.440 n_{rel}^{-2} + 0.710 n_{rel}^{-1} + 0.668 + 0.0636 n_{rel}. \tag{15.137d}$$

An example of the Farrell model is given in Fig. 15.36, in which a Monte Carlo simulation for a typical situation is compared.

This model is implemented in the program, together with the simple model given in (15.133), for different values for n.

Farrell et al. also extended the model given above by assuming that the effective source extends along the Z-axis, obeying a Lambert-Beer-like attenuation law with $\mu_a + \mu_s'$ as the attenuation coefficient, but this results in expressions that are not very tractable.

Fig. 15.37 Comparison of the ratio of reflected vs. injected photon numbers, calculated with the Farrell model and with Monte Carlo simulations. *Upper panel*: varying absorption coefficient μ_a; $\mu_s = 10.4$ mm^{-1}; $g = 0.90$; $\mu_s' = 1.04$ mm^{-1}. *Lower panel*: varying reduced scattering coefficient μ_s'; $g = 0.90$; parameter: μ_a [mm^{-1}]. Here the difference for zero absorption and low scattering may be caused by the limited thickness of the sample (65 mm)
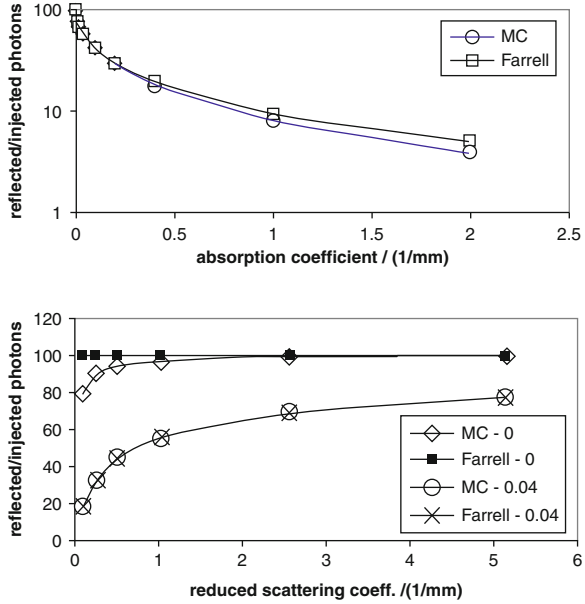
15.8.4.2 Total Reflection

The approximations given above can be integrated over the surface, using

$$I_{total} = \int_0^\infty I(r).2\pi r.dr \tag{15.138}$$

and this will lead to

$$I_{total} = c \ (\pi/\mu_{eff})^{\frac{3}{2}}; \quad = c \ 2\pi/\mu_{eff}; \quad = \infty \quad \text{for } b = \frac{1}{2}; \ 1; \ 2 \tag{15.139a}$$

and for the Farrell model

$$I_{total} = \tfrac{1}{2} \, Pa' \, \exp(-\mu_{eff} z_0)\left[1 + \exp\left\{-\tfrac{4}{3}A \, \mu_{eff} z_0\right\}\right] \tag{15.139b}$$

with a' as the reduced albedo: $a' = \mu_s'/(\mu_a + \mu_s')$. It turns out that the correspondence of the Farrell model with simulated data, for values of the optical constants typical for tissue, is rather satisfactory. This is reflected in Fig. 15.37, where the ratios of reflected and injected photons in the simulation and in the model are compared.

Table 15.1 Moments of Lorentzian and Gaussian Power Spectra (after integration over ω from 0 to ∞)

Model	M_0	M_1	M_2	M_1/M_0	$\sqrt{(M_2/2\,M_0)}$
Gaussian	$\frac{1}{2}\,s\sqrt{\pi}$	$\frac{1}{2}\,s^2$	$\frac{1}{4}\,s^3\sqrt{\pi}$	$s/\sqrt{\pi}$	$\frac{1}{2}\,s$
Lorentzian	s	s^2	$2\,s^3$	s	s

15.8.4.3 Doppler Power Spectrum Approximations

In Sect. 15.7.1, the option of including particle velocities, leading to Doppler frequency spectra, was treated. In Sect. 15.8.1, the possibility for calculating the moments of the Doppler power spectra was mentioned.

The program offers the option of fitting those spectra with predefined functions, since Bonner et al. [5] showed that sometimes these spectra might correspond to simple Lorentzian or Gaussian time functions.

For a *Gaussian* function, suppose the frequency distribution $f(\omega)$ looks like

$$f(\omega) = \exp(-\omega^2/s^2), \tag{15.140a}$$

as is known with interval $\Delta\omega$, then the homodyne power spectrum (for $\omega \geq 0$ only!) will have the form

$$S(\omega) = \sqrt{\frac{1}{2}\pi}.s.\exp(-\omega^2/(2s^2))\,\Delta\omega, \tag{15.140b}$$

and so the maximum (at $\omega = 0$) and the width of $S(\omega)$ will be $\sqrt{(\pi/2)}.s.\Delta\omega$, and $\sqrt{2}$ ($= 1.414$) times the maximum and the width of $f(\omega)$, respectively.

The moments are listed below, in Table 15.1.

For a *Lorentzian* function, suppose the frequency distribution $f(\omega)$ is given by

$$f(\omega) = \exp(-|\omega|/s), \tag{15.141a}$$

then

$$S(\omega) = (\omega + s)\,\exp(-\omega/s)\,\Delta\omega, \tag{15.141b}$$

and the maximum and the width of $S(\omega)$ will now be $s.\Delta\omega$ and $1.67835\,s$, respectively, while those of $f(\omega)$ are 1 and $s.\ln2$ ($= 0.69315\,s$), respectively, a broadening with a factor of 2.4213.

15.9 Conclusions

We have described the physics and mathematics behind the Monte Carlo light scattering simulation program as developed in our group. It offers a large number of

options and extra features. Among the options are inclusion of various structures, like tubes and spheres, in the layer system; working with different concentrations of particles with different optical characteristics; investigating reflection, transmission, and absorption; studying path length and time-of-flight distributions; inclusion of frequency-modulation spectra and ultrafast transillumination phenomena; handling of Doppler frequency shifts upon scattering at moving particles; calculation of photoacoustic response from sources of absorbing particles; and performance of Raman and fluorescence spectroscopy. The light source might be a pencil beam, a broad parallel beam, or a divergent beam, from an external or an internal focus, or photons produced at the positions where (in previous simulations) photons were absorbed.

The output options include distribution plots of a number of variables, such as the position of detection, the angles at detection, the number of scattering events, the path length (either optical or geometrical), and the Doppler frequency shift. Detection might occur in reflection and transmission, i.e., at the surface or at the bottom of the sample, or internally, e.g., at the inner surface of an embedded sphere.

In addition to the simulations, a number of approximations is present, namely for the Doppler power spectra, the intensity curves, and the frequency-modulation distributions of the phase and the modulation depth.

15.10 Book Editor's Comments

The advantage of the described method of "sudden death" photons, is, that it is easy to incorporate "objects" in the stattering/absorbing medium, like layers, blocks, spheres, cylinders, mirrors, cones and even torusses, with different optical characteristics. Also, Raman and fluorescence can be performed easy: just run the simulations in "absorbing" mode. Then the program stores the positions of places where photons are absorbed, and those positions can be used as sources of Raman or fluorescence scattering in a subsequent run. Or you can do photo-acoustics, by calculating the photo-acoustic response from those absorbed photons, and accumulating those responses on a (simulated) "piezo-detector".

The most current and recently developed Monte Carlo (MC) studies have used publically available MCML code or its modified version [13, 31–33]. The MCML is based on the photon weight variance reducing, i.e., the weight of each photon packet during the propagation within a medium is attenuated exponentially according to scattering and absorption coefficients of the medium. When the actual weight W becomes too small, the technique, so-called "Russian roulette," is applied, which gives each photon packet a chance m to survive with a weight $m*W$. This approach was originally used for counting fluence rate distribution and tends to balance energy of incident radiation with the energy of radiation absorbed and scattered within the medium. Such an assigning of the additional weight to randomly selected photon packets results in unjustified increasing of their path lengths within the medium. This affects the final distribution of the photon paths and may give an uncertainty to the method.

Another approach combines the statistical weight scheme and effective simulation of optical photon paths [34]. The simulation is based on the modeling of a large number of possible trajectories of the photon packets from the area of injection of photons into the medium to the site where the photon packet leaves the medium. The initial and final states of the photons are entirely determined by the source and the detector geometries, numerical apertures, spatial distribution of the intensity of incident light, detector sensitivity, etc. Assuming the independence of absorption and scattering along the photon trajectory allows for simulating these events separately. Therefore, during the propagation within a medium, the weight of each photon packet is attenuated only due to the partial reflection and/or refraction on the medium boundaries, i.e., total internal reflection is taken into account [35]. Thus, accumulating a sufficient number of the photon packets ($\sim 10^6$–10^8) between source and detector areas the statistical weight of each photon packet is recalculated by exponential attenuation according tp its total path length and absorption coefficient of the medium. This allows for rapid recalculation of the intensity for a set of the medium absorption assigned for particular wavelengths. Thus, tissue reflectance, transmittance and fluorescence spectra, OCT images, and so on can be simulated with ease. The great advantage of this approach is that time of simulation is independent of the absorption of the medium and the modeling avoids the energy conservation problem that occurs in roulette-based MC techniques. With the further recent developments, this MC approach has been generalized for a number of applications [36] and is available on-line [37].

MC modeling is widely used in calculations of tissue fluorescence. Suggested models [38, 39] have assumed that the fluorescence is emitted uniformly from the scattering sites in random directions. An algorithm, described in Ref. [40], accounts for spatial distribution of fluorophores within the skin as an example of a tissue. The MC algorithms for calculation of skin reflectance spectra [34, 41] and for optically cleared skin [42] have been designed. The coherent multiple scattering effects in the framework of MC modeling are discussed in Refs. [43, 44]. The MC algorithm for simulation of real image transfer through disperse turbid medium [45] and the MC imitation modeling of 2D OCT images accounting for polarization, coherence, and speckles [46, 47] are available.

The first application of MCML to GPU parallel computing for high-speed simulation of photon migration has been done [48] and the first Online Object Oriented MC-algorithm utilized CUDA NVIDEA GPU technology and unified for multiple applications in tissue optics, including skin color, reflectance spectra, and polarization simulation, is described [36, 37].

Three-dimensional MC code for photon migration through complex heterogeneous media, including the adult human head, has been described [49]. In Ref. [50], three different MC programs of polarized light transport in scattering media are carefully compared. New closed-form approximation for skin chromophore mapping was tested by comparing it to the MCML simulation model [51].

An effective MC-algorithm for simulation of the photoelectric current in laser Doppler flowmetry of blood in skin can be found in the literature [52]. A quantitative description of optical properties of blood using inverse MC (IMC)

algorithms has been provided and the absorption (μ_a) and scattering (μ_s) coefficients and the anisotropy factor (g) of human blood were evaluated from experimental data by IMC simulations in various physiological conditions [53–55]. The IMC algorithm was also designed for the analysis of blood optical properties in flows [56]. The changes of optical properties in flows were speculated as related to deformation, distribution, and orientation of erythrocytes caused by a share stress in a cell flow. The optical properties derived using conventional MC codes, however, do not represent the actual interaction between photons and erythrocytes. In particular, estimation of the anisotropy factor presents a difficult problem. Because erythrocytes have a nonspherical biconcave shape, the scattering depends on the incident photon direction; in addition, their deformability in the flow significantly complicates the scattering problem. In Refs. [57, 58], the MCML-algorithm based on Henyey-Greenstein phase function was suggested for modeling of light scattering by erythrocytes. Detailed analysis of the impact of phase function on MC modeling can be found in Refs. [59, 60].

To overcome the shortcomings of conventional MC methods, a photon-cell interactive Monte Carlo (pciMC) code that tracks photon propagation through both the extra- and intra-cellular spaces of erythrocyte without the need for the macroscopic scattering phase function and anisotropy factor was proposed [61]. In the pciMC approach, 3-D biconcave erythrocytes are described by the input parameters including volume, shape, and hematocrit. The interaction of photons at the plasma-cell boundary is expressed by the geometric optics, since normally hemoglobin is more or less homogeneously distributed in cytoplasm of a erythrocyte, the size of which is much more than the wavelength. Therefore, the pciMC code can follow the scattering changes depending on the cell volume, shape, and orientation, as well as the intracellular hemoglobin concentration.

Description of IMC algorithms for reconstruction of optical parameters of tissues (skin, subcutaneous, and muscle tissues) can be found in an overview paper [62].

References

1. K.M. Case, P.F. Zweifel, *Linear Transport Theory* (Addison-Wesley, Reading, 1967)
2. A. Ishimaru, Diffusion of light in turbid material. Appl. Opt. **28**, 2210–2215 (1989)
3. A. Ishimaru, Wave Propagation and Scattering in Random Media, vols. 1, 2. (Academic, San Diego, 1978)
4. R.A.J. Groenhuis, H.A. Ferwerda, J.J. ten Bosch, Scattering and absorption of turbid materials determined from reflection measurements, 1: Theory. Appl. Opt. **22**, 2456–2462 (1983); 2: Measuring method and calibration. Appl. Opt. **22**, 2463–2467 (1983)
5. R.F. Bonner, R. Nossal, S. Havlin, G.H. Weiss, Model for photon migration in turbid biological media. J. Opt. Soc. Am. A **4**, 423–432 (1987)
6. M.S. Patterson, B. Chance, B.C. Wilson, Time resolved reflectance and transmittance for the non-invasive measurement of tissue optical properties. Appl. Opt. **28**, 2331–2336 (1989)
7. T.J. Farrell, M.S. Patterson, B.C. Wilson, A diffusion theory model of spatially resolved, steady-state diffuse reflectance for the noninvasive determination of tissue optical properties in vivo. Med. Phys. **19**, 879–888 (1992)

8. R.C. Haskell, L.O. Svaasand, T.T. Tsay, T.C. Feng, M.S. McAdams, B.J. Tromberg, Boundary conditions for the diffusion equation in radiative transfer. J. Opt. Soc. Am. A **11**, 2727–2741 (1994)

9. A. Kienle, M.S. Patterson, N. Dögnitz, R. Bays, G. Wagnières, H. van den Bergh, Noninvasive determination of the optical properties of two-layered media. Appl. Opt. **37**, 779–791 (1998)

10. A. Kienle, T. Glanzmann, In vivo determination of the optical properties of muscle with time-resolved reflecntance using a layered model. Phys. Med. Biol. **44**, 2689–2702 (1999)

11. F.F.M. de Mul, M.H. Koelink, M.L. Kok, P.J. Harmsma, J. Greve, R. Graaff, J.G. Aarnoudse, Laser Doppler velocimetry and Monte Carlo simulations on models for blood perfusion in tissue. Appl. Opt. **34**, 6595–6611 (1995)

12. For further information: see the general site of the University Twente, click to "Faculties" or "Departments", then to "Applied Physics", "Research", "Biophysics", "Biomedical Optics", "courses"

13. L. Wang, S.L. Jacques, Hybrid model of Monte-Carlo simulation and diffusion theory for light reflectance by turbid media. J. Opt. Soc. Am. A **10**, 1746–1752 (1993)

14. V.G. Kolinko, F.F.M. de Mul, J. Greve, A.V. Priezzhev, On refraction in Monte-Carlo simulations of light transport through biological tissues. Med. Biol. Eng. Comp. **35**, 287–288 (1997)

15. H.C. van de Hulst, *Light Scattering by Small Particles* (Dover, New York, 1957, 1981)

16. G. Yao, L.V. Wang, Propagation of polarized light in turbid media: simulated animation sequences. Opt. Express **7**, 198–203 (2000)

17. M.J. Rakovic, G.W. Kattawar, Theoretical analysis of polarization patterns from incoherent backscattering of light. Appl. Opt. **37**, 3333–3338 (1998)

18. M.J. Rakovic, G.W. Kattawar, M. Mehrubeoglu, B.D. Cameron, L.V. Wang, S. Rastegar, G.L. Coté, Light backscattering polarization patterns from turbid media: theory and experiment. Appl. Opt. **38**, 3399–3408 (1999)

19. W.S. Bickel, W.M. Bailey, Stokes vectors, Mueller matrices and polarized light. Am. J. Phys. **53**, 468–478 (1985)

20. S. Bartel, A.H. Hielscher, Monte-Carlo simulations of diffuse backscattering Mueller matrix for highly scattering media. Appl. Opt. **39**, 1580–1588 (2000)

21. X. Wang, G. Yao, L.V. Wang, Monte Carlo model and single-scattering approximation of the propagation of polarized light in turbid media containing glucose. Appl. Opt. **41**, 792–801 (2002)

22. M. Born, E. Wolf, *Principles of Optics*, 6th edn. (Cambridge University Press, Cambridge, 1980–1993)

23. J.R. Zijp, J.J. ten Bosch, Pascal program to perform Mie calculations. Opt. Eng. **32**, 1691–1695 (1993)

24. L.G. Henyey, J.L. Greenstein, Diffuse radiation in the galaxy. Astrophys. J. **93**, 70–83 (1941)

25. C.G.A. Hoelen, F.F.M. de Mul, R. Pongers, A. Dekker, Three-dimensional photoacoustic imaging of blood vessels in tissue. Opt. Lett. **23**, 648–650 (1998)

26. C.G.A. Hoelen, F.F.M. de Mul, A new theoretical approach to photoacoustic signal generation. J. Acoust. Soc. Am. **106**, 695–706 (1999)

27. C.G.A. Hoelen, A. Dekker, F.F.M. de Mul, Detection of photoacoustic transients originating from microstructures in optically diffuse media such as biological tissue. IEEE – UFFC **48**, 37–47 (2001)

28. C.G.A. Hoelen, F.F.M. de Mul, Image reconstruction for photoacoustic scanning of tissue structures. Appl. Opt. **39**, 5872–5883 (2000)

29. R. Graaff, K. Rinzema, Practical improvements on photon diffusion theory: application to isotropic scattering. Phys. Med. Biol. **46**, 3043–3050 (2001)

30. M. Keijser, W.M. Star, P.R. Storchi, Optical diffusion in layered media. Appl. Opt. **27**, 1820–1824 (1988)

31. L.V. Wang, S.L. Jacques, Source of error in calculation of optical diffuse reflectance from turbid media using diffusion theory. Comput. Meth. Progr. Biomed. **61**, 163–170 (2000)

32. L.V. Wang, H.-I. Wu, *Biomedical Optics: Principles and Imaging* (Wiley-Interscience, Hoboken, 2007)
33. ftp://ftp.wiley.com/public/sci_tech_med/biomedical_optics
34. I.V. Meglinski, Modeling the reflectance spectra of the optical radiation for random inhomogeneous multi-layered highly scattering and absorbing media by the Monte Carlo technique. Quant. Electr. **31**(12), 1101–1107 (2001)
35. D.Y. Churmakov, I.V. Meglinski, D.A. Greenhalgh, Influence of refractive index matching on the photon diffuse reflectance. Phys. Med. Biol. **47**(23), 4271–4285 (2002)
36. A. Doronin, I. Meglinski, Online object oriented Monte Carlo computational tool for the needs of biomedical optics. Biomed. Opt. Express **2**(9), 2461–2469 (2011)
37. Meglinski I. SPIE News, website http://biophotonics.otago.ac.nz (2012)
38. M. McShane, S. Rastegar, M. Pishko, G. Cote, Monte Carlo modeling of implantable fluorescent analyte sensors. IEEE Trans. Biomed. Eng. **47**(5), 624–632 (2000)
39. K. Vishwanath, B. Pogue, M. Mycek, Quantitative fluorescence spectroscopy in turbid media: comparison of theoretical, experimental and computational methods. Phys. Med. Biol. **47**(18), 3387–3405 (2002)
40. D.Y. Churmakov, I.V. Meglinski, S.A. Piletsky, D.A. Greenhalgh, Analysis of skin tissues spatial fluorescence distribution by the Monte Carlo simulation. J. Phys. D: Appl. Phys. **36**(14), 1722–1728 (2003)
41. I.V. Meglinski, S.J. Matcher, Quantitative assessment of skin layers absorption and skin reflectance spectra simulation in visible and near infrared spectral region. Physiol. Meas. **23**(4), 741–753 (2002)
42. I.V. Meglinski, D.Y. Churmakov, A.N. Bashkatov, E.A. Genina, V.V. Tuchin, The enhancement of confocal images of tissues at bulk optical immersion. Laser Phys. **13**(1), 65–69 (2003)
43. V.L. Kuzmin, I.V. Meglinski, Coherent multiple scattering effects and Monte Carlo method. JETP Lett. **79**(3), 109–112 (2004)
44. I.V. Meglinski, V.L. Kuzmin, D.Y. Churmakov, D.A. Greenhalgh, Monte Carlo simulation of coherent effects in multiple scattering. Proc. Royal Soc. A **461**(2053), 43–53 (2005)
45. E. Berrocal, I.V. Meglinski, D.A. Greenhalgh, M.A. Linne, Image transfer through the complex scattering turbid media. Laser Phys. Lett. **3**(9), 464–468 (2006)
46. I.V. Meglinski, M. Kirillin, V.L. Kuzmin, R. Myllylä, Simulation of polarization-sensitive optical coherence tomography images by a Monte Carlo method. Opt. Lett. **33**(14), 1581–1583 (2008)
47. M. Kirillin, I. Meglinski, E. Sergeeva, V.L. Kuzmin, R. Myllylä, Simulation of optical coherence tomography images by Monte Carlo modeling based on polarization vector approach. Opt. Express **18**(21), 21714–21724 (2010)
48. E. Alerstam, T. Svensson, S. Andersson-Engels, Parallel computing with graphics processing units for high-speed Monte Carlo simulation of photon migration. J. Biomed. Opt. **13**, 060504 (2008)
49. D.A. Boas, J.P. Culver, J.J. Stott, A.K. Dunn, Three dimensional Monte Carlo code for photon migration through complex heterogeneous media including the adult human head. Opt. Express **10**(3), 159–170 (2002)
50. J. Ramella-Roman, S. Prahl, S. Jacques, Three Monte Carlo programs of polarized light transport into scattering media: part I. Opt. Express **13**(12), 4420–4438 (2005)
51. P. Valisuo, I. Kaartinen, V. Tuchin, J. Alander, New closed-form approximation for skin chromophore mapping. J. Biomed. Opt. **16**(4), 046012-1–046012-10 (2011)
52. T. Binzoni, T.S. Leung, D. Van De Ville, The photo-electric current in laser-Doppler flowmetry by Monte Carlo simulations. Phys. Med. Biol. **54**(14), N303–N318 (2009)
53. A.N. Yaroslavsky, I.V. Yaroslavsky, T. Goldbach, H.-J. Schwarzmaier, The optical properties of blood in the near infrared spectral range. Proc. SPIE. **2678**, 314–324 (1996)
54. A.N. Yaroslavsky, I.V. Yaroslavsky, T. Goldbach, H.-J. Schwarzmaier, Different phase function approximations to determine optical properties of blood: a comparison. Proc. SPIE. **2982**, 324–330 (1997)

55. A.N. Yaroslavsky, I.V. Yaroslavsky, T. Goldbach, H.-J. Schwarzmaier, Influence of the scattering phase function approximation on the optical properties of blood determined from the integrating sphere measurements. J. Biomed. Opt. **4**(1), 47–53 (1999)
56. A. Roggan, M. Friebel, K. Dorschel, A. Hahn, G. Müller, Optical properties of circulating human blood in the wavelength range 400–2500 nm. J. Biomed. Opt. **4**(1), 36–46 (1999)
57. D. Chicea, I. Turcu, Testing a new multiple light scattering phase function using RWMCS. J. Optoelectr. Adv. Mater. **8**(4), 1516–1519 (2006)
58. D. Chicea, I. Turcu, RWMCS – An alternative random walk Monte Carlo code to simulate light scattering in biological suspensions. Optik **118**, 232–236 (2007)
59. E. Berrocal, D. Sedarsky, M. Paciaroni, I.V. Meglinski, M.A. Linne, Laser light scattering in turbid media part I: experimental and simulated results for the spatial intensity distribution. Opt. Express **15**, 10649–10665 (2007)
60. E. Berrocal, D. Sedarsky, M. Paciaroni, I.V. Meglinski, M.A. Linne, Laser light scattering in turbid media part II: spatial and temporal analysis of individual scattering orders via Monte Carlo simulation. Opt. Express **17**, 13792–13809 (2009)
61. D. Sakotam, S. Takatani, Photon-cell interactive Monte Carlo model based on the geometrical optics theory for photon migration in blood by incorporating both extra and intra-cellular pathways. J. Biomed. Opt. **15**(6), 065001, 1–14 (2010)
62. A.N. Bashkatov, E.A. Genina, V.V. Tuchin, Optical properties of skin, subcutaneous, and muscle tissues: a review. J. Innov. Opt. Health Sci. **4**(1), 9–38 (2011)

Optical Coherence Tomography

Optical Coherence Tomography: Light Scattering and Imaging Enhancement

16

Ruikang K. Wang and Valery V. Tuchin

Contents

R.K. Wang (✉)
University of Washington, Seattle, WA, USA
e-mail: wangrk@u.washington.edu

V.V. Tuchin
Department of Optics and Biophotonics, Saratov State University, Saratov, Russian Federation

Precision Mechanics and Control, Institute of the Russian Academy of Sciences, Saratov, Russian Federation

Optoelectronics and Measurement Techniques Laboratory, University of Oulu, Oulu, Finland
e-mail: tuchinvv@mail.ru

Abstract

The fundamental aspects of optical coherence tomography and a brief description of its applications in medicine and biology are presented. The impact of multiple scattering in tissues on OCT imaging performance, and developments in reducing the overwhelming multiple scattering effects and improving imaging capabilities by the use of immersion technique are discussed. A novel technique based on the use of biocompatible and hyperosmotic chemical agents to impregnate the tissue and to enhance the OCT images is described. The mechanisms for improvements in imaging depth and contrast are discussed, primarily through the experimental examples.

16.1 Introduction

Over the last two decades, noninvasive or minimally invasive spectroscopy and imaging have witnessed widespread and exciting applications in biomedical diagnostics. Optical techniques that use the intrinsic optical properties of biological tissues, such as light scattering, absorption, polarization, and autofluorescence, have many advantages over the conventional X-ray computed tomography, MRI, and ultrasound imaging in terms of safety, cost, contrast, and resolution features. Time-resolved and phase-resolved optical techniques are capable of deep-imaging of the tissues that could provide information of tissue oxygenation states and detect brain and breast tumors [1, 2], whereas confocal microscopy and multi-photon excitation imaging have been used to show cellular and subcellular details of superficial living tissues [3, 4]. However, most biological tissues strongly scatter the probing light within the visible and near-infrared range, i.e., the therapeutic and/or diagnostic optical window. The multiple scattering of light is severely detrimental to imaging contrast and resolution, which limits the effective probing depth to several hundred micrometers for the confocal microscopy and multi-photon excitation imaging techniques. However, some clinical applications, such as early cancer diagnosis, require the visualization of intermediate depth range of the localized anatomical structures with micron-scale resolution.

Optical coherence tomography (OCT) fills a nice niche in this regard. It uses low-coherence interferometry to image internal tissue structures to the depth up to 2 mm with micron-scale resolution [5, 6]. Its first applications in medicine were reported more than 20 year ago [7–11], but its roots lie in early work on white-light

interferometry that led to the development of optical coherence-domain reflectometry (OCDR), a one-dimensional optical ranging technique [12]. Although OCDR was developed originally for finding faults in fiber-optic cables and network components [13], its ability to probe the eye [14–16] and other biological tissues [17] was soon realized. The superb axial resolution is achieved by exploiting the short temporal coherence of a broadband light source. Borrowing the concept of confocal microscopy, OCDR was quickly extended to section the biological tissues [7] through the point-by-point scan, so-called optical coherence tomography. OCT enables microscopic structures in biological tissue to be visualized at a depth beyond the reach of conventional confocal microscopes. Probing depth exceeding 2 cm has been reported for transparent tissues, including the eye [18] and frog embryo [19]. To date, successful stories of in vitro and in vivo OCT applications in medicine have been delivered in a wide number of areas, for example, ophthalmology [20], gastrointestinal tract [21–25], dental [26], and dermatology [27–29]. OCT is becoming viable as a clinical diagnostic tool with the recent advent of high-power, low-coherence sources and near real-time image scanning technology [30]. The high resolution (<10 μm) and high dynamic range (>100 dB) of OCT would allow for in vivo tissue imaging approaching the resolution of excisional biopsy. An advantage that OCT has over high-frequency ultrasonic imaging, a competing technology that achieves greater imaging depths but with low resolution [31], is its relative simplicity and cost-effectiveness of the hardware on which OCT systems are based.

This chapter introduces the fundamental aspects of optical coherence tomography and briefly discusses its applications in medicine and biology. In the later parts of chapter, we will discuss how multiple scattering of tissue would impact the OCT imaging performance, and the developments in reducing the overwhelming multiple scattering effects and improving imaging capabilities by the use of immersion techniques.

16.2   Optical Coherence Tomography: The Techniques

16.2.1 Introduction

OCT is analogous to ultrasonic imaging that measures the intensity of reflected infrared light rather than reflected sound waves from the sample. Time gating is employed so that the time for the light to be reflected back, or echo delay time, is used to assess the intensity of backreflection as a function of depth. Unlike ultrasound, the echo time delay of an order of femtosecond cannot be measured electronically due to the high speed associated with the propagation of light. Therefore, the time-of-flight technique has to be engaged to measure such ultrashort time delay of light backreflected from the different depth of sample. OCT uses an optical interferometer to solve this problem. Central to OCT is a low-coherence optical reflectometry (LCR) that can be realized by a Michelson or a Mach-Zehnder interferometer illuminated by a low coherent light source.

16.2.2 Low Coherence Reflectometry

LCR, or "white light interference," has been used for centuries in industrial metrology, e.g., to measure the thickness of thin film [32], as a position sensor [33], and with other measurands that can be converted to a displacement [34]. At present, all OCT techniques use LCR to obtain the depth-resolved information of a sample, an example of which is shown in Fig. 16.1.

One arm of the interferometer is replaced by the sample under measurement. The reference mirror is translated with a constant velocity v_r to produce interference modulation with Doppler frequency $f_D = 2v_r/\lambda_0$ for optical heterodyne detection, where λ_0 is the central wavelength of a low-coherence light source. Then the interference can occur only when the optical path lengths of light in both the sample arm and reference arm are matched to within the coherence length of light source.

The principle of LCR can be analyzed in terms of the theory of two-beam interference for partially coherent light. Assuming that the polarization effects of light are neglected, $E_s(t - L_s/c)$ and $E_r(t - L_r/c)$ are scalar complex functions that represent the light fields from the sample and reference arms of a Michelson interferometer, respectively. L_s and L_r are the corresponding optical path lengths. Given the assumption that the photodetector captures all of the light from the reference and sample arms, due to time invariance of the light field, the resultant intensity at detector PD is then:

$$I_d(\tau) = \langle [E_s(t) + E_r(t + \tau)][E_s(t) + E_r(t + \tau)]^* \rangle, \tag{16.1}$$

where the angular brackets denote the time average over the integration time at the detector; $\tau = \Delta L/c$ is the time delay corresponding to the round-trip optical path length difference between the two beams, i.e., $\Delta L = L_s - L_r = 2n_0(l_{s0} - l_{r0})$; $n_o \cong 1$, is the refractive index of air; and l_{s0} and l_{r0} are the geometric lengths of two arms, as indicated in Fig. 16.1. Because $I_s = \langle E_s(t)E_s^*(t) \rangle$ and $I_r = \langle E_r(t + \tau)E_r^*(t + \tau) \rangle$, equation (16.1) can then be written as:

$$I_d(\tau) = I_s + I_r + 2\text{Re}\{<E_s(t)E_r^*(t + \tau)>\}. \tag{16.2}$$

The last term in the above equation, which depends on the optical time delay τ set by the position of the reference mirror, represents the amplitude of interference fringes that carry information about the structures in the sample. The nature of the interference fringes, or whether any fringes form at all, depends on the degree to which the temporal and spatial characteristics of E_s and E_r match. Thus, the interference functions as a cross-correlator and the amplitude of interference signal generated after integration on the surface of the detector provides a measure of the cross-correlation amplitude. The first two terms in (16.1) contribute to the dc signal only in the interference signal detected by photodetector. To facilitate the separation of cross-correlation amplitude from the dc component of detected intensity, various techniques have been realized to modulate the optical time delay, i.e., τ. A few of these techniques will be discussed later.

Fig. 16.1 Schematic of
low-coherence interferometer
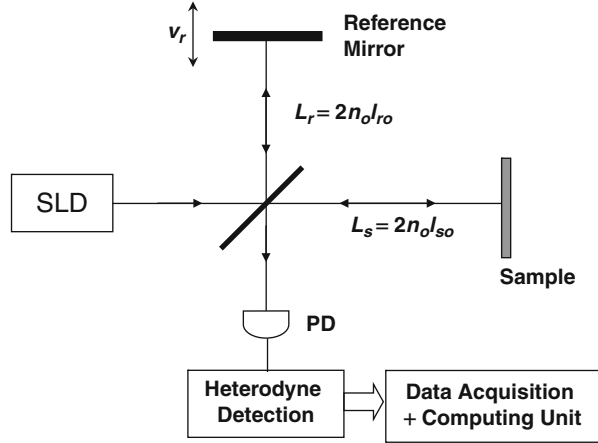
Under the assumption that the sample behaves as a perfect mirror that leaves the
sample beam unchanged, the correlation amplitude depends on the temporal-
coherence characteristics of the source, according to

$$\text{Re}\{<E_s(t)E_r^*(t+\tau)>\} = |G(\tau)|\cos[2\pi f_0\tau + \phi(\tau)], \tag{16.3}$$

where is the central frequency of the source with c the speed of light, and $G(\tau)$ is its
complex temporal coherence function with an argument of $\phi(\tau)$. According to the
Wiener-Khinchin theorem, $G(\tau)$ is related to the power spectral density of the
source, $S(f)$, as [35, 36]

$$G(\tau) = \int_0^\infty S(f)\exp(-j2\pi\tau)df. \tag{16.4}$$

It follows from this relationship that the shape and width of the emission
spectrum of the light source are important variables in the low-coherence interfer-
ometry, and thereby OCT, because of their influence on the sensitivity of the
interferometer to the optical path length difference between the sampling and
reference arms. Light sources with broad bandwidth are desirable because they
produce interference signals of short temporal extent. The relationship between $S(f)$
and $G(\tau)$ can be seen clearly when both are represented by Gaussian functions:

$$S(f) \leftrightarrow G(\tau) \tag{16.5}$$

with

$$S(f) = \frac{2\sqrt{\ln 2/\pi}}{\Delta f}\exp\left[-4\ln 2\left(\frac{f-f_0}{\Delta f}\right)^2\right], \tag{16.6}$$

and

$$G(\tau) = \exp\left[-\left(\frac{\pi\Delta f\tau}{2\sqrt{\ln 2}}\right)^2\right]\exp(-j2\pi f_{0\tau}). \tag{16.7}$$

In these equations, the full-width-half-maximum bandwidth Δf represents the spectral width of the source in the optical frequency domain. The corresponding measure of the correlation width, derived from (16.7), is the correlation length (in free space), given by

$$l_c = \frac{2c\ln 2}{\pi}\cdot\frac{1}{\Delta f} \approx 0.44\frac{\lambda_0^2}{\Delta\lambda}, \tag{16.8}$$

where $\Delta\lambda$ is the full-width of the coherence function at half-maximum measured in wavelength units. Other definitions of the coherence length yield similar expressions, but with a different constant factor. For example, defined as the speed of light in medium times the area under the squared amplitude of the normalized temporal coherence function, $l_c \approx 0.66\,\lambda_0^2/\Delta\lambda$ [35]. In the OCT community, (16.8) is often used.

16.2.3 Noise

One of the main noise sources in LCR is mechanical $1/f$ noise. To achieve shot-noise-limited detection, a heterodyne technique can be used. The most straightforward and simplest technique in optics is to use the Doppler effect, e.g., simply moving the reference mirror with constant speed v. Thus the time delay will be

$$\tau = \frac{2vt}{c}. \tag{16.9}$$

Then we have the ac term of detected interference signal time-modulated by

$$\text{Re}\{<E_s(t)E_r^*(t+\tau)>\} = |G(\tau)|\cos[4\pi f_0 vt/c + \phi(\tau)]. \tag{16.10}$$

From here, the central Doppler frequency will be

$$f = \frac{2f_0 v}{c} = \frac{2v}{\lambda_0}. \tag{16.11}$$

Figure 16.2a shows an example of a time-modulated interference signal detected by the photodetector. The detected ac signal is bandpass filtered with respect to the central Doppler frequency as the center frequency, then rectified and low-pass filtered. The output of the low-pass filter is the envelope of the time-modulated ac interference signal, which is equivalent to the cross-correlation amplitude
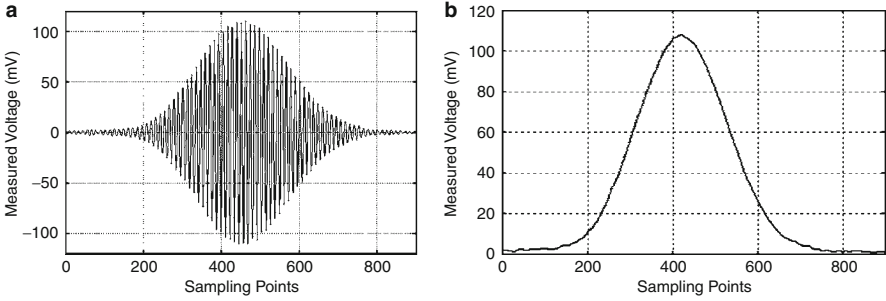
Fig. 16.2 (**a**) Time-modulated ac term of interference signal, (**b**) corresponding cross-correlation amplitude, i.e., envelope

mentioned above. Figure 16.2b gives an example of the detected envelope corresponding to Fig. 16.2a.

In addition to 1/*f* noise, there are several other noise sources such as quantum noise, shot noise, and electronic noise. The impact of these noise disturbances on the measurement can be described by signal-to-noise ratio (SNR), which is the ratio of the expected mean photocurrent power to its standard deviation. The dynamic range (DR) of an instrument is defined by the ratio of the maximum to the minimum measurable photocurrent power P of the interference signal:

$$DR = 10 \log \frac{P_{max}}{P_{min}} = 10 \log(SNR_{max}). \tag{16.12}$$

Photocurrent power P is proportional to the square of the light intensity impinging at the photodetector, hence

$$\frac{P_{max}}{P_{min}} = \frac{R_{max}^2}{R_{min}^2} = \frac{1}{R_{min}^2} \quad \Rightarrow DR = -20 \log(R_{min}), \tag{16.13}$$

where R_{min} is the minimal reflectivity in the sample beam producing a photodetector signal power equal to the standard deviation of the photocurrent power generated by a reflectivity of $R_{max} = 1$. In case of LCR and OCT, the intensity at photodetector is caused by the interference of the sample beam with the reference beam. Hence, according to the interference law, the signal intensity at the photodetector is proportional to the square root of the object intensity and we have in this case:

$$DR = -10 \log(R_{min}). \tag{16.14}$$

The LCR and OCT have been designed near the shot noise limit by choosing a proper Doppler frequency to avoid low frequency 1/*f* noise [13], a proper balanced-detector scheme to reduce the excess photon noise [37], and a proper

transimpedance amplifier resistance voltage to overcome thermal noise [38]. The simplest method for choosing a proper Doppler frequency is to mount the reference mirror on a linear translation stage moving at a chosen constant velocity. The other methods include the fiber stretching via a piezoelectric crystal [39], and frequency domain scanning by introduction of a grating-based phase control delay line [40].

16.2.4 Optical Coherence Tomography

Optical coherence tomography performs cross-sectional imaging by measuring the time delay and magnitude of optical echoes at different transverse positions, essentially by the use of a low-coherence interferometry. A cross-sectional image is acquired by performing successive rapid axial measurements while transversely scanning the incident sample beam onto the sample (see Fig. 16.3). The result is a two-dimensional data set, which represents the optical reflection or backscattering strength in a cross-sectional plane through a material or biological tissue. OCT was first demonstrated in 1991 [7]. Imaging was performed in vitro in the human retina and in atherosclerotic plaque as examples of imaging in transparent, weakly scattering media, as well as highly scattering media. The system implemented by the optic fiber couplers, matured in the telecommunication industry, offers the most advantage for the OCT imaging of biological tissues because it can be integrated into almost all currently available medical imaging modalities, for example, endoscope and microscope. Figure 16.4 gives an example of the optic-fiber versions of OCT [25, 29]. In this type of optic-fiber version of interferometer, light from a low-coherence light source is coupled to a single-mode fiber coupler where half of light power is conducted through the single-mode fiber to the reference mirror. The remaining half enters the sample via proper focusing optics. The distal end of the fiber in the sample arm serves a dual role as a coherent light receiver and spatial filter analogous to a confocal pinhole. Because the dc signal and intensity noise generated by the light from the reference arm add to the interference signal, it makes the system prone to the photon excess noise. One way to reduce this type of noise is to use a balanced detection configuration as shown in Fig. 16.4 that would make the background noise components cancelled by subtracting the photocurrents generated by two photodetectors. The interference signals at the output of the detectors add because they vary out of phase [50].

OCT has the advantage that it can achieve very high axial image resolution independent of the transverse image resolution. The axial resolution is determined by the coherence length of light source used, i.e., (16.8), which is independent of the sampling beam focusing conditions. From (16.8), the axial resolution is inversely proportional to the spectral bandwidth of light source. Thus, the higher axial resolution can be achieved by the use of a wider spectral bandwidth of light sources. Table 16.1 lists characteristics of a variety light sources suitable for use in OCT systems [6]. The most commonly used sources in the current OCT systems are the superluminescent diodes (SLDs) with peak emission wavelengths in either 820 nm

Fig. 16.3 OCT images are generated by performing measurements of the echo time delay and magnitude of back-scattered light over a range of transverse positions. OCT are two- or three-dimensional data sets that represent the optical backscattering in a cross section or volume of the tissue (Courtesy of Cranfield Biophotonics Group)
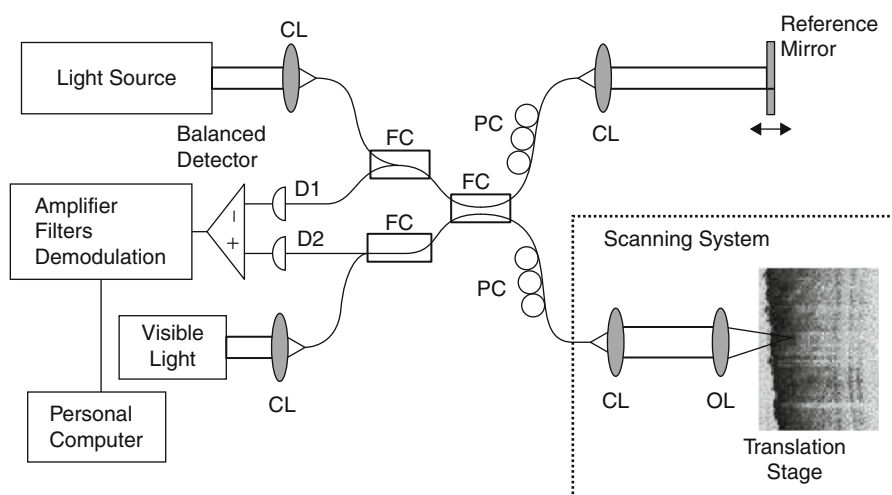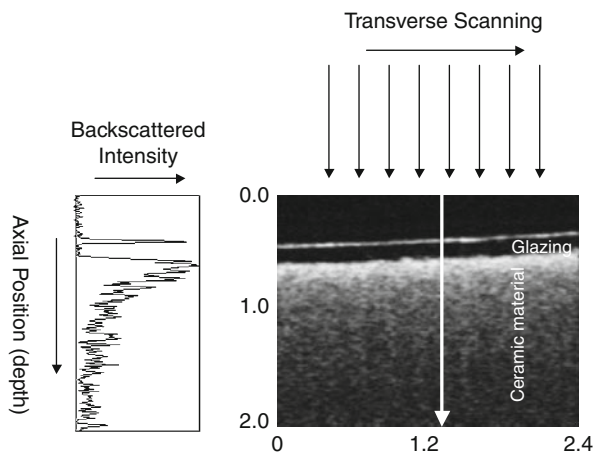
Fig. 16.4 Example of the fiber-optic versions of OCT systems where *CL* is the collimating lens, *FC* the fiber coupler, *PC* the polarization controller, *OL* the objective lens, and *D* the detector

or 1,300 nm fiber-optic telecommunication bands because of their high irradiance, compactness, and relatively low cost. However, the spectral bandwidth of the available SLDs is usually limited, which determines the achievable axial resolution at 7–10 μm for 800 nm and 10–20 μm for 1,300 nm band light sources, which are sometimes not sufficient to meet the resolution requirement for some medical and industrial applications. In order to enhance the axial resolution, a light source with broader spectral bandwidth has to be applied. Researchers attempted to integrate a number of SLDs with non-overlapping central wavelengths into a single broadband source for resolution improvement [41], but the improvement is suboptimal in

Table 16.1 Low-coherence light sources suitable for use in OCT systems

Light source	Central wavelength (nm)	Bandwidth (nm)	Emission power	Reference
Edge-emitting LED	1,300, 1,550	50–100	20–300 μW	[53]
SLD	800, 1,300	20–50	1–10 mW	[41]
Multiple QW	800	90	15 mW	[55]
LED/SLD	1,480	90	5 mW	[56]
Laser-pumped fluorescent organic dye	590	40	9 mW	[54]
Mode-locked Ti:Al_2O_3 laser	820	50–200	400 mW	[42]
Mode-locked Cr^{4+}forsterite laser	1,280	75	30 mW	[42]
Superfluorescent optical fibers:				
Er-doped	1,550	40–80	10–100 mW	[52]
Tm-doped	1,800	80	7 mW	[52]
Nd-/Yb-doped	1,060	65	108 mW	[51]
Supercontinuum	Selectable	200–300	2 W	[49]

terms of emitting wavelength of the multiplexed SLD that is typically centered at >900 nm, overlapping the water absorption at 980 nm that may affect the imaging depth. A number of reports (e.g., [11, 42–44]) have demonstrated the use of state-of-the-art femtosecond lasers to achieve a 2–3 μm axial resolution, but with the disadvantage of being expensive and bulky limits its uses to a few research laboratories. Being spectrally very broad and visually very bright, supercontinuum (SC) light sources have attracted notice as an excellent alternative for OCT imaging to achieve subcellular axial resolution [45–49]. There have also been developments in diode-pumped superfluorescent fiber sources [51, 52] that gained attention because of their low cost and compactness. The high power and wide bandwidth of these light sources make them attractive alternatives for fast, high-resolution OCT imaging of in vivo biological tissues.

The lateral or transverse resolution achieved with an OCT imaging system is determined by the focused spot size limited by the numerical aperture of the lens used to deliver the light onto the sample, and the optical frequency of incident light as in conventional microscopy [57]. The transverse resolution can be written

$$\Delta x = \frac{4\lambda f}{\pi d}, \tag{16.15}$$

where d is the spot size on the objective lens and f is its focal length. High transverse resolution can be achieved by the use of a large numerical aperture of lens and focusing the beam to a small spot size. In addition, the transverse resolution is also related to the depth of focus or confocal parameter, b. The confocal parameter is

twice the Raleigh range, $2z_R$. Its relationship to transverse resolution is described by the formula:

$$b = 2z_R = \pi\Delta x^2/2\lambda. \tag{16.16}$$

In addition to its high-resolution feature, advantages of OCT for medical imaging include its broad dynamic range, rapid data acquisition rate, and compact portable structure. The frame rates for OCT systems are currently at four to eight frames per second [40]. At the beginning of OCT development, the path length in the reference arm was scanned via the use of a moving mirror or galvanometer [7]. However, such scanning would require approximately 40 s to perform imaging of non-transparent tissue [58]. A system similar to this is still in use for imaging the transparent tissue of the eye, and sometimes is sufficient for use as a research tool. Fiber-stretching with a piezoelectric crystal [28] in the reference arm offers a rapid scanning of the optical path length. However, there are disadvantages in the use of such technique, including polarization mode dispersion, hysteresis, crystal breakdown, and high voltage requirement. Presently, the most popular OCT systems employ a variable optical group delay in the reference arm through the introduction of a grating-based phase control delay line [39]. This configuration was originally designed for shaping femtosecond pulses that employ a grating-lens combination and an oscillating mirror to form an optical delay line [59]. It was reported to achieve high data acquisition rates up to 4–8 frames per second [61]. In addition to its high data acquisition rate, the system has two other advantages over the previous configurations. The optical group delay can be varied separately from the phase delay, and the group velocity dispersion can be varied without the introduction of a separate prism [60, 61].

The OCT system described above is the backbone of current OCT system developments, particularly in stimulating new concepts and ideas. This is usually called the time domain approach (TDOCT), i.e., the first generation of the OCT development. There are varieties of other systems developed that operate at different domains or reveal different functionalities of the tissue, but essentially the same mechanism, for example, dual beam OCT [8, 62], en-face OCT [63, 64] (see also ▶ Chap. 19), Fourier domain OCT [65–67], whole-field OCT [68, 69], and functional OCT including polarization sensitive OCT [70–72] (see also ▶ Chap. 21), Doppler OCT [73–78] (see also ▶ Chap. 22), and spectroscopic OCT [79]. For detailed information regarding the different forms of OCT systems, please refer to recent comprehensive review papers [80, 81] and a monograph [82].

With the current shift of OCT application to in vivo imaging applications, one of the most important parameters that must be considered is the imaging speed, because the faster the imaging speed, the better we can manage to minimize the motion artifacts that are inevitable for any in vivo imaging applications. Being the first generation, TDOCT is capable of only up to ~8,000 A-lines per second (with most systems having up to 2 kHz A-scan rate), which is mainly restricted by the employment of a mechanically scanning mirror in the reference arm to provide

depth-resolved axial information of the sample. With this imaging speed, it is sometimes difficult for TDOCT to achieve in vivo 3D scanning. For example, in retinal imaging, only several cross-sectional images could be captured before eye blinking and movements happen [83], which is inevitable for human studies. To increase the imaging speed, a new interferogram detection scheme, Fourier domain OCT (FDOCT), is proposed to directly achieve depth-resolved reconstruction of the biological tissue without the need of mechanically scanning the reference arm [66, 84], a development that represents the second OCT generation (2gOCT). In FDOCT, the interference spectrograms are detected either with a broadband light source and a high-speed spectrometer (i.e., spectral domain OCT [SDOCT]) [66, 84] or a wavelength swept laser and ultrahigh-speed photodetector (swept source OCT [SSOCT]) [85, 86]. Compared with TDOCT, FDOCT has proven to have dramatically improved system sensitivity [87–89], thereby affording much higher imaging speed without losing useful information about the sample. Beginning in 2002 [90], FDOCT has gradually become dominant in OCT development [91–97], allowing a scanning rate at dozens of kilo-A-lines per second (up to $\sim$40 kHz). With this imaging speed, it is possible to visualize the sample in a 3D mode, offering much flexibility in the comprehensive analysis and quantification of the sampled volume. In addition, based on the high-speed FDOCT, several novel imaging processing algorithms have been made possible to achieve in vivo 3D functional imaging of the tissue sample, for example, the blood flow and microvasculature imaging [98–110].

Although 2gOCT has been demonstrated great success in the past few years, the imaging speed is still a barrier to achieve satisfactory 3D imaging on untrained patients due to the inevitable motion during the in vivo imaging. It is now clear that one of the solutions to reduce the motion artifacts in the final results is to further improve the system imaging speed. Recently, the ultrahigh-speed (hundreds of kHz line rate) FDOCT system (the third-generation (3 g) OCT) has become increasingly attractive by employing the frequency domain mode locking (FDML) technology [111–114] in SSOCT and high-speed line scan CMOS camera in SDOCT [115–117]. For example, the 20-MHz system based on a 1,310 nm swept laser source was demonstrated in Ref. [118]. At a different operating wavelength, the 1.3-MHz 1,050 nm system was reported in Ref. [119]. So far, the fastest retinal FDOCT system, which can maintain both the high axial resolution ($\sim$7 μm) and the ultrafast imaging speed, is reported in Ref. [111], in which the authors developed an 1-μm SSOCT system running at $\sim$400 k-A-lines per second, realized by combining FDML with a multi-spot detection strategy. It is reported that it is possible with this system to further improve imaging speed to 684 kHz [119]. However, the commercial utilization of such SSOCT is yet to be approved by the FDA. Currently, the commercially available retinal OCT systems are still based on SDOCT, with the imaging speed directly determined by the camera employed in the spectrometer. Until now, the fastest retinal SDOCT system reported is a system working at a 312 kHz A-line rate [115]. However, to reach 312 kHz, it has to sacrifice the spectral resolution by using a part of the CMOS sensor array (576 pixels out of 4,096 pixels). In consequence, the detectable depth is shallow ($\sim$2 mm in air) and

the system sensitivity rolling off is relatively high ($\sim$25 dB over 2-mm ranging distance). To further increase the imaging speed while maintaining the system axial resolution at less than 10 μm, the acceptable performances, e.g., system sensitivity rolling off and detectable depth range, are still a challenge in the development of a retinal SDOCT system.

16.3   OCT in Imaging

16.3.1 Introduction

OCT was originally developed to image the transparent tissue of the eye at unprecedented resolution [7]. It has been used clinically to evaluate a wide range of retinal-macular diseases [120–122]. Recently, the technology has been advanced to image nontransparent tissue, where penetration of light is limited [125, 126]. Nontransparent tissue has high light scattering in nature, which limits the light penetration depth for OCT imaging. To partially resolve this problem, most OCT imaging of nontransparent tissues is implemented with light having an incident wavelength near 1,300 nm, rather than 820 nm used in the relatively transparent tissues. At the wavelength of 1,300 nm, light scattering is low relative to scattering of light in the visible region. Absorption is low because this wavelength is too long to result in large amounts of electron transitions but is too short to induce extensive vibrational transitions in water. Another method to enhance the OCT imaging depth for nontransparent tissue is to use the immersion technique to interrogate the tissue with biocompatible chemical agents. This will be described later in this chapter.

16.3.2 Ophthalmology

Due to the relatively transparent nature of human eye tissue to near-infrared light, its weakly scattering structures, including the retina, can be imaged by OCT to the full depth with a resolution at 20 μm without difficulty [8, 18, 19, 127, 128]. The diagnostic potential of OCT for non-contact biometry segment of abnormalities of the eye was first demonstrated by Izatt et al. [16]. Using the reflectometer technique at a central wavelength of 1,310 nm, structures such as cornea, sclera, iris, and lens anterior capsule can be clearly visualized. With the 820 nm central wavelength, detailed layered structures within the human retina can now be delineated with high resolution. See Fig. 16.5 for examples.

Many retinal diseases are accompanied by changes in retinal thickness. Hence, high depth resolution is an important feature of any imaging techniques used to diagnose retinal pathology. Current diagnostic tools such as the confocal scanning ophthalmoscope are limited to a depth resolution no better than 300 μm [129]. Towards this, OCT offers a great potential to advance the diagnostic techniques because of its high resolution. Using a wavelength of 830 nm, it can easily differentiate the large-scale anatomical features, such as the fovea, optic disk, and
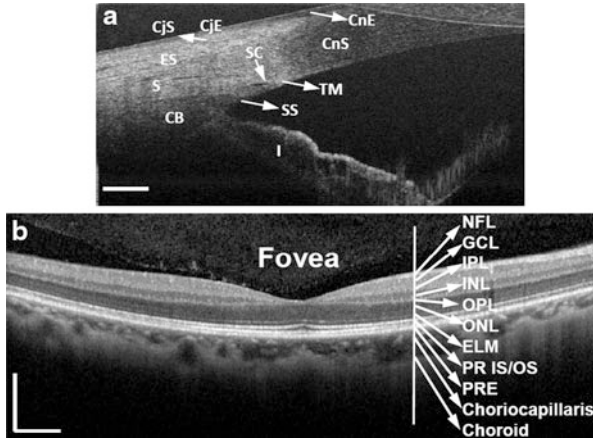
Fig. 16.5 (**a**) In vivo microstructure imaging of the human corneo-scleral limbus from a temporal location, where CnE, corneal epithelium; CnS, corneal stroma; CjE, conjunctival epithelium; CjS, conjunctival stroma; ES, episclera; S, sclera; SS, scleral spur; CB, ciliary body; I, iris; TM, trabecular meshwork; SC, Schlemm's canal. (**b**) In vivo OCT reveals detailed morphological features within retina and choroid, where NFL, Nerve fiber layer; GCL, ganglion cell layer; IPL, inner plexiform layer; INL, inner nuclear layer; OPL, outer plexiform layer; ONL, outer nuclear layer; ELM, external limiting membrane; PR IS/OS, photoreceptor inner and outer segments; RPE, retinal pigment epithelium. The scale bar represents 500 μm (Courtesy of Biophotonics and Imaging Laboratory, University of Washington)

retinal profiles. It can also quantitatively assess retinal thickening caused by macular edema and other diseases. Further studies have shown that the potential of OCT to quantify the amount of serous retinal detachments, macular holes, and macular edema, [130, 131] and to assess glaucoma [132].

With the use of a laboratory-based ultra-broadband femtosecond titanium–sapphire laser light source, an axial resolution of OCT for ophthalmologic applications has been recently advanced to about 1–3 μm [133, 134], enabling unprecedented in vivo imaging of intraretinal subcellular structures. The availability of this technology for clinical research and patient care will depend mainly on the availability of suitable sources for ultra-broad-bandwidth light, but it will no doubt have enormous impact on the future care of our vision.

16.3.3 Developmental Biology

Some of the exciting applications of OCT have occurred in the basic science of developmental biology. Studies have shown the promises of OCT to monitor in real time the developing neural and embryonic morphology [19, 29, 136–143] of *Xenopus laevis, Rana pipiens, Brachydanio rerio*, and chicken and rodent embyros.

Figure 16.6 shows in vivo 3D OCT images scanned from a 5-day-old chicken embryo, the time point at which its heart is nearly proper formed. The images have
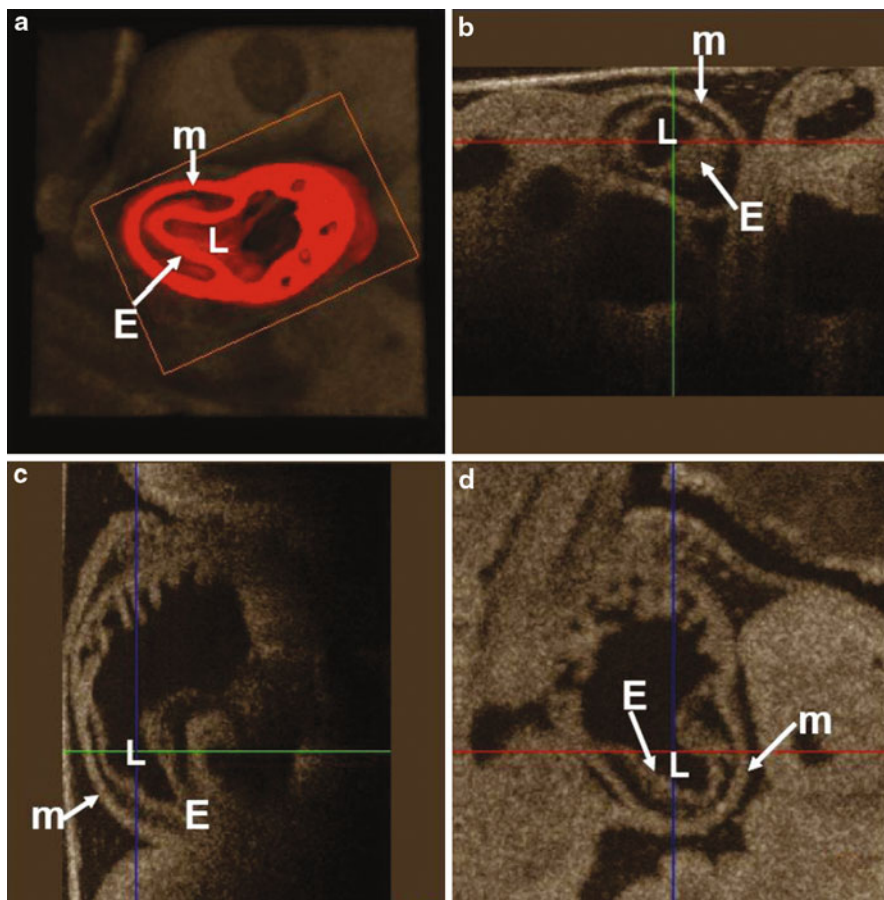
Fig. 16.6 In vivo 3D OCT images scanned from a 5-day-old chicken embryo. The 3D dataset enables the accurate segmentation of the heart, as shown in (**a**): (**b**) the sagittal scan, (**c**) the longitudinal scan, and (**d**) the transverse scan, where *m* denotes the myocardium, *E* the endocardium, and *L* the lumen (Courtesy of Biophotonics and Imaging Laboratory, University of Washington)

resolutions of 8 μm (axial) and 20 μm (transversal) where the gray level corresponds to the logarithm of back-scattered light intensity collected by the optical system, with white representing the highest backscattered signal. These images show high-resolution details of pathologically important internal structures, including myocardium, endocardium, and lumen.

The current imaging speed of the OCT system of more than hundreds of kilo-Hz enables the dynamic heart microstructures to be captured in vivo at the early development stage, useful for further understanding of the dynamic interaction of genetic and environmental factors that determine the generation of the basic elements, such as cells, extracellular matrix, adhesion molecules, and how these
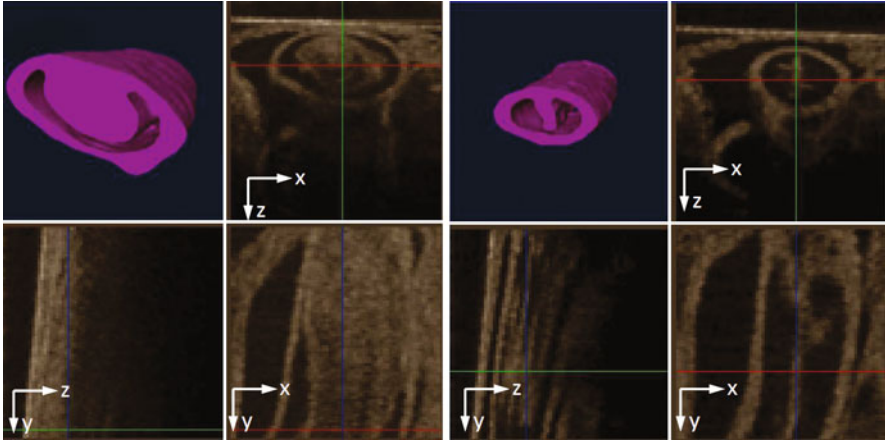
Fig. 16.7 High-speed OCT system enables 3D imaging of chicken embryos at the early development stage. Shown are the 3D images captured at the time instant when the out-flow tract was maximally dilated (*left panel*) and maximally constricted (*right panel*) (Courtesy of Biophotonics and Imaging Laboratory, University of Washington)

basic elements are assembled into a properly functional heart. Figure 16.7 illustrates results obtained from a 92-kHz OCT system that captures the beating heart of a chicken embryo at 3 days old, at the time point when the heart is merely in a form of a tube, the so-called out-flow-tract (OFT). With the help of post-data processing, 4D non-gated cardiac OCT images can be synchronized to obtain useful morphological information of the dynamic heart [140]. Figure 16.7a shows the 3D OCT image captured at the time instant when the chick OFT was maximally dilated, while Fig. 16.7d demarcates the 3D image captured when the OFT was maximally constricted. Although the current OCT system does not permit the imaging of individual cells due to its limited resolution, it performs well in imaging larger tissue and organ morphology, the structures that are too large to image in vivo with confocal microscopy. The above results demonstrate that OCT has applications to developmental biology because it can image biological species noninvasively and in real time. Such noninvasive 3D imaging of the embryonic internal organs could make OCT a powerful monitoring tool for developmental biology.

16.3.4 Dermatology

Dermatology appeared to be another promising application field for OCT due to the obvious ease of access [27]. However, it turned out that skin is a much less favorable subject for OCT imaging than previously thought because of strong scattering of the probe light and poor optical contrast between structural components in clinically important areas. OCT penetration depth covers the stratum corneum, the living epidermis, and the dermis consisting mainly of a network of collagen and elastin fibers and fibroblasts. Nevertheless, it does offer potential for
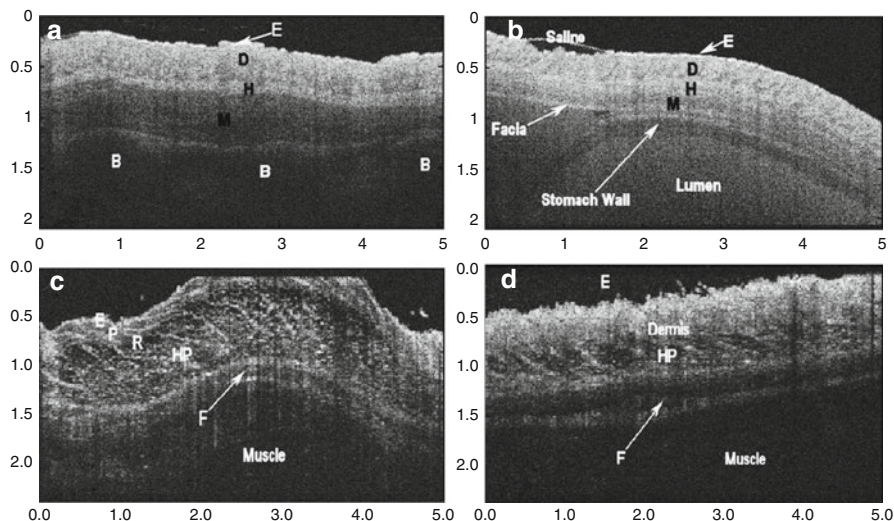
Fig. 16.8 Seeing through the rat skin with high resolution: (**a**) at the chest site and (**b**) at the abdomen site. (**c, d**) high-resolution imaging of pathological skin layers and features [29]

early detection of malignant melanoma [144, 145]. However, the successful application to this problem will depend on establishing correlations with the standard histopathology through a vast amount of experimental studies. Whether sufficient optical contrast exists between normal and pathological tissue at a cellular scale is a critical question that needs to be addressed in the future.

Figure 16.8 illustrates the ex vivo OCT images from a 5-day-old rat at (a) the chest and (b) the abdomen. It clearly demonstrates that OCT has the capability of seeing through the skin of the species with high resolution. Different layers and features starting from skin surface are delineated sharply, including epidermis (E), dermis (D), hypodermis (H), muscle (M), fascia (F), bone (B), stomach, hair follicles, and other features.

High-resolution delineation of the skin structures with OCT are shown in Fig. 16.8c, d, where a whole body of an adult Wistar rat was used in the experiments. Skin imaging with OCT has traditional difficulties because of the skin has high scattering properties to the near-infrared light which limit light penetration into deep skin. To reduce the light scattering in the skin, chemical agents were used in the experiments, including glycerol and propylene glycol, agents known to provide a bed for refractive index matching inside the superficial tissue [29, 184]. After topical applications of the chemical agent solutions onto the skin surface, OCT imaging allows us to visualize clearly the different layers and features in the skin, including epidermis (E), epidermal basement (EB), papillary dermis (P), reticular dermis (R), hypodermis (HP), fascia (F), muscle, and hair follicles. Far more detailed structures are delineated in the dermis zone. Note that the experiments were done with topical applications of glycerol solution, Fig. 16.8c, and propylene glycol solution, Fig. 16.8d.
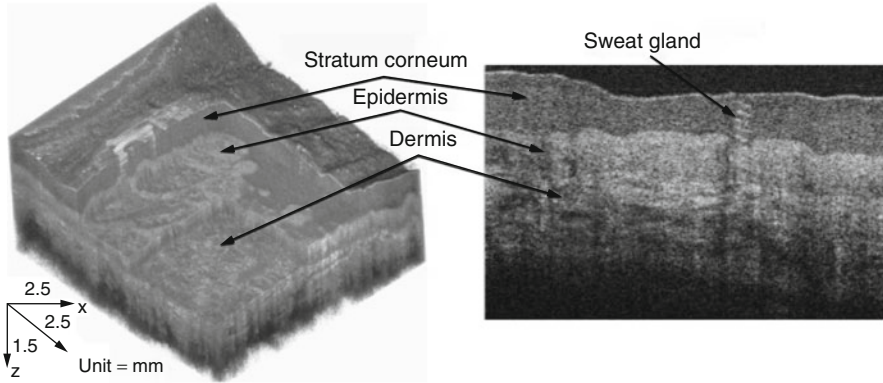
Fig. 16.9 High-resolution visualization of human skin layers and features in vivo (Courtesy of Biophotonics and Imaging Laboratory, University of Washington)

With the advancement of continuous OCT development in terms of imaging speed and spatial resolution, it is now possible to image detailed pathological features and important layers within the human skin in vivo. Figure 16.9 shows such an example captured using a 1,310 nm OCT system with 180 kHz A-scan rate and ∼5 μm spatial resolutions from a human palm region of a volunteer. The powerful ability of OCT in delineating the microstructures within skin promises future clinical utility of OCT in the diagnosis, treatment, and management of skin diseases, such as cancer, port-wine stain, and psoriasis.

16.3.5 Gastroenterology

Gastrointestinal disorders, including cancer, represent a major international health problem. Conventional gastrointestinal endoscopic diagnosis is predicated on the gross morphological characteristics of mucosal and submucosal abnormalities [146]. However, endoscopic diagnosis is less successful in clinical situations where the underlying morphological or biochemical premalignant changes do not alter gross architecture. Due to its high resolution and in-depth imaging capability, OCT has potential in the future routine clinical application in gastrointestinal endoscopy [147]. The depth range of OCT imaging, however limited, is sufficient to penetrate the mucosal lining of endoscopically accessible organs of the gastrointestinal tract to provide in-depth images with a resolution superior to currently available clinical imaging techniques [21–24].

OCT images of the normal esophagus, Fig. 16.10a, and esophago-gastric junction, Fig. 16.10b, allow the visualization of morphology of the mucosa and submucosa, and distinguish the transitional features from esophagus to stomach. From Fig. 16.10a, the upper portion of the mucosa, including stratified squamous epithelial (SE) and lamina propria (LP), appears homogeneous in the OCT image.
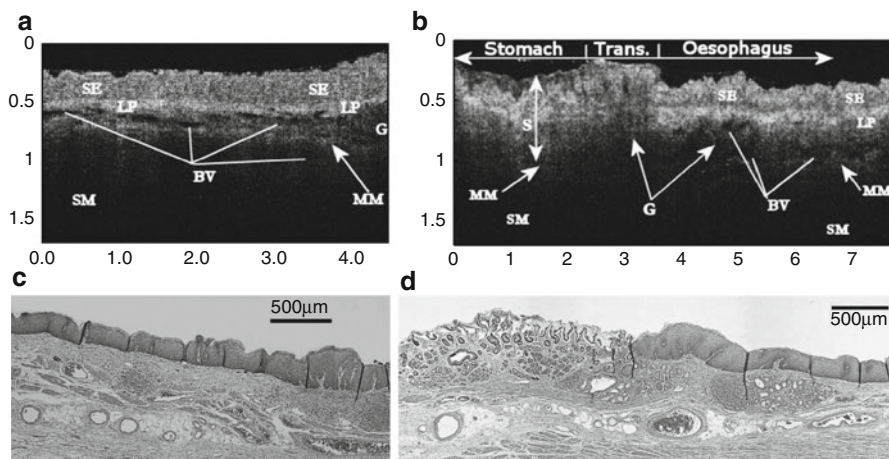
Fig. 16.10 High-resolution OCT images of normal (**a**) esophagus and (**b**) esophago-gastric junction, where *S* denotes the secretory glands, *SE* the stratified squamous epithelium, *LP* the lamina propria, *MM* the muscularis mucosae, *ED* the excretory ducts, *BV* the blood vessels, and *SM* the submucosa; and their corresponding histology (**c**) and (**d**), respectively (Courtesy of Cranfield Biophotonics Group)

The muscularis mucosa (MM) is more highly reflective than the mucosa. Numerous blood vessels can be identified in the lamina propria zone.

The transition from the esophageal to the gastric tissues was clearly visualized by the OCT images as shown in Fig. 16.10b. It demonstrated that the mucosa of the tract undergoes an abrupt transition from a protective stratified squamous epithelium (SE) to a tightly packed glandular secretory mucosa (S). The lamina propria (LP) appears highly reflecting and homogeneous in the esophagus. The muscularis mucosae (MM) is continuous across the junction, though it is less easily seen in the stomach, where it lies immediately beneath the base of the gastric glands. Other architectural features such as the excretory ducts, blood vessels, and esophageal glands were also clearly delineated in the OCT images.

The OCT images of normal colonic tissue allow visualization of the morphology of the mucosa (M), submucosa (SM), and muscle layers (ML). This is presented in Fig. 16.11a. A distinct feature of mucosa for the large intestine is its unbranched simple tubular glands (crypts of Lieberkuhn), which extend through the lamina propria to the muscularis mucosae (MM). Such a feature is clearly delineated in the OCT images, where they lie immediately above the muscularis mucosae, while the latter is seen as a high reflecting layer (see upper portion of Fig. 16.11a). The muscle layer of the colon is seen as a dark layer because the muscle highly attenuates the incoming light. The regular horizontal lining seen in the muscle layer (see bottom of Fig. 16.11a) probably demonstrates the fiber-bundle arrangement of muscularis externa.

The eventual target for endoscopic OCT includes real-time, in situ characterization of gastrointestinal premalignant changes such as dysplasia, as well as the identification
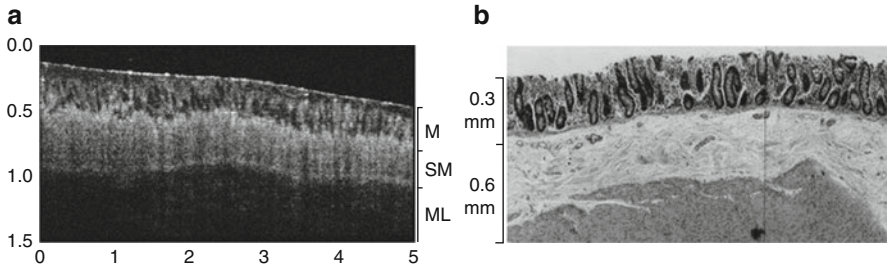
Fig. 16.11 High-resolution OCT image of (**a**) normal human colon and (**b**) its corresponding histology, where the mucosa (*M*), submucosa (*SM*), muscularis propria layer (*ML*), lymph nodule, and cryptscan be visualized (Courtesy of Cranfield Biophotonics Group)

and staging of small, superficial cancers. Endoscopic implementations of OCT in vivo have been recently reported with some success [148, 149]. As OCT technology matures, however, accurate primary diagnosis and staging by OCT could have a significant impact on clinical care because small, early stage malignancies would be amendable to immediate curative therapy at the time of endoscopy. This capability would enable physicians to make diagnostic and therapeutic decisions at the time of examination without referring to the histopathological diagnosis that normally requires a time frame of 1 week.

16.3.6 Other Biomedical Applications

The distinct features of optical coherence tomography, e.g., high resolution, relative high penetration depth, and a potential for functional imaging, make OCT a suitable candidate for optical biopsy. It offers a wide range of promising applications across all biomedical imaging disciplines. Apart from the applications stated above, we mention below briefly a few other examples of high-resolution and functional OCT.

Due to optic-fiber implementation of system, OCT is predestined as an endoscopic modality for high-resolution intraluminal imaging of organ systems, including intravascular walls. Preliminary studies have shown that OCT can detect intramural collections of lipid within the intimal vessel wall [123, 150]. Compared with high-frequency (30 MHz) ultrasound, OCT (1,300 nm wavelength) yielded superior structural information [151, 152].

Colston et al. presented a fiber-optics-based dental OCT system operating at a central wavelength at 1,300 nm [153]. Penetration depth varied from 3 mm in hard tissues to 1.5 mm in soft tissues. Hard tissue structures identified were enamel, dentin, and dento-enamel junction (see Fig. 16.12, for example). In the early investigations, birefringence induced artifacts in the enamel OCT imaging [153, 154]. These can be eliminated by measuring the polarization state of the returned light using a polarization-sensitive OCT (PSOCT). Birefringence detected by PSOCT, however, has been shown to be useful as a contrast mechanism indicating pre-carious or carious lesions in both enamel and dentin [155, 156].

Fig. 16.12 OCT imaging of human tooth near the gingiva (*left*). Image size is 1.8 × 4 mm (Courtesy of Cranfield Biophotonics Group)
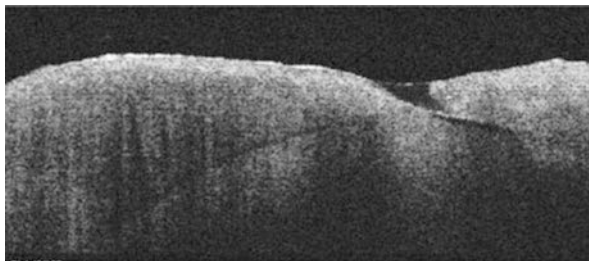
Fig. 16.13 OCT image of ceramics of a dish plate. The *top* is the glaze layer
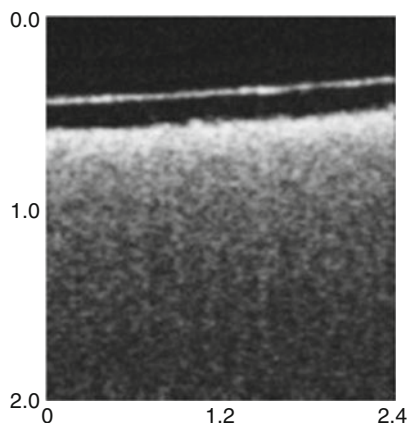
16.3.7 Industrial Applications

As stated previously, low-coherence interferometry has already been used in optical production technology and metrology [32–34]. With the current OCT technique, Dunker et al. [157] analyzed the applicability of OCT for nondestructive evaluation of highly scattering polymer-matrix composites to estimate residual porosity, fiber architecture, and structure integrity. OCT has also found its application to detect the subsurface extent of the Hertzian crack on the surface of a silicon nitride ball that has good agreement when compared with the predictions from crack propagation theories based on principal stresses and on maximum strain energy release [158]. Nondestructive evaluation of paints and coatings is another promising non-medical OCT application [159]. Operating in a confocal mode, OCT imaging though an 80-µm-thick highly scattering polymeric two-component paint layer (corresponding to an equivalent thickness of ten mean free paths) has been demonstrated by a light source with central wavelength at 800 nm and bandwidth of 20 nm [159].

Figure 16.13 gives an example of OCT light penetration depth through a hard industrial material of a ceramic dish plate where the light source used is 820 nm central wavelength and 25 nm spectral bandwidth [160]. Despite the high scattering nature of ceramic materials, the imaging depth beyond 2.5 mm is possible.

16.4 Effects of Light Scattering on OCT

16.4.1 Introduction

Thus far, OCT has been seen to have the capability to delineate noninvasively sub-surface microstructures, which has the potential to improve the diagnostic limits of currently available imaging techniques, allowing a wide range of clinical disorders to be addressed at an early stage. However, the reality is that OCT relies on the penetration and back-scattering of light into tissue to construct cross-sectional, tomographic images. It collects the back-scattered photons that have experienced less scattering, i.e., ballistic or least-scattered photons. However, unlike the transparent ocular organs where OCT found its most successful applications [18], there is no evidence that an OCT imaging depth beyond 2 mm for opaque biological tissues is possible [126]. This is largely due to the multiple scattering inherent in the interactions between the probing light and the targeted tissue, which limits light penetration into the tissue, and therefore prevents the deep microstructures from imaging. Generally, multiple scattering could degrade signal attenuation and localization, leading to an image artifact that reduces the imaging depth, degrades the signal localization and affects the image contrast.

Smithies et al. [161] developed a Monte Carlo (MC) model according to their specific OCT system geometry to investigate how signal attenuation and localization are influenced by multiple scattering effects, where two specific media (Intralipid and blood) are considered, representing moderately and highly anisotropic scattering, respectively. The multiple scattering effects were clearly demonstrated in terms of the spreading of the point spread function (PSF). In the meantime, Yao and Wang [162] developed a MC model to simulate how multiple scattering degrades the OCT signal attenuation into the tissue, by separate considerations of least scattering and multiple-scattered photons.

More recently, Wang [126] systematically investigated the multiple scattering effects on the OCT imaging performances including imaging depth, resolution degradation, and signal localization. Generally from the results, it was found that signal localization and attenuation are dependent on the optical properties of tissue. The high scattering coefficient and the low degree of forward scattering are the primary causes for the degradation of signal localization and attenuation, leading to complication of interpretation of the measured OCT signals. More importantly, it was found that the imaging resolution is a function of the probing depth within the medium, as opposed to the claimed OCT system resolution. This fact has been overlooked recently in the OCT imaging applications. The imaging resolution is greatly reduced with increasing depth; this case is even more severe for the highly scattering medium. Therefore, attention must be paid to this fact when applying the OCT to the human organs because of the high scattering nature of tissue.

Let us revisit the OCT system by looking closely the backscattering light from the high scattering medium that has the possibility to contribute to the interference signal. A simple schematic of OCT system when probing the highly scattering medium is illustrated in Fig. 16.14, where the sample beam progressively loses its

Fig. 16.14 Simple schematic of OCT system showing scattering interactions between a probing beam and biological tissue. Three types of interactions are backscattered from within the tissue: single scatter *a*, small-angle scatter *b*, and wide-angle scatter *c*. A layer with a thickness Δz at the depth of *z* is the expected layer for OCT localization
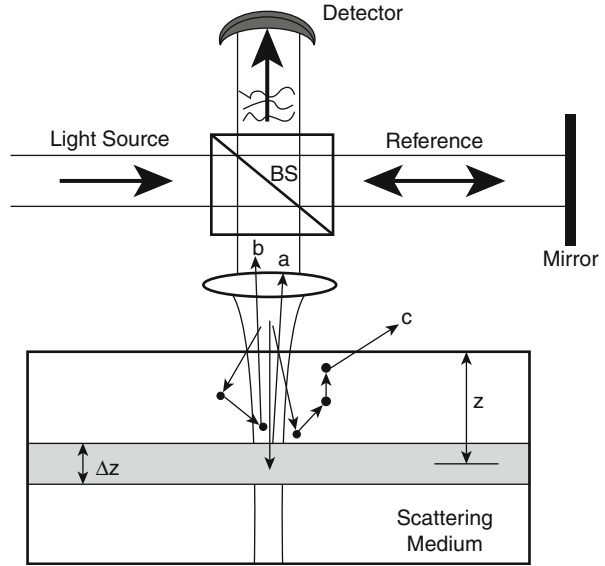
spatial coherence as it penetrates a turbid biological tissue. This loss of coherence results from the scattering by a variety of cellular structures with sizes ranging from less than one wavelength (e.g., cellular organelles) to several hundreds of micrometers (e.g., the length of a collagen fiber). As illustrated in Fig. 16.14, the dominant scattering interaction of the probing beam in the turbid medium can be categorized into three types [126, 163]: (1) single backscatter *a*, (2) small angle forward scatter *b*, and (3) extinction by absorption or wide angle scatter *c* (i.e., light scattered out of the view of the interferometric receiver). The detector will only receive the first two categories of scatters because of the heterodyne detection characteristics of the OCT system. Furthermore, the low-coherence light source used, as stated in the Sect. 16.2, provides a time gate to enable the detector to only receive those photons that travel beneath the tissue surface, with their optical path lengths matched to the optical path length in reference arm to within coherence length of the light source. Consequently, the OCT system in reality plays a role to sieve all the backscattering photons emerging at the detector according to their arrival times, or equivalently the optical path lengths that photons have traveled. For simplicity, we only consider the optical path length of the photon traveling beneath the tissue surface, i.e., the tissue surface is assumed to correspond with the zero position of reference mirror. Therefore, to enable the detector to produce the signal, the following criteria must be fulfilled:

$$|L_p - 2nz|, < \frac{L_c}{2}, \tag{16.17}$$

where L_p is the optical path length that the photon has traveled within the tissue, n is the refractive index of the medium, and z is the depth of a layer whose distance from the tissue surface matches the scanning distance of mirror, nz, in the reference arm.

For the signal localization, we normally expect that the detected photons be backscattered from the layer whose thickness is determined by

$$2n\Delta z = L_c. \tag{16.18}$$

However, because of multiple scattering there are possibilities for those photons contributing to the detected signal that are not backscattered from the expected layer, z, but fulfill the criteria of (16.17). As a consequence, this part of the photons degrades the signal attenuation, localization, and resolution because they are not from the desired layer, leading to a signal artifact complicating the interpretation of OCT image. To gain insight into how single and multiple scattering effects would influence the signal attenuation and localization, it is therefore useful to classify the photons according to their localization information. We could classify the detected photons into those photons being backscattered from the desired layer, z, and those backscattered otherwise but fulfilling the criterion of (16.17). Due to the requirement of matching the optical path lengths, the photons in the former must undergo fewer scattering events and very small-angle scattering including the single back-scattering events, we therefore term this part of photons as the least scattered photons (LSP). Those photons that satisfy (16.17) but are backscattered from a depth other than the desired layer are treated as the multiple scattered photons (MSP) that have experienced a wider-angle scattering. Clearly, the LSP signal is particularly useful as it provides localized optical information about the targeted layer; whereas the MSP signal consists of multiply scattered photons that are not from the desired layer, leading to the degradation of detected signal.

There is a clear relationship between the scattering interaction types described earlier in this section and the photon classifications that will be used in this study. The MSP comes solely from the interaction type b, while the LSP includes the interaction type a and part of type b because the photons backscattered from the desired layer might be subject to multiple scattering but with very small-angle scattering. A distinct difference between them is that the LSP and MSP have been sorted according to their optical pathlengths, thereby enabling the investigation of their influence on the OCT signal attenuation and localization.

With these conventions in mind, we now turn to look at some ways that multiple scattering affects OCT imaging performance by the use of the Monte Carlo simulation technique. For details, please see reference [126].

16.4.2 The Effects of LSP and MSP on Attenuation

To investigate the influence of the photons coming back from the specific layer of interest, it is best to investigate separately the LSP and MSP signals on the backscattering profiles. Figure 16.15 illustrates such results for $\mu_s = 40 \text{ mm}^{-1}$
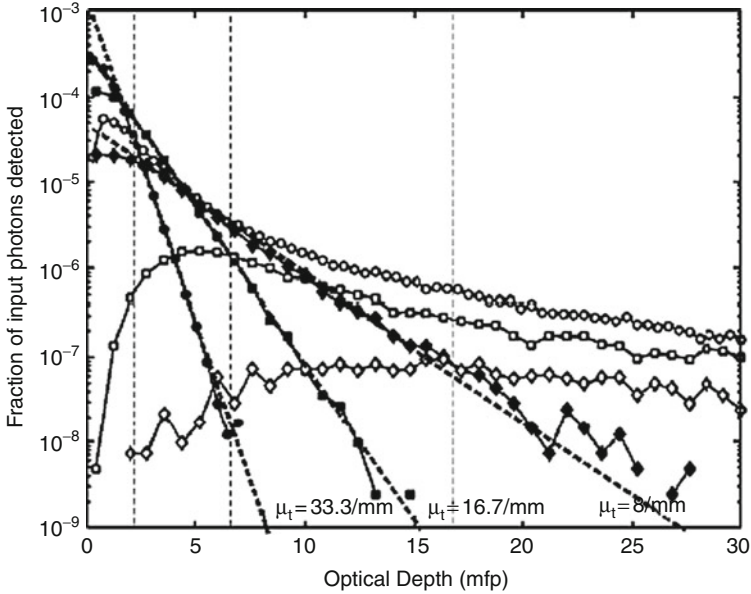
Fig. 16.15 The profiles are shown as the backscattering intensities separately for the LSP and MSP photons for the media with optical properties of $g = 0.7$ (*circle*), 0.9 (*square*), and 0.98 (*diamond*), respectively, while $\mu_s = 40$ mm^{-1} is kept the same for all the media. The *curves with solid symbols* represent the LSP photons, and those *with hollow symbols* the MSP photons. The *vertical dashed lines* from left to right indicate the critical imaging depth for $g = 0.7, 0.9$, and 0.98, respectively. *Thick dashed lines* represent the least square fits of the LSP signals

with $g = 0.7, 0.9$, and 0.98, respectively. It can be seen that the strength of the MSP signal increases with decreasing g in the medium at any optical depth of light penetration. This indicates that the photons that have reached a depth that does not correspond to the desired layer have a greater chance of emerging at the detector for the less anisotropic medium, leading to a greater degree of uncertainty in signal localization. The signal from LSP has an approximately logarithmic linear relationship with the probing depth for all cases but with different slopes. The slopes for the media investigated are calculated as 33.3, 16.7, and 8.0 mm^{-1} for $g = 0.7, 0.9$, and 0.98, respectively. These values deviate significantly from the theoretical value of 40 mm^{-1}, with the worst case for the highest g. This is probably understandable because the higher the value of g, the greater the degree of forward scattering of photons in the medium, leading to a greater chance of the photons reaching the detector while satisfying the criterion of (16.17). Obviously such photons are able to survive more scattering events because of small-angle scattering.

Because the OCT signal is the summation of the MSP and LSP, it appears that the critical depth for optical imaging is the depth where the signal from the LSP equals that from the MSP as the imaging contrast beyond this depth will be less than 1. These depths are illustrated in Fig. 16.15 as vertical dashed lines from left to right

Fig. 16.16 Photons detected plotted as a function of the number of scattering events, backscattered from the specific depths at 50 μm (*circle*) and 100 μm (*square*), respectively. *Solid curves* are from LSP signals, while *dashed curves* are from MSP signals. Note that the number of detected photons backscattered from 100 μm is artificially magnified by five times to facilitate the comparisons
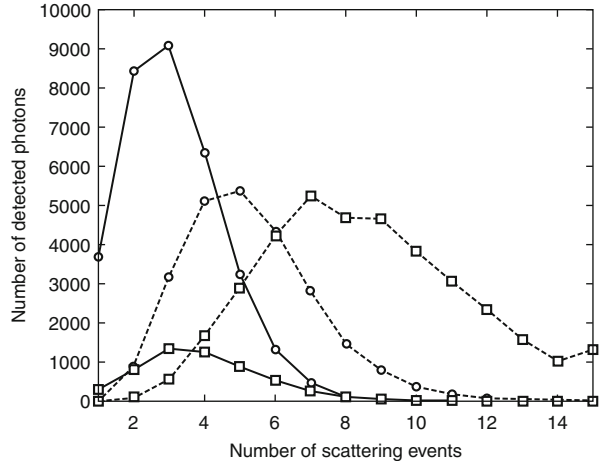
for $g = 0.7$, 0.9, and 0.98, respectively, corresponding to 2 MFP, 6.65 MFP, and 17 MFP, where MFP represents mean free path length measured as optical depth of $\mu_s d$. It should be noted that the critical depth, at which the MSP signal levels with the LSP signal, should actually be greater because the simulations do not take into account the polarization effects. The MSP photons undergo more scattering events than the LSP photons; the average scattering events increase much faster for the MSP photons with increasing depth. This is illustrated in Fig. 16.16, where the detected photons are plotted as a function of the number of scattering events for the LSP and MSP signals backscattered from the depths of 50 and 100 μm, respectively. The optical parameters used for Fig. 16.16 are $\mu_s = 67 \text{ mm}^{-1}$ and $g = 0.7$. Please note that the number of detected photons for the case of 100 μm has been artificially magnified by five times to facilitate the comparisons. All the curves are skewed towards the lesser number of scattering events. The average number of scatterings from the LSP signal has only a slight increase from the depth of 50–100 μm, that is, from 2.5 to 2.8 scattering events, respectively, while for the MSP signal, the average scattering increases much faster from 50 to 100 μm, that is, from 4.6 to 7.4 times. As multiple scattering depolarizes the light, the MSP photons are progressively and rapidly randomized with the increase in probing depth. As a consequence, the actual signal from MSP should be much lower than the calculated signals.

Despite the greater degree of degradation of signal attenuation, the probing critical depth increases dramatically with the increase of the anisotropic factor of the medium as illustrated in Fig. 16.15. This is particularly useful in the optical clearing of blood by the use of biocompatible dextrans, where the dextrans induce blood cell aggregation, an effect that might increase the forward direct scattering of the blood solution, leading to an enhanced optical imaging depth for OCT imaging through the blood [117, 124].

16.4.3 Signal Localization

As a photon penetrates the turbid biological tissue, it progressively loses its spatial coherence due to the tendency of having a greater chance of being scattered by the tissue. In the meantime, the photons multiply backscatter from within the tissue at a greater depth, and those that are merged at the detector will have a greater chance of fulfilling the criterion of (16.17) for the photon categories of either MSP or LSP. It is the MSP that degrades signal localization because it is from a depth other than the expected layer, leading to reduced axial resolution of the OCT image. Signal localization was thus investigated systematically by means of the point-spread function (PSF) at the specific depth, for different optical properties to illustrate how the LSP and MSP contribute to signal localization.

Figure 16.17 gives examples of depth point spread function (zPSF) at different probing depths for the turbid media representing moderate scattering in the left column ($\mu_s = 10$ mm^{-1}) and high scattering in the right ($\mu_s = 67$ mm^{-1}). The figures were obtained for $g = 0.7$, 0.9, and 0.98 from top to bottom, respectively, to allow us to scrutinize the influence of the anisotropic parameter of the medium on the signal localization. The depths monitored are indicated in each figure. The filled symbol curves are the actual PSFs that are the summation of LSP and MSP signals from a specific depth. However, to investigate the effects of LSP and MSP signals separately on the PSFs, the signals from the LSP alone are plotted in each case, represented by the hollow symbol curves.

First, it is obvious that the worst case is from the medium with the highest scattering coefficient and lowest degree of forward scattering, i.e., $\mu_s = 67$ mm^{-1} and $g = 0.7$ in this case (see the top right figure), where signal localization is merely discerned at a depth of 50 μm. Even at this depth, the contribution from an MSP signal is large enough to degrade the signal localization, where it can be seen that the PSF curve is skewed towards the nominal probing depth, indicating that the photons multiply scattered within the medium before this depth have more chances of surviving to reach the detector. Moreover, the photons backscattered from a very shallow depth at approximately 5 μm still survive the scattering to meet the criterion of equation (16.17) for depth localization at 50 μm. With an increase in probing depth to 150 μm, the PSF is overwhelmed by the MSP signal with only a few photons belonging to the LSP category. At this depth the signal localization is totally lost for OCT imaging. Furthermore, the axial resolution and imaging contrast are greatly reduced. The claim of high-resolution optical imaging of OCT is therefore questionable for highly scattering biological tissues. The axial resolution of OCT imaging is dependent on the optical properties of tissue and is a function of depth.

Figure 16.18 illustrates the measured axial resolution from the simulation results as a function of depth for the cases of $(\mu_s, g) = (67$ mm$^{-1}, 0.7)$, $(67$ mm$^{-1}, 0.9)$, and $(10$ mm$^{-1}, 0.9)$, respectively. The axial resolution of the OCT system is merely kept up to the depth of 50 μm for the case of $(\mu_s, g) = (67$ mm$^{-1}, 0.7)$. After this depth, the actual axial resolution degrades exponentially with the increase of depth, where it becomes approximately 220 μm at the depth of 200 μm as opposed to the system
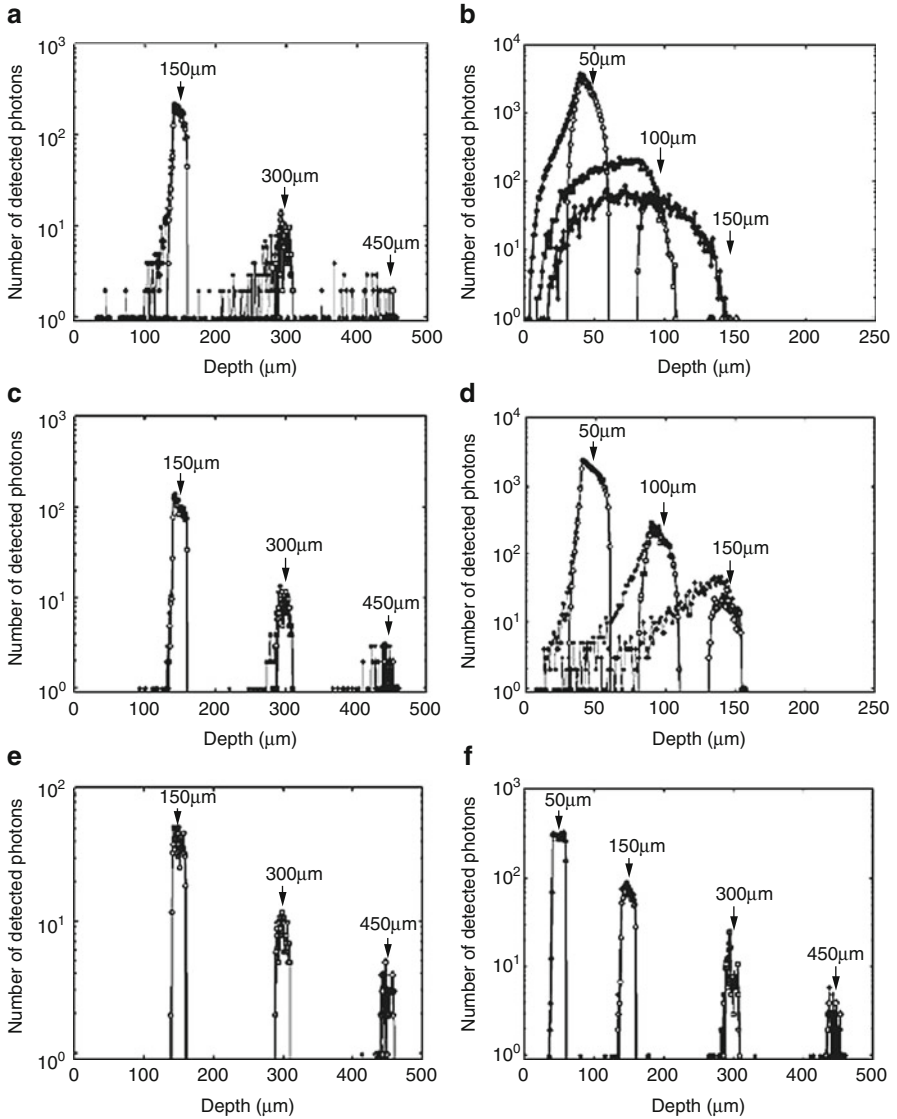
Fig. 16.17 Depth point spread functions (*solid symbol curves*) at different probing depths as indicated, for the turbid media representing moderate scattering ($\mu_s = 10$ mm^{-1}) in the *left column* and high scattering ($\mu_s = 67$ mm^{-1}) in the *right*. From *top* to *bottom*, $g = 0.7$, 0.9, and 0.98, respectively. The LSP photons are plotted as the curves with *hollow symbols*

resolution of 40 μm. With the increase of g to 0.9, this performance has been improved, with system resolution retained up to a depth of 100 μm. If, in the meantime, the scattering coefficient of the medium is reduced, for example, to $\mu_s = 10$ mm^{-1} in this case, the probing depth at which imaging resolution is

Fig. 16.18 The measured axial resolution from the simulation results plotted as a function of the probing depth for $(\mu_s, g) = (67$ mm^{-1}, 0.7) (*circle*), (67 mm^{-1}, 0.9) (*square*), and (10 mm^{-1}, 0.9) (*diamond*), respectively
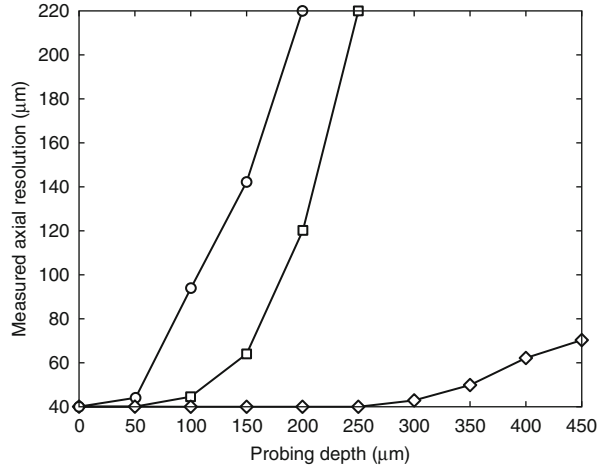
retained to the theoretical value would dramatically improve. This result is particularly welcome for the optical clearing of tissues with the purpose of enhancing the imaging depth of OCT, which will be discussed in the next section.

With the reduction of the scattering coefficient (compare the left and right columns in Fig. 16.17), signal localization improves, with the lesser MSP signal contributing to the depth of PSFs. This indicates that the low scattering medium offers the more localized signal at any probing depth, which alternatively implies that the light penetration depth, i.e., optical imaging depth, is enhanced with less deterioration of the imaging resolution as stated above. On the other hand, it can be clearly seen from Fig. 16.17 that, with increasing g, the signal localization at any depth for the scattering medium improves dramatically, where the highly forward scattering medium, i.e., $g = 0.98$, offers the best signal localization for all the cases investigated; see the bottom two figures for $\mu_s = 10$ mm^{-1}and $\mu_s = 67$ mm^{-1}, respectively. In these cases, only a few photons from the MSP category survive the scattering to contribute to final PSF at a depth of up to 600 μm.

However, the results shown in Fig. 16.17 do not give us the information as to how many times a photon has been scattered within the medium for both the LSP and the MSP signal before reaching the detector. Figure 16.19 gives such information of the average scattering event of the photons within the medium as a function of the probing depth for the media with $(\mu_s, g) = (10$ mm^{-1}, 0.7 or 0.9) and (67 mm^{-1}, 0.7 or 0.9), respectively. It is clear that the higher the scattering coefficient, the greater the number of scattering events of the photons at any depth before emerging at the detector in both LSP and MSP. For both the LSP and MSP photons, the average number of scattering events has an approximate linear relationship, with the probing depth for all the cases investigated; but this relationship is stronger for the MSP.

For the high scattering medium, $\mu_s = 67$ mm^{-1}, the average number of scattering events for MSP is close to 15 times at a depth of about 120 μm. Please note that,

Fig. 16.19 The average number of scattering events for the LSP (*hollow symbols*) and MSP (*solid symbols*), plotted as a function of probing depth for (**a**) $\mu_s = 10$ mm^{-1} with $g = 0.7$ (*circle*) or 0.9 (*square*), and (**b**) $\mu_s = 67$ mm^{-1} with $g = 0.7$ (*circle*) or 0.9 (*square*), respectively
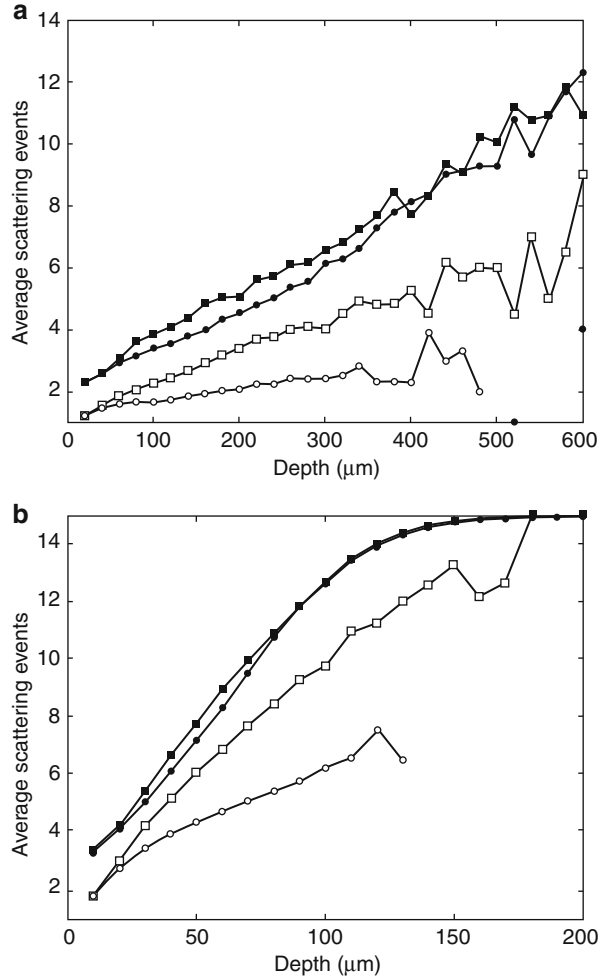
after this depth, the curve looks like running into a flat region for MSP; this is an artifact due to the fact that the maximum scattering number of photons monitored in our MC program is set to 15 times in order to save the memory for computing. In the meantime, with the increase in g, the average number of scattering events increases with increasing probing depth for both the LSP and MSP; however, the pace for LSP is faster than that for MSP. For example, at a depth of 300 µm for $\mu_s = 10$ mm^{-1} medium, the average number of scattering events for the LSP signal increases from 2.4 to 4.2, while for the MSP signal it only increases from 6.1 to 6.5. Bear in mind that the LSP photons have survived the criterion of equation (16.17), which alternatively means that they undergo a much smaller angle scattering than MSP photons.

Generally speaking, the average number of scattering events is much greater for MSP photons than for LSP photons. This is good in that the multiply scattered

Fig. 16.20 Measured PSF mean positions plotted against the probing depths for the media with g = 0.7 (*circles*), 0.9 (*squares*), and 0.98 (*diamonds*) and (**a**) $\mu_s = 10$ mm^{-1} and (**b**) $\mu_s = 67$ mm^{-1}, respectively. The *dashed lines* represent the nominal depth positions for PSFs
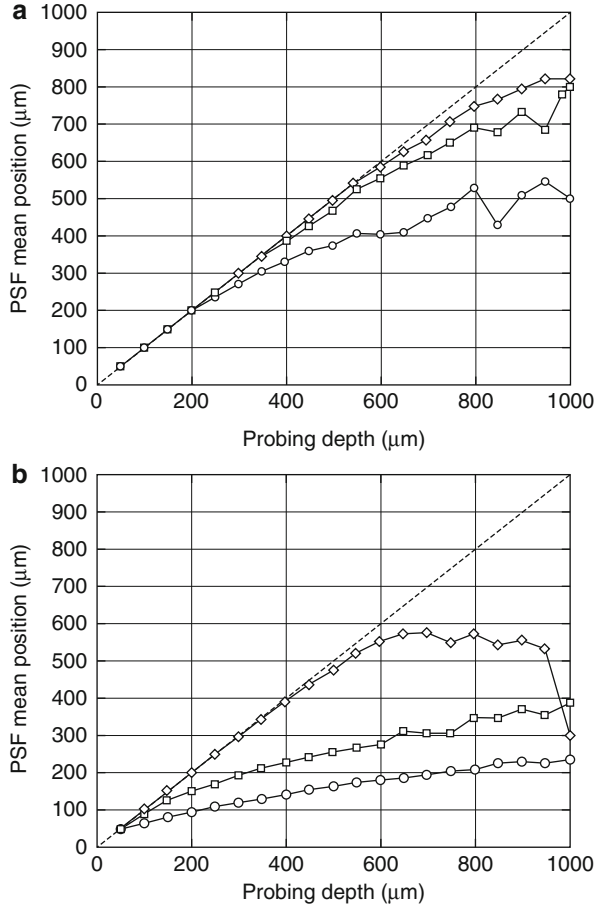
photons lose their polarization state progressively with an increase in scattering events, and thus actually contribute less to the final signal measured. The increased number of scattering events for increasing g accounts for the fewer slopes for LSP signals observed in Fig. 16.15, and is the primary cause of the degradation of signal attenuation. To investigate how signal localization depends on the optical properties, for example, μ_s and g, Fig. 16.20 gives such information for the determined PSF mean position from the simulations as a function of the probing depth for the media with g = 0.7, 0.9, and 0.98 and (a) $\mu_s = 10$ mm^{-1} and (b) $\mu_s = 67$ mm^{-1}, respectively. The broken lines in the figure represent the nominal depth positions for PSFs. It can be seen that for a less scattering medium with high g value, for example, $\mu_s = 10$ mm^{-1} and g = 0.98 in Fig. 16.20a, the best accuracy of signal localization throughout the depth monitored is given; the opposite is true for the highest scattering medium and lowest g investigated. For $\mu_s = 67$ mm^{-1} and g = 0.7, the accuracy of signal localization is only reliable up to a depth of 50 µm.

With increasing probing depth the ability of OCT to provide signal localization is greatly reduced. This is because the MSP photons progressively overwhelm the LSP photons with increasing depth. This effect makes OCT lose its localization capability, while the increase of g value dramatically improves signal localization, where it can be seen that for $\mu_s = 67 \text{ mm}^{-1}$ and $g = 0.98$ the signal localization is maintained up to about 600 μm. After this depth the accuracy starts to level off. Generally, the accuracy of signal localization is improved by either the reduction of the scattering coefficient or the increase of the degree of forward scattering of the medium.

Thus, overall, it can be concluded that the signal localization or imaging depth can be improved by either reduction of the scattering coefficient or increasing the anisotropic value of the medium, or both. It can also be seen that the manipulation of g towards a high value is more efficient than that of the scattering coefficient. This conclusion is particularly useful for the optical clearing of tissues by the use of biocompatible chemical agents for the purpose of enhancing the optical imaging depth for high-resolution optical imaging techniques. A recent study indicated that the mechanisms for improving the light penetration depth for the dextran-mediated blood is due to both the refractive matching and red blood cell (RBC) aggregation and disaggregation induced by the dextrans [78, 117]. The index-matching effect causes the reduction of the scattering coefficient of the medium, while RBC aggregation probably increases the anisotropic factor for the blood, leading to increased light penetration depth.

The above analysis has used the Monte Carlo simulation technique as a tool to illustrate the multiple scattering effects on the OCT imaging performance. It is worth noting that there are analytical models developed for analyzing the multiple scattering effects as well. Schmitt and Knüttel described an OCT model by the use of a mutual coherence function based on the extended Huygens–Fresnel principles of light propagation in homogeneous turbid media [165]. It was later extended by Thrane et al. by incorporating the so-called "shower curtain effect" (see also ▶ Chap. 17). This model considers the OCT signal as the summation of singly back-scattered light (coherent) and multiply scattered light (partially coherent) [166]. Most recently, Feng et al. further simplified Thrane's model through approximating the focusing optics in the sampling arm by an imaginary lens proximal to the tissue surface [167]. The advantage of the latter model is that it avoids the consideration of backscattering light from traveling in the free space between the focusing lens and tissue surface before mixing with the reference beam, i.e., observing the object embedded in scattering medium at the mixing plane through a non-scattering distance. The detailed description of the analytical models for OCT will be covered in ▶ Chap. 17.

16.5 New Technique to Enhance OCT Imaging Capabilities

16.5.1 Introduction

From the last section, we have seen that multiple scattering is a detrimental factor that limits OCT imaging performances, for example, imaging resolution, depth, and localization. To improve the imaging capabilities, the multiple

scattering of tissue must be reduced. Tissue as a scattering medium shows all optical effects that are characteristic of a turbid physical system. It is well known that turbidity of a dispersive physical system can be effectively controlled using immersion effect matching of refractive indices of the scatters and the ground material [168–171]. The living tissue allows one to control its optical (scattering) properties using various physical and chemical actions such as compression, stretching, dehydration, coagulation, UV irradiation, exposure to low temperature, and impregnation by chemical solutions, gels, and oils [171–182]; see also ▶ Chap. 5. Such methods of controlling optical properties of tissue have been explored to enhance the optical imaging capabilities of OCT [25, 124, 183–189]. The possible mechanisms of enhancing OCT imaging depth and contrast have been suggested [124, 167, 171, 183–192].

The depth of penetration for near-infrared light into a biological tissue depends on the scattering characteristics and absorptivity of the tissue. Optically, tissue can be described as a spatial distribution of refractive index on the microscopic scale that could be classified into those of the extracellular and intracellular components [192, 194]. Estimated from the dissolved fractions of proteins and carbohydrates, the intracellular and extracellular fluids have the approximate refractive index between 1.34 and 1.36 [195]. The results of earlier studies suggest that the tissue elements that contribute most to the local refractive index variations are the connective tissue fibers (bundles of elastin and collagen), cytoplasmic organelles (e.g., mitochondria), and cell nuclei [195, 196]. The refractive index of the connective fiber is about 1.47, which corresponds to 55 % hydration of collagen [197]. The nucleus and cytoplasmic organelles in mammalian cells that contain similar concentrations of proteins and nucleic acids, such as mitochondria and ribosome, have refractive indices that span within a relatively narrow range between 1.39 and 1.42 [198, 199]. However, other cytoplasmic inclusions, particularly pigment granules, can have much higher refractive indices [195]. Therefore, the local refractive index within the tissue can vary from anywhere within the background refractive index, i.e., 1.34, and 1.50, depending on what type of soft tissue is concerned. It is this variation of refractive index distribution within the tissue that causes a strong light scattering. Unfortunately, as stated in the last section, the light scattering limits light penetration depth and degrades the imaging contrast [126]. For non-interacting Mie scatterers, the reduced scattering coefficient of spheres is determined by the ratio of refractive indices of scattering center and ground matter [200, 201]. If the mismatch between scattering centers and the ground substance decreases, it would result in less scattering at the interface between the ground substance and cellular components, leading to the decrease of reduced scattering coefficient of tissue [167, 171, 187].

To describe theoretically the optical scattering in tissues, attempts have been made using the particle model with some success [192, 194]. Based on the model, the biological tissue is treated as that consisting of the discrete scattering centers with different sizes, randomly distributed in the background media. According to the Rayleigh-Gans approximation, the reduced scattering, μ'_s, of turbid media is

related to the reduced cross section, σ'_s, and the total number of scattering particles per unit volume, i.e., number density, ρ:

$$\mu'_S = \sum_{i=1}^{n} \rho_i \sigma'_{Si} = \sum_{i=1}^{n} \frac{3\varphi_i}{4\pi a_i^3} \sigma'_{Si}, \tag{16.19}$$

and

$$\sigma'_{Si} = \frac{9}{256\pi} \left| \frac{m_i^2 - 1}{m_i^2 + 2} \right| \left(\frac{\lambda}{n_0} \right)^2$$
$$\int_0^\pi (\sin u_i - u_i \cos u_i)^2 \frac{(1 + \cos^2\theta) \sin \theta (1 - \cos \theta)}{\sin^6(\theta/2)} \, d\theta \tag{16.20}$$

where $u_i = 2(2\pi a_i n_0/\lambda) \sin (\theta/2)$, $m_i = n_{Si}/n_0$ with n_{Si} and n_0 being the refractive indices of the i-th scattering centers and background medium, φ_i the volume fraction of the i-th particles and a_i the radius of the i-th scatterer. It can be seen that the reduced scattering coefficient of scattering medium is dependent on both the refractive index ratio, m_i, and the size of the scattering centers.

The most popular method in enhancing OCT imaging performances is to use the biochemical and hyperosmotic chemical agents to interrogate the tissue. Below we give some examples to intuitively illustrate to what degree the multiple scattering can be reduced and how the imaging depth and contrast of OCT imaging can be improved by the use of impregnation of tissue with the biochemical agents. The agents used in these examples are glycerol and dimethyl sulfoxide (DMSO).

16.5.2 Enhancement of Light Transmittance

The light transmittance and scattering after the application of chemical agents can be assessed quantitatively by the use of the near-infrared spectroscopic method. With the use of Varian Cary 500 spectrophotometer with an internal integrating sphere (Varian UK Ltd), Fig. 16.21a, b illustrates the shift of transmittance and diffuse reflectance spectra, respectively, over the range of 800–2,200 nm as a function of time when the native porcine stomach pyloric mucosa specimen was applied with 80 % glycerol. The curves shown in the figure were obtained at the time intervals of 0, 5, 10, 20, and 30 min, respectively, from bottom to top for transmittance (Fig. 16.21a) and from top to bottom for reflectance (Fig. 16.21b). It can be seen from Fig. 16.21 that, over the whole wavelength range investigated, the transmittance was increased with time. Diffuse reflectance was decreased over the range of 800–1,370 nm. The greatest increase in transmittance was at 1,278 nm, and the greatest decrease in reflectance was at 1,066 nm.

Figure 16.22a, b show the similar results from the samples with the application of 50 % DMSO, respectively, at the time intervals of 0, 5, 10, 20, and 30 min. Transmittance was enhanced and diffuse reflectance was reduced with the time course.
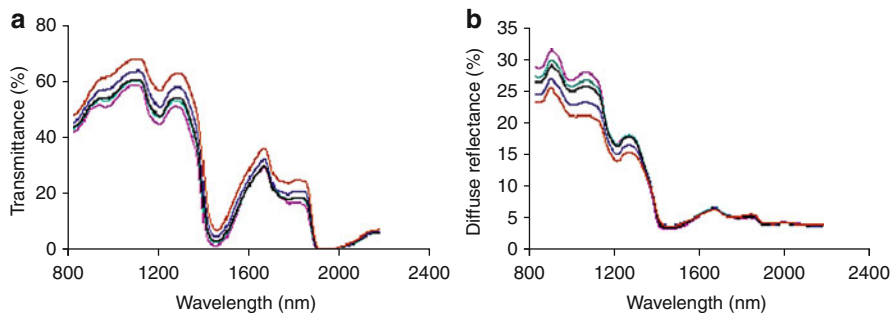
Fig. 16.21 Optical changes for porcine stomach pyloric mucosa before and after application of 80 % glycerol over the range from 800 to 2,200 nm measured by spectrophotometer. (**a**) Transmittance after application of the agent at the time intervals of 0, 5, 10, 20, and 30 min (from *bottom to top*), respectively. (**b**) Diffuse reflectance at the time intervals the same as in (**a**) (from *top to bottom*) [189]
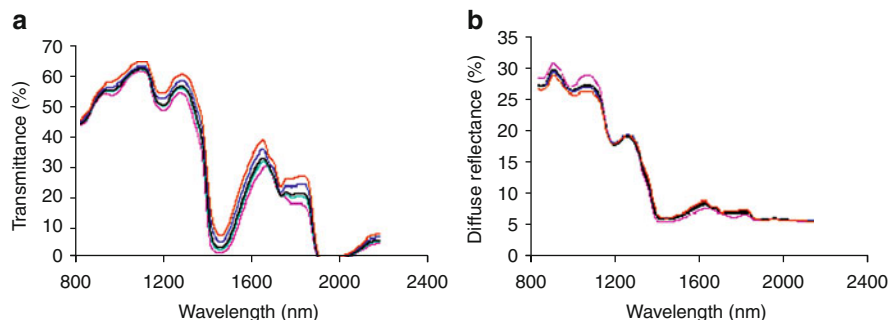
Fig. 16.22 Optical changes for porcine stomach pyloric mucosa before and after application of 50 % DMSO over the range from 800 to 2,200 nm measured by spectrophotometer. (**a**) Transmittance after application of the agent at the time intervals of 0, 5, 10, 20, and 30 min (from *bottom to top*), respectively. (**b**) Diffuse reflectance at the time intervals the same as in (**a**) (from *top to bottom*) [189]

From Figs. 16.21 and 16.22, it is clear that both glycerol and DMSO have the ability to clear the tissue, thereby enhancing the light transmittance through the tissue.

It is found that there is a strong correlation between optical clearing and water desorption [189–191]. The water activities for 80 % glycerol and 50 % DMSO measured with a water activity meter (Aqua Lab Model Series 3 TE, Labcell Ltd) yield 0.486 and 0.936, respectively. Figure 16.23 shows the water content measurements at 30 min after the treatment, where 80 % glycerol caused 15 % water loss, whereas 50 % glycerol and 50 % DMSO caused 9 % and 7 %. The patterns of optical clearing are similar to those of water desorption.

Because most of OCT system uses the light source with a central wavelength at 1,300 nm, Fig. 16.24 shows experimental results of the transmittance enhancement at about 1,300 nm after application of different chemical agent solutions, where it is

Fig. 16.23 Correlation between the NIR absorbance (measured at 1,936–1,100 nm) and time of application of 50 % glycerol and 50 % DMSO, respectively [189]
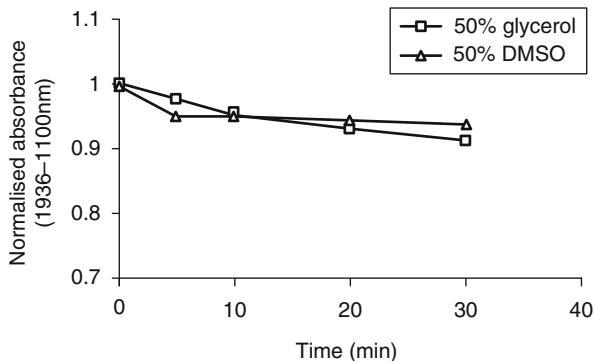
Fig. 16.24 Changes in transmittance at 1,278 nm against time for porcine stomach pyloric mucosa treated with 80 %, 50 % glycerol or 50 % DMSO [189]
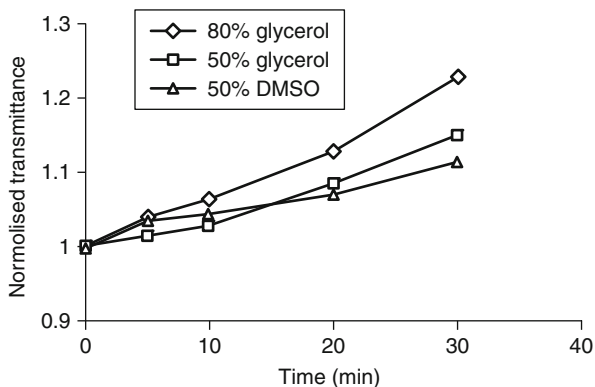
seen that transmittance was increased by approximately 23 % at 30 min after the application of 80 %, while 15 % and 11 % were received after the treatment with 50 % glycerol and 50 % DMSO, respectively.

The optical clearing induced by the agents studied is a time-dependent process [188, 189, 192]. This implies that the clearing effect occurs as a consequence of the diffusion of water out of the tissue, leading to dehydration [189, 190], and the diffusion of chemical agents into the tissue [189, 192], respectively. For tissue dehydration, the water will migrate from within tissue, where there is higher water potential and a lower osmotic potential, to the outside, where there is lower water potential and higher osmotic potential, because the applied agents have the higher osmotic potential than that of tissue fluids. The migration of water will be terminated if the osmotic pressure is balanced inside and outside of the tissue if the agent is impermeable to the tissue.

However, the glycerol and DMSO are both permeable to tissue, indicating that the agents will diffuse into the tissue at the same time when the water leaves the

tissue. The mass transport of the chemical agents within tissue is a complicated phenomenon that involves the bulk tissue and its constituent cells and fiber structures. Because tissue occupies the intracellular (and/or fibrillar) and extracellular (and/or extrafibrillar) spaces, we assume that the agent will first transport into the extracellular (and/or extrafibrillar–interstitial) space, and then into the intracellular (and/or fibrillar) space, leading to an activity for water in and out of the surrounding interstitial space (and/or cells). The general rule of water migration will apply, that is, the water will transport from an area with the higher water potential and lower osmotic pressure to an area with the lower water potential and higher osmotic pressure. When the agent transports from the inserted (topically or by injection) area into surrounding space, it induces a higher osmotic potential around and thus causes the water to migrate out from the surrounding interstitial space and to leave the intrafibrillar (and/or intracellular) space, causing the fibers and/or cells to shrink. As a rule, this is a second stage of the process. In the meantime, the glycerol and DMSO are membrane permeable, suggesting that the agent will diffuse into the intracellular space after it arrives at the extracellular space. The transmembrane permeability for glycerol and DMSO is much lower than that of water (water is on the order of 10^{-2} cm/min, whereas glycerol and DMSO are on the order of 10^{-5} cm/min [202, 203]), which accounts for an initial decrease in cell volume as water leaves much faster than the agent migrates into it. Therefore, much of the intracellular water leaves the cell while the clearing agent continues to migrate into the cell, leading to a gradual increase in volume that stabilizes with the time course. Because both the anhydrous glycerol and DMSO have the refractive indices of 1.47 [204], after the agent migrates into the extracellular and intracellular space, a refractive index matching environment is created by simply matching the chemical agents with the main scattering components within the tissue, leading to the enhanced light penetration together with the dehydration effect. It should be noted that this is different from the refractive index matching created by the dehydration where the matching is produced by the more closely packed scattering constituents.

On the other hand, the mass transport process is dependent on the permeability of water and the agents to the membrane, and the tissue as a whole. Among the glycerol and DMSO, the former has lower permeability than the latter. As a consequence, DMSO penetrates the membrane and tissue rapidly [205], and even across the stratum corneum of skin [204], which glycerol is not able to do. The study on the hamster skin by Vargas et al. [186] also showed that DMSO has a greater effect in enhancing the light transmittance than that of glycerol. However, the stomach tissue in the present study has different characteristics in allowing the agents diffusing into the tissue because it does not have a barrier of the stratum corneum for the skin case. In addition, the mucosa layer of stomach is composed of loosely packed cells, and glands and ducts with narrow lumens are rich, which would facilitate the agents diffusing into the tissue. Thus, the mass transport process would happen much quicker than that of the skin, with the DMSO faster than the glycerol. As a consequence, with the progress of agent transport, a spatial gradient is created because water efflux will occur at the surface first and then deeper as the diffusion front moves [206]. The move of diffusion front for DMSO is much more

rapid than that of the glycerol, indicating that the water efflux at the surface is occurring for a much longer time with glycerol than with DMSO.

Accordingly, the changes in optical properties are observed almost linearly with time with the application of 50 % glycerol (see Figs. 16.23 and 16.24), probably because the solution diffuses into tissue at almost the same rate as the water efflux at the surface. It is also understandable that 80 % glycerol has a greater slope for both the transmittance and reflectance because it has the stronger ability in dehydration. For the samples treated with 50 % DMSO, in the first 5 min, DMSO permeates faster and replaces water faster (Figs. 16.23, 16.24), and its optical clearing effect is greater than 50 % glycerol. After 30 min treatment, dehydration caused by 50 % glycerol is slightly higher than that by 50 % DMSO. Consequently, the optical clearing effect induced by 50 % glycerol is slightly greater than that by 50 % DMSO within the time period investigated, although they both have the same refractive indices. The better effect caused by DMSO at the beginning stage results from the different mass transport process of DMSO and glycerol, as stated above.

16.5.3 Enhancement of OCT Imaging Capabilities

In the last section, we clearly see that the chemical administration of tissue would increase light transmittance through the tissue, the effect of which would no doubt increase the imaging depth for OCT. Figure 16.25 shows dynamic OCT structural images of porcine stomach with the topical application of 50 % glycerol solution, which was recorded at the time intervals of 0, 10, 20, 30, 40, and 50 min, respectively.

The OCT system used was working at wavelength of 1,300 nm with axial and transverse resolutions at 15 and 20 μm, respectively. A metal needle was inserted into the tissue approximately 1 mm beneath the surface. The signals reflecting back from the needle surface were used to suggest improvement of back reflectance signal caused by the chemical clearing. The OCT image of the porcine stomach without the administration of glycerol has a visualization depth of approximately 1.0 mm, as shown in Fig. 16.25a. It can be seen that a significant improvement of the imaging depth is clearly demonstrated after the topical application of glycerol. The penetration depth has increased to about 2.0 mm after 50 min application of glycerol, as shown in Fig. 16.25f. Tissue shrinkage occurs after the administration of the agents to tissue, see Fig. 16.25b–f. The needle embedded in the tissue becomes brighter with the increase of the time duration, see Fig. 16.25b–f. It should be pointed out that the imaging contrast of Fig. 16.25c, d is also greatly improved. Such features as lamina propria (LP) and muscularis mucusae (MM) are clearly visualized in Fig. 16.25c, d. The neck, base, and MM layers of the tissue could be differentiated after 20–30 min application of glycerol. The reflection from the needle surface is also sharp within this period of time. But it is interesting to find out that, with the increase of time, the imaging contrast improvement disappears gradually with the further increase of time course, as shown in Fig. 16.25e, f.

Figure 16.26 is the dynamic OCT structure images of porcine stomach with the topical application of 50 % DMSO solution, which was again recorded at the time
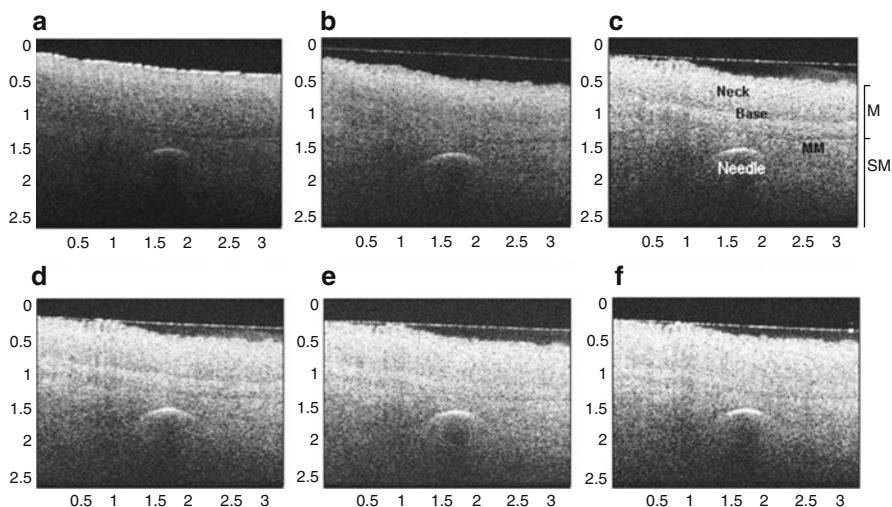
Fig. 16.25 Dynamic OCT images obtained at the time (**a**) 0, (**b**) 10, (**c**) 20, (**d**) 30, (**e**) 40, and (**f**) 50 min after the topical application of 50 % glycerol solution onto the porcine stomach tissue. All the units presented are in millimeters, and the vertical axis presents the imaging depth [188]
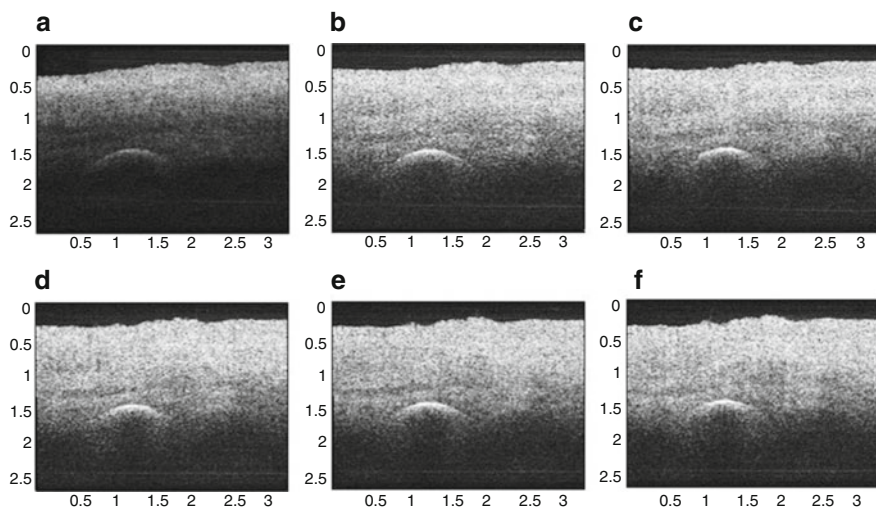
Fig. 16.26 Dynamic OCT images obtained at the time (**a**) 0, (**b**) 10, (**c**) 20, (**d**) 30, (**e**) 40, and (**f**) 50 min after the topical application of 50 % DMSO solution onto the porcine stomach tissue. All the units presented are in millimeters, and the vertical axis presents the imaging depth [188]

intervals of 0, 10, 20, 30, 40, and 50 min, respectively. Like the case with glycerol, it is also demonstrated that a significant improvement of the imaging depth is achieved in Fig. 16.26b–f when compared with Fig. 16.26a after the application of DMSO. The penetration depth has increased to about 2.0 mm after 50 min
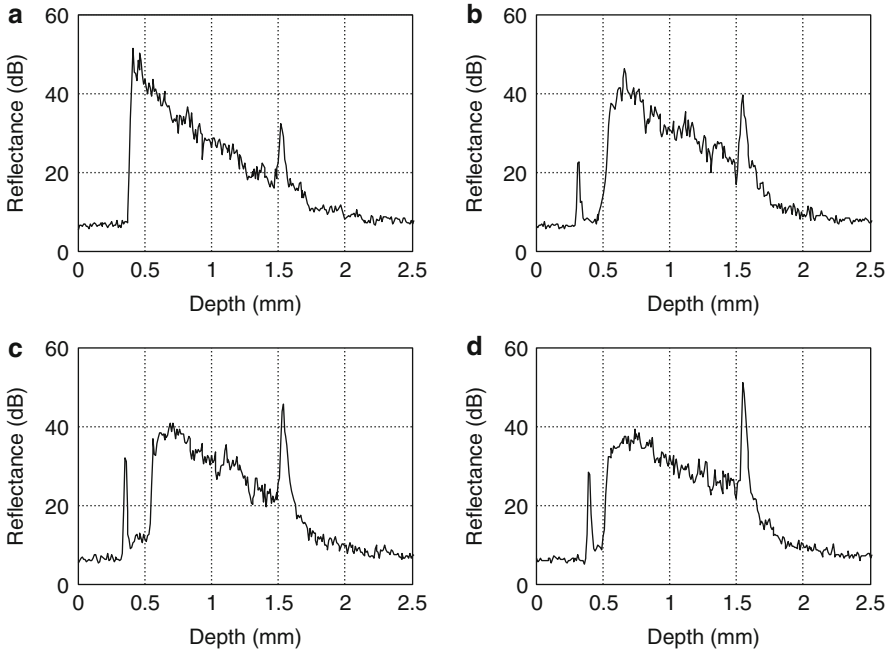
Fig. 16.27 The measured OCT in-depth back-reflectance profiles at the following times: (**a**) 0, (**b**) 10, (**c**) 30, and (**d**) 50 min after topical application of glycerol solution [188]

application of DMSO, as shown in Fig. 16.26f. However, image contrast enhancement was hardly observed during any period of time in the experiments. Tissue shrinkage due to the dehydration of the tissue is not clear, as seen from Fig. 16.26b–f. The reflection signal from the needle surface is approximately the same level from Fig. 16.26b–f.

To further illustrate the different dynamics induced by the two agents, back-reflectance signals along with depth from the stomach tissue with glycerol and DMSO administrations are quantitatively plotted in Figs. 16.27 and 16.28, respectively. The signals were obtained at the different time intervals of 0, 10, 30, and 50 min, respectively, at the same spatial point, but averaged over 10 repeated scans to minimize the random noise. It can be seen from Fig. 16.27a that, after application of glycerol, the strength of the reflectance signal is reduced gradually, starting from the superficial layers, while the signals coming from the needle surface are gradually raised from about 32, 40, and 45 dB to 50 dB, as shown in Fig. 16.27a–d. This suggests that the scattering property of tissue is reduced that is a function of the time duration. However, for the DMSO case, as shown in Fig. 16.28, the reflectance signal from the needle surface was increased from about 28 to 50 dB immediately after the application of agent; see Fig. 16.28a, b for comparison. After about 1 min, the signals from the tissue surface, deeper layer of tissue, and the needle surface remain almost the same level; see Fig. 16.28b–d.
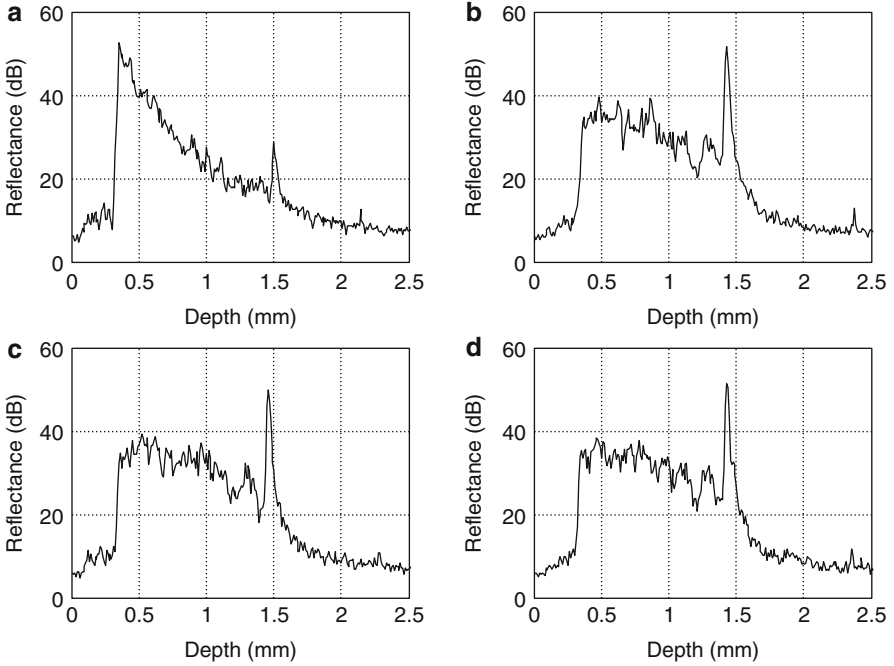
Fig. 16.28 The measured OCT in-depth back-reflectance profiles at the following times: (**a**) 0, (**b**) 10, (**c**) 30, and (**d**) 50 min after topical application of DMSO solution [188]
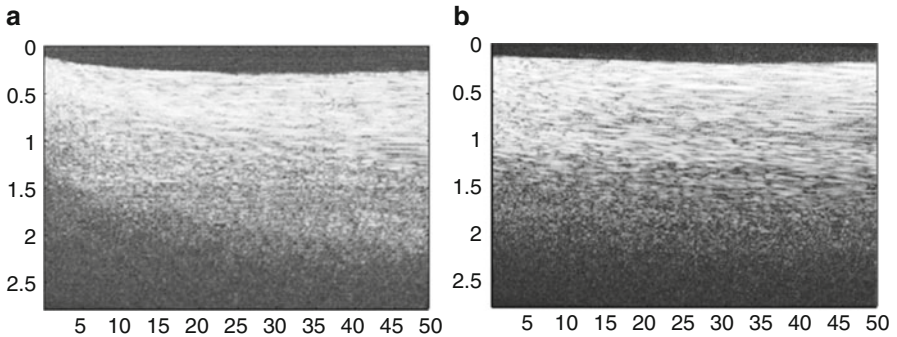
Fig. 16.29 Comparison of the time course of repeated A-scans of the porcine stomach tissue with the application of (**a**) glycerol and (**b**) DMSO, respectively. The horizontal and vertical axes present the time (min) and the imaging depth (mm), respectively [188]

Figure 16.29 illustrates the M-mode OCT images obtained from the repeated A-scans of the porcine stomach with the application of (a) glycerol and (b) DMSO. Because the system used required re-localization of the tissue surface manually after topical application of agents, the registration of OCT signal starts

Fig. 16.30 The dynamic
dehydration effect of glycerol
and DMSO. Data represent
average ± SD from three
independent experiments
[188]
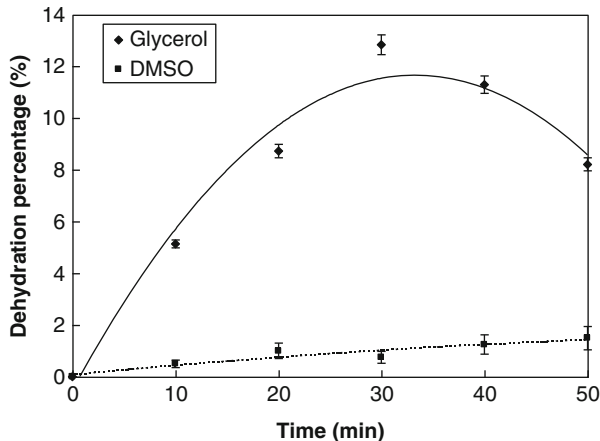
at the time of about 0.5 min after the agent application. From the image obtained
with glycerol application, it is clearly seen that the penetration depth increases
gradually with the increase of time duration. However, from Fig. 16.29b, a sig-
nificant depth improvement appears at the time immediately after the application
of DMSO. This indicates that DMSO could fulfill tissue clearing within a very
short time period. There is a slope of the surface of the tissue. The downward
trend of the tissue surface is attributed to the tissue dehydration induced by the
chemical agents.

Figure 16.30 shows the dynamics of dehydration effects after the application of
the glycerol and DMSO solutions, respectively. It is shown that the application of
glycerol causes a greater water loss of stomach tissue than that of DMSO does.
During the time period between 0 and 30 min, dehydration induced by glycerol
application increases with the time duration; and this reaches a maximum of
approximately 12 % at about 32 min. After this time, the curve goes down to
8 %, with the further increase of time to 50 min. It seems that the re-hydration
occurs. Water re-enters the tissue, making it swollen. The application of DMSO
only causes a small percentage (about 1 %) of dehydration of tissue, and
the re-hydration effect was not observed during the time period investigated.
These results were consistent with the continuous A-scan experiments as shown
in Fig. 16.29.

After glycerol was administrated on the surface of the tissue, it will come to the
first diffusion stage mentioned in the last subsection. Note that the tissues used here
were stomach tissues. The glycerol would diffuse into the intercellular space of the
stomach tissue relatively fast because the epithelial layers of the internal organs are
composed of loosely packed cells, and glands and ducts with narrow lumens are
rich in the mucosa of the gastrointestinal tract. However, it should be understood
that this diffusion rate would still slower than that at which water migrates out from
the tissue because of the high osmolarity of the solution and the large molecule of

this agent. This causes tissue dehydration, as observed in Fig. 16.25a–d. After glycerol is diffused into the tissue, it will play its role in not only drawing intercellular fluids out of tissue but also drawing the interstitial water further from cells and fibers. This decreases microscopically the local volume fraction of the scattering centers and the subcellular structure within the cells, thereby increasing the back reflective light signal. On the other hand, this diffusion increases the refractive index of the ground substances. Consequently, such dehydration effect would therefore increase the local reflectance signals leading to the increase of both imaging contrast and depth because OCT actually probes the refractive index difference between macroscopic structures limited by the OCT system resolution, at least in the current study. The concurrent enhancement of imaging depth and contrast are evident from Fig. 16.25c, d.

Glycerol has been found to enter and exit cells by passive diffusion [202]. Therefore, with the elapsing of time, glycerol will further diffuse into the cells, i.e., the second diffusion stage mentioned above. This causes a full refractive index matching with the subcellular structure. After glycerol enters into cells, it could draw the water back into cells due to its water affinity property, leading to tissue re-hydration, as observed in Fig. 16.29a and 16.30 respectively. During this period, the volume of scattering centers in cells could be enlarged by the re-hydration, and the increase of the local reflectance signals does not occur. However, light scattering still remains small because of the refractive index matching environment created between the chemical agents and the scattering centers within tissue. This explains the OCT images of Fig. 16.25e, f, respectively, where there is the improvement of imaging depth, but the imaging contrast is gradually reduced.

For DMSO, the first-stage diffusion is much faster because of its strong penetration ability (refer to the discussions in the last Sect. 16.5.3). Employing (^{35}S) DMSO, Kolb et al. [207] evaluated the absorption and distribution of DMSO in lower animals and humans. It was reported [207] that 10 min after the cutaneous application in rat, radioactivity was measured in the blood. In humans, radioactivity appeared in the blood 5 min after cutaneous application. One hour after application of DMSO to the skin, radioactivity could be detected in the bones. DMSO has also been found to be one of the most effective agents across cell membranes [208, 209]. These experiments indicate that the duration of the aforementioned second diffusion stage of DMSO also happens within a very short time frame. The fast diffusion rate of DMSO could decrease the osmolarity of the solution rapidly, although the original one is high. Therefore, the application of DMSO will cause lighter dehydration of the tissue than glycerol does. This is confirmed by the experimental results, as shown in Fig. 16.29b and 16.30. This also indicates that a little volume decrease of the scattering centers would occur, and the back reflective light signal would not increase once the agent diffuses into tissue. Consequently, no image contrast enhancement was observed with the OCT measurements, as shown in Fig. 16.26. In other words, the application of DMSO causes a rapid full refractive index matching with the subcellular scattering centers of turbid tissue, leading to the imaging depth but not contrast improvement.
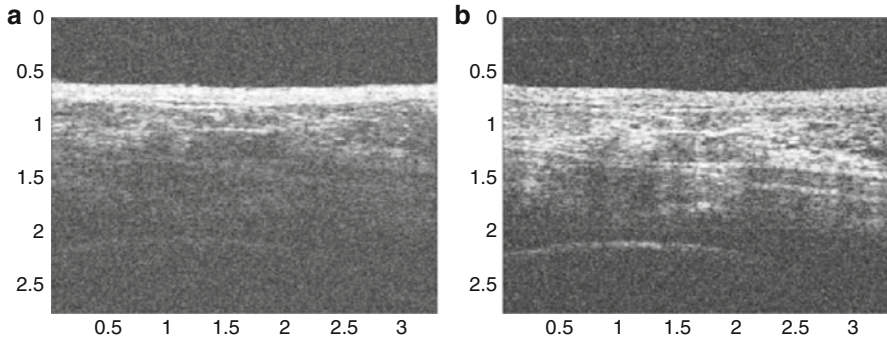
Fig. 16.31 OCT images of chicken skin tissue (**a**) without and (**b**) with 20 min application of glycerol. Both the imaging depth and contrast were enhanced in (**b**) compared with (**a**)

Figure 16.31 shows an even more convincing case for the action of glycerol to the tissue, where the OCT imaging depth and contrast are dramatically improved when comparing the images before and after the application of glycerol agent.

The experimental results by comparison of the tissue clearing dynamics of glycerol and DMSO not only allow us to understand its mechanism, but also are important in the selection of chemicals for the different applications. The above results indicate that DMSO may be more suitable for such applications where high light energy penetration and fast process are desired, for example, photodynamic therapy. Glycerol may be more suitable for the OCT imaging applications where the improvement of both the penetration depth and imaging contrast are required.

It should be pointed out that the above experiments were performed in vitro on biological tissues. The dynamic optical clearing effect induced by the chemical agent would differ from that of the in vivo case. Because of the cell self-regulation and blood circulation, the living tissues would have a less dehydration after the application of hyperosmotic chemical agent. However, a study conducted by Wang et al. [187] showed that the application of the propylene glycol agent solution to the human tissue in vivo has the effect of enhancement of both the imaging depth and contrast. See Fig. 16.32 for an example. Whether this is due to the simultaneous actions of dehydration and chemical diffusion, as suggested in the current study, remains unclear.

Thus far, we have used the examples to illustrate that the impregnation of tissue with a biocompatible chemical can enhance OCT imaging capabilities through the optical clearing and chemical mass transport upon diffusion mechanisms. However, such imaging capability enhancement is agent selectable, particularly for the imaging contrast enhancement. The mechanisms for light penetration enhancement have been well established, i.e., in the framework of the refractive index matching approach, which can improve the OCT imaging depth and resolution. The expla-nations for imaging contrast enhancement, thereby the improvement of OCT
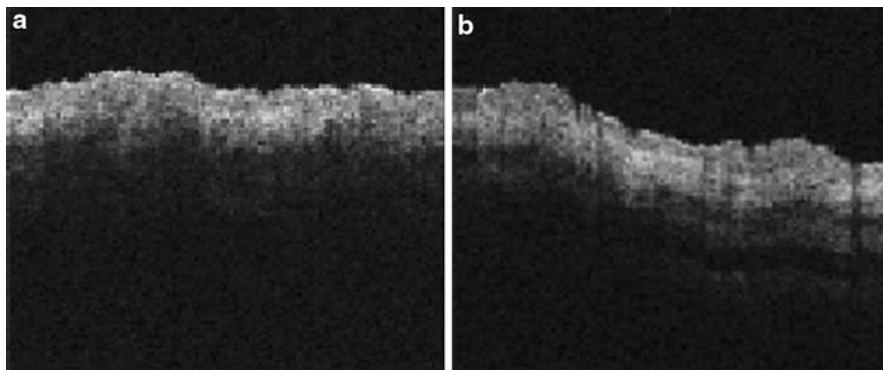
Fig. 16.32 OCT images captured from human forearm in vivo (**a**) without and (**b**) with 50 % topical application of propylene glycol solution. Image sizes: 1.8×1.6 mm [187]

localization capability, are based on the dehydration induced by the chemicals and chemical mass transport characteristics. The exact mechanism behind the contrast enhancement remains to be explored.

16.5.4 Imaging through Blood

As follows from above discussion, OCT is a powerful technique for the study of the structure and dynamics of highly scattering tissues and blood, including imaging of the vascular system for the diagnosis of atherosclerotic lesions. In vitro studies performed on human aorta have shown that OCT is able to identify structural features such as lipid collections, thin intimal caps, and fissures characteristic of plaque vulnerability [123, 151, 152, 210]. In in vivo OCT imaging of the rabbit aorta through a catheter, a vascular structure was defined, but saline infusion was required during imaging since blood led to significant attenuation of the optical signal [152]. Eliminating the need for saline or minimization of its concentration would represent a substantial advance for intravascular OCT imaging.

Refractive index mismatch between erythrocyte cytoplasm and blood plasma causes strong scattering of blood that prevents getting high-quality images of intravascular structures through whole blood. The refractive index of erythrocyte cytoplasm is mostly defined by hemoglobin concentration (blood hematocrit) [211]. The scattering properties of blood are also dependent on erythrocyte volume and shape, which are defined by blood plasma osmolarity [211, 212] and aggregation or disaggregation ability [124, 164, 213, 214]. Recently, the feasibility of index matching as a method to overcome the limited penetration through blood for getting of OCT tissue images has been demonstrated [124, 164, 185]. Glucose, low and high molecular dextrans, X-ray contrasting, glycerol, and other biocompatible agents were used to increase the refractive index of blood plasma closer to that of the erythrocyte cytoplasm to improve penetration depth of OCT images.

The 1,300 nm OCT system was used for taking images of the reflector through circulated blood in vitro [185]. The total intensity of the signal off the reflector was used to represent penetration. As immersion substances, dextran (group refractive index – 1.52) and IV contrast (group refractive index – 1.46) were taken. Both dextran and IV contrast were demonstrated to increase penetration through blood: 69 ± 12 % for dextran and 45 ± 4 % for IV contrast.

Studies of blood scattering reduction by the immersion technique using various hyperosmotic solutions, which are biocompatible with blood, like glucose, glycerol, propylene glycol, trazograph (X-ray contrasting substance for intravenous injection), and dextran were also described [124, 164]. The 820 and 1,310 nm OCT systems were applied for taking images of the reflector through a 1-mm layer of uncirculating fresh whole blood. It was shown that for uncirculating blood, the sedimentation plays an important role in blood clearing using the immersion technique, and OCT allows for precise monitoring of blood sedimentation and aggregation.

The mean square of the photodetector heterodyne signal current $<i^2(z)>$ received by an OCT system from the probing depth z is a product of two factors: the mean square heterodyne signal in the absence of scattering $<i^2>_0$ and the heterodyne efficiency factor $\Psi(z)$, describing the signal degradation due to the scattering [166, 215–217], i.e.,

$$<i^2(z)> = <i^2>_0 \Psi(z), \qquad (16.21)$$

where the factor $<i^2>_0$ is defined as

$$<i^2>_0 = \beta^2 P_R P_S \sigma_b / \pi (w_H)^2 \qquad (16.22)$$

with β being the power-to-current conversion factor, P_R and P_S the power of the reference and input sample arm beams, σ_b the effective backscattering cross-section, and w_H the $1/e$ irradiance radius at the probing depth in the absence of scattering, respectively. More precisely, w_H is defined in Refs. [166, 215].

The heterodyne efficiency factor $\Psi(z)$ contains the scattering effects. It has been shown [166, 215] that for only the single scattering contribution

$$\Psi(z) \approx \exp\{-2\mu_s z\}. \qquad (16.23)$$

The factor 2 in the exponent of (16.23) accounts for the round-trip attenuation to and from depth z in the sample arm. In the absence of absorption, the scattering coefficient μ_s can be determined from the slope of the OCT signal. For media with absorption and described by the single scattering approximation, the light travels in a ballistic way and Beer's law can be applied to calculate the total OCT attenuation coefficient: $\mu_t = \mu_s + \mu_a$. Consequently, μ_s can be obtained by subtracting the absorption coefficient from the total attenuation coefficient obtained from the slope of the OCT signal.

Thus, the measured signal in the OCT system is defined as [166, 215–217]

$$\left(\langle i^2(z) \rangle\right)^{1/2} \approx \left(\langle i^2 \rangle_0\right)^{1/2} \left(\exp\left(-2\mu_t z\right)\right)^{1/2}. \tag{16.24}$$

The result of the OCT study is the measurement of optical backscattering or reflectance, $R(z) \propto \left(\langle i^2(z) \rangle\right)^{1/2}$, from the RBCs versus axial ranging distance, or depth, z. The reflectance depends on the optical properties of blood, i.e., the total attenuation coefficient μ_t. For optical depths less than 4, reflected power can be approximately proportional to $-\mu_t z$ in exponential scale according to the single scattering model [124, 164], i.e.,

$$R(z) = I_0 \alpha(z) \exp(-\mu_t z). \tag{16.25}$$

Here, I_0 is the optical power launched into the blood sample and $\alpha(z)$ is the reflectivity of the blood sample at the depth of z.

Optical clearing (enhancement of apparent transmittance) ΔT by an agent application can be estimated using the following expression:

$$\Delta T = \left[(R_{\text{agent}} - R_{\text{saline}})/R_{\text{saline}}\right] \times 100\%, \tag{16.26}$$

where R_{agent} is the reflectance from the backward surface of the vessel within a blood sample with an agent, and R_{saline} is that with a control blood sample (whole blood with saline).

Measurement of OCT reflectance for two depths, z_1 and z_2, allows one to evaluate approximately the attenuation coefficient and its temporal behavior due to reduction of the blood scattering coefficient at agent immersion if reflectivity $\alpha(z)$ is considered as weakly dependent on depth for a homogeneous blood layer

$$R(z_1, t)/R(z_2, t) \approx \exp\{-\mu_t(t)[z_1 - z_2]\} \tag{16.27}$$

or

$$\mu_t(t) = \frac{1}{\Delta z} \ln\left[\frac{R(z_1, t)}{R(z_2, t)}\right], \tag{16.28}$$

where $\Delta z = |z_1 - z_2|$.

The OCT system used is described in Sect. 16.2, and it yields 12 μm axial resolution in free space. This determines the imaging axial resolution, which is comparable with the dimensions of RBCs or small aggregates.

A few different glass vessels of 0.2–2 mm of thickness were used as blood sample holders. For some holders to enhance reflection from the bottom interface, a metal reflector was applied. The sample holder was mounted on a translation stage at the sample arm and was placed perpendicular to the probing beam. The amplitude of reflected light as a function of depth at one spatial point within the sample

Table 16.2 Influence of dextrans (2.43 gdL^{-1}) on light attenuation property of the sample containing 65 % blood and 35 % saline [164]. Data was corrected accounting for algorithm expressed by equation (16.28)

Agent	μ_t (cm^{-1})	ΔT (%)
Saline	74.2	–
Dextran10	76.4	11.9
Dextran70	59.4	100.1
Dextran500	62.4	86.7

was obtained. The result is the measurement of optical backscattering or reflectance, $R(z)$, from the RBCs versus axial ranging distance, or depth, z, described by (16.25). Optical clearing (enhancement of transmittance) ΔT by an agent application was estimated using (16.26). Averaging for a few tenths of z-scans was employed.

Venous blood was drawn from healthy volunteers and stabilized by K2E EDTA K2. For example, blood samples containing dextrans were prepared immediately after blood taking by gently mixing blood and dextran-saline solution with low rate manual rotating for 1 min before each OCT measurement. Four groups of the blood samples with various hematocrit values were investigated in this study [164]. The dextrans used in the experiments were D×10, D×70, and D×500 with the molecular weights (MW) at 10,500, 65,500, and 473,000, respectively.

Table 16.2 gives the results from 65 % blood (from a 24-year-old male volunteer) with 35 % dextran saline solution. The concentration of dextrans used was 2.43 gdL^{-1}. The measurement started immediately after the addition of dextran. It can be seen from Table 16.2 that D×500 and D×70 are effective agents to decrease the light attenuation of blood compared with the saline control (blood with saline), with the total attenuation coefficient decreased from 74.2 cm^{-1} for the saline control to 62.4 and 59.4 cm^{-1}, respectively. The optical clearing capability ΔT was approximately 90 % and 100 % for D×500 and D×70, respectively.

It is interesting that D×500, providing a higher refraction, had less effect than that of D×70 at the same concentration. Moreover, the increase in concentration (refraction power) cannot always achieve higher optical clearance, thus, 0.5 gdL^{-1} D×500 had a stronger effect than 5 gdL^{-1} D×500 in 20 % blood with 80 % saline samples. Better transmittance does not always correlate with lesser scattering coefficient (see Dextran 10).

The changes in scattering property brought above by the addition of dextran solution may first be explained by the refractive index matching hypothesis [184, 185]. It can be seen that scattering can be reduced when the refractive index of plasma is increased.

The refractive index of dextran saline solution was increased with concentration in all molecular weight groups. The measured indices of blood samples with dextrans were in good agreement with the theoretical values calculated according to the equation $n = c_b n_b + (1 - c_b) n_s$, where c_b is the volume fraction (20 %) of whole blood in the diluted sample and n_s is the index of saline with or without dextrans. As expected, the refractive index of blood with dextran increases as the concentration of the added dextran increases due to an increase of the index of the ground matter of the sample.

Fig. 16.33 A summary of effects of dextrans compared with that of the saline control on light transmission after 10 min sedimentation. Lower concentration Dx500 and Dx70 had significant effects in enhancing light transmission. Efficiency of higher concentration dextrans was much lower than that of the saline control [164]
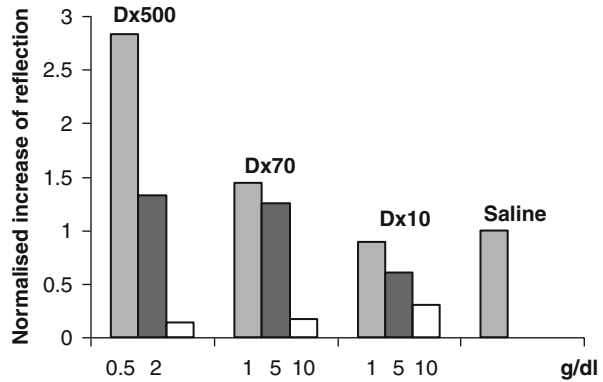
Blood optical property can be altered by dextrans-induced refractive index matching between RBCs and plasma. However, refractive index matching is not the only factor affecting blood optical properties. Obviously, this discrepancy resulted from the assumption of only refractive index influence. Thus, other factors should be taken into account, particularly, the cellular aggregation effect induced by dextrans [164].

As the aggregation process is time dependent, the blood sample was allowed 10 min sedimentation in this study after the measurement at the beginning stage of the addition of dextrans. Figure 16.33 shows the summary of the effect of dextrans compared with the saline control on light transmission for the sample with 20 % blood and 80 % saline after 10 min sedimentation. It can be seen from Fig. 16.33 that the influence of dextran on the light transmission was different compared with that at the beginning of mixing dextrans in blood. The lower concentration (0.5 gdL^{-1}) D×500 still had the strongest effect on reducing the scattering of light in blood, with a 2.8-fold stronger effect than that of the saline control. However, enhancement by the highest concentration of D×500 (5 gdL^{-1}) and D×70 (10 gdL^{-1}) was dramatically lower than that of the saline control. At the beginning, they both had a very high blood optical clearing capability with 67.5 % and 76.8 % ΔT, respectively. In addition, the effect was decreased with the increase of dextran in blood within all three groups, contrary to the expectation of the refractive index matching hypothesis.

The decreased aggregation capability of dextran with concentration explained well that light transmission decreased less with the increase of dextran for both types (mid-molecular and large-molecular). Over a range of concentrations, D×500 and D×70 induced RBC aggregation. However, dextrans have been known to exert a biphasic effect on RBC aggregation; they induce aggregation at low concentration and disaggregation at high concentration [214]. For example, with D×70, the maximal aggregation size is obtained at approximately 3 %, above which the size decreases. In our OCT measurements, 2 gdL^{-1} D×500 and 5 gdL^{-1} D×70 in 20 % blood with 80 % saline appeared to be the critical concentration to affect RBC aggregation. Their aggregation parameters became smaller than those of

$0.5\,\mathrm{gdL}^{-1}\,\mathrm{D}\times 500$ and $1\,\mathrm{gdL}^{-1}\,\mathrm{D}\times 70$. When the concentration increased to $5\,\mathrm{gdL}^{-1}$ for $\mathrm{D}\times 500$ and $10\,\mathrm{gdL}^{-1}$ for $\mathrm{D}\times 70$, they played a role of disaggregation. That is the reason why the cells are much less packed than with the saline control, accounting for the reduced light transmission. Although refractive index matching suggested a higher light transmission, it can be seen that the aggregation-disaggregation effects are now dominant.

The behavior of RBCs in flow is dependent on the processes of aggregation-disaggregation, orientation, and deformation. Increased RBC aggregability has been observed in various pathological states, such as diabetes and myocardial infarction, or following trauma. The aggregation and disaggregation properties of human blood can be used for the characterization of the hemorheological status of patients suffering different diseases [213]. Our work suggests that OCT may be a useful noninvasive technique to investigate rheology for diagnosis, together with its additional advantage of monitoring blood sedimentation [124].

It is well established that RBCs are very sensitive to changes in blood plasma osmolarity [211]. As osmolarity increases due to cell dehydration, the RBC volume decreases, hemoglobin concentration within the cell increases, and index of refraction increases. For example, glucose injection in blood causes the linear increase of plasma osmolarity with glucose concentration, up to 6,000 mOsm/L at glucose concentration in blood plasma of 1.0 g/mL. Using data of Ref. [211], the following empirical relation was suggested to describe RBC volume change with osmolarity [218, 219]:

$$V_{RBC}(osm) = V_{RBC}(300)\left(0.463 + 1.19\exp\left\{-\frac{osm}{376.2}\right\}\right), \qquad (16.29)$$

where $V_{RBC}(osm)$ is the RBC volume in $\mu\mathrm{m}^3$ at given osmolarity expressed in mOsm/L and $V_{RBC}(300)$ is the RBC volume at isotonic osmolarity $osm = 300$ mOsm/L. At glucose injection, the local blood hematocrit (Hct) decreases. If Hct before injection of glucose was 45 % at $osm = 300$ mOsm/L; then at $C_{gl} = 0.05$ g/mL, $osm = 580$ mOsm/L and Hct = 32 %; at $C_{gl} = 0.1$ g/mL, $osm = 850$ mOsm/L and Hct = 26 %; and at $C_{gl} = 0.2$ g/ml, $osm = 1{,}400$ mOsm/l and Hct = 22 %. At further increase of glucose concentration (0.3–1.0 g/mL), hematocrit stays constant, Hct $\cong$ 21 %, in spite of linear increase of blood plasma osmolarity (2,000–6,000 mOsm/L).

Results of modeling of the scattering properties control for a whole blood at its immersion (local intravessel injection in the vicinity of the endoscopic OCT probe) by a glucose solution at different concentrations accounting for RBC polidispersity (150 volume fractions of volume (size) distribution) [220, 221], packing function in the form $F(\mathrm{Hct}) = (1 - \mathrm{Hct})$ [222, 223], osmolarity, and hematocrit effects are presented in Refs. [219, 224]. The scattering coefficient and scattering anisotropy factor were calculated. The scattering coefficient behavior with concentration and the wavelength is defined by: (1) the change in blood plasma osmolarity (increase of scattering for all wavelengths far from Soret band caused by RBC shrinkage and increase of refractive index for low concentration of glucose; (2) reduction of blood hematocrit (plays some role in the scattering decrease for glucose concentration less

than 0.3 g/mL); (3) refractive index matching – the main effect (a significant reduction of scattering for glucose concentration from 0.5 to 0.7 g/mL in dependence of the wavelength); and (4) dispersion of hemoglobin absorbing bands (within a strong Soret band (415 nm) it does not allow a significant reduction of scattering and modifies slightly the position of the dip and the depth of scattering damping for other lower-absorbing hemoglobin bands, 542 and 575 nm). For applications, especially when OCT endoscopy is used, concurrent reduction of scattering and increase of g-factor at immersion agent administration is important. The transport scattering coefficient, $\mu'_s = (1 - g)\mu_s$, decreases and transport free path length for a photon, $l_{tr} \cong 1/\mu'_s$ increases dramatically, thus a larger amount of photons, which carry information about the hidden object (for example, thin-wall plaques in the coronary arteries) can be detected. For the wavelength 900 nm, the scattering coefficient of blood is changed from 1,200 cm^{-1} to approximately 50 cm^{-1} and g-factor from 0.991 to 0.994 at glucose immersion, thus the transport free path length increases more than 35 times [219, 224]. Correspondingly, the depolarization depth of blood [225, 226], which is proportional to l_{tr}, should be much larger at optical clearing. The described method for immersed blood modeling is applicable for any other biocompatible immersion agent administration, such as dextrans, glycerol, and trazograph (see Table 16.2 and Refs. [164, 227]).

There also exists another possibility of blood immersion, using the local blood hemolysis that can be also provided in the vicinity of the fiber-optic endoscopic probe [228]. Free hemoglobin is the immersion agent in that case. The local increase of hemoglobin concentration in plasma can lead to local change of plasma osmolarity [218]:

$$osm' = osm + \frac{C_{bpHe}}{M_{Hb}}, \qquad (16.30)$$

where osm is the plasma osmolarity under physiological condition (280–300 mOsm/L), C_{bpHb} is the concentration of plasma hemoglobin, g/L, and M_{Hb} is the molar mass of hemoglobin ($M_{Hb} = 66{,}500$ g/M). The expected change of RBC volume calculated using empirical (16.29) is not more than 0.1 % at hemolysis less than 20 %. For simplicity, the polydispersity of RBC can be taken into account on the basis of the six-fraction blood model [228]. Modeling of optical properties of whole blood at normal conditions and at local hemolysis with the packing function $F(Hct) = (1 - Hct)(1.4 - Hct)$ [222] showed that, in contrast to the small changes of absorption coefficient, more significant changes of the scattering properties of blood have been observed at increase of free hemoglobin concentration in plasma [228]. A spectrally smooth decrease of scattering coefficient for all wavelengths with free hemoglobin release at hemolysis was found. At a hemolysis rate of 20 %, the decrease of the scattering coefficient for two typical wavelengths, 633 and 820 nm, was calculated as 40 %, while the anisotropy factor, at 633 nm, increases from 0.9940 to 0.9952, and at 820 nm from 0.9919 to 0.9929.

The described method can be realized not only at blood hemolysis but also at local free hemoglobin injection. Hemoglobin administration also may serve as

a clearing agent for tissue clearing, when clearing is needed in the spectral range far from the strong absorption bands of hemoglobin.

This concept was experimentally proved by using a quantitative phase microscopy for investigating RBC morphology and dynamics with subnanometer pathlength sensitivity at the millisecond time scales [229]. The ability to quantify noninvasively the hemoglobin flow out of the cell during hemolysis due to cell refractive index mismatching/matching with surroundings was demonstrated. RBC volume and dynamic morphology were investigated.

A number of experimental studies have demonstrated that glucose and dextrans improve OCT blood penetration [124, 164, 185, 218, 219, 224, 227, 228]. The safety and usefulness of the non-occlusion method for OCT image acquisition with low-molecular-weight dextran L (LMD-L) (Dextran 40) via a guiding catheter were recently demonstrated in clinical studies [230, 231]. The intracoronary frequency-domain optical coherence tomography (FD-OCT) system used in this investigation normally required injection of contrast media for image acquisition, which may lead to the impairment of renal function. To compare the image quality and quantitative measurements between contrast media and LMD-L for FD-OCT image acquisition in coronary stented lesions, 22 patients with 25 coronary stented lesions were enrolled. Using the continuous-flushing method via a guiding catheter, contrast media and LMD-L were infused at a rate of 4 mL/s by an autoinjector. It was shown that, with regard to image quality, the prevalence of clear image segments was comparable between contrast media (97.9 %) and LMD-L (96.5 %), $p = 0.90$, with excellent correlations between both flushing solutions at application to minimal and mean lumen, as well as mean stent areas. The total volumes of contrast media and of LMD-L needed for OCT image acquisition were similar. Thus, LMD-L may have the potential to reduce the total amount of more toxic contrast media without loss of OCT image quality and in the near future could be widely adopted in clinical practice, especially in patients with renal insufficiency. As follows from the above discussion (see Fig. 16.33 and Table 16.2), the high-molecular-weight dextrans are more efficient and we have the prospect of total replacement of contrasting agents.

16.6   Monitoring of Drug Delivery

To describe the relationship between the depth of penetration and the signal strength at a particular depth, a method based on OCT signal slope (*OCTSS*) or OCT amplitude (*OCTA*) analysis can be used [232–236]. In a single scattering approximation [see (16.28)], the *OCTSS* plotted on a logarithmic scale is proportional to the total attenuation coefficient of the tissue, μ_t:

$$OCTSS \equiv \ln\left[\frac{I(z)}{I_0}\right] = -\mu_t z \qquad (16.31)$$

The *OCTSS* method allows one to evaluate the average permeability rate of the tissue layer for a chemical agent or molecules of a drug. The permeability rate can

be simply calculated by dividing the thickness of the region used to measure the *OCTSS* by the time of molecular permeation in this region

$$\bar{P} = z_{\text{region}}/t_{\text{region}}. \tag{16.32}$$

Prior to the addition of molecules, the baseline signal would remain relatively constant. Only after application will the changes in the *OCTSS* be observed. The time interval can be calculated as the time when saturation was achieved (after diffusion) minus the time at which the molecules first reached the region of interest (t_{region}). Alternatively, the *OCTA* method of measurement can be used to calculate the permeability rate at specific depths within the tissue from

$$P(z) = z_i/t_{zi}, \tag{16.32}$$

where z_i is the distance from the surface of the tissue where the measurements are performed and t_{zi} is the time of the agent diffusion to that depth.

Many studies have been performed on the effect of OCAs on different biological samples. Optical clearing can be estimated by the change in the optical signal obtained from the tissue, after the addition of the clearing agent, as a percentage change. Formally, percentage change at a certain depth of a tissue can be defined as

$$\% \, clearing = \frac{I_2 - I_1}{I_1} \times 100\%, \tag{16.33}$$

where, I_1 is the optical intensity prior to addition of the clearing agent and I_2 is the optical intensity after the clearing agent has diffused through that particular depth. For example, Ghosn et al. showed that 40 % glucose can induce around 10 % clearing effect in the upper layer of rabbit sclera, which increases to 22 % in the layers below [234]. Larina et al. showed how glycerol can be used as a clearing agent that can help better visualize deeper layers in mice embryo [237]. Sudheendran et al. monitored the changes in tissue as different concentrations of glucose solution diffused through pig skin [238].

It has been demonstrated that the concentration change of OCA in different tissues changes its optical properties [239–253]. Most recently, a method that allows for the quantification of the permeation rates of different compounds in tissues using *OCTSS* has been developed [232–235, 246–251]. Permeation of various molecules and drugs has been quantified in the sclera and the cornea of the eye, monkey skin in vivo, and various vascular tissues. Table 16.3 shows an example for the permeation rates of various molecules and drugs in the rabbit sclera and cornea measured using the *OCTSS* method [234].

In this study [234], an aqueous solution of 40 % glucose is added to rabbit sclera in vitro, where depth-resolved permeability coefficients and optical clearing are measured with OCT. The permeability rate in the upper 80- to 100-µm region is found to be different from that in the deeper 100-µm region: $(6.01 \pm 0.37) \times 10^{-6}$ cm/s and $(2.84 \pm 0.68) \times 10^{-5}$ cm/s, respectively. A difference in percent

Table 16.3 Permeation rates of various drugs in rabbit cornea and sclera

Drug	Permeability (rate ± standard deviation, cm/s) Cornea	Sclera
Mannitol	$(1.46 \pm 0.08) \times 10^{-5}$ $(n = 4)$	$(6.18 \pm 1.08) \times 10^{-6}$ $(n = 5)$
Ciprofloxacin	$(1.85 \pm 0.27) \times 10^{-5}$ $(n = 4)$	$(1.41 \pm 0.38) \times 10^{-5}$ $(n = 3)$
Dexamethasone	$(2.42 \pm 1.03) \times 10^{-5}$ $(n = 7)$	–
Metronidazole	$(1.59 \pm 0.43) \times 10^{-5}$ $(n = 5)$	$(1.31 \pm 0.29) \times 10^{-5}$ $(n = 4)$
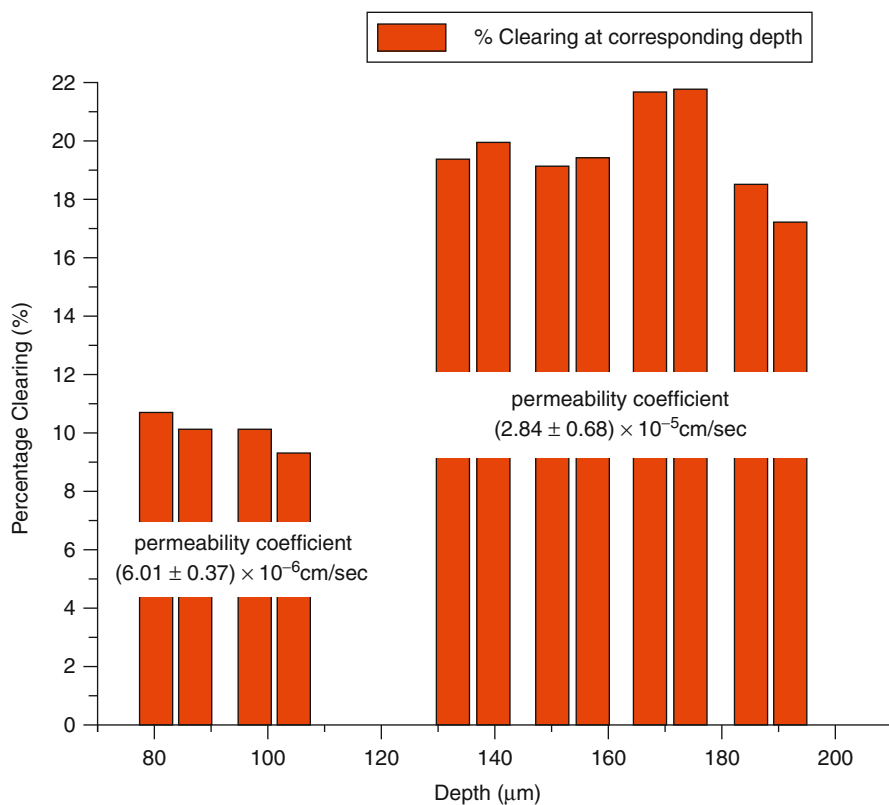
Fig. 16.34 Optical clearing at different depths in rabbit sclera during the 40 % glucose diffusion experiment [234]

clearing is also noted. Optical clearing of the upper region is about 10 % and increased to 17–22 % in the one beneath. These results demonstrate the capability of OCT-based methods to not only measure the diffusion rate and optical clearing of a tissue, but also its ability of functional differentiation between layers of epithelial cells and stroma (see Fig. 16.34).

Recently, OCT has been employed to quantify the permeability rates of glucose and different lipoproteins (very low density lipoprotein (VLDL), low density

Table 16.4 Permeation rates of lipoproteins and glucose in human carotid endarterectomy tissues at 20 °C and 37 °C

Lipoprotein	Permeability (rate ± standard deviation, cm/s) × 10^5			
	Normal, 20 °C	Normal, 37 °C	Diseased, 20 °C	Diseased, 37 °C
VLDL	1.13 ± 0.26	1.20 ± 0.25	1.50 ± 0.21	1.75 ± 0.34
LDL	3.16 ± 0.37	4.77 ± 0.48	1.97 ± 0.34	2.01 ± 0.23
HDL	1.57 ± 0.26	2.42 ± 0.24	2.01 ± 0.32	2.43 ± 0.31
20 % Glucose	3.51 ± 0.27	3.70 ± 0.44	6.31 ± 0.61	5.70 ± 0.48

lipoprotein (LDL), and high density lipoprotein (HDL)) in vascular tissues (porcine aorta and human carotid endarterectomy tissue) [252, 253]. It is also known that structural organization of cells and fibrils composing a tissue could significantly impact the molecular permeability rate and, thus, allow early detection of tissue abnormalities by quantifying permeability rate in normal versus pathological tissues. For example, the permeability rate of 20 % glucose solution in normal vascular tissues was calculated to be $(6.80 ± 0.18) × 10^{-6}$ cm/s, while it significantly increased during formation of early arteriosclerotic disease: $(2.69 ± 0.42) × 10^{-5}$ cm/s [250].

The influx of lipoproteins is a significant factor in studying the physiological mechanisms that contribute towards the formation of atherosclerosis in vascular tissues. OCT can also be used to measure the perfusion through yet another biological system, the intimal layer of the carotid arterial wall. This layer is obtained from human carotid endarterectomy (CEA) specimens, which contain *normal* healthy segments and *diseased* atherosclerotic segments that included lipidic, calcific, hemorrhagic, and/or fibrotic components. The permeation rates of glucose and different lipoproteins were studied at room temperature (20 °C) as well as physiological temperature (37 °C). The results of these permeation studies are summarized in Table 16.4 [236, 252, 253].

As discussed above and as described in general in Ref. [224], OCT in conjunction with uploading tissue by an OCA holds promise as a research tool for analysis of identifying the boundaries between normal and diseased tissue in vitro and in vivo. Depth- and time-resolved profiles for OCT signal at optical clearing allow one to differentiate human cancer and normal breast tissues [254, 255]. The permeability coefficients [(16.32)] and the percentages of OCT signal enhancement [(16.33)] for normal and cancerous breast tissues have been investigated in vitro for 60 % glycerol [254], 20 % glucose, 40 % glucose, and 20 % mannitol [255]. The OCT slope signals of breast tissues decreased as OCA diffusing into tissues. For example, the permeability coefficient of glycerol in cancer tissues was 3.54-fold larger than that in normal tissues. The permeability coefficient of 60 % glycerol was $(3.14 ± 0.07) × 10^{-5}$ cm/s in breast cancer tissues and $(0.89 ± 0.02) × 10^{-5}$ cm/s in normal breast tissues [254]. Obtained results indicate that the OCA permeability coefficient in breast cancer tissue is prominently larger than that in normal breast tissue, while the percentage of optical clearing is lower. The results suggest that OCT has the ability to distinguish cancer tissue from different aspects [255] that are related to tissue morphology and OCA impact on tissue.

Pilot results on in vitro quantification of glucose diffusion permeability in normal esophageal epithelium and esophageal squamous cell carcinoma (ESCC) human tissues by using OCT technique were also reported [256]. The permeability coefficient of 40 % glucose was found to be $(1.74 \pm 0.04) \times 10^{-5}$ cm/s in normal esophagus and $(2.45 \pm 0.06) \times 10^{-5}$ cm/s in ESCC tissues. Therefore, a 1.41-fold greater permeability coefficient than that for normal tissues was found for ESCC, however, similar to breast tissue, the OCT light penetration depth for the diseased tissue is significantly smaller than that of normal esophagus tissues in the same time interval.

It was also found that the glucose permeability is nonlinear through the esophagus tissue and increases with depth for both normal and ESCC tissues [257]. The OCT images were acquired continuously for 120 min, and the depth-resolved and average permeability coefficients for the 40 % glucose solution have been extracted from experimental data using the OCT amplitude (*OCTA*) method [232–236]. The depth-resolved permeability coefficient for 40 % glucose solution increases from $(3.30 \pm 0.09) \times 10^{-6}$ and $(1.57 \pm 0.05) \times 10^{-5}$ cm/s at the mucous membrane of normal esophagus and ESCC tissues to $(1.82 \pm 0.04) \times 10^{-5}$ and $(3.53 \pm 0.09) \times 10^{-5}$ cm/s at the submucous layer ~742 μm apart from the epithelial surface of normal esophagus and ESCC tissues, respectively. This result fits well with data from Fig. 16.34, where difference between diffusivity of epithelial cells and stroma is underlined. It is also important to note that the cancer epithelial cell layer becomes 5.5 times more permeative than the normal tissue layer, but the permeability of the stromal layer increases only 2.2 times. The results presented could support the use of OCT in conjunction with OCA application in functional esophageal tissues imaging.

Another important application of OCT is for diagnostics of disease-caused structural changes in dental tissues [258–260]. Monitoring of the molecular diffusion processes was studied in hard tissues such as human tooth [261, 262] and nail [263]. Diffusion of water and dental liquor is necessary for teeth functioning and affects tooth hardness [264]. The permeability of dental tissues to exogenous chemical agents and drugs is important for dental disease treatment and tooth cosmetics [265]. The study of water and glycerol application to dentin samples was implemented in two geometries [261, 262]: (1) the sample placed in a cuvette and OCT-scanning performed through the liquid layer, covering the sample (front application); (2) the sample glued to a window in the cuvette side face (back application). The sample was coated with hermetic varnish except a window for OCA diffusion and light penetration in the case of one side OCA application and two windows on the opposite sides of the sample in the case of backward OCA application. In both cases, OCT-scanning was performed repeatedly over a few hours. The difference found between A-scans for front and backward OCA application is due to competition between the mean attenuation and the back reflectance coefficients. Both parameters decrease at application of diffusing immersion agent, but reduction of the attenuation coefficient leads to OCT signal increase from the sample depth, as the back reflectance decrease causes the corresponding decrease of OCT signal. A remarkable finding is that, in both

Table 16.5 Tooth tissue structural and diffusion parameters obtained from microscopy and OCT

Agent	Sample thickness, mm	Mean tubule diameter, μm	Saturation time, min	Permeability rate, cm/s
Water	0.9	0.60 ± 0.10	78	$(3.04 \pm 0.13) \times 10^{-6}$
Water	1.3	2.30 ± 0.15	9	$(4.02 \pm 0.24) \times 10^{-5}$
Water	1.2	1.60 ± 0.13	154	$(2.09 \pm 0.65) \times 10^{-6}$
44 % glycerol	0.8	2.4 ± 0.55	54	$(4.91 \pm 0.67) \times 10^{-6}$

cases, the mean slope of the OCT signal decreases with time and the ultimate damping time constants agree well. Backward OCA application is free of artifacts introduced by the liquid layer over the sample and hence was used in further experiments with other agents.

Similar measurements were carried out for other samples for water and 44 % glycerol aqueous solution (summarized in Table 16.5). The results demonstrate some correlation of the diffusion rate and time of OCT signal saturation with tissue structure, i.e., the tubules' diameter and their number density. The glucose diffusion and glucose impact on the dentin permeability that is important for *diabetes mellitus* patients were also studied. It has been found that the permeability coefficient for 35 % aqueous solution of glucose is about two orders of magnitude smaller than that for water (naturally, due to the greater molecule size and, possibly, due to molecular binding). The diffusion process of water in tooth samples was investigated before and after the long-term (5 days) incubation of a sample with 35 % glucose. The permeability coefficients of intact and incubated samples were found to be $(2.59 \pm 1.63) \times 10^{-4}$ cm/s and $(3.86 \pm 0.39) \times 10^{-4}$ cm/s, respectively. Thus, the long-term glucose impact on the tooth dentin results in irreversible changes of the tissue properties that may result from the glycation-induced change of the intertubular dentin density and, hence, the increased tubule looseness.

An in vivo study of molecular diffusion in a volunteer's partly removed nail was also performed [263]. OCT measurement allowed for identification of each tissue layer (nail and underlying tissue) and evaluation of its optical thickness and attenuation (scattering) coefficient. The effect of glycerol diffusion and mechanical compression (see Sect. 16.8) was clearly seen for all layers.

Overall, these results demonstrate the capability of OCT technology to quantify time- and depth-dependent diffusion processes in many soft and hard tissues. Moreover, the difference in diffusion rates between normal and diseased tissues measured with OCT could assist in tissue classification/pathology efforts.

16.7 Glucose Sensing

Significant efforts were undertaken in the field of glucose sensing in tissues with OCT and encouraging results were obtained in several studies [240, 242, 245, 266–275]. Glucose concentration monitoring is based on the similar phenomena as tissue optical

clearing and drug delivery and uses matching of refractive indices of the interstitial fluid, where glucose migrates from blood vessels, and tissue scattering constituents. By registering changes in scattering that are seen as the OCT signal slope changes, it is possible to evaluate changes in glucose concentration. Fortunately, as was proved in pioneering papers by Esenaliev et al. [245] and Larin et al. [240, 242], a high sensitivity of OCT slope measurement allows for in vivo monitoring of glucose at physiological levels in tissues of animals and humans.

Glucose clamping experiments were performed in the animal studies [240]. The clamping technique allowed slow, controlled intravenous administration of glucose at desired rates to simulate normal physiological changes in blood glucose concentration. A dextrose solution (50 % w/w) was administrated for approximately 1 h using a digital pump at a rate of 1.2 mL per min. This resulted in an increase of blood glucose concentration from a baseline level of 100 mg/dL ($\sim$5.5 mM) to 400 mg/dL ($\sim$22.2 mM). The *OCTSS* was measured at the depth from 300 to 400 µm and changed approximately 53 % in the range from 100 to 400 mg/dL. The lag time between an increase of blood glucose concentration and a decrease of the OCT signal slope was approximately 14 min and can be explained by glucose diffusion from bloodstream to skin.

An 80 % decrease of the slope of the OCT signal at the depth of 380–480 µm as the blood glucose increased from 144 mg/dL to 600 mg/dL (3.2 %/mM) was observed in an experiment with rabbit lip [240]. Good linear correlation between the OCT signal slope and blood glucose concentration with a correlation coefficient of 0.93 and a *p*-value less than 0.01 was demonstrated.

For healthy human volunteer [242], the slopes changed significantly: $\sim$17 %, with changes in glucose concentration from 90 to 140 mg/dL. These results also demonstrated good correlation between changes in slopes of noninvasively measured OCT signals and actual blood glucose concentration. On average, the slope changed 1.9 % per 10 mg/dL change of the blood glucose concentration.

16.8   Compression Clearing and Contrasting

A mechanical stress on a soft tissue in the form of compressing or stretching causes a significant increase in its optical transmission due to less overall light scattering [175, 224, 236, 276–287]. For living tissues, the major mechanisms behind this phenomenon are: (1) increased optical tissue homogeneity due to removal of blood and extracellular fluid from the compressed site; (2) closer packing of tissue components, leading to constructive interference (cooperative) effects; and (3) less tissue thickness.

The estimation of biomechanical properties of tissue is critical to many areas of the health sciences, including monitoring of the tension in wound closures, skin flaps, and tissue expanders. Optical and especially OCT techniques are helpful in such studies.

Askar'yan [277] was the first to study the propagation of a laser beam through the soft tissue phantoms and human palm at mechanical compression. The reduction of extinction coefficient after tissue compression and prolongation

of optical clearing effect after removing pressure for some time interval were successfully demonstrated.

As a tissue that is well-supplied with blood, the skin's spectral properties can be effectively controlled by applying an external localized pressure in in vivo experiments when UV-induced erythema (skin redness) is developed [287]. For that particular case, extra blood in the skin dermis resulting from a physiological reaction to UV light is pushed out by compression, thus providing better light transmittance within the bands of hemoglobin even the induced erythema without compression is rather strong.

The squeezing-induced effects in tissues containing little or no blood, such as eye sclera, are characterized by a marked inertia (a few minutes) [224, 284]. This happens because of the relatively slow diffusion of water from the compressed site. Due to water displacement from the interspace between collagen fibrils, concentration of the proteins and mucopolysaccharides increases in this space. Since these proteins and sugars have a refractive index closer to that of the collagen fibrils, a more index-matched environment can be created.

On the other hand, compression reduces specimen thickness d, which might increase the effective scatterer concentration inside the tissue. Therefore, compression may also give rise to an increase in tissue scattering coefficient μ_s. Sometimes the increase in scatterer concentration is likely to be more dominant than the reduction in index mismatch [175]. In addition, reduction of tissue thickness causes an increase in local chromophore concentration, and thus the absorption coefficient μ_a increases. However, the total effect on optical properties changes, which is proportional to the product of $(\mu_s + \mu_a)d$, and is characterized by less light attenuation due to the smaller thickness of compressed soft tissue (up to 72 %) [175, 285, 286]; cooperative effects also may have a great influence in reduction of the overall scattering [224].

Steady-state diffuse reflectometry with a variable source-detector separation r_{sd} allows one to characterize properties of light propagation in a tissue at mechanical tension, including its anisotropy following the stretching direction [283]. At external forced tension, more significant damping of scattering along the direction of mechanical stress is expected. In vivo human experiments showed that the specular reflection from skin changes with stretch [280]. For small values of skin stretch, the specular reflectivity measured for He:Ne laser ($\lambda = 633$ nm) beam with the 45° angle of incidence increases linearly with strain, showing considerable anisotropic properties.

All above-mentioned early studies of tissue compression have stimulated application of this technology to OCT, where the penetration depth and image contrast issues are critical. The authors of Ref. [279] used a hemispherically tipped glass rod (borosilicate, $n_{\text{glass}} = 1.474$) 20 mm long with a 3-mm tip diameter, as a probe for localized skin compression and concurrent OCT imaging at mean wavelength 1,310 nm (swept source OCT system). The glass rod did not add any perceivable distortions to the OCT signal. It was demonstrated that for similar effective tissue strain, air dehydration and mechanical compression produce similar changes in refractive index and water volume fraction. These data directly prove the concept
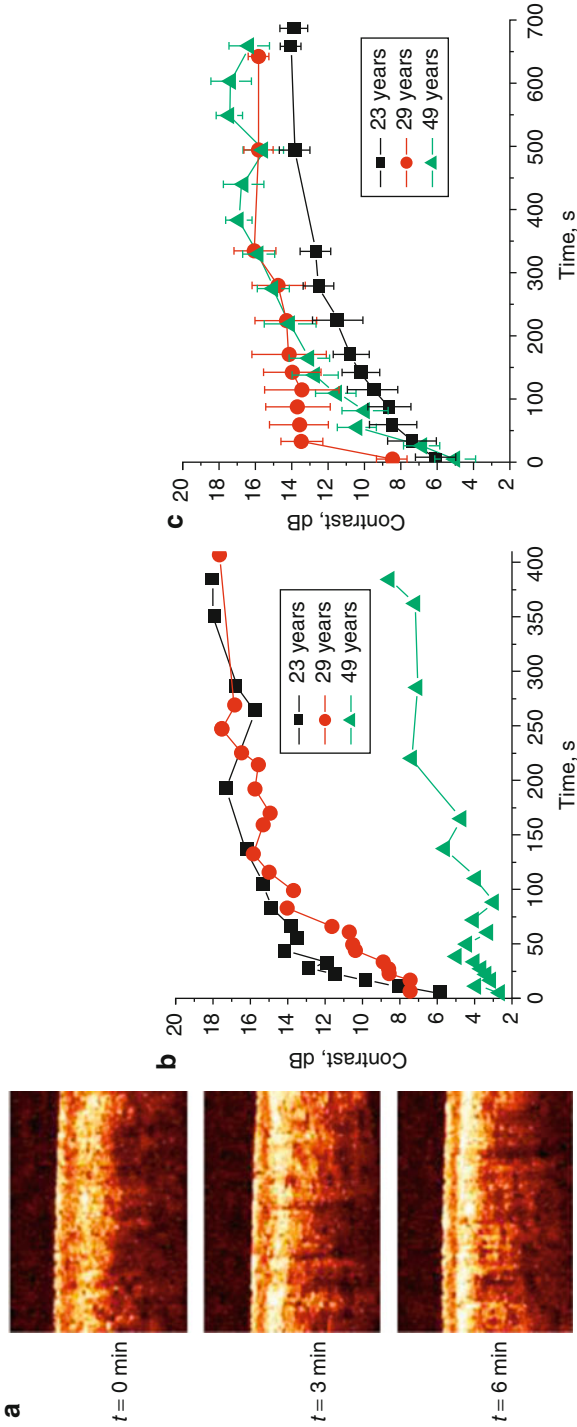
Fig. 16.35 (**a**) OCT images of thin skin of 29-year-old male volunteer immediately after compression started ($t = 0$), at 3 min, and at 6 min for high-pressure regime (0.35 N/mm^2); (**b**, **c**) temporal characteristics of contrast of epidermis–dermis junction for three volunteers of different age for low-pressure (0.07 N/mm^2) (**b**) and high-pressure (0.35 N/mm^2) compression [282]

that mechanical compression may cause local water removal within compressed tissue sites. This water may then be transported from the compressed site laterally along interstitial pressure gradients, increasing local protein concentration. Mechanical compression results in higher OCT signal intensity, i.e., higher contrast and thus better imaging capability. The localized mechanical compression of skin decreases tissue thickness and water content and increases refractive index and OCT signal intensity. Mechanical loading may also decrease absorption and scattering in the compressed region, particularly at 1,310 nm, near the 1,450 nm absorption peak of water (low concentration of water due to its displacement).

The effect of mechanical compression on the contrast between epithelial and stromal layers of human rectum ex vivo in OCT images was studied in Ref. [276]. Due to different mechanical properties and water content of these layers, the changes of scattering properties induced by compression are different, which leads to better contrasting of these layers in OCT images. The same group has reported studies on continuous mechanical compression of human thin skin in vivo [282]. The OCT images (mean wavelength 910 nm, axial and transverse spatial resolution of 15 and 25 μm in air, respectively) were obtained for three male volunteers of different ages at low and high mechanical pressures. The OCT probe was placed in a special holder allowing for control of the force of pressure on the skin and keeping it constant. The probe was pressed onto human skin with force varying from 0.4 N (pressure 0.07 N/mm^2) to 2 N (0.35 N/mm^2) and was held in such a position for 10–15 min while the OCT images of the skin were acquired continuously at a rate of one image every 5 s. The OCT signal (A-scan) was averaged over the transverse direction in the region uniform in the transverse (in respect to probe beam) direction of 200 μm-width (Fig. 16.35a); from this averaged A-scan OCT signals (in dB) for particular layers were extracted; the difference of these signals for neighboring layers was attributed as image contrast corresponding to the ratio of the OCT signals indicated in dB (Fig. 16.35b, c). The temporal dependencies of OCT image contrast for the epidermis–dermis junction measured at low and high pressures are presented in Fig. 16.35b, c.

For the 23-year-old volunteer, the image contrast increased monotonously with time for both the low- and high-pressure regimes. The maximal contrast was reached much faster for the high pressure than for the lower, less than 1 min was enough to reach the similar contrast for which at the low pressure more than 3 min was needed. The skin of the older volunteer (49 years old) demonstrates an increase in junction contrast, especially at the high-pressure regime that reaches a similar maximum as for younger skin at the sixth min. Evidently, these changes could be associated with the different dynamics of water inflow, in particular connected with the different balance of free and bounded water for the young and aged skin.

16.9 Summary

In summary, we have discussed in this chapter the basic principles of an optical coherence tomography system and have shown briefly its applications, both medical and non-medical. The emphasis was placed on the low-coherence

interferometry that consists of the building block for optical coherence tomography. OCT based on the time modulation of the interference signal, i.e., modulation of the time delay in order to increase the signal-to-noise ratio of the system, was discussed, while other variations of OCT systems were left for readers to refer to the existing literatures. Several features of OCT suggest that it will be an important technique for both biomedical imaging and industrial applications. These features include: (1) high axial resolution of 1–15 μm, one to two orders of magnitude higher than conventional ultrasound; (2) noninvasive and non-contact, which imply that the imaging can be performed without the contact with the sample and without the need to excise the specimen; (3) high speed, enabling real-time imaging; (4) flexibility, in that it can be integrated into almost all medical imaging modalities; (5) cost-effectiveness and portability, because the system can be implemented by optic-fibers commercially available in the telecommunication industrials.

For further reading on OCT advanced systems and broader biomedical applications, we recommend the following comprehensive OCT monographs: [82, 135, 288].

Human tissue is highly scattering in nature to the near infrared light that is usually used to illuminate the OCT systems. In the second part of this chapter, it was shown that multiple scattering of tissue is a detrimental factor that limits OCT imaging performance, for example, the imaging resolution, depth, localization, and contrast. In order to improve the imaging capabilities for OCT systems, the multiple scattering of tissue must be reduced.

The last part of this chapter introduced a novel technique, i.e., using a biocompatible and hyperosmotic chemical agent to impregnate the tissue, to enhance the OCT imaging performances through the tissue. The mechanisms for such improvements, for example, imaging depth and contrast, were discussed, with primary through the experimental examples. It is assumed that when chemical agents are applied onto the targeted sample, there are two approaches concurrently applied to the tissue. The imaging depth, or light penetration depth, is enhanced by the refractive index matching of the major scattering centers within the tissue with the ground material induced by the chemical agents, usually through the diffusions of the interstitial liquids of tissue and the chemical agents. The imaging contrast enhancement is caused by the tissue dehydration due to the high osmotic characteristics of the chemical agents, which is also dependent on the mass transport of chemical agents within tissue.

Additional information on tissue optical clearing mechanisms, biomedical applications, benefits, and limitations, including toxicity issues, can be found in monographs, special issues of journals, and overview publications [168, 224, 236, 266, 289–298]. Tissue optical clearing is an exciting field of research, specifically in further development of OCT technologies. In particular, it allows one to image of superficial skin vessels using a compact low-power OCT Doppler system [299, 300]. The development of OCT technology in conjunction with optical clearing stimulates designing of novel biocompatible OCAs and compositions with enhancers [301, 302].

References

1. A. Yodh, B. Chance, Spectroscopy and imaging with diffusing light. Phys. Today **48**, 34–40 (1995)
2. D. Delpy, Optical spectroscopy for diagnosis. Phys. World **7**, 34–39 (1994)
3. B.R. Masters, P.T.C. So (eds.), *Handbook of Biomedical Nonlinear Optical Microscopy* (Oxford University Press, New York, 2008)
4. M. Rajadhyaksha, M. Grossman, D. Esterowitz, R. Webb, R. Anderson, In-vivo confocal scanning laser microscopy of human skin – melanin provides strong contrast. J. Invest. Dermatol. **104**, 946–952 (1995)
5. A.F. Fercher, Optical coherence tomography. J. Biomed. Opt. **1**, 157–173 (1996)
6. J.M. Schmitt, Optical coherence tomography (OCT): a review. IEEE J. Sel. Top. Quantum Electron. **5**, 1205–1215 (1999)
7. D. Huang, E.A. Swanson, C.P. Lin, J.S. Schuman, W.G. Stinson, W. Chang, M.R. Hee, T. Flotte, K. Gregory, C.A. Puliafito, J.G. Fujimoto, Optical coherence tomography. Science **254**, 1178–1181 (1991)
8. A.F. Fercher, C.K. Hitzenberger, W. Drexler, G. Kamp, H. Sattmann, In vivo optical coherence tomography. Am. J. Ophthalmol. **116**, 113–114 (1993)
9. J.M. Schmitt, A. Knüttel, M. Yadlowsky, R.F. Bonner, Optical coherence tomography of a dense tissue: statistics of attenuation and backscattering. Phys. Med. Biol. **42**, 1427–1439 (1994)
10. J.G. Fujimoto, M.E. Brezinski, G.J. Tearney, S.A. Boppart, B.E. Bouma, M.R. Hee, J.F. Southern, E.A. Swanson, Optical biopsy and imaging using optical coherence tomography. Nat. Med. **1**, 970–972 (1995)
11. G.J. Tearney, M.E. Brezinski, B.E. Bouma, S.A. Boppart, C. Pitris, J.F. Southern, J.G. Fujimoto, In vivo endoscopic optical biopsy with optical coherence tomography. Science **276**, 2037–2039 (1997)
12. R.C. Youngquist, S. Carr, D.E.N. Davies, Optical coherence domain reflectometry: a new optical evaluation technique. Opt. Lett. **12**, 158–160 (1987)
13. K. Takada, I. Yokohama, K. Chida, J. Noda, New measurement system for fault location in optical waveguide devices based on an interferometric technique. Appl. Opt. **26**, 1603–1606 (1987)
14. A.F. Fercher, K. Mengedoht, W. Werner, Eye-length measurement by interferometry with partially coherent light. Opt. Lett. **13**, 1867–1869 (1988)
15. C.K. Hitzenberger, W. Drexler, A.F. Fercher, Measurement of corneal thickness by laser Doppler interferometry. Invest. Ophthalmol. Vis. Sci. **33**, 98–103 (1992)
16. J.A. Izatt, M.R. Hee, E.A. Swanson, C.P. Lin, D. Huang, J.S. Schuman, C.A. Puliafito, J.G. Fujimoto, Micrometer-scale resolution imaging of the anterior eye with optical coherence tomography. Arch. Ophthalmol. **112**, 1584–1589 (1994)

17. W. Clivaz, F. Marquis-Weible, R.P. Salathe, R.P. Novak, H.H. Gilgen, High-resolution reflectometry in biological tissue. Opt. Lett. **17**, 4–6 (1992)

18. M.R. Hee, J.A. Izatt, E.A. Swanson, D. Huang, C.P. Lin, J.S. Schuman, C.A. Puliafito, J.G. Fujimoto, Optical coherence tomography of the human retina. Arch. Ophthalmol. **113**, 326–332 (1995)

19. S.A. Boppart, M.E. Brezinski, B.E. Bouma, G.J. Tearney, J.G. Fujimoto, Investigation of developing embryonic morphology using optical coherence tomography. Dev. Biol. **177**, 54–63 (1996)

20. C.A. Puliafito, M.R. Hee, C.P. Lin, J.G. Fujimoto, Imaging of macular disease with optical coherence tomography. Ophthalmology **102**, 217–229 (1995)

21. C. Pitris, C. Jesser, S.A. Boppart, D. Stamper, M.E. Brezinski, J.G. Fujimoto, Feasibility of optical coherence tomography for high resolution imaging of human gastrointestinal tract malignancies. J. Gastroenterol. **35**, 87–92 (2000)

22. S. Brand, J.M. Poneros, B.E. Bouma, G.J. Tearney, C.C. Compton, N.S. Nishioka, Optical coherence tomography in the gastrointestinal tract. Endoscopy **32**, 796–803 (2000)

23. B.E. Bouma, G.J. Tearney, C.C. Compton, N.S. Nishioka, High-resolution imaging of the human esophagus and stomach in vivo using optical coherence tomography. Gastrointest. Endosc. **51**, 467–574 (2000)

24. S. Jackle, N. Gladkova, F. Feldchtein, A. Terentieva, B. Brand, G. Gelikonov, V. Gelikonov, A. Sergeev, A. Fritscher-Ravens, J. Freund, U. Seitz, S. Schroder, N. Soehendra, In vivo endoscopic optical coherence tomography of the human gastrointestinal tract – toward optical biopsy. Endoscopy **32**, 743–749 (2000)

25. R.K. Wang, J.B. Elder, Propylene glycol as a contrasting agent for optical coherence tomography to image gastro-intestinal tissues. Lasers Surg. Med. **30**, 201–208 (2002)

26. B.W. Colston, M.J. Everett, L.B. Da Silva, L.L. Otis, P. Stroeve, H. Nathel, Imaging of hard- and soft-tissue structure in the oral cavity by optical coherence tomography. Appl. Opt. **37**, 3582–3585 (1998)

27. J.M. Schmitt, M.J. Yadlowsky, R. Bonner, Subsurface imaging of living skin with optical coherence tomography. Dermatology **191**, 93–98 (1995)

28. N.D. Gladkova, G.A. Petrova, N.K. Nikulin, S.G. Radenska-Lopovok, L.B. Snopova, Y.P. Chumakov, V.A. Nasonova, V.M. Geilkonov, G.V. Geilkonov, R.V. Kuranov, A.M. Sergeev, F.I. Feldchtein, In vivo optical coherence tomography imaging of human skin: norm and pathology. Skin Res. Technol. **6**, 6–16 (2000)

29. R.K. Wang, J.B. Elder, High resolution optical tomographic imaging of soft biological tissues. Laser Phys. **12**, 611–616 (2002)

30. J.G. Fujimoto, B.E. Bouma, G.J. Tearney, S.A. Boppart, C. Pitris, J.F. Southern, M.E. Brezinski, New technology for high speed and high resolution optical coherence tomography. Ann. N. Y. Acad. Sci. **838**, 95–107 (1998)

31. C. Passmann, H. Ermert, A 100 MHz ultrasound imaging system for dermatologic and ophthalmologic diagnostics. IEEE Trans. Ultrason. Ferroelect. Freq. Control **43**, 545–552 (1996)

32. P.A. Flournoy, White light interferometric thickness gauge. Appl. Opt. **11**, 1907–1915 (1972)

33. T. Li, A. Wang, K. Murphy, R. Claus, White light scanning fibre Michelson interferometer for absolute position measurement. Opt. Lett. **20**, 785–787 (1995)

34. Y.J. Rao, Y.N. Ning, D.A. Jackson, Synthesised source for white light sensing system. Opt. Lett. **18**, 462–464 (1993)

35. J.W. Goodman, *Statistical Optics* (Wiley, New York, 1985), pp. 164–169

36. R.K. Wang, Resolution improved optical coherence-gated tomography for imaging through biological tissues. J. Mod. Opt. **46**, 1905–1913 (1999)

37. A. Podolenau, D.A. Jackson, Noise analysis of a combined optical coherence tomograph and a confocal scanning ophthalmoscope. Appl. Opt. **38**, 2116–2127 (1999)

38. P.R. Gray, R.G. Meyer, *Analysis and Design of Integrated Circuits*, 2nd edn. (Wiley, New York, 1984)

39. V.M. Gelikonov, G.V. Gelikonov, N.D. Gladkova et al., Coherent optical tomography of microscopic inhomogeneities in biological tissues. JETP Lett. **61**, 149–153 (1995)
40. G.J. Tearney, B.E. Bouma, S.A. Boppart, B. Golubovic, E.A. Swanson, J.G. Fujimoto, Rapid acquisition of in vivo biological images by use of optical coherence tomography. Opt. Lett. **21**, 1408–1410 (1996)
41. T. Ko, D. Adler, J. Fujimoto, D. Mamedov, V. Prokhorov, V. Shidlovski, S. Yakubovich, Ultrahigh resolution optical coherence tomography imaging with a broadband superluminescent diode light source. Opt. Express **12**, 2112–2119 (2004)
42. B.E. Bouma, G.J. Tearney, S.A. Boppart, M.R. Hee, M.E. Brezinski, J.G. Fujimoto, High-resolution optical coherence tomographic imaging using a mode-locked Ti: Al_2O_3 laser source. Opt. Lett. **20**, 1486–1488 (1995)
43. W. Drexler, U. Morgner, F.X. Kärtner, C. Pitris, S.A. Boppart, X.D. Li, E.P. Ippen, J.G. Fujimoto, In vivo ultrahigh-resolution optical coherence tomography. Opt. Lett. **24**, 1221–1223 (1999)
44. R. Leitgeb, W. Drexler, A. Unterhuber, B. Hermann, T. Bajraszewski, T. Le, A. Stingl, A. Fercher, Ultrahigh resolution Fourier domain optical coherence tomography. Opt. Express **12**, 2156–2165 (2004)
45. B. Považay, K. Bizheva, A. Unterhuber, B. Hermann, H. Sattmann, A.F. Fercher, W. Drexler, A. Apolonski, W.J. Wadsworth, J.C. Knight, P.S. Russell, M. Vetterlein, E. Scherzer, Submicrometer axial resolution optical coherence tomography. Opt. Lett. **27**, 1800–1802 (2002)
46. S. Kray, F. Spoler, M. Forst, H. Kurz, High-resolution simultaneous dual-band spectral domain optical coherence tomography. Opt. Lett. **34**, 1970–1972 (2009)
47. F. Spoler, S. Kray, P. Grychtol, B. Hermes, J. Bornemann, M. Forst, H. Kurz, Simultaneous dual-band ultra-high resolution optical coherence tomography. Opt. Express **15**, 10832–10841 (2007)
48. P. Cimalla, J. Walther, M. Mehner, M. Cuevas, E. Koch, Simultaneous dual-band optical coherence tomography in the spectral domain for high resolution in vivo imaging. Opt. Express **17**, 19486–19500 (2009)
49. Z.W. Zhi, J. Qin, L. An, R.K. Wang, Supercontinuum light source enables in vivo optical microangiography of capillary vessels within tissue beds. Opt. Lett. **36**, 3169–3171 (2011)
50. K. Takada, H. Yamada, M. Horiguchi, Optical low coherence reflectometer using [3 × 3] fiber coupler. IEEE Photonics Technol. Lett. **6**, 1014–1016 (1994)
51. R. Paschotta, J. Nilsson, A.C. Tropper, D.C. Hanna, Efficient superfluorescent light sources with broad bandwidth. IEEE J. Sel. Top. Quantum Electron. **3**, 1097–1099 (1997)
52. B.E. Bouma, L.E. Nelso, G.J. Tearney, D.J. Jones, M.E. Brezinski, J.G. Fujimoto, Optical coherence tomographic imaging of human tissue at 1.55 μm and 1.81 μm using Er- and Tm-doped fiber sources. J. Biomed. Opt. **3**, 76–79 (1998)
53. D.J. Derickson, P.A. Beck, T.L. Bagwell, D.M. Braun, J.E. Fouquet, F.G. Kellert, M.J. Ludowise, W.H. Perez, T.R. Ranganath, G.R. Trott, S.R. Sloan, High-power, low-internal-reflection, edge emitting light-emitting diodes. Hewlett-Packard J. **46**, 43–49 (1995)
54. H.H. Liu, P.H. Cheng, J.P. Wang, Spatially coherent white-light interferometer based on a point fluorescent source. Opt. Lett. **18**, 678–680 (1993)
55. C.F. Lin, B.L. Lee, Extremely broadband AlGaAs/GaAs superluminescent diodes. Appl. Phys. Lett. **71**, 1598–1600 (1997)
56. P.J. Poole, M. Davies, M. Dion, Y. Feng, S. Charbonneau, R.D. Goldberg, I.V. Mitchell, The fabrication of a broad-spectrum light-emitting diode using high-energy ion implantation. IEEE Photonics Technol. Lett. **8**, 1145–1147 (1996)
57. T.R. Cole, G.S. Kino, *Confocal Scanning Optical Microscopy and Related Imaging Systems* (Academic, San Diego, 1990)
58. J.M. Schmitt, A. Knüttel, M. Yadlowsky, M.A. Eckhaus, Optical coherence tomography of a dense tissue: statistics of attenuation and backscattering. Phys. Med. Biol. **39**, 1705–1720 (1994)

59. C.B. Su, Achieving variation of the optical path length by a few millimeters at millisecond rates for imaging of turbid media and optical interferometry: a new technique. Opt. Lett. **22**, 665–667 (1997)

60. G.J. Tearney, B.E. Bouma, J.G. Fujimoto, High speed phase and group-delay scanning with a grating-based phase control delay line. Opt. Lett. **22**, 1811–1813 (1997)

61. A.M. Rollins, M.D. Kulkarni, S. Yazdanfar, R. Ung-Arunyawee, J.A. Izatt, In vivo video rate optical coherence tomography. Opt. Express **3**, 219–229 (1998)

62. W. Drexler, O. Findl, R. Menapace, A. Kruger, A. Wedrich, G. Rainer, A. Baumgartner, C.K. Hitzenberger, A.F. Fercher, Dual beam optical coherence tomography: signal identification for ophthalmologic diagnosis. J. Biomed. Opt. **3**, 55–65 (1998)

63. J.A. Izatt, M.R. Hee, G.M. Owen, E.A. Swanson, J.G. Fujimoto, Optical coherence microscopy in scattering media. Opt. Lett. **19**, 590–592 (1994)

64. A.G. Podoleanu, Unbalanced versus balanced operation in an optical coherence tomography system. Appl. Opt. **39**, 173–182 (2000)

65. A.F. Fercher, C.K. Hitzenberger, G. Kamp, S.Y. El Zaiat, Measurement of intraocular distances by backscattering spectral interferometry. Opt. Commun. **117**, 43–8 (1995)

66. G. Häusler, M.W. Lindner, Coherence radar and spectral radar – new tools for dermatological diagnosis. J. Biomed. Opt. **3**, 21–31 (1998)

67. Y. Yasuno, Y. Sutoh, M. Nakama, S. Makita, M. Itoh, T. Yatagai, M. Mori, Spectral interferometric optical coherence tomography with nonlinear beta-barium borate time gating. Opt. Lett. **27**, 403–405 (2002)

68. E. Beaurepaire, A.C. Boccara, M. Lebec, L. Blanchot, H. Saint-Jalmes, Full-field optical coherence microscopy. Opt. Lett. **23**, 244–2466 (1998)

69. L. Vabre, A. Dubois, A.C. Boccara, Thermal-light full-field optical coherence tomography. Opt. Lett. **27**, 530–532 (2002)

70. C.E. Saxer, J.F. de Boer, B. Hyle Park, Y. Zhao, Z. Chen, J.S. Nelson, High-speed fiber-based polarization-sensitive optical coherence tomography of in vivo human skin. Opt. Lett. **25**, 1257–355 (2000)

71. J.E. Roth, J.A. Kozak, S. Yazdanfar, A.M. Rollins, J.A. Izatt, Simplified method for polarization-sensitive optical coherence tomography. Opt. Lett. **26**, 1069–1071 (2001)

72. S. Jiao, L.V. Wang, Two-dimensional depth-resolved Mueller matrix of biological tissue measured with double-beam polarization-sensitive optical coherence tomography. Opt. Lett. **27**, 101–103 (2002)

73. Z. Chen, T.E. Milner, D. Dave, J.S. Nelson, Optical Doppler tomographic imaging of fluid flow velocity in highly scattering media. Opt. Lett. **22**, 64–66 (1997)

74. J.A. Izatt, M.D. Kulkarni, S. Yazdanfar, J.K. Barton, A.J. Welch, In vivo bidirectional color Doppler flow imaging of picoliter blood volumes using optical coherence tomograghy. Opt. Lett. **22**, 1439–1441 (1997)

75. Y. Zhao, Z. Chen, C. Saxer, X. Shaohua, J.F. de Boer, J.S. Nelson, Phase-resolved optical coherence tomography and optical Doppler tomography for imaging blood flow in human skin with fast scanning speed and high velocity sensitivity. Opt. Lett. **25**, 114–116 (2000)

76. Y. Zhao, Z. Chen, Z. Ding, H. Ren, J.S. Nelson, Real-time phase-resolved functional optical coherence tomography by use of optical Hilbert transformation. Opt. Lett. **27**, 98–100 (2002)

77. S.G. Proskurin, Y. He, R.K. Wang, Determination of flow-velocity vector based on Doppler shift and spectrum broadening with optical coherence tomography. Opt. Lett. **28**, 1224–1226 (2003)

78. S.G. Proskurin, I.A. Sokolova, R.K. Wang, Imaging of non-parabolic velocity profiles in converging flow with optical coherence tomography. Phys. Med. Biol. **48**, 2907–2918 (2003)

79. U. Morgner, W. Drexler, F.X. Kartner, X.D. Li, C. Pitris, E.P. Ippen, J.G. Fujimoto, Spectroscopic optical coherence tomography. Opt. Lett. **25**, 111–113 (2000)

80. A.F. Fercher, W. Drexler, C.K. Hitzenberger, T. Lasser, Optical coherence tomography – principles and applications. Rep. Prog. Phys. **66**, 239–303 (2003)

81. P.H. Tomlins, R.K. Wang, Theory, development and applications of optical coherence tomography. J. Phys. D: Appl. Phys. **38**, 17 (2005)
82. W. Drexler, J.G. Fujimoto (eds.), *Optical Coherence Tomography: Technology and Applications* (Springer, Berlin, 2008)
83. C.K. Hitzenberger, P. Trost, P.W. Lo, Q.Y. Zhou, Three-dimensional imaging of the human retina by high-speed optical coherence tomography. Opt. Express **11**, 9 (2003)
84. A.F. Fercher, C.K. Hitzenberger, G. Kamp, S.Y. Elzaiat, Measurement of intraocular distances by backscattering spectral interferometry. Opt. Commun. **117**, 6 (1995)
85. S.R. Chinn, E.A. Swanson, J.G. Fujimoto, Optical coherence tomography using a frequency-tunable optical source. Opt. Lett. **22**, 3 (1997)
86. U. Haberland, P. Jansen, V. Blazek, H.J. Schmitt, Optical coherence tomography of scattering media using frequency-modulated continuous-wave techniques with tunable near-infrared laser. Proc. SPIE **2981**, 9 (1997)
87. J.F. de Boer, B. Cense, B.H. Park, M.C. Pierce, G.J. Tearney, B.E. Bouma, Improved signal-to-noise ratio in spectral-domain compared with time-domain optical coherence tomography. Opt. Lett. **28**, 3 (2003)
88. M. Choma, M. Sarunic, C. Yang, J. Izatt, Sensitivity advantage of swept source and Fourier domain optical coherence tomography. Opt. Express **11**, 6 (2003)
89. R. Leitgeb, C. Hitzenberger, A. Fercher, Performance of Fourier domain vs. time domain optical coherence tomography. Opt. Express **11**, 6 (2003)
90. M. Wojtkowski, R. Leitgeb, A. Kowalczyk, T. Bajraszewski, A.F. Fercher, In vivo human retinal imaging by Fourier domain optical coherence tomography. J. Biomed. Opt. **7**, 7 (2002)
91. B. Cense, N. Nassif, T. Chen, M. Pierce, S.-H. Yun, B. Park, B. Bouma, G. Tearney, J. de Boer, Ultrahigh-resolution high-speed retinal imaging using spectral-domain optical coherence tomography. Opt. Express **12**, 13 (2004)
92. D.M. de Bruin, D. Burnes, J. Loewenstein, Y. Chen, S. Chang, T. Chen, D. Esmaili, J.F. de Boer, In vivo three-dimensional imaging of neovascular age related macular degeneration using optical frequency domain imaging at 1050 nm. Invest. Ophthalmol. Vis. Sci. **49**(10), 4545–4552 (2008)
93. E.C. Lee, J.F. de Boer, M. Mujat, H. Lim, S.H. Yun, In vivo optical frequency domain imaging of human retina and choroid. Opt. Express **14**, 9 (2006)
94. H. Lim, M. Mujat, C. Kerbage, E.C. Lee, Y. Chen, T.C. Chen, J.F. de Boer, High-speed imaging of human retina in vivo with swept-source optical coherence tomography. Opt. Express **14**, 7 (2006)
95. M. Wojtkowski, V. Srinivasan, T. Ko, J. Fujimoto, A. Kowalczyk, J. Duker, Ultrahigh-resolution, high-speed, Fourier domain optical coherence tomography and methods for dispersion compensation. Opt. Express **12**, 19 (2004)
96. R. Leitgeb, W. Drexler, A. Unterhuber, B. Hermann, T. Bajraszewski, T. Le, A. Stingl, A. Fercher, Ultrahigh resolution Fourier domain optical coherence tomography. Opt. Express **12**, 10 (2004)
97. V.J. Srinivasan, R. Huber, I. Gorczynska, J.G. Fujimoto, J.Y. Jiang, P. Reisen, A.E. Cable, High-speed, high-resolution optical coherence tomography retinal imaging with a frequency-swept laser at 850 nm. Opt. Lett. **32**, 3 (2007)
98. A.H. Bachmann, M.L. Villiger, C. Blatter, T. Lasser, R.A. Leitgeb, Resonant Doppler flow imaging and optical vivisection of retinal blood vessels. Opt. Express **15**, 15 (2007)
99. L. An, R.K. Wang, In vivo volumetric imaging of vascular perfusion within human retina and choroids with optical micro-angiography. Opt. Express **16**, 15 (2008)
100. B.J. Vakoc, R.M. Lanning, J.A. Tyrrell, T.P. Padera, L.A. Bartlett, T. Stylianopoulos, L.L. Munn, G.J. Tearney, D. Fukumura, R.K. Jain, B.E. Bouma, Three-dimensional microscopy of the tumor microenvironment in vivo using optical frequency domain imaging. Nat. Med. **15**, 8 (2009)

101. B.R. White, M.C. Pierce, N. Nassif, B. Cense, B.H. Park, G.J. Tearney, B.E. Bouma, T.C. Chen, J.F. de Boer, In vivo dynamic human retinal blood flow imaging using ultra-high-speed spectral domain optical coherence tomography. Opt. Express **11**, 8 (2003)

102. J. Fingler, R.J. Zawadzki, J.S. Werner, D. Schwartz, S.E. Fraser, Volumetric microvascular imaging of human retina using optical coherence tomography with a novel motion contrast technique. Opt. Express **17**, 11 (2009)

103. L. An, H.M. Subhush, D.J. Wilson, R.K. Wang, High-resolution wide-field imaging of retinal and choroidal blood perfusion with optical microangiography. J. Biomed. Opt. **15**, 066022 (2010)

104. L. Yu, Z. Chen, Doppler variance imaging for three-dimensional retina and choroid angiography. J. Biomed. Opt. **15**, 016029 (2010)

105. M. Szkulmowski, A. Szkulmowska, T. Bajraszewski, A. Kowalczyk, M. Wojtkowski, Flow velocity estimation using joint spectral and time domain optical coherence tomography. Opt. Express **16**, 18 (2008)

106. R.K. Wang, L. An, S. Saunders, D.J. Wilson, Optical microangiography provides depth-resolved images of directional ocular blood perfusion in posterior eye segment. J. Biomed. Opt. **15**, 020502 (2010)

107. S. Makita, F. Jaillon, M. Yamanari, M. Miura, Y. Yasuno, Comprehensive in vivo micro-vascular imaging of human eye by dual-beam-scan Doppler optical coherence angiography. Opt. Express **19**, 13 (2011)

108. S. Makita, Y. Hong, M. Yamanari, T. Yatagai, Y. Yasuno, Optical coherence angiography. Opt. Express **14**, 20 (2006)

109. S. Zotter, M. Pircher, T. Torzicky, M. Bonesi, E. Götzinger, R.A. Leitgeb, C.K. Hitzenberger, Visualization of microvasculature by dual-beam phase-resolved Doppler optical coherence tomography. Opt. Express **19**, 11 (2011)

110. Y.K. Tao, K.M. Kennedy, J.A. Izatt, Velocity-resolved 3D retinal microvessel imaging using single-pass flow imaging spectral domain optical coherence tomography. Opt. Express **17**, 12 (2009)

111. B. Potsaid, B. Baumann, D. Huang, S. Barry, A.E. Cable, J.S. Schuman, J.S. Duker, J.G. Fujimoto, Ultrahigh speed 1050 nm swept source/Fourier domain OCT retinal and anterior segment imaging at 100,000 to 400,000 axial scans per second. Opt. Express **18**, 20 (2010)

112. C.M. Eigenwillig, T. Klein, W. Wieser, B.R. Biedermann, R. Huber, Wavelength swept amplified spontaneous emission source for high speed retinal optical coherence tomography at 1060 nm. J. Biophotonics **4**(7–8), 552–558 (2010)

113. M. Gora, K. Karnowski, M. Szkulmowski, B.J. Kaluzny, R. Huber, A. Kowalczyk, M. Wojtkowski, Ultrahigh-speed swept source OCT imaging of the anterior segment of human eye at 200 kHz with adjustable imaging range. Opt. Express **17**, 15 (2009)

114. V.J. Srinivasan, D.C. Adler, Y. Chen, I. Gorczynska, R. Huber, J. Duker, J.S. Schuman, J.G. Fujimoto, Ultrahigh-speed optical coherence tomography for three-dimensional and *en face* imaging of the retina and optic nerve head. Invest. Ophthalmol. Vis. Sci. **49**(11), 5103–5110 (2008)

115. B. Potsaid, I. Gorczynska, V.J. Srinivasan, Y.L. Chen, J. Jiang, A. Cable, J.G. Fujimoto, Ultrahigh speed spectral/Fourier domain OCT ophthalmic imaging at 70,000 to 312,500 axial scans per second. Opt. Express **16**, 21 (2008)

116. D.Y. Kim, J. Fingler, J.S. Werner, D.M. Schwartz, S.E. Fraser, R.J. Zawadzki, In vivo volumetric imaging of human retinal circulation with phase-variance optical coherence tomography. Biomed. Opt. Express **2**, 10 (2011)

117. R.K. Wang, L. An, P. Francis, D.J. Wilson, Depth-resolved imaging of capillary networks in retina and choroid using ultrahigh sensitive optical microangiography. Opt. Lett. **35**, 3 (2010)

118. W. Wieser, B.R. Biedermann, T. Klein, C.M. Eigenwillig, R. Huber, Multi-megahertz OCT: high quality 3D imaging at 20 million A-scans and 4.5 GVoxels per second. Opt. Express **18**, 20 (2010)

119. T. Klein, W. Wieser, C.M. Eigenwillig, B.R. Biedermann, R. Huber, Megahertz OCT for ultrawide-field retinal imaging with a 1050 nm Fourier domain mode-locked laser. Opt. Express **19**, 19 (2011)

120. M.R. Hee, J.A. Izatt, E.A. Swanson, D. Huang, J.S. Schuman, C.P. Lin, C.A. Puliafito, J.G. Fujimoto, Optical coherence tomography of the human retina. Arch. Opthalmol. **113**, 325–332 (1995)

121. C.A. Puliafito, M.R. Hee, C.P. Lin, E. Reichel, J.S. Schuman, J.S. Duker, J.A. Izatt, E.A. Swanson, J.G. Fujimoto, Imaging of macular diseases with optical coherence tomography. Ophthalmology **120**, 217–229 (1995)

122. C.A. Puliafito, M.R. Hee, J.S. Schumann, J.G. Fujimoto, *Optical Coherence Tomography of Ocular Diseases* (Slack, Thorofare, 1995)

123. M.E. Brezinski, G.J. Tearney, B.E. Bouma, J.A. Izatt, M.R. Hee, E.A. Swanson, J.F. Southern, J.G. Fujimoto, Optical coherence tomography for optical biopsy: properties and demonstration of vascular pathology. Circulation **93**, 1206–1213 (1996)

124. V.V. Tuchin, X. Xu, R.K. Wang, Dynamic optical coherence tomography in optical clearing, sedimentation and aggregation study of immersed blood. Appl. Opt. **41**, 258–271 (2002)

125. P. Parsa, S. Jacques, N. Nishioka, Optical properties of rat liver between 350 and 2200 nm. Appl. Opt. **28**, 2325–2330 (1989)

126. R.K. Wang, Signal degradation by multiple scattering in optical coherence tomography of dense tissue: a Monte Carlo study towards optical clearing of biotissues. Phys. Med. Biol. **47**, 2281–2299 (2002)

127. D. Huang, J. Wang, C.P. Lin, C.A. Puliafito, J.G. Fujimoto, Micron-resolution ranging of cornea anterior chamber by optical reflectometry. Lasers Surg. Med. **11**, 419–425 (1991)

128. A.F. Fercher, C.K. Hitzenberger, G. Kemp, S.Y. Elzaiat, Measurement of intraocular distances by backscattering spectral interferometry. Opt. Commun. **117**, 43–48 (1995)

129. K. Rohrschneider, R.O. Burk, F.E. Kruse, H.E. Volcker, Reproducibility of the optic nerve head topography with a new laser tomographic scanning device. Ophthalmol. **101**, 1044–1049 (1994)

130. M.R. Hee, C.A. Puliafitom, C. Wong, E. Reichel, J.S. Duker, J.S. Schuman, E.A. Swanson, J.G. Fujimoto, Optical coherence tomography of central serous chorioretinopathy. Am. J. Ophthalmol. **120**, 65–74 (1995)

131. M.R. Hee, C.A. Puliafito, C. Wong, E. Reichel, J.S. Duker, J.S. Schuman, E.A. Swanson, J.G. Fujimoto, Optical coherence tomography of macular holes. Ophthalmol. **102**, 748–756 (1995)

132. J.S. Schuman, M.R. Hee, C.A. Puliafito, C. Wong, T. Pedutkloizman, C.P. Lin, E. Hertzmark, J.A. Izatt, E.A. Swanson, J.G. Fujimoto, Quantification of nerve fibre layer thickness in normal and glaucomatous eyes using optical coherence tomography. Arch. Ophthalmol. **113**, 586–596 (1995)

133. W. Drexler, U. Morgner, R.K. Ghanta, F.X. Kartner, J.S. Schuman, J.G. Fujimoto, Ultrahigh-resolution ophthalmic optical coherence tomography. Nat. Med. **7**, 502–507 (2001)

134. I. Hartl, T. Ko, R.K. Ghanta, W. Drexler, A. Clermont, S.E. Bursell, J.G. Fujimoto, In vivo ultrahigh resolution optical coherence tomography for the quantification of retinal structure in normal and transgenic mice. Invest. Ophthalmol. Vis. Sci. **42**(Suppl. 4), 4252 (2001)

135. B.E. Bouma, G.J. Tearney (eds.), *Handbook of Optical Coherence Tomography* (Marcel-Dekker, New York, 2002)

136. S.A. Boppart, B.E. Bouma, M.E. Brezinski, G.J. Tearney, J.G. Fujimoto, Imaging developing neural morphology using optical coherence tomography. J. Neurosci. Methods **70**, 65–72 (1996)

137. S.A. Boppart, G.J. Tearney, B.E. Bouma, J.F. Southern, M.E. Brezinski, J.G. Fujimoto, Noninvasive assessment of the developing *Xenopus* cardiovascular system using optical coherence tomography. Proc. Natl. Acad. Sci. U.S.A. **94**, 4256–4261 (1997)

138. S. Rugonyi, C. Shaut, A.P. Liu, K. Thornburg, R.K. Wang, Changes in wall motion and blood flow in the outflow tract of chick embryonic hearts observed with optical coherence tomography after outflow tract banding and vitelline-vein ligation. Phys. Med. Biol. **53**, 5077–5091 (2008)

139. A. Liu, R.K. Wang, K.L. Thornburg, S. Rugonyi, Dynamic variation of hemodynamic shear stress on the walls of developing chick hearts: computational models of the heart outflow tract. Eng. Comput. **25**, 73–86 (2009)

140. A. Liu, R.K. Wang, K.L. Thornburg, S. Rugonyi, Efficient post-acquisition synchronization of 4D non-gated cardiac images obtained from optical coherence tomography: application to 4D reconstruction of the chick embryonic heart. J. Biomed. Opt. **14**(4), 044020 (2009)

141. Z. Ma, A. Liu, X. Yin, A. Troyer, K. Thornburg, R.K. Wang, S. Rugonyi, Measurement of absolute blood flow velocity across outflow tract of HH18 chicken embryo based on 4D reconstruction using spectral domain optical coherence tomography. Biomed. Opt. Express **1**(3), 798–811 (2010)

142. I.V. Larina, K. Furushima, M.E. Dickinson, R.R. Behringer, K.V. Larin, Live imaging of rat embryos with Doppler swept-source optical coherence tomography. J. Biomed. Opt. **14**, 050506-1–050506-3 (2009)

143. K.V. Larin, I.V. Larina, M. Liebling, M.E. Dickinson, Live imaging of early developmental processes in mammalian embryos with optical coherence tomography. J. Innov. Opt. Health Sci. **2**, 253–259 (2009)

144. N.D. Gladkova, G.A. Petrova, N.K. Nikulin, S.G. Radenska-Lopovok, L.B. Snopova, Y.P. Chumakov, V.A. Nasonova, V.M. Gelikonov, G.V. Gelikonov, R.V. Kuranov, A.M. Sergeev, F.I. Feldchtein, In vivo optical coherence tomography imaging of human skin: norm and pathology. Skin Res. Technol. **6**, 6–16 (2000)

145. J. Welzel, Optical coherence tomography in dermatology: a review. Skin Res. Technol. **7**, 1–9 (2001)

146. C.B. Williams, J.E. Whiteway, J.R. Jass, Practical aspects of endoscopic management of malignant polyps. Endoscopy **19**(Suppl. 1), 31–37 (1987)

147. K. Kobayashi, H.S. Wang, M.V. Sivak, J.A. Izatt, Micron-resolution sub-surface imaging of the gastrointestinal tract wall with optical coherence tomography. Gastrointest. Endosc. **43**, 29–29 (1996)

148. J.A. Izatt, Micron scale in vivo imaging of gastrointestinal cancer using optical coherence tomography. Radiology **217**(Suppl. S), 385 (2000)

149. A. Das, M.V. Sivak, A. Chak, R.C.K. Wong, V. Westphal, A.M. Rollins, J. Willis, G. Isenberg, J.A. Izatt, High-resolution endoscopic imaging of the GI tract: a comparative study of optical coherence tomography versus high-frequency catheter probe EUS. Gastrointest. Endosc. **54**, 219–224 (2001)

150. J.G. Fujimoto, M.E. Brezinski, G.J. Tearney, S.A. Boppart, B.E. Bouma, M.R. Hee, J.F. Southern, E.A. Swanson, Optical biopsy and imaging using optical coherence tomography. Nature Med. **1**, 970–972 (1995)

151. M.E. Brezinski, G.J. Tearney, N.J. Weissman, S.A. Boppart, B.E. Bouma, M.R. Hee, A.E. Weyman, E.A. Swanson, J.F. Southern, J.G. Fujimoto, Assessing atherosclerotic plaque morphology: comparison of optical coherence tomography and high frequency intravascular ultrasound. Heart **77**, 397–403 (1997)

152. J.G. Fujimoto, S.A. Boppart, G.J. Tearney, B.E. Bouma, C. Pitris, M.E. Brezinski, High resolution in vivo intra-arterial imaging with optical coherence tomography. Heart **82**, 128–133 (1999)

153. B.W. Colston, U.S. Sathyam, L.B. DaSilva, M.J. Everett, P. Stroeve, L.L. Otis, Dental OCT. Opt. Express **3**, 230–238 (1998)

154. Y. Yang, L. Wu, Y. Feng, R.K. Wang, Observations of birefringence in tissues from optic-fibre based optical coherence tomography. Meas. Sci. Technol. **14**, 41–46 (2003)

155. A. Baumgartner, C.K. Hitzenberger, H. Sattmann, W. Drexler, A.F. Fercher, Signal and resolution enhancements in dual beam optical coherence tomography of the human eye. J. Biomed. Opt. **3**, 45–54 (1998)

156. G. Yao, L.V. Wang, Two-dimensional depth-resolved Mueller matrix characterization of biological tissue by optical coherence tomography. Opt. Lett. **24**, 537–539 (1999)

157. J.P. Dunkers, R.S. Parnas, C.G. Zimba, R.C. Peterson, K.M. Flynn, J.G. Fujimoto, B.E. Bouma, Optical coherence tomography of glass reinforced polymer composites. Composites **30A**, 139–145 (1999)

158. M. Bashkansky, D. Lewis III, V. Pujari, J. Reintjes, H.Y. Yu, Subsurface detection and characterization of Hertzian cracks in Si_3N_4 balls using optical coherence tomography. NDT E-Int. **34**, 547–555 (2001)

159. F. Xu, H.E. Pudavar, P.N. Prasad, Confocal enhanced optical coherence tomography for nondestructive evaluation of paints and coatings. Opt. Lett. **24**, 1808–1810 (1999)

160. R.K. Wang, J.B. Elder, Optical coherence tomography: a new approach to medical imaging with resolution at cellular level. Proc. MBNT 1–4, ISSBN: 0951584235 (1999)

161. D.J. Smithies, T. Lindmo, Z. Chen, J.S. Nelson, T. Miller, Signal attenuation and localisation in optical coherence tomography by Monte Carlo simulation. Phys. Med. Biol. **43**, 3025–3044 (1998)

162. G. Yao, L.V. Wang, Monte Carlo simulation of an optical coherence tomography signal in homogeneous turbid media. Phys. Med. Biol. **44**, 2307–2320 (1999)

163. J.M. Schmitt, A. Knüttle, M.J. Yadlowsky, M.A. Eckhaus, Optical coherence tomography of a dense tissue: statistics of attenuation and backscattering. Phys. Med. Biol. **39**, 1705–1720 (1994)

164. X. Xu, R.K. Wang, J.B. Elder, V.V. Tuchin, Effect on dextran-induced changes in refractive index and aggregation on optical properties of whole blood. Phys. Med. Biol. **48**, 1205–1221 (2003)

165. J.M. Schmitt, A. Knüttel, Model of optical coherence tomography of heterogeneous tissue. J. Opt. Soc. Am. A **14**, 1231–1242 (1997)

166. L. Thrane, H.T. Yura, P.E. Andersen, Analysis of optical coherence tomography systems based on the extended Huygens-Fresnel principle. J. Opt. Soc. Am. A **17**, 484–490 (2000)

167. Y. Feng, R.K. Wang, J.B. Elder, A theoretical model of optical coherence tomography for system optimization and characterization. J. Opt. Soc. Am. A **20**, 1792–1803 (2003)

168. V.V. Tuchin, *Tissue Optics: Light Scattering Methods and Instruments for Medical Diagnosis*, vol. PM 166, 2nd edn. (SPIE Press, Bellingham, 2007)

169. V.V. Tuchin, Light scattering study of tissue. Phys. Usp. **40**, 495–515 (1997)

170. V.V. Tuchin, I.L. Maksimova, D.A. Zimnyakov, I.L. Kon, A.H. Mavlutov, A.A. Mishin, Light propagation in tissues with controlled optical properties. J. Biomed. Opt. **2**, 401–417 (1997)

171. V.V. Tuchin, Coherent optical techniques for the analysis of tissue structure and dynamics. J. Biomed. Opt. **4**, 106–124 (1999)

172. V.V. Tuchin (ed.), *Handbook of Optical Biomedical Diagnostics*, vol. PM107 (SPIE Press, Bellingham, 2002)

173. B. Beauvoit, T. Kitai, B. Chance, Contribution of the mitochondrial compartment to the optical properties of rat liver: a theoretical and practical approach. Biophys. J. **67**, 2501–2510 (1994)

174. J.T. Bruulsema, J.E. Hayward, T.J. Farrell, M.S. Patterson, L. Heinemann, M. Berger, T. Koschinsky, J. Sandahl-Christiansen, H. Orskov, M. Essenpreis, G. Schmelzeisen-Redeker, D. Böcker, Correlation between blood glucose concentration in diabetics and noninvasively measured tissue optical scattering coefficient. Opt. Lett. **22**(3), 190–192 (1997)

175. E.K. Chan, B. Sorg, D. Protsenko, M. O'Neil, M. Motamedi, A.J. Welch, Effects of compression on soft tissue optical properties. IEEE J. Sel. Top. Quantum Electron. **2**, 943–950 (1996)

176. B. Chance, H. Liu, T. Kitai, Y. Zhang, Effects of solutes on optical properties of biological materials: models, cells, and tissues. Anal. Biochem. **227**, 351–362 (1995)

177. I.F. Cilesiz, A.J. Welch, Light dosimetry: effects of dehydration and thermal damage on the optical properties of the human aorta. Appl. Opt. **32**, 477–487 (1993)

178. M. Kohl, M. Essenpreis, M. Cope, The influence of glucose concentration upon the transport of light in tissue-simulating phantoms. Phys. Med. Biol. **40**, 1267–1287 (1995)

179. H. Liu, B. Beauvoit, M. Kimura, B. Chance, Dependence of tissue optical properties on solute-induced changes in refractive index and osmolarity. J. Biomed. Opt. **1**, 200–211 (1996)

180. J.S. Maier, S.A. Walker, S. Fantini, M.A. Franceschini, E. Gratton, Possible correlation between blood glucose concentration and the reduced scattering coefficient of tissues in the near infrared. Opt. Lett. **19**, 2062–2064 (1994)

181. X. Xu, R.K. Wang, A. El Haj, Investigation of changes in optical attenuation of bone and neuronal cells in organ culture or 3 dimensional constructs in vitro with optical coherence tomography: relevance to cytochrome-oxidase monitoring. Eur. Biophys. J. **32**, 355–362 (2003)

182. V.V. Tuchin, A.N. Bashkatov, E.A. Genina, Y.P. Sinichkin, N.A. Lakodina, In vivo investigation of the immersion-liquid-induced human skin clearing dynamics. Tech. Phys. Lett. **27**, 489–490 (2001)

183. G. Vargas, E.K. Chan, J.K. Barton, H.G. Rylander III, A.J. Welch, Use of an agent to reduce scattering in skin. Lasers Surg. Med. **24**, 133–141 (1999)

184. R.K. Wang, X. Xu, V.V. Tuchin, J.B. Elder, Concurrent enhancement of imaging depth and contrast for optical coherence tomography by hyperosmotic agents. J. Opt. Soc. Am. **B18**, 948–953 (2001)

185. M. Brezinski, K. Saunders, C. Jesser, X. Li, J. Fujimoto, Index matching to improve OCT imaging through blood. Circulation **103**, 1999–2003 (2001)

186. G. Vargas, K.F. Chan, S.L. Thomsen, A.J. Welch, Use of osmotically active agents to alter optical properties of tissue: effects on the detected fluorescence signal measured through skin. Lasers Surg. Med. **29**, 213–220 (2001)

187. R.K. Wang, V.V. Tuchin, Enhance light penetration in tissue for high resolution optical imaging techniques by use of biocompatible chemical agents. J. X-Ray Sci. Technol. **10**, 167–176 (2002)

188. Y. He, R.K. Wang, Dynamic optical clearing effect of tissue impregnated by hyperosmotic agents: studied with optical coherence tomography. J. Biomed. Opt. **9**, 200–206 (2004)

189. R.K. Wang, X. Xu, Y. He, J.B. Elder, Investigation of optical clearing of gastric tissue immersed with the hyperosmotic agents. IEEE J. Sel. Top. Quantum Electron. **9**, 234–242 (2003)

190. X. Xu, R.K. Wang, The role of water desorption on optical clearing of biotissue: studied with near infrared reflectance spectroscopy. Med. Phys. **30**, 1246–1253 (2003)

191. X. Xu, R.K. Wang, J.B. Elder, Optical clearing effect on gastric tissues immersed with biocompatible chemical agents studied by near infrared reflectance spectroscopy. J. Phys. D: Appl. Phys. **36**, 1707–1713 (2003)

192. A.N. Bashkatov, E.A. Genina, Y.P. Sinichkin, V.I. Kochubey, N.A. Lakodina, V.V. Tuchin, Determination of diffusion coefficients of glucose in the human eye sclera. Biophysics **48**(3), 309–313 (2003)

193. J.M. Schmitt, G. Kumar, Optical scattering properties of soft tissue: a discrete particle model. Appl. Opt. **37**, 2788–2797 (1998)

194. R.K. Wang, Modeling optical properties of soft tissue by fractal distribution of scatters. J. Mod. Opt. **47**, 103–120 (2000)

195. A. Dunn, R. Richards-Kortum, Three-dimensional computation of light scattering from cells. IEEE J. Sel. Top. Quantum Electron. **2**, 898–905 (1996)

196. S.L. Jacques, Origins of tissue optical properties in the UVA, visible, and NIR regions, in *Selected Papers on Tissue Optics: Applications in Medical Diagnostics and Therapy*, ed. by V.V. Tuchin. SPIE Milestone Series, vol. MS 102 (SPIE Press, Bellingham, 1994), pp. 364–371

197. V. Twersky, Transparency of pair-correlated, random distributions of small scatters, with applications to the cornea. J. Opt. Soc. Am. **65**, 524–530 (1975)

198. R. Barer, K.F. Ross, S. Tkaczyk, Refractometry of living cells. Nature **171**, 720–724 (1953)

199. P. Brunsting, P. Mullaney, Differential light scattering from spherical mammalian cells. Biophys. J. **14**, 439–453 (1974)

200. C.F. Bohren, D.R. Huffman, *Absorption and Scattering of Light by Small Particles* (Wiley, New York, 1983)
201. R. Graaff, J.G. Aarnoudse, J.R. Zijp, P.M.A. Sloot, F.F. de Mul, J. Greve, M.H. Koelink, Reduced light scattering properties for mixtures of the optical properties: a simple approximation derived from Mie calculation. Appl. Opt. **31**, 1370–1376 (1992)
202. J. Firm, P. Mazur, Interactions of cooling rate, warming rate, glycerol concentration and dilution procedure on the viability of frozen-thawed human granulocytes. Cryobiology **20**, 657–676 (1983)
203. N. Songsasen, B.C. Bucknell, C. Plante, S.P. Leibo, In vitro and in vivo survival of cryopreserved sheep embryos. Cryobiology **32**, 78–91 (1995)
204. D. Martin, H. Hauthal, *Dimethyl Sulphoxide* (Wiley, New York, 1975)
205. W.M. Bourne, D.R. Shearer, L.R. Nelson, Human corneal endothelial tolerance to glycerol, dimethysulphoxide, 1,2-propanediol, and 2,3-butanediol. Cryobiology **31**, 1–9 (1994)
206. J.O.M. Karlsson, M. Toner, Long term storage of tissue by cryopreservation: critical issues. Biomaterials **17**, 243–256 (1996)
207. K.H. Kolb, G. Janicke, M. Kramer, P.E. Schulze, G. Raspe, Absorption, distribution and elimination of labeled dimethyl sulfoxide in man and animals. Ann. N. Y. Acad. Sci. **141**, 85–95 (1967)
208. R. Herschler, S.W. Jacob, The case of dimethyl sulfoxide, in *Controversies in Therapeutics*, ed. by L. Lasagna (W.B. Saunders, Philadelphia, 1980)
209. A. Walter, J. Gutknecht, Permeability of small nonelectrolytes through lipid bilayer membranes. J. Membr. Biol. **90**, 207–217 (1986)
210. P. Patwari, N.J. Weissman, S.A. Boppart, C.A. Jesser, D. Stamper, J.G. Fujimoto, M.E. Brezinski, Assessment of coronary plaque with optical coherence tomography and high frequency ultrasound. Am. J. Cardiol. **85**, 641–644 (2000)
211. A. Roggan, M. Friebel, K. Dorschel, A. Hahn, G. Mueller, Optical properties of circulating human blood in the wavelength range 400-2500 nm. J. Biomed. Opt. **4**, 36–46 (1999)
212. S.Y. Shchyogolev, Inverse problems of spectroturbidimetry of biological disperse systems: an overview. J. Biomed. Opt. **4**, 490–503 (1999)
213. A.V. Priezzhev, O.M. Ryaboshapka, N.N. Firsov, I.V. Sirko, Aggregation and disaggregation of erythrocytes in whole blood: study by backscattering technique. J. Biomed. Opt. **4**, 76–84 (1999)
214. S.M. Bertoluzzo, A. Bollini, M. Rsia, A. Raynal, Kinetic model for erythrocyte aggregation. Blood Cells Mol. Dis. **25**(22), 339–349 (1999)
215. D. Levitz, L. Thrane, M.H. Frosz, P.E. Andersen, C.B. Andersen, S. Andersson-Engels, J. Valanciunaite, J. Swartling, P.R. Hansen, Determination of optical scattering properties of highly-scattering media in optical coherence tomography images. Opt. Express **12**, 249–259 (2004)
216. Y. Yang, T. Wang, N.C. Biswal, X. Wang, M. Sanders, M. Brewer, Q. Zhu, Optical scattering coefficient estimated by optical coherence tomography correlates with collagen content in ovarian tissue. J. Biomed. Opt. **16**(9), 090504-1–090504-3 (2011)
217. V.M. Kodach, D.J. Faber, J. van Marle, T.G. van Leeuwen, J. Kalkman, Determination of the scattering anisotropy with optical coherence tomography. Opt. Express **19**(7), 6131–6140 (2011)
218. D.M. Zhestkov, A.N. Bashkatov, E.A. Genina, V.V. Tuchin, Influence of clearing solutions osmolarity on the optical properties of RBC. Proc. SPIE **5474**, 321–330 (2004)
219. A.N. Bashkatov, D.M. Zhestkov, E.A. Genina, V.V. Tuchin, Immersion optical clearing of human blood in the visible and near infrared spectral range. Opt. Spectrosc. **98**(4), 638–646 (2005)
220. A.G. Borovoi, E.I. Naats, U.G. Oppel, Scattering of light by a red blood cell. J. Biomed. Opt. **3**(3), 364–372 (1998)
221. M. Hammer, D. Schweitzer, B. Michel, E. Thamm, A. Kolb, Single scattering by red blood cells. Appl. Opt. **37**(31), 7410–7418 (1998)

222. J.M. Steinke, A.P. Shephard, Diffusion model of the optical absorbance of whole blood. J. Opt. Soc. Am. A **5**, 813–822 (1988)

223. A. Ishimaru, *Wave Propagation and Scattering in Random Media* (IEEE Press, New York, 1997)

224. V.V. Tuchin, *Optical Clearing of Tissues and Blood*, vol. PM 154 (SPIE Press, Bellingham, 2006)

225. A.H. Hielsher, J.R. Mourant, I.J. Bigio, Influence of particle size and concentration on the diffuse backscattering of polarized light from tissue phantoms and biological cell suspensions. Appl. Opt. **36**, 125–135 (1997)

226. V. Shankaran, J.T. Walsh Jr., D.J. Maitland, Comparative study of polarized light propagation in biological tissues. J. Biomed. Opt. **7**(3), 300–306 (2002)

227. V.V. Tuchin, X. Xu, R.K. Wang, Sedimentation of immersed blood studied by OCT. Proc. SPIE **4241**, 357–369 (2001)

228. V.V. Tuchin, D.M. Zhestkov, A.N. Bashkatov, E.A. Genina, Theoretical study of immersion optical clearing of blood in vessels at local hemolysis. Opt. Express **12**, 2966–2971 (2004)

229. G. Popescu, T. Ikeda, C.A. Best, K. Badizadegan, R.R. Dasari, M.S. Feld, Erythrocyte structure and dynamics quantified by Hilbert phase microscopy. J. Biomed. Opt. **10**(6), 060503-1–060503-3 (2005)

230. H. Kataiwa, A. Tanaka, H. Kitabata, T. Imanishi, T. Akasaka, Safety and usefulness of non-occlusion image acquisition technique for optical coherence tomography. Circ. J. **72**, 1536–1537 (2008)

231. Y. Ozaki, H. Kitabata, H. Tsujioka, S. Hosokawa, M. Kashiwagi, K. Ishibashi, K. Komukai, T. Tanimoto, Y. Ino, S. Takarada, T. Kubo, K. Kimura, A. Tanaka, K. Hirata, M. Mizukoshi, T. Imanishi, T. Akasaka, Comparison of contrast media and low-molecular-weight dextran for frequency-domain optical coherence tomography. Circ. J. **76** (2012). doi:10.1253/circj. CJ-11-1122 released online Feb. 3, 2012

232. M. Ghosn, V.V. Tuchin, K.V. Larin, Depth-resolved monitoring of glucose diffusion in tissues by using optical coherence tomography. Opt. Lett. **31**, 2314–2316 (2006)

233. M.G. Ghosn, V.V. Tuchin, K.V. Larin, Nondestructive quantification of analyte diffusion in cornea and sclera using optical coherence tomography. Invest. Ophthalmol. Vis. Sci. **48**, 2726–2733 (2007)

234. M.G. Ghosn, E.F. Carbajal, N. Befrui, V.V. Tuchin, K.V. Larin, Differential permeability rate and percent clearing of glucose in different regions in rabbit sclera. J. Biomed. Opt. **13**, 021110-1–021110-6 (2008)

235. K.V. Larin, V.V. Tuchin, Functional imaging and assessment of the glucose diffusion rate in epithelial tissues with optical coherence tomography. Quantum Electron. **38**, 551–556 (2008)

236. K.V. Larin, M.G. Ghosn, A.N. Bashkatov, E.A. Genina, N.A. Trunina, V.V. Tuchin, Optical clearing for OCT image enhancement and in-depth monitoring of molecular diffusion. IEEE J. Sel. Top. Quantum Electron. **18**(3), 1244–1259 (2012)

237. I.V. Larina, E.F. Carbajal, V.V. Tuchin, M.E. Dickinson, K.V. Larin, Enhanced OCT imaging of embryonic tissue with optical clearing. Laser Phys. Lett. **5**, 476–480 (2008)

238. N. Sudheendran, M. Mohamed, M. Ghosn, V.V. Tuchin, K.V. Larin, Assessment of tissue optical clearing as a function of glucose concentration using optical coherence tomography. J. Innov. Opt. Health Sci. **3**, 169–176 (2010)

239. K.V. Larin, T. Akkin, R.O. Esenaliev, M. Motamedi, T.E. Milner, Phase-sensitive optical low-coherence reflectometry for the detection of analyte concentrations. Appl. Opt. **43**, 3408–3414 (2004)

240. K.V. Larin, M. Motamedi, T.V. Ashitkov, R.O. Esenaliev, Specificity of noninvasive blood glucose sensing using optical coherence tomography technique: a pilot study. Phys. Med. Biol. **48**, 1371–1390 (2003)

241. A.I. Kholodnykh, I.Y. Petrova, K.V. Larin, M. Motamedi, R.O. Esenaliev, Precision of measurement of tissue optical properties with optical coherence tomography. Appl. Opt. **42**, 3027–3037 (2003)

242. K.V. Larin, M.S. Eledrisi, M. Motamedi, R.O. Esenaliev, Noninvasive blood glucose monitoring with optical coherence tomography – a pilot study in human subjects. Diabetes Care **25**, 2263–2267 (2002)

243. G. Vargas, A. Readinger, S.S. Dozier, A.J. Welch, Morphological changes in blood vessels produced by hyperosmotic agents and measured by optical coherence tomography. Photochem. Photobiol. **77**, 541–549 (2003)

244. A.T. Yeh, J. Hirshburg, Molecular interactions of exogenous chemical agents with collagen – implications for tissue optical clearing. J. Biomed. Opt. **11**, 014003 (2006)

245. R.O. Esenaliev, K.V. Larin, I.V. Larina, M. Motamedi, Noninvasive monitoring of glucose concentration with optical coherence tomography. Opt. Lett. **26**, 992–994 (2001)

246. M. Ghosn, E.F. Carbajal, N. Befrui, V.V. Tuchin, K.V. Larin, Concentration effect on the diffusion of glucose in ocular tissues. Opt. Lasers Eng. **46**, 911–914 (2008)

247. E.A. Genina, A.N. Bashkatov, V.V. Tuchin, M. Ghosn, K.V. Larin, T.G. Kamenskikh, Cortexin diffusion in human eye sclera. Quantum Electron. **41**, 407–413 (2011)

248. M. Ghosn, N. Sudheendran, M. Wendt, A. Glasser, V.V. Tuchin, K.V. Larin, Monitoring of glucose permeability in monkey skin in vivo using optical coherence tomography. J. Biophotonics **3**, 25–33 (2010)

249. M.G. Ghosn, S.H. Syed, N.A. Befrui, M. Leba, A. Vijayananda, N. Sudheendran, K.V. Larin, Quantification of molecular diffusion in arterial tissues with optical coherence tomography and fluorescence microscopy. Laser Phys. **19**, 1272–1275 (2009)

250. M.G. Ghosn, E.F. Carbajal, N. Befrui, A. Tellez, J.F. Granada, K.V. Larin, Permeability of hyperosmotic agent in normal and atherosclerotic vascular tissues. J. Biomed. Opt. **13**, 010505-1–010505-3 (2008)

251. K.V. Larin, M.G. Ghosn, S.N. Ivers, A. Tellez, J.F. Granada, Quantification of glucose diffusion in arterial tissues by using optical coherence tomography. Laser Phys. Lett. **4**, 312–317 (2007)

252. M.G. Ghosn, M. Mashiatulla, S.H. Syed, M.A. Mohamed, K.V. Larin, J.D. Morrisett, Permeation of human plasma lipoproteins in human carotid endarterectomy tissues: measurement by optical coherence tomography. J. Lipid Res. **52**(7), 1429–1434 (2012)

253. M.G. Ghosn, M. Mashiatulla, M.A. Mohamed, S.H. Syed, F. Castro-Chavez, J.D. Morrisett, K.V. Larin, Time dependent changes in aortic tissue during cold storage in physiological solution. Biochim. Biophys. Acta **1810**, 555–560 (2011)

254. H.Q. Zhong, Z.Y. Guo, H.J. Wei, C.C. Zeng, H.L. Xiong, Y.H. He, S.H. Liu, Quantification of glycerol diffusion in human normal and cancer breast tissues in vitro with optical coherence tomography. Laser Phys. Lett. **7**(4), 315–320 (2010)

255. Z. Zhu, G. Wu, H. Wei, H. Yang, Y. He, S. Xie, Q. Zhao, X. Guo, Investigation of the permeability and optical clearing ability of different analytes in human normal and cancerous breast tissues by spectral domain OCT. J. Biophotonics **5**(5–6), 1–8 (2012). doi:10.1002/jbio.201100106

256. Q.L. Zhao, J.L. Si, Z.Y. Guo, H.J. Wei, H.Q. Yang, G.Y. Wu, S.S. Xie, X.Y. Li, X. Guo, H.Q. Zhong, L.Q. Li, Quantifying glucose permeability and enhanced light penetration in *ex vivo* human normal and cancerous esophagus tissues with optical coherence tomography. Laser Phys. Lett. **8**(1), 71–77 (2011)

257. Q. Zhao, Z. Guo, H. Wei, H. Yang, S. Xie, In vitro investigation hyperosmotic agents diffusion of different depths in normal and malignant human esophagus tissues by optical coherence tomography. Quantum Electron. **41**(10), 950–955 (2011)

258. L.S. de Melo, R.E. de Araujo, A.Z. Freitas, D. Zezell, N.D. Vieira, J. Girkin, A. Hall, M.T. Carvalho, A.S. Gomes, Evaluation of enamel dental restoration interface by optical coherence tomography. J. Biomed. Opt. **10**, 064027 (2005)

259. D.P. Popescu, M.G. Sowa, M.D. Hewko, L.P. Choo-Smith, Assessment of early demineralization in teeth using the signal attenuation in optical coherence tomography images. J. Biomed. Opt. **13**, 054053 (2008)

260. P. Wilder-Smith, L. Otis, J. Zhang, Z. Chen, Dental OCT, in *Optical Coherence Tomography*, ed. by W. Drexler, J.G. Fujimoto (Springer, Berlin/Heidelberg, 2008), pp. 1151–1182

261. N.A. Trunina, V.V. Lychagov, V.V. Tuchin, OCT monitoring of diffusion of water and glycerol through tooth dentine in different geometry of wetting. Proc. SPIE **7563**, 75630U-1–75630U-7 (2010)

262. N.A. Trunina, V.V. Lychagov, V.V. Tuchin, Study of water diffusion in human dentin by optical coherent tomography. Opt. Spectrosc. **109**(2), 162–168 (2010)

263. V.V. Tuchin, A.N. Bashkatov, E.A. Genina, V.I. Kochubey, V.V. Lychagov, S.A. Portnov, N.A. Trunina, D.R. Miller, S. Cho, H. Oh, B. Shim, M. Kim, J. Oh, H. Eum, Y. Ku, D. Kim, Y. Yang, Finger tissue model and blood perfused skin tissue phantom. Proc. SPIE **7898**, 78980Z-1–78980Z-10 (2011)

264. A. Kishen, S. Vedantam, Hydromechanics in dentine: role of dentinal tubules and hydrostatic pressure on mechanical stress-strain distribution. Dent. Mater. **23**, 1296–306 (2007)

265. C.T. Hanks, J.C. Fat, J.C. Wataha, J.F. Corcoran, Cytotoxicity and dentin permeability of carbamide peroxide and hydrogen peroxide vital bleaching materials, in vitro. J. Dent. Res. **72**, 931–938 (1993)

266. V.V. Tuchin (ed.), *Handbook of Optical Sensing of Glucose in Biological Fluids and Tissues* (CRC Press/Taylor & Francis Group, London, 2009)

267. K.V. Larin, V.V. Tuchin, Monitoring of glucose diffusion in epithelial tissues with optical coherence tomography, in *Handbook of Optical Sensing of Glucose in Biological Fluids and Tissues*, ed. by V.V. Tuchin (CRC Press/Taylor & Francis Group, London, 2009), pp. 623–656

268. A.N. Bashkatov, E.A. Genina, V.V. Tuchin, Measurement of glucose diffusion coefficients in human tissues, in *Handbook of Optical Sensing of Glucose in Biological Fluids and Tissues*, ed. by V.V. Tuchin (CRC Press/Taylor & Francis Group, London, 2009), pp. 587–621

269. E.A. Genina, A.N. Bashkatov, V.V. Tuchin, Glucose-induced optical clearing effects in tissues and blood, in *Handbook of Optical Sensing of Glucose in Biological Fluids and Tissues*, ed. by V.V. Tuchin (CRC Press/Taylor & Francis Group, London, 2009), pp. 657–692

270. K.V. Larin, M.G. Ghosn, V.V. Tuchin, Noninvasive assessment of molecular permeability with OCT, in *Handbook of Photonics for Biomedical Science*, ed. by V.V. Tuchin (CRC Press/Taylor & Francis Group, London, 2010), pp. 410–428

271. E.A. Genina, K.V. Larin, A.N. Bashkatov, V.V. Tuchin, Glucose and other metabolites sensing in skin, in *Handbook of Biophotonics, Vol. 2: Photonics for Health Care*, ed. by J. Popp, V. Tuchin, A. Chiou, S.H. Heinemann (Wiley, Weinheim, 2011), pp. 835–853

272. M. Kinnunen, R. Myllylä, T. Jokela, S. Vainio, In vitro studies toward noninvasive glucose monitoring with optical coherence tomography. Appl. Opt. **45**(10), 2251–2260 (2006)

273. M. Kinnunen, S. Tausta, R. Myllylä, S. Vainio, Monitoring changes in the scattering properties of mouse skin with optical coherence tomography during an in vivo glucose tolerance test. Proc. SPIE **6535**, 65350B-1–65350B-10 (2007)

274. M. Kinnunen, R. Myllylä, S. Vainio, Detecting glucose-induced changes in in vitro and in vivo experiments with optical coherence tomography. J. Biomed. Opt. **13**(2), 021111-1–021111-7 (2008)

275. A. Popov, A. Bykov, S. Toppari, M. Kinnunen, A. Priezzhev, R. Myllylä, Glucose sensing in flowing blood and intralipid by laser pulse time-of-flight and optical coherence tomography techniques. IEEE J. Sel. Top. Quantum Electron. **18**(4), 1335–1342 (2012)

276. P.D. Agrba, M.Y. Kirillin, A.I. Abelevich, E.V. Zagaynova, V.A. Kamensky, Compression as a method for increasing the informativity of optical coherence tomography of biotissues. Opt. Spectrosc. **107**, 853–858 (2009)

277. G.A. Askar'yan, The increasing of laser and other radiation transport through soft turbid physical and biological media. Sov. J. Quantum Electron. **9**, 1379–1383 (1982)

278. C. Drew, T.E. Milner, C.G. Rylander, Mechanical tissue optical clearing devices: evaluation of enhanced light penetration in skin using optical coherence tomography. J. Biomed. Opt. **14**, 064019 (2009)

279. A.A. Gurjarpadhye, W.C. Vogt, Y. Liu, C.G. Rylander, Effect of localized mechanical indentation on skin water content evaluated using OCT. Int. J. Biomed. Imaging **2011**, 817250 (2011)

280. N. Guzelsu, J.F. Federici, H.C. Lim, H.R. Chauhdry, A.B. Ritter, T. Findley, Measurement of skin stretch via light reflection. J. Biomed. Opt. **8**, 80–86 (2003)

281. A.P. Ivanov, S.A. Makarevich, A.Y. Khairulina, Propagation of radiation in tissues and liquids with densely packed scatterers. J. Appl. Spectrosc. **47**, 662–668 (1988)

282. M.Y. Kirillin, P.D. Agrba, V.A. Kamensky, In vivo study of the effect of mechanical compression on formation of OCT images of human skin. J. Biophotonics **3**, 752–758 (2010)

283. S. Nickell, M. Hermann, M. Essenpreis, T.J. Farrell, U. Kramer, M.S. Patterson, Anisotropy of light propagation in human skin. Phys. Med. Biol. **45**, 2873–2886 (2000)

284. P. Rol, P. Niederer, U. Dürr, P.-D. Henchoz, F. Fankhauser, Experimental investigation on the light scattering properties of the human sclera. Laser Light Ophthalmol. **3**, 201–212 (1990)

285. C.G. Rylander, O.F. Stumpp, T.E. Milner, N.J. Kemp, J.M. Mendenhall, K.R. Diller, A.J. Welch, Dehydration mechanism of optical clearing in tissue. J. Biomed. Opt. **11**, 041117 (2006)

286. H. Shangguan, S. Prahl, S.L. Jacques, L.W. Casperson, K.W. Gregory, Pressure effects on soft tissues monitored by changes in tissue optical properties. Proc. SPIE **3254**, 366–371 (1998)

287. Y.P. Sinichkin, N. Kollias, G. Zonios, S.R. Utz, V.V. Tuchin, Reflectance and fluorescence spectroscopy of human skin in vivo, in *Optical Biomedical Diagnostics*, ed. by V.V. Tuchin (SPIE Press, Bellingham, 2002), pp. 725–785

288. M.E. Brezinski, *Optical Coherence Tomography: Principles and Applications* (Academic, Amsterdam/Boston, 2006)

289. V.V. Tuchin, Optical clearing of tissue and blood using immersion method. J. Phys. D: Appl. Phys. **38**, 2497–2518 (2005)

290. V.V. Tuchin, Optical immersion as a new tool to control optical properties of tissues and blood. Laser Phys. **15**(8), 1109–1136 (2005)

291. V.V. Tuchin, A clear vision for laser diagnostics. IEEE J. Sel. Top. Quantum Electron. **13**(6), 1621–1628 (2007)

292. E.A. Genina, A.N. Bashkatov, V.V. Tuchin, Tissue optical immersion clearing. Expert Rev. Med. Devices **7**(6), 825–842 (2010)

293. V.V. Tuchin, R.K. Wang, A.T. Yeh, Optical clearing of tissues and cells. J. Biomed. Opt. **13**, 021101-1 (2008)

294. V.V. Tuchin, M. Leahy, D. Zhu, Optical clearing for biomedical imaging in the study of tissues and biological fluids. J. Innov. Opt. Health Sci. **3**(3) (2010). doi:10.1142/S1793545810001076

295. V.V. Tuchin, Tissue and blood optical properties control, in *Advances in Biophotonics*, ed. by B. Wilson, V. Tuchin, S. Tanev. NATO Science Series I. Life and Behavioural Sciences, vol. 369 (Ios Press, Amsterdam, 2005), pp. 79–122

296. S. Tanev, W. Sun, N. Loeb, V. Tuchin, The finite-difference time-domain approach and its application to the modelling of light scattering by biological cells in absorbing and controlled extra-cellular media, in *Advances in Biophotonics*, ed. by B. Wilson, V. Tuchin, S. Tanev. NATO Science Series I. Life and Behavioural Sciences, vol. 369 (Ios Press, Amsterdam, 2005), pp. 45–78

297. R.K. Wang, V.V. Tuchin, Optical tissue clearing to enhance imaging performance for OCT, in *Optical Coherence Tomography: Technology and Applications*, ed. by W. Drexler, J.G. Fujimoto (Springer, Berlin, 2008), pp. 851–882

298. E.A. Genina, A.N. Bashkatov, K.V. Larin, V.V. Tuchin, Light–tissue interaction at optical clearing, in *Laser Imaging and Manipulation in Cell Biology*, ed. by F.S. Pavone (Wiley, Weinheim, 2010)
299. S.G. Proskurin, I.V. Meglinski, Optical coherence tomography imaging depth enhancement by superficial skin optical clearing. Laser Phys. Lett. **4**(11), 824–826 (2007)
300. M. Bonesi, S.G. Proskurin, I.V. Meglinski, Imaging of subcutaneous blood vessels and flow velocity profiles by optical coherence tomography. Laser Phys. **20**(4), 891–899 (2010)
301. J. Wang, Y. Liang, S. Zhang, Y. Zhou, H. Ni, Y. Li, Evaluation of optical clearing with the combined liquid paraffin and glycerol mixture. Biomed. Opt. Express **2**(8), 2329–2338 (2011)
302. X. Wen, S.L. Jacques, V.V. Tuchin, D. Zhu, Enhanced optical clearing of skin in vivo and OCT in-depth imaging. J. Biomed. Opt. **17**, 066022 (2012)

Optical Coherence Tomography: Advanced Modeling **17**

Peter E. Andersen, Lars Thrane, Harold T. Yura, Andreas Tycho, and Thomas M. Jørgensen

Contents

P.E. Andersen (✉) • L. Thrane • A. Tycho • T.M. Jørgensen
Department of Photonics Engineering, Technical University of Denmark, Kongens Lyngby, Denmark
e-mail: peta@fotonik.dtu.dk, lath@fotonik.dtu.dk, tmjq@fotonik.dtu.dk

H.T. Yura
Electronics and Photonics Laboratory, The Aerospace Corporation, Los Angeles, CA, USA
e-mail: hal.t.yura@aero.org

Abstract

Analytical and numerical models for describing and understanding the light propagation in samples imaged by optical coherence tomography (OCT) systems are presented. An analytical model for calculating the OCT signal based on the extended Huygens-Fresnel principle valid both for the single- and multiple-scattering regimes is derived. An advanced Monte Carlo model for calculating the OCT signal is also derived, and the validity of this model is shown through a mathematical proof based on the extended Huygens-Fresnel principle. From the analytical model, an algorithm for enhancing OCT images is developed, the so-called true-reflection algorithm in which the OCT signal may be corrected for the attenuation caused by scattering. The algorithm is verified experimentally and by using the Monte Carlo model as a numerical tissue phantom. Applications of extraction of optical properties from tissue are discussed. Finally, the Wigner phase-space distribution function is derived in a closed-form solution, which may have applications in OCT.

17.1   Introduction

Optical coherence tomography (OCT) has developed rapidly since its potential for applications in clinical medicine was first demonstrated in 1991 [1]. OCT performs high-resolution, cross-sectional tomographic imaging of the internal microstructure in materials and biologic systems by measuring backscattered or backreflected light.

Mathematical models [2–9] have been developed to promote understanding of the OCT imaging process and thereby enable development of better imaging instrumentation and data processing algorithms. One of the most important issues in the modeling of OCT systems is the role of the multiple-scattered photons, an issue, which only recently has become fully understood, the works of Thrane et al. [10] and Turchin et al. [11] representing the most comprehensive modeling. Hence, such modeling, capable of describing both the single- and multiple-scattering regimes simultaneously in heterogeneous media, is essential in order to completely describe the behavior of OCT systems.

Experimental validation of models on realistic sample structures, for example, layered sample structures, would require manufacturing of complex tissue phantoms with well-controlled optical properties. However, a useful alternative to validate the analytical predictions on such geometries is to apply a Monte Carlo

(MC)-based simulation model [12], since there are few limitations on which geometries that may be modeled using MC simulations. MC models for analyzing light propagation are based on simulating the radiative equation of transfer by tracing a large number of energy packets, each considered to represent a given fraction of the incident light energy [13, 14]. Hence, as a numerical experiment, one has full control of all parameters.

The scope of this chapter is the presentation of analytical and numerical models that are able to describe the performance of OCT systems including multiple-scattering effects in heterogeneous media. Such models, where the contribution to the OCT signal from multiple-scattering effects has been taken into account, are essential for the understanding and in turn optimization of OCT systems. Moreover, establishing a valid MC model of OCT systems is important, because such a model may serve as a numerical phantom providing data that are otherwise cumbersome to obtain experimentally. In general, these models, analytical as well as numerical, may serve as important tools for improving interpretation of OCT images.

17.1.1 Organization of This Chapter

The chapter is divided into four sections, covering specific topics in modeling OCT systems. In Sect. 17.2, an analytical model for the detected OCT signal is derived based on the extended Huygens-Fresnel principle. In the field of biomedical optics, Monte Carlo simulations have already proved their value. In Sect. 17.3, an advanced Monte Carlo model for calculating the OCT signal is presented, and comparisons to the analytical model are made. The analytical model, in Sect. 17.4, is then used to derive the optical properties of a scattering medium, which forms the basis of the so-called true-reflection algorithm. The algorithm is verified using MC simulations as well as experiments. The Wigner phase-space distribution function has been proposed as an alternative to OCT. In Sect. 17.5, we demonstrate the applicability of using the extended Huygens-Fresnel principle to calculate the Wigner phase-space distribution function and to derive a novel method of OCT imagery.

17.2 Analytical OCT Model Based on the Extended Huygens-Fresnel Principle

Since the first paper describing the use of the OCT technique for noninvasive cross-sectional imaging in biological systems [1], various theoretical models of the OCT system have been developed. The primary motivation has been optimization of the OCT technique, thereby improving the imaging capabilities. The first theoretical models were based on single-scattering theory [2, 3]. These models are restricted to superficial layers of highly scattering tissue in which only single scattering occurs. Single scattering or single backscattering refers to photons which do not undergo scattering either to or from the backscattering plane of interest, that is, ballistic photons.

At larger probing depths, however, the light is also subject to multiple scattering. The effects of multiple scattering have been investigated on an experimental basis [4] and by using a hybrid Monte Carlo/analytical model [5], analysis methods of linear systems theory [6], on the basis of solving the radiative transfer equation in the small-angle approximation [7], a model based on the extended Huygens-Fresnel (EHF) principle [8], and MC simulations [9]. Note that modeling using MC simulations is treated in greater detail in Sect. 17.3.3.

In the present context, the main objective is the analysis of multiple-scattering effects. As shown by several investigations, the primary effects of multiple scattering are a reduction of the imaging contrast and resolution of the OCT system.

In Ref. [15], the authors suggested solving the multiple-scattering problem by using the EHF principle [8] known from atmospheric propagation of laser beams [16]. Their analysis contains one important inaccuracy because in their end result, the ballistic component is included twice, leading to erroneous calculations. As a result, their analysis should be applied with care. In addition, the effects of the so-called shower-curtain effect [16] are not accounted for in their analysis. Thrane et al. [10] succeeded in applying the EHF principle for the OCT geometry (see below). Following their analysis, Feng et al. [17] aimed at expanding on the use of EHF in modeling the OCT geometry. In particular, their aim is to simplify the analysis, but several mistakes are introduced in the attempt: Firstly, an imaginary lens is introduced with the purpose of obviating the shower-curtain effect, leading to errors in the final calculation of the OCT signal. Secondly, an erroneous lateral coherence length is introduced, that is, the lateral coherence length should be calculated as resulting from reflecting off a rough surface and not, as done in Ref. [17], a specular surface. Hence, their model should be approached with caution.

A statistical optics approach to adequately model the effects of multiple scattering was proposed by Karamata et al. [18]. However, their analysis, based on a heuristic argument, is misleading and incorrect. The main error is due to their assumption regarding spatial coherence, where it is alleged that transverse spatial coherence is not degraded due to multiple scattering. The argument used by Karamata et al. [18] is valid only for the case of a focused beam reflecting off a rough surface with no scattering medium in between the reflection site and the collection aperture (see, e.g., pages 210–211 of Ref. [19]). This is definitely not the case for OCT in turbid media (i.e., tissue). The degradation of spatial coherence of a beam propagating through a multiple-scattering media is well known and documented in the literature (see Ref. [20] and references therein). Therefore, the analysis given in Ref. [18] is not considered further, and the results and conclusions should not be used in modeling light propagation in turbid media.

Recently, Turchin et al. [11] expanded the analysis of Dolin [7] to an OCT geometry. Their analysis is based on the radiative transfer equation (RTE) in the small-angle approximation, of which Arnush [21] first obtained the closed-form solution. It should be noted that in this approximation, the solution of the RTE and the EHF is identical [22, 23]. In general, the analysis of Ref. [11] is consistent with that of the EHF model, which is presented below. However, technically there are two important differences that need to be pointed out. Firstly, the choice of

scattering phase function in Ref. [11]: as in Ref. [10], the forward scattered part is modeled by a Gaussian distribution, but additionally a small backscattered fraction is included. This way of taking into account tissue backscattering was previously suggested by Raymer and coworkers [24] and discussed by Yura et al. [23]. However, it was not included in the EHF analysis of the OCT geometry [10], but it can be readily adopted [25]. Hence, the RTE [11] and EHF [10] descriptions are equivalent. Secondly, Thrane et al. [10] present an analytic engineering expression for the OCT signal current based on an accurate analytical approximation for the irradiance distribution in the backscatter plane (see Sect. 17.7 for details). Turchin et al. [11] do not use this approximation, and consequently their end results require numerical computations, which yield highly accurate values for the OCT signal current. They also obtain accurate results in the extraction of optical scattering properties of the sample, which is further addressed in at the end of this chapter. Furthermore, it is noted that the analysis of Turchin et al. [11] is restricted to the special case where the focusing lens in the sample arm is in direct contact with the tissue being investigated. This is in contrast to the analysis of Ref. [10] where the ABCD ray-matrix formalism was used to readily include an arbitrary configuration of the sample arm. Finally, in contrast to the totally numerical results of Ref. [11], the multiple-scattering EHF analysis presented below yields accurate analytic expressions for the OCT signal for a wide range of optical configurations that are both amenable to physical interpretation and are desirable for use in parametric studies for OCT system optimization.

In this section, a general theoretical description [10, 26–28] of the OCT technique when used for imaging in highly scattering tissue is presented. The description is based on the EHF principle. It is shown that the theoretical model, based on this principle and the use of mutual coherence functions, simultaneously describes the performance of the OCT system in both the single- and multiple-scattering regimes. In a standard OCT system [1] with diffuse backscattering from the tissue discontinuity being probed, and a distance between the focusing lens and the tissue, the so-called shower-curtain effect [16, 29, 30] is present. This effect has been omitted in previous theoretical models [8]. However, it is demonstrated in this section that inclusion of this effect is of utmost importance in the theoretical description of an OCT system.

17.2.1 The Extended Huygens-Fresnel Principle

When an optical wave propagates through a random medium, for example, tissue, both the amplitude and phase of the electric field experience random fluctuations caused by small random changes in the index of refraction. Several different theoretical approaches have been developed for describing these random amplitude and phase fluctuations, based upon solving the wave equation for the electric field of the wave or for the various statistical moments of the field. By assuming a sinusoidal time variation in the electric field, it has been shown [31–34] that

Maxwell's equations for the vector amplitude $\mathbf{E}(\mathbf{R})$ of a propagating electromagnetic wave through a non-absorbing refracting medium lead directly to

$$\nabla^2 \mathbf{E} + k^2 n^2(\mathbf{R})\mathbf{E} + 2\nabla[\mathbf{E} \cdot \nabla \ln n(\mathbf{R})] = 0, \tag{17.1}$$

where $\mathbf{R}$ denotes a point in space, k is the wave number of the electromagnetic wave, and $n(\mathbf{R})$ is the index of refraction whose time variations have been suppressed. We now assume that the magnitude of the index of refraction fluctuations is small in comparison with unity. Hence, the index of refraction $n(\mathbf{R}) = \langle n(\mathbf{R}) \rangle + n_f(\mathbf{R})$, where $n_f(\mathbf{R})$ is the small fluctuating part of the index of refraction with zero mean and a root-mean-square value much less than unity. This assumption is in general valid for tissue [35]. In this case, it has been shown that the last term on the left-hand side of (17.1), which is related to the change in polarization of the wave as it propagates, is negligible if the wavelength of the radiation $\lambda \ll 2\pi\, l_0$, where l_0 is a measure of the smallest random inhomogeneities in the medium [33, 34]. The structures that dominate light propagation in tissue, for example, cells, have a size of 2 μm or more, which means that the criteria for neglecting the depolarization term are fulfilled in the case of interest where $\lambda \sim 1.0$ μm. By dropping this term, (17.1) simplifies to

$$\nabla^2 \mathbf{E} + k^2 n(\mathbf{R})\mathbf{E} = 0, \tag{17.2}$$

which is now easily decomposed into three scalar equations, one for each component of the field $\mathbf{E}$. If we let $U(\mathbf{R})$ denote one of the scalar components transverse to the direction of propagation along the positive z-axis, then (17.2) may be replaced by the scalar stochastic equation

$$\nabla^2 U + k^2 n^2(\mathbf{R})U = 0. \tag{17.3}$$

Equation (17.3) cannot be solved exactly in closed form. Some early attempts to solve (17.3) were based on the geometric optics approximation [36], which ignores diffraction effects, and on perturbation theories widely known as the Born approximation and Rytov approximation [32]. One approach to solving (17.3) by other than perturbation methods was developed, independent of each other, by Lutomirski and Yura [37] and by Feizulin and Kravtsov [38]. This technique is called the extended Huygens-Fresnel (EHF) principle. As the name indicates, it is an extension of the Huygens-Fresnel principle to a medium that exhibits a random spatial variation in the index of refraction. That is, the field due to some arbitrary complex disturbance specified over an aperture can be computed, for propagation distances that are large compared with the size of the aperture, by superimposing spherical wavelets that radiate from all elements of the aperture. This principle follows directly from Green's theorem [39] and the Kirchhoff approximation [39] applied to the scalar wave equation together with a field reciprocity theorem between an observation point and a source point of spherical waves in the random medium. On the basis of this principle, the geometry of the problem, that is, the

aperture field distribution, can be separated from the propagation problem, which is determined by the way a spherical wave propagates through the medium. Furthermore, Yura and Hanson [40, 41] have applied the EHF principle to paraxial wave propagation through an arbitrary ABCD system in the presence of random inhomogeneities. An arbitrary ABCD system refers to an optical system that can be described by an ABCD ray-transfer matrix [42]. In the cases of interest in this section, the ABCD ray-transfer matrix is real, and the field in the output plane is then given by [40]

$$U(\mathbf{r}) = \int U_0(\mathbf{p})G(\mathbf{p}, \mathbf{r})d\mathbf{p}, \tag{17.4}$$

where $\mathbf{r}$ and $\mathbf{p}$ are two-dimensional vectors transverse to the optical axis in the output plane and input plane, respectively. Throughout this chapter it is understood that spatial integrals are to be carried out over the entire plane in question.

The quantity $U_0(\mathbf{p})$ is the field in the input plane, and $G(\mathbf{p},\mathbf{r})$ is the EHF Green's function response at $\mathbf{r}$ due to a point source at $\mathbf{p}$ given by [37, 40]

$$G(\mathbf{p}, \mathbf{r}) = G_0(\mathbf{p}, \mathbf{r}) \exp[i\varphi(\mathbf{p}, \mathbf{r})], \tag{17.5}$$

where $G_0(\mathbf{p},\mathbf{r})$ is the Huygens-Fresnel Green's function for propagation through an ABCD system in the absence of random inhomogeneities and $\varphi(\mathbf{p},\mathbf{r})$ is the random phase of a spherical wave propagating in the random medium from the input plane to the output plane. The Huygens-Fresnel Green's function $G_0(\mathbf{p},\mathbf{r})$ is given by [40]

$$G_0(\mathbf{p}, \mathbf{r}) = -\frac{ik}{2\pi B} \exp\left[-\frac{ik}{2B}\left(Ap^2 - 2\mathbf{p} \cdot \mathbf{r} + Dr^2\right)\right], \tag{17.6}$$

where A, B, and D are the ray-matrix elements for propagation from the input plane to the output plane. In the following, it is assumed that φ is a normally distributed zero-mean random process.

17.2.2 The OCT Signal

A conventional OCT system [1] consists of a superluminescent diode (SLD), a Michelson interferometer with movable reference mirror, and a photodetector. The rotationally symmetric sample arm geometry of the OCT system is shown in Fig. 17.1. The tissue discontinuity being probed arises from a refractive index discontinuity between two tissue layers ($n \neq n_1$ in Fig. 17.1). Therefore, the discontinuity, located at a depth z in the tissue, is characterized by a Fresnel reflection coefficient R_d. A lens with focal length f is placed at a distance d from the tissue surface. In the system of interest, the focal plane coincides with the tissue discontinuity. Furthermore, the reference arm optical path length in the Michelson interferometer is matched to the focal plane optical depth.

Fig. 17.1 Sample arm
geometry of the OCT system
(From Ref. [10])
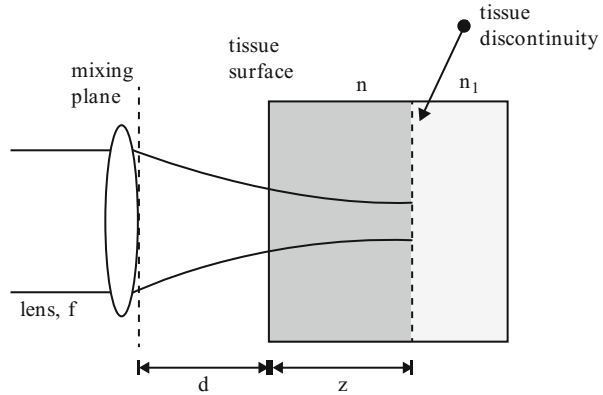
In the case of human skin, light scattering in the bulk tissue is predominantly in the forward direction for the wavelengths of interest in the NIR region [43]. Hence, we neglect bulk backscattering and use the EHF principle [37, 38] to describe the light propagation in the bulk tissue. This is justified by the fact that the EHF principle is based on the paraxial approximation and therefore valid for small-angle forward scattering. In particular, it can be shown that the paraxial approximation is valid up to 30°, that is, 0.5 rad [42]. Because most tissues are characterized by *rms* scattering angles below this limit, the EHF principle may be used to describe light propagation in tissue, retaining both amplitude and phase information. Also, the bulk tissue absorption is neglected [43]. Thus, the bulk tissue is characterized by a scattering coefficient μ_s, a root-mean-square scattering angle θ_{rms} or asymmetry parameter g [44], and a mean index of refraction n. Furthermore, the bulk tissue is modeled as a material with scatterers randomly distributed over the volume of interest. Note that in the present analysis, polarization effects are excluded.

By mixing the sample field U_S reflected from the discontinuity in the tissue at depth z, with the reference field U_R on the photodetector of the OCT system, we obtain that the heterodyne signal current $i(z)$ can be expressed as [8]

$$i(z) \propto \mathrm{Re}\left[\int U_R(\mathbf{p}, t)U_S^*(\mathbf{p}, t + \tau)d\mathbf{p}\right], \qquad (17.7)$$

where the integration is taken over the area of the photodetector, Re denotes the real part, and τ is the difference between the propagation times of the reference and sample beams. In practice, the heterodyne signal current $i(z)$ is measured over a time much longer than the source coherence time. In this case, it can be shown that [8]

$$i(z) \propto |g(\tau)|\mathrm{Re}\left[\int U_R(\mathbf{p})U_S^*(\mathbf{p})d\mathbf{p}\right], \qquad (17.8)$$

where $|g(\tau)|$ is the modulus of the normalized temporal coherence function of the source (notice that $g(\tau)$ is not related to the asymmetry parameter g).

Because the detailed structure of the tissue is unknown a priori, it is necessary and appropriate to treat the optical distortions as a random process and, as is commonly done in the literature, to specify certain measures of the average performance, for example, the mean (i.e., ensemble average) square heterodyne signal current. It can be shown that the mean square heterodyne signal current $\langle i^2(z) \rangle$, which is proportional to the heterodyne signal power, is given by [8, 29]

$$\langle i^2(z) \rangle = 2\alpha^2 |g(\tau)|^2 \mathrm{Re} \left[\int\int \Gamma_S(\mathbf{p}_1, \mathbf{p}_2; z) \Gamma_R(\mathbf{p}_1, \mathbf{p}_2) d\mathbf{p}_1 d\mathbf{p}_2 \right], \qquad (17.9)$$

where

$$\Gamma_R(\mathbf{p}_1, \mathbf{p}_2) = U_R(\mathbf{p}_1) U_R^*(\mathbf{p}_2), \qquad (17.10)$$

$$\Gamma_S(\mathbf{p}_1, \mathbf{p}_2; z) = \langle U_S(\mathbf{p}_1; z) U_S^*(\mathbf{p}_2; z) \rangle \qquad (17.11)$$

are the mutual coherence functions of the reference and the reflected sample optical fields in the mixing plane. The angular brackets denote an ensemble average both over the statistical properties of the tissue and the reflecting discontinuity. For simplicity, the heterodyne mixing process has been chosen to take place directly behind the lens at the side facing the tissue, and $\mathbf{p}_1$, $\mathbf{p}_2$ are two-dimensional vectors in this plane transverse to the optical axis. The quantity α is a conversion factor for power to current and equals $(q_e \eta / h\nu)$, where q_e is the electronic charge, η the detector quantum efficiency, ν the optical frequency, and h the Planck's constant. In the case of interest, the reference arm optical path length in the Michelson interferometer is always matched to the sample arm optical path length, from which it follows that $|g(\tau)| = |g(0)| = 1$ [8].

For the heterodyne detection scheme, the spatial coherence properties of the sample field contained in the mutual coherence function Γ_S are of utmost importance in the determination of the corresponding signal. In particular, if the spatial coherence of the sample field is degraded with respect to the reference field, one obtains a corresponding degradation in the signal-to-noise ratio.

The reference field and the input sample field U_{Si} in the lens plane impinging on the sample are assumed to be of Gaussian shape and given by

$$U_R(\mathbf{p}, t) = \sqrt{\frac{P_R}{\pi w_0^2}} \exp\left[-\frac{p^2}{2}\left(\frac{1}{w_0^2} + \frac{ik}{f} \right) \right] \exp[i\omega_R t + \varphi_R(t)], \qquad (17.12)$$

$$U_{Si}(\mathbf{p}, t) = \sqrt{\frac{P_R}{\pi w_0^2}} \exp\left[-\frac{p^2}{2}\left(\frac{1}{w_0^2} + \frac{ik}{f} \right) \right] \exp[i\omega_S t], \qquad (17.13)$$

where P_R and P_S are the powers of the reference and input sample beams, respectively, w_0 is the $1/e$ intensity radius of these beams in the lens plane, $k = 2\pi/\lambda$, where λ is the center wavelength of the source in vacuum, ω_R and ω_S are the angular frequencies of the reference and input sample beams, respectively, and φ_R is the phase of the reference field relative to the input sample field.

In the determination of the mutual coherence function Γ_S, we use the EHF principle to obtain a viable expression for $U_S(\mathbf{p};z)$, that is, the reflected sample optical field in the mixing plane. Using (17.4), we have

$$U_S(\mathbf{p};z) = \int U_B(\mathbf{r};z)G(\mathbf{r},\mathbf{p};z)d\mathbf{r}, \qquad (17.14)$$

where $U_B(\mathbf{r};z)$ is the reflected sample field in the plane of the tissue discontinuity, $\mathbf{r}$ is a two-dimensional vector in this plane transverse to the optical axis, and $G(\mathbf{r},\mathbf{p};z)$ is the EHF Green's function response at $\mathbf{p}$ due to a point source at $\mathbf{r}$, which includes the effects of scattering in the intervening medium. Combining (17.11) and (17.14) yields

$$\Gamma_S(\mathbf{p}_1, \mathbf{p}_2; z) = \int \int \langle U_B(\mathbf{r}_1; z)U_B(\mathbf{r}_2; z)G(\mathbf{r}_1, \mathbf{p}_1; z)G^*(\mathbf{r}_2, \mathbf{p}_2; z)\rangle d\mathbf{r}_1 d\mathbf{r}_2, \quad (17.15)$$

where $\mathbf{r}_1$, $\mathbf{r}_2$ are two-dimensional vectors in this plane transverse to the optical axis. For simplicity in notation, we omit in the following the explicit dependence of the various quantities on z.

We next assume that the statistical properties of the bulk tissue and the tissue discontinuity are independent and that the propagation to the tissue discontinuity is statistically independent from the corresponding reflected propagation path. The former seems to be a reasonable assumption for a medium like tissue. The latter means that enhanced backscattering is neglected. Enhanced backscattering and the criterion for neglecting it are discussed in Sect. 17.5. From these assumptions, it follows that

$$\begin{aligned} \langle U_B(\mathbf{r}_1)U_B^*(\mathbf{r}_2)G(\mathbf{r}_1, \mathbf{p}_1)G^*(\mathbf{r}_2, \mathbf{p}_2)\rangle = \\ \langle U_B(\mathbf{r}_1)U_B^*(\mathbf{r}_2)\rangle \langle G(\mathbf{r}_1, \mathbf{p}_1)G^*(\mathbf{r}_2, \mathbf{p}_2)\rangle. \end{aligned} \qquad (17.16)$$

The first term on the right-hand side of (17.16) relates to both the mean value over statistics of the bulk tissue in propagating from the lens plane to the tissue discontinuity and the reflection statistics of the discontinuity. The second term on the right-hand side of (17.16) relates to the corresponding average over the statistics of the bulk tissue when propagating back from the discontinuity to the mixing plane. Assuming diffuse backscattering from the tissue discontinuity, we have [29, 45]

$$\langle U_B(\mathbf{r}_1)U_B^*(\mathbf{r}_2)\rangle = \frac{4\pi}{k^2}\delta(\mathbf{r}_1 - \mathbf{r}_2)\langle I_B(\mathbf{r}_1)\rangle, \qquad (17.17)$$

where $\delta(\mathbf{r})$ is the two-dimensional Dirac delta function and $I_B(\mathbf{r}_1)$ is the mean backscattered irradiance distribution in the plane of the discontinuity. An adequate analytic approximation for this mean backscattered irradiance distribution is obtained by multiplying the approximate expression for the mean irradiance distribution, derived in Sect. 17.2.3, by the reflection coefficient R_d. The expression, which is valid for arbitrary values of the optical depth $\mu_s z$, is given by

$$\langle I_B(r) \rangle = \frac{R_d P_S}{\pi} \left[\frac{e^{-\mu_s z} \exp\left[-r^2/w_H^2\right]}{w_H^2} + \frac{(1 - e^{-\mu_s z}) \exp\left[-r^2/w_S^2\right]}{w_S^2} \right]. \tag{17.18}$$

The first term in the brackets on the right-hand side of (17.18) can be interpreted to represent the attenuated distribution obtained in the absence of the inhomogeneities, and the corresponding second term represents a broader halo resulting from scattering by the inhomogeneities. The quantities w_H and w_S are the $1/e$ irradiance radii or spot sizes in the discontinuity plane in the absence and presence of scattering, respectively, given by

$$w_H^2 = w_0^2 \left(A - \frac{B}{f} \right)^2 + \left(\frac{B}{k w_0} \right)^2, \tag{17.19}$$

$$w_S^2 = w_0^2 \left(A - \frac{B}{f} \right)^2 + \left(\frac{B}{k w_0} \right)^2 + \left(\frac{2B}{k \rho_0} \right)^2. \tag{17.20}$$

A and B are the ray-matrix elements for propagation from the lens plane to the discontinuity plane. For the geometry of interest, A and B are given by $A = 1$ and $B = f = d + z/n$ [42]. The quantity ρ_0 appearing in (17.20) is the lateral coherence length of a spherical wave in the lens plane due to a point source in the discontinuity plane [29]. The lateral coherence length is discussed in detail in Ref. [10].

Combining (17.15), (17.16), and (17.17) and simplifying yield

$$\Gamma_S(\mathbf{p}_1, \mathbf{p}_2) = \frac{4\pi}{k^2} \int \langle I_B(\mathbf{r}) \rangle \langle G(\mathbf{r}, \mathbf{p}_1) G^*(\mathbf{r}, \mathbf{p}_2) \rangle d\mathbf{r}. \tag{17.21}$$

Using (17.5), the second term in the integral on the right-hand side of (17.21) may be written as

$$\langle G(\mathbf{r}, \mathbf{p}_1) G^*(\mathbf{r}, \mathbf{p}_2) \rangle = G_0(\mathbf{r}, \mathbf{p}_1) G_0^*(\mathbf{r}, \mathbf{p}_2) \Gamma_{pt}(\rho), \tag{17.22}$$

where $G_0(\mathbf{r}, \mathbf{p})$ is the Huygens-Fresnel Green's function when propagating from the discontinuity plane to the lens plane and Γ_{pt} is the mutual coherence function of a point source located in the discontinuity plane and observed in the lens plane given by

$$\Gamma_{pt} = \langle \exp[i\{\phi(\mathbf{p}_1) - \phi(\mathbf{p}_2)\}] \rangle. \tag{17.23}$$

The mutual coherence function Γ_{pt} contains the effects of the scattering inhomogeneities. Using (17.6), the Green's function $G_0(\mathbf{r},\mathbf{p})$ is given by

$$G_0(\mathbf{r},\mathbf{p}) = -\frac{ik}{2\pi B_b} \exp\left[-\frac{ik}{2B_b}\left(A_b r^2 - 2\mathbf{r}\cdot\mathbf{p} + D_b p^2\right)\right], \qquad (17.24)$$

where A_b, B_b, and D_b are the ray-matrix elements for backpropagation to the lens plane. These quantities are given by $A_b = D = 1$, $B_b = B = d + z/n$, and $D_b = A = 1$ [40]. In order to obtain an analytical solution, we have to use an approximate expression for the mutual coherence function Γ_{pt}. The expression, derived in Sect. 17.2.3, is given by

$$\Gamma_{pt}(\rho) \cong e^{-\mu_s z} + (1 - e^{-\mu_s z})\exp\left[-\rho^2/\rho_0^2\right], \qquad (17.25)$$

where $\rho = |\mathbf{p}_1 - \mathbf{p}_2|$.

Substituting (17.10), (17.12), (17.18), (17.21), (17.22), (17.24), and (17.25) into (17.9) and performing the indicated Gaussian integrations over $\mathbf{p}_1,\mathbf{p}_2$ and simplifying yield

$$\begin{aligned}
\langle i^2(z)\rangle =& \frac{2\alpha^2 P_R P_S \sigma_b}{\pi^2} \\
&\times \int \left[\frac{e^{-\mu_s z}\exp\left[-r^2/w_H^2\right]}{w_H^2} + \frac{(1 - e^{-\mu_s z})\exp\left[-r^2/w_S^2\right]}{w_S^2}\right]d\mathbf{r},
\end{aligned} \qquad (17.26)$$

where the effective backscattering cross section of the tissue discontinuity $\sigma_b = 4\pi R_d/k^2$. It is important to note that the algebraically simple result given in (17.26) is, strictly speaking, valid only for propagation geometries where $A = D$, as is obtained in the case of interest. Performing the integration over the discontinuity plane in (17.26) and simplifying, we obtain the following expression for the mean square heterodyne signal current

$$\begin{aligned}
\langle i^2(z)\rangle =& \frac{\alpha^2 P_R P_S \sigma_b}{\pi w_H^2} \\
&\times \left[e^{-2\mu_s z} + \frac{2e^{-\mu_s z}(1 - e^{-\mu_s z})}{1 + \frac{w_S^2}{w_H^2}} + (1 - e^{-\mu_s z})^2\frac{w_H^2}{w_S^2}\right] \\
\equiv& \langle i^2\rangle_0 \Psi(z).
\end{aligned} \qquad (17.27)$$

The quantity $\langle i^2\rangle_0 = \alpha^2 P_R P_S \sigma_b/\pi(w_H)^2$ is the mean square heterodyne signal current in the absence of scattering, and the terms contained in the brackets are the heterodyne efficiency factor $\Psi(z)$. A comparison between the analytic approximation of $\Psi(z)$, given in (17.27), and the exact numerical calculation is given in Ref. [46]. Physically, $\Psi(z)$ can be looked upon as the reduction in the heterodyne signal-to-noise ratio due to the scattering of the tissue. The first term in the brackets

of (17.27) represents the contribution due to single scattering. The corresponding third term is the multiple-scattering term, and the second term is the cross term. Physically, the cross term is the coherent mixing of the unscattered and the multiple-scattered light.

17.2.2.1 Dynamic Focusing: Diffuse Reflectance

When the focal plane coincides with the tissue discontinuity, that is, $fA = B$ with $A = 1$, we obtain from (17.19) and (17.20)

$$w_H^2 = \left(\frac{f}{kw_0}\right)^2; \quad \frac{w_H^2}{w_S^2} = \frac{1}{1 + \left(\frac{2w_0}{\rho_0(z)}\right)^2}. \tag{17.28}$$

The quantity $\rho_0(z)$ is the lateral coherence length of the reflected sample field in the mixing plane. For lateral separations much less (greater) than $\rho_0(z)$, the field can be considered to be mutually coherent (incoherent). Because of the diffuse back-scattering from the tissue discontinuity, $\rho_0(z)$ is determined only by the propagation back through the tissue from the tissue discontinuity to the mixing plane. As a consequence, $\rho_0(z)$ is the lateral coherence length of a point source located in the tissue discontinuity plane, as observed in the mixing plane. For the geometry of interest, it can be shown [46] that

$$\rho_0(z) = \sqrt{\frac{3}{\mu_s z} \frac{\lambda}{\pi \theta_{rms}} \left(1 + \frac{nd(z)}{z}\right)}, \tag{17.29}$$

where $d(z) = f - (z/n)$ and $\theta_{rms} \approx [2(1 - g)]^{1/2}$. The second term in the brackets of (17.29) indicates that the lateral coherence length increases with increasing distance between the tissue surface and the mixing plane.

This well-known dependence of the lateral coherence length on the position of the scattering medium relative to the observation plane is the so-called shower-curtain effect [29, 30]. In general, the shower-curtain effect implies that the lateral coherence length obtained for the case when the scattering medium is close to the radiation source is larger than for the case when the scattering medium is close to the observation plane. Physically, this is due to the fact that a distorted spherical wave approaches a plane wave as it further propagates through a non-scattering medium. As a consequence, for example, from a distance, one can see a person immediately behind a shower curtain, but the person cannot see you. The effect is well known for light propagation through the atmosphere as discussed by Dror et al. [30] but has been omitted in previous theoretical OCT models [8]. However, due to the finite distance between the focusing lens and the tissue, the effect is inevitably present in practical OCT systems and could facilitate system optimization [46]. Finally, the reflection characteristics of the tissue discontinuity play a vital role for the shower-curtain effect.

17.2.2.2 Dynamic Focusing: Specular Reflectance

If we, instead of diffuse backscattering, had a specular reflection at the tissue discontinuity, the corresponding mutual coherence function for plane waves would apply. Using this mutual coherence function, we have

$$\Psi(z) = \left[e^{-2\mu_s z} + \left(1 - e^{-2\mu_s z} \right) \frac{w_H^2}{w_S^2} \right] \tag{17.30}$$

and

$$\rho_0(z) = \sqrt{\frac{1}{2\mu_s z} \frac{\lambda}{\pi \theta_{rms}}}. \tag{17.31}$$

It is obvious from (17.31) that the shower-curtain effect would not be present in the case of specular reflection at the tissue discontinuity, in contrast to the case of diffuse backscattering. However, it is important to note that it is diffuse backscattering which actually occurs in the case of (skin) tissue.

17.2.2.3 Collimated Sample Beam

In the case of a collimated sample beam, the expressions for w_H and w_S in (17.19) and (17.20) need to be rewritten:

$$w_H^2 = \lim_{f \to \infty} \left[w_0^2 \left(1 - \frac{d + \frac{z}{n}}{f} \right)^2 + \left(\frac{d + \frac{z}{n}}{kw_0} \right)^2 \right] = w_0^2 + \left(\frac{d + \frac{z}{n}}{kw_0} \right)^2 \tag{17.32}$$

$$w_S^2 = \lim_{f \to \infty} \left[w_H^2 + \left(\frac{2\left(d + \frac{z}{n}\right)}{k\rho_0} \right)^2 \right] = w_0^2 + \left(\frac{d + \frac{z}{n}}{kw_0} \right)^2 + \left(\frac{2\left(d + \frac{z}{n}\right)}{k\rho_0} \right)^2, \tag{17.33}$$

where it has been used that $A = 1$ and $B = d + z/n$ and note that now $B \neq f$. In order to find the heterodyne efficiency factor, these expressions must be inserted in (17.27), and moreover, the expression for ρ_0 should be chosen in accordance with the reflection characteristics of the probed discontinuity.

17.2.2.4 Numerical Results

The heterodyne efficiency factor $\Psi(z)$ is shown as a function of depth z of the tissue discontinuity in Fig. 17.2 for typical parameters of human skin tissue with diffuse backscattering and the shower-curtain effect included (dashed) and specular reflection (solid), respectively. For comparison, we show the case of diffuse backscattering with exclusion of the shower-curtain effect (dash-dot) and the case of pure single scattering (dotted). At shallow depths, single backscattering dominates. Due to multiple scattering, the slope is changed and $\Psi(z)$ becomes almost constant for three cases (curves 1–3). The important difference is, however, that the change of

Fig. 17.2 $\Psi(z)$ as a function of z for diffuse backscattering with the shower-curtain effect included (curve 1) and for specular reflection (curve 3). Curve 2 is calculated for diffuse backscattering without the shower-curtain effect, and curve 4 is the case of pure single backscattering; $\lambda = 814$ nm, $\mu_s = 20$ mm^{-1}, $g = 0.955$ ($\theta_{rms} = 0.3$ rad), $n = 1.4, f = 5$ mm, $w_0 = 0.5$ mm (From Ref. [10])
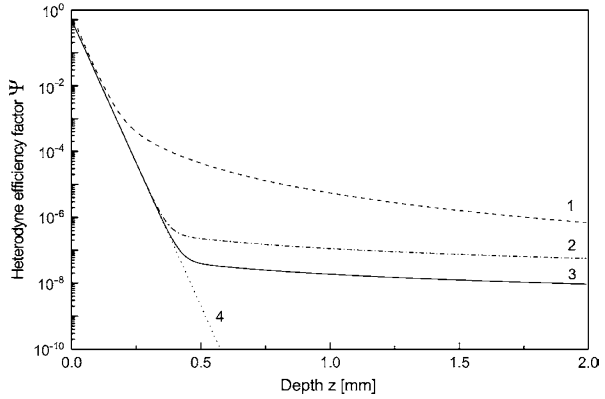
Fig. 17.3 $\Psi(z)$ as a function of z for $\mu_s = 10$ mm^{-1} and three values of g. The curves are for the case of a diffuse backscattering at the discontinuity and inclusion of the shower-curtain effect ($\lambda = 814$ nm, $n = 1.4$, $f = 5$ mm, $w_0 = 0.5$ mm)
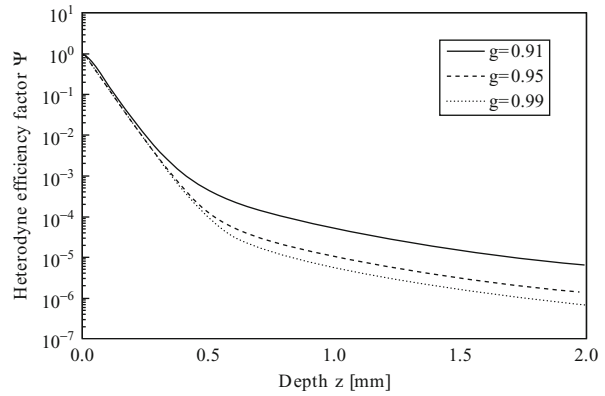
slope occurs at different depths. This is due to the shower-curtain effect leading to an appreciable enhancement of $\Psi(z)$, and with it the heterodyne signal, which is obtained by comparing curves 1 and 2 in Fig. 17.2. Physically, this increase in the heterodyne signal is due to an enhanced spatial coherence of the multiple-scattered light.

In Fig. 17.3, $\Psi(z)$ is shown as a function of depth z for $\mu_s = 10$ mm^{-1} and three values of g within the range of validity of the EHF principle. The curves are computed for the case of diffuse backscattering at the discontinuity and inclusion of the shower-curtain effect. This figure demonstrates the degree of sensitivity of the heterodyne efficiency factor with respect to changes in the asymmetry parameter. Moreover, in Fig. 17.4, $\Psi(z)$ is shown as a function of depth z for $g = 0.95$ and three values of μ_s within the range of interest with respect to tissue [43]. The curves are computed for the case of diffuse backscattering at the discontinuity and inclusion of the shower-curtain effect. This figure demonstrates the degree of sensitivity of the heterodyne efficiency factor with respect to changes in the scattering coefficient.

Fig. 17.4 $\Psi(z)$ as a function of z for $g = 0.95$ and three values of μ_s within a range of interest with respect to tissue. The curves are for the case of a diffuse backscattering at the discontinuity and inclusion of the shower-curtain effect ($\lambda = 814$ nm, $n = 1.4$, $f = 5$ mm, $w_0 = 0.5$ mm)
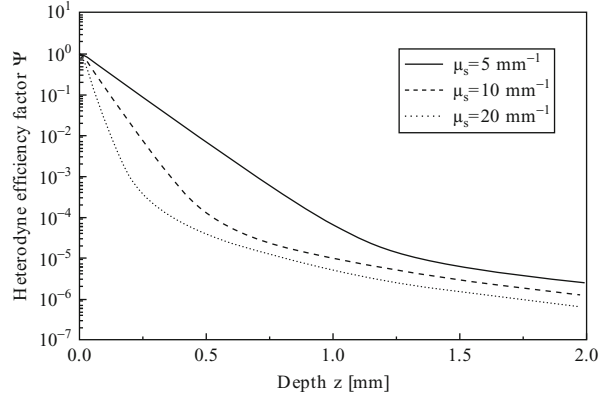
17.2.2.5 Choice of Scattering Function

In the present modeling of the OCT geometry, we use a Gaussian volume scattering function [19], as discussed in Sect. 17.2.3 below. The motivation for this choice of scattering function is the ability to obtain an accurate analytic engineering approximation, valid for all values of the optical depth. In the case of the Henyey-Greenstein scattering function [47], which is widely used in approximating the angular scattering dependence of single-scattering events in some biological media [43, 48], the corresponding analytic approximation is not as accurate as for the case of a Gaussian scattering function. However, a numerical computation using the exact expressions may be carried out instead. Hence, both scattering functions may be used in the modeling of the OCT geometry presented in this chapter.

17.2.2.6 Signal-to-Noise Ratio (SNR)

Without loss of generality, an OCT system with shot-noise-limited operation is considered in a calculation of the signal-to-noise ratio (SNR). The only significant source of noise is the shot-noise caused by the reference beam. For a photoconductive detector, the mean square noise power N_p can then be expressed as [49]

$$N_p = 2\alpha q_e G_{ca}^2 R_l B_w P_R, \tag{17.34}$$

where R_l is the resistance of the load, G_{ca} the gain associated with the current amplifier, and B_w the system bandwidth. The corresponding mean heterodyne signal power $S(z)$ is given by [50]

$$S(z) = \langle i^2(z) \rangle G_{ca}^2 R_l, \tag{17.35}$$

where $\langle i^2(z) \rangle$ is given by (17.27). Hence, the mean signal-to-noise ratio $SNR(z)$ is given by

$$SNR(z) = \frac{S(z)}{N_p} = (SNR)_0 \Psi(z), \tag{17.36}$$

where the signal-to-noise ratio in the absence of scattering $(SNR)_0$ is given by

$$(SNR)_0 = \frac{\eta P_S}{2hvB_w}\left(\frac{\sigma_b}{\pi w_H^2}\right). \tag{17.37}$$

In the case of interest where the focal plane coincides with the tissue discontinuity, we get the following expression for $(SNR)_0$

$$(SNR)_0 = \frac{2\eta P_S}{hvB_w}\left(\frac{w_0}{f}\right)^2 R_d, \tag{17.38}$$

where it has been used that $\sigma_b = 4\pi R_d/k^2$.

Calculation of the Maximum Probing Depth

The maximum probing depth is of considerable interest in the characterization and optimization of an OCT system when used for imaging in highly scattering tissue. The maximum probing depth may be calculated by using the model presented above. Details of the calculation are found in Ref. [27], where the calculation of the maximum probing depth z_{max} is based on the minimum acceptable SNR in the case of shot-noise-limited detection. In the calculations, a value of 3 is used as the minimum acceptable signal-to-noise ratio, that is, $SNR(z_{max}) = 3$.

An important conclusion of Ref. [27] is that, in general, z_{max} depends on the focal length at small values of the scattering coefficient but is independent of the focal length at larger values of the scattering coefficient. A similar behavior is observed for z_{max} as a function of μ_s and the $1/e$ intensity radius of the sample beam being focused. This behavior is due to multiple scattering of the light in the tissue. At scattering coefficients found in human skin tissue [43, 51], for example, it is concluded that the maximum probing depth is independent of the focal length f. This is an important conclusion because the depth of focus and the lateral resolution of the OCT system may then be chosen independently of z_{max}. For example, if no scanning of the focal plane in the tissue is desirable and, therefore, a large depth of focus has been chosen, the same maximum probing depth is obtained as for a system with a short depth of focus where the focal plane is scanned to keep it matched to the reference arm. This conclusion is not surprising or contrary to assumptions already held in the field. However, the theoretical analysis in this section provides a theoretical foundation for such statements. Moreover, this agreement may also be taken as a further validation of the OCT model presented here.

17.2.3 The OCT Lateral Resolution

As already discussed, the lateral resolution of an OCT system is determined by the spot size at the depth being probed in the tissue. Therefore, we determine the mean

irradiance distribution or the intensity pattern of the optical field as a function of the probing depth z in the tissue. In highly scattering tissue, the mean irradiance distribution, and with it the lateral resolution, is dependent on the scattering properties of the tissue. The formalism presented in this chapter enables the calculation of the lateral resolution in highly scattering tissue, which is shown below.

For small-angle scattering, where the paraxial approximation is valid, the EHF principle yields that the mean irradiance distribution is given by [40]

$$\langle I(r) \rangle = \left(\frac{k}{2\pi B} \right)^2 \int K(\rho) \exp\left\{ \frac{ik}{B} \boldsymbol{\rho} \cdot \mathbf{r} \right\} \Gamma_{pt}(\rho) d^2\rho, \qquad (17.39)$$

where

$$K(\rho) = \int \exp\left\{ -\frac{ikA}{B} \boldsymbol{\rho} \cdot \mathbf{P} \right\} U_{Si}(\mathbf{P} + \boldsymbol{\rho}/2) U_{Si}^*(\mathbf{P} - \boldsymbol{\rho}/2) d^2P, \qquad (17.40)$$

and $\boldsymbol{\rho} = \mathbf{p}_1 - \mathbf{p}_2$. For an OCT system focusing at a depth z in the tissue, $A = 1$ and $B = f$. The mutual coherence function Γ_{pt} can be expressed as [45]

$$\Gamma_{pt} = \langle \exp\{i[\phi(\mathbf{p}_1) - \phi(\mathbf{p}_2)]\} \rangle = \exp\{-s[1 - b_\phi(\rho)]\}, \qquad (17.41)$$

where we have assumed that the phase ϕ is a normally distributed zero-mean random process. The quantity s is the phase variance, and $b_\phi(\rho)$ is the normalized phase autocorrelation function for a point source whose origin is at the probing depth z. It can be shown [52] that the phase variance $s = \mu_s z$, which is equal to the optical depth. The normalized phase autocorrelation function $b_\phi(\rho)$ is given by [45]

$$b_\phi(\rho) = \frac{\int\limits_0^L dz' \int\limits_0^\infty \sigma(\theta; z') J_0(kp_s\theta)\theta d\theta}{\int\limits_0^L dz' \int\limits_0^\infty \sigma(\theta; z')\theta d\theta}, \qquad (17.42)$$

J_0 is the Bessel function of the first kind of order zero,

$$p_s = \frac{B_b(z')}{B_b}\rho, \qquad (17.43)$$

where $B_b(z')$ is the B-matrix element for backpropagation from the probing depth z to a distance z' and $\sigma(\theta; z')$ is the volume scattering or phase function with θ being the scattering angle. For the OCT geometry, $B_b(z') = z'/n$ for $0 \leq z' \leq z$, $L = d + z$, and

$\sigma(\theta; z') = \sigma(\theta)$ for $0 \le z' \le z$, and zero otherwise. In this model, we use a Gaussian volume scattering function, which in the small-angle approximation is given by

$$\sigma(\theta) = \exp\left[-\theta^2/\theta_0^2\right], \tag{17.44}$$

where $g = \langle\cos\theta\rangle \approx 1 - \langle\theta^2\rangle/2$ and $\theta_0 = \langle\theta^2\rangle^{1/2} \approx [2(1-g)]^{1/2}$. Substituting (17.43) and (17.44) into (17.42) and performing the indicated integrations yield the following equation for the normalized phase autocorrelation function

$$b_\phi(\rho) = \frac{\sqrt{\pi}}{2}\frac{\rho_\phi}{\rho}\,\mathrm{erf}\left(\rho\big/\rho_\phi\right), \tag{17.45}$$

where $\mathrm{erf}(\rho/\rho_\phi)$ denotes the error function and ρ_ϕ is the phase correlation length given by

$$\rho_\phi = \frac{\lambda}{\pi\sqrt{2(1-g)}}\left(1 + \frac{nd}{z}\right). \tag{17.46}$$

Hence, the mutual coherence function Γ_{pt} is given by (17.41) with $b_\phi(\rho)$ given by (17.45). Thus, for specific values of both s and g, the mutual coherence function is completely determined, and for a given value of the initial optical wave function U_{Si}, numerical results for the mean irradiance can be obtained directly from (17.39). Here, U_{Si} is given by (17.13), and we get the following equation for the mean irradiance distribution at the probing depth z in the tissue

$$\langle I(\mathbf{r})\rangle = \frac{P_S}{2\pi(f/kw_0)^2}\int\limits_0^\infty \exp\left\{-\frac{x^2}{4}\right\}xJ_0(ux)\Gamma_{pt}(xw_0)dx, \tag{17.47}$$

where J_0 is the Bessel function of the first kind of order zero and

$$u = \frac{r}{f/kw_0} \tag{17.48}$$

is a normalized transverse coordinate.

As indicated above, numerical results can readily be obtained. However, it is useful to have an analytic approximation so that OCT system parameter studies can be performed. Examination of (17.41) reveals for large values of the optical depth that Γ_{pt} is nonzero for $s\{1 - b_\phi(\rho)\}$ less than the order unity, that is, for $b_\phi(\rho)$ near unity. Expanding $b_\phi(\rho)$ in powers of ρ and retaining the first two nonzero terms yields from (17.45) that $b_\phi(\rho) \approx 1 - \rho^2/3(\rho_\phi)^2$, from which it follows that

$$\Gamma_{pt} \approx \exp\left[-\rho^2/\rho_0^2\right], \quad s >> 1, \tag{17.49}$$

where $\rho_0 = \rho_\phi (3/s)^{1/2}$. We expect that the ballistic, that is, unscattered, component of the irradiance pattern is proportional to $e^{-\mu_s z}$. Thus, we approximate the mutual coherence function as

$$\Gamma_{pt} \approx e^{-\mu_s z} + (1 - e^{-\mu_s z}) \exp\{-\rho^2/\rho_0^2\}. \tag{17.50}$$

Substituting (17.13) and (17.50) into (17.39) and performing the integration yield the following approximate expression for the mean irradiance distribution at the probing depth z in the tissue

$$\langle I(\mathbf{r}) \rangle \approx \frac{P_S}{\pi} \left[\frac{e^{-\mu_s z} \exp\{-r^2/w_H^2\}}{w_H^2} + \frac{(1 - e^{-\mu_s z}) \exp\{-r^2/w_S^2\}}{w_S^2} \right]. \tag{17.51}$$

The first term in the brackets on the right-hand side of (17.51) can be interpreted to represent the attenuated distribution obtained in the absence of the inhomogeneities, and the corresponding second term represents a broader halo resulting from scattering by the inhomogeneities. The quantities w_H and w_S are the $1/e$ irradiance radii in the absence and presence of scattering, respectively, given by

$$w_H^2 = w_0^2 \left(A - \frac{B}{f} \right)^2 + \left(\frac{B}{kw_0} \right)^2, \tag{17.52}$$

$$w_S^2 = w_0^2 \left(A - \frac{B}{f} \right)^2 + \left(\frac{B}{kw_0} \right)^2 + \left(\frac{2B}{k\rho_0} \right)^2. \tag{17.53}$$

For the OCT system, we have

$$w_H = \frac{f}{kw_0}, \tag{17.54}$$

$$w_S = \sqrt{w_H^2 + \left(\frac{2f}{k\rho_0} \right)^2}. \tag{17.55}$$

It is only in the very superficial layers of highly scattering tissue that it is possible to achieve diffraction-limited focusing. In this region, the lateral resolution is given by $2w_H$. At deeper probing depths, the lateral resolution is dependent on the scattering properties and given by $2w_S$. It is seen from (17.55) and (17.29) that the lateral resolution is degraded due to multiple scattering when the probing depth is increased. This is illustrated in Fig. 17.5, where the intensity pattern is shown as a function of the probing depth z in the tissue using (17.51). Finally, from (17.55) and (17.29), it is important to note that the shower-curtain effect leads to an increased lateral resolution.

Fig. 17.5 The intensity pattern as a function of the probing depth z in the tissue ($\lambda = 814$ nm, $\mu_s = 10$ mm^{-1}, $g = 0.955$ ($\theta_{rms} = 0.3$ rad), $n = 1.4$, $f = 5$ mm, $w_0 = 0.5$ mm)
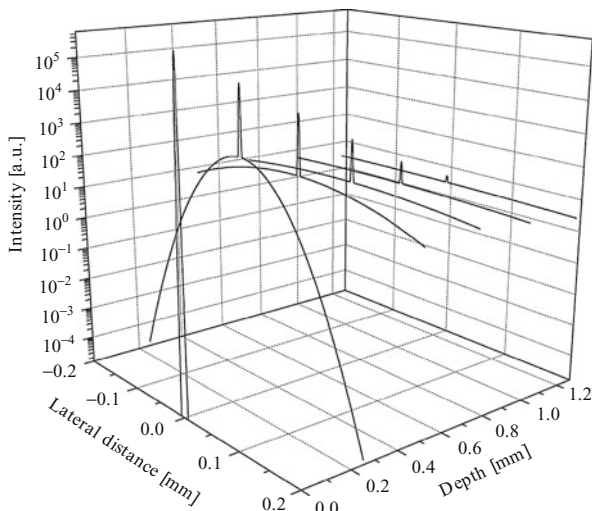
17.3 Advanced Monte Carlo Simulation of OCT Systems

In the previous section, the extended Huygens-Fresnel model was applied to model a generalized OCT setup, where the OCT signal from a diffusely reflecting discontinuity within the sample was found. In the following, we refer to this model as the EHF model. Also the so-called heterodyne efficiency factor Ψ was investigated, which describes the degradation of the OCT signal due to scattering. The predictions from the EHF model have been demonstrated to compare well with experiments carried out on aqueous suspensions of microspheres [10]. In this section, we describe the derivation of a Monte Carlo (MC) model of the OCT signal. As stated in the introduction, our motivation for applying MC simulation is to develop a model which may serve as a numerical phantom for further theoretical studies.

It is important to note that the MC method only describes the transport of energy packets along straight lines and therefore the approach is incapable of describing coherent interactions of light. These energy packets are often referred to as photon packets or simply photons, and this is adopted here. However, it should be emphasized that no underlying wave equation is guiding or governing these photons. Accordingly, any attempt to relate these to real quantum mechanical photons should be done with great care as argued in Ref. [53] regarding a suggested approach of including diffraction effects into MC simulations [54]. An MC photon packet represents a fraction of the total light energy, and for some applications, especially continuous wave, it may be useful to think of the path traveled by a photon as one possible path in which a fraction of the power flows. A collection of photon packets may then be perceived as constituting an intensity distribution due to an underlying field, and it can, accordingly, seem tempting to infer behavior

known to apply to fields upon photon packets. Consider, as an example, that one wishes to determine whether the photon packets are able to enter an optical fiber. It can then seem intuitively correct to restrict the access of photons impinging on the fiber end to those which fall within the numerical aperture of the fiber. However, such an angular restriction may not be correct, because the individual photon packet do not carry information of the entire field and its phase distribution. It is therefore not possible to determine whether a portion of the energy carried by a photon packet will enter the fiber due to a mode match between the fiber mode and the field underlying the collective intensity distribution of the photon packets. This discussion is treated in greater detail in Ref. [12].

With the above discussion of MC photons in mind, it may seem futile to investigate if MC simulation is applicable to estimate an OCT signal, which is the result of heterodyne mixing, and thus depends upon the coherence properties of the light. However, the problem may be reformulated to investigate whether or not the effect of the lack of coherence information in an MC simulation may be circumvented or at least minimized. Others [55–58] have attempted to model similar optical geometries by interpreting the heterodyne process as a rejection process in which the detected photons must conform to a set of criteria on position and angle. We refer to such a set of criteria as a detection scheme. However, these criteria were found by ad hoc considerations of the optical system, which may easily lead to incorrect results as exemplified above. Instead a mathematical derivation of the true criteria of the detection scheme will be given in this section.

In Sect. 17.3.1, the EHF principle is used to derive an expression for the OCT signal depending on the intensity of the light only. This is obtained by calculating the mixing of the reference and sample beams in the plane conjugate to the discontinuity plane in the sample probed by the system. The result is surprising, because the expression for the signal given in (17.9) depends on the coherence properties of the light. However, it is shown that the formula used for calculating the OCT signal in this particular plane is mathematically identical to the result in (17.9). These results are valid for the, from a biomedical point of view, important case of a signal arising from a diffusely reflecting discontinuity embedded in a scattering sample. As a novelty, this proves the viability of MC simulation to model the OCT technique, because it is shown that only intensity, and not field and phase, is necessary for this case. In Sect. 17.3.2, the necessary advanced method of simulating focused Gaussian beams in MC simulation is discussed. The results of Sects. 17.3.1 and 17.3.2 are then combined in Sect. 17.3.3 to form an MC model of the OCT signal. The results using this model are then compared to those of the EHF model in Sect. 17.3.4.

17.3.1 Theoretical Considerations

The optical geometry of the sample arm is shown in Fig. 17.6, and it should be noted that the enclosed section corresponds to the geometry used for the EHF calculation in Sect. 17.2.2. An optical fiber end is positioned in the *p*-plane.

Fig. 17.6 Sample arm setup of the OCT system. The lenses L1 and L2 are considered to be identical, perfect, and have infinite radius. The setup is essentially a 4F system (From Ref. [12])
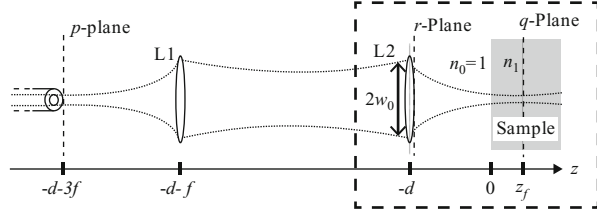
The fiber emits a beam, which hits the collimating lens L1. The focusing lens L2 is positioned in the *r*-plane, and in this plane, the beam is a Gaussian beam with $1/e$ width, w_0, of the intensity. The beam is focused by L2 upon a diffusely reflecting discontinuity positioned at the depth z_f inside a scattering sample a distance d from L2. The sample is taken to be a slab infinite in the transverse direction. The part of the light that is reflected from the discontinuity propagates out through the sample, through lenses L2 and L1 to the optical fiber, where it is collected. The lenses L1 and L2 have the focal length f and are taken to be identical, perfect, and infinite in radius. This means that the *q*- and *p*-planes are conjugate planes with magnification one.

The OCT signal is produced by the mixing of the light from the reference and sample arms on the photodetector of the OCT system. Due to the symmetry of the system, in Sect. 17.2.2, the EHF prediction of the mixing between signal and reference beam was conveniently calculated at the *r*-plane. The mean square of the signal current $\langle i^2 \rangle$ is given by (17.9) and rewritten according to the notation in Fig. 17.6 to yield

$$\langle i^2 \rangle = 2\alpha^2 |g(\tau)|^2 \operatorname{Re}\left[\iint \Gamma_R(\mathbf{r}_1, \mathbf{r}_2)\Gamma_S(\mathbf{r}_1, \mathbf{r}_2)\, d\mathbf{r}_1 d\mathbf{r}_2 \right] \equiv \Psi_r \langle i_0^2 \rangle, \qquad (17.56)$$

where $\Gamma_R(\mathbf{r}_1, \mathbf{r}_2) = U_R(\mathbf{r}_1)U_R^*(\mathbf{r}_2)$ is the cross correlation of the scalar reference field, $\Gamma_S(\mathbf{r}_1, \mathbf{r}_2) = \langle U_S(\mathbf{r}_1)U_S^*(\mathbf{r}_2) \rangle$ is the cross correlation of the sample field, and $\mathbf{r}_1$ and $\mathbf{r}_2$ are vectors in the *r*-plane (see Fig. 17.6). Ψ_r is the heterodyne efficiency factor (defined in (17.27); subscript *r* refers to it being calculated in the *r*-plane), which quantifies the reduction in signal due to scattering, and $\langle i_0^2 \rangle$ is the OCT signal current in the absence of scattering. The angle brackets denote an ensemble averaging over both the statistical properties of the scattering medium and the discontinuity, and the function $g(\tau)$ is the normalized temporal coherence function of the field, where τ is the time difference of propagation between the two fields.

It is important to note that by using the EHF principle, the investigation is limited to the paraxial regime as discussed above. In addition, most tissues are highly forward scattering in the near-infrared regime in which most OCT systems operate. It is assumed that the coherence length of the light source is short enough that signal powers from other reflections than the probed discontinuity are negligible. On the other hand, the coherence length is assumed long enough so that the temporal distortion of the sample field, or the path length distribution of the reflected photons, is assumed negligible compared to the coherence length of

the light source. Assuming that the optical path length of the reference beam and sample beam reflected from the discontinuity are perfectly matched, then $g(\tau) \approx 1$. To obtain the best comparison with the EHF model, the MC model presented in this section adopts this approximation.

The approximation of $g(\tau) \approx 1$ is a justified approximation for highly forward scattering tissues [8]. However, it does render the EHF model unsuitable to investigate the effect of scattering on the axial resolution of an OCT system in general, because the coherence gate due to the limited coherence length of the light source is not incorporated. Others have suggested using MC simulation and the total optical path length traveled by a photon packet to determine the influence of the coherence gate [9, 58, 59]. While this may very well be a valid approach, it is clear from the above discussion of photon packets and coherence that, how intuitively correct it may seem, this may not be the case. However, no efforts have been published to establish the meaning of a photon packet in such a temporal mixing of fields, so future work is required to establish such a relation. It is the intention that the MC model of the OCT signal presented in this chapter may be instrumental in such studies.

The OCT signal depends upon the lateral cross correlation of the light from the scattering sample (see (17.27)) and the lateral coherence length ρ_0 of the sample field in the r-plane for a single layer in front of the discontinuity is given by (17.29). With a nonzero lateral coherence length, ρ_0, it is seen that the OCT signal depends heavily upon the coherence properties of the field from the sample. As discussed above, an MC simulation does not describe the spatial coherence properties of light, and thus, a direct simulation of (17.56) is not possible. Like in Sect. 17.2.2, we assume that the discontinuity is diffusely reflecting and this infers that the lateral coherence will be zero immediately after reflection. Our motivation for envisioning the system geometry considered in Sect. 17.2.2 as part of a 4 F setup is to obtain a conjugate plane to the q-plane, here the p-plane (see Fig. 17.6). Through the conjugate relation, it is given that, in the absence of scattering, the lateral coherence length in the p-plane will also be zero. Hence, the sample field will be delta-correlated [19], and the OCT signal will only depend upon the intensities of the reference and sample field. In Appendix A, we show that within the paraxial regime, the sample field is delta-correlated even in the presence of scattering. We also show that the heterodyne efficiency factor calculated in the p-plane Ψ_p is mathematically identical to the heterodyne efficiency factor calculated in the r-plane, so that

$$\Psi_p = \frac{\langle i^2 \rangle}{\langle i_0^2 \rangle} = \frac{\int I_R(\mathbf{p})\langle I_S(\mathbf{p})\rangle d^2\mathbf{p}}{\int I_R(\mathbf{p})\langle I_{S0}(\mathbf{p})\rangle d^2\mathbf{p}} = \Psi_r, \qquad (17.57)$$

where I_R is the intensity at the reference beam and I_S, I_{S0} are the received intensities of the sample beam with and without scattering, respectively. The quantity $\mathbf{p}$ is a vector in the p-plane (see Fig. 17.6). Equation (17.57) shows the viability of applying an MC simulation to an OCT system provided a good estimate of the intensity distribution of the sample field is achieved. This requires a method to

simulate a focused Gaussian beam, and a novel method for modeling such a beam using MC simulation is reviewed in Sect. 17.3.2. Note that the identity proven in (17.57) is only strictly valid within the approximations of the EHF principle and thus also within the paraxial regime. However, for geometries with scattering that is not highly forward directed, we expect coherence effects to be of even less importance, and thus, (17.57) should at least be a good first approximation even when the paraxial approximation is not strictly valid.

17.3.2 Modeling a Focused Gaussian Beam with Monte Carlo Simulation

Monte Carlo models have previously been applied to model the focusing of light beams in tissue. The motivations have been to study the distribution of absorbed power for photodynamic therapy (PDT) [60], the performance of confocal microscopy [55, 56, 59], the efficiency of 1- and 2-photon excitation microscopy [57, 61], OCT [9], and the distribution within turbid media in general [60, 62]. In the absence of scattering, the focusing behavior of the beam is simply determined from the initial coordinates and propagation angles of the photons being launched. By carrying out MC simulations, one may then determine the distortion caused by scattering and other structures. Previously, two different ways of modeling the focusing have been employed:

Geometric-focus method: The initial position of the photon launch is found stochastically according to the initial intensity distribution, and the photon packets are simply directed toward the geometric focus of the beam [9, 60, 62, 63]. The geometric-focus method is obviously only a good approximation to a Gaussian beam for a very hard focus, but even then, the infinite photon density of the unscattered photons at the geometric focus may pose a problem.

Spot-focus method: After the initial position has been found as in the geometric-focus method, the photon packets are then directed toward a random position within an area in the focal plane of the beam [55–57]. The position within the chosen spot in the focal plane may be chosen according to different probability distributions. If future applications of the proposed MC model involve the use of the path lengths of the received photon packets to study the effect temporal distortion of the light due to scattering, the stochastic nature of the photon paths may pose a problem.

We have developed a method of choosing initial coordinates and angles for the photons so that the full 3D spatial intensity distribution of a Gaussian beam, that is, both the correct beam waist and finite spot size at focus, is obtained. This may be realized by utilizing the hyperbolic nature of a Gaussian beam, and we denote this approach the *hyperboloid method*. It is important to notice that this method does not require more simulation time than the two methods discussed above. Moreover, since the photons are still launched along straight lines, the incorporation of the scheme into most MC simulation programs for light propagation will be straightforward. Details of the hyperboloid method may be found in Ref. [12].
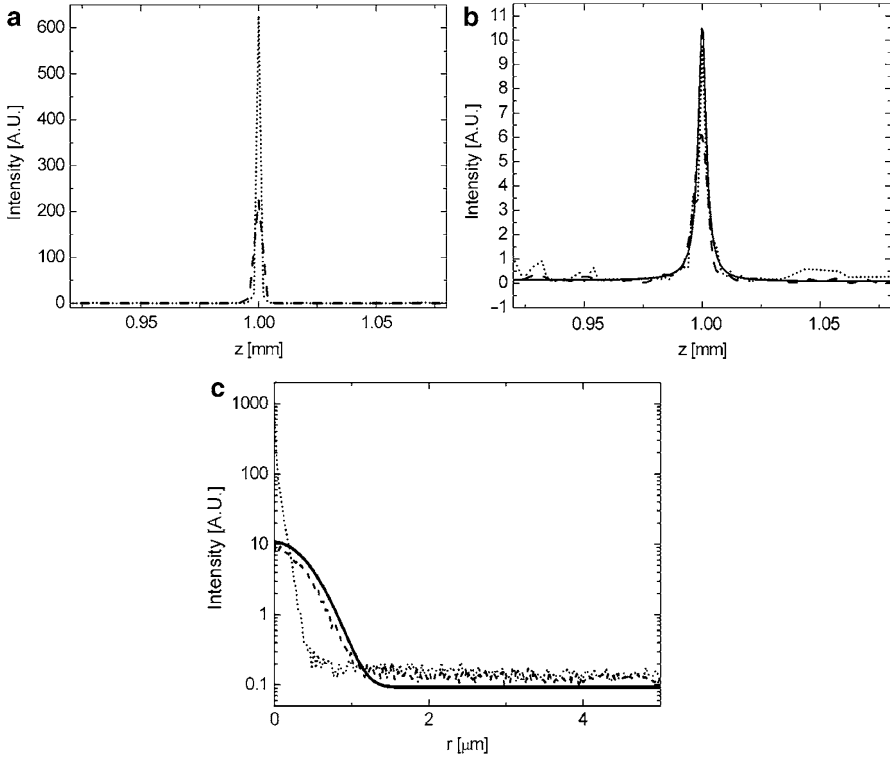
Fig. 17.7 The axial focus of a beam described in the text. All distributions have been normalized to unity for $(r, z) = (0, 0)$. (**a**) The axial intensity estimated using the geometric-focus method. *Dashed* curve is obtained with the *larger grid* and *dotted* curve with the smaller grid (see text). (**b**) Similar curves obtained with the hyperboloid method. The *solid* curve is the intensity distribution obtained from the integral expression (17.39). (**c**) The transverse intensity distribution (*small grid*) in the focal plane: *dotted* curve: the geometric-focus method; *dashed* curve: hyperboloid method; *solid* curve: the integral expression

As an illustration of the performance of the hyperboloid method, the intensity distribution of a collimated beam has been found using three different methods: MC with the hyperboloid method, MC with the geometric-focus method (the most commonly used method in the literature), and an integral expression (see (17.39)). The intensity distributions found using each method are shown in Fig. 17.7. The modeled beam is a collimated beam with $1/e$ intensity radius $w_0 = 0.4$ mm, which is focused by a lens with $f = 4.0$ mm at a depth of 1.0 mm into a scattering medium with $\mu_s = 10$ mm^{-1} and $g = 0.92$. The light propagation has been simulated using $50 \cdot 10^9$ photons for two sizes of the spatial discretization grid, $\Delta z = 4$ μm, $\Delta q = 0.5$ nm, and $\Delta z = 2$ μm, $\Delta q = 0.25$ nm. The resulting intensity distributions have all been normalized to unity at $(q,z) = (0,0)$.

In Fig. 17.7a and b, the axial intensity distributions predicted by the geometric-focus and the hyperboloid method are shown, respectively. The dotted curves are

the results of using the small grid size, whereas the dashed curves are the results of using the larger grid size. The solid curve in Fig. 17.7b is the result found by using integral expression in (17.39). For the large grid size, the geometric-focus method overestimates the peak height relative to the integral expression with a factor of 14, whereas the hyperboloid method underestimates the peak height with a factor of 0.5. We see that when the resolution is increased, the hyperboloid method approaches the result of the integral expression in (17.39) to a factor of 0.95, whereas the peak height estimated by the geometric-focus method increases even further to a factor of 41. The latter is a result of the infinite photon density of the unscattered photons in the geometric-focus method. It is noted that the high-resolution curve for the hyperboloid method (dotted curve in Fig. 17.7b) seems noisier than its counterpart from the geometric-focus method (dotted curve in Fig. 17.7a). In fact, the variance of the data used for the two curves is practically identical but less noticeable in Fig. 17.7a due to the scale necessary to show the peak intensity estimated by the geometric-focus method. In Fig. 17.7c, the transverse intensity distribution in the focal plane estimated by the geometric-focus method (dotted), the hyperboloid method (dashed), and the integral expression (solid) are plotted, respectively. From Fig. 17.7a and c, we see that the geometric-focus method is an inappropriate method for estimating the detailed intensity distribution around the focus. Figure 17.7b and c show an excellent agreement between the hyperboloid method and the integral expression. Thus, for modeling applications, where spatial resolution is important, as in OCT, the hyperboloid method should be used when doing MC simulation of focused Gaussian beam.

17.3.3 Monte Carlo Simulation of the OCT Signal

In Sect. 17.3.1, we found that the heterodyne efficiency factor of the OCT signal may be found using the knowledge of the intensity distributions of the sample and reference fields in the p-plane (see Fig. 17.6), where the fiber end is situated:

$$\Psi_p = \frac{\int I_R(\mathbf{p})\langle I_S(\mathbf{p})\rangle d^2\mathbf{p}}{\int I_R(\mathbf{p})\langle I_{S0}(\mathbf{p})\rangle d^2\mathbf{p}}. \tag{17.58}$$

In the EHF principle, the effect of a scattering medium is treated as a random phase distortion added to the deterministic phase of the light as it propagates through the medium. In the derivation of (17.58) (see Sect. 17.7), it is necessary to assume that the phase distortion added to the light propagating toward the discontinuity is statistically independent from the phase distortion added to the light propagating away from the discontinuity. It is important to note that this assumption is inherently fulfilled by MC methods such as that used by the MCML computer code [64]: A photon is traced through a dynamic medium in the sense that the distance to the next scattering event and scattering angle is a random variable independent upon the past of the photon. Hence, after each

stochastic event, the photon experiences a different realization of the sample. Therefore, an ensemble averaging over the stochastic sample in (17.58) is carried out through a single simulation. Moreover, to also obtain an averaging in the modeling of the diffusely reflecting discontinuity, each reflected photon must experience a new realization of the discontinuity. Thus, we use the macroscopic intensity distribution of a Lambertian emitter [19] to sample the reflected angle:

$$I_r(\theta_r) = I_T \cos \theta_r. \tag{17.59}$$

Here, I_T is the reflected intensity at $\theta_r = 0$ and θ_r is the reflected angle. By following the method outlined by Prahl et al. [65] of sampling a physical quantity using a computer-generated pseudorandom, we obtain the relations

$$\theta_r = \arcsin (\xi), \tag{17.60}$$

$$\varphi_r = 2\pi\zeta, \tag{17.61}$$

where φ_r is the azimuthal angle of the reflected photon and ξ and ζ are both random numbers evenly distributed between 0 and 1.

Accordingly, the method of simulating the OCT signal is carried out as follows. The MC photon packet is launched from the focusing lens in the r-plane (see Fig. 17.6) using the new hyperboloid method described in Sect. 17.3.2. The interfacing with specular surfaces, such as the sample surface and the propagation through the scattering medium, is carried out using the MCML computer code. When a photon packet is reflected off the diffusely reflecting discontinuity, (17.60) and (17.61) are used to determine the direction of the photon after reflection. As a photon exits the sample after interaction with the discontinuity, its position and angle is used to calculate its position in the p-plane after propagation through the 4F system. To evaluate (17.58), numerically consider that the m'th photon packet exiting the medium contributes to the intensity at the point p_m in the p-plane by the amount

$$I_{S,m} \propto \frac{w_m}{\Delta p^2}, \tag{17.62}$$

where w_m is the energy, or weight, carried by the photon packet and Δp^2 is a differential area around p_m. Using this and (17.58), the MC estimated heterodyne efficiency factor Ψ_{MC} is then given by

$$\Psi_{MC} = \frac{\sum_m^M I_R(p_m)I_{S,m}\Delta p^2}{\langle i_0^2 \rangle} = \frac{\sum_m^M I_R(p_m)w_m}{\langle i_0^2 \rangle}, \tag{17.63}$$

where $I_R(p)$ is the intensity distribution of the reference beam in the p-plane, and it is noted that the reference beam has a Gaussian intensity distribution of width w_f

in the p-plane. The signal in the absence of scattering $\langle i_0^2 \rangle$ may be either simulated or calculated. The latter is straightforward, because with the conjugate relationship between the p- and q-plane, the intensity distribution of the sample beam will be identical to that of the reference beam in the absence of scattering.

Equation (17.63) reveals the important detection criterion of the MC simulation of the OCT signal: a photon must hit the p-plane within the extent of the reference beam. While detection schemes of previously published MC models of OCT also incorporate that photons must hit the detector, the novelty of this detection scheme is the analytically derived size and necessary position in the p-plane. Furthermore, contrary to these schemes, the model does not incorporate an angular criterion that a photon packet must fulfill in order to contribute to the signal. It may seem counterintuitive that photon packets contribute to the desired signal without penalty regardless of angle of incidence upon the fiber in the p-plane. However, as demonstrated in Ref. [12], the inclusion of an angular criterion related to the angular extent of the incident beam, or equivalently the numerical aperture of the fiber, yields incorrect results.

17.3.4 Numerical Validation

17.3.4.1 Beam Geometries for Numerical Comparison

A set of beam geometries has been selected for numerical comparison between the EHF model and the MC model. These geometries are selected so that the two approaches are compared for different degrees of focusing and distances between the lens L2 and the sample. The selected cases are listed in Table 17.1 and are referred to as cases 1 through 4, respectively.

For all cases, the mean refractive index of the sample before the discontinuity and the surroundings are assumed to be matched so that $n_0 = n_1 = 1$. We wish to investigate the effect of scattering on the OCT signal. A difference in the refractive index between the sample and the surrounding will impose a Snell's law refraction at the interface, which in turn imposes a focus distortion not treated in the paraxial approximation ($\sin\theta \approx \theta$) and thus not described by the EHF model. Such a distortion will be difficult to separate from the effects of scattering and is thus omitted here. As discussed in Ref. [62], there is only a severe distortion for very tightly focused beams.

In all cases discussed in the following, the wavelength of the light is chosen to be 814 nm, which is one relevant wavelength for biomedical applications of OCT. The sample is assumed to exhibit scattering described by a Gaussian scattering function (see, e.g., Chap. 13 in Ref. [32]). The motivation for this choice is to enable comparison to analytical models of the propagation of Gaussian beams in random media [40] and the OCT signal (see Sect. 17.2.2), which both apply the Gaussian scattering function. The comparisons presented here are carried out for different degrees of scattering and for two relevant values of the asymmetry parameter in tissue [43]: very highly forward scattering ($g = 0.99$)

Table 17.1 Beam geometries for the four cases

Case number	f [mm]	d [mm]	z [mm]	w_0 [mm]	w_0/f
1	16.0	15.5	0.5	0.125	0.008
2	8	7.5	0.5	0.4	0.05
3	0.5	0.0	0.5	0.125	0.25
4	16.0	15.0	1.0	4	0.25

and highly forward scattering ($g = 0.92$). The value $g = 0.92$ was the value of the asymmetry factor in the experiments performed to validate the EHF model by Thrane et al. [10] With these two cases, the two approaches are compared for a sample geometry where the paraxial approximation is well satisfied and for a sample geometry, which is close to the limit of the paraxial approximation. Accordingly, it is expected that the best agreement will be found for $g = 0.99$.

Comparison

In Fig. 17.8, Ψ is plotted for cases 1 through 4 as a function of the scattering coefficient μ_s, and for reference, the case of single backscattering, that is, $\Psi_{single} = \exp(-2\mu_s z)$, has been included.

Three important observations may be made from Fig. 17.8. Firstly, we observe fine agreement between the MC method and the EHF model for the four cases tested. Thus, we consider these plots as validation of the MC model. Secondly, it is inferred that the OCT signal for high optical depths is a result of multiple-scattering effects in agreement with Sect. 17.2.2. This is seen by comparing the single-scattering curve to the plots of the MC and EHF. Finally, an important result of Sect. 17.2.2 was the inclusion of the so-called shower-curtain effect [29]. It is an effect caused by multiple scattering and thus plays an important role in calculating the OCT signal as the optical depth increases. Omitting this effect leads to an underestimation of the OCT signal of several orders of magnitude. Due to the fine agreement between the EHF model (with the shower-curtain effect included) and the MC model, we obtain the important result that the MC model inherently takes the effect into account.

For cases where the approximation of the EHF model is well satisfied, we attribute the observed deviation between the EHF and MC models to be caused by coherence effects in the intensity distribution of the sample field. Apparently, from Fig. 17.8, the lack of coherence information leads to an underestimation of Ψ, but the specific cause for this has yet to be determined. Ψ is by definition unity in the absence of scattering, and for large optical depths, coherence effects are expected to be negligible. Accordingly, we expect the two models to agree for small and large values of the optical depth of the discontinuity, whereas some deviation is to be expected in the intermediate region. As a highly forward scattering event perturbs the field only to a small degree, it is expected to distort coherence effects less than a more isotropic scattering case. In order to plot the relative deviation as a function of the effective distortion of the coherence, we plot the
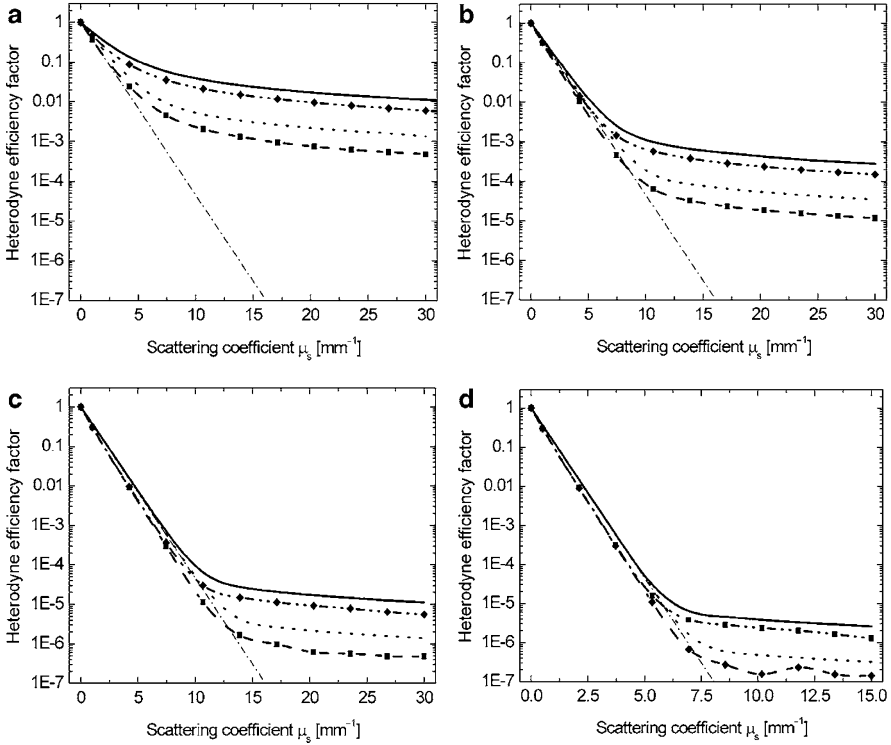
Fig. 17.8 Heterodyne efficiency factors estimated using, respectively, the EHF model and the MC method for two cases of *g*. (**a**), (**b**), (**c**), and (**d**) show the estimated values for geometries 1, 2, 3, and 4 in Table 17.1, respectively. The *solid line* and *dotted line* curves are the results of the EHF model for *g* = 0.99 and *g* = 0.92, respectively. *Dash-dot-dot* and *dashed curves* are the results of the MC simulations for *g* = 0.99 and *g* = 0.92, respectively. Diamonds (♦) and squares (■) mark the actual data points obtained by the MC simulation method. For comparison, the exponential reduction in signal due to scattering obtained by a single-scatter model is shown as a *dash-dot* curve

ratio Ψ_{EHF}/Ψ_{MC} as a function of the transport reduced optical depth of the discontinuity given by

$$S_{tr} = \mu_z Z_f (1 - g). \tag{17.64}$$

The relative difference between the EHF model and the MC method behaves, qualitatively, identical as a function of s_{tr} independent of beam geometry and *g*. This is illustrated in Fig. 17.9 for cases 2 (*g* = 0.92 and 0.99), 3 (*g* = 0.92), and 4 (*g* = 0.92), respectively. The difference between the two approaches increases as a function of s_{tr} until $s_{tr} \approx 0.5$ after which it evens out. We mainly attribute this to the coherence effects in the intensity distribution discussed above. The more abrupt behavior of the curve for geometry 4 is attributed to a higher numerical uncertainty

Fig. 17.9 The relative
numerical difference between
the results of the EHF model
and the MC model from
Fig. 17.8 for a representative
selection of the considered
geometries. The ratio $\Psi_{EHF}/$
Ψ_{MC} is plotted for case 2 and
$g = 0.99$ with symbols ($\blacklozenge$)
and *solid* curve, for case 2 and
$g = 0.92$ with symbols ($\blacksquare$)
and *dash-dot-dot* curve, for
case 3 and $g = 0.92$ with
symbols ($\blacktriangledown$) and *dashed*
curve, and for case 4 and
$g = 0.92$ with symbols ($\bullet$) and
dotted curve (From Ref. [12])
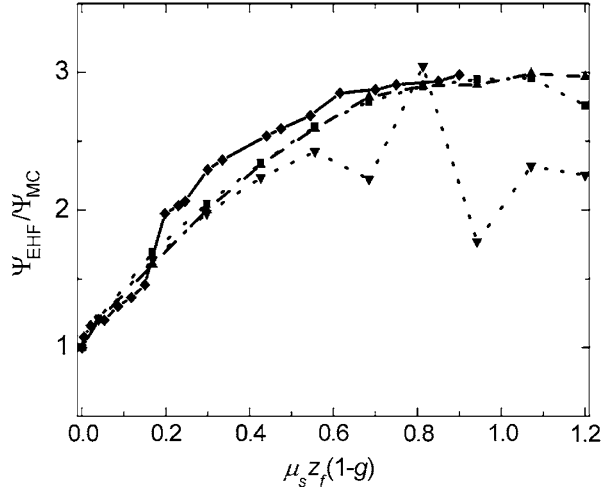
in the case, caused by a more tightly focused beam. According to the new detection
scheme, this implies that fewer photons will contribute to the signal resulting in an
increased variance.

In summary, due to the fine agreement between the results of the EHF model and
MC simulations borne out in Figs. 17.8 and 17.9, we conclude that the MC
simulation presented in this section is a viable method of simulating the heterodyne
efficiency factor of an OCT signal.

17.4 True-Reflection OCT Imaging

The interpretation of conventional OCT images may be a difficult task. One reason for
this is the fact that an OCT signal, measured at a given position in a non-absorbing
scattering medium, is a result of not only the amount of light reflected at the given
position but also the attenuation due to scattering when the light propagates through
the scattering medium. Therefore, to make images, which give a direct measure of the
amount of light reflected at a given position, thereby making interpretation of OCT
images easier, it is necessary to be able to separate reflection and scattering effects.

In this section, we present the concept of a so-called true-reflection OCT
imaging algorithm [46] based on the analytical model described in Sect. 17.2.
With this algorithm, it is possible to remove the effects of scattering from conven-
tional OCT images and create so-called true-reflection OCT images. This kind of
post-processing is similar to the correction for attenuation well known in ultrasonic
imaging. In that field, a mathematical model describing the relationship between the
received signal and the two main acoustic parameters, backscatter and attenuation,
has been considered [66]. The model has then been used to guide the derivation of
a processing technique with the aim of obtaining ultrasonic images that faithfully
represents one acoustic parameter, such as backscatter [66]. Due to the similarity

between the ultrasonic case and the situation encountered in OCT, this forms a strong basis for introducing the concept of a true-reflection OCT imaging algorithm. The principle of the true-reflection OCT imaging algorithm is demonstrated experimentally by measurements on a solid scattering phantom in Sects. 17.4.2 and 17.4.3 on a heterogeneous sample simulated by using the MC model presented in Sect. 17.3.

17.4.1 True-Reflection OCT Imaging Algorithm

It was shown in Sect. 17.2.2 that the mean square heterodyne signal current for light reflected at depth z in the tissue may be expressed as $\langle i^2(z) \rangle = \langle i^2(z) \rangle_0 \Psi(z)$, where $\langle i^2(z) \rangle_0$ is the mean square heterodyne signal current in the absence of scattering and $\Psi(z)$ is the heterodyne efficiency factor, which includes all of the scattering effects. The maximum of the envelope of the measured interference signal corresponds to $\left[\langle i^2(z) \rangle \right]^{1/2}$. Thus, by dividing the envelope of the measured interference signal with $[\Psi(z)]^{1/2}$, we are able to correct for the scattering effects, that is, compensate for attenuation, and determine the envelope that would be obtained in the absence of scattering. It is important to note that in addition to the system parameters λ, f, and w_0, knowledge about μ_s, θ_{rms}, and n of the scattering medium is necessary in order to enable calculation of $[\Psi(z)]^{1/2}$. However, in practice, μ_s and θ_{rms} may be obtained by fitting the expression for $\left[\langle i^2(z) \rangle \right]^{1/2}$ to a measured depth scan of the homogeneous backscattering tissue using an estimated value of n and the appropriate system parameters. Implementing this procedure as an option in the imaging program provides the opportunity to make what may be labeled *true-reflection OCT images*.

17.4.2 Experimental Demonstration of the True-Reflection OCT Imaging Algorithm

The principle of the true-reflection OCT imaging algorithm is demonstrated experimentally by measurements on a solid scattering phantom using a conventional OCT system comprised by a superluminescent diode with a center wavelength of 814 nm (22.8 nm spectral bandwidth (FWHM), 1.9 mW output power), a fiber-optic Michelson interferometer with movable reference mirror, and a silicon photodetector. The two system parameters f and w_0 are 16 mm and 0.125 mm, respectively [67].

The solid phantom having three discontinuities, A, B, and C, with identical reflection coefficients, is shown in Fig. 17.10. It consists of scattering microspheres (approximate diameter size 10 μm) in a polymer. The optical parameters of the solid phantom, that is, the asymmetry parameter, the scattering coefficient, and the absorption coefficient, were determined by carrying out integrating sphere and collimated transmission measurements and using the inverse adding-doubling method [68]. It turned out that the phantom had negligible absorption.

Fig. 17.10 A schematic of
the solid phantom used in the
demonstration of the true-
reflection OCT imaging
algorithm
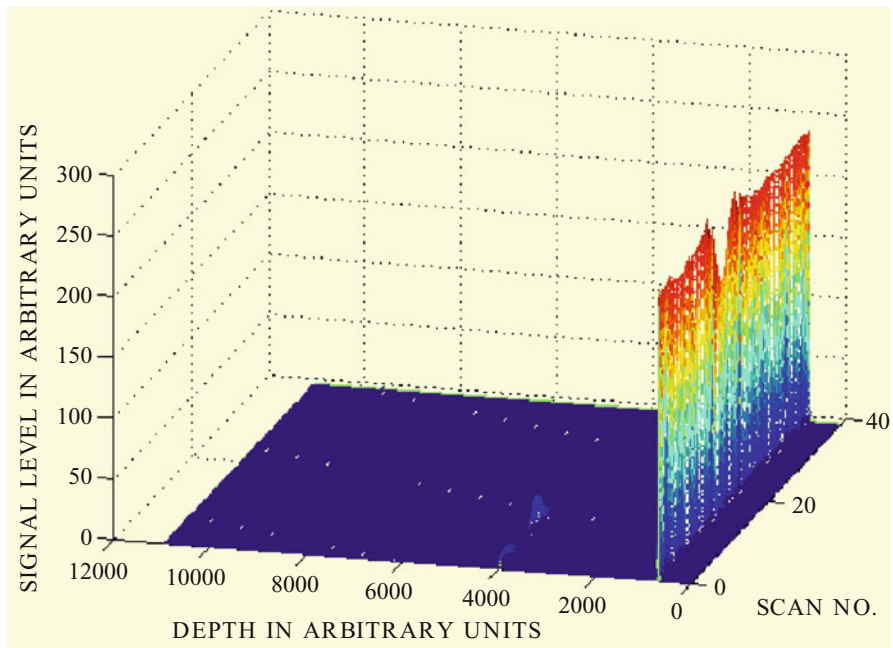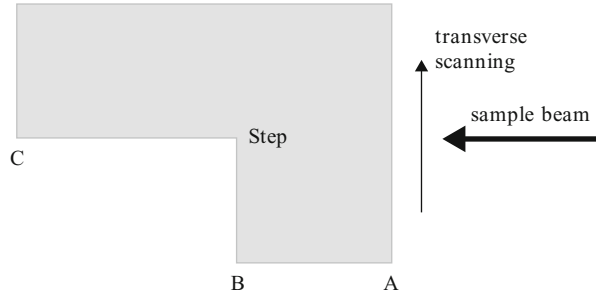
Fig. 17.11 The original unprocessed envelopes of the 40 longitudinal scans (From Ref. [67])

In the experiment, 40 longitudinal (horizontal) scans are performed across the
step as indicated in Fig. 17.10. The distance between adjacent longitudinal scans is
10 μm, and only one longitudinal scan is taken in every lateral position. The light is
reflected at the air-phantom discontinuity A ($z = 0.0$ mm) and at the two phantom-
air discontinuities at $z = 2.0$ mm (B) and $z = 5.2$ mm (C), respectively, which all
give a diffuse backscattering. The backscattering from the bulk of the phantom is
negligible and cannot be detected.

The original unprocessed envelopes of the 40 longitudinal scans are shown in
Fig. 17.11 with the use of a linear palette. The orientation is similar to the
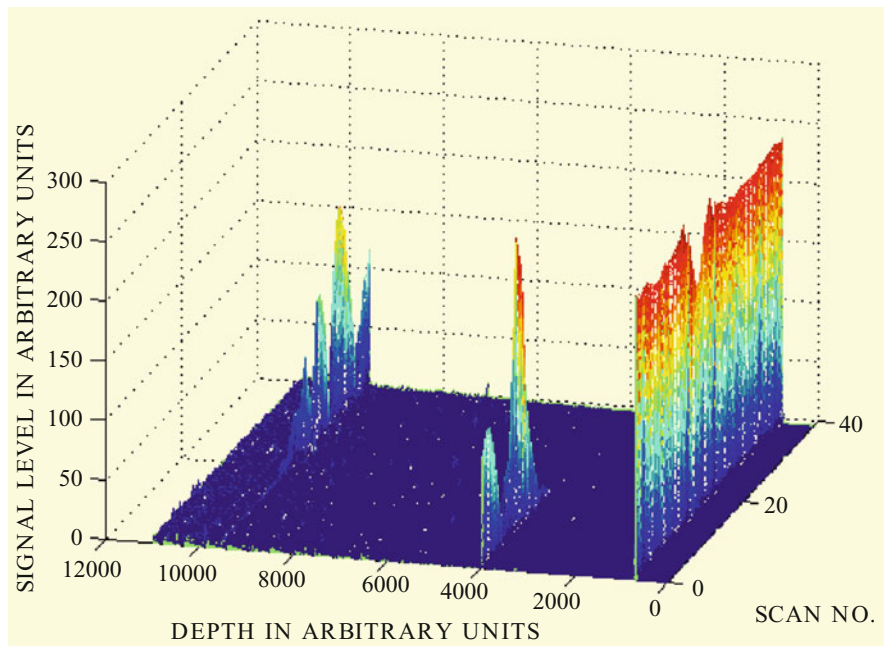
Fig. 17.12 The result of using the true-reflection OCT imaging algorithm on an OCT image of a solid phantom having three discontinuities (pos. A, B, and C) with identical values of their reflection coefficients (From Ref. [67])

orientation in Fig. 17.10. For a better visualization of the effect of the true-reflection OCT imaging algorithm, the envelopes are shown as a 3D plot. The first signal from the right is due to light reflected at the air-phantom discontinuity A, which will be denoted *the first discontinuity* in the following. The signal from the phantom-air discontinuity B at $z = 2.0$ mm (*the second discontinuity*) and the signal from the phantom-air discontinuity C at $z = 5.2$ mm (*the third discontinuity*) cannot be distinguished in Fig. 17.11. This is due to the scattering of the light in the phantom, which attenuates the signal.

By using the true-reflection OCT imaging algorithm described above to correct for the scattering effects, we get the envelopes shown in Fig. 17.12. The optical parameters of the solid phantom, which were used in the algorithm, are $\mu_s = 1.815$ mm^{-1}, $\theta_{rms} = 0.1096$ rad ($g = 0.994$), and $n = 1.5$. As expected, the three signals from the discontinuities A, B, and C are nearly equal in strength after using the algorithm. A plausible explanation of the lateral variations of the signal is speckle [19], which is a well-known effect in OCT [69]. In addition, variation of the signal close to the step (see Fig. 17.10) is likely due to a partly reflection of the beam.

The experimental errors of the measured values of μ_s and g of the solid phantom have been estimated to be ± 5 % and ± 1 %, respectively. Values of μ_s +5 % and -5 % have been used in the algorithm, but the changes of the signal levels were
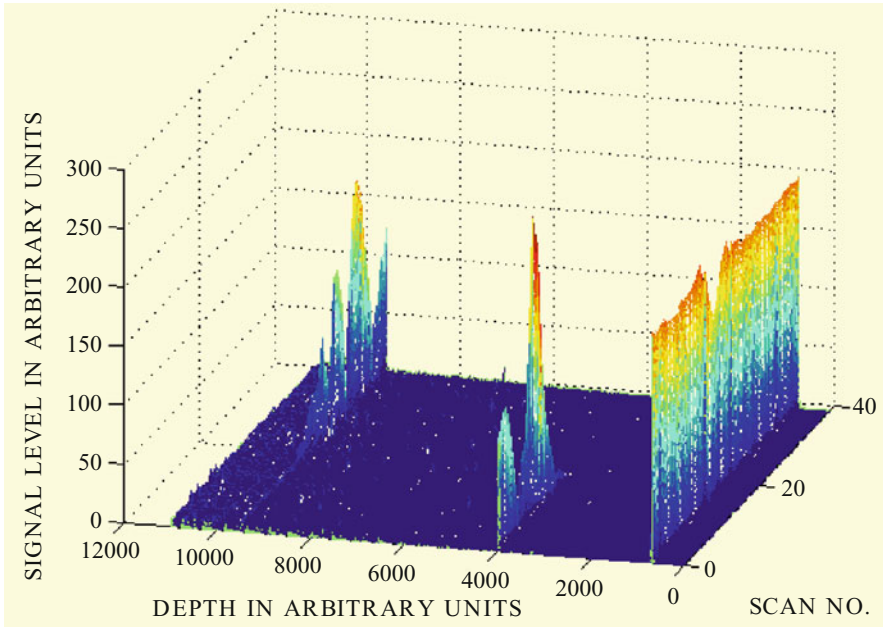
Fig. 17.13 The envelopes of the 40 longitudinal scans when the true-reflection OCT imaging algorithm has been used together with a value of $g - 1$ % (From Ref. [67])

very small. This is in contrast to the observation when a value of $g - 1$ % was used in the algorithm, and the envelopes are shown in Fig. 17.13. Note that the maximum signal of the second discontinuity is now slightly larger than the signal from the first discontinuity. However, the maximum signal levels of the second and third discontinuities seem to be closer to the signal level of the first discontinuity as compared to Fig. 17.12.

Figure 17.14 shows, for comparison, the envelopes obtained if only the single-scattering term is used in the expression for Ψ. Due to a large overestimate of the signal from the third discontinuity in this case, the signals from the first and second discontinuities are too small in amplitude to be observed in Fig. 17.14. Thus, it is obvious that the single-backscattering model is not sufficient, and furthermore, it demonstrates the importance of taking multiple-scattering effects into account.

The experiment demonstrates the feasibility of the new algorithm for a homogeneously scattering medium. However, the algorithm may be extended to cover heterogeneously scattering media, for example, skin tissue. *True-reflection OCT images* may be easier to interpret than conventional OCT images, and improved diagnosis may be envisioned due to a better differentiation of different tissue types.
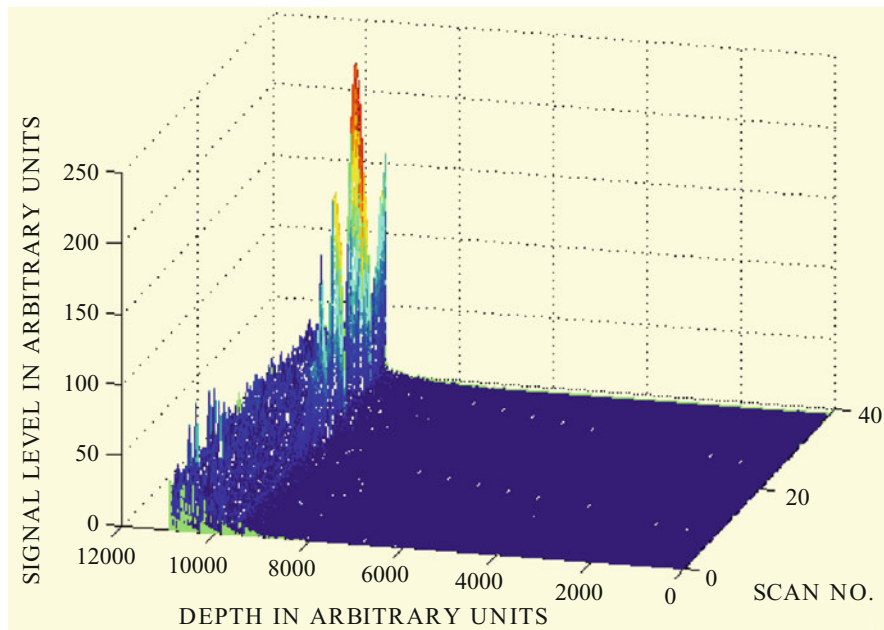
Fig. 17.14 The envelopes obtained by using the true-reflection OCT imaging algorithm when only the single-scattering term is used in the expression for Ψ (From Ref. [67])

17.4.3 True-Reflection OCT Imaging on an MC-Simulated Heterogeneous Multilayered Sample

The MC model presented in Sect. 17.3 may be used as a numerical phantom, which, for example, could be used to investigate the performance of the EHF model for sample geometries difficult to produce in the laboratory or for which one or more of the approximations made in the EHF model do not hold. It is important to note that the predictions from the EHF model have been demonstrated to compare well with experiments carried out on single-layered phantoms consisting of aqueous suspensions of microspheres [10]. In this section, we demonstrate the true-reflection OCT imaging algorithm on a heterogeneous multilayered sample using the MC model following the outline in Ref. [70].

Multilayered structures are at best difficult to manufacture, and the simulation of such structures using the MCML computer code is well established. Thus, we use the MC model to simulate the OCT signal for a two-layer sample in order to demonstrate the true-reflection OCT imaging algorithm on a heterogeneous sample. Through the incorporation of the ABCD matrix formalism in the EHF theory, it is straightforward to model the OCT system applied to a multilayered sample (see Appendix A of Ref. [10]). Thus, to demonstrate the true-reflection algorithm, we fit the two-layer EHF expression for the OCT signal to the MC simulation,

Fig. 17.15 MC simulation of the OCT signal for a two-layer sample (*squares*); EHF fit to the first and second layers (*solid line*); the MC simulation of the OCT signal after use of the true-reflection algorithm (*triangles* connected with a *dashed line*) (From Ref. [70])
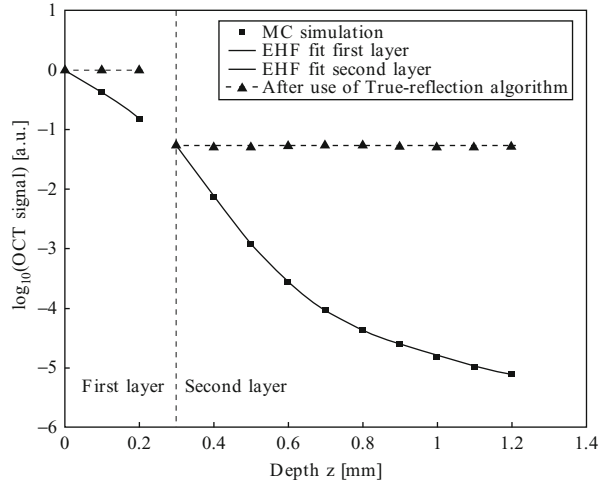
Table 17.2 The input parameters of the MC simulation, together with the extracted parameters obtained by using the EHF model, and the percentage difference

Layer no.	Input μ_s [mm^{-1}]	Fitted μ_s [mm^{-1}]	Difference [%]	Input g	Fitted g	Difference [%]
1	5.00	4.92	−1.6	0.9900	0.9834	−0.67
2	10.00	10.22	2.2	0.9200	0.8586	−6.67

extract the optical properties of the two layers, and use these values of the optical properties in the algorithm to correct for the attenuation caused by scattering.

As in the previous MC simulations in Sect. 17.3, the refractive indices of the sample and the surroundings are matched and equal to unity. The system parameters in this case are $\lambda = 800$ nm, $w_0 = 0.4$ mm, and $f = 8.0$ mm. The first layer is 0.3 mm thick and has a constant scattering coefficient of $\mu_{s1} = 5.0$ mm^{-1} and $g_1 = 0.99$. The second layer is 0.9 mm thick and has a constant scattering coefficient of $\mu_{s2} = 10.0$ mm^{-1} and $g_2 = 0.92$. The MC simulation of the mean square heterodyne signal current is shown as squares in Fig. 17.15. The fit of the two-layer EHF model to the MC simulation is shown as a solid line in Fig. 17.15, and the hereby extracted optical properties μ_s and g (n is not a fitting parameter) of the two layers are shown in Table 17.2 together with the input parameters of the MC simulation. The relatively large point separation of the MC simulation in the z-direction makes the gap between the last point of the first layer and the first point of the second layer rather distinct in this case.

The small percentage difference shown in Table 17.2 between the MC input parameters and the extracted parameters demonstrates the capability of the EHF model to extract optical properties from a heterogeneous multilayered sample, for example, human skin. The extracted optical properties of the two layers may now be used in the true-reflection algorithm. Thus, the MC simulation of the OCT signal

after use of the true-reflection algorithm, that is, after correction for the attenuation caused by scattering, is shown as triangles in Fig. 17.15 connected by a dashed line. The distinct signal levels obtained for the two different layers after using the true-reflection algorithm strongly indicate that a better differentiation of different tissue types may be obtained in OCT images of real tissue by using the true-reflection algorithm. This is expected to result in an improved diagnosis.

17.5 Applications of Modeling in OCT

Extraction of optical scattering parameters from OCT images is a method to obtain more quantitative information from these images in order to improve the diagnostics, that is, an alternative method of functional imaging. Accordingly, one may envisage a novel functional imaging method where, in addition to tissue morphology, parameters such as the scattering parameters, g and/or μ_s, or mean refractive index are obtained. In the following, the viability of the suggested approach in OCT is briefly discussed.

17.5.1 Extraction of Optical Scattering Properties from Tissues

As mentioned above, attenuation compensation is widely accepted within ultrasound [66]. Therefore, it has also been among the first attempts to improve on OCT imagery. In fact, attenuation compensation is a method to remove the attenuation caused by scattering in OCT images. This should improve the diagnostic capabilities due to a better differentiation of different tissue types. Until now, there have been few attempts to do attenuation compensation in OCT images of tissue by using the single-scattering OCT model [71]. However, due to the fact that multiple-scattered photons contribute to the OCT signal, the single-scattering OCT model is insufficient for this purpose. Attenuation compensation was verified on a single-layer phantom by using an OCT model taking multiple-scattering effects into account [67].

The optical scattering properties themselves, however, also contain information about the tissue. For example, cell mitochondria is affected or changed in several malignant conditions, and through these changes, the scattering changes. Conversely, provided that information about the scattering properties can be obtained with good accuracy and good (high) spatial resolution, new diagnostics can be performed. This fact is one important motivation for attempting to extract optical scattering properties in order to improve the diagnostic potential of OCT.

By using the single-scattering OCT model [2], studies have been carried out with the aim to extract only the scattering coefficient μ_s from OCT images of tissue. This approach was applied in various important applications. For example, glucose monitoring was investigated by using the single-scatter approach [72] and more recently expanded to include phase-sensitive OCT [73]. Although these investigations are of high clinical importance, more work is still needed in this area.

Determining optical scattering properties of blood is also of high importance. Faber et al. [74, 75] demonstrated that the optical absorption spectra of oxygenated and

deoxygenated hemoglobin, corrected for optical scattering, may be obtained by using spectral OCT. The underlying OCT modeling was based on a single-scattering approach. Subsequent investigations, however, have led to the conclusion that improved modeling needs to be developed in order to satisfactorily include multiple-scattering effects [76]. Single-scattering-based modeling might be applicable as demonstrated by Kodach et al. [77] showing that anisotropy and scattering parameters can be obtained from non-absorbing samples. It should be emphasized that the values for the anisotropy (approximately 0.35) is much different from those of biological tissues (approximately >0.85). Accordingly the results might not be transferred to biological tissues.

An important contribution by the group of van Leeuwen has been made in in vitro characterization of atherosclerotic plaque [78]. Although the model applied was based on a single-scattering model, their findings provide important data on the optical scattering coefficient of these plaques, which may influence OCT-based diagnostics in this area.

Provided an OCT model is used that takes into account multiple scattering, both μ_s and the anisotropy factor g may be extracted. Extraction for a two-layer geometry has been carried out [70, 79], where both μ_s and g were obtained for each (tissue) layer. In Ref. [70], MC simulations were used as numerical phantom as discussed in detail in the previous subsection.

A number of in vitro studies have been reported. Characterization of atherosclerotic plaque using a single, multiple-scattering layer model has been reported [80]. The method of extracting the optical scattering properties was verified using well-controlled and calibrated, single-layer tissue-like phantoms. The study provided the optical scattering properties in the 1,300-nm range for lesions in different stages including the anisotropy parameter. Based on the extracted parameters, normal tissue could be separated from malignant tissue. It should be noted that some discrepancies occur between the reported values for the scattering coefficients in Refs. [80] and [78]. Possible explanations for the differences may be due to different sample handling and fit to different models. The results reported in both Refs. [80] and [78] are encouraging, although further studies are required to fully establish these criteria and thereby demonstrate the feasibility of the method in this particular area.

In Ref. [11], an excellent study presented a rigorous application of the RTE modeling (small-angle approximation) in the extraction of optical parameters. First, the authors verified their modeling on a well-controlled tissue-like phantom. By estimating covariance and confidence regions for the extracted optical properties, they point to specific regimes of the OCT signal decay where extraction is likely to fail. These regimes depend on both the optical properties and sample beam geometry. Hence, their findings provide important insight of how to optimize the OCT system for a specific application. The authors applied their method to cervical tissue (cervical dysplasia 2–3 and leukoplakia). In their in vitro investigation, they demonstrated that cervical dysplasia 2–3 and leukoplakia could be distinguished on the basis of the extracted optical scattering properties. Hence, their excellent contribution should be an encouragement for expanding to other clinical applications and finally in vivo applications.

Related to this work, Samatham et al. [81] develop a method for extracting optical properties of skin samples (from a mouse) based on reflectance-mode

confocal laser scanning microscopy. Their approach might be relevant for optical coherence microscopy and even find applications in OCT extraction of optical properties in vivo.

In vivo studies are sparse; however, Knüttel et al. [82] took the approach of extracting optical scattering properties and refractive index aiming at relating the effects of skin hydration to the optical properties extracted from OCT images. Their investigation showed the applicability of the approach and the potential in dermatology to provide new diagnostic information.

17.6 Wigner Phase-Space Distribution Function for the OCT Geometry

Recently, the Wigner phase-space distribution [83] for multiple light scattering in biological media has received considerable attention. This is because it has been suggested by numerous authors that new venues for medical imaging may be based on coherence tomography using measurements of Wigner phase-space distributions [23, 24, 84–86]. It has been suggested that the Wigner phase-space distribution is particularly useful for biomedical imaging because the phase-space approach provides maximum information, that is, both space and momentum (angular) information, about the light being used. This section is devoted to the derivation of a closed-form solution for the Wigner phase-space distribution function [23] obtained directly from the EHF [37] solution for the optical field.

In all cases considered in this section, as well as in Refs. [24, 84–86], the Wigner phase-space distribution function is positive definite, and hence, the Wigner function and the specific radiance may be used interchangeably. We are primarily concerned with a standard OCT propagation geometry shown in Fig. 17.1, and as such, we consider a sample beam reflected at a discontinuity giving rise to diffuse backscattering. This section deals with the reflection geometry only; for the transmission geometry, the reader is referred to Refs. [23, 85].

17.6.1 General Considerations

Consider a cw quasi-monochromatic optical wave propagating through a non-absorbing random small-angle scattering medium, reflecting off a discontinuity giving a diffuse reflection, and subsequently propagating back to the initial plane. Denote the resulting optical field in the initial plane, perpendicular to the optic axis, by $U(\mathbf{P})$, where $\mathbf{P}$ is a two-dimensional vector in this plane. For simplicity in notation, we omit the time dependence. The Wigner phase-space distribution, $W(\mathbf{P},\mathbf{q})$, may be written as [87]

$$W(\mathbf{P}, \mathbf{q}) = \int \frac{d\mathbf{p}}{(2\pi)^2} \langle U(\mathbf{P} + \mathbf{p}/2) U^*(\mathbf{P} - \mathbf{p}/2) \rangle \exp[i\mathbf{q} \cdot \mathbf{p}], \qquad (17.65)$$

where angular brackets denote the ensemble average. That is, the Wigner phase-space distribution function is a two-dimensional Fourier transform of the indicated mutual coherence function $\langle U(\mathbf{P} + \mathbf{p}/2)U^*(\mathbf{P} - \mathbf{p}/2)\rangle$ and, as such, contains the same information about the optical field as does the mutual coherence function. The quantity $\mathbf{q}$ is a transverse momentum, and in the small-angle approximation, its magnitude q can be related directly to the scattering angle simply as $q = 2k\sin\theta/2 \approx k\theta$, where is the free-space wave number. In addition, because in the small-angle approximation the differential element of solid angle $d\Omega = 2\pi\sin\theta d\theta \approx 2\pi\theta d\theta = 2\pi q dq/k^2$, it is easily verified that the integral of $W(\mathbf{P},\mathbf{q})$ over all $\mathbf{q}$ (i.e., over solid angle) equals the intensity $I(\mathbf{P})$, that is, $|U(\mathbf{P})|^2$, at the observation point $\mathbf{P}$. Hence, to within a multiplicative constant, the Wigner phase-space distribution is equal to the specific radiance distribution of the optical field at the observation point of interest for those cases where the Wigner phase-space distribution is positive definite. To be specific, the specific radiance distribution $N(\mathbf{P},\theta) = k^2 W(\mathbf{P},k\theta)$ in those cases.

Here, we neglect polarization effects, bulk backscattering, and enhanced backscattering, which is obtained very close to the optical axis. In random media where the scattering particles are large compared to the wavelength and the index of refraction ratio is near unity, the bulk backscatter efficiency is much smaller than the scattering efficiency. Moreover, the scattering is primarily in the forward direction, which is the basis of using the paraxial approximation. Therefore, the bulk backscattering may be neglected when considering the light propagation problem, since its contribution is small. An example of this is skin tissue (cell sizes of 5–10-μm diameter and index of refraction ratio of 1.45/1.4 = 1.04).

It is well known that a medium with random scattering inhomogeneities will produce an amplification effect of the mean intensity in the strictly backward direction, as compared to the corresponding intensity obtained in the homogeneous medium [88]. This so-called enhanced backscattering is due to multichannel coherence effects (i.e., interference at a source point between waves transmitted in the forward and backward directions by the same inhomogeneities in the medium). Additionally, because of conservation of energy, enhanced backscattering is accompanied by a corresponding reduction in intensity in directions close to the strictly backward direction. In general, as discussed in Ref. [88], the linear dimension of the region surrounding the strictly backward direction where enhanced backscattering is obtained is of the order or less than the transverse intensity correlation length, l. The corresponding reduction of intensity occurs near the surface of a cone of angle of the order l/Z, where Z is the (one way) propagation distance in the medium. Strictly speaking, enhanced backscattering effects are obtained in situations where the linear dimensions of the illuminated region, a, in the backscattering plane satisfy $a^2 << \lambda Z$, where λ is the wavelength. When the radiation at some point $\mathbf{P}$ in the observation plane results from illuminated regions that are large compared to $[\lambda Z]^{1/2}$, $\mathbf{P}$ will not be in the strictly backscattered direction with respect to the reflected light and, as a consequence, enhanced backscattering will not be manifested. In all cases considered here, $a >> [\lambda Z]^{1/2}$ and, therefore, enhanced backscattering effects are neglected.

As indicated in Fig. 17.1, the signal of interest results from diffuse reflection at the discontinuity of interest only. As discussed above, the statistics of the forward and back propagating optical waves are assumed here to be independent. This case has been treated in Sect. 17.2, and from (17.21) with $\mathbf{p}_{1,2} = \mathbf{P} \pm \mathbf{p}/2$, the EHF solution for the mutual coherence function for diffuse reflection in the discontinuity plane, and observation in the lens plane, is given by

$$\langle U(\mathbf{P} + \mathbf{p}/2)U^*(\mathbf{P} - \mathbf{p}/2)\rangle = \frac{4\pi}{k^2} \int d\mathbf{r} \langle I_B(\mathbf{r})\rangle G_0(\mathbf{r}, \mathbf{P} + \mathbf{p}/2)G_0^*(\mathbf{r}, \mathbf{P} - \mathbf{p}/2)\Gamma_{pt}(\rho). \tag{17.66}$$

$\langle I_B(r)\rangle$ is the mean backscattered irradiance distribution in the plane of the discontinuity, $\Gamma_{pt}(p)$ is the mutual coherence function of a point source located in the discontinuity plane and observed in the lens plane, where $p = |\mathbf{p}_1 - \mathbf{p}_2|$, and $G_0(\mathbf{r}, \mathbf{p})$ is the Huygens-Fresnel Green's function for homogeneous media given, in general, by [40]

$$G_0(\mathbf{r}, \mathbf{p}) = -\frac{ik}{2\pi B_b} \exp\left[-\frac{ik}{2B_b}\left(A_b r^2 - 2\mathbf{r} \cdot \mathbf{p} + D_b p^2\right)\right], \tag{17.67}$$

where A_b, B_b, and D_b are the (real) ABCD ray-matrix elements for backpropagation through the optical system (because we are dealing with "real" ABCD optical systems, we tacitly assume that $B \neq 0$). To be as general as possible, we assume an arbitrary ABCD optical system between the lens and discontinuity planes, respectively. For the OCT geometry, we have $A_b = D_b = 1$ and $B_b = d + z/n$, where d is the distance from the lens to the tissue surface, n is the mean index of refraction of the tissue, and z is the depth of the discontinuity. In (17.66), the positive definite quantity Γ_{pt} is the mutual coherence of a point source located in the discontinuity plane and observed in the initial lens plane, that is, the mutual coherence function for backward propagation through the medium. This quantity is given by [45]

$$\Gamma_{pt}(p) = \exp\left\{-s\left[1 - b_\phi(p)\right]\right\}, \tag{17.68}$$

where the optical depth $s = \mu_s z$. The quantity μ_s is the bulk scattering coefficient, and $b_\phi(p)$ is the normalized phase autocorrelation function of a point source whose origin is in the discontinuity plane given by [45]

$$b_\phi(p) = \frac{\int_0^z dz' \int_0^\infty \sigma(\theta; z')J_0(kp_s\theta)\theta d\theta}{\int_0^z dz' \int_0^\infty \sigma(\theta; z')\theta d\theta}, \tag{17.69}$$

J_0 is the Bessel function of the first kind of order zero,

$$p_s = \frac{B_b(z')}{B_b}p, \tag{17.70}$$

where $B_b(z')$ is the B-matrix element for backpropagation from the discontinuity plane to a distance z' and $\sigma(\theta;z')$ is interpreted as the volume scattering function as a function of position measured from the discontinuity plane in the optical system [40]. Strictly speaking, (17.68) applies to the case where the scattering is in the near-forward direction and all of the scattered light being contained within the collection solid angle of the optical system being used. For propagation in an inhomogeneous medium where appreciable light is scattered outside of the collection solid angle, the mutual coherence function of (17.68) becomes $\Gamma_{pt}(p) = \exp\{-s_W - s_N[1 - b_\phi(p)]\}$, where the subscripts N and W refer to the near-forward and wide-angle contributions to the optical depth, respectively [23, 24, 86]. That is, the portion of the light scattered outside of the collection solid angle thus appears much like an effective absorption coefficient for propagation in the near-forward direction. We note that all correlation functions of interest here can be expressed directly in terms of the spectral densities via the relation $\sigma(\theta) = 2\pi k^4 \Phi_n(k\theta)$, where Φ_n is the three-dimensional spectrum of the index of refraction inhomogeneities, and we have omitted the functional dependence on path length for notational simplicity [52]. For the OCT geometry, we have $\sigma(\theta;z') = \sigma(\theta)$ for $0 \le z' \le z$, and 0 otherwise; $B_b(z') = z'/n$ for $0 \le z' \le z$ and $B_b(z') = z/n + z' - z$ for $z \le z' \le d + z$.

In this section, it is tacitly assumed that we are dealing with a statistically stationary and isotropic random medium. Then, it is well known that all second-order spatial correlation functions of the optical field, such as $\Gamma_{pt}(p)$, are functions of the magnitude of the difference of the spatial coordinates and satisfy the identity $\Gamma_{pt}(-p) = \Gamma_{pt}^*(p)$ [52].

Because the point source mutual coherence function given in (17.68) is valid for arbitrary values of the optical depth s [52], the results given below for the Wigner phase-space distribution function are valid in both the single- and multiple-scattering regimes, that is, arbitrary values of s.

Substituting (17.66) and (17.67) into (17.65) and simplifying yield

$$W(\mathbf{P}, \mathbf{q}) = \frac{1}{\pi B^2} \int \frac{d\mathbf{p}}{(2\pi)^2} \exp\left[i\mathbf{p} \cdot \left(\mathbf{q} - \frac{kD}{B}\mathbf{P}\right)\right] \Gamma_{pt}(p) H(\mathbf{p}), \qquad (17.71)$$

where

$$H(\mathbf{p}) = \int d\mathbf{r} \langle I_B(\mathbf{r}) \rangle \exp\left[i\frac{k}{B_b}\mathbf{p} \cdot \mathbf{r}\right] \qquad (17.72)$$

is related to the Fourier transform of $\langle I_B(\mathbf{r}) \rangle$. In Ref. [23], it is shown that

$$H(\mathbf{p}) = R_d \Gamma_{pt}(-p) K(-\mathbf{p}) = R_d \Gamma_{pt}^*(p) K(-\mathbf{p}), \qquad (17.73)$$

where R_d is the reflection coefficient of the discontinuity,

$$K(\mathbf{r}) = \int d\mathbf{R} \, U_{Si}(\mathbf{R} + \mathbf{r}/2) U_{Si}^*(\mathbf{R} - \mathbf{r}/2) \exp\left[-i\frac{kA}{B}\mathbf{r} \cdot \mathbf{R}\right], \qquad (17.74)$$

and $U_{Si}(\mathbf{r})$ is the initial optical wave function. Substituting (17.73) into (17.71) yields

$$
\begin{aligned}
W(\mathbf{P}, \mathbf{q}) &= \frac{R_d}{\pi B_b^2} \int \frac{d\mathbf{p}}{(2\pi)^2} |\Gamma_{pt}(p)|^2 K(-\mathbf{p}) \exp\left[i\mathbf{p} \cdot \left(\mathbf{q} - \frac{kD_b}{B_b}\mathbf{P}\right)\right] \\
&= \frac{R_d}{2\pi^2 B_b^2} \int_0^\infty dp\, p\, |\Gamma_{pt}(p)|^2 K(p) J_0\left(\left|\mathbf{q} - \frac{kD_b}{B_b}\mathbf{P}\right| p\right)
\end{aligned}
\tag{17.75}
$$

$$
\text{(for axially symmetric } U_{Si}\text{).}
$$

This is the required general solution for the Wigner phase-space distribution function for diffuse reflection in the paraxial approximation. That is, for a given initial optical wave function and a medium whose scattering function is known, (17.75) is the solution for the Wigner phase-space distribution function, that is, specific radiance. Note that $I(\mathbf{P}) = \int W(\mathbf{P},\mathbf{q})d\mathbf{q} = R_d P_0 / \pi B_b^2$, where P_0 is the transmitted power. As expected for diffuse reflection, the intensity in the observation plane is constant, independent of position.

17.6.1.1 Comments

For general scattering functions $\sigma(\theta)$, the integral indicated in (17.75) cannot be obtained analytically, although numerical results can be readily obtained. However, some general features of the Wigner phase-space distribution function can be obtained by direct examination of the general formula. First, examination of (17.75) reveals that, in general, the Wigner phase-space distribution attains its maximum along the line given by $\mathbf{P} = B_b\mathbf{q}/kD_b = B_b\boldsymbol{\theta}/D_b$. Additionally, because $\Gamma_{pt}(p)$ in (17.68) can be rewritten as

$$
\Gamma_{pt}(p) = e^{-s} + e^{-s}\left(\exp\left[sb_\phi(p)\right] - 1\right),
\tag{17.76}
$$

we can conclude, from (17.75) and (17.76), that, in general, the Wigner phase-space distribution function consists of three terms. The square of the first term on the right-hand side of (17.76), which corresponds to the ballistic photons, leads to an attenuated distribution of what would be obtained in the absence of the scattering inhomogeneities. The square of the corresponding second term represents a broader halo resulting from multiple scattering in the medium. The third term is a cross term between the ballistic and multiple-scattering contributions, respectively. Physically, the cross term is the coherent mixing of the unscattered and multiple-scattered light.

Next, for sufficiently large values of the optical depth s, examination of (17.68) reveals that Γ_{pt} is nonzero for $s[1 - b_\phi(p)]$ less than the order unity, that is, for $b_\phi(p)$ near unity. Expanding $b_\phi(p)$ in powers of p and retaining the first two nonzero terms allows one to obtain asymptotic results. In the limit $s \gg 1$, for all cases of practical concern, the resulting width of $|\Gamma_{pt}(p)|^2$ is much narrower than $K(p)$, and without loss of generality, we may replace $K(p)$ by its value at the origin $K(0) = P_0$, the transmitted power (see (17.74)).

17.6.2　Applications to Optical Coherence Tomography

It follows from the analysis in Sect. 17.2 that the signal-to-noise ratio (*SNR*) in a standard OCT system can be expressed as

$$SNR = \text{constant} \times \text{Re}\left[\iint \Gamma_R(\mathbf{P} + \mathbf{p}/2, \mathbf{P} - \mathbf{p}/2)\Gamma_S(\mathbf{P} + \mathbf{p}/2, \mathbf{P} - \mathbf{p}/2)d\mathbf{P}d\mathbf{p}\right], \tag{17.77}$$

where denotes the real part and Γ_R and Γ_S are the mutual coherence functions of the (deterministic) reference beam and sample beam in the mixing plane, respectively. Because the Wigner phase-space distribution function and the mutual coherence function are Fourier transform related (see (17.65)), the *SNR* can be rewritten as

$$SNR = \text{constant} \times \text{Re}\left[\iint W_R(\mathbf{P}, -\mathbf{q})W_S(\mathbf{P}, \mathbf{q})d\mathbf{P}d\mathbf{q}\right], \tag{17.78}$$

where W_R and W_S are the corresponding Wigner phase-space distribution functions of the reference and sample beams, respectively. Equation (17.78) indicates, in particular, that the *SNR* of a standard OCT system is related globally to the Wigner phase-space distribution function of the sample beam. That is, images obtained from standard OCT systems contain global, rather than local, information of the Wigner phase-space distribution function of the sample beam. Improved OCT imagery can thus only be obtained from systems that make use of the local properties of the Wigner phase-space distribution function, rather than globally where information is inevitably lost. Below, we derive expressions for the Wigner phase-space distribution function of the sample beam for a standard OCT geometry for both classes of scattering functions discussed in Ref. [23].

Consider an OCT system where the initial optical wave function (i.e., immediately following the lens) is given by

$$U_{Si}(r) = \sqrt{\frac{P_0}{\pi w_0^2}}\exp\left[-\frac{r^2}{2}\left(\frac{1}{w_0^2} + \frac{ik}{f}\right)\right]. \tag{17.79}$$

For an OCT system, focusing at a tissue discontinuity at depth z, we then get the following equation for $K(r)$

$$K(r) = P_0 \exp\left[-\frac{r^2}{4w_0^2}\right], \tag{17.80}$$

and using (17.78), the heterodyne efficiency factor for the OCT signal for such a system may be written as

$$\Psi \equiv \frac{SNR}{SNR_0} = \frac{\int |K(\mathbf{p})|^2|\Gamma_{pt}(\mathbf{p})|^2 d\mathbf{p}}{\int |K(\mathbf{p})|^2 d\mathbf{p}}. \tag{17.81}$$

We now obtain analytic engineering approximations for the Wigner phase-space distribution function, valid for all values of s, for b_ϕ that are quadratic near the origin. Substituting (17.17) in Ref. [23] and (17.80) into (17.75) and simplifying yield

$$W(\mathbf{P}, \mathbf{q}) \cong \frac{R_d P_0 4 w_0^2}{(2\pi f)^2} \left[e^{-2s} \exp\left(-Q^2 w_0^2\right) + e^{-s}(1 - e^{-s}) \frac{\tilde{\rho}_0^2}{4 w_0^2} \exp\left(-\frac{Q^2 \tilde{\rho}_0^2}{4}\right) \right.$$
$$\left. + (1 - e^{-s})^2 \frac{\tilde{\rho}_0^2}{8 w_0^2} \exp\left(-\frac{Q^2 \tilde{\rho}_0^2}{8}\right) \right],$$

$$\tag{17.82}$$

where

$$\frac{1}{\tilde{\rho}_0^2} = \frac{1}{\rho_0^2} + \frac{1}{4 w_0^2}, \tag{17.83}$$

$$\rho_0 = \sqrt{\frac{3}{s}} \frac{\lambda}{\pi \theta_{rms}} \left(\frac{nf}{z}\right). \tag{17.84}$$

Here, $Q = |\mathbf{q} - (k/f)\mathbf{P}|$. The first, second, and third terms on the right-hand side of (17.82) represent the ballistic, cross, and multiple-scattering contributions to the Wigner phase-space distribution function discussed below (17.76), respectively.

In the limit of $s << 1$, examination of (17.82) reveals that for $\mathbf{P} = \mathbf{0}$, the $1/e$ transverse momentum width, Δ_q, of the Wigner phase-space distribution is given by $\Delta_q = 1/w_0$. Furthermore, in the limit $s >> 1$, $\Delta_q = 2\sqrt{2}\tilde{\rho}_0^{-1}$, where $\tilde{\rho}_0 \cong \rho_0$. In this case, $\Delta_q \propto z^{3/2}$ in the presence of the shower-curtain effect, which manifests itself in the standard OCT geometry. For comparison, $\Delta_q \propto z^{1/2}$ in the absence of the shower-curtain effect.

We have not been able to obtain a corresponding analytic approximation, valid for all values of s, for the Henyey-Greenstein type of scattering function [23]. For this case, we can only conclude that

$$W(\mathbf{P}, \mathbf{q}) \cong \frac{R_d P_0}{(2\pi f)^2} (1 - 2s) \exp\left[-Q^2 w_0^2\right], \quad s << 1, \tag{17.85}$$

and

$$W(\mathbf{P}, \mathbf{q}) \cong \frac{R_d P_0}{\pi (2\pi f)^2} \left(\frac{r_0}{s}\right)^2 \frac{1}{\left(1 + \left(\frac{r_0}{s}\right)^2 \left|\mathbf{q} - \frac{k}{f}\mathbf{P}\right|^2\right)^{3/2}}, \quad s >> 1, \tag{17.86}$$

where $r_0 = \{[\lambda g^{1/2}]/[2\pi(1 - g)]\}[nf/z]$. In the limit of $s << 1$, examination of (17.85) reveals that for $\mathbf{P} = \mathbf{0}$, the $1/e$ transverse momentum width, Δ_q,

of the Wigner phase-space distribution is given by $\Delta_q = 1/w_0$. Furthermore, in the limit $s \gg 1$, it is obtained from (17.86) that $\Delta_q = s/r_0$. In this case, $\Delta_q \propto z^2$ in the presence of the shower-curtain effect. For comparison, $\Delta_q \propto z$ in the absence of the shower-curtain effect.

It is important to note that for both types of scattering functions, the momentum width increases with increasing depth as z^γ, with considerably larger values of γ being obtained in the presence of the shower-curtain effect. Furthermore, the actual value of γ is highly dependent on the details of the scattering function [23].

As shown above, it is possible to determine the lateral coherence length of the sample field from measurements of the Wigner phase-space distribution. As is evident from (17.84), the lateral coherence length depends on the optical parameters of the tissue, that is, n, μ_s, and θ_{rms}. Therefore, it is feasible to create images based on measurements of the lateral coherence length as a function of position in the tissue. In contrast to OCT signals used to create conventional OCT images, the lateral coherence length is related only to the propagation of the light in the tissue, and its magnitude is independent of the amount of light backscattered or reflected at the probed depth.

In general, a discontinuity between two tissue layers is characterized by a change of the scattering coefficient, the backscattering coefficient, and the index of refraction. The relative change of the scattering coefficient and the backscattering coefficient is markedly greater than the corresponding relative change in the index of refraction [43]. In human skin tissue, for example, the scattering coefficients of epidermis and dermis are 50 and 21.7 mm^{-1}, respectively, while the indices of refraction are lying in the range 1.37–1.5 [43]. On this basis, it can be shown from the analysis above that an imaging system, based on measurements of the lateral coherence length, may have a higher sensitivity to changes in the scattering coefficient than the conventional OCT system probing the corresponding change in the backscattering coefficient. The higher sensitivity may lead to an improved contrast in the obtained image. This model and the above discussion give more insight into the ideas presented recently that new venues for medical imaging may be based on coherence tomography using measurements of Wigner phase-space distributions [23, 24, 84–86].

17.7 Appendix A

The 4F system described in Sect. 17.3.1 is inspected where we have designated three transverse coordinate planes (see Fig. 17.6): the p-plane coinciding with the optical fiber, the q-plane coinciding with the diffusely reflecting discontinuity within the sample, and the r-plane coinciding with the right side of the thin focusing lens at $z = -d$. By applying approximations identical to those used in Ref. [10], we now wish to show the following two statements. Firstly, that the heterodyne efficiency factor, defined by the cross correlations of the sample

and reference fields at the p-plane, may be written in terms of their respective intensities only, so that

$$\Psi_p = \frac{\langle i^2 \rangle}{\langle i_0^2 \rangle} = \frac{\int I_R(\mathbf{p})\langle I_s(\mathbf{p})\rangle d^2\mathbf{p}}{\int I_R(\mathbf{p})\langle I_{s0}(\mathbf{p})\rangle d^2\mathbf{p}}, \tag{17.A1}$$

where the integrals are taken over the p-plane and I_R, $\langle I_S(\mathbf{p})\rangle$, and $\langle I_{S0}(\mathbf{p})\rangle$ are the intensities of the reference, the ensemble average of the reflected light from the discontinuity, and the ensemble average of the reflected light from the discontinuity in the absence of scattering, respectively. Secondly, that this calculation of the heterodyne efficiency factor Ψ in the p-plane, Ψ_p, is mathematically identical to calculating Ψ in the r-plane, Ψ_r, as given by (17.57), so that

$$\begin{aligned} \Psi_r &= \frac{\mathrm{Re}\left[\iint \Gamma_R(\mathbf{r}_1, \mathbf{r}_2)\langle \Gamma_S(\mathbf{r}_1, \mathbf{r}_2)\rangle d\mathbf{r}_1 d\mathbf{r}_2\right]}{\mathrm{Re}\left[\iint \Gamma_R(\mathbf{r}_1, \mathbf{r}_2)\langle \Gamma_{S0}(\mathbf{r}_1, \mathbf{r}_2)\rangle d\mathbf{r}_1 d\mathbf{r}_2\right]} \\ &= \frac{\mathrm{Re}\left[\iint \Gamma_R(\mathbf{p}_1, \mathbf{p}_2)\langle \Gamma_S(\mathbf{p}_1, \mathbf{p}_2)\rangle d\mathbf{p}_1 d\mathbf{p}_2\right]}{\mathrm{Re}\left[\iint \Gamma_R(\mathbf{p}_1, \mathbf{p}_2)\langle \Gamma_{S0}(\mathbf{p}_1, \mathbf{p}_2)\rangle d\mathbf{p}_1 d\mathbf{p}_2\right]} = \Psi_p. \end{aligned} \tag{17.A2}$$

To outline the derivation, the proof will be initiated by finding the field U_S due to an initial field propagating from the r-plane toward the sample and reflecting off the discontinuity. This field is then used to calculate the cross correlation $\langle \Gamma_S(\mathbf{p}_1, \mathbf{p}_2)\rangle = \langle U_S(\mathbf{p}_1)U_S^*(\mathbf{p}_2)\rangle$, and it is shown that U_S is delta-correlated [19] and thus the validity of (17.A1) is demonstrated. It is then demonstrated that the obtained expression for Ψ_p is identical to (17.81). Because we are only concerned with the ratio Ψ, any multiplicative constant not related to the properties of the scattering medium is omitted.

Using the Huygens-Fresnel principle, the field at the p-plane, U_S, due to a field immediately to the right of the focusing lens in the r-plane, U_r, is given by

$$U_s(\mathbf{r}, \mathbf{p}) = \int U_r(\mathbf{r})G_{r-p}(\mathbf{r}, \mathbf{p})d^2\mathbf{r}, \tag{17.A3}$$

where $G_{r\text{-}p}(\mathbf{r},\mathbf{p})$ is the Huygens-Fresnel Green's function for propagation from the r-plane to the p-plane. For a general ABCD matrix system, this Green's function is given by [40]

$$G_0(\mathbf{r}, \mathbf{p}) = -\frac{ik}{2\pi B} \exp\left[-\frac{ik}{2B}\left(Ar^2 - 2\mathbf{r}\cdot\mathbf{p} + Dp^2\right)\right], \tag{17.A4}$$

where A, B, and D are the matrix elements and the notation r denotes the length of the vector $\mathbf{r}$. For the propagation from r to p, $A = -1$, $B = f$, and $D = -1$. The field

at the r-plane due to a field, U_q, impinging upon the discontinuity is found using the EHF principle

$$U_r(\mathbf{r}) = \int \eta(\mathbf{q}) U_q(\mathbf{q}) G_f(\mathbf{q}, \mathbf{r}) \exp[i\varphi(\mathbf{q}, \mathbf{r})] d^2\mathbf{q}, \tag{17.A5}$$

where G_f is the Green's function for propagating the optical distance f given by (17.A4) with the matrix elements $A = 1$, $B = f$, and $D = 1$. $\varphi(\mathbf{q}, \mathbf{r})$ is the stochastic phase added to the phase of a spherical wave propagating from $\mathbf{q}$ to $\mathbf{r}$ due to the scattering medium, and $\eta(\mathbf{q})$ is a complex reflection coefficient due to the discontinuity. Calculating the cross correlation of the field U_S yields

$$\begin{aligned}\Gamma_s(\mathbf{p}_1, \mathbf{p}_2) = \iiiint &G_f(\mathbf{q}, \mathbf{r}) G_f^*(\mathbf{q}', \mathbf{r}') G_{r-p}(\mathbf{r}, \mathbf{p}_1) G_{r-p}^*(\mathbf{r}', \mathbf{p}_2) \\ &\times \langle U_q(\mathbf{q}) U_q^*(\mathbf{q}') \rangle \langle \eta(\mathbf{q}) \eta(\mathbf{q}') \rangle \\ &\times \langle \exp[i\varphi(\mathbf{q}, \mathbf{r}) - i\varphi(\mathbf{q}', \mathbf{r}')] \rangle d^2\mathbf{r} d^2\mathbf{r}' d^2\mathbf{q} d^2\mathbf{q}', \end{aligned} \tag{17.A6}$$

where primed variables are related to $U_S{}^*$, and we have assumed that the scattering medium and the properties of the diffusely discontinuity are independent. It should also be noted that in writing $\langle U_q(\mathbf{q}) U_q^*(\mathbf{q}') \exp[i\varphi(\mathbf{q}, \mathbf{r}) - i\varphi(\mathbf{q}', \mathbf{r}')] \rangle = \langle U_q(\mathbf{q}) U_q^*(\mathbf{q}') \rangle \times \langle \exp[i\varphi(\mathbf{q}, \mathbf{r}) - i\varphi(\mathbf{q}', \mathbf{r}')] \rangle$, it has been assumed that the phase distortion due to the scattering medium added to the field propagating from L2 to the discontinuity is statistically independent of that added to the field propagating from the discontinuity to L2. The validity of this assumption in MC simulations is discussed in Sect. 17.3.3. Because the discontinuity is diffusely reflecting $\langle \eta(\mathbf{q}) \eta(\mathbf{q}') \rangle = (4\pi/k^2) \delta(\mathbf{q} - \mathbf{q}')$, where $\delta(\mathbf{r})$ is the two-dimensional Dirac's delta function [39]. This yields

$$\begin{aligned}\Gamma_s(\mathbf{p}_1, \mathbf{p}_2) = \iiint &G_f(\mathbf{q}, \mathbf{r}) G_f^*(\mathbf{q}, \mathbf{r}') G_{r-p}(\mathbf{r}, \mathbf{p}_1) G_{r-p}^*(\mathbf{r}', \mathbf{p}_2) \\ &\times \langle I_q(\mathbf{q}) \rangle \Gamma_{PT}(\mathbf{r} - \mathbf{r}') d^2\mathbf{r} d^2\mathbf{r}' d^2\mathbf{q}, \end{aligned} \tag{17.A7}$$

where Γ_{PT} is given by (17.41) and I_q is the intensity of the field U_q. The average intensity $\langle I_q(\mathbf{q}) \rangle$ can be found from (17.39), and it is noted that the difference vector, $\boldsymbol{\rho}$, in (17.39) is independent of $\mathbf{r}$ and $\mathbf{r}'$ in (17.A7). Now, invoking the sum and difference coordinates $\mathbf{R} = \frac{1}{2}(\mathbf{r} + \mathbf{r}')$ and $\boldsymbol{\rho} = \mathbf{r} - \mathbf{r}'$ and performing the q-integration and the ρ-integration originating from (17.39) yield

$$\begin{aligned}\Gamma_s(\mathbf{p}_2, \mathbf{p}_2) = \iint &\exp\left[-\frac{ik}{2f}\{p_2^2 - p_1^2 - \boldsymbol{\rho} \cdot (\mathbf{p}_1 + \mathbf{p}_2) + 2\mathbf{R} \cdot (\mathbf{p} - \mathbf{p}_1)\}\right] \\ &\times |\Gamma_{PT}(\boldsymbol{\rho})|^2 K(-\boldsymbol{\rho}) d^2\boldsymbol{\rho} d^2\mathbf{R}, \end{aligned} \tag{17.A8}$$

where we have used the relation

$$\int \exp[i\mathbf{m}\cdot(\mathbf{u}+\mathbf{v})]d^2\mathbf{m} = (2\pi)^2\delta(\mathbf{u}+\mathbf{v}). \qquad (17.\text{A}9)$$

Carrying out the $\mathbf{R}$-integration then yields

$$\Gamma_s(\mathbf{p}_2,\mathbf{p}_1) = \delta(\mathbf{p}_2-\mathbf{p}_1)\int \exp\left[-\frac{ik}{2f}\{p_2^2-p_1^2-\boldsymbol{\rho}\cdot(\mathbf{p}_1+\mathbf{p}_2)\}\right] \\ \times |\Gamma_{PT}(\boldsymbol{\rho})|^2 K(-\boldsymbol{\rho})d^2\boldsymbol{\rho} \qquad (17.\text{A}10)$$

which shows the sample U_S to be delta-correlated, and thus, (17.A1) is proven.

To calculate (17.A1), we consider (17.A8) for the case $\mathbf{p}_1 = \mathbf{p}_2 = \mathbf{p}$, which then yields the intensity

$$\langle I_s(\mathbf{p})\rangle = A_{lens}\int \exp\left[-\frac{ik}{f}\boldsymbol{\rho}\cdot\mathbf{p}\right]|\Gamma_{PT}(\boldsymbol{\rho})|^2 K(-\boldsymbol{\rho})d^2\boldsymbol{\rho}, \qquad (17.\text{A}11)$$

where A_{lens} is the area of the focusing lens.

To find the OCT signal $\langle i^2\rangle$, we now insert (17.A11) into the numerator of (17.A1)

$$\langle i^2\rangle = \iint \exp\left[-\frac{ik}{2f}(-2\boldsymbol{\rho}\cdot\mathbf{p})\right]|\Gamma_{PT}(\boldsymbol{\rho})|^2 K(-\boldsymbol{\rho})I_R(\mathbf{p})d^2\boldsymbol{\rho}d^2\mathbf{p} \\ = \int |\Gamma_{PT}(\boldsymbol{\rho})|^2|K(\boldsymbol{\rho})|^2 d^2\boldsymbol{\rho}, \qquad (17.\text{A}12)$$

where we have used that the reference field impinging on the reference mirror may be calculated using (17.39) with $\Gamma_{PT}=1$ and $A=1$ and $B=f$. Because the p-plane is the conjugate plane to the plane of the reference mirror, the field here is identical to that impinging upon the reference mirror. Γ_{PT} is unity in the absence of scattering, so it is now easy to see that Ψ may be calculated through

$$\Psi_p = \frac{\int |\Gamma_{PT}(\boldsymbol{\rho})|^2|K(\boldsymbol{\rho})|^2 d^2\boldsymbol{\rho}}{\int |K(\boldsymbol{\rho})|^2 d^2\boldsymbol{\rho}}. \qquad (17.\text{A}13)$$

Note that the integration is over the r-plane. It is seen that Ψ_p is identical to Ψ_r given by (17.81). It has thus been proven that within the approximation of the EHF principle, the heterodyne efficiency factor of the OCT system depends solely upon the intensity distributions of the reference and sample fields in the p-plane. Furthermore, it is straightforward to prove that this will be true for any conjugate plane to a diffusely reflecting discontinuity plane within the sample.

One should note that there exists an ambiguity between obtaining a delta function in (17.A10) and obtaining a finite area of the focusing lens in (17.A11). Firstly, this area is irrelevant for the heterodyne efficiency factor, and no assumption of a finite lens area is made in Sect. 17.2.2. Furthermore, it is easy to show that (17. A13) is just as well obtained by inserting (17.A10) into (17.A2). Secondly, a finite radius of the focusing lens would have yielded an Airy function in R_A ($\mathbf{p}_1 - \mathbf{p}_2$) instead of a delta function, where R_A is the radius of aperture. Thus, if the aperture is large, the sample field will be essentially delta-correlated in the p-plane.

References

1. D. Huang, E.A. Swanson, C.P. Lin, J.S. Schuman, W.G. Stinson, W. Chang, M.R. Hee, T. Flotte, K. Gregory, C.A. Puliafito, J.G. Fujimoto, Optical coherence tomography. Science **254**, 1178–1181 (1991)
2. J.M. Schmitt, A. Knüttel, R.F. Bonner, Measurement of optical properties of biological tissues by low-coherence reflectometry. Appl. Opt. **32**, 6032–6042 (1993)
3. J.M. Schmitt, A. Knüttel, A.S. Gandjbakhche, R.F. Bonner, Optical characterization of dense tissues using low-coherence interferometry. Proc. SPIE **1889**, 197–211 (1993)
4. M.J. Yadlowsky, J.M. Schmitt, R.F. Bonner, Multiple scattering in optical coherence microscopy. Appl. Opt. **34**, 5699–5707 (1995)
5. M.J. Yadlowsky, J.M. Schmitt, R.F. Bonner, Contrast and resolution in the optical coherence microscopy of dense biological tissue. Proc. SPIE **2387**, 193–203 (1995)
6. Y. Pan, R. Birngruber, R. Engelhardt, Contrast limits of coherence-gated imaging in scattering media. Appl. Opt. **36**, 2979–2983 (1997)
7. L.S. Dolin, A theory of optical coherence tomography. Radiophys. Quant. Electron. **41**, 850–873 (1998)
8. J.M. Schmitt, A. Knüttel, Model of optical coherence tomography of heterogeneous tissue. J. Opt. Soc. Am. A **14**, 1231–1242 (1997)
9. D.J. Smithies, T. Lindmo, Z. Chen, J.S. Nelson, T.E. Milner, Signal attenuation and localization in optical coherence tomography studied by Monte Carlo simulation. Phys. Med. Biol. **43**, 3025–3044 (1998)
10. L. Thrane, H.T. Yura, P.E. Andersen, Analysis of optical coherence tomography systems based on the extended Huygens-Fresnel principle. J. Opt. Soc. Am. A **17**, 484–490 (2000)
11. I.V. Turchin, E.A. Sergeeva, L.S. Dolin, V.A. Kamensky, N.M. Shakhova, R. Richards-Kortum, Novel algorithm of processing optical coherence tomography images for differentiation of biological tissue pathologies. J. Biomed. Opt. **10**, 064024 (2005)
12. A. Tycho, T.M. Jørgensen, H.T. Yura, P.E. Andersen, Derivation of a Monte Carlo method for modeling heterodyne detection in optical coherence tomography systems. Appl. Opt. **41**, 6676–6691 (2002)
13. H. Kahn, T.E. Harris, Estimation of particle transmission by random sampling, in *Monte Carlo Methods*. National Bureau of Standards Applied Mathematics Series, vol. 12 (U. S. Government Printing Office, Washington, DC, 1951)
14. B.C. Wilson, G. Adam, A Monte Carlo model for the absorption and flux distributions of light in tissue. Med. Phys. **10**, 824–830 (1983)
15. J.M. Schmitt, A. Knüttel, M. Yadlowsky, M.A. Eckhaus, Optical-coherence tomography of a dense tissue: statistics of attenuation and backscattering. Phys. Med. Biol. **39**, 1705–1720 (1994)
16. H.T. Yura, Signal-to-noise ratio of heterodyne lidar systems in the presence of atmospheric turbulence. Opt. Acta **26**, 627–644 (1979)

17. Y. Feng, R. Wang, J. Elder, Theoretical model of optical coherence tomography for system optimization and characterization. J. Opt. Soc. Am. A **20**, 1792–1803 (2003)

18. B. Karamata, M. Laubscher, M. Leutenegger, S. Bourquin, T. Lasser, P. Lambelet, Multiple scattering in optical coherence tomography. I. Investigation and modeling. J. Opt. Soc. Am. A **22**, 1369–1379 (2005)

19. J.W. Goodman, *Statistical Optics* (Wiley, New York, 1985)

20. R.G. Frehlich, M.J. Kavaya, Coherent laser radar performance for general atmospheric refractive turbulence. Appl. Opt. **30**, 5325–5352 (1991)

21. D. Arnush, Underwater light-beam propagation in the small-angle-scattering approximation. J. Opt. Soc. Am. **62**, 1109–1111 (1972)

22. H.T. Yura, A multiple scattering analysis of the propagation of radiance through the atmosphere, in *Proceedings of the Union Radio-Scientifique Internationale Open Symposium*, La Baule, 1977, pp. 65–69

23. H.T. Yura, L. Thrane, P.E. Andersen, Closed-form solution for the Wigner phase-space distribution function for diffuse reflection and small-angle scattering in a random medium. J. Opt. Soc. Am. A **17**, 2464–2474 (2000)

24. M.G. Raymer, C. Cheng, D.M. Toloudis, M. Anderson, M. Beck, Propagation of Wigner coherence functions in multiple scattering media, in *Advances in Optical Imaging and Photon Migration*, vol. 2 of *OSA Trends in Optics and Photonics Series*, eds. by R.R. Alfano, J.G. Fujimoto (Optical Society of America, Washington, DC, 1996), pp. 236–238; C.-C. Cheng, M.G. Raymer, Long-range saturation of spatial decoherence in wave-field transport in random multiple-scattering media. Phys. Rev. Lett. **82**, 4807–4810 (1999); M.G. Raymer, C.-C. Cheng, Propagation of the optical Wigner function in random multiple-scattering media, in *Laser-Tissue Interaction XI: Photochemical*, *Photothermal, and Photomechanical*, eds. by D. D. Duncan, J.O. Hollinger, S.L. Jacques. Proc. SPIE **3914**, 376–380 (2000)

25. P.E. Andersen, T.M. Jørgensen, L. Thrane, A. Tycho, H.T. Yura, Modeling light–tissue interaction in optical coherence tomography systems, in *Optical Coherence Tomography: Technology and Applications*, ed. by W. Drexler, J.G. Fujimoto (Springer, New York, 2008), pp. 73–113 (Chap. 3). ISBN 3540775498

26. L. Thrane, H.T. Yura, P.E. Andersen, Optical coherence tomography: new analytical model and the shower curtain effect. Proc. SPIE **4001**, 202–208 (2000)

27. L. Thrane, H.T. Yura, P.E. Andersen, Calculation of the maximum obtainable probing depth of optical coherence tomography in tissue. Proc. SPIE **3915**, 2–11 (2000)

28. P.E. Andersen, L. Thrane, H.T. Yura, A. Tycho, T.M. Jørgensen, Modeling the optical coherence tomography geometry using the extended Huygens-Fresnel principle and Monte Carlo simulations. Proc. SPIE **3914**, 394–406 (2000)

29. H.T. Yura, Signal-to-noise ratio of heterodyne lidar systems in the presence of atmospheric turbulence. Opt. Acta **26**, 627–644 (1979)

30. I. Dror, A. Sandrov, N.S. Kopeika, Experimental investigation of the influence of the relative position of the scattering layer on image quality: the shower curtain effect. Appl. Opt. **37**, 6495–6499 (1998)

31. V.I. Tatarskii, *Wave Propagation in a Turbulent Medium* (McGraw-Hill, New York, 1961)

32. A. Ishimaru, *Wave Propagation and Scatteringin Random Media* (IEEE Press, Piscataway, 1997)

33. J. Strohbehn (ed.), *Laser Beam Propagation in the Atmosphere* (Springer, New York, 1978)

34. R.L. Fante, Wave propagation in random media: a systems approach, in *Progress in Optics XXII*, ed. by E. Wolf (Elsevier, New York, 1985)

35. J.M. Schmitt, G. Kumar, Turbulent nature of refractive-index variations in biological tissue. Opt. Lett. **21**, 1310–1312 (1996)

36. S.M. Rytov, Y.A. Kravtsov, V.I. Tatarskii, Principles of statistical radiophysics, in *Wave Propagation Through Random Media*, vol. 4 (Springer, Berlin, 1989)

37. R.F. Lutomirski, H.T. Yura, Propagation of a finite optical beam in an inhomogeneous medium. Appl. Opt. **10**, 1652–1658 (1971)

38. Z.I. Feizulin, Y.A. Kravtsov, Expansion of a laser beam in a turbulent medium. Izv. Vyssh. Uchebn. Zaved. Radiofiz. **24**, 1351–1355 (1967)
39. J.W. Goodman, *Introduction to Fourier Optics*, 2nd edn. (McGraw-Hill, Singapore, 1996)
40. H.T. Yura, S.G. Hanson, Optical beam wave propagation through complex optical systems. J. Opt. Soc. Am. A **4**, 1931–1948 (1987)
41. H.T. Yura, S.G. Hanson, Second-order statistics for wave propagation through complex optical systems. J. Opt. Soc. Am. A **6**, 564–575 (1989)
42. A.E. Siegman, *Lasers* (University Science, Mill Valley, 1986), pp. 626–630
43. M.J.C. Van Gemert, S.L. Jacques, H.J.C.M. Sterenborg, W.M. Star, Skin optics. IEEE Trans. Biomed. Eng. **36**, 1146–1154 (1989)
44. C.F. Bohren, D.R. Huffman, *Absorption and Scattering of Light by Small Particles* (Wiley, New York, 1983)
45. H.T. Yura, S.G. Hanson, Effects of receiver optics contamination on the performance of laser velocimeter systems. J. Opt. Soc. Am. A **13**, 1891–1902 (1996)
46. L. Thrane, Optical coherence tomography: modeling and applications, PhD dissertation Risø National Laboratory, Denmark, 2000. ISBN 87-550-2771-7
47. L.G. Henyey, J.L. Greenstein, Diffuse radiation in the galaxy. Astro-Phys. J. **93**, 70–83 (1941)
48. S.L. Jacques, C.A. Alter, S.A. Prahl, Angular dependence of He-Ne laser light scattering by human dermis. Lasers Life Sci. **1**, 309–333 (1987)
49. C.M. Sonnenschein, F.A. Horrigan, Signal-to-noise relationships for coaxial systems that heterodyne backscatter from the atmosphere. Appl. Opt. **10**, 1600–1604 (1971)
50. D.L. Fried, Optical heterodyne detection of an atmospherically distorted signal wave front. Proc. IEEE **55**, 57–67 (1967)
51. V.V. Tuchin, S.R. Utz, I.V. Yaroslavsky, Skin optics: modeling of light transport and measuring of optical parameters, in *Medical Optical Tomography: Functional Imaging and Monitoring*, ed. by G. Mueller, B. Chance, R. Alfano et al., vol. IS11 (SPIE Press, Bellingham, 1993), pp. 234–258
52. V.I. Tatarskii, *The Effects of the Turbulent Atmosphere on Wave Propagation* (National Technical Information Service, Springfield, 1971)
53. A. Tycho, T.M. Jørgensen, Comment on 'Excitation with a focused, pulsed optical beam in scattering media: diffraction effects. Appl. Opt. **41**, 4709–4711 (2002)
54. V.R. Daria, C. Saloma, S. Kawata, Excitation with a focused, pulsed optical beam in scattering media: diffraction effects. Appl. Opt. **39**, 5244–5255 (2000)
55. J. Schmitt, A. Knüttel, M. Yadlowsky, Confocal microscopy in turbid media. J. Opt. Soc. A **11**, 2226–2235 (1994)
56. J.M. Schmitt, K. Ben-Letaief, Efficient Monte Carlo simulation of confocal microscopy in biological tissue. J. Opt. Soc. Am. A **13**, 952–961 (1996)
57. C.M. Blanca, C. Saloma, Monte Carlo analysis of two-photon fluorescence imaging through a scattering medium. Appl. Opt. **37**, 8092–8102 (1998)
58. Y. Pan, R. Birngruber, J. Rosperich, R. Engelhardt, Low-coherence optical tomography in turbid tissue – theoretical analysis. Appl. Opt. **34**, 6564–6574 (1995)
59. G. Yao, L.V. Wang, Monte Carlo simulation of an optical coherence tomography signal in homogeneous turbid media. Phys. Med. Biol. **44**, 2307–2320 (1999)
60. Z. Song, K. Dong, X.H. Hu, J.Q. Lu, Monte Carlo simulation of converging laser beams propagating in biological materials. Appl. Opt. **38**, 2944–2949 (1999)
61. C.M. Blanca, C. Saloma, Efficient analysis of temporal broadening of a pulsed focused Gaussian beam in scattering media. Appl. Opt. **38**, 5433–5437 (1999)
62. L.V. Wang, G. Liang, Absorption distribution of an optical beam focused into a turbid medium. Appl. Opt. **38**, 4951–4958 (1999)
63. A.K. Dunn, C. Smithpeter, A.J. Welch, R. Richards-Kortum, Sources of contrast in confocal reflectance imaging. Appl. Opt. **35**, 3441–3446 (1996)
64. L.-H. Wang, S.L. Jacques, L.-Q. Zheng, MCML – Monte Carlo modeling of photon transport in multi-layered tissues. Comput. Methods Programs Biomed. **47**, 131–146 (1995)

65. S.A. Prahl, M. Keijzer, S.L. Jacques, A.J. Welch, A Monte Carlo model for light propagation in tissue, in *Dosimetry of Laser Radiation in Medicine and Biology*, ed. by S.A. Prahl. SPIE Institute Series, vol. IS5 (SPIE Press, Bellingham, 1998)

66. D.I. Hughes, F.A. Duck, Automatic attenuation compensation for ultrasonic imaging. Ultrasound Med. Biol. **23**, 651–664 (1997)

67. L. Thrane, T.M. Jørgensen, P.E. Andersen, H.T. Yura, True-reflection OCT imaging. Proc. SPIE **4619**, 36–42 (2002)

68. S.A. Prahl, M.J.C. van Gemert, A.J. Welch, Determining the optical properties of turbid media by using the adding-doubling method. Appl. Opt. **32**, 559–568 (1993)

69. J.M. Schmitt, S.H. Xiang, K.M. Yung, Speckle in optical coherence tomography. J. Biomed. Opt. **4**, 95–105 (1999)

70. L. Thrane, M.H. Frosz, A. Tycho, T.M. Jørgensen, H.T. Yura, P.E. Andersen, Extraction of optical scattering parameters and attenuation compensation in optical coherence tomography images of multi-layered tissue structures. Opt. Lett. **29**, 1641–1643 (2004)

71. G.J. Tearney, S.A. Boppart, B.E. Bouma, M.E. Brezinski, N.J. Weissman, J.F. Southern, J.G. Fujimoto, Scanning single-mode fiber optic catheter-endoscope for optical coherence tomography. Opt. Lett. **21**, 543–545 (1996)

72. R.O. Esenaliev, K.V. Larin, I.V. Larina, M. Motamedi, Noninvasive monitoring of glucose concentration with optical coherence tomography. Opt. Lett. **26**, 992–994 (2001)

73. K.V. Larin, T. Akkin, R.O. Esenaliev, M. Motamedi, T.E. Milner, Phase-sensitive optical low-coherence reflectometry for the detection of analyte concentrations. Appl. Opt. **43**, 3408–3414 (2004)

74. D.J. Faber, M.C.G. Aalders, E.G. Mik, B.A. Hooper, M.J.C. van Gemert, T.G. van Leeuwen, Oxygen saturation-dependent absorption and scattering of blood. Phys. Rev. Lett. **93**, 028102-1–028102-4 (2004)

75. D.J. Faber, E.G. Mik, M.C.G. Aalders, T.G. van Leeuwen, Toward assessment of blood oxygen saturation by spectroscopic optical coherence tomography. Opt. Lett. **30**, 1015–1017 (2005)

76. D.J. Faber, T.G. van Leeuwen, Are quantitative attenuation measurements of blood by optical coherence tomography feasible? Opt. Lett. **34**, 1435–1437 (2009)

77. V.M. Kodach, D.J. Faber, J. van Marle, T.G. van Leeuwen, J. Kalkman, Determination of the scattering anisotropy with optical coherence tomography. Opt. Express **19**, 6131–6140 (2011)

78. F.J. van der Meer, D.J. Faber, D.M.B. Sassoon, M.C. Aalders, G. Pasterkamp, T.G. van Leeuwen, Localized measurement of optical attenuation coefficients of atherosclerotic plaque constituents by quantitative optical coherence tomography. IEEE Trans. Med. Imaging **24**, 1369–1376 (2005)

79. N.M. Shakhova, V.M. Gelikonov, V.A. Kamensky, R.V. Kuranov, I.V. Turchin, Clinical aspects of the endoscopic optical coherence tomography: a method for improving the diagnostic efficiency. Laser Phys. **12**, 617–626 (2002)

80. D. Levitz, L. Thrane, M.H. Frosz, P.E. Andersen, C.B. Andersen, J. Valanciunaite, J. Swartling, S. Andersson-Engels, P.R. Hansen, Determination of optical scattering properties of highly-scattering media in optical coherence tomography images. Opt. Express **12**, 249–259 (2004)

81. R. Samatham, S.L. Jacques, P. Campagnola, Optical properties of mutant versus wild-type mouse skin measured by reflectance-mode confocal scanning laser microscopy (rCSLM). J. Biomed. Opt. **13**, 041309 (2008)

82. A. Knüttel, S. Bonev, W. Knaak, New method for evaluation of in vivo scattering and refractive index properties obtained with optical coherence tomography. J. Biomed. Opt. **9**, 265–273 (2004)

83. E.P. Wigner, On the quantum correction for thermodynamic equilibrium. Phys. Rev. **40**, 749–759 (1932)

84. S. John, G. Pang, Y. Yang, Optical coherence propagation and imaging in a multiple scattering medium. J. Biomed. Opt. **1**, 180–191 (1996)

85. A. Wax, J.E. Thomas, Measurement of smoothed Wigner phase-space distributions for small-angle scattering in a turbid medium. J. Opt. Soc. Am. A **15**, 1896–1908 (1998)
86. C.-C. Cheng, M.G. Raymer, Propagation of transverse optical coherence in random multiple-scattering media. Phys. Rev. A **62**, 023811-1–023811-12 (2000)
87. M. Hillery, R.F. O'Connel, M.O. Scully, E.P. Wigner, Distribution functions in physics: fundamentals. Phys. Rep. **106**, 121–167 (1984)
88. V.A. Banakh, V.L. Mironov, *LIDAR in a Turbulent Atmosphere* (Artech House, Boston, 1987)

Flying Spot En-Face OCT Imaging

18

Adrian Podoleanu

Contents

A. Podoleanu
School of Physical Sciences, University of Kent at Canterbury, Canterbury, UK
e-mail: A.G.H.Podoleanu@kent.ac.uk

Abstract

En face optical coherence tomography (OCT) delivers slices in the tissue with an orientation similar to that of confocal microscopy and of thickness determined by the coherence length of the broadband excitation source. En face OCT has progressed along two main avenues, full-field and flying spot. In the flying spot implementation, the path modulation introduced by the transverse scanners may be employed to generate en face OCT images. En face OCT is a time domain method. In an era dominated by spectral domain methods, en face OCT has unique features not achievable via spectral domain methods, such as versatile operation in A, B, C scanning regimes, compatibility with simultaneous confocal imaging, dynamic focus, simultaneous imaging at several depths and measurement of topography, and orientation of surfaces in a single frame

18.1 Different Scanning Procedures

To obtain 3D information about the object, any imaging system, operating on the flying spot concept, is equipped with three scanning means, one to scan the object in depth and two others to scan the object transversely. Depending on the order that these three scanners are operated, and on the scanning direction associated with the line displayed in the raster of the final image delivered, different possibilities exist.

18.1.1 A-Scan

Low-coherence interferometry has evolved as an absolute measurement technique which allows high-resolution ranging [1] and characterization of optoelectronic components [2, 3]. This technique typically outputs a one-dimensional (1D) reflectivity profile in depth in the sample, called A-scan, as shown in Fig. 18.1 [4]. The first application in the biomedical optics field was for the measurement of the eye length [5]. A low-coherence interferometry system is generally based on a two-beam interferometer. The A-scan technique in time domain OCT is facilitated by a technical advantage: when moving the mirror in the reference
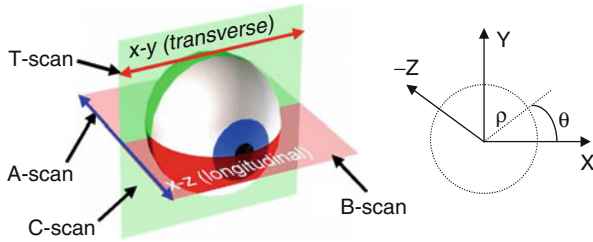
Fig. 18.1 Relative orientation of the axial scan (A-scan), transverse or 1D en face scan (T-scan), 2D cross-sectional or longitudinal slice (B-scan), and 2D en face or transverse slice (C-scan) (Reproduced with OSA's permission from [10] and copyright M. Seeger [4])

path of the interferometer, not only is the depth scanned but a radio frequency carrier is also generated. The carrier frequency is the Doppler shift produced by the longitudinal scanner itself (moving along the axis of the system, Z, to explore the sample in depth).

18.1.2 A-Scan-Based B-Scan

By adding a transversal scanner to a low-coherence interferometer equipped to produce A-scans, cross-sectional images can be obtained in the sample. The high resolution of such images allows for tomographic investigation of the inside of the object volume. To express this capability, researchers at MIT proposed to denominate the technique as optical coherence tomography (OCT) [6]. B-scan OCT images, analogous to ultrasound B-scan, are generated by collecting many A-scans for different and adjacent transverse positions, as shown in Fig. 18.2(i). B-scans are two-dimensional (2D) maps. The lines in the raster generated correspond to A-scans, i.e., the lines are oriented along the depth coordinate. The transverse scanner (operating along X or Y, or along the polar angle θ in polar coordinates in Fig. 18.1, with X shown in Fig. 18.2(i)) advances at a slower pace to build a B-scan image. The imaging technology used to generate the image in Fig. 18.2(i) is often referred to as longitudinal OCT, irrespective if time domain or spectral domain principles are used. In time domain OCT, the signal bandwidth, given by the speed the depth pixel size is scanned, determines an enlargement of the Doppler frequency component in the spectrum of the photodetected signal. The image bandwidth is practically identical with the signal bandwidth required to process an individual A-scan (as the lateral movement of the beam is at a much slower speed than the scanning in depth and does not contribute to any bandwidth enlargement). The majority of time domain OCT reports in literature [7–11] refer to this way of operation. Historically, the first OCT image was a B-scan image of the retina [6] made from A-scans, using flying spot time domain longitudinal OCT technology.
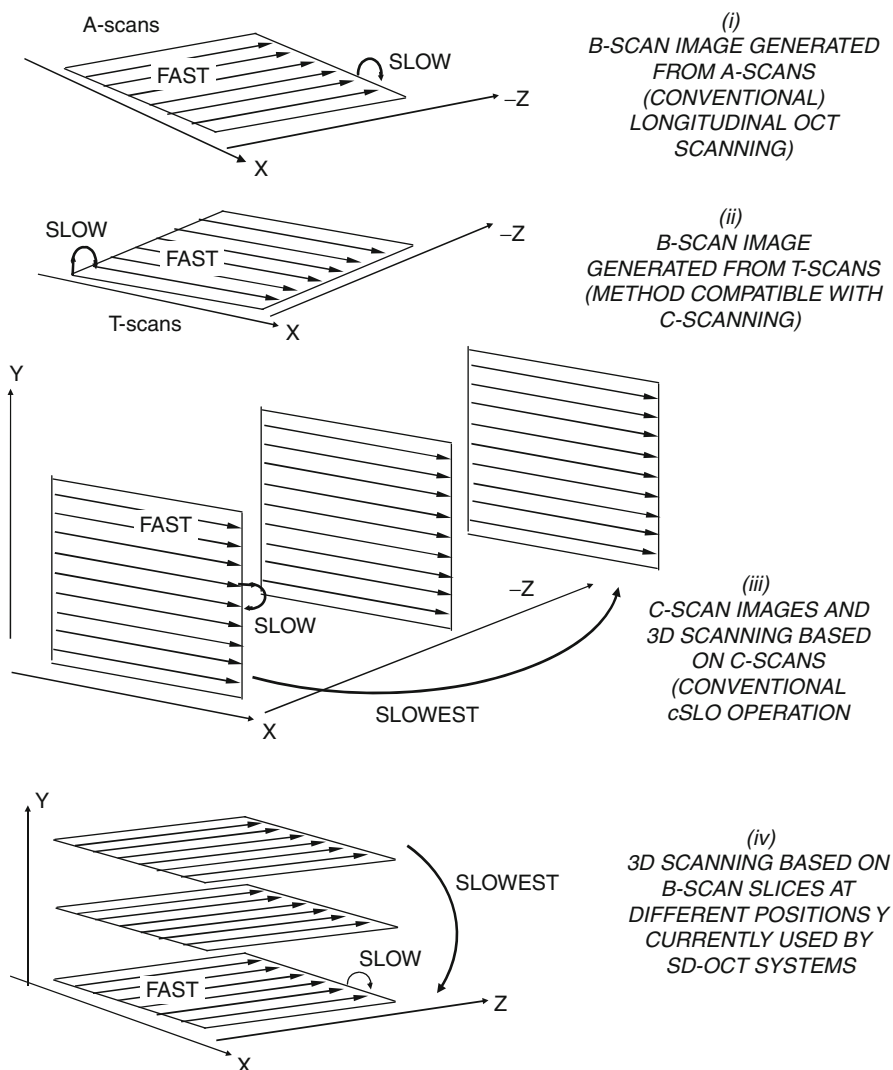
Fig. 18.2 Different modes of operation of the three scanners in a 3D flying spot imaging system. Lateral scanning along the X and Y axes is implemented using an XY or a 2D transverse scanner in both confocal microscopy (CM) and OCT systems. The scanning in depth along the axis Z, differs, implemented using focus change in CM and OPD change in OCT (Reproduced with Elsevier's permission from [11])

18.1.3 T-Scan-Based B-Scan

In en face OCT, the transverse scanner produces the fast lines in the image [12–14]. We call each such image line as a T-scan. This can be produced by controlling either the transverse scanner along the X-coordinate or along the Y-coordinate or

along the polar angle θ, with the other two scanners fixed. The example in Fig. 18.2(ii) illustrates the generation of a T-scan-based B-scan, where the X-scanner produces the T-scans and the axial scanner advances slower in depth, along the Z-coordinate. As it will be shown in this chapter, this procedure has a net advantage in comparison with the A-scan-based B-scan procedure as it allows real-time production of OCT transverse (or en face) images for a fixed reference path, images called C-scans.

18.1.4 C-Scan

C-scan images, as shown in Fig. 18.2(iii), are made from many T-scans along either X, Y, ρ, or θ coordinates, repeated for different values of the other transverse coordinate Y, X, θ, or ρ respectively in the transverse plane. The repetition of T-scans along the other transverse coordinate is performed at a slower rate than that of the T-scans, called the frame rate. In this way, a complete raster is generated. In order to tomographically investigate the whole volume of the sample, different transverse slices are collected for different depth values Z, either by advancing the optical path difference in the OCT in steps after each complete transverse (XY) or (ρ,θ) scan, or continuously at a much slower speed than the frame rate. For correct sampling in depth of the tissue volume, the speed of advancing in depth should be such that on the duration of the frame, the depth variation be no more than half the depth resolution.

18.1.5 Collecting 3D Data

3D complete information could be collected in different ways, either acquiring many longitudinal OCT images (B-scans) at different en face positions [15, 16] or many en face OCT images (C-scans) at different depth positions [17–19]. In principle, the volume rendered by either procedure from the tissue should be equivalent. However, the devices used to scan the object in the three directions are not identical. They are chosen or designed according to the scanning method used, either longitudinal, based on A-scans as in Fig. 18.2(i), or en face, based on T-scans as in Fig. 18.2(ii).

To produce longitudinal OCT images as in Fig. 18.2(i), two different categories of devices can be employed, depending whether time domain (TD) or spectral domain (SD)-OCT is used. In TD-OCT, a fast scanner to generate A-scans such as a turbine-driven mirror [20] or a fast galvanometer mirror or a resonant scanner in a spectral scanning line using a diffraction grating [21] is employed. Such fast axial scanner is paired with a slower scanning device to perform the advance in the transverse plane, using a piezo or a galvanometer scanner. In SD-OCT, FFT of the reading of a linear camera in a spectrometer or FFT of the photodetected signal collected in the time interval required for tuning a swept optical source leads to A-scans.

To produce B-scan en face OCT images as in Fig. 18.2(ii), a fast galvanometer scanner, a resonant scanner, or a polygon mirror to generate T-scans is paired to a slower scanning device for scanning the depth along depth, such as a translation stage or a piezo device.

This dedicated design determines the way the 3D information is collected using the flying spot concept.

In confocal microscopy (CM), the depth scanning requires the axial movement of a lens to alter the focus, as the lens is heavy, the scanning cannot be fast. Electrically adjustable lenses may provide a solution for fast axial scanning in CM; however, there is no motivation for development in that direction in view of the much better resolution obtained using OCT.

OCT systems, using CCD cameras or arrays of sensors or arrays of emitters eliminate the need of scanning the beam. However, the same scanning terminology applies in such cases as well, where the ray scanning is replaced by different forms of electronic scanning.

In spectral domain OCT, scanning strategies as described by (ii) and (iii) in Fig. 18.2 cannot be implemented.

For 3D acquisition, either longitudinal B-scan OCT images are acquired at different transverse coordinates as shown in Fig. 18.2(iv) or C-scan OCT images are acquired at different depths as shown in Fig. 18.2(iii). Obviously, the longitudinal OCT B-scans shown in Fig. 18.2(iv) can be replaced with the en face B-scans in Fig. 18.2(ii).

18.2   Sampling Function in En Face OCT

In order to generate C-scan images at a fixed depth, a path imbalance modulator is needed in order to create a carrier for the image bandwidth. This will obviously require the introduction of a phase modulator in one of the arms of the interferometer, which would complicate the design and introduce dispersion [22]. Research has shown that the X or Y scanning device itself introduces a path modulation which plays a similar role to the path modulation created by the longitudinal scanner employed to produce A-scans or A-scan-based B-scans. Theoretical analysis has shown that the generation of a C-scan OCT image can be interpreted as interrogating the object with a specific sampling function. Depending on the position of the incident beam on the scanner mirror and on the interface optics used, the sampling function could look either as Newton rings or as a regular grid of lines. The sampling function is in fact a fringe pattern in transverse section. Consequently, when the beam scans the target, the OCT signal is modulated by this fringe pattern. As the pattern is not regular, the transverse resolution varies across the target and different frequencies result in contrast to the generation of A-scans, where the carrier frequency is constant. However, for sufficiently large image size, the errors introduced in the image by the variable sampling pattern can be neglected.

18.2.1 Newton Rings

Figure 18.3 shows the beam being deflected from point O on the galvanometer mirror MX by tilting this mirror at different angles β. In this simplified approach,
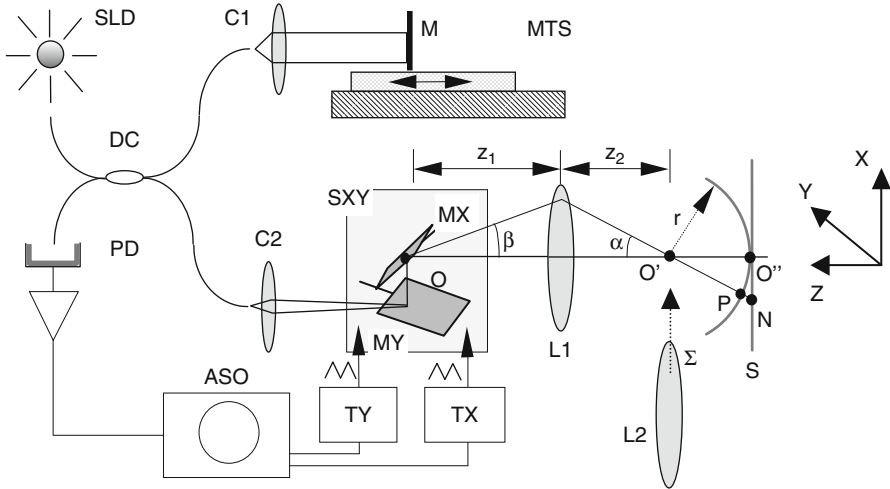
Fig. 18.3 SLD: Superluminescent diode; DC: directional coupler; C1, C2: microscope objectives; M: mirror; MTS: micrometer translation stage; SXY: galvanometer scanning mirror system; MX, MY: scanner mirrors; L1: lens; PD: photodetector; ASO: analogue storage oscilloscope; TX, TY: triangle waveform generators (Reproduced with OSA's permission from [12])

the distance between galvanometer mirrors MX and MY is neglected in comparison with the distance z_1 to lens L1, i.e., as regards scanning along Y, the beam may also be considered as originating from point O. The conjugate point of O is O′, and therefore, the optical path lengths of all the reflected rays measured between mirror MX and O′ are equal. Let us consider a flat surface S as the object under test, perpendicularly oriented to the system axis and intersected by the scanned beam at N.

The coherence surface Σ, defined by the length of the reference arm, is given by the spherical surface of radius r centered in O′. For each scanning angle β, two beams are superposed on the photodetector, one being reflected from the point N and the second reflected by mirror M, which may be equivalently considered as originating from point P on surface Σ. The optical path difference (OPD) between the reference and the sensing arm is [12]

$$OPD = 2(O'N - O'P) = 2\left[\frac{r}{\cos \alpha} - r\right]. \tag{18.1}$$

Maxima are obtained when

$$OPD = 2\,M\,\frac{\lambda}{2}, \tag{18.2}$$

where λ is the central wavelength and M an integer. The variation in the angle β measured about the point O between adjacent rays corresponding to two maxima in the photodetected signal is connected to the variation in angle α measured about the point O′ and is given by

$$\delta\beta = \frac{z_2}{z_1}\delta\alpha = \frac{z_2}{z_1}\frac{\lambda\cos^2\alpha}{2r\sin\alpha} \approx \frac{z_2}{z_1}\frac{\lambda}{2r\alpha}, \tag{18.3}$$

where we have taken into account the distances z_1 and z_2 in Fig. 18.3 and assumed small angles in (18.3). If mirror MX is driven by a triangular voltage signal of amplitude U and frequency F_x, then

$$\beta(t) = 4kUtF_x, \tag{18.4}$$

where k is measured in rad/V and represents the scanner angular efficiency. Using (18.1), (18.2), (18.3), and (18.4), the frequency ν at which maximums are encountered in the photodetected signal can be obtained as

$$\nu = \frac{8kUz_1F_x}{z_2}\frac{r\alpha}{\lambda}. \tag{18.5}$$

A similar expression can be obtained by considering the speed of OPD variation when performing A-scanning, in which case a reference mirror, M, is moved at a constant speed, v, and the frequency of the Doppler beat signal amounts to $\nu = 2v/\lambda$. Comparing this with (18.5) leads to an equivalent depth scanning speed:

$$v = \frac{4kUx_1F_x}{z_2}r\alpha. \tag{18.6}$$

The geometrical locus of the points on the surface S of maximum interference according to (18.2) is described by rings of radius $RM = O''N$. For small angles and a low-order M, the radius of such rings is given by

$$R_M \approx \sqrt{Mr\lambda}, \tag{18.7}$$

which shows that the locus of maximum interference is given by a similar relation to that describing Newton rings. However, the configuration in Fig. 18.3 differs from the Newton rings configuration presented in classical optics textbooks based on a spherical element in contact with a planar element [23]. Here, the interfering rays producing Newton rings are coming from two different arms of the interferometer.

Given the coherence length l_c of the source, the target area sampled by these Newton rings is limited to

$$A \approx \frac{\pi}{2}l_cr. \tag{18.8}$$

The analysis shows that the object is being interrogated with a sampling function which in the particular case of the setup in Fig. 18.3 looks like concentric circles
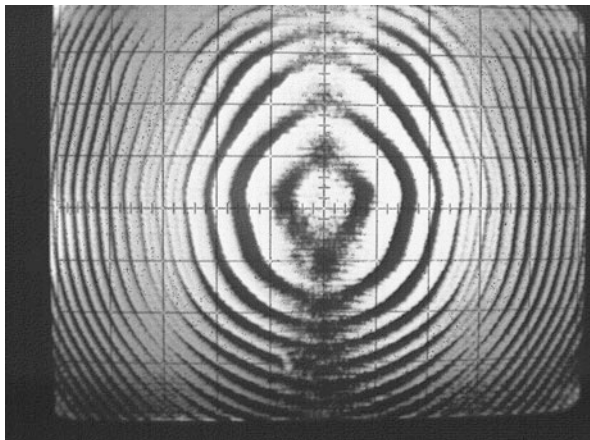
centered on the system axis. When the object is a mirror, the T-scans map the
sampling function and the returned signal is modulated in intensity at the frequency
ν given by (18.5).

In order to improve the transverse resolution, another lens L2, may be placed in
O′. The previously obtained relations are still valid with r replaced by f_2, the focal
length of lens L2.

An image from a mirror displays the sampling function pattern described by
Newton rings, as shown in Fig. 18.4. Such an image was obtained by using a lens L2
of 2.5-cm focal length and by driving the horizontal and vertical scanners with
signals at $F_x = 20$ Hz (signal generator GX) and 0.25 Hz (signal generator GY),
respectively. The amplitude of both signals was 0.25 V, and galvo-scanners with
k = 69.81 rad/V were used.

The main advantages of this imaging method are its simplicity and quick display
capability.

18.2.2 Grid Sampling Function

The incident beam direction is shifted by δ away from the rotation center of the line
scanner, chosen to be the X-scanner in Fig. 18.5. For simplicity, let us consider that
the scanning head XY is reduced to one mirror, X. To obtain incidence of the beam
off-pivot on the X-mirror, the scanner is displaced toward the objective C2 in
Fig. 18.3 by a distance δ, and then, the support holding the fiber and collimator
C2 is moved in such a way as to shift the launching beam parallel with itself by the
same distance δ, toward lens L1. In this way, for β = 0, the incoming ray is incident
on the galvanometer mirror in a point B on the optical axis (of the lens L1), situated
at $z_1 - δ$ away from lens L1. Two rays undergoing reflection at mirror MX are
shown in Fig. 18.5, when MX is tilted at an angle β/2 = 0 (impact point B, ray
deflected by an angle β from the axis) and when MX is tilted at an angle β ≠ 0
(impact point C). The ray deflected from C intersects the optical axis in A.

Fig. 18.5 The object beam in Fig. 18.3 is incident on the galvanometer scanner at a distance δ away from the center of rotation. Axes X and Z (shown in Fig. 18.3) are in the plane of the drawing (Reproduced with OSA's permission from [13])
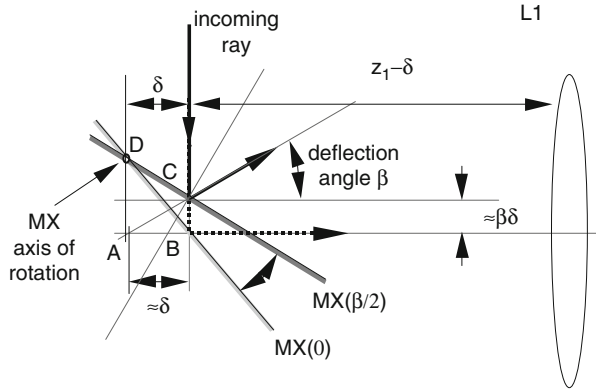
For small scanning angles β, the segment AB ≈ δ. In these circumstances, it can be shown that the path imbalance OPD introduced between the central ray (deflected from B along the optic axis) and the ray deflected from C at an angle β from the optic axis is given by the equation [13]:

$$\text{OPD} \approx -2\delta\beta + f_2 \frac{z_1^2}{z_2^2}\beta^2. \tag{18.9}$$

The first term in (18.9) can be intuitively thought of as arising from the double pass of light along segment BC (to and from the object), although the exact calculations are more elaborate. The second term gives the path imbalance responsible for Newton rings imaging in which case the ray geometry and formula were presented in the previous paragraph. Point A at a distance z_1 in front of L1 and point O′ at a distance z_2 behind L1 (Fig. 18.3) are conjugate by virtue of L1.

The frequency of the photodetected signal due to scanning a mirror placed in the focal plane of lens L2, perpendicular to the optic axis, is given by

$$\nu = \frac{8kF_xU}{\lambda}[\delta - 4kUf_2 \frac{z_1^2}{z_2^2}F_xt], \tag{18.10}$$

where the same notations as in (18.5) were used. During a scan, the frequency ν varies between

$$\nu_{\text{min,max}} = \nu_c \pm \nu_n = \frac{8kF_xU}{\lambda}[\delta \pm f_2 \frac{z_1^2}{z_2^2}\beta_m], \tag{18.11}$$

where ν_c is the central frequency and ν_n the frequency spread owing to the nonlinear OPD dependence on β in (18.10) (this is also the maximum component in the spectrum in the centered beam case in Fig. 18.3, Newton rings sampling function case).
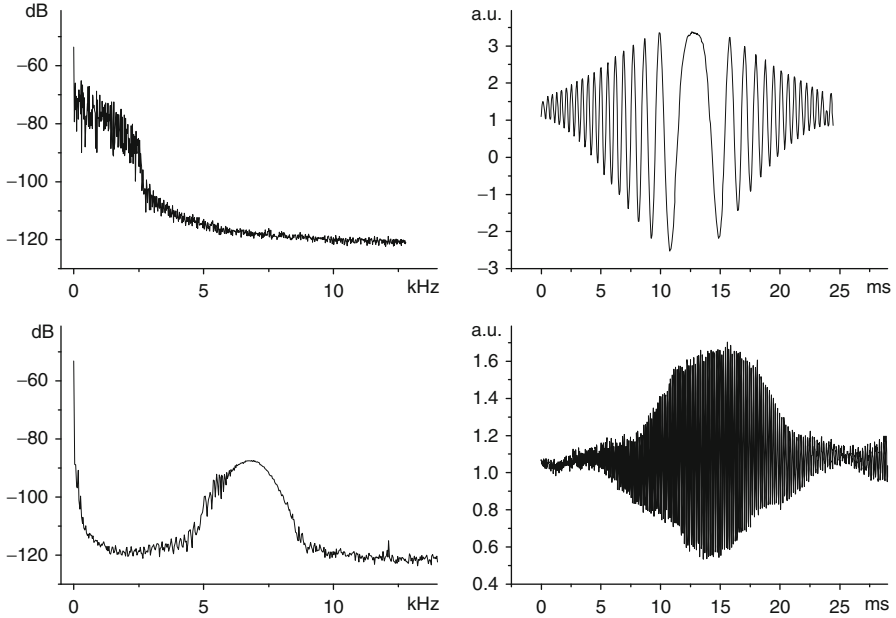
Fig. 18.6 Spectra (*left*) of the photodetected signal (*right*) for optical beam centered (*top*) and shifted by $\delta = 3$ mm (*bottom*). $z_1 = 14.5$ cm, $z_2 = 10.2$ cm, triangular drive signal of amplitude U = 0.17 V, and frequency $F_x = 20$ Hz applied to the X-scanner, Y-scanner not driven (Reproduced with OSA's permission from [13])

Interference occurs as long as the $|OPD|$ is less than the coherence length of the source, l_c. The maximum angle $|\beta|$ for which $|OPD| = l_c$ is β_c. For $|\beta| > \beta_c$, β_m in (18.11) is β_c, while for $|\beta| < \beta_c$, $\beta_m = kU$. Based on the Airy disk size of a pixel defined on a target situated in the focal plane of lens L2 (focal length f_2), for a beam diameter D, the image bandwidth is

$$B_i = 0.82 \frac{F_x D}{\lambda} \frac{\Delta X}{f_2}, \tag{18.12}$$

where ΔX is the width of the T-scan on the target.

The linear term in (18.10) becomes dominant when the shift δ is large enough, giving a first limiting condition for the minimum value of δ. A second condition results from $\nu_c - \nu_n > B_i$. It can be shown that the second condition prevails, resulting in

$$\delta > \frac{z_1}{z_2} \sqrt{f_2 l_c + 0.04 D^2}. \tag{18.13}$$

A "carrier" is distinguishable as shown in Fig. 18.6 bottom left (beam displaced by $\delta = 3$ mm), in comparison with the nondisplaced beam spectrum shown in Fig. 18.6 top left.

Fig. 18.7 Grid sampling
function. Horizontal and
vertical scale: 10 mV/div
(Reproduced with OSA's
permission from [13])

For example, values of $\nu_c = 6.86$ kHz and $\nu_n = 1.6$ kHz are obtained from
(18.10), in agreement with Fig. 18.6 bottom left, when $F_x = 20$ Hz, $\lambda = 0.83$ μm,
$D = 2$ mm, $f_2 = 3$ cm, and $\Delta X = 2$ mm. Equation (18.12) gives $B_i = 5.27$ kHz. To
produce a lateral scan $\Delta X = 2$ mm for $z_1 = 14.5$ cm and $z_2 = 10.2$ cm, the value of
the applied voltage is $U = 0.34$ V. Using (18.13) with $l_c = 31.9$ μm, δ should be
larger than 2.1 mm.

The sampling function takes the form of a grid of regular lines, as shown in
Fig. 18.7. This was obtained by driving the X- and Y-scanners with ramp signals of
amplitude 0.17 V, $F_x = 20$ Hz, and $F_y = 0.2$ Hz for $\delta = 3$ mm and using the same
scanner head as that used to generate the sampling function in Fig. 18.4.

Using the conversion factor of 29 μm/mV, the period of the grid of lines on
the target is found to be about 6 μm which indicates that the minimum feature
size which can be imaged using this sampling function is 12 μm. In comparison
with the Newton rings case, the spatial sampling rate is constant across the area
displayed.

To reduce the contribution of 1/f noise, a high modulation frequency is desirable.
By driving the X-galvo-scanner with a ramp signal at a frequency of 300 Hz,
amplitude 2 V, and $\delta = 3$ mm (maximum permissible by the size of the scanning
mirror), a value of ν_c in excess of 200 kHz was obtained.

Compared to the case of the nondisplaced beam Newton rings sampling func-
tion, the coherence surface now changes from spherical to conical. For small angles
β, the conical surface can be approximated with a plane perpendicular on the plane
of the diagram in Fig. 18.3, forming an angle $90° - \varphi$ with the optical axis and
intersecting it in O'', with $\tan \varphi \approx \delta/f_2$.

By generating a carrier, the features of the object in the center of the image are
now sampled at the same rate as those at the periphery of the image, in opposition to
the $\delta = 0$ case (Newton rings). This method has similarities with topographical
methods such as Moiré fringe pattern imaging. The sampling function acts as
a selective topographic function, with only those features of the object sampled
for which $|OPD| < l_c$.

In a different development, the frequency shift introduced by placing the incidence point away from the pivot was suggested as a frequency shifting modality essential in implementing a simple and effective solution to eliminate the mirror terms in spectral domain OCT [24].

18.2.3 Using a Phase Modulator

Ideally, to ensure constant sampling rate within the C-scan image, a phase modulator should be introduced in the interferometer. This is especially required for imaging small size features, less than the sampling spatial period (determined by the distance between Newton rings in Fig. 18.4 or the lines in the grid in Fig. 18.7). However, for sufficiently large size images, a phase modulator may not be required. To illustrate the contribution that phase modulation has to the creation of a C-scan image, depending on its size, a phase modulator PM based on a piezo cylinder was introduced in an OCT interferometer [14] and driven at 30 kHz. The X-galvo-scanner was driven by ramp signals of frequency Fx = 600 Hz and different amplitudes U. The Y-galvo-scanner was not driven. Figure 18.8 shows the ratio between the amplitudes of the components in the spectrum of the photodetected current in a bandwidth of 5 kHz centered about 60 (90) kHz obtained with and without the sinusoidal modulation of PM at 30 kHz. The amplitudes were averaged over 100 measurements. These graphs show that for voltages over $U_c = 0.6$ V, corresponding to a lateral image size of 1.6 mm, the external phase modulation does not add any noticeable contribution to the demodulated signal. Consequently, for an image size larger than 1.6 mm, the phase modulation created by the X-galvo-scanner is sufficient. Little enhancement is brought about by the PM in the range 0.3–0.6 V. For voltages applied to the X-scanner less than $U_3 = 0.32$ V, the modulation introduced by a PM becomes more important, as proved by the graphs in Fig. 18.8. This corresponds to a lateral image size of less than 0.8 mm for the configuration used in Fig. 18.3, where L1 has a focal length of 12 cm and a lens L2 of 2 cm.

The carrier frequency needs to be larger than the bandwidth. Therefore, for video rate OCT, only fast PMs can be used, which work at over few MHz, such as electro-optic modulators. However, such modulators introduce dispersion [22]. Nondispersive modulation methods rely on piezo-vibration of tiny mirrors or on stretching fiber. Such methods cannot however approach 1 MHz required for fast OCT imaging. Utilization of such modulators limits the acquisition time. For instance, in reference [19], microscopic size C-scan images of 0.6 × 0.35 mm of a frog embryo were obtained with piezo-modulation at 120 kHz. The external phase modulation was essential in this case, as the scanners were moved relatively slow (acquisition of a 10^6 voxel in 5 min).

Transillumination tomography [25] has been demonstrated using the same principle, where the phase modulator was implemented in fiber. Utilization of a low-frequency phase modulator was made possible by the slow transverse scanning (8 min for a 200 × 50 pixels images), so the carrier frequency generated by the
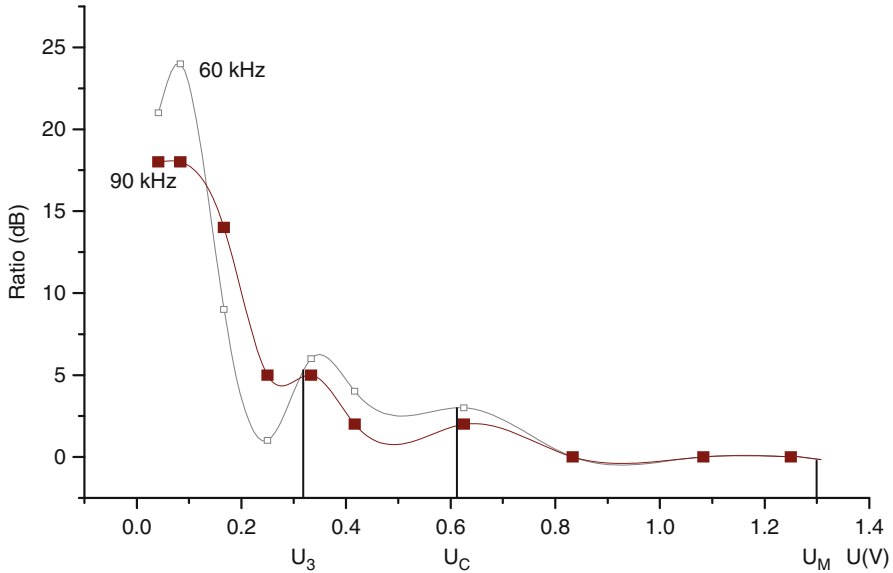
Fig. 18.8 Ratio of the amplitudes of the 60 kHz (and 90 kHz) components in the spectrum with and without the sinusoidal modulation applied to the phase modulator versus the amplitude U of the ramp signal driving the X-scanner. Fx = 600 Hz, the Y-galvo-scanner not driven (Reproduced with SPIE's permission from [14])

external phase modulator was much larger than the image bandwidth. The small band required allowed a high dynamic range of 130 dB.

18.3 T-Scan-Based C-Scan and B-Scan OCT Images Acquired from Different Objects

The images in Figs. 18.4 and 18.7 above display the sampling function when the object is a flat mirror. When imaging scattering elements of a rough surface, or a tilted surface, the sampling function is distorted. However, a C-scan image could still be generated, as proven by the examples below.

18.3.1 Profilometry

Four C-scan images at 20-μm depth intervals are shown in Fig. 18.9 obtained from the rough surface of a 5 pence coin.

What is important for imaging is the generation of fringe cycles when the features are at coherence. The amplitudes of these cycles are rectified and presented as proportional brightness on the screen. The roughness itself, compounded with the

Fig. 18.9 Images obtained from a 5 pence coin. The reference path was increased in steps of 20 μm between *top left* and *bottom right* image; 370 μm/div both horizontally and vertically (Reproduced with OSA's permission from [12])
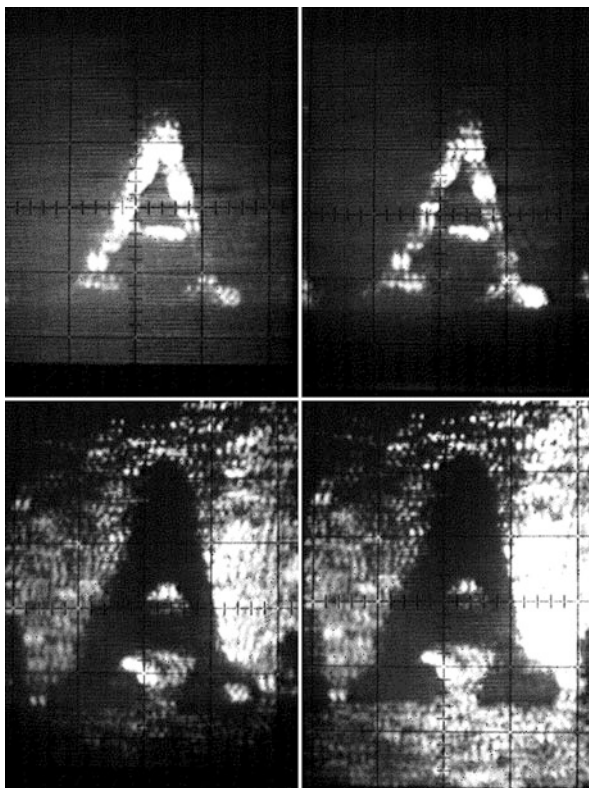
aberrations of the interface optics, introduces phase changes which lead to the modulation of interference signal under the form of spikes. The variations in the signal due to roughness may be denser across the transverse coordinate than that due to the sampling function. If such variation exists, then it is presented as an ac voltage to the rectifier. The amplitudes of the spikes so generated in the photodetected signal are proportional to the local reflectivity, and a high detailed image can be produced.

When imaging very small features, it is expected to "see" the sampling function superposed on the image [12, 13]. The sampling function is noticeable in Fig. 18.9, especially in the image in the top raw right.

In practice, when scanning a beam over tiny features, a similar effect to that encountered in anemometry happens. In anemometry, the beam is stationary and particles intersect the beam. The interference pattern is modulated by fluctuations of the moving particles.

The same happens in en face OCT, where the particles (object features) are stationary and the beam is scanned over. The fluctuations in the interference signal strength are rectified and produce brightness variation in images from scattering targets, such as tissue, as demonstrated below.
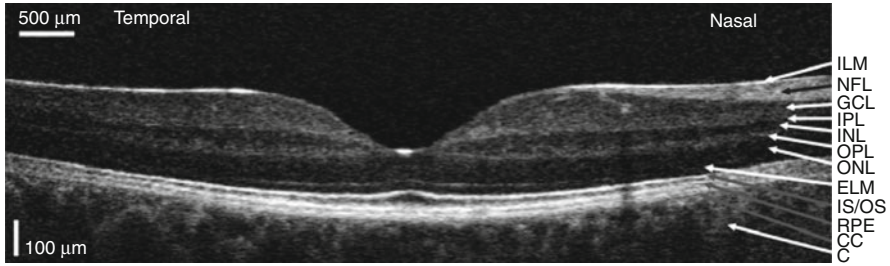
Fig. 18.10 En face ultrahigh-resolution OCT B-scan of the macular region of the human retina in vivo. ILM: the inner limiting membrane; NFL: nerve fiber layer; GCL: ganglion cell layer; IPL: inner plexiform layer; INL: inner nuclear layer; OPL: outer plexiform layer; ONL: outer nuclear layer; ELM: external limiting membrane; IS/OS: junction between the inner and outer photoreceptors; RPE: retinal pigment epithelium; CC: choriocapillaris; C: choroid (Reproduced with OSA's permission from [26])

18.3.2 T-Scan-Based B-Scan Images

Figure 18.10 presents a T-scan-based B-scan OCT image using a broadband SLD as a source [26], which determines an axial resolution of 3.2 μm in the retina. The image in Fig. 18.10, collected from the retina in the eye of a volunteer, shows with high resolution the succession of layers in the retina structure.

18.3.3 En Face OCT for Art Restoration

A particular application direction is that of assessing the capability of OCT for art conservation. We have proven that en face OCT can be used to monitor the thickness of varnish layers during conservation work of painting [27].

En face OCT is particularly suited to the imaging of underdrawings, since it can produce an image at the depth at which the underdrawing is located [28]. In addition, OCT in general offers greater resolution and dynamic range than any direct imaging method. Figure 18.11 shows that the en face OCT image of underdrawing on a test panel is far superior than even the images from the state-of-the-art infrared camera SIRIS using InGaAs technology [29]. The liquid droplets of the ink and the direction in which it is drawn can be seen in the C-scan OCT image.

OCT can be used not only for paintings but for imaging of transparent art objects, such as glass, faience, ceramics, and wood. C-scan OCT images of an Egyptian core-formed glass sample are shown in Fig. 18.12.

Some details of the 3D structure of the colored glass threads can be observed to a depth of approximately 500 μm. The principle feature of the images is the clear demarcation between the glaze and quartz layers [30].
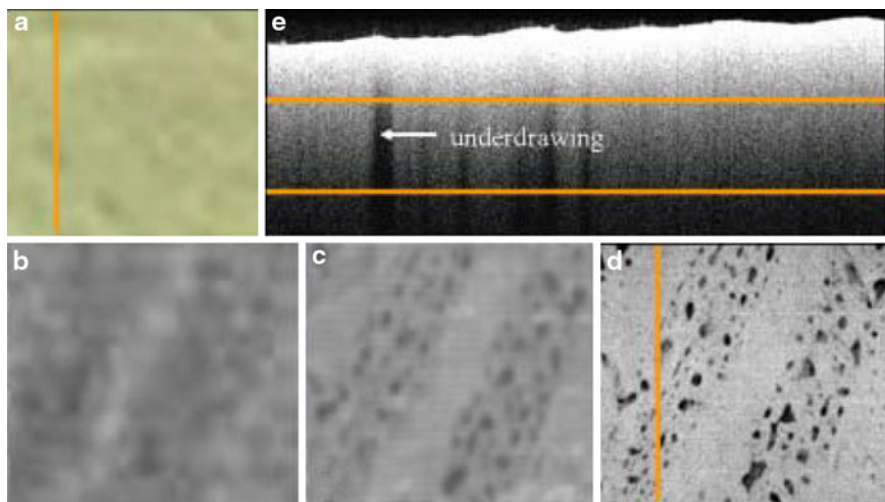
Fig. 18.11 Near-infrared images of a painted patch of two layers of lead-tin yellow over underdrawing of bone black in gum executed with a quill pen: (**a**) color image; (**b**) near-infrared Vidicon image; (**c**) near-infrared image from SIRIS, an InGaAs camera; (**d**) 1,300-nm OCT image, obtained by averaging C-scan OCT images collected from the depth interval between the horizontal lines in (**e**), where the underdrawing information is located; (**e**) B-scan OCT image obtained from T-scans along the line marked in the images (**a**) and (**d**) (Reproduced with International Council of Museums's permission from [28])
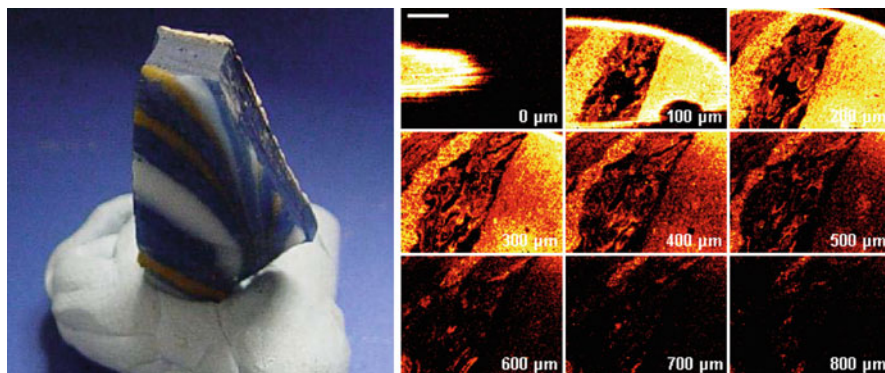
Fig. 18.12 Egyptian core-formed glass sample (British Museum Research Laboratory, No. 36458). *Left*: photograph (Reproduced with permission of the British Museum Research Laboratory); *Right*: C-scan OCT slices at 100-μm depth intervals (Copyright, Michael Hughes [30]). The 3D structure of the colored glass layers can be observed. The scale bar is 2 mm

Images in Figs. 18.9, 18.10, 18.11, and 18.12 demonstrate the capability of the T-scanning procedure in building C-scan and B-scan OCT images from a large variety of objects, from the surface, as well as from inside of rough structures and tissue, without recurring to an external modulator.
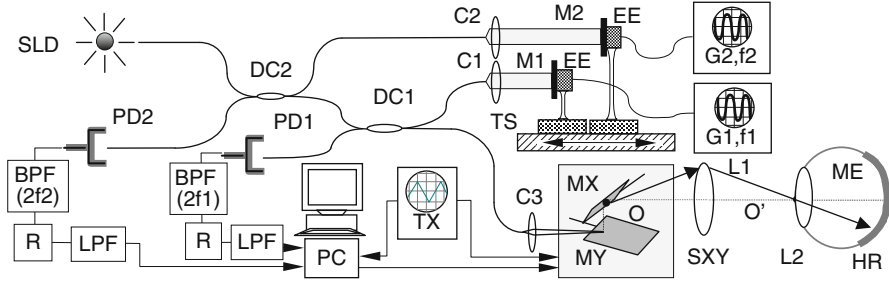
Fig. 18.13 SLD: superluminescent diode (850 nm); C1, C2, C3: microscope objectives; DC1, DC2: directional couplers; M1, M2: mirrors; PD1, PD2: photodetectors; SXY: orthogonal galvo-scanners; MX(MY): mirror of the X(Y) scanner; ME: model eye consisting of a lens, L2, and HR, human postmortem retina; BPF: band-pass filter; R: rectifier; LPF: low-pass filters; TS: computer-controlled translation stage; EE: electrostrictive element; G1, G2; sinusoidal generators (Reproduced with OSA's permission from [31])

18.4 Parallel OCT

The time to investigate the tissue in volume using en face OCT could be reduced by simultaneously acquiring several C-scan OCT images from different depths. This can be achieved by using multiple optical paths interferometer configurations. Several such configurations are presented.

18.4.1 Multiple Coupled Interferometers

Several interferometers, sharing the object arm toward the sample, tuned to different optical path differences, can provide simultaneously multiple C-scan OCT images from different depths. A configuration with two coupled interferometers is shown in Fig. 18.13. Light from a pigtailed superluminescent diode, SLD, is injected into a single-mode directional coupler, DC2. The transmitted light from one of the output ports is injected into a second single-mode coupler, DC1, while the light from the other port is directed to mirror M2. The elements in the object arm following DC1 up to the tissue are similar to those used in Fig. 18.3.

Two Michelson interferometers are formed using this arrangement. The reference arm in each interferometer consists of a microscope objective, C1 (C2), and a mirror, M1 (M2). Mirrors M1 and M2 are vibrated by two electrostrictive elements, EE, driven by sinusoidal generators G1 and G2 at f1 = 30 kHz and f2 = 22.5 kHz, respectively. Both mirrors are mounted on the same computer-controlled translation stage, TS. The tissue required a range of exploration in depth of 1 mm. Therefore, to generate distinct images, the difference between the depths of the two interferometers was chosen 1/4 from the range, i.e., 250 μm. This was adjusted by shifting the supports of the fiber ends and collimators C1, C2 relative to mirrors M1 and M2. Two photodetectors, PD1 and PD2, collect the returned optical

signals. After photodetection, the signals in the two channels are band-pass filtered (BPF) at 2f1 (2f2) in order to avoid the residual intensity modulation on the fundamental frequency.

The signals are then rectified (R) and low-pass filtered (LPF). The amplitude of the driving signals was adjusted to maximize the modulation at 2f1 and 2f2. The triangle generator TX drives the horizontal line scanner, MX, and triggers the acquisition of the two analog signals via an A/D interface. Data acquisition and hardware commands are synchronized under the control of a LabVIEW™ Virtual Instrument (VI). This VI also produces incremental voltage steps via a D/A interface to drive the vertical scanner, MY. The method is illustrated by acquiring and simultaneously displaying two en face images from the retina of a postmortem human eye, collected from different depths [31]. With MX driven at 20 Hz, peak to peak amplitude 1 V, and MY driven over 100 steps from -0.5 V to 0.5 V, the images in Fig. 18.14 were obtained. It can be noticed that the upper image in the set for z = 250 μm becomes similar to the lower image in the set for z = 0 μm. Due to the low-frequency phase modulation and scanning rate used, the display of the pairs of images required 3 s.

The production of two images is not done at the expense of speed or signal-to-noise ratio in the first interferometer. The addition of a second coupler (and interferometer) is compensated for by a corresponding increase in optical power, so there is no penalty for adding a second interferometer (if one neglects the increase in Rayleigh scattering due to longer fiber lengths).

However, the image quality obtained in the second interferometer may not be as good as in the first interferometer, as shown in the following.

This method could be extended to display several layers in depth by applying the principle illustrated in the setup in Fig. 18.15. The diagram in Fig. 18.15 shows the concept extended to 4 interferometers.

Considering the power from the SLD launched into the fiber to be P_0, the photodetectors to have sensitivity η, the directional couplers DC to have zero loss, the reflectivity of mirrors M_j to be R_j, and the eye to return a fraction O of the incident power (both R_j and O adjusted to include coupling losses in and out of fiber), the photodetected signal delivered by the last photodetector, PDn, is given by

$$i_n = \eta P_0 \left[\begin{array}{l} \dfrac{O}{2^{2n}} + \dfrac{1}{4}\sum_{j=1}^{n}\dfrac{R_j}{2^{2(n-j)}} + \dfrac{(-1)^{n-1}}{2^n}\sqrt{OR_n}\,\gamma(d_{On})\cos(\dfrac{2\pi}{\lambda}d_{On}) \\[2mm] + \sum_{j=1}^{n-1}c_j(n)\sqrt{OR_j}\,\gamma(d_{Oj})\cos(\dfrac{2\pi}{\lambda}d_{Oj}) \\[2mm] + \sum_{j,p=1}^{n}e_{jp}(n)\sqrt{R_pR_j}\,\gamma(d_{pj})\cos(\dfrac{2\pi}{\lambda}d_{pj}) \end{array} \right], \quad (18.14)$$

where γ stands for the modulus of the optical field correlation function, d_{Oj} is the OPD in interferometer j, d_{pj} is the OPD between mirrors Mj and Mp, c_j and e_{jp} are numerical coefficients, and λ is the central wavelength of the SLD. The first two terms represent a bias; the third one is the useful signal, periodic with components at multiples of f_n. The fourth term represents interference events between the object
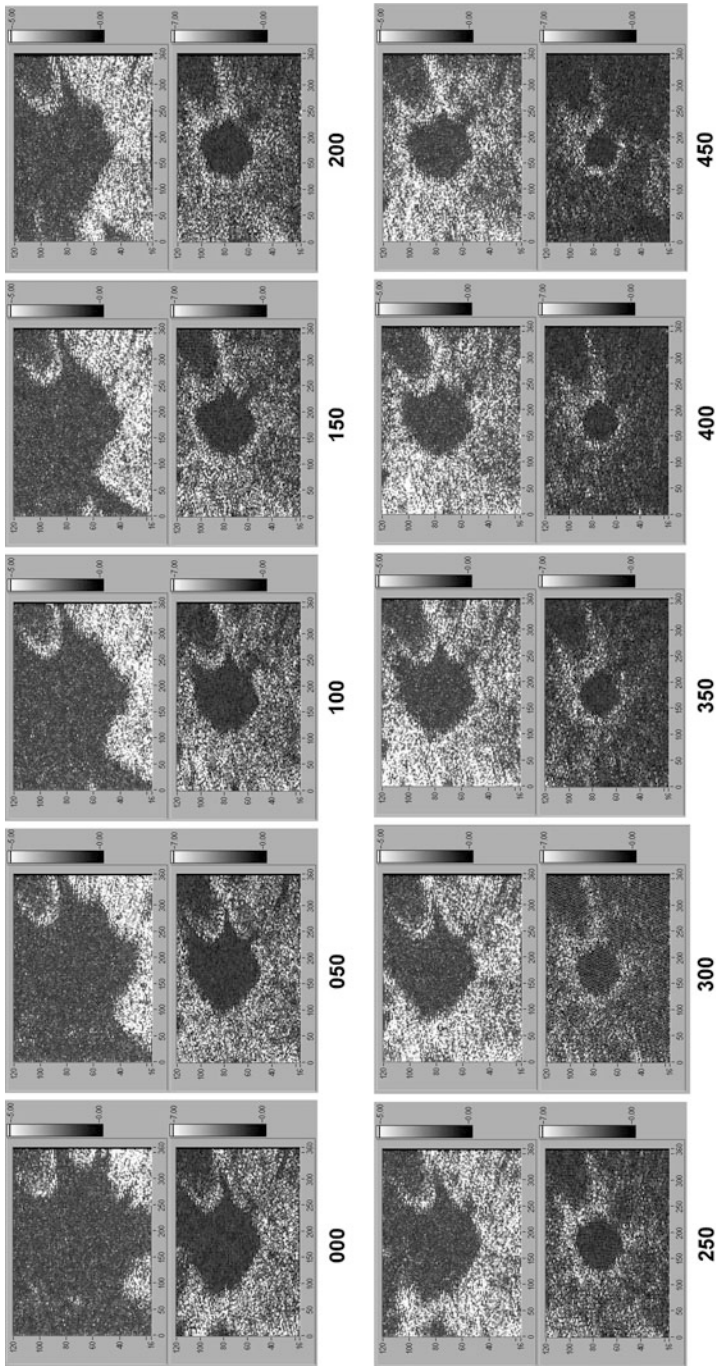
Fig. 18.14 Twelve pairs of 4 × 4 mm C-scan OCT images taken at 50-μm intervals from an in vitro retina tissue (Reproduced with OSA's permission from [31])
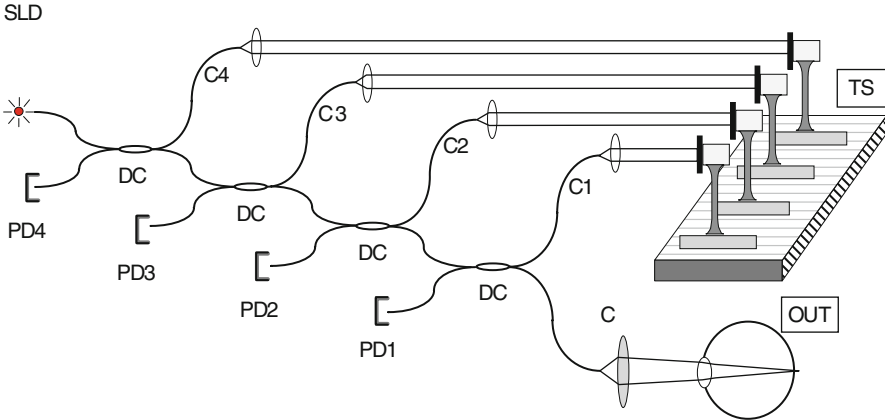
Fig. 18.15 System with four couplers (interferometers) for the simultaneous display of four en face layers. SLD: superluminescent diode; DC:50:50 single-mode directional couplers; PD1-4: photodetectors; M1-4: mirrors; TS: computer-controllable translation stage; C1-5: microscope objectives; OUT: object under test (Reproduced with OSA's permission from [31])

wave and the waves reflected by the reference mirrors in the interferometers closer to the object, j = 1,...n-1. These are periodic terms at multiples of frequencies f_j which can be sufficiently attenuated by band-pass filters tuned to f_n, if the frequency values f_j are correctly selected. The last term represents interference events between the signals reflected by the mirrors M_j and M_p with p = j. These are insignificant when the OPD increment from mirror to mirror exceeds the coherence length (due to the small value of $\gamma(d_{pj})$ in (18.14)). For instance, in the configuration shown in Fig. 18.13, d_{12} = 250 μm, which is much longer than the 25 μm coherence length of the source.

It can be shown that from one interferometer to the next, the object power decreases with the reference power increasing by the same factor. Consequently, a similar amplitude for the useful interference signal given by the third term in (18.14) results for all photodetectors.

An increase in the number of layers should be accompanied by a corresponding increase in the optical source power to ensure sufficient signal strength in comparison to noise. For safety reasons, the power of the beam should be limited to a safety value P_s, with $P_0/2^n = P_s$ in the third term in (18.14). It is clearly seen that the useful term is maintained constant as n increases if the source power is correspondingly increased. This increase in power is feasible with existing large bandwidth optical sources. The images in Fig. 18.14 were obtained with an SLD of 0.7 mW optical power. In principle, up to P_s = 1 mW CW power could be injected in the eye at 800 nm [32] when the beam is scanned. Given that the average power of solid state large bandwidth lasers [33], such as a Kerr lens mode-locked $Ti:Al_2O_3$ laser, can exceed 400 mW, a very large number of interferometers may in principle be operated simultaneously.

Another important constraint on increasing the number of layers (and accordingly of interferometers) derives from the fact that the interferometers are not

physically independent. The interference signal from the first interferometer is present on the photodetector in the second interferometer, the interference signal from the second is present in the third interferometer, and so on. The electronics in the nth interferometer has to filter out n − 1 interference signals, as given by the fourth term in (18.14).

In addition, the higher the number n, the higher the bias in (18.14) and the shot noise. These two contributions act as a noise source. The noise given by the fourth term in (18.14) can be reduced by a correct selection of frequencies f_j. Electrostrictive and tiny piezo-elements can vibrate millimeter size mirrors slightly over 100 kHz. For a 20-Hz period of the signal applied to the horizontal scanner, a bandwidth enlargement of up to 0.5 kHz was measured. With Q = 20 for the band-pass filter, a minimum carrier frequency of at least 20 kHz is needed. In the range 20 − 100 kHz, 4 carriers could be placed safely, in such a way that no multiples of any one carrier fit inside the bandwidth of any other channel and the nearest component is at least 4 kHz away from the tuned frequency. Higher modulation frequencies could be achieved by using electro-optic crystals, in which case, another unmodulated crystal should be placed in the sensing arm to compensate for dispersion.

The contribution to noise of the constant power on the detector, represented by the first two terms in (18.14), could be kept low only by reducing the bandwidth, i.e., increasing the image acquisition time. Considering that all BPFs have the same bandwidth, that all the unwanted interference signals (the fourth term in (18.14)) are largely attenuated, and assuming O<<Rj $\cong$ 1, a calculation in the shot noise limited case based on the shot noise value given by the second term in (18.14) reveals that compared to the first interferometer, the signal-to-noise ratio decreases by about 4 dB in the second interferometer, by 7 dB in the third interferometer, and 10 dB in the fourth interferometer.

The diagrams in Figs. 18.13 and 18.15 represent proofs of concept configurations; however, they may suffer from excess photon noise. To reduce such noise, a balance photodetection configuration is required. A possible solution is described in the next paragraph.

18.4.2 Simultaneous C-Scan OCT Imaging at Two Depths Using a Double Path Electro-optic Modulator

Simultaneous en face OCT imaging at multiple depths and rejection of excess photon noise are possible using an integrated modulator. A configuration with two channels [34] is shown in Fig. 18.16. The scheme employs only one interferometer with radio frequency multiplexing-demultiplexing.

The configuration is based on two single-mode couplers. Light from a pigtailed superluminescent diode, SLD, is injected into a single-mode coupler, DC1. The SLD delivers 120 μW to the object, has a central wavelength at 860 nm, and has a spectral FWHM of 18 nm. Assuming a Gaussian spectral profile, the coherence length, l_c = 32 μm, gives a depth sampling interval of 16 μm in air. In the object
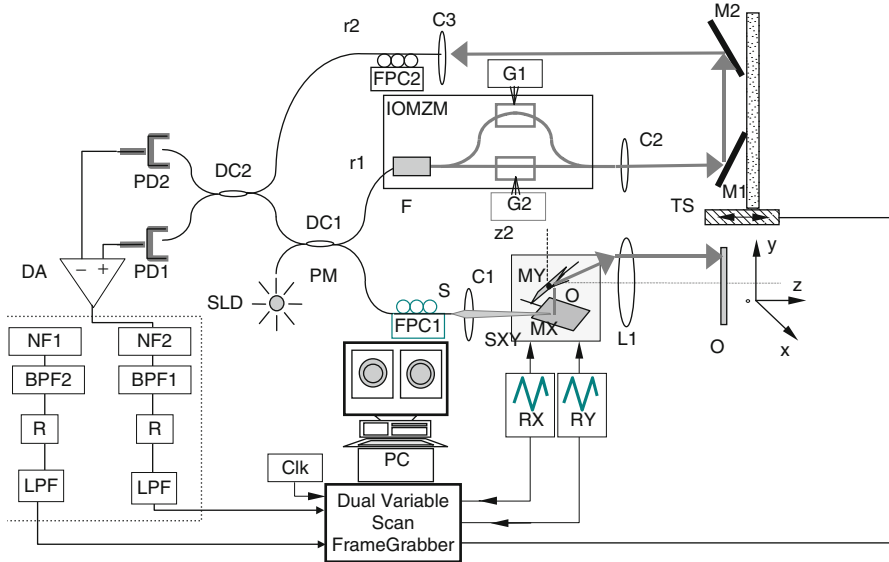
Fig. 18.16 Experimental setup for en face OCT imaging at two depths (Reproduced with Elsevier's permission from [34])

arm, the light propagates from the port S via a microscope objective, C1, the galvanometer scanner head, SXY, and then, passes through lens L1, focal length 6 cm to the object, O. Two sawtooth generators, RX and RY, drive mirrors MX and MY of the SXY galvo-scanning head. The transmitted light from the other port of DC1 (the reference beam), which is of much higher power than the signal beam, is transferred via ferrule, F, to the integrated optic Mach-Zehnder modulator, IOMZM. The ferrule F is in direct contact with the input guide of the IOMZM (Fig. 18.17).

The light at its output is collected via a microscope objective, C2, and then rerouted by mirrors M1 and M2 to the second coupler DC2. The two IOMZM electrodes are driven by sinusoidal signals from two generators G1 and G2 at $f_1 = 1.5$ MHz and $f_2 = 5$ MHz, respectively. The mirrors serving to recirculate the light in the reference arm are mounted on a computer-controlled translation stage TS to enable coherence matching of the reference and the object arm. Polarization controllers, FPC1,2, are mounted in the sensing and in the reference arms. Two photodetectors, PD1 and PD2, collect the returned optical signals from the coupler DC2.

The photodetected signals are applied to the two inputs of a differential amplifier, DA, in a balanced detection configuration. After DA, the signal is split into two electronic channels, each equipped with a notch filter, NF1 and NF2, and band-pass filters, BPF1 and BPF2, a rectifier, R, and a low-pass filter, LPF. The system has consequently two channels, providing two C-scan OCT images. Two variable scan rate frame grabbers are used to simultaneously display the two images.

Fig. 18.17 Depth sectioning interval of the two channels measured using a mirror as object, normally oriented to the system axis Z (Reproduced with Elsevier's permission from [34])
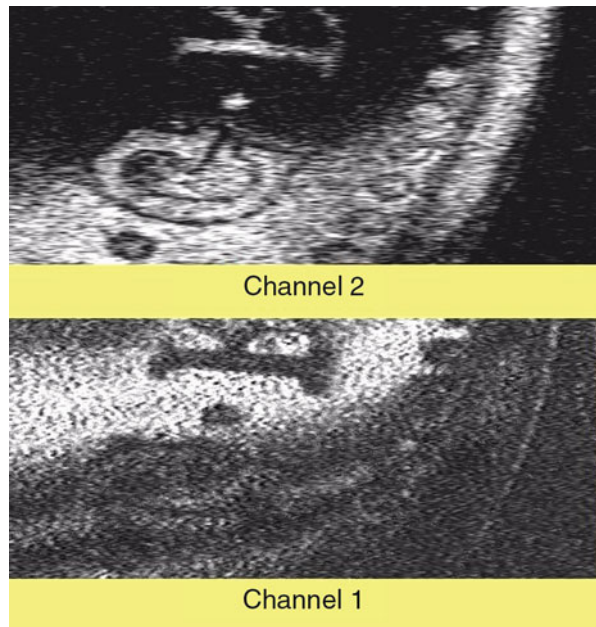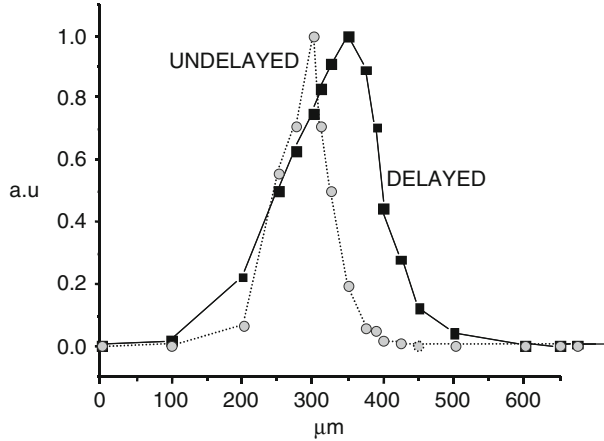
Fig. 18.18 Simultaneous C-scan OCT imaging at two depths from a 5 pence coin. Transverse size: 3 × 3 mm (Reproduced with Elsevier's permission from [34])

Sawtooth signals, of 700 Hz and of 2 Hz, are applied to the X- and Y-galvanometer scanners, respectively. For an image size of 150 × 150 pixels, the image bandwidth required is ≈100 kHz.

Modulating only one electrode at a time and processing the signal received from a mirror used as a target on the corresponding frequency, the correlation profile shown in Fig. 18.18 was obtained. Channel 2 uses the straight guide (undelayed) and exhibits a FWHM sectioning interval of 40 μm. Channel 1 uses the bent waveguide (delayed) and exhibits 120 μm. The sectioning intervals in both

channels larger than the value of 16 μm (given by half of the coherence length l_c) shows dispersion in the system with a larger dispersion component in the bent waveguide channel.

The simultaneous en face OCT imaging at two depths is illustrated using a 5 pence coin as object, O (the coin has a diameter of 18 mm). The amplitude on the two galvanometer scanners was such as to cover an area of 3 × 3 mm at the back of the lens L1. Both BPFs were set at pass bands of ≈100 kHz and the low-pass filter cutoff was adjusted to ≈150 kHz. The coin is an example of a two-layer object in depth separated by ≈60 μm, one layer, the plane of the coin background and the second layer, the top of the embossed letters. In channel 1 (Fig. 18.18, bottom), the background around the letter R is displayed, while in channel 2 (Fig. 18.18, top), the top of the letter R and some of the areas surrounding the letter G, showing that the coin is inclined with respect to the OZ axis.

The first implementation of such modulator and its coupling to the configuration was such that it could not be applied successfully to obtain images from tissue. Especially the presence of dispersion in the curved waveguide affected the achievable performances of the system. Progress in the technology of integrated optic modulators and more efficient coupling into fiber are envisaged in the near future. This will allow such a configuration to be applied to imaging of tissue.

18.4.3 Multiple Path Interferometer Configuration

The solutions previously studied exhibited increased losses with the number of channels [31] or mismatched dispersion in multiple path modulators [34]. These problems limited the number of channels to a reduced number, and the waveguide modulator solution in [34] is not reconfigurable either.

In this paragraph, a different configuration is presented which allows interrogation of multiple depths separated by an interval which could be easily adjusted from zero to values less, larger, or much larger than the coherence length of the optical source. Key to the new configuration presented is the use of recirculating loops in both reference and sample arms of a low-coherence interferometer [35], as shown in Fig. 18.19.

Light from a broadband source, BBS, central wavelength 1,060 nm, full width at half maximum 50 nm (Multiwave Photonics, Porto, Portugal), is split into a main sample arm and a main reference arm by the directional coupler, DC. Each main arm of the interferometer incorporates an acousto-optic frequency shifter, $AOFS_1$ ($AOFS_2$), which shifts the optical frequency upward by the frequency of the driving signal f_1, (f_2). The setup is based on a Mach-Zehnder interferometer, where each main arm feeds a separate optical ring, with adjustable path length. To compensate for the losses, identical semiconductor optical amplifiers, SOA_1 and SOA_2 (QPhotonics, QSOA-1050), are incorporated in the two rings. In this way, multiple depths can be interrogated, separated by the difference between the optical path lengths of the two rings, OPL_{Diff}.

The multiple delays thus introduced are encoded on the frequency given by the beating of signals at f_1 and f_2. After the $AOFS_1$ ($AOFS_2$), light is injected into the
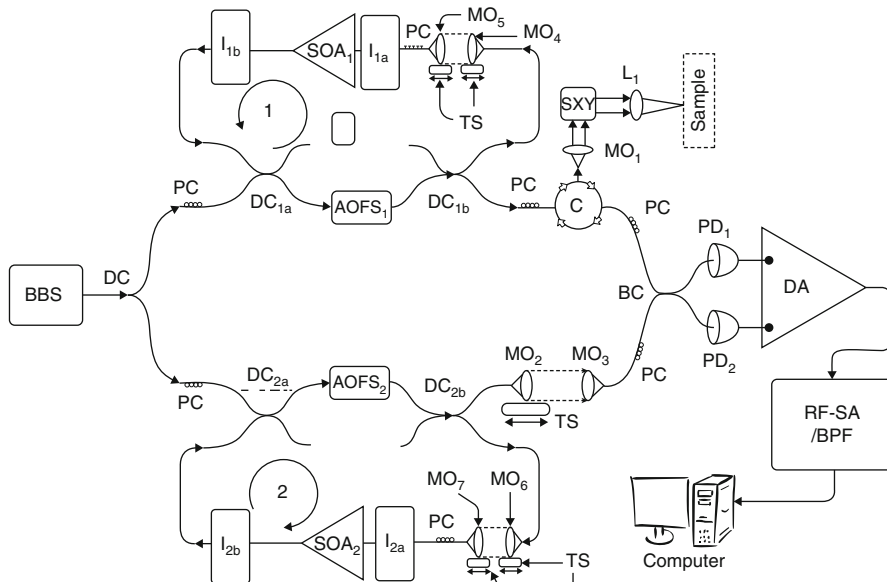
Fig. 18.19 Multiple paths configuration for en face OCT (Reproduced with OSA's permission from [35])

main loop as well as into a sample (reference) ring via a coupler DC_{1b} (DC_{2b}). Optical isolators I_{1a}, I_{1b} (I_{2a}, I_{2b}) placed at the input and at the output of the SOA_1 (SOA_2) protect their operation from stray reflections. The amplified light is reinjected into the main loop by a coupler DC_{1a} (DC_{2a}). For every pass of light through the sample (reference) ring, the optical frequency is shifted, by f_1 (f_2). The main sample arm contains an optical circulator C, microscope objective MO_1, a pair of orthogonal galvo-scanners SXY, and a lens L_1, sending 1 mW toward the sample. Its focal length of 2 cm and the $MO_1 \times 10$ determine a spot size on the sample of 10 μm. The multiple waves from the reference path interfere with the multiple waves from the sample path at the directional balanced coupler BC, producing a beat $f = n|f_1 - f_2| = n\Delta f$, where n is the number of recirculations of light in the two rings. The BC output signals are sent to a balanced photodetector unit, consisting of two pin photodetectors, PD_1 and PD_2, and a differential amplifier, DA. In this way, the OCT signal collected by en face imaging of the target is placed around a carrier of frequency $n\Delta f$. The $AOFS_1$ is driven at $f_1 = 40$ MHz, while $AOFS_2$ is driven from a generator which allows tuning of f_2 to adjust Δf.

A radio frequency spectrum analyzer RF-SA can be tuned on different frequencies $n\Delta f$. This operates as a tunable band-pass filter (BPF). The signals at $n\Delta f$ are generated simultaneously, and in principle, a signal processing interface can be designed to process all images at $n\Delta f$ simultaneously.
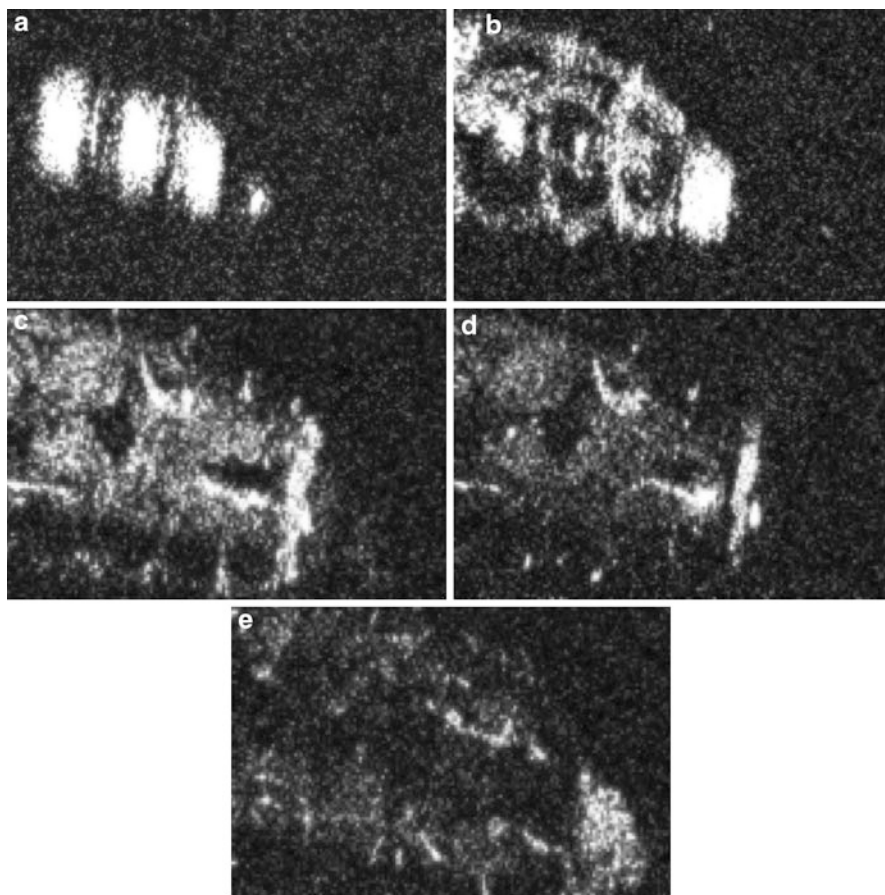
Fig. 18.20 Simultaneously generated C-scan OCT images of a *Drosophila* larva with its dorsal side up (posterior to the *right*) from five different depths, selected when the RF-SA was tuned on f = 1 MHz (**a**), 2 MHz (**b**), 3 MHz (**c**), 4 MHz (**d**), and 5 MHz (**e**) (Reproduced with OSA's permission from [35])

For a 500-Hz line rate, the bandwidth of the OCT signal is in the range of hundreds of kHz. Therefore, f_2 has been chosen as 41 MHz to determine a carrier frequency $\Delta f = 1$ MHz.

The optical path length in the rings can be adjusted using the micrometer screws of the translation stages, TS, that allow axial movement of microscope objectives, MO_4–MO_7, and fiber receptacles together. The difference in the optical paths of the two rings, OPL_{Diff}, can thus be adjusted. The number of recirculation passes through the rings determines the number of C-scan OCT images that can be collected for different depth positions of the coherence gate, at intervals determined by OPL_{Diff} measured from the depth in the sample where the main OPD is zero.

To prove such capability, the system was used to simultaneously acquire images from a *Drosophila* in its third larval instar stage prepared as described in [36]. Five such C-scan OCT images are shown in Fig. 18.20. The OPL$_{Diff}$ was set on 50 μm. In this way, multiple interference signals were produced via multiple recirculations at progressive 50-μm steps in depth in the fly. Images of 2.1 mm (horizontal) and 1.1 mm (vertical) in size were obtained by driving two galvo-scanners with ramps at 500 and 2 Hz, respectively (each image of 500 lines).

18.4.4 Multiple Delay Element in the Reference Arm

We have been exploring the possibility of reducing the time required for measurement of the cornea shape by taking multiple transverse scans at different depths at the same time. This application is different from the task in previous paragraphs, of collecting C-scan images at different depths. Here, we are interested in the topography of single-layer objects only, and a simplified method is proposed, based on en face OCT imaging, where all C-scans at several depths are superposed together. To this goal, a reference path composed of multiple optical path lengths is used. This is achieved by introducing a multiple delay element (MDE) in the OCT reference arm [37]. An MDE is constructed from stacked thin microscope glass slides. We will refer to an MDE-equipped OCT system as an MDE-OCT. A MDE-OCT C-scan image is obtained in the time normally required to obtain a single C-scan, yet it contains the information needed to determine the three-dimensional shape of curved objects, with applications in topography of the cornea. Since the measurement time is reduced in comparison with either scanning at multiple depths in case of a C-scan-based OCT system or at different polar orientations in case of a B-scan-based OCT system, the result is less affected by eye movement. Using this method, the axial position of or the radius of a spherical object can be measured.

The schematic diagram of the en face MDE-OCT setup is shown in Fig. 18.21. The system employs a two-coupler configuration, and the source is a 1,300-nm superluminescent diode sending 1-mW optical power toward the cornea. The depth resolution of the system is 18 μm in air. A low numerical aperture is used, by employing an achromatic lens of 4-cm focal length between the XY scanning block and the cornea. A galvanometric optical scanner pair is used to transversely scan the beam across the cornea in the transverse plane (X, Y). The X-scanner is driven at 500 Hz while the *Y*-scanner at 2 Hz. The axial position of the scan is controlled by moving the mirrors M which are mounted on a 1-μm-precision translation stage, TS. The reference beam intersects the MDE, which generates multiple optical path delays. A combined C-scan image is generated that is formed from the superposition of C-scan OCT images obtained for each optical path in the MDE in the reference arm.

18.4.4.1 Eye Topography

Topography of an eye obtained with an MDE with five plates is shown in Fig. 18.22.

The combined C-scan OCT image can be used to generate cornea topography, as the height of the cornea shape is coded in the radius of contours corresponding to
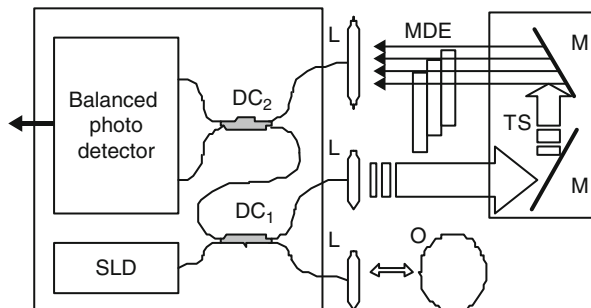
Fig. 18.21 Diagram of the multiple delay OCT system (SLD: superluminescent diode; DC_1, DC_2: single-mode directional couplers; L: lenses; M: mirrors; MDE: multiple delay element with three layers, which introduces four different length reference paths; TS: translation stage; O: object to be measured) (Reproduced with SPIE's permission from [37])
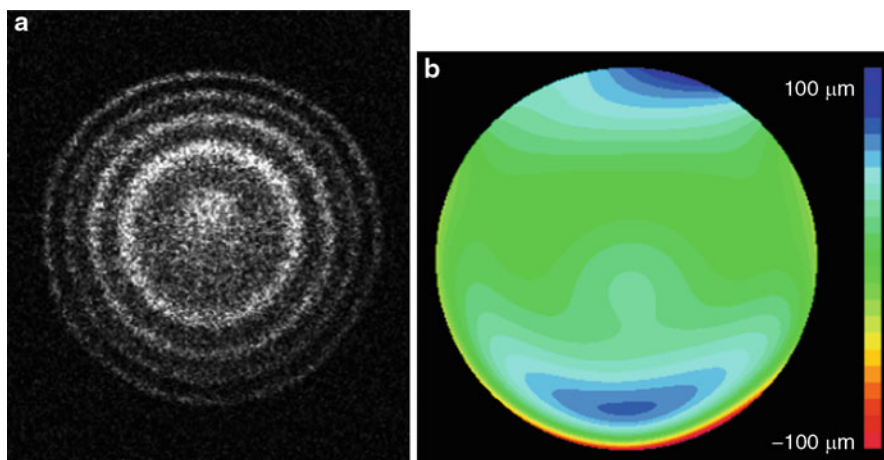
Fig. 18.22 (**a**) MDE-OCT C-scan image of the cornea of a volunteer and (**b**) cornea elevation map obtained from the image at (**a**) (Reproduced with SPIE's permission from [37])

the interface between air and the cornea. The acquired multiple contours C-scan is measured and analyzed by a computer program, identifying cornea surface locations that are placed at a specific axial distance, which can be used to produce a three-dimensional cornea topography dataset.

The method can be extended to measurement of topography of any single-layer reflective object. In the time required to produce one combined C-scan frame (the same as the time required for a single C-scan), all contours are obtained.

The same principle was also tested using a full-field OCT setup and a 2D camera [38] to measure the curvature of a metal ball in one shot.

18.5   Pixel-to-Pixel Correspondence En Face OCT and Confocal Imaging

It is simply to note that once the OCT image is oriented en face, it has the same aspect with that of images generated by using confocal microscopy (CM) [39, 40]. The following five reasons have led to a new imaging instrument [41] which blends together the two principles, OCT and CM:

1. In both imaging technologies, the en face OCT and CM, the fast scanning is en face and the depth scanning (optical path change in the OCT case and focus change in the CM case) is much slower (performed at the frame rate).
2. The better the depth resolution, the more fragmented the C-scan OCT image looks like. A single C-scan image from the tissue may contain only a few fragments and may be challenging to interpret.
3. In order to produce a B-scan OCT image, adjacent imaging instruments are required to guide the OCT system in directions perpendicular to the optical axis, toward the part of the tissue to be imaged.
4. The usefulness of the C-scan OCT images for the ophthalmologists can be greatly improved if the fragments of the fundus sampled by OCT channel are uniquely put in correspondence with fundus images produced by a CM channel.
5. In addition, the ophthalmologists have built large data bases of SLO images for diseased eyes. In order to exploit this knowledge in the interpretation of C-scan OCT images, it would be useful to produce simultaneously an SLO image. Having a witness image, with sufficient contrast, could lead to an improvement in the overall OCT imaging procedure for retinal assessment.

In order to implement a dual OCT/CM channel imaging instrument, a confocal channel was added to the en face OCT system by making the most of the components used to generate the OCT image. The two C-scan images produced by the two channels are naturally pixel-to-pixel correspondent [41, 42]. This helps with the guidance, especially in imaging the eye. When imaging the retina, the confocal channel provides an image similar to that of a confocal scanning laser ophthalmoscope (SLO) [43].

The combination of confocal imaging and imaging based on interference for scattering media has already been discussed in microscopy [44, 45].

A possible configuration for a dual-channel OCT/CM (SLO) instrument is shown in Fig. 18.23. Light from a pigtailed superluminescent diode, SLD, is injected into a single-mode directional coupler, DC1. Light in the object arm propagates via the microscope objective C3 and plate beam splitter PB and then enters the orthogonal scanning mirror pair, MX and MY. The converging lens L1 sends the beam toward the object under investigation, typically the retina, HR, of the human eye, HE. Lens L1 brings the fan of rays to convergence at the eye lens, EL. The reference beam is directed via microscope objectives C1 and C2 and the corner cube CC to coupler DC2. The corner cube CC is mounted on a computer-controlled translation stage, TS, used to alter the reference path length. The light back reflected from the object and transferred via DC1 to DC2 interferes with the reference signal in the coupler DC2. Two photodetectors, PD1 and PD2, collect the signal, and their outputs are applied to the two inputs of a differential amplifier, DA,

in a balanced detection configuration. The OCT signal is then demodulated in the demodulator block, DMOD, which drives the OCT input of a dual variable scan frame grabber, VSG, under control of a personal computer, PC.

Ramp generators TX,Y drive the transverse scanners equipped with the mirrors MX and MY, respectively, and also trigger signal acquisition by the frame grabber.

OCT configuration with balance detection is chosen here in order to attenuate (a) the intensity modulation resulting from vibrations in the translation stage, TS, moving the corner cube, CC; (b) the excess photon noise, not possible with an unbalanced configuration when the OCT acquires data fast [46]. As an additional bonus, recirculation of the reference power avoids a large power beam being sent back to the SLD, known being that these devices are prone to oscillations.

A separate confocal receiver is used based on a plate beam splitter PB (or a directional coupler), which reflects a percentage χ of the returned light from the object to a photodetector PD3 via a lens L2 and a pinhole H. The confocal signal is subsequently amplified in A and applied to the other input of the variable frame grabber VSG.

Two types of photodetectors are employed, silicon pin diodes for the photodetectors PD1 and PD2 in the OCT and an avalanche photodiode (APD) for the photodetector PD3 in the separate confocal receiver.

18.5.1 Choosing the Beam Splitter Ratio

Different criteria can be devised to find the most suitable value for the percentage of light, χ, diverted by the beam splitter PB toward the confocal receiver. However, due to the fact that the two systems employ different principles, comparisons of parameters to be balanced are difficult. An optimum design should address the trade-off between χ and the confocal channel depth resolution. The larger the percentage of light χ, the higher the intensity of the signal collected by the confocal photodetector, PD3, which allows for a smaller size for the pinhole H to be used before reaching the noise floor. The smaller the pinhole size, the better the depth resolution in the confocal channel [36]. However, at the same time, with the increase in χ, the signal-to-noise ratio in the OCT image worsens, as quantitatively described in reference [39].

18.5.2 Dual-Channel OCT/CM for Imaging the Retina (the OCT/SLO Instrument)

The en face OCT/SLO system described in Fig. 18.23 was applied to imaging several conditions of the eye. The scanning procedure is similar to that used in any SLO system, where the fast scanning is en face to produce a T-scan (as in Fig. 18.1, this determines the line rate, using the scanning mirror MX) and the frame scanning is much slower (at the frame rate, using the scanning mirror MY). The MX mirror is
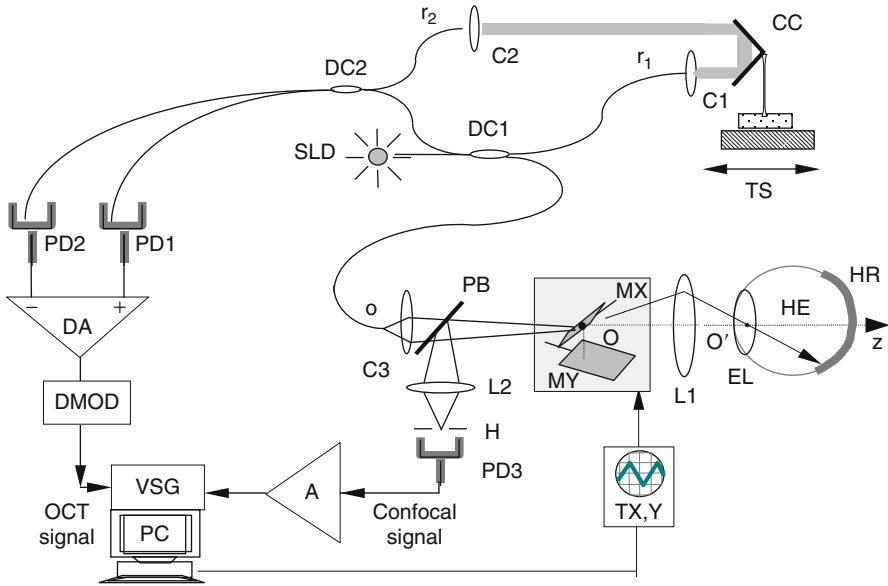
Fig. 18.23 Detailed schematic diagram of the apparatus using a plate beam splitter to divert light to a confocal receiver. SLD: superluminescent diode; C1, C2, C3: microscope objectives; DC1, DC2: directional couplers; TS: computer-controlled translation stage; CC: corner cube; M1, M2: mirrors; MX, MY: orthogonal galvanometer mirrors; TX(Y): ramp generators; DMOD: demodulation block; L1: convergent lens; PD1, PD2: photodetectors; DA: differential amplifier; PD3 and A: photodetector and amplifier respectively for the confocal receiver; H: pinhole; PB: plate beam splitter; HE: patient's eye; EL: eye lens; HR: human retina; PC: personal computer; VSG: dual input variable scan frame grabber for displaying and manipulating two images simultaneously (Reproduced by permission of the Institution of Engineering and Technology from [41])

driven with a ramp at 500 Hz, while the MY mirror is driven with a ramp at 2 Hz. In this way, a C-scan OCT image in the plane (x, y) is generated at constant depth. The next C-scan OCT image at a new depth is then generated by altering the length of the reference path of the OCT interferometer by controlling the translation stage TS in the reference path and repeating the (x, y) scan.

The system can operate in different regimes [10]. In the B-scan OCT regime, only one galvo-mirror of the galvanometer scanning pair is driven with a ramp at $500 - 1,000$ Hz, and the translation stage is moved for the depth range required in 0.2–1 s. In this case, an OCT B-scan image is produced either in the plane (x,z) or (y,z). A B-scan OCT image from the optic nerve in the plane (x,z) is shown at the top of the left pair of images in Fig. 18.24. The multilayer structure is clearly visible.

In the C-scan OCT regime, one galvo-scanner is driven with a ramp at 500–1,000 Hz and the other galvo-scanner with a ramp at 1–5 Hz. In this way, a C-scan image, in the plane (x,y), is generated, at constant depth. Then the depth is changed by moving TS in the reference arm of the interferometer, and a new C-scan image is collected.
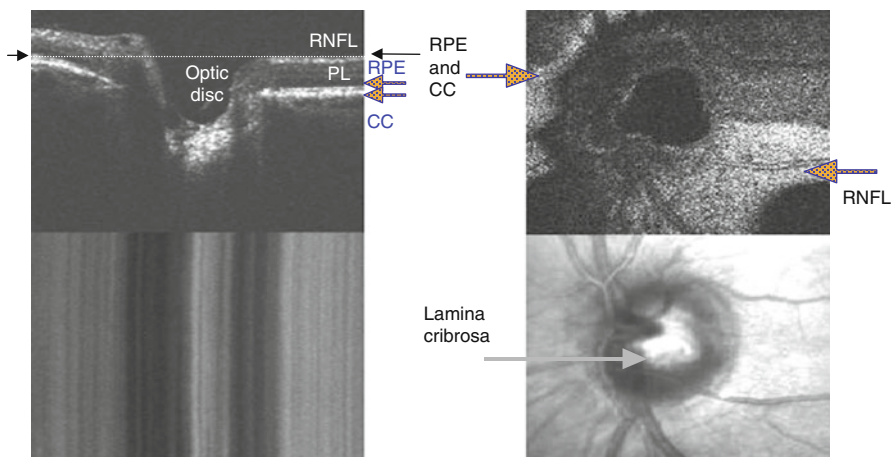
Fig. 18.24 Pair of images from the optic nerve acquired with the standalone OCT/confocal system. *Top* images: OCT, *Bottom* images: confocal. *Left*: B-scan regime at y = 0; *Right*: C-scan regime. The C-scan OCT image on the *right* is collected from the depth shown by the *double arrow* in the B-scan OCT image in the *left*. RNFL (*bright*): retinal nerve fiber layer; PL (*dark*): photoreceptor layer; RPE (*bright*): retinal pigment epithelium; CC (*bright*): choriocapillaris. 3 mm horizontal size in all imaging, *Left*: vertical coordinate in the OCT image is 2 mm depth measured in air, while in the confocal image, it corresponds to the acquisition time of the B-scan OCT image, 0.5 s. The lateral variations of the shades indicate lateral movements of the eye during the acquisition. *Right*: vertical coordinate is 3 mm (Reproduced with OSA's permission from [10])

An example of such C-scan OCT image is shown at the top of the right pair of images in Fig. 18.24. The bottom images in Fig. 18.24 are confocal, and they do not bear any depth significance. The brightness of each pixel in the confocal image is an integration of the signal received over the depth of focus determined by the interface optics and the pinhole in the confocal channel. Because the focus is not changed when altering the path imbalance in the OCT, the linear variation of the intensity received along the axis X in Fig. 18.24 bottom left and the (x,y) map of the intensity in Fig. 18.24 bottom right do not change with the depth z.

The combination of the C-scan OCT and C-scan SLO imaging was tested on eyes with pathology, such as exudative ARMD, macular hole, central serous retinopathy, RPE detachment, polypoidal choroidal vasculopathy, and macular pucker [11].

OCT/SLO images of a case of central serous retinopathy are shown in the top of Fig. 18.25. A pattern of concentric alternating dark and light rings are seen in the C-scan OCT image (right). This results from the convex splaying of adjacent hyper- and hyporeflective layers of the sensory retina. There is no border of intense hyperreflectivity as seen in an RPE detachment.

The images in Figs. 18.24 and 18.25 show two challenging features of the high-resolution C-scan imaging: patchy fragments and display of depth structure for the tilted parts of the tissue. The combined display of sections in the eye is extremely

Fig. 18.25 Central serous retinopathy. *Top*: SLO (*left*) and C-scan OCT image (*right*). *Bottom*: B-scan OCT image, lateral size 22° and 1.3 mm in depth (measured in air). The B-scan image was collected along the line in the middle of the SLO image, as shown in the *inset* beneath the B-scan, on the *right*. The SLO image in the inset underneath on the *left* is the image simultaneously generated by the SLO channel when the system operates in the B-scan regime. The verticality of lines proves that the eye has not moved laterally during the B-scan acquisition (Reproduced with Elsevier's permission from [11])
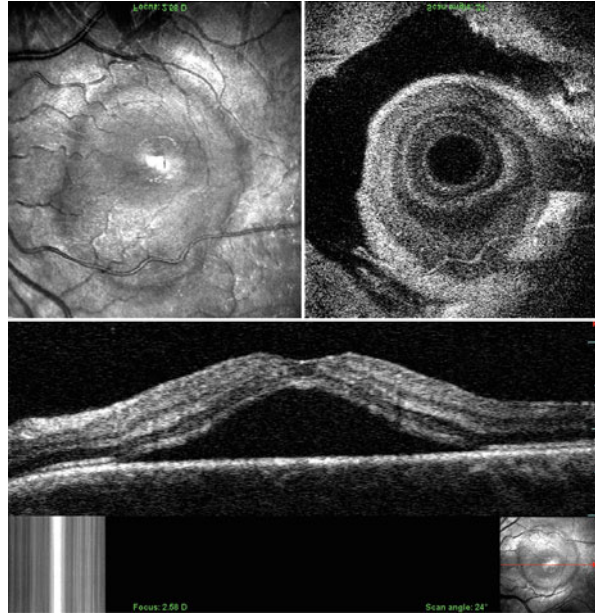
useful in interpreting these images. Similar aspect looking images with those produced by the SLO channel are obtained in real time using C-scan OCT. The confocal image in the dual-channel OCT/confocal system was found helpful in orientating and positioning the eye. It was much more difficult to align the eye using the OCT channel alone, as an image is displayed only when at coherence.

18.5.3 Beam-Splitter-less OCT/CM(SLO) Instrument

18.5.3.1 Sequential En Face OCT/SLO Imaging

Switching off the reference beam in a configuration as that in Fig. 18.23 removes the high value of photodetected intensity and the noise associated with the high-power reference beam falling on the photodetectors. In this way, the photodetectors can reproduce a noise-free SLO signal. Elimination of the constant terms means that high-gain photodetectors such as avalanche photodiodes (APD)s and photomultipliers can be employed, which however need to be swapped for low-gain photodetectors such as pin diodes when the reference beam is reinstated on the photodetectors in the OCT regime. A technical solution is presented in Ref. [47], where APDs are used in both regimes, and a self-switching APD regime is employed based on the voltage drop on the resistors in series with the APDs. The advantage of such a configuration is its simplicity and also its efficiency in using the whole signal returned from the retina to produce either an OCT or an SLO image, i.e., no splitting of the signal is required.

18.5.3.2 Quasi-simultaneous En Face OCT/SLO Imaging

Quasi-simultaneous imaging in the two regimes, OCT and CM, is achieved by using a chopper instead of the opaque screen, chopper which is controlled via a synchronization mechanism. This allows line-by-line operation, with a fast switching on the fly between the two regimes of operation, during the raster line of a dual frame image. The sensitivity of the OCT channel is not lowered, since no splitter is required. An additional difficulty was raised by the need to employ avalanche photodetectors (APD) in order to achieve sufficient signal-to-noise ratio in the CM channel. Low-noise electronics and optimization of APD voltage combined with the optical power level in the reference beam lead to a signal-to-noise ratio in the OCT regime close to that achieved when using PIN photodetectors.

The system [48], as shown in Fig. 18.26, is based on a two-splitter low-coherence hybrid interferometer optimized for broad bandwidth sources. Light from a superluminescent diode (SLD, Superlum, Moscow) centered at 810 nm with an 18-nm bandwidth is launched into the system through a single-mode optical fiber port and then is split by a plate beam splitter, BS, into an object and reference arm. The returned light from both arms is then routed into a second splitter, a broadband single-mode directional coupler, DC. In the object arm of the interferometer, a pair of XY galvanometer scanners is employed to direct the beam via the interface optics to the object.

A Fourier domain-optical delay line scheme in the reference arm is employed for dispersion compensation and depth scanning. This works in transmission and exhibits low losses by traversing the diffraction grating only twice [49]. The delay line uses a diffraction grating DG, a lens L, and a tilting mirror GS in a 2f configuration. The grating disperses a collimated beam, which is then imaged by an achromatic lens L at a distance f away. A galvanometer scanner, GS, with its pivot located in the other focal plane of the lens, causes a linear phase ramp on the spectrum and redirects the rays back to the DG through L. Here, the spectrum is recombined into a collimated beam. The outgoing beam exits the DG at a different point, O', parallel to the incoming beam. The amount of mirror tilt, θ, translates into a group delay for the output beam. This is based on the well-known property of the Fourier theorem that a linear phase in frequency domain corresponds to a group delay in time domain. To eliminate the walk-off, mirrors M_1 and M_2 are used to send the recombined beam back to GS, where the angular tilt is descanned.

A chopper (SR540, Stanford Research Systems) is used to square-wave modulate the intensity of the reference beam. The chopper is powered by an adjustable voltage power supply, which is set to rotate the chopper at a repetition frequency of 500 Hz. The TTL pulses delivered by the chopper are then fed into a function synthesizer (8116A Pulse/Function Generator, 50 MHz, Hewlett-Packard) that outputs a triangle waveform at 500 Hz to drive the line scanner. Mechanical and electric delays in the scanners require adjustment of the correct timing when the reference beam is toggled on and off. A delay is introduced by the block "line trigger delay" in the line delivering the TTL signal to the line frequency generator,
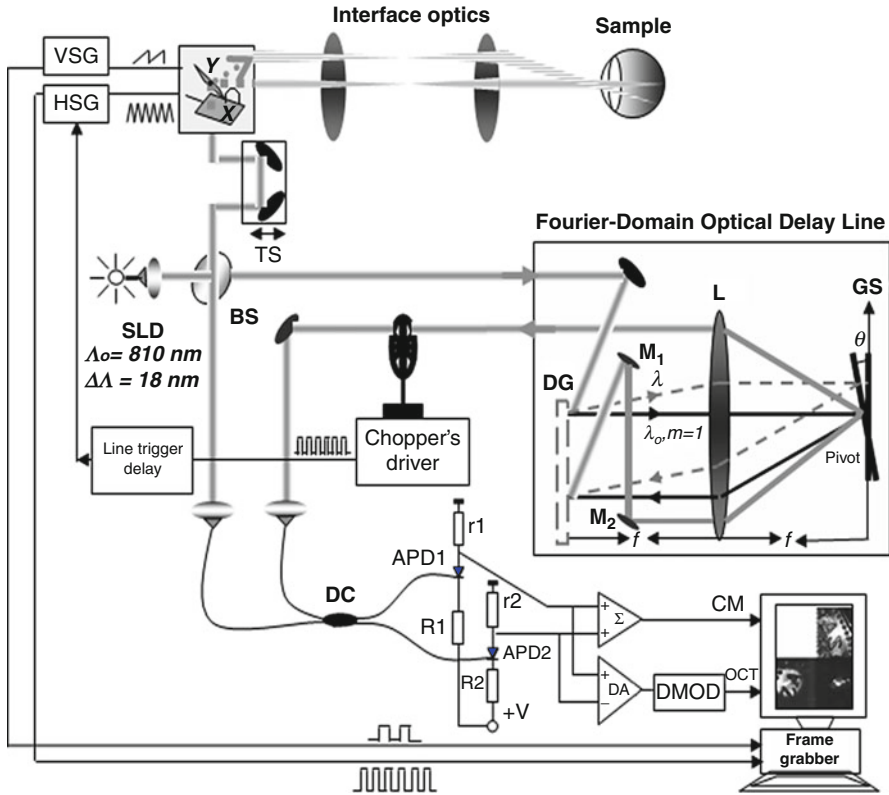
Fig. 18.26 Schematic diagram of the quasi-simultaneous en face OCT/SLO system. SLD, superluminescent diode (Superlum 361); BS, beam splitter; DC, broadband directional coupler; DG, diffraction grating; M_1 and M_2, mirrors; GS, galvano scanner mirror; $APD_{1,2}$ avalanche photodetectors; VSG, vertical signal generator; HSG, horizontal signal generator; Σ, summing amplifier; DA, differential amplifier; DMOD, demodulator block; $R_{1,2}$, ballast resistors; $r_{1,2}$ determine the sensitivity of the photodetection (Reproduced with SPIE's permission from [48])

and this is adjusted accordingly, in order to synchronize the start of ray deflection over the object with the moment of toggling the reference beam power on and off. The chopper's frequency was sufficiently stable not to require any adjustments during the imaging. The frame scanner in the XY-pair is driven by a vertical signal generator, VGS, with a sawtooth waveform at 1.5 Hz. The system operates differently during each ramp of the triangle sent to the line scanner. A similar approach was reported for generation of quasi-simultaneous OCT/OCT images with different depth resolutions [50], where a different coherence length source was used during each ramp. Here, the same source is employed, but the regime of operation is toggled from OCT to SLO synchronous with the X-scanner.

The system can be used to generate cross-sectional images by using either transverse priority or depth priority scanning, and it is suitable for compensating the dispersion when scanning in depth [51]. However, for the present study, we used
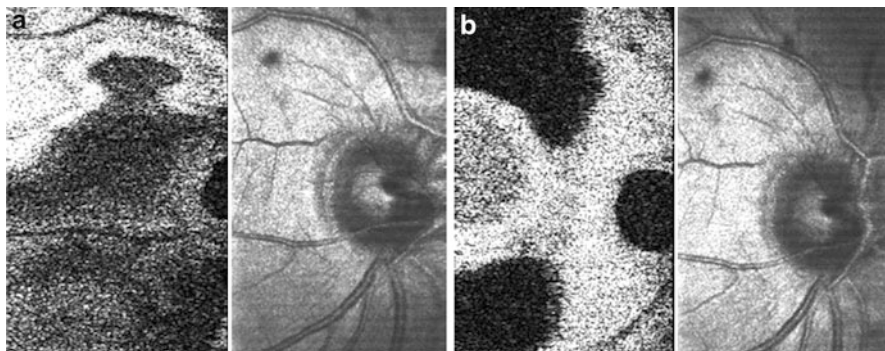
Fig. 18.27 Pairs of quasi-simultaneous C-scan OCT (*top*)/confocal (*bottom*) images of the optic nerve in vivo at different depths in the OCT channel. Image size: 4 mm (horizontal) × 7.5 mm (vertical). The images here have been cropped from the originals, and the OCT images were horizontally reverted to correspond to the SLO images (Reproduced with SPIE's permission from [48])

only T-scans, where the carrier for the image bandwidth was created by the path modulation introduced by the galvo-scanner determining the line in the final raster [12, 13]. The detection unit employs two avalanche photodetectors, APD1 and APD2 (Mitsubishi PD1002). Essential for the operation regime here is their self-switching [52] depending on the optical power applied and the value of the ballast resistors, r_1 and r_2. Therefore, we have designed a special amplifier board which has allowed adjustment of the ballast resistor values and of the transimpedance in order to optimize the S/N ratio.

The CM signal is provided by the summing amplifier (Σ), where the two photodetected signals collected from resistors r_1 and r_2 are added up. The OCT signal is available at the output of the differential amplifier (DA) after demodulation in the demodulator block (DMOD). A dual-channel variable frame grabber (BitFlow, Raven) is used to display the two images.

Ideally, during the first half ramp applied to the line galvo-scanner (X), of *1ms* (ascending slope), the reference beam is on and the system provides the OCT signal (while the CM channel is saturated). During the second half ramp of *1ms* (descending slope), the reference beam is blocked and the confocal signal is displayed (while the OCT channel provides a distorted CM image). For every line of *2ms* in the raster, *1ms* corresponds to the OCT regime and the next to the SLO (CM) regime of operation. Images of the optic nerve area obtained in these two regimes are shown in Fig. 18.27. The delay in producing SLO and OCT images is small, equal to the ramp duration; therefore, images can be considered as quasi-simultaneously obtained. They are, however, pixel-to-pixel correspondent.

In practice, there is a delay between the signal applied to the transversal scanner and the actual galvo-mirror tilt, as well as other delays in the electronics circuitry, which requires correction via the "line trigger delay." The OCT and SLO images captured by the system are mirror-inverted with respect to the median of the frame grabber display window.

Fig. 18.28 The anatomy of the dual OCT/CM imaging system. SLD: superluminescent diode; MO and MOi: microscope objectives; BSi: beam splitters; Li: achromatic lenses; PDi: photodetectors, APD: avalanche photodetector; PM: phase modulator; TS: translation stage; M: flat mirrors; DA: differential amplifier; SX, SY: galvanometer scanning mirrors (Reproduced with SPIE's permission from [53])
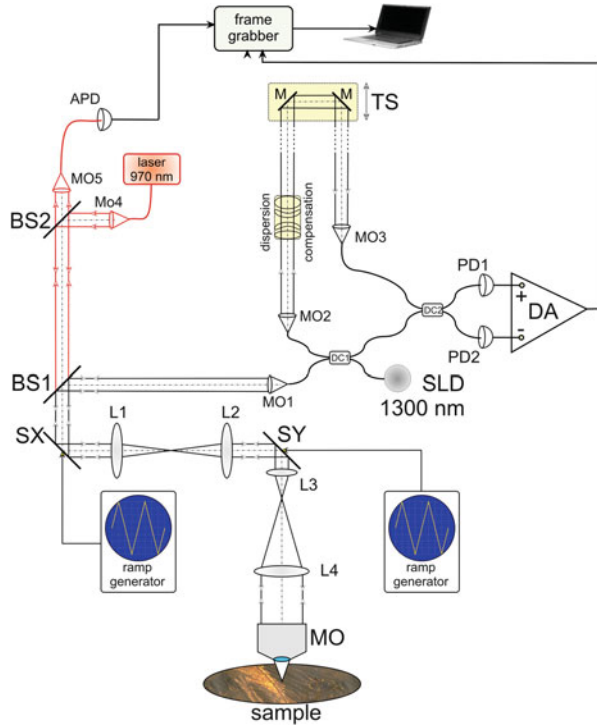
18.5.4 Dual OCT/CM in Imaging *Drosophila* Embryos

For microscopy, 1,300 nm is better suited due to less scattering. However, combination with CM requires a highly sensitive photodetector.

As avalanche photodiodes for this wavelength do not exist, a second optical source, emitting at 970 nm was used to drive a silicon APD amplifier [53], as shown in Fig. 18.28. Arrhythmia in *Drosophila* heart [54] was studied using such an en face OCT system. It was also found useful to record Doppler shifts of the signal after carefully positioning the beam on the heart and stopping the lateral scanning. Noninvasive live recording of the heart activity with the system provided series parameters from heart organ and single cardiomyocyte level.

Such a dual OCT/CM system was used to image *Drosophila* embryo and larval heart, by simultaneously acquiring OCT C-scan images with high depth resolution and CM images with low speckle noise.

The system could be easily switched to B-scan imaging. The imaging instrument has proven useful in distinguishing certain tissue structures in late embryo stage, as shown in Fig. 18.29, and monitoring the movement of the heartbeat cycle with high resolution. Although the acquisition speed could not cover all the process of the cardiac cycle, the system proved to be a useful tool in investigating some of the heart functions.
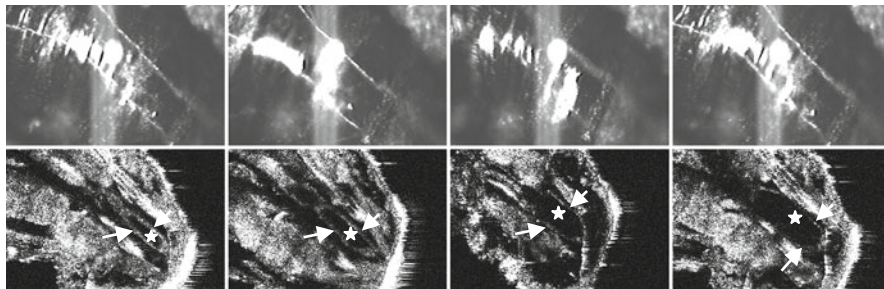
Fig. 18.29 Dual C-scan OCT (*bottom*) and CM (*top*) images of the heart of the *Drosophila* third instar larvae. The heart wall (*white arrow*) and the lumen (*stars*) of the heart at the contracting (systolic) and resting (diastolic) were recorded. Image size: 900 × 600 µm (Reproduced with SPIE's permission from [53])

18.5.5 Dual En Face OCT/CM in Imaging the Anterior Chamber of the Eye

Continuous examination from the cornea to the lens is not possible using the same optical design confocal microscope [55]. The reflection from the tear film in front of the epithelium is 2 %. If a confocal instrument is built to image the lens, then it can be used for imaging the cornea with limited success. The low numerical aperture of the interface optics precludes separation of the different layers in the cornea from the strong reflection at the air-tear film interface. Due to the low reflectivity of the transparent tissue in the anterior eye structure, there is a lack of contrast.

OCT addresses all these disadvantages and ensures the same depth resolution from the cornea level up to very deep in the anterior chamber [56].

An OCT/CM instrument was reported for collecting images from the cornea and the anterior chamber [57]. An SLD at 850 nm which delivers 300 µW to the eye was used, depth resolution in air slightly below 20 µm.

To visualize the cornea only, a numerical aperture of the interface optics of 0.1 was used. This gave a transverse resolution of better than 20 µm and a depth of focus of 0.25 mm in both the OCT and confocal channel (the values are larger than those theoretically expected due to aberrations). The C-scan images in Fig. 18.30 show the multilayer structure of the cornea. The top raw shows sections from the epithelium.

The Bowman layer is visible in transverse section; its separation from the epithelium is transferred to the distance between the external contour and first internal contour. The bottom raw displays C-scan OCT images from the endothelium.

In order to collect images in the anterior chamber as deep as from the lens, a lower NA aperture interface optics was used, of 0.02. This gives a long depth of focus with the disadvantage that the signal strength is just sufficient to allow visualization of the most important features in the anterior chamber. Figure 18.31 shows a couple of pairs of C-scan images so obtained, confocal and OCT, deep in
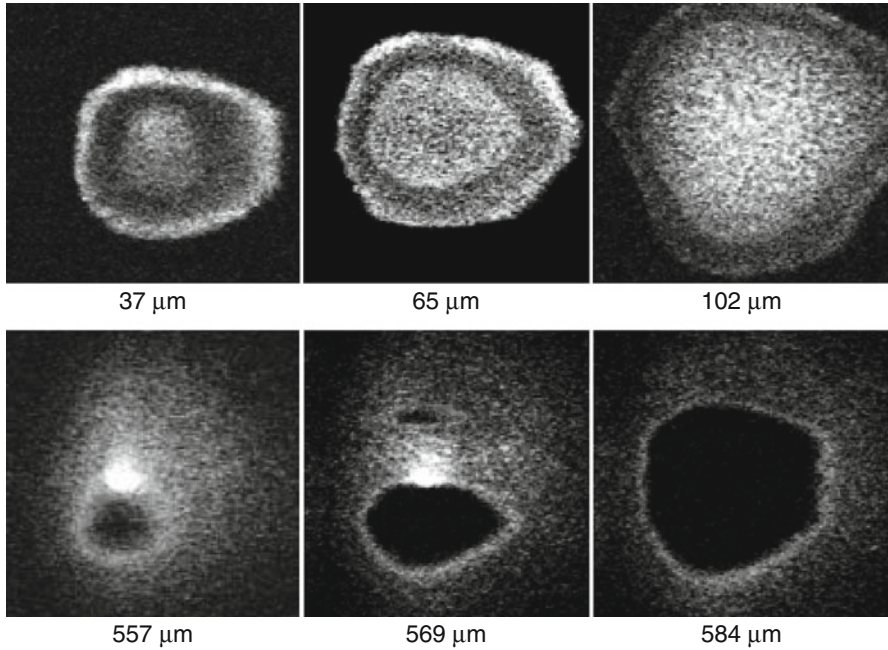
Fig. 18.30 C-scan OCT images of the cornea, 3×3 mm. All depths are measured in air relative to the top of the cornea (Reproduced with SPIE's permission from [57])
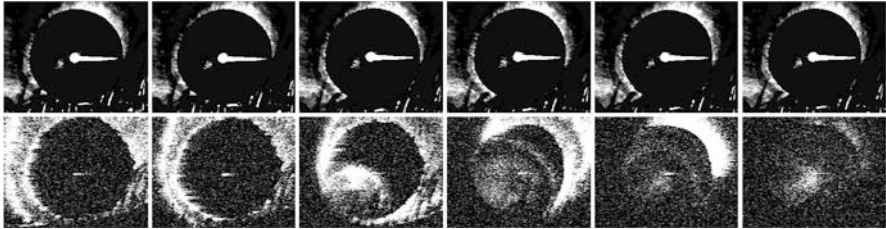
Fig. 18.31 Pairs of confocal (top) and OCT (*bottom*) C-scan images deep in the anterior chamber. Confocal images show the Purkinje reflections and the iris. Deeper, the lens is seen, offset from the optic axis, around the third Purkinje image. Differential axial separation between OCT images is 0.12 mm measured in air. Lateral size: 6×6 mm (Reproduced with SPIE's permission from [57])

the anterior chamber. The iris and the lens are visible. The images have been collected at a rate of 1 frame of pair images per second. The images in the top raw are the confocal images. Scanning deep in the anterior chamber using the OCT channel, the iris appears at a depth of 3.5 mm. The irregularities of the iris rim
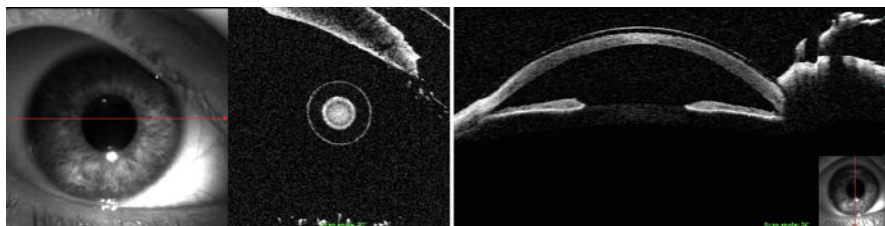
Fig. 18.32 Rigid contact on keratoconic cornea. *Left*: pair of camera image (*left*) and C-scan OCT image (*right*). The C-scan OCT image shows the apex of cornea surrounded by thin outline of contact lens. The distance to the outer ring reveals the fluid space between the *nipple* on the apex of the cornea and the lens. *Right*: B-scan OCT image shows the contact lens on the cornea but does not reveal the fine profile of the *nipple*. The *inset* image shows the orientation of the B-scan cut along a vertical line over the eye (Reproduced with Springer's permission from [58])

and the meshwork-like structure of the iris stroma are clearly visible at this magnification.

Then, at 4 mm depth, the lens becomes visible. The images in the bottom raw in Fig. 18.31 show the C-scan sections around the Purkinje reflected spots. The offset of the lens from the center of the image indicates how sensitive C-scan imaging is at off-axis orientation in comparison with the B-scan OCT imaging. The Purkinje reflections may be useful in aligning the eye axially, information difficult to handle when generating B-scan OCT images. The first two Purkinje images are visible in the confocal channel in Fig. 18.31. The clinical value of C-scan OCT images for examination of the anterior segment can be demonstrated with a variety of examples where the pathology in question is so asymmetric that single B-scan OCT images are inadequate to image the anatomy [58].

The advantage of the C-scan perspective is further demonstrated in a series of images (Fig. 18.32) of a cornea with keratoconus fitted with a rigid gas-permeable contact lens. While the cross-sectional OCT on the right shows the lens well fitted to the cornea, the coronal perspective on the left side, right image, actually reveals the fine disparity between the peak of the keratoconus nipple and the surrounding apex of the cornea.

18.5.6 Dual En Face OCT/CM in Dentistry

Several reports [59, 60] proved the ability of OCT to provide high-resolution images of dental tissues including caries lesion in enamel. However, these early reports on time domain OCT as well as the current reports on spectral OCT refer to longitudinal OCT imaging only. The information which can be collected cutting the object axially is obviously limited. It would be more natural to generate C-scan OCT slices in the tooth as their orientation is similar to that we are used to see when looking through a microscope. Therefore, en face OCT was extended to the imaging of dental tissue structures.

Fig. 18.33 Single frame of C-scan OCT and confocal images from a bovine tooth showing the demineralized part. Lateral size: 5 × 5 mm. Depth in the OCT image, 0.25 mm from the top of the tooth (Reproduced with SPIE's permission from [61])
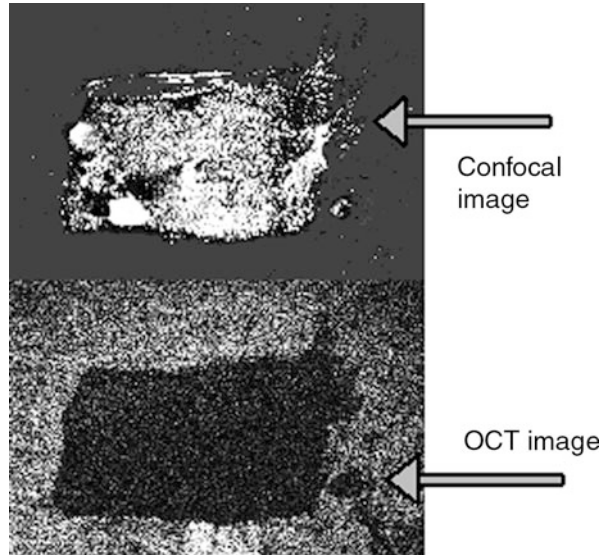
18.5.6.1 Evaluation of Demineralization

Demineralization of bovine teeth [61, 62] was assessed employing a dual imaging OCT/CM system. The teeth were painted with two coats of a nonfluorescent acid-resistant colorless nail varnish, except for an exposed window (2 × 2 mm) on the labial surface of the teeth. Caries-like lesions were then produced on each window by 3-day demineralization of the teeth in acidic buffer solution, as described in reference [63]. A pair of en face OCT image and confocal image is displayed in Fig. 18.33. Both C-scan and B-scan OCT images showed the caries lesion as volumes of reduced reflectivity. The caries appears bright in the confocal image. The confocal image displays an integral of the reflectivity over a large depth, 1 mm, and therefore, the high reflectivity of the superficial layer is expected to dominate any confocal variations in depth.

Again, the confocal channel was instrumental in guiding the investigation.

18.5.6.2 Investigation of Material Defects of Dental Prostheses and of Microleakage at Prosthetic Interfaces

An important goal in conservative dentistry is the evaluation of the microleakage in cavities filled with restorative materials. Presently, the methods used for assessing marginal microleakages are invasive and are performed in vitro only [64]. The OCT potential for clinical evaluation of dental restoration [65] has been demonstrated on interfaces between enamel and dental amalgam.

En face OCT was also proved instrumental in imaging gaps between the dental interfaces and material defects [66]. For best stability of orthodontic appliances, ideally, the resin shape should match the tooth shape. OCT can identify mismatches of the resin and the tooth shape. Voids may occur due to contraction caused by the curing process or due to an inadequate application of the composite resin. OCT has

Fig. 18.34 Dual C-scan images, confocal (*A*) and OCT (*B*); lateral size: 1 × 1 mm in both channels; (*a*) gutta-percha cone, (*b*) root canal sealer, (*c*) root canal walls, (*d*) microleakage area (Reproduced with Springer's permission from [67])
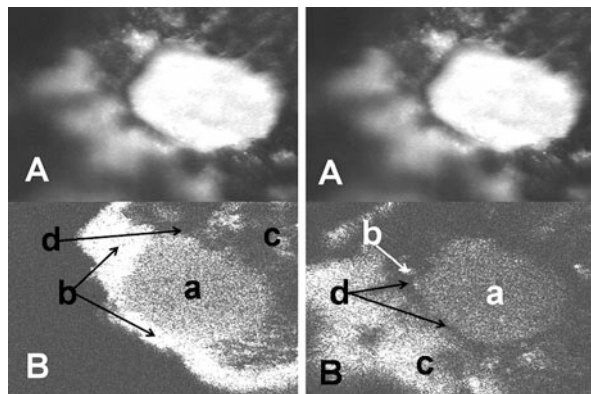
the potential for both investigating the bracket bonding technique as well as assessing the material defects inside the used composite resin.

All-ceramic restorations have recently entered the field of prosthodontics, offering improvements in esthetics. Early detection of substance defects within their layers is important in order to plan corrections before the restorations are inserted into the oral cavity.

En face OCT imaging was also used to investigate the apical microleakage after laser-assisted endodontic treatment [67] using a high-power 980-nm laser diode. Laser irradiation has the ability to remove debris and smear layer from the root canal walls following biomechanical instrumentation. After biomechanical preparation of the radicular spaces, the second important step in the endodontic treatment is the root canal filling. En face OCT imaging proved that laser processing leads to good preparation of root canal filling and reduction of microleakage, as investigated by producing images as shown in Fig. 18.34. Such images allow identification of a large numbers of defects within the control group.

These studies have proven that by versatile use of C-scans and B-scans, OCT can detect early caries lesions, show the depth of the lesion into the tissue, image and quantify the level of demineralization, and identify defects in dental structures.

18.5.7 Combination of Dual En Face OCT/CM(SLO) with Fluorescence Imaging

18.5.7.1 Applications in Ophthalmology

The dual-channel OCT/CM(SLO) instrument can in principle be customized to perform fluorescence imaging of either the indocyanine green (ICG), fluorescein, or both. ICG angiography and OCT appear well suited to operate together because they share similar spectral bands. The most widely used band for retinal OCT is 820–920 nm, while ICG is usually excited at 806 nm and fluoresces in the band 810–860 nm with a peak at 830 nm. Operating in similar bands allows the same source to be used for ICG excitation as well as for the production of an OCT image.

A chromatic splitter [68, 69, 70] is used in Fig. 18.35 to divert some of the light to a separate confocal receiver. This separates the retina-scattered light at the excitation wavelength 792 nm guided into the OCT channel, from the fluorescence signal, centered at 830 nm, guided toward the fluorescence confocal receiver. The residual transmission of the chromatic splitter (approx. 4 %) at the OCT wavelength is sufficient to generate an SLO image.

The fluorescence signal and the residual signal at the excitation wavelength are separated by a chromatic splitter, a cold mirror with a transition wavelength λ_{tr} between the excitation band and the ICG fluorescence band. To enhance the contrast of fluorescence in the confocal receiver, a supplementary filter "fluorescence emission filter" is used in the fluorescence channel to attenuate any excitation band light that penetrated the chromatic splitter. Superlum Moscow developed a comparatively powerful SLD for this project, with an output power of 5-mW ex-fiber at $\lambda = 792$ nm and $\Delta\lambda = 21$ nm spectral full width half maximum (FWHM) which determines a depth resolution in the tissue in the OCT channel of less than 9 μm (considering an index of refraction n ≈ 1.4).

Figure 18.36 further demonstrates the utility of the system in evaluation of a retina of a patient with polypoidal choroidal vasculopathy, a peculiar variant of neovascular macular degeneration [70]. Figure 18.36a–c presents the coronal aspect captured at 15, 28, and 60 s after the ICG injection.

Figure 18.36d shows the display in the B-scan regime, captured at 3 min and 18 s after the injection. The C-scans on the left were the last images collected in the OCT and ICG channels just before switching the instrument to the B-scan regime.
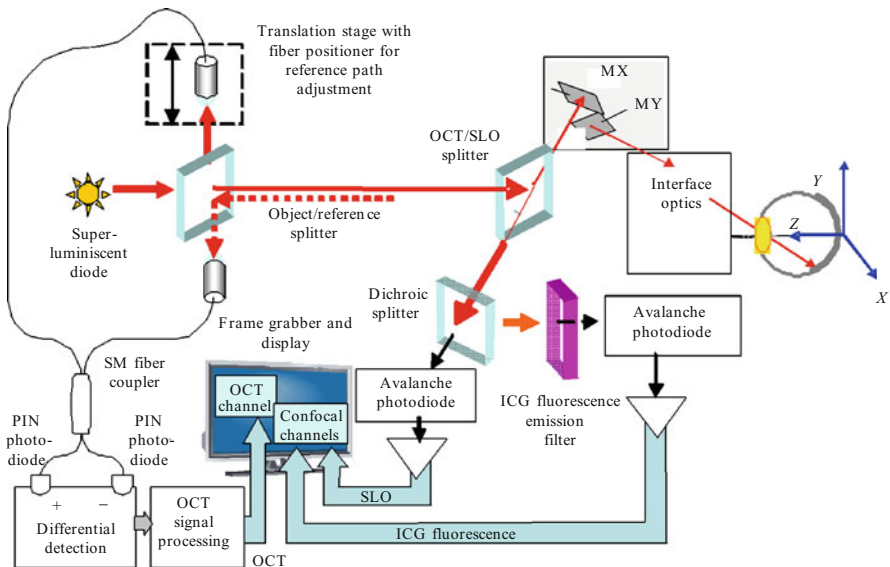
Fig. 18.35 Combined OCT/SLO/ICG system (MX, MY: galvanometer mirrors of the *XY* scanning pair); the confocal channels display a standard SLO image and an ICG fluorescence image (Reproduced with OSA's permission from [69])
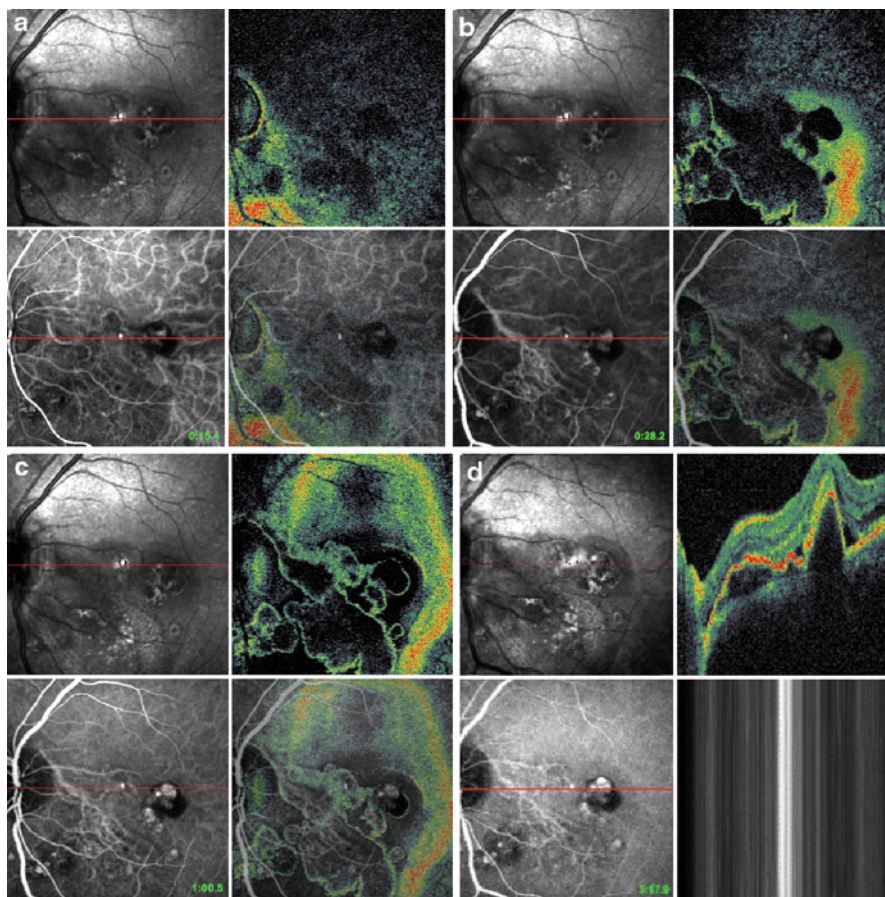
Fig. 18.36 ICG/OCT/SLO sets of a patient with polypoidal choroidal neovascularization. (**a**) Early arterial phase of ICG sequence reveals lobular choroidal vessels. OCT depth is within the choroid and shows evidence of shadowing. (**b**) Mid-arterial-venous phase demonstrates leash of deep abnormal vessels with hyperfluorescent bulbous endings. OCT image outlines the overlying serous elevation surrounding the vessels and hot spots. (**c**) Full venous phase of the ICG angiogram shows increased leakage at vessel endings. The OCT reveals the outlines of the serous cuff around the vessels and enlarging fluorescence accumulations. (**d**) Late-phase ICG with B-scan OCT through area of leakage (*top left*). The OCT reveals corrugated elevation of the RPE. The SLO image in the lower right (collected at the same time with the B-scan) confirms good alignment with minimal movement artifacts. The Z-axis of the B-scan is expanded by the configuration of the multichannel display producing an exaggeration of the aspect ratio. In all C-scan images, lateral size: $12° \times 12°$; B-scan OCT image, lateral size $12°$ and 1.3 mm in depth (measured in air) (© Copyright 2009 IOVS, [70])

The lateral size is the same as that of C-scan images, while the vertical axis is oriented along the depth coordinate.

The ICG angiography images reveal a leash of abnormal vessels which originate near the nerve, extend inferotemporally, and terminate with bulbous endings.

The accompanying OCT images capture the sausage-shaped cuff of fluid surrounding the vessels which accounts for the lumpy polypoidal appearance in the SLO images in the upper left quadrants of the display and in the cross-sectional B-scan OCT in Fig. 18.36d upper right. The overlay channel in Fig. 18.36a–c bottom right highlights the relationship between the vascular structures and the anatomic effect of the fluid leakage by displaying the vessels within the resulting cavitations.

The pixel-to-pixel correspondence inherent in the design of this system allows an integrated and potentially more accurate analysis of the association between morphology and function within the retina and choroid than is currently possible with separate instruments.

In these images, blood vessels are well defined in the ICG images while inconsistently revealed within the OCT images. At the same time, the depth resolution in the ICG channel is orders of magnitude lower than the OCT axial resolution, and morphology cannot be assessed accurately. Therefore, we believe that such a system can have valuable applications by combining the complementary information supplied by the two data channels. Regions of leakage, visible in the ICG image, can be selectively examined in depth by acquiring B-scan cross sections in the OCT channel.

18.5.7.2 Applications in Microscopy

The combination of OCT/CM imaging with fluorescence concept, as implemented in Fig. 18.35, can also be extended to microscopy. However, here, a large variety of fluorophores have excitation wavelengths in visible. This requires a technical solution with two sources to implement configurations similar to that in Fig. 18.28.

For imaging fast events, however, such as monitoring the movement of the heart wall in *Drosophila*, spectral domain OCT is better suited. As described in Ref. [36], a CM channel and a fluorescence channel produce C-scan images, while the OCT channel produces B-scan OCT images along cuts decided by observing the CM or fluorescence image. Such a system may also incorporate two sources. In Ref. [36], the fluorescence channel was tuned on the fluorescence emission of green fluorescein protein, and excitation was produced with a separate laser, at 488 nm, while the OCT channel used a longer wavelength to benefit from less scattering of 840 nm.

18.5.8 Synergy Between the Channels

When a confocal channel is added to an OCT imaging instrument, further versatility is gained. The same orientation of both images relative to the object investigated is possible with en face OCT only. The design described above ensures a strict pixel-to-pixel correspondence between the two C-scan images (OCT and confocal). This helps in two respects: for small movements of the tissue, the confocal image can be used to track the movements between frames and for subsequent transverse alignment of the OCT image stacks; for large movements, like blinks when imaging the eye or movement of the *Drosophila* larva in microscopy, the confocal image gives a clear indication of the OCT frames which need to be eliminated from the collected stack.

As a reference for the aligning procedure, the first artifact-free confocal image in the set is used. For example, in Fig. 18.24 bottom left, in the left inset in Fig. 18.25 bottom, and in Fig. 18.36d bottom right, lateral movements of the eye, if any, would distort the sequence of confocal traces. Each horizontal line in the confocal image corresponds to a depth position. The relative eye movement, proven by any lateral deviation of vertical shadows, can easily be transferred to the B-scan OCT image for correction.

18.5.9 New Challenge

New imaging technology brings not only new information to the clinician but, with it, the requirement of interpretation. En face OCT is no exception in this respect. The OCT images shown so far illustrate the challenges in interpreting and using the C-scan images.

First, the C-scan OCT image looks fragmented, and on its own, such an image cannot be interpreted. The higher the resolution of the OCT system, the more fragmented the C-scan OCT image looks like [14, 17, 18]. As the imaging proceeds at a few frames a second, the inherent eye movements may result in significant changes in the size of fragments sampled out from the tissue. The fragmentation (Figs. 18.9 and 18.24 right) is especially visible when imaging inclined layers.

Second, variations in tissue inclination with respect to the coherence wave surface alter the sampling of structures within the depth in the tissue, producing novel slice orientations [71] which are often challenging to interpret. The bright patches in the OCT image represent the intersection of the surface of optical path difference (OPD) = 0 with the tissue.

Additional complication is brought about the particular way the tissue is scanned. The retina is scanned, with a fan of rays converging on the eye pupil, so the surface of OPD = 0 is an arc circle with the center in the eye pupil. When the depth is explored, the radius of the arc is altered. If the arc has a small radius, it may just only intersects the top of the optic nerve with the rest of the arc in the aqueous. The radius of the arc is changed by changing the length of one of the arms of the interferometer in the OCT channel to explore the retina up to the RPE and choroid.

When scanning the cornea and the skin, the scanning ray is moved parallel to itself and with a normal to the tissue. Any curvatures in the tissue will alter the curvature of the C-scan image. When imaging the cornea, for instance, the pixels in the C-scan images in Fig. 18.30 do not belong to a plane perpendicular to the eye axis but to a curved surface. Normally, the curvature of deep C-scan surfaces follows the curvature of the external surface of the tissue, while in B-scan images, deep layers are curved against the external surface curvature of the tissue.

The layers at the back of the eye are also not planar, and this complicates the interpretation of the image even further.

Consequently, despite cutting images en face, along the T-scan direction, C-scan images may display the structure in depth like in any B-scan OCT image. For instance, the C-scan images in Fig. 18.30 top raw display the Bohman layer.

As far as the fragmentation problem is concerned, this can be addressed by providing a confocal image which guides the user and by collecting many C-scan images at different depths and subsequently building the 3D profile. However, the display of structures in depth in the C-scan OCT images requires education of the interpretation process.

18.5.10 Adaptive Optics-Assisted En Face OCT/CM(SLO)

The transverse resolution in OCT imaging is governed by the optics of the eye and its aberrations. In a flood-illuminated eye, adaptive optics (AO) was employed to demonstrate that transverse resolution could be improved to the point where it was possible to distinguish the cones in the fovea [72]. AO utilizes two devices operating in closed loop. In an AO closed loop system, a wave front sensor (WFS) [73] measures the deviations of the wave front from a plane and uses this information to actuate a wave front corrector, a deformable mirror, or a liquid crystal [74].

A flying spot ophthalmoscope incorporating AO elements [75] was reported with an estimated resolution of 2.5 μm transverse and 100 μm axial.

The application of AO correction to the OCT/SLO dual imaging system would appear to be a natural fit; however, it is not straightforward. Implementing AO in OCT raises a number of issues not present in the simpler cases of the scanning laser ophthalmoscope or the fundus camera. Matching the beam diameter to that of the corrector, to the aperture of the XY transverse scanner, with the size of the lenslet array in the Shack-Hartmann wave front sensor and with the SLO confocal receiver aperture raises constructive and engineering problems.

Figure 18.37 shows a schematic diagram of an OCT/SLO system, where aberrations are reduced by using a closed adaptive optics loop [76]. A superluminescent diode, SLD, is used with central wavelength at 831 and 17 nm bandwidth (which determines a depth resolution of approximately 13 μm in the eye). The source beam is collimated and then split by a beam splitter (90 % transmission), BS1, into a reference and a probing beams. The probing beam is reflected by the deformable mirror, DM, and then sent via a Badal defocus corrector, BDC, then via the XS and YS galvo-scanners to the subject's eye. The YS and XS scanners are driven at 2 and 700 Hz, respectively.

A series of telescopes built using pairs of spherical mirrors are used. Mirrors have been chosen rather than lenses to avoid the stray reflections from lens surfaces that may affect the performance of the wave front sensor, WFS. These telescopes conveniently alter the diameter of the beam in order to match the aperture of different elements in the probing path and convey a probing beam of 6 mm in diameter through the subject's pupil plane. The telescopes also ensure that the
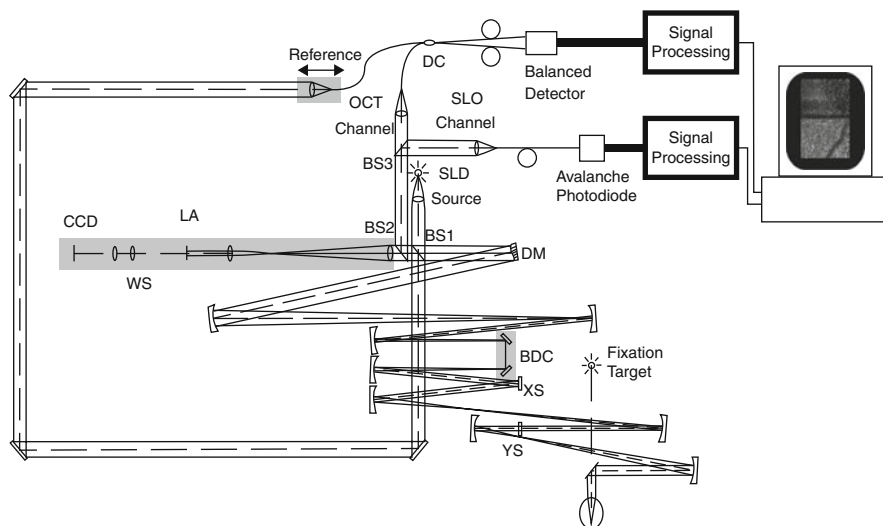
Fig. 18.37 Adaptive optics-assisted en face OCT/SLO system; BS1, BS2, BS3: beam splitters; DM: deformable mirror; BDC: Badal defocus corrector; XS: X-scanner; YS: Y-scanner; WS: wave front sensor; LA: lenslet array; DC: directional coupler (Reproduced with OSA's permission from [76])

subject's pupil plane is conjugate to the XS, YS, and DM planes. The system uses a double-pass configuration [77].

This and the utilization of large focal length mirrors determined a large size layout, and in consequence, the object and reference arms are quite long (the object arm is ∼5 m in length one way).

This may lead to thermal fluctuations of the optical path difference and launching problems. Therefore, an isolated optical bench was used.

Light scattered back from the patient's retina passes a second time through the object arm and reaches a second beam splitter, BS2 (1 % transmission). Light transmitted through BS2 is collected by a Shack-Hartmann WFS. Light reflected at BS2 reaches a third beam splitter, BS3, to divert 30 % of the incoming beam to the SLO channel and transmit the rest into the OCT channel. In both channels, light is injected into single-mode fibers. This ensures a high confocal parameter in both channels and good spatial rejection of multiple-scattered light. The other end of the fiber in the SLO channel is connected to an avalanche photodiode. In the OCT channel, light is guided toward a single-mode directional coupler, DC, where it interferes with that coming from the reference arm. Both output fibers from the DC are connected to two pin photodetectors in a balanced photodetection unit. The last focusing element and the fiber end in the reference arm are fixed on a translation stage that has a range of 2.5 cm, useful to allow coherence matching for different lengths of the volunteer's eyes.

Figure 18.38 left shows two pairs of en face OCT/SLO images collected at two different depths in the OCT channel [71]. The blobs in the bottom images, delivered
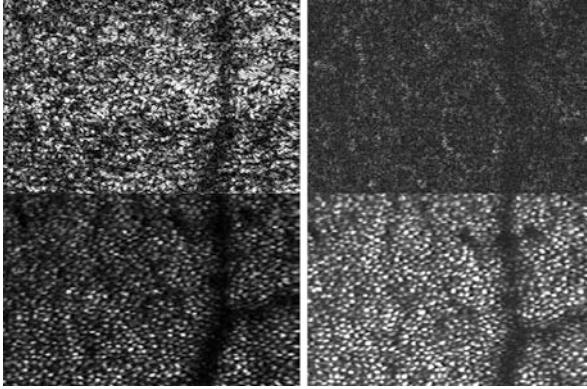
Fig. 18.38 Pairs of C-scan OCT and SLO images simultaneously acquired and displayed via AO closed loop correction in an OCT/SLO system (each image size: 330 × 500 μm; *top*: OCT C-scan image; *bottom*: SLO image; the depth in the OCT channel is at the junction of inner segment and outer segment (*left*) and approximately 50 μm above (*right*), displaying microvasculature) (Reproduced with OSA's permission from [76])

by the SLO channel, are photoreceptors, well resolved due to the AO closed loop. In the top images, delivered by the OCT channel, the blobs are fragmented by fringes; this illustrates that even after round-trip traversal of several hundred of microns through a scattering tissue such as the retina, the signal retains specular reflection characteristics.

The en face OCT/SLO instrument is particularly well suited for identifying the depth origin of the regular pattern seen in the SLO image. Using the pixel-to-pixel correspondence, the pattern can be traced to the depth shown in the OCT B-scan. Clear pattern regularity seen in the SLO images can be associated to the layer in depth exhibiting such regularity in the B-scan [11]. The determination of depth origin of patterns seen in small size imaging of the fovea using fundus cameras and SLOs is consistent with the explanation previously given for an en face OCT system without AO correction [78] and for an AO corrected FD-OCT system [79].

The studies by the OCT groups in Vienna and Kent on small size imaging employing T-scan-based OCT suggest that when combined with AO, this is superior to the A-scan-based OCT combinations because the T-scan-based OCT method is compatible with dynamic focus. Dynamic focus is critical if aberrations are well corrected, since the resulting confocal profile narrowing in the core of the OCT channel markedly reduces the signal outside focus. Despite this, the majority of recent reports on OCT/AO refer to combinations of SD-OCT with AO emphasizing the better S/N ratio or higher acquisition speed of the SD-OCT method in comparison with the TD-OCT, without considering the negative impact that a good AO correction could have on the sensitivity variation with depth, due to shrinkage of the confocal profile. This phenomenon is easily counterbalanced in time domain OCT by implementing dynamic focus.

18.6   Coherence-Gated Wave Front Sensor

18.6.1 Insensitivity to Depth Variations of Aberrations of a Standard Shack-Hartmann Wave Front Sensor

Due to the limited numerical aperture in the beams associated with each microlens in the lenslet array, a Shack-Hartmann wave front sensor has little sensitivity to the position in depth in the object where the signal comes from. This makes the Shack-Hartmann wave front sensor (SH/WFS) insensitive to depth variations of aberrations, or more precisely, the spots are deviated from the ideal wave front grid by quantities which represent averages of aberrations over the depth of focus of the equivalent confocal microscopy channel associated with each microlens in the lenslet array.

Due to the insensitivity to depth mentioned above, stray reflections from the interface optics cannot be rejected, and therefore, supplementary spatial filters need to be employed in the interface optics. However, when imaging the eye, reflections from the cornea and the eye lens cannot be entirely attenuated using spatial filters.

To address the problems mentioned above, en face OCT can be applied, in its version of full field, to implement coherence-gated wave front sensing. In opposition
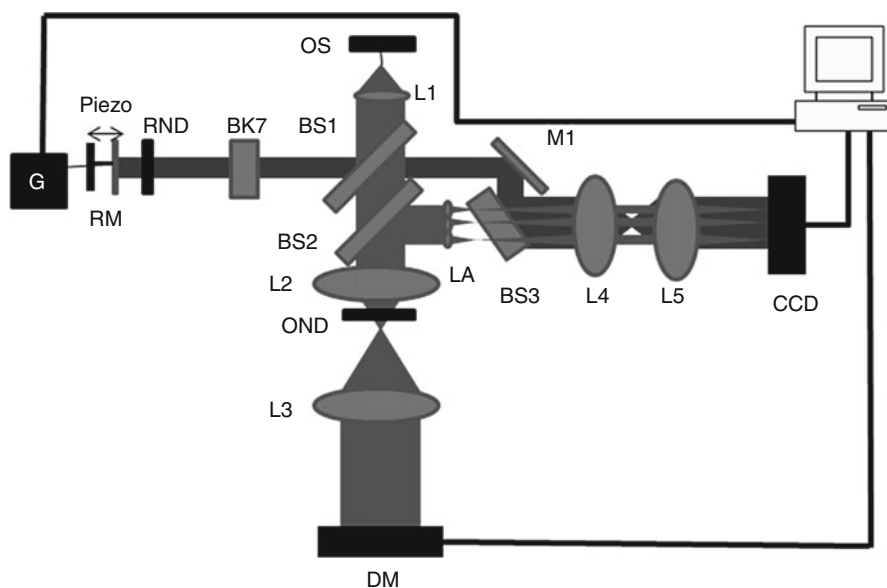
Fig. 18.39 Schematic diagram for the evaluation of full-field en face optical coherence tomography applied to a Shack-Hartmann wave front sensor. OS: optical source; OND: neutral density filter in the object path; RND: neutral density filter in the reference path; RM: reference mirror; BS1 and BS2: 50/50 beam splitters; BS3: 55/45 beam splitter; LA: lenslet array; BK7: dispersion compensating glass; DM: deformable mirror; L1: 10× microscope objective; L2: 3 cm focal length lens; L3: 15 cm focal length lens; L4 and L5: 7.5 cm focal length lenses (Reproduced with OSA's permission from [80])
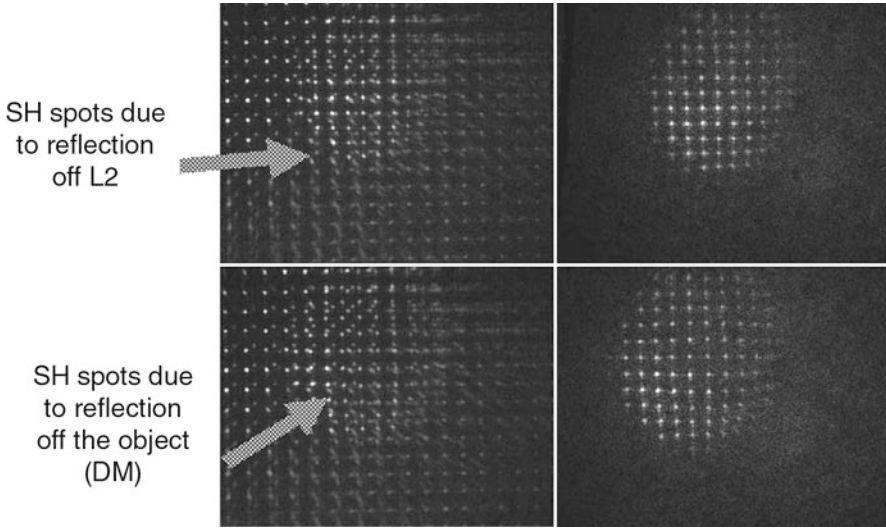
Fig. 18.40 Images in the *top* row were of the SH spots with no deformation of the mirror. Images in the *bottom* row were obtained with further aberrations introduced by deforming the DM, obtained by applying −0.18 V on electrode 30 of the DM. Images in the *left* column were obtained with the reference arm blocked and according to the conventional procedure in an SH/WFS while in the *right* column, images were obtained based on the principle of time domain coherence-gated SH/WFS (Reproduced with OSA's permission from [80])

to the paragraphs above, where the beam was scanned over the target, in the full-field OCT, the target is illuminated over all its transversal pixels at once. The same happens in an SH/WFS. A collimated beam is sent toward the whole aperture of the optics whose wave front needs correction, a lens or the eye lens in ophthalmology.

18.6.2 Time Domain En Face Coherence-Gated Wave Front Sensor

A preliminary study has investigated the interference on a CCD array between multiple beamlet outputs by the lenslet array and a reference beam provided by the same optical source used to illuminate the target [80]. The schematic diagram of such a coherence-gated SH/WFS is shown in Fig. 18.39. This is driven by a source with large bandwidth (a superluminescent diode) and operates based on principles of phase-shifting interferometry to recover a C-scan image of the spot pattern.

Due to the aberrations encountered by the beam toward and backward from the target (in double-pass configurations) or coming from the target only (in single pass configurations), the beamlets suffer various deflections on the CCD array. Irrespective of these deflections, interference with the reference beam still takes place, as the reference beam is uniformly spread over the CCD array.

Figure 18.40 shows the SH spots on the CCD camera. The images in the top raw were obtained with the DM flat, while the images on the bottom raw were obtained

with the DM deformed by applying -0.18 V to its electrode number 30. Images in the left column were obtained with the reference arm blocked, and therefore, the SH spots correspond to a conventional SH/WFS. These images contain SH spots due to the stray reflections from lens L2 (seen as thick diagonal small traces), superposed on the SH spots created by the object, DM.

The images in the right column were obtained with the reference beam on and after using four phase-shift steps. These images represent spatial cropping of spots as determined by the coherence gate. The SH spots due to reflections from lens L2 were totally eliminated, and the only SH spots in the image are due to the object. If the reference arm is blocked and the same phase-shifting algorithm was applied, most of the SH spots disappeared, apart from small remnants due to random shot noise. All images had 400 by 400 pixels, the camera was run at 10 Hz, and the system provided an en face image of SH spots (after phase shifting) at 2.5 Hz. Furthermore, when working with 200 by 200 pixels^2, the camera operated at 40 Hz and an en face image of SH spots could be delivered at 10 Hz. Using a camera with a higher frame rate could increase the acquisition speed even further [81]. Successful elimination of stray reflections opens the possibility of using lenses in a double-pass configurations as presented in Fig. 18.37 for imaging the retina and extending the SH/WFS principle to microscopy.

18.7   Conclusion

The method of en face OCT offers certain advantages. First, T-scans can be used to generate B-scans as well as coronal-plane-oriented scans (C-scans) [17, 26]. This allows quick alternating imaging sessions in orthogonal planes by instantly switching scanning regimes [51]. Second, the technology is compatible with live and simultaneous generation of a conventional fundus image (coronal-plane oriented) [11], or similar to that produced by scanning laser ophthalmoscopy (SLO). In microscopy, simultaneous pixel-to-pixel correspondence is achievable with a confocal microscopy channel. Such combinations also open the avenue towards fluorescence imaging and the possibility of assembling multiple imaging channels in the same instrument.

The en face OCT belongs to the category of time domain OCT methods. The sensitivity and acquisition speed in en face OCT is therefore less than in spectral domain OCT. However, spectral domain OCT methods present the following disadvantages: (1) decay of sensitivity with optical path difference, (2) all points in the A-scan are measured under the same focus position, and (3) mirror terms. En face OCT does not present such disadvantages. However, when imaging the retina of the human eye with spectral domain OCT, disadvantages (1) and (2) have little significance. In terms of (1), this is because the retina is thin, approx. 1 mm, so the decay of sensitivity in 1 mm range can be tolerated by an instrument with an axial range of over 5 mm typically. In terms of (2), this is because the human eye length is relatively large, determining a depth range for the confocal profile comparable with the retina thickness. Therefore, fixed focus can be tolerated.

However, disadvantage (2) can become a stumbling point when imaging smaller eyes, such as the case of animal eyes. With lengths of several mm, the confocal profile becomes smaller than the retina thickness. If spectral OCT is performed, then needs to be repeated for different focus positions. This disadvantage may also become more evident as progress toward improving AO technology applications to the eye imaging continues. An ideal correction for the human eye can lead to a confocal profile narrower than 10 % of the retina thickness of the human eye [75].

In addition, if transversal resolution is paramount, then high-focus interface optics is needed, which requires dynamic focus, applicable to time domain OCT methods only. En face OCT is ideal for dynamic focus as the focus adjustment needs to be performed at a slow speed, determined by the frame rate, and not at the line rate required by A-scan based time domain OCT.

Due to recent achievements in the increase of the acquisition speed of swept source based OCT applied to eye imaging [82], return to time domain OCT (including en face OCT) looks unlikely. However, with the tendency in extending OCT to fields outside ophthalmology, such as to microscopy, where the sample is stationary and high transversal resolution is required, time domain OCT will have a role to play.

References

1. S.A. Al-Chalabi, B. Culshaw, D.E.N. Davies, Partially coherent sources in interferometric sensors, in *Book of Abstracts, First International Conference on Optical Fibre Sensors*, 26–28 April 1983 (I.E.E., London, 1983), p. 132–135
2. R.C. Youngquist, S. Carr, D.E.N. Davies, Optical coherence-domain reflectometry: a new optical evaluation technique. Opt. Lett. **12**, 158–160 (1987)

3. H.H. Gilgen, R.P. Novak, R.P. Salathe, W. Hodel, P. Beaud, Submillimeter optical reflectometry. Lightwave Technol. **7**, 1225–1233 (1989)

4. M. Seeger, 3-D imaging using optical coherence radar, PhD thesis, University of Kent, 1997

5. A.F. Fercher, E. Roth, Ophthalmic laser interferometry. Proc. SPIE **658**, 48–51 (1986)

6. D. Huang, E.A. Swanson, C.P. Lin, J.S. Schuman, W.G. Stinson, W. Chang, M.R. Hee, T. Flotte, K. Gregory, C.A. Puliafito, J.G. Fujimoto, Optical coherence tomography. Science **254**, 1178–1181 (1991)

7. J.A. Izatt, M.R. Hee, D. Huang, J.G. Fujimoto, E.A. Swanson, C.P. Lin, J.S. Shuman, C. Puliafito, Ophthalmic diagnostics using optical coherence tomography. Proc. SPIE **1877**, 136–144 (1993)

8. J.A. Izaat, M.R. Hee, G.M. Owen, E.A. Swanson, J.G. Fujimoto, Optical coherence microscopy in scattering media. Opt. Lett. **19**, 590–592 (1994)

9. A.M. Rollins, M.D. Kulkarni, S. Yazdanfar, R. Ungarunyawee, J.A. Izatt, *In vivo* video rate optical coherence tomography. Opt. Express **3**, 219–229 (1998)

10. J.A. Rogers, A.G. Podoleanu, G.M. Dobre, D.A. Jackson, Topography and volume measurements of the optic nerve using en-face optical coherence tomography. Opt. Express **9**(10), 533–545 (2001)

11. A.G. Podoleanu, R.B. Rosen, Combinations of techniques in imaging the retina with high resolution. Prog. Retin. Eye Res. **27**(4), 464–499 (2008)

12. A.G. Podoleanu, G.M. Dobre, D.J. Webb, D.A. Jackson, Coherence imaging by use of a Newton rings sampling function, Opt. Lett. **21**, 1789–1791 (1996)

13. A.G. Podoleanu, G.M. Dobre, D.A. Jackson, *En-face* coherence imaging using galvanometer scanner modulation. Opt. Lett. **23**, 147–149 (1998)

14. A.G. Podoleanu, M. Seeger, G.M. Dobre, D.J. Webb, D.A. Jackson, F. Fitzke, Transverse and longitudinal images from the retina of the living eye using low coherence reflectometry. J. Biomed. Opt. **3**, 12–20 (1998)

15. Y. Pan, D. Farkas, Non-invasive imaging of living human skin with dual-wavelength optical coherence tomography in two and three dimensions. J. Biomed. Opt. **3**, 446–455 (1998)

16. S.A. Boppart, G.J. Tearney, B.E. Bouma, J.F. Southern, M.E. Brezinski, J.G. Fujimoto, Noninvasive assessment of the developing *Xenopus* cardiovascular system using optical coherence tomography. Proc. Natl. Acad. Sci. U.S.A. **94**, 4256–4261 (1997)

17. A.G. Podoleanu, G.M. Dobre, H.M. Seeger, D.J. Webb, D.A. Jackson, F.W. Fitzke, G.A.S. Halfyard, Low coherence interferometry for en-face imaging of the retina. Lasers Light Ophthalmol. **8**, 188–192 (1998)

18. A.G. Podoleanu, J.A. Rogers, D.A. Jackson, S. Dunne, Three dimensional OCT images from retina and skin. Opt. Express **7**, 292–298 (2000)

19. B. Hoeling, A. Fernandez, R. Haskell, E. Huang, W. Myers, D. Petersen, S. Ungersma, R. Wang, M. Williams, S. Fraser, An optical coherence microscope for 3-dimensional imaging in developmental biology. Opt. Express **6**, 136–145 (2000)

20. L. Giniunas, R. Danielius, R. Karkockas, Scanning delay line with a rotating-parallelogram prism for low-coherence interferometry. Appl. Opt. **38**, 7076–7079 (1999)

21. A.V. Zvyagin, E.D.J. Smith, D.D. Sampson, Delay and dispersion characteristics of a frequency-domain optical delay line for scanning interferometry. J. Opt. Soc. Am. **20**, 333–341 (2003)

22. C.K. Hitzenberger, A. Baumgartner, A.F. Fercher, Dispersion induced multiple signal peak splitting in partial coherence interferometry. Opt. Commun. **154**, 179–185 (1998)

23. A.F. Leung, J.E. Lee, Newton's rings: a classroom demonstration with a He-Ne laser. Am. J. Phys. **59**, 663–664 (1991)

24. L. An, R.K. Wang, Use of a scanner to modulate spatial interferograms for *in vivo* full-range Fourier-domain optical coherence tomography. Opt. Lett. **32**(23), 3423–3425 (2007)

25. M.R. Hee, J.A. Izatt, E.A. Swanson, J.G. Fujimoto, Femtosecond transillumination tomography in thick tissues. Opt. Lett. **18**(13), 1107–1110 (1993)

26. R.G. Cucu, A.G. Podoleanu, A. Rogers, J. Pedro, R.B. Rosen, Combined confocal scanning ophthalmoscopy/en face T-scan based ultrahigh resolution OCT of the human retina in vivo. Opt. Lett. **31**(11), 1684–1687 (2006)

27. H. Liang, M.G. Cid, R. Cucu, G.M. Dobre, J. Pedro, D. Saunders, A.G. Podoleanu, Application of optical coherence tomography to examination of easel paintings. Opt. Express **13**(16), 6133–6144 (2005)
28. M.J. Spring, H. Liang, B. Peric, D. Saunders, A.G. Podoleanu, Optical coherence tomography – a tool for high resolution non-invasive 3D-imaging of the subsurface structure of paintings, in *International Council of Museums Conservation Committee Triennial Meeting ICOM-CC*, New Delhi, 22–26 September 2008, vol. II, p. 633–640
29. D. Saunders, R. Billinge, J. Cupitt, N. Atkinson, H. Liang, A new camera for high-resolution infrared imaging of works of art. Stud. Conserv. **51**, 277–290 (2006)
30. M. Hughes, Optical coherence tomography for art conservation and archaeology: methods and applications, PhD thesis, University of Kent, 2010
31. A.G. Podoleanu, G.M. Dobre, D.J. Webb, D.A. Jackson, Simultaneous *En-face* Imaging of Two Layers in Human Retina. Opt. Lett. **22**, 1039–1041 (1997)
32. *American National Standard for the Safe Use of Lasers: ANSI Z 136.1* (Laser Institute of America, New York, 1993)
33. B. Bouma, D.J. Tearney, S.A. Boppart, M.R. Hee, M.E. Brezinski, J.G. Fujimoto, High-resolution optical coherence tomograhic imaging using a mode-locked Ti:Al$_2$O$_3$ laser source. Opt. Lett. **20**, 1486–1488 (1995)
34. A.G. Podoleanu, J.A. Rogers, R.C. Cucu, D.A. Jackson, B. Wacogne, H. Porte, T. Gharbi, Simultaneous low coherence interferometry imaging at two depths using an integrated optic modulator. Opt. Commun. **191**, 21–30 (2001)
35. L. Neagu, A. Bradu, L. Ma, J.W. Bloor, A.G. Podoleanu, Multiple-depth en face optical coherence tomography using active recirculation loops. Opt. Lett. **35**(13), 2296–2298 (2010)
36. A. Bradu, L. Ma, J.W. Bloor, A. Podoleanu, Dual optical coherence tomography/fluorescence microscopy for monitoring of *Drosophila melanogaster* larval heart. J. Biophoton. **2**(6–7), 380–388 (2009)
37. L. Plesea, A.G. Podoleanu, Direct corneal elevation measurements using multiple delay *en-face* OCT. J. Biomed. Opt. **13**(5), 054054 (2008)
38. J. Wang, C. Dainty, A. Podoleanu, Multiple delay lines full-field optical coherence tomography. Proc. SPIE **7139**, 71390A (2008)
39. T. Wilson, *Confocal Microscopy* (Academic, London, 1990)
40. R. Rajadhyaksha, R. Anderson, R. Webb, Video-rate confocal scanning laser microscope for imaging human tissues in vivo. Appl. Opt. **38**, 2105–2115 (1999)
41. A.G. Podoleanu, D.A. Jackson, Combined optical coherence tomograph and scanning laser ophthalmoscope. Electron. Lett. **34**, 1088–1090 (1998)
42. A.G. Podoleanu, D.A. Jackson, Noise analysis of a combined optical coherence tomography and confocal scanning ophthalmoscope. Appl. Opt. **38**, 2116–2127 (1999)
43. R.H. Webb, Scanning laser ophthalmoscope, in *Noninvasive Diagnostic Techniques in Ophthalmology*, ed. by B.R. Masters (Springer, New York, 1990), pp. 438–450
44. R. Juskaitis, T. Wilson, Scanning interference and confocal microscopy. J. Microsc. **176**, 188–194 (1994)
45. M. Kempe, W. Rudolph, E. Welsch, Comparative study of confocal and heterodyne microscopy for imaging through scattering media. J. Opt. Soc. Am. **13**, 46–52 (1996)
46. A.G. Podoleanu, Unbalanced versus balanced operation in an OCT system. Appl. Opt. **39**, 173–182 (2000)
47. A.G. Podoleanu, G.M. Dobre, R.G. Cucu, R.B. Rosen, Sequential OCT and confocal imaging. Opt. Lett. **29**(4), 364–366 (2004)
48. I. Trifanov, M. Hughes, A.G. Podoleanu, R.B. Rosen, Quasi-simultaneous optical coherence tomography and confocal imaging. J. Biomed. Opt. **13**(4), 044015 (2008)
49. C.C. Rosa, J. Rogers, A.G. Podoleanu, Fast scanning transmissive delay line for optical coherence tomography. Opt. Lett. **24**, 3263–3265 (2005)

50. A.G. Podoleanu, R.G. Cucu, R.B. Rosen, G.M. Dobre, J.A. Rogers, D.A. Jackson, Quasi-simultaneous OCT en-face imaging with two different depth resolutions. J. Phys. D: Appl. Phys. **36**, 1696–1702 (2003)

51. C.C. Rosa, J. Rogers, J. Pedro, R. Rosen, A.G. Podoleanu, Multiscan time-domain optical coherence tomography for retina imaging. Appl. Opt. **46**(10), 1795–1808 (2007)

52. R. Cernat, A. Podoleanu, Avalanche photodiode based optical coherence tomography. Proc. SPIE **5459**, 185–191 (2004)

53. A. Bradu, L. Ma, J. Bloor, A. Podoleanu, Versatile confocal/optical coherence tomography system for embryonic developmental imaging. Proc. SPIE **6847**, 68471W (2008)

54. L. Ma, A. Bradu, A.G. Podoleanu, J.W. Bloor, Arrhythmia caused by a *Drosophila tropomyosin* mutation is revealed using a novel optical coherence tomography instrument. PLoS One **5**(12), 1–8 (2010). e14348

55. P. Furrer, J.M. Mayer, R. Gurny, Confocal microscopy as a tool for the investigation of the anterior part of the eye. J. Ocul. Pharmacol. Ther. **13**, 559–578 (1997)

56. S. Radhakrishnan, A.M. Rollins, J.E. Roth et al., Real-time optical coherence tomography of the anterior segment at 1310 nm. Arch. Ophthalmol. **119**, 1179–1185 (2001)

57. A.G. Podoleanu, J.A. Rogers, G.M. Dobre, R.G. Cucu, D.A. Jackson, *En-face* OCT imaging of the anterior chamber. Proc. SPIE **4619**, 240–243 (2002)

58. R.B. Rosen, P. Garcia, A.G. Podoleanu, R.G. Cucu, G. Dobre, M.E.J. Van Velthoven, M.D. de Smet, J.A. Rogers, M. Hathaway, J. Pedro, R. Weitz, En-face flying spot OCT/ophthalmoscope, in *Optical Coherence Tomography Technology and Applications*, ed. by W. Drexler, J.G. Fujimoto. Biomedical Engineering, Biological and Medical Physics, vol. XXVIII, 1357 (Springer, Berlin/Heidelberg, 2008), pp. 448–474

59. B.W. Colston Jr., M.J. Everett, L.B. DaSilva, L.L. Otis, P. Stroeve, H. Nathel, Imaging of hard – and soft – tissue structure in the oral cavity by optical coherence tomography. Appl. Opt. **37**, 3582–3585 (1998)

60. F.I. Feldchtein, G.V. Gelikonov, V.M. Gelikonov, R.R. Iksanov, R.V. Kuranov, A.M. Sergeev, N.D. Gladkova, M.N. Ourutina, J.A. Warren Jr., D.H. Reitze, In vivo OCT imaging of hard and soft tissue of the oral cavity. Opt. Express **3**, 239–250 (1998)

61. B.T. Amaechi, A.G. Podoleanu, S.M. Higham, D. Jackson, Correlation of quantitative light-induced fluorescence and optical coherence tomography applied for detection and quantification of early dental caries journal. J. Biomed. Opt. **8**(4), 642–647 (2003)

62. B. Amaechi, A. Podoleanu, S.M.G. Komarov, J. Rogers, S. Higham, D. Jackson, Application of optical coherence tomography for imaging and assessment of early dental caries lesions. Laser Methods Med. Biol. **13**(5), 703–710 (2003)

63. B.T. Amaechi, S.M. Higham, W.M. Edgar, Factors affecting the development of carious lesions in bovine teeth in vitro. Arch. Oral Biol. **43**, 619–628 (1998)

64. K.I.M. Delme, P.J. Deman, R.J.G. De Moor, Microleakage of class V resin composite restorations after conventional and Er:YAG laser preparation. J. Oral Rehabil. **32**, 676–685 (2005)

65. L.S.A. De Melo, R.E. De Araujo, A.Z. Freitas, D. Zezell, N.D. Vieira Jr., J. Girkin, A. Hall, M.T. Carvalho, A.S.L. Gomes, Evaluation of enamel dental restoration interface by optical coherence tomography. J. Biomed. Opt. **10**, 064027 (2005)

66. C. Sinescu, M.L. Negrutiu, C. Todea, C. Balabuc, L. Filip, R. Rominu, A. Bradu, M. Hughes, A.G. Podoleanu, Quality assessment of dental treatments using en-face optical coherence tomography. J. Biomed. Opt. **13**(5), 054065 (2008), 044015-1–044015-7

67. C. Todea, C. Balabuc, C. Sinescu, L. Filip, C. Kerezsi, M. Calniceanu, M. Negrutiu, A. Bradu, M. Hughes, A.G. Podoleanu, En face optical coherence tomography investigation of apical microleakage after laser-assisted endodontic treatment. Lasers Med. Sci. **25**(5), 629–639 (2010)

68. A.G. Podoleanu, G.M. Dobre, R. Cernat, J.A. Rogers, J. Pedro, R.B. Rosen, P. Garcia, Investigations of the eye fundus using a simultaneous optical coherence tomography/indocyanine green fluorescence imaging system. J. Biomed. Opt. **12**(1), 014019 (2007)

69. R.B. Rosen, M. Hathaway, J. Rogers, J. Pedro, G. Patricia, P. Laissue, G.M. Dobre, A.G. Podoleanu, Multidimensional en-face OCT imaging of the retina. Opt. Express **17**(5), 4112–4133 (2009)
70. R.B. Rosen, M. Hathaway, J. Rogers, J. Pedro, P. Garcia, G.M. Dobre, A.G. Podoleanu, Simultaneous OCT/SLO/ICG imaging. Invest. Ophthalmol. Vis. Sci. **50**(2), 851–860 (2009)
71. M. Ohmi, K. Yoden, M. Haruna, Optical reflection tomography along the geometrical thickness. Proc. SPIE **4251**, 76–80 (2001)
72. J. Liang, D.R. Williams, Aberrations and retinal image quality of the normal human eye. J. Opt. Soc. Am. **14**(11), 2873–2883 (1997)
73. J. Fernandez, I. Iglesias, P. Artal, Closed-loop adaptive optics in the human eye, Opt. Lett. **26**, 746–748 (2001)
74. J.C. Dainty, A.V. Koryabin, A.V. Kudryashov, Low-order adaptive deformable mirror. Appl. Opt. **37**(21), 4663–4668 (1998)
75. A. Roorda, F. Romero-Borja, W.J. Donnelly III, H. Queener, T.J. Herbert, M.C.W. Campbell, Adaptive optics scanning laser ophthalmoscopy. Opt. Express **10**, 405–412 (2002)
76. D. Merino, C. Dainty, A. Bradu, A.G. Podoleanu, Adaptive optics enhanced simultaneous *en-face* optical coherence tomography and scanning laser ophthalmoscopy. Opt. Express **14**(8), 3345–3353 (2006)
77. R. Zawadzki, S. Jones, S. Olivier, M. Zhao, B. Bower, J. Izatt, S. Choi, S. Laut, J. Werner, Adaptive-optics optical coherence tomography for high-resolution and high-speed 3D retinal in vivo imaging. Opt. Express **13**, 8532–8546 (2005)
78. M. Pircher, E. Gotzinger, R. Leitgeb, H. Sattmann, O. Findl, C.K. Hitzenberger, Imaging of polarization properties of human retina *in vivo* with phase resolved transversal PS-OCT. Opt. Express **12**, 5940–5951 (2004)
79. Y. Zhang, J.T. Rha, R.S. Jonnal et al., Adaptive optics parallel spectral domain optical coherence tomography for imaging the living retina. Opt. Express **13**, 4792–4811 (2005)
80. S. Tuohy, A.G. Podolean, Depth-resolved wavefront aberrations using a coherence-gated Shack-Hartmann wavefront sensor. Opt. Express **18**(4), 3458–3476 (2010)
81. K. Grieve, A. Dubois, M. Simonutti, M. Paques, J. Sahel, J.F. Le Gargasson, C. Boccara, *In vivo* anterior segment imaging in the rat eye with high speed white light full-field optical coherence tomography. Opt. Express **13**, 6286–6295 (2005)
82. T. Klein, W. Wieser, C.M. Eigenwillig, B.R. Biedermann, R. Huber, Megahertz OCT for ultrawide-field retinal imaging with a 1050 nm Fourier domain mode-locked laser. Opt. Express **19**, 3044–3062 (2011)

Polarization Sensitive Optical Coherence Tomography

19

Phase-Sensitive Interferometry for Multifunctional Imaging

Johannes F. de Boer

Contents

Abstract

The principle of the determination of Stokes parameters in OCT by the coherent detection of interference fringes is explored. The implementation of a real-time fiber-based PS-OCT system, the associated behavior of polarization states in

J.F. de Boer
Institute for Lasers, Life and Biophotinics (LaserLaB) Amsterdam, Department of Physics, VU University, Amsterdam, The Netherlands
e-mail: jfdeboer@few.vu.nl

single-mode fibers, and optimal polarization modulation schemes will be described. Processing of PS-OCT signals to extract polarization properties of tissue, such as birefringence, optical axis orientation, and diattenuation, will be explained.

19.1   Introduction

Optical coherence tomography (OCT) is an emerging technology for minimally invasive high-resolution imaging (1–10 μm) of tissue in two or three dimensions up to a depth of 2–3 mm [1]. OCT images tissue reflectivity by measuring the spatially resolved backscattered intensity in turbid media. In contrast to ultrasound, the velocity of light prohibits time-resolved measurement of the time delay of short temporal pulses backscattered from tissue. OCT measures the time delay by means of interferometry. OCT instrumentation uses a spectrally broadband light source and a two-beam interferometer (e.g., Michelson) with the reflector in one path (i.e., sample arm) replaced by a turbid medium. Depth ranging in the turbid medium is possible because interference fringes are observed only for light in sample and reference arms that has traveled equal optical path lengths to within the source coherence length. By scanning optical path length in the reference arm and amplitude detection of the interference fringes, a depth scan (A-scan) can be recorded that maps sample reflectivity. Temporal coherence length of the source light determines axial resolution of a system, while numerical aperture of the focusing optics determines lateral resolution. The availability of sources with shorter coherence length over the past decade has increased the axial (depth) resolution of OCT from 15 μm to approximately 1 μm. Lateral scanning mechanisms allow two- and three-dimensional recording of images from consecutive A-scans. Although light is frequently treated as a scalar wave, many applications require a description using transverse electromagnetic waves. The transverse nature of light is distinguished from longitudinal waves (e.g., sound), by the extra degree of freedom, which is described by the polarization state of light. Polarization-sensitive OCT (PS-OCT) uses the information encoded in the polarization state of the recorded interference fringe intensity to provide additional contrast in images of the sample under study. PS-OCT provides high-resolution spatial information on the polarization state of light reflected from tissue that is not discernible using existing diagnostic optical methods. In this chapter, a review will be presented of PS-OCT, the theory of calculation of the Stokes vectors, implementation of PS-OCT in fiber-based systems for clinical applications, and recent results in the field of dermatology and ophthalmology.

19.1.1 Optical Properties of Tissue That Influence Polarization

Scattering is the principle mechanism that modifies the polarization state of light propagating through biological tissue. The polarization state of light after a single scattering event depends on the scatterer, direction of scatter, and incident

polarization state. In many turbid media such as tissue, scattering structures have a large variance in size and are distributed/oriented in a complex and sometimes apparently random manner. Because each scattering event can modify the incident polarization state differently, the scrambling effect of single scattering events accumulates, until finally the polarization state is completely random (i.e., uncorrelated with the incident polarization state).

An important exception is when the media consists of organized linear structures, such as fibrous tissues that can exhibit form birefringence. Many biological tissues exhibit form birefringence, such as tendons, muscle, nerve, bone, cartilage, and teeth. Form birefringence arises when the relative optical phase between orthogonal polarization components is nonzero for forward scattered light. After multiple forward scattering events, relative phase difference accumulates and a delay (δ) similar to that observed in birefringent crystalline materials (e.g., calcite) is introduced between orthogonal polarization components. For organized linear structures, the increase in phase delay may be characterized by a difference (Δn) in the effective refractive index for light polarized along, and perpendicular to, the long axis of the linear structures. The phase retardation, δ, between orthogonal polarization components is proportional to the distance x traveled through the birefringent medium

$$\delta = \frac{2\pi \Delta n x}{\lambda}.$$

(19.1)

The advantage in using PS-OCT is the enhanced contrast and specificity in identifying structures in OCT images by detecting induced changes in the polarization state of light reflected from the sample. Moreover, changes in birefringence may, for instance, indicate changes in functionality, structure, or viability of tissues.

19.2   Theory

19.2.1 Historical Overview

Application of laser interferometry to characterize the polarization state of light reflected from optical components was reported by Hazebroek and Holscher in 1973 [2]. More recently, bright broadband light sources that emit in a single spatial mode have provided the basis for novel applications in testing of optical components and biomedical imaging. For example, Newson et al. [3] constructed a combined Mach-Zehnder/Michelson interferometer (configured in tandem) that used a low-coherence semiconductor light source and polarization-sensitive detection to measure temperature changes in a birefringent fiber. Kobayashi et al. [4] reported an early demonstration of a polarization-sensitive fiber Michelson interferometer using a low-coherence light source for testing optical components.

The emphasis in optical coherence tomography (OCT) has been on the reconstruction of two-dimensional maps of tissue reflectivity while neglecting the

polarization state of light. In 1992, Hee et al. [5] reported an optical coherence ranging system able to measure the changes in the polarization state of light reflected from a sample. Using an incoherent detection technique, they demonstrated birefringence-sensitive ranging in a wave plate, an electro-optic modulator, and calf coronary artery. In 1997, the first two-dimensional images of birefringence in bovine tendon were presented, and the effect of laser-induced thermal damage on tissue birefringence was demonstrated [6], followed in 1998 by a demonstration of the birefringence in porcine myocardium [7]. To date, polarization-sensitive OCT measurements have attracted active interest from several research groups. Potential biomedical applications that are being explored include determination of thermal injury for burn depth assessment [8] and retinal nerve fiber layer birefringence determination for early detection of glaucoma [9, 10]. For an overview of the earlier developments in PS-OCT and a discussion of the theory in the context of bulk optical interferometers, we refer to de Boer and Milner [11].

19.2.2 Stokes Vector and Poincaré Sphere

The Stokes vector is composed of four elements, I, Q, U, and V (sometimes denoted S_0, S_1, S_2, and S_3), and provides a complete description of the light polarization state. Historically, Stokes vectors were developed because they describe observable quantities of light. I, Q, U, and V can be measured with a photodetector and linear and circular polarizers. Let us call I_t the total light irradiance incident on the detector, $I_{0°}$, $I_{90°}$, $I_{+45°}$, and $I_{-45°}$ the irradiances transmitted by a linear polarizer oriented at an angle of, respectively, $0°$, $90°$, $+45°$, and $-45°$ to the horizontal. Let us define also I_{rc} and I_{lc} as the irradiances transmitted by a circular polarizer opaque to, respectively, left and right circularly polarized light. Then, the Stokes parameters are defined by

$$
\begin{aligned}
lI &= I_t, \\
Q &= (I_{0°} - I_{90°}), \\
U &= (I_{+45°} - I_{-45°}), \\
V &= (I_{rc} - I_{lc}).
\end{aligned}
\tag{19.2}
$$

After normalizing the Stokes parameters by the irradiance I, Q describes the amount of light polarized along the horizontal ($Q = +1$) or vertical ($Q = -1$) axes, U describes the amount of light polarized along the $+45°$ ($U = +1$) or $-45°$ ($U = -1$) directions, and V describes the amount of right ($V = +1$) or left ($V = -1$) circularly polarized light. Figure 19.1 shows the definition of the normalized Stokes parameters with respect to a right-handed coordinate system, where we have adopted the definition of a right-handed vibration ellipse (positive V parameter) for a clockwise rotation as viewed by an observer who is looking toward the light source. Positive rotation angles are defined as counterclockwise rotations.
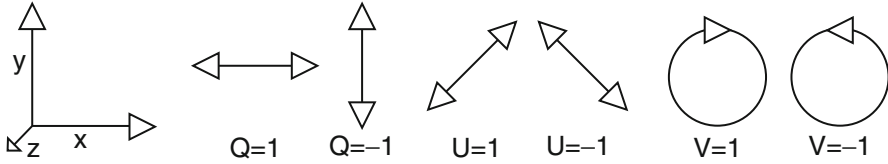
Fig. 19.1 Definition of the Stokes parameters with respect to a right-handed coordinate system. The light is propagation along the positive z-axis, that is, toward the viewer. Q and U describe linear polarizations in frames rotated by 45° with respect to each other. The V parameter describes circular polarized light
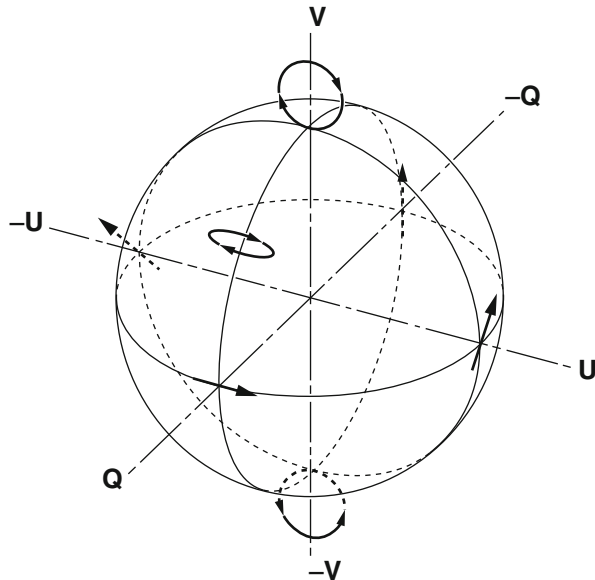
Fig. 19.2 Poincaré sphere representation of the Stokes parameters (Adapted from [12])

For practical reasons, the Stokes vector is sometimes represented in the Poincaré sphere system [12], where it is defined as the vector between the origin of an x-, y-, z-coordinate system and the point defined by (Q,U,V). The ensemble of normalized Stokes vectors with the same degree of polarization ($0 < P < 1$) defines a sphere with radius that varies between 0 for natural light and 1 for totally polarized light (Fig. 19.2).

The Poincaré sphere is a convenient geometrical tool to analyze change in polarization state due to linear, circular, or elliptical birefringence. The transformation by a linear retarder of a Stokes vector representing the incident polarization state is given by a rotation around an axis in the Q-U plane of the Poincaré sphere. The orientation of the rotation axis corresponds to the orientation of the optic axis with respect to the horizontal. For example, when the optic axis of the linear retarder is at 45° with respect to the horizontal, the rotation axis on the Poincaré sphere is coincident with the positive U-axis. The angle of rotation about the axis on

the Poincaré sphere equals the amount of phase retardation. From the Poincaré sphere, it is clear that a circular polarization state ($V = +/-1$) is always perpendicular to a rotation axis in the Q-U plane and, thus, will always be modified by a linear retarder, regardless of the orientation of the optic axis. When a linear polarization state is incident parallel to the optic axis of a linear retarder, the state is unchanged. The retardation and orientation of the optic axis of a linear retarder can be determined from the transformation of the Stokes vector in the Poincaré sphere by finding the three-dimensional rotation matrix with a rotation axis in the Q-U plane that describes the transformation. Circular birefringence (optical activity) is a rotation around the V-axis. Linear dichroism, that is, the differences in the absorption and scattering coefficients for linearly polarized light, is described by an evolution of the Stokes vector over an arc in the Poincaré sphere toward the equator (Q-U plane). Circular dichroism, that is, the differences in the absorption and scattering coefficients for circularly polarized light, is described by an evolution of the Stokes vector over an arc in the Poincaré sphere toward the poles ($V = 1$ or $V = -1$). A more detailed description of these transformations in the Poincaré sphere is given in Sect. 19.4.4.

19.2.3 Calculating the Stokes Parameters of Reflected Light

Combining the principles of interferometric ellipsometry and OCT, the depth-resolved Stokes parameters of reflected light can be determined. Polarimetry requires in general four measurements of the intensity in preselected polarization states to determine the Stokes vector of light. An interferometric technique, however, allows recovery of not only the intensity but also the relative phase between the electromagnetic fields in orthogonal polarization states. Preserving this phase information allows determination of the Stokes vector of the reflected light as a function of depth in the sample with a single measurement. The amplitude *and* relative phase of the interference fringes in each orthogonal polarization channel will be used to derive the depth-resolved Stokes vector of reflected light. The use of interferometry to characterize the polarization state of laser light specularly reflected from a sample was first demonstrated by Hazebroek and Holscher [2]. In their work, coherent detection of the interference fringe intensity in orthogonal polarization states formed by He-Ne laser light in a Michelson interferometer was used to determine the Stokes parameters of light reflected from a sample. Using a source with short temporal coherence adds path length discrimination to the technique, since only light reflected from the sample with an optical path length equal to that in the reference arm within the coherence length of the source will produce interference fringes. When using incoherent detection techniques, only two of the four Stokes parameters can be determined simultaneously. In the present analysis, we demonstrate that coherent detection of the interference fringes in two orthogonal polarization states allows determination of all four Stokes parameters simultaneously. Before giving a mathematical description, the principles underlying calculation of the Stokes vector will be discussed. We assume that the
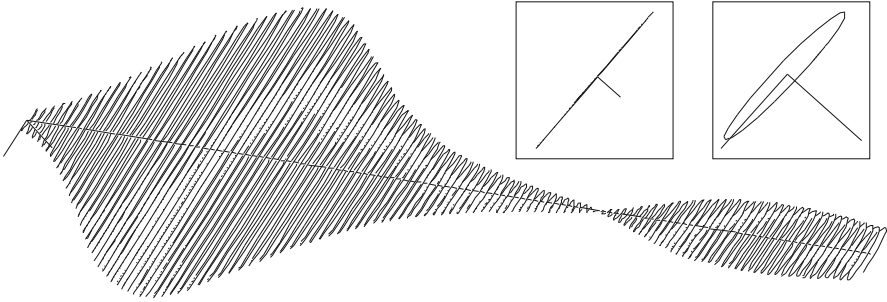
Fig. 19.3 Evolution of the electric component of the electromagnetic wave of the reflected light propagating through birefringent mouse muscle. The electric field is reconstructed from the horizontal A_H and vertical A_V polarized components and relative phase of the interference fringes. The displayed section is a small part of a longitudinal scan. Length of the section is 38 μm in a sample with refractive index $n = 1.4$. The beginning of the section shows the reflection from the sample surface modulated by the coherence envelope. The inserts show cross sections of the electric field over a full cycle perpendicular to the propagation direction taken at, respectively, 5.7 and 35.7 μm from the beginning of the section. As can be seen from the inserts, the initial polarization state of reflected light is linear along one of the displayed axes, changing to an elliptical polarization state for reflection deeper in the tissue (Reprinted from [13] with permission of the Optical Society of America)

polarization state of light reflected from the reference arm is perfectly linear, at an angle of 45° with the horizontal axis. After the polarizing beam splitter in the detection arm, the horizontal and vertical field components of light in the reference arm will have equal amplitude *and* phase. Light reflected from the sample will interfere with that from the reference, and the amplitude and *relative phase difference* of the interference fringes in each polarization channel will be proportional to the amplitude and *relative phase difference* between horizontal and vertical electric field components of light in the sample arm. The electric field vector of light reflected from the sample arm can be reconstructed by plotting the interference term of the signals on the horizontal and vertical detectors along the x and y axes, respectively.

Figure 19.3 shows a reconstruction of the electric field vector over a trace of 38 μm. The plot does not reflect the actual polarization state reflected from the sample, since the light has made a return pass through the quarter wave plate in the sample arm before being detected. The plot indicates change in polarization state from a linear to an elliptic state as a consequence of tissue birefringence.

The Stokes parameters can be determined from the detected interference fringe intensity signals. Figure 19.4 shows three examples interference fringes detected in the orthogonal polarization channels that correspond to Stokes parameters $Q = 1$, $U = 1$, and $V = 1$, respectively. For instance, if the interference fringes are maximized on one detector, and minimal on the other, the polarization state is linear in either the horizontal or vertical plane, which corresponds to the Stokes parameter Q being 1 or -1. If the interference fringes on both detectors are of equal amplitude and in phase, or π out of phase, the polarization state is linear, at 45° with the

Fig. 19.4 Determination of
the Stokes vector from the
detected interference fringe
amplitude and phase in the
horizontal and vertical
polarized detection channel.
From *top to bottom*, examples
of fringe amplitude and phase
are given for three Stokes
vectors, $Q = 1$, $U = 1$, and
$V = 1$, respectively
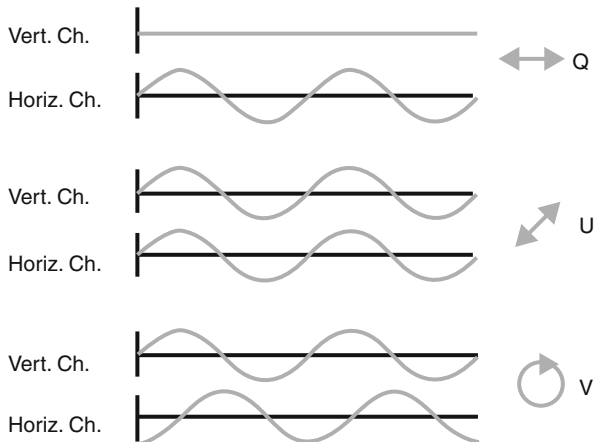
horizontal or vertical, corresponding to the Stokes parameter U being 1 or -1. If the
interference fringes on both detectors are of equal amplitude and are exactly $\pi/2$ or
$-\pi/2$ out of phase, the polarization state is circular, corresponding to the Stokes
parameter V being 1 or -1.

In the more mathematical description given in Refs. [11, 14, 15], the Stokes
vector was calculated by Fourier transforming the interference fringes in each
channel over a length of approximately the coherence length, and computing the
relative phase difference and amplitude of the Fourier components at each wave
number.

In conclusion, determination of the amplitude *and* relative phase of interference
fringes in orthogonal polarized detection channels gives access to all four Stokes
parameters, while applying an incoherent detection technique that does not com-
pute the relative phase between fringes in orthogonal detection channels allows
determination of only two of the four Stokes parameters from a single A-line scan.

19.2.4 The Degree of Polarization

The complete characterization of the polarization state of reflected light by means
of the Stokes parameters permits the calculation of the degree of polarization P,
defined as

$$P = \frac{\sqrt{Q^2 + U^2 + V^2}}{I}. \tag{19.3}$$

For purely polarized light, the degree of polarization is unity, and the Stokes
parameters obey the equality $I^2 = Q^2 + U^2 + V^2$, while for partially polarized light,
the degree of polarization is smaller than unity, leading to $I^2 > Q^2 + U^2 + V^2$.
Natural light, characterized by its incoherent nature, has (by definition) a degree of

polarization of zero. An interferometric gating technique such as OCT measures only the light reflected from the sample arm that does interfere with the reference arm light. On first inspection, this suggests that the degree of polarization will always be unity, since only the coherent part of the reflected light is detected. We will demonstrate, however, that the degree of polarization can be smaller than unity and is a function of the interval Δz over which the degree of polarization is calculated.

An input beam with $P < 1$ can be decomposed into purely polarized beams ($P = 1$). After propagation through an optical system, the Stokes parameters of the purely polarized beam components are added to give the Stokes parameters for the original input beam. In Bohren and Huffman's words, "If two or more quasi-monochromatic beams propagating in the same direction are superposed *incoherently*, that is to say there is no fixed relationship between the phases of the separate beams, the total irradiance is merely the sum of individual beam irradiances. Because the definition of the Stokes parameters involves only irradiances, it follows that the Stokes parameters of a collection of incoherent sources are additive" ([16], p. 53).

Implicit in our analysis is that a broadband OCT source may be viewed as an incoherent superposition of beams with different wave numbers or wavelengths and the observation that scattering and polarization properties of samples have a spectral dependence.

If the source was monochromatic, the degree of polarization of reflected light as measured in a PS-OCT system would always be 1. However, an OCT source ideally is broadband to obtain high axial resolution. In addition, the polarizarion properties of the sample will have a spectral dependence, meaning that different wavelength will be reflected from the sample in different polarization states. As an example, consider an OCT source emitting two monochromatic beams in the same polarizaton state at different wavelength, and assume that the light reflected from the sample at these two wavelengths is in orthogonal polarization states. Using the above quoted description by Bohren and Huffman, Stokes parameters of incoherently superposed beams are summed, and the light source has a degree of polarization of unity, while the light reflected from the sample has a degree of polarization of zero, that is, the reflected light is completely unpolarized. For a broadband source, the degree of polarization of reflected light is determined by the vector sum of Stokes vectors at independent wavelengths, divided by the sum of intensities over the independent wavelengths. Using the Poincaré sphere representation, one can visualize that the magnitude of a sum of Stokes vectors will be greatest if the direction of all components is collinear. For instance, directly after a polarizer, all wavelength components are in the same polarization state, and the Stokes vectors add collinearly, resulting in a degree of polarization of unity. For the reflected light, the Stokes vectors for different wavelengths are not necessarily collinear, leading to a degree of polarization that can be smaller than unity.

As stated above, the degree of polarization for light reflected from a particular depth in the sample depends on the length of the interval Δz over which the degree of polarization is calculated. This can be understood by considering that the wavelength resolution in Fourier transform spectrometry is proportional to the scan range. For instance, two wavelengths can only be discriminated if the number

of oscillations within a scan range Δz differs by an integral number. Thus, the number of independent wavelengths that contribute to the vector sum of Stokes vectors depends on the length of the interval Δz. The longer the interval, the more independent wavelengths contribute to the vector sum, increasing the probability that the length of the vector sum is smaller than the sum of intensities, which leads to a degree of polarization less than unity. When the interval Δz is so small that the wavelength resolution is coarser than the spectral width of the source, there will be only one independent wavelength, and the degree of polarization is necessarily unity.

An alternative argument will lead to the same conclusion. The reconstruction of the electric field vector in Fig. 19.3 shows that the Stokes parameters can be determined over a single cycle of the field, where at each cycle the degree of polarization will be (very close to) unity. The Stokes parameters over an interval Δz are the sum of the Stokes parameters of single cycles of the electric field vector within the interval. The degree of polarization P of the depth-resolved Stokes vector will be a function of the interval length Δz, since Stokes parameters can vary from cycle to cycle.

The reduction of the degree of polarization with increasing depth, which is demonstrated in Fig. 19.6, can be attributed to several factors: first, spectral components that may have traveled over different paths with equal lengths through the sample; second, spectral dependence of the Stokes parameters of light forward or backscattered by (irregularly shaped) particles; third, presence of multiple scattered light and speckle in the pupil of the sample arm; fourth, a decrease in the signal to noise ratio. Note that elastic (multiple) scattering does not destroy the coherence of the light in the sense of its ability to interfere with the source light (or the reference arm light). However, spectral phase variations within or between polarization channels may reduce the coherence envelope in a manner similar to the effect of dispersion. Inelastic interactions, such as incoherent Raman scattering or fluorescence, do destroy the coherence and interference with source light is lost.

19.3 Determination of the Sample Polarization Properties

From the Stokes parameters, the birefringence and optic axis of the sample can be determined, assuming that the orientation is constant with depth. The values of Q and U depend on the choice of the reference frame (i.e., the orientation of the polarizing beam splitter in the detection arm). The reference frame, or laboratory frame, is determined by the orientation of orthogonal polarization states exiting the polarizing beam splitter, which in our case is along the horizontal and vertical axes. The Mueller matrix for an ideal retarder is given by

$$\begin{pmatrix} 1 & 0 & 0 & 0 \\ 0 & C^2 + S^2 \cos \delta & SC(1 - \cos \delta) & -S \sin \delta \\ 0 & SC(1 - \cos \delta) & S^2 + C^2 \cos \delta & C \sin \delta \\ 0 & S \sin \delta & -C \sin \delta & \cos \delta \end{pmatrix}, \tag{19.4}$$

where $C = \cos 2\alpha$, $S = \sin 2\alpha$, with α the angle of the optic axis with the horizontal, and δ the retardance. Equation (19.4) is the Mueller matrix representation of a linear retarder, with $\delta = k_0 z \Delta n$, k_0 the wave vector, z the distance traveled through the birefringent material, and Δn the birefringence. Upon specular reflection inside the sample, the Stokes parameters U and V change sign. The angle α of the optic axis of the Mueller matrix for the linear retarder on the return pass changes sign because the coordinate handedness is changed (the propagation direction of the light is reversed). After the return pass through the retarder, the combined Mueller matrix of propagation, reflection, and return pass is given by

$$\begin{pmatrix} 1 & 0 & 0 & 0 \\ 0 & C^2 + S^2 \cos\delta & SC(1 - \cos\delta) & -S\sin\delta \\ 0 & -SC(1 - \cos\delta) & -S^2 - C^2\cos\delta & -C\sin\delta \\ 0 & -S\sin\delta & C\sin\delta & -\cos\delta \end{pmatrix}, \tag{19.5}$$

with $\delta = 2k_0 z \Delta n$. For example, when right circularly polarized light is incident onto a sample with linear retardance, the reflected light polarization state can be defined by the product of the Stokes vector (1,0,0,1) and the above matrix. The reflected light Stokes vector is

$$\begin{pmatrix} I \\ Q \\ U \\ V \end{pmatrix} = \begin{pmatrix} 1 \\ -\sin 2\alpha \sin 2k_0 z \Delta n \\ -\cos 2\alpha \sin 2k_0 z \Delta n \\ -\cos(2k_0 z \Delta n) \end{pmatrix}. \tag{19.6}$$

From (equation 19.6), it is immediately clear that the birefringence can be determined from the Stokes parameter V and the optic axis orientation α can be determined from the Q and U parameters, $\tan\alpha = Q/U$.

Figure 19.5 shows a graphical depiction of the transformation of a Stokes vector due to a birefringent medium as described in (19.6). An incident circular polarization state is shown that is transformed by a rotation over an angle (δ) around an optical axis in the Q-U plane oriented at angle 2α.

19.3.1 Depth-Resolved Imaging of Stokes Parameters

As an example, two-dimensional images of the spatially resolved Stokes parameters of light reflected from ex vivo rodent muscle are shown in Fig. 19.6. Rodent muscle was mounted in a chamber filled with saline and covered with a thin glass cover slip to avoid dehydration during measurement. Figure 19.6 shows images of Stokes parameters for right circularly polarized incident light. Several periods of normalized U and V, cycling back and forth between 1 and −1, are observed in muscle, indicating that the sample is birefringent, further demonstrated by the averages of the Stokes parameters over all depth profiles in Fig. 19.7a.

Fig. 19.5 Rotation of the
Stokes vector for a circular
polarization state (1,0,0,1) by
a birefringent medium with
retardation δ and optic axis at
an angle α with respect to the
horizontal plane. F and
S denote fast and slow optic
axis orientation, respectively
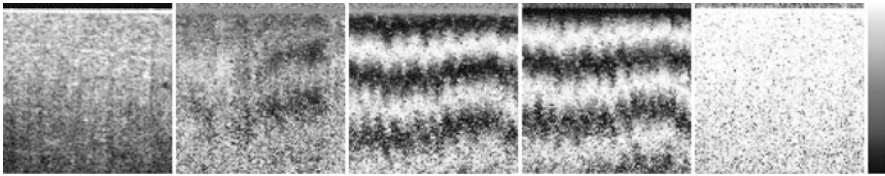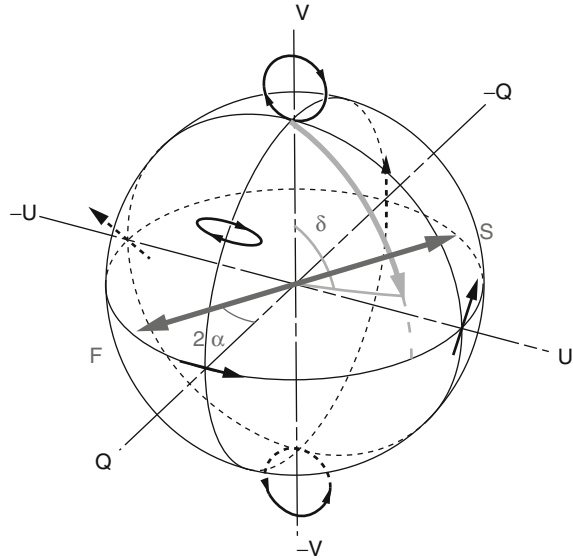
Fig. 19.6 PS-OCT images of ex vivo rodent muscle, 1×1 mm, pixel size 10×10 μm. From *left to right*, the Stokes parameter I, normalized parameters Q, U, and V in the sample frame for right circularly polarized incident light, and the degree of polarization P. The *gray scale* to the *right* gives the magnitude of signals, 35 dB range for I, from 1 (*white*) to -1 (*black*) for Q, U, and V, and from 1 (*white*) to 0 (*black*) for P (Reprinted from [14] with permission of the Optical Society of America)

To verify experimentally the orientation of the optical axis, light incident on the sample was prepared in three linear polarization states with electric fields parallel, perpendicular, and at an angle of 45° to the experimentally determined optical axis of the birefringent muscle. Figure 19.7b shows the average of the normalized Stokes parameter Q over all depth profiles at the same sample location. The negligible amplitude of oscillation in Q for light polarized parallel and perpendicular to the optical axis verified the experimentally determined orientation. When light is incident at an angle of 45° to the optical axis of the sample, Q oscillates with increasing sample depth as expected for a birefringent sample. The similarity of the reflected intensity for circular, parallel, and perpendicular light (shown in Fig. 19.7c) indicates that the polarization state changes are not due to dichroism
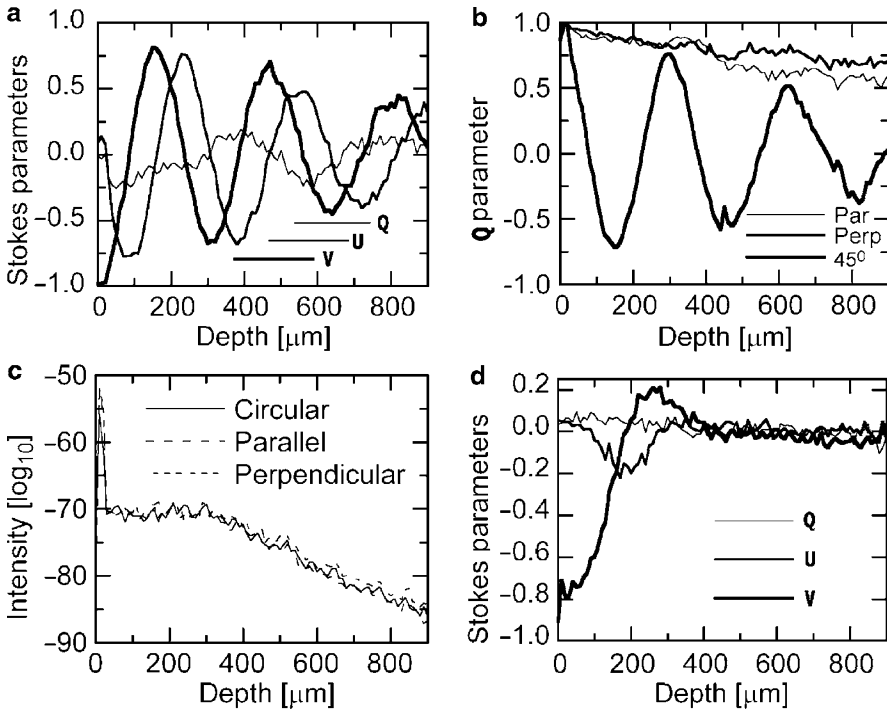
Fig. 19.7 Averages of Stokes parameter *I* and normalized parameters *Q*, *U*, and *V* in the sample frame over all depth profiles of, respectively, (**a**) rodent muscle, right circular incident polarization, (**b**) rodent muscle, linear incident polarization, parallel, perpendicular, and at 45° with the optical axis, (**c**) rodent muscle, right circular, parallel, and perpendicular incident polarization, (**d**) in vivo rodent skin, right circular incident polarization (Reprinted from [14] with permission of the Optical Society of America)

of the muscle fibers. The birefringence Δn was determined by measuring the distance of a full *V* period, which corresponds to a phase retardation of $\pi = k_0 z \Delta n$, giving $\Delta n = 1.4 \times 10^{-3}$.

19.3.2 Polarization Diversity Detection

To summarize, PS-OCT is important not only to measure birefringence but also for accurate interpretation of OCT images. Most fibrous structures in tissue (e.g., muscle, nerve fibers) are form birefringent due to their structural anisotropy. Single detector OCT systems can generate images that show structural properties by a reduction in tissue reflectivity, solely due to polarization effects. Polarization diversity detection is defined as the depth-resolved measurement of the *I* component of the Stokes vector of light reflected from the sample. Intuitively, one might expect that use of unpolarized sources may be advantageous for polarization diversity detection.

Although a polarized light source was assumed, the presented analysis is easily extended to include unpolarized sources. An unpolarized source can be described by the addition of two orthogonally polarized sources that are mutually incoherent. The interference fringes at the detector(s) need to be analyzed separately for the two pure polarization states, and the total interference fringe pattern at the detector(s) is given by the sum of the fringe patterns generated by each pure polarization state.

An OCT system with an unpolarized source and a single detector does not necessarily provide polarization diversity detection. On the contrary, this system is even more sensitive to polarization effects than a system with a polarized source.

Consider polarized source light incident on a birefringent sample acting as linear retarder with optic axis at 45° with respect to the incident light polarization axis. The polarization state of reflected light from some depth has undergone a π phase retardation and is orthogonal to the incident polarization state. Since orthogonally polarized states cannot interfere, light from the sample and reference arms do not produce interference fringes. The same holds for each of the orthogonally polarized states in the decomposition of an unpolarized source into linear states at 45° and −45° with the optic axis. Therefore, for the unpolarized source, no interference fringes will be detected. Suppose now that the decomposition of the unpolarized source is chosen differently for the above-mentioned birefringent sample such that the two orthogonal linearly polarized mutually incoherent states are along and perpendicular to the optic axis. Both orthogonal polarization states reflected from the sample are unaltered by the birefringence and will produce interference fringes with the reference arm light. However, at the same depth as above, the interference fringes for orthogonal polarization states are exactly π out of phase and cancel after summation on the single detector, and no interference fringe pattern is observed. Thus, in this example, the unpolarized source will not produce interference fringes at one depth regardless of the orientation of the optic axis (as is expected from symmetry arguments). In contrast, a polarized source would produce interference fringes if the state is polarized (partially) along the optic axis.

19.3.3 Summary

PS-OCT systems can be constructed with bulk optical components. These systems are too cumbersome to work with for practical application of this technique in a clinical setting. For portable, robust systems, implementation of the technique in optical fiber is necessary. In addition, probing with a single polarization state results in incomplete polarization properties' information of the sample. As an example, consider a circular polarization state incident on a birefringent sample. At some point in depth, this circular state will be converted to a linear state. If at this depth the optical axis of the sample changes to one collinear with the linear polarization state, the polarization will remain unchanged, that is, no change in polarization state will be detected. To remedy this erroneous result, the sample needs to be interrogated with more than one polarization state. In the next section, implementation of

PS-OCT systems in optical fiber will be described, and optimal polarization modulation schemes will be discussed to accurately determine the polarization properties of samples under study.

19.4   Fiber-Based PS-OCT Systems

Previous PS-OCT systems were air-spaced interferometers using bulk optical components that allowed precise control over the polarization state of light in the sample and reference arms [5–7, 14, 17]. Fiber-based interferometers offer distinct advantages in terms of system alignment and handling but pose design problems due to polarization changes induced in optical fibers. Polarization-maintaining (PM) fibers have a large birefringence with a beat length of 2–3 mm. The energy of wave components along the primary axes of the fiber is preserved, but the relative phase is lost due to the difference in experienced optical path length. In order to determine the Stokes parameters, such phase information is needed [14]. Recently, an OCT system was demonstrated where the difference in optical path length in PM fiber was compensated for by splicing two matching sections with orthogonal orientation of the optic axis [18].

19.4.1 Polarization Mode Dispersion and Differential Group Delay

Single-mode (SM) fibers (and the above-described compensated PM fibers) have polarization mode dispersion (PMD). Due to random birefringence, induced by core ellipticity, noncircularly symmetric stresses, and fiber bends, SM fibers propagate two nearly degenerate orthogonal polarization states. Differential phase delay (DPD) and differential group delay (DGD) between these two states cause, respectively, an evolution of the polarization states along the fiber and a broadening of the interferogram in an OCT system. With respect to DPD, which describes fiber birefringence, and thus the polarization state change while the light propagates through the fiber, the spectral dependence should be kept minimal to minimize the effect of spectral components transforming to different polarization states. DGD, which describes the difference in group delay between orthogonal polarization states, should at least result in an optical path length difference less than the source coherence length. The mode coupling length h describes the distance in the fiber with a constant orientation of the optic axis. It can be interpreted similarly to the mean free path (the distance between scattering events) in a random walk model of light diffusion. For fiber length L shorter than the mode coupling length h, DPD and DGD are directly proportional to fiber length. This relationship changes to a square root dependence for $L >> h$, indicating the underlying one-dimensional random walk nature of PMD [19]. We used a single-mode fiber (Corning SMF-28) with a PMD $\leq 0.1[ps/\sqrt{km}]$ if $L > h$ and $\leq 0.1\sqrt{km}/\sqrt{h}[ps/km]$ if $L < h$, resulting in an optical path length difference between orthogonal polarization states that is in either case less than 2 μm for 4.4 m of fiber.
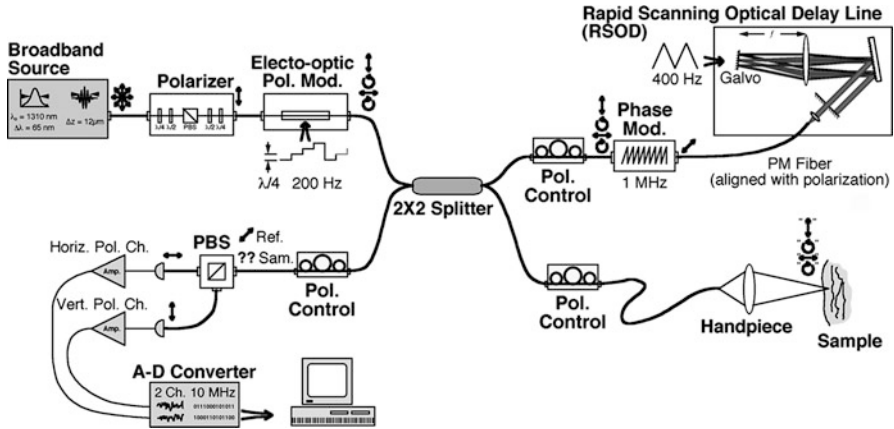
Fig. 19.8 Schematic of the fiber-based PS-OCT system

19.4.2 Fiber-Based PS-OCT Instrument

In Fig. 19.8, a single-mode fiber-based PS-OCT system is presented, which was described earlier [20]. A low-coherence source (AFC Technologies) with a FWHM bandwidth of 80 nm centered at 1,310 nm was polarized by a bulk polarizer and coupled back into the fiber. Quarter and half wave plates before the polarizer were used to select the polarization state of the source with the highest power (8 mW). Quarter and half wave plates after the polarizer prepared the polarization such that after a short fiber length (15 cm) the light emerged with equal magnitude wave components parallel and perpendicular to the optic axis of a bulk electro-optic polarization modulator (New Focus 4104). The modulator allows control of the polarization state over a grand circle on Poincaré sphere.

A four-step driving function, where each step introduces a $\pi/2$ phase shift, cycles the light over four Stokes vectors. In Fig. 19.9, the numbered black dots on the black grand circle indicate the polarization states immediately after the modulator, before a fiber 2×2 coupler. Due to the sample arm fiber circular and linear birefringence (or equivalently the DPD), the polarization state at the tip of the sample arm fiber is unknown. However, in a lossless fiber (with a total DGD smaller than the coherence time of the light), the transformations in Poincaré sphere are orthonormal, preserving the angles between the four Stokes vectors. The numbered gray dots on the gray grand circle in Fig. 19.9 indicate a possible realization of the four polarization states at the fiber tip. The sample arm consists of a fiber with a collimator and focusing lens, mounted on a motorized linear translation stage.

In the reference arm, a static polarization controller is aligned such that for all four polarization states, half of the light is transmitted through a PM fiber pigtailed phase modulator (JDS Uniphase) which by its structure polarizes the light. The PM fiber is also used to couple the light into a rapid-scanning optical delay
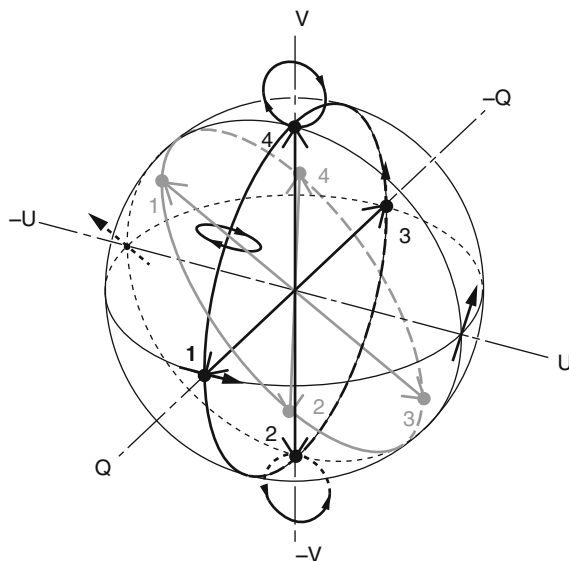
Fig. 19.9 The *black dots* numbered 1 through 4 on the *black* grand circle and axes show the four polarization states with 90° retardance increments after the polarization modulator. The *gray dots* numbered 1 through 4 on the *gray* grant circle show a possible realization of the polarization states at the sample arm fiber tip. In the absence of polarization-dependent loss, the 90° angle between the Stokes vectors after the polarization modulator is maintained at the sample arm fiber tip. The random orientation of circular and linear birefringence in the fiber transforms the light after the polarization modulator by a rotation in the Poincaré sphere

line (RSOD) [21, 22], which was operated with the spectrum centered on the galvo mirror. The RSOD thus only generates a group delay and no phase delay; the carrier of the interferometric signal at the detector is only generated by the phase modulator. The phase modulator is driven by a sawtooth waveform at 1 MHz, generating a maximum 2π phase shift after double passage.

In the detection arm, a static polarization controller before the polarizing beam splitter is aligned such that the reference arm light is split equally over both detectors. Electronic signals were high pass filtered, amplified, and digitized by a 12-bit dual-channel 10 M samples/s per channel A/D board (Gage Applied Sciences Inc.).

19.4.3 Fiber-Based PS-OCT Data Processing

Data processing consists of lock-in detection in software of the sine and cosine components at the reference frequency of 1 MHz. The sine and cosine components of 5-µm segments in each A-line (depth profile) of 2 mm length are processed to obtain the Stokes parameters as described earlier [14, 23]:

Fig. 19.10 Stokes parameter images I, Q, U, and V for each of the four input polarization states for in vivo human skin. Image size is 2×2 mm, gray scale coded on a logarithmic scale for the I parameter, and linearly gray scale coded from *black* to *white* for Q, U, and V values between 1 and -1
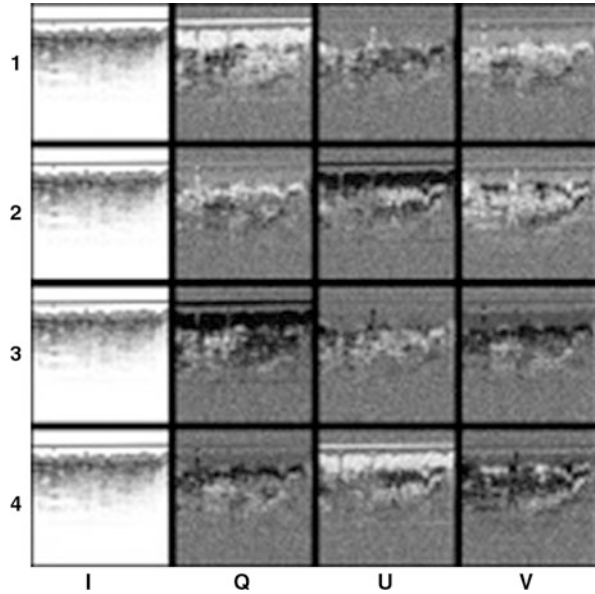
$$
\begin{aligned}
I &= \sin^2_H + \cos^2_H + \sin^2_V + \cos^2_V, \\
Q &= \sin^2_H + \cos^2_H - \sin^2_V - \cos^2_V, \\
U &= 2\sin_H * \sin_V + 2\cos_H * \cos_V, \\
V &= 2\sin_H * \cos_V - 2\cos_H * \sin_V.
\end{aligned}
\tag{19.7}
$$

Figure 19.10 shows 16 images of the four Stokes parameters for each of the four input states. A close look at these images reveals that the Stokes parameter images Q, U, and V for input polarization state 1 and 3 form an (nearly) identical pair that only differs in sign. In the images, this is apparent by an opposite gray scale color. Input polarization states 2 and 4 form a similar pair. The four input states form two pairs of orthogonal polarizations. In the Poincaré sphere representation, two orthogonal states are collinear vectors pointing to opposite points on the sphere. In a purely birefringent medium, two orthogonal states will undergo the exact same transformation and one Stokes vector can be obtained from the corresponding orthogonally polarized vector by a mirror operation in the origin. The pairs 1,3 and 2,4 carry independent information and are necessary to determine tissue birefringence properties. The lack of control over the polarization state incident on the sample due to the unknown polarization state change in the sample arm fiber could lead to the undesirable situation that the polarization state for pair 1,3 is linear and aligned with the optic axis of the medium. In this case, the polarization state will remain unchanged while propagating through the birefringent medium. In the Poincaré sphere representation, the incident Stokes state is collinear with the rotation. However, Stokes vector pair 2,4 is oriented at an angle of 90° with pair

1,3, which was collinear with the axis of rotation. Thus, pair 2,4 makes a right angle with the rotation axis and, thus, will be transformed over a grand circle.

In conclusion, any set of two polarization states that make an angle of 90° in the Poincaré sphere will necessarily be transformed by sample birefringence. In contrast, a collinear set (180° angle in the Poincaré sphere) is not necessarily transformed by sample birefringence. By calculating a single rotation matrix that transforms both pairs simultaneously, the birefringence of the sample can be determined, regardless of the actual realization of the polarization states at the fiber tip or the orientation of the sample optic axis. Pure diattenuation in the sample will lead to different transformations for orthogonally polarized Stokes vector pairs; the Stokes vectors of a pair do not remain collinear.

The effect of diattenuation in the measurement can be eliminated by averaging these 16 images as follows: for each pair of orthogonal incident polarizations, the I images are averaged by addition and the Q, U, and V images are averaged by subtraction since they have opposite signs. Any diattenuation contribution to the transformation of the remaining two Stokes vectors is eliminated. The resulting eight images (one set of I, Q, U, and V images per input pair) define two Stokes vectors that are described by lengths I_1 and I_2 and three component (Q, U, and V) vectors $\mathbf{I_1}$ and $\mathbf{I_2}$ with unit length (Fig. 19.11).

The incident polarization states $\mathbf{I_1}$ and $\mathbf{I_2}$ are now determined by the polarization state of light returning from the surface of the sample. $\mathbf{I_1}$ and $\mathbf{I_2}$ are compared to Stokes vectors returning from deeper in the sample, denoted by states $\mathbf{I_1}'$ and $\mathbf{I_2}'$. The calculation involves first determining an optic axis and then a degree of phase retardation about that axis. A single rotation, for example, from $\mathbf{I_1}$ to $\mathbf{I_1}'$, determines a plane of possible optic axes spanned by the sum and cross product of the two states. The intersection of the two planes, one determined by $\mathbf{I_1}$ and $\mathbf{I_1}'$ (Fig. 19.12b) and the other determined from $\mathbf{I_2}$ and $\mathbf{I_2}'$ (Fig. 19.12c), is taken as the overall optic axis, $\mathbf{A}$ (Fig. 19.12d). The final step in the analysis is determining the degree of phase retardation over this optic axis. θ_1 may be defined as the degree of rotation about $\mathbf{A}$ that takes $\mathbf{I_1}$ to $\mathbf{I_1}'$, and θ_2 is defined analogously. The expectation is that the two rotation angles are equal; however, in practice, they differ slightly due to noise. The overall phase retardation is taken as the intensity weighted average of the angles

$$\theta = \frac{\left|\overrightarrow{I_1}'\right| \theta_1 + \left|\overrightarrow{I_2}'\right| \theta_2}{\left|\overrightarrow{I_1}'\right| + \left|\overrightarrow{I_2}'\right|}. \tag{19.8}$$

These values are encoded on a gray scale with black and white representing rotation of 0 and π radians, respectively. A more elaborate expression for (19.8) was given in B.H. Park et al. [24].

Currently, a single rotation matrix is calculated at each depth in the sample, which assumes that the optical axis is constant. In a more advanced approach, the
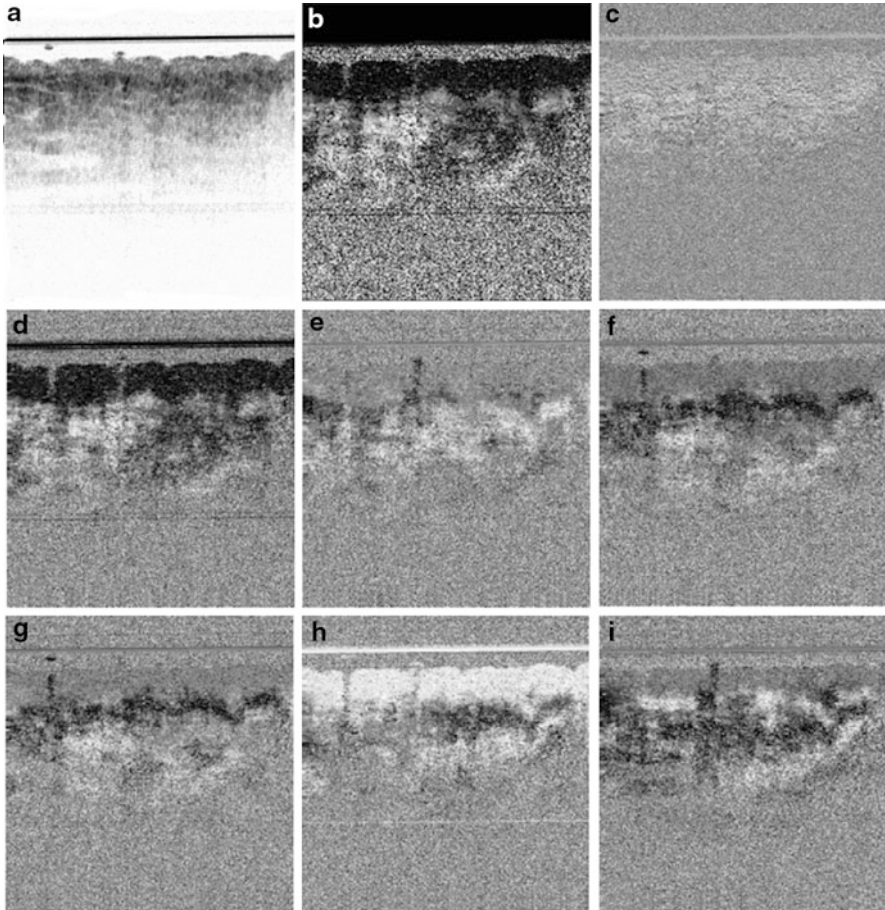
Fig. 19.11 Polarization-sensitive OCT images of in vivo human skin of the (*inside*) ventral forearm. (**a**) Conventional intensity image averaged from four scans with different incident polarizations. (**b**) Retardation phase map indicating the minimum amount of retardation to shift the incident polarization vector to the polarization state reflected back from a given depth. (**c**) Orthogonality image depicting the value of the cross product of the Stokes vectors. The remaining six images depict the polarization components of the Stokes vectors of the backscattered light for the pairs of polarizations that have been averaged: polarization 1 (**d**) Q, (**e**) U, (**f**) V, polarization 2 (**g**) Q, (**h**) U, (**i**) V

rotation matrix could be calculated between consecutive Stokes vectors along a depth profile, which would take into account variations in the orientation of the optic axis with depth. The total encountered birefringence would be the sum of the absolute values of the consecutive rotation angles. However, the presence of speckle noise would likely lead to a significant overestimation of the total phase retardation.
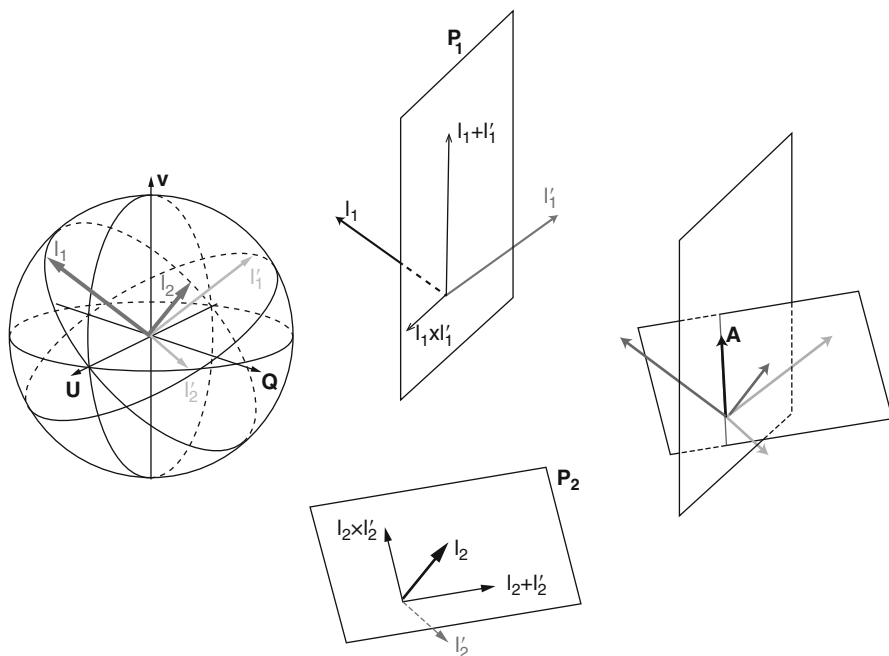
Fig. 19.12 These figures illustrate an example of a birefringence calculation. The polarization states at the surface, I_1 and I_2, are depicted on Poincaré sphere along with the polarization states reflected from a particular point in the sample, I_1' and I_2'. Plane P_1 is determined from I_1 and I_1'. Plane P_2 is determined from I_2 and I_2'. The intersections of planes P_1 and P_2 are taken as the combined optic axis A (Reprinted from [8] with permission of the Society of Photo-Optical Instrumentation Engineers)

19.4.4 Polarization Modulation Schemes

In order to evaluate the optimal choice of polarization states with which to interrogate the sample to determine the polarization properties, the possible polarization changes in the sample will be analyzed in the framework of Jones matrices and transformations in the Poincaré sphere. In the description discussed so far, the amplitude and the electric field components in orthogonal polarization channels were used to calculate the Stokes vector, and the polarization properties of tissue were analyzed by transformations in the Poincaré sphere. Equivalently, the amplitude and the electric field components can be used to perform an analysis using Jones matrix formalism [25, 26]. A Jones matrix is a complex 2×2 transfer matrix describing the transformation of the electric field components propagating through matter. Since a common phase factor can be extracted, a Jones matrix has seven independent variables. The polarization properties can be separated into four fundamental effects: linear birefringence (LB), circular birefringence (CB), linear diattenuation (LD), and circular diattenuation (CD). A sample that acts as

a polarizer can be described by diattenuation. The transmission Jones matrices for the above-described effects are given by, respectively,

$$\text{LB:} \begin{pmatrix} \cos\alpha & -\sin\alpha \\ \sin\alpha & \cos\alpha \end{pmatrix} \begin{pmatrix} e^{-i\delta/2} & 0 \\ 0 & e^{i\delta/2} \end{pmatrix} \begin{pmatrix} \cos\alpha & \sin\alpha \\ -\sin\alpha & \cos\alpha \end{pmatrix}, \qquad (19.9)$$

$$\text{CB:} \begin{pmatrix} \cos\gamma & \sin\gamma \\ -\sin\gamma & \cos\gamma \end{pmatrix}, \qquad (19.10)$$

$$\text{LD:} \begin{pmatrix} \cos\alpha & -\sin\alpha \\ \sin\alpha & \cos\alpha \end{pmatrix} \begin{pmatrix} P_1 & 0 \\ 0 & P_2 \end{pmatrix} \begin{pmatrix} \cos\alpha & \sin\alpha \\ -\sin\alpha & \cos\alpha \end{pmatrix}, \qquad (19.11)$$

$$\text{CD:} \begin{pmatrix} e^{i\pi/4} & -e^{i\pi/4} \\ e^{-i\pi/4} & e^{-i\pi/4} \end{pmatrix} \begin{pmatrix} P_1 & 0 \\ 0 & P_2 \end{pmatrix} \begin{pmatrix} e^{-i\pi/4} & e^{i\pi/4} \\ -e^{-i\pi/4} & e^{i\pi/4} \end{pmatrix}, \qquad (19.12)$$

with α the orientation of the birefringence or diattenuation optic axis with the horizontal, δ and γ the linear and circular phase retardance, respectively, and P_1 and P_2 the diattenuation coefficients with a value between 0 and 1.

A sample can be described by the matrix product of these Jones matrices. Since these matrices do not commute, the order does matter. The corresponding transformations in the Poincaré sphere for these four effects are depicted in Fig. 19.13. The transformation in the Poincaré sphere for a product of Jones matrices is given by a subsequent application to the Stokes vector of the corresponding transformations in the Poincaré sphere.

As discussed previously, a single polarization state will not suffice to determine uniquely the polarization properties, since the incident state could coincide with the optic axis for birefringence, or the convergence point for diattenuation. For birefringent tissue and a circular input polarization state, the polarization state will be converted to a linear state at some depth in the tissue. If at that depth the orientation of the optic axis changes to be collinear with the linear polarization state, no additional change in the polarization state will be detected from that depth on.

The minimal number of polarization states needed to uniquely determine the polarization properties in reflection is two. Due to the Jones reversibility theorem, the Jones matrix for light propagating forth and back through the same optical element is transpose symmetric [27]. Because of this symmetry, the number of independent parameters in the Jones matrix is reduced from seven to five [26]. A single measurement results in three known quantities: the electric field amplitudes in orthogonal polarization channels and their relative phase. Two measurements with different polarization states yield six known quantities, more than sufficient to determine the five independent parameters in the Jones matrix [26]. The elimination of two independent parameters in the Jones matrix is a consequence of the cancellation of circular birefringence and circular diattenuation upon forth and back propagation through the same optical element.
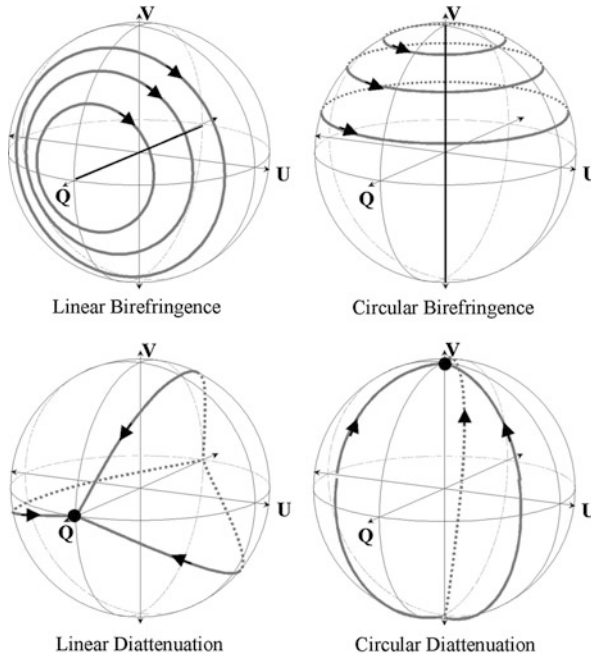
Fig. 19.13 Representation of the transformations in the Poincaré sphere for linear and circular birefringence (*top panel*) and linear and circular diattenuation (*bottom panel*). Linear birefringence is described by a rotation around an axis in the Q-U plane (in this example the Q-axis). Circular birefringence is described by a rotation around the V-axis. Linear diattenuation is described by a transformation of the Stokes vector over trajectories converging toward a point on a grant circle in the Q-U plane (in this example the $Q = 1$ point). Circular diattenuation is described by a transformation of the Stokes vector over trajectories converging toward the poles on the V-axis. Diattenuation is associated with loss. In these examples, the Stokes vectors were normalized on the intensity to obtain length unity

This can be verified by taking the matrix product of the Jones matrix for reflection sandwiched between the Jones matrix for circular birefringence or circular diattenuation, respectively. The resulting matrix is a diagonal matrix with opposite sign of the diagonal elements, representative of the Jones matrix for reflection. The effects of circular birefringence and circular diattenuation are eliminated from the resulting matrix.

The optimal choice for the two polarization states with which to probe the sample is given by two states that make a right angle in the Poincaré sphere representation [8, 10, 20, 28], for example, a $V = 1$ and a $Q = 1$ pair, or a $Q = 1$ and a $U = 1$ pair. As is evident from the transformations associated with birefringence as depicted in Fig. 19.13, if one state is an eigenvector of the transformation, the other state of the pair will trace out the longest arc on the sphere under the transformation.

The optimal choice for two polarization states was based on the assumption of probing the sample in sequential A-lines (depth profiles) with two states. In the next section, the Jones formalism will be expanded to analyze the result of polarization-sensitive OCT configurations that incorporate optical fiber. At the end, a polarization modulation scheme will be discussed where the polarization state will be modulated within a single A-line. In the latter case, the optimal polarization states are opposite in the Poincaré sphere representation (i.e., a horizontal and a vertical polarization state) with the assumption that the phase in the interference fringes between the two polarization states is stable.

19.4.5 Jones Formalism

The nondepolarizing polarization properties of an optical system can be completely described by its complex Jones matrix, $\mathbf{J}$, which transforms an incident polarization state, described by a complex electric field vector, $\mathbf{E} = \begin{bmatrix} H, & V \end{bmatrix}^T$, to a transmitted state, $\mathbf{E}' = \begin{bmatrix} H', & V' \end{bmatrix}^T$, and can be decomposed in the form $\mathbf{J} = \mathbf{J}_R\mathbf{J}_P = \mathbf{J}_{P'}\mathbf{J}_{R'}$ [29]. Birefringence, described by $\mathbf{J}_R$, can be parameterized by three variables: a degree of phase retardation η about an axis defined by two angles, γ and δ. Diattenuation, described by $\mathbf{J}_P$, is defined as $d = \left(P_1^2 - P_2^2\right)\big/\left(P_1^2 + P_2^2\right)$ and can be parameterized by four variables, where P_1 and P_2 are the attenuation coefficients parallel and orthogonal, respectively, to an axis defined by angles Γ and Δ. These seven independent parameters, along with an overall common phase $e^{i\psi}$, account for all four complex elements of a general Jones matrix $\mathbf{J}$. Assuming that birefringence and diattenuation arise from the same fibrous structures in biological tissue and thus share a common axis ($\delta = \Delta$ and $\gamma = \Gamma$) [25], the number of independent parameters is reduced by two. An incident and reflected polarization state yield three relations involving the two orthogonal amplitudes and the relative phase between them [9]. Therefore, it is possible to use the six relationships defined by two unique pairs of incident and reflected polarization states to exactly solve for the Jones matrix of a sample.

In general terms, a PS-OCT system sends polarized light from a broadband source into the sample and reference arms of an interferometer, and reflected light from both arms is recombined and detected. Define $\mathbf{J}_{\text{in}}$ as the Jones matrix representing the optical path from the polarized light source to the sample surface, $\mathbf{J}_{\text{out}}$ as that going from the sample surface to the detectors, and $\mathbf{J}_S$ as the round-trip Jones matrix for light propagation through a sample [30]. This nomenclature can be applied to all PS-OCT systems, ranging from bulk-optic systems [5–7, 9, 17, 31], to those with fibers placed such that they are traversed in a round-trip manner [32], to time-domain [20, 33] (Fig. 19.14) and spectral-domain [34] PS-OCT systems with the unrestricted use of optical fiber and nondiattenuating fiber components, and even for retinal systems [35], where the polarization effects of the cornea can be included in $\mathbf{J}_{\text{in}}$ and $\mathbf{J}_{\text{out}}$. The electric field of light reflected from the sample surface, $\mathbf{E}$, can be expressed as $\mathbf{E} = e^{i\psi}\mathbf{J}_{\text{out}}\mathbf{J}_{\text{in}}\mathbf{E}_{\text{source}}$, where ψ represents a common phase and $\mathbf{E}_{\text{source}}$ represents the electric field of light coming from the polarized source.
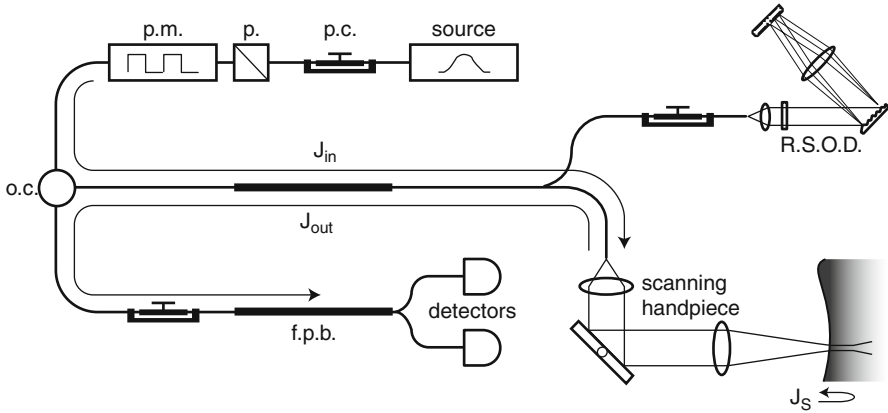
Fig. 19.14 Schematic of the fiber-based PS-OCT system (*p.c.* polarization controller, *p.* polarizer, *p.m.* polarization modulator, *o.c.* optical circulator, *R.S.O.D.* rapid-scanning optical delay, *f.p.b.* fiber polarizing beam splitter). $\mathbf{J}_{in}$, $\mathbf{J}_{out}$, and $\mathbf{J}_S$ are the Jones matrix representations for the one-way optical path from the polarization modulator to the scanning handpiece, the one-way optical path back from the scanning handpiece to the detectors, and the round-trip path through some depth in the sample, respectively (Reprinted from Fig. 19.1 of Ref. [30] with permission of the Optical Society of America)

Likewise, the electric field of light reflected from some depth within the tissue may be described by $\mathbf{E}' = e^{i\psi'}\mathbf{J}_{out}\mathbf{J}_S\mathbf{J}_{in}\mathbf{E}_{source}$. These two measurable polarization states can be related to each other such that $\mathbf{E}' = e^{i\Delta\psi}\mathbf{J}_T\mathbf{E}$, where $\mathbf{J}_T = \mathbf{J}_{out}\mathbf{J}_S\mathbf{J}_{out}^{-1}$ and $\Delta\psi = \psi' - \psi$.

If the optical system representing $\mathbf{J}_{out}$ is nondiattenuating, $\mathbf{J}_{out}$ can be treated as a unitary matrix with unit determinant after separating out a common attenuation factor. $\mathbf{J}_S$ can be decomposed into a diagonal matrix $\mathbf{J}_C = \left[P_1 e^{i\eta/2}, \; 0; \; 0, \; P_2 e^{i\eta/2}\right]$, containing complete information regarding the amount of sample diattenuation and phase retardation, surrounded by unitary matrices with unit determinant that define the sample optic axis. $\mathbf{J}_T$ can be reformed such that $\mathbf{J}_T = \mathbf{J}_{out}\mathbf{J}_S\mathbf{J}_{out}^{-1} = \mathbf{J}_{out}\left(\mathbf{J}_A\mathbf{J}_C\mathbf{J}_A^{-1}\right)\mathbf{J}_{out}^{-1} = \mathbf{J}_U\mathbf{J}_C\mathbf{J}_U^{-1}$, where $\mathbf{J}_U = \mathbf{J}_{out}\mathbf{J}_A$. Since unitary matrices with unit determinant form the special unitary group SU(2) [36], $\mathbf{J}_U$ must also be a unitary matrix with unit determinant by closure and can be expressed in the form

$$\mathbf{J}_U = e^{i\beta}\begin{bmatrix} C_\theta e^{i(\phi-\varphi)} & -S_\theta e^{i(\phi+\varphi)} \\ S_\theta e^{-i(\phi+\varphi)} & C_\theta e^{-i(\phi-\varphi)} \end{bmatrix}. \tag{19.13}$$

An alternative formulation for $\mathbf{J}_T$ can be obtained by combining information from two unique incident polarization states, $\left[H'_1, \; H'_2; \; V'_1, \; V'_2\right] = e^{i\Delta\psi_1}\mathbf{J}_T\left[H_1, \; e^{i\alpha}H_2; \; V_1, \; e^{i\alpha}V_2\right]$, where $\alpha = \Delta\psi_2 - \Delta\psi_1$. The polarization properties of interest can be obtained by equating the two expressions for $\mathbf{J}_T$ to yield

$$e^{i\Delta\psi_1}\begin{bmatrix} P_1 e^{i\eta/2} & 0 \\ 0 & P_2 e^{-i\eta/2} \end{bmatrix} = \begin{bmatrix} C_\theta & S_\theta \\ -S_\theta & C_\theta \end{bmatrix}\begin{bmatrix} e^{-i\phi} & 0 \\ 0 & e^{i\phi} \end{bmatrix}\begin{bmatrix} H'_1 & H'_2 \\ V'_1 & V'_2 \end{bmatrix}.$$

$$\begin{bmatrix} H_1 & e^{i\alpha}H_2 \\ V_1 & e^{i\alpha}V_2 \end{bmatrix}^{-1}\begin{bmatrix} e^{i\phi} & 0 \\ 0 & e^{-i\phi} \end{bmatrix}\begin{bmatrix} C_\theta & -S_\theta \\ S_\theta & C_\theta \end{bmatrix} \qquad (19.14)$$

In principle, parameters θ, ϕ, and α can be solved for with the condition that the off-diagonal elements of the matrix product on the right-hand side of (19.14) are equal to zero. In practice, real solution cannot always be found, as measurement noise can induce nonphysical transformations between incident and transmitted polarization states. To account for this, (19.14) can be solved by optimizing parameters θ, ϕ, and α to minimize the sum of the magnitudes of the off-diagonal elements. In principle, this can be achieved using two unique incident polarization states to probe the same volume of a sample. However, when two orthogonal incident polarization states are used [32], birefringence cannot be retrieved under all circumstances [37]. A better choice is to use two incident polarization states perpendicular in a Poincaré sphere representation to guarantee that polarization information can always be extracted [20, 24, 33–35, 38]. The degree of phase retardation can easily be extracted through the phase difference of the resulting diagonal elements, and the diattenuation by their magnitudes. It should be noted that these phase retardation values range from $-\pi$ to π and can therefore be unwrapped to yield overall phase retardations in excess of 2π.

As a control measurement, a series of OCT intensity images with varying single linear incident polarization states were acquired from chicken tendon and muscle tissue. The orientations for which the reflected polarization states from within the tissue varied minimally as a function of depth were chosen as those where the incident state was aligned parallel or orthogonal to the sample optic axis. The corresponding intensity profiles described attenuation parameters P_1 and P_2, from which depth-resolved control diattenuation plots were derived. PS-OCT scans were then acquired of the same tissue regions. After correcting for slight imbalances between the gains for the two orthogonal detectors, depth-resolved plots of both diattenuation and phase retardation were calculated. The resulting single-pass diattenuation plots are shown in Fig. 19.15. Numerical simulation revealed that the average angular displacement of a polarization state on the Poincaré sphere for a small diattenuation, d, is approximately $(40d)^\circ$. Given that the a standard deviation of the order of 5° for individual polarization states reflected from the surface was found, the control and PS-OCT-derived diattenuation per unit depth of chicken muscle, 0.0380 ± 0.0036/mm versus 0.0622 ± 0.0533/mm, and tendon, 0.5027 ± 0.0353/mm versus 0.3915 ± 0.0365/mm, were within reasonable agreement. These diattenuation values correspond to angular displacement on the order of $1.5 - 2.5^\circ$/mm and $15 - 20^\circ$/mm for muscle and tendon, respectively. The slopes of the respective phase retardation plots, 179.7°/mm and
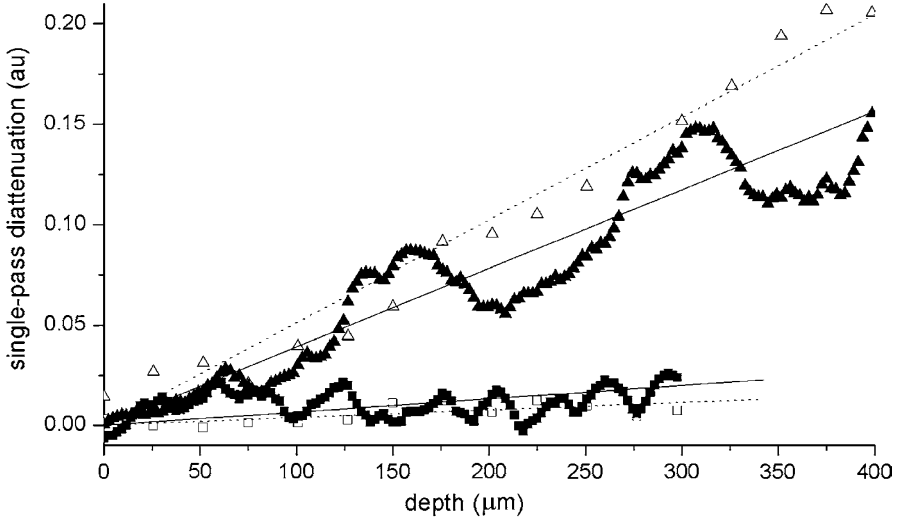
Fig. 19.15 Single-pass diattenuation as a function of depth. The open triangles and squares represent control diattenuation values of chicken tendon and muscle, respectively, calculated from comparison of the reflectivity profiles for linear incident polarization states along and orthogonal to the fiber direction. The *solid triangles* and *squares* are diattenuation values derived from PS-OCT images acquired from the same tissues. Linear least-squares fits are shown for all plots (Reprinted from Fig. 19.3 of Ref. [30] with permission of the Optical Society of America)

$1184.4°/$mm for tendon, are well within expected parameters. The angular displacement of the Stokes vectors as a result of diattenuation is negligible compared with those due to birefringence in both cases, implying that for these samples, birefringence can be determined with accuracy even ignoring diattenuation.

A relative optic axis can be derived from ϕ and θ, given in Stokes parameter form by $\mathbf{A} = [\, 1, \quad C_{2\phi}C_{2\theta}, \quad C_{2\phi}S_{2\theta}, \quad S_{2\phi} \,]^T$. However, determination of this relative optic axis in a fiber-based system has a fundamental ambiguity. All members of the SU(2) group can be mapped to rotations in SO(3), and so $\mathbf{J}_{out}$, $\mathbf{J}_A$, and $\mathbf{J}_U$ all represent rotations in a Poincaré sphere representation. This means that $\mathbf{J}_C$, $\mathbf{J}_S$, and $\mathbf{J}_T$ are related by unitary transforms and are equivalent except for their respective coordinate systems. Therefore, the amount of phase retardation and diattenuation in $\mathbf{J}_C$, $\mathbf{J}_S$, and $\mathbf{J}_T$ is the same. The three matrices differ only in their eigenvectors, and their optic axis equivalents, in a well-defined manner dictated by $\mathbf{J}_{out}$. In other words, the optic axis of $\mathbf{J}_T$ is the product of the sample optic axis defined by $\mathbf{J}_A$ and the fiber transformations represented by $\mathbf{J}_{out}$.

Due to the round-trip nature of detected light propagation in tissue, the circular components of birefringence and diattenuation in the sample cancel. Only the linear components of these properties can be measured using PS-OCT. In mathematical terms, the optic axes of $\mathbf{J}_S$, defined by its eigenvectors, can represent only linear birefringence and diattenuation; the *V*-component (describing circular

polarization effects) of the equivalent Stokes vector must equal zero. Therefore, all possible optic axes for $\mathbf{J}_S$ lie on the QU-plane of a Poincaré sphere. Since $\mathbf{J}_T$ and $\mathbf{J}_S$ differ only by an overall rotation of their coordinate systems, the plane of all possible optic axes for $\mathbf{J}_T$ can be rotated off the QU-plane to some arbitrary plane passing through the origin. The optic axes of $\mathbf{J}_T$ can then have circular components that are entirely due to rotations of the coordinate system arising from system fiber. To verify this analysis, PS-OCT images were taken of a chicken muscle sample, its surface oriented orthogonal to the incident beam, and rotated in $40°$ increments to span a full $360°$. Details of the fiber-based PS-OCT system, capable of imaging at 2,048 depth scans per second, were presented by Pierce et al. [33]. It should be noted that the sample itself was rotated and that the fibers in the system were left untouched. Two different analysis methods, the vector-based method and the Jones-matrix-based method, were used to analyze the data, providing nearly identical results. The resulting optic axes, along with a plane determined by least-squares fitting, are shown in the inset of Fig. 19.16. The rotation away from the QU-plane is evident, as is the coplanarity of the calculated optic axes.

One method of determining optic axis orientation is to simply determine the orientation as an angle on this tilted plane, as shown in Fig. 19.16. The resulting orientations, relative to that at $0°$, are plotted as a function of the set orientation and show that the relative optic axis orientation can be recovered accurately. A second method is to rotate the calculated plane of optic axes back down onto the QU-plane of the Poincaré sphere. The change in coordinate system due to optical fibers in the system can be decomposed into two parts: a rotation within the plane of possible measured optic axes and a tilting of the plane about some arbitrary axis in the QU-plane. The rotation within the plane causes an overall offset in the calculated orientation that has been discussed in previous publications [32, 37–39] and implies that only relative orientation angles, not absolute angles, can be determined from a fiber-based PS-OCT system. The tilting of the plane leads to what can be termed a π-ambiguity, or an indeterminacy in the sign of the orientation angle [39].

One proposed method to compensate for this tilting uses the reflection from the surface of a sample to determine the rotation needed to tilt the plane back onto the QU-plane by solving $\mathbf{E} = e^{i\psi} \mathbf{J}_{in}^T \mathbf{J}_{in} \mathbf{E}_{source}$, where $\mathbf{J}_{in}$ represents the sample arm fiber only [32]. Four possible solutions to $\mathbf{J}_{in}$ can be found that map to two unique rotations in SO(3) corresponding to common phase factors ψ differing by π. In geometrical terms, this is the equivalent of the fact that there are two ways to rotate the plane of measured optic axes onto the QU-plane of the Poincaré sphere (face-up and face-down). This results in an ambiguity in the sign of the orientation angle. In other words, as the set optic axis orientation of a sample rotates in one direction, the measured optic axis orientation, depending on the correction chosen, could move in either direction. Thus, the sign of the orientation angle cannot be determined explicitly, only the absolute value, or magnitude, of change from one location to the next. The slope of Fig. 19.16, relating the calculated orientation to the set orientation for a set of data where the same correction could be used throughout, could be positive or negative with equal validity. This π-ambiguity is inherent to all
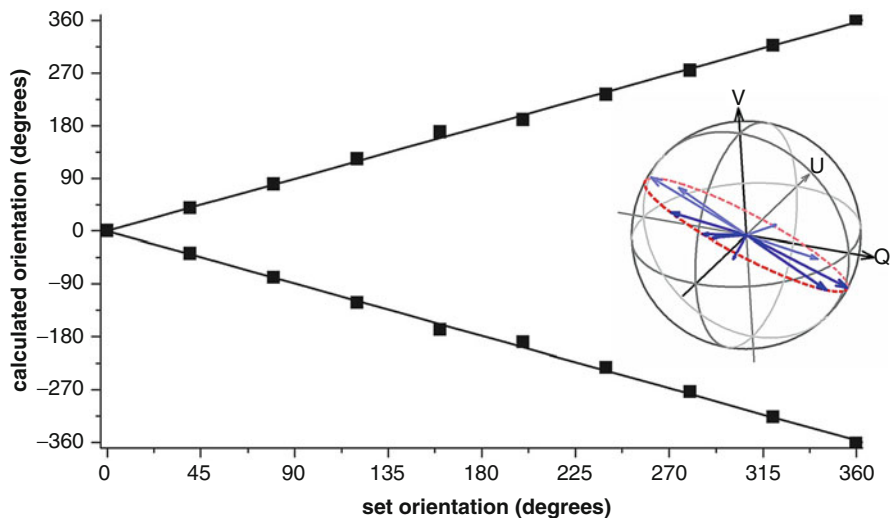
Fig. 19.16 Calculated optic axis orientation as a function of set orientation relative to $0°$ (*squares*, measured orientation; *lines*, linear fit to the data). As a result of the π-ambiguity (see text), the measured orientation can have both a positive and a negative slope with equal likelihood. *Inset*, Poincaré sphere representation of the calculated optic axes (*arrows*) for various set orientations of the tissue sample optic axis. The plane (*dashed circle*) in which these optic axes lie was determined by least-squares fitting (Reprinted from Fig. 19.1 of Ref. [39] with permission from the Optical Society of America)

fiber-based PS-OCT systems and implies that although the relative optic axis within an image can be determined, the direction of change in optic axis orientation cannot be compared from image to image absolutely without a priori knowledge.

19.4.6 Rapid Polarization Modulation Within an A-Line (Depth Profile)

The polarization modulation schemes presented above assumed that the polarization was modulated between consecutive A-lines (depth profiles). Yamanari et al. presented in 2008 a polarization modulation scheme where the polarization was rapidly modulated within an A-line (depth profile) [40]. Modulation within an A-line removes the arbitrary phase α in (19.14) that was introduced to account for phase instabilities between consecutive A-line scans in the Jones matrix formalism. Eliminating the arbitrary phase α by the fast modulation scheme also alters the choice of optimal incident polarization states: the optimal polarization states become opposite in the Poincaré sphere representation (i.e., a horizontal and a vertical polarization state) under the condition that the phase α in the interference fringes between the two polarization states is stable.

19.5 Future Directions in PS-OCT

The potential biological and medical applications of PS-OCT are just beginning to be explored. Much work remains for further development of PS-OCT. We anticipate progress will proceed in three major areas; these include instrumentation, biological and medical applications, and data interpretation/image processing. Many clinical applications of PS-OCT require a fiber-based instrument that can record images at high frame rates. Especially the progress made in SD-OCT and OFDI allow for high-speed systems [41–44]. Because many components in biological materials contain intrinsic and/or form birefringence, PS-OCT is an attractive technique for providing an additional contrast mechanism that can be used to image/identify structural components. Moreover, because functional information in some biological systems is associated with transient changes in birefringence, the possibility of functional PS-OCT imaging should be explored. PS-OCT may hold considerable potential for monitoring, in real-time, laser surgical procedures involving birefringent biological materials. Because many laser surgical procedures rely on a photothermal injury mechanism, birefringence changes in subsurface tissue components measured using PS-OCT may be used as a feedback signal to control laser dosimetry in real time. The loss of birefringence in thermally denatured collagen might provide a means for in vivo burn depth assessment [6, 8, 45]. Changes in birefringence of the retinal nerve fiber layer might provide an early indication of the onset of glaucoma. Finally, many features of PS-OCT interference fringe data require additional interpretation and study. Because polarization changes in light propagating in the sample may be used as an additional contrast mechanism, the relative contribution of light scattering and birefringence-induced changes requires further study and clarification. In principle, one would like to distinguish polarization changes due to scattering and birefringence at each position in the sample and utilize each as a potential contrast mechanism. In conclusion, we anticipate PS-OCT will continue to advance rapidly and be applied to novel problems in clinical medicine and biological research.

References

1. D. Huang, E.A. Swanson, C.P. Lin, J.S. Schuman, W.G. Stinson, W. Chang, M.R. Hee, T. Flotte, K. Gregory, C.A. Puliafito, J.G. Fujimoto, Optical coherence tomography. Science **254**, 1178–1181 (1991)
2. H.F. Hazebroek, A.A. Holscher, Interferometric ellipsometry. J. Phys. E Sci. Instrum. **6**, 822–826 (1973)

3. T.P. Newson, F. Farahi, J.D.C. Jones, D.A. Jackson, Combined interferometric and polarimetric fiber optic temperature sensor with a short coherence length source. Opt. Commun. **68**, 161–165 (1988)

4. M. Kobayashi, H. Hanafusa, K. Takada, J. Noda, Polarization-independent interferometric optical-time-domain reflectometer. J. Lightwave Technol. **9**, 623–628 (1991)

5. M.R. Hee, D. Huang, E.A. Swanson, J.G. Fujimoto, Polarization-sensitive low-coherence reflectometer for birefringence characterization and ranging. J. Opt. Soc. Am. B **9**, 903–908 (1992)

6. J.F. de Boer, T.E. Milner, M.J.C. van Gemert, J.S. Nelson, Two-dimensional birefringence imaging in biological tissue by polarization-sensitive optical coherence tomography. Opt. Lett. **22**, 934–936 (1997)

7. M.J. Everett, K. Schoenenberger, B.W. Colston, L.B. Da Silva, Birefringence characterization of biological tissue by use of optical coherence tomography. Opt. Lett. **23**, 228–230 (1998)

8. B.H. Park, C. Saxer, S.M. Srinivas, J.S. Nelson, J.F. de Boer, In vivo burn depth determination by high-speed fiber-based polarization sensitive optical coherence tomography. J. Biomed. Opt. **6**, 474–479 (2001)

9. M.G. Ducros, J.F. de Boer, H.E. Huang, L.C. Chao, Z.P. Chen, J.S. Nelson, T.E. Milner, H.G. Rylander, Polarization sensitive optical coherence tomography of the rabbit eye. IEEE J. Sel. Top. Quant. Electron. **5**, 1159–1167 (1999)

10. B. Cense, T.C. Chen, B.H. Park, M.C. Pierce, J.F. de Boer, In vivo depth-resolved birefringence measurements of the human retinal nerve fiber layer by polarization-sensitive optical coherence tomography. Opt. Lett. **27**, 1610–1612 (2002)

11. J.F. de Boer, T.E. Milner, Review of polarization sensitive optical coherence tomography and Stokes vector determination. J. Biomed. Opt. **7**, 359–371 (2002)

12. W.A. Shurcliff, S.S. Ballard, *Polarized Light* (Van Nostrand, New York, 1964)

13. J.F. de Boer, T.E. Milner, J.S. Nelson, Two dimensional birefringence imaging in biological tissue using phase and polarization sensitive optical coherence tomography, in *Trends in Optics and Photonics (TOPS): Advances in Optical Imaging and Photon Migration* (OSA, Washington, DC, 1998)

14. J.F. de Boer, T.E. Milner, J.S. Nelson, Determination of the depth-resolved Stokes parameters of light backscattered from turbid media by use of polarization-sensitive optical coherence tomography. Opt. Lett. **24**, 300–302 (1999)

15. J.F. de Boer, T.E. Milner, M.G. Ducros, S.M. Srinivas, J.S. Nelson, Polarization-sensitive optical coherence tomography, in *Handbook of Optical Coherence Tomography*, ed. by B.E. Bouma, G.J. Tearney (Marcel Dekker, New York, 2002), pp. 237–274

16. C.F. Bohren, D.R. Huffman, *Absorption and Scattering of Light by Small Particles* (Wiley, New York, 1983)

17. G. Yao, L.V. Wang, Two-dimensional depth-resolved Mueller matrix characterization of biological tissue by optical coherence tomography. Opt. Lett. **24**, 537–539 (1999)

18. D.P. Davé, T. Akkin, T.E. Milner, Polarization-maintaining fiber-based optical low coherence reflectometer for birefringence characterization and ranging. Opt. Lett. **28**, 1775–1777 (2003)

19. C.D. Poole, Statistical treatment of polarization dispersion in single-mode fiber. Opt. Lett. **13**, 687–689 (1988)

20. C.E. Saxer, J.F. de Boer, B.H. Park, Y.H. Zhao, Z.P. Chen, J.S. Nelson, High-speed fiber-based polarization-sensitive optical coherence tomography of in vivo human skin. Opt. Lett. **25**, 1355–1357 (2000)

21. G.J. Tearney, B.E. Bouma, J.G. Fujimoto, High-speed phase- and group-delay scanning with a grating-based phase control delay line. Opt. Lett. **22**, 1811–1813 (1997)

22. A.M. Rollins, M.D. Kulkarni, S. Yazdanfar, R. Ung-arunyawee, J.A. Izatt, In vivo video rate optical coherence tomography. Opt. Express **3**, 219–229 (1998)

23. J.F. de Boer, S.M. Srinivas, B.H. Park, T.H. Pham, Z.P. Chen, T.E. Milner, J.S. Nelson, Polarization effects in optical coherence tomography of various biological tissues. IEEE J. Sel. Top. Quant. Electron. **5**, 1200–1204 (1999)

24. B.H. Park, M.C. Pierce, B. Cense, J.F. de Boer, Real-time multi-functional optical coherence tomography. Opt. Express **11**, 782–793 (2003)
25. S.L. Jiao, L.H.V. Wang, Two-dimensional depth-resolved Mueller matrix of biological tissue measured with double-beam polarization-sensitive optical coherence tomography. Opt. Lett. **27**, 101–103 (2002)
26. S.L. Jiao, L.H.V. Wang, Jones-matrix imaging of biological tissues with quadruple- channel optical coherence tomography. J. Biomed. Opt. **7**, 350–358 (2002)
27. N. Vansteenkiste, P. Vignolo, A. Aspect, Optical reversibility theorems for polarization – application to remote-control of polarization. J. Opt. Soc. Am. A Opt. Image Sci. Vis. **10**, 2240–2245 (1993)
28. M.C. Pierce, B.H. Park, B. Cense, J.F. de Boer, Simultaneous intensity, birefringence, and flow measurements with high speed fiber-based optical coherence tomography. Opt. Lett. **27**, 1534–1536 (2002)
29. J.J. Gil, E. Bernabeu, Obtainment of the polarizing and retardation parameters of a non-depolarizing optical system from the polar decomposition of its Mueller matrix. Optik **76**, 67–71 (1987)
30. B.H. Park, M.C. Pierce, B. Cense, J.F. de Boer, Jones matrix analysis for a polarization-sensitive optical coherence tomography system using fiber-optic components. Opt. Lett. **29**, 2512–2514 (2004)
31. C.K. Hitzenberger, E. Gotzinger, M. Sticker, M. Pircher, A.F. Fercher, Measurement and imaging of birefringence and optic axis orientation by phase resolved polarization sensitive optical coherence tomography. Opt. Express **9**, 780–790 (2001)
32. S.L. Jiao, W.R. Yu, G. Stoica, L.H.V. Wang, Optical-fiber-based Mueller optical coherence tomography. Opt. Lett. **28**, 1206–1208 (2003)
33. M.C. Pierce, B.H. Park, B. Cense, J.F. de Boer, Simultaneous intensity, birefringence, and flow measurements with high-speed fiber-based optical coherence tomography. Opt. Lett. **27**, 1534–1536 (2002)
34. B.H. Park, M.C. Pierce, B. Cense, S.H. Yun, M. Mujat, G.J. Tearney, B.E. Bouma, J.F. de Boer, Real-time fiber-based multi-functional spectral-domain optical coherence tomography at 1.3 μm. Opt. Express **13**, 3931–3944 (2005)
35. B. Cense, T.C. Chen, B.H. Park, M.C. Pierce, J.F. de Boer, In vivo depth-resolved birefringence measurements of the human retinal nerve fiber layer by polarization-sensitive optical coherence tomography. Opt. Lett. **27**, 1610–1612 (2002)
36. W.K. Tung, *Group Theory in Physics* (World Scientific, Philadelphia, 1985)
37. B.H. Park, M.C. Pierce, J.F. de Boer, Comment on "optical-fiber-based Mueller optical coherence tomography". Opt. Lett. **29**, 2873–2874 (2004)
38. B.H. Park, C. Saxer, S.M. Srinivas, J.S. Nelson, J.F. de Boer, In vivo burn depth determination by high-speed fiber-based polarization sensitive optical coherence tomography. J. Biomed. Opt. **6**, 474–479 (2001)
39. B.H. Park, M.C. Pierce, B. Cense, J.F. de Boer, Optic axis determination accuracy for fiber-based polarization-sensitive optical coherence tomography. Opt. Lett. **30**, 2587–2589 (2005)
40. M. Yamanari, S. Makita, Y. Yasuno, Polarization-sensitive swept-source optical coherence tomography with continuous source polarization modulation. Opt. Express **16**, 5892–5906 (2008)
41. M. Wojtkowski, R. Leitgeb, A. Kowalczyk, T. Bajraszewski, A.F. Fercher, In vivo human retinal imaging by Fourier domain optical coherence tomography. J. Biomed. Opt. **7**, 457–463 (2002)
42. N. Nassif, B. Cense, B.H. Park, M.C. Pierce, S.H. Yun, B.E. Bouma, G.J. Tearney, T.C. Chen, J.F. de Boer, In vivo high-resolution video-rate spectral-domain optical coherence tomography of the human retina and optic nerve. Opt. Express **12**, 367–376 (2004)
43. N. Nassif, B. Cense, B.H. Park, S.H. Yun, T.C. Chen, B.E. Bouma, G.J. Tearney, J.F. de Boer, In vivo human retinal imaging by ultrahigh-speed spectral domain optical coherence tomography. Opt. Lett. **29**, 480–482 (2004)
44. S.H. Yun, G.J. Tearney, J.F. de Boer, N. Iftimia, B.E. Bouma, High-speed optical frequency-domain imaging. Opt. Express **11**, 2953–2963 (2003)
45. J.F. de Boer, S.M. Srinivas, A. Malekafzali, Z. Chen, J.S. Nelson, Imaging thermally damaged tissue by polarization sensitive optical coherence tomography. Opt. Express **3**, 212–218 (1998)

Doppler Optical Coherence Tomography

20

Zhongping Chen and Gangjun Liu

Contents

Abstract

This chapter describes Doppler optical coherence tomography (D-OCT). This is an imaging modality that combines Doppler principles with optical coherence tomography to image tissue structure and blood flow velocity

Z. Chen (✉) • G. Liu

Department of Biomedical Engineering, Beckman Laser Institute, University of California, Irvine, Irvine, CA, USA
e-mail: z2chen@uci.edu, gangjun@gmail.com

simultaneously. We will review the principle and technology of D-OCT and illustrate a few examples of its applications.

20.1 Introduction

Noninvasive techniques for imaging in vivo blood flow are of great value for biomedical research and clinical diagnostics where many diseases have a vascular etiology or component. In dermatology, for example, the superficial dermal plexus alone is particularly affected by the presence of disease (e.g., psoriasis, eczema, scleroderma), malformation (e.g., port-wine stain, hemangioma, telangiectasia), or trauma (e.g., irritation, wound, burn). In these situations, it would be most advantageous to the clinician if blood flow and structural features could be isolated and probed at user-specified discrete spatial locations in either the superficial or deep dermis. In ophthalmology, many ophthalmic diseases may involve disturbances in ocular blood flow, including diabetic retinopathy, low tension glaucoma, anterior ischemic optic neuritis, and macular degeneration. For example, in diabetic retinopathy, retinal blood flow is reduced and the normal autoregulatory capacity is deficient. Ocular hemodynamics is altered in patients with glaucoma, and severe loss of visual function has been associated with reduced macular blood flow. Simultaneous imaging of tissue structure and blood flow can provide critical information for early diagnosis of ocular disease. Finally, three-dimensional mapping of microcirculation may also provide important information for the diagnosis and management of cancer. It is known that the microvasculature of mammary tumors has several distinct differences from normal tissues. Tumor vasculature provides significant additional information for the differentiation of benign and malignant tumors [1]. The mapping of in vivo blood changes following pharmacological intervention is also important for the development of antiangiogenic drugs for cancer treatment.

Currently, techniques, such as Doppler ultrasound (DUS) and laser Doppler flowmetry (LDF), are used for blood flow velocity determination. DUS is based on the principle that the frequency of ultrasonic waves backscattered by moving particles is Doppler shifted. However, the relatively long acoustic wavelengths required for deep tissue penetration limit the spatial resolution of DUS to approximately 200 μm. Although LDF has been used to measure mean blood perfusion in the peripheral microcirculation, high optical scattering in biological tissue prevents its application for tomographic imaging.

Optical coherence tomography (OCT) is a noninvasive imaging modality for cross-sectional imaging of biological tissue with micrometer scale resolution [2]. OCT uses coherence gating of backscattered light for tomographic imaging of tissue structure. Variations in tissue scattering due to inhomogeneities in the optical index of refraction provide imaging contrast. However, in many instances and especially in the early stages of disease, the change in tissue-scattering properties between normal and diseased tissue is small and difficult to measure. One of the great challenges for extending the clinical applications of OCT is to find more contrast mechanisms that can provide physiological information in addition to morphological structure.

Doppler OCT (D-OCT) (also named optical Doppler tomography (ODT)) combines the Doppler principle with OCT to obtain high-resolution tomographic images of static and moving constituents simultaneously in highly scattering biological tissues [5–7]. The first use of coherence gating to measure localized flow velocity was reported in 1991, where the one-dimensional velocity profile of the flow of particles in a duct was measured [3]. In 1997, the first two-dimensional in vivo D-OCT imaging was reported using the spectrogram method [4, 5]. The spectrogram method uses a short-time fast Fourier transformation (STFFT) or wavelet transformation to determine the power spectrum of the measured fringe signal [4–9]. Inasmuch as detection of the Doppler shift using STFFT requires sampling the interference fringe intensity over at least one oscillation cycle, the minimum detectable Doppler frequency shift, f_D, varies inversely with the STFFT window size [7–10]. Therefore, velocity sensitivity, spatial resolution, and imaging speed are coupled. This coupling prevents the spectrogram method from achieving simultaneously both high imaging speed and high velocity sensitivity, which are essential for measuring flow in small blood vessels where flow velocity is low [4–6].

Phase-resolved D-OCT was developed to overcome these limitations [10, 11]. This method uses the phase change between sequential line scans for velocity image reconstruction [10–13]. Phase-resolved D-OCT decouples spatial resolution and velocity sensitivity in flow images and increases imaging speed by more than two orders of magnitude without compromising spatial resolution and velocity sensitivity [10, 11]. The minimum flow velocity that can be detected using an A-line scanning speed of 1,000 Hz is as low as 10 μm/s while maintaining a spatial resolution of 10 μm. The significant increases in scanning speed and velocity sensitivity make it possible to image in vivo tissue microcirculation in human skin [10, 11, 14]. A real-time phase-resolved D-OCT system that uses polarization optics to perform Hilbert transformation was demonstrated [13]. A number of real-time, phase-resolved D-OCT systems using hardware and software implementations of a high-speed processor have also been reported [15, 16].

One of the limitations of using the Doppler shift to study blood flow is that the Doppler shift is only sensitive to the flow velocity parallel to the probing beam. However, in many biological cases where flow direction is not known, Doppler shift measurement alone is not enough to fully quantify the flow. Furthermore, there are many clinical applications, such as ocular blood flow, in which vessels are in the plane perpendicular to the probing beam.

Several methods have been reported to measure the vector flow, including multiple angle measurements. However, sequential measurements with different angles of incident beam will only be useful for measuring steady state flow. A dual-channel, optical low-coherence reflectometer has been demonstrated that performs simultaneous measurements from two incident beams with different angles from two polarization channels [17]. The advantage of the dual-channel method is that two incident angle measurements are performed simultaneously. The disadvantage is that probing beams involve polarization optics and may not be suitable for endoscopic applications. A method to measure transverse flow velocity using the bandwidth (standard deviation) of the Doppler spectrum was

reported in 2002 [18]. The advantage of this technique is that a single measurement of the Doppler spectrum will provide both transverse and longitudinal flow velocity.

In many clinical applications, the mapping of the microvasculature is more important than the measurement of the flow velocity. Doppler variance (or standard deviation) tomography developed by our group provides an excellent method for mapping microvasculature [11, 12, 14, 19–22]. It was demonstrated that Doppler variance imaging has the advantages of being less sensitive to the pulsatile nature of the blood flow and the complex variation of incident angle. Recently, several groups have successfully extended a number of similar methods for mapping blood vessel networks. Yasuno et al. demonstrated an intensity-based binarization method named scattering optical coherence angiography (S-OCA) to map fine vasculature in the retinal and choroid layers [23–25]. Wang et al. proposed a method called optical microangiography (OMAG) technology to separate the static and moving signals with a modified Hilbert transform that remove low-frequency static signals [26–28]. Szkulmowski et al. designed a joint spectral and time domain OCT for the detection of capillary level blood vessels [29, 30]. In addition, intensity variation-based methods have also been proposed for mapping blood vessels [31–35].

Due to its exceptionally high spatial resolution and velocity sensitivity, D-OCT has a number of applications in biomedical research and clinical medicine. Several biomedical applications of D-OCT have been demonstrated, including screening vasoactive drugs, monitoring changes in image tissue morphology and hemodynamics following pharmacological intervention and photodynamic therapy, evaluating the efficacy of laser treatment in port-wine stain patients, assessing the depth of burn wounds, mapping cortical hemodynamics for brain research, and imaging tumor microvasculature [7, 8, 10–12, 14, 20, 36–39]. Clinical application of D-OCT in ophthalmology and gastrointestinal tracts has also been demonstrated [19, 22, 27, 40–49].

In this chapter, we will review the principle and technology of D-OCT and describe a few examples of potential applications of D-OCT.

20.2 Principle and Technology of D-OCT

20.2.1 Doppler Principle

D-OCT combines the Doppler principle with OCT to obtain high-resolution tomographic images of static and moving constituents in highly scattering biological tissues. When light backscattered from a moving particle interferes with the reference beam, a Doppler frequency shift (f_D) occurs in the interference fringe:

$$f_D = \frac{1}{2\pi}(\mathbf{k}_s - \mathbf{k}_i) \bullet \mathbf{v},\qquad(20.1)$$

Fig. 20.1 Schematic of flow direction and probe beam angle
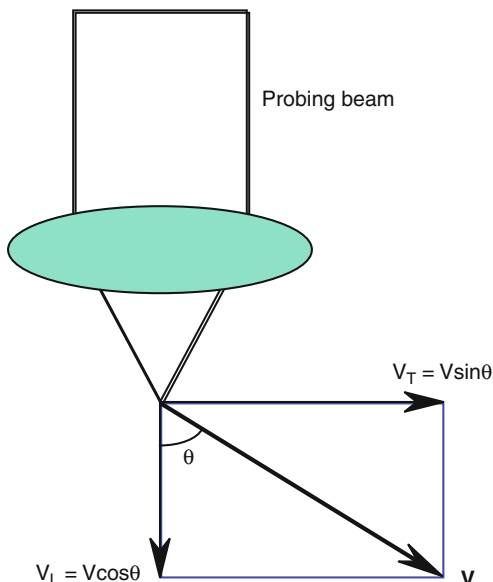
where $\mathbf{k}_i$ and $\mathbf{k}_s$ are wave vectors of incoming and scattered light, respectively, and $\mathbf{v}$ is the velocity of the moving particle (Fig. 20.1). Since D-OCT measures the backscattered light, assuming the angle between flow and sampling beam is θ, the Doppler shift equation is simplified to

$$f_D = \frac{2V \cos \theta}{\lambda_0},$$

(20.2)

where λ_0 is the vacuum center wavelength of the light source. Longitudinal flow velocity (velocity parallel to the probing beam) can be determined at discrete user-specified locations in a turbid sample by measurement of the Doppler shift. Transverse flow velocity can also be determined from the broadening of the spectral bandwidth due to the finite numeric aperture of the probing beam [18].

20.2.2 Spectrogram Method

The optical system of D-OCT is similar to that of OCT. The primary difference is in signal processing. Figure 20.2 shows a D-OCT instrument that uses a fiber-optic Michelson interferometer with a broadband light as a source [4, 6–8]. Light from a broadband partial coherence source is coupled into a fiber interferometer by a 2×2 fiber coupler and then split equally into reference and target arms of the interferometer. Light backscattered from the turbid sample is coupled back into the fiber and forms interference fringes with the light reflected from the reference arm. High longitudinal (axial) spatial resolution is possible because interference fringes are observed only when the path length differences between the light from the sample arm and reference
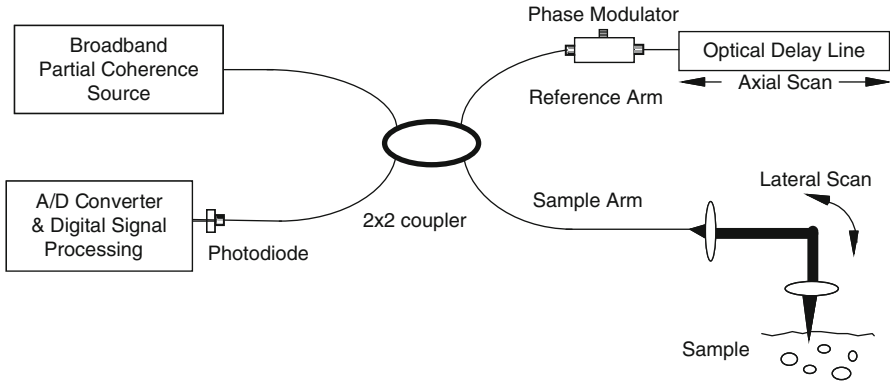
Fig. 20.2 Schematic of the prototype D-OCT instrument
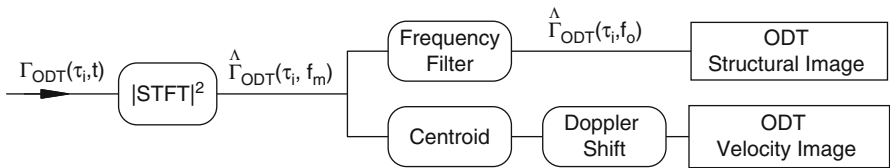
Fig. 20.3 Signal processing algorithms for D-OCT structural and velocity images

arm are within the coherence length of the source. A rapid-scanning optical delay (RSOD) line is used for group phase delay and axial scanning. Because RSOD can decouple the group delay from the phase [50], an electro-optical phase modulator is introduced to produce a stable carrier frequency. Temporal interference fringe intensity ($\Gamma_{\text{D-OCT}}(\tau)$) is measured by a single-element silicon photovoltaic detector, where τ is the time delay between light from the reference and sample arms, and is related to the optical path length difference (Δ) by $\tau = \Delta/c$. The interference fringe intensity signal is amplified, band-pass filtered, and digitized with a high-speed analog-to-digital (A/D) converter. The signal processing is carried out at the same time as data is transferred to the computer, and real-time display can be accomplished with the use of a digital signal processing board.

Time-frequency analysis can be used to calculate the Doppler shift. Signal processing algorithms to obtain structural and velocity images from recorded temporal interference fringe intensities using the spectrogram method are illustrated in Fig. 20.3.

The spectrogram is an estimate of the power spectrum of the temporal interference fringe intensity ($\hat{\Gamma}_{\text{ODT}}(\tau_i, f_j)$) in the i'th time delay window [51]. The power spectrum of the temporal interference fringe at the i'th pixel corresponding to time delay τ_i in the structural and velocity images is calculated by a short-time fast Fourier transformation (STFFT) or a wavelet transformation:

$$\hat{\Gamma}_{ODT}(\tau_i, f_m) = \left| STFT(f_m; \Gamma_{ODT}(\tau)) \right|^2, \tag{20.3}$$

where f_m is the discrete frequency value. A tomographic structural image is obtained by calculating the value of the power spectrum at the phase modulation frequency (f_0). Because the magnitude of the temporal interference fringe intensity decreases exponentially with increasing depth in the turbid sample, a logarithmic scale (20.4) is used to display the D-OCT structural images:

$$S_{ODT}(i) = 10 \cdot \log(\hat{\Gamma}_{ODT}(\tau_i, f_o)). \tag{20.4}$$

Fluid flow velocity is determined from the Doppler frequency shift (f_D), which is the difference between the carrier frequency established by the optical phase modulation (f_0) and the centroid (f_c) of the measured power spectrum at the i'th pixel:

$$v_{ODT}(i) = \frac{\lambda_o f_D}{2\bar{n}\cos(\theta)} = \frac{\lambda_o(f_c - f_o)}{2\bar{n}\cos(\theta)}, \tag{20.5}$$

where we have assumed $\mathbf{k}_s = -\mathbf{k}_i$ and θ is the angle between $\mathbf{k}_i$ and $\mathbf{v}$ (20.2). The centroid of the measured power spectrum is determined by

$$f_c = \sum_m f_m \hat{\Gamma}_{ODT}(\tau_i, f_m) \Big/ \sum_m \hat{\Gamma}_{ODT}(\tau_i, f_m). \tag{20.6}$$

Lateral and axial spatial resolutions are limited by the beam spot size and source coherence length (L_c). Velocity resolution is dependent on pixel acquisition time (Δt_p) and the angle (θ) between flow velocity (v) and the incoming light direction ($\mathbf{k}_i$) in the turbid sample; velocity resolution may be improved with a smaller angle (θ) or longer pixel acquisition time (Δt_p).

Figure 20.4 shows the first in vivo structural and blood flow images from a chick chorioallantoic membrane (CAM), which is a well-established model for studying the microvasculature and the effects of vasoactive drugs on blood vessels [4]. In the structural image (Fig. 20.4a), the lumen wall, chorion membrane, and yolk sac membrane are observed. In the velocity image (Fig. 20.4b), static regions ($v = 0$) in the CAM appear dark, while blood flowing at different velocities appears as different brightnesses on the gray scale. The velocity profile taken from a horizontal cross section passing through the center of the vessel is shown in Fig. 20.4c.

20.2.3 Phase-Resolved D-OCT Method

Although spectrogram methods allow simultaneous imaging of in vivo tissue structure and flow velocity, the velocity sensitivity is limited for high-speed imaging. When STFFT or a wavelet is used to calculate flow velocity, the resolution is determined by the window size of the Fourier transformation for each pixel [4–6].

Fig. 20.4 D-OCT images of
in vivo blood flow in a CAM
vein. (**a**) structural image; (**b**)
velocity image; and (**c**)
velocity profile taken from
a horizontal cross section
passing through the center of
the vein, where the *open
circles* are experimental data
and the *solid line* is
a parabolic fit (From Ref. [4])
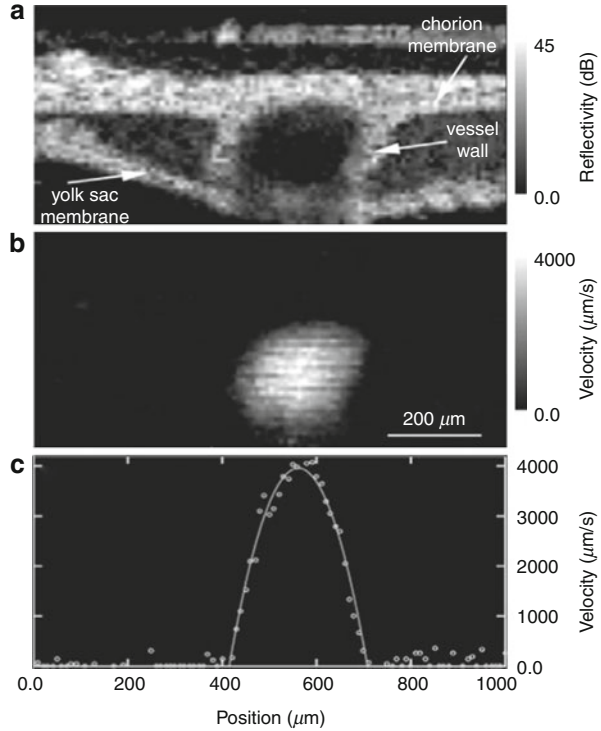
The minimum detectable Doppler frequency shift, f_D, varies inversely with the
STFFT window size (i.e., $\Delta f_D \approx 1/\Delta t_p$). With a given STFFT window size, velocity
resolution ($v_{D\text{-}OCT}(\text{min})$) is given by

$$v_{ODT}(\text{min}) = \frac{\Delta f_D(\text{min}) \ \lambda_o}{2\bar{n}\cos(\theta)}. \tag{20.7}$$

Because pixel acquisition time is proportional to the STFFT window size, the
image frame rate is limited by velocity resolution. Furthermore, spatial resolution,
Δx_p, is also proportional to the STFFT window size. Therefore, a large STFFT
window size increases velocity resolution while decreasing spatial resolution. This
coupling between velocity sensitivity, spatial resolution, and imaging speed pre-
vents the spectrogram method from achieving simultaneously both high imaging
speed and high velocity sensitivity, which are essential for measuring flow in small
blood vessels where flow velocity is low [4–6].

Phase-resolved D-OCT overcomes the compromise between velocity sensitivity
and imaging speed by using the phase change between sequential scans to construct
flow velocity images (Fig. 20.5) [10, 11, 13, 14].

Fig. 20.5 Schematic signal processing diagram for the phase-resolved D-OCT system
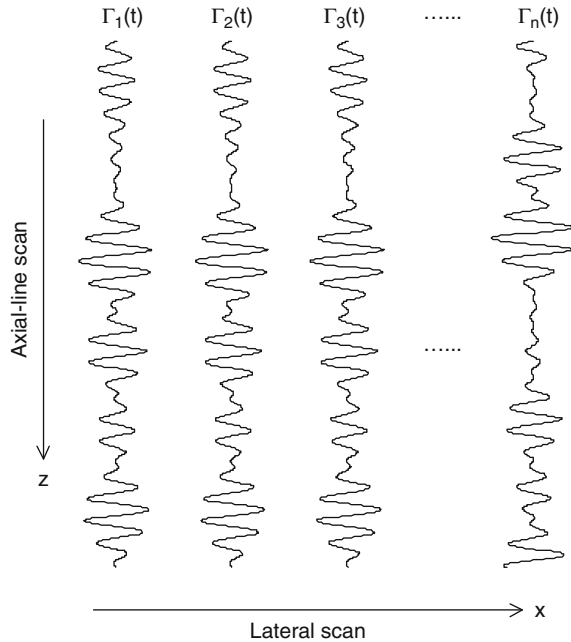
The phase information of the fringe signal can be determined from the complex analytical signal $\tilde{\Gamma}(t)$, which is determined through analytic continuation of the measured interference fringe function, $\Gamma(t)$, using a Hilbert transformation [10, 13]:

$$\tilde{\Gamma}(t) = \Gamma(t) + \frac{i}{\pi} P \int_{-\infty}^{\infty} \frac{\Gamma(\tau)}{\tau - t} d\tau = A(t) e^{i\phi(t)}, \tag{20.8}$$

where P denotes the Cauchy principle value, i is the complex number, and $A(t)$ and $\phi(t)$ are amplitude and phase of $\tilde{\Gamma}(t)$, respectively. Because the interference signal $\Gamma(t)$ is quasi-monochromatic, the complex analytical signal can be determined by [13]

$$\tilde{\Gamma}(t) = 2 \int_0^{+\infty} \int_0^{+\tau} \Gamma(t') \exp(-2\pi i v t') dt' \exp(2\pi i v t) dv, \tag{20.9}$$

where τ is the time duration of the fringe signal in each axial scan.

A digital approach to determine the complex analytical signal using Hilbert transformation is shown in Fig. 20.6, where FFT denotes the fast Fourier transformation and $H(v)$ is the Heaviside function given by

$$H(v) = \begin{cases} 0 & v < 0 \\ 1 & v \geq 0 \end{cases}, \tag{20.10}$$
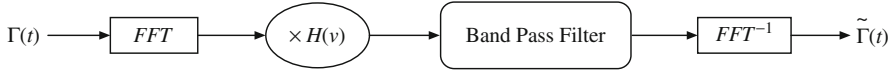
Fig. 20.6 Block diagram for calculating complex analytical signal using Hilbert transformation

and FFT^{-1} denotes the inverse fast Fourier transformation. Multiplication of the Heaviside function is equivalent to performing an operation that discards the spectrum in the negative frequency region.

The Doppler frequency shift (f_n) at n'th pixel in the axial direction is determined from the average phase shift between sequential A-scans. This can be accomplished by calculating the phase change of sequential scans from the individual analytical fringe signal [10, 11]:

$$f_n = \frac{\Delta \phi}{2\pi T} = \frac{1}{2\pi T} \sum_{m=(n-1)M}^{nM} \sum_{j=1}^{N} \left[\tan^{-1} \left(\frac{\mathrm{Im} \tilde{\Gamma}_{j+1}(t_m)}{\mathrm{Re} \tilde{\Gamma}_{j+1}(t_m)} \right) - \tan^{-1} \left(\frac{\mathrm{Im} \tilde{\Gamma}_{j}(t_m)}{\mathrm{Re} \tilde{\Gamma}_{j}(t_m)} \right) \right].$$

(20.11)

Alternatively, the phase change can also be calculated by the cross-correlation method [10, 11]:

$$f_n = \frac{1}{2\pi T} \tan^{-1} \left(\frac{\mathrm{Im} \left[\sum_{m=(n-1)M}^{nM} \sum_{j=1}^{N} \tilde{\Gamma}_j(t_m) \cdot \tilde{\Gamma}_{j+1}^*(t_m) \right]}{\mathrm{Re} \left[\sum_{m=(n-1)M}^{nM} \sum_{j=1}^{N} \tilde{\Gamma}_j(t_m) \cdot \tilde{\Gamma}_{j+1}^*(t_m) \right]} \right),$$

(20.12)

where $\tilde{\Gamma}_j(t_m)$ and $\tilde{\Gamma}_j^*(t_m)$ are the complex signals at axial time t_m corresponding to the jth A-scan and its respective conjugate; $\tilde{\Gamma}_{j+1}(t_m)$ and $\tilde{\Gamma}_{j+1}^*(t_m)$ are the complex signals at axial time t_m corresponding to the next A-scan and its respective conjugate; M is an even number that denotes the window size in the axial direction for each pixel; N is the number of sequential scans used to calculate the cross correlation; and T is the time duration between A-scans, which can be the delay between sequential A-scans or sequential B-scans. Because T is much longer than the pixel time window within each scan used in the spectrogram method, high velocity sensitivity can be achieved.

Phase-resolved D-OCT decouples spatial resolution and velocity sensitivity in flow images and increases imaging speed by more than two orders of magnitude without compromising spatial resolution and velocity sensitivity. In addition, because two sequential A-line scans are compared at the same location, speckle modulations in the fringe signal cancel each other and, therefore, will not affect the phase difference calculation. Consequently, the phase-resolved method reduces speckle noise in the velocity image. Furthermore, if the phase difference between

sequential frames is used, then the velocity sensitivity can be further increased. Real-time imaging with velocity sensitivity on the order of 10 μm/s has been demonstrated.

A Doppler flow image is very sensitive to environmental disturbances, such as sample motions. However, because we are interested in the relative motion of blood flow with respect to the tissue, motion artifacts can be minimized by choosing the tissue as a stable reference point for phase measurement in each axial scan [12].

In addition to digital processing of the fringe signal using Hilbert transformation, the complex analytical signal can also be achieved through hardware implementation. Optical Hilbert transformation using polarization optics has been implemented for real-time phase-resolved D-OCT imaging [13]. Real-time D-OCT imaging using hardware demodulation of the D-OCT signal has also been demonstrated by several groups [15, 16, 52].

20.2.4 Phase-Resolved Fourier Domain D-OCT

Fourier domain OCT (also named spectral domain OCT) uses the spectral information from the interference signal for tomographic image reconstruction. It was first developed by Fercher et al. in 1995 [53]. It has the advantage that no optical delay line is required. Recently, it has also been demonstrated that Fourier domain OCT can achieve high signal to noise ratio over time domain OCT [54–56]. In addition, there is no need to scan the reference arm [54, 57]. However, it requires a high-speed spectrometer or a high-speed spectral sweeping source. Two methods have been developed to employ the Fourier domain technique: a spectrometer-based system that uses a high-speed line-scan camera [58, 59] or a swept laser source-based system that uses a single detector [60–64].

Fourier domain D-OCT combines Doppler principle with Fourier domain OCT [65–67]. A schematic diagram of a spectrometer-based Fourier domain D-OCT system is shown in Fig. 20.7. The signal from the Michelson interferometer is directly coupled to a spectrometer that records the spectral fringe pattern. The temporal interference fringe can be calculated by a Fourier transform of the spectral fringe pattern. The Doppler shift can then be determined from the phase shift between sequential scans using the phase-resolved D-OCT algorithm described in previous sections.

To understand spectral domain D-OCT, we first look at the relation between time and spectral domain fringe signals. Let us denote $U(t)$ as a complex-valued analytical signal of a stochastic process representing the field amplitude emitted by a low-coherent light source and $\bar{U}(v)$ as the corresponding spectral amplitude at optical frequency v. The amplitude of a partially coherent light coupled into the interferometer at time t is written as a harmonic superposition

$$U(t) = \int_0^\infty \overline{U}(v)e^{2\pi i v t}dv. \tag{20.13}$$
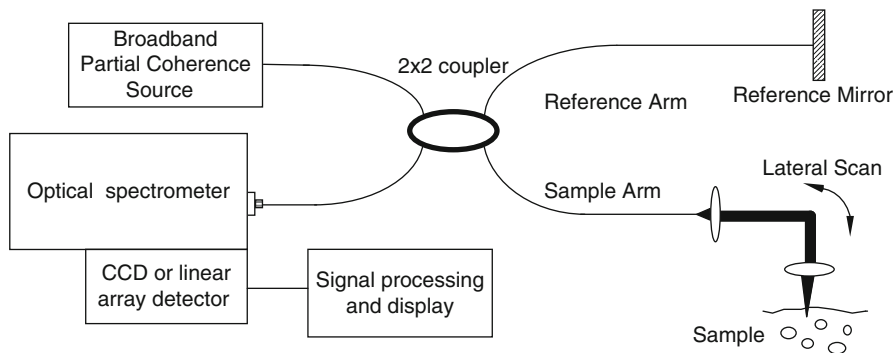
Fig. 20.7 Schematic diagram of a spectral domain D-OCT instrument

Because the stochastic process of a partially coherent light source is stationary, cross spectral density of $\overline{U}(v)$ satisfies

$$\left\langle \overline{U}^*(v)\overline{\mathrm{U}}(v')\right\rangle = S_o(v)\delta(v-v'), \tag{20.14}$$

where $S_o(v)$ is the source power spectral density and $\delta(v-v')$ is the Dirac delta function. Assuming that light couples equally into the reference arm and sample arm with a spectral amplitude of $\overline{U}_0(v)$, the light coupled back to the detectors from the reference, $\overline{U}_r(v)$, and sample, $\overline{U}_s(v)$, is given by (20.15) and (20.16), respectively:

$$\overline{U}_r(v) = e^{2\pi i v(2L_r + L_d)/c}K_r(v)e^{i\alpha_r}\overline{U}_o(v), \tag{20.15}$$

$$\overline{U}_s(v) = e^{2\pi i v(2L_s + L_d)/c}K_s(v)e^{i\alpha_s}\overline{U}_o(v), \tag{20.16}$$

where L_r and L_s are the optical path lengths from the beam splitter to the reference mirror, respectively; L_d is the optical path from the beam splitter to the detector; and $K_r(v)e^{i\alpha r(v)}$ and $K_s(v)e^{i\alpha s(v)}$ are the amplitude reflection coefficients of light backscattered from the reference mirror and turbid sample, respectively.

The total power detected at the interferometer output is given by a time-average of the squared light amplitude

$$P_d = \left\langle |U_s(t) + U_r(t)|^2 \right\rangle. \tag{20.17}$$

Combining harmonic expansions for $U_s(t)$ and $U_r(t)$ and applying (20.14) when computing a time-average, total power detected is a sum of three terms representing reference (I_r), sample (I_s), and the interference fringe intensity ($\Gamma_{D\text{-}OCT}(\Delta_d)$):

$$\begin{aligned}
P_d &= \int_0^\infty \left(\mathrm{P}_r(v) + P_s(v) + P_{ODT}(v)\right)dv \\
&= I_r + I_s + \Gamma_{ODT}(\Delta_d)
\end{aligned} \tag{20.18}$$

with

$$P_r(v) = S_o(v)|K_r(v)|^2, \tag{20.19}$$

$$P_s(v) = S_o(v)|K_s(v)|^2, \tag{20.20}$$

$$P_{ODT}(v) = 2S_o(v)K_r(v)K_s(v)\cos[2\pi v\Delta_d/c + \alpha_s(v) - \alpha_r(v)], \tag{20.21}$$

and

$$I_r = \int_0^\infty P_r(v)dv, \tag{20.22}$$

$$I_s = \int_0^\infty P_s(v)dv, \tag{20.23}$$

$$\Gamma_{OCT}(\Delta_d) = \int_0^\infty P_{ODT}(v)dvdv, \tag{20.24}$$

where Δ_d determines the optical phase delay between light traveled in the sample and reference arms. Light scattered from a moving particle is equivalent to a moving phase front; therefore, Δ_d can be written as

$$\Delta_d = \Delta + \bar{n}v_z t, \tag{20.25}$$

where Δ is the optical path length difference between light in the sampling and reference arms, v_z is the velocity of a moving particle parallel to the probe beam, and $\bar{n}$ is the refractive index of flow media. To simplify the computation, we assume α_s and α_r are constant over the source spectrum and can be neglected. The spectral domain fringe signal, $P_{D\text{-}OCT}(v)$, is simplified to

$$P_{ODT}(v) = 2S_o(v)K(v)_r K_s(v)\cos[2\pi v(\Delta + \bar{n}v_z t)/c]. \tag{20.26}$$

The corresponding time domain signal, $\Gamma_{ODT}(\Delta)$, is given by

$$\Gamma_{ODT}(\Delta) = 2\int_0^\infty S_o(v)K(v)_r K_s(v)\cos[2\pi v(\Delta + \bar{n}v_z t)/c]dv. \tag{20.27}$$

Equation 20.26 shows that $P_{D\text{-}OCT}(v)$ contains information on both location and velocity of moving particles. Spectral interference fringe intensity of single

backscattered light from the static particle ($v_z = 0$) is a sinusoidal modulation of the power spectral density. A moving particle in the sample path results in a phase shift in the spectral domain signal. A comparison of (20.26) and (20.27) shows that there is a Fourier transformation relation between the spectral domain and time domain signal. The phase shift due to the moving particle can be determined from the Fourier transformations of two sequential spectral fringe signals. The Doppler frequency can then be calculated using (20.11) or (20.12) of the phase-resolved method.

20.2.5 Transverse Flow Velocity Determination

One of the limitations of using Doppler shift to determine the flow is that the technique is only sensitive to longitudinal flow velocity (flow velocity along the probing beam direction, V_L). If one knows the flow direction, Doppler shift measurement can fully quantify the flow. However, in many biological cases where flow direction is not known, Doppler shift measurement alone is not enough to fully quantify the flow. Furthermore, there are many clinical cases, such as ocular blood flow, where vessels are in the plane perpendicular to the probing beam. When flow direction is perpendicular to the probing beam (V_T), the Doppler shift is not sensitive to transverse blood flow. Therefore, a method to measure transverse flow velocity is essential to clinical applications of D-OCT.

We have developed a method that uses standard deviation of the Doppler spectra to determine the transverse flow [18]. The technique is based on the fact that D-OCT imaging uses a relatively large numeric aperture lens in the sampling arm. The beam from different sides of the edges will produce different Doppler shifts f_1 and f_2 as indicated in Fig. 20.8 [18]. Consequently, the Doppler spectra will be broadened by the transverse flow. In a simple geometrical consideration, the broadening can be calculated as

$$f_1 = 2V\cos(\theta - \gamma)/\lambda, \tag{20.28}$$

$$f_2 = 2V\cos(\theta + \gamma)/\lambda, \tag{20.29}$$

$$B = f_1 - f_2 = \frac{4V\sin\theta NA_{eff}}{\lambda}. \tag{20.30}$$

If we assume that the incident beam has a Gaussian spectral profile and contributions from Brownian motion and other sources independent of the macroscopic flow velocity are included, we can find a linear relation between standard deviation of the Doppler spectra and transverse flow velocity, $V_T = V\sin\theta$:

$$\sigma = \frac{\pi V \sin\theta NA_{eff}}{8\lambda} + b, \tag{20.31}$$

Fig. 20.8 Effect of
numerical aperture and
transverse flow velocity on
Doppler bandwidth
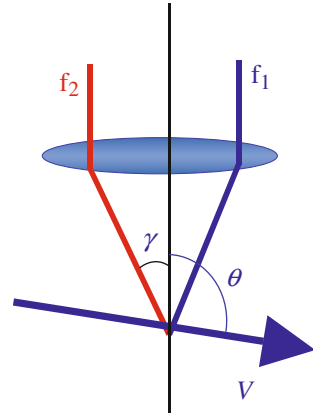
where b is a constant and NA_{eff} is the effective numeric aperture. The standard deviation can be determined from the measured analytical fringe signal:

$$
\sigma^2 = \frac{1}{2\pi^2 T^2} \left(1 - \frac{\left| \sum_{m=(n-1)M}^{nM} \sum_{j=1}^{N} \tilde{\Gamma}_j(t_m) \cdot \tilde{\Gamma}^*_{j+1}(t_m) \right|}{\frac{1}{2} \sum_{m=(n-1)M}^{nM} \sum_{j=1}^{N} \left[\tilde{\Gamma}_j(t_m) \cdot \tilde{\Gamma}^*_j(t_m) + \tilde{\Gamma}_{j+1}(t_m) \cdot \tilde{\Gamma}^*_{j+1}(t_m) \right]} \right),
$$

$$(20.32)$$

where $\tilde{\Gamma}_j(t_m)$ and $\tilde{\Gamma}^*_j(t_m)$ are the complex signals at axial time, t_m, corresponding to the jth A-scan and its respective conjugate; $\tilde{\Gamma}_{j+1}(t_m)$ and $\tilde{\Gamma}^*_{j+1}(t_m)$ are the complex signals at axial time, t_m, corresponding to the next A-scan and its respective conjugate; M is an even number that denotes the window size in the axial direction for each pixel; N is the number of sequential scans used to calculate the cross correlation; and T is the time duration between A-scans.

The measured standard deviation as a function of transverse flow velocity is shown in Fig. 20.9. It is found that above a certain threshold level, the Doppler bandwidth is a linear function of flow velocity, and the effective numerical aperture of the optical objective in the sample arm determines the slope of this dependence. This result indicates that standard deviation can be used to determine the transverse flow velocity.

Since both longitudinal, V_L, and transverse flow velocity, V_T, can be measured by the Doppler shift and standard deviation, respectively, flow direction can be determined from a single measurement of the Doppler fringe signal [11, 68, 69]. Figure 20.10 shows the angle of the flow direction measured by the Doppler shift and standard deviation. The result indicates that the angle determined by the Doppler shift and standard deviation of the Doppler spectrum fits with the predicted value very well.

Fig. 20.9 Standard deviations as a function of flow velocity for two different numeric apertures at a Doppler angle of 77° (From Ref. [18])
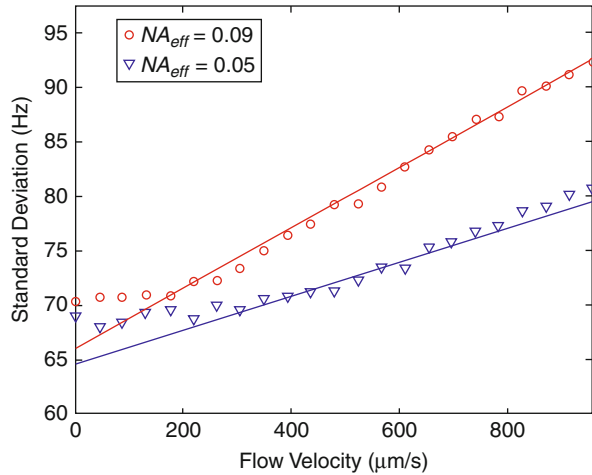
Fig. 20.10 Relationship between the measured Doppler angle by D-OCT and predicted Doppler angle. The *solid line* is a linear fit of the measured data (From Ref. [70])
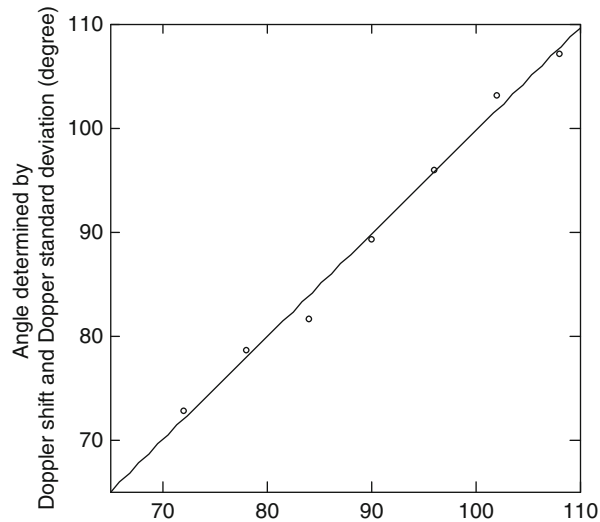
We have demonstrated that an arbitrary velocity vector can be determined from a single measurement by generating multiple $\Delta\mathbf{k}$ vectors with different path length delays simultaneously [71]. A beam divider which has three parts with different thicknesses of 0, t, and 2 t was inserted in the sample arm as shown in Fig. 20.11a. After passing through the focusing lens, the divider produced five independent $\Delta\mathbf{k}$'s and divided a probe beam to have five independent viewpoints and path length delays (Fig. 20.11b). Figure 20.11c shows Doppler images of a scattering fluid flowing through a microtube from a single scan. The five Doppler images correspond to five different $\Delta\mathbf{k}$ with different path lengths. The velocity vector field can
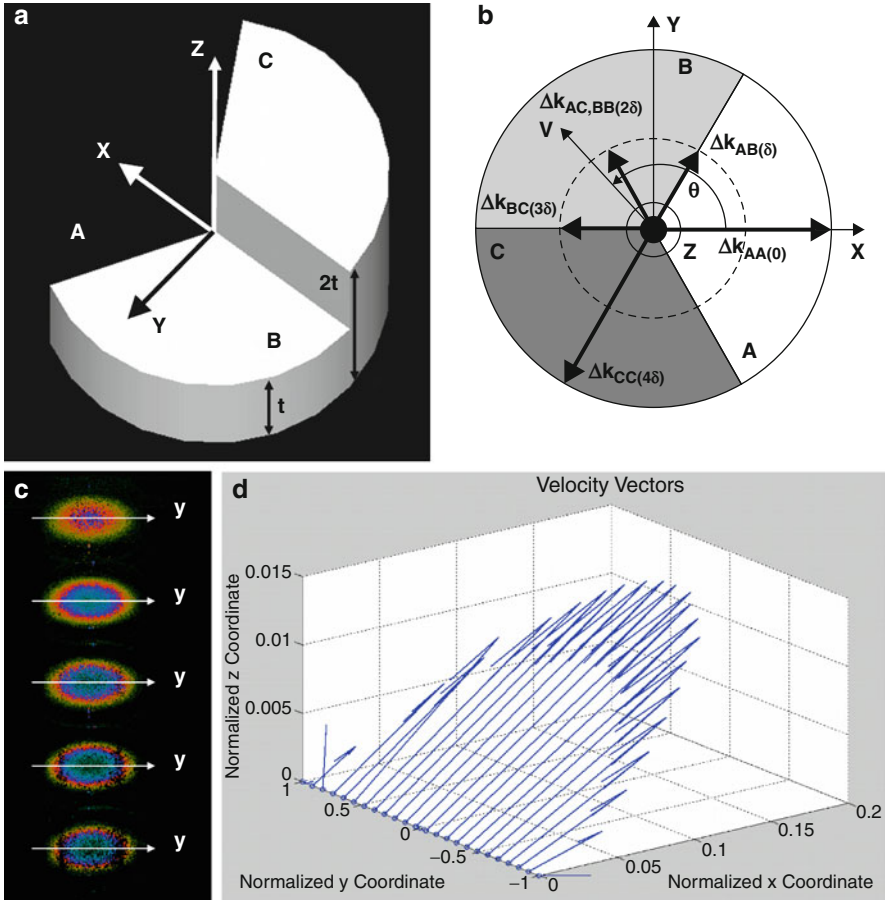
Fig. 20.11 The beam divider that generates five independent **Δk** with different path length delays (**a**, **b**). D-OCT imaging from five different path length and wave vectors (**c**). Velocity vector field measured by the multi-angle D-OCT along the diameter of the microtube (**d**), determined from the five Doppler images in (**b**) (From Ref. [71])

be quantified by solving a three-dimensional minimization problem from five Doppler images. The results are shown in Fig. 20.11d and has good agreement with the actual values [71].

20.2.6 Microvasculature Mapping and Optical Microangiogram

The mapping of microvascular network is essential for diagnosis and management of many diseases that have a vascular etiology. Although phase-resolved D-OCT provides high-sensitivity measurement of flow velocity, the technology is very sensitive to phase stability of the OCT system, the motion artifact, and the orientation of the

vasculature. In applications where absolute flow velocity is less important than vessel distribution, Doppler variance (or standard deviation) tomography developed by our group provides an excellent method for mapping microvasculature [11, 12, 14, 19–22]. It was demonstrated that Doppler variance has the advantage of being less sensitive to the pulsatile nature of the blood flow and the complex variation of incident angle. Doppler/phase variance technology has been used for imaging three-dimensional retina and choroid vessels for angiography and for imaging localized ischemic stroke in a mouse model [20, 35].

For a phase-stable system, Doppler phase variance can be calculated from the standard deviation of the measured analytical fringe signal:

$$\sigma^2 = \frac{1}{2\pi^2 T^2}\left(1 - \frac{\left|\sum\limits_{m=(n-1)M}^{nM}\sum\limits_{j=1}^{N}\tilde{\Gamma}_j(t_m)\cdot\tilde{\Gamma}_{j+1}^*(t_m)\right|}{\frac{1}{2}\sum\limits_{m=(n-1)M}^{nM}\sum\limits_{j=1}^{N}\left[\tilde{\Gamma}_j(t_m)\cdot\tilde{\Gamma}_j^*(t_m) + \tilde{\Gamma}_{j+1}(t_m)\cdot\tilde{\Gamma}_{j+1}^*(t_m)\right]}\right).$$

(20.33)

Doppler phase variance is not sensitive to gradient phase changes and can be used without bulk motion correction for in vivo imaging [22]. In the phase-instable situation where there is phase jumping or jittering between adjacent A-lines, the variance value will be affected greatly by the abrupt change in phase terms. The phase instability may produce artifacts, and the performance of the phase variance methods will be degraded. An intensity-based variance method can minimize the artifact from the phase instability [31–35]. The intensity-based variance can be calculated by [35]

$$\sigma^2 = \frac{1}{2\pi^2 T^2}\left(1 - \frac{\left|\sum\limits_{m=(n-1)M}^{nM}\sum\limits_{j=1}^{N}\left|\widehat{\Gamma}_j(t_m)\cdot\widehat{\Gamma}_{j+1}^*(t_m)\right|\right|}{\frac{1}{2}\sum\limits_{m=(n-1)M}^{nM}\sum\limits_{j=1}^{N}\left[\widehat{\Gamma}_j(t_m)\cdot\widehat{\Gamma}_j^*(t_m) + \widehat{\Gamma}_{j+1}(t_m)\cdot\widehat{\Gamma}_{j+1}^*(t_m)\right]}\right).$$

(20.34)

Intensity-based methods do not require a phase-stabilized system and can be used for a phase-instable situation, such as a swept source-based Fourier domain OCT system. Figure 20.12 shows an optical microangiogram of choroidal blood vessels using intensity-based Doppler variance imaging with a swept source OCT. Depth-resolved choroidal blood vascular networks are clearly visible.

20.3 Applications of D-OCT

The high velocity sensitivity and high imaging speed of phase-resolved D-OCT have made it possible to image in vivo tissue microcirculation. We describe in the following sections a few examples of applications.

Fig. 20.12 Optical microangiogram of choroidal blood vessels using intensity-based Doppler variance imaging (From Ref. [35])
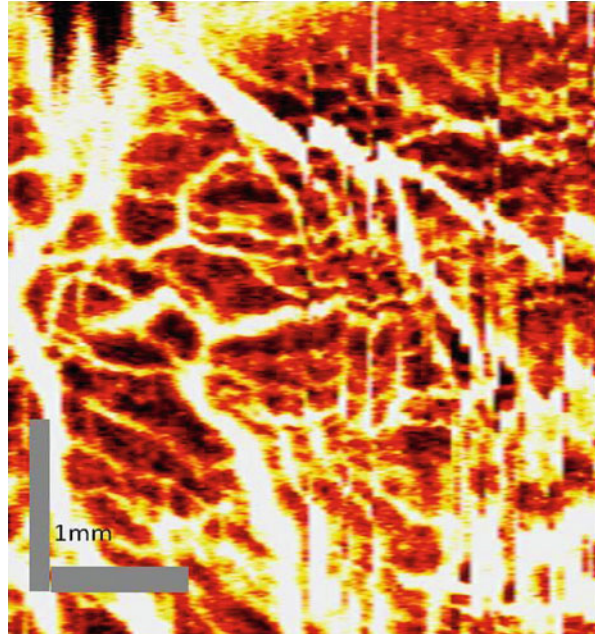
20.3.1 Drug Screening

Noninvasive drug screening is essential for the rapid development of new drugs. To demonstrate the potential applications of D-OCT for in vivo blood flow monitoring after pharmacological intervention, the effects of nitroglycerin (NTG) on the CAM artery and vein were investigated [7]. Changes in arterial vascular structure and blood flow dynamics are shown in Fig. 20.13-I, where Figs. 20.13A and B are structural and velocity images, respectively, before, and Figures A′ and B′ are after, topical application of NTG. The arterial wall can be clearly identified, and dilation of the vessel after nitroglycerin application is observed in the structural images. Although velocity images appear discontinuous due to arterial pulsation (Figs. 20.13B and B′), enlargement of the cross-sectional area of blood flow is evident. Peak blood flow velocity at the center of the vessel increased from 3,000 to 4,000 μm/s after NTG application.

The effects of NTG on CAM venous blood flow are shown in Fig. 20.13-II, where Figs. 20.13A and B are structural and velocity images, respectively, before, and A′ and B′ are corresponding images after, topical application. Dilation of the vein due to nitroglycerin is observed in both structural and velocity images. In contrast to the artery, the peak velocity at the center of the vein decreased from 2,000 to 1,000 μm/s after NTG application.

NTG is a vasodilator used in the treatment of ischemic and congestive heart disease. Figure 20.13 indicates that the degree of CAM arterial dilation is greater than the venous in response to NTG. This is probably due to the reversal of
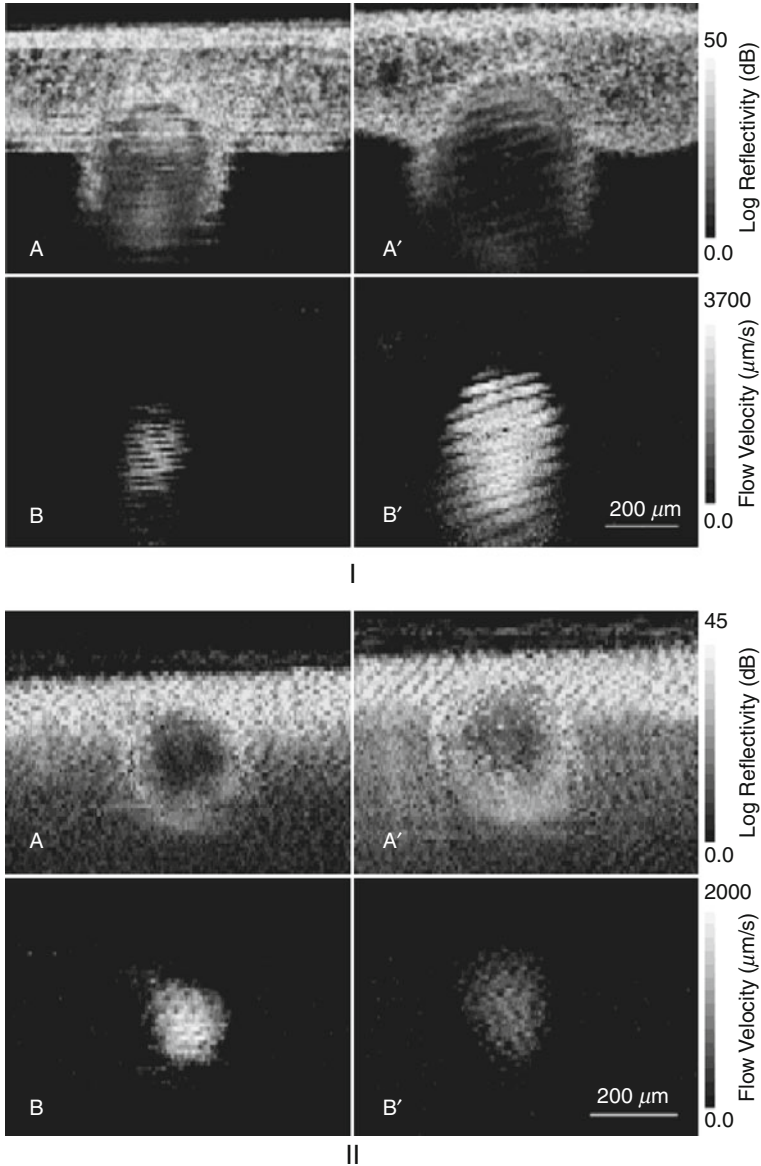
Fig. 20.13 Effects of topical NTG on blood flows in CAM artery (I) and vein (II), respectively. OCT/D-OCT structural and velocity images, respectively, before (*A*, *B*) and after (*A'*, *B'*) drug application (from Ref. [7])

oxygenation in the CAM vasculature where arteries and veins are oxygen poor and rich, respectively, because the embryo oxygenates itself from the surrounding air through the shell. The reversal of oxygenation could result in a reversal in selectivity, making NTG arterioselective in the CAM.

Fig. 20.14 Vessel structure and blood flow dynamics in rodent mesenteric artery after PDT. D-OCT structural and velocity images, respectively, prior to laser irradiation (A, A′), 16 min (B, B′) and 71 min (C, C′) after laser irradiation (From Ref. [7])
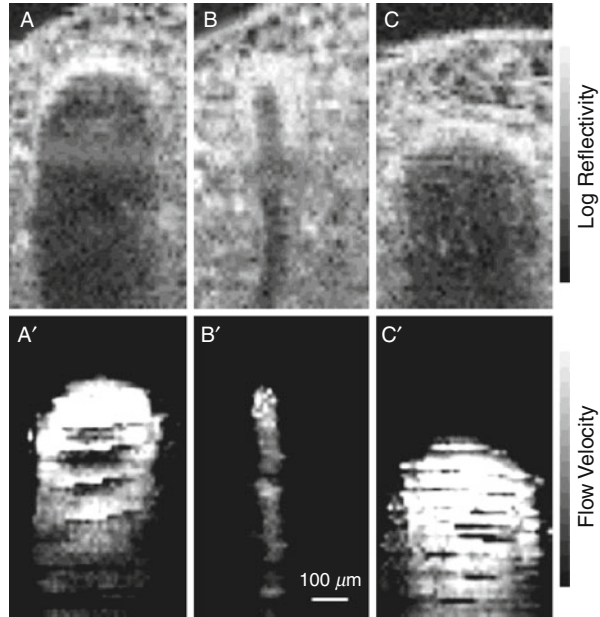
20.3.2 In Vivo Blood Flow Monitoring During Photodynamic Therapy (PDT)

The potential application of D-OCT for in vivo blood flow monitoring during PDT was investigated in rodent mesentery after benzoporphyrin derivative (BPD) injection and laser irradiation (Fig. 20.14) [7]. D-OCT structural and velocity images, respectively, were recorded before laser irradiation (Figs. 20.14A and A′), 16 (Figs. 20.14B and 14B′) and 71 min after laser irradiation (Figs. 20.14C and 14C′). The results indicate that the artery goes into vasospasm after laser exposure, and compensatory vasodilatation occurs in response to PDT-induced tissue hypoxia.

The pharmacokinetics of the PDT drug can also be studied with D-OCT. D-OCT images were taken at different intervals between photosensitizer injection and laser irradiation. Rodents were given a PDT sensitizing drug 20 min, 4 h, and 7 h before mesenteric laser irradiation, and the changes in arterial diameter and flow were calculated from D-OCT images (Fig. 20.15). The results indicate that the effects of PDT are strongly dependent on the time interval between drug injection and light irradiation. For a drug-light time interval of 20 min, the arterial diameter (Fig. 20.15a) decreased by 80% after light irradiation followed by a rebound with vasodilative overshoot. Mesenteric arterial flow (Fig. 20.15b) mirrored changes in diameter with an initial reduction with a subsequent rebound. These effects are significantly reduced with longer postinjection times due to progressive diffusion of the photosensitizer out of the vasculature. These results suggest that characterizing

Fig. 20.15 Changes in relative arterial diameter (**a**) and flow rate (**b**) in rodent mesentery following PDT as a function of postirradiation time (From Ref. [72])
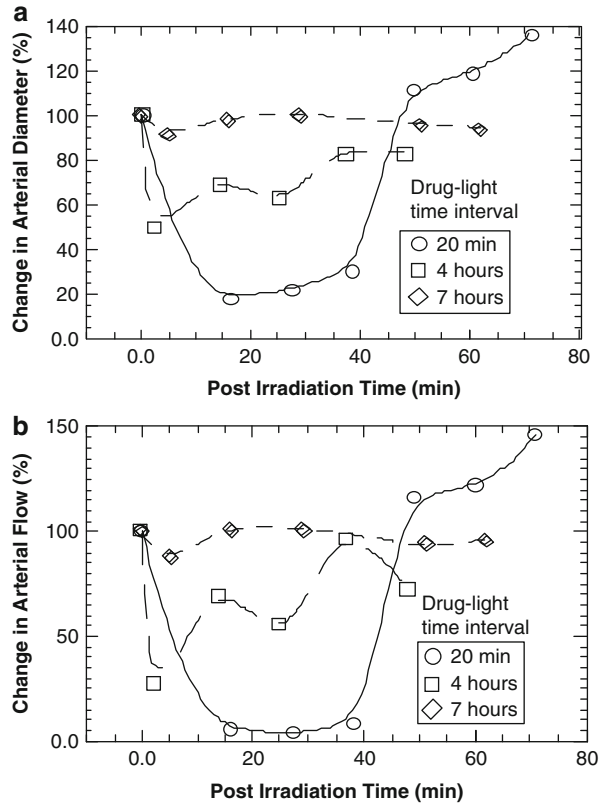
intratumoral hemodynamics by D-OCT not only provides insight into understanding the mechanism(s) of PDT but could also be used to monitor the progress of treatment in real time.

20.3.3 D-OCT Images of Brain Hemodynamics

D-OCT has also been used to image brain hemodynamics in the cerebral cortex of the brain. The cerebral cortex is generally believed to be composed of functional units, called "columns," that are arranged in clusters perpendicular to the surface of the cortex [73]. Alterations in the brain's blood flow are known to be coupled to regions of neuronal activity [73]. A number of techniques, such as positron-emission tomography (PET), functional magnetic resonance imaging (fMRI), and diffuse reflectance spectra, have been used to study brain hemodynamics. However, the resolution of PET and fMRI is too low to resolve the columns. Although optical spectral reflectance techniques can map out *en face* cortex hemodynamics, it does not provide depth resolution. Currently, two-photon microscopy has been used for mapping cortex activity. However, this technique

Fig. 20.16 D-OCT image of in vivo blood flow in the rat cerebral cortex
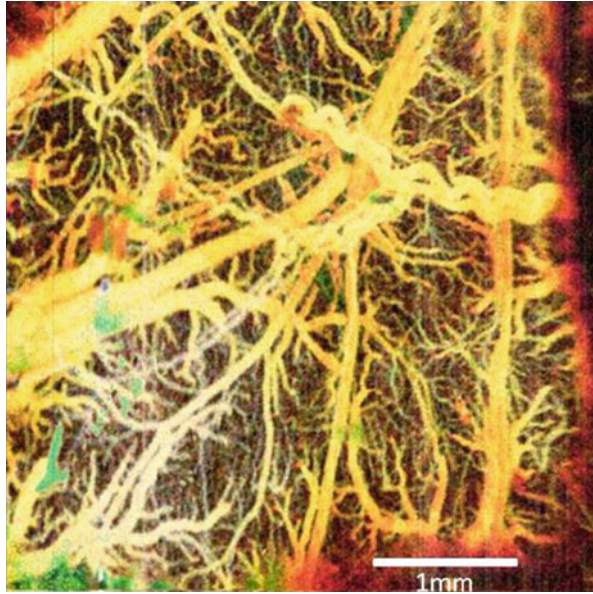
requires the injection of a fluorescent dye and has limited penetration depth. The noninvasive and tomographic capability of D-OCT makes it an ideal technique for mapping depth-resolved blood flow in the cortex. Figure 20.16 shows an *en face* D-OCT image of in vivo blood flow in the rat cerebral cortex. The parietal cortex of an anesthetized rat was imaged through a dural incision. This preliminary investigation demonstrated that D-OCT can map blood flow in the cortex with high axial resolution. D-OCT shows great promise in brain research for imaging the entire depth of the cortex, and it can be used to measure stimulus-induced changes in blood flow [8] and to evaluate and monitor brain ischemia and trauma [20, 36].

20.3.4 In Vivo Monitoring of the Efficacy of Laser Treatment of Port-Wine Stains

The high spatial resolution and high velocity sensitivity of D-OCT has many potential clinical applications. The first clinical application of D-OCT is the in vivo monitoring of the efficacy of laser treatment of port-wine stains (PWS) [10, 11, 14]. PWS is a congenital, progressive vascular malformation of capillaries in the dermis of human skin that occurs in approximately 0.7% of children. Histopathological studies of PWS show an abnormal plexus of layers of dilated blood vessels located 150–750 μm below the skin surface in the dermis, having diameters varying on an individual patient basis, and even from site to site on the
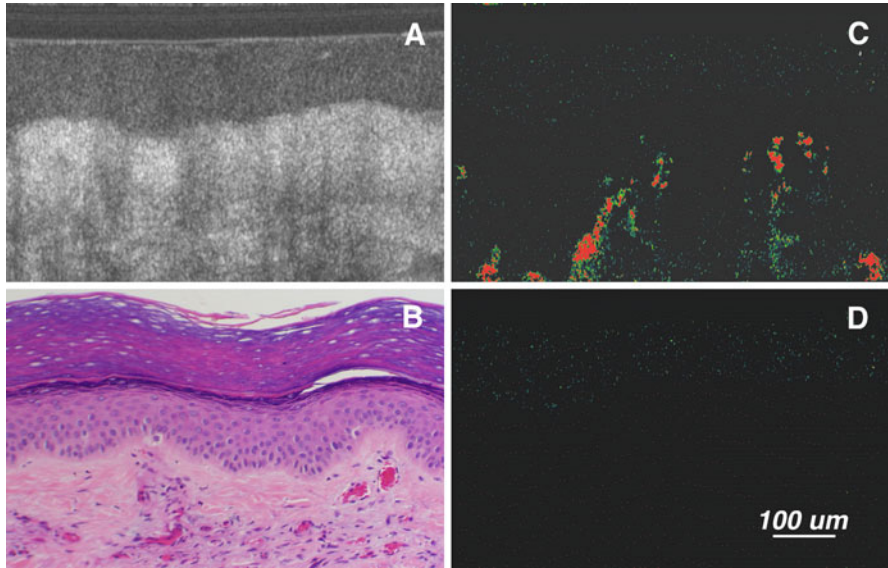
Fig. 20.17 Phase-resolved Doppler OCT images taken *in situ* from PWS human skin. (**a**) Structural image; (**b**) histological section from the imaged site; (**c**) Doppler standard deviation image before laser treatment; and (**d**) Doppler standard deviation image after laser treatment (From Ref. [14])

same patient, over a range of 10–150 μm. The pulsed dye laser can coagulate selectively PWS vessels by inducing microthrombus formation within the targeted blood vessels. However, currently there is no technique to evaluate efficacy of therapy immediately after the laser treatment. Phase-resolved Doppler OCT provides a means to evaluate the efficacy of laser therapy in real time.

Figure 20.17 shows D-OCT structural and flow velocity images of a patient with PWS before and after laser treatment, respectively. For comparison, we also include a histology picture taken at the same site. The vessel location from the D-OCT measurement and histology agree very well. Furthermore, the destruction of the vessel by laser can be identified since no flow appears on the Doppler flow image after laser treatment. This result indicates that D-OCT can provide a fast semiquantitative evaluation of the efficacy of PWS laser therapy *in situ* and in real time.

20.3.5 Three-Dimensional Images of a Microvascular Network

It is known that the microvasculature of mammary tumors has several distinct differences from normal tissues. Three-dimensional images of a microvascular network may provide additional information for cancer diagnosis. This can be accomplished in D-OCT by stacking the 2-D scans together [12]. Figure 20.18

Fig. 20.18 Three-dimensional D-OCT images of multiple blood vessels in human skin from a patient with a PWS birthmark (From Ref. [12])
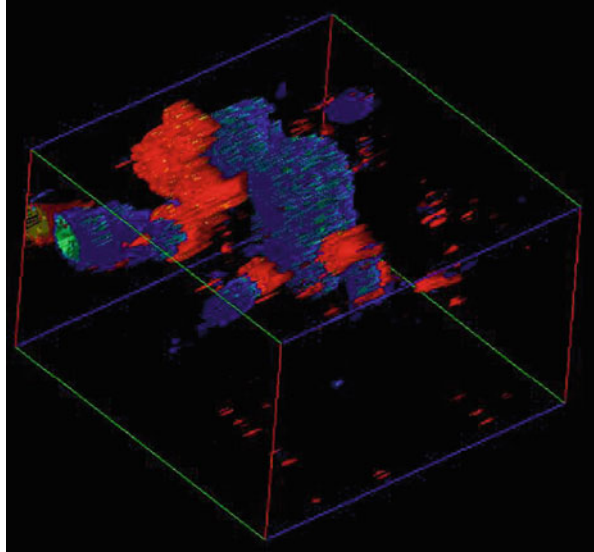
shows multiple blood vessels imaged in human skin from a patient with a PWS birthmark. Different colors represent different signs of the Doppler shift, which depends on the angle between the direction of the flow and probing beam. The convoluted nature of the blood vessels is consistent with the typical vasculature observed in PWS patients.

20.3.6 Imaging and Quantification of Flow Dynamics in MEMS Microchannel

Currently, there is great interest in miniaturizing biochemical analysis instruments on a small chip using the microelectromechanical systems (MEMS) technology. One of the most important components in BioMEMS is microfluidic flow handling, including microfluidic channel, valve, and mixing chamber. However, currently there is no technology that can measure and quantify the structure and flow dynamics of BioMEMS devices simultaneously. Conventional metrology and imaging techniques, such as scanning transmission electronic microscopy, has been widely used in the semiconductor industry. However, it is not versatile enough to image BioMEMS devices consisting of different materials. In addition, it is also a destructive technique that requires coating. More importantly, these techniques cannot image and measure flow dynamics in microfluidic devices. Particle imaging velocimetry can produce velocity field maps over a large region within the focal plane of the imaging system. However, it cannot provide a cross-sectional structure and velocity imaging for complex geometries. For many BioMEMS devices for biomedical diagnosis, the structural dimension is on the order of 10–500 μm, and flow dynamics depends strongly on the surface characteristics of the microfluidic channel.
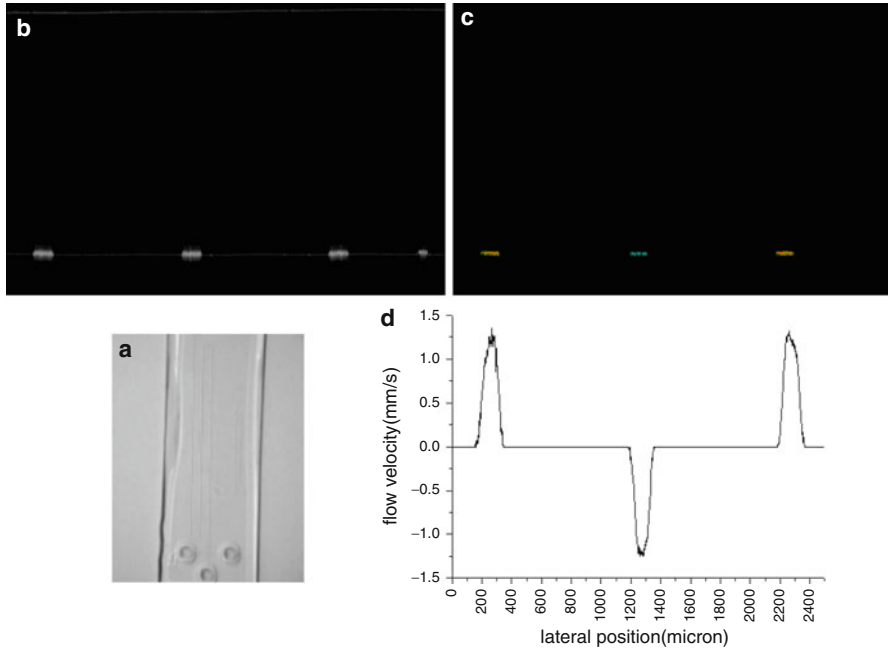
Fig. 20.19 Imaging and quantification of geometry and flow velocity of an S-shaped microchannel with cross-sectional dimension of 30×150 µm. (**a**) Polymer chip with an S-shaped channel; (**b**) structural image; (**c**) velocity image; and (**d**) velocity profile (From Ref. [75])

A nondestructive imaging and metrology technique that can image both structure and flow velocity of a microfluidic device simultaneously is essential for the development of integrated system technologies for BioMEMS applications [67, 74].

D-OCT can provide cross-sectional imaging of channel geometry and flow velocity within a microfluidic channel with a spatial resolution on the order of a micrometer and a velocity sensitivity of 10 µm/s. Figure 20.19a shows an S-shaped polymer microchannel with a cross-sectional dimension of 30×150 µm. D-OCT structural and velocity images are shown in Fig. 20.19b and c, respectively. The scan is perpendicularly through three parallel channels. The structure of three channels is clearly visible in Fig. 20.19b. The upper surface of the PDMS channel layer and the interface between the PDMS layer and glass substrate can also be observed. The velocity image provides a background-free picture of the velocity of the moving intralipid. The velocity profile along the horizontal direction near the center of the channel is shown in Fig. 20.19d. The velocity profile in each channel is close to a parabolic shape, which agrees with the predicted profile of a pressure driven laminar flow. The direction of the flow velocity is also shown.

One of the best examples to show the advantage of D-OCT is to diagnose velocity and mixing pattern in a bubble-train flow through a meandering microchannel [76, 77]. Two liquids are to be mixed in liquid slugs spaced by gas bubbles. Convective two-liquid mixing is enhanced by not only the alternating
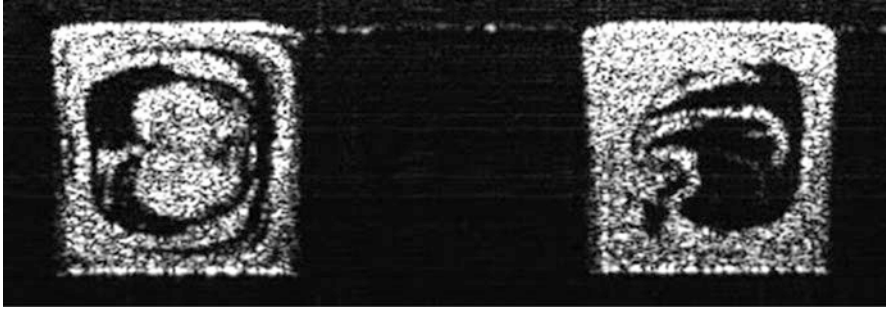
Fig. 20.20 Transient mixing patterns enhanced by the bubble-train flow in a meandering microchannel (From Ref [77])

curvature of the meandering microchannel but also the gas bubble. Scattering particles are seeded in only one of the two liquids to make a contrast. Fourier domain Doppler OCT is able to image interfaces among three fluids (two liquids and gas) and velocity as well. Figure 20.20 shows transient mixing patterns enhanced by the bubble-train flow.

In addition to imaging mixing patterns, D-OCT can also be used to simultaneously image and quantify the secondary flow, which plays a critical role in mixing in microchannels [77]. Aqueous suspension of polystyrene beads with a diameter of 0.2 μm and concentration of 20.5 mg/cc was injected into both inlets of the Y branch device of a meandering microchannel with a square cross section as shown in Fig. 20.21. The probe beam of the D-OCT was adjusted to be approximately perpendicular to the plane of the microchannel (x-z plane). Because primary flow is in the x-z plane and the probe beam is in the y-direction, D-OCT is not sensitive to the primary flow in such a probe configuration. Consequently, only the secondary flow along the y-direction will contribute to the Doppler signal. The y-component of the secondary flow velocity $V_y(x,y,z)$ was imaged and quantified with D-OCT (Fig. 20.21). Counter-rotating vortices in the x-y and y-z planes as well as alternating flow direction of the secondary flow at different depths in the x-z plane can be clearly visualized. This result clearly demonstrates that D-OCT can be used to image and quantify secondary flow [77].

In addition to imaging, D-OCT can also be used to measure osmotic mobility, quantify size of the scattering particle, and study flow dynamics of microfluid in microchannels of different materials, geometry, and surface treatment [67, 76–81].

20.3.7 In Vivo Imaging of Human Retinal Blood Vessel and Vascular Network

OCT has become the one of the standard clinical diagnostic tools for retinal and glaucoma diseases. As a functional extension of OCT, Doppler OCT can provide useful information for the diagnosis and management of vascular-related eye diseases.
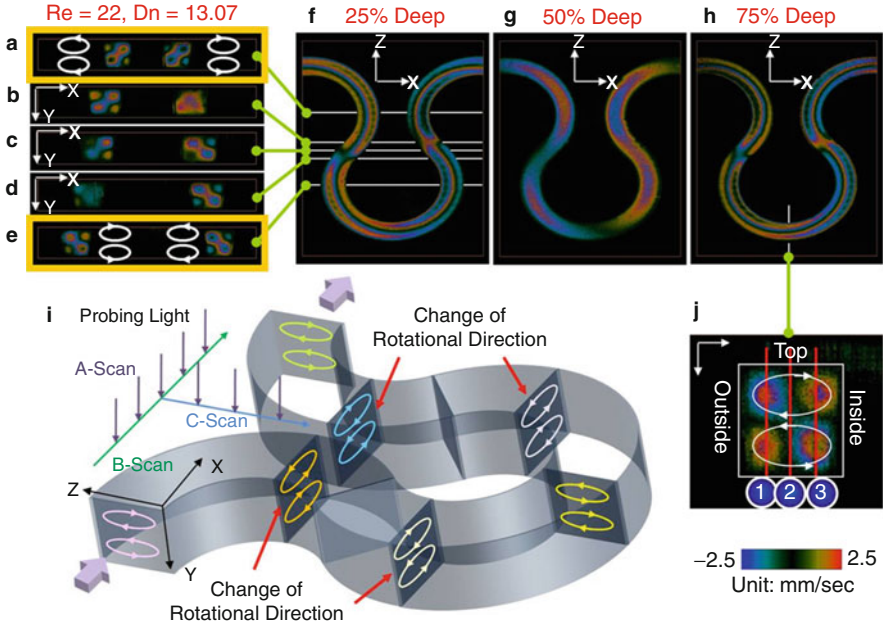
Fig. 20.21 Three-dimensional images of secondary flow velocity along the out-of-plane (*y*-direction). The out-of-plane velocity fields sectioned by *x-y* planes (**a–e**), *x-z* planes (**f–h**), and *y-z* plane (**j**). In the *x-y* and *y-z* plane, the velocity field shows a pair of counter-rotating vortices (**a–e**, **i**). Since the curvature is alternating, the rotational direction of the vortices is also alternating (**a–e**) at different locations in the curved channel. Alternating flow direction of the secondary flow at different depths in the *x-z* plane can be clearly visualized (**f–h**) (From Ref [77])

D-OCT has been used to quantify blood velocity profiles in human retina blood vessels, determine vessel boundaries, and analyze time-dependent bidirectional flow dynamics in retinal artery-vein pairs [19, 22, 27, 40–46, 49]. However, the blood flow is pulsatile, and the flow is changing within the cardiac cycle. The development of high-speed Fourier domain D-OCT allows fast scanning of a single blood vessel multiple times over a cardiac cycle. Spectral Doppler wave-forms can be obtained by performing spectral analysis of the time sequences of Doppler images [45]. The quantitative information, such as maximum velocity envelope, mean velocity envelope, and flow-volume rate envelope, can be derived accordingly [45]. Doppler-angle-independent flow indices, such as flow resistance and flow pulsatility, can be determined from this measurement [45]. The spectral Doppler method provides an alternative way to quantify retinal blood flow with Doppler-angle-independent flow indices that may provide insight on the retinal flow in many vascular-related eye diseases. Figure 20.22 shows the spectral Dopp-ler wave forms that show the change of axial velocity and flow-volume rate within a time span of 7.9 s [45].

Another application of D-OCT in ophthalmology is imaging the human retina and choroid microvascular network, which provides important information
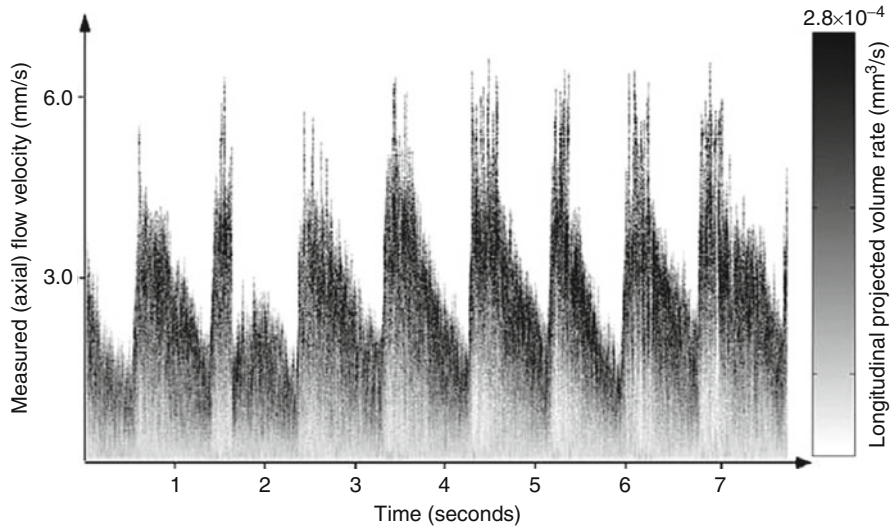
Fig. 20.22 Spectral Doppler waveforms that show the change of average flow velocity and flow-volume rate from a single vessel in the human retina within a time span of 7.9 s (the *right-gray* scale bar is used to represent the volume rate contribution for a given velocity) (From Ref. [45])

for the diagnosis and management of ocular diseases, such as glaucoma, diabetic retinopathy, and age-related macular degeneration. In contrast to traditional angiography methods, such as fluorescein angiography (FA) and indocyanine green angiography (ICGA), D-OCT is a label-free technique and has three-dimensional imaging capability. By extracting the *en face* images from the 3D image volume, the FA or ICGA-like angiography images can be obtained. In addition, the projection images can be obtained by summing up the *en face* images at different depths [19, 22, 27, 40–42, 45, 46, 49]. Figure 20.23 shows the projection OCT structure, Doppler variance and color Doppler images of human retina. The images were obtained by summing up all the layers below the retinal pigment epithelium layer. Color Doppler projection images can provide information about the blood vessel, such as blood flow direction (pink and blue colors represent different directions), blood flow speed, etc. However, due to the pulsatile nature of human blood flow, the blood flow direction and blood flow speed are not constant inside a single blood vessel. The incident angle dependent nature of Doppler OCT makes the situation more complex. A Doppler variance projection image provides a fine microvascular network image which is more continuous and results in a better mapping of the vascular network. This image is similar to images from traditional angiography. However, D-OCT has the advantage of being contrast agent free and the capability to section vesicular mapping in different depth regions.
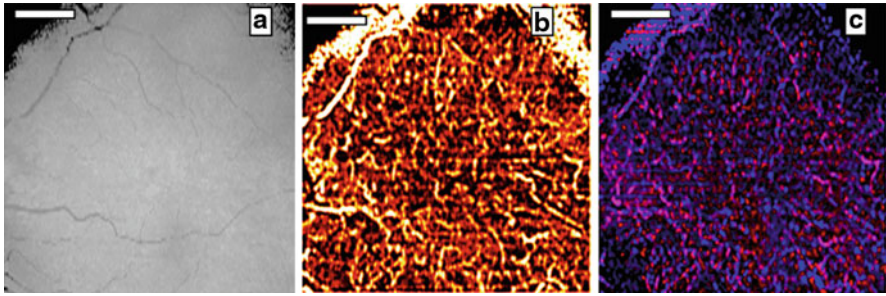
Fig. 20.23 Projection images of human retina. (**a**) OCT projection, (**b**) Doppler variance projection, and (**c**) color Doppler projection images of choroidal vessels. Scale bar: 1 mm (From Ref. [22])

20.4 Conclusion

D-OCT is a rapidly developing imaging technology with many potential applications. New developments in all components of an OCT system can be integrated to a D-OCT system, including new light sources for high-resolution OCT, new scanning probes for endoscopic imaging, and new processing algorithms. Integration of D-OCT with other functional OCT, such as polarization-sensitive OCT, spectroscopic OCT, and second harmonic OCT, can greatly enhance the potential applications of this technology. Given the noninvasive nature and exceptionally high spatial resolution and velocity sensitivity, functional OCT that can simultaneously provide tissue structure, blood perfusion, birefringence, and other physiological information has great potential for basic biomedical research and clinical medicine.

References

1. P.L. Carson, D.D. Adler, J.B. Fowlkes, Enhanced color flow imaging of breast cancer vasculature: continuous wave Doppler and three-dimensional display. J. Ultrasound Med. **11**, 77 (1992)
2. D. Huang, E.A. Swanson, C.P. Lin, J.S. Schuman, W.G. Stinson, W. Chang, M.R. Hee, T. Flotte, K. Gregory, C.A. Puliafito, J.G. Fujimoto, Optical coherence tomography. Science **254**, 1178–1181 (1991)

3. V. Gusmeroli, M. Martnelli, Distributed laser Doppler velocimeter. Opt. Lett. **16**, 1358–1360 (1991)
4. Z. Chen, T.E. Milner, S. Srinivas, X.J. Wang, A. Malekafzali, M.J.C. van Gemert, J.S. Nelson, Noninvasive imaging of in vivo blood flow velocity using optical Doppler tomography. Opt. Lett. **22**, 1119–1121 (1997)
5. J.A. Izatt, M.D. Kulkarni, S. Yazdanfar, J.K. Barton, A.J. Welch, In vivo bidirectional color Doppler flow imaging of picoliter blood volumes using optical coherence tomography. Opt. Lett. **22**, 1439–1441 (1997)
6. Z. Chen, T.E. Milner, D. Dave, J.S. Nelson, Optical Doppler tomographic imaging of fluid flow velocity in highly scattering media. Opt. Lett. **22**, 64–66 (1997)
7. Z. Chen, T.E. Milner, X.J. Wang, S. Srinivas, J.S. Nelson, Optical Doppler tomography: imaging in vivo blood flow dynamics following pharmacological intervention and photodynamic therapy. Photochem. Photobiol. **67**, 56–60 (1998)
8. Z. Chen, Y. Zhao, S.M. Srinivas, J.S. Nelson, N. Prakash, R.D. Frostig, Optical Doppler tomography. IEEE J. Sel. Top. Quant. Electron. **5**, 1134–1141 (1999)
9. M.D. Kulkarni, T.G. van Leeuwen, S. Yazdanfar, J.A. Izatt, Velocity-estimation accuracy and frame-rate limitations in color Doppler optical coherence tomography. Opt. Lett. **23**, 1057–1059 (1998)
10. Y. Zhao, Z. Chen, C. Saxer, S. Xiang, J.F. de Boer, J.S. Nelson, Phase-resolved optical coherence tomography and optical Doppler tomography for imaging blood flow in human skin with fast scanning speed and high velocity sensitivity. Opt. Lett. **25**, 114–116 (2000)
11. Y. Zhao, Z. Chen, C. Saxer, Q. Shen, S. Xiang, J.F. de Boer, J.S. Nelson, Doppler standard deviation imaging for clinical monitoring of in vivo human skin blood flow. Opt. Lett. **25**, 1358–1360 (2000)
12. Y. Zhao, Z. Chen, Z. Ding, H. Ren, J.S. Nelson, Three-dimensional reconstruction of in vivo blood vessels in human skin using phase-resolved optical Doppler tomography. IEEE J. Sel. Top. Quant. Electron. **7**, 931–935 (2001)
13. Z. Ding, Y. Zhao, H. Ren, S.J. Nelson, Z. Chen, Real-time phase resolved optical coherence tomography and optical Doppler tomography. Opt. Express **10**, 236–245 (2002)
14. J.S. Nelson, K.M. Kelly, Y. Zhao, Z. Chen, Imaging blood flow in human port-wine stain in situ and in real time using optical Doppler tomography. Arch. Dermatol. **137**, 741–744 (2001)
15. V.X. Yang, M.L. Gordon, A. Mok, Y. Zhao, Z. Chen, R.S.C. Cobbold, B.C. Wilson, I.A. Vitkin, Improved phase-resolved optical Doppler tomography using the Kasai velocity estimator and histogram segmentation. Opt. Commun. **208**, 209–214 (2002)
16. V. Westphal, S. Yazdanfar, A.M. Rollins, J.A. Izatt, Real-time, high velocity-resolution color Doppler optical coherence tomography. Opt. Lett. **27**, 34–36 (2002)
17. D.P. Dave, T.E. Milner, Doppler-angle measurement in highly scattering media. Opt. Lett. **25**, 1523–1525 (2000)
18. H. Ren, M.K. Breke, Z. Ding, Y. Zhao, J.S. Nelson, Z. Chen, Imaging and quantifying transverse flow velocity with the Doppler bandwidth in a phase-resolved functional optical coherence tomography. Opt. Lett. **27**, 409–411 (2002)
19. L. Yu, Z. Chen, Doppler variance imaging for three-dimensional retina and choroid angiography. J. Biomed. Opt. **15**, 016029 (2010)
20. L. Yu, E. Nguyen, G. Liu, B. Choi, Z. Chen, Spectral Doppler optical coherence tomography imaging of localized ischemic stroke in a mouse model. J. Biomed. Opt. **15**, 066006 (2010)
21. G. Liu, M. Rubinstein, A. Saidi, W. Qi, A. Foulad, B. Wong, Z. Chen, Imaging vibrating vocal folds with a high speed 1050 nm swept source OCT and ODT. Opt. Express **19**, 11880–11889 (2011)
22. G. Liu, W. Qi, L. Yu, Z. Chen, Real-time bulk-motion-correction free Doppler variance optical coherence tomography for choroidal capillary vasculature imaging. Opt. Express **19**, 3657–3666 (2011)
23. S. Makita, Y. Hong, M. Yamanari, T. Yatagai, Y. Yasuno, Optical coherence angiography. Opt. Express **14**, 7821–7840 (2006)

24. Y. Hong, S. Makita, M. Yamanari, M. Miura, S. Kim, T. Yatagai, Y. Yasuno, Three-dimensional visualization of choroidal vessels by using standard and ultra-high resolution scattering optical coherence angiography. Opt. Express **15**, 7538–7550 (2007)

25. Y. Yasuno, Y. Hong, S. Makita, M. Yamanari, M. Akiba, M. Miura, T. Yatagai, In vivo high-contrast imaging of deep posterior eye by 1-micron swept source optical coherence tomography and scattering optical coherence angiography. Opt. Express **15**, 6121–6139 (2007)

26. L. An, R.K. Wang, In vivo volumetric imaging of vascular perfusion within human retina and choroids with optical micro-angiography. Opt. Express **16**, 11438–11452 (2008)

27. R.K. Wang, L. An, P. Francis, D.J. Wilson, Depth-resolved imaging of capillary networks in retina and choroid using ultrahigh sensitive optical microangiography. Opt. Lett. **35**, 1467–1469 (2010)

28. R.K. Wang, L. An, S. Saunders, D.J. Wilson, Optical microangiography provides depth-resolved images of directional ocular blood perfusion in posterior eye segment. J. Biomed. Opt. **15**, 020502 (2010)

29. M. Szkulmowski, I. Grulkowski, D. Szlag, A. Szkulmowska, A. Kowalczyk, M. Wojtkowski, Flow velocity estimation by complex ambiguity free joint spectral and time domain optical coherence tomography. Opt. Express **17**, 14281–14297 (2009)

30. I. Grulkowski, I. Gorczynska, M. Szkulmowski, D. Szlag, A. Szkulmowska, R.A. Leitgeb, A. Kowalczyk, M. Wojtkowski, Scanning protocols dedicated to smart velocity ranging in spectral OCT. Opt. Express **17**, 23736–23754 (2009)

31. J. Barton, S. Areomaki, Flow measurement without phase information in optical coherence tomography. Opt. Express **13**, 5483–5493 (2005)

32. A. Mariampillai, B.A. Standish, E.H. Moriyama, M. Khurana, N.R. Munce, M.K. Leung, J. Jiang, A. Cable, B.C. Wilson, I.A. Vitkin, V.X. Yang, Speckle variance detection of microvasculature using swept-source optical coherence tomography. Opt. Lett. **33**, 1530–1532 (2008)

33. A. Mariampillai, M.K. Leung, M. Jarvi, B.A. Standish, K. Lee, B.C. Wilson, A. Vitkin, V.X. Yang, Optimized speckle variance OCT imaging of microvasculature. Opt. Lett. **35**, 1257–1259 (2010)

34. E. Jonathan, J. Enfield, M.J. Leahy, Correlation mapping method for generating microcirculation morphology from optical coherence tomography (OCT) intensity images. J. Biophotonics **4**, 583–587 (2010)

35. G. Liu, L. Chou, W. Jia, W. Qi, B. Choi, Z. Chen, Intensity-based modified Doppler variance algorithm: application to phase instable and phase stable optical coherence tomography systems. Opt. Express **19**, 11429–11440 (2011)

36. Y. Jia, M.R. Grafe, A. Gruber, N.J. Alkayed, R.K. Wang, In vivo optical imaging of revascularization after brain trauma in mice. Microvasc. Res. **81**, 73–80 (2010)

37. Y. Jia, R.K. Wang, Optical micro-angiography images structural and functional cerebral blood perfusion in mice with cranium left intact. J. Biophotonics **4**, 57–63 (2011)

38. V.J. Srinivasan, S. Sakadzic, I. Gorczynska, S. Ruvinskaya, W. Wu, J.G. Fujimoto, D.A. Boas, Quantitative cerebral blood flow with optical coherence tomography. Opt. Express **18**, 2477–2494 (2010)

39. B.J. Vakoc, R.M. Lanning, J.A. Tyrrell, T.P. Padera, L.A. Bartlett, T. Stylianopoulos, L.L. Munn, G.J. Tearney, D. Fukumura, R.K. Jain, B.E. Bouma, Three-dimensional microscopy of the tumor microenvironment in vivo using optical frequency domain imaging. Nat. Med. **15**, 1219–1223 (2009)

40. S. Yazdanfar, A.M. Rollins, J.A. Izatt, Imaging and velocimetry of the human retinal circulation with color Doppler optical coherence tomography. Opt. Lett. **25**, 1448–1450 (2000)

41. R.A. Leitgeb, L. Schmetterer, W. Drexler, A.F. Fercher, R.J. Zawadzki, T. Bajraszewski, Real-time assessment of retinal blood flow with ultrafast acquisition by color Doppler Fourier domain optical coherence tomography. Opt. Express **11**, 3116–3121 (2003)

42. B.R. White, M.C. Pierce, N. Nassif, B. Cense, B.H. Park, G.J. Tearney, B.E. Bouma, T.C. Chen, J.F. de Boer, In vivo dynamic human retinal blood flow imaging using ultra-high speed spectral domain optical Doppler tomography. Opt. Express **25**, 3490–3497 (2003)

43. Y. Wang, A. Fawzi, O. Tan, J. Gil-Flamer, D. Huang, Retinal blood flow detection in diabetic patients by Doppler Fourier domain optical coherence tomography. Opt. Express **17**, 4061–4073 (2009)

44. Y. Wang, B.A. Bower, J.A. Izatt, O. Tan, D. Huang, In vivo total retinal blood flow measurement by Fourier domain Doppler optical coherence tomography. J. Biomed. Opt. **12**, 041215 (2007)

45. B. Rao, L. Yu, H.K. Jiang, L.C. Zacharias, R.M. Kurtz, B.D. Kuppermann, Z. Chen, Imaging pulsatile retinal blood flow in human eye. J. Biomed. Opt. **5**, 040505 (2008)

46. R.K. Wang, L. An, Doppler optical micro-angiography for volumetric imaging of vascular perfusion in vivo. Opt. Express **17**, 8926–8940 (2009)

47. V.X. Yang, M.L. Gordon, S. Tang, N.E. Marcon, G. Gardiner, B. Qi, S. Bisland, E. Seng-Yue, S. Lo, J. Pekar, B.C. Wilson, I.A. Vitkin, High speed, wide velocity dynamic range Doppler optical coherence tomography (part III): in vivo endoscopic imaging of blood flow in the rat and human gastrointestinal tracts. Opt. Express **11**, 2416–2424 (2003)

48. V.X. Yang, S.J. Tang, M.L. Gordon, B. Qi, G. Gardiner, M. Cirocco, P. Kortan, G.B. Haber, G. Kandel, I.A. Vitkin, B.C. Wilson, N.E. Marcon, Endoscopic Doppler optical coherence tomography in the human GI tract: initial experience. Gastrointest. Endosc. **61**, 879–890 (2006)

49. D.Y. Kim, J. Fingler, J.S. Werner, D.M. Schwartz, S.E. Fraser, R.J. Zawadzki, In vivo volumetric imaging of human retinal circulation with phase-variance optical coherence tomography. Biomed. Opt. Express **2**, 1504–1513 (2011)

50. G.J. Tearney, B.E. Bouma, J.G. Fujimoto, High-speed phase- and group-delay scanning with a grating-based phase control delay line. Opt. Lett. **22**, 1811–1813 (1997)

51. F. Hlawatsch, G.F. Boudreaux-Bartels, Linear and quadratic time-frequency signal representations. IEEE Spectr. **4**, 21–67 (1992)

52. S. Yazdanfar, A.M. Rollins, J.A. Izatt, Ultrahigh velocity resolution imaging of the microcirculation in vivo using colar Doppler optical coherence tomography. Proc. SPIE **4251**, 156 (2001)

53. A.F. Fercher, C.K. Kitzenberger, G. Kamp, S.Y. El-Zaiat, Measurement of intraocular distances by backscattering spectral interferometry. Opt. Commun. **117**, 43–48 (1995)

54. R. Leitgeb, C.K. Hitzenberger, A.F. Fercher, M. Kulhavy, Performance of Fourier domain vs. time domain optical coherence tomography. Opt. Express **11**, 889–894 (2003)

55. M.A. Choma, M.V. Sarunic, C. Yang, J.A. Izatt, Sensitivity advantage of swept source and Fourier domain optical coherence tomography. Opt. Express **11**, 2183–2189 (2003)

56. J.F. de Boer, B. Cense, B.H. Park, M.C. Pierce, G.J. Tearney, B.E. Bouma, Improved signal-to-noise ratio in spectral-domain compared with time-domain optical coherence tomography. Opt. Lett. **28**, 2067–2069 (2003)

57. B.E. Bouma, G.J. Tearney, *Handbook of Optical Coherence Tomography* (Marcel Dekker, New York, 2002)

58. M. Wojtkowski, V.J. Srinivasan, T. Ko, J.G. Fujimoto, A. Kowalczyk, J.S. Duker, Ultrahigh-resolution high speed Fourier domain optical coherence tomography and methods for dispersion compensation. Opt. Express **12**, 2404–2422 (2004)

59. B. Cense, N. Nassif, T.C. Chen, M.C. Pierce, S.H. Yun, B.H. Park, B.E. Bouma, G.J. Tearney, J.F. de Boer, Ultrahigh-resolution high-speed retinal imaging using spectral-domain optical coherence tomography. Opt. Lett. **12**, 2435–2447 (2004)

60. S.H. Yun, G.J. Tearney, J.F. de Boer, N. Iftimia, B.E. Bouma, High speed optical frequency domain imaging. Opt. Express **11**, 2593–2963 (2003)

61. S.H. Yun, C. Boudoux, G.J. Tearney, B.E. Bouma, High-speed wavelength-swept semiconductor laser with a polygon-scanner-based wavelength filter. Opt. Lett. **28**, 1981–1983 (2003)

62. J. Zhang, J.S. Nelson, Z. Chen, Removal of mirror image and enhancement of signal to noise ratio in Fourier domain optical coherence tomography using an electro-optical phase modulator. Opt. Lett. **30**, 147–149 (2005)

63. J. Zhang, J.S. Nelson, Z. Chen, Full range polarization-sensitive Fourier domain optical coherence tomography. Opt. Express **12**, 6033–6039 (2004)

64. M.V. Sarunic, M.A. Choma, C. Yang, J.A. Izatt, Instantaneous complex conjugate resolved spectral domain and swept-source OCT using 3×3 fiber couplers. Opt. Express **13**, 957–967 (2005)

65. Z. Chen, in *Optical Doppler Tomography for High Resolution Imaging of* In Vivo *Microcirculation.* Whitake Foundation, 1997

66. R. Leitgeb, L. Schmetterer, M. Wojtkowski, M. Sticker, C.K. Hitzenberger, A.F. Fercher, Flow velocity measurement by frequency domain short coherence interferometry. Proc. SPIE **4619**, 16 (2002)

67. L. Wang, X. Wei, Y. Wang, M. Bachaman, G.P. Li, Z. Chen, Imaging and quantifying of microflow by phase-resolved optical Doppler tomography. Opt. Commun. **232**, 25–29 (2004)

68. D. Piao, L.L. Otis, Q. Zhu, Doppler angle and flow velocity mapping by combine Doppler shift and Doppler bandwidth measurements in optical Doppler tomography. Opt. Lett. **28**, 1120 (2003)

69. S. Proskurin, Y. He, R. Wang, Determination of flow velocity vector based on Doppler shift and spectrum broadening with optical coherence tomography. Opt. Lett. **28**, 1227 (2003)

70. L. Wang, *Development of Phase-Resolved Optical Doppler Tomography for Imaging and Quantifying Microflow Dynamics and Particle Size in Microfluidic Channels* (Department of Electrical and Computer Engineering, University of California, Irvine, Irvine, 2004)

71. Y.-C. Ahn, W. Jung, Z. Chen, Quantification of a three-dimensional velocity vector using spectral-domain Doppler optical coherence tomography. Opt. Lett. **32**, 1587–1589 (2007)

72. A. Major, S. Kimel, S. Mee, T.E. Milner, D.J. Smithies, S.M. Srinivas, Z. Chen, J.S. Nelson, Microvascular photodynamic effects determined in vivo using optical Doppler tomography. IEEE J. Sel. Top. Quant. Electron. **5**, 1168–1175 (1999)

73. R.D. Frostig, E.E. Lieke, D.Y. Ts'o, A. Grinvald, Cortical functional architechture and local coupling between neuronal activity and the microcirculation revealed by in vivo high-resolution optical imaging of intrinsic signals. Proc. Natl. Acad. Sci. USA **87**, 6082–6086 (1990)

74. Y. Chen, Z. Chen, Y. Zhao, J.S. Nelson, M. Bachman, Y. Chiang, C. Chu, G.P. Li, Test channels for flow characterization of processed platic microchannels, in *1999 Fall MRS Conference* (MRS, Boston, 1999)

75. Y. Chen, In vivo measurement and characterization of fluid flow in microchannels using OCT/ODT system, in *Electrical Engineering* (University of California, Irvine, Irvine, 2001), p. 100

76. Y.-C. Ahn, W. Jung, J. Zhang, Z. Chen, Investigation of laminar dispersion with optical coherence tomography and optical Doppler tomography. Opt. Express **13**, 8164–8171 (2005)

77. Y.-C. Ahn, W. Jung, Z. Chen, Optical sectioning for microfluidics: secondary flow and mixing in a meandering microchannel. Lab on a Chip **8**, 125–133 (2008)

78. L. Wang, Y. Wang, M. Bachaman, G.P. Li, Z. Chen, Frequency domain Phase-resolved optical Doppler and Doppler variance tomography. Opt. Comm. **242**, 345–347 (2004)

79. L. Wang, W. Xu, M. Bachaman, G.P. Li, Z. Chen, Phase-resolved optical Doppler tomography for imaging flow dynamics in microfluidic channels. Appl. Phys. Lett. **85**, 1855–1857 (2004)

80. R.K. Wang, High-resolution visualization of fluid dynamics with Doppler optical coherence tomography. Meas. Sci. Technol. **15**, 725–733 (2004)

81. Y.-C. Ahn, W. Jung, Z. Chen, Tubid two-phase slog flow in a microtube simultaneous visualizaion of structure and velocity field. Appl. Phys. Lett. **89**, 064109 (2006)

Doppler Optical Coherence Tomography Signals: Analysis in Low and High Scattering Media

21

Alexander V. Bykov and Jeroen Kalkman

Contents

Abstract

In this chapter, Doppler OCT signals (OCT magnitude and flow velocity profile) for low and high scattering media are analyzed. For low scattering media, we demonstrate the use of the single scattering model to determine the optical properties of the sample. For high scattering media, the effects of multiple scattering are stronger and the single scattering description breaks down. An alternative approach, based

A.V. Bykov (✉)
Optoelectronics and Measurement Techniques Laboratory, University of Oulu, Oulu, Finland
e-mail: bykov@ee.oulu.fi

J. Kalkman
Biomedical Engineering & Physics, Academic Medical Center, University of Amsterdam,
Amsterdam, The Netherlands
e-mail: j.kalkman@amc.uva.nl

on Monte Carlo simulations, is proposed as it gives a more appropriate description of the Doppler OCT signal by taking into account multiple scattering effects. Using Monte Carlo simulations, we analyze the deviation of the OCT slope from the value predicted by the single scattering model and analyze the distortions in the measured Doppler OCT flow profile. Monte Carlo simulations are compared to Doppler OCT measurements for Intralipid and blood.

21.1 Introduction

Optical coherence tomography (OCT) is a relatively new biomedical imaging technique that is used in clinical diagnostics, treatment monitoring, and disease prevention (screening). OCT is based on low-coherence interferometry and provides micrometer resolution images of turbid media up to a few millimeters deep. Besides morphological images, OCT also can be used to determine functional tissue parameters such as the light attenuation coefficient [1], (blood) flow [2], and tissue birefringence [3]. Since its invention [4], OCT has been applied in ophthalmology, vascular imaging, dermatology, and many other areas.

In this chapter, we analyze the Doppler OCT signal in low and high scattering media. For low scattering media the Doppler OCT signal is well described by the single scattering model, which is discussed in Sect. 21.2 As described in Sect. 21.3 optical properties such as the scattering coefficient, the scattering cross section, and the scattering anisotropy can be extracted directly from the OCT signal using the single scattering model. The single scattering model also provides a good description of the Doppler OCT signal and is used to quantify flow. In Sect. 21.4 we show that for high scattering media, the single scattering approximation is no longer an appropriate model to describe the Doppler OCT signal. To describe the Doppler OCT signal for high scattering media, we use Monte Carlo simulations, as explained in Sect. 21.5 to simulate the Doppler OCT signal as shown in Sect. 21.6. We focus on Intralipid and blood as scattering media as they differ in their scattering coefficient and scattering anisotropy. Finally in Sect. 21.7 we compare the Monte Carlo simulations to the Doppler OCT measurements for Intralipid and blood. We observed good agreement between our simulations and the measurements.

21.2 Single Scattering Description of the Doppler OCT Signal

In its most basic form, OCT is based on single backscattering imaging. Light incident on the sample travels in a ballistic straight path through the scattering medium until a single backscatter event reflects the light back into the sample arm optics. Multiple scattered light is rejected by the combination of confocal detection and coherent gating. In confocal detection, axial and lateral out of focus light is rejected due to the lower back-coupling efficiency. Moreover, out of focus light has traveled a longer path length and therefore is mapped onto larger depths in the sample, thereby reducing its effect on the shallower OCT signals. For low scattering

media multiple scattered light is efficiently rejected from the OCT signal and the single scattering approximation is a valid description for the OCT signal.

For the single scattering approximation of the OCT signal, we assume a loss less time-domain OCT system without focus tracking. The OCT detector current $i_{det}(z)$ as a function of depth z, is equal to the backscatter profile of the sample as a function of z convoluted with the complex coherence function $\gamma\ (2z/c)$ [5]. For a single perfect mirror in air positioned in the sample arm located at $z = 0$, the OCT detector current signal is

$$i_{\det}(z) = \eta \text{Re}\left\{\gamma\left(\frac{2z}{c}\right)\right\} \otimes r_{mirror}h(z)\delta(z)\sqrt{P_{ref}P_{sample}}, \qquad (21.1)$$

where η is the detector conversion factor from the incident light power to the electric current, Re{} is the real part of the complex coherence function, c is the speed of light, r_{mirror} is the field reflection coefficient of the mirror, $h(z)$ is the confocal point spread function [6], $\delta(z) = 1$ for $z = 0$ and $\delta(z) = 0$ for all other z. The powers P_{ref} and P_{sample} are the powers incident on the reference and sample arm, respectively. Performing the convolution in (21.1) and taking the square of the OCT signal at $z = 0$, we find

$$i_{\det}(z = 0)^2\big|_{mirror} = \eta^2\ r_{mirror}^2 P_{ref}P_{sample}, \qquad (21.2)$$

where it is assumed that $h(0) = 1$, i.e., the mirror is in the focus of the sample arm focusing lens. For a scattering medium without absorption, the situation is more complicated. A one-dimensional single scattering model is assumed where homogenously distributed scatterers all add coherently to the OCT signal. Assuming that the OCT signal for a homogenous scattering medium is the sum of all scattering contributions, the detector current is

$$i_{\det}(z) = \eta \text{Re}\left\{\gamma\left(\frac{2zn_{med}}{c}\right)\right\} \otimes h(z)\sqrt{P_{ref}P_{sample}}\sqrt{\mu_{b,NA}}\sqrt{\exp(-2\mu_s z)}, \quad (21.3)$$

with n_{med} the group refractive index of the medium, $\mu_{b,NA}$ the effective backscattering coefficient (quantifying the part of the light that is backscattered into the detection numerical aperture (NA) of the OCT system). The scattering coefficient μ_s is equal to the concentration of scatterers C and their cross section σ_s, i.e., $\mu_s = C\sigma_s$. The factor 2 in the exponent of (21.3) accounts for the round-trip attenuation to and from depth z. In a scattering medium with attenuation μ_s, the amplitude of the OCT signal can be found by extrapolating the attenuated OCT signal to $z = 0$. The square of the OCT signal at the interface is

$$i_{\det}(z = 0)^2\big|_{scat} = \eta^2 \frac{l_c}{n_{med}}P_{ref}P_{sample}\mu_{b,NA}\,Q, \qquad (21.4)$$

where the coherence length l_c is defined in single pass according to Schmitt et al. [7] and Goodman [5]. Note that this coherence length definition is a factor $(\pi/8\ln2)^{1/2} \approx 0.75$ smaller than the commonly used definition related to the axial resolution in OCT that is defined as the full width at half maximum of the Gaussian–shaped coherence point spread function of the OCT amplitude [8].

The constant Q describes the heterodyne intensity back-coupling efficiency from a scattering medium compared to that of a mirror and ranges from 0 to 1. There are two main reasons that cause a reduction of the heterodyne detection efficiency Q for a homogenous distribution of scatterers compared to a mirror to values less than 1. First, the OCT magnitude for a sum of scatterers depends on the random axial position of the scatterers in the sample (causing speckle). As a result, the envelope of the OCT signal (e.g., the mean value of the speckle pattern) is smaller than the addition of all individual particle envelopes. Second, the OCT backscatter efficiency for small particles depends on the lateral offset of the scatterer in the focused beam. For particles not on the optical axis, the spherical wave originating from a particle is less efficiently coupled back to the single mode fiber compared to the planar wavefront reflected from the mirror.

From this analysis, it can be observed that μ_b can be determined by dividing (21.2) by (21.4). The backscattering coefficient is

$$\mu_{b,NA} = \frac{i_{\det}(z=0)^2\big|_{scat}}{i_{\det}(z=0)^2\big|_{mirror}} \frac{n_{med}r^2_{mirror}}{l_c Q} = p_{NA}\mu_s, \tag{21.5}$$

with the backscattering coefficient μ_b equal to the scattering coefficient times the phase function integrated over the *NA* in the backscattering direction, p_{NA}. Note that by taking the ratio of two OCT measurements additional loss factors in the OCT system do not influence the determination of μ_b. In the absence of absorption, the scattering coefficient μ_s can be determined from the slope of the OCT signal. For media with absorption and described by the single scattering approximation, light travels in a ballistic way and Beer's law can be applied to calculate the total OCT attenuation coefficient μ_t, which equals $\mu_t = \mu_s + \mu_a$. Consequently, μ_s can be obtained by subtracting the absorption coefficient from the total attenuation coefficient obtained from the slope of the OCT signal. The scattering phase function in the backscattering direction can be obtained by integrating the scattering phase function $p(\theta)$ over angles from π-*NA* to π. The phase function integrated over the *NA*, p_{NA}, describes the fraction of scattered photons that are detected by the OCT system, i.e., $p_{NA} = \mu_{b,NA}/\mu_s$. Consequently, p_{NA} can be determined using (21.5) and μ_s

$$p_{NA} \equiv \int_{\pi-NA}^{\pi} p(\theta)2\pi\sin(\theta)d\theta = \frac{\mu_{b,NA}}{\mu_s} = \frac{n_{med}r^2_{mirror}}{l_c Q \mu_s} \frac{i_{\det}(z=0)^2\big|_{scat}}{i_{\det}(z=0)^2\big|_{mirror}}. \tag{21.6}$$

Since p_{NA} is related to the phase function, the scattering anisotropy g can be determined from a determination of p_{NA} if the NA and the shape of the phase function is known a priori.

In the single scattering approximation, light is backscattered once and the Doppler frequency shift $f_{Doppler}$ of the backscattered light is determined by the incident angle θ, refractive index of the medium n, wavelength λ, and the flow speed v according to

$$f_{Doppler} = \frac{2vn}{\lambda} \cos \theta. \tag{21.7}$$

Note that for forward scattering the Doppler frequency shift is zero.

21.3 Determination of Optical Properties and Flow from Doppler OCT Signals of Low Scattering Media

The optical parameters of low scattering media are determined using a home-built time-domain OCT system, which is described in detail in Ref. [9]. The time-domain OCT system is based on a filtered Fianium light source with the center wavelength at 1,300 nm. The axial resolution of this system is 9.7 ± 0.1 μm as was determined from the full width at half maximum of the OCT magnitude point spread function. The Gaussian beam waist of the focusing lens is 9.6 ± 0.2 μm, corresponding to a numerical aperture $NA = 0.043 \pm 0.001$. Prior to the experiment, the OCT system is calibrated for quantitative measurements of the backscattered power. Due to the limited dynamic range of the OCT system, the power from the mirror is measured using different calibrated neutral density filters in the sample arm. From the dependence of the OCT signal on the optical attenuation the reflected power and the OCT magnitude can be directly compared to the signals for the scattering sample in (21.6) (i.e., with no optical attenuation in the sample arm).

OCT measurements on suspensions of scatterers are performed in a 1 mm thick glass cuvette, placed in the sample arm at $\sim 70°$ angle relative to the incident beam. The sample arm beam is focused at the first glass-medium interface. Measurements for every solution are performed independently for five times, averaging 100 A-scans per measurement. After background subtraction the OCT signal magnitude is corrected for the confocal point spread function [6], the optical path length is converted to depth using the refractive index of water [10]. The OCT attenuation coefficient is determined with a two parameter single exponential fit of the measured OCT signal in depth. To reduce the effects of multiple scattering, the concentration of scatterers is kept low to create samples with scattering coefficients below 5 mm^{-1} (as calculated with Mie theory). In addition, only OCT signals starting at ~ 60 μm depth after the sample front surface and extending 190 μm in depth is used for fitting the single exponential decay. The scattering coefficient μ_s is calculated by subtracting the water absorption coefficient ($\mu_a = 0.2$ mm^{-1}) from the fitted attenuation coefficient μ_t. Finally, the scattering cross section σ_s is calculated
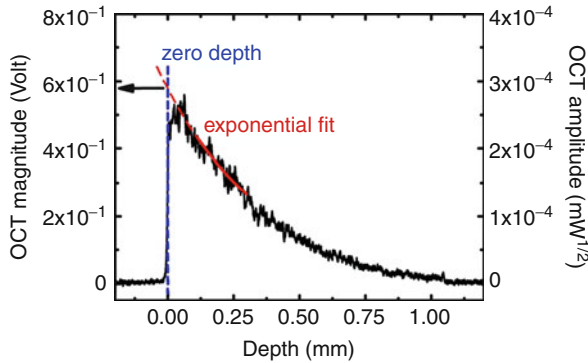
Fig. 21.1 OCT measurement of backscattered power from a suspension of 400 nm diameter polystyrene microspheres in water. The vertical scale on the *left* is converted to absolute units of square root of power using the power calibration and is indicated on the *right*. The attenuation coefficient is determined from the single exponential decay fit (*solid red line*); the amplitude of the OCT signal from the sample surface is determined by extending the exponential (*dashed red line*) fit to intersect with a drop line at zero depth (*dashed blue line*)

by dividing the scattering coefficient by the known particle concentration. The OCT signal amplitude at the front glass-sample interface is determined from the exponential fit by extending the fitting line to zero depth, as is shown in Fig. 21.1. The zero depth location is determined from the crossing of the OCT signal with the vertical drop line at half height of the OCT signal. Using our calibration method, the OCT signal magnitude is determined on an absolute scale in $mW^{1/2}$ units, which is indicated in Fig. 21.1 on the right hand side scale for a measurement of a scattering medium for 400 nm diameter particles. The peak of the backscattered power in the heterodyne (OCT) signal is of the order of 90 pW.

Polystyrene microspheres (Thermo Scientific, USA) are used as scatterers with the concentration of the sample calculated based on the used dilution (1 wt% concentration). The microspheres have mean diameters of 203 ± 5, 400 ± 9, 596 ± 6, 799 ± 9, and 994 ± 10 nm and size distribution standard deviations of 4.7, 7.3, 7.7, 4.8, and 10 nm, respectively. Mie calculations are performed based on mean diameters to calculate the scattering cross section and phase function of the polystyrene particles. The refractive index of water ($n_{water} = 1.32$ [10]) and polystyrene are used ($n_{polyst} = 1.57$ [11]) as input. From Mie calculations, the scattering anisotropy, i.e., the g of these microspheres, is calculated to be: 0.07, 0.29, 0.62, 0.73, and 0.81 for increasing sphere diameter. Also, from the calculated phase functions, the scattering efficiency in the backscattering direction p_{NA} is calculated by integrating the phase function over the NA of the sample arm focusing lens.

Measurements performed on Intralipid samples are used as an example of our technique to a polydisperse medium. Intralipid is an aqueous suspension of polydisperse lipid droplets, which is often used as a tissue phantom for optical measurements. To reduce any effects of multiple scattering, we performed measurements for low concentrations Intralipid (0.63, 1.25, and 2.5 wt%).

Fig. 21.2 Results of Mie calculations and experimental measurements of: (**a**) scattering cross section of polystyrene microspheres (error bars are smaller than symbols); (**b**) scattering phase function p_{NA} of polystyrene microspheres (error bars are standard deviations); the *dashed line* indicates the measured value of p_{NA} for Intralipid (standard deviation is given in the text); (**c**) Mie calculations of g versus particle diameter at 1,300 nm for polystyrene microspheres. *Arrows* show the average particle diameter and the g of Intralipid
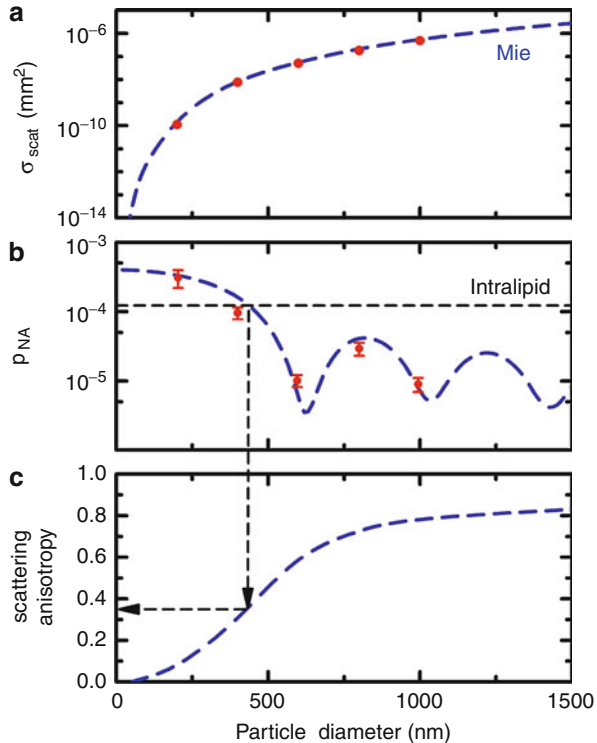
The samples are prepared by dilution of a single batch of 20 wt% Intralipid (Fresenius-Kabi) with deionized water. The refractive indices used for Mie calculations of Intralipid are: $n_{water} = 1.32$ [10] for water; $n_{lip} = 1.46$ for lipid droplets [12].

From an OCT measurement as shown in Fig. 21.1, the scattering coefficient for a solution of particles is determined. Figure 21.2a shows the scattering cross section of polystyrene microspheres for the different diameters obtained from the scattering coefficient. The experimental results are compared to Mie calculations and good agreement is observed (typical error is within 10 %). Consequently, it can be assumed that multiple scattering effects are negligible and that the single scattering model is valid for a description of the OCT signal. From the data in Fig. 21.2a and the measured OCT magnitude at the interface, p_{NA} is determined using (21.6). Measurements of p_{NA} for all diameters are used to calculate the average heterodyne intensity back-coupling efficiency $Q = 0.26 \pm 0.04$, which is used to compare p_{NA} to Mie calculations in Fig. 21.2b. The experimental points match the calculated values reasonably well and the oscillations in p_{NA} due to the particle diameter dependent lobe structure of the backscattering efficiency are clearly observable.

The phase function in the backscattering direction p_{NA} can be used to estimate the average size of the scatterers and, consequently, g. To determine the average diameter, the crossing point of the horizontal line through the experimental p_{NA} and

Fig. 21.3 (**a**) OCT signal
and (**b**) Doppler OCT flow
measurement of 0.5 vol%
Intralipid solution under flow.
The flow profile is measured
in a cylindrical flow channel
(see *inset*), the *vertical line*
indicates the location of the
flow measurement
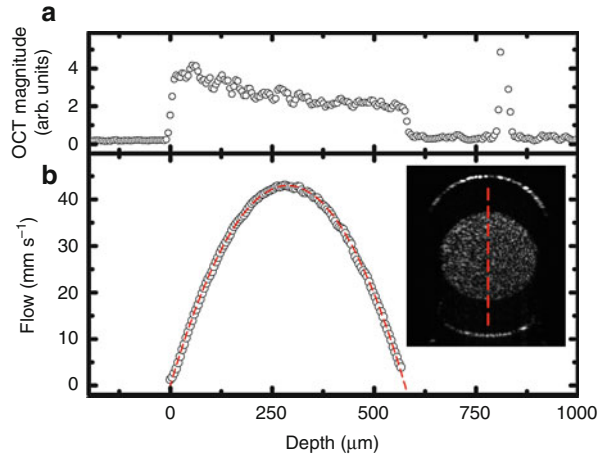
the calculated p_{NA} curve for varying scatterer size has to be found. The obtained
crossing point specifies the average particle diameter (Fig. 21.2b). Finally, the
average particle diameter corresponds to a scattering anisotropy g (Fig. 21.2c).
To demonstrate our method on non-calibrated samples we apply it to Intralipid,
which is a polydisperse suspension of scatterers. Following the same procedure as
for polystyrene microspheres, p_{NA} of Intralipid is determined. For low particle
concentration, p_{NA} is independent of the concentration of scatterers and the p_{NA}
values for all measured Intralipid concentrations (1.30×10^{-4}, 1.26×10^{-4} and
1.11×10^{-4} for 0.63, 1.25 and 2.5 wt% Intralipid, respectively) are averaged.
The resulting value, $p_{NA} = (1.22 \pm 0.21) \times 10^{-4}$, is plotted in Fig. 21.2b. Note
that although the refractive indices of polystyrene spheres and Intralipid droplets
are different, this has negligible influence on the calculated p_{NA}. From Fig. 21.2b,
the crossing point of the line of the calculated p_{NA} of polystyrene microspheres and
the measured p_{NA} of Intralipid corresponds to a particle diameter of 438 ± 21 nm.
Consequently, from Fig. 21.2c where we calculate g for varying particle diameter,
this particle diameter corresponds to the scattering anisotropy $g = 0.35 \pm 0.03$.
This value agrees very well with previously reported measurements of g for
Intralipid at 1,300 nm $g = 0.32 \pm 0.07$ [13].

Doppler OCT experiments are conducted on a home-built spectral-domain (SD)
OCT system operating at a center wavelength $\lambda_c = 1,300$ nm wavelength [14].
Doppler OCT measurements are performed by calculating the incremental phase
change per A-line [15]. For low scattering media quantitative flow measurements
can be performed using Doppler OCT. Figure 21.3 shows a Doppler OCT
flow measurement on a 0.5 vol% Intralipid solution flowing through a glass
capillary with 0.55 mm inner and 0.98 mm outer diameter. After calibration of
the Doppler angle θ, quantitative flow measurements can be performed. The
parabolic flow profile, predicted by the Navier–Stokes equations, is accurately
measured using Doppler OCT.

21.4 Multiple and Dependent Scattering Effects in Doppler OCT Measurements of High Scattering Media

For low scattering media, the single scattering model is a good description of the Doppler OCT signal. At high particle concentrations and/or high scattering cross sections the scattering coefficient becomes high and multiple scattering is much stronger. Due to the nonzero collection *NA* and coherence length, multiple scattered light cannot be sufficiently rejected from the Doppler OCT signal, thereby affecting the measured Doppler OCT signal. As a result, the single scattering approximation is no longer valid and a quantitative analysis of the Doppler OCT signals is much more difficult.

Multiple scattering can lead to non-single-exponential decay, thereby making a quantitative determination of the scattering coefficient more difficult [16, 17]. Moreover, since in OCT the path length of the detected light is mapped one on one to a geometrical location in the sample, multiple scattering can also affect depth ranging and it can lead to spatial resolution loss [18]. For Doppler OCT flow measurements, it has been shown theoretically [19], with Monte Carlo (MC) simulations [20], and experimentally [21] that multiple scattering can increase or decrease the Doppler frequency for light penetrating deep into highly scattering media. Consequently, for a quantitative analysis of Doppler OCT data, e.g., to correctly determine flow and/or shear rate parameters [22], the effect of multiple scattering has to be taken into account.

In addition to multiple scattering, the scattering coefficient is also influenced by coherent light scattering effects, i.e., due to close packing of particles the coherent addition of light can lead to a reduction in the scattering coefficient. This effect is called dependent scattering; a dependence of the scattering strength on the separation between the particles. In this case, the scattering coefficient μ_s does not follow the linear relation $\mu_s = C\sigma_s$, but instead the Mie scattering cross section σ_s depends in a complex way on particle concentration C and therefore the relation $\mu_s = C\sigma_s(C)$ holds. As already shown in other light scattering experiments [23, 24], dependent scattering leads to a reduction in the scattering coefficient and thus can lead to a decrease of the OCT signal attenuation. In addition, the single scattering approximation of the scattering coefficient does not hold anymore and the scattering coefficient, in general, cannot be described as the sum of the contributions from the single scatterers. In this case, the scattering cross section becomes concentration dependent and coherent addition of waves scattered from different particles has to be taken into account.

To study multiple and dependent scattering effects, we perform Doppler OCT measurements of Intralipid and diluted blood solutions under flow with the SD-OCT system. For both samples the scattering strength varies with particle concentration. However, blood has a much higher scattering coefficient and scattering anisotropy than Intralipid. We will observe how these two effects influence multiple and dependent scattering.

As a scattering medium we use Intralipid. For Intralipid, we use dilutions of a single batch of 20 wt% Intralipid (Fresenius-Kabi) with distilled water. The

Intralipid (particle) volume concentration is calculated from the dilution of the batch solution by assuming that only the soybean oil and the egg-phospholipid are in the solid state, with the rest of the constituents (glycerol and water) in solution [25]. For blood, fresh porcine blood is drawn and anticoagulated before use. It is washed, centrifuged at 3,500 rpm, and the supernatant is replaced with phosphate buffered saline. Solutions with varying hematocrit (HCT) are made from the initial solution by adding phosphate buffered saline to the blood. For every solution a sample is taken right after the Doppler OCT measurement and analyzed with an XE-5000 automated hematology system to determine the mean cell volume (MCV) and HCT. Flow is generated by a precision syringe pump (Perfusor fm, B. Braun AG) that pumps the Intralipid solution at a flow of 50 or 100 mL/h through a 500 μm thickness glass flow cuvette with rectangular cross section.

Similar to the measurements with the time-domain OCT system, the SD-OCT signal magnitude is corrected for the signal background, confocal point spread function, and in addition, the spectral-domain depth detection sensitivity. Optical path length is converted to physical depth by dividing with an effective refractive index based on the relative concentrations of water ($n_{water} = 1.32$ [10]) and/or Intralipid ($n = 1.46$, soybean oil) and hemoglobin ($n_{Hb} = 1.40$, extrapolated from [26]). The Doppler frequencies are converted to flow using (21.7), the estimated refractive index, and the measured Doppler angle θ.

The OCT signal attenuation coefficient is determined by a 2-parameter single exponential fit (attenuation rate μ_{OCT} and amplitude) over a range in the cuvette where the signal shows a single exponential decay. Since the OCT signal at any depth z (path length) in the sample is attenuated by absorption according to $\exp(-\mu_a z)$, the fitted OCT attenuation coefficient is corrected for absorption by subtraction of the water and/or HCT dependent μ_a from μ_{OCT}. In this way, the OCT attenuation coefficient due to scattering only is obtained, which we call $\mu_{OCT,s}$.

Figure 21.4a and b show Doppler OCT measurements for 23 vol% Intralipid and (c) and (d) for HCT = 15 % blood. These concentrations are the highest concentrations we measured for Intralipid and blood. For Intralipid, the OCT signal attenuation is well described by a single exponential fit over the whole depth range of the cuvette, described by $\mu_{OCT,s} = 4.9 \text{ mm}^{-1}$. At this scattering coefficient the Doppler flow profile is not a parabola, as would be expected, but is severely distorted. The flow profile maximum is shifted from the center of the cuvette toward smaller depths and a large offset is observed at the bottom boundary of the cuvette. For blood, the OCT signal in the first 150 μm increases, thereafter it decreases with a single exponential decay, as described by $\mu_{OCT,s} = 4.9 \text{ mm}^{-1}$. The Doppler OCT flow profile for blood is distorted and shows, similar to Intralipid, a large offset at the bottom boundary of the flow profile.

The fits to the OCT signal decay in depth result in an estimation of $\mu_{OCT,s}$ for both Intralipid and blood as a function of concentration and is shown in Fig. 21.5. For both samples $\mu_{OCT,s}$ increases nonlinearly with increasing concentration. For Intralipid, $\mu_{OCT,s}$ is relatively close to μ_s as reported in literature [12, 13]. For similar volume concentrations $\mu_{OCT,s}$ for blood is close to that for Intralipid.
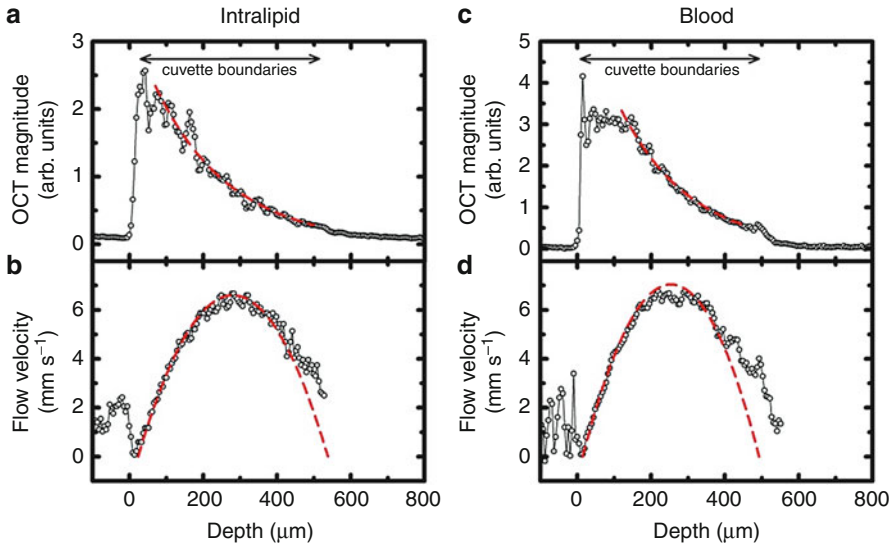
Fig. 21.4 (**a**) OCT and (**b**) Doppler OCT measurement for 23 vol% Intralipid and (**c**) OCT and (**d**) Doppler OCT for HCT = 15 % blood. Measured data is shown with *open circles*. Single exponential fits to the measured OCT signal are shown with *dashed line* in (**a**) and (**c**). Parabolic flow profile fits to the Doppler OCT signal are shown with a *dashed line* in (**b**) and (**d**)

However, we expect it to be much larger, since the scattering coefficient μ_s for blood is known to be much higher [27] than for Intralipid [12, 13].

21.5   Monte Carlo Simulations of Light Tissue Interaction in Scattering Media

Monte Carlo (MC) simulations are a powerful tool for simulating signals for a variety of experimental arrangements. Monte Carlo simulations of light tissue interaction have been widely used in OCT and Doppler OCT [18, 20]. Monte Carlo simulations of light tissue interaction are based on calculating the trajectories of a large numbers of photons randomly propagating in a scattering medium. Optical properties of the medium such as absorption coefficient, scattering coefficient, and scattering anisotropy determine the length and the shape path of individual photon trajectories. We use a traditional MC algorithm for simulation of light propagation in multilayered media described in Ref. [28], which is modified for simulation of OCT and Doppler OCT signals by accounting for the coherence gating and the geometry of the sample arm (shown in Fig. 21.6). Details of the Monte Carlo algorithm for OCT signal simulation can be found in [20]. To improve the calculation performance, a parallel message-passing-interface-based MC code was implemented on a computer cluster system based on Intel Xeon 3 GHz processors. For the simulation of a single OCT A-line scan, the trajectories of 10^{11} photons

Fig. 21.5 Scattering coefficient $\mu_{OCT,s}$ measured with OCT for varying Intralipid concentration and blood HCT
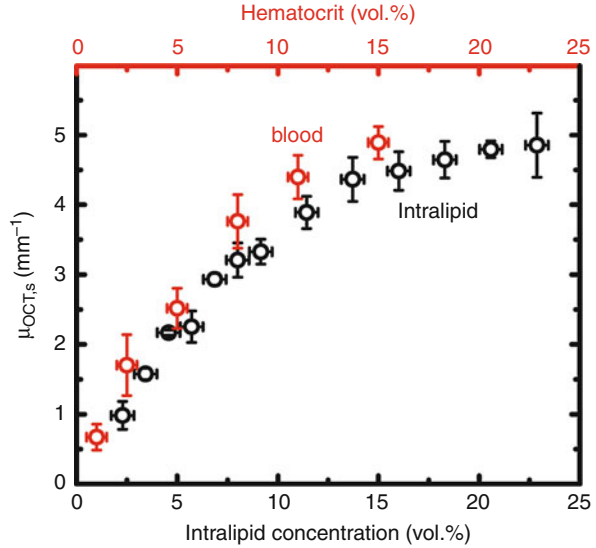
were generated and analyzed. The incoming photons are modeled in the form of a pencil beam. Photons are considered to be coherent if their single pass optical path length is within half a coherence length of their maximum penetration depth. The outgoing photons are detected using a finite size detector located at the focal distance from the medium under study. We performed MC simulations for the SD-OCT system geometry and media describing Intralipid and blood. The sample arm geometry of this setup is shown in Fig. 21.6.

21.6 Monte Carlo Simulations of the Doppler OCT Signal

21.6.1 Monte Carlo Simulations of Doppler OCT Signals from Intralipid

To determine the role of multiple and dependent scattering on the OCT and Doppler OCT signal, we performed MC simulations using the developed MC code. First, we focus on Intralipid solutions, which have intermediate scattering coefficient and low scattering anisotropy. Figure 21.7 shows the simulated OCT signal as a function of depth calculated for the measured $\mu_{OCT,s}$ for three Intralipid concentrations (in Fig. 21.5). These simulations are performed using a Henyey-Greenstein function with $g = 0.33$ as a valid approximation of scattering phase function of Intralipid [13]. As can be seen from the figure, the simulated OCT signal decay is close to the expected scattering coefficient $\mu_{OCT,s}$, but for all Intralipid concentrations the slope of the single exponential part of the simulated OCT attenuation, indicated on the right hand side of the graph, is slightly lower ($\sim$13 %) than the input μ_s.

Fig. 21.6 Schematics of the sample arm configuration with focusing lens and flow cuvette. MC simulations are based on the geometry and experimental parameters: l_c is the coherence length of the source, f is the focal length of the sample arm lens, λ_c is the OCT center wavelength, NA is the numerical aperture of the lens, and θ is the Doppler angle
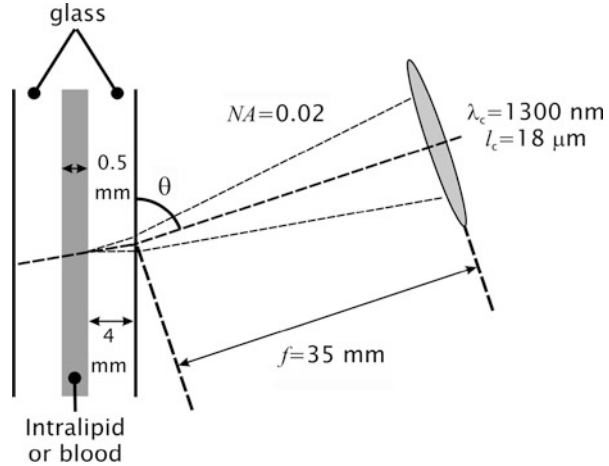
Fig. 21.7 Monte Carlo simulations of the OCT signal attenuation in depth for varying Intralipid concentration. The simulations are performed with $\mu_s = 1$, 2.9, and 4.9 mm^{-1}, for 2, 7, and 23 vol% Intralipid, respectively. Indicated on the *right* are the effective OCT attenuation coefficients $\mu_{OCT,s}$ obtained for these simulations
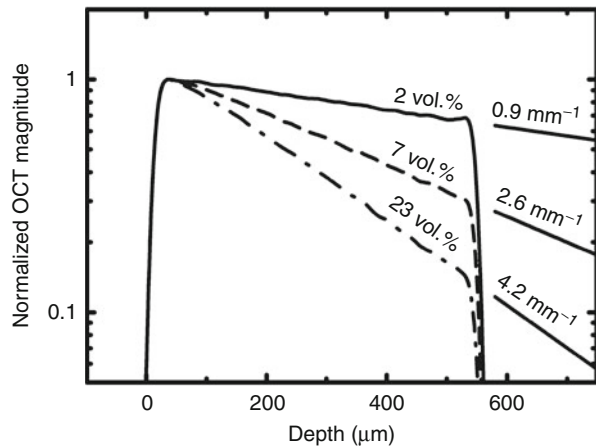
This phenomenon is clarified by an analysis of the contribution of multiple scattered photons, as is shown in Fig. 21.8.

Focusing on the highest Intralipid concentration, as shown in Fig. 21.8, the OCT signal from the single (back) scattered photons has an attenuation of μ_s, as expected. However, due to the finite collection numerical aperture and coherence length, multiple scattered photons are also detected. For depths larger than 200 μm the number of multiple scattered photons (scattered more than one time) exceeds the number of single scattered photons and since multiple scattered photons are found to have a lower attenuation rate with depth, their addition to the OCT signal from the single backscattered photons leads to a decrease of the attenuation coefficient from μ_s to $\mu_{OCT,s}$. Therefore, the OCT signal attenuation becomes slightly non-single exponential as it changes from mainly single backscattering
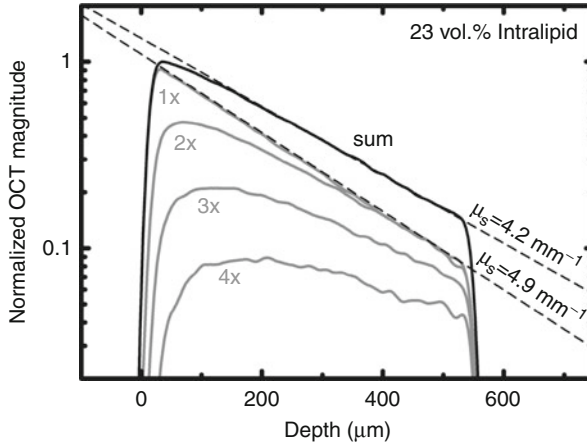
Fig. 21.8 Monte Carlo simulation of the OCT signal attenuation for 23 vol% Intralipid. The simulated OCT signal is decomposed into the contribution of the number of scattering events per photon (indicated). For single backscattering the attenuation is equal to the input μ_s. Multiple scattering adds signal to the OCT amplitude thereby decreasing the OCT attenuation coefficient from $\mu_s = 4.9$ mm^{-1} to $\mu_{OCT,s} = 4.2$ mm^{-1} ($\sim$13 %)

(depth < 200 μm) to mainly multiple scattered (depth > 200 μm). From the MC simulations, we derive that we consistently underestimate the single scattering coefficient μ_s by $\sim$13 % if we compare the MC simulations to the measured OCT signal attenuation slope.

Next, we perform MC simulations of the Doppler OCT signal for flowing Intralipid. Figure 21.9 shows the simulated OCT Doppler signal using a normalized input flow for three different Intralipid concentrations. It demonstrates that for increasing Intralipid concentration the flow maximum shifts to a larger depth (+5 % relative to the center) and that the Doppler frequency at the rear border of the cuvette increases (+29 % of the peak flow), both are observed in our measurements (see Fig. 21.4b). Also, the peak flow decreases. This effect is difficult to observe in our measurements due to the flow variations of the syringe pump, dependence of the Doppler frequency on the refractive index of the Intralipid, and incidence angle variations due to the refractive index of the Intralipid. As expected, for single scattered photons the simulated Doppler flow profile is equal to the input parabolic flow profile (not shown).

21.6.2 Doppler OCT Signals for Varying Anisotropy Factor

In comparison with the single scattering description of the OCT signal, multiple scattering decreases the slope of the OCT signal in depth and affects the Doppler OCT flow profile at large depths. In general, these multiple scattering effects increase with increasing scattering coefficient. However, the effect of the scattering

Fig. 21.9 Monte Carlo simulation of the Doppler OCT signal for varying Intralipid concentration. The *dashed line* indicates the input flow profile. The effect of increasing amounts of multiple scattering on the Doppler OCT signal is indicated by *arrows*
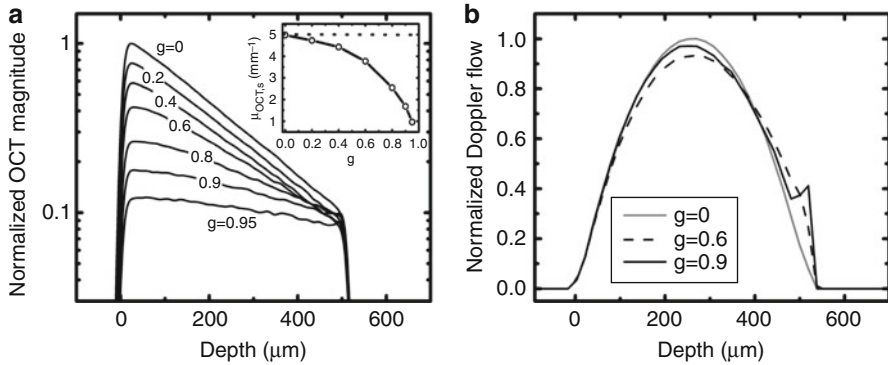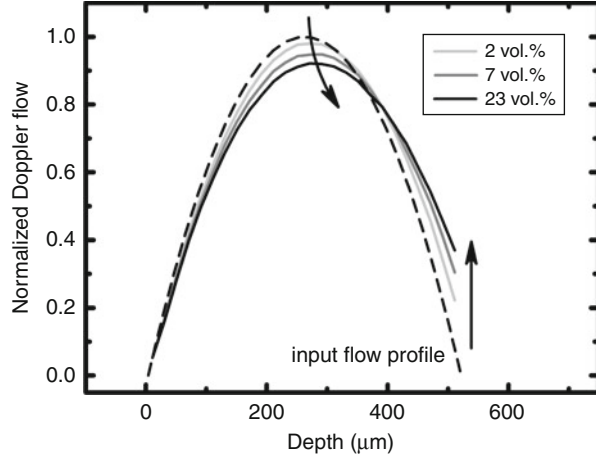
Fig. 21.10 (**a**) MC simulations of the OCT signal for different anisotropy factor g (values are indicated on the graph). The inset shows $\mu_{OCT,s}$ derived from the slope of the OCT signal for varying g-factor. (**b**) Normalized Doppler OCT flow profiles at selected g (indicated)

anisotropy g is more complicated, especially on the Doppler OCT flow profile. Figure 21.10 shows MC simulations using a constant $\mu_s = 5$ mm^{-1} and varying g (using a Henyey-Greenstein phase function). The simulations are performed for our experimental geometry. The absorption of the scattering medium is considered to be negligible small.

Figure 21.10a shows that the slope of the OCT signal decreases with increasing g due to increasing amounts of multiple scattered photons in the OCT signal. For $g = 0$, the slope of the OCT signal attenuation is close to that described by the single scattering model, which means that for this scattering anisotropy multiple scattered photons are effectively filtered out from the beam. For high scattering anisotropies (e.g., $g = 0.95$) many of the multiple scattered photons stay in the beam, thus

contributing to the OCT signal and decreasing its slope. This is further indicated in the inset where $\mu_{OCT,s}$ is estimated from the single exponential part of the decay and plotted against g. Figure 21.10b shows MC simulations for the Doppler OCT flow profiles at three different scattering anisotropies. For $g = 0$, the input flow profile is accurately reproduced because the Doppler OCT signal is formed mostly by single scattered photons. For $g = 0.6$ the flow profile is significantly distorted, and finally for $g = 0.9$, the flow profile again is slightly distorted, however, for this g the contribution of multiple scattered photons is significant. This effect can be explained by the interplay between the Doppler shift per scattering event and the average number of scattering events that a detected photon experiences. For very low g, the Doppler shift per scattering event is very large, however, these photons are very rapidly scattered sideways out of beam and do not contribute to the OCT signal. On the other hand, for very high g, photons are scattered mainly in the forward direction. These photons stay in the beam and contribute to the OCT signal, however, they have a very low Doppler shift per scattering event (strictly forward scattered photons have zero scattering angle and do not gain any Doppler shift). Therefore, the effect of multiple scattering on the measured Doppler OCT flow profile is largest at intermediate g, i.e., $g = 0.6$ where a significant fraction of the detected light is multiple scattered and these multiple scattered photons also experience a significant Doppler shift per scattering event. Forward scattering, which occurs at high g, also leads to the appearance of a small peak at the backside interface of the Doppler flow profile (Fig. 21.10b) even though the specularly reflected beam does not hit the detector (the capillary is tilted relative to the probe beam). This peak is formed by multiple (forward) scattered photons that are not present in the case when only single scattering is dominant.

21.6.3 Monte Carlo Simulations of Doppler OCT Signals from Blood

For high scattering media, such as blood, the effect of multiple scattering is expected to be much stronger than for Intralipid. For the OCT attenuation, this results in an underestimation of the scattering coefficient and a nonlinear increase of the scattering coefficient with HCT [17]. These effects are attributed to multiple scattering and concentration-dependent scattering, respectively. Here we use Monte Carlo (MC) simulations to model the Doppler OCT signal for flowing blood. It is well known that the Henyey-Greenstein function is not a good approximation for the red blood cell (RBC) phase function [29]. In addition, the experimentally obtained $\mu_{OCT,s}$ of blood is inadequately low to expect a good result of MC simulation using this parameter as input scattering coefficient. Therefore, the scattering cross section of an RBC is estimated using the discrete dipole approximation (DDA), calculated with the ADDA code [30]. The calculations are performed for $\lambda_c = 1,300$ nm using the RBC's dimensions (determined from the measured MCV as input parameter. The RBCs are modeled by oblate spheroid particles, this shape being the simplest nonspherical approximation for the RBC. For the refractive index contrast ratio we choose $|m| = 1.05$ [26]. The refractive index of the medium is estimated at $n_{med} = 1.33$. The ratio of the short over the long

axis lengths of the oblate spheroid is estimated to be 0.25 using Ref. [31]. As output of the DDA calculations, we obtain Mueller matrices for all scattering angles. For oblate spheroids, these Mueller matrices are calculated for two extreme orientations (short axis in the direction of the beam and short axis perpendicular to the beam). The M_{11} Mueller matrix elements (isotropic polarization scattering) are integrated over all scattering angles to obtain the scattering cross section and g. The scattering cross sections σ_s are converted to μ_s using the concentration C derived from the measured HCT and MCV values and the relation $\mu_s = C\sigma_s$, no concentration-dependent scattering effects are accounted in this calculation. The average phase function $p(\theta)$ is calculated, using the phase functions $p_0(\theta)$ and $p_{90}(\theta)$ and the scattering coefficients $\mu_{s,0}$ and $\mu_{s,90}$ at the two extreme orientations, according to [32] $p(\theta) = (\mu_{s,0}p_0(\theta) + \mu_{s,90}p_{90}(\theta))/(\mu_{s,0} + \mu_{s,90})$. The results of the calculations are shown in Fig. 21.11.

As expected, the calculated scattering coefficients for blood are significantly higher than the measured OCT scattering attenuation coefficient $\mu_{OCT,s}$. For very low HCT the difference between the calculated scattering coefficient and $\mu_{OCT,s}$ decreases. Figure 21.11a also shows the scattering coefficient determined by Roggan et al. [27] with the integrating sphere method at $\lambda = 1{,}300$ nm and HCT = 5 % for human RBCs. Since the size of human RBCs is close to those of porcine RBCs [33] we expect that this value closely matches our DDA calculations, as is observed. Figure 21.11(b) shows the phase function integrated over the polar angle. The MC simulation uses the calculated RBC orientation-averaged phase function as input. The corresponding scattering anisotropy is $g = 0.98$.

Using the μ_s and phase function calculated with DDA as described above, we performed MC simulations for HCT = 8 %. This is the highest measured HCT below 10 % for which the linear relation between scattering coefficient and concentration holds (see Fig. 21.5 and Refs. [34, 35]) and avoids any concentration-dependent scattering effects.

Figure 21.12 shows the results of the MC simulations calculated with $\mu_s = 27$ mm^{-1} (HCT = 8 %, Fig. 21.11), $\mu_a = 0.37$ mm^{-1}, and the orientation-averaged phase function. MC simulations are shown for the sum of all detected photons and for contributions according to the number of scattering events N a detected photon experienced. As can be seen, higher scattering orders are mainly deeper in the sample. The rise of the OCT signal in the first 100 μm is due to the buildup of higher scattering order signals. At the backside of the cuvette, most of photons have experienced more than 20 scattering events. The decay as a function of depth indicates much lower attenuation of the OCT signal compared to the single scattering model, i.e., $\mu_{OCT,s} = 3.8$ mm^{-1} versus $\mu_s = 27$ mm^{-1}. Remarkably, $\mu_{OCT,s}$ estimated from the MC simulated OCT signal corresponds very well to the experimentally measured value (see Fig. 21.5). In Fig. 21.12b one can see that the Doppler OCT flow profile clearly deviates, albeit by a small amount, from a parabola, especially at the back end of the cuvette due to the multiple scattered photons contribution. Such a small deviation at a relatively high number of scattering events can be only explained by the high g of blood, which results in a very low Doppler shift per scattering event.

Fig. 21.11 (**a**) Orientation-averaged scattering coefficients calculated using DDA for oblate spheroids (shown with *black* color) and measured scattering coefficient $\mu_{OCT,s}$ (*red* color). The value for human RBCs [27] is indicated with a *star*. (**b**) Calculated RBC scattering phase function as a function of azimuthal angle: RBC short axis perpendicular to beam (*dashed light gray*), short axis parallel to beam (*dashed dark gray*), and average (*solid black*)
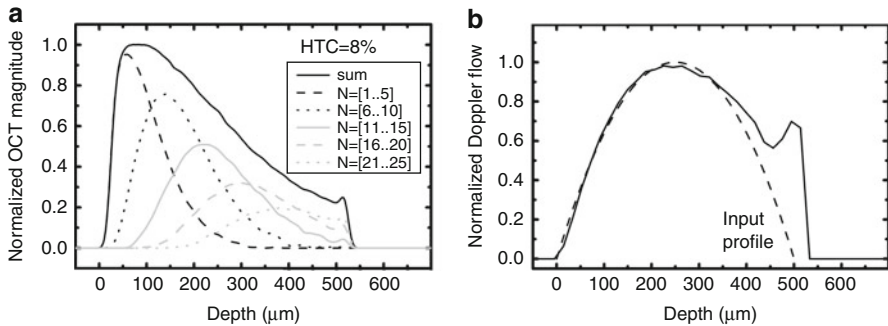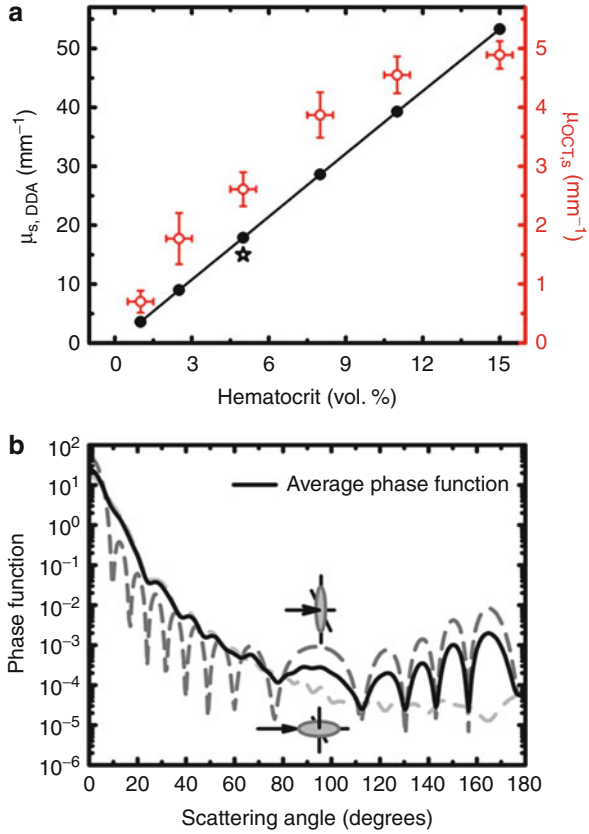
Fig. 21.12 (**a**) MC simulation of OCT signal from the porcine blood with HCT = 8 % for the sum over all photons (*black solid line*), and for different scattering orders N (see legend). (**b**) MC simulation of Doppler OCT signal (*black solid line*), and the input flow profile (*dashed line*)
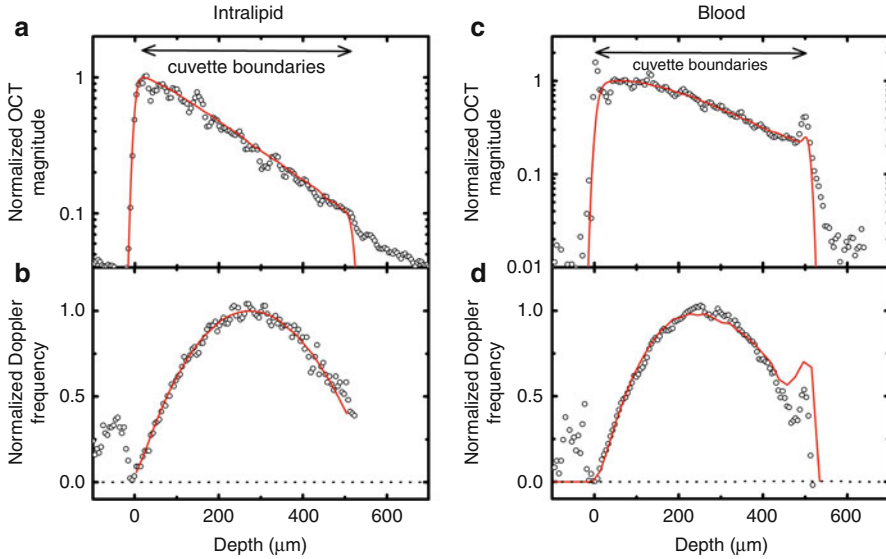
Fig. 21.13 (**a**) and (**b**) show the comparison of the measured OCT and Doppler OCT signals (*open dots*) with the results of MC simulation (*solid line*) (OCT amplitude signal and flow velocity profile) for 23 vol% Intralipid and (**c**) and (**d**) for HCT = 8 % blood

21.7 Comparison of Monte Carlo Simulations and Doppler OCT Measurements

To estimate the scattering coefficient of Intralipid at 23 vol% for which the experimental data and the MC simulation show good agreement, we performed a series of calculations for varying scattering coefficient. Good agreement is observed using $\mu_s = 5.6$ mm^{-1} as input parameter (see Fig. 21.13a). The input μ_s is 15 % higher than the scattering coefficient estimated from the OCT slope with the single scattering model ($\mu_{OCT,s} = 4.9$ mm^{-1}). A relatively good single-exponential fit is also achieved for lower Intralipid concentrations (not shown). From a comparison of our OCT measurements and MC simulations, we conclude that for all Intralipid concentrations the scattering coefficient μ_s is approximately 15 % higher than the measured OCT signal attenuation rate due to multiple scattering effects. The MC simulation of Doppler OCT flow profile is compared to the experimental data and shown in Fig. 21.13b. Good agreement can be observed between the MC simulation and the measurements. Especially notable is that the offset of the flow at the deepest cuvette wall increases with Intralipid concentration in accordance with the measurements.

For blood with HCT = 8 % a good agreement in experimental and simulated OCT signal slopes was obtained with $\mu_s = 27$ mm^{-1}. This value is also predicted by the DDA calculation using the simplified RBC model. The comparison of experimental and simulated data is shown in Fig. 21.13c. The increasing OCT signal at the

first glass/blood interface and the slope of the OCT signal as well as the small peak at the second blood/glass interface are well reproduced by the MC simulation. In Fig. 21.13d it can be observed that the MC simulation of the Doppler OCT flow profile matches the measured flow profile and is close to the single scattering model parabolic flow profile. The increase of the Doppler frequency at the second blood/glass interface is reproduced by the MC simulations albeit that the distortion of the MC simulated flow profile is larger than measured. For Doppler OCT measurements with HCT smaller than 8 %, similar agreement between Doppler OCT measurements and MC simulations is observed with the deviation between the single scattering model and measurements being smaller (not shown).

From our consistent agreement between the simulations and the measurements for both OCT signal attenuation and Doppler OCT data supports the interpretation of our data. Multiple scattering influences flow parameters measured with Doppler OCT such as peak flow, peak flow location, flow volume, and shear rate. To accurately quantify these parameters from Doppler OCT measurements in highly scattering media, multiple scattering effects have to be taken into account.

21.8   Conclusion

In this chapter, we have compared the Doppler OCT signals for low and high scattering media. We have shown that the single scattering model is an appropriate description for low scattering media. For low scattering media, parameters such as the scattering cross section, scattering anisotropy, and Doppler flow profile can be directly determined from the Doppler OCT signal.

For high scattering media, the single scattering model does not describe the OCT signal very well. Usually, the slope of the OCT signal is much lower than the scattering coefficient of the medium and the Doppler OCT flow profile is distorted. Both effects are caused by multiple scattered light that contributes to the OCT signal. The difference between the single scattering model description and the measured Doppler OCT signal depends on parameters of the sample under study (e.g., anisotropy factor) and parameters of the OCT setup (e.g., coherence length). We have shown that the scattering anisotropy is of paramount importance in the quantification of multiple scattering effects. For a medium with low scattering anisotropy (e.g., Intralipid, with $g = 0.32$ at 1,300 nm) the difference between the real scattering coefficient and the scattering coefficient estimated from the slope of the OCT signal is quite small. For the medium with a high scattering anisotropy (e.g., blood, with $g = 0.98$ at 1,300 nm) the scattering coefficient is much higher than predicted from the slope of the OCT signal using the single scattering description. Doppler OCT flow profiles are most strongly distorted at intermediate $g \sim 0.6$.

References

1. F.J. van der Meer, D.J. Faber, D.M. Baraznji Sassoon, M.C. Aalders, G. Pasterkamp, T.G. van Leeuwen, Localized measurement of optical attenuation coefficients of atherosclerotic plaque constituents by quantitative optical coherence tomography. IEEE Trans. Med. Imaging. **24**, 1369–1376 (2005)
2. Z. Chen, T.E. Milner, S. Srinivas, X. Wang, A. Malekafzali, M.J.C. van Gemert, J.S. Nelson, Noninvasive imaging of in vivo blood flow velocity using optical Doppler tomography. Opt. Lett. **22**, 1119–1121 (1997)
3. J.F. de Boer, T.E. Milner, M.J.C. van Gemert, J.S. Nelson, Two-dimensional birefringence imaging in biological tissue by polarization-sensitive optical coherence tomography. Opt. Lett. **22**, 934–936 (1997)
4. D. Huang, E.A. Swanson, C.P. Lin, J.S. Schuman, W.G. Stinson, W. Chang, M.R. Hee, T. Flotte, K. Gregory, C.A. Puliafito, J.G. Fujimoto, Optical coherence tomography. Science **254**, 1178–1181 (1991)
5. J.W. Goodman, *Statistical Optics* (Wiley, New York, 1985)
6. T.G. van Leeuwen, D.J. Faber, M.C. Aalders, Measurement of the axial point spread function in scattering media using single-mode fiber-based optical coherence tomography. IEEE J. Sel. Top. Quant. Electron. **9**, 227–233 (2003)
7. J.M. Schmitt, A. Knüttel, R.F. Bonner, Measurement of optical properties of biological tissues by low-coherence reflectometry. Appl. Opt. **32**, 6032–6042 (1993)
8. C. Akcay, P. Parrein, J.P. Rolland, Estimation of longitudinal resolution in optical coherence imaging. Appl. Opt. **41**, 5256–5262 (2002)
9. V.M. Kodach, J. Kalkman, D.J. Faber, T.G. van Leeuwen, Quantitative comparison of the OCT imaging depth at 1300 nm and 1600 nm. Biomed. Opt. Express **1**, 176–185 (2010)
10. M. Daimon, A. Masumura, Measurement of the refractive index of distilled water from the near-infrared region to the ultraviolet region. Appl. Opt. **46**, 3811–3820 (2007)
11. A. Unterhuber, B. Povazay, B. Hermann, H. Sattmann, W. Drexler, V. Yakovlev, G. Tempea, C. Schubert, E.M. Anger, P.K. Ahnelt, M. Stur, J.E. Morgan, A. Cowey, G. Jung, T. Le, A. Stingl, Compact, low-cost Ti:Al$_2$O$_3$ laser for in vivo ultrahigh-resolution optical coherence tomography. Opt. Lett. **28**, 905–907 (2003)
12. H.J. van Staveren, C.J.M. Moes, J. van Marle, S.A. Prahl, M.J.C. van Gemert, Light scattering in Intralipid-10 % in the wavelength range of 400–1100 nm. Appl. Opt. **30**, 4507–4514 (1991)
13. C. Chen, J.Q. Lu, H. Ding, K.M. Jacobs, Y. Du, X. Hu, A primary method for determination of optical parameters of turbid samples and application to intralipid between 550 and 1630 nm. Opt. Express **14**, 7420–7435 (2006)
14. J. Kalkman, A.V. Bykov, D.J. Faber, T.G. van Leeuwen, Multiple and dependent scattering effects in Doppler optical coherence tomography. Opt. Express **18**, 3883–3892 (2010)
15. L. Wang, Y. Wang, S. Guo, J. Zhang, M. Bachman, G.P. Li, Z. Chen, Frequency domain phase-resolved optical Doppler and Doppler variance tomography. Opt. Commun. **242**(4–6), 345–350 (2004)
16. L. Thrane, H.T. Yura, P.E. Andersen, Analysis of optical coherence tomography systems based on the extended Huygens–Fresnel principle. J. Opt. Soc. Am. A **17**(3), 484–490 (2000)
17. D.J. Faber, T.G. van Leeuwen, Are quantitative attenuation measurements of blood by optical coherence tomography feasible? Opt. Lett. **34**(9), 1435–1437 (2009)
18. R.K. Wang, Signal degradation by multiple scattering in optical coherence tomography of dense tissue: a Monte Carlo study towards optical clearing of biotissues. Phys. Med. Biol. **47**(13), 2281–2299 (2002)
19. H.T. Yura, L. Thrane, P.E. Andersen, Analysis of multiple scattering effects in optical Doppler tomography. Proc. SPIE **5861**, 5861B (2005)
20. A.V. Bykov, M.Y. Kirillin, A.V. Priezzhev, Monte Carlo simulation of an optical coherence Doppler tomography signal: the effect of the concentration of particles in a flow on the reconstructed velocity profile. Quant. Electron. **35**(2), 135–139 (2005)

21. J. Moger, S.J. Matcher, C.P. Winlove, A. Shore, The effect of multiple scattering on velocity profiles measured using Doppler OCT. J. Appl. Phys. D. **38**(15), 2597–2605 (2005)
22. T.G. van Leeuwen, M.D. Kulkarni, S. Yazdanfar, A.M. Rollins, J.A. Izatt, High-flow-velocity and shear-rate imaging by use of color Doppler optical coherence tomography. Opt. Lett. **24**(22), 1584–1586 (1999)
23. G. Göbel, J. Kuhn, J. Fricke, Dependent scattering effects in latex-sphere suspensions and scattering powders. Waves Rand. Comp. Med. **5**, 413–426 (1995)
24. G. Zaccanti, S. Del Bianco, F. Martelli, Measurements of optical properties of high-density media. Appl. Opt. **42**, 4023–4030 (2003)
25. R. Michels, F. Foschum, A. Kienle, Optical properties of fat emulsions. Opt. Express **16**, 5907–5925 (2008)
26. M. Friebel, M. Meinke, Determination of the complex refractive index of highly concentrated hemoglobin solutions using transmittance and reflectance measurements. J. Biomed. Opt. **10**, 064019 (2005)
27. A. Roggan, M. Friebel, K. Dörschel, A. Hahn, G. Müller, Optical properties of circulating human blood in the wavelength range 400–2500 nm. J. Biomed. Opt. **4**, 36–46 (1999)
28. L. Wang, S.L. Jacques, L. Zheng, MCML – Monte Carlo modeling of light transport in multi-layered tissues. Comput. Methods Programs Biomed. **47**(2), 131–146 (1995)
29. A.N. Yaroslavsky, I.V. Yaroslavsky, T. Goldbach, H.-J. Schwarzmaier, Influence of the scattering phase function approximation on the optical properties of blood determined from the integrating sphere measurements. J. Biomed. Opt. **4**(1), 47–53 (1999)
30. M.A. Yurkin, V.P. Maltsev, A.G. Hoekstra, The discrete dipole approximation for simulation of light scattering by particles much larger than the wavelength. J. Quant. Spectrosc. Radiat. Transfer **106**, 546–557 (2007)
31. A.V. Cardoso, A.O. Camargos, Geometrical aspects during formation of compact aggregates of red blood cells. Mater. Res. **5**, 263–268 (2002)
32. V.M. Kodach, D.J. Faber, J. van Marle, T.G. van Leeuwen, J. Kalkman, Determination of the scattering anisotropy with optical coherence tomography. Opt. Express **19**, 6131–6140 (2011)
33. J.E. Smith, N. Mohandas, S.B. Shohet, Variability in erythrocyte deformability among various mammals. Am. J. Physiol. **236**, 725–730 (1979)
34. J.M. Steinke, A.P. Shepherd, Role of light scattering in whole blood oximetry. IEEE Trans. Biomed. Eng. **33**, 294–301 (1986)
35. M. Meinke, G. Müller, J. Helfmann, M. Friebel, Empirical model functions to calculate hematocrit-dependent optical properties of human blood. Appl. Opt. **46**, 1742–1753 (2007)

Optical Coherence Tomography: Principles and Applications of Microvascular Imaging

22

Beau A. Standish, Adrian Mariampillai, Michael K. K. Leung, and
I. Alex Vitkin

Contents

B.A. Standish (✉) • A. Mariampillai
Department of Electrical and Computer Engineering, Ryerson University, Toronto, Canada
e-mail: standish@ee.ryerson.ca, a.mariampillai@ryerson.ca

M.K.K. Leung
Departments of Medical Biophysics and Radiation Oncology, University of Toronto, Toronto,
Canada
e-mail: michaelkk.leung@utoronto.ca

I.A. Vitkin
Departments of Medical Biophysics and Radiation Oncology, University of Toronto, Toronto,
Canada

Division of Biophysics and Bioimaging, Ontario Cancer Institute/University Health Network,
Toronto, Canada
e-mail: Alex.Vitkin@rmp.uhn.on.ca

Abstract

Microvascular detection and quantification with optical coherence tomography is an exciting and growing research field and is the topic of this chapter. Specifically, the fundamental principles of OCT microvascular imaging are described, encompassing phase-resolved and power-based methods, and the use of exogenous contrast agents. Representative biomedical applications of microvascular OCT imaging are presented, with emphasis on treatment monitoring and tissue response assessment. A discussion of outstanding challenges and future outlook concludes the chapter.

22.1 Introduction

A healthy vascular supply is essential for normal function in biological tissues, whereas anomalies in the vascular supply are associated with disease processes such as abnormal cellular proliferation in cancer [1], age-related macular degeneration [2], and atherosclerosis [3]. Of these examples, cancer represents one of the most diverse environments for neovasculature as the pathophysiology of solid tumors constantly recruits and develops new microvascular networks in a process called tumor angiogenesis. If these modified vascular networks can be identified early in the disease progression, then appropriate risk stratification/screening strategies may benefit patient management; further, therapies aimed at disrupting the neovascular supply, and monitoring the efficacy of this disruption, may enable more efficacious treatments.

Tumor vessels are chaotic, lack hierarchy, and exhibit abnormal spatial patterns and volumetric densities. Tumor endothelial cells lining its vessel walls also have different phenotypic properties compared to those in normal vasculature [4]. As a consequence, tumor vasculature has functional abnormalities such as unstable velocity and direction of blood flow, high vascular resistance, and structural fragility. Furthermore, flow is often erratic, displaying stasis or even reversal in certain vessels [5]. As there are such drastic differences between normal and tumor blood vessels, these may provide contrast mechanisms for the detection of cancer (potentially at its premalignant or early stage) along with monitoring strategies for developing and optimizing vascular-targeted therapies.

Clinical imaging methods such magnetic resonance imaging (MRI), computed tomography (CT), positron emission tomography (PET), and ultrasound (US) all have the ability to detect various aspects of tissue blood flow but lack the spatial resolution to directly image the microscopic vascular structures such as capillaries, venules, arterioles, or the lymphatic vessels. Therefore, the scope of this book chapter will focus on optical methods that can detect in vivo microvascular networks. Currently, vascular detection and assessment methods used for cancer prognosis largely rely on ex vivo microscopic examination of static vessel structures in resected tissue specimens. Following biopsy and fixation, vessels are stained, and metrics such as planar 2D microvessel density (MVD, used to assess

tumor angiogenesis) and 2D intercapillary distance (ICD, thought to indicate tumor oxygenation) are derived [6]. In several human tumor types, particularly breast cancer, these can serve as independent prognostic factors to predict relapse-free and overall survival in patients [7]. MVD can also be used to stratify patients for different treatment regimes and may be predictive of their response to chemotherapy [8]. One method to obtain these vascular metrics is by counting individual or clusters of endothelial cells lining the insides of the vessel walls. Usually, only regions with the highest MVD, or "hot spots," are analyzed on the purported basis that these areas are most biologically important [7].

This histological "gold standard" for microvascular assessment has many important flaws. It is disruptive and painful to the patient, suffers from poor sampling statistics associated with localized tissue excision, is limited to 2-dimension (2D) analysis of thin planar tissue slices, reports on vessel anatomy and structure, and is generally unable to provide useful information on blood flow physiology and or functionality. Furthermore, the counting process is laborious, somewhat subjective, and is prone to variations in the number of vessels highlighted by the staining process depending on the antibody used [9]. Hence, MVD and other vessel architectural metrics are difficult to use and incorporate into the existing patient management process supported by standard pathology services. These histologically derived detection methods have a major additional shortcoming in that they are not practical for continuous patient monitoring, as physical biopsy specimens are required. Therefore, there exists an extensive opportunity to develop new noninvasive in vivo imaging techniques to compliment biopsy for tissue microvascular detection, such as high-resolution optical imaging strategies to directly visualize microcirculation details. This represents a paradigm shift from the ex vivo, geometrical/anatomical assessment of the tissue microvasculature (as reported by histology) for tumor detection/diagnosis and therapy response, to that of in vivo physiologically relevant metrics of blood perfusion. Several promising in vivo optical techniques, such as diffuse correlation spectroscopy, confocal microscopy, laser speckle contrast imaging, and optical coherence tomography, are under development to detect and quantify microvascular blood flow. These and other promising novel approaches (e.g., photoacoustics [10, 11]) may assume a significant role in biomedicine through detection, quantification, and response monitoring of various pathologies with significant microvascular involvement.

22.2   Brief Overview of Optical Vascular Detection Methods and Representative Uses

Diffuse correlation spectroscopy (DCS) has been used in vivo to monitor the relative blood flow fraction (rBF) as a function of various treatment parameters in photodynamic therapy (PDT, see Sect. 22.5.2) in animal tumor models, with promising correlations to the biological endpoint of tumor growth delay [12]. The major components of a DCS system are a CW laser, a non-contact probe with multiple delivery and detector fibers, and a camera to collect the diffusely reflected

light [13]. Employing an optical switching methodology, the light is directed through each of the source delivery fibers in a consecutive manner, followed by collection via the detection fibers. The detected signal intensity fluctuations of the diffuse light are sensitive to the motion of tissue scatterers within the sampled volume of tissue for the particular excitation – detection fiber geometry – and hence can give a relative indication of blood flow within the interrogated volume of tissue. For example, Yodh et al. [12] have shown that PDT-induced changes in the DCS-derived rBF metric were predictive of the treatment response. Specifically, mice that exhibited a slower decline in the rBF during the PDT treatment went on to have slower-growing tumors. An advantage of this technique is that it can continuously and noninvasively monitor tissue blood flow, as the probes do not require contact with tissue. However, this technique has several disadvantages; for example, the overall size of the DCS distal probe implies that primarily only near-surface regions contribute to the detected signal. Moreover, DCS is a bulk tissue assessment tool, presenting its metrics averaged over the sampling volume. In other words, it lacks the ability to resolve localized regions of tissue blood flow, since the technique does not directly image or visualize the tissue microvasculature. This is potentially an important limitation: in vascular-targeted therapies, such as prostate PDT, for example, optimal monitoring techniques should be able to provide spatially resolved (laterally and in-depth) local vascular feedback for targeted pathology regions or for nearby organs at risk, such as sensitive urethral or rectal wall structures.

Confocal microscopy is a widely used optical microscopy technique for examining tissue that has been resected, preserved, and histologically stained to yield submicron resolution images, with the additional benefit of functional assessment via fluorescent markers. This technique is the gold standard for imaging ex vivo tissue microvasculature referred to earlier, where bloods vessels can be identified through the histochemical staining of vascular endothelial cells [14]. The functionality of vessels can be assessed using exogenous contrast agents that are injected into the circulatory system prior to tissue excision and fixation. In addition to its important ex vivo microscopy role, several attempts at its in vivo extension have been recently reported in the context of intravital microscopy and microendoscopy [15, 16]. There have been a limited number of in vivo preclinical animal models, where intravital multiphoton confocal microscopy (MPCM) has been used in conjunction with fluorescence vascular contrast agents (e.g., FITC dextran) to image the microvascular network [17, 18]. However, MPCM suffers from a number of drawbacks that severely limits this technology to preclinical imaging scenarios and will impede its potential clinical adoption: (1) MPCM is slow (e.g., a 5 mm × 5 mm region can take ∼1 h to image); (2) fluorescent dyes can be difficult to work with in a patient setting (safety and regulatory issues), and their leaking out of the vascular network makes longitudinal imaging difficult; and (3) the exquisite axial and lateral resolution (submicron level) comes at a cost of limited depth of penetration (<400 μm).

Laser speckle contrast imaging (LSCI) is another optical approach that was developed in the 1980s, where full-field tissue images are acquired by a camera,

obtaining a quick snapshot of the speckle pattern [19]. The surface region of tissue is then imaged over subsequent snapshots, where blood flow can be inferred from the calculated spatial and temporal statistics of the resultant speckle modulation pattern. The LSCI technique has matured over the last 20 years, with success in imaging blood flow in the skin and excellent potential for monitoring brain function in animal models. The former was one of the original clinical applications of LSCI [20], using it as a feedback mechanism to optimize the laser therapy of port wine stain [21].

Similar to DCS, one of the drawbacks of LSCI is the inherent lack of depth resolution. Despite this limitation, LSCI has demonstrated particular utility in imaging the brain, when a portion of the skull is thinned or removed in animal models. As the majority of the microvascular network of the brain is superficial, LSCI has been used to monitor the changes in cerebral blood flow to map the oxygenation of the brain following sensory activation [22]. Subsequently, LSCI imaging has become a very useful tool for stroke research and for monitoring cerebral blood flow changes in the ischemic brain tissue in several animal models [23, 24]. For example, LSCI was used to monitor the collateral blood flow during acute stroke in a rat, highlighting the potential benefits of identifying the presence of collateral blood flow in selecting appropriate poststroke therapies [22]. The LSCI technique is inexpensive and easy to implement, readily yielding. However, the advantage of LSCI's inherent camera-based quick full-field imaging is also a disadvantage: it has proven difficult to package the LSCI platform into intracavity, endoscopic, or interstitial imaging scenarios, limiting its range of potential clinical uses to readily reachable surfaces. This, in combination with the lack of subsurface-depth-resolved information, will likely limit its biomedical uses to near-surface and small animal imaging.

Optical coherence tomography (OCT) is a promising emerging imaging modality that overcomes several limitations of the above vascular detection techniques and will be the focus of this chapter. Specifically, OCT is portable and inexpensive, can obtain high-resolution depth-resolved topographic images, is sensitive to blood flow down to the capillary level, and has recently become commercially available, with demonstrated variety of clinical uses and successes (e.g., ophthalmology, as discussed below). Its major drawback is arguably its limited imaging depth (1–3 mm in most tissues), so care must be taken in selecting imaging scenarios where this penetration depth probes suitable tissue of interest (e.g., mucosal linings of various body cavities, intravascular plaque assessment, retinal imaging, and model studies in small animals). OCT is somewhat analogous to ultrasound, but instead of backscattered pressure waves, OCT measures backscattered photons. Interferometric detection is used, relying on coherence gating (thus the "C" in OCT) to obtain depth-resolved information, thereby avoiding the difficult task of directly measuring the time of flight of the backscattered light. Recent state-of-the-art OCT systems have demonstrated submicron spatial resolutions [25], allowing for the in vivo detection of subcellular features. Additionally, several OCT vascular detection approaches have been developed to move beyond structural imaging. We will now describe their scientific fundamentals along with selected illustrative examples of preclinical/clinical applications.

22.3   Microvascular Imaging with Optical Coherence Tomography

Over the past decade, there have been many advances in tissue microvascular imaging using OCT. Algorithms and techniques developed over this time period can be broadly divided into two groups: (1) those that attempt to quantify blood flow (e.g., velocity, direction) and (2) those that simply visualize microvasculature. (1) The majority of the techniques that attempt to quantify velocity, such as color Doppler imaging, are based on measuring the mean frequency shift induced by moving scatterers (red blood cells) across multiple A-scans [26, 27]. It is also possible to measure flow rates by examining speckle spatial frequencies in OCT intensity (B-mode) images [28]. However, this approach is only able to estimate the flow rate to within an arbitrary scaling factor. (2) On the other hand, the methods developed to only visualize, but not quantify, vascular flow measure the power (intensity) in the signal attributed to moving scatterers. These techniques include power Doppler, optical microangiography, intensity-modulated phase variance, and speckle variance [29–32].

To obtain an intuitive understanding of how these two different classes of measurement techniques are related, it is useful to consider the simple imaging scenario in which a planar reflector is moving with constant velocity in the direction of the optical axis. For frequency domain OCT, the measured signal from this target at time $t = 0$ and $t = \tau$ can be written as

$$I(0, k) = 2S(k)E_R a(z_1) \cos[2knz_1] \tag{22.1}$$
$$I(\tau, k) = 2S(k)E_R a(z_1) \cos[2kn(z_1 - v\tau)].$$

Here, $S(k)$ is the source spectrum, E_R is the light reflected from reference arm, $a(z_1)$ is the reflectivity of the plane reflector located at position z_1, n the index of refraction of the medium, and v the velocity of the planar reflector. These equations describe a translating set of fringes (i.e., sequentially obtained at offset lateral positions) in time for a frequency domain system. The basic principles of OCT Doppler detection employing a subset of the N A-scans acquired from the reflector at the depth z_1 are shown in Fig. 22.1.

The sampled signal traced out along the dashed black line (single k value) is termed the slow-time signal. Its mean angular frequency can be calculated from the power spectrum, $P(\omega)$, of the slow-time signal using

$$\varpi = \frac{\int \omega P(\omega) d\omega}{\int P(\omega) d\omega}. \tag{22.2}$$

This mean frequency $f = \varpi/2\pi$ of the slow-time signal is commonly referred to as the Doppler frequency, f_D, and can be related to the velocity of the moving plane reflector by

$$v = \frac{\lambda f_D}{2n}. \tag{22.3}$$
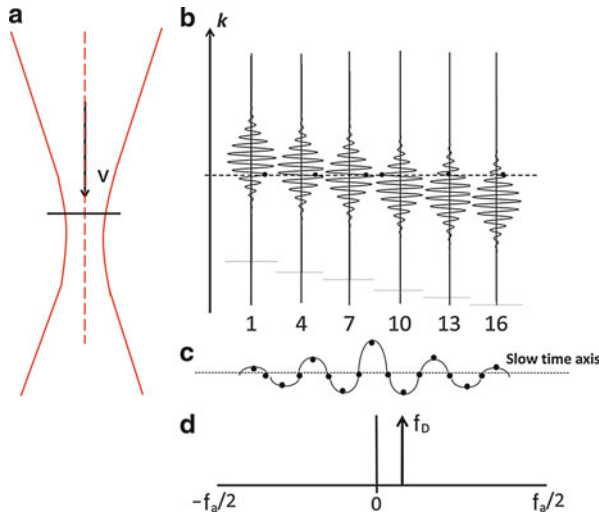
Fig. 22.1 Principles of OCT Doppler imaging. (**a**) A simple reflector propagating with a velocity v along the interrogating beam. (**b**) Subset of acquired fringes from the sample, the *green dashed line* representing the depth location of interest. The numbers label the sequential depth scans (referred to as A-scans). (**c**) The slow-time signal, with its sampled points at positions where the labeled A-scans in (**b**) intersect the *dashed green line* (points from additional A-scans also shown). (**d**) Power spectrum of the slow-time signal, where f_a is the A-scan rate of the OCT system

In the more general case where the reflector is moving at an angle θ with respect to the optical axis, the velocity is given by

$$v = \frac{\lambda f_D}{2n \, \cos(\theta)} \tag{22.4}$$

The Doppler frequency is most commonly measured through an autocorrelation approach, which calculates the phase shift between sequential A-scans, as discussed in the following section.

Alternatively, instead of measuring the frequency of the slow-time signal, one could also estimate the power in the slow-time signal corresponding to moving scatterers. This concept becomes the basis for power-based methods:

$$I_{PD} = \int P(\omega)d\omega. \tag{22.5}$$

In the idealized example of Fig. 22.1, all of the power is contained in the frequency band centered at f_D. In reality, the OCT field of view will encompass both moving (mostly blood) and stationary (mostly tissue) scatterers, and the power spectrum will have additional complicating features. A more accurate schematic of the slow-time power spectrum, although still idealized, is shown in Fig. 22.2.
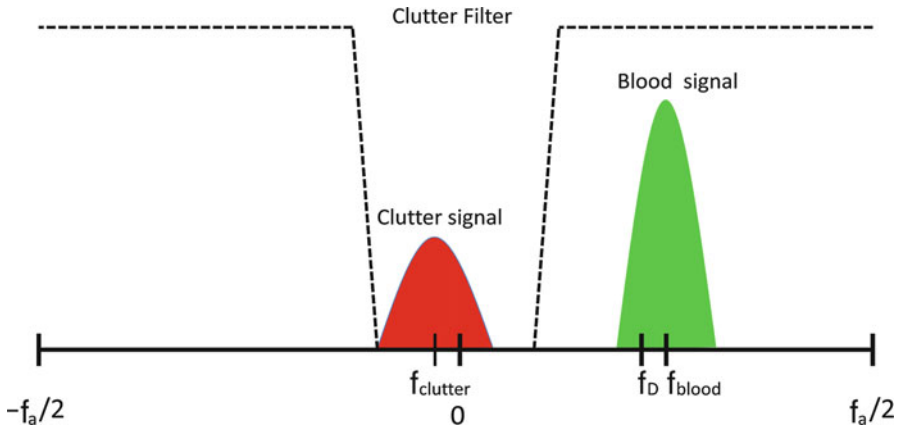
Fig. 22.2 Schematic power spectrum of slow-time signal from B-mode image of tissue. The moving blood signal is centered about f_D, and the tissue clutter signal is centered about $f_{clutter}$. If the background tissue is truly stationary, the latter is centered about zero frequency. Often, there is also bulk tissue motion, causing a shift in the $f_{clutter}$ distribution away from the baseband. In the illustration above, the tissue is moving away from the interrogating beam, hence the negative frequency location of the clutter signal. The *dotted lines* represents an idealized clutter rejection band-stop filter that suppresses the clutter signal frequencies, in order to generate accurate Doppler images representative of tissue blood flow

The spectrum now has two components: (1) tissue scatterers, generally termed clutter, with mean frequency $f_{clutter}$ and (2) moving scatterers in the blood with mean frequency f_{blood}. As described in the figure caption, the clutter signal arises from stationary tissue but can also have a bulk tissue motion component. In the presence of clutter, an estimate of the mean frequency f_D, using (22.1), (e.g., as needed for color Doppler imaging) will be distorted by the presence of the stationary or slowly moving tissue signal. However, this distortion is generally negligible for mean frequency measurements, as the OCT voxel size ($\sim$10 μm $\times$ 10 μm $\times$ 10 μm) is small enough that it can be considered to be fully filled with blood or not at all (i.e., both clutter and blood signals are unlikely to be present in the same voxel). On the other hand, estimation of the power in these clinically relevant situations must account the presence of the clutter spectrum, with a band-stop filter (also referred to clutter filters or wall filters in the ultrasound literature) applied to remove it (dotted line in Fig. 22.2), before the power in the remaining blood signal can be accurately calculated and displayed. Thus, to accurately estimate the slow-time signal frequency and power, a number of different factors must be considered to yield optimized blood flow detection as follows:

1. The number of slow-time samples used in the estimates and the time between successive samples
2. Finite displacement between adjacent A-scans resulting from lateral scanning schemes (which induce broadening of the slow-time signal spectrum)
3. The presence of static or slowly moving scattering structures (tissue clutter)

In the next two sections, the implications of these factors on the measurement of the mean frequency and power will be discussed.

22.3.1 Phase-Resolved Methods

When acquiring two A-scans taken at the same position at slightly different times, the slow-time (Doppler) frequency can be estimated by measuring the phase shift, in the direction of the optical beam, which is induced by the scattering particles using autocorrelation analysis. To perform the autocorrelation analysis, two or more consecutive A-scans are acquired from approximately the same location. Typically, using a larger number of samples (e.g., $N = 16$ or 32) improves the estimate of the phase shift, where N is referred to as the packet length. The frequency of the slow-time signal can then be related to the phase shift via the equation

$$f_d = \Omega f_a, \tag{22.6}$$

where Ω is the measured phase shift and f_a is the A-scan rate (assuming a linear change of phase with time) over the time interval $\Delta t = 1/\mathfrak{f}_a$.

In practice, the Doppler frequency can be estimated using the Kasai velocity estimator [33]

$$f_d = \frac{f_a}{2\pi} \arctan \left\{ \frac{\frac{1}{M(N-1)} \sum_{m=1}^{M} \sum_{n=1}^{N-1} I_{m,n+1} Q_{m,n} - Q_{m,n+1} I_{m,n}}{\frac{1}{M(N-1)} \sum_{m=1}^{M} \sum_{n=1}^{N-1} Q_{m,n+1} Q_{m,n} + I_{m,n+1} I_{m,n}} \right\}. \tag{22.7}$$

Here, I and Q are the in-phase and quadrature components of the demodulated detector signal, and m is the axial averaging index. The index n represents adjacent A-scans in the lateral direction, in which the autocorrelation analysis takes place. This estimator provides a computationally efficient way to estimate the Doppler shift over a packet length of N A-scans [26]. Figure 22.3 shows an example of structural and color Doppler imaging from the heart of *Xenopus laevis* tadpole employing this phase-resolved flow detection technique. Due to the limited A-scan frequency of the OCT system used in this experiment (16 kHz), aliasing occurred in the spiral valve of the truncus arteriosus (TA), where detected frequencies were greater than the aliasing frequency of $f_a/2$ (from [34]).

A number of factors influence the sensitivity (minimum measurable phase shift and thus minimum detectable blood velocity) of a Doppler OCT system. Most important is the influence of the structural signal-to-noise ratio (SNR) on the Doppler noise floor. To estimate the SNR-limited Doppler noise floor, consider the simple theoretical model, which defines the SNR as

$$SNR = \left(\frac{\overrightarrow{|E|}}{\overrightarrow{|n|}} \right)^2. \tag{22.8}$$
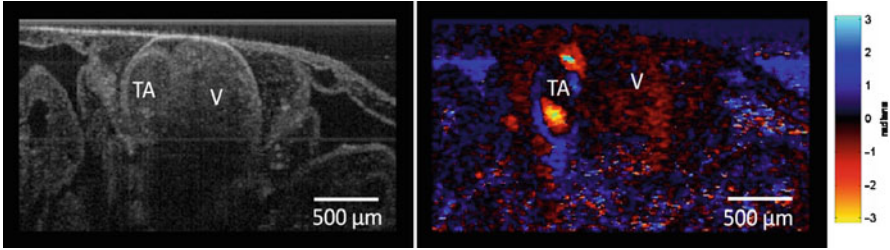
Fig. 22.3 Structural and Doppler flow image showing blood being ejected out of the truncus arteriosus (TA) in the *Xenopus laevis* tadpole heart. To the right of the truncus arteriosus is the ventricle (V)

Here, $\vec{n}$ is a random noise vector and $\vec{E}$ is the reflected electric field at the detector. In the regime where high *SNR* is observed ($|E| \gg |n|$), the standard deviation of the phase shift between two A-scans is given by [29]

$$\sigma_{\Delta\varphi} = \frac{1}{SNR^{1/2}}. \tag{22.9}$$

The SNR-limited phase noise is the lowest phase shift that can be measured between two A-scans. For optimal Doppler detection, the system should always be operating as close to this threshold as possible.

Another important factor that contributes to the DOCT noise floor is the fact that the majority of OCT systems use only a single linearly scanned beam to generate B-mode images; in other words, consecutive A-scans are not sampling exactly the same spatial location. This introduced lateral displacement between each A-scan during B-mode imaging, which increases the Doppler noise floor (broadening of the clutter signal spectrum) [26]. Standard protocols to minimize these effects include extensive lateral oversampling. However, this reduces the effective frame rate of the system [35, 36]. A related noise issue is that of physiological motion (sometimes referred to bulk tissue motion), which can shift the center frequency of the clutter spectrum. This can make it very difficult to interpret color Doppler images, due to large bulk phase shifts that are superimposed on the Doppler signals. A number of techniques have been developed to address this problem, where two of the most commonly used include (1) the simple subtraction of the mean phase shift from each line in the Doppler image and (2) the histogram rejection technique [35, 37].

It is important to note that ongoing technical advances in Fourier-domain OCT systems (faster swept sources and/or spectrometers) for volumetric OCT imaging can actually be counterproductive for phase-resolved Doppler detection, as these blood flow measurement schemes require phase buildup between successive A-scans. Therefore, as the time between consecutive A-scans becomes smaller (inversely proportional to the A-scan rate of OCT system), there is less time for a measurable phase difference to be measured. In the best-case scenario, when the

phase noise floor remains constant, as the A-scan rate increases, there is a linear reduction in the minimum detectable velocity. This can be overcome by a proportional increase in the packet length N (number of A-scans used in the Kasai, or other, velocity estimator). However, this slows the imaging frame rate, diminishing the advantages afforded by increased A-scan rates.

Typical minimum detectable velocities for phase-resolved methods lie in the range of 100–500 μm/s. These values are directly dependent on the imaging system and sample characteristics for signal detection. Physiologically, this lower limit implies phase-resolved methods are able to detect flow in larger arterioles and venules, but smaller vessels and capillaries will not be detected. Although the phase-resolved methods suffer from a variety of complication as mentioned above (along with additional complications arising from Doppler angle requirements and aliasing), phase-resolved methods do provide a robust method of calculating blood flow velocity in OCT.

22.3.2 Power-Based Methods

Power Doppler OCT (PD-OCT) imaging was first applied to time-domain OCT systems [26, 38]. PD-OCT is based on first filtering out the stationary or slowly moving tissue component (clutter) of the slow-time power spectrum using a high-pass filter and subsequently quantifying the remaining signal intensity. In the idealized case shown in Fig. 22.2, the clutter rejection filter centered at zero frequency has sufficient bandwidth to remove the clutter signal (centered at $f_{clutter}$), while leaving the Doppler signal from blood (centered at f_{blood}) unaffected. In practical in vivo imaging scenarios, it is crucial to match the clutter filter characteristics to that of the clutter signal in order to obtain sufficient rejection of the tissue clutter components. This filter matching is complicated by the same factors that degrade color Doppler imaging: low SNR and the use of a linearly scanned beam that broadens the clutter spectrum. Therefore, a broader bandwidth clutter rejection filter must be used, which inevitably removes a finite fraction of the low velocity blood signals. Bulk tissue motion shifts the center of the clutter spectrum in a motion-dependent fashion, necessitating the use of adaptive filters which compensate for these effects [39] or the use of very broad band filters. Finally, as in the case of phase-resolved methods, the ever-increasing OCT A-scan speeds afforded by faster lasers and spectrometers allow very little time for the slow-moving blood spectrum to separate from the clutter spectrum, resulting in partial removal of the blood spectrum signal by the clutter signal filter.

Recently, a technique known as optical angiography (OAG) has also been developed for frequency domain OCT [30]. This technique is similar to PD-OCT except that the filtering of the tissue clutter, from the slow-time power spectrum, occurs in the frequency domain via a Hilbert transform [30]. Overall, the greatest benefit of power Doppler and OAG imaging, compared to phase-sensitive techniques, is that averaging multiple lines and frames from the same location (an approach known as persistence in ultrasonography) increases the system's
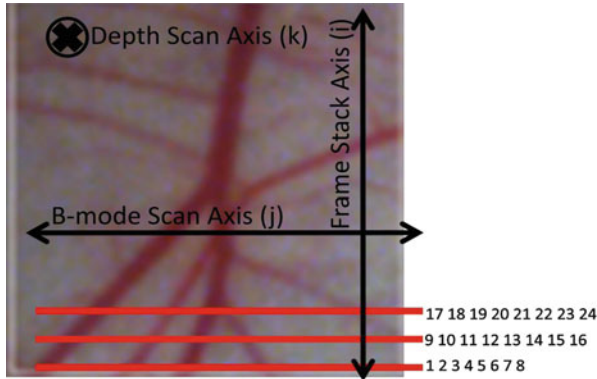
Fig. 22.4 Interframe scanning pattern used to perform high-sensitivity vascular imaging with techniques such as speckle variance (SV) OCT. Acquisition of multiple B-mode frames at each location (indicated by their numerical index on the *right* of the figure, at a representative B-mode location) minimizes decorrelation of static structures, thus maximizing vascular contrast

sensitivity to smaller vessels. Additionally, PD-OCT imaging does not suffer from aliasing and angle dependence as seen in CD-OCT, making it easier to interpret for real-time application where flow velocity is not needed. PD-OCT can also be color-coded to indicate the directionality of flow. This is accomplished by first applying the clutter filter and then applying a filter that either removes all positive components or negative components resulting in two separate power Doppler images – one that displays only positive components of the power spectrum and one that only displays the negative components. These two images are typically color-coded red and blue, respectively, and merged into a single directional power Doppler image [40].

However, even with the use of large amounts of averaging, the smallest vessels cannot be detected using standard PD-OCT techniques, as current OCT A-scan rates (on the order of tens of kHz) do not allow enough time for the blood flow spectrum to separate from the low-frequency tissue clutter spectrum. An elegant solution is to move away from intraframe measurements (where the slow-time sampling frequency is f_a) to interframe techniques (axis i in Fig. 22.4) This increases the integration time between successive measurements, allowing the blood scatterers to move sufficient physical distances to uncouple f_D signals from $f_{clutter}$ signals.

This idea forms the basis for OCT techniques such as ultrahigh-sensitivity OMAG (UHS-OMAG) [41], phase variance [29], intensity-modulated phase variance [31], and speckle variance (SV) [32]. In these techniques, where the interframe time between measurements becomes large, the blood component of the slow-time power spectrum (now in the frame direction) becomes uniformly distributed in frequency, as shown in Fig. 22.5. This uniform distribution of phases arises from complete decorrelation of the OCT signal, on the order of the interframe timescale.

Clutter signals can now be filtering out using a high-pass filter, leaving the power associated with moving blood scatterers to generate highly sensitive vascular maps.
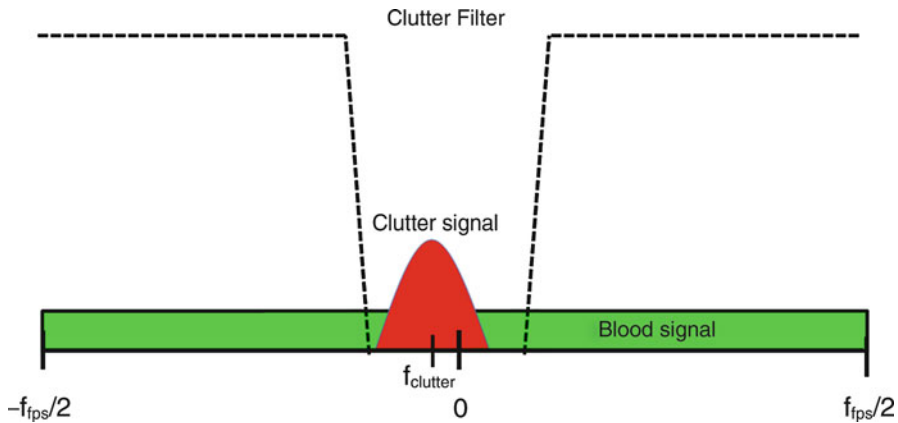
Fig. 22.5 Power spectrum of slow-time signal taken in the frame stack direction. The effective sampling rate now becomes the frame rate of the system in frames per second (fps)

For example, the algorithm for generating speckle variance images requires calculating the variance of pixels from a set of N B-mode images (here, N is known as the gate length), acquired from the same spatial location using the equation

$$SV_{ijk} = \frac{1}{N} \sum_{i=1}^{N} \left(I_{ijk} - \frac{1}{N} \sum_{i=1}^{N} I_{ijk} \right)^2. \tag{22.10}$$

Here, i, j, and k are indices for the frame, transverse, and axial pixels, respectively, and I is the corresponding pixel intensity value. For clarity, a schematic representation of a typical data set and pixel indices is shown in Fig. 22.6.

Figure 22.7 demonstrates a highly sensitivity color-coded vascular projection map of a tumor obtained with the above SV-OCT approach. Features closest to the surface have been encoded as green yellow, while deeper features are encoded with orange red, and the transparency of each pixel is determined by the speckle variance intensity [42]. As seen, these blood flow detection techniques now have the ability to directly visualize the 3D capillary bed in vivo to a depth of ∼1 mm. The next section discusses further improvements in the robustness of this approach (especially in the presence of tissue motion) and imaging depth (potentially with the introduction of exogenous contrast agents).

The recent development of interframe power-based blood flow detection techniques has enabled hitherto unavailable in vivo sensitive detection of the entire vascular network throughout several millimeters of tissue. These new approaches, in combination with high A-scan rate Fourier-domain OCT systems, have yielded imaging tools that are capable of providing 3D morphological and vascular data sets in mere seconds. This unprecedented ability to provide volumetric vascular perfusion maps in vivo may have widespread preclinical and clinical applications, ranging from model small animal studies to wound healing to disease detection to

Fig. 22.6 Schematic
representation of an acquired
speckle variance data set of *N*
frames, and the corresponding
indices used to label the frame
(*i*), transverse pixel location
(*j*), and the axial pixel
location (*k*)
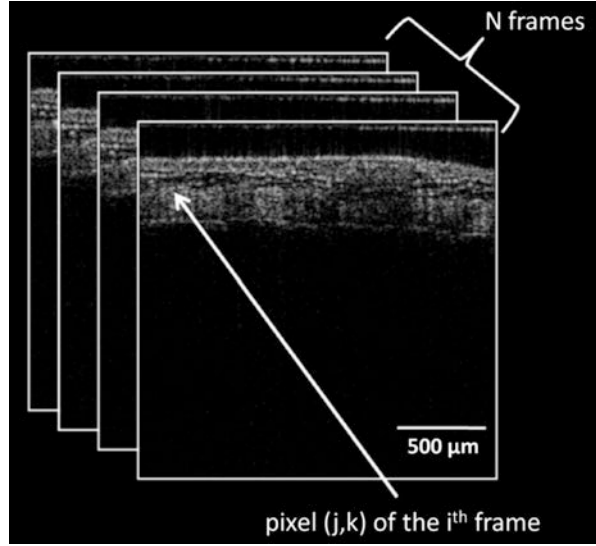
Fig. 22.7 Depth-encoded
color projection image of 9L
gliosarcoma tumor imaged
9 days after implantation in
the dorsal skinfold window
chamber model. Features
closest to the coverslip are
encoded with *green yellow*,
while deeper features are
encoded with *orange red*. The
transparency of a pixel is
determined by the speckle
variance intensity. The image
shows a significant amount of
intratumoral microvascular
heterogeneity [43]
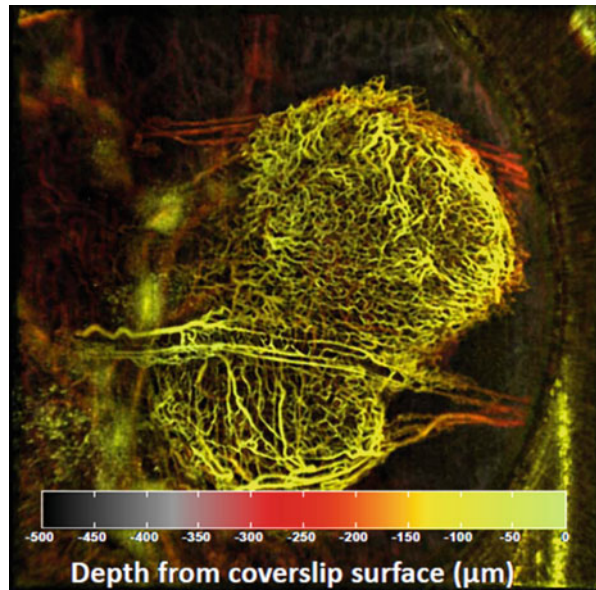
treatment monitoring/optimization. As with all imaging modalities, each of these
specific vascular detection schemes has their advantages and disadvantages, and the
researcher or clinician must take great care in choosing a vascular detection scheme
that is optimal for the specific application in question.

22.4   Contrast Agents to Improve Microvascular Detection

The OCT vascular detection techniques described above are based on Doppler shift, power Doppler, or speckle modulation and inherently assume the imaging background is essentially stationary, and that the only moving components are due to the presence of blood (either due to convective flow or due to natural Brownian motion even in the absence of flow as in the case of speckle modulation). Thus, the motion of the scatterers in blood is the overarching source of vascular contrast in OCT. In some cases, however, it may be advantageous if additional exogenous contrast can be localized in the vasculature, in order to better reject background (nonvascular) signals and decrease the reliance on the motion detection algorithm. Vascular contrast-enhancing agents are present in many other biological imaging modalities, making feasible the detection of vascular network, and recognizing regions of altered perfusion. They include iodinated agents in computed tomography, gadolinium in magnetic resonance imaging, and microbubbles for ultrasound. In optical imaging, a prevalent modality that relies on contrast agents is fluorescence imaging. A wide variety of fluorescently tagged molecules are used in confocal and multiphoton microscopy. One common vascular detection method involves the use of fluorescently tagged high molecular weight Dextran, which acts as a blood pooling agent and has been successfully used to diagnose vascular anomalies in the eye [44]. However, one of the primary drawbacks of fluorescence imaging for clinical applications is the limited depth of penetration. The use of contrast agents for OCT has the potential to enable high specificity of the imaging target, with an order of magnitude increase in imaging depth. However, a confounding factor to this potential for OCT deep vessel detection is that fluorescence is an incoherent process and is therefore unsuitable for OCT. Therefore, OCT must rely on actual changes in the (scattering and absorption) optical properties of the tissue to be imaged [45].

One potential mechanism for enhanced vascular contrast is thus to utilize agents with strong scattering or absorbing properties that can be localized in the blood. The following section discusses strategies to enable contrast-agent-enhanced vascular detection. Note that contrast agents for OCT imaging extend far beyond vascular imaging, where developments have been primarily focused on the detection of cellular biomarkers. Interested readers are referred to a review by Yang [46].

There are many commercially available near-infrared (NIR) absorbing dyes, which can alter the spectral properties of an imaging target within localized regions. The NIR dye indocyanine green, for example, has been FDA-approved and has found applications in ophthalmic angiography [47]. NIR dyes may be used as a contrast agent when combined with spectroscopic OCT, which can probe the spectral information of a sample [48, 49]. Dyes that have absorption peaks that are off-centered from the center wavelength of the OCT light source are chosen. Their presence causes a regional shift in the spectrum of the backscattered light where they are located. This shift can be detected using spectroscopic OCT, where the concentration of the dye may be determined by the amount of spectral shift from the

center wavelength of the light source. This has been successfully applied to the imaging of the vascular bundles of a celery stalk [50].

Microbubbles and microspheres are another type of contrast agent, relying on scattering alterations, that could potentially be utilized for vascular detection using OCT. Gas-filled microbubbles are highly scattering due to the large index of refraction mismatches that they create in tissue. They may also find applications for combined OCT and ultrasound imaging. Barton et al. demonstrated the OCT detection of phospholipid-coated perfluorobutane microbubbles in the femoral vessels of a mouse hind limb [51]. Other scatterers with refractive indices that are significantly different from tissue, such as gold and iron oxides, have also been encapsulated in microspheres for use as contrast agent in OCT [52]. However, an inherent difficulty with using either strong absorbers or high scatterers as contrast agent for OCT is that the biological tissues themselves generate a large range of backscattered signal. Combined with the presence of speckle, this makes differentiation of intrinsic contrast from an exogenous probe difficult, based on intensity alone. This may help explain the rather subtle improvements in vascular detection using microbubbles reported by Barton et al. [51].

To enhance the separation of contrast agents from the tissue background signal, it is possible to use a dynamic modulation method by observing the changes between a pair of images (B-mode) or between adjacent depth profiles (A-scans), while the absorbing or scattering properties of the contrast agent are altered. That is, a baseline acquisition is performed, the properties of the contrast agent are modified, and then a second acquisition is taken. The difference between the two B-mode images (or two A-scans) can be used to identify the location of the contrast agents. For example, methylene blue has a modifiable absorption peak that can be changed from 650 nm at ground state to 830 nm at an excited state by optical pumping. Difference images can be obtained by turning the pump on and off, as has been demonstrated by Rao et al. in what they termed "pump-probe OCT" [53]. The main difficulty with using methylene blue is its short excitation lifetime, requiring high pumping light intensity to allow a sufficient time window for image acquisition. Other molecules with longer transition times, such as phytochrome A, have also been explored [54]. Another modulated contrast agent is that of ferromagnetic particles. In magnetomotive optical coherence tomography [55], magnetic nanoparticles are mechanically modulated with an external magnetic field during OCT imaging. Background rejection is accomplished by performing an additional scan when the magnetic field is off. In principle, these modifiable contrast agents could be encapsulated within engineered microspheres to remain within vasculature. Alternatively, surface modifications could be performed on the microspheres to label diseased blood vessels as markers for arthrosclerosis or tumor angiogenesis [52]. These exogenous contrast agents for OCT have yet to become widely used or widely available to the OCT research community. Although signal improvement has been demonstrated, the inherent physiological implications and associated toxicities of these contrast agents remain unknown. Extensive preclinical testing is required prior to their acceptance as a technique to improve the viability of contrast-enhanced vascular OCT.

22.5 Representative Applications

22.5.1 Vascular OCT for Retinal Assessment

Mutation in the vascular network of the retina has been associated with various diseases including vascular occlusion disease, diabetic retinopathy, and glaucoma. Therefore, an opportunity exists to quantify the relative or absolute blood flow pattern of the retina as a way to gain a physiologically relevant understanding of these retinal diseases. Quantitative imaging of blood vessels, via color Doppler OCT, was first reported in 1997 [56, 57] and extended to retinal imaging by Yazdanfar et al. [58] in 2000. This concept of using the inherent blood flow as a contrast mechanism was employed to differentiate the stationary tissue from the moving red blood cells and to visualize the morphology of the blood vessels in the ocular fundus and is now termed optical coherence angiography (OCA) [59]. With recent advances in computer hardware and an increase in the A-scan rate of OCT systems, three-dimensional (3D) scans can now occur at multiple times per second, where the vascular information can be used to differentiate between retinal and choroidal vascular networks. Although fluorescein angiography (FA) is still the gold standard for vascular detection in the eye, recently developed inherent-contrast OCT blood detection techniques such as speckle variance, phase variance, and optical microangiography have the potential to replace FA as the accepted standard of care in the near future.

OCT is in fact becoming a standard of care for many ophthalmic diseases, and many ocular OCT studies have been reported. This has translated to and increased use of microvascular OCT imaging in the eye [60, 61]. For example, a recent Doppler OCT pilot study by Wang et al. [62] has demonstrated how ocular blood flow characteristics in retinal and optic nerve diseases could be used to stratify patients with and without disease. Subjects were subdivided into five groups – normal, glaucoma, nonarteritic ischemic optic neuropathy (NAION), diabetic retinopathy (PDR), and branch retinal vein occlusion (BRVO) – and their blood flow was detected and quantified, via the Doppler OCT velocity profiles, in a regions around the optic nerve head. It was found that the total retinal blood flow in normal patients averaged 47.6 ± 5.4 µL/min, whereas eyes with glaucoma (34.1 ± 4.9 µL/min), NAION (28.2 ± 8.2 µL/min), or PDR (15.8 ± 10.1 µL/min) had a significantly decreased blood supply ($P < 0.001$). In addition, there was a statistically significant correlation between the loss of normal blood flow in the eye and visual field loss in glaucoma patients ($P = 0.003$). This is but one example demonstrating how Doppler OCT retinal blood flow imaging can help identify and quantify diseases of the posterior chamber of the eye.

As OCT blood flow detection algorithms and techniques continue to be validated by preclinical and clinical research, several imaging and workflow advantages may allow these techniques to assume routine use in the clinic. These advantages include inherent (endogenous) vascular contrast without the need for exogenous contrast agent injection (e.g., fluorescein), no need for surface contact (cf. ultrasound), and OCT's ability to yield coregistered high-resolution morphological information and sensitive blood flow detection maps simultaneously.

22.5.2 Vascular OCT Monitoring of Photodynamic Therapy

Photodynamic therapy (PDT) is a non- or minimally invasive treatment that combines the effect of three nontoxic agents – photosensitizer, oxygen, and light – to produce a cytotoxic photochemical reaction. PDT is approved for treating a variety of solid tumors, dysplasias, and other oncologic and nononcologic pathologies [63, 64]. Several advantages of PDT as an oncotherapy include ability to preferentially target tumor while sparing adjacent normal tissues (owing to selective accumulation of photosensitizer and focal light irradiation strategies), reduced systemic phototoxicity using recently developed photosensitizers, ability to target either cellular or vascular tumor compartments, good cosmesis outcome (owing to sparing of the connective tissue and stroma), and lack of treatment resistance buildup (allowing for retreatments as necessary to improve response). Some disadvantages of PDT include systemic photosensitivity with previous generation of photosensitizers, inability to treat large tumors (related to limitations imposed by light propagation in tissue), overall complexity of the treatment (correct mixture of light, drug, and oxygen "doses"), and the need for a viable blood supply to ensure continuous oxygenation (which can prove difficult in a hypoxic tumor environment [65]).

When the photosensitizer is excited to a higher energy state by the PDT treatment light source, it can return to its ground energy level via nonradiative relaxation, fluorescence, or through an intermediate triplet state. It is this triplet state which is of most interest to the PDT effect, as the photosensitizer can undergo a type 1 or type 2 reaction. The type 2 reaction is considered to be the main cytotoxic PDT path leading to cell death [66], where the photosensitizer reacts with molecular oxygen to produce singlet oxygen [67]. As the singlet oxygen reacts with the tissue, cell destruction can occur via plasma membrane damage [68], bleb formation [68], reduction of active transport [69], depolarization of the plasma membrane [70], and cell lysis [65]. DNA damage has also been implicated in PDT, often mitochondrial and not nuclear, owing to the details of photosensitizer subcellular localization; unlike the mode of damage of ionizing radiation, however, the induced DNA base oxidative damage, strand breaks, and cross-links may be such that the damage is sublethal [71, 72].

In addition to (or perhaps instead of) cellular damage, tumor vasculature is also an attractive target during PDT, as the tumor environment requires a functional vascular system for the delivery of nutrients and for removal of toxic wastes associated with cellular metabolism of its rapidly proliferating cells. The tumor vasculature is significantly different from normal vasculature in both vessel architecture (tortuosity, irregular branching, lack of basement membrane in endothelial cells) and function (e.g., blood pooling, increased vessel permeability, perfusion) [73]. These differences provide a potential framework for preferentially targeting tumorous vasculature to disrupt or modulate vessel architecture/function, while limiting damage to normal vascular tree. An important benefit of vascular targeting, when compared to cellular targeting, is that not all endothelial cells need to be affected to disrupt tumor vascular function. Instead, damaging a single endothelial cell or small section of a blood vessel may induce catastrophic results, as thousands

of tumor cells may die since they were dependent on that single vessel section for their blood supply [74].

These PDT vascular impairment effects are complex and dynamic, but potentially useful; as such, they may be monitored, quantified, and perhaps optimized in real time via OCT. The vascular changes, if measurable, can offer a metric for quantifying the biological response of PDT, further elucidating its mechanisms of action and providing an early assessment of therapeutic efficacy. This may overcome some of the PDT dosimetry challenges and provide potential feedback information for therapy improvement and individualization.

OCT's ability to simultaneously image tissue structure and blood flow information is very promising for biomedical applications and is well suited for monitoring the vascular changes associated with PDT treatments. Doppler OCT (DOCT) is capable of producing high-resolution structural images while also acquiring blood flow characteristics at the microcirculation level. However, due to the shallow penetration depth of OCT (1–3 mm in scattering tissues), new technologies are needed to obtain DOCT images of deeply situated tissue for clinical applications such as prostate or brain cancer.

Yang et al. [75] first demonstrated the feasibility of using a needle-based OCT probe to minimally invasively image the microstructure and microvasculature of hamster leg muscle. Note that this approach does not improve the OCT imaging depth of 1–3 mm per se but rather enables its placement anywhere in 3D space (via a minimally invasive high-gauge needle, under radiologic guidance). This design was miniaturized ($\sim$400 μm diameter OCT probe) and used in several follow-up studies to monitor and quantify PDT in preclinical animal studies under varying treatment conditions. Standish et al. [76] demonstrated that interstitial (IS) DOCT was able to detect and monitor microvascular changes during and post-PDT, deep within the tumor in real time, by providing quantitative differences in the vascular response to varying irradiance rates. This study monitored dynamic changes in vascular blood flow and defined a new quantitative metric called the vascular shutdown rates. This IS-DOCT metric was then used by Standish et al. [77] to predict the biological endpoint of tumor necrosis after PDT treatment in a Dunning prostate tumor rat model. Figure 22.8 demonstrates typical blood flow detection images throughout a PDT treatment and corresponding changes in the vascular index. Note only a couple of vessels have been highlighted in Fig. 22.8a for ease of displaying the detected blood flow.

Figure 22.9 demonstrates the PDT-induced vascular shutdown within the treatment region of multiple rats. A resonable correlation ($R^2 = 0.72$) between the percent tumor necrosis at 24 h post treatment and the vascular shutdown rate was observed slower vascular shutdown rate corresponded to higher treatment efficacy (larger volume of tumor necrosis).

These results demonstrate the potential for clinical measurements of the vascular effects of PDT via Doppler OCT, laying the groundwork for further work to improve vascular detection along with new imaging protocols and platforms for detecting and quantifying tissue microvascular network including the capillary bed [32, 34, 42].

a Before PDT

| 0 min | 5 min | 10 min |

During PDT

| 10 min | 15 min | 20 min |

| 25 min | 30 min | 35 min |

Post PDT

| 35 min | 40 min | 45 min |

500 μm

Reflectivity [dB]: 6 21 36

Doppler [kHz]: −4 0 +4

b

$32 \, \text{mWcm}^{-2}$
$48 \, \text{Jcm}^{-2}$

VI_{max}

VI_{min}

Vascular Index

Time (min)

c

$60 \, \text{mWcm}^{-2}$
$90 \, \text{Jcm}^{-2}$

Vascular Index

Time (min)
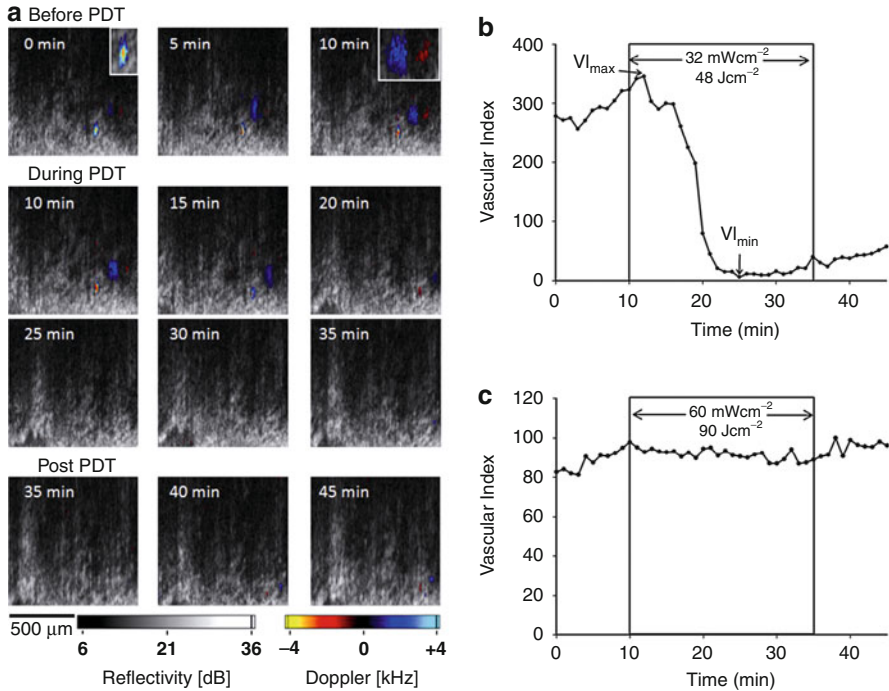
Fig. 22.8 Photofrin-mediated PDT, treatment time = 25 min. (**a**) IS-DOCT imaging sequence of color Doppler blood detection overlaid onto structural OCT images before, during, and post-PDT treatment. The inserts are 2× magnifications showing aliasing (0 min) and counterpropagating flows (10 min). (**b**) Vascular index VI as a function of time in a single animal showing the vascular shutdown during PDT light exposure and the definitions of VI_{max} and VI_{min}. (**c**) Control animal (light, no photosensitizer). Fluence rates and fluence listed in (**b**) and (**c**) are subsurface values at the depth of the IS-DOCT probe

Fig. 22.9 Correlation between percent tumor necrosis and DOCT flow reduction rate in PDT-treated rats carrying Dunning prostate tumor xenografts. PDT-treated group showed a marked and a statistically significant ($R^2 = 0.723$) decrease in PDT treatment efficacy with the increased rate of vascular shutdown. Vascular index VI is a quantification of the relative blood flow fraction detected in Doppler OCT images

$y = -0.002x + 0.43$
$R^2 = 0.723$

Necrosis (%)

Vascular shutdown Rate (% VI/min)

○ PDT treated tumors
— Linear regression
□ Controls
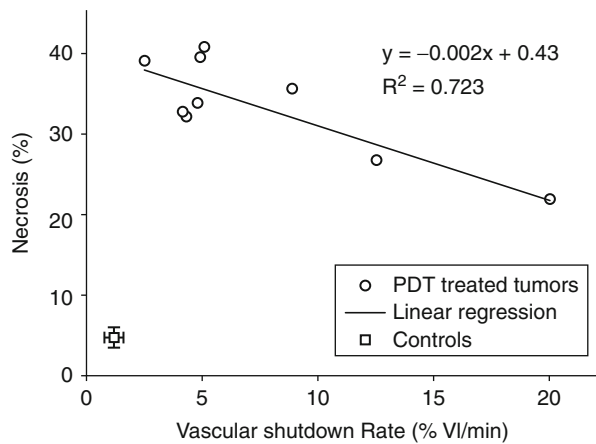
22.5.3 Vascular OCT in a Murine Window Chamber Model

Window chamber models for visualizing tissue development in vivo have been established since the 1920s [78]. In this approach, surgery is performed at the site of interest to implant an optically transparent window that allows for direct intravital imaging of otherwise inaccessible regions. The rabbit ear chamber, cranial chamber, dorsal skinfold chamber (DSWC), and other body organ windows (such as the kidney) have been demonstrated for different research areas [79]. All these models provide long-term (days, weeks, months) intravital observation of the organ of interest using high-resolution optical microscopy. The advantages of repeated longitudinal imaging studies in a well-controlled in vivo environment are beneficial to tumor implantation and development, controlled manipulation, disease treatments, and multimodality assessments and are highly beneficial for preclinical studies. The DSWC in particular has been used to study the microvasculature, with applications ranging from the studies of perfusion to monitoring various transplanted cells or tissues in the chamber to spatio/temporal quantification of responses to various treatments.

Figure 22.10a shows an example of a DSWC Swiss nude mouse commonly used for preclinical research. The model is convenient for DSWC implantation as the mouse is nude, avoiding the need for hair removal and skin irritation; its suppressed immune system permits the growth of various human xenografts tumor cell lines. The DSWC allows for direct observation of the cells, connective tissues and blood vessels of the normal dorsal skin environment, and, importantly, implanted tumor. Figure 22.10b demonstrates the different components of the window chamber frame.

Typically, the tissue thickness ranges from 500 μm to ∼1 mm; for tumor experimentation, a bolus of tumor cells is implanted through the underside of the dorsal skinfold. The lifetime of the DSWC is approximately 2–4 weeks, depending on its implantation details and postsurgery care. Figure 22.10 shows typical OCT structural images of the DSWC with and without tumor implantation. The glass cover slip appears transparent, apart from the glass to air/tissue interfaces. The thickness of the dorsal skin tissue can vary significantly, as exemplified in Fig. 22.11a–d. When investigating tumor growth, the cells are left to grow for approximately 1 week before imaging and appear as a tissue mass that bulges out toward the back side of the DSWC, away from the imaging surface (Fig. 22.11c). Proper segmentation of structural OCT images may allow quantitative evaluation of the tumor volume. Some blood vessels may be observed from structural images. Figure 22.11d (arrows) displays large blood vessels whose texture is clearly distinct from the surrounding tissue. The contrast is based on the time-varying speckle pattern of fluids, which causes the region to be smeared out when averaged, whereas static features (solid tissue) would not. When speckle variance signal processing is performed on the 3D data set (22.9), vascular detection down to the capillary level can be observed in the dorsal skin of the window chamber animal model, as seen in Fig. 22.11e.

As such, the DSWC animal model has proven an invaluable tool to allow for an in vivo imaging environment that provides the direct observation of cells, connective tissues, and vascular network. It also provides a continuous longitudinal testing
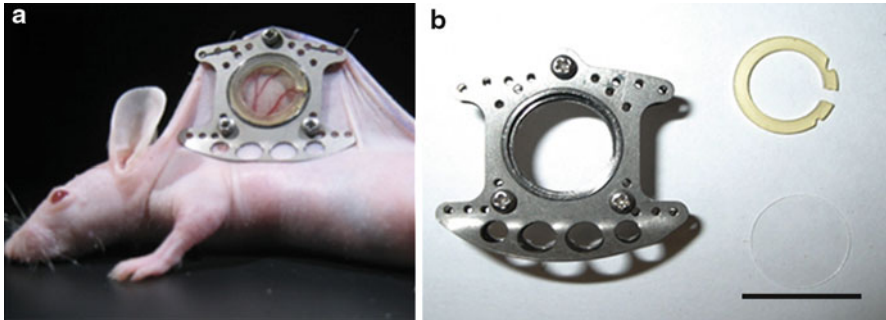
Fig. 22.10 (**a**) A Swiss nude mouse whose dorsal skin had been implanted with a titanium window chamber. (**b**) The titanium chamber, glass cover slip (diameter = 0.8 cm), and plastic fastener are shown. Scale bar = 1 cm
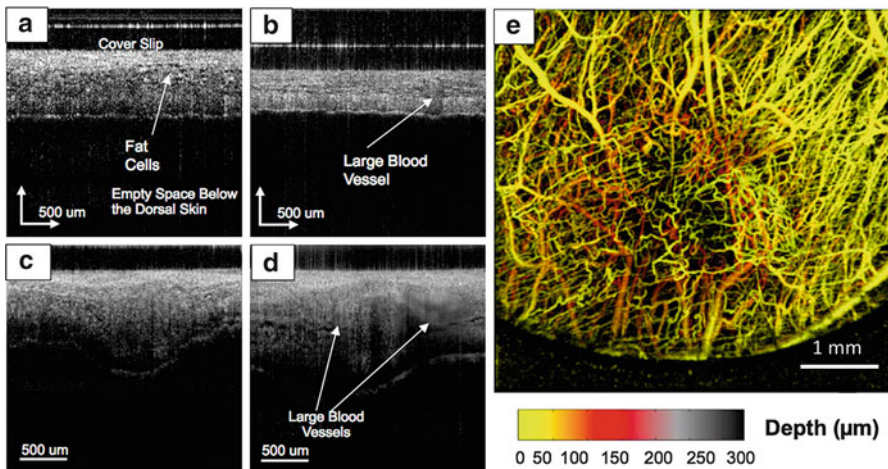
Fig. 22.11 Structural optical coherence tomography images of the dorsal skinfold window chamber from different mice. Each image has a depth of view of 3 mm in air or approximately 2 mm in tissue. (**a**, **b**) Two examples of normal nude mouse skin. (**c**, **d**) Two examples of tumor-bearing nude mouse skin, 1 week posttumor cell implantation. (**a**) Dorsal skin of a nude mouse. The fat cells are visible (labeled). (**b**) Dorsal skin with visible vessel. (**c**) Mouse implanted with ME-180 tumor cells. A tumor mass is present, which manifests as a protrusion on the dermal side of the tissue. (**d**) In another location of the same mouse, prominent blood vessels are seen. (**e**) Speckle variance OCT en face projection image of the mouse dorsal skin, where the colored map indicates the relative depth of the vessels (cf. Fig. 22.7)

environment to optically track and quantify disease progression, cancer therapies, and vascular network development. However, there are several areas of improvement that could further increase the utility of this optical imaging platform. Technically, WC is difficult to implant, requiring specialized surgical tools and frames, and the resulting limited lifetime (1–3 weeks) precluded longer-term observations.

Additionally implanted tumors take on a "pancake" shape, typically 2–4 mm in diameter and ∼1–1.5 mm thick. It could be argued that they may not fully represent the physiology of larger tumors in terms of 3D effects, solute transport, and other physiology [80]. Nevertheless, in many cases, the ability to serially image the cellular/vascular/stromal tumor compartments in vivo over extended periods of time (for monitoring disease progression, detailed spatiotemporal response patterns to various types of therapies, etc.) outweighs these disadvantages.

22.5.4 Vascular OCT for Radiation Response Monitoring

Radiation therapy (RT) is one of the most common treatments for cancer. Over half of all cancer patients are treated with RT, either alone or in combination with chemotherapy or surgery [81]. The therapy involves the use of ionizing radiation to kill cancer cells and shrink tumors by primarily damaging their genetic material, which impairs their ability to grow and divide. The therapy is used to treat most types of solid tumors. The radiation dose delivered to each site depends on the location, type, and stage of the cancer, as well as the presence of nearby organs that may be damaged by radiation [82].

RT plays a central role in cancer management. However, its efficacy is also highly influenced by the tumor's surrounding environment or the microenvironment. A nonexhaustive list includes the interaction of tumors with the cells of the immune system and the inflammatory response, oxygen deprivation, and associated signaling molecules [80]. Of particular interest in this chapter is the role of blood vessels.

Development of a functional vascular supply is essential for the successful growth of solid tumors. Typically, existing blood vessels can only support tumor growth to a few millimeters in size before the neoplastic cell population exceeds the nutritional needs [83]. What follows is the initiation of new vascular networks, in a process called angiogenesis [84]. The new blood vessels play several roles for tumor cells: (1) They provide them with nutrients and oxygen for survival, (2) they allow removal of toxic waste from cellular metabolism, and (3) they are the principal route for cancer metastasis [85].

As alluded to previously, tumor blood vessels are very different than that of normal tissues. Structurally, they are chaotic, lack hierarchy, and have an abnormal density. Compositionally, they are incomplete in nature, having missing layers such as basement membranes, endothelial lining, as well as receptors. Tumor endothelial cells also have different phenotypic properties than that of normal vasculature [4]. These characteristics result in vascular networks that are unable to supply sufficient oxygen and nutrient to the tumor mass [86]. Using the window chamber model and custom radiation delivery apparatus, the interplay between tumors and vessels after radiation therapy may be studied with high spatial resolution using OCT.

Here, we present preliminary results that demonstrate the utility of vascular-sensitive OCT in monitoring the vascular changes following a single dose of radiation. The Swiss nude mouse was fitted with a dorsal skinfold window chamber, and tumor cells (ME-180, human cervical carcinoma) were implanted. The tumor
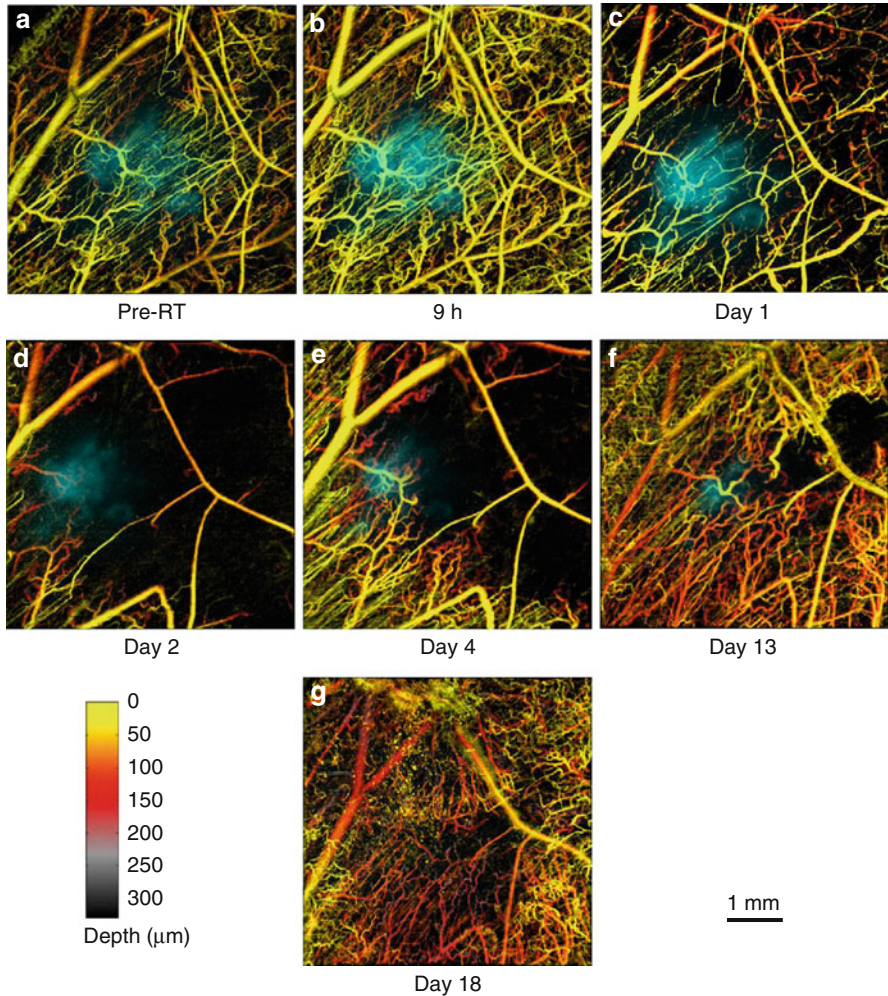
Fig. 22.12 Pseudocolored intravital images demonstrating changes in tumor mass (*cyan-colored*) and vascular architecture (color-coded for depth, see Figs. 22.7 and 22.11e) induced by radiation exposure (30 Gy) using speckle variance OCT and fluorescence microscopy in vivo in the DSWC. The circular treatment region is 4 mm in diameter centered on the tumor. Eight different imaging time points (**a–g**) were performed over a period of 18 days. A dramatic decrease in vasculature post-RT occurred within 2 days, followed by gradual revascularization

cells were stably transfected with the DsRed2 fluorescent protein to facilitate the monitoring of in vivo cellular tumor growth by fluorescence microscopy. The nude mouse was treated with single 30 Gy dose of ionizing radiation collimated to the window chamber region and monitored over 18 days. A wide-field fluorescence microscope observed the progression of the tumor, and the vasculature was imaged with speckle variance OCT. Images from both modalities were coregistered to produce the images shown in Fig. 22.12. By day 18, fluorescence signal from the

tumor mass has completely vanished, indicating absence of tumor cells. Most large vessels (arterioles, venules) remained present, but destruction of the majority of the capillaries was observed in day 2, followed by a gradual reperfusion of the tissue.

These OCT vascular results may be used to provide initial feedback or may even predict the long-term efficacy of the radiation therapy treatment as has been the case for other cancer therapies such as PDT studies discussed above [77]. These images may be further processed to obtain quantitative information, such as vascular area or density after skeletonization [87]. With the identification of relevant vascular imaging metrics, these vascular OCT techniques could be used as a feedback mechanism to alter treatment regimes and have the potential to provide individualized patient therapy, based on point-of-care vascular feedback measurements. However, it is important to note that extensive preclinical and clinical testing is required prior to the widespread adoption of OCT vascular monitoring as a means to improve existing radiation therapy treatments.

22.6 Conclusion, Challenges, and Future Outlook

A variety of optical approaches have been developed for structural and functional assessment of intact biological tissues. Of these, OCT is particularly promising owing to its high-micron-scale spatial resolution approaching histological/microscopic levels, portability, relative affordability, and fiber-optic compatibility enabling a variety of clinical scenarios. Further, functional extensions of OCT – spectroscopic, elastographic, polarimetric, textural, Doppler, speckle variance, etc. – allow the acquisition of further useful biological information, often at levels previous inaccessible by other techniques. The latter variants of these extensions, as described in this chapter, are uniquely suited to visualize tissue vasculature at the perfusion and microcirculation levels. Illustrative examples of the utility of microvascular detection and quantification, in the contexts of disease diagnosis and therapeutic monitoring, have been provided.

It is interesting to note that OCT is most often grouped under the "optical diagnostics" rubric of biophotonics, implying its primary role in diagnosis and detection of pathologies. While the important role of early detection and differential diagnosis in oncology cannot be marginalized, there is a growing realization that OCT (and other optical and nonoptical medical imaging techniques) may address other unmet needs in modern medicine. One outstanding opportunity is to provide adjunct information to compliment cancer treatments. Consider radiation therapy and chemotherapy two of the three major weapons at an oncologist's disposal (the other one being surgery). These therapies are essentially blind, in the sense that the success (or failure) of therapy is often not known for weeks or months following their completions, typically assessed by a posttherapy CT or MRI scan. Yet by that time, the delivery of the therapeutic agent, be it ionizing radiation or a chemotherapeutic drug, is over. It would be ideal if some medical imaging or tissue assessment modality could provide feedback on the progress of therapy *during* the course of its delivery so that patient-specific optimization of the

remaining therapeutic regimen could ensue. Such beneficial fusion of diagnostic and therapeutic technologies will clearly benefit patient management (termed "theragnostics" or alternatively "theranostics") and may indeed bring us a step closer to the elusive promise of personalized molecular medicine.

Research in this direction is on the rise. In radiation therapy, while imaging has been widely used for advanced geometric targeting to ensure increased dose conformity (the field of image-guided radiotherapy or IGRT), it is starting to be used for tumor response monitoring as well. Specifically, changes in tumor volume and quantification of tumor shrinkage are starting to be assessed between therapeutic fractions, over the course of a multifractioned radiation delivery. This is a step in the right direction, but clearly, gross anatomical volume changes in the cm^3 range must be preceded by much earlier, more sensitive metrics of radiobiological response. Functional PET studies in radiotherapy patients are also beginning to appear, with the intent of evaluating the changes in the metabolic status of tumors as a result of irradiation [88–90]. But the outstanding issues of resolution, complexity, radiation damage and safety, practicality, and cost are still to be properly addressed.

It is in this context of therapeutic monitoring, feedback, optimization, and "shedding light on therapy" that the vascular OCT techniques discussed in this chapter may have a significant impact. As evidenced by illustrative examples, tissue microvasculature is a sensitive, dynamic, and crucial functional tissue metric that is readily detectable by OCT and may indeed be modulated by a variety of noninvasive therapies such as PDT, chemotherapy, and radiation therapy. The outstanding challenges are many – improve microvascular detectability, quantify the resultant microvascular metrics, test whether the detected blood flow changes are indeed specific to the therapy, determine if these detected changes are indicative of the eventual treatment outcome, and so forth. Some of these challenges have been initially addressed as summarized in this chapter, but clearly much work remains to be done in the exciting field of OCT microvascular imaging.

References

1. R.S. Kerbel, Tumor angiogenesis. N. Engl. J. Med. **358**, 2039–2049 (2008)
2. W. Wang, D. Dean, H. Kaplan, Age-related macular degeneration. Discov. Med. **9**, 13–15 (2010)
3. P.R. Moreno, K. Purushothaman, Neovascularization in human atherosclerosis. Circulation **113**, 2245–2252 (2006)
4. A. Eberhard, S. Kahlert, V. Goede, B. Hemmerlein, K.H. Plate, H.G. Augustin, Heterogeneity of angiogenesis and blood vessel maturation in human tumors: implications for antiangiogenic tumor therapies. Cancer Res. **60**, 1388–1393 (2000)
5. J.R. Less, T.C. Skalak, E.M. Sevick, R.K. Jain, Microvascular architecture in a mammary carcinoma: branching patterns and vessel dimensions. Cancer Res. **51**, 265–273 (1991)
6. C.M.L. West, R.A. Cooper, J.A. Loncaster, D.P. Wilks, M. Bromley, Tumor vascularity: a histological measure of angiogenesis and hypoxia. Cancer Res. **61**, 2907–2910 (2001)
7. S.B. Fox, R.D. Leek, M.P. Weekes, R.M. Whitehouse, K.C. Gatter, A.L. Harris, Quantitation and prognostic value of breast cancer angiogenesis: comparison of microvessel density, Chalkley count, and computer image analysis. J. Pathol. **177**, 275–283 (1995)

8. E. Protopapa, G.S. Delides, L. Revesz, Vascular density and the response of breast carcinomas to mastectomy and adjuvant chemotherapy. Eur. J. Cancer A Gen. Top. **29**, 1391–1393 (1993)

9. E.R. Horak, R. Leek, N. Klenk, S. LeJeune, K. Smith, N. Stuart, M. Greenall, K. Stepniewska, A.L. Harris, Angiogenesis, assessed by platelet/endothelial cell adhesion molecule antibodies, as indicator of node metastases and survival in breast cancer. Lancet **340**, 1120–1124 (1992)

10. H.F. Zhang, K. Maslov, M.-L. Li, G. Stoica, L.V. Wang, In vivo volumetric imaging of subcutaneous microvasculature by photoacoustic microscopy. Opt. Express **14**, 9317–9323 (2006)

11. M.C. Pilatou, N.J. Voogd, F.F.M.D. Mul, W. Steenbergen, L.N.A.V. Adrichem, Analysis of three-dimensional photoacoustic imaging of a vascular tree in vitro. Rev. Sci. Instrum. **74**, 4495–4499 (2003)

12. G. Yu, T. Durduran, C. Zhou, H.W. Wang, M.E. Putt, H.M. Saunders, C.M. Sehgal, E. Glatstein, A.G. Yodh, T.M. Busch, Noninvasive monitoring of murine tumor blood flow during and after photodynamic therapy provides early assessment of therapeutic efficacy. Clin. Cancer Res. **11**, 3543–3552 (2005)

13. C. Menon, G.M. Polin, I. Prabakaran, A. Hsi, C. Cheung, J.P. Culver, J.F. Pingpank, C.S. Sehgal, A.G. Yodh, D.G. Buerk, An integrated approach to measuring tumor oxygen status using human melanoma xenografts as a model. Cancer Res. **63**, 7232–7240 (2003)

14. M.P. Pusztaszeri, W. Seelentag, F.T. Bosman, Immunohistochemical expression of endothelial markers CD31, CD34, von Willebrand factor, and Fli-1 in normal human tissues. J. Histochem. Cytochem. **54**, 385–395 (2006)

15. P. Hsiung, J. Hardy, S. Friedland, R. Soetikno, C. Du, A. Wu, P. Sahbaie, J. Crawford, A. Lowe, C. Contag, Detection of colonic dysplasia in vivo using a targeted heptapeptide and confocal microendoscopy. Nature **14**, 454–458 (2008)

16. A. Meining, D. Saur, M. Bajbouj, V. Becker, E. Peltier, H. HoÃàfler, C.H. von Weyhern, R.M. Schmid, C. Prinz, In vivo histopathology for detection of gastrointestinal neoplasia with a portable, confocal miniprobe: an examiner blinded analysis. Clin. Gastroenterol. Hepatol. **5**, 1261–1267 (2007)

17. M. Khurana, H.A. Collins, E.H. Moriyama, A. Mariampillai, H.L. Anderson, B.C. Wilson, Multi-modality optical imaging of vascular responses to photodynamic therapy in mouse window chamber model. Presented at the BIOMED conference, St. Petersburg, Florida (2008)

18. M. Khurana, E.H. Moriyama, A. Mariampillai, B.C. Wilson, Intravital high resolution optical imaging of individual vessel response to photodynamic treatment. J. Biomed. Opt. **13**, 040502 (2008)

19. A. Fercher, J. Briers, Flow visualization by means of single-exposure speckle photography. Opt. Commun. **37**, 326–330 (1981)

20. J.D. Briers, S. Webster, Laser speckle contrast analysis (LASCA): a nonscanning, full-field technique for monitoring capillary blood flow. J. Biomed. Opt. **1**, 174–179 (1996)

21. Y.C. Huang, T.L. Ringold, J.S. Nelson, B. Choi, Noninvasive blood flow imaging for real-time feedback during laser therapy of port wine stain birthmarks. Lasers Surg. Med. **40**, 167–173 (2008)

22. A.K. Dunn, A. Devor, A.M. Dale, D.A. Boas, Spatial extent of oxygen metabolism and hemodynamic changes during functional activation of the rat somatosensory cortex. Neuroimage **27**, 279–290 (2005)

23. H.K. Shin, A.K. Dunn, P.B. Jones, D.A. Boas, M.A. Moskowitz, C. Ayata, Vasoconstrictive neurovascular coupling during focal ischemic depolarizations. J. Cereb. Blood Flow Metab. **26**, 1018–1030 (2005)

24. H.K. Shin, A.K. Dunn, P.B. Jones, D.A. Boas, E.H. Lo, M.A. Moskowitz, C. Ayata, Normobaric hyperoxia improves cerebral blood flow and oxygenation, and inhibits peri-infarct depolarizations in experimental focal ischaemia. Brain **130**, 1631–1642 (2007)

25. K. Bizheva, A. Unterhuber, B. Hermann, B. Povazay, H. Sattmann, A.F. Fercher, W. Drexler, M. Preusser, H. Budka, A. Stingl, T. Le, Imaging ex vivo healthy and pathological human brain tissue with ultra-high-resolution optical coherence tomography. J. Biomed. Opt. **10**, 11006 (2005)

26. V.X.D. Yang, M.L. Gordon, B. Qi, J. Pekar, S. Lo, E. Seng-Yue, A. Mok, B.C. Wilson, I.A. Vitkin, High speed, wide velocity dynamic range Doppler optical coherence tomography (Part I): system design, signal processing, and performance. Opt. Express **11**, 794–809 (2003)

27. B.J. Vakoc, S.H. Yun, J.F. De Boer, G.J. Tearney, B.E. Bouma, Phase-resolved optical frequency domain imaging. Opt. Express **13**, 5483–5493 (2005)

28. J. Barton, S. Stromski, Flow measurement without phase information in optical coherence tomography images. Opt. Express **13**, 5234–5239 (2005)

29. J. Fingler, D. Schwartz, C. Yang, S.E. Fraser, Mobility and transverse flow visualization using phase variance contrast with spectral domain optical coherence tomography. Opt. Express **15**, 12636–12653 (2007)

30. R.K. Wang, S.L. Jacques, Z. Ma, S. Hurst, S.R. Hanson, A. Gruber, Three dimensional optical angiography. Opt. Express **15**, 4083–4097 (2007)

31. B.J. Vakoc, R.M. Lanning, J.A. Tyrrell, T.P. Padera, L.A. Bartlett, T. Stylianopoulos, L.L. Munn, G.J. Tearney, D. Fukumura, R.K. Jain, B.E. Bouma, Three-dimensional microscopy of the tumor microenvironment in vivo using optical frequency domain imaging. Nat. Med. **15**, 1219–1223 (2009)

32. A. Mariampillai, B.A. Standish, E.H. Moriyama, M. Khurana, N.R. Munce, M.K.K. Leung, J. Jiang, A. Cable, B.C. Wilson, I.A. Vitkin, V.X.D. Yang, Speckle variance detection of microvasculature using swept-source optical coherence tomography. Opt. Lett. **33**, 1530–1532 (2008)

33. C. Kasai, K. Namekawa, A. Koyano, R. Omoto, Real-time two-dimensional blood flow imaging using an autocorrelation technique. IEEE Trans. Sonics Ultrason. **32**, 458–464 (1985)

34. A. Mariampillai, B.A. Standish, N.R. Munce, C. Randall, G. Liu, J.Y. Jiang, A.E. Cable, I.A. Vitkin, V.X.D. Yang, Doppler optical cardiogram gated 2D color flow imaging at 1000 fps and 4D in vivo visualization of embryonic heart at 45 fps on a swept source OCT system. Opt. Express **15**, 1627–1638 (2007)

35. T.C. Chen, B. Cense, M.C. Pierce, N. Nassif, B.H. Park, S.H. Yun, B.R. White, B.E. Bouma, G.J. Tearney, J.F. De Boer, Spectral domain optical coherence tomography ultra-high speed, ultra-high resolution ophthalmic imaging. Arch. Ophthalmol. **123**, 1715–1720 (2005)

36. B.J. Vakoc, G.J. Tearney, B.E. Bouma, Statistical properties of phase-decorrelation in phase-resolved Doppler optical coherence tomography. IEEE Trans. Med. Imaging **28**, 814–821 (2009)

37. V.X.D. Yang, M.L. Gordon, A. Mok, Y. Zhao, Z. Chen, R.S.C. Cobbold, B.C. Wilson, I. Alex Vitkin, Improved phase-resolved optical Doppler tomography using the Kasai velocity estimator and histogram segmentation. Opt. Commun. **208**, 209–214 (2002)

38. H. Ren, Y. Wang, J.S. Nelson, Z. Chen, Power optical Doppler tomography imaging of blood vessel in human skin and M-mode Doppler imaging of blood flow in chick chrioallantoic membrane. *Proceedings of SPIE*, vol. 4956 (2003)

39. L. An, R.K. Wang, In vivo volumetric imaging of vascular perfusion within human retina and choroids with optical micro-angiography. Opt. Express **16**, 11438–11452 (2008)

40. R.K. Wang, Directional blood flow imaging in volumetric optical microangiography achieved by digital frequency modulation. Opt. Lett. **33**, 1878–1880 (2008)

41. G. van Soest, T. Goderie, E. Regar, S. Koljenovi, G. van Leenders, N. Gonzalo, S. van Noorden, T. Okamura, B. Bouma, G. Tearney, Atherosclerotic tissue characterization in vivo by optical coherence tomography attenuation imaging. J. Biomed. Opt. **15**, 011105 (2010)

42. A. Mariampillai, M.K.K. Leung, M. Jarvi, B.A. Standish, K. Lee, B.C. Wilson, A. Vitkin, V.X.D. Yang, Optimized speckle variance OCT imaging of microvasculature. Opt. Lett. **35**, 1257–1259 (2010)

43. A. Mariampillai, Development of a high resolution microvascular imaging toolkit for optical coherence tomography. Thesis from the Department of Medical Biophysics, University of Toronto, Toronto, 2010

44. E.G. Atkinson, S. Jones, B.A. Ellis, D.C. Dumonde, E. Graham, Molecular size of retinal vascular leakage determined by FITC-dextran angiography in patients with posterior uveitis. Eye **5**, 440–446 (1991)
45. J.M. Schmitt, A. Knüttel, Model of optical coherence tomography of heterogeneous tissue. J. Opt. Soc. Am. A Opt. Image Sci. Vis. **14**, 1231–1242 (1997)
46. C. Yang, Molecular contrast optical coherence tomography: a review. Photochem. Photobiol. **81**, 215–237 (2005)
47. L.A. Yannuzzi, J.S. Slakter, J.A. Sorenson, D.R. Guyer, D.A. Orlock, Digital indocyanine green videoangiography and choroidal neovascularization. Retina **12**, 191–223 (1992)
48. U. Morgner, W. Drexler, F.X. Kärtner, X.D. Li, C. Pitris, E.P. Ippen, J.G. Fujimoto, Spectroscopic optical coherence tomography. Opt. Lett. **25**, 111–113 (2000)
49. F. Robles, R.N. Graf, A. Wax, Dual window method for processing spectroscopic optical coherence tomography signals with simultaneously high spectral and temporal resolution. Opt. Express **17**, 6799–6812 (2009)
50. C. Xu, J. Ye, D.L. Marks, S.A. Boppart, Near-infrared dyes as contrast-enhancing agents for spectroscopic optical coherence tomography. Opt. Lett. **29**, 1647–1649 (2004)
51. J.K. Barton, J.B. Hoying, C.J. Sullivan, Use of microbubbles as an optical coherence tomography contrast agent. Acad. Radiol. **9**, S52–S55 (2002)
52. S.A. Boppart, A.L. Oldenburg, C. Xu, D.L. Marks, Optical probes and techniques for molecular contrast enhancement in coherence imaging. J. Biomed. Opt. **10**, 041208 (2005)
53. K.D. Rao, M.A. Choma, S. Yazdanfar, A.M. Rollins, J.A. Izatt, Molecular contrast in optical coherence tomography by use of a pump probe technique. Opt. Lett. **28**, 340–342 (2003)
54. C. Yang, M.A. Choma, L.E. Lamb, J.D. Simon, J.A. Izatt, Protein-based molecular contrast optical coherence tomography with phytochrome as the contrast agent. Opt. Lett. **29**, 1396–1398 (2004)
55. A.L. Oldenburg, V. Crecea, S.A. Rinne, S.A. Boppart, Phase-resolved magnetomotive OCT for imaging nanomolar concentrations of magnetic nanoparticles in tissues. Opt. Express **16**, 11525–11539 (2008)
56. Z. Chen, T.E. Milner, D. Dave, J.S. Nelson, Optical Doppler tomographic imaging of fluid flow velocity in highly scattering media. Opt. Lett. **22**, 64–66 (1997)
57. J.A. Izatt, M.D. Kulkarni, S. Yazdanfar, J.K. Barton, A.J. Welch, In vivo bidirectional color Doppler flow imaging of picoliter blood volumes using optical coherence tomography. Opt. Lett. **22**, 1439–1441 (1997)
58. S. Yazdanfar, A.M. Rollins, J.A. Izatt, Imaging and velocimetry of the human retinal circulation with color Doppler optical coherence tomography. Opt. Lett. **25**, 1448–1450 (2000)
59. S. Makita, Y. Hong, M. Yamanari, T. Yatagai, Y. Yasuno, Optical coherence angiography. Opt. Express **14**, 7821–7840 (2006)
60. J.S. Schuman, C.A. Puliafito, J.G. Fujimoto, *Optical Coherence Tomography of Ocular Diseases* (Slack, Thorofare, NJ, 2004)
61. V. Gupta, A. Gupta, M. Mangat Ram Dogra, *Atlas Optical Coherence Tomography of Macular Diseases and Glaucoma* (Jaypee Brothers Medical, New Delhi, India, 2010)
62. Y. Wang, A.A. Fawzi, R. Varma, A.A. Sadun, X. Zhang, O. Tan, J.A. Izatt, D. Huang, Pilot study of optical coherence tomography measurement of retinal blood flow in retinal and optic nerve diseases. Invest. Ophthalmol. Vis. Sci. **52**, 840–845 (2011)
63. T.J. Dougherty, C.J. Gomer, B.W. Henderson, G. Jori, D. Kessel, M. Korbelik, J. Moan, Q. Peng, Photodynamic therapy. J. Natl. Cancer Inst. **90**, 889–905 (1998)
64. Z. Huang, A review of progress in clinical photodynamic therapy. Technol. Cancer Res. Treat. **4**, 283–293 (2005)
65. Z. Luksiene, Photodynamic therapy: mechanism of action and ways to improve the efficiency of treatment. Medicina (Kaunas) **39**, 1137–1150 (2003)
66. M.S. Patterson, S.J. Madsen, B.C. Wilson, Experimental tests of the feasibility of singlet oxygen luminescence monitoring in vivo during photodynamic therapy. J. Photochem. Photobiol. B Biol. **5**, 69–84 (1990)

67. C.M. Moore, I.M. Hoh, S.G. Bown, M. Emberton, Does photodynamic therapy have the necessary attributes to become a future treatment for organ-confined prostate cancer? BJU Int. **96**, 754–758 (2005)

68. G. Volden, T. Christensen, J. Moan, Photodynamic membrane damage of hematoporphyrin derivative-treated NHIK 3025 cells in vitro. Photobiochem. Photobiophys. **3**, 105–111 (1981)

69. J. Moan, J. McGhie, P.B. Jacobsen, Photodynamic effects on cells in vitro exposed to hematoporphyrin derivative and light. Photochem. Photobiol. **37**, 599–604 (1983)

70. K.G. Specht, M.A. Rodgers, Depolarization of mouse myeloma cell membranes during photodynamic action. Photochem. Photobiol. **51**, 319–324 (1990)

71. A. Ketabchi, A. MacRobert, P.M. Speight, J.H. Bennett, Induction of apoptotic cell death by photodynamic therapy in human keratinocytes. Arch. Oral Biol. **43**, 143–149 (1998)

72. G. Buggiani, M. Troiano, R. Rossi, T. Lotti, Photodynamic therapy: off-label and alternative use in dermatological practice. Photodiagnosis Photodyn. Ther. **5**, 134–138 (2008)

73. D. Fukumura, R.K. Jain, Tumor microvasculature and microenvironment: targets for anti-angiogenesis and normalization. Microvasc. Res. **74**, 72–84 (2007)

74. B. Chen, C. He, P. de Witte, P.J. Hoopes, T. Hasan, B.W. Pogue, Vascular targeting in photodynamic therapy, in *Advances in Photodynamic Therapy: Basic, Translational, and Clinical*, ed. by M.R. Hamblin, P. Mroz (Artech House, Norwood, 2008), pp. 179–191

75. V.X.D. Yang, Y.X. Mao, N. Munce, B. Standish, W. Kucharczyk, N.E. Marcon, B.C. Wilson, I.A. Vitkin, Interstitial Doppler optical coherence tomography. Opt. Lett. **30**, 1791–1793 (2005)

76. B.A. Standish, X. Jin, J. Smolen, A. Mariampillai, N.R. Munce, B.C. Wilson, I.A. Vitkin, V.X.D. Yang, Interstitial Doppler optical coherence tomography monitors microvascular changes during photodynamic therapy in a Dunning prostate model under varying treatment conditions. J. Biomed. Opt. **12**, 034022 (2007)

77. B. Standish, K. Lee, X. Jin, A. Mariampillai, N. Munce, M. Wood, B. Wilson, I. Vitkin, V. Yang, Interstitial Doppler optical coherence tomography as a local tumor necrosis predictor in photodynamic therapy of prostatic carcinoma: an in vivo study. Cancer Res. **68**, 9987–9995 (2008)

78. J.C. Sandison, The transparent chamber of the rabbit's ear giving a complete description of improved techniques of construction and introduction and general account of growth and behavior of living cells and tissues as seen with the microscope. Am. J. Anat. **41**, 447–472 (1928)

79. G.E. Koehl, A. Gaumann, E.K. Geissler, Intravital microscopy of tumor angiogenesis and regression in the dorsal skin fold chamber: mechanistic insights and preclinical testing of therapeutic strategies. Clin. Exp. Metastasis **26**, 329–344 (2009)

80. M.W. Dewhirst, Y. Cao, B. Moeller, Cycling hypoxia and free radicals regulate angiogenesis and radiotherapy response. Nat. Rev. Cancer **8**, 425–437 (2008)

81. J.B. Owen, L.R. Coia, G.E. Hanks, Recent patterns of growth in radiation therapy facilities in the United States: a patterns of care study report. Int. J. Radiat. Oncol. Biol. Phys. **24**, 983–986 (1992)

82. B. Emami, J. Lyman, A. Brown, L. Coia, M. Goitein, J.E. Munzenrider, B. Shank, L.J. Solin, M. Wesson, Tolerance of normal tissue to therapeutic irradiation. Int. J. Radiat. Oncol. Biol. Phys. **21**, 109–122 (1991)

83. D.W. Siemann, M.R. Horsman, Chapter 8 – Significance of the tumour microenvironment in radiotherapy, in *Cancer Microenvironment and Therapeutic Implications*, ed. by G. Baronzio, G. Fiorentini, C.R. Cogle (Springer, 2009)

84. J. Folkman, Angiogenesis in cancer, vascular, rheumatoid and other disease. Nat. Med. **1**, 27–31 (1995)

85. O. Stöltzing, L.M. Ellis, The role of microvasculature in metastasis formation, in *Vascular-Targeted Therapies in Oncology*, ed. by D.W. Siemann (Wiley, Chichester, 2006), pp. 31–62

86. P. Vaupel, Tumor microenvironmental physiology and its implications for radiation oncology. Semin. Radiat. Oncol. **14**, 198–206 (2004)

87. T.C. Lee, R.L. Kashyap, C.N. Chu, Building skeleton models via 3-D medial surface axis thinning algorithms. CVGIP: Graph. Model Image Process. **56**, 462–478 (1994)
88. I. Madani, W. Duthoy, C. Derie, W. De Gersem, T. Boterberg, M. Saerens, F. Jacobs, V. Grégoire, M. Lonneux, L. Vakaet, B. Vanderstraeten, W. Bauters, K. Bonte, H. Thierens, W. De Neve, Positron emission tomography-guided, focal-dose escalation using intensity-modulated radiotherapy for head and neck cancer. Int. J. Radiat. Oncol. Biol. Phys. **68**, 126–135 (2007)
89. T. Gupta, S. Jain, J.P. Agarwal, V. Rangarajan, N. Purandare, S. Ghosh-Laskar, K.A. Dinshaw, Diagnostic performance of response assessment FDG-PET/CT in patients with head and neck squamous cell carcinoma treated with high-precision definitive (chemo)radiation. Radiother. Oncol. **97**, 194–199 (2010)
90. D.S. Yoo, T.Z. Wong, D.M. Brizel, The role of adaptive and functional imaging modalities in radiation therapy: approach and application from a radiation oncology perspective. Semin. Ultrasound CT MRI **31**, 444–461 (2010)

Ocular Imaging Combining Ultrahigh Resolution and High Speed OCT

23

Tilman Schmoll and Rainer A. Leitgeb

Contents

Abstract

The impact of ultrahigh-resolution and ultrahigh-speed OCT technique on corneal and retinal imaging is shown. The capabilities of advanced OCT system for imaging of the cornea and the thickness determination of the tear film, corneal epithelium, and Bowman's layer over a wide field of view are demonstrated. The high transverse and axial resolution of OCT system allowing one to image individual nerve fiber bundles, the parafoveal capillary network, and individual cone photoreceptors is described.

23.1   Introduction

Over the past 20 years, optical coherence tomography (OCT) rapidly passed several important milestones. Starting from the idea to use laser interferometry to measure ocular distances, soon the first 2D scan of the human eye fundus was presented by Fercher at the ICO-15 satellite conference in 1990 [1–3]. This technique was

T. Schmoll (✉) • R.A. Leitgeb
Center for Medical Physics and Biomedical Engineering, Medical University Vienna, Vienna, Austria
e-mail: t.schmoll@meditec.zeiss.com, rainer.leitgeb@meduniwien.ac.at

quickly picked up by others and named optical coherence tomography [4]. During the following years, it has proven its potential for in vivo cross-sectional imaging of the human retina [5, 6]. The next important step toward a noninvasive optical biopsy was to increase the resolution of OCT by an order of magnitude from 10–15 μm to below 1 μm [7–10]. Another milestone was then reached with the introduction of Fourier/spectral domain OCT (FDOCT/SDOCT) [11]. By acquiring a complete axial scan instantaneously a tremendous improvement in imaging speed was realized which consequently led to a significant sensitivity advantage compared to former time domain OCT techniques [12–14]. Very recently, the next advancement has been made regarding imaging speed using fast swept source laser technology [15]. These systems increased the line rates of OCT systems from several tens of kHz up to several MHz axial scan rates while maintaining reasonable sensitivity [16, 17].

High acquisition speed is not only necessary to improve patient comfort but also to reduce motion artifacts to a minimum. The fast acquisition of volumes and therefore a minimum of motion blurring is crucial for high transverse resolution in vivo imaging. In order to support the optical resolution ultrahigh-resolution OCT volumes require a fairly dense sampling. This is though only achievable in a reasonable amount of time with very high acquisition speed. Therefore, ultrahigh resolution and ultrahigh speed are closely linked. By combining both, microscopic details such as the parafoveal capillaries or individual photoreceptors can be resolved in vivo [18, 19]. High-resolution imaging is however not only useful for retinal diagnostics. For corneal imaging, especially, high axial resolution is required to resolve thin subcorneal layers such as the Bowman's layer. Gaining knowledge of the thickness profile of such layers is of significant interest for, e.g., the planning and follow-up monitoring of refractive surgery.

In this chapter, we illustrate the impact of ultrahigh resolution and ultrahigh speed advancements in OCT on corneal as well as retinal imaging. We show the capabilities of state-of-the-art optical coherence tomography for imaging of the cornea and the thickness determination of the tear film, corneal epithelium, and Bowman's layer over a wide field of view. Furthermore, we demonstrate the resolution capabilities of an OCT system, which incorporates high transverse resolution as well as high axial resolution to resolve microscopic retinal features such as individual nerve fiber bundles, the parafoveal capillary network, and individual cone photoreceptors.

23.2 Corneal Imaging

SDOCT is a powerful tool when it comes to thickness measurements of closely separated tissue layers. The human cornea represents a well-suited sample for ultrahigh-resolution OCT, as the light does not have to travel through large distances of dispersive media, which could compromise the resolution. Therefore, one can make full use of the axial resolution to determine the thickness of even very thin corneal layers. The measurement of the total corneal thickness as well as the

thickness measurement of sublayers hold substantial value for several diagnostic and surgical applications, such as monitoring of corneal edema and endothelial function, planning refractive surgery, and also follow-up examinations of, e.g., the flap interface [20]. A variety of techniques already exist to image the cornea and assess topographic thickness of the cornea and its layers [21–26]. However, each of these methods suffers from some significant limitations. Ultrasound pachymetry only provides one-dimensional measurements at a single spot in depth. Very high frequency ultrasound imaging does provide measurement data of a wider field of view even of the epithelial thickness profile. Yet it is comparably slow and does not reach the resolution of ultrahigh-resolution optical coherence tomography and therefore fails to resolve the Bowman's layer. Confocal microscopy provides comparable resolution but is limited to a very small field of view. This makes it almost impossible to measure the same spot multiple times in follow-up examinations. Another significant drawback of this technique is its very short working distance, which raises the risk of causing corneal lesions. Electron microscopy of course surpasses the resolution capabilities of ultrahigh-resolution OCT and is however only available for histopathologic examinations of excised cornea. With state-of-the-art optical coherence tomography systems one is able to overcome these shortcomings [8, 27]. Its very high speed enables motion artifact free measurements over a large range across the cornea and its resolution even permits to resolve the Bowman's layer with high precision [28]. Gaining knowledge of the epithelial and Bowman's layer thickness profile may prove as a successful diagnostic tool for diseases of the cornea as, e.g., keratoconus, where the epithelium becomes thinner over the region of the cone and does in some cases lead to epithelial breakdown. Also the precision of refractive surgery may be improved by more accurate thickness data of these corneal sublayers but by more precise measurements of the corneal flap. A feature of ultrahigh-resolution OCT, which makes it especially interesting for dry eye diagnostics and pharmaceutical studies, is its ability to resolve the thin tear film on top of the cornea. Making good use of the high temporal resolution, even time-resolved studies of the tear film thickness and its breakup are feasible.

By using a Ti:Sapph laser with a broadband width Gaussian-shaped spectrum as a light source and carefully choosing the optical components of the interferometer as well as of the spectrometer with respect to their suitability for broad band optical transmittance and wavelength-dependent losses, one is able to design an ultrahigh-resolution OCT system for corneal imaging, which achieves a resolution of approximately 1 μm in tissue [8, 28, 29]. In a very recent study, we demonstrated the use of ultrahigh-resolution OCT for thickness measurements of the Bowman's layer and the epithelium [28]. A Ti:Sapph laser was used, which provided a spectral bandwidth of 155 nm, centered at 800 nm. This led to an axial resolution of 1.3 μm in tissue. At the same time, we equipped this system with a fast spectrometer, using a CMOS camera. The high acquisition speed of 100,000 A-scans/s reduces the motion artifacts to a minimum. The ultrahigh resolution combined with the high speed has proven to be a useful method for the in vivo thickness determination of these layers over a large field of view. This system was capable of capturing full 3D
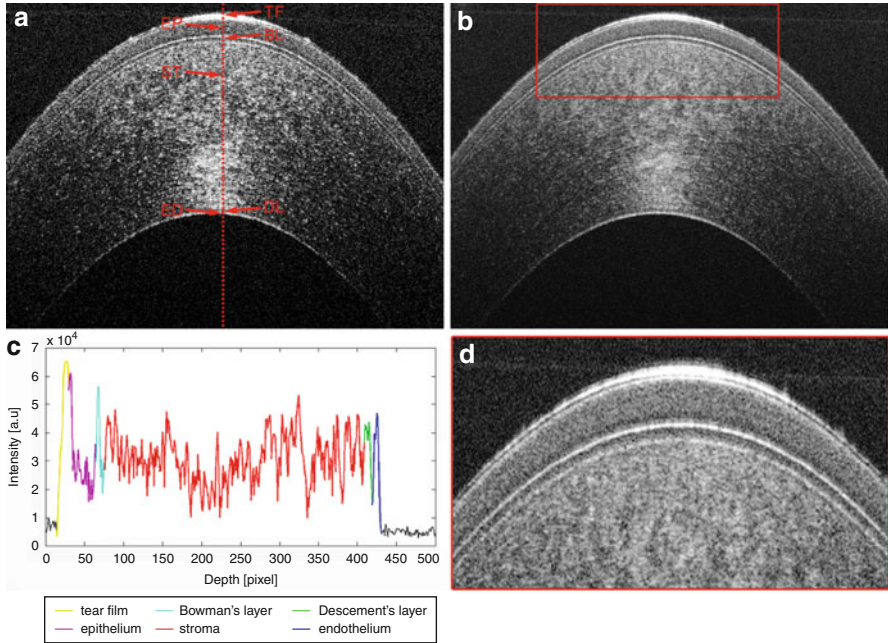
Fig. 23.1 Ultrahigh-resolution and ultrahigh-speed OCT scans of the cornea. (**a**) Single B-scan of the central cornea. The *dotted line* indicates the lateral position of (**c**). *TF* tear film, *EP* epithelium, *BL* Bowman's layer, *ST* stroma, *DL* Descement's layer, *ED* endothelium. (**b**) High definition B-scan, created by averaging five B-scans at the same position as (**a**). The *red box* indicates the region of (**d**). (**c**) A-scan at the position indicated in (**a**). (**d**) Magnification of the region indicated in (**b**)

volumes of the cornea with a size of 8.4 × 8.4 × 2.7 mm (horizontal × vertical × depth), containing 1,000 × 100 × 2,688 pixels, within 1 s.

Figure 23.1a shows a single B-scan, covering 8.4 mm across the central cornea, acquired within only 0.01 s using this ultrahigh resolution and speed SDOCT system. With such a system one is not only able to resolve the corneal epithelium (EP), the Bowman's layer (BL), the stroma (ST), the Descement's layer (DL), and the endothelium (ED), but even the very thin tear film (TF) on top of the cornea, which cannot be resolved by standard resolution OCT systems. In Fig. 23.1c, we plotted an A-scan, which further illustrates the capability of this system to detect closely separated tissue layers. To further enhance the image contrast as well as to reduce speckle noise within a tomogram one can also use the high acquisition speed to capture multiple B-scans at the same lateral position and then average these scans to create high definition OCT B-scans, as presented in Fig. 23.1b, d. In those scans, the individual layers can be distinguished even easier.

For the thickness evaluation of the acquired 3D volumes, a Canny edge detection algorithm was used during post-processing in order to extract the boundaries of air–epithelium, epithelium–Bowman's layer, and Bowman's layer–stroma (Fig. 23.2 a).
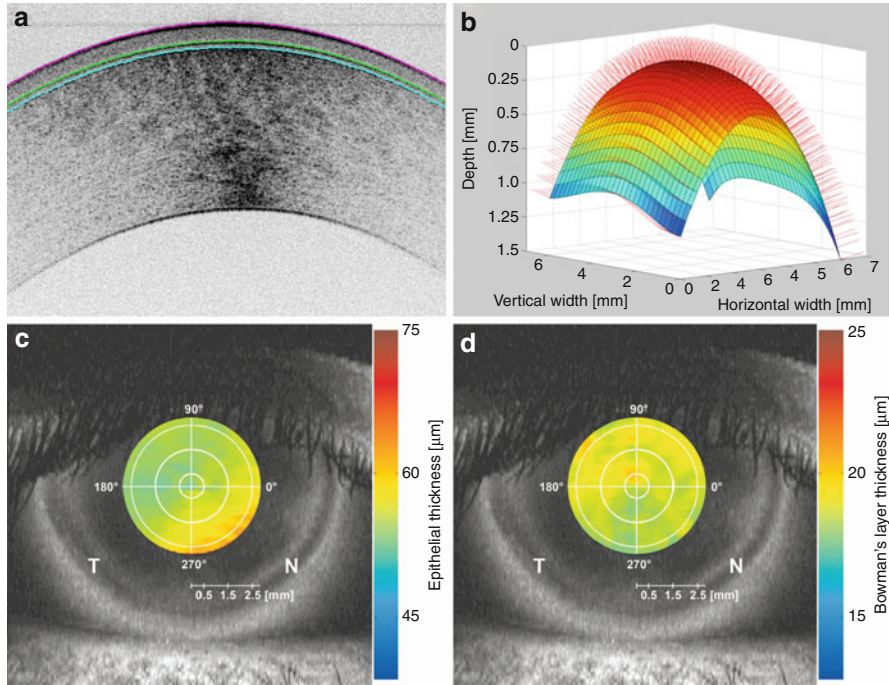
Fig. 23.2 Topographical thickness measurements of the epithelium and Bowman's layer. (**a**) shows the segmentation by the Canny edge algorithm. (**b**) Illustrates the surface normals across a detected corneal surface. (**c**) Epithelial thickness map of a healthy eye. (**d**) Bowman's layer thickness map of a healthy eye

This detection algorithm however still required user supervision to detect and correct false positive segmentations. The extracted boundaries were smoothed by a local regression algorithm using weighted linear least squares. In a next step, the surface normals were calculated for each point of the boundary surfaces (Fig. 23.2b). The thickness was then determined by measuring the distance between two corresponding intersection points of the surface normal and the layer boundary surfaces. In a next step, this data was plotted in 2D thickness maps for both epithelial thickness and Bowman's layer thickness. These measurements were performed over the full field of view of 8.4×8.4 mm, we however only chose to present the thicknesses for a diameter of 6 mm across the central cornea, because in the periphery the edge detection algorithm sometimes failed to reliably detect the layer boundaries due to reduced signal-to-noise ratio. But also in the exact center of the cornea, the measured values might hold a slightly increased uncertainty due to the central specular hyper-reflective reflex. Figure 23.2c, d shows the described thickness maps for the epithelial thickness as well as for the Bowman's layer thickness, overlaid over an intensity projection of a large field of view 3D OCT data set (15×15 mm) of the same eye. For determining the thickness of thicker corneal layers (e.g., the stroma) or the complete corneal thickness it is in principle

Table 23.1 Average epithelial and Bowman's layer thickness values for different measurement techniques

Investigator	Method	Bowman's layer thickness
D. Z. Reinstein et al. [22]	Very high frequency ultrasound	53.7 μm
J. G. Pérez et al. [32]	Optical pachymeter	48 μm
H. F. Li et al. [24]	Confocal microscopy through focusing	50.6 μm
N. Hutchings et al. [27]	1,060 nm optical coherence tomography	58.4 μm
A. Tao et al. [33]	800 nm optical coherence tomography	52.5 μm
T. Schmoll et al. [28]	800 nm optical coherence tomography	55.8 μm
Y. Komai et al. [26]	Electron microscopy	8–12 μm
H. F. Li et al. [24]	Confocal microscopy through focusing	16.6 μm
N. Hutchings et al. [27]	1,060 nm optical coherence tomography	18.3 μm
A. Tao et al. [33]	800 nm optical coherence tomography	17.7 μm
T. Schmoll et al. [28]	800 nm optical coherence tomography	18.7 μm

necessary to first correct the shape of the cornea due to refraction at the front surface of the cornea [30]. However, as we were in this study only interested at the rather thin epithelium and Bowman's layer at the surface of the cornea, one could avoid the excessive computational effort of a ray tracing correction. All optical distances were divided by the average group refractive index of 1.387 in order to receive geometrical distances [31]. Another factor which would gain importance when imaging structures at larger depths would be dispersion. The dispersion introduced by the superjacent tissue and fluids would significantly disturb the high resolution of this system.

In this study a total of 14 healthy eyes were evaluated. We received an average epithelial thickness of 55.8 ± 3.3 μm and an average Bowman's layer thickness of 18.7 ± 2.5 μm. These values match very well with values found in other publications. Table 23.1 gives an overview of measured average thickness values for different measurement techniques. The lower value for the Bowman's layer thickness found with electron microscopy may not be attributed to its superior resolution capabilities compared to the other techniques, but rather to the preparation steps prior to the imaging, which include slicing, fixation, clearing, and dehydration.

Figure 23.1 already exposed the ability of ultrahigh-resolution SDOCT to resolve the tear film on top of the cornea. Using the high temporal resolution of OCT one is also able to perform time-resolved studies of the tear film and its breakup. This can be done by acquiring B-scan time series at the same lateral position. In this case a temporal resolution of 100 B-scans/s is not even necessary, which is why the acquisition rate can be reduced to 30 kHz A-scan rate in order to further enhance the sensitivity. This acquisition rate still results in a temporal resolution of 30 B-scans/s. In post-processing, the thickness of the tear film is then monitored as a function of time. Figure 23.3a shows such a B-scan of a tearing healthy eye directly after blinking. A thickness M-scan is presented in Fig. 23.3b,
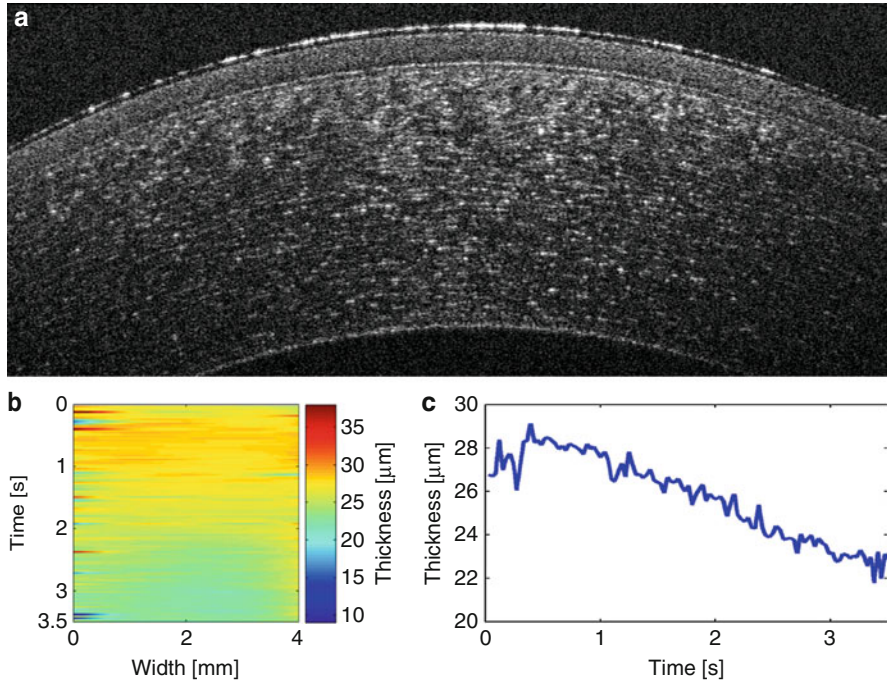
Fig. 23.3 Dynamic tear film thickness monitoring. (**a**) Ultrahigh-resolution B-scan of a tearing eye after blinking. (**b**) Tear film thickness M-scan. (**c**) Average tear film thickness as a function of time

where the color encoded tear film thickness is plotted in time across the central 4 mm of the cornea. Here also an inhomogeneous decrease of the tear film can be seen for different lateral positions. In Fig. 23.3c, we plotted the average thickness of the entire range as a function of time. Shortly after blinking the tear film thickness slightly increases before it linearly decreases over the following seconds. To further increase the value of such time-resolved tear film studies using OCT also volume series could be acquired. Either by using a lower temporal resolution or by using alternative scanning patterns, such as a radial scan pattern. Alternatively, one could use a multiple beam OCT system or parallel OCT system to further increase the acquisition speed, while maintaining the resolution [34].

The ultrahigh resolution and ultrahigh speed opens new perspectives for corneal diagnostics. It enhances the diagnostics of several corneal diseases and may be used to improve the accuracy of refractive surgery. In the future, ultrahigh-resolution and ultrahigh-speed OCT systems might even be directly integrated in machines for refractive surgery to monitor the surgery in quasi real time. The ability to perform precise time-resolved imaging of the tear film may in the future be used to investigate dry eye disease, pharmacological studies of artificial tears, or the effect of contact lenses on the tear film.
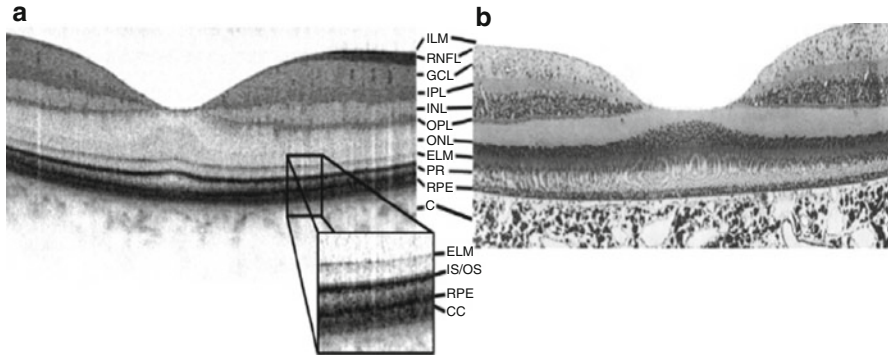
Fig. 23.4 (**a**) UHR OCT tomogram taken across the central fovea. The retinal layers can easily be identified by cross-correlation with histology (**b**) (The histology was copied from [35])

23.3 Retinal Imaging

The development of Ti:Sapph lasers provided broad optical bandwidths in the interesting therapeutic window at 800 nm, where water absorption and scattering is low. This enabled OCT imaging with high axial resolution–ultrahigh-resolution OCT (UHR OCT). First implementations for retinal imaging brought a quantum step in imaging performance, and detail. The drawback of UHR OCT based on time domain OCT however was the inverse scaling of the signal-to-noise ratio (SNR) with the optical bandwidth. At the time, retinal UHR-OCT equipped with Ti:Sapph lasers achieved A-scan rates of less than 100 Hz. Nevertheless, the new degree of detail allowed for a precise interpretation of retinal layers, resulting also in a better diagnosis of retinal diseases based on OCT scans. The next quantum step in retinal imaging brought Fourier domain OCT (FDOCT), which allowed for unprecedented high speed imaging without suffering the SNR drawback of TDOCT. Soon, UHR FDOCT images were presented revealing impressive structural details in full three-dimensional volumes. The higher speed can be used for high-density scans to improve the tissue contrast. Current UHR FDOCT systems provide details that can be well compared with histological sections (Fig. 23.4).

On the other hand, it is possible to average several tomograms and to remove the speckle noise. The price in resolution is completely outweighted by the gain in image quality. Current developments of sensor technology and light source technology enable recording of full-time series with volume rates of more than 10 Hz. The principle of Fourier domain mode locking (FDML) for swept source OCT opened another quantum leap in speed performance breaking already the 1 MHz A-scan rate barrier [15–17].

Figure 23.5 shows the effect of tomogram averaging using UHR FDOCT for imaging the central retina. The tomograms were obtained at 100 kHz A-scan rate and an axial resolution of better than 3 μm. A single tomogram is shown in Fig. 23.5a.B with a zoom into the squared regions A and B. The effect of averaging
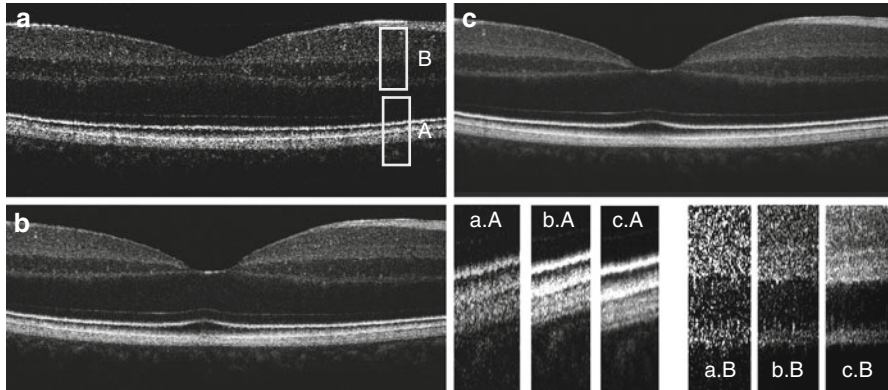
Fig. 23.5 (**a**) Influence of speckle averaging by summing tomograms. The number of averaged tomograms changes are 0(a), 3(b), 7(c). The rectangular areas of interest show substructure in the photoreceptor layer (*A*) and in the inner plexiform layer (*B*) that become visible by speckle reduction. Higher averaging smoothes out the capillary structure in *D*

is seen from Fig. 23.5 B.b–c, for using 3 and 7 tomograms. Speckle averaging reveals details that are otherwise hidden, such as the splitting of the retinal pigment layer (A) or the three layer substructure of the inner plexiform layer (B).

Having improved the axial resolution for retinal imaging to less than three micrometers, the next question is how to deal with the lateral resolution. The unique advantage of OCT is the decoupling of axial and lateral resolution. Hence, even with low numeric aperture (NA) objectives an axial resolution of less than 1 μm is feasible if the optics supports the large optical bandwidth. However, the lateral resolution in the focus scales linearly with the NA as in confocal microscopy. The change in lateral resolution along the optical axis still depends on the depth of focus (DOF) range as given by the Rayleigh range of Gaussian optics. The DOF scales to the power of two with the inverse NA. Thus, improving the resolution by a factor of two decreases the DOF by a factor of four. In case of retinal imaging, the maximum lateral resolution is limited by the iris dilatation. According to Gaussian optics, we have in the diffraction limit the following relation between spot size σ and beam diameter d, $\sigma = 4\lambda f/(\pi d)$, where λ_0 is the central wavelength of the light source, and f is the effective focal length of a standard eye. Assuming $f = 24.46$ mm and $\lambda_0 = 800$ nm yields the plot of Fig. 23.6.

Even for a full pupil size of 7 mm one obtains a theoretical diffraction limited lateral spot size of 3.6 μm. In practice, it is not recommended to use the total aperture given by the fully dilated iris. As the beam diameter at the cornea increases, ocular aberrations will become more prominent. Those aberrations cannot be corrected by simple spectacles correcting for defocus and astigmatism. They involve higher order deformations of the wavefront that can only be properly treated with the use of adaptive optics (AO). AO was originally developed for astronomy, and was used for correcting the influence of air turbulences of the atmosphere to the imaging performance of ground-based telescopes. The principle

Fig. 23.6 Diffraction limited spot size on the retina for central wave length $\lambda_0 = 800$ nm
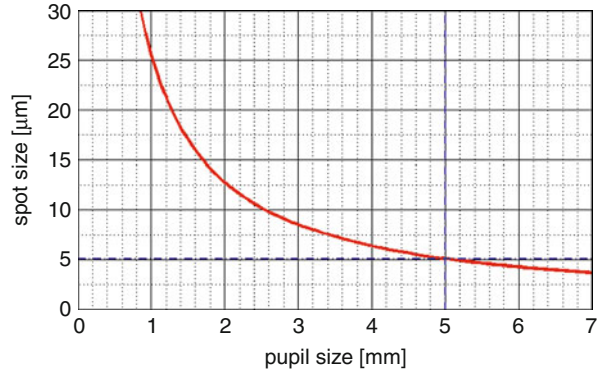
has been adapted for improving retinal imaging systems and has recently been successfully combined with OCT. AO OCT would allow for retinal imaging with high isotropic resolution in all three dimensions. As compared to Scanning Laser Opthalmology, OCT has the advantage of better axial resolution and efficient rejection of out-of-focus or out-of-coherence-gate light.

Nevertheless, motion artifacts especially for in vivo imaging often limit the performance of systems with nominal high lateral resolution. Therefore, resolution and imaging speed are closely linked. For example, the cone photoreceptor mosaic could already be visualized without the use of AO, but with high speed en face OCT [36]. The fast acquisition of several tens of en face images per second preserved the integrity of lateral structures. The same has been observed recently with high speed FDOCT systems based on CMOS technology [18, 19]. CMOS sensors have the advantage as compared to CCD sensors that the frame rate can be increased by decreasing the number of active pixels. For example, a common CMOS sensor for high speed OCT has 4,096 pixels and a frame rate of 70 kHz (Basler Sprint spL4096-140 km). Reducing the number of pixels to 512 allows for more than 300 kHz frame rate. Clearly, the reduced number of pixels results in smaller spectral bandwidth and lower resolution (keeping the same optics and grating configuration in the spectrometer), or in reduced depth range. Figure 23.7 plots the experimentally determined sensitivity of the detector for various speed settings, keeping the number of pixels constant. The sensitivity decay is displayed in Fig. 23.7a for two camera line-rate settings, 20 and 200 kHz. With both settings there is a loss of -9 dB over 2 mm, indicating no observable pixel cross talk change with line rate. Figure 23.7b displays the measured sensitivities for used camera line rates. Since sensitivity scales with exposure time rather than line rate, the actual exposure time is plotted. There is -11 dB change in sensitivity from 20 to 200 kHz as should be expected, since the exposure times change by an order of magnitude from 48.3 to 3.3 μs. The sensitivity might be partially recovered using alternative interferometer configurations employing fiber circulators or different splitting ratios. Nevertheless, even at 200 kHz there is still sufficient sensitivity >90 dB for retinal in vivo imaging.
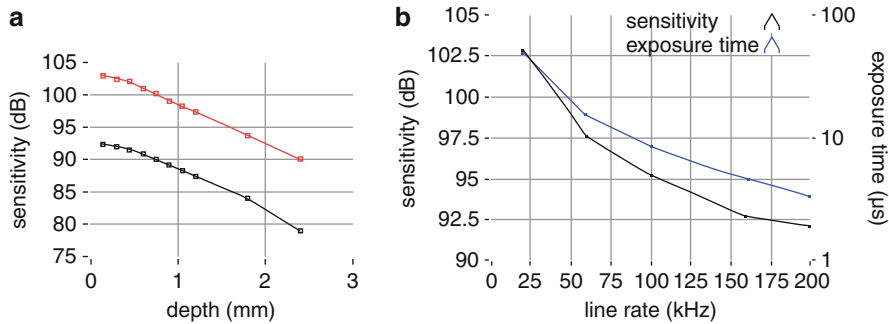
Fig. 23.7 (**a**) Sensitivity decay with depth (*red* line 20 kHz, *black* line 200 kHz). (**b**) Sensitivity decay with line rate (*black*), and actual exposure time (*blue*)

The current chapter is devoted to demonstrate the performance of high speed UHR FDOCT to resolve microscopic retinal details without the technologically complex and expensive AO extension. The interested reader is referred, e.g., to the review article of Pircher and Zawadzki [37]. Of course, it is then important to avoid large aberrations caused by filling the maximum iris diameter with the illumination. The usable pupil size that exhibits minimum optical aberrations varies from subject to subject. In average a larger pupil size than 3–4 mm only results in degradation of lateral resolution on the retina.

On the one hand, the visualization of microscopic retinal details needs a densely sampled volume. On the other hand, recording times need to be small in order to keep motion artifacts low. To give an example: if the spot size on the retina is only 5 μm, then a small patch on the retina covering 1.5 × 1.5 mm needs at least a sampling of 600 × 600 points. Thus, even at high acquisition speed of 100 kHz, the recording takes already more than 3 s. This stresses again the strong link of high resolution and imaging speed. Motion artifacts can roughly be divided into large-scale motion due to eye drift or heart beat, and small saccadic movements in the order of a few microseconds. The influence of the first kind of motion can be minimized by keeping the acquisition times small often at the price of undersampling. Having a fast OCT system at hand, it is possible to study the motion artifacts in 3D by acquiring volume series [38]. Fig. 23.8a shows an en face map taken at the photoreceptor layer of a single volume obtained at 200 kHz A-scan rate, and 10 Hz volume rate. The photoreceptor mosaic is well appreciated. Registration of the individual volumes allows tracing the relative displacements in the en face direction as shown in Fig. 23.8d. The trace is followed over a time course of 2 s and shows the movement of an eye that fixates on a target. Even for a trained person, that fixates well, the amplitude varies from 10 to 50 μm within 100 ms. Figure 23.8c shows a small region where saccadic motion occurs. The duration of the saccade is about 10 ms. Saccadic motion happens at a much smaller timescale and is therefore difficult to avoid. The amount of saccades changes not only from subject to subject, but might also vary for a single subject. However, it is interesting to observe that the eye returns back to the original fixation point with good precision.
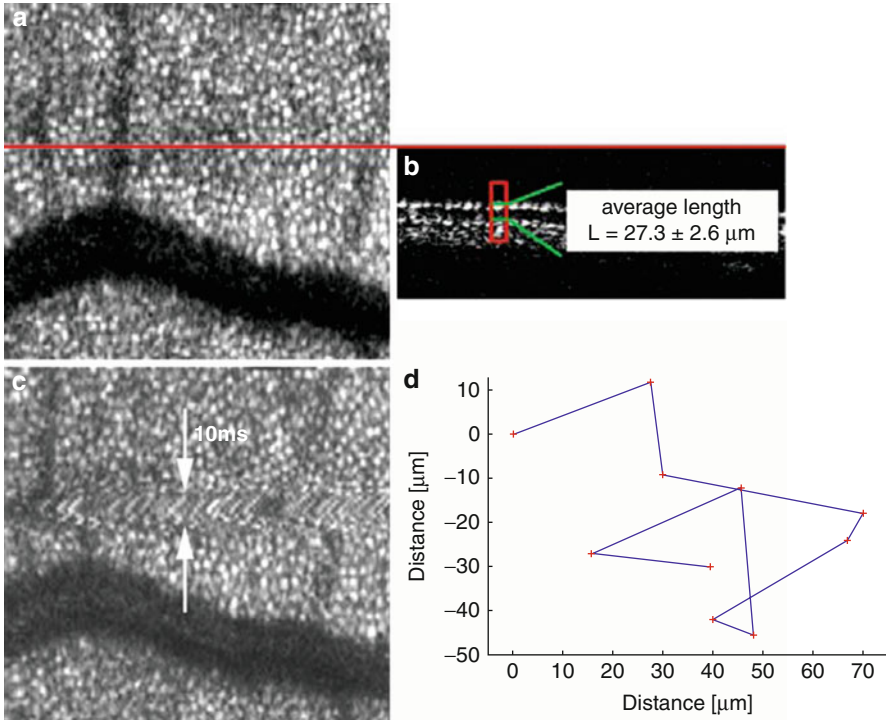
Fig. 23.8 (**a**) En face projection of a high speed OCT volume (300 × 300 μm) acquired at 200 kHz taken at the inner/outer segment photoreceptor junction. (**b**) Tomogram extracted at the indicated line demonstrating the measurement of the photoreceptor outer segment length. (**c**) En face view that contains a micro-saccade. (**d**) Reconstructed path of eye motion during 2 s

Resolving individual photoreceptors in 3D gives access to study structural details with high precision. Figure 23.8b shows a B-scan taken at the position indicated in Fig. 23.8a. The outer photoreceptor segment is well visible as delimited by the inner-outer segment junction and the end-tips signal. FDOCT is in fact optimal for measuring axial distances with high precision, since they are not distorted by any axial motion. It is easy to extract, for example, the average length of the outer cone photoreceptor length as 27.3 ± 2.6 μm. The axial resolution in this case was approximately 3 μm in tissue. Of particular interest are longitudinal studies of the evolution of the outer photoreceptor length [39, 40]. The cones are renewed by phagocytosis at the end tip of the photoreceptor. Pathologic changes might alter this renewal rate, which could therefore be a highly sensitive parameter for diagnosis, in particular of AMD. Alternatively, the photoreceptors have been measured with en face OCT, a method that can be viewed as SLO with coherent axial gating. The axial gate can be slowly shifted in order to record 3D maps of photoreceptors. Nevertheless, the slow tuning of the axial coordinate is sensitive to axial motion, and special care must be taken to correct for those artifacts [41].

Fig. 23.9 Imaging of individual nerve fibers in the parafoveal region
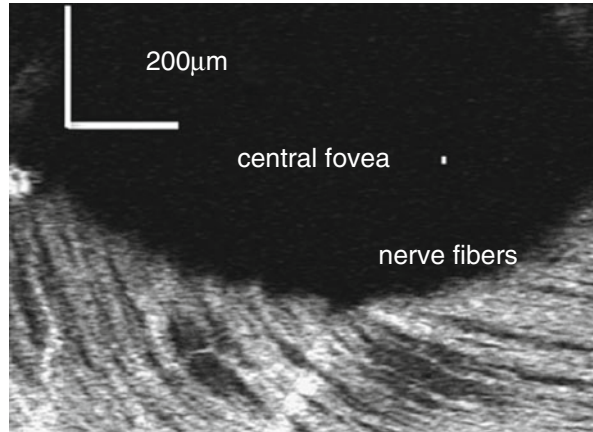
Another important microscopic structure that can be visualized comprehensively are individual nerve fiber bundles. Analysis of their structure has high relevance for diagnosis of glaucoma, or other diseases that attack the integrity and function of the nerve fiber tissue, like multiple sclerosis. Figure 23.9 shows an en face slice at the surface of the parafoveal region that allows differentiating individual nerve fiber bundles and even their substructure.

Additional contrast might be gained by complementing the intensity information with polarization sensitive (PS) contrast [42]. PS OCT is sensitive to form birefringence that is caused by the refractive index change at fiber interfaces. On the other hand, loss of degree of polarization is a sensitive label-free indicator of pigmented structure, such as the retinal pigment epithelium, or of pathologically disordered tissue. PS OCT has recently as well been demonstrated with ultrahigh speed based on FDOCT with a CMOS sensor (Fig. 23.10) [43, 44]. This is the first important step toward microscopic retinal in vivo imaging with PSOCT.

Probably, the most fascinating retinal microstructure is the retinal capillary network [45]. Typically, one can separate three capillary vessel layers: the radial peripapillary capillaries in the retinal nerve fiber layer (RNFL), the inner layer capillaries in the ganglion cell layer (GCL), and the outer layer of capillaries of the inner nuclear layer (INL) [46]. In fact, we observed that the third layer can be distinguished into another two sublayers: Those at the border of the inner plexiform layer (IPL) and INL, and another network at the INL and outer plexiform layer (OPL) boundary. The arrangement of those capillary layers is nicely seen from the cross-sections (bright spots) in the UHR OCT tomogram of Fig. 23.11(a). In the following, the inner layer capillaries of the GCL and IPL (Segment 1), and the outer layer capillaries of the INL (Segment 2) are distinguished. Although one would not expect any capillaries below the OPL within healthy eyes, certain pathologies, such as telangiectasia imply abnormal vessel growth from the INL down toward the photoreceptors. Therefore, segment 2 includes the OPL, outer nuclear layer (ONL), and the external limiting membrane (ELM) down to the inner segment/outer
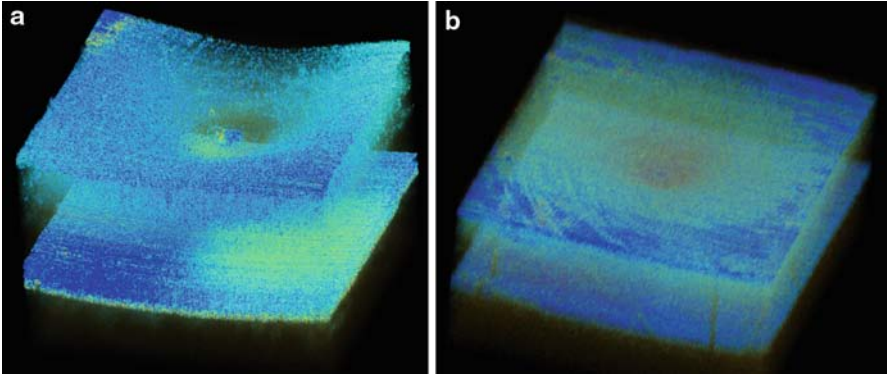
Fig. 23.10 High-speed PSOCT retardation maps across fovea recorded at 160 kHz (**a**) The impact of the Henle fibers is well visible from the typical hour glass pattern at the inner/outer segment photoreceptor junction. (**b**) Individual nerve fiber bundles are contrasted
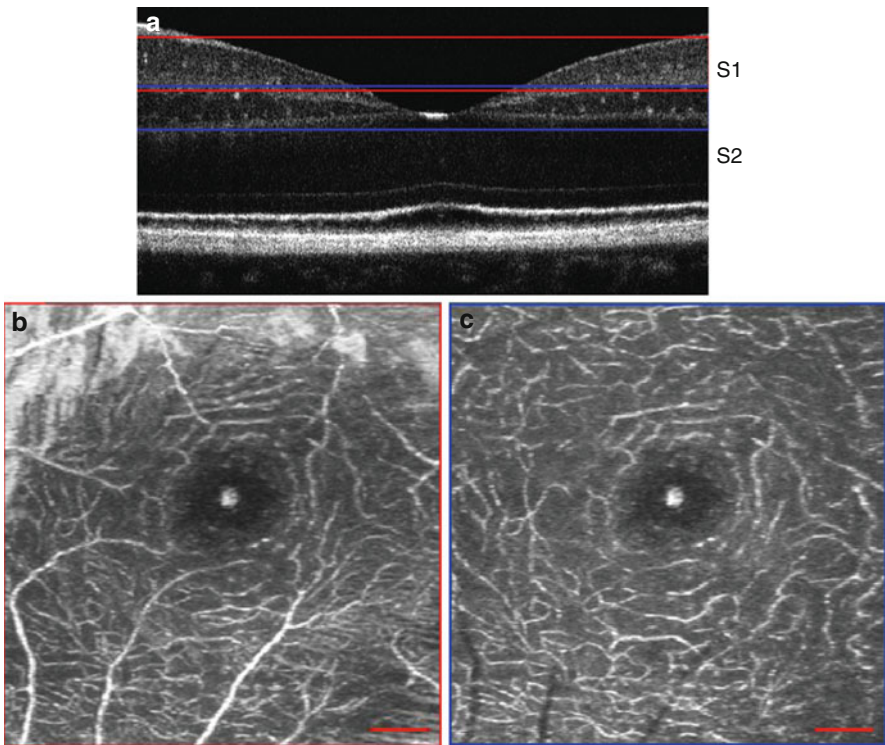
Fig. 23.11 (**a**) B-scan across the central fovea. *Red* lines indicate the segmentation of segment 1 (S1). *Blue* lines indicate the segmentation of segment 2 (S2). (**b**) En face projection of S1, indicated in (**a**). (**c**) En face projection of S2, indicated in (**a**). *Red* scale bars denote 200 μm
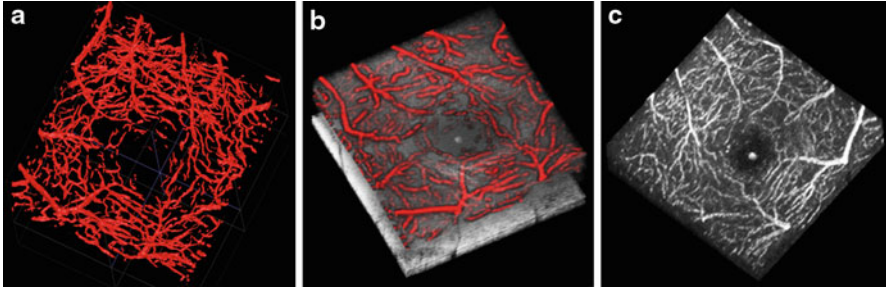
Fig. 23.12 Annotation of the foveal capillary network of a healthy eye. (**a**) 3D view of the segmented capillary network. (**b**) Overlay of the annotation and the OCT intensity volume without the retinal nerve fiber layer. (**c**) Multiplication of the annotation with the inner retinal layers of the intensity volume

segment (IS/OS) of the photoreceptors. Figure 23.11b and c are en face maximum intensity projections of segment 1 (Fig. 23.11a S1) and segment 2 (Fig. 23.11a S2) from a retinal 3D volume of a healthy subject. The segmentation of the retinal layers within the individual B-scans is done semiautomatically using a Canny edge detection algorithm. The maximum intensity projections are obtained by displaying the maximum intensity along the depth axis at each transverse position. The vascular structure is well resolved down to the size of the smallest capillaries. Also the foveal avascular zone (FAZ) is clearly visible. The good contrast for retinal vasculature is a result of the high scattering of blood relative to the surrounding naturally low scattering retinal tissue. Pure intensity imaging in combination with simple thresholding and spatial frequency filtering allows therefore already extracting the complex capillary network. Of course, this simple method has its limitations, as in particular in the plexiform layers the contrast is not as good as in the INL. Advanced methods apply machine learning algorithms adapted for OCT [47].

Expert viewer annotation may serve as a ground truth for testing any automated filtering method. The annotation of the capillaries of a healthy volunteer can be seen in Fig. 23.12a. In Fig. 23.12b an overlay of the annotation with the intensity volume can be seen. The retinal nerve fiber layer was removed in order to reveal the underlying capillary network. Figure 23.12c shows the multiplication of the annotation with the inner retinal layers of the intensity volume.

The result of filtering the microvasculature is shown in Fig. 23.13 for the same data set as presented in Fig. 23.12. Figure 23.13a shows the maximum intensity projection of the segmented INL. In Fig. 23.13b the result of the FFT band pass filter is displayed. One can clearly observe that the signal from the surrounding tissue was removed and only the capillary network remains. In the center of the maximum intensity projection the central foveal reflex is visible. It is also visible within the filter result, as it has not been removed by the FFT band pass filter. Having segmented the capillaries, we obtain the vessel centerlines by transforming the filter result to a binary image before skeletonizing the capillary network as
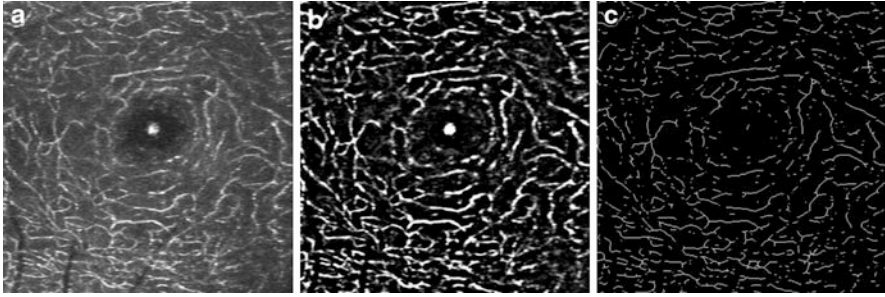
Fig. 23.13 (**a**) Maximum intensity projection of the INL; (**b**) Result of band pass filtering (**a**). (**c**) Skeleton of (**b**)
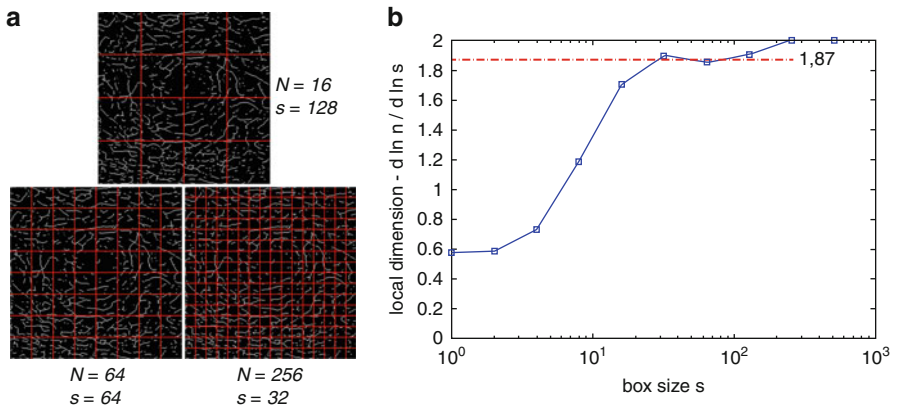
Fig. 23.14 Demonstration of box count method for determination of fractal dimension (Following [50, 51])

displayed in Fig. 23.13c. By skeletonizing the boundary pixels of the capillaries within the binary image are removed until each capillary consists of a single line, but does not break apart. This operation is performed by the Matlab function bwmorph, which uses an algorithm described by W. K. Pratt [48].

The skeletonized representation of the vasculature can be used as basis for characterizing the capillary integrity and structure. The index that describes the vascular branching pattern is the fractal dimension (FD) of the vessel lines. The fractal dimension has been used before to characterize 3D tumor vessel growth [49]. Obviously, it should be an early indicator of vascular growth disorder. A decrease of this index as compared to the healthy case indicated pathologic vessel deformation, or capillary degradation due to vessel occlusion. There are different methods to determine the FD. The easiest method to implement is the box count method [50, 51]. It is based on calculating the number of vessel pixels that are covered after tiling the image area in boxes of different sizes (Fig. 23.14a). The FD
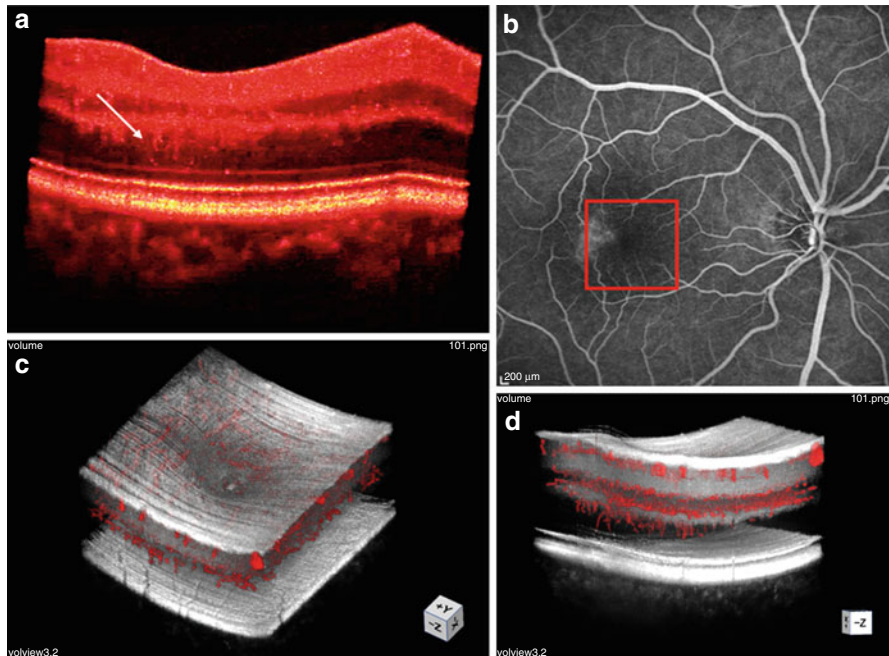
Fig. 23.15 Atypical vessel growth in telangiectasia. (**a**) Intensity volume, white arrow points to capillaries growing toward photoreceptors; (**b**) Fundus fluorescein angiogram, square indicates section imaged with OCT. (**c**) Overlay of intensity volume and annotation; (**d**) Overlay of intensity volume and annotation showing capillaries growing toward photoreceptors

is given by determining a plateau of the local slope in the *ln N* versus *ln s* plot, where *s* is the size of the box, and *N* is the number of boxes that cover the vessels (Fig. 23.14b).

To compare healthy and diseased case data of patients suffering from early stage telangiectasia are taken (Fig. 23.15). The ultrahigh-resolution and high-speed system reveals for the first time small pathologic growing disorders of capillaries from the INL, through the OPL and ONL, down toward the photoreceptors. These capillaries can already be observed within the intensity volume rendering without any filtering (Fig. 23.15a) and are even better visible within the overlay of the expert annotation with the intensity volume (Fig. 23.15c, d). The area of the abnormal vessel growth corresponds to areas in the fundus fluorescence angiography, where leakages are clearly visible (Fig. 23.15b).

In general, the FD can be calculated for the total measured 3D volume. However, it was seen that the fractal dimension of 2.35 for the healthy retina differed only slightly from that of the diseased retina of 2.33 [45].

The fractal volume analysis gives a gross overview about the entire parafoveal capillary network. If one investigates the capillary network of the telangiectasia eyes, one observes pathologic changes especially in the second segment S2. Figure 23.16 plots the FD of the two healthy and two diseased retinas for

Fig. 23.16 Fractal dimension for segments of two healthy subjects and two patients suffering from telangiectasia
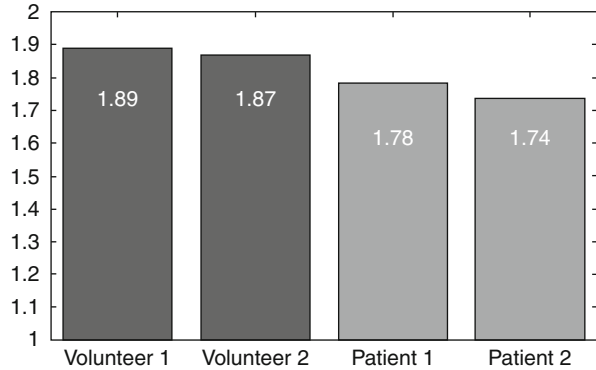
segments 2 (cf. Fig. 23.11a) showing larger values for the healthy layers as compared to the diseased ones. This result is a first indication that local fractal dimensional analysis might indeed be used for distinguishing healthy from diseased retinal capillary structure.

Of course, the published results so far show only a tendency that needs to be further investigated based on a larger number of patient data. It will be of main interest in further studies how sensitive the index is to early small changes in the capillary structure. Nevertheless, the fact that one has now access to those structures with high speed and ultrahigh-resolution retinal tomography systems opens new perspectives in early retinal diagnosis.

23.4 4D Capillary Imaging

We have seen that the imaging speed of current research OCT systems already reaches several hundred to a few million axial scans per second [16–19]. This opens completely new perspectives for microscopic in vivo imaging of dynamic tissue processes. It is now not only possible to record single cross-sectional scans or single volumes, but also a series of volumes with high temporal sampling. With the fastest systems even video rate volume series of 25–50 volumes/s can are achievable. With such a system one is now able to capture dynamic processes in 4D (3D plus time), opposed to B-scan time series which of course only hold cross-sectional information [19]. Figure 23.17 shows 5 volumes of such a 4D acquisition of the parafoveal capillaries. This time series was recorded at 200,000 A-scans/s and a sampling of 150 A-scans $\times$ 100 B-scans per volume, which resulted in a volume rate of 13.3 volumes/s. Each volume covers the same patch of 0.6 deg $\times$ 0.4 deg on the retina, approximately 1 deg nasal to the fovea. Axial motion artifacts induced by the heart beat were corrected using correlation-based image registration. The transverse resolution was approximately 5 μm. The axial resolution defined by the bandwidth of the used super luminescence diode (SLD) was 6.7 μm in air. The power at the cornea was measured to be 550 μW.

Fig. 23.17 4D acquisition of parafoveal capillaries recorded at a volume rate of 13.3 volumes/s. (**a**) The retinal nerve fiber layer (RNFL) was removed to reveal a larger capillary within the ganglion cell layer (GCL). (**b**) The RNFL, GCL and inner plexiform layer (IPL) were removed to reveal the capillaries within the inner nuclear layer (INL). The fluctuating bright spots from volume to volume represent blood cells traveling through the capillaries
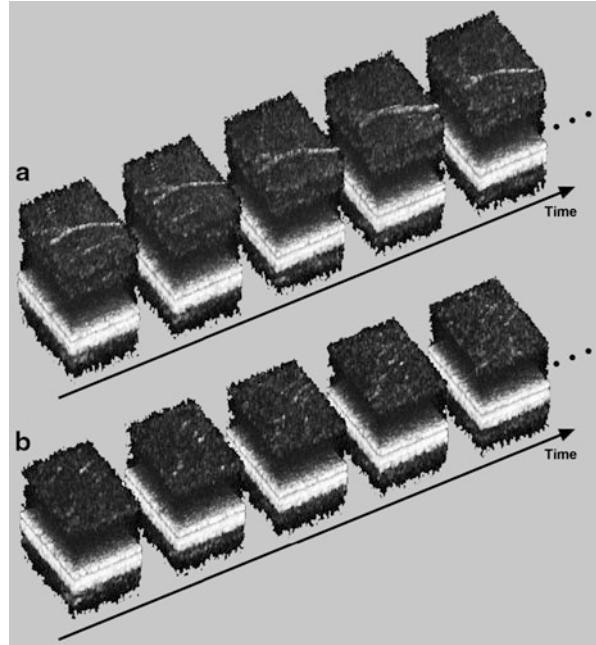
In Fig. 23.17a the retinal nerve fiber layer (RNFL) was removed to reveal a larger capillary within the ganglion cell layer (GCL). The intensity fluctuation within this capillary from one volume in time to the next is an indication for blood flowing through this capillary. Below in Fig. 23.17b in addition to the RNFL also the GCL as well as the inner plexiform layer (IPL) has been removed in order to reveal the small capillaries of the inner nuclear layer (INL). The shifting bright spots within this layer represent blood cells traveling through the capillaries.

Although flow quantification cannot be demonstrated within such time series, it offers for the first time the observation of pulsation phase-coherent volumetric perfusion images. Such information will certainly impact on the way retinal flow beds are understood in their interaction with different retinal structures and layers and might eventually lead to a better understanding of retinal function and pathophysiology.

23.5   Conclusion and Outlook

For in vivo imaging high resolution needs the support of high acquisition speed. Technological development in light source as well as sensor technology is continuously pushing the performance of OCT systems. The benefit for the patient is increased comfort due to shorter measurement procedures, but also better diagnosis as a result of improved quality of images. With the integration of functional extensions such as 4D flow imaging or polarization contrast OCT, further enhances the diagnostic capabilities of high speed OCT. The access to comprehensive microstructural details

such as the nerve fiber bundles or the capillary network opens exciting perspectives for ophthalmic research and early diagnosis. Resolving the photoreceptors in 3D gives access to a better understanding of dynamic physiologic processes. The response of individual photoreceptors to stimulation might, for example, give insight into signal pathways in a completely noninvasive and noncontact way.

The next generation of ophthalmic systems employs multiple beams in order to decrease the measurement times or parallelize the acquisition. Broad bandwidth sources might become even more compact and cheaper, which opened the way for commercializing also UHR OCT. Finally, it is up to the medical researchers to properly exploit the new fascinating possibilities that are available through latest technological mile steps in OCT.

References

1. A.F. Fercher, Ophthalmic laser interferometry. Proc. SPIE **658**, 48–51 (1986)
2. A.F. Fercher, K. Mengedoht, W. Werner, Eye-length measurement by interferometry with partially coherent light. Opt. Lett. **13**, 186–188 (1988)
3. A.F. Fercher, Ophthalmic interferometry, in *Optics in Medicine, Biology and Environmental Research. Selected Contributions to the First International Conference on Optics Within Life Sciences (OWLSI), Garmisch-Partenkirchen, Germany, 12–16 August 1990 (ICO-15SAT)*, ed. by G. von Bally, S. Khanna (Elsevier, Amsterdam/London/New York/Tokyo, 1993), pp. 221–228
4. D. Huang, E.A. Swanson, C.P. Lin, J.S. Schuman, W.G. Stinson, W. Chang, M.R. Hee, T. Flotte, K. Gregory, C.A. Puliafito et al., Optical coherence tomography. Science **254**, 1178–1181 (1991)
5. A.F. Fercher, C.K. Hitzenberger, W. Drexler, G. Kamp, H. Sattmann, *In vivo* optical coherence tomography. Am. J. Ophthalmol. **116**, 113–114 (1993)
6. E.A. Swanson, J.A. Izatt, M.R. Hee, D. Huang, C.P. Lin, J.S. Schuman, C.A. Puliafito, J.G. Fujimoto, In vivo retinal imaging by optical coherence tomography. Opt. Lett. **18**, 1864–1866 (1993)
7. W. Drexler, U. Morgner, F.X. Kartner, C. Pitris, S.A. Boppart, X.D. Li, E.P. Ippen, J.G. Fujimoto, In vivo ultrahigh-resolution optical coherence tomography. Opt. Lett. **24**, 1221–1223 (1999)
8. W. Drexler, U. Morgner, R.K. Ghanta, F.X. Kartner, J.S. Schuman, J.G. Fujimoto, Ultrahigh-resolution ophthalmic optical coherence tomography. Nat. Med. **7**, 502–507 (2001)
9. W. Drexler, H. Sattmann, B. Hermann, T.H. Ko, M. Stur, A. Unterhuber, C. Scholda, O. Findl, M. Wirtitsch, J.G. Fujimoto, A.F. Fercher, Enhanced visualization of macular pathology with the use of ultrahigh-resolution optical coherence tomography. Arch. Ophthalmol. Chic **121**, 695–706 (2003)
10. W. Drexler, Ultrahigh-resolution optical coherence tomography. J. Biomed. Opt. **9**, 47–74 (2004)

11. A.F. Fercher, C.K. Hitzenberger, G. Kamp, S.Y. Elzaiat, Measurement of intraocular distances by backscattering spectral interferometry. Opt. Commun. **117**, 43–48 (1995)
12. R. Leitgeb, C. Hitzenberger, A. Fercher, Performance of Fourier domain vs. time domain optical coherence tomography. Opt. Express **11**(889–894) (2003)
13. J.F. de Boer, B. Cense, B.H. Park, M.C. Pierce, G.J. Tearney, B.E. Bouma, Improved signal-to-noise ratio in spectral-domain compared with time-domain optical coherence tomography. Opt. Lett. **28**, 2067–2069 (2003)
14. M. Choma, M. Sarunic, C. Yang, J. Izatt, Sensitivity advantage of swept source and Fourier domain optical coherence tomography. Opt. Express **11**, 2183–2189 (2003)
15. R. Huber, M. Wojtkowski, J.G. Fujimoto, Fourier domain mode locking (FDML): a new laser operating regime and applications for optical coherence tomography. Opt. Express **14**, 3225–3237 (2006)
16. W. Wieser, B.R. Biedermann, T. Klein, C.M. Eigenwillig, R. Huber, Multi-megahertz OCT: high quality 3D imaging at 20 million A-scans and 4.5 GVoxels per second. Opt. Express **18**, 14685–14704 (2010)
17. T. Klein, W. Wieser, C.M. Eigenwillig, B.R. Biedermann, R. Huber, Megahertz OCT for ultrawide-field retinal imaging with a 1050 nm Fourier domain mode-locked laser. Opt. Express **19**, 3044–3062 (2011)
18. B. Potsaid, I. Gorczynska, V.J. Srinivasan, Y. Chen, J. Jiang, A. Cable, J.G. Fujimoto, Ultrahigh speed spectral/Fourier domain OCT ophthalmic imaging at 70,000 to 312,500 axial scans per second. Opt. Express **16**, 15149–15169 (2008)
19. T. Schmoll, C. Kolbitsch, R.A. Leitgeb, Ultra-high-speed volumetric tomography of human retinal blood flow. Opt. Express **17**, 4166–4176 (2009)
20. V. Christopoulos, L. Kagemann, G. Wollstein, H. Ishikawa, M.L. Gabriele, M. Wojtkowski, V. Srinivasan, J.G. Fujimoto, J.S. Duker, D.K. Dhaliwal, J.S. Schuman, In vivo corneal high-speed, ultra high-resolution optical coherence tomography. Arch. Ophthalmol. Chic **125**, 1027–1035 (2007)
21. Y.S. Rabinowitz, K. Rasheed, H. Yang, J. Elashoff, Accuracy of ultrasonic pachymetry and videokeratography in detecting keratoconus. J. Cataract Refract. Surg. **24**, 196–201 (1998)
22. D.Z. Reinstein, T.J. Archer, M. Gobbe, R.H. Silverman, D.J. Coleman, Epithelial thickness in the normal cornea: three-dimensional display with Artemis very high-frequency digital ultrasound. J. Refract. Surg. **24**, 571–581 (2008)
23. B.R. Masters, A.A. Thaer, Real-time scanning slit confocal microscopy of the in vivo human cornea. Appl Opt **33**, 695–701 (1994)
24. H.F. Li, W.M. Petroll, T. Moller-Pedersen, J.K. Maurer, H.D. Cavanagh, J.V. Jester, Epithelial and corneal thickness measurements by in vivo confocal microscopy through focusing (CMTF). Curr. Eye Res. **16**, 214–221 (1997)
25. I. Jalbert, F. Stapleton, E. Papas, D.F. Sweeney, M. Coroneo, In vivo confocal microscopy of the human cornea. Br. J. Ophthalmol. **87**, 225–236 (2003)
26. Y. Komai, T. Ushiki, The three-dimensional organization of collagen fibrils in the human cornea and sclera. Invest. Ophthalmol. Vis. Sci. **32**, 2244–2258 (1991)
27. N. Hutchings, T.L. Simpson, C. Hyun, A.A. Moayed, S. Hariri, L. Sorbara, K. Bizheva, Swelling of the human cornea revealed by high-speed, ultrahigh-resolution optical coherence tomography. Invest. Ophthalmol. Vis. Sci. **51**, 4579–4584 (2010)
28. T. Schmoll, A. Unterhuber, C. Kolbitsch, T. Le, A. Stingl, R.A. Leitgeb, Precise thickness measurements of Bowman's layer, epithelium and tear film. Optom. Vis. Sci. **89**(5), E795–E802 (2012)
29. B. Povazay, K. Bizheva, A. Unterhuber, B. Hermann, H. Sattmann, A.F. Fercher, W. Drexler, A. Apolonski, W.J. Wadsworth, J.C. Knight, P.S. Russell, M. Vetterlein, E. Scherzer, Submicrometer axial resolution optical coherence tomography. Opt. Lett. **27**, 1800–1802 (2002)
30. M. Zhao, A.N. Kuo, J.A. Izatt, 3D refraction correction and extraction of clinical parameters from spectral domain optical coherence tomography of the cornea. Opt. Express **18**, 8923–8936 (2010)

31. S.R. Uhlhorn, D. Borja, F. Manns, J.M. Parel, Refractive index measurement of the isolated crystalline lens using optical coherence tomography. Vision Res. **48**, 2732–2738 (2008)

32. J.G. Perez, J.M. Meijome, I. Jalbert, D.F. Sweeney, P. Erickson, Corneal epithelial thinning profile induced by long-term wear of hydrogel lenses. Cornea **22**, 304–307 (2003)

33. A. Tao, J. Wang, Q. Chen, M. Shen, F. Lu, S.R. Dubovy, M.A. Shousha, Topographic thickness of Bowman's layer determined by ultra-high resolution spectral domain-optical coherence tomography. Invest. Ophthalmol. Vis. Sci. **52**, 3901–3907 (2011)

34. B. Grajciar, M. Pircher, A. Fercher, R. Leitgeb, Parallel Fourier domain optical coherence tomography for in vivo measurement of the human eye. Opt. Express **13**, 1131–1137 (2005)

35. E. Wolff, R.J. Last, *Anatomy of the Eye and Orbit, Including the Central Connections, Development, and Comparative Anatomy of the Visual Apparatus* (H. K. Lewis, London, 1968)

36. M. Pircher, B. Baumann, E. Gotzinger, H. Sattmann, C.K. Hitzenberger, Simultaneous SLO/OCT imaging of the human retina with axial eye motion correction. Opt. Express **15**, 16922–16932 (2007)

37. M. Pircher, R.J. Zawadzki, Combining adaptive optics with optical coherence tomography: unveiling the cellular structure of the human retina in vivo. Expert Rev. Ophthalmol. **2**, 1019–1035 (2007)

38. T. Schmoll, C. Kolbitsch, R.A. Leitgeb, In vivo functional retinal optical coherence tomography. J. Biomed. Opt. **15**(4), 041513 (2010)

39. R.S. Jonnal, J.R. Besecker, J.C. Derby, O.P. Kocaoglu, B. Cense, W. Gao, Q. Wang, D.T. Miller, Imaging outer segment renewal in living human cone photoreceptors. Opt. Express **18**, 5257–5270 (2010)

40. M. Pircher, J.S. Kroisamer, F. Felberer, H. Sattmann, E. Gotzinger, C.K. Hitzenberger, Temporal changes of human cone photoreceptors observed in vivo with SLO/OCT. Biomed. Opt. Express **2**, 100–112 (2010)

41. M. Pircher, B. Baumann, E. Gotzinger, H. Sattmann, C.K. Hitzenberger, Simultaneous SLO/OCT imaging of the human retina with axial eye motion correction. Opt. Express **15**, 16922–16932 (2007)

42. M.R. Hee, D. Huang, E.A. Swanson, J.G. Fujimoto, Polarization-sensitive low-coherence reflectometer for birefringence characterization and ranging. J. Opt. Soc. Am. B **9**, 903–908 (1992)

43. T. Schmoll, E. Götzinger, A. Unterhuber, C.K. Hitzenberger, R.A. Leitgeb, Ultra-high-speed polarization sensitive OCT in the human retina using a single spectrometer. Proc. SPIE **7889**, 7889 0U (2011)

44. T. Schmoll, E. Gotzinger, M. Pircher, C.K. Hitzenberger, R.A. Leitgeb, Single-camera polarization-sensitive spectral-domain OCT by spatial frequency encoding. Opt. Lett. **35**, 241–243 (2010)

45. T. Schmoll, A.S. Singh, C. Blatter, S. Schriefl, C. Ahlers, U. Schmidt-Erfurth, R.A. Leitgeb, Imaging of the parafoveal capillary network and its integrity analysis using fractal dimension. Biomed. Opt. Express **2**, 1159–1168 (2011)

46. R.E. Records, *Physiology of the Human Eye and Visual System* (Harper & Row, Hagerstown, 1979)

47. E. Dittrich, R. Neij, T. Schmoll, S. Schriefl, C. Ahlers, R.A. Leitgeb, G. Langs, Detection of capillary vessels in optical coherence tomography based on a probabilistic kernel. Med. Image Underst. Anal. **13**, 37–41 (2009)

48. W.K. Pratt, *Digital Image Processing* (Wiley, New York, 1991)

49. B.J. Vakoc, R.M. Lanning, J.A. Tyrrell, T.P. Padera, L.A. Bartlett, T. Stylianopoulos, L.L. Munn, G.J. Tearney, D. Fukumura, R.K. Jain, B.E. Bouma, Three-dimensional microscopy of the tumor microenvironment in vivo using optical frequency domain imaging. Nat. Med. **15**, 1219–1223 (2009)

50. J.W. Baish, R.K. Jain, Fractals and cancer. Cancer Res. **60**, 3683–3688 (2000)

51. F. Moisy, Boxcount (Matlab Central, 2006). http://www.mathworks.com/matlabcentral/fileexchange/13063-boxcount

OCT Fundamentals and Clinical Applications of Endoscopic OCT

24

Lev S. Dolin, Grigory V. Gelikonov, Valentin M. Gelikonov,
Natalia D. Gladkova, Rashid R. Iksanov, Vladislav A. Kamensky,
Roman V. Kuranov, Alexander M. Sergeev, Natalia M. Shakhova,
and Ilya V. Turchin

Contents

L.S. Dolin (✉) • G.V. Gelikonov • V.M. Gelikonov • R.R. Iksanov • V.A. Kamensky •
R.V. Kuranov • A.M. Sergeev • N.M. Shakhova • I.V. Turchin
Institute of Applied Physics of the Russian Academy of Sciences, Nizhny Novgorod, Russian
Federation
e-mail: Lev.Dolin@hydro.appl.sci-nnov.ru, grig@ufp.appl.sci-nnov.ru, gelikon@ufp.appl.sci-
nnov.ru, rir@ufp.appl.sci-nnov.ru, vlad@ufp.appl.sci-nnov.ru, rkuranov@yahoo.com, ams@ufp.
appl.sci-nnov.ru, shakh@ufp.appl.sci-nnov.ru, ilya@ufp.appl.sci-nnov.ru

N.D. Gladkova
Medical Academy, Nizhny Novgorod, Russian Federation

Abstract

This chapter is devoted to different aspects of optical coherence tomography. First, the theory of OCT image formation is discussed from the standpoint of the wave and energy approaches. The next section discusses the development and creation of optical elements based on polarization-maintaining fiber for the "heart" of the OCT scheme – the Michelson interferometer. Then, various modifications of OCT such as "two-color," 3D, cross-polarized, and endoscopic OCT modalities are discussed briefly. Following the theoretical and technical discussion of OCT, the chapter overviews its clinical applications. OCT's criteria of norm and pathology, diagnostic value, and clinical indications are discussed. Influence of tissue compression and various chemical agents on OCT images are also shown. Finally, a mathematical algorithm for postprocessing of OCT images is demonstrated and results of recovering of tissue scattering properties are discussed.

24.1 Introduction

In the past decade, an increasing interest in new optical bioimaging modalities and rapid development of relevant optical technologies has stimulated elaboration of a number of optical coherence tomography (OCT) schemes that resulted in various laboratory setups. A wide range of optical components such as femtosecond lasers, superluminescent and thermal light sources, fiber optical and air interferometers, mechanical and piezo-optical scanning systems, and highly sensitive detectors of interference signals with a large dynamic range were mastered for applications in OCT for the entire infrared frequency band.

Selection of a scheme and creation of a specific OCT setup is guided primarily by the problem OCT is intended to solve. The main purpose of the study, the results of which are presented in this chapter, was creation of an endoscopic OCT device and application of this device for multi-disciplinary clinical studies. Obviously, in order to comply with the above requirements, this OCT device is to be compact, reliable, easy to use in a clinical environment, and potentially be compatible with the majority of modern standard endoscopic equipment. These requirements determined the choice of fiber optical interferometry based on polarization maintaining (PM) fiber and superluminescent light sources as main components of an endoscopic OCT system. Use of PM fibers

allows implementing a flexible sample arm of an interferometer, which facilitates access to internal organs; superluminescent light sources are apparently preferable to femtosecond lasers, primarily due to the complexity, cost, and size of the latter.

Creation of the proposed OCT scheme was accompanied by solving several optical engineering problems. First, a new system for fast piezo-optical scanning of the pathlength difference between the interferometer arms was devised, which allowed getting rid of mechanically moving parts in the interferometer and creation of an all-optical-fiber OCT device. Second, a miniature optical probe performing lateral scanning of a probing beam was invented and constructed; the size of the optical probe is sufficiently small to fit biopsy channels of standard endoscopic equipment. Third, fiber optical elements with unique characteristics allowed creation of ultra-broadband and multicolor OCT schemes. All these inventions were put together and lead to development of the whole range of compact OCT devices, which were successfully introduced into research clinical practice. This chapter discusses theoretical issues of OCT image formation and experimental and technical aspects of the OCT scheme used, and also presents some clinical results obtained by means of the created OCT devices.

24.2 Theoretical Models for OCT Imaging

From the standpoint of optical theory, the problems of detecting a foreign object embedded in a turbid medium and imaging separate elements of the medium (i.e., its tomography) are very closely related. In each case, the ability to perform remote sensing is limited by three factors. First, light that propagates from the source to the object (or a specific element of the medium) and from the object to the detector can be either absorbed or scattered out of the propagation path, resulting in signal attenuation. Second, due to scattering, photons coming from the object change their direction of propagation and contribute to "strange" elements in the image. It results in the so-called multiplicative noise. Finally, light that has scattered out of the propagation path can re-scatter back into the path and be detected, but with a different phase. This is an additive noise source resulting from multiple light scattering events in the volume of the turbid medium. The first limitation can be mitigated by choosing an appropriate operating wavelength that suffers the least losses and employing a source that delivers a sufficiently large number of photons to the detector. The influence of the other two factors can be attacked using special methods of control of the illumination field and selective detection of the received signals. Such methods were developed for radar and hydroacoustic sensing [1, 2]; their application in optics became possible with the advent of lasers. In particular, the technique of optical sounding was developed and used for observation of light scattering layers in the ocean and atmosphere with depth resolution of about a meter. With the advent of femtosecond lasers, it became tempting to apply the lidar technique to imaging of biological tissue with micrometer-scale resolution. However, unlike nanosecond oceanic optical ranging experiments, direct time-of-flight measurements are difficult in the femtosecond temporal regime and usually require cumbersome nonlinear-optical-gating techniques. This problem does not

Fig. 24.1 A principal scheme of OCT setup. SLD (superluminescent diode), M (reference mirror), EF (optical fiber end), L (lens), PD (photodetector), S (OCT signal)
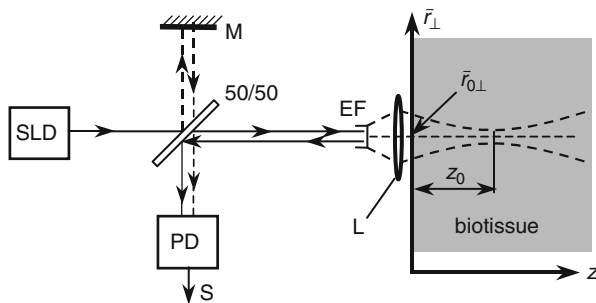
arise in optical coherence tomography [3–10] that realizes the sounding technique based on coherent reception of a broadband continuous signal.

An OCT image is formed by a continuous optical signal radiated and received by the tip of a single-mode optical fiber (Fig. 24.1). The radiation is transmitted to the medium as a narrow focused beam. Separate observation of reflections from tissue elements that are located at different depths (z) is performed by measuring the cross-correlation function of the reflected optical signal and the reference signal. The reference signal is a copy of the probing signal and is formed by launching the source light to the reference arm of the optical fiber Michelson interferometer. The received and reference waves are recombined on a photodetector. The tomographic signal is obtained as a result of detection of Doppler beats that emerge in the photodetector current in response to variation of the length of the interferometer reference arm. The image in the $z = $ const plane is formed due to the shift of the OCT system aperture along the tissue surface.

Although OCT and pulsed methods use different ways of forming the image versus depth, this difference has no impact on the informative properties of the image. Therefore, models of OCT images are constructed by analogy with lidar signal models. Solutions of radiative transfer equation (RTE) or results of modeling of photon migration in a scattering medium by the Monte Carlo method are usually used for this purpose.

It should be noted that energy (or corpuscular) description of a light field does not take into consideration two factors affecting characteristics of OCT images; namely, (1) high coherence (regularity) of a signal formed at the input of the OCT system during observation of a point object and (2) identity of spatial structures of the wave fields radiated and received by the OCT system because the OCT optical system selectively detects a phase-conjugated wave only. These factors are taken into account by the wave model of a backscattered signal [11].

24.2.1 Similarity Relations for the Signals of Coherence and Pulsed Sounding

Let the emitted wave inside the optical fiber be

$$u_e = M(\vec{r}') \, S_e(t - z'/c'),$$

where $\vec{r}\,'$ is the radius vector of a point in the fiber cross section Σ, and z' is the coordinate along the fiber axis. Function $M(\vec{r}\,')$ characterizes the transverse structure of the fiber mode and satisfies the normalization condition

$$\int_{\Sigma} M^2 \, d^2\vec{r}\,' = 1,$$

c' is the phase velocity of the mode. Emitted signal $S_e(t)$ is a random stationary process with zero mean $\bar{S}_e = 0$, center frequency ω_0, bandwidth $\Delta\omega_0 \ll \omega_0$, power spectrum $W(\omega)$, and autocorrelation function

$$B(\tau) = \overline{S_e(t+\tau) \cdot S_e(t)} = \int_{-\infty}^{\infty} W(\omega)\cos(\omega\tau)d\omega = P_e \cdot b(\tau) \cdot \cos(\omega_0\tau), \quad (24.1)$$

P_e is the average emitted power, and $b(0) = 1$. The received wave inside the optical fiber is

$$u_r = M(\vec{r}\,')\, S_r(\vec{r}_{0\perp}, \ t + z'/c'),$$

where $S_r(\vec{r}_{0\perp}, t)$ is the received signal as a function of the transverse coordinate $(\vec{r}_{0\perp})$ where the light-beam axis crosses the medium surface (see Fig. 24.1).

According to similarity relations for the signals of coherence and pulsed sounding [11], the "useful" current at the output of OCT heterodyne detector

$$i(\vec{r}_{0\perp}, t_0) = \eta\sqrt{2P_{ref}/P_e} \cdot \overline{S_r(\vec{r}_{0\perp}, t)S_e(t - t_0)}, \quad (24.2)$$

can be expressed as

$$i(\vec{r}_{0\perp}, t_0) = \eta\sqrt{\tau_0 P_e P_{ref}} \ \widehat{S}_r(\vec{r}_{0\perp}, t_0), \quad \tau_0 = \int_{-\infty}^{\infty} b^2(\tau)d\tau, \quad (24.3)$$

where t_0 is the delay time of the reference signal with respect to the probing signal, η is the photodetector sensitivity [A/W], P_e, P_{ref} stand for the power of emitted and reference signals, respectively, and $\widehat{S}_r(\vec{r}_{0\perp}, t)$ is the received signal inside the optical fiber in the case of a pulsed probing signal

$$\widehat{S}_e(t) = \sqrt{(2/\tau_0)}\, b(t)\, \cos(\omega_0 t) \quad (24.4)$$

with spectrum

$$f_e(\omega) = \frac{1}{2\pi} \int_{-\infty}^{\infty} \widehat{S}_e(t)\exp(-i\omega t)dt = \sqrt{(2/\tau_0)} \cdot P_e^{-1} \cdot W(\omega),$$

power

$$\widehat{P}_e(t) = \overline{\overline{(\widehat{S}_e)^2}} = \frac{1}{\tau_0} b^2(t), \tag{24.5}$$

and energy $\widehat{W}_e = \int\limits_{-\infty}^{\infty} \widehat{P}_e \, dt = 1$ [the double bar in (24.5) means averaging over a time interval $2\pi/\omega_0$]. If the coherence time (τ_c) of the signal $S_e(t)$ and duration (d_e) of the pulse [see (24.4)] are determined from the following relations $\tau_c^2 = \tau_0^{-1} \int\limits_{-\infty}^{\infty} \tau^2 b^2(\tau) d\tau, \quad d_e^2 = \int\limits_{-\infty}^{\infty} t^2 \widehat{P}_e dt$, then $d_e = \tau_c$.

24.2.2 Model of Random Realization of a Backscattered Signal

The biological tissue is considered as a medium with random distribution of dielectric permittivity

$$\varepsilon(\vec{r}) = \langle \varepsilon \rangle \, [1 + \varepsilon_1 \, (\vec{r}) + \varepsilon_2 \, (\vec{r})], \quad <\varepsilon_{1,2}> = 0$$

(angle brackets $< >$ denote statistical averaging). The term ε_1 describes the fluctuations of ε with spatial scale $l_1 \gg \lambda_0$, and ε_2 are the fluctuations with scale $l_2 < \lambda_0$, where $\lambda_0 = 2\pi c/\omega_0$, c is the light velocity in a medium. The fields $\varepsilon_{1,2}(\vec{r})$ are characterized by correlation functions

$$B_{1,2} \, (\vec{r}, \rho) = <\varepsilon_{1,2} \, (\vec{r} + \vec{\rho} / 2) \, \varepsilon_{1,2}^* \, (\vec{r} - \vec{\rho} / 2)>,$$

and spatial spectra

$$\Phi_{1,2} \, (\vec{r}, \kappa) = (2\pi)^{-3} \iiint\limits_{\infty} B_{1,2}(\vec{r},\rho) \exp(-i\vec{\kappa}\vec{\rho}) d^3\vec{\rho}, \quad \kappa = |\vec{\kappa}|.$$

The model of a pulsed signal reflected by the medium, $\widehat{S}_r(\vec{r}_{0\perp}, t)$, is constructed under certain assumptions. It is assumed that backscattering of a probing pulse $\widehat{S}_e(t)$ occurs on small-scale heterogeneities (ε_2), and large-scale heterogeneities (ε_1) do not reflect light but rather work as a source of multiplicative noise. We denote by $U_\omega(\vec{r}_{0\perp}, \vec{r}) \cdot \exp(i\omega t)$ the field formed in the medium with permittivity $\varepsilon(\vec{r}) = \langle \varepsilon \rangle \, [1 + \varepsilon_1(\vec{r})]$ when the emitted wave inside the optical fiber is $M(\vec{r}') \, \exp[i\omega(t - z'/c)]$. Then, in the single backward scattering approximation one can write

$$\widehat{S}_r(\vec{r}_{0\perp}, t) = -(2c)^{-1} \iiint\limits_{z>0} \varepsilon_2(\vec{r}) \left[\int\limits_{-\infty}^{\infty} i\omega f_e(\omega) \cdot U_\omega^2(\vec{r}_{0\perp}, \vec{r}) \cdot e^{i\omega t} d\omega \right] d^3\vec{r}.$$

Based on the equation

$$U_\omega(\vec{r}_{0\perp}, \vec{r}) = A(\vec{r}_{0\perp}, \vec{r}) \exp(-ik\varphi(\vec{r}_{0\perp}, \vec{r})),$$

where A, φ are the wave amplitude and eikonal, $k = \omega/c$, the pulsed response of medium will be

$$\widehat{S}_r(\vec{r}_{0\perp}, t) = -(2c)^{-1} \iiint\limits_{z>0} \varepsilon_2(\vec{r}) A^2(\vec{r}_{0\perp}, \vec{r}) \frac{d}{dt} \widehat{S}_e(t - 2\varphi(\vec{r}_{0\perp}, \vec{r})/c) \, d^3\vec{r} \approx$$

$$\approx \frac{k_0}{\sqrt{2\tau_c}} \iiint\limits_{z>0} \varepsilon_2(\vec{r}) \sin[\omega_0(t - 2\varphi/c)] A^2(\vec{r}_{0\perp}, \vec{r}) \, b(t - 2\varphi/c) \, d^3\vec{r},$$

(24.6)

where $k_0 = \omega_0/c$. Assuming $\varphi = z + \Delta\varphi$, $\Delta\varphi << z$ one can see that backscattering of the probing signal occurs in the sinusoidal component of ε_2 with spatial period of about $\lambda_0/2$. Factor A^2 in (24.6) describes a distribution of field intensity in a continuous illumination beam with allowance for focusing medium parameters and light scattering on large-scale heterogeneities. Factor b determines the position and longitudinal size of the medium element from which the signal originates at a given moment of time. This signal is noise-like due to the random nature of ε_2 and of functions A, φ; the correlation time of the signal is equal to τ_c, $<\widehat{S}_r> = 0$.

24.2.3 Model of a Statistically Averaged Backscattered Signal

The scales of spatial fluctuations of A and φ are assumed to be large compared with l_2, and the fields ε_1 and ε_2 are assumed to be statistically independent. Then, power of the signal $\widehat{S}_r$ averaged over an ensemble of spatial series of ε_1 and ε_2 yields

$$\widehat{P}_r = <\overline{\widehat{S}_r^2}> = 2\pi^3 k_0^2 \iiint\limits_{z>0} \Phi_2(\vec{r}, \, 2k_0) <A^4 \widehat{P}_e(t - 2\varphi/c)> d^3\vec{r}. \tag{24.7}$$

Under some additional assumptions we can express the integrand factor $<A^4\widehat{P}_e>$ through energy characteristics of the illumination field, which can be found from a radiative transfer equation (RTE). Let us represent U_ω as a sum of nonscattered and scattered fields and assume that fluctuations of the scattered field amplitude and phase are not cross-correlated; the amplitude is distributed according to the Rayleigh law and the phase is distributed uniformly in the interval from 0 to 2π.

Then, taking into consideration that the backscattering coefficient (the effective area of backscattering of a unit medium volume) is $\sigma_0(\vec{r}) = 2\pi^2 k_0^4 \Phi_2(\vec{r}, 2k_0)$, we can write (24.7) in the form

$$\widehat{P}_r(\vec{r}_{0\perp}, t) = (\lambda_0^2/4\pi) \iint\limits_{z>0}\int \sigma_0(\vec{r}) \mathrm{K}(\vec{r}_{0\perp}, \vec{r}, t)\, d^3\vec{r}, \qquad (24.8)$$

$$\mathrm{K}(\vec{r}_{0\perp}, \vec{r}, t) = \left[2E^2(\vec{r}_{0\perp}, \vec{r}) - E_{ns}^2(\vec{r}_{0\perp}, \vec{r}) \right] \int\limits_{-\infty}^{\infty} \widehat{P}_e(t - t') T\left(\vec{r}_{0\perp}, \vec{r}, \frac{t'}{2} \right) \frac{dt'}{2}, \quad (24.9)$$

$$T(\vec{r}_{0\perp}, \vec{r}, t) = \widehat{E}_\delta(\vec{r}_{0\perp}, \vec{r}, t)/E(\vec{r}_{0\perp}, \vec{r}), \qquad (24.10)$$

where E, E_{ns} are the total irradiance and irradiance by nonscattered light from the stationary illumination beam with power $P_e = 1$, $\widehat{E}_\delta$ is the irradiance in the medium from a pulsed source with power $\widehat{P}_e(t) = \delta(t)$, and T denotes photon distribution in the time of flight from point $\vec{r}_{0\perp}$ to point $\vec{r}$.

Note for comparison that calculations on the basis of RTE of received signal power give a different expression for K

$$\mathrm{K}(\vec{r}_{0\perp}, \vec{r}, t) = E^2 \int\limits_{-\infty}^{\infty} \widehat{P}_e(t - t') T_1(\vec{r}_{0\perp}, \vec{r}, t') dt', \qquad (24.11)$$

$$T_1(\vec{r}_{0\perp}, \vec{r}, t) = \int\limits_{-\infty}^{\infty} T(\vec{r}_{0\perp}, \vec{r}, t') T(\vec{r}_{0\perp}, \vec{r}, t - t') dt'. \qquad (24.12)$$

24.2.4 Comparison of Wave and Energy Models of an OCT Signal

The OCT optical fiber couples only the scattered field component whose spatial structure is similar to that of the probing beam, i.e., a phase-conjugated wave. Therefore, OCT images feature the phenomena of backscattering amplification and dispersion doubling of a received wave's phase fluctuations [12], which is caused by passage of the probing and reflected wave through the same large-scale heterogeneities (ε_1). The wave model of a statistically averaged backscattered signal [(24.8)–(24.10)] takes these effects into account and the energy model [(24.8), (24.11), and (24.12)] neglects them. We can illustrate this on an example of a signal from a "point" object with effective area of scattering Σ located at point $\vec{r}_1$ of a medium containing large-scale heterogeneities. This signal is calculated according to the formulas

$$\widehat{P}_r(\vec{r}_{0\perp}, t) = \alpha \mathrm{K}(\vec{r}_{0\perp}, \vec{r}_1, t), \quad \alpha = \lambda_0^2(\Sigma/4\pi), \qquad (24.13)$$

which are obtained from (24.8) with assumption of $\sigma_0(\vec{r}) = \Sigma\delta(\vec{r} - \vec{r}_1)$.

When an object is illuminated primarily by ballistic photons (the light scattered "forward" does not make any significant contribution to irradiance E), we can make use of the relations $E \approx E_{ns}$, $T(\vec{r}_{0\perp}, \vec{r}, t) \approx \delta(t - z/c)$. In this case, two sets of

(24.9), (24.10), (24.13) and (24.11)–(24.13) yield the same result: power and energy of the received signal are expressed as

$$\widehat{P}_r(\vec{r}_{0\perp}, t) = \alpha E_{ns}^2(\vec{r}_{0\perp}, \vec{r}_1)\widehat{P}_e(t - 2z_1/c), \quad \widehat{W}_r = \int_{-\infty}^{\infty} \widehat{P}_r dt = \alpha E_{ns}^2(\vec{r}_{0\perp}, \vec{r}_1),$$

where arrival time of a signal "center of gravity" is given by $t_r = (\widehat{W}_r)^{-1}\int_{-\infty}^{\infty} t\widehat{P}_r dt = 2z_1/c$, and characteristic duration of the signal is

$$d_r = \left[(\widehat{W}_r)^{-1}\int_{-\infty}^{\infty}(t - \bar{t})^2\widehat{P}_r dt\right]^{1/2} = d_e.$$

However, these models are not equivalent in a general case. According to the wave model

$$\widehat{W}_r = \alpha\left[2E^2(\vec{r}_{0\perp}, \vec{r}_1) - E_{ns}^2\right], \quad t_r = 2\bar{t}, \quad d_r = \sqrt{d_e^2 + 4d^2},$$

where

$$\bar{t} = \int_{-\infty}^{\infty} tT(\vec{r}_{0\perp}, \vec{r}_1, t)dt, \quad d^2 = \int_{-\infty}^{\infty}(t - \bar{t})^2T(\vec{r}_{0\perp}, \vec{r}_1, t)dt$$

are average value and dispersion of photon propagation time from point $\vec{r}_{0\perp}$ to point $\vec{r}_1$, whereas the energy model gives $\widehat{W}_r = \alpha E^2(\vec{r}_0, \vec{r}_1)$, $t_r = 2\bar{t}$, $d_r = \sqrt{d_e^2 + 2d^2}$. Comparison of the wave and energy models shows that for $E_{ns} \ll E$, $d_e \ll d$ the energy model gives underestimated values for energy of the received signal (by a factor of two) and yields axial blurring of the image (by a factor of $\sqrt{2}$ times). Such error will also manifest in modeling of images by the Monte Carlo method.

24.2.5 Formulas for Calculating OCT Image

As follows from (24.3), mean-square current at the input of a heterodyne receiver of an OCT system is expressed through a pulsed response of a medium in the following form:

$$<\overline{\overline{i^2(\vec{r}_0, t_0)}}> = \eta^2\tau_0 P_e P_{ref}\widehat{P}_r(\vec{r}_0, t_0) \tag{24.14}$$

(the double bar in the left-hand side of (24.14) denotes averaging over time interval π/ω_1, where $\omega_1 = \omega_0[dt_0(t)/dt]$ is an intermediate frequency). Consequently, the (24.8)–(24.10) can be used straightforwardly for calculation of images formed by an OCT system with a quadratic video signal detector.

If we suppose that a signal with delay t_0 comes from depth $z_0 = ct_0/2$, then the structure of three-dimensional image of the medium can be described by a dimensionless function $P(\vec{r}_{0\perp}, z_0) = \tau_0 \bar{P}_r(\vec{r}_{0\perp}, 2z_0/c)$ related to current i by $\overline{\langle i^2(\vec{r}_{0\perp}, t_0)\rangle} = \eta^2 P_e P_{ref} P(\vec{r}_{0\perp}, ct_0/2)$. Given statistical homogeneity of field ε_1 in the $z = const$ plane, we have

$$P(\vec{r}_{0\perp}, z_0) = (\lambda_0^2/4\pi) \iiint_{z>0} \sigma_0(\vec{r}_\perp, z) Q(\vec{r}_{0\perp} - \vec{r}_\perp, z_0, z)\, d^2\vec{r}_\perp dz, \qquad (24.15)$$

$$Q(\vec{r}_\perp, z_0, z) = \left[2\bar{E}^2(\vec{r}_\perp, z) - \bar{E}_{ns}^2(\vec{r}_\perp, z)\right] \int_{-\infty}^{\infty} b^2(2t - 2z_0/c)\bar{T}(\vec{r}_\perp, z, t)dt, \quad (24.16)$$

where $\vec{r}_\perp$ is the component of $\vec{r}$ in the $z = 0$ plane,

$$\bar{E}(\vec{r}_\perp, z) = E(0, \vec{r}), \quad \bar{E}_{ns}(\vec{r}_\perp, z) = E_{ns}(0, \vec{r}), \quad \bar{T}(\vec{r}_\perp, z, t) = T(0, \vec{r}, t).$$

Employing the relationships $\bar{E} = \int_{-\infty}^{\infty} \widehat{E}_\delta(0, \vec{r}, t)dt$, $\bar{T} = \widehat{E}_\delta(0, \vec{r}, t)/\bar{E}$ we can express function Q through irradiance $\widehat{E}_\delta$ from a supplementary δ-pulse source in a medium with volume scattering function $\beta_1(z, \theta) = 0.5\pi k_0^4 \Phi_1(z, 2k_0 \sin(\theta/2))$. Therefore, calculation of OCT images based on (24.15) and (24.16) may be made using the energy models of light pulse propagation in a medium with strongly anisotropic scattering [13–15]. In the case when duration of a δ-pulse signal at depth z_0 is short compared with d_e, we obtain a simpler expression for Q: $Q = \left[2\bar{E}^2 - \bar{E}_{ns}^2\right] b^2(2(z - z_0)/c)$. It contains only characteristics of a continuous illumination beam that are described well by analytical solutions of RTE in the small-angle approximation [13, 14].

Note that statistically average current at the output of a linear video signal detector is $\overline{\langle |i(\vec{r}_0, t_0)|\rangle} \approx \sqrt{\overline{\langle i^2(\vec{r}_0, t_0)\rangle}}$. Hence, (24.15) and (24.16) can be also used for calculation of images formed by an OCT system with a linear video signal detector.

The model of a random realization of an OCT signal [(24.3) and (24.6)] also allows evaluating the fluctuations that generate speckle noise in the image. In particular, if the amount of small-scale heterogeneities in the resolution element is large, then, according to this model, coefficients of variation of a video signal for linear and quadratic detectors are 0.523 and 1, respectively.

24.3 Methods and Element Basis for PM Fiber Optical Interferometry

As was shown in the previous section, information about optical heterogeneities of a turbid medium may be recovered from a nonscattered (or weakly scattered) coherent component, which is usually a few orders of magnitude smaller than thr

background formed by a noninformative strongly scattered component of probing radiation. Discrimination of such a weakly scattered component is effectively accomplished by means of optical interferometry with broadband light sources in the visible and near-infrared (IR) frequency ranges. An interference signal is detected only when the optical path length difference between the sample and reference arms of the interferometer are matched within the coherence length that is determined by the bandwidth of the probing radiation. Therefore, by changing the reference and/or probing arm length one can perform in-depth scanning. The interference signal is contributed mostly by backscattering on tissue heterogeneities. Since the informative signal decreases exponentially with depth of the medium, its detection with an acceptable dynamic range is challenging and demands new engineering ideas and their experimental realizations.

Imaging modalities should meet a number of technical requirements, i.e., adequate imaging depth, appropriate image contrast, high acquisition rate, etc. The main requirements for the optical coherence tomography (OCT) device were dictated by the planned object of study, namely, soft mucosal tissues of human organs. The requirements were the following: spatial resolution of about 10 μm, imaging depth of several millimeters, low non-invasive probing power, and combined acquisition and visualization time for an image with 200×200 pixels of about 1 s. Since the OCT device was intended primarily for clinical use, additional requirements were simplicity of using the device in a clinical environment and, in particular, compactness.

The "heart" of OCT is an optical interferometer, consequently, the main challenge was to devise an interferometer that would satisfy all the requirements listed above and to fabricate necessary fiber optical parts. We chose the Michelson scheme for the interferometer and decided to build it using polarization-maintaining (PM) fibers. PM fiber allowed constructing of the interferometer with a flexible sample arm and provided stable detection of the interference signal. Flexibility of a sample arm facilitates access to the examined site of biological tissue, which is vital for diagnosis of, for instance, internal organs. The interferometer comprised several fiber optical elements with unique characteristics, which were developed and fabricated by our research team. Another important part of the OCT device is a light source. The commercially available quantum sources of broadband optical radiation in the near IR range with short coherence duration and high cross-sectional spatial coherence were employed as light sources.

All the ideas and expertise of the research team resulted in creation of the compact OCT device based on PM fiber, a commercially available low-coherent light source, and unique fiber optical elements. The device featured wide dynamic range and high-speed lateral and longitudinal scanning. The miniaturized OCT optical probe was optimized and suited for a variety of clinical applications.

24.3.1 Optical Interferometers Based on PM Fiber

Low-coherence fiber interferometry proved to be a convenient tool for image acquisition in turbid media. It is highly effective for rejecting non-informative

multiply scattered light and for detecting the informative component formed by nonscattered or weakly scattered light propagating at almost rectilinear trajectories ("snake photons"). Calculations and model experiments in media similar to biological tissue verify that the effect of multiple scattering blurs the image generated by the informative component at the depth of 6–8 of mean free path of a photon. Due to low reflectivity of biological tissue structures, it is necessary to detect backscattered light, which is attenuated to the level of 90–100 dB compared with the incident light. High signal-to-noise ratio for detecting such weak signals in the developed OCT setups was attained by minimizing power losses in the optics, heterodyning of the detected signal at the shot noise level, and reducing the influence of various parasitic effects leading to appearance of false "spurious" signals. In order to eliminate the latter, we investigated the dynamic characteristics, fluctuations, and parasitic phenomena in anisotropic fiber interferometers with broadband light sources. This allowed us to formulate technical requirements and, as a result, develop all interferometer components with improved qualitative and quantitative characteristics.

The dynamic range of a signal is a basic characteristic influencing the maximum imaging depth. It depends on the interferometer scheme used. The quality of the optical elements, their alignment, and the level of noise induced during fiber splicing are the parameters determining quality of the interferometer. It was found that the major limitation of a dynamic range in a Michelson interferometer used in our experimental OCT device is primarily caused by interaction of fiber waveguide modes during their propagation in anisotropic fiber. Technically, there are four single-mode waveguides for light waves in a two-arm interferometer. Two waves oriented along the "fast" and "slow" anisotropy axes of fiber can propagate in each arm, respectively. When orthogonal modes are launched into an interferometer, the fiber waveguide modes with orthogonal polarizations interfere in pairs independently. Practically, parameters of anisotropic fiber vary over length and, thus, cause large-scale fluctuations of group velocity modes propagating along the slow and fast axes. Consequently, zero path length difference for different modes occurs at slightly different arm lengths. As a result, when a mirror is placed into a sample arm that is a standard procedure for adjusting the interferometer and checking its quality, there appear two cross-correlation functions (CCF) with a time delay, i.e., the real image and a parasitic copy of the real image. In addition, more parasitic signals may arise in CCF due to undesired coupling of modes in fiber elements such as couplers, polarizers, and so on at the sites of fiber splicing. This obviously leads to a reduction in the dynamic range of the interferometer.

Due to the low coherence nature of radiation employed in OCT, it is more convenient to speak about different speed of delays for different waveguide modes of fiber rather than about modulation of a polarization state by means of a phase modulator. This leads to different values of the Doppler frequency for orthogonal polarizations. In case of SLDs emitting partially polarized light and a linearly varying path length difference between the interferometer arms, two independent CCF are observed at close Doppler frequencies. The presence of two

Fig. 24.2 Illustration of the spikes' appearance on the two PM (*A*, *B*) fiber joint: interferometer arms (*1*, *2*), 3 dB splitter (*3*), photoreceiver (*4*)
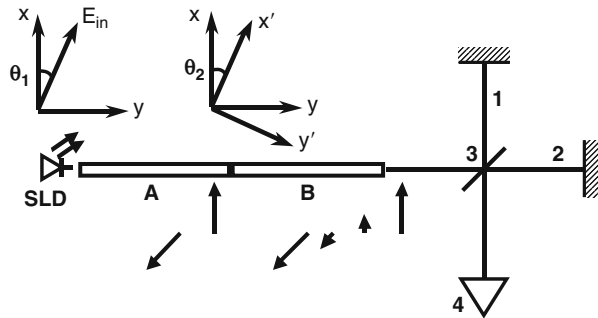
close frequencies in the signal results in beating. This parasitic effect is removed by polarization filtering of one of the orthogonal modes.

Parasitic coupling of orthogonal fiber modes may also manifest in OCT images when only one linearly polarized mode is excited initially. Experiments demonstrated that such mode coupling was induced at the sites of anisotropic fiber splicing and in the regions of mechanical stresses. This type of coupling excites a weak wave with orthogonal polarization and a group velocity different from that of a primary wave. Due to the secondary parasitic coupling of orthogonal modes, part of the parasitic wave power may return to the initial wave down the propagation path, thus producing another coherent component with a time delay. Secondary coupling may have the same origin as the primary one and may be formed in a polarizer and coupler [16, 17]. In this case the appearance of the echo-like parasitic spikes in the interferometric signal is caused by the defects of anisotropy of the optical tract that limits the dynamic range of an interferometer [18].

The appearance of such spikes can be illustrated on the example of two spliced anisotropic fibers (Fig. 24.2) using the time correlation approach. This approach in the general case considers propagation of individual coherent pulse trains; each of these trains is considered to be a source of secondary coherent pulse trains. A Michelson interferometer is employed here to estimate the quality of the mutual orientation of axes of spliced fibers.

Let the radiation from a superluminescent diode $\vec{E}(t) = \vec{E}_{in}E_0(t)$ be linearly polarized at an angle of θ_1 to the eigen axes x',y' of the first fiber A, while the axes of the second fiber B are directed at an angle of θ_2 with respect to the axes of the first fiber. Here, $E_0(t)$ is the time dependence of the electric field at the input of the first fiber and $\vec{E}_{in}$ is the dimensionless vector describing the polarization state and the field amplitude $\vec{E}(t)$ at the input of the first fiber. In this case, one coherent pulse train will propagate with delays τ_{1x} and τ_{1y} along each of the axes x' and y', respectively, at the output from the first fiber (further we will omit primes in x and y for brevity). The amplitudes of the trains propagating along axes x and y are $A_x = E_{in} \cos \theta_1$ and $A_y = E_{in} \sin \theta_1$, respectively. Because the axes of the first and second fibers do not coincide, each of the trains gives the projections on both the x and y axes, so these two pulse trains will propagate along each of the axes in the second fiber.

Therefore, two trains with delays $\tau_{1x} + \tau_{2x}$ and $\tau_{1y} + \tau_{2x}$ and amplitudes $B_{1x} = \cos\theta_1\cos\theta_2 E_{in}$ and $B_{2x} = \sin\theta_1\sin\theta_2 E_{in}$ will propagate along the x axis of the second fiber, and two trains with delays $\tau_{1y} + \tau_{2y}$ and $\tau_{1x} + \tau_{2y}$ and amplitudes $B_{1y} = \sin\theta_1\cos\theta_2 E_{in}$ and $B_{2y} = -\cos\theta_1\sin\theta_2 E_{in}$ will propagate along the y axis. The parameters of secondary coherent pulse trains are analyzed with a Michelson interferometer, whose axes are made coincident with the axes of the second fiber. Assuming that a beamsplitter shown in Fig. 24.2 is isotropic, i.e., the power division coefficients for radiation with x and y polarizations are equal ($\kappa_x = \kappa_y = \kappa$), we can express the components of the autocorrelation function along x and y axes in the form:

$$G_x(\tau \pm \Delta\tau) = 2\kappa(1-\kappa)\{(\cos^2\theta_1\cos^2\theta_2 + \sin^2\theta_1\sin^2\theta_2)\cdot E_{in}^2 G_0(\tau) + \\ + \sin\theta_1\cos\theta_1\sin\theta_2\cos\theta_2 E_{in}^2 G_1(\tau \pm \Delta\tau)\}, \quad (24.17)$$

$$G_y(\tau \pm \Delta\tau) = 2\kappa(1-\kappa)\{(\sin^2\theta_1\cos^2\theta_2 + \cos^2\theta_1\sin^2\theta_2)\cdot E_{in}^2 G_0(\tau) - \\ - \sin\theta_1\cos\theta_1\sin\theta_2\cos\theta_2 E_{in}^2 G_1(\tau \pm \Delta\tau)\}, \quad (24.18)$$

where $G_0(\tau) = \langle E_0(t)\cdot E_0(t+\tau)\rangle$ is the initial autocorrelation function of the light source (the random process $E_0(t)$ is assumed to be stationary); the angle brackets denote time averaging; $G_1(\tau \pm \Delta\tau)$ is the cross-correlation function; $\Delta\tau = \tau_{1x} - \tau_{1y}$ is the difference of delays for radiations with x and y polarizations in the first fiber. The sign $\pm$ reflects the symmetry of the autocorrelation function, which physically means that the situation when the first arm of the interferometer is shorter than the second one is equivalent to the situation when the second arm is shorter than the first one (Fig. 24.2).

One can see from (24.17) and (24.18) that, in the absence of dichroism of the optical tract or anisotropy of the division coefficient, for each of the trains propagating along the x axis with the nonzero delay (the condition $\tau = 0$ means the equality of the interferometer arms), there will be a pulse train that propagates along the y axis with the same delay and the same amplitude but with an opposite sign. Such trains will cancel each other out [see (24.19)]. Therefore, the term $G_1(\tau \pm \Delta\tau)$ in (24.17) and (24.18) corresponding to the propagation of trains with different polarizations in the first fiber will disappear from the total autocorrelation function

$$G(\tau) = G^x(\tau) + G^y(\tau) = 2k(1-k)\left|\vec{E}_{ex}\right|^2 G_0(\tau) = 2k(1-k)\cdot I_0\cdot G_0(\tau), \quad (24.19)$$

where I_0 is the initial radiation intensity entering the interferometer. In the absence of dichroism or anisotropy of the division coefficient the mutual orientation of the spliced fibers cannot be determined. In the presence of anisotropy of the division coefficient in the interferometer ($\kappa_x \neq \kappa_y$), the subtraction of the trains will be incomplete. The subtraction depth is defined by the coefficient:

$$\eta = \frac{\left| \sqrt{\kappa_x \cdot (1 - \kappa_x)} - \sqrt{\kappa_y \cdot (1 - \kappa_y)} \right|}{\sqrt{\kappa_x \cdot (1 - \kappa_x)} + \sqrt{\kappa_y \cdot (1 - \kappa_y)}}, \tag{24.20}$$

where $\eta = 0$ corresponds to the complete subtraction and $\eta = 1$ to the absence of subtraction.

Let us assume that the first fiber is longer than the depolarization length $L_d = \lambda_0^2/(\Delta\lambda\Delta n_a)$, where λ_0 is the central wavelength of the light source in vacuum; $\Delta\lambda$ is the spectral width of the light source; Δn_a is the difference of the refractive indices of polarization axes of fibers. In the presence of dichroism or anisotropy of the division coefficient, the interference pattern will have a separate interference region (hereafter, the correlation or interference peak) with a delay $\Delta\tau$. Two trains propagating with different initial polarizations and the same time delay will separate when the propagation length will exceed the depolarization length, which will result in appearance of an additional interference peak. For a light source with spectral width of 20 nm, the central wavelength of 0.8 mm, and the birefringent refractive index of $\Delta n_a = 1.5 \cdot 10^{-4}$, the corresponding depolarization length is 21 cm.

Therefore, a separate correlation peak can already be induced by splicing two relatively short pieces of PM fibers. As one can see from (24.17) and (24.18), the best condition for the observation of this peak (when the peak amplitude is maximal for given θ_2) is attained when the polarization modes of the first fiber are excited at the same rate, and radiation with one of the polarizations is not sent to a photodetector. In this case, the subtraction is completely absent.

The wave with one of the polarizations can be suppressed by placing a polarizer between the second fiber and a photodetector whose axis is oriented to coincide with one of the axes of the second fiber [18]. The amplitude of the correlation peak depends on the angle between the axes of spliced fibers and changes from zero (when the axes are coincident or orthogonal) to the maximum equal to the half amplitude of the main peak (when the angle between the axes of the fibers is 45°). The correlation peak amplitude also depends on the angle between the transmission axis of the polarizer and the axis of the output fiber and varies from the maximum (when the axes are coincident or orthogonal) to zero (when the angle between axes is 45°). The appearance of new components with given polarization from components with orthogonal polarization (energy transfer) upon splicing two PM fibers can be described with a rotational matrix $O(\theta_2)$ where θ_2 is the angle between the intrinsic axes of spliced fibers.

$$O(\theta_2) = \begin{pmatrix} \cos\theta_2 & \sin\theta_2 \\ -\sin\theta_2 & \cos\theta_2 \end{pmatrix}. \tag{24.21}$$

In this case, the fields along the axes x and y at the output of the second fiber can be written as:

$$E_x = E_{in} \cdot \left(E_1(t + \tau_{1x}) \cos\theta_1 \cos\theta_2 + E_2(t + \tau_{1y}) \sin\theta_1 \sin\theta_2 \right)$$
$$E_y = E_{in} \cdot \left(-E_1(t + \tau_{1x}) \cos\theta_1 \sin\theta_2 + E_2(t + \tau_{1y}) \sin\theta_1 \cos\theta_2 \right) \qquad (24.22)$$

Such a representation of the output field components is convenient for analysis of more complicated systems, for example, systems with distributed heterogeneities, multiple defects of anisotropy, and so on.

It can be shown that distributed defects of anisotropy induce transferring of part of the power from initial polarization into orthogonal polarization [18]. The amplitude of the power with orthogonal polarization is determined by two basic parameters: maximum angle between intrinsic polarization axis and induced axis and ratio of the defect length (L_i) to the beat length of fiber $L_b = 2\pi/\Delta\beta$, where $\Delta\beta$ – is the difference between propagation constants of fiber for orthogonal polarizations.

The appearance of new pulse trains in orthogonal polarizations can be described by the time correlation analysis. In this case, propagation of low-coherence radiation can be mathematically represented by transformation of a pair of complex vectors with dimension $2n$

$$\boldsymbol{V}_{2n} = \begin{pmatrix} \mathbf{a}^{nx} \\ \mathbf{a}^{ny} \end{pmatrix}, \quad \begin{array}{l} \mathbf{a}^{nx} = \left(a_1^{nx}, a_2^{nx}, \ldots, a_n^{nx} \right) \\ \mathbf{a}^{ny} = \left(a_1^{ny}, a_2^{ny}, \ldots, a_n^{ny} \right) \end{array}. \qquad (24.23)$$

Each of n elements of the vector $\mathbf{a}^{nx} - a_j^{nx} = A_j^{nx} e^{i\varphi_j^{nx}}$ corresponds to the single random process (pulse train) with a certain time delay $\Delta\tau_j^{nx} = \varphi_j^{nx}(\omega_0)/\omega_0$ and amplitude A_j^{nx} with polarization along the x axis; the same relations are held for each element of vector a^{ny} but for the y axis.

Transformation of radiation with polarization along x and y axes on the $m + 1$ defect of anisotropy yields a pair of vectors $\boldsymbol{V}_{2nx}^u = \hat{U}_{m+1}\boldsymbol{V}_{2nx}$ and $\boldsymbol{V}_{2ny}^u = \hat{U}_{m+1}\boldsymbol{V}_{2ny}$, where $\hat{U}_{m+1}$ is the Jones matrix of the defect of anisotropy and $\boldsymbol{V}_{2nx} = \begin{pmatrix} \mathbf{a}^{nx} \\ 0 \end{pmatrix}$; $\boldsymbol{V}_{2ny} = \begin{pmatrix} 0 \\ \mathbf{a}^{ny} \end{pmatrix}$. It should be noted that when defects of anisotropy are short compared with the depolarization length, the dependence of the Jones matrix elements could be neglected. In addition, when the length of a piece of a fiber with anisotropy defects is short compared with the depolarization length, the frequency dependence of the Jones matrix elements could be neglected [18].

Total transformation on the defect of anisotropy for x and y polarizations is given by a pair of vectors $\boldsymbol{V}_{4n}$

$$\boldsymbol{V}_{4n} = \boldsymbol{V}_{2nx}^u + \boldsymbol{V}_{2ny}^u = \begin{pmatrix} u_{11}^{m+1}\mathbf{a}^{nx}, & u_{12}^{m+1}\mathbf{a}^{ny} \\ u_{21}^{m+1}\mathbf{a}^{nx}, & u_{22}^{m+1}\mathbf{a}^{ny} \end{pmatrix} = \begin{pmatrix} \mathbf{a}^{2nx} \\ \mathbf{a}^{2ny} \end{pmatrix}, \qquad (24.24)$$

the pair of vectors $\boldsymbol{V}_{4n}$ is twice as long the initial pair of vectors $\boldsymbol{V}_{2n}$.

While propagating between two defects of anisotropy, each pulse train acquires different time delays for x and y polarizations:

$$V'_{4n} = \begin{pmatrix} e^{0.5i\Delta\beta L} & 0 \\ 0 & e^{-0.5i\Delta\beta L} \end{pmatrix} \begin{pmatrix} a^{2nx} \\ a^{2ny} \end{pmatrix}, \tag{24.25}$$

where L is the distance between two defects of anisotropy. The dimension of the pair of vectors is not changed by this operation.

Using this approach, one can describe the propagation of low-coherence radiation in the arms of an interferometer independently. A pair of vectors $V1_{4n1}$ and $V2_{4n2}$ with dimensions of $4n1$ and $4n2$ are needed for description of the interferometric signal on the input of a photodetector. The above pair of vectors will contain the final set of delays and amplitudes in the first and second arms of the interferometer, respectively.

The final correlation function of the system can be written using the following formula:

$$G_{x,y}(\tau) = \sum_{j1=1}^{n1} \sum_{j2=1}^{n2} A1_{j1}^{x,y} \cdot A2_{j2}^{x,y} \cdot N1_{j1j2}^{x,y}\left(\tau - \Delta\tau_{j1j2}^{x,y}\right), \tag{24.26}$$

where

$$N1_{j1j2}^{x,y}(\tau - \Delta\tau_{j1j2}^{x,y}) = \int_{-\infty}^{\infty} S(\omega) \cdot e^{i\cdot\Delta\varphi_{j1j2}^{x,y}(\omega)} \cdot e^{i\cdot\omega\cdot\tau} d\omega. \tag{24.27}$$

$A1_{j1}^{x,y}$ and $A2_{j2}^{x,y}$ are the modules of a pair of vectors $V1_{4n1} = \begin{pmatrix} a1^{2n1x} \\ a1^{2n1y} \end{pmatrix}$ and $V2_{4m} = \begin{pmatrix} a2^{2n2x} \\ a2^{2n2y} \end{pmatrix}$ correspondingly. All possible variations of phase differences between $a1_{j1}^{2n1x,y}$ and $a2_{j2}^{2n2x,y}$ are normalized on the central frequency of a light source ω_0 and used as delays $\Delta\tau_{j1j2}^{x,y}$.

The number of elements required for calculations increases as 2^m, where m is the number of defects of anisotropy. For instance, 50 defects of anisotropy in the optical tract would require a pair of vectors with $1.1*10^{15}$ elements. The number of elements can be reduced by applying the perturbation theory. This theory is valid when power transferred to the orthogonal polarization on the defect of anisotropy is much smaller than power in the initial polarization. Mathematically, this can be expressed by the following inequality:

$$|u_{12}| \ll 1, \; |u_{21}| \ll 1, \tag{24.28}$$

where $|u_{12}|$ and $|u_{21}|$ are non-diagonal elements of the Jones matrix. The theory of perturbations of the s-order considers series terms from zero to s-th order inclusively. For example, if the initial pulse train is of the 0-order; then, on the defect of anisotropy it generates the pulse train of the 1-order with orthogonal polarization.

In this case, it is convenient to split the Jones matrix describing appearance of the new field components on the next defect of anisotropy into two matrices:

$$\hat{U}_{m+1} = \hat{U}1_{m+1} + \hat{U}2_{m+1} = \begin{pmatrix} u_{11}^{m+1} & 0 \\ 0 & u_{22}^{m+1} \end{pmatrix} + \begin{pmatrix} 0 & u_{12}^{m+1} \\ u_{21}^{m+1} & 0 \end{pmatrix}. \qquad (24.29)$$

When the first term in (24.29) is multiplied on the pair of vectors, the order of the perturbation series does not change; conversely, the second term in (24.29) being multiplied on the pair of vectors causes an increase in the order by 1. Therefore, application of the perturbation theory decreases the number of elements required for calculations to m^s. For instance, for 50 defects of anisotropy and pulse trains up to the second order inclusively, the required number of elements is 2.5×10^3.

In addition to the primary mode, coupling can occur before entering the interferometer. The OCT image tomogram features symmetrical stripes parallel to the object surface following the bright structures of the image. Such parasitic stripes generated by excitation of orthogonal modes at the site of splicing of the isotropic fiber output of the light source and the anisotropic fiber input of the polarizer were removed by compensating the delay difference according to the method described in Ref. [19]. The idea of the method is to splice the input fiber of a polarizer with a piece of same type of fiber of the same length, but with the anisotropy axis turned by 90°. Such a compensator makes the total delays for the orthogonally polarized modes equal prior to entering the polarizer, thus effectively decreasing the parasitic signal by 20–25 dB.

An alternative method of compensating optical birefringence in single-mode optical waveguides was proposed and investigated in Refs. [20, 21]. In this approach, 45° Faraday cells are placed at the end of each interferometer arm through which light passes twice. As a result, both regular and parasitic fiber anisotropies are compensated completely and the initial polarization state of light is restored with its axis turned by 90°. This approach was investigated theoretically by means of the apparatus of the Jones matrices. This method can provide a handy tool for fabricating the OCT interferometer partially or completely based on isotropic single mode fiber.

The principal limitation of the compensation method described above is dispersion of light in a Faraday cell. However, our experiments using a light source with a central wavelength of 1.3 μm and bandwidth of 50 nm and a Faraday cell based on a YIG crystal in an oversaturated magnetic field demonstrated that regular and parasitic anisotropy can be compensated, at least, up to level of 40 dB.

A 45° Faraday cell was also used for creation of an interferometer in the setup for polarization OCT described in Sect. 24.4.4. The Faraday cell was placed, for example, in one reference arm, thus, linearly polarized light returning to the coupler had orthogonal polarization. Therefore, interference occurred only with a part of the backscattered wave in the sample arm, which also had polarization orthogonal to the initial one. The orthogonal polarization appeared in backscattered light due to reflection from of the sample with a change in polarization. This approach introduces additional suppression of non-informative components, which is a limiting

factor for OCT imaging, Moreover, simultaneous acquisition of images in initial and orthogonal polarizations provided a basis for development of the method of cross-polarization OCT [22, 23].

Another original interferometer scheme was elaborated for "color" optical coherence tomography, i.e., for imaging of the same sample regions at several wavelengths simultaneously. This is of great interest, because optical properties of biological tissues noticeably vary in the short and long wavelength regions of the "therapeutic transparency window" (e.g., at wavelengths of about 0.8 and 1.3 μm). We fabricated a fiber optical interferometer that was built using a single-mode fiber and optimized for wavelengths of 0.8 and 1.3 μm simultaneously [24]. Group delays and dispersion in both interferometer arms were simultaneously compensated at both wavelengths, even though the material and waveguide dispersion of fiber were quite different at these wavelengths. The idea was to insert into both arms of the interferometer two sections of additional optical fiber whose optical properties differ strongly from those of the primary fiber. Thus, the interferometer scheme was artificially extended to include additional degrees of freedom provided by optical parameters of the additional fiber sections. By optimizing the latter, optical paths were made equal and the duration of cross-correlation functions for signals at both wavelength were minimized. The setup for "color" OCT is described in detail in Sect. 24.4.2.

24.3.2 Fabrication of Fiber Optical Elements Based on PM Fiber

A polished 3-dB coupler based on single-mode isotropic fiber and a polarizer based on the half of a coupler were developed for low-coherent interferometry. The 3-dB coupler was optimized to yield stable coupling of waveguide modes in a wide temperature range with good orthogonal mode decoupling and losses less than 0.1 dB.

The couplers and polarizers for OCT based on PM fiber were fabricated employing the technologies developed earlier [25, 26]. The most challenging problem was to increase accuracy of orienting anisotropy axes of fibers relative to the symmetry axes of the optical elements. Among a variety of anisotropic fibers, we chose PANDA anisotropic fiber because its structure allows the most precise optical control of alignment of fiber axes. The fiber axes were aligned relative to the axes of the optical element with accuracy of 1°. Custom-designed equipment for accurate angular orientation of fibers allowed aligning without twisting; the quality of alignment was optically controlled using the CCD array. The results of subsequent computer data analysis were further used for correction of alignment. The specially designed correlometer described in Ref. [18] controlled appearance of local coupling of fiber modes in fiber during its installation and fixing in a profiled groove of the basic optical element of the polarizer or coupler. Each individual basic optical element was then grinded and polished. Then, these basic elements were used as halves of the assembled coupler. The basic elements employed for polarizers were preliminary processed by depositing dielectric and metal layers.

The parameters of deposited structures were simulated numerically and further tested experimentally. The polarizer extinction, whose maximum value depended on parasitic mode mixing, was measured by a correlometer. As a result, for wavelengths of 0.83 and 1.3 μm we obtained the following unique parameters of a polarizer based on anisotropic fiber: extinction coefficient of about 35–40 dB and the level of induced losses less than 0.2 dB.

Analogous anisotropic fiber elements were used to fabricate 3 dB couplers with crosstalk less than −40 dB and the level of induced losses less than 0.1 dB. We also developed a unique technique and fabricated a 3-dB coupler working on two distant wavelengths of 0.83 and 1.3 μm simultaneously.

In-depth OCT scanning was realized by changing the optical path length difference between the sample and reference arms according to a linear law. This was attained by elastically stretching the fibers of the interferometer arms in counter phase. Optical fibers were glued to piezoceramic actuators, which provided fiber stretching with relative elongation of up to 10^{-4}. Given a sufficient fiber length, the absolute path length difference between the interferometer arms could achieve several thousand wavelengths.

24.4 Experimental OCT Systems

Successful creation of experimental OCT setups became possible due to a combination of several factors, namely, promising results of the theory of vision in turbid media described in Sect. 24.2, development of methods for precision fiber optical interferometry, and fabrication of unique fiber optical elements.

24.4.1 Compact OCT Device Based on Michelson Fiber Optical Interferometer

The schematic of the optical coherence tomography device is depicted in Fig. 24.3. The setup features a broadband light source in the near IR frequency range, the Michelson interferometer based on PM fiber, the electron-mechanical system performing in-depth scanning by means of modulation of lengths of interferometer arms, the electro-mechanical system for lateral scanning of the sample (optical probe), the system for photodetection of the interference signal, the electron system for analog signal processing, and a personal computer for digital signal processing, image visualization and storage, and for general control of the OCT device.

In different OCT designs we used as light sources superluminescent diodes (SLD) with central wavelengths ranging from 0.83 to 1.28 μm, bandwidths ranging from 25 to 50 nm, and power in a single mode fiber output from 1 mW to 10 mW. For experimental purposes we also employed femtosecond lasers (a titanium-sapphire (Ti:Sa) laser with a central wavelength of 0.8 μm, bandwidth up to 70 nm and output power up to 200 mW; a chromium-forsterite laser with a central wavelength of 1.3 μm, bandwidth up to 30 nm and power up to 100 mW). Novel
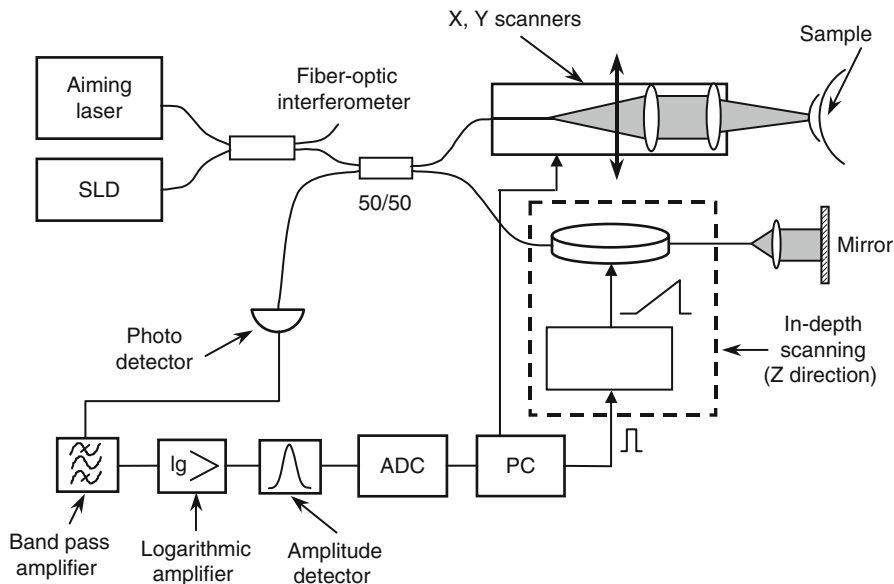
Fig. 24.3 OCT functional scheme

semiconductor superluminescent sources operating in the IR frequency range with bandwidth up to 100 nm are expected to appear in the near future. These sources [27] would be competitive with femtosecond Ti:Sa lasers that are currently the sources of coherent radiation with the widest broadband.

The heterodyne detection is attained by modulating the path length difference between interferometer arm lengths, ΔL, according to a linear law $\Delta L = \dot{\Delta L} \cdot t$. The general principle of low-coherence interferometry states that the depth h within the sample from which the OCT signal is detected changes with velocity $\dot{h} = \dot{\Delta L}\frac{n_{fgr}}{n_{mgr}}$, where n_{fgr} and n_{mgr} are the group refractive indices of the fiber material and of the sample, respectively. The detector discriminates from the total measured signal an interference component at the Doppler frequency $F = \frac{2\,\dot{\Delta L}\,n_f}{\lambda_0} = 2n_{mgr}\frac{\dot{h}}{\lambda_0}\frac{n_f}{n_{fgr}}$, where n_f is the phase refractive index of the fiber material and λ_0 is the vacuum wavelength of probing light. For example, for the wavelength of 1.3 µm, the scanning velocity of 65 cm/s corresponds to the Doppler frequency of 1 MHz.

The modulation speed of the arm path length difference and its stability are critical OCT parameters. The scanning velocity of 50 cm/s is required to acquire images with a size of 2.5×4 mm^2 (axial size $\times$ lateral size), resolution of 20×20 µm^2, and acquisition rate of 1 image/s. The scanning velocity should be maintained constant with an accuracy of at least of 1 % to confine the Doppler frequency signal within the detection band. Resonance properties of currently available mechanical systems cannot guarantee constant velocity with required accuracy throughout the modulation period. For our OCT setups, we developed and fabricated a scanning system based on the original fiber optical piezoelectric

modulator [28]. This modulator is capable of scanning the path length difference between the interferometer arms at the rate of 50 cm/s up to 4 mm in depth. Another advantage of our scanning system is almost inertia-free response within the working amplitude and modulation frequency range that substantially simplifies detection of the informative signal at the Doppler frequency.

The probing beam is moved along the sample surface by means of a custom-designed one- or two-coordinate scanner embedded inside of the optical at the distal end of the sample arm. The probing light is focused by a system of lenses with fixed magnification into a 10–20 μm spot at the certain sample depth that can be adjusted mechanically. The fiber tip is swung transversally in the focal plane of the lens system, thus, causing transversal movement of a probing beam within the sample. The scanning process is fully automated and computer controlled.

The interference signal is detected by a photodiode with an optical fiber input that is characterized by high quantum yield (>0.8) and low noise level. The photodiode is coupled with a circuit filtering the electrical signal and extracting the Doppler component with a central frequency of about 1 MHz. The signal consequently passes a linear pre-amplifier characterized by the intrinsic noise level lower than the shot noise of detected light, then a system of filters, a multicascade logarithmic amplifier, and finally an amplitude detector. The logarithmic amplifier with the dynamic range exceeding 70 dB was necessary for detection of extremely low signals because backscattered light intensity decreases exponentially with depth. After analog processing, the signal is fed to a computer through the analog-digital converter for further processing, data recording, and displaying of OCT images.

As was shown in Sect. 24.1, the measured signal is proportional to the logarithm of tissue backscattering. The two-dimensional map of tissue backscattering obtained by scanning in depth (by varying the optical path length difference between the interferometer arms) and by scanning along the sample surface (by moving the probing beam transversally) is displayed on a computer monitor and stored for further use and processing. Such 2D OCT images are called tomograms.

A general view of the compact OCT device is shown in Fig. 24.4. The device is portable ($15'' \times 14'' \times 5.5''$; weight 18 lb); the data acquisition board is internal and is connected via an interface cable to a standard PC printer port. The image acquisition is automated and controlled by a computer. Developed software controls the instrument, processes the data, and displays the images.

24.4.2 "Two-Color" OCT System

The scattering and absorbing properties of samples generally depend on the probing wavelength. Back in the days of early OCT experiments, there appeared an idea of "color" low-coherence imaging in turbid media. The idea was to measure OCT images of the same sample regions at two or more wavelengths simultaneously and then superimpose these images using different colors and relative amplitudes for different wavelengths. We developed and built a system for two-color optical

Fig. 24.4 General view of the portable optical coherence OCT device
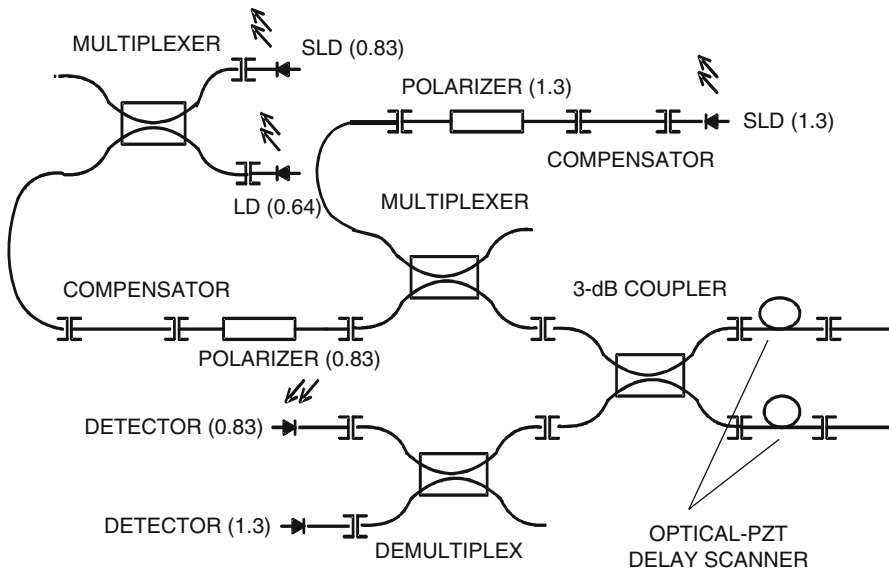
Fig. 24.5 The schematic for two-color OCT setup

coherence tomography [24] that could acquire OCT images at two wavelengths simultaneously using only one interferometer and focusing system.

The schematic of the setup is shown in Fig. 24.5. The light source consisted of two SLDs with central wavelengths of 0.83 and 1.3 μm, spectral bandwidths of 25 and 50 nm (corresponding axial coherence lengths of 13 and 19 μm), and power of 1.5 and 0.5 mW, respectively. The light from both SLDs was coupled to the same Michelson interferometer. The incident radiation was split into two equal parts between the sample and reference arms by a fiber coupler with 3-dB light separation at both wavelengths. The path length difference between the interferometer arms

was modulated by means of the piezoceramic modulator (see Sect. 24.2.2), providing in-depth scanning as deep as 3 mm. The most challenging problem was compensation of wave dispersion in interferometer arms for two different wavelengths simultaneously. This problem was solved by inserting an additional piece of fiber whose dispersion properties were quite different from those of the principal fiber into one of the arms of the interferometer. Cross-correlation function width was minimized by changing the lengths of the principal and compensating fibers for both probing wavelengths. The corresponding attained in-depth spatial resolution for wavelengths of 0.83 and 1.3 μm was 15 and 34 μm, respectively.

24.4.3 3D OCT Imaging

In the optical probe for two-dimensional OCT imaging, the trajectory of a probing beam is linear. For 3D imaging, the electromechanical system of beam deflection was improved to allow an arbitrary trajectory of a probing beam. This type of optical probe permits recording of three-dimensional OCT images with an arbitrary shape of regions within the scattering medium. The simplest way to obtain three-dimensional images is to record a series of two-dimensional images of parallel sections of a sample and then fuse them together. For better visualization, we developed software for animation and presentation of 3D OCT images in the form of semitransparent three-dimensional structures, which greatly simplified perception of large data amounts of tomographic information [22].

24.4.4 Cross-Polarization OCT Setup

Multiple experiments conducted by different research groups have shown that OCT is sensitive to structural alterations in biological objects that occur at the level of cell groups and tissue layers [29–32]. Nevertheless using standard OCT imaging, it is very difficult to differentiate inflammatory processes, papillomatosis, cancer, and scar changes [23].

In many pathologies, structural violations are preceded by biochemical and initial morphological changes. It is known that some structural components of biotissue, e.g., stromal collagen fibers that constitute the basis of healthy mucosa, can strongly depolarize incident radiation. Also, fibrous tissues such as collagens have linear birefringency, i.e., they change the polarization state of light, depending on the value of birefringence and penetrated tissue depth. Both these processes lead to the appearance of cross-polarized component in backscattered light. Pathological processes with different origins are characterized by the difference in both the amount of collagen fibers and their spatial organization. Therefore, a comparative analysis of cross-polarization backscattering properties of biological objects may be taken as an underlying point of the technique for early diagnosis of neoplastic processes.

The specificity of standard OCT can be improved by studying polarization properties of probing radiation when it propagates through a biological object.
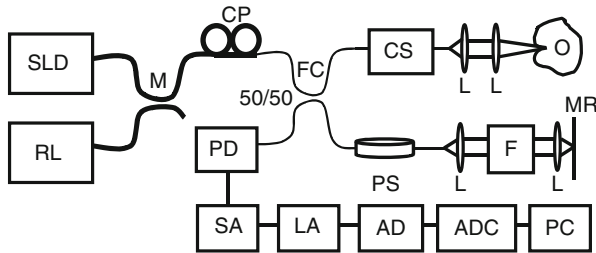
Fig. 24.6 The experimental setup for the cross-polarization OCT: cross-sectional scanner (CS), investigated object (O), longitudinal piezo-scanner (PS), lenses (L), photodiode (PD), selective amplifier (SA), logarithmic amplifier (LA), amplitude detector (AD), analog to digital converter (ADC), personal computer (PC). *Bold line* corresponds to single-mode fiber; *thin line* illustrates polarization maintaining fiber

This approach was implemented in the polarization-sensitive OCT technique (PS OCT), which is described in detail in ► Chap. 19 by J.F. de Boer. At present, in the majority of studies on PS OCT, the criterion of pathological changes in tissue is a sharp decrease in its macroscopic birefringence. For early diagnostics of neoplastic processes, a reliable signal reception at depths 400–700 μm is required. To correctly determine phase characteristics, such as birefringence, the signal-to-noise ratio should be not less than 10–15 dB, which is difficult to achieve when studying layers at depths more than 300–500 μm. For deeper layers (up to 1.5 mm) a variant of PS OCT – the cross-polarization OCT (CP OCT) – can be employed. OCT setups may be equipped with a means for recording images with polarization orthogonal to that of incident probing light. It is a new realm of tomographic information because only regions of the medium that depolarize backscattered light contribute to the interference signal. In order to detect the OCT signal in the orthogonal polarization, a 45° YIG Faraday cell was inserted into the reference arm of the interferometer. The CP OCT technique is based on the detection of a backscattered component that is orthogonal to linearly polarized probing radiation [22, 33].

A sketch of the experimental setup used for measuring OCT and cross-polarized OCT images is shown in Fig. 24.6. Using a multiplexer low-coherence IR radiation from a superluminescent diode (SLD) with wavelength of 1.3 μm and coherence length of 21 μm is combined with radiation from a semiconductor red laser (RL) used for alignment purposes. Then, one of polarization Eigen modes of a PM 3-dB fiber coupler is selected by means of a Lefevre polarization controller (CP). PM fiber is used to transport radiation with a certain polarization state in both the signal and reference arms of the interferometer. When there is no Faraday rotator (F) in the reference arm, a co-polarized component of backscattered radiation is recorded. The Faraday rotator performs rotation of an arbitrary polarization state by a specified angle, and the direction of the rotation depends only on the direction of the magnetic field inside the rotator and does not depend on the propagation direction of the radiation [20]. Therefore, in the case of the 45° Faraday rotator the radiation passes through it, is reflected by a mirror, goes back through the rotator,

and becomes orthogonally polarized in the reference arm. As a result, only the cross-polarized component of light backscattered by a biological object would interfere with light from the reference arm. In Ref. [33], a quarter wave plate oriented at 45° to the incident polarization was used for this purpose. We use a Faraday rotator instead because it does not require the angular alignment, therefore, minimizing the realignment time for the whole system. The readjustment of the system takes approximately 30 s. The acquisition time of one OCT image is 1 s. For all OCT images, the logarithmic intensity scale is used. Lateral resolution of the system determined by the diameter of the probing beam in the focus is chosen close to axial (in-depth) resolution, which is determined by coherence length and in our case is 21 μm. It should be noted that when the system is readjusted to obtain images in the orthogonal polarization, the probe should be held still. Therefore, both types of images (OCT and CP OCT) are obtained from the same tissue site.

Because this design is based on PM fiber, a portable setup with a flexible probe can be created, thus making it easy to use in clinical applications (e.g., endoscopically).

24.4.5 Miniature Probe for Endoscopic OCT

The main problem to be solved for endoscopic implementation of OCT is to provide reliable and convenient access of low-coherence probing radiation to the surface of internal organs. This problem includes several optical, engineering, and biomedical aspects such as creation of an OCT interferometer with a flexible arm, development of a remotely controlled miniaturized optical probe, and acquisition of OCT data in parallel with standard endoscopic imaging. The implementation of the endoscopic OCT (EOCT) system required integration of a sample arm of an all-optical-fiber interferometer into a standard endoscope using the biopsy channel to deliver probing light to investigated tissue. As a result, a whole family of diagnostic EOCT devices suitable for studying different internal organs has been created [34].

To probe the surface of an internal organ we have developed a miniaturized electromechanical unit (optical probe) controlling and performing lateral scanning (Fig. 24.7). This probe is located at the distal end of the sample arm and its size allows fitting the diameter and the curvature radius of standard biopsy channels of endoscopes. Figure 24.8a demonstrates the head of an endoscope for GI investigations with the integrated OCT scanner. A schematic diagram of the optical scanning probe and how it is positioned against a studied object is shown in Fig. 24.8b. The probing beam is swung along the tissue surface with amplitude of 2 mm. The beam deviation system embodies the galvanometric principle, and the voltage with the maximum of 5 V is supplied to the distal end of the endoscope. The distance between the output lens and a sample varies from 5 to 7 mm; the focal spot diameter is 20 μm. The optical scanning probe and the part of the flexible sample arm that is inserted in the endoscope are both sealed, therefore, the conventional cleaning procedure and sterilization can be performed before applying the setup clinically.

Implementation of an extended flexible arm of the OCT interferometer became feasible due to use of polarization maintaining fibers as a means for transportation

Fig. 24.7 Miniature probe for endoscopic OCT
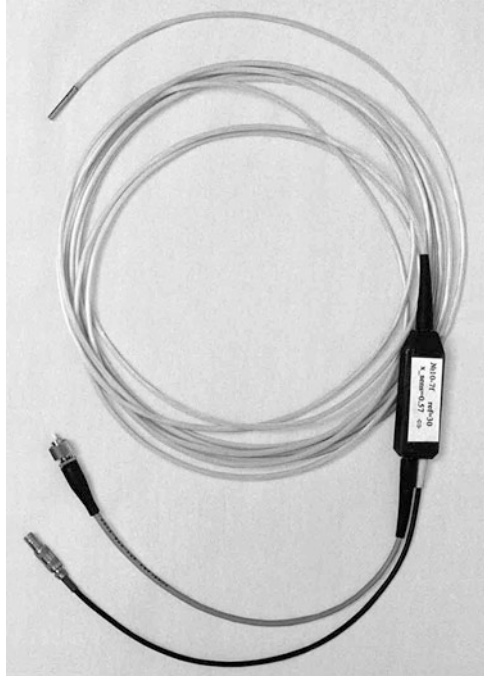
of the low-coherence probing light. This allows eliminating polarization fading caused by polarization distortions at the sites of bending of the endoscope arm. The device features high-quality fiber polarizers and couplers. The "single-frame" dynamic range of our OCT scheme determined as the maximum variation of the reflected signal power within a single-image frame attains 35–40 dB. With the scanning rate of 45 cm/s and the image depth of 3 mm (in free space units), an OCT picture with 200 × 200 pixels is acquired for approximately 1 s. This acquisition rate is sufficient to eliminate influence of moving of internal organs (moving artifact) on the image quality.

The combination of the OCT device with the standard endoscopic equipment has proven to be convenient for clinical studies. A clinician can perform standard observation of internal organs and, in the case of interest, can also extend the analysis by noninvasive optical biopsy simultaneously of as many tissue sites as desired.

24.5 Clinical Applications of OCT

24.5.1 Motivation for OCT Use in Clinical Practice

A majority of pathological processes are accompanied by structural alterations of tissue. Information on these tissue changes is decisive for diagnosis and choosing

Fig. 24.8 (**a**) Distal end of gastroscope with OCT probe introduced through biopsy channel; (**b**) schematic diagram of scanning unit: *1* – output lens, *2* – output glass window, *3* – sample
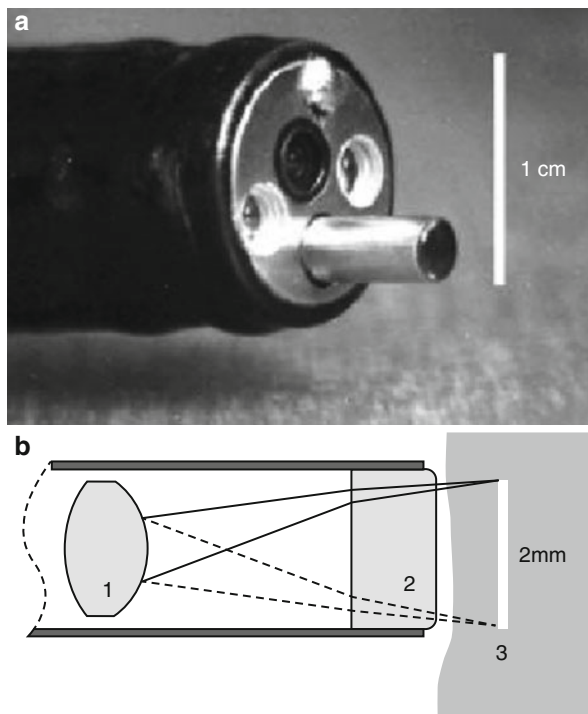
a treatment strategy. The conventional method for obtaining such information is histological study of biopsy specimens of tissue. Biopsy is considered to be the "gold standard." A tissue site to be biopsied is typically chosen using additional modalities such as microscopy, endoscopy, and so on. These methods, however, can provide information only about the surface of the studied object. Meanwhile, it is known that neoplastic and inflammatory processes primarily involve parabasal and basal layers, the basement membrane, and components of the lamina propria of mucosa and rarely affect the surface layers of the epithelium. Structural alterations in these portions of the epithelium cannot be detected by surface-imaging methods. Therefore, a clinician is to rely on indirect subtle superficial manifestations of pathological processes in order to perform a guided biopsy that eventually leads to a high rate of false-negative results of biopsy [35].

Information on the internal structure of biological tissues is essential not only for diagnosis of disease, but also for planning of the extent of treatment, control of treatment adequacy, and follow-up. In these situations, application of an invasive method such as biopsy is impractical and sometimes contraindicated.

Optical coherence tomography (OCT) is a promising imaging modality characterized by high spatial resolution, noninvasiveness, and high rate of image acquisition. An OCT device developed at IAP RAS (Nizhny Novgorod, Russia) is compact, portable, and easy to operate; the device is equipped with miniature

optical probes compatible with working channels of standard endoscopes, which provides an additional advantage for clinical applications.

Our experience of clinical studies using OCT can be divided into three stages: determination of OCT criteria for norm and pathology for various human tissues, evaluation of diagnostic efficiency of the method, and development of OCT procedures for different clinical situations.

24.5.2 OCT Criteria of Normal and Pathological Tissue

At the first stage, we performed ex vivo and in vivo OCT studies of various human organs. OCT images were compared with the results of standard histology and, based on this comparative analysis, the optical criteria of the states of human tissues were determined. It was established that due to different scattering properties of different tissue layers, OCT images reveal the stratified structure. Mucosa of different organs, skin of various localization, and hard dental tissues have a specific structure with distinctive optical patterns, which makes these objects favorable for OCT.

Figures 24.9 and 24.10 illustrate examples of parallel OCT and histological study of healthy mucosa of the esophagus (Fig. 24.9a and b), uterine cervix (Fig. 24.9c and d), and larynx (Fig. 24.9e and f), which are covered by the stratified squamous epithelium; of the urinary bladder whose internal layer is represented by the transitional epithelium (Fig. 24.10a and b), and of the colon (Fig. 24.10c and d), which is covered by the simple single-layer epithelium atop irregular basement membrane forming glands or crypts. All histological layers inherent to mucosa are evident in these OCT images. It is known that the stratified (transitional) epithelium is separated from the underlying stroma by a smooth basement membrane. Due to different scattering properties of the epithelium and stroma, the location of the basement membrane is clearly seen on these tomograms. In the case of the colon, the basement membrane is irregular and its form is difficult to define accurately. However, the intestinal crypts and the structure of subepithelial layers are well visualized. Mucous glands are also visualized as poorly scattering shadows but their borders are much less distinct (Fig. 24.9e).

A typical endosonographic image of healthy esophagus is shown in Fig. 24.11. The zone of OCT imaging is also depicted in the same figure. Obviously, spatial resolution of endoscopic ultrasound is not sufficient for revealing details of the mucosal structure; OCT, however, easily visualizes the layered optical pattern (Fig. 24.9a).

OCT images of the skin (Fig. 24.12a and b) differ from those of mucosa in the relatively weak optical contrast between structural components. This is likely caused by strong reflection of probing light from the tissue surface due to keratinization. Nevertheless, the tomograms clearly demonstrate the morphological features of thick and thin skin.

In vivo OCT imaging of dental tissues showed that the effective penetration depth of probing radiation in teeth was 2–2.5 mm. The structure and content of
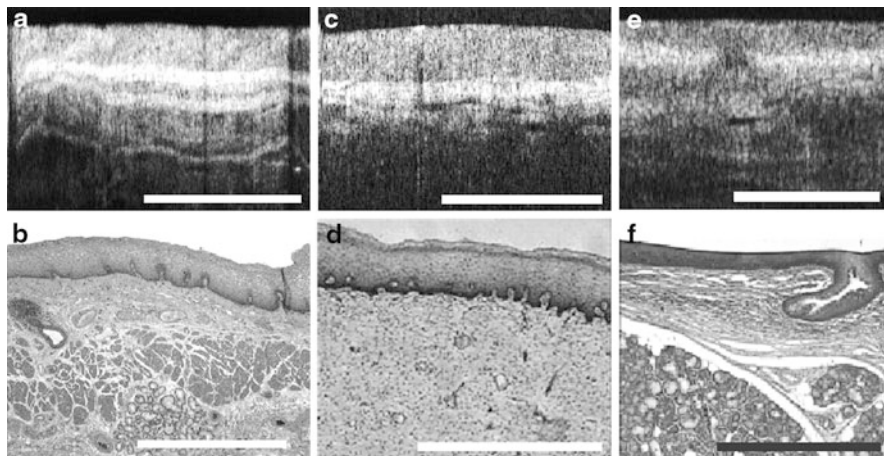
Fig. 24.9 OCT images and histology of healthy mucosa of esophagus (**a**, **b**), uterine cervix (**c**, **d**), and larynx (**e**, **f**) covered by stratified squamous epithelium
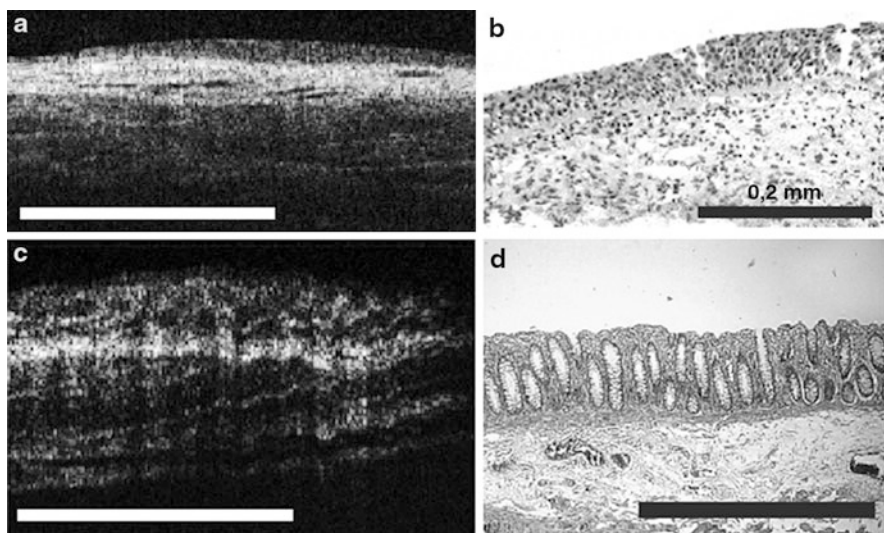
Fig. 24.10 OCT images and histology of urinary bladder covered by transitional epithelium (**a**, **b**) and colon covered by the simple single-layer epithelium (**c**, **d**)

dentin is known to be considerably different from those of enamel, thus, allowing differentiation between dentin and enamel and estimation of the state of the dentino-enamel junction (Fig. 24.13a and b).

Therefore, due to different optical properties, OCT can differentiate tectorial and hard dental tissues, revealing their regular layered structure. The type of the

Fig. 24.11 Typical endosonographic image of healthy esophagus
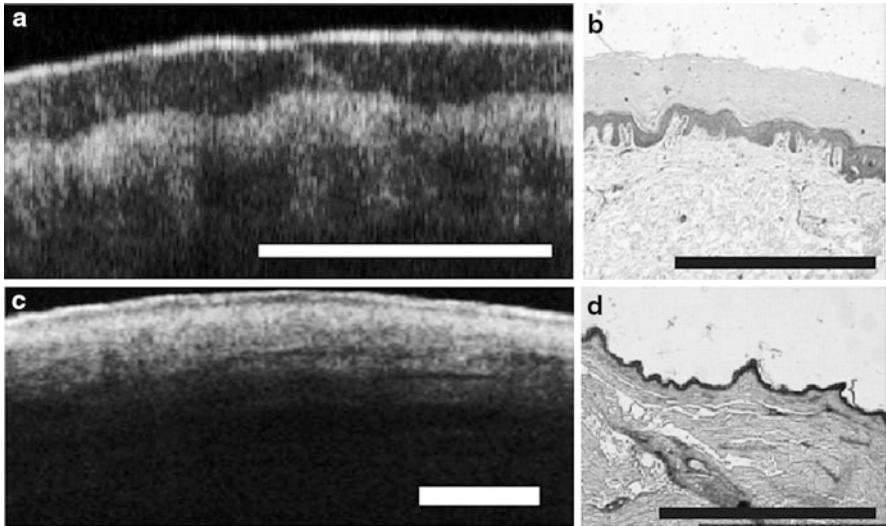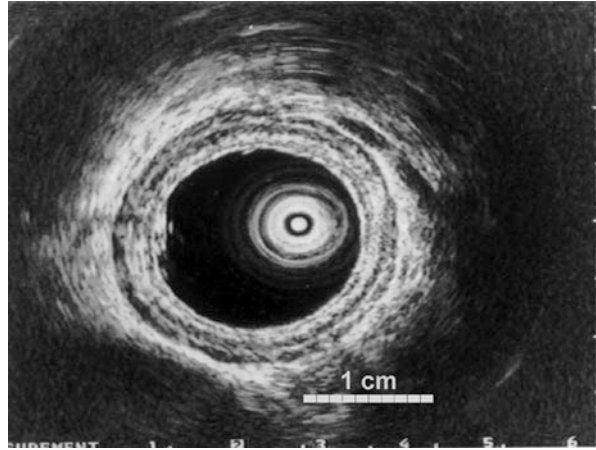
Fig. 24.12 OCT images and histology of thick (**a**, **b**) and thin skin (**c**, **d**)

epithelium, keratinization processes, and the architecture of the basement membrane affect the OCT pattern of tectorial tissues. Because optical properties of mucous glands are considerably different from those of the stroma, OCT can both reliably identify and quantify them throughout the entire range of sizes, limited only by spatial resolution of the OCT method. Interestingly, healthy human tissues, which do not have the layered structure, appear unstructured in OCT images. A good example of such tissue is cartilage covering articulating surfaces of bones (Fig. 24.14a and b).

Fig. 24.13 OCT image and histology of hard dental tissues (**a**, **b**)
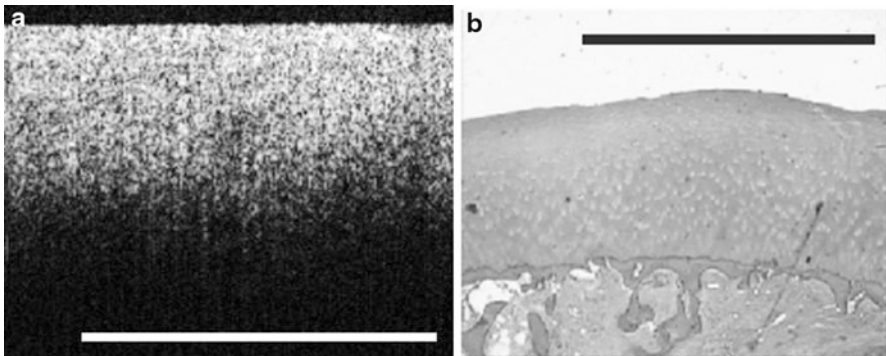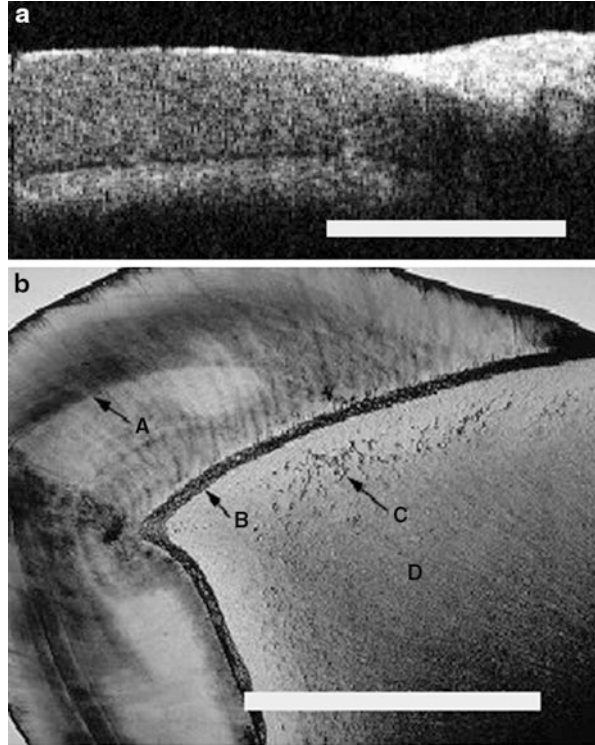
Fig. 24.14 OCT image and histology of cartilage covering articulating surfaces of bones (**a**, **b**)

We performed clinical studies using OCT in various fields of medicine, such as gastroenterology, urology, laryngology, gynecology, dermatology, and dentistry, and involving some 2,000 patients. These studies show that there are a number of universal OCT patterns corresponding to different structural alterations, which are in turn caused by different pathological processes [22, 32, 36–39]. Figure 24.15a

Fig. 24.15 OCT image of
chronic inflammatory process
in the uterine cervix (**a**) as
compared with the norm (**b**)
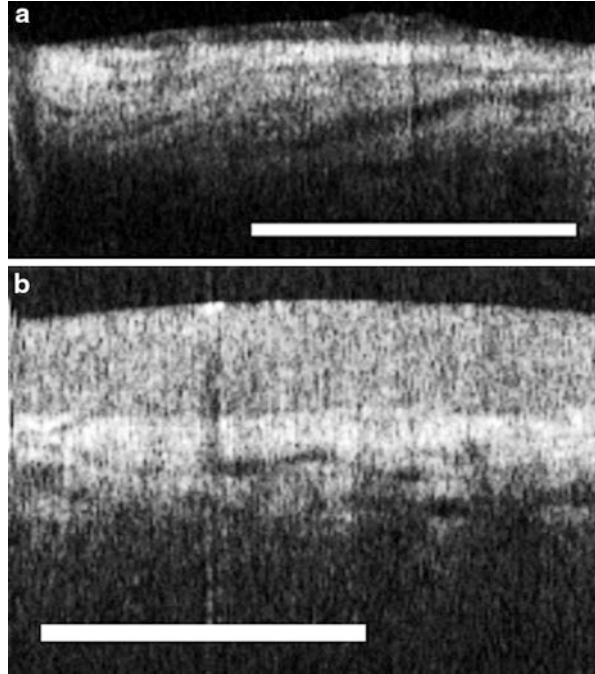
demonstrates a typical OCT image of a chronic inflammatory process in the uterine cervix accompanied by atrophy of the epithelium. The OCT manifestation of the above processes is a decrease in the thickness of the upper moderately bright layer down to 50 μm (in comparison to 300–350 μm in norm, see Fig. 24.15b). The identical optical signs of epithelial atrophy are found also in other localizations.

Hyperplasia (hypertrophy) of the epithelium manifests in OCT images as an increase in the thickness of the epithelial layer (corresponding examples of the transitional epithelium of the urinary bladder are shown in Fig. 24.16a and b); the stratified squamous epithelium of a vocal fold is shown in Fig. 24.16c and d. In these cases of epithelial hypertrophy, the basement membrane is not affected and, hence, the two-layered optical pattern with high contrast is preserved.

Hypertrophy with acanthosis and papillomatosis alters not only the thickness but also the optical properties of the epithelium (increasing the level of epithelial backscattering) and the course of the basement membrane (making it winding). All these phenomena lead to a decrease in the contrast of the characteristic two-layer pattern of mucosae. Figure 24.17 presents a tomogram (a) and parallel histology (b) and (c) of acanthosis and papillomatosis of mucosa in the uterine cervix where stromal papillae come up to the epithelial surface. Each papilla contains an enlarged terminal vessel, which is visualized in the image as a dark area. Note that these alterations of the epithelium are benign and the two-layer architecture of tectorial tissue is preserved.
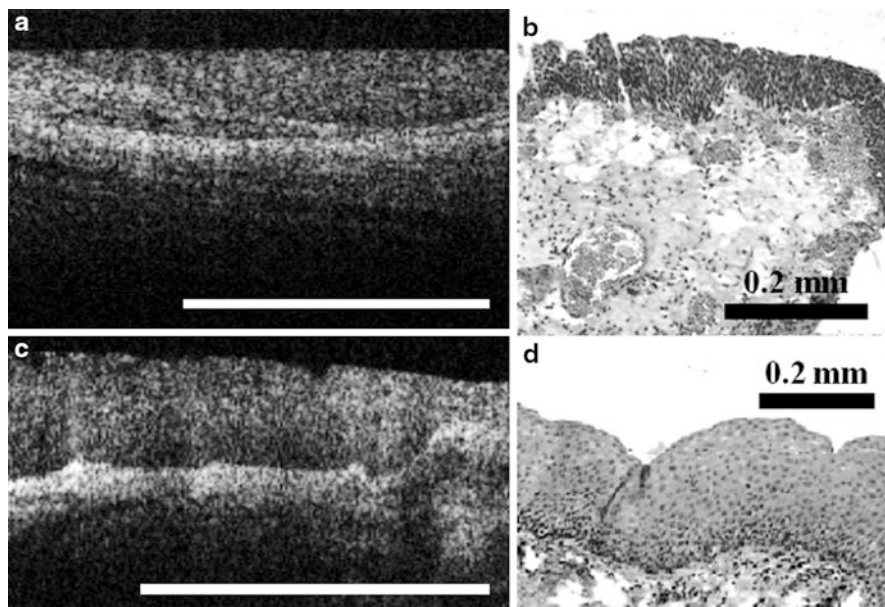
Fig. 24.16 OCT image and histology of epithelial hyperplasia. Transitional epithelium in the urinary bladder (**a**, **b**); stratified squamous epithelium in the vocal fold (**c**, **d**)

OCT can be also used for imaging of the metaplastic processes. Figure 24.18 demonstrates an OCT image and parallel histology of metaplasia of the stratified squamous epithelium of the esophagus into the columnar specialized epithelium in Barrett's esophagus (Fig. 24.18a and b). An OCT image of healthy esophagus is shown in Fig. 24.18c for comparison. The tomogram of benign Barrett's esophagus indicates the layered architecture of esophageal mucosa; only at the sites of the uniform moderately scattering squamous epithelium is a so-called glandular mucosa visualized by alternating dark (corresponding to the glandular epithelium) and light (corresponding to connective tissue layers of lamina propria) horizontal stripes. The OCT image of squamous metaplasia of urinary bladder mucosa (Fig. 24.19a and b) is characterized by an increase in the thickness of the epithelium, as compared with urothelium inherent to this mucosa in norm (Fig. 24.19c), and a higher brightness of the epithelial layer due to hyperkeratosis.

Thus, various benign processes occurring in the epithelium manifest in OCT images as changes in the epithelial thickness, scattering properties, and the course of the basement membrane.

OCT can detect changes that occur not only in the epithelium but in the stromal component of mucosa as well. Pathological processes of different origin can be accompanied by either stromal edema or accumulation of liquid with formation of cavities and cystic structures. Different types of liquid accumulation are presented in Fig. 24.20. Figure 24.20a shows an OCT image of the skin from a shoulder with a subcorneal blister in a patient with paraneoplastic skin eruption. An OCT image of
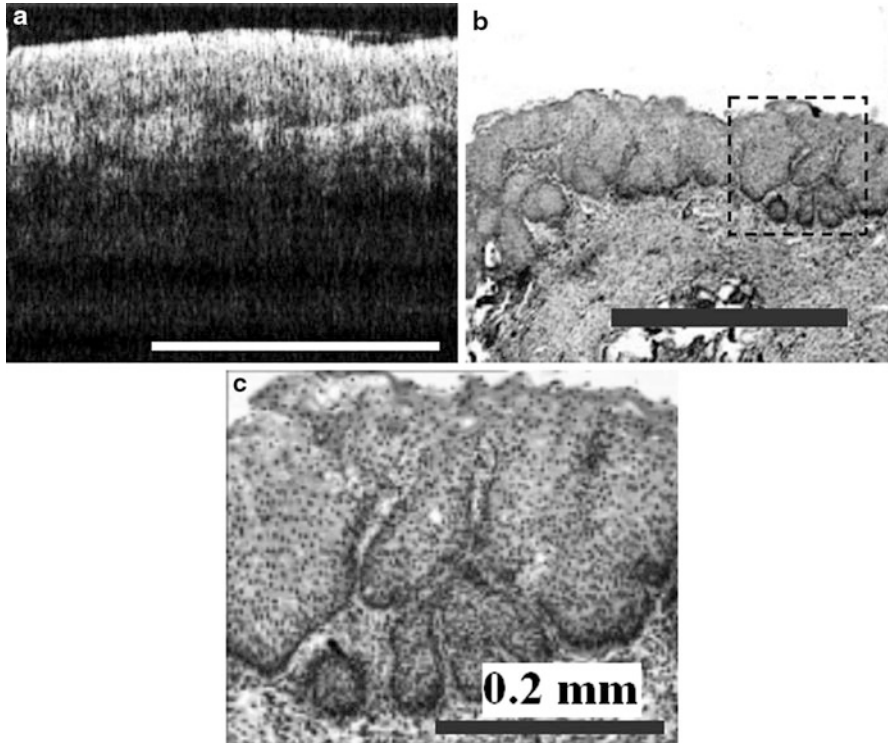
Fig. 24.17 OCT image (**a**) and parallel histology (**b** and **c**) of acanthosis and papillomatosis of uterine cervix mucosa

the uterine cervix in pregnancy (Fig. 24.20b) shows accumulation of liquid inside of tissue and disconnection of connective tissue fibers (so-called physiological edema) and indicates that the well-organized structure of the connective-tissue layer is destroyed which results in appearance of dark irregular areas. OCT can clearly visualize various glandular structures: enlarged glands of esophageal mucosa in Barrett's metaplasia (Fig. 24.20c) and Brunn's nests in cystitis cystica (Fig. 24.20d). These examples demonstrate the capability of OCT not only to visualize hollow structures but also to detect their form and localization precisely.

The information on the structure of objects provided by OCT can be used for tumor detection. Although our OCT device has spatial resolution of about 10–20 μm and, thus, cannot detect neoplastic changes at the cellular level, but its spatial resolution is sufficient to reveal certain specific features of the tissue architecture accompanying the malignization process, such as abnormal accumulation of cells, penetration of the epithelium into the stroma, and, conversely, of the stroma into the epithelium without disruption of the basal membrane (leading to changes in optical properties of the epithelium and loss of the optical contrast between the epithelium and stroma) and an increase in the amount of blood vessels.
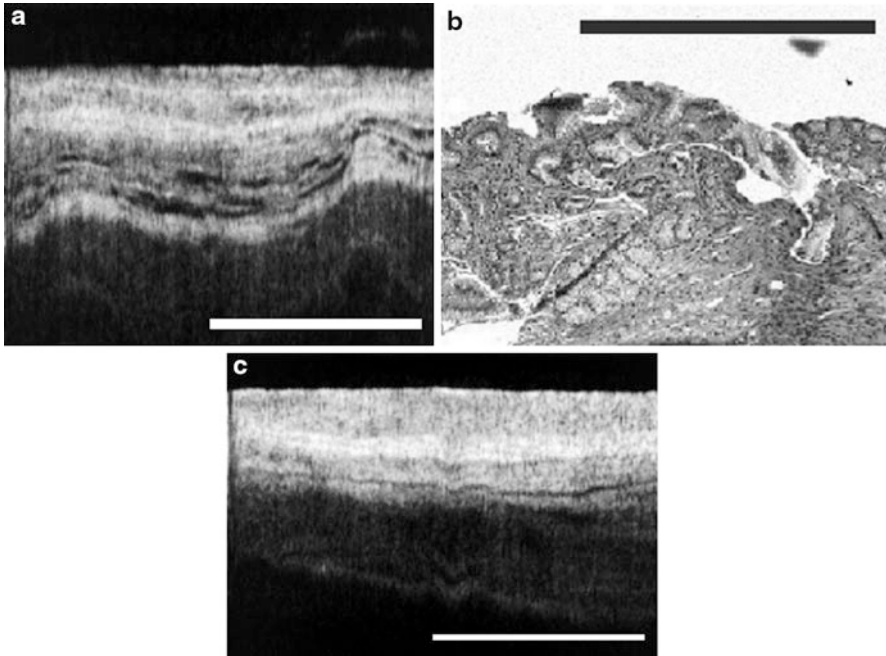
Fig. 24.18 OCT images of metaplasia of stratified squamous epithelium of esophagus (**c**) into columnar specialized epithelium in Barrett's esophagitis (**a**), parallel histology (**b**)

Result of our OCT study demonstrate:

1. Low-grade dysplasia almost does not change optical properties of the epithelium and, thus, preserves the layered optical pattern with good contrast, which is typical for benign mucosa (Fig. 24.21);
2. High-grade dysplasia changes optical properties of the epithelium and underlying connective tissue and, therefore, considerably reduces contrast between the epithelium and the stroma in OCT images (Figs. 24.22a, b, 24.23a, b, and 24.24a, b);
3. Microinvasive cancer is characterized by local disappearance of the basement membrane and leads to further changes of optical properties of the epithelium and stroma; as a result, OCT images of microinvasive cancer appear weakly structured (Figs. 24.22c, d, 24.23c, d, and 24.24c, d);
4. Invasive cancer is an extreme stage of malignization; it is visualized by OCT as a bright homogeneous pattern. The effective imaging depth in this case is sufficiently smaller (Figs. 24.25, 24.26, and 24.27).

24.5.3 OCT Diagnostic Value

To evaluate the efficiency of the OCT method for detection of different stages of malignization, three independent blind tests were performed using OCT images of the uterine cervix, urinary bladder, and larynx. The studies showed that OCT is
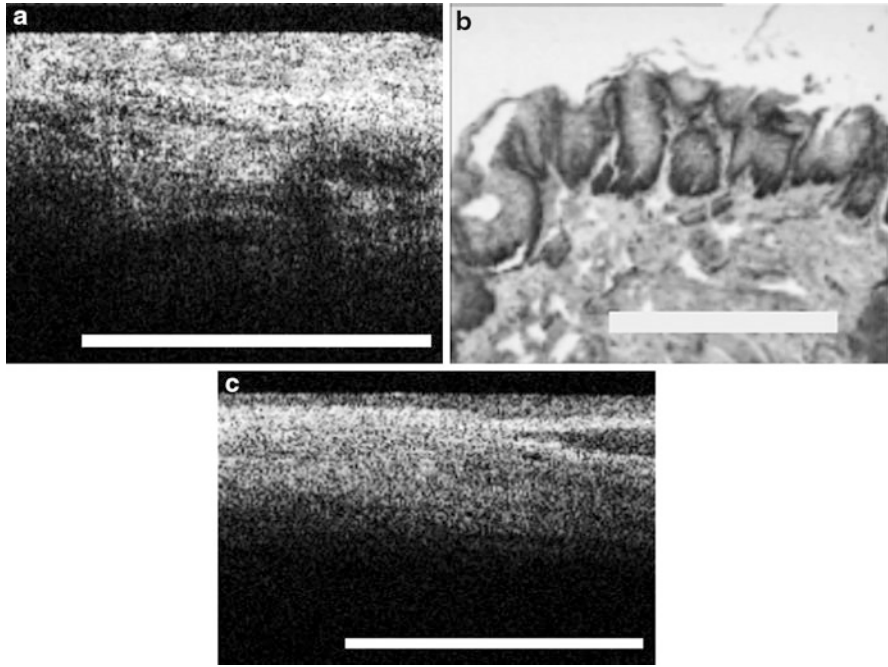
Fig. 24.19 OCT image and histology of squamous metaplasia of urinary bladder mucosa (**a**, **b**), OCT image of normal urothelium (**c**)
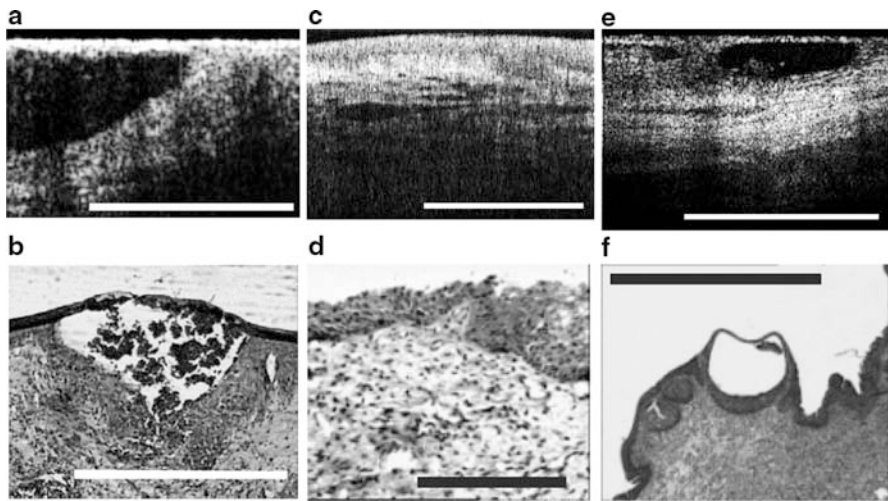
Fig. 24.20 OCT images and histology of different types of liquid accumulation: subcorneal blister (**a**, **b**), uterine cervix at pregnancy (**c**, **d**), Brunn's nests in cystitis cystica (**e**, **f**)
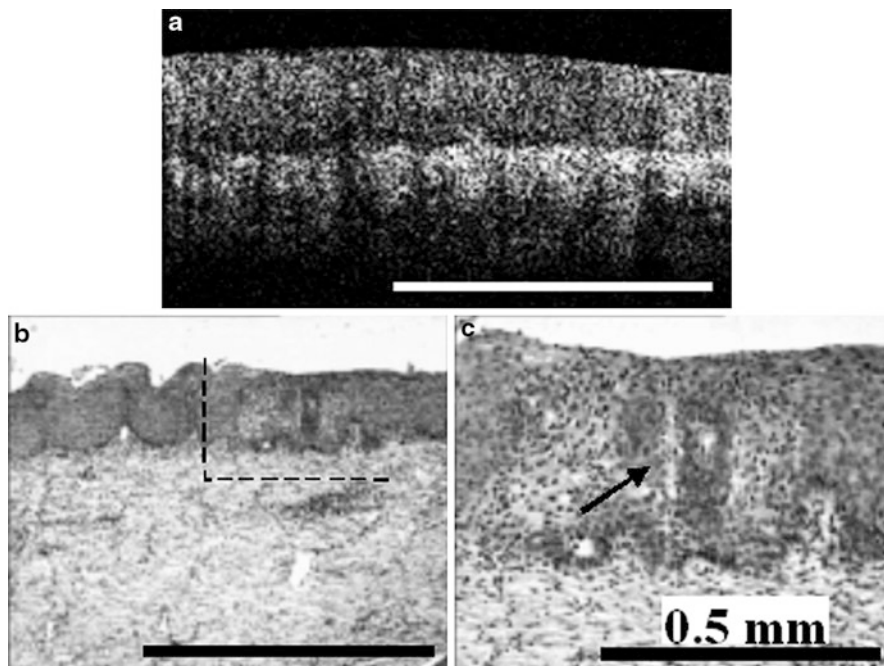
Fig. 24.21 OCT image of low-grade dysplasia accompanied by hyperplastic stratified squamous epithelium of uterine cervix with signs of acanthosis and papillomatosis (**a**), parallel histology (**b**, **c**)

highly efficient for diagnosing of mucosal neoplasia of the uterine cervix, urinary bladder, and larynx: OCT sensitivity was 82 %, 98 %, and 77 %, respectively; specificity was 78 %, 71 %, and 96 %; diagnostic accuracy was 81 %, 85 %, 87 % with significantly good agreement index of clinicians kappa – 0.65, 0.79, 0.83 (confidence intervals: 0.57–0.73; 0.71–0.88; 0.74–0.91). Error in detection of high-grade dysplasia and microinvasive cancer was 21.4 % on average.

24.5.4 Clinical Indications for OCT

OCT can provide information on the internal structure of biological tissues in real time with high resolution and noninvasively. These capabilities of OCT can be used to improve current diagnostic methods. This would benefit oncology, where exact knowledge of morphological alterations is essential for choosing treatment strategy.

Nonaltered tissues with different internal structure have specific optical patterns determined by certain features of their structure. Loss of tissue specificity accompanying neoplastic changes makes tissues look similar without any architectural and optically structure. Figures 24.28 and 24.29 present tomograms and histological sections of patients with carcinoma of the larynx, uterine cervix, urinary bladder, and rectum. Results of histology show the presence of a distinct border between
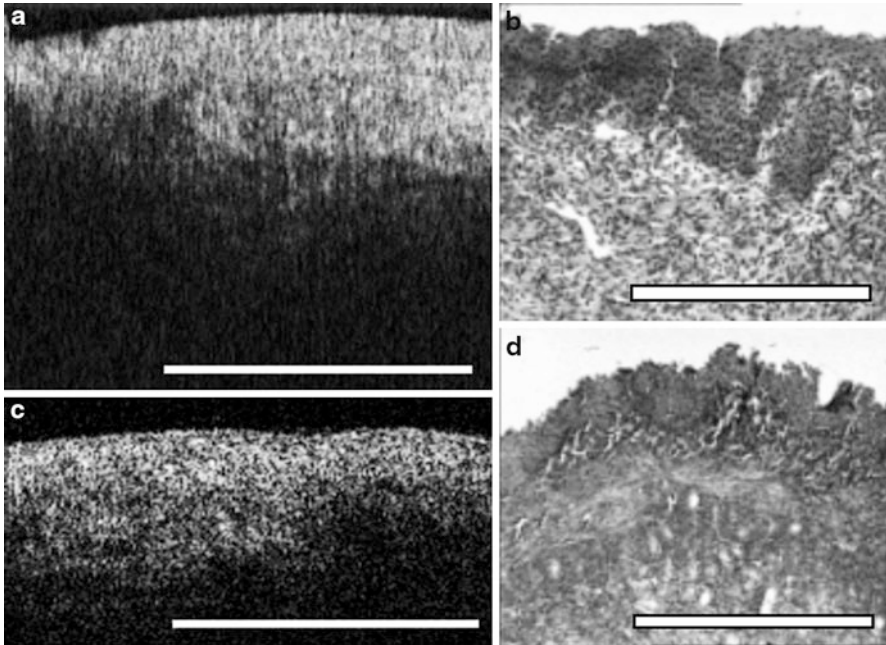
Fig. 24.22 OCT image of high-grade dysplasia of uterine cervix (**a**), parallel histology (**b**); OCT image of microinvasive cancer of uterine cervix (**c**), parallel histology (**d**)

malignant tumor and benign mucosa (Figs. 24.28b, d, 24.29b, d, and e). The transition from a structureless optical pattern with high backscattering from sub-surface layers typical of malignant tumors into a structured optical pattern with a clearly detectable, layered organization is clearly seen in the OCT images (Figs. 24.28a, c, and 24.29a, c). Therefore, OCT is capable not only to detect tissue regions suspicious for neoplasia but also to accurately and reliable determine their borders.

This fact is very important clinically. First, OCT data may be critical for choosing a tissue site for excisional biopsy when conventional methods are inadequate. For instance, biopsy sampling from the areas of the uterine cervix suspicions for cancer is routinely guided colposcopy. So-called abnormal colposcopic findings are indicative of malignization. However, these abnormal colposcopic findings are not pathognomic signs of malignant growth and can be found in benign lesions as well [40]. In our opinion, additional information on the tissue structure provided by OCT can improve the specificity of colposcopy and optimize target biopsy of uterine cervix pathology. In laryngology, OCT imaging proves to as helpful as in gynecology. Currently, even when the state-of-the-art microlaryngoscopy is used, from 7 % to 20 % of patients need to come back to have biopsy repeated in order to confirm the laryngeal carcinoma diagnosis [41, 42]. This may cause serious complications, especially for such a vulnerable organ as the larynx.
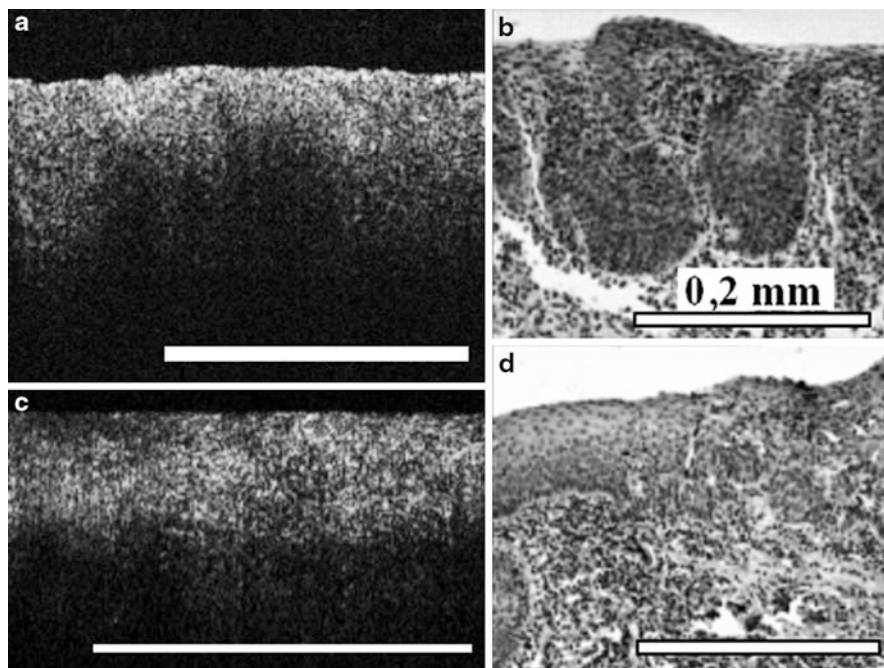
Fig. 24.23 OCT image of high-grade dysplasia of the epithelium of a vocal fold (**a**), parallel histology (**b**); OCT image of microinvasive cancer of a vocal fold (**c**), parallel histology (**d**)

Second, the capability of OCT to detect tumor borders and their linear dimensions can be employed for staging of the malignant process in clinical situations for which the linear extent of tumor is essential.

Third, information provided by OCT can be used to plan a resection line in the course of organ-preserving operations and to control adequacy of resection. The main requirements for successful organ-preserving surgeries are adequacy of resection of a pathological region and minimal damage of healthy surrounding tissues. Necessity for such surgeries is dictated by the need to preserve the organ function. For example, at the initial stage of uterine bladder cancer, it is still possible to perform transurethral resection (TUR), when the organ is totally preserved, or partial resection followed by plastic surgery of the bladder, the latter is feasible only if the sphincter is preserved. According to existing rules, the resection line should be 2 cm away from the visual tumor border at TUR and not less than 3 cm from the urinary bladder cervix at partial resection. Such stringent requirements limit the number of patients in whom the organ-preserving surgery can be performed. However, notwithstanding such a strict approach, the recurrence rate for partial resection is as high as 40–80 % [43]. The same situation takes place with rectal tumors where the recurrence rate attains 78 %. It was shown that the high recurrence rate is caused by deficient resection of tumors [44]. Reported data proves that existing methods for monitoring of organ-preserving operations in most of the
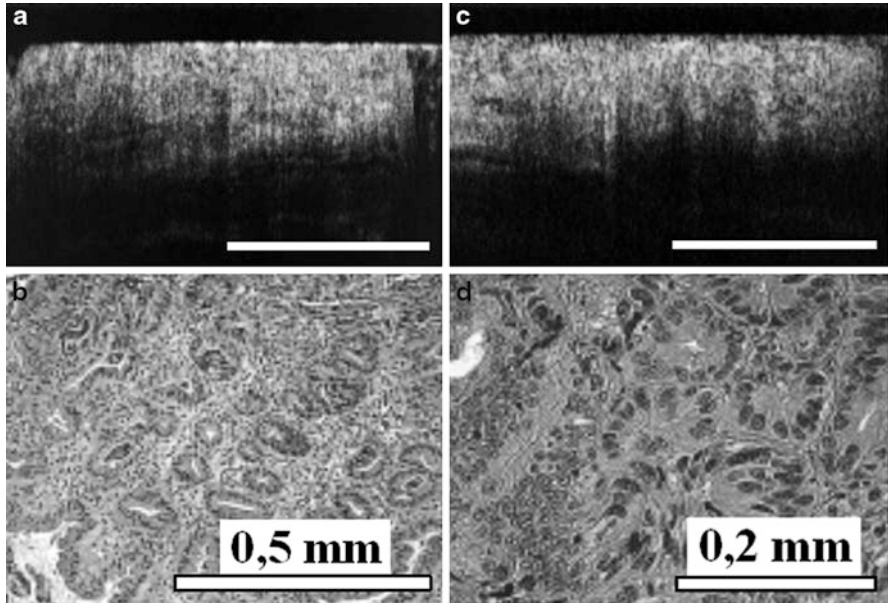
Fig. 24.24 OCT image of high-grade dysplasia of metaplastic epithelium in Barrett's esophagus (**a**), parallel histology (**b**); OCT image of microinvasive adenocarcinoma of the esophagus (**c**), parallel histology (**d**)

cases are inadequate. The OCT technology can definitely be helpful and aid conventional methods in solving this problem. The method provides high spatial resolution images in real-time, thus allowing using OCT intraoperatively. OCT is noninvasive (no tissue damage, no side effects); therefore, one can perform monitoring of surgeries. Compatibility of OCT probes with working channels of standard endoscopes permits applying OCT endoscopically.

Fourth, since information on the tissue structure is obtained in vivo, OCT imaging can be used during both surgery and conservative treatment to monitor whether reparative processes are timely and adequate, and to detect early recurrence during follow-up.

24.5.5 Development of Clinical Procedures for OCT

At the present stage of its development, OCT has a number of disadvantages and limitations. Most prominent of them are the following. First, spatial resolution of 15–20 μm is sufficient to identify cellular layers but too low to visualize single cells. Consequently, in situations where detection of changes occurring at the cellular level is critical, OCT cannot provide adequate specificity. Second, the informative imaging depth of OCT is limited to 2 mm, which is a serious limitation, especially for oncology where estimation of the depth of tumor invasion into underlying tissue is of high importance.
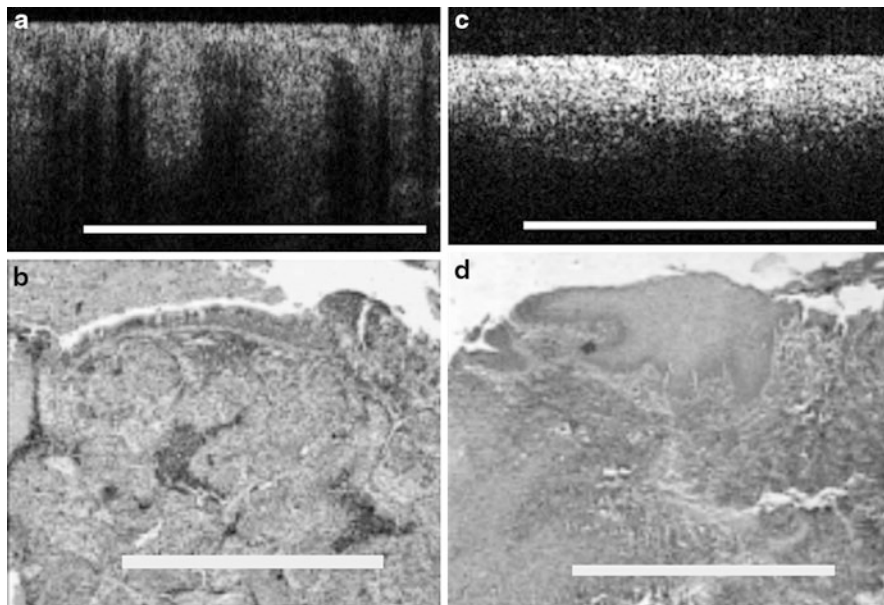
Fig. 24.25 OCT image of invasive squamous cell carcinoma of segmented bronchus (**a**), parallel histology (**b**); OCT image of invasive squamous cell carcinoma of vocal fold (**c**), parallel histology (**d**)

These disadvantages and limitations are rather technical. At the same time, the diagnostic value of OCT can also be decreased by drawbacks of the imaging procedure, which affect the quality of images, namely, lower brightness and contrast and introduce movement artifacts. On the one hand, these factors to some extent impede extensive application of OCT in clinical practice, but on the other hand, it is a strong reason for further improvement of the OCT technology.

There are several ways of improving OCT imaging, which can be grouped as follows:

- Development of OCT procedures taking into account both specific features of objects being studied and particular clinical tasks
- Modification of standard OCT
- Additional processing of OCT images

24.5.5.1 Effects of Biotissue Compression

One of the most important practical problems in the development of OCT technology is creation of OCT procedures taking into account both clinical tasks and specific features of objects being studied. One of requirements for obtaining of high-quality images is the absence of movement artifacts. For this, an OCT probe must be fixed relative to the object. The latter can be eliminated by keeping the OCT probe still and by slightly pressing it against the tissue region being studied. However, soft biological tissues are very elastic and, consequently, even slight
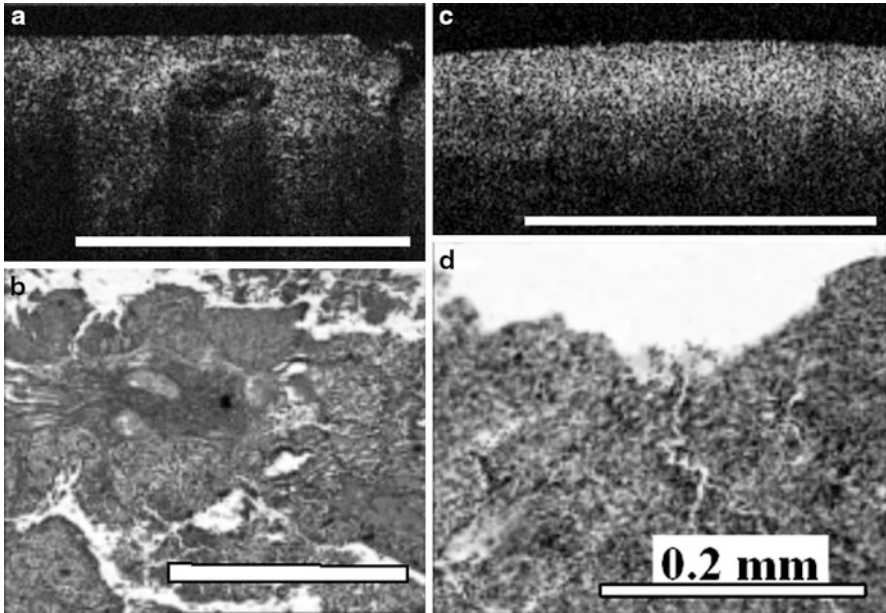
Fig. 24.26 OCT image of invasive transitional cell carcinoma of urinary bladder (**a**), parallel histology (**b**); OCT image of invasive squamous cell carcinoma of uterine cervix (**c**), parallel histology (**d**)
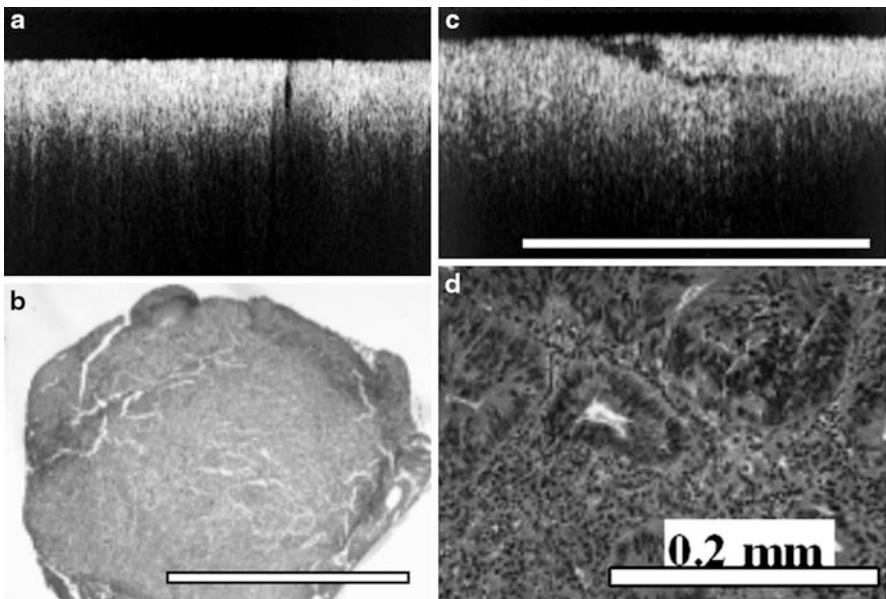
Fig. 24.27 OCT image of invasive adenocarcinoma of esophagus (**a**), parallel histology (**b**); OCT image of invasive adenocarcinoma of rectum (**c**), parallel histology (**d**)
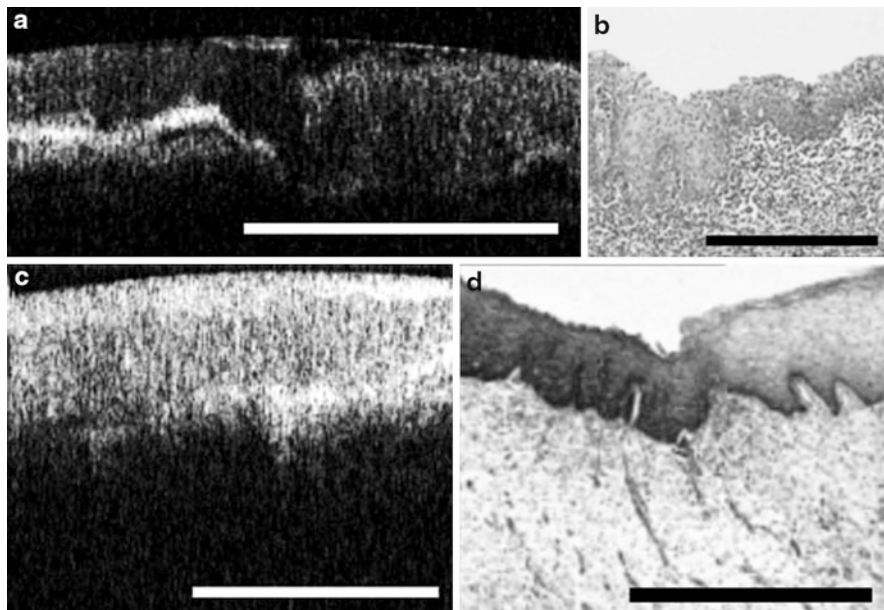
Fig. 24.28 OCT images (**a**, **c**) and parallel histology (**b**, **d**) of carcinoma of larynx (**a**, **b**); benign mucosa (to the *left*), high grade dysplasia (to the *right*). Uterine cervix (**c**, **d**); benign mucosa (to the *right*), high grade dysplasia (to the *left*)

pressure leads to compression of the object, which affects measured OCT information. Figure 24.29 shows ex vivo tomograms of the sigmoid colon clearly demonstrating that OCT images depend on the degree of object's compression. As pressure increases, the contrast between layers improves, which is most likely caused by the induced increase in the tissue density. Moreover, at the maximum compression (Fig. 24.30c) all layers of the intestinal wall were visible in the OCT image. The thickness of the wall surely exceeds 2 mm, therefore, compression technically allowed to image tissue layers below the effective OCT imaging depth.

24.5.5.2 Effects of Chemical Agents

One of the approaches to improve OCT penetration depth is based on biological tissue clearing using biocompatible chemical agents [45, 46]. Hyperosmolar chemical agents such as glycerol, propylene glycol, and concentrated glucose solutions reduce the refractive index mismatch on the air-tissue boundary and upon penetration into tissue also facilitate matching of refractive indices of tissue constituents, which leads to a decrease in scattering of tissue components. For instance, refractive indices of glycerol (1.47) and propylene glycol (1.43) are slightly different that of the skin (1.47) [45, 46]. Application of these agents allows one to increase the effective depth of OCT imaging and to improve image contrast. The effect of clearing is shown in Fig. 24.31. The OCT image of skin with psoriatic erythrodermia acquired in 60 min after application of glycerol (Fig. 24.31b) differs
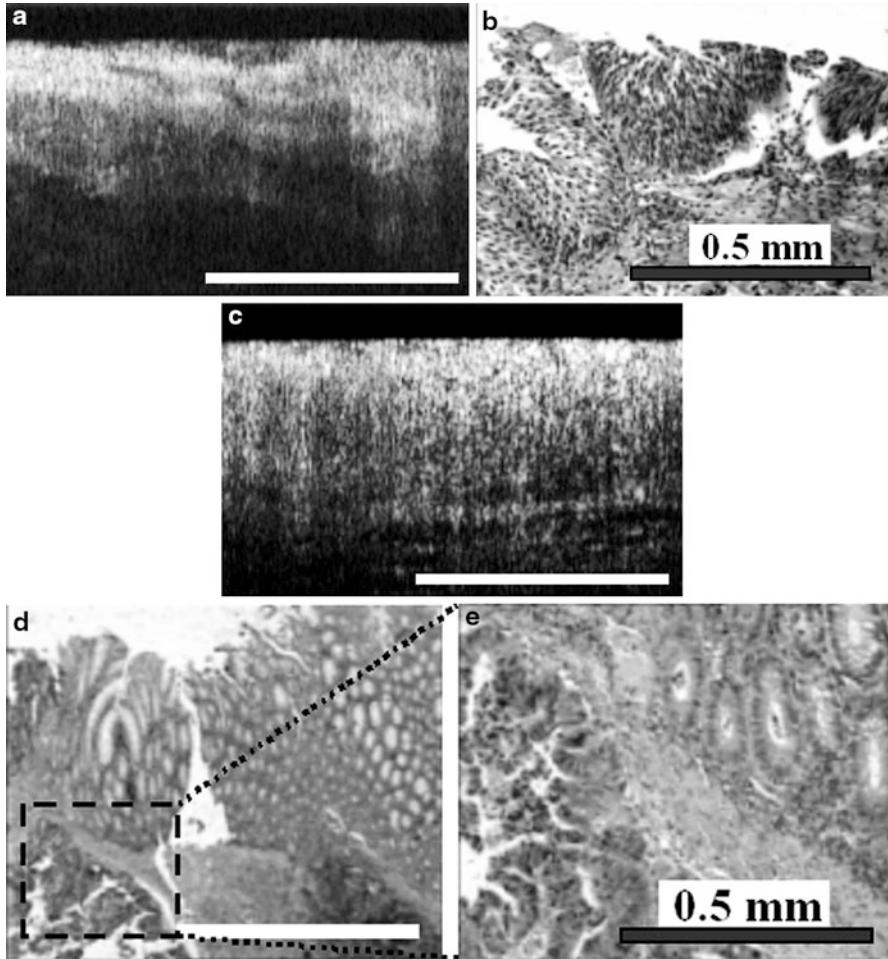
Fig. 24.29 OCT images (**a**, **c**) and parallel histology (**b**, **d**) urinary bladder (**a**, **b**, to the *left* – benign mucosae, to the *right* – high grade dysplasia) and rectum (**c–e**, to the *right* – benign mucosae, to the *left* – invasive carcinoma)

from the initial image (Fig. 24.31a) in greater penetration depth and better contrast. These image improvements facilitate identifying of important morphological phenomenon of acanthosis (Fig. 24.31c). It is known that tissue clearing depends on time and the type of tissue. Development of a clinical procedure for various pathological processes and types of biological tissue requires accurate choice of chemical agents and optimal exposure times.

24.5.5.3 Cross-Polarization OCT
The specificity of standard OCT can be improved by studying collected light reflected back from a biological object with respect to polarization. In many
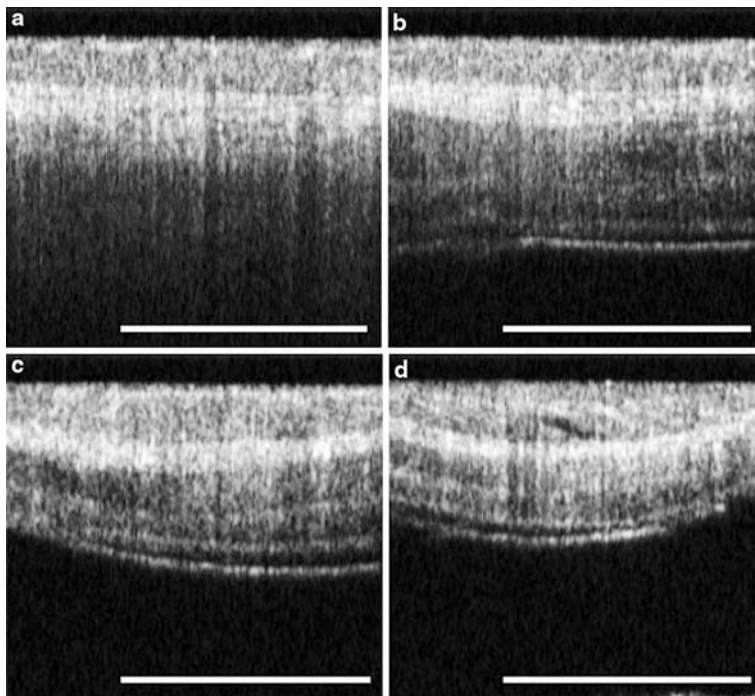
Fig. 24.30 Ex vivo OCT images of sigmoid colon, demonstrating the dependence of image character on the degree of compression of the object (**a–d**)

pathologies severe structural alterations are preceded by biochemical and initial mild morphological changes. It is known that several structural components of biological tissue, e.g., stromal collagen fibers constituting the basis of healthy mucosa, can strongly scatter and also depolarize incident radiation [47]. Both these phenomena can lead to the appearance of the cross-polarized component in backscattered light. Pathological processes of different origin are characterized by various spatial organization and density of collagen fibers that would affect the OCT signal intensity detected in orthogonal polarization. Therefore, analysis of cross-polarization backscattering properties of biological objects may provide a new way for diagnosis of different pathological processes.

OCT images in initial and orthogonal polarizations were acquired ex vivo on the resected esophagus (no later than 60 min after extirpation) and in vivo during esophagoscopy. It should be noted that, when the system was readjusted to measure images in the different polarizations while probe was kept still for 30 s, OCT and cross-polarization (CP) OCT images were verified by comparing with results of parallel analysis of biopsy H&E and Van Gieson stained samples. The Van Gieson staining is specific for collagen fibers of connective tissue [48].

The results of the OCT study of the healthy esophagus are presented in Fig. 24.32. Tomograms of unaltered esophageal mucosa obtained in both
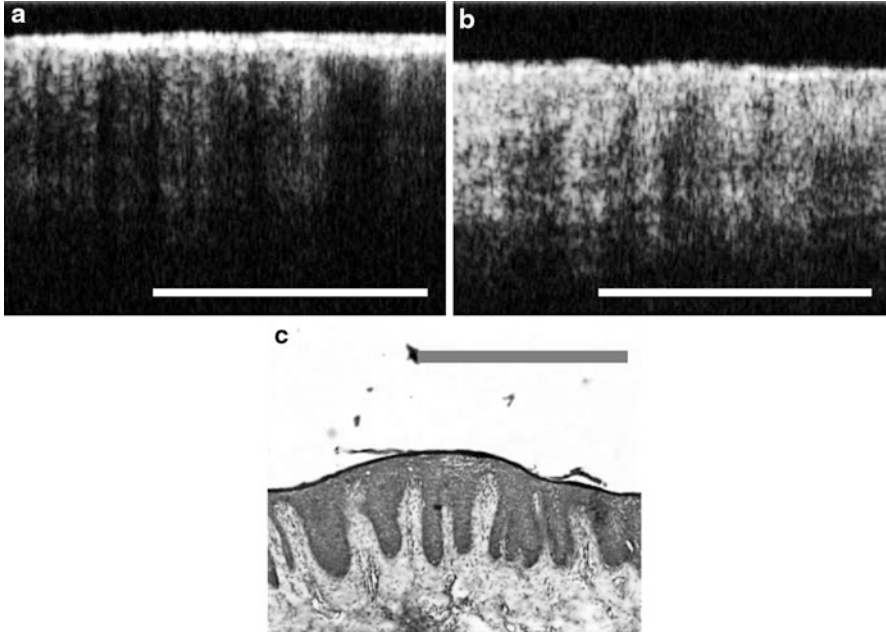
Fig. 24.31 OCT images of skin with psoriatic erythrodermia (**a**) before application of glycerin, (**b**) 60 min after application of glycerin, (**c**) parallel histology

polarizations have an organized pattern that is layered horizontally. In the initial polarization (Fig. 24.32a), the epithelium appears as a moderately scattering layer with a distinct boundary atop the bright underlying stroma characterized by higher backscattering. In the orthogonal polarization (Fig. 24.32b), the epithelium conversely appears as a very poorly scattering layer. The main fibrous component of the stroma is collagen fibers (red staining in Fig. 24.32d and e), which are responsible for efficient depolarization and birefringence of the tissue [47, 49]. Depolarizing collagen fibers explain presence of an intense signal in the CP OCT images; horizontally oriented stripes on the OCT images may be explained by birefringence nature of collagen. These structures correlate well with collagen fiber bundles (Fig. 24.32e). The transversal size of these collagen bundles shown in Fig. 24.32e and of the striped structures in Fig. 24.32b is approximately 70–80 μm.

OCT and CP OCT images of carcinoma and scar tissue of the esophagus are shown in Figs. 24.33 and 24.34, respectively. Standard OCT images of carcinoma and scar tissue (Figs. 24.33a and 24.34a) are barely distinguishable; both images are structureless. Therefore, it is difficult to differentiate neoplastic and scar changes using standard OCT. Meanwhile, CP OCT images of these pathologies (Figs. 24.33b and 24.34b) are considerably different. Cancer cells almost do not change polarization of the probing light, and the signal level on the average is substantially (about 10 dB) lower than that of CP OCT images of healthy tissue. In the CP OCT images, vertically oriented regions of a stronger signal are visible
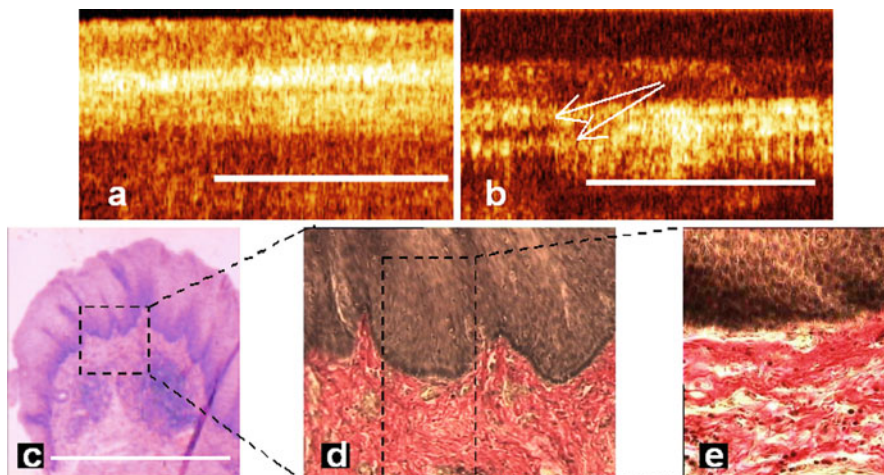
Fig. 24.32 (**a**) Standard OCT image, (**b**) CP OCT image, (**c**) H&E histology, (**d**) and (**e**) Van Gieson histology at different magnifications of healthy esophagus. *White bar* corresponds to 1 mm
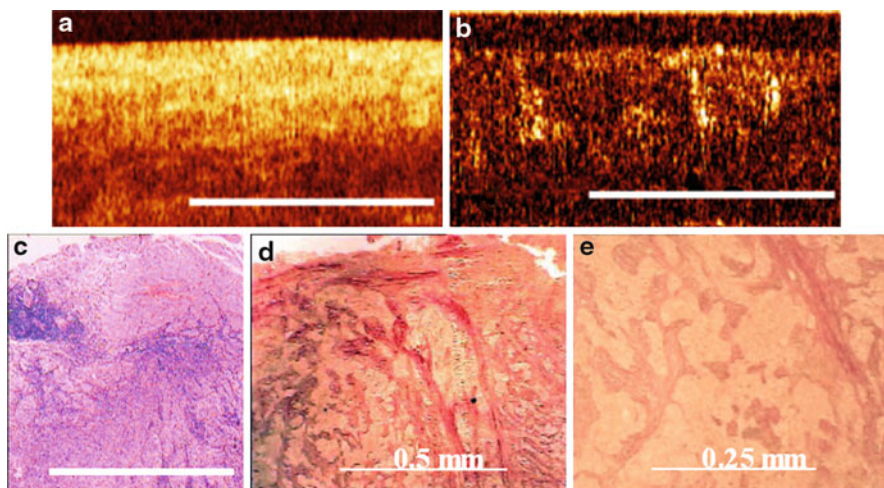
Fig. 24.33 (**a**) Standard OCT image, (**b**) CP OCT image, (**c**) H&E histology, (**d**) and (**e**) Van Gieson histology at different magnification of cancerous esophagus. *White bar* corresponds to 1 mm where not specially marked

against the weak background (Fig. 24.32b). These images correlate well with single vertically oriented collagen fibers shown in Fig. 24.32d, where they are visualized as red elongated individual structures. CP OCT images of scar tissue of the esophagus demonstrate levels of the signal comparable to those of healthy tissue (Fig. 24.33b). At the same time, in the CP OCT image one can note a large number
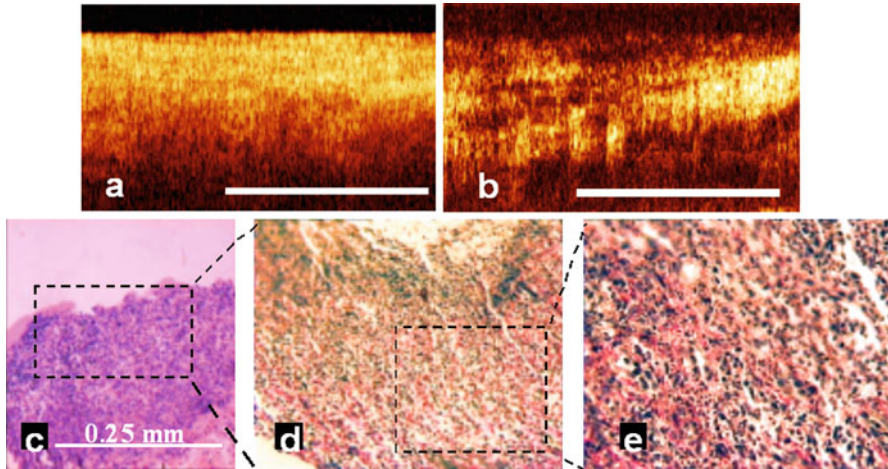
Fig. 24.34 (**a**) Standard OCT image, (**b**) CP OCT image, (**c**) H&E histology, (**d**) and (**e**) Van Gieson histology at different magnification of scarred esophagus. *White bar* corresponds to 1 mm where not specially marked

of chaotically oriented regions of both intense and weak signal. This is due to the nature of scar tissue, whose organization is different than that of cancer. As can be seen from Fig. 24.34d, collagen fibers are one of the main components of immature scar tissue (pink regions in the image correspond to maturing collagen). In Fig. 24.34d the collagen regions are alternating with regions of accumulation of cells forming granular tissue, which correlates well with the signal behavior in the CP OCT image of scar. The difference in structural features of collagen fibers in cancer and scar tissue provides the basis for differentiation of these pathologies because their cross-polarization backscattering properties are determined, in a considerable degree, by anisotropic structures, i.e., by collagen fibers.

Presented results demonstrate that CP OCT providing additional information on cross-polarization backscattering properties of biological tissues, thereby can improve the diagnostic value of standard OCT.

24.5.6 OCT Image Processing

Numerous experiments carried out independently by different research groups proved that the method of OCT was sufficiently sensitive to detect abnormality of biological tissue at the level of cell groups and tissue layers [6, 34]. Generally, only visual analysis of OCT images is performed in order to detect the type of pathology. The transformations of biological tissue, such as the alternation of the number of tissue layers or the emergence of contrast inclusions in OCT images, can be revealed visually [22, 34]. However, some pathological processes develop without disruption of the layered structure of tissue, but proceed by inducing changes in

scattering properties. In some cases, in spite of a tremendous change in optical characteristics of tissue layers, pathological processes can hardly be detected by visual analysis [50]. Nevertheless, it was observed that additional numerical processing of OCT images facilitated detection of such processes [29, 51].

In this chapter we propose an OCT image processing algorithm based on the theoretical model of the OCT signal versus depth [11]. Biological tissue is considered to be a stratified scattering medium described by a set of parameters specified for each layer, namely, total scattering coefficient and backscattering coefficient. These parameters are varied in order to fit the measured OCT curve with a theoretical OCT signal. The best-fit values are assumed to be true biological tissue properties.

24.5.6.1 Theoretical Model of the OCT Signal

The major requirements for an OCT theoretical model are the following: (1) it should be universal and valid for different types of biological tissue (healthy tissue and different stages of various pathologies), (2) it should be based on an adequate model of scattering properties of tissue and take into account the characteristics of a probing light beam, (3) it should use as few parameters as possible to describe the medium, and (4) the analytical expressions for the signal should be simple in order to decrease computational time of fitting. The last requirement is necessary if one wants to include numerical processing of OCT images as a part of a real-time medicine procedure.

As far as optical scattering is concerned, biological tissue contains a variety of scatterers with sizes smaller than, comparable to, and larger than the wavelength and, in a general scatterer, size distribution is given by a complicated function [52]. The majority of soft biological tissues are characterized by strong forward scattering. Correct description of light propagation within tissue should take into account the effects of multiple small-angle scattering, which start contributing significantly for depth larger than one mean free path. In contrast to previous publications [6, 51, 53] where OCT signal attenuation with the probing depth is described using only total and diffusion scattering, we do not neglect the changes in the beam structure caused by small-angle scattering at small depths and by light diffusion at large depths. This problem is solved based on the stationary radiance-transfer equation in small-angle approximation. Because light is scattered mainly in a forward direction, the probability of backscattering is a small parameter and it is reasonable to use single backscattering approximation to calculate the OCT signal. According to this approximation, the scattering phase function can then be presented as a sum of a small-angle scattering phase function $x_1(z, \theta)$ that tends to zero for $\theta > \pi/2$, and a constant that corresponds to isotropic scattering [11]:

$$x(z, \theta) = (1 - 2p_b(z))x_1(z, \theta) + 2p_b(z). \tag{24.30}$$

Backscattering probability, p_b, is determined by the part of the light energy scattered into the backward semisphere:

$$p_b(z) = \frac{1}{2} \int\limits_{\pi/2}^{\pi} x(z,\theta)\sin\theta d\theta. \tag{24.31}$$

As a result, the expression for the OCT signal was derived in a simple single-integral form [11]. Thereby, the developed theoretical model appeared to take tissue properties into account adequately and, at the same time, it is not too time consuming and computationally demanding in comparison with Monte Carlo modeling [6, 54].

The theoretical OCT signal formed by single backscattered photons is given by average intensity $I_{th}(z)$ versus depth z. The signal undergoes squared detection, and is normalized on its value at the tissue boundary [11, 51]

$$I_{th}(z)/I_{th}(0) = 2A^2(0)\frac{\mu_{bs}(z)}{\mu_{bs}(0)}\exp\left(-2\int\limits_0^z \mu_s(z')dz'\right) \times$$

$$\times \left[\int\limits_0^\infty \exp\left(-\frac{A^2(z)h^2}{2} + 2\int\limits_0^z \mu_{fs}(z-z')\tilde{x}_1(z',hz')dz'\right)hdh - \frac{1}{2A^2(z)}\right], \tag{24.32}$$

where $\mu_s(z)$ is the total scattering coefficient; $\mu_{bs}(z) = \mu_s(z)p_b(z)$ is backscattering coefficient; $\mu_{fs} = \mu_s - 2\mu_{bs}$ is forward scattering coefficient; $\tilde{x}_1(z,p) = \frac{1}{2}\int\limits_0^\pi x_1(z,\theta)J_0(p\theta)\sin\theta d\theta$ is spectrum of the small-angle scattering phase-function $x_1(z,\theta)$, which was defined by (24.30); and $A^2(z) = A_0^2 + (z-f)^2\lambda^2\big/(2\pi n A_0)^2$ is radius of a Gaussian probing beam with focusing depth f, minimum beam waist A_0, and wavenumber $k = 2\pi n/\lambda$ in a non-scattering medium with a refractive index n. Along with the initial beam shape and the attenuation of the OCT signal due to total scattering on the way to the reflection side and back, (24.32) accounts for the effects of multiple small-angle scattering, expressed by the convolution integral $\int\limits_0^z \mu_{fs}(z-z')\tilde{x}_1(z',hz')dz'$.

24.5.6.2 Biological Tissue Scattering Properties

Equation (24.32) contains the following scattering characteristics of a stratified scattering medium: distributions of a total scattering coefficient $\mu_s(z)$, a backscattering coefficient $\mu_{bs}(z)$, and a small-angle phase function $x_1(z,\theta)$. Generally, the inverse problem of reconstructing these distributions from an OCT image does not have a unique solution. Nevertheless, in the case when the phase function is described by a few parameters and tissue consists of a limited number of homogeneous layers, the solution is unique and can be found numerically. The numerical algorithm implemented the Henyey-Greenstein phase-function [8]. This function is characterized by a single parameter, the anisotropy factor, and well represents experimental scattering for a wide range of tissue types. The anisotropy

factor for each i-th biotissue layer can be expressed via total scattering coefficient $\mu_{s,i}$ and a backscattering one $\mu_{bs,i}$, therefore each layer is described by two parameters, $\mu_{s,i}$ and $\mu_{bs,i.}$

24.5.6.3 Algorithm for Reconstruction of Tissue Scattering Properties

In the current algorithm, the total scattering coefficient of i-th tissue layer $\mu_{s,i}$, its backscattering coefficient $\mu_{bs,i}$, and the position of the layer boundary l_i are recovered via fitting of the experimental OCT signal versus depth $I_{ex}(z)$ by the theoretical curve $I_{th}\left(z, \vec{\mu}_s, \vec{\mu}_{bs}, \vec{l}\right); \vec{\mu}_s = \left(\mu_{s,1}, \ldots, \mu_{s,N}\right), \vec{\mu}_{bs} = \left(\mu_{bs,1}, \ldots, \mu_{bs,N}\right), \vec{l} = (l_1, \ldots, l_N)$, where N is the total number of tissue layers. A mean-square deviation of the logarithms of the experimental and fitting theoretical curves yields the discrepancy for the varying set of tissue parameters. In this case, the "true" medium parameters are obtained as a result of minimizing the integral within the given range of values

$$\left(\vec{\mu}_s, \vec{\mu}_{bs}, \vec{l}\right) = \arg \min_{\left(\vec{\mu}_s, \vec{\mu}_{bs}, \vec{l}\right)} \int_0^L \log^2\left(I_{th}\left(z, \vec{\mu}_s, \vec{\mu}_{bs}, \vec{l}\right)/I_{ex}(z)\right) dz, \qquad (24.33)$$

where L is the maximum depth of the OCT signal. Finding the global minimum of (24.33) with I_{th} defined in (24.32) is time consuming and computationally intensive. We applied the genetic algorithm [55] to minimize integral (24.33), which allowed a reduction in time in comparison with conventional methods.

Figure 24.35 shows an example of fitting an experimental OCT signal with a theoretical curve in the case of a relatively homogeneous tissue. Before the fitting procedure is applied, a certain region of the tomogram, where the parameters of the medium are to be estimated, is selected. Within this window, the in-depth OCT profiles are added together in order to reduce the noise level and yield an average OCT signal, which is used for fitting. Both the noise dispersion in the experimental curve I_{ex} and the covariance of the recovered tissue parameters decrease as the width of the window is increased. Let us consider an example of the window composed of 20 adjacent OCT scans spaced with a 10-μm lateral step (Fig. 24.35a). Reconstruction of tissue parameters using the theoretical model described in (24.32) takes about 1 min for each OCT experimental curve.

It is clearly seen in the Fig. 24.35 that the theoretical dependence describes well the main features of the experimental OCT signal. According to the theoretical model, the fast decrease of the OCT signal at small depth is mainly caused by attenuation of the probing light beam due to small-angle scattering. This "fast" attenuation obeys Beer's law (the dotted line in the figure), and the slope of the curve corresponds to the doubled coefficient of small-angle scattering $2\mu_{fs} = 2(\mu_s - 2\mu_{bs})$. At larger depth, the regular beam structure collapses due to diffusion and backscattering, which, in fact, is weaker than small-angle scattering, and the rate of OCT signal attenuation slows down. Both regions of fast and slow attenuation are observed in the experimental OCT images obtained from homogeneous tissue (Fig. 24.35b).
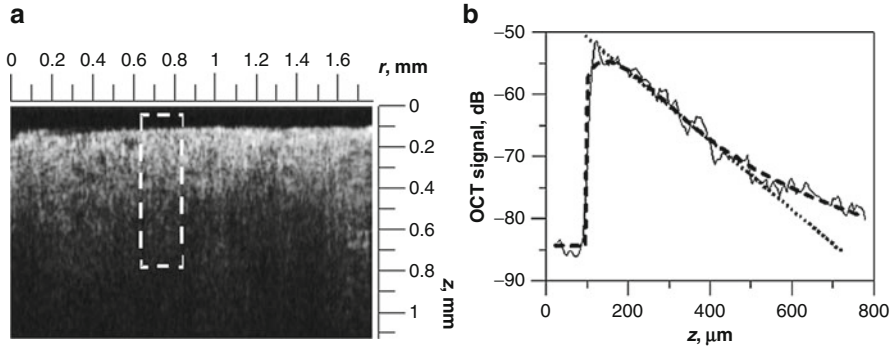
Fig. 24.35 An example of fitting of an OCT signal from single layered tissue; (**a**) a typical in vivo OCT image of cervical cancer; (**b**) an OCT signal averaged out over the selected window (*solid line*), a theoretical fitting curve (*dashed line*); Beer's law approximation of the fast attenuating part of the experimental curve (*dotted line*). Recovered tissue parameters are: $\mu_s = 223$ 1/cm, $\mu_{bs} = 1.3$ 1/cm
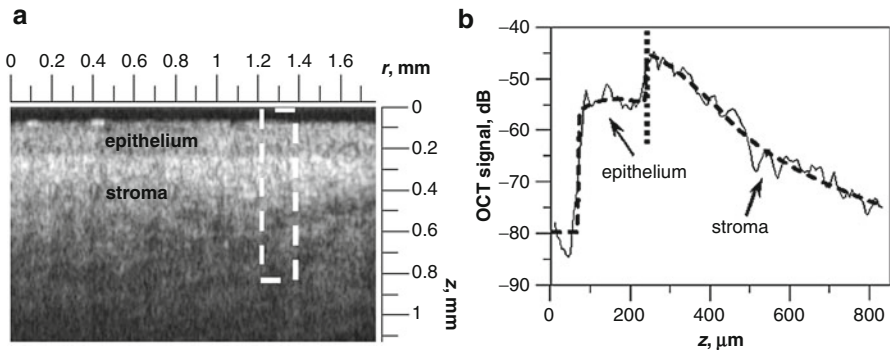
Fig. 24.36 An example of fitting of an OCT signal from two-layered tissue; (**a**) a typical in vivo OCT image of healthy cervical mucosa; (**b**) an OCT signal averaged out over the selected window (*dashed line*), a theoretical fitting curve (*thick line*). Recovered parameters are: (epithelium) $\mu_s = 75$ 1/cm, $\mu_{bs} = 0.28$ 1/cm; (stroma) $\mu_s = 284$ 1/cm, $\mu_{bs} = 3.3$ 1/cm

Figure 24.36 demonstrates an example of fitting of the experimental OCT signal and recovering scattering parameters of the two-layered tissue (epithelium and stroma). The jump in the OCT signal at the depth of 250 μm is caused by the mismatch of backscattering coefficients between the first layer (epithelium) and the second layer (stroma).

24.5.6.4   Algorithm Testing

To test the performance of the algorithm, an experimental OCT setup with the following technical characteristics was used: wavelength of 1.3 μm, the same axial and transversal resolution of 15 μm, scanning depth of 1–2 mm, acquisition time for a 2D image of 1.5 s.
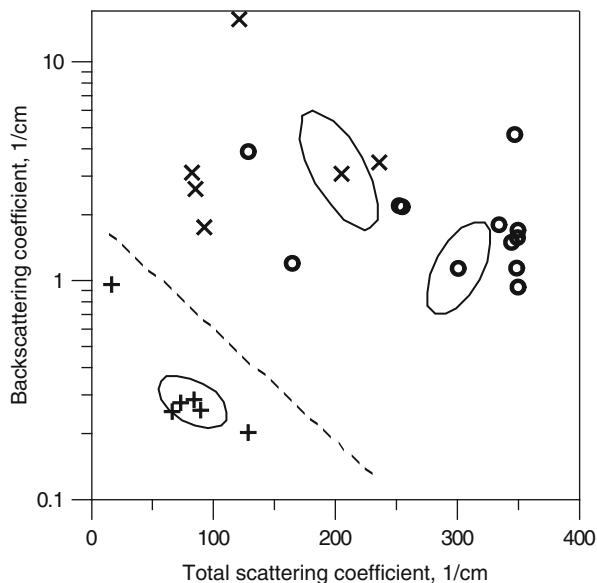
Fig. 24.37 Result of processing of OCT images obtained from a patient with cervical cancer (one clinical example). Both healthy and neoplastic areas of tissue were included in analysis. Points on the plane correspond to recovered scattering parameters for the epithelium and the stroma in the case of healthy mucosa and one parameter in the case of cancer. Scattering parameters of healthy areas: + – epithelium and × – stroma; parameters of cervical cancer: O. *Ellipses* are the confidence areas of the estimated parameters. The *dashed line* separates scattering parameters corresponding to the healthy epithelium and cancer

The OCT images of healthy and neoplastic areas in a patient with cervical cancer were obtained in vivo using a flexible probe with diameter of 2.5 mm. The results of reconstruction of scattering parameters are given in Fig. 24.37. Each layer of each processed tomogram is characterized by a point at the scattering parameter plane. In the reconstruction algorithm, the two-layered model of the OCT signal is used for OCT images of healthy areas (epithelium and stroma) and one-layered model for neoplastic areas. Results of processing of the obtained data show that the estimated values of the total scattering coefficient are in a good agreement with the reported data for these types of tissue [8]. For all processed images, recovered scattering parameters of healthy epithelium and neoplastic tissue are localized in two separate, non-overlapping regions on the scattering parameter plane. The boundary between these regions is marked with the dashed line (Fig. 24.37). We believe that during progression of a neoplastic process, the scattering parameters of the epithelium gradually increase from low values of total and backscattering coefficients to higher values, thus, crossing the boundary between domains of scattering parameters. This fact can provide a basis for identification of the abnormal changes in tissue structure.

24.6 A New Approach to Cross-Polarization Optical Coherence Tomography Based on Common Path Optical Fiber System

The PM fiber-based OCT scheme described above has some drawbacks, which have been revealed in practice. The main drawback of the OCT system for endoscopic applications is a long optical path of the Michelson interferometer arm due to a long probe. Because of insufficiently high repeatability of fiber parameters, this results in poor probe reproducibility. The second variant of the CP OCT technique, which is more important for practical applications, is based primarily on isotropic fiber and uses a measuring Fizeau interferometer and a Michelson interferometer as a correlometer. The concept of CP OCT described here is based on the idea of common path OCT, where reference and probe radiation propagate along the same fiber and therefore change the polarization properties together, maintaining parallel or orthogonal orientation even when individual polarization is changing.

24.6.1 Method Validation

The intrinsic property of single-mode initially isotropic optical fibers to maintain polarization orthogonality of light waves, even in the presence of phase perturbations, is essential for isotropic-fiber-based CP OCT. The only requirement is the absence of anisotropic losses. It can be easily shown that any two initially orthogonal arbitrarily polarized waves maintain their orthogonality when passing through a single-mode isotropic optical fiber, despite the change in their polarization state. Indeed, according to the well-known optical equivalence theorem, any set of elements with phase anisotropy can be represented by an equivalent element that consists of an optical rotator (rotator of polarization plane) and a linear wave plate [56]. This theorem is equally valid for a piece of single-mode optical fiber. The Jones matrix of such an optical system $\hat{A} = [a_{ik}]$ in the absence of anisotropic losses is unitary, and the condition $\hat{A}^{\dagger}\hat{A} = \hat{A}\hat{A}^{\dagger} = \hat{I}$ is satisfied. Here, $\hat{A}^{\dagger} \equiv \left[a_{ki}^{*}\right]$ is a Hermitian conjugate matrix of $\hat{A}$, and $\hat{I}$ is a unity matrix. (Note that in the description of optical light propagation in a single-mode isotropic optical fiber presented in [37–39] an overstringent condition of no losses is imposed to maintain angles between Stokes vectors on the Poincare sphere.) If at the entrance to the optical fiber described by the matrix $\hat{A}$ there is an elliptically polarized wave with an arbitrarily polarized electric vector $\overrightarrow{E}_{u} = \begin{bmatrix} m \\ n \end{bmatrix}$ and an orthogonal wave $\overrightarrow{E}_{v} = \begin{bmatrix} -n^{*} \\ m^{*} \end{bmatrix}$, for both of which the orthogonality condition is fulfilled $\left(\overrightarrow{E}_{u}, \overrightarrow{E}_{v}\right) = 0$, then the orthogonality condition $\left(\overrightarrow{E}_{u}^{out}, \overrightarrow{E}_{v}^{out}\right) = (\hat{A}\overrightarrow{E}_{u}, \hat{A}\overrightarrow{E}_{v}) \equiv (\overrightarrow{E}_{u}, \hat{A}^{\dagger}A\overrightarrow{E}_{v}) = (\overrightarrow{E}_{u}, \overrightarrow{E}_{v}) = 0$ will also be fulfilled for outcoming waves with

vectors $\overrightarrow{E}_u^{out} = \hat{A}\overrightarrow{E}_u$ and $\overrightarrow{E}_v^{out} = \hat{A}\overrightarrow{E}_v$. From a mathematical point of view, this means that the scalar product of two vectors is maintained when the vectors are multiplied by a unitary operator [57]. Note that, in a single-mode optical fiber, the orthogonality condition for the two waves does not imply in the general case that the waves coincide with normal waves. It is important for CP OCT that the property of waves to preserve their orthogonality in isotropic optical fiber should certainly refer to backscattered waves as well.

The second idea underlying our CP OCT system consists of creating at the entrance to the optical scheme two strictly orthogonally polarized waves with a predetermined time delay between coherent regions. In the general case, these waves may have arbitrary ellipticity under condition of their strict mutual orthogonality. This may be achieved in several ways. In a simple and preferred embodiment, it is enough to insert a piece of PM fiber (with a definite length) before an optical scheme and excite in it two linearly polarized Eigen modes with equal efficiency. At the exit from this piece of birefringent optical fiber, slow and fast linear waves should follow each other at a distance ΔL equal to the scanning depth. Exactly at the entrance to the single-mode optical fiber, the two initially orthogonal waves are linearly polarized. As they further propagate along the fiber, each of them may change their polarization state, but their mutual orthogonality is maintained.

By means of a Fizeau interferometer in the optical probe, either of the two waves may then be split into a reference wave and a probing wave, without changing their polarization and strict orthogonality. Below we present the description of the suggested optical scheme.

24.6.2 Experiment

A schematic of the CP OCT system using orthogonal polarization modes in an isotropic optical fiber is shown in Fig. 24.38. The CP OCT system operates at a wavelength of 1,300 nm with a spectral bandwidth of 35 nm (light source SLD 561 HP2) and is based on isotropic fiber SMF-28. The description of a prototype optical scheme can be found in Refs [58, 59].

The CP OCT scheme described in Refs. [58, 59], which comprises a fiber-based Fizeau interferometer, a common path for signal and reference waves [60], and an autocorrelator based on a Michelson interferometer with Faraday mirrors [58, 59], is optimal when isotropic optical fiber is used. The fiber-optic Fizeau interferometer was used for the first time, to the best of our knowledge, in Ref [60], and proved to be highly efficient for measurements of subangstrom vibrations. When operating in the simplest mode, the Fizeau interferometer provides heterodyne detection of weak scattered light with maximum possible and stable visibility of the interference fringes. Indeed, when the directional pattern of optical probe is identical for emitted and received light, a wave scattered from non-depolarizing structures and a wave reflected from the fiber tip have identical polarization states. An additional benefit of this optical scheme is that Faraday mirrors in the autocorrelator can compensate
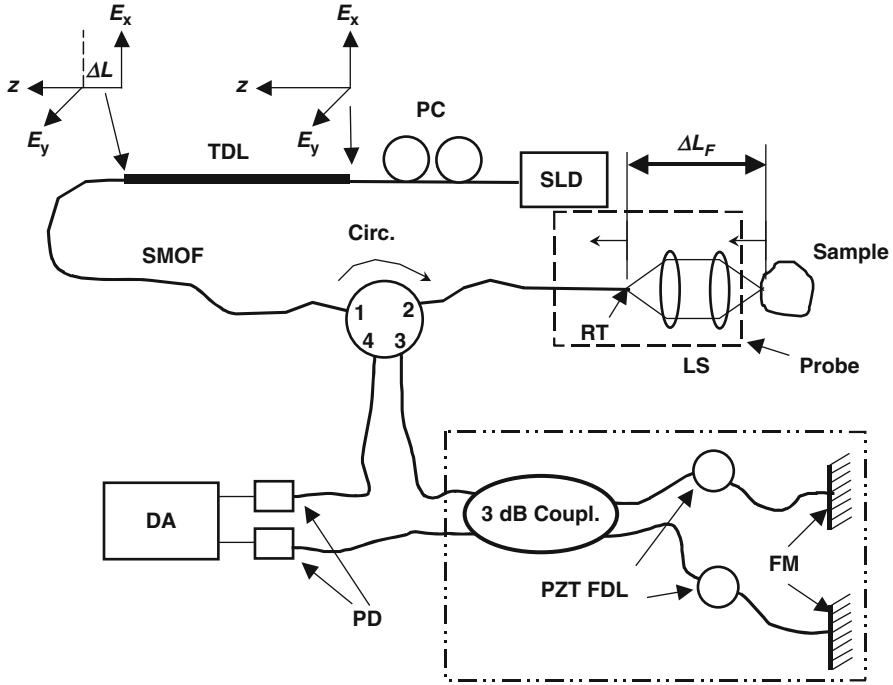
Fig. 24.38 Optical scheme of CP OCT: SLD – superluminescent diode; PC – polarization controller; TDL – time-delay line consisting of a piece of birefringent fiber; SMOF – single-mode optical fiber; Circ. – 4-port circulator; RT – reflecting tip of the fiber; LS – lens system; Sample – sample under study; 3 dB coupler – 0.5 × 0.5 coupler; PZT FDL – piezoelectric fiber delay line; FM – 45° Faraday mirrors; PD – photo diodes; DA – differential amplifier. The *dashed box* indicates an optical probe, the *dashed-dotted box* shows a compensating Michelson interferometer that also performs longitudinal A-scanning

for not only regular anisotropy in the fiber arms but also the result of random weak couplings of the orthogonal modes.

Note that the method for compensating arbitrary anisotropy in single-mode optical waveguides was first suggested and demonstrated in our earlier work using a fiber-optic Michelson interferometer with Faraday mirrors [61, 62]. Later, this compensation method was also suggested and investigated in Ref. [63].

The optical scheme operates as follows. Partially polarized light from a superluminescent diode (SLD) with a central wavelength of $\lambda = 1,300$ nm is delivered along a single-mode fiber to a polarization controller (PC). By means of the PC placed at the entrance of a time-delay line (TDL) formed by a piece of birefringent (PM) fiber, two orthogonal linearly polarized normal waves $\vec{x}_0 E_x$, $\vec{y}_0 E_y$ with equal intensity are excited (notations in accompanying coordinates). In TDL, the orthogonal waves travel along different optical path lengths, the train of the fast wave $\vec{y}_0 E_y$ being ahead of the train of the slow wave $\vec{x}_0 E_x$ by a fixed base length interval ΔL that slightly exceeds (by 10–20 %) the depth of A-scan (in our

Fig. 24.39 Evolution of the Stokes vectors for light propagating in the optical scheme up to a compensating interferometer. The two *curved heavy lines* indicate changes of the Stokes vectors in single-mode fiber
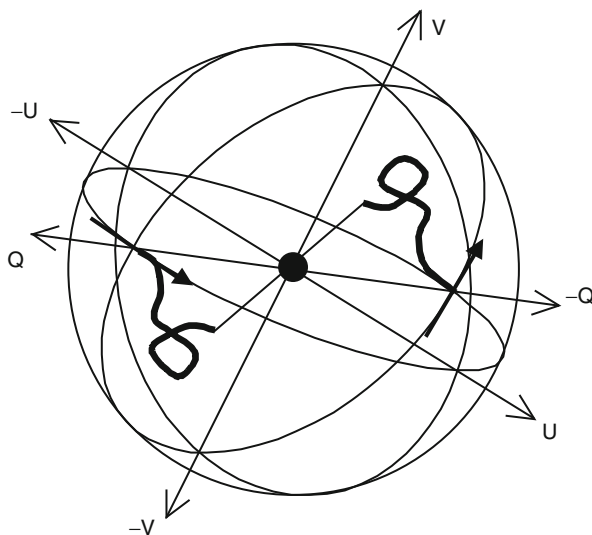
system $\Delta L = 2$ mm). At high Eigen birefringence of this PM fiber piece, the orthogonality of output waves at the exit from BS is quite strict. Then, both waves are directed into a single-mode fiber (SMF) to excite two orthogonally polarized waves $\vec{x}_0 E_x$ and $\vec{y}_0 E_y$ with the same optical path difference. In the remaining part of the optical scheme, only single-mode isotropic fiber is used, and the mutual polarization orthogonality of the both waves is maintained while their polarization state in this fiber can change depending on perturbations the fiber experiences. These perturbations, in particular, may be from fiber bending in the optical probe. In the general case, the polarization state of each orthogonal wave can be elliptical with an arbitrary angle of inclination of the long axis.

The transformation of a partially polarized low-coherent wave in a single-mode fiber path is clearly described using the Stokes vector formalism $\mathbf{S} = \{S_0, S_1, S_2, S_3\} \equiv \{I, Q, U, V\}$ [64]. The four Stokes parameters, I, Q, U, and V, are defined through the total intensity I_t, Cartesian intensity components of the transverse electric field $I_{0°}$, $I_{90°}, I_{+45°}, I_{-45°}$, and intensities I_{rc} and I_{lc}, respectively, for the right and left circular components in the form:

$$I = I_t, \quad Q = (I_{0°} - I_{90°}), \quad U = (I_{+45°} - I_{-45°}), \quad V = (I_{rc} - I_{lc}). \qquad (24.34)$$

The evolution of light polarizations represented using Stokes subspace (Q, U, V) in the scheme described herein is shown in Fig. 24.39.

At the exit from the PM fiber, both waves are completely polarized and mutually orthogonal, so the points representing the polarization state lie at the intersections of the axis Q with the surface of the Poincare sphere ($Q = \pm 1$). The evolution of the polarization state of the two waves is random and depends on the total perturbations affecting the isotropic fiber. A possible evolution of the Stokes vectors showing the preservation of strict mutual orthogonality between polarization states in each fiber
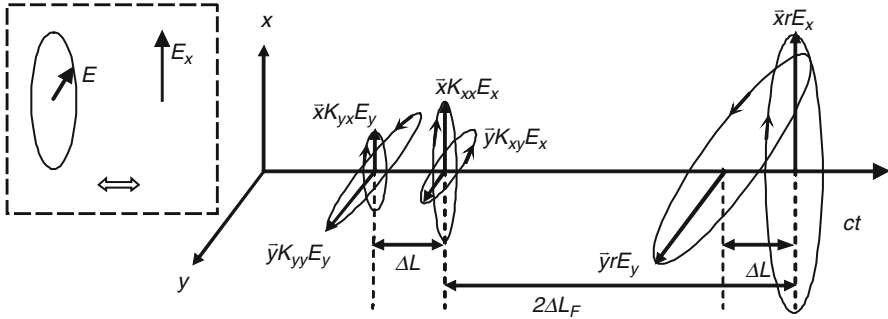
Fig. 24.40 Time delays for reference and scattered waves

region is indicated by the heavy lines in Fig. 24.39. The polarization states in each cross-section of the isotropic fiber (the fiber length not exceeding the depolarization length) are represented by two diametrically opposite points on the sphere at the intersection of a respective line passing through the center of the sphere.

Let us consider the structure of reflected waves in the Fizeau interferometer. The Fizeau interferometer with the length ΔL_F is formed by the fiber face end of the optical probe and the sample. For simplicity, we introduce a Cartesian coordinate frame (x, y) at the exit of the optical probe, which is oriented along the long axes of polarization ellipses of outcoming orthogonally polarized waves. For demonstration purposes, we will also replace orthogonal elliptical waves at the exit of the optical probe by orthogonal linear waves, with electric vectors, directed along the long axes of polarization ellipses (see example enframed by a dashed line on the left in Fig. 24.40). We will denote the state of these orthogonally polarized waves by $\bar{x}E_x$ and $\bar{y}E_y$. Light then passes through ports 1 and 2 of the circulator (CIRC) and comes into the single-mode fiber of the optical probe indicated by the dashed line in Fig. 24.38. The end face of the reflecting tip (RT) is slightly tilted to receive a portion (proportional to r^2) of light reflected from the end face. This portion comprises two reference waves $\bar{x}rE_x$ and $\bar{y}rE_y$ with the same path length difference ΔL that the waves initially had in the anisotropic fiber (see Fig. 24.40). The value of r is chosen to effectively reduce excessive noise [65]. A larger portion of light is focused onto the sample by a lens system. In the general case, the backscattered portion contains four waves (we will consider them in the laboratory frame). Backscattering of wave $\bar{x}E_x$ will create waves with initial $\bar{x}K_{xx}E_x$ and orthogonal polarization $\bar{y}K_{xy}E_x$, while backscattering of wave $\bar{y}E_y$ will create a wave with the same polarization $\bar{y}K_{yy}E_y$ and also a wave with polarization orthogonal to it $\bar{x}K_{yx}E_y$. Scattering coefficients in the initial and orthogonal polarizations are related for a chaotic medium as: $K_{xx} = K_{yy}$ and $K_{xy} = K_{yx}$. The both groups of backscattered waves coming to the entrance end of the optical fiber have the same baseline delay ΔL with respect to each other as the reference waves. The relative delay of the beginning of the reference wave group relative to the backscattered wave group is equal to a doubled length of the Fizeau interferometer – $2\Delta L_F$. Both light portions pass through ports 2 and 3 of the circulator and come to the Michelson

interferometer that is formed by a 3-dB coupler and single-mode fiber arms with Faraday mirrors at their ends. A schematic diagram of the relative delays for the reference and backscattered waves before they come to the Michelson interferometer is shown in Fig. 24.40.

The Michelson interferometer is adjusted to have a respective initial path length difference between its two arms ($2\Delta L_F - \Delta L$) for compensation of the initial delay. When the path length difference between the two arms is changed with a constant speed, mutual coherence between the wave trains with a relative Doppler shift of their optical spectra is gradually restored. The path length difference is modulated by means of piezoelectric fiber delay lines (PZT FDL) [66]. The combined waves from one interferometer output are directed to the first photo diode, while those from the other interferometer output come through circulator ports 3 and 4 to the second photo diode. Signals with Doppler frequency shift are then summed in a differential amplifier, which is known to lead to doubling of antiphase interference signals and subtraction of in-phase components of interfering signals and noise.

Let us consider the mechanism for formation of signals with orthogonal polarizations during consecutive A-scanning the depth of the sample by the Michelson interferometer. In fact, this is a way of extracting registration channels for light scattered into a wave with initial and orthogonal polarization. As was said earlier, two groups of reference and backscattered waves with a mutual spatial shift $2\Delta L_F$ travel along the single-mode fiber and come to the Michelson interferometer with preserved coherence and orthogonality but with an arbitrary polarization state. Because the 3-dB coupler in the Michelson interferometer is isotropic, the waves have identical polarization states in the initial segments of the optical fiber in the interferometer arms. It is known that when 45° Faraday mirrors are used in the Michelson interferometer, the polarization state at the exit from the interferometer differs from that at its entrance only by 90°. So corresponding groups of scattered and reference waves preserve their mutual orthogonality.

To compensate for the optical path difference between the coherent components with initial and orthogonal polarizations it is necessary to choose different delays by controlling the path length difference between the two arms of the Michelson interferometer. As can be clearly seen from Fig. 24.40, at delay $2\Delta L_F - \Delta L$ the reference wave with the initial polarization $\vec{y}rE_y$ will interfere with the backscattered wave with orthogonal polarization $\vec{y}K_{xy}E_x$ (orthogonal channel). At delay $2\Delta L_F$, reference and backscattered waves with initial polarizations will interfere in pairs, respectively: $\vec{x}rE_x$ and $\vec{x}K_{xx}E_x$, and $\vec{y}rE_y$ and $\vec{y}K_{yy}E_y$ (parallel channel). The interference between the reference wave $\vec{x}rE_x$ and the backscattered wave $\vec{x}K_{yx}E_y$ will occur at delay $(2\Delta L_F + \Delta L)$ (second orthogonal channel). It is clear that when estimating the scattering coefficients one needs to take into account that two pairs of waves interfere at delay $2\Delta L_F$, and only one pair at delays $(2\Delta L_F - \Delta L)$ and $(2\Delta L_F + \Delta L)$. One should also consider the existence of a slight non-coherent component in the reference wave of the orthogonal channels, which is due to incomplete polarization of the light source. Apparently, if the longitudinal A-scan depth overlaps all above-mentioned delays, then two or three interference fringes, respectively, will be consecutively imaged during one enlarged A-scan.
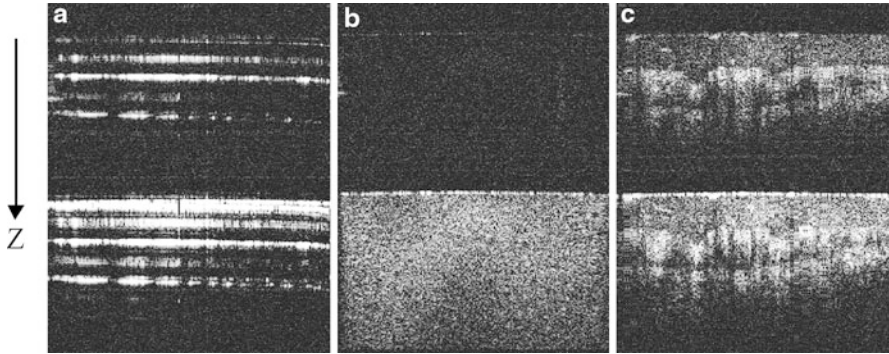
Fig. 24.41 In-depth scattering patterns (along Z) in two model samples: Polaroid film (**a**) and vacuum lubricant (**b**), and in biological tissue – human finger skin (**c**)
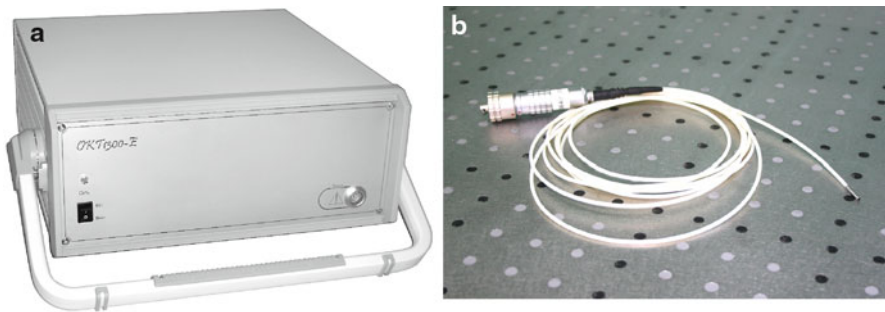
Fig. 24.42 General view of the portable optical coherence OCT device (**a**) and fiber optic endoscope probe (**b**)

Comparative images of scattering in two model media and in a biological sample are shown in Fig. 24.41a and b. Figure 24.41a presents images of light scattering from the internal structure of a Polaroid film successively from top to bottom in orthogonal and initial polarizations. Figure 24.41b demonstrates images of scattered signal in two polarizations in a weakly depolarizing medium – a vacuum lubricant. It can be clearly seen that there is almost no scattered signal with the orthogonal polarization. Figure 24.41b also shows a high dynamical range for orthogonal polarization detection (about 40 dB), which, as estimated, is determined by residual noise of a differential detection system.

Figure 24.41c presents images of a birefringent biological tissue (human finger skin) in the orthogonal and initial polarizations, showing good correspondence of details that is typical of the CP OCT method.

The above-described method for acquiring information in orthogonal polarizations has an additional advantage. It allows parallel detection in orthogonal channels when scanning a narrowband-source frequency over a broad bandwidth that determines the ultimate limit of the axial resolution. Because of the different delays

between coherent wave components – $\tau_1 = (2\Delta L_F - \Delta L)/c$, $\tau_2 = \Delta L_F/c$, $\tau_3 = (2\Delta L_F + \Delta L)/c$ – mean frequencies of the signals will be different and will be $\frac{dv}{dt}\tau_i$. This allows separation of scattering patterns in the initial and orthogonal polarizations by means of frequency selection in the radio channel.

24.6.3 Conclusion

The CP OCT method has been embodied in a compact optical device that is based on a single-mode isotropic optical fiber and performs consecutive scans of the path length difference between interferometric arms. An isotropic-fiber-based flexible micro-probe analogous in design to that described previously in Ref. [34] has been created and modified to meet CP OCT requirements. Experiments have demonstrated high reliability of the CP OCT method, high quality of images acquired in the both polarizations, and absence of any noticeable artifacts.

A specific feature of the suggested CP OCT method is that light scattered from a biological medium with strictly orthogonal polarizations is received in the interferometric scheme based on isotropic fiber. High-quality images can be obtained simultaneously in both polarizations with a dynamical range that is limited by residual noise only. Flexible isotropic-fiber paths can be used in the whole measurement optical scheme, thus considerably simplifying fabrication of OCT devices and exchangeable optical probes. Both a sequential method of information acquisition by scanning the path length difference between two arms of the interferometer and a high-speed method in parallel with the use of tunable lasers can be implemented. This CP OCT approach makes possible not only investigation of the depolarizing properties of biological tissues but also determination of birefringence parameters.

The developed portable isotropic-fiber-based CP OCT system is designed for use in a clinical environment. The general view of the portable OCT device is shown in Fig. 24.42. The OCT device may be completed with any of the three types of fiber-optic endoscope probes (with 2.7, 2.4, or 1.8 mm outer diameter) that have LEMO electronic and fiber-optic connectors.

The polarization technique and its experimental validation are discussed in [67–70].

24.7 Discussion and Future Directions

The described algorithm can aid visual analysis of OCT images by providing an additional tool for quantitative assessment of biological tissue optical properties and, thus, improving capabilities of OCT in identification of pathological processes. Since a one-dimensional model of the OCT signal is employed in the algorithm, the processed region of a tomogram is to be stratified. The speckle noise of the average OCT signal and the covariance of estimated parameters can be reduced significantly by choosing a wider region of an OCT image for averaging out. Tomograms of mucosa of the uterine cervix, larynx, esophagus, and so on are most appropriate for such processing, because the architecture of these types of biological tissue is close

to plane stratified. Reliable differentiation of pathologies using reconstructed scattering parameters can be attained only when the confidence areas of these parameters do not overlap (see the confidence areas marked with ellipses in Fig. 24.37). As can be seen from Fig. 24.37, the dispersion of the estimated parameters is determined not only by speckle noise but also by patient-to-patent variations of optical properties within the same state of tissue. This problem has not been adequately studied, and this will be addressed in future investigations. The increase of dispersion can also be caused by the imperfection of the theoretical model applied in the algorithm. For example, the scattering phase function needs to be studied more carefully for different states of tissue. Additional parameters may be required in scattering phase function to provide more adequate description for light scattering in tissue. These characteristics can be then included in the fitting procedure using (24.33) together with the total scattering coefficient and backscattering coefficient. On the other hand, additional fitting parameters would increase computational time and make interpretation of the obtained results more difficult. The theoretical model of the OCT signal is based on some approximations described above, which also need to be verified. Moreover, the radiative transfer theory does not take into account wave phenomena such as interference of light fields.

In summary, an improved phase function to describe tissue scattering and an advanced model for an OCT signal are needed and will be developed in future.

References

1. M.I. Skolnik (ed.), *Radar Handbook* (McGraw-Hill, New York, 1970)
2. R.J. Urick (ed.), *Principles of Underwater Sound for Engineers*, 2nd edn. (McGraw-Hill, New York, 1975)
3. D. Huang, E.A. Swanson, C.P. Lin, J.S. Schuman, W.G. Stinson, W. Chang, M.R. Hee, T. Flotte, K. Gregory, C.A. Puliafito, J.G. Fujimoto, Optical coherence tomography. Science **254**, 1178–1181 (1991)
4. V.M. Gelikonov, G.V. Gelikonov, R.V. Kuranov, K.I. Pravdenko, A.M. Sergeev, F.I. Feldchtein, Y.I. Khanin, D.V. Shabanov, N.D. Gladkova, N.K. Nikulin, G.A. Petrova, V.V. Pochinko, Coherent optical tomography of microscopic inhomogeneties in biological tissues. JETP Lett. **61**, 158–162 (1995)
5. A.F. Fercher, Optical coherence tomography. J. Biomed. Opt. **1**(2), 157–173 (1996)
6. J.M. Schmitt, Optical coherence tomography (OCT): a review. IEEE J. Select. Tops Quant. Electr. **5**(4), 1205–1215 (1999)
7. J.G. Fujimoto, W. Drexler, U. Morgner, F. Kartner, E. Ippen, Optical coherence tomography: high resolution imaging using echoes of light. Opt. Photon. News **11**, 24–31 (2000)

8. V.V. Tuchin, *Tissue Optics: Light Scattering Methods and Instruments for Medical Diagnosis* (SPIE Press, Bellingham, 2000)

9. A.M. Sergeev, L.S. Dolin, D.H. Reitze, Optical tomography of biotissues: past, present, and future. Opt. Photon. News **12**, 28–35 (2001)

10. B.E. Bouma, G.J. Tearney (eds.), *Handbook of Optical Coherence Tomography* (Marcel Dekker, New York, 2002)

11. L.S. Dolin, A theory of optical coherence tomography. Radiophys. Quant. Electr. **41**(10), 850–873 (1998)

12. Y.A. Kravtsov, A.I. Saichev, Effects of double transition of waves in random-inhomogeneous media. Uspekhi Fizicheskikh Nauk **137**, 501–527 (1982)

13. A. Ishimaru, *Wave Propagation and Scattering in Random Media* (Academic, New York, 1978)

14. L.S. Dolin, I.M. Levin, Optics underwater, in *Encyclopedia of Applied Physics*, vol 12 (VCH Publishers, Berlin, 1995), pp. 571–601

15. J.W. McLean, J.D. Freeman, R.E. Walker, Beam spread function with time dispersion. Appl. Opt. **37**(21), 4701–4711 (1998)

16. I.A. Andronova, D.D. Gusovskii, V.M. Gelikonov, V.I. Leonov, Y.A. Mamaev, A.A. Turkin, A.S. Yakhnov, Fluctuation characteristics of an all-fiber Sagnac interferometer at a wavelength of 0.85 mcm. Sov. Phys. Tech. Phys. **35**, 270–272 (1990)

17. I.A. Andronova, V.M. Gelikonov, Y.A. Mamaev, A.A. Turkin, Performance of a Sagnac fiber interferometer as a phasemeter. Radiophys. Quant. Electr. **34**, 346–350 (1991)

18. V.M. Gelikonov, R.V. Kuranov, A.N. Morozov, Time correlation analysis of the propagation of low-coherence radiation in an optical channel with imperfections anisotropy. Quant. Electr. **32**, 59–65 (2002)

19. V.M. Gelikonov, M.N. Kucheva, G.B. Malykin, Measurement of optical fiber birefringence with a wide-band radiation source. Radiophys. Quant. Electr. **34**, 598–599 (1991)

20. V.M. Gelikonov, D.D. Gusovskii, V.I. Leonov, M.A. Novikov, Birefringence compensation in single-mode optical fibers. Sov. Tech. Phys. Lett. **13**, 322–323 (1987)

21. V.M. Gelikonov, V.I. Leonov, M.A. Novikov, Optical anisotropy induced in a round trip through single-mode optical waveguides and methods for suppression of this anisotropy. Sov. J. Quant. Electr. **19**, 1227–1230 (1989)

22. F.I. Feldchtein, G.V. Gelikonov, V.M. Gelikonov, R.R. Iksanov, R.V. Kuranov, A.M. Sergeev, N.D. Gladkova, M.N. Ourutina, J.A. Warren Jr., D.H. Reitze, In vivo OCT imaging of hard and soft tissue of the oral cavity. Opt. Express **3**, 239–250 (1998)

23. R.V. Kuranov, V.V. Sapozhnikova, I.V. Turchin, E.V. Zagainova, V.M. Gelikonov, V.A. Kamensky, L.B. Snopova, N.N. Prodanetz, Complementary use of cross-polarization and standard OCT for differential diagnosis of pathological tissues. Opt. Express **10**, 707–713 (2002)

24. S.N. Roper, M.D. Moores, G.V. Gelikonov, F.I. Feldchtein, N.M. Beach, M.A. King, V.M. Gelikonov, A.M. Sergeev, D.H. Reitze, In vivo detection of experimentally induced cortical dysgenesis in the adult rat neocortex using optical coherence tomography. J. Neurosci. Meth. **80**, 91–98 (1998)

25. V.M. Gelikonov, D.D. Gusovskii, Y.N. Konoplev, V.I. Leonov, Y.A. Mamaev, A.A. Turkin, Investigation of a fiber-optic polarizer with a metal film and a dielectric buffer layer. Sov. J. Quant. Electr. **20**, 76–78 (1990)

26. V.M. Gelikonov, Y.N. Konoplev, M.N. Kucheva, Y.A. Mamaev, A.A. Turkin, Effect of buffer layer on extinction coefficient of fiber-optic polarizer with metallic coating. Opt. Spectrosc. **71**, 397–398 (1991)

27. V.K. Batovrin, I.A. Garmash, V.M. Gelikonov, G.V. Gelikonov, A.V. Lyubarskii, A.G. Plyavenek, S.A. Safin, A.T. Semenov, V.R. Shidlovskii, M.V. Shramenko, S.D. Yakubovich, Superluminescent diodes based on single-quantum-well (GaAl)As heterostructures. Quant. Electr. **26**, 109–114 (1996)

28. V.M. Gelikonov, G.V. Gelikonov, N.D. Gladkova, V I. Leonov, F.I. Feldchtein, A.M. Sergeev, Y.I. Khanin, Optical fiber interferometer and piezoelectric modulator, USA Patent #5835642, 1998

29. N.M. Shakhova, V.M. Gelikonov, V.A. Kamensky, R.V. Kuranov, I.V. Turchin, Clinical aspects of the endoscopic optical coherence tomography and the ways for improving its diagnostic value. Laser Phys. **12**, 617–626 (2002)

30. M.E. Brezinski, J.G. Fujimoto, Optical coherence tomography: high resolution imaging in nontransparent tissue. IEEE J. Select. Tops Quant. Electr. **5**, 1185–1192 (1999)

31. C. Pitris, C. Jesser, S.A. Boppart, D. Stamper, M.E. Brezinski, J.G. Fujimoto, Feasibility of optical coherence tomography for high-resolution imaging of human gastrointestinal tract malignancies. J. Gastroenterol. **35**, 87–92 (2000)

32. N.D. Gladkova, G.A. Petrova, N.K. Nikulin, S.G. Radenska-Lopovok, L.B. Snopova, Y.P. Chumakov, V.A. Nasonova, V.M. Gelikonov, G.V. Gelikonov, R.V. Kuranov, A.M. Sergeev, F.I. Feldchtein, In vivo optical coherence tomography imaging of human skin: norm and pathology. Skin Res. Technol. **6**, 6–16 (2000)

33. J.M. Schmitt, S.H. Xiang, Cross-polarized backscatter in optical coherence tomography of biological tissue. Opt. Lett. **23**, 1060–1062 (1998)

34. A.M. Sergeev, V.M. Gelikonov, G.V. Gelikonov, F.I. Feldchtein, R.V. Kuranov, N.D. Gladkova, N.M. Shakhova, L.B. Snopova, A.V. Shakhov, I.A. Kuznetzova, A.N. Denisenko, V.V. Pochinko, Y.P. Chumakov, O.S. Streltzova, In vivo endoscopic OCT imaging of precancer and cancer states of human mucosa. Opt. Express **1**, 432–440 (1997)

35. E.H. Hopman, P. Kenemans, T.J. Helmerhorst, Positive predictive rate of colposcopic examination of the cervix uteri: an overview of literature. Obstet. Gynecol. Surv. **53**, 97–106 (1998)

36. S. Jackle, N.D. Gladkova, F.I. Feldchtein, A.B. Terentieva, B. Brand, G.V. Gelikonov, V.M. Gelikonov, A.M. Sergeev, A. Fritscher-Ravens, J. Freund, U. Seitz, S. Schruder, N. Soehendra, In vivo endoscopic optical coherence tomography of the human gastrointestinal tract – toward optical biopsy. Endoscopy **32**, 743–749 (2000)

37. E.V. Zagainova, O.S. Strelzova, N.D. Gladkova, L.B. Snopova, G.V. Gelikonov, F.I. Feldchtein, A.N. Morozov, In vivo optical coherence tomography feasibility for bladder disease. J. Urology **167**, 1492–1497 (2002)

38. N.D. Gladkova, A.V. Shakhov, F.I. Feldchtein, Capabilities of optical coherence tomography in laryngology, in *Handbook of Optical Coherence Tomography*, ed. by B.E. Bouma, G.J. Tearney (Marcel Dekker, New York, 2002), pp. 705–724

39. N.M. Shakhova, F.I. Feldchtein, A.M. Sergeev, Applications of optical coherence tomography in gynecology, in *Handbook of Optical Coherence Tomography*, ed. by B.E. Bouma, G.J. Tearney (Marcel Dekker, New York, 2002), pp. 649–672

40. E. Burghardt, H. Pickel, F. Girardi (eds.), *Colposcopy, Cervical Pathology: Textbook and Atlas* (Thieme, New York, 1998)

41. A.I. Panches (ed.), *Head and Neck Tumors* (De-Yure, Moscow, 1996)

42. H. Welge-Luessen, C. Glanz, P. Arens, R. Oberholzer, Probst, "Die mehrmalige Biopsie bei der Diagnosestellung von Kehlkopfkarzinomen". Laryngorhinootologie **75**, 611–615 (1996)

43. N.P. Dandekar, H.B. Tongaonkar, A.V. Dalal et al., Partial cystectomy for invasive bladder cancer. J. Surg. Oncol. **60**, 24–29 (1995)

44. L. Blomqvist, Rectal adenocarcinoma: assessment of tumor involvement of the lateral resection margin by MRI of resected specimen. Brit. J. Radiol. **72**, 18–23 (1999)

45. V.V. Tuchin, X. Xu, R.K. Wang, Dynamic optical coherence tomography in studies of optical clearing, sedimentation, and aggregation of immersed blood. Appl. Opt. **41**, 258–271 (2002)

46. R.K. Wang, J.B. Elder, Propylene glycol as a contrasting agent for optical coherence tomography to image gastrointestinal tissues. Lasers Surg. Med. **30**, 201–208 (2002)

47. S.L. Jacques, J.R. Roman, K. Lee, Imaging superficial tissues with polarized light. Lasers Sur. Med. **26**, 119–129 (2000)

48. R.D. Lillie (ed.), *Histopathologic Technique and Practical Histochemistry* (McGraw-Hill, New York/Toronto/Sydney/London, 1965), Chap. 15; http://www.ebsciences.com/staining/van_gies.htm

49. D.J. Maitland, J.T. Walsh, Quantitative measurements of linear birefringence during heating of native collagen. Lasers Sur. Med. **20**, 310–318 (1997)
50. G. Zuccaro, N.D. Gladkova, J. Vargo, F.I. Feldchtein, J. Dumot, E.V. Zagaynova, D. Conwell, G.W. Falk, J.R. Goldblum, J. Ponsky, G.V. Gelikonov, J.E. Richter, Optical coherence tomography (OCT) in the diagnosis of Barrett's esophagus (BE), high grade dysplasia (HGD), intramucosal adenocarcinoma (ImAC) and invasive adenocarcinoma (InvAC). Gastrointest. Endosc. **53**, 330 (2001)
51. J.M. Schmitt, A. Knüttel, Measurement of optical-properties of biological tissues by low-coherence reflectometry. Appl. Opt. **32**, 6032–6042 (1993)
52. J.M. Schmitt, G. Kumar, Optical scattering properties of soft tissue: a discrete particle model. Appl. Opt. **37**, 2788–2797 (1998)
53. L. Thrane, H.T. Yura, Analysis of optical coherence tomography systems based on the extended Huygens-Fresnel principle. J. Opt. Soc. Am. A **17**, 484–490 (2000)
54. G. Yao, L. Wang, Monte Carlo simulation of an optical coherence tomography signal in homogeneous turbid media. Phys. Med. Biol. **44**, 2307–2320 (1999)
55. L. Davis (ed.), *Handbook of Genetic Algorithms* (Van Nostrand Reinhold, New York, 1991)
56. H. Hurwitz, R.C. Jones, A new calculus for the treatment of optical systems. II. Proof of three general equivalence theorems. JOSA **31**, 493–499 (1941)
57. G.A. Korn, T.M. Korn, *Mathematical Handbook* (McGraw-Hill, New York, 1961)
58. J. Bush, P.G. Davis, M.A. Marcus, All-fiber coherence domain interferometric techniques, in *Fiber Optic Sensor Technology II*, ed. by E. A. Culshaw, *Proc SPIE 4204A-08*, pp. 71–80 (2001)
59. J. Bush, F. Feldchtein, G. Gelikonov, V. Gelikonov, S. Piyevsky, Cost effective all-fiber autocorrelator for optical coherence tomography imaging, in *17th International Conference on Optical Fibre Sensors, Bruges, Belgium, SPIE*, pp. 254–257 (2005)
60. D. Drake, D.C. Leiner, Fiber-optic interferometer for romote subangstrom vibration measurement. Rev. Sci. Instrum. **55**, 162–165 (1984)
61. V.M. Gelikonov, V.I. Leonov, M.A. Novikov, Fiber-optic sensor. Patent Inventor certificate SU 1315797 A1 (1987), priority May 4, 1984
62. V.M. Gelikonov, D.D. Gusovskii, V.I. Leonov, M.A. Novikov, Birefringence compensation in single-mode optical fibers. Sov. Tech. Phys. Lett. **13**, 775–779 (1987)
63. M. Martinelli, A universal compensator for polarization changes induced by birefringence on a retracing beam. Opt. Commun. **72**, 341–344 (1989)
64. R.M.A. Azzam, N.M. Bashara, *Ellipsometry and Polarized Light* (North-Holland, Amsterdam/New York/Oxford, 1977)
65. W.V. Sorin, D.M. Baney, A simple intensity noise-reduction technique for optical low-coherence reflectometry. IEEE Photon. Technol. Lett. **4**, 1404–1406 (1992)
66. V.M. Gelikonov, G.V. Gelikonov, N.D. Gladkova, V.I. Leonov, F.I. Feldchtein, A.M. Sergeev, Y.I. Khanin, Optical fiber interferometer and piezoelectric modulator. Patent US 5,835,642, 1998
67. V.M. Gelikonov, G.V. Gelikonov, New approach to cross-polarized optical coherence tomography based on orthogonal arbitrarily polarized modes. Laser Phys. Lett. **3**, 445–451 (2006)
68. V.M. Gelikonov, G.V. Gelikonov, Fibreoptic methods of cross-polarisation optical coherence tomography for endoscopic studies. Quantum Electron. **38**, 634–640 (2008)
69. V. Gelikonov, G. Gelikonov, M. Kirillin, N. Shakhova, A. Sergeev, N. Gladkova, E. Zagainova, Fiber based OCT: from optical design to clinical applications, in *Handbook of Photonics for Biomedical Science*, ed. by V. Tuchin (CRC Press/Tailor and Francis Group LLC, Boca Raton, 2010), pp. 423–443
70. N. Gladkova, O. Streltsova, E. Zagaynova, E. Kiseleva, V. Gelikonov, G. Gelikonov, M. Karabut, K. Yunusova, O. Evdokimova, Cross-polarization optical coherence tomography for early bladder-cancer detection: statistical study. J. Biophoton. **4**, 519–532 (2011). Special Issue: Advanced Endoscopy

Needle Probes in Optical Coherence Tomography

25

Robert A. McLaughlin, Dirk Lorenser, and David D. Sampson

Contents

R.A. McLaughlin (✉) • D. Lorenser

Optical + Biomedical Engineering Laboratory, School of Electrical, Electronic, and Computer Engineering, University of Western Australia, Perth, WA, Australia
e-mail: Robert.McLaughlin@uwa.edu.au, Dirk.Lorenser@uwa.edu.au

D.D. Sampson

Optical + Biomedical Engineering Laboratory, School of Electrical, Electronic, and Computer Engineering, University of Western Australia, Perth, WA, Australia

Centre for Microscopy, Characterisation and Analysis, University of Western Australia, Perth, WA, Australia
e-mail: david.sampson@uwa.edu.au

Abstract

The development and deployment of OCT needle-probe technologies are reviewed. Their use through several different clinical applications, including demarcation of breast cancer tumor margins and lung imaging, is demonstrated.

25.1   Introduction

Fiber-optic probes are being developed for a rapidly increasing range of clinical applications. Greater opportunities are due both to improvements in the technology and to our increased understanding of the interaction of light with diseased tissue. A key optical imaging modality is optical coherence tomography (OCT) [1–4]. OCT acquires images of tissue structure through the detection of backscattered near-infrared light. It enables the acquisition of very-high-resolution images, in some situations allowing imaging of individual cells. Such imaging is of a much higher resolution than is possible with other clinical modalities, such as CT, MRI, or ultrasound, and is more similar to the level of detail achievable by histology. While histological analysis allows imaging of smaller structures than are visible in OCT, its key disadvantage is that it may only be used on excised tissue and requires processing of the tissue. In contrast, optical imaging modalities have the potential to be used in vivo and in real time, avoiding the need to excise tissue and allowing minimally invasive imaging of disease in situ. The promise of such high-resolution optical imaging has been referred to as an "optical biopsy" [2].

Despite the potential of this technology, OCT imaging has been restricted in clinical applications by its extremely limited imaging depth, typically only 2–3 mm in tissue. In turbid tissue, the imaging depth is limited by both scattering and absorption, with scattering being the dominant attenuation mechanism [5].

Miniaturized fiber-optic probes offer the potential to image deep within the body. It is possible to miniaturize the distal scan head and encase it within a medical needle – an *OCT needle probe*. Such a probe may then be inserted through the tissue until it reaches the area to be imaged.

In this chapter, we will review the development and deployment of OCT needle-probe technologies and examine their use through several different clinical applications.

25.2   Optical Coherence Tomography

OCT is an interferometric imaging technique that is analogous to ultrasound but uses near-infrared light waves instead of sound waves. Light covering a broad spectral bandwidth is split into two paths by an optical beam splitter. One path, the reference arm, is terminated by a mirror that reflects light back along the path. The second path, referred to as the sample arm, is weakly focused into the tissue sample under examination. A small percentage of the light is backscattered from
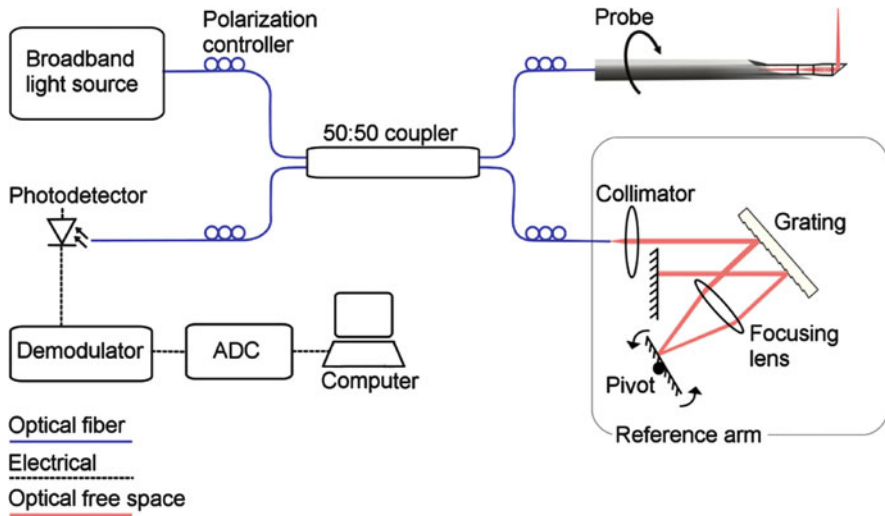
Fig. 25.1 Schematic of a time-domain OCT system and needle probe (Image adapted from Ref. [15])

multiple depths within the tissue sample and captured by the system. Reflected light from the reference arm and backscattered light from the sample arm are combined, and light that has traveled the same optical path length in both arms coherently interferes, giving rise to a signal indicative of the backscatter from a particular depth in the tissue sample. The extent of the coherent interference is limited by the optical bandwidth available. A large optical bandwidth conveys a narrow range of depths adequately matched to produce a signal, giving rise to OCT's defining optical sectioning property.

By varying the optical path length of the reference arm, it is possible to assess the tissue backscatter at different depths. In a time-domain OCT (TD-OCT) system [6], the optical delay is varied, typically by moving a mirror, yielding a one-dimensional scan over a predefined depth into the tissue sample. A typical setup is illustrated in Fig. 25.1. The movement of the mirror in the reference arm is a major limitation to the scanning speed of a TD-OCT system. To maximize scanning speed, the most commonly used design for the reference arm is the Fourier-domain rapid-scanning optical delay line (also referred to as the frequency-domain optical delay line) [7, 8].

An alternative hardware configuration avoids the need for a moving mirror by analyzing the spectrum of the interferometer output, which is related to the time-domain response by the Fourier transform [9–11]. This approach is therefore referred to as spectral-domain OCT (SD-OCT). SD-OCT is capable of acquiring depth scans at a rate that is an order of magnitude or more faster than is possible with TD-OCT and achieves much higher sensitivity. Two variants of SD-OCT have evolved. The first variant uses a spectrometer at the output of the interferometer, with all other components being identical to a TD-OCT system except that the
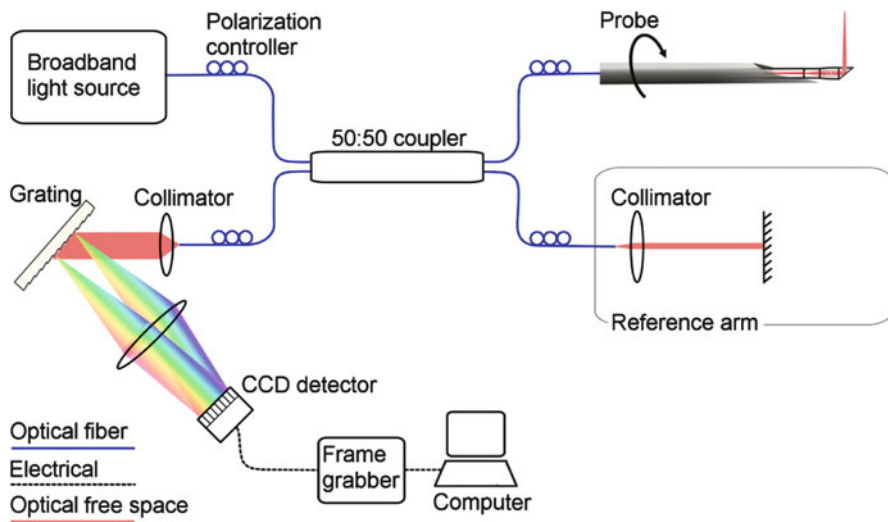
Fig. 25.2 Schematic of a spectrometer-based SD-OCT system and needle probe (Image adapted from [15])

reference-arm delay remains stationary. A representative setup is illustrated in Fig. 25.2. In practice, it is often referred to as FD-OCT (for Fourier domain), although this terminology is problematic as it can also be understood as a general name for all OCT techniques that employ Fourier-transform techniques, thereby conflicting with the term SD-OCT. We therefore choose to call it spectrometer-based SD-OCT. The second variant uses a swept single optical frequency instead of broadband light, thereby encoding the spectral information contained in the interferometer output in a temporal waveform that can be detected with a single photodetector (avoiding the need for high-resolution and high-speed spectrometers). It is, therefore, appropriately referred to as swept-source OCT (SS-OCT) [12], and it can achieve acquisition rates and sensitivities comparable to spectrometer-based SD-OCT systems.

The stationary mirror in SD-OCT makes it particularly suitable for common-path (or single-arm) OCT. In this configuration, a single path is used for both the sample and reference arms. The stationary reference reflection is a strong interface in this path. For example, in some OCT probe designs, this may be the glass–air interface where the light beam leaves the focusing optics or an interface between two components of the focusing optics. Alternative designs have been proposed to incorporate a miniaturized beam splitter with the focusing optics of the probe [13]. Common-path OCT is "down-lead insensitive," avoiding issues of polarization or dispersion mismatch between the reference and sample arms [14].

Terminology in OCT has been taken from ultrasound. A one-dimensional depth scan into a tissue sample is referred to as an A-scan. A two-dimensional (2D) image is referred to as a B-scan and is generated by moving the light beam laterally across

the tissue sample. This may be done by translating or rotating the scanning probe. A sequence of B-scans may be reconstructed into a three-dimensional (3D) volume and is referred to as a C-scan.

The choice of operating wavelength in OCT is a function of the light propagation properties of tissue and the operating wavelength ranges of available components. Light propagation in tissue depends upon the scattering and absorption properties of the tissue's components: cells, cell organelles, and various fiber structures. In the near infrared, scattering is the dominant attenuation mechanism [16]. The transparency of most tissues reaches a maximum in this spectral range, as scattering decreases with increasing wavelength [5]. Depending upon the specific tissues being imaged, the optimal operating wavelength is typically in the range 600–1,600 nm, referred to as the diagnostic window, the upper limit of which is set by rapidly increasing absorption by water [17]. Most OCT systems will utilize a light source with a center wavelength in either the 800 or 1,300 nm region.

As illustrated in Figs. 25.1 and 25.2, the vast majority of modern OCT systems are based on fiber-optic components rather than bulk-optics and free-space arrangements. Fiber-optic systems are alignment insensitive and robust, and their implementation is facilitated by the serendipitous fact that the most attractive OCT operating wavelength region around 1,300 nm coincides with a fiber-optic telecommunications wavelength band for which a wide range of high-performance and cost-effective components are readily available. Such fiber-optic systems exclusively utilize single-mode fiber (SMF) for constructing OCT interferometers because multimode fiber would allow the optical signals to propagate through the system via a number of modes with different group delays, thereby corrupting the OCT signal or at least making the system highly complex and alignment sensitive.

Image resolutions [4, 18] in the direction of the light beam (axial) and perpendicular to this (transverse) are decoupled in an OCT system. In both the axial and the transverse directions, the resolution in OCT is defined as the full width at half maximum (FWHM) of the system response to a point scatterer. The axial resolution is determined by the coherence length of the broadband light (larger spectral bandwidth corresponds to a shorter coherence length, which implies a better axial resolution). For a light source with a Gaussian power spectral density, the axial resolution expressed in units of optical (group) path length is [4]

$$\Delta \tilde{l}_{FWHM} = \frac{2 \ln(2)}{\pi} \frac{\overline{\lambda}^2}{\Delta \lambda}, \tag{25.1}$$

where $\overline{\lambda}$ is the mean vacuum wavelength and $\Delta \lambda$ is the FWHM spectral bandwidth. The above expression takes into account the double pass in the interferometer, and it implicitly contains the group refractive index n_g of the sample medium in the definition $\Delta \tilde{l}_{FWHM} = n_g \Delta l_{FWHM}$, where Δl_{FWHM} is the physical one-way path length difference in the interferometer (in accordance with [4], we denote optical path lengths with a tilde to distinguish them from physical lengths). This means that the axial resolution is always better in a medium than in air (a typical value for

biological tissue is $n_g = 1.4$). The axial resolution may be degraded by dispersion mismatch in the sample and reference arms, by electrical filtering in a TD-OCT system, or by nonlinearities in the spectral sampling in an SD-OCT system.

The transverse resolution is equal to the FWHM of the optical point spread function (PSF) of the OCT system in the transverse spatial dimension. The optical PSF in a fiber-based OCT system is equivalent to that of a reflection-mode fiber-optic confocal microscope [19], and its magnitude is equal to the transverse intensity profile of the probe beam at the respective axial location in the sample. Assuming an ideal Gaussian beam profile (and, thus, no truncation by the focusing lens) with a $1/e^2$ radius w, the FWHM is related to the $1/e^2$ beam diameter (or "spot size") $d_{1/e^2} = 2w$ by

$$\Delta x_{FWHM} = \sqrt{\frac{\ln(2)}{2}} d_{1/e^2} = 0.59 \cdot d_{1/e^2}. \tag{25.2}$$

The transverse resolution is, therefore, determined only by the numerical aperture (NA) of the focusing optics, which focus the probe beam to a spot size $d_{1/e^2} = 2\bar{\lambda}/(\pi NA)$, where $\bar{\lambda}$ is the mean vacuum wavelength. There is an inherent compromise between transverse resolution and depth of focus (DOF), which is defined as twice the Rayleigh range for an ideal Gaussian beam. A higher NA will give a smaller beam waist (hence improved transverse resolution), but the beam will diverge more rapidly away from the beam waist, giving a reduced DOF.

Typical systems achieve axial and transverse resolutions in the range 10–20 μm. Ultrahigh-resolution systems [20–25] have been reported with axial resolutions in air of 1–3 μm and transverse resolutions of ∼5 μm, but none of these have yet been implemented in conjunction with an OCT needle probe.

25.3   Design of OCT Needle Probes

Needle probes replace the sample-arm optics of a conventional OCT scanner. The tasks of the sample-arm optics are to scan and focus the incident light and to collect the weak backscattered light from the sample with high efficiency. Therefore, they define or significantly influence a number of key performance parameters of the OCT system, such as

- Transverse resolution
- Depth of focus (DOF)
- Sensitivity
- Imaging speed

Losses or back reflections in the sample-arm optics will reduce the system sensitivity, whereas aberrations and alignment errors will negatively impact the transverse resolution and DOF. In a well-designed conventional free-space sample-arm setup consisting of a collimator, galvanometer mirrors, and a compound scan lens, minimal losses and diffraction-limited probe beam quality over the entire field

Fig. 25.3 Output beam characteristics of a fiber-based needle probe. The schematic illustration of the needle probe depicts a distal focusing scheme using a gradient-index lens, which refocuses the approximately Gaussian mode emitted from the single-mode fiber into the sample volume. *WD* working distance, *DOF* depth of focus
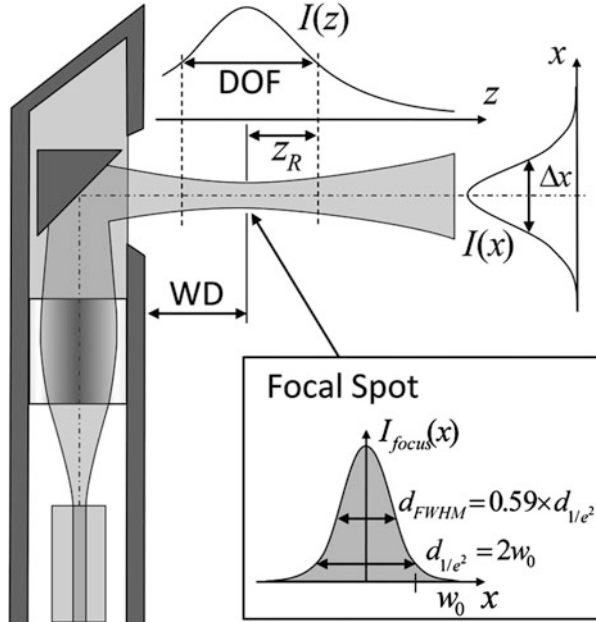
of view can easily be simultaneously achieved using high-quality antireflection-coated optics which are designed for the OCT operating wavelength. In the case of miniaturized sample-arm optics, such as endoscopic or needle probes, the small dimensions and the employed fabrication methods typically force the designer to make trade-offs which will negatively impact the sensitivity and resolution of the OCT system.

25.3.1 Beam Parameters

The probe beam determines the transverse resolution and the DOF of the OCT system. In most cases, the probe beam can be described as a Gaussian beam that results from refocusing the mode emitted from the sample-arm fiber by the distal focusing optics, as illustrated in Fig. 25.3. The relevant parameters for OCT imaging are the working distance (WD), spot size, and DOF. In the OCT literature, the spot size generally refers to the $1/e^2$ diameter $d_{1/e^2} = 2w_0$ of the beam waist. As outlined in the introductory section, the transverse resolution is equal to the FWHM of the beam intensity profile, with $\Delta x_{FWHM} = 0.59 \cdot d_{1/e^2}$. In the case of an ideal Gaussian beam, the double Rayleigh range is used as a measure of the DOF. The double Rayleigh range equals the FWHM of the axial intensity profile, and its boundaries mark the points at which the beam diameter has expanded by a factor of $\sqrt{2}$ compared to the value at the beam waist. The DOF can then be expressed as

Fig. 25.4 Forward-viewing
(**a**) and side-viewing (**b**)
probes
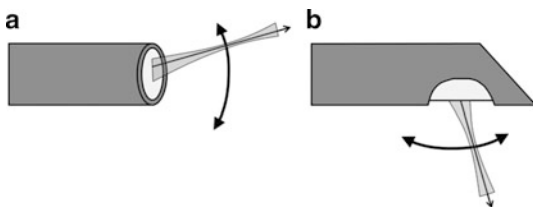
$$DOF_{Gauss} = 2z_R = 2\frac{n\pi w_0^2}{\bar{\lambda}}, \qquad (25.3)$$

where n is the refractive index of the sample medium and $\bar{\lambda}$ is the mean vacuum
wavelength.

25.3.2 Scan Mechanisms

Imaging, as opposed to single-point measurements, is only possible if the probe
beam can be scanned within the sample. Many different ways of scanning the probe
beam have been devised, and the development of novel scan mechanisms is a very
active ongoing field of research. In the following, we will give a categorization of
scanning probes, based on mechanical and optical principles, which is independent
of the technical details of the scan mechanism implementation. This categorization
will allow us to gain some insight into the advantages and disadvantages of
different classes of currently employed scan mechanisms, and it is general enough
to accommodate future developments.

Firstly, probes can be categorized into forward-viewing and side-viewing types
(see Fig. 25.4). Generally, the requirements of the application dictate which of these
two is preferable.

Furthermore, probes can be categorized according to their scan mechanisms.
There are two main categories of scan mechanisms: beam scanning and probe
scanning. The two categories and some of their variations are illustrated in
Fig. 25.5. Beam scanning involves a movement of the beam path inside the probe
housing, allowing the probe to remain stationary during the scan. Probe scanning,
on the other hand, mechanically actuates the entire probe (or a mechanical
subcomponent thereof which defines the emitting beam aperture), while the beam
path inside the probe is unchanged. Beam scanning probes are more challenging to
miniaturize, as they require moving parts inside the probe housing. For this reason,
probes with submillimeter dimensions generally utilize probe scanning.

In beam scanning, the moving beam is projected out of the probe housing into
the sample by the probe optics. The probe optics form an imaging system which
images scattered light from the sample (the object) onto the sample-arm fiber tip
(the image). Using terminology from imaging optics, we can therefore further
subdivide beam scanning techniques as "image-space scanning" (Fig. 25.5a),
"pupil scanning" (Fig. 25.5b), or as "object-space scanning" (Fig. 25.5c). Although

Fig. 25.5 Overview of some basic scan mechanisms, categorized into "beam scanning" and "probe scanning." (**a**) Image-space scanning (using an oscillating fiber tip in this example). (**b**) Pupil scanning (the white dashed rectangle represents a beam deflection mechanism, which can be implemented using various technologies – see text for practical examples). (**c**) Object-space scanning. (**d**) Rotation/pullback scanning. (**e**) Linear scanning using a linearly actuated probe inside a protective outer housing or catheter
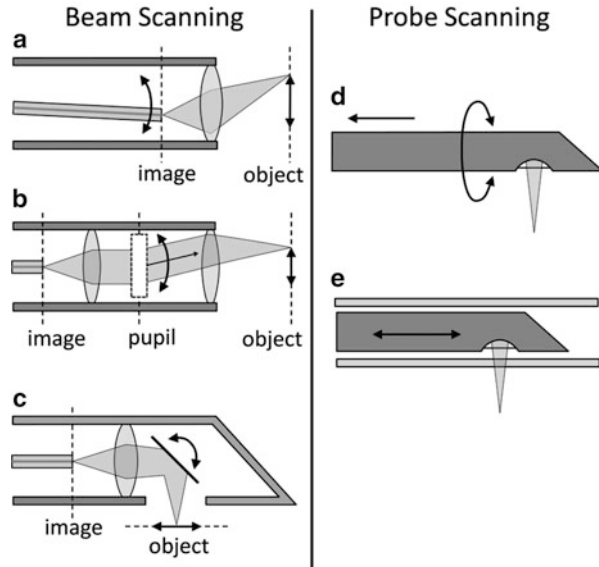
Fig. 25.5a and b shows forward-viewing configurations for pupil and image-space scanning, they can in principle also be realized as side-viewing types by adding mirrors or prisms to deflect the beam outward at right angles.

Image-space scanning involves actuating the tip of the sample-arm fiber. The probe-beam focal spot is thereby scanned in the sample over a range, which is determined by the magnification of the probe optics. The concept of image-space scanning has been implemented in endoscopic probe designs using oscillating fiber tips [26], but miniaturization of these designs to submillimeter diameters has proven to be challenging. Small-diameter forward-viewing OCT probes of this type have been reported with outer diameters of 2.4 mm and 2.2 mm using tubular four-quadrant piezoelectric actuators [27] and electrostatic actuators [28], respectively.

Pupil scanning involves an angular deflection of the collimated beam in the pupil plane of the imaging optics. This is the principle of conventional beam scanning solutions based on galvanometer mirrors, which are positioned in the back focal plane of the scan lens. Beam deflection mechanisms for pupil-scanning probes have been realized with MEMS mirrors [29, 30] and with counterrotating wedged gradient-index (GRIN) lens pairs (paired-angle-rotation scanning, PARS [31]). In pupil-scanning arrangements, MEMS mirror solutions require a folded-beam path geometry, resulting in relatively large probe diameters of several millimeters. However, PARS probes have been miniaturized to needle dimensions as small as 21 gauge (21 G, diameter 0.82 mm) in a forward-viewing configuration for OCT imaging of the eye [32].

Object-space scanning arrangements sacrifice some of the working distance of the probe optics, but they are often used in side-viewing miniaturized MEMS

mirror probes [33, 34] because the MEMS mirror can conveniently serve as the output beam deflector, which directs the beam sideways out of the probe. Although probes of this type with diameters down to 2.6 mm have been demonstrated [34], MEMS technology does not yet seem to allow the miniaturization to submillimeter dimensions at the time of writing and is, therefore, mainly targeted toward endoscopic OCT applications. An overview of endoscopic OCT probes using MEMS technology can be found in [35] and [15].

An elegant variation of beam scanning involves the use of long and thin GRIN relay rods, which can be inserted into hypodermic needles. By scanning the incident light at the proximal end face of the GRIN relay rod, the relayed and focused beam is scanned in object space at the distal end of the relay. The key advantage of this approach is that the scan mechanism does not need to be miniaturized to the diameter of the needle and can be relocated into a larger-diameter housing to which the needle is attached. Submillimeter diameter needle probes of this kind were first demonstrated for multiphoton [36] and confocal microscopy [37], and a forward-viewing OCT needle probe with an outer diameter of 740 μm which incorporated a 500-μm-diameter GRIN relay rod was recently demonstrated [38]. In these needle probes, the GRIN relay rod is an integral part of the distal focusing optics. Depending on the scanning mechanism at the proximal end face of the relay (e.g., by scanning the sample-arm fiber tip [37] or scanning an image of it using a galvanometer mirror and objective lens [38]), they can be classified as either image-space or pupil scanning types, respectively.

In order to achieve the highest degree of miniaturization to submillimeter "needle-probe" dimensions, probe-scanning techniques (see Fig. 25.5d and e) are typically used, with the smallest reported probe of this kind being encased in a 30-G needle (diameter 0.31 mm) [39]. Since the probe can only be actuated via rotation and/or translation (along the probe axis), probe-scanning designs must be side viewing in order to enable at least 2D scanning capability. The most straightforward and common approach is the rotation/pullback method of Fig. 25.5d [39, 40], where B-scans are acquired over one probe rotation and then stacked along the translation direction to generate a 3D image. An alternative is to perform a fast translation along the probe axis to acquire a 2D image, as illustrated in Fig. 25.5e, and needle probes of this design have been demonstrated with sizes down to 22 G (0.72 mm diameter) for use in interstitial Doppler imaging [41, 42].

25.3.3 Probe Optics

The probe optics assembly typically consists of a number of miniaturized lenses, spacers, mirrors, and optical windows. The quality of the probe optics is of fundamental importance for the imaging performance of the OCT system. Losses and back reflections will degrade the OCT system sensitivity, and aberrations will degrade the resolution and DOF.

Early designs of miniaturized probes used discrete micro-optic components. Some examples are shown in Fig. 25.6. The first demonstrated OCT needle probe
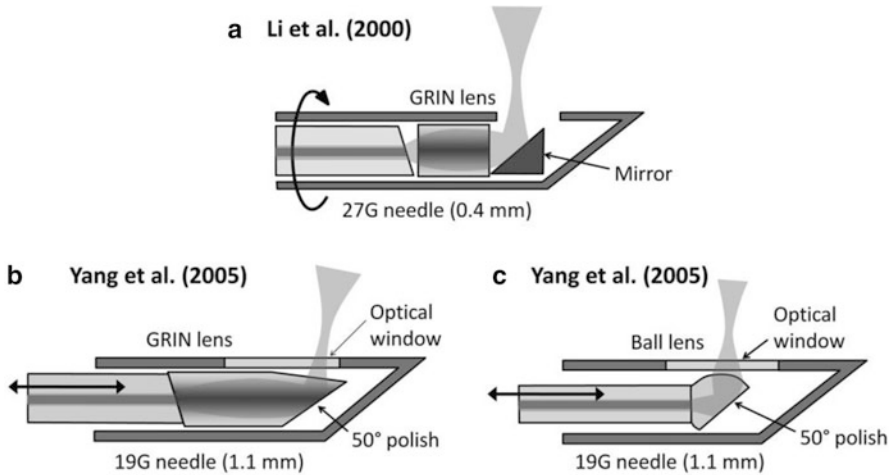
Fig. 25.6 Examples of early OCT needle-probe designs. (**a**) The first demonstrated needle probe [43] using a discrete GRIN lens and a micromirror inside the needle. (**b**) Linear-scanning needle probe using an angle-polished GRIN lens under total internal reflection [41]. (**c**) Linear-scanning needle probe using an angle-polished ball lens under total internal reflection [41]

(see Fig. 25.6a) used a 250-μm-diameter GRIN lens and a micromirror which were assembled inside a 27-G (0.41 mm diameter) needle and held in place using optical adhesive [43]. In order to avoid back reflections from the fiber–lens interface, the SMF was angle cleaved at 8°. A similar design for linear-scanning operation (see Fig. 25.6b) was demonstrated in which the angle-polished GRIN lens was adhesive-bonded to the end of the angle-cleaved SMF [41]. Instead of using a micromirror, the end of the GRIN lens was polished at 50° in order to enable total internal reflection. Since this design cannot operate when immersed in fluid, the side opening in the needle was sealed with an optical window. A variation of this design using a ball lens (see Fig. 25.6c) was shown in the same paper. The dimensions of the optics and the optical window imposed restrictions on the degree of miniaturization, making this probe relatively large (19 G, 1.1 mm diameter).

Later needle-probe designs made use of sections of multimode GRIN fiber spliced to the end of the SMF [44, 45], as shown in Fig. 25.7. Multimode GRIN fibers have a parabolic refractive-index profile (although there are some inherent deviations from the ideal parabolic profile due to the MOCVD process used in manufacturing the preforms [44]) and can, therefore, be used as a substitute for GRIN rod lenses in applications that are tolerant of a certain amount of aberration. Fortunately, this is the case in the low-NA beams used in OCT. This technique, originally developed for fabricating lensed fibers for telecommunications applications [46], offers two significant advantages over the previous approaches using discrete micro-optics. Firstly, the design is amenable to fabrication using established fusion-splicing technology, which is reproducible and self-aligning. Secondly, the fusion-spliced optics assembly eliminates back reflections from
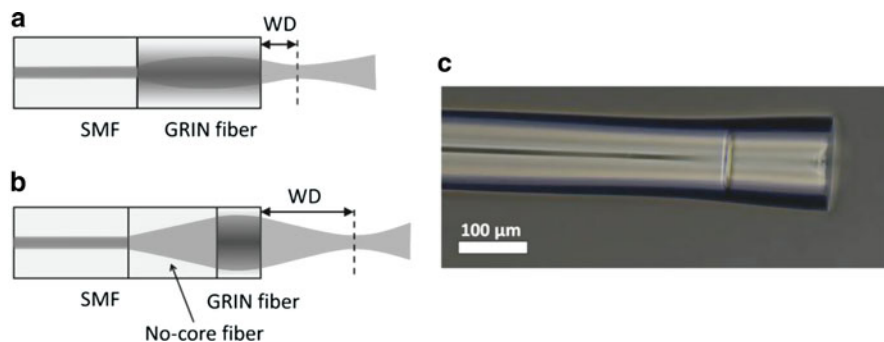
Fig. 25.7 Lensed fibers fabricated by fusion-splicing a section of multimode GRIN fiber to the end of a SMF. (**a**) Simple lensed-fiber design with the GRIN fiber joined directly to the SMF. (**b**) Improved lensed-fiber design with longer working distance using a section of no-core fiber to expand the beam from the SMF. (**c**) Phase contrast microscope image of a lensed fiber. The GRIN fiber has a cladding diameter of 140 μm; therefore, the junction to the thinner 125-μm-diameter SMF is clearly visible

optical interfaces between the SMF and the focusing optics that could otherwise degrade OCT sensitivity and cause image artifacts. In order to obtain a long working distance (which is desirable in side-viewing probes in order to obtain a focus outside of the needle-probe housing), an improved design using a spacer made of coreless silica fiber ("no-core fiber") between the SMF and the GRIN fiber can be used, as illustrated in Fig. 25.7b.

Many current miniaturized probes for OCT have adopted the GRIN fiber design, with some examples shown in Fig. 25.8. The fusion-splicing process allows addition of an extra section of no-core fiber after the GRIN lens, which can be angle-polished to form a reflector, thereby eliminating the need to fabricate and align a separate micromirror inside the probe housing. The first such probe used the angle-polished reflector under total internal reflection inside an enclosing catheter [42], as shown in Fig. 25.8a. By applying a reflection coating to the angle-polished end face of the probe, it is possible to eliminate the need for an enclosing catheter, thereby enabling the realization of an ultrathin side-facing probe with dimensions that are only limited by the outer diameter of the optical fiber. An ultrathin needle probe using such a reflection-coated angle-polished reflector (see Fig. 25.8d) has been demonstrated successfully, and the 125-μm cladding diameter of the various fibers allowed it to be inserted into a 30-G needle (0.31 mm outer diameter), making it the smallest side-facing OCT needle probe published to date [39]. A minor limitation of this probe design is the astigmatism which the beam acquires as it exits from the side of the fiber cladding, which behaves as a cylindrical lens. However, it was shown in [39] that the astigmatism is strongly reduced under the near-index-matched conditions when the probe is inserted into tissue. Most side-facing probe designs using capillaries or catheters have this problem to some extent when it is not possible to index match all interfaces. An improved needle-probe design (see Fig. 25.8c) using a flat-polished capillary output window has been
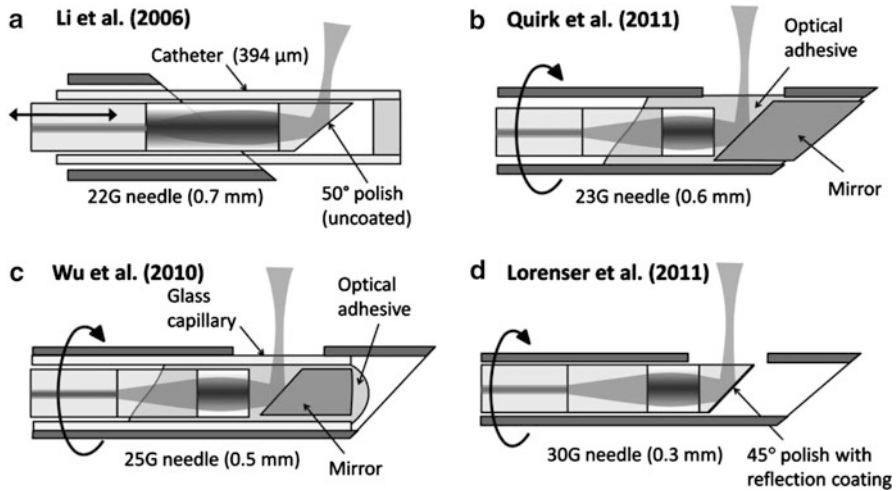
Fig. 25.8 Examples of some improved probe designs using sections of GRIN fiber in their distal focusing optics. (**a**) A linear-scanning probe using an angle-polished section of no-core fiber under total internal reflection inside a catheter [42]. (**b**) A needle probe using a lensed fiber in combination with a polished metal mirror embedded in optical adhesive [40]. (**c**) A probe design similar to (**b**) but using a glass capillary to form a robust optical-quality output window interface [47]. (**d**) The smallest demonstrated side-viewing probe, using a reflection-coated angle-polished section of no-core fiber as the output mirror [39]

demonstrated to address this problem [47]. It was shown that the astigmatism could be almost completely eliminated using this approach and the glass capillary provides a robust optical-quality output window interface, but the enclosing capillary increases the probe diameter compared to simpler designs that trade off beam quality in favor of ultrasmall probe dimensions.

25.3.4 Optical Design of OCT Needle Probes

The design techniques for miniaturized optical systems are somewhat different from classical lens design in that the approximations of ray optics are often no longer satisfied. Therefore, ray-tracing methods, as employed by lens-design-oriented optical engineering software packages, will not be adequate to properly calculate parameters such as working distance and spot size. Scalar-wave theory is required to properly account for diffraction of the probe beam and its transformation by the optical elements of the probe. While many optical engineering software packages offer such functionality (e.g., "Physical Optics Propagation" in ZEMAX), their cost and complexity make them unsuitable for sporadic use and quick iterative design calculations.

A simple but very effective alternative to a full scalar-wave simulation is the paraxial ray-matrix formalism for Gaussian beams [48]. Since the beam emitted by

a single-mode fiber can be well approximated by a fundamental Gaussian mode, paraxial ray matrices can be used to describe its transformation by the optical elements of the probe. If no limiting apertures are present in the optics, this formalism fully accounts for diffraction and will yield results that are sufficiently accurate for practical work. The ray-matrix formalism lends itself to implementation in technical computing tools such as MATLAB or Mathematica, making it ideal for fast and flexible design calculations. The fabrication of miniaturized probes involves dealing with significant variations from the simulated situation due to manufacturing tolerances, as well as nonideal properties of optical components. Accordingly, the probe fabrication process will generally involve an iterative experimental optimization procedure and, therefore, approximate initial design calculations will be sufficient in most cases.

The Gaussian beam is a solution to the paraxial wave equation. It has a normalized complex envelope given by [49]

$$A(\rho, z) = \sqrt{\frac{2}{\pi}} \frac{q_0}{w_0 q(z)} \exp\left(-i \frac{k \rho^2}{2 q(z)}\right) \qquad \left(\rho = \sqrt{x^2 + y^2}\right), \quad (25.4)$$

where ρ is the distance from the optical axis and $k = n \, 2\pi/\lambda_0$ is the propagation constant in a medium with refractive index n for a wave with a vacuum wavelength of λ_0 and w_0 is the waist radius. It can be seen from (25.4) that for every axial position z, $A(\rho, z)$ is completely defined by the complex beam parameter $q(z)$. For a beam with a waist located at $z = 0$, the complex beam parameter as a function of z is
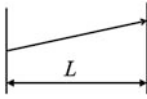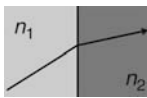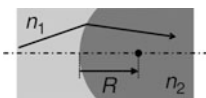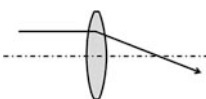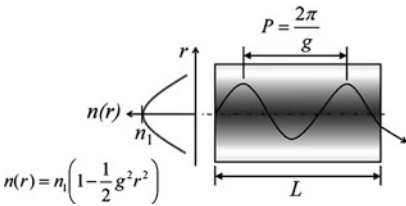
$$q(z) = z + i \, z_R \qquad (q_0 = q(0) = i z_R), \quad (25.5)$$

where $z_R = k \, w_0^2/2 = n\pi \, w_0^2/\lambda_0$ is the Rayleigh range. The complex beam parameter $q(z)$ is related to the more intuitive quantities $R(z)$ (radius of curvature of the wavefront) and $w(z)$ (beam radius) via

$$\frac{1}{q(z)} = \frac{1}{R(z)} - i \frac{2}{k \, w^2(z)}. \quad (25.6)$$

If the complex beam parameter q in a region of free-space propagation is known at a certain axial position, we can see from (25.5) that we can extract the distance from the focus via $z = \text{Re}\{q\}$ and the waist radius (which is directly related to the Rayleigh range) via $z_R = \text{Im}\{q\}$. Therefore, the Gaussian beam can be plotted as a function of z in that entire region, and it can be propagated to the next optical interface or optical element via (25.5) (after shifting the z-coordinate to correspond to the optical system coordinates). At every optical element in the system, the complex beam parameter is transformed via

Table 25.1 Ray matrices of some basic optical elements

Free-space propagation		$\begin{bmatrix} 1 & L \\ 0 & 1 \end{bmatrix}$
Refraction at an interface		$\begin{bmatrix} 1 & 0 \\ 0 & \frac{n_1}{n_2} \end{bmatrix}$
Refraction at a curved interface (convex $\rightarrow R > 0$)		$\begin{bmatrix} 1 & 0 \\ -\frac{(n_2-n_1)}{n_2 R} & \frac{n_1}{n_2} \end{bmatrix}$
Thin lens		$\begin{bmatrix} 1 & 0 \\ -\frac{1}{f} & 1 \end{bmatrix}$
Graded-index material		$\begin{bmatrix} \cos(gL) & \frac{1}{g}\sin(gL) \\ -g\sin(gL) & \cos(gL) \end{bmatrix}$

$$q_2 = \frac{Aq_1 + B}{Cq_1 + D} \qquad M = \begin{bmatrix} A & B \\ C & D \end{bmatrix}, \qquad (25.7)$$

where M is the ray matrix of the optical element.

A list of ray matrices of some optical elements useful in the design of probe optics is shown in Table 25.1. Most probes can be modeled as a sequence of the elements shown in the table, and, therefore, the beam propagation from the end face of the single-mode fiber to the output of the probe can be calculated by an iterative application of (25.7). Since the beam launched from the SMF has its waist at the fiber end face, the complex beam parameter at the input to the probe is $q_{in} = in\pi w_{in}^2/\lambda_0$, where w_{in} is equal to half the mode-field diameter (MFD) of the fiber and n is the refractive index of silica.

An example of such a simulation at an operating wavelength of 1,310 nm is shown in Fig. 25.9. The fiber-optic probe consists of sections of no-core fiber and GRIN fiber with lengths of 360 and 210 μm, respectively, spliced to the end of SMF-28 with a MFD of 9.2 μm. The GRIN fiber has a gradient constant of

Fig. 25.9 Simulation of
beam propagation in a fiber-
optic probe using the ray-
matrix method. The output
beam propagation is shown in
air. *SMF* single-mode fiber,
NCF no-core fiber, *GRIN*
gradient-index fiber. See text
for explanation
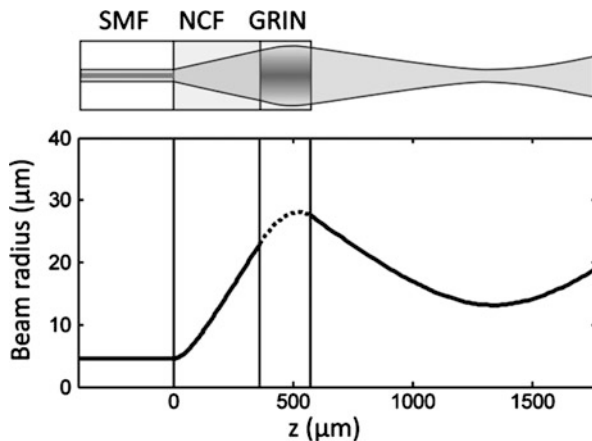
$g = 3.76$ mm^{-1}, and its length corresponds to 0.13 pitch. The output beam has
a spot size of 26 μm located at a working distance of 766 μm in air. The NA of the
output beam is 0.03.

The main source of error when designing GRIN fiber probes using paraxial ray-
matrix theory lies in the deviation of the refractive-index profile of real gradient-
index materials from the idealized parabolic profile. This becomes particularly
apparent when working with commercial multimode GRIN fiber, which is typically
drawn from preforms manufactured using a modified chemical-vapor-deposition
(MCVD) process. This results in a prominent central refractive-index dip that causes
strong distortions of the beam profile when they are employed as gradient-index
lenses. This problem was already recognized in early work and was addressed by
more advanced preform fabrication techniques based on a vapor-phase axial depo-
sition (VAD) process [46]. More recently, efforts to make higher-bandwidth
multimode GRIN fibers have led to MCVD processes which yield preforms that
are nearly free of the central index depression [44]. When using commercial GRIN
fibers, it is therefore advisable to obtain a measured refractive-index profile from the
manufacturer to check for the presence and the severity of the central index depres-
sion. Even in the cases where the refractive-index dip is negligible, the refractive-
index profile will typically exhibit slight deviations from the ideal parabolic profile,
which result in on-axis aberrations. In most cases, these aberrations will manifest
themselves in a discrepancy between the simulated and measured working distances
of the probe. For this reason, a thorough characterization of the beam profile of
fabricated probes is of utmost importance, as will be shown in the following section.

25.3.5 Fabrication and Testing

The technique of fabricating fusion-spliced distal focusing optics consisting of
precisely controlled lengths of no-core and GRIN fiber has been widely adopted,

Fig. 25.10 Fabrication steps of an ultrathin 30-G needle probe. (**a**) Fiber probe with fusion-spliced distal focusing optics and an angle-polished section of no-core fiber, which serves as the beam deflection mirror. (**b**) Fiber probe after deposition of metal coating. (**c**) Close-up view of the tip of the assembled 30-G needle probe, showing the electrochemically etched side window opening
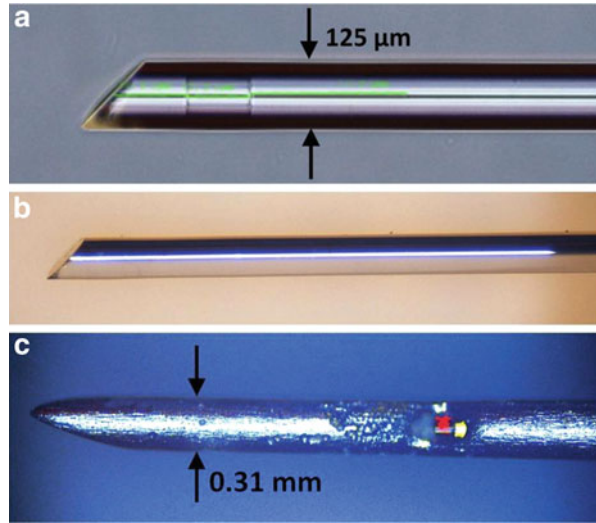
and it is relatively straightforward using commercial splicers and fiber cleavers. However, in order to build a side-facing needle probe that is capable of generating 2D or 3D images via the probe-scanning mechanisms shown in Fig. 25.5d and e, it is also necessary to fabricate a beam deflection mirror and a side window. These two fabrication steps are very challenging, and different solutions have been implemented depending on the specific requirements of the application (simplicity, optical quality, robustness).

For the fabrication of the beam deflection mirror, our group has taken two approaches. In the first approach, for probe designs of the type shown in Fig. 25.8b, we use polished metal mirrors which are manufactured in-house from 0.3-mm-diameter copper wire using a custom-made polishing machine with a series of silicon carbide (30 and 9 μm) and aluminum oxide (0.3 μm) polishing films (Krell Technologies, Morganville, NJ, USA). In the second approach, for ultrathin probe designs of the type shown in Fig. 25.8d, we angle-polish and metal-coat an additional section of no-core fiber, which is spliced to the end of the GRIN section (see Fig. 25.10a). The angle polishing is performed on a commercial fiber-connector polishing machine (SpecPro 4L, Krelltech, USA) using a custom fiber chuck that holds the fiber at an angle of 45°. The metal coating consists of a 10-nm chrome adhesion layer and a 300-nm gold layer. It is applied using a thermal vacuum deposition process, which is ideal for this application since the metal atoms travel on a line-of-sight trajectory from the source to the sample. Thus, the simultaneous coating of the beam output interface of the angle-polished fiber probe is avoided by orienting it in the coating chamber such that it faces away from the deposition source. An example of such a metal-coated angle-polished fiber tip is shown in Fig. 25.10b.

The side window opening in the needle also poses several challenges, as it must be fabricated precisely and without sharp burrs. Our group has developed an

electrochemical etching procedure using a customized setup in which the needle is connected as the anode in a bath of concentrated sulfuric acid. The current density is directed to the desired location using a sharp-tipped cathode, thereby preferentially etching away the steel at that point. An example of such a side window opening fabricated using this method is shown in Fig. 25.10c. While this method causes some degradation of the surface quality of the needle (this is especially pronounced in the close vicinity of the hole as can be seen in Fig. 25.10c), it creates relatively clean holes compared to methods such as drilling, grinding, or filing which tend to produce sharp burrs and edges.

When a side opening has been created in the needle, the question arises of how to form a well-defined optical interface to the sample. In the ultrathin 30-G needle probe shown in Fig. 25.10c, the side opening is not sealed, allowing water or other fluids to enter the probe housing during scanning. The optical interface is thereby formed by the glass/water interface of the fiber cladding at the point where the beam exits the side-facing probe. The fiber cladding is a durable and optical-quality interface, but it introduces significant astigmatism to the output beam [39]. The problem of creating an optical-quality interface without astigmatism in side-facing needle probes has recently been addressed by Wu et al. [47]. They employed a novel design in which a side-facing fiber probe assembly is encased in a glass capillary which is polished flat on one side, thereby providing a robust planar glass/ sample interface. However, the glass capillary increases the diameter of the probe, and the smallest demonstrated probe of this type was encased in a 25-G needle. A less robust but very simple solution is to seal the side opening of the needle with optical adhesive. This approach is used in our needle probes of the type shown in Fig. 25.8b, where the focusing optics and the copper mirror are held rigid by embedding in optical adhesive (Norland, NJ, USA), which also serves as the sealant for the output window and as the optical interface to the sample medium. However, the surface of the optical adhesive is susceptible to mechanical and chemical wear, and we have observed that the optical quality degrades after prolonged usage of the probe.

As mentioned in the section on optical design of fiber probes, a thorough characterization of the output beam is necessary after fabrication in order to verify the design calculations or to make iterative adjustments until the desired spot size and working distance are obtained. Figure 25.11 shows the results of a beam profile measurement of an 800-nm fiber probe using a camera-based near-field beam profiler (SP620U, Ophir-Spiricon, USA). The fiber probe consists of sections of no-core fiber (length 294 μm, POFC, Taiwan) and GRIN fiber (length 129 μm, GIF625, Thorlabs, USA) spliced to SMF (SM800, Fibercore, UK). The plot of the fitted $1/e^2$ beam diameters versus distance shows that the probe has a working distance of 600 μm in air and a focal spot diameter of 20 μm.

25.3.6 Sensitivity

There are two main causes of sensitivity loss when using a needle probe in place of a free-space sample arm. The first is due to losses in the probe optics. These losses
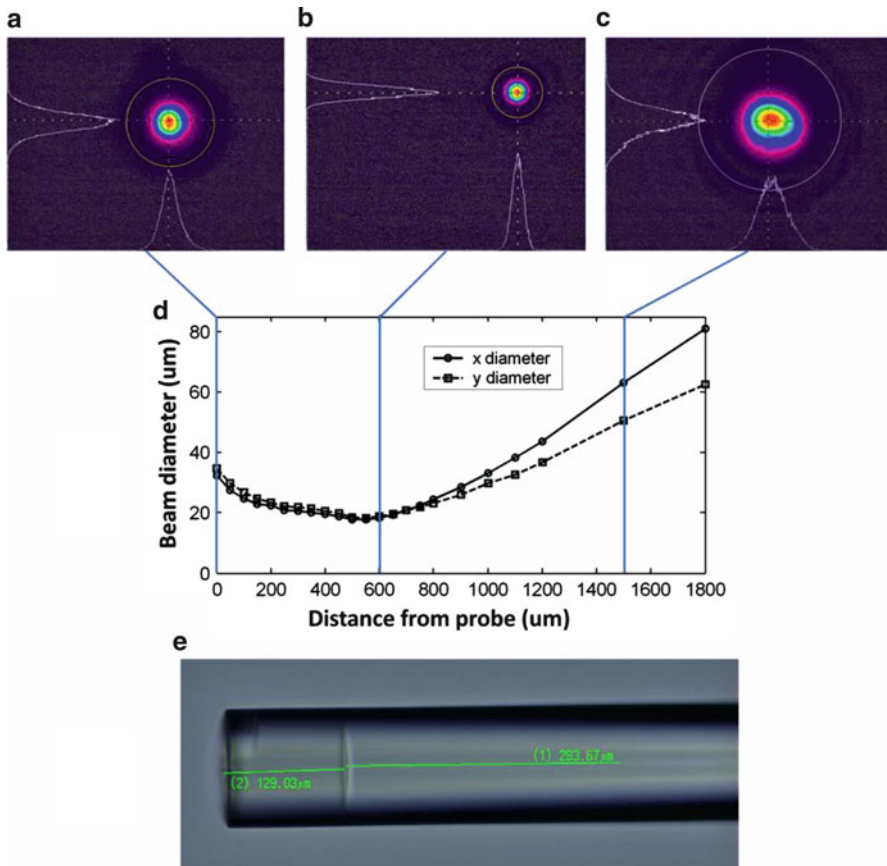
Fig. 25.11 Characterization and testing of a fabricated 800-nm fiber probe. (**a–c**) Measured beam profiles at distances of 0 μm, 600 μm, and 1,500 μm from the end face of the fiber probe. (**d**) Beam diameters ($1/e^2$) obtained from Gaussian fits of the transverse beam profiles in the *x*- and *y*-directions. (**e**) Microscope image of the fabricated probe, showing the measurements of the GRIN and no-core fiber sections

are serious because they typically act in double pass and can arise from a multitude of effects, such as:

- Refractive-index discontinuities and uncoated interfaces
- Imperfectly polished optical surfaces and nonideal reflection coatings
- Beam clipping due to the finite aperture of micro-optical elements (e.g., GRIN lenses, microreflector prisms)
- Scattering in thick sections of optical adhesive which may contain flaws such as gas bubbles caused by the curing process

The second cause of sensitivity loss is due to back-reflected power from interfaces and optical elements in the probe, which reduces the dynamic range of the detector as well as introducing shot and beat noise [50, 51].
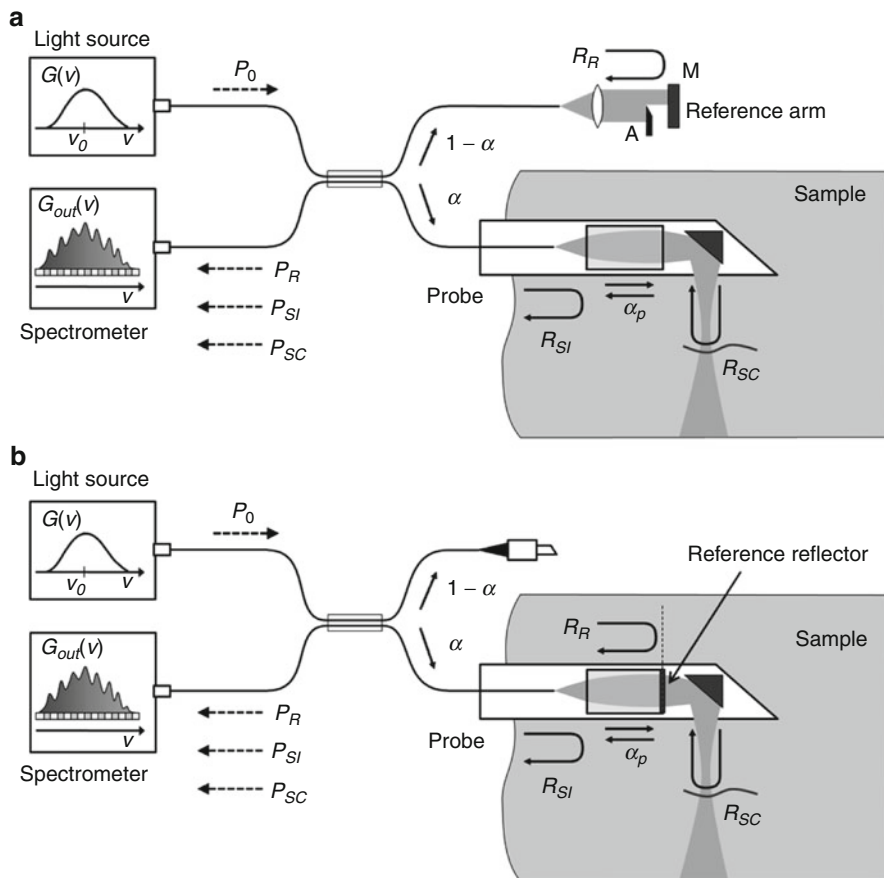
Fig. 25.12 Schematic of fiber-based SD-OCT systems with a needle-probe sample arm in (**a**) Michelson and (**b**) common-path (Fizeau) configuration. *M* mirror, *A* attenuator

We will briefly review the sensitivity analysis of OCT systems with a view toward the specific causes of sensitivity loss in needle-probe systems. While most early work with needle probes was done with TD-OCT systems [41, 43], recent developments [39, 47] have followed the trend toward SD-OCT (swept source as well as spectrometer based) due to its inherent sensitivity advantage [52]. We will, therefore, limit our discussion to SD-OCT. A schematic of a spectrometer-based all-fiber SD-OCT system with a needle-probe sample arm is shown in Fig. 25.12, in two commonly employed configurations. Figure 25.12a shows a Michelson inter-ferometer configuration with a reference arm that is matched to the optical path length of the needle probe and which allows adjustment of the returning reference power level via an optical attenuator. Figure 25.12b shows a common-path (Fizeau) interferometer configuration, in which a back reflection from the probe optics serves as the reference reflector. As outlined at the beginning of this chapter, this

configuration has the significant advantage of almost completely eliminating problems associated with dispersion matching as well as "down-lead sensitivity" resulting from polarization fading due to fiber movement during needle scanning [14]. The main drawback of the common-path configuration is that the reference reflectivity cannot be adjusted during operation and must therefore be optimally chosen beforehand, and it thus becomes an integral part of the probe design and fabrication process [13, 14, 53].

The results of our sensitivity analysis of needle-based SD-OCT systems will be applicable without modifications to both the Michelson and the common-path configurations, as the reference and sample signals traverse the fiber coupler via the transmitted as well as the coupled path on their way from the source to the spectrometer arm of the interferometer in both cases, as can be verified by tracing their paths through the two systems shown in Fig. 25.12. In the following, we will therefore limit our discussion to the Michelson configuration of Fig. 25.12a, because it represents the most general situation. Broadband light with average power P_0 is split into the sample and reference arms of the Michelson interferometer built around a fiber coupler with power splitting ratio α. In the reference arm, the reference reflectivity R_R can be adjusted via an optical attenuator. In the sample arm, the incident power is collimated and refocused into the sample by the probe optics. It is attenuated by the single-pass probe attenuation α_P resulting from the losses and back reflections in the probe optics. Some of the lost power from the probe back reflections will be back-coupled into the sample-arm fiber. This signal will generally be outside of the coherence volume of the OCT system; therefore, we denote the source of this back-reflected power as an "incoherent" reflectivity R_{SI} (it will generally be the cumulative effect of a number of interfaces and scatterers inside the probe, but for this discussion, it suffices to represent them by a single effective reflector). By contrast, the actual OCT signal will result from reflectors within the coherence volume. For the signal-to-noise (SNR) analysis, we consider the sample to consist of only a single reflector with a "coherent" reflectivity R_{SC}, as illustrated in Fig. 25.12. The power reflected from the sample reflector R_{SC} and collected by the probe optics will again be attenuated by the single-pass probe attenuation α_P. In the output arm of the interferometer, the returning powers P_R, P_{SI}, and P_{SC} from the reference and sample arms are

$$P_R = P_0\alpha(1 - \alpha)R_R = P_0\gamma_R R_R, \tag{25.8}$$

$$P_{SC} = P_0\alpha(1 - \alpha)\alpha_P^2 R_{SC} = P_0\alpha(1 - \alpha)\gamma_P R_{SC} = P_0\gamma_S R_R \tag{25.9}$$

$$P_{SI} = P_0\alpha(1 - \alpha)R_{SI}, \tag{25.10}$$

where P_R is the coherent reference-arm power and P_{SC} and P_{SI} are the coherent and incoherent sample-arm powers, respectively. The factors γ_R and γ_S represent the fraction of the source power P_0 returning from the reference and sample arms for a unity reflector ($R_R = R_{SC} = 1$), in accordance with the notation in [52]. We have

also defined the round-trip attenuation $\gamma_P = \alpha_P^2$ of the probe for a unity reflector placed at the working distance. The round-trip attenuation γ_P is a very useful parameter because it can be measured easily. It is indicative of the sensitivity loss caused by the needle probe and can therefore be used as a figure of merit for assessing its optical quality [39].

The signal-to-noise ratio (SNR) of an OCT system is defined as [52]

$$\text{SNR} = \frac{|S|^2}{\sigma_{noise}^2} = \frac{|S|^2}{\sigma_{shot}^2 + \sigma_{excess}^2 + \sigma_{receiver}^2}, \tag{25.11}$$

where $|S|^2$ is the absolute squared peak signal amplitude from a single reflector and σ_{noise}^2 is the total noise variance which consists of three main contributions: shot noise, excess noise, and receiver noise. In the case of a spectrometer-based SD-OCT system, the receiver noise encompasses the dark noise and readout noise of the array detector. Under the assumption that $P_{SC} << P_{SI}$, the SNR expression for a spectrometer-based SD-OCT system can be written as [52]

$$\text{SNR} = \frac{\left(\frac{\eta}{h\nu_0}\right)^2 \tau P_R P_{SC}}{\left(\frac{\eta}{h\nu_0}\right)(P_R + P_{SI}) + \frac{(1+\Pi^2)}{2\Delta\nu_{eff}}\left(\frac{\eta}{h\nu_0}\right)^2 \left(P_R^2 + P_{SI}^2 + 2P_R P_{SI}\right) + \frac{N}{\tau}\sigma_{receiver}^2}, \tag{25.12}$$

where η is the total spectrometer efficiency (comprising the grating efficiency, optical losses, and the array detector response), τ is the exposure time, h is Planck's constant, ν_0 is the mean optical center frequency of the broadband light, $\Delta\nu_{eff}$ is the effective spectral linewidth of the broadband light source [50], Π is the degree of polarization, and N is the number of spectrometer pixels. The excess noise term in (25.12) has been expanded to include beat noise [4] by adding a cross-beat term $2P_R P_{SI}$ which is often neglected in noise analyses of OCT systems.

If the incoherent back reflections from the probe are sufficiently suppressed, it is possible to operate the SD-OCT system in the shot-noise-limited regime by adjusting the reference-arm power level such that the shot noise (the first term in the denominator of (25.12)) dominates. In this case, (25.12) simplifies to

$$\text{SNR}_{SNL} = \left(\frac{\eta}{h\nu_0}\right)\tau P_{SC} = \frac{\eta\tau P_0}{h\nu_0}\gamma_S R_{SC}, \tag{25.13}$$

and the sensitivity Σ, defined as the inverse of the minimum measurable sample reflectivity (SNR equal to one), becomes

$$\Sigma_{SNL} = \frac{1}{R_{SC,min}} = \frac{\eta\tau P_0 \gamma_S}{h\nu_0}. \tag{25.14}$$

This result shows that the sensitivity of the OCT system is directly proportional to the round-trip attenuation of the probe for a unity reflector, γ_P, because $\gamma_S = \alpha(1-\alpha)\gamma_P$. Equation 25.14 has also been shown to be valid for swept-source OCT systems [54], where η is equal to the photodetector efficiency, P_0 is the average power of the wavelength-swept laser, and τ is the sweep duration.

While state-of-the-art SD-OCT systems with carefully built free-space scanning sample arms routinely attain sensitivities which are very close to the theoretical shot-noise limit (SNL), it is more difficult to achieve this in needle-based SD-OCT systems due to the reasons listed at the beginning of this section. While some of these reasons are intuitively clear, the negative effects of incoherent sample-arm back reflections require a more detailed analysis. In order to investigate these effects, we can obtain from (25.12) the full expression for the sensitivity of an SD-OCT system with all noise sources taken into account:

$$\Sigma = \frac{\left(\frac{\eta}{h\nu_0}\right)^2 P_0^2 \tau \, \gamma_S \gamma_R R_R}{\left(\frac{\eta}{h\nu_0}\right)(R_R + R_{SI})\gamma_R P_0 + \frac{(1+\Pi^2)}{2\Delta\nu_{eff}}\left(\frac{\eta}{h\nu_0}\right)^2 \left(R_R^2 + R_{SI}^2 + 2R_R R_{SI}\right)\gamma_R^2 P_0^2 + \frac{N}{\tau}\sigma_{receiver}^2}.$$

$$(25.15)$$

In Fig. 25.13, the sensitivity calculated from (25.15) is plotted versus reference-arm power for a typical spectrometer-based SD-OCT system of the type shown in Fig. 25.12. In the plot, the four curves show the total sensitivity (solid line) as well as the sensitivity if it was limited only by shot noise (dashed), excess noise (dotted), or receiver noise (dot-dash) alone. The calculation assumes a fully polarized 840-nm SLD light source with a FWHM spectral bandwidth of 50 nm and 20-mW output power. It further assumes the coupling ratio α of the interferometer is 50 %, and a spectrometer with an efficiency of $\eta = 15\%$ incorporating a CCD array detector with 2,048 pixels, a receiver noise $\sigma_{receiver}$ of 90 electrons, and a full well depth of 180,000 electrons. The exposure time τ is 50 μs. The round-trip attenuation γ_P of the probe is 50 %, yielding $\gamma_S = 0.125$.

Figure 25.13a shows the ideal case of no incoherent sample-arm back reflections ($R_{SI} = 0$). The system can attain a near shot-noise limited sensitivity of 108 dB (the theoretical SNL is 109 dB) for an optimum reference-arm reflectivity around −30 dB. For higher reference-arm reflectivities, excess noise begins to dominate the SNR, but the system will not enter this regime in this configuration due to the onset of detector saturation in the CCD sensor array. Figure 25.13b shows the sensitivity of the same system when we introduce an incoherent sample-arm back reflection of $R_{SI} = -30$ dB. Two significant effects become evident. Firstly, the additional incoherent back-reflected power causes the detector to saturate at much lower levels of reference reflectivity (around −36 dB). Secondly, the shot noise of the incoherent back-reflected power begins to dominate the SNR for the entire useful range of reference reflectivities. Both effects reduce the maximum sensitivity that the system can reach in this configuration to

Fig. 25.13 Calculated sensitivity of a spectrometer-based SD-OCT system as a function of reference-arm reflectivity illustrating the negative effects of incoherent sample-arm back reflections. (**a**) Idealized system with no incoherent sample-arm back reflections. (**b**) Nonideal system with an incoherent sample-arm reflectivity R_{SI} of −30 dB. See text for discussion
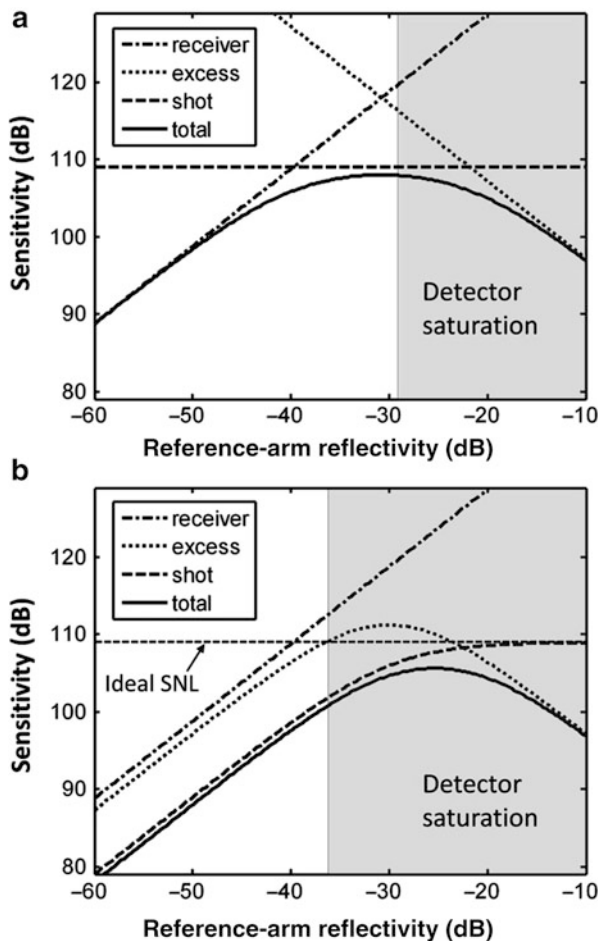
Table 25.2 Fresnel back reflections at planar interfaces between commonly encountered optical materials

		Fresnel back reflection (dB)			
n @ 800 nm		Fused silica	BK7	Water	UV adhesive
Fused silica	1.45				
BK7	1.51	−33.9			
Water	1.33	−27.3	−24.0		
UV adhesive	1.56	−28.7	−35.8	−22.0	
Air	1.00	−14.7	−13.8	−17.0	−13.2

about 101 dB. As can be seen in Table 25.2, it is not uncommon to obtain back reflections on the order of −30 dB or more at interfaces in optical assemblies unless special precautions, such as angled interfaces or antireflection coatings, are taken. Back reflections from fiber-to-fiber connections are specified to be on the

order of −60 dB or below for the angled FC/APC connector standard which is commonly used in OCT, and they are therefore unlikely to cause problems unless the connectors are damaged or worn.

25.4 Review of Previous Applications

The first demonstration of an OCT needle probe, reported in 2000 [43], showed an image of muscle tissue taken from the leg of a live hamster. The 90° segment of a radial B-scan image was taken with a rotating, side-directed 27-G needle and showed muscle fascicles (bundles of muscle fibers) and evidence of signal fading induced by birefringence. This work was closely followed by the use of even smaller probes inserted (bare without the use a hypodermic needle) into rat brain to monitor brain motion in single A-scans [44].

Subsequently, a parallel field to OCT needle probes emerged [55], in which GRIN rod lenses have been used to construct bare glass, high-NA imaging probes for high-resolution, one-photon, and two-photon fluorescence microscopy in live rat and mouse brains. Such lenses, with diameters in the range 350–1,000 μm and a few tens of millimeters in length, are not sufficiently robust to be used for application in humans without protective coatings. However, such a 350-μm lens was incorporated into a 20-G needle and used to image live human muscle tissue in situ [56]. Recently, a novel design was realized by our group and demonstrated to be capable of revealing sarcomeres at 15 mm depth in bovine muscle tissue [37]. Such fluorescence-based approaches record en face images at depth in tissue by scanning the proximal end face of the GRIN rod lens, and 3D imaging is possible through axial motion of the lens ("probe scanning"). Much higher resolution is achieved than in OCT but at much shallower depth, with smaller field of view and the requirement for a fluorescent exogenous agent to be present.

The first OCT needle probe capable of Doppler measurements was demonstrated in 2005, employing a 19-G (1.06 mm outer diameter) "echogenic" needle, as employed in interventional radiology to provide visibility under ultrasound, X-ray, or CT guidance [41]. Linear B-scan images showing superimposed Doppler signals were shown for several locations and features in a live rat, including an artery–vein pair, likely the femoral profunda, gluteal muscle, and abdomen. In 2006, an improved 22-G version was used to demonstrate the feasibility of monitoring microvascular changes deep within a tumor mass in response to photodynamic therapy in a rat xenograft model of Dunning prostate cancer [42]. This work, incorporating high-frequency ultrasound guidance, was then extended into more extensive studies [57]. Linear B-scans in these works showed the reductions in flow monitored over time that resulted from the therapy. A strong relationship was established between the percent tumor necrosis at 24 h post treatment and the vascular shutdown rate. This correlation between a biological end point and a direct and localized measurement of microvascular changes led the authors to suggest a potential clinical role for real-time microvascular monitoring for optimizing treatment efficacy in individual patients, which is a very interesting prospect.

In 2007, the use of OCT needle probes to monitor refractive index was proposed via two methods: A-scan measurements that record optical path length for known physical path length [58] or the strength of a signal recorded from a glass–tissue interface [59]. Only single-point measurements recorded in solutions were reported, although there have been separately reported measurements, without the use of needle probes, of OCT-measured refractive index correlated to tissue status in breast cancer [60].

The first proposal to use OCT needle probes in the eye was published in 2008 [32]. A novel forward-looking design combining two rotating GRIN rod lenses, first described in 2006 by the same group [31], was improved and incorporated into a 21-G needle (0.82 mm outer diameter). The motivation was in aiding vitrectomy, which is the surgical removal of the vitreous humor. Vitrectomy is a required precursor to other surgeries for the treatment of severe eye diseases such as retinal detachment. Its success depends on the complete local removal of the vitreous humor, which is difficult to visualize through a light pipe inserted through an incision in the patient's eye. OCT could aid in this procedure by providing better images through its close proximity to the retinal surface and sensitivity to scattering. Radial B-scan segment images (approx. 30°) of the retina of an enucleated porcine eye, with cornea, lens, and vitreous removed, were reported.

The first application of an OCT needle probe for human applications was demonstrated in 2005 on excised breast cancer specimens [61]. The objective was to develop a guide for fine-needle aspiration biopsy in which small quantities of human breast tissue are extracted. The premise is that better guidance will lead to fewer sampling errors and, thus, greater use of fine-needle aspiration biopsy, which is less invasive and costs less than other biopsy procedures. The 23-G probe comprised a bare single-mode fiber, and forward-looking A-scans were recorded from adipose, fibroglandular, invasive ductal carcinoma tissues. Subsequently, in 2009, the same group used an improved system on 89 excised tissue samples and designed a classifier which achieved 80% sensitivity and 84% specificity in correctly identifying adipose, normal, and tumor tissue types [62].

In 2010, the group led by Li, who pioneered OCT needle probes [43], published new results [47] showing radial and linear B-scans from needles inserted into various excised animal tissues, including porcine spleen and pancreas, and murine esophagus. Example B-scan images are shown in Fig. 25.14, reproduced from Ref. [47].

The first paper to show full three-dimensional OCT imaging in a needle probe was recently published by our group [40] in lung tissue, and this has been closely followed by several other works in lung tissues and breast cancer [39, 63] to be described in the case studies in the next section.

Two key challenges have restricted the application of OCT needle probes to date – the difficulty of maintaining high-sensitivity and high-resolution OCT imaging while miniaturizing the probe, and the difficulty inherent in many applications of not having available full three-dimensional information. This latter challenge is faced by OCT imaging in general and has seen the wide emergence of three-dimensional imaging systems. Such systems are generally necessary in order to create closely corresponding OCT images and histopathology, which is
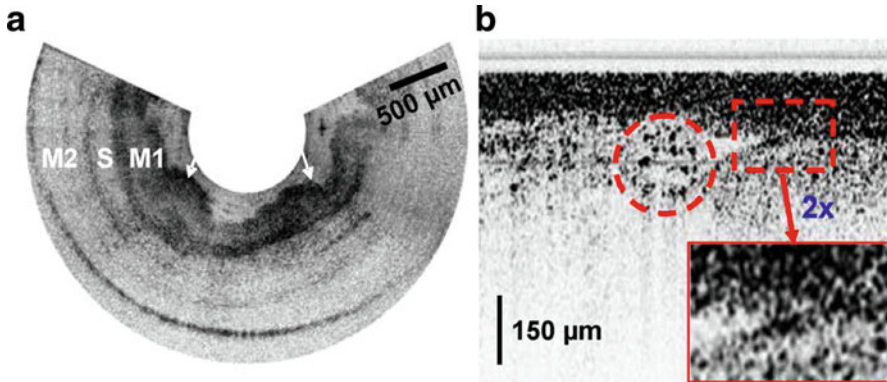
Fig. 25.14 (**a**) Ex vivo OCT radial B-scan segment of fresh mouse esophageal tissue. *M1* mucosa, *S* submucosa, *M2* muscularis. *Arrows* indicate epithelium. (**b**) Ex vivo OCT linear B-scan of fresh pig pancreatic tail. The structure indicated by the *circle* may be related to islets of Langerhans (Reproduced from [47])

a prerequisite for effective engagement with the pathologists who are essential in interpreting OCT images [64]. As a result, most studies reported to date remain proof of principle, predominantly imaging in animal models. An important aspect of needle probes is guidance to the correct site for imaging, and there has yet to be widespread uptake of needle-probe guidance with other imaging modalities, although use of ultrasound has been reported [65]. The most substantial studies reported to date have been in the assessment of photodynamic therapy in the rat model, employing Doppler OCT – a major technical achievement in itself, and the A-scan studies on human breast cancer samples. This latter study highlights the general difficulty in extracting sufficient information from A-scans to make definitive assessments. The range and promise of these early needle-based studies augurs well for OCT needle probes to make significant clinical impact in the future. Further evidence for this is contained in the next section.

25.5   Case Study: Breast Cancer Tumor Margins

In this section, we explore the potential use of OCT needle probes through a specific clinical case study.

Invasive breast cancer is the second leading cause of cancer-related female deaths in the USA, with annually over 180,000 new cases identified and over 40,000 deaths [66]. Surgical excision of the malignant tissue forms the central component of treatment. When excising the tumor, standard surgical practice is to remove an adjacent margin of benign breast tissue to minimize residual malignancy and so minimize local recurrence. However, accurate identification of the extent of malignant tissue is difficult during surgery, and up to 34% of patients undergoing breast-conserving surgery will have involved margins (i.e., containing malignant

tissue) or inadequate clearance ($<$5 mm) [67], resulting in an increased risk of local recurrence and often requiring further surgery.

Histological assessment is the gold-standard method to evaluate margin status, but can only be performed ex vivo, after processing and staining of the tissue. Specimen X-ray or ultrasound may also be performed on the excised fresh specimen, but microscopic areas of disease close to margins may easily be missed. OCT needle probes have the potential to provide surgical guidance when delineating the tumor margin prior to excision.

OCT acquired through the surface of fresh, excised human breast cancer samples has been shown to provide real-time microscopic images to a depth of 2 mm [68–70], and computational techniques have been proposed to differentiate tissue types [60, 62]. However, intraoperative surgical guidance requires assessment of the tissue prior to excision, where such tissue is significantly beyond the 2–3-mm image penetration depth of OCT.

In this section, we demonstrate the use of an OCT needle probe to acquire images significantly deeper in the tissue, showing the interface between tumor and the adjacent healthy tissue. The sample under investigation was obtained from a 70-year-old female with a 21-mm, grade 3 invasive ductal carcinoma, undergoing a left mastectomy.

The side-facing needle probe used in these experiments was of the type shown in Fig. 25.8b, encased in a 23-G needle (outer diameter 640 μm) with a length of 30 mm. The focusing optics yielded a spot with a $1/e^2$ diameter of $\sim$20 μm at a distance of 300 μm from the side window of the needle. The fabrication of the mirror and output window is described in the earlier section on fabrication and testing.

The probe was mounted on a stepper motor and counterrotated at 2 Hz to acquire 2D radial B-scans. Only clockwise rotations were used to form the reconstructed 3D OCT data set to minimize artifacts from tissue drag. A linear translation stage was used to insert and retract the needle at 7 μm per rotation, giving a velocity of 14 μm/s, and enabling acquisition of a 3D data volume.

The needle probe was interfaced with a spectrometer-based SD-OCT system. The source was a superluminescent diode (Superlum, Ireland) with output power of 19 mW, a central wavelength of 836 nm, and a source bandwidth of 50 nm giving an axial resolution of 7.6 μm in air. Data was sampled at 900 pixels per A-scan and 800 A-scans per radial B-scan. The OCT system was operated in a common-path or Fizeau configuration. Such a configuration provides inherent dispersion matching of the sample and reference paths of the interferometer if sample dispersion can be neglected.

The fresh specimen was imaged within 15 min of excision. The OCT needle probe was inserted and positioned at the edge of the tumor. The probe was withdrawn to acquire a sequence of radial images. Using the angle of acquisition of each A-scan, the radial images were reformatted into rectangular Cartesian coordinates, using linear interpolation to compute values for pixels not positioned directly along an A-scan. The images were then stacked to form a cylindrical 3D OCT data volume (length 2.36 mm, diameter 1.60 mm, assuming a group refractive index for tissue of $n = 1.4$), with spacing between slices specified by the step size of

Fig. 25.15 (**a**) H&E section of a tumor margin. (**b**) Longitudinal reconstructed OCT image of the tumor margin, with the horizontal axis aligned with the direction of needle retraction during scanning (Images taken from [63])
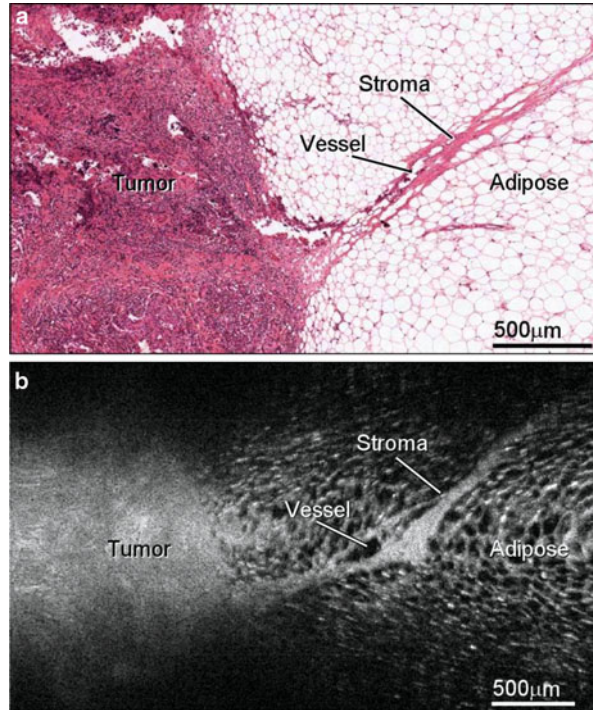
the needle's translation stage (7 μm per rotation). The data was displayed using in-house visualization software developed in C++, which allowed for the extraction of an arbitrary oblique imaging plane from the OCT volume.

To validate the OCT image, the specimen was then fixed in formalin, processed in accordance with standard laboratory procedures, and hematoxylin and eosin (H&E)-stained sections prepared. The H&E sections were digitally micrographed using a ScanScope XT system (Aperio Technologies, Vista, CA, USA) and manually coregistered against the optimal oblique slice extracted from the 3D OCT data volume.

Figure 25.15 shows H&E histology and the matching coregistered OCT image of the tumor margin, displaying a clear distinction between an area of dense tumor and the honeycomb structure evident in the surrounding adipose tissue. This image was acquired approximately 20 mm below the surface of the tissue. Note that an image plane parallel and adjacent to the needle probe was selected; thus, the needle shaft is not visible in this OCT image. This longitudinal image was constructed by orienting the image plane so that the horizontal axis of the image was aligned along the direction of the needle retraction. Each vertical column of the image intersects a different radial B-scan. The image bounds are defined such that a horizontal section through the center of the image is closest to the probe. The reduced signal at the top and bottom of the image corresponds to tissue that is more distant from the probe.

Malignant tissue appears as a homogeneous region of high backscatter (light gray) in the OCT, corresponding to an area of invasive carcinoma. A band of normal fibrous stroma extends from the area of malignancy, containing a vascular space labeled in both images (Vessel). The H&E section was cut along the direction of OCT needle retraction (corresponding to the horizontal axis in the OCT image), highlighting that the length of the field of view of the OCT image is only limited by the extent of needle retraction.

Note that the limited field of view of the OCT scan will only image a portion of the tumor boundary. Comprehensive assessment of a tumor margin would involve multiple acquisitions around the proposed area of excision. However, such an assessment could potentially be performed intraoperatively, immediately prior to excision, and could be of value in maximizing tissue preservation and reducing rates of inadequate excision.

25.6   Case Study: Lung Imaging

In this case study, we outline the potential of OCT needle probes for lung imaging.

The lungs comprise a network of branching airways, originating from the major bronchi, extending to the bronchioles, and terminating with the alveolar sacs. Structural and mechanical properties of the alveoli regulate function: the walls of the alveoli are interlaced with an anastomosing network of capillaries which facilitates gas exchange, and elastin fibers within the alveoli walls allow the alveoli to expand as they fill with gas during inhalation and contract during exhalation. There are numerous fatal pathologies that alter the structure of the alveoli and impair function [71]. Emphysema, predominantly caused by long-term exposure to cigarette smoke, is characterized by permanent enlargement of the airspaces distal to the terminal bronchioles and destruction of the alveoli walls. Pulmonary fibrosis results in a thickening of the alveoli walls with fibrotic tissue (scar tissue). This may be secondary to other processes (e.g., asbestosis or rheumatoid arthritis) or appear without any known cause (idiopathic pulmonary fibrosis). Emphysema and pulmonary fibrosis together account for over three quarters of all lung transplants [72].

Ex vivo studies have shown the potential of optical coherence tomography (OCT) to image individual alveoli [73, 74]. In vivo imaging of alveoli in mice [75] and rabbit models [76] has been demonstrated through use of a thoracic window, in which muscle and skin are resected from between the ribs to allow OCT imaging, and has been validated against confocal microscopy [77]. The opening can be resealed with a transparent membrane through which imaging is possible. While suitable for nonrecovery animal studies, the use of a thoracic window is undesirably invasive for human subjects.

In this section, we demonstrate the use of an OCT needle probe to acquire images within the lungs, without the need for a thoracic imaging window.

The side-facing OCT needle follows the design described in the previous case study, with the distal focusing optics consisting of no-core and GRIN fiber affixed
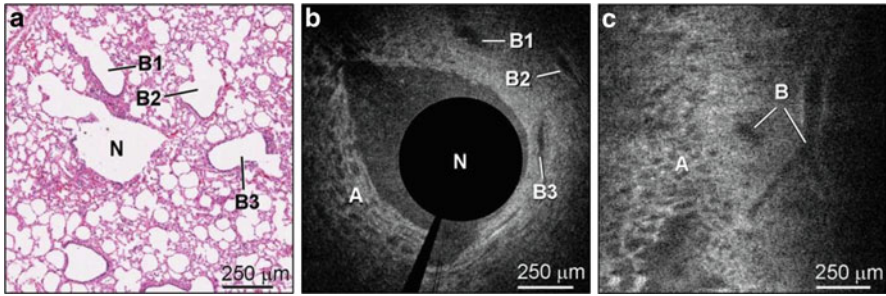
Fig. 25.16 (**a**) H&E. (**b**) Radial OCT B-scan. (**c**) Orthogonal OCT plane. *N* needle hole, *B* bronchiole, *A* alveoli (Image taken from [40])

to a length of single-mode fiber; a copper mirror to redirect the light beam and the entire assembly encased within a 23-G needle. The probe was interfaced to the spectrometer-based SD-OCT system described previously.

The sample under investigation was a fresh, intact sheep lung. The lung was filled with normal saline until visually inflated. The OCT needle probe was inserted into several different lobes and images acquired as the needle was rotated and retracted over a distance of 2.4 mm. To validate the OCT images, tissue around each needle insertion was subsequently excised along each needle trajectory. The excised tissue was fixed, embedded in paraffin, and sectioned at 250 μm intervals, and H&E sections were prepared. Multiplanar formatting was applied to the 3D OCT volumetric data sets to extract the 2D image plane with an optimal visual match to the histological sections, and multiple features were correlated and followed through adjacent OCT B-scans and multiple histological slices.

Figure 25.16 shows H&E histology and the matching OCT radial scan. The needle hole (labeled N) is located at the center of the images, surrounded by alveoli (labeled A in the OCT image). Each alveolar space presents as a small region of low backscatter (dark gray), delineated by the more highly backscattering alveoli walls (light gray). In the H&E image, the needle tract appears as a localized defect rimmed by trauma-induced tissue artifact. Three bronchioles (labeled B1, B2, B3) can be seen adjacent to the needle hole, showing the strong geometrical correspondence between both the H&E and OCT images. Figure 25.16c shows an image taken in a plane orthogonal to the radial B-scans, parallel to the direction of needle retraction. The geometry of this image is comparable to Fig. 25.15. It shows a longitudinal view of a bronchiole, appearing as a tubular area of low backscatter (dark), bifurcating into the next generation of airways.

Figure 25.17 shows H&E and OCT images of an adjacent lobe, displaying the presence of both bronchioles and a blood vessel. Some linear reconstruction artifacts appear in this OCT image due to camera settings. Adjacent radial B-scans allowed the geometry of the bronchioles and vessels to be tracked while within the field of view of the 3D OCT scan, and bifurcation of the bronchiole can be seen in the orthogonal view shown in Fig. 25.17c.
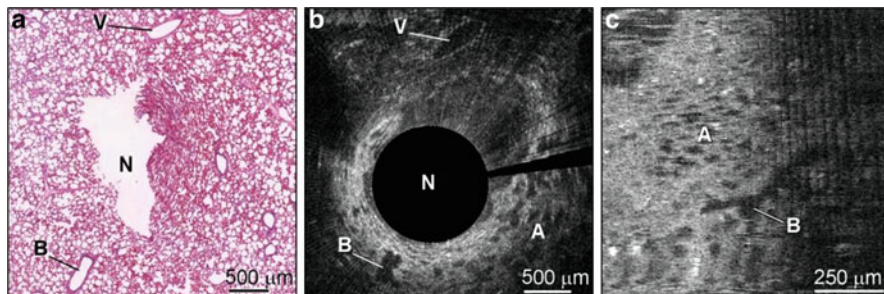
Fig. 25.17 (**a**) H&E. (**b**) Radial OCT B-scan. (**c**) Orthogonal OCT plane. *N* needle hole, *B* bronchiole, *A* alveoli, *V* blood vessel (Image taken from [40])
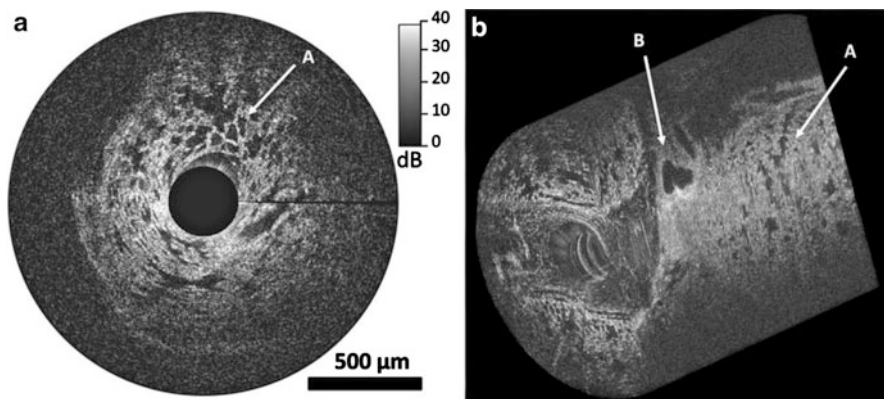
Fig. 25.18 OCT images of a lamb lung obtained with a 30-G needle probe. (**a**) Radial B-scan. (**b**) Cutaway view of a rendered volume consisting of 400 B-scans. *A* alveoli, *B* bronchiole (Images taken from [39])

Note that OCT images of air-filled lungs suffer poor image penetration. This is due to the large difference in the refractive indices of tissue and air, resulting in strong reflections at each air–tissue interface and rapid attenuation of the OCT signal. The images displayed here used saline to reduce refractive-index mismatch, resulting in improved image penetration depth. Localized immersion with saline, referred to as bronchoalveolar lavage [78], can be performed in vivo and is used clinically as a diagnostic test for interstitial lung disease. A bronchoscope is endoscopically positioned in the airway and used to both flush the airway and aspirate the saline for subsequent histological analysis. More extensive flushing of the whole lung is used as treatment for pulmonary alveolar proteinosis [79]. Note that by varying the pressure of the saline and performing longitudinal imaging of a lung region, it may be feasible to assess the viscoelastic properties of the lung tissue, in a manner similar to that described by Williamson et al. [80]. The use of a saline lavage also serves to reduce the effects of surface tension on the measured

volume–pressure curve [81], so that measurements reflect the intrinsic elastic properties of parenchymal tissue.

The H&E histology images of Figs. 25.16 and 25.17 show that the OCT needle probe causes some local trauma to pulmonary structures. While the OCT needle probe is significantly smaller than the needles used for lung biopsies, further reductions in the size of the probe are feasible. Lorenser et al. [39] demonstrated the use of a 30-G side-facing OCT needle probe (OD 310 μm) for lung imaging, as shown in Fig. 25.18, resulting in significantly less tissue deformation than was observed with a 23-G OCT needle probe. The use of these smaller needles also reduces the risk of complications such as pneumothorax.

25.7 Conclusion

In this chapter, we have presented a comprehensive overview of OCT needle probes. The principles behind the probe optical design and scanning systems have been described, emphasizing the prevalence of multiple-element fused in-line probe designs generally realized in custom laboratory facilities in gauge sizes ranging from 31 to 19 G. The full characterization of such probes has been rarely presented, but the framework for characterization presented in this chapter provides a good model for future reports, including a framework for assessing sensitivity. Issues such as the merits of common-path probes and how to create them, the elimination of unwanted reflections, the optical quality of windows and mirrors, and the depth of focus and resolution of probes all remain to be further explored and optimized. Scanning systems for OCT needle probes are in their infancy. The first 3D scans are only just being reported, and it is apparent that there remains much scope for innovation leading to shorter scan times. The application of OCT needle probes is likewise yet to be exploited clinically. Early examples cover a wide range of tissues. The most comprehensive use of needle probes has been in the study of blood flow using Doppler OCT in a rat prostate model. The first human applications have been in breast cancer for guiding biopsy and for intraoperative tumor margin identification. Otherwise, most other reports focus on technology and report images by way of example. The most recent reports on 3D imaging and the high image quality achieved suggest the technology is maturing and that the time is right for a more extensive investigation of the candidate clinical applications of OCT needle probes.

References

1. J.G. Fujimoto, M.E. Brezinski, G.J. Tearney, S.A. Boppart, B. Bouma, M.R. Hee, J.F. Southern, E.A. Swanson, Optical biopsy and imaging using optical coherence tomography. Nat. Med. **1**(9), 970–972 (1995)
2. J.G. Fujimoto, Optical coherence tomography for ultrahigh resolution in vivo imaging. Nat. Biotechnol. **21**(11), 1361–1367 (2003)

3. W. Drexler, J.G. Fujimoto, SpringerLink (Online service), eBrary Inc., *Optical Coherence Tomography: Technology and Applications*. Biological and Medical Physics, Biomedical Engineering, 1st edn. (Springer, Berlin/New York, 2008)

4. D.D. Sampson, T.R. Hillman, Optical coherence tomography, in *Lasers and Current Optical Techniques in Biology*, ed. by G. Palumbo, R. Pratesi. Comprehensive Series in Photochemical and Photobiological Sciences, vol. 4 (The Royal Society of Chemistry, Cambridge, UK, 2004), pp. 481–571

5. V.V. Tuchin, *Tissue Optics: Light Scattering Methods and Instruments for Medical Diagnosis*, 2nd edn. (SPIE/International Society for Optical Engineering, Bellingham, WA, 2007)

6. D. Huang, E.A. Swanson, C.P. Lin, J.S. Schuman, W.G. Stinsin, W. Chang, M.R. Hee, T. Flotte, K. Gregory, C.A. Puliafito, J.G. Fujimoto, Optical coherence tomography. Science **254**, 1178–1181 (1991)

7. Z. Hu, A.M. Rollins, Optical design for OCT, in *Optical Coherence Tomography: Technology and Applications*, ed. by W. Drexler, J.G. Fujimoto. Biological and Medical Physics, Biomedical Engineering, 1st edn. (Springer, Berlin/New York, 2008), pp. 379–404

8. A.V. Zvyagin, E.D.J. Smith, D.D. Sampson, Delay and dispersion characteristics of a frequency-domain optical delay line for scanning interferometry. J. Opt. Soc. Am. A **20**(2), 333–341 (2003)

9. A.F. Fercher, C.K. Hitzenberger, G. Kamp, S.Y. El-Zaiat, Measurement of intraocular distances by backscattering spectral interferometry. Opt. Commun. **117**, 43–48 (1995)

10. G. Häusler, M.W. Lindner, "Coherence radar" and "Spectral radar" – new tools for dermatological diagnosis. J. Biomed. Opt. **3**(1), 21–31 (1998)

11. M. Wojtkowski, R. Leitgeb, A. Kowalczyk, T. Bajraszewski, A.F. Fercher, In vivo human retinal imaging by Fourier domain optical coherence tomography. J. Biomed. Opt. **7**(3), 457–463 (2002)

12. S.R. Chinn, E.A. Swanson, J.G. Fujimoto, Optical coherence tomography using a frequency-tunable optical source. Opt. Lett. **22**(5), 340–342 (1997)

13. A.R. Tumlinson, J.K. Barton, B. Považay, H. Sattman, A. Unterhuber, R.A. Leitgeb, W. Drexler, Endoscope-tip interferometer for ultrahigh resolution frequency domain optical coherence tomography in mouse colon. Opt. Express **14**(5), 1878–1887 (2006)

14. U. Sharma, N.M. Fried, J.U. Kang, All-fiber common-path optical coherence tomography: Sensitivity optimization and system analysis. IEEE J. Sel. Top. Quantum Electron. **11**(4), 799–805 (2005)

15. R.A. McLaughlin, D.D. Sampson, Clinical applications of fiber-optic probes in optical coherence tomography. Opt. Fiber Technol. **16**(6), 467–475 (2010)

16. J. Qu, C. MacAulay, S. Lam, B. Palcic, Optical properties of normal and carcinomatous bronchial tissue. Appl. Opt. **33**(31), 7397–7405 (1994)

17. T.R. Hillman, D.D. Sampson, The effect of water dispersion and absorption on axial resolution in ultrahigh-resolution optical coherence tomography. Opt. Express **13**(6), 1860–1874 (2005)

18. W. Drexler, Y. Chen, A. Aguirre, B. Považay, A. Unterhuber, J.G. Fujimoto, Ultrahigh resolution optical coherence tomography, in *Optical Coherence Tomography: Technology and Applications*, ed. by W. Drexler, J.G. Fujimoto. Biological and Medical Physics, Biomedical Engineering, 1st edn. (Springer, Berlin/New York, 2008), pp. 239–279

19. M. Gu, C.J.R. Sheppard, X. Gan, Image formation in a fiber-optical confocal scanning microscope. J. Opt. Soc. Am. A **8**(11), 1755–1761 (1991)

20. W. Drexler, U. Morgner, F.X. Kärtner, C. Pitris, S.A. Boppart, X.D. Li, E.P. Ippen, J.G. Fujimoto, In vivo ultrahigh-resolution optical coherence tomography. Opt. Lett. **24**(17), 1221–1223 (1999)

21. R.A. Leitgeb, W. Drexler, A. Unterhuber, B. Hermann, T. Bajraszewski, T. Le, A. Stingl, A.F. Fercher, Ultrahigh resolution Fourier domain optical coherence tomography. Opt. Express **12**(10), 2156–2165 (2004)

22. A.M. Kowalevicz, T. Ko, I. Hartl, J.G. Fujimoto, M. Pollnau, R.P. Salathé, Ultrahigh resolution optical coherence tomography using a superluminescent light source. Opt. Express **10**(7), 349–353 (2002)
23. B. Hermann, E.J. Fernández, A. Unterhuber, H. Sattmann, A.F. Fercher, W. Drexler, P.M. Prieto, P. Artal, Adaptive-optics ultrahigh-resolution optical coherence tomography. Opt. Lett. **29**(18), 2142–2144 (2004)
24. H. Lim, Y. Jiang, Y. Wang, Y.-C. Huang, Z. Chen, F.W. Wise, Ultrahigh-resolution optical coherence tomography with a fiber laser source at 1 microm. Opt. Lett. **30**(10), 1171–1173 (2005)
25. M. Wojtkowski, V.J. Srinivasan, T.H. Ko, J.G. Fujimoto, A. Kowalczyk, J.S. Duker, Ultrahigh-resolution, high-speed, Fourier domain optical coherence tomography and methods for dispersion compensation. Opt. Express **12**(11), 2404–2422 (2004)
26. E.J. Seibel, Q.Y.J. Smithwick, Unique features of optical scanning, single fiber endoscopy. Lasers Surg. Med. **30**(3), 177–183 (2002)
27. X. Liu, M.J. Cobb, Y. Chen, M.B. Kimmey, X. Li, Rapid-scanning forward-imaging miniature endoscope for real-time optical coherence tomography. Opt. Lett. **29**(15), 1763–1765 (2004)
28. N.R. Munce, A. Mariampillai, B.A. Standish, M. Pop, K.J. Anderson, G.Y. Liu, T. Luk, B.K. Courtney, G.A. Wright, I.A. Vitkin, Electrostatic forward-viewing scanning probe for Doppler optical coherence tomography using a dissipative polymer catheter. Opt. Lett. **33**(7), 657–659 (2008)
29. Y. Pan, H. Xie, G.K. Fedder, Endoscopic optical coherence tomography based on a microelectromechanical mirror. Opt. Lett. **26**(24), 1966–1968 (2001)
30. T. Xie, H. Xie, G.K. Fedder, Y. Pan, Endoscopic optical coherence tomography with new MEMS mirror. Electron. Lett. **39**(21), 1535–1536 (2003)
31. J. Wu, M. Conry, C. Gu, F. Wang, Z. Yaqoob, C. Yang, Paired-angle-rotation scanning optical coherence tomography forward-imaging probe. Opt. Lett. **31**(9), 1265–1267 (2006)
32. S. Han, M.V. Sarunic, J. Wu, M. Humayun, C. Yang, Handheld forward-imaging needle endoscope for ophthalmic optical coherence tomography inspection. J. Biomed. Opt. **13**, 020505 (2008)
33. J. Sun, S. Guo, L. Wu, L. Liu, S.W. Choe, B.S. Sorg, H. Xie, 3D in vivo optical coherence tomography based on a low-voltage, large-scan-range 2D MEMS mirror. Opt. Express **18**(12), 12065–12075 (2010)
34. L. Liu, L. Wu, J. Sun, E. Lin, H. Xie, Miniature endoscopic optical coherence tomography probe employing a two-axis microelectromechanical scanning mirror with through-silicon vias. J. Biomed. Opt. **16**(2), 6006 (2011)
35. J. Sun, H. Xie, MEMS-based endoscopic optical coherence tomography. Int. J. Opt. (2011). doi:10.1155/2011/825629
36. J.C. Jung, M.J. Schnitzer, Multiphoton endoscopy. Opt. Lett. **28**(11), 902–904 (2003)
37. R.S. Pillai, D. Lorenser, D.D. Sampson, Deep-tissue access with confocal fluorescence microendoscopy through hypodermic needles. Opt. Express **19**(8), 7213–7221 (2011)
38. C.P. Liang, J. Wierwille, T. Moreira, G. Schwartzbauer, M.S. Jafri, C.M. Tang, Y. Chen, A forward-imaging needle-type OCT probe for image guided stereotactic procedures. Opt. Express **19**(27), 26283–26294 (2011)
39. D. Lorenser, X. Yang, R.W. Kirk, B.C. Quirk, R.A. McLaughlin, D.D. Sampson, Ultrathin side-viewing needle probe for optical coherence tomography. Opt. Lett. **36**(19), 3894–3896 (2011)
40. B.C. Quirk, R.A. McLaughlin, A. Curatolo, R.W. Kirk, P.B. Noble, D.D. Sampson, In situ imaging of lung alveoli with an optical coherence tomography needle probe. J. Biomed. Opt. **16**(3), 036009 (2011)
41. V.X.D. Yang, Y.X. Mao, N. Munce, B. Standish, W. Kucharczyk, N.E. Marcon, B.C. Wilson, I.A. Vitkin, Interstitial Doppler optical coherence tomography. Opt. Lett. **30**(14), 1791–1793 (2005)

42. H. Li, B.A. Standish, A. Mariampillai, N.R. Munce, Y. Mao, S. Chiu, N.E. Marcon, B.C. Wilson, A. Vitkin, V.X.D. Yang, Feasibility of interstitial Doppler optical coherence tomography for in vivo detection of microvascular changes during photodynamic therapy. Lasers Surg. Med. **38**(8), 754–761 (2006)

43. X. Li, C. Chudoba, T. Ko, C. Pitris, J.G. Fujimoto, Imaging needle for optical coherence tomography. Opt. Lett. **25**(20), 1520–1522 (2000)

44. W.A. Reed, M.F. Yan, M.J. Schnitzer, Gradient-index fiber-optic microprobes for minimally invasive in vivo low-coherence interferometry. Opt. Lett. **27**(20), 1794–1796 (2002)

45. Y. Mao, S. Chang, S. Sherif, C. Flueraru, Graded-index fiber lens proposed for ultrasmall probes used in biomedical imaging. Appl. Opt. **46**(23), 5887–5894 (2007)

46. W. Emkey, C. Jack, Analysis and evaluation of graded-index fiber lenses. IEEE J. Lightwave. Technol. **5**(9), 1156–1164 (1987)

47. Y. Wu, J. Xi, L. Huo, J. Padvorac, E. Shin, S.A. Giday, A.A. Lennon, M.F. Canto, J.F. Hwang, X.F. Li, Robust high-resolution fine OCT needle for side-viewing interstitial tissue imaging. IEEE J. Sel. Top. Quantum Electron. **16**(4), 863–869 (2010)

48. A.E. Siegman, *Lasers* (University Science, Mill Valley, CA, 1986)

49. B.E.A. Saleh, M.C. Teich, *Fundamentals of Photonics*. Wiley Series in Pure and Applied Optics, 1st edn. (Wiley, New York, 1991)

50. A.M. Rollins, J.A. Izatt, Optimal interferometer designs for optical coherence tomography. Opt. Lett. **24**(21), 1484–1486 (1999)

51. R.C. Haskell, D. Liao, A.E. Pivonka, T.L. Bell, B.R. Haberle, B.M. Hoeling, D.C. Petersen, Role of beat noise in limiting the sensitivity of optical coherence tomography. J. Opt. Soc. Am. A **23**(11), 2747–2755 (2006)

52. R. Leitgeb, C. Hitzenberger, A. Fercher, Performance of fourier domain vs. time domain optical coherence tomography. Opt. Express **11**(8), 889–894 (2003)

53. U. Sharma, J.U. Kang, Common-path optical coherence tomography with side-viewing bare fiber probe for endoscopic optical coherence tomography. Rev. Sci. Instrum. **78**, 113102 (2007)

54. S. Yun, G. Tearney, J. de Boer, N. Iftimia, B. Bouma, High-speed optical frequency-domain imaging. Opt. Express **11**(22), 2953–2963 (2003)

55. A.T. Yeh, B. Kao, W.G. Jung, Z. Chen, J.S. Nelson, B.J. Tromberg, Imaging wound healing using optical coherence tomography and multiphoton microscopy in an in vitro skin-equivalent tissue model. J. Biomed. Opt. **9**(2), 248–253 (2004)

56. M.E. Llewellyn, R.P.J. Barretto, S.L. Delp, M.J. Schnitzer, Minimally invasive high-speed imaging of sarcomere contractile dynamics in mice and humans. Nature **454**(7205), 784–788 (2008)

57. B.A. Standish, X. Jin, J. Smolen, A. Mariampillai, N.R. Munce, B.C. Wilson, I.A. Vitkin, V.X.D. Yang, Interstitial Doppler optical coherence tomography monitors microvascular changes during photodynamic therapy in a Dunning prostate model under varying treatment conditions. J. Biomed. Opt. **12**(3), 034022 (2007). doi:10.1117/1.2744068

58. A.M. Zysk, S.G. Adie, J.J. Armstrong, M.S. Leigh, A. Paduch, D.D. Sampson, F.T. Nguyen, S.A. Boppart, Needle-based refractive index measurement using low-coherence interferometry. Opt. Lett. **32**(4), 385–387 (2007)

59. A.M. Zysk, D.L. Marks, D.Y. Liu, S.A. Boppart, Needle-based reflection refractometry of scattering samples using coherence-gated detection. Opt. Express **15**(8), 4787–4794 (2007)

60. A.M. Zysk, S.A. Boppart, Computational methods for analysis of human breast tumor tissue in optical coherence tomography images. J. Biomed. Opt. **11**(5), 054015 (2006)

61. N.V. Iftimia, B.E. Bouma, M.B. Pitman, B. Goldberg, J. Bressner, G.J. Tearney, A portable, low coherence interferometry based instrument for fine needle aspiration biopsy guidance. Rev. Sci. Instrum. **76**(6), 064301 (2005)

62. M. Mujat, R.D. Ferguson, D.X. Hammer, C. Gittins, N. Iftimia, Automated algorithm for breast tissue differentiation in optical coherence tomography. J. Biomed. Opt. **14**(3), 034040 (2009)

63. R.A. McLaughlin, B.C. Quirk, A. Curatolo, R.W. Kirk, L. Scolaro, D. Lorenser, P.D. Robbins, B.A. Wood, C.M. Saunders, D.D. Sampson, Imaging of breast cancer with optical coherence tomography needle probes: feasibility and initial results. IEEE J. Sel. Top. Quantum Electron. **18**(3), 1184–1191 (2012)

64. R.A. McLaughlin, L. Scolaro, P. Robbins, S. Hamza, C. Saunders, D.D. Sampson, Imaging of human lymph nodes using optical coherence tomography: Potential for staging cancer. Cancer Res. **70**(7), 2579–2584 (2010)

65. B.A. Standish, K.K.C. Lee, X. Jin, A. Mariampillai, N.R. Munce, M.F.G. Wood, B.C. Wilson, I.A. Vitkin, V.X.D. Yang, Interstitial Doppler optical coherence tomography as a local tumor necrosis predictor in photodynamic therapy of prostatic carcinoma: An in vivo study. Cancer Res. **68**(23), 9987–9995 (2008)

66. American Cancer Society, *Cancer Facts & Figures 2008* (American Cancer Society, Atlanta, 2008)

67. M.F. Dillon, A.D.K. Hill, C.M. Quinn, E.W. McDermott, N. O'Higgins, A pathologic assessment of adequate margin status in breast-conserving therapy. Ann. Surg. Oncol. **13**(3), 333–339 (2006)

68. P.-L. Hsiung, D.R. Phatak, Y. Chen, A.D. Aguirre, J.G. Fujimoto, J.L. Connolly, Benign and malignant lesions in the human breast depicted with ultrahigh resolution and three-dimensional optical coherence tomography. Radiology **244**(3), 865–874 (2007)

69. F.T. Nguyen, A.M. Zysk, E.J. Chaney, J.G. Kotynek, U.J. Oliphant, F.J. Bellafiore, K.M. Rowland, P.A. Johnson, S.A. Boppart, Intraoperative evaluation of breast tumor margins with optical coherence tomography. Cancer Res. **69**(22), 8790–8796 (2009)

70. C. Zhou, D.W. Cohen, Y. Wang, H.-C. Lee, A.E. Mondelblatt, T.-H. Tsai, A.D. Aguirre, J.G. Fujimoto, J.L. Connolly, Integrated optical coherence tomography and microscopy for ex vivo multiscale evaluation of human breast tissues. Cancer Res. **70**(24), 10071–10079 (2010)

71. A.N. Husain, V. Kumar, The lung, in *Robbins and Cotran Pathologic Basis of Disease*, ed. by V. Kumar, A.K. Abbas, N. Fausto, 7th edn. (Elsevier Saunders, Philadelphia, 2005), pp. 711–772

72. E.P. Trulock, L.B. Edwards, D.O. Taylor, M.M. Boucek, B.M. Keck, M.I. Hertz, Registry of the International Society for Heart and Lung Transplantation: Twenty-second official adult lung and heart-lung transplant report–2005. J. Heart Lung Transplant. **24**(8), 956–967 (2005)

73. S.A. Boppart, B.E. Bouma, C. Pitris, G.J. Tearney, J.G. Fujimoto, Forward-imaging instruments for optical coherence tomography. Opt. Lett. **22**(21), 1618–1620 (1997)

74. N. Hanna, D. Saltzman, D. Mukai, Z. Chen, S. Sasse, J. Milliken, S. Guo, W. Jung, H. Colt, M. Brenner, Two-dimensional and 3-dimensional optical coherence tomographic imaging of the airway, lung, and pleura. J. Thorac. Cardiovasc. Surg. **129**(3), 615–622 (2005)

75. M. Mertens, A. Tabuchi, S. Meissner, A. Krueger, K. Schirrmann, U. Kertzscher, A.R. Pries, A.S. Slutsky, E. Koch, W.M. Kuebler, Alveolar dynamics in acute lung injury: heterogeneous distension rather than cyclic opening and collapse. Crit. Care Med. **37**(9), 2604–2611 (2009)

76. S. Meissner, L. Knels, C. Schnabel, T. Koch, E. Koch, Three-dimensional Fourier domain optical coherence tomography in vivo imaging of alveolar tissue in the intact thorax using the parietal pleura as a window. J. Biomed. Opt. **15**(1), 016030 (2010)

77. J. Bickenbach, R. Dembinski, M. Czaplik, S. Meissner, A. Tabuchi, M. Mertens, L. Knels, W. Schroeder, P. Pelosi, E. Koch, W.M. Kuebler, R. Rossaint, R. Kuhlen, Comparison of two in vivo microscopy techniques to visualize alveolar mechanics. J. Clin. Monit. Comput. **23**(5), 323–332 (2009)

78. U. Costabel, *Atlas of Bronchoalveolar Lavage (trans: Mitchell JN)* (Oxford University Press, London, 1999)

79. M. Beccaria, M. Luisetti, G. Rodi, A. Corsico, M.C. Zoia, S. Colato, P. Pochetti, A. Braschi, E. Pozzi, I. Cerveri, Long-term durable benefit after whole lung lavage in pulmonary alveolar proteinosis. Eur. Respir. J. **23**(4), 526–531 (2004)

80. J.P. Williamson, R.A. McLaughlin, W.J. Noffsinger, A.L. James, V.A. Baker, A. Curatolo, J.J. Armstrong, A. Regli, K.L. Shepherd, G.B. Marks, D.D. Sampson, D.R. Hillman, P.R. Eastwood, Elastic properties of the central airways in obstructive lung diseases measured using anatomical optical coherence tomography. Am. J. Respir. Crit. Care Med. **183**(5), 612–619 (2011)

81. J. Mead, J.L. Whittenberger, E.P. Radford Jr., Surface tension as a factor in pulmonary volume-pressure hysteresis. J. Appl. Physiol. **10**(2), 191–196 (1957)

Assessment of Cardiovascular Disease Using Permeability Rates: Quantification by Optical Coherence Tomography

26

Mohamad G. Ghosn, Maleeha Mashiatulla, Joel D. Morrisett, and Kirill V. Larin

Contents

Abstract

In order to prevent major damage to the cardiovascular system, it is of vital importance to monitor molecular changes in vascular tissues. Symptoms of cardiovascular diseases frequently do not manifest themselves until it is too late for effective treatment; therefore, methodologies that facilitate early

M.G. Ghosn (✉)
Department of Medicine, Baylor College of Medicine, Houston, TX, USA

Department of Biomedical Engineering, University of Houston, Houston, TX, USA
e-mail: moghoson22@yahoo.com

M. Mashiatulla
Department of Biomedical Engineering, University of Houston, Houston, TX, USA

J.D. Morrisett
Department of Medicine, Baylor College of Medicine, Houston, TX, USA

K.V. Larin
Department of Biomedical Engineering, University of Houston, Houston, TX, USA

Department of Optics and Biophotonics, Saratov State University, Saratov, Russian Federation
e-mail: klarin@Central.UH.EDU

detection are crucial. Atherosclerosis is a major underlying cause of many cardiovascular diseases; thus, elucidating the mechanisms of atherosclerosis is essential for shedding light on the initiation and progression of atherosclerotic lesions. Atherosclerosis includes an inflammatory process in arterial tissue that involves subintimal accumulation of lipoproteins particles, mainly low-density lipoprotein and lipoprotein[a]. Measurement of the permeation rates of these particles should extend our understanding of this disease and lead to methods for early disease detection. Over the past decade, optical coherence tomography (OCT) has become widely used in research and, more recently, has been used as a high-resolution imaging technique, capable of quantifying molecular permeability in biological tissues. OCT enables highly sensitive and accurate measurement of permeability rates of molecules and particles in vascular tissue. This sensitivity is due to high in-depth and transverse resolution along with a high dynamic range. In this chapter, we discuss the permeation of molecules and particles through human and animal vascular tissue.

26.1 Introduction: Cardiovascular Disease

Cardiovascular disease is the number one cause of death in the United States, claiming the lives of more than half a million people each year [1, 2]. Atherosclerosis is the most common underlying cause of vascular disease, including cardiovascular, cerebrovascular, and peripheral vascular disease. Atherosclerosis, originating from the Greek word athero (paste) and sclerosis (hardening), is a process whereby lipids, calcification, thrombus, and fibrotic material accumulate in the arterial wall to form a plaque. Plaque accumulates in the intimal layer of arteries, causing partial narrowing or complete occlusion. The accumulation of plaque may begin as early as childhood, but signs and symptoms do not usually appear until much later in life. Although it is initially a slowly progressing disease, it is capable of progressing much more rapidly in later years. Rupture of the plaque tends to occur when it contains a lipid-rich core and a thin fibrous cap. Ruptured plaques may trigger the formation of a thrombus at or near the rupture site. If a clot forms in a coronary artery, the risk of a heart attack dramatically increases [1, 2]. Hence, early identification of plaque is important in order for effective treatment to be administered.

The solubility of cholesterol in water is extremely low ($<10^{-9}$ M); hence, in order for cholesterol to travel in the circulatory system, it must partition into lipid-transporting particles termed lipoproteins. The major lipoprotein classes are high-density lipoprotein (HDL), low-density lipoprotein (LDL), and very-low-density lipoprotein (VLDL) [2]. LDL is a cholesteryl-ester-rich lipoprotein that can move across the artery wall into the subintimal space where it becomes oxidized and subsequently taken up by macrophages and becomes transformed into cholesterol-laden foam cells [3]. As isolated foam cells are formed, a complex inflammation mechanism is initiated. Endothelial cells directly above the foam cells express

adhesion molecules that bind various classes of leukocytes [4]. Cholesterol exists in two forms – unesterified and esterified. Unesterified cholesterol in the artery wall can be taken up by HDL, thereby reducing plaque size, then transported to the liver. Esterified cholesterol is not easily removed from the arterial wall, and hence its accumulation leads to progression of the atherosclerotic lesion [5].

The risk of cardiovascular disease may be assessed by the net cholesterol flux which is calculated as the difference between the amount of cholesterol brought into the artery wall by LDL and the amount taken out by HDL [6–8]. Cholesterol levels below 200 mg/dL are considered to be normal, while those above 240 mg/dL are considered to confer a high cardiovascular risk. Levels of LDL above 130 mg/dL and levels of HDL below 35 mg/dL are also considered to confer high risk [6]. The rate of plaque size increase and decrease may be dependent on the rate at which lipoproteins traverse the arterial wall [1, 2, 6]. Several studies suggest that increased arterial permeability contributes to the endothelial lining adaptation to different localized shear stresses acting on the wall [9–13]. These results imply that permeability might be increased where the endothelium is exposed to a changing shear stress environment and, thus, the variability of hemodynamics at the artery wall may actually change the regional susceptibility to atherosclerosis. However, to date, rather little experimental evidence has been obtained to elucidate the spatial variation in endothelial permeability and local changes in permeability [7, 14, 15]. In order to understand the initiation, progression, and regression of atherosclerosis, it is essential to understand the movement of lipoproteins across the arterial wall. For this reason, there is a need for a noninvasive imaging technology with the capability of detecting and measuring changes occurring during the formation of plaques.

Several techniques have been employed to detect and assess atherosclerosis [16–19]. The most common technique utilized to detect plaque accumulation and evaluate cardiovascular risk has been the ultrasonic measurement of the carotid intima-media thickness (CIMT) [20, 21]. Recently, magnetic resonance imaging (MRI) has been employed successfully to identify plaques in carotid and femoral vessels [22, 23]. While structural imaging is still the conventional way of identifying plaques and monitoring cardiovascular disease, there is a need for a functional method to monitor plaque dynamics.

The permeability rate of particles and molecules through selected media has been determined using a number of different functional imaging modalities. Ultrasound has been employed to quantify permeability rates [24], but its applications are limited due to a (1) need for tissue contact and (2) relatively low resolution. MRI has also proven to be an excellent tool for studying diffusion rates in the brains of live rats and distribution of drugs in the eye globe [25, 26]. Optical coherence tomography (OCT) is a relatively novel imaging modality which overcomes limitations presented by other techniques. OCT has the capability of real-time imaging with high resolution (2–20 μm) and could be used noninvasively. OCT has been used in studies to measure the permeation rates of lipoproteins and glucose in various biological tissues [27–30]. This chapter will discuss studies conducted to quantify the permeability rates of molecules and particles in cardiovascular tissue.

26.2 OCT Systems

OCT is a relatively new noninvasive optical technique that renders images with spatial resolution of a few microns and depth of a few millimeters. OCT is a promising diagnostic imaging technology which can be used to perform in vivo high-resolution, cross-sectional imaging of microstructure in biological tissues. Since its introduction in the early 1990s, OCT has become widely used in biology and medicine. The image resolution with OCT is 10–100 times greater than that of standard ultrasound. Table 26.1 compares the differences in characteristics of commonly used imaging modalities.

The basic objective of the OCT system is to detect backscattered photons from the tissue of interest within a coherence length of the laser source by using a two-beam interferometer. OCT is similar to B-mode ultrasound, the major difference being the use of light rather than sound. Broadband low-coherence laser light passes through a beam splitter. The light is divided into a reference beam, directed toward a reference mirror, and a specimen path, directed toward the sample tissue. Light scattered by the specimen is collected and combined with the light reflected by the reference mirror, and a photodiode detects the resulting interferometric signal. The gathered data at points across the surface can be used to construct a 2D cross section in real time with resolution of a few micrometers and penetration of several millimeters in depth. Using the acquired 2D images, a single 1D graph representing the scattering of light in tissue (in logarithmic scale) can be calculated by averaging the images. Optical properties of the specimen can also be obtained by analyzing the light attenuation profile [31–34]. There are two classifications of OCT: time domain OCT (TDOCT) and Fourier domain OCT (FDOCT). Hereafter, we will be discussing only TDOCT. A schematic for a TDOCT system is shown in Fig. 26.1.

The major advantage of OCT compared to other imaging modalities is its relatively high resolution (Table 26.1). An important characteristic of OCT is decoupling of the axial and lateral resolutions that are independent from each other. Axial resolution is determined by the coherence length of the source used in the OCT system, whereas the lateral resolution depends on focusing properties of the lens. Improving the axial resolution in OCT has been a focus of research since its introduction [35–39]. High axial resolution can be achieved by introducing light sources with a broad emission spectrum. Axial resolution may be approximated by using the expression

$$\Delta z = \frac{2\ln(2)}{\pi} \frac{\lambda^2}{\Delta\lambda},$$

(26.1)

where Δz is the axial resolution, λ is the central wavelength of the source used, and $\Delta\lambda$ represents the bandwidth of the source [40]. The lateral resolution, on the other hand, is calculated by

$$\Delta x = \frac{4\lambda}{\pi} \frac{f}{d},$$

(26.2)

Table 26.1 Typical performance of commonly used medical imaging techniques

Technique	Resolution	Imaging depth	Cost	Comments
CT	1–2 mm	>50 cm	High	Radiation
MRI	1 mm	>50 cm	Very high	Slow
Ultrasound	50–150 μm	15 cm	High	Requires contact
OCT	1–25 μm	Few mm	Low	Limited penetration depth
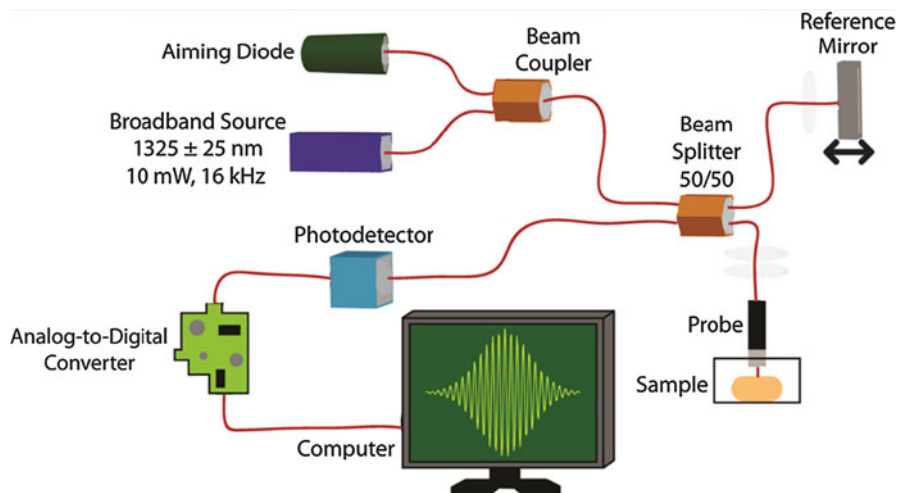
Fig. 26.1 Schematic diagram of time domain OCT

where Δx is the lateral resolution, f is the focal length of the lens, and d is the spot size of the objective lens. High lateral resolution can be obtained by using a large numerical aperture and focusing the beam to a small spot size; therefore, increasing the lateral resolution results in a decrease in the depth of focus.

The process of permeation of chemical compounds (agents, particles, drugs, etc.) changes the tissue scattering properties due to a number of biophysical processes [31, 34, 41–44]. The concept of two fluxes, one substance into tissue and bulk water out, which may be relatively independent or interacting fluxes, defines the dynamic properties of tissue optical clearing and demonstrates its efficiency [41]. Optical clearing agents' (OCA) diffusion inside tissue and interstitial space leads to an increase in refractive index of the interstitial fluid (ISF), thus matching the refractive index to collagen fibers (and other tissue components – scatterers) and ISF. A hyperosmotic OCA may induce an intensive water flow from tissue, thereby causing its strong dehydration and corresponding alteration of the tissue's morphological and optical properties by:

1. Refractive index matching/mismatching (generally for whole tissue matching and locally mismatching may take place)
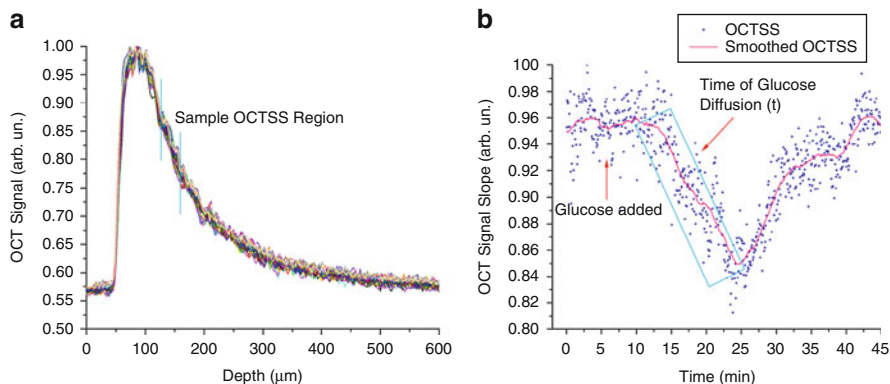
Fig. 26.2 (**a**) OCT signals recorded from porcine aorta indicating region and depths for OCTSS measurements; (**b**) a section of OCT signal slope used to analyze permeation rate

2. Increase of tissue collagen fiber packing density (ordering of scatterers)
3. Decrease of tissue thickness

Tissue collagen reorganization also may take place [44].

Similar to all optical methods, as the OCT beam penetrates deeper into a tissue, the signal strength diminishes due to optical attenuation. Therefore, there is a relationship between the depth of penetration and the signal strength at a particular depth; this can be described in terms of the OCT signal slope (OCTSS) which has previously been explained [27, 29, 30, 45–48].

The permeability rates of different analytes, such as lipoproteins, and drugs passing through biological tissues can be calculated using the OCT signal slope (OCTSS) method. The two-dimensional OCT images are averaged in the lateral (*x* axial) direction into a single curve to obtain an OCT signal that represents a one-dimensional distribution of intensity in-depth; this can be seen in Fig. 26.2. Average permeability rate is computed by analyzing OCTSS changes induced from analyte or drug diffusion in a specific depth region. A linear region from 1D OCT signal is chosen, and its thickness (z_{region}) is calculated. The local increase of permeating drug or analyte concentration in the chosen region causes the scattering coefficient to decrease, which is clearly reflected in the OCTSS graph. The time (t_{region}) is calculated from the point where OCTSS starts to decrease until a reverse process takes place. The reverse process is believed to arise from the difference in the concentration gradients on both sides of the tissue causing the fluid to travel from the region of lower concentration to higher concentration; water reenters the tissue after diffusing out due to the action of the permeating species. The permeability rate ($\bar{P}$) is calculated by dividing the measured thickness of the selected region by the time required for the agent to permeate the vessel: $\bar{P} = \frac{z_{region}}{t_{region}}$.

26.3   Cardiovascular Tissue

26.3.1 OCT Experiments on Porcine Aorta

Alterations in the structure and morphology of vascular tissue can be caused by the development of an atherosclerotic plaque. A change in the organization of cells and fibers that compose the tissue could significantly impact the permeability rate of molecules (e.g., drugs, glucose), particles (e.g., lipoproteins), and cells (e.g., macrophages). Therefore, knowledge of permeation values obtained using OCT could potentially aid in diagnosing diseases and help in differentiating between normal and diseased specimens. This section deals with quantification of glucose perfusion in normal and atherosclerotic regions of porcine aorta.

The permeation rates were measured in normal and diseased sections of a fresh hypercholesterolemic porcine aorta. Continuous imaging was performed for approximately 1 h for each specimen. Glucose was chosen for molecular permeation in porcine aorta since it has been extensively used in other studies conducted on various tissues [27, 29, 32, 34, 45–49]. According to our preliminary studies, glucose is also one of the most available, potent molecules that significantly affect tissues' scattering properties and, thus, is easily detectable with high signal-to-noise ratio.

The 2D OCT images of a normal and an atherosclerotic porcine aorta tissue sample are presented in Fig. 26.3. There is no significant difference between OCT images of normal tissue and tissue showing first onset of atherosclerotic disease (Fig. 26.3a and b, respectively). Figure 26.3c shows the histological section of a normal sample, whereas Fig. 26.3d shows the histology of a diseased section.

A typical OCTSS graph for a normal porcine aorta during glucose permeation is shown in Fig. 26.3e. The tissue sample was submerged in saline solution and monitored for ∼10 min to establish a baseline before the glucose was added to the solution. The OCT signal slope eventually decreased due to the reduction of scattering within the tissue, directly caused by the local increase of glucose concentration. The glucose solution reached the monitored region approximately 20 min after administration and another 20 min was required for it to completely permeate through the sample tissue. The consequent increase in OCTSS could have resulted from diffusion via concentration gradient differences on either side of the tissue; the net fluid (mainly water) movement from areas of low concentration to those of higher concentration prevails until equilibrium is reached. The permeability rate of 20 % glucose was determined to be $(6.80 \pm 0.18) \times 10^{-6}$ cm/s (n = 4). Figure 26.3f illustrates an atherosclerotic porcine aortic tissue OCTSS graph. The same procedure is implemented as used for the normal tissue experiments. The specimen was imaged for ∼10 min to establish a baseline before glucose was added to the saline bath. Diffusion of glucose in the monitored region started ∼7 min after the onset of diffusion with the same reverse process occurring 12 min later. The permeability rate of 20 % glucose in atherosclerotic aortic tissues was calculated to be $(2.69 \pm 0.42) \times 10^{-5}$ cm/s (n = 7) (see Fig. 26.4).
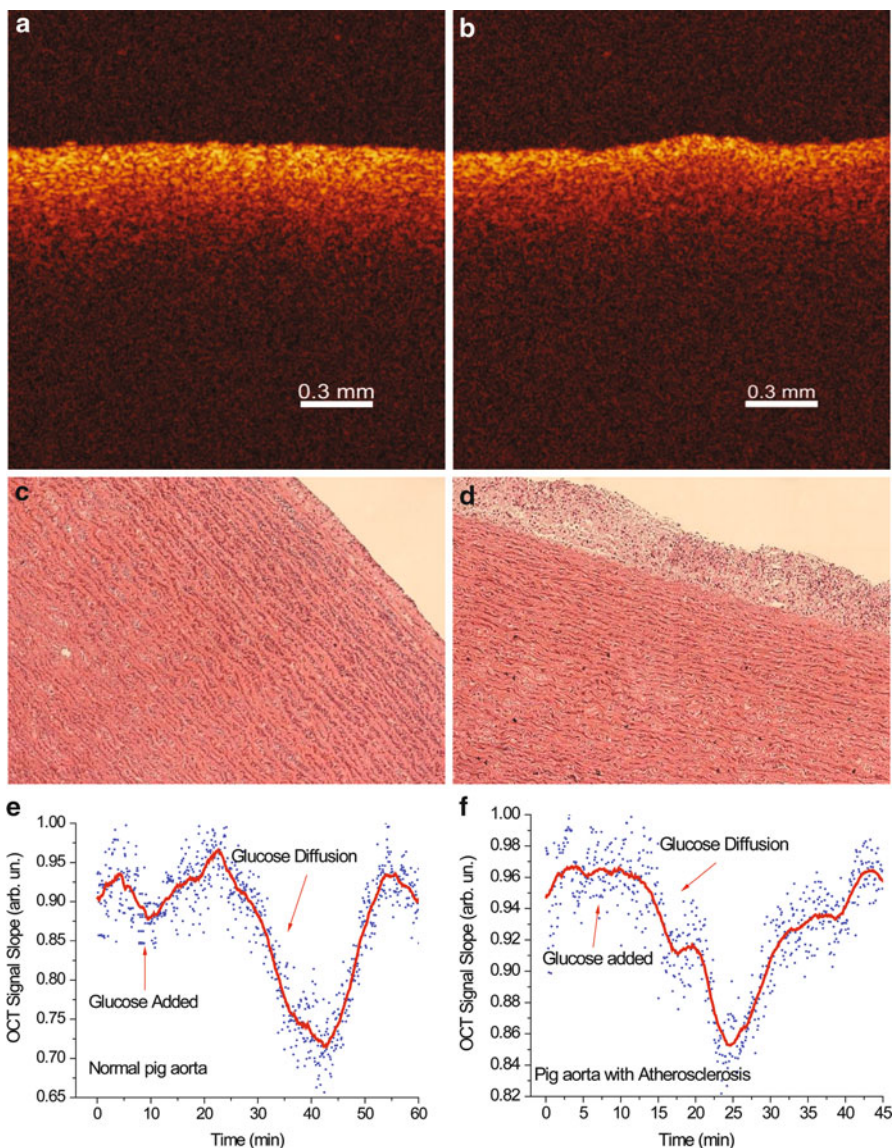
Fig. 26.3 (**a**, **b**) OCT images of a normal and atherosclerotic porcine aortic tissue, respectively; (**c**, **d**) histological sections (10 μm) for the normal and atherosclerotic specimens; (**e**, **f**) typical OCTSS graphs as a function of time recorded from a normal porcine aorta sample and an atherosclerotic porcine sample, respectively, during glucose permeation experiments

The results from this study indicate that glucose permeates atherosclerotic tissue more rapidly than it permeates normal tissue. These results suggest that the atherosclerotic tissue has more interstitial defects, rendering it "leaky and porous."

Fig. 26.4 A schematic illustrating the greater permeability rate of glucose through atherosclerotic aorta compared to normal aorta

$P_{diseased} = (2.69 \pm 0.42) \times 10^{-5}$ cm/s

$P_{normal} = (6.80 \pm 0.18) \times 10^{-6}$ cm/s
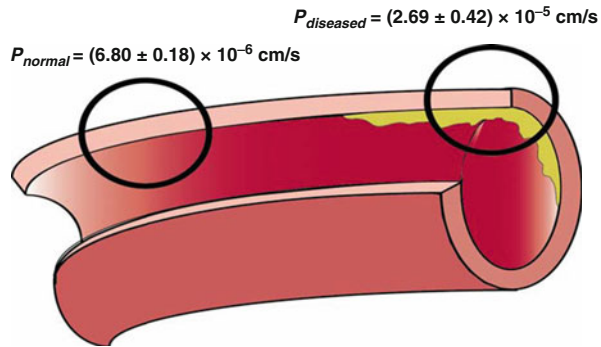
These defects may be due to calcified nodules or plates that do not pack efficiently or to disruptions of fibrin, collagen, or elastin packing.

The structural OCT images obtained from our experiments did not allow differentiation of normal from diseased tissues as shown in Fig. 26.3a and b, respectively. However, the functional images provided by the OCT system allowed effective differentiation between normal and abnormal tissue regions (Fig. 26.4). If particle and molecular permeation through arterial tissue is controlled by particle size, it would be reasonable to hypothesize that lipoproteins of increasing size will permeate at decreasing rate. Hence, the order of permeation rate should be HDL (0.25×10^6 Da) > LDL (2.1×10^6 Da) > VLDL (4.5×10^6 Da).

26.3.2 OCT Experiments on Human Carotid Endarterectomy Tissues

The relative rates of influx and efflux of lipoproteins are significant factors to be considered in studying the physiological mechanisms that contribute to the formation of atheroma. In the present study, we have used OCT to measure perfusion through yet another biological system, the intimal layer of the carotid arterial wall. This layer is obtained from human carotid endarterectomy (CEA) specimens, which contain *normal* healthy segments and *diseased* atherosclerotic segments which included lipidic, calcific, hemorrhagic, and/or fibrotic components (Fig. 26.5). Each OCT experiment was performed within 24 h after receiving the CEA specimen. Progression of this process is thought to involve the accumulation of modified LDL [50] in the subintimal space, while regression is believed to involve removal of cholesterol by HDL [51, 52] (reverse cholesterol transport). This study has been directed toward measuring and comparing the rates of VLDL, LDL, and HDL [53] influx into *normal* and atherosclerotic CEA tissue with the expectation that the results will provide new insights into the mechanisms of atherogenesis.

Tissue viability was quantitatively measured with the live/dead cell assay described by Allison et al. [54]. About 300-μm sections were stained in 4-μM calcein AM and 2-μM ethidium homodimer then viewed by confocal microscopy. Live cells bind calcein AM at their surface and emit light at 515 nm (green) when

Fig. 26.5 CEA specimen illustrating normal tissue in the proximal common (*PC*) and external (*EC*) segments (*black arrows*), and diseased tissue in the bifurcation (*BC*) and internal (*IC*) segments (*white arrows*)
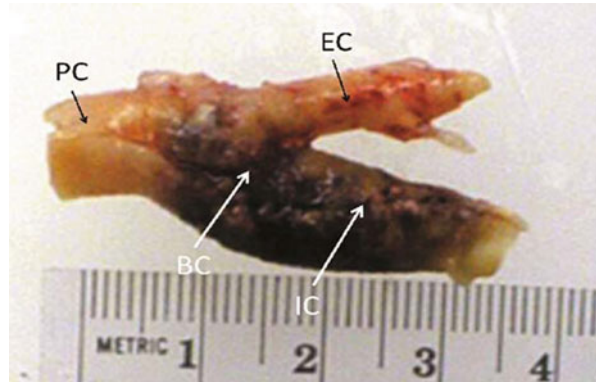
Fig. 26.6 Magnified photograph of a 6-mm-diameter carotid tissue sample immersed in PBS buffer in a well of a 96-well microtiter plate
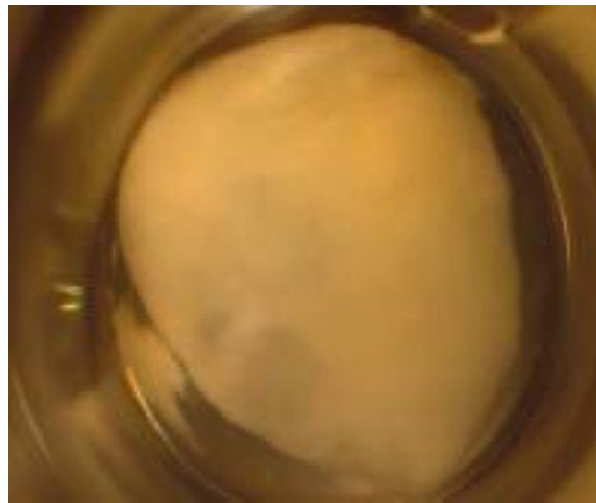
excited at 495 nm. Dead cells allow entrance of ethidium and hence fluoresce at 635 nm (red) when excited at 495 nm. Unstained tissue (negative control) was used to determine tissue autofluorescence. Tissue treated with 70 % ethanol for 30 min served as a positive control for dead cells. Positive control for live cells was a 3D culture of aortic smooth muscle cells.

Each tissue sample was immersed in PBS and imaged for 5 min to acquire baseline data (Fig. 26.6). Subsequently, a particular analyte (VLDL, LDL, HDL, or glucose) was added to the well containing the tissue sample, and image acquisition continued for another 40 min. A schematic representation of the methods used for these experiments is shown in Fig. 26.7, and the permeability rates of the various experiments are summarized in Fig. 26.8.

The viability of the CEA tissues used is demonstrated in Fig. 26.9. Ethidium diffused within all the cells treated with ethanol as shown in Fig. 26.9a serving as
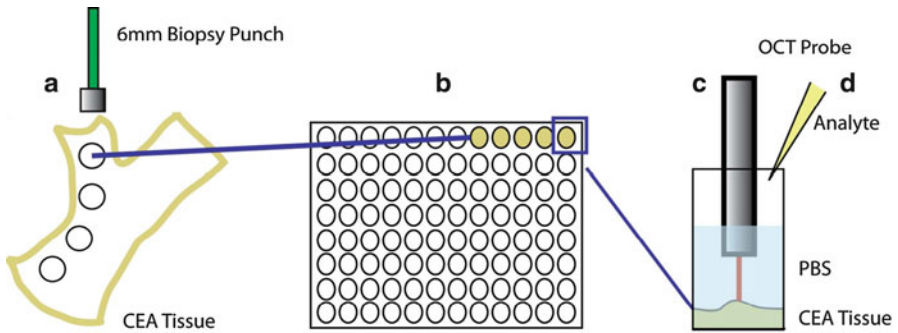
Fig. 26.7 Schematic representation of the tissue preparation and experimental procedure. (**a**) Tissue disks were cut using a 6-mm-diameter biopsy punch, (**b**) tissues were transferred in PBS to a microtiter plate, (**c**) functional imaging was performed using an OCT system, and (**d**) an analyte was added after acquiring 50 images for baseline data
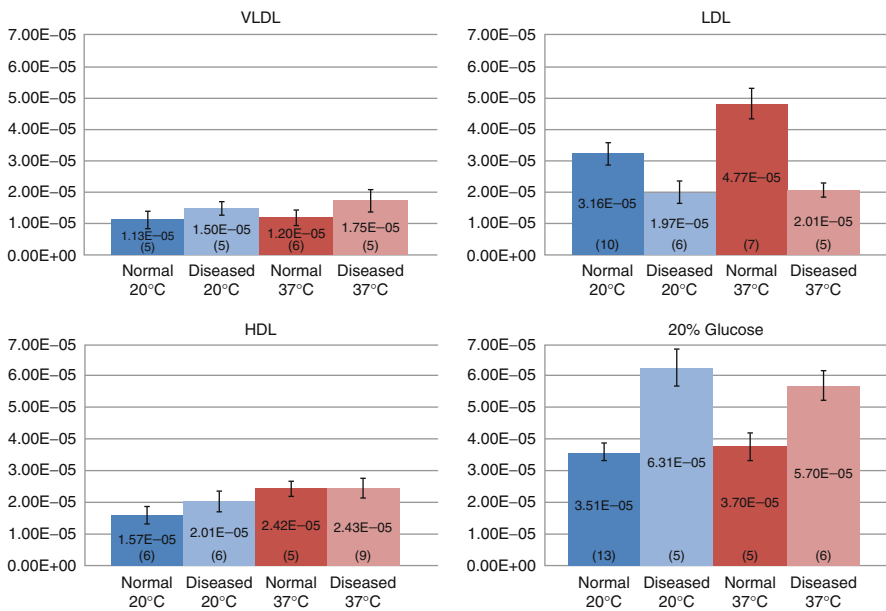
Fig. 26.8 Comparative data acquired from lipoprotein perfusion experiments; analyte type vs. permeability rate for VLDL, LDL, HDL, and glucose in both normal and diseased human carotid endarterectomy tissue samples, at 20 °C and 37 °C. (n) represents the number of tissue disks analyzed

a positive control for dead cells. The live aortic smooth muscle cells did not allow penetration of ethidium, yet the calcein bound to the outer membranes of the cells provided a positive control for live cells (Fig. 26.9b). Note the presence of live cells in both normal and diseased CEA tissues, demonstrating the viability of these specimens as shown in Fig. 26.9c and d.
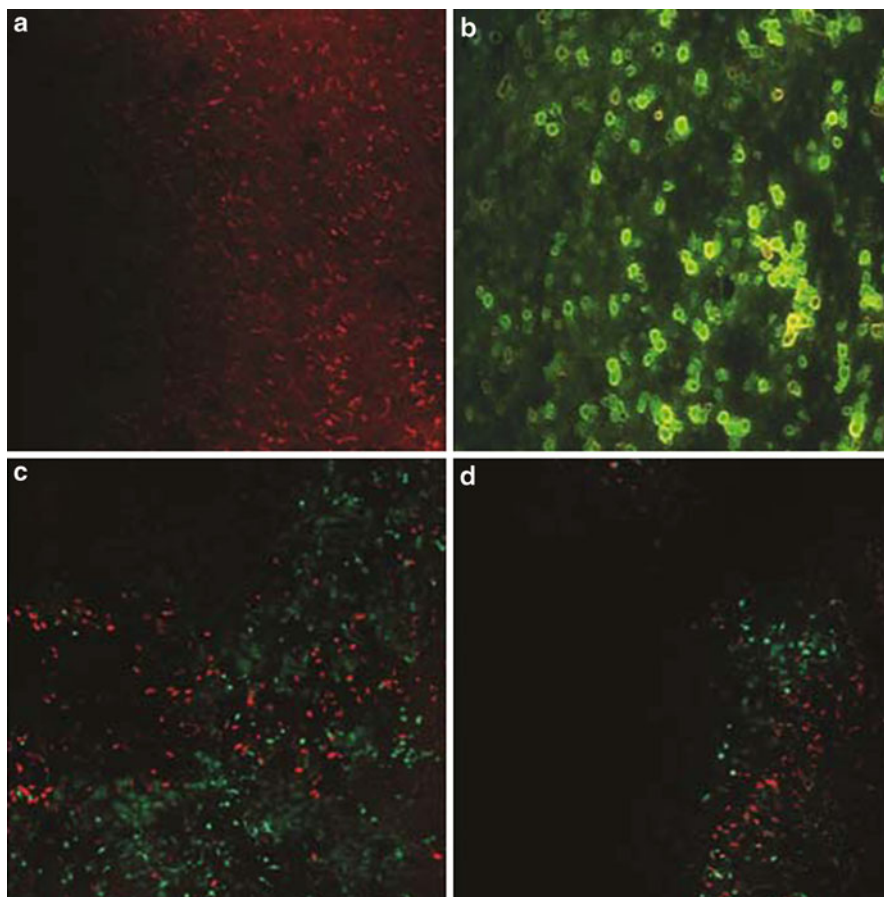
Fig. 26.9 Tissue viability test. (**a**) SMC treated with ethanol (negative control); (**b**) 3D culture of SMC (positive control), (**c**) normal CEA tissue, and (**d**) calcified CEA tissue. *Green* = live cells; *red* = dead cells

The initial hypothesis was that increasing temperature would be attended by increasing permeation rates for each lipoprotein. This was in fact the case for all three lipoproteins permeating through normal and diseased tissues. The mean increase for VLDL, LDL, and HDL through normal tissue was 37.0 %. The mean increase for these lipoproteins through diseased tissue was 13.2 %. The most striking effect of temperature increase on permeability rate was observed with LDL in normal tissues which exhibited an increase of 50.9 %.

The second hypothesis was that the permeation rate would be inversely related to lipoprotein size (i.e., increasing size correlates with decreasing rate). This hypothesis proved valid for VLDL, the lipoprotein with the largest diameter (>80 nm) and smallest permeation rate. However, this hypothesis did not hold for LDL. Its permeation rate through normal tissue at 37 °C $\{(4.77 \pm 0.48) \times 10^{-5}$ cm/s$\}$ was

97.1 % greater than the rate for HDL {$(2.42 \pm 0.24) \times 10^{-5}$ cm/s} under the same conditions. This property of LDL prevailed only with normal tissues. With diseased tissues at 20 °C, the rates increased ($1.50 \rightarrow 1.97 \rightarrow 2.01$) with decreasing particle size (VLDL $\rightarrow$ LDL $\rightarrow$ HDL). A similar trend was observed at 37 °C ($1.75 \rightarrow 2.01 \rightarrow 2.43$).

The third hypothesis was that diseased tissue would be more permeable than normal tissue. This hypothesis proved valid for VLDL (mean = 38.5 %) and HDL (mean = 14.2 %). For LDL, however, the normal tissue exhibited 47.7 % greater mean permeability than diseased tissue. For normal carotid tissues at physiological temperature (37 °C), the permeability rate of LDL was significantly higher than that of glucose. This result suggests the presence of a cellular transport mechanism specific to LDL. Previous reports have indicated that LDL permeates the endothelial layer of aortic tissue primarily by two pathways: vesicles [55, 56] and leaky junctions [57–59]. Leaky junctions within the endothelium originate from apoptotic events and the formation of lesions due to an increase in the rate of cellular turnover. An in vitro study of LDL transport compared the significance of these two pathways and found that leaky junctions account for >90 % of LDL flux, whereas vesicles account for <10 % [60]. Leaky junctions are temperature dependent, being more abundant and greater in size at 37 °C than at 20 °C. These differences could account for the dramatic increase in the permeability rate of LDL at 37 °C.

The glucose permeation measurements reveal interesting properties of the normal and diseased arterial wall. The rate of glucose permeation through normal tissue is not significantly increased by raising the temperature from 20 °C to 37 °C ($3.51 \rightarrow 3.70$), suggesting that the normal intimal permeability to small molecules is at or near its maximal value in this temperature range. Similarly, glucose permeation through diseased tissue is not considerably changed upon raising the temperature from 20 °C to 37 °C ($6.31 \rightarrow 5.70$). Significantly, the glucose permeation rate through diseased tissue at 20 °C (37 °C) is 79.9 % (54.0 %) greater than through normal tissue. The higher permeation rates for the diseased tissues suggest the presence of defects that permit influx of small molecules like glucose, but not large particles like lipoproteins.

This study benefited from several unique advantages: (1) OCT does not perturb the CEA tissue or permeating species. (2) Both *normal* and *diseased* tissues could be obtained from the same tissue specimen. (3) The amount of tissue and permeating species required was small, allowing adequate experiment replication. However, the study did have significant limitations: (1) The permeating species were not competed by other components that would be present in normal blood. (2) Measurements were performed using static, nonflowing solutions. (3) The CEA tissue contained only the intimal layer and plaque, not the media or adventitial layers.

Our observation that LDL permeates CEA tissue faster than other lipoproteins is consistent with a much earlier report that ^{125}I-LDL enters the normal arterial wall rapidly and interacts with it [61]. This interaction includes both binding to the arterial wall and degradation of the radiolabeled LDL protein. These studies were extended later in the balloon de-endothelialized rabbit aorta, which was injected

with ^{125}I-LDL. Anterior scintigrams demonstrated sequestration of the labeled lipoprotein by the aorta [61]. In a separate study, ^{125}I-LDL was also shown to accumulate in the carotid arteries of patients previously injected with the labeled lipoprotein [62]. The retention of LDL in the arterial wall may be controlled by atherin, a protein that avidly binds LDL and is found only in atherosclerotic lesions, not in normal intima [61].

26.3.2.1 CEA Experiments Summary

The permeability rate of VLDL, LDL, HDL, and glucose in normal and diseased human CEA tissue at 20 °C and 37 °C was measured using OCT. A significant difference ($p < 0.05$) between 20 °C and 37 °C in normal tissue was found for the permeability rate of LDL, $(3.16 \pm 0.37) \times 10^{-5}$ cm/s and $(4.77 \pm 0.48) \times 10^{-5}$ cm/s, respectively, supporting previous suggestions for an arterial transport mechanism specific to LDL. The permeability rate of LDL in diseased tissue was significantly lower than that in normal tissue (consistent with the greater abundance of LDL in diseased tissue). OCT has proven to be a noninvasive and nondestructive method for determining the permeability rates of lipoproteins, and other small analytes, in CEA tissues. Direct experimental measurement of depth-resolved lipoprotein influx rates for normal and diseased vasculature is essential for our understanding of the complexities of arteriosclerotic plaque formation.

26.4   Validation of OCT Using Fluorescent Microscopy

In previously described studies, effective OCT-based methods have been developed for the determination of diffusivity of molecules and drugs by detecting changes in tissue's optical properties as the analytes perfuse through extracellular matrix [27, 47–49, 63, 64]. However, in order to determine the effectiveness of OCT in noninvasive permeation studies, a comparison with a conventional, well-established method already in use (the gold standard) had to be made. The focus of this study was to compare the permeability rate of dextran tetramethylrhodamine fluorescent dye in vascular tissues measured with both the OCT system (completely nondestructively) and a fluorescence microscope (FM), via standard histological examination.

Freshly excised porcine aortas were transported to the lab while submerged in chilled saline solution. A sagittal incision was made on the aorta creating a 2D sheet, which was then cut into 1 cm square samples. The permeability of dextran tetramethylrhodamine dye (MW 3,000) was monitored comprehensively using OCT and fluorescence microscopy. Experiments in both imaging methods were begun simultaneously after the tissue was obtained, ensuring the accuracy of the study. The dye solution used in the experiments was prepared by diluting 1 mg of the dextran in 10 ml of distilled water, and the resulting solution was kept at 4 °C and protected from exposure to light to prevent photobleaching. The acquired image data was obtained through the OCT system.

Fig. 26.10 OCT signal slope graph of dye diffusion experiment in porcine aorta
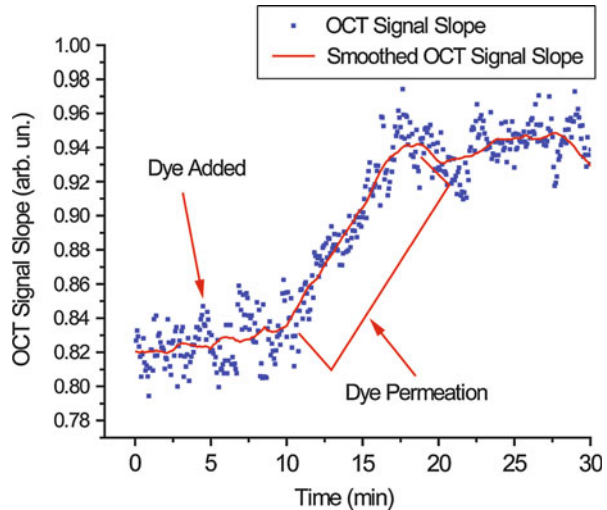
An aorta sample was placed on top of saline solution on a glass slide in order to preserve hydration of the tissue during the course of imaging. The fluorescent dye was added about 5 min after the onset of imaging after a baseline was established, and the tissue was continuously imaged for 30 min. The permeability rate was calculated for these images by implementing the OCTSS method.

The histological examination of the time-dependent dye diffusion was executed by using a standard fluorescent microscope (Olympus BX61). Excised 1 cm^2 square aorta samples were taken from saline solution and placed on individual glass slides to which 0.5 ml of dye solution was added simultaneously. The control and tissues with the dye were placed on a 35-mm-diameter cryocassette disk and covered with cryochrome and frozen on dry ice. The aorta tissues were then segmented laterally in 10 μm slices and, eventually, were mounted on microscope slides for imaging. These tissue samples were frozen at different time increments (10, 15, 20, 25, and 30 min) after the addition of the dye solution. The same procedure was repeated to prepare slides for all tissue samples [65].

All of the images acquired by fluorescence microscopy were normalized to the maximum value from the control sample, thus eliminating the background autofluorescence created by the tissue itself. The distance traveled by the dye in the tissue was measured at each time increment, thus allowing an accurate calculation of the permeability rate of the fluorescent dye, which was estimated by dividing the distance traveled at each time increment.

A sample OCTSS graph for a porcine aorta during a dye diffusion experiment is shown in Fig. 26.10. The tissue was first imaged for about 5 min to establish a baseline before adding 0.5 ml of the dye solution. A region inside the artery which was 140 μm thick (z_{region}) was selected to calculate the permeability rate. Figure 26.10 indicates a rise in the OCTSS region labeled dye diffusion which demonstrates that the absorption rate increased as the dye solution reached the monitored region.
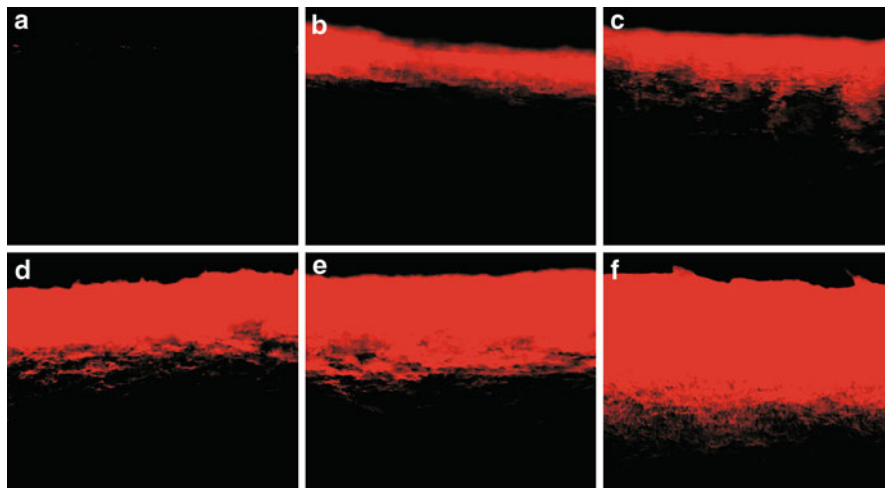
Fig. 26.11 Microscope images of porcine aorta in a dye diffusion experiment at times 0, 10, 15, 20, 25, and 30 min corresponding to images (**a**), (**b**), (**c**), (**d**), (**e**), and (**f**), respectively [65]

Table 26.2 Permeability rate of glucose in porcine aorta found using OCT compared to permeability rate determined by fluorescence microscopy

	OCT (n = 3)	Fluorescence microscopy (n = 8)
Permeability rate (cm/s)	$(2.45 \pm 0.46) \times 10^{-5}$	$(2.08 \pm 0.31) \times 10^{-5}$

After the dye penetrated through the entire monitored region in the tissue, a saturation stage was reached, as illustrated by a flat line in the OCTSS graph. To obtain the time interval required for the dye to diffuse through the indicated area, the region where the slope increased in the OCTSS graph was taken, and the time interval was estimated to be approximately 10 min. From this information, the permeability rate was computed to be 2.59×10^{-5} cm/s [65].

Figure 26.11a depicts the control image where no dye was introduced, and Fig. 26.11b–f shows images of dye in aorta at 5-min intervals. The distances that the dye traveled in these images were measured to be 120, 181, 191, 263, and 350 µm, respectively, which correspond to an average permeability rate of 1.86×10^{-5} cm/s. The permeability rate of the dye was found to be $(2.45 \pm 0.46) \times 10^{-5}$ cm/s (n = 3) from the OCT method and $(2.08 \pm 0.31) \times 10^{-5}$ cm/s (n = 8) from the fluorescence microscopic measurement. Comparison of the two permeability rates can be found in Table 26.2. Thus, the results obtained from OCT experiments correlate reasonably well to those acquired using fluorescence microscopy.

Slight differences in the averaged values and standard deviations from the two experimental methods could be attributed to the mechanical changes the aorta

tissues underwent in the fluorescent microscopic trials. It is well-known that freezing and mechanical slicing of the samples can alter their thickness, explaining the variations in estimation of the dye diffusion region. Another potential source of error is that the average refractive index for aorta was assumed to be 1.4 in all calculations performed with the OCT method. Even though this assumption is not entirely accurate, it did not affect the measured permeability rate values since the error margin fell within the standard deviation.

Overall, the results obtained by OCT and fluorescence microscopy indicate that OCT is a valid technique for measuring molecular permeation through biological tissues. The technique is completely noninvasive, making it a good candidate for clinical application in the future.

26.5 Conclusion

This chapter demonstrates the capability for OCT to noninvasively and nondestructively measure the permeation rates of various analyte in vascular tissue. Permeation rates of a small molecule (glucose) and large particles (VLDL, LDL, and HDL) through porcine aortic tissue and CEA samples were demonstrated. Temperature-dependent experiments were conducted. The permeation of glucose did not change significantly when the temperature was elevated from 20 °C to 37 °C, while the permeation of LDL increased almost twofold with the same temperature elevation. This suggests that the tissue is freely permeable to small molecules over this temperature range, while this increase in temperature alters the structure of the arterial intima in a way that allows it to become much more permeable to large particles on the order of 20 nm in diameter. Unexpectedly, at 37 °C, the permeation of LDL was 1.3-fold greater than that of glucose, suggesting that at this physiological temperature the movement of LDL across the intimal boundary is enhanced by an active mechanism in addition to passive diffusion.

The permeability rates of VLDL, LDL, HDL, and glucose in normal and *diseased* human CEA tissue were measured. With the exception of LDL, the permeation rates of these particles/molecules were higher in the *diseased* samples. This supports previous suggestions for an arterial transport mechanism specific to LDL in normal arterial tissue.

In summary, OCT is a well-suited imaging modality for conducting permeation trials. Such studies could improve the understanding of the penetration and accumulation of lipoproteins in arterial wall and, thus, could enhance our knowledge for the treatment of atherosclerosis.

References

1. H. Robenek, N.J. Severs, *Cell Interactions in Atherosclerosis* (CRC, Boca Raton, 1992)
2. L.M. Shin, K. Bellenir, *Blood and Circulatory Disorders Sourcebook: Basic Information about Blood and Its Components* (Omnigraphics, Detroit, MI, 1999)
3. Y. Imanaga, N. Sakata, S. Takebayashi, A. Matsunaga, J. Sasaki, K. Arakawa, R. Nagai, S. Horiuchi, H. Itabe, T. Takano, In vivo and in vitro evidence for the glycoxidation of low density lipoprotein in human atherosclerotic plaques. Atherosclerosis **150**(2), 343–355 (2000)
4. P. Libby, Inflammation in atherosclerosis. Nature **420**(6917), 868–874 (2002)
5. P.E. Szmitko, C.H. Wang, R.D. Weisel, J.R. de Almeida, T.J. Anderson, S. Verma, New markers of inflammation and endothelial cell activation: Part I. Circulation **108**(16), 1917–1923 (2003)
6. M.H. Friedman, D.L. Fry, Arterial permeability dynamics and vascular disease. Atherosclerosis **104**(1–2), 189–194 (1993)
7. E. Falk, Pathogenesis of atherosclerosis. J. Am. Coll. Cardiol. **47**(8 Suppl), C7–C12 (2006)
8. J.M. Tarbell, Mass transport in arteries and the localization of atherosclerosis. Annu. Rev. Biomed. Eng. **5**, 79–118 (2003)
9. M. Lei, C. Kleinstreuer, J.P. Archie, Hemodynamic simulations and computer-aided designs of graft-artery junctions. J. Biomech. Eng. **119**(3), 343–348 (1997)
10. M.Z. Darbeau, R.J. Lutz, W.E. Collins, Simulated lipoprotein transport in the wall of branched arteries. ASAIO J. **46**(6), 669–678 (2000)
11. C.R. Ethier, Computational modeling of mass transfer and links to atherosclerosis. Ann. Biomed. Eng. **30**(4), 461–471 (2002)
12. A.L. Hazel, D.M. Grzybowski, M.H. Friedman, Modeling the adaptive permeability response of porcine iliac arteries to acute changes in mural shear. Ann. Biomed. Eng. **31**(4), 412–419 (2003)
13. M. Prosi, P. Zunino, K. Perktold, A. Quarteroni, Mathematical and numerical models for transfer of low-density lipoproteins through the arterial walls: a new methodology for the model set up with applications to the study of disturbed lumenal flow. J. Biomech. **38**(4), 903–917 (2005)
14. K.S. Cunningham, A.I. Gotlieb, The role of shear stress in the pathogenesis of atherosclerosis. Lab. Invest. **85**(1), 9–23 (2005)
15. A.M. Shaaban, A.J. Duerinckx, Wall shear stress and early atherosclerosis: a review. AJR Am. J. Roentgenol. **174**(6), 1657–1665 (2000)
16. M.A. Calfon, A. Rosenthal, G. Mallas, A. Mauskapf, R.N. Nudelman, V. Ntziachristos, F.A. Jaffer, In vivo near infrared fluorescence (NIRF) intravascular molecular imaging of inflammatory plaque, a multimodal approach to imaging of atherosclerosis. J. Vis. Exp. **54**, 2257 (2011)
17. C. Yuan, W.S. Kerwin, MRI of atherosclerosis. J. Magn. Reson. Imaging **19**(6), 710–719 (2004)
18. D. Gao, N. Ning, Y. Guo, W. Ning, X. Niu, J. Yang, Computed tomography for detecting coronary artery plaques: a meta-analysis. Atherosclerosis **219**(2), 603–609 (2011)
19. R. Diletti, H.M. Garcia-Garcia, J. Gomez-Lara, S. Brugaletta, J.J. Wykrzykowska, N. van Ditzhuijzen, R.J. van Geuns, E. Regar, G. Ambrosio, P.W. Serruys, Assessment of coronary atherosclerosis progression and regression at bifurcations using combined IVUS and OCT. JACC Cardiovasc. Imaging **4**(7), 774–780 (2011)
20. R. Tang, M. Hennig, M.G. Bond, R. Hollweck, G. Mancia, A. Zanchetti, Quality control of B-mode ultrasonic measurement of carotid artery intima-media thickness: the European Lacidipine Study on atherosclerosis. J. Hypertens. **23**(5), 1047–1054 (2005)
21. E. de Groot, S.I. van Leuven, R. Duivenvoorden, M.C. Meuwese, F. Akdim, M.L. Bots, J.J. Kastelein, Measurement of carotid intima-media thickness to assess progression and regression of atherosclerosis. Nat. Clin. Pract. Cardiovasc. Med. **5**(5), 280–288 (2008)
22. C. Karmonik, P. Basto, K. Vickers, K. Martin, M.J. Reardon, G.M. Lawrie, J.D. Morrisett, Quantitative segmentation of principal carotid atherosclerotic lesion components by feature

space analysis based on multicontrast MRI at 1.5T. IEEE Trans Biomed Eng **56**(2), 352–360 (2009)

23. R. Brown, C. Karmonik, G. Brunner, A. Lumsden, C. Ballantyne, S. Johnson, Y. Wang, J. Morrisett, Simultaneous bilateral magnetic resonance imaging of the femoral arteries in peripheral arterial disease patients. J. Magn. Reson. Imaging **34**(1), 150–156 (2011)

24. D. Bommannan, H. Okuyama, P. Stauffer, R.H. Guy, Sonophoresis. I. The use of high-frequency ultrasound to enhance transdermal drug delivery. Pharm. Res. **9**(4), 559–564 (1992)

25. V.G. Roullin, J.R. Deverre, L. Lemaire, F. Hindre, M.C. Venier-Julienne, R. Vienet, J.P. Benoit, Anti-cancer drug diffusion within living rat brain tissue: an experimental study using [3H](6)-5-fluorouracil-loaded PLGA microspheres. Eur. J. Pharm. Biopharm. **53**(3), 293–299 (2002)

26. H. Kim, M.J. Lizak, G. Tansey, K.G. Csaky, M.R. Robinson, P. Yuan, N.S. Wang, R.J. Lutz, Study of ocular transport of drugs released from an intravitreal implant using magnetic resonance imaging. Ann. Biomed. Eng. **33**(2), 150–164 (2005)

27. M.G. Ghosn, E.F. Carbajal, N.A. Befrui, A. Tellez, J.F. Granada, K.V. Larin, Permeability of hyperosmotic agent in normal and atherosclerotic vascular tissues. J. Biomed. Opt. **13**(1), 010505 (2008)

28. M.G. Ghosn, M. Leba, A. Vijayananda, P. Rezaee, J.D. Morrisett, K.V. Larin, Effect of temperature on permeation of low-density lipoprotein particles through human carotid artery tissues. J. Biophotonics **2**(10), 573–580 (2009)

29. M.G. Ghosn, M. Mashiatulla, M.A. Mohamed, S. Syed, F. Castro-Chavez, J.D. Morrisett, K.V. Larin, Time dependent changes in aortic tissue during cold storage in physiological solution. Biochim. Biophys. Acta **1810**(5), 555–560 (2011)

30. M.G. Ghosn, M. Mashiatulla, S.H. Syed, M.A. Mohamed, K.V. Larin, J.D. Morrisett, Permeation of human plasma lipoproteins in human carotid endarterectomy tissues: measurement by optical coherence tomography. J. Lipid Res. **52**(7), 1429–1434 (2011)

31. K.V. Larin, M.S. Eledrisi, M. Motamedi, R.O. Esenaliev, Noninvasive blood glucose monitoring with optical coherence tomography: a pilot study in human subjects. Diabetes Care **25**(12), 2263–2267 (2002)

32. K.V. Larin, M. Motamedi, T.V. Ashitkov, R.O. Esenaliev, Specificity of noninvasive blood glucose sensing using optical coherence tomography technique: a pilot study. Phys. Med. Biol. **48**(10), 1371–1390 (2003)

33. M. Kinnunen, R. Myllyla, T. Jokela, S. Vainio, In vitro studies toward noninvasive glucose monitoring with optical coherence tomography. Appl. Opt. **45**(10), 2251–2260 (2006)

34. R.O. Esenaliev, K.V. Larin, I.V. Larina, M. Motamedi, Noninvasive monitoring of glucose concentration with optical coherence tomography. Opt. Lett. **26**(13), 992–994 (2001)

35. G. Wollstein, L.A. Paunescu, T.H. Ko, J.G. Fujimoto, A. Kowalevicz, I. Hartl, S. Beaton, H. Ishikawa, C. Mattox, O. Singh, J. Duker, W. Drexler, J.S. Schuman, Ultrahigh-resolution optical coherence tomography in glaucoma. Ophthalmology **112**(2), 229–237 (2005)

36. V.J. Srinivasan, M. Wojtkowski, A.J. Witkin, J.S. Duker, T.H. Ko, M. Carvalho, J.S. Schuman, A. Kowalczyk, J.G. Fujimoto, High-definition and 3-dimensional imaging of macular pathologies with high-speed ultrahigh-resolution optical coherence tomography. Ophthalmology **113**(11), 2054 (2006)

37. T. Mumcuoglu, G. Wollstein, M. Wojtkowski, L. Kagemann, H. Ishikawa, M.L. Gabriele, V. Srinivasan, J.G. Fujimoto, J.S. Duker, J.S. Schuman, Improved visualization of glaucomatous retinal damage using high-speed ultrahigh-resolution optical coherence tomography. Ophthalmology **115**(5), 782–789 (2008)

38. T.H. Ko, J.G. Fujimoto, J.S. Duker, L.A. Paunescu, W. Drexler, C.R. Baumal, C.A. Puliafito, E. Reichel, A.H. Rogers, J.S. Schuman, Comparison of ultrahigh- and standard-resolution optical coherence tomography for imaging macular hole pathology and repair. Ophthalmology **111**(11), 2033–2043 (2004)

39. J. Rogowska, M.E. Brezinski, Evaluation of the adaptive speckle suppression filter for coronary optical coherence tomography imaging. IEEE Trans. Med. Imaging **19**(12), 1261–1266 (2000)

40. B.E. Bouma, G.J. Tearney, *Handbook of Optical Coherence Tomography* (Marcel Dekker, New York, 2002)

41. V.V. Tuchin, *Tissue optics: Light Scattering Methods and Instruments for Medical Diagnosis* (SPIE, Bellingham, 2007)

42. V.V. Tuchin, I.L. Maksimova, D.A. Zimnyakov, I.L. Kon, A.H. Mavlyutov, A.A. Mishin, Light propagation in tissues with controlled optical properties. J. Biomed. Opt. **2**, 401–417 (1997)

43. G. Vargas, K.F. Chan, S.L. Thomsen, A.J. Welch, Use of osmotically active agents to alter optical properties of tissue: effects on the detected fluorescence signal measured through skin. Lasers Surg. Med. **29**(3), 213–220 (2001)

44. A.T. Yeh, J. Hirshburg, Molecular interactions of exogenous chemical agents with collagen– implications for tissue optical clearing. J. Biomed. Opt. **11**(1), 014003 (2006)

45. M.G. Ghosn, E.F. Carbajal, N.A. Befrui, V.V. Tuchin, K.V. Larin, Differential permeability rate and percent clearing of glucose in different regions in rabbit sclera. J. Biomed. Opt. **13**(2), 021110 (2008)

46. M.G. Ghosn, N. Sudheendran, M. Wendt, A. Glasser, V.V. Tuchin, K.V. Larin, Monitoring of glucose permeability in monkey skin in vivo using Optical Coherence Tomography. J. Biophotonics **3**, 25–33 (2009)

47. M.G. Ghosn, V.V. Tuchin, K.V. Larin, Depth-resolved monitoring of glucose diffusion in tissues by using optical coherence tomography. Opt. Lett. **31**(15), 2314–2316 (2006)

48. M.G. Ghosn, V.V. Tuchin, K.V. Larin, Nondestructive quantification of analyte diffusion in cornea and sclera using optical coherence tomography. Invest. Ophthalmol. Vis. Sci. **48**(6), 2726–2733 (2007)

49. K.V. Larin, M.G. Ghosn, Influence of experimental conditions on drug diffusion in cornea. Quantum Electron. **36**(12), 1083–1088 (2006)

50. L.B. Nielsen, Transfer of low density lipoprotein into the arterial wall and risk of atherosclerosis. Atherosclerosis **123**(1–2), 1–15 (1996)

51. A.M. Gotto, H.J. Pownall, *Manual of Lipid Disorders: Reducing the Risk of Coronary Heart Disease* (Williams & Wilkins, Baltimore, 1999)

52. A. von Eckardstein, J.R. Nofer, G. Assmann, High density lipoproteins and arteriosclerosis. Role of cholesterol efflux and reverse cholesterol transport. Arterioscler. Thromb. Vasc. Biol. **21**(1), 13–27 (2001)

53. D.A. Warrell, *Oxford Textbook of Medicine* (Oxford University Press, Oxford/New York, 2003)

54. D.D. Allison, J.A. Drazba, I. Vesely, K.N. Kader, K.J. Grande-Allen, Cell viability mapping within long-term heart valve organ cultures. J. Heart Valve Dis. **13**(2), 290–296 (2004)

55. E. Vasile, M. Simionescu, N. Simionescu, Visualization of the binding, endocytosis, and transcytosis of low-density lipoprotein in the arterial endothelium in situ. J. Cell Biol. **96**(6), 1677–1689 (1983)

56. I. Snelting-Havinga, M. Mommaas, V.W. Van Hinsbergh, M.R. Daha, W.T. Daems, B.J. Vermeer, Immunoelectron microscopic visualization of the transcytosis of low density lipoproteins in perfused rat arteries. Eur. J. Cell Biol. **48**(1), 27–36 (1989)

57. S.J. Lin, K.M. Jan, S. Chien, Role of dying endothelial cells in transendothelial macromolecular transport. Arteriosclerosis **10**(5), 703–709 (1990)

58. S.J. Lin, K.M. Jan, G. Schuessler, S. Weinbaum, S. Chien, Enhanced macromolecular permeability of aortic endothelial cells in association with mitosis. Atherosclerosis **73**(2–3), 223–232 (1988)

59. S. Weinbaum, G. Tzeghai, P. Ganatos, R. Pfeffer, S. Chien, Effect of cell turnover and leaky junctions on arterial macromolecular transport. Am. J. Physiol. **248**(6), 945–960 (1985)

60. L.M. Cancel, A. Fitting, J.M. Tarbell, In vitro study of LDL transport under pressurized (convective) conditions. Am. J. Physiol. Heart Circ. Physiol. **293**(1), H126–H132 (2007)

61. A.M. Lees, A.E. Deconinck, B.D. Campbell, R.S. Lees, Atherin: a newly identified, lesion-specific, LDL-binding protein in human atherosclerosis. Atherosclerosis **182**(2), 219–230 (2005)

62. P. Lu, P. Zanzonico, J. Lister-James, S.M. Goldfine, E. Herrold, R.S. Lees, A.M. Lees, R.T. Dean, B.R. Moyer, J.S. Borer, Biodistribution and Autoradiographic Localization of I-125–Labeled Synthetic Peptide in Aortic Atherosclerosis in Cholesterol-Fed Rabbits. Am. J. Ther. **3**(10), 673–680 (1996)
63. K.V. Larin, V.V. Tuchin, Functional imaging and assessment of the glucose diffusion rate in epithelial tissues in optical coherence tomography. Quantum Electron+ **38**(6), 551–556 (2008)
64. K.V. Larin, M.G. Ghosn, S.N. Ivers, A. Tellez, J.F. Granada, Quantification of glucose diffusion in arterial tissues by using optical coherence tomography. Laser Phys. Lett. **4**(4), 312–317 (2007)
65. M.G. Ghosn, S.H. Syed, N.A. Befrui, M. Leba, A. Vijayananda, N. Sudheendran, K.V. Larin, Quantification of molecular diffusion in arterial tissues with optical coherence tomography and fluorescence microscopy. Laser Phys. **19**(6), 1272–1275 (2009)

Part 5

Coherent-Domain Microscopy

Optical Coherence Microscopy

27

Grigory V. Gelikonov, Valentin M. Gelikonov, Sergey U. Ksenofontov, Andrey N. Morosov, Alexey V. Myakov, Yury P. Potapov, Veronika V. Saposhnikova, Ekaterina A. Sergeeva, Dmitry V. Shabanov, Natalia M. Shakhova, and Elena V. Zagainova

Contents

G.V. Gelikonov (✉) • V.M. Gelikonov • S.U. Ksenofontov • A.N. Morosov • A.V. Myakov • Y.P. Potapov • V.V. Saposhnikova • E.A. Sergeeva • D.V. Shabanov • N.M. Shakhova
Institute of Applied Physics of the Russian Academy of Sciences, Nizhny Novgorod, Russian Federation
e-mail: grig@ufp.appl.sci-nnov.ru, gelikon@ufp.appl.sci-nnov.ru, xen@appl.sci-nnov.ru, morozov@ufp.appl.sci-nnov.ru, Myakov@mera.ru, p_up@mail.ru, rkuranov@yahoo.com, sea@ufp.appl.sci-nnov.ru, dvshab@ufp.appl.sci-nnov.ru, shakh@ufp.appl.sci-nnov.ru

E.V. Zagainova
Medical Academy, Nizhny Novgorod, Russian Federation
e-mail: ezagaynova@gmail.com

Abstract

This chapter presents the practical embodiment of two types of optical coherence microscope (OCM) modality that differ by probing method. The development and creation of a compact OCM device for imaging internal structures of biological tissue at the cellular level is presented. Ultrahigh axial resolution of 3.4 μm and lateral resolution of 3.9 μm within tissue was attained by combining broadband radiations of two spectrally shifted SLDs and implementing the dynamic focus concept, which allows in-depth scanning of a coherence gate and beam waist synchronously. This OCM prototype is portable and easy to operate; creation of a remote optical probe was feasible due to use of polarization maintaining fiber. The chapter also discusses the results of a theoretical investigation of OCM axial and lateral resolution degradation caused by light scattering in biological tissue. We demonstrate the first OCM images of biological objects using examples of plant and human tissue ex vivo.

Another variant of OCM is based on a broadband digital holographic technique. The final section of the chapter concerns 2D or 3D optical coherence tomography (OCT) imaging of the internal structure of strongly scattering media with micrometer-scale resolution by processing 200 sets of 2D holographic complex reconstructions at interference reception of backscattered light obtained at different wavelengths separated by a fixed spectral interval in the wavelength region of tens of nanometers. This technique of internal structure visualization apparently has a number of advantages over the known time-domain and spectral OCT methods, including the absence of transverse scanning systems at 3D visualization, and transverse spatial resolution has no limitations inherent in the correlation and spectral OCT techniques.

27.1 Compact Optical Coherence Microscope

27.1.1 Introduction. Overview of the Main Approaches to OCM Design

Optical coherence microscopy (OCM) is a new biomedical modality for cross-sectional subsurface imaging of biological tissue combining the sectioning abilities of optical coherence tomography (OCT) with confocal microscopy (CM). In OCM, spatial sectioning due to tight focusing of the probing beam and pinhole rejection provided by CM is enhanced by additional longitudinal sectioning provided by OCT coherence gating. For the first time, the OCT technique was used to enhance optical resolution of confocal microscopy by Izatt et al. [1]. Later, the OCM method and its potential for clinical application were studied and discussed in Ref. [2]. In that study, OCM images of a 5-μm layer located at the depth of 500 μm of the normal human colon specimen were acquired. The OCM images clearly demonstrated structures with resolution at the cellular level.

One of the main challenges of OCM is to provide high axial resolution by means of ultra-broadband light sources. As in OCT, the longitudinal resolution in OCM depends on bandwidth of a light source. Axial OCM resolution at a subcellular level was reported in Ref. [3], where a Kerr-lens mode-locked Ti:sapphire laser with double-chirped mirrors with a bandwidth up to 350 nm was used. At the wavelength of 0.8 μm, the authors attained 1-μm longitudinal resolution and 3-μm transverse resolution in biotissue. In Ref. [4], a superluminescent Ti:Al$_2$O$_3$ crystal was demonstrated as a possible light source for ultra-high-resolution OCT. This new source yielded light with power of 40 μW and bandwidth of 138 nm, which provided longitudinal resolution of 2.2 μm in air and 1.7 μm in tissue.

The feasibility of ultra-high axial resolution using supercontinuum generation was demonstrated by Hartl et al. [5]. The authors developed a broadband OCT imaging system with bandwidth of 370 nm and central wavelength of 1.3 μm. The longitudinal resolution of 2.5 μm in air and 2 μm in tissue was attained. An unprecedented axial resolution using supercontinuum generation was reported in Ref. [6]. The optical spectrum of generated light extended from 550 to 950 nm ($\lambda = 725$ nm, $P_{out} = 27$ mW); the corresponding axial resolution in air was 0.75 and 0.5 μm in biological tissue.

Nowadays, semiconductor diodes are the most compact broadband IR light sources. In Ref. [7], the authors combined radiations of several broadband luminescent diodes (LEDs) in order to improve longitudinal resolution of OCM by broadening the probing light spectrum. As a result, resolution was sufficient to successfully image microspheres with a diameter of 6 μm up to the depth of 500 μm in a scattering medium containing a suspension of 0.2-μm particles. For the same purpose of improving axial resolution, radiations of two superluminescent diodes (SLDs) with central wavelengths separated by 25 nm (830 and 855 nm, respectively) were combined [8]. The effective bandwidth of 50 nm was achieved, which corresponded to axial resolution of 6–7 μm in tissue. Although the semiconductor sources cannot yet provide axial resolution attainable by other sources, the field of IR optics is nevertheless rapidly evolving.

A second major challenge in OCM is to perform synchronous axial scanning of a sharply focused focal spot and the coherence gate while keeping their spatial alignment constant. For this purpose, in Refs. [1] and [2], the object itself was moved through a high-aperture lens and OCM images of a thin layer of the object near the focal area were acquired. In Refs. [3] and [4], several individual images obtained with the focus at different depths were fused to yield a composite image. The problem of synchronous scanning was partially solved when the dynamic focus method was proposed [6, 7]. In this method, the coherence gate and the sharply focused area of the probing beam are spatially aligned and moved in the axial direction simultaneously. In some designs the dynamic focus was attained by mounting an output objective of the signal arm and a retroreflector in the reference arm on the same scanning platform. However, this schematic provides satisfactory results only for relatively short scanning distances, because the mismatch between the coherence gate and sharply focused area is compensated only partially. In the alternative approach of dynamic coherence focus described in Ref. [9], the optical

length of the sample arm does not change during scanning. As a result, the coherence gate remains in the beam focus, requiring no additional adjustment of the reference arm. In Ref. [10], the authors describe another realization of the method for precise alignment of the focal area and coherence gate. Synchronous scanning is attained by moving the tip of the output fiber and a lens inside of the objective. This approach was successfully applied to determine refractive indices of different subsurface layers of biological tissue in vivo.

In our study we developed and fabricated a prototype of a compact OCM with a flexible sample arm and a remote optical probe for laboratory and clinical environment. To achieve axial resolution at the cellular level, a light source with effective bandwidth of 100 nm was developed. It comprised two semiconductor SLDs based on one-layer quantum-dimensional (GaAl)As-heterostructures with shifted spectra. Radiations from both SLDs were coupled into polarization-maintaining (PM) fiber by means of a specially designed multiplexer. The multiplexer was spectrally adjusted in order to achieve the minimum width of auto-correlation function (ACF). To broaden the bandwidth of a Michelson interferometer, the polished coupler based on anisotropic fiber with broadband of 3 dB was developed.

We also solved the problem of the dynamic focus by scanning the output lens of the objective located at the very end of the sample arm. The lens movement was controlled by the electronic system, thus allowing alignment of the sharply focused focal spot with the coherence gate spatially during their simultaneous scanning depth of 0.5–0.8 mm in biological tissue.

A method for suppression of spectral side lobes caused by non-uniformity of the light source spectrum was developed and successfully applied; the suppression efficiency was also estimated.

In addition, the problem of light propagation in a scattering medium was solved numerically. The dependence of axial resolution on the probing depth was studied for different parameters of the scattering and absorbing medium and the incident spectrum of probing radiation.

27.1.2 Interferometer for Compact OCM

A diagram of a compact OCM interferometer based on the traditional OCT scheme using PM fiber is shown in Fig. 27.1. The fiber optical Michelson interferometer employed for OCM comprises sample and reference arms. The use of anisotropic fiber allows the signal arm to be flexible, which is important for clinical applications. A light source consisted of two SLDs based on one-layer quantum-dimensional (GaAl)As-heterostructures with central wavelengths of 907 and 948 nm, bandwidths of approximately 53.4 and 72 nm, and initial power of 0.9 and 3 mW, respectively.

The probing light produced by the light source is passed through the sample arm to the optical probe. The probe comprises the optical and mechanical systems that perform focusing of the beam and also axial and lateral scanning. At the same time, the probe collects light backscattered by the object. The reference arm delivers
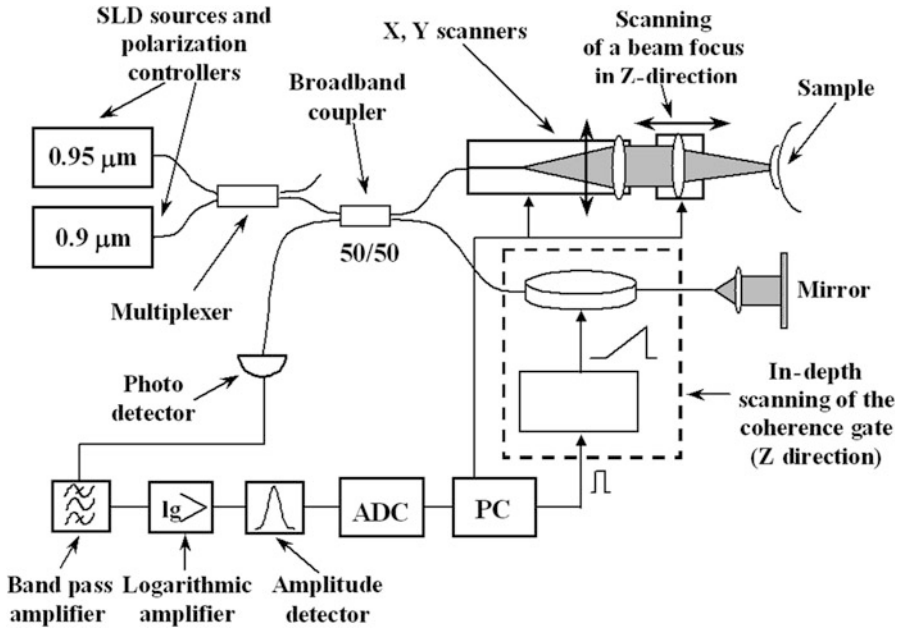
Fig. 27.1 OCM functional scheme

light onto a reference mirror and transports it back to the beamsplitter. At the beamsplitter, the light from both arms of the interferometer is combined. The light backscattered by the object would produce interference fringes with light reflected from the reference mirror only if the path-length difference between the arms does not exceed the coherence length of the source. The interference fringes are detected by the photo diode. The path-length difference between the arms of the interferometer (ΔL) was modulated by a linear law $\Delta L = \Delta \dot{L} \cdot t$ to perform heterodyne detection of the interference signal. This was attained by elastically stretching and contracting in antiphase the fibers using modulators based on piezoelectric converters [11]. In this case, the probing depth h inside of the object, from which the signal is measured, varies at a rate $\dot{h} = \Delta \dot{L} \frac{n_{fgr}}{n_{mgr}}$, where n_{fgr} and n_{mgr} are group-refractive indices of a fiber material and the object, respectively. When the path-length difference between the arms is changed linearly at the rate of $\Delta \dot{L}$, optical frequencies in the interferometer arms differ by a value of the Doppler shift. Therefore, the interference signal contains the component at a Doppler frequency $F = \frac{2\Delta \dot{L} n_f}{\lambda_0} = 2 n_{mgr} \frac{\dot{h}}{\lambda_0} \frac{n_f}{n_{fgr}}$, where n_f is the fiber phase refractive index, and λ_0 is the vacuum wavelength of probing radiation. For instance, at the wavelength of 0.94 μm and the Doppler frequency of 0.4 MHz the optical path-length difference between the interferometer arms is changed at the rate of $\Delta \dot{L} n_f \sim 0.13$ m/s.

The optical probe comprises a scanner that provides the "dynamic focus" by longitudinally scanning an output lens of the objective in the axial direction. The

scanner also moves the probing beam in the lateral directions, thus, generating both 2D and 3D images. The optical layout of a scanner consists of a two-lens objective; therefore allowing use of the maximum numerical aperture of the output lens. The objective magnification is equal to unity; the diameter of the focal spot is less than 4 μm. In the current design, the effective "dynamic focus" is implemented up to the depths at which sharp beam focusing starts to degrade due to multiple scattering of light.

Movement of an optical beam along the object surface is attained by moving an additional lens of the objective transversely. Scanning is performed by an electro-mechanical system that is incorporated into an optical probe at the end of the sample arm of the interferometer. The scanning process is fully automated and computer controlled.

The interference signal was detected using a photo diode with a fiber optical input characterized by a high quantum yield (>0.8) and low noise level. After analog processing, the signal is fed to a computer through an analog-digital converter. The computer is further utilized for digital signal processing, recording, and displaying of images.

According to the scheme of signal detection and analog processing, the resulting signal comprises a component that is proportional to the logarithm of the coefficient of tissue backscattering. The two-dimensional field of tissue backscattering coefficient obtained by scanning in depth (by changing the optical path-length difference between the interferometer arms) and along the object surface (by moving the probing beam laterally) is displayed on a computer monitor and stored for further processing. In contrast to many other indirect modalities of imaging of turbid media, reconstruction of both OCT and OCM images from the measured signal does not require solution of the complex inverse problem. Each in-depth element of an image corresponds to the certain time of light propagation to this element and back, i.e., the certain path-length difference between the interferometer arms. Therefore, the obtained images are relatively easy to interpret because they do not require any post processing and can be displayed in real time during scanning.

27.1.3 Development of Broadband Light Source and Interferometer Elements

Miniature superluminescent emitters and fiber elements of the interferometer are the basis for creation of compact portable devices that are suitable for clinical and industrial environments. The superluminescent semiconductor diodes based on one-layer quantum-dimensional (GaAl)As-heterostructures with central wavelengths of 907 and 948 nm, spectral widths of about 53.4 and 72 nm, and initial radiation power in the output of the single-mode fibers of 0.9 and 3 mW were employed as a light source. Spectra and corresponding ACFs of SLDs used are shown in Fig. 27.2.

The spectra of the both SLDs have complicated shapes that are inherent for quantum-dimensional heterostructures [12, 13]. When the radiations of two SLDs are mixed, the spectrum of resulting radiation considerably depends on the ratio of initial powers of each SLD. Figure 27.3a illustrates several resulting spectra

Fig. 27.2 (**a**) Spectral characteristics of superluminescent diodes. (**b**) Autocorrelation functions
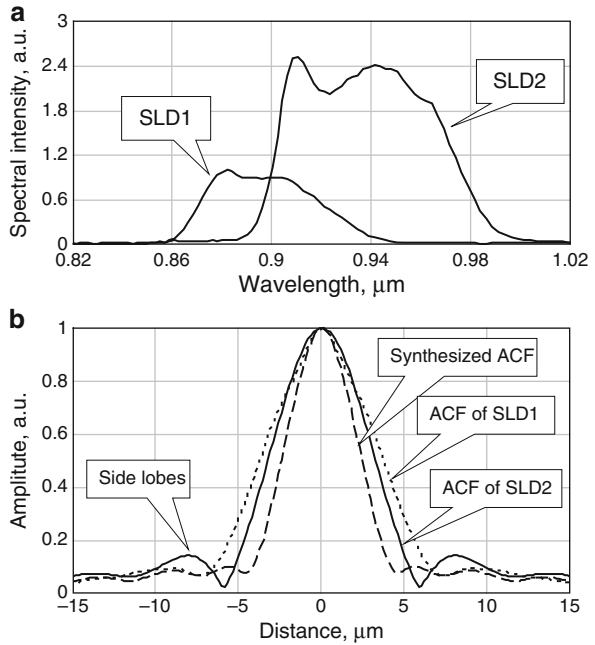
Fig. 27.3 Synthesis of broadband signal at different values of attenuation factor α of the second source (SLD2). (**a**) Synthesized spectrum, (**b**) corresponding autocorrelation function

obtained at the fixed power (0.9 mW) of a 907 nm SLD and varying power of
a 948 nm SLD (relative attenuation α of the initial power of the 948 nm SLD is
attained by lowering the pumping current). Corresponding ACFs are shown in
Fig. 27.3b. The resulting optimal spectrum was of a complex shape; bandwidth of
generated light was slightly wider than 100 nm and corresponding minimum width
of the central ACF lobe was 4.9 μm (free space). The side lobes of ACF were
suppressed to the level of 17.5 dB as compared to the central main peak.

Spectral tuning of the fiber optic multiplexer combining optical radiations from
two SLDs in one fiber was found to be critical. By controlling the parameters of the
multiplexer during assembly, the multiplexer output was optimized to provide
the narrowest ACF, which automatically provided the widest bandwidth of
the resulting spectrum. The multiplexer was made of halves of a polished coupler
using anisotropic fiber. The final assembly of the multiplexer was performed with
light introduced into both halves; the output ACF of the resulting radiation was
controlled with a correlometer and optimized as described above until the minimum
width of the resulting ACF was attained.

Figure 27.4 shows several curves of the resulting ACF width versus total output
power of the multiplexer. Parameter α was a ratio of current power of 948 nm SLD
to the initial power of 3 mW. The narrowest achieved ACF width corresponded to
4.75 μm in air.

The interferometer comprised a fiber optical 3-dB coupler built of polished
elements. There was observed optical coupling of modes in the polished elements
due to interaction of exponentially decreasing fields occurring mostly in fiber
coating. Polished couplers in contrast to welded ones usually provide a higher
degree of isolation of polarization modes with the extinction coefficient of at
least 35 dB. However, typical couplers of this type have bandwidths that are
insufficiently wide for use in interferometers with bandwidths of light sources at
the order of 100 nm. In our study, we analyzed the possibility of increasing the
broadband of the 3-dB coupler by optimizing its parameters. As a result, we
determined a more optimal domain of parameters and developed a 3-dB coupler

Fig. 27.5 Coupling efficiency, forward and backward pass, (*a*) with conventional broadbandness, and (*b*) enhanced broadbandness
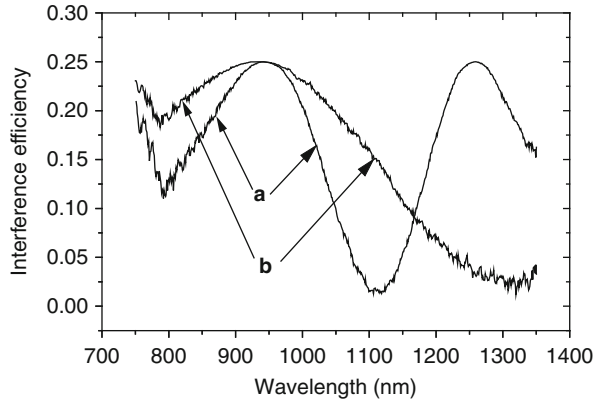
Fig. 27.6 Dependence of OCM lateral resolution versus depth for different initial waist sizes of probing beam
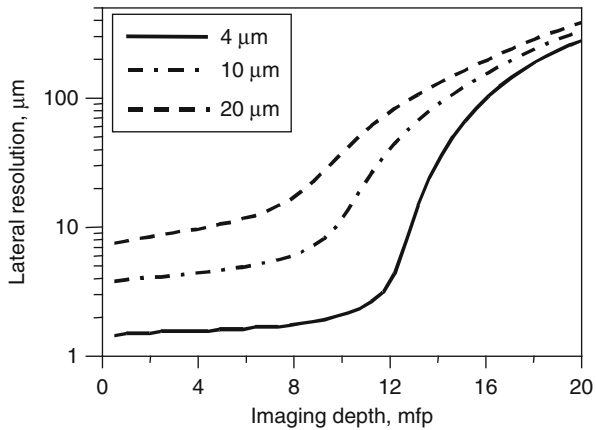
with improved broadband. Figure 27.5 presents experimental curves of the transfer coefficient during successive propagation and coupling in conventional and novel couplers. As can be seen from the graph, the novel design provides broadband approximately twice that of a conventional design. The parameters of the novel 3-dB fiber optical coupler are listed below: spectral bandwidth of 150 nm with central wavelength of 0.94 μm, insertion losses less than 0.2 dB, and the level of cross-talk between the polarization modes less than 35 dB.

27.1.4 Influence of Light Scattering on OCM Spatial Resolution

Multiple small-angle scattering affects spatial resolution of the OCM method significantly. In the transparent non-scattering medium, in-depth spatial resolution of the method is defined by a longitudinal coherence length (l_c) that is related to a coherence time (τ_c) and the velocity of light in the medium (v_n): $l_c = \frac{v_n \tau_c}{2}$. OCM sub-micron lateral resolution is determined by the waist size of the probing beam

Fig. 27.7 The contrast of the layer with spatially modulated backscattering coefficient for various initial beam waist sizes
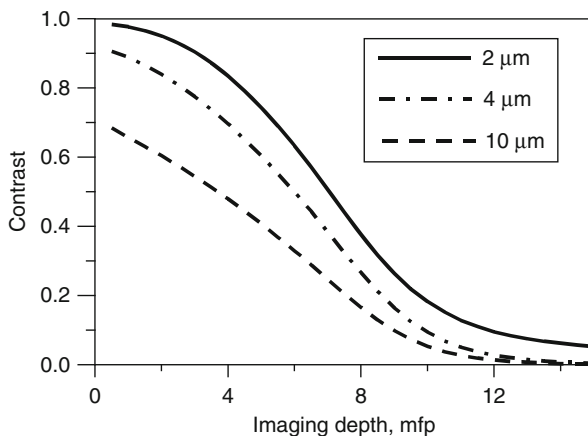
and is attained by using large numerical apertures. However, at typical imaging depths within biological tissue, multiple small-angle scattering becomes the dominant reason responsible for reducing the quality of obtained OCM images. Owing to multiple small-angle scattering, the radius of the focal spot increases, thus resulting in degradation of OCM lateral resolution. Moreover, the phenomenon of small-angle scattering also decreases OCM axial resolution due to multipass of photons.

However, the analysis of OCM resolution performed on the basis of the above-discussed theoretical model allows us to conclude that loss of spatial resolution due to scattering can be reduced by strong focusing of the probing beam, and in this way both lateral and axial resolution can be improved.

Figure 27.6 shows a dependence of OCM lateral resolution versus imaging depth for various waist sizes of the probing beam waist. It is assumed that an OCM image is reconstructed by synchronous in-depth scanning of the beam focal spot and the length of the reference arm while keeping the beam waist size constant. The lateral resolution was estimated by the FWHM of an OCM image of a point object obtained from the theoretical OCT model described in ▶ Chap. 24 (▶ Sect. 24.2) [14, 15]. (All presented dependences are calculated for a medium with scattering coefficient $\mu_s = 10$ mm^{-1}, anisotropy factor $g = 0.9$, and initial longitudinal coherence length $l_c = 5$ μm.) As is seen from the Fig. 27.6, OCM lateral resolution is preserved for larger imaging depths for probing beams with smaller initial sizes of beam waists. Starting from 10 mean free paths (mfp), a considerable loss of lateral resolution occurs due to diffuse widening of the probing beam at the focal depth. Under these conditions, the focusing effect also disappears and the behavior of lateral resolution versus depth becomes asymptotic and universal for all initial sizes of beam waists.

The idea of how OCM lateral resolution is lost can be deducted from imaging the layer with sinusoidal spatial modulation of the backscattering coefficient. Figure 27.7 demonstrates contrast of such a structure, i.e., the relative modulation amplitude of detected intensity versus the layer depth within scattering medium.

Fig. 27.8 OCM axial
resolution versus the imaging
depth for different waist sizes
of probing beam
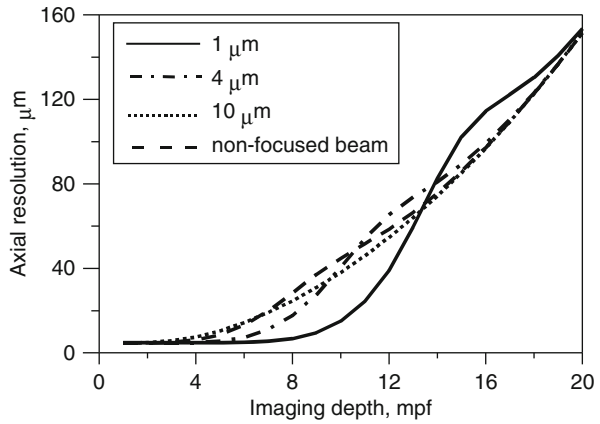
Fig. 27.9 OCM resolution
degradation versus beam
waist size at various imaging
depths
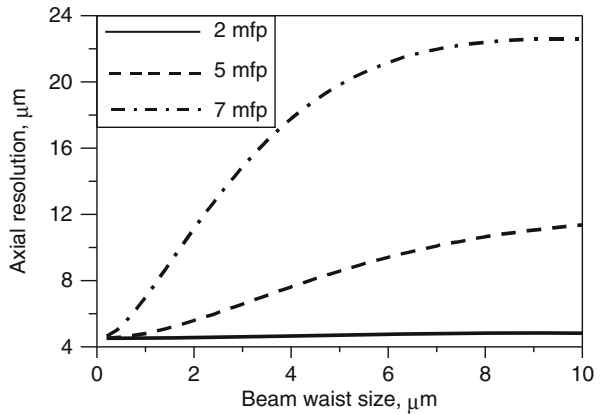
The contrast depends on the structure scale significantly. At shallow depth, the
structures for which the scale is comparable to the size of the beam waist have far
less contrast than those with the scale on the order of 10 diameters of the beam
waist. Contrast degradation with the imaging depth can be explained by beam
widening at the focal volume, the beam waist first becomes comparable with the
structure scale and then exceeds it.

It is important to point out that axial resolution of the method of OCM benefits
from tight focusing of the probing beam due to retaining of the longitudinal
coherence length for larger imaging depth in comparison to non-focused or weakly
focused beams. OCM axial resolution is defined as the width of an OCM image of
a thin backscattering layer. Figure 27.8 shows the dependence of OCM axial
resolution on the imaging depth for different sizes of beam waists. At shallow
depth, strong focusing provides better axial resolution because ballistic photons of
a highly focused beam contribute greater to the total light distribution at the focal

volume. However, at larger depths one can notice a sharper decrease of axial resolution for beams with smaller widths. This effect can originate from the fact that, for a beam focused deep inside of a scattering medium, the backscattered OCM signal is registered not from the focal volume precisely but from a closer distance due to group retardation of photons. In the case of tight focusing, the beam volume that contributes to the detected signal is larger than that of a weakly focused beam. Therefore, the OCM image is formed by photons undergoing more scattering events, which results in a significant loss of axial resolution. Figure 27.9 shows the behavior of OCM axial resolution for various imaging depths as the beam waist increases.

In summary, the analysis of OCM spatial resolution shows that tight focusing of the probing beam allows preserving both lateral and axial resolution up to the depth of 10 mfp due to increased contribution of ballistic photons to an OCM signal.

27.1.5 Electro-mechanical System for Dynamic Focus

The optical probe comprising the focusing system and the means for transversal beam scanning is located at the distal end of the sample arm of the interferometer. The optical layout of the focusing system consists of two lenses with effective magnification of unity. The lateral focal spot size was equal to 3.9 μm, i.e., to the diameter of fiber mode of the sample arm. The second lens allows using the objective aperture with maximum efficiency. The dynamic focus is attained in this OCM prototype by moving the output lens axially and thus providing longitudinal movement of the focal spot through the object (Fig. 27.10a). The relationship between the axial displacement of the focal spot in a medium and the coherence gate while they are simultaneously scanned and the path-length difference between the arms of the interferometer is established below. If the focal spot during lens scanning is placed inside of a uniform medium with a refractive index n, then, as shown in Ref. [9], the lens displacement Δz_L will correspond to the increase in the optical path length of the sample arm by $n n_g \Delta z_L$. Here, n_g is the group refractive index of the medium. Therefore, when the lens is moved, the distance between centers of the focal and coherence zones gets shifted by $n n_g \Delta z_L$. In our interferometer, an additional modulator is used to scan the optical path-length difference between the interferometer arms [11]. The path length difference of Δz in free space corresponds to the displacement of the coherence zone in the medium of $\Delta z / n_g$. Obviously, the initially aligned focal spot and coherence gate centers will not diverge during scanning only if the following condition is satisfied $n n_g \Delta z_L = \Delta z$. At the fixed rate of the path length difference scanning that determines a Doppler frequency, the rate of the axial movement of the output lens should be $\Delta \dot{z}_L = \Delta \dot{z} / (n \cdot n_g)$.

The typical length of the focal area (Rayleigh waist), say, for a focal spot diameter of 3.9 μm is 26 μm. Therefore, spatial alignment of the coherence gate and the focal spot should be quite accurate. The output lens was hanged in flexible suspension and scanned according to the triangular law by an electromagnetic
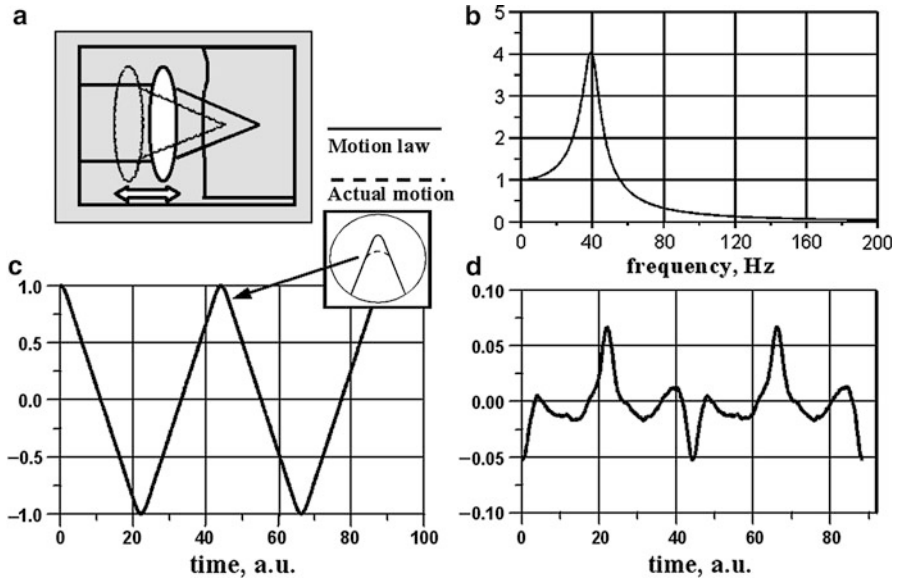
Fig. 27.10 Dynamic focusing in OCM
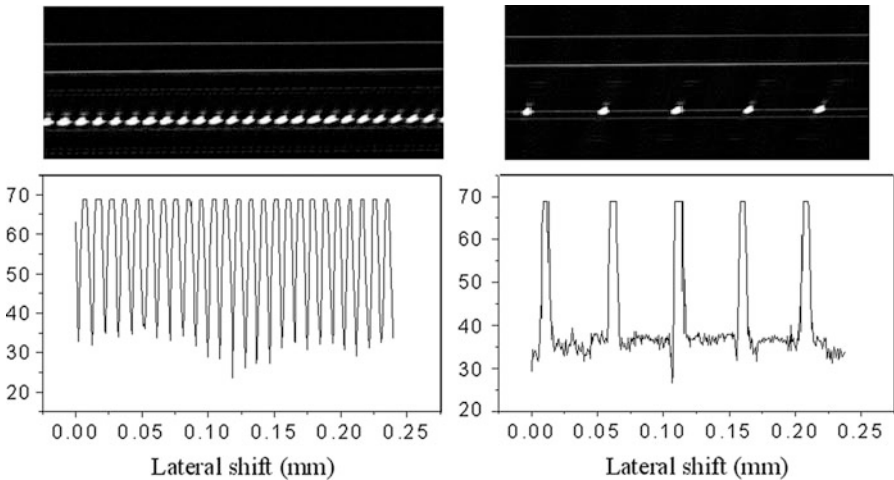
Fig. 27.11 OCM images of periodic patterns

controller with frequency of 100 Hz (Fig. 27.10c). The amplitude-frequency characteristic of the mechanical system was typical for resonance mechanical systems with a resonance frequency of ∼40 Hz and a Q factor of ∼4 (Fig. 27.10b). Since the frequency of lens scanning was close to the resonance frequency of the system, the control triangular signal was pre-distorted to compensate for the resonance response. As a result, it was measured that for the amplitude of

lens oscillations of 0.6 mm, the difference between the real motion and the theoretical one did not exceed 2 % for approximately 80 % of the movement range (Fig. 27.10d). The lateral resolution of OCM was analyzed using a grating with a step of 10 μm. The OCM images of the periodic pattern were recorded for several longitudinal positions of the sample. In a typical image shown in Fig. 27.11, the contrast of the image is about 30 dB. This corresponds well with the computational results for a Gaussian beam with a waist of 3.9 μm in diameter.

Of course, it is not always possible to precisely align the coherence gate and focal zone in real biotissue. This can be caused by deviations of refraction index from its mean, which are typical for biotissue layers [10]. In fairly thick layers of biological tissue, the misalignment can exceed the size of the focal zone. However, this misalignment can be eliminated in a single layer by correcting the lens movement law. To obtain an image with maximum resolution over the whole scanning range, it is necessary to acquire several 2D images with corrected focusing for particular layers of biological tissue and then fuse these 2D images.

27.1.6 Digital Signal Processing as a Tool to Improve OCM Resolution

As was described in Sect. 27.1.2, the radiation from two spectrally separated SLDs was combined in one fiber. It was observed that the resulting radiation had a spectrum of a non-Gaussian shape. This phenomenon led to the appearance of side lobes in ACF at the distance of ± 10 μm from the main center peak with amplitude of -18 dB. To suppress the side lobes, we developed a method of regularization of the spectrum of the Doppler signal by means of digital signal processing. The idea of the method is to devise a regularization function that could be used to multiply the original ACF with side lobes and the product would yield ACF with nearly Gaussian shape with suppressed side lobes. Using this function, the recorded radio-frequency (RF) signal was converted and an OCM image was reconstructed.

Figure 27.12 shows the ACF shape before and after spectrum regularization. It can be seen that the side lobes were suppressed approximately by 17 dB. Figure 27.13 presents spectra of the Doppler signal before and after regularization and the spectrum of the regularizing function. Note that along with the correction of the spectrum, the regularization procedure eliminated noise outside of the Doppler detection band. Figure 27.14 illustrates an example of an OCM signal from two thin scattering boundaries separated from each other by 18 μm, before and after regularization.

It can be seen from this figure that the side lobes of responses from two boundaries overlap. Obviously, the resulting side lobes in the OCM signal in between the central peaks of boundary responses depend on the phase difference between the latter. As a result, the suppression of these combined side lobes by means of regularization would also depend on a distance between responses. In this
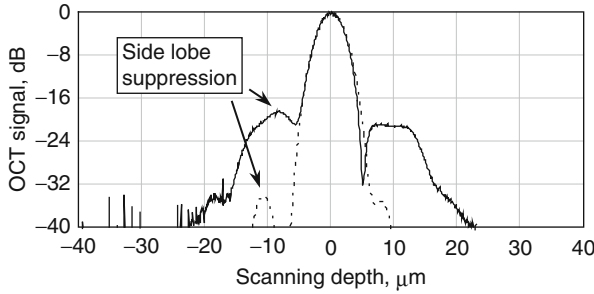
Fig. 27.12 Autocorrelation function before (*bold line*) and after (*dotted line*) regularization procedure
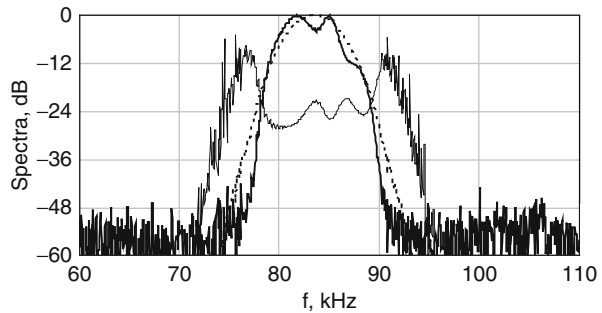
Fig. 27.13 Spectra of the Doppler signal before (*bold solid line*) and after regularization (*bold dotted line*) and the spectrum of the regularizing function (*solid thin line*)
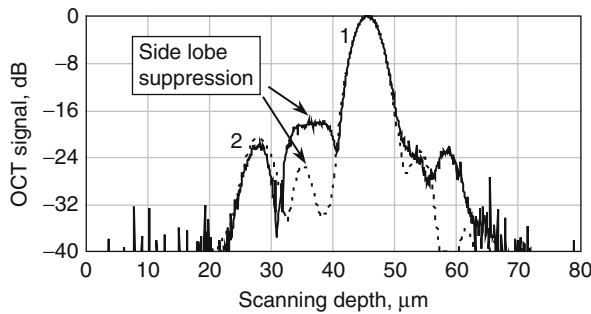
Fig. 27.14 *Bold line*: OCT signal obtained from two reflectors, peaks *1* and *2*, correspondingly; *dotted line*: OCT signal after spectra regularization procedure. The amplitude of a side lobe between peaks *1* and *2* is larger than the amplitude of peaks *2* and thus produces a false target on a tomogram. Regularization method allows one to suppress side lobes significantly

particular case, the side lobes were suppressed by 8 dB. If the distance between neighboring imaging elements exceeds the coherence length, the degree of side lobe suppression by regularization will be the same as for ACF and will be equal to 17 dB.

Fig. 27.15 General view of OCM

27.1.7 Experimental OCM prototype

All the ideas and approaches described above were implemented in our experimental compact OCM prototype. The OCM setup features a flexible signal arm and a remote optical probe at the distal end. The probe is equipped with a three-coordinate scanning device that controls a focal zone position. The size of the optical probe in the largest dimension does not exceed 5 cm. The studied object is placed atop the output window with immersion. Figure 27.15 presents a general view of the compact optical coherence microscope and the remote optical probe connected to the main body by flexible optical and electrical cables. The dimensions of the OCM device in this configuration do not exceed $12 \times 30 \times 40$ cm^2, weight is about 7 kg. The OCM requires standard AC power network, device power consumption is no more than 25 W. The OCM device can be operated and images can be recorded and stored using a personal desktop or portable computer with a processor 486DX-33 or higher. The OCM device in the current design may be applied for intraoperative express analysis of human tissues ex vivo.

27.1.8 Biomedical Applications

Preliminary biomedical experiments using OCM were carried out on model media and on biological materials ex vivo, namely, plant leaves and excised human tissues were studied. Plant leaves were observed immediately after separation from the stem in order to minimize influence of a decrease in cellular turgor on the quality of images. Postoperative samples of human tissue were placed into physiological solution right after excision and were studied during next 40 min. to avoid postmortal tissue alterations.

Figure 27.16 shows OCM and OCT images of tomato and tradescantia leaves. Images clearly demonstrate morphological features of studied objects. Advantages of OCM over OCT are obvious: while OCT allows differentiation of mostly cellular

OCT

OCM
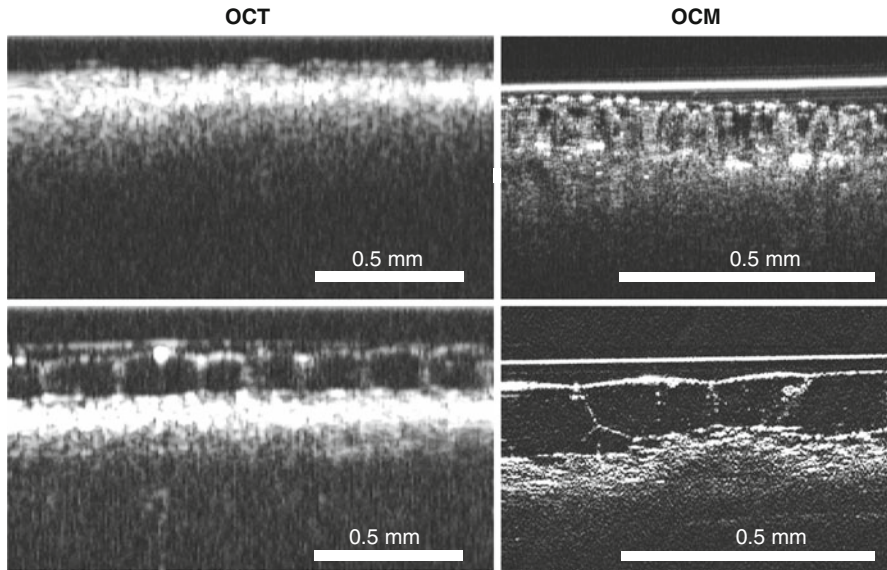
Fig. 27.16 OCT and OCM images of tomato and tradescantia leaves
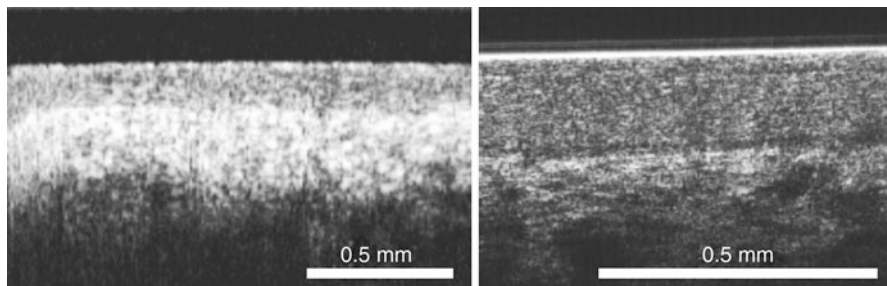
Fig. 27.17 OCT and OCM images of uterine cervix ex vivo

layers, and rarely large cells with a size of 50–100 μm, OCM easily visualize both cellular layers and single cells with a size of 10–20 μm constituting these layers.

Quality of visualization of intracellular structures is determined not only by spatial resolution of the method but also by the chosen plane of scanning because sometime 2D scans miss cellular nuclei. 3D scanning of the object with a step of several microns between the 2D planes allowed reconstruction of the true 3D structure of the object, detecting cellular nuclei and accurate estimating of cellular shapes and sizes.

Based on our experience with OCT where the most informative were tissues with a stratified internal structure for the OCM study we chose organs covered with the squamous epithelium. The idea of the study was to compare OCM and OCT performances. Results of the study are shown in Fig. 27.17. Comparative analysis

revealed that while standard OCT could visualize the tissue layers, namely, the epithelium and underlying stroma, OCM could distinguish single cells constituting the epithelium up to depth of 500 μm.

Therefore, clinical and biological experiments clearly demonstrate that spatial resolution of OCM is sufficient for visualizing single cells. High spatial resolution of OCM advances us to the realization of the idea of absolutely non-invasive "optical" biopsy. We believe that another promising application of OCM is monitoring of plants in vivo with a purpose of dynamic control of structural alterations. Non-invasive investigation of internal structures of plants would allow studying the influence of various environmental factors (external and internal). Such studies would definitely benefit selections, ecology, and cosmic biology.

27.1.9 Conclusion

This part of the chapter presents development and fabrication of a compact OCM based on broadband PM fiber elements. OCM combines advantages of ultra-broadband OCT and high numerical aperture confocal microscopy. An ultra-broadband light source was devised and constructed using two SLDs with spectra covering the wavelength range of 0.88–0.98 μm. The light source provided axial resolution of 4.75 μm in air. The optical layout of the OCM probe comprised two micro lenses transposing the fiber tip with magnification of 0.8–1 and provided lateral resolution of about 3.9 μm. The focal volume of the probing beam and the coherence gate were spatially matched and scanned in-depth synchronously using the principle of the dynamic focus. For this purpose we developed and created a three-coordinate electro-mechanical system. We also proposed and investigated a method for correction of distortion of the ACF form caused by the non-Gaussian shape of the light source spectrum. This method corrects the envelope shape and suppresses the spectral side lobes by regularizing the spectrum of the Doppler signal at the stage of digital signal processing. The dependences of axial and lateral spatial resolutions of the optical coherence microscope on imaging depth in media with scattering parameters typical for tissue were investigated theoretically. OCM images of model media and biological objects ex vivo were acquired.

27.2 A New Optical Coherence Microscope Approach Based on Broadband Digital Holography

The broadband digital holographic method allows getting high-resolution 3D images of depth structure of biotissue (or other turbid matters) by IR radiation without axial and lateral scanning. Absence of any mechanical scanning, unlike time domain (TD) and spectral domain (SD) OCT methods, removes restriction on time of reception of 3D OCT images.

27.2.1 Introduction

Much attention has been given to developing methods for visualizing internal structure of biological objects such as optically turbid layered media with spatial resolution of several microns. These include time domain (correlation) OCT [16] and spectral OCT [17] based on low-coherence interferometry, as well as confocal microscopy (CM) [18]. Cross-sectional, micron-scale imaging of internal structure of the studied object is based on reception of a spatially localized component of backscattered and back-reflected radiation with suppression of the influence of background noisy multiple scattering. A raster (2D) pattern of cross-sectional imaging is attained by means of transverse scanning. The use of transverse scanning with lens translation in low-coherence interferometry gave rise to both, the term OCT and the OCT technique [16]. Later, transverse scanning was accomplished by including various systems driving a fiber tip, e.g., [19], as well as some other mechanical methods [20]. Scanning methods as well as principles of formation of longitudinal and transverse elements of spatial resolution are different in different OCT modalities and CM, hence, limitations and drawbacks of the latter are also different, which can be illustrated by some examples. For instance, in the time domain OCT technique, a probing wave beam is formed with Rayleigh length equal to the entire observation length so as to ensure uniform illumination of the object. Scattered light at each time instant can be received only from the region whose depth is equal to the radiation coherence length [16] and is much smaller than the Rayleigh length. As the scattered radiation components coming from other regions do not take part in interference, the power of probing optical radiation is used inefficiently. In the spectral OCT technique, each received spectral component has equivalent coherence length exceeding a possible area of study, and optical power is used more effectively. The drawback of this technique is a possibility of coherent noise [21, 22]. Confocal microscopy [18] has higher longitudinal and transverse resolution but the signal decays faster with increasing observation depth than in the case of OCT. Note that for CM and OCT depth enhancement, the method of optical clearing is currently under way [23–25]. The OCM technique that combines the principles of OCT and CM [1, 26] provides larger observation depth and better spatial resolution. A second major challenge in OCM is to perform synchronous axial scanning of a sharply focused focal spot and the coherence gate while keeping their spatial alignment constant. The difficulties encountered with the use of the OCM technique relate mainly to accuracy of controlling the focusing lens motion, especially when scanning multilayered biological objects. The transverse and longitudinal scanning systems in all of the above-mentioned techniques are based on mechanical devices whose resonance properties limit the speed and accuracy of motion. In addition, some applications, such as endoscopy, demand compact systems for transverse scanning that may introduce additional difficulties.

Some papers address development of a method for visualizing 3D objects without longitudinal and transverse scanning. Holographic reception of scattered

light is used for digital 2D or 3D imaging of the object [27–29]. For example, the method of determining complex amplitude of the field scattered from an object holographically recorded on CCD matrix is described in the Ref. [27], where the image of a flat object recorded in monochromatic light at the wavelength of 514 nm was reconstructed. The longitudinal position of the object was set to an accuracy of Rayleigh length of effective Gaussian beam determined by the size of the CCD matrix and distance to the object. Longitudinal spatial resolution in the holographic method may be increased by processing a series of holograms obtained at different wavelengths separated by a fixed spectral interval [28, 29]. Thus, the spatial resolution of 3 cm obtained in [28] using 11 holograms in the 10 GHz laser-tuned interval (595 nm central wavelength) allowed resolving two plane layers spaced 18 cm apart. A method of transverse spatial harmonics expansion for 3D imaging from a hologram was described in [29]. It was demonstrated that this method has better processing speed and signal-to-noise ratio than imaging by the Fresnel diffraction formula for different distances between the object and the hologram. For example, surface structure of a coin was reconstructed from 20 holograms obtained in the 575–605 nm wavelength range. Thus, fundamental principles of using holographic photoreceiver matrix records of scattered light for digital 2D and 3D imaging of object surfaces were considered in [27–29].

The holographic method of recording interference pattern and subsequent digital reconstruction and imaging of the object may be employed in the OCT technique for imaging the internal structure of scattering media (biological objects). In conventional holography an object is illuminated by a monochromatic source of light, and the result of interference between the light scattered or refracted by the object surfaces and the reference wave is 2D recorded. Holographic imaging of several semitransparent internal structures is also possible. Rayleigh length is an element of longitudinal spatial resolution in 3D imaging. One of the ways to further improve longitudinal spatial resolution is to use low-coherence radiation similarly to the time domain [16] and spectral [17] OCT techniques. Still another resource for increasing longitudinal spatial resolution in holographic recording is reduction of effective Rayleigh length by increasing the angular aperture of scattered light reception like in confocal microscopy [18], which is especially interesting for detailed drafting of small-size objects [30].

The goal of the current work is implementation in experiments with a broadband digital OCT holographic technique for visualizing external and internal structure of layered scattering media with a resolution of several microns and analysis of its merits and drawbacks.

27.2.2 Fundamentals of the Technique

In the current work, as in [27–29], information about backscattered radiation was obtained by means of 2D recording of a holographic picture instead of transverse X-Y scanning by probing light. Longitudinal resolution was enhanced, similarly to [28, 29], using a series of holograms recorded at several wavelengths

separated by a fixed spectral interval in a broad spectral band. Probing and reference waves had spherical and plane wave fronts, respectively.

In a digital hologram, a signal of each matrix element is proportional to optical field intensity. Two-dimensional records of the signal represented for simplicity in continuous coordinates may be written in the following form:

$$
\begin{aligned}
S(x, y) = I_R(x, y) + I_S(x, y) + 2 \cdot \sqrt{I_R(x, y) \cdot I_S(x, y)} \cdot \\
\cdot \cos[\varphi_R(x, y) - \varphi_S(x, y)],
\end{aligned}
\tag{27.1}
$$

where $I_R(x, y)$, $I_S(x, y)$ are the intensities at the (x, y) point on the CCD-matrix plane of the reference and scattered wave fields, respectively, and $\varphi_R(x, y)$ and $\varphi_S(x, y)$ are the phases of these fields. In addition, for simplicity, we omitted in the interference term in formula (27.1) the visibility factor numerically equal to the cosine of the angle between wave vectors of the interfering waves. The quantities entering (27.1) are real; however, complex representation of the signal is needed to remove conjugate components for image reconstruction. For this it is necessary to make three digital sets of records of signals from the CCD matrix with the phase difference between the waves $\Delta\varphi = 0, \pi/2$ and π. By subtracting the result of the first records from the second one, and of the second from the third, and taking into account that the reference wave intensity and phase are independent of the transverse coordinate, we obtain the following two expressions:

$$
\begin{aligned}
S_2(x, y) - S_1(x, y) = \sqrt{2} \cdot A_S(x, y) \cdot \cos(\varphi_S(x, y) - C) \text{ and} \\
S_3(x, y) - S_2(x, y) = \sqrt{2} \cdot A_S(x, y) \cdot \sin(\varphi_S(x, y) - C),
\end{aligned}
\tag{27.2a}
$$

where $C = const + \frac{3 \cdot \pi}{4}$, and $A_S(x, y) = \sqrt{I_S(x, y)}$ is the amplitude of the field.

Expressions (27.2a) may be transformed to a complex form of the field in the CCD-matrix plane $S_C(x, y)$:

$$
S_C(x, y) = A_S(x, y) \cdot \exp(i \cdot \varphi_S(x, y) - C).
\tag{27.2b}
$$

The field at the object site at distance z from the CCD-matrix plane is reconstructed as follows. First, the field scattered by the object must be expanded in terms of plane waves at $z = 0$. For this the $S_C(x, y)$ field is 2D Fourier transformed:

$$
FFF2d_C(k_x, k_y)_0 = \iint S_C(x, y) \cdot \exp(i \cdot k_x \cdot x + i \cdot k_y \cdot y) \cdot dx \cdot dy,
\tag{27.3}
$$

where k_x, k_y are the transverse spatial frequencies that are projections of the wave vectors of these plane waves on the X and Y axes, respectively. With such a digital hologram representation, the conditions of Kotelnikov-Nyquist's criterion should

be met for transverse spatial harmonics of the field scattered by an object. The absolute value of wave vector projections onto the XY-plane of the matrix should not exceed $\frac{\pi}{d}$, where d is the size of the matrix element. This condition determines the magnitude of minimal distance to the object.

As the observation plane is moving from the matrix plane along the Z-axis, the complex value of the 2D Fourier transform (27.3) for a definite direction in the k-representation (k_x, k_y, k_z) will only change the phase with velocity $\partial \phi / \partial z = k_z$. The resulting 2D Fourier transform in the z-plane has the form

$$FFF2d_c(k_x, k_y)_z = FFF2d_c(k_x, k_y)_0 \cdot \exp(-i \cdot z \cdot \sqrt{k^2 - k_x{}^2 - k_y{}^2}). \qquad (27.4)$$

The inverse Fourier transform of the $FFF2d_c(k_x, k_y)_Z$ array gives the representation of the field from the object at distance z from the CCD matrix at the wavelength $\lambda = 2 \cdot \pi / k$.

Figure 27.18 shows the real part of the reconstructed field for different depths z, presented in intensity scale for a single scattering object.

The resolution attained with such a technique may be calculated (approximately) by formulas for the transverse $2\omega_0$ and longitudinal size $2Z_R$ of the waist of the Gaussian beam focused by a lens having diameter d equal to the size of the CCD matrix and focal distance f equal to the distance from the matrix to the object, respectively:

$$2 \cdot \omega_0 = \frac{4 \cdot \lambda}{\pi} \cdot \left(\frac{f}{d}\right), \qquad (27.5)$$

$$2 \cdot Z_R = \frac{\pi \cdot 4 \cdot \omega_0^2}{2 \cdot \lambda}. \qquad (27.6)$$

Note that the radiation coherence length of a tunable source should exceed the depth of the studied area. To increase longitudinal in-depth resolution (along z), like in spectral OCT, the radiation source with spectral bandwidth $\delta\lambda$ should be tuned discretely within the spectral range $\Delta\lambda$ with step $\Delta\lambda/N$. As a result, using the procedure described above one can obtain N complex holograms for this set of N wavelengths. The result of 3D field distribution in complex form is calculated for each n-th wavelength. 3D representation of the signal $S_C(x, y, z)$ is calculated by summarizing in complex form all N 3D field distributions obtained above:

$$S_C(x, y, z) = \sum_{n=1}^{N} \iint FFT2d_C\left(k_x, k_y, \frac{2\pi}{\lambda_n}\right) \cdot \exp\left(-i \cdot z \cdot \sqrt{\left(\frac{2\pi}{\lambda_n}\right)^2 - k_x{}^2 - k_y{}^2}\right)$$
$$\cdot \exp(-i \cdot k_x \cdot x - i \cdot k_y \cdot y) \cdot dk_x \cdot dk_y,$$
$$(27.7)$$

which allows increasing resolution along the z-axis at 3D imaging. In our case, when $k^2 >> k_x{}^2 + k_y{}^2$, expression (27.7) may be simplified as follows:
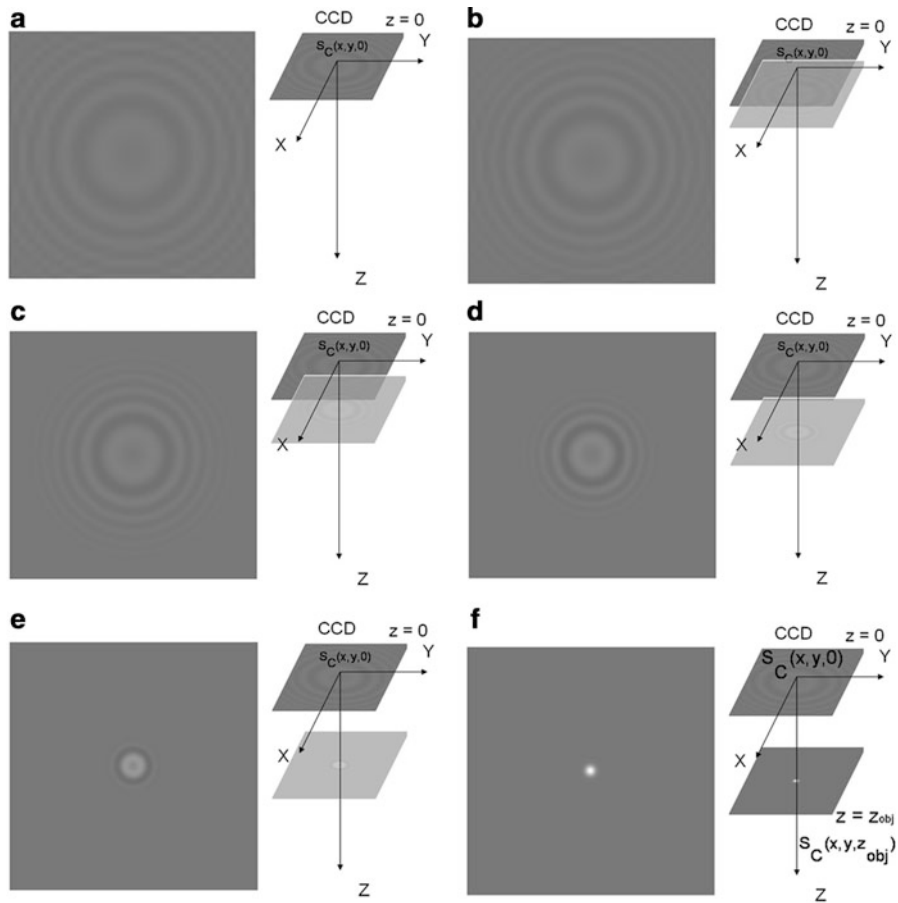
Fig. 27.18 2D optical field reconstruction for different z – distance to CCD plane. Fragment f corresponds to scatterer location

$z \cdot \sqrt{k^2 - k_x^2 - k_y^2} \approx k \cdot z - z_0 \cdot \frac{k_x^2 + k_y^2}{2 \cdot k^2}$, where z_0 is the coordinate of the object border.

Thus, expression (27.7) is represented as a 3D Fourier transform written for simplicity in integral form

$$S_C(x,y,z) = \iiint FFF3d_C(k_x, k_y, k) \cdot \exp(-i \cdot k_x \cdot x - i \cdot k_y \cdot y - i \cdot k \cdot z) \cdot dk_x \cdot dk_y \cdot dk.$$

$$(27.8)$$

Formula (27.8) is calculated by a standard algorithm of fast Fourier transform. Here
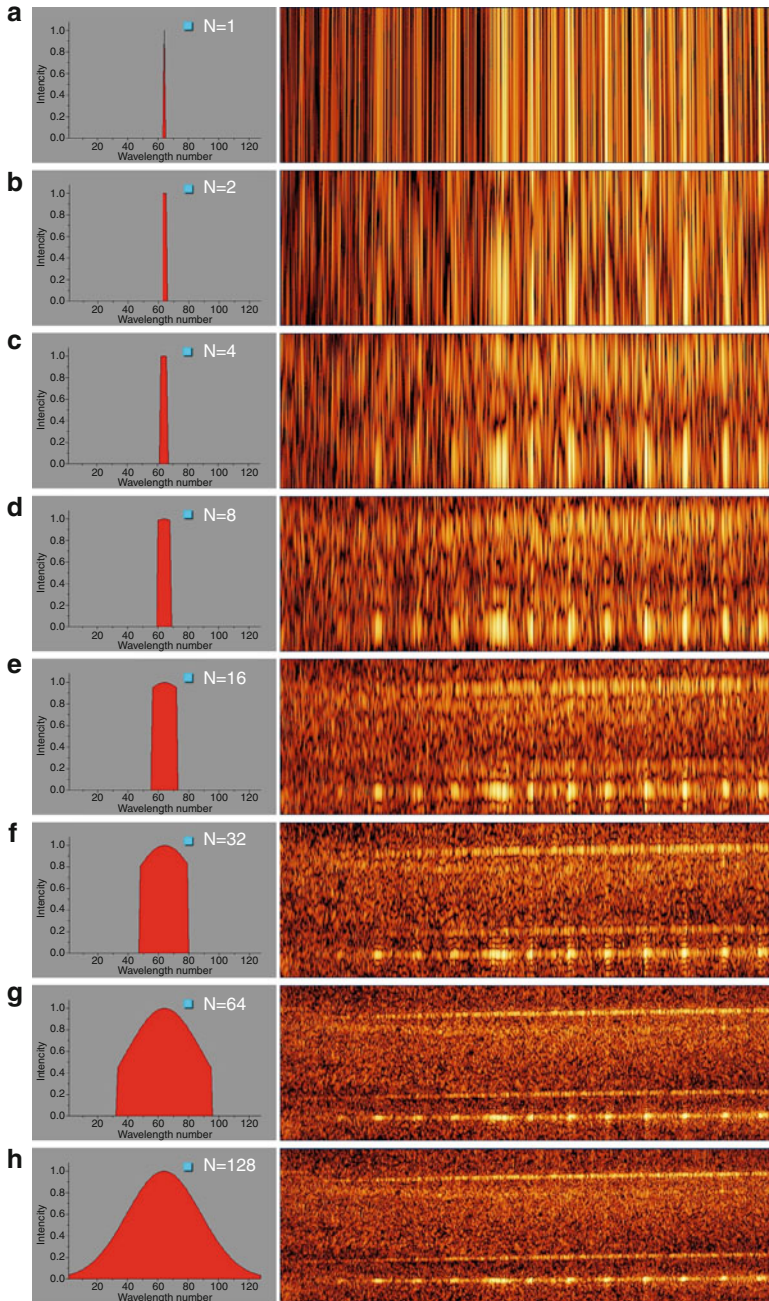
Fig. 27.19 Dependence of axial resolution on the number of spectral lines registered independently. Left column – spectral shapes; right column – X-Z planes of the corresponding reconstructions of "metric circle crosshair contact reticle"

Fig. 27.20 Optical scheme of the holographic OCT technique
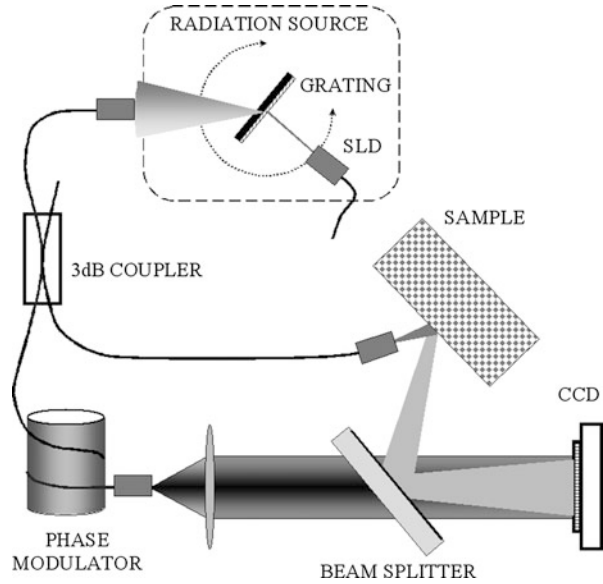
$$FFT3d_C(k_x, k_y, k) = FFT2d_c(k_x, k_y, k) \cdot \exp\left(i \cdot z_0 \cdot \frac{k_x^2 + k_y^2}{2 \cdot k}\right)$$

Note that, unlike the holographic image obtained by means of monochromatic radiation, a multiwave 3D image has longitudinal spatial distribution determined by the width of the spectral range of light source tuning

$$\Delta z = \frac{2 \cdot \ln 2}{\pi} \cdot \left(\frac{\lambda^2}{\Delta \lambda}\right),$$

rather than by equivalent Rayleigh length.

Experimentally, Fig. 27.19 demonstrates the decreasing of axial resolution element while increasing of a number N of spectral lines registered independently.

27.2.3 Experiment

The setup for implementing the holographic OCT technique is shown schematically in Fig. 27.20.

A prototype of a narrowband radiation source with coherence wavelength of several millimeters (2–3 mm) tuned in the 30-nm spectral range with the central wavelength of 850 nm was created for the experiment. Radiation of a broadband superluminescent source was subjected to spectral discrimination with a diffraction grating (1,200 grooves per millimeter) and, further, radiation in the spectral interval
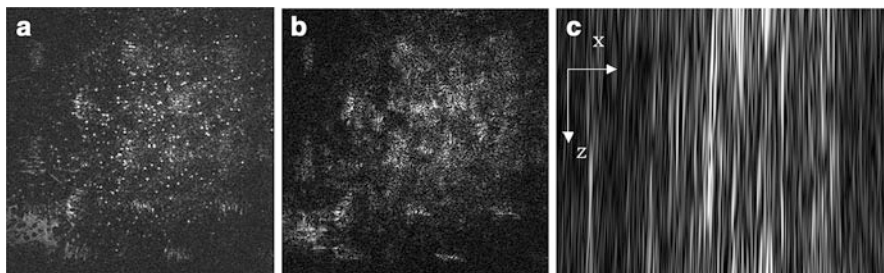
Fig. 27.21 Image of the object section in the planes $z = 43$ mm (**a**), $z = 44$ mm (**b**), and result of in-depth section imaging (in the x-z plane) in the 42–44 mm interval (**c**)

$\delta\lambda$ was collimated into a single-mode fiber. The operating wavelength was changed by the collimator angle of turn relative to the grating. The source radiation power was about 2 μW.

Wavelength tunable IR radiation was separated by means of a fiber optic coupler (Fig. 27.20) into a probing and a reference wave in 9/1 ratio. The probing wave was emitted into free space from a single-mode fiber with natural divergence determined by the mode size. The reference wave that was also emitted into free space was then collimated into a plane wave. The wave scattered by the object was added to the reference wave on the CCD matrix that recorded the result of their interference. In our experiment we used a CCD matrix with 1024×768 elements, each being 4.65×4.65 μm in size. With such a density of matrix elements, the Kotelnikov-Nyquist's criterion was met at distances to the object not less than 40 mm. An example of digital reconstruction of field amplitude from complex holograms recorded at one wavelength is shown in Fig. 27.21 for a fiberglass plastic sample – scattering material with coarse-fiber structure located 43 mm away from the CCD matrix. Pictures of the reconstructed field 2.37×2.37 mm in size (500×500 points) for the surface of the object ($z = 43$ mm) in the transverse x-y plane are shown in Fig. 27.21a, and for the section 1-mm deep inside the object ($z = 44$ mm) in Fig. 27.21b.

The first section corresponding to the surface of the object shows the image of surface micro-inhomogeneities with diffraction resolution. This is due to location of the object's surface near the focus of the equivalent confocal system digitally reconstructed from one complex hologram. The image in the second section corresponds to detuning from the focal plane by the depth of about $10 \cdot Z_R$.

The in-depth reconstruction of the cross-section (in the x-z plane) for the same studied sample is presented in Fig. 27.21c, where z (the vertical axis) varies from 42 to 44 mm, the size along the horizontal is 2.37 mm. This plane image is reconstructed from a complex hologram using a coherence source at 0.85 μm. The extended structures represent the Rayleigh regions (27.6) $2 \cdot Z_R$ in size. Here, the longitudinal resolution is analogous to confocal reception. In our case, for $\lambda = 0.85$ μm, $f = 43$ mm, and $d = 5$ mm we have: $2 \cdot \omega_0 \approx 10 \mu m$ and $2 \cdot Z_R \approx 200 \mu m$. It is clear from Fig. 27.21 that the holographic image obtained at one length has good transverse and poor longitudinal resolution.
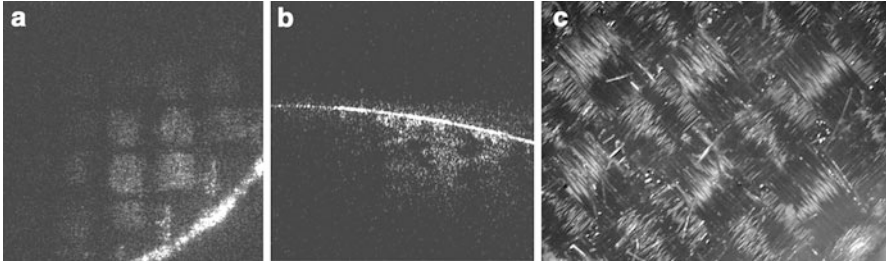
Fig. 27.22 Reconstructed fragments of bulk image in the X-Y plane (**a**) and in the X-Z plane (**b**). (**c**) Photographic image of the object, cleft in plane X-Y on the same depth
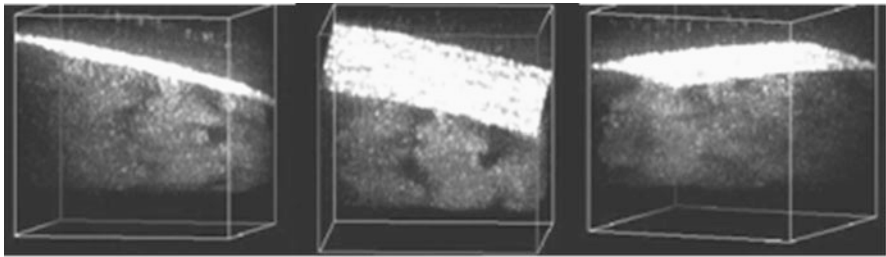
Fig. 27.23 Fragments fiberglass plastic 3D images under different angles of observation

To increase resolution along the *z*-coordinate we obtained 200 complex holograms using the procedure described above for equidistant wavelengths in the 30 nm spectral range with center at 0.85 μm. The fragments of bulk image reconstructed by formula (27.7) are given in Fig. 27.22 in the form of two sections (parallel and normal to its surface) at the depth of ∼0.5 mm.

The regions of the object in Fig. 27.22 have the size of 2.5 × 2.5 mm. Figure 27.22 demonstrates potentialities of digital image reconstruction with high spatial resolution from a series of complex holograms obtained without a focusing system. In our case, for the effective value $\Delta\lambda = 30$ nm, the theoretical maximum of longitudinal spatial resolution is $\Delta z \approx 11$ μm.

In Fig. 27.23, various projections of fiberglass plastic 3D image obtained in a Mach-Zehnder interferometer setup are presented. Images are presented for various angles of observation for the object part, bounded in *x-y* plane (approximately 1 × 1 mm). On images through the artificial cube lateral sides, the fiberglass plastic internal structure is visible.

The surface curvature visible in the figures is attributed to probing wave divergence and may be removed by means of the corresponding correction during imaging.

Other images were obtained using commercial tunable laser source BS840-02 by Superlum (Russia). Output optical power is about 1 mW, tuning range is from 825 to 875 nm, and laser line width is $\delta\lambda = 0.1$ nm. The test object was comprised of
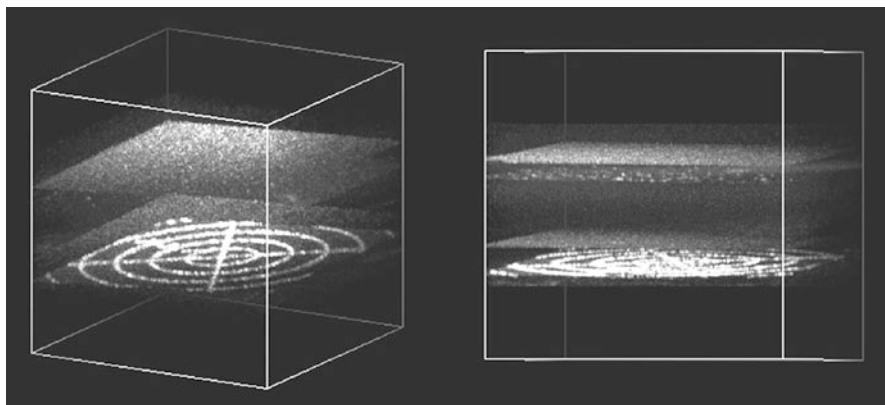
Fig. 27.24 3D images of the test object acquired with a tunable laser source

a NT39-454 Metric circle crosshair contact reticle (Edmund Optics) and piece of semitransparent tape on the surface. Some fragments of the 3D image of the test object are represented in Fig. 27.24.

27.2.4 Conclusion

In this chapter we presented results of development of two versions of the OCM technique based on low-coherence interferometry. First, we described results of creating OCM in which time-domain OCT and confocal microscopy are combined. One of the principal features of this OCM variety is the use of several scanning systems for high spatial resolution imaging (3-4 μm) along the X,Y,Z coordinates. These include the transverse scanning system and the system of synchronous axial scanning of a sharply focused focal spot and a coherence gate while keeping their spatial alignment constant.

In the second part of the chapter we considered practical application of OCM technique based on broadband digital holography. Thus, this chapter described further development of the earlier research [27–29, 31]. Full-range 3D OCT imaging of in-depth layered structure of the object is based on the digital holographic method of recording scattered signal using a wavelength-tunable IR radiation source and digital reconstruction.

This technique of internal structure visualization apparently has a number of advantages over the known TD-OCT [16] and SD-OCT [17] methods. Firstly, digital holographic recording of scattered signal in OCT eliminates the need in transverse scanning systems for 3D visualization, as well as systems of longitudinal scanning of a sharply focused focal spot and a coherence gate. Secondly, holographic recording ensures a much larger reception aperture of scattered radiation and higher signal-to-noise ratio. In the third place, transverse spatial resolution has no limitations inherent in the correlation and spectral OCT techniques. Resolution

can be improved up to the wavelength (and even submicron) size when using a large digital-aperture lens or small pixel size of the matrix. The considered broadband digital holographic technique is a good instrument for investigation of biological objects. But it is important to ensure fast hologram recording to eliminate the influence of phase disturbance by living objects moving during the total exposure time. With the state-of-the-art computer speed, a 3D image with 512 elements along each coordinate may be processed during about 1 sec.

References

1. J.A. Izatt, M.R. Hee, G.M. Owen, E.A. Swanson, J.G. Fujimoto, Optical coherence micros-copy in scattering media. Opt. Lett. **19**, 590–592 (1994)
2. J.A. Izatt, M.D. Kulkarni, H.-W. Wang, K. Kobayashi, M.V. Sivak Jr., Optical coherence tomography and microscopy in gastrointestinal tissues. IEEE J. Sel. Top. Quant. Electron. **2**, 1017–1028 (1996)
3. W. Drexler, U. Morgner, F.X. Kartner, C. Pitris, S.A. Boppart, X.D. Li, E.P. Ippen, J.G. Fujimoto, *In vivo* ultrahigh resolution optical coherence tomography. Opt. Lett. **24**, 1221–1223 (1999)
4. A.M. Kovalevicz, T. Ko, I. Hartl, J.G. Fujimoto, M. Pollnau, R.P. Salathe, Ultrahigh resolu-tion optical coherence tomography using a superluminescent light source. Opt. Express **10**, 349–353 (2002)
5. I. Hartl, X.D. Li, C. Chudoba, R.K. Ghanta, T.H. Ko, J.G. Fujimoto, J.K. Ranka, R.S. Windeler, Ultrahigh-resolution optical coherence tomography using continuum generation in an air-silica microstructure optical fiber. Opt. Lett. **26**, 608–610 (2001)
6. B. Povazay, K. Bizheva, A. Unterhuber, B. Hermann, H. Sattmann, A.F. Fercher, W. Drexler, A. Apolonski, W.J. Wadsworth, J.C. Knight, P.S.J. Russel, M. Vetterlein, E. Scherzer, Submicrometer axial resolution optical coherence tomography. Opt. Lett. **27**, 1800–1802 (2002)
7. J.M. Schmitt, S.L. Lee, K.M. Yung, An optical coherence microscope with enhanced resolv-ing power in thick tissue. Opt. Commun. **142**, 203–207 (1997)
8. A. Baumgartner, C.K. Hitzenberger, H. Sattmann, W. Dresler, A.F. Fercher, Signal and resolution enhancements in dual beam optical coherence tomography of the human eye. J. Biomed. Opt. **3**, 45–54 (1998)
9. F. Lexer, C.K. Hitzenberger, W. Drexler, S. Molebny, H. Sattmann, M. Sticker, A.F. Fercher, Dynamic coherent focus OCT with depth-independent transversal resolution. J. Mod. Opt. **46**, 541–553 (1999)
10. A. Knuttel, M. Boehlau-Godau, Spatially confined and temporally resolved refractive index and scattering evaluation in human skin performed with optical coherence tomography. J. Biomed. Opt. **5**, 83–92 (2000)
11. V.M. Gelikonov, G.V. Gelikonov, N.D. Gladkova, V.I. Leonov, F.I. Feldchtein, A.M. Sergeev, Y.I. Khanin, Optical fiber interferometer and piezoelectric modulator. US 5835642, 1998

12. V.K. Batovrin, I.A. Garmash, V.M. Gelikonov, G.V. Gelikonov, A.V. Lyubarskii, A.G. Plyavenek, S.A. Safin, A.T. Semenov, V.R. Shidlovskii, M.V. Shramenko, S.D. Yakubovich, Superluminescent diodes based on single-quantum-well (GaAl) As heterostructures. Quant. Electron. **26**, 109–114 (1996)

13. V.K. Batovrin, I.A. Garmash, V.M. Gelikonov, G.V. Gelikonov, A.V. Lyubarskii, A.G. Plyavenek, S.A. Safin, A.T. Semenov, V.R. Shidlovskii, M.V. Shramenko, S.D. Yakubovich, Superluminescent diodes based on single-quantum-well (GaAl) As heterostructures. Kvantovaya Elektronika Moskva **23**, 113–118 (1996)

14. L.S. Dolin, A theory of optical coherence tomography. Quant. Electron. **41**, 850–873 (1998)

15. L.S. Dolin, On the passage of a pulsed light signal through an absorbing medium with strong anisotropic scattering. Izvestiya Vysshikh Uchebnykh Zavedenii, Radiofizika **26**, 300–309 (1983)

16. D. Huang, E.A. Swanson, C.P. Lin, J.S. Schuman, W.G. Stinson, W. Chang, M.R. Hee, T. Flotte, K. Gregory, C.A. Puliafito, J.G. Fujimoto, Optical coherence tomography. Science **254**, 1178–1181 (1991)

17. A.F. Fercher, C.K. Hitzenberger, G. Kamp, S.Y. Elzaiat, Measurement of intraocular distances by backscattering spectral interferometry. Opt. Commun. **117**, 43–48 (1995)

18. T. Wilson, *Confocal Microscopy* (Academic, San Diego/London, 1990), p. 426

19. V.M. Gelikonov, G.V. Gelikonov, R.V. Kuranov, N.K. Nikulin, G.A. Petrova, V.V. Pochinko, K.I. Pravdenko, A.M. Sergeev, F.I. Feldchtein, Y.I. Khanin, D.V. Shabanov, Coherent optical tomography of microscopic inhomogenities in biological tissues. J. Exp. Theor. Phys. Lett. **61**, 149–153 (1995)

20. B.E. Bouma, G.J. Tearney (eds.), in *Handbook of Optical Coherence Tomography*, 1st edn. (Marcel Dekker, New York, 2002), p. 741

21. E. Gotzinger, M. Pircher, R.A. Leitgeb, C.K. Hitzenberger, High speed full range complex spectral domain optical coherence tomography. Opt. Express **13**, 583–594 (2005)

22. J. Ai, L.V. Wang, Synchronous self-elimination of autocorrelation interference in Fourier-domain optical coherence tomography. Opt. Lett. **30**, 2939–2941 (2005)

23. V.V. Tuchin, Optical clearing of tissues and blood using the immersion method. J. Phys. D (Appl. Phys.) **38**, 2497–2518 (2005)

24. S.G. Proskurin, I.V. Meglinski, Optical coherence tomography imaging depth enhancement by superficial skin optical clearing. Laser Phys. Lett. **4**, 824–826 (2007)

25. I.V. Larina, E.F. Carbajal, V.V. Tuchin, M.E. Dickinson, K.V. Larin, Enhanced OCT imaging of embryonic tissue with optical clearing. Laser Phys. Lett. **5**, 476–479 (2008)

26. C.J. Koester, *Handbook of Biological Confocal Microscopy* (Plenum, New York, 1990)

27. T. Zhang, I. Yamaguchi, Three-dimentional microscopy with phase-shifting digital holography. Opt. Lett. **23**, 1221–1223 (1998)

28. M.K. Kim, Wavelength-scanning digital interference holography for optical section imaging. Opt. Lett. **24**, 1693–1695 (1999)

29. L. Yu, M.K. Kim, Wavelength-scanning digital interference holography for tomographic three-dimensional imaging by use of the angular spectrum method. Opt. Lett. **30**, 2092–2094 (2005)

30. J. Lademann, J. Shevtsova, A. Patzelt, H. Richter, N.D. Gladkowa, V.M. Gelikonov, S.A. Gonchukov, Optical method for the screening of doping substances. Laser Phys. Lett. **5**, 908–911 (2008)

31. D.V. Shabanov, G.V. Gelikonov, V.M. Gelikonov, Broadband digital holographic technique of optical coherence tomography for 3-dimensional biotissue visualization. Laser Phys. Lett. **6**, 753–758 (2009)

Confocal Laser Scanning Microscopy Using Scattering as the Contrast Mechanism

28

Steven L. Jacques

Contents

Abstract

Confocal laser scanning microscopy (CLSM) is best known and widely used for fluorescence imaging. However, any commercial CLSM can be operated in reflectance mode by setting the microscope's detector to accept the excitation laser wavelength. In this mode, the images are based on the scattering properties of the cell or tissue. This chapter discusses reflectance-mode CLSM (rCLSM), the mechanisms of contrast involved in such images, and examples of how rCLSM is being used to study tissue properties.

28.1 Introduction

Confocal laser scanning microscopy (CLSM) offers a means of obtaining images that are optimally sharp in detail because CLSM rejects photons that contribute to blurring of the image. Such blurring photons can be the background fluorescence of

S.L. Jacques
Oregon Health & Science University, Portland, OR, USA
e-mail: jacquess@ohsu.edu

the tissue, or background photons multiply scattered by the tissue. So the primary key advantage of CLSM is the ability to acquire sharp images within the first few hundred micrometers of a tissue, by collecting light originating from the focus of the objective lens and rejecting photons originating from outside the focus. Reflectance-mode CLSM (rCLSM) is based on the backscattered fraction of the incident light delivered to the tissue. Any standard CLSM can be operated in rCLSM mode by setting the collection filter to accept the "excitation" wavelength being delivered.

This chapter discusses the signals obtained during rCLSM and how to obtain the optical properties (scattering coefficient, μ_s, and anisotropy of scattering, g) of a homogeneous tissue. These optical properties can be used as the contrast parameter for an image.

28.2 The Basic Method

Figure 28.1 illustrates a basic rCLSM system. rCLSM involves coordinating the focus within a tissue and the focus at a pinhole in front of the detector (or, alternatively, the focus at an optical fiber acting as a pinhole and carrying light to the detector). The objective lens has a focus within the tissue, creating a focal volume. Photons that originate from this focal volume, whether fluorescence or scattered reflectance, and escape the tissue without significant deflection by scattering will be recollimated by the objective lens and then refocused into the pinhole in front of the detector. Hence, the detector sees only the photons that originate from the focus and pass through the pinhole. A low background signal occurs due to lucky multiply scattered photons that by chance escape into the solid angle of collection that reaches the pinhole.

Scanning mirrors translate the focus along the lateral x-y axes of the field of view, while the focus at the pinhole remains stationary. Hence, the "scanning" aspect of the rCLSM surveys the field of view, while the single detector acquires a signal as a function of time during the scanning. The computer can reformat the time-resolved signal during an x-y scan with the focus at z into a dataset denoted here as $R(x, y)@z$, where R indicates reflectance.

There are two approaches toward scanning versus depth along the z-axis. The tissue sample can be translated along the z-axis, using a sample stage under computer control to move the sample closer to or further from the objective lens. Alternatively, a piezo-driven objective lens can move the focus to different depths within the tissue. By repeating the $R(x, y)@z$ acquisition for a series of z positions, a full 3D dataset can be generated, $R(x, y, z)$.

The objective lens is coupled to the tissue by a coupling medium, usually saline or gel. There is a factor $\partial z_f/\partial h$ that relates the height of the objective lens above the tissue (h) and the depth position of the focus relative to the tissue surface (z_f), which depends on the refractive index mismatch at the coupling medium/tissue interface: $\partial z_f/\partial h = \tan(\theta_1)/\tan(\theta_2)$, where $\theta_1 = \arcsin(NA/n_{medium})$ and $\theta_2 = \arcsin(NA/n_{tissue})$, where NA is the numerical aperture of the lens. The focus is located within

Fig. 28.1 A basic rCLSM system. Light delivered to and reflected from the focus of the objective lens, which is within the sample, is returned through a pinhole to the detector. Scanning optics use a galvo mirror and a pair of relay lenses to send collimated light into the objective lens at varying angles, which causes the focus to scan laterally (x, y) within the tissue. The objective lens is water or gel coupled to the tissue. The depth position of the focus within the sample is scanned by either moving the sample or moving the objective lens along z
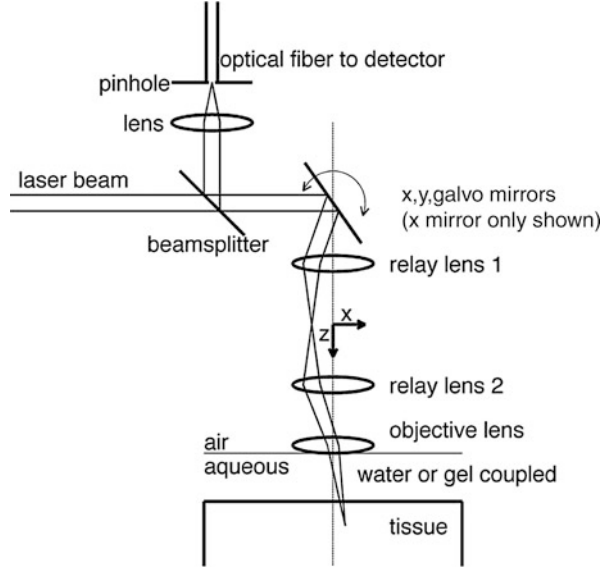
the tissue at a depth $z_f = (FL\text{-}h)\partial z_f/\partial h$, where FL is the focal length of the lens in the coupling gel. If $h = FL$, then $z_f = 0$ and the focus is at the tissue surface. If $h < FL$, then z_f is deeper than $FL\text{-}h$. For $NA = 0.90$, $n_{medium} = 1.33$ and $n_{tissue} = 1.40$, $\partial z_f/\partial h = 1.095$. In the following equations, the parameter z is assumed to be the depth z_f after correction for this refraction at the tissue surface.

In summary, light is delivered to a focus and a fraction of the backscattered light from the focus is able to escape the tissue without significant deflection by scattering. The trajectory of the escaping light allows collection by the objective lens and refocusing into the pinhole of detection. The transport from the objective lens into the tissue to the focus is here called T_{in}. The reflectance of photons from the focus with a trajectory aimed toward collection by the objective lens is called ρ. The transport out of the tissue from the focus to the objective lens is called T_{out}.

$$R = T_{in}\rho T_{out}. \tag{28.1}$$

The terms T_{in} and T_{out} are actually identical. The ability of collimated light to be focused by an objective lens and reach the focus is the same as the ability of light to scatter from the focus and be recollimated by the objective lens then focused into the pinhole. Hence, (28.1) can be expressed simply as $R = T_{in}^2\rho$. So what is the nature of T_{in}^2?

The term T_{in} is most simply expressed as a Beer's law attenuation $T_{in} = \exp(-\mu_s L)$, where L is path length, and hence $T_{in}^2 = \exp(-\mu_s 2z)$, since L is the round-trip photon path to/from a depth z. This expression has been used by several investigators to describe the observed exponential decay of R as the focus is moved down into a tissue,

Fig. 28.2 The relationship a versus g (see (28.2)). The ability of μ_s to attenuate the ability of photons to reach the focus decreases as $a(g)$ decreases, as the anisotropy g increases due to more forward-directed scattering. The simulations from Gareau [5], Samatham [6], and this chapter are shown
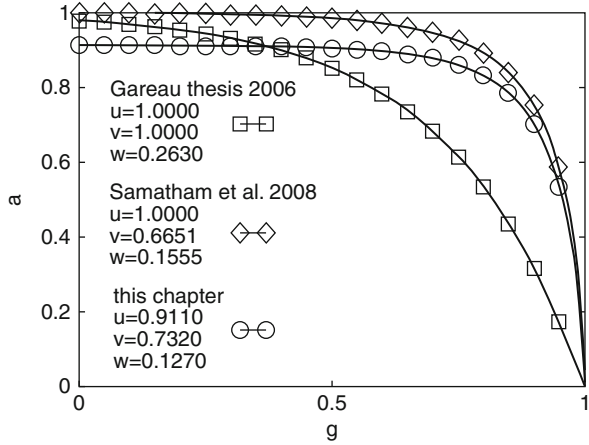
for example [1–3]. A more complete review is in [4]. In my laboratory, we have developed a modified version of this expression for T_{in}^2:

$$T_{in}^2 = e^{-(a\mu_s + \mu_a)2Gz} = e^{-\mu z}, \tag{28.2}$$

where

$a = 0 < a < 1$ mitigates the effect of scattering

μ_s = scattering coefficient [cm^{-1}]

μ_a = absorption coefficient [cm^{-1}]

2 = accounts for path into/out of the tissue

G = accounts for oblique delivery/collection

z = depth position of the focus within the tissue [cm]

$\mu = (a\mu_s + \mu_a)2G$, the in/out attenuation coefficient

The factor a modifies the ability of scattering to prevent photons from reaching the focus or escaping to reach the pinhole. For the case of isotropic scattering (i.e., the anisotropy of scattering, g, is equal to 0), the value of a is $\sim$1, and μ_s is maximally able to attenuate the reflectance R. For the case of very forward-directed light (g approaching 1), the value of a drops toward zero and the effectiveness of μ_s drops proportionately. In other words, despite multiple scattering, if the scattering is highly forward directed, then the photon can still reach the focus. An approximate and purely descriptive expression for a as a function of the anisotropy g is

$$a \approx u(1 - e^{-(1-g)^v/w}). \tag{28.3}$$

Figure 28.2 shows the shape of a versus g based on Monte Carlo simulations [5, 6].

The role of the absorption coefficient, μ_a, is included in (28.2). Experiments were conducted by Fu [7] in phantom tissues in which μ_a was varied at significant levels relative to μ_s to demonstrate changes in R that were consistent with (28.2). However, in most biological tissues, $\mu_a << \mu_s$. This chapter will neglect the role of μ_a.

The term $2G$ relates the apparent average in/out photon path to the depth of the focus, z. The factor 2 is obvious, since photons travel into then out of the tissue. The factor G is due to the extra photon path as photons travel obliquely to the focus when delivered by a high numerical aperture (NA) lens. For a low NA, as in optical coherence tomography (OCT), the value of G is close to unity. But for a 0.9-NA lens, the value of G is $\sim$1.13.

The calculation of G involves integration over the angles of photon delivery by the objective lens. The path length for each angle of incidence (θ) entering the tissue surface at z is z/cosθ. Longer path lengths are attenuated more than shorter path lengths. The photons entering at smaller θ suffer less attenuation and hence contribute more to T_{in}. The contribution to the total T_{in} from each angle is $\exp(-(a\mu_s + \mu_a)z/\cos\theta)$, and the total T_{in} is the expectation value for this factor over the range of θ values:

$$T_{\text{in}} = \left\langle e^{\frac{-(a\mu_s+\mu_s)z}{\cos\theta}} \right\rangle = \frac{\displaystyle\int_{\theta=0}^{\arcsin(NA/n_{\text{tissue}})} \frac{E(\theta)}{P_o} e^{\frac{-(a\mu_s+\mu_s)z}{\cos\theta}} 2\pi \sin\theta d\theta}{\displaystyle\int_{\theta=0}^{\arcsin(NA/n_{\text{tissue}})} \frac{E(\theta)}{P_o} 2\pi \sin\theta d\theta}, \tag{28.4}$$

where $E(\theta)$ (W/sr) is the incident focused beam power per incremental solid angle entering the tissue surface at an angle of θ_{in} within the tissue. The total beam power is P_o (W) = integral(E(θ) $2\pi\sin\theta d\theta$, θ = 0 to θ_{in}). The focused beam $E(\theta)$ can vary in shape, usually somewhere between Gaussian and flat field, and can be truncated by the aperture imposed by the objective lens. Rearranging (28.2), the value of G is

$$G = \frac{-\ln(T_{in})}{(a\mu_s + \mu_a)z}, \tag{28.5}$$

where T_{in} is given by (28.4).

Figure 28.3 shows the relationship between G and the NA of the objective lens for the case of a water immersion lens ($n_{\text{medium}} = 1.33$) and a tissue ($n_{\text{tissue}} = 1.4$).

The factor ρ in (28.1) describes the fraction of light backscattered from the focus at a trajectory that can be collected by the objective lens. The expression for ρ is

$$\rho = \mu_s \Delta z b, \tag{28.6}$$

where
Δz = axial extent of focus, $\Delta z = 1.4\lambda/(NA/n_{\text{tissue}})^2$
$\mu_s\Delta z$ = fraction of light reaching the focus that is scattered within the focus
$b = 0 \leq b \leq 1$ is the fraction of light scattered within the focus into a trajectory that can be collected by the objective lens

Fig. 28.3 The path length
factor G versus numerical
aperture (NA) of the objective
lens such that the apparent
total in/out photon path length
equals $2Gz$ (see (28.2)). This
curve is for the case of a water
immersion lens
($n_{\text{medium}} = 1.33$, $n_{\text{tissue}} = 1.4$)
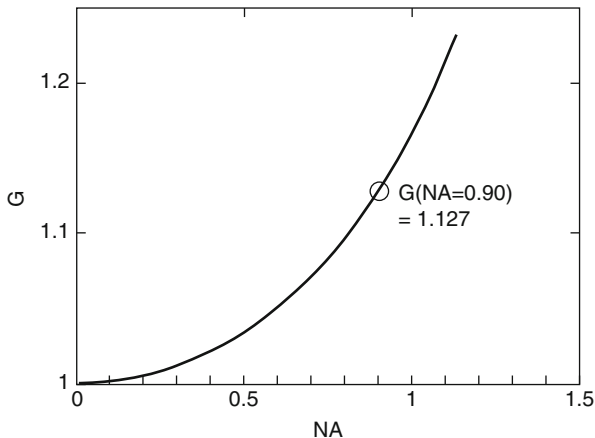
The factor b equals 1 if a mirror is located in the center of the focus. For a tissue with a scattering function $p(\theta)$ (sr^{-1}), the value of b is calculated:

$$b = \int_{\theta=\pi}^{\pi-\arcsin(NA/n_{\text{tissue}})} p(\theta)2\pi \sin\theta d\theta, \tag{28.7}$$

where the angle θ extends over the solid angle of collection of the objective lens. The forward direction is $\theta = 0$, and the backward direction is $\theta = \pi$ radians. A typical tissue might have an anisotropy $g = 0.90$, which is well described by the Henyey-Greenstein function:

$$p(\theta) = \frac{1}{4\pi} \frac{1 - g^2}{(1 + g^2 - 2g\cos\theta)^{3/2}}, \tag{28.8}$$

such that

$$1 = \int_{\theta=0}^{\pi} p(\theta)2\pi \sin\theta d\theta \tag{28.9}$$

and

$$g = \int_{\theta=0}^{\pi} p(\theta)\cos(\theta)2\pi \sin\theta d\theta. \tag{28.10}$$

For the example in Fig. 28.4, the value of b is 0.045. The dependences of b on NA and on g are depicted in Fig. 28.5. Decreasing g or increasing NA will increase b.
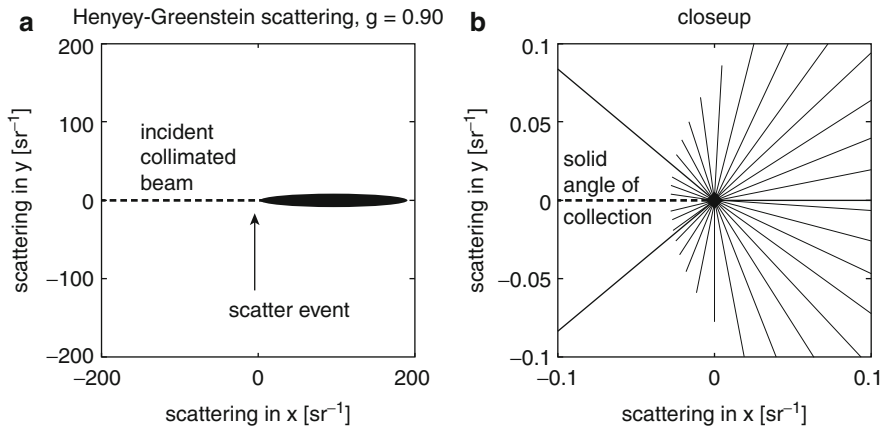
Fig. 28.4 Henyey-Greenstein scattering. For the case of NA = 0.90, n_{tissue} = 1.4, and g = 0.90, the value of b is 0.045 (see (28.7)). (**a**) Polar plot of $p(\theta)$ (sr^{-1}), illustrating very forward-directed scatter. (**b**) Close-up of same $p(\theta)$, illustrating the small amount of light backscattered into the solid angle of collection of the objective lens
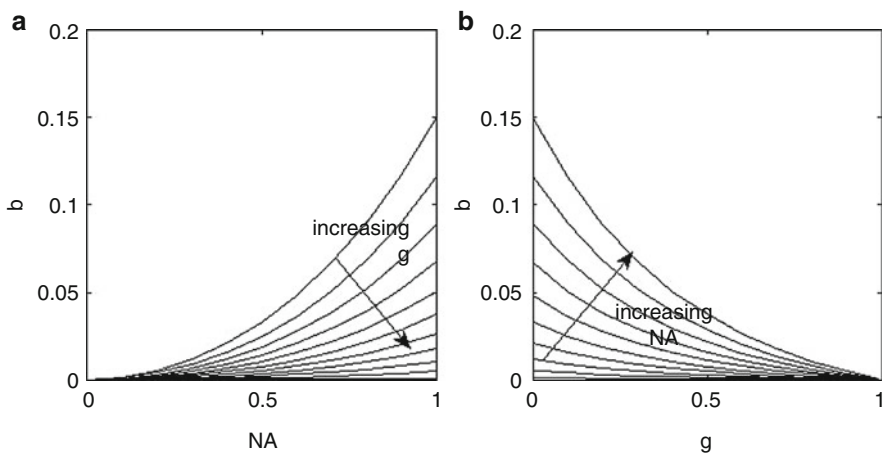
Fig. 28.5 (**a**) The dependence of the backscatter collection factor b versus the NA of the objective lens, for various g = [0:0.1:0.9 0.99]. (**b**) The dependence of b on g, for various NA = [0:0.1:1]

The above term Δz referred to the axial resolution of a confocal microscope: $\Delta z = 1.4\lambda/(NA/n_{tissue})^2 = 2.71$ μm for NA = 0.90, n_{tissue} = 1.4, λ = 800 nm. However, an optical coherence tomography (OCT) system is also a confocal microscope operating in reflectance mode, with its pinhole being either the optical fiber that collects light or the detector surface area in a free-beam system. The above analysis applies to OCT measurements as well. For OCT, the Δz of the axial resolution of the coherence gate is $\Delta z = 0.44\lambda^2/\Delta\lambda = 0.282$ μm, for λ = 800 nm,

Fig. 28.6 Ratio μ/ρ versus g, for the case of NA = 0.90, $n_{tissue} = 1.4$. As g exceeds 0.5, the ratio μ/ρ exceeds the simple expression $\mu/\rho = Ae^{kg}$. The two solid curves are for $\mu_s = 10$ and 10^4 cm^{-1}, illustrating the ratio μ/ρ is insensitive to the value of μ_s
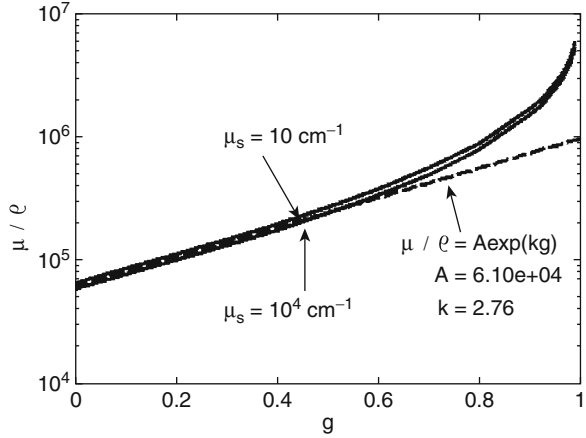
$\Delta\lambda = 100$ nm. For OCT, the smaller of the two Δz values, the value due to the objective lens or the value due to the coherence gate, should be used. It should be mentioned that this choice of Δz is a convention we currently use. However, the issue of the appropriate value of Δz for a confocal microscope is still a topic under study. For OCT using a high NA, the correct Δz may be a synergistic combination of the Δz due to the objective lens and the coherence gate.

In summary, the rCLSM reflectance signal, $R(z)$, where z is the depth position of the focus relative to the tissue surface, falls exponentially as z increases:

$$R(z) = \rho e^{-\mu z}, \tag{28.11}$$

where

$$\mu = (a\mu_s + \mu_a)2G, \tag{28.12}$$

$$\rho = \mu_s \Delta z b. \tag{28.13}$$

The factors a, b, and G are functions of the anisotropy of scattering (g) and the numerical aperture (NA): $a(g)$, $b(g, \text{NA})$, and $G(\text{NA})$. The role of μ_a is usually negligible but can become significant if absorption is strong.

Since (28.12) and (28.13) both contain μ_s, it is interesting to point out that the ratio μ/ρ cancels μ_s and yields

$$\frac{\mu}{\rho} = \frac{2aG}{b\Delta z}. \tag{28.14}$$

Figure 28.6 illustrates the relation between μ/ρ and g. Below $g \approx 0.5$, the ratio follows a simple exponential $\mu/\rho = Ae^{kg}$. At higher g, the ratio exceeds the simple exponential expression.

28.3   The Analysis Grid

Given (28.11), (28.12), and (28.13), it is possible to graphically portray the relationship between the experimental observables, μ and ρ, and the tissue optical properties, μ_s and g. Figure 28.7 graphically depicts the relationship and is here called an "analysis grid." The x and y axes are the observables, μ and ρ. The grid within the figures plots the iso-g and iso-μ_s contours. The grid is generated by choosing a series of g values and a series of μ_s values, and using (28.12) and (28.13) to generate corresponding values of μ and ρ.

If the wavelength (λ) decreases (or increases), the grid shifts left (or right) proportional to λ, since Δz is proportional to λ and ρ is proportional to Δz (see (28.6)).

If the NA decreases (or increases), the grid shifts left (or right) since b increases with NA (see Fig. 28.5) and ρ is proportional to b (see (28.6)).

Experimentally, one measures an axial profile $R(z)@x,y$ at a particular position x and y. The $R(z)$ profile is fit to the simple exponential $R(z) = \rho\exp(-\mu z)$ to specify μ and ρ. Then, this pair of observables (μ, ρ) is mapped to the corresponding properties (μ_s, g).

28.4   Computer Simulation of rCLSM

A Monte Carlo computer simulation of the rCLSM measurements simulated the focusing of a collimated flat-field beam by an objective lens to a focus at a depth of 400 μm within a tissue. The NA of the lens was 1.26 and the n_{tissue} was 1.4, such that the factor $NA/n_{\text{tissue}} = 0.90$. The scattering coefficient μ_s was varied from 3.75 to 625 cm^{-1}. The value of the anisotropy (g) was varied over $g = [0.10\ 0.50\ 0.70\ 0.80\ 0.90\ 0.95\ 0.99]$.

Figure 28.8 shows the transport $T(z)$ (cm^{-2}) such that the fluence rate distribution $\phi(z)$ (W/cm^2) was equal to $P_oT(z)$, where P_o (W) was the total power of the incident focused beam, for the two cases of $g = 0.10$ and 0.99. The transport to the focus fell as the value of μ_s was increased. It was more difficult for light to reach the focus when scattering was stronger. However, at high g the effect of μ_s was less strong than for low g. The forward-directed scattering allowed photons to reach the focus despite multiple scattering.

The value of $T(z)$ for $z = 400$ μm was normalized by the value of $T(z)$ in the absence of scattering to specify the value of T_{in}:

$$T_{\text{in}} = \frac{T(z = 400\ \mu m, \mu_s)}{T(z = 400\ \mu m, \mu_s = 0)}. \tag{28.15}$$

Figure 28.9 plots T_{in} versus the optical depth (OD), defined as

$$OD = \mu_s z, \tag{28.16}$$

Fig. 28.7 An analysis grid. The experimental observables, μ and ρ, map to the tissue optical properties, μ_s and g. This grid is for $\lambda = 800$ nm, NA $= 0.90$, and $n_{tissue} = 1.4$
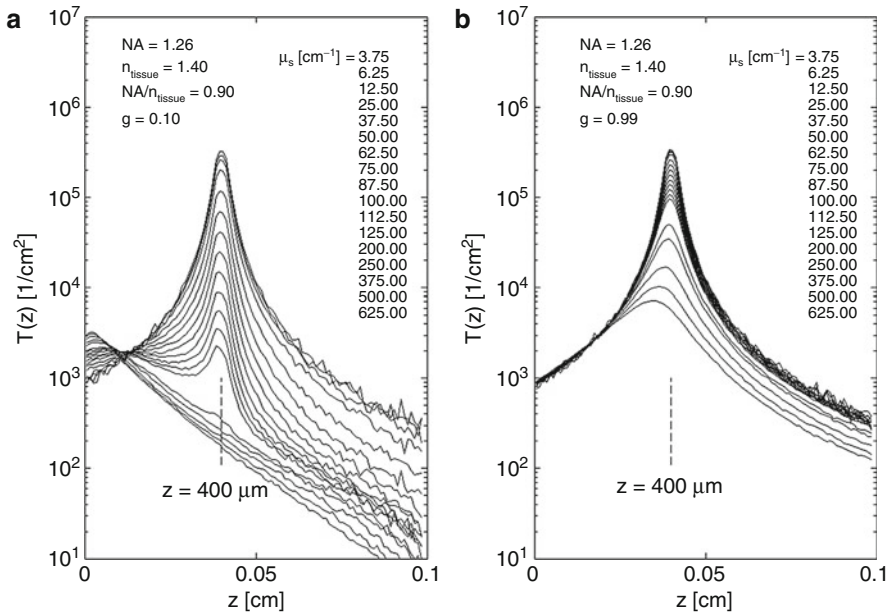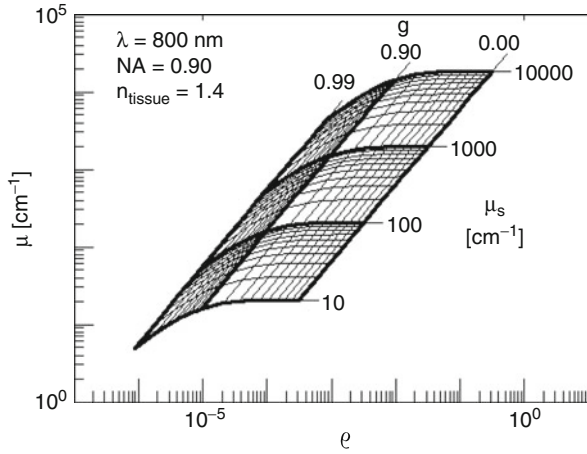
Fig. 28.8 The transport $T(z)$ ($1/cm^2$) of a focused beam into tissue of varying optical scattering coefficient (μ_s) (Monte Carlo simulations). The $T(z)$ at the focus at $z = 0.04$ cm fell as the μ_s was increased. (**a**) The anisotropy of scattering (g) was 0.10. The $T(z = 400 \ \mu m)$ decays rapidly as μ_s is increased. (**b**) The g was 0.99. The $T(z = 400 \ \mu m)$ decays more slowly as μ_s is increased
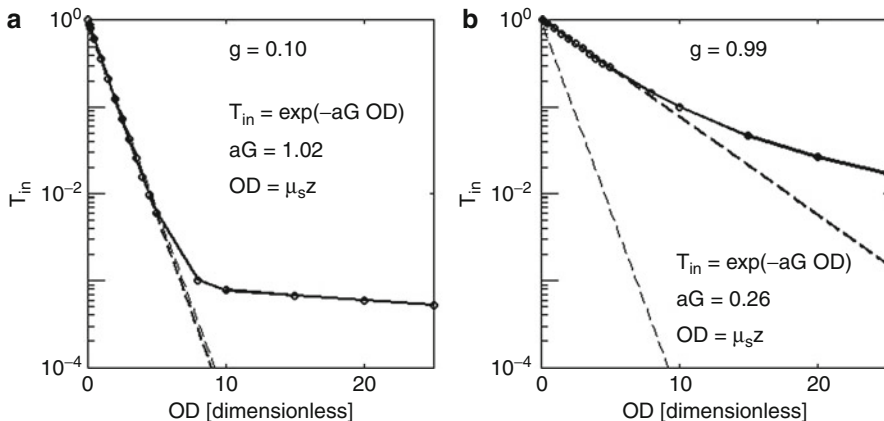
Fig. 28.9 The transport to the focus (T_{in}) is plotted versus the optical depth (OD $= a\mu_s Gz$, $z = 400$ μm), using the data in Fig. 28.8. The value $T_{in}(OD) = T(z = 400$ μm, $\mu_s)/T(z = 400$ μm, $\mu_s = 0)$, which is dimensionless. The *thin dashed line* shows $T_{in} = \exp(-OD)$. The *bold dashed line* fits the early data before the background of multiply scattered light becomes dominant, $T_{in} = \exp(-aG$ OD). (**a**) $g = 0.10$. The factor aG is close to unity. (**b**) $g = 0.99$. The factor aG is 0.26

where $z = 0.04$ cm. The data is fit by the expression:

$$T_{in} = e^{-aG\,OD} + \text{background signal}, \qquad (28.17)$$

where the background signal is due to lucky multiply scattered photons that by chance escape with a trajectory that can reach the pinhole. The early exponential decay of $T_{in}(OD)$ specifies the value of the product aG. Analysis of several $T_{in}(OD)$ using different values of g yielded values of the aG for each value of g. Fig. 28.10 shows the aG versus g data and the fit.

To separate the lumped parameter aG into the distinct parameters a and G, the following procedure was followed for each of the g values:
1. An initial value of G was assumed, $G = 1.13$.
2. The value of a was assigned the value aG/G.
3. Equation 28.4 was used to calculate T_{in} using these a and G.
4. Equation 28.5 was used to calculate a new value of G.
5. Then, steps 2–4 were repeated. Only a couple repetitions achieved stable values of a and G that matched the factor aG.

The results of this procedure are shown in Fig. 28.11, which plots a versus g and G versus g. The value of a falls from an initial value of 0.911 at $g = 0$, to $a = 0.533$ at $g = 0.95$, to $a = 0.216$ at $g = 0.99$. Simultaneously, G increases as g exceeds about 0.5, rising from $G = 1.13$ at $g = 0$ (consistent with Fig. 28.3), to $G = 1.157$ at $g = 0.95$, to $G = 1.125$ at $g = 0.99$. The fall in a with increasing g is expected, as

Fig. 28.10 Plot of the factor
aG versus *g* based on a series
of Monte Carlo simulations
similar to Figs. 28.8 and 28.9
using different values of
anisotropy (*g*)

$$aG = u(1-\exp(-((1-g)^v)/w)$$

u = 1.018
v = 0.699
w = 0.132

$$a = u(1-\exp(-((1-g)^v)/w/G$$
u = 0.911
v = 0.732
w = 0.127

NA = 0.90

NA = 0.90
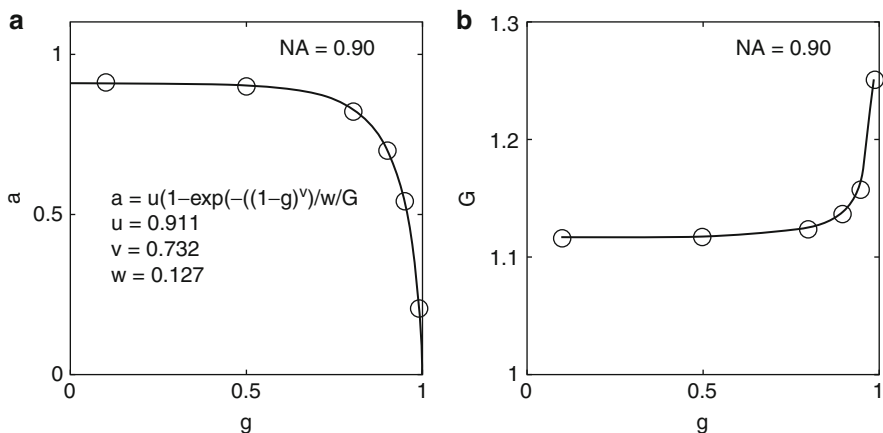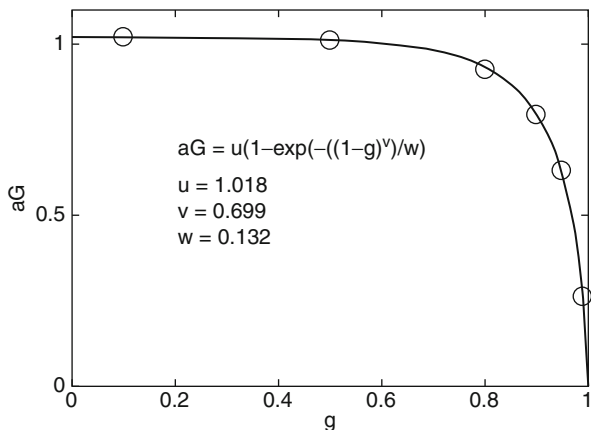
Fig. 28.11 Separating the factor *aG* into the factors *a* and *G*. (**a**) Plotting *a* versus *g*. (**b**) Plotting
G versus *g*

discussed earlier. The rise in *G* with increasing *g* is understood as the forward-directed scattering allowing more photons to successfully traverse the tissue through the larger angles delivered by the objective lens. Hence, the *G* increases.

28.5   History of This Work

A review of the previous literature cites the various reports of the simple expression
$R(z) = \rho\exp(-\mu_s 2z)$ [8].

The development of the model for rCLSM, as described in this chapter, introduced the behavior of $a(g)$ as well as revisiting $b(g)$ and $G(NA)$. The work has

Fig. 28.12 Results of studies on freshly excised murine tissues using a 488-nm rCLSM are plotted on the analysis grid. The results show the approximate values of μ_s and g for these tissues at the 488 nm (*blue*) wavelength
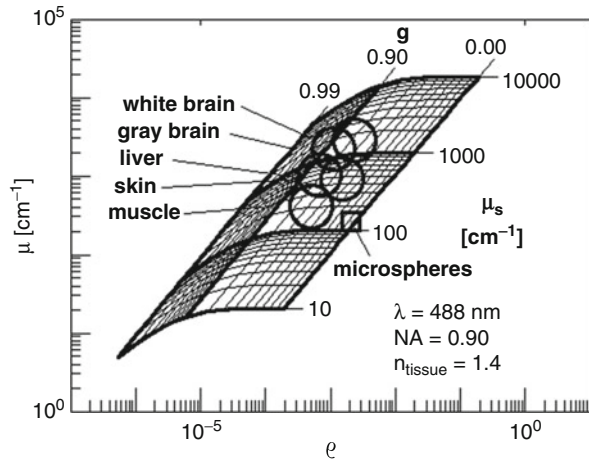
involved my graduate students and postdoctoral trainees. The model began while working with Dan Gareau, whose PhD thesis involved building a 488-nm rCLSM system [5]. Dan generated the relation $a(g)$ using Monte Carlo simulations and conducted the first ex vivo murine tissue experiments. Ravikant Samatham (graduate student) and Niloy Choudhury (postdoc) improved the rCLSM system, and Samatham conducted further ex vivo experiments on tissues. Felix Truffer contributed to improving the calculations of G. Yongji Fu conducted experiments showing the influence of absorption (μ_a) on the measurements and analysis [7]. David Levitz and Choudhury implemented the work using 1,310-nm OCT [9, 10]. Levitz argued for the usefulness of the μ/ρ ratio. Samatham used rCLSM to study the effects of optical clearing on excised murine dermis [11]. Colleagues at the University of Western Australia, Robert McLaughlin et al., applied the method to imaging excised nodes containing metastasized breast cancer [12]. Kevin Phillips conducted in vivo rCLSM measurements of epidermal hyperplasia in mouse skin [13] and in vivo OCT measurements of inflammation in mouse ears [14], induced by topical drug applications.

28.6   Experimental Results

Experimental studies on gels, ex vivo murine tissues, and in vivo murine studies have been conducted. Figure 28.12 shows the results for rCLSM studies of freshly excised murine tissues using a 488-nm wavelength (blue light). There is a large variation in the values of μ_s between the different tissue types that were measured, ranging from 200 to 2,000 cm^{-1}. The anisotropy values were in the range of 0.6–0.90. The value of $1 - g$ therefore varied from 0.1 to 0.4. The diffusion of light depends on the product $\mu_s(1 - g)$, so the term $1 - g$ is important.

28.7 Conclusion

In conclusion, rCLSM can determine the optical scattering properties of a tissue, if it is sufficiently homogenous. Microscale heterogeneity usually does not violate this restriction, since light transport averages over the microscale of these fluctuations in tissue properties. Heterogeneities, however, do remain a challenge to the method.

The μ_s and g derived from such analysis of an $R(x,y,z)$ dataset can serve as the contrast for an image $\mu_s(x,y)$ or $g(x,y)$. Alternatively, one can work with the raw observable parameters, μ and ρ, as did McLaughlin et al. [12] who used the μ parameter to create image contrast in images of lymph nodes with breast cancer metastases. The $g(x,y)$ images are especially interesting since g maps into the submicron size scale of tissue structure. Samatham et al. followed the change in the structure of collagen fibers of skin in mice with one gene change (osteogenesis imperfecta) [6]. Levitz et al. followed the disruption of collagen fibers by metal metalloproteinases [9]. Samatham et al. followed the changes in dermal collagen when soaked in glycerol [11].

This rCLSM project has been motivated by the desire to extract information about a tissue rather than simply provide images of tissue landmarks such as an interface between tissue types. We believe the optical scattering properties themselves are an important contrast mechanism for imaging.

References

1. J.M. Schmitt, A. Knüttel, R.F. Bonner, Measurement of optical properties of biological tissues by low-coherence reflectometry. Appl. Opt. **32**, 6032–6042 (1993)
2. T. Collier, M. Follen, A. Malpica, R. Richards-Kortum, Sources of scattering in cervical tissue: determination of the scattering coefficient by confocal microscopy. Appl. Opt. **44**, 2072–2081 (2005)
3. D. Levitz, L. Thrane, M.H. Frosz, P.E. Andersen, C.B. Andersen, J. Valanciunaite, J. Swartling, S. Andersson-Engels, P.R. Hansen, Determination of optical scattering properties of highly-scattering media in optical coherence tomography images. Opt. Express **12**, 249–259 (2004)
4. S.L. Jacques, D. Levitz, R. Samatham, N. Choudhury, F. Truffer, D.S. Gareau, Specifying tissue optical properties using confocal reflectance microscope, in *Biomedical Applications of Light Scattering*, ed. by V. Backman, A. Wax (McGraw-Hill, New York, 2009)
5. D.S. Gareau, In Vivo Confocal Microscopy in Turbid Media, Ph.D. Dissertation, Oregon Health & Science University, Portland, 2006
6. R. Samatham, S.L. Jacques, P. Campagnola, Optical properties of mutant vs wildtype mouse skin measured by reflectance-mode confocal scanning laser microscopy (rCSLM). J. Biomed. Opt. **13**(4), 041309 (2008)
7. Y. Fu, Using Optical Methods to Monitor and Administer Photodynamic Therapy to Oral Bacteria, Ph.D. Dissertation, Oregon Health & Science University, Portland, 2008
8. S. Jacques, R. Samatham, N. Choudhury, and D.S. Gareau, Specifying tissue optical properties using axial dependence of confocal reflectance images: confocal scanning laser microscopy and optical coherence tomography, in *Biomedical Applications of Light Scattering*, *Proc. of SPIE*, ed. by A. Wax, V. Backman, **6446**, 64460N (2007)

9. D. Levitz, M.T. Hinds, N. Choudhury, N.T. Tran, S.R. Hanson, S.L. Jacques, Quantitative characterization of developing collagen gels using optical coherence tomography. J. Biomed. Opt. **15**(2), 026019 (2010)
10. D. Levitz, M.T. Hinds, A. Ardeshiri, S.R. Hanson, S.L. Jacques, Non-destructive label-free monitoring of local smooth muscle cell remodeling of collagen gels using optical coherence tomography. Biomaterials **31**(32), 8210–8217 (2010)
11. R. Samatham, K.G. Phillips, S.L. Jacques, Assessment of optical clearing agents using reflectance-mode confocal scanning laser microscopy. J. Innov. Opt. Health Sci. **3**(3), 183–188 (2010)
12. R.A. McLaughlin, L. Scolaro, P. Robbins, C. Saunders, S.L. Jacques, D.D. Sampson, Parametric imaging of cancer with optical coherence tomography. J. Biomed. Opt. **15**(4), 046029 (2010)
13. K.G. Phillips, R. Samatham, P. Thuillier, S.L. Jacques, In vivo measurement of epidermal thickness changes associated with tumor promotion in murine models. J. Biomed. Opt. **15**(4), 041514 (2010)
14. K.G. Phillips, Y. Wang, D. Levitz, N. Choudhury, E. Swanzey, J. Lagowski, M. Kulesz-Martin, S.L. Jacques, Dermal reflectivity determined by optical coherence tomography is an indicator of epidermal hyperplasia and dermal edema within inflamed skin. J. Biomed. Opt. **16**(4), 040503 (2011)

Part 6

Applications of Coherent-Domain Optical Methods

Mueller Matrix Polarimetry in Material Science, Biomedical and Environmental Applications

29

Sergey N. Savenkov

Contents

Abstract

This chapter describes approaches to understanding the physics of the interaction of polarized beams with natural scenes and to searching for informative and useful polarimetric discriminants to identify objects of various natures in optical and radar polarimetry. We start with a general introduction to the Mueller polarimetry. In particular, the multiplicative and additive matrix models of deterministic and depolarizing objects are discussed. Then, several important applications of optical and radar polarimetry, including biomedical tissues, vegetation, soil, atmosphere, oil and chemical contaminations, and man-made targets, are considered.

S.N. Savenkov
Department of Radiophysics, Kyiv Taras Shevchenko University, Kyiv, Ukraine
e-mail: sns@univ.kiev.ua

29.1   Introduction

To develop polarimetric methods for object identification and classification, one needs to understand the relation between polarimetric and physical properties of the objects. As light interacts with or propagates through a medium, its polarization state changes, as does its intensity. Polarization properties of the scattered light contain extensive information on morphological and functional properties of the medium. For example, because depolarization of scattered polarized light depends on the morphological and physical parameters of scatterers (i.e., density, size, distribution, shape, refractive index, etc.) present in the studied object [16, 256], this information can be utilized for developing identification techniques for the objects. Many constituents of an object also exhibit polarization properties such as birefringence, dichroism, and depolarization that might serve to discriminate between surface and volume scattering as well.

The enormous importance of the Mueller matrix is that it contains all the information (birefringence, dichroism, and depolarization) that one can obtain from light scattered by a medium [7, 22, 27, 50, 235]. The information contained in the Mueller matrix has many useful applications in such diverse fields as interaction with various optical systems ([7, 27, 50, 235]), cloud diagnostics [22, 133, 171, 172, 263], remote sensing of the ocean, atmosphere, and planetary surfaces [20, 131–133, 175, 185], and biological tissue optics [206, 255, 256].

Hence, the Mueller matrix shows great promise for the efficient quantification of polarization parameters, i.e., sizes, shapes and orientation of the medium structural elements as well as birefringence, dichroism, an depolarization of the medium. To extract this information and interpret experimental results on scattering, one needs an appropriate polarimetric matrix model for the particular object in question. There are two concepts that are currently used for object modeling. First, an object can be modeled as a discrete ensemble of scatterers [256, 263, 276]; and second, the object can be modeled as a medium with a continuous distribution of optical parameters [7, 27, 70, 230, 254]). The choice of concept is completely determined by both the structural features of the object in question and the type of scattering characteristics that are to be obtained. In the first case, the Mueller matrix contains information related to the optical properties, size, shape, and composition of the constituent scatterers [22, 263], while in the second case, the Mueller matrix contains information related to the anisotropy of the medium, viz., linear and circular dichroism and birefringence (i.e., amplitude and phase anisotropies) [14, 140]. In both cases, the Mueller matrix can contain information on depolarization [40, 82, 170]. The methods of interpretation of the Mueller matrices have been developed by many authors [44, 85, 112, 151, 152, 160, 225, 226, 228, 280].

Our main focus in this chapter is on the Mueller matrix interpretation intended for the characterization of the objects of various natures both in optical range and in radar polarimetry. An example of important polarimetric applications that do not involve the measurement of the Mueller matrix is beyond the scope of our discussion. Hence, our reference list should by no means be considered exhaustive and is merely intended to provide initial reference points for the interested reader.

29.2 Mueller Matrices of Deterministic and Depolarizing Objects

In the Mueller matrix calculus, the polarization state of light can be completely characterized by a Stokes vector, while the polarization transforming properties of a medium can be completely characterized by a Mueller matrix:

$$\mathbf{S}^{out} = \mathbf{M}\mathbf{S}^{inp}, \tag{29.1}$$

where the four-component Stokes column vector (with "out" and "inp" denoting the Stokes vectors of the output and input light, respectively) consists of the following parameters:

$$\mathbf{S} = \begin{pmatrix} I \\ Q \\ U \\ V \end{pmatrix} = \begin{pmatrix} s_1 \\ s_2 \\ s_3 \\ s_4 \end{pmatrix} = \begin{pmatrix} \langle |E_x|^2 + |E_y|^2 \rangle \\ \langle |E_x|^2 - |E_y|^2 \rangle \\ \langle E_x^* E_y + E_x E_y^* \rangle \\ i \langle E_x^* E_y + E_x E_y^* \rangle \end{pmatrix}, \tag{29.2}$$

with $i = (-1)^{1/2}$. Among the pioneering contributions to this field of research, we note those by Solleillet [244], Perrin [202], Mueller [180], and Parke [198, 199].

The Stokes parameter I is proportional to the total energy flux of the light beam. The Stokes parameters Q and U represent the differences between two components of the flux in which the electric vectors oscillate in mutually orthogonal directions. The Stokes parameter V is the difference between two oppositely circularly polarized components of the flux. As indicated by the angular brackets, the Stokes parameters s_i are ensemble averages (or time averages in the case of ergodic, stationary processes). This implies that no coherence effects are considered.

The Stokes vectors and Mueller matrices represent operations on intensities and their differences, i.e., incoherent superpositions of light beams; they are not adequate to describe either interference or diffraction effects. However, they are well suited to describe partially polarized and unpolarized light. Extensive lists of various Mueller matrices have been presented by several authors (e.g., [75, 129, 235]).

The Stokes parameters obey the inequality

$$s_1^2 \geq s_2^2 + s_3^2 + s_4^2. \tag{29.3}$$

This inequality is called the Stokes−Verdet criterion and is a consequence of the Schwartz (or Couchy−Buniakovski) theorem [8]. The degree of polarization p is defined by

$$p = \sqrt{s_2^2 + s_3^2 + s_4^2}/s_1. \tag{29.4}$$

In (29.3), the equality holds for a completely polarized (pure) beam of light. In this case, $p = 1$. Another limiting case, $p = 0$, occurs when $s_2^2 + s_3^2 + s_4^2 = 0$,

i.e., when the electric vector vibrates in all directions randomly and with no preferential orientation. An intermediate case, $0 < p < 1$, implies that light contains both polarized and depolarized components and is, therefore, called partially polarized.

The inequality (29.3) plays an important role in polarimetry because it allows one to classify the character of the light–medium interaction. Assume first that the input light is completely polarized. In this case, the equality in (29.3) implies that the medium is non-depolarizing. Note that the terms *non-depolarizing* and *deterministic* or "pure" are not, in general, identical. The term *deterministic* means that the Mueller matrix describing such a medium can be derived from the corresponding Jones matrix [3, 83, 89, 237]. This condition is more rigid than the condition of a non-depolarizing medium [222]. Hereinafter, we call this class of matrices pure Mueller matrices [106]. If the output light results in an inequality in (29.3) then the scattering medium is not deterministic. If, in addition, the transformation matrix in (29.1) can be represented as a convex sum of deterministic Mueller matrices [44, 81, 82] then the result is a depolarizing Mueller matrix (hereinafter Mueller matrix); otherwise, the result is a Stokes transformation matrix, i.e., the transformation matrix ensures the fulfillment of the Stokes−Verdet criterion only. The properties of matrices transforming Stokes vectors into Stokes vectors, i.e., those satisfying the Stokes−Verdet criterion, have been studied by many authors [86, 88, 186, 245, 266, 267, 285].

Any pure Mueller matrix $\mathbf{M}$ can be transformed to the corresponding Jones matrix $\mathbf{T}$ using the following relation ([7, 63, 199]):

$$\mathbf{M} = \mathbf{A}(\mathbf{T} \otimes \mathbf{T}^*)\mathbf{A}^{-1}, \tag{29.5}$$

where the asterisk denotes the complex-conjugate value,

$$\mathbf{T} = \begin{pmatrix} t_1 & t_4 \\ t_3 & t_2 \end{pmatrix}, \tag{29.6}$$

$$\mathbf{A} = \begin{pmatrix} 1 & 0 & 0 & 1 \\ 1 & 0 & 0 & -1 \\ 0 & 1 & 1 & 0 \\ 0 & i & -i & 0 \end{pmatrix}, \tag{29.7}$$

the t_i are, in general complex, and $\otimes$ is the tensorial (Kronecker) product.

Since the element m_{11} is a gain for unpolarized incident light, it must satisfy the following inequality:

$$m_{11} > 0. \tag{29.8}$$

Furthermore, the elements of the Mueller matrix must obey the following conditions:

$$m_{11} \geq |m_{ij}|, \tag{29.9}$$

$$\mathrm{Tr}(\mathbf{M}) \geq 0, \tag{29.10}$$

$$\mu\,\mathbf{T} \sim |\mu|^2 \mathbf{M}, \tag{29.11}$$

where Tr denotes the trace operation and μ is an arbitrary real or complex constant.

Note that the last relation defines the ability of the Jones and Mueller matrices to represent a "physically realizable" medium [3, 82, 151] and implies the physical restriction according to which the ratio g of the intensities of the emerging and incident light beams (the gain or intensity transmittance) must always be in the interval $0 \leq g \leq 1$. This condition is called the gain or transmittance condition and can be written in terms of the elements of the Mueller matrix as follows [9]:

$$
\begin{aligned}
m_{11} + \left(m_{12}^2 + m_{13}^2 + m_{14}^2\right)^{1/2} &\leq 1, \\
m_{11} + \left(m_{21}^2 + m_{31}^2 + m_{41}^2\right)^{1/2} &\leq 1.
\end{aligned}
\tag{29.12}
$$

While a Jones matrix has generally eight independent parameters, the absolute phase is lost in (29.5), yielding only seven independent elements for a pure Mueller matrix. Evidently, this results in the existence of interrelations for the elements of a general pure Mueller matrix. This fact was pointed out for the first time, although without a derivation of their explicit form, by van de Hulst [263]. Since then, this subject has been studied by many authors (e.g., [1, 73, 109]). In the most complete and refined form these interrelations are presented in Hovenier [106].

In particular one can derive the following important equation for the elements of a pure Mueller matrix:

$$\sum_{i=1}^{4} \sum_{j=1}^{4} m_{ij}^2 = 4m_{11}^2. \tag{29.13}$$

This equality was obtained for the first time by Fry and Kattawar [73]. However, the question of whether this is a sufficient condition for $\mathbf{M}$ to be a pure Mueller matrix has been the subject of extensive discussions (see, e.g., [3, 26, 28, 83, 106, 127, 137, 138, 237, 238]). Under the premise that the Mueller matrix in question can be represented as a convex sum of pure Mueller matrices, (29.13) is both a necessary and a sufficient condition for $\mathbf{M}$ to be a pure Mueller matrix [82].

In addition to the equalities presented above, a set of inequalities can be derived to characterize the structure of the pure Mueller matrix, as follows [109]:

$$
\begin{aligned}
m_{11} + m_{22} + m_{12} + m_{21} &\geq 0, \\
m_{11} - m_{22} - m_{12} + m_{21} &\geq 0, \\
m_{11} + m_{22} - m_{12} - m_{21} &\geq 0, \\
m_{11} - m_{22} + m_{12} - m_{21} &\geq 0, \\
m_{11} + m_{22} + m_{33} + m_{44} &\geq 0, \\
m_{11} + m_{22} - m_{33} - m_{44} &\geq 0, \\
m_{11} - m_{22} + m_{33} - m_{44} &\geq 0, \\
m_{11} - m_{22} - m_{33} + m_{44} &\geq 0.
\end{aligned}
\tag{29.14}
$$

Equation (29.5) can be used to derive interrelations between the structures of a Jones matrix and the corresponding pure Mueller matrix. For example, the successive application of transposition and sign reversal for the off-diagonal elements of the Jones matrix in (29.6) yields

$$
\begin{pmatrix} t_1 & -t_3 \\ -t_4 & t_2 \end{pmatrix} \leftrightarrow \begin{pmatrix} m_{11} & m_{21} & -m_{31} & m_{41} \\ m_{12} & m_{22} & -m_{32} & m_{42} \\ -m_{13} & -m_{23} & m_{33} & -m_{43} \\ m_{14} & m_{24} & -m_{34} & m_{44} \end{pmatrix}.
\tag{29.15}
$$

Physical reasons for the above relations are quite clear. Indeed, (29.15) originates from the operation of interchanging the incident and emerging light beams, the principle of reciprocity [205, 229, 231, 273], and mirror symmetry [104, 105].

The effect of the symmetry of the individual scatterers and collections of scatterers on the structure (number of independent parameters) of the Mueller matrix has been considered by van de Hulst [263]. In particular, he demonstrated that the collection of scatterers containing equal numbers of particles and their mirror particles possesses the following Mueller matrix:

$$
\begin{pmatrix} m_{11} & m_{12} & 0 & 0 \\ m_{21} & m_{22} & 0 & 0 \\ 0 & 0 & m_{33} & m_{34} \\ 0 & 0 & m_{43} & m_{44} \end{pmatrix}.
\tag{29.16}
$$

If in (29.6) $t_3 = t_4$, then $m_{11}^2 - m_{12}^2 - m_{33}^2 - m_{34}^2 = 0$, $m_{22} = m_{11}$, $m_{33} = m_{44}$, and $m_{34} = -m_{43}$, see (29.5).

If, in addition, the collection of scatterers contains equal numbers of particles in positions described by (29.6) and (29.15) and those corresponding to the transposition and sign reversal of the off-diagonal elements of the Jones matrix (29.6), then $m_{12} = m_{21}$.

The Mueller matrix of (29.16) plays a key role in many light-scattering applications. Some of them will be discussed later in this section. The structure of (29.16) can be caused by a symmetry of individual particles and a collection of particles in single and multiple scattering [170, 263] as well as by illumination-observation geometries for backward [289] and forward [227] scattering.

The model of a medium described by the Mueller matrix of (29.16) has been used in studies of optical characteristics of oceanic water [132, 275]; ensembles of identical, but randomly oriented fractal particles [134]; dense spherical particle suspensions in the multiple-scattering regime [123]; ice clouds consisting of nonspherical ice crystals in the multiple-scattering regime [143]; polydisperse, randomly oriented ice crystals modeled by finite circular cylinders with different size distributions [286]; cylindrically shaped radially inhomogeneous particles [158]; and small spherical particles (ranging in diameter from 0.2 to 1.5 μm) sparsely seeded on the surface of a crystalline silicon c-Si wafer [122]. Other applications included measurements of the complex refractive index of isotropic materials as matrices of isotropic and ideal metal mirror reflections [55]; the development of a symmetric three-term product decomposition of a Mueller−Jones matrix [195]; and the description of very general and practically important cases of (1) randomly oriented particles with a plane of symmetry [108] and/or (2) equal numbers of particles and their mirror particles [172]. This list of applications can be extended significantly.

An example of the situation in which the Mueller matrix has the structure of (29.16) and contains information on the strong dependence of depolarization and depolarization on the polarization state of the input light is the exact forward scattering of polarized light by a slab of inhomogeneous linear birefringent medium [227].

The scattering angles 0°(exact forward direction) and 180°(exact backward direction) deserve special attention owing to their importance in numerous practical applications, including the scattering by biological tissues. For the first time, the general form of angles was derived by van de Hulst [263]. Hu et al. [110] presented a comprehensive study of forward and backward scattering by an individual particle in a fixed orientation. For forward scattering, they distinguished 16 different symmetry shapes which were classified into 5 symmetry classes; for backward scattering, 4 different symmetry shapes were identified and classified into 2 symmetry classes. A large number of relations were derived in this way. The structures of Mueller matrices for various collections of particles in the cases of forward and backward scattering can be found elsewhere [107, 263].

It is important to note that although analyses of the internal structure of a general pure Mueller matrix, the symmetry relations between matrix elements caused by interchanging the incident and emerging light beams, and the principle of reciprocity have historically been carried out in the framework of light scattering by discrete particles these results are also relevant to pure Mueller matrices in the continuous-medium approximation.

In this section, we consider the problem of Mueller matrix interpretation in the framework of the approach wherein the medium studied is modeled as a medium with a continuous (and possibly random) distribution of optical parameters. The polarization of light changes if the amplitudes and phases of the components of the

electric vector $\mathbf{E}$ change separately or simultaneously ([7, 27, 235]). It is, therefore, customary to distinguish between the corresponding classes of anisotropic media: dichroic (or possessing amplitude anisotropy), influencing only the amplitudes; birefringent (or possessing phase anisotropy), influencing only the phases; and "all other" (possessing both amplitude and phase anisotropy) affecting both the amplitudes and the phases of the components of the electric field vector. Among these classes, four types of anisotropic mechanisms are recognized as basic or, after Jones, elementary [112, 116–118, 120]: linear and circular phase and linear and circular amplitude anisotropies.

Linear birefringence is described by the following pure Mueller matrix:

$$
\mathbf{M}^{LP} = \begin{pmatrix}
1 & 0 & 0 & 0 \\
0 & \cos^2 2\alpha + \sin^2 2\alpha \cos \varDelta & \cos 2\alpha \sin 2\alpha \left(1 - \cos \varDelta\right) & -\sin 2\alpha \sin \varDelta \\
0 & \cos 2\alpha \sin 2\alpha \left(1 - \cos \varDelta\right) & \sin^2 2\alpha + \cos^2 2\alpha \cos \varDelta & \cos 2\alpha \sin \varDelta \\
0 & \sin 2\alpha \sin \varDelta & -\cos 2\alpha \sin \varDelta & \cos \varDelta
\end{pmatrix}
\tag{29.17}
$$

where $\varDelta$ is the phase shift between two orthogonal linear components of the electric field vector and α is the azimuth of the anisotropy.

The Mueller matrix describing linear dichroism is

$$
\mathbf{M}^{LA} = \begin{pmatrix}
1 + P & (1 - P) \cos 2\gamma & (1 - P) \sin 2\gamma & 0 \\
(1 - P) \cos 2\gamma & \cos^2 2\gamma \left(1 + P\right) + 2\sin^2 2\gamma \sqrt{P} & \cos 2\gamma \sin 2\gamma \left(1 - \sqrt{P}\right)^2 & 0 \\
(1 - P) \sin 2\gamma & \cos 2\gamma \sin 2\gamma \left(1 - \sqrt{P}\right)^2 & \sin^2 2\gamma \left(1 + P\right) + 2\cos^2 2\gamma \sqrt{P} & 0 \\
0 & 0 & 0 & 2\sqrt{P}
\end{pmatrix},
\tag{29.18}
$$

where P is the relative absorption of two linear orthogonal components of the electric vector and γ is the azimuth of the anisotropy.

The Mueller matrix describing circular birefringence is

$$
\mathbf{M}^{CP} = \begin{pmatrix}
1 & 0 & 0 & 0 \\
0 & \cos 2\varphi & \sin 2\varphi & 0 \\
0 & -\sin 2\varphi & \cos 2\varphi & 0 \\
0 & 0 & 0 & 1
\end{pmatrix},
\tag{29.19}
$$

where φ is the induced phase shift between two orthogonal circular components of the electric vector.

Finally, in terms of the Mueller-matrix calculus, circular amplitude anisotropy is described by the following matrix:

$$
\mathbf{M}^{CA} = \begin{pmatrix}
1 + R^2 & 0 & 0 & 2R \\
0 & 1 - R^2 & 0 & 0 \\
0 & 0 & 1 - R^2 & 0 \\
2R & 0 & 0 & 1 + R^2
\end{pmatrix},
\tag{29.20}
$$

where R is the magnitude of anisotropy, i.e., the relative absorption of two orthogonal circular components of the electric vector. The six quantities α, Δ, P, γ, φ, and R are called anisotropy parameters.

It can be seen that the matrices describing linear and circular birefringence belong to the class of unitary matrices (in the case of matrices with real-valued elements – orthogonal matrices). The matrices of linear, (29.18), and, circular (29.20), dichroism belong to the class of Hermitian matrices (in the case of matrices with real-valued elements – symmetric matrices).

The Mueller matrices of (29.17)−(29.20) represent media exhibiting individual types of anisotropy. Experimental measurements of these matrices or of the corresponding informative matrix elements allow one to interpret and characterize anisotropy properties of media. However, more often two or more types of anisotropy are exhibited by a medium simultaneously. Evidently, such cases require the development of more sophisticated polarimetric matrix models [44, 85, 112, 152, 195, 196, 226].

The matrix model that is used most extensively in optical polarimetry for decoupling constituent polarization properties of optical medium is the polar decomposition proposed by Lu and Chipman [152]. This model is based on the so-called polar decomposition theorem [141], according to which an arbitrary matrix $\mathbf{M}$ can be represented by a product

$$\mathbf{M} = \mathbf{M}_P\,\mathbf{M}_R \quad \text{or} \quad \mathbf{M} = \mathbf{M}_R\,\mathbf{M}'_P, \tag{29.21}$$

where $\mathbf{M}_P$ and $\mathbf{M}'_P$ are Hermitian matrices and $\mathbf{M}_R$ is a unitary one. The Hermitian matrix is associated with amplitude anisotropy, while the unitary matrix describes phase anisotropy [280]. The matrices $\mathbf{M}_P$ and $\mathbf{M}_R$ are called the dichroic and the phase polar form [85, 152, 280].

The polar decomposition was first employed by Whitney [280] without finding explicit expressions for $\mathbf{M}_P$ and $\mathbf{M}_R$. They were proposed later, independently by Gil and Bernabeu [85] and Lu and Chipman [152]. Alternatively, the dichroic and phase polar forms can be derived using spectral methods of linear algebra [7].

The phase polar form $\mathbf{M}_R$ (using notation from [152]) is given by

$$\mathbf{M}_R = \begin{pmatrix} 1 & \vec{0}^{\,T} \\ \vec{0} & \mathbf{m}_R \end{pmatrix},$$

$$(m_R)_{ij} = \delta_{ij}\cos R + a_i a_j (1 - \cos R) + \sum_{k=1}^{3} \varepsilon_{ijk} a_k \sin R, \tag{29.22}$$

where $\vec{0}$ is the 3×1 zero vector; $\begin{bmatrix} 1 & a_1 & a_2 & a_3 \end{bmatrix}^T = \begin{bmatrix} 1 & \widehat{R}^T \end{bmatrix}^T$ is the normalized Stokes vector for the fast axis of $\mathbf{M}_R$; δ_{ij} is the Kronecker delta; ε_{ijk} is the Levi−Civita permutation symbol, $\mathbf{m}_R$ is the 3×3 submatrix of $\mathbf{M}_R$ obtained by striking out the first row and the first column of $\mathbf{M}_R$; and R is the birefringence given by

$$R = \arccos\left(\frac{1}{2} Tr\, \mathbf{M}_R - 1\right). \tag{29.23}$$

The dichroic polar form $\mathbf{M}_P$ is as follows:

$$\mathbf{M}_P = T_u \begin{pmatrix} 1 & \vec{\mathbf{D}}^T \\ \vec{\mathbf{D}} & \mathbf{m}_P \end{pmatrix},$$

$$\mathbf{m}_P = \sqrt{1 - D^2}\,\mathbf{I} + \left(1 - \sqrt{1 - D^2}\right)\widehat{\mathbf{D}}\,\widehat{\mathbf{D}}, \tag{29.24}$$

where $\mathbf{I}$ is the 3×3 identity matrix; $\widehat{\mathbf{D}} = \vec{\mathbf{D}}\big/|\vec{\mathbf{D}}|$ is the unit vector in the direction of the diattenuation vector $\vec{\mathbf{D}}$; T_u is the transmittance for unpolarized light; and the value of diattenuation can be obtained as

$$D = \left\{ 1 - 4\,|\det(\mathbf{T})|^2 \big/ [Tr(\mathbf{T}^*\mathbf{T})]^2 \right\}^{1/2}. \tag{29.25}$$

The models of anisotropic media based on the polar decomposition contain six independent parameters, three for the phase polar form $\mathbf{M}_R$ and three for the dichroic polar form $\mathbf{M}_P$. It can be seen that the phase polar form is a unitary (orthogonal) matrix and the dichroic polar form is a Hermitian (symmetric) matrix. Note that unitarity (orthogonality) of the phase polar form, (29.22), is in complete agreement with the first Jones' equivalence theorem [112], and is a general model of elliptically birefringent media. The situation with the dichroic polar form is more complex [225, 228]. Mathematically, the complexity originates from the fact that, in contrast to unitary matrices, the product of Hermitian matrices is generally not a Hermitian matrix [141].

If the incident light is fully polarized and the output light is characterized by an inequality in (29.3) then the equalities for matrix elements obtained in Hovenier [106] and (29.13), which determine the structure of the Mueller matrix as a deterministic matrix, are lost. In this case, the output light is composed of several incoherent contributions, and the medium as a whole cannot be represented by a Jones matrix. However, the medium can be considered as a parallel set of deterministic media, each one being described by a well-defined Jones matrix, in such a way that the light beam is shared among these different media. It is important to point out that the same result could be obtained by considering the medium as an ensemble [127] so that each realization i, characterized by a well-defined Jones matrix $\mathbf{T}^i$, occurs with a probability p^i.

If a Mueller matrix can be represented by a convex sum of pure Mueller matrices [44, 46, 82, 238] then it is called a depolarizing Mueller matrix. It is important to note that this class of matrices does not coincide with the class of matrices, called Stokes matrices, satisfying the Stokes−Verdet criterion, i.e., matrices transforming Stokes vectors into Stokes vectors, see (29.3). Any physical Mueller matrix is a Stokes matrix, but the converse is not, in general, true [82]. On the other hand,

no method has been quoted to physically realize a Stokes matrix that cannot be represented as a convex sum of deterministic Mueller matrices.

Linear inequalities for the elements of a pure Mueller matrix are also valid for a depolarizing Mueller matrix $\mathbf{M}$ [108], in particular:

$$
\begin{aligned}
&m_{11} \geq 0; \quad m_{11} \geq |m_{ij}|, \\
&m_{11} + m_{22} + m_{12} + m_{21} \geq 0, \\
&m_{11} + m_{22} - m_{12} - m_{21} \geq 0, \\
&m_{11} - m_{22} + m_{12} - m_{21} \geq 0, \\
&m_{11} - m_{22} - m_{12} + m_{21} \geq 0.
\end{aligned}
\tag{29.26}
$$

In this case, the following quadratic inequalities are also valid [73]:

$$
\begin{aligned}
(m_{11} + m_{12})^2 - (m_{21} + m_{22})^2 &\geq (m_{31} + m_{32})^2 + (m_{41} + m_{42})^2, \\
(m_{11} - m_{12})^2 - (m_{21} - m_{22})^2 &\geq (m_{31} - m_{32})^2 + (m_{41} - m_{42})^2, \\
(m_{11} + m_{21})^2 - (m_{12} + m_{22})^2 &\geq (m_{13} + m_{23})^2 + (m_{14} + m_{24})^2, \\
(m_{11} - m_{21})^2 - (m_{12} - m_{22})^2 &\geq (m_{13} - m_{23})^2 + (m_{14} - m_{24})^2, \\
(m_{11} + m_{22})^2 - (m_{12} + m_{21})^2 &\geq (m_{33} + m_{44})^2 + (m_{34} - m_{43})^2, \\
(m_{11} - m_{22})^2 - (m_{12} - m_{21})^2 &\geq (m_{33} - m_{44})^2 + (m_{34} + m_{43})^2,
\end{aligned}
\tag{29.27}
$$

while (29.13) becomes an inequality as well:

$$
\sum_{i=1}^{4} \sum_{j=1}^{4} m_{ij}^2 \leq 4m_{11}^2.
\tag{29.28}
$$

The study and characterization of depolarization is of considerable importance owing to the fact that depolarization phenomena are encountered in many theoretical and experimental applications of polarimetry to discrete random media and media with bulk and surface inhomogeneities. Note that the light–medium interaction with depolarization is heretofore studied in considerably less detail than the problem described by Mueller–Jones matrices discussed above.

Depolarization is the result of decorrelation of the phases and the amplitudes of the electric field vectors and/or selective absorption of polarization states [27]. Depolarization can be observed in both single and multiple light scattering and depends on geometrical and physical characteristics of the scattering particles: shape, morphology, refractive index, size parameter (ratio of the particle circumference to the wavelength of the incident light), and orientation with respect to the reference frame [170]. Furthermore, multiple scattering results in depolarization of the output light even in the case of a collection of spherically symmetric particles and often reinforces depolarization caused by particle nonsphericity [170, 173].

Our purpose here is to consider the depolarization phenomenon using the Mueller-matrix formalism; in particular, we intend to discuss single-number depolarization metrics and Mueller matrices of depolarization. The notion of depolarization Mueller-matrix factorization has long existed in the literature and will be considered in this section, below.

Depolarization metrics provide a single scalar number that varies from zero, thereby corresponding to a totally depolarized output light, to a certain positive number corresponding to a totally polarized output light. All intermediate values are associated with partial polarization.

The depolarization index was introduced by Gil and Bernabeu [83, 84]:

$$DI\left(\mathbf{M}\right) = \sqrt{\sum_{i,j=1}^{4} m_{ij}^2 - m_{11}^2 \Big/ \left(\sqrt{3}m_{11}\right)}. \tag{29.29}$$

The depolarization index is bounded according to $0 \leq DI(\mathbf{M}) \leq 1$. The extreme values of $DI(\mathbf{M})$ correspond to the case of unpolarized and totally polarized output light, respectively.

An "analog" to the degree of polarization, (29.4), for linearly polarized input light in terms of Mueller matrix elements, the so-called index of linear polarization, was introduced by Bueno [30]:

$$G_L = \frac{\sqrt{3}}{2m_{11}} \left(m_{21}^2 + m_{31}^2 + \frac{1}{3} \sum_{i=1}^{4} \left(m_{2i}^2 + m_{3i}^2\right) \right)^{1/2}. \tag{29.30}$$

It can be seen that G_L is the ratio of the mean of the sum of the squares of matrix elements corresponding to linear polarization of the output light and the value of the corresponding averaged intensity normalized by the maximum value of this ratio that occurs for a linear polarizer: $(G_L)_{\max} = 2/3^{1/2}$. The former implies the following range of variation: $0 \leq G_L \leq 1$.

The average degree of polarization was defined by Chipman [42] as follows:

$$Average \, DoP(\mathbf{M}) = \frac{1}{4\pi} \int_{0}^{\pi} \int_{-\pi/2}^{\pi/2} p\left[\mathbf{MS}(\varepsilon, \zeta)\right] \cos \varepsilon \, d\varepsilon \, d\zeta. \tag{29.31}$$

The term $\cos \varepsilon \, d\varepsilon \, d\zeta$ scans the incident polarization state over the Poincaré sphere, with the latitude ε and longitude ζ. The Stokes vector $\mathbf{S}(\varepsilon, \zeta)$ is a function of ellipticity and orientation azimuth of the polarization ellipse of light:

$$\mathbf{S}(\varepsilon, \zeta) = \begin{bmatrix} 1 & \cos 2\varepsilon \cos 2\zeta & \cos 2\varepsilon \sin 2\zeta & \sin 2\varepsilon \end{bmatrix}^{\mathbf{T}}, \tag{29.32}$$

where T stands for "transposed."

The so-called $Q(\mathbf{M})$ metrics is defined as follows [68]:

$$Q(\mathbf{M}) = \sum_{i=2}^{4} \sum_{j=1}^{4} m_{ij}^2 \bigg/ \sum_{j=1}^{4} m_{1j}^2 = \left\{ 3 \left[DI(\mathbf{M})\right]^2 - \left[D(\mathbf{M})\right]^2 \right\} \bigg/ \left\{ 1 + \left[D(\mathbf{M})\right]^2 \right\},$$

(29.33)

where $D(\mathbf{M}) = (m_{12}^2 + m_{13}^2 + m_{14}^2)^{1/2}$ is the diattenuation parameter and $0 \leq D(\mathbf{M}) \leq 1$. The metric $Q(\mathbf{M})$ is bounded according to $0 \leq Q(M) \leq 3$. Specifically, $Q(\mathbf{M}) = 0$ corresponds to a totally depolarizing medium; $0 < Q(M) < 1$ describes a partially depolarizing medium; $1 \leq Q(M) < 3$ represents a partially depolarizing medium if, in addition, $0 < DI(M) < 1$; otherwise, it represents a non-depolarizing diattenuating medium; finally, $Q(M) = 3$ for a non-depolarizing non-diattenuating medium.

Thus, the depolarization metrics provide a summary of the depolarizing property of a medium via a single number. The depolarization index $DI(\mathbf{M})$ and the $Q(\mathbf{M})$ metrics are directly related to the Mueller matrix elements only and, in contrast to the average degree of polarization *Average DoP*, require no scan of the whole Poincaré sphere of the input polarizations. Furthermore, $Q(\mathbf{M})$ provides more detailed information about depolarization properties of a medium.

Quantities referring to the intrinsic depolarization properties of light have had wide applications in polarimetry as well. These are the linear, δ_L, and circular, δ_C, depolarization ratios defined according to [169, 170]

$$\delta_L = (s_1 - s_2)/(s_1 + s_2),$$

(29.34)

$$\delta_C = (s_1 + s_4)/(s_1 - s_4).$$

(29.35)

The interest in these parameters is explained by the fact that they are susceptible to particle nonsphericity. Indeed, for spherical particles both ratios are equal to zero identically, whereas for nonspherical scatterers both δ_L and δ_C can substantially deviate from zero [169]. The former means that if the incident light is linearly polarized then the backscattered light is completely linearly polarized in the same plane, whereas if the incident light is circularly polarized then the backscattered light is completely circularly polarized in the opposite sense. For nonspherical particles this is generally not the case.

Chipman [40] introduced somewhat different versions of the degrees of linear and circular polarization:

$$DoLP = \sqrt{s_2^2 + s_3^2}/s_1,$$

(29.36)

$$DoCP = s_4/s_1.$$

(29.37)

These parameters turn out to be very useful for applications in meteorology, astronomy, ophthalmology, and optical fibers (e.g., [30] and references therein).

Some media depolarize all polarization states equally. Other depolarizing media partially depolarize most polarization states but may not depolarize one or some incident states. Depolarization depends significantly on the polarization state of the input light in the multiple-scattering regime ([17, 128, 214], and references therein). In particular, Bicout et al. [17] studied numerically and experimentally how depolarization evolves for linear and circular input polarizations as the size of the particles increases from very small (Rayleigh regime) to large (Mie regime) in the case of a forward scattering geometry.

A single-number metric providing a summary of depolarization by a medium cannot give detailed information about all features of depolarization. Such information can only be obtained from Mueller-matrix models of depolarization. The case when for all polarizations of the input light the degree of polarization p of the output light is the same is called isotropic depolarization. When the degree of polarization of the output light is a function of parameters of the input polarization, one speaks of anisotropic depolarization.

There seems to be a consensus regarding the form of the Mueller matrix model describing isotropic depolarization [27, 41]:

$$\mathrm{diag}\begin{bmatrix} 1 & p & p & p \end{bmatrix}. \tag{29.38}$$

It can be seen that the properties of this type of depolarization are the following:
1. The transmittance is the same for all polarizations of the incident light;
2. p of the output light is the same for all input polarizations.

On the other hand, there is no consensus in the literature concerning the Mueller matrix for the case of anisotropic depolarization. Apparently, one of the most accepted forms of the Mueller matrix describing the dependence of p of the output light on the incident polarization is the following [27, 41, 196, 234]:

$$\mathrm{diag}\begin{bmatrix} 1 & a & b & c \end{bmatrix}. \tag{29.39}$$

The elements a, b, and c are interpreted physically in the following manner: a and b are the degrees of linear depolarization, while c is the degree of circular depolarization. If $a = b = c = 0$ then the Mueller matrix represents an ideal depolarizer. Bicout et al. [17] discussed the depolarization arising in multiple scattering of light by spherical scatterers in the Rayleigh regime and given by (29.39) with $a = b$.

The most general expression for the Mueller matrix describing depolarization was suggested by Lu and Chipman [152]:

$$\begin{pmatrix} 1 & \vec{\mathbf{O}}^T \\ \vec{\mathbf{P}}_\Delta & \mathbf{m}_\Delta \end{pmatrix}, \quad \mathbf{m}_\Delta^T = \mathbf{m}_\Delta, \tag{29.40}$$

where $\vec{\mathbf{P}}_\varDelta$ denotes the so-called polarizance vector. The polarizance vector describes the state of polarization generated by this Mueller matrix from unpolarized incident light. The Mueller matrix of (29.40) has 9° of freedom, and this is of interest because this matrix along with a generalized deterministic Mueller matrix are jointly characterized by 16° of freedom. This means that in this way one obtains the generalized Mueller matrix of an arbitrary medium that has 16° of freedom and linearly interacts with polarized light.

The product of Mueller matrices of the polar forms (29.22) and (29.24) and the depolarizing Mueller matrix (29.40)

$$\mathbf{M} = \mathbf{M}_\varDelta \, \mathbf{M}_R \, \mathbf{M}_P, \tag{29.41}$$

is the generalized polar decomposition and a multiplicative matrix model of an arbitrary Mueller matrix [81, 82, 152].

The product of the phase polar form and the depolarizing matrices can then be obtained as

$$\mathbf{M}_\varDelta \, \mathbf{M}_R = \mathbf{M}' = \mathbf{M} \, \mathbf{M}_P^{-1}. \tag{29.42}$$

Then

$$\vec{\mathbf{P}}_\varDelta = (\vec{\mathbf{P}} - \mathbf{m}\vec{\mathbf{D}})/(1 - D^2), \tag{29.43}$$

where $\vec{\mathbf{P}} = (1/m_{11}) \begin{bmatrix} m_{21} & m_{31} & m_{41} \end{bmatrix}^T$ and $\mathbf{m}$ is the submatrix of the initial matrix $\mathbf{M}$. The $\mathbf{m}'$ is the submatrix of $\mathbf{M}'$ and can be written as

$$\mathbf{m}' = \mathbf{m}_\varDelta \, \mathbf{m}_R. \tag{29.44}$$

The submatrix $\mathbf{m}_\varDelta$ can be calculated as follows:

$$\begin{aligned} \mathbf{m}_\varDelta = &\pm[\mathbf{m}' \, (\mathbf{m}')^T + (\sqrt{\lambda_1 \lambda_2} + \sqrt{\lambda_2 \lambda_3} + \sqrt{\lambda_1 \lambda_3}) \, \mathbf{I}]^{-1} \\ &\times[(\sqrt{\lambda_1} + \sqrt{\lambda_2} + \sqrt{\lambda_3}) \, \mathbf{m}' \, (\mathbf{m}')^T + \sqrt{\lambda_1 \lambda_2 \lambda_3} \, \mathbf{I}], \end{aligned} \tag{29.45}$$

where λ_i are the eigenvalues of $\mathbf{m}' \, (\mathbf{m}')^T$. The sign "+" or "−" is determined by the sign of the determinant of $\mathbf{m}'$. The net depolarization coefficient $\varDelta$ can be calculated according to

$$\varDelta = 1 - \frac{1}{3} \, | \, \mathrm{Tr} \, (\mathbf{M}_\varDelta) - 1 \, |. \tag{29.46}$$

In conclusion of this section, we consider the additive Mueller matrix model of depolarizing object suggested by Cloude [44] and extensively employed in optical

and radar polarimetry (see, e.g., [47, 48, 182–184, 219, 224, 274]). The Cloude coherence matrix $\mathbf{J}$ is derived from the corresponding arbitrary Mueller matrix as follows:

$$
\begin{aligned}
&J_{11} = (1/4)(m_{11} + m_{22} + m_{33} + m_{44}) \quad &&J_{12} = (1/4)(m_{12} + m_{21} - im_{34} + im_{43}) \\
&J_{13} = (1/4)(m_{13} + m_{31} + im_{24} - im_{42}) \quad &&J_{14} = (1/4)(m_{14} - im_{23} + im_{32} + m_{41}) \\[6pt]
&J_{21} = (1/4)(m_{12} + m_{21} + im_{34} - im_{43}) \quad &&J_{22} = (1/4)(m_{11} + m_{22} - m_{33} - m_{44}) \\
&J_{23} = (1/4)(im_{14} + m_{23} + m_{32} - im_{41}) \quad &&J_{24} = (1/4)(-im_{13} + im_{31} + m_{24} + m_{42}) \\[6pt]
&J_{31} = (1/4)(m_{13} + m_{31} - im_{24} + im_{42}) \quad &&J_{32} = (1/4)(-im_{14} + m_{23} + m_{32} + im_{41}) \\
&J_{33} = (1/4)(m_{11} - m_{22} + m_{33} - m_{44}) \quad &&J_{34} = (1/4)(im_{12} - im_{21} + m_{34} + m_{43}) \\[6pt]
&J_{41} = (1/4)(m_{14} + im_{23} - im_{32} + m_{41}) \quad &&J_{42} = (1/4)(im_{13} - im_{31} + m_{24} + m_{42}) \\
&J_{43} = (1/4)(-im_{12} + im_{21} + m_{34} + m_{43}) \quad &&J_{44} = (1/4)(m_{11} - m_{22} - m_{33} + m_{44})
\end{aligned}
\tag{29.47}
$$

It can be seen that coherence matrix $\mathbf{J}$ is positive semidefinite Hermitian and, hence, has always four real eigenvalues. The eigenvalues of the coherence matrix, λ_i, can be combined to form a quantity that is a measure of the depolarization, depolarization metric, of the studied medium. This quantity is called entropy and is defined as:

$$
H = -\sum_{i=1}^{N} \left(\lambda_i \bigg/ \sum_j \lambda_j \right) \log_N \left(\lambda_i \bigg/ \sum_j \lambda_j \right)
\tag{29.48}
$$

Given eigenvalues λ_i of coherence matrix $\mathbf{J}$, we have for initial Mueller matrix:

$$
\mathbf{M} = \sum_{k=1}^{4} \lambda_k \mathbf{M}_{\mathrm{D}}^{k}; \qquad \mathbf{M}_{\mathrm{D}}^{k} \Leftrightarrow \mathbf{T}^{k},
\tag{29.49}
$$

here $\mathbf{M}_{\mathrm{D}}^{k}$ are the pure Mueller matrices obtained from the Jones matrices by (29.5). The Jones matrix, $\mathbf{T}$, in turn, is obtained in the following manner:

$$
\begin{aligned}
t_{11}^{(k)} = \Psi_1^{(k)} + \Psi_2^{(k)}, \quad & t_{12}^{(k)} = \Psi_3^{(k)} - i\Psi_4^{(k)} \\
t_{21}^{(k)} = \Psi_3^{(k)} + i\Psi_4^{(k)}, \quad & t_{22}^{(k)} = \Psi_1^{(k)} - \Psi_2^{(k)} \quad k = \overline{1,4}
\end{aligned},
\tag{29.50}
$$

where $\boldsymbol{\Psi}^{(k)} = (\Psi_1 \quad \Psi_2 \quad \Psi_3 \quad \Psi_4)_k^T$ is k-th eigenvector of coherence matrix $\mathbf{J}$.

Thus, the substance of the Cloude's coherency matrix concept, which, in essence, is an additive matrix model of depolarizing Mueller matrix, (29.49), is the representation of the initial depolarizing Mueller matrix as a weighted convex sum of four pure Mueller matrices.

If three of the eigenvalues of **J** vanish, then the entropy $H = 0$ and initial matrix **M** is a deterministic Mueller-Jones matrix. If all four eigenvalues of **J** are not equal to zero and $H \leq 0.5$, then the pure Mueller matrix, which corresponds to the maximal eigenvalue, is the dominant type of deterministic polarization transformation of the studied object. So, this model allows the possibility of studying the anisotropy properties of depolarizing objects on the one hand and, on the other hand, is a necessary and sufficient criterion for given 4×4 real matrix to be Mueller matrix (the case when all four eigenvalues of **J** are non-negative) and pure Mueller matrix (the case when three of the eigenvalues vanish) [182–184, 274].

29.3 Mueller Matrix Measurements

The aim of this section is to discuss the general concept of the Mueller matrix measurement. An ample number of practical schemes of the Stokes and Mueller polarimeters can be found elsewhere [6, 40, 96].

The Mueller matrix polarimeter at visible and infrared is composed of a polarization state generator (PSG) and polarization state analyzer (PSA), as shown in Fig. 29.1.

The PSG forms the particular polarization state of incident light on the studied object. The PSA is operated to measure either the full Stokes vector or some of the Stokes parameters of the scattered light. Both PSG and PSA consist of retarders and diattenuators that are capable of analyzing the polarization state of the scattered beam.

Nearly all existing Mueller matrix polarimeters are configured so that the entire Mueller matrix has to be measured [40]. Such an approach is required to make up the conditioned set of 16 equations for matrix elements in order to reconstruct the full 4×4 Mueller matrix. The approach has been determined by structure of the so-called characteristic or data-reduction matrix of generalized measurement equation. The data-reduction matrix describes the conversion of a set of polarized-intensity measurements into the Mueller matrix that is represented as a 16×1 vector. For any PSG and PSA, the total flux measured by the detector is

$$g = \mathbf{QML} = \sum_{i=1}^{4} \sum_{j=1}^{4} q_i m_{ij} l_j, \tag{29.51}$$

where **L** is the Stokes vector produced by PSG; **M** is the object Mueller matrix; and **Q** is the Stokes vector corresponding to the first row of the Mueller matrix representing the PSA.

To measure the full Mueller matrix, $N \geq 16$ of flux measurements (29.51) are required. Flattening the Mueller matrix **M** into 16×1 Mueller vector of the form $\vec{\mathbf{M}} = [\, m_{11} \quad m_{12} \quad m_{13} \quad m_{14} \quad \cdot \quad \cdot \quad \cdot \quad m_{43} \quad m_{44} \,]^T$ the polarimetric measurement equation can be represented as follows:

Fig. 29.1 Schematic overview to measure the Mueller matrices
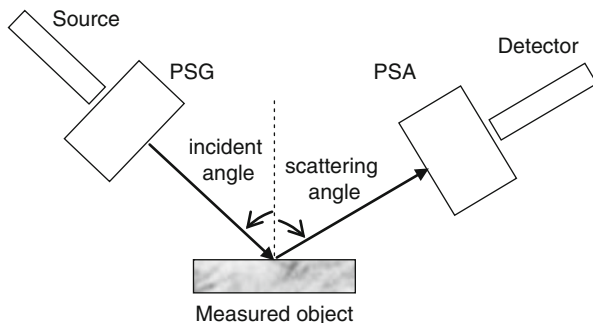
$$\mathbf{G} = \mathbf{W}\vec{\mathbf{M}} = \begin{pmatrix} q_1^1 l_1^1 & q_1^1 l_2^1 & q_1^1 l_3^1 & \cdot & q_4^1 l_4^1 \\ q_1^2 l_1^2 & q_1^2 l_2^2 & q_1^2 l_3^2 & \cdot & q_4^2 l_4^2 \\ q_1^3 l_1^3 & q_1^3 l_2^3 & q_1^3 l_3^3 & \cdot & q_4^3 l_4^3 \\ \cdot & \cdot & \cdot & \cdot & \cdot \\ q_1^N l_1^N & q_1^N l_2^N & q_1^N l_3^N & \cdot & q_4^N l_4^N \end{pmatrix} \begin{pmatrix} m_{11} \\ m_{12} \\ m_{13} \\ \cdot \\ m_{44} \end{pmatrix}, \tag{29.52}$$

where $\mathbf{G}$- $N \times 1$ vector, whose components are the fluxes measured by detector; $\mathbf{W}$ is $N \times 16$ general characteristic or data reduction matrix with elements $w_{ij}^N = q_i^N l_j^N$.

Equation (29.52) is a system of generally N algebraic equations for Mueller matrix elements m_{ij}. The simplest case of the system (29.52) occurs when 16 independent measurements are performed. In this case $N = 16$, $\mathbf{W}$ is of rank 16, and inverse matrix $\mathbf{W}^{-1}$ is unique. Then all 16 Mueller matrix elements are

$$\vec{\mathbf{M}} = \mathbf{W}^{-1}\mathbf{G}. \tag{29.53}$$

Most Mueller matrix polarimeters are configured so that $N > 16$. This makes $\vec{\mathbf{M}}$ overdetermined, and $\mathbf{W}^{-1}$ does not exist. The optimal (least-squares) estimation of $\vec{\mathbf{M}}$ can be obtained using the pseudoinverse matrix $\tilde{\mathbf{W}}$ of $\mathbf{W}$ [141]:

$$\vec{\mathbf{M}} = \tilde{\mathbf{W}}\mathbf{G} = \left(\mathbf{W}^{\mathrm{T}}\mathbf{W}\right)^{-1}\mathbf{W}^{\mathrm{T}}\mathbf{G}. \tag{29.54}$$

In mathematics there exist a variety of pseudoinverse matrices (e.g., one-sided inverse, Drazin inverse, group inverse, Bott-Duffin inverse, etc.). Here we use the so-called Moore-Penrose pseudoinverse matrix [19, 176, 201]. Note that the characteristic matrix $\mathbf{W}$ in (29.7) is or can evidently be reduced to those of the full column rank.

This approach is called complete Mueller polarimetry. The theory of operation and calibration of Mueller matrix polarimetry was developed in [40], and the general formalism has been applied by many authors to the optimization of Mueller matrix polarimeters in the presence of noise and measurement error [53, 220, 241, 258]. This procedure is repeated at different scattering angles in order to determine the angular profile of the Mueller matrix.

However, in many applications reconstruction of the full Mueller matrix is not necessary [193, 220, 221, 259]. First of all, some subset of matrix elements might completely describe scattering that is of interest and, hence, these subsets can be considered as initial information for the solution of corresponding classes of inverse problems. Another factor making the measurement of complete Mueller matrix unnecessary is matrix symmetry. Illustrative example is the pure Mueller matrix with symmetry determining by the first Jones equivalence theorem [106, 112]. This matrix is widespread in the literature [247, 248] because it describes linear crystal optics without absorption. This approach is termed incomplete or partial Mueller polarimetry [221, 259].

The exact sets of matrix elements, i.e., structures of incomplete Mueller matrices, which can be measured in the framework of any of measurement strategies (time sequential, dynamic, etc.), are also determined by structure of the data-reduction matrix of generalized measurement equation (29.51). This corresponds to the third case in (29.51) occurring when $N < 16$ and $\mathbf{W}$ is of rank less than 16. The optimal estimation of $\vec{\mathbf{M}}$ is again obtained using the pseudoinverse matrix $\tilde{\mathbf{W}}$. However, only 15 or fewer Mueller matrix elements can be determined from the system (29.54), i.e., polarimetry is "incomplete" or "partial."

29.4 Radar Polarimetry

Radar polarimetry is a special class of equipment to carrying out the polarization measurements at micro- and radiowave. Monostatic radars use the same antenna to transmit and receive electromagnetic radiation and are limited to measurements at the exact backscattering direction. Bistatic radars use one or more additional receiving antennas that provide supplementary polarization information.

For radar polarimetry, the Stokes vector is not the most effective way to characterize the data since there are effectively two measurements of polarization to quantify – one for each of the orthogonal transmitted waves. The radar transmits a horizontal polarized wave, measures the echo polarization, transmits a vertical polarized wave and measures the polarization of that echo. At least two Stokes vectors would then be required [283]. Since the polarimetric measurements of the echoes are made as orthogonal measurements it is convenient to define an alternative notion of the Jones matrix, (29.6), called in radar polarimetry a scattering matrix [45, 178]

$$\mathbf{S} = \begin{pmatrix} s_{VV} & s_{VH} \\ s_{HV} & s_{HH} \end{pmatrix}, \tag{29.55}$$

where s_{HV} denotes a transmitting antenna of a horizontal polarization and a receiving antenna of a vertical polarization. $\mathbf{S}$ becomes symmetric if the target is reciprocal, $s_{HV} = s_{VH}$.

In (29.6) and (29.55) there are two major conventions currently used for coordinates systems, the forward-scatter alignment (FSA) convention and the backscattered

alignment (BSA) convention [21, 91, 271]. If BSA convention is used, then the scattering matrix defined in (29.18) relates the scattered wave viewed approaching the receiving antenna to the incident wave viewed receding from the transmitting antenna [272]. In optical or transmission polarimetry, the FSA convention is used.

The **S** matrix, which is expressed in the BSA coordinates, is referred to as the Sinclair matrix [21, 91, 126, 239, 287].

When we say in (29.1) that the input and output Stokes vectors are connected through the Mueller matrix, it assumes utilization of the FSA convention. Using the BSA convention, the Stokes vector of the backscattered wave is related to the incident-wave Stokes vector through the Kennaugh matrix, **K** [21, 125, 263, 272]. Thus, the Mueller matrix **M** and the Kennaugh matrix **K** are formally related by [21, 91, 153]

$$\mathbf{M} = diag\begin{bmatrix} 1 & 1 & 1 & -1 \end{bmatrix} \cdot \mathbf{K}. \tag{29.56}$$

For symmetrical targets the matrices **S**, **K**, and **M** are characterized by only five parameters.

In addition to **M** and **K**, two matrices named the target covariance matrix and the target coherence matrix might be used for characterization of partially polarized waves.

The scattering matrix of (29.18) can be represented in the vector form as follows

$$\vec{\mathbf{S}} = \begin{bmatrix} s_{HH} & s_{HV} & s_{VH} & s_{VV} \end{bmatrix}^T. \tag{29.57}$$

An ensemble average of the complex product between $\vec{\mathbf{S}}$ and $\vec{\mathbf{S}}^{*T}$ leads to the so-called covariance matrix **C** [24, 270]:

$$\mathbf{C} = <\vec{\mathbf{S}} \cdot \vec{\mathbf{S}}^{*\mathrm{T}}>. \tag{29.58}$$

The Hermitian positive semi-definite matrix **C** has precisely the same elements as the Kennaugh matrix **K** and the Mueller matrix **M** but with different arrangements. The full established properties of Hermitian matrices make convenient the use of **C** in some applications [24, 135, 190, 249, 269].

The coherency marix (29.47) introduced by Cloude [44] can per analogy with (29.58) be written as

$$\mathbf{J} = <\vec{\mathbf{k}} \cdot \vec{\mathbf{k}}^{*\mathrm{T}}>. \tag{29.59}$$

where $\vec{\mathbf{k}}$ is the target scattering vector [44] and is given by

$$\vec{\mathbf{k}} = \begin{bmatrix} s_{HH} + s_{VV} & s_{HH} - s_{VV} & s_{HV} + s_{HV} & i(s_{HV} - s_{VH}) \end{bmatrix}^T. \tag{29.60}$$

Note that **C** and **J** are unitarily similar. The two matrices carry the same information; both are Hermitian positive semidefinite and both have the same eigenvalues but different eigenvectors [47].

Once reciprocity, $s_{HV} = s_{VH}$, has been assumed the elements of **S** and may be stacked into a three-element vector $\vec{\mathbf{k}} = [\, s_{VV} \quad s_{HV} \quad s_{HH} \,]^T$. The linear basis is not always the most efficient way of dealing with the analysis of polarimetric data, and the Pauli basis of the target vector

$$\vec{\mathbf{k}}_P = [\, s_{HH} - s_{VV} \quad 2s_{HV} \quad s_{HH} + s_{VV} \,]^T \tag{29.61}$$

Is, for many applications, more useful as it helps to emphasize the phase difference between the HH and VV terms. Double-interactions are dominated by the first term, multiple (volume) scattering is dominated by the second term, and direct scattering is dominated by the third term. Equation (29.59) gives in these cases the 3×3 coherency matrix and corresponding three components decomposition of the target Mueller matrix. Using normalized eigenvalues of coherency matrix $p_i = \lambda_i \big/ \sum_{i=1}^{3} \lambda_i$ [49], one more important single metric, the scattering anisotropy A, can be introduced

$$A = (p_2 - p_3)/(p_2 + p_3). \tag{29.62}$$

Scattering anisotropy A varies between zero and one defining the relation between the second and the third eigenvalues, i.e., the difference of the secondary scattering mechanisms. Entropy for smooth surfaces becomes zero, implying a non-depolarizing scattering process described by a single scattering matrix and increasing with surface roughness. Depolarizing surfaces are characterized by nonzero entropy values. However, A can be zero even for rough surfaces. For surfaces characterized by intermediate entropy values, a high scattering anisotropy A indicates the presence of only one strong secondary scattering process, while a low anisotropy indicates the appearance of two equally strong scattering processes. For azimuthally symmetric surfaces $p_2 = p_3$ and A becomes zero [47]. In this sense, the anisotropy provides complementary information to the entropy and facilitates the interpretation of the surface scatterer.

The scattering patterns are described by four independent variables, the ellipticity and orientation of the incident wave, and the ellipticity and orientation of the backscattered wave. However, using all four of these variables would result in a response that would be too cumbersome and complicated to interpret. Therefore, for clearness, only two variables are used at a time to interpret the scattering patterns – the ellipticity and orientation angle of the incident wave. This yields two signatures – the co-polarization and cross-polarization signatures introduced in [2, 272], see Fig. 29.2. In the co-polarization case, the polarization of the scattered wave is the same as the polarization of the incident wave; while in the cross-polarization case, the polarization of the scattered wave is orthogonal to the polarization of the incident wave.

The height of the pedestal is an indicator of the presence of an unpolarized scattering component, and thus the degree of polarization of a scattered wave [272]. Signatures with significant pedestals are typical of targets that are dominated by

Fig. 29.2 Example of polarization signature
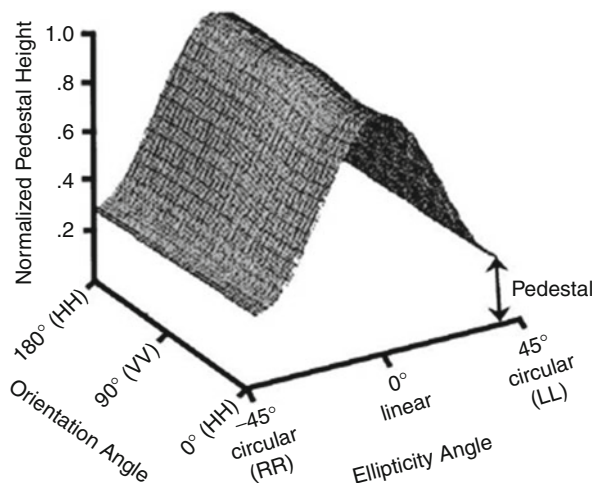
volume scattering or multiple surface scattering. Evans et al. [69] reported that pedestal height was directly proportional to vegetation density. Ray et al. [212] and van Zyl [268] noted that pedestal height was related to surface roughness with increases in roughness resulting in higher pedestals.

Although being not unique, polarization signature capturing many scattering characteristics of the target, at all polarizations, is informative and can indicate the scattering mechanisms dominating the target response. Inasmuch as different scattering mechanisms give different polarization signatures, they could be extracted from the measured Mueller matrix. The "building block" of such interpretation of the measured Mueller matrix are the following scattering mechanisms: (1) double bounce scattering; (2) Bragg scattering; (3) single (odd) bounce scattering; (4) cross scattering (see, for example, [61]). Because measurements for independent scattering mechanisms can be added incoherently ([127, 263]), the total Mueller matrix can be represented as a sum of the above basic scattering mechanisms. A number of additive decompositions of the scattering and Mueller matrix can be found elsewhere [47, 48, 250].

Double bounce scattering models typically the scattering from the dihedral-corner-reflector-like structures such as the trunk-ground structure in forested areas and the wall-ground structures in urban areas. It has been shown [59] that the scattering matrix for this mechanism can be written as

$$\mathbf{S}_1 = \begin{pmatrix} 1 & 0 \\ 0 & (1/\sqrt{\alpha})\exp(i\delta) \end{pmatrix}, \tag{29.63}$$

where α and δ are referred to as polarization index defined as the ratio of *HH* to *VV* polarization response and polarization phase difference defined as the phase difference between *HH* and *VV* backscattered responses. For trunk-ground structure, $\alpha \approx 4 - 6$ and $\delta \approx 140$–$160°$ [60]. The Mueller matrix for the double bounce scattering has the form

$$\mathbf{M}_1 = \begin{pmatrix} (\alpha+1)/2\alpha & (\alpha-1)/2\alpha & 0 & 0 \\ (\alpha-1)/2\alpha & (\alpha+1)/2\alpha & 0 & 0 \\ 0 & 0 & (1/\sqrt{\alpha})\cos\delta & -(1/\sqrt{\alpha})\sin\delta \\ 0 & 0 & -(1/\sqrt{\alpha})\sin\delta & -(1/\sqrt{\alpha})\cos\delta \end{pmatrix}. \quad (29.64)$$

Bragg scattering models the scattering from slightly rough surfaces, for example, sea surface [66, 262]. The Mueller matrix of the Bragg scattering is

$$\mathbf{M}_2 = \begin{pmatrix} (\alpha+1)/2\alpha & (\alpha-1)/2\alpha & 0 & 0 \\ (\alpha-1)/2\alpha & (\alpha+1)/2\alpha & 0 & 0 \\ 0 & 0 & (1/\sqrt{\alpha}) & 0 \\ 0 & 0 & 0 & -(1/\sqrt{\alpha}) \end{pmatrix}, \quad (29.65)$$

where the mean polarization index value $\alpha < 1$; the mean polarization phase difference value δ is zero, the Bragg scattering undergoes a single bounce.

The single bounce scattering models the direct specular reflections from the ground surfaces or from building roofs perpendicular to incident waves. The Mueller matrix for this mechanism is

$$\mathbf{M}_3 = \begin{pmatrix} 1 & 0 & 0 & 0 \\ 0 & 1 & 0 & 0 \\ 0 & 0 & 1 & 0 \\ 0 & 0 & 0 & -1 \end{pmatrix}. \quad (29.66)$$

The co-polarized response from forest crown volume backscattering can be included in this mechanism. If the orientations of leaves, twigs, and small branches are assumed to be uniformly distributed, the backscattering response will be independent of polarization, giving the same *HH* and *VV* responses. The backscattering from the trihedral-corner-reflector-like, wall-wall-ground structures can also be classified into this mechanism, since the scattering undergoes odd bounces [61].

The polarimetric response of a point or distributed target can generally consist of the co- and cross-polarized responses. If the total cross-polarized component is of interest, it can be assumed theoretically that the total cross-polarized response is caused by a hypothetical cross-scattering mechanism whose scattering matrix is

$$\mathbf{S}_4 = \begin{pmatrix} 0 & 1 \\ 1 & 0 \end{pmatrix}, \quad (29.67)$$

and the corresponding Mueller matrix

$$\mathbf{M}_4 = \begin{pmatrix} 1 & 0 & 0 & 0 \\ 0 & -1 & 0 & 0 \\ 0 & 0 & 1 & 0 \\ 0 & 0 & 0 & 1 \end{pmatrix}. \quad (29.68)$$

29.5   Applications of Mueller Matrix Polarimetry

Optical Mueller polarimetry and polarimetric remote sensing have recently demonstrated their unique abilities in anisotropic media and point and distributed targets of various nature identification, characterization, and classification. Some of their applications will be discussed in this section.

A comprehensive survey would here be impossible through, in the limited space of this chapter, and, all applications considered below deserve their own individual volumes. Thus, we select a few representative examples taken from different areas and concentrate only on some of their features affecting polarization of incidence EM wave.

29.5.1 Biomedical Applications

In this subsection we restrict ourselves to consideration of the structures and information content of Mueller matrices in the framework of the dichotomy of biological tissue modeling: the cases of a discrete ensemble of scatterers and of a continuous distribution of optical parameters. The understanding of the nature of light interaction with biological tissues is relevant to a number of noninvasive medical diagnostic techniques for cancer and other tissue pathologies. More comprehensive discussions of the interaction between polarized light and biomedical tissues, including the aspects suggesting no Mueller matrix measurements, can be found, for example, in the following excellent books Tuchin [255] and Tuchin et al. [256].

29.5.1.1 Polarization Properties of Tissues: The Case of a Discrete Ensemble of Scatterers

Based on the results of the above sections, the following features can be pointed out that allow one to classify scattering parameters of tissues or other biomedical structural components, by interpreting their Mueller matrices.

The ratio $-m_{21}/m_{11}$ is called the degree of linear polarization for unpolarized incident light [134, 170]. It is often negative for most scattering angles. This means that the vibrations of the electric field vector occur predominantly in the plane perpendicular to the scattering plane. For single spheres, the ratio $-m_{21}/m_{11}$ at scattering angles 0 and π is identically equal to zero. Mishchenko et al. [172] pointed out that the most prominent feature of nonspherical scattering appears to be the bridge of positive linear polarization at scattering angles near $120°$.

The ratio m_{22}/m_{11} is equal to unity for spherical particles at any scattering angle [172]. Therefore, the deviation of m_{22}/m_{11} from unity can be used as an indicator of particle nonsphericity sensitive, at least in some cases, to the particle size and aspect ratio [169, 210]. The angular features of this ratio have been studied for different kinds of pollen [16] and marine organisms [148, 275]. However, similar features can be caused by multiple scattering in turbid collections of spherical particles (e.g., [173]).

He et al. [98] showed that characteristic scattering features of the skeletal muscle (bovine *Sternomandibularis*) can be described by sphere–cylinder scattering because the element m_{22} has an asymmetry in the image scattering pattern characteristic of the scattering by cylinders. The Mueller matrix element patterns of the skeletal muscle found by He et al. are similar to those reported in other studies [147, 211].

The ratio m_{34}/m_{11} describes the transformation of the linearly polarized incident light into the circularly polarized output light. The m_{34}/m_{11} decreases with the particle refractive index. Bickel et al. [16] and Bickel and Stafford [15] have found a high specificity of the normalized element m_{34}/m_{11} for every type of biological scatterers. Strong distinctions are revealed in the values of m_{34}/m_{11} for spores of two mutant varieties of bacteria, which are distinguished by variations in their structures not detectable by traditional scattering techniques. The sensitivity of other matrix elements to these types of scatterers appears to be significantly weaker.

If scattering is well described by the Rayleigh–Gans approximation, then $m_{34} = 0$. Thus, a non-zero value for this element can be related to a deviation of the particle characteristics from those satisfying the Rayleigh–Gans scattering regime [22].

As noted in Bickel et al. [16], Bickel and Stafford [15], Hoekstra and Sloot [102, 103], Bronk et al. [25], and van de Merwe et al. [264, 265], the element m_{34} is sensitive to properties of various biological microorganisms, in particular, to small morphological alterations in scatterers. It has been shown that m_{34} is affected by a small surface roughness of a sphere [102]. It has also been demonstrated that measurements of m_{34} can be a basis for determining the diameters of rod-shaped bacteria (*Escherichiacoli* cells), which are difficult to characterize using other techniques [25]. The angular dependences of the normalized element m_{34}/m_{11} for different bacteria turn out to be oscillating functions whose maxima positions are very sensitive to varying sizes of the bacteria [25, 264, 265] thus allowing bacterial growth to be traced. Mueller matrix measurements have been used to examine the formation of liposome complexes with plague capsular antigens [253, 256] and various particle suspensions, e.g., those of spermatozoid spiral heads [115, 217].

The ratio m_{33}/m_{11} describes the reduction of the degree of circular polarization for circularly polarized incident light. Like for m_{22}/m_{11}, the behavior of the element ratios m_{33}/m_{11} and m_{44}/m_{11} also represents asymmetric particle shapes, i.e., the deviation of m_{44}/m_{11} from m_{33}/m_{11} indicates a nonspherical morphology of particles [172, 286]. The polarization characteristics of suspensions of biological particles have been described by Lopatin et al. [149], who analyzed the sensitivity of different matrix elements to variations in scatterer shapes and sizes. It was noted that the values of the elements m_{33} and m_{44} in the backward scattering direction may serve as indicators of biological particle nonsphericity.

By experimentally measuring backscattering Mueller matrix patterns, it was demonstrated in Antonelli et al. [4] that for the tumoral and healthy parts of a sample of ex vivo human colon tissue, the absolute value of m_{22} and m_{33} was larger for the diseased tissue than in healthy regions. The same difference between

cancerous and healthy regions was observed in the m_{44} element. For both kinds of tissue, the following inequality holds:

$$|m_{22}| = |m_{33}| > |m_{44}|. \tag{29.69}$$

Note that this trend seems to be quite general. Indeed, it has been observed for healthy and cancerous cell suspensions by Hielscher et al. [101] and Sankaran et al. [218] for a variety of tissues (fat, tendon, arterial wall, myocardium, blood) in transmission. Only whole blood displayed the opposite trend,

$$|m_{22}| = |m_{33}| < |m_{44}|, \tag{29.70}$$

with lower depolarization for circularly polarized incident light.

Many tissues are characterized by optical activity manifesting itself in circular dichroism and circular birefringence. The optical activity of tissues may be caused by the optical activity of the substances they are formed from and by their structural features. Circular intensity differential scattering is the difference between scattered intensities for left- and right-hand circularly polarized incident light. Circular intensity differential scattering effects can be studied by measuring the matrix element m_{14} [22]. The so-called "form circular intensity differential scattering" is an anisotropy resulting from the helical structure of a scatterer [103]. Dorman and Maestre [62] were likely the first to point out that the matrix element m_{14} could be useful in studies of helical structures. Indeed, Maestre et al. [156] reported large m_{14} values for octopus sperm heads of the species *Eledone cirrhosa*. In Shapiro et al. [232], the Mueller matrix elements for a model of DNA plectonemic helix were calculated using the coupled dipole approximation. The calculations of the Mueller matrix elements were carried out for two and four turn helices versus scattering angle. It was shown that the elements m_{12} and m_{14} exhibit the largest change with respect to the number and position of nodes, maxima, and minima for the calculation performed at $\lambda = 20$ nm and allow one to discriminate between the cases of two and four turn helices. In Shapiro et al. [233], the matrix element m_{14} was used for the determination of the average DNA orientation of this scatterer. In [11, 58, 288] it was reported that m_{14} appears sensitive to the higher order of DNA structures, namely the pitch and radius of the polynucleosomal helical arrangements

29.5.1.2 Polarization Properties of Tissues: The Case of a Continuous Distribution of Optical Parameters

Biological tissues are often optically anisotropic ([111, 256] and references therein; [12, 43, 70, 145, 187, 257]) and, in principle, can exhibit all the elementary types of anisotropy (29.17)–(29.20).

Tissues are primarily characterized by the linear birefringence caused by fibrous structures, which are common constituents of many connective tissues. A large variety of tissues, such as eye cornea, tendon, cartilage, eye sclera, dura mater, testis, muscle, nerve, retina, bone, arteries, myocardium, myelin, and so on, exhibit

birefringence. All of these tissues contain uniaxial and/or biaxial birefringent structures. The refractive index of the medium is greater along the length of the fibers than across the width. Reported birefringence values for tendon, muscle, coronary artery, myocardium, sclera, cartilage, and skin are on the order of 10^{-3} ([51, 52, 142, 256] and references therein, [260, 284]).

Linear dichroism (diattenuation), i.e., differential wave attenuation for two orthogonal polarizations, in systems formed by long cylinders or plates is defined by the difference between the imaginary parts of the effective refractive indices. For example, the linear dichroism of the retinal nerve's fiber layer gives rise to partial polarization of an unpolarized laser beam that has passed the retinal fiber layer twice [12, 150, 187]. Naoun et al. [187] reported significant differences in dichroism between normal and glaucomatous eyes. The magnitudes of birefringence and diattenuation are related to the density and other properties of the collagen fibers, whereas the orientation of the fast axis indicates the orientation of the collagen fibers.

In addition to linear birefringence and dichroism, many tissue components exhibit optical activity. There are a number of effects, generically called optical activity, resulting from the molecule's chirality that stems from its asymmetric structure [5, 10, 92, 157, 246]. A well-known manifestation of optical activity is the ability to rotate the plane of linearly polarized light about the axis of propagation. The angle of rotation depends on the chiral molecular concentration, the path length through the medium, and the wavelength of light. Interest in optically active turbid media is caused by the possibility of noninvasive in situ optical monitoring of the glucose in diabetic patients.

Many tissues demonstrate effects of optical activity resulting in circular dichroism. An example is the difference between the scattered intensities for left- and right-handed circularly polarized incident light (the so-called circular intensity differential scattering) resulting from the helical structure of scatterers [11, 31, 58, 90, 288].

Note that the interpretation of the individual contributions of several types of anisotropy occurring simultaneously is made considerably more complicated by multiple scattering in optically thick turbid media (such as most biological tissues), resulting in strong depolarization. Depolarization is controlled by a large number of tissue parameters such as the concentration, size, shape, and refractive index of the scatterers, the detection geometry, and the incident light's state of polarization [17, 76, 218].

Using the polar decomposition model in (29.41), Manhas et al. [157] showed that the change in the orientation angle of the polarization vector of light propagating through a chiral turbid medium arises not only due to the circular birefringence property of the medium but also is caused by linear diattenuation and linear birefringence of light scattered at large angles. Measurements were carried out on chiral turbid samples prepared using known concentrations of scatterers and glucose molecules. This research can potentially facilitate the determination of the concentration of chiral substances present in a turbid medium using the measured Mueller matrix.

Structurally, each muscle fiber consists of many myofibrils, which appear striated due to the periodic sarcomere structure [256]. Sarcomeres are the fundamental functional unit in each muscle fiber. Using the bovine *Sternomandibularis* muscle as an example, Li and Yao [145] applied the polar decomposition to study the effect of sarcomere lengths, which is closely related to force generation in

skeletal muscles, by comparing polarization images of muscle samples in their original states and after stretching along the muscle fibers.

Many forms of precancerous changes in tissues are difficult to detect using conventional techniques, which require a histological examination of biopsies obtained from visible lesions or random surveillance biopsies. On the other hand, it is known that cancerous tissues depolarize light less than their surrounding tissues, whereas noncancerous tissues have the same depolarizing properties as the surrounding tissue [240]. This effect is caused by changes in the subsurface structures of cancerous tissues that prevent light from penetrating inside the tissue as deeply as it would in the case of a normal tissue. These facts are indicative of the likely potential of the polarimetric approach to noninvasive cancer detection.

This potential was demonstrated by Chung et al. [43] based on the polar decomposition of in vivo Mueller matrix image patterns of nine cheek pouches in female golden Syrian hamsters (*Mesocricetus auratus*). The histological features in this model have been shown to correspond closely with those of premalignancy and malignancy in human oral mucosa. Figure 29.3 shows in vivo depolarization and birefringence images for normal and precancerous tissues, respectively. These images were taken from three different hamster cheek pouches, and the imaged fields were 2.25 × 2.25 mm.

Thus, depolarization and birefringence images can be used to identify quantitatively the dysplastic region of a tissue. Apparently, this suggests that depolarization and birefringence results will facilitate earlier and more sensitive diagnosis of precancerous changes and improve the monitoring of disease progression, the identification of region boundaries, and the assessment of cancer response to therapy. Ghosh et al. [78] used the polar decomposition methodology for monitoring regenerative treatments of myocardial infarction. To this end, the Mueller matrices were measured in the transmission mode for 1-mm-thick ex vivo myocardial samples from Lewis rats harvested after myocardial infarction, both with and without the stem cell treatment. The measured Mueller matrices were analyzed with the polar decomposition method to obtain the values of linear birefringence. The results are shown in Fig. 29.4. It can be seen that significant differences in the derived linear birefringence values exist between normal and infracted regions as well as between infracted regions with and without the stem-cell treatment. An increase in birefringence in the infracted regions of the treated hearts indicates reorganization and re-growth, as confirmed by a histologic examination.

Several important problems related to the validation of the generalized polar decomposition for the quantification and interpretation of all the intrinsic polarization parameters of a complex turbid medium have been analyzed in Ghosh et al. [77, 79, 80] and Wood et al. [282]. The gist of this issue is that the generalized polar decomposition, (29.41), represents the initial Mueller matrix as an ordered product of the Mueller matrices of the constituent polarization effects, thus implying that they act in succession. However, in actual tissues, all the polarization effects are exhibited simultaneously and not in an ordered sequential manner. To realize the potential of the polar decomposition approach for real tissues, Ghosh et al. [77, 80] have tested the validity of the decomposition process in the case of multiply-scattering media exhibiting simultaneous linear birefringence, optical activity,

and depolarization for the forward and backward directions. The simultaneous effects of linear birefringence and optical activity have been accounted for by using the Jones N-matrix formalism [119, 281] in a Monte Carlo simulation of light propagation between successive scattering events. The simulation results for the forward direction were found to corroborate the experimental findings and demonstrate that the Mueller matrix decomposition methodology can successfully extract the individual polarization characteristics of a medium that exhibits simultaneous linear birefringence, optical activity, and multiple-scattering effects. In the backward geometry, it was shown that the simultaneous determination of the intrinsic values of linear and circular birefringence can be accomplished by decomposing the Mueller matrix measured at a distance from the point of illumination greater than the transport mean free path.

In Wood et al. [282], the validity of the polar decomposition was demonstrated in vivo by carrying out intravital measurements in a dorsal skin window chamber mouse model using collagenase to induce changes in tissue structure and birefringence. In the window chamber model, the skin layer of the mouse was removed from a 10 mm diameter region on the dorsal surface, and a titanium saddle was sutured in place to hold the skin flap vertically. The treatment and measurements were carried out under general anesthesia. The values for linear and circular birefringence, depolarization, and diattenuation were extracted from the experimentally derived Mueller matrices at successive moments in time. The properties of the referenced and treated tissues were alternatively controlled by the histological examination.

In Fig. 29.5, the values of the birefringence δ and the net depolarization coefficient Δ, (29.46), in treated and control regions of the tissue are plotted as functions of time following the collagenase injection. The birefringence ranges from 1.2 to 0.3 rad, in contrast to the control region where the values remain essentially constant at 1 rad. The decrease in birefringence is likely due to the denaturation of the collagen fibers, which reduces the structural anisotropy. This reduction in depolarization (Δ decreases from 0.63 to 0.45) is also due to the destruction of the collagen fibers, since these represent one of the primary scattering structures in the tissue. These results were confirmed by histology.

It is evident that, due to the non-commuting nature of the matrix multiplication, the multiplication order in (29.41) is ambiguous. This results in the possibility of six different decomposition orders of multiplication that can be grouped into two families, depending upon the position of the depolarizer and the diattenuator matrices [152, 177, 197]. The three decompositions with the depolarizer set after the diattenuator form the first family, while the three decompositions with the depolarizer preceding the diattenuator constitute the second family:

$$
\begin{array}{ll}
\text{First family} & \text{Second family} \\
\left\{
\begin{array}{l}
\mathbf{M}_\Delta \, \mathbf{M}_R \, \mathbf{M}_P \\
\mathbf{M}_\Delta \, \mathbf{M}_P \, \mathbf{M}_R \\
\mathbf{M}_R \, \mathbf{M}_\Delta \, \mathbf{M}_P
\end{array}
\right.
&
\left\{
\begin{array}{l}
\mathbf{M}_P \, \mathbf{M}_R \, \mathbf{M}_\Delta \\
\mathbf{M}_R \, \mathbf{M}_P \, \mathbf{M}_\Delta \\
\mathbf{M}_P \, \mathbf{M}_\Delta \, \mathbf{M}_R
\end{array}
\right.
\end{array}
\tag{29.71}
$$

In Ghosh et al. [79], the influence of the multiplication order for two cases from both families represented by the first rows in (29.71) was studied.

The experimental Mueller matrices were measured for the dermal tissue of an athymic nude mouse (NCRNU-M, Taconic), in vivo from a dorsal skinfold window chamber mouse model, using a high-sensitivity turbid-polarimetry system [282]. Table 29.1 shows the experimental Mueller matrix (in transmission),

a Depolarization image   **b** Retardance image

I

Fig. 29.3   (continued)

a   **Depolarization image**   **b**   **Retardance image**

II
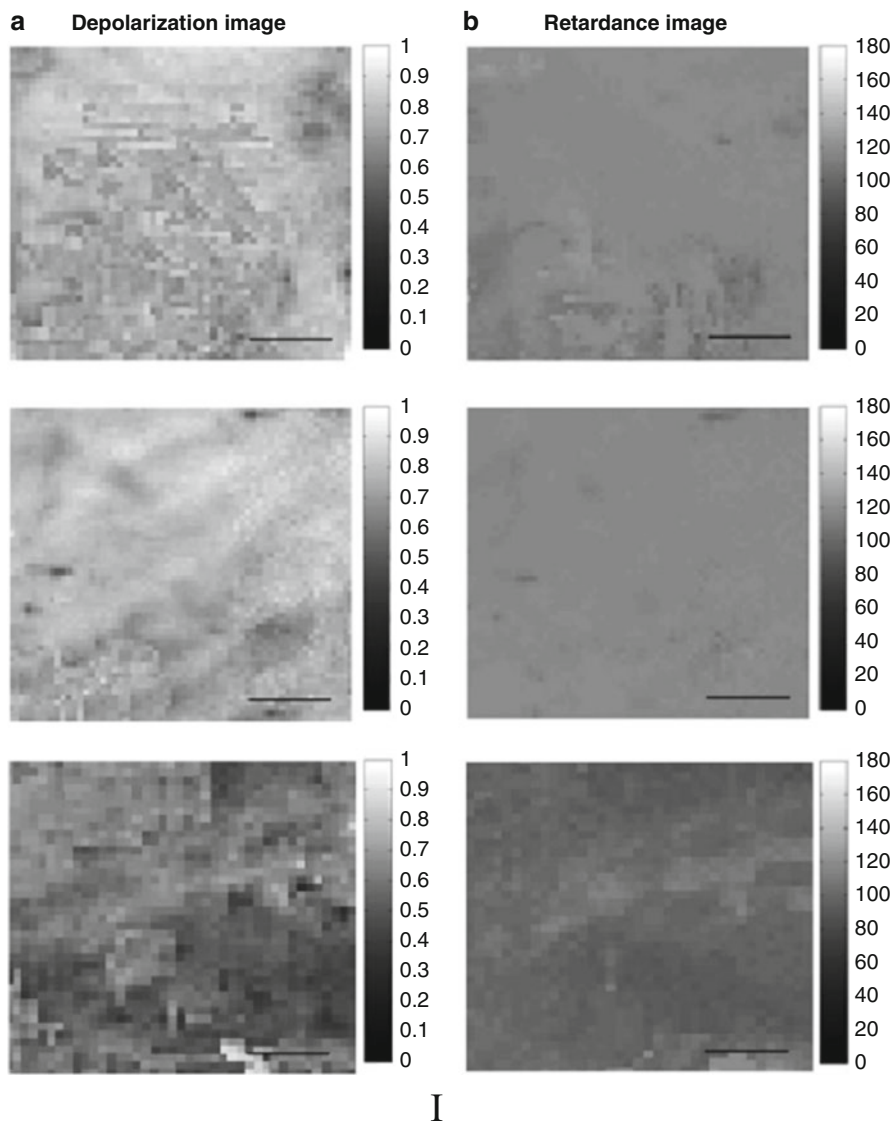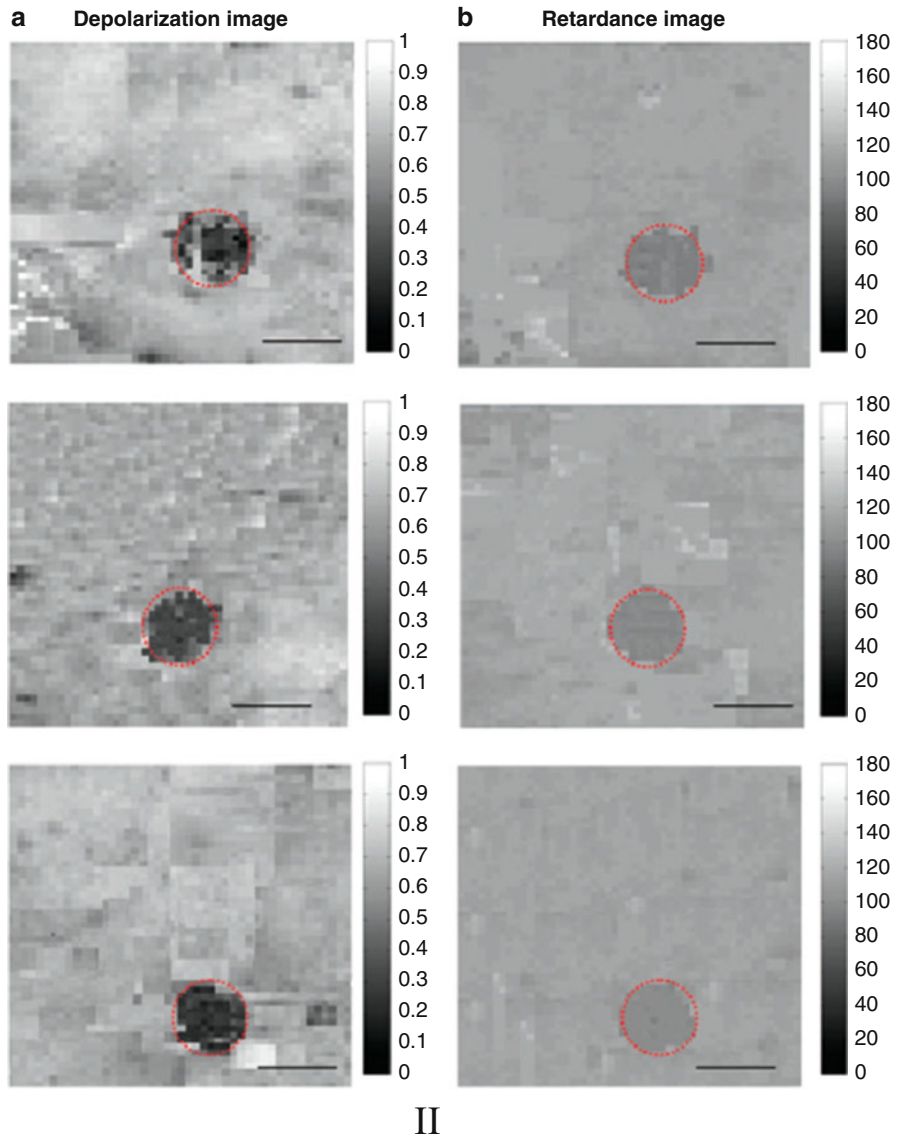
Fig. 29.3 (*a*) Depolarization images, and (*b*) birefringence images for the m_{33} element of the Mueller matrix of (**I**) healthy tissues and (**II**) precancerous tissues. The scale bars are 0.5 mm (After Chung et al. [43])

the corresponding decomposed constituent matrices, and the determined values of the polarization parameters. The constituent matrices obtained via the decomposition according to the first rows of (29.71) ($\mathbf{M}_\varDelta \, \mathbf{M}_R \, \mathbf{M}_P$ and $\mathbf{M}_P \, \mathbf{M}_R \, \mathbf{M}_\varDelta$) are shown in the second and third rows, respectively. The results summarized in the

Fig. 29.4 The results of
linear birefringence
measurements from the
controls and the stem-cell
treated groups of infracted
tissues (After Ghosh at al.
[77])
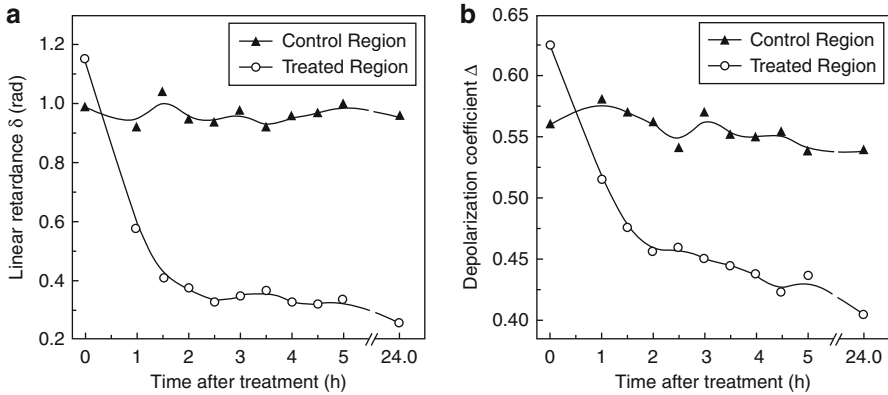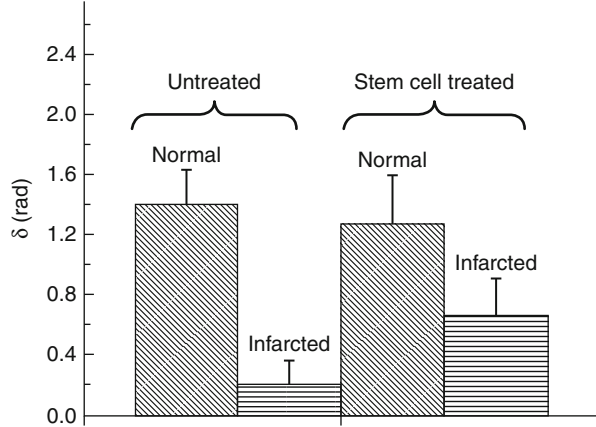
Fig. 29.5 (**a**) Birefringence and (**b**) depolarization as a function of time after collagenase
injection in the treated and control regions (After Wood et al. [282])

table show that the polar decompositions using the two selected multiplication
orders of the constituent matrices give similar values for the retrieved polariza-
tion parameters. An insignificant difference is observed in the linear dichroism
value only, the other parameters being almost identical. We can thus conclude
that the individual polarization parameters of the tissue could be decoupled and
quantified despite their simultaneous occurrence, even in the presence of multi-
ple scattering.

It should be noted that, although almost all existing polarimetric matrix models
assume successive multiplication of the constituent Mueller matrices, the physical
nature of the interrelation between this successive multiplication and the actual
simultaneity of the polarization effects in real anisotropic media has not been
clarified completely. Therefore, the results of Ghosh et al. [77, 79, 80] and Wood
et al. [282] have the utmost practical importance.

Table 29.1 *Top*: the experimental Mueller matrix and the decomposed constituent matrices from dermal tissue. The constituent matrices obtained via decomposition with the order of (2.1) ($\mathbf{M}_\Delta\mathbf{M}_R\mathbf{M}_P$ and $\mathbf{M}_P\mathbf{M}_R\mathbf{M}_\Delta$) are shown in the second and the third rows respectively. *Bottom*: The values for the polarization parameters extracted from the decomposed matrices (After Wood et al. [282])

$$M$$

$$\begin{bmatrix} 1 & 0.0707 & 0.0348 & -0.0060 \\ 0.0480 & 0.4099 & 0.0077 & 0.0650 \\ 0.0162 & -0.0184 & 0.2243 & -0.3580 \\ 0.0021 & -0.0465 & 0.3571 & 0.1783 \end{bmatrix}$$

$$M_\Delta \qquad\qquad M_R \qquad\qquad M_D$$

$$\begin{bmatrix} 1 & 0 & 0 & 0 \\ 0.0193 & 0.4006 & 0 & 0 \\ 0.0076 & 0 & 0.4596 & 0 \\ -0.0060 & 0 & 0 & 0.3768 \end{bmatrix} \begin{bmatrix} 1 & 0 & 0 & 0 \\ 0 & 0.9935 & 0.0697 & 0.0897 \\ 0 & 0.0435 & 0.4960 & -0.8673 \\ 0 & -0.1049 & 0.8655 & 0.4897 \end{bmatrix} \begin{bmatrix} 1 & 0.0707 & 0.0348 & -0.0060 \\ 0.0707 & 0.9994 & 0.0012 & 0 \\ 0.0348 & 0.0012 & 0.9975 & 0 \\ -0.0060 & 0 & 0 & 0.9969 \end{bmatrix}$$

$$\begin{bmatrix} 1 & 0.0516 & 0.0301 & -0.0037 \\ 0 & 0.3994 & 0 & 0 \\ 0 & 0 & 0.4588 & 0 \\ 0 & 0 & 0 & 0.3758 \end{bmatrix} \begin{bmatrix} 1 & 0 & 0 & 0 \\ 0 & 0.9935 & 0.701 & 0.0898 \\ 0 & 0.0436 & 0.4960 & -0.8672 \\ 0 & -0.1047 & 0.8655 & 0.4898 \end{bmatrix} \begin{bmatrix} 1 & 0.0480 & 0.0162 & 0.0021 \\ 0.0480 & 0.9999 & 0.0004 & 0 \\ 0.0162 & 0.0004 & 0.9988 & 0 \\ 0.0021 & 0 & 0 & 0.9987 \end{bmatrix}$$

Parameters	Estimated values using the order of Eq. (2.1)	Estimated values using the order of Eq. (2.4)
d	0.079	0.051
Δ	0.58	0.59
ψ (°)	0.51	0.50
δ (rad)	1.06	1.058

29.5.2 Vegetation

Complete radar polarimetry has proven inherent advantages over optical polarimetry in vegetation monitoring due to their ability to penetrate the vegetation cover and obtain information of the underlying soil surface. Several experimental and theoretical studies have been carried out in last few decades to investigate the sensitivity of microwave polarization sensors to the vegetation and soil parameters. In this subsection we concentrate on results of radar polarimetry of different types of vegetation and trees. Some recent results obtained in optical range, in particular, Mueller polarimetry of the different types of leaves at visible, are discussed as well.

Imhoff et al. [113] and Hess et al. [100] demonstrated that when the incident wave propagates through the entire canopy and reaches an underlying highly reflecting surface, mangrove forests and flooded vegetation exhibit the enhancement of the back scattering coefficient for the co-polarizations *HH* and *VV* by a factor up to 10 dB, depending on the magnitude of canopy attenuation and thus on radar parameters and vegetation type. This originates from double-bounce returns or multiple scattering between the water surface and forest components [67, 213, 277, 278]. At the same time, the cross-polarization *HV* originating from multiple scattering within the canopy layer does not exhibit any particular enhancement.

In [179] experimental results obtained over mangrove forests of French Guiana with the NASA/JPL AIRSAR has been presented. The further challenge is to provide a physically based interpretation of observed polarimetric radar signatures of mangroves forests [207]. To this end, it seems reasonable to use the polarimetric scattering model of Karam et al. [124] to simulate the response of mangrove canopies aimed at identifying the dominant scattering mechanisms in the

radar–forest interactions. In compliance with this model, the forest is treated as a multilayer medium over a rough surface. The layers represent the canopy volume, and the rough surface delineates the soil interface. Each layer contains the tree constituents; i.e., trunks, branches, and leaves. The branches and trunks are modeled as randomly oriented finite cylinders, and the leaves are modeled as randomly oriented elliptic discs. All the scatterers are assumed to be uniformly oriented in the azimuth direction.

The study site, named Crique Fouillee (52°19′W, 4°52′N), is a 2.5 km × 32.5 km area allocated along the coast of French Guiana. On this test site, three development stages of mangrove forests are present: pioneer, mature, and declining stages. The pioneer stage consists of a very homogeneous canopy dominated by the gray mangrove (*Laguncularia racemosa*). Tree density is high, ranging from about 10,000 to 40,000 stems per hectare. Mean tree height lies between 0.8 m and 7.7 m. The mature stage is dominated by the white mangrove (*Avicennia germinans*) with a tree density ranging between 500 and 2,000 stems per hectare. Mean tree height is about 15 m, reaching a maximum of 25 m for the dominant species. The declining stage shows more heterogeneous canopies, including two strata: a high single-species stratum composed of the white mangrove and a lower stratum of the red mangrove (*Rhizophora* ssp.). Tree density is low, from about 300 to 600 stems per hectare. Overall, the considered forest stands consist of closed canopies. The topography of the study site is nearly flat (more details about study site can be found in Fromard et al. [72], Mougin et al. [179], and Proisy et al. [207]).

From the delivered data, the average Mueller matrix is formulated and then used to determine the following quantities for each frequency: the backscattering coefficients σ_{VV}, σ_{HH}, and σ_{HV} (for the *HH*, *VV*, and *HV* polarizations, respectively), the co-polarized σ_{VV}/σ_{HH} ratio, and the two cross-polarized σ_{HH}/σ_{HV} and σ_{VV}/σ_{HV} ratios.

Preliminary experimental observations on the relations between mangrove parameters and backscattering coefficients were reported in [179]. Results show that, for all frequencies, there is a positive relation between σ_{ii} and total biomass, with the largest sensitivity to biomass found at P-band (0.44 GHz) *HV* and L-band (1.225 GHz) *HV*. Moreover, strong differences are observed between polarizations at L- and P-band below a biomass value of about 100–150 tDM/ha (tons of dry matter per hectare). Above this threshold, co- and cross-polarization ratios reach small and constant values.

The mangrove stands are modeled as multilayer media above a rough semi-infinite interface. The young stands are modeled with one or two layers, whereas three layers are necessary for the oldest stands (Fig. 29.6).

Figure 29.7a shows the comparison between simulated backscattering coefficients versus total biomass and observed backscatter at C-, L-, and P-band. The three main contributions to the total response also are plotted – namely, the soil scattering component, the volume scattering component, and the double-bounce scattering component (see Fig.29.7b). The soil term is the surface response attenuated by the canopy layer. The volume term consists of the scattering from the tree components up to the second order. The double-bounce term corresponds to the interaction between the tree components and the ground.
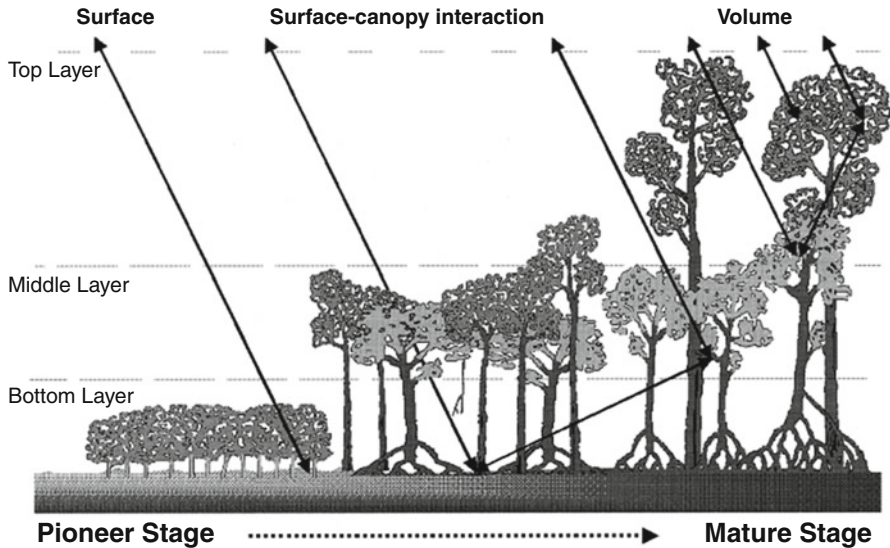
Fig. 29.6 Geometry of the mangrove forest model (After Proisy et al. [207])

On the whole, P-band provides the most pronounced polarimetric patterns. Among the polarimetric parameters, the polarization ratio is found to be most informative and useful for analyzing scattering mechanisms for discriminating between various forest stages.

Validation of the above-mentioned three-layer canopy model is carried out for another type of canopy – coniferous trees [124]. This is done in two steps. First, computed backscattering coefficients are compared with experimental data. The computed backscattering coefficient is broken down into individual contributions from different scattering mechanisms in order to develop an understanding of the relation between the backscattering coefficients and different forest biophysical parameters. The microwave data were retrieved from multipolarization, multifrequency SAR images acquired over a coniferous forest in Les Landes Forest, in southwestern France, near Bordeaux, during the MAESTRO-I campaign. The data were acquired with the NASA 1 JPL AIRSAR system, which operates at P-band (0.44 GHz), L-band (1.225 GHz), and C-band (5.3 GHz) [99].

This test site is the largest pine plantation forest in Europe. The forest is almost totally formed of maritime pine (*Pinus pinaster*). It is managed in a consistent fashion in order to ensure that the canopy remains homogeneous. The test site under consideration consists of an area 7 km × 10 km, comprising quasi-uniform large stands with a mean area of about 25 ha. The stands are rectangular in shape and delimited by fire protection tracks. Most of the stands are artificially sown, generally in rows of 4 m spacing. The rows follow an east-west direction on the test site. The test area includes many clear-cuts and a range of classes, varying from seedlings to stands over 46 years old. Consequently, these stands provide a wide range of variability of the relevant forest parameters to the model, such as density,

diameter at breast height (dbh), tree height, and standing biomass. In particular, standing biomass ranges from 0 to 150 t of dry matter per hectare.

As an example, Fig. 29.8a shows the prediction of the three-layer model against experimental data for P-bands. Each figure shows *VV*, *VH*, and *HH* polarizations. Figure 29.8b shows the individual contributions from those scatterers, which, according to the model, most affect the total backscattering coefficient. The contributions shown are limited to those from bare soil; single-bounce scattering from the needles, branches, and trunks; and double bounce scattering involving the needles, branches, trunks, and the ground.

In Fig. 29.8a, more dynamic range is obtained in the case of cross-polarization than co-polarization. Fig. 29.8b shows that, for younger trees, both the single-
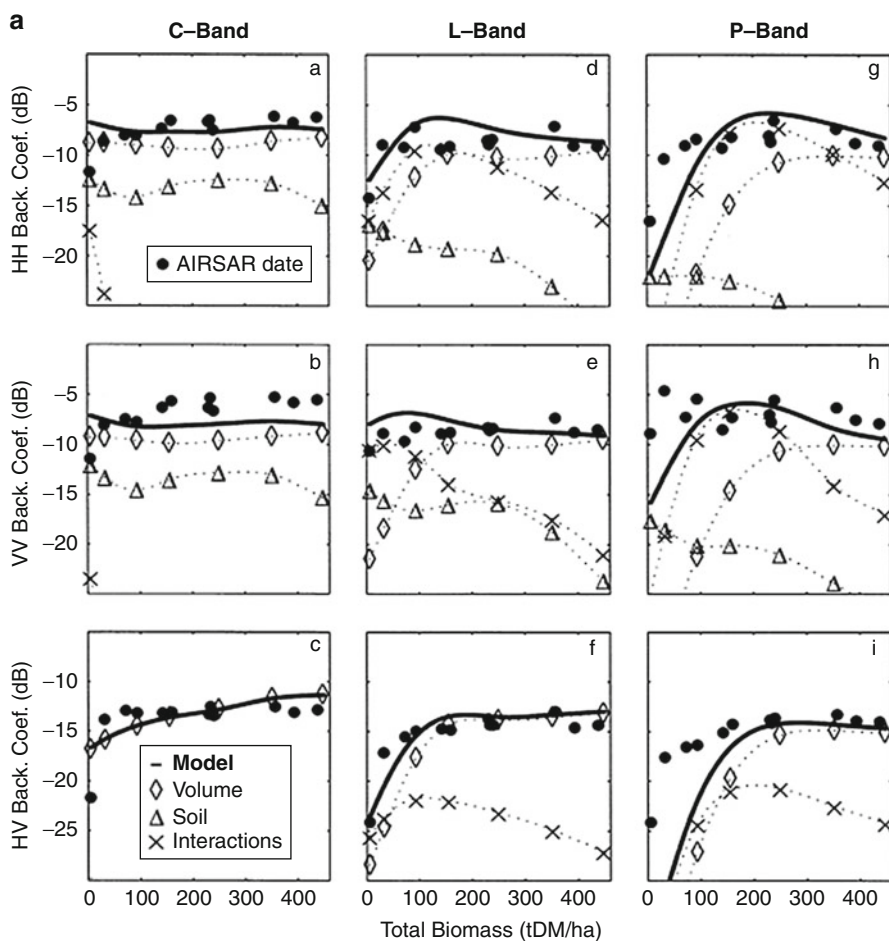
Fig. 29.7 (continued)
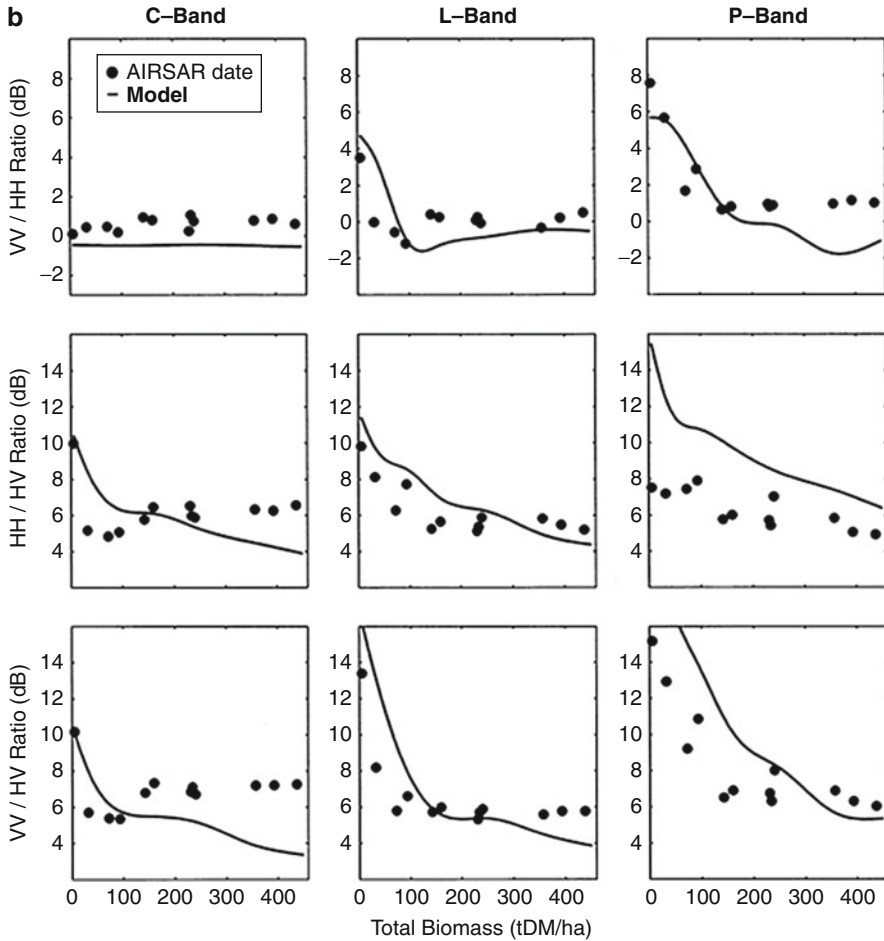
Fig. 29.7 Simulated (—) and experimental data (•) versus total biomass at C-, L-, and P-band: (**a**) backscattering coefficients and (**b**) polarization ratios (After Proisy et al. [207])

bounce scattering from branches and the double-bounce scattering of the trunk-ground interaction make significant contributions. As the trees grow older, the trunk-ground contribution becomes less significant, and the contribution from the branch dominates. This dominance is more obvious in the case of VV polarization than HH. On the other hand, the VH backscattering coefficient is due almost solely to the long branches, for all ages. Therefore, for P-band and VH polarization, the dynamic range observed reflects the physiological changes in the long branches as the canopy age increases.

An empirical relation between biomass and age reflecting the fact that the growth of trees tends to slow down as the canopy becomes older has been suggested in the form
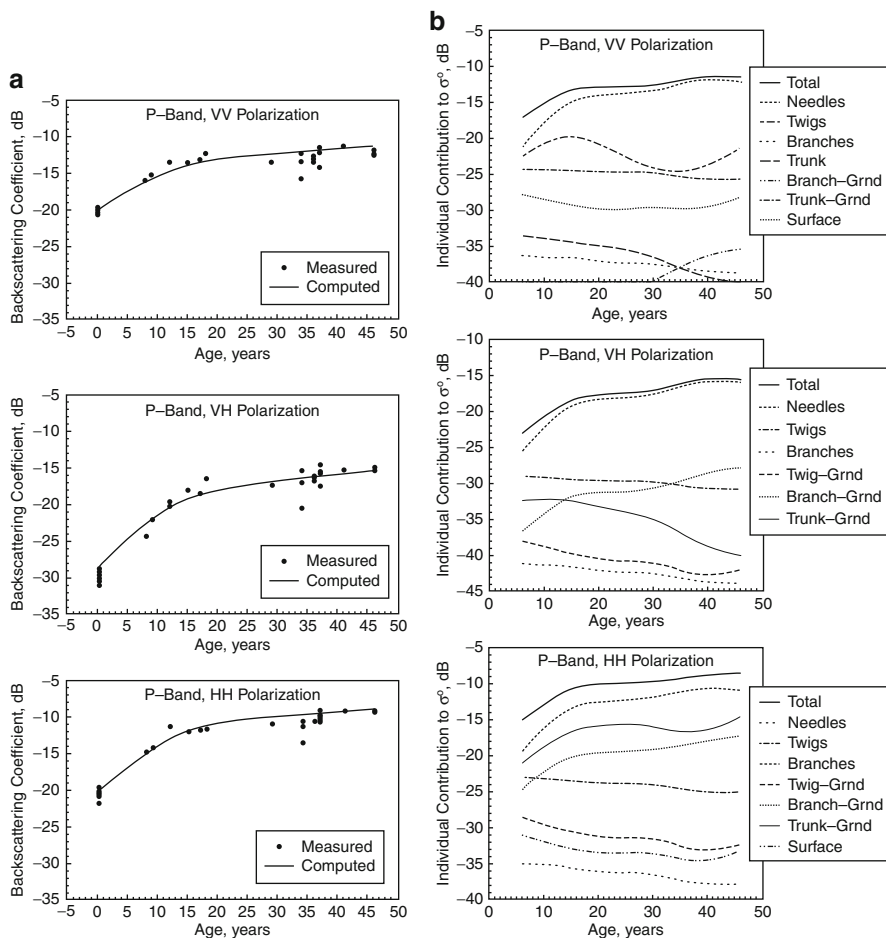
Fig. 29.8 (**a**) Comparison between computed and measured values of the backscattering coefficients at P-band as a function of the tree age; (**b**) backscattering coefficients at P-band as a function of the tree age. The contributions are broken down into single-bounce and double-bounce scattering (After Karam et al. [124])

$$Biomass = \sqrt{463.85\ age - 2,938}. \tag{29.72}$$

The relation (29.72) was used to obtain the total aboveground biomass for the ages (excluding the clear cuts) for which ground truth was available, see Fig. 29.9 for biomass as a function of tree age.

The Lear Area Index (LAI) is a dimensionless variable that measures the amount of leaf area per area unit ground surface, and may be used to describe the health of the forest after, for example, aninsect attack (e.g., [216, 243]). The use of

Fig. 29.9 (a) Comparison between computed and measured backscattering coefficient as a function of total tree biomass showing VH polarization and (b) biomass as a function of tree age both at P-band (After Karam et al. [124])
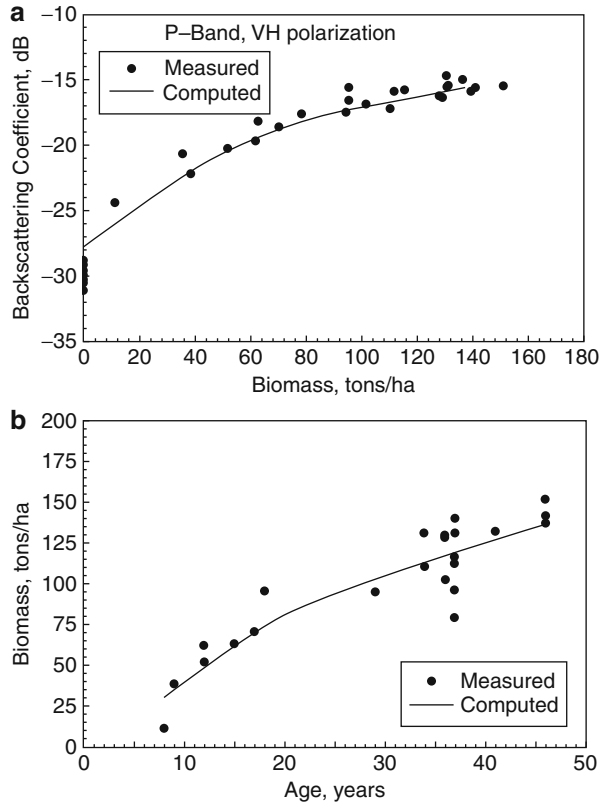
polarimetric radar data has shown a great potential for obtaining precise estimates of the LAI of boreal forests [159], rice fields [65] and corn, sorghum, and wheat [261].

A few models exist of the backscatter as a function of LAI for forest vegetation. These models are, in general, very complex, and an inverse function (i.e., a function describing LAI as a function of radar backscatter) is more or less impossible to obtain [71]. Manninen et al. [159] showed that LAI of Norway spruce and Scots pine were well explained by the backscattering ratio VV/HH. In their study they obtain for single measurement

$$LAI = a_0 + a_1(\sigma_{VV}/\sigma_{HH}),\tag{29.73}$$

and for multiple measurements

$$LAI = a + b_1(\sigma_{VV1}/\sigma_{HH1}) + \ldots + b_K(\sigma_{VVK}/\sigma_{HHK}),\tag{29.74}$$

where k-measurement number.

In Salberg et al. [216] a simple quadratic model to predict the LAI from the backscatter measurements has been used:

$$LAI = a_0 + a_1\sigma_{HH} + a_2\sigma_{HH}^2 + a_3\sigma_{XX} + a_4\sigma_{XX}^2 + a_5\sigma_{VV} + a_6\sigma_{VV}^2 \qquad (29.75)$$

where σ_{HH}, σ_{VV} and σ_{XX} denote the backscatter with horizontal, vertical and cross polarization, respectively.

The area of investigation is situated at Palokangas, in the east of Finland, about $62°52'23''$N, $30°54'10''$E. The image of the test site (acquired by August 28, 2007) is shown in Fig. 29.10.

Figure 29.11 shows the estimates of the LAI from backscatter *HH* and *VV* (Fig. 29.10). Here, the cross polarization terms are not included.

The main elements within a forest canopy are individual trees, leaves, branches, and trunks. All of these elements act as scatters and may strongly influence the backscatter patterns. The magnitude of each one of these backscatter components depends on wavelength, polarization, angle of incidence, and many other terrain and canopy parameters. Therefore, the scattering by these elements are individual problems, which are important for studying of scattering and polarization properties of these elements by themselves and play a crucial role in understanding of canopy scattering as a whole. Further, we consider the scattering of microwaves and optic radiation by different trees and leaves.

In [23, 37, 163, 164, 188] measurements of the Mueller matrices at 95 GHz (3.07 mm) and 225 GHz (1.3 mm) of four individual trees: eastern cottonwood and weeping willow, which have vertically oriented leaves (erectophil); silver maple, which has horizontally oriented leaves (planophil); and white pine, a conifer having needles which are less than 0.5λ in diameter have been carried out.

Measured co-polarized and cross-polarized signatures for all four trees are shown in Fig. 29.12a–h. Note that the signatures at $\tau = \pm45^0$ are nonzero as a result of unpolarized energy in the scattered wave. The greater unpolarized energy in the white pine's response is illustrated in Fig. 29.13d, where for all four trees the power-weighted histograms of the receive polarization state as a function of azimuth φ and ellipticity τ for vertical transmit polarization are presented.

As can be seen at 225 GHz, the two erectophil trees (cottonwood and willow) are the most highly polarized, the white pine (conifer) is the least polarized, and the silver maple (planophil) falls roughly in between.

These results are of interest when compared with the complete polarimetric data presented in [61] for eucalyptus at P-, L-, and C-bands measured in Gippsland, Australia (see Fig. 29.14).

It can be seen that pedestals are high for all bands. Authors explained this by the significance of the responses of *RR* (right-handed transmission and right-handed receiving) and *LL* (left-handed transmission and receiving) circular polarizations. The *VH* component also contributes to the pedestals. Eucalyptus in the studied site is quite sparse, with less than 25 % closure of their crowns. This can manifest double bounce scattering between underlying vegetation and the ground surface.

Fig. 29.10 Images of the scene with 20 × 20 m pixel resolution. *Upper/left*: HH-polarized. *Upper/right*: HV-polarized. *Lower/left*: VV-polarized. *Lower/right*: Linear decomposition RGB = (HV,HH,VV) (After Salberg et al. [216])
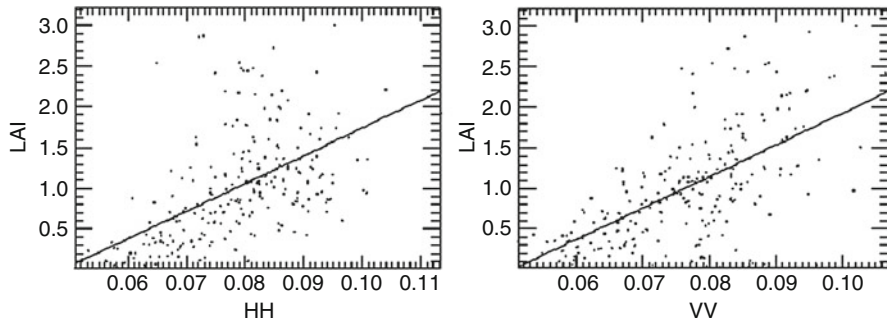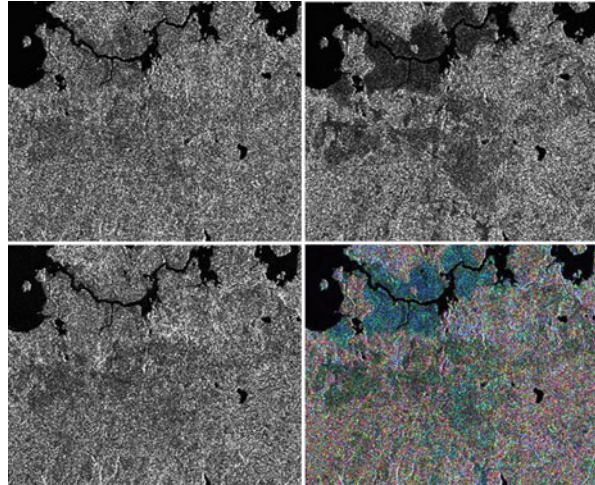
Fig. 29.11 LAI versus backscatter HH (*right*) and VV (*left*) (August 28, 2008) (After Salberg et al. [216])

To study the dependence of scattering on leaf orientation, in [164], the variability of percent polarization versus footprint location within a single tree canopy was measured. Figure 29.15 shows the approximate locations of the center of the radar footprints (A–F) within the tree crown of an eastern cottonwood tree that was approximately 20 m tall by 10 m wide and results for the percent polarization for the three linear transmit polarizations V, H, −45° and right-handed circular polarization.

From Fig. 29.15, there is a considerable difference in percent polarization for the central measurement point A versus the measurement point F at the edge of the crown. This difference relates apparently to the predominant orientation of leaves for these points: at point A, leaves perpendicular to the direction of the propagation, whereas, the average leaf normal near the edge of the crown (points F and E) is more likely to be a large angle with respect to the direction of propagation. At the same time, for point A, the percent polarization measured for the eastern

Fig. 29.12 Co-polarized and cross-polarized signatures: (**a**) and (**b**) eastern cottonwood; (**c**) and (**d**) weeping willow; (**e**) and (**f**) silver maple, and (**g**) and (**h**) white pine trees, respectively (After Mead and McIntosh [164])
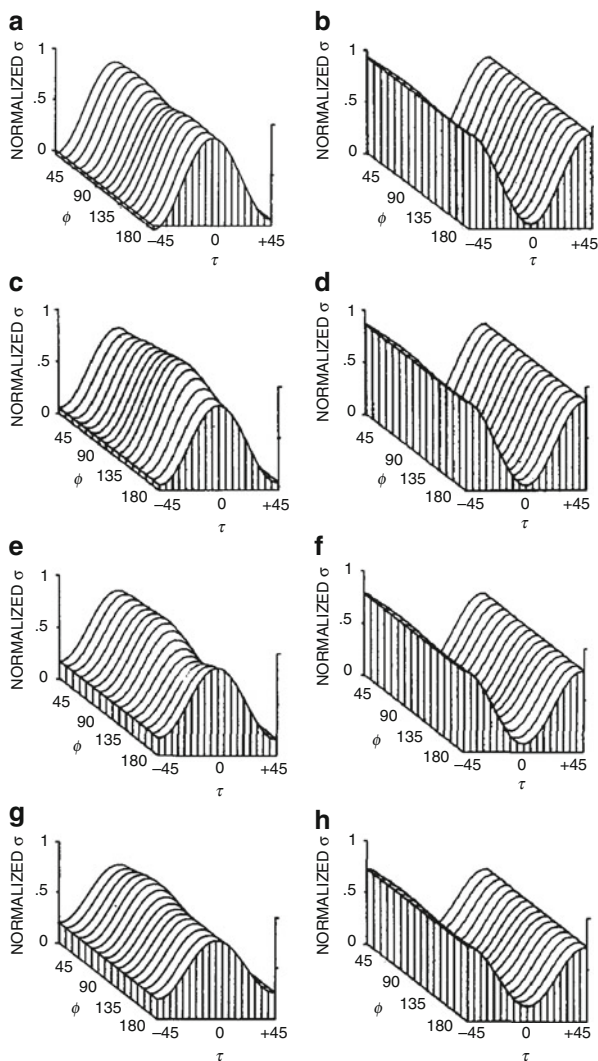
cottonwood and weeping willow trees, which have significantly different leaf shapes, turned out to be nearly equal. This suggests that the angular distribution of the leaves is dominant for scattering compared with the leaf shape and size, provided that the leaves are significantly larger than a wavelength in length and width.

Thus, the polarization characteristics of the trees are varied according to species and location on crown. A further important aspect is whether there exists any variability of the polarimetric behavior for a given tree species. Evidently, it would be reasonable to make such measurements for coniferous trees, because white pine has an angular distribution of needles that is practically uniform and the
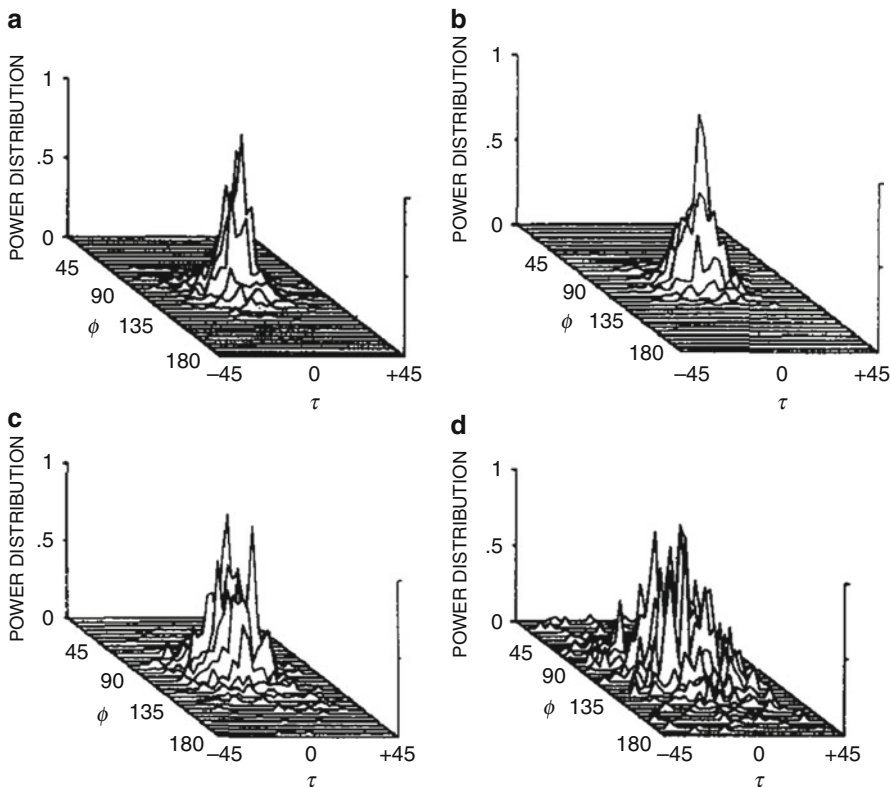
Fig. 29.13 Scatter plots of received polarization state: (**a**) eastern cottonwood; (**b**) weeping willow, (**c**) silver maple, and (**d**) white pine (After Mead and McIntosh [164])

scattering is expected to depend on the footprint location. The Mueller matrices of 11 independent footprints from 7 individual white pine trees were measured [164]. The averaged Mueller matrix and the standard deviation matrix are

$$
\begin{pmatrix}
1.044 & -0.006 & 0.007 & -0.011 \\
-0.097 & 0.739 & 0.020 & -0.005 \\
-0.021 & -0.027 & 0.749 & 0.144 \\
0.003 & -0.014 & 0.088 & -0.532
\end{pmatrix}
\text{ and }
\begin{pmatrix}
0.0073 & 0.0129 & 0.0129 & 0.0110 \\
0.0085 & 0.0097 & 0.0093 & 0.0073 \\
0.0076 & 0.0091 & 0.0091 & 0.0076 \\
0.0040 & 0.0123 & 0.0082 & 0.0081
\end{pmatrix}
\tag{29.76}
$$

This indicates little variability between the polarimetric behavior for a given tree species.

Light scattering from leaves has been the subject of many previous studies (see, for example, [161] and references therein) but only a few (e.g., [139, 161, 204, 219, 223, 224]) address the Mueller matrix measurements, and these have mainly been single wave length (633 nm), multiple incidence angle measurements.
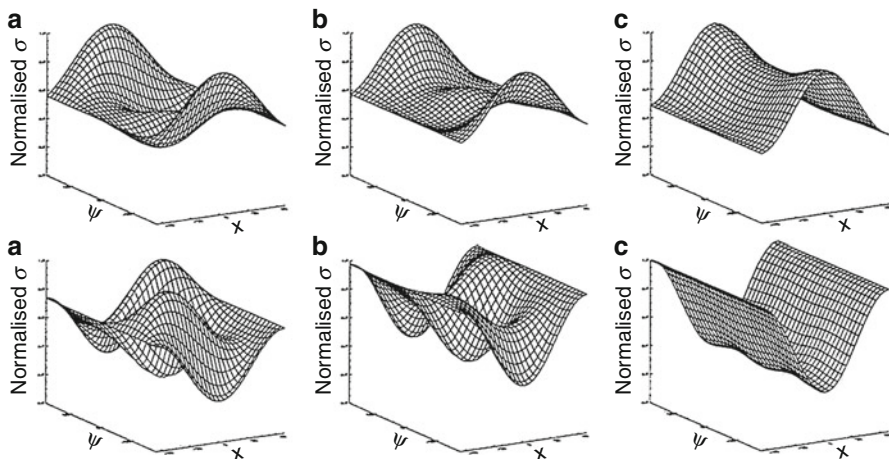
Fig. 29.14 Co- (*top*) and cross-polarization (*bottom*) signatures for eucalyptus at (**a**) P-, (**b**) L-, and (**c**) C-bands (After Dong et al. [61])

location	V	H	-45^0	RC
A	93.2	92.4	94.4	88.9
B	89.7	88.7	92.3	84.3
C	89.1	91.0	88.6	83.1
D	87.7	88.4	89.8	82.3
E	87.8	85.1	89.9	81.5
F	84.5	83.7	87.0	78.6
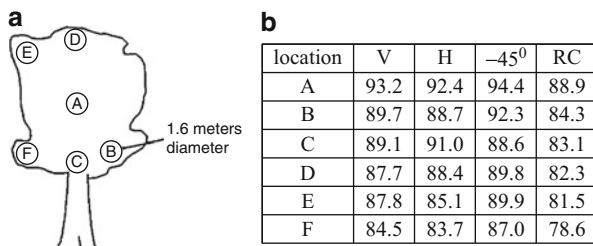
Fig. 29.15 (**a**) Locations of the center of the footprints (A–F) within the tree crown of an eastern cottonwood tree; (**b**) results for the percent polarization for the three linear transmit polarizations V, H, -450 and right-handed circular polarization (After Mead and McIntosh [164])

Savenkov et al. [224] reported Mueller matrices at a fixed wavelength (633 nm) with normal incidence and backscattering angles for English oak and wheat leaves. Krishnan and Nordine [139] reported Mueller matrices for yew and maple leaves at 633 nm with a fixed incidence angle of 400 measuring the reflected light from the leaf surface. In [161], measurement geometry assumes the angle of incidence on the sample is 45° and the light scattered is measured at a fixed angle of 135°. The spectral range is from 345 to 1,020 nm, with gap at 510–550 nm for three leaf samples, *Arabidopsis thaliana* (aka Thale Cress), English oak (*Quercus robur*), and *Ficus benjamina*. Results for English oak presented in [224] are consistent with that measured in [161] at 630 nm.

Structures of the Mueller matrices for transmitted and backscattered light reported in [224] have the forms
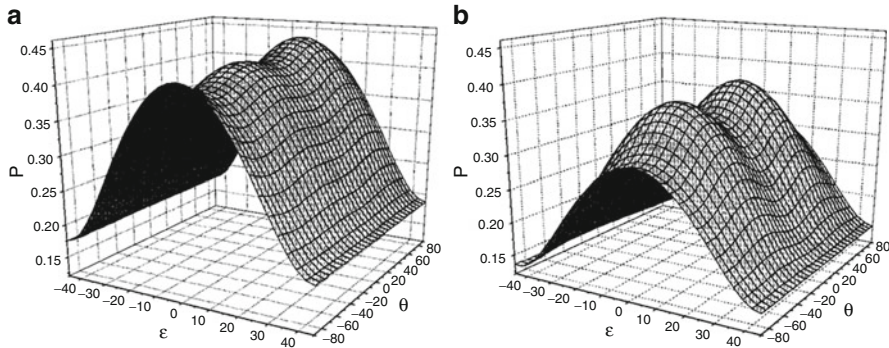
Fig. 29.16 Degree of polarization as a function of input light azimuth and ellipticity for (**a**) a fresh leaf and (**b**) a day-old leaf for transmitted light at observation angle 0° (After Savenkov et al. [224])

$$\mathbf{M}^{tr} = \begin{pmatrix} m_{11}^{tr} & 0 & 0 & 0 \\ 0 & m_{22}^{tr} & 0 & 0 \\ 0 & 0 & m_{33}^{tr} & 0 \\ 0 & 0 & 0 & m_{44}^{tr} \end{pmatrix} \text{ and } \mathbf{M}^{bsc} = \begin{pmatrix} m_{11}^{bsc} & m_{12}^{bsc} & 0 & 0 \\ m_{21}^{bsc} & m_{22}^{bsc} & 0 & 0 \\ 0 & 0 & m_{33}^{bsc} & 0 \\ 0 & 0 & 0 & m_{44}^{bsc} \end{pmatrix}.$$

(29.77)

It is interesting that Krishnan and Nordine [139] obtained the same structure of the Mueller matrices as (29.77) for yew and maple leaves, however, with considerably greater (negative) values for elements m_{12} and m_{21} The degree of polarization of light reflected by plant-leaf surfaces in their experiments was largely explained as the result of higher external and smaller internal scattering by the leaves.

It turned out that the most informative parameters for leaf type identification (coniferous or deciduous) [139], for estimation of changes to water vapor concentration [224], and for testing of leaf virus infection [219] were the single depolarization metrics: degree of polarization (linear and/or circular), (29.4), and Cloude's entropy, (29.48). Figures 29.16 and 29.17 show the degree of polarization as a function of input light for a fresh leaf and a day-old leaf for transmitted (observation angle 0°) and backscattered (observation angle 170°) light, respectively. Figure 29.18 shows the Cloude's entropy for wheat infected by WSMV (the wheat streak mosaic virus) with various infection developments for forward and backscattered light.

29.5.3 Soil

The sensitivity of microwaves to the dielectric properties and geometrical surface structure of bare soil surfaces makes radar remote sensing applicable to a wide
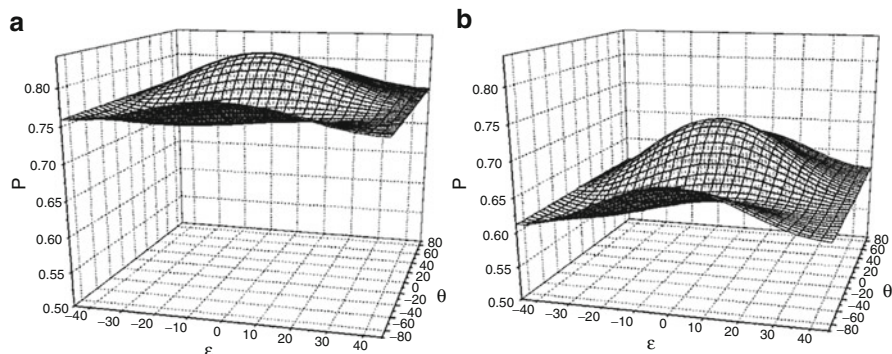
Fig. 29.17 Degree of polarization as a function of input light azimuth and ellipticity for (**a**) a fresh leaf and (**b**) a day-old leaf for backscattered light at observation angle 170° (After Savenkov et al. [224])
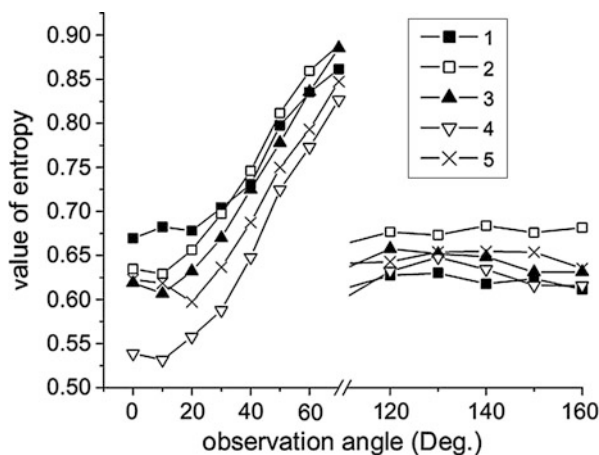
Fig. 29.18 Dependencies of the entropy versus the observation angle for the wheat leaves grown under field conditions: (*1*) wheat infected with WSMV (infection development 4 points); (*2*) wheat infected with WSMV (infection development 3 points); (*3*) wheat infected with WSMV (infection development 2 points); (*4*) healthy wheat; (*5*) wheat infected with WSMV (infection development 1 points) (After Savenkov et al. [219])

range of environmental issues relating to soil. In particular, the potential to retrieve soil moisture with high spatial and/or temporal resolution represents a significant contribution to predictive modeling in hydrology and meteorological modeling, as well as to economical optimization of agricultural procedures. A major problem in the quantitative estimation of either soil moisture or surface roughness is the separation of their individual contributions to the backscattered radar signal. In this subsection we consider the use of fully polarimetric measurements to obtain independent estimates of surface roughness and soil moisture.

Soil surfaces are characterized in terms of their material (dielectric) and geometrical properties. One of the key material parameters is the volumetric soil moisture content that affects the radar backscatter, primarily through its strong influence to the dielectric constant. Soil moisture is determined by gathering soil samples with a probe of known volume, weighing them with a portable scale, and drying them in a microwave oven. By using wet M_1 and dry M_2 soil masses and the volume V, the volumetric soil moisture values is calculated as $((M_1 - M_2)/V) \cdot 100$ %. On the other hand, the geometric properties of surfaces are described by the spatial roughness scales in both the horizontal and vertical directions, through the surface rms height and the surface correlation length, respectively.

In the absence of any simple relationship between the backscattered signal and the surface parameters, polarimetry plays an important role allowing a direct or indirect separation of roughness and moisture-induced effects.

In [94], the quantitative estimation of roughness and dielectric constant over a wide range of natural bare surfaces from polarimetric data based on the model that is an extension of the small perturbation model have been carried out. The used model has two components: a Bragg scattering term and a roughness-induced rotation symmetric disturbance. In order to decouple the real part of the dielectric constant from surface roughness, the model is addressed in terms of the polarimetric scattering entropy H, scattering anisotropy A, and alpha angle α that are derived from the eigenvalues and eigenvectors of the polarimetric coherency matrix [48].

The performance of the proposed inversion algorithm is tested using fully polarimetric L-band (HH, VV, HV, VH) data against ground measurements collected over two different test sites: the flat terrain of the river Elbe, characterized by dry and rough surface conditions, and the hilly terrain of the Weiherbach watershed, characterized by wet and slight-to-moderate surface roughness. Experimental polarimetric data with a spatial resolution of the single-look complex data in azimuth of about 0.75 m and in range of about 1.5 m were acquired in April and August 1997 along two 15-km-long and 3.2-km-wide strips over two test sites.

The experimental scattering matrix data are transformed into a coherency matrix form. Then the coherency matrix data were eigendecomposed to compute the entropy H – (29.48), anisotropy A – (29.62), and alpha angle α [48]. This allows identifying dominant surface scattering areas. The areas for which $H > 0.5$ and alpha $\alpha > 45^0$ are not considered in the following. Results for surface roughness ks and volumetric soil moisture m_v are presented in Figs. 29.19 and 29.20.

The application of the model to experimental data shows good agreement between the inverted values and ground measurements for surface roughness ks and soil moisture m_v. The inversion accuracy is high enough to point out the seasonal variation effects: the rms errors for the Weiherbach test site are much smaller for the upper soil layer (flight campaign in March), while for the Elbe-Auen test site the rms error is smaller in the deeper soil layer (flight campaign in August).

In [93] it has been shown that the model permits robust roughness estimation largely independent of topographic variations of test areas. However, a challenging problem and the main limitation for surface parameter estimation from polarimetric
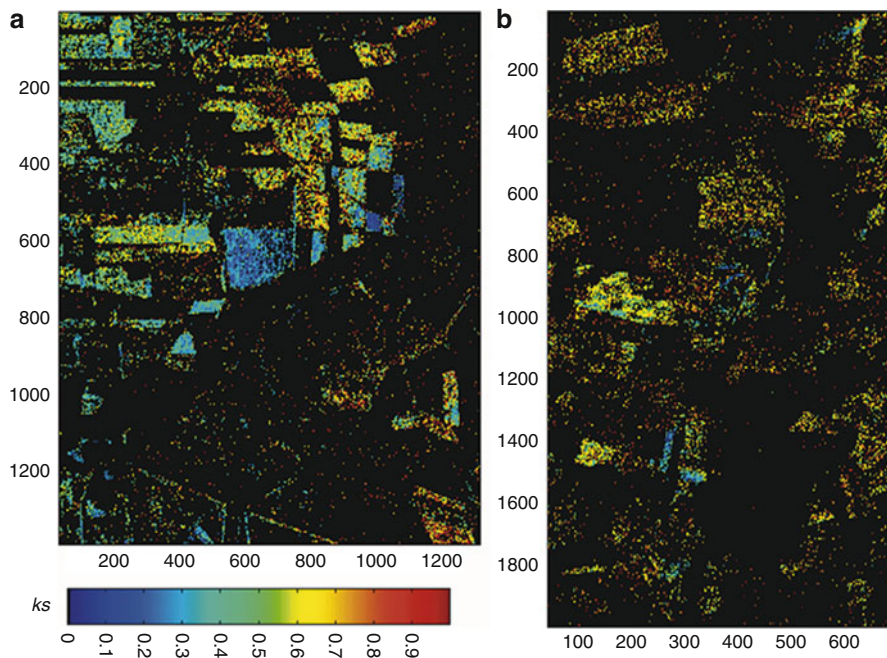
Fig. 29.19 Estimated surface roughness *ks*, ranging from 0 to 1; invalid areas are indicated with black. (**a**) Elbe-Auen test site. (**b**) Weiherbach test site (After Hajnsek et al. [94])

data is the presence of vegetation. This leads to overestimations of the surface roughness and complex dielectric constant; the former due to increasing of the entropy and decreasing the anisotropy and the latter through increasing of the alpha angle.

The most popular scattering model for vegetated surfaces is the radiative transfer model [251]. This scattering model, however, is too complicated to be used for the inversion algorithm. In DeRoo et al. [56], to retrieve soil moisture from radar response the regression models for the backscattering coefficients of a specific vegetation canopy have been used. An approach assuming an inversion of a simplified scattering model, the so-called water-cloud model, which represents the vegetation canopy as uniformly distributed water particles like a cloud, was proposed by Bindlish and Barros [18] and Sikdar et al. [236]. The parameters of the water-cloud model are derived by fitting the model with experimental data.

The backscattering coefficients for a tall-grass field, the biomasses, leaf moisture contents, and soil moisture contents are measured in [194] with a polarimetric L-band scatterometer. For computing the radar backscattering coefficients of vegetated surfaces, the radiative transfer model was suggested. This model includes five basic scattering mechanisms, as shown in Fig. 29.21: (1) direct backscattering from the vegetation canopy, (2) forward-scattering from the vegetation layer and then reflecting from the soil surface, (3) reflecting from the soil surface and then
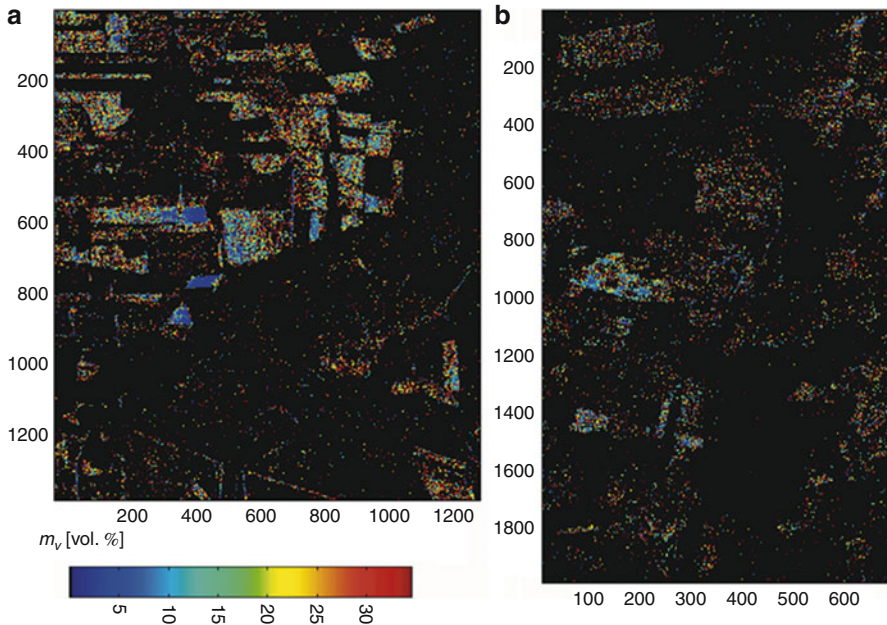
Fig. 29.20 Estimated volumetric soil moisture, m, ranging from 0 to 40 (vol%); invalid areas are indicated with black. (**a**) Elbe-Auen test site. (**b**) Weiherbach test site (After Hajnsek et al. [94])

forward-scattering from the vegetation layer, (4) reflecting from the soil surface, then backscattering from the vegetation layer, and reflecting again from the soil surface, and (5) direct backscatter contribution of the underlying soil surface with two-way attenuations through the vegetation layer.

The proposed model was used for analysis of a set of polarimetric measurement data acquired using the Hongik Polarimetric Scatterometer system at 1.85 GHz from a tall-grass field at an incidence angle of 40° for a period of 2 months in 2006 with various soil moisture conditions and a fixed surface roughness. The measured ground-truth data have the following values; the vegetation height $h = 72$ cm, averaged leaf length $L_{leaf} = 60$ cm, averaged leaf width $W_{leaf} = 2$ cm, leaf density $N_{leaf} = 800$ m^{-2}, surface RMS height $s = 2.35$ cm, and surface correlation length $l = 34.5$ cm. The measured volumetric soil moisture contents m_v have a range from 0.17 cm^3/cm^3 to 0.38 cm^3/cm^3 during the experiment period.

The measured co-polarized ratio $p = \sigma_{HH}/\sigma_{VV}$ and cross-polarized ratio $q = \sigma_{HV}/\sigma_{VV}$ of the tall-grass field, as well as the *HH*-, *VV*-, and *HV*-polarized backscattering coefficients (σ_{VV}, σ_{HH}, and σ_{HV}), were used to retrieve the soil moisture and surface roughness. Figure 29.22 demonstrates that the scattering model agrees quite well with the measured parameters.

The crop residue classification by radar polarimetry was addressed in McNairna et al. [162]. This is of great importance for land use, the economy, and agricultural production. In this analysis polarimetric data (*HH*, *VV*, and *HV*) for the Altona site,

Fig. 29.21 Scattering
mechanisms of the radiative
transfer model (After Oh
[194])
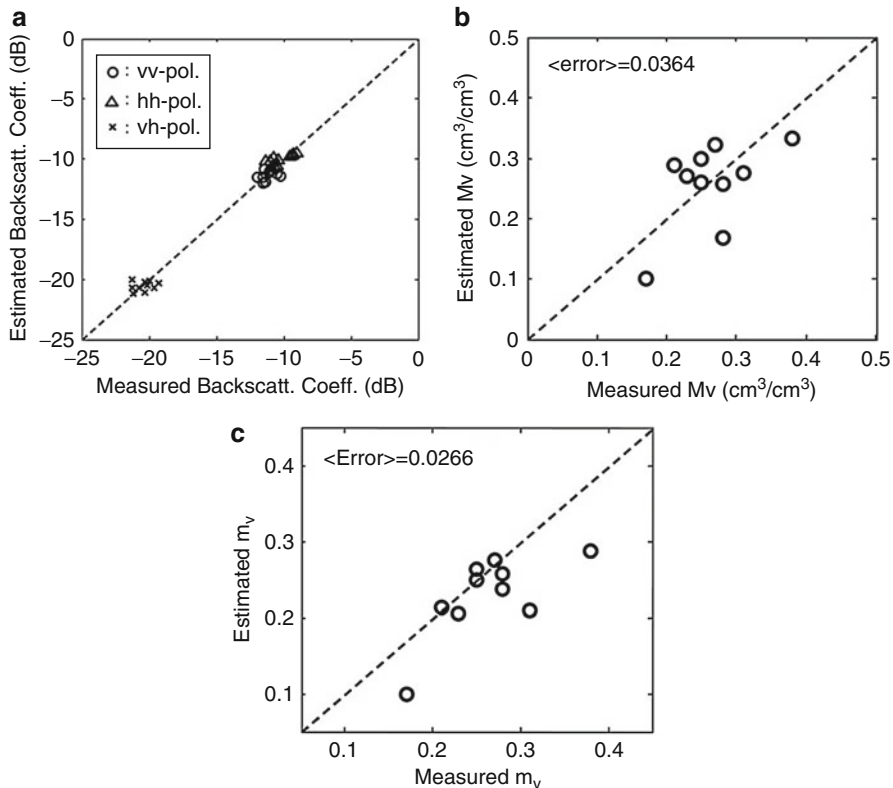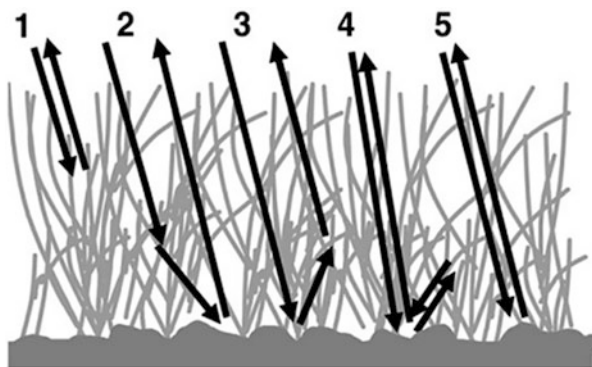
Fig. 29.22 Comparison between the estimated and measured (**a**) backscattering coefficients; soil
moisture contents using (**b**) co- and cross-polarized measurements, and (**c**) only co-polarized
measurements (After Oh [194])

southern Manitoba, acquired in April 12 and October 5, 1994 were used. In April, the Altona test site consisted of bare agricultural fields with varying surface roughness and amounts of crop residue cover. The site conditions in October were similar, although some crops had not yet been harvested.

The incidence angle was approximately 44° at the center of the site for the April, and 51° for the October measurements. Results for L-band co-polarization signatures are presented in Fig. 29.23.

From Fig. 29.23a it can be seen that these surfaces are not rough enough and do not have enough vegetation to cause significant multiple or volume scattering. These are the typical cases of surface scattering. The cases of no-till residue fields, Fig. 29.23b, and senesced crops, Fig. 29.23c, are dominated by multiple and volume scattering. Evidently, one of the most informative parameters for given test fields characterization is the pedestal height. Larger pedestals associated with standing crops and no-till fields. This demonstrates the sensitivity of pedestal height to multiple and volume scattering.

29.5.4 Atmosphere

Evidently, Solar's radiation budget plays a key role for all living beings on the Earth and it can be dramatically affected by volcanic eruptions, injecting into the atmosphere active gases and solid aerosol particles. They can remain there for months to several years changing the composition of the atmosphere [192, 209, 242, 252]. The composition and size distribution of the volcanic aerosols can significantly affect the climate changes [95].

After eruption of Eyjafjallajökull in Iceland, April 2010, it is well known that volcanic ash clouds formed right after the eruption can disrupt the air traffic of the whole continent. Ash clouds are extremely dangerous to jets. Jet engines are affected by volcanic ash particles, and these can also produce acid abrasion of windshields and other surfaces [13, 215].

The climate can be strongly affected by anthropogenic atmospheric aerosols as well, in particular, by fly ash clouds which is a by-product (consisting mainly of clays) of the combustion of coal in electricity power plants [38].

Therefore, studying the scattering and polarization properties of ash particles is important and useful in order to estimate their effect on Earth's climate as a whole and, in particular, in industrial regions where the concentration of anthropogenic aerosols can be high. Unfortunately, theoretical and numerical techniques are not suited for realistic polydispersions of volcanic ash particles, because of their wide ranges of sizes and shapes. Therefore, experimental studies remain an important source of information on scattering properties of irregular ash particles.

In [183, 184, 274], laboratory measurements of complete Mueller matrices as functions of the scattering angle in the range from 5° to 173°, of several different samples of volcanic ashes and in [182] of fly ash particles at 633-nm wavelength have been reported.

A

a) Pea Residue
(25% residue cover)

b) Lentil Residue
(25% residue cover)

c) Canola Residue
(40% residue cover)

d) Wheat/Barley Residue
(20% residue cover)

e) Sunflower Residue
(40% residue cover)

B

f) Pea Residue

g) Corn Residue

h) Canola Residue

i) Wheat/Barley Residue

j) Sunflower Residue
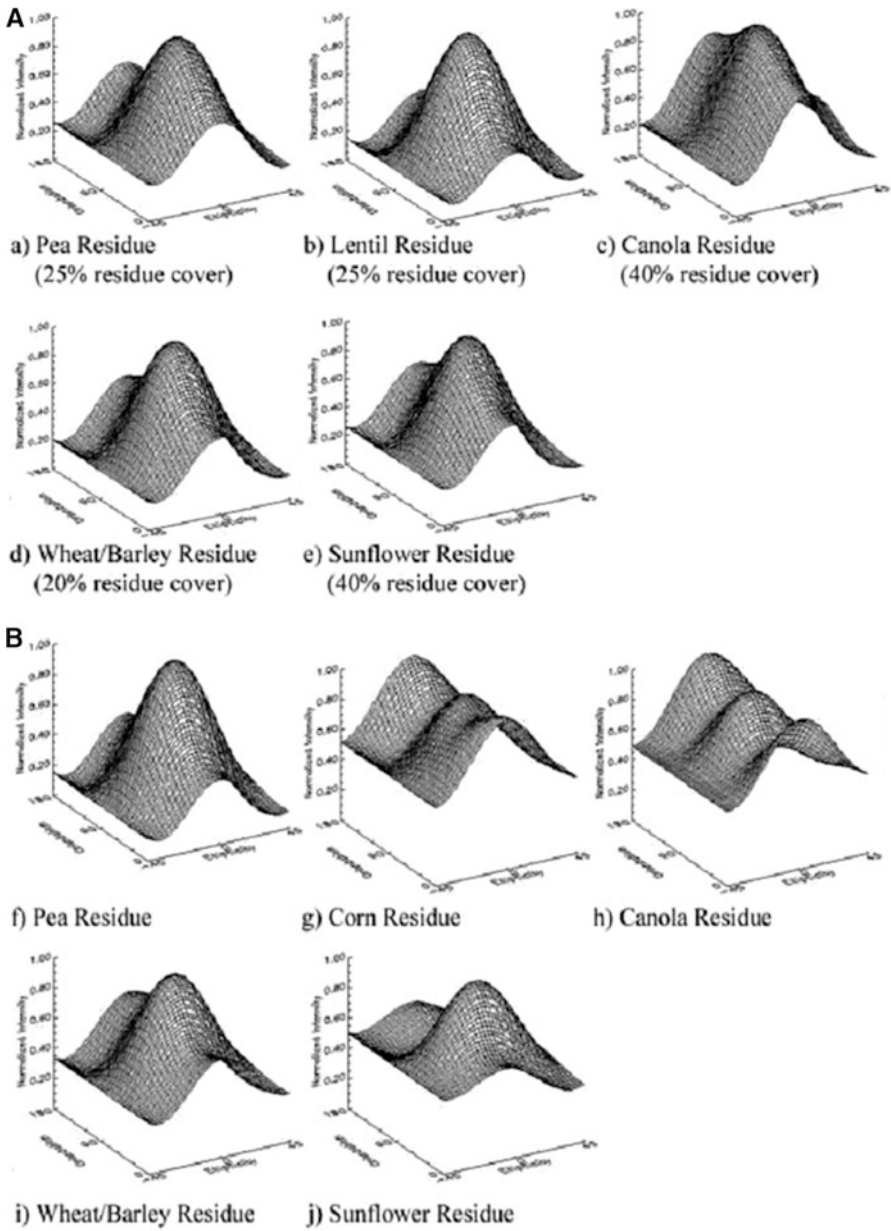
Fig. 29.23 (continued)
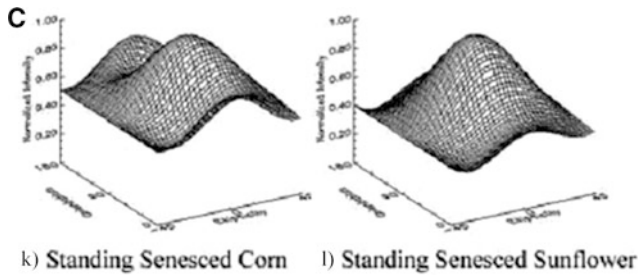
Fig. 29.23 L-Band co-polarization signatures: (**A**) tilled fields with lower amounts of residue; (**B**) no-till fields; (**C**) senesced crop prior to harvest (After McNairna et al. [162])

The samples of volcanic ashes include the following: (1) sample of dacitic pyroclastic flow from the 1989 to 1990 eruption of Mount St. Helens, Washington; (2) andesitic samples from the 1989 to 1990 eruption of Redoubt Volcano, Alaska; (3) andesitic ashes from the 18 August 1992 eruption of Crater Peak, Mount Spurr, Alaska; (4) two andesitic ash samples from the 17–18 September 1992 eruption of Crater Peak, Mount Spurr, Alaska and some other. Details of the volcanic ashes and fly ash particle's parameters and of measurement procedures are in [182, 184]. Particles presented are the examples of the two classes of small irregular particles [154]: fly ash (aggregates) and the volcanic ashes (compact particles).

Figure 29.24 presents elements of the complete Mueller matrices as functions of the scattering angle for the randomly oriented particles of fly ash. The same for the Mount St. Helens sample of volcanic ash has been presented in Fig. 29.25.

For all samples considered, the elements F_{13}/F_{11}, F_{14}/F_{11}, F_{23}/F_{11}, and F_{24}/F_{11} are zero within the experimental errors in the complete measured scattering angle range. Therefore, their Mueller matrices have a block-diagonal structure, see (29.16). This allows assuming that these scattering samples consist of randomly oriented particles with equal amounts of particles and their mirror particles.

The phase functions F_{11} for the fly ash particles show a relatively strong increase at backscattering angles, which seems to be related to their shape, compared with experimental results obtained for all samples of volcanic ashes. For all volcanic ashes, the phase functions F_{11} are smooth functions of the scattering angle showing a strong forward peak; they are featureless and flat at side-scattering angles and have almost no structure at backscattering angles. This scattering behavior can probably be considered as general property of ensembles of mineral irregular particles [114, 174, 274, 279]. The measured $-F_{12}/F_{11}$ curves for fly ash particles are found to differ appreciably from the ones for volcanic ashes. This means that the values of the degree of linear polarization for the fly ash are generally lower. The shape of F_{22}/F_{11} with an increase around $130°$ observed for fly ash was also obtained by Mackowski and Mishchenko [155] for monodisperse aggregates of N spheres with a size parameter of the single sphere of 5 and N ranging from 2 to 5.

The Mueller matrix elements for the volcanic ash samples show relatively little differences. Nevertheless, differences cannot evidently be attributed to the shapes
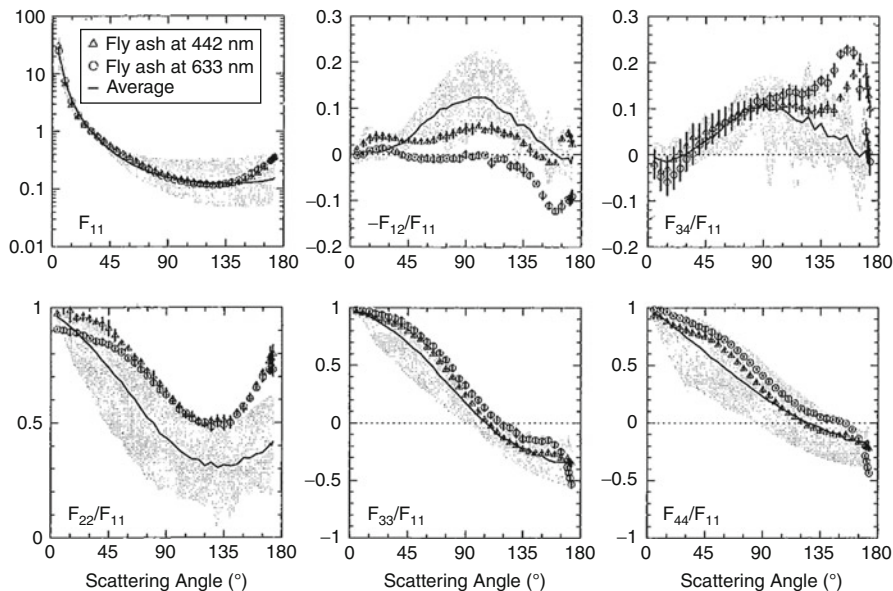
Fig. 29.24 Measured Mueller matrix as functions of the scattering angle for fly ash particles at 442 nm (*triangles*) and 633 nm (*circles*). *Solid lines* correspond to the average mineral scattering matrix for compact particles. The domains occupied by the aerosol measurements presented by Volten et al. [274] are indicated by *shading* (After Munoz et al. [182])

of the volcanic particles rather to the size and color of these samples. Through the relatively small observed differences, Munoz et al. [184] suggested constructing an average Mueller matrix for volcanic ashes that can be used for many purposes, in particular, in studies of climatic effects of volcanic eruptions when the actual properties of the volcanic ash are unknown.

One more factor that can make a significant radiative impact on climate is dust clouds. In many regions of the Earth the atmospheric aerosol component is dominated by mineral dust. The main source of mineral dust over the globe is probably Saharan dust. Indeed, large quantities of dust are transported from sources in North Africa across the Atlantic, covering very large areas [39, 146, 208].

In Munoz et al. [290], the complete Mueller matrices as a function of the scattering angle of a Sahara sand sample were measured. The samples of particles were collected from the upper part of a dune in Libya. Thus, these samples mainly consist of large particles since small particles were blown up by the wind. The Libyan sand particles in this experiment have the effective radius $r_{eff} = 124.75$ μm and effective variance $v_{eff} = 0.15$ and a wide variety of irregular, round and elongated shapes with occasional sharp edges [121, 136, 189]. Such particles are composed of a variety of different minerals. Taking into account previous data [64, 130, 200] it is assumed for the sample's refractive indices an average value $m = 1.5 + 4 \cdot 10^{-3} i$ at 632.8 nm. Results of the Mueller matrix element measurements are presented in Fig. 29.26.
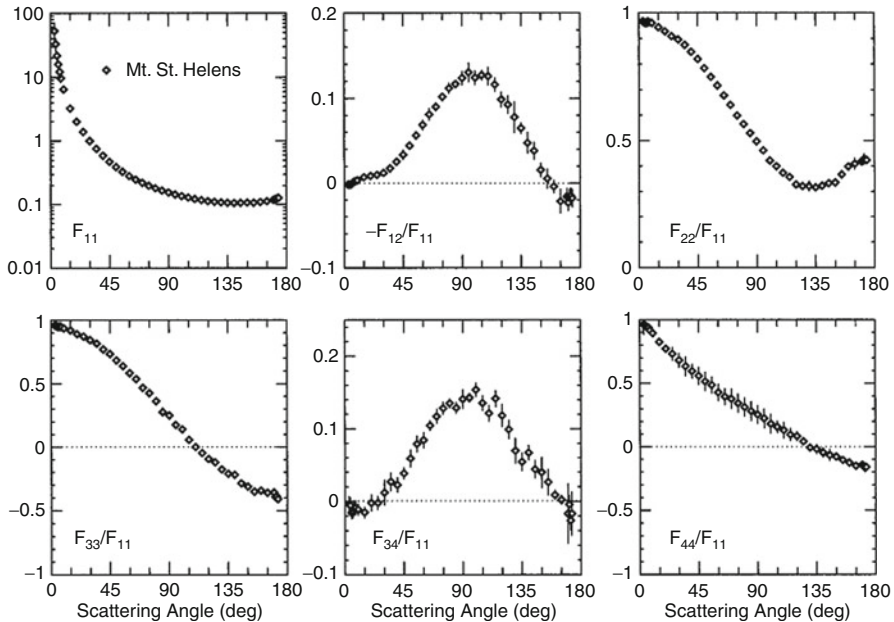
Fig. 29.25 Measured scattering matrix elements as functions of the scattering angle at 632.8 nm for the Mount St. Helens sample. Error is indicated by *bars* or is within the size of the symbols (After Munoz et al. [184])

In spite of considerable difference in size, the measured Mueller matrix elements for the Libyan sand sample, the same as volcanic ashes samples, follow the general trends presented by irregular mineral particles (see, e.g., [174, 274]). Numerical simulations show that the single scattering properties of the Libyan sand particles can be reasonably modeled with accounting for the effects of surface roughness, i.e., very spiky shapes of the particles combined with Lambertian surface elements.

Obtained results are expected to improve the accuracy of remote sensing of desert surfaces. In addition, it is important for the understanding of the scattering properties of asteroid surfaces apparently composed of particles that large compared with the wavelength in the visible range [181].

29.5.5 Contamination

29.5.5.1 Ocean

Almost a decade ago, the use of the microwave polarimetric measurements for oil slick observation was suggested [29]; the first results appeared unsatisfactory [74], however, and it was not further developed. Only recently have new studies showed the usefulness of these fully and partially polarimetric SAR measurements (see, e.g., [165, 167, 191] and references therein).
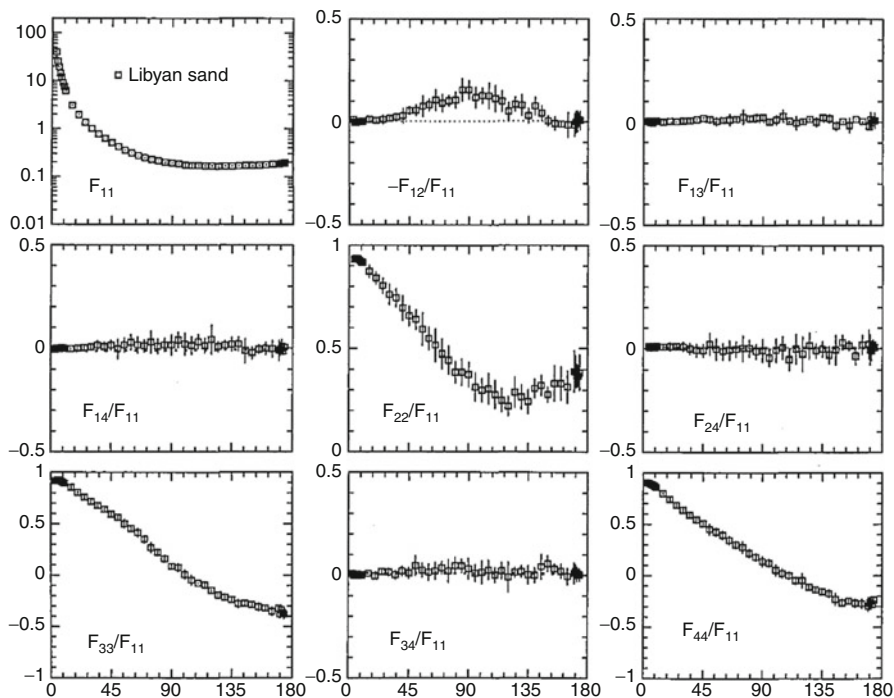
Fig. 29.26 Measured scattering matrix elements as functions of the scattering angle at 632.8 nm for the Libyan sand sample. Errors are indicated by error *bars* or are within the symbols (After Munoz et al. [290])

Sea oil spills and pollution is a matter of great concern since it affects ruinously and sometimes irretrievably both the environment and human health. Oil slick detection is determinative for effective planning of restorative countermeasures and to minimize pollution fatal consequences. In this sense, through its all-weather day-and-night capabilities [29], the full polarimetric radar data is undoubtedly recognized as the most informative and useful tool for global and regional environment monitoring, disaster management support, and resource surveys.

The oil spill detection approach is based on the different sea surface scattering mechanisms expected with and without surface slicks (non-Bragg and Bragg, respectively) [167, 191] and, therefore, they are characterized by different polarimetric features (see Table 29.2).

In [168], two approaches to the Mueller matrix analysis of three data samples (one an oil spill accident and two of look-alikes) are presented. First, the Mueller matrix analysis approach assumes using the co-polarized signatures (see Sect. 29.4). Migliaccio et al. [166] shows that a sea surface without a slick, characterized by low unpolarized backscattered energy (see Table 29.2), yields a copolarized signature with a small pedestal height. The larger pedestal height

Table 29.2 Oil-free and oil-covered polarimetric features (After Migliaccio et al. [168])

	Oil-free	Oil-covered
Polarimetric entropy	Low	High
Unpolarized energy	Low	High
HH-VV correlation	High	Low
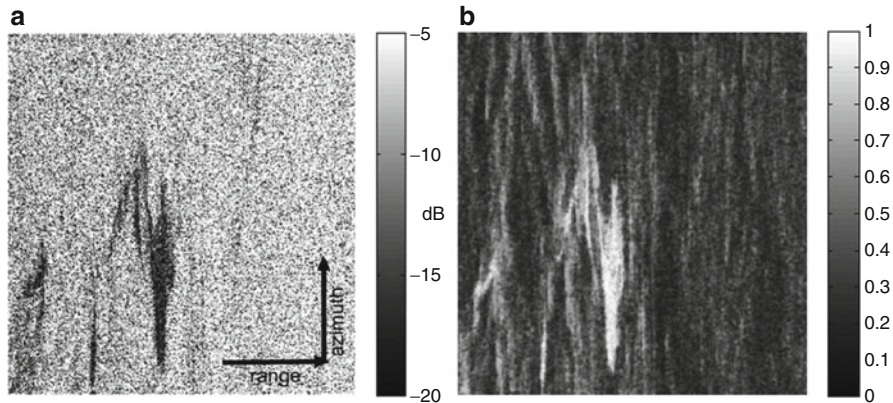
Fig. 29.27 (**a**) Polarimetric L-band SAR data (VV) for the accident area; (**b**) polarimetric entropy (After Migliaccio et al. [168])

corresponds to the case of a sea surface with slick, characterized by a large, unpolarized backscattered signal. The second approach is based on the use of the Cloude entropy, (29.48). In the scope of this approach in the case of a sea surface without slick, low entropy is evidently expected, and high entropy is characteristic to the case of a sea surface with slick.

The first data sample is a oil spill accident that occurred with the tanker Solar I in August 11, 2006, which sank in 640 m of water about 24 km off the southern coast of Lusaca Point, Guimaras Island of the Philippines, causing a heavy oil spill (approximately 200,000 L) from the tanker.

In Fig. 29.27a, polarimetric L-band SAR data (VV) for the accident area are presented. Fig. 29.27b depicts this area in the polarimetric entropy terms. It can be seen that, as predicted in [166], the entropy values for the oil-covered area are larger than the surrounding sea.

The normalized co-polarized signature has been synthesized for both the oil-free, Fig. 29.28a, and the oil-covered, Fig. 29.28b, sea surfaces by considering two regions of interest of equal size. Again, comparison of the two polarization signatures shows that, in accordance with [166] the oil slick, increasing the amount of unpolarized backscattered energy, yields the higher pedestal.

Two other cases relate to two look-alikes belonging to the acquisition on March 10, 2007, off the coasts of Da Nang (Vietnam). Figure 29.29a shows polarimetric
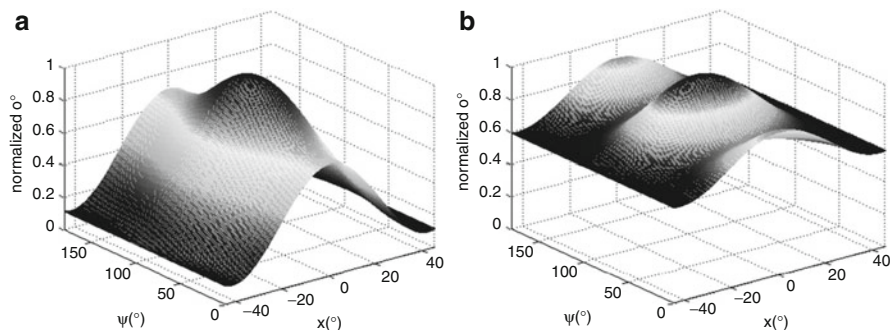
Fig. 29.28 The normalized copolarized signatures: (**a**) oil-free and (**b**) oil-covered sea surfaces (After Migliaccio et al. [168])
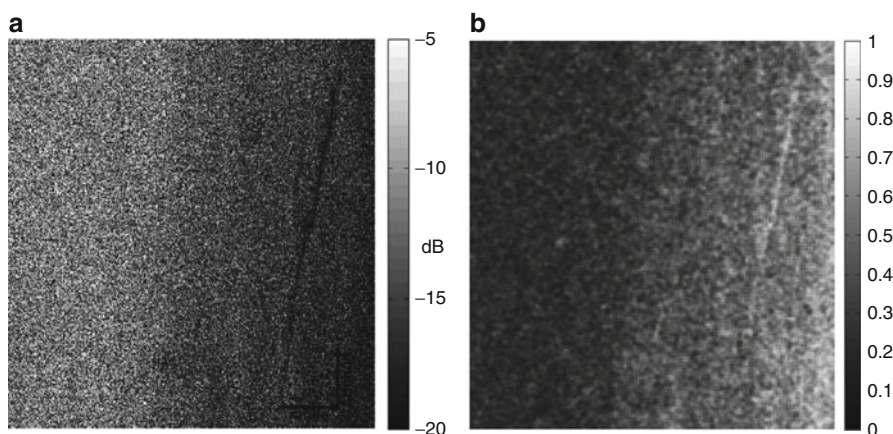
Fig. 29.29 (**a**) Polarimetric L-band SAR data (VV) for look-alike area; (**b**) polarimetric entropy (After Migliaccio et al. [168])

L-band SAR data (VV) for one of look-alike areas, in which a dark elongated feature is visible. Figure 29.29b is the same in the polarimetric entropy terms. In Fig. 29.30, the normalized co-polarized signature, synthesized for both the slick-free sea surface (a) and the dark area (b), are presented.

The polarimetric entropy, Fig. 29.29b, does not show any reliable features that can be attributed to the dark area in Fig. 29.29a. Comparison of the two co-polarized signatures, Fig. 29.30, shows low and almost equal pedestals for the slick-free sea surface and the dark area. These allow classifying the dark area in Fig. 29.29a as a look-alike.

The experimental results obtained show the effectiveness and the usefulness of the polarimetric L-band SAR data for sea oil slick observation.
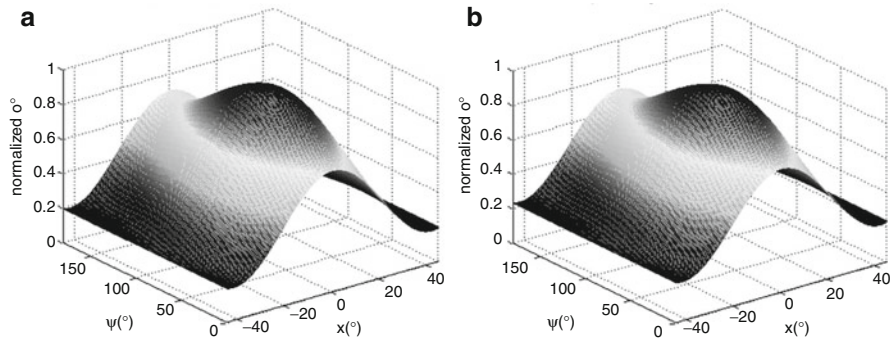
Fig. 29.30 Normalized copolarized signatures for (**a**) the slick-free sea surface and (**b**) the dark area (After Migliaccio et al. [168])

29.5.5.2 Chemical-Biological Materials

Undoubtedly, a need for the rapid and reliable identification of toxic chemical-biological materials and their derivatives in the atmosphere or on remote surfaces at safe distances (standoff detection) is urgent for military, industrial, and civilian defense practices ([57, 203] and references therein). It is even more crucial because only long-range and beforehand detection and classification of toxic chemical-biological materials will allow one to take appropriate countermeasures minimizing their environmental and population consequences.

In [32–36, 97], an approach to detect the presence of particular compounds in the atmosphere or on remote surfaces named differential absorption Mueller matrix spectroscopy (DIAMMS) has been suggested. The approach consists of twice measuring the Mueller matrix of the suspected contaminant in the backscattering direction, using two CO_2 laser emission lines as the light sources. The matter is that the Mueller matrices would not normally be measurably differently for two close wavelengths. However, if one of the wavelengths is selected to coincide with a known IR absorption band of the suspected contaminant, a significant difference can occur in 1 or more of the 16 Mueller matrix elements in switching between wavelengths.

This approach was tested on number of materials, in particular, crystalline samples comprising amino acids, sugars, enantiomorphs, aerosolized γ-irradiated *Bacillus subtilus*, and protein *chicken egg white albumen*. These materials were chosen because they are nontoxic, easy to handle, have some polarization properties that are inherent in the more complex biological organisms and act as biological warfare agent surrogates.

Samples of crystalline organic materials were prepared by pressing the powder to form the wafers, which could then be vertically arranged in a polarimeter. The sample Mueller matrix for backscattering was measured for the orientation angle, which is normal incidence ±20°. For aerosol measurements, materials were dispersed inside windowless pneumatic chambers, and then irradiated across
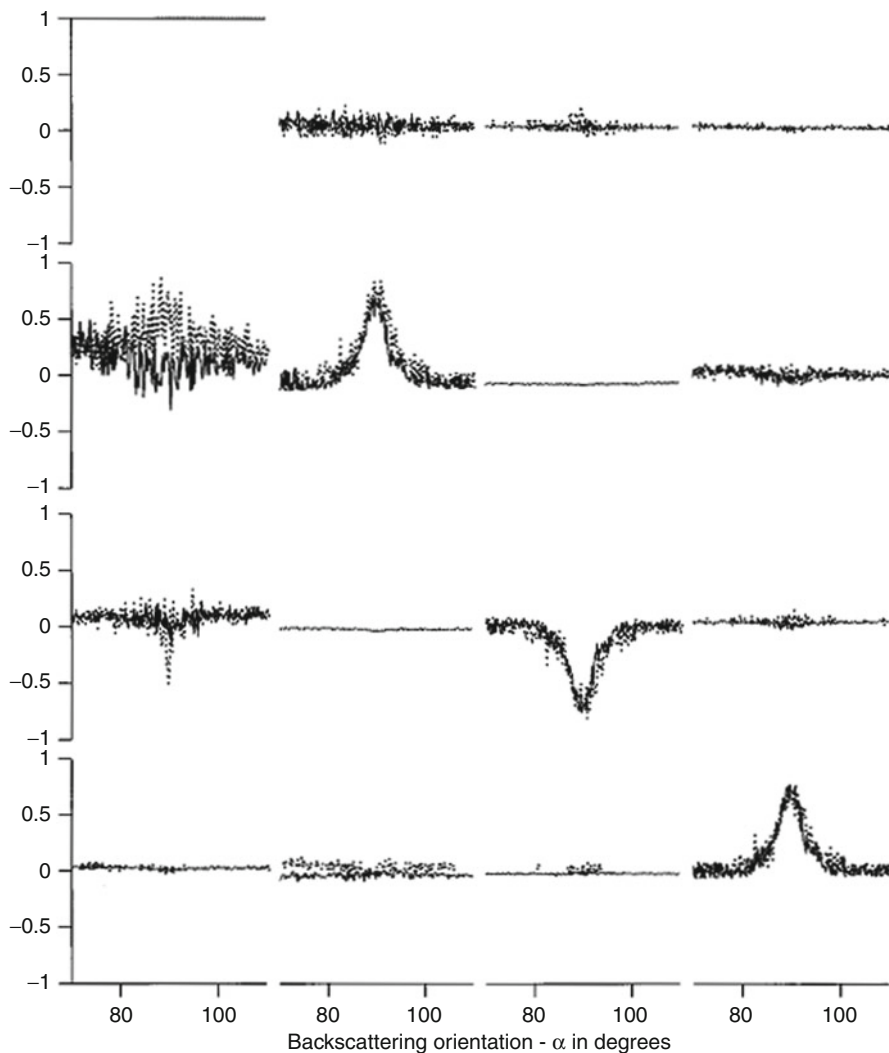
Fig. 29.31 Normalized Mueller matrix elements as a function of backscattering orientation for L-tartaric acid off and on vibration resonance (*solid line* 1,029.9 cm^{-1} and *dotted line* 1,082.3 cm^{-1}, respectively) (After Carrieri et al. [34])

9.1–12.0 μm optical bandwidth. Each aerosol was interrogated between 30 and 94 beam wavelengths, and at least one fundamental molecular vibration or vibration-rotation resonance mode in the analyte is stimulated from these infrared probing beams.

Figure 29.31 displays the example of results of the Mueller matrix element measurements for L-tartaric acid. The dotted curves represent data acquired with a laser line coincident with an absorption band in L-tartaric acid (1,082.3 cm^{-1}); the

Table 29.3 Measured polarization signatures of L-tartaric acid

Matrix element	Off-resonance 1,029.9 cm^{-1}	On-resonance 1,082.3 cm^{-1}	Scaled difference Δm_{ij}
m_{13}	0.058	0.188	0.105
m_{21}	0.208	0.704	1.587
m_{31}	0.120	−0.310	−1.101
m_{34}	−0.039	0.131	0.099
m_{43}	−0.038	0.011	0.003

solid curve data were taken at a wavelength off resonance (1,029.9 cm^{-1}). The data in Fig. 29.31 are qualitatively typical of all the samples. The dependence on the orientation angle is observed only in the diagonal elements and the rapid and seemingly random fluctuations in amplitude as the orientation angle is scanned are not electronic detector noise – the pattern is reproduced in detail as the orientation angle is scanned back and forth.

The DIAMMS approach requires that the detection of the suspected contaminant is based on the Mueller matrix elements whose values differ when the probe beam is switched between on- and off-resonance wavelengths not less than the sum of the standard deviations associated with each of the two measurements. The analysis of the data presented in Fig. 29.31 indicates that, for L-tartaric acid, five Mueller matrix elements correspond to this requirement, see Table 29.3.

The column "Scaled difference" in Table 29.3 presents a quantity related to the simple difference between matrix elements on- and off-resonance and is computed by

$$\Delta m_{ij} = \left(\Delta m_{ij}(\alpha, \lambda_o, \lambda_r) - \langle \Delta m_{ij}(\alpha, \lambda_o, \lambda_r)\rangle\right)/4 \cdot SD, \qquad (29.78)$$

where $\Delta m_{ij}(\alpha, \lambda_o, \lambda_r) = m_{ij}(\alpha, \lambda_o) - m_{ij}(\alpha, \lambda_r)$ and the subscripts o and r refer to off- and on-resonance wavelengths, respectively; $< >$ is the average, SD denotes standard deviations for matrix elements.

Figure 29.32 is an example of DIAMMS data of biological aerosol protein *chicken egg white albumen* irradiated at beam wavelengths $\lambda = 9.155$ μm and $\lambda^* = 10.458$ μm.

Normalized and averaged ordinate and abscissa of plots are $m_{ij}^o(\lambda) = \langle m_{ij}(\lambda)/m_{11}(\lambda)\rangle$ and $m_{ij}^a(\lambda^*) = \langle m_{ij}(\lambda^*)/m_{11}(\lambda^*)\rangle$; respectively, the intersection of ordinate and abscissa red dotted lines at $\left(m_{ij}^o, m_{ij}^a\right)$ are average M-elements coordinates, and separation widths of paired ordinate and abscissa green solid lines are standard deviations in $\left(m_{ij}^o, m_{ij}^a\right)$ data sets. The perpendicular distance from coordinate $\left(m_{ij}^o, m_{ij}^a\right)$ to the diagonal line in each M-element block is

$$\rho_{ij} = 2^{-1/2}\left(\left(m_{ij}^o\right)^2 + \left(m_{ij}^a\right)^2\right)^{1/2}\left[\cos\left(\arctan\left(m_{ij}^a/m_{ij}^o\right)\right) - \sin\left(\arctan\left(m_{ij}^a/m_{ij}^o\right)\right)\right]$$

$$(29.79)$$
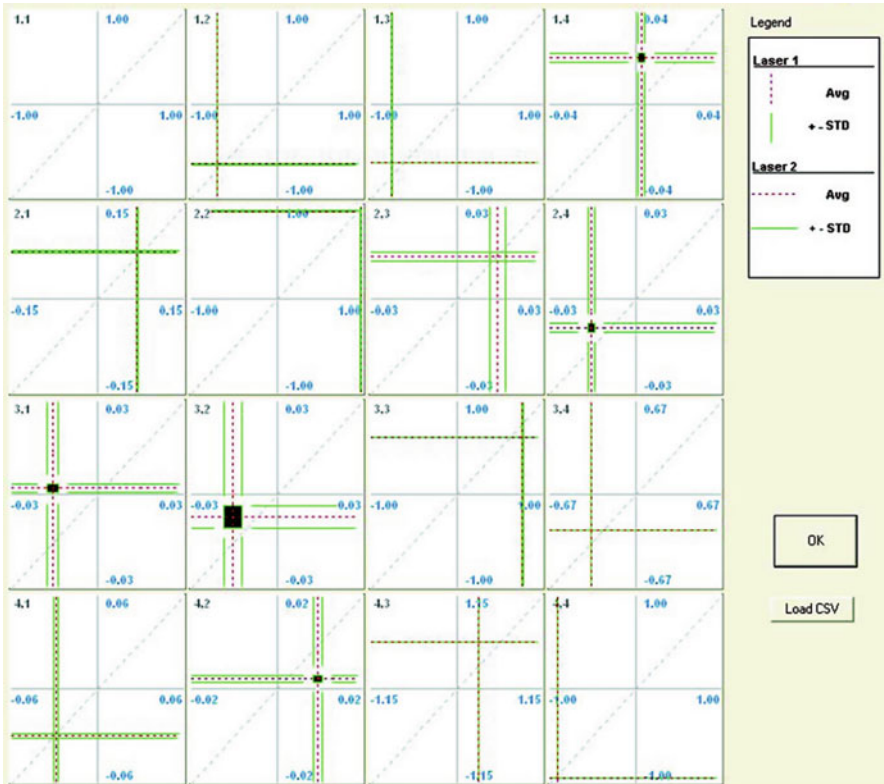
Fig. 29.32 Mueller matrix elements of biological aerosol protein *chicken egg white albumen*. Mantissa, measurement at $\lambda = 9.155$ μm; abscissa, measurement at $\lambda^* = 10.458$ μm (After Carrieri et al. [36])

where $i,j = 1, 2, 3, 4$ and $\neq 11$. Quantities ρ_{ij} are measures of analyte susceptibility and key identification parameters of the dual-beam-interrogated aerosol. In the example of Fig. 29.32, for instance, the eight most significant values of ρ_{ij} for *chicken egg white albumen* are grouped in the Mueller space (m_{14}, m_{24}, m_{31}, m_{32}, m_{33}, m_{34}, m_{42}, m_{43}) denoted by solid rectangles in Fig. 29.32.

Some common conclusions relating the results have to be noted: (1) a complete Mueller matrix is not required for establishing biosimulant materials features; (2) diagonal matrix elements undergo the error test rarely; (3) matrix elements m_{12}, m_{21}, m_{13}, m_{31}, m_{24}, m_{42}, m_{34}, and m_{43} seem to be the most informative detection matrix elements.

29.5.6 Urban and Manmade Targets

A primary motivation for research in scatter polarimetry is to gain an understanding of the physical nature of the interaction of polarized beams with natural scenes and

Table 29.4 Manmade samples characterized by scatter polarimetry (After DeBoo et al. [54])

Sample	Description
Metal box part	Smooth metal painted dark green
Nylon plastic material	Dark green color, lightweight material
Canvas with paint splotches	Varies in color and material, underlying cloth is greenish-khaki
Sidewalk concrete	Flat, rough surface
Glass diffuser	Frosted on only one side
Gold-coated glass diffuser	Similar to glass diffuser, roughened surface has thin coating of gold
Screen mesh	Finely meshed material, as used for a window screen

to search for useful discriminants to classify objects at a distance. The main subject of interest in this section is polarimetry of various manmade objects, as diverse as buildings and automobile paints.

In [54], the Mueller matrix data of different manmade samples (e.g., fabric, concrete, metal) as well as their reduced polarimetric data (e.g., depolarization and diattenuation) are studied as a function of scattering geometry at 808 nm (laser diode Hamamatsu L-8446). The seven manmade samples measured are presented in Table 29.4.

As an example, Fig. 29.33 depicts the Mueller matrix elements as a function of sample rotation angle for (a) a green-painted metal sample and (b) canvas material.

The Mueller matrix data allows making some common conclusions on polarization properties of the samples considered. The green-painted metal and the gold-coated diffuser are characterized by large m_{11} peaks at the origin and, hence, exhibit pronounced specular components. Diffusely scattering samples (the nylon plastic, screen mesh fabric, and concrete) exhibit small specular components yielding nearly flat m_{11} curves. The majority of the non-zero matrix elements for all samples are m_{11}, m_{12}, m_{21}, m_{22}, m_{23}, m_{32}, m_{33}, and m_{44}. Correspondingly, nearly zero elements are m_{13}, m_{14}, m_{24}, m_{31}, m_{34}, m_{41}, m_{42}, and m_{43}. Utilization of polar decomposition (29.41) shows that these samples, while being very different, all have negligible retardance and a small diattenuation and polarizance oriented with the s or p planes, but all exhibit high depolarization.

The depolarization index (29.29) versus sample rotation angle is shown for five samples in Fig. 29.34I.

The depolarization profiles in Fig. 29.34I with changing sample rotation angle resemble inverted Gaussian curves. However, depolarization profiles of the screen mesh and nylon plastic material, which are depicted in Fig. 29.34II, not well fit by Gaussian curves.

For most samples, the depolarization separately of each linear state and of both circular states are nearly equal. However, the depolarization difference between linear and circular states is significant; circular states are depolarized more than linear states. This is consistent with previous results [144, 169]. Less difference between the depolarization of circular and linear states is observed for three of the more reflective samples, the green-painted metal and the two diffuser samples.
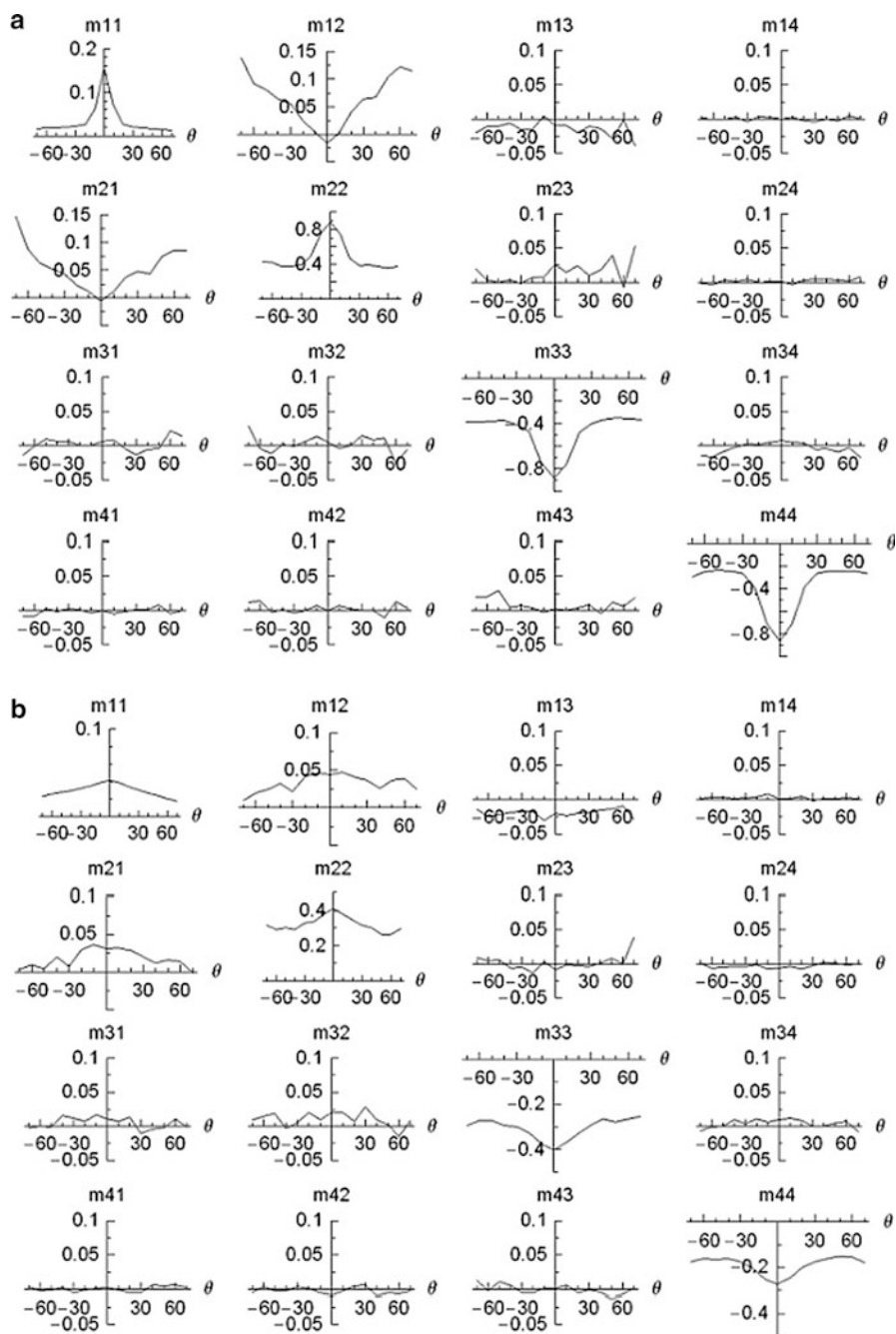
Fig. 29.33 Normalized Mueller matrix elements for (**a**) a green-painted metal sample; (**b**) canvas material as a function of sample rotation angle (After DeBoo et al. [54])
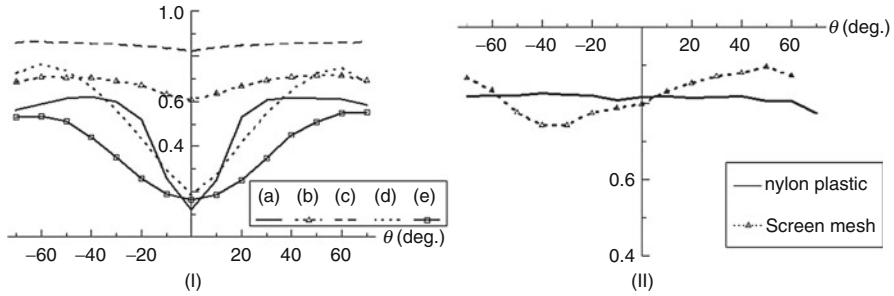
Fig. 29.34 Depolarization index versus sample rotation angle for (**I**) samples with Gaussian profiles ((*a*) painted metal; (*b*) canvas; (*c*) concrete; (*d*) glass diffuser, and (*e*) gold-coated diffuser); (**II**) the screen mesh and nylon plastic material (After DeBoo et al. [54])
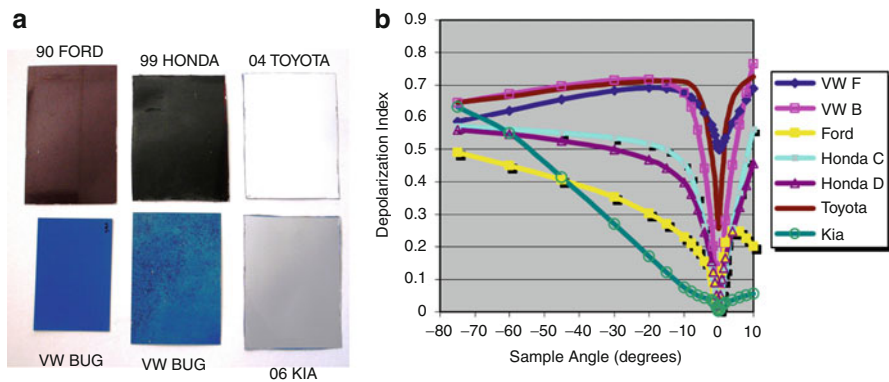
Fig. 29.35 (**a**) Automobile panel samples and (**b**) depolarization index versus sample angle at 1.06

Mueller matrix measurements and depolarization index calculations were used in [87] for identification of samples of totally different nature, namely, automobile panel samples at the range 0.7–2.6 μm. The samples selected are very shiny: 1990 Ford (mean roughness 0.37 μm), 2004 Toyota, and 2006 Kia; shiny but somewhat dulled: 1999 Honda; a satin finish: back of the VW bug (mean roughness 0.62 μm); and very aged and rough: front of the VW bug (mean roughness 1.66 μm), see Fig. 29.35a. Depolarization index versus sample angle at 1.06 μm is presented in Fig. 29.35b.

Again, depolarization index features enable reliable discrimination between automobile panel samples. However, it seems reasonable to use other depolarization metrics, see Sect. 29.2, for improving further the discrimination procedure. Thus, depolarization offers an extremely informative metrics for identification of both surface scattering properties such as roughness or reflectivity and bulk scattering with large dynamic range.
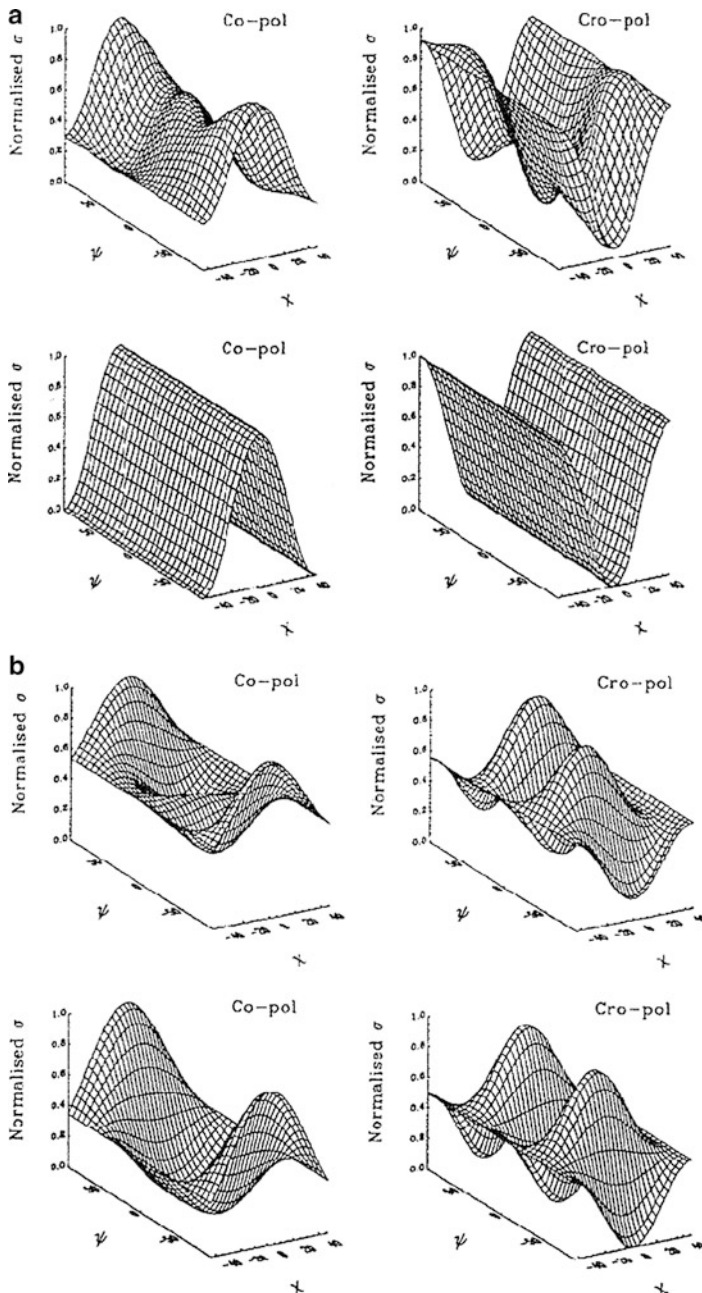
Fig. 29.36 P-band polarization signatures for two groups of buildings: (**a**) at incidence angle of 300 and (**b**) at incidence angle 600 (After Dong et al. [61])

Table 29.5 Scattering components as a percentage of the total *HH* backscattering response

Incidence angle	Single, %	Double, %	Bragg, %	Error, %
30°	65	35	0	3.4
60°	25	75	0	3.2

In [61], the comparison of two groups of buildings in the test site of Sydney (complete polarimetric data acquired in Sydney, Australia, in August-September 1993 at P-band) has been carried out. The motivation was to study the features of polarization signatures of two groups of buildings, which are similar to one another, but are seen for radar at different angles: one group in the near range at 30° and the other in the far range at 60°. Figure 29.36 shows measured P-band polarization signatures (top row) for these two groups of buildings: (a) at incidence angle of 30° and (b) at incidence angle 60°.

For analysis of polarization signatures measured, the approach to decompose them into a combination of contributions by four basic scattering mechanisms was suggested. These four basic mechanisms are (see Sect. 29.4 for details): (1) double bounce scattering; (2) Bragg scattering; (3) single (odd) bounce scattering, and (4) cross scattering. The bottom row of Fig. 29.36 presents the theoretic polarization signatures by (a) single bounce and (b) double bounce scattering for comparison.

Table 29.5 lists the percentages of single, double, and Bragg scattering components of *HH* polarization for two groups of buildings considered at P-band. The last column, "Error," presents the error between measured and predicted by decomposition suggested values.

The results obtained indicate that at incidence angle 30°, single bounce scattering is a dominant mechanism, whereas at 60° there is a pronounced double bounce scattering. The reason is that the roofs of most of buildings covered by plain tiles are tilted about 30–35° from vertical. So, in the near range at incidence angle 30°, the pronounced specular reflections from the roofs are expected. In far range, the roofs are not almost normal to the radar and strong double bounce scattering from wall-ground structures is observed.

References

1. K.D. Abhyankar, A.L. Fymat, Relations between the elements of the phase matrix for scattering. J. Math. Phys. **10**, 1935–1938 (1969)
2. A.B. Agrawal, W.M. Boerner, Redevelopment of Kennaugh's target characteristic polarization state theory using the polarization transformation ratio formalism for the coherent case. IEEE Trans. Geosci. Remote Sens. **27**, 2–14 (1989)
3. D.G.M. Anderson, R. Barakat, Necessary and sufficient conditions for a Mueller matrix to be derivable from a Jones matrix. J. Opt. Soc. Am. A **11**, 2305–2319 (1994)
4. M.-R. Antonelli, A. Pierangelo, T. Novikova et al., Mueller matrix imaging of human colon tissue for cancer diagnostics: how Monte Carlo modeling can help in the interpretation of experimental data. Opt. Express **18**, 10200–10208 (2010)

5. J. Applequist, Optical activity: Biot's bequest. Am. Sci. **75**, 59–67 (1987)
6. R.M. Azzam, Mueller-matrix ellipsometry: a review. Proc. SPIE **3121**, 396–405 (1997)
7. R.M. Azzam, N.M. Bashara, *Ellipsometry and Polarized Light*, 1st edn. (North-Holland, New York, 1987)
8. R. Barakat, Theory of the coherency matrix for light of arbitrary spectral bandwidth. J. Opt. Soc. Am. **53**, 317–322 (1963)
9. R. Barakat, Conditions for the physical realizability of polarization matrices characterizing passive systems. J. Mod. Opt. **34**, 1535–1544 (1987)
10. L.D. Barron, *Molecular Light Scattering and Optical Activity* (Cambridge University Press, Cambridge, UK, 1982)
11. A. Belmont, S. Zietz, C. Nicolini, Differential scattering of circularly polarized light by chromatin modeled as a helical array of dielectric ellipsoids within the born approximation. Biopolymers **24**, 1301–1321 (1985)
12. A.-M. Benoit, O.K. Naoun, V. Louis-Dorr et al., Linear dichroism of the retinal nerve fiber layer expressed with Mueller matrices. Appl. Opt. **40**, 565–569 (2001)
13. A. Bernard, W.I. Rose, The injection of sulfuric acid aerosol in the stratosphere by El Chichon volcano and its related hazard to international air traffic. Nat. Hazards **3**, 59–67 (1990)
14. M.V. Berry, M.R. Dennis, The optical singularities of birefringent dichroic chiral crystals. Proc. R. Soc. Lond. Ser. A **459**, 1261–1292 (2003)
15. W.S. Bickel, M.E. Stafford, Biological particles as irregularly shaped particles, in *Light Scattering by Irregularly Shaped Particles*, ed. by D. Schuerman (Plenum, New York, 1980), pp. 299–305
16. W.S. Bickel, J.F. Davidson, D.R. Huffman, R. Kilkson, Application of polarization effects in light scattering: a new biophysical tool. Proc. Natl. Acad. Sci. USA **73**, 486–490 (1976)
17. D. Bicout, C. Brosseau, A.S. Martinez, J.M. Schmitt, Depolarization of multiply scattered waves by spherical diffusers: influence of the size parameter. Phys. Rev. E. **49**, 1767–1770 (1994)
18. R. Bindlish, A.P. Barros, Parameterization of vegetation backscatter in radar-based, soil moisture estimation. Remote Sens. Environ. **76**, 130–137 (2001)
19. A. Bjerhammar, Application of calculus of matrices to method of least squares; with special references to geodetic calculations. Trans. Inst. Technol. (Stockholm), **49** (1951)
20. W.-M. Boerner, *Direct and Inverse Methods in Radar Polarimetry* (Kluwer, Dordrecht, 1992)
21. W.M. Boerner, H. Mott, E. Luneburg, C. Livingstone, B. Brisco, R.J. Brown, J.S. Paterson, S.R. Cloude, E. Krogager, J.S. Lee, D.L. Schuler, J.J. van Zyl, D. Randall, P. Budkewitsch, E. Pottier, Polarimetry in radar remote sensing: basic and applied concepts, in *Manual of Remote Sensing: Principles and Applications of Imaging Radar*, ed. by F.M. Henderson, A.J. Lewis (Wiley, New York, 1998)
22. C.F. Bohren, E.R. Huffman, *Absorption and Scattering of Light by Small Particles* (Wiley, New York, 1983)
23. C.C. Borel, R.E. McIntosh, Millimeter wave backscatter from deciduous trees. IEEE Trans. Antennas Propagat. **38**, 1391–1398 (1990)
24. M. Borgeaud, R.T. Shin, J.A. Kong, Theoretical models for polarimetric radar clutter. J. Electromagn. Waves Appl. **1**, 73–89 (1987)
25. B.V. Bronk, S.D. Druger, J. Czege, W.P. van de Merwe, Measuring diameters of rod-shaped bacteria in vivo with polarized light scattering. Biophys. J. **69**, 1170–1177 (1995)
26. C. Brosseau, Analysis of experimental data for Mueller polarization matrices. Optik **85**, 83–86 (1990)
27. C. Brosseau, *Fundamentals of Polarized Light: A Statistical Optics Approach* (Wiley, New York, 1998)
28. C. Brosseau, C.R. Givens, A.B. Kostinski, Generalized trace condition on the Mueller−Jones polarization matrix. J. Opt. Soc. Am. A **10**, 2248–2251 (1993)

29. C.E. Brown, M.F. Fingas, Synthetic aperture radar sensors: viable for marine oil spill response? in *Proceedings of the 26th AMOP* (2003), pp. 299–310

30. J.M. Bueno, Indices of linear polarization for an optical system. J. Opt. A: Pure Appl. Opt. **3**, 470–476 (2001)

31. C. Bustamante, M.F. Maestre, D. Keller, I. Tinoco Jr., Differential scattering (CIDS) of circularly polarized light by dense particles. J. Chem. Phys. **80**, 4817–4823 (1984)

32. A.H. Carrieri, Neural network pattern recognition by means of differential absorption Mueller matrix spectroscopy. Appl. Opt. **38**, 3759–3766 (1999)

33. A.H. Carrieri, D.J. Owens, J.C. Schultz, Infrared Mueller matrix acquisition and preprocessing system. Appl. Opt. **47**, 5019–5027 (2008)

34. A.H. Carrieri, J.R. Bottiger, D.J. Owens, E.S. Roese, Differential absorption Mueller matrix spectroscopy and the infrared detection of crystalline organics. Appl. Opt. **37**, 6550–6557 (1998)

35. A.H. Carrieri, D.J. Owens, E.S. Roese, K.C. Hung, P.I. Lim, J.C. Schultz, M.V. Talbard, Photopolarimetric lidar dual-beam switching device and Mueller matrix standoff detection method. J. Appl. Remote Sens. **1**, 013502 (2007)

36. A.H. Carrieri, J. Copper, D.J. Owens, E.S. Roese, J.R. Bottiger, R.D. Everly, K.C. Hung, Infrared differential-absorption Mueller matrix spectroscopy and neural network-based data fusion for biological aerosol standoff detection. Appl. Opt. **49**, 382–393 (2010)

37. P.S. Chang, J.B. Mead, Ph.M. Langlois, R.E. McIntosh, Millimeter-wave measurements of natural surfaces at 35, 95, and 225 GHz, in *Proceedings of the ISAP* (1992), pp. 541–544

38. R.J. Charlson, S.E. Schwartz, J.M. Hales, R.D. Cess, J.A. Coakley Jr., J.E. Hansen, D.J. Hofmann, Climate forcing by anthropogenic aerosols. Science **255**, 423–431 (1992)

39. I. Chiapello, C. Moulin, J.M. Prospero, Understanding the long-term variability of African dust transport across the Atlantic as recorded in both Barbados surface concentrations and large-scale Total Ozone Mapping Spectrometer (TOMS) optical thickness. J. Geophys. Res. **110**, D18S10 (2005)

40. R.A. Chipman, Polarimetry, in *Handbook of Optics*, vol. II, ed. by M. Bass (McGraw Hill, New York, 1995)

41. R.A. Chipman, Depolarization. Proc. SPIE **3754**, 14–20 (1999)

42. R.A. Chipman, Depolarization index and the average degree of polarization. Appl. Opt. **44**, 2490–2495 (2005)

43. J. Chung, W. Jung, M.J. Hammer-Wilson et al., Use of polar decomposition for the diagnosis of oral precancer. Appl. Opt. **46**, 3038–3045 (2007)

44. S.R. Cloude, Group theory and polarization algebra. Optik **7**, 26–36 (1986)

45. S.R. Cloude, *Polarization: Applications in Remote Sensing* (Oxford University Press, New York, 2010)

46. S.R. Cloude, E. Pottier, Concept of polarization entropy in optical scattering. Opt. Eng. **34**, 1599–1610 (1995)

47. S.R. Cloude, E. Pottier, A review of target decomposition theorems in radar polarimetry. IEEE Trans. Geosci. Remote Sens. **34**, 498–518 (1996)

48. S.R. Cloude, E. Pottier, An entropy based classification scheme for land applications of polarimetric SAR. IEEE Trans. Geosci. Remote Sens. **35**, 68–78 (1997)

49. S.R. Cloude, K.P. Papathanassiou, E. Pottier, Radar polarimetry and polarimetric interferometry. IEICE Trans. Electron. **E84-C**, 1814–1822 (2001)

50. E. Collett, *Polarized Light: Fundamentals and Applications* (Marcel Decker, New York, 1993)

51. J.F. de Boer, T.E. Milner, Review of polarization sensitive optical coherence tomography and Stokes vector determination. J. Biomed. Opt. **7**, 359–371 (2002)

52. J.F. de Boer, T.E. Milner, M.J.C. van Gemert, J.S. Nelson, Two dimensional birefringence imaging in biological tissue by polarization-sensitive optical coherence tomography. Opt. Lett. **22**, 934–936 (1997)

53. A. De Martino, Y.-K. Kim, E. Garcia-Caurel, B. Laude, B. Drevillon, Optimized Mueller polarimeter with liquid crystals. Opt. Lett. **28**, 616–618 (2003)

54. B.J. DeBoo, J.M. Sasian, R.A. Chipman, Depolarization of diffusely reflecting man-made objects. Appl. Opt. **44**, 5434–5445 (2005)
55. L.L. Deibler, M.H. Smith, Measurement of the complex refractive index of isotropic materials with Mueller matrix polarimetry. Appl. Opt. **40**, 3659–3667 (2001)
56. R.D. DeRoo, Y. Du, F.T. Ulaby, M.C. Dobson, A semi-empirical backscattering model at L-band and C-band for a soybean canopy with soil moisture inversion. IEEE Trans. Geosci. Remote Sens. **39**, 864–872 (2001)
57. P.A. Demirev, A.B. Feldman, J.S. Lin, Chemical and biological weapons: current concepts for future defenses. Johns Hopkins APL Tech. Dig. **26**, 321–333 (2005)
58. A. Diaspro, C. Nicolini, Circular intensity differential scattering and chromatin DNA-structures. Cell Biophys. **10**(10), 45–60 (1987)
59. Y. Dong, J.A. Richards, Studies of the cylinder-ground double bounce scattering mechanism in forest backscatter models. IEEE Trans. Geosci. Remote Sens. **33**, 229–231 (1995)
60. Y. Dong, J.A. Richards, Forest discrimination using SAR multifrequency and multipolarization data, in *Proceedings of the IGARSS* (1995)
61. Y. Dong, B.C. Forster, C. Ticehurst, Decompositions of radar polarization signatures from built and natural targets. Int. Arch. Photogramm. Remote Sens. **XXXI**(Part B7), 196–202 (1996)
62. B.P. Dorman, M.F. Maestre, Experimental differential light scattering corrections to the circular dichroism of T2 bacteriophage. Proc. Natl. Acad. Sci. USA **70**, 255–259 (1973)
63. P.C. Dubois, I. Norikane, Data volume reduction for imaging radar polarimetry, in *Proceedings of the IGARSS* (1987), pp. 691–696
64. O. Dubovik, B.N. Holben, T. Lapyonok, A. Sinyuk, M.I. Mishchenko, P. Yang, I. Slutsker, Non-spherical aerosol retrieval method employing light scattering by spheroids. Geophys. Res. Lett. **29**(10), 1415 (2002)
65. S.L. Durden, L.A. Morrissey, G.P. Livingston, Microwave backscatter and attenuation dependence on leaf area index for flooded rice fields. IEEE Trans. Geosci. Remote Sens. **33**, 807–810 (1995)
66. C. Elachi, *Introduction to the Physics and Techniques of Remote Sensing* (Wiley, New York, 1987)
67. N. Engheta, C. Elachi, Radar scattering from a diffuse vegetation layer over a smooth surface. IEEE Trans. Geosci. Remote Sens. **20**, 212–216 (1982)
68. R. Espinosa-Luna, E. Bernabeu, On the Q(M) depolarization metric. Opt. Commun. **277**, 256–258 (2007)
69. D.L. Evans, T.G. Farr, J.J. van Zyl, H.A. Zebker, Radar polarimetry: analysis tools and applications. IEEE Trans. Geosci. Remote Sens. **26**, 774–789 (1988)
70. F. Fanjul-Vélez, J.L. Arce-Diego, Polarimetry of birefringent biological tissues with arbitrary fibril orientation and variable incidence angle. Opt. Lett. **35**, 1163–1165 (2010)
71. A. Freeman, S.L. Durden, A three-component scattering model for polarimetric SAR data. IEEE Trans. Geosci. Remote Sens. **36**, 345–351 (1998)
72. F. Fromard, H. Puig, E. Mougin, G. Marty, J.L. Betoulle, L. Cadamuro, Structure, above-ground biomass and dynamics of mangrove ecosystems: new data from French Guiana. Oecologia **115**, 39–53 (1998)
73. E.S. Fry, G.W. Kattawar, Relationships between elements of the Stokes matrix. Appl. Opt. **20**, 2811–2814 (1981)
74. M. Gade, W. Alpers, H. Huhnerfuss, H. Masuko, T. Kobayashi, Imaging of biogenic and anthropogenic ocean surface films by the multifrequency/multipolarization SIR-C/X-SAR. J. Geophys. Res. **103**, 18851–18866 (1998)
75. A. Gerrard, J.M. Burch, *Introduction to Matrix Methods in Optics* (Wiley, New York, 1975)
76. N. Ghosh, H.S. Patel, P.K. Gupta, Depolarization of light in tissue phantoms – effect of a distribution in the size of scatterers. Opt. Express **11**, 2198–2205 (2003)
77. N. Ghosh, M.F.G. Wood, I.A. Vitkin, Mueller matrix decomposition for extraction of individual polarization parameters from complex turbid media exhibiting multiple scattering, optical activity, and linear birefringence. J. Biomed. Opt. **13**, 044036 (2008)

78. N. Ghosh, M.F.G. Wood, I.A. Vitkin, Polarimetry in turbid, birefringent, optically active media: a Monte Carlo study of Mueller matrix decomposition in the backscattering geometry. J. Appl. Phys. **105**, 102023 (2009)

79. N. Ghosh, M.F.G. Wood, I.A. Vitkin, Influence of the order of the constituent basis matrices on the Mueller matrix decomposition-derived polarization parameters in complex turbid media such as biological tissues. Opt. Commun. **283**, 1200–1208 (2010)

80. N. Ghosh, M.F.G. Wood, S.-h. Li et al., Mueller matrix decomposition for polarized light assessment of biological tissues. J. Biophoton. **2**, 145–156 (2009)

81. J.J. Gil, Characteristic properties of Mueller matrices. J. Opt. Soc. Am. A **17**, 328–334 (2000)

82. J.J. Gil, Polarimetric characterization of light and media. Eur. Phys. J. Appl. Phys. **40**, 1–47 (2007)

83. J.J. Gil, E. Bernabeu, A depolarization criterion in Mueller matrices. Opt. Acta **32**, 259–261 (1985)

84. J.J. Gil, E. Bernabeu, Depolarization and polarization indexes of an optical system. Opt. Acta **33**, 185–189 (1986)

85. J.J. Gil, E. Bernabeu, Obtainment of the polarizing and retardation parameters of a non-depolarizing optical system from the polar decomposition of its Mueller matrix. Optik **76**, 67–71 (1987)

86. C.R. Givens, A.B. Kostinski, A simple necessary and sufficient condition on physically realizable Mueller matrices. J. Mod. Opt. **40**, 471–481 (1993)

87. D.H. Goldstein, Polarization measurements of automobile paints. Proc. of SPIE **6972**, 69720V–69721V (2008)

88. A.V. Gopala Rao, K.S. Mallesh, Sudha, On the algebraic characterization of a Mueller matrix in polarization optics. I. Identifying a Mueller matrix from its N matrix. J. Mod. Opt. **45**, 955–987 (1998)

89. A.V. Gopala Rao, K.S. Mallesh, Sudha, On the algebraic characterization of a Mueller matrix in polarization optics. II. Necessary and sufficient conditions for Jones-derived Mueller matrices. J. Mod. Opt. **45**, 989–999 (1998)

90. C.T. Gross, H. Salamon, A.J. Hunt et al., Hemoglobin polymerization in sicklecells studied by circular polarized light scattering. Biochim. Biophys. Acta **1079**, 152–160 (1991)

91. A. Guissard, Mueller and Kennaugh matrices in radar polarimetry. IEEE Trans. Geosci. Remote Sens. **32**, 590–597 (1994)

92. K.C. Hadley, I.A. Vitkin, Optical rotation and linear and circular depolarization rates in diffusively scattered light from chiral, racemic, and achiral turbid media. J. Biomed. Opt. **7**, 291–299 (2002)

93. I. Hajnsek, Inversion of surface parameters from polarimetric SAR. *DLR Res. Rep. FB*, 2001-30 (2001)

94. I. Hajnsek, E. Pottier, S.R. Cloude, Inversion of surface parameters from polarimetric SAR. IEEE Trans. Geosci. Remote Sens. **41**, 727–744 (2003)

95. J. Hansen, A. Lacis, R. Ruedy, M. Sato, Potential climate impact of Mount Pinatubo eruption. Geophys. Res. Lett. **19**, 215–218 (1992)

96. P.S. Hauge, Recent developments in instrumentation in ellipsometry. Surface Sci. **96**, 108–140 (1980)

97. S.M. Haugland, E. Bahar, A.H. Carrieri, Identification of contaminant coatings over rough surfaces using polarized infrared scattering. Appl. Opt. **31**, 3847–3852 (1992)

98. H. He, N. Zeng, R. Liao et al., Application of sphere–cylinder scattering model to skeletal muscle. Opt. Express **18**, 15104–15112 (2010)

99. D.N. Held, W.E. Brown, A. Freeman, J.D. Klein, H. Zebker, T. Sato, T. Miller, Q. Nguyen, Y. Lou, The NASA/JPL multifrequency, multipolarization airborne SAR system, in *Proceedings of the ICARSS* (1988, pp. 345–349)

100. L.L. Hess, J.M. Melack, D.S. Simonett, Radar detection of flooding beneath the forest canopy: a review. Int. J. Remote Sens. **14**, 1313–1325 (1990)

101. A.H. Hielscher, A.A. Eick, J.R. Mourant et al., Diffuse backscattering Mueller matrices of highly scattering media. Opt. Express **1**, 441–453 (1997)
102. A.G. Hoekstra, P.M.A. Sloot, Dipolar unit size in coupled-dipole calculations of the scattering matrix elements. Appl. Opt. **18**, 1211–1213 (1993)
103. A.G. Hoekstra, P.M.A. Sloot, Biophysical and biomedical applications of nonspherical scattering, in *Light Scattering by Nonspherical Particles: Theory, Measurements, and Applications*, ed. by M.I. Mishchenko, J.W. Hovenier, L.D. Travis (Academic, San Diego, 2000), pp. 585–602
104. J.W. Hovenier, Symmetry relations for scattering of polarized light in a slab of randomly oriented particles. J. Atmos. Sci. **26**, 488–499 (1969)
105. J.W. Hovenier, Principles of symmetry for polarization studies of planets. Astron. Astrophys. **7**, 86–90 (1970)
106. J.W. Hovenier, Structure of a general pure Mueller matrix. Appl. Opt. **33**, 8318–8324 (1994)
107. J.W. Hovenier, D.W. Mackowski, Symmetry relations for forward and backward scattering by randomly oriented particles. J. Quant. Spectrosc. Radiat. Transf. **60**, 483–492 (1998)
108. J.W. Hovenier, C.V.M. van der Mee, Basic relationships for matrices describing scattering by small particles, in *Light Scattering by Nonspherical Particles: Theory, Measurements, and Applications*, ed. by M.I. Mishchenko, J.W. Hovenier, L.D. Travis (Academic, San Diego, 2000), pp. 61–85
109. J.W. Hovenier, H.C. van de Hulst, C.V.M. van der Mee, Conditions for the elements of the scattering matrix. Astron. Astrophys. **157**, 301–310 (1986)
110. C.-R. Hu, G.W. Kattawar, M.E. Parkin, P. Herb, Symmetry theorems on the forward and backward scattering Mueller matrices for light scattering from a nonspherical dielectric scatterer. Appl. Opt. **26**, 4159–4173 (1987)
111. D.G. Hunter, J.C. Sandruck, S. Sau et al., Mathematical modeling of retinal birefringence scanning. J. Opt. Soc. Am. A **16**, 2103–2111 (1999)
112. H. Hurwitz, C.R. Jones, A new calculus for the treatment of optical systems. II. Proof of three general equivalence theorems. J. Opt. Soc. Am. **31**, 493–499 (1941)
113. M. Imhoff, M. Story, C. Vermillion, F. Khan, F. Polcyn, Forest canopy characterization and vegetation penetration assessment with space-borne radar. IEEE Trans. Geosci. Remote Sens. **24**, 535–542 (1986)
114. D.L. Jaggard, C. Hill, R.W. Shorthill, D. Stuart, M. Glantz, F. Rosswog, B. Taggard, S. Hammond, Light scattering from particles of regular and irregular shape. Atmos. Environ. **15**, 2511–2519 (1981)
115. R.G. Johnston, S.B. Singham, G.C. Salzman, Polarized light scattering. Comments Mol. Cell. Biophys. **5**, 171–192 (1988)
116. R.C. Jones, A new calculus for the treatment of optical systems. I. Description and discussion of the calculus. J. Opt. Soc. Am. **31**, 488–493 (1941)
117. R.C. Jones, A new calculus for the treatment of optical systems. IV. J. Opt. Soc. Am. **32**, 486–493 (1942)
118. R.C. Jones, A new calculus for the treatment of optical systems. V. A more general formulation and description of another calculus. J. Opt. Soc. Am. **37**, 107–110 (1947)
119. R.C. Jones, A new calculus for the treatment of optical systems. VII. Properties of the N-matrices. J. Opt. Soc. Am. **38**, 671–685 (1948)
120. R.C. Jones, A new calculus for the treatment of optical systems. VIII. Electromagnetic theory. J. Opt. Soc. Am. **46**, 126–131 (1956)
121. O.V. Kalashnikova, I.N. Sokolik, Modeling the radiative properties of nonspherical soil-delivered mineral aerosols. JQSRT **87**, 137–166 (2004)
122. B. Kaplan, B. Drevillon, Mueller matrix measurements of small spherical particles deposited on a c-Si wafer. Appl. Opt. **41**, 3911–3918 (2002)
123. B. Kaplan, G. Ledanois, B. Drevillon, Mueller matrix of dense polystyrene latex sphere suspensions: measurements and Monte Carlo simulation. Appl. Opt. **40**, 2769–2777 (2001)

124. M.A. Karam, F. Amar, A.K. Fung, E. Mougin, A. Lopes, D.M. Le Vine, A. Beaudoin, A microwave polarimetric scattering model for forest canopies based on vector radiative transfer theory. Remote Sens. Environ. **53**, 16–30 (1995)

125. K. Kennaugh, Effects of type of polarization on echo characteristics. Tech. Rep. **OH 389-4**, 35, **OH 381-9**, 39 (1951)

126. K. Kennaugh, Polarization properties of radar reflections. M.Sc. thesis, The Ohio State University, Columbus, Ohio (1952)

127. K. Kim, L. Mandel, E. Wolf, Relationship between Jones and Mueller matrices for random media. J. Opt. Soc. Am. A **4**, 433–437 (1987)

128. Y.L. Kim, P. Pradhan, M.H. Kim, V. Backman, Circular polarization memory effect in low-coherence enhanced backscattering of light. Opt. Lett. **31**, 2744–2746 (2006)

129. D.S. Kliger, J.W. Lewis, C.E. Randall, *Polarized Light in Optics and Spectroscopy* (Academic, New York, 1990)

130. P. Koepke, M. Hess, I. Shultz, E.P. Shettle, Global aerosol data set. *Rep. 44*, Max Planck Inst. for Meteorol. (1997)

131. A.A. Kokhanovsky, *Light Scattering Media Optics: Problems and Solutions* (Praxis, Chichester, 2001)

132. A.A. Kokhanovsky, Parameterization of the Mueller matrix of oceanic waters. J. Geophys. Res. **108**, 3175 (2003)

133. A.A. Kokhanovsky, *Polarization Optics of Random Media* (Praxis, Chichester, 2003)

134. A.A. Kokhanovsky, Optical properties of irregularly shaped particles. J. Phys. D: Appl. Phys. **36**, 915–923 (2003)

135. J.A. Kong, A.S. Swartz, H.A. Yueh, L.M. Novak, R.T. Shin, Identification of terrain cover using the optimum polarimeter classifier. J. Electromagn. Waves Appl. **2**, 171–194 (1987)

136. I. Koren, E. Ganor, J.H. Joseph, On the relation between size and shape of desert dust aerosol. J. Geophys. Res. **106**, 18037–18045 (2001)

137. A.B. Kostinski, Depolarization criterion for incoherent scattering. Appl. Opt. **31**, 3506–3508 (1992)

138. A.B. Kostinski, C.R. Givens, J.M. Kwiatkowski, Constraints on Mueller matrices of polarization optics. Appl. Opt. **32**, 1646–1651 (1993)

139. S. Krishnan, P.C. Nordine, Mueller-matrix ellipsometry using the division-of-amplitude photopolarimeter: a study of depolarization effects. Appl. Opt. **33**, 4184–4192 (1994)

140. L.D. Landau, E.M. Lifshitz, L.P. Pitaevskii, *Electrodynamics of Continuous Media* (Pergamon Press, Oxford, 1984)

141. P. Lankaster, M. Tismenetsky, *The Theory of Matrices* (Academic, San Diego, 1985)

142. B. Laude-Boulesteix, A. De Martino, B. Drevillon, L. Schwartz, Mueller polarimetric imaging system with liquid crystals. Appl. Opt. **43**, 2824–2832 (2004)

143. R. Lawless, Y. Xie, P. Yang et al., Polarization and effective Mueller matrix for multiple scattering of light by nonspherical ice crystals. Opt. Express **14**, 6381–6393 (2006)

144. G.D. Lewis, D.L. Jordan, E. Jakeman, Backscatter linear and circular polarization analysis of roughened aluminum. Appl. Opt. **37**, 5985–5992 (1998)

145. X. Li, G. Yao, Mueller matrix decomposition of diffuse reflectance imaging in skeletal muscle. Appl. Opt. **48**, 2625–2631 (2009)

146. X. Li, H. Maring, D. Savoie, K. Voss, J.M. Prospero, Dominance of mineral dust in aerosol light scattering in the North Atlantic trade winds. Nature **380**, 416–419 (1996)

147. X. Li, J.C. Ranasinghesagara, G. Yao, Polarization-sensitive reflectance imaging in skeletal muscle. Opt. Express **16**, 9927–9935 (2008)

148. K.D. Lofftus, M.S. Quinby-Hunt, A.J. Hunt et al., Light scattering by Prorocentrum micans: a new method and results. Appl. Opt. **31**, 2924–2931 (1992)

149. V.N. Lopatin, A.V. Priezzhev, A.D. Apanasenko et al., *Methods of Light Scattering in the Analysis of Dispersed Biological Media* (Fizmatlit, Moscow, 2004) (in Russian)

150. V. Louis-Dorr, K. Naoun, P. Allé et al., Linear dichroism of the cornea. Appl. Opt. **43**, 1515–1521 (2004)

151. S.-Y. Lu, R.A. Chipman, Homogeneous and inhomogeneous Jones matrices. J. Opt. Soc. Am. A **11**, 766–773 (1994)
152. S.-Y. Lu, R.A. Chipman, Interpretation of Mueller matrices based on polar decomposition. J. Opt. Soc. Am. A **13**, 1106–1113 (1996)
153. E. Lueneburg, Principles of radar polarimetry-using the directional Jones vector approach. IEICE Trans. Electron. **E78-C**, 1339–1345 (1995)
154. K. Lumme, Scattering properties of interplanetary dust particles, in *Light Scattering by Nonspherical Particles* (Academic, San Diego, 2000)
155. D.W. Mackowski, M.I. Mishchenko, Calculation of the T matrix and the scattering matrix for ensembles of spheres. J. Opt. Soc. Am. A **11**, 2266–2278 (1996)
156. M.F. Maestre, C. Bustamante, T.L. Hayes et al., Differential scattering of circularly polarized light by the helical sperm head from the octopus Eledone cirrhosa. Nature **298**, 773–774 (1982)
157. S. Manhas, M.K. Swami, P. Buddhiwant et al., Mueller matrix approach for determination of optical rotation in chiral turbid media in backscattering geometry. Opt. Express **14**, 190–202 (2006)
158. S. Manickavasagam, M.P. Menguc, Scattering-matrix elements of coated infinite-length cylinders. Appl. Opt. **37**, 2473–2482 (1998)
159. T. Manninen, P. Stenberg, M. Rautiainen, P. Voipio, H. Smolander, Leaf area index estimation of boreal forest using ENVISAT ASAR. IEEE Trans. Geosci. Remote Sens. **43**, 2627–2635 (2005)
160. V.V. Mar'enko, S.N. Savenkov, Representation of arbitrary Mueller matrix in the basis of matrices of circular and linear anisotropy. Opt. Spectrosc. **76**, 94–96 (1994)
161. W.E. Martin, E. Hesse, J.H. Hough, W.B. Sparks, C.S. Cockell, Z. Ulanowski, T.A. Germer, P.H. Kaye, Polarized optical scattering signatures from biological materials. JQSRT. **111**, 2444–2459 (2010)
162. H. McNairna, C. Duguay, B. Brisco, T.J. Pultz, The effect of soil and crop residue characteristics on polarimetric radar response. Remote Sens. Environ. **80**, 308–320 (2002)
163. J.B. Mead, R.E. McIntosh, A 225 GHz polarimetric radar. IEEE Trans. Microw. Theory Tech. **38**, 1252–1257 (1990)
164. J.B. Mead, R.E. McIntosh, Polarimetric backscatter measurements of deciduous and coniferous trees at 225 GHz. IEEE Trans. Geosci. Remote Sens. **29**, 21–28 (1991)
165. M. Migliaccio, A. Gambardella, M. Tranfaglia, SAR polarimetry to observe oil spills. IEEE Trans. Geosci. Remote Sens. **45**, 506–511 (2007)
166. M. Migliaccio, F. Nunziata, A. Gambardella, Polarimetric signature for oil spill observation. *Proceedings of the US/EU-Baltic International Symposium* (2008), pp. 1–5
167. M. Migliaccio, F. Nunziata, A. Gambardella, On the copolarised phase difference for oil spill observation. Int. J. Remote Sens. **30**, 1587–1602 (2009)
168. M. Migliaccio, A. Gambardella, F. Nunziata, M. Shimada, O. Isoguchi, The PALSAR polarimetric mode for sea oil slick observation. IEEE Trans. Geosci. Remote Sens. **47**, 4032–4041 (2009)
169. M.I. Mishchenko, J.W. Hovenier, Depolarization of light backscattered by randomly oriented nonspherical particles. Opt. Lett. **20**, 1356–1358 (1995)
170. M.I. Mishchenko, L.D. Travis, Polarization and depolarization of light, in *Light Scattering from Microstructures*, ed. by F. Moreno, F. González (Springer, Berlin, 2000), pp. 159–175
171. M.I. Mishchenko, J.W. Hovenier, L.D. Travis (eds.), *Light Scattering by Nonspherical Particles: Theory, Measurements, and Applications* (Academic, San Diego, 2000)
172. M.I. Mishchenko, L.D. Travis, A.A. Lacis, *Scattering, Absorption, and Emission of Light by Small Particles* (Cambridge University Press, Cambridge, UK, 2002)
173. M.I. Mishchenko, L.D. Travis, A.A. Lacis, *Multiple Scattering of Light by Particles. Radiative Transfer and Coherent Backscattering* (Cambridge University Press, Cambridge, UK, 2006)

174. M.I. Mishchenko, W.J. Wiscombe, J.W. Hovenier, L.D. Travis, Overview of scattering by nonspherical particles, in *Light Scattering by Nonspherical Particles*, ed. by M. Mishchenko, J. Hovenier, L. Travis (Academic, San Diego, 2000)

175. M.I. Mishchenko, V.K. Rosenbush, N.N. Kiselev, D.F. Lupishko, V.P. Tishkovets, V.G. Kaydash, I.N. Belskaya, Y.S. Efimov, N.M. Shakhovskoy, *Polarimetric Remote Sensing of Solar System Objects* (Akadempperiodyka, Kyiv, 2010)

176. E.H. Moore, On the reciprocal of the general algebraic matrix. Bull. Am. Math. Soc. **26**, 394–395 (1920)

177. J. Morio, F. Goudail, Influence of the order of diattenuator, retarder, and polarizer in polar decomposition of Mueller matrices. Opt. Lett. **29**, 2234–2236 (2004)

178. H. Mott, *Remote Sensing with Polarimetric Radar* (Wiley, New York, 2007)

179. E. Mougin, C. Proisy, G. Marty, F. Fromard, H. Puig, J.L. Betoulle, J.P. Rudant, Multifrequency and multipolarization radar backscattering from mangrove forests. IEEE Trans. Geosci. Remote Sens. **37**, 94–102 (1999)

180. H. Mueller, The foundation of optics. J. Opt. Soc. Am. **38**, 661 (1948)

181. K. Muinonen, J. Piironen, Yu, G. Shkuratov, A. Ovcharenko, B.E. Clark, Asteroid photometric and polarimetric phase effects, in *Asteroids III* (University of Arizona Press, Tucson, 2002)

182. O. Munoz, H. Volten, J.F. de Haan, W. Vassen, J.W. Hovenier, Experimental determination of scattering matrices of fly ash and clay particles at 442 and 633 nm. J. Geophys. Res. **106**, 22833–22844 (2001)

183. O. Munoz, H. Volten, J.F. de Haan, W. Vassen, J.W. Hovenier, Experimental determination of the phase function and degree of linear polarization of El Chichon and Pinatubo volcanic ashes. J. Geophys. Res. **107**(D13), 4174 (2002)

184. Q. Munoz, H. Volten, J.W. Hovenier, B. Veihelmann, W.J. van der Zande, L.B.F.M. Waters, W.I. Rose, Scattering matrices of volcanic ash particles of Mount St. Helens, Redoubt, and Mount Spurr Volcanoes. J. Geophys. Res. **109**, D16201 (2004)

185. R.S. Muttiah (ed.), *From Laboratory Spectroscopy to Remotely Sensed Spectra of Terrestrial Ecosystems* (Kluwer, Dordrecht, 2002)

186. D.I. Nagirner, Constrains on matrices transforming Stokes vectors. Astron. Astrophys. **275**, 318–324 (1993)

187. O.K. Naoun, V. Louis-Dorr, P. Allé et al., Exploration of the retinal nerve fiber layer thickness by measurement of the linear dichroism. Appl. Opt. **44**, 7074–7082 (2005)

188. R.M. Narayanan, C.C. Borel, R.E. McIntosh, Radar backscatter characteristics of trees at 215 GHz. IEEE Trans. Geosci. Remote Sens. **26**, 217–228 (1988)

189. T. Nousiainen, K. Muinonen, P. Raisanen, Scattering of light by large Saharan dust particles in a modified ray optics approximation. J. Geophys. Res. **108**(D1), 4025 (2003)

190. L.M. Novak, M.C. Burl, Optimal speckle reduction in polarimetric SAR imagery. IEEE Trans. Aerosp. Electron. Syst. **26**, 293–305 (1990)

191. F. Nunziata, A. Gambardella, M. Migliaccio, On the mueller scattering matrix for SAR Sea oil slick observation. IEEE Geosci. Remote Sens. Lett. **5**, 691–695 (2008)

192. V.R. Oberbeck, E.F. Danielsen, K.G. Snetsinger, G.V. Ferry, Effect of the eruption of El Chichon on stratospheric aerosol size and composition. J. Geophys. Lett. **10**, 1021–1024 (1983)

193. E.A. Oberemok, S.N. Savenkov, Structure of deterministic Mueller matrices and their reconstruction in the method of three input polarizations. J. Appl. Spectrosc. **70**, 224–229 (2003)

194. Y. Oh, Radar remote sensing of soil moisture and surface roughness for vegetated surfaces. Korean J. Remote Sens. **24**, 427–436 (2008)

195. R. Ossikovski, Interpretation of nondepolarizing Mueller matrices based on singular-value decomposition. J. Opt. Soc. Am. A **25**, 473–482 (2008)

196. R. Ossikovski, Analysis of depolarizing Mueller matrices through a symmetric decomposition. J. Opt. Soc. Am. A **26**, 1109–1118 (2009)

197. R. Ossikovski, A. De Martino, S. Guyot, Forward and reverse product decompositions of depolarizing Mueller matrices. Opt. Lett. **32**, 689–691 (2007)
198. N.G. Parke III, Matrix optics. Ph.D. thesis, Massachusetts Institute of Technolody, Cambidge, MA, 1948
199. N.G. Parke III, Optical algebra. J. Math. Phys. **28**, 131–139 (1949)
200. E.M. Patterson, D.A. Gillete, B.H. Stockton, Complex index of refraction between 300 and 700 nm for Saharan aerosols. J. Geophys. Res. **82**(C21), 3153–3160 (1977)
201. R. Penrose, A generalized inverse for matrices. Proc. Cambridge Philos. Soc. **151**, 406–413 (1955)
202. F. Perrin, Polarization of light scattering by isotropic opalescent media. J. Chem. Phys. **10**, 415–427 (1942)
203. M.W.P. Petryk, Promising spectroscopic techniques for the portable detection of condensed-phase contaminants on surfaces. Appl. Sp. Rev. **42**, 287–343 (2007)
204. M.M. Pospergelis, Spectroscopic measurements of the four stokes parameters for light scattered by natural objects. Sov. Phys. Astronom. **12**, 973–976 (1969)
205. R.J. Potton, Reciprocity in optics. Rep. Prog. Phys. **67**, 717–754 (2004)
206. A.V. Priezzhev, V.V. Tuchin, L.P. Shubochkin, *Laser Diagnostics in Biology and Medicine* (Nauka, Moscow, 1989) (in Russian)
207. C. Proisy, E. Mougin, F. Fromard, M.A. Karam, Interpretation of polarimetric radar signatures of mangrove forests. Remote Sens. Environ. **71**, 56–66 (2000)
208. J.M. Prospero, P.J. Lamb, African droughts and dust transport to the Caribbean: climate change implications. Science **302**, 1024–1027 (2003)
209. R.F. Pueschel, P.B. Russell, D.A. Allend, G.V. Ferry, K.G. Snetsinger, J.M. Livingston, S. Verma, Physical and optical properties of the Pinatubo volcanic aerosol: aircraft observations with impactors and a Sun-tracking photometer. J. Geophys. Lett. **99**(12), 915–922 (1994)
210. M.S. Quinby-Hunt, P.G. Hull, A.J. Hunt, Polarized light scattering in the marine environment, in *Light Scattering by Nonspherical Particles: Theory, Measurements, and Applications*, ed. by M.I. Mishchenko, J.W. Hovenier, L.D. Travis (Academic, San Diego, 2000), pp. 525–554
211. J.C. Ranasinghesagara, G. Yao, Imaging 2D optical diffuse reflectance in skeletal muscle. Opt. Express **15**, 3998–4007 (2007)
212. T.W. Ray, T.G. Farr, J.J. van Zyl, Detection of land degradation with polarimetric SAR. Geophys. Res. Lett. **19**, 1587–1590 (1992)
213. J.A. Richards, P.W. Woodgate, A.K. Skidmore, An explanation of enhanced radar backscattering from flooded forests. Int. J. Remote Sens. **18**, 1319–1332 (1987)
214. L.F. Rojas-Ochoa, D. Lacoste, R. Lenke et al., Depolarization of backscattered linearly polarized light. J. Opt. Soc. Am. A **21**, 1799–1804 (2004)
215. W.I. Rose, Interaction of aircraft and explosive eruption clouds: a volcanologist's perspective. AIAA J. **25**, 52 (1986)
216. A.-B. Salberg, S. Solberg, D.J. Weydahl, R. Astrup, Leaf Area Index Estimation using ENVISAT ASAR and Radarsat-2. *Note No.SAMBA/30/09* (Norwegian Computing Center, NR, 2009)
217. G.C. Salzmann, S.B. Singham, R.G. Johnston, C.F. Bohren, Light scattering and cytometry, in *Flow Cytometry and Sorting*, ed. by M.R. Melamed, T. Lindmo, M.L. Mendelsohn (Wiley, New York, 1990), pp. 81–107
218. V. Sankaran, J.T. Walsh Jr., D.J. Maitland, Comparative study of polarized light propagation in biologic tissues. J. Biomed. Opt. **7**, 300–306 (2002)
219. S.N. Savenkov, L.T. Mishchenko, R.S. Muttiah, Y.A. Oberemok, I.A. Mishchenko, Mueller polarimetry of virus-infected and healthy wheat under field and microgravity conditions. JQSRT **88**, 327–343 (2004)
220. S.N. Savenkov, Optimization and structuring of the instrument matrix for polarimetric measurements. Opt. Eng. **41**, 965–972 (2002)

221. S.N. Savenkov, Analysis of generalized polarimetric measurement equation. Proc SPIE **6682**, 668214 (2007)
222. S.N. Savenkov, K.E. Yushtin, New classes of objects in polarimetry including the isotropic depolarization. Radiotechnika **116**, 3–11 (2000) (in Russian)
223. S.N. Savenkov, R.S. Muttiah, Inverse polarimetry and light scattering from leaves, in *Photopolarimetry in Remote Sensing*, ed. by G. Videen, Y. Yatskiv, M. Mishchenko (Springer, Dordrecht, 2004)
224. S.N. Savenkov, R.S. Muttiah, Y.A. Oberemok, Transmitted and reflected scattering matrices from an English oak leaf. Appl. Opt. **42**, 4955–4962 (2003)
225. S.N. Savenkov, O.I. Sydoruk, R.S. Muttiah, The conditions for polarization elements to be dichroic and birefringent. J. Opt. Soc. Am. A **22**, 1447–1452 (2005)
226. S.N. Savenkov, V.V. Marienko, E.A. Oberemok, O.I. Sydoruk, Generalized matrix equivalence theorem for polarization theory. Phys. Rev. E. **74**, 056607 (2006)
227. S.N. Savenkov, R.S. Muttiah, K.E. Yushtin, S.A. Volchkov, Mueller-matrix model of an inhomogeneous, linear, birefringent medium: single scattering case. J. Quant. Spectrosc. Radiat. Transf. **106**, 475–486 (2007)
228. S.N. Savenkov, O.I. Sydoruk, R.S. Muttiah, Eigenanalysis of dichroic, birefringent, and degenerate polarization elements: a Jones-calculus study. Appl. Opt. **46**, 6700–6709 (2007)
229. D.S. Saxon, Tensor scattering matrix for electromagnetic fields. Phys. Rev. **100**, 1771–1775 (1955)
230. J.M. Schmitt, G. Kumar, Turbulent nature of refractive-index variations in biological tissue. Opt. Lett. **21**, 1310–1312 (1996)
231. Z. Sekera, Scattering matrices and reciprocity relationships for various representations of the state of polarization. J. Opt. Soc. Am. **56**, 1732–1740 (1966)
232. D.B. Shapiro, P.G. Hull, A.J. Hunt, J.E. Hearst, Calculations of the Mueller scattering matrix for a DNA plectonemic helix. J. Chem. Phys. **101**, 4214–4221 (1994)
233. D.B. Shapiro, M.F. Maestre, W.M. McClain, P.G. Hull, Y. Shi, M.S. Quinby-Hunt, J.E. Hearst, A.J. Hunt, Determination of the average orientation of DNA in the octopus sperm *Eledone cirrhossa* through polarized light scattering. Appl. Optics. **33**, 5733–5744 (1994)
234. Y. Shindo, Applications of polarized modulator technique in polymer science. Opt. Eng. **34**, 3369–3384 (1995)
235. W.A. Shurcliff, *Polarized Light: Production and Use* (Harvard University Press, Harvard, 1962)
236. M. Sikdar, S. MacIntosh, I. Cumming, B. Brisco, Incorporating a vegetation index into a soil moisture retrieval model: results from Conair-580 SAR data, in *Proceedings of the IGARSS* (2005), pp. 383–386
237. R. Simon, The connection between Mueller and Jones matrices of polarization optics. Opt. Commun. **42**, 293–297 (1982)
238. R. Simon, Mueller matrices and depolarization criteria. J. Mod. Opt. **34**, 569–575 (1987)
239. G. Sinclair, Transmission and reception of elliptically polarized waves. Proc. IRE **38**, 148–151 (1950)
240. M.H. Smith, Interpreting Mueller matrix images of tissues. Proc. SPIE **4257**, 82–89 (2001)
241. M.H. Smith, Optimization of a dual-rotating-retarder Mueller matrix polarimeter. Appl. Opt. **41**, 2488–2495 (2002)
242. K.G. Snetsinger, G.V. Ferry, P.B. Russell, R.F. Pueschel, V.R. Oberbeck, Effects of El Chichon on stratospheric aerosols late 1982 to early 1984. J. Geophys. Res. **92**(14), 761–771 (1987)
243. S. Solberg, A. Brunner, K.H. Hanssen, H. Lange, E. Nusset, M. Rautiainen, P. Stenberg, Mapping LAI in a Norway spruce forest using airborne laser scanning. Remote Sens. Environ. **113**, 2317–2327 (2009)
244. P. Solleillet, Sur les paramètres caractérisant la polarisation partielle de la lumière dans les phénomènes de fluorescence. Ann. Phys. Biol. Med. **12**, 23–97 (1929)

245. R. Sridhar, R. Simon, Normal form for Mueller matrices in polarization optics. J. Mod. Opt. **41**, 1903–1915 (1994)

246. R.C.N. Studinski, I.A. Vitkin, Methodology for examining polarized light interactions with tissues and tissue-like media in the exact backscattering direction. J. Biomed. Opt. **5**, 330–337 (2000)

247. M.K. Swami, S. Manhas, P. Buddhiwant, N. Ghosh, A. Uppal, P.K. Gupta, Polar decomposition of 3x3 Mueller matrix: a tool for quantitative tissue polarimetry. Opt. Express **14**, 9324–9337 (2006)

248. S.T. Tang, H.S. Kwok, 3x3 Matrix for unitary optical systems. J. Opt. Soc. Am. A **18**, 2138–2145 (2001)

249. R. Touzi, A. Lopes, The principle of speckle filtering in polarimetric SAR imagery. IEEE Trans. Geosci. Remote Sens. **32**, 1110–1114 (1994)

250. R. Touzi, W.M. Boerner, J.S. Lee, E. Lueneburg, A review of polarimetry in the context of synthetic aperture radar: concepts and information extraction. Can. J. Remote Sensing **30**, 380–407 (2004)

251. L. Tsang, J.A. Kong, R.T. Shin, *Theory of Microwave Remote Sensing* (Wiley, New York, 1985)

252. S.R. Tsitas, Y.L. Yung, The effect of volcanic aerosols on ultraviolet radiation in Antarctica. Geophys. Res. Lett. **23**, 157–160 (1996)

253. V.V. Tuchin, Lasers light scattering in biomedical diagnostics and therapy. J. Laser Appl. **5**, 43–60 (1993)

254. V.V. Tuchin (ed.), *Selected Papers on Tissue Optics Applications in Medical Diagnostics and Therapy* (SPIE Press, Bellingham, 1994)

255. V.V. Tuchin (ed.), *Handbook of Optical Biomedical Diagnostics* (SPIE Press, Bellingham, 2002)

256. V.V. Tuchin, L.V. Wang, D.A. Zimnyakov, *Optical Polarization in Biomedical Applications* (Springer, Berlin, 2006)

257. K.M. Twietmeyer, R.A. Chipman, A.E. Elsner et al., Mueller matrix retinal imager with optimized polarization conditions. Opt. Express **16**, 21339–21354 (2008)

258. K. Twietmeyer, R.A. Chipman, Optimization of Mueller polarimeters in the presence of error sources. Opt. Express **16**, 11589–11603 (2008)

259. J.S. Tyo, Z. Wang, S.J. Johnson, B.G. Hoover, Design and optimization of partial Mueller matrix polarimeters. Appl. Opt. **49**, 2326–2333 (2010)

260. N. Ugryumova, S.V. Gangnus, S.J. Matcher, Three-dimensional optic axis determination using variable-incidence-angle polarization-optical coherence tomography. Opt. Lett. **31**, 2305–2307 (2006)

261. F.T. Ulaby, C.T. Allen, G. Eger III, Relating the microwave backscattering coefficient to leaf area index. Remote Sens. Environ. **14**, 113–133 (1984)

262. G.R. Valenzuela, Depolarization of EM waves by slightly rough surfaces. IEEE Trans. Antennas Propagat. **AP-15**(4), 552–557 (1967)

263. H.C. van de Hulst, *Light Scattering by Small Particles* (Wiley, New York, 1957)

264. W.P. van de Merwe, D.R. Huffman, B.V. Bronk, Reproducibility and sensitivity of polarized light scattering for identifying bacterial suspensions. Appl. Opt. **28**, 5052–5057 (1989)

265. W.P. van de Merwe, Z.-Z. Li, B.V. Bronk, J. Czege, Polarized light scattering for rapid observation of bacterial size changes. Biophys. J. **73**, 500–506 (1997)

266. C.V.M. van der Mee, An eigenvalue criterion for matrices transforming Stokes parameters. J. Math. Phys. **34**, 5072–5088 (1993)

267. C.V.M. van der Mee, J.W. Hovenier, Structure of matrices transforming Stokes parameters. J. Math. Phys. **33**, 3574–3584 (1992)

268. J.J. van Zyl, Unsupervised classification of scattering behavior using radar polarimetry data. IEEE Trans. Geosci. Remote Sens. **27**, 37–45 (1989)

269. J.J. van Zyl, Application of Cloude's target decomposition theorem to polarimetric imaging radar data. Proc. SPIE **1748**, 184–191 (1992)

270. J.J. van Zyl, F.T. Ulaby, Scattering matrix representation for simple targets, in *Radar polarimetry for geosciences applications*, ed. by F.T. Ulaby, C. Elachi. (Artech House, Norwood, 1990)

271. J.J. van Zyl, H.A. Zebker, Imaging radar polarimetry, in *PIER 3, Progress in Electromagnetics Research* (Elsevier, New York, 1990)

272. J.J. van Zyl, H.A. Zebker, C. Elachi, Imaging radar polarization signatures: theory and observation. Radio Science **22**, 529–543 (1987)

273. N. Vansteenkiste, P. Nignolo, A. Aspect, Optical reversibility theorems for polarization: application to remote control of polarization. J. Opt. Soc. Am. A **10**, 2240–2245 (1993)

274. H. Volten, O. Munoz, E. Rol, J.F. de Haan, W. Vassen, J.W. Hovenier, K. Muinonen, T. Nousianen, Scattering matrices of mineral aerosol particles at 441.6 nm and 632.8 nm. J. Geophys. Res. **106**, 17, 375 (2001)

275. K.J. Voss, E.S. Fry, Measurement of the Mueller matrix for ocean water. Appl. Opt. **23**, 4427–4436 (1984)

276. L.V. Wang, G.L. Coté, S.L. Jacques (eds.), Special section on tissue polarimetry. J. Biomed. Opt. **7**, 278–397 (2002)

277. Y. Wang, M.L. Imhoff, Simulated and observed L-HH radar backscatter from tropical mangrove forests. Int. J. Remote Sens. **14**, 2819–2828 (1993)

278. Y. Wang, L.L. Hess, S. Filoso, J.M. Melack, Understanding the radar backscattering from flooded and non flooded Amazonian forests: results from canopy backscatter modeling. Remote Sens. Environ. **54**, 324–332 (1995)

279. R.A. West, L.R. Doose, A.M. Eibl, M.G. Tomasko, M.I. Mishchenko, Laboratory measurements of mineral dust scattering phase function and linear polarization. J. Geophys. Res. **102**, 16871–16881 (1997)

280. C. Whitney, Pauli-algebraic operators in polarization optics. J. Opt. Soc. Am. **61**, 1207–1213 (1971)

281. M.F.G. Wood, X. Guo, I.A. Vitkin, Polarized light propagation in multiply scattering media exhibiting both linear birefringence and optical activity: Monte Carlo model and experimental methodology. J. Biomed. Opt. **12**, 014029 (2007)

282. M.F.G. Wood, N. Ghosh, E.H. Moriyama et al., Proof-of-principle demonstration of a Mueller matrix decomposition method for polarized light tissue characterization in vivo. J. Biomed. Opt. **14**, 014029 (2009)

283. I.H. Woodhouse, Predicting backscatter-biomass and height-biomass trends using a macroecology model. IEEE Trans. Geosci. Remote Sens. **GRS-44**, 871–877 (2006)

284. T. Xie, S. Guo, J. Zhang, Z. Chen, G.M. Peavy, Use of polarization-sensitive optical coherence tomography to determine the directional polarization sensitivity of articular cartilage and meniscus. J. Biomed. Opt. **11**, 064001 (2006)

285. Z.-F. Xing, On the deterministic and nondeterministic Mueller matrix. J. Mod. Opt. **39**, 461–484 (1992)

286. L. Xu, J. Ding, A.Y.S. Cheng, Scattering matrix of infrared radiation by ice finite circular cylinders. Appl. Opt. **41**, 2333–2348 (2002)

287. F.A. Zebker, J.J. van Zyl, Imaging radar polarimetry: a review. Proc. IEEE **79**, 1583–1606 (1991)

288. S. Zietz, A. Belmont, C. Nicolini, Differential scattering of circularly polarized light as an unique probe of polynucleosome superstructures. Cell Biophys. **5**, 163–187 (1983)

289. E. Zubko, Y.G. Shkuratov, G. Videen, Coherent backscattering effect for non-zero elements of Mueller matrix of discrete media at different illumination-observation geometries. J. Quant. Spectrosc. Radiat. Transf. **89**, 443–452 (2004)

290. O. Munoz, H. Volten, J.W. Hovenier, T. Nousiainen, K. Muinonen, D. Guirado, F. Moreno, L.B.F.M. Waters, Scattering matrix of large Saharan dust particles: experiments and computations. J. Geophys. Res. **112**, D13215 (2007)

Nonlinear Laser Fluorescence Spectroscopy of Natural Organic Compounds

30

Victor V. Fadeev and Evgeny A. Shirshin

Contents

Abstract

Principles of nonlinear laser fluorescence spectroscopy of complicated organic compounds and of the method capable of determining photophysical parameters are considered in this chapter. Special attention is paid to the peculiarities of the method connected with specific photophysical processes in natural organic

V.V. Fadeev (✉) • E.A. Shirshin
Moscow State University, Moscow, Russian Federation
e-mail: victor_fadeev@mail.ru, eshirshin@gmail.com

compounds, especially in proteins, and to the major role of intramolecular energy transfer and presence of localized donor-acceptor pairs (LDAP) of fluorophores within single macromolecules. These facts stimulated the development of models based on the collective states formalism describing fluorescent response of LDAP to pulsed laser excitation. Unique features of the method are illustrated by the example of proteins (proteins with intrinsic fluorescence (HSA, BSA) and fluorescent protein mRFP1) that can be used as fluorescent tags of intracellular processes while their photophysical parameters can be used as the information channel.

30.1   Introduction

The use of lasers (laser radiation) has dramatically changed optics and optical spectroscopy [1–3]. Many of the traditional methods of spectroscopy had a rebirth, the most striking examples being spectroscopy of spontaneous Raman scattering [2, 4], opto-kalorimetric methods (the method of termolens, optoacoustic spectroscopy, etc.) [2, 3]. Of greater scientific interest and practical importance are the "true laser" techniques, based on the nonlinearity and coherent optical response of the medium on laser radiation. For example, these methods include intracavity laser spectroscopy [3], laser spectroscopy within the Doppler line [2], coherent anti-Stokes Raman spectroscopy (CARS) [2], nonlinear spectroscopy of surface (SERS, the second and the third harmonic spectroscopy [1]), and parametric scattering of light spectroscopy [1, 2, 5].

For a long time, the method of fluorescence spectroscopy stood apart from this process, though this method has high sensitivity [6]. The principal limitations of classical fluorometry are its low selectivity caused by broad and unstructured fluorescence emission bands and the fact that this method is very limited at the solution of the inverse problem (i.e., at determination of photophysical characteristics of fluorescent molecules). In the early 1970s, the prospects of using fluorescence in remote laser (lidar) sensing of the atmosphere and, especially, the hydrosphere were demonstrated [7], and extensive application of laser diagnostics in medicine and biology [8] became incentives for seeking ways of making fluorometry more informative.

These studies led to the creation of the method of nonlinear laser fluorescence spectroscopy [9–11]. In this method, fluorescence saturation curves (nonlinear dependencies of fluorescence intensity on the exciting radiation) are used as the input data for solving of the inverse problem. In the framework of solving just one inverse problem, using a single saturation curve measured on a single spectrometer, one can simultaneously determine the photophysical characteristics (absorption cross section, the lifetime of the excited state, the rates of energy transfer, etc.), measuring which in classical spectroscopy would require the use of different tools and techniques, and, moreover, it can be done without a priori information required for classical methods, such as the concentration of molecules (for determining the absorption cross section), the lifetime of the excited state of the donor in the absence of the acceptor (for determining the rate of energy transfer), and so on.

Laser fluorometry turned out to be a unique method of studying natural organic compounds, photosynthetic organisms [12], proteins [13–15] (especially fluorescent proteins [14, 15]), and humic substances [16], which, moreover, can be used as fluorescent descriptors and indicators of the ecosystem state to which they belong. An important property of the majority of natural complex organic compounds (COC) in scope of optical spectroscopy is a high local concentration of absorbing (chromophores) and fluorescing (fluorophores) groups located within a single macromolecule, while the concentrations of these macromolecules in media are usually low. This fact predetermines a major role of intramolecular energy transfer. Some of the natural COC typically have a determined countable number of chromophores/fluorophores with a possible energy transfer between them (e.g., localized donor-acceptor pairs [14]). All these require the development of novel methods based on the laser fluorescence spectroscopy technique.

This chapter outlines the basis of nonlinear laser fluorescence spectroscopy of complex organic compounds. The possibilities of laser fluorometry are illustrated by the results of its application in the research and diagnostics of extremely important natural organic compounds - proteins, including fluorescent proteins that are of great interest as indicators of living cells' state. The choice of these objects has been determined both by their importance in nature and the variety of photophysical processes that allows illustration of unique possibilities of nonlinear laser fluorometry.

In this chapter, human and bovine serum albumins (HSA and BSA [13, 14]) and red fluorescent protein mRFP1 [14, 15] are represented. The complexity of photophysical processes in this sequence increases and requires the development of the analysis method.

30.2 Fundamentals of Nonlinear Laser Fluorescence Spectroscopy of Complex Organic Compounds (COC)

30.2.1 Photophysical Processes in COC. Photophysical Parameters

Both classical (linear) and laser fluorescence spectroscopy of complex organic compounds (COC) are based on the phenomenon of fluorescence. The model of fluorescence response formation under optical excitation operates with a set of photophysical parameters – the absorption (or excitation) cross section, fluorescence quantum yield, the rates of radiative and non-radiative excited state relaxation, the rate of singlet-triplet conversion, and the rate of intermolecular energy transfer, including energy transfer between similar molecules in the excited state (singlet-singlet annihilation). The processes and capabilities of classical fluorescence spectroscopy (fluorometry) are presented in many monographs (see, e.g., [6]). The information below is provided to present the foundations of nonlinear laser fluorometry.

Fluorescence, or fast luminescence, is the result of the allowed radiative transitions from the excited electronic state to the ground one. The diagram of the lowest
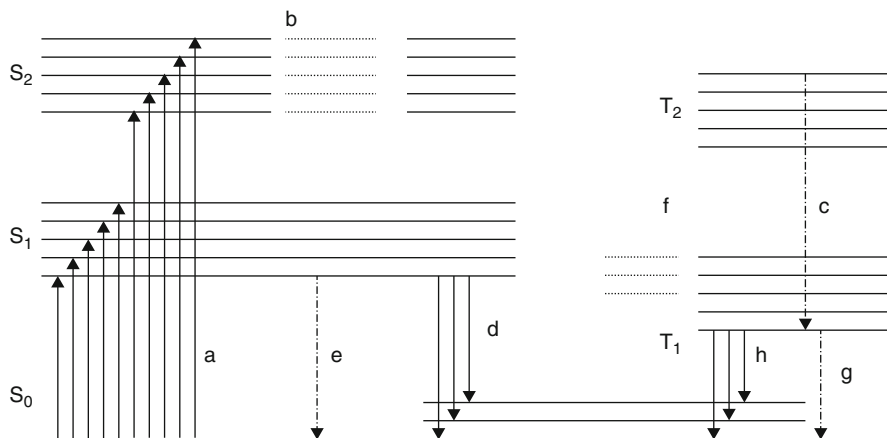
Fig. 30.1 Lowest energy levels of COC molecule and possible photophysical processes: a – absorption; b – internal conversion; c, e, g – nonradiative decay; d – fluorescence emission; f – singlet-triplet conversion; h – phosphorescence

molecules' energy levels is presented on Fig. 30.1. For the majority of molecules with an even number of electrons in ground state, all the molecular orbitals (MO) are filled with pairs of electrons (i.e., the orbital contains an even number of electrons).

According to the Pauli exclusion principle, electrons of the same MO have opposite spins, hence, the resultant spin quantum number (S) for the molecules in the ground state is zero ($S = 0$) and the multiplicity $J = |2S + 1| = 1$. However, when one electron goes to the upper orbital, its spin can be oriented in either the same or the opposite direction to that of the remainder of the lower orbital electron. In the first case, $S = 0$, $J = 1$, and the excited state is singlet; in the second, $S = 1$, $J = 3$, and the state of the molecule is triplet.

Each electronic level of an organic molecule splits into a series of vibrational levels, and each vibrational level into a series of closely spaced rotational sublevels. Collision of molecules and electrostatic perturbation induced by the surrounding solvent molecules leads to broadening of the vibrational-rotational sublevels. As a result, a quasicontinuum of energy states appears. Therefore, absorption and fluorescence spectra of COC molecules in solution are usually unstructured bands with a width of a few tens of nanometers [6].

A COC molecule in ground state absorbs photon with a probability equal to σF, where σ is the absorption cross section (cm^2), and F is the excitation photon flux density (cm^{-2} s^{-1}). A number of processes lead to relaxation of the excited state.

The typical excited state lifetime of COC molecule is $\tau_F \approx 10^{-9}$ s. Relaxation between vibrational energy levels m and n ($m > n$) within the same electronic level i $S_i^m \rightarrow S_i^n$ is called internal conversion (typical time $\tau_{IC} \approx 10^{-12} \div 10^{-13}$ s). Radiative $S_1 \rightarrow S_0$ transition is called fluorescence. Non-radiative $S_1 \rightarrow S_0$ transitions can also occur; rates of these processes determine fluorescence quantum yield. Nonradiative $S_i \rightarrow T_i$ transitions are called singlet-triplet conversion ($\tau_{ST} \approx 10^{-7}$ s), and radiative

$T_1 \rightarrow S_0$ transitions are called phosphorescence ($\tau_P \approx 10^{-3} \div 10^2$ s). Transitions between energy levels with different multiplicity are spin-forbidden and become partially allowed for COC as the result of spin-orbit coupling.

Radiative transitions from higher energy levels S_i and T_i can also occur, however, for COC, probability of such processes is quite low [6]. When the concentration of fluorescing COC molecules in solution or in an organic complex is high, bimolecular energy transfer processes are possible. One of these processes is singlet-singlet annihilation: when two excited molecules are close enough, energy transfer can occur if the necessary conditions are fulfilled (e.g., in case of fluorescence resonance energy transfer (FRET), the donor's emission band and the acceptor's absorption band must overlap). As the result, one of the molecules comes to the ground state. This effect plays a major role in fluorescent response to pulsed laser excitation of photosynthetic organisms due to high (up to 1 M) local concentration of chlorophyll a [12, 17, 18].

Since internal conversion leads to fast deactivation of higher COC molecule energy states S_i and T_i ($i > 1$) and of higher vibrational levels of S_1 and T_1, one can use a three-level model of COC energy states, involving transitions (absorption and excited state relaxation) between S_0, S_1, and T_1 levels (Fig. 30.2).

The balance of S_0, S_1, and T_1 states populations (n_1, n_3, n_2, respectively) for a COC molecule can be described by the system of differential equations (30.1):

$$\begin{cases} \dfrac{\partial n_1(t, \vec{r})}{\partial t} = (K_{31} + K'_{31})n_3(t, \vec{r}) - F(t, \vec{r})\sigma n_1(t, \vec{r}) + \gamma n_3^2(t, \vec{r}) \\[2mm] \dfrac{\partial n_2(t, \vec{r})}{\partial t} = K_{32}n_3(t, \vec{r}) \\[2mm] \dfrac{\partial n_3(t, \vec{r})}{\partial t} = F(t, \vec{r})\sigma n_1(t, \vec{r}) - (K_{31} + K'_{31} + K_{32})n_3(t, \vec{r}) - \gamma n_3^2(t, \vec{r}) \end{cases} \quad (30.1)$$

where

K_{31}, K'_{31}, K_{32} are the rates of radiative and nonradiative $S_1 \rightarrow S_0$ transitions and the rate of singlet-triplet conversion (see Fig. 30.2)

$\tau^{-1} = K_{31} + K'_{31} + K_{32}$ is the total rate of S_1 state deactivation

σ is the COC molecule's absorption cross section (in the general case, the COC molecule's excitation cross section taking into account all the possible pathways of excitation: direct absorption, energy transfer, etc.)

γ is the constant of the singlet-singlet annihilation rate, caused by energy transfer between two excited fluorophores (Fig. 30.2)

$F(t, \vec{r})$ is the excitation photon flux density

$\vec{r} = \{x, y\}$ are coordinates in the beam cross section

The relation between n_1, n_2, and n_3 is determined by the conservation law:

$$n_0 = n_1 + n_2 + n_3,$$

where n_0 is the total concentration of COC molecules (in cm^{-3}).
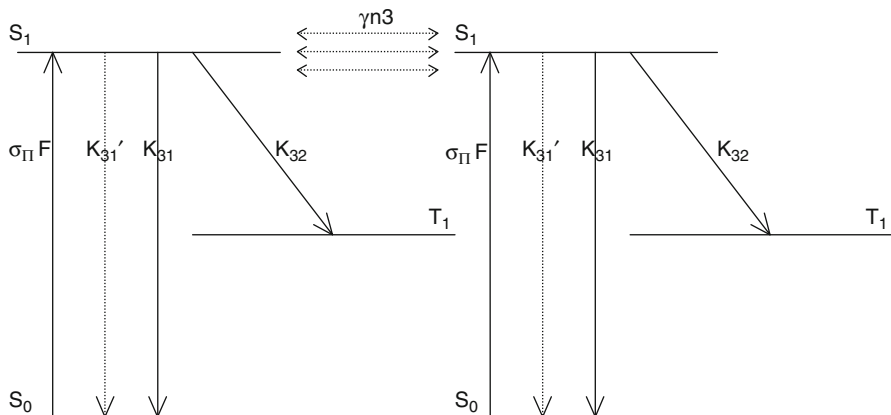
Fig. 30.2 Three-level model of COC molecule energy levels (including singlet-singlet annihilation)

When writing (30.1), the following factors are neglected:

- Excited state absorption from S_1 and T_1 states – if this process does not cause photobleaching (e.g., photoionization), it does not affect the kinetics of the energy level's population due to fast internal conversion,

- Stimulated transitions from S_1 to S_0 (here we suppose the excitation to be non-resonant);

- $T_1 \rightarrow S_0$ transitions (it is supposed that the duration of exciting laser pulse $t_{pulse} << 1/K_{21} << f^{-1}$, where K_{21} is the rate of T_1 state relaxation, and f is the pulse repetition rate; i.e., triplet state T_1 is some kind of "trap," accumulating COC molecules, that completely depopulates between two excitation pulses). Here we consider pulsed laser radiation because of its high photon flux density that can cause nonlinear dependency of fluorescence intensity on the excitation intensity.

Let us consider a diluted solution of the COC molecules that is irradiated with light pulses propagating along the z axis. We regard an optically thin layer of thickness l ($n_0 \cdot \sigma \cdot l << 1$) bounded by two planes perpendicular to the z axis with the coordinates z and $z + l$. Let's consider the fluorescent response of the selected layer to the excitation laser pulse.

The exciting pulse can be represented as a group of photons propagating along the z axis. We suppose the distribution of photons in the beam cross section to be axisymmetric; this allows use of cylindrical coordinates $\{z, r\}$ $\left(z = z, \ r^2 = \sqrt{x^2 + y^2} \right)$.

We introduce the distribution function of photons per pulse $g(t/t_p, r/r_0)$, which describes the probability density for a photon of the exciting radiation to be at time t at the point with coordinate r (here, t_p, r_0 are effective pulse duration and beam radius). Let's introduce the following notation: $\xi = t/t_p$, $\rho = r/r_0$, then, by definition,

the probability of a photon to be in the ring of $dV = 2\pi\rho \cdot d\rho \cdot d\xi$ volume is determined by $g(\xi,\rho)dV$. Therefore, the function $g(\xi,\rho)$ must obey the normalization condition:

$$\int_{-\infty}^{+\infty} \int_{-\infty}^{+\infty} g(\xi, \rho) \cdot 2\pi\rho \cdot d\rho \cdot d\xi = 1. \tag{30.2}$$

Let $g(\xi, \rho)$ be a factorized distribution $g(\xi, \rho) = g_\xi(\xi) \cdot g_\rho(\rho)$. The effective pulse duration τ_p and the beam radius r_0 can be defined as follows:

$$\begin{aligned} g_\xi(\pm 0.5) &= 0.5 \cdot g_\xi(0) \\ g_\rho(1) &= 0.5 \cdot g_\rho(0) \end{aligned} \tag{30.3}$$

Possible $g_\xi(\xi)$ distributions include Gauss distribution in time

$$g_{\xi\Gamma}(\xi) = \sqrt{\frac{4 \cdot \ln(2)}{\pi}} \cdot \exp(-4 \cdot \ln(2) \cdot \xi^2) \tag{30.4}$$

and in the beam cross section

$$g_{\rho\Gamma}(\rho) = \frac{\ln(2)}{\pi} \cdot \exp(-\ln(2) \cdot \rho^2). \tag{30.5}$$

These distribution functions [(30.4) and (30.5)] satisfy (30.3), and their combinations satisfy (30.2).

Let us select a ring volume $dV = 2\pi\rho \cdot d\rho \cdot d\xi$. The number of exciting pulse photons in dV is $N_{dV} = F(t, r) \cdot 2\pi r \cdot dr \cdot dt$, where $F(t, r)$ is the photon flux density. From the other side, $N_{dV} = N \cdot g(\xi,\rho) \cdot 2\pi\rho \cdot d\rho \cdot d\xi$, where N stands for the total number of photons in the pulse. Hence, $F(t,r) \cdot r_0^2 \cdot t_p = N \cdot g(\xi,\rho)$. The value $F_{eff} = \frac{N}{t_p \pi r_0^2}$ is called the effective photon flux density of the exciting radiation and

$$F(t,r) = \pi \cdot g(t/t_p, r/r_0) \cdot F_{eff} = \pi \cdot g(\xi,\rho) \cdot F_{eff}. \tag{30.6}$$

In cylindrical coordinates $\left(z = z, \ r^2 = \sqrt{x^2 + y^2}\right)$, assuming an optically thin layer system, (30.1) is transformed into

$$\begin{cases} \dfrac{\partial n_1(t,r)}{\partial t} = (K_{31} + K'_{31})n_3(t,r) - \pi \cdot g(t/t_p, r/r_0) \cdot F_{eff}\sigma n_1(t,r) + \gamma n_3^2(t,r) \\[2mm] \dfrac{\partial n_2(t,r)}{\partial t} = K_{32}n_3(t,r) \\[2mm] \dfrac{\partial n_3(t,r)}{\partial t} = \pi \cdot g(t/t_p, r/r_0) \cdot F_{eff}\sigma n_1(t,r) - (K_{31} + K'_{31} + K_{32})n_3(t,r) - \gamma n_3^2(t,r) \end{cases}$$

$$\tag{30.7}$$

Integrating the system (30.7) and taking into account the conservation law, one can obtain an expression for the population of the first excited singlet state of fluorescent molecules $n_3(t, \boldsymbol{r})$. Using this expression, it is possible to find the number of fluorescence photons emitted from the selected layer of the solution as a result of excitation by the laser pulse:

$$
\begin{aligned}
N_{fl} &= K_{31} \times \int\limits_{z}^{z+l} dz \cdot \int\limits_{0}^{\infty} 2\pi r \cdot dr \cdot \int\limits_{-\infty}^{\infty} n_3\big(K_{31}, K'_{31}, K_{32}, \sigma, \gamma, F_{eff}, t, r\big) \cdot dt \\
&= K_{31} \cdot l \times \int\limits_{0}^{\infty} 2\pi r \cdot dr \cdot \int\limits_{-\infty}^{\infty} n_3\big(K_{31}, K'_{31}, K_{32}, \sigma, \gamma, F_{eff}, t, r\big) \cdot dt
\end{aligned}
\tag{30.8}
$$

30.2.2 Fluorescence Saturation of COC Under Pulsed Laser Excitation. Basics of the Nonlinear Fluorometry

With increasing intensity of the exciting radiation, the dependence of COC molecules' fluorescence photons [see (30.8)] on the photon flux density becomes nonlinear (Fig. 30.3a). This effect is called fluorescence saturation. In the framework of the adopted three-level model (for single-component solution of COC), there are two basic mechanisms of fluorescence saturation [9, 12, 17]: depletion of the ground state of fluorescent molecules (absorption bleaching) and singlet-singlet annihilation.

Nonlinear laser fluorometry is based on the fluorescence saturation effect and operates with the measured dependence of the number of fluorescence photons N_{fl} on the photon flux density F of the exciting laser radiation – $N_{fl}(F)$. At typical F values for pulsed lasers ($F \geq 10^{20}\,\text{cm}^{-2}\,\text{s}^{-1}$), deviation of $N_{fl}(F)$ from the linear law appears, in varying degrees for different COC. For diluted solutions of organic dyes, nonlinearity becomes significant at F values $F \geq 10^{24}\text{cm}^{-2}\text{c}^{-1}$ [9] and for objects with a high local concentration of fluorophores (e.g., photosynthetic organisms), it is already apparent at $F \geq 10^{19}\,\text{cm}^{-2}\,\text{s}^{-1}$ [12, 17].

The next step is the inverse problem solution: determination of photophysical parameters used in the model describing experimental fluorescence saturation curves $N_{fl}(F)$. As usual, the inverse problem solution consists of two stages: direct problem solution (evaluation of $N_{fl}(F)$ for a given set of photophysical parameters) and the inverse problem solution itself: determination of the set of parameters that gives minimum discrepancy between theoretical and experimental saturation curves. For this purpose, different algorithms – the traditional variational, such as gradient descent methods and nonlinear regression, and neural networks [10] – are used. Some unique capabilities of nonlinear fluorometry (NLF) will be presented in Sect. 30.3 using the example of concrete proteins. As with any other method, NLF has its limitations: because of the monotonous character of the saturation curves,

Fig. 30.3 Fluorescence saturation curve in different axes: (**a**) $N_{fl}(F)$, (**b**) $\Phi^{-1}(F)$, (**c**) $\Gamma(F)$. Dependencies in the absence of fluorescence saturation are shown with *dotted lines*
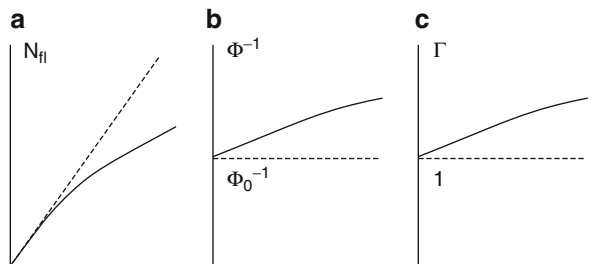
the dimension of an inverse problem with a sustainable solution is no more than three (detailed analysis of sustainability and uniqueness of NLF inverse problem solution is given in [11]). This limitation is partially overcome in the so-called matrix method of laser fluorometry, synthesizing nonlinear and time-resolved (kinetic) fluorometry [19]. Fundamentals of this method are described in Sect. 30.2.4, which is preceded by a description of the method of time-resolved fluorometry (Sect. 30.2.3).

In real experiments, the value $N_{fl}(F)$ is measured in arbitrary units (a.u.), since the procedure for measuring the absolute values of fluorescence photons is cumbersome and fraught with errors. In order to obtain quantities that can be measured in absolute terms and compared with those calculated from the adopted model, it is necessary to make the normalization of the number of detected fluorescence protons N_{fl} some reference signal N_{ref} that depends linearly on the photon flux density of exciting radiation. The intensity of laser radiation measured by the second photodetector or the signal of Raman scattering (RS) of light by water molecules or other solvent [9, 20] can be used as a reference signal. The ratio $\Phi = N_{fl}/N_{ref}$ is called the fluorescence parameter.

To characterize the degree of fluorescence saturation, the saturation factor $\Gamma = \frac{N_{fl}^0}{N_{fl}}$ is introduced, where $N_{fl}^0 = F \times \lim\limits_{F \to 0} \frac{dN_{fl}}{dF}$ is the number of photons that would have been emitted by the molecule in the absence of saturation. Fluorescent parameter Φ is connected with Γ by the following equation: $\Gamma = \frac{\Phi_0}{\Phi}$, where $\Phi_0 = \lim\limits_{F \to 0} \Phi(F)$ is the unsaturated fluorescence parameter that does not depend on F. In absence of fluorescence saturation, $N_{fl} \sim F$ and $\Gamma = 1$. When $N_{fl}(F)$ becomes nonlinear, $\Gamma(F)$ ceases to be a unit (Fig. 30.3). The dependencies $N_{fl}(F)$ (Fig. 30.3a), $\Phi^{-1}(F)$ (Fig. 30.3b), and $\Gamma(F)$ (Fig. 30.3c) are called fluorescence saturation curves in corresponding axes.

30.2.3 Fluorescence Kinetics of COC Molecules. Principles of Time-Resolved Fluorometry

The classical method of time-resolved fluorometry [2] is based on analysis of the fluorescence decay curves after the exciting pulse with much shorter

duration than the lifetime of the excited state. For typical COC molecules, this method requires the use of picosecond pulses. However, information about the relaxation of the excited state of COC molecules can be also obtained with nanosecond excitation.

In Ref. [21], the suggested variant of time-resolved fluorometry COC solution is excited laser pulses with duration $\tau_p = 10$ ns. The fluorescence signal is detected with intensified CCD camera with mini/mum gate width $\tau_{gate} = 10$ ns and gating resolution $\Delta\tau = 2.5$ ns. It was shown that, using this equipment it, becomes possible to determine COC molecules' lifetimes down to 1 ns, despite the fact of large τ_p and τ_{gate} values.

Here, the dependence of the number of photons in the ICCD gate t_g on the delay time t_{del} after the exciting laser pulse is called the kinetic curve. According to (30.8), $N_{fl}(t_{del})$ is given by:

$$N_{fl} = K_{31} \cdot l \times \int_0^\infty 2\pi r \cdot dr \int_{-t_g/2+\tau_{del}}^{t_g/2+\tau_{del}} n_3(t,r) \cdot dt \qquad (30.9)$$

Delay time t_{del} changes discretely proportional to the number of the gating steps i: $t_{del} = i \times t_{\text{step}}$.

When using this technique, the key point is selection of the zero point, that is, the moment when $t_{del} = 0$; for example, this point can be chosen from the condition that at $t_{del} = 0$ the maximum of the laser pulse and the center of the ICCD gate coincide. This point can be chosen using the maximum of Raman scattering by water molecules as a reference (RS signal is almost inertialess; the elementary act of scattering occurs at $10^{-11} - 10^{-12}$ s timescales).

Fluorescence intensity is measured in a.u., so in order to compare for experimental and calculated kinetic curves the normalized values of intensity are used:

$$I_{fl}(t_{del}) = \frac{N_{fl}(t_{del})}{N_{fl}(0)}$$

where $Nfl(t_{del})$ is the number of photons registered at t_{del} delay at the same gate width. This normalization is used during processing of experimental data.

30.2.4 Matrix Method in COC Fluorometry

As already mentioned, capabilities of NLF are limited by the number of photophysical parameters that can be recovered from smooth fluorescence saturation curves. In many cases, this can be enough, for example, in the case of monofluorophoric solution absorption cross section (in absence of a priori information about concentration; see Sect. 30.3 for details), excited state lifetime, the

rate of singlet-triplet conversion, or the rate of singlet-singlet annihilation can be determined. However, in case of a bifluorophoric system when energy transfer appears, this set of parameters can appear to be insufficient. This situation is mathematically described by a system of kinetic equations:

$$
\begin{cases}
\dfrac{dn_1}{dt} = F(t)\sigma_1(n_{01} - n_1) - \dfrac{n_1}{\tau} - \gamma n_1^2 - K_{12}(n_{02} - n_2) \\
\dfrac{dn_2}{dt} = F(t)\sigma_2(n_{02} - n_2) - \dfrac{n_2}{\tau} - \gamma n_2^2 + K_{12}(n_{02} - n_2)
\end{cases}
\tag{30.10}
$$

with the following abbreviations:

n_1, n_2 – concentrations of the excited molecules of the corresponding fluorophores;

n_{01}, n_{02} – initial concentrations of the molecules of the corresponding fluorophores;

τ_1, τ_2 – lifetimes of the excited molecules of the corresponding fluorophores;

γ_1, γ_2 – constants of singlet-singlet annihilation of the corresponding fluorophores;

σ_1, σ_2 – excitation cross sections of the corresponding fluorophores;

$F(t)$ – photon flux density of the exciting radiation;

K_{12} – constant of intermolecular energy transfer from the first to the second fluorophore.

Having determined $n_1(t,F)$ and $n_2(t,F)$, it is possible to calculate the fluorescence intensity $I(F,T)$ in a receiver gate delayed for time T with respect to the exciting laser pulse for the given value of photon flux density F [21].

In this model we do not separate singlet-triplet conversion from the common channel of intermolecular relaxation of excited state of fluorophores, that is, from the total time of this relaxation, τ_1 and τ_2. Nevertheless, there are nine model parameters, which cannot be determined simultaneously neither with the kinetic fluorometry method, nor with the nonlinear fluorometry method, nor by the sequential use of these methods. These considerations have led to the idea to perform a synthesis of these methods [19]. To do so, the following matrix needs to be measured:

$$
M_{FT} =
\begin{bmatrix}
I_{F_1 T_1} & \cdots & I_{F_1 T_t} \\
\vdots & \vdots & \vdots \\
I_{F_W T_1} & \cdots & I_{F_W T_t}
\end{bmatrix}
$$

where I_{FnTm} is the fluorescence intensity of the COC mixture for the exciting radiation photon flow density F_n and for the gate delayed for time T_m with respect to the laser pulse.

The rows of this matrix are the points on kinetic curves at different photon flux densities F; the columns are the points on fluorescence saturation curves at different gate delays T. The range of F should be selected in such a way that, at its minimal value, there would be no saturation of fluorescence, and at its maximum value saturation would be significant. The degree of saturation at maximum F is chosen based on the peculiarities of the specific problem.

From physical considerations, it may be expected that different matrix elements have different dependences on photo-physical parameters. Consequently, under rational choice of matrix elements, all photo-physical parameters can be determined.

It should be noted that this approach is in principle different from the matrix method, suggested in [22, 23] and aimed at determination of partial concentrations of components in a mixture where the following matrix is used:

$$M_{\lambda T} = \begin{bmatrix} I_{\lambda_1 T_1} & \cdots & I_{\lambda_1 T_t} \\ \vdots & \vdots & \vdots \\ I_{\lambda_W T_1} & \cdots & I_{\lambda_W T_t} \end{bmatrix}$$

Here, the matrix elements are the values of intensity measured at different wavelength within the overall fluorescence band at different ICCD gate delay with respect to the laser pulse.

30.2.5 Laser Fluorometry of Localized Donor-Acceptor Pairs. Collective States of Donor-Acceptor Pair

The systems with excitation energy transfer in which the donor has only one possible acceptor (localized donor-acceptor pairs) are finding increasing wider application [24, 25]. Commonly, the systems of this kind are constructed artificially out of pairs of organic compounds (e.g., out of dye molecules or fluorescent protein macromolecules). A description of the fluorescence response of such systems in terms of the conventional approach becomes inapplicable, because the situation is possible when the donor and the acceptor of a LDA pair are simultaneously in an excited state; therefore, the energy transfer in the framework of a conventional scheme [see (30.10)] is impossible. The model presented in this section makes it possible to describe the energy transfer inside a LDA pair, but disregarding the energy transfer between the pairs.

We employ the following notations: S_{0D}, S_{1D} are the ground and the first excited states of the donor, S_{0A}, S_{1A} are the same for the acceptor. Let us to introduce a notion of the collective states of a LDA pair, each of these states simultaneously describes both the donor state and the acceptor state:

- Collective state 1: the donor and the acceptor are in the ground state S_{0D} and S_{0A}, respectively; the concentration of such molecules is denoted as $n_1 \equiv n_1(t, \vec{r})$;
- Collective state 2: the donor is in the state S_{1D}, and the acceptor is in the state S_{0A}; the concentration of such molecules is denoted as $n_2 \equiv n_2(t, \vec{r})$;
- Collective state 3: the donor is in the state S_{0D}, and the acceptor is in the state S_{1A}; the concentration of such molecules is denoted as $n_3 \equiv n_3(t, \vec{r})$;
- Collective state 4: the donor and the acceptor are in the first excited state S_{1D} and S_{1A}, respectively; the concentration of such molecules is denoted as $n_4 \equiv n_4(t, \vec{r})$

The collective states of a LDA pair can be illustrated by the diagrams, see Fig. 30.4.
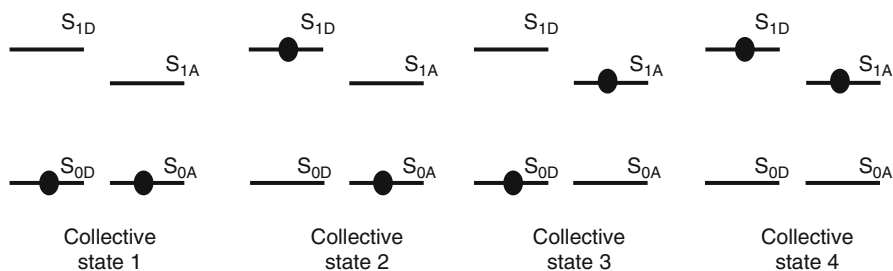
Fig. 30.4 The collective states of the localized donor-acceptor pair (in each collective state the left scheme of the energy levels is attributed to the donor of the LDA pair (levels S_{0D} and S_{1D}) and the right one to the acceptor (levels S_{0A} and S_{1A}))

The dynamics of variation in the concentrations of these four collective states of the LDA pair (disregarding singlet-triplet conversion and single-singlet annihilation process) is mathematically described by the following system of the kinetic (30.11):

$$
\begin{cases}
\dfrac{\partial n_1}{\partial t} = -F(t,\vec{r}) \cdot (\sigma_D + \sigma_A) \cdot n_1 + \dfrac{n_2}{\tau_3^D} + \dfrac{n_3}{\tau_3^A} \\[2ex]
\dfrac{\partial n_2}{\partial t} = -F(t,\vec{r}) \cdot \sigma_A \cdot n_2 - \dfrac{n_2}{\tau_3^D} - K_{DA} \cdot n_2 + F(t,\vec{r}) \cdot \sigma_D \cdot n_1 + \dfrac{n_4}{\tau_3^A} \\[2ex]
\dfrac{\partial n_3}{\partial t} = -F(t,\vec{r}) \cdot \sigma_D \cdot n_3 - \dfrac{n_3}{\tau_3^A} + F(t,\vec{r}) \cdot \sigma_A \cdot n_1 + \dfrac{n_4}{\tau_3^D} + K_{DA} \cdot n_2 \\[2ex]
\dfrac{\partial n_4}{\partial t} = F(t,\vec{r}) \cdot \sigma_A \cdot n_2 + F(t,\vec{r}) \cdot \sigma_D \cdot n_3 - \dfrac{n_4}{\tau_3^D} - \dfrac{n_4}{\tau_3^A} \\[2ex]
n_1 + n_2 + n_3 + n_4 = n_0,
\end{cases}
\tag{30.11}
$$

where the symbols D and A denote the donor and the acceptor, respectively; τ is the lifetime of excitation state of the donor or acceptor molecules; σ is the absorption cross section corresponding to the $S_0 \rightarrow S_1$ transition; K_{DA} is the rate of the energy transfer from the excited donor to the unexcited acceptor; n_0 is the total concentration of molecules containing a LDA pair.

It should be noted that that the parameter K_{DA} in (30.11) has the meaning of the energy transfer rate, whereas in the conventional model (30.10) it is the constant of the energy transfer rate, that is, the rate normalized to a unitary concentration of the unexcited acceptor molecules. This is the consequence of the fact that the model described by (30.11) suggests the presence of only one donor and one acceptor in a macromolecule (it should be noted that the model can be generalized for the case when a macromolecule contains several donors and acceptors). In this case, the energy transfer rate can assume two fixed values: $K_{DA} = 0$ (in the collective state 4) and $K_{DA} = $ const (in the collective state 2). In the conventional model, the donor is surrounded by a large quantity of the acceptor molecules and,

consequently, the rate of energy transfer can assume a continuous series of values from 0 to some maximum value, which is equal to $K_{DA}^{*} \times M_{0A}$, here K_{DA}^{*} is the constant of energy transfer rate, and M_{0A} is the concentration of the acceptor molecules.

Knowing the law of variation in the concentration of fluorescent molecules in the excited state, one can calculate the number of fluorescence photons N_{Fl}, emitted under the influence of a laser pulse:

For the donor:

$$N_{Fl}^{D}(\lambda) \propto \int_{0}^{\infty} 2\pi r \cdot dr \int_{-\infty}^{+\infty} (n_2(t,r) + n_4(t,r)) dt; \tag{30.12}$$

For the acceptor:

$$N_{Fl}^{A}(\lambda) \propto \int_{0}^{\infty} 2\pi r \cdot dr \int_{-\infty}^{+\infty} (n_3(t,r) + n_4(t,r)) dt. \tag{30.13}$$

In the model described by (30.11), the fluorescence saturation occurs due to the finite time of return of fluorescent molecules from the excited state S_1 to the ground state S_0, and due to a decrease in the number of molecules in the collective state 2 (the saturation of the energy transfer channel). As the conventional model, model (30.11), operating with the collective states of a LDA pair, could be supplemented with other mechanisms of the fluorescence saturation (the singlet-triplet conversion, singlet-singlet annihilation, photochemical processes in an excited state, etc.).

30.3 Laser Fluorescent Spectroscopy of Proteins

30.3.1 Optical Properties of Protein Macromolecules

It is well known [26] that protein molecules obtain intrinsic luminescence in the UV region of spectrum due to the presence of aromatic amino acids – tryptophan (Trp), tyrosine (Tyr), and phenylalanine (Phe). About 90 % of the total fluorescence of proteins is usually due to tryptophan residues. This natural fluorophore is extremely sensitive to the polarity of the environment. Spectral shifts of its absorption and fluorescence bands are often the consequence of several phenomena, among which are the ligand binding, protein-protein association and denaturation. Proteins absorb light near 280 nm, the maxima of fluorescence spectra lie in the region 320–350 nm (Fig. 30.5). Excited state lifetimes of tryptophan residues usually ranged from 1 to 6 ns.

Tyrosine fluoresces intensively in solution, but its emission intensity in proteins is much weaker. Protein denaturation usually increases tyrosine emission.

Fig. 30.5 Irreversible changes in the absorption (**a**) and fluorescence (**b**) spectra of the tryptophan solution during its irradiation by UV light: before irradiation (*solid curve*), after irradiation for 15 min (*dashed curve*), after irradiation for 30 min (*circles*), and within 6 h after the end of 30-min irradiation (*triangles*) for the photon flux density $F = 10^{25}$ cm^{2}s^{-1}. The inset shows the dependence of the change in the optical density of the aqueous solution of tryptophan at 278 nm due to the photoproduct formation on the exciting photon flux density. The irradiation time is 30 min [27]
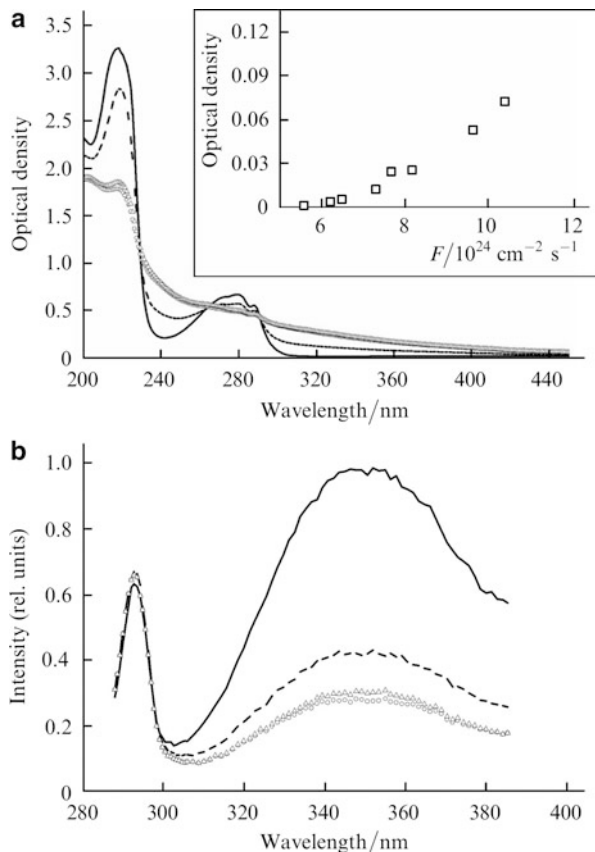
Phenylalanine's fluorescence quantum yield in proteins is small (less than 1 %), so its impact on protein fluorescence can usually be neglected.

A detailed analysis of the intrinsic fluorescence of proteins is hampered by the number of factors that affect the fluorescence and the presence of several different aromatic amino acid residues in one protein molecule. Since each residue is in a different environment, its spectral properties may differ. Emission spectra of all residues overlap, and it is difficult to separate the spectral contributions of each of them, for example, in a multitryptophan protein. In addition, the emission spectra and fluorescence relaxation kinetics are rather complicated, even for free tryptophan and proteins containing a single tryptophan residue. For example, for most proteins with a single tryptophan residue multiexponential fluorescence decay is observed; for this reason we can't simply interpret the data of time-resolved fluorometry in terms of the behavior of individual residues in multitryptophan proteins. A detailed review of data on amino acids and proteins fluorescence can be found, for example, in Ref. [26].

30.3.2 Nonlinear Laser Fluorometry of Tryptophan

As already noted, many proteins fluoresce in the near UV region due to the presence of tryptophan, tyrosine, and phenylalanine residues (aromatic amino acid residues) [26]. Because the parameters of fluorescence spectra (position, shape, intensity, etc.) of aromatic amino acids (fluorophores) characterize their interaction with the environment, they can be used to obtain information about the properties of protein molecules. To obtain more complete information, it is also important to know the molecular photophysical parameters of fluorophores such as absorption cross sections, singlet-triplet conversion constants, and so on. Of special importance is studying the nature of fluorescence of tryptophan molecules because this fluorescence dominates in the so-called intrinsic fluorescence of proteins [26].

Although the fluorescence of tryptophan in solutions and proteins has been investigated in many papers (see review in Ref. [26]), the nature of the fluorescence band of this amino acid cannot be considered explained so far. The determination of the entire set of photophysical parameters of a tryptophan molecule and their dependence on the environment factors is promising for the development of the method of fluorescence diagnostics of proteins.

In Ref. [27] the results of measuring the molecular photophysical parameters of tryptophan in aqueous solution by the method of nanosecond laser fluorometry based on the simultaneous recording (by using one laser spectrometer) of the kinetic and fluorescence saturation curves are presented. The solution of L-tryptophan (Ajinomoto, Japan) in mQ water (MilliPor, USA) was studied. Absorption spectra were recorded at the tryptophan concentration of 1.3×10^{-4} M; fluorescence spectra and fluorescence saturation curves were obtained at the tryptophan concentration of 2×10^{-9} M. All the experiments were carried out at temperature 25 °C ± 1 °C.

Excitation of tryptophan molecules by UV radiation can induce a number of photophysical processes and photochemical reactions involving the excited state. Although the photophysical parameters of tryptophan molecules have been studied in many papers, the mechanisms of their phototransformations have not been completely established. The values of photophysical parameters corresponding to these processes reported in the literature differ considerably [28–33] (see Table 30.1 below).

The following deactivation mechanisms of the first excited singlet state can be distinguished, which affect the fluorescence response of a low-concentration tryptophan solution excited by nanosecond laser pulses:

1. Radiative and nonradiative transitions to the ground state
2. Singlet-triplet conversion
3. Spontaneous ionization
4. Photoionization. This process was not considered in detail anywhere; it was also pointed out that it occurs and ionization products are similar to products formed upon one-step ionization [28–30]. This process, as with process 3, is reversible, with recombination times at the micro-to-millisecond scale [29].

Table 30.1 Photophysical parameters of tryptophan molecules in an aqueous solution.

Parameter	Values	
	NLF-based method [27]	Other (linear) methods
τ_3, ns	2.8 ± 1	3.13 (amplitude $= 0.93$), 0.53 [28]
σ, 10^{-17} cm^2	1.6 ± 0.3	1.9 [28]
$\eta_T + \eta_i$	0.17 ± 0.5	$\eta_T = 0.12$ [28]; $\eta_i = 0.25$ [29]; $\eta_i = 0.08$ [28, 30]
$K_{32} + K_{3i}$, 10^7 c^{-1}	6 ± 2	
$(\sigma_{3i} + \sigma_{ph})$, 10^{-18} cm^2	2.2 ± 0.7	

5. Formation of a non-recoverable photoproduct. The existence of such an irreversible mechanism is pointed out in [28]; however, like process 4, it has not been quantitatively studied. It seems that this process, as process 4, is caused by the absorption of a photon by a tryptophan molecule in the first excited singlet state (and, hence, is a two-step process as a whole). This is confirmed by the fact that the dependence of the product formation rate on the radiation intensity deviates from a linear dependence (inset in Fig. 30.5a), and the product formation is manifested in a gradual decrease in the fluorescence intensity (during UV irradiation) and optical density in the first and second singlet absorption bands of a sample (Fig. 30.5).

The two-step processes 4 and 5 are poorly studied since the experimental measurement of the quantum yield of ions and a photoproduct in the case of a two-photon reaction involves considerable difficulties because it is necessary to know the concentration of excited molecules absorbing the second photon and also their extinction coefficient at the excitation wavelength. Thus, it is difficult to describe these processes quantitatively within the framework of traditional classical approaches. The authors of most papers (e.g., on flash photolysis [29, 30]) deliberately selected the energy parameters of setups to minimize the contributions of two-step processes (specially specifying this fact) to the quantitative characteristics being determined. When molecular photophysical parameters are measured by the method of nonlinear fluorometry upon excitation by high-power radiation, processes 4 and 5 can make a noticeable contribution to the fluorescence response, and therefore their neglect can lead to errors in the measurements of other parameters. Moreover, the consideration of these processes in the method of nonlinear fluorometry allows one to obtain their quantitative parameters.

In the laser fluorometer used in Refs. [13–15, 27], fluorescence was excited by 10-ns, 0.7-mJ, 266-nm fourth-harmonic pulses from a Nd:YAG laser with a pulse repetition rate of 10 Hz. Fluorescence was recorded with an optical multichannel analyzer consisting of a polychromator and a multichannel camera (DeltaTech, Moscow State University Scientific Park), which gave a two-dimensional optical image in the plane of the polychromator exit slit. The camera was coupled with a PC equipped with the software allowing operation both in the continuous (nonlinear fluorometry) and gated (kinetic fluorometry) regimes. The gate duration was 10 ns, the delay time step was 2.5 ns. The fluorescence intensity was measured
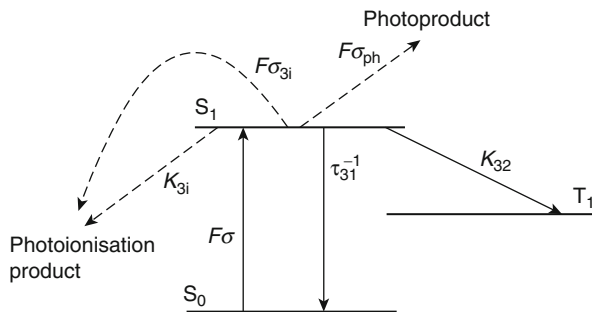
Fig. 30.6 Energy level diagram of a polyatomic organic molecule, corresponding to the system of kinetic (balance) (30.13). The arrows indicate processes considered above ($F\sigma$ is the probability of photon absorption from the S_0 state; $\tau_{31}{}^{-1}$ is the total rate of radiative and nonradiative transitions from the excited S_1 single t state to the S_0 ground state; K_{32} and K_{3i} are the rate constants of singlet-singlet conversion and spontaneous ionization, respectively; $F\sigma_{3i}$ and $F\sigma_{ph}$ are the probabilities of induced photoionization and product formation, respectively)

by varying the laser photon flux density F from 2×10^{24} to 5×10^{25} cm^{2}s^{-1}. For a fixed value of F (and a fixed delay time in the case of kinetic measurements [21]), the fluorescence signal was obtained by averaging over 100 pulses. The dynamics of photoproduct formation was studied by the methods of absorption and fluorescence spectroscopy by using a tryptophan solution of volume 3 mL. Nonlinear and kinetic fluorometry was performed by using a continuous-flow system to exclude the photoproduct accumulation. Absorption spectra were recorded with a Lambda 25 PerkinElmer spectrophotometer.

The model of a fluorescence response, which is used in the methods of nonlinear and kinetic fluorometry and takes into account processes pointed out above, is described by the system of kinetic equations for populations of the energy states of a polyatomic organic molecule (Fig. 30.6), where, in comparison with models from Sect. 30.4, photophysical processes involving the excited state are taken into account:

$$
\begin{cases}
\dfrac{\partial n_3(t,\vec{r})}{\partial t} = F(t,\vec{r})\sigma \cdot n_1(t,\vec{r}) - \dfrac{n_3(t,\vec{r})}{\tau_{31}} - (K_{32} + K_{3i})n_3(t,\vec{r}) - \\
\quad - F(t,\vec{r})(\sigma_{3i} + \sigma_{ph})n_3(t,\vec{r}) \\
\dfrac{\partial n_2(t,\vec{r})}{\partial t} = K_{32}n_3(t,\vec{r}) \\
\dfrac{\partial n_i(t,\vec{r})}{\partial t} = K_{3i}n_3(t,\vec{r}) + F(t,\vec{r})\sigma_{3i}n_3(t,\vec{r}) \\
\dfrac{\partial n_{ph}(t,\vec{r})}{\partial t} = F(t,\vec{r})\sigma_{ph}n_3(t,\vec{r}) \\
n_0 = n_1 + n_2 + n_3 + n_i + n_{ph}
\end{cases}
\tag{30.14}
$$

where n_0 is the sum of concentrations of initial polyatomic molecules and their photoproducts; n_3, n_2, and n_1 are concentrations of molecules in the first excited S_1

singlet (level 3), the first excited T_1 triplet (level 2), and the S_0 ground (level 1) states, respectively; n_i is the total concentration of reversibly ionized and photoionized molecules; n_{ph} is the concentration of reversibly photoionized and irreversibly photodegraded molecules; $F(t, r)$ is the photon flux density of exciting radiation at the instant t at the point with coordinate $r = \{x, y\}$ in the plane perpendicular to the laser beam direction (the dependence of parameters on the coordinate z along the beam direction is neglected, i.e., the optically thin layer approximation is used); σ is the absorption cross section of the fluorophore; $\tau_{31} = 1/(K_{31} + K'_{31})$, where K_{31} and K'_{31} are the rate constants of radiative and nonradiative transitions from the excited S_1 singlet state to the S_0 ground state (level 1); K_{32} is the rate constant of singlet-triplet conversion; K_{3i} is the rate constant of spontaneous ionization from the S_1 state; σ_{3i} and σ_{ph} are the cross sections for photoionization and photodegradation of molecules from the S_1 state induced by irradiation.

The total lifetime of a molecule in the S_1 state (fluorescence decay time) in this model is described by the expression

$$\tau_3^{-1} \equiv K_3 = \tau_{31}^{-1} + K_{32} + K_{3i} + F \cdot (\sigma_{3i} + \sigma_{ph}), \qquad (30.15)$$

which at low excitation intensities (when the absorption of radiation by molecules in the S_1 state can be neglected) has the form

$$\tau_3^{-1} \equiv K_3 = \tau_{31}^{-1} + K_{32} + K_{3i}. \qquad (30.16)$$

The lifetimes of the $T_1 \rightarrow S_0$ transition and recombination of ions can lie in the micro- and millisecond ranges, which greatly exceeds the laser pulse duration but is smaller than the time between laser pulses (0.1 s). This allows us to neglect these processes in the system, described by (30.15) [28–30].

Knowing variations in molecular concentrations $n_3(t, r)$, we can calculate the number N_{fl} of fluorescence photons emitted upon excitation by a laser pulse. For an axially symmetric beam, N_{fl} is determined with (30.8).

The fluorescence saturation in the model under study is caused by a finite $S_1 \rightarrow S_0$ fluorescence decay time, the singlet-triplet conversion, mechanisms of ionization and photoionization and the formation of a photoproduct. The method of nonlinear fluorometry involves the measurement (by solving the inverse problem) of molecular photophysical parameters of organic compounds from the saturation curve $N_{fl}(F)$. It is convenient to normalize the number N_{fl} of detected fluorescence photons to the reference signal N_{ref}, which can be a Raman scattering line of water (or other solvent).

In principle, all photophysical parameters of the model, described by (30.14), can be determined from the fluorescence saturation curve. However, the practical stability of the solution of the corresponding inverse problem allows one, at present, to determine no more than three parameters [10, 11]. Therefore, along with the measurement of the saturation curve, we recorded the fluorescence kinetics by using the same laser spectrometer.

The lifetime τ_3 found from the kinetic curve $N_{fl}(t_{del})$ recorded at low-intensity laser pulses ($F < 10^{23}$ cm^{2}s^{-1}) was a fixed parameter in the model describing the saturation curve. The combined use of kinetic and nonlinear fluorometry allows us to solve the four-parameter inverse problem with a sufficient practical stability. However, as follows from (30.16), by using the method of kinetic fluorometry, two parameters, $\alpha_3^{-1} = \tau_{31}^{-1} + K_{32} + K_{3i}$ and $\beta \equiv (\sigma_{3i} + \sigma_{ph})$, can also be determined by recording several (minimum, two) kinetic curves for different values of F.

It was shown in papers [31, 32] that the fluorescence decay of the aqueous solution of tryptophan excited by picosecond laser pulses was described by two exponentials: the long-lived ($\sim$3 ns) component making a dominant contribution (85–95 %) and the short-lived ($\sim$0.5 ns) component. So far, no convincing mechanisms were proposed that would predict the nonexponential fluorescence decay of tryptophan. For this reason, and also taking into account the nanosecond duration of the exciting pulse and the nanosecond time resolution of a detector, in [27] the inverse problem of kinetic fluorometry by using a model with one excited-state lifetime $\tau_3 = (\tau_{31}^{-1} + K_{32} + K_{3i})^{-1}$ was solved.

Figure 30.7 presents one of the kinetic curves obtained in [27]. The processing of such curves by the variation method gave $\tau_3 = 2.8 \pm 1$.

Figure 30.8 shows one of the fluorescence saturation curves. The solution of the three-parametric inverse problem with the fixed parameter $\tau_3 = 2.8$ ns gave the following values of the other model parameters: $\sigma = (1.6 \pm 0.3) \times 10^{-17}$ cm^2; $\sigma_{3i} + \sigma_{ph} = (2.2 \pm 0.7) \times 10^{-18}$ cm^2; $K_{32} + K_{3i} = (6 \pm 2) \times 10^7$ s^{-1}. These values give the sum of triplet and ionization quantum yields ($\eta_T + \eta_i$) = 0.17 $\pm$ 0.5.

The parameter $\beta \equiv (\sigma_{3i} + \sigma_{ph})$ was also determined from kinetic measurements by measuring two kinetic curves for low and high values of F. For $F = 10^{23}$ cm^{-2} s^{-1}, the calculated lifetime was 2.8 $\pm$ 1 ns, while for $F = 10^{26}$ cm^{-2} s^{-1} this time was $\tau_3 = 2 \pm 1$ ns. Then, by using (30.16), $\sigma_{3i} + \sigma_{ph} = (1.2 \pm 0.4) \times 10^{-18}$ was determined, which agrees (taking the confidence interval into account) with the value obtained from the saturation curve.

Since the influence of the intersystem crossing (the rate K_{32}) and spontaneous ionization (the rate K_{3i}) on the fluorescence kinetics and saturation curves is indistinguishable, one can determine within the framework of the NLF method only the total rate of these processes. A similar situation takes place for cross sections for reversible photoionization (σ_{3i}) and formation of a stable photoproduct (σ_{ph}).

Table 30.1 compares the results obtained [27] with the use of the complex method including NLF with the data, obtained with the use of classical spectroscopy.

30.3.3 Nonlinear Laser Fluorometry of Proteins Containing One and Two Tryptophan Residues. Application of the Formalism of Localized Donor-Acceptor Pairs

Tryptophan is used as a natural "intrinsic tag" whose fluorescence can bring information about the changes in the protein molecule properties under an external action [26].

Fig. 30.7 Fluorescence kinetic curve of tryptophan excited by a 10-ns laser pulse with $F < 10^{23}$ cm^{2}s^{-1}; *squares* are experimental data, the *solid curve* is the theoretical dependence
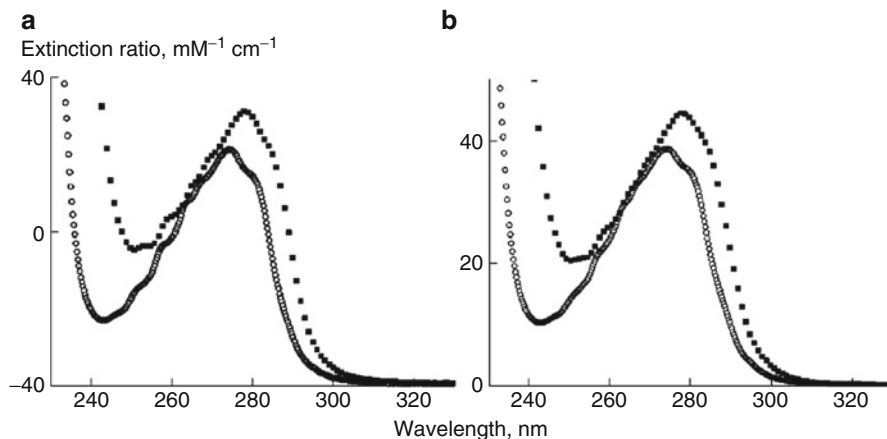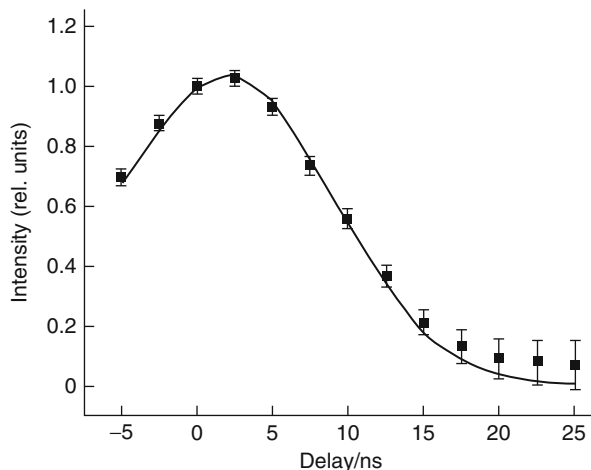
Fig. 30.8 Absorption spectra of (**a**) HSA (*squares*) and an equimolar solution of tryptophan, tyrosine, and phenylalanine (1:18:31) (*circles*) and (**b**) BSA (*squares*) and an equimolar solution of tryptophan, tyrosine, and phenylalanine (2:20:27) (*circles*)

However, information obtained using conventional methods of fluorescence spectroscopy is often insufficient for the interpretation of the structural organization of proteins and use as the descriptors of living systems. The analysis can be significantly improved by using laser methods (such as nonlinear, kinetic, and, especially, "matrix" laser fluorometry), which, in addition to traditional fluorescent parameters describing the shape and position of fluorescence bands, allows one to determine the molecular photophysical parameters of fluorophores (such as the lifetime, absorption cross section, rate of energy transfer, etc.) under a lack of a priori information necessary for conventional methods (see Sect. 30.2). These parameters can be used as diagnostic identifiers.

In Ref. [13], an approach based on the use of the nonlinear laser fluorometry method that allows one to determine in the experiment the individual photophysical parameters of fluorophores in single-tryptophan-containing (using the example of human serum albumin) and two-tryptophan-containing (using the example of bovine serum albumin) proteins is suggested and developed. The latter can exhibit the excitation energy transfer between tryptophan residues within one protein macromolecule (intramolecular energy transfer); therefore, the solution of this protein is an example of an ensemble of localized donor–acceptor pairs. Individual photophysical parameters of the mentioned proteins have been determined for the first time. The values of the photophysical parameters received for concrete objects (albumins) can be used for the diagnostics of biological systems containing these proteins.

Serum albumins are globular proteins accomplishing the transport function in blood plasma. The structure and biological functions of albumins can be found in Ref. [34]. Tryptophan, tyrosine, and phenylalanine (with relative contents of 1:18:31 in HSA and 2:20:27 in BSA [34]) are the absorption groups (chromophores) in proteins, including albumins. The tyrosine fluorescence in HSA and BSA (as in many other natural proteins) is quenched due to the effect of adjacent peptide bonds, polar groups (such as CO, NH_2), and other factors [26], and phenylalanine has a low fluorescence quantum yield [26]. Therefore, the fluorescence signal in these proteins is determined mainly by tryptophan residues. As described in Ref. [34], HSA and BSA have a similar amino acid sequence and spatial structure. However, HSA contains one tryptophan residue in the protein matrix (Trp214), and BSA contains two residues (Trp212 and Trp134). Trp212 in BSA and Trp214 in HSA have a similar microenvironment and, hence, their spectral properties are similar [35]. Tryptophans of BSA are not spectrally identical due to the stronger integration of Trp212 into the protein's structure and the more hydrophobic environment of Trp212 in comparison with Trp134 [35]. The distance between tryptophans in BSA is about 3.5 nm [34]. This fact makes the intramolecular energy transfer between them using the Forster resonance energy transfer (FRET [6]) mechanism possible.

The absorption spectra of the objects under study and (for comparison) the corresponding equimolar solutions (solution of tryptophan, tyrosine, and phenylalanine at the same ratio as they are contained in protein) are shown in Fig. 30.8. It is seen that the parameters of the absorption bands of proteins do not coincide with the corresponding parameters for the equimolar solutions.

The fluorescence spectra of the proteins and the solution of the free tryptophan (the tryptophan in a water solution was investigated in Ref. [13]) are presented in Fig. 30.9. One can see that the fluorescence of the proteins is blue shifted relative to the tryptophan fluorescence (353 nm) in a buffer solution. This is due to a decrease in the tryptophan environment polarity in the proteins. The maximum of the HSA fluorescence (332 nm) is blue shifted in comparison with BSA (342 nm). Because the fluorescence spectrum of the tryptophan residues reflects the polarity of their nearest environment, and since the properties of the environments of Trp212 in BSA and Trp214 in HSA are similar [35], such a shift can be related to the fact that

Fig. 30.9 Fluorescence spectra of HSA (*circles*), BSA (*triangles*), and tryptophan (*squares*) in a phosphate buffer with a concentration of 10^{-5} M
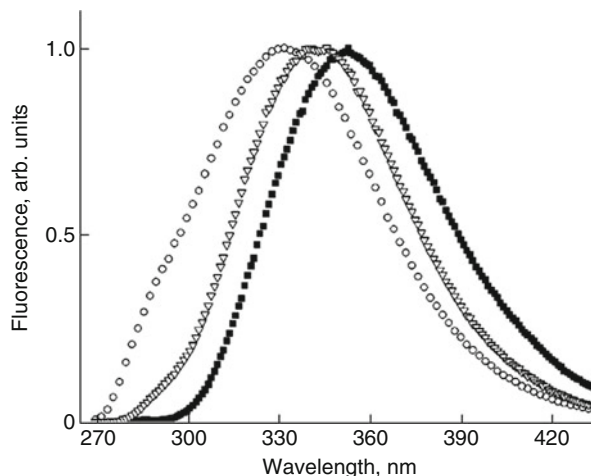
BSA contains tryptophan Trp134 located in the environment with a higher polarity (in comparison with Trp212). Thus, the total fluorescence spectrum of BSA is red shifted.

In Ref. [13], application of NLF in complex with time-resolved fluorometry to diluted solutions of HSA and BSA yielded new information about their photophysical characteristics. The results of the investigation performed are presented below.

In this work, solutions of human serum albumin (HSA) (>96 %, Sigma) and of bovine serum albumin (BSA) (>98 %, MP Biomedicals) in a phosphate buffer (0.01 M, pH 7.4) were used. The concentrations were 10^{-5} (during the measurement of the absorption spectra and the fluorescence spectra at spectrofluorometer) and 10^{-9} M (during the measurement of the fluorescence spectra, kinetic curves, and nonlinear curves at the laser fluorometer). All of the experiments were performed at a temperature of 25 °C ± 1 °C.

Fluorescence saturation curves and fluorescence kinetics were measured with the use of a spectrometer described in Sect. 30.3.2. Experimental data were processed using the models of fluorescence response given in Sect. 30.2.

The fluorescence bands at several values of photon flux density F of the exciting laser radiation are shown in Fig. 30.10. One can see that the maximum of the HSA fluorescence band does not change its position when F is changed. This is due to the fact that HSA contains one saturating fluorophore. However, the BSA fluorescence band is blue shifted (from 340 to 335 nm) when F is increased, owing to the fact that BSA contains two fluorophores in different environments (therefore, with different spectral properties), which exhibit different degrees (factors) of saturation. Taking into account the blue shift of the HSA fluorescence spectrum (in comparison with the BSA fluorescence spectrum) and the similarity of the properties of Trp214 in HSA and Trp212 in BSA, one can assume that, in the system of two tryptophans of BSA, Trp212 serves as the donor of the energy, and Trp314 is the acceptor (i.e., its fluorescence spectrum is presumably shifted towards long wavelengths).
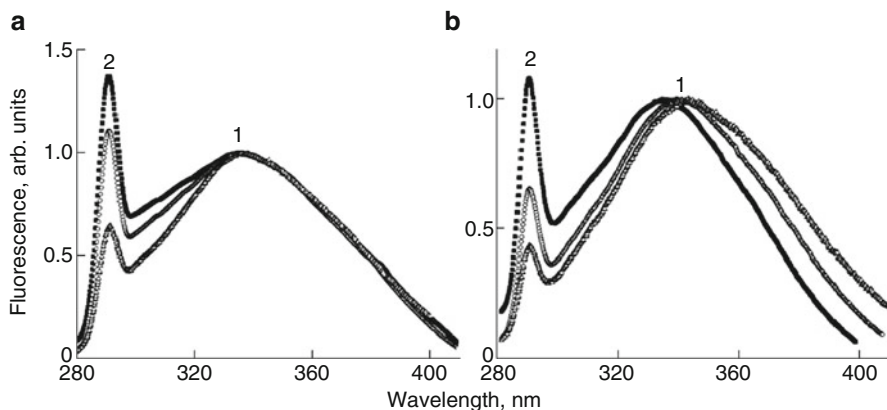
Fig. 30.10 Fluorescence bands (*1*) of proteins HSA (**a**) and BSA (**b**) and Raman scattering from water molecules (*2*) at several values of photon flux density (*F*). The band with a maximum value of F ($F = 4 \cdot 10^{25}\,\mathrm{cm}^{-2}\,\mathrm{s}^{-1}$) corresponds to the maximum value of the Raman scattering from water molecules

The kinetic curves and the fluorescence saturation curves of BSA are shown in Fig. 30.11. For BSA, the saturation curves depend on the registration wavelength in the wavelength range 310–390 nm. This is due to the fact that the BSA fluorescence band is a superposition of the bands of two tryptophans possessing different spectral properties. A similar difference in the curves for HSA is negligible.

For the determination of the photophysical parameters of HSA fluorophore, the inverse problems of nonlinear fluorometry were solved with the model, described by (30.8) and (30.9) (see Sect. 30.2). For the determination of the individual photophysical parameters of fluorophores of BSA, the inverse problems of nonlinear and kinetic fluorometry were also solved, but, in this case, the model described by (30.11) and Eqs. (30.12) and (30.13) was used; the fluorescence signal was measured at 310 nm (when the kinetic curves and the fluorescence saturation curves for the donor were constructed) and 390 nm (when similar curves were constructed for the acceptor). The resulting values of the parameters of protein fluorophores are presented in Table 30.2.

As one can see from Table 30.2, the values of photophysical parameters σ and τ_3 of Trp214 in HSA and Trp212 in BSA are similar. This result should have been expected based on a comparison of the structures of these proteins. The rates of energy transfer in BSA from excited donor to unexcited acceptor (K_{DA}) and to excited acceptor (K_{SS}) are small in comparison with the rate of intramolecular relaxation (τ_3^{-1}). This can be due to the following reasons: (A) In BSA, the tryptophan residues in the D–A pair are located at a distance that is insufficient for a noticeable energy transfer between them. According to the data on the BSA structure [34], the distance between two tryptophans in the molecule is about 3.5 nm. For comparison, the Forster radius for the energy transfer between free tryptophans ranges from 0.6 to 1.2 nm [26] (depending on the solvent). (B) Perhaps, the mutual orientation of the transition dipoles of fluorophores impedes the energy transfer [6].
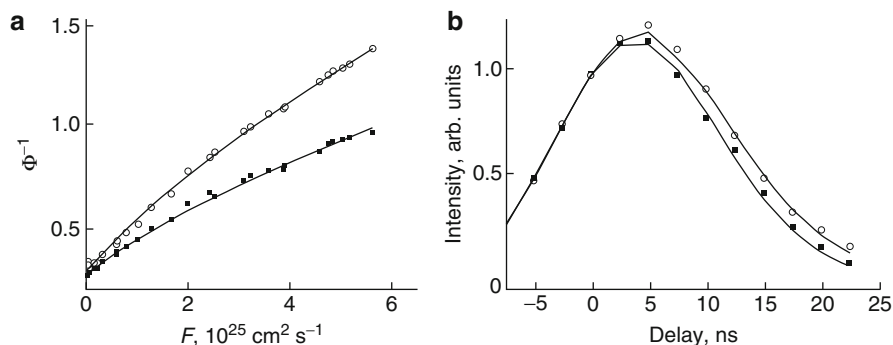
Fig. 30.11 (**a**) Saturation and (**b**) kinetic curves for BSA (registration wavelengths at 390 (*squares*) and 310 nm (*circles*)). *Lines* are plotted using model (30.11) and (Eqs. 30.12) and (30.13) for the parameters presented in the Table 30.2

Table 30.2 Photophysical parameters of fluorophores (tryptophan residues) in human serum albumin (HSA) and bovine serum albumin (BSA)

Protein	Parameters	Tryptophan residues	
HSA		Trp214	
	τ_3, ns	4.5	
	$\sigma, 10^{-17}$ cm^2	1.3	
	K_{32}, s^{-1}	$<10^7$	
BSA		Trp134	Trp212
	τ_3, ns	6.2	5
	$\sigma, 10^{-17}$ cm^2	3	1
	K_{DA}, s^{-1}	$<10^7$	
	K_{SS}, s^{-1}	$<10^7$	

It is significant that the values of the absorption cross section determined using the method of nonlinear fluorometry are true values for fluorophores and they are obtained without a priori information about the contribution of other groups into absorption at a specific wavelength and about the concentration of fluorophores. This is a unique feature of nonlinear fluorometry. In the literature (see, e.g., Ref. [36]), the absorption cross section of the tryptophan residue in protein is assumed to be equal to the absorption cross section of free tryptophan in solution, because it is supposed that this parameter is weakly dependent on the environment.

However, it is clear that such an assumption is only an estimate. A comparison of the equimolar solution and protein solution absorption spectra (Fig. 30.8) shows that these spectra do not coincide. The absorption cross section for tryptophan in solution is equal to $1.6 \cdot 10^{-17}$ cm^2 [26] (at 266 nm in an aqueous solution); now, it can be compared with the true values of the absorption cross section of tryptophan residues in native proteins (see Table 30.2), which were determined for the first time in Ref. [13].

Nonlinear fluorometry provides a unique possibility to determine one more parameter; namely, the energy transfer rate in a localized D–A pair, in which the measurement of the donors' lifetime in the absence of an acceptor (which is necessary information for the application of a traditional method [6]) is impossible. In BSA as a representative of a macromolecule with a localized donor–acceptor pair, the values of the interfluorophore energy transfer rates KDA and KSS was 1–2 orders of magnitude lower than the value of the intrafluorophore energy transfer rate; with the use of the suggested method, it became possible to give the upper estimate these values: $K_{\mathrm{DA}}, K_{\mathrm{SS}} < 10^7 \, \mathrm{s}^{-1}$.

30.3.4 Nonlinear Laser Fluorometry of Red Fluorescent Protein mRFP1

Fluorescent proteins (FP) are a special class of proteins that have a distinguishing property to form inner fluorescent (and/or absorbing), in a visible wavelength range, center (heterogroup) without involvement of any additional cofactors and ferments (autocatalytic reaction), except for molecular oxygen [37–39]. That center is called a chromophore, even in the case when it produces fluorescence, i.e., it is a fluorophore (as in FP mRFP1). The interest in FPs is determined by several factors: (a) the possibilities to use them as indicators of processes in living cells [37–39]; (b) the structure features [38, 39]; (c) the features of photophysical processes in FPs, which make it possible to use them as model systems with LDA pairs [40, 41].

According to the investigations of the mRFP1 three-dimensional structure [42], there is a tryptophan (tryptophan residue) at the distance of 15 Å from the protein chromophore, which could be a potential partner (the donor of energy) for inductive resonance energy transfer (FRET) to the protein chromophore. It is known [43–47] that the water solution of mRFP1 (and the water solutions of mRFP1 homologs) is a mixture of two or three (it depends on external factors) chemically nonidentical types of molecules (spectral forms). In the literature these forms are called the B, G, and R form of a protein and they have a difference only in chemical structure of the protein chromophore [43, 45–47]. Thereby, one can say that mRFP1 molecule contains a LDA pair and an ensemble of molecules of the protein is a multicomponent ensemble of such pairs.

It is known [43–47] that the balance between B and G forms of FP can be disturbed with a change of the solution acidity (pH indicator) or as a result of light (from the UV, blue, or green spectral range) influence on the protein. Irradiation of the protein molecules by the light from the green spectral range provokes a conversion of G-form molecules to the molecules of B form; as a result, the protein solution will represent a mixture of only two forms (the sum of two sub-ensembles of molecules containing a LDA pair), namely, B and R. An incremental change of the protein solution pH to 9 leads to nearly total transfer of the B-form molecules to the G-form ones. In [15], these procedures decreased the amount of simultaneously existing forms in the mRFP1 solution and the method of the

Fig. 30.12 The absorption (*solid curve*) and fluorescence excitation (*dotted curve*, registration wavelength is 607 nm) spectra of mRFP1. The spectra are normalized to the value of the signal intensity at 584 nm
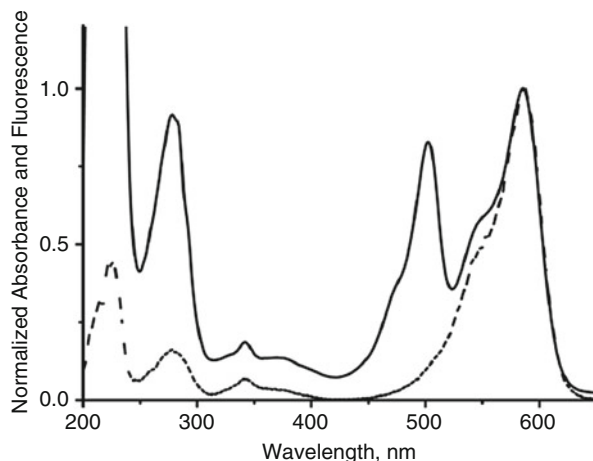
nonlinear fluorometry (combined with kinetic fluorometry) for determining photophysical parameters was used. The experimental setup is described in Sect. 30.3.2. Kinetic curves were obtained with the use of a picosecond fluorometer. Combined use of both methods allows for such a complex object as three-component solution of fluorescent protein (FP) to identify the most relevant set of photophysical parameters that describes the main features of photophysical processes in FP and can be used to diagnose its condition in the environment.

The acceptor fluorescence decay under excitation of an ensemble of donor-acceptor pairs by δ-pulse is described [48] as:

$$I_A(t) = B \times \exp\left(-t/\tau_A\right) - A \times \exp(-t/\tau_{D+A}), \tag{30.17}$$

where $B = A + [A^*]_0$, $[A^*]_0$ is the excited acceptor molecules concentration at a time point $t = 0$ (immediately after the excitation pulse is over); $A = [D^*]_0 \times K_{DA}/(1/\tau_{D+A} - 1/\tau_A)$; $[D^*]_0$ is the excited donor molecules concentration at a time point $t = 0$; $\tau_{D+A} = (1/\tau_D + K_{DA})^{-1}$ is the fluorescence lifetime of the donor in the presence of the acceptor; other designations are given above.

The excitation pulse duration and the detector instrument function's width of the spectrometer used in Ref. [15] are an order of magnitude less than the fluorescence lifetimes measured in the experiments. Therefore, after an approximation of the experimental time dependence of object fluorescence intensity by function (30.17), one can determine the lifetimes τ_A, τ_{D+A}, and the partial contributions of B and A components of the fluorescence decay curve.

As has been mentioned, the obtained preparation of the mRFP1 is a mixture of three chemically nonidentical sub-ensembles of molecules (G, B, and R forms of protein). The excitation of the protein solution by irradiation at a wavelength of 270 nm (the absorption maximum of the tryptophan in the protein [49], see Fig. 30.12) leads to appearance in the signal spectrum not only of an UV band (maximum at 330 nm), which corresponds to the tryptophan fluorescence in the
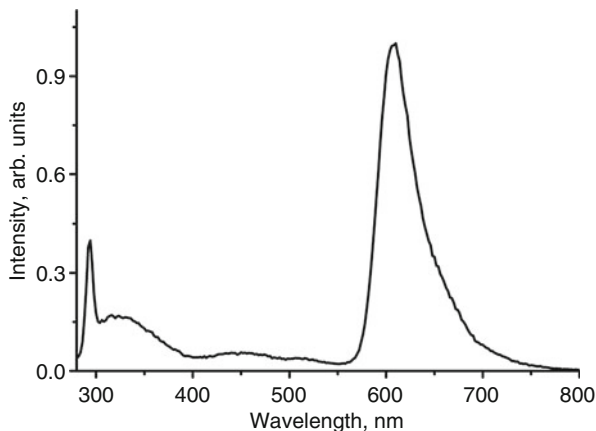
protein matrix [49], but also of a band in the visible region of wavelengths
(maximum at 607 nm) corresponding to fluorescence of the chromophore mRFP1
R form (Fig. 30.13) [50]. The chromophore of B and G forms of the protein is
nonfluorescent [50].

In principle, there are two possible mechanisms of the R-chromophore fluorescence band appearance under UV-light (the wavelength around 270 nm) excitation:
(a) direct light absorption by the chromophore; in this case the chromophore is
transferred to a higher state than the first excited singlet one, with further
nonradiative relaxation to the first excitation level; (b) the energy transfer from
tryptophan to the chromophore, through a higher than the first, excited level of the
chromophore. By using only absorption, fluorescence excitation, and emission
spectra one cannot define the contributions of these two mechanisms.

The method of nonlinear fluorometry allowed in [15] to reveal that, under
UV-light irradiation (the wavelength around 270 nm, namely, 266 nm), the
predominant mechanism of the fluorescence band (which we mentioned above) –
excitation – is the energy transfer from tryptophan. Moreover, using this method
one can obtain the value of the energy transfer rate and the values of other
significant photophysical parameters. Below we describe the procedure of resolving
this task according to Ref. [15].

The processing of the fluorescence decay curve of the mRFP1 using (30.17),
which was obtained under picosecond pulsed laser excitation (excitation wavelength is 266 nm) and registered in the range of the R-form chromophore fluorescence (other forms' chromophores are not fluorescent), allowed determination of
the lifetime values $\tau_A = 3$ ns and $\tau_{D+A} = 0.24$ ns [15].

The values of pre-exponential coefficients B and A in (30.4) were found to be
practically equal. This is indicative of the absence of the direct excitation of the
acceptor [48], therefore, in the (30.11), we can assume $\sigma_A = 0$ (under excitation at
$\lambda_{ex} = 266$ nm) and for this reason, the acceptor fluorescence (under this wavelength
excitation) is a result of the energy transfer from the tryptophan to the chromophore.

Fig. 30.14 The saturation curves of the donor (*circles*, fluorescence registration at 330 nm) and the acceptor (*squares*, fluorescence registration at 607 nm) in mRFP1 for the mixture of the R and G forms
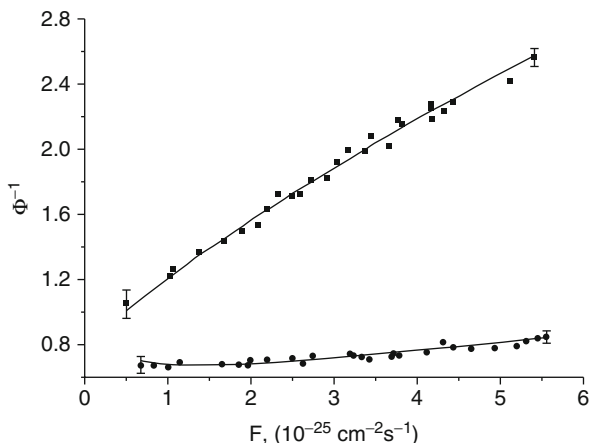
At the value of pH = 7.4, the mRFP1 solution is represented as a sum of three sub-ensembles of molecules with the LDA pair, each having its own set of photophysical parameters. It is difficult to resolve the inverse task of the nonlinear fluorometry in such a situation, because the number of unknown parameters is too large. But, as we have mentioned above, there are the techniques that allow reducing the number of simultaneously presented forms to two.

In Ref. [15] the following procedure was performed:

(a) The value of the protein solution pH was kept near 9; in this situation, the protein solution contains only protein molecules of R and G forms. After that, two saturation curves were under excitation at the wavelength of 266 nm and registration at 330 nm (the fluorescence saturation curve of the donor, which is determined by the fluorescence signal from tryptophan contained in protein molecules of the R and G forms) and at 607 nm (the fluorescence saturation curve of the acceptor, which is determined by the chromophore fluorescence signal only from the protein molecules of the R-form). Resolving the inverse task of nonlinear fluorometry, in which the fluorescence response formation is described by the model of the collective states of the LDA pair (see Sect. 30.2.5) and the values of the parameters τ_{D+A}, τ_A, $\sigma_A = 0$ for R-form of the protein are considered to be known (see above), the values of K_{DA} (for the R and G forms) and τ_A (for the G form) were determined.

The experimental dependences $\Phi^{-1}_D(F)$ and $\Phi^{-1}_A(F)$ for case (a) are presented in Fig. 30.14. In order to obtain the saturation curves $\Phi^{-1}_D(F)$ and $\Phi^{-1}_A(F)$, the first and second orders of RS valence band of water molecules (the wavelengths are 291 and 582 nm, correspondingly) were used as a reference signal; the excitation was at $\lambda_{ex} = 266$ nm.

Having performed this procedure by the use of the model of collective states of the LDA pair, the photophysical parameters (see Table 30.3) were determined. The parameters measured in Ref. [15] by the complex of methods based on the nonlinear fluorometry formed a practically complete set of the parameters that describe the photophysical processes in the molecules of three sub-ensembles of the protein mRFP1, containing a LDA pair.

Table 30.3 The values of the photophysical parameters of the LDA pairs in mRFP1 protein

Parameter[a]	R-form	B-form	G-form
$\sigma_D(\lambda_{ex} = 266)$, cm^2	$(1 \pm 0.2) \times 10^{-16}$		
$\sigma_A(\lambda_{ex} = 266)$, cm^2	0	Not defined	Not defined
K_{DA}	$(3.7 \pm 0.7) \times 10^9$	$(7.8 \pm 1) \times 10^9$	$(2.5 \pm 0.7) \times 10^9$
E	0.89	0.94	0.84
$\tau_3{}^A$, ns	3 ± 0.15	1.9 ± 0.4	1.7 ± 0.4
$\tau_3{}^D$, ns	2.1 ± 0.5		

[a]In the table:

$\sigma_D(\lambda_{ex} = 266)$ and $\sigma_A(\lambda_{ex} = 266)$ – the absorption cross section of the donor and the acceptor at the wavelength of 266 nm;

K_{DA} and $E = K_{DA}/(K_{DA} + 1/\tau_3{}^D)$ – the rate and efficiency of the energy transfer from the excited donor to the unexcited acceptor;

$\tau_3{}^D$ and $\tau_3{}^A$ – the excited state lifetimes of the donor (in the absence of the acceptor) and the acceptor

As the result, it is important to point out that:

(a) The nonlinear fluorometry method makes it possible to determine the true (not distorted by the effect of other sources of light attenuation at a given wavelength) absorption cross section of a fluorescent molecule in the absence of information on the molecule concentration (which is necessary in the traditional methods of absorption spectroscopy). It is interesting to compare the value obtained for tryptophan in the FP mRFP1 with the values of this parameter for tryptophan in an aqueous solution ($\sigma_{266} = 1.6 \times 10^{-17}$ cm^2 [27]), human serum albumin ($\sigma_{266} = 1.3 \times 10^{-17}$ cm^2 [13]), and bovine serum albumin ($\sigma^D{}_{266} = 1 \times 10^{-17}$ cm^2 and $\sigma^A{}_{266} = 3 \times 10^{-17}$ cm^2 [13]).

(b) We emphasize that the lifetime of the excited state of the donor in the absence of the acceptor has been obtained without the removal of the acceptor. For FP mRFP1, this value also has been obtained first in Ref. [15]. For tryptophan in an aqueous solution, $\tau_D = 2.8$ ns [27]; for tryptophan in human serum albumin, $\tau_D = 4.5$ ns [13]; and for tryptophan in bovine serum albumin, $\tau_D = 5$ ns and $\tau_A = 6.2$ ns [13].

(c) The value τ_A for the chromophore of the R form obtained in Ref. [15] coincides within the error with the parameter obtained in Ref. [51] in the direct excitation to the absorption band of the chromophore. Simultaneously, the excited state lifetime values of the chromophores of the B and G form have been obtained (although the chromophores of these forms are nonfluorescent).

(d) The obtained results show that the high volume ($E = 0.89$) of the energy transfer efficiency from the tryptophan to the chromophores in all three forms of the protein is of special scientific and practical interest. This permits employing mRFP1 as a promising fluorescence indicator that makes use of its own inner LDA pair (an alternative is the preparation of such pairs of two proteins [46, 47]). Let us note that the application of the nonlinear fluorometry enabled us to determine this parameter on conditions that the concentration of the acceptor cannot be changed or the acceptor cannot be totally removed

(in conventional methods of the energy transfer rate measurement, this procedure is assumed [48]) without any preparative actions on the protein (in our case, for the native protein).

30.4   Conclusion

The material presented in the chapter covers the fundamentals of nonlinear fluorometry. This method is not widely used in spectroscopy of COC, although it has some unique features. Among them are the following capabilities that can be of interest for spectroscopists:

- The nonlinear fluorometry method makes it possible to determine the true (not distorted by the effect of other sources of light attenuation at a given wavelength) absorption cross section of a fluorescent molecule in the absence of information on the molecule concentration (which is necessary in the traditional methods of absorption spectroscopy).
- The lifetime of the excited state of the donor in the absence of the acceptor has been obtained without the removal of the acceptor.

These possibilities have been illustrated by the example of proteins (including fluorescent proteins) that attract attention as potential fluorescent tags and indicators of state of the cells, where they can be introduced using gene expression. An approach based on NLF that allows one to determine photophysical parameters of fluorophores within a single protein macromolecule has been developed. In the case of red fluorescent protein mRFP1, these fluorophores are a pair consisting of tryptophan residue and the chromophore that fluoresces in the visible area of spectrum.

The approach uses the formalism of the collective states of a LDA pair and was applied to a ternary ensemble (solution) of the red FP mRFP1 for determination of its photophysical parameters. This allowed quantitative investigation of the photophysical processes in FP macromolecules.

It was shown that the basic channel of the chromophore fluorescence excitation in the R form of the protein under UV radiation at a wavelength of 266 nm is the energy transfer from the tryptophan residue. The rate values of energy transfer from the tryptophan residue to the chromophore for each of three forms coexisting in the ensemble of FP mRFP1 and the individual photophysical parameters (the absorption cross sections and excited state lifetimes) have been determined. It was shown that the tryptophan residue and chromophore in each protein form formed a LDA pair with a high efficiency of energy transfer (approximately 90 %), which makes it possible to use the FP mRFP1 as a prospective fluorescent indicator of the states of living systems. Another advantage of this indicator is the fact that the LDA pair is contained directly in the protein molecule and does not need to be constructed artificially. Thereby, using a rather complex object such as the ternary ensemble of the FP mRFP1 molecules, the abilities of the nonlinear fluorometry method (with excitation by 10 ns pulses of laser radiation) were demonstrated. A wide set of the photophysical parameters have been obtained after processing only two experimental dependences: namely, the fluorescence saturation and kinetic curves.

References

1. Y.R. Shen, *The Principles of Nonlinear Optics* (Wiley, New York, 1984)
2. W. Demtröder, *Laser Spectrocopy* (Springer, New York, 1982)
3. D.S. Kliger (ed.), *Ultrasensitive Laser Spectrocopy* (Academic, New York, 1983)
4. J.J. Laserna (ed.), *Modern Techniques in Raman Spectroscopy* (Wiley, New York, 1996)
5. D.N. Klyshko, *Photons and Nonlinear Optics* (Nauka, Moscow, 1980) [translation: Gordon and Breach, New York, 1988]
6. J.R. Lakowicz, *Principles of Fluorescence Spectroscopy*, 2nd edn. (Kluwer/Plenum, New York, 1999)
7. R.M. Measures, *Laser Remout Sensing* (Wiley, New York, 1984)
8. Q. Peng et al., Lasers in medicine. Rep. Prog. Phys. **71**(056701) (2008)
9. V.V. Fadeev, T.A. Dolenko, E.M. Filippova, V.V. Chubarov, Saturation spectroscopy as a method for determining the photophysical parameters of complicated organic compounds. Opt. Commun. **166**, 25–33 (1999)
10. S.A. Dolenko, T.A. Dolenko, V.V. Fadeev, E.M. Filippova, O.V. Kozyreva, I.G. Persiantsev, Solution of inverse problem in nonlinear laser fluorimetry of organic compounds with the use of artificial neural networks. Pattern Recogn. Image Anal. **9**(3), 510–515 (1999)
11. I.V. Boychuk, T.A. Dolenko, A.R. Sabirov, V.V. Fadeev, E.M. Filippova, Study of the uniqueness and stability of the solution of inverse problem in saturation fluorimetry. Quantum Electron. **30**(7), 611–616 (2000)
12. T.S. Gostev, V.V. Fadeev, Determination of photophysical parameters of chlorophyll a in photosynthetic organisms using the method of nonlinear laser fluorimetry. Quantum Electron. **41**(5), 414–419 (2011)
13. A.A. Banishev, E.A. Shirshin, V.V. Fadeev, Laser fluorimetry of proteins containing one and two tryptophan residues. Laser Phys. **18**(7), 861–867 (2008)
14. E.A. Shirshin, A.A. Banishev, V.V. Fadeev, Localized donor-acceptor pairs of fluorophores: determination of the energy transfer rate by nonlinear fluorimetry. JETP Lett. **89**(10), 475–478 (2009)
15. A.A. Banishev, E.A. Shirshin, V.V. Fadeev, Determination of photophysical parameters of red fluorescent protein mRFP1 under ultraviolet excitation by methods of laser fluorimetry. Appl. Opt. **49**(34), 6637–6644 (2010)
16. E.M. Filippova, V.V. Fadeev, V.V. Chubarov, S.M. Glushkov, T.A. Dolenko, Laser fluorescence spectroscopy as a method for studying humic substance. Appl. Spectrosc. Rev. **36**(1), 87–117 (2001)
17. D.V. Maslov, E.E. Ostroumov, V.V. Fadeev, Saturation fluorimetry of complex organic compounds with high local concentration of fluorophores (by the example of phytoplankton). Quantum Electron. **36**(2), 163–168 (2006)
18. V.Z. Pashenko, L.B. Rubin, Laser spectroscopy of the photosynthesis energy conversion. Sov. J. Quantum Electron. **5**(10), 2196–2205 (1978)
19. V.V. Fadeev, T.A. Dolenko, D.V. Il'in, P.N. Litvinov, A.A. Meshkantsov, Matrix method of laser fluorimetry of complex organic compounds in water. EARSeL eProc. **3**(1), 191–196 (2004)
20. V.V. Fadeev, Possibility of standardisation of normalized fluorescent parameters as a measure of organic admixtures concentration in water and atmosphere. Proc. SPIE **3821**, 458–466 (1999)
21. S.A. Dolenko, T.A. Dolenko, V.V. Fadeev, I.V. Gerdova, M. Kompitsas, Time-Resolved Fluorimetry of Two-Fluorophore Organic Systems Using Artificial Neural Networks. Opt. Commun. **213**(4), 309–324 (2002)
22. F. Lewitzka, U. Bunting, P. Karelischek, M. Niederkruger, G. Marowsky, Quantitative analysis of aromatic molecules in water by laser induced fluorescence spectroscopy and multivariate calibration techniques, in *International Conference of "Envirosense" (Europto series)*, Munich, Germany, vol. 3821 (1999), pp. 331–338

23. P. Karlischek, F. Lewitzka, U. Bunting, M. Niederkruger, G. Marowsky, Detection of aromatic pollutants in the environment by using UV-laser-induced fluorescence. Applied Physics B **67**, 497–504 (1998)
24. L. Stryer, Fluorescence energy transfer as a spectroscopic ruler. Annu. Rev. Biochem. **47**, 819–846 (1978)
25. G. Srinivas, A. Yethiraj, B. Bagchi, FRET by FET and dynamics of polymer folding. J. Phys. Chem. B **105**, 2475–2478 (2001)
26. E.A. Permyakov, *Metod sobstvennoi lyuminestsentsii belka (Method of the Intrinsic Protein Luminescence)* (Nauka, Moscow, 2003)
27. A.A. Banishev, E.A. Shirshin, V.V. Fadeev, Determination of photophysical parameters of tryptophan molecules by methods of laser fluorimetry. Quantum Electron. **38**, 77–81 (2008)
28. R.J. Robbins, G.R. Fleming, G.S. Beddard, G.W. Robinson, P.J. Thistlethwaite, G.J. Woolfe, The photophysics of aqueous tryptophan: pH and temperature effects. J. Am. Chem. Soc. **102**, 6271–6277 (1980)
29. D. Bryant, R. Santus, L.I. Grossweiner, Laser flash photolysis of aqueous tryptophan. J. Phys. Chem. **79**(25), 2711–2716 (1975)
30. R. Klein, I. Tatischeff, M. Bazin, R. Santus, Photophysics of Indole. Comparative study of quenching, solvent, and temperature effects by laser flash photolysis and fluorescence. J. Phys. Chem. **85**, 670–677 (1981)
31. P.S. Sherin, O.A. Snytnikova, Y.P. Tsentalovich, Tryptophan photoionization from prefluorescent and fluorescent state. Chem. Phys. Lett. **391**, 44–49 (2004)
32. D. Creed, The photophysics and photochemistry of the near-uv absorbing amino acids-I. Tryptophan and its simple derivatives. Photochem. Photobiol. **39**(4), 537–562 (1984)
33. B. Finstrom, F. Tfibel, L. Lindqvist, One- and two-photon ionization of aqueous tryptophan by the harmonics of the Nd laser. Chem. Phys. Lett. **71**(2), 312–316 (1981)
34. T. Peters Jr, *All About Albumin: Biochemistry, Genetics, and Medical Applications* (Academic, San Diego, 1996)
35. M. Eftink, C.A. Ghiron, Exposure of tryptophanyl residues and protein dynamics. Biochemestry **16**, 5546–5557 (1977)
36. C.N. Pace, F. Vajdos, L. Fee, G. Grimsley, T. Gray, How to measure and predict the molar absorption coefficient of a protein. Protein Sci. **4**, 2411–2423 (1995)
37. R.Y. Tsien, The green fluorescent protein. Annu. Rev. Biochem. **67**, 509–544 (1998)
38. O. Shimomura, *The Discovery of Green Fluorescent Protein* (Wiley, New York, 1998)
39. B.W. Hicks, *Green Fluorescent Protein: Applications and Protocols* (Humana Press, New Jersey, 2002)
40. B. Lounis, J. Deich, F.I. Rosell, S.G. Boxer, W.E. Moerner, Photophysics of DsRed, a red fluorescent protein, from the ensemble to the single-molecule level. J. Phys. Chem. B **105**, 5048–5054 (2001)
41. R. Steinmeyer, A. Noskov, C. Krasel, I. Weber, C. Dees, G.S. Harms, Improved fluorescent proteins for single-molecule research in molecular tracking and co-localization. J. Fluoresc. **15**, 707–721 (2005)
42. D. Yarbrough, R. Wachter, K. Kallio, M. Matz, S. Remington, Refined crystal structure of DsRed, a red fluorescent protein from coral, at 2.0-A resolution. Proc. Natl. Acad. Sci. USA **98**, 462–467 (2001). http://www.rcsb.org/pdb/explore.do?structureId=1G7K
43. V.V. Verkhusha, D.M. Chudakov, N.G. Gurskaya, S. Lukyanov, K.A. Lukyanov, Common pathway for the red chromophore formation in fluorescent proteins and chromoproteins. Chem. Biol. **11**, 845–854 (2004)
44. M. Chattoraj, B.A. King, G.U. Bublitz, S.G. Boxer, Ultra-fast excited state dynamics in green fluorescent protein: multiple states and proton transfer. Proc. Natl. Acad. Sci. USA **93**, 8362–8367 (1996)
45. A.F. Bell, D. Stoner-Ma, R.M. Wachter, P.J. Tonge, Light-driven decarboxylation of wild-type green fluorescent protein. J. Am. Chem. Soc. **125**, 6919–6926 (2003)

46. A.A. Pakhomov, N.Y. Martynova, N.G. Gurskaya, T.A. Balashova, V.I. Martynov, Photoconversion of the chromophore of a fluorescent protein from *Dendronephthya* sp. Biochem. (Moscow) **69**, 901–908 (2004)
47. S. Habuchi, M. Cotlet, T. Gensch, T. Bednarz, S. Haber-Pohlmeier, J. Rozenski, G. Dirix, J. Michiels, J. Vanderleyden, J. Heberle, F.C. Schryver, J. Hofkens, Evidence for the isomerization and decarboxylation in the photoconversion of the red fluorescent protein DsRed. J. Am. Cchem. Soc. **127**(8977–8984) (2005)
48. B. Valeur, Resonance energy transfer and its applications, in *Molecular Fluorescence. Principles and Applications*, ed. by B. Valeur. (Wiley-VCH, Weinheim, 2002), pp. 247–272. http://www.sigmaaldrich.com/catalog/product/sigma/m0566?lang=en&region=RU
49. H. Mizuno, A. Sawano, P. Eli, H. Hama, A. Miyawaki, Red fluorescent protein from discosoma as a fusion tag and a partner for fluorescence resonance energy transfer. Biochemistry **40**, 2502–2510 (2001)
50. R.E. Campbell, O. Tour, A.E. Palmer, P.A. Steinbach, G.S. Baird, D.A. Zacharias, R.Y. Tsien, A monomeric red fluorescent protein. Proc. Natl. Acad. Sci. USA **99**, 7877–7882 (2002)
51. A.A. Banishev, E.P. Vrzheshch, D.V. Dmitrienko, V.L. Drutsa, D.V. Maslov, V.Z. Pashchenko, E.A. Shirshin, P.V. Vrzheshch, V.V. Fadeev, A method for determining the individual optical characteristics of posttranslational fluorescent forms of fluorescent proteins with the use of nonlinear laser fluorimetry. Biofizika **52**, 792–798 (2007)

Triplet-Triplet Annihilation Assisted Upconversion: All-Optical Tools for Probing Physical Parameter of Soft Matter

31

Andrey A. Turshatov and Stanislav B. Baluschev

Contents

Abstract

A description of the energetically conjoined triplet-triplet annihilation upconversion (TTA-UC) process in a soft matter environment is provided. Material parameters of the organic system assuring efficient TTA and TTA-UC are discussed. TTA-UC-based stable and reproducible sensing of local temperature in thin polymer films and a water environment is suggested.

A.A. Turshatov (✉)
Max-Planck-Institute for Polymer Research, Mainz, Germany
e-mail: turshat@mpip-mainz.mpg.de

S.B. Baluschev
Max-Planck-Institute for Polymer Research, Mainz, Germany

Organic Optoelectronics Laboratory, Optics and Spectroscopy Department, Sofia University, "St. Kliment Ochridski", Sofia, Bulgaria
e-mail: balouche@phys.uni-sofia.bg

31.1 Introduction

Rapid progress in the synthesis and processing of materials has lead to a drastic reduction in sample characteristic dimensions – down to sub-micrometer length scales ($<10^{-6}$ m) and specific volume in the range of picoliters ($\sim 10^{-12}$ m^3). This development has created a demand for greater scientific understanding and technological control of the physical parameters such as temperature, thermal transport or viscosity in microscale devices, individual nanostructures, and nanostructured materials. Direct quantitative sensing of the local temperature or the local viscosity is still a considerable challenge. Even more complicated is the definition of two-dimensional (2D) spatial and/or temporal temperature profiles in ultra-thin (sub-100 nm) films and small (sub-micrometer) objects. The challenges in obtaining quantitative information about the local temperature distribution increase significantly when the thin films are included in complicated multilayer structures and/or are locally heated – a typical example of which being the process of optical addressing in memory devices, where diffraction limited spots are used.

A universal representative of sensing problems with sub-micrometer length scales is the definition of 2D-spatial and/or 2D-temporal temperature profiles of the studied sample. A bright pallet of thermal sensing techniques has been developed. The scanning thermal microscope technique (SThM) [1] delivers quantitative data for lateral thermal distribution with ultra-high spatial resolution. Despite rapid progress made in the field of SThM, some severe problems remain [2], namely, the role of near-field radiation in tip-sample heat transfer, especially in a vacuum environment; the propagation of phonons and electrons through a point contact that is on the order of their wavelength; and the dependence of the tip-sample thermal resistance on surface topography. As a consequence, a topography-related artifact [2] in thermal images remains a problem. The time-domain thermo-reflectance method (TDTR) [3] has a high temporal sensitivity, but it is inherently limited only to metallic samples, or samples that can be coated with a thin metal film. Direct imaging with infrared cameras [4] has a natural limitation of the spatial resolution (until about 1.1 μm used in confocal geometry) caused by the wavelengths used from the infrared region.

Further experimental complications are created if the microscale device is included in a life-science sample of interest. In addition to the problem of scaling down the sensing techniques, the necessity of non-contact measurement tools becomes imperative. The application of all-optical sensing tools in the field of life science has additional complications in terms of spectral mismatch: there are strongly contradictive requirements for the wavelength of the excitation light and, as a consequence of the tissue transparency properties, only wavelengths higher than $\lambda \approx 700$ nm are well transmitted, whereas only photons with enough high energy, namely $\lambda << 700$ nm, can initiate biochemical processes and serve as a sensing tool.

31.1.1 Material Parameters of the One-Component Organic System Assuring Efficient Triplet-Triplet Annihilation (TTA)

Metallated macrocycles (MM) such as porphyrins and phthalocyanines are known as efficient phosphorescent emitters [5, 6]. The dependence of the integral phosphorescence emission or the decay time of the phosphorescence is widely used as a thermal or oxygen sensor [7, 8]. The sensing process includes optical excitation of the MM molecule and registration of the decreased phosphorescence or phosphorescence decay time as a function of the increased sample temperature or oxygen content [9, 10].

The main experimental drawback of this sensing technique is that the phosphorescence emission is an integral parameter, depending on the series of experimental parameters, many of them difficult to control, including local changes in molecular concentration, local variation of the sensing layer thickness, and instability of the probing laser intensity. All these experimental parameters are interconnected through their dependence on the excitation light intensity. A powerful solution to this problem demonstrates the use of the process of TTA: instead a single material response on the acting parameter (temperature), a ratiometric material response is obtained, ensuring *inherent* and *instantaneous* compensation for the local changes of the sample parameters.

In the following, the TTA–sensing procedure will be elucidated using the example of palladium octaethyl porphyrin (PdOEP), the structure of which is shown in the inset of Fig. 31.1. It is important to note that all experimental results can be transferred to the other MM with different extension of the π-conjugated system by annelated aromatic rings and, consequently, with different excitation and emission spectra.

In Fig. 31.2, a Jablonski diagram is shown for the molecule of PdTBP together with the energetic schema of the process of TTA. Both singlet bands, Soret- and Q-band, have a common response on optical excitation.

The absorption of a photon into the Soret-band is followed by fast relaxation (on the order of 200–1,000 ps), depending on the structure of the macromolecule and the type of central atom [5, 6], and emission-less relaxation to the bottom of the S_1 band:

$$S_0 + h v_1 \rightarrow S_2^* \xrightarrow{\text{fast}} S_1. \tag{31.1}$$
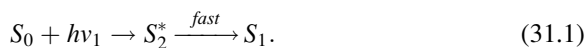
Similarly, the absorption of a photon into the Q-band is followed by fast relaxation to the bottom of the S_1 band:

$$S_0 + h v_2 \rightarrow S_1^* \xrightarrow{\text{fast}} S_1 \tag{31.2}$$
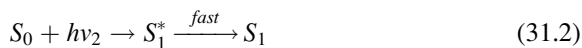
Two competing processes lead to depopulation of the S_1–singlet state. The first represents the prompt fluorescence:

$$S_1 \xrightarrow{F} S_0 + h v_3 \tag{31.3}$$

Fig. 31.1 Normalized
absorption spectrum (*left*) and
normalized luminescence
spectrum (*right*) of PdOEP. In
order to represent the
fluorescence ($\lambda_{max} = 550$ nm)
and the phosphorescence
($\lambda_{max} = 662$ nm) with
comparable intensity, for the
wavelength higher than
600 nm, additional signal
attenuation (more than 50
times) is introduced. *Inset:*
Structure of the sensitizer –
(2,7,8,12,13,17,18-octaethyl-
porphyrinato)Pd(II) (PdOEP)
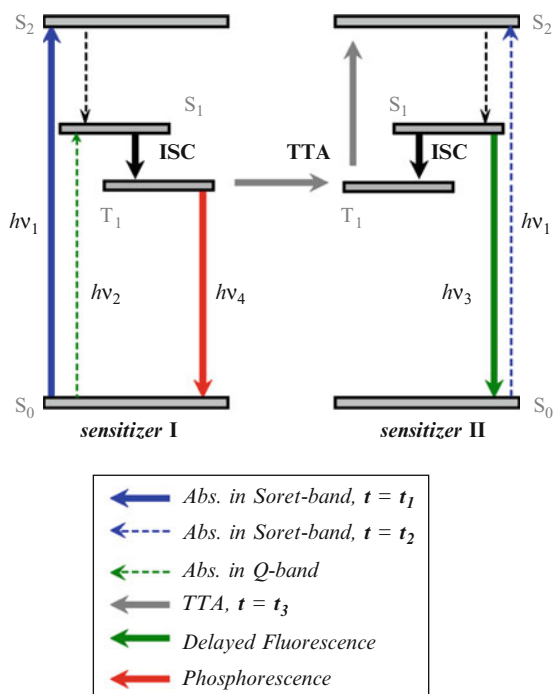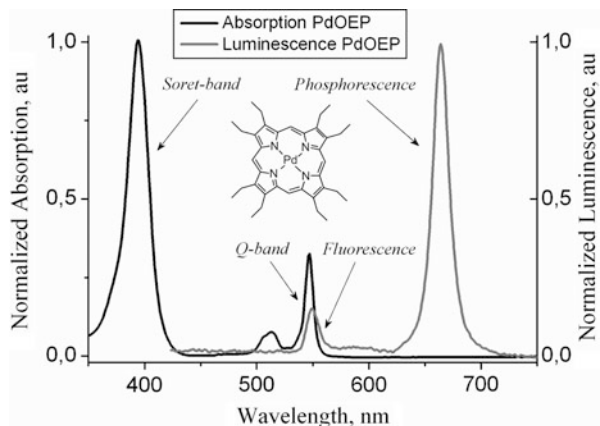
Fig. 31.2 Energetic schema
of the process of TTA in
metallated macrocycles

The probability for emissive depopulation of the S_1–porphyrin singlet state is
very low; therefore porphyrin fluorescence is rarely reported. At higher tempera-
tures, – on order of 300 °C, the S_1 fluorescence becomes stronger and so-called
"hot-band emission" [6] is observed.

The second relaxation process is the inter-system crossing (ISC), which is
strongly enhanced by the spin-orbit coupling to the metal center of the MM

sensitizer molecules [11, 12]. The efficient ISC within the sensitizer molecules (for instance, the ISC-probability is almost 1 for metallated porphyrins [6]) ensures an efficient population of the sensitizer triplet level via single photon absorption:

$$S_1 \xrightarrow{ISC} T_1. \tag{31.4}$$

The probability of ISC at the molecules of the MM is high and depends strongly on the mass of the central metal ion [5, 6]. In the case of heavy metals, the yield of the ISC approaches 0.95–0.995 and the metastable triplet state is populated. The sensitizer triplet states, with their relatively long lifetimes (which exceed several tens of microseconds in the case of the MM in this work)s serve as an energy reservoir. The depopulation channels for these triplet states include radiative decay (phosphorescence) and nonradiative energy dissipation. The MM are known [6] as very efficient phosphorescent emitters. For instance, the phosphorescence quantum yield of PdOEP in toluene solution (1×10^{-6} M) is 0.5. At small molecular concentrations ($\sim 1 \times 10^{-6}$ M), the interactions between the exited triplet states can be neglected.

When the molar concentration of the optically active molecules is increased up to 1×10^{-4} to 1×10^{-3} M, the interaction between the molecules of the MM cannot be neglected. The probability of the process of TTA grows remarkably and, at specific experimental conditions, could become the main relaxation mechanism. Schematically, the process of TTA is shown in Fig. 31.2. Note that the population of the triplet states participating at the process of TTA can be completed in independent time intervals:

$$S_0 + hv_1 \rightarrow S_2 \xrightarrow{fast} S_1 \xrightarrow{ISC} T^{(1)}{}_1, \quad t = t_1 \tag{31.5}$$

$$S_0 + hv_1 \rightarrow S_2 \xrightarrow{fast} S_1 \xrightarrow{ISC} T^{(2)}{}_1, \quad t = t_2 \tag{31.6}$$
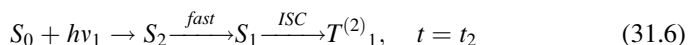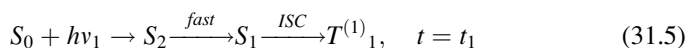
where the upper index $^{(i)}$ represents the triplet states created at the moments $t = t_i$, $i = 1, 2$ correspondingly.

As a consequence of the TTA process, one of the excited MM molecules returns to the ground state S_0, but the other MM molecule is excited to the higher lying singlet state S_2. After fast intramolecular relaxation, the S_1 singlet state is again populated. Furthermore, this singlet state can participate in one of the competing relaxation processes described earlier, namely emitting fluorescent photons or performing ISC to the metastable triplet state. The process of TTA and the following relaxation can be described as:

$$T_1^{(1)} + T_1^{(2)} \xrightarrow{TTA} S_0 + S_2 \xrightarrow{fast} S_0 + S_1 \Rightarrow \begin{cases} \xrightarrow{DF} 2 \times S_0 + hv_3, & t = t_3 \\ \text{or} \\ \xrightarrow{ISC} S_0 + T^{(3)}{}_1, & t = t_4 \end{cases} \tag{31.7}$$
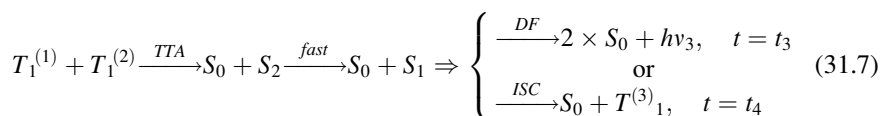
It is important to note that the emitted photon hv_3 belongs to the particular fluorescent spectrum (delayed fluorescence (DF)) of the studied molecule, but it will be emitted at the moment $t = t_4$, much longer after cancelation of the optical excitation pulse. Practically, the moment t_3 is 2–3 orders of magnitude longer than the specific lifetime of the prompt fluorescence.

Furthermore, the triplet state $T^{(i)}_1$ can participate in one of the competing processes – phosphorescence:

$$T^{(i)}_1 \xrightarrow{Ph} S_0 + hv_4, \quad i = 1, 2, 3 \qquad (31.8)$$
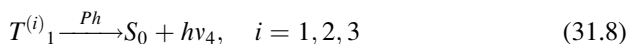
or again in the process of TTA, but now interacting with a third molecule in the excited triplet state.

As an outcome of the processes, described by (31.3)–(31.8), delayed fluorescence (31.7) is added to the trivial relaxation channels of the optical excitation (hv_1 or hv_2) including phosphorescence (31.8) and prompt fluorescence (31.3), the particular intensity of which is predetermined by the efficiency of the TTA process. The energy of the delayed fluorescence photons results from the excitation energy stored at the triplet ensemble. Therefore, emission of delayed fluorescence photons leads to a remarkable decrease of the emitted phosphorescent photons and will change significantly the temporal characteristics of the residual phosphorescence.

Though the process of TTA is a diffusion-controlled process, and the efficiency of the TTA will depend on material parameters of the system such as molar concentration of the MM, physical parameters of a matrix, intensity of excitation, and temperature of the sample. These dependencies can be successfully used as sensing tools because of TTA ratiometric response.

31.1.2 Material Parameters of the Two-Component Organic System Assuring Efficient Triplet-Triplet Annihilation Upconversion (TTA-UC)

The process of TTA-UC incorporates a chain of mutually complementary processes: ISC, triplet-triplet transfer (TTT), TTA, and consequent emitter fluorescence [13–15]. The energetic schema of the process of TTA–UC in a two-component molecular system is shown in Fig. 31.3.

The first process in the chain is the ISC, which is strongly enhanced by the spin-orbit coupling to the metal center of the MM sensitizer molecules. The efficient ISC within the sensitizer molecules ensures an efficient population of the sensitizer triplet level via single photon absorption.

On the other hand, the weak ISC of the emitter molecules (its probability for various aromatic hydrocarbon derivatives has vanishing values [6]) substantially prohibits the depopulation of the excited emitter triplet states via phosphorescence and thus stores the created triplet population of the emitter for the process of TTA.

Fig. 31.3 Energetic schema of the process of a TTA–UC two-component organic system
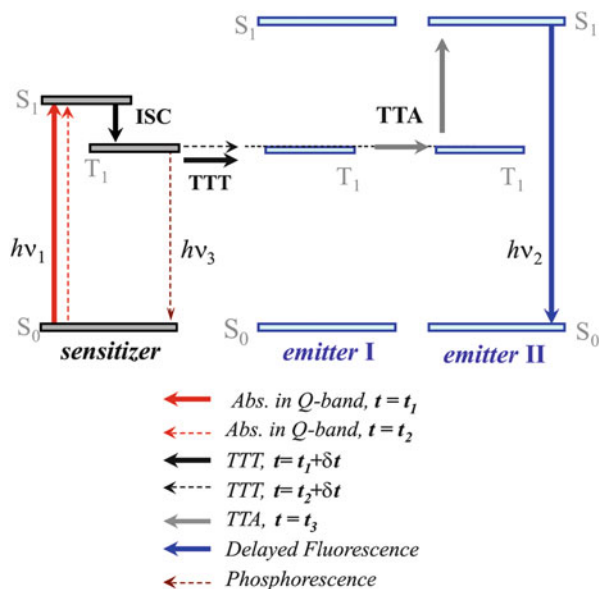
Therefore, the first requirement of the molecular system is that a large difference between the ISC coefficients of the sensitizer and emitter molecules must exist:

$$c_{ISC}^{s} \gg c_{ISC}^{e} \tag{31.9}$$

where the upper indexes ^{s} and ^{e} represent the sensitizer or emitter energy state, respectively.

The second process in the chain of TTA-UC is the transfer of the excitation of the sensitizer triplet to the emitter triplet: TTT [16]. Those processes can be expressed through the equation:

$$S_0 + h\nu_1 \to S_1^s \xrightarrow{ISC} T_1^{s(1)} \xrightarrow{TTT} T_1^{e(1)}, \quad t = t_1 + \delta t. \tag{31.10}$$

$$S_0 + h\nu_1 \to S_1^s \xrightarrow{ISC} T_1^{s(2)} \xrightarrow{TTT} T_1^{e(2)}, \quad t = t_2 + \delta t \tag{31.11}$$
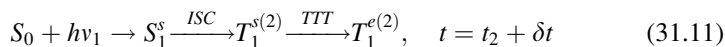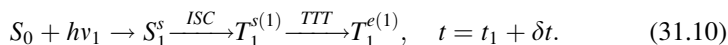
where the upper index $^{(i)}$ represents the sensitizer or emitter triplet states created at the moments $t = t_i$, $i = 1, 2$, correspondingly. The sensitizer triplet ensemble is essentially depopulated by the process of TTT [17]. Nevertheless, the sensitizer triplet state $T^{(i)}_1$ can participate in the competing depopulation process and phosphorescence of the MM:

$$T^{s(i)}_1 \xrightarrow{Ph} S_0 + h\nu_3, \quad i = 1, 2 \tag{31.12}$$
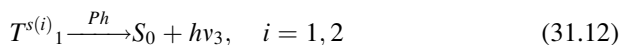
As a consequence of the effective quenching of the sensitizer triplet state, the dynamical parameters of the residual sensitizer phosphorescence such as the intensity of the integral sensitizer phosphorescence and decay time of the sensitizer phosphorescence are strongly influenced. Furthermore, their change relative the undisturbed sensitizer triplet ensemble can be used as a prompt experimental proof for the efficiency of the TTT process.

The efficiency of the TTT is determined by the extent of overlap of the sensitizer and emitter triplet manifolds, thus the second requirement [13] of the molecular system is:

$$\Delta E \longrightarrow 0 \quad in \quad E_{triplet}^s + \Delta E = E_{triplet}^e \tag{31.13}$$

Particularly if the emitter triplet energy level requires involvement of thermal energy in order to match the sensitizer triplet level (i.e., $\Delta E > 0$), this reduces the efficiency of the TTT process significantly.

The third process is the subsequent TTA [5]. In a two-component molecular system, the process of TTA happens mostly between the identical triplet states of the emitter molecules (*homo* TTA, process 31.14). As a consequence of this process, one of the emitter molecules returns to the ground state, but the other emitter molecule is excited to the higher singlet state and strongly blue-shifted emission is observed [18–20]. The *hetero* TTA (processes 16 and 17), i.e., annihilation of one emitter triplet state and one sensitizer triplet state, has significantly lower probability because the concentration of the excited sensitizer triplet states is much lower than the concentration of the excited emitter triplet states [21]. The probability of *homo* TTA (process 31.14) between the triplet states of the sensitizer is even lower.

$$T_1^e + T_1^e \xrightarrow{TTA} S_0^e + S_1^e \longrightarrow 2 \times S_0^e + h\nu_2 \tag{31.14}$$

$$T_1^s + T_1^s \xrightarrow{TTA} S_2^s + S_0^e \xrightarrow{fast} S_1^s + S_0^e \xrightarrow{ISC} T_1^s + S_0^s \tag{31.15}$$

$$T_1^s + T_1^e \xrightarrow{TTA} \begin{cases} S_0^s + S_1^e \to S_0^s + S_0^e + h\nu_2 \\ S_2^s + S_0^e \xrightarrow{fast} S_1^s + S_0^e \xrightarrow{ISC} T_1^s + S_0^e \end{cases} \tag{31.16, 31.17}$$
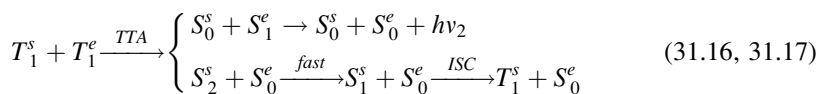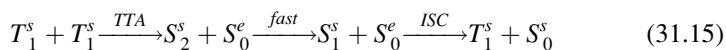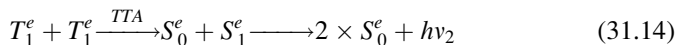
The requirement for effective TTA-UC (process 31.14) is the fulfillment of the (31.18) without the need for thermal energy:

$$\Delta E \to 0 \quad in \quad 2 \times E_{triplet}^e + \Delta E = E_{singlet}^e. \tag{31.18}$$

In other words, this requirement ensures that the sum-energy of two excited emitter triplet states is enough to populate the first excited singlet state of the emitter molecule without using thermal energy.

The last requirement is related to the structure of the absorption spectrum of the sensitizer. In order to reduce the re-absorption of the UC emission generated via

Fig. 31.4 Normalized absorption spectrum (*left*) of the sensitizer molecule (PdTBP, structure is shown in Fig. 31.6a) and the normalized fluorescence spectrum (*middle*) of the emitter molecule. *Inset:* structure of the emitter – 3,10-Bis(3,3-dimethylbut-1-ynyl) Dibenz[*de,kl*] anthracene
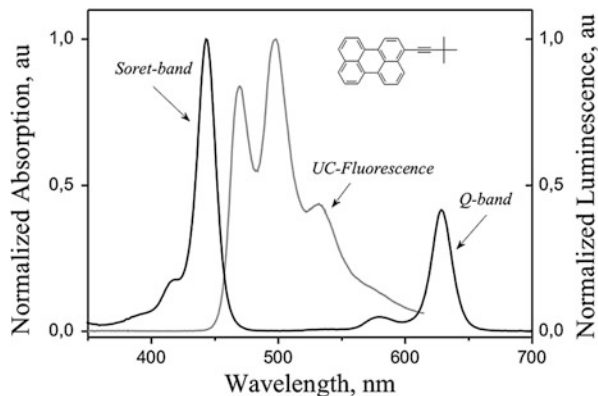
the sensitizer molecules in ground state, the so-called "transparency window" of the sensitizer molecule has to be sufficiently large. Serendipitously, MMs such as porphyrins and phthalocyanines have a band-like absorption spectrum, with only two strong bands – the Soret-band and the Q-band. Therefore, photons with energies lying far enough away from these two local absorption maxima will hardly be absorbed. For the energy positions of the absorption maxima of the sensitizer and the first excited singlet state of the emitter, the third requirement of the molecular system follows from the above:

$$E^s_{Soret-band} > E^e_{singlet} \gg E^s_{Q-band} \qquad (31.19)$$

In summary, the main outcome of these theoretically and experimentally determined requirements of multi-component organic systems is that, if the requirements specified in (31.9), (31.13), (31.18), and (31.19) are fulfilled, then it follows that it is likely that (31.10) and (31.14) will also be fulfilled, and thus efficient energetically conjoined TTA-UC will be observed. A typical sensitizer absorption spectrum and UC fluorescence spectrum are shown in Fig. 31.4.

Special attention must be drawn to the fact that all molecular energy levels involved in the process of TTA-UC are real molecular levels; consequently, no virtual energetic levels are involved. The processes of intramolecular relaxation happen on a time scale of picoseconds [6]. The characteristic time scale of the process of TTA is predetermined by the decay time of the delayed emitter fluorescence (time scale of 100 μs) and the diffusion-controlled process of triplet-triplet energy transfer (TTT) [22] (time scale of microseconds). Therefore, the processes of internal energy relaxation (i.e., thermalization of the electronic states of the molecules involved) and, consequently, their influence on the energetic schema of the process of TTA-UC cannot be neglected. As a consequence, the processes of internal energy conversion lead to a noticeable loss of excitation photon energy, therefore, the up-converted emission a priori has a frequency lower than the doubled frequency of the excitation light.

It is important to note that the observed time-dependent dynamic of the remaining sensitizer phosphorescence has a multi-exponential time behavior as a consequence of the complexity of the depopulation process. The depopulation efficiency of the sensitizer triplet state depends on experimental parameters such as concentration of the excited triplet states (which is continuously changed during the process), concentration of the emitter molecules, local temperature, and excitation intensity. Ignoring this complexity and defining the decay time as the time necessary to drop the phosphorescence signal amplitude down to 1/e level, consistent and valuable results could be obtained.

The quantum yield (η_{TTA-UC}) of the TTA-UC process is certainly of decisive importance. The studied TTA-UC process incorporates a chain of mutually complementary processes (as mentioned earlier, ISC, TTT, TTA, and consequent emitter fluorescence), all with particular efficiency (η_{ISC}, η_{TTT}, η_{TTA}, and η_{F}, respectively). The value of the TTA-UC quantum yield (independent of its particular definition [17, 23]) is an integral parameter.

$$\eta_{TTA-UC} = \eta_{ISC} \times \eta_{TTT} \times \eta_{TTA} \times \eta_F \qquad (31.20)$$

It has to be pointed out that a classical term (such as quantum yield) is attributed to a complex system like the TTA-UC process. By using such a term that is clear and noncontradictive, knowledge about the ratio of absorbed excitation photons to emitted UC-photons can be derived [17]. Any other definition (such as internal efficiency [24] or amount of participating emitter triplet states [23]) can only lead the reader to inconsistency of the real UC photon flux expected. Thus, we recommend using the term *quantum yield* in its classical meaning: the "absorption" of the UC media will be determined by the absorption of the used sensitizer, and the "emission" will be attributed to the UC fluorescence of the emitter species:

$$\eta_{TTA-UC} = N_{absorbed}^{photons} \Big/ N_{emitted}^{photons} \qquad (31.21)$$

In this context, it is important to compare UC systems with the same amount of emitter chromophores (i.e., systems with the same molar ratio sensitizer/emitter chromophores).

31.2 Sensing tools based on TTA-UC

A realistic sensing alternative in cases of nontrivial scaling-down could be the process of TTA in multi-component organic systems. The proposed process has three crucial advantages:

First, it is *inherently* a micro-scale sensing technique. The sensing function is carried out by ensembles of organic (organometallic) macromolecules. Therefore, the mass and the heat capacity of the sensor itself are comparable or significantly lower than the mass and heat capacity of the micro-scale sample.

Second, the TTA sensing function is performed in an *all-optical* regime. The mechanical contact (even in near-field meaning) is not obligatory. Furthermore, the optical intensities needed are low – at the level of Wcm^{-2}. This low excitation intensity keeps the radiation stress on the living tissue at an acceptable level.

Finally, the sensing properties and the efficiency of the process of TTA do not depend on the *coherence characteristics* of the light used. The TTA sensing function also resolves another shortcoming of the conventional methods for all-optical sensing: the necessity to excite the samples with extremely bright optical sources (e.g., lasers). Excitation sources emitting light with extremely low spectral power density (down to 125 μWnm^{-1}) can generate efficient TTA emission [13]. The sensing molecules have broad absorption spectra, in some cases even up to 80 nm (FWHM). As a consequence, optical sources with flexible chosen emission wavelengths can be used without any consequence to the TTA emission spectra or TTA efficiency.

31.2.1 Sensing of Local Temperature in Thin Polymer Films

The temperature dependence of the process of TTA between the MM dispersed in polymer matrix ("solid solution") for a broad range of temperatures will be demonstrated. This results directly in strong temperature dependence of the phosphorescence and the fluorescence emission for this class of metallated porphyrin molecules. Therefore, the ratio between the intensities of the fluorescence and the phosphorescence emission for different temperatures represents a real-time temperature probe with ratiometric response [25] for a broad temperature interval. The temperature-sensing systems, based on up-conversion processes [26], have the additional experimental advantage of relative easy optical separation between the pump and the signal wavelengths.

In Fig. 31.5, the dependence of the sample phosphorescence on the temperature is demonstrated. Indeed, there is a strong decrease in the phosphorescent signal when the sample temperature increase is known for a number of MMs [6]. Conversely, the strong (more than 8 times) increase of the sample fluorescent signal when the sample temperature also increases is rarely demonstrated.

The absolute as well as the relative values of the integral phosphorescence and integral fluorescence of certain samples are completely reproducible, at multiple increases or decreases of the sample temperature. Nevertheless, there are two important requirements for free reproducibility. First, the residual concentration of the molecular oxygen must not exceed the value of 1–3 ppm. The second is related to the matrix material: the sample temperature should not exceed the specific glass transition temperature (T_G) of the optically inactive polymer matrix.

For many bio applications it is important that the sensing light does not interact with the sample causing unwanted light-triggered processes. A typical example is generation of oxygen-dependent reactions of free-radical species during the excitation of fluorescent proteins or dye molecules with surrounding cellular components [27]. An elegant solution of this problem might be the excitation wavelength

Fig. 31.5 Dependence of the phosphorescence and the fluorescence of a thin polymer film (PS 20 kD blended with 3 % wt PdOEP) on the sample temperature. The film is prepared in a nitrogen-filled glove box with residual oxygen less than 3 ppm. Quartz substrate, the film thickness is 80 nm. Excitation laser with $\lambda = 405$ nm, laser power $= 2$ mW (stability better than 1 %), excitation spot diameter ~ 300 μm; $T_G = 98$ °C
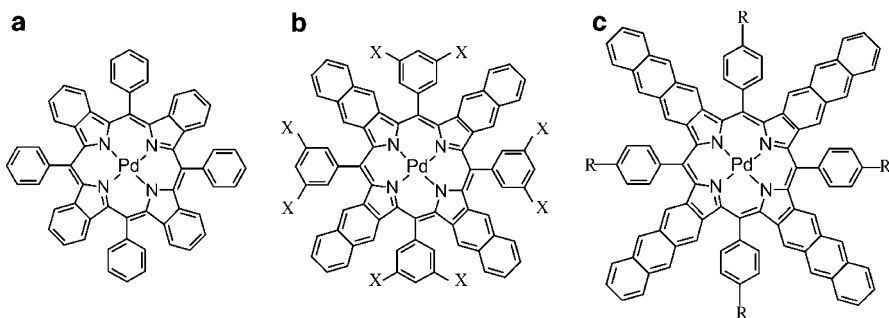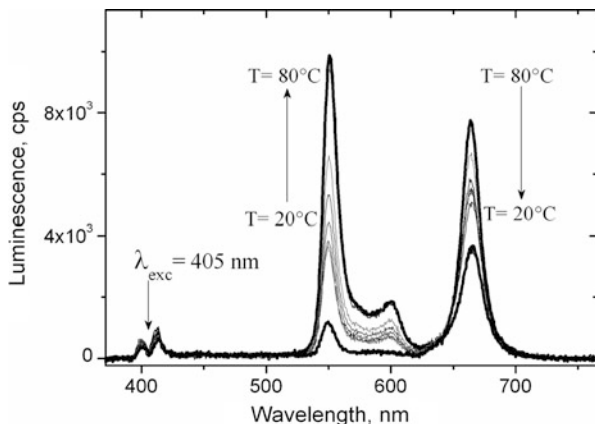
Fig. 31.6 Structures of sensing molecules: (**a**) *meso*-Tetraphenyl-tetrabenzoporphyrin Palladium (PdTBP); (**b**) *meso*-Tetraphenyl-octamethoxide-tetranaphtho[2,3]porphyrin Palladium (PdTNP), X = OMe (**c**) *tetrakis*-5,10,15,20-(*p*-Methoxycarbonylphenyl) tetraanthra[2,3-*b,g,l,q*]porphyrin (PdTAP), R = COOH

tuning of the MM used in sensing. If the probing light is adequately red-shifted, then it will be not absorbed and unwanted interactions will be avoided.

The extension of the π-conjugated system in the metallated porphyrins by annulated aromatic rings results in a noticeable red shift in the absorption and emission spectra. Porphyrins, such as tetranaphthoporphyrins [28] and tetraanthra-porphyrins [29], have expanded excitation spectra down to the IR-A region of the visible spectrum (Fig. 31.6).

The absorption spectra of the extended porphyrins are shown in Fig. 31.7. The Soret-band of the sensing molecule demonstrates less expressed red-shift of the absorption maxima, whereas the corresponding Q-bands are remarkably red-shifted.

An example of the sensing molecule PdTBP will be shown where the sensing properties do not depend in any way on the excitation wavelength used. In other

Fig. 31.7 Normalized absorption spectrum of the materials shown in Fig. 31.6, as follows, PdTBP (*black line*), PdTNP (*dark gray line*), and PdTAP (*gray line*)
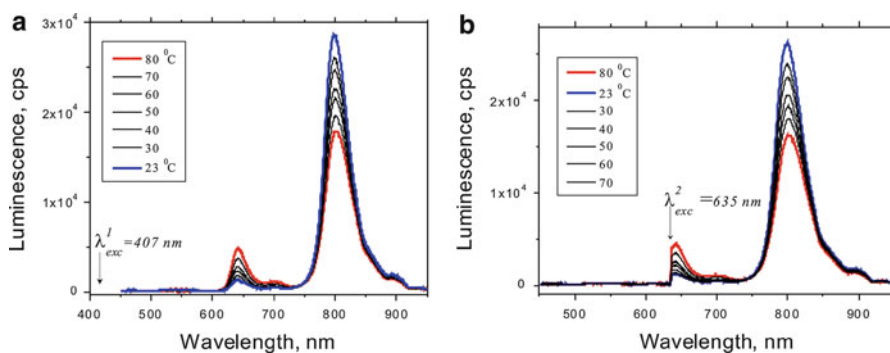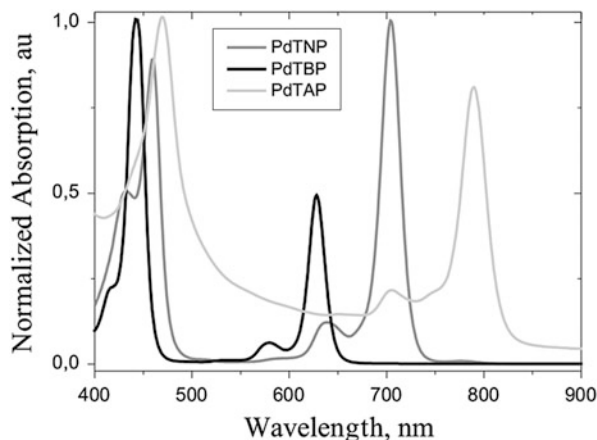
Fig. 31.8 (a) Dependence of the luminescence of a thin polymer film of PS (film thickness 80 nm) on the sample temperature. Optical excitation into the Soret-band, $\lambda = 407$ nm, cw-laser power ~ 1 mW, laser spot diameter 300 μm. Optical density of the sample at the excitation wavelength: $OD_{407} = 0.27$; (b) Dependence of the luminescence of a thin polymer film of PS on the sample temperature. Optical excitation into the Soret-band, $\lambda = 635$ nm, cw-laser power ~ 0.5 mW, laser spot diameter 300 μm. Optical density of the sample at the excitation wavelength: $OD_{635} = 0.72$

words, the temperature evaluation is not affected in which the absorption maxima of the MM is excited optically. Two samples consisting of polystyrene (PS 30 kD) thin film blended with 5 % wt PdTBP on quartz substrates were prepared in a nitrogen-filled glove box with a residual oxygen concentration of $O_2 \sim 3$ ppm (Fig. 31.8).

As shown in Fig. 31.9, the thermal evolution of the triplet ensembles of the MM molecules created via excitation in the Soret-band or Q-band is identical. As a rule of thumb, the optical excitation in the Q-band is more desirable, mainly because of the possibility to tune significantly the pump wavelength deep in the red optical region. Additionally, the energy difference between the Soret-band and Q-band is substantial, therefore the amount of excitation energy that is dissipated as heat

Fig. 31.9 Temperature
calibration curve: excitation
into the Soret-band (*filled
circles*) and into the Q-band
(*stars*)
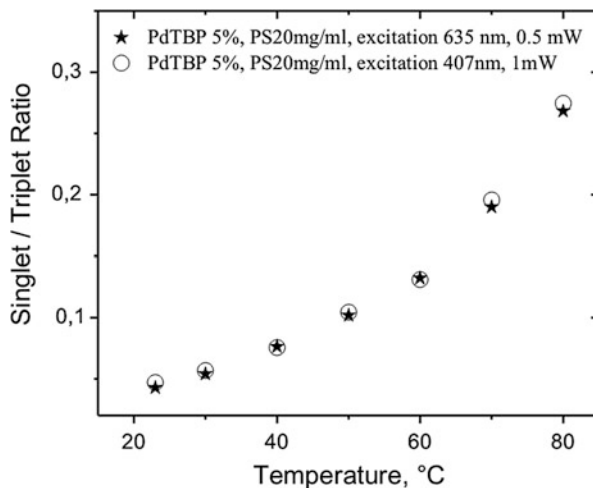
through the sample must be considered when extremely sensitive applications are
planned.

Thus far, the temperature-sensing properties of the time-integrated temperature
dependencies of MM fluorescence and MM phosphorescence have been discussed.
Another way to increase the sensitivity of the measuring process is to use the strong
dependence of the decay time of the delayed MM fluorescence and the decay time
of the MM phosphorescence as sensing tool.

In the classical description of the TTA process in organic molecular crystals [6],
it is postulated in axiomatic manner that the concentration of the singlet states
created via the process of TTA depends *only* on the concentration of the excited
triplet states:

$$[S] \sim [T] \times [T] \tag{31.22}$$

Therefore, the intensity of the DF signal depends on the quadrate of the excita-
tion intensity, $I_{DF} \sim I^2_{excitation}$, and, consequently, the decay time of the delayed
fluorescence (τ_{DF}) and the phosphorescence decay time (τ_{Phos}) are related by
$\tau_{DF} = \tau_{Phos}/2$.

As has been demonstrated in our experiments, the temporal evolution of the MM
blended in polymer films shows strong temperature dependence, not generalized by
the classical theory of the TTA process (Fig. 31.10).

Note that the signal amplitudes are not normalized in order to show how not only
the time-dependent parameters but also the integral characteristics of the signal are
changed with the temperature. The excitation pulse duration is long enough to reach
steady-state conditions of the build-up of the excited state triplet ensemble. The
repetition rate (100 Hz) ensures cross-talk-free operation; the time between the
excitation pulses is much longer than the $5\times$ decay time of the longer process.
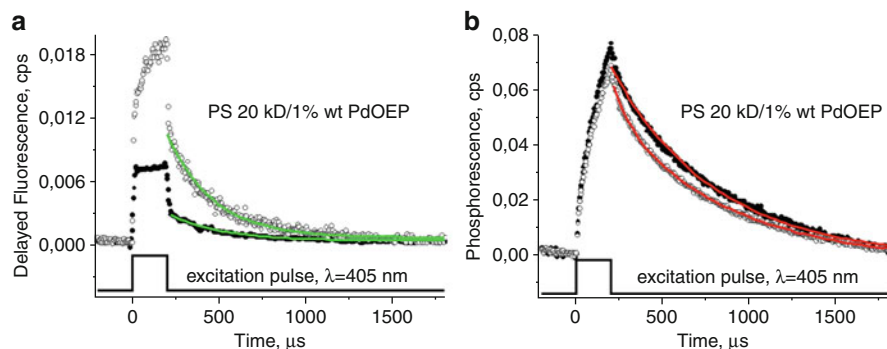
Fig. 31.10 Time-resolved fluorescence and phosphorescence intensity of sample consisting of PS 20 kD and PdOEP for two temperatures: 24 °C (*filled circles*) and 90 °C (*open circles*). Excitation pulse duration 200 μs, peak intensity 0.4 kWcm^{-2}, repetition rate 100 Hz, $\lambda = 405$ nm, film thickness 40 nm. The lines serve to guide the eye

Again, the observed time-dependent dynamic of the sensing macrocycle phosphorescence, as well as the time-dependent dynamic of the delayed fluorescence, have a multi-exponential time behavior, a consequence of the complexity of the depopulation processes. Ignoring this complexity, one can define the decay time as the time necessary to drop the phosphorescence signal amplitude down to the 1/e level.

The working hypothesis, giving a physical description of the experimentally observed phenomenon of temperature dependence of the TTA efficiency in optically excited MM ensembles, is as follows: at increased sample temperatures, the viscosity of the optically inactive polymer matrix, where the MM molecules are dispersed, is decreased (Fig. 31.11). The lower viscosity leads to temperature-dependent increase of the local mobility of the dispersed molecules, and the required optimal steric alignment of the participating molecules for the process of TTA is reached faster. Therefore, the signal directly related to the process of TTA, the delayed fluorescence signal, grows remarkably.

This working hypothesis successfully explains why, in the boundary cases regarding the viscosity of the matrix, with vanishing viscosity (organic solutions) or with infinite viscosity (macromolecular organic crystals), the efficiency of the TTA process (and, therefore, the delayed fluorescence) does not depend on the sample temperature. In the first case, the viscosity is so low that it cannot be decreased by a reasonable amount, but in the second case it remains great, independent of the sample temperature.

For application in the field of life science, two additional experimental issues must be addressed. The first of them is to ascertain the sample (local) temperature in an aqueous environment, maintaining the advantages of the all-optical sensing TTA technique. This means that the TTA process must be transferred from the hydrophobic environment (organic solvent) to the hydrophilic one. The second problem is that the intensity used at the temperature measurement via
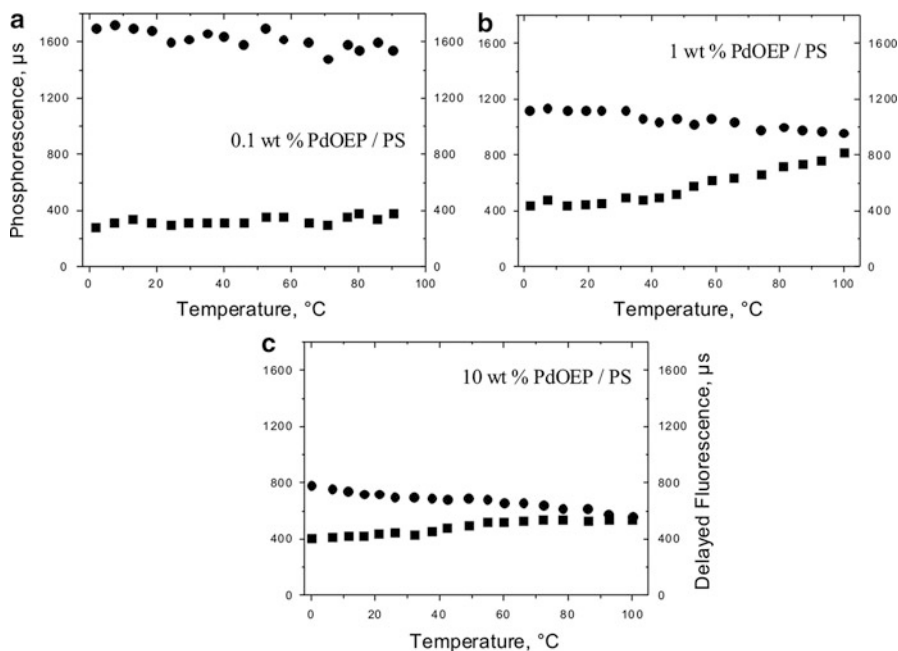
Fig. 31.11 Dependence of the decay time of phosphorescence (*filled circles*) and decay time of the delayed fluorescence (*squares*) on the temperature for different mass concentrations of the PdOEP: (**a**) 0.1 % wt.; (**b**) 1 % wt.; (**c**) 10 % wt

the TTA process in MM molecules (on the order of 0.4 kWcm^{-2}) could be too high for certain sensitive biological applications. Therefore, there is a tough need to further decrease the required all-optical temperature-sensing excitation intensity.

The temperature-sensing potential of the process of TTA-UC in water environment under extremely low excitation intensities will be discussed below.

31.2.2 Sensing of Local Temperature in Water Environment

The process of TTA-UC was demonstrated earlier for metallated porphyrins and aromatic hydrocarbon dyes (serving, respectively, as sensitizer and emitter) in various organic media: volatile or nonvolatile organic solvents [30] and styrene oligomers [31]. Replacing the organic solvent by an aqueous medium would enable a cluster of unique applications in the fields of material and life science.

Practically, solubilization in water can be achieved by various methods, including chemical modification of the sensitizer and emitter in order to enhance their solubility in highly polar solvents, and encapsulation (or embedding) of the optically active hydrophobic dyes in colloidal carriers (such as micelles of an appropriate surfactant or nanoparticles of a polymer or inorganic nature).

Of the mentioned techniques, the solubilization by encapsulation in micelles of nonionic surfactants is a powerful method, widely used for the delivery and controlled release of bioactive hydrophobic components [32, 33]. Recently, efficient solubilization of substances with low water-solubility was demonstrated using amphiphilic block-copolymers from the family of polyoxyethanyl α-tocopheryl sebacate (PTS) as a surfactant [34]. The chemical structure of PTS is presented in Fig. 31.1a. It has been shown that PTS surfactant forms spherical micelles with diameter on the order of 20–25 nm that possess a high capacity for loading strongly hydrophobic materials; for instance, the highly water insoluble Q10 coenzyme has been successfully solubilized in PTS and delivered into the human body [35]. In a typical formulation, the molar ratio between PTS and Q10 coenzyme was 2 to 1. Thus, very high solubility is achieved. For instance, 5 % wt. solution of PTS in water can solubilize nearly 1.8 % wt (or 21 mM) of the Q10 coenzyme. Therefore, we expected that concentrations of sensitizer and emitter from 10 μM up to 10 mM are obtainable. It should be noted that the local concentration of sensitizer and emitter dyes inside the PTS micelles is nearly one order of magnitude higher, and therefore more than sufficient to observe effective TTA-UC. Furthermore, PTS micelles have also been used as nanoreactors: chemical transformations such as Heck and Suzuki coupling, olefin metathesis, and ring-closing metathesis were conducted with good yield at ambient conditions [36]. These chemical processes are only possible if the core of the micelles has a liquid-like nature and the reactants diffuse freely. This suggests that the requirement of high local mobility of the active substances necessary to achieve efficient TTA-UC is also met in this system. Therefore, these micelles are ideal candidates for transferring an efficient TTA-UC process from an organic solvent environment to a biologically relevant aqueous environment.

Using the example of the UC system, consisting of a sensitizer – palladium benzoporphyrin (Fig. 31.12b) – and an emitter – bis(butylphenyl)perylene (Fig. 31.12c) – embedded at the PTS micelles (Fig. 31.12a), the sensing properties of the process of TTA-UC in a water environment will be demonstrated.

In Fig. 31.13, the luminescence spectra of the UC system PdTBP/BTP in two different solvents is compared. It is important to note that the only wavelength-selective element in the experimental setup is a notch filter, designed to suppress the excitation wavelength (central wavelength $\lambda = 632$ nm, FWHM ~ 18 nm). Therefore, for the chosen UC system, the intensities of the delayed fluorescence (the UC signal) and the residual phosphorescence are comparable. This demonstrates the efficiency of the TTA-UC process and explains why the sensing intensity can be lower by more than 2 orders of magnitude, down to excitation intensities of 1 Wcm^{-2}. If a further decrease of the sensing intensity is needed, as a fast solution of the problem, the observation time can be increased so that enough sensing photons will be collected, even at intensities on the order of 1 mWcm^{-2}.

The dependences of integral UC fluorescence in an organic solvent and PTS/water mixture on the excitation intensity are shown in Fig. 31.14. The solid lines are power law fits: $I_{UpConv} = a * I_{exc}^{b}$ with $b = 1.11$ for the TTA-UC in toluene solution (Fig. 31.14, filled circles) and $b = 1.18$ for the TTA-UC in the micellar system
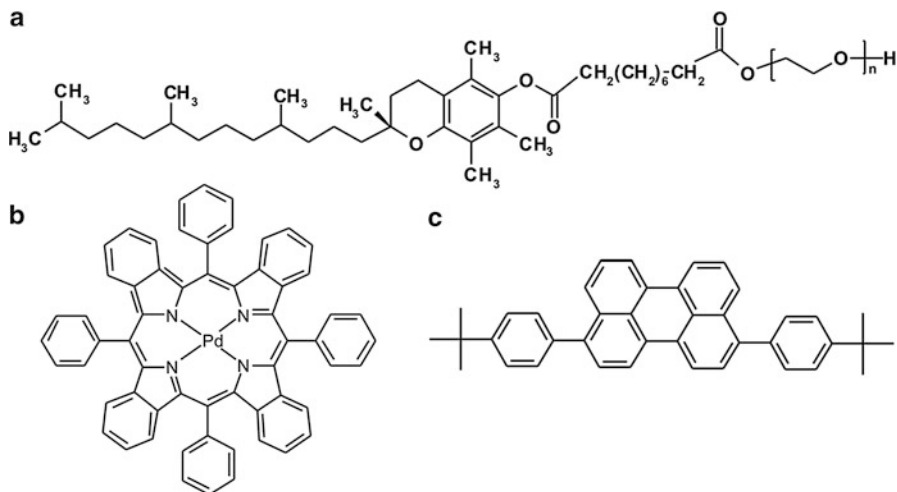
Fig. 31.12 Structures of the: (**a**) Polyoxyethanyl α-tocopheryl sebacate (PTS); (**b**) *meso*-Tetraphenyl-tetrabenzoporphine Palladium (PdTBP) and (**c**) 3,10-Bis(4-*tert*-butylphenyl) Dibenz [*de,kl*]anthracene (BTP)

(Fig. 31.14, filled triangles). It is important to note that the region of excitation intensities, where the UC molecular system shows an intensity dependence that is well approximated with a sub-linear function, is more than 3 orders of magnitude broad.

The dependence of luminescence of the UC system PdTBP/BTP/Igepal®CA-630 (1×10^{-6} M/1×10^{-5} M/5 wt%) in an aqueous environment on the sample temperature is shown in Fig. 31.15.

As in the case of TTA between optically excited MM blended in a polystyrene matrix, the Igepal®CA-630 micelles ensure for the TTA-UC process an optically inactive matrix for which the viscosity has strong dependence on temperature. A well-expressed ratiometric response to the sample temperature is observed. The ratio (Fig. 31.15b) of the integral UC fluorescence regarding the integral residual phosphorescence changes more than 6 times for a temperature interval of 60 K. Such a strong change ensures a temperature sensitivity of 0.1 K.

The flexibility to choose a specific excitation wavelength is demonstrated in Figs. 31.16 and 31.17, where porphyrins with tunable π-conjugation (including π-contraction or π-extension) obtained from tetrabenzo building blocks are demonstrated.

On one hand, the replacement of benzo- rings with naphto- or anthro- groups will induce a significant red shift of the Q-band. Such a red shift will allow matching of the excitation spectrum with the transparency window of the living tissue. On the other hand, the removal of benzo- rings or their replacement with an alkyl substituent will cause a significant blue shift of the Q-band absorption. Following this synthetic strategy, a fine tuning of the absorption maxima of the porphyrin Q-bands by addition or removal of one, two, or three benzo- rings is possible. This also

Fig. 31.13 Dependence of
the sample luminescence on
the excitation light intensity
for the UC couple PdTBP/
BTP in different solvents:
(**a**) in toluene $(1 \times 10^{-6}$ M/
1×10^{-5} M); (**b**) in 5 wt%
PTS/water mixture
$(1 \times 10^{-6}$ M/1×10^{-5} M).
Pump wavelength
$\lambda = 635$ nm, excitation spot
diameter ~ 400 μm, maximal
light intensity <3 Wcm^{-2}
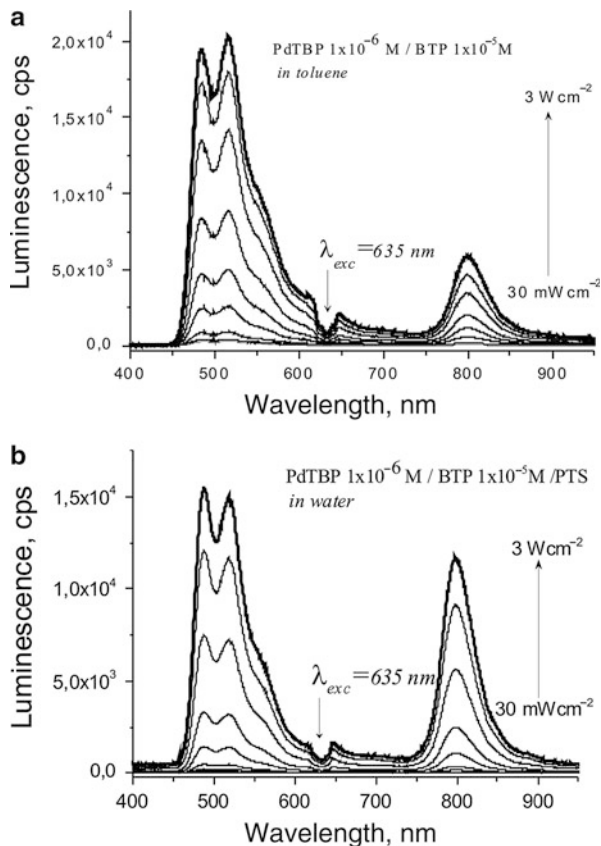
Fig. 31.14 Dependence of
the integral TTA-UC
fluorescence on the excitation
light intensity for the UC
couple PdTBP/BTP in
different solvents: *filled
circles* – in toluene
$(1 \times 10^{-6}$ M/1×10^{-5} M);
filled triangles – in 5 wt%
PTS/water mixture
$(1 \times 10^{-6}$ M/1×10^{-5} M)
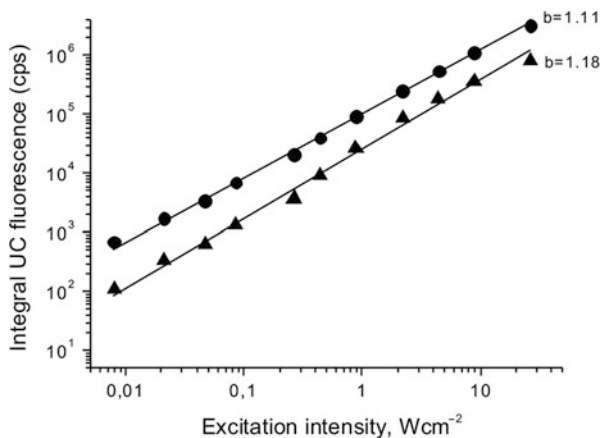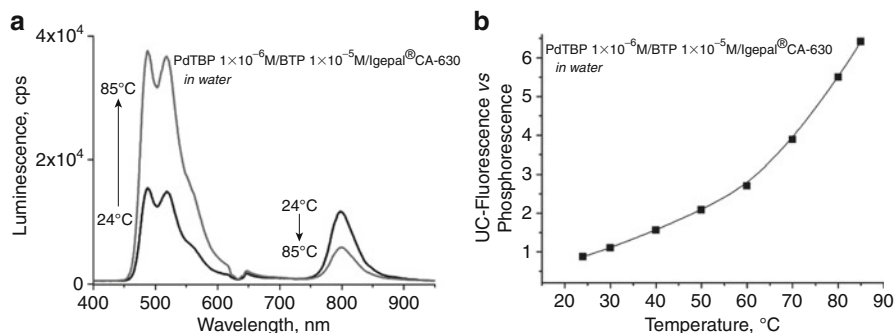
Fig. 31.15 (**a**) Dependence of the luminescence of the UC system PdTBP/BTP/Igepal®CA-630 in an aqueous environment on the sample temperature. Optical excitation $- \lambda = 635$ nm, cw-laser intensity ~ 3 Wcm^{-2}, laser spot diameter 400 mm. (**b**) Temperature calibration curve
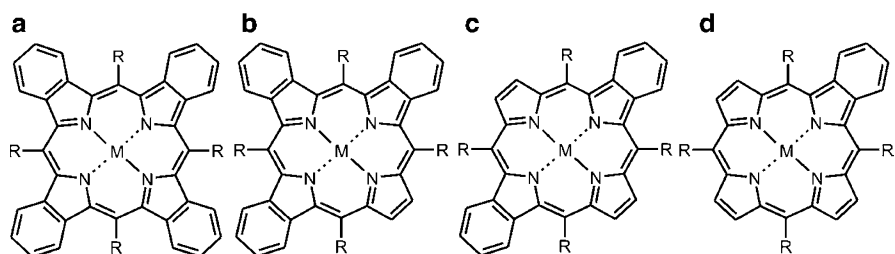
Fig. 31.16 Chemical structures of: (**a**) tetraphenyltetrabenzo, (**b**) tribenzo-, (**c**) dibenzo-, and (**d**) monobenzotetraphenyl-porphyrins. Sensitizers for emitters from the blue part of the visible spectrum
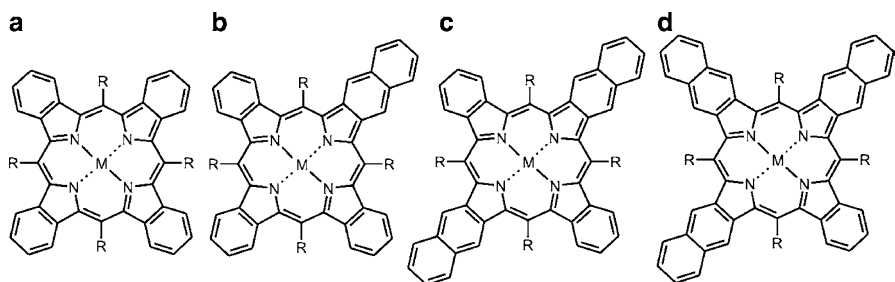
Fig. 31.17 Chemical structures of: (**a**) tetraphenyltetrabenzo-, (**b**) mononaphthotribenzo-, (**c**) dinaphthodibenzo-, and (**d**) trinaphthomonobenzo-porphyrins. Sensitizers for emitters from the green part of the visible spectrum

means a fine tuning of the porphyrin triplet states energies. In a nonprecise manner, exchanging one benzo- ring with one naphto- ring will lead to $\Delta\lambda \sim 30$ nm red-shift of the corresponding Q-band absorption. Conversely, the exchange of one

benzo- ring with one alkyl substituent will lead to $\Delta\lambda \sim 25$ nm blue-shift of the corresponding Q-band absorption.

Additionally, the absorption spectra of the sensitizer molecules used are broad, in some cases up to 80 nm (FWHM); therefore, optical sources with various emission wavelengths can be used, allowing flexibility in choosing the excitation wavelength without any consequence on the TTA-UC sensing properties or efficiency. Another important feature of the TTA-UC is the sub-linear dependence of the UC emission on the excitation intensity. This behavior helps to predict precisely the necessary radiation dose and to avoid unwanted optical stress of the bio-samples.

31.3 Conclusion

In summary, the temperature-sensing properties of the processes of triplet-triplet annihilations in thin polymer films and the energetically conjoined triplet-triplet annihilation-assisted photon energy upconversion in a water environment were demonstrated. Those noninvasive and all-optical sensing techniques are applicable to a wide sample family and experimental environment. This temperature-sensing technique is based on the ratiometric luminescence response and provides stabile and reproducible results.

References

1. C.C. Williams, H.K. Wickramasinghe, Scanning thermal profiler. Appl. Phys. Lett. **49**, 1587–1589 (1986)
2. D.G. Cahill, W.K. Ford, K.E. Goodson, G.D. Mahan, A. Majumdar, H.J. Maris, R. Merlin, S. R. Phillpot, Nanoscale thermal transport. J. Appl. Phys. **15**, 793–818 (2003)
3. D.N. Messias, M.V.D. Vermelho, A.S. Gouveia-Neto, J.S. Aitchison, All optical integrated upconversion fluorescence-based point temperature sensing system using Er3 + -doped silica-on-silicon waveguides. Rew. Sci. Instrum. **73**, 476–479 (2002)
4. G. Albright, J. Stump, C. Li, H. Kaplan, in Quantum Focus Instruments Corporation, Honeyhill Technical Company, http://www.quantumfocus.com/publications.htm
5. J.B. Birks, *Photophysics of Aromatic Molecules* (Wiley – Interscience, London, 1970)
6. M. Pope, C. Swenberg, *Electronic Processes in Organic Crystals* (Clarendon, Oxford, 1982)
7. M.I.J. Lorenz, S.H. Fischer, O.S. Wolfbeis, Multiple fluorescent chemical sensing and imaging. Chem. Soc. Rev. **39**, 3102–3114 (2010)
8. S.M. Grist, L. Chrostowski, K.C. Cheung, Optical oxygen sensors for applications in microfluidic cell culture. Sensors **10**, 9286–9316 (2010)
9. A. Fercher, S.M. Borisov, A.V. Zhdanov, I. Klimant, D.B. Papkovsky, Intracellular O_2 sensing probe based on cell-penetrating phosphorescent nanoparticles. ACS Nano **5**(7), 5499–5508 (2011)
10. S.M. Borisov, P. Lehner, I. Klimant, Novel optical trace oxygen sensors based on platinum(II) and palladium(II) complexes with 5,10,15,20-meso-tetrakis-(2,3,4,5,6-pentafluorphenyl)-porphyrin covalently immobilized on silica-gel particles. Anal. Chim. Acta **690**, 108–115 (2011)
11. M. Kasha, Characterization of electronic transitions in complex molecules. Discuss. Faraday Soc. **9**, 14–19 (1950)
12. R.L. Fulton, M. Gouterman, Vibronic coupling 1. Mathematical treatment for 2 electronic states. J. Chem. Phys. **35**, 1059–1064 (1961)

13. S. Baluschev, V. Yakutkin, T. Miteva, G. Wegner, T. Roberts, G. Nelles, A. Yasuda, S. Chernov, S. Aleshchenkov, A. Cheprakov, A general approach for non-coherently excited annihilation up-conversion: transforming the solar-spectrum. New J. Phys. **10**, 013007 (2008)

14. J.E. Auckett, Y.Y. Chen, T. Khoury, R.G.C.R. Clady, N.J. Ekins-Daukes, M.J. Crossley, T.W. Schmidt, Efficient up-conversion by triplet-triplet annihilation. J. Phys. Conf. Ser. **185**, 012002 (2009)

15. S.K. Sugunan, U. Tripathy, S.M.K. Brunet, M.F. Paige, R.P. Steer, Mechanisms of low-power noncoherent photon upconversion in metalloporphyrin-organic blue emitter systems in solution. J. Phys. Chem. A **113**, 8548–8556 (2009)

16. C.-P. Hsu, The electronic couplings in electron transfer and excitation energy transfer. Account Chem. Res. **42**(4), 509–518 (2009)

17. T.N. Singh-Rachford, F.N. Castellano, Triplet sensitized red-to-blue photon upconversion. J. Phys. Chem. Lett. **1**, 195–200 (2010)

18. P.E. Keivanidis, S. Baluschev, T. Miteva, A. Yasuda, G. Nelles, G. Wegner, Up-conversion in polyfluorene doped with metal (II)-octaethyl. Adv. Mater. **15**(24), 2095–2998 (2003)

19. R.R. Islangulov, D.V. Kozlov, F.N. Castellano, Chem. Commun. **30**, 3776–3778 (2005)

20. S. Baluschev, T. Miteva, V. Yakutkin, G. Nelles, A. Yasuda, G. Wegner, Up-conversion fluorescence: non-coherent excitation by sun-light. Phys. Rev. Lett. **97**, 143903 (2006)

21. T. Miteva, V. Yakutkin, G. Nelles, S. Baluschev, Annihilation assisted upconversion: all-organic, flexible and transparent multicolour display. New J. Phys. **10**, 103002 (2008)

22. D.L. Andrews, C. Curutchet, G.D. Scholes, Resonance energy transfer: beyond the limits. Laser Photon. Rev. **5**(1), 114–123 (2011)

23. Y.Y. Cheng, T. Khoury, R.G.C.R. Clady, M.J.Y. Tayebjee, N.J. Ekins-Daukes, M.J. Crossley, T.W. Schmidt, On the efficiency limit of triplet-triplet annihilation for photochemical upconversion. Phys. Chem. Chem. Phys. **12**, 66–71 (2010)

24. P. Du, R. Eisenberg, Energy upconversion sensitized by a platinum(II) terpyridyl acetylide complex. Chem. Sci. **1**, 502–506 (2010)

25. G.A. Baker, S.N. Baker, T.M. McCleskey, Noncontact two-color luminescence thermometry based on intramolecular luminophore cyclization within an ionic liquid. Chem. Comm. **39**(23), 2932–2933 (2003)

26. D.N. Messias, M.V.D. Vermelho, A.S. Gouveia-Neto, J.S. Aitchison, All optical integrated upconversion fluorescence-based point temperature sensing system using Er3 + -doped silica-on-silicon waveguides. Rev. Sci. Instrum. **73**, 476–480 (2002)

27. M.M. Frigault, J. Lacoste, J.L. Swift, C.M. Brown, Live-cell microscopy – tips and tools. J. Cell Sci. **122**(6), 753–767 (2009)

28. O.S. Finikova, A.V. Cheprakov, P.J. Carroll, S.A. Vinogradov, Novel route to functionalized tetraaryltetra[2,3]naphthaloporphyrins via oxidative aromatization. J. Org. Chem. **68**(19), 7517–7520 (2003)

29. N. Kobayashi, W.A. Nevin, S. Mizunuma, H. Awaji, M. Yamaguchi, Ring-expanded porphyrins as an approach towards highly conductive molecular semiconductors. Chem. Phys. Lett. **205**, 51–54 (1993)

30. V. Yakutkin, S. Aleshchenkov, S. Chernov, T. Miteva, G. Nelles, A. Cheprakov, S. Baluschev, Towards the IR limit of the triplet-triplet annihilation-supported up-conversion: tetraanthraporphyrin. Chem. Eur. J. **14**, 9846–9850 (2008)

31. T. Miteva, V. Yakutkin, G. Nelles, S. Baluschev, Annihilation assisted upconversion: all-organic, flexible and transparent multicolour display. New J. Phys. **10**, 103002 (2008)

32. M.C. Branco, J.P. Schneider, Self-assembling materials for therapeutic delivery. Acta Biomaterialia **5**, 817–831 (2009)

33. E.V. Batrakova, A.V. Kabanov, Pluronic block copolymers: evolution of drug delivery concept from inert nanocarriers to biological response modifiers. J Control Release. **130**, 98–106 (2008)

34. H. Borowy-Borowski, C. Sodja, J. Docherty, P.R. Walker, M. Sikorska, Unique technology for solubilization and delivery of highly lipophilic bioactive molecules. J. Drug Target. **12**(7), 415–424 (2004)
35. J. Naderi, M. Somayajulu-Nitu, A. Mukerji, P. Sharda, M. Sikorska, H. Borowy-Borowski, B. Antonsson, S. Pandey, Water-soluble formulation of Coenzyme Q10 inhibits Bax-induced destabilization of mitochondria in mammalian cells. Apoptosis **11**, 1359–1369 (2006)
36. B.H. Lipshutz, B.R. Taft, Heck couplings at room temperature in nanometer aqueous micelles. Org. Lett. **10**(7), 1329–1332 (2008)

Index